Wave-Length Dependence of the Quantum Efficiency and Absorption of Powder Phosphors

Yasuo Uehara, Iso Masuda, and Yoshimasa Kobuke

Matsuda Research Laboratory, Tokyo Shibaura Electric Company, Kawasaki, Japan

ABSTRACT

A number of powder phosphors have been measured by a direct optical method. Results are compared with other published values. Although slight discrepancies are found for magnesium and calcium tungstate at the 2537Å position, the maximum quantum efficiency for magnesium tungstate is in good agreement with the published values. Good agreement is also found for impurity-activated phosphors. New data are presented for a number of orthophosphates. The quantum efficiency curves decrease more rapidly than the absorption curves toward both longer and shorter wave lengths from the peak position. The peaks of the quantum efficiency curves lie at longer wave lengths than those of the absorption curves. Reasons for these differences are discussed.

Knowledge of the wave-length dependence of the quantum efficiency and absorption of phosphors provides an important foundation for the theoretical interpretation of luminescent properties as well as for the development or technical application of phosphors.

The quantum efficiency of powder phosphors has been measured by several methods (1), i.e., by direct optical, lamp efficiency calculation, calorimetric, and comparison methods. The second method used by Thayers and Barnes (2) and others (3-6) consists of comparing the measured luminous efficiency of a fluorescent lamp with its calculated maximum efficiency. This method involves some ambiguous assumptions concerning the optical characteristics of the phosphor layer in the fluorescent lamp. With the third or calorimetric method (1, 7) it is difficult to carry out the measurement over a wide range of exciting wave lengths, because an intense source of ultraviolet radiation is required but not available. The comparison method (1, 6, 8) is unsuitable to determine the absolute value of the quantum efficiency. In the present investigation, therefore, the first or direct optical method (9-11) was used to measure the wave-length dependence of many powder phosphors.

Experimental Apparatus

The arrangement of the experimental apparatus is similar to that reported by Botden and Kröger (10) and is shown schematically in Fig. 1. The radiation from a low-pressure hydrogen lamp L is reflected by two concave mirrors A and B, then falls on the entrance slit of a Beckmann type monochromator MN. The monochromatic beam from the exit slit is projected on the layer of phosphor P or magnesium oxide Q through a 5-mm circular hole in the ellipsoidal aluminum mirror M of 100 mm diameter. The samples are placed interchangeably on the first focus of the mirror whose position is 2 mm from the plane of aperture of the mirror in order to concentrate the entire flux of reflected light from the sample onto the second focus of the ellipsoidal mirror. The phosphor sample consists of a 3-mm thick layer prepared by compressing the phosphor powder into a rectangular recess of approximate size 3 x 10 x 18 mm which is cut or machined into a rectangular metal block of slightly larger size. The layer of magnesium oxide powder is in turn covered with a freshly smoked layer of magnesium oxide. Thus the thickness of the magnesium oxide layer is also about 3 mm. The two samples are interchangeable by 180° rotation about the rotation axis of the sample holder R. Their geometrical positions are adjustable so as to be accurately identical after rotation.

The radiation reflected from the phosphor or magnesium oxide is concentrated by the ellipsoidal mirror onto a photomultiplier PM (RCA 1P28) placed at the second focus of the mirror. With a phosphor in the measuring position, filters with a cut-off at about 3500Å or 4000Å are inserted between the photomultiplier and sample in order to separate the fluorescent light from the reflected radiation. The spectral sensitivity of the photomultiplier was determined by comparing it with a vacuum thermopile at various wave lengths in the spectral region from 2200 to 8500Å. In this experiment, a 500-w Xe lamp (Osram XB0501) and an incandescent lamp with a tungsten ribbon filament

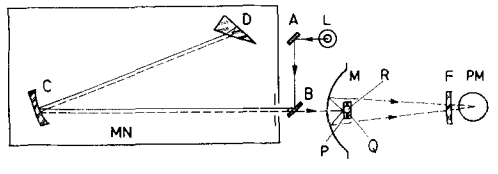

Fig. 1. Arrangement of experimental apparatus. L, light source A, B, and C, concave mirrors; D, quartz prism; MN, Beckmann type monochromator; M, ellipsoidal aluminum mirror; P, phosphor layer; Q, plaque of smoked magnesium oxide; R, axis of rotation of sample holder; F, filter; and PM, photomultiplier.

were used as the source for ultraviolet and visible radiation, respectively.

For the measurement of the spectral energy distribution of fluorescence, a Zeiss Three Glass Prism Spectrometer combined with a photomultiplier (RCA 1P22) was used, as reported in a previous paper (12). All of the experiments mentioned above were made at room temperature.

Experimental Procedure

In order to measure the relative reflectance of the aluminum mirror M, a fragment cut from its flange was placed at the position of sample P in Fig. 1, and the intensity of monochromatic radiation reflected by it and then by the ellipsoidal mirror was measured at various wave lengths relative to that of monochromatic radiation projected directly onto the photomultiplier. The relative spectral reflectivity of the plaque of smoked magnesium oxide was measured in the same manner. Let i, i_A, and i_o be the photocurrents produced by the incident monochromatic radiation, by the monochromatic radiation reflected from the piece of the aluminum mirror, and from the plaque of magnesium oxide, respectively, then the relative spectral reflectance of the aluminum mirror R_M and that of magnesium oxide R_1 are determined by the following relations:

$$R_M \equiv K_1 R_A = \left\{ \frac{i_A}{i} \right\}^{1/2} \qquad [1]$$

and

$$R_1 \equiv K_2 R_o = \frac{i_o}{i R_M} \qquad [2]$$

where R_A and R_o are the absolute values of the spectral reflectance of the aluminum mirror and magnesium oxide, respectively, and K_1 and K_2 are proportionality constants. In these equations, the influence of the multiple reflection between the samples and the mirror on the radiation reflected by the samples and then by the mirror was neglected. The measured results are shown in Fig. 2. Curve (2) for magnesium oxide shows no noticeable selectivity over a wide range of the spectrum from about 3500 to 6000Å, in contrast to curve (1) for the aluminum mirror. This result suggests that the influence of the multiple reflection on the measurement is negligibly small, as assumed above.

In order to determine the quantum efficiency of pure phosphors such as magnesium tungstate, it is necessary to know the absolute value of the spectral reflectivity of magnesium oxide, which is known to be close to unity in the visible region of the spectrum (13). One can, therefore, accept the spectral reflectivity of magnesium oxide normalized to unity as the absolute one with a probable error of about 0.2% (13).

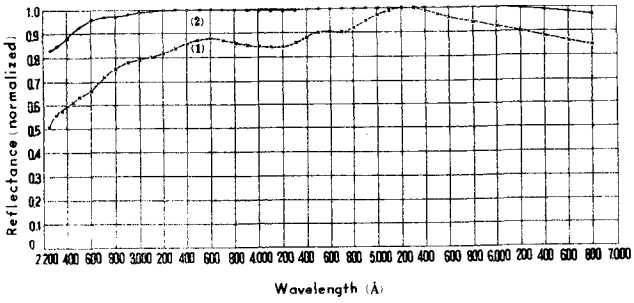

Fig. 2. Normalized reflection curves of aluminum mirror, 1, and magnesium oxide, 2.

It was verified by experiments that the transmittance for ultraviolet and visible light through a 3-mm thick layer of samples was practically zero. For such a layer, the relation between reflectivity R and absorptance A is given by

$$A = 1 - R \qquad [3]$$

Using this relation, one can determine the spectral absorptance by measuring the spectral reflectivity. The spectral reflectivity of unactivated phosphor base, of pure phosphor, and of impurity-activated phosphor is given by the following relations, respectively

$$R_b = \frac{i_b}{i_o} \cdot R_o \qquad [4a]$$

$$R_p = \frac{i_p}{i_o} \cdot R_o \qquad [4b]$$

and

$$R_a = \frac{i_a}{i_o} \cdot R_o \qquad [4c]$$

where i_b, i_p, *and* i_a are, respectively, the photocurrents produced with the layer of unactivated phosphor base, of pure phosphor, and of impurity-activated phosphor. Putting these relations in Eq. [3], the spectral absorptance of the pure and the impurity-activated phosphor is determined as follows:

$$A_p = 1 - R_p = \frac{i_o - i_p \cdot R_o}{i_o} \qquad [5a]$$

and

$$A_a = R_b - R_a = \frac{(i_b - i_a) R_o}{i_o} \qquad [5b]$$

Referring to Eq. [5b], it should be noted that A_a expresses the spectral absorptance due solely to the activators in the impurity-activated phosphor.

We shall define the quantum efficiency of the pure and the impurity-activated phosphors by the ratio of the emitted quanta to the quanta absorbed by the pure phosphor and by the activators in the impurity-activated phosphor, respectively. Then, the wave-length dependencies for the quantum efficiency of the pure and the impurity-activated phosphor are given by

$$\eta_p = \frac{i_{f,p} \cdot R_M \cdot S}{i_a / R_o - i_p} \times \frac{\int_o^\infty \lambda/\lambda e \cdot E_p \cdot d\lambda}{\int_o^\infty R_M \cdot S \cdot E_p \cdot d\lambda} \qquad [6a]$$

and

$$\eta_a = \frac{i_{f,a} \cdot R_M \cdot S}{i_b - i_a} \times \frac{\int_o^\infty \lambda/\lambda e \cdot E_a \cdot d\lambda}{\int_o^\infty R_M \cdot S \cdot E_a \cdot d\lambda} \qquad [6b]$$

where E_p and E_a are the respective energy distributions of the fluorescent emission, S is the spectral sensitivity of the photomultiplier, $i_{f,p}$ and $i_{f,a}$ are,

respectively, the photocurrents produced by the fluorescent emission with the pure and the impurity-activated phosphor, and λ and λ_e denote the wave length of the fluorescent and exciting radiation, respectively.

Since the spectral distribution of the emission of the phosphors measured was practically independent of the wave length of exciting radiation from 2200 to 4000Å, the integration of Eq. [6] can be carried out easily by numerical calculation. In order to measure the wave-length dependence of the quantum efficiency due to sensitizer and activator in the sensitized phosphors such as calcium halophosphate activated with Sb and Mn, the measured fluorescence spectrum was resolved into two bands due to sensitizer and activator. For example, the relative energy distribution curve of the Sb-band in calcium halophosphate activated with Sb and Mn was determined so as to fit it with that of the phosphor activated with Sb alone. By subtracting this curve from the energy distribution curve of the sensitized phosphor, the energy distribution of the Mn-band was determined.

In Eq. [6], the effect of absorption loss of fluorescent light through the powder on the measured quantum efficiency was neglected. Taking into account the absorption loss in the powder, Bril and Klasens (14) have already given the following approximate formula for the intrinsic quantum efficiency of fluorescence:

$$\eta_i = \frac{2}{1 + R_\infty}\eta_m \qquad [7]$$

where η_i and η_m are, respectively, the intrinsic and the measured quantum efficiency, and R_∞ is the reflectance of the thick phosphor layer for its fluorescent light. If the value for R_∞ is larger than 0.9, the correction factor according to Eq. [7] is less than 5%. On the other hand, the experimental errors in this experiment were about ±5%. The correction by Eq. [7], therefore, will be necessary only for phosphor layers whose reflectance in the visible region of the spectrum is smaller than 0.9.

Preparation of Phosphors and Experimental Results

Magnesium tungstate phosphors.—Three types of magnesium tungstate phosphors were measured. The first and second type had compositions of $MgWO_4$ and Mg_2WO_5, respectively. They were prepared by firing together the required proportions of magnesium nitrate and ammonium tungstate $[(NH_4)_2O \cdot 7WO_3 \cdot 6H_2O]$, with or without Pb and Cd in amounts of 1 mole %. Firing was at 980°C for 30 min followed by intimate grinding and a second firing at 1000°C for 1 hr. The third type phosphors were commercial products obtained from Sylvania Electric Products Inc. and from our factory.

Results for the first series of phosphors with and without Pb are shown in Fig. 3. The data for the second and third types of phosphors without added impurities were practically identical with those labeled (1) in Fig. 3, except for the Sylvania product whose quantum efficiency was about 5% smaller than that of the other magnesium tungstate phosphors. Addition of 1 mole % Cd to magnesium

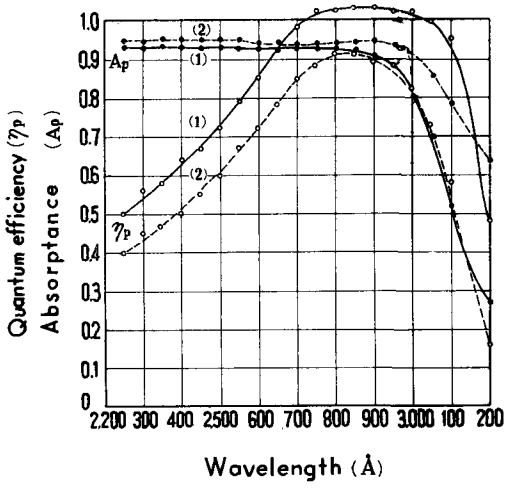

Fig. 3. Wave-length dependence of quantum efficiency and absorption for magnesium tungstate phosphors with or without Pb. 1, $MgWO_4$; 2, $MgWO_4$:Pb (10^{-2} mole).

tungstate of composition Mg_2WO_5 gave essentially the same curves as (2) in Fig. 3. Considering the experimental errors, the quantum efficiency of magnesium tungstate without added impurities is thus practically independent of its composition and close to unity in the spectral region from about 2750 to 3000Å. It is 0.75-0.80 at wave length 2537Å.

Calcium tungstate phosphors.—Six samples of calcium tungstate phosphors were measured. They were prepared by firing mixtures of 1 mole calcium nitrate and 1/7 mole ammonium tungstate with or without 0.4 mole calcium sulfate or 0.01 mole lead fluoride for two half-hour periods at 1000°C with intimate grinding between firings. In order to investigate the existence of nonluminescent compounds in the phosphor which absorb ultraviolet radiation uselessly (15), two samples of calcium tungstate phosphors with or without added calcium sulfate were washed with 5 wt % hot ammonium hydroxide aqueous solution.

Results for calcium tungstates are shown in Fig. 4. The phosphor with 0.4 mole calcium sulfate gave almost the same curves as those labeled (1) in Fig. 4. Washing with ammonium hydroxide decreases

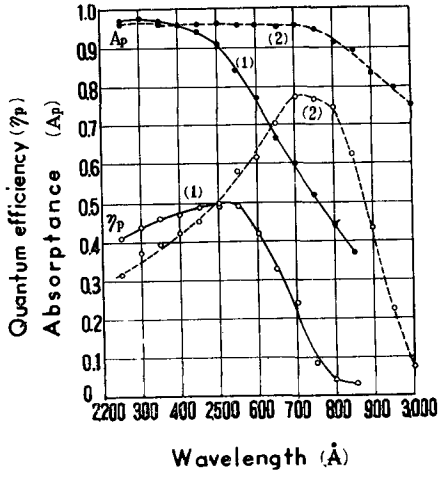

Fig. 4. Wave-length dependence of quantum efficiency and absorption for calcium tungstate phosphors with or without Pb. 1, $CaWO_4$; 2, WO_4:Pb (10^{-2} mole).

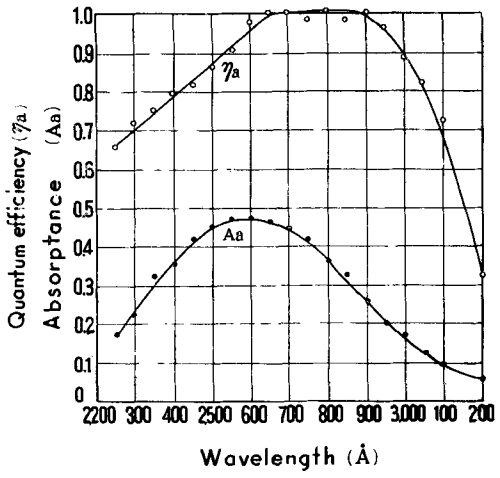

Fig. 5. Wave-length dependence of quantum efficiency and absorption for β-calcium orthophosphate activated with Cu, i.e., β-$Ca_{2.7}P_2O_8$:Cu (5×10^{-3} moles).

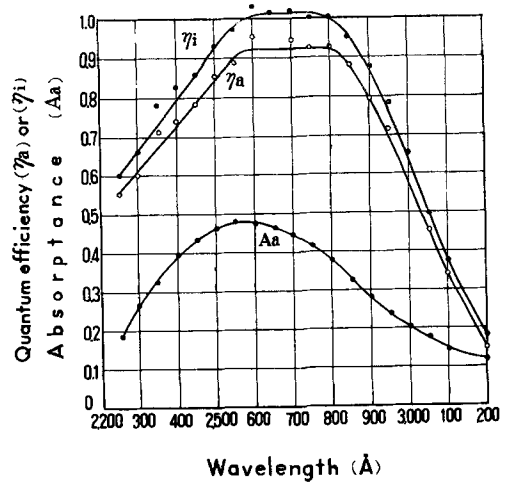

Fig. 6. Wave-length dependence of quantum efficiency and absorption for β-calcium-zinc orthophosphate activated Cu, i.e., β-$Ca_{2.7}Zn_{0.2}P_2O_8$:Cu(5×10^{-3} moles). η_a and η_i denote the measured and the intrinsic quantum efficiency, respectively.

the absorption of calcium tungstate phosphors with or without calcium sulfate slightly, while the quantum efficiency of both phosphors is increased by 5-10%. The maximum quantum efficiency of pure calcium tungstate phosphors, including the washed samples, is 0.50-0.62 at about 2537Å. The addition of 1 mole % Pb produces a remarkable increase in absorption and in the quantum efficiency in the spectral region above about 2500Å. In the spectral region below 2500Å, the quantum efficiency is slightly lowered by the addition of Pb. The maximum value of the quantum efficiency of calcium tungstate sensitized with Pb is about 0.77 at 2700Å.

Cu-activated β-calcium orthophosphate and related phosphors.—Data for Cu-activated β-calcium, β-calcium·magnesium, and β-calcium·zinc orthophosphate, together with those for pure orthophosphates without activators (used for the measurements) are shown in Fig. 5 and 6; the phosphors were prepared as reported in a previous paper (12).

The quantum efficiency of Cu-activated β-calcium orthophosphate is close to unity in the spectral region from about 2650 to 2900Å, as shown in Fig. 5, while that of Cu-activated β-calcium·zinc orthophosphate is about 0.92 in the same spectral region, as shown by the η_a-curve in Fig. 6. The spectral reflectivity of Cu-activated β-calcium and β-calcium magnesium orthophosphate averaged over the entire visible region of the spectrum was about 0.94, while that of Cu-activated β-calcium·zinc orthophosphate was about 0.81. Using Eq. [7], the intrinsic quantum efficiency of the latter phosphor was calculated. It is shown by the η_i-curve in Fig. 6. The curve for calcium·magnesium orthophosphate is quite similar to the η_i-curve in Fig. 6, but it is slightly lower; the maximum quantum efficiency of this phosphor is 0.99 around 2700Å. The absorption curve of this phosphor is in good agreement with that shown in Fig. 6.

Tin-activated calcium orthophosphate and related phosphors.—β-calcium orthophosphate phosphors activated with Sn and with Sn and Mn were prepared by firing mixtures of 1 mole calcium hydroxide, 2 moles dibasic calcium phosphate and 0.1 mole stannous chloride with or without 0.1 mole manganese carbonate for 30 min in air at 950°C and 1100°C, respectively, followed by firing in a reducing atmosphere (mixture of 25% H_2 and 75% N_2) for the same period and at the same temperature after an intimate grinding between firings. Pure β-calcium orthophosphate without activators was prepared by the same method.

Results are shown in Fig. 7. The curve for the quantum efficiency of the Sn-activated phosphor resembles somewhat that of the Cu-activated material, while the absorption curves are noticeably different. On the other hand, the absorption curves of the Sn and the (Sn + Mn) activated orthophosphate are quite close to each other, while the wave length dependencies of the quantum efficiencies are remarkably different.

As reported by Butler, the α-form of Sn-activated calcium orthophosphate is easily produced by firing at temperatures above 1175°C with low amounts of Sn, while the transition from the β- to the α-form of the phosphor is inhibited by the addition of

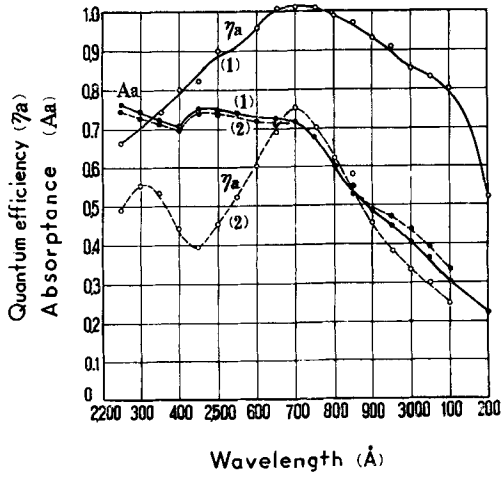

Fig. 7. Wave-length dependence of quantum efficiency and absorption for β-calcium orthophosphate phosphors activated with Sn and Mn.
1, $Ca_3P_2O_8$:Sn (0.1 mole); 2, $Ca_3P_2O_8$:Sn (0.1 mole), Mn (0.1 mole).

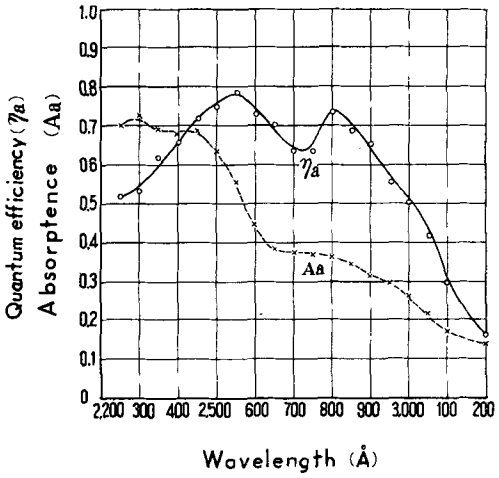

Fig. 8. Wave-length dependence of quantum efficiency and absorption for α-calcium orthophosphate activoted with 4 mole % Sn and containing 0.45 mole silica, fired at about 1200°C.

rather large amounts of Sn of the order of 4 mole %. It was found by the present authors that the conversion from the β- to the α-form with rather large amounts of Sn was promoted by the addition of silica during the preparation of phosphors. A series of Sn-activated calcium orthophosphate phosphors containing various amounts of silica were prepared by firing mixtures of 2 moles dibasic calcium phosphate, 0.9 mole calcium carbonate, silica in various amounts from 0.01 to 0.8 moles, and 0.04 mole stannous chloride for 30 min at about 1200°C in air, and then in a reducing atmosphere for the same period and at the same temperature after an intimate grinding between firings. Pure α-calcium orthophosphates without activators were prepared by the same method.

Results for Sn-activated α-calcium orthophosphate containing 0.45 mole silica are shown in Fig. 8. It was proved by x-ray analysis and by measurement of the fluorescent spectrum that it was typical α-calcium orthophosphate. The wave-length dependence of the quantum efficiency for Sn-activated α-phosphors is practically independent of the amount of added silica. It is quite different from that for the Sn-activated β-phosphor and resembles the curve for β-calcium orthophosphate activated with Sn and Mn. The absorption curves for Sn-activated α- and β-phosphors are rather different, and the intensity of the absorption band peaking at about 2800Å for α-phosphor is lower than that for β-phosphor.

Calcium·cadmium silicate phosphor activated Pb *and* Mn.—Calcium·cadmium silicate containing less than 30 mole % Cd and activated with Pb and Mn was described by Schulman (16). The phosphors used for the present measurements were prepared by firing a mixture of 0.8 mole calcium carbonate, 0.2 mole cadmium carbonate, and 1.2 mole silica with or without 8 x 10^{-3} mole lead fluoride and 0.1 mole manganese chloride for two 2-hr periods at 1180°C with an intimate grinding between firings. Results are shown in Fig. 9. Also shown as a dotted line (2) is the corresponding curve for the total (Pb+Mn) emission of calcium silicate activated with

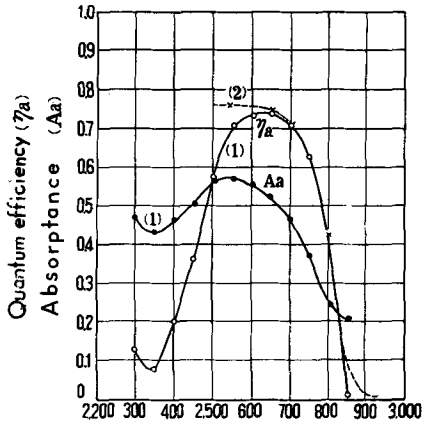

Fig. 9. Wave-length dependence of quantum efficiency and absorption for calcium · cadmium silicate activated with Pb and Mn, compared with Botden and Kroger's data on calcium silicate.
1, $Ca_{0.8}Cd_{0.2}$ · $1.2SiO_2$:Pb(8×10^{-3} moles), Mn (0.1 mole), (Mn-emission);
2, calcium silicate: Pb, Mn (observed by Botden and Kroger).

Pb and Mn, as reported by Botden and Kröger (10). The two curves for the quantum efficiency are in good agreement in the spectral region above about 2650Å.

Calcium halophosphate phosphors activated with Sb or with Sb and Mn.—Calcium halophosphate phosphors of composition $3\,Ca_x\cdot P_2O_8\cdot 0.6\,CaF_2\cdot 0.4\,CaCl_2$ ($x = 2.7 - 2.8$) and activated with 0.3 mole Sb and various amounts of Mn ranging from 0 to 0.18 moles per mole calcium halophosphate, together with pure halophosphate without activators, were prepared by firing calcium carbonate and dibasic calcium phosphate with or without added Sb or Mn for two half-hour periods at 1100°C, with intimate grinding between firings.

Results for typical samples are shown in Fig. 10 and 11. The quantum efficiency of the phosphor

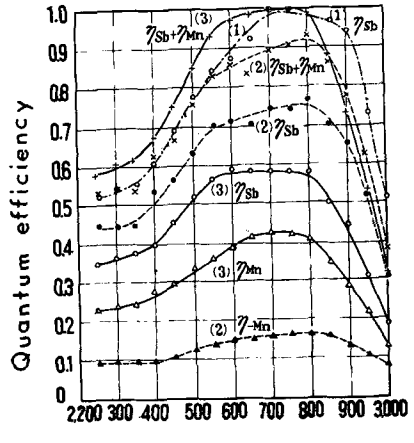

Fig. 10. Wave-length dependence of quantum efficiency for calcium halophosphate phosphors activated with Sb and with Mn. η_{Sb} and η_{Mn} denote the quantum efficiencies for the individual Sb-and Mn-bands.
1, $3\,Ca_{2.7}P_2O_8$ · $0.6\,CaF_2$ · $0.4\,CaCl_2$:Sb (0.3 moles),
2, $3\,Ca_{2.8}P_2O_8$ · $0.6\,CaF_2$ · $0.4\,CaCl_2$:Sb (0.3 moles), Mn (3×10^{-2} moles),
3, $3\,Ca_{2.8}P_2O_8$ · $0.6\,CaF_2$ · $0.4\,CaCl_2$:Sb (0.3 moles), Mn (9×10^{-2} moles).

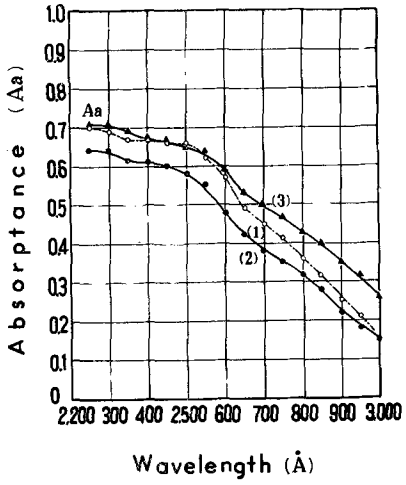

Fig. 11. Spectral distribution of obsorption (Aa) due to activators for calcium halophosphate phosphors. The samples are the same as in Fig. 10.

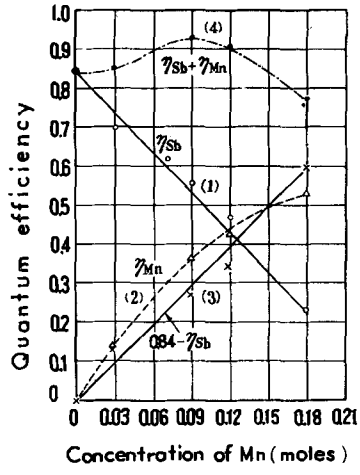

Fig. 12. Relation between quantum efficiency and concentration of Mn for calcium halophosphate phosphors activated with 0.3 mole Sb and various amounts of Mn from 0 to 0.18 mole per mole phosphor, excited with 2537Å. η_{Sb} and η_{Mn} denote the quantum efficiencies for the individual Sb- and Mn-bands.

activated with Sb alone is close to unity at wave lengths around 2750Å and 0.84 at 2537Å.

The relation between quantum efficiency and concentration of Mn for phosphors excited with 2537Å is shown in Fig. 12. With increasing concentration of Mn, the quantum efficiency for the Sb-emission, η_{Sb}, decreases almost linearly, while that for the Mn-emission, η_{Mn}, increases nonlinearly. Thus the total quantum efficiency of fluorescence, $\eta_{Sb} + \eta_{Mn}$, depends on the concentration of Mn. The straight line given by $0.84 - \eta_{Sb}$ expresses the concentration dependence of the quantum efficiency for the Mn-emission which might be obtained if the excitation energy absorbed by the Sb-centers were transferred to the Mn-centers with the same efficiency as that of Sb-centers alone. By comparing the observed with the calculated $(0.84-\eta_{Sb})$ values, it is seen that a part of the excitation energy, which is dissipated as heat energy in the Sb-centers, is transferred to Mn-centers in the sensitized phosphor and it leads to Mn-emission at concentrations below 15 mole % Mn; when the concentration of Mn ex-

Table I. Quantum efficiency of various phosphors

Phosphors	Quantum efficiency: Excited by 2537Å	Quantum efficiency: Maximum value	Wave length at maximum Q.E., Å	Method	Reference
Magnesium tungstate	0.7			Lamp efficiency	Thayer and Barnes, 1939 (2)
	0.9-1	1	2800	Direct	Fonda, 1944 (9)
	0.9			Lamp efficiency	Thayer, 1945 (2)
	0.84			Lamp efficiency	Jerome, 1953 (6)
	0.90			Lamp efficiency	Tregellas-Williams, 1958 (1)
$MgWO_4$ and Mg_2WO_5	0.75-0.80	1	2750-3000	Direct	This paper
:Pb	0.68	0.91	2750-2900	Direct	This paper
:Cd	0.70	0.95	2750-2900	Direct	This paper
Calcium tungstate	0.70			Lamp efficiency	Thayer and Barnes, 1939 (2)
	0.7			Direct	Kröger, 1948 (10)
	0.50-0.62	0.50-0.62	2537-2550	Direct	This paper
:Pb	0.55-0.60	0.77	2700	Direct	This paper
Calcium orthophosphate: Cu	0.91	1	2650-2900	Direct	This paper
Calcium·magnesium Orthophosphate: Cu	0.93	0.99	2650-2800	Direct	This paper
Calcium·zinc Orthophosphate: Cu	0.88	0.92	2650-2900	Direct	This paper
Calcium orthophosphate: Sn	0.92	1	2650-2750	Direct	This paper
Calcium orthophosphate: Sn, Mn	0.52	0.75	2700	Direct	This paper
Calcium orthophosphate: Sn	0.78-0.83	0.78-0.83	2500-2550	Direct	This paper
Calcium·cadmium silicate: Pb, Mn (Mn-em.)	0.70	0.73	2650	Direct	This paper
Calcium halophosphate					
:Sb	0.87-0.96	1	2600-2800	Comparison	Fonda, 1954 (8)
	0.95			Lamp efficiency	Tregellas-Williams, 1958 (1)
	0.84	1	2750	Direct	This paper
:Sb, Mn	0.52-0.76			Comparison	Fonda, 1954 (8)
	0.85			Comparison	Fonda, 1954 (8)
	0.74			Direct	Butaeva, *et al.* 1959 (18)
	0.77-0.92	1	2700-2750	Direct	This paper

ceeds 15 mole %, it is partly dissipated as thermal energy by the action of concentration quenching in the Mn-center. The absorption spectrum of these phosphors shown in Fig. 11 resembles that of Sn-activated α-calcium orthophosphate.

Discussion

Values for the measured quantum efficiency are summarized in Table I, compared with values reported in the literature. Our value for the quantum efficiency of magnesium tungstate at 2537Å is somewhat smaller than that reported by Fonda (9). This discrepancy does not seem to be due to phosphor differences but mainly due to the accuracy of measurements since the quantum efficiency of pure magnesium tungstate phosphors was independent of the samples used, as mentioned before. The maximum quantum efficiency and its wave length showed rather good agreement with the values reported by Fonda (9). The discrepancy of the quantum efficiency around 2537Å may be ascribed to the errors of the calibration of the photomultiplier or photocell used in these measurements. Furthermore, it should be noted that the quantum efficiency obtained by the lamp efficiency calculation method is likely to turn out too high because of neglect of the contribution of mercury lines other than the line 2537Å, for example, the line at 1850Å, to the luminous flux of the fluorescent lamp (18). Our value of the quantum efficiency of pure calcium tungstate is also somewhat smaller than that reported by the other authors. This discrepancy between these values may be due to the same reason as that for magnesium tungstate. The quantum efficiency of magnesium tungstate was decreased by the addition of Pb or Cd, while that of calcium tungstate was increased remarkably by the addition of Pb, as mentioned before. This fact is theoretically interesting with respect to the configuration of the luminescent center of tungstate phosphors.

In the impurity-activated phosphors, the quantum efficiency should be defined by the ratio of the emitted quanta to the quanta absorbed solely by activators, as shown by Eq. [6b]. Such a caution is especially important for the case in which the phosphor base shows a rather strong absorption in the ultraviolet region. It should be noted that the quantum efficiency of impurity-activated phosphors, based on the above definition, can be measured only by the direct optical method. Considering the sample differences, the quantum efficiency of halophosphate activated with Sb and with Sb and Mn shows good agreement with that reported by the other authors. The measured quantum efficiencies for the other impurity-activated phosphors seem to be reasonable.

In general, the quantum efficiency curves decrease more rapidly than the absorption curves at both longer and shorter wave lengths compared with the peak. For example, in the typical cases of magnesium and calcium tungstate, the quantum efficiency curves decrease gradually in the short wave-length region in which the absorption curves are flat, as shown in Fig. 3 and 4. The peaks of the quantum efficiency curves lie at a longer wave-length region than those of the absorption curves.

In principle, the wave-length dependence of the quantum efficiency of phosphors containing a single emitting state in the activator center should be flat over a wide range of the absorption spectrum, if the absorption is allowed only between the ground and the emitting state. If the absorption spectrum contains other absorption bands which are not responsible for the emission, the quantum efficiency should be reduced to small values in the corresponding spectral region. The rapid decrease of the quantum efficiency at longer wave lengths may be thus explained.

The decrease of the quantum efficiency at short wave lengths, however, seems to be attributable to another mechanism. It may be explained by a mechanism similar to that suggested by Dexter, Klick, and Russell (19) as an explanation for the low efficiency of F-center emission in alkali halides. We assume that the higher the vibration state in the excited state to which an electron makes a transition from the ground state, the larger becomes the nonradiative quenching of the excited state. The quantum efficiency will then decrease in the shorter wave-length region of the absorption spectrum. As a result, the peaks of the quantum efficiency curves will shift toward long wave lengths.

Acknowledgment

The authors wish to express their sincere thanks to Dr. Tsuneo Harada, the Director of Matsuda Research Laboratory of Tokyo Shibaura Electric Co., for his continuous support and encouragement. Part of this paper was presented at the Spring Meeting of The Physical Society of Japan, Fukuoka, April 9-11, 1957.

Manuscript received April 13, 1959.

Any discussion of this paper will appear in a Discussion Section to be published in the December 1960 JOURNAL.

REFERENCES

1. For general review and references see: J. Tregellas-Williams, *This Journal*, **105**, 173 (1958).
2. R. N. Thayer and B. T. Barnes, *J. Opt. Soc. Amer.*, **29**, 131 (1939); R. N. Thayer, *Trans. Electrochem. Soc.*, **87**, 413 (1945).
3. J. H. Schulman, *J. Appl. Phys.*, **17**, 902 (1946).
4. H. C. Froelich, *Trans. Electrochem. Soc.*, **91**, 241 (1947); *This Journal*, **93**, 101 (1948); *ibid.*, **98**, 402 (1951).
5. A. A. Shklover, *J. Techn. Phys. (USSR)*, **7**, 1239 (1947).
6. C. W. Jerome, *This Journal*, **100**, 586 (1953).
7. Z. Bodó, *Acta Phys. Acad. Sci. Hung.*, **3**, 23 (1953); Gy. Gergely, *J. Phys. radium*, **672**, 698 (1956).
8. G. R. Fonda, *J. Appl. Phys. Suppl.*, **4**, 69 (1954); *ibid.*, **4**, 17 (1954).
9. G. R. Fonda, *J. Phys. Chem.*, **43**, 561 (1939); *ibid.*, **48**, 303 (1944).
10. P. J. Botden and F. A. Kröger, *Physica*, **14**, 553 (1948); F. A. Kröger, "Some Aspects of the Luminescence of Solids," Elsevier Publishing Co., New York (1948); P. J. Botden, *Philips Research Repts.*, **6**, 425 (1951).
11. V. V. Antonov-Romanovsky and M. T. Epstein, *C. R. Acad. Sci. U.R.S.S.*, **64**, 483 (1949); V. V. Antonov-Romanovsky, *J. Phys. radium*, **17**, 694 (1956).
12. Y. Uehara, Y. Kobuke, and I. Masuda, *This Journal*, **106**, 200 (1959).

13. See, for example: M. G. Mellon, "Analytical Absorption Spectroscopy," p. 263, John Wiley & Sons, Inc., New York (1950).
14. A. Bril and H. A. Klasens, *Philips Tech. Rev.*, **15**, 63 (1953).
15. J. L. Ouweltjes and W. L. Wanmaker, *This Journal*, **103**, 160 (1956); W. A. Roberts, U.S. Pat. 2,312,267.
16. J. H. Schulman, U.S. Pat. 2,471,082.
17. F. A. Kröger, *Physica*, **6**, 774 (1939).
18. F. A. Butaeva, B. A. Fabricant, and A. L. Nedospasov, CIE XIV Sessions, Brussels (1959), Preprint P-59.4.
19. D. L. Dexter, C. C. Klick, and G. A. Russell, *Phys. Rev.*, **100**, 603 (1955).

Microscopic Observations on Electroluminescent Phosphors

A. Kremheller

Sylvania Research Laboratories, Bayside, New York

ABSTRACT

The electroluminescent brightness of single phosphor particles is studied microscopically in liquid dielectric cells. A simple visual technique in conjunction with a microscope permits one to analyze the brightness distribution within and among electroluminescent particles. Some experimental results are presented on the nonuniformity of the emission, the influence of ball milling and acid etching on the brightness, the improvement of brightness by particle separation, the analysis of the integrated light output as a function of the processing temperature, and the brightness changes due to particle orientation, contact, and irradiation.

Many investigations which aim at improving the brightness[1] of electroluminescent (EL) lamps are concerned with the integrated light output in evaluating the influence of the processing parameters in phosphor preparation. Although this approach is useful in testing and comparing finished products with each other, one does not learn much about the behavior of the single particles composing the EL layer. Even if one observes that a certain treatment improves the integrated light output, it is not evident how the improvement affects the phosphor particles, e.g., does an increased number of particles become electroluminescent, does every particle become brighter, or does the brightness distribution of particles change in some other way. These questions can be answered by observing the single EL particles. In this way, it is hoped that the analysis of the components of the integrated light output will finally lead to improved EL lamps by means of synthesis of the improved components. This paper shows in several examples that such an improvement can be attained by the microscopic study of single phosphor particles.

Experimental

Various EL phosphors have been studied in liquid, plastic, and glass dielectric cells. Some phosphors are of an experimental nature, while others are commercially available. Most brightness measurements are conducted with an adjustable-gap sandwich cell using castor oil as the liquid dielectric. The study of particle orientation, contact, and alignment is facilitated by using a gap-like cell. Its electrodes are about 0.5 mm high to avoid excessive edge effects with respect to the electric field.

[1] "Electroluminescent brightness" as used here is a measure of the luminous flux per unit emissive area of a single particle. (See also the definition of "brightness" in American Institute of Physics Handbook, Dwight E. Gray, New York, 1957, page 6-3.)

The particle brightness is determined by a method similar to that described by Zalm, Diemer, and Klasens (1) and has been adapted for our purpose. In this method, a relative estimate of the EL brightness of phosphor particles is obtained by employing photographic, neutral-density step filters in conjunction with a microscope. The filter is inserted into the optical path of the microscope until the EL particle remains just visible to the adapted eye; the step number is then a measure of the particle brightness. The opacity of the filter doubles with every two filter steps, so that 20 steps correspond to a change in particle brightness B by a factor of $2^{10} = 1024$. The logarithmic sequence of the opacity facilitates the plotting of log B if $2^{1/2}$ is used as the base of the logarithms. This simple visual technique permits comparison of the brightness from various regions within a single particle and among phosphor particles.

Nonuniformity of EL Emission

The importance of studying the EL brightness of single phosphor particles becomes apparent when an EL lamp is viewed under a microscope, and the considerable brightness variations from particle to particle are observed (Fig. 1). Only a minority of particles electroluminesces brightly, while some particles do not emit any EL light and others appear fairly dim.

Microscopic investigation of single particles permits one to measure their brightness and to produce a frequency diagram of the EL brightness (Fig. 2). The diagram indicates the degree of brightness variation. Since the base $2^{1/2}$ is used for log B, the brightness range is such that the brightest particles are about 50 times brighter than the dim ones. Actually, there are about 20% of the particles which do not

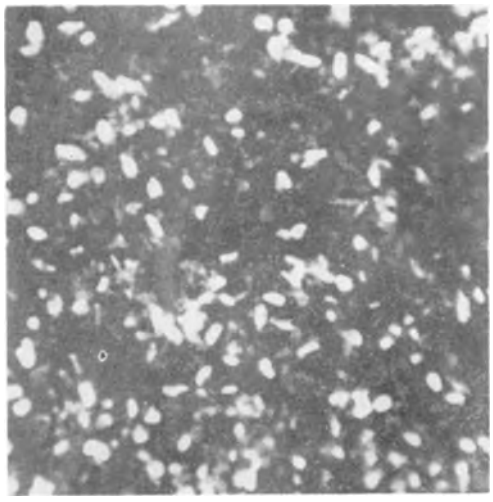

Fig. 1. Brightness variation among particles. Average particle diameter about 25 μ.

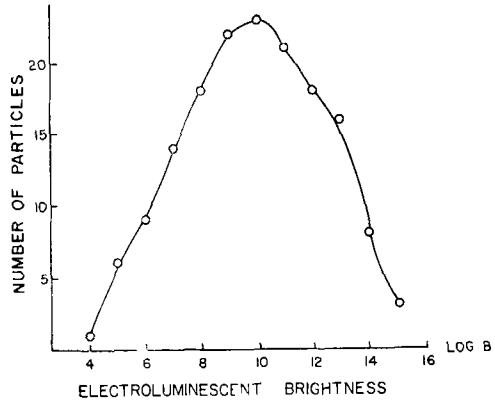

Fig. 2. Brightness distribution of electroluminescent phosphor particles; log B to the base $2^{1/2}$.

electroluminesce at all. Some of these "dead" particles do not show up in the photograph, others get some light from adjacent bright particles and can be seen. There is a most frequent particle brightness which is about 8 times the lowest brightness measured. The brightness-frequency diagram varies somewhat from phosphor to phosphor. In some cases a relatively flat peak or even 2 maxima have been observed.

Besides the brightness nonuniformity among particles, considerable brightness variation also occurs within single particles, as shown in Fig. 3. The emission seems to originate from particle regions[2] (usually the edges of particles) which appear opaque in transmitted visible light; it is also observed that the same opaque regions become photoluminescent under ultraviolet irradiation. The photoluminescence is, however, somewhat more uniform than the electroluminescence, as pointed out by other researchers (2). In addition to electroluminescent emission from extended areas, there is emission from spots (3); this spot emission is not observed during photoluminescence. The spot emission predominates at high frequencies (several kc) of the applied electric field. The spots occur usually in line arrange-

[2] In the review of this paper it was indicated that "the emission is, very likely, created only in small spots, and that the area emission is simulated mainly, or exclusively, by multiple reflections inside the crystals." The author feels that this statement is definitely valid at high frequencies, although primary area emission may occur at very low frequencies of the applied electric field.

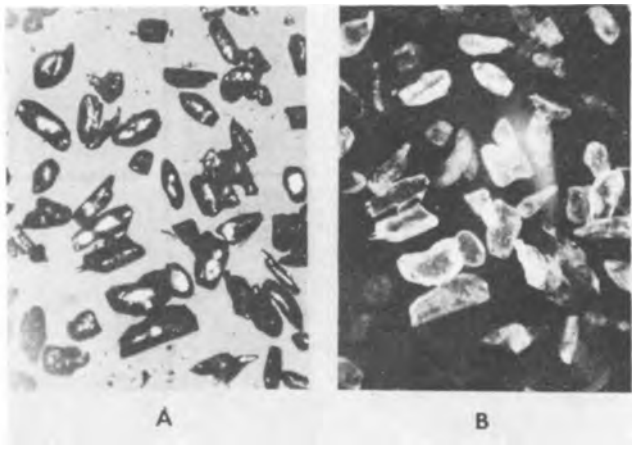

Fig. 3. Microscopic observation of phosphor particles: (a) in transmitted light; (b) under their own EL illumination. Average particle diameter about 120 μ.

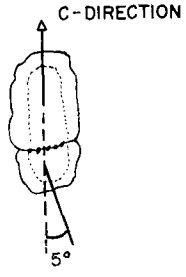

Fig. 4. Disorientation and spot emission along crystallite boundary.

ments, apparently located in fissures parallel to the c-plane (or 111-plane for cubic structure). It appears that these fissures separate contiguous crystallographic regions which are in many cases disoriented. The misalignment often amounts to 5° (Fig. 4), as the difference in extinction angle between crossed nicols indicates. Sometimes emission colors from spots and from areas are different; for instance, some (Zn,Cd) (S,Se) : Cu,Cl phosphors emit greenish-orange area and greenish-blue spot electroluminescence. It is possible that these color differences are caused by the nonuniformity of the electric field (4), or by the preferential optical absorption of the short-wavelength light in the bulk of the crystallite.

Ball Milling and Acid Etching

Another series of EL phosphors differs in that they have been ball milled prior to a final thermal treatment. Microscopic observation indicates that the milled phosphors exhibit an improved uniformity in EL brightness among and within single particles. The integrated light output increases in a typical case by 30% due to milling. As an attendant effect, milling introduces enough damage to particles to make most of them appear opaque in transmitted light. It is plausible that the particle damage during milling may contribute to an improved activator distribution (5) in the thermal processing step. In addition to this effect, it appears that surface damage increases the EL brightness by facilitating light emission which is otherwise lost by absorption due to internal multiple reflections.

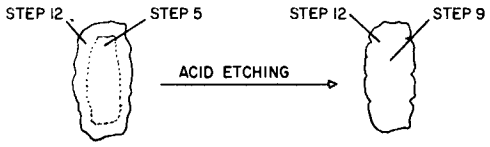

Fig. 5. Increase of emission uniformity by acid etching; the opacity values of the step filter indicate the relative brightness.

This hypothesis has been tested by acid etching of phosphor particles. A single phosphor particle (Fig. 5) is observed in a gap cell in castor oil. It is found that the edge has about 10 times greater EL brightness than the center region of the particle. The particle is removed from the cell, etched with concentrated HCl for a few minutes, and returned into the cell. The opacity of the center region in transmitted light is considerably increased by acid etching. The center region is now 4 times brighter electroluminescent than in the case of the original grain. The use of the step filter permits an estimate of the brightness improvement of the center region as a result of the acid treatment. The acid etching is not uniform over the whole grain; there is some preferential dissolution along grain boundaries, strained regions, and in strongly birefringent regions.

An increase in brightness and uniformity is also indicated by the slight shift of the brightness distribution (Fig. 6), which represents a large number of particles in the test cell. While there is no change in the maximum particle brightness, one obtains a slight increase in the most frequent brightness. The integrated light output is also measured, and an increase of 30% is observed which is due to the acid etching.

Particle Separation

Since the EL brightness of individual particles differs widely, attempts have been made to select bright particles for separate examination. This selection is sometimes comparatively simple; for instance, the bright particles may differ in size from the rest. A Zn(S,Se):Cu,I phosphor exhibited an unusual frequency diagram of the brightness distribution in that 2 peaks are observed (Fig. 7). The peak at high brightness is mainly due to the bright large particles. This green EL phosphor is fractionated so that particles above 80 and below 20 μ could be studied separately, since microscopic

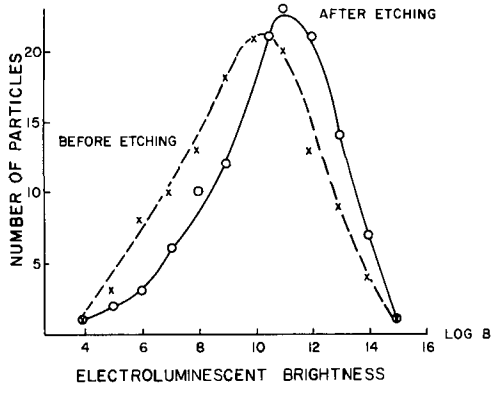

Fig. 6. Frequency diagram of brightness change with acid etching.

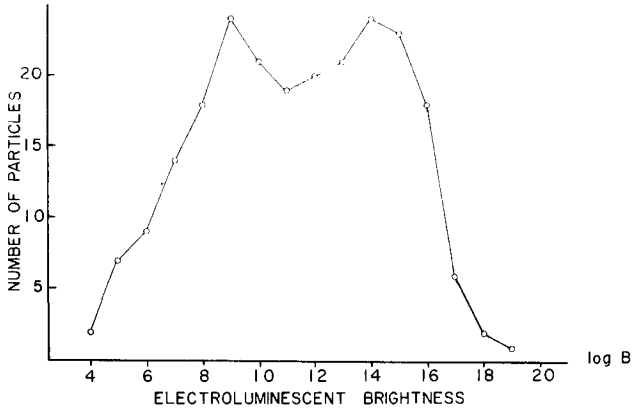

Fig. 7. Brightness distribution of a Zn(S,Se):Cu,1 phosphor

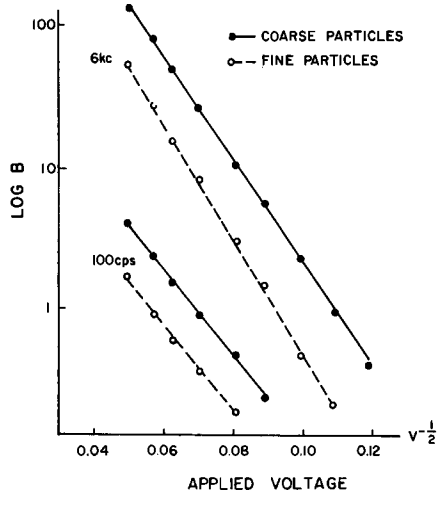

Fig. 8. Brightness vs. voltage for two particle fractions

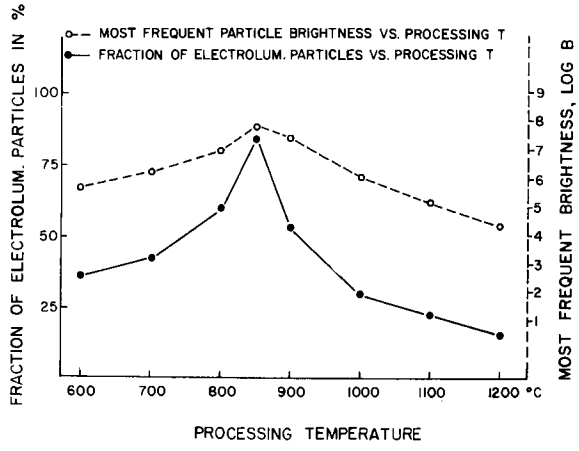

Fig. 9. Components of integrated light output vs. processing temperature.

observations had indicated that the large particles were brighter than the small ones. Measurements on the fractionated material show that the integrated light output from a liquid dielectric sandwich cell containing the coarse particles is up to 5 times as high as that from a cell containing the same weight of the fine particle size fraction (Fig. 8).[3]

Analysis of Integrated Light Output

Microscopic observation of single particles also permits analysis of the brightness characteristics as

[3] Measured by Dr. P. Goldberg of our laboratory.

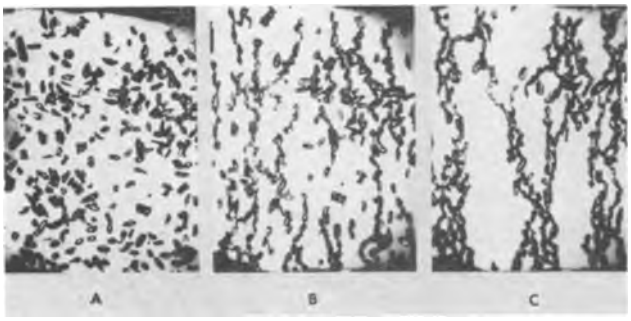

Fig. 10. Influence of electric field and irradiation on particle orientation: (a) random particle distribution, (b) orientation due to electric field, and (c) re-alignment due to irradiation with visible light. Average particle diameter about 70 μ.

a function of processing parameters, such as the preparation temperature. A series of blue-emitting EL phosphors has been studied for which the thermal treatment had been carried out at various temperatures between 600° and 1200°C. The integrated light output had been shown to be at a maximum for the material processed at 850°C. The study of the brightness of single particles reveals that this maximum in integrated light output results from optimization in two respects at this temperature, as indicated in Fig. 9. First, the fraction of particles which are electroluminescent peaks sharply at 850°C, and second, the most frequent particle brightness of the various frequency-brightness distribution curves is also at a maximum at this temperature.

Particle Orientation, Contact, and Irradiation

Phosphor particles in castor oil dielectric cells are readily oriented by electric a-c and d-c fields (6, 7). A change in voltage or frequency causes motion and reorientation of particles; some particles exhibit translational and rotational motion even at constant voltage and frequency. Especially the very small particles move erratically and appear to be charged and discharged by collisions with other particles. Randomly distributed particles (Fig. 10a) are oriented in an electric field; Fig. 10b shows the orientation with 1250 v/cm applied at 500 cps. During the orientational motion some particles become attached to one electrode while most particles become attached to other particles. The particles form oriented chains, with their elongation parallel to the electric field, and aggregates between the electrodes. Alignment and contact increase the EL brightness of many particles; although some particles remain nonelectroluminescent, others turn brightly electroluminescent. A brightness increase by a factor of 4 can be observed readily in many cases.

Although most particles align themselves with their elongation parallel to the applied electric field, there are some internally misaligned particles (some with adjacent crystallite regions disoriented by up to 10°, cf. Fig. 4) which align themselves with their aggregate elongation perpendicular to the electric field. It appears that this mode of alignment occurs when there is only little electrical contact between adjacent, elongated single crystal regions, which are consequently aligned with their single crystal elongation parallel to the electric field. This anomalous particle orientation is also connected with a marked increase in the EL brightness of such particles.

Irradiation with ultraviolet or visible light facilitates particle alignment and changes the brightness distribution. The threshold field for particle alignment under strong irradiation is considerably below that for the start of alignment in the dark. When partially aligned particles (Fig. 10b) are irradiated with visible light, the alignment as well as chain and aggregate formation continue until a new, fairly stationary arrangement is achieved, as shown in Fig. 10c. Besides this re-alignment, irradiation causes a redistribution of the local light emission from the phosphor particles in the test cell. The electroluminescence emission from single particles and particle regions frequently increases or decreases. It appears likely that most of these brightness changes, due to various parameters discussed above, are caused by the concomitant changes in the local electric field.

Summary and Conclusions

A simple visual method employing a logarithmically graded, neutral-density step filter enables one to study microscopically the brightness variation among and within single EL phosphor particles.

It has been shown that a relation exists between the opacity and the light emission from single particles, in that acid etching increases both. Sometimes it is possible to make use of the nonuniformity of light emission in improving the lamp brightness, for instance by particle separation. The integrated light output as a function of processing temperature is analyzed, and it is found that the phosphor sample of optimum integrated brightness contains the largest fraction of EL particles and the maximum brightness value for the most frequent particle fraction. Particle orientation, particle-to-particle and particle-to-electrode contact enhance the electroluminescence emission. External irradiation with visible or ultraviolet light exerts also a marked influence on the brightness distribution within and among single phosphor particles.

Microscopic studies consequently can contribute to the preparation and selection of bright particles, so that the integrated light output of EL lamps can also be increased. The method is that of analysis and synthesis. That is, one looks first at single particles and attempts to optimize the components contributing to the integrated light output. The second step is then the synthesis of the optimized components which leads to the improvement of the brightness of EL lamps, as has been demonstrated above in some typical cases.

Manuscript received Aug. 17, 1959. This paper was prepared for delivery before the Philadelphia Meeting, May 3-7, 1959.

Any discussion of this paper will appear in a Discussion Section to be published in the December 1960 JOURNAL.

REFERENCES

1. P. Zalm, G. Diemer, and H. A. Klasens, *Philips Research Repts.*, **10**, 205 (1955).

2. K. H. Butler, C. W. Jerome, and J. F. Waymouth, *Elec. Eng.*, **73**, 524 (1954).
3. J. F. Waymouth and F. Bitter, *Phys. Rev.*, **95**, 941 (1954).
4. L. Burns, *This Journal*, **100**, 572 (1953).
5. A. H. McKeag and E. G. Steward, *ibid.*, **104**, 41-4 (1957).
6. W. Lehmann, *ibid.*, **103**, 24 (1956); **105**, 585 (1958).
7. W. C. Gungle, *et al.* (to Sylvania Electric Products Inc.), U. S. Pat. 2,728,870, Dec. 27, 1955.

Hydrothermal Preparation of Two-Component Solid Solutions from II-VI Compounds

A. Kremheller, A. K. Levine,[1] and G. Gashurov

Sylvania Research Laboratories, A Division of Sylvania Electric Products Inc., Bayside, New York

ABSTRACT

The hydrothermal synthesis of binary solid solutions of inorganic phosphors and photoconductors is described. This method depends on the increased reactivity between the components and ease of crystal growth in an aqueous solution maintained at high temperature under a confining pressure. The hydrothermal method offers the advantages of a sealed system and easily reproducible experimental conditions. Solid solutions of ZnS-HgS, CdS-HgS, and ZnS-CdS have been prepared by this method. Results of optical absorption measurements, x-ray analysis, microscopic studies, and the spectral photoresponse of the solid solutions formed are presented.

The conventional preparation of binary solid solutions from group II—group VI systems recently has been of interest (1,2), since these materials (such as zinc-inter-chalcogenides, zinc sulfo-and seleno-tellurides) permit one to study the correlation between crystal structure and their electronic behavior as photoconductors and phosphors. The usual synthesis (3) of stoichiometrically controlled two-component solid solutions is difficult if the vapor pressures of the compounds involved differ greatly, so that preferential evaporation occurs. In such cases solid solution is sometimes achieved by a vapor phase process in high-pressure furnaces (4), or by coprecipitation in aqueous solutions (5).

Utilizing processing techniques introduced by Allen and Crenshaw (6), Kremheller and Levine (7) succeeded in hydrothermally preparing electronically active II-VI compounds, such as photoconductive cadmium sulfide and various related luminescent materials. This paper reports on the extension of these investigations to the synthesis of binary solid solutions of II-VI compounds. The hydrothermal method was chosen because it employs a lower temperature than is required in dry processing. Low-temperature synthesis is possible under hydrothermal conditions because the formation of mixed crystals is effected by solution transport, whereas in conventional processing crystal formation and growth take place mainly by vapor transport.

Experimental

The hydrothermal method has been described in some detail in previous publications (7); therefore, only a brief account of the method is given here. Hydrothermal synthesis employs aqueous or liquid solution of the component materials, sometimes with certain additives, at temperatures considerably above the normal boiling point of the solution and under pressures of several hundred atmospheres.

Hydrothermal synthesis is carried out by placing the finely divided component solids, say zinc sulfide and mercuric sulfide in a typical case, into a quartz vial which then is filled partially with deionized water and sealed. The quartz vial is enclosed in a high-pressure steel autoclave which also contains water. As long as there is a liquid phase in equilibrium with a vapor, the pressure will depend only on the temperature and not on the amount of each phase. Therefore, at temperatures below the critical temperature, the pressure outside of the quartz vial can be equal to the pressure inside even though the degree of filling of the autoclave is not the same as that in the vial. For example, the temperature-density diagram for water shows that two phases are present at 350°C as long as the degree of filling is in the range of about 20 to 50% (8). The autoclave is put in place, and its temperature is raised very slowly so that the temperature of the water in the vial is almost the same as that of the water outside it. Under these conditions the pressure inside the sealed quartz vial is sufficiently close to that in the autoclave so that the quartz vial neither explodes nor implodes. After the desired time at temperature, the autoclave is cooled slowly until the pressure is atmospheric; the vial is taken out and the processed material is removed. A large number of vials can be processed at the same time under identical conditions without danger of sample-to-sample contamination.

Results

Most experiments were carried out at temperatures around 350°C and under pressures of several

[1] Chemistry Department, Brooklyn College, Brooklyn, N. Y.; Consultant, Research Laboratories, Sylvania Electric Products Inc., Bayside, N. Y.

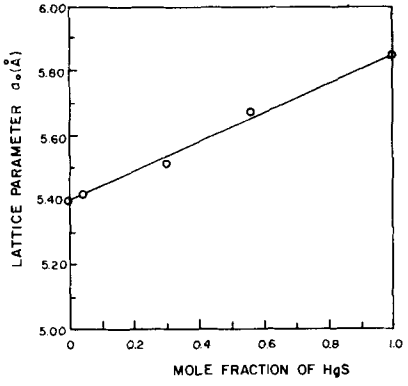

Fig. 1. Lattice parameter as a function of composition, ZnS-HgS system.

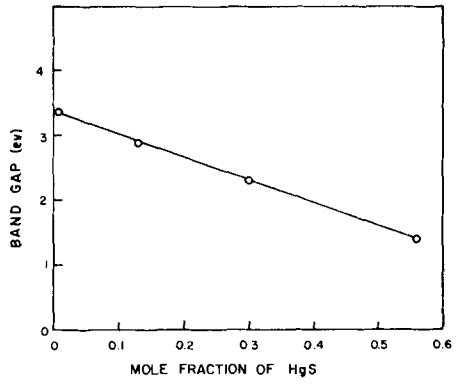

Fig. 2. Band gap as a function of composition, ZnS-HgS system.

hundred atmospheres. It was found that heat-treatment under these conditions for two or three days was sufficient usually to produce solid solutions of ZnS-HgS, CdS-HgS, and ZnS-CdS. In some experiments, equilibrium was reached in shorter time.

Solid solutions of ZnS-HgS.—Since the solubility rather than the vapor pressure is responsible for the formation of solid solutions by the hydrothermal processing technique, it is feasible to prepare quantitatively controlled solid solutions of components exhibiting greatly different vapor pressures under conventional processing conditions. For example, attempts were made conventionally to prepare solid solutions of (Zn,Hg)S by mixing ZnS with HgS and heating. However, after 30 min at 800°C, it was found that all the mercuric sulfide had volatilized leaving only ZnS. When a mixture of ZnS and HgS was processed hydrothermally for 50 hr at 350°C, solid solutions of (Zn,Hg)S were obtained, as indicated by the results of x-ray diffraction analysis of a series of such solid solutions (Fig. 1). These solid solutions are of the zinc blende structure, and within the limit of experimental error they exhibit a change of lattice constant with chemical composition in agreement with Vegard's law. A further proof of the formation of solid solution for the ZnS-HgS system was obtained from optical reflection measurements which show a shift in the absorption edge toward longer wave lengths as the mercury content increases. The reflection measurements were made with a Beckman Model DU Spectrophotometer with a MgO cell as the standard. The change of the energy band gap determined from these measurements

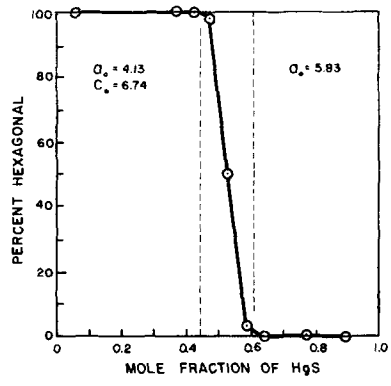

Fig. 3. Results of x-ray analysis, CdS-HgS system.

is shown in Fig. 2. The values of the band gap were calculated from the wave lengths corresponding to the intersection of the straight-line extrapolation above and below the short wave length knee of the reflectance curve, i.e., the same procedure was used as that employed by Larach, Shrader, and Stocker (2).

Solid solutions of CdS-HgS.—Solid solutions of (Hg,Cd)S can also be prepared readily by the hydrothermal synthesis. Figure 3 shows x-ray results for the CdS-HgS system. For HgS additions up to 43 mole % all the samples were of the wurtzite structure, and within the limit of experimental error no shift in the lattice parameters could be detected, the lattice parameters being essentially those of hexagonal CdS. The energy gap change in these samples (Fig. 4) indicates that formation of solid solutions was achieved, and it appears that CdS takes up HgS without any apparent structural changes.

For HgS additions of 60 mole % and higher only the zinc blende structure could be detected in CdS-HgS samples, and these cubic solid solutions have the same cell constant of 5.83Å. There is also an intermediate region in the CdS-HgS system extending from 43 to 60 mole % of HgS in which both the hexagonal (a = 4.13Å, c =6.74Å) and the cubic (a = 5.83Å) phases are present. The ratio of hexagonal phase to cubic appears to change gradually with the change in composition so that the sample to which 53 mole % of HgS were added contains both phases in equal amounts. To investigate further the nature of the intermediate region, microscopic observations were made on CdS-HgS samples and some results are given in Fig. 5. Figure 5a shows the sample con-

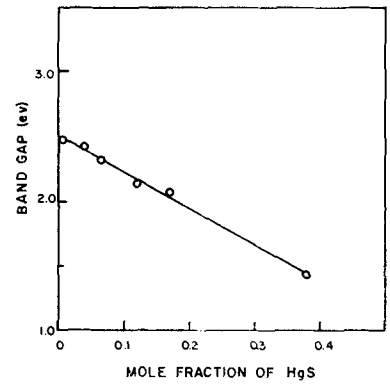

Fig. 4. Band gap as a function of composition, CdS-HgS system.

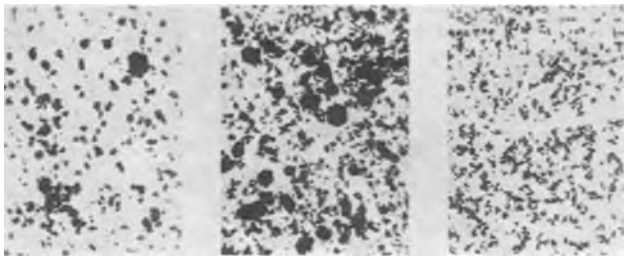

Fig. 5. Photomicrographs of CdS-HgS preparations: (a) (left) 43 mole % HgS (hexagonal), (b) (center) 53 mole % HgS (hexagonal:cubic, 1:1), and (c) (right) 77 mole % HgS (cubic). Figures have the same magnification; largest particle diameter about 50 μ.

taining 43 mole % of HgS in which only the hexagonal phase was found by x-ray analysis. One observes that the sample consists of large hexagons and small particles of indefinite shape. Under higher magnification it is observed that the small particles are also either hexagonal in shape or that they are fractions of large hexagons. The sample 5c containing 77 mole % of HgS consists of small particles which are found by x-ray analysis to be aggregates of cubic crystallites. The sample shown in the center, Fig. 5b, in which both hexagonal and cubic phases were found in equal amounts, consists of hexagons similar to those in Fig. 5a and small particles of the same kind as those in Fig. 5c. It appears that the sample containing 53% of HgS is a physical mixture of two solid solutions: the hexagonal (a = 4.13Å, c = 6.74Å) and the cubic (a = 5.83Å).

Solid solutions of ZnS-CdS.—Self-activated (Zn,Cd)S solid solutions have also been prepared by hydrothermal synthesis. The single crystallites exhibit good crystallinity; they are below 5μ in diameter, which is considerably smaller than the size of particles prepared by dry processing. Their luminescence and photoconductivity properties are comparable to those of conventionally prepared solid solutions. Luminescence under ultraviolet excitation (3650Å) shifts from blue to red with the increase in CdS concentration, while photosensitivity decreases with increasing ZnS concentration.

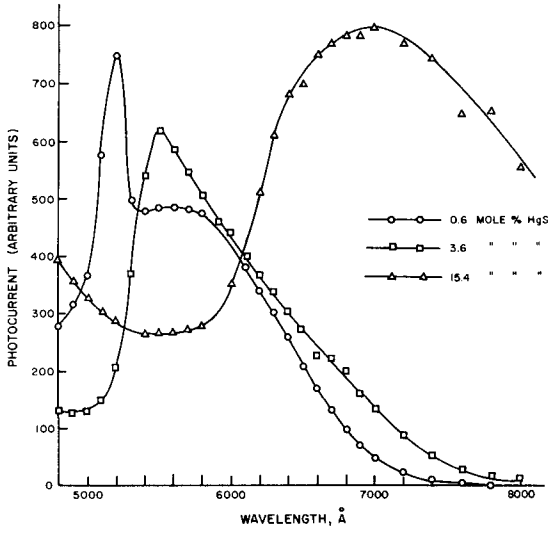

Fig. 6. Spectral response of photoconductive (Cd,Hg)S:Cu, Cl.

Activated solid solutions.—Solid solutions of (Zn,Hg)S, (Zn,Cd)S, and (Cd,Hg)S were made photoconductive or luminescent by proper activation. Activation was accomplished by adding copper or silver together with chlorine or aluminum to the host components. The luminescence of (Zn,Hg)S solid solutions under ultraviolet excitation (3650Å) shifts from green to red with the increase in HgS concentration. No visible photoluminescence is exhibited by (Zn,Hg)S solid solutions containing over 30 mole % of HgS because of a shift to the infrared. (Cd,Hg)S solid solutions were found to show photoluminescence and photoconductivity. Figure 6 shows the spectral response curves for this system. In every case 0.3 mole % of copper, 1 mole % of chlorine, relative to the sulfide was added to the solution in the vial. The photoconductivity peak shifts toward longer wave lengths with increasing HgS, as one would expect from the decrease in the width of the energy gap (Fig. 4). The photosensitivity in general decreases and the dark current increases with increase in HgS concentration.

Conclusions

Complete solid solution is obtained throughout the whole range for the ZnS-HgS system. These solid solutions appear to show a linear variation of lattice constant with composition. Corresponding to the continuous range of solid solution in this system, there occurs a linear variation of the energy gap at least up to 56 mole % of HgS. It is clear, however, that the energy gap cannot vary linearly in the whole range since the straight line in Fig. 2 extrapolates to a negative value for the band gap of pure cubic HgS.

HgS and CdS form solid solutions over the entire range, but the crystal system depends on the composition. Hexagonal solid solution of the wurtzite structure is obtained in the 0-43 mole % HgS range, while cubic solid solution of the zinc blende type is obtained for HgS additions above 60 mole %. Within the limits of experimental error neither of these solid solutions showed any shift in lattice parameters with composition. Hexagonal and cubic solid solutions are present in the 43-60 mole % region, the ratio of cubic to hexagonal solid solutions increasing continuously with increasing HgS concentration. These results agree essentially with those reported by Rittner and Schulman (5), who obtained (Cd,Hg)S solid solutions by coprecipitating CdS and HgS in concentrated ammonium sulfide solution. Solid solutions of (Zn,Hg)S, (Zn,Cd)S, and (Cd,Hg)S were made photoconductive and luminescent by proper activation.

Acknowledgment

Grateful acknowledgment is made to V. A. Brophy for carrying out the x-ray determinations, and to J. T. Ragusin and S. Faria for valuable assistance with the experimental work.

Manuscript received Aug. 24, 1959. This paper was prepared for delivery at the Philadelphia Meeting, May 3-7, 1959.

Any discussion of this paper will appear in a Discussion Section to be published in the December 1960 JOURNAL.

REFERENCES

1. S. Larach, W. H. McCarroll, and R. E. Shrader, *J. Phys. Chem.*, **60**, 604 (1956).
2. S. Larach, R. E. Shrader, and C. F. Stocker, *Phys. Rev.*, **108**, 587 (1957).
3. H. W. Leverenz, "Luminescence of Solids," Chap. 3, John Wiley & Sons, Inc., New York (1950).
4. L. Wesch, "Leuchten und Struktur fester Stoffe," R. Tomaschek, Editor, pp. 124-146, R. Oldenburg (publisher), Munich and Berlin (1943).
5. E. S. Rittner and J. H. Schulman, *J. Phys. Chem.*, **47**, 537 (1943).
6. E. T. Allen and J. L. Crenshaw, *Am. J. Sci.*, **34**, 341 (1912).
7. A. Kremheller and A. K. Levine, Spring Meeting of the ACS, Miami, April 9, 1957; *J. Appl. Phys.*, **28**, 746 (1957); *Sylvania Technologist*, **10**, 67 (1957).
8. A. Neuhaus, *Chemie-Ing.-Techn.*, **5**, 355 (1956).

Tin-Activated Alkaline-Earth Pyrophosphate Phosphors

R. C. Ropp and R. W. Mooney

Chemical and Metallurgical Division, Sylvania Electric Products Inc., Towanda, Pennsylvania

ABSTRACT

The preparation and properties of the Group II metal pyrophosphates activated by tin are described. It is shown that the fluorescent emission is strongly dependent on the matrix shifting toward higher wave lengths with increasing size of the cation of the pyrophosphate. Excitation and emission spectra of many of the phosphors are given. The most useful of these phosphors is $Sr_2P_2O_7$:Sn, a very efficient blue phosphor emitting at 452 mμ.

During the past few years there have been several investigations of tin-activated phosphates. These phosphors present certain problems in preparation since the tin atoms function as activators only when in a partially reduced state, commonly thought to be the Sn^{2+} oxidation state. Except for this minor problem, the tin-activated phosphates are easily prepared and a wealth of new phosphors may be obtained by changing the cationic constituent of the lattice and the crystal structure if the compound exists in polymorphic forms.

The tin-activated orthophosphates were studied in detail by Butler (1) and several efficient phosphors discovered. Starting from titanium-activated barium pyrophosphate (2), Ranby and co-workers (3) made a study of the tin-activated alkaline-earth pyrophosphates giving the visually detected luminescent colors obtained by varying the ratio of one cation to another in the three binary systems and the spectral energy distributions of selected pyrophosphates activated by tin and manganese. All three alkaline-earth pyrophosphates were found to be polymorphic, but only in the barium pyrophosphate system did a change in structure from the low-temperature to the high-temperature form produce a change in emission, specifically from green to red. The high-temperature forms (commonly referred to as the α-forms) and the low-temperature or β-forms of calcium and strontium pyrophosphate both were stated to fluoresce blue under 254 μ excitation. A concurrent study of the tin-activated strontium and barium pyro- and tetraphosphates by McKeag and Steward (4) yielded several different phosphors in the barium system, but the blue emission of the strontium system was relatively unaffected by changes in the Sr/P ratio or firing temperature.

The present study was undertaken to investigate in greater detail the optical properties of the tin-activated alkaline-earth pyrophosphates and modifications thereof, especially with regard to the effects of crystal structure changes on the emission and excitation spectra of these phosphors. It will be shown that the spectral properties are even more dependent on crystal structure than was previously realized, thus leading to the discovery of several new phosphors. The most useful phosphor in this system is $Sr_2P_2O_7$:Sn, a deep-blue emitter, which has found practical application in fluorescent lamps.

Experimental Method

The pyrophosphates of calcium, strontium, and barium were readily obtained by ignition of their respective secondary phosphates. The compounds $CaHPO_4$ and $BaHPO_4$ were precipitated by the usual methods of adding a solution of $(NH_4)_2HPO_4$ to a solution of $CaCl_2$ or $BaCl_2$, each solution having been previously purified by sulfide separation of the heavy metals. Anomalies in the precipitation of $SrHPO_4$ led to an investigation of this material from which it was found that $SrHPO_4$ is dimorphic with each polymorph exhibiting slightly different behavior on ignition (5). In general, a slight excess of phosphate ion was used and the tin concentration varied from 0.01-0.20 gram-atom tin per gram-mole of pyrophosphate. It was found that phosphor characteristics were independent of activator concentration over this range, and therefore all phosphors were prepared at the same added concentration of 0.05 gram-atom tin per gram-mole of pyrophosphate. For the magnesium- and zinc-modified phosphors, the compounds $MgNH_4PO_4$ and $ZnNHPO_4$ were precipitated by standard techniques (13). The firing techniques used in the preparation of these phosphors followed the methods described in detail by several previous authors (1-3) and are not described here, except to state that various requisite

temperatures were employed to form the diverse polymorphic crystalline forms.

The crystal structures of the phosphors were determined by conventional x-ray diffraction techniques using CuKα radiation from a Philips Norelco unit. In the majority of cases, identification was made by means of Debye-Scherrer powder patterns taken on large diameter (114.6 mm) cameras. In a few cases, diffractometer tracings were taken on a Norelco wide-range goniometer at a scanning speed of ¼°/min. As would be expected, the two methods were in excellent agreement.

The excitation-emission radiometer[1] used for the measurements of excitation and emission spectra will be described in detail elsewhere (6). Basically, it is a double monochromator system with a high-pressure xenon arc source and a 1P28 photomultiplier detector. A combination of optical and electrical components provides for constant-energy-level illumination of the sample during excitation measurements and gives an emission spectrum which is proportional to the true energy output of the sample regardless of source fluctuations or detector sensitivity as a function of wave length. The relative efficiency measurements were made on a plaque tester of conventional design (7).

Experimental Results in Single-Component Pyrophosphates

Spectral characteristics of the tin-activated polymorphic modifications of calcium, strontium, and barium pyrophosphate are summarized below. In general, there were no changes in spectra with tin content.

Calcium pyrophosphates.—Excitation and emission spectra of β- and α-$Ca_2P_2O_7$:Sn are shown in Fig. 1. (λ_x refers to the wave length of excitation, and λ_e, the emission wave length at which the excitation was measured.) No fluorescence was observed for γ-$Ca_2P_2O_7$:Sn.

The low-temperature or β-form of $Ca_2P_2O_7$:Sn is primarily an ultraviolet emitter with a broad band peaking at 369 mμ. The excitation spectrum is also broad with the primary band peaking at 238 mμ. Both the emission and excitation spectra suggest the presence of a second band in each at lower energies. However, the emission spectrum remained essentially as shown in Fig. 1 for all energies of excitation which gave fluorescence. These results agree with the emission spectrum for β-$Ca_2P_2O_7$:Sn presented by Bril and Klasens (8).

As the crystal structure changed from β-$Ca_2P_2O_7$ to α-$Ca_2P_2O_7$, the high-temperature form, the spectra also varied. With high excitation energies, the emission spectrum closely resembled that of β-$Ca_2P_2O_7$:Sn with the peak shifted very slightly to higher energies at 364 mμ. The excitation spectrum for this band was, however, different with the strongest absorption band at 254 mμ and a weaker band at about 232 mμ. As the energy of excitation decreased, a second band appeared in the emission spectrum at about 430 mμ until with $\lambda_x = 276$ mμ the fluorescent spectrum shown in Fig. 1 was obtained. The excitation spectrum obtained for emission in this band also showed two peaks, the stronger at 240 mμ and the weaker at 260 mμ. An inspection of Fig. 1 shows that the positions of the bands in the excitation spectra are not equivalent for the two different emission bands.

[1] Built by the Perkin-Elmer Corporation, Norwalk, Conn.

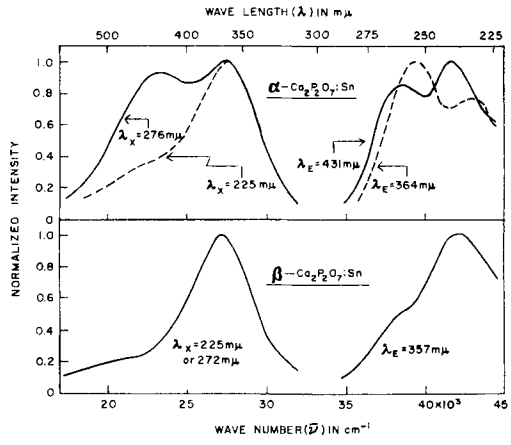

Fig. 1. Excitation-emission spectra for $Ca_2P_2O_7$:Sn phosphors. Firing temperature, 1300° and 1175°C, respectively.

Strontium pyrophosphates.—The low-temperature or β-form of $Sr_2P_2O_7$:Sn is also primarily an ultraviolet emitter (see Fig. 2) with its main band at 364 mμ and evidence of another weaker band in the visible. Its excitation spectrum has two bands, the stronger peaking at 234 mμ and the weaker at about 260 mμ. The similarities between the excitation and emission spectra of β-$Ca_2P_2O_7$:Sn and β-$Sr_2P_2O_7$:Sn are striking with the bands shifted very slightly to higher energies for β-$Sr_2P_2O_7$:Sn.

The α-form of $Sr_2P_2O_7$:Sn has a single emission band peaking at 464 mμ and the usual two excitation bands at 256 mμ and approximately 238 mμ. Again, a similarity may be noted between α-$Sr_2P_2O_7$:Sn and the lower-energy emission band in α-$Ca_2P_2O_7$:Sn with the spectrum of the strontium compound shifted to lower energies. The bands in the excitation spectra of α-$Sr_2P_2O_7$:Sn and α-$Ca_2P_2O_7$:Sn for $\lambda_E = 431$ mμ occur at almost identical energies although the relative intensities of the bands are reversed.

Barium pyrophosphates.—The low-temperature form of $Ba_2P_2O_7$, which Ranby (3) has designated as α-$Ba_2P_2O_7$ has a single weak emission band peaking

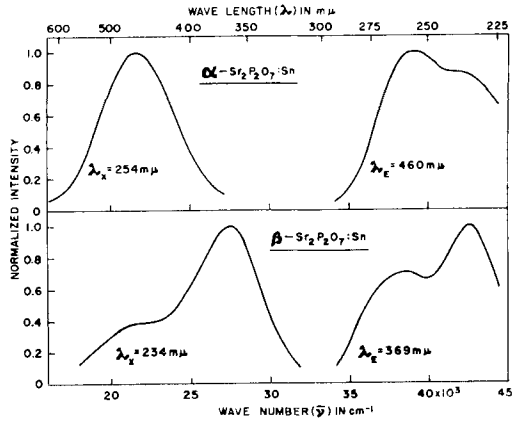

Fig. 2. Excitation-emission spectra for $Sr_2P_2O_7$:Sn phosphors. Firing temperature, 1100° and 650°C, respectively.

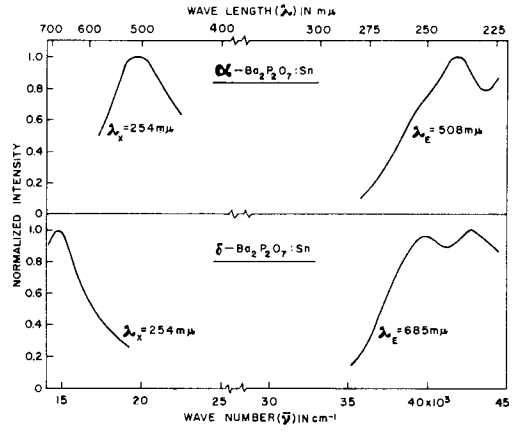

Fig. 3. Excitation-emission spectra for $Ba_2P_2O_7$:Sn phosphors. Firing temperature, 650° and 980°C, respectively.

at 505 mμ (see Fig. 3). The main excitation band peaks at 239 mμ and there is evidence of a weaker band at lower energies in the general vicinity of 256 mμ. Thus this phosphor also has spectral characteristics in common with α-$Ca_2P_2O_7$:Sn and α-$Sr_2P_2O_7$:Sn with the emission peak shifted to lower energies, but the positions of the two excitation bands relatively unchanged.

The δ-$Ba_2P_2O_7$ structure is unique and has no simple relationship to the other alkaline-earth pyrophosphates. Therefore, it is not surprising that the phosphor δ-$Ba_2P_2O_7$:Sn is also unique having a single emission band peaking in the deep red at 676 mμ and two excitation bands at 233 mμ and 250 mμ.

Experimental Results on Binary Metal Pyrophosphates

The effect of varying the ratio of one cation to another in the three possible binary combinations of the alkaline-earth pyrophosphates is shown in Fig. 4 in which the relative red and blue plaque readings, using Corning 2424 and 5543 plus 3389 filters, respectively, (7) are plotted against composition. The data given in Fig. 4 represent three separate systems. On the right is shown the binary combinations of the strontium calcium pyrophosphates activated by tin. The section in the middle represents barium strontium pyrophosphates activated by tin, and the left hand section represents barium calcium pyrophosphate activated by tin. In general, the combination of a pair of red and blue plaque readings represents the response of a single phosphor composition. Changes in fluorescent color were observed, and these changes are represented at the top of the figure. An increase or decrease in blue or red plaque readings should be correlated together to determine the relative chromaticities of the three systems to each other. The firing temperature was selected to give the high-temperature modification of each pyrophosphate, i.e., the α-modifications of $Ca_2P_2O_7$ and $Sr_2P_2O_7$ and the δ-modification of $Ba_2P_2O_7$ since the high-temperature forms were more efficient, visually, than their low-temperature modifications. Data on each system are summarized below.

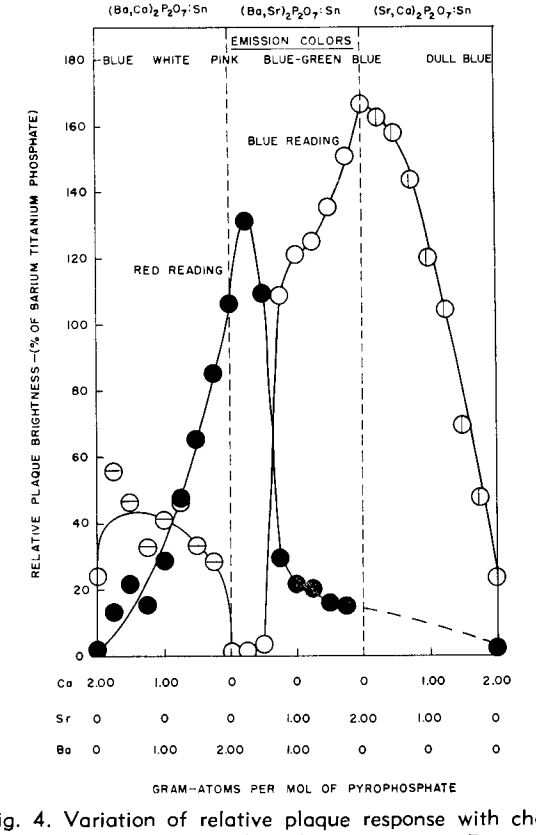

Fig. 4. Variation of relative plaque response with change in cationic constituents in three binary systems. Firing temperature, 1100°C.

Calcium-strontium pyrophosphates.—The plaque data of Fig. 4 show a continuous increase in blue emission as the Sr/Ca ratio is increased in $(Sr,Ca)_2P_2O_7$:Sn (right portion of Fig. 4). Identification of the compounds present by x-ray diffraction showed that the phosphors were mixtures of α-$Ca_2P_2O_7$ and α-$Sr_2P_2O_7$ with the relative amount of each being determined by the relative amounts of the cations. Therefore, it was not surprising that the emission spectra also showed the ultraviolet emission band at about 361 mμ characteristic of α-$Ca_2P_2O_7$:Sn and the visible band at about 464 mμ characteristic of α-$Sr_2P_2O_7$:Sn. Again, the amount of each emission band present was determined by the relative amount of the particular compound in the mixture. The excitation spectra were not examined in detail.

Strontium-barium pyrophosphates.—The fluorescent color of $(Ba,Sr)_2P_2O_7$:Sn changed from blue to blue-green to pink in agreement with Ranby, *et al.* (3) as the Ba/Sr ratio increased (middle portion of Fig. 4). It is evident that there is a sharp change in fluorescent color in going from $Sr_{0.75}Ba_{1.25}P_2O_7$:Sn to $Sr_{0.50}Ba_{1.50}P_2O_7$:Sn. The emission spectra of the system exhibited only a single band whose peak wave number varied with the alkaline-earth ratio. The discontinuity mentioned above is readily shown in Fig. 5 where the peak emission energy is plotted against this ratio. The x-ray data paralleled the optical measurements. Thus the diffraction pattern showed a continuous change from α-$Sr_2P_2O_7$ to a pattern closely resembling α-$Ba_2P_2O_7$ in going from $Sr_2P_2O_7$ to $Sr_{0.75}Ba_{1.25}P_2O_7$. Phosphors with higher barium contents than the latter had essentially the δ-$Ba_2P_2O_7$ structure and the characteristic red emission of δ-$Ba_2P_2O_7$:Sn. The data of Fig. 4 seem to imply that the phosphor $Sr_{0.25}Ba_{1.75}P_2O_7$:Sn has more emission in the red than δ-$Ba_2P_2O_7$:Sn. However, this result is due to the greater sensitivity of the photo-

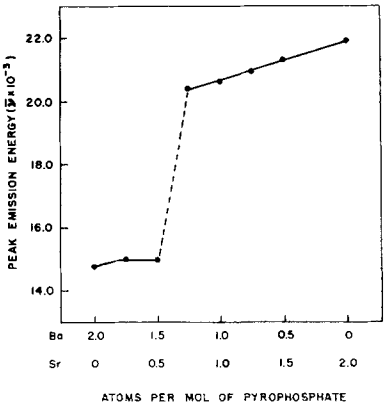

Fig. 5. Peak emission changes in the $(Sr,Ba)_2P_2O_7$:Sn systems.

multiplier as the peak emission shifts toward the green. In this system also, there was no detailed study of excitation spectra.

Barium-calcium pyrophosphates.—It is apparent from the results given in Fig. 4 (left portion) that the $(Ba,Ca)_2P_2O_7$:Sn phosphors are low in efficiency. For this reason, and since they melted very easily giving fused materials, this sytem was not studied in detail.

Other binary pyrophosphates.—With two exceptions, other Group II binary pyrophosphates activated by Sn were generally inefficient and uninteresting. The exceptions were $(Sr, Mg)_2P_2O_7$:Sn and $(Sr,Zn)_2P_2O_7$:Sn. These phosphors displayed a decrease in blue plaque efficiency similar to that shown in Fig. 4 for $(Sr,Ca)_2P_2O_7$:Sn as the Sr/Mg or Sr/Zn ratio decreased. Measurements of emission spectra disclosed that although $Mg_2P_2O_7$:Sn and $Zn_2P_2O_7$:Sn are essentially inert, the addition of small amounts of strontium produces ultraviolet-emitting phosphors. As an example, the emission and excitation spectra of $Mg_{1.75}Sr_{0.25}P_2O_7$:Sn and $Zn_{1.75}Sr_{0.25}P_2O_7$:Sn are given in Fig. 6. Both have a strong emission band peaking at 333 mμ and evidence of the α-$Sr_2P_2O_7$:Sn band appearing at lower energies. As the Sr/Mg ratio or Sr/Zn is increased, this band at about 464 mμ increases in intensity while the one at 333 mμ decreases. The excitation spectra are composed of two bands, on at about 248 mμ and a second at about 226 mμ. X-ray identification showed the presence of α-$Sr_2P_2O_7$ as well as compounds having diffraction patterns similar, but not identical, to $Mg_2P_2O_7$ and $Zn_2P_2O_7$. A comparison of the emission spectra data in Fig. 1 and 2 with those in Fig. 5 reveals no interrelation or similitude to previous data.

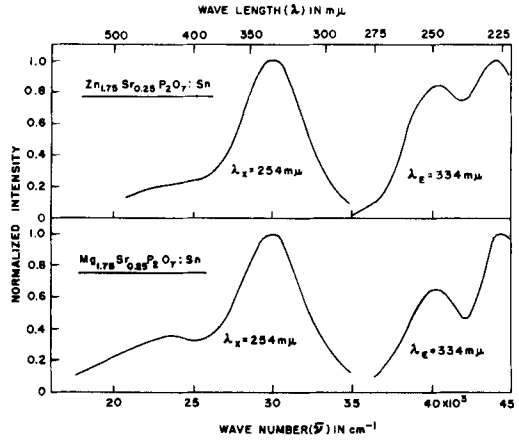

Fig. 6. Excitation-emission spectra for $(Mg,Sr)_2P_2O_7$:Sn and $(Zn,Sr)_2P_2O_7$:Sn phosphors. Firing temperature, 1120°C.

Discussion

The results of this investigation are in general agreement with those reached earlier by Ranby, *et al.* (3), namely, that the emission spectra are determined primarily by the crystal structure of the matrix. This conclusion is also applicable to the excitation spectra. However, while there is general agreement with previous work, there are several areas in which previous views must be modified. For instance, the tin-activated calcium strontium pyrophosphates exhibit considerable change in emission in going from $Ca_2P_2O_7$:Sn to $Sr_2P_2O_7$:Sn and in going from the β-form to the α-form. Thus, both β-$Ca_2P_2O_7$:Sn and β-$Sr_2P_2O_7$:Sn are primarily ultraviolet emitters, but neither is very efficiently excited by 254 mμ excitation. On the contrary, α-$Sr_2P_2O_7$:Sn is a blue phosphor and is very efficiently excited by 254 mμ, while α-$Ca_2P_2O_7$:Sn is both a blue and an ultraviolet emitter, but the blue band is only weakly excited by a low-pressure mercury-vapor arc. Therefore, under this excitation the $(Sr,Ca)_2P_2O_7$:Sn phosphors show changes in relative intensity but little change in position of the emission bands. The band at 464 mμ attributed to α-$(Ca,Sr)_2P_2O_7$:Sn (3) is therefore, in reality, due to α-$Sr_2P_2O_7$:Sn as shown in Fig. 2. The emission data on the barium pyrophosphates are in fair agreement with previous results (3,4).

The $(Sr,Ba)_2P_2O_7$:Sn system is interesting in view of its continuous change in the position of the emission peak with composition as shown in Fig. 5. Starting from α-$Sr_2P_2O_7$:Sn and replacing strontium by barium, the emission peak energy decreased linearly approaching that of the α-$Ba_2P_2O_7$:Sn phosphor. The d-spacings in the x-ray diffraction patterns showed a similar continuous shift, and therefore it is concluded that $Sr_2P_2O_7$ and $Ba_2P_2O_7$ form a continuous series of solid solutions up to an alkaline-earth content of 75% barium. At this point, the α-phase is no longer stable and the δ-$Ba_2P_2O_7$:Sn phosphor is formed as evidenced by the x-ray diffraction pattern and the spectra. It should be noted that the most efficient phosphors having the blue-green emission characteristic of α-$Ba_2P_2O_7$:Sn are prepared by stabilizing this structure with strontium as, for instance, in the phosphor $Ba_{1.25}Sr_{0.75}P_2O_7$:Sn, since it is difficult to prepare α-$Ba_2P_2O_7$:Sn with high efficiency due to the tendency to form δ-$Ba_2P_2O_7$:Sn at temperatures necessary to promote the requisite crystallinity and ultraviolet response of the phosphor.

The $(Sr,Ba)_2P_2O_7$:Sn system is therefore very different from the $(Sr,Ca)_2P_2O_7$:Sn, $(Sr,Mg)_2P_2O_7$:Sn, and $(Sr,Zn)_2P_2O_7$:Sn systems where the x-ray diffraction patterns of each individual component are readily discernible and where the emission spectra of both components appear, as for example the bands due to α-$Sr_2P_2O_7$:Sn and α-$Ca_2P_2O_7$:Sn in $(Sr,Ca)_2P_2O_7$:Sn. One is therefore led to believe that in these systems the phosphor components

Table I. Ultraviolet emission bands

Phosphor	Peak wave length in mμ		
	Emission	Excitation	
β-$Ca_2P_2O_7$: Sn	369	260	238
β-$Sr_2P_2O_7$: Sn	364	260	234
α-$Ca_2P_2O_7$: Sn	362	253	232

Table II. Visible emission bands

Phosphor	Peak wave length in mμ		
	Emission	Excitation	
α-$Ca_2P_2O_7$: Sn	429	261	240
α-$Sr_2P_2O_7$: Sn	463	256	238
α-$Ba_2P_2O_7$: Sn	505	256	239

exist as separate species, in contrast to the $(Sr,Ba)_2P_2O_7$: Sn system.

It was noted earlier that the emission spectra of the β-forms of $Ca_2P_2O_7$: Sn and $Sr_2P_2O_7$: Sn were similar and apparently related to one of the bands in α-$Ca_2P_2O_7$: Sn. This relationship is easily seen by a compilation of the peak energies.

Inspection of Table I shows that the peaks in the emission and excitation bands occur at almost identical energies. A corresponding tabulation of the peak energies of the α-forms of calcium, strontium and barium pyrophosphate is given in Table II. These three forms are closely related structure-wise and have orthorhombic symmetry (3).

For the visible emission bands there is a definite trend toward lower energies with increasing size of the alkaline-earth cation; however, again the excitation bands peak at almost identical energies.

The relative heights of the two excitation bands given in Tables I and II vary for each phosphor. If one assumes that the lower-energy emission bands, i.e., the visible, are associated with the lower-energy excitation bands, and the higher-energy emission bands, i.e., the ultraviolet, are associated with the higher-energy excitation bands, one obtains a direct correspondence between the strong excitation and the strong emission bands with both strontium systems and with β-$Ca_2P_2O_7$: Sn. However, the correspondence is very poor for α-$Ba_2P_2O_7$: Sn where the phosphor absorbs in the higher-energy band and emits in what we have arbitrarily called the lower-energy band, i.e., at 505 mμ. A similar, but even more puzzling anomaly exists in the α-$Ca_2P_2O_7$: Sn system where, considering only the excitation data, one would predict that irradiation with low-energy ultraviolet would yield the ultraviolet band. Actually, just the reverse results were obtained for the emission spectra, i.e., irradiation with 225 mμ energy gave the ultraviolet band and irradiation with 276 mμ energy gave both ultraviolet and visible bands. Thus the emission data are, by themselves, consistent with the other calcium and strontium systems.

In order to illustrate the trends in emission spectra with changes in structure, the peak emission energies of all phosphors are plotted against the alkaline-earth cationic radii in Fig. 7. The grouping

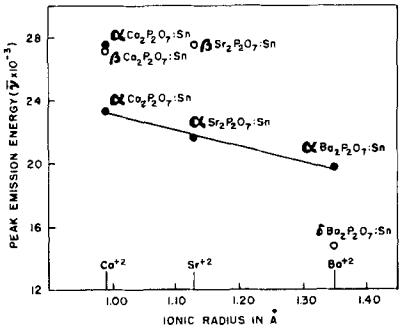

Fig. 7. Effect of cationic radius and structure on emission of tin-activated alkaline-earth pyrophosphate phosphors.

together of the ultraviolet bands is obvious as is the linear relationship between the peak energies in the α-pyrophosphates vs. cationic radii. The emission of δ-$Ba_2P_2O_7$: Sn falls into neither grouping. It is very apparent from Fig. 7 that there is an over-all trend toward lower emission energies or longer wave lengths with increasing cationic size. Unfortunately, this is in direct conflict with the results on several other phosphor systems as summarized by Fonda (9). However, with three exceptions all of the phosphors listed by Fonda were activated by manganese either as a primary or secondary activator. These exceptions were the alkaline-earth sulfides activated by europium (10), the self-activated vanadates of the alkaline-earth metals (11), and the alkaline-earth orthophosphates activated by tin (1). However, in the latter case the results were conflicting since, in one case, an increase in cationic size shifted the emission to shorter wave lengths, whereas in the other a shift to longer wave lengths was observed.

Fonda also points out several exceptions to his general rule that the spectral position of the emission band should shift to longer wave lengths as the lattice spacing is decreased. For these exceptions, the activators are thallium, silver, copper and in two cases, manganese. It is interesting that, ignoring the two manganese cases above, all of the other activators together with tin share the property that their bonding electrons are s-electrons, not d-electrons as is the case with manganese and europium. We are, therefore, led to agree with Fonda that the effects of polarizability lead to the reversal of his general rule stated above, but going a step further we believe that the effects of polarizability are more apt to be found in systems with activators whose bonding electrons are symmetrical s-electrons than in those whose bonding electrons are d-electrons, as for instance, manganese. The results on the tin-activated alkaline-earth pyrophosphates are explained, therefore, by assuming that the tin in a barium site has a greater effective radius than in a calcium site and is, therefore, more easily polarizable leading to a greater overlapping of the electronic orbits and a consequent shrinkage in the energy difference between the excited and ground states. Generalizing, it would appear that it is dangerous to treat all activator centers as identical and, specifically, it is very dangerous to use manganese-activated systems as typical. This conclusion is equally applicable to properties other than optical spectra

since, for instance, it has been shown that the tin- and manganese-activated phosphates do not exhibit the same type of variation of fluorescent efficiency with temperature (12).

Finally, one might assign the visible emission bands in the α-structures to the $^3P_1^0 \rightarrow {}^1S_0$ transition of the tin center and the ultraviolet emission bands to the $^1P_1^0 \rightarrow {}^1S_0$ transition. Corresponding assignments in the reverse direction could also be made to the excitation bands, although there are many unexplained phenomena that do not correspond exactly to these assignments.

Acknowledgment

The authors are indebted to T. J. Veleker and C. W. W. Hoffman for their x-ray identifications of the structures.

Manuscript received July 6, 1959. This paper was prepared for delivery before the Philadelphia Meeting, May 3-7, 1959.

Any discussion of this paper will appear in a Discussion Section to be published in the December 1960 JOURNAL.

REFERENCES

1. K. H. Butler, *This Journal*, **100**, 250 (1953).
2. S. T. Henderson and P. W. Ranby, *ibid.*, **98**, 479 (1951).
3. P. W. Ranby, D. H. Mash, and S. T. Henderson, *Brit. J. Appl. Phys.*, Supplement #4, S18 (1955).
4. A. H. McKeag and E. G. Steward, *ibid.*, Supplement #4, S26 (1955).
5. R. W. Mooney, M. A. Aia, C. W. W. Hoffman, and R. C. Ropp, *J. Am. Chem. Soc.*, **81**, 826 (1959).
6. W. Slavin, R. W. Mooney, and D. T. Palumbo, To be published.
7. K. H. Butler and R. W. Mooney, *Sylvania Technologist*, **9**, 121 (1956).
8. A. Bril and H. A. Klasens, *Philips Research Repts.*, **7**, 421 (1952).
9. G. R. Fonda, *J. Opt. Soc. Amer.*, **47**, 877 (1957).
10. P. M. Jaffe and E. Banks, *This Journal*, **102**, 518 (1955).
11. H. Gobrecht and G. Heinsohn, *Z. Physik*, **147**, 350 (1957).
12. R. W. Mooney, *This Journal*, **105**, 456 (1958).
13. I. M. Kolthoff and E. B. Sandell, "Textbook of Quantitative Inorganic Analysis," Macmillan Co., New York, p. 362, (1949).

Voltage Dependence and Particle Size Distribution of Electroluminescent Phosphors

Willi Lehmann

Research Department, Westinghouse Electric Corporation, Bloomfield, New Jersey

ABSTRACT

The particle sizes of electroluminescent zinc sulfide phosphors prepared by common firing techniques usually range over broad distributions which always have the same shape. Every phosphor of this "normal" particle size distribution shows a voltage (V) dependence of electroluminescent brightness (L) which, over many decades of L, can closely be described by $L = L_o \exp [-(V_o/V)^{0.5}]$. Every deviation of the particle size distribution from the "normal" form also causes a deviation of the measurable $L(V)$ dependence from this expression. Measurements on phosphor particles and on uniform phosphor films indicate that the basic excitation mechanism of electroluminescence follows the voltage dependence $L = L_o \exp [-(V_o/V)]$ and that the square root in the exponent of the usual equation is due mainly to the broad particle size distribution of regular phosphors. This view is supported also by a mathematical analysis.

The time-average of the emission intensity, L, of electroluminescent (EL) zinc sulfide powders generally increases rather rapidly with increasing amplitude of the exciting alternating voltage, V. Based on rough theoretical considerations, Destriau originally proposed to describe this dependence by

$$L = L_o \exp [-(V_o/V)] \qquad [1]$$

with L_o and V_o as constants (1). It developed, however, that the fit of this equation to experimental results is not too good, and a great variety of other mathematical forms have been proposed by various workers since that time (2-17). One of them

$$L = L_o \exp [-(V_o/V)^{0.5}] \qquad [2]$$

differs from Eq. [1] only by the square root in the exponent, and its agreement with experimental results is amazingly good in many cases and can extend over six or more decades of L. This agreement has repeatedly been considered to be a proof for the validity of the exhaustion barrier theory (9, 18-20) from which Eq. [2] originally was deduced (9). It cannot be denied, however, that deviations from Eq. [2] have been observed frequently.

The suggestion by Lehmann (21) that Eq. [2] is a result of the well-known nonuniformity of the emission in a phosphor powder could not, at that time, be supported by experimental results.

A somewhat unexpected answer to the problem came from investigations of particle size effects on

EL. If a common phosphor having the usual broad particle size distribution is separated into fractions of different mean particle sizes, then these fractions also show different $L(V)$ dependences. The first reliable experimental results in this respect apparently were reported by Milch and Mazenko (22). They separated their phosphor into fractions of fairly small distribution widths and used a generalized modification of Eq. [2]

$$L = L_0 V^n \exp\ [-(V_0/V)^{0.5}] \qquad [3]$$

to describe their measured $L(V)$ dependences. They found that not only L_0 and V_0 in Eq. [3] depend on the mean particle size, but also that a proper fit could be obtained only with values of the exponent, n, ranging between $n = -11$ and $n = +0.67$. Later, Goldberg (23) and Lehmann (24) independently made similar experiments with apparently less sharply separated phosphor fractions and described the $L(V)$ dependence of these fractions by Eq. [2]. They found, too, that both constants in Eq. [2], L_0 and V_0, depend on the mean particle size of the phosphor.

These experimental results immediately permit a conclusion. If the $L(V)$ dependence of a single phosphor particle depends in some fashion on its size, and if a phosphor has a broad particle size distribution (which is normally always the case), then the $L(V)$ dependence of the whole phosphor must be determined not only by the $L(V)$ dependence of a single particle but also by the form of the particle size distribution of the phosphor. In other words, there must be a correlation between the particle size distribution of a phosphor and its measurable $L(V)$ dependence, i.e., the $L(V)$ dependences of two otherwise identical phosphors, one of a broad and the other of a narrow particle size distribution, should be different even if the mean particle sizes of both samples are equal. The $L(V)$ dependence of normal phosphors with broad particle size distributions can be described fairly well by Eq. [2]. Consequently, a phosphor with a very narrow particle size distribution can be expected to show an $L(V)$ dependence which does not closely follow Eq. [2]. The significance of an experimental confirmation of this conclusion for all theoretical efforts to understand the mechanism of electroluminescence is obvious.

Particle Size Distributions of Regular Phosphors

Particle size distributions of normal phosphors, as obtained by common preparation procedures, were determined by means of a projection microscope. The approximate diameters of some 200-300 particles of each sample were measured. The resulting distributions of all these phosphors had essentially the same shape. An example in the form of a frequency-diameter histogram is shown in Fig. 1. Such a typical distribution curve has been shown earlier by Leverenz (25). It is not symmetrical and cannot be described closely by a Gaussian function, but a relatively good fit was obtained empirically by the function

$$y = ax^2 \exp\ (-2x/x_0) \qquad [4]$$

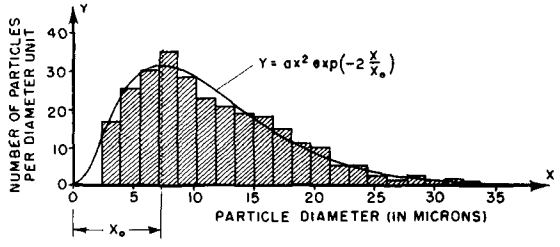

Fig. 1. Typical particle size distribution of a normal (i.e., unseparated) phosphor.

where x is the particle diameter, x_0 that particular particle diameter which corresponds to the peak of the function $y(x)$, a is a constant, and ydx is the number of particles between the size limits x and $x + dx$. The close fit of this function to the experimental distribution is shown also in Fig. 1. Variations of the several parameters of preparation (e.g., firing temperature and time, concentration of impurities, etc.) seem to cause only a shift of the peak size, x_0, to smaller or larger values but do not alter the general form of the particle size distribution. To what extent Eq. [4] may find a theoretical foundation (possibly in statistical considerations) is unknown. Nevertheless, it is at least a good approximation.

The $L(V)$ dependence of the phosphor sample whose particle size distribution is shown in Fig. 1 is given in Fig. 2. The agreement of the experimental points with straight lines, i.e., the agreement of the $L(V)$ dependence with Eq. [2], is almost exact over the whole measured range.

Behavior of Phosphor Fractions of Very Narrow Particle Size Distributions

The most desirable goal, fractions of almost uniform particle sizes separated out of common phosphor powders, could not be reached because of a lack of available techniques. There seems to be no

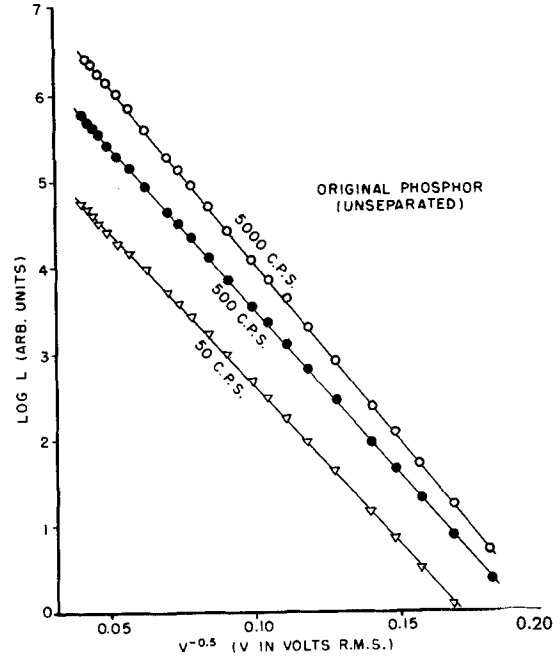

Fig. 2. The L(V) dependence of a normal phosphor can closely be described by Eq. [2].

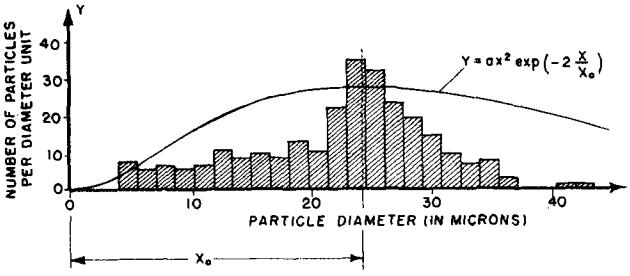

Fig. 3. Particle size distribution of a small fraction separated out of the normal phosphor of Fig. 1.

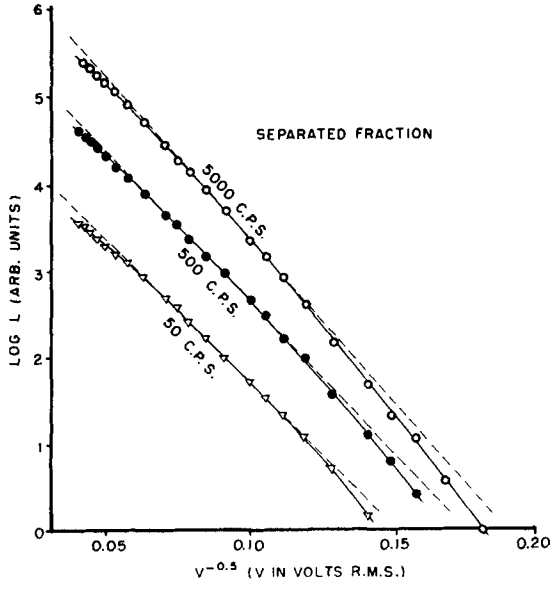

Fig. 4. The L(V) dependence of the separated fraction of Fig. 3 cannot closely be described by Eq. [2].

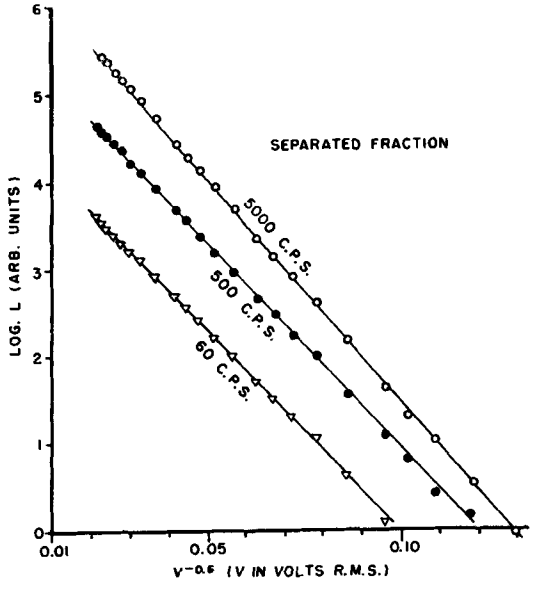

Fig. 5. The L(V) dependence of the separated fraction of Fig. 3 can closely be described by Eq. [5] with $\alpha = 0.6$.

known method permitting such narrow separations. As an example of what actually could be obtained in these experiments, Fig. 3 shows the distribution of a fraction of large diameter separated out of the phosphor whose original distribution is shown in Fig. 1. Although the distribution of Fig. 3 still has a considerable width, it is much smaller than that of the original, and it is obvious that there is no longer agreement with Eq. [4] as shown by the smooth curve in Fig. 3. The $L(V)$ dependence of this separated fraction is given in Fig. 4 as log L as a function of $V^{-0.5}$. The experimental points are not on straight lines here, so that this $L(V)$ dependence cannot be described closely by Eq. [2]. But if Eq. [2] is arbitrarily generalized by replacing the exponent 0.5 by an arbitrary constant

$$L = L_0 \exp\left[-(V_0/V)^{\alpha}\right] \qquad [5]$$

it turns out that $\alpha = 0.6$ now gives a good fit, much better than $\alpha = 0.5$, as shown in Fig. 5. This value of $\alpha = 0.6$, of course, is purely incidental and has no physical meaning except that it indicates the influence of the still present width of the particle size distribution on the $L(V)$ dependence of the phosphor.

An extrapolation may be permitted here. If the $L(V)$ dependence of the original phosphor with its broad particle size distribution can be described by $\alpha = 0.5$ while the separated sample with the smaller but still considerable particle size distribution gives a better fit with $\alpha = 0.6$, then a phosphor with a still narrower particle size distribution probably would require a still higher value of α. An approach to $\alpha = 1$, i.e., toward Eq. [1], for ideally uniform particles seems likely but cannot, of course, be deduced rigorously from an extrapolation.

Behavior of Single Phosphor Particles

Most of all the geometrical complexity of a phosphor powder can be eliminated by consideration of single particles. However, a part of the complexity remains here also. Real single particles always have somewhat irregular shapes, may contain lattice disorders, and may be differently oriented with respect to the direction of the electric field. It is also known that the emission inside the phosphor crystals mainly originates from relatively small spots (5, 26, 27), and microscopic examination shows that every particle may contain one or more such emitting spots. Sometimes, the spots appear to be extended to lines, and the direction of these lines seems to follow the direction of some striped pattern, probably stacking faults (28-30), which can be seen when the crystal is illuminated by white light. Figure 6 shows a typical example of such nonuni-

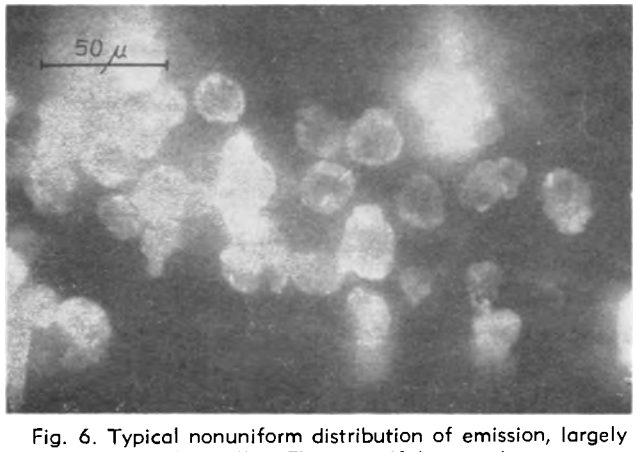

Fig. 6. Typical nonuniform distribution of emission, largely concentrated in "spots," of EL zinc sulfide particles.

form emission, largely concentrated in spots of single phosphor particles. Despite these complications, an $L(V)$ dependence of single particles somewhat simpler than that of complete phosphor powders can be expected.

The light emission of one single phosphor particle is too weak to be measured over a wide range by usual photomultipliers. Therefore, a visual method was used in these experiments. The phosphor to be measured (a few particles only) was placed in an oil cell and viewed through a microscope with low magnification. The starlike image of one luminescent particle was compared with the controlled and calibrated brightness of an artificial star (a pinhole in a piece of black paper illuminated by an incandescent lamp). Since a judgment of equality of the visual brightnesses of the two spots, even if they are visible side by side, always has a considerable uncertainty, each measurement was repeated ten times and the final value obtained by the arithmetic average of the ten single values. This technique gave fairly accurate results but was rather tiring to the eyes and time consuming so that only six single particles were completely measured.

The results obtained differ somewhat from particle to particle and are somewhat in contrast to results reported by Waymouth and Bitter (5) and by Zalm, Diemer, and Klasens (26). One particle out of the six had an $L(V)$ dependence which, over the whole measured range, can be described by Eq. [1] but not by Eq. [2] (see Fig. 7). Three other particles had $L(V)$ dependences which could not be described completely by either Eq. [1] or [2] but which can be understood easily by a superposition of two terms each of which has the form of Eq. [1]. Obviously in these three cases the curves are due to two emitting spots, with different voltage characteristics, inside the particles. Finally, the last two particles had $L(V)$ dependences which could be described in either way, by two terms of Eq. [1] or by one term of Eq. [2]. Since it seems unlikely that two totally different excitation mechanisms would be present in different particles of the same phosphor, we draw the conclusion that the emission of these two particles was due to two (or more) emitting spots inside the particles.

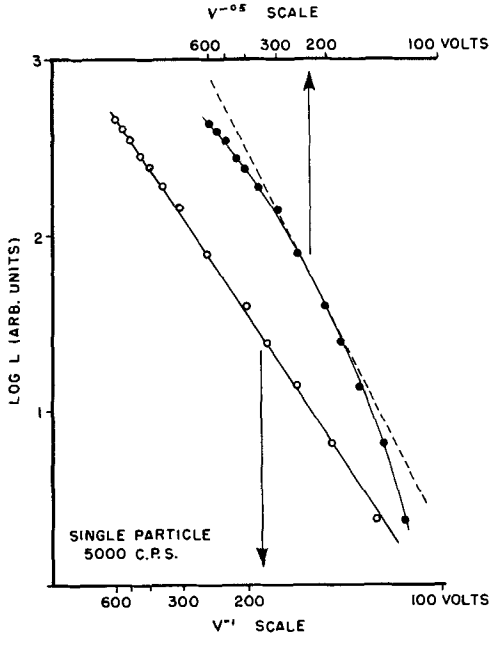

Fig. 7. The L(V) dependence of one single particle measured can closely be described by Eq. [1] but not by Eq. [2].

Behavior of Thin Phosphor Films

A uniform continuous film is obviously the simplest geometrical structure an EL phosphor can have. Its "particle size" is identical with its thickness, and variations of the thickness have the same effect as a finite particle size distribution of a powder phosphor; they cause a nonuniform distribution of the emission over the film area. The over-all emission of such nonuniform films in many cases can be described also by Eq. [2] fairly well, although deviations from this dependence occur rather frequently (31).

Most significant in this respect is, of course, the behavior of highly uniform films. Results obtained on specially selected uniform films[1] are shown in Fig. 8 and 9. These particular films (blue and green-emitting ZnS:Cu,Cl) were relatively thin (1 or 2 μ) and directly in contact with both electrodes (evaporated aluminum and the SnO_2 layer of conducting glass). The films appeared uniform and glassy under the microscope. Their electroluminescence was also uniform over their whole areas and without any emitting "spots" as are observed in powder phosphors. The experimental points deviate strongly from straight lines in Fig. 8 where log L is plotted as a function of $V^{-0.5}$. The points are on straight

[1] Made and kindly furnished by W. A. Thornton of this laboratory.

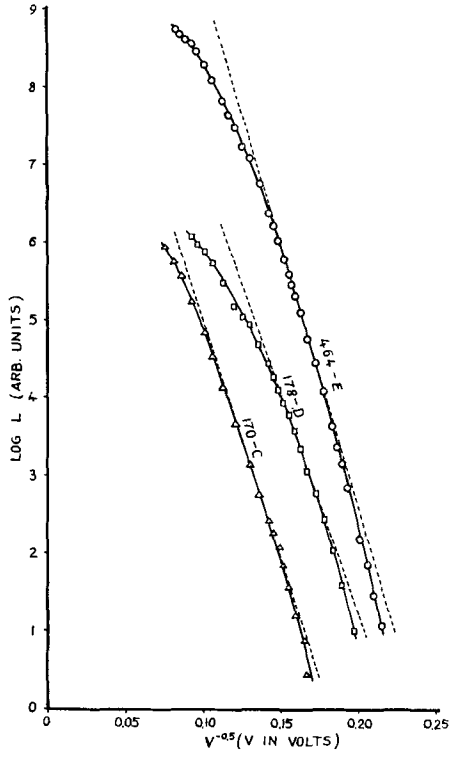

Fig. 8. The L(V) dependences of uniform zinc sulfide films do not follow Eq. [2].

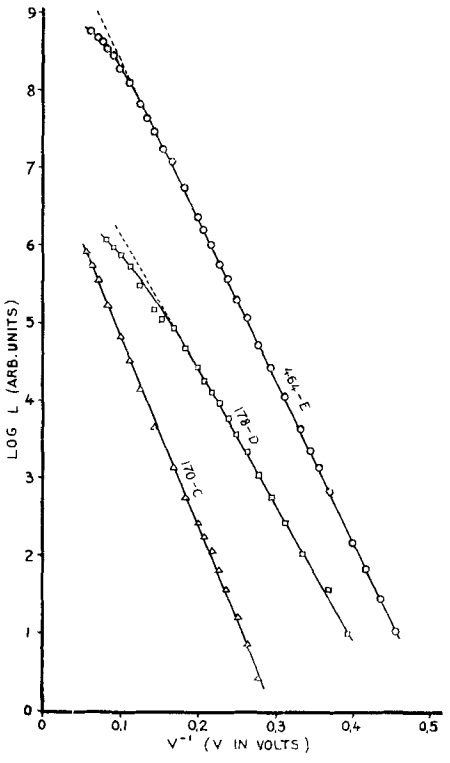

Fig. 9. The L(V) dependences of uniform zinc sulfide films follow Eq. [1] over many decades of L.

lines[2] in Fig. 9 over many decades of L, however, if log L is plotted as a function of V^{-1}.

Mathematical Treatment

The above experimental results indicate that, most likely, the process of excitation and emission of electroluminescence closely follows Eq. [1] if geometrical complexities are eliminated, and that the square root in Eq. [2] results only by the nonuniform geometry of the phosphor, i.e., mainly by the finite particle size distribution. Neglecting other possible reasons of nonuniformity (e.g., irregular particle shapes, orientations of stacking faults and barriers, etc.), it is possible even to draw a direct mathematical connection between the distribution function [4] and the emission function [1] on the one hand, and function [2] on the other hand.

A model phosphor may have a particle size distribution according to Eq. [4]. Every particle of this model phosphor may emit a light intensity described by

$$l = l_o \exp\ (-v_o/v) \qquad [6]$$

where l_o and v_o are constants and where v denotes the voltage drop across the whole particle. The two equations [1] and [6] are essentially identical concerning the voltage dependence. The particle size dependence enters Eq. [6] in two terms. The pre-exponential factor, l_o, may depend on the particle size, x, in a way which approximately may be described by $l_o = cx^m$ where c is a constant and where m is in the order of unity. Much stronger, however, seems to be the dependence v (x) since it enters Eq. [6] in the exponent. The ratio of the particle voltage, v, to the cell voltage, V, is essentially the ratio of the particle size, x, to the cell spacing, S, modified only by a factor, K, in the order of unity denoting the influence of the different dielectric constants of phosphor and embedding material

$$Kv/V = x/S \qquad [7]$$

The emission intensity of the whole phosphor is given by the integral

$$L = \int_o^\infty y(x)\ l(x,V)\,dx \qquad [8]$$

and introduction of [4], [6], and [7] into [8] gives

$$L = ac \int_o^\infty x^n \exp\left[-\left(2\frac{x}{x_o} + \frac{Kv_oS}{xV}\right)\right]dx \qquad [9]$$

where $n = m + 2$.

No simple analytical solution of this integral seems to exist, so a numerical integration was made with the assumption of reasonable values for the constants. The assumed values were $x_o = 8.7\ \mu$, and $(Kv_oS) = 2.3 \times 10^4\ v\mu$ (this corresponds, for instance, to $v_o = 100$ v, $S = 100\ \mu$, and $K = 2.3$). The value of the factor ac in Eq. [9] is unimportant. With these values, the integrand in Eq. [9], i.e., of

$$Y = x^n \exp\left[-\left(2\frac{x}{x_o} + \frac{Kv_oS}{xV}\right)\right] \qquad [10]$$

was computed for different values of n and of V. It develops that the value of the exponent, n, is only of very minor influence so that the presentation of the case $n = 2$ in Fig. 10 may be sufficient here (the curves for the cases $n = 0$, 1, or 3 are almost the same). The results of the numerical integrations are shown in two different ways, in Fig. 11 as log L as a function of $V^{-0.5}$ and in Fig. 12 as log L as a function of V^{-1}. In Fig. 11, the curves very closely approach straight lines over many decades of L, almost independent of the particular value of n. The curves deviate from straight lines at the highest voltages,

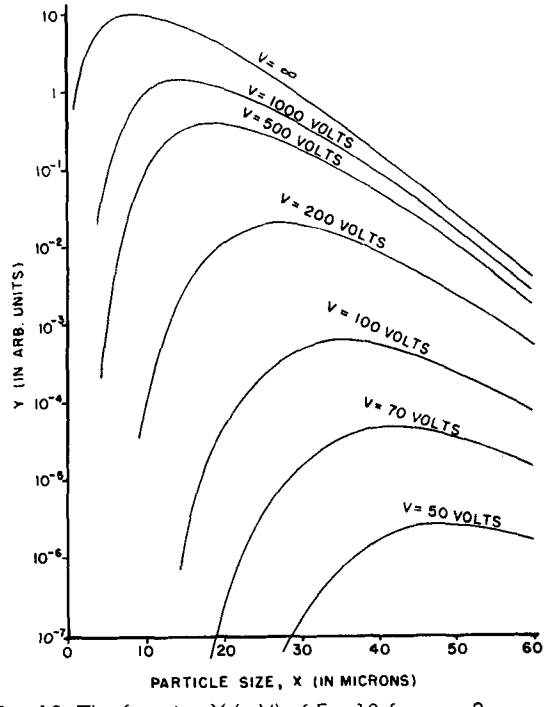

Fig. 10. The function Y (x,V) of Eq. 10 for n = 2, x_o = 8.7 μ, and Kv_oS = 2300 Vμ.

[2] The deviation of two curves at the highest voltages in Fig. 11 is probably due to thermal quenching. The films became noticeably warm under the highest loads and the emission changed from blue to greenish.

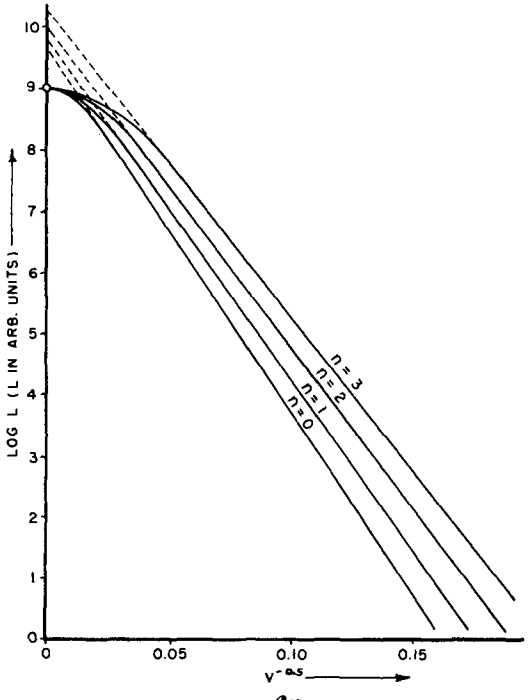

Fig. 11. The function $L = \int_0^\infty Y dx$ (Eq. [9]) approaches Eq. [2] very closely for low and moderate voltages.

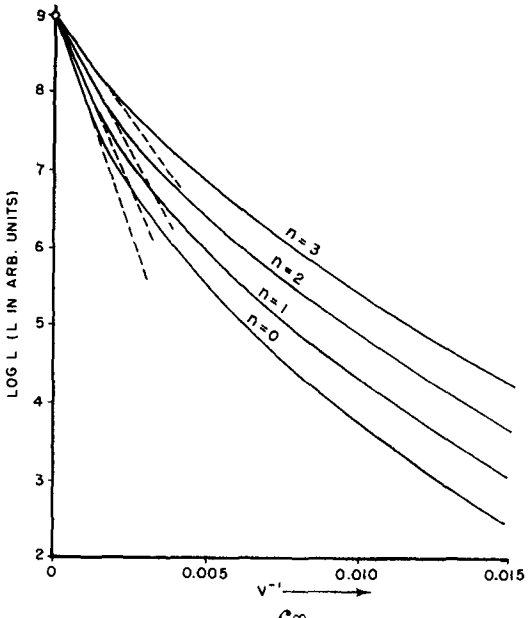

Fig. 12. The function $L = \int_0^\infty Y dx$ (Eq. [9]) does not closely follow Eq. [1] except at the highest voltages.

however, approaching "saturation" values considerably below the intersections of the straight lines with the axis $V = \infty$ (i.e., below the constant L_0 in Eq. [2]). In Fig. 12, on the other hand, the curves do not approach straight lines at all except at the very highest voltages. This behavior is in agreement with experimental observations (15, 21).

Figure 10 also shows another effect, namely, a shift of these particle sizes which contribute most to the over-all light emission with a variation of the voltage, V. At low voltages, only the few largest particles contribute noticeably to the over-all light emission while the many fine particles are still practically dead. Increasing voltage causes the emission from the fine particles to increase faster than that from the coarse particles so that the fine particles dominate at high voltages because they are more numerous. This different contribution of the particles of a real phosphor at different voltages is qualitatively well known (3, 27).

Conclusions

The main results outlined in this paper permit the following conclusion:

(*a*) There is a correlation between the particle size distribution of an EL phosphor and the form of its $L(V)$ dependence. The particle size distribution of common EL zinc sulfide phosphors can be described closely by Eq. [4], and the $L(V)$ dependence of such phosphor follows closely Eq. [2] over many decades of L. Every deviation of the particle size distribution from Eq. [4] also causes a deviation of the $L(V)$ dependence from Eq. [2]. It is possible by a suitable form of the particle size distribution to obtain, within certain limits, any desired form of the $L(V)$ dependence of a phosphor.

(*b*) The fundamental process of electroluminescence, if geometrical complexities are eliminated, most likely follows Eq. [1].

Manuscript received July 29, 1959. This paper was prepared for delivery before the Philadelphia Meeting, May 3-7, 1959.

Any discussion of this paper will appear in a Discussion Section to be published in the December 1960 JOURNAL.

REFERENCES

1. G. Destriau, *J. chim. phys.*, **34**, 117 (1937).
2. G. Destriau, *Compt. rend.*, **209**, 36 (1939).
3. P. Zahm, G. Diemer, and H. A. Klasens, *Philips Research Repts.*, **9**, 81 (1954).
4. B. T. Howard, H. F. Ivey, and W. Lehmann, *Phys. Rev.*, **96**, 799 (1954).
5. J. F. Waymouth and F. Bitter, *ibid.*, **95**, 941 (1954).
6. R. Goffaux, *Bull. acad. roy. Belg., Cl. Sci.*, **40**, 808 (1954).
7. H. Gobrecht, D. Hahn, and H. E. Gumlich, *Z. Phys.*, **136**, 612 (1954).
8. G. F. Alfrey, *Brit. J. Appl. Phys., Suppl. No. 4*, p. 44 (1955).
9. J. B. Taylor, *ibid.*, 45 (1955).
10. P. Zahm, *ibid.*, 48 (1955).
11. W. W. Piper and F. E. Williams, *ibid.*, 39 (1955).
12. F. A. Schwertz, J. J. Mazenko, and E. R. Michalik, *Phys. Rev.*, **98**, 1133 (1955).
13. B. T. Howard, *ibid.*, **98**, 1544 (1955).
14. E. E. Loebner, *ibid.*, **98**, 1545 (1955).
15. G. Destriau and H. F. Ivey, *Proc. I.R.E.*, **43**, 1911 (1955).
16. S. Nudelman and F. Matossi, *This Journal*, **103**, 34 (1956).
17. E. Nagy, *Acta Phys. Acad. Sci. Hung.*, **6**, 153 (1956).
18. P. Zalm, *Philips Research Repts.*, **11**, 417 (1956).
19. G. Diemer, H. A. Klasens, and P. Zalm, *This Journal*, **104**, 130C (1957).
20. G. F. Alfrey and K.N.R. Taylor, *Helv. Phys. Acta*, **30**, 206 (1957).
21. W. Lehmann, *This Journal*, **103**, 667 (1956).
22. A. Milch and J. J. Mazenko, Quarterly Report No. 9, Second Series Computer Components Fellowship No. 347, Mellon Institute, Dec. 31, 1955, page V-40 (Contract No. CLN AF19(604)-943).
23. P. Goldberg, *This Journal*, **106**, 34 (1959).
24. W. Lehmann, *ibid.*, **105**, 585 (1958).

25. H. W. Leverenz, "An Introduction to Luminescence of Solids," p. 50, John Wiley and Sons, New York (1950).
26. P. Zalm, G. Diemer, and H. A. Klasens, *Philips Research Rept.*, **10**, 205 (1955).
27. A. Kremheller, Paper presented at Electrochem. Soc. Meeting, Philadelphia, May 1959 (Abstract 49).
28. M. A. Short, E. G. Steward, and T. B. Tomlinson, *Nature*, **177**, 240 (1956).
29. A. H. McKeag and E. G. Steward, *This Journal*, **104**, 41 (1957).
30. L. W. Strock; Intern. Union of Crystallography, Montreal, July 1957; *Acta Crystal.*, **10**, 840 (1957).
31. W. A. Thornton, *J. Appl. Phys.*, **30**, 123 (1959).

Gallium-Arsenide Diffused Diodes

J. Lowen and R. H. Rediker

Lincoln Laboratory, Massachusetts Institute of Technology, Lexington, Massachusetts

ABSTRACT

Gallium arsenide has been used to fabricate variable reactance and computer diodes which compare favorably with the best commercially available of germanium and silicon. The diodes have been fabricated by zinc diffusion into n-type gallium arsenide. Ohmic contact to the n-type material has been made with an antimony-gold alloy and to the p-type side with indium. Etching is used to remove the p-type diffused skin from everywhere but under the indium contact, thereby forming the mesa and defining the p-n junction area. Rectification ratios (at 2 v) as high as 10^{10} have been achieved. The diodes have been operated successfully in a variable reactance amplifier at S-band (2800 mcps) and in millimicrosecond-switching computer circuits.

Gallium arsenide, because its energy gap is larger than that of silicon, its electron mobility larger than that of germanium, and its dielectric constant smaller than both germanium and silicon, is a very attractive material for use in high-frequency as well as high-temperature devices. Recently it has been reported (1) that the electron lattice scattering mobility in GaAs may be as high as 12,000 $cm^2\ v^{-1}\ cm^{-1}$ and that material with electron mobilities as high as 6000 $cm^2\ v^{-1}\ cm^{-1}$ is now being produced. Point-contact gallium arsenide microwave diodes have been reported by Jenney (2) and Sharpless (3). These point-contact diodes have operated efficiently as first detectors at 6 Kmc (2), and at 11 Kmc and 60 Kmc (3). Jenney (4) has described the very low lifetime of the minority carriers in presently available gallium arsenide and the consequent difficulties in the fabrication of conventional bipolar transistors from the material. This very low lifetime, however, is one of the reasons for the very short switching times (10^{-9}-10^{-10} sec) reported (2, 3) for the point-contact gallium arsenide diode.

This paper describes the fabrication techniques and electrical properties of gallium arsenide diffused diodes. These diodes were designed for use as variable capacitors in parametric amplifiers. Because of the low lifetime for minority carriers in the gallium arsenide, the diodes also could be used in high-speed computer applications, since their switching times were in the order of 10^{-9} sec. The rectification ratios for these diodes are orders of magnitude larger than those for point-contact (2, 3) or alloy junction (5) gallium arsenide diodes previously reported.

Fabrication

The fabrication of the gallium arsenide diffused diodes can be divided into two sets of processes, the first set related to the diffusion step, the second including the assembly of the diode and the making of the ohmic contacts.

Diffusion is accomplished in a sealed quartz ampoule as shown in Fig. 1. All components are carefully etched and washed before being introduced into the ampoule. Referring to Fig. 1, the n-type gallium arsenide wafer which is about 0.050 cm thick has been cut from single crystal material so that its faces are perpendicular to the <111> direction. The face sitting on the flat quartz plate has been polished with 600 mesh SiC, but the exposed face has been polished to a mirror finish, the final abrasive being 0.1 μ alumina. The flat quartz plate is used to avoid the possibility of producing strains in the wafer during the diffusion cycle. About 250 mg of coarse crushed gallium arsenide is added below the quartz plate to provide an arsenic atmosphere and preserve the mirror-like finish during the diffusion. Without this added gallium arsenide the surface becomes stained and under extreme conditions of temperature and vacuum shows droplets of gallium. About 200 millionths of a gram of zinc, the p-type dopant, has been weighed into a quartz capillary which is inserted into the ampoule with due precaution to prevent contact between the zinc and the gallium arsenide. The quartz ampoules which have been used have a volume of about 20

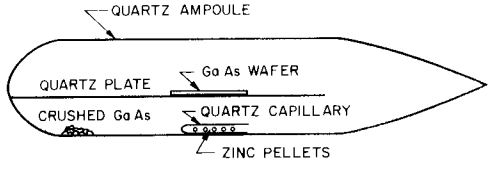

Fig. 1. Sealed diffusion ampoule just prior to being inserted into furnace.

ml; thus, the concentration of zinc in the vapor phase during diffusion is approximately 10^{17} atoms/ml. The loaded quartz ampoule is attached to a high vacuum system, pumped down to about 5 x 10^{-7} mm Hg, and then sealed off under vacuum. The heating cycle is programmed to heat to temperature rapidly, remain at that temperature for the desired period of time, and to allow for a slow cool down, between 1-2°C/min. Diodes have been fabricated from gallium arsenide indiffused with zinc at 650° and 700°C, and times of diffusion have been varied from 3 to 72 hr. There are indications that temperatures as low as 600°C can be used. For a 66-hr diffusion run at 650°C, we measured a junction depth of 8 μ, using a potassium hydroxide, potassium ferricyanide etch to delineate the junction.

The zinc indiffused gallium arsenide wafer then is diced and the rough side lapped to remove the p-type skin and to reduce the wafer thickness to between 0.003 to 0.005 in. Ohmic contact to this n-type side is made by bonding in a hydrogen atmosphere at about 450°C to an antimony gold plated Kovar rod. Ohmic contact to the p-type skin is made by alloying in an indium sphere 0.003-0.005 in. in diameter at 250°-300°C in a hydrogen atmosphere with aluminum chloride as a flux. The wafer is cleaned and then etched with a solution of equal parts of HNO_3, HAc, and HF. In this etching the p-n junction area is defined since the p-type skin is removed from the die everywhere but where it is masked by the indium alloy contact. An artist's conception of a section through a completed diode is shown in Fig. 2. This figure shows a pressure contact to the indium.

Electrical Properties

The voltage-current characteristic of a diode fabricated as described above is shown in Fig. 3. This characteristic has been plotted to logarithmic scale to show clearly the operating range of the diode. Note that below 5 v the reverse current is less than 2 x 10^{-11} amp and at 2 v the rectification ratio is about 10^{10}. For the diode of Fig. 3, the current in the forward direction obeys to a close approximation an $I = I_o \exp(qV/2kT)$ law between 10^{-11} and 10^{-2} amp. Larger area diodes have exhibited forward characteristics where, as the current is increased the exp $(qV/2kT)$ relationship changes to exp (qV/kT) before the ohmic series resistance masks the junction properties. This change in exponential behavior is consistent with the theory of Sah, Noyce, and Shockley (6).

The variation of diode capacitance with voltage is illustrated in Fig. 4. Plotted as abscissa is the applied voltage plus an assumed junction built-in-potential of 1.2 v. This assumed built-in-potential has been determined from the internal contact potential calculated from the impurity distribution. It is well known, however, that for germanium (7) and silicon the built-in-potential is usually less than this internal contact potential. The capacitance-voltage data is not sufficiently detailed to exclude by reason of poor fit to a power law the use of built-in-po-

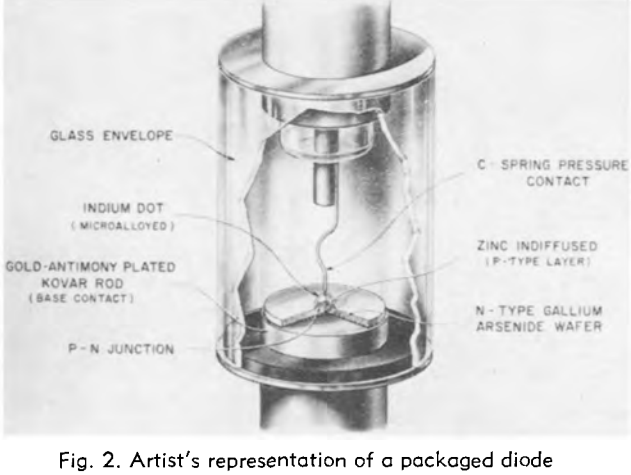

Fig. 2. Artist's representation of a packaged diode

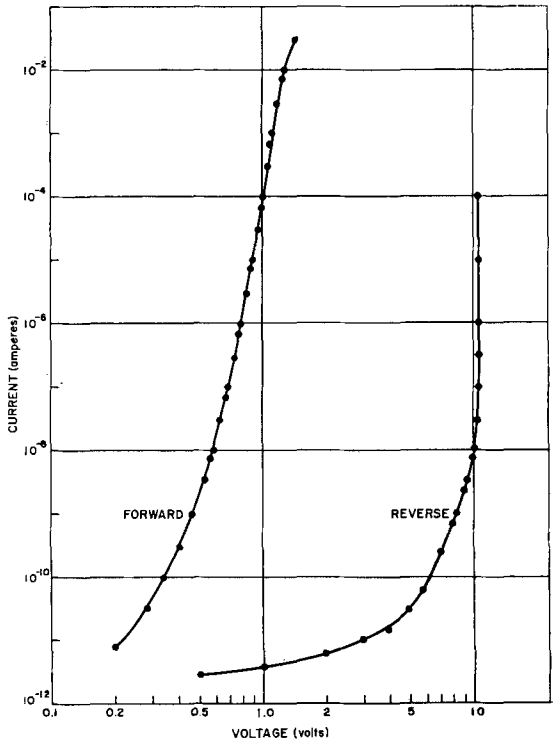

Fig. 3. Logarithmic presentation of voltage-current characteristics of GaAs diode. This diode was fabricated from material with a net donor density of 3.5 x 10^{16} cm^{-3} and electron mobility ~4000 cm^2/v sec. The diameter of the p-n junction was about 0.005 in.

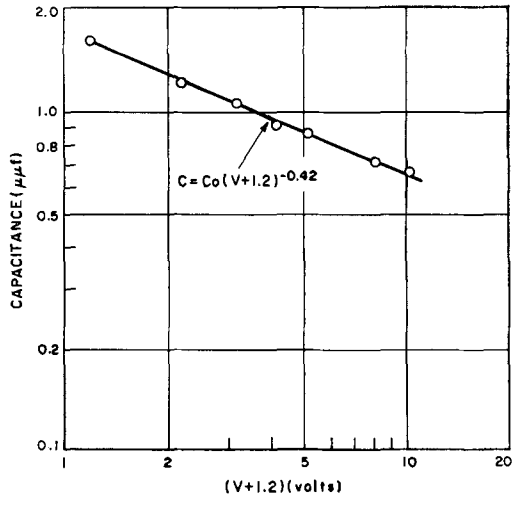

Fig. 4. Capacitance as a function of voltage for diode of Fig. 3.

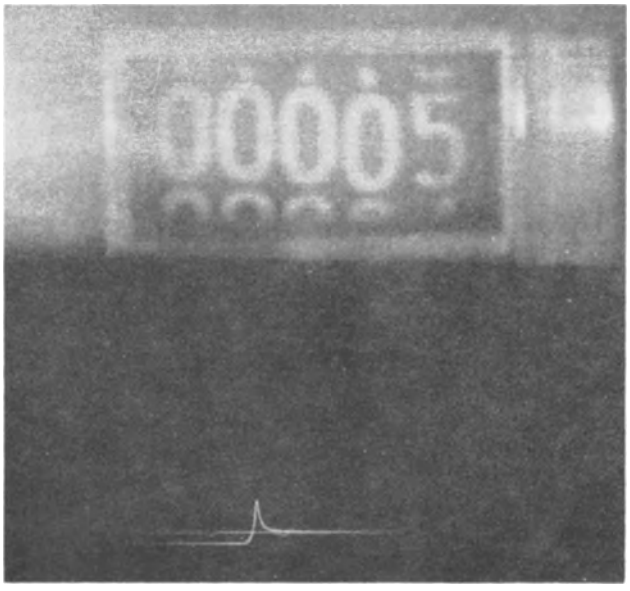

Fig. 5. Traveling-wave oscilloscope presentation of the reverse recovery transient for conditions described in text for diode of Fig. 3. Also shown is the zero diode current line on which two markers 6 mμsec apart have been superimposed.

tentials as low as 0.6 v. Using 1.2 v as shown in Fig. 5, the capacitance can be approximated by

$$C = \frac{C_o}{(V + 1.2)^{0.42}} \qquad [1]$$

indicating that the p-n junction is intermediate between an abrupt junction where the $V^{-1/2}$ law applies and the linear junction where the $V^{-1/3}$ law applies. If a built-in-potential of 0.7 v is used, on the other hand, the capacitance-voltage data can be fit by a $V^{-1/3}$ law.

Use as a Variable Capacitor

A figure of merit that has been proposed (8) for variable reactance diodes is the cutoff frequency

$$f_c = (2\pi R_s C_{min})^{-1} \qquad [2]$$

where C_{min} is the diode capacitance (given in Eq. [1]) just short of breakdown and R_s is the semiconductor series bulk resistance through which the capacitance charging current must flow. This cutoff frequency is the highest frequency for which the quality factor Q of the variable reactance can be unity or larger. The intrinsic value of gallium arsenide as the semiconductor in variable reactance diodes lies in its high electron mobility even at high doping levels, which makes possible lower values of series resistance, R_s, than can be achieved in either germanium or silicon. The ratio of the cutoff frequency for diffused diodes of different semiconducting materials but of identical geometry and impurity concentration is

$$\frac{f_{c1}}{f_{c2}} = \frac{\mu_1}{\mu_2} \cdot \frac{\epsilon_2}{\epsilon_1} \qquad [3]$$

where ϵ is the dielectric constant and μ is the mobility of majority carriers in the bulk material. The cutoff frequency should be larger for GaAs than for Si or Ge because (*a*) the dielectric constant of 11 for GaAs is smaller than the values of 12 for Si and 16 for Ge, and (*b*) the electron mobility in GaAs is significantly larger, and for very heavily doped material ($n > 10^{18}$ cm^{-3}) almost an order of magnitude larger, than that in germanium and silicon. The comparison of cutoff frequencies has been given in Eq. [3] assuming the breakdown voltage for a given impurity distribution is independent of the semiconducting material. Actually, for the more heavily doped material ($n > 10^{18}$ cm^{-3}) diodes made of gallium arsenide seems to exhibit a higher breakdown voltage than similar diodes of germanium or silicon.

The diode whose electrical characteristics are shown in Fig. 3 and 4 has been used successfully in a variable reactance amplifier at S-band (2800 mcps). It had a cutoff frequency measured at 5 v reverse bias of about 30 Kmc which corresponds to a series bulk resistance of about 6.5 ohms. This value of resistance can be explained in terms of a true bulk resistance alone if one remembers that near the diffused junction the resistivity is much higher than the 0.04 ohm-cm resistivity of the starting material and that it is in this region (which is in the mesa) that the diode cross section is limited. On the other hand, contributions to the resistance by the contacts cannot be excluded.

By further refinements of technique we have been able, using the same resistivity material, to fabricate diodes with about 3 times the high frequency capabilities of the diode described above (9). This resistivity, however, is by no means optimum for diodes to be used as variable capacitors. For a given semiconductor the figure of merit, given in Eq. [2], is related to the material properties by

$$f_c \propto n^{1/2} \mu \qquad [4]$$

where n is the net impurity concentration and μ is the mobility. Lower resistivity gallium arsenide than has been used here should yield significantly better figures of merit. The full exploitation of the advantages of this relatively new intermetallic semiconductor for variable capacitors and other applications awaits a more abundant supply of good single crystal gallium arsenide of controlled resistivity. One application, however, for which present day gallium arsenide with its very low minority carrier lifetime is eminently suited is the fast-switch computer diode.

Use as a Computer Diode

Because of the very low lifetime in the GaAs now available, minority carrier storage which limits the switching speed in most germanium and silicon diodes is minimized. Diodes, which were fabricated as described above primarily for use as variable capacitors, when used in computer circuits have had switching times of the order of millimicroseconds. Figure 5 is a photograph of the reverse recovery transient as seen on a traveling wave oscilloscope of the diode whose characteristics are illustrated in Fig. 3 and 4. The diode was switched from 10 ma forward current to 5 v reverse bias with a loop impedance of 120 ohms. The time to recover to 1 ma reverse current is less than 3 mμsec.

Acknowledgments

The authors wish to thank Mrs. M. Barney and F. Sullivan for help in fabricating the diodes, and R. H. Kingston for evaluating the diodes in his S-band variable reactance amplifier. For our supply of single crystal gallium arsenide we are indebted to the RCA Semiconductor Division and the RCA Laboratories and to the Wright Air Development Center and the Air Materiel Command who sponsored their work, as well as to P. Moody and Mrs. C. Kolm of our laboratory.

Manuscript received June 24, 1959. This paper was prepared for delivery at the Philadelphia Meeting, May 3-7, 1959. The work reported in this paper was performed by Lincoln Laboratory, a center for research operated by Massachusetts Institute of Technology with the joint support of the U.S. Army, Navy, and Air Force.

Any discussion of this paper will appear in a Discussion Section to be published in the December 1960 JOURNAL.

REFERENCES

1. F. J. Reid and R. K. Willardson, *J. of Electronics and Control*, **5**, 54 (1958); see also, L. R. Weisberg, J. R. Woolston, and M. Glicksman, *J. Appl. Phys.*, **29**, 1514 (1958).
2. D. A. Jenney, *Proc. IRE*, **46**, 717 (1958).
3. W. M. Sharpless, *Bell System Tech. J.*, **38**, 259 (1959).
4. D. A. Jenney, *Proc. IRE*, **46**, 959 (1958).
5. S. M. Ku and H. T. Minden, Paper presented at ECS Meeting, Philadelphia, May 1959.
6. C. T. Sah, R. N. Noyce, and W. Shockley, *Proc. IRE*, **45**, 1228 (1957).
7. D. R. Muss, *J. Appl. Phys.*, **26**, 1514 (1955).
8. A. Uhlir, Jr., *Proc. IRE*, **46**, 1099 (1958).
9. J. Halpern, Private communication.

Purification of $SiCl_4$ by Adsorption Techniques

H. C. Theuerer

Bell Telephone Laboratories, Inc., Murray Hill, New Jersey

ABSTRACT

Silicon tetrachloride may be purified using adsorption columns filled with hydrous oxides or silicates. Hydrogen reduction of this purified halide leads to higher purity silicon than is obtainable otherwise. Data for the adsorption efficiency of various materials are presented using infrared spectroscopy and radioactive tracer techniques as the basis of comparison.

Several methods currently in use for the preparation of high-purity silicon require silicon tetrachloride as a source material. The quality of the silicon obtained depends on the purity of the silicon tetrachloride used, boron and phosphorus chlorides being the residual impurities of most concern. Removal of these impurities usually has been accomplished by distillation methods in conjunction with complexing additives (1-3). Such additives react with boron and phosphorus chlorides to form low vapor pressure compounds which remain in the still during distillation.

A new method for the purification of silicon tetrachloride using columns filled with hydrous adsorbents has led to significantly better results. It has been found that boron and phosphorus, as well as heavy metal chlorides, are removed efficiently by adsorption. Hydrogen reduction of the purified silicon tetrachloride to produce silicon rods, followed by floating-zone refining, has resulted in p-type crystals with resistivities above 8000 ohm-cm and minority carrier lifetimes of 1 msec. Using distillation methods for purification, comparative rods have resistivities of about 1000 ohm-cm and lifetimes of the same order as those obtained with the purer silicon.

In establishing the best adsorption techniques for the purification of silicon tetrachloride, it was necessary to evaluate various classes of adsorbents. Since hydrogen reduction and floating-zone refining are time consuming, several analytical methods were developed for these evaluations. Infrared absorption spectroscopy was used for the detection of BCl_3 and PCl_3 in $SiCl_4$. In the case of phosphorus, PCl_3 containing radioactive P32 with a half life of 14 days also was used for detection.

Evaluation of Adsorbents by Infrared Analysis for BCl_3 and PCl_3 in $SiCl_4$

Infrared spectra revealed that BCl_3 had a characteristic band at 1313 cm^{-1}, and PCl_3 had a series of bands at 1415, 1368, and 1345 cm^{-1}. $SiCl_4$ does not absorb in these regions. For calibration purposes, a series of $SiCl_4$ standards containing known amounts of BCl_3 and PCl_3 was prepared and analyzed. Strict adherence to Beer's law was not observed due to molecular interaction between BCl_3 and PCl_3, and the results are therefore semiquantitative with a detection sensitivity of 0.01%. Using this detection method and working with $SiCl_4$ containing 1% each of BCl_3 and PCl_3, it was possible to evaluate the relative efficiencies of various adsorbents for the removal of these impurities. Although the concentrations of impurities normally found in $SiCl_4$ are much lower than the detection limit of 0.01%, the above method gave much valuable information concerning the purification efficiency of various adsorbents.

In initial experiments, silica gel, activated alumina, coconut charcoal, and "molecular sieves" (sodium-calcium-alumino silicate) were evaluated for

Table I. Purification of $SiCl_4$ containing 1% PCl_3 and BCl_3 by various adsorbents

Adsorbent	First 10 cc eluted		Remaining drainable fractions	
	BCl_3, %	PCl_3, %	BCl_3, %	PCl_3, %
Silica gel 6-16 mesh	<0.01	<0.01	<0.01	<0.01
Activated alumina 8-14 mesh	<0.01	<0.01	<0.01	<0.01
Coconut charcoal 6-14 mesh	<0.01	0.1	0.1	0.1
Molecular sieves (sodium calcium alumino silicate) 1/16 in. pellets	1.0	<0.01	1.0	1.0

the removal of BCl_3 and PCl_3 from $SiCl_4$. Prior to use, the adsorbents were activated by treating in air at 270°C for 16 hr. The adsorbents then were added to 50 ml burettes to form columns 0.4 in. in diameter and 10 in. long. Thirty milliliters of $SiCl_4$ containing 1% each of BCl_3 and PCl_3 were allowed to drip into the columns at the rate of 1 ml/min. After standing 1 hr, 10 ml samples were drained from the burettes at a rate of 0.8 ml/min. A second set of samples comprising the remaining drainable $SiCl_4$ (approximately 12 ml) was collected also. All samples then were analyzed by the infrared absorption technique, with the results shown in Table I. It is apparent from these results that the hydrous oxides of silica and alumina are quite effective for removal of BCl_3 and PCl_3 from $SiCl_4$, the other adsorbents being relatively ineffective.

In addition to the above, various classes of adsorbents, including ion exchange resins, were tested for adsorption of BCl_3 and PCl_3 from $SiCl_4$ using the infrared technique. In a number of instances desired materials were not readily available, and in these cases, they were prepared specially. Where possible, the adsorbents were precipitated in gelatinous form for maximum surface area. The methods of preparation used are listed in Appendix I.

In the case of ion exchange resins, while $SiCl_4$ solutions are essentially nonionic, physical adsorption of impurities on these resins seemed possible, since they are porous and have a high surface area. Because such resins normally are furnished in a moist condition, prior to use with $SiCl_4$, it was necessary to remove the water by drying in a vacuum desiccator. After several days of pumping, these materials no longer hydrolyzed $SiCl_4$ and were then in satisfactory condition for adsorption studies.

In testing the adsorption efficiencies of the various materials, 5 cc of solid adsorbent, activated as listed in Table II, were added to 20 ml of $SiCl_4$ containing 1% each of BCl_3 and PCl_3. The mixtures were shaken intermittently for 1 hr, after which the $SiCl_4$ was filtered through glass wool and analyzed by infrared spectroscopy. Results are summarized in Table II.

It will be seen that hydrous oxides and silicates adsorb both BCl_3 and PCl_3 from $SiCl_4$. Those materials which were in gel form were most effective, probably due to their large surface area. Dehydration of several of the active oxides destroyed their adsorption efficiency, suggesting that chemisorption involving OH groupings is at least a part of the purification mechanism. Ion exchange resins were inoperative for the removal of boron and phosphorus chlorides.

Adsorption Studies Using Radioactive PCl_3 and PCl_5 in $SiCl_4$

In determining the effectiveness of adsorption columns for the removal of phosphorus chlorides

Table II. Purification of $SiCl_4$ containing 1% BCl_3 and PCl_3 by various adsorbents

Adsorbent	Activation	PCl_3, %	BCl_3, %
Silica gel 6-14 mesh	270°C-18 hr	0.01	<0.01
Silica gel 6-14 mesh deactivated	1000°C-18 hr	1	1
Silica gel from hydrolyzed $SiCl_4$	270°C-18 hr	<0.01	<0.01
$Mg(OH)_2$ powdered	120°C-4 hr	0.01	0.01
MgO anhydrous	120°C-18 hr	1	1
CaO	270°C-30 hr	1	1
$CaCO_3$	270°C-30 hr	1	1
$Fe(OH)_3$ gel	270°C-4 hr	<0.01	<0.01
TiO_2 gel	270°C-18 hr	<0.01	<0.01
Fullers earth	120°C-18 hr	<0.01	<0.01
Tungstic acid	—	0.1	0.1
Cellite #545 (treated diatomaceous earth)	120°C-18 hr	0.1	0.1
Decalso (alumino silicate gel)	120°C-18 hr	0.1	0.1
Zeo Dur (hydrous silicate greensand)	25°C-vacuum dried	0.01	0.01
Permutet H-70 (carboxylic acid resin)	25°C-vacuum dried	1	1
Permutet Q (sulfonated polystyrene)	25°C-vacuum dried	1	1
Permutet S-2 (quarternary amine polystyrene)	25°C-vacuum dried	1	1

from $SiCl_4$, solutions containing 0.001% by volume of PCl_3 containing radioactive P32 were used. Where desired, the PCl_3 was converted to PCl_5 by the addition of Cl_2 to the $SiCl_4$ solution. In these studies, samples of the eluent were analyzed, and autoradiographs of the columns were made. The detection sensitivity for phosphorus in the $SiCl_4$ was initially 1×10^{-8} mole %. In this work, activated alumina and silica gel were used as the adsorbents; these were activated by heating in air prior to use at 270°C for 18 hr. The initial exploratory work was done with 0.4 in. diameter x 10 in. long columns in 50 ml burettes using 6-14 mesh adsorbents. In these experiments, autoradiographs showed that the PCl_3 was dispersed throughout the adsorbents, suggesting that channeling of the liquid was occurring in the columns resulting in some elution of PCl_3. To prevent channeling, finer adsorbents were required, and all subsequent experiments were done with 80-200 mesh adsorbents. For these experiments, columns, such as the one shown in Fig. 1, were used. With these columns, the $SiCl_4$ was allowed to drip through the adsorbent at a rate of about 1 cc/min until a liquid head formed in the top of the tube. The column then was allowed to equilibrate for several hours before sample collection was begun at a rate of 1 ml/min, controllable with the Teflon valve in the apparatus. Radioactivity measurements on samples of eluent taken during the purification, and autoradiographs of the columns were made at the end of each experiment. Table III gives a summary of the analytical data obtained with variations of the adsorption practice. It will be seen that using 60-200 mesh silica gel or activated alumina eliminated the channeling found with the 6-14 mesh adsorbents, and in consequence, better phosphorus removal was obtained. Autoradiographs of the columns containing the finer adsorbents showed that the phosphorus was banded for a distance extending 3 in. down from the top, no phosphorus being detected below this point.

In the course of this work, as shown in Table III, it was found that best results were obtained when the $SiCl_4$ contained free chlorine or a combination of chlorine and aluminum chloride prior to adsorption purification. In these cases, 10 ml of liquid chlorine per liter of $SiCl_4$ were added; where $AlCl_3$ was used, 30 g/l of granular anhydrous $AlCl_3$ were added. After standing overnight, the undissolved $AlCl_3$ was filtered off. The purpose of the chlorine addition was to convert PCl_3 to PCl_5. The use of $AlCl_3$ results in the formation of the coordination compound, $PCl_5 \cdot AlCl_3$ (2, 4). Using either of these pretreatments, with activated alumina as the adsorbent, no phosphorus was detected in the eluent after 3525 ml had passed through the columns. In both cases tight banding of the phosphorus was observed at the top of the columns. The width of this band increased with the quantity of $SiCl_4$ eluted and after 3525 ml had passed through extended down from the top of the column for a distance of about 1 in. For phosphorus removal, no advantage was found in adding $AlCl_3$ in conjunction with the chlorine. However, for reasons not completely understood, use of the combination of $AlCl_3$ and Cl_2 in the purification of $SiCl_4$ leads to silicon lower in boron. It has been observed that both PCl_3 and PCl_5 form coordination compounds with BCl_3. The complex $BCl_3 \cdot PCl_5$ has a solubility of about 0.033 mole % in $SiCl_4$ and sublimes below 100°C. It may be that the $AlCl_3$ breaks this complex by forming $AlCl_3 \cdot PCl_5$, thus freeing the BCl_3

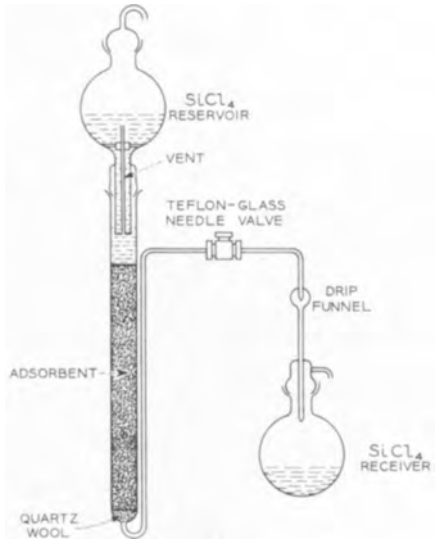

Fig. 1. Adsorption column for purification of $SiCl_4$

Table III. Purification of $SiCl_4$ containing 0.001% radioactive PCl_3 by adsorption on silica gel and activated alumina

Adsorbent	Additive	Quantity of $SiCl_4$ eluted, ml	Mole % P in eluent	Autoradiograph results
Silica gel 6-16 mesh	—	185	9.8×10^{-5}	Adsorption spotty throughout column channeling of $SiCl_4$
Activated alumina 6-14 mesh	—	185	—	As above
Silica gel 60-200 mesh	—	185	6.9×10^{-6}	Banding of PCl_3 top 3 in. of column
Activated alumina 80-200 mesh	—	185	Not detected $<7.7 \times 10^{-8}$	As above
		1500	4.2×10^{-6}	
Activated alumina 80-200 mesh	Cl_2*	3525	Not detected $<8.6 \times 10^{-7}$	Tight band extending 1 in. down column
Activated alumina 80-200	Cl_2+ $AlCl_3$*	3525	Not detected $<8.4 \times 10^{-8}$	As above

* 10 ml of liquid chlorine per liter, and 30 g $AlCl_3$ per liter of $SiCl_4$ were used.

for more effective adsorption. These complexes of phosphorus and boron chlorides also may be the source of the difficulty normally encountered in distillation procedures for the removal of these impurities.

Removal of Heavy Metal Chlorides and Sulfur Compounds from $SiCl_4$

In operating adsorption columns, such as shown in Fig. 1, filled with either activated alumina or silica gel, it is observed that after several liters of $SiCl_4$ have been eluted, a brown band forms at the top of the column for a distance of about ½ in. This band gradually broadens with continued use. Spectrochemical analysis of the adsorbent in the banded region shows traces of B, Cu, Fe, Mn, and Mg. These impurities are not detected lower in the column and are not detectable in hydrolyzed samples of the initial $SiCl_4$. These results clearly indicate that the adsorption technique is quite effective in removing heavy metal chlorides from $SiCl_4$.

Commercially available $SiCl_4$ may contain sulfur compounds at mole ratios as high as 1.1×10^{-4}. These compounds, probably $SiCl_3HS$ and $SiCl_2S$, liberate H_2S on hydrolysis of the $SiCl_4$, and this may be used as a basis of detection. While adsorption methods remove these compounds, it is expedient to reflux the $SiCl_4$ with copper turnings for 16 hr prior to column purification, which effectively removes the sulfur. Sulfur compounds in $SiCl_4$ react with copper to form black CuS. In the absence of sulfur, the copper turnings remain bright.

Summary

It has been shown that adsorption columns filled with hydrous oxides or silicates offer an attractive method of purifying $SiCl_4$ for use in the preparation of very high-purity silicon. In using the method, the $SiCl_4$ is first refluxed with copper turnings to remove sulfur compounds. It is then preferably treated with $AlCl_3$ and Cl_2 and passed through an adsorption column containing either activated alumina or silica gel. The purified $SiCl_4$ contains Cl_2 which, if objectionable, may be removed by refluxing in a stream of dry nitrogen or hydrogen. On reduction of the purified $SiCl_4$ in hydrogen on tantalum tubes, polycrystalline rods suitable for floating-zone refining are obtained. After removal of the tantalum, such rods, if given several zone passes in dry hydrogen, are n-type with a resistivity of 50-100 ohm-cm in the region of the crystal where refining does not occur. Subsequent zone refining to eliminate the donors, principally phosphorus, results in p-type silicon with resistivities above 8000 ohm-cm. After two zone passes, the lifetimes of the crystals are of the order of 1 msec and no evidence of trapping centers is found. Subsequent refining does not further improve the lifetime.

The source of the phosphorus in this silicon is not known. It is unlikely that the phosphorus originates from the purified $SiCl_4$ in view of the radioactivity results, which show tight banding of phosphorus at the top of the column and no detectable phosphorus in the eluent. It seems probable that the donors are introduced during the reduction process either from the reactants or the apparatus itself.

Although a detailed study has not been made, exploratory experiments indicate that column methods using hydrous oxides as adsorbents can purify other halides such as $SiHCl_3$ and $GeCl_4$ effectively. Attempts to purify SiI_4 by passing through a heated column, or by dissolving the iodide in n-heptane or toluene prior to column elution, have not been promising. SiI_4 reacts with the adsorbents tried (activated alumina and silica gel) with the liberation of iodine.

Acknowledgments

The author is greatly indebted to a number of his colleagues at Bell Telephone Laboratories for much of the work in this investigation. D. L. Wood and J. P. Luongo were responsible for the infrared spectroscopy; J. D. Struthers was responsible for the radioactive tracer analyses; J. E. Jamieson purified the silicon tetrachloride and made the hydrogen reduced silicon; and D. D. Bacon did the zone refining work.

Manuscript received July 10, 1959. This paper was prepared for delivery before the Philadelphia Meeting, May 3-7, 1959.

Any discussion of this paper will appear in a Discussion Section to be published in the December 1960 JOURNAL.

REFERENCES

1. I. J. Krchma, U.S. Pat. 2,820,698.
2. J. M. Whelan, U.S. Pat. 2,821,460.
3. F. H. Winslow, U.S. Pat. 2,812,235.
4. W. Fischer and O. Juberman, *Z. anorg. u. allgem. Chem.*, **235**, 337 (1938).

APPENDIX I

Method of Preparing Various Adsorbents

Silica gel from hydrolyzed $SiCl_4$.—Fifty milliliters of $SiCl_4$ were hydrolyzed in 500 ml of deionized water at 0°C. An opalescent liquid was obtained which set to a gel in about 2 hr. After aging overnight, the gel was broken up and washed copiously to remove the HCl formed during hydrolysis. The gel was dried for 2 days in a vacuum desiccator followed by air drying at 100°C for 24 hr and activation at 270°C for 18 hr.

Silica gel anhydrous.—Commercial silica gel, 6-14 mesh, was deactivated at 1000°C for 18 hr in air with a weight loss of 5.2%.

MgO *and* $Mg(OH)_2$.—Anhydrous MgO powder was heated for 18 hr at 120°C prior to use as an adsorbent. To hydrate this oxide, a batch of the above MgO was dissolved in 6*N* HCl and filtered. The clear solution was made alkaline with ammonium hydroxide to precipitate $Mg(OH)_2$. This was filtered, washed, and dried at 120°C. The resulting hard cake of $Mg(OH)_2$ was crushed in an agate mortar and dried for 4 hr at 120°C before use.

Titania gel.—Twenty-five milliliters of tetraisopropyl titanate were stabilized against rapid hydrolysis with 5 ml of 12*N* HCl. To the above solution, 75 ml of H_2O were added and the mixture heated to 80°C. Ammonium hydroxide then was added until a curdy gelatinous precipitate formed. After standing for several hours, the gelatinous mass was made strongly alkaline with ammonium hydroxide. The curd then was aged overnight, washed free of ammonia, and dried for 24 hr in a vacuum desiccator. This was followed by air drying at 120°C and activation for 18 hr at 270°C.

$Fe(OH)_3$ *gel.*—$Fe(OH)_3$ was dissolved in a small excess of 6*N* HCl and the solution filtered. This was made strongly alkaline with NH_4OH precipitating gelatinous $Fe(OH)_3$. After aging overnight, the precipitate was filtered, washed free of NH_4OH and NH_4Cl, and dried overnight. It then was dried for 24 hr at 120°C and activated at 270°C for 4 hr

Purification of Tantalum Obtained by Vacuum Arc Melting

M. L. Torti

National Research Corporation, Cambridge, Massachusetts

ABSTRACT

The purest commercially available tantalum powder was consolidated by a single, vacuum, consumable-arc melting operation yielding ingots of considerably higher purity than the original powder. Interstitial and metallic impurity analyses are presented for a large number of heats made under consistent conditions of ingot and electrode size, arc current, and furnace pressure. The effect of carbon addition to an oxygen-rich starting material was investigated, and the optimum carbon-oxygen ratio for maximum refinement has been located approximately. Under favorable conditions, the oxygen content is reduced by approximately one order of magnitude.

Tantalum metal has traditionally been produced by the powder metallurgy route in which a lengthy high-temperature vacuum sintering treatment is utilized for refining to the purity necessary for fabrication.

The general extension of vacuum arc melting as a method for consolidating the refractory metals has prompted a wide interest in the arc melting of tantalum. Although fabricable ingots have been produced from tantalum powder of conventional purity, the purity and ductility of these ingots has not matched good sintered bar material. Indeed, doubt is commonly expressed as to whether any refinement at all occurs during arc melting.

When a relatively pure tantalum powder became commercially available the arc melting procedure gained new promise. Ingots are now being produced by a single melt which can be fabricated cold from ingot to 0.0005 in. thick strip without intermediate anneals. The excellent ductility and superior purities are due in a large degree to the initial purity of the tantalum powder. However, substantial purification does occur during arc melting with respect to both interstitial and metallic impurities.

Description of Equipment and Procedure

All melting was done in a conventional cold-mold arc furnace. Power was supplied by a bank of welding generators capable of supplying 5600 amp. A 1000 CFM mechanical-booster high-vacuum pump, backed by a 100 CFM mechanical pump, comprised the pumping system. This system blanks off below 1 μ and has a pumping speed of over 1000 CFM between 10 and 1000 μ. A nominal 4 in. diameter cold mold was used. Since double extra heavy copper pipe was installed as the mold liner, the actual inner mold diameter was 3.5 in. Melt stock was National Research Corporation melting grade tantalum powder −12 +325 mesh. Bars 1¾ to 2 in. in diameter were hydrostatically pressed from this powder. These bars were given a quick premelting treatment in which direct resistance heating was used to heat the bars to 1500°C for approximately 1 min in vacuum. This operation dimensionally stabilizes the bars and improves the already excellent green strength. No significant purification is obtained for such a short heating period. The bars are then welded into the electrode using a tungsten permanent electrode in an argon atmosphere. Strong, ductile welds are obtained on high-purity powder. Brittle welds may occur if powder containing over 1000 ppm total interstitial impurities is used.

Melts were run at 30 v, 4500-5000 amp under 2-5 μ pressure measured in the furnace body. A melting rate of 0.5 lb/min resulted. This corresponds to a power input of approximately 4.5 kwh/lb. The molten pool was stirred by a 500 turn d-c adjustable-amperage stirring coil. Normally 3 amp was sufficient to stabilize the arc and gently stir the pool without undue agitation. At that amperage the measured magnetic field in the center of the empty mold is 40 gauss.

During melting the arc is observed visually. A thin film of deposited vapor is seen above the melt. This layer is partially driven ahead of the melt level and partially redissolved in the melt, resulting in the higher impurity levels reported for the ingot tops.

The 70-90 lb ingots are lathe conditioned, then slices are cut from the top and bottom for analytical samples. Chunks from the interior of the samples are used for the oxygen and nitrogen samples. Dry drillings are used for the other samples. For some elements both spectrographic and wet analyses are reported, and two spectrographic procedures were employed.

Experimental Results

Table I reports carbon and oxygen analysis for 2-in. diameter pressed-bar electrodes and the resulting 3½ in. diameter ingot. In this series no carbon was added to the melt stock. Note that signifi-

cant amounts of oxygen are removed, particularly at the ingot bottom. The oxygen is probably removed as tantalum oxides which deposit on the mold wall above the melt. Since this oxide film must be either driven up or redissolved in the melt it is not surprising that the oxygen level at the ingot top, although slightly lower than the melt stock, is double the oxygen content at the ingot bottom. The carbon present in the melt stock is decreased to or below the analytical limits indicating that some carbon removal, probably as carbon monoxide, is occurring. Occasional analyses report higher oxygen content for the ingot than for the melt stock. This is attributed to individual sampling and analytical determination errors, and indicates the necessity for averaging the results from a large number of heats.

Table I also reports analytical data for 1¾-in. diameter electrodes to which fine graphite powder was added. Since the melt rate, pressure, ingot condition, and metallic refinement were the same as for the 2-in. diameter electrodes, it is assumed that except for the carbon addition, melting conditions for this series are identical to those for the 2-in. electrodes. The initial carbon content of the tantalum was 10-20 ppm. Additional carbon in the form of fine graphite powder was thoroughly mixed with the tantalum powder. Sufficient carbon was added to raise the carbon-oxygen ratio to 50% of the stoichiometric ratio for carbon monoxide.

The average oxygen content in the electrode was 239 ppm, the average oxygen content in the ingots was 65 ppm top and 34 ppm bottom. The total carbon in the electrode was 111 ppm which was reduced to 23 ppm top and 30 ppm bottom for the ingots. Thus an average of 73% of the oxygen content of the electrode was removed at the top of the ingots and 85% at the ingot bottom. This compares to a 25% oxygen reduction at the ingot top and 67% at the ingot bottom for the melts (Table I) to which no carbon was added. Furthermore, carbon additions appear to cut down the fluctuations in oxygen content from ingot to ingot.

Table I. Tantalum vacuum arc melting

I. Oxygen and carbon refinement for no carbon addition, average of 14 melts

	O (ppm)		C (ppm)	
	Top	Bottom	Top	Bottom
Electrode	140		10-20	
Ingot	106	46	<10	13

II. Oxygen and carbon refinement with 50% stoichiometric carbon addition, average of 11 melts

	O (ppm)		C (ppm)	
	Top	Bottom	Top	Bottom
Electrode	239		111	
Ingot	65	34	23	30

III. Oxygen and carbon refinement with 100% stoichiometric carbon addition, average of 2 melts, high oxygen powder used

	O (ppm)		C (ppm)	
	Top	Bottom	Top	Bottom
Electrode	950		800	
Ingot	120	—	360	—

IV. Other impurity refinement (ppm), average of 25 melts

	N	Fe	Cr	Ni	Nb	Si
Electrode	28	95	86	111	112	<250
Ingot	27	30	14	28	40	30

The final carbon-oxygen ratio appears quite good, particularly at the ingot bottom. Earlier in the program tantalum powder of 1000 ppm oxygen content was mixed with sufficient carbon to bring the carbon-oxygen ratio to 100% of the stoichiometric ratio for carbon monoxide removal. Table I shows the results of two melts. Considerable oxygen was removed, but the final carbon content was 2-3 times that of the oxygen. When one of these ingots was remelted, the decrease in oxygen was less than expected.

Table I reports analytical data for several other elements. The ingot analyses were taken at the ingot top. Three analytical procedures are used; wet chemical, pellet spectrographic, and carrier spectrographic.

Very little difference is noted between the nitrogen analysis for the ingots and electrodes so that it appears that little, if any, nitrogen removal occurs during melting at the low nitrogen levels encountered in this program.

Iron is definitely removed on melting, being reduced by a factor of two or three. The amount of refinement is somewhat vague for several melts due to the starting concentration being below the level of detection for the method used.

Nickel is present in the same amounts as iron and is removed to the same degree.

Chromium is quite volatile and considerable refinement occurs, generally resulting in an ingot content below the level of detection.

The data indicate a removal of niobium on the same level as iron and nickel. This is somewhat surprising since the vapor pressure of niobium is considerably lower than that of iron at the tantalum melting point. Two possible mechanisms may be postulated. The vapor pressure of the niobium suboxides may be higher than that tantalum suboxide vapor pressure resulting in the preferential removal of niobium oxides. Unfortunately, values of the vapor pressures have not been reported in the published literature. Iron and nickel form intermetallic compounds with tantalum while niobium does not. Thus the activity coefficient of niobium in tantalum may be higher than that for iron or nickel in tantalum. The resulting impurity partial pressures may then be more nearly equal.

The data for silicon unfortunately do not locate the silicon level in the electrode until the last few runs. However, these rather sparse data do indicate significant removal during melting.

Hydrogen analyses were not always run, but the electrode hydrogen content varies between 25 and 50 ppm, while the ingot hydrogen varies between 1 and 5 ppm.

Conclusions

Consumable arc melting of tantalum can, under favorable conditions, result in considerable refine-

ment of the metal. Oxygen can be removed both as tantalum oxides and as carbon monoxide. Of the combinations studied, the lowest, most uniform oxygen analyses in the ingot result when the carbon in the electrode is 50% of the stoichiometric carbon-oxygen ratio for carbon monoxide removal.

Nitrogen is not significantly reduced at the low nitrogen levels encountered. Metallic impurities with vapor pressures equal to or greater than nickel are significantly reduced. Niobium appears to be partially removed although the mechanism is not completely clear.

Acknowledgment

Grateful acknowledgment is given for the analytical services of Messrs. F. Pink, L. McGowan, and J. Martin, the analytical supervision of Dr. F. Benner, the melting operations of Mr. R. Malatesta, and the invaluable consultations of Mr. John Ham.

Mansucript received June 29, 1959. This paper was prepared for delivery before the Philadelphia Meeting, May 3-7, 1959.

Any discussion of this paper will appear in a Discussion Section to be published in the December 1960 JOURNAL.

Heat Transfer Rates of an Argon Plasma Jet

C. S. Stokes, W. W. Knipe,[1] and L. A. Streng

The Research Institute of Temple University, Philadelphia, Pennsylvania

ABSTRACT

Heat flux measurements were made on a small argon plasma jet. Experimental values as high as 4.5 kcal/cm² sec were obtained for the transient-heating rate of a small copper slug. The heat-flux variation with energy supplied and the energy distribution to cathode, anode, and plasma are presented.

Arcs have been of interest as high-temperature sources for a number of years. The development of the plasma jet has provided a convenient tool for studying gases at these temperatures, without electrode interference. A number of investigators (1-3) have devised plasma-jet apparatus of various kinds. This paper presents the measurements of the heat transfer rates of an argon plasma jet.

Apparatus and Procedure

A drawing of the plasma generator is shown in Fig. 1. The generator consists of a water-cooled ⅛ in.-2% thoriated tungsten cathode with an annulus for feeding the argon gas. The copper anode, which has a 0.157 in.-hole for the plasma jet, is water cooled. A ¼ in.-Teflon gasket insulates the anode from the cathode.

A 600-amp d-c welder was used as the power source. Appropriate electrical meters guided the operation. Argon[2] was metered through a Fisher and Porter flowmeter. The plasma jet was approximately 1 in. long and expanded to a diameter of about ¼ in.

The heat transfer measurements were made with a transient probe consisting of a piece of copper ⅛ in. in diameter and ¼ in. long, embedded in a ⅝ in.-diameter piece of "Transite" ½ in. long. This assembly was placed in a 1½ in.-diameter by 1 in.-long piece of laminated fiberglass (see Fig. 2). The probe was mounted on a high-speed air-piston cylinder which thrust the probe into the jet approximately 1 mm below the anode. A 30-gauge iron-constantan thermocouple was inserted into the copper slug 0.050 in. from the back surface.

Two separate high-speed measuring apparatus were used to obtain the time-temperature curves for

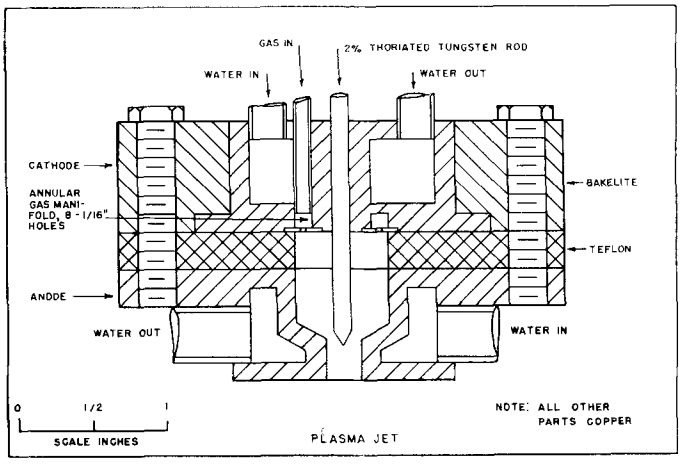

Fig. 1. Schematic of plasma jet apparatus

the copper slugs. One consisted of a d-c-modulated high response time potentiometer. The low voltage from the thermocouple modulated a 160-kc carrier wave which was shown on an oscilloscope with a triggered-sweep duration of 2 sec. The other system used was a Tektronix type-533 oscilloscope with a type-53/54D calibrated high-gain d-c preamplifier.

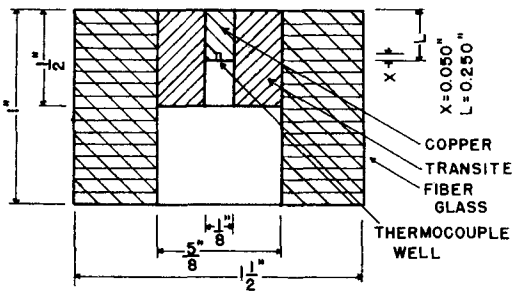

Fig. 2. Transient heat probe

[1] Present address: Pennsalt Chemicals Corp., Philadelphia, Pa.
[2] Obtained from Air Reduction Co.

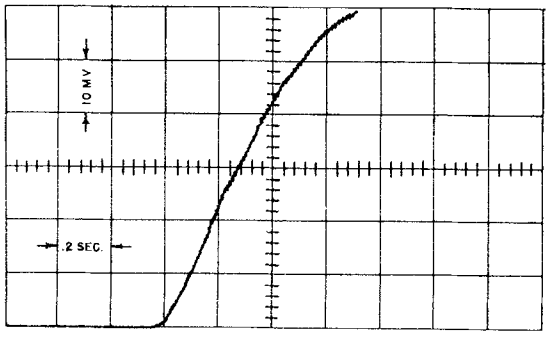

Fig. 3. Trace of the tektronix system. Ordinate, 10 mv per large division; abscissa, 0.2 sec per large division.

Both systems produced similar results. The modulation system cut out most of the "noise" produced by the arc but was more difficult to calibrate than the other. A typical trace of the Tektronix system is given in Fig. 3.

Calculation of Heat Transfer Rates

The general method of data reduction used is described by Sutton (4).

The equations for a transient one-dimensional system are:

$$\frac{T - T_o}{Q} = \frac{L}{K} Z \qquad [1]$$

$$Z = 2\sqrt{X} \sum_{0}^{\infty} (\text{ierfc } z + \text{ierfc } z') \qquad [2]$$

$$X = \frac{Kt}{dL^2 C_p} \qquad [3]$$

$$N = x/L \qquad [4]$$

$$z = (2r + 1 - N)/2\sqrt{X} \qquad r = 0, 1, 2, \ldots$$

$$z' = (2r + 1 + N)/2\sqrt{X}$$

Where: Q is heat transfer rate; T_o, initial temperature; T, temperature after time t; L, length of slug; K, thermal conductivity; N, position ratio; d, density of slug; C_p, heat capacity of slug at constant pressure; and x, distance of thermocouple from back of slug. Tables of Z have been tabulated by Kaye and Yeh (5) as a function of X and N.

The change in temperature was read from the photographs for the time increment 0.1 to 0.2 sec, making t equal to 0.1 sec. Values of X and N then were calculated and Z was read from the tables. From this value Q was computed. An example follows for the copper slug described previously: For copper: K, is 0.842 cal/cm sec °C; d, 8.94 g/cm^3; C_p, 0.1057 cal/g °C; L, 0.635 cm; x, 0.127 cm; t, 0.1 sec;

X is $\dfrac{(0.842)(0.1)}{(8.94)(0.1057)(0.635)^2} = 0.222$; and N, $\dfrac{0.127}{0.635} = 0.20$.

For the above values of X and N, $Z = 0.095$. Therefore,

$$\frac{T - T_o}{Q} = \frac{L}{K}(0.095) = \frac{(0.635)(0.095)}{0.842} = 0.0715$$

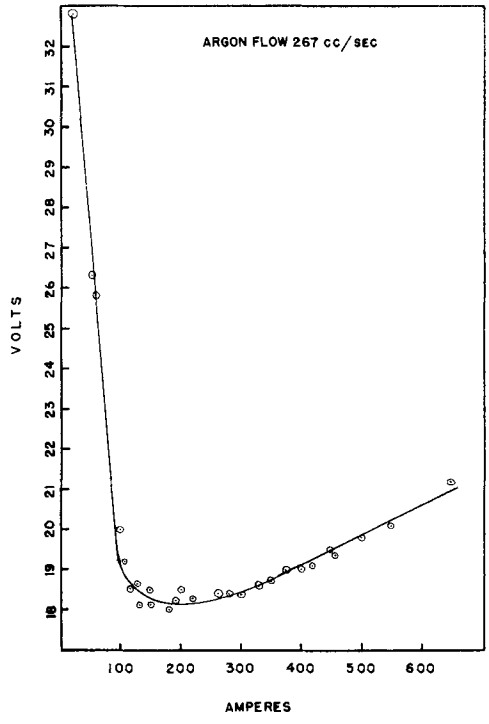

Fig. 4. Electrical characteristics of the argon plasma jet

letting $\Delta T = T - T_o$

$$Q = 1.4 \times 10^{-2} \Delta T \text{ in kcal/cm}^2 \text{ sec}$$

where ΔT is in °C.

Figure 4 shows the electrical characteristics of the arc jet. It will be noted that the high-intensity region starts at approximately 200 amp. Measurements of heat flux were made only in the high-intensity region because the jet becomes unsteady on the low-intensity side.

Results

The results of the heat transfer measurements are given in Fig. 5 and Table I. As can be seen, for the range of power used and for an argon flow of 16 liters/min, the heat flux falls between 0.5 and 4.5 kcal/cm^2 sec. These values are about 4 or 5 times those obtained from rocket motors and make possible tests on the stability of materials at extremely high temperatures and high heat fluxes. The values obtained are compared with the theoretical heat balance of the arc as shown in Fig. 6. The theoretical

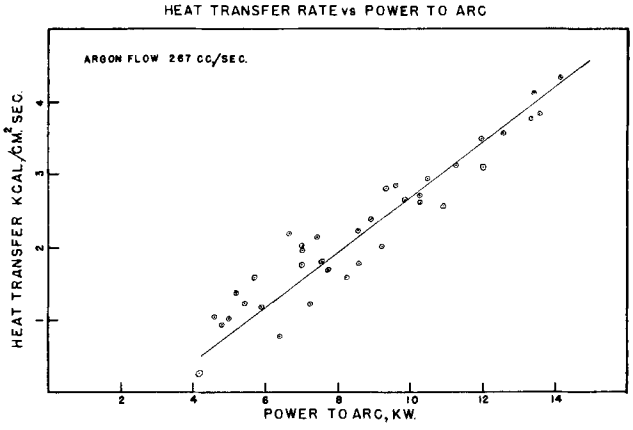

Fig. 5. Heat transfer rates vs. power to arc

Table I. Heat transfer rates of the argon plasma jet at a constant argon flow of 16 liters/min

Power to Arc, kw	Heat transfer rates, kcal/cm² sec
4.13	0.28
4.60	1.03
4.80	0.94
5.00	1.00
5.15	1.38
5.41	1.22
5.66	1.60
5.90	1.18
6.40	0.75
6.65	2.19
6.95	1.79
7.01	1.96
7.05	2.04
7.24	1.22
7.41	2.14
7.56	1.78
7.69	1.71
8.25	1.58
8.60	2.24
8.62	1.76
8.94	2.38
9.25	2.02
9.40	2.80
9.61	2.90
9.90	2.64
10.20	2.65
10.30	2.71
10.49	2.94
11.06	2.50
11.30	3.19
12.00	3.50
12.25	2.85
12.60	3.59
13.40	3.79
13.45	4.16
13.60	3.84
14.20	4.35

curve was calculated by dividing the power to the plasma in kcal/sec by the average cross-sectional area of the plasma jet in cm². Experimental values fall below the theoretical as would be expected, since some of the energy is dissipated by radiation and other processes. The energy in the plasma was arrived at by evaluating the losses to the water-cooling system. It was found that approximately 56% of the total energy to the arc goes into the plasma jet, 5% to cathode heating and the remainder to heating the anode. Figure 7 shows the experimental points.

By using the Saha ionization equation (6), average plasma temperatures were calculated. These

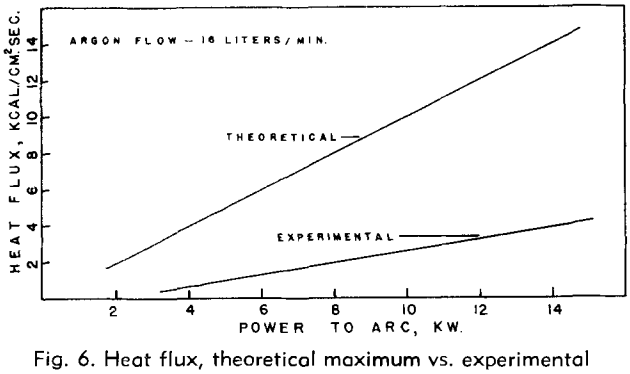

Fig. 6. Heat flux, theoretical maximum vs. experimental

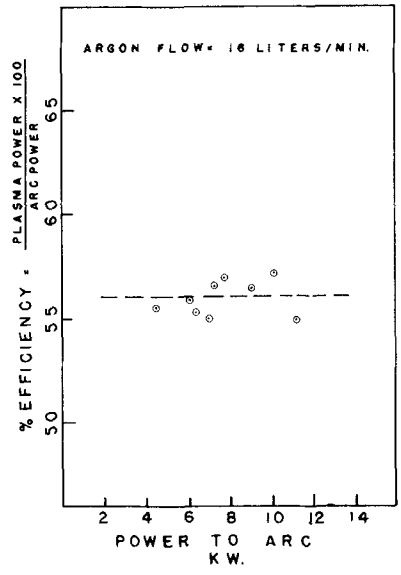

Fig. 7. Efficiency of arc

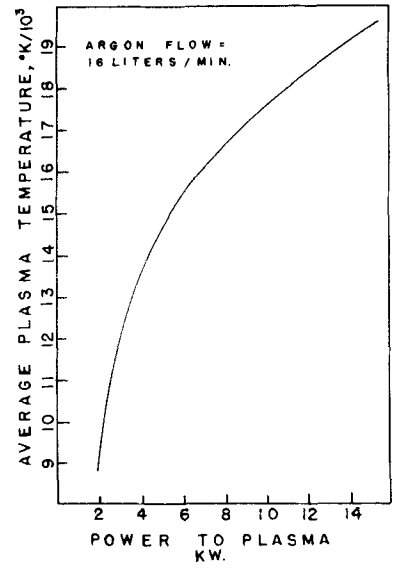

Fig. 8. Calculated temperature of the arc

temperatures are based on the total argon flow and the amount of energy actually in the plasma (56%). Figure 8 shows the results of these calculations. The temperatures range from 9000°K at 2 kw to 19000°K at 14 kw. There is some doubt whether these temperatures are actually the true ones, because a "frozen" composition of the jet is required by the Saha equation.

Acknowledgment

The authors wish to thank Dr. A. V. Grosse and Mr. W. L. Doyle for their helpful suggestions.

The research was supported by the U. S. Army through the U. S. Army Ballistic Missile Agency under Contract No. DA-36-034-ORD-2328.

Manuscript received May 4, 1959. This paper was prepared for delivery before the Ottawa Meeting, Sept. 28-Oct. 2, 1958.

Any discussion of this paper will appear in a Discussion Section to be published in the December 1960 JOURNAL.

REFERENCES

1. "The Symposium on Arcs in Inert Atmospheres and Vacuum," W. E. Kuhn, Editor, John Wiley & Sons, Inc., New York, (1956).
2. "High Intensity Arc Symposium," S. D. Mark, Jr., Editor, The Carborundum Co., Niagara Falls, N. Y. (1958).
3. "Conference on Extremely High Temperatures," Fisher and Mansur, Editors, John Wiley & Sons Inc., New York (1958).
4. G. W. Sutton, Real Gas Technical Memorandum No. 10, General Electric Company, MOSD, Philadelphia, Pa., May 23, 1956.
5. J. Kaye and V.C.M. Yeh, *J. Aeronaut. Sci.*, **22**, 755 (1955).
6. Saha, *Phil. Mag.*, **1**, 1025 (1920).

The Preparation of a New Crystalline Modification of Boron, and Notes on the Synthesis of Boron Triiodide

L. V. McCarty[1] and D. R. Carpenter

Research Laboratory, General Electric Company, Schenectady, New York

ABSTRACT

Boron triiodide has been made in yields as high as 70% from boron and iodine at 900°C. An equilibrium apparently limits the yield to 49% at 1050°C. An approximate free energy equation, $\Delta F^\circ_T = -43{,}000 + 31\ T$ cal/mole of BI_3, has been derived for the reaction $B_{(c)} + 3/2\ I_{2(g)} \leftrightarrows BI_{3(g)}$. Molybdenum metal may catalyze the reaction.

A new and denser form of crystalline boron has been deposited on tantalum in the temperature range 800°-1000°C from boron triiodide. Small portions of the deposit occur as red crystals with a density of 2.459_5 at 22.6°. The main impurity is 0.04% iodine. The red boron is composed of units of nearly regular icosahedra in a slightly deformed cubic close packing.

The preparation and properties of pure boron prior to 1942 have been reviewed by Laubengayer, Newkirk, and Brandauer (1). A short time later Laubengayer, Hurd, Newkirk, and Hoard (2) published their preparation of pure boron by the hydrogen reduction of purified boron tribromide. This technique probably makes the purest boron that has been described to date.

At least three other methods have been described since. These include sodium reduction of boron trichloride or boron trifluoride (3, 4), the electrolytic reduction of fused salt baths of fluoborates and alkali borates (5), and the hydrogen reduction of boron trichloride on hot carbon (6, 7) or titanium (7) rods. The first two of these three and the deposition on titanium lead to contamination of the boron with other metals which can be leached from the samples at least in part. Boron prepared on carbon rods may have as much as 5% carbon contamination, which is difficult to remove.

One of the chief advantages of the hydrogen reduction of boron tribromide is that it can be accomplished at temperatures as low as 600°C, and contamination by alloying with the filament substrate is not as serious a problem. Thermodynamic estimates indicate that boron triiodide would not be reduced as readily, but it would be expected to decompose directly to iodine and boron below 1000°C.

A possible advantage might be realized in the purification of boron triiodide (bp 209.5°C) by distillation. Aside from tetraiodoethylene (bp 187°C) iodine is the next lower boiling material (bp 184.35°C). The possible presence of tetraiodoethylene cannot be dismissed lightly because of the importance of carbon as an impurity, but its formation seems unlikely in our method of preparing boron triiodide. Phosphorus triiodide (bp approx. 220°C) is the nearest higher boiling iodide. Its removal may be difficult because there is only a 10° or 11° difference in the boiling points. During the decomposition of boron triiodide, phosphorus might react to form boron phosphide which would not volatilize as readily as elemental phosphorus. The next higher boiling compound anticipated is silicon tetraiodide (bp 301.5°C) which should not be difficult to remove.

Since phosphorus will not affect the electrical properties as much as silicon or carbon, its presence in our product is perhaps not as serious as the latter two. Efforts to make very pure boron from fractionally distilled boron triiodide resulted in a new crystalline modification some of which occurred as small, transparent red crystals.

Preparation and Purification of Boron Triiodide

Boron triiodide was made from the elements according to the method described by Moissan (8). U.S. Borax crystalline grade boron was placed in vertical reactors, and reagent grade iodine was vaporized slowly by boiling into a stream of about 50 cc/min of argon.

Boron triiodide vapor attacks quartz and alumina reactors at the optimum temperature of preparation. This problem was solved only partially by lining

[1] Present address: Lamp Development Department, General Electric Company, Nela Park, Cleveland, Ohio.

Table I. Iodination of U. S. Borax crystalline boron

Reaction temp, °C	Reaction time, hr	Wt of boron in bed, g	Wt of I_2 vaporized, g	I_2 converted to crude BI_3, %
Batch No. 1 (−4 to +100 mesh)				
800*	25	173	2869	22
900‡	31.3	151	2060	62
900*	18.3	165	2639	70
1050*	14	177	1416	49
Batch No. 3 (−20 to +100 mesh)				
900*	14	187	2032	57
900**	34	812	10,550	17
900†	9	124	3473	9

* Boron contained in vertical quartz reactor 1⅛ in. OD by 12 in. lined with molybdenum sheet.
‡ Boron contained in vertical quartz reactor 1 in. OD by 12 in.
** Boron contained in vertical quartz reactor 2 in. OD by 12 in. lined with molybdenum sheet.
† Boron contained in vertical quartz reactor 1⅛ in. OD by 12 in. with graphite liner ¾ in. ID.

quartz reactors with molybdenum sheet, because a brittle molybdenum boride was formed which crumbled eventually in use. Graphite was also used, but it is so porous that it did not protect the quartz. Thermodynamic estimates indicate that beryllia reactors might be stable to boron triiodide, but these were not tried.

The product contained considerable quantities of unreacted iodine which was stripped off in preliminary distillations in a 30-plate Pyrex distillation column. Material remaining in the still pot was weighed as crude boron triiodide.

Table I presents data from several runs. In the series with boron batch No. 1 the yield of crude boron triiodide goes through a maximum at 900°C. We interpret the decrease in yield at 1050° to be the result of having achieved equilibrium conditions for an exothermic reaction. An identical yield was observed with another grade of boron powder at 1050°C. As the temperature increases for an exothermic reaction the equilibrium constant normally decreases. By combining these data with Brewer's (9) estimate of the free energy of formation of crystalline boron triiodide, an approximate free energy equation

$$\Delta F^\circ_T = -43{,}000 + 31\,T \text{ cal/mole of } BI_3$$

(T = °K; range 298°-1323°)

can be derived based on the reaction $B_{(c)} + 3/2\ I_{2(g)} \leftrightarrows BI_{3(g)}$, after allowing for the decrease in molecular iodine concentration due to dissociation.[2] Equilibrium constants calculated from this free energy equation indicate that our yields at 900°C could be improved upon.

Boron batch No. 3 was somewhat less reactive than batch No. 1 in the usual reactors, but astonishingly less reactive in larger reactors and graphite lined reactors. Molybdenum is quite likely acting as a catalyst even though it is one of the most inert materials toward iodine attack.

Several lots of crude boron triiodide were combined in a 2-liter Pyrex distillation flask which could be attached to a 1-in. OD Pyrex distillation column by means of a Teflon gasketed standard taper joint. The remaining parts of the column were sealed together in such a way that liquid boron triiodide was delivered through a heated tube to a receiving flask with a nitrogen blanket maintained around the connection. The column was packed with helices and had an estimated efficiency equivalent to about 30 theoretical plates. The reflux ratio was never less than 30/1. About 10-15% was taken off in the first cut which was rejected and 60-70% in the heart cut for decomposition to boron.

Purified boron triiodide was discolored by the presence of iodine which seemed to form in small amounts throughout the distillation. The still pot became very dark colored and essentially opaque during distillation. Undoubtedly it contained the B_xI_y, where $x > y$, that Schumb, Gamble, and Banus (10) described. Little, if any, of this latter compound appeared in the distillate which sublimed cleanly and completely in the experiments described below.

Decomposition of Boron Triiodide

The decomposition reaction occurs on an electrically heated wire or rod in an evacuated apparatus similar to that used for the decomposition of silicon tetraiodide (11, 12). Temperatures were read with an optical pyrometer and have not been corrected for transmission of quartz or emissivity of the boron. The temperature of the boron triiodide was adjusted to maintain estimated vapor pressures in the range 0.1-1.0 mm.

Tantalum, molybdenum, and tungsten as deposition substrates.—Previous work (2, 7) is in conflict with respect to tantalum as a satisfactorily nonreactive surface for the preparation of very pure boron. Conditions in this work differ from the work with boron tribromide or trichloride in that hydrogen was not used in the reduction. Hydrogen might influence the formation of tantalum boride indirectly, so three kinds of wires were coated with boron in order to determine their suitability for iodide boron deposition. Hairpins formed from 20 in. of 10-mil diameter wires were heated to 1000° for 1 hr in boron triiodide vapor coming from a reservoir at 0°C (vapor pressure of the order of 0.1 mm). About 17-18 mg of boron was deposited on each wire. They were sectioned, polished, and a photomicrograph of each was prepared.

In Fig. 1 two distinct layers have formed on the tantalum. The inner zone is quite well defined and is very probably a tantalum-boron alloy, but no work was done to try to identify it. Other evidence obtained later indicates that the outer, rather irregular zone is pure boron. It is so brittle that it has fractured rather badly during the sectioning. A close examination indicates the boron has a crystalline appearance.

Figure 2 is a similar photomicrograph for boron on molybdenum filaments. The alloy zone is much broader, and relatively little free boron is evident. Figure 3 shows the results obtained with tungsten. No adherent alloy zone is evident, and the nature of the material that has separated from the tungsten sur-

[2] The authors are indebted to Mr. A. C. Loonam for suggesting the correct method of calculating the free energy from the equilibrium constant at 1050°C.

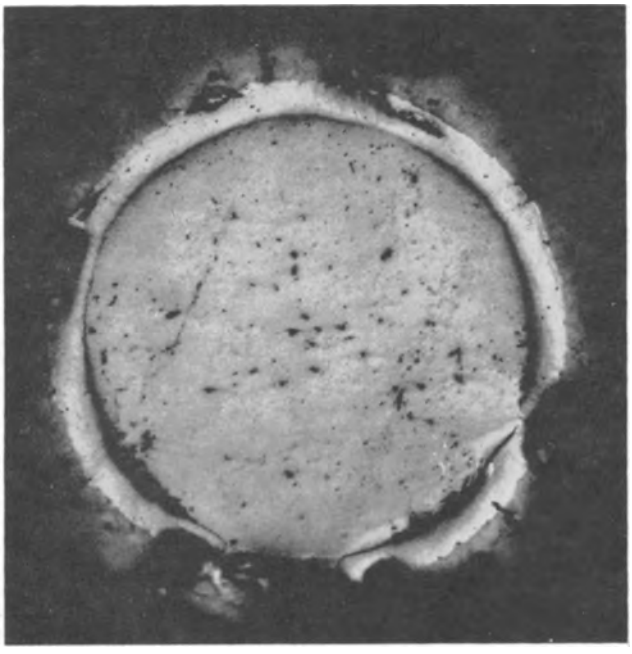

Fig. 1. Section of iodide boron deposit on 10-mil tantalum wire.

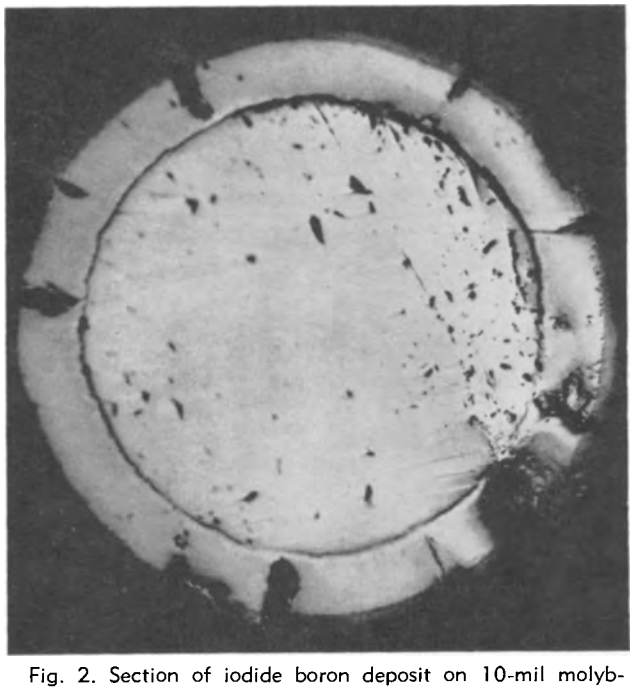

Fig. 2. Section of iodide boron deposit on 10-mil molybdenum wire.

face is unknown. Later work with tantalum at a lower temperature produced a similar flaky deposit that contained substantial amounts of tantalum. Since a densely adherent deposit was desired, the flaky type of product was unattractive.

Tantalum metal is not an ideal deposition substrate for this work, but it seems to be the best of the three refractory metals investigated. Tungsten might make a satisfactory surface at higher temperatures, but it would require further investigation.

Deposition of iodide boron on tantalum wire.— Two 4½ in. pieces of 3-mil tantalum wire were heated at 1000°C for 4½ hr in the vapor from boron triiodide kept at room temperature. The wire grew

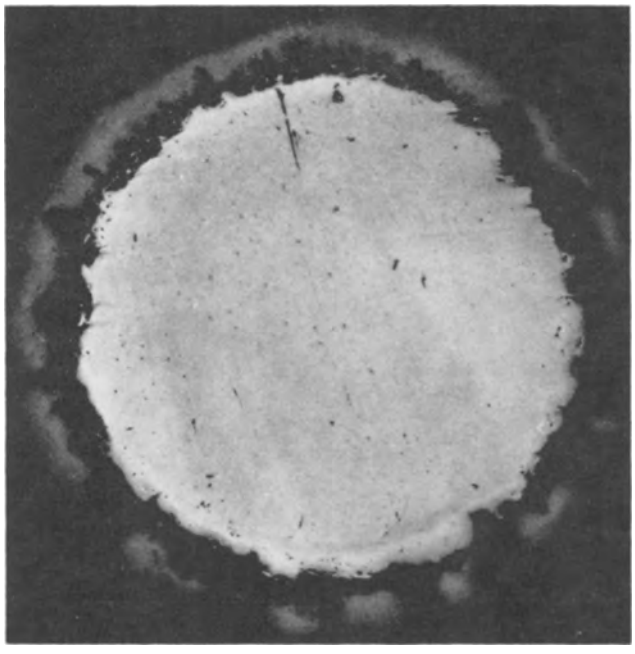

Fig. 3. Section of iodide boron deposit on 10-mil tungsten wire.

to approximately 70 mils in diameter when it broke revealing a cluster of red crystals surrounding the tantalum wire which were clearly visible to the unaided eye. In this same sample Horn (19) found a wedge-shaped band of orange-colored boron in a fractured portion of the rod which started as a narrow band at the tantalum core and expanded as it grew out to the surface. Neither the orange-colored band nor the red crystals were evident from the external appearance.

Deposition of iodide boron on tantalum rods.— Boron was deposited from boron triiodide on ⅛-in. x 36-in. tantalum rods in the form of a hairpin at the three temperatures shown in Table II. The deposit at 800°C was black, or nearly so, and very flaky. It peeled off the rod throughout the run and fell into the boron triiodide reservoir. X-ray powder photographs disclosed the presence of two components in this material: a low temperature crystal form of boron (13, 14), and considerable amounts of a tantalum boride. X-ray emission analysis of this sample confirmed the presence of approximately 78% tantalum, which was unexpected. The original purpose in preparing this sample was to compare its x-ray powder pattern with the 900°C sample which

Table II. Thermal decomposition of boron triiodide (tantalum rods)

Temp,* °C	BI_3 temp, °C	Time, hr	Wt of deposit, g	Yield, %
800	0-~25	73½	10.3	Not determined**
900	20	23	11	43
1000	~25	16	56.6†	78
1000	~25	48.3		

* Uncorrected temperature read with an optical pyrometer.
** Boron did not adhere well to the tantalum in this run and kept peeling and falling off.
† Combined weight of deposit.

Fig. 4. Fragment of iodide boron made at 900°C

Fig. 5. Fragment of iodide boron made at 900°C

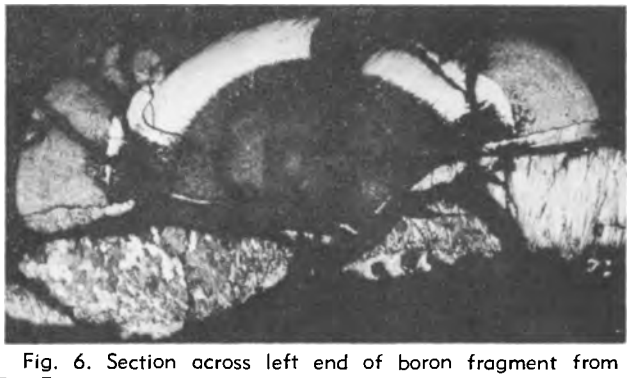

Fig. 6. Section across left end of boron fragment from Fig. 5.

was actually prepared first. There was no difference in the powder pattern from the boron, but the 900°C sample had only a very small amount of tantalum boride in it.

The boron sample prepared at 900°C adhered to the rod well during deposition and exhibited several features not seen at higher or lower temperatures. Two kinds of very regular growths about 0.060 in. in diameter developed on the surface of the boron during the run which are shown in Fig. 4 and 5. The two kinds of growth are probably related, but those shown in Fig. 4 have not been investigated for their structure. The central portion of the kind shown in Fig. 5 appeared to be a dark-colored glassy phase when viewed from above. A fracture in the boron deposit across one of the spots permitted examination of a cross section of the growth. The most dramatic feature revealed was that the glassy layer was clear red by transmitted light.

This particular sample was mounted by the Metallography Section of the G.E. Research Laboratory, polished, and photographed as shown in Fig. 6. The boron is so brittle that it has fractured during the polishing operation, but enough of the structure remains so that the chief features are easily discerned. The glassy layer referred to previously is the well-defined curved portion near the top about 4 mils in width.

The major portion of the exterior of the boron deposited at 900°C had a dull, matte-like texture with a brownish, slightly purple cast to it which contrasted sharply with the more metallic, crystalline appearance of the hemispherical growths of Fig. 4 and deposits made at higher temperatures.

The sample was subjected to several kinds of analysis after removing it from the tantalum rod by wrapping it in a polyethylene sheet and flexing gently. The analytical results are: carbon, 0.007 $\pm 0.002\%$;[3] tantalum, 0.03%; iodine, present by x-ray emission analysis; nickel, trace by x-ray emission analysis, but not detected by spectrographic emission analysis, $<0.01\%$. The tantalum was estimated from an uncalibrated x-ray emission analysis.

The sample of boron deposited on the tantalum rod at 1000°C warped the hairpin so badly that it moved close to the quartz wall of the deposition chamber and would have touched it if the experiment had continued. The experiment was interrupted to reposition the tantalum rod and then continued. The boron was removed from the tantalum by wrapping in aluminum foil and flexing in order to eliminate polyethylene as a source of carbon contamination. The carbon content of this sample was determined as $0.003 \pm 0.002\%$.

X-ray powder photographs of the 1000° sample showed some differences in line intensities compared to the 900°C sample, but the characteristic phase seemed to be the low temperature form of boron. Horn (19) found that the solid seemed to consist of several phases when examined under a microscope. By leaching with warm concentrated nitric acid he recovered red sandy, red glassy, and red microcrystalline material. Clear red crystals about 0.25 mm long were collected from this product. When examined by x-ray emission the red crystals showed about 0.04 wt % of iodine, but no other impurities of atomic number 13 or larger in concentration greater than 0.001% (the limit of detection for the amount of sample available). The density was measured as 2.459_6 at 22.6°C which is considerably greater than the density of the high temperature rhombohedral form obtained from melted boron, 2.33 at 22.6°C (13).

X-ray powder patterns of the various types of colored crystals present showed no significant differences (19), but there are very large differences in the electrical resistivities (15). The red colored crystals of the low-temperature rhombohedral form of boron apparently have impurities occupying very shallow levels near the band edge which contrasts with the deeper levels found in boron made at higher temperatures. The black portions of the deposits of low-temperature rhombohedral boron are probably more impure than the clear red crystals.

Kasper and Decker determined the crystal structure (14) of the red boron which is composed of units of nearly regular icosahedra in a slightly deformed cubic close-packing. The space group is $R\bar{3}m$ with $a_o = 5.07$Å and $\alpha = 58°1'$. The theoretical density calculated from the dimensions of this structure agrees very well with Horn's experimental values.

[3] Carbon analyses performed by a combustion-conductimetric technique fluxed with iron in a commercially available apparatus.

Discussion

The marked amount of tantalum contamination observed in the 800° deposition (cf. Table II) contrasts sharply with the experience of Laubengayer, Hurd, Newkirk, and Hoard in their work on the hydrogen reduction of boron tribromide (2). The formation of tantalum boride at 800°C in the present work may involve the formation of a tantalum iodide compound that is unstable at higher temperatures, while the corresponding tantalum bromide may simply never form because of the reducing action of hydrogen.

On the other hand, the small amount of contamination experienced in the 900° and 1000°C deposits on tantalum contrasts just as markedly with the experience of Stern and Lynds [cf. Table II, ref. (7)], who observed considerable diffusion of tantalum into boron at 975°-1025°C. Greater temperature gradients in the latter work could have increased the rate of diffusion in the solid phases, and, logically, at least comparable amounts of tantalum should have been found in Stern and Lynds' 1200°-1250°C sample, but it is not reported. It is difficult to reconcile the various observations on the basis of a physical mechanism such as simple diffusion. The chemistry of the various phases that can form at the tantalum surface may depend very strongly on the particular halide used and the presence or absence of hydrogen.

Among the elements not covered by our analytical techniques, the most probable contaminants are nitrogen and oxygen. Nitrogen should not be a problem during the deposition of the boron in an evacuated system. Richter (16) has shown that evaporated boron films will react with nitrogen of the air, however, to form crystalline boron nitride. It would not be surprising to find a surface film of nitrogen on most boron samples.

Oxygen is more of a problem because of the difficulty of removing water vapor completely from a quartz vessel. The reactor and boron triiodide container was prepared for use by flaming it with an air-gas mixture while it was being flushed with dry nitrogen with a dew point of less than −50°C. Boron triiodide vapor would be expected to react with most of the residual water vapor at or near the walls of the vessel. The work of Kaiser, Keck, and Lange (17) on the quantity of oxygen dissolved in floating zone purified silicon, suggests that iodide boron may contain less than 0.001% oxygen.

The band gap in the high-temperature rhombohedral boron formed from the melt is about 1.6 ev (18), and this kind of boron should be transparent to visible light in the far red end of the visible spectrum when pure enough. The "low-temperature" form of boron obtained as clear red crystals in this work may have a band gap as high as 2 ev (15), which could be the chief reason for the red transparency. It is true that high purity may be necessary too, but the purity requirements are, perhaps, not as stringent as for the "high-temperature" form in order to insure red transparency.

The red crystals observed within the deposit on the 3-mil tantalum wire were clustered around the wire core in such a way that the presence of the tantalum may have influenced the nature of the deposit. From the analysis of the red crystals of another deposit it seems clear that no significant amount of tantalum is necessarily present in the crystals. There remains the possibility that tantalum may be acting as a "getter" for impurities and thus promoting the growth of a red phase locally. Again, the presence of tantalum is not a necessary condition for the red glassy phase was observed in the center of the "bull's eyes" which grew on the exterior of the deposit as shown in Fig. 5.

The question of why the various kinds of growth and different colors occur in these deposits is a fascinating subject for speculation. The color of the crystals is very likely related to the impurity content. Apparently only one crystalline phase is involved, yet there must be subtle differences in the way the crystals grow in order to cause the segregation observed.

Acknowledgment

The authors are indebted to F. H. Horn for his interest and work on the properties of "red" boron. J. S. Kasper and Mrs. B. F. Decker performed most of the x-ray crystallographic work. A. E. Newkirk has been interested in the morphology of boron deposits for many years. His advice and encouragement were extremely valuable.

Manuscript received June 12, 1959.

Any discussion of this paper will appear in a Discussion Section to be published in the December 1960 JOURNAL.

REFERENCES

1. A. W. Laubengayer, A. E. Newkirk, and R. L. Brandaur, *J. Chem. Ed.*, **19**, 382 (1942).
2. A. W. Laubengayer, D. T. Hurd, A. E. Newkirk, and J. L. Hoard, *J. Am. Chem. Soc.*, **65**, 1924 (1943).
3. J. S. Spevack, U.S. Pat. No. 2,685,501 (1954).
4. Heinz Hoag, U.S. Pat. No. 2,794,708 (1957).
5. N. F. Murphy, R. S. Tinsley, and G. F. Meenaghan, *Bull. Va. Polytech. Inst.*, **50**, Eng. Expt. Sta. Ser. No. 115, **4**, 18 pp. (1957).
6. G. H. Fetterly, U.S. Pat. No. 2,542,916 (1951).
7. D. R. Stern and L. Lynds, *This Journal*, **105**, 676 (1958).
8. H. Moissan, *Compt. rend.*, **112**, 717 (1891).
9. "Chemistry and Metallurgy of Miscellaneous Materials: Thermodynamics," National Nuclear Energy Series IV-19B, Laurence L. Quill, Editor, McGraw-Hill Book Co. (1950). Cf. paper 6 by L. Brewer, L. A. Bromley, P. W. Gilles, and N. L. Lofgren.
10. W. C. Schumb, E. L. Gamble and M. D. Banus, *J. Am. Chem. Soc.*, **71**, 3225 (1949).
11. F. B. Litton and H. C. Andersen, *This Journal*, **101**, 287 (1954).
12. L. V. McCarty, *ibid.*, **106**, 1036 (1959).
13. L. V. McCarty, J. S. Kasper, F. H. Horn, B. F. Decker, and A. E. Newkirk, *J. Am. Chem. Soc.*, **80**, 2592 (1958).
14. B. F. Decker and J. S. Kasper, *Acta Cryst.*, **12**, 503 (1959).
15. F. H. Horn, *J. Appl. Physics*, **30**, 1611 (1959).
16. H. Richter, *Physik Z.*, **44**, 406 (1943).
17. W. Kaiser, P. H. Keck, and C. F. Lange, *Phys. Rev.*, **101**, 1264 (1956).
18. W. C. Shaw, D. E. Hudson, and G. C. Danielson, *Phys. Rev.*, **107**, 419 (1957).
19. F. H. Horn, Private communication.

Electrolytic Reduction of Thorium Oxide

L. H. Meyer

Savannah River Laboratory, E. I. du Pont de Nemours & Company, Aiken, South Carolina

ABSTRACT

Thorium metal was prepared by electrolytic reduction of thorium oxide in two systems, a fused KF-ThF_4 mixture and a fused NaCl-KCl-$ThCl_4$ mixture. The average decomposition potential measured in both systems was 1.92 v. Electrolysis in the fluoride melt proved to be a superior process, the metal product having higher purity and larger average particle size than the product from the chloride melt. In addition, the recovery of thorium from recycle streams proved to be much simpler in the fluoride process than in the chloride process. The feasibility was demonstrated for all the essential steps of a complete process for production of the metal in the fluoride system.

A satisfactory method for production of thorium metal requires (*a*) a simple preparation of feed material, (*b*) a successful reduction of the thorium feed compound to thorium metal, and (c) an efficient recovery of the metal after reduction. A simple recycle of nonrecoverable metal fines and other thorium-containing materials is also frequently desirable. Existing techniques utilize electrolytic or metallothermic reduction of a thorium halide as a means of producing the metal. However, preparation of an anhydrous thorium halide suitable for feed to a continuous reduction process is at best a difficult operation. Production of thorium metal through reduction of its oxide offers the advantage of eliminating the halogenation step and substituting for it the relatively simple preparation of thorium oxide.

This investigation was undertaken to determine the feasibility of a process based on electrolytic reduction of thorium oxide. This technique, which is closely analogous to the Hall process for producing aluminum, was suggested as a possible method for thorium production in a 1931 patent by Driggs (1). Electrolytic rather than metallothermic reduction of the oxide was selected because the former lends itself more readily to continuous operation and because other attempts (2) at the latter have resulted in a product with an average particle size of only 7-8 μ. Previous work (3) indicated that electrolytic reduction should produce a metal having larger particle size and lower impurity content.

The results of this experimental study form the basis for a proposed process for producing thorium metal by electrolytic reduction of its oxide. All steps essential to continuous operation have been demonstrated.

Experimental

Apparatus.—Electrolysis cells.—The cells, which also served as the anodes during electrolysis, were CS-312 graphite crucibles, 18 in. high and 5 in. in diameter with 0.5-in. walls. They were obtained from the National Carbon Company. During operation, the cell was inserted into a stainless steel sleeve to prevent loss of the melt in event of cell rupture.

Housing.—The cell was contained in a dry box provided with equipment to handle the internal manipulations. During operation the box atmosphere could be maintained at 99+% helium.

Instrumentation.—The instrumentation was standard. The Pt-Pt, 10% Rh thermocouple was housed in a stainless steel well which was immersed in the melt.

Materials.—Potassium thorium fluoride.—The compound $KThF_5$ was prepared by the method of Driggs and Lilliendahl (4). The anhydrous double salt precipitated upon adding an excess of aqueous potassium fluoride to aqueous thorium nitrate. The precipitation of Th^{+4} from the solution was virtually complete, the filtrate analyzing $<6\times10^{-6}$M Th^{+4}.

Thorium chloride.—The anhydrous NaCl-KCl-$ThCl_4$ mixture was obtained from Horizons, Inc., Cleveland, Ohio.

Thorium oxide.—Fisher Scientific Co. C. P. thorium oxide was used in all runs.

Cathode metals.—Six-millimeter molybdenum rod was used as cathode material in most of the electrolyses. The molybdenum and the tantalum were obtained from the Fansteel Metallurgical Corporation, North Chicago, Illinois. Titanium was obtained from Rem-Cru Titanium, Inc., Midland, Pennsylvania; and the thorium used for cathodes was obtained from the Atomic Energy Commission.

Procedures.—Electrolysis.—Prior to each electrolysis, the cell was filled with salt plus the desired quantity of oxide. The cathodes were hung on racks, and all electrical connections were made. The front window then was put in place, and the helium purge and heating were started simultaneously. Two to three hours were required to reach operating temperature.

After thermal equilibrium at the desired temperature had been attained, the cathode was immersed in the melt and electrolysis started immediately. At the conclusion of the electrolysis, the cathode was withdrawn slowly to allow maximum drainage of the molten salt. The cathode with its metallic deposit was hung on a rack to cool. A second cathode then

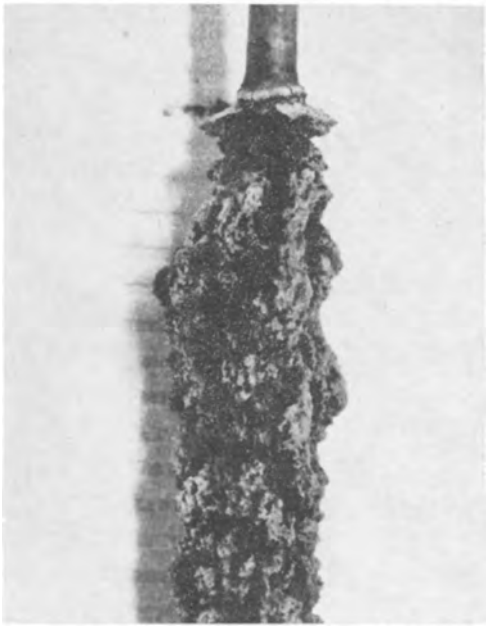

Fig. 1. Typical cathode deposit obtained by electrolysis of ThO_2 in a KF-ThF_4 melt.

could be immersed and the process could be repeated. A helium atmosphere was maintained throughout the cooling period to prevent oxidation of the deposited metal. Figure 1 is a photograph of a typical cathode deposit.

Metal recovery.—Fluoride system.—The metal produced by electrolysis in the fluoride system was recovered by stripping the deposit from the cathode, crushing, screening, and leaching. After the deposit was crushed, 20 to 40% passed a 200-mesh screen. This fraction, containing from 5 to 14% of the metal, was not processed further. The +200 mesh fraction was leached for 10 to 20 min in boiling aqueous aluminum nitrate (~1M). A white or gray near-colloidal dispersion formed in the supernatant liquor during the leaching operation. This dispersion, which consisted of finely divided thorium oxide and thorium metal, could be coagulated and precipitated by centrifugation. After the leaching operation, the metal was visibly free of salt, as shown in Fig. 2.

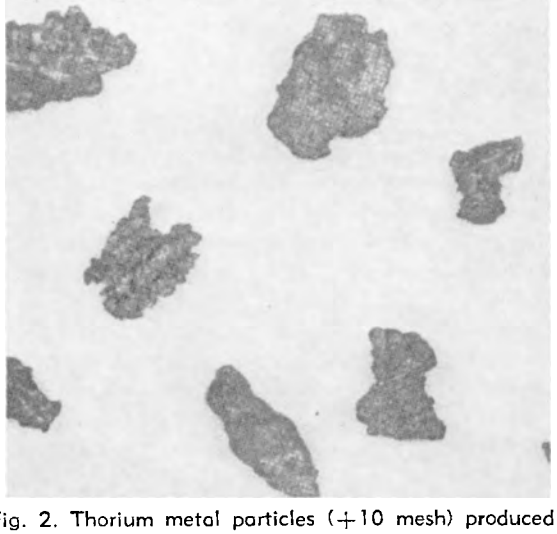

Fig. 2. Thorium metal particles (+10 mesh) produced by electrolysis of ThO_2 in a KF-ThF_4 melt, following leach with hot aqueous aluminum nitrate.

Table I. Anode gas analyses during electrolysis of ThO_2 in a KF-ThF_4 melt*

Constituent	Before start	8 min after start	18 min after start	3 min after conclusion	16 min after conclusion
He	95.4	70.0	72.1	94.1	96.6
CO	1.77	22.2	25.8	4.62	2.33
CO_2	0.17	7.02	1.23	0.10	0
N_2	0.15	Trace	Trace	Trace	Trace
O_2	0.03	0	0	0	0
H_2	2.45	0.69	0.88	1.10	1.10
F-containing gas	0	0	0	0	0

* All figures given in mole per cent.

Table II. Anode gas analyses during electrolysis of ThO_2 in a NaCl-KCl-$ThCl_4$ melt*

Constituent	Before start	5 min after start	20 min after start	Immediately after conclusion	10 min after conclusion
He	98.4	71.6	73.2	93.8	98.0
CO	0	5.33	6.96	2.53	0.15
CO_2	0.10	20.4	17.8	1.78	0.24
N_2	0.10	0.41	0.51	0.22	0.09
O_2	0	0.05	0	0	0
H_2	1.35	2.10	1.55	1.64	1.56
Cl-containing gas	0	0	0	0	0

* All figures given in mole per cent.

Metal recovery.—Chloride system.—The recovery scheme following electrolysis in the chloride melt differed from that for the fluoride system. The procedure consisted of stripping the deposit from the cathode, crushing, and leaching with water. Screening yielded no effective separation of metal from salt due to the very small average particle size of the metal. Leaching was accomplished easily, since the chloride salts of the melt are all highly soluble in water.

Cathode pretreatment.—During the course of the experimentation, it was found that pretreating the cathode decreased the porosity and improved the adherence of the metallic deposit. This pretreatment consisted of sanding to roughen the surface, degreasing with trichloroethylene vapor, and pickling for 3-5 min with an agent suitable for the cathode material. Following the pickling, the cathodes were washed in distilled water and dried in air.

Results and Discussion

Electrolysis of thorium oxide.—The composition of the anode gas evolved during electrolysis in both the fused fluoride and the fused chloride systems established thorium oxide as the compound undergoing decomposition. The oxygen resulting from decomposition of the oxide was liberated at the graphite anodes as carbon dioxide and carbon monoxide. The large increase in the oxide content of the gas surrounding the anode during electrolysis is evident from the analyses listed in Tables I and II. The anode gas contained no fluorine or chlorine compounds. The presence of such compounds would have been observed had the halides been decomposed during the electrolysis.

Decomposition potential.—The decomposition potential of thorium oxide in both systems was determined

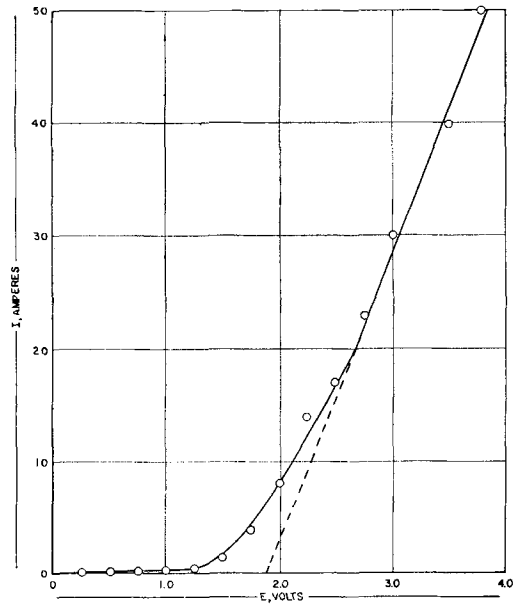

Fig. 3. Current-voltage curve for electrolysis of ThO_2 in o KF-ThF_4 melt.

in the conventional manner from current-voltage graphs. A typical plot is shown in Fig. 3. A variation from 1.67 to 2.15 v was found over fourteen independent determinations in the fused fluoride system, yielding a value of 1.92 ±0.11 v. Ten determinations in the fused chloride system gave a value of 1.92 ±0.27 v.

Solubility of thorium oxide.—The solubility of thorium oxide in a KF-ThF_4 melt, 70% ThF_4 by weight, was found to be approximately 1%. No reliable result was obtained for the solubility of thorium oxide in the NaCl-KCl-$ThCl_4$ melt.

Leaching agents.—A solvent was required for the constituents of each of the melts in order to leach the occluded salt from the metal. No problem was encountered in the chloride system, since all the salts in the melt are water soluble. Thorium fluoride and its double salts with potassium fluoride are insoluble in water but dissolve satisfactorily in boiling aqueous aluminum nitrate.

Product purity.—The product was identified as thorium metal by x-ray diffraction. Determination of the HCl-insoluble content yielded the amount of dissolved or occluded thorium oxide, which averaged 0.63% in the product from the fluoride process, but ran as high as 12.2% in the product from the chloride process. One complete spectroscopic analysis of the metal produced by electrolysis in the fluoride melt (Run 3D) is listed below:

600 ppm Al	35 ppm Mg
9 ppm B	40 ppm Mn
90 ppm Ca	300 ppm Ni
<0.5 ppm Cd	400 ppm Si
700 ppm Cr	<1 ppm U
250 ppm Cu	80 ppm Zn
1000 ppm Fe	<50 ppm Zr

Remainder Th

The source of impurities was assumed to be the fluoride salt.

Operating and performance data.—*Fused fluoride system.*—Table III lists the operating and performance data for seventeen electrolyses carried out in the fused fluoride system. Runs with a common numeral were made in the same salt bath. The recovery efficiency listed in the table is the per cent recovery of the metal theoretically deposited by the passage of the given charge, assuming a quadrivalent thorium ion in the molten salt solution. The HCl-insoluble content indicates the quantity of oxide dissolved in the metal.

Examination of the data reveals that the first electrolysis with each salt bath resulted in poor yields. This effect is ascribable to impurities in the salt, the presence of which decreases the mean particle size

Table III. Operating and performance data for the electrolyses of ThO_2 in a KF-ThF_4 melt

Run	Cathode material	Cathode pretreatment	Temperature, °C	Current density amp/dm²	Recovery efficiency, %	Wt. fraction of recovered metal*	Wt. % recovered metal +40 mesh	Wt. % deposit −200 mesh	Wt. % metal in −200 mesh deposit	Per cent HCl-insolubles
1A	Mo	None	990	160	2.5	0.025	0	—	—	—
1B	Mo	None	1000	280	9.6	0.221	38.7	—	—	2.30
1C	Mo	None	980	56	14.7	0.228	16.7	—	—	—
1D	Mo	None	950	63	8.2	0.276	69.0	—	—	1.10
1E	Mo	None	940	103	24.6	0.583	95.0	—	—	0.43
1F	Mo	None	960	280	10.3	0.210	63.4	—	—	0.14
2A	Mo	None	1000	193	0	—	—	—	—	—
2B	Mo	None	1000	380	18.5	0.182	32.4	—	—	0.44
2C	Mo	None	990	380	21.5	0.473	69.0	34.3	6.9	0.94
3A	Mo	8M HNO_3	950	174	12.0	—	1.5	—	18.8	2.70
3B	Mo	8M HNO_3	965	104	7.8	0.478	63.5	39.2	—	0.32
3C	Mo	8M HNO_3	970	35	19.1	0.596	65.1	27.2	—	0.26
3D	Mo	8M HNO_3	980	174	41.0	0.679	91.4	18.8	—	0.10
3E	Mo	8M HNO_3	1010	182	25.8	0.400	74.1	31.4	20.7	0.23
3F	Th	6M HCl	1000	53	8.2	0.129	2.0	66.7	21.8	0.21
3G	Ti	6M HCl	1000	136	10.2	0.084	0	80.6	39.0	2.60
3H	Ta	8M HNO_3	1000	167	12.3	0.058	0	88.0	40.0	0.25

* $\frac{\text{Weight of recovered metal}}{\text{Total weight of deposit}}$ (includes occluded salt and oxide)

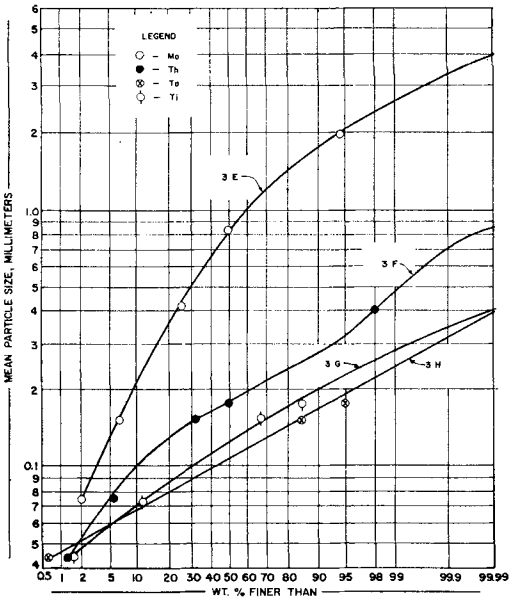

Fig. 4. Particle-size distribution for electrolyses with varied cathode material.

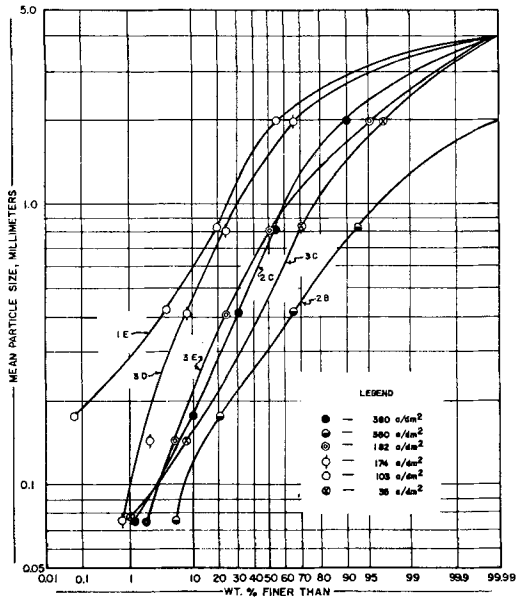

Fig. 5. Particle-size distribution for electrolyses at varied current densities.

(5) and consequently the recovery efficiency. The first electrolysis with each bath apparently served as a scavenging run, after which performance improved.

From the data in Table III the superiority of molybdenum as a cathode material over the other metals tested is apparent. If the results of the scavenging runs are discounted, the recovery efficiency, based on a quadrivalent thorium cation, for the electrolyses with molybdenum cathodes varied from 8.2 to 41.0%, averaging 18.3%.[1] The ratio of the weight of the recovered metal to the total weight of the deposit (including occluded salt and ThO_2) averaged 39.3%, with a total variation from 18.2 to 67.9%. An average of 61.7% of the recovered metal exceeded 40 mesh in size, and the amount of metal fines in the −200 mesh fraction ranged from only 2 to 7% of the total weight of the deposit. The HCl-insoluble content varied from 0.10 to 2.30%, averaging 0.63%. Performance with thorium, titanium, and tantalum cathodes was much less satisfactory. In particular, the particle size distribution of the product was less favorable than with the molybdenum cathodes, since much larger fractions of the thorium metal were produced as irrecoverable fines with the other three cathode materials tested. Figure 4 illustrates the differences in particle size distributions for the four cathode materials.

Current density was varied from 35 to 380 amp/dm² for the electrolyses listed in Table III. No good correlation was observed, however, between current density and any of the performance criteria. Figure 5 shows the particle size distributions for electrolyses run at different current densities.

Beginning with Run 3A, the cathodes were given a pretreatment with a pickling agent in an attempt to improve the adherence of the deposit. Improvement was not pronounced; however, the metal particles plated on pickled electrodes had a firmer structure, which facilitated separation of the metal from the salt.

Operating and performance data.—Fused chloride system.—Fourteen electrolyses were performed in the chloride system. Recovery efficiency, based on Th^{+4} in solution, varied from 13.9 to 55.0%, averaging 27.2%. The ratio of the weight of recovered metal to the total weight of the deposit averaged 22.5%, ranging from 10.9 to 43.3%. The HCl-insoluble content was high, 1.92 to 12.2%. The particle size distribution was considerably less favorable than that resulting from the electrolyses in the fluoride system. In only one of the fourteen runs did any of the metal particles exceed 80 mesh in size. Virtually all the product was −100 mesh, with sizable fractions in the 10 to 50 μ range.

Comparison of Processes in the Fluoride and Chloride System

The experimental results indicate that the production of thorium metal by electrolysis of thorium oxide in the fused fluoride system is superior to the analogous process in the chloride system. The chloride melt has a lower fusion temperature (~800°C) than the fluoride system (~1000°C), plus a high water solubility of the bath constituents, which facilitates the leaching operation. However, these advantages are inadequate to compensate for the lower purity and smaller particle size of the product. Moreover, there is no simple technique for recycling the occluded chloride salts that are removed with the cathode deposit. Unless methods can be found for depositing larger metal particles from the chloride melt, electrolysis of thorium oxide in this system does not appear to be competitive with the fluoride process.

Flowsheet for Proposed Process

Figure 6 is the proposed flowsheet of the complete process for the production of thorium metal in the fused fluoride system. A brief discussion of each of the steps is presented below.

[1] A sizable loss resulted from lack of proper equipment to strip the tightly adhering thorium deposit efficiently from the cathodes.

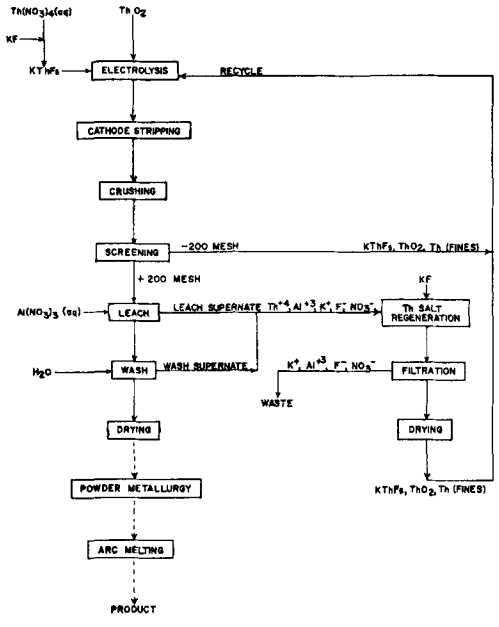

Fig. 6. Proposed flowsheet for production of thorium metal in fused fluoride system.

Electrolysis.—Electrolysis is performed in graphite-lined cast iron cells. The liners, serving as anodes, are replaced as they are consumed. An inert atmosphere chamber must be provided for removal and cooling of the cathodes following electrolysis.

Cathode stripping.—Conventional techniques and equipment are available for stripping the deposit from the cathodes.

Crushing and screening.—The gross physical separation of metal from salt is based on the fact that the salt crystals are reduced in size easily by crushing, while the metal particles are not. It is proposed that the metal in the +200 mesh (U. S. Standard Series) fraction, which contains 80 to 95% metal by weight, be leached, while the −200 mesh fraction which averages only 15% metal be recycled.

Leaching.—The salt not removed by the physical separation can be dissolved in hot aqueous aluminum nitrate. Boiling 10 to 20 min in 1M aluminum nitrate gives satisfactory removal of salt.

Metal processing.—After the leaching operation, the metal is separated from the supernatant liquor by decantation. The metal then is washed with water and air dried. The drying step is followed by a powder metallurgical forming of electrodes for subsequent arc melting.

Recycle (−200 mesh screening fraction).—The composition of this fraction averages 15% thorium metal, 0.4% thorium oxide, and the remainder salt. Two alternatives are available for treatment of these fines. An oxygen roast converts the metal to thorium oxide, after which this fraction can be returned to the electrolysis cells; or the −200 mesh fraction may be recycled directly to the cells, and a periodic oxygen sparge may be employed to re-oxidize the thorium metal. The latter alternative is favored, since an oxygen sparge is probably necessary to re-oxidize the nonadhering metal product, which collects at the bottom of the cells during electrolysis. Any such treatment with oxygen requires careful control to prevent excessive attack on the graphite liners.

Recycle (leach and wash supernatant liquors).—The leach and wash supernatant liquors contain thorium in the form of soluble Th^{+4} ion plus dispersed oxide and metal fines. The dissolved thorium can be recovered by adding KF in quantity sufficient to precipitate all the thorium as $KThF_5$. Some care must be observed in order not to precipitate any of the potassium aluminum fluorides. Control is not too critical, however, since less than 80% of the KF required for incipient precipitation from a blank 1M aluminum nitrate solution precipitates essentially all of the Th^{+4} from a 1M aluminum nitrate solution saturated with $KThF_5$. A well-agitated precipitation should succeed in coagulating and carrying down the dispersed particles as well. Following filtration, the precipitate is dried and recycled to the electrolysis cells.

Waste.—The only waste stream in the process is the filtrate from the $KThF_5$ regeneration step. Thorium concentration in this stream is less than 10^{-5}M.

Manuscript received May 25, 1959. The information contained in this article was developed during the course of work under contract AT(07-2)-1 with the U.S. Atomic Energy Commission.

Any discussion of this paper will appear in a Discussion Section to be published in the December 1960 JOURNAL.

REFERENCES

1. F. H. Driggs, U. S. Pat. 1,815,054 (1931).
2. B. Kopelman, International Conference on the Peaceful Uses of Atomic Energy, Paper No. 531 (1955).
3. W. C. Lilliendahl, "Rare Metals Handbook," C. F. Hampel, Editor, pp. 429-454, Reinhold Publishing Corp., New York (1954).
4. F. H. Driggs and W. C. Lilliendahl, *Ind. Eng. Chem.*, **22**, 1302 (1930).
5. C. C. Ma, *ibid.*, **44**, 342 (1952).

Mass Transfer at the Streaming (Jet) Mercury Electrode

Theoretical Calculation of Limiting Currents

Kameo Asada, Fumio Hine, Shiro Yoshizawa, and Shinzo Okada

Department of Industrial Chemistry, Faculty of Engineering, Kyoto University, Kyoto, Japan

ABSTRACT

Mass transfer at the streaming or jet mercury electrode has been studied theoretically. Momentum equations for both the mercury jet and the surrounding solution layer have been solved simultaneously on the assumption of laminar flow in both mercury jet and surrounding solution envelope. Limiting currents were measured for the reduction of Tl^+, Pb^{++}, and Zn^{++} at 25°C with 0.1M KCl as supporting electrolyte. Experimental results are in good agreement with predictions based on theoretical analysis.

The streaming or jet mercury electrode has been studied and used in various forms of polarography (1-12). Its application to routine analytical purposes is restricted by the large amount of mercury consumed, the high charging currents, and the inconvenience in reproducing stream geometry. On the other hand, the streaming electrode, if used along with the dropping electrode, appears promising in studies of kinetic currents (6, 7) and irreversible electrode processes (12). Furthermore, the rapid renewal of the mercury surface makes it useful in studies of the mercury-solution interface (2, 4, 8, 11). Toshima and Mizuno (13) successfully applied a mercury stream to the production of caustic soda from crude brine.

It is of interest to know how the mercury jet drags the solution around it and how the rate of mass transfer of the ions (limiting current) is related to the conditions of operation, such as flow rate of mercury, length of jet, etc. Ríus, *et al.* (8) obtained an expression for the limiting current based on the assumption that the radius of the mercury jet is constant, the curvature negligible, and the velocity of the jet and of the adjacent solution uniform everywhere. Weaver and Parry (12) showed the invalidity of these assumptions and presented a semi-empirical equation for the limiting current, using observed values of the jet diameter, interfacial velocity, and velocity gradient. The present paper gives an analysis of jet characteristics by methods of fluid dynamics, which have already been applied successfully to many instances of ionic mass transfer (14-17), and describes methods for the calculation of limiting currents without the use of empirical information on jet geometry.

Stream Characteristics

Theoretical.—Although the turbulent flow of gases from nozzles (18) and the breakup of liquid streams (19) have both been considered in fluid mechanics, no theory adaptable to working conditions of the streaming mercury electrode was available. Throughout this paper it will be assumed that (*a*) the flow of the mercury within the capillary is laminar (Hagen-Poiseulle flow without slip), (*b*) the mercury jet, after leaving the capillary, and the solution boundary layer formed around it are cylindrical and undergo laminar flow, and (c) there is no slip between the mercury jet and the solution boundary layer. The cylindrical coordinates are chosen as shown in Fig. 1, z being the logitudinal distance from the capillary tip and r the radial distance from the center of the jet.[1] The mercury jet and the solution flow are distinguished from each other by subscripts m and s, respectively.

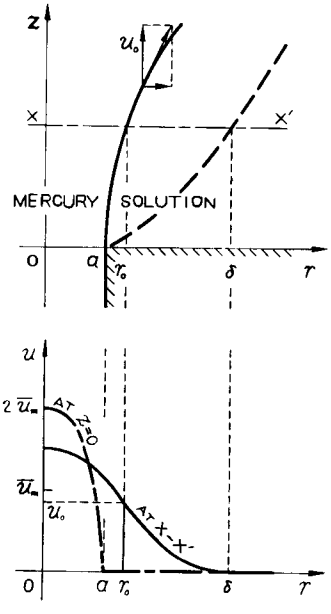

Fig. 1. Model for theoretical analysis; coordinates and velocity profiles.

As a rigorous simultaneous solution of the Navier-Stokes equations and the continuity equations for noncompressible fluids is very difficult, the Kármán momentum equation method (20, 21) is applied, a boundary layer of definite thickness being assumed. In order to simplify the mathematical model, parabolic velocity profiles are assumed, that is, the ve-

[1] A glossary of symbols is given at the end of this paper.

locity components in the z direction, u_m and u_s, are expressed by

$$\left.\begin{aligned} u_m/u_o &= 1 + [(\mu_s/\mu_m)r_o/(\delta - r_o)][1 - (r/r_o)^2] \\ u_s/u_o &= [(\delta - r)/(\delta - r_o)]^2 \end{aligned}\right\} \quad [1]$$

which satisfies the following conditions

$$\left.\begin{aligned} &\text{at } r = 0,\ \partial u_m/\partial r = 0 \\ &\text{at } r = r_o,\ u_m = u_s \equiv u_o \text{ and} \\ &\quad \mu_m \cdot \partial u_m/\partial r = \mu_s \cdot \partial u_s/\partial r \\ &\text{at } r = \delta,\ u_s = \partial u_s/\partial r = 0 \end{aligned}\right\} \quad [2]$$

In the above μ is the dynamic viscosity, r_o the radius of the mercury stream, δ the thickness of the boundary layer measured from the center of the stream ($r = 0$), and u_o the interface velocity component in the z direction. The last three quantities are unknown parameters dependent on z alone and are determined by the momentum equations

$$\left.\begin{aligned} &-d[\rho_m \textstyle\int_0^{r_o} u_m^2\, r\, dr]/dz + g(\rho_m - \rho_s)r_o^2/2 \\ &= -\mu_m r_o(\partial u_m/\partial r)_{r=r_o} = -\mu_s r_o(\partial u_s/\partial r)_{r=r_o} \\ &= d[\rho_s \textstyle\int_{r_o}^{\delta} u_s^2\, r\, dr]/dz \end{aligned}\right\} \quad [3]$$

and by the equation of conservation of mass for the mercury stream

$$d[\textstyle\int_0^{r_o} u_m r\, dr]/dz = 0 \quad [4]$$

ρ being the density and g the acceleration due to gravity (g is negative when the stream flows upward).[2] In Eq. [3] the bracketed terms are equivalent to the momenta of the mercury jet and of the solution envelope. The third and fourth terms correspond to the shearing stresses per unit length. Hence Eq. [3] implies that the momentum of the moving mercury jet, after ejection from the capillary, is consumed by work against gravitational force (or *vice versa*) or is transferred to the surrounding solution through the shearing stress at the interface. The second equality in Eq. [3] means absence of slippage at the interface [assumption (*c*)] and so perfect momentum transfer. It follows from assumption (*a*) that the boundary conditions in the z coordinate are

$$\text{at } z = 0,\ u_m/\bar{u}_m = 2[1 - (r/a)^2] \text{ and } u_s = 0 \quad [5]$$

where u_m is the mean velocity of the mercury jet and a the inner radius of the capillary.

Equation [1] is introduced into Eqs. [3] and [4], which then are integrated with respect to r and Eq. [5] is taken into consideration. One obtains

$$\left.\begin{aligned} &dM_s/dz' = 3(u_o/\bar{u}_m)\mu'\phi/(1 - \phi) \\ &M_m + M_s = 1 + g' \textstyle\int_0^{z'} (r_o/a)^2\, dz' \\ &(r_o/a)^2(u_o/\bar{u}_m)[2 + \mu'\phi/(1 - \phi)] = 2 \end{aligned}\right\} \quad [6]$$

where

$$\left.\begin{aligned} &z' = \nu_m z/a^2\bar{u}_m,\ \mu' = \mu_s/\mu_m,\ \rho' = \rho_s/\rho_m,\ \phi = r_o/\delta \\ &M_m = \tfrac{1}{4}(r_o/a)^2(u_o/\bar{u}_m)^2 \cdot \\ &\quad [3 + 3\mu'\phi/(1 - \phi) + (\mu')^2\phi^2/(1 - \phi)^2] \\ &M_s = (\rho'/20)(r_o/a)^2(u_o/\bar{u}_m)^2 \cdot \\ &\quad (1 - \phi)(1 + 5\phi)/\phi^2 \\ &g' = \tfrac{3}{4}(1 - \rho')\, ga^2/\nu_m\bar{u}_m \end{aligned}\right\} \quad [7]$$

ν being the kinematic viscosity ($=\mu/\rho$). The quantities M_m and M_s are the momenta of the mercury jet and of the solution envelope, respectively, expressed as fractions of the initial momentum of the mercury on ejection from the capillary.

The ratios r_o/a and $u_o/\bar{u}_m$ may be eliminated from Eq. [6] if the gravity term of the second expression is left in the integral form. When the effect of gravity is assumed negligible ($g' = 0$), one has an ordinary differential equation with separable variables, whose numerical integral is available (22) if values of μ' and ρ' are specified. Calculations including the gravity term may be carried out by means of successive approximations.

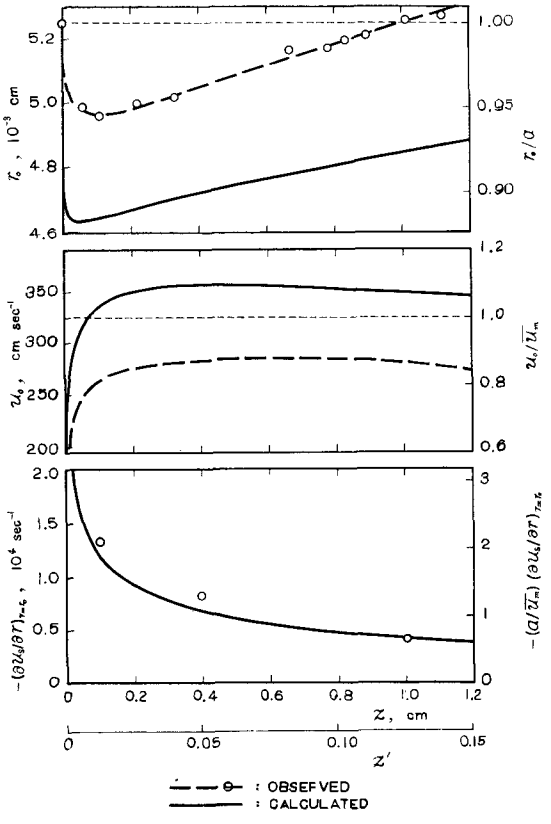

Fig. 2. Mercury jet diameter, interface velocity, and interface velocity gradient, from top to bottom; comparison between calculated and observed results for an upward mercury jet with $a = 0.0052_5$ cm and $\bar{u}_m = 325$ cm sec^{-1}. (Although the dashed curve in the middle figure is not for u_o but for the interface velocity, there is no appreciable difference except near the base of the stream.)

Results and Discussion

The above analysis was applied to some practical systems, and the results were discussed in comparison with experimental findings of Weaver and Parry (12). These authors obtained the jet diameter photographically, the interface velocity by measurements of charging currents, and the interface velocity gradient at the solution side by adding aluminum dust therein. Theoretical results for the foregoing three quantities for a 0.1M KCl solution at 25°C[3]

[2] Equations [3] and [4] may be obtained by integration of the Navier-Stokes equations and the equations of continuity.

[3] The following values were adopted for the physical properties of this system: $\mu_s = 0.008298$ g cm^{-1} sec^{-1}, $\mu_m = 0.01527$ g cm^{-1} sec^{-1}, $\rho_s = 1.0018$ g cm^{-3}, and $\rho_m = 13.534$ g cm^{-3} (from International Critical Tables and Landolt-Börnstein Tabellen).

Table I. Comparison of observed and calculated results of $(r_o/a)^2(u_o/\bar{u}_m)$

z'	Observed	Calculated	Deviation, % calc.—obs.
0.01	0.72	0.779	+9
0.02	0.75	0.837	+12
0.04	0.79	0.875	+11
0.06	0.82	0.894	+9
0.1	0.85	0.914	+7
0.15	0.87	0.927	+6
0.2	—	0.935	—

(the gravity term is neglected) are shown in Fig. 2 together with the experimental values of Weaver and Parry.

Qualitative agreement is good and supports the model described by Eqs. [3]-[5]. The initial increase of u_o is simply a result of acceleration of the outer slow layers of the mercury jet by the inner fast ones through viscous shear. This means that the velocity distribution within the jet becomes more and more uniform; hence the mercury jet should tend to contract in order to conserve its mass velocity, so far as its momentum remains unchanged. But, since momentum transfer from the mercury jet to the solution envelope occurs gradually, the jet slows down and its diameter enlarges because, in the extreme example of infinitesimal momentum, an infinitely wide stream alone can sustain definite mass velocity.

Quantitative failure in the values of r_o and u_o arises in part from the parabolic velocity distribution approximation (Eq. [1]).[4] Since momentum is being transferred at the interface, the deceleration of the mercury jet due to drag of the solution moves from the interface into the interior; thus the velocity distribution profile should have an inflection point. Attempts to improve the velocity distribution function through introduction of higher terms (definite in number) led to a discontinuity in Eq. [5]. However, the momentum equation method is not designed to give individual values for r_o and u_o but is designed to yield products such as $r_o^2u_o$ and $r_o^2u_o^2$. Since the rate of reversible reduction (mass transfer) of ions at the streaming mercury electrode depends chiefly on the former product (12) and since the theoretical values of this product are in reasonable agreement with the experimental (Table I), this failure does not preclude an application of the analysis to problems of mass transfer (and thus to electrochemical measurements).

Although gravitational force was considered as a variable in the original analysis, its effect on an actual situation is negligible. For example, consideration of the gravity term raises r_o by 0.3% and reduces u_o by 0.6% at $z' = 0.14$ in the case of Fig. 2.

Limiting Current

Theoretical.—Limiting currents were evaluated by the following four methods:

1. The approximate solution of the problem by Ríus and his coauthors [(8) see also (16)]

$$I = 4n\mathbf{F}C_o a(\pi D\bar{u}_m l)^{\frac{1}{2}} \qquad [8]$$

[4] Although the experimental values are not specified as to temperature, minute change in physical properties does not account for such a large deviation.

where I is the limiting current, n the number of Faradays per mole or gram-ion reacting, **F** the Faraday, C_o the bulk concentration of the reactive species in moles per cubic centimeter, D its diffusion coefficient, and l the effective length of the jet or streaming mercury electrode.

2. Introduction of the jet characteristics observed by Weaver and Parry (dashed curves on Fig. 2) into their rigorous equation (12)

$$I = \pi n\mathbf{F}DC_o\left\{2\int_0^l r_o^2u_o[\pi D\int_o^z r_o^2u_o dz]^{-\frac{1}{2}}dz + l + \tfrac{1}{2}\int_o^l (r_o/u_o)(\partial u_s/\partial r)_{r=r_o}\,dz + \ldots\right\}^{-\frac{1}{2}} \qquad [9]$$

3. Introduction of the calculated characteristics (solid curves on Fig. 2) into Eq. [9],

4. Solution of the equation of mass transfer with an approximate method similar to that applied to the stream, as shown in the following.

A profile of the concentration C of the reactive species

$$C/C_o = 1 - [(\delta' - r)/(\delta' - r_o)]^2 \qquad [10]$$

is adopted, where δ' is the thickness of the diffusion layer in the same sense as $\delta(\delta' < \delta)$. If Eq. [1] and [10] are put into

$$d[\int_{r_o}^{\delta'} u_s(C - C_o)r\,dr]/dz = -Dr_o(\partial C/\partial r)_{r=r_o} \qquad [11]$$

one obtains (the gravity term on Eq. [6] is neglected)

$$\frac{60\psi}{\sigma(1-\psi)} = \frac{d}{dz'}\cdot\left\{\frac{(1-\psi)}{[2(1-\phi)+\mu'\phi](1-\phi)\psi^4}\cdot [5\psi^2(1+3\psi) - 4\phi\psi(1+3\psi+6\psi^2) + \phi^2(1+3\psi+10\psi^3)]\right\} \qquad [12]$$

where $\sigma = \nu_m/D$ and $\psi = r_o/\delta'$. Equation [12] can be solved numerically (22), and limiting currents are calculated through

$$I = n\mathbf{F}D\int_o^l 2\pi r_o(\partial C/\partial r)_{r=r_o}\,dz \qquad [13a]$$

or

$$I' = I\nu_m/4\pi n\mathbf{F}DC_o a^2\bar{u}_m = \int_o^{l'} \psi(1-\psi)^{-1}\,dz' \qquad [13b]$$

where $l' = \nu_m l/a^2\bar{u}_m$.

The dimensionless group I' in Eq. [13] corresponds to a Nusselt number divided by the Reynolds number of the mercury stream within the capillary. The mass transfer correlation is expressed as a relationship among the dimensionless parameters I', l', σ, μ', ρ', and g', the last three being of minor influence. It is not easy to measure a and $\bar{u}_m$ separately, but they appear both in I' and l' as the product $a^2\bar{u}_m$, which may be replaced by the mass velocity

$$\bar{m} = \pi\rho_m a^2\bar{u}_m \qquad [14]$$

Experimental, Results and Discussion

Valenta (9) reported that the limiting current was proportional to the square root of $\bar{m}l$ in accordance with Eq. [8], while Weaver and Parry (12) demonstrated that this proportionality required some correction with their equation, Eq. [9] above.

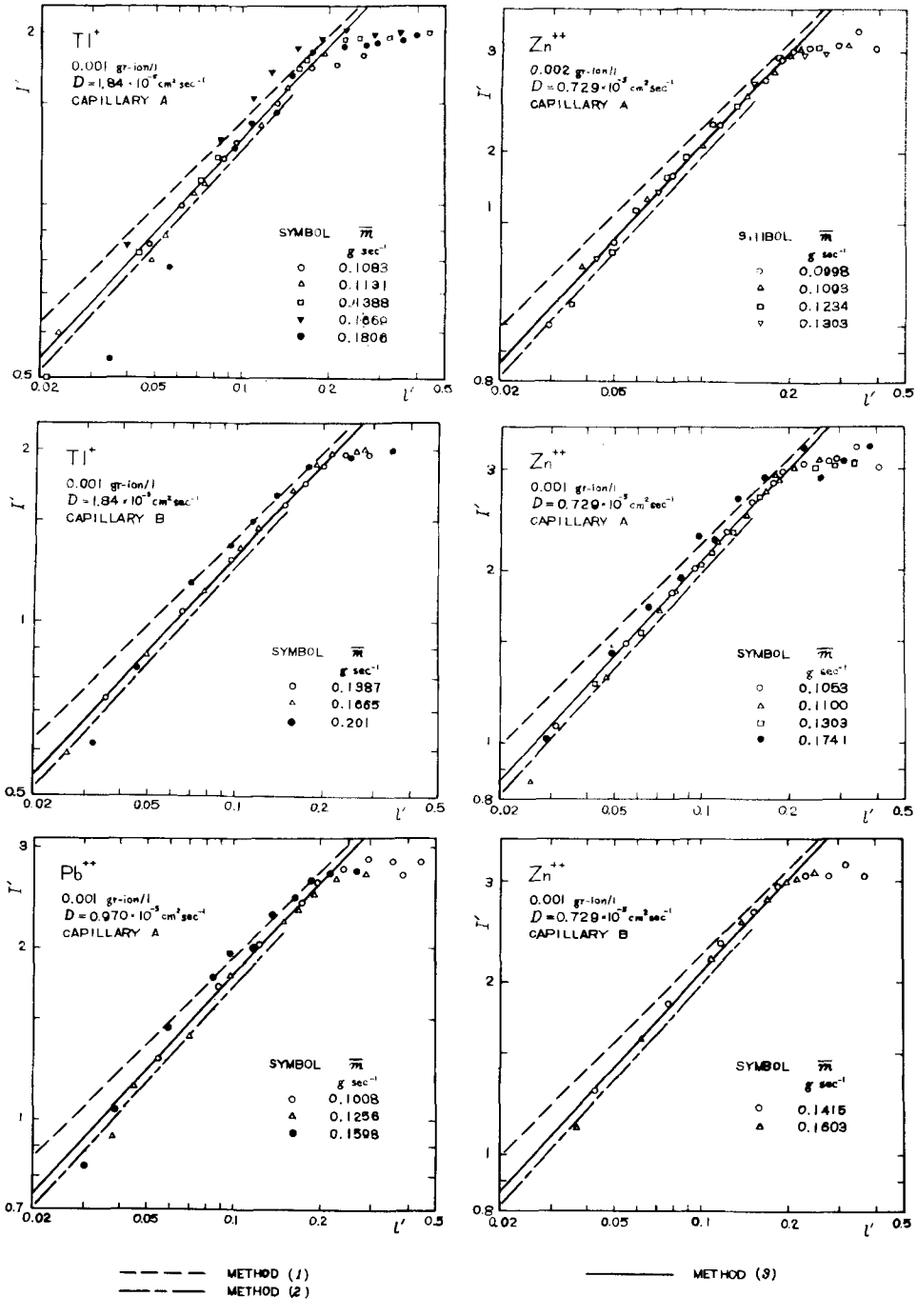

Fig. 3. Mass transfer correlation. Open symbols refer to laminar mercury streaming; solid symbols, to turbulent.

As neither of these data was specified as to temperature, measurements were made with an apparatus essentially similar to that used by Bieber and Trümpler (5), mounted in a bath controlled at 25°C. The solutions studied were 0.1M in KCl and 0.001 or 0.002M in TlCl, $PbCl_2$, or $ZnCl_2$. These systems were chosen since diffusion coefficients of the tracer ions of the reactive species are known: 10^5D (cm^2 sec^{-1}) = 1.84 (Tl^+), 0.970 (Pb^{++}), 0.729 (Zn^{++}) in 0.1M KCl (23). The limiting current I was measured at different values of the mass velocity $\overline{m}$ and the electrode length l, and the results are summarized in Fig. 3 in a dimensionless correlation between I' and l'.

In measuring I, a polarographic apparatus was not employed because anodic polarization and ohmic drop were large. Since charging currents are relatively high at streaming mercury electrodes (7), it was necessary to evaluate them separately. This was achieved by making measurements on solutions with and without the reactive species present.

The mercury mass velocity $\overline{m}$ is dependent both on the characteristics of the capillary and on the mercury head. Two capillaries designated A and B were used; although the mercury flow rate for B was almost twice as large as that for A under the same pressure head, no differences between A and B appear in Fig. 3. $\overline{m}$ was measured by weighing the ejected mercury, and results were plotted against the pressure head in order to check linearity between them or to confirm assumption (*a*). If this assumption is valid, assumption (*b*) is expected to be true, for the path of the mercury stream is rather short. On Fig. 3. open symbols refer to runs within the limit of laminar flow, while solid symbols refer to runs in

which $\overline{m}$ was larger and the mercury stream was turbulent. In the latter case the data were scattered.

The length l (more precisely speaking, the length of the upward mercury jet between the capillary tip and the solution level) was varied from 0.05 through 2.5 cm and measured by use of a cathetometer. When l was very small, polarization curves had discontinuities due to disappearance of charging currents. According to Valenta (9) it is caused by slippage at the interface, and so has a close connection with assumption (c) (accordingly, with Eq. [3]). Slippage at the mercury solution interface is dependent on surface tension; application of surface active agents has been supposed necessary to prevent it, in connection with polarographic maxima (24) and the rotated dropping mercury electrode (25). Although no surface active agent was added in the present study, the discontinuity was observed rather rarely, and besides the experimental results in Fig. 2 show clearly the drag of the solution; hence, slippage would not invalidate the theory. But rather low results for runs for $l' < 0.05$ may be due to this slippage (9). Although slipping was no serious problem, another trouble appeared. The solution coned up around the mercury stream above the solution level (9, 12) and some correction (reduction) was required for observed limiting currents. When l was too large or $\overline{m}$ too small, the limiting current increased no more because of decay and breakup of the stream. The critical value of l' was found to be around 0.2 at −1.4 v vs. S.C.E.

Within these restrictions (turbulence, and upper and lower limits of l'), the observed values ranged themselves on a single correlation for a species, justifying the choice of the dimensionless groups.

The limiting current was calculated by the four methods listed in the theoretical part and represented on Fig. 3 and Table II (method 4 was applied only to reduction of thallous ions). Equation [8] by Ríus and his coauthors (method 1) gives values which are too high. Methods 3 and 4, based on theoretical stream characteristics, gave results within about 2% of each other, suggesting that the approximations used are of fairly high reliability. Methods 2 and 3 give curves which, although nearly parallel, deviate from each other by about 6%. The experimental data follow well curves for these two methods. But no correction for coning of the solution was applied to the measured I values. The fractional correction should vary with the electrode length (larger as l' becomes smaller). It is not easy to obtain the magnitude of the "tail-cone correction," but Weaver and Parry estimated it at about 5-7% for $l' = 0.126$ in 0.1M KCl solution. In conclusion, the present theory of the stream characteristics allows prediction of limiting currents with an accuracy of a few per cent at worst.

Table II. Comparison of methods for calculating l' (reduction of Tl^+, $D = 1.84 \times 10^{-5}$ cm² sec⁻¹)

l'	Method 1	Method 2	Method 3	Method 4
0.01	0.442	0.35	0.367	0.373
0.02	0.625	0.51	0.541	0.552
0.04	0.884	0.75	0.793	0.810
0.06	1.082	0.94	0.989	1.009
0.1	1.397	1.24	1.310	1.333
0.15	1.711	1.55	1.623	1.649
0.2	1.976	—	1.893	1.921

Acknowledgment

The authors are grateful to Dr. T. Sato of Kyoto University for his kind advice on fluid dynamics. Their thanks also go to Dr. R. W. Parry of the University of Michigan, who reviewed and offered a number of helpful suggestions in the preparation of the manuscript.

Manuscript received Sept. 17, 1958. This paper was abstracted from the dissertation of one of the authors (K.A.), Kyoto University, 1958. The theoretical part of the paper was presented before the Polarographic Discussion Meeting, Tokyo, Nov. 20 and 21, 1956.

Any discussion of this paper will appear in a Discussion Section to be published in the December 1960 JOURNAL.

REFERENCES

1. J. Heyrovsky and J. Forejt, *Z. phys. Chem.*, **193**, 77 (1943).
2. J. Heyrovsky, F. Sorm, and J. Forejt, *Coll. Czech. Chem. Comm.*, **12**, 11 (1947).
3. J. Heyrovsky, *Faraday Soc. Discussions*, **1**, 212 (1947).
4. J. Heyrovsky and M. Matyás, *Coll. Czech. Chem. Comm.*, **16**, 455 (1951).
5. R. Bieber and G. Trümpler, *Helv. chim. Acta*, **30**, 971 (1951).
6. J. Koryta and I. Kossler, *Coll. Czech. Chem. Comm.*, **15**, 241 (1950).
7. J. Koryta, *ibid.*, **19**, 433 (1954); **20**, 1125 (1955).
8. A. Rius, *et al.*, *Chem. Abstr.*, **41**, 4725g (1947); **44**, 5233i, 8267a (1950); **45**, 50a, 7454g,h (1951); **46**, 10963e (1952); **47**, 11037h (1953); **48**, 6289g (1954).
9. P. Valenta, *Coll. Czech. Chem. Comm.*, **16**, 239 (1951).
10. P. Léveque, *J. chim. phys.*, **49**, 269 (1952).
11. J. W. Loveland and P. J. Elving, *J. Phys. Chem.*, **56**, 250 (1952).
12. J. R. Weaver and R. W. Parry, *J. Am. Chem. Soc.*, **76**, 6258 (1954); **78**, 5542 (1956).
13. S. Mizuno and S. Toshima, *J. Electrochem. Soc., Japan*, **27**, 391 (1959).
14. J. N. Agar, *Faraday Soc. Discussions*, **1**, 26 (1947).
15. C. W. Tobias, M. Eisenberg, and C. R. Wilke, *This Journal*, **99**, 359C (1952).
16. P. Delahay, "New Instrumental Methods in Electrochemistry," Chap. 9, Interscience Publishing Co., New York (1954).
17. S. Yoshizawa, *J. Electrochem. Soc., Japan*, **25**, 584 (1957).
18. W. Forstall and A. H. Shapiro, *J. Appl. Mech.*, **17**, 399 (1950).
19. R. M. Christiansen and A. N. Hixon, *Ind. Eng. Chem.*, **49**, 1017 (1957).
20. S. Goldstein, Editor, "Modern Developments in Fluid Dynamics," Clarendon Press, Oxford (1938).
21. E. R. G. Eckert, "Introduction to Transfer of Heat and Mass," McGraw-Hill Book Co., New York (1950).
22. K. Hidaka, "Suchi-sekibun-ho (Numerical Integration)," vol. I, Iwanami Book Co., Tokyo (1936).
23. J. H. Wang, *J. Am. Chem. Soc.*, **76**, 1528, 1584 (1954).
24. B. Levich, *Faraday Soc. Discussions*, **1**, 37 (1947).
25. Y. Okinaka and I. M. Kolthoff, *J. Am. Chem. Soc.*, **79**, 3326 (1957).

GLOSSARY OF SYMBOLS

a — radius of capillary (cm)
C — concentration of reactive species (moles/cm³)
C_o — bulk concentration of reactive species (moles/cm³)
D — diffusion coefficient of reactive species (cm²/sec)
$\mathbf{F}$ — the Faraday (amp sec/eq)
g — acceleration of gravity (cm/sec²)
g' — modified Froude number, defined by Eq. [7] (dimensionless)
I — limiting current (amp)
I' — reduced limiting current, defined by Eq. [13] (dimensionless)
l — electrode length (cm)
l' — reduced electrode length, defined by Eq. [13] (dimensionless)
$\overline{m}$ — mass velocity of mercury stream (g/sec)
M — fractional momentum, relative to that possessed by the mercury jet on ejection from capillary (dimensionless)
n — number of Faradays per mole or gram-ion (eq/mole)
r — radial distance (cm)
r_o — radius of mercury jet (cm)
u — velocity component in the z-direction (cm/sec)
u_o — interface velocity component in the z-direction (cm/sec)
$\bar{u}_m$ — mean velocity of mercury jet (cm/sec)
z — distance in the direction of streaming (cm)
z' — $= \nu_m z/a^2\bar{u}_m$ (dimensionless)
δ — thickness of boundary layer (cm)
δ' — thickness of diffusion layer (cm)
μ — dynamic viscosity (g/cm-sec)
μ' — $= \mu_s/\mu_m$ (dimensionless)
ν — kinematic viscosity ($= \mu/\rho$) (cm²/sec)
σ — $= \nu_m/D$ (dimensionless)
ρ — density (g/cm³)
ρ' — $= \rho_s/\rho_m$ (dimensionless)
ϕ — $= r_o/\delta$ (dimensionless)
ψ — $= r_o/\delta'$ (dimensionless)
$_m$ — mercury (jet)
$_s$ — solution (flow)

On the Parabolic Rate Law

W. B. Jepson

Department of Chemistry, University of Exeter, Exeter, England

ABSTRACT

The parabolic rate constant k_p is reformulated in terms of the defect concentration at one interface only by introducing the free energy change of the oxidation reaction ΔG. The pressure dependence of k_p then follows naturally, and k_p is shown to have an exponential dependence on ΔG.

Of the various rate laws which have been found to describe the oxidation kinetics of metals, the parabolic relation

$$X^2 = k_p t \qquad [1]$$

connecting the thickness of the layer of reaction product X with the time of oxidation t is probably the most familiar and widely applicable. The relation between the parabolic rate constant k_p and the mobility of the moving particles has attracted considerable interest, and there have been a number of derivations (1-5).

The purpose of this paper is to re-formulate k_p in terms of the defect concentration at one interface only.

We consider a metal whose rate of oxidation is controlled by the rate of diffusion of metal ions across the oxide layer; the attacking gas is oxygen and any simultaneous anionic diffusion is assumed to be negligible. The derivation by Mott (4, 5) of k_p is easily extended to give, for an n-type oxide, the result:

$$k_p = AD_i[n_i(\mathrm{O}) - n_i(\mathrm{X})]$$
$$\mathrm{A} = 2(z+1)\Omega \qquad [2]$$

for an interstitial ion of valence z where D_i is the diffusion coefficient of the interstitial ion, Ω is the volume of oxide per metal ion, and $n_i(\mathrm{O})$ and $n_i(\mathrm{X})$ are the concentrations of interstitial metal ions at the metal/oxide and gas/oxide interface, respectively. In deriving Eq. [2], the following assumptions are made: (*a*) the regions of space charge at the two interfaces can be neglected (4); (*b*) the problem can be treated as one of steady-state diffusion through a slab of constant thickness (6, 7); and (*c*) the dissolved metal atoms are fully dissociated into ions and quasi-free electrons which in turn form an ideal-dilute solution in the oxide; to the same approximation the concentration gradient of interstitial ions across the oxide layer is linear.

Now the defect concentrations at the two interfaces are determined by the equilibria:

$$2\mathrm{M} = 2\mathrm{M}_o^{z+} + 2ze \qquad [3]$$

$$\frac{z}{2}\mathrm{O}_2 + 2\mathrm{M}_o^{z+} + 2ze = \mathrm{M}_2\mathrm{O}_z \qquad [4]$$

at the metal/oxide and gas/oxide interfaces, respectively, the symbol M_o^{z+} denotes a metal ion occupying an interstitial position. It is easy to show that

$$2\ln n_i(\mathrm{X})n_e^z(\mathrm{X}) - 2\ln n_i(\mathrm{O})n_e^z(\mathrm{O}) = \Delta G/RT \qquad [5]$$

where $n_e(\mathrm{O})$ and $n_e(\mathrm{X})$ are the concentrations of quasi-free electrons at the metal/oxide and gas/oxide interfaces, respectively, and ΔG is the free energy change per mole of the oxidation reaction

$$2\mathrm{M} + \frac{z}{2}\mathrm{O}_2 = \mathrm{M}_2\mathrm{O}_z \qquad [6]$$

at temperature T and an oxygen pressure of p atm. By assumption (a), $n_e = zn_i$ so that, after simplifying Eq. [5] and inserting in Eq. [2], we obtain:

$$k_p = AD_i n_i(O)\left[1 - \exp\left\{\frac{\Delta G}{2(1+z)RT}\right\}\right] \quad [7]$$

which shows the dependence of k_p on the driving force of the reaction.

Since $n_i(O)$ is determined by the equilibrium represented in Eq. [3], the only pressure dependent term in Eq. [7] is ΔG,

$$\Delta G = \Delta G_o - \frac{z}{2} RT \ln p \quad [8]$$

where ΔG_o is the standard free energy change per mole of the oxidation reaction. Hence

$$k_p = AD_i n_i(O)[1 - \alpha p^{-s}] \quad [9]$$

where

$$\alpha = \exp \frac{\Delta G_o}{2(1+z)RT}$$

$$s = \frac{z}{4(1+z)} \quad [10]$$

If the metal ions are diffusing between vacant cation sites then, making the same approximations as before, the result is

$$k_p = AD_v n_v(X)\ [1 - \alpha p^{-s}] \quad [11]$$

where D_v is the diffusion coefficient of the vacancy (of valence z) and α and s are as defined in Eq. [10]; $n_v(X)$ the concentration of vacant cation sites at the gas/oxide interface is determined by the equilibrium:

$$2M^{z+} + 2ze + \frac{z}{2} O_2 = M_2O_z + 2M^{z+}\square + 2ze\square \quad [12]$$

where $M^{z+}\square$ and $e\square$ denote a vacant cation site and a positive hole, respectively. Equation [12] is sometimes formulated with the oxygen in the adsorbed state (12). By Eq. [12],

$$n_v(X) = n_v^{\circ} p^s \quad [13]$$

where n_v° is the concentration of vacant cation sites in equilibrium with an oxygen pressure of one atmosphere. Equations [11] and [13] give

$$k_p = AD_v n_v^{\circ} p^s (1 - \alpha p^{-s}) \quad [14]$$

The relations in Eq. [9] and [14] are of course equivalent to the alternative formulation (8) in terms of the partial pressures of oxygen at the metal/oxide and gas/oxide interfaces, but in the author's opinion they have two advantages: the dependence of k_p on the driving force of the reaction ΔG is clearly brought out (cf. Eq. [7]) and both the pressure dependence of k_p for an n-type oxide and what may be termed the additional pressure dependence for a p-type oxide follow naturally from Eq. [8]. Thus if $\alpha << p^s$, k_p will either be independent of pressure [n-type oxide] or will vary according to p^s [p-type oxide].[1] Values of α are given in Table I for some metal oxidation reactions which satisfy the parabolic rate law and whose pressure dependence has been examined. For the first three examples it is clear that the term αp^{-s} is negligible except at very low pressures: taking nickel oxidation as an example, the term αp^{-s} is only 0.076 with $p = 10^{-3}$ atm. For copper oxidation on the other hand, $\alpha = 0.163$ and k_p is not proportional to p^s (with $p = 10^{-2}$ atm., $\alpha p^{-s} = 0.290$); the procedure adopted by Baur, Bridges, and Fassell (12) of plotting log k_p against log p to determine s as an experimental quantity is therefore incorrect. It would also appear that the generalized rate expression for pressure sensitive oxidation reactions, developed by the same authors, should be modified to include the term in αp^{-s}.

Finally, it is of interest to note that if ΔG is sufficiently small for the exponential term in Eq. [7] to be written

$$\exp\left\{\frac{\Delta G}{2(1+z)RT}\right\} = 1 + \frac{\Delta G}{2(1+z)RT}$$

the parabolic rate constant becomes

$$k_p = A \frac{D_i n_i(O)}{2(1+z)RT} (-\Delta G)$$

so that k_p is now proportional to the driving force of the reaction or alternatively to the electromotive force of the equivalent electrical cell, a result equivalent to that derived by Hoar and Price (3) for a film substance of constant specific conductivity.

Manuscript received July 13, 1959.

Any discussion of this paper will appear in a Discussion Section to be published in the December 1960 JOURNAL.

REFERENCES

1. C. Wagner, *Z. phys. Chem.*, **21B**, 25 (1933).
2. W. Jost, "Diffusion in Solids, Liquids and Gases," p. 383, Academic Press Inc., New York (1952).
3. T. P. Hoar and L. E. Price, *Trans. Faraday Soc.*, **34**, 867 (1938).

[1] The value of s found experimentally is usually different from that predicted (see Table I): for copper oxidation, the discrepancy has been attributed to the fact that the defects do not form an ideal-dilute solution in the oxide (8).

Table I. Values of the parameter α (11)

Oxidation reaction	Ref.	Temp, °C	α	s Predicted	s Observed
$2Ni + O_2 = 2NiO$	(8)	1000	2.4×10^{-2}	1/6	1/4
$2Co + O_2 = 2CoO$	(9)	1148	2.8×10^{-2}	1/6	1/3
$2Fe + S_2 = 2FeS$	(10)	670	1.4×10^{-2}	1/6	1/7, 1/4
$2Cu + \frac{1}{2}O_2 = Cu_2O$	(8)	1000	1.63×10^{-1}	1/8	1/7
$2Zn + O_2 = 2ZnO$	(8)	400	5.4×10^{-8}	(0)	(0)

4. N. F. Mott, *J. chim. phys.*, **44**, 172 (1947).
5. N. Cabrera and N. F. Mott, *Repts. Prog. in Phys.*, **12**, 163 (1949).
6. F. Booth, *Trans. Faraday Soc.*, **44**, 796 (1948).
7. W. J. Moore, *This Journal*, **100**, 302 (1953).
8. C. Wagner and K. Gruenewald, *Z. phys. Chem.*, **40B**, 455 (1938).
9. R. E. Carter and F. D. Richardson, *J. Metals*, Trans. AIME, 336 (1955).
10. K. Hauffe and A. Rahmel, *Z. phys. Chem.*, **199**, 152 (1952).
11. Calculated from the data listed by: O. Kubaschewski and E. LL. Evans, "Metallurgical Thermochemistry," Pergamon Press, New York (1956).
12. J. P. Baur, D. W. Bridges, and W. M. Fassell, Jr., *This Journal*, **103**, 273 (1956).

Magnetism of the Electrodeposited Films as Revealed by Electron Diffraction

S. Yamaguchi

Institute of Physical and Chemical Research, Tokyo, Japan

The path of an electron beam is deflected in a magnetic field as the result of the Lorentz effect. This phenomenon is observable in electron diffraction of a ferromagnetic substance. The magnetic induction of a ferromagnetic film was measurable from the diffraction pattern obtained from it.

Experimental

A process of double exposure was utilized in order to measure the deflection of an electron beam caused by a ferromagnetic specimen. The diffraction pattern from a nonferromagnetic substance (gold foil) was photographed beforehand, and then that of a ferromagnetic specimen was superposed on it. In this process the wave length of the electrons applied as well as the position of the photographic plate were kept fixed. Diffraction rings from these two substances were not cocentric, because the specimen had the Lorentz effect on the electrons, whereas the nonferromagnetic gold foil showed no magnetic effect on them.

Nickel Film

Nickel was deposited electrolytically on a foil of brass from an aqueous solution of nickel sulfate (1). The deposited layer of nickel was divorced from the brass foil with a dilute solution of nitric acid. The area and thickness of the nickel film prepared for the experiment were 10 x 10 mm and about 5 μ, respectively. The specimen was magnetized as illustrated in Fig. 1a. A small piece of permanent magnet (size: about 0.5 mm, coercive force: 400 Oersted) was attracted at the edge of the film. An electron beam passed through a pin hole (about 0.1 mm) found in the nickel film (see Fig. 1a). Such pin holes were formed frequently in an electrodeposited film. Figure 2a was obtained by the double exposure process with the specimen and with a nonferromagnetic gold foil. In this double diagram it is recognizable that the diffraction rings from the specimen and those from

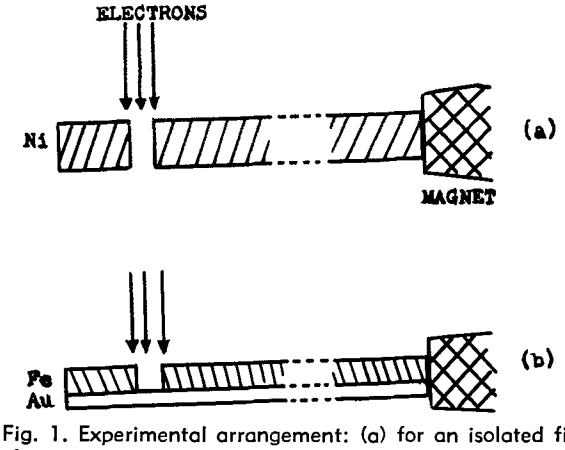

Fig. 1. Experimental arrangement: (a) for an isolated film, (b) for a composite film.

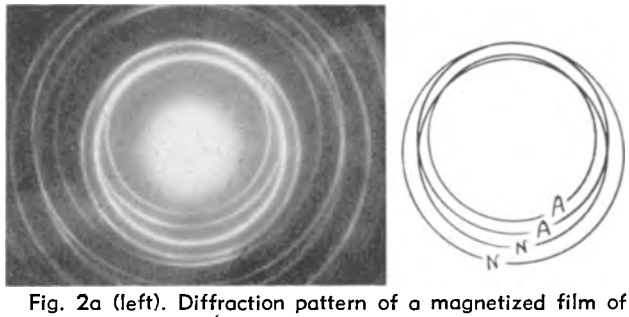

Fig. 2a (left). Diffraction pattern of a magnetized film of nickel and that of gold are superposed. The diffraction rings are eccentric as the result of the Lorentz effect. Wave length: 0.0327Å; camera length: 495 mm: Positive enlarged 2.3 times before reduction for publication. Fig. 2b (right). The main rings corresponding to Ni and to Au in (a) are indicated. N: Ni. A: Au.

the gold foil are eccentric as the result of the Lorentz effect. The main rings corresponding to the two substances are indicated in Fig. 2b (N: the nickel specimen, A: gold).

The deflection ΔZ of the incident beam caused by the magnetic specimen is measurable from the ring

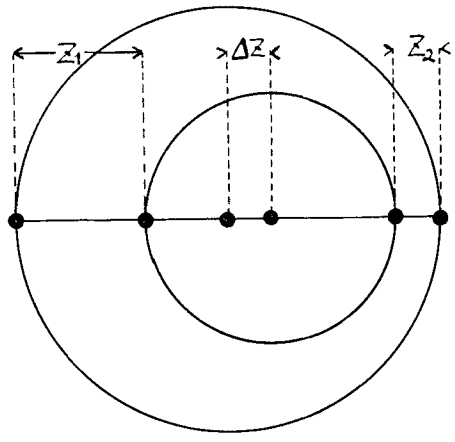

Fig. 3. Illustration for the calculation of the magnetic deflection ΔZ of the incident beam from the ring eccentricity.

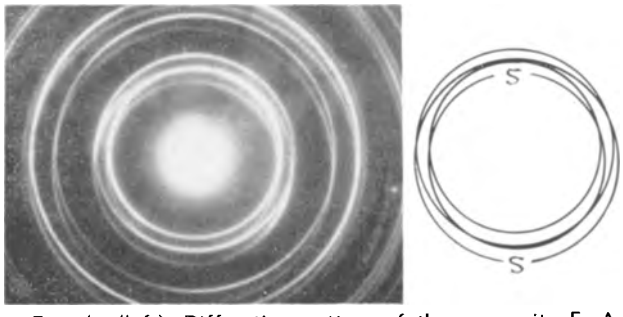

Fig. 4a (left). Diffraction pattern of the composite Fe-Au film and that of gold are superposed. Wave length: 0.0332Å. Lorentz effect. Fig. 4b (right). S shows the rings from the Fe-Au film.

eccentricity, as illustrated in Fig. 3. That is

$$\Delta Z = \frac{1}{2}(Z_1 - Z_2)$$

Under the experimental arrangement in Fig. 1 and 2 we have a relation between ΔZ and the magnetic induction B:

$$\Delta Z = \frac{eL}{mv}\int_0^l Bdl = \frac{eL\lambda}{h}\int_0^l Bdl \qquad [1]$$

where e is electron charge (1.6×10^{-20} emu), m is electron mass, v the velocity of the electrons, L the camera length (495 mm), λ the wave length of the electrons, and l the magnetic field region traversed by the electron beam. λ was determined with the diffraction rings of gold observed in Fig. 2. As seen from Fig. 1, l is approximately equal to the film thickness of the specimen (5 μ). In Fig. 2 we measure $\Delta Z = 0.142$ cm and $\lambda = 0.0327$Å. We obtain, therefore, $B \cong 7 \times 10^3$ gausses for the nickel film according to Eq. [1].

Iron Film

Iron was electrodeposited on a gold foil from an aqueous solution of ammonium ferrous sulfate. A composite Fe-Au film thus prepared, in which the thickness of the iron layer and that of the gold film were about 10^4Å and 5×10^2Å, respectively, was readily investigated by the present process (see Fig. 1b). Figure 4a is a double diagram obtained with the specimen and with a single film of gold. In Fig. 4b the main rings from the specimen are indicated with "S." In this diagram we recognize the ring eccentricity resulted from the magnetic effect. Here we measure $\Delta Z = 0.109$ cm and $\lambda = 0.0332$Å. According to Eq. [1], therefore, we obtain $B \cong 3 \times 10^4$ gausses.

Discussion

Figure 4 shows mainly the existence of the diffraction rings from gold. In this figure it is difficult to determine the rings characteristic of iron. This is because the electrodeposited layer of iron is not so crystalline as the gold film. In the present process, the magnetic state of the ferromagnetic layer is studied indirectly through the diffraction rings from the crystalline gold layer in the composite film. This method is suitable for the study of the magnetism of an amorphous film.

The magnetic inductions of the nickel and the iron film here measured (7×10^3 and 3×10^4 gausses) coincide with the known saturation inductions of these two substances (2). As seen from Eq. [1], it is possible to measure the thickness l of a film if the induction B of the film is known.

The successful result of a blank test for the present magnetic analysis was already shown with the two nonferromagnetic substances, i.e., here all diffraction rings were cocentric in a double exposure diagram (3).

It is of significance that the B-values determined in the present process are absolute, because Eq. [1] contains only the universal constants.

Manuscript received Oct. 20, 1958.

Any discussion of this paper will appear in a Discussion Section to be published in the December 1960 JOURNAL.

REFERENCES

1. Cf. A. G. Gray, "Modern Electroplating," p. 299, John Wiley & Sons, Inc., New York (1953).
2. R. M. Bozorth, "Ferromagnetism," p. 870, D. Van Nostrand Co., Princeton, New Jersey (1956).
3. S. Yamaguchi, *This Journal*, **106**, 268 (1959).

Polarography in Formamide

I. Some Transition Metal Ions, Zinc and Cadmium Ions

Glenn H. Brown and Hsiao-shu Hsiung

Department of Chemistry, University of Cincinnati, Cincinnati, Ohio

Formamide is a good solvent for a large number of inorganic salts as well as organic compounds. It has a very high dielectric constant (109.5 at 25°C) (1), a convenient liquid range (freezing point 2.5°C, boiling point 193°C), a very low vapor pressure (1 mm Hg at 70.5°C), and its solutions have a moderate electrical resistance. Formamide is very easily deoxygenated thus making it a good solvent for use in polarography. Moreover, formamide with anhydrous sodium perchlorate as a supporting electrolyte has a decomposition potential of −1.6 v vs. a saturated calomel electrode. Even though this voltage does not allow the voltage range of usefulness afforded by N-N′-dimethylformamide (2) (−2.4 v vs. a mercury pool) it is nevertheless a sufficiently high voltage to make it a useful solvent for polarography of many inorganic salts. The solvent has a high viscosity (3.359 cp at 25°C), but this is not a serious objection to its use.

Formamide is a very good solvent for a large number of different kinds of inorganic compounds; Colton and Brooker (3) have obtained solubility values for 47 salts. Although we have not made quantitative measurements of solubility for our polarographic studies, we have found that perchlorates are quite soluble in formamide. Also, the salts K_2NbF_7, K_2ZrF_6, K_2TaF_7, and K_2HfF_6 are all somewhat soluble in the solvent.

There appear to be only four papers in the literature concerned with the polarography of inorganic salts in formamide. Zan'ko and Mannsova (4) studied the polarography of cadmium sulfate, lead nitrate, tin (II) chloride, and zinc chloride. No supporting electrolyte was used in this study since the authors report that there is sufficient ammonium chloride (origin in synthesis of formamide) in the formamide to function as a supporting electrolyte. Letaw and Gropp (5) investigated the polarography of organic compounds such as acetophenone and anisaldehyde in formamide. They also obtained polarographic data on zinc sulfate, thallium (I) sulfate, and lead nitrate. Their supporting electrolyte was 0.1M KCl for the zinc and lead and 0.1M KNO_3 for thallium. Hook, Letaw, and Gropp (6) studied these same metal ions in formamide-acetamide mixtures. Their $E_{1/2}$ values in formamide are close to those for the same ions in water, and those in the mixed solvent are close to those in formamide.

Bruss and DeVries (7) in a study of the effect of solvents on the polarographic reduction of cations observed the $E_{1/2}$ values of bismuth, cadmium, chromium (III), and zinc ions against a silver-silver chloride electrode in a number of different solvents of which formamide was one. Their values for cadmium and zinc ions check with ours when one considers the different reference electrodes used. However, they did not report on $E_{1/2}$ value for Cr (II) to Cr (0), but did report an $E_{1/2}$ value for Cr (III) to Cr (II). We found the wave for the Cr (III) to Cr (II) to be ill-defined but were able to assign an approximate value of −0.9 v vs. S.C.E. to this transition which is close to the value of −0.83 v vs. Ag-AgCl electrode reported by Bruss and DeVries.

This paper deals with the polarography of some transition metal ions, zinc and cadmium in formamide. In this study we chose the hydrates of the salts of the electroreducible ions instead of anhydrous salts. Further studies of stability constants in nonaqueous solvents are now in progress using different ligands with some of the ions reported herein. When these studies are completed, data on the anhydrous salts will be discussed in light of the systems under observation.

Experimental

Materials.—The practical grade of formamide, obtained from Matheson Company, Inc., was purified by double vacuum distillation (2-3 mm Hg, bp 90°C). However, small amounts of water do not alter the decomposition potential of the solvent. It was found in this work that up to 3 ml of water in 25 ml of formamide did not change the decomposition potential of the formamide.

Anhydrous sodium perchlorate was used as the supporting electrolyte in this study. Anhydrous sodium perchlorate of "reagent" quality purchased from the G. Frederick Smith Chemical Company was used without further purification. The decomposition potential of a 0.2M solution of sodium perchlorate in formamide is −1.6 v vs. a saturated calomel electrode.

All perchlorates used in this study were "reagent" quality, obtained from the G. Frederick Smith Chemical Company and were used without further purification. These salts were dried in a current of dry air and dissolved as the hydrates. The cadmium sulfate was the "Baker Analyzed" reagent manufactured by the J. T. Baker Chemical Company. It was used without further purification.

In a few cases, maxima occurred in the polarographic wave and when these were found, they could be depressed by the use of gelatin.

Apparatus.—All polarograms were obtained using a L&N recording "Electro-Chemograph." The electromotive force recorded by the instrument was

checked with a "Queen Model" E-3040, three-range potentiometer manufactured by the Gray Instrument Co., Philadelphia, Pennsylvania. All diffusion currents were corrected for residual current, which never exceeded 1.5 μamp for any potential at which the diffusion current was measured.

The polarographic cell was constructed according to one described by Kolthoff and Coetzee (8) in order to eliminate the transference of water or potassium chloride into the electrolysis cell during the time required to complete the polarogram. The half-wave potentials were measured against a saturated calomel electrode.

All diffusion currents were corrected for iR drop across the electrolysis cell. The resistance of the solutions was measured with an Industrial Instruments, Inc., Model R C 16 conductance bridge. A 0.2M sodium perchlorate solution in formamide gave a resistance of 9600 ±50 ohms. In the iR corrections average values of i and R were used.

The capillary was made of Corning marine barometer tubing, which has a capillary of 28.4 μ radius, and was 10 cm in length. The capillary (open circuit) had the following characteristics: $m = 1.01$ mg/sec, and $t = 5.83$ sec/drop for $h = 64$ cm. The relationship of $m^{2/3}t^{1/6}$ was studied as a function of applied voltage for the capillary. These values for several applied voltages are: −0.4 v, 1.34; −0.8 v, 1.33; −1.20 v, 1.31; and −1.60 v, 1.26. These values were used at the appropriate places in the handling of the data.

The cell was immersed in a water bath at a temperature of 25 ±0.5°C. The electrolytic solutions were deaerated by bubbling tank nitrogen, obtained from the National Cylinder Company, through them.

Results and Discussion

Well-defined waves were obtained for the metal ions considered in this investigation. The concentrations of the electroreducible ions were varied from 0.6 to 4 mM in 0.2M $NaClO_4$ as the supporting electrolyte. In all cases the diffusion currents were proportional to the concentration. If one uses the criterion that an experimental value of the slope of a

$$\text{plot of } -E_{d.e.} \text{ vs. } \log \frac{i}{i_d - i} \text{ is } \frac{0.0591}{n} \text{ volts at } 25°C$$

and must agree with the theoretical value within 3-5 mv for a system to be reversible (9), then only one of the ions studied undergoes a reversible process (i.e., manganese). Zinc and cadmium approach reversibility while each of the other ions shows irreversibility in its electroreducible process. The copper reduction gave only a one-step wave, the same as in water.

The polarographic data on the ions investigated are to be found in Table I. The I_d values were calculated using values for t which were taken at the decomposition potential of the particular ion.

In formamide, as in water, the reduction stage of iron which gives a true curve is that from iron (II) to iron (0). On starting with iron (III) the first wave is not a true one since the reduction of iron (III) sets in at a potential which is more positive than the anodic dissolution of mercury.

Chromium (III) ion gives a stepwise reduction to chromium (II) and then to chromium (0). The first wave is not well-defined and makes the determination of the $E_{1/2}$ (approximately −0.9 v) for this step uncertain. Also, it might be pointed out that the height of the second wave is somewhat greater than twice that of the first. The chromium (II) to chromium (0) wave is well defined and can be used for evaluation of polarographic data.

Table I. Polarographic characteristics of some transition metal ions, zinc and cadmium in formamide (0.2M $NaClO_4$ as supporting electrolyte).

Salt	conc, mM/l	I_d	$-E_{1/2}$ v vs. S.C.E.	D cm²/sec x 10^5	0.059/n
$Cr(ClO_4)_3 \cdot 6H_2O$	2	1.65	1.56*	0.184	0.119
$Mn(ClO_4)_2 \cdot 6H_2O$	2	1.78	1.57	0.216	0.035
$Fe(ClO_4)_3 \cdot 6H_2O$	2	0.91	1.40†	0.056	0.059
$Co(ClO_4)_2 \cdot 6H_2O$	1	1.81	1.20	0.292	0.072
$Ni(ClO_4)_2 \cdot 6H_2O$	2	0.99	0.98	0.066	0.083
$Cu(ClO_4)_2 \cdot 6H_2O$	2	1.28	0.12	0.110	0.077
$Zn(ClO_4)_2 \cdot 6H_2O$	2	1.71	1.07	0.197	0.043
$3CdSO_4 \cdot 8H_2O$	2	1.85	0.69	0.229	0.049

* Value is for chromium (II) to chromium (0).
† Value is for iron (II) to iron (0).

Manuscript received May 22, 1959.

Any discussion of this paper will appear in a Discussion Section to be published in the December 1960 JOURNAL.

REFERENCES

1. G. R. Leader, *J. Am. Chem. Soc.*, **73**, 856 (1951).
2. G. H. Brown and R. Al-Urfali, *ibid.*, **80**, 2113 (1958).
3. E. Colton and R. E. Brooker, *J. Phys. Chem.*, **62**, 1595 (1958).
4. A. M. Zan'ko and F. A. Mannsova, *J. Gen. Chem. (U.S.S.R.)*, **10**, 1171 (1940); *C.A.*, **35**, 2808 (1941).
5. H. Letaw, Jr., and A. H. Gropp, *J. Phys. Chem.*, **57**, 964 (1953).
6. J. H. Hook, H. Letaw, Jr., and A. H. Gropp, *ibid.*, **58**, 81 (1954).
7. D. B. Bruss and T. DeVries, *J. Am. Chem. Soc.*, **78**, 733 (1956).
8. I. M. Kolthoff and J. F. Coetzee, *ibid.*, **79**, 870 (1957).
9. L. Meites, "Polarographic Techniques," p. 104, Interscience Publishers, Inc., New York (1955).

Technical Review

Fabrication, Properties, and Applications of Some Metallic Silicides

R. D. Grinthal

American Electro Metal Division of Firth Sterling Inc., Yonkers, New York

Recent requirements for higher and higher operating temperatures in the rocket and missile field, nuclear reactors, and many other applications have led to the consideration of the so-called "refractory hardmetals" for use as one class of structural materials in the temperature ranges where today's superalloys are no longer useful.

The term refractory hardmetals includes compounds of the transition metals with boron, carbon, nitrogen, silicon, and sulfur. These materials are characterized in general as hard, brittle interstitial compounds which have very high melting points. They differ from the corresponding oxides mainly in their electrical and thermal behavior which is distinctly metallic. They are good conductors of electricity and heat. Many are even better in this respect than austenitic stainless steel and titanium which are among the poorer conducting metals. Thus the term refractory hardmetals serves to distinguish this class of materials from high melting metals such as tungsten and molybdenum and from the more refractory oxides.

Table I. Physical properties of some metallic silicides.

Silicide	Crystal structure	Density g/cm³	Melting point, °C	Hardness, kg/mm² (100 g load)	Electrical resistivity, microohm-cm
Ti_5Si_3				986	170
$TiSi_2$	Orthorhombic	4.4	1540	618	123
$ZrSi_2$	Orthorhombic	4.9	1520	1030	161
V_3Si	Cubic	5.7	2000		
VSi_2	Hexagonal	4.7	1750	1090	9.5
$NbSi_2$	Hexagonal	5.3	1950	1050	6.3
$TaSi_2$	Hexagonal	8.8	2400	1560	8.5
Cr_3Si	Cubic	6.5	1730	1100	43
CrSi	Cubic	5.3	1600	1230	139
$CrSi_2$	Hexagonal	4.4	1570	1150	600
Mo_3Si	Cubic	9.0	2100	1310	
$MoSi_2$	Tetragonal	6.2	1870	1260	21.5
WSi_2	Tetragonal	9.3	2150	1090	334
$ThSi_2$	Tetragonal	7.8	1600	1120	
USi	Orthorhombic	10.4	1600		
$USi_2(\alpha)$	Tetragonal	9.0			
$USi_2(\beta)$	Hexagonal	9.2	1700		
YSi_2	Orthorhombic	4.5	1500		
$LaSi_2$	Tetragonal	5.0	1500		
$EuSi_2$	Tetragonal	5.5	1500		
$GdSi_2$	Orthorhombic	6.4	1500		
$DySi_2$	Orthorhombic	6.8	1500		

Their stability in oxidizing atmospheres at high temperature falls between that of the refractory metals and the oxides. Some of these hardmetals have excellent resistance to oxidation at elevated temperatures while others must be protected or used in nonoxidizing atmospheres. This discussion is concerned only with metallic silicides, which are among the most stable of the refractory hardmetals under oxidizing conditions.

Table I lists physical properties of some silicides of the transition metals and metals of the lanthanide and actinide series. A great variety of crystal structures are encountered in these materials, from the orthorhombic $TiSi_2$ through the cubic V_3Si, tetragonal $MoSi_2$, and hexagonal $CrSi_2$. While most monocarbides and mononitrides are isomorphous with each other and most diborides are isomorphous with each other, this is not true of the silicides.

The melting points of the silicides which are known are quite high, although not as high as the corresponding borides or carbides in most cases. The disilicides in particular, however, have outstanding chemical stability, and resistance against oxidation and attack by acids is maintained over large temperature ranges.

Production

Silicides are produced by several methods, the most important of which are as follows.

Direct combination of the metal and silicon.—This can be accomplished by either fusion or sintering. Fusion temperatures are extremely high, necessitating electric arc or carbon tube furnaces. Sintering of mixtures of powders produces a violently exothermic reaction at temperatures ranging from 900°-1500°C, depending on the material. In many instances the metal hydride can be substituted for the metal powder. Protective atmospheres of argon, hydrogen, or vacuum are necessary to prevent oxidation.

Reduction of metal oxides with silicon.—Silicon can reduce metal oxides in the same manner as boron or carbon, but extremely high temperatures (above 1500°C) are necessary, and the silica which forms as a reaction product is difficult to remove completely. If the reduction is carried out in vacuum, however, the silica contamination is held to a minimum by

removal of the more volatile SiO before it can condense on the furnace charge.

Reaction between metal oxides and silica in the presence of carbon.—This process is similar to direct reduction with silicon except that the carbon serves to reduce both the metal oxide and the silica, forming CO and CO_2 which do not contaminate the reaction product. This process is best carried out at high temperature in an electric arc furnace.

The aluminothermic process.—The reaction of metal oxide, quartz, and either aluminum or magnesium, performed in clay crucibles in the presence of sulfur, yields fused silicides which can be treated chemically to remove undesirable reaction products. The sulfur serves to form a liquid slag which is decomposed readily by water.

Reaction of metal with silicon halide.—Silicon tetrachloride, when passed over heated metal powder in the presence of hydrogen, reacts to form the metal silicide and HCl at temperatures ranging from 1100°-1800°C, depending on the material. This method is also used to siliconize metal surfaces and produce protective coatings in place.

Fused salt electrolysis.—By electrolysis of fused alkali fluosilicate baths containing metal oxides, silicide crystallites are deposited on the cathode.

Fabrication

Bodies may be fabricated from the silicide powders by several powder metallurgical methods. Hot pressing (simultaneous application of heat and pressure) is done in graphite dies and produces dense parts. Limitations of this process, however, only allow production of fairly small, simple shapes which have regular cross section, no undercuts, and no thin walls. Since the graphite dies cannot be used more than once or twice, this is not a means of achieving high production rates.

Cold pressing followed by sintering allows the use of steel or carbide dies and can be adapted for fairly high volume production. The same limitations in size and shape apply here as were described for hot pressing. Long time sintering in a protective atmosphere consolidates and densifies the part, but the shrinkage which occurs makes it more difficult to hold close dimensional tolerances. This can be compensated for in long run production by allowing for shrinkage in the die design. Cold pressed and sintered parts may have slightly different mechanical properties than hot pressed parts.

Extrusion of the silicide powder after it has been mixed with plastic is also possible. This method is limited to simple cross sections which have straight sides, but for certain parts it can be a high volume production process. The sintered piece may be slightly porous due to voids left when the plastic burns out, but this is not a serious drawback in most cases.

Slip casting is a ceramic process which is currently being applied successfully to metal powders. The shape of the part produced by this method is far more unrestricted than any previously described, but the process at present is in a developmental state and, although some materials are produced in quantity, most would require considerable experimentation before usable parts could be produced on a volume basis. Using this method, however, re-entry angles, undercuts, thin-walled sections are all possible. Size is restricted only by the weight that the green piece can support without collapsing during sintering.

Another fabrication method which may be employed in special cases is flame spray forming. Here the silicide is extruded into rod, which is sintered, then fed through a flame spray gun and deposited on a pattern as a coating. The coating is built up to any desired thickness and the substrate removed chemically, leaving a strong, formed body which does not require further sintering. Density is 80-90% of theoretical. If this is not satisfactory for the application, it can be improved somewhat by sintering. This method may also be used, of course, to produce protective coatings on substrate materials which are subjected to oxidizing conditions which they cannot withstand normally. The coatings are slightly porous and quite brittle, but the porosity is not interconnected and is usually sealed by the protective silicate which forms during high-temperature oxidation.

Properties

The mechanical properties of these materials are generally similar. They are hard, brittle, and have appreciable compressive and transverse rupture strength which is retained at temperatures up to 1000°-1200°C. Like most interstitial compounds, they are sensitive to impact loading and cannot be relied on in applications where tensile strength is necessary. The properties of any given material can be varied somewhat by changes in the fabrication method or by the presence of small amounts of impurities which may come from various methods of preparation. Porosity exerts a major influence in this respect and, since most test samples are prepared by powder metallurgical methods, some porosity is almost always present.

Some of the properties of $MoSi_2$, chosen here as a typical example, are listed in Table II. This material is perhaps the best known silicide and may be closest to having real commercial application. The figures given should be taken only as representative values, since the properties can vary over a wide range when variations in fabrication technique or impurity content are employed.

Modifications

Several attempts have been made to apply the cermet principal to the hardmetals and improve impact strength by addition of a third metal, which is intended to act as a binder as in the case of WC-Co

Table II. Mechanical properties of $MoSi_2$

Hardness		80-87 RA
Compressive strength		100-350,000 psi
Modulus of elasticity		59×10^6 psi
Modulus of transverse rupture	20°C	36-67,000 pst
	1000°C	51-86,000 psi
Tensile strength	1300°C	41,000 psi
Stress to rupture (100 hr life)	1000°C	13,000 psi
Oxidation resistance	Excellent to 1700°C	

and TiC-Ni. These two cases, however, have proved to be the exception rather than the rule. Several factors must be considered in choosing a metal addition to a silicide system. First, the metal to be added should be one which does not form silicides readily and, second, the silicide should be the lowest possible in the system. If, for instance, copper should be added to $MoSi_2$, the result would not be a two-phase system consisting of $MoSi_2$ in a copper matrix. The copper would react with the $MoSi_2$ forming a copper silicide and leaving a lower molybdenum silicide such as Mo_5Si_3 or Mo_3Si. These materials are all brittle and, in addition, do not have the excellent oxidation resistance of $MoSi_2$. The same results are obtained when cobalt, platinum, nickel, chromium, or titanium are added to $MoSi_2$. When metallurgical equilibrium is obtained, the starting materials are never present in their original form but always react to form new compounds, solid solutions, or ternary compounds which are sometimes even more brittle and less stable than the original materials.

Several investigators have worked with the silicide-silicide systems which, in many cases, act like binary systems between elements. It is possible in this manner to produce modifications of some silicide structures by addition of only a few mole per cent of a second silicide. For instance, $TiSi_2$ and $MoSi_2$ are not isomorphous, and $TiSi_2$ is practically insoluble in $MoSi_2$. However, a few mole per cent $MoSi_2$ added to $TiSi_2$ changes the orthorhombic structure to a hexagonal one which is intermediate between $TiSi_2$ and the tetragonal $MoSi_2$. The two compounds form a third phase which has a wide range of homogeneity and, although similar to the parent compounds, it possesses unique properties of its own.

$MoSi_2$ and WSi_2 are isomorphous, and behavior similar to the above was also noted with $TiSi_2$ and WSi_2. $CrSi_2$ and $MoSi_2$ are mutually soluble in one another in very large amounts, with a narrow two-phase region between them in the center of the diagram. Other pseudobinary systems investigated include $ZrSi_2$-$TiSi_2$, WSi_2-$CrSi_2$, VSi_2-$TiSi_2$, $CrSi_2$-$TaSi_2$, USi_2-$MoSi_2$, $MoSi_2$-WSi_2. The last pair forms a complete series of solid solutions. Investigation of systems like these may lead to methods of changing physical, electrical, or mechanical properties of these materials so that they can be tailored to suit specific applications.

Applications

Many of the silicides have been tested for potential applications in various fields. $MoSi_2$ is perhaps the best known of the group and the one closest to commercial use. A new type of heating element has been developed which is based on this material. It can be heated in air for long periods at temperatures up to 1650°C without damage. The excellent stability of $MoSi_2$ has led to its use as a protective coating for molybdenum. This coating can be applied by flame spraying or by siliconizing a molybdenum surface. It has also been found to be resistant to corrosion by molten boron oxide at elevated temperatures. Other potential applications where impact loading is not a factor may be in rocket nozzles, afterburners (as a coating), or as refractory brick.

Some investigation has been carried out concerning the possible use of solid solutions of $MoSi_2$ and USi_2 as nuclear fuel elements. This may allow high reactor temperatures and minimize the distortion usually encountered when uranium metal or alloys are used as fuel elements.

A great deal of interest has developed lately in the use of the so-called refractory metals molybdenum, tungsten, tantalum, and niobium for very high-temperature applications. If the atmosphere is oxidizing, these materials must be protected, and the possibility of coating each with its corresponding silicide is certainly an interesting one.

$CrSi_2$ and $TiSi_2$ may find applications where the combination of high temperature stability and light weight are of interest.

Among the rare earth silicides, gadolinium disilicide has been considered as a possible control rod material, dysprosium disilicide has been used as a counter for neutron flux density measurements, and europium disilicide has been fabricated for a nuclear application.

As more information is compiled about these materials, other applications will undoubtedly be suggested and investigated, and one or two will find commercial outlets. When this happens, the whole class of hardmetal materials will begin to come into more popular use, and it is hoped that the fear of using brittle materials will subside finally.

Manuscript received June 4, 1959. This paper was prepared for delivery before the Philadelphia Meeting, May 3-7, 1959.

Any discussion of this paper will appear in a Discussion Section to be published in the December 1960 JOURNAL.

REFERENCES

1. P. Schwarzkopf and R. Kieffer, "Refractory Hard Metals," Macmillan Co., New York (1953).
2. R. D. Grinthal, WADC, TR 53-190, Part VI, "New High Temperature Materials" (May 1958).
3. I. Campbell, Editor, "High Temperature Technology," John Wiley & Sons, Inc., New York (1956).
4. Climax Molybdenum Co., Bulletin Cdb-6, (January 1956).
5. R. Kieffer and F. Benesovsky, "Silicides of the Transition Metals of the 4th, 5th, and 6th Group of the Periodic Table." Powder Metallurgy (1954), The Iron and Steel Institute (Dec. 1954).

Brief Communication

Nodule Growth on Al_2O_3 Coatings

R. J. Jaccodine

Bell Telephone Laboratories, Incorporated, Allentown, Pennsylvania

This communication concerns the growth of nodules or hillocks on surfaces of heaters sprayed with Al_2O_3 coatings.

In studying heater-cathode breakdown phenomena, the method used (1) involved helically winding a bare tungsten heater or other bare metals about the Al_2O_3 coated heater: these were pumped and sealed off at 10^{-5} mm Hg. A variable heater voltage then was applied to both heaters to obtain the desired thermal conditions (Al_2O_3 coated heater at 1200°C optical and bare tungsten heater 900°C optical), and a d-c voltage of 180 v with coated heater positive was applied between both heaters to set up a potential gradient. During the course of this study, it was observed that nodules or hillocks of Al_2O_3 surface to the outside tungsten heater. These growths appeared gradually over a period of several months. The size of the nodule seemed to be limited by the gap formed between the outside base tungsten heater and the alumina surface. Figure 1 shows the hillock growth with the helically wound outside heater in place. Figure 2 shows the nodules with the outside heater removed. As can be noted, the nodules are aligned helically and occur only under the outside heater. The tops of the hillocks appear loosely packed and powdered as compared to the more substantial-looking base region. However, upon probing with a fine metal probe, the whole hillock and the region immediately adjacent to and under its base was found to be powdered, less adherent, and more loosely packed than adjacent normal regions of the coating.

Fig. 1. Hillock growth with helically wound outside heater in place.

Fig. 2. Nodules with outside heater removed

The presence of hillocks might be explained by several possible mechanisms. There may be an Al_2O_3-W (or impurities in W) reaction; bulk and/or surface diffusion under the influence of thermal and electrical gradients and also reaction involving vapor phase constituents.

The question of an Al_2O_3-W reaction at elevated temperatures remains open. Brewer and Searcy (2) claim Mo and W are nonreactive toward Al_2O_3. Wartenberg (3) and also Ackermann and Thorn (4) claim Al_2O_3 and W do react at high temperatures and form AlO.

Vapor phase reactions have been noted by various workers. Brewer and Searcy (2) give data on the Al-Al_2O_3 system, particularly the pressure of gaseous species over liquid Al_2O_3 and over liquid Al and solid Al_2O_3 mixture. Webb and Forgeng (5) account for the growth of single crystal Al_2O_3 whiskers by a vapor phase reaction in which AlO is adsorbed on an aluminum oxide surface where disproportionation takes place according to the reaction

$$3AlO(g) = 3AlO(surface) = Al_2O_3(s) + Al(l)$$

They noted globules of aluminum metal at the tips of their Al_2O_3 single crystal whiskers.

There seems a good possibility that the nodules grow as a result of an interaction of the above mechanisms. A reaction of Al_2O_3 with tungsten or the impurities in tungsten (carbon, for example) to give AlO and other vapor species, and the chemical disproportionation might be indicated by the identification of aluminum which coats in spots the wound outside heater and after longer periods slightly darkens the inside of the tube bulb. Chemical identification of these bright metallic spots was made by removing the outside tungsten heater and having qualitative spectrochemical analysis made of these areas. In Fig. 1, some of these spots can be seen on the outside base tungsten heater. Diffusion mechanism can be invoked to aid in the buildup of the nodules and could account for the observation that the regions immediately adjacent to the base of the nodules are loosely packed and in some instances are concave or moat-like.

These hillocks have also been observed in tubes in which the outside "heater" was made of nickel.

Manuscript received Sept. 3, 1959.

Any discussion of this paper will appear in a Discussion Section to be published in the December 1960 JOURNAL.

REFERENCES

1. R. J. Jaccodine, *This Journal*, **106**, 530 (1959).
2. L. Brewer and A. W. Searcy, *J. Am. Chem. Soc.*, **73**, 5308 (1951).
3. H. V. Wartenberg, *Ceramic Abstracts*, **7**, 110 (1928).
4. R. J. Ackermann and R. J. Thorn, *J. Am. Chem. Soc.*, **78**, 4169 (1956).
5. W. W. Webb and W. D. Forgeng, *J. Appl. Phys.*, **28**, 1448 (1957).

The Reaction of Germanium with Aqueous Solutions

II. Dissolution Kinetics in Electrolytes and the Role of Specific Adsorption

Walter W. Harvey and Harry C. Gatos

Lincoln Laboratory, Massachusetts Institute of Technology, Lexington, Massachusetts

ABSTRACT

The dissolution of single-crystal germanium has been studied in electrolyte solutions containing dissolved oxygen. The following electrolytes were considered: KF, KCl, KBr, KI, $NaNO_3$, Na_2SO_4, CsCl, $BaCl_2$, and $LaCl_3$. In the range 10^{-6} to 1.0N, the dissolution rate typically goes through a maximum as the electrolyte concentration is increased. The concentration corresponding to maximum dissolution rate is different for the various electrolytes but, in general, is less than $10^{-2}N$. In the case of KF, two distinct maxima were observed; in $BaCl_2$ solutions the maximum is followed by a minimum. The activation energy for the reaction in O_2-saturated KCl solutions was found to be about 19 kcal/mole. At very low oxygen partial pressures, the activation energy was less than 5 kcal/mole, indicative of diffusion-controlled kinetics.

For single-crystal as well as for powdered germanium samples, the reaction rates were not altered measurably by changes in mobile-carrier concentration brought about by doping or illumination. The experimental results are related to germanium electrode behavior and can be interpreted on the basis of specific adsorption rather than solution conductance and oxygen solubility. The interaction of germanium surface atoms with aqueous solutions is discussed in terms of probable electronic configurations.

In a previous communication (1) it was reported that, in the absence of dissolved oxygen, germanium is inert to water and nonoxidizing electrolytes up to 100°C and over a broad range of *p*H. In oxygen-saturated water, the germanium dissolution rate at room temperature is approximately 1 $\mu g/cm^2/hr$, and the reaction is controlled by the activated reduction of oxygen. The dissolution mechanism was found to be the same for the various surface orientations, although the absolute dissolution rates decreased in the order {100} > {110} > {111} [see also Ellis (2)].

An unusual feature of the surface chemistry of germanium is that its common oxide, hexagonal GeO_2, is moderately soluble in water and aqueous electrolytes [forming metagermanic acid (3)], whereas germanium itself is not attacked by nonoxidizing acids (including HF) and bases. As a result, it is possible to follow the reaction of properly prepared germanium surfaces with mild oxidizing agents in aqueous solutions without the complicating effects of surface oxides. Germanium surfaces prepared by conventional etching techniques, however, generally are covered with an oxide layer consisting at least in part of an insoluble modification (possibly tetragonal GeO_2). With the chemical polishing agent CP-4[1] difficultly soluble surface oxide is likely formed by continued reaction of the etchant on removal of the germanium from the etching bath [cf. Ellis (4)]. The formation of the difficultly soluble oxide is avoided by displacing the etchant[2] with a large volume of water or dilute HF. It is believed that in this way, oxide-free germanium surfaces are obtained, whose subsequent behavior is independent of their prior etching treatment.

The obvious advantages of studying the surface properties of a semiconductor without the complicating effects of a surface oxide, as well as the continued importance of surface reactions in the science and technology of semiconductor materials, motivated this study of the influence of electrolytes in the reaction of germanium with aqueous solution. Elucidation of the role of the adsorptive properties of various ions was considered of particular importance. Our earlier finding (1), that changes in the mobile carrier concentration in germanium are without effect on the kinetics of the reaction with water containing dissolved oxygen, in contrast to the results reported by Schwab (6), was confirmed using both single-crystal and powdered germanium samples. Furthermore, no mobile-carrier effect was found in the presence of added electrolyte.

Experimental

The experimental techniques employed were, in many respects, similar to those described earlier (1). The reagent grade salts employed were not further purified, since consistent results were obtained with such salts from different sources. The KHF_2 was purified by recrystallization. Certain improvements in the procedure for single-crystal samples, as well as the technique employed with powdered samples, will be described briefly.

Powdered samples.—These experiments were performed using a conventional Warburg apparatus.

[1] CP-4 consists of conc. HNO_3 (5 parts by volume), glacial CH_3COOH (3 parts), 48% HF (3 parts), and Br_2 (0.06 part).

[2] A similar technique has been employed for cleaning silicon surfaces (5).

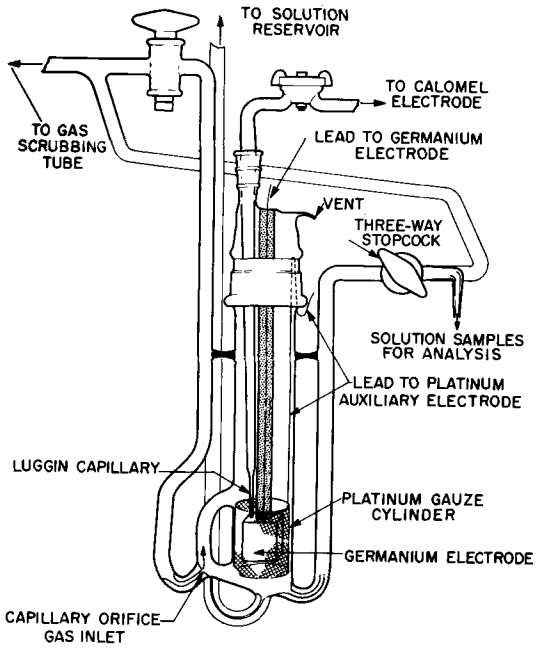

Fig. 1. Cell for dissolution and electrochemical measurements.

The method is similar to that employed by Schwab, *et al.* (6). Consumption of oxygen gas during the reaction was measured by means of a differential micromanometer to within 1 microliter. Our illuminating source consisted of two fluorescent lamps, providing an incident intensity of about 6500 meter-candles, or a photoflood lamp providing approximately 20,000 meter-candles. Radiation from the latter source was filtered through 1 in. of water.

The powdered samples were prepared by crushing germanium crystals of known type under water in an agate mortar. The particle size varied up to several hundred microns; extremely fine particles were removed by washing. For certain runs, powders of nearly uniform particle size were obtained by sieving. In a number of cases, on completion of the run, the solution was analyzed for total dissolved germanium for the purpose of comparison with the total amount of oxygen consumed.

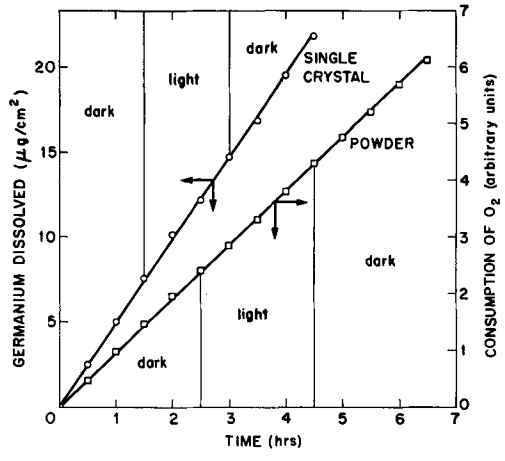

Fig. 2. Typical results of photo experiments with single-crystal and powdered germanium samples in oxygen-saturated solutions at 30°C and pH 6. ○ = 10^{-4}N Na_2SO_4; □ = 10^{-4}N KCl.

Single-crystal samples.—The single crystals employed were rectangular parallelepipeds measuring initially 1.5 x 1.5 x 2.5 cm, all faces having {100} orientation. This geometry was chosen for convenience. An electrical lead was soldered to the crystal, which was mounted as shown in Fig. 1. A thin layer of Apiezon W wax held the sample against the flat end of a heavy-walled capillary tube, through which the electrical lead passed. The saturating gas was introduced through a side tube so as to provide vigorous circulation of the solution past the specimen without permitting direct contact between gas bubbles and germanium. The partial pressure and, hence, the concentration of dissolved oxygen was varied by means of metered admixtures of nitrogen. A platinum auxiliary electrode made possible electrolytic pretreatment of the germanium whenever this procedure was required for the establishment of a stable rest potential. During pretreatment and subsequent equilibration, the solution in the cell was replaced continuously with presaturated solution from the reservoir.

Dissolution rates were obtained by withdrawing portions of solution periodically and analyzing for germanium. At least four samples were taken for each rate reported. For investigating photoeffects, sequences of three stages of alternating darkness and strong light were used in order to distinguish illumination effects from occasional small variations of rate due to other causes. Under the conditions of the experiment, illumination resulted in a considerable enhancement of the minority carrier densities.

Results

Role of mobile carriers.—In agreement with our earlier findings with single-crystal samples, no change in dissolution rate resulted from illumination of either n- or p-type germanium powder. This was the case not only in water, but also in 0.1*N* and 10^{-4}*N* KCl. Similarly, light was without effect on the reaction of n- and p-type germanium single crystals in electrolytes generally. In the latter experiments, total bulk carrier densities ranged from 5 x 10^{13} (intrinsic) to about 10^{18} carrier/cm^3. Typical results are shown in Fig. 2.

It is also significant that the average activation energy for the dissolution of powdered samples was found to be 20 kcal/g-atom, in agreement with the value previously reported for single-crystal samples (1). Furthermore, absolute dissolution rates for the sieved powders were the same as for single crystals, within the uncertainty of estimating actual surface areas. The ratio of moles of O_2 consumed to gram-atoms of germanium dissolved had an average value of 0.85 in 13 runs. However, in view of the experimental uncertainties in the quantitative determination of oxygen consumption, no significance is attached to the deviation of the average value from unity.

Influence of solution variables.—In a given electrolyte solution, as in pure water, the germanium dissolution rate remained constant with time for periods exceeding those employed in this study. With increasing electrolyte concentration, the dissolution rate goes through a maximum, as shown

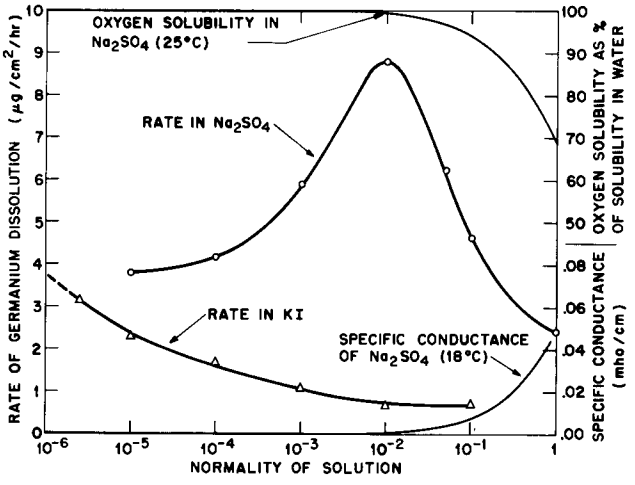

Fig. 3. Germanium dissolution rate, oxygen solubility, and specific conductance in Na_2SO_4 solutions. Oxygen solubility data from ref. (11). Conductance data from ICT 6:231, 236, 240. The maximum rates in KI and Na_2SO_4 solutions occur at the lowest and highest concentrations, respectively, of the electrolytes studied.

in Fig. 3 for Na_2SO_4 solutions. In addition to the dependence on electrolyte concentration, the effects of *p*H, oxygen partial pressure, and temperature were studied systematically with the following results.

It was found that the dissolution rate of germanium is not affected by *p*H changes below approximately *p*H 6. Above this value, the dissolution rate increases with increasing *p*H, as shown in Fig. 4(b) for O_2-saturated 0.1*N* KCl. The average of 12 determinations in the *p*H range 3 to 6.5 was 1.09 ± 0.11 μg/cm²/hr. (This value also indicates the degree of reproducibility of the data generally.) There is evidence that in certain more concentrated solutions, e.g., 1*N* CsCl, the rate in alkaline solutions is even more strongly dependent on *p*H, but this behavior was not studied in detail. Since working at low *p*H values would preclude consideration of very dilute salt solutions, all studies were carried out at *p*H 6.0 ± 0.1, unless otherwise specified.

The dependence of the dissolution rate on the concentration of dissolved oxygen is shown in Fig. 5 for 0.1*N* and $10^{-4}N$ KCl. Although rates are higher

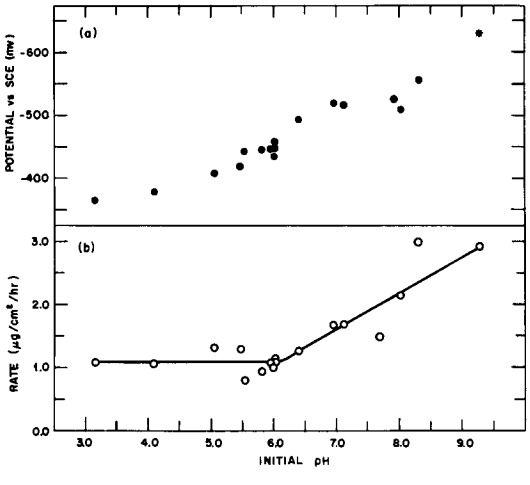

Fig. 4. Variation of (a) mixed potential and (b) dissolution rate with pH in 10^{-1}N KCl at 30°C.

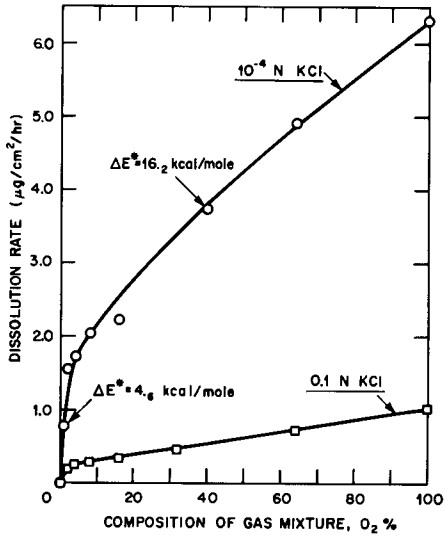

Fig. 5. Effect of oxygen partial pressure on the dissolution rate in 10^{-1}N and 10^{-4}N KCl at 30°C and pH 6.

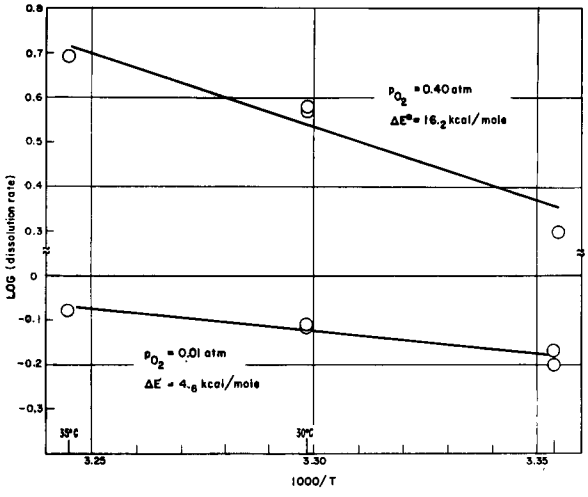

Fig. 6. Temperature dependence of the dissolution rate in 10^{-4}N KCl at two concentrations of dissolved oxygen.

in the latter, the general features of the oxygen dependence are the same in the two solutions, namely, an approximately linear decrease of rate with decreasing oxygen partial pressure, down to about 0.04 atm, and a more rapid decrease (to zero) below this value.

The temperature dependence of the reaction rate in $10^{-4}N$ KCl is shown in Fig. 6 for two values of P_{O_2}. The activation energy at 0.4 atm was 16 kcal/mole, in contrast to the value of less than 5 kcal/mole at 0.01 atm. These results indicate that diffusion is rate limiting only at low concentrations of dissolved oxygen.

Nature of the electrolyte.—The nature of the anion has a marked influence on the dissolution kinetics, as illustrated in Fig. 7 for the potassium halides. In view of the fact that in pure water the dissolution rate is 0.7 μg/cm²/hr at the same temperature, the maximum for KI evidently occurs at concentrations below $10^{-6}N$.[8] Considering for the present only the second of the two maxima in KF

[8]Actually, the maximum occurs below 10^{-7}M I⁻, as found by extending the concentration range to this value using H_2SO_4, rather than HI, for adjusting the pH to 6. The dissolution rate at 10^{-7}M I⁻ was 5.4 μg/cm²/hr.

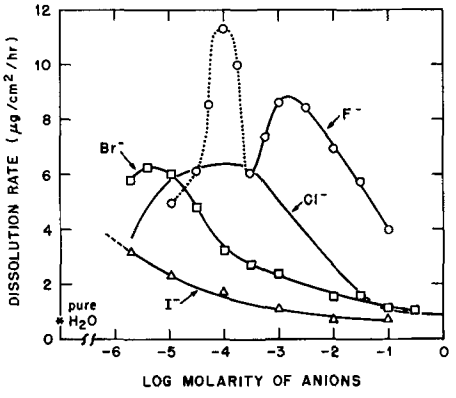

Fig. 7. Specific effects of halogen ions on the dissolution rate-oxygen-saturated solutions of potassium salts at 30°C and pH 6. The anion molarities have been corrected for additions of the corresponding acids in pH adjustments. The experimental points for KCl, omitted for clarity, are included in Fig. 8.

(full line in Fig. 7), a systematic shift of the maximum rate toward higher concentrations occurs in going from KI to KF.

The influence of the nature of the cations present was studied in a series of chlorides (Fig. 8). With the exception of $BaCl_2$, the maximum rates occur at nearly the same Cl^- ion concentration. There is, however, a significant variation in the absolute value of the maximum rate. It is also of interest to note that for $BaCl_2$, the dissolution rate does not decrease indefinitely with concentration after the initial maximum.

Electrode potential measurements.—The electrode behavior of germanium in aqueous solutions presents

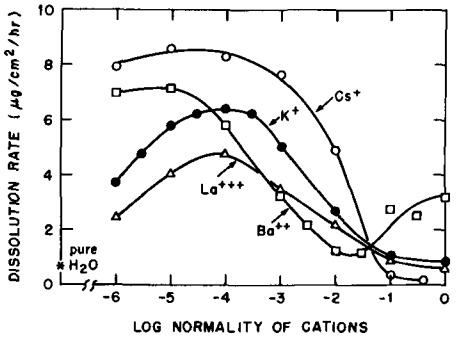

Fig. 8. Specific effects of cations on the dissolution rate-oxygen-saturated chloride solutions at 30°C and pH 6.

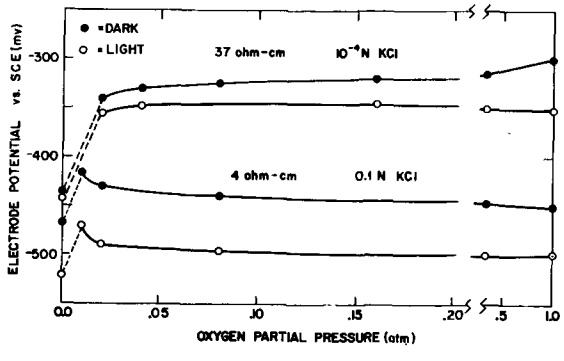

Fig. 9. Variation of the steady-state electrode potential with concentration of dissolved oxygen for n-type germanium electrodes and the effect of illumination.

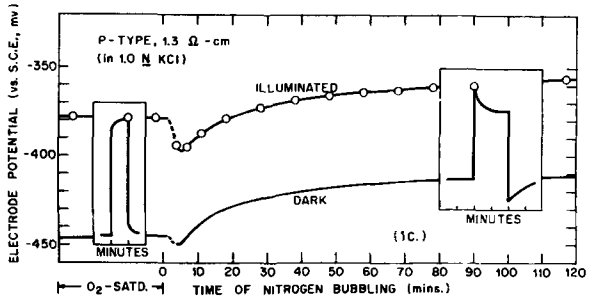

Fig. 10. Transient behavior of the photopotential of a p-type germanium electrode in moderately concentrated electrolyte.

certain aspects peculiar to semiconductors. Effects of oxygen and electrolytes on certain electrical properties of the surface have been described elsewhere (7). Some observations pertinent to the electrochemistry of the dissolution reaction are presented here. In dilute electrolytes, the steady-state mixed potential becomes more cathodic with increasing partial pressure of oxygen, as shown in Fig. 9 for an n-type electrode in $10^{-4}N$ KCl. The photopotentials obtained in the same solutions under steady illumination also are shown in Fig. 9. In more concentrated electrolytes, however, the steady-state potential becomes somewhat more anodic with increasing oxygen partial pressure, following a cathodic shift at very low oxygen partial pressures (illustrated in Fig. 9 for an n-type electrode in $0.1N$ KCl).

From Fig. 10 it will be noted that the combination of p-type electrode and moderately concentrated electrolyte results in a mixed potential which becomes more cathodic with light (i.e., the surface region is more n-type than the bulk). In the example shown, the potential under steady light in nearly oxygen-free solution undergoes a relaxation with a time constant of the order of tens of seconds. Comparably slow changes of the photopotential under no external polarization were not observed in dilute electrolytes for germanium of either type.

The mixed potentials recorded during steady-state dissolution in $10^{-4}N$ KCl at various pH's are plotted in Fig. 4(a) above the corresponding dissolution rates. The dependence of mixed potential on pH was studied more quantitatively in O_2-satu-

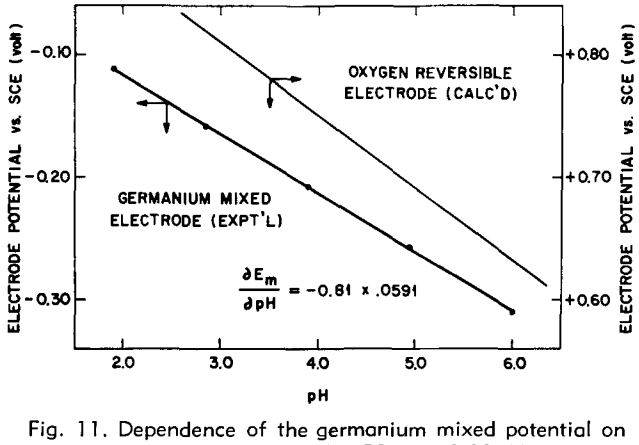

Fig. 11. Dependence of the germanium mixed potential on pH in oxygen-saturated 1.0N Na_2SO_4 + 0.001M GeO_2 + H_2SO_4.

rated 1.0N Na_2SO_4 solutions (sulfate-bisulfate buffers). Here the potential varied linearly with pH (Fig. 11) with a slope equal to −0.0478 v/pH unit at room temperature. It will be noted that the mixed potential is far removed from the oxygen reversible potential in these solutions.

Discussion

Comparison with Metal Behavior

The dependence of the germanium dissolution rate on the concentration of inert electrolyte resembles the behavior of metals in similar environments. In the case of metals, however, the maximum in dissolution rate occurs in the vicinity of 0.5N (8) and is attributed by Akimov (9) to the combined effects of solution conductivity and oxygen solubility. Thus, the increase in rate with increasing electrolyte concentration is ascribed to the increase in solution conductivity, leading in turn to an increase in the corrosion current. The subsequent decrease in rate in concentrated solutions is attributed to a decrease in oxygen solubility with electrolyte concentration. Evans (10) treats the subject in a more quantitative way but on a similar basis.

In the case of the germanium dissolution reaction, the maxima in rate occur at electrolyte concentrations below $10^{-2}N$. In this range, the solubility of oxygen is the same to within less than 1% as that in pure water (11), so that the decrease in rate with increasing concentration of electrolyte cannot be ascribed solely to diminishing oxygen solubility, although this is a contributory factor at concentrations greater than approximately 0.1N It is also unlikely that solution conductance alone is responsible for the initial increase of rate with concentration, since, at very low concentrations of electrolyte, marked differences in dissolution rate are observed in solutions of comparable conductivity.[4] Furthermore, for a given electrolyte, a maximum in rate is reached while the solution conductance continues to increase and the oxygen solubility remains essentially unchanged. This is shown in Fig. 3 for Na_2SO_4 and KI solutions, which represent the extremes of behavior observed in our experiments.

Clearly, the interpretation proposed for the dependence of the corrosion rates of metals on the concentration of electrolyte (9, 10) cannot account for the present findings. In fact, it appears that, even in the case of metals, it is inconsistent with some experimental results. For example, Schaschl and Marsh (12) have found recently that in inert electrolyte solutions at concentrations as low as $10^{-3}N$, the dissolution of iron is controlled by the amount of dissolved oxygen and is independent of conductivity and pH.

Specific Adsorption of Anions

In view of the dependence of the dissolution rate on the nature of the anion (Fig. 7) and the fact that the electrolytes considered are chemically inert toward germanium and oxygen, we believe that anions influence the kinetics of the dissolution process through specific adsorption. Specifically adsorbed anions are considered to be bonded covalently to the metal surface (13). The present results suggest that specific adsorption of anions onto germanium may be represented as follows

$$Ge\cdot + X^- \rightarrow Ge\text{-}X + e^- \qquad [1]$$

where Ge· is a surface atom having an unpaired electron (dangling bond) resulting from termination of the covalent lattice. The transfer of the anionic charge according to Eq. [1] presumably facilitates the reduction of oxygen at an adjacent site. Adsorbed anions regain their charge on detachment of underlying germanium atoms and in essence function as catalysts for the reduction of oxygen. With increasing concentration of adsorbable anions, however, competition for active surface sites between anions and oxygen molecules results eventually in a decrease in the number of sites available for the adsorption and reduction of oxygen and, hence, in a decrease in the dissolution rate. The more strongly adsorbed the anion, the more dilute the solution in which the maximum dissolution occurs. Based on this argument, the data of Fig. 3 and 7 indicate that the anions studied adsorb onto germanium in the order

$$I^- > Br^- > Cl^- > F^- > SO_4^=$$

(in the case of F^- ions the maximum occurring at $10^{-3}N$ is considered as the pertinent one in this regard, as will be discussed below). The same order of specific adsorbability of the halides has been found for mercury (14) and platinum (15). The tendency of sulfate ions to adsorb less than the halogen ions is consistent with data on other solid surfaces (16). In nitrate solutions, the position of the maximum dissolution rate was poorly defined. The unsatisfactory reproducibility of the measured rates may have been due to the presence of adsorbable impurities, especially NO_2^- ion. Nevertheless, the data indicate that the adsorbability of NO_3^- ion on germanium is close to that of Cl^- ion.

Fluoride Solutions

While it is generally considered that F^- ions are not specifically adsorbed on mercury (17), it is possible that they adsorb on germanium, especially since not only the tetrafluoride but also stable fluogermanates (18) are known. The possibility exists that one of the two maxima in KF solutions is associated with a change in the anodic mechanism, e.g., oxidation of germanium to H_2GeF_6 rather than H_2GeO_3. However, this is unlikely in view of the fact that measured solubilities of high-purity GeO_2 in 0.1N solutions of KI, KBr, KCl, KF, as well as in $10^{-4}N$ KF, all at pH 6, were the same as that measured in pure water. The absence of complexing action by the principal anions considered is thus indicated.

It is likely that the "anomalous" maximum occurring at $10^{-4}N$ in KF solutions is associated with specific adsorption of HF molecules rather than HF_2^- for the following reasons: (*a*) the residual bonding power of the HF molecule is indicated by the formation of H_2F_2 in the vapor and pure liquid and by the formation of HF_2^- in F^- solutions, and

[4] The conductivity of germanium is orders of magnitude greater than that of very dilute electrolyte solutions. At room temperature the conductivity of intrinsic germanium is 0.02 mho/cm.

(*b*) in the solution considered, the concentration of HF is about $10^{-7}N$ while that of HF_2^- is about $10^{-10}N$ (Table I). The subsequent increase of dissolution rate at higher KF concentrations probably results from displacement of adsorbed HF. At still higher concentrations, adsorption of F^- ions results in the eventual decline of the dissolution rate (Fig. 7).

The displacement of adsorbed HF is considered to result from association with F^- to form HF_2^-

$$HF_{(adsorbed)} + F^- \rightarrow HF_2^- \qquad [2]$$

The postulated interface reaction corresponds to the association of HF and F^- in the solution phase. Adsorption and displacement of HF may be considered as the net result of competition between F^- ions in the double layer and surface atoms having an unshared electron pair (—Ge:$^-$ or $\diagup\diagdown$Ge: —see below.)

The foregoing interpretation was tested with solutions of KHF_2. In the range 10^{-5} -10^{-3}M F^-, the concentrations of HF and HF_2^- are greater in the KHF_2 solutions than in the corresponding KF solutions and, moreover, increase much more rapidly with increasing $[F^-]$ (Table I). Accordingly, it was found that the anomalous maximum shifted from $[F^-] = 10^{-4}$M in KF to $F^- < 10^{-5}$M in KHF_2. The "normal" maximum also was observed in KHF_2 solutions, but could not be mapped accurately owing to chemical attack of the glassware.

Specific Effects of Cations

Figure 8 shows that the nature of the cation modifies the influence of the anion on the kinetics of the germanium dissolution reaction. No differences were observed between Na^+ and K^+ ions. The case for specific adsorption of inorganic cations is not nearly as well established as that for anions. Owing to the greater polarizability of anions, however, it is likely that their electrical centers are displaced closer to the electrode surface than those of cations. Thus, the larger the charge and the closer the approach of the cation, the greater is its effect in opposing the transfer of anionic charge and, hence, the smaller is the rate of oxygen reduction for equal concentrations of the same anion. For the cations considered, the charge-to-radius ratios are in the order $La^{+++} > Ba^{++} > K^+ > Cs^+$. The data for Cs^+, K^+, and La^{+++} are consistent with this interpretation over a very wide range of concentration (Fig. 8).

Of the cations considered, Cs^+ ions are most likely to undergo specific adsorption (19) and in the present case this seems to occur at concentrations greater than about 0.05*N*. The sharply reduced dissolution rates may be accounted for by specific adsorption of Cs^+ ions leading to increased polarization of the cathodic step, i.e., increase in the potential barrier for electron transfer to oxygen (or hole transfer to germanium).

The minimum in the dissolution rate at about $10^{-2}N$ $BaCl_2$ suggests a change in sign of the electrical double layer such as encountered in the coagulation of collodial particles by electrolytes. Since there is nothing unusual in the chemistry of Ba^{++} ion, its unique behavior suggests specific interaction with the germanium surface. A further study of this phenomenon could prove of special interest.

In view of the predominant role of adsorption in the kinetics of the germanium dissolution process, it is clear that solution conductance can have no more than a minor effect. Rather, it is suggested that in the case of metals, the dissolution rates in inert electrolytes containing dissolved oxygen are not entirely controlled by solution conductance and oxygen solubility, but are also influenced by specific adsorption. Recently, in fact, a correlation has been made between adsorption of anions and the pitting corrosion behavior of stainless steels(20).

Chemical Model of Interactions at Germanium Surfaces

Surface atoms[5] triply bonded to the lattice ($\diagup\diagdown$Ge· or, simply, Ge·) are considered to have each of their four valence electrons in sp^3 hybrid orbitals, three of which are involved in bond formation and the fourth constituting a "dangling bond." Doubly bonded surface atoms ($\diagup\diagdown$Ge: or, simply, Ge:) are usually described as possessing two dangling bonds; however, it is probably more accurate to consider their electrons as being in sp^2 hybrid orbitals, with two electrons forming a lone electron pair [cf. Handler (21)].

[5] Taking into account irregularities of atomic dimensions, any real germanium surface must consist of atoms doubly and triply bonded to the lattice; atoms attached to the crystal by a single bond are probably capable of only transitory existence at a surface in contact with an aqueous solution.

Table I. Composition of fluoride and bifluoride solutions*

KF (pH adj. to 6.0)				KHF_2			
M_{KF}	[HF]	$[HF_2^-]$	$[F^-]$	M_{KHF_2}	[HF]	$[HF_2^-]$	pH
1.0×10^{-6}	3.0×10^{-9}	2.3×10^{-14}	2×10^{-6}	1.0×10^{-6}	3.0×10^{-6}	2.3×10^{-14}	6.0
9.0×10^{-6}	1.5×10^{-8}	5.8×10^{-13}	1×10^{-5}	6.0×10^{-6}	7.4×10^{-8}	2.9×10^{-12}	5.3
9.9×10^{-5}	1.5×10^{-7}	5.8×10^{-11}	1×10^{-4}	5.3×10^{-5}	6.9×10^{-6}	2.7×10^{-9}	4.3
1.0×10^{-3}	1.5×10^{-6}	5.8×10^{-9}	1×10^{-3}	7.1×10^{-4}	4.3×10^{-4}	1.6×10^{-6}	3.5
1.0×10^{-2}	1.5×10^{-5}	5.8×10^{-7}	1×10^{-2}	9.7×10^{-3}	8.8×10^{-3}	3.4×10^{-4}	3.2
0.10	1.5×10^{-4}	5.8×10^{-5}	0.1	0.137	9.9×10^{-2}	3.8×10^{-2}	3.2
1.0	1.5×10^{-3}	5.8×10^{-3}	1	4.85	1.00	3.86	3.2

Note: All concentrations are expressed as gram-formula weights per liter of solution.
* Calculations are based on the equilibrium data of Broene and DeVries, *J. Am. Chem. Soc.*, **69**, 1644 (1947).

Processes such as trapping, generation, and recombination of carriers can be visualized more readily in terms of triply bonded surface atoms and will be described accordingly. Conduction electrons and/or holes may be captured by surface atoms having unpaired electrons; an atom capturing both an electron and a hole functions as a recombination center:

$$\underset{\text{electron trap}}{\text{—Ge}^{+}} \; e^{+} \; \underset{\text{recombination center}}{\text{—Ge}\cdot} \; e^{-} \; \underset{\text{hole trap}}{\text{—Ge}^{-}}: \qquad [3]$$

Charged surface atoms may trap electrons or holes, as in Eq. [3], and so constitute localized surface states. Surface states on clean germanium generally are considered to be "fast," whereas "slow" states are believed to lie either in the oxide layer or at the oxide-gas interface (22). Long-time changes in the photopotential (Fig. 10) in moderately concentrated electrolytes[6] indicate that slow states may also result from adsorptive interaction of ions with an oxide-free surface.

In water or very dilute electrolyte solutions, oxygen makes the germanium electrode potential more cathodic and the surface more p-type (Fig. 9); this behavior is consistent with the nature of the oxygen molecule as an electron acceptor. The tendency of dissolved oxygen to drive the surface p-type is opposed by anions of the electrolyte (ref. 7 and Fig. 9 and 10), suggesting that nonoxidizing anions behave as electron donors during the dissolution reaction. This result further supports the view that adsorbed anions are covalently bonded to the lattice; adsorption of anions without transfer of charge would lead to changes in electrode potential and surface conductivity opposite to those observed.

Mechanism of the Dissolution Reaction

The insensitivity of the rates to changes in carrier concentration as brought about by illumination and doping indicates that holes and electrons are in adequate supply for the reaction of germanium with dissolved oxygen in aqueous solutions. Actually, the highest rates observed correspond to a corrosion current density of only about 15 μamp/cm^2, which is well below the region of measured limiting carrier currents (23). Moreover, the existence of an electron-limiting current recently has been disputed (24, 25).

Evidently, the rate-limiting step of the over-all dissolution reaction lies in the activated transfer, rather than supply, of electrons to oxygen. Although formal mechanisms can be written for the reduction of O_2 at Ge· and Ge: sites, the decrease in surface recombination velocity on adsorption of O_2 from aqueous solution (7) indicates that the former sites are involved in the first stage of the reduction.

The following mechanism[7] is compatible with the results of the previous discussion, including the pH dependence of the dissolution rate and mixed potential:

$$\text{acid solution} \begin{cases} O_2 + H^+ + e^- \rightarrow -O_2H & \text{(cathodic)} \quad [4] \\ Ge\cdot + H_2O \rightarrow Ge\text{-}OH + H^+ + e^- & \text{(anodic)} \quad [5] \end{cases}$$

$$\text{alkaline solution} \begin{cases} O_2 + H_2O + e^- \rightarrow -O_2H + OH^- & \text{(cathodic)} \quad [6] \\ Ge\cdot + OH^- \rightarrow Ge\text{-}OH + e^- & \text{(anodic)} \quad [7] \end{cases}$$

where $-O_2H$ represents the surface intermediate $\begin{matrix} H\text{—}O \\ | \\ \text{—Ge—O} \end{matrix}$. Subsequent steps in the mechanism can lead to the formation of metagermanic acid, $OGe(OH)_2$ [or $HGeO_3^-$ in alkaline solution (3)]. In this mechanism, the intermediate formation of GeO or GeO_2 is not essential [cf. Rösner (26)].

Provided the equilibrium between holes and electrons in the germanium is not disturbed, as by carrier injection or illumination, the measured potentials are the same for n-type and p-type electrodes. Hence, the quantity $\partial E_m/\partial pH$ (Fig. 11) measures the same variation of potential as for a metal electrode, irrespective of possible changes of the space charge potential drop inside the germanium. Generalizing the treatment given by Ammar and Riad (20) for the dependence upon pH of the mixed potential of a metal corroding by reaction with dissolved oxygen, we obtain for the case of activation controlled kinetics:

$$\partial E_m/\partial pH = -\frac{(\nu_c - \nu_a)}{n_c\beta_c + n_a\beta_a} \times \frac{RT \ln 10}{\mathbf{F}} \qquad [8]$$

where ν's are the chemical coefficients of H^+ (negative for OH^-) in the rate-determining anodic and cathodic steps; n's, the numbers of electrons transferred; β's, the corresponding symmetry factors; and $RT \ln 10/\mathbf{F} = 0.0591$ at room temperature. Assuming symmetrical energy barriers ($\beta_c = \beta_a = 0.5$), the mechanism represented by Eq. [4] and [5] or by [6] and [7] gives $\partial\epsilon_m/\partial pH = -0.0591$ v/pH unit. The experimental slope (Fig. 11) is -0.81×0.0591. The experimental value of $\partial E_m/\partial pH$ can be reconciled with the mechanism proposed and Eq. [8] if the reasonable assumption is made that the energy barrier for germanium dissolution is lower than that for the reverse process.

From a study of the anodic dissolution of germanium, Turner (27) concluded that the rate-determining step involves the capture of two holes. This has been considered improbable by Beck and Gerischer (28), who propose that one hole and one OH^- are required in the limiting step during anodic dissolution. These mechanisms are not discussed further here, since the anodic partial process of the reaction with O_2 and H_2O is not necessarily identical with the mechanism of electrolytic anodic dissolution. Moreover, we have made no attempt to distinguish on the basis of purely chemical evidence between the roles of conduction and valence electrons in the dissolution mechanism.

[6] Depending on the type and resistivity of the electrode and the composition of the solution, transient behavior can be more complicated than for the system shown in Fig. 10.

[7] The symbol e^- in the equations is used for valence as well as conduction electrons. It is recognized that holes can be consumed by the anodic reaction and that holes may be injected by the cathodic reaction, but these features are not essential to the present discussion.

The increase of dissolution rate with increasing pH (Fig. 4) is ascribed to depolarization of the cathodic reaction in alkaline solutions as a result of specific adsorption of OH^- ions on sites adjacent to those of adsorbed oxygen:

$$\begin{matrix} Ge\cdot + O_2 & & Ge-O_2H & \\ & + H_2O \rightarrow & & + OH^- \\ Ge\cdot + OH^- & & Ge-OH & \end{matrix} \qquad [9]$$

This is similar to the scheme proposed earlier in this discussion for the accelerating effect of anions. However, since both $-O_2H$ and $-OH$ are consumed in the formation of H_2GeO_3, it is readily understandable that the germanium dissolution rate increases continuously with increasing OH^- concentration in contrast to the behavior with other anions. Actually, experiments showed that differences in rate for the various electrolytes virtually are eliminated in strongly alkaline solutions.

The only previously published work on the reaction of germanium with oxygen in aqueous solutions is that reported by Schwab (6), who proposed that the reaction takes place according to

$$Ge \rightarrow Ge^+ + e^- \text{ and } O_2 + e^- \rightarrow O_2^- \qquad [10]$$

This mechanism does not account for the dependence of mixed potential on pH, and in other respects is incompatible with the results of our experiments.

The barrier-layer theory of chemisorption (29), applied with considerable success to reactions at the semiconductor-gas interface, leads in charge-transfer adsorption to a coverage whose magnitude is determined by the carrier density in the semiconductor bulk. For the reacting system germanium-aqueous solution, on the other hand, our results indicate that the steady-state surface configuration in a given environment is the same for n- and p-type germanium [cf. Bohnenkamp and Engell (30)], at least under mildly oxidizing conditions. In fact, for the reactions studied, the arrangement and predominantly covalent character of the bonds in the germanium crystal are of considerably greater significance than its semiconductor properties.

Acknowledgment

The authors are indebted to A. A. Menna, W. J. LaFleur, and M. J. Button for technical assistance, to A. P. P. Malinauskas for conducting the experiments with the powdered samples, and to S. Sheff for confirming some of the authors' results and performing the experiments in KHF_2 solutions.

Manuscript received June 22, 1959. The work reported in this paper was performed by Lincoln Laboratory, a center for research operated by Massachusetts Institute of Technology with the joint support of the U.S. Army, Navy, and Air Force. This paper was prepared for delivery before the Ottawa Meeting, Sept. 28-Oct. 2, 1958.

Any discussion of this paper will appear in a Discussion Section to be published in the December 1960 JOURNAL.

REFERENCES

1. W. W. Harvey and H. C. Gatos, *This Journal*, **105**, 654 (1958).
2. R. C. Ellis, Jr., *J. Appl. Phys.*, **25**, 1497 (1954).
3. Mme. Lourijsen-Teyssèdre, *Bull. soc. chim. France*, **1955**, 1118.
4. S. G. Ellis, *J. Appl. Phys.*, **28**, 1262 (1957).
5. H. E. Farnsworth, R. E. Schlier, T. H. George, and R. M. Burger, *ibid.*, **29**, 1150 (1958).
6. G.-M. Schwab, "Semiconductor Surface Physics," p. 294, R. H. Kingston, Ed., University of Pennsylvania Press, Philadelphia (1957); "Advances in Catalysis," Vol. IX, p. 234, A. Farkas, Ed., Academic Press, New York (1957).
7. W. W. Harvey and H. C. Gatos, *J. Appl. Phys.*, **29**, 1267 (1958).
8. C. W. Borgmann, *Ind. Eng. Chem.*, **29**, 814 (1937).
9. G. V. Akimov, "Théorie et Méthodes d'Essai de la Corrosion des Métaux," p. 218, Dunod, Paris (1957).
10. U. R. Evans, "Metallic Corrosion, Passivity and Protection," 2nd ed., p. 347, Edward Arnold and Co., London (1946).
11. C. G. MacArthur, *J. Phys. Chem.*, **20**, 495 (1916).
12. E. Schaschl and G. A. Marsh, *Corrosion*, **13**, 243t (1957).
13. B. Breyer, *Rev. Pure and Appl. Chem.*, **6**, 249 (1956).
14. D. C. Grahame, *Chem. Rev.*, **41**, 441 (1947); D. C. Grahame, M. A. Poth, and J. I. Cummings, *J. Am. Chem. Soc.*, **74**, 4422 (1952).
15. P. V. Popat and N. Hackerman, *J. Phys. Chem.*, **62**, 1198 (1958).
16. N. A. Balaschova, *Z. physik. Chem. (Leipzig)*, **207**, 340 (1957).
17. D. C. Grahame and B. A. Soderberg, *J. Chem. Phys.*, **22**, 449 (1954).
18. O. H. Johnson, *Chem. Rev.*, **51**, 431 (1952).
19. B. B. Damaskin, N. V. Nikolaeva-Fedorovich, and A. N. Frumkin, *Doklady Akad. Nauk*, **121**, 129 (1958).
20. M. A. Streicher, *This Journal*, **103**, 375 (1956).
21. P. Handler, "Semiconductor Surface Physics," p. 23, R. H. Kingston, Editor, Univeristy of Pennsylvania Press, Philadelphia (1957).
22. R. H. Kingston, *J. Appl. Phys.*, **27**, 101 (1956).
23. W. H. Brattain and C. G. B. Garrett, *Bell System Tech. J.*, **34**, 129 (1955).
24. H. Gerischer and F. Beck, *Z. physik. Chem.*, **13**, 389 (1957).
25. E. A. Efimov and I. G. Erusalimchik, *Zhur. Fiz. Khim.*, **32**, 1967 (1958).
26. O. Rösner, *Z. Metallk.*, **46**, 225 (1955); *ibid*, **48**, 137 (1957).
27 D. R. Turner, *This Journal*, **103**, 252 (1956).
28. F. Beck and H. Gerischer, *Z. Elektrochem.*, **63**, 500 (1959).
29. A number of references to the original literature are tabulated by F. S. Stone, "Chemisorption," p. 188, W. W. Garner, Editor, Academic Press, New York (1957).
30. K. Bohnenkamp and H. J. Engell, *Z. Elektrochem.*, **61**, 1184 (1957).

Corrosion Mechanisms in the Reaction of Steel with Water and Oxygenated Solutions at Room Temperature and 316°C

Mary Boehm Strauss and M. C. Bloom

U. S. Naval Research Laboratory, Washington, D. C.

ABSTRACT

The corrosion products developed by steel when reacting with water of varying oxygen content at room temperature and at 316°C are described. The reaction was carried out in sealed steel capsules and followed by pH measurement of the solution and by microscopic, x-ray, and electron diffraction analysis of the corrosion product films. Data on the transformation behavior of the corrosion products involved and a summary of some of their physical properties are included.

Although the literature dealing with aqueous corrosion in ferrous systems is discouragingly voluminous, the amount of material dealing directly with the nature of the corrosion product films formed has, until recent years, been rather meager. A literature review (1) in 1955 indicated that the available information was far short of that needed for analysis of corrosion mechanisms of interest in connection with naval and nuclear steam generation problems, and a long-range program for obtaining some of the needed data was undertaken. This is a report of the preliminary explorations of that program. The conditions chosen for this preliminary exploration were room temperature (25°C) on the one hand and 316°C (600°F) on the other, a choice dictated by the practical considerations of naval and nuclear power steam generation applications.

Before discussing the experimental work, it may be useful to recall a few of the properties of the corrosion products with which we are concerned. These properties are listed in Table I. Neglecting FeO, with which we will not be concerned in this work, we see that color can sometimes be useful in distinguishing various forms. The structures are readily distinguishable by diffraction techniques with the exception of the two spinels Fe_3O_4 and γ-Fe_2O_3 which are built on the same framework. It may be noted that these two oxides are the only ferromagnetic species in this corrosion product system.

Experimental Techniques

The technique which was the major basis of the experiments was the use of mild steel specimens in the form of sealed capsules completely filled with the solution under test (17). The test specimens were prepared from mild steel tubing the composition of which appears in Table II. Attention is directed to the manganese content which will come into discussion later. Before fabrication into capsules, the steel tubing was hydrogen annealed 1 hr at 875°C, cooled

Table I. Corrosion products of iron

Composition (Mineral name)	Color	Structural type (3)	Magnetic character	Electrical resistivity	Density	Thermal behavior
$Fe_{0.950}O$ to $Fe_{0.833}O$ (Wustite) (2)	Black	NaCl	Paramagnetic (4)	Semiconductor (3)	5.4-5.73 (2, 11)	Melts at 1371°-1424°C. Below 570°C decomposes to Fe and Fe_3O_4 (2)
$Fe(OH)_2$	White	$Mg(OH)_2$ (Brucite)	Paramagnetic (5)	Insulator*	3.40 (12)	Decomposes at about 100°C to Fe_3O_4 and H_2† (14)
Fe_3O_4 (Magnetite)	Black	Spinel	Ferromagnetic (4)	Electronic conductor (8)	5.20 (4)	Melts at 1597°C (2)
γ-FeOOH (Lepidocrocite)	Orange	γ-FeOOH (Lepidocrocite)	Paramagnetic (6)	Insulator*	3.97 (13)	Dehydrates to‡ γ-Fe_2O_3 at about 200°C (16)
α-FeOOH (Goethite)	Yellow	α-FeOOH (Goethite)	Paramagnetic (6, 7)	Insulator (9)	4.20 (13)	Dehydrates to‡ α-Fe_2O_3 at about 200°C (16)
γ-Fe_2O_3 (Maghemite)	Brown	Spinel (with vacancies)	Ferromagnetic (4)	Semiconductor to insulator (10)	4.88 (4)	Transforms to‡ α-Fe_2O_3 above 250°C (16)
α-Fe_2O_3 (Hematite)	Brick red to black	Al_2O_3 (Corundum)	Paramagnetic (4)	Insulator (10)	5.25 (4)	Decomposes to magnetite at 1457°C and 1 atm (2)

* Color indicates that these are insulators.
† In contact with traces of oxygen $Fe(OH)_2$ is unstable at room temperature and transforms to γ-FeOOH, α-FeOOH, or Fe_3O_4 depending on the conditions of the system (15).
‡ Presence of water causes conversion to α-Fe_2O_3 at lower temperature.

Table II. Analysis of steel

Constituent	Weight %
C	0.09
P	0.017
S	0.032
N	0.007
Mn	0.57
Si	0.07
Cr	0.10
Ni	0.07
Fe (by difference)	99.05

in the hydrogen atmosphere to 60°C and then removed to the atmosphere of the room; subsequently, the tubing was annealed 1 hr at 875°C in a vacuum furnace maintained at a pressure of less than 10^{-5} mm Hg and cooled to room temperature in the furnace. The electron diffraction pattern obtained from the metal after this treatment was that of α-iron with occasional traces of the 311-line, the strongest line of the spinel pattern.

The prepared capsule specimens were exposed in sets of 6 to 12 each. The specimens were prepared, treated at room temperature for selected lengths of time, and then opened. Additional capsules were treated at room temperature for specific times, then placed in an oven at 316°C for one week, or twelve weeks, cooled to room temperature, and opened immediately thereafter. A typical capsule is shown in Fig. 1. The capsules were opened by carefully filing one corner until the metal was so thin that it could be punctured with a stainless steel syringe needle. The liquid was removed from each capsule into a glass syringe and the *p*H of the liquid measured promptly to avoid reaction with carbon dioxide from the atmosphere. The *p*H measurements were made using a Beckman "one drop" glass electrode and Model G *p*H meter. The individual measurements showed considerable scatter. The value reported is the average. In some cases samples of the liquid were dropped on copper electrodes coated with Apiezon wax, evaporated to dryness under an infrared lamp, and analyzed by emission spectroscopy. When liquid was withdrawn from a capsule, a magnet was used to test suspended solids for the presence of the spinel type oxides, Fe_3O_4 and γ-Fe_2O_3, which as previously indicated are the only ferromagnetic species in this corrosion product system. Solids suspended in the capsule liquids were collected on a Millipore filter and dried in a desiccator over Drierite (anhydrous calcium sulfate), x-ray diffraction patterns being obtained from the dry solids.

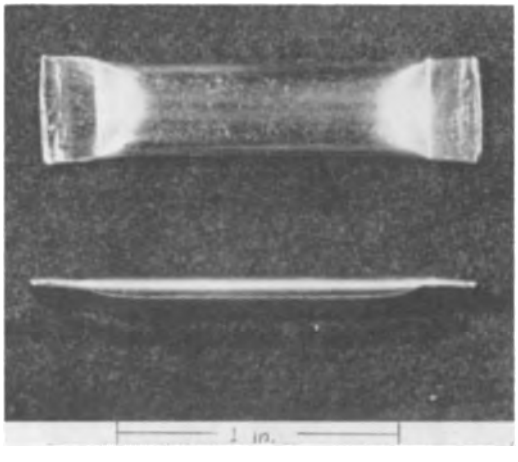

Fig. 1. Typical capsule

After removal of the liquid from the capsules, the walls were prepared for examination by filing away the lengthwise edges and shearing the transverse edges to yield two opposite wall surfaces. These were examined by use of a Geiger counter x-ray spectrometer using cobalt $K\alpha$ radiation as well as by use of the diffraction attachment of an RCA (EMU-2) electron microscope. The x-ray patterns served to characterize the bulk of the corrosion product film when this film was thick enough. The electron diffraction patterns served for characterization of very thin films on the metal surfaces and of the exterior surface layers of thicker corrosion product films.

The corroded capsule walls also were examined microscopically to determine the character and extent of the corrosive attack as well as the appearance of the corrosion products.

In most cases, no attempt was made in this exploratory work to distinguish between Fe_3O_4 and γ-Fe_2O_3.

Corrosion Products Generated in Air-Saturated Distilled Water

The data obtained in the characterization of the corrosion products formed at room temperature in capsules initially filled with distilled water are shown in Table III. Each *p*H value reported in this and subsequent tables is the average of a number of measurements usually 6-12. An indication of the scatter can be seen from the following which show typical scatter for data in Table III:

Measured *p*H after 6 hr: 9.48, 9.72, 9.57, 9.40, 8.91, 9.30, average 9.4; after 1 week: 9.7, 9.4, 10.1, 10.0, 9.7, 9.6, average 9.8; after 52 weeks: 9.93, 9.96, 9.90, 9.71, 10.02, average 9.9.

The water was initially air-saturated and the small variation in *p*H at the outset is probably due to differences in the carbon dioxide content of the laboratory atmosphere. It may be noted that after 6 hr the *p*H has risen to 9.4. This is approximately the *p*H of a saturated solution of $Fe(OH)_2$. This rise in *p*H indicates that all the oxygen has been consumed (20). The *p*H thereafter steadily rises to 9.9 where it is found one year later. The rise to so high a *p*H puzzled us for some time, but seems explicable as due to the simultaneous presence of $Fe(OH)_2$ and $Mn(OH)_2$. Using the known solubility product data for these two hydroxides one may calculate the *p*H in the presence of both to be 9.92. A calculation of the amount of manganese required (5.5×10^{-7} g) to produce this amount of $Mn(OH)_2$ shows that 10^{-4} g of steel would be required to be dissolved to give this quantity of manganese. This seems a very reasonable quantity to expect to have been dissolved in the 12 week period where this *p*H is shown to be developed. An independent series of experiments confirmed the conclusion that the calculated equilibrium of 9.92 would be achieved by allowing mixtures of carbonyl

Table III. Corrosion products formed by the action of water* in mild steel capsules at 25°C

Solution pH before reaction†	Time metal was exposed to solution	Solution pH after reaction†	Appearance of solution	Appearance of metal	Corrosion products on metal
5.9	1 hr	8.5	Yellow tinge	Speckled with brownish yellow islands	γ-FeOOH
5.6	6 hr	9.4	Clear, colorless	Same as above	γ-FeOOH and possibly spinel
6.0	24 hr	9.5	Clear, colorless	Same as above	γ-FeOOH and spinel
6.0	1 wk	9.8	Clear, colorless	Same as above	γ-FeOOH and spinel
6.0	12 wk	9.9	Clear, colorless	Thin gray brown film	Spinel and some γ-FeOOH
6.0	52 wk	9.9	Few particles of spinel	Continuous black film	Spinel

* The water was initially air saturated.
† Each value represents the mean of 6 capsules.

Table IV. Corrosion products formed by the action of 0.2% H_2O_2 in mild steel capsules at 25°C

Solution pH before reaction	Time metal exposed to solution	Solution pH after reaction†	Solid corrosion products filtered from solution	Appearance of metal	Corrosion products on metal	Residual oxygen pressure
5.9	1 hr	7.1	*	Yellow islands on shiny metal	γ-FeOOH	Yes
5.9	24 hr	6.8	Spinel and some γ-FeOOH	Same as above	γ-FeOOH and spinel	No
5.8	1 wk	7.4	Spinel	Yellow islands on black film	Spinel and some γ-FeOOH	No
5.8	4 wk	8.6	Spinel	Few yellow islands on black film	Spinel and some γ-FeOOH	No
5.7	52 wk	10.0	Spinel	Nearly covered with brownish-black film	Spinel	No

* Insufficient material for analysis.
† Each value represents the mean of 8 to 12 capsules.

Table V. Corrosion products formed by the action of 1% H_2O_2 on mild steel capsules at 25°C

Solution pH before reaction	Time metal exposed to solution	Solution pH after reaction*	Solid corrosion products filtered from solution	Appearance of metal	Corrosion products on metal	Residual oxygen pressure
5.8	1 hr	6.9	None	Yellow islands on shiny metal	γ-FeOOH	Yes
5.9	24 hr	7.3	γ-FeOOH	Same as above	γ-FeOOH	Yes
5.7	1 wk	8.0	α-FeOOH	Yellow film covers metals	γ-FeOOH and α-FeOOH	Yes
5.9	4 wk	8.2	α-FeOOH	Same as above	γ-FeOOH and α-FeOOH	Yes

* Each value represents the mean of 8 to 12 capsules.

Table VI. Corrosion products formed by the action of 4% H_2O_2 in mild steel capsules at 25°C

Solution pH before reaction	Time metal exposed to solution	Solution pH after reaction*	Solid corrosion products filtered from solution	Appearance of metal	Corrosion products on metal	Residual oxygen pressure
5.8	1 hr	7.1	None	Shiny metal	γ-FeOOH	Yes
6.0	24 hr	7.3	γ-FeOOH	Nearly covered with yellow film	γ-FeOOH	Yes
5.9	1 wk	8.2	α-FeOOH	Same as above	γ-FeOOH and α-FeOOH	Yes
5.9	4 wk	8.6	α-FeOOH	Same as above	γ-FeOOH and α-FeOOH	Yes
Not measured	61 wk	8.5	α-FeOOH	Same as above	α-FeOOH and trace of γ-FeOOH	Yes(?)

* Each value represents the mean of 8 to 12 capsules.

iron and electrolytic manganese to corrode in water. These metals had a total metallic impurity content of the order of 100 ppm and a nitrogen content in the neighborhood of 20 ppm. In these experiments, metallic powders were allowed to remain in sealed platinum-lined capsules for 3 weeks at 25°C prior to sampling. The solutions then gave the following pH values

Powder	Observed pH	pH Calculated for saturation
Fe	9.37	9.32
Mn	9.95	9.92
Fe-Mn mixture	9.95	9.92

Next, attention is called to the fact that the initial product of reaction is γ-FeOOH. The approximately 8 ppm of oxygen introduced with the air-saturated water apparently has produced the ferric ions necessary for its formation. This phase shows up as islands on the otherwise unattacked metal.

Finally, it may be noted that within 24 hr, the spinel phase has made its appearance and eventually spreads over the entire surface of the specimen. The fact that the pH of the solution has reached 9.4 [approximately the equilibrium pH of $Fe(OH)_2$] at the time that the spinel phase appears suggests that $Fe(OH)_2$ is present also, and the rise to 9.9 is taken as an indication of the presence of solid $Mn(OH)_2$ along with the $Fe(OH)_2$. Linnenbom (18) has shown that under these pH conditions $Fe(OH)_2$ does not break down to form Fe_3O_4 in impurity-free solutions, but Evans and Wanklyn (19), as well as Shipko and Douglas (14), have shown that impurities may catalyze the reaction

$$3Fe(OH)_2 \rightarrow Fe_3O_4 + 2H_2O + H_2$$

and this would appear to be what is happening here unless nuclei of Fe_3O_4 formed by reduction of γ-FeOOH are serving a similar catalytic purpose.

Tables IV-VI show some data concerning the effect of the presence of more oxygen in these systems. The data were obtained by utilizing solutions of H_2O_2 in the capsules. These solutions decompose readily in the presence of ferrous or ferric ions to liberate oxygen and thus provide a simple means for introducing oxygen into the capsules. When the capsules were opened, fluid squirted out whenever the residual oxygen pressure was in excess of atmospheric and this phenomenon was used to give a qualitative indication of oxygen exhaustion inside the capsules. The column marked residual oxygen pressure is based on this criterion.

Table IV shows the data obtained using 0.2% H_2O_2 solutions at room temperature. The pH of 5.7 to 5.9 exhibited by the solution before reaction is undoubtedly due to absorption of carbon dioxide from the atmosphere. No explanation is offered for the apparent drop in pH during the first 24 hr. Perhaps this is experimental error. Attention is, however, called to the fact that no residual oxygen pressure was observed after 24 hr and that thereafter the solution pH began to rise as it did previously in the case where no peroxide was added. It may be noted that γ-FeOOH is the initial reaction product which gives way to spinel as the oxygen content decreases and the pH increases finally reaching the vicinity of the 9.9 associated with oxygen-free solutions.

Table V exhibits analogous data obtained with a 1% H_2O_2 solution. It may be observed that a residual oxygen pressure in excess of atmospheric was present in all cases. We note that the pH again rises with time of exposure but that now a new corrosion product, α-FeOOH, appears when the pH reaches 8. Data obtained using a 4% solution of H_2O_2 are shown in Table VI. Again we note the appearance of α-FeOOH when the pH gets above 8, and we may now note that the pH seems to reach a plateau in the neighborhood of 8.5-8.6 which it maintains even after a year of exposure.

The following explanation is suggested for the arrest of the pH in the 8.5 region when oxygen is present. In the presence of oxygen, saturation of the solution with $Fe(OH)_2$ is not attained due to oxidation of Fe^{++} (20) and the consequent generation of FeOOH instead of $Fe(OH)_2$. FeOOH is so insoluble (21) that a pH in excess of 7 would not be anticipated from this source.

In the manganese system we might expect that analogously $Mn(OH)_2$ would be oxidized by dissolved oxygen as this is the basis of the Winkler test (22) for dissolved oxygen in water. However, the nature of the corrosion product generated and the corresponding pH has apparently not been investigated. Therefore, a brief exploration was undertaken of the corrosion of manganese by dissolved oxygen at room temperature. For this purpose fragments of electrolytic manganese were immersed in water in a quartz-glass flask and exposed to an atmosphere of oxygen which had been purified by being passed through sulfuric acid, water, and basic barium chloride. At weekly intervals the pH of the water was measured. Starting at 6.4, the pH of the water rose to 8.8 in the first week and remained there for 2 additional weeks. The major corrosion product which accumulated out of contact with the metal was a brown powder with an x-ray diffraction pattern not included in the ASTM card index. It has similarities to the pattern of γ-FeOOH and is perhaps the manganese analogue of that structure.

It seems probable therefore that the pH arrest noted in the capsules in the region of pH 8.5-8.6 was due to the genesis of manganese oxidation products.

As an aid to interpretations of observations from the capsule corrosion studies, exploratory studies of the transformation behavior of the various oxides and hydroxides were conducted. Samples of the desired compounds, obtained from commercial sources, (see Table VII) were subjected to the following treatments: (*a*) treatment in mild steel capsules at 25°C in the presence of water, (*b*) treatment in platinum-lined capsules at 316°C in the presence and absence of water, (*c*) treatment in mild steel capsules at 316°C in the presence and absence of water. The nature of the transformation products was determined by x-ray diffraction, chemical analysis for Fe(II) and Fe(III) and observation of the presence or absence of ferromagnetism. The results of these experiments are shown in Tables VIII-X. The data indicated that when in contact with corrod-

Table VII. Chemical analyses of oxides and hydrated oxides

Material	Fe_2O_3	Fe_3O_4	Water	Al_2O_3	MnO	SiO_2	CaO	SnO_2	MgO	Total
γ-FeOOH	85.24	0.14	13.09	1.07	0.09	0.08	—	—	—	99.71
α-FeOOH	86.23	0.05	12.56	1.38	0.06	0.03	—	—	—	100.31
γ-Fe_2O_3	90.90	6.52	0.65	1.63	0.03	0.53	—	0.07	—	100.33
α-Fe_2O_3	97.51	0.20	0.50	1.86	0.05	0.06	—	—	—	100.18
Fe_3O_4	21.76	77.22	—	—	—	0.22	1.00	—	0.20	100.40

Table IX. Summary of observations on products formed when iron oxides and hydrated oxides are heated in sealed platinum-lined nickel capsules at 316°C

Substance	Treatment	Time at 316°C	Color of product	Ferromagnetic	Result of treatment
γ-FeOOH	Heated with H_2O	24 hr	Brick-red	No	Converted to α-Fe_2O_3
γ-FeOOH	Heated dry with air	24 hr	Brick-red	No	Converted to α-Fe_2O_3
α-FeOOH	Heated with H_2O	24 hr	Maroon	No	Converted to α-Fe_2O_3
α-FeOOH	Heated dry with air	24 hr	Brick-red	No	Converted to α-Fe_2O_3
γ-Fe_2O_3	Heated with H_2O	24 hr	Maroon	Partially	All but a slight amount converted to α-Fe_2O_3
γ-Fe_2O_3	Heated dry with air	24 hr	Brown	Yes	Unchanged
α-Fe_2O_3	Heated with H_2O	24 hr	Brick-red	No	Unchanged
α-Fe_2O_3	Heated with H_2O	2 wk	Brick-red	No	Unchanged
α-Fe_2O_3	Heated dry with air	24 hr	Brick-red	No	Unchanged
Fe_3O_4	Heated with H_2O	24 hr	Black	Yes	Unchanged
Fe_3O_4	Heated dry with air	24 hr	Black	Yes	Unchanged

Table X. Summary of observations on products formed when iron oxides and hydrated oxides are heated in sealed mild steel capsules at 316°C

Substance	Treatment	Time at 316°C	Color of product	Ferromagnetic	Result of treatment
γ-FeOOH	Heated with H_2O	Up to 4 hr (before cracking)	Red-brown	Partially	Converted to α-Fe_2O_3 and some Fe_3O_4
γ-FeOOH	Heated with H_2O	(All capsules tested cracked and leaked within 6 hr)			
γ-FeOOH	Heated dry with air	24 hr	Red	No	Converted to α-Fe_2O_3 and trace Fe_3O_4
α-FeOOH	Heated with H_2O	24 hr	Black-red	Yes	Reduced to Fe_3O_4 with trace α-Fe_2O_3
α-FeOOH	Heated dry with air	24 hr	Brick-red	No	Converted to α-Fe_2O_3 with trace Fe_3O_4
γ-Fe_2O_3	Heated with H_2O	24 hr	Black-brown	Yes	Converted to α-Fe_2O_3 and Fe_3O_4
γ-Fe_2O_3	Heated dry with air	24 hr	Brown (unchanged)	Yes	Slight reduction to Fe_3O_4 at Fe interface
α-Fe_2O_3	Heated with H_2O	24 hr	Brick-red (unchanged)	No	Slight reduction to Fe_3O_4
α-Fe_2O_3	Heated with H_2O	7 days	Very dark red	Partially	Considerable reduction to Fe_3O_4
α-Fe_2O_3	Heated dry with air	24 hr	Brick-red (unchanged)	No	Unchanged
Fe_3O_4	Heated with H_2O	24 hr	Black (unchanged)	Yes	Unchanged
Fe_3O_4	Heated dry with air	24 hr	Black (unchanged)	Yes	Unchanged

ing steel at room temperature, anhydrous oxides were more resistant to reduction to Fe_3O_4 than the hydrous ones and that the α-Fe_2O_3 was most resistant to this action. This reduction could be a reaction with corrosion-generated hydrogen or a precipitation reaction involving divalent iron from the corroding steel and dissolved species from the trivalent solids. A probable mechanism is the following: $Fe^{++} + 2FeO_2^- \rightarrow Fe_3O_4$. Evidence of rapid direct reaction of this kind is found in the experiments of Forrest, Roetheli, and Brown (23) in which "gelatinous precipitates of ferrous and ferric hydroxides" were mixed to produce Fe_3O_4.

It may be noted that at elevated temperatures in the absence of corroding steel the transformation of all trivalent species to α-Fe_2O_3 is markedly accelerated by the presence of water in accord with the observations of Gheith (16). The reduction of all trivalent oxides to Fe_3O_4 at the elevated temperature is most probably due to reduction by corrosion-generated hydrogen. The fact that γ-Fe_2O_3 did not transform to α-Fe_2O_3 when heated at 316° in the dry state is undoubtedly due to stabilization by the presence of the aluminum present as an impurity (24). The cracking of the capsules when heated with γ-FeOOH slurries was shown to be a stress corrosion phenome-

Table VIII. Behavior of iron oxide and hydrated oxide slurries in mild steel capsules at room temperature

Iron compound in prepared slurry	Solids present in slurry after 48 hr	Solids present in slurry after 4 wk
Fe_3O_4	Apparently unchanged	No change
γ-FeOOH	Apparently unchanged	γ-FeOOH and spinel*
γ-Fe_2O_3	Apparently unchanged	γ-Fe_2O_3 and traces of Fe_3O_4
α-FeOOH	Apparently unchanged	α-FeOOH and spinel*
α-Fe_2O_3	Apparently unchanged	Unchanged

* Chemical analysis was not used for these cases since Fe_3O_4 seems to be the only spinel species which could be developed. In both cases, prior experimentation (16) indicates complete stability to dehydration up to temperatures in the neighborhood of 100°C. Thus γ-Fe_2O_3 could not be developed by dehydration of γ-FeOOH. In the case of α-FeOOH, even dehydration would produce only the stable α-Fe_2O_3. Thus the only feasible way in which the spinel structure could be developed here is by reduction to Fe_3O_4.

non induced by the presence of a chloride impurity. This will be discussed in a subsequent publication.

All the data thus far discussed are summarized in Table XI, and the results of heating capsules to 316°C after 24 hr of room temperature exposure are shown in Tables XII and XIII.

The following conclusions may be drawn:

1. Steel in contact with air saturated water at 25°C in these capsules develops γ-FeOOH within an hour. This γ-FeOOH appears as islands on the metallic surface. The pH rises within 24 hr from an initial value of about 6.0 to 9.5, approximately the equilibrium value in contact with $Fe(OH)_2$, and continues to rise to 9.9 where it apparently remains indefinitely. This pH of 9.9 is the equilibrium pH of a solution in contact with both $Fe(OH)_2$ and $Mn(OH)_2$. This rise in pH is accompanied by the gradual elimination of γ-FeOOH and its replacement with a spinel which eventually covers the entire specimen as the oxygen is used up and the pH rises.

2. Steel in contact with H_2O_2 solutions under these conditions also develops γ-FeOOH which appears as islands on the metal within an hour. The rise in pH in this case, however, is much more gradual. With sufficient oxygen present ($\geqq$ 1% H_2O_2) γ-FeOOH is at first produced, and then as the pH rises with time to a value of 8.0 or above, α-FeOOH appears. With sufficient oxygen present the pH reaches a plateau in the neighborhood of 8.5.

3. On long standing (1 year) with exhaustion of oxygen, the spinel phase appears and the pH rises to the vicinity of 9.9, the equilibrium value in contact with $Fe(OH)_2$ and $Mn(OH)_2$.

4. On heating at 316°C, any $Fe(OH)_2$ or γ-FeOOH generated by room temperature exposure of steel to water is converted to magnetite within 24 hr with a corresponding drop in pH to the neutral region.

5. On heating at 316°C, any γ- or α-FeOOH generated by room temperature exposure in H_2O_2 solutions is converted to α-Fe_2O_3 within 24 hr with a corre-

Table XI. Summary of corrosion products formed by the action of water and H_2O_2 solutions in mild steel capsules at 25°C

Time of exposure	H_2O		0.2% H_2O_2		1% H_2O_2		2% H_2O_2		4% H_2O_2	
	pH	Product	pH	Product	pH	Product	pH	Product	pH	Product
1 hr	8.5	γ-FeOOH	7.1	γ-FeOOH	6.9	γ-FeOOH	7.3	γ-FeOOH	7.1	γ-FeOOH
24 hr	9.5	γ-FeOOH and spinel	6.8	Spinel and some γ-FeOOH	7.3	γ-FeOOH	7.3	γ-FeOOH	7.3	γ-FeOOH
1 wk	9.8	γ-FeOOH and spinel	7.4	Spinel	8.0	α-FeOOH	8.3	α-FeOOH	8.2	α-FeOOH
4 wk	—	—	8.6	Spinel	8.2	α-FeOOH	8.1	α-FeOOH	8.6	α-FeOOH
1 yr	9.9	Spinel	10.0	Spinel	—	—	—	—	8.5	α-FeOOH

Table XII. Corrosion products formed by the action of water in mild steel capsules at 316°C

Solution pH before 316°C treatment	Time metal was treated at 316°C*	Solution pH after 316°C treatment†	Appearance of solution	Appearance of metal	Corrosion products on metal	Thickness of surface oxide
9.5	24 hr	6.9	Clear, colorless	Continuous gray black film	Spinel	Less than 1μ
9.5	1 wk	7.0	Clear, colorless	Same as above	Spinel	Less than 1μ
9.5	14 wk	7.0	Clear, colorless	Same as above	Spinel	1 to 3μ
9.5	52 wk	6.9	Clear, colorless	Same as above	Spinel	2 to 6μ

* The metal was exposed at room temperature for 24 hr before treatment at 316°C.
† Each value represents the mean of at least 5 capsules.

Table XIII. Summary of the corrosion products formed by the action of H_2O_2 solutions in mild steel capsules at 316°C

Solution and initial pH	Exposure at 25°C	Products on metals	Solution pH after 25°C treatment	Exposure at 316°C	Products on metal	Solution pH after 316°C treatment
0.2% H_2O_2	24 hr	γ-FeOOH and spinel	6.8	1 wk	Spinel and trace α-Fe_2O_3	6.8
5.8-5.9	1 wk	Spinel and some γ-FeOOH	7.4	1 wk	Spinel	7.2
				12 wk	Spinel	6.7
1.0% H_2O_2	24 hr	γ-FeOOH	7.3	1 wk	α-Fe_2O_3 and some spinel	6.4
5.7-5.9	1 wk	γ-FeOOH and α-FeOOH	8.0	1 wk	α-Fe_2O_3 and some spinel	6.4
				12 wk	Spinel and trace α-Fe_2O_3	6.9
2.0% H_2O_2	24 hr	γ-FeOOH	7.3	1 wk	α-Fe_2O_3 and some spinel	6.1
5.4-5.7	1 wk	γ-FeOOH and α-FeOOH	8.3	1 wk	α-Fe_2O_3 and some spinel	6.0
				12 wk	α-Fe_2O_3 and spinel	6.0
4.0% H_2O_2	24 hr	γ-FeOOH	7.3	1 wk	α-Fe_2O_3 and some spinel	6.1
5.9-6.0	1 wk	γ-FeOOH and α-FeOOH	8.2	1 wk	α-Fe_2O_3 and some spinel	5.9
				12 wk	α-Fe_2O_3 and spinel	5.8

sponding drop in pH to the neutral region. As the oxygen is consumed by the reaction, this α-Fe_2O_3 is slowly reduced to spinel (Fe_3O_4).

Acknowledgments

The authors are indebted to W. A. Fraser and G. N. Newport for assistance throughout the course of this work; to C. O. Timmons for the preparation and treatment of many of the specimens; to Evelyn Cisney and W. G. Sadler for x-ray diffraction patterns; to D. M. Price for metallography, to the Analytical Branch of this organization for chemical analyses, to A. J. Pollard for aid in the exploration of the oxidation of manganese, to Jeanne B. Burbank for assistance with the electron diffraction patterns, and to Dr. Morris Cohen of the Canadian Research Council for helpful discussion of the kinetics of $Fe(OH)_2$ oxidation.

Manuscript received July 16, 1959. This paper was prepared for delivery before the Ottawa Meeting, Sept. 28-Oct. 2, 1958.

Any discussion of this paper will appear in a Discussion Section to be published in the December 1960 JOURNAL.

REFERENCES

1. M. J. Boehm and M. C. Bloom, *Corrosion*, **13**, No. 2, 44 (1957).
2. L. S. Darken and R. W. Gurry, *Metals Handbook*, p. 1212, American Society for Metals (1948).
3. W. Huckel, "Structural Chemistry of Inorganic Compounds," Elsevier Publishing Co., New York (1951).
4. B. Mason, *Geol. Foren. i. Stockholm Forh.*, **65**, 97 (1943).
5. A. Quartaroli, *Gazz. chim. ital.*, **46 ii**, 224 (1916).
6. H. W. Albrecht, *Ber.*, **62**, 1475 (1929).
7. G. F. Huttig and H. Kittel, *Z. anorg. Chem.*, **199**, 129 (1931).
8. E. J. Verwey and J. H. deBoer, *Rec. trav. chim.*, **55**, 531 (1936).
9. T. W. Case, *Phys. Rev.*, **9**, (2), 305 (1917).
10. H. Sachse, *Z. Phys.*, **70**, 539 (1931).
11. E. R. Jette and F. Foote, *J. Chem. Phys.*, **1**, 29 (1933).
12. G. Natta and E. Casazza, *Atti accad. naz. Lincei*, **5**, (6), 803 (1927).
13. J. Bohm, *Z. Krist.*, **68**, 568 (1928).
14. F. J. Shipko and D. L. Douglas, *J. Phys. Chem.*, **60**, 1519 (1956).
15. J. E. O. Mayne, *J. Chem. Soc.*, 129 (1953).
16. a-M. A. Gheith, "Stability Relations of Ferric Oxides and Their Hydrates," Ph.D. Thesis, Univ. of Minn. (1951).
    b-L. A. Welo and O. Baudisch, *Chem. Rev.*, **15**, 45 (1934).
17. M. C. Bloom and M. Krulfeld, *This Journal*, **104**, No. 5, 265 (1957).
18. V. J. Linnenbom, *ibid.*, **105**, No. 6, 322 (1958).
19. U. R. Evans and J. N. Wanklyn, *Nature*, **162**, 27 (1948).
20. M. J. Pryor and M. Cohen, *This Journal*, **100**, No. 5, 208 (1953).
21. K. H. Gayer and L. Woontner, *J. Phys. Chem.*, **60**, 1569 (1956).
22. ASTM Standards, Part 10, p. 1004 (1958).
23. H. O. Forrest, B. E. Roetheli, and R. H. Brown, *Ind. and Eng. Chem.*, **23**, No. 6, 650 (1931).
24. F. E. DeBoer and P. W. Selwood, *J. Am. Chem. Soc.*, **76**, 3365 (1954).

Corrosion of Nickel Coated Mild Steel

B. C. Banerjee[1]

National Chemical Laboratory, Poona, India

ABSTRACT

A dissolution rate study of iron from mild steel disks coated with electrodeposited nickel having (100), (10$\bar{1}$0) + (211), (110), and (210) orientations has revealed that, in hydrochloric acid solution, coatings with (210) orientation gave the best protection to the iron. On the other hand, in neutral sodium chloride solution appreciable difference in the dissolution rate has not been observed. These results have been discussed with reference to the precipitation of basic iron salts, the electrochemical anisotropy of different faces of a single crystal, and also to the texture of the deposits.

The corrosion of a metal can be minimized by a coating of a nobler metal, for example, by electrodeposition of nickel on iron. Under the conditions of electroplating used in practice, the coating will be more or less porous and the protection efficiency is supposed to depend largely on the porosity of the coating (1, 2). It may be mentioned in this connection that the polycrystalline nickel coating is made up of a large number of single crystals. Such a coating may, however, develop different crystal orientations under varying conditions of deposition (3, 4) and thus affect the corrosion rate of the base metal due to electrochemical anisotropy of different faces of a single crystal (5-8). It was previously thought (3, 4) that the lateral growth of electrodeposited metals of the f.c.c. type, defined by the orientation of the more densely packed atomic planes such as (111), (100), or (10$\bar{1}$0) + (211) parallel to the substrate surface gives better protection than the outgrowth type of deposits defined by (110) or (210) orientations. For industrial electroplating, bath conditions corresponding to the former were therefore recommended (4). In what follows some preliminary results of dissolution of iron from a mild steel disk coated with electrodeposited nickel suggest a different type of behavior.

Experimental Results

Mild steel disks of 2 cm diameter were made out of a rod supplied by "TISCO" (India). They were carefully polished and the nonsignificant portions were thickly plated with nickel, and then covered with collodion. The significant surfaces (area 3.14 cm^2) of one set of such disks were hand polished with emery of different grades ranging from 1F down to 4/0 and the surfaces of another set were machine polished on a polishing cloth containing jeweller's rouge soaked with a continuous supply of xylene as lubricant. Machine polishing of different sets of disks also was carried out with jeweller's rouge soaked continuously with benzene, toluene, dioxane, decaline, etc., respectively. The machine polished disks contained no visible scratches, but a few scratches could be seen in hand polished disks. The surfaces thus obtained were cleaned thoroughly with acetone (A.R. grade) and distilled water to make them free from grease, etc., and then coated with nickel from a bath consisting of 280 g/l of nickel sulfate, 48 g/l of nickel chloride, and 31 g/l of boric acid. All chemicals were of C. P. grade. The bath was purified initially by electrolyzing the solution at a low current density, with a dummy brass cathode and a very pure nickel foil as anode. The *p*H of the bath was adjusted by adding an appropriate quantity of the acid or nickel carbonate. The solutions thus prepared were filtered to remove any suspended matter in them. In order to prevent possible leakage of iron through nonsignificant surfaces of a disk during experiments, thick coatings of beeswax also were applied on them. The deposit orientations, (210), (100), and (10$\bar{1}$0) + (211) were obtained at 25°C at *p*H of 2.1, 3.9, and 5.1, respectively, whereas the (110) orientation was developed at any one of the *p*H's at 60°C. The current density was 10 ma/cm^2 in all the above cases of deposition. The time of deposition which ensured an average thickness of 5.75 μ of nickel coating was noted from reference curves, previously determined for each one of the crystal orientations, by a method suggested by Blum and Hogaboom (1). The orientations were checked from electron diffraction patterns (reflection type, ~55 kv electrons, camera length ~50 cm).

The experiments on dissolutions of the plated disks were carried out in Pyrex beakers containing 40 cc of 0.5% HCl (*p*H $\approx$ 1) or 5% NaCl (*p*H $\approx$ 7) at 25°C with the disks immersed vertically for the specified time intervals in the stagnant solutions, kept open to air all the time. The disk was washed with distilled water, dried with filter paper, and dipped in a fresh solution every time. The solutions containing iron mostly in the form of Fe^{2+} ions were oxidized to the Fe^{3+} state by adding 3 cc of 4*N* nitric acid and boiling for 5 min. Then the concentration of iron was estimated spectrophotometrically after adding KCNS solution with a Unicam spectrophotometer using a light of $\lambda = 500$ mμ (10).

Figure 1 presents results for the dissolutions in 0.5% HCl solutions at 25°C when the initial surface was hand polished, Fig. 2 for machine polished surfaces (jeweller's rouge soaked with xylene as lubri-

[1] Present address: Department of Physics, Pennsylvania State University, University Park, Pa.

cant), and Fig. 3 for dissolution in 5% NaCl solution from the machine polished plated disks. However, results similar to Fig. 1 also were obtained with machine polished plated disks if benzene, toluene, dioxane, decaline, and many other similar hydrocarbons were used as soaking liquid for jeweller's rouge during machine polishing of initial surfaces of mild steel disks instead of xylene. In all the above cases averages from five different experiments are given. It may be seen that the rate of dissolution as given by the slope is higher initially and becomes steady after a few minutes. In the case of (210) orientation the initial rate of dissolution is higher compared with other orientations (Fig. 1 and 2), but later the rate becomes the lowest of all, irrespective of the method of polishing of the initial iron surfaces. This indicates that (210) orientation of nickel coating or the texture of the coating obtained under the stated bath conditions on mild steel ultimately gives the better protection from corrosion in the wet environments studied above.

In the salt solution (Fig. 3), however, no appreciable difference in the corrosion rates was observed

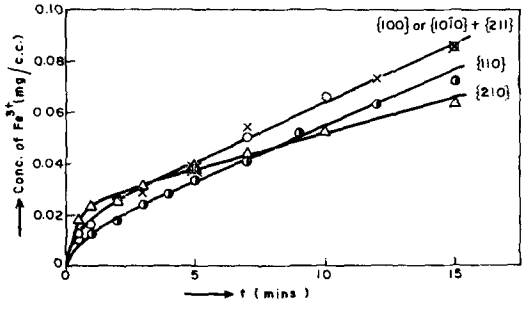

Fig. 1. Dissolution of Fe from hand-polished disk, coated with orientated nickel in 0.5% HCl solution.

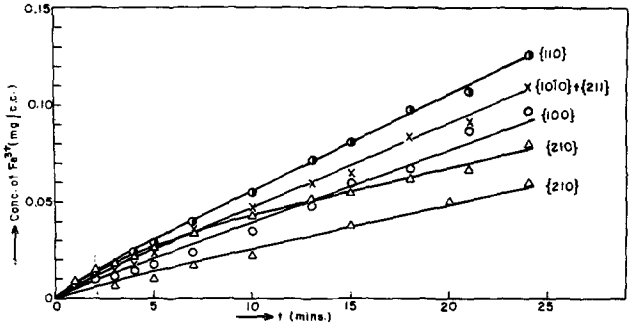

Fig. 2. Dissolution of Fe from machine-polished disk (xylene as soaking liquid) coated with orientated nickel in 0.5% HCl solution, (the lowest curve 0.25% HCl).

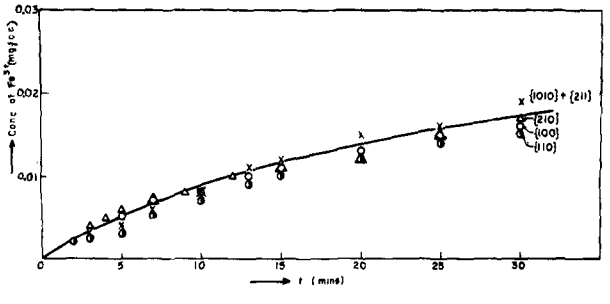

Fig. 3. Dissolution of Fe from machine-polished disk, coated with orientated nickel in 5.0% NaCl solution.

for the various crystal orientations. The higher dissolution observed in the case of hand-polished, compared to machine-polished, coated disks is obviously due to more irregularities on the surface leading to a less efficient protection by the coating.

Discussion

The corrosion of metals in acid solution involves essentially the transfer of one or more electrons by the metal atom to another species, followed by solvation in the aqueous solution. It could be assumed that the rate of dissolution will, *inter alia,* be dependent on the area of the exposed iron. The important question of the texture of the deposit involving such considerations as size, grain boundaries, orientations, and mutual arrangement of the discontinuities of the intercrystallites should be considered primarily (7-9).

It may be inferred that bath conditions depositing nickel with (210) plane parallel to the substrate surface might have produced the least porous surface. However, qualitative estimates of porosity by the usual hot water dip and ferrocyanide methods reveal that deposits with (210) and (1010) + (211) orientations are distinctly more porous and the results are in agreement with those of Rotinyan (13). This also can be appreciated in view of the fact that appreciable evolution of hydrogen occurs during the deposition of nickel with (210) crystal orientation and small gas bubbles would stick to cathode surface when the deposition is carried out (3-5). Although the above tests for porosity (1) do not give any quantitative estimate of the total area exposed as a result of discontinuities, etc., in the deposits, it is enough to suggest that the dissolution rate (vide Fig. 1 and 2) is not determined entirely by this exposed area, and the crystal orientation might have influenced the results (7-9).

It may be noted that the dissolution behavior as represented in Fig. 1 for (110) and (100) orientations of nickel coating is completely reversed in Fig. 2. This may be due to the adsorption of xylene (in some form or other) on the iron surface during machine polishing and the adsorbed matter could not possibly be removed by washing. Thus during electrodeposition of nickel on such surfaces, the adsorbed matter might have been trapped in the pores or other forms of discontinuities of nickel deposits and hence in the local corrosion cells during dissolution experiments. These trace quantities of trapped impurities (12) might have been responsible for influencing anodic and cathodic processes in each corrosion cell, ultimately giving the reversal effect.

It is well known that different single crystal faces have different electrochemical potentials (5, 6) and hence the oxidation and reduction rates differ considerably between them (7-9). We can visualize the existence of local cells at each pore consisting of large cathodes (oriented nickel) and small anodes (polycrystalline iron). The potentials of such cells are dependent on the orientations of nickel to such an extent as to affect the rate of dissolutions in the order suggested by our results. Further, the significant influence of other textural features as mentioned earlier cannot be ruled out.

Evans (2) pointed out that the combination of a large cathode and small anode gives rise to intense attack by corrosive agents. This will lead to a higher current density in the local corrosion cells favoring the dissolution of iron. In the prevailing stagnant condition of the acid solution in the pore, there will soon arise high anodic polarization due to the accumulation of Fe-ions which will oppose dissolution of iron progressively. Further, owing to the discharge of hydrogen at the cathode the liquid in the nickel/solution interfacial region will tend to be alkaline. Since the anode and the cathode are so near each other, iron/solution interface also will be at a pH much higher than that of the bulk solution. The precipitation of basic salts of iron in the pore thus are facilitated, and this decreases the dissolution rate with time. The absence of any appreciable difference in dissolution behavior of specimens having different crystal orientations in 5% sodium chloride solution in contrast with their behavior in dilute hydrochloric acid solutions may be attributed to the instantaneous formation of a protective oxide coating on the exposed areas in presence of neutral solution in the pores.

Acknowledgments

The author expresses his gratitude to Dr. A. B. Biswas for various suggestions and encouragements during the progress of the work and to Drs. A. P. B. Sinha, M. K. Gharpurey, and Hira Lal for stimulating discussions.

Manuscript received May 28, 1959.

Any discussion of this paper will appear in a Discussion Section to be published in the December 1960 JOURNAL.

REFERENCES

1. W. Blum and G. B. Hogaboom, "Principles of Electroplating and Electroforming," 3rd Ed., pp. 141 and 104, McGraw-Hill Book Co., New York (1949).
2. U. R. Evans, "An Introduction of Metallic Corrosion," Edward Arnold and Co., London (1950).
3. B. C. Banerjee and A. Goswami, *J. Sci. Ind. Res. (India)*, **14B**, 322 (1955).
4. B. C. Banerjee and A. Goswami, *This Journal*, **106**, 20 (1959).
5. H. Leidheiser, Jr., and A. T. Gwathmey, *Trans. Electrochem. Soc.*, **91**, 95 (1947).
6. W. E. Tragert and W. D. Robertson, *This Journal*, **102**, 86 (1955).
7. F. W. Young, Jr., J. V. Cathcart, and A. T. Gwathmey, *Acta Met.*, **4**, 145 (1956).
8. K. R. Lawless and A. T. Gwathmey, *ibid.*, **4**, 153 (1956).
9. "Semiconductor Surface Physics," R. H. Kingston Editor, p. 336, University of Pennsylvania Press (1956).
10. A. Vogel, "A Textbook of Quantitative Inorganic Analysis, Theory and Practice," p. 702, Longmans, Green and Co., London (1943).
11. A. L. Rotinyan, *et al*, *J. Appl. Chem. (U.S.S.R.)* (English edition), **30**, 756 (May 9, 1957).
12. B. C. Banerjee and A. Goswami, *J. Sci. Ind. Res. (India)*, **16B**, 144 (1957).

The Kinetics of the Corrosion of Low-Hafnium Zirconium in Aqueous Sulfuric Acid Solutions

Tennyson Smith

Atomics International, Canoga Park, California

ABSTRACT

The rates of corrosion of low-hafnium zirconium in aqueous sulfuric acid solutions, over the concentration range 9-97% by weight, have been studied. Corrosion was detected by measuring the concentration of zirconium in solution with a radioactive tracer, Zr^{95}. The samples first were etched in an aqueous hydrofluoric-nitric acid solution, then placed directly into the sulfuric acid solution. The initial corrosion followed a parabolic rate law which was followed by a constant rate. Corrosion during the constant reaction rate period was faster, by an order of magnitude or more, than rates reported in the literature (1-4) for unetched samples under similar conditions. This is thought to be due to the removal of the protective oxide film on etching and the subsequent growth of some less protective film in the sulfuric acid solution.

The corrosion rate was found to be first-order with respect to undissociated sulfuric acid over the concentration range 0.2-9M, "undissociated sulfuric acid," [31.4 to 81.1% H_2SO_4 by weight (5)]. An equation relating the corrosion rate and the concentration of undissociated sulfuric acid at 44°C and with pre-etching, is: $R = 4.0 \times 10^{-5} \times (H_2SO_4) + 1.0 \times 10^{-5}$, g cm^{-2} hr^{-1}. An approximate value for the activation energy determined over the temperature range 20°-72°C, is 7-8 kcal mole^{-1}. A discussion of possible mechanisms is given with suggestions for further research.

This paper reports the second part of a study to elucidate the kinetics of the corrosion of low-hafnium zirconium in aqueous acid solutions. Part one of this study has been reported previously (6) and concerned the dissolution of zirconium in aqueous hydrofluoric acid solutions.

Little has been reported in the literature about the kinetics of the corrosion of zirconium. Most of the work has been reported as engineering data, that is, spot checks at various temperatures and acid concentrations. The work reported here, although preliminary in nature, throws light on the mechanism of the corrosion of zirconium in sulfuric acid solutions and points the way to further experimentation.

To help understand the mechanism of the corrosion phenomenon, it is important to know the concentrations of the various species in solution. Much work has been done to identify the species present in aqueous sulfuric acid solutions. Most of the work has been done with the use of Raman spectra. It has been found that different species have characteristic lines, which are peculiar to them alone, the intensity of which is proportional to the concentration. Although most of the work has been concerned with identifying the Raman spectra with the individual species, two publications have been made which report the concentrations of the various species (H^+, $SO_4^=$, HSO_4^-, and undissociated H_2SO_4, hereafter represented as H_2SO_4) as a function of the stoichiometric sulfuric acid concentration. In 1949, Young and Blatz (5) reported calculations, based on the work of Rao (7), of the specific concentration of H^+, $SO_4^=$, HSO_4^-, and H_2SO_4 in aqueous sulfuric acid solutions. In 1951, Young (8) reported later work on the concentrations of these species.

The following reaction rate data are analyzed in terms of the specific concentrations of the various species in solution.

Experimental Procedure

Low-hafnium zirconium samples 5 x 5 x 0.32 cm had been irradiated with neutrons at the Oak Ridge National Laboratory. The isotope Zr^{95} (half life 65 days) was used as a tracer in these experiments. A detailed description of the zirconium history and the isotope detection apparatus is given in a previous paper (6). In brief, weighed samples were taken from the zirconium plates and were dissolved in hydrofluoric acid solutions. These solutions were used as standards for comparison with unknown concentrations of zirconium in solution. The apparatus, which continuously recorded the zirconium concentration in the hydrofluoric acid work (6), was not used because of the extremely slow corrosion rates in sulfuric acid below 80%.

The solutions were made with conductivity water and reagent grade sulfuric acid. All concentrations recorded in per cent refer to per cent by weight.

Four zirconium samples were suspended by polyethylene strings in four separate beakers which were in a constant temperature bath. Each beaker contained 750 ml of the appropriate sulfuric acid solution. Initial experiments showed that the corrosion of unetched zirconium samples in aqueous sulfuric acid solutions was too slow to be studied in the time available with the proposed experimental technique. Even samples that had been etched in aqueous hydrofluoric acid solutions, then rinsed in distilled water, corroded very slowly. Except for a few initial experiments, the zirconium samples were first etched for 1 min in a 4% hydrofluoric, 30% nitric acid, aqueous solution to remove any oxide film. The sample was then placed immediately into the sulfuric acid solution. Experiment showed that a sample etched then placed immediately into water put about 1 x 10^{-4} g of zirconium in solution as reaction products from the etchant. After placing samples in the sulfuric acid solution, samples of the solution were taken immediately and at regular time intervals and counted in the scintillometer. The amount of zirconium (1 x 10^{-4} to 2 x 10^{-4} g) in the first solution-sample then was subtracted from subsequent measurements, to determine the amount of corrosion.

In many of the initial experiments the solution was stirred at various rates (stirrer speed 0 to 1500 rpm), since no effect from stirring could be detected over the concentration and temperature range of the experiments stirring was discontinued.

Results

Figures 1, 2, and 3 show a few examples of 42 experiments that were made over a range of 9 to 97% sulfuric acid. Figure 1 shows the amount of zirconium that dissolved in a 16.9% solution of sulfuric acid as a function of time. Nine independent experiments were made at this concentration. Experiments 1, 2, 3, and 4 in Fig. 1 illustrate a phenomenon that occurred only a few times during the study, that of a sudden increase in the rate, or break away for a period of time, after which the corrosion rate returned to approximately the original value. These four experiments were started at the same time and were all in the same constant temperature bath. For simplicity, only curves showing trends are drawn through the points.

Figure 2 illustrates the shape of the curves that resulted when the weight of dissolved zirconium vs. time was plotted for 24.4% sulfuric acid solutions at 44°C. In most of the experiments, a constant rate was observed after the initiation period.

Figure 3 shows a plot of the corrosion of zirconium in 31.4% and 55% sulfuric acid over a period of 800 hr. The temperature was changed during some of the experiments to find the effect on the reaction rate. It is seen that the corrosion of zirconium in sulfuric acid, under the conditions of these experiments, is linear with respect to time over long periods.

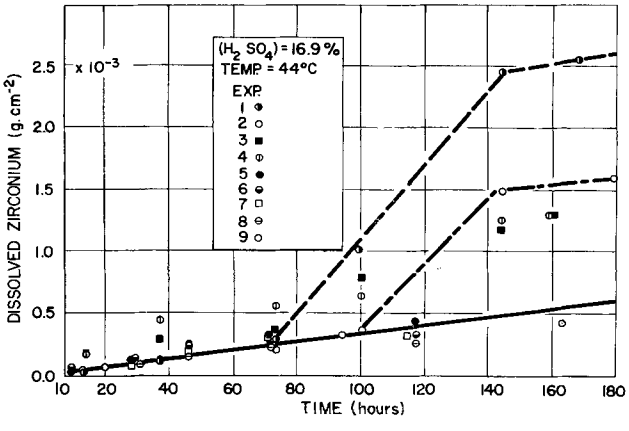

Fig. 1. Dissolved zirconium vs. time for a 16.9% sulfuric acid solution at 44°C. Shows break-away phenomenon.

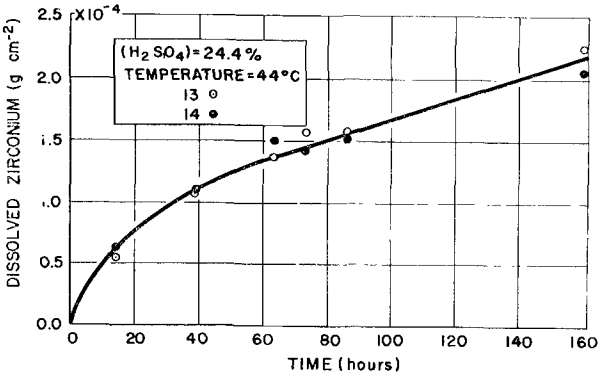

Fig. 2. Corrosion of zirconium in a 24.4% sulfuric acid solution at 44°C. Initial reaction follows the parabolic rate law.

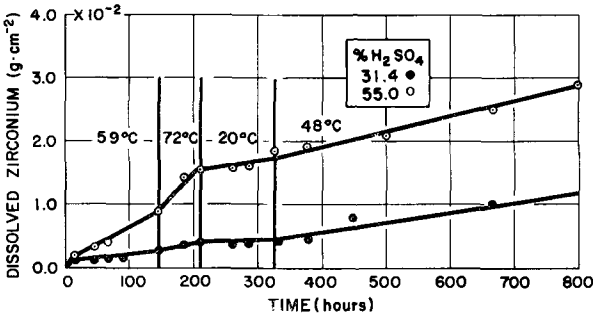

Fig. 3. Corrosion of zirconium in a 31.4 and 55% sulfuric acid solution, as a function of time and temperature.

Figure 4 is an Arrhenius plot for two experiments, one at 31.4% and the other at 55% sulfuric acid. An estimate of the activation energy from the experiment at 31.4% and 55% is about 7-8 kcal/mole.

Recorded in Table I is the rate of corrosion of zirconium at various concentrations of sulfuric acid, in weight per cent. The molarity of the sulfuric acid and the corresponding concentrations of the H^+, HSO_4^-, $SO_4^=$, and H_2SO_4 also have been recorded. These concentrations were estimated from the data given in the two reports by Young and Blatz (5) and Young (8) mentioned above.

Corrosion in solutions 9% or less was too slow to be detected in the time of the experiments. Between

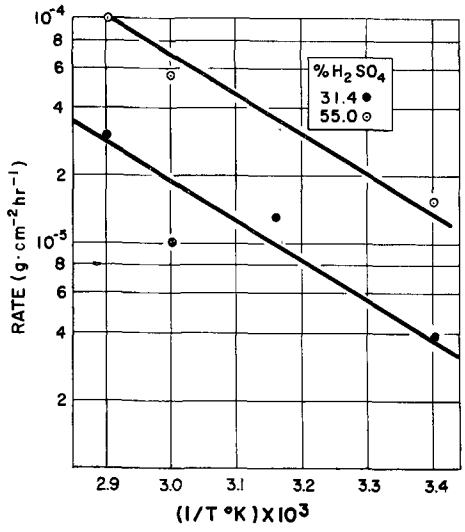

Fig. 4. An Arrhenius plot for zirconium corrosion in a 31.4 and 55% sulfuric acid solution.

9 and about 80% sulfuric acid the reaction rate was rapid at first then slowed down with time to a steady state. The samples had a clean metallic appearance while corrosion occurred, but were not bright. They appeared to have a very thin film that dulled their luster. At higher concentrations (around 80% or above) a white layer formed; some of this was scraped off and analyzed by x-ray diffraction. The x-ray diffraction pattern matched that of zirconium disulfate tetrahydrate as reported by Startzky and Singr (9) and also later by the National Bureau of Standards (10). At the highest concentrations (above 80%) the reaction rate was very fast and not reproducible. Black films formed that spalled and flaked off. The black material proved to be amorphous, giving broad peaks on x-ray analysis; many of the major peaks matched well in "d" value with those reported for ϵ zirconium hydride (ϵ-ZrH) by Hagg (11).

A weighed sample of zirconium turnings was reacted to completion in 96% sulfuric acid; the gas that evolved was collected and tested by infrared spectroscopy and by Orsat analysis. The gas proved to be

Table I. Corrosion rate of zirconium in sulfuric acid solutions as a function of concentration at 44°C

H_2SO_4, % by wt	Stoichiom conc. H_2SO_4, M	(H^+) M		$(SO_4^=)$ M		(HSO_4^-) M		(H_2SO_4) M		Rate‡ g cm^{-2} hr^{-1} x 10^{-4}	Rate, mdd
		*	†	*	†	*	†	*	†		
16.9	1.87	2.6	1.9	0.6	0.1	1.4	1.7	—	0.08	0.033	7.9
24.4	2.80	3.8	2.7	0.9	0.1	2.0	2.5	—	0.18	0.086	20.6
31.4	3.74	5.0	3.6	1.2	0.2	2.6	3.2	—	0.29	0.230	55.2
37.9	4.67	6.2	4.4	1.5	0.2	3.2	4.0	—	0.47	0.230	55.2
44.0	5.61	7.2	5.3	1.6	0.3	4.0	4.7	—	0.67	0.380	91.2
55.0	7.48	9.1	6.5	1.7	0.3	5.7	5.9	—	1.22	0.670	160
64.7	9.35	10.6	7.3	1.4	0.3	7.8	6.7	—	2.35	1.04	250
69.1	10.28	11.2	7.3	1.2	0.3	8.8	6.7	—	3.30	1.46	350
73.3	11.22	12.2	6.8	1.0	0.2	10.2	6.4	—	4.71	2.30	552
77.3	12.15	13.0	5.9	0.8	0.1	11.4	5.7	—	6.53	2.60	624
81.1	13.09	13.6	4.0	0.5	0.0	12.6	4.0	—	8.85	3.60	876
88.0	14.96	12.6	2.6	0.0	0.0	12.6	2.6	2.0	12.50	—	—
94.0	16.83	8.0	1.3	0.0	0.0	8.01	1.3	8.1	15.60	—	—
100.0	18.70	0.0	0.0	0.0	0.0	0.0	0.0	15.0	18.70	—	—

* Concentrations estimated from Fig. 4, Ref. (8).
† Concentrations estimated from Table II, Ref. (5).
‡ Rates were determined over the period 20-100 hr, and are an average of a number of experiments at each concentration.

pure hydrogen; the amount was stoichiometrically correct for the oxidation of zirconium to the +4 state. The product of the reaction in solution would be zirconyl sulfate tetrahydrate according to Blumenthal (12).

To determine if the rate was affected by oxygen concentration, an experiment was conducted for which the solution had been boiled, cooled in an argon atmosphere, and saturated with argon. No change in the rate could be detected by thus changing the oxygen concentration.

Many of the experiments were made stirring the solutions at different rates, but no effect on the reaction rate could be noted.

One experiment was conducted with a solution approximately 1.5% sulfuric acid, for about 3 hr at varying temperature and pressure to see if corrosion would increase appreciably. The temperature ranged from 38° to 177°C and the pressure from 200 to 800 psig. No corrosion could be detected for zirconium in this short time experiment, although the titanium liner of the autoclave showed marked dissolution, forming a blue complex in solution.

Pitting corrosion was not observed during this study.

Discussion

Very low corrosion rates for unetched samples is in accord with rates reported in the literature (1-4), and this is usually ascribed to a protective layer of oxide on the zirconium surface.

To help understand the mechanism by which the reaction between zirconium and sulfuric acid is inhibited, samples were placed directly from the aqueous hydrofluoric acid solution into the sulfuric acid solution. It was felt that in this manner any oxide film adhering to the zirconium would be stripped off in the etchant, leaving a clean surface for the initial corrosion in sulfuric acid. In this way, the growth of any new film could be followed by the rate zirconium dissolved in solution.

Although the reaction during the initial period (20-60 hr) was not very reproducible, the curves generally had the shape as shown in Fig. 2.

A log log plot of the data in Fig. 2 is linear with a slope of 0.5. The initial corrosion follows a parabolic rate law which can be associated then with the growth of a corrosion product film (13).

The greatly increased corrosion rates that followed the initiation period, as compared to rates reported in the literature, indicate that this film is not an oxide film as found on unetched samples, but much more pervious. An attempt to discover the structure or composition of the film by x-ray analysis of the surface of a flat plate of zirconium proved unsuccessful. One can speculate that the composition is similar to that found at the higher acid concentrations, zirconium disulfate tetrahydrate, or zirconium hydride. Another possibility might be the formation of a film with small amounts of fluoride which acts as a catalyst to promote corrosion. The few instances where break-away took place (1, 2, 3, and 4, Fig. 1) may be attributed to the formation of an unstable film which occasionally breaks down, causing higher corrosion rates for a short interval until the film reforms.

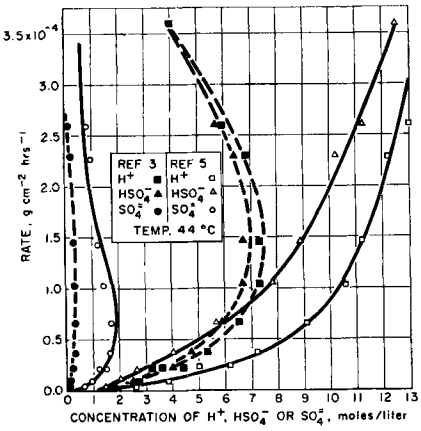

Fig. 5. Rate of corrosion of zirconium as a function of the concentration of H^+, HSO_4^-, and $SO_4^=$ ions.

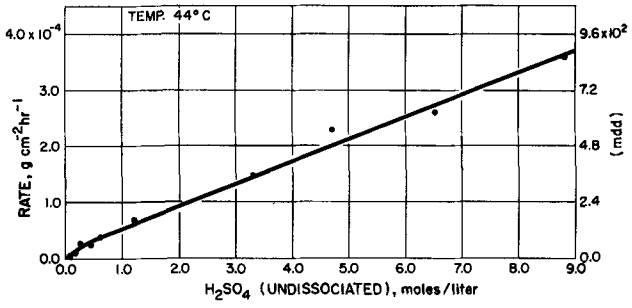

Fig. 6. Rate of corrosion of zirconium at various concentrations of undissociated H_2SO_4.

To find the effect of the individual ionic species on the rate of reaction, the steady-state corrosion rates were plotted as a function of the concentration of the ionic species separately in Fig. 5 and 6. The articles by Young and Blatz (5) and the later article by Young (8) report that, at low stoichiometric sulfuric acid concentrations, the major species are H^+ and HSO_4^-; at high acid concentrations H_2SO_4 increases rapidly. The article by Young and Blatz (5) reports that H^+, HSO_4^-, and $SO_4^=$ go through a maximum starting at a stoichiometric sulfuric acid concentration of about 6 to 7M. The later article by Young (8) gives the maximum for H^+ and HSO_4^- species at a much higher concentration, approximately 14M.

Figure 5 is a plot of the rate as a function of the concentrations of the H^+, $SO_4^=$, and HSO_4^- ions estimated from the two above mentioned articles. It is seen that, if the earlier report by Young and Blatz is correct, the rate is double valued for all of these species, and it can be concluded that the rate is independent of any of them. If the article by Young (8) is correct, the rate is still double valued for the sulfate ion and, although the curves for the H^+ and HSO_4^- ions are not double valued until much higher concentrations are reached, the shapes of the curves are such that it seems unlikely that the rate is a function of these ions in any case.

Figure 6 shows a plot of the rate as a function of the undissociated sulfuric acid concentration, based on the article by Young and Blatz (5). Within experimental error, the rate is directly proportional to the concentration of H_2SO_4. The points in Fig. 6 are

experimental, and the curve is a visual fit of these points.

Although the temperature at which Rao (7) did his work was not reported by him (he mentioned that he cooled his solutions by water), the temperature was probably close to room temperature or not far above this. Young (8) reported his later work was done at 25°C. The solutions used for the experiments reported in Table I were held at 44°C. In view of all the uncertainties involved, the values plotted in Fig. 5 and 6 probably have considerable error; however, the relative values and the shape of the curves should be reliable.

It seems reasonable to conclude that the species that controls the reaction rate is the undissociated sulfuric acid molecule, at least at the higher concentrations, and probably to as low as 0.5M. An equation for the linear portion of the curve in Fig. 6 is: $R = 4.0 \times 10^{-5} (H_2SO_4) + 1.0 \times 10^{-5}$ g cm^{-2} hr^{-1}, where R is the rate in grams of zirconium dissolving into solution per square centimeter of sample per hour.

By way of summary, the following observations have been made: under the conditions of these experiments the initiation reaction usually lasts from 20-40 hr and obeys a parabolic rate law. The initiation reaction is followed by a constant reaction rate which is somewhat higher than for unetched zirconium. The constant reaction rate appears to be a function of the undissociated H_2SO_4 concentration alone and is first order with respect to this species. At 44°C the specific reaction rate constant is 4.0×10^{-5} g cm^{-2} hr^{-1} moles^{-1} liter. The activation energy for the reaction slow step is 7-8 kcal mole^{-1}. No effect on the rate could be detected by stirring the solution or changing the oxygen concentration. No change in the appearance of the samples is detected until the solution becomes saturated with corrosion products, which crystallize as loose white crystals. The samples have a clean metallic appearance while corrosion occurs, but are not bright. They appear to have a very thin film that dulls their luster. Reaction of zirconium in solutions 80% sulfuric acid or higher gives rapidly increasing reaction rates, while loose films are formed that proved to be zirconium disulfate tetrahydrate. At the higher concentrations black films that flaked off are also formed; they are probably partly zirconium hydride. The gaseous reaction product is pure hydrogen; the amount evolved corresponds to that needed for zirconium to be oxidized to the +4 state.

Although these observations do not permit a very detailed account of the corrosion mechanism, they do allow the elimination of many of the possible mechanisms and point to further research which will narrow down the remaining possibilities.

The first order rate dependence on the undissociated sulfuric acid molecule and the low activation energy suggest the slow step to be some physical phenomenon involving this species, such as adsorption or diffusion. The initial reaction which follows a parabolic rate law indicates the growth of a reaction product barrier through which the reactants must diffuse. When the film reaches a limiting thickness, the reaction comes to a steady state as shown by the constant reaction rate which follows the initiation period. Another possibility could be that, as the reaction product film grows, it cracks, exposing only a small portion of the surface to reactants and that after the initiation period, exposure and closing off of reaction surface reaches a steady state.

Further experiments that would help elucidate the mechanism of corrosion of zirconium in sulfuric acid solution could be: electropolish the zirconium samples rather than etch them in hydrofluoric acid; weigh and measure the dimensions of both irradiated and unirradiated samples during corrosion, as a check on the tracer method, to see if irradiation affected the rate, and so that a material balance could be made accounting for the corrosion products that remained on the sample and that which dissolved in solution; investigate the reaction product film that adheres to the zirconium by electron diffraction and chemical analysis, if possible; and investigate the current potential relationships during the dissolution of zirconium in sulfuric acid solutions.

Acknowledgment

This research was supported by a grant from the Atomic Energy Commission. This paper was abstracted from a thesis submitted to the faculty of the University of Utah, Dept. of Fuel Technology, in partial fulfillment of the requirement for a Ph.D. degree, June 1956.

Manuscript received March 19, 1959.

Any discussion of this paper will appear in a Discussion Section to be published in the December 1960 JOURNAL.

REFERENCES

1. B. Lustman and F. Kerze, Jr., "The Metallurgy of Zirconium," McGraw-Hill Book Co., New York (1955).
2. L. B. Golden, "Zirconium and Zirconium Alloys," p. 305, American Society for Metals, Cleveland, Ohio, May (1953).
3. R. J. Gegner and W. L. Wilson, "The Corrosion Resistance of Titanium and Zirconium in Chemical Plant Exposures," Paper presented at the 15th annual conference, N.A.C.E., Chicago, Illinois, March 12-20, 1959.
4. W. E. Kuhn, "More Zr Facts", Col. 1, No. 2, p. 5, (1957), Publication of the Carborundum Metals Co., Akron, New York.
5. T. F. Young and L. A. Blatz, *Chem. Rev.*, **44**, 102 (1949).
6. T. Smith and G. R. Hill, *This Journal*, **105**, 117 (1958).
7. N. R. Rao, *Indian J. Phys.*, **14**, 143 (1940).
8. T. F. Young, *Record Chem. Prog.*, **12**, 81 (1951).
9. E. Startzky and J. Singr, *Anal. Chem.*, **28**, 553 (1956).
10. Nat. Bur. Standards *Circular* 539, **7**, p. 66 (1957).
11. G. Hagg, *Z. Phys. Chem.*, **11**, 433 (1930).
12. W. B. Blumenthal, *Ind. Eng. Chem.*, **46**, 528 (1954).
13. H. H. Uhlig, Editor, "The Corrosion Handbook," John Wiley & Sons, Inc., New York (1948).

The Relationship between Brightness and Structure in Electroplated Nickel

R. Weil and R. Paquin

Department of Metallurgy, Stevens Institute of Technology, Hoboken, New Jersey

ABSTRACT

Nickel deposits of various brightnesses were plated from Watts baths containing several different addition agents. The as-plated surfaces of the deposits were examined by electron microscopy. All bright deposits had a very fine-grained structure. However, some fine-grained deposits showed surface crevices and were therefore not bright. A linear relationship between the fraction of the surface area having a roughness less than 0.15 μ and the logarithm of light reflected as measured with a photocell was found. There is no direct relationship between the degree of preferred orientation and brightness, but the fiber axis is related to the type of structure observed, i.e., platelet, equiaxed crystallite, or spiral-type, and the addition agents in the plating bath.

The relationship between the light-reflecting property generally referred to as the brightness and the structure of electrodeposits has been the subject of many investigations. These studies have led to two theories. One theory advanced by Kohlschütter (1), Liebreich (2), and others states that electrodeposits are bright if their microstructure consists of crystallites smaller than the wave lengths of visible light, i.e., smaller than 0.4 μ. However, Read and Weil (3) and Denise and Leidheiser (4) have shown that not all very fine-grained deposits are bright.

The second theory which, among others, Hume-Rothery and Wyllie (5) and Blum, Beckman, and Meyer (6) have formulated, states that the more oriented the grain structure, the brighter the deposit. Smith, Keeler, and Read (7) and Denise and Leidheiser (4) found this relationship not to hold.

Therefore, the need for further study to determine what structural features determine brightness was indicated and this investigation was undertaken.

Experimental Procedure

Nickel electrodeposits having a range of brightnesses from dull gray to specular were plated from Watts baths containing the various addition agents listed in Table I. The baths were agitated by pumping solution from the region near the cathode into the anode bag, which also served as a filter. Three deposits were plated from each bath to a thickness of about 50 μ; for two deposits, the starting cathode was electropolished copper sheet and for the third, mechanically polished, mild steel.

The microstructures of the as-plated surfaces were examined by electron microscopy. Collodion replicas made in the manner described by Weil and Read (8) and carbon replicas prepared according to the method of Grube and Rouze (9) were used. In view of the claims found in the literature (10) that the microstructure of bright deposits cannot be resolved by electron microscopy, a thin surface layer of the deposit was examined directly in order to eliminate possible extraneous structural features resulting from shadowing or the replicating medium.

The thin surface layers were obtained by partially immersing one of the deposits plated on copper sheet in a copper-cyanide bath immediately after removal from the nickel-plating bath and rinsing in water. A copper layer approximately 1000Å thick was deposited. After rinsing again, part of the copper-plated nickel deposit was immersed again in the

Table I. Plating conditions and addition agents

Bath composition: 400 g/l $NiSO_4 \times 6H_2O$, 45 g/l $NiCl_2 \times 6H_2O$, 45 g/l H_3BO_3

Plating conditions: pH:4.0; temperature 60° ±2°C, current density 5 amp/dm²

Specimen No.	Addition agent
3000	None
3001	0.2 g/l 1-5 Naphthalene disulfonic acid
3002	0.4 g/l 1-5 Naphthalene disulfonic acid
3003	0.6 g/l 1-5 Naphthalene disulfonic acid
3004	0.6 g/l 1-5 Naphthalene disulfonic acid + 0.2 g/l chloral hydrate
3005	0.6 g/l 1-5 Naphthalene disulfonic acid + 0.6 g/l chloral hydrate
3006	1.0 g/l 1-5 Naphthalene disulfonic acid + 0.6 g/l chloral hydrate
3007	0.2 g/l p-Toluene sulfonamide
3008	0.6 g/l p-Toluene sulfonamide
3009	0.6 g/l p-Toluene sulfonamide + 0.2 g/l chloral hydrate
3010	0.6 g/l p-Toluene sulfonamide + 0.6 g/l chloral hydrate
3011	1.0 g/l Zinc + 0.6 g/l 1-5 naphthalene disulfonic acid
3012	1.0 g/l Zinc + 1.0 g/l 1-5 naphthalene disulfonic acid
3013	0.09 g/l Aniline
3014	0.18 g/l Aniline
3015	0.31 g/l Benzoic acid
3016	0.08 g/l Saccharin
3017	0.20 g/l Saccharin
3018	0.40 g/l Saccharin
3019	0.60 g/l Saccharin
3020	Harshaw Chemical Co. Nubrite addition agents

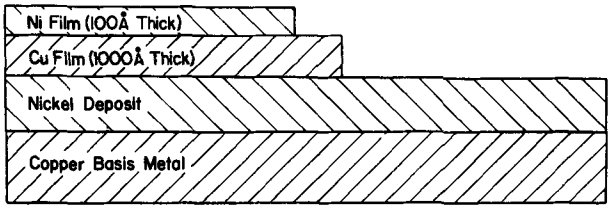

Fig. 1. Schematic representation of deposits for obtaining transparent nickel films.

original nickel bath and a thin nickel film, approximately 100Å thick, plated over the copper layer. Thus, the surface of this sample consisted partly of the original nickel plate, partly of the thin copper layer, and partly of the second nickel deposit as schematically represented in Fig. 1. Collodion replicas from the surfaces of the original nickel deposit, the copper film, and the nickel film were examined electron microscopically as were carbon replicas from the original nickel deposit and the nickel film. The purpose of these examinations was to determine if the nickel and copper films had copied the structure of the original nickel deposit. When this was found to be so, the nickel film was stripped by dissolving the copper layer in an aqueous solution of 50 g/l H_2SO_4 and 500 g/l CrO_3.

The light-reflecting properties of the deposits were determined by directing a beam from a zirconium arc through a slit onto the specimen and measuring the reflected light with a photocell. The incident beam made an angle of 10° with the normal to the sample and the photocell was placed along a line 10° to the normal on the other side. The brightnesses of the three areas of the sample represented in Fig. 1 as well as of the other two deposits were measured. In spite of the polishing there were some irregularities in the starting-cathode surface which resulted in lower brightness measurements. Therefore, the maximum reading is recorded in Table II. The various deposits also were arranged in five classifications of brightness as judged by eye. These data are also included in Table II. The order of brightness by eye evaluation, with one exception, was the same as that obtained with photocell measurements.

Table II. Experimental results

Specimen No.	Quantity of light reflected, ft. candles	Eye evaluation brightness group*	Percentage of area with roughness less than 0.15μ	Fiber axis‡
3000	4.5	I	7.4	(100)s
3001	47.5	IV	86.4	(311)+(111)w
3002	58.5	IV	93.4	(311)+(111)w
3003	58.5	IV	95.5	(311)+(111)w
3004	95.0	V	99.7	(100)s
3005	28.0	II	66.8	(100)s
3006a†	80.0	V	81.1	(100)s
3006b†	43.0	IV	100	(100)s
3007	53.5	IV	86.2	(100)s
3008	48.5	IV	84.5	(100)vs
3009	50.0	IV	84.9	(100)vs
3010	50.0	IV	84.0	(100)vs
3011	66.0	IV	93.4	(311)+(111)w
3012	>100	V	99.4	(311)+(111)w
3013	4.0	I	2.8	(110)m
3014	4.0	I	3.4	(110)m
3015	6.3	II	19.4	(110)m
3016	13.0	II	41.0	(100)m
3017	35.0	III	74.1	(100)s
3018	29.0	III	69.2	(100)s
3019	25.0	III	65.0	(100)s
3020	>100	V	100	(311)+(111)w

* Brightness increases with group number.
† Part of deposit was hazy (a), part bright (b).
‡ s = strong, vs = very strong, m = medium, w = weak.

The fiber axis of the deposits was determined by x-ray diffraction. The nickel deposit first was stripped off the copper basis-metal by dissolving the copper in the sulfuric acid-chromium oxide mixture mentioned previously. The nickel deposit was bent into a convex shape through an arc of a circle of 10 cm radius and an x-ray beam was directed along its surface. The results of these determinations are recorded also in Table II.

For reasons which will be explained later, measurements to determine the fraction of the surface area which had a roughness less than 0.15 μ were made on electron photomicrographs of collodion replicas. Polystyrene latex spheres which were 0.514 μ ±0.011 μ in diameter, obtained from the Dow Chemical Company, Midland, Michigan, were placed on the replicas and palladium evaporated on them subsequently. The heights of the various structural components were determined from the ratio of their shadows to those of the latex spheres. The area occupied by those components of the structure more than 0.15 μ above or below the surface then was measured with a planimeter and the value subtracted from the total area of the photograph in order to get that fraction of the whole surface which was reflecting light. The results of these measurements also are included in Table II.

Experimental Results

Three structural types corresponding to the three different fiber axes were observed in the deposits plated in the baths containing the various addition agents. The type of structure was affected by the addition agent, but the structures of all deposits plated from a given bath were the same regardless of the basis metal.

The deposits having a (100) fiber axis[1] were found to consist of platelets. A number of platelets were stacked parallel to each other and comprised a colony. In most of the deposits exhibiting this type of structure, a depression in the surface resembling a grain boundary existed between colonies of platelets. The thickness and the spacing of the platelets within a colony varied widely between deposits from different baths. Figure 2 shows coarsely spaced and relatively thick platelets and a large colony size. Figure 3 shows a finer spacing and a smaller colony size. A structure with still finer platelets, although possessing a larger colony size than shown in Fig. 3, can be seen in Fig. 4. The x-ray diffraction patterns of the structures with the (100) fiber axis showed the anomalous intensity maximum at the meridian which Clark and Simonsen (11) explained on the basis of a twinning relation between the platelets. Structures with platelets were found in deposits

[1] The term, fiber axis is used here in the same sense as in Ref. (7).

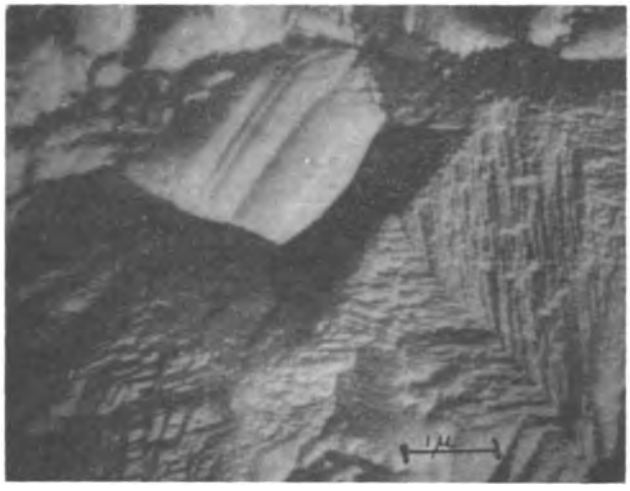

Fig. 2. Electron micrograph of nickel deposit showing coarse platelets and large colony size.

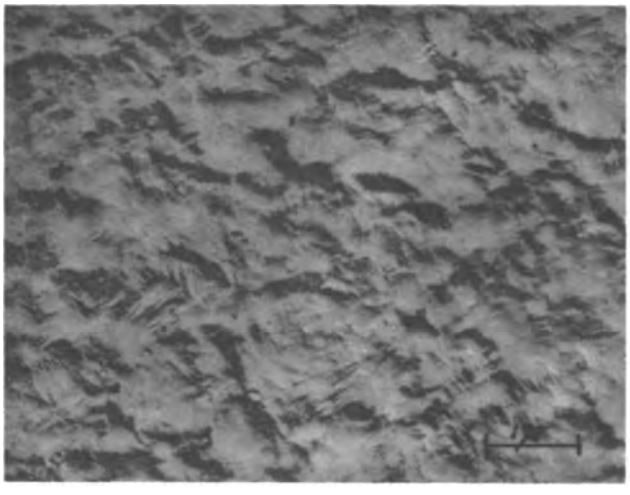

Fig. 3. Electron micrograph of nickel deposit showing medium-fine platelets and small colony size.

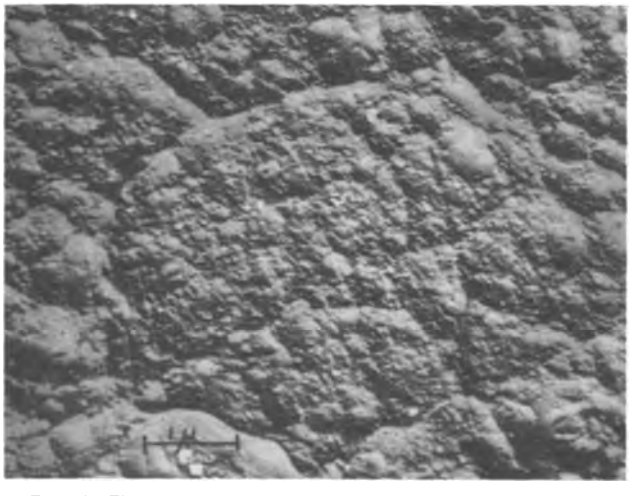

Fig. 4. Electron micrograph of nickel deposit showing fine platelets, but large colony size.

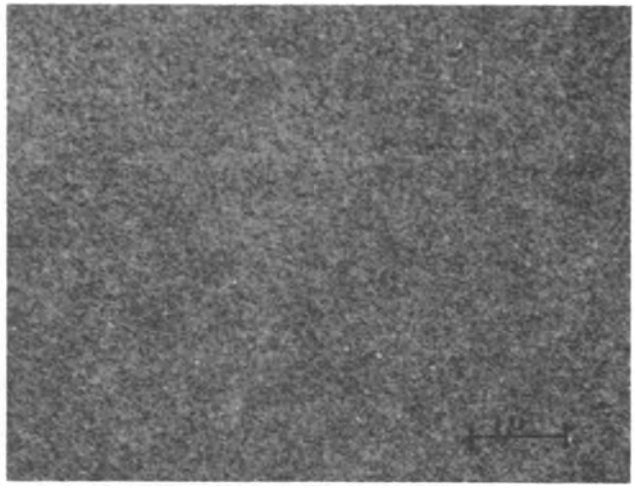

Fig. 5. Electron micrograph of specular nickel deposit

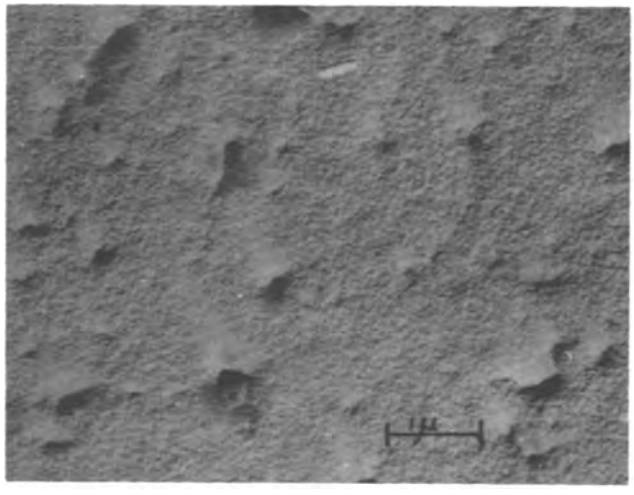

Fig. 6. Electron micrograph of hazy nickel deposit showing fine-grained structure with crevices.

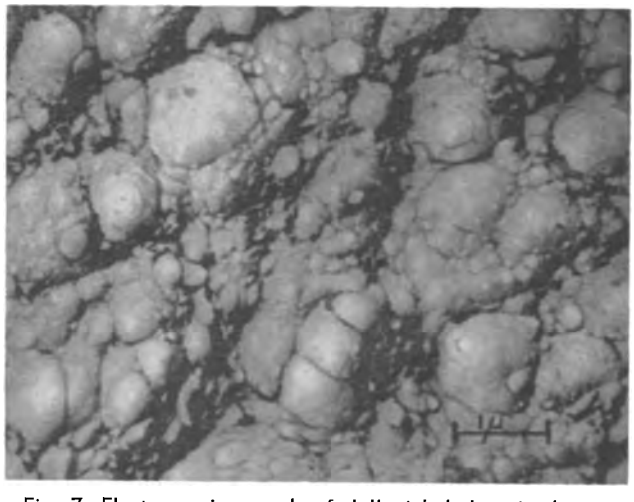

Fig. 7. Electron micrograph of dull nickel deposit showing spiral-type growth.

from plain Watts bath and from baths with chloral hydrate, p-toluene sulfonamide, and saccharin additions.

The second structural type, which was associated with a (311) + (111) fiber axis, consisted of fine crystallites which appeared equiaxed in the surface plane of the deposits. Most of the bright deposits exhibited this type of structure, but so did some hazy ones. Figure 5 shows the structure of a specular deposit as seen by transmission through the thin nickel surface film. In hazy deposits with this type of structure, depressions in the surface were observed. These depressions appear as dark areas in Fig. 6, which is an electron micrograph of a negative collodion replica, shadowed with palladium. The raised portions in

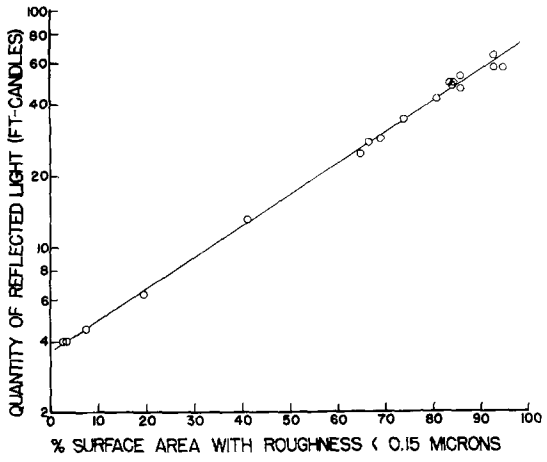

Fig. 8. Relationship between amount of light reflected and the fraction of the area with roughness less than 0.15 μ.

the replica result from depressions in the surfaces of the electrodeposit. Baths containing naphthalene disulfonic acid without chlorate hydrate and the bath containing the Harshaw Chemical Company proprietary brightener resulted in deposits of the second type.

Spiral growth was found in electrodeposits having a (110) fiber axis. This structure, represented by Fig. 7, was found in nickel plated from Watts baths containing aniline and benzoic acid. It is noteworthy that some deposits plated in an all-chloride bath without additives in connection with some other work performed by a graduate student at this institution also showed spiral-type growth. These deposits were found to have a (110) fiber axis. Banerjee and Goswami (12) reported the same preferred orientation under the same plating conditions. All deposits of this type were dull.

In attempting to relate microstructure and brightness, it was noted that all bright nickel samples in addition to having very small structural components also showed no crevices, deep grain boundaries, or protrusions which extended more than 0.15 μ from the surface plane. It therefore was assumed arbitrarily that only that fraction of the surface area with a roughness less than 0.15 μ specularly reflects light. This light-reflecting area was measured in the way previously described. A graph of brightness vs. fraction of surface area with a roughness less than 0.15 μ is shown in Fig. 8.

Discussion

It is apparent from Fig. 8 that the brightness depends on the degree to which the structural components of the surface of electrodeposits are in one plane. This, in turn, is determined by several factors such as grain size and orientation, the degree of preferred orientation, and codeposition of foreign substances. The grain size is important because the boundaries between large grains appear as deep crevices in the surface of electrodeposits. Structures composed of large platelets will show coarse steps between the plates. It is therefore necessary for bright deposits to be very fine-grained. However, it is also apparent from data in Table II that a small grain size is not a sufficient condition for brightness. The deposits showing spiral-type structures were dull even though some were fine grained because this type of growth results in crystals which have no light-reflecting plane parallel to the surface and consequently the tops of the grains protrude above the intergranular crevices. The orientation of the crystals which determines whether a light-reflecting plane is parallel to the surface therefore affects the brightness.

The size of the crevice between neighboring grains is certainly influenced by their relative orientations. It is expected that a group of crystallites with a common fiber axis would have very small crevices between them. As the degree of preferred orientation is only one of several factors which determines the surface roughness, it is not to be expected that there is a unique relationship between preferred orientation and brightness. Certainly, the findings previously cited (4, 7) that preferred orientation is not proportional to brightness have been substantiated. Even for a given fiber axis, no direct correlation has been found.

The smoothness of the surface has been shown by Beacon and Riley (13) to be dependent on the distribution of addition agents. By means of brighteners containing a radioactive atom, they showed that preferential codeposition takes place at protrusions, hindering crystal growth at these sites and thereby tending to eliminate the crevices. This could explain why there were no depressions in the surface with certain addition-agent concentrations.

The scatter of data for high light-reflecting values in Fig. 8 is probably due to the fact that, when most of the area has a roughness less than 0.15 μ, smaller changes in the morphology of the surface become significant. The photocell was also not as accurate at high light intensities as at lower ones. In the deposits with over 99% of their area having a roughness less than 0.15 μ, an increase in brightness and decreasing grain size was noted. The number of samples was not sufficient to definitely establish a relationship between brightness and grain size.

Conclusions

1. A direct relationship exists between the fraction of the surface roughness less than 0.15 μ and brightness in electroplated nickel.

2. The observations of others that fine-grained deposits need not be bright have been confirmed and explained.

3. A correlation between type of microstructure and fiber axis has been found.

4. There is no unique relationship between brightness and the degree to which the fiber axis is parallel to the corresponding crystallographic direction in each grain of the deposit.

Acknowledgments

Professor Harold J. Read of the Pennsylvania State University and Professors Alfred Bornemann and Theodore Gela of Stevens Institute of Technology read the manuscript and made valuable suggestions.

The work described in this paper was sponsored by the Office of Ordnance Research, U. S. Army.

Manuscript received Aug. 10, 1959. This paper was prepared for delivery before the Columbus Meeting, Oct. 18-22, 1959.

Any discussion of this paper will appear in a Discussion Section to be published in the December 1960 JOURNAL.

REFERENCES

1. V. Kohlschüter, *Trans. Electrochem. Soc.*, **45**, 229 (1924).
2. E. Liebreich, *Trans. Faraday Soc.*, **31**, 1188 (1935).
3. H. J. Read and R. Weil, *Plating*, **37**, 1239 (1950).
4. F. Denise and H. Leidheiser, Jr., *This Journal*, **100**, 490 (1953).
5. W. Hume-Rothery and H. R. Wyllie, *Proc. Royal Soc. (London)*, **181A**, 331 (1943).
6. W. Blum, A. O. Beckman, and W. R. Meyer, *Trans. Electrochem. Soc.*, **30**, 249 (1941).
7. W. Smith, J. H. Keeler, and H. J. Read, *Plating*, **36**, 355 (1949).
8. R. Weil and H. J. Read, *Metal Finishing*, **53**, [11], 60 (1955).
9. W. L. Grube and J. R. Rouze, *Proc. ASTM*, **52**, 573 (1952).
10. K. M. Gorbunova, J. Popova, A. A. Sutyagina, and V. M. Polukarvo, "Crystal Growth, Report of First Conference, 1956," p. 46, Consultants Bureau (English Transl.), New York (1958).
11. G. L. Clark and S. H. Simonsen, *This Journal*, **98**, 110 (1951).
12. B. C. Banerjee and A. Goswami, *ibid.*, **106**, 21 (1959).
13. S. E. Beacon and B. J. Riley, *General Motors Engrg. J.*, **6**, [2], 21 (1959).

The Adhesion of Electrodeposited Nickel to Chromium at Elevated Temperatures

Walter E. Reid, Jr. and Fielding Ogburn

Chemistry Division, National Bureau of Standards, Washington, D. C.

ABSTRACT

The use of a composite coating of electrodeposited nickel and chromium to protect molybdenum from oxidation at elevated temperatures has certain practical limitations. Examination of the composite coating showed that the problems of blister formation, weakening of the bond between nickel and chromium, and edge separation were interrelated. Blister formation was eliminated and edge separation reduced slightly by an improved treatment of the chromium surface prior to nickel plating. The weakening of the bond between nickel and chromium appears to be inherent in the coating system.

The application of a composite coating of electrodeposited nickel and chromium to protect molybdenum from oxidation at elevated temperatures has been described by Couch and co-workers (1). The use of this coating at elevated temperatures (800°-1200°C) has associated with it certain problems caused by the difference in the properties of the metals involved. Heating and thermocycling tests of the composite coating showed that (*a*) heating to 800° or 1000°C frequently, but not consistently, resulted in the formation of blisters between the chromium and nickel layers, (*b*) prolonged heating weakened the bond between the nickel and chromium layers, and (*c*) thermocycling between room temperature and 800° or 1000°C caused a separation of the nickel from the chromium, principally at sharp edges or corners.

An investigation of these three closely interrelated problems was necessary, since they represent practical limitations to the use of the coating system.

Blister Formation

Blister formation was observed on a number of specimens, electroplated with 0.007 in. of nickel over 0.001 in. of chromium, after they had been heated in a helium atmosphere to 850°C. These had been plated by the procedure described by Couch and co-workers. Examination of the blisters revealed that they always formed within the nickel-chromium diffusion alloy and not at the original nickel-chromium interface. Both nickel and chromium were detected chemically on the entire inner surface of the blister. Also the occurrence of blisters usually was accompanied by poor adhesion of the nickel to chromium on other parts of the specimen where blistering had not occurred.

Since blister formation is often caused by improper cleaning prior to plating, we examined a number of modifications in the plating cycle between the chromium and Watts nickel plating steps. Modifications included anodic and cathodic treatment of the chromium surface in different solutions, elimination of the water rinse, variation of current density for the nickel strike, and the immersion time in the nickel strike bath prior to electroplating.

The only change which eliminated blistering was the substitution of anodic etching in an acetic acid solution for the hydrochloric acid etch.

Acetic Acid Etch

Glacial acetic acid, to which had been added 10 to 15% H_2SO_4 by volume to increase the conductivity, constituted the etch solution. An inert cathode was used. Specimens were etched anodically in the solution at current densities of 3-7 amp/dm^2 until the surface of the chromium was covered uniformly with

a dark brown film. They were rinsed rapidly in water and placed in the Wood's nickel bath with electrical contact made beforehand so that plating began as the specimen was immersed. The specimens were plated at 25-30 amp/dm^2 for 2 to 4 min, then transferred directly to a Watts nickel bath.

A brief study of the etching process showed that an etching time of 5 min at 4 amp/dm^2 was usually sufficient. The time of exposure of the specimen to air after the water rinse and prior to insertion of the specimen into the Wood's nickel strike bath was not critical as long as it was brief and the specimen did not become dry. After adoption of this etch procedure in the plating cycle, blister formation was not encountered.

Adhesion

No difficulty was encountered with the adhesion of nickel to chromium in the "as plated" condition when either the plating procedure described by Couch and co-workers (1) or the acetic acid etch was used.

Heat treatment, however, caused a weakening of the bond between the chromium and nickel. This occurred when the nickel-chromium plated specimens were heated to 850°C in helium and held at this temperature for 1 hr. Very good adhesion was obtained with the acetic acid etch of chromium, even after extension of the heat treatment to 24 hr or with thermocycling (10 min in oven at 850°C, 10 min at room temperature) in air for 24 hr. Only a few such specimens were subjected to these more severe tests, but each one retained good bonding between the chromium and nickel.

A still more severe heat treatment of the same specimens, either at higher temperatures or for longer periods, resulted in a weakened bond. Thus, while it has been possible to improve the performance of the coating system with respect to bond failure, the problem still exists for prolonged heating at higher temperatures.

To gain additional insight into the weakening of the bond, a few experiments were conducted with short lengths of chromium plated nickel rods which were heat-treated to alloy the chromium and nickel. Additional nickel was plated over the chromium to serve as a grip for the measurement of the bond strength between the chromium and nickel rod by the Ollard method. Duplicate specimens were heated in helium at 850°C for 24 and 66 hr and compared with duplicate specimens in the as-plated condition. While the bond strength measurements were not highly reproducible, they showed a reduction in bond strength of 75 to 90%. This shows that bond strength is lost on heating when chromium is plated on nickel, just as when nickel was plated on chromium in the earlier experiments. Hence, it would appear that deterioration of the bond is an inherent property of the nickel-chromium system no matter how the nickel-chromium interface is prepared and is the result of the interdiffusion of nickel and chromium. The diffusion process leads to the formation of a weak layer which becomes the plane of separation. This weak layer could be simply an alloy of low tensile strength. It could also consist of a line of voids formed by the diffusion process (2) or a line of inclusions as observed by Couch and co-workers (1).

In summary, two factors can affect adversely the adhesion of the coating: (*a*) passivity of the chromium surface, and (*b*) alloying of the nickel and chromium. The first can be reduced by proper pretreatment of the chromium, but the second appears to be a property of the coating system.

Adhesion of Chromium to Molybdenum

As indicated above, the problem of blister formation was associated with the deposition of nickel on chromium. Usually, the adhesion of chromium to molybdenum was not a problem; however, an occasional lack of adhesion was encountered.

In the anodic etching of molybdenum in the sulfuric-phosphoric acid solution prior to plating, the metal becomes covered with a viscous film which is not entirely removed by simple rinsing in water. It was found that a subsequent short immersion in an acidified chromic acid solution (3) resulted in excellent adhesion. The composition of the immersion solution is given below. Other compositions were not considered, since no case of poor adhesion was encountered after adoption of this cleaning procedure.

Procedure.

1. Clean and anodically etch molybdenum in 1:1 H_2SO_4 (95%)-H_3PO_4 (85%) at 5-20 amp/dm^2 for 2 to 3 min.
2. Rinse thoroughly in water.
3. Immerse molybdenum for 3 min in an aqueous solution containing: 6% of CrO_3 by weight, 15% of H_2SO_4 by volume, and 15% of concentrated HCl by volume.
4. Rinse thoroughly in water.
5. Place in chromium bath about 30 sec before making electrical contact.
6. Plate in the chromium bath at 120 amp/dm^2 and 80° to 85°C.

"Edge Separation"

The resistance to thermal shock of a number of molybdenum specimens with a composite coating of chromium and nickel was evaluated by thermocycling them in air between room temperature and 800°-1100°C. The thermocycling was accomplished by lowering the specimens into a tube furnace at the desired temperature for 10 min and then withdrawing them to cool for 10 min. This cycle was repeated automatically for the duration of the test.

Microscopic examination of cross sections of specimens which had been cycled 6 times to 800°C revealed a slight parting within the coating in the immediate vicinity of a sharp corner or edge of a rectangular specimen. Specimens cycled for longer periods of time or at higher temperatures showed that the size of the void increased and also extended along the flat surfaces. In an extreme case, the separation of the coating extended over the entire circumference of a rod 0.25 in. in diameter after being cycled 16 times to 1100°C. The coating was intact, but was only very loosely held to the rod.

The "edge separation" always was observed as occurring within the nickel-chromium diffusion al-

loy. In view of this, the phenomenon of "edge separation" may be considered as another manifestation of the problem associated with the formation of a weak layer between the nickel and chromium.

Stresses due to Unequal Expansion of the Metals

A major factor contributing to the deterioration of the bond between the nickel and chromium when plated on molybdenum is the difference in the coefficients of expansion of the three metals. The expansion coefficient for nickel is about 2½ times that for molybdenum. Heating therefore would be expected to cause stresses which would tend to fracture the composite coating, especially where the radius of curvature is small. The equations used by Lander and Germer to explain spalling (4) also can be applied to this problem.

In these equations plastic flow is neglected and it is considered that a cylinder of metal A is plated with a metal B. They give for the normal pressure at the interface

$$P = \frac{2h}{d} (\alpha_B - \alpha_A) E_B t$$

and for the circumferential stress per unit area

$$S = (\alpha_B - \alpha_A) E_B t$$

where*: E is modulus of elasticity; α, coefficient of thermal expansion; d, diameter of cylinder; h, thickness of coating; and t, degrees Centigrade above room temperature. Though these equations do not include all the factors involved, they do help us to understand the stresses involved.

Since initial edge separation is governed by the stresses normal to the surface, the first equation is of primary interest. Consider a molybdenum surface with a radius of curvature of 0.3 in. plated with 0.008 in. of nickel over 0.001 in. of chromium. If this is heated to 800°C, the calculated normal stress is 5200 psi at the nickel-chromium interface and 1000 psi at the chromium-molybdenum interface. Thus the normal stress is greatest at the nickel-chromium interface and is of the order of the nickel-chromium (5) bond strength. The equation leads us to expect coating separation if the radius of curvature is small or the coating is thick.

These predictions are in qualitative agreement with the experimental evidence. Edge separation occurs initially at corners of rectangular specimens where the radius of curvature is small and at the chromium-nickel interface. If the corners are rounded off by increasing the thickness of chromium, edge separation is less likely. For example, two specimens were cycled 50 times to 980°C. One specimen had been plated with 0.004 in. of chromium and 0.006 in. of nickel, and the other with 0.001 in. of chromium and 0.006 in. of nickel. Edge separation occurred to a much greater extent on the specimen with the thinner layer of chromium.

The predicted low normal stress at the chromium-molybdenum interface is also verified by experiments for which rectangular molybdenum specimens were plated with 0.009 in. of chromium. After cycling 50 times to 980°C, no coating separation was observed.

Once the coating separation has been initiated, the analysis of the situation is different. Heating of the specimen causes the loose nickel layer to expand and the result is a high concentration of stress where the nickel joins the underlying metal. This stress concentration causes an extension of the void so that a peeling action of the coating occurs with continued thermocycling.

* The following quantities are used in the present discussion:

$\alpha_{Mo} = 5.5 \times 10^{-6}/°C$
$\alpha_{Cr} = 8.1 \times 10^{-6}$
$\alpha_{Ni} = 13.7 \times 10^{-6}$
$E_{Ni} = 30 \times 10^{6}$ psi
$E_{Cr} = 20 \times 10^{6}$ psi

Acknowledgment

The authors express appreciation to the Navy Department Bureau of Aeronautics, for financial support of the project and for permission to publish the results. Acknowledgment is also made to D. E. Couch and H. Shapiro, who did most of the experimental work on "edge separation."

Manuscript received July 30, 1959.

Any discussion of this paper will appear in a Discussion Section to be published in the December 1960 JOURNAL.

REFERENCES

1. D. E. Couch, H. Shapiro, J. K. Taylor, and A. Brenner, *This Journal*, **105**, 450 (1958).
2. R. S. Barnes and D. J. Mazey, *Acta Met.*, **6**, 1 (1958); R. S. Barnes, *Proc. Phys. Soc.*, **B65**, 512 (1952).
3. *Welding Engineer*, **44**, 41 (1959).
4. J. J. Lander and L. H. Germer, *Metals Tech.*, **14**, No. 2259 (1947).
5. A. Brenner, P. Burkhead, and C. W. Jennings, *Proc. Amer. Electroplaters' Soc.*, **34**, 32 (1947).

Temperature and Space-Charge Effects in Liquid Hydrocarbons

R. Coelho[1] and M. Bono[2]

Laboratory for Insulation Research, Massachusetts Institute of Technology, Cambridge, Massachusetts

ABSTRACT

Preliminary results on the residual d-c conduction and space-charge polarization in n-hexane and n-heptane under highly inhomogeneous field conditions (thin wire in coaxial cylinder) are presented. A residual current is observed under high applied voltage for either polarity of the test cell. At 20°C the current is one order of magnitude larger when the wire is the positive electrode. As temperature is increased, the residual current for the wire positive decreases and for the wire negative increases, until at 50°C it is about the same for both polarities. By heating only the wire, observations supporting and extending these findings were made. The gross features of the current-voltage characteristics can be explained by dissociation of polar impurities in the region of high field strength. The dependence on polarity can be explained by space-charge distortion of the field. For negative wire, field emission appears to occur from the wire, surrounding it with a current-limiting space charge.

For a number of years, work in this laboratory has emphasized the importance of field emission for certain types of electric breakdown in gases (1), liquids (2), and solids (3), and the role of space-charge buildup in front of the cathode as a means of providing the required gradient. Also, the charging-up of surface layers comes into play, as demonstrated impressively, for example, in the Malter effect (4) and in the work of Llewellyn Jones and co-workers (5).

The present investigation deals with space-charge phenomena in n-hexane and n-heptane, in continuation of the work by Green (2). His principal findings on d-c currents under nearly homogeneous field were that the current-voltage characteristics consist of a low-field region, dominated by the ions of the liquid, and of a high-field region in which the decisive role is played by the cathode as a source of field emission.

The main purpose of our measurements was to extend the study to a highly inhomogeneous electrode configuration (thin wire in large coaxial cylinder) that allows separation of anodic and cathodic effects.

Experimental

The test cell (Fig. 1) consisted of a platinum wire (1 mil diameter) stretched along the axis of a carefully polished platinum cylinder (about 10 mm diameter and 30 mm long) with ends rounded to avoid edge effects. The geometrical field strength on the wire is roughly 400 times greater than that on the cylinder surface. The cylinder was connected, through a 50-megohm resistor, to a reversible high-voltage 30-kv power supply (Beta Electric Co.) driven by a Sorensen a-c voltage regulator. The maximum ripple, observed with an oscilloscope, was less than 1.5 v peak to peak at 10 kv. The wire was connected to a vibrating-reed electrometer whose output was sent through a General Electric self-balancing potentiometer into an Esterline-Augus recorder (Fig. 2). The equipment in its shielded cage was tested up to 20 kv for the absence of corona.

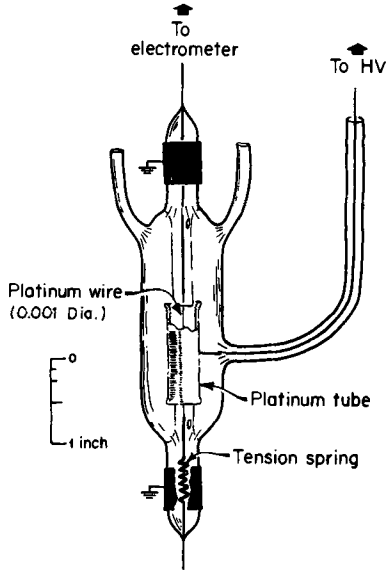

Fig. 1. Schematic drawing of the test cell

Test Samples and Procedures

"Pure grade" n-hexane and n-heptane (Philips Petroleum Co.) were repurified by passage through a 2-ft column of silica gel and an ultrafine fritted-glass filter; the initial fraction of the filtrate was discarded.

Ultraviolet absorption spectra, taken with a Cary spectrophotometer before and after treatment, show that bands initially observed around 2500Å are removed. This treatment seems to reduce the initial current slightly, but no significant change in residual current has been recorded.

Before final readings were taken, the cell was "conditioned" as follows.[3] After slowly raising the

[1] Present address: Laboratoire Central des Industries Electriques, Fontenay-aux-Roses, France.

[2] Present address: Torino, Italy.

[3] A similar technique has been used by House (6).

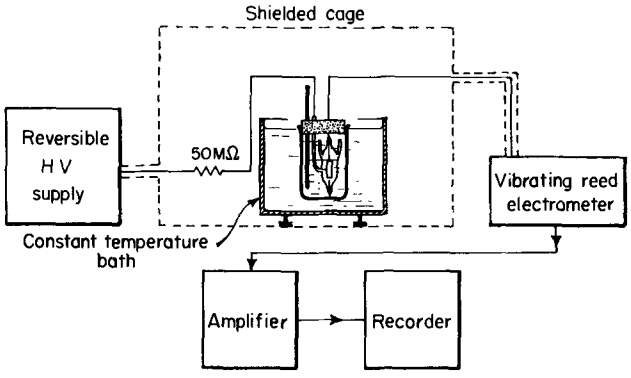

Fig. 2. Block diagram of the experimental setup

voltage to the onset of an erratic current, it was kept constant to permit the fluctuating current to decay gradually toward a steady state. Then the cycle was repeated three or four times until voltages of the order of 15 kv were reached. It is worth noting here that voltages up to 18 kv (which corresponds to 2.3 mv/cm at the wire for space-charge-free configuration) have been reached by this procedure. This treatment has a particularly strong effect in the negative-wire polarity (Fig. 3) supporting the belief that conditioning eliminates spots of high emissivity. The reproducibility of the final curves is shown by shaded areas which indicate the spread of the current values over a period of several weeks. The residual current is always noisy, especially when the wire is negative, and sudden fluctuations, superimposed on this noise, occasionally occur even after conditioning periods of 15 days. Hence, the current measured at intervals of several days was rarely reproducible within less than 40%.

In a second series of measurements, the test cell was thermostated to ±0.05°C and the steady current measured at constant voltage for various values of temperature as well as at constant temperature for different applied voltages.[4]

In a third series of experiments the wire alone was heated by a battery current and the average temperature of the wire estimated from its increment in resistance and the known temperature coefficient $d\rho/dt$ for platinum (4×10^{-3} ohm x cm x degree^{-1} between 0° and 100°C). In order to make sure that the leakage resistance to ground was not reduced when the heating current was turned on, the battery was connected permanently by one of its poles, and the whole circuit, including the switch, carefully insulated from ground. Potentials of 1.5, 3, 4.5, and 6 v were applied across the wire; at higher voltages the liquid at the wire surface started to boil. Since the volume of the wire is six orders of magnitude smaller than that of the liquid, only a very small fraction of the liquid near the wire surface is heated appreciably during the 1-min heating runs.

Time recordings of the charging and depolarization currents were also taken.

Behavior of the Residual Current

The residual current subsisting under both polarities after careful conditioning of the cell is shown in

[4] Since n-heptane is a liquid between −90.5° and +98.4°C, the data, thus far taken only over the range +13° to +50°C, should be extended. Some preliminary measurements in the wider range have been made but must be confirmed in detail before being reported.

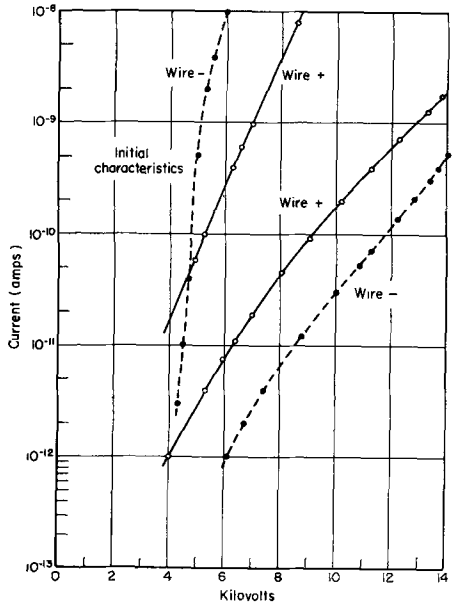

Fig. 3. Current-voltage characteristics in n-hexane showing the effect of conditioning. The shaded areas contain all the data taken over a period of several weeks, the points referring to the latest measurements.

Fig. 3 as a function of the applied voltage. The two curves, plotted on a log scale, are very similar in shape but the one corresponding to i_+ (positive wire configuration) lies above that corresponding to i_- (negative wire configuration).

Essentially the same results were obtained with a 1-mil diameter tungsten wire as the center electrode, although its surface roughness was much greater than that of the platinum wire. The residual current was larger under both polarities but the ratio i_+/i_- was nearly the same as for platinum (Fig. 4). Furthermore, fairly good agreement between the two sets of curves was obtained by scaling along the V axis. This seems to indicate that the highest field locally present in the cell, rather than the nature of the electrodes, is the significant factor.

The curves of Fig. 5, showing the temperature dependence of the current in n-heptane for various applied voltages, were obtained directly by varying the temperature under constant voltage. The same

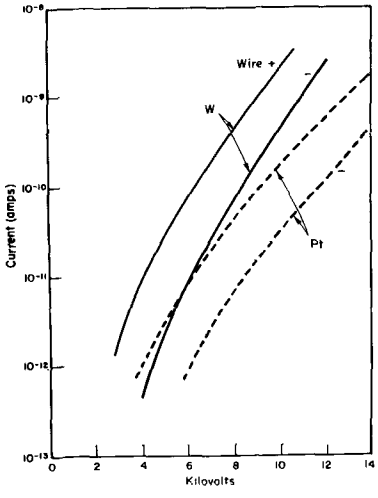

Fig. 4. Comparison of the current-voltage characteristics obtained with platinum and tungsten wire.

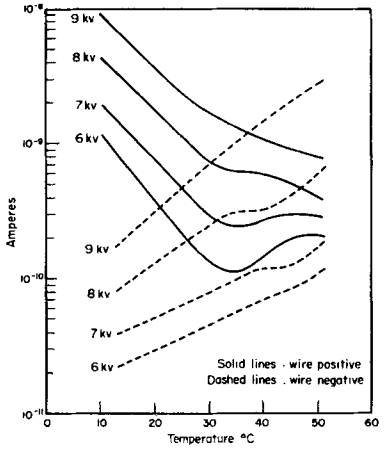

Fig. 5. Residual current vs. temperature in n-heptane for various applied voltages.

type of curves, constructed from a set of current-voltage characteristics at different temperatures, agree fairly well with those of Fig. 4. Although some details in the curves are not significant, the general trend shows that i_+ and i_- vary oppositely with temperature. While at room temperature i_+ is ten to twenty times larger than i_-, the two currents are of comparable magnitude at 50°C.

Current vs. Time (Wire Heated)

The results obtained when the wire was heated with 6 v applied are summarized in Fig. 6, which reproduces the essential trends of actual recordings. When the heating current is applied, the current drops suddenly regardless of polarity; then while i_+ keeps decreasing slowly, i_- tends to increase. When the wire current is switched off, the cell current rises sharply at first and then recovers its original value more slowly.

This effect is independent of the orientation (vertical or horizontal) of the test cell, the polarity of the battery, and the characteristics of the external circuit. Consequently, the sudden drop of the current must be caused by the heating of the wire and its immediate surroundings. However, transient phenomena related to the appearance of the thermal gradient are probably involved and complicate the interpretation. The slow variation, caused by the propagation of heat through the cell, is consistent

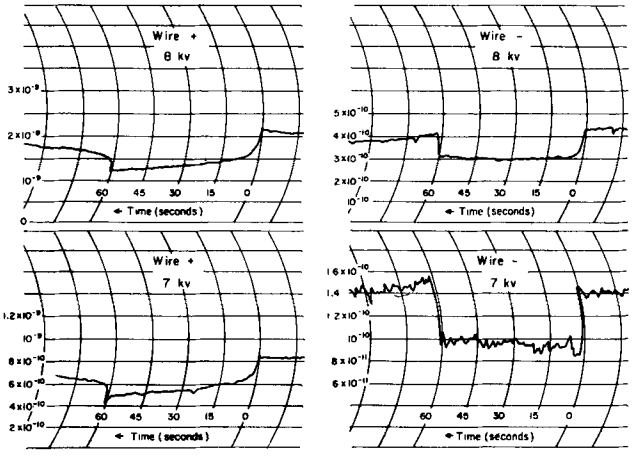

Fig. 6. Current recordings showing the effects of heating the wire alone.

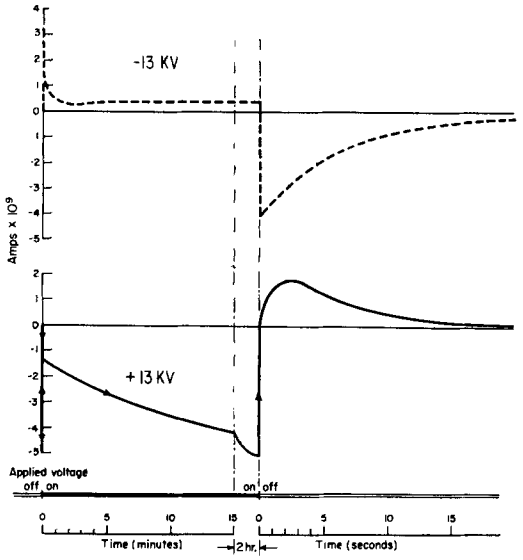

Fig. 7. Polarization and depolarization currents for both polarities.

with the results obtained by homogeneous heating of the whole cell. Table I shows the initial current drop in its relation to the wire temperature.

Polarization Currents

The cell generates a slowly decaying depolarization current when the applied voltage is removed after a steady state is reached. However, as Fig. 7 shows, the initial rise of this current is polarity dependent. When the applied voltage is restored, the current, after an initial jump, slowly recovers its initial value. It should be noted that i_+ increases significantly with time.

Discussion

The significant facts are: above a certain applied voltage, a residual current can be measured for both polarities. The current-voltage characteristics for i_+ and i_-, while of similar shape, vary oppositely when temperature is changed. The ratio i_+/i_-, of the order of 10 at 20°C, approaches unity around 50°C.

A detailed analysis, due to Onsager (7), of the influence of an external field E on the dissociation constant K of a weak electrolyte shows that for the high-field limit,

$$K(E) = K(O)\ (2/\pi)^{1/2}\ (8b)^{-3/4} \exp \sqrt{8b} \qquad [1]$$

where $8b = 77.2\ E/\kappa T^2$.

Table I. Initial current drop through the cell upon heating of the wire

Voltage across the wire, v	Current in wire, ma	Resistance of wire, ohm	Temperature at wire surface, °C*	Initial current drop through cell, %
0	0	13.40†	20.5 (R.T.)	0
1.5	102.5	14.65	38.7	7
3.0	189	15.90	64.0	12-22
4.5	260	17.30	77.5	18-22
5.95	318	18.75	97	27-30

* Calculated from the formula $R_T = 0.725\ R_{20.5}\ (1 + \alpha T)/(1 + \alpha \times 20.5)$. The factor 0.725 accounts for the difference between the temperature of the wire at its periphery and its average temperature. It was estimated from the fact that boiling started when the average temperature was about 135°C.

† Obtained by graphical extrapolation for zero current.

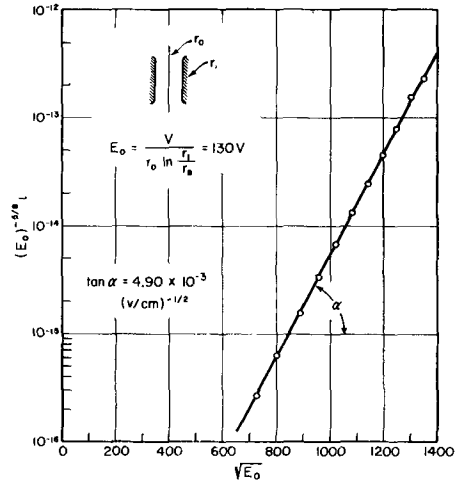

Fig. 8. Final characteristics of Fig. 3 (wire positive), plotted for a check of Onsager's theory.

Assuming that the dissociation products of both signs contribute equally to the current and that the mobility of the carriers does not vary in the field range of interest, the current is expected to vary with the field as $E\sqrt{K(E)}$, i.e. (in hexane at room temperature, $8b = 4.5 \times 10^{-4} E$), as

$$i \propto E^{5/8}\, 10^{1.6 \times 10^{-3} \sqrt{E}} \qquad [2]$$

In fact, if the residual characteristic for positive wire (cf. Fig. 3) is replotted on a log scale (Fig. 8) as $iE^{-5/8}$ vs. $\sqrt{E}$, the points fall on a straight line of angular coefficient 4.0×10^{-3}, as compared with the theoretical value of 4.6×10^{-3}. [5]

In view of the approximations involved in Eq. [1] and of the presence of the space charge which may distort the field at the wire, the agreement can be considered very good and strongly indicates that the carriers are created primarily by field ionization of impurities near the wire. Furthermore, the results obtained by other workers [in particular by House (6)] with more homogeneous field are consistent with this model. However, this mechanism fails to predict the temperature dependence of the residual current, in particular the effect of polarity (cf. Fig. 5). Since the polarization and depolarization currents (Fig. 7) suggest the presence of a different kind of space-charge for each polarity, it is logical to investigate whether the polarity effect can be ascribed to space-charge phenomena.

Let us call E_w^0 the field at the wire surface in the absence of space charge, and E_w^+ and E_w^- the actual field strengths at the wire positive and negative, respectively. If the wire is positive, a negative ionic space charge builds up at the wire surface, and $E_w^+ > E_w^0$ (Fig. 9). For increasing temperature the space charge expands by diffusion, hence E_w^+ decreases. For wire negative, field emission can occur. [6]

[5] The "effective radius" of the cell, defined as

$$\bar{r} = \int_{r_{in}}^{r_{out}} \left\{K[E(r)]\right\}^{1/2} r\,dr \Big/ \int_{r_{in}}^{r_{out}} \left\{K[E(r)]\right\}^{1/2} dr$$

with $E(r) = V/[r \ln(r_{out}/r_{in})]$ and $V = 9000$ v, has been calculated and found to be about twice the radius of the wire. Hence, no error in order of magnitude is made by using the geometric field $E(r_{in})$ in the plot of Fig. 7.

[6] E_w^0 is of the order of 10^6 v/cm for 8 to 10 kv applied. Surface irregularities make the field locally higher; furthermore, the potential barrier at the electrode is decreased by the dielectric.

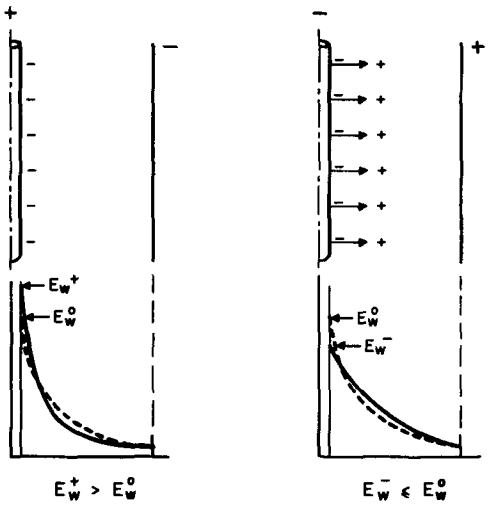

Fig. 9. Hypothetical model for the field distribution under both polarities (schematic).

The emitted electrons trapped by the liquid create a negative space charge, so that $E_w^- \leqq E_w^0$; as temperature increases, the space charge expands and E_w^- increases.

The inequality $E_w^- \leqq E_w^0 < E_w^+$ predicts the relative value of the current for both polarities, and the fact that E_w^- and E_w^+ become closer to E_w^0 as temperature increases is also in agreement with the observed temperature dependence.

To summarize, some evidence is given that the carriers are produced by field-induced dissociation and that the polarity dependence indirectly results from the fact that field emission is possible when the wire is negative. The species that dissociate under high field, the mobility of the charge carriers, and other problems of detail remain to be investigated. Experiments with other liquids and over a wider temperature range should help in clarifying the situation.

Acknowledgments

The authors are deeply grateful to Professor A. R. von Hippel for valuable discussions which contributed to the interpretation of the results, and to Mr. J. Kalnajs of this laboratory for his unfailing help in the realization of the experiment.

Manuscript received Sept. 16, 1959. This paper was prepared for delivery before the Philadelphia Meeting, May 3-7, 1959. Work on this paper was sponsored by the U.S. Office of Naval Research, Army Signal Corps, Air Force, and Atomic Energy Commission.

Any discussion of this paper will appear in a Discussion Section to be published in the December 1960 JOURNAL.

REFERENCES

1. A. von Hippel, Z. *Physik*, **80**, 19 (1933); D. R. Young, *J. Appl. Phys.*, **21**, 222 (1950).
2. W. B. Green, *J. Appl. Phys.*, **26**, 1257 (1955); **27**, 921 (1956).
3. A. von Hippel and R. S. Alger, *Phys. Rev.*, **76**, 127 (1949); A. von Hippel, E. P. Gross, J. G. Jelatis, and M. Geller, *ibid.*, **91**, 568 (1953); M. Geller, *ibid.*, **101**, 1685 (1956).
4. L. Malter, *ibid.*, **49**, 478 (1936).
5. F. Llewellyn Jones, *Repts. Prog. in Phys.*, **16**, 216 (1953).
6. H. House, *Proc. Phys. Soc. (London)*, **A170**, 913 (1957).
7. L. Onsager, *J. Chem. Phys.*, **2**, 599 (1934).

Silicon Nitride Thin Film Dielectric

Charles R. Barnes and Charles R. Geesner

Electronic Technology Laboratory, Wright Air Development Center, Wright-Patterson Air Force Base, Ohio

ABSTRACT

Thin adherent nonporous films of pure silicon nitride have been deposited from the vapor phase on hot molybdenum substrates by pyrolytic deposition. Such films, when incorporated between molybdenum plates to form capacitors, were found to maintain satisfactory dielectric properties up to and above 600°C. Silicon nitride coatings, deposited by the method herein described, also offer a convenient and effective method of encapsulation for protecting metal surfaces from atmospheric oxidation up to and above 1000°C.

As a result of the need for high temperature resistant electronic materials and miniaturized electronic equipment for use in space vehicles and satellites, thin films of silicon nitride were deposited pyrolytically and developed as a new dielectric material for capacitors capable of operating satisfactorily up to and above 600°C.

Pyrolytic deposition may be defined to include the following three chemical processes of deposition of materials on the surface of hot substrates: (*a*) the thermochemical decomposition of a properly selected chemical compound existing in the vapor state, (*b*) the reaction between two or more chemical vapors at the hot surface, and (*c*) the reaction of a vapor with the hot substrate itself. In the present case a process like (*b*) above was used.

The literature shows no record of the use of thin adherent nonporous films of pure silicon nitride as a dielectric for capacitors capable of satisfactory operation at 600°C. From the thermodynamic data of Kellogg (1), Brewer, Bromley, Gilles, and Lofgren (2), Powell (3) in a search for high-temperature protective coatings for metals predicted that silicon nitride might be vapor plated by means of the reaction of the combined vapors of silicon tetrachloride, hydrogen, and nitrogen at a substrate temperature of 1000°-1600°C. Powell further states that the probable deposit would be composed of a mixture of elemental silicon and silicon nitride.

In the present investigation it was imperative that a high temperature resistant dielectric material should not only be of high purity but should be pore-free in order to function properly in a thin film capacitor. To prevent the formation of pores in the deposit and to obtain a pure silicon nitride film the following precautions and requirements were adopted: (*a*) The metal substrate surface must be smooth and thoroughly cleansed. (*b*) Its temperature must be accurately controlled during the deposition. (*c*) A volatile silicon compound is required, such as silicon tetrabromide, capable of being relatively easily reduced to silicon which should react with nitrogen at temperatures below 1000°C to form pure Si_3N_4. (*d*) The reactant carrier gases, hydrogen and nitrogen, must be thoroughly purged of water vapor and oxygen.

Deposition of Silicon Nitride Dielectric

The silicon nitride dielectric films were deposited on smooth polished molybdenum disks 1 in. in diameter and 0.005 in. thick by means of the apparatus shown in Fig. 1. Before introducing the molybdenum disk into the plating apparatus, its surface is cleaned in succession with acetone, a hot water solution of sodium hydroxide, hot chromic acid, distilled water, and finally wiped dry with a fine clean grade of untreated tissue paper. The disk is then placed on the graphite core of the plating chamber (G), heated to the desired temperatures to be discussed later, deoxidized with hydrogen, and finally plated with silicon nitride dielectric.

In the actual plating process for silicon nitride dielectric illustrated in Fig. 1, commercial grades of hydrogen and nitrogen are allowed to flow through calibrated flowmeters (A) at the following flow rates expressed in milliliters per minute: 300 for hydrogen and 1100 for nitrogen. Both hydrogen and nitrogen gases then pass through deoxidizing units (B) and (C), respectively, for the purpose of removing con-

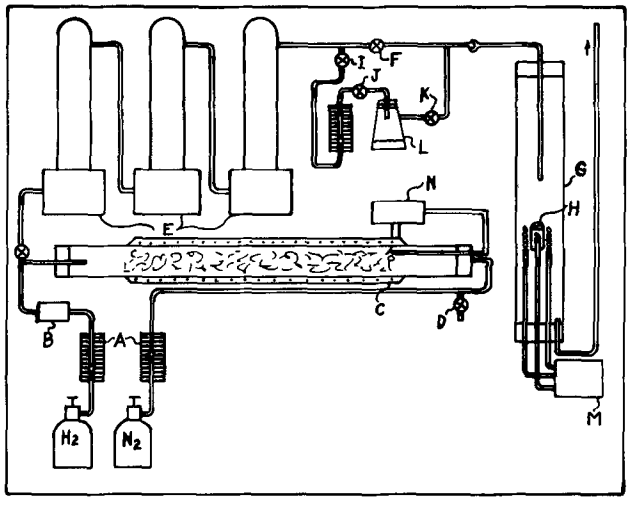

Fig. 1. Apparatus for depositing silicon nitride: (A) Flowmeters for hydrogen and nitrogen; (B) and (C) deoxidizers; (D) back-flush valve; (E) calcium hydride drying towers; (F), (I), (J), and (K) vapor control valves; (G) deposition chamber; (H) substrate; (L) silicon bromide evaporator; (M) induction heater with temperature controller; (N) deoxidizer temperature control.

taminating oxygen. For the hydrogen purification a Baker and Company Deoxo unit Model D is employed. The nitrogen gas is purified by passing over copper turnings maintained at a temperature of 750°C. The advantage of using a separate deoxidizing unit for the nitrogen is that the copper can be reactivated between runs by back flushing hydrogen through the hot oxidized copper turnings. As a result, a large quantity of water is removed from the system through outlet valve (D). This water would otherwise rapidly consume the drying agent in subsequent drying towers (E). The hydrogen and nitrogen both flow together through three drying towers each of which contains a bed of —4 to 40 mesh calcium hydride that is 7 in. in depth and 2 in. in diameter. The mixed purified carrier gases then flow through valve (F) and enter the plating chamber (G) through Vycor nozzle. Thus the carrier gases blow directly on the clean molybdenum disk substrate, the upper surface of which is maintained at a temperature of 960° ±2°C as measured by an optical pyrometer. The source of heat is a 7.5 kw induction heater whose water-cooled coils surround a cylindrical graphite core. By induction the graphite core is heated to approximately 1000°C which in turn heats the molybdenum disk substrate (H) resting on top. Finally the exhaust gases leave the heating chamber through the exhaust stack.

In starting the plating operation the carrier gases are allowed to flow until all air and moisture are flushed from the plating chamber. The induction heater is turned on and the temperature of the substrate raised to and maintained at 600°C for 10 min during which time the nitrogen flow is turned down to a trickle and hydrogen valve is opened to allow a flow of 1000 ml/min. The purpose of this short operation is to deoxidize and clean the substrate surface with hydrogen.

After the above purging operation the hydrogen and nitrogen flow rates are readjusted to 300 and 1100 ml/min, respectively, and the gas flow allowed to continue until equilibrium of the gas mixture is established in the Pyrex glass plating chamber. The temperatures of the graphite core and molybdenum disk are then increased until a substrate surface temperature of 960° ± 2°C is reached and maintained. To start the deposition of silicon nitride on the substrate, valves (I), (J), and (K) are opened and valve (F) is partially closed. By manipulation of valves (F) and (I) simultaneously the amount of carrier gas by-passed through the silicon bromide evaporator (L) is adjusted to 100 ml/min. As the gas mixture passes over the surface of the liquid, silicon bromide vapor is picked up and blown directly on the molybdenum disk substrate which is located 4¼ in. from the nozzle. Subsequently a deposit of silicon nitride (Si_3N_4) appears immediately on the molybdenum substrate discernible only by the moving rainbow formations which continue to grow as the deposition progresses. After continuing the deposition process for 1 hr, a silicon nitride dielectric film of 0.5 mil approximate thickness has grown on the molybdenum substrate. Finally, after turning off the silicon bromide vapor flow and in a few minutes shutting down the heater, the substrate with deposited film is allowed to cool and may be removed.

Although experiment showed that silicon nitride films can be deposited over a temperature span of 930°-1000°C, the best quality dielectric films were obtained at a substrate surface temperature of 960°C. These were smooth, clear, transparent, colorless, very adherent, free of pores, and suitable for capacitor construction. It was further determined that, by increasing the flow-rate of the carrier gases and silicon tetrabromide vapor, the deposition rate can also be increased. However, the best quality dielectric films were those which required at least 1 hr to obtain a thickness of 0.4-0.6 mil.

Construction of Silicon Nitride Capacitor

In order to measure the dielectric properties of silicon nitride a number of thin film capacitors were constructed and tested utilizing the dielectric films deposited on molybdenum disks as described above.

Before constructing the capacitor the molybdenum disk with a dielectric film of silicon nitride 0.5 mil thick on one side is turned over and plated on the opposite side with a coating of silicon nitride 0.3 mil thick which serves to encapsulate the molybdenum plate after it is incorporated in a capacitor.

Thickness of the films were measured by a metallurgical microscope with a mechanical stage graduated with one scale division equal to 1 μ of stage movement.

To construct the capacitor, a thin film of molybdenum of 0.5 mil thickness is plated on the silicon nitride dielectric which was previously deposited on the molybdenum substrate. As a source of molybdenum its pentachloride vapor carried by hydrogen gas to the substrate is employed, a procedure recommended by Powell (4). In the present case the apparatus of Fig. 1 is modified by removing the head assembly of the plating chamber and replacing with another (not shown) which contains an evaporator for furnishing molybdenum pentachloride vapor at a temperature of 195°C to the hydrogen carrier gas blowing at 1000 ml/min. The silicon nitride substrate surface temperature is 800°C. Five minutes are required to deposit a molybdenum film of 0.5 mil thickness. After cooling and removing the capacitor from the plating chamber the edge of the molybdenum film is etched back from the outer circumference for a distance of 1/32 in. Also a spot is etched away where it is desired to scratch through the silicon nitride dielectric in order to solder a lead to the base plate.

Platinum wire leads are then soldered with metallic gold, one to the molybdenum base plate and the other to the molybdenum film. To accomplish the gold soldering the capacitor is placed in the plating chamber and platinum wire leads are supported in such a manner that one tip of each rests against the bare molybdenum and adjacent to a tiny bead of gold placed at the attachment areas. Soldering is then accomplished in an atmosphere of hydrogen by heating the whole capacitor to the fluxing temperature of gold.

After the leads are attached the capacitor remains in the plating chamber and a final encapsulating film

Table I. Dielectric properties of silicon nitride

Temp, °C	Resistance in megohms at 100 V.D.C.	Volume resistivity, ohm-cm	Capacity at 1 kc	Dielectric constant at 1 kc	Dissipation factor at 1 kc	RC product, megohm-microfarads	Dielectric strength, v/mil
25	1.5×10^8	4.1×10^{16}	2714	12.7	<0.0001	407,000	1000
100	8.5×10^7		2719		<0.0001	231,000	
200	1.7×10^7		2725		<0.0001	46,300	
300	1.7×10^6		2737		<0.0001	4,600	
400	5.0×10^5		2747		0.0003	1,375	
500	3.2×10^5		2757		0.0006	881	
600	5.7×10^4	1.6×10^{18}	2763	13.5	0.0033	157	660

of silicon nitride 0.3 mil thick is plated over the molybdenum film and the attachment areas of the leads. The construction of an encapsulated high temperature thin film silicon nitride capacitor is now complete.

Summary of Dielectric Properties of Silicon Nitride

Several of the capacitors were recycled stepwise three times in a muffle furnace over a temperature range of 25°-600°C. Each capacitor was supported by two Vycor tubes through which the leads were passed. The tubes extended separately from the capacitor in the furnace through the port hole to the outside without touching each other or the walls of the furnace. Representative results of the temperature exposures up to 600°C are presented in Table I. Furthermore it is interesting to note that in one case a capacitor was heated to 1000°C in a flame without damage.

Manuscript received Sept. 18, 1959.

Any discussion of this paper will appear in a Discussion Section to be published in the December 1960 JOURNAL.

REFERENCES

1. H. H. Kellogg, *J. Metals*, **2**, 862 (1950).
2. L. Brewer, L. A. Bromley, P. W. Gilles, and N. L. Lofgren, "The Chemistry and Metallurgy of Miscellaneous Materials," L. L. Quill, Editor, pp. 40-75, McGraw-Hill Book Co., New York (1950).
3. C. F. Powell, I. E. Campbell, and B. W. Gonser, "Vapor Plating," p. 97, John Wiley & Sons, Inc., New York (1955).
4. C. F. Powell, I. E. Campbell, and B. W. Gonser, *J. (and Trans.) Electrochem. Soc.*, **93**, 258 (1948).

Tin-Activated Calcium Orthosilicate Phosphors

Richard W. Mooney

Chemical and Metallurgical Division, Sylvania Electric Products Inc., Towanda, Pennsylvania

ABSTRACT

A study of the tin-activated calcium orthosilicates disclosed two phosphors: a blue-emitting phosphor with a very broad excitation band having the β-Ca_2SiO_4 structure and a yellow-emitting phosphor with fair response to high-pressure mercury-vapor radiation having the α'-Ca_2SiO_4 structure. The β-Ca_2SiO_4: Sn phosphor is the more efficient of the two, comparing very favorably with other well-known blue phosphors. The efficiency of β-Ca_2SiO_4: Sn was studied as a function of activator concentration and compared with similar results for β-$CaSiO_3$: Sn. The difference in behavior between β-Ca_2SiO_4: Sn and β-$CaSiO_3$: Sn is attributed to differences in crystal structure.

The orthosilicates of calcium having the composition $2CaO \cdot SiO_2$ or Ca_2SiO_4 have been the subject of many investigations, since they are found commonly in blast furnace and open-hearth slags and used extensively in Portland cement and certain types of refractories. The present ideas on the chemistry and crystallography of dicalcium orthosilicate began in 1943 with the work of Bredig (1) whose ideas since have been confirmed and extended by many authors (2-6). It is now generally accepted that dicalcium orthosilicate occurs in four polymorphic modifications: namely, an alpha (α) or high-temperature modification stable above 1450°C; an alpha prime (α') modification occurring between 850° and 1450°C; a beta (β) modification, metastable at room temperature; and a gamma (γ) modification, which is stable at room temperature. The γ-, β-, and α'-modifications are found in nature and have the mineralogical names: calcio-olivine, larnite, and bredigite, respectively. It has been shown also that the additions of small amounts of many of the common oxides change the temperatures of both the α-β and the β-γ inversions, resulting in some cases in the stabilization of high-temperature forms (7, 8). For instance, less than 0.2 mole % of Na_2O will inhibit the β-γ transformation (9). Thus the specific crystallographic species formed by high-temperature solid-state reaction will be determined not only by the temperature of firing, but also by the particular modifying compounds present.

The only calcium orthosilicate phosphor previously reported was β-Ca_2SiO_4: Pb which, according to Studer and Fonda (10), emits at 334 mμ under 254 mμ excitation. The present investigation was undertaken as part of a general study of the tin-activated calcium silicates. The preparation and optical properties of the tin-activated calcium metasilicates were reported in a previous paper (11) while this paper gives corresponding data on the calcium orthosilicates activated by tin.

Experimental Procedure

Calcium carbonate and silicic acid were mixed in mole ratios which varied from 2CaO/0.95 SiO_2 to 2CaO/1.50 SiO_2 with 0.01-10.0 mole % of stannic or stannous oxide. The mixture was pebble-milled in a deionized water slurry, dried at 110°-120°C, and fired in silica trays at temperatures varying from 870°-1320°C. For maximum efficiency it was necessary to fire in a steam atmosphere, and since tin-activated phosphors luminesce only when the tin is in a lower valence state, a reducing atmosphere, usually a mixture of hydrogen, nitrogen, and steam, was maintained. All gas flows were controlled carefully in order to obtain reproducible results with optimum efficiencies being obtained at a nitrogen to hydrogen ratio of approximately unity.

The methods used for structure identification by x-ray diffraction, measurement of excitation and emission spectra, and determination of per cent tin by quantitative analyses were the same as those previously reported (11). In this paper the activator contents are expressed as gram-atom tin per gram-atom of calcium in the fired phosphor.

Relative efficiency measurments under 254 mμ excitation were made on a plaque tester of conventional design (12). Efficiency measurements under high-pressure mercury-vapor (HPMV) excitation were made on a similar instrument using as sources two General Electric C85H3 lamps with ultraviolet-transmitting envelopes. The predominant wave lengths present in the HPMV source were 313 and 365 mμ. The instrument was so constructed that efficiencies of various phosphors could be compared at room temperature, or the temperature dependence of fluorescence of a sample could be measured by raising the temperature of the sample at a constant heating rate of approximately 2°C/min. The output of a 1P21 photomultiplier detector was amplified by a Photovolt Model 520-M unit and fed into the Y-axis of a Mosely Autograf X-Y recorder. The signal from a chromel-alumel thermocouple imbedded in the phosphor sample was fed to the X-axis, thus giving a continuous plot of efficiency vs. temperature for a particular sample.

Results with β-Ca_2SiO_4:Sn

A deep blue-emitting phosphor having the β-Ca_2SiO_4 structure was formed over wide temperature and composition limits with temperatures between 1150° and 1230°C and compositions between 2.0 CaO/1.00 SiO_2 and 2.0 CaO/1.10 SiO_2 giving the best results. There was no evidence in any of the firings of the presence of γ-Ca_2SiO_4. The most efficient phosphors were produced at a SiO_2 content

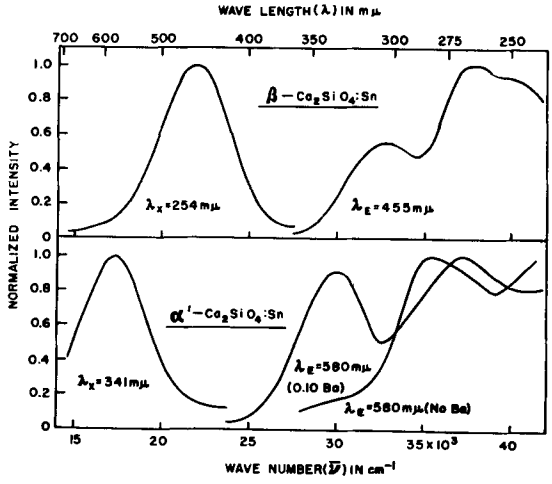

Fig. 1. Excitation and emission spectra of β-Ca_2SiO_4:0.003 Sn and α'-Ca_2SiO_4:0.003 Sn.

that gave a slight excess of SiO_2 over the theoretical Ca_2SiO_4 composition. The presence of a slight excess of CaO was extremely deleterious to phosphor brightness.

The excitation and emission spectra of β-Ca_2SiO_4:Sn are shown in the top half of Fig. 1. The emission spectrum consists of a single band peaking at 22,000 cm^{-1} or 455 mμ regardless of the energy of excitation. The excitation spectrum is broad, giving efficient excitation by both 254 mμ and HPMV radiation. The brightness of β-Ca_2SiO_4 compares very favorably with that of other blue-emitting phosphors. For instance, with 254 mμ excitation β-Ca_2SiO_4: 0.003 Sn is 25% brighter than $Sr_2P_2O_7$: Sn, which has its peak emission at 452 mμ, and under HPMV excitation it is 15% brighter than magnesium tungstate. Both comparisons were made at room temperature.

Results with α'-Ca_2SiO_4:Sn

As the firing temperature exceeded 1200°C for phosphors having a composition close to the theoretical Ca_2SiO_4 composition, there was a gradual decrease in blue emission and an equally gradual increase in yellow emission. This effect was most pronounced as the composition approached the Ca_2SiO_4 stoichiometric formulation and decreased as the excess SiO_2 increased. Concurrent with the shift in emission, there occurred a corresponding shift in the excitation spectrum with the yellow component being excited more easily by HPMV radiation than by 254 μ excitation. The yellow-emitting phosphor was identified by x-ray diffraction as α'-Ca_2SiO_4: Sn with emission and excitation spectra as given in the bottom half of Fig. 1.

The emission is dependent on the wave length of excitation, giving a single band at 17,300 cm^{-1} (578 mμ) when excited by 341 mμ. As the energy of the exciting wave length is increased, the position of the main emission band shifts from 578 mμ under 341 mμ excitation to 559 mμ under 268 mμ excitation, and in addition a very weak emission band develops at about 370 mμ. From the excitation data it is apparent that the intensity of the band in the neighborhood of 570 mμ is greatest at the peak in the excitation curve, i.e., under 285 mμ radiation.

It was also found that the substitution of small amounts of Mg, Zn, Sr, or Ba, in the range 0.10 gram-atom of modifying Group II metal, for an equivalent amount of Ca in the calcium orthosilicate formulation tended to promote the transition to the yellow-emitting α'-Ca_2SiO_4:Sn. A comparison of the results showed that the greater the difference in ionic size between calcium and the modifying cation, the greater the effect, i.e., barium and magnesium were more efficient in promoting the transition than zinc or strontium while cadmium had little, if any, effect. The most efficient yellow-emitting phosphor having the α'-Ca_2SiO_4 structure had the composition $Ca_{1.92}Ba_{0.08}SiO_4$:0.003 Sn. The excitation spectrum of the Ba-modified α'-Ca_2SiO_4:Sn phosphor as shown in the bottom half of Fig. 1 is very different from the unmodified sample as evidenced by the strong absorption of radiation at about 30,000 cm^{-1} (333 mμ) caused by the addition of barium. The addition of small amounts of alkali metals as, for example, 0.013 gram-mole of Li_2CO_3 to a Ba-modified Ca_2SiO_4:Sn phosphor was also effective in increasing the efficiency to HPMV radiation by increasing the absorption of 30,000 cm^{-1} radiation still further. Calcium orthosilicate phosphors fired at 1316°C displayed no evidence of fusion even in the presence of well-known fluxes such as Li_2CO_3 or $BaCO_3$.

Effect of Activator Concentration on β-Ca_2SiO_4:Sn

The effect of activator concentration, expressed as atom Sn found in the fired phosphor per atom Ca, on the relative efficiency of β-Ca_2SiO_4:Sn was studied and compared to similar results on the more efficient of the tin-activated calcium metasilicates, namely, β-$CaSiO_3$:Sn. The results for 254 mμ excitation for both β-Ca_2SiO_4:Sn and β-$CaSiO_3$:Sn are shown in the top half of Fig. 2. The normalized efficiency data were fitted to the equation

$$\eta = \frac{c(1-c)^z}{c + (\sigma/\sigma')(1-c)}$$

where η is the relative efficiency, c is the activator concentration in atom Sn per atom Ca, and Z and σ/σ' are adjustable parameters (13). The parameter σ/σ' is the ratio of the capture cross sections of non-activators to the capture cross sections of luminescent activators, while the parameter Z is defined as the number of lattice positions surrounding a given activator such that, if any one of these sites is occupied by another activator, luminescence is quenched. The efficiency of β-Ca_2SiO_4:Sn is relatively insensitive to activator concentration over the range 0.001-0.020 atom Sn/atom Ca for 254 mμ excitation, whereas the efficiency of β-$CaSiO_3$:Sn is sharply peaked at an activator concentration of about 0.001 atom Sn/atom Ca. The ratio of the capture cross section of nonactivators to activators is approximately constant for both phosphors, whereas Z increases by a factor of six in going from 10 for β-Ca_2SiO_4:Sn to 60 for β-$CaSiO_3$:Sn.

Since β-Ca_2SiO_4:Sn is also excited by HPMV radiation, the effect of activator concentration on the HPMV response was also studied, with results as given in the bottom half of Fig. 2. The efficiencies at elevated temperatures were calculated from the

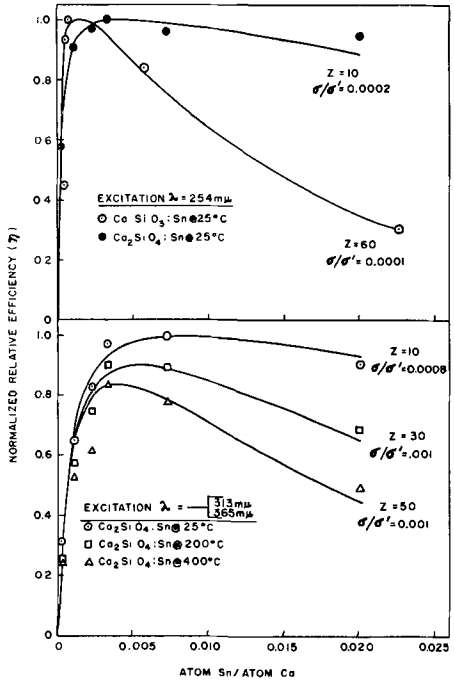

Fig. 2. Relative efficiency vs. activator concentration for β-Ca_2SiO_4:Sn with ultraviolet excitation.

room-temperature efficiencies and measurements of the temperature dependence of fluorescence. The β-Ca_2SiO_4:Sn phosphors showed a gradual decrease in efficiency with temperature with the phosphor having the highest tin concentration giving the greatest drop in efficiency. Since the decrease in brightness is very gradual, the error due to non-equilibrium measurements should be negligible. As would be expected the maximum in the plot of efficiency vs. activator content shifts to lower activator concentrations with increasing temperature.

Values of Z and σ/σ' for β-Ca_2SiO_4:Sn at 25°, 200°, and 400°C were calculated. The σ/σ' values for all three temperatures were approximately equal, i.e., about 0.001 or an order of magnitude greater than the σ/σ' values for 254 mμ excitation. The Z value found was the same at room temperature for low and HPMV excitation, but increased from 10 at room temperature to 50 at 400°C for HPMV excitation.

It is interesting that most of the tin added to the phosphor mix is lost during the firing process. Thus, for β-Ca_2SiO_4:Sn, 44% of the original tin present is retained at the lowest activator concentration. This amount decreases to a value of 13% in the neighborhood of the optimum activator concentration and then increases rapidly again to 40% for 0.10 gram-atom Sn added per gram-mole of Ca_2SiO_4. The per cent tin retained in β-$CaSiO_3$:Sn goes through a similar minimum starting at 45%, decreasing to a minimum of 2.5%, and increasing again to 42%.

Discussion

The predominance of the β-Ca_2SiO_4 structure and the complete lack of any evidence of the γ-Ca_2SiO_4 structure in the Ca_2SiO_4:Sn phosphors indicate that tin has a strong stabilizing effect on the metastable β-Ca_2SiO_4 crystal lattice. Another stabilizing influence on the β-Ca_2SiO_4 structure might be the small

particle size since Guinier and Yannaguis (5) found that, with crystals less than 10 μ in size, the β-phase only was stable. At very high temperature it is necessary to introduce a distorting cation whose radius is markedly different from that of calcium in order to promote the β-α' transition and stabilize the α'-structure at room temperature. The necessity of a slight excess of SiO_2 over the Ca_2SiO_4 composition for optimum efficiency is generally accepted in phosphor technology as is the use of reducing atmospheres for the firing of tin-activated phosphors.

It is interesting to compare the σ/σ' and Z values obtained on β-Ca_2SiO_4:Sn and β-$CaSiO_3$:Sn with those of another tin-activated phosphor, namely $Sr_{2.65}Zn_{0.20}(PO_4)_2$:Sn, recently studied (14). For 254 mμ excitation at room temperature, the σ/σ' values are all approximately constant, varying from 0.0001 and 0.0002 for the tin-activated silicates to 0.0005 for the tin-activated phosphate. The Z values of 10 and 60 for the silicates are higher than the previous $Z = 1$ value for the above phosphate, although a strict comparison of these figures is not entirely valid, since in the previous paper (14) the activator concentrations were expressed in terms of the unfired mix, whereas in the present paper they are given in terms of the tin actually present in the phosphor after firing. The latter method is much to be preferred due to the large and variable loss of tin during firing.

A comparison of the response of β-Ca_2SiO_4:Sn with $Sr_{2.65}Zn_{0.20}(PO_4)_2$: Sn under HPMV excitation gives similar results. Thus, σ/σ' is not changed very much, being in the neighborhood of 0.001 for the tin-activated silicates and varying with temperature from 0.003 to 0.005 for the tin-activated phosphate. The increase in Z with temperature is according to expectation, and at elevated temperatures there is good correlation between the Z value for $Sr_{2.65}Zn_{0.20}(PO_4)_2$:Sn of 36 at 377°C and the values of 30 and 50 for temperatures of 200° and 400°C, respectively, for β-Ca_2SiO_4:Sn.

Generalizing these results, it would appear that the ratio of the capture cross section of nonactivators to luminescent activators is relatively unaffected by environment, being a function largely of the activator itself and the energy of the exciting radiation. However, the parameter Z, which is related to the number of neighboring sites occupied sufficient to cause concentration quenching, is a function of the phosphor matrix.

More specifically, why is β-$CaSiO_3$:Sn with a Z value of 60 much more sensitive to activator concentration than is β-Ca_2SiO_4:Sn with a Z value of 10. One possible explanation for the difference lies in the fundamental difference in structure between wollastonite (β-$CaSiO_3$) and larnite (β-Ca_2SiO_4). Thus the structure of larnite has been shown by Midgley (15) to consist of isolated SiO_4 tetrahedra and Ca ions. On the other hand, the wollastonite structure has recently been reinvestigated (16, 17) and found to consist of infinite chains of Si_6O_{17} radicals arranged along endless columns of Ca-octahedra. Thus the activator sites in wollastonite, assuming isomorphous replacement of calcium by tin, are found in these Ca-octahedra columns, whereas the sites in β-Ca_2SiO_4:Sn are more or less randomly distributed among the isolated calcium sites in the crystal. It is proposed that the association of the activator sites by this column-type structure leads to a greater interaction between neighboring activators and therefore a greater sensitivity to concentration quenching as evidenced by a Z value of 60 for β-$CaSiO_3$:Sn vs. a Z value of 10 for β-Ca_2SiO_4:Sn.

The appreciable loss of tin during firing is undoubtedly explained by the work of Platteeuw and Meyer (18) who showed that at high temperatures SnO is a stable gas with an appreciable vapor pressure. The presence of H_2 in the gas mixture would undoubtedly favor the formation of SnO and thus lead to its subsequent dispersal through the system and partial loss to the surroundings. The presence of the activator in the vapor state might also explain the generally high efficiencies of tin-activated phosphors due to uniform incorporation in the lattice. The increase in the tin retained at the higher concentrations is evidently due to the inability of the phosphor to rid itself of excess tin during the period of firing used.

An analysis of the spectra of the Sn-activated calcium orthosilicates is considerably more difficult than that for the metasilicates. Studer and Fonda (10) found one emission band at 334 mμ for β-Ca_2SiO_4:Pb. However, recent measurements in this laboratory indicate that there are at least four emission bands with a corresponding number of excitation bands. As a consequence, it is completely impossible to relate the excitation or emission bands in β-Ca_2SiO_4:Sn to those in β-Ca_2SiO_4:Pb at this time.

Acknowledgment

The author is indebted to several of his colleagues for their help with the preparations and measurements. Specifically, he wishes to thank Dr. C. W. W. Hoffman for the x-ray identifications and Mr. G. J. Meisenhelter for the analytical determinations. The author also wishes to acknowledge the advice and encouragement of Dr. J. S. Smith during the progress of this work.

Manuscript received Aug. 26, 1959. This paper was prepared for delivery before the Philadelphia Meeting, May 3-7, 1959.

Any discussion of this paper will appear in a Discussion Section to be published in the December 1960 JOURNAL.

REFERENCES

1. M. A. Bredig, *Am. Mineral.*, **28**, 594 (1943); *J. Phys. Chem.*, **49**, 537 (1945); *J. Am. Ceram. Soc.*, **33**, 188 (1950).
2. G. Trömel, *Naturwissenschaften*, **36**, 88 (1949).
3. G. Yamaguchi, H. Miyabe, K. Amano, and S. Komatsu, *Yogyo Kyokai Shi*, **65**, 99 (1957).
4. N. A. Toropov, B. V. Volkonskii, and V. I. Sadkov, *Doklady Akad. Nauk S.S.S.R.*, **112**, 467 (1957).
5. A. Guinier and N. Yannaguis, *Compt. rend.*, **244**, 2613 (1957).
6. D. M. Roy, *J. Am. Ceram. Soc.*, **41**, 293 (1958).
7. E. S. Newman and L. S. Wells, *J. Research Nat. Bur. Standards*, **36**, 137 (1946).
8. G. V. Kukolev and M. T. Mel'nik, *Doklady Akad. Nauk S.S.S.R.*, **109**, 1012 (1956).
9. E. Thilo and H. Funk, *Z. anorg. u. allgem. Chem.*, **273**, 28 (1953).

10. F. J. Studer and G. R. Fonda, *J. Optical Soc. Am.*, **39**, 655 (1949).
11. R. W. Mooney, *This Journal*, **106**, 955 (1959).
12. K. H. Butler and R. W. Mooney, *Sylvania Technologist*, **9**, 121 (1956).
13. P. D. Johnson and F. E. Williams, *J. Chem. Phys.*, **18**, 1477 (1950).
14. R. W. Mooney, *This Journal*, **105**, 456 (1958).
15. C. M. Midgley, *Acta Cryst.*, **5**, 307 (1952).
16. K. Dornberger-Schiff, F. Liebau, and E. Thilo, *ibid.*, **8**, 752 (1955).
17. Kh. S. Mamedov and N. V. Belov, *Doklady Akad. Nauk. S.S.S.R.*, **107**, 463 (1956).
18. J. C. Platteeuw and G. Meyer, *Trans. Faraday Soc.*, **52**, 1066 (1956).

Luminescent Properties of Silver-Activated Magnesium Borate Phosphors

Yasuo Uehara, Yoshimasa Kobuke, and Isoo Masuda

Matsuda Research Laboratory, Tokyo Shibaura Electric Co., Ltd., Kawasaki, Japan

ABSTRACT

Silver-activated magnesium borate phosphors are extremely sensitive to reducing agents in the presence of water or moist air. With progressive reduction, the color of fluorescence turns from bluish white to green, yellow, orange, and red under excitation by 3650Å. At the same time the color of the phosphor powders changes from white to gray or black. Similar properties were found in some other crystals containing Ag. The characteristics of these phosphors show some similarities with photographic materials.

The fluorescence due to atomic silver in glasses and crystals containing silver has already been reported by Weyl and others (1). Reduction of the silver ions in these substances was effected by means of hydrogen, electron bombardment, and exposure to x- or γ-rays. It was found by the present authors that Ag-activated magnesium borate can be reduced by common reducing agents in the form of solutions and thus be made strongly fluorescent. These phosphors are extremely sensitive to reducing agents, and their fluorescence color under excitation by 3650Å radiation varies from an original whitish blue to orange or red with increasing degree of reduction; eventually they become nonfluorescent and dark gray. These phosphors are of interest in providing an analogy to photographic processes.

Preparation of Phosphor

Silver-activated magnesium borate phosphors of various compositions were prepared by firing mixtures of purified boric acid (H_3BO_3), basic magnesium carbonate ($3MgCO_3 \cdot MgO \cdot 4H_2O$), and silver nitrate with or without added aluminum hydroxide, for two 0.5 or 1 hr periods at 950°C. The initial firing was always made in air, and the second firing was carried out in various atmospheres, such as in air, oxygen, or nitrogen, after an intimate grinding between firings. Pure magnesium borates without added impurities were also prepared by the same method. The compositions studied were as follows: boric acid, 2 moles; basic magnesium carbonate, 0.5, 0.375, 0.25, and 0.125 moles; silver nitrate, $0\text{-}2\times10^{-2}$ moles; and aluminum hydroxide, $0\text{-}5\times10^{-2}$ moles. Furthermore, magnesium borates of composition $MgO \cdot B_2O_3$ containing 1 mole % Cu, Li, Be, Hg, Al, La, Tl, Ti, Ge, Zr, Sn, Pb, V, As, Sb, Bi, Se, Mn, Ce, Sm, U, and Th were prepared by the same method, except for phosphors with Ce and Sn which were fired in air or in a reducing atmosphere in the second heat treatment.

Reduction of phosphors.—A small amount of the phosphor is placed in a glass dish and wetted with an extremely dilute solution of a reducing agent. For most of the experiments, $10^{-5}N$ sodium sulfite ($Na_2SO_3 \cdot 7H_2O$) solution or the solution prepared by dissolving 1 cc Elon-Hydroquinon Borax (D-76) developer in 100 liters of water were used as reducing agents. With these dilute solutions of reducing agents, the fluorescence color of Ag-activated phosphors changes from an original whitish blue to green, yellow, orange, or red within a few minutes, while with concentrated solutions of reducing agents, such as D-76 developer itself, the phosphors turn into nonfluorescent black powders. On the other hand, pure magnesium borates of various compositions remained unchanged by the same reducing agents.

Filter paper or common white paper can also be used as convenient reducing agents. If a small amount of the dry phosphor powders is spread on a sheet of dry white paper in a layer of a few millimeter thickness, the reduction of the phosphor due to traces of reducing agents such as sulfite, which may be originally contained in the paper, occurs gradually and progresses from the interface between powder layer and paper to the upper layer of the powders. For example, the bluish white fluorescing phosphor spread on a sheet of paper turned completely into a green fluorescent phosphor during a few hours in air of about 70% relative humidity at room temperature, while the sample spread in a clean glass dish and wetted with distillated water showed no change of fluorescence color for a long time.

If the phosphor is first placed on a sheet of paper for several tens of minutes and then stored in a clean glass bottle, it turns into the reduced phosphor during a few months' time. Indeed, a phosphor spread on a sheet of paper for 30 min and then stored in a bottle in the dark for about five years turned into a dark gray powder producing only extremely weak red fluorescence under excitation by 3650Å, while the same phosphor stored from the beginning in a clean glass bottle turned into a strongly green fluorescent powder during the same length of time. The speed of reduction of the phosphor depends on temperature and moisture, as well as on the concentration of reducing agents. If the phosphor on a sheet of paper is moistened with hot steam, the color of fluorescence under excitation by 3650Å changes from whitish blue to green, yellow, orange or red, and finally to reddish dark gray within a few minutes. For the measurements of the optical properties of the reduced phosphor, the sample reduced on paper in air at room temperature was used since it was difficult to stop the reduction at the desired stage with reducing solutions.

Silver-activated phosphors reduced by electron bombardment or by means of hydrogen diluted with nitrogen in a third heat treatment at temperatures from 100° to 200°C showed weak fluorescence of various colors depending on the degree of reduction. When these phosphors were exposed to 2537 or 3650Å radiation and x- or γ-rays for 1 hr at room temperature they showed no changes of fluorescence color.

Emission and reflection spectra.—The spectral distribution of fluorescence under excitation by 3650Å and that of reflection were measured at room temperature by the same method as reported in a previous paper (2).

Experimental Results

Emission Characteristics

Silver-activated magnesium borate phosphors of approximate composition $MgO \cdot B_2O_3$:Ag (10^{-2} mole) and prepared by firing in air show a weak whitish blue fluorescence under excitation by 2537 or 3650Å, but not under excitation by cathode rays. The detailed hue of color and the intensity of fluorescence fluctuate from sample to sample, even when they are prepared under as nearly identical conditions as possible. This fluctuation of the luminescent properties may be due to slight differences of the atmosphere during preparation. The phosphors prepared by firing in oxygen or nitrogen in the second heat treatment are similar to those prepared by firing in air. At liquid air temperature, all of these phosphors produce strong bluish green or green fluorescence under excitation by 2537Å and 3650Å. The fluorescence of Ag-activated phosphors with different mole ratios of $MgO:B_2O_3$ was similar in color to that of the phosphor mentioned above, but weak in intensity. Pure magnesium borate showed no fluorescence under excitation by ultraviolet or cathode rays at room or liquid air temperature.

Silver-activated phosphors treated with reducing agents show a strong fluorescence whose color varies from bluish green to dark red depending on the degree of reduction of the phosphor, but only under excitation by 3650Å. The brightest fluorescence after reduction was obtained when the composition was $MgO \cdot B_2O_3$:Ag ($1\text{-}2\times10^{-2}$ moles). The fluorescent intensity of the phosphors emitting green, yellow or orange fluorescence is comparable to that of Cu-activated zinc or zinc·cadmium sulfide phosphors under excitation by 3650Å. Since the body color of the phosphor powder deepens from white to black with increasing degree of reduction, the intensity of the emerging red fluorescence of the gray colored powder is weak. The fluorescent intensity of Ag-activated phosphors of different mole ratios of $MgO:B_2O_3$ is weak after treatment with reducing agents as before. Pure magnesium borate without added impurities shows no fluorescence at all after reduction by the same reducing agents.

Among magnesium borates containing various elements other than Ag, several phosphors such as the ones containing Mn (red fluorescence under excitation by 3650Å or cathode rays), Tl (weak blue, 2537Å), Sm (orange, cathode rays), Ce(Ce^{3+}: strong violet, 2537Å) and Sn(Sn^{2+}: weak yellow white, 2537Å), produced fluorescence, but none of these phosphors showed a change of fluorescence color after treatment with the same reducing agents as before. Phosphors with 1 mole % Ag and increasing amounts of Al from 0.1 to 5 mole % showed a decreasing sensitivity to reducing agents as the Al concentration was increased. Thus a sample with 0.1 mole % Al was still strongly green fluorescent after the reduction, while one with 1% Al was already very weak.

The fluorescent spectrum of the bluish green phosphor obtainable by slight reduction on paper is shown by curve 1 in Fig. 1. After the phosphor was allowed to stand in air for 3 hr at room temperature, it gave the fluorescent spectrum shown by curve 2. As seen in this diagram, the normalized fluorescent spectra consist of at least two main bands peaking at about 4200 and 5300Å. With increasing degree of reduction, the intensity of the blue band decreases, while that of the green band increases.

The fluorescent spectrum of the green phosphor, which was reduced on paper in air, is shown by curve 1 in Fig. 2. The peak position is at about 5200Å in approximate agreement with that of the green band

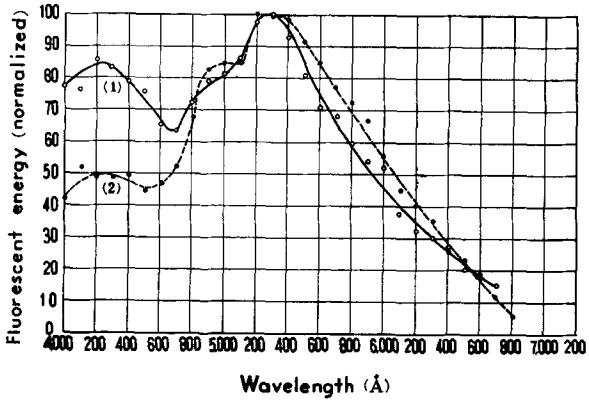

Fig. 1. Fluorescent spectrum of bluish white fluorescent magnesium borate phosphors with 1 mole % Ag, fired for two 0.5 hr periods at 950°C in air, under excitation by 3650Å at room temperature.

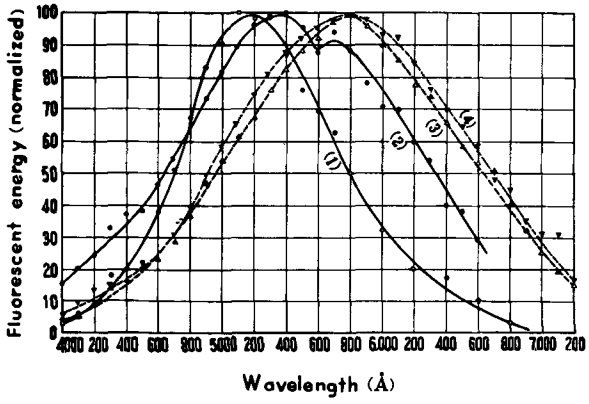

Fig. 2. Fluorescent spectrum of magnesium borate phosphors with 1 mole % Ag, fired for two 0.5 hr periods at 950°C in air, producing green (curve 1), yellow (curve 2) and orange (curves 3 and 4) fluorescence after reduction, under excitation by 3650Å at room temperature.

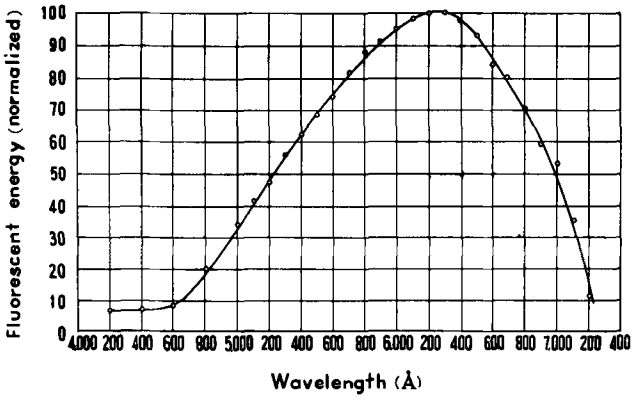

Fig. 3. Fluorescent spectrum of magnesium borate phosphor with 1 mole % Ag, fired for two 0.5 hr periods at 950°C in air, producing red fluorescence after reduction, under excitation by 3650Å at room temperature.

shown in Fig. 1. The fluorescent spectrum of the same phosphor exposed to 3650Å radiation for 6 hr in air at room temperature after the measurement of curve 1 in Fig. 1 is shown by curve 2 in Fig. 2. This spectrum shows two bands peaking at about 5400 and 5700Å which correspond to the bands peaking at about 5200 and 5800Å to be described below. The shift in peak position of the two bands may be due to the overlap of the two bands peaking at about 5200 and 5800Å.

The fluorescent spectra of samples which were allowed to stand in the dark in air for 24 hr, or for 18 hr followed by exposure to 3650Å for 12 hr, after the measurement of the spectrum shown by curve 2 in Fig. 2 was made, are shown by curves 3 and 4 in Fig. 2, respectively. The time required for the measurement of the respective fluorescent spectra mentioned above was about 30 min. The spectra shown by curves 3 and 4 in Fig. 2 are essentially identical and the peak wave length of the spectra is about 5800Å.

The fluorescent spectrum of a phosphor reduced on paper under irradiation by 2537Å for 30 hr at room temperature is shown in Fig. 3. The peak wave length of the spectrum is about 6300Å.

Reflection Spectra

The spectral reflection of pure magnesium borate of composition $MgO \cdot B_2O_3$ is shown by curve 1 in Fig. 4, relative to that of magnesium oxide. The reflection spectra of typical phosphors whose fluorescence spectra are illustrated by curve 1 in Fig. 1, by curves 1 and 2 in Fig. 2, and by Fig. 3 are shown by curves 2, 3, 4, and 5 in Fig. 4. All of these curves have a rather similar shape and show no narrow absorption bands over a wide range of the spectrum from about 2400 to 4800Å.

Discussion

Since the change of fluorescence color of phosphors treated with reducing agents was confined to the phosphors activated with Ag, the origin of this phenomenon must be ascribed to the presence of Ag. In Ag-activated magnesium borate phosphor prepared in oxidizing or neutral atmosphere, silver may be introduced into the matrix in the form of Ag^+ ions replacing Mg^{++} ions at the lattice sites. An O^{--} ion vacancy may be generated by the replacement of two Mg^{++} ions by two Ag^+ ions in order to satisfy the condition of charge neutrality in the phosphor, as has already been suggested for the Cu-activated calcium orthophosphate (2). The blue fluorescence band peaking at 4200Å may be ascribed to an Ag^+ activator center adjacent to an O^{--} ion vacancy.

Extending the assumption made above, the green, orange, and red bands in the reduced phosphor may be attributed to activator centers adjacent to O^{--} ion vacancies in which one, two, and three electrons are trapped, respectively. It is plausible to assume that one of the trapped electrons will combine with an Ag^+ ion and form an Ag-atom. If Ag-atoms aggregate into the colloidal form the phosphor powder will become gray or black colored.

It is further proposed that the surface O^{--} ions of the phosphor crystals react chemically with adsorbed reducing agents in the presence of water. For ex-

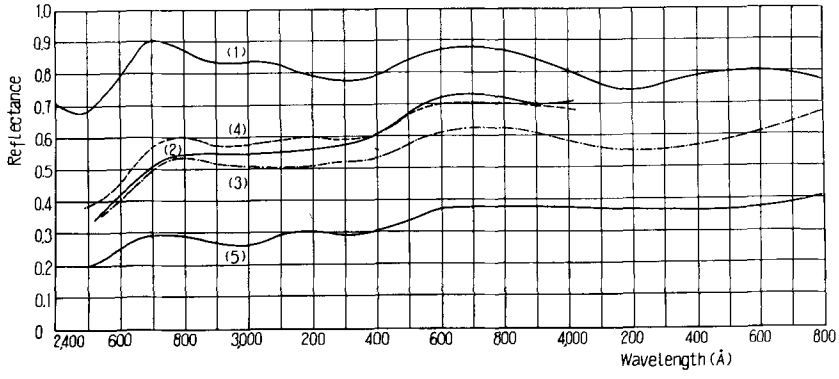

Fig. 4. Reflection spectrum of pure and Ag-activated magnesium borates: curve 1, pure magnesium borate; 2, bluish white fluorescent phosphor; 3, green fluorescent phosphor; 4, yellow fluorescent phosphor; and 5, red fluorescent phosphor.

ample, sulfite ions are thus oxidized to sulfate ions with the simultaneous release of free electrons. These free electrons then enter into the crystal via the conduction band and become trapped at O^{--} vacancies adjacent to Ag^{+} ions. This may lead to a reduction of Ag^{+} ions to Ag atoms. As a result, the concentration of surface O^{--} ions is greatly decreased. This establishes a steep gradient of O^{--} ion concentration in the region near the crystal surface, causing more O^{--} ions from the crystal interior to diffuse to to the surface. Repetition of these processes then leads to the progressive disintegration of the crystal until the last stage of reduction, namely the form of a black powder, is reached.

The strong interaction between activator center and lattice in the phosphor or the loose binding of trapped electrons with Ag^{+} ions in the activator centers will be responsible for the rather flat reflection spectra shown in Fig. 4. Since the intensity of fluorescence of the phosphors producing green to orange fluorescence is comparable with that of Cu-activated zinc or zinc·cadmium sulfide whose quantum efficiencies have been reported to be about 0.5 at 3650Å, the quantum efficiency of these Ag-activated magnesium borate phosphors will be close to unity at 3650Å. This is estimated on the basis of their much lower absorption of 3650Å radiation compared with the sulfides.

With the incorporation of aluminum into Ag-activated magnesium borate, the number of O^{--} ion vacancies will decrease, since aluminum will be introduced into the matrix as Al^{+++} ions replacing Mg^{++} ions at the lattice sites. The effect of aluminum in lowering the intensity of fluorescence of the reduced phosphor is thus explained.

The properties of these phosphors resemble somewhat those of Ag-activated alkali halides or of pure silver halides as reported by Weyl and others (1, 3), but they are more complicated. In addition to the phosphors described, a number of other Ag-activated phosphors were prepared and reduced by the same method. Many phosphors, such as Ca or Sr silicate containing Ag, showed similar properties, but their intensity of fluorescence after reduction was lower than that of Ag-activated magnesium borate. Furthermore, it was found that silver nitrate crystals purified by repeated recrystallizations and stored in a clean glass bottle for about five years in the dark developed a number of bright specks under excitation by 3650Å, while nonpurified silver nitrate crystals turned into nonfluorescent gray crystals under the same conditions. The color and intensity of the fluorescent specks in the pure crystals were similar to those of magnesium borate phosphors shown by curves 3 or 4 in Fig. 2. These crystals containing orange fluorescent specks turned into nonfluorescent dark gray crystals after reduction by the same reducing agents as mentioned before. The luminescent centers of these crystals, therefore, seem to be identical with those of Ag-activated magnesium borates. We suggest that Ag^{+} ions adjacent to negative ion vacancies in the phosphors correspond to the latent image in the photographic emulsion.

Acknowledgment

The authors wish to express their sincere thanks to Dr. Tsuneo Harada, the Director of Matsuda Research Laboratory, Tokyo Shibaura Electric Co., for his continuous support and encouragement. A major portion of this paper was presented at the Annual Symposium on Photochemistry, sponsored by The Chemical Society of Japan, The Photographic Society of Japan, and The Phosphor Circles of Japan, Tokyo, September 25, 1954.

Manuscript received April 22, 1959.

Any discussion of this paper will appear in a Discussion Section to be published in the December 1960 JOURNAL.

REFERENCES

1. W. A. Weyl, J. H. Schulman, R. J. Ginther, and L. W. Evans, *This Journal*, **95**, 70 (1949); J. H. Schulman, R. J. Ginther, C. C. Klick, R. S. Alger, and R. A. Levy, *J. Appl. Phys.*, **22**, 1479 (1951).
2. Y. Uehara, Y. Kobuke, and I. Masuda, *This Journal*, **106**, 200 (1959).
3. K. V. Shalimova and A. V. Belkina, *Zhur. Eksptl. Teoret. Fiz.*, **21**, 326 (1951); M. L. Kats, *Doklady Akad. Nauk S.S.S.R.*, **85**, 539 (1952); *Zhur, Eksptl. Teoret. Fiz.*, **23**, 720 (1952).

Chemical Etching of Silicon

II. The System HF, HNO_3, H_2O, and $HC_2H_3O_2$

H. Robbins and B. Schwartz

Hughes Semiconductors, Newport Beach, California

ABSTRACT

The kinetics of the reaction of silicon with solutions of hydrofluoric acid, nitric acid, and acetic acid are reported as a function of the composition of the etchant. The system qualitatively behaves in the same manner as the system hydrofluoric acid, nitric acid, and water, which has been reported previously. Quantitatively, the acetic acid diluted system shows a much higher tolerance for the diluent than does the water diluted system. The greater tolerance for acetic acid has been explained on the basis of the lesser ionization of nitric acid in acetic acid than in water. The reaction mechanisms postulated for the water diluted system have been found to apply equally well to the acetic acid diluted system.

Acetic acid is used widely as an additive to silicon etching solutions composed of hydrofluoric acid and nitric acid. This study was undertaken with the object of determining the role played by the acetic acid in the reaction, and also in the expectation that an understanding of the behavior of the acetic acid diluted system would lead to a better understanding of the water diluted system (1).

Experimental Procedure[1]

The kinetics of the system were determined by measuring the change in the dimensions of a silicon die, initially 0.125 x 0.125 in. in area and 0.025 in. thick, as a function of the composition of the etchant at constant initial temperature (25°C). The data were taken over the composition range where the decrement in die thickness exceeded 0.0001 in./min. The dice were n-type of approximately 3 ohm-centimeter resistivity; the two large surfaces were oriented along the (111) plane with an accuracy of approximately 90 min, whereas the remaining four surfaces were randomly oriented in the 111 zone. All surfaces were lapped with an abrasive grit; they were work damaged to an estimated depth of about ¼ mil.

The etching solutions consisted of mixtures, in various proportions, of nitric acid, hydrofluoric acid, and glacial acetic acid. No water was added to the solution. The only water in the solution was that contained in the concentrated hydrofluoric acid (51% H_2O) and nitric acid (30% H_2O). Before etching was begun, 20 ml of etching solution was placed in a small Teflon beaker and brought to 25°C in a constant temperature bath.

Two dice were placed in a small perforated polyethylene basket and etched simultaneously. Turbulent agitation was provided by rapidly swirling the basket through the solution, and quenching at the proper time was effected by rapidly transferring the basket to a large volume of water in a separate beaker. The decrement in die thickness was measured with a micrometer to ±0.0001 in.

The dice were etched three times, in separate portions of the same solution, and they were measured after each etch. The first etch was performed on an initially work damaged surface. The second etch was performed on a surface free from work damage, and the third etch was performed in the presence of a catalytic trace of sodium nitrite.[2]

Results and Discussion

Figure 1 depicts the etch rate corresponding to the catalyzed system as a function of the composition of the etchant. The solid curves correspond to the etching system in which acetic acid is the diluent, whereas the dashed curves correspond to the system in which water is the diluent. The curves are seen to converge on the zero diluent line, and to diverge as the amount of diluent is increased.

[1] Essentially the same experimental procedure was used here as was described in the first paper of this series.

[2] Small amounts of sodium nitrite have been found to enhance the rate of reaction in those instances where the supply of reagent by diffusion was not rate limiting (see below). Larger amounts of sodium nitrite caused inhibition of the reaction by formation of a protective film. This film is formed also in the presence of KNO_2 or NH_4NO_2, and on the basis of x-ray diffraction it has been identified as a fluosilicate.

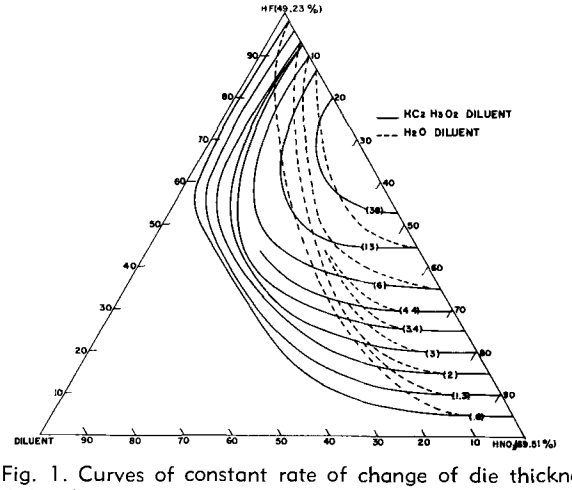

Fig. 1. Curves of constant rate of change of die thickness (mils/min) as a function of etchant composition in the system 49% HF, 70% HNO_3, and diluent.

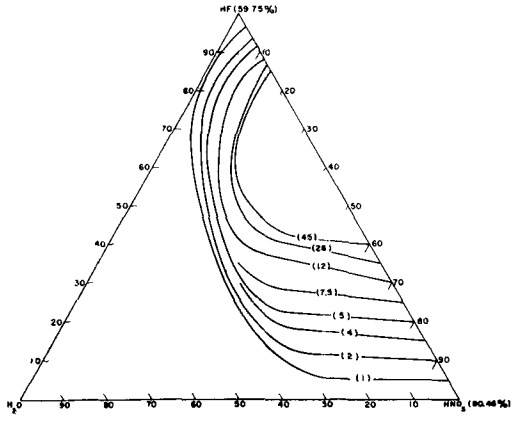

Fig. 2. Curves of constant rate of change of die thickness (mils/min) as a function of etchant composition in the system 60% HF, 90% HNO_3, and H_2O.

The etching behavior of the acetic acid diluted system is similar qualitatively to that of the water diluted system. The similarity is more striking when the acetic acid diluted system is compared with the more concentrated water diluted system shown in Fig. 2. There are three areas of general interest: the high nitric acid region, the high hydrofluoric acid region, and the region in the vicinity of the maximum etch rate. In the high nitric acid region the curves run parallel with lines of constant hydrofluoric acid, indicating that the hydrofluoric acid plays the kinetically important role here. In the high hydrofluoric acid region the course of the curves parallel with lines of constant nitric acid indicates that here the kinetically important reagent is nitric acid. In the region near the maximum etch rate both reagents play an important kinetic role.

The interpretation of the mechanism of the reaction in the water diluted system appears to be applicable also to the acetic acid diluted system. The mechanism involves a diffusion limited supply of reagents to the silicon surface, modified by autocatalytic factors as described earlier (1).

Effect of Diluent on the Reaction

The principal difference between the water diluted system and the acetic acid diluted system lies in the much greater tolerance of the latter for the diluent. Both systems initially show an indifference toward the addition of diluent in both the high hydrofluoric acid region and the high nitric acid region. When a critical amount of diluent has been added, however, the rates vanish rapidly upon the further addition of a small amount of diluent. In the high hydrofluoric acid region, the water diluted system of Fig. 1 already contains the critical amount of diluent so that no additional water can be tolerated if the etch rates are to retain their diffusion limited values.

Briner and co-workers (2, 3) have shown that the oxidizing power of nitric acid in concentrated solutions depends on the undissociated species, probably in the form of the pseudo acid $HONO_2$, which is involved directly in the oxidation. Cretella and Gatos (4) take a similar position with respect to the necessary role of undissociated nitric acid. They find that the rate of oxidation of germanium is proportional to the product of HNO_2 and undissociated HNO_3. They base their argument on the mechanism postulated by Vetter (5) as follows:

$$HNO_2 + HNO_3 \rightleftarrows N_2O_4 + H_2O$$

(slow and rate determining) [1]

$$N_2O_4 \rightleftarrows 2NO_2 \quad \text{(fast)} \quad [2]$$

$$NO_2 + e^- \rightleftarrows NO_2^- \quad \text{(fast)} \quad [3]$$

Here the active species is NO_2, which takes an electron from the germanium to form the nitrite ion. The nitrite ion then combines with a proton to regenerate the nitrous acid required for step [1]. This mechanism is in accord with the observed autocatalytic behavior of the reaction.

An additional possible interpretation of the mechanism is based on a paper by Schmid and Spahn (6) which considers the various equilibria involving nitrogen oxides and nitrous acid. The latter authors accept the basic ideas of Abel, *et al.* (7-9) that the active oxidizing agent is HNO_2 such that

$$2HNO_2 + R \rightarrow RO + 2NO + H_2O$$

(R = reducing agent) [4]

and that the formation of HNO_2 is rate determining.

$$HNO_2 + H^+ + NO_3^- \rightleftarrows N_2O_4 + H_2O$$

(slow, rate determining) [5]

$$N_2O_4 + 2NO + 2H_2O \rightleftarrows 4HNO_2 \quad \text{(fast)} \quad [6]$$

A portion of the HNO_2 is recycled through [5], and the remainder either reacts with the reducing agent to form more NO, which is again involved in the regeneration of HNO_2 as in [6], or diffuses away into the bulk of the solution. The net result is:

$$HNO_3 + R = RO + HNO_2 \quad [7]$$

On the basis of these equilibria which involve water, Schmid and Spahn come to the conclusion that there must be a maximum in the oxidizing ability of nitric acid at an optimum water content, since the removal of water past that point causes the reversal of Eq. [6] and thus a decrease in the concentration of the actual reactive species. As applied to the present research, this peak in the oxidizing ability of nitric acid would be leveled into a plateau by the diffusion mechanism, but would, in accord with our results to be discussed below, account for the ultimate falling off of the etch rates as the amount of water is decreased. We are not inclined to favor the point of view of Schmid and Spahn, since we have observed that in many instances the slowdown of the oxidation by nitric acid as the water content is decreased can be attributed to the formation of an insoluble film, and that in instances where the formation of the film does not take place, e.g., in the oxidation of substances such as sulfur, selenium, or phosphorus, the rates continue to increase monotonically as the amount of water is decreased. A further complication is the fact that the etching of silicon will take place in the presence of a slight excess of permanganate or cerate ions, which quantitatively remove all of the nitrogen existing in lower valence states, and which themselves attack silicon but slowly, if at

all. Under these conditions only the mechanism of Briner is possible. We are inclined to consider that it is this process that initiates the reaction, generating a surface concentration of catalyst that leads to the build-up of the etch rate to the steady-state value. In the steady state, the reaction probably takes a parallel path through the intermediate formation of HNO_2 within the boundary film in a mechanism similar to that postulated by Schmid and Spahn (6).

The difference between the two systems tolerance for diluent, shown in Fig. 1, reflects the difference in the basicity and dielectric constant of the diluents. Since the oxidizing power of nitric acid has been shown to depend on the undissociated HNO_3 molecule, the etch rates at constant nitric acid concentration should decrease as water is added to the system. However, as long as the reaction is diffusion governed, the reaction rates will remain constant in spite of the decreasing oxidizing power of the nitric acid as diluent is added. Upon the further addition of water, however, a point is reached ultimately where the oxidation potential has been reduced to the extent that the rate of oxidation of the suface during the induction period becomes slightly less than the possible rate of supply of reagents by diffusion. At this point, the reduction products of nitric acid begin to play a kinetically observable role, and, since the reaction is now sensitive to the catalyst concentration, there results a very rapid decrease in the rate of the initiation reaction on the further addition of only a small amount of diluent. Since a 49% HF solution already contains the critical amount of water, it is necessary to employ a 60% solution to observe this behavior.

When acetic acid is the diluent, it must be remembered that in the high HF region and at constant HNO_3 concentration, diluent is being substituted for an aqueous HF solution. Thus a very weak base of low dielectric constant is being substituted for a somewhat stronger base, water, and a substance having moderately acidic properties, HF. Initially this should result in a decrease in the dissociation of the nitric acid, since the solvent is initially more than 50% water. Because of the diffusion limitation, the etch rates do not respond to the increased free nitric acid concentration. On further dilution with acetic acid, the removal of HF, which is a stronger acid than acetic acid, probably counteracts the effect of the substitution of acetic acid for water, so that the concentration of undissociated HNO_3 probably goes through a maximum and then decreases. A critical composition with respect to diluent thus is reached ultimately, and the rates vanish on the slight further addition of acetic acid, for the same reason as in the water diluted system.

The same argument can be used to interpret the abrupt change of the curvature of the rate contours with increasing diluent in the high nitric acid region. The question may be raised that, if in the high HF region the reaction can be noncritical at 5% HNO_3, why does it become critical at 50% HNO_3 in the high nitric acid region of the acetic acid diluted system, and at a still higher value of HNO_3 in the water diluted system? We can only suggest that the difference lies in the nature of the silicon surface. In the high HF region the surface is essentially stripped of oxide, and the rapid decrease in the etch rate is the result of the slowdown of the oxidation reaction. In the high HNO_3 region the surface is essentially covered with an oxide mask. As the concentration of HNO_3 is decreased, this oxide becomes more tenuous, until a point is reached at which the HF reaction begins to slow down. The slowdown in the HF reaction causes a slowdown in the over-all reaction which then further affects the oxidation step through the mechanism of reduced catalyst production. This condition then requires an increased HF concentration to restore the etch rate to its previous value. It can be seen that in the critical region the rate contours run in the direction of constant acetic acid concentration, suggesting that the decrease in reactivity of the nitric acid as the latter is decreased in concentration may be compensated by the increase in the HF concentration. In this region the reaction is probably not strictly diffusion limited, since there is a finite surface concentration of both reagents. However, diffusion still plays a role in that the surface concentration does not equal the bulk concentration of reagents, and both the surface concentration of reagents and the nature of the surface itself affect the kinetics.

Chemical etching in solutions the compositions of which lie in the critical regions of Fig. 1 can be extremely frustrating. As an example, a mixture of 4.50 ml HF, 7.50 ml HNO_3, and 8.00 ml of $HC_2H_3O_2$ has always been found to etch a work damaged specimen, and etching always continued at the same rate even after all of the damage had been removed. A fresh solution did re-etch the specimen if the solution had been made up from 48.9% HF, but it did not re-etch the specimen if it had been made up from 48.5% HF. Furthermore, the addition of one drop of acetic acid to 20 ml of the solution that had been made up from 48.9% HF caused the solution to lose its ability to re-etch. The addition of a few milligrams of sodium nitrite then caused the solution to regain its etching ability. If an etching die were transferred to a fresh solution made up from 48.5% HF, it usually would continue to etch at the same rate, since a trace of catalyst reinitiates the reaction. If this die were transferred rapidly to a solution of the same composition, swirled to dissipate the catalyst, and then transferred to a third solution of the same composition, etching invariably would be quenched. In all cases, the etching rate was either in the vicinity of 1.8 mil/min or 0.

In view of this behavior, the reaction must proceed first through an induction period in which the autocatalytic factors cause a build-up of the etch rate to the steady-state value. The induction period depends greatly on the condition of the silicon surface. A work damaged surface has a short induction period, whereas an undamaged surface has a relatively long induction period, owing to the absence of catalyst initially. Whether or not the etch rate can build up to the steady-state value then depends on whether the catalyst can be conserved in the vicinity

of the surface in sufficient quantity to assure its involvement in the propagation of the reaction. The etch rates thus seem to be the result of a balance struck between the autocatalytic factors, which are explosive in nature, and some rate limiting mechanism. Since the rates are the result of the difference between these two large quantities, the system may be inherently unstable, and this may cause the measured etch rates to be nonreproducible.

Conclusions

The role of acetic acid in the etchant is primarily that of a diluent. As such it is able to provide control over the rate of the reaction by reducing the concentration of the kinetically important species. However, this function also can be performed with nitric acid as diluent in the compositions rich in nitric acid, or with hydrofluoric acid in the compositions rich in hydrofluoric acid. Excessive addition of acetic acid can cause the etch rates to become erratic and extremely critical with respect to small changes in composition. Water also can be used as a diluent, except that in the high hydrofluoric acid region the system is critical with respect to the addition of diluent.

The kinetics in the acetic acid diluted system are governed by the same factors that operate in the water diluted system. Thus the reaction rates are determined by the rate of diffusion of the kinetically important species to the surface of the specimen. The autocatalytic factors that operate in the water diluted system play the same role in the acetic acid diluted system. The quantitative differences between the two systems can be explained on the basis of the difference in the basicity and dielectric constant of the two diluents.

Manuscript received April 6, 1959. This paper was prepared for delivery before the Ottawa Meeting, Sept. 28-Oct. 2, 1958.

Any discussion of this paper will appear in a Discussion Section to be published in the December 1960 JOURNAL.

REFERENCES

1. H. Robbins and B. Schwartz, *This Journal*, **106**, 505 (1959).
2. E. Briner, *Helv. Chim. Acta*, **18**, 363 (1935).
3. E. Briner and P. Bolle, *ibid.*, **18**, 368 (1935).
4. M. Cretella and H. Gatos, *This Journal*, **105**, 487 (1958).
5. K. Vetter, *Z. physik. Chem.*, **194**, 199 (1950).
6. G. Schmid and H. Spahn, *Z. Metallkunde*, **45**, 128 (1955).
7. E. Abel and H. Schmid, *Z. physik. Chem.*, **132**, 55 (1928).
8. E. Abel and H. Schmid, *ibid.*, **134**, 279 (1928).
9. E. Abel, H. Schmid, and S. Babad, *ibid.*, **136**, 135 (1928).

High-Purity Silicon from an Iodide Process Pilot Plant

Carlyle S. Herrick and James G. Krieble[1]

Research Laboratory, General Electric Company, Schenectady, New York

ABSTRACT

Silicon tetraiodide is formed from commercial silicon and iodine in a fluid-bed reactor. Impurities are rejected by solvent recrystallization followed by fractional distillation. High-purity silicon is formed by thermal decomposition of the iodide on a silicon surface. Silicon made this way has a resistivity over a 1000 ohm-cm. Reproducible results are obtained which suggest the product quality is controlled by back-contamination from the decomposition and crystal growing steps. Data from the decomposition of silicon tetraiodide at 1000°C and low pressure are correlated by the relation:

$$\log p = 2.18 - \frac{m}{0.305}$$

where p = lb SiI_4 vapor feed/hr/ft^2 heated surface and m = fraction of $SiI_{4(g)}$ converted to $Si_{(s)}$. It is postulated that this reaction reaches equilibrium.

Iodide chemistry was developed by Van Arkel and de Boer (1) into a useful method for reducing the oxygen, nitrogen, or carbon content of such refractory materials as titanium, zirconium, hafnium, and silicon. Other impurities, aluminum, beryllium, boron, iron, and copper, are not rejected effectively by this simple iodide cycle and, as a result, further development of the iodide method has been necessary to produce the purity required in semiconductor silicon. The most fruitful approach has been to remove the iodide intermediate from the reaction system, subject it to additional purification, then decompose it to form a purer material.

Recrystallization (2), distillation (2-4), sublimation (5), and zone refining (5, 6) have been reported to be useful for the intermediate purification of sili-

[1] Present address: Lamp Metals & Components Department, General Electric Company, Cleveland, Ohio.

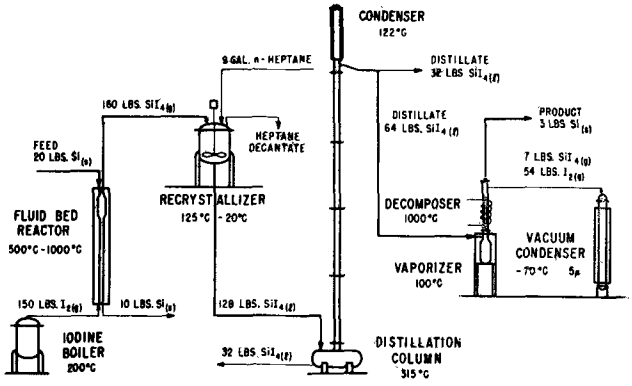

Fig. 1. Iodide process flowsheet

con tetraiodide. McCarty (2) in this laboratory has shown that silicon of 500 ohm-cm resistivity can be prepared by using a recrystallization step followed by a distillation step. The present work has been directed toward finding answers to the questions:

1. Can silicon of even higher purity be made by chemical means?
2. Can this silicon be made in large quantities?

Both questions can be answered in the affirmative when an iodide process is used.

Process Description

The flow sheet for this iodide process, Fig. 1, shows reaction of silicon and iodine to form silicon tetraiodide, purification of tetraiodide by recrystallization, then distillation, and decomposition to high-purity elemental silicon and iodine. This same sequence of events was used by McCarty (2); however the character of the reaction step, distillation and decomposition step used here have been modified substantially to improve their effectiveness.

Silicon tetraiodide is formed in a fluid bed reactor using commercial 99.9% silicon and research grade iodine at atmospheric pressure. The bed, charged with 44-100 μ diameter silicon powder is fluidized entirely by iodine vapor, although an inert gas diluent may be used if desired. Fluidization provides excellent heat transfer between particles and creates a uniform temperature throughout the bed. It has the advantage that an exothermic reaction involving a poor heat conducting solid can take place at constant temperature. Of course, constant reaction temperature means a constant reactivity for silicon and its impurities and a better separation between them based on reaction energies. Previously described small scale reactors have used the fixed bed principle and thus have not realized the full separating potential of the reaction step. Close observation of a fixed bed using iodine and silicon discloses that lack of temperature control causes a reaction zone to travel through the bed as a "hot spot," usually incandescent. Such lack of control is characteristic of fixed beds. Unreacted silicon enriched in impurities is discharged from the fluid bed at the end of an experiment.

Iodine residence time in the bed is short, 1-2 sec; however the reaction is rapid enough for the yield to be quantitative. As iodine is consumed from the vapor stream, the silicon tetraiodide product takes over the job of fluidizing the bed. Since the reaction appears to involve only iodine atoms and silicon, there is a 4 to 1 volume change during the reaction according to Eq. [1].

$$4\ I_{(g)} + Si_{(s)} \rightarrow SiI_{4(g)} \qquad [1]$$

This decrease in top-bed fluidizing velocity helps reduce powder entrainment.

Silicon tetraiodide leaving the reactor condenses in the recrystallizer where n-heptane is added in 1 to 1 mole ratio. The resultant slurry is warmed and then cooled to dissolve and recrystallize the tetraiodide. The n-heptane containing dissolved impurities is decanted, then the operation is repeated. The over-all yield for two recrystallizations is about 80%.

In the distillation column the tetraiodide is divided into a bottom fraction containing the less volatile impurities, a top fraction containing the more volatile impurities, and a second distillate of purified tetraiodide comprising 50% of the column charge.

This purified tetraiodide is fed to the vaporizer where evacuating and heating produce a low-pressure tetraiodide atmosphere around a heated silicon rod. Now the tetraiodide dissociates to the diiodide (7) and then to solid silicon according to reactions [2] and [3].

$$SiI_{4(g)} \rightarrow SiI_{2(g)} + 2\ I_{(g)} \qquad [2]$$

$$SiI_{2(g)} \rightarrow Si_{(s)} + 2\ I_{(g)} \qquad [3]$$

A deposit of high quality product silicon forms on the heated rod while the iodine atoms recombine after cooling and flow to the vacuum condenser along with unreacted tetraiodide. The diffusion rates of many impurities in silicon are comparable with the rate of product accumulation. Commercial semiconductor silicon was used for the heated decomposer surface to minimize diffusional contamination of the product silicon. The yield for this step was about 50%.

In the stoichiometry of Fig. 1, 20 lb of silicon and 150 lb of iodine are fed to the reactor for each 3 lb deposit of product silicon. It does not take account of the existing opportunities to reuse and recycle waste streams to bring consumption and production into better balance.

Except for impurities added during processing, it is assumed that impurities are present as iodides in silicon tetraiodide. Vapor pressure data from Brewer (8) and from Schäfer and Hönes (9) are shown in Fig. 2. Vapor pressures of Nb, Hg, Ga, Ge, Al, As, and Sb iodides fall in a band between those of tin and tantalum. Vapor pressures of most metal iodides are lower than for silicon tetraiodide so they will remain in the reboiler during distillation. Phosphorus and boron iodides are more volatile and must be removed at the top of the distillation column before purified silicon tetraiodide can be distilled overhead. At 1 atm CI_4 boils 19°C higher than SiI_4 and PI_3 63°C lower. The calculated relative volatilities are 3.4 for PI_3 with respect to SiI_4 and 1.4 for SiI_4 with respect to CI_4. Both volatilities are large enough to permit extensive separations with a moderate number of theoretical distillation plates.

This process scheme imposes stringent requirements on the materials of construction. Silicon tetra-

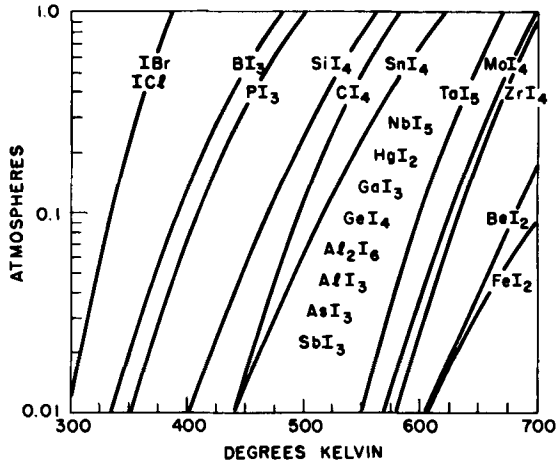

Fig. 2. Iodide vapor pressures

iodide in process is usually accompanied by some iodine and hydrogen iodide and this mixture is quite aggressive toward container materials at elevated temperatures. Quartz, due to its high chemical stability, was selected for the reactor, the distillation column, and the decomposer.

Process Equipment

The fluid bed reactor is a 4-in. diameter quartz tube 8 ft long mounted vertically in a furnace, Fig. 3. A porous-type gas distributor was used to eliminate stagnant zones and get uniform fluidization (10). Heat of reaction is removed from the bed by direct radiation to the furnace walls which are maintained about 50°C cooler than reaction temperature. The electric heating elements in the furnace are internally exposed to get maximum heat transfer and

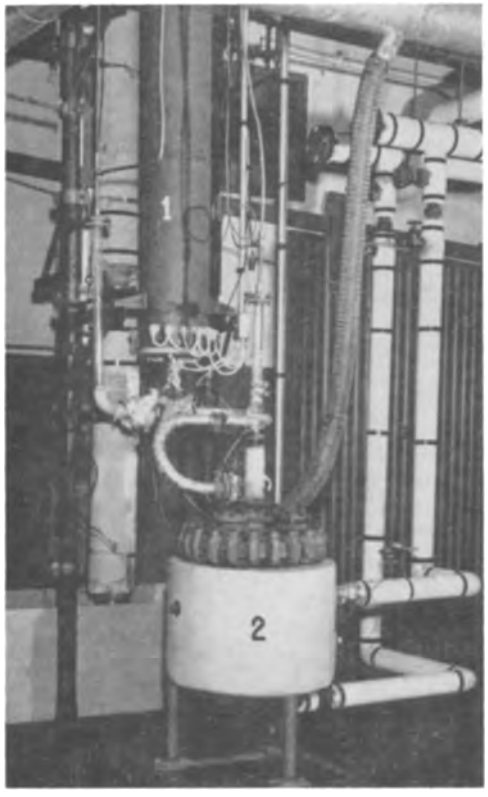

Fig. 3. Fluid bed reactor: 1, reactor furnace; 2. iodine boiler.

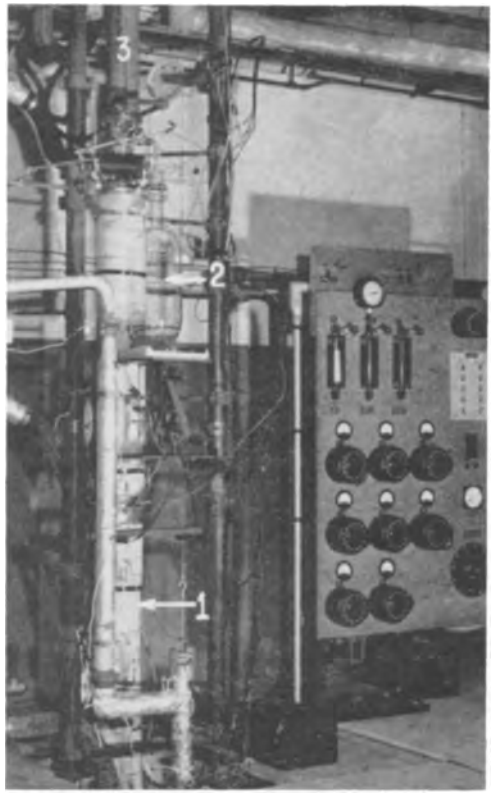

Fig. 4. Distillation column: 1, column upper sections; 2, product receiver; 3, condenser.

controllability. Iodine is vaporized in a 10-gal glass-lined steel iodine boiler jacketed with 230°C hot oil.

The recrystallizer is a 20-gal glass-lined steel agitated vessel jacketed for steam heating or water cooling. It is mounted on a base which permits weighing without disturbing the quartz piping connections.

The all-quartz distillation column consists of reboiler, four lengths of 3-in. diameter tubing, and a condenser, with an over-all height of 24 ft. At the bottom the 10-gal reboiler is heated by Calrod®[2] units inserted in quartz tubes sealed lengthwise through the lower sector of the vessel. Direct radiant heat transfer from heater to boiling SiI_4 gives fast response and minimum superheating.

At the top of the distillation column, Fig. 4, a 3-ft length of 4-in. tubing serves as a condenser. It is provided with a 6-in. stainless steel jacket and a circulating hot oil coolant system. Each of the four column sections is packed with ⅜-in. quartz rashig rings with quartz packing supports and distributor plates. The entire asesmbly is supported by a system of weights and pulleys and is arranged for adiabatic operation. Thirty-two theoretical plates were measured at 1 atm using a n-heptane methylcyclohexane test mixture (11) and the Fenske equation (12).

Silicon tetraiodide is removed from the column in a 3-gal quartz receiver and placed in the vaporizer to become the bottom portion of the decomposer assembly. Figure 5 shows a Pyrex receiver of the same size holding 45 lb of tetraiodide. The discoloration is caused by iodine released by a photochemical oxidation which has not yet been identified. Heating silicon tetraiodide from room temperature to 100°C

[2] ® Registered Trademark.

Fig. 5. Product receiver

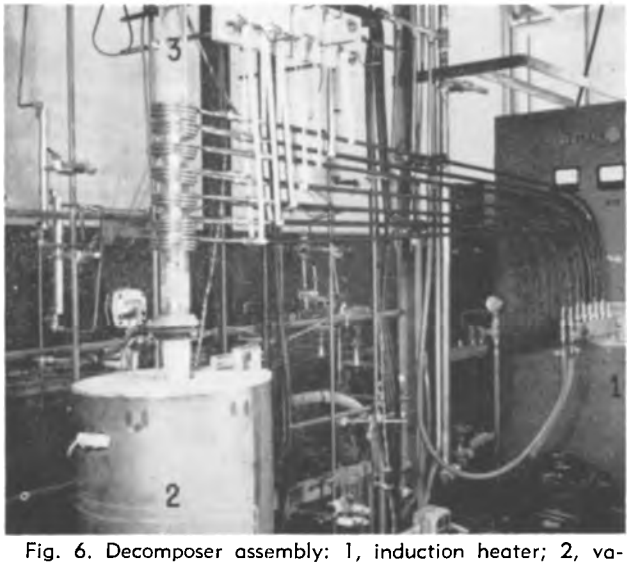

Fig. 6. Decomposer assembly: 1, induction heater; 2, vaporizer; 3, decomposer.

causes expansion forces strong enough to break glass or quartz containers. Melting the outer layer of the SiI_4 cake and reforming along one side of the vessel creates ample room for expansion without breakage.

The decomposer consists of a vertical 2-in. quartz tube mounted atop a 3 gal SiI_4 receiver just described. A silicon rod, $\frac{5}{8}$ in. in diameter and 14 in. long, mounted inside the tube, is heated to 1000°C by external coils connected to an induction heater, Fig. 6. As SiI_4 decomposes in contact with the heated surface, silicon deposits on the rod which increases in diameter. Adjustment of the heating coils along the rod is necessary to obtain a uniform deposit.

Figure 7 shows a typical deposit obtained by heating a 10 in. length of rod. It is 1.25 in. in diameter

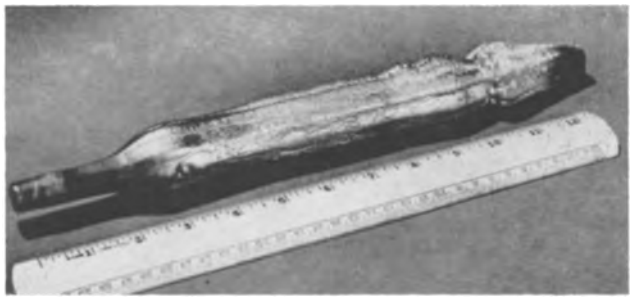

Fig. 7. Product silicon

and contains 1 lb of new silicon. Deposit and rod are separated by a sawing operation which produces sizes and shapes required for crystal growing.

Product Silicon Evaluation

Resistivity measurements were made on single crystals prepared by the Czochralski technique (13). The four point probe method (14) was used to measure resistivity profiles. Minority carrier lifetime was measured by the infrared photoconducting decay method (15).

Experimental results are listed in Table I. It should be recognized that the four point probe measurement is subject to large errors above 1000 ohm-cm. Furthermore, the crucible method of crystal growing contaminates the silicon, and at high resistivities this causes the seed end resistivity to change rapidly along the crystal so the region of maximum resistivity is difficult to locate. This effect is noticeable in Table I where resistivity values are reported at approximate 1-in. intervals along the crystals.

Resistivities as high as 3500 ohm-cm have not been reported previously for crucible grown silicon. Dissolution of quartz in molten silicon during crystal growth is known to occur (16, 17), and the accompanying impurities are expected to limit the maximum obtainable resistivity values. Practical values for such a limit have not yet been reported. Hannay (17) reports that the limit is higher than 300 ohm-cm p-type while Taft and Horn (16) report exceeding 300 ohm-cm in practice. The present work suggests that the practical limit is above 1000 ohm-cm p-type under the most favorable experimental conditions, i.e., minimum time elapses between the onset of melting and the cooling-off of the seed end of the pulled crystal.

Examinations in a cryostat for deep level compensation showed these effects to be absent. Each crystal did exhibit a photo-emf in ambient light; however, type reversals were not detectable by potentiomet-

Table I. Product silicon resistivity and lifetime

Lot No.	Decomposer Rod material	Rectification type	Speed end	Resistivity, ohm-cm		Sprout end	Lifetime, μsec
1	ZR	p	3400	1100	500	200	100
2	C	n	70	78	65	130	50
3	ZR	p	3500	700	400	130	100
4	ZR	p	3200	900	400	140	350

ZR—Zone refined silicon, 130 ohm-cm p-type.
C—Commercial grade silicon, 2 ohm-cm n-type.

ric probing or by applying an electric field to a barium titanate coated surface. The source of the photo-emf is not understood at present. While it did interfere somewhat with lifetime measurements, the values obtained are in a medium range for high-quality crucible grown silicon.

With all factors considered, it is concluded that the product silicon quality corresponds to a resistivity over 1000 ohm-cm. Measurements on crucible grown silicon in this resistivity range do not warrant a more quantitative statement at the present time.

The Table I data are a full sequence of lots without deletions or selections; thus the agreement between 3400, 3500, and 3200 ohm-cm resistivities is remarkable in view of the measurement uncertainties and may be fortuitous. The weight of evidence indicates to the authors, however, that this agreement is more real than circumstantial. It is believed to result from improved effectiveness and reproducibility in the processing steps and from skillful handling of the crystal growing problem.

Two different grades of silicon were used for the decomposer surface. One, the zone refined, had a resistivity of 130 ohm-cm; the other was a premelt rod of 2 ohm-cm commercial grade silicon. Both were prepared by the techniques of Taft and Horn (16). The low resistivity of product silicon in the second experiment correlates with the low resistivity of the silicon rod used in the decomposer. Since relative volumes of silicon and time of deposit were roughly equal in the four experiments, the data suggest that a proportional dilution effect controls product resistivity at about 27 times greater than the starting rod resistivity. It further suggests that the effect is roughly independent of resistivity over the range covered by the experiments.

Macroscopic examination of a transverse fraction in the product silicon gives the impresion of close-packed needlelike crystals with major axes radiating outward from the center of the rod. Hölbling (18) shows similarly oriented columnar crystals from the hydrogen reduction of SiI_4 on a carbon rod. Sangster, Maverick, and Croutch (19), on the other hand, show propagation of the original crystal structure when $SiBr_4$ is hydrogen reduced on a heated silicon filament.

The product silicon in this work was found to propagate the crystal structure of the original silicon rod. Figure 8 shows several crystal faces present after 2×10^5 atom layers of silicon have been deposited. The same crystal pattern was present in the rod before deposition. Microscopic examination of the product shows the individual crystals to have a large number of defects, presumably twins, Fig. 9. These twin lines are highly oriented in the growth direction. This degree of defect alignment would account for the observed fraction pattern as well as for the observation that the product material is much weaker when stressed in the transverse direction than is the original rod.

Impurity Separations During Processing

A resistivity of 3500 ohm-cm requires the electrically active impurity content of the silicon to be about 8 atoms per hundred billion atoms. The contribution of each process step to the total separation has been estimated in Table II to indicate whether this purity level is a reasonable achievement for the process. Impurity concentrations are indicated only as to order of magnitude which is about the accuracy warranted by much of the supporting data. The starting silicon was commercial acid-leached 99.9% silicon. Spectrographic analyses of this material gave results in agreement with those reported by Szekely (4). The most concentrated impurity was present less than 1×10^{-3} atoms per atom Si. Analysis of the SiI_4 product from the fluid bed reactor by the same means shows the maximum impurity concentration to be a few parts per million. Similarly after the recrystallization step the impurity content is below the sensitivity of the analytical method. It is interesting to note that detectable amounts of boron are rejected in the solvent.

An indirect approach is necessary to estimate distillation column output purity. Calculations for the PI_3-SiI_4 system using the Fenske equation (12) and a relative volatility modified to dilute solution conditions according to the experience of Green and

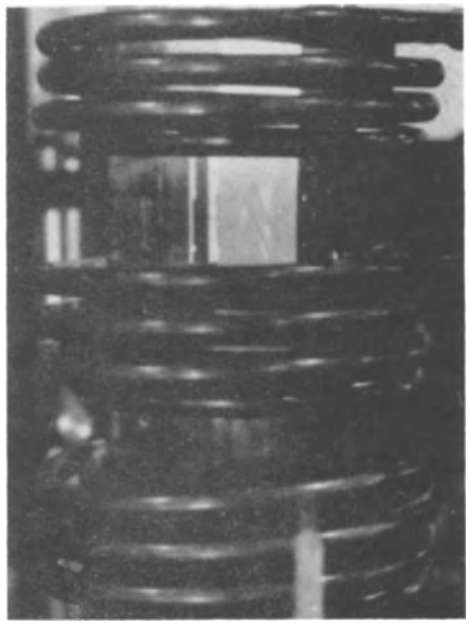

Fig. 8. Crystal faces preserved during deposition

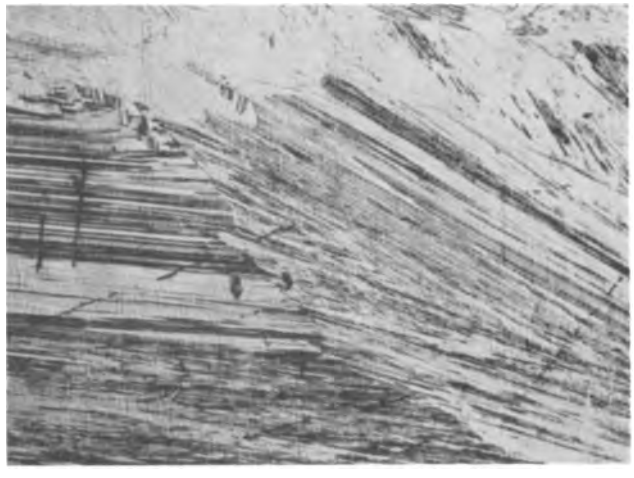

Fig. 9. Product silicon crystal structure. Magnification 200 X before reduction for publication.

Table II. Impurity separating ability of process steps

Process step	Atoms of most concentrated impurity per silicon atom		Separation factor
	Input	Output	
Fluid bed reactor	1×10^{-3}	10^{-6}	10^{3}
Recrystallizer	10^{-6}	10^{-8}	10^{2}
Distillation column	10^{-8}	10^{-13}	10^{5}
Silicon surface decomposer	10^{-13}	10^{-11}	10^{-2}

Kafalas (20) indicate a maximum separation factor of 5.5 x 10^{6} for this column and feed. It is probable, however, that column performance is limited to a factor of 10^{5} by an aerosol entrainment mechanism according to Manowitz, Bretton, and Horrigan (21). This factor applies to all iodide impurities except CI_4. Since carbon is one of the elements most effectively rejected by iodide chemistry the lower separation factor for this compound has not caused special problems.

The decomposer separation factor calculated as the difference between known input and output impurity levels gives 10^{-2} or a hundredfold contamination. This is consistent with the observed dependence of product purity on silicon rod purity. Moreover, the magnitude of the effect is reasonable for the impurity level of this step.

Two conclusions can be drawn from this analysis. First, product silicon in the 10^{-11} impurity range is within the capability of this process. Second, improvements in the decomposition step will probably yield product silicon of still higher purity.

SiI_4 Decomposition

The experimental observations on the decomposition step made at the General Electric Research Laboratory including this work and that of McCarty are correlated in Fig. 10. Equation [4] expresses the linear correlating function.

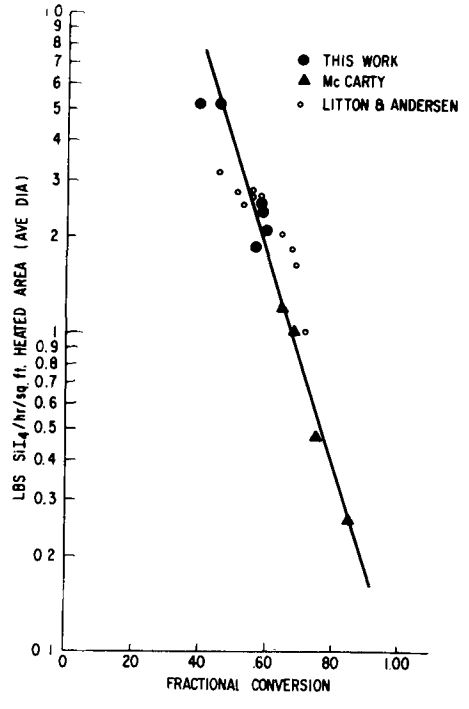

Fig. 10. Correlation of decomposition reaction data

$$\log p = 2.18 - \frac{m}{0.305} \qquad [4]$$

when p = pounds of SiI_4 vapor feed to the decomposer per hour per square foot of heated surface (arithmetic average) and m = fractional conversion of SiI_4 to Si.

The correlation holds for the over-all reaction of Eq. [5] at 1000°C and a condenser pressure of 1 to 10 μ.

$$SiI_{4(g)} \rightleftharpoons Si_{(s)} + 2\,I_{2(g)} \qquad [5]$$

The basic significance of this correlation is not understood at present, and no theoretical treatment exists to support it. Undeniably it correlates the data well. The results of Litton and Andersen (3), who have published the only data on thermal decomposition of SiI_4, have been recalculated and are compared with Eq. [4] in Fig. 10. Although the Litton and Andersen data show some scatter, the quantitative agreement is good. The decomposer vessels used in these three investigations differ widely in geometry. In this work decomposition occurred on a 5/8-in. diameter rod in a 2-in. diameter vessel. McCarty decomposed inside a 1.25-in. diameter cylinder while Litton and Andersen decomposed on a 0.1-in. diameter wire formed into an open helix inside a 2.75-in. diameter vessel. The fact that data taken under such widely different circumstances fit the same correlation suggests that chemical equilibrium exists in each type of equipment over the experimental range covered.

It is interesting to note that in all three studies each datum is really the average result of an entire experiment conducted at a continuously changing iodide vaporization rate, hence the instantaneous conditions corresponded with the average for a short time only. The form of the correlating equation $p = e^{m}$ is such that the derivative dp/dm is also equal to e^{m}. In this case, if the average diameter is replaced by the instantaneous diameter, the correlation will apply to the variables on an instantaneous basis. This condition is a prerequisite to having Eq. [4] represent an equilibrium relation.

One should note that the units, pounds per hour per square foot heated area, are actually unconventional units of pressure. Although no investigator has yet reported decomposer pressure measurements for reasons of contamination and corrosion, in principle sufficient data are now available to calculate an experimental equilibrium constant. The constant for equilibrium Eq. [5] is given by [6].

$$K_p = \frac{[I_2]^2}{[SiI_4]} \qquad [6]$$

In Table III experimental pressure values taken from the correlation have been recalculated to the more familiar units microns Hg. K_p has been calculated on the hypothesis that the experimental pressure is the total pressure in the system, i.e., the plug flow case or flow with no back-mixing. The variation between values of K_p is less than a factor

Table III. Experimental equilibrium constant

Lb SiI_4/hr/ft²	Pressure, μHg	K_p, mm
0.20	0.94	1.3×10^{-3}
0.30	1.4	1.2
1.0	4.4	1.4
3.0	13	1.9
6.0	25	2.2

of 2 which is firm evidence for equilibrium conditions during the decomposition reaction.

Acknowledgments

The authors appreciate the guidance and assistance of L. V. McCarty throughout the work, also C. B. Collins, F. H. Horn, and R. O. Carlson who took part in many helpful discussions. R. O. Carlson and G. W. Ludwig evaluated the product silicon, and W. C. Dash supplied silicon rods for the decomposer. R. J. Sullivan, R. L. Richard, and D. A. Reed assisted in carrying out the experimental work.

Manuscript received Jan. 22, 1959. This paper was prepared for delivery before the Buffalo Meeting, Oct. 6-10, 1957.

Any discussion of this paper will appear in a Discussion Section to be published in the December 1960 JOURNAL.

REFERENCES

1. A. E. Van Arkel and J. H. deBoer, *Z. anorg. u. allgem. Chem.*, **148**, 345 (1925).
2. L. V. McCarty, *This Journal*, **106**, 1036 (1958).
3. F. B. Litton and H. C. Andersen, *ibid.*, **101** 287 (1954).
4. G. Szekely, *ibid.*, **104**, 663 (1957).
5. B. Rubin, G. H. Moates, and J. R. Weiner, *ibid.*, **104**, 656 (1957).
6. G. H. Moates and B. Rubin, Paper presented before Electronics Division 113th meeting, Electrochem. Soc., New York, April 1958.
7. H. Schäfer and B. Morcher, *Z. anorg. u. allgem. Chem.*, **290**, 279 (1957).
8. Brewer, *et. al.*, "The Chemistry and Metallurgy of Miscellaneous Materials, Thermodynamics," L. L. Quill, Editor, McGraw-Hill Book Co., New York (1950).
9. H. Schäfer and W. J. Hönes, *Z. anorg. u. allgem. Chem.*, **238**, 68 (1956).
10. E. W. Grohse, *AIChE Journal*, **1**, 358 (1955).
11. E. C. Bromily and D. Quiggle, *Ind. Eng. Chem.*, **25**, 1136 (1933).
12. M. R. Fenske, *ibid.*, **24**, 482 (1932).
13. J. Czochralski, *Z. Physik Chem.*, **92**, 219 (1918).
14. A. Coblenz and H. L. Owens, "Transistors: Theory and Measurement," p. 208, McGraw-Hill Book Co., New York (1955).
15. R. L. Watters and G. W. Ludwig, *J.Appl. Phys.*, **27**, 489 (1956).
16. E. A. Taft and F. H. Horn, *This Journal*, **105**, 81 (1958).
17. N. B. Hannay, "Recent Advances in Silicon," Progress in Semiconductors, Vol. 1, p. 7, Heywood, London (1956).
18. R. Hölbling, *Z. Angew. Chem.*, **40**, 655 (1927).
19. R. C. Sangster, E. F. Maverick, and M. L. Croutch, *This Journal*, **104**, 317 (1957).
20. M. Green and J. A. Kafalas, *J. Chem. Soc.*, **5943**, 1604 (1955).
21. B. Manowitz, R. H. Bretton, and R. V. Horrigan, *Chem. Eng. Prog.*, **51**, 313 (1955).

The Preparation and Properties of Aluminum Antimonide

W. P. Allred, W. L. Mefferd, and R. K. Willardson

Battelle Memorial Institute, Columbus, Ohio

ABSTRACT

An improved method of growing single crystals of aluminum antimonide is described. Oxide from the aluminum has been eliminated by a vacuum heat-treating technique which also removes volatile impurities. The mobility of the positive carriers in AlSb at 300°K is found to be greater than 400 cm²/v-sec. Values as high as 5000 cm²/v-sec have been measured at 50°K. The p-type impurities have an activation energy of about 0.02 ev in AlSb. A maximum is observed at 4000 gauss in the magnetic-field dependence of the Hall coefficient at 77°K.

Considerable interest has been shown over the past few years in the development of semiconductors which are capable of operating at high ambient temperatures. The electrical properties of some of the Group III-V compounds are especially interesting for this application. Among these compounds, aluminum antimonide, with an energy gap of 1.6 electron volts (ev) shows particular promise. The major problem in producing device-quality aluminum antimonide is concerned with the removal of impurities from the compound or its constituents (1). Schell (2) reports that zone refining AlSb has produced p-type material with resistivities as high as 14 ohm-cm and carrier concentrations of 3 x 10^{15}/cm³. However, these samples have low carrier mobilities, 150 cm²/v-sec. Aluminum antimonide crystals with resistivities as high as 30 ohm-cm have been obtained by doping p-type AlSb with selenium (3). Again, the mobility of the positive carriers in the base p-type AlSb was low, about 100 cm²/v-sec. Resistivities as high as 200 ohm-cm have been obtained by adding lithium to aluminum antimonide (4). In this case, the mobility was extremely low, about 0.02 cm²/v-sec. While doping can produce interesting samples for optical studies, it drastically decreases the carrier mobilities and the purity of the

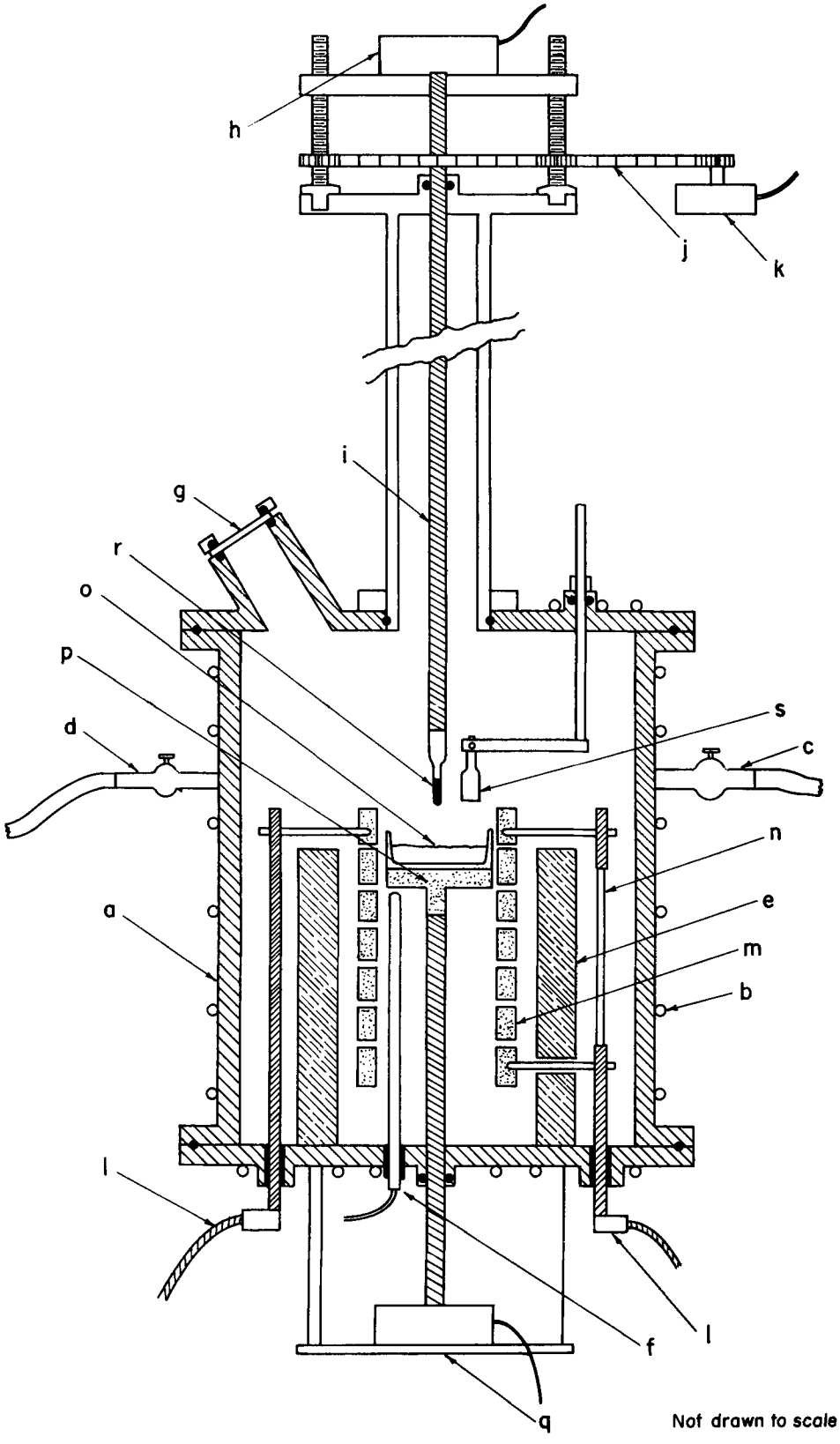

Fig. 1. Crystal growing furnace

aluminum antimonide. Nasledov and Slobodchikov (5) have prepared p-type aluminum antimonide with hole mobilities as high as 240 cm^2/v-sec and carrier concentrations of nearly $10^{18}/cm^3$.

Results of this investigation show that the majority of the p-type impurities found in aluminum antimonide come from the aluminum. It also shows that the concentration of the major p-type impurity in aluminum antimonide can be reduced by heat treating the aluminum at 1000°C in a vacuum. A relatively easy method for heat treating the aluminum and producing p-type aluminum antimonide single cystals with mobilities as high as 400 cm^2/v-sec and carrier concentrations in the $10^{16}/cm^3$

range is described. The purity of the aluminum antimonide is indicated by the temperature dependence of the Hall coefficient and the mobility data.

Growing of Single Crystals

The crystal-growing furnace shown in Fig. 1 is a steel vacuum tank (a) surrounded by cooling coils (b). Helium gas used for atmosphere while growing crystals enters the furnace through valve (c). A vacuum pump is connected to valve (d). Fused quartz is used for shielding (e) in this system, and the thermocouple well (f) is porcelain.

The viewing port (g) at the top is so located as to reduce condensation of volatile materials on the viewing glass. An electric motor (h) rotates the stainless steel seed holder (i). This motor is attached to a platform that is raised or lowered by the rotation of two long screws which are turned by a chain (j) driven by a variable-speed motor (k). The electrical feed-throughs (l) are stainless steel which contact the graphite heating element (m) through molybdenum rods. One side of the heating element is mechanically supported by a porcelain rod (n). The Morganite Al_2O_3 crucible (o) is mounted on an AUC graphite pedestal (p) and rotated counterclockwise by motor (q), while the seed (r) rotates clockwise. Both the seed and the crucible are normally rotated at 6 rpm, giving a net rotational rate of the seed with respect to the melt of 12 rpm.

Although aluminum is etched prior to its reaction with antimony, it still retains an oxide surface that floats on the aluminum antimonide melt and provides nucleation centers which produce additional crystals when the oxide particles come in contact with the seed or the crystal being pulled.

Originally this oxide was removed by lowering the aluminum oxide paddle (s) into the melt. The entire surface of aluminum antimonide was allowed to freeze to the paddle. Then this surface plus the oxide could be lifted out of the crucible, leaving a melt clear of oxide.

The oxide coating on the seed is a second source of nucleation. In order to minimize this nucleation, the crystal being grown is necked down to approximately ⅛ in. before it is allowed to grow out to the desired diameter. This necking down forces out crystals nucleated by the oxide on the surface of the seed.

During the pulling of aluminum antimonide crystals, it was observed that single crystals could not be grown when pulling at speeds above 3 in./hr. Pulling rates exceeding this value caused the ingot to grow as if pulled from a nonstoichiometric melt. This and other experiments indicate that the maximum pulling rate for single crystal growth depends on the magnitude of the deviation of the melt from the stoichiometric ratio. The greater the deviation from stoichiometry the more slowly the crystal must be pulled.

At pulling speeds less than ½ in./hr it was observed frequently that the ingot was covered with a yellow-white glasslike substance. This coating was identified as vitreous antimony trioxide by index-of-refraction measurements. The vitreous coating of Sb_2O_3 varied from 8 to 26 μ in thickness. It is expected therefore that all of the aluminum antimonide crystals pulled from the melt have a thin coating of antimony trioxide glass. Based on oxide coating thickness found at different pulling rates, ingots pulled at 2 in./hr would have a coating of Sb_2O_3 about 4 μ thick. This thickness would of course vary with the pressure of the inert gas and the amount of oxygen present.

Starting Materials

Since neither the antimony nor the aluminum was of sufficient purity as a starting material, purification by zone refining was attempted. The aluminum was given 20 zone-melting passes at 2 in./hr, while the antimony was given 20 passes at 1 in./hr. Both the aluminum and the antimony were zone refined in AUC graphite boats. Following the zone refining, both elements were etched to remove oxides from their surfaces. The aluminum was etched in a solution composed of 95% phosphoric acid and 5% nitric acid, and the antimony was etched in CP-4. Deionized water was used for washing the materials after etching.

In general, pulled aluminum antimonide crystals produced from zone-refined aluminum and antimony reacted in an aluminum oxide crucible contain p-type impurities on the order of $6 \times 10^{17}/cm^3$. Since high-purity indium antimonide can be made with antimony of the same quality as that used in the preparation of aluminum antimonide, the impurity content of the antimony is at least two orders of magnitude below this $6 \times 10^{17}/cm^3$ level.

To investigate the possibility of the melt being doped with contaminants in the aluminum oxide crucibles, two aluminum antimonide crystals were pulled from a high-purity, single-crystal sapphire crucible. These crystals showed no significant differences in electrical properties from the previously obtained material. It was concluded that this level of p-type impurities, i.e., $6 \times 10^{17}/cm^3$, does not come from the crucible.

Therefore, it is probable that the source of the observed impurities in aluminum antimonide is the aluminum. Various impurities which should act as acceptors in aluminum antimonide are found (spectrographically) in the aluminum. Significant quantities of magnesium and copper are among these impurities. An ingot of aluminum antimonide was pulled from a melt doped with 1 part magnesium to 10^4 parts aluminum. As would be expected, the acceptor concentration increased from 6×10^{17} to $2.5 \times 10^{18}/cm^3$. More significantly, little change in carrier concentration along the crystal was observed, indicating that magnesium segregates slowly in aluminum antimonide.

Heat Treatment of the Aluminum

The aluminum was heat treated in vacuum at 1000°C for several hours in an attempt to reduce the concentration of volatile impurities. Magnesium should be one of these impurities removed, since the vapor pressure of magnesium is quite high with respect to that of aluminum. After evacuating and flushing the system with dry helium several times, the system was maintained at 1×10^{-3} mm Hg. Then

Table I. Electrical properties of crystals pulled from AlSb Melts (300°K)

Crystal	Hall coefficient, cm^3/coulomb	Mobility, cm^2/v-sec	Number of carriers, n/cm^3	Preparation of aluminum
1	10.3	230	6.0×10^{17}	As received
4	11.0	230	5.6×10^{17}	Zone refined
8	14.6	250	4.5×10^{17}	Heat treat 1000°C for 7 hr
10	41.0	300	1.5×10^{17}	Heat treat 1000°C for 16 hr
16	53.3	340	1.2×10^{17}	Heat treat 1000°C for 40 hr
15	66.2	330	9.4×10^{16}	Heat treat 1000°C for 54 hr

the aluminum, in an aluminum oxide crucible, was heated to 1000°C for several hours. After heating the aluminum about 3 or 4 hr, the oxide skin which always appears on the aluminum began to disappear. The mechanism involved is probably the Al_2O_3 reduction by aluminum to Al_2O, which subsequently evaporates (6).

After the heat treatment of the aluminum, the system was filled with dry helium and a positive pressure of 10 psi maintained. The antimony which had been fastened to the aluminum oxide probe during the heat-treatment of the aluminum was lowered into the hot zone and allowed to melt into the crucible. This method allowed the aluminum and the antimony to react without the necessity of opening the system; a surface completely clear of oxide particles was produced.

Table I shows the electrical properties of crystals pulled from aluminum antimonide melts when using as-received, zone refined, and heat-treated aluminum. It is apparent from these properties that zone refining the aluminum does very little to reduce the p-type impurities in aluminum antimonide crystals. However, the crystals pulled from melts containing aluminum that had been heat treated had p-type impurity concentrations almost an order of magnitude lower than those observed for crystals made from as-received aluminum.

Figure 2 is a graphical presentation of a portion of the data in Table I. The concentration of p-type impurities in pulled aluminum antimonide crystals is plotted as a function of heat-treatment time of the

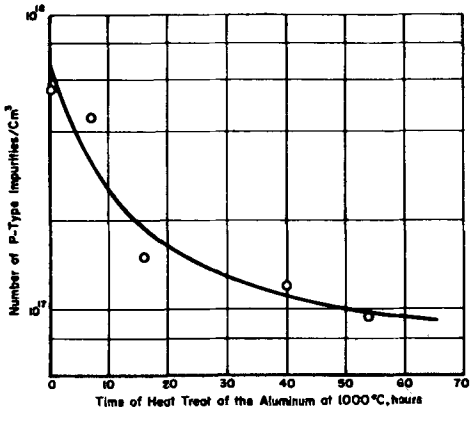

Fig. 2. Concentration of p-type impurities in pulled crystals of AlSb as a function of heat-treating time.

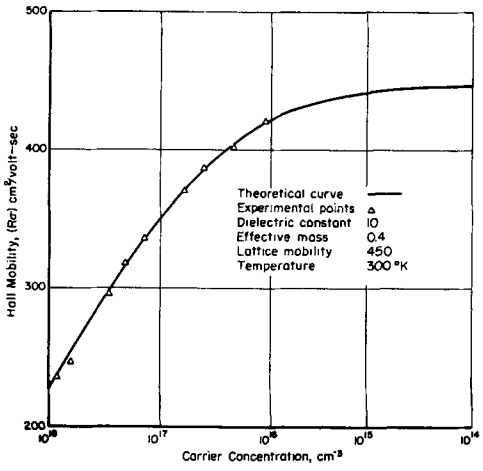

Fig. 3. Hole mobility at 300°K vs. carrier concentration of AlSb.

aluminum. As has been noted, initially the surfaces of the aluminum melts are covered with oxide, which gradually disappears as the aluminum is retained in the molten state. The vaporization of magnesium and other volatile impurities from the melt is inhibited undoubtedly by the oxide coating, which may be a cause of the scatter of points observed in the initial part of the curve in Fig. 2. Since the rate of the removal of p-type impurities seems to decrease rapidly at heat-treatment times above 16 hr, it is probable that most of the volatile impurities have been removed by this time and that the remaining impurities are not highly volatile and therefore are difficult to remove by this method. Such an impurity could be copper, which is known to be present in the aluminum also.

In Fig. 3 the mobility of the positive carriers in aluminum antimonide is shown as a function of carrier concentration. The theoretical curve was calculated on the basis of a dielectric constant of 10 for aluminum antimonide, an effective mass of 0.4 m_o, and a lattice mobility of 450 cm^2/v-sec at 300°K. The close agreement of the experimental points to the theoretical curve indicates that vacuum heat treatment of the aluminum significantly reduces the impurities in aluminum antimonide. The observed re-

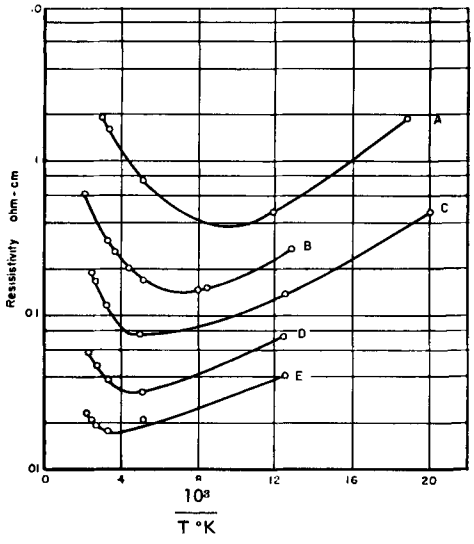

Fig. 4. Resistivity as a function of temperature for single crystals of AlSb.

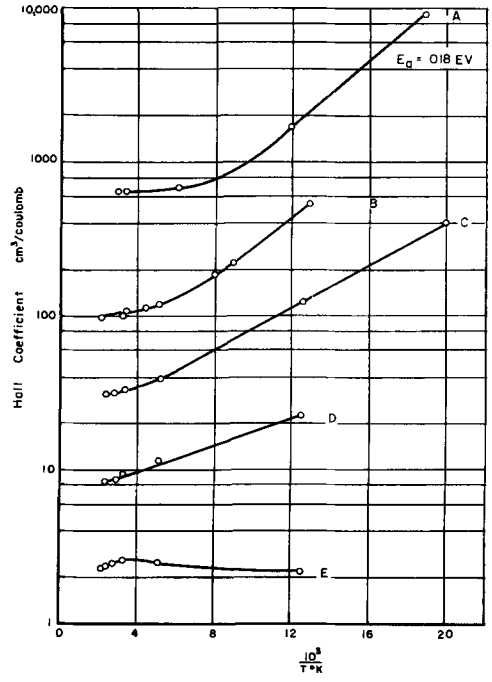

Fig. 5. Hall coefficient as a function of temperature for single crystals of AlSb.

duction in carrier concentrations therefore is not due to compensation.

Figure 4 shows the resistivity as a function of temperature of Hall samples cut from pulled aluminum antimonide crystals. Samples A, B, and C were taken from crystals pulled from melts containing aluminum that had been vacuum heat treated at 1000°C for 16 hr. Sample D is from an aluminum antimonide crystal made from aluminum that had been zone refined but not heat treated. Crystals grown from melts containing zone-refined aluminum show little, if any, improvement over crystals grown from melts containing aluminum in as-received condition. Sample E was cut from the aluminum antimonide crystal that had been doped with 1 part magnesium to 1 x 10^4 parts of aluminum.

Figure 5 shows the Hall coefficient as a function of temperature for the five crystals in Fig. 4. The slope of curve A was used to compute the energy level of the acceptor impurity. The energy level calculated from this slope is 0.018 ev. The minority impurity concentration calculated is consistent with the amount of compensation predicted by a comparison of the mobility data with the theoretical curve in Fig. 3.

The Hall sample cut from the magnesium-doped crystal giving curve E is degenerate throughout the entire temperature range of measurement. The critical concentration of p-type impurities in AlSb for which the ionization energy disappears is about 2 x 10^{18}/cm³, compared with 6.5 x 10^{18}/cm³ for silicon (7). It is expected that the effective activation energy will increase somewhat from 0.018 ev as the acceptor concentration is decreased and that it will be different for the various p-type impurities. However, it appears likely that the acceptor levels in AlSb are, in general, nearer to the valence band than those in silicon; probably the activation energies in AlSb are about a factor of two less than those in silicon.

Figure 6 is a plot of mobility as a function of temperature, as computed from the resistivity and Hall coefficient curves in Fig. 4 and 5. The mobility of the positive carriers decreases more steeply than $T^{-3/2}$ in the lattice-scattering range. In fact, the slope of the lattice mobility vs. temperature appears to be greater than T^{-2}. Magnetoresistance data suggest the presence of both light and heavy mass valence bands in AlSb. Thus, with the relatively impure samples presently available and the uncertainty in the values of r relating the Hall coefficient at a given magnetic field to the carrier concentration, the only conclusion possible is that the temperature dependence of the mobility in p-type AlSb is similar to that of p-type germanium and silicon.

Measurements of the Hall coefficient as a function of magnetic field between 600 and 20,000 gauss have

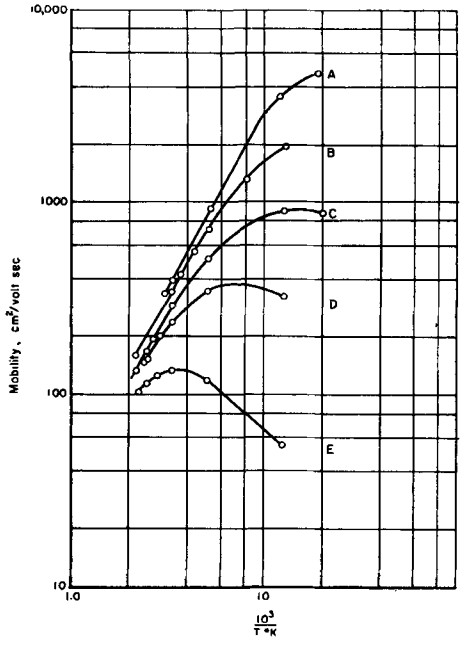

Fig. 6. Mobility as a function of temperature for single crystals of AlSb.

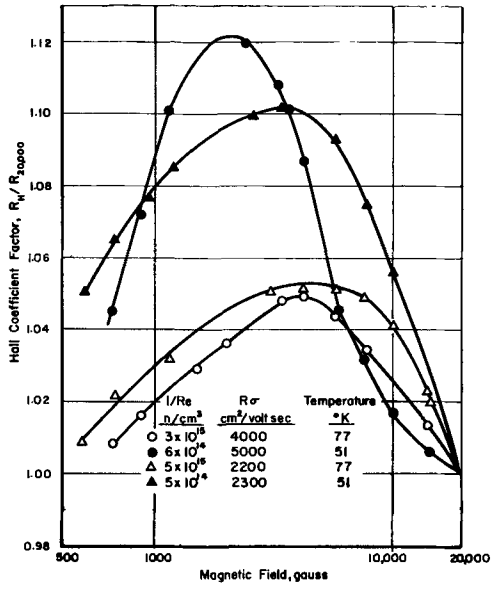

Fig. 7. Magnetic field dependence of the Hall coefficient in p-type AlSb.

been made at 77° and 51°K on a 1.6 ohm-cm sample of p-type aluminum antimonide with an $R\sigma$-value of 400 cm²/v-sec at room temperature. These measurements (shown in Fig. 7) indicate a maximum in the Hall coefficient at about 4000 gauss at 77°K and 2000 gauss at 51°K. A maximum also has been reported in the Hall coefficient of silicon at 77°K and a magnetic field of 20,000 gauss (8). In the case of silicon this maximum appears to be caused by a warping of the heavy mass band. One might expect a similar situation in p-type AlSb. It should be pointed out however that the maximum in the Hall coefficient occurs at a much lower magnetic field in AlSb. This could imply that the maximum in the Hall coefficient in p-type AlSb is related to the structure of the light mass band (9). Other factors, such as the polar character of the zinc blende structure, might affect the magnetic-field dependence of the Hall coefficient.

Summary

The p-type impurities in AlSb have been reduced by an order of magnitude by heat treating the aluminum. The major impurity remaining is probably copper; therefore, methods for removing minute amounts of copper and other nonvolatile impurities from the aluminum need to be developed. The oxide that hinders the growth of single crystals of aluminum antimonide can be eliminated completely by vacuum heat treatment of the aluminum. The activation energies of p-type impurities in AlSb are about one-half those for silicon. The mobility and the temperature dependence of the mobility of the majority carrier in p-type AlSb are almost identical with those in silicon. Finally, as in silicon, a maximum is observed in the magnetic-field dependence of the Hall coefficient in p-type AlSb.

Acknowledgments

The authors wish to thank Dr. H. L. Goering and Dr. A. C. Beer for helpful suggestions. They are especially indebted to F. J. Reid and J. J. Duga for making the electrical measurements. They also wish to acknowledge helpful conversations with R. L. Batdorf of the Bell Telephone Laboratories.

Manuscript received July 21, 1959. This research was supported by the Aeronautical Research Laboratory, Wright Air Development Center. This paper was prepared for presentation at the Philadelphia Meeting, May 5, 1959.

Any discussion of this paper will appear in a Discussion Section to be published in the December 1960 JOURNAL.

REFERENCES

1. W. P. Allred, B. Paris, and M. Genser, *This Journal*, **105**, 93 (1958).
2. H. A. Schell, *Z. Metallkunde*, **49**, 140 (1958).
3. A. Herczog, R. R. Haberecht, and A. E. Middleton, *This Journal*, **105**, 533 (1958).
4. F. Kover, "On the Electrical and Optical Properties of Aluminum Antimonide," International Conference on Solid State Physics in Electronics and Telecommunications, Brussels, June 2-7, 1958.
5. D. N. Nasledov and Slobodchikov, *J. Tech. Phys. (U.S.S.R.)*, **28**, 715 (1958).
6. R. F. Porter, P. Schissel, and M. G. Inghram, *J. Chem. Phys.*, **23**, 339 (1955).
7. G. L. Pearson and J. Bardeen, *Phys. Rev.*, **75**, 865 (1949).
8. A. C. Beer and R. K. Willardson, *ibid.*, **110**, 1286 (1958).
9. A. C. Beer, *J. Phys. Chem. Solids*, **8**, 507 (1959).

A Phase Equilibrium Study of the System Na_2WO_4-Na_2CO_3-H_2O

R. L. Pilloton and G. E. Crawley, Jr.

Metals Research Laboratories, Union Carbide Metals Company, Division of Union Carbide Corporation, Niagara Falls, New York

ABSTRACT

A phase equilibrium diagram representing the binary system Na_2WO_4-H_2O between −7.5° and +35°C was constructed. This curve shows the regions of stability of the dihydrate and decahydrate of sodium tungstate. There is a eutectic point for the system ice-$Na_2WO_4 \cdot 10H_2O$ at −7.5°C and 30.1% Na_2WO_4, a transformation point for $Na_2WO_4 \cdot 10H_2O$-$Na_2WO_4 \cdot 2H_2O$ at 6.2°C, and 42.5% Na_2WO_4 and a metastable eutectic point for ice-$Na_2WO_4 \cdot 2H_2O$ at −13°C and 42.5% Na_2WO_4. Phase equilibria for the ternary system Na_2CO_3-Na_2WO_4-H_2O between −8° and +35°C are represented by a ternary diagram. Projections showing temperature contours and crystallization paths are given. The regions of initial crystallization of the various salts are presented. Applications of the diagram to fractional crystallizations are discussed.

Although solutions of sodium tungstate and of sodium tungstate plus sodium carbonate play an important part in the metallurgy of tungsten, information concerning phase equilibria of these systems is still incomplete. Published values for the solubility of sodium tungstate in water at low temperature (1, 2) are based on work done by Funk in 1900 (3). He indicated the existence of sodium tungstate decahydrate but did not study the exact range of stability of this salt. Furthermore, his solubility measurements are not sufficient to construct phase diagrams representing phase equilibria of the system Na_2WO_4-H_2O at low temperatures.

The only recent investigation of the ternary sys-

tem Na_2CO_3-Na_2WO_4-H_2O was reported by Sei and co-workers (4) in 1954 and concerns solubilities only at 19° and 29°C.

The first objective of the present work was to study the phase equilibria of the systems Na_2WO_4-H_2O and Na_2WO_4-Na_2CO_3-H_2O in the temperature and concentration regions close to those found in industrial applications. A second objective was to use the data for investigating the fractional crystallization of sodium carbonate from aqueous solutions containing both sodium carbonate and sodium tungstate.

General Procedures

To determine the solubilities, solutions of reagent-grade sodium carbonate and sodium tungstate containing an excess of one salt were agitated for several hours at constant temperature and the resulting solutions analyzed.

For experiments at or above 0°C, the samples were equilibrated in a water bath, the temperature of which was kept constant within 0.1°C. For experiments below 0°C, a glycol bath in a low-temperature chamber was used. After attainment of equilibrium, samples of the solution were withdrawn and filtered in the chamber at constant temperature. The length of time necessary to attain equilibrium was determined by analyzing aliquots from a number of solutions at regular intervals.

The densities of the solution samples were measured with a Westphal balance at room temperature. The dissolved sodium tungstate was determined by precipitating the tungsten as WO_3 in an acidified solution in the presence of cinchonine, igniting and weighing the oxide. Sodium carbonate was determined by weighing the $BaCO_3$ formed by absorption of the acid-displaced CO_2 in $Ba(OH)_2$ solution. Water was determined by difference. All analytical results were converted to weight percentages for the graphical representation. These results were found to be reproducible within a precision of 0.5%. The hydrate formulas were calculated from chemical analyses of the crystals which separated on cooling the solutions. Any solution attached to these crystals was carefully separated by absorption with filter paper. Crystals of ice were also analyzed to verify that they did not contain any Na_2WO_4 or Na_2CO_3.

In order to verify the course of crystallization, particularly in the "ice" region of the tungstate-carbonate diagram, a number of thermal analyses were made. In these experiments, solutions containing known quantities of Na_2CO_3 and Na_2WO_4 were cooled and time-temperature curves drawn. In most cases, a 4°C supercooling was observed. The temperatures of initial crystallization were determined from the curves.

Experimental results of the solubility measurements are given in Table I and represented by the phase diagram of Fig. 1.

The experiments showed that in most cases only crystals of $Na_2WO_4 \cdot 2H_2O$ were obtained even when saturated solutions of sodium tungstate were cooled to −5°C. The points representing the composition of the solution were then on branch FG of the curve in Fig. 1. However, by completely freezing a sodium tungstate solution at −15°C and then slowly raising the temperature to 0°C, long needles of a new hydrate were obtained. This compound was identified as $Na_2WO_4 \cdot 10\,H_2O$ by chemical analysis. The colorless crystals of this hydrate turned white and converted to $Na_2WO_4 \cdot 2H_2O$ and water at +6.2°C. By keeping the decahydrate at a low temperature, it was possible to prevent its decomposition and to

Table I. Solubility of Na_2WO_4 in water

Temp, °C	Density d^{26}_{25}	Weight % Na_2WO_4	Weight % Water	Solid phase
−1.7	—	9.6	90.4	Ice
−3.5	—	17.2	82.8	Ice
−4.7	1.27	23.6	76.4	Ice
−4.8	—	24.3	75.7	Ice
−5.6	—	25.7	74.3	Ice
−6.1	—	27.2	72.8	Ice
−6.8	—	28.2	71.8	Ice
−6.7	—	28.4	71.6	Ice
−7.2	—	29.4	70.6	Ice
−7.6	—	30.4	69.6	Ice
−8.0	—	32.2	67.8	Ice
−8.6	1.41	33.2	66.8	Ice
−9.8	—	35.5	64.5	Ice
−6.7	1.35	31.1	68.9	$Na_2WO_4 \cdot 10H_2O$
−6.0	1.37	31.4	68.6	$Na_2WO_4 \cdot 10H_2O$
−4.7	1.39	32.5	67.5	$Na_2WO_4 \cdot 10H_2O$
0.5	—	37.5	62.5	$Na_2WO_4 \cdot 10H_2O$
5.0	—	41.5	58.5	$Na_2WO_4 \cdot 10H_2O$
29.9	—	42.2	57.8	$Na_2WO_4 \cdot 2H_2O$
15.0	—	42.5	57.5	$Na_2WO_4 \cdot 2H_2O$
20.0	—	42.9	57.1	$Na_2WO_4 \cdot 2H_2O$
5.0	1.56	42.7	57.3	$Na_2WO_4 \cdot 2H_2O$ metastable
5.0	1.57	42.5	57.5	$Na_2WO_4 \cdot 2H_2O$ metastable
0.0	1.56	43.0	57.0	$Na_2WO_4 \cdot 2H_2O$ metastable
0.0	1.56	42.5	57.5	$Na_2WO_4 \cdot 2H_2O$ metastable
−2.5	1.56	42.5	57.5	$Na_2WO_4 \cdot 2H_2O$ metastable
−4.5	1.56	42.4	57.6	$Na_2WO_4 \cdot 2H_2O$ metastable

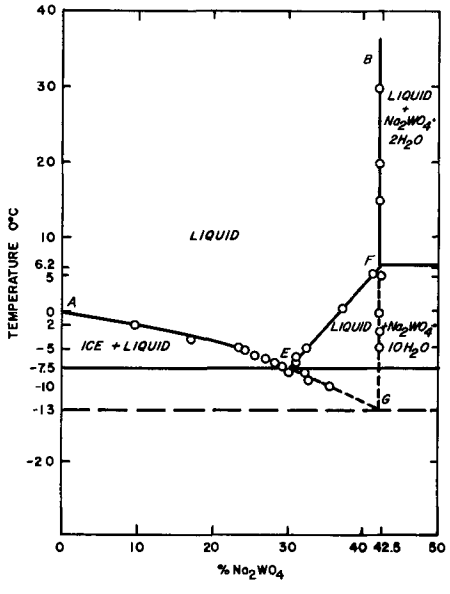

Fig. 1. Phase diagram for the system sodium tungstate-water.

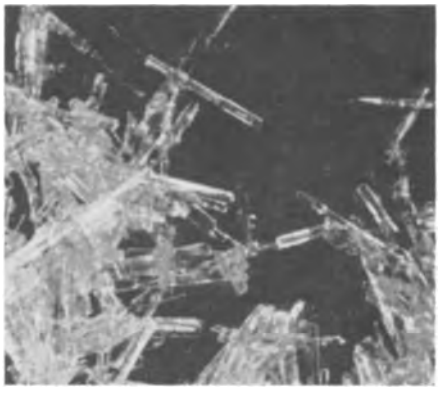

Fig. 2. Crystals of $Na_2WO_4 \cdot 10H_2O$. Magnification ~10X

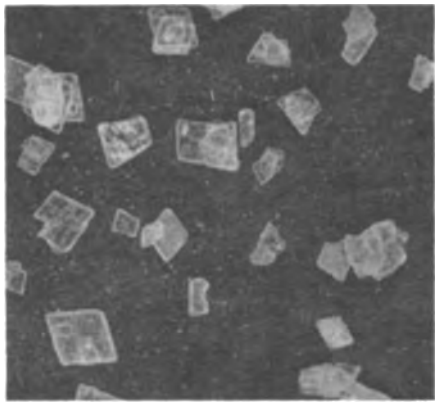

Fig. 3. Crystals of $Na_2WO_4 \cdot 2H_2O$. Magnification ~10X

use the crystals to seed other solutions. Branch EF of the curve was obtained by the procedure of seeding the solution after cooling below 6°C. Crystals of $Na_2WO_4 \cdot 10\,H_2O$ and $Na_2WO_4 \cdot 2H_2O$ are shown in Fig. 2 and 3.

The diagram shows that the freezing points of the solutions vary from 0 to −7.5°C along branch AE of the curve when the sodium tungstate concentration is lower than 30.1%. An aqueous solution containing 30.1% Na_2WO_4 by weight freezes invariantly at −7.5°C to give a binary eutectic E consisting of crystals of ice and of $Na_2WO_4 \cdot 10\,H_2O$. When the composition is lower than 42.5% and higher than 30.1% Na_2WO_4, crystals of $Na_2WO_4 \cdot 10\,H_2O$ may form between −7.5° and +6.2°C along branch EF of the diagram. However, in many cases, because of a "metastable supercooling" phenomenon, crystals of ice are formed along EG or crystals of $Na_2WO_4 \cdot 2H_2O$ along branch FG. Point F gives the temperature and

Table II. Solubility of Na_2CO_3-Na_2WO_4 in water

Temp, °C	Density d^{25}_{25}	Solubility-weight %			Solid phase
		Na_2CO_3	Na_2WO_4	Water	
−2.5	—	1.7	9.1	89.2	Ice
−3.0	—	3.5	9.2	87.3	Ice
−3.8	1.12	5.0	9.1	85.9	Ice
−4.1	—	1.7	17.0	81.3	Ice
−4.6	—	3.1	16.7	80.2	Ice
−5.9	—	1.5	24.7	73.8	Ice
−6.0	1.53	1.8	24.7	73.5	Ice
+20	1.40	11.7	20.9	67.4	$Na_2CO_3 \cdot 10H_2O$
+20	1.33	13.6	15.3	71.1	$Na_2CO_3 \cdot 10H_2O$
+20	—	15.8	8.1	76.1	$Na_2CO_3 \cdot 10H_2O$
+15	1.40	8.7	24.6	66.7	$Na_2CO_3 \cdot 10H_2O$
+15	1.31	10.0	17.5	72.5	$Na_2CO_3 \cdot 10H_2O$
+15	1.22	11.9	9.2	78.9	$Na_2CO_3 \cdot 10H_2O$
+15	1.52	5.3	33.2	61.5	$Na_2CO_3 \cdot 10H_2O$
+10	1.40	5.6	26.7	67.7	$Na_2CO_3 \cdot 10H_2O$
+10	1.30	7.3	20.2	72.5	$Na_2CO_3 \cdot 10H_2O$
+10	1.20	8.6	9.6	81.8	$Na_2CO_3 \cdot 10H_2O$
+10	1.25	9.1	9.8	81.1	$Na_2CO_3 \cdot 10H_2O$
+10	1.52	3.9	36.2	59.9	$Na_2CO_3 \cdot 10H_2O$
+10	1.52	5.4	29.8	64.8	$Na_2CO_3 \cdot 10H_2O$
+5	1.39	4.1	27.8	68.1	$Na_2CO_3 \cdot 10H_2O$
+5	1.29	4.8	19.7	75.5	$Na_2CO_3 \cdot 10H_2O$
+5	1.18	6.8	11.3	81.9	$Na_2CO_3 \cdot 10H_2O$
+5	1.25	9.3	6.6	84.1	$Na_2CO_3 \cdot 10H_2O$
+5	1.56	4.0	35.6	60.4	$Na_2CO_3 \cdot 10H_2O$
+5	1.54	3.9	34.2	61.9	$Na_2CO_3 \cdot 10H_2O$
0	1.38	3.7	29.2	67.1	$Na_2CO_3 \cdot 10H_2O$
0	1.29	4.2	22.0	73.8	$Na_2CO_3 \cdot 10H_2O$
0	1.17	5.9	11.8	82.3	$Na_2CO_3 \cdot 10H_2O$
0	1.25	7.7	9.4	82.9	$Na_2CO_3 \cdot 10H_2O$
−3.8	—	5.0	9.1	85.9	$Na_2CO_3 \cdot 10H_2O + H_2O$
−4.6	—	3.1	16.7	80.2	$Na_2CO_3 \cdot 10H_2O + H_2O$
−6.7	—	3.0	22.0	75.0	$Na_2CO_3 \cdot 10H_2O + H_2O$
+15	1.51	2.6	38.8	58.6	$Na_2WO_4 \cdot 2H_2O$
+10	1.51	2.4	37.3	60.3	$Na_2WO_4 \cdot 2H_2O$
0	1.54	1.4	34.9	63.7	$Na_2WO_4 \cdot 10H_2O$
−2	1.54	1.5	33.2	65.3	$Na_2WO_4 \cdot 10H_2O$
−4	1.54	1.2	31.8	67.0	$Na_2WO_4 \cdot 10H_2O$

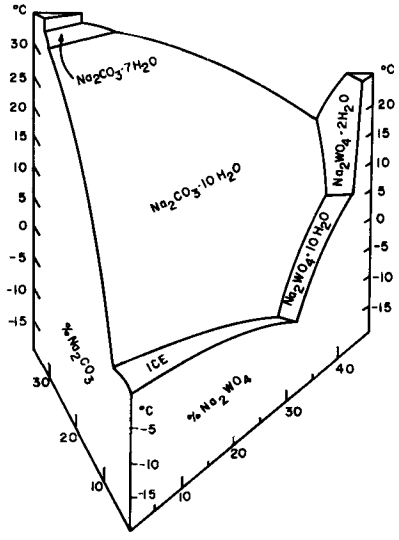

Fig. 4. Surface of initial crystallization for the system Na_2CO_3-Na_2WO_4-H_2O.

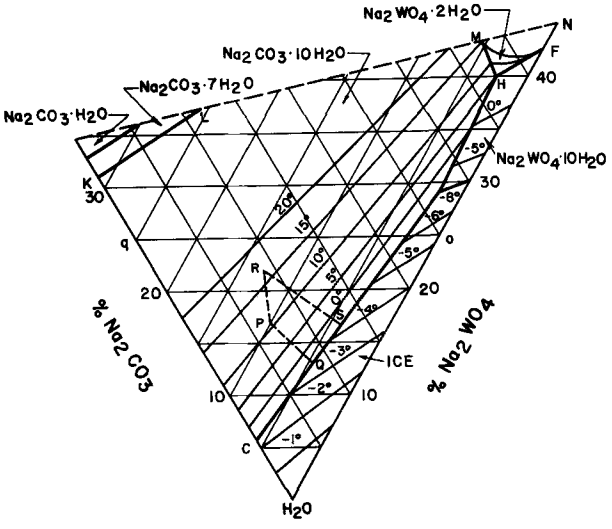

Fig. 5. Projectian of the system Na_2CO_3-Na_2WO_4-H_2O showing temperature contours.

composition of the liquid in equilibrium with both di- and decahydrate. Point G, at −13°C, is the metastable binary eutectic point of the dihydrate and ice. Branch FB of the curve corresponding to saturation of the dihydrate is nearly vertical, indicating that there is little solubility change above +6.2°C.

The System Na_2CO_3-Na_2WO_4-H_2O

Graphical representation.—The three dimensional representation derived from the solubility measure-

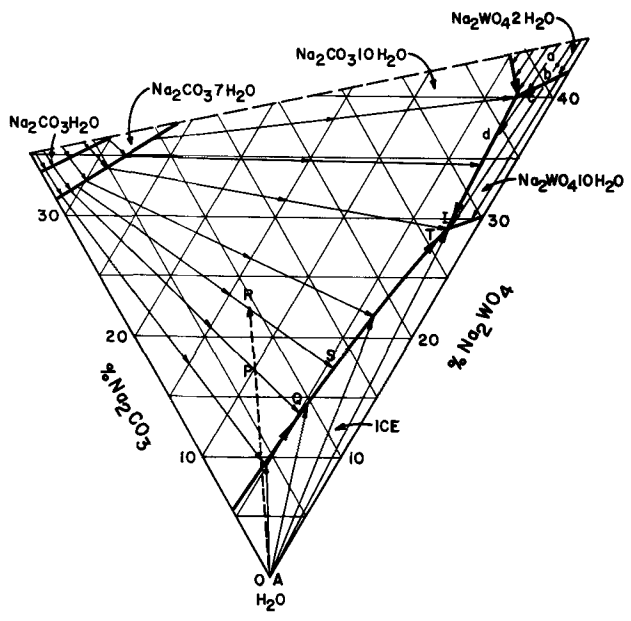

Fig. 6. Projection for the system Na_2CO_3-Na_2WO_4-H_2O showing crystallization paths.

ments given in Table II is shown in Fig. 4. This diagram covers concentrations up to 35% Na_2CO_3 and 45% Na_2WO_4. Figures 5 and 6 are projections showing temperature contours and crystallization paths, respectively.

The different regions and the most important points and lines are lettered. Table III summarizes the state of the phases for various compositions with corresponding letters.

Peritectic reactions.—The "ice" region is a region of congruent crystallization; in other words, the composition of the solid phase being formed lies within the boundaries of its field of primary crystallization. On the other hand, solutions in the region corresponding to crystallizations of $Na_2CO_3 \cdot 10\,H_2O$ and of $Na_2WO_4 \cdot 10\,H_2O$ undergo incongruent crystallizations. Because of these phenomena, conversions of one crystal species into another are observed at the upper borders of these regions. For example, on cooling solution a in Fig. 6, crystals of $Na_2WO_4 \cdot 2H_2O$ are obtained first while the composition of the solution moves from a to b. From b to c, the crystals of $Na_2WO_4 \cdot 2H_2O$ are converted into $Na_2WO_4 \cdot 10\,H_2O$. At c, when all the dihydrate has been converted to decahydrate, the point representing the composition of the solution leaves the binary eutectic line and moves across the field $Na_2WO_4 \cdot 10\,H_2O$ to reach the binary eutectic

Table III. Salient features in the system Na_2WO_4-Na_2CO_3-H_2O

System composition	State of phases	Solid phases	Temp, °C
C	Binary eutectic	H_2O-$Na_2CO_3 \cdot 10H_2O$	−2.1
K	Binary peritectic	H_2O-$Na_2CO_3 \cdot 10H_2O$-$Na_2CO_3 \cdot 7H_2O$	31.2
E	Binary eutectic	H_2O-$Na_2WO_4 \cdot 2H_2O$	−7.5
F	Binary peritectic	H_2O-$Na_2WO_4 \cdot 2H_2O$-$Na_2WO_4 \cdot 10H_2O$	+6.2
H	Ternary peritectic	$Na_2WO_4 \cdot 2H_2O$-$Na_2WO_4 \cdot 10H_2O$-$Na_2CO_3 \cdot 10H_2O$	+5
I	Ternary eutectic	H_2O-$Na_2WO_4 \cdot 10H_2O$-$Na_2CO_3 \cdot 10H_2O$	−8
KLMHIC	One component saturation	$Na_2CO_3 \cdot 10H_2O$	−8 to 32
CIEA	One component saturation	H_2O	0 to −8
EIHF	One component saturation	$Na_2WO_4 \cdot 10H_2O$	−8 to 6.2
FHM	One component saturation	$Na_2WO_4 \cdot 2H_2O$	Above +5

line corresponding to crystallization of a mixture of $Na_2CO_3 \cdot 10\,H_2O$ and $Na_2WO_4 \cdot 10\,H_2O$. Upon further cooling, the invariant point I is reached, and the whole solution freezes solid to give a mixture of crystals of ice, $Na_2CO_3 \cdot 10\,H_2O$, and $Na_2WO_4 \cdot 10\,H_2O$.

Application to the crystallization of sodium carbonate.—The diagrams show that large quantities of sodium carbonate can be crystallized by cooling solutions containing both sodium tungstate and sodium carbonate in quantities comparable to those found in industrial sodium tungstate liquors. The course of the crystallization can be followed on Fig. 6. An example of a possible solution is represented by point P, which is in the Na_2CO_3-$10\,H_2O$ region. Upon cooling, the composition of the solution varies first from P to Q, while crystals of $Na_2CO_3 \cdot 10\,H_2O$ are formed. At Q, around −3°C, the binary eutectic line is reached, and a mixture of crystals of ice and of $Na_2CO_3 \cdot 10\,H_2O$ appears. More of these crystals form when the temperature is lowered further and the composition of the solution moves toward I along line QI. The temperature to each composition is found in Fig. 5. If cooling is stopped before a temperature of −8°C is reached at point I of the diagram, only crystals of ice and of sodium carbonate are formed, and there is no precipitation of sodium tungstate. Since sodium tungstate stays in solution, the amount of sodium carbonate and of water per gram of Na_2WO_4 before and after cooling indicates the yield of the crystallization. For example, point P of the diagram corresponds to the composition (by weight) $Na_2CO_3 = 10.2\%$, $Na_2WO_4 = 7.2\%$, water = 82.6%; consequently, there are 1.42 g of Na_2CO_3 and 11.5 g of water per gram of Na_2WO_4. At the end of the crystallization at, say, −7°C, the composition T is $Na_2CO_3 = 2.0\%$, $Na_2WO_4 = 28\%$, water = 70% which corresponds to 0.071 g of Na_2CO_3 and 2.5 g of water per gram of Na_2WO_4. The percentages of sodium carbonate and of water separated by crystallization are, respectively:

$$Na_2CO_3 \text{ .....} \frac{1.42 - 0.07}{1.42} \times 100 = 95.0\%$$

$$H_2O \text{ .....} \frac{11.5 - 2.5}{11.5} \times 100 = 78.3\%$$

The compositions of the final solutions and the percentages of water and of sodium carbonate removed by crystallization when solution P is cooled down to −4°, −5°, −6°, and −7°C are given in Table IV.

Table IV. Water and sodium carbonate crystallization from solution P (Fig. 6) at various temperatures

Final Temp, °C	Final composition, %			Removed percentage	
	Na_2WO_4	Na_2CO_3	Water	Na_2CO_3	Water
−3	8.5	5.0	86.5	56.5	11.3
−4	10.0	5.0	85.0	64.8	26.1
−5	16.0	4.4	79.6	80.6	56.7
−6	22.0	3.0	75.0	90.4	70.4
−7	28.0	2.0	70.0	95.0	78.3

If water is evaporated from the solution prior to cooling, the point representing the solution moves from P to R on line APR. The temperature at which crystallization of R starts is given by the temperature contour passing through R in Fig. 5. Upon cooling the solution, the composition follows paths RS and SI (Fig. 6).

Conclusions

This study of the solubility of sodium tungstate in water indicates that solid phases existing at temperatures between −7.5° and +35°C are ice, $Na_2WO_4 \cdot 10\,H_2O$, and $Na_2WO_4 \cdot 2H_2O$. The eutectic point for ice-$Na_2WO_4 \cdot 10\,H_2O$ is at −7.5°C and 30.1% Na_2WO_4, the peritectic point for $Na_2WO_4 \cdot 2H_2O$-$Na_2WO_4 \cdot 10\,H_2O$ at +6.2% and 42.5% Na_2WO_4, and the metastable eutectic point for ice-$Na_2WO_4 \cdot 2H_2O$ at −13°C and 42.5% Na_2WO_4.

The ternary diagram representing the system Na_2CO_3-Na_2WO_4-H_2O shows a ternary eutectic containing 2% Na_2CO_3, 27% Na_2WO_4, and 71% H_2O at −8°C. This diagram indicates that large quantities of sodium carbonate can be crystallized fractionally from solutions containing quantities of Na_2WO_4 and Na_2CO_3 comparable to those present in industrial liquors.

Manuscript received May 18, 1959. This paper was prepared for delivery before the New York Meeting, April 27-May 1, 1958.

Any discussion of this paper will appear in a Discussion Section to be published in the December 1960 JOURNAL.

REFERENCES

1. K. C. Li and Chung Yu Wang, "Tungsten," p. 284, Reinhold Publishing Co., New York (1956).
2. Gmelin's Hanbuch der anorganischen Chemie, 8 Auflage, System Number 54, Wolfram, 215 (1933).
3. R. Funk, *Ber.*, **33**, 3696 (1900).
4. Rempei Sei, Genichi Nakazawa, and Koichi Ito, *J. Mining Inst. Japan*, **70**, 513 (1954).

Production of Thorium Powder by Calcium Reduction of Thorium Oxide

N. Fuhrman,[1] R. B. Holden,[1] and C. I. Whitman

Sylvania-Corning Nuclear Corporation, Bayside, New York

ABSTRACT

A process for the preparation of high-purity thorium powder by calcium reduction of thorium oxide has been developed, Calcined thorium oxide is reduced in an inert atmosphere at 950°C with high-purity calcium metal in the presence of calcium chloride. The reduction vessel is fabricated of type 446 stainless steel to avoid pick up of iron and nickel impurities and permit break out of the reduction cake. The thorium powder so produced has essentially the same purity as the thorium oxide starting material. Important factors controlling yield and quality of the thorium powder are discussed.

The purpose of this investigation was to examine the direct reduction of thorium oxide with calcium as a potential production process, to determine the yields and the quality of the metal so obtained, and to develop a standard procedure for preparing small batches of metal by this process.

Investigations of the calcium reduction of thorium oxide date back to the beginning of this century. Huppertz (1) suggested the use of calcium vapor, and Burger (2) employed this method with some success. Kuzel and Wedekind (3) subsequently patented a process using calcium vapor, and Wedekind (4) carried out further studies.

Results of the first critical study of thorium metal preparation were presented by Marden and Rentschler (5, 6) who, with the aim of producing a metal powder capable of being consolidated into homogeneous metallic bodies, conducted an investigation of calcium reduction of the oxide. Their method involved the reduction of thoria with a three-mole excess of calcium and one part of calcium chloride to one part of the oxide. The authors claim that after compacting and sintering, the solid metal assayed was 99.7 to 99.8% thorium.

Kroll (7) also investigated this process, essentially following the procedure of Marden and Rentschler. This method was also used on a large scale with some modifications in Germany during World War II, as reported by Espe (8, 9).

Rentschler, *el al.* (10) eliminated the calcium chloride in the charge and used a thin-walled molybdenum cup instead of the steel bomb. The reduction took place in a Vycor bell jar under argon at a maximum temperature of 1400°C, the heat being supplied by high-frequency induction. The thorium powder was recovered by leaching the charge directly out of the cup.

A variation of the above procedure was used by Marden (11) in the experimental preparation of several 12-lb batches of powder.

[1] Present address: Metallurgical Laboratories, Olin Mathieson Chemical Corporation, New Haven, Connecticut.

Meyerson (12) has described the development of the calcium reduction process in the U.S.S.R. Except for the production of thorium powder of much lower purity, his results are in agreement with those of the present work. Although the efforts were entirely independent, some of his reported procedures are similar to those developed here.

Process Description

The raw materials in the charge for reduction are: (*a*) thorium oxide, (*b*) redistilled calcium metal, and (*c*) anhydrous calcium chloride. Thorium fines may be added as a means of recycling the relatively impure metal powder which is not recovered as primary material in the leaching step.

The thorium oxide employed in the charge was supplied by the U.S. Atomic Energy Commission. A typical analysis of AEC thorium oxide is presented in Table I. It is apparent that special attention has been given to the removal of impurities of high thermal neutron absorption cross section. The overall quality of the material was fairly consistent from lot to lot. Raw thoria is fired for removal of absorbed carbon dioxide prior to preparation of the charge. Two methods have been used to accomplish this (*a*) continuous calcining at about 880°C in an experimental rotary unit, and (*b*) batch calcining in stainless steel boats for 40 hr or more at 800°C. The fired oxide is then handled in a CO_2-free atmosphere during the charge preparation and reduction. This procedure substantially reduces the carbon content of the metal product.

Redistilled calcium metal[2] was utilized as-received in the form of 6-mesh nodules. Typical analyses of the Domal and Nelco redistilled calcium indicate that they are of similar quality. Anhydrous calcium chloride, meeting the American Chemical Society specifications, is obtained in the form of 20-mesh granules and is used in the charge as-received.

[2] Obtainable from either Dominion Magnesium, Ltd. or Nelco Metals, Inc.

Table I. Comparison of impurity levels of thorium metal powder and thorium oxide feed material

Impurity spectrochemical	ThO_2— Lot FP-125* (oxide basis)	Thorium powder run 84† (metal basis)
Ag		a 0.5
Al	<10	<10
As		<5
B	0.2	<0.2
Be	<1	—
Bi	<2	<1
Ca	200	a 200
Cd	<0.2	<0.1
Co	1	—
Cu	35	a 30
Fe	35	55
Mg	15	120
Mn	2	a 6
Mo	2	—
Ni	20	7
P	<40	—
Pb	25	2
Sb		—
Si	<10	a 25
Sn	2	<2
V	<10	—
Zr	<10	—

Notes: All values are ppm. a = approximate; — = not detected; < = less than.
* Analysis supplied by National Lead of Ohio.
† Analysis performed by New Brunswick Laboratory of AEC.

The following charge composition is typical for the runs involving thorium fines recycle: 7000 g prefired ThO_2; 925 g thorium fines; 2800 g anhydrous $CaCl_2$; 2760 g redistilled calcium. The amount of $CaCl_2$ is 40% of the weight of ThO_2. The amount of calcium is 30% more than that required to react with the ThO_2. Whether or not thorium fines are recycled in this manner depends on the quality of thorium powder desired as a product.

The charge ingredients are weighed in an argon dry box into a 5-gal can which is then sealed and tumbled on a drum roller. Because of occasional poor yields of metal resulting from incomplete reduction, it is believed that blending may not be thorough enough with this equipment. An alternate blending method utilizes a 0.33 ft^3 double cone blender in which about half the charge is tumbled at one time. The latter procedure, on the basis of a limited number of experiments, appears to produce higher yields.

Fig. 1. Calcium reduced thorium oxide reduction cake. Type 446 stainless steel reduction vessel.

The blended charge is transferred to a tapered reactor fabricated of type 446 stainless steel. A flat reactor cover is secured to the reduction vessel, shown in Fig. 1, by means of a clamping ring. A pipe welded to the reactor cover admits argon into the reactor during the fastening operation as well as during the subsequent heating period, so that the reduction may take place in an inert atmosphere. An argon head of 5 in. of Hg is usually employed.

The loaded reactor is heated to 950°C by high-frequency induction heating and held there while the charge is soaked for about 5 hr. After reduction, the reactor generally is quenched in water to hasten the cooling process. The reduction product remains under argon until it is cold.

After cooling, the head is removed from the reactor and the reduction product or "cake" broken out by jolting the inverted reactor once or twice. A typical reduction cake is shown in Fig. 1.

Primary size reduction of the reduction cake is performed by crushing the cake between flat plates with a hydraulic press. Normally, about a 20- to 30-ton load is required to crack the cake. The large chunks are further reduced in size with a jaw crusher. A uniform crushed cake of about ¼ in. particle size is thus obtained.

A leaching apparatus consisting of a 55-gal stainless steel drum and a ½ hp "Lightnin" mixer, is used to disintegrate the crushed cake. First, the crushed reduction product is introduced into 35 gal of agitated tap water. After 15 to 30 min hydrogen evolution has almost ceased and agitation may be stopped. Any remaining unleached cake is allowed to disintegrate statically. After 2 hr the reduction cake is almost completely leached; however, in current practice, it is allowed to stand overnight. The supernatant liquor, containing suspended thorium fines, as well as $Ca(OH)_2$, is pumped to a settling tank for later recovery of the fines. The resulting thorium powder is then subjected to from three to five successive tap water washes to remove more of the $Ca(OH)_2$ leach product. These washes are carried out in a 20-gal stainless steel pot with agitation provided by a ¼ hp "Lightnin" mixer. After a settling interval of about 5 min, the supernatant liquor is pumped to the settling tanks. When practically all of the $Ca(OH)_2$ has been removed by this method, the thorium powder is ready for acid washing.

The powder is subjected to two successive washes of 1:8 nitric acid and then successive washes with demineralized water until the supernatant liquor is neutral. This treatment removes residual calcium and $Ca(OH)_2$ from the powder.

The wet powder is filtered and washed on a 9 in. diameter stainless steel Buchner funnel with three rinses of acetone followed by three rinses with petroleum ether (boiling range, 30° to 60°C) and then vacuum dried overnight at a pressure of <1 mm of Hg.

The wet powder can also be dried in a vacuum shelf dryer. The thorium powder is sufficiently dry when a vacuum of 35 μ of Hg is attained. It should be noted that in this drying method there is a possibility of obtaining an incompletely dried product which, because of its possible sensitiveness to ignition, is a safety hazard.

Thirty-seven reductions were carried out on an 11-lb. scale (the largest nominal batch size produced during the development program) with yields running as high as 91% of theoretical. The term "yield" refers to the coarse thorium powder obtained after the drying process. Early in this work it was shown that the yield of metal averaged over 99% when the metal fines were included and hence the conversion of oxide to metal is essentially complete.

The usual procedure for determining the quality of the thorium powder is chemical analysis. The following impurities are determined in each run: (*a*) carbon, (*b*) nitrogen, (c) hydrochloric acid insolubles (ThO_2), (*d*) iron, and (*e*) chromium. Occasionally, spectrochemical analyses are obtained, especially for elements with a high thermal neutron absorption cross section.

A typical spectrochemical analysis of the thorium powder produced is presented in Table I along with that of the ThO_2 starting material. A comparison of the two indicates that there is no substantial pickup of impurities in the process. In this case, an exception is magnesium which is readily removed, however, during consolidation by arc melting. Table II shows the chemical analyses of thorium powder produced during a series of ten consecutive runs on the 11-lb scale when the process was under control and before significant changes were made in the operating conditions. It is seen that the calcium reduction process is capable of consistently producing a high-purity thorium in good yield.

As a supplement to chemical analysis, another approach to quality measurement has been found useful, namely, the evaluation of the hardness and the surface appearance of arc melted buttons. For this evaluation, a 30-g sample of thorium powder is melted in an argon atmosphere of 7 in. of Hg absolute pressure in an arc furnace (button type). The Rockwell F hardness and button density are then determined. Since the button hardness is very sensitive to a small quantity of carbon and larger amounts

Table II. Thorium powder chemical analyses, button hardness and yield data for a series of 11-lb scale production runs

Run No.	Chemical analysis					Button hardness, R_F	Yield % of theoretical
	Nitrogen, ppm	Carbon, ppm	ThO_2, %	Iron, ppm	Chromium, ppm		
60	40	160	0.16	11	11	40	83
61	50	140	0.19	35	13	35	78
62	40	210	0.15	46	9	41	80
63	40	200	0.14	44	10	36	91
64	30	150	0.24	41	17	31	85
65	30	200	0.17	46	22	34	88
66	40	120	0.57	43	20	40	80
67	40	190	0.12	42	17	38	86
68	40	200	0.17	39	28	36	85
69	50	140	0.04	48	26	36	78

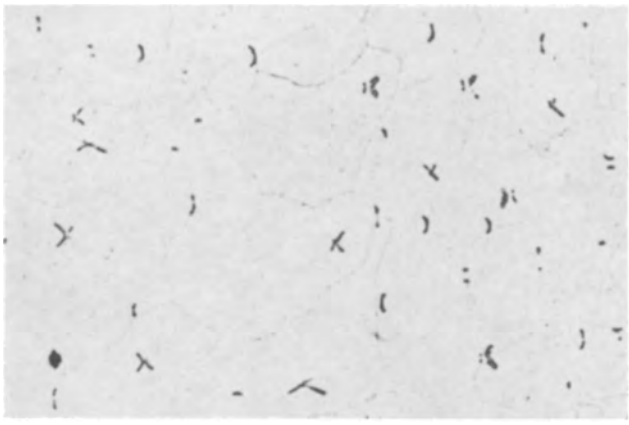

Fig. 2. Arc melted thorium button, run No. 58, bright field, 200X, 0.37% ThO_2.

of metallic impurities such as nickel, this method serves as a rapid means of determining relative quality. The presence of an unusually high oxide content is easily ascertained from the appearance of an oxide film on the button surface. Powder with a low oxide content (less than 0.3% HCl insolubles) normally results in a bright metallic surface. Button hardnesses of the material produced in the ten runs cited above are also shown in Table II.

A typical photomicrograph of an arc melted button is presented in Fig. 2. The main inclusion constituent is probably ThO_2, since chemical analysis indicates the presence of 0.37% HCl insolubles in the button.

To recover the very fine thorium powder which has been pumped to settling tanks during the leaching and acid washing steps for recycle through the reduction step, the settled thorium sludge is washed with 1:8 HNO_3. Enough nitric acid is added to insure the complete dissolution of $Ca(OH)_2$. After a 1-hr settling period, the supernatant liquor is pumped to the settling tanks. The supernatant liquor contains a small amount of dissolved thorium which may be periodically recovered as the hydroxide by precipitation with NH_4OH. The thorium fines are then washed with demineralized water at least three times to remove the acid. The fines are collected and dried by either of the two drying methods described previously.

Coarse thorium powder has been stored for periods as long as 4 months in air without any detectable deterioration. The usual practice is to store the powder from each run in a separate metal container. During the course of the development program described in this report, no case of spontaneous ignition of the powder was ever observed. However, at the termination of the project, a serious explosion did occur when some scrap fines were being burned in a disposal operation. It is suggested, therefore, that thorium powder be handled by procedures recommended for the handling of zirconium metal powders.

Various methods of consolidating thorium metal powder have been investigated extensively at this laboratory. These methods are: (*a*) consumable electrode arc melting (14), (*b*) hot compaction (15-17), and (c) cold compaction and sintering (17). By far, the most advantageous of these is the

first, since such impurities as calcium, magnesium, and hydrogen are reduced by a factor of about 10 during the arc melting. In addition, ingot densities as high as 11.69 g/cc [theoretical is 11.71 g/cc (18)] are obtained in a single melting operation.

Process Development

The standard operating procedure described in the previous section evolved from fifty-seven experiments made on a smaller scale. In these experiments the important factors controlling the yield and quality of thorium metal powder produced were ascertained. The most important results of these experiments are summarized below.

According to the thermodynamic data compiled by Coughlin (13), the equilibrium for the reduction of thorium oxide with calcium is favorable below the boiling point of calcium. It appears from our work that the reduction is not highly exothermic, i.e., there is no sudden increase in the temperature of the reactor as it is heated slowly to the reduction temperature. A calculation of the heat of reaction at 950°C predicts a value of −12.4 kcal for the reduction of a gram mole of thorium oxide with liquid calcium as follows:

$$ThO_2 + 2Ca \rightarrow 2CaO + Th$$

This small quantity of heat evolved is apparently easily dissipated.

In practice, a calcium metal excess of 25% or more is usually added to effect complete reduction. In addition calcium chloride is required to provide a fluid medium for contact between the reactants. It has been suggested by Marden and Rentschler (5) that the compound $CaO \cdot CaCl_2$ is formed (between the flux and the reaction product CaO), which removes the CaO as it is formed, driving the reaction to completion. This assumption cannot be entirely correct since it was found in the present work that complete reduction is attained with a relatively small amount of $CaCl_2$, much less than that contained in the compound $CaO \cdot CaCl_2$.

The subsequent leaching of the thorium metal from the reduction product releases heat through reaction of CaO and excess Ca metal with water and acid. For removal of this heat, some cooling mechanism must be provided; otherwise, local overheating may cause excessive oxidation of the thorium metal. The leaching and acid washing may be carried out with a large volume of water to dissipate the heat, or a cooling coil may be introduced into the leaching tank.

It was found that impurities in the calcium and calcium chloride such as nitrogen and aluminum would appear in the thorium metal product. The use of redistilled calcium and calcium chloride granules which conformed to American Chemical Society specifications reduced the nitrogen content from greater than 100 to less than 60 ppm and aluminum from greater than 2000 ppm to less than 10 ppm. Carbon in the thorium metal product was traced to the absorption of CO_2 from the atmosphere by thorium oxide raw material. For example, small samples of thoria were found to contain 80 ppm carbon immediately after calcining. This same material, after exposure to an air stream for 30 min was found to have increased in carbon content to 400 ppm. Either batch or continuous calcining of the thoria was found to be a suitable technique for reducing the carbon content in the thorium metal product to levels rarely exceeding 200 ppm.

The development of a suitable container for carrying out the reduction proved to be a major problem in this program. Ordinary steel is unsuitable because of its lack of oxidation resistance. When a nickel stainless steel or Inconel container was used, the reduction cake adhered so firmly to the container wall that it was necessary to leach the charge in place in the container. Also, the thorium metal produced generally contained several hundred ppm of nickel impurity. Lining of the reactor with overlapped sheets of molybdenum was not satisfactory in preventing nickel pickup. A calcium oxide liner was dissolved in the reduction melt. A graphite liner eliminated the breakout problem but resulted in carbon contents of about 500 ppm.

It was found eventually that the use of a tapered reactor of type 446 stainless steel (which contains no nickel) reduced the nickel content in the product to as low as 7 ppm and also permitted removal of the reduction cake by the simple process of inverting the container and jolting it on a hard surface. In addition, to minimize atmospheric contamination, it was found necessary to admit argon throughout the reduction process through a tube leading into the cover of the reactor.

Experiments were made with varying proportions of calcium and calcium chloride, reduction times, and reduction temperatures. In general, a longer reduction time resulted in an increased yield of thorium powder, probably through agglomeration of fine thorium particles into larger ones. This was counter-balanced by a slightly increased pickup of such impurities as iron and chromium from the reactor. When the excess of calcium was decreased from 50% down to 25%, it became necessary to increase the soaking time from 2½ hr to 5 hr to insure complete reduction of thorium oxide. An optimum temperature for reduction is 950°C because at higher temperatures breakout difficulty can be encountered and, in addition, impurities in the thorium powder increase.

It was noted that increased periods of agitation during the leaching of the reduction cake had an adverse effect on thorium yield because larger particles are comminuted to fines. Both impeller agitation and tumbling barrel techniques were satisfactory for leaching thorium powder.

A typical analysis of fines is illustrated in Table III. It should be noted that the impurity level is somewhat higher than in primary yield thorium powder. These fines can be recycled into the process in several ways. If necessary, fines can be dissolved, reprecipitated as thorium oxalate, and calcined to form thorium dioxide, although economically this is least attractive. As noted earlier, fines can also be introduced directly into the metal reduction charge and with good results. Finally, the fines can be consolidated directly with the primary yield coarse thorium

Table III. Chemical analysis of thorium fines

	%
Nitrogen	0.010
Carbon	0.036
HCl insol.	0.83
Iron	0.012
Chromium	0.0058

powder at an apparent sacrifice in the quality of the metal produced. This was demonstrated in an experiment by comparing the button hardness of the product resulting from the two latter methods of recycle using the same lot of fines and a 15% recycle basis. The hardness of the metal produced by direct consolidation was R_F 58 and that prepared by recycle to the reduction step was R_F 47.

Conclusions

It has been shown that the calcium reduction of thorium oxide is capable of producing a high-purity thorium metal. This can be accomplished only through use of high-purity starting materials and by careful attention to charge preparation, reduction conditions, containers, materials, and powder leaching procedure. Extension of the process to manufacture of larger quantities should be straightforward.

Manuscript received Nov. 17, 1958. This paper was prepared for delivery before the Philadelphia Meeting, May 3-7, 1959. The work was sponsored by the U. S. Atomic Energy Commission at the Atomic Energy Division of Sylvania Electric Products, Inc., now Sylvania-Corning Nuclear Corporation.

Any discussion of this paper will appear in a Discussion Section to be published in the December 1960 JOURNAL.

REFERENCES

1. H. Huppertz, *Chem. Zentr.*, **1**, 1383 (1904).
2. K. Burger, Dissertation, Basel (1907); Gmelin Kraut, "Handbuch der Anorganische Chemie," III, Part 1, 1207.
3. H. Kuzel and E. Wedekind, U. S. Pat. 1,088,909 (1914).
4. E. Wedekind, *Edel-Erden und-Erze*, (3) Nos. 19-20, 109 (1922).
5. J. W. Marden and H. C. Rentschler, *Ind. Eng. Chem.*, **19**, 97 (1927).
6. J. W. Marden and H. C. Rentschler, U. S. Pat. 1,814,-719 (1931).
7. W. Kroll, *Z. Metallkunde*, **26**, 30 (1936).
8. W. Espe, *Powder Met. Bull.*, **3**, 100 (1948).
9. W. Espe, *ibid.*, **4**, 257 (1949).
10. H. C. Rentschler, W. C. Lilliendahl, and J. Gray, U. S. Pat. 2,446,062 (1948).
11. J. W. Marden, AEC Research and Development Report No. N-2139.
12. G. A. Meyerson, "Powder Metallurgy of Thorium," 1955 Geneva Conference A/Conf. 8/P/635.
13. J. P. Coughlin, Bulletin 542, Bureau of Mines (1954).
14. R. Witt, AEC Report, SEP-209, "Consumable Electrode Arc-Melting of Cold Compacted Thorium Powder," April 19, 1956.
15. R. H. Witt, J. Nylin, and H. M. McCullough, AEC Report, SEP-221, "A Study of the Hydride Process for Producing Thorium Powder," June 10, 1956.
16. R. H. Witt and H. M. McCullough, AEC Report, SEP-224, "Hot Pressing of Electrolytic Dehydrided and Calcium-Reduced Thorium Powders," Oct. 9, 1956.
17. R. B. Wagner and S. Storchheim, AEC Report, SEP-168, "Preparation and Consolidation of Thorium and Thorium Hydride Powders," August 9, 1954.
18. H. A. Saller and J. R. Keeler, "The Fabrication and Properties of Thorium," presented at the Nuclear Engineering and Science Congress, Dec. 12-16, 1955, Cleveland, Ohio.

Batteries with Solid Ion-Exchange Membrane Electrolytes

II. Low-Temperature Hydrogen-Oxygen Fuel Cells

W. T. Grubb and L. W. Niedrach

Research Laboratory, General Electric Company, Schenectady, New York

ABSTRACT

Hydrogen-oxygen fuel cells employing a commercial ion-exchange membrane as the electrolyte are described. Some performance data on this type of cell operating at room temperature with a cation membrane in the hydrogen form and with hydrogen and oxygen at 1 atm are presented. The open circuit EMF is about 0.3 v below the value of 1.23 expected for a reversible cell. This deficiency is found to be caused by the oxygen electrode which does not achieve the reversible half-cell potential. Equilibration of the membrane electrolyte with sulfuric acid prior to cell assembly results in improved polarization characteristics. Favorable features of these cells include their simple construction and their small unit thickness. In addition, the presence of as much as 67% CO_2 in the hydrogen feed gas is found to have little effect upon performance. Since the electrolyte is a cross-linked, water-saturated polymer, the electrolyte is locked into the structure and cannot be leached from the cell when it is operated within the stability limits of the polymer. No dilution occurs from the water formed at the oxygen electrode during cell operation because it is rejected from the saturated electrolyte.

In previous work (1), the behavior of ion-exchange membranes as electrolytes in cells employing metal electrodes was described. Their behavior suggests a strong analogy with aqueous solution elec-

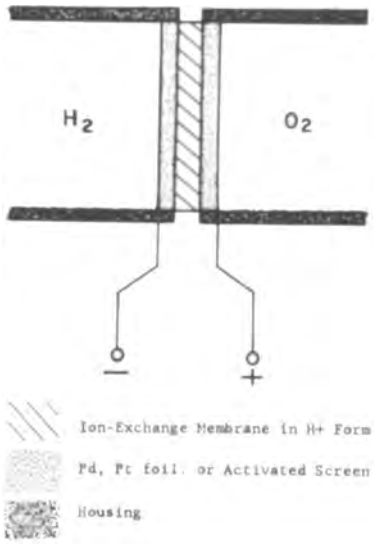

Fig. 1. Schematic diagram of ion-exchange membrane fuel cell.

Fig. 2. Type 1 ion-exchange membrane fuel cell, active area, 25 cm².

trolytes. Since the permeability of gases through ion-exchange membranes is low, they appeared to be ideally suited to serve as both the gas separator and the electrolyte in fuel cells (2, 3). The present work was undertaken therefore to study the properties of some simple systems of this type. This has resulted in a new type of low-temperature, hydrogen-oxygen fuel cell.

Experimental

Two types of cells were used in the experimental work. In both cases construction was such that the electrodes were in intimate contact with the electrolyte material as shown schematically by the diagram in Fig. 1. Immediately adjacent to the electrodes, gas chambers for the hydrogen and oxygen were formed by the cell housings.

A commercially available ion-exchange membrane was used in all of this work. For this purpose Amberplex C-1[1] was selected. This is a heterogeneous membrane consisting of particles of sulfonated, cross-linked polystyrene bonded into sheet form with an inert binder. These membranes, which were employed in the hydrogen form, have a conductivity that approximates that of a 0.1*N* H_2SO_4 solution (4). They are also stable chemically and have high flexibility and mechanical strength. Some electrochemical properties of Amberplex C-1 have been reported by Winger, *et al* (5).

Nickel screens activated by platinum black were used as the electrodes in most cases although a few experiments were performed with platinized platinum and palladium foil electrodes. Platinizing of the nickel screens was accomplished by simply immersing the screen into an acidified platinum chloride solution containing a trace of lead acetate (6). When palladium or platinum was employed, electrodeposition of the black was necessary, and the method of Reilly and Rae (6) was used.

A photograph of the simple cell (type 1) employed for the first experiments is shown in Fig. 2. The effective cell area was 25 cm² and the thickness of the electrolyte layer 0.06 cm to provide a cell constant of about 420. This type of cell was used with both screen and foil electrodes. Because of the relatively small area and the use of flat electrodes, good contact was obtained between the electrolyte and the electrodes with only the pressure of the flanges on the periphery of the housing.

In later work a larger version of the cell was designed. Two views of this cell (type 2) are shown in Fig. 3 and 4. In this model the electrodes were held in place against the membrane by backing plates with suitable baffles arranged to promote gas distribution. A uniform pressure was applied to the electrodes by placing rubber spacers between the backing plates and the face plates of the cell. These

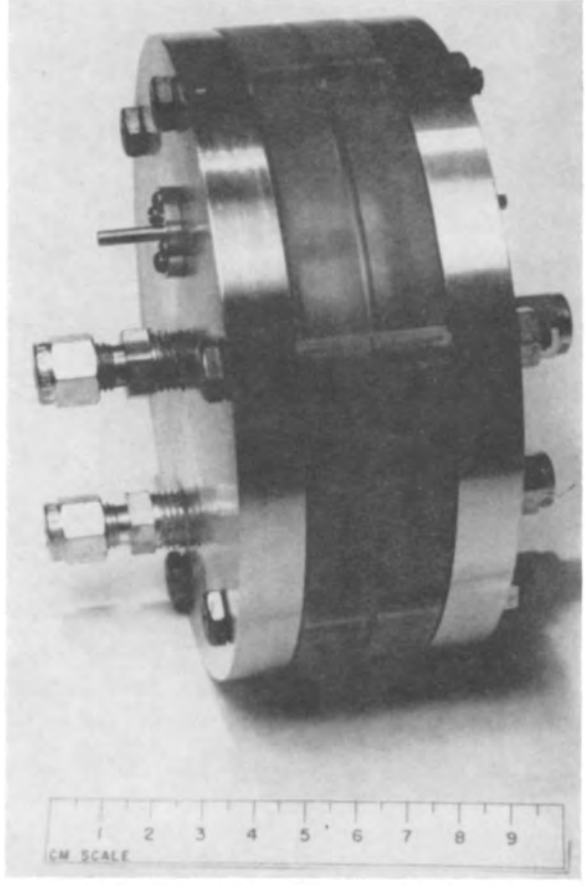

Fig. 3. Type 2 ion-exchange membrane fuel cell, assembled, active area, 50 cm².

[1] Rohm and Haas Co., Philadelphia, Pa. A similar product is available as Permaplex C-10 from Permutit Corp. Ltd., London, England.

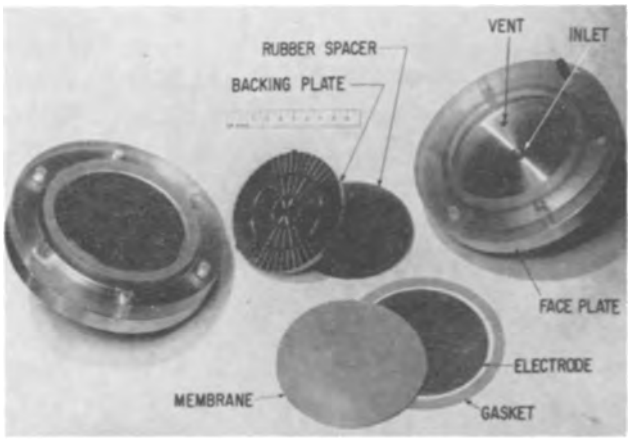

Fig. 4. Type 2 cell, not assembled

parts are shown in Fig. 4. In operation the feed gases were admitted through inlets on the axis of the cell. After radial distribution over the electrodes, the waste gases were then vented through the exit ports. Silicone rubber gaskets were employed as seals. Over-all diameter of the cell was 12.7 cm (5 in.) and the diameter of the electrodes was 8.3 cm (3¼ in.). Total active area was approximately 50 cm².

The cells were operated by admitting hydrogen and oxygen, respectively, to the two gas chambers and measuring the electrical output. In order to maintain ion exchange membranes in highly conducting form, they must be kept at 100% humidity, and this was accomplished by bubbling the input gases through water. Water formed by the cell in operation can help to maintain the hydration of the membranes. Actual dilution of the electrolyte cannot occur since the membranes reject water when they are saturated.

Polarization curves were obtained under various conditions by measuring currents with a sensitive galvanometer and cell potentials with a Rubicon potentiometer. In the initial work with the type 1 cells (Fig. 2), measurements were taken 10 sec after applying the load. This procedure has been recommended by Davtyan (7) and proved adequate for the purpose of comparing various modifications. In the work with type 2 cells, steady-state data were obtained. Establishment of equilibrium generally required several minutes after a change in load was made. All of the data were obtained at room temperature (25° ± 3°C).

In order to permit comparison of data obtained with the two types of cells, all current measurements were converted to current densities. This was done by dividing the measured current by the geometrical area covered by the circular electrodes.

Results and Discussion

The initial polarization curves, shown in Fig. 5, were obtained on type 1 cells with platinum foil electrodes. Platinized platinum foils as thin as 0.0002 cm (0.08 mil) were used in order to minimize diffusion effects through the metal. Only fairly low currents could be obtained from these cells. For this reason, attention was quickly directed toward cells with metal screen electrodes.

Polarization curves obtained with the type 1 cell using platinized screen electrodes are depicted in Fig. 6. All screen cells were found to afford higher currents than the foil types. The screen electrodes were made from nickel screen 150 x 150 (per inch) mesh. This mesh is woven from 0.0076 cm (0.003 in.) diameter nickel wire. The original screen thickness is 0.015 cm (0.006 in.) at the points where the wires of the mesh cross. The three curves were obtained with screens that had been rolled to different thicknesses before being platinized. It was observed that, as a result of the successive rolling, the surface of the screen became flatter and facilitated a larger area of contact between the electrode and electrolyte. This correlates with the fact that less polarization occurs with the more extensively rolled samples since lower effective current densities at the electrode surface would result from the better contact. The best type 1 cell achieved 60 ma at 0.75 v after 10 sec under load and a steady-state current of about 40 ma on the same load resistance.

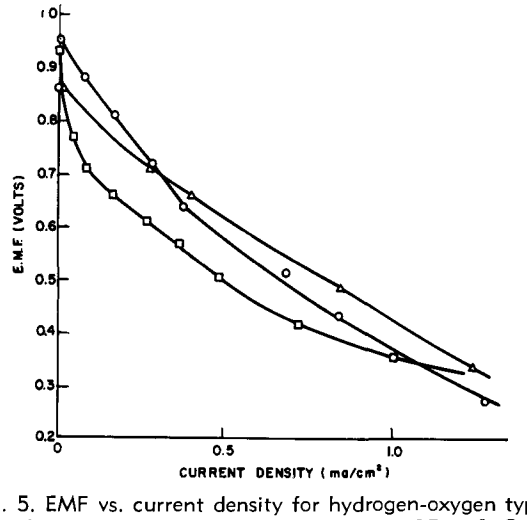

Fig. 5. EMF vs. current density for hydrogen-oxygen type 1 cells with platinum foil electrodes; cell area, 25 cm². ○, 0.5 mil foil platinized; △, 0.08 mil foil platinized; □, 0.05 mil lightly platinized.

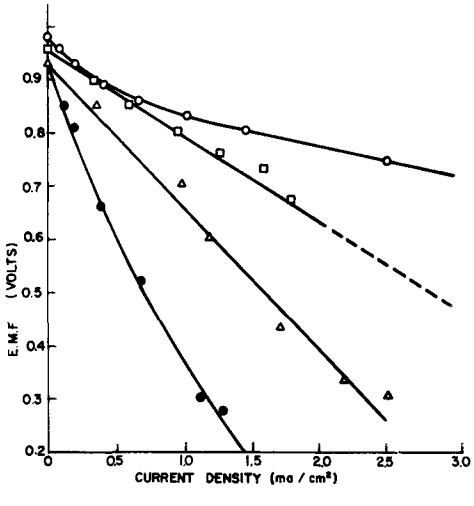

Fig. 6. EMF vs. current density for hydrogen-oxygen type 1 cells with various electrodes; cell area, 25 cm². ○, rolled screen* 2 mil thickness; □, rolled screen* 4 mil thickness; △, unrolled screen* 6 mil thickness; •, 0.08 mil foil cell (cf. Fig. 5).

* Platinized nickel screen.

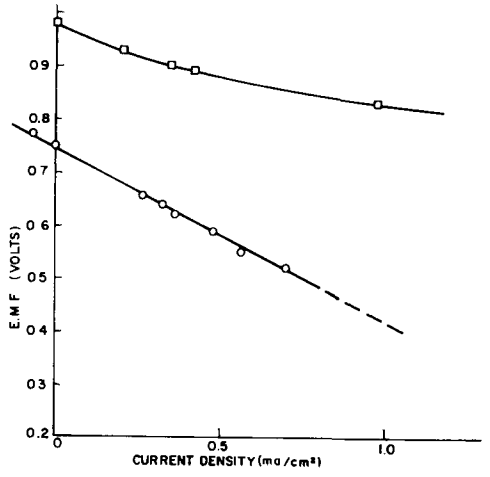

Fig. 7. EMF vs. current density for zinc-hydrogen and oxygen-hydrogen cells with plotinized nickel screen electrodes. Cell, type 1; area, 25 cm². □, H_2-O_2 cell; ○, H_2-Zn cell.

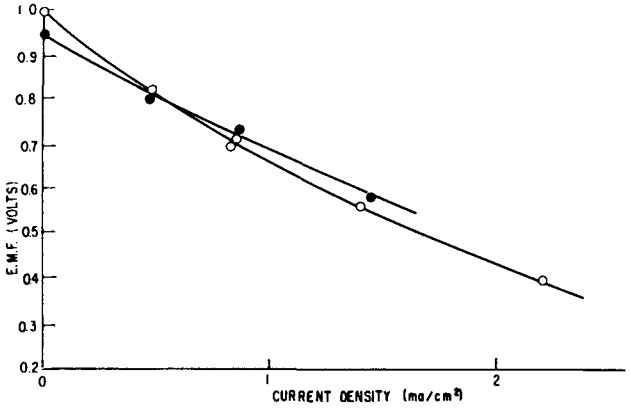

Fig. 8. Steady-state EMF vs. current density for type 2 cell operating on dry O_2 (flow rate 7 cc/min) and a 1:2M mixture of H_2 and CO_2 saturated with water (flow rate 10 cc/min). ○, Initial operation; ●, after 15 hr of operation at 1 ma/cm². Electrodes 500X 500 mesh nickel screen activated with platinum black.

The form of the polarization curves and the value of the open-circuit voltage both suggest irreversibility at one or both electrodes in this cell. In order to separate the effects of the anode and cathode, the hydrogen electrode was placed in a separate cell against a zinc electrode which is already known to behave reversibly (1). The following cell was used: zinc metal/zinc ion membrane/hydrogen ion membrane/platinized screen/hydrogen gas at 1 atm. The polarization curve of this cell is plotted in Fig. 7 along with that of the best cell of Fig. 6 for comparison. The emf of the H_2-Zn cell at zero current is observed to be 0.75 v, whereas in the analogous cell in which aqueous solutions at 25°C are employed with unit ionic activities the emf is 0.763 v (8). It is concluded that the H_2/platinized screen/H^+ membrane half-cell must be operating approximately at the reversible emf. The open-circuit emf of the H_2-O_2 cell is 0.90-0.96 v as compared with 1.23 v to be expected from the value of free energy of formation of water at 25°C. A deficiency of about 0.25-0.30 v at the O_2 electrode must therefore be present. This result is not surprising in view of published work on the behavior of platinum electrodes with oxygen at room temperature in sulfuric acid solutions (9).

The data presented above were obtained during short periods of operation using the type 1 cell of Fig. 2. It was of interest to consider performance under continuous operation. For this purpose a test run of approximately 15-hr duration was made on the type 2 cell of Fig. 3 and 4. In this run platinized nickel electrodes were used. In addition, the fuel gas was a mixture of 2 moles CO_2 to 1 mole of H_2. Flowing gases were used. At the start of the run the current was 45 ma at 0.69 v. After approximately 15-hr operation the cell current was 47 ma at 0.73 v. Initial and final polarization curves for this run are shown in Fig. 8.

Since it is known that ion-exchange membranes have a capacity for free acid, it was of interest to determine the effect of such acid on cell performance. For this purpose a membrane was equilibrated with 6M H_2SO_4 and after being blotted dry was assembled into a cell. The pronounced effect of the free acid on cell performance is shown by a comparison of the two curves in Fig. 9. The lower curve in the figure is representative of steady-state performance of cells operating with untreated membranes on pure hydrogen and oxygen.

While addition of free acid to the membrane does improve the cell performance, this does not appear to be a satisfactory, long range approach because of the corrosion problems that are thereby introduced. In addition, this acid can be leached from the membrane by the water produced in the cell reaction unless proper conditions are maintained to remove water by evaporation.

Summary and Conclusions

The use of ion-exchange membranes as the electrolyte in hydrogen-oxygen fuel cells is attractive. As solid, nonleachable electrolytes, these membranes permit the construction of cells that require a minimum of external components and controls, e.g., pumps, etc. Another important advantage of the ion-exchange membrane electrolyte is its very favorable geometry. The cells described here have a total active thickness of less than 1 mm. Such a favorable space factor helps to compensate for the lower current density of this cell relative, for example, to that of Bacon (3). In addition, because such membranes are used in their acid form, operation on gases containing large amounts of CO_2 is possible and has been demonstrated.

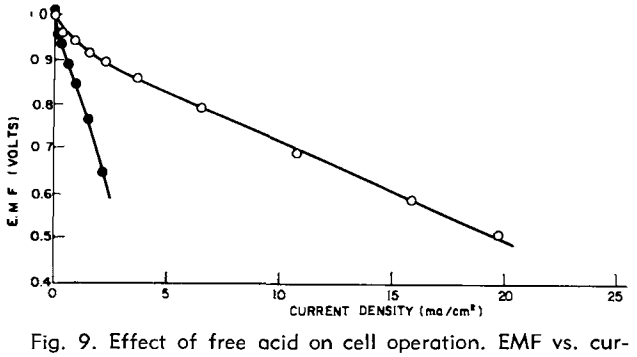

Fig. 9. Effect of free acid on cell operation. EMF vs. current density for type 2 cell with 200 x 200 mesh nickel screen electrodes (rolled to 0.002 in. thickness) platinum activated. ●, Leached membrane H^+ form; ○, membrane H^+ form in equilibrium with 6M H_2SO_4 and wiped dry superficially.

Saturation of the membrane-electrolyte with sulfuric acid improves the performance of the cell. The treatment has some disadvantage in that it causes corrosion problems and other complications related to the dilution and leaching out of the free acid.

The indicated directions of improvement for cells of this kind are in mechanical construction to improve the electrical contact between the electrodes and the membrane and in the oxygen electrode surface to provide a more nearly reversible O_2 half-cell.

Acknowledgment

The authors are indebted to Drs. H. A. Liebhafsky, J. L. Weininger, and D. L. Douglas for a number of helpful discussions during the course of this investigation.

Manuscript received Oct. 2, 1959.

Any discussion of this paper will appear in a Discussion Section to be published in the December 1960 JOURNAL.

REFERENCES

1. W. T. Grubb, *This Journal*, **106**, 275 (1959) (Part I of this series).
2. R. G. H. Watson, *Research*, **7**, 34 (1954).
3. F. T. Bacon, *Beama Journal*, January (1954).
4. W. T. Grubb, *J. Phys. Chem.*, **63**, 55 (1959).
5. A. G. Winger, G. W. Bodamer, and R. Kunin, *This Journal*, **100**, 179 (1953).
6. J. Reilly and W. R. Rae, "Physico-Chemical Methods," Vol. 2, p. 608, D. Van Nostrand Co. Inc., New York (1953).
7. O. K. Davtyan, "Direct Conversion of Energy of Fuels to Electrical Energy," pp. 1-48, Academy of Science of the USSR, Moscow (1947).
8. W. M. Latimer, "Oxidation Potentials," 2nd ed., Prentice-Hall, Inc., New York (1952).
9. J. O'M. Bockris and A. K. M. S. Huq, *Proc. Royal Soc. (London)*, **237A**, 277 (1956).

The Influence of Cations on the Differential Capacity of the Dropping Mercury Electrode in Solutions of Electrolytes in Methanol and Ethanol

S. Minc and J. Jastrzebska

Department of Electrochemistry, University of Warsaw, Warsaw, Poland, and Department of Electrochemistry, Polish Academy of Sciences, Warsaw, Poland

ABSTRACT

Differential capacities of the electrical double layer of LiCl, NaCl, $MgCl_2$, and $SrCl_2$ in methanol have been measured. The capacities have been found to be higher in the presence of large cations (of low polarizability), which undergo chemisorption according to Frumkin's theory, by comparison with values observed in the presence of cations of high polarizability. In addition, the effect of concentration of the electrolyte on the differential capacity increases with decreasing polarizability of the cation. The solvent effect on the differential capacity has been found to be greatest near the zero charge potential, the decrease of the differential capacity relative to its value in water solutions being proportional to the decrease in dielectric constant.

In recent papers on electrocapillary phenomena, two different points of view have been advanced regarding the effect of cations on the structure of the electrical double layer. According to Grahame (1-3) the differential capacity of the inner part of the double layer is independent of the kind of cation if it is monatomic. Small differences of capacity observed for aqueous solutions in the region of strong cathodic polarization in the presence of different cations are due, according to Grahame's theory (4), to incomplete dielectric saturation of the solvent by some cations. There are more facts which could hardly be explained by Grahame's theory. For instance, it is known that the presence of large cations in the solutions increases the rate of electroreduction of some anions, e.g., $S_2O_8^{2-}$, and/or shifts the potential of desorption of anions toward more negative values (5-7).

Frumkin has concluded (6, 8) that some large cations, e.g., Rb^+, Cs^+, are chemisorbed at the surface of mercury. The aim of our work has been to contribute further experimental data to the solution of this problem (9). It was expected that the effects of chemisorption of cations ought to be more pronounced in some organic solvents. Methyl and ethyl alcohols have been chosen as solvents because of their high compressibility, high electrostriction in electrical fields, and their ease of dielectric saturation (10, 11). In consequence, the influence of cations on the structure of the double layer should be determined more precisely.

Experimental

An a-c symmetrical bridge was used in measurements of the differential capacity of the dropping mercury electrode. Our circuit differed from that of Grahame (12, 13) in that the stray capacitances of the bridge ratio resistors were balanced. A ferrite core choke or large inductance was introduced into the circuit (14). The application of balanced ratio

resistors and a large inductance in measurements with organic solvent solutions of low conductivity resulted in greater accuracy. The polarization of the dropping mercury electrode was achieved by a conventional polarographic technique.

Differential capacities were measured for potentials between —0.1 v and —1.8 v, with the aqueous saturated calomel electrode (S.C.E.) as reference. The surface area was evaluated by Grahame's method. The calculated differential capacity per unit area has been plotted against the potentials in Fig. 1-10.

Methyl and ethyl alcohols were distilled on a 30-plate column and the appropriate fractions collected. Water was distilled three times through a quartz condenser. Its specific conductivity was 4×10^{-6} ohm^{-1} cm^{-1}. Magnesium chloride, after being recrystallized from water, was heated in mixture with ammonium chloride at 360°C in platinum. Sodium chloride was brought down from a saturated solution by means of gaseous hydrogen chloride. Other salts were recrystallized from methyl alcohol and dried at 180°C to constant weight. Mercury was washed with dilute nitric acid, then with water, and finally distilled in vacuum. Nitrogen used for removing oxygen from the solutions was purified by means of activated carbon, potassium hydroxide solution, and silica gel impregnated with Cu_2O (15). The purity of solutions was checked polarographically.

Results and Discussion

Figure 1 shows differential capacity curves for 0.1M LiCl, 0.1M NaCl, and saturated KCl (about

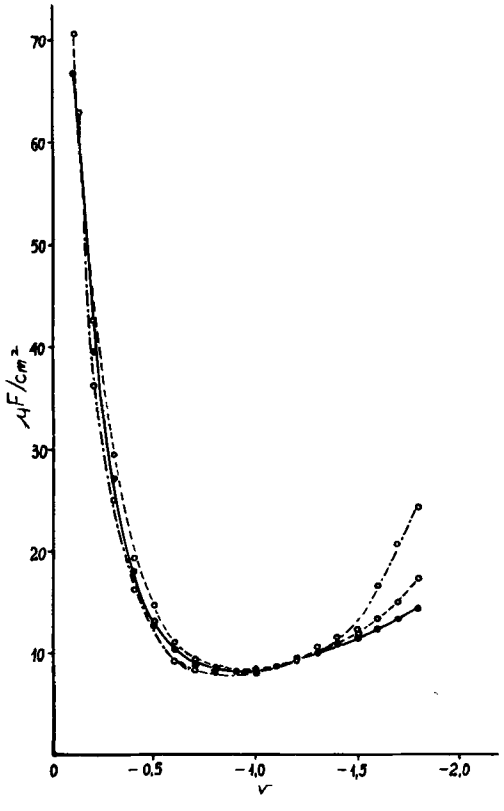

Fig. 1. •— 0.1M LiCl in methanol; o— — 0.1M NaCl in methanol; o- — satd. KCl in methanol.

Figs. 1-10. In the ordinate is the differential capacity of the mercury-solution interface in microfarads per square centimeter, the abcissa is the potential relative to the aqueous S.C.E., in volts.

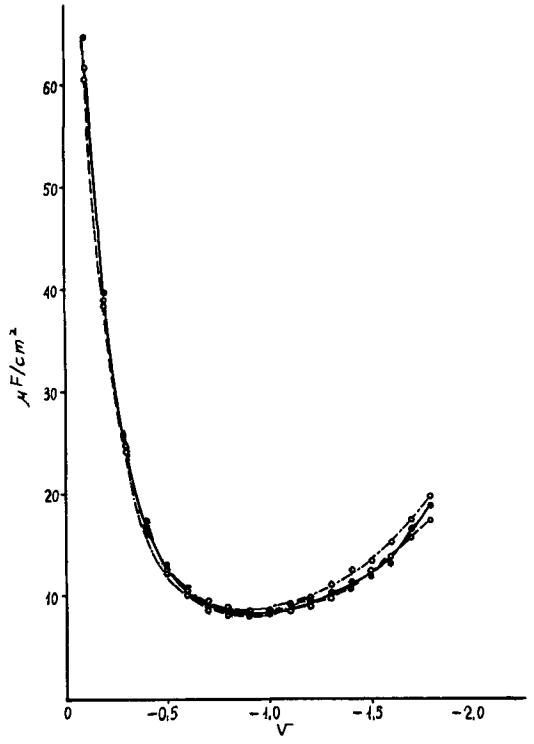

Fig. 2. •— 0.1M $MgCl_2$ in methanol; o— — 0.1M $CaCl_2$ in methanol; o- — 0.1M $SrCl_2$ in methanol.

0.05M) in methyl alcohol. In the region of high cathodic polarization the differential capacities differ in the presence of different cations and increase from Li^+ to K^+ in a manner similar to that observed for water solutions, except that the effect is more pronounced in alcohol. Similar curves determined for 0.1M methanol solutions of $MgCl_2$, $CaCl_2$, and $SrCl_2$ are shown in Fig. 2. The divalent cations affect the differential capacity only slightly and then only in the region of high cathodic polarization. In summary, it may be said that the differential capacity of the electrical double layer on mercury in the cathodic region is higher in the presence of cations of low polarizability (large radii). These ions, according to Frumkin's theory, undergo specific adsorption (chemisorption). There is no doubt that the high compressibility and electrorestriction of methyl alcohol molecules cause a more pronounced interaction of cations with the metal surface.

Results shown in Fig. 1 and 2 make it clear, however, that the differential capacity is affected not only by the nature of the solvent, as postulated by Grahame (11, 16), but also by the nature of cations, especially those of low polarizability. If Frumkin's hypothesis of specific adsorption of some cations is true, an unusually strong effect of concentration of the electrolyte on the differential capacity is to be expected when these cations are present in solution. The measurements performed to test this expectation are presented in Fig. 3-8. The differential capacities have been measured for aqueous, methanol, and ethanol solutions of LiCl and KF in the concentration range from 0.05 to 0.5M.

For aqueous solutions of LiCl and KF the effect of concentration on the differential capacity is small and nearly the same for both cations in the cathodic region (Fig. 3 and 4). This is in accordance with the

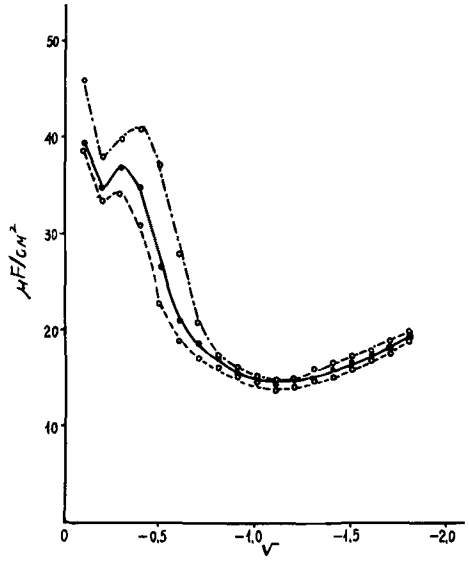

Fig. 3. Effect of concentration o— — 0.05 M LiCl in water; •— 0.1 M LiCl in water; o- — 0.5 M LiCl in water.

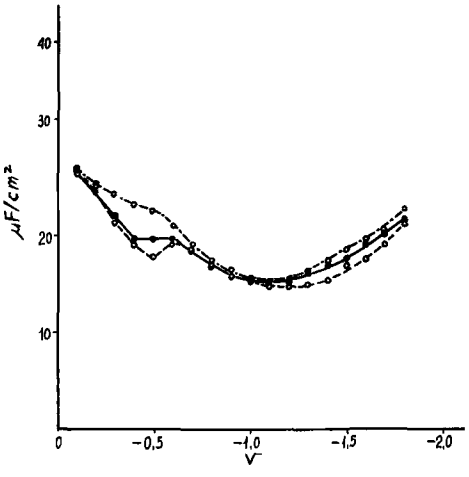

Fig. 4. Effect of concentration. o— — 0.05M KF in water; •— 0.1M KF in water; o- — 0.5M KF in water.

conclusion that neither Li^+ nor K^+ are chemisorbed on mercury from water. The small effect of concentration on the differential capacity of LiCl solutions in all three solvents (Fig. 3, 5, and 6) may be accounted for on the basis of the theory of electrostatic interaction of ions with metal surface developed by Grahame (1, 2, 11).

The marked concentration dependence found for high cathodic polarizations in alcoholic KF solutions (Fig. 7 and 8) cannot be due to the effect of concentration on the capacity of the diffuse part of the double layer as this effect could not be so different for the two cations investigated. It may be considered as evidence in support of the hypothesis of chemisorption of K^+ ion from methanol and ethanol.

Further measurements were undertaken to determine the desorption potentials of halide ions in methanol (Fig. 9 and 10). The only reason for the lower differential capacities in the cathodic region for saturated (about 0.05M) KCl in methanol as compared with 0.1M solutions of the potassium halides (Fig. 10) is evidently the difference in concentration. The differential capacities of saturated KCl (Fig. 1) and of 0.05M KF (Fig. 7) are practically the same. It is worth stressing that the desorption potentials found in this work for F^- and Cl^- ions in the presence of K^+ ion in methyl alcohol are nearly the same as those given by Grahame (11) for the same anions and solvent in the presence of NH_4^+.

In order to characterize the solvent effect, the curves for 0.1M LiCl in water (Fig. 3), methanol

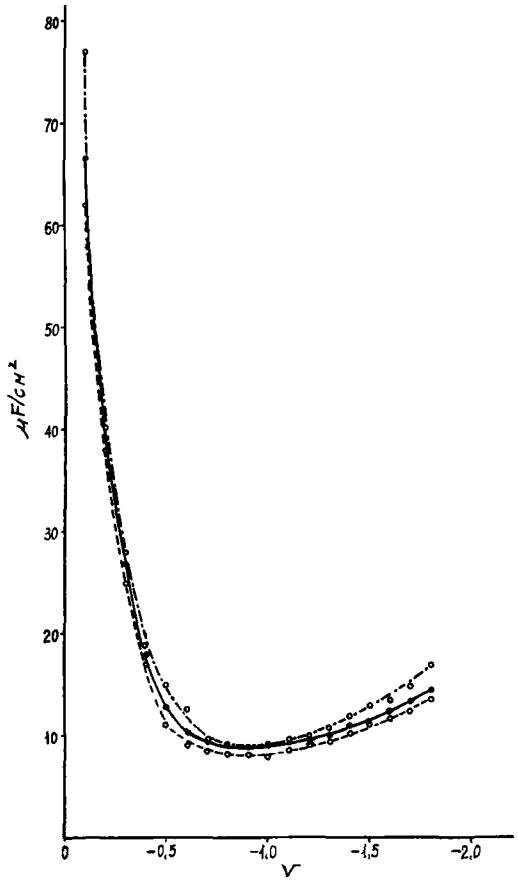

Fig. 5. Effect of concentration. o— — 0.05M LiCl in methanol; •— 0.1M LiCl in methanol; o- — 0.5M LiCl in methanol.

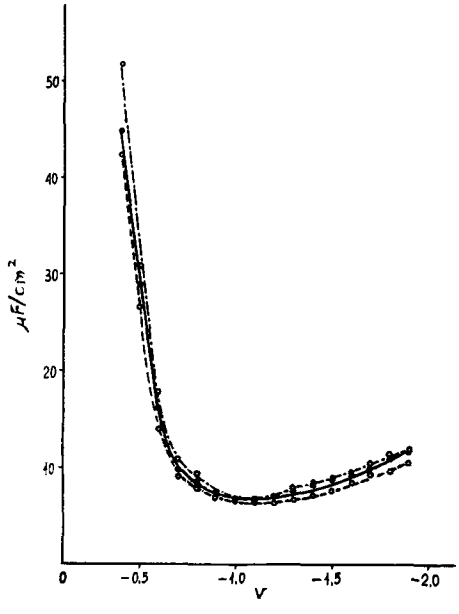

Fig. 6. Effect of concentration. o— — 0.05M LiCl in ethanol; •— 0.1M LiCl in ethanol; o- — 0.5M LiCl (satd.) in ethanol.

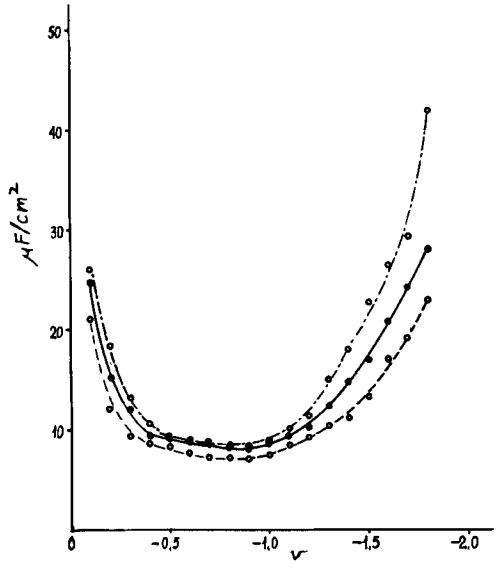

Fig. 7. Effect of concentration. o— — 0.05M KF in methanol; •— 0.1M KF in methanol; o- — 0.5M KF in methanol.

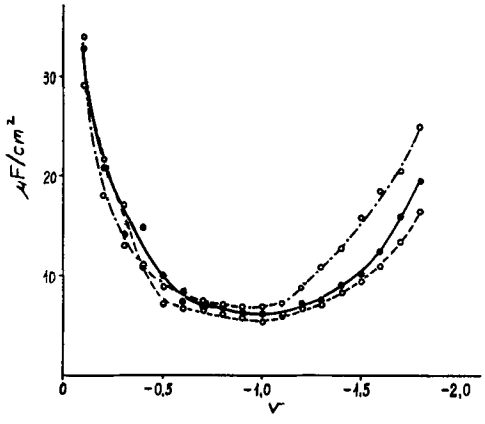

Fig. 8. Effect of concentration. o— — 0.05M KF in ethanol; •— 0.1M KF in ethanol; o- — satd. KF in ethanol.

(Fig. 1 and 5), and ethanol (Fig. 6) can be compared. The strongest effect of the solvent occurs near the zero charge potential (about —0.6 v). In this region, the decrease of the differential capacity when water is replaced by alcohol is nearly proportional to the decrease of the dielectric constant of the solvent. Also worth noting is the fact that the differential capacities of alcohol solutions show no peaks in the region of low anodic polarizations (about —0.3 to —0.4 v to S.C.E.); such peaks are observed in aqueous solutions (Fig. 3). This observation seems to favor the explanation given by Grahame (16) according to which this effect is due to the pseudocrystallic structure of water.

Manuscript received June 11, 1959.

Any discussion of this paper will appear in a Discussion Section to be published in the December 1960 JOURNAL.

REFERENCES

1. D. C. Grahame, *Chem. Rev.*, **41**, 441 (1947).
2. D. C. Grahame and B. A. Soderberg, *J. Chem. Phys.*, **22**, 449 (1954).
3. D. C. Grahame, *Z. Elektrochem.*, **59**, 773 (1955).
4. D. C. Grahame, *This Journal*, **98**, 343 (1951).
5. A. N. Frumkin, *Izvesti Akad. Nauk S.S.S.R.*, **12**, 1421 (1957).

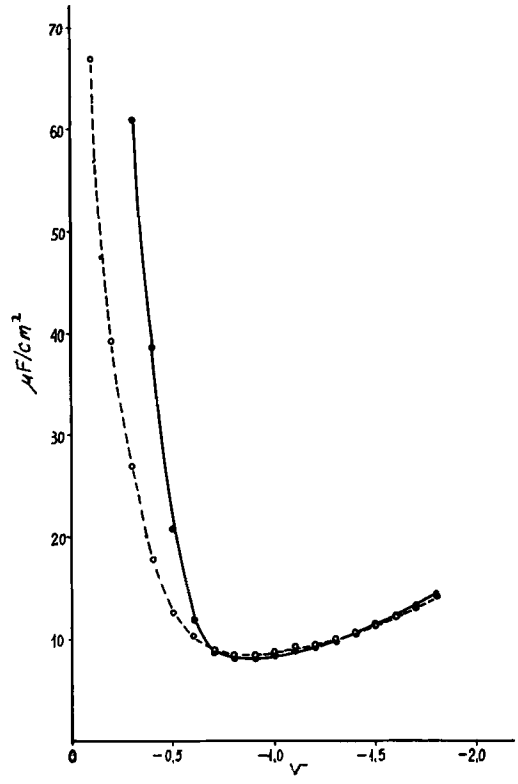

Fig. 9. Differential capacity in presence of specific adsorption of some anions. o— — 0.1M LiCl in methanol; •— 0.1M LiBr in methanol.

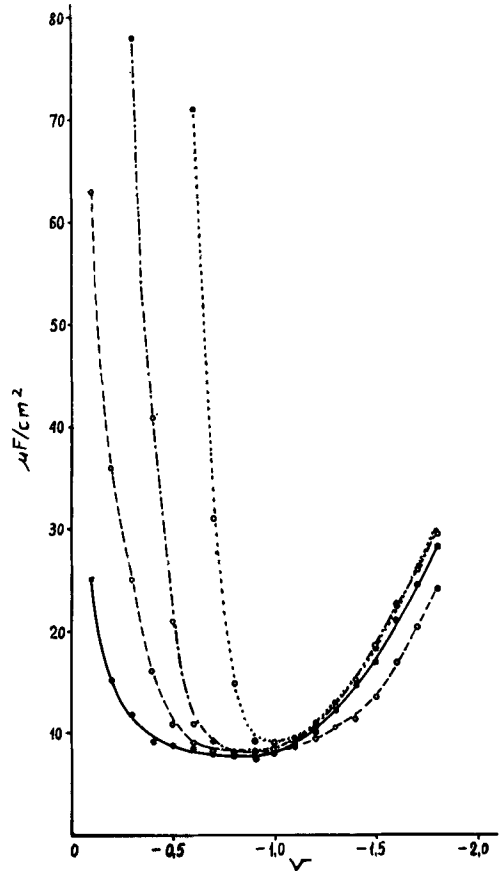

Fig. 10. Differential capacity in presence of specific adsorption of some anions. •— 0.1M KF in methanol; o— — satd. KCl in methanol; o- — 0.1M KBr in methanol; o- - - - - 0.1M KI in methanol.

6. A. N. Frumkin, B. Damackin, and N. Nikolajeva-Fiedorovic, *Doklady Akad. Nauk S.S.S.R.*, **115**, 751 (1957).
7. J. J. Lothe and L. B. Rogers, *This Journal*, **101**, 258 (1954).
8. B. Damackin, N. Nikolajeva-Fedorovic, and A. N. Frumkin, *Doklady Akad. Nauk S.S.S.R.*, **121**, 129 (1958).
9. S. Minc and J. Jastrzebska, *ibid.*, **120**, 114 (1958).
10. R. J. Macdonald, *J. Chem. Phys.*, **25**, 364 (1956).
11. D. C. Grahame, *Z. Elektrochem.*, **59**, 740 (1955).
12. D. C. Grahame, *J. Am. Chem. Soc.*, **63**, 1207 (1941).
13. D. C. Grahame, *ibid.*, **71**, 2975 (1949).
14. S. Minc and J. Jastrzebska, *Rocz. Chem.*, **31**, 1339 (1957).
15. F. Meyer and G. Konge, *Angew. Chem.*, **52**, 637 (1939).
16. D. C. Grahame, *J. Am. Chem. Soc.*, **79**, 2093 (1957).

Technical Notes

Chloride Content of the Diffusion Layer at a Silver Anode

Paul A. Krasley[1]

Chemistry Division, National Bureau of Standards, Washington, D. C.

A technique for isolating the diffusion layer at an electrode was developed by Yannakopoulos and Brenner (1). It involves the drawing off of the diffusion layer through a microporous electrode. These authors applied the method only to the study of the decrease of metal concentration that occurred at a cathode during metal deposition. The study reported here is an extension of the method and deals with the depletion of chloride ion that occurs at an attackable anode of silver.

The diffusion layer that forms at a silver anode during electrolysis of a sodium chloride solution contains a lower concentration of salt than the body of the solution, and the lowest concentration exists at the interface of the solution and the anode. The reduction in concentration results from the precipitation of chloride ions as silver chloride and the migration of sodium ions toward the cathode.

Experimental

Preparation of a microporous silver electrode.— Yannakopoulos and Brenner used a microporous, cylindrical, stainless steel electrode in their experiments. This shape has the advantage of providing a large electrode surface and a small volume. Efforts to prepare a microporous cylinder from porous silver sheet were unsuccessful for several reasons. The pores in the silver sheet were closed through cold-welding during the fabrication of the cylinder, and the sheet was so brittle that it cracked in shaping. A silver plated stainless steel cylinder was unsatisfactory because the stainless steel was attacked anodically through the pores in the silver coating.

Plane microporous silver anodes 2 in. in diameter were made by placing "spherical silver powder" in a soapstone form, covering with a disk of soapstone, and sintering in a preheated furnace at 900°C for 0.5 hr. This procedure yielded disks having a ratio of voids to volume of 30-50%. Both acicular and electrolytic silver powder were also tried in the fabrication, but the spherical silver powder was most satisfactory.

Attempts to form the silver disks by the application of pressure alone, up to 2000 lb/in.^{2}, were not successful, because the silver did not cold-weld sufficiently to form a mechanically strong disk. The combination of compacting by pressure followed by sintering at 900°C had no advantage over heating alone.

The porous silver disks were made as thin as possible in order to reduce the amount of solution required to rinse the porous disks before collecting a sample of the interface of the bath. Disks having a thickness of about 0.09 in. were the thinnest able to withstand the handling in the cleaning procedure and the slight vacuum applied during sampling.

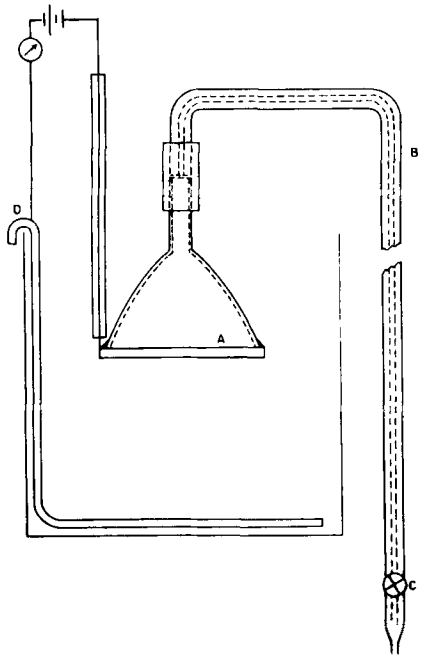

Fig. 1. Apparatus for desalting water: A, microporous silver anode; B, siphon; C, pinchcock; D, nickel anode.

[1] Present address: Bureau of Engraving and Printing, Washington, D. C.

Apparatus and Procedure

The apparatus shown in Fig. 1 consisted of a microporous silver anode, A, attached to an inverted funnel with Apiezon wax. The funnel was provided with a long capillary syphon, B. A pinchcock, C, regulated the rate of sampling of the interface. The nickel cathode, D, was bagged to minimize turbulence due to hydrogen evolution.

The apparatus was made ready for an experiment in the following way. The inverted funnel attached to the silver anode was filled with an organic liquid immiscible with water. To do this the anode assembly was partially immersed in water while the organic liquid was poured in from the top. An organic liquid more dense than water was chosen so that the aqueous solution subsequently collected would rise to the top. The following liquids were tried: a toluene-chloroform mixture (density 1.07^{20}), perfluorotriethylamine (density 2.7^{20}), and tetrabromoethane (density 2.95^{20}). Tetrabromoethane was used in most of the experiments.

The filled anode assembly was attached to the capillary syphon and was suspended in the bath. Electrolyses at various anodic current densities and rates of sampling were performed. Since the pores of the silver anode were filled with the water, the first several milliliters of liquid collected in an experiment were discarded before a sample representative of the electrode-solution interface was collected.

Results

The data in Table I represent typical results for the electrolysis of sodium chloride solutions. One disk was used for the 3% electrolysis and another disk was used for the 1% electrolysis. Because the formation of silver chloride plugged the interstices of the disk and caused a considerable increase in resistance both to current flow and to the flow of liquid, a single disk could not be used to make many successive experiments for determining effects of current density and of the rate of collection of the sample. For this reason the concentration of sodium chloride was reduced to 1%. The order of collection of data was the same as appears in Table I. Run No. 9 and definitely Run No. 10 can be attributed to the plugging of the disk. The plugging is accompanied by the evolution of gas which doubtless disturbs the diffusion layer.

Table I. Results of the electrolysis of NaCl solutions using porous silver anodes

Run No.	Conc. of electrolyte, %	Current density, amp/dm²	Rate of sampling of diffusion layer, min/ml	Reduction in chloride, %
1	3	2	3.3	17.8
2	3	3	3.3	24.5
3	3	1	7	39.4
4	3	2	7	45.6
5	1	0.25	7	18.5
6	1	0.50	7	34.3
7	1	0.25	14	32.2
8	1	0.5	14	73.0
9	1	0.75	14	80.9
10	1	0.75	17.5	27.0

Discussion

The investigation of the removal of chloride ion in the diffusion layer of a silver anode was carried only far enough to indicate that the process was theoretically feasible. The plugging of the silver disks showed that the use of this particular electrode was impracticable as a means of desalting water. However, it is possible that a more satisfactory electrode system can be developed.

Theoretically, a continuous desalting process could be devised which would utilize two porous silver-silver chloride electrodes. They would be placed close together, and initially the desalted water would be collected from one electrode. At intervals the direction of the current would be changed to regenerate the electrode and at the same time the collection of the desalted water from the other electrode would be started. If the two electrodes were placed close together to lessen resistance, the consumption of electrical energy would be small.

The desalting of water by the continuous collection of solution at the anode-solution interface differs in principle from the removal of chloride ion by use of a silver anode and cathode in a confined volume of solution. In the latter process, even though all the chloride ion were eventually removed by the silver anode, an equivalent content of sodium hydroxide would replace it, so that the solution would not be demineralized. The microporous electrode method, on the other hand, is envisaged to operate in a large volume of flowing solution, such as an ocean, so that the anode is always immersed in a solution of constant composition and the products formed at the cathode are swept away.

Murphy (2) has utilized silver-silver chloride electrodes to separate dissolved chlorides by an electro-gravitational method. His method is not directly comparable with the microporous electrode method, since its operation depends on the continued treatment of a solution for several hours either in a fixed volume or as it flows along the electrodes.

Manuscript received Aug. 19, 1959.

Any discussion of this paper will appear in a Discussion Section to be published in the December 1960 JOURNAL.

REFERENCES

1. Theodore Yannakopoulos and Abner Brenner, *This Journal*, **105**, 521 (1958).
2. G. W. Murphy, *ibid.*, **97**, 405 (1950); G. W. Murphy and D. Batzer, *ibid.*, **99**, 520 (1952).

Oxidation Rates of K and Rb between -79°C and -20°C

J. V. Cathcart and G. P. Smith

Metallurgy Division, Oak Ridge National Laboratory, Union Carbide Corporation, Oak Ridge, Tennessee

A study of the oxidation characteristics of the alkali metals was undertaken as a part of an investigation of the factors which determine the degree of protectiveness of thin oxide films formed on metals. Previously published data (1) relative to the oxidation kinetics of Na indicated that in purified oxygen Na formed a highly protective oxide film at room temperature or below but that the film became nonprotective after long periods of oxidation in the vicinity of 50°C. A similar study of the oxidation rates of K and Rb between —79° and —20°C showed that these metals likewise formed protective films at low temperatures but that the transition from protective to nonprotective oxidation occurred at a lower temperature than for the case of Na.

Experimental Procedure

Oxidation rates of K and Rb were determined by measuring the changes in pressure in a closed reaction chamber as oxidation proceeded. A sensitive differential manometer served as the pressure sensing device. Samples of K and Rb were purified by careful vacuum distillation (2), and the oxidation specimens were prepared by depositing relatively thick films of K or Rb on the walls of the oxidation chamber at a pressure of approximately 10^{-7} mm Hg. Details of the apparatus and the experimental procedure have been described elsewhere (1).

Results and Discussion

Rate measurements were made for K at —79°, —50°, —20°C and for Rb at —79° and —50°C. Results of typical experiments are shown in Fig. 1 and 2. In each figure the number of moles of oxygen consumed per square centimeter of apparent surface area is plotted against the time of oxidation measured in minutes.

Both K and Rb exhibited a marked lack of reactivity in pure oxygen in the temperature range cited. If it is assumed that the oxide formed as a uniform surface layer on the specimens, the films produced on K at —50° and —79°C were not more than 100Å thick after 100,000 min (about 70 days) of oxidation. At higher temperatures, —20°C for K and —50°C for Rb, the maximum film thicknesses attained were probably between 2000 and 3000Å. More precise figures are not given for the film thicknesses because of the uncertainty as to the exact oxide compositions and because of the likelihood that thickness inhomogeneities existed in the films (3).

It will be noted that the oxide films formed on K at —50° and —79°C were almost completely protective, but at —20°C a transition from protective to nonprotective oxidation was observed. A similar transition occurred in oxide films formed on Rb at —50° and —79°C. These results are also consistent with the oxidation characteristics of Na for which a comparable behavior was observed at 48°C. Thus a transformation from protective to nonprotective oxidation occurred for all three of the alkali metals investigated, and the temperature at which this transformation was observed varied inversely with the electropositive character of the metals.

Because of the extreme thinness of the oxide films and their sensitivity to moist air, no satisfactory method has as yet been devised for determining their compositions. The super oxides, KO_2 and RbO_2 have been reported as the major products formed during the burning of K and Rb in oxygen (4). However, several other oxides have been reported in the literature for both K and Rb (5), although complete metal-oxygen phase diagrams are available

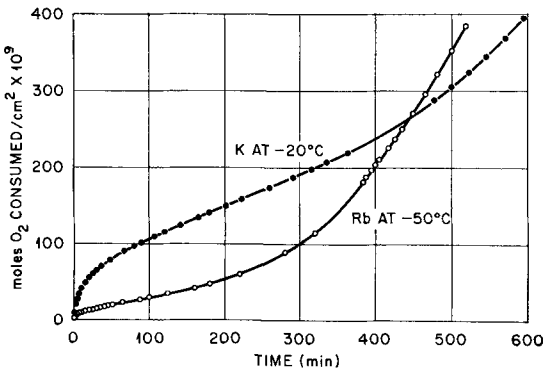

Fig. 1. Oxidation of K at —20°C and Rb at —50°C

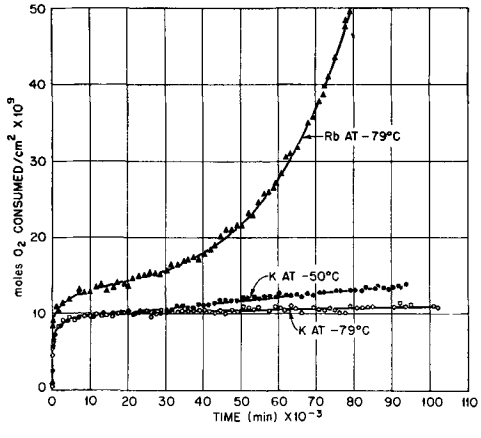

Fig. 2. Oxidation of K at —50° and —79°C and Rb at —79°C.

for neither. Since the metal was by no means completely consumed in the experiments reported here, it is probable that the oxide films consisted of several oxide phases in addition to the super oxides.

Efforts to determine rate curves at temperatures higher than −50°C for Rb and −20°C for K were unsuccessful because the rates of oxidation were too rapid to be measured with the manometric technique utilized in this research. At room temperature, actual burning of the metal occurred. It was noted, however, that, if the specimens were first exposed to oxygen at a lower temperature, e.g., −79°C, and then the system brought to room temperature, a drastic reduction in the oxidation rate occurred. Instead of the burning such as occurred when the clean metal was exposed to oxygen at room temperature, a slow uptake of gas was found to take place over a period of several days. Thus the oxidation rates of K and Rb, as is the case for many other metals, proved to be markedly dependent on the prior history, especially the surface condition, of the metal specimens.

Manuscript received March 23, 1959.

Any discussion of this paper will appear in a Discussion Section to be published in the December 1960 JOURNAL.

REFERENCES

1. J. V. Cathcart, L. L. Hall, and G. P. Smith, *Acta Met.*, 5, 245 (1957).
2. G. W. Horsley, "The Purification of Commercial Potassium," Atomic Energy Research Establishment No. M/R 1371.
3. W. W. Harris, F. Ball, and A. T. Gwathmey, *Acta Met.*, 5, 574 (1957).
4. H. Remy, "Lehrbuch der Anorganischen Chemie," Vol. 1, p. 165, Akademische Verlasgesellschaft, Leipzig (1953).
5. L. Brewer, *Chem. Rev.*, 52, 1 (1953).

The A-C Resistance of a Polarized Stainless Steel Wire Cathode

G. M. Schmid and Norman Hackerman

Department of Chemistry, University of Texas, Austin, Texas

Resistance measurements are used currently to determine the amounts of adsorbed gas on thin metal films (1). It also should be possible, in principle, to determine the growth of an oxide layer on a thin metal film in solution by this method. However, it is uncertain how the resistance of an electrode is affected by the solution and by a polarizing current.

The a-c resistance of palladium wires increases when the metal is in certain electrolyte solutions while being cathodically charged (2-4). Prolonged charging at higher current densities results in a resistance decrease. The increase is due to H_2 absorption and it has been suggested by Knorr and coworkers (5, 6) that the decrease is due to leakage through the surrounding electrolyte. Conductivity by way of the electrolyte must occur via a coupling which is provided by disturbing of the electrical double layer (edl). In order to eliminate the effect of H_2 absorption the a-c resistance of stainless steel electrodes was followed in this study. The structure of the edl was altered by passing a d-c polarizing current of 1-40 ma/cm^2.

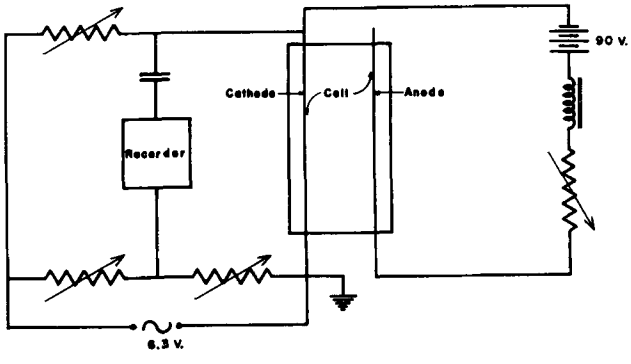

Fig. 1. Circuit diagram

Experimental and Results

The cell consisted of a glass tube and two straight type 302 stainless steel wires, 0.038 cm in diameter and 30-100 cm long (Fig. 1). The a-c resistance of the wire serving as the cathode was measured. The second wire was the anode and was held parallel to the first, generally more than 0.1 cm away. The electrolyte was 0.01-1.0M Na_2SO_4.

The resistance measurements, with or without d-c polarization, were obtained with a standard Wheatstone-Bridge, using 60 cps a-c. A Brown-Honeywell recorder with its converter stage by-passed was used as an automatic balancing instrument. Any d-c pickup was eliminated by the transformer in the automatic balancing unit of the recorder and by using a 100 μf capacitor in the circuit. The voltage drop along the grounded cathode was about 0.1 v. Resistance changes of 0.005 ohm could be measured easily. The polarizing current was furnished by a 90 v battery using a set of resistors to control the current and a 10 henry choke to minimize a-c pickup from the bridge circuit. In order to get significant resistance changes the cathode had to be polarized to the hydrogen evolution potential (at least to −1.1 v vs. SCE).

Addition of solution alone has no influence on the resistance of the cathode, causing changes of no more than 0.01 ohm, provided the anode was more than 1 mm away. On the other hand, Fig. 2 shows that the resistance of the cathode drops when polarized at current densities greater than 0.5 ma/cm^2, thus indi-

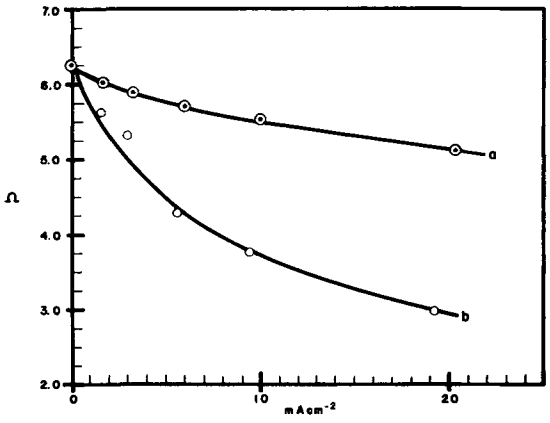

Fig. 2. Dependence of resistance on electrode-distance, cathode surface area 11.1 cm^2, 18-8 stainless steel, 1.0M Na_2SO_4. Curve a, electrode-distance 2.1 cm; curve b, electrode-distance 0.1 cm.

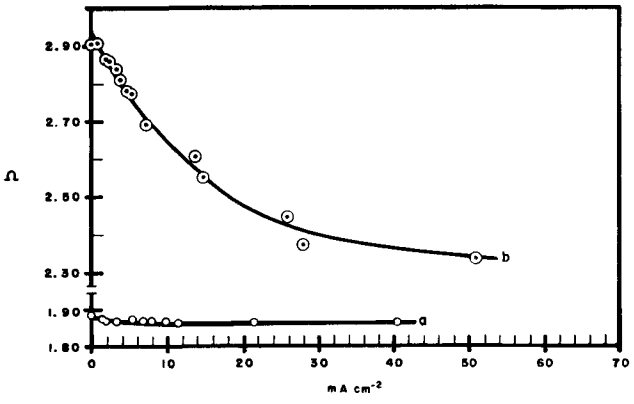

Fig. 3. Dependence of resistance on electrolyte concentration, electrode-distance 1.0 cm. Curve a, 0.01M Na_2SO_4, length of wire 29 cm, surface area 3.5 cm^2; curve b, 1.0M Na_2SO_4, length of wire 44 cm, surface area 5.2 cm^2.

cating additional conduction by the surroundings. The resistance changes are related nonlinearly to the length of the wire in solution.

Aside from immersed wire length, the resistance decrease at constant polarizing current density was influenced by the distance between anode and cathode. This indicates that the anode as well as the electrolyte is part of the a-c conducting system at small separations (Fig. 2). The influence of solution concentration is shown in Fig. 3. Under the same conditions except with 0.001M Na_2SO_4 there was no resistance change.

In all cases the resistance changes occurred in less than 2 sec, indicating the absence of hydrogen diffusion effects. The i^2R-effect was negligibly small, values obtained being steady over a 5-min period. The changes were reversible and, for a given electrolyte, a given distance between anode and cathode, and a given "air" resistance of anode and cathode, entirely reproducible.

Discussion

Coehn and Specht (7) carried out similar experiments on palladium and also observed drops in resistance proportional to the polarizing current. They explained their effects by the additional conductivity by hydrogen in the metal in excess of saturation concentration. This explanation is not suitable for stainless steel because of the rapid resistance changes and the rapid recovery of original resistance after switching off the d-c polarizing current. This makes diffusion effects highly improbable.

The transition resistance between cathode and surroundings seems to be very high as long as the cathode is not polarized. After the polarizing current has shifted the potential of the electrode to a high enough negative value, the a.c. is able to oxidize and reduce some species according to its own frequency, thus passing into solution. Moreover, with increasing current density, i.e., increasing negative potential, the cathode metal is sufficiently displaced from its zero point of charge so that there should be an adsorbed layer of cations and oriented water dipoles in close contact. This may cause a further drop in resistance.

The same effect, with reverse sign, should be expected at the anode, and this was verified experimentally. The resistance changes are in the same order of magnitude.

It seems therefore that the resistance of the system in a polarized state consists of the resistance of the cathode and the anode plus a transition resistance or coupling capacitance on either side plus the resistance contributed by the electrolyte. All these additional resistivities cannot be considered as parallel to the cathode but rather as diffuse and effective over the whole cathode surface. Thus a linear relationship between resistance change and length of the cathode should not be expected.

In order to get conclusive data concerning oxide films on thin working electrodes by observing its resistance change, one has to work in electrolytes of very low conductivity, otherwise the data taken during the flow of a d-c polarizing current are meaningless.

Further studies in this field should include the frequency dependence of the transition resistance and the effects of specifically adsorbed ions and surface active substances.

Acknowledgment

This work was carried out as part of Contract Nonr 375(02) with the Office of Naval Research. The authors take this opportunity to express their appreciation for this aid. Financial assistance by the Robert A. Welch Foundation is also appreciated.

Manuscript received June 5, 1959.

Any discussion of this paper will appear in a Discussion Section to be published in the December 1960 JOURNAL.

REFERENCES

1. Especially Suhrmann and co-workers, e.g., *Z. Elektrochem.*, **63**, 155 (1959).
2. F. Fischer, *Ann. phys.*, **20**, 503 (1906).
3. A. Coehn and H. Juergens, *Z. Phys.*, **71**, 179 (1931).
4. D. P. Smith, "Hydrogen in Metals," University of Chicago Press, Chicago (1948).
5. C. A. Knorr and E. Schwartz, *Z. Elektrochem.*, **39**, 281 (1933).
6. Just as this paper was being submitted an abstract of a paper given by Knorr and Roemer at the Bunsen-Meeting 1959 in Darmstadt/Germany on "Dependence between Polarization Resistance and Resistance of Hydrogen-Containing Palladium Wires" was received.
7. A. Coehn and W. Specht, *Z. Phys.*, **62**, 1 (1930).

Brief Communication

Measurement of the Segregation Coefficients of Impurity Elements in Aluminum Antimonide

D. Hazelby and J. L. Parmee

B.T.H. Group Research Laboratory, Rugby, England

Some approximate figures have already been quoted (1) for segregation coefficients in aluminum antimonide, but it was considered necessary to obtain accurate values for those elements which influence the electrical properties of the compound, and also those which are common impurities.

The technique adopted was to use radioactive tracers, prepared by irradiating each impurity in the B.E.P.O. pile at Harwell. Since no suitable isotope of carbon could be made by this method, carbon-14 was obtained from the radiochemical center at Amersham. It was found convenient to measure activities with a liquid counter. As the energy of the beta radiation from carbon-14 and from sulfur-35 was too weak to be detected with this counter, they were precipitated with carriers as barium sulfate and carbonate, respectively, and measured with an end window Geiger counter. Magnesium was used in the inactive form and estimated with a mass spectrograph, although the accuracy of this method was somewhat less than would be obtained by the radiochemical method.

The impurity concentration at any point along an ingot produced by normal freezing is

$$C = kC_o\,(1-g)^{k-1} \qquad [1]$$

where C is the concentration at the point where a fraction g of the ingot has solidified, C_o is the original concentration in the melt, and k is the segregation coefficient.

At the front of the ingot, where g is almost equal to zero, the equation becomes

$$C = kC_o \qquad [2]$$

Thus, by measuring the concentration at the front of the ingot and the average concentration, k can be determined.

The conditions of our experiment did not conform strictly to those required for equilibrium segregation and so the measured values of k can be regarded only as observed values, i.e., as would be encountered in practice.

Milligram quantities of each impurity element were melted by high-frequency induction heating with 35 g of aluminum antimonide in a "Purox" alumina boat in an atmosphere of pure, dry argon. The melt was held at 1200°C for 5 min, during which time the stirring induced by the high-frequency field produced thorough mixing. The boat then was drawn out of the furnace at a rate of 5 in. hr^{-1}, causing normal freezing along the whole length of the charge.

The front 5% of the ingot was cut off, and this and the remaining piece weighed and dissolved in a mixture of hydrochloric and nitric acids. A suitable aliquot was taken from each solution and the activity was measured. The activity of the smaller piece gave the concentration of the front of the ingot C, and that of the larger piece was taken to be the average concentration C_o. The slope of the normal freezing curve at the front of the ingot is small for all values of k; there is thus no significant loss of accuracy in taking C to be the average concentration of the front 5%. The segregation coefficients of several elements are quoted in Table I.

It was noticed in some cases that an appreciable amount of activity was being lost by volatilization. Consideration of vapor pressures indicated that this was likely with zinc, cadmium, sulfur, selenium, and tellurium. This loss increased along the length of the ingot, being greatest at the end which was last to freeze, and so lowered the impurity concentration and hence the measured value of C_o. This gave a very high apparent value for the segregation coefficient, using Eq. [2].

In the practical use we are interested in the overall purification by both evaporation and segregation.

Table I.

Impurity element	Segregation coefficient	Purification factor
Magnesium	0.1	
Carbon	0.6	
Silicon	0.1	
Germanium	1.2	
Tin	1.0	
Iron	0.02	
Copper	0.01	
Manganese	0.01	
Cobalt	0.002	
Zinc		0.02
Cadmium		0.002
Sulfur		0.003
Selenium		0.003
Tellurium		0.01

This can be obtained by taking the ratio of the concentration of the activity in the front 5% of the ingot, to that of the impurity originally added, and gives an indication of the purification obtained under conditions in which volatilization is occurring. These ratios, which we have described as purification factors, are also given in Table I. Although they are clearly dependent on the conditions of the experiment, they do give an indication of the behavior of these impurities that could be expected on zone refining aluminum antimonide.

Acknowledgments

The authors express indebtedness for encouragement and assistance in this work to colleagues in the B.T.H. Group Research Laboratory.

Manuscript received Oct. 12, 1959.

Any discussion of this paper will appear in a Discussion Section to be published in the December 1960 JOURNAL.

REFERENCE

1. W. P. Allred, B. Paris, and M. Genser, *This Journal*, **105**, 93 (1958).

Corrections

In the discussion of the paper by P. E. Lake and E. J. Casey, "The Anodic Oxidation of Cadmium, I. Mechanism of Film Formation," which appeared in the June 1959 JOURNAL, in column 1 on page 533 it should read $R_2 = \frac{I\,t'_p}{t_s + t'_p}$ rather than $R_2 = \frac{I\,t'_p}{t_s\,t'_p}$.

* * *

In the paper by B. Schwartz, "The Use of Organo-Substituted Hydrolyzable Silanes on Silicon Devices," which appeared in the October 1959 JOURNAL, the following corrections should be made:

Page 871, column 1, paragraph 2, line 4—". . . while R is an organic . . ." should read ". . . where R is an organic . . ."

Page 871, column 2, paragraph 1, line 5—". . . this technique is the one preferred to . . ." should read ". . . this technique is the one referred to . . ."

Page 872, Table I, column 6, and Table III, column 1—"I_b, μa" should read "I_b, $m\mu a$"

Page 873, column 2, paragraph 3, line 3—". . . creating a silicon coating on the surface . . ." should read ". . . creating a silicone coating on the surface . . ."

Page 873, Reference 3—"*General Electric Rec.*" should read "*General Electric Rev.*"

Observations on the Fe-Cr-O System

A. U. Seybolt

Research Laboratory, General Electric Company, Schenectady, New York

ABSTRACT

An isothermal phase diagram for the Fe-Cr-O system is presented for 1300°C which, with a minor modification, holds for 1000°C. It is observed that Fe-Cr alloys containing over 13% Cr are in equilibrium with Cr_2O_3 containing a little dissolved Fe_2O_3. Alloys of lower chromium content are in equilibrium with iron chromite of variable composition of the type $FeCr_2O_4$. Evidence is presented indicating that when the spinel forms next to the metal a pronounced internal oxidation occurs. However, higher chromium alloys with Cr_2O_3 next to the metal show no tendency for internal oxidation. An oxygen pressure-composition diagram for the entire system is also presented. Marker experiments made during the oxidation of 20% Cr and 30% Cr alloys suggest that Cr_2O_3 is formed almost entirely by cation (Cr^{+3}) diffusion.

Many investigators have been concerned with the oxidation kinetics of the industrially important Fe-Cr alloys. However, before the kinetics can be evaluated properly, the equilibria involved should be well established. The work of Yearian, Randell, and Longo (1), conducted between 700° to 1160°C, was primarily a kinetic study, but these workers presented an approximate phase diagram which agrees in many essentials with the present investigation and with the slightly later work of Woodhouse and White (2). The investigation of Yearian, *et al.* (1) as just mentioned was not primarily an equilibrium study, and in addition the scales they observed were influenced by the presence of significant amounts of manganese, silicon, and carbon in the commercial steels they studied.

The work of Richards and White (3), and in particular the closely related investigation of Woodhouse and White (2), presented considerable information on equilibria in this system. Only very little of the findings of Richards and White (3) can be compared directly with the present study since these investigators were more concerned with the effects of rather wide variation in temperature than with establishing phase boundaries at constant temperature, as in the present case. In addition, they studied equilibria which were stable in the partial pressure of oxygen in air. On the other hand, their qualitative findings relating to the M_2O_3-M_3O_4 equilibria are in agreement with results presented here.

However, the tentative isothermal phase diagram presented by Woodhouse and White (2) (for temperatures between 560°C and the solidus) can be compared directly and qualitatively with the present investigation. It should be emphasized that Woodhouse and White considered their Fe-Cr-O isothermal phase diagram as only semiquantitative. Considering the limited amount of information available to these investigators, it is remarkable that their estimation of the nature of the system should agree so well, on a qualitative basis, with the findings to be reported in the present investigation. This agreement is particularly remarkable in view of the fact that Woodhouse and White conducted no equilibrium studies involving a metal phase, but confined themselves experimentally to the study of oxide equilibria.

It would require an inordinate amount of space to review in detail the results of the various observations made on the oxidation of Fe-Cr type materials, including stainless steels. However, the nature of the scales observed in a few of the more significant papers might be listed briefly. Rickett and Wood (4) oxidized 12-28% Cr-Fe alloys in oxygen at 980° and 1090°C and found spinel ($FeCr_2O_4$) and Cr_2O_3 on the inside and Fe_2O_3 on the outside of the scale. The nature and number of the layers depended on chromium content and temperature. McCullough and Fontana (5) found that on stainless steels heated in oxygen to 980°C spinel formed next to the metal, but as the oxidation proceeded Fe_2O_3 was predominant in the scale. Caplan and Cohen (6) used commercial Fe-Cr alloys containing 11-26% Cr with 0.3% Si, and oxidized their alloys at 1600°F to 2000°F in dry and moist air. Cr_2O_3 and spinel in various proportions were observed as the principal scale components. No essentially pure iron oxides, such as Fe_2O_3, were observed apparently under the conditions of their experiments. Moreau (7) studied a wide range of Fe-Cr alloys at 800°-1250°C and is one of the few authors who reports FeO as a stable oxide (mixed with $FeCr_2O_4$) next to the metal. Moreau apparently observed this mixed scale regardless of the chromium concentration. Yearian, Randell, and Longo (1) found practically all possible oxides depending on the parameters of composition and temperature. Their main findings can be summarized as characterizing two kinds of scale: type A (low rates of attack) consisting primarily of Cr_2O_3 with some dissolved Fe_2O_3, and type

B scales where attack is severe. In the latter scales, the spinel of the type $FeCr_2O_4$ is predominant.

In reviewing the literature of the oxidation of Fe-Cr alloys, the somewhat confused summary just presented is quite typical. This lack of agreement is due primarily to the fact that the types of scale formed are a sensitive function of temperature, chromium content, atmosphere, time of exposure, impurities present, and possibly other factors. However, it seems reasonably clear that the following oxides can be present depending on composition and oxygen partial pressure: FeO, Fe_3O_4, Fe_2O_3, Cr_2O_3, and $FeCr_2O_4$. These last two oxides require additional discussion. It has been established by Wretblad (8) and by others that Fe_2O_3 and Cr_2O_3 form a continuous series of solid solutions. In addition, Yearian, *et al.* (1) and Caplan and Cohen (6) found evidence for some Fe_2O_3 dissolved in the Cr_2O_3-type scales. The spinel $FeCr_2O_4$ is not necessarily stoichiometric, but this cubic oxide forms a solid solution series with Fe_3O_4. This has been demonstrated very well by Yearian, Kartwright, and Langenheim (9) who found that the lattice parameter of these solid solutions is not a single valued function of the composition, due to lattice sites being occupied differently as Cr^{+3} ions are replaced by Fe^{+3} ions.

In the work which follows, the primary object has been to outline the isothermal sections at 1000° and 1300°C. The oxygen equilibrium pressure is in general different in different parts of the system.

Experimental Methods

Fe-Cr alloys in the range 1-70% Cr were made using Ferrovac (vacuum-melted electrolytic iron) and hydrogen-treated electrolytic chromium. In order to maintain good control over composition, the alloys were prepared as 50-g buttons in an inert arc furnace. After homogenizing heat treatments at 1000°C or above in a hydrogen atmosphere during the processing, the alloys were mainly finished as hot-rolled (600°C) strip 0.015 in. thick. Samples used for the oxidation treatment were usually ½ x 1 in. rectangles, whose flat surfaces were abraded with various grades of wet or dry carborundum paper. The 180 grade of paper was found to be better than some of the finer grits because the oxide formed subsequently during high-temperature oxidation treatments tended to be better anchored to the sample. It was desired to keep the oxide on the metal surface to secure equilibration with the metal phase.

The general procedure for oxidation was to form a thin oxide layer on the surface and then to "equilibrate" the oxide with the metal by heating at 1000° or 1300°C in an argon atmosphere. By forming a comparatively thin oxide layer on the surface, insufficient metal was used up in forming the oxide to change the alloy composition appreciably, at least in most instances. Where considerable oxidation occurred, the experiment was repeated or the sample was not used for determining a phase boundary. True equilibration between the metal and oxide phase would require accurate control of the oxygen partial pressure and, in general, each Fe-Cr alloy would require a different oxygen pressure. However, as will be demonstrated shortly, most of the alloys are in equilibrium with Cr_2O_3 containing a small amount of Fe_2O_3. Since the dissociation pressure of Cr_2O_3 is so low, about 10^{-16} atm at 1300°C, the rate of breakdown of Cr_2O_3 in pure argon would be very small. Hence, the practical difference between controlling the oxygen pressure at 10^{-16} atm and using argon is negligible for equilibria involving Cr_2O_3. This same reasoning can be applied to cases where $FeCr_2O_4$ or more accurately, $Fe\ Fe_{(2-x)}\ Cr_xO_4$ [$x=O-2$] solid solution, is stable. This is true for compositions near $FeCr_2O_4$ but not for spinels of low chromium content. In the vicinity of Fe_3O_4 or Fe_2O_3, the dissociation pressure is sufficiently high so that rapid breakdown of the oxides in argon occurs.

The primary object of the phase equilibrium study was to establish the tie lines between metal phase and oxide phase. While the identification of the oxide-oxide equilibria was of secondary importance, it was possible to establish these boundaries also.

Alloy-Oxide Equilibration Experiments

It is obvious of course that as long as one is using alloys far removed from a phase boundary, the amount of chromium removed from the alloy during oxidation is not critical. However, if one is close to a critical composition, one should not remove an appreciable fraction of chromium from the alloy if the phase boundary is to be located with a high degree of accuracy. The accuracy aimed at was about ± 1% Cr.

In general, the small ½ x 1 in. strips were oxidized briefly in 1 atm of dry oxygen for 1-5 min at temperatures ranging from 600° to 1000°C depending on chromium content. The higher chromium alloys required more severe oxidizing conditions to secure enough scale for Debye camera x-ray or electron diffraction identification. After a few milligrams of oxide were formed on the surface, the samples were transferred to a furnace operated at 1000° or 1300°C and equipped with a vacuum-tight mullite tube containing a stagnant argon atmosphere. The equilibration treatment was usually at least 24-hr long and sometimes over 65 hr in duration. The samples standing on edge on a ceramic boat could be pushed into or out of the hot zone without disturbing the argon atmosphere. The object of the equilibration was twofold: (*a*) to allow sufficient time for the composition of the oxide to adjust to the equilibrium composition of the metal phase, and (*b*) to smooth out local concentration gradients in the metal at the metal/oxide interface. Because the surface of the alloy was robbed to some extent of chromium to form a chromium-containing scale, the equilibration treatment served to reestablish a uniform chromium content across the thickness of the sheet.

For very low chromium alloys where oxidation was severe, or in cases where better control over the degree of oxidation was necessary, samples were

sealed in SiO_2 capsules. In these capsules, samples were mounted on molybdenum brackets to prevent contact with SiO_2. Also sealed into the capsule was a small amount of FeO wrapped in iron foil. The Fe/FeO equilibrium pressure at 1300°C is about 10^{-11} atm, which was more than enough to stabilize any equilibrium scale in the entire system. These capsules were partially filled with purified argon, after exhausting the air, to prevent collapse of the SiO_2 at 1300°C. Equilibrations usually were carried out on the encapsulated samples by again encapsulating them in a SiO_2 tube without the FeO.

Experimental Results

Oxidizing and equilibrating runs are summarized in Tables I and II, which give x-ray and electron diffraction results, visual and metallographic observations at 1000° and 1300°C, respectively. It will be noted that spinel solid solution ($FeFe_{(2-x)}Cr_xO_4$) was formed at low chromium concentrations, and that Cr_2O_3 constituted the scale at high chromium contents; this was true both at 1000° and 1300°C. However, at a chromium level centering about 13%, both Cr_2O_3 and the spinel were sometimes observed. It will be noted, however, that as the chromium content gradually increases, the spinel pattern becomes weaker, and the Cr_2O_3 pattern becomes correspondingly stronger. This is indicated in both Table I and II.

It was sometimes observed that the color of the scale could be a very sensitive indicator of composition, particularly since Cr_2O_3 and the spinel are so different in color. Note the visual observations in center of Table I near 14% Cr. According to this, the critical composition for spinel or Cr_2O_3 formation is between 12.8 and 13.6% Cr, whereas the x-ray data showed no Cr_2O_3 for the 13.6% Cr alloy. This last result is probably due to the fact that x-ray diffraction frequently fails to indicate a phase present in minor amount.

While in the absence of a subscale two oxide layers would signify lack of equilibrium, this is not true for the subscales formed here in the vicinity of 13% Cr. This is because, as will be demonstrated shortly, at this composition a three-phase field makes its appearance. This three-phase field widens with increasing oxygen content, and it is therefore to be expected that if much internal oxidation occurs, both spinel and Cr_2O_3 as well as the alpha solid solution can coexist.

However, for this same reason it was desired, in establishing the critical Fe-Cr alloy composition which divides Cr_2O_3 scales from the spinel scales, to avoid excessive oxidation, both external and internal. This was necessary in order to shrink the composition width over which both oxides coexist to a point on the Fe-Cr binary boundary of the isothermal phase diagram. In order to accomplish this aim the capsule experiment described above under experimental methods was used. In this manner, by the use of the decomposition pressure of iron-saturated FeO at 1000° and 1300°C, it was possible to form such a thin film of oxide (about 200 $\mu g/cm^2$) that an inconsequential amount of chromium was used up. Hence, concentration variations across the critical chromium content could be avoided, and

Table I. 1000°C scaling experiments

% Cr analysis	Oxidation treatment	Equilibration in argon	X-ray or electron diffraction results	Visual & metallographic exam.	Run No.
0.954	1 min O_2 1000°C	24 hr 1000°C	Spinel		915
1.94	1 min O_2 1000°C	24 hr 1000°C	Spinel		916
2.87	1 min O_2 1000°C	24 hr 1000°C	Spinel		917
3.91	1 min O_2 1000°C	24 hr 1000°C	Spinel	Metallography qualitatively the same	918
4.95	1 min O_2 1000°C	24 hr 1000°C	Spinel + small amt. FeO		919
5.86	1 min O_2 1000°C	24 hr 1000°C	—		920
6.83	1 min O_2 1000°C	24 hr 1000°C	Spinel		921
7.90	1 min O_2 1000°C	24 hr 1000°C	—		922
8.84	1 min O_2 1000°C	24 hr 1000°C	Spinel + some αFe_2O_3		923
9.94	5 min O_2 1000°C	64 hr 1000°C	Spinel		927
10.78	5 min O_2 1000°C	64 hr 1000°C	Spinel		928
11.02	5 min O_2 1000°C	64 hr 1000°C	Spinel		929
12.8	5 min O_2 1000°C	64 hr 1000°C	Spinel	No sign of green Cr_2O_3	930
13.6	5 min O_2 1000°C	64 hr 1000°C	Spinel	Some green color	931
14.4	5 min O_2 1000°C	64 hr 1000°C	Cr_2O_3 + spinel	More green color	932
16.4	5 min O_2 1000°C	64 hr 1000°C	Strong Cr_2O_3 weak spinel		933
18.7	5 min O_2 1000°C	64 hr 1000°C	Strong Cr_2O_3 v. weak spinel		934
20	1½ hr O_2 1000°C	64 hr 1000°C	Cr_2O_3		853
30	1½ hr O_2 1000°C	64 hr 1000°C	Cr_2O_3		854
40	1½ hr O_2 1000°C	64 hr 1000°C	Cr_2O_3		855
48.3	1½ hr O_2 1000°C	64 hr 1000°C	Cr_2O_3		856
59.5	1½ hr O_2 1000°C	64 hr 1000°C	Cr_2O_3		857
68.0	1½ hr O_2 1000°C	64 hr 1000°C	Cr_2O_3		858
			Results of SiO_2 Capsule Experiments		
10.78	FeO 30 min 1000°C	48 hr 1000°C	Spinel		1018
11.02	FeO 30 min 1000°C	48 hr 1000°C	Spinel		
12.8	FeO 30 min 1000°C	48 hr 1000°C	Spinel		
13.6	FeO 30 min 1000°C	48 hr 1000°C	Cr_2O_3		

Table II. 1300°C scaling experiments

% Cr analysis	Oxidation treatment	Equilibration in argon	X-ray or electron diffraction results	Visual & metallographic exam.	Run No.
0.954	2 min O_2 800°C	24 hr 1300°C	Spinel	Metallographic results were essentially the same for all these alloys. Some Cr_2O_3 present.	948
3.91	2 min O_2 800°C	24 hr 1300°C	Spinel		951
4.95	1 min O_2 1000°C	24 hr 1300°C	Spinel		943
5.86	1 min O_2 1000°C	24 hr 1300°C	—		944
6.83	1 min O_2 1000°C	24 hr 1300°C	—		945
7.90	1 min O_2 1000°C	24 hr 1300°C	—		946
8.84	1 min O_2 1000°C	24 hr 1300°C	Spinel		947
9.94	5 min O_2 1000°C	24 hr 1300°C	—		938
10.78	5 min O_2 1000°C	24 hr 1300°C	Mostly spinel, some Cr_2O_3 SS*		939
11.02	5 min O_2 1000°C	24 hr 1300°C	—	Visual examination showed mostly spinel	940
11.02	1 min O_2 1000°C	88 hr 1300°C	Mostly spinel, some Cr_2O_3		969
12.8	5 min O_2 1000°C	24 hr 1300°C	Spinel + Cr_2O_3		941
12.8	5 min O_2 1000°C	24 hr 1300°C	Strong spinel, weak Cr_2O_3		957
12.8	1 min O_2 1000°C	88 hr 1300°C	—	Visual observation showed mostly spinel	970
12.8	5 min O_2 800°C	67 hr 1300°C	Spinel	Very thin film	995
13.6	5 min O_2 1000°C	64 hr 1300°C	Spinel + Cr_2O_3	Metallography showed nearly 100% Cr_2O_3	955
13.6	5 min O_2 1000°C	24 hr 1300°C	Stronger Cr_2O_3, weaker spinel	Metallography showed nearly 100% Cr_2O_3	958
14.4	1 min O_2 1000°C	88 hr 1300°C	Weak spinel, strong Cr_2O_3	Metallography showed nearly 100% Cr_2O_3	972
15.7	5 min O_2 1000°C	24 hr 1300°C	Weak spinel, strong Cr_2O_3	Metallography showed nearly 100% Cr_2O_3	960
16.4	5 min O_2 1000°C	24 hr 1300°C	Weak spinel, strong Cr_2O_3	Metallography showed nearly 100% Cr_2O_3	961
20	1½ hr O_2 1000°C	23 hr 1300°C	—	Cr_2O_3 only	896
30	1½ hr O_2 1000°C	24 hr 1300°C	Cr_2O_3		877
48.3	1½ hr O_2 1000°C	24 hr 1300°C	Cr_2O_3		879
68	1½ hr O_2 1000°C	24 hr 1300°C	Cr_2O_3		881
			Results of SiO_2 Capsule Experiments		
10.78	FeO, 30 min 1000°C	20 hr 1300°C	Spinel		1016
11.02	FeO, 30 min 1000°C	20 hr 1300°C	Spinel		
12.8	FeO, 30 min 1000°C	20 hr 1300°C	Spinel		
13.6	FeO, 30 min 1000°C	20 hr 1300°C	Cr_2O_3		

* Cr_2O_3-Fe_2O_3 solid solution.

single equilibrium scales could be observed by electron diffraction as recorded in the last part of Tables I and II.

X-ray and electron diffraction observations on "equilibrated" oxide films may be summarized by stating that the transition between the spinel at low chromium content and Cr_2O_3 at high chromium contents lies at about 13% Cr ± 0.5% Cr.

Metallography

Besides the primary tool of scale identification by x-ray or electron diffraction and the occasional assistance provided by visual color observations, metallography was found to be only second in importance to x-ray diffraction. It was found possible to make a sharp division more readily between compositions which form Cr_2O_3 and those which form spinel by this technique than by use of x-rays. The pronounced separation between these two classes of alloys was made possible by the fact that alloys which form the spinel show very prominent internal oxidation, while the alloys richer in chromium, which oxidize to Cr_2O_3, do not. This is made clear in the following photomicrographs (Fig. 1-8).

The oxidized strips were given an evaporated silver coating and after a flash of copper were nickel plated to prevent washing out of the oxide layer during metallographic preparation. Four different compositions were chosen to show characteristic scales for both spinel-type and Cr_2O_3-type oxidation. Two compositions near 5 and 10% Cr in the spinel region, one near the critical 13% Cr composition and one well into the Cr_2O_3 region are shown. Figures 1 and 2 show a layer of alpha iron next to the nickel plate. The black layer between the iron layer and the beginning of the internal oxidation is spinel. The reason for the presence of an iron layer appears to be as follows: Because the chromium content is

Fig. 1. 4.95% Cr oxidized 1½ hr, 1000°C; equilibrated 64 hr argon, 1000°C. Note layer of internal spinel. Magnification 100X before reduction for publication.

Fig. 2. 9.94% Cr oxidized 1½ hr, 1000°C; equilibrated 64 hr argon, 1000°C. Note layer of internal spinel. Magnification 100X before reduction for publication.

fairly low in these two alloys, some iron oxide, perhaps both Fe_2O_3 and Fe_3O_4, are formed during the oxidation treatment in pure oxygen gas. These oxides form at the surface, while the more stable spinel forms next to the metal. During the subsequent argon "equilibration" treatment the iron oxides decompose to pure iron because their dissociation pressures are quite high and, hence, the kinetics tend to be fast. However, the spinel with its very low dissociation pressure and sluggish decomposition kinetics remains after heating in argon. It is interesting to note that Fig. 3 shows both the internal oxide and areas where only the surface scale of Cr_2O_3 is present; hence this sample represents a transition structure. Since Cr_2O_3 shows a brilliant green under polarized light, while the spinel appears red to yellow depending on thickness, it was easy to ascertain that the surface scale was essentially pure Cr_2O_3 while the internal oxide was mostly all spinel. Some samples showed very small particles of Cr_2O_3 as an internal oxide which occurred with the more massive and prominent spinel. The existence of spinel above 13% Cr or of Cr_2O_3 below this concentration was always insignificant in amount compared with the major oxide present.

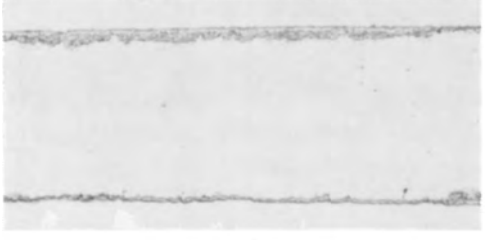

Fig. 3. 12.8% Cr oxidized 5 min, 1000°C; equilibrated 65 hr argon, 1000°C. Note transition scale: partly internal oxide, partly surface oxide. Magnification 100X before reduction for publication.

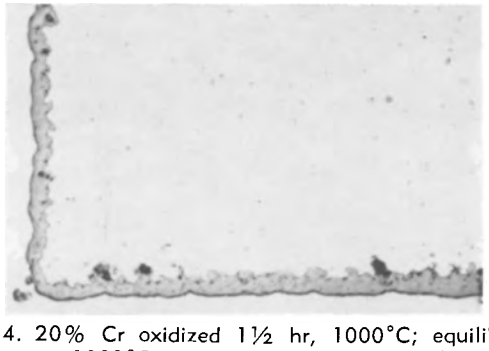

Fig. 4. 20% Cr oxidized 1½ hr, 1000°C; equilibrated 64 hr argon, 1000°C. All surface oxide. Internal oxide inclusions were present in sheet prior to oxidation. Magnification 500X before reduction for publication.

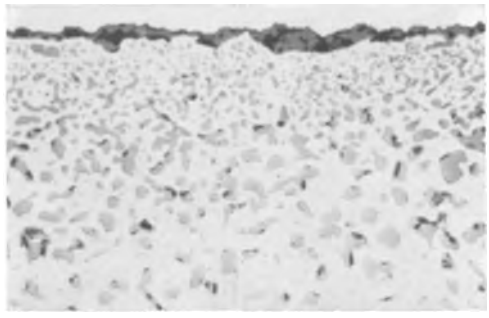

Fig. 5. 4.95% Cr oxidized 1 min, 1000°C; equilibrated 24 hr argon, 1300°C. Exaggerated internal oxidation apparently caused by some air leakage at 1300°C. Large particles are spinel. Magnification 500X before reduction for publication.

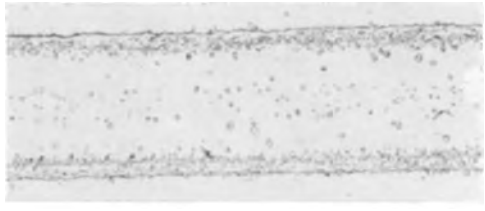

Fig. 6. 10.78% Cr oxidized 5 min, 1000°C; equilibrated 24 hr argon, 1300°C. Prominent internal oxidation. Oxide phase is spinel. Magnification 100X before reduction for publication.

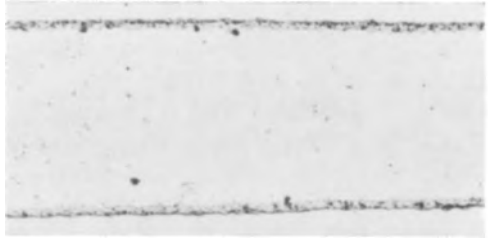

Fig. 7. 13.6% Cr oxidized 5 min 1000°C; equilibrated 24 hr argon, 1300°C. Note absence of internal oxidation. Magnification 100X before reduction for publication.

Therefore, it caused no confusion in interpretation, nor in allowing the choice of about 13% Cr as the critical chromium concentration. Although not shown here, there was essentially no difference in scale appearance nor in its kinetics of formation once the chromium content exceeded about 20%.

Figure 8 is of particular interest from the standpoint of oxidation mechanism. It is shown here that a 1-mil platinum wire spot-welded to a 30% Cr-Fe strip becomes covered with Cr_2O_3 during oxi-

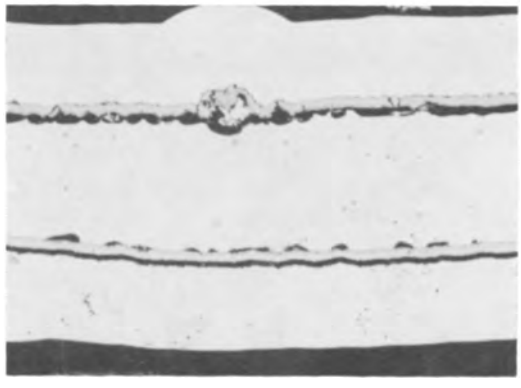

Fig. 8. 30% Cr oxidized 1½ hr, 1300°C; equilibrated 22½ hr argon, 1300°C. Note oxide covering platinum marker. Magnification 100X before reduction for publication.

Table III. Per cent Fe_2O_3 found in Cr_2O_3 scales

Alloy	Oxidation	Equilibration	% Fe_2O_3 in scale
1st sample 20% Cr-Fe	5 min 1000°C—O_2	1000°C—45 hr argon	2.7
			2.3 (check analysis)
	5 min 1000°C—O_2	1300°C—40 hr argon	0.32
		1300°C—40 hr argon	0.7 (check analysis)
2nd sample	5 min 1000°C—O_2	1000°C—64 hr argon	2.57
	5 min 1000°C—O_2	1300°C—16 hr argon	0.46

dation at 1300°C. It will be noted that many (Kirkendall) voids were formed just below the oxide layer, suggesting one-way diffusion of chromium to the scale without any countercurrent diffusion into the alloy. This observation corroborates the platinum marker behavior. Identical behavior was observed at 1000°C except that no voids just below the scale were observed. In addition, the same behavior was noted at both temperatures for a 20% Cr-Fe alloy. Since no oxide at all was formed underneath the wires, the tentative conclusion is that Cr_2O_3 on binary Fe-Cr alloys forms by cation (Cr^{+3}) diffusion, and that no appreciable diffusion of oxygen anions occurs from the gas phase. This mechanism is also suggested by the nature of the defect structure of Cr_2O_3 (10, 11).

Composition of the Two Equilibrium Scales

It has been shown above that from x-ray and metallographic evidence only two kinds of scale can be in equilibrium with binary Fe-Cr alloys: iron chromite or spinel below about 13% Cr, and Cr_2O_3 above this composition. So far, however, no evidence has been presented on the composition of these scales. To check the amount of Fe_2O_3 dissolved in Cr_2O_3, the following experiment was carried out. Two different samples of 20% Cr-Fe sheet were given a thin scale of Cr_2O_3 by a 5-min oxidation treatment in pure oxygen at 1000°C. The oxide film thus formed was equilibrated in argon at 1000° and 1300°C with the results indicated in Table III.

An alloy well over 13% Cr was chosen deliberately so that, in forming some Cr_2O_3 on the surface, the alloy would not be robbed of chromium to the point where spinel would make its appearance. However, on the basis of experience obtained in these experiments, it seems safe to assume that the nominal 20% Cr was not altered significantly by the very short oxidation treatments given this alloy. The reason for the lack of agreement between the check analyses at 1300°C must lie in the analytical technique since it was the same sample of scale. However, the main point is that if 0.5% Fe_2O_3 is taken as the average for the solubility of Fe_2O_3 in Cr_2O_3 on a 20% Cr alloy scale at 1300°C then there is an increase by a factor of five in Fe_2O_3 content by lowering the temperature to 1000°C.

The lattice parameters of the spinel phase from pure Fe_3O_4 to $FeCr_2O_4$ has been studied by Yearian, Kartwright, and Langenheim (9) as mentioned previously. While lattice parameters in this system cannot be used alone as an indication of composition, it can be used in conjunction with auxiliary information. For example, if the composition of the spinel is between approximately $Fe_{1.7}Cr_{1.3}O_4$ and $FeCr_2O_4$, one then can make use of the data of Yearian, *et al.* (9) to find the spinel composition. Fortunately, it developed that a key spinel composition fell within this range. Therefore, it was possible by suitable oxide phase equilibrations to determine all of the most important phase boundaries in the isothermal section. Before proceeding with the spinel equilibria and spinel compositions, it will be helpful to show the isothermal section of the Fe-Cr-O system at 1300° or 1000°C (Fig. 9). All of the evidence (except the maximum Fe_2O_3 solubility in Cr_2O_3) points to essentially no shift in phase boundaries between these two temperatures. At least any shift, if it occurs, seems to be less than 1% in composition. Starting at the top of the diagram, the first horizontal line joining Fe_2O_3 and Cr_2O_3 represents the continuous series of solid solutions formed by these two oxides. Just below it is the horizontal join between Fe_3O_4 and $FeCr_2O_4$; the latter composition is denoted at point S_3 in Fig. 9. The Fe_3O_4-$FeCr_2O_4$ join has a finite width according to the accepted Fe-O phase diagram and according to Yearian, *et al* (9). These authors find that $FeCr_2O_4$ contains a maximum of 0.002 cation vacancies per mole or about 2.9% vacancies, corresponding to somewhat less than 2 a/o maximum excess oxygen. Fe_3O_4 at 1300°C appears to have a homogeneity range of approximately 0.6 a/o oxygen (13). This indicates that the Fe_3O_4-$FeCr_2O_4$ join is actually a narrow band of something like 1 a/o oxygen average width. This width is indicated by the extra heavy line in Fig. 9.

The diagram can best be described by referring to the three, three-phase fields starting at the left with γ Fe, FeO, spinel and then proceeding to the right to the α Fe, γ Fe, spinel, and finally to spinel,

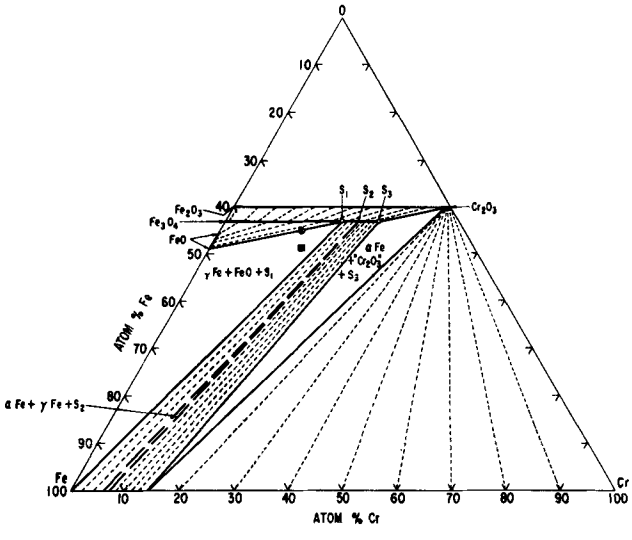

Fig. 9. Isothermal phase diagram at 1300°C for Fe-Cr-O system.

α Fe or (13 wt % Cr-Fe), "Cr_2O_3". The quotation marks around Cr_2O_3 refer to the fact that this oxide contains some Fe_2O_3 in solution. It has already been demonstrated that there are two kinds of two-phase equilibria involving the metal phase: Fe, spinel; and Fe, "Cr_2O_3." It will, of course, be understood that the spinel is of different composition in each of the three-phase fields mentioned above, and that its composition as a scale is a function of the alloy composition.

Spinel-FeO Equilibria and the Adjoining Spinel-FeO-Fe Equilibrium

The spinel composition S_1 corresponds to approximately $Fe_{1.5}Cr_{1.5}O_4$ or 21.4 a/o Cr as against 28.6 a/o Cr for $FeCr_2O_4$(S_8). The location of point S_1 was determined by heating together FeO (high iron) and $FeCr_2O_4$ at 1300°C. Samples were prepared by mixing −200 mesh FeO powder prepared by H_2/H_2O treatment of Fe_2O_3, and $FeCr_2O_4$ prepared by synthesis from FeO and Cr_2O_3. The starting composition was 50% by weight FeO and 50% by weight $FeCr_2O_4$. In one experiment the 2-g pressed compact was heated to 1300°C in argon for 20 hr with some FeO present to supply a small oxygen pressure. Metallographic examination and x-ray diffraction results showed a mixture of FeO and spinel of lattice parameter 8.398Å. The original lattice parameter of the $FeCr_2O_4$ used had a lattice parameter of 8.377Å which agrees with the value given by Yearian, *et al.* (9) for stoichiometric spinel. Yearian's curve shows that, if the composition is near $FeCr_2O_4$, a lattice parameter of 8.398Å corresponds to $Fe_{1.5}Cr_{1.5}O_4$ or 21.4 a/o Cr as indicated above. Chemical analysis of this oxide mixture yielded 49.5% total iron, 0% free iron, and 23.2% Cr. This analysis corresponds to 29.1 a/o Fe and 14.7 a/o Cr. If this composition is plotted on the isothermal section, it falls on the phase boundary between FeO and point S_1, as it should, at the spot marked with a circled X. Hence, the lattice parameter-located point S_1 agrees with the chemical analysis of the oxide mixture.

Two additional 50-50 wt % mixtures of FeO-$FeCr_2O_4$ were made at 1300°C but sintered in argon without using FeO to supply some oxygen. In these cases some decomposition of the FeO allowed the formation of free iron, resulting in one instance in the following analysis: free iron, 14.6%; total iron 51.6%; chromium, 24.7%. Plotting this point in terms of atom per cent results in the point in the three-phase field marked with an x inside a square. The lattice parameter (8.397Å) of spinel phase in all these three-phase compacts was within the experimental error the same as in the two-phase mixture.

Figure 10 shows the microstructure of the three-phase FeO + spinel + Fe specimen. The bright spots are iron and the lighter of the two oxide phases is the FeO phase. It will be noted that the dark chromite phase is completely surrounded by the FeO, and that it has many flat sides and sharp corners evidently indicating crystallographic growth from a liquid. Therefore, it appears that this composition touches the solidus surface at 1300°C. Not enough liquid was formed to allow deformation of the pressed compacts; there was no slumping or rounding off of sharp edges.

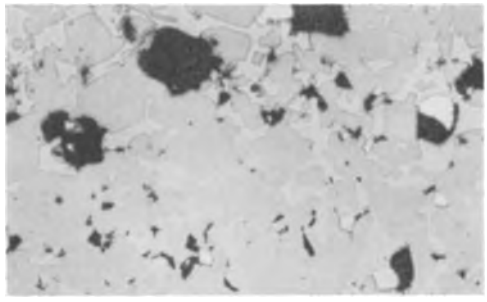

Fig. 10. αFe(γ at temperature), FeO, and spinel, demonstrating three-phase equilibrium. As polished. Black areas are voids. Magnification 250X before reduction for publication.

The FeO-$FeCr_2O_4$ experiments just cited seem to leave no doubt that the three-phase region of FeO, spinel, Fe exists as shown with the spinel composition as given above.[1] Furthermore, there appears to be no doubt that FeO of variable composition is in equilibrium with spinel of variable composition, as indicated qualitatively by the dotted tie lines. It must be emphasized, however, that these tie lines are purely qualitative, and are shown for purposes of illustration only; the precise location of these lines has *not* been determined.

Spinel-Rhombohedral Solid Solution Equilibria

The existence of this equilibria was first demonstrated by Richards and White (3), and was observed here by heating an equimolar mixture of Fe_3O_4 and Cr_2O_3 at 1800°C for 1 hr in a gas kiln. X-ray diffraction of the resulting body showed a mixture of iron chromite (spinel) and rhombohedral solution of approximately 50% Cr_2O_3 by weight. It was not possible to estimate the composition of the spinel phase from the x-ray pattern.

Figure 11 shows the microstructure of the spinel and rhombohedral solid solution compact. The black areas are voids (as in Fig. 10). The light phase which has formed on the boundary of the grains is the rhombohedral solid solution, and the darker of the two oxides is the spinel or chromite phase. Evidently at 1800°C the structure was principally spinel, but

[1] *Note added after MS preparation*: Birchenall (12) has evidence that in very dilute Fe-Cr alloys containing about 0.2% Cr, a FeO layer is formed *below* the spinel layer, e.g., next to the alloy. This evidently indicates a small amount of Cr solubility in FeO, and makes necessary a narrow two-phase region of gamma Fe solid solution—$FeO_{(Cr)}$ along the inside of the Fe-O side of the isothermal phase diagram (Fig. 9).

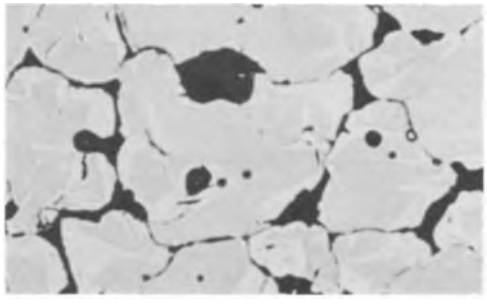

Fig. 11. Spinel (dark) plus Cr_2O_3-Fe_2O_3 solid solution (light). Black areas are voids. As polished. Magnification 500X before reduction for publication.

on cooling to lower temperatures the spinel becomes more susceptible to oxidation to the rhombohedral solid solution. Nucleation of the rhombohedral solution evidently occurred at the edges of the spinel grains where there was ready access to air, and as cooling progressed, the rhombohedral solid solution fingered into the interior of the cubic iron chromite (spinel) grains.

It has already been mentioned in connection with the spinel-FeO equilibria that the location of the tie lines were not determined but are only shown approximately for purposes of illustration. The same statement must be made about the spinel-rhombohedral solid solution equilibria. The tie lines could be established if it were possible to analyze either of these two equilibrium oxide systems for chromium, and both bivalent and trivalent iron. However, no current technique seems to be available for dissolving such oxide mixtures without oxidizing the Fe^{+2} to Fe^{+3}. In principle, probably it would be possible to obtain these tie lines merely from a knowledge of the chromium and total iron content together with lattice parameter measurements. This procedure, however, would have at least two drawbacks: (*a*) because of the lattice parameter of the spinel phase is not a single-valued function of composition, some trial and error would be involved, and (*b*) in some of the oxide mixtures the x-ray diffraction patterns may not be of sufficiently good quality to obtain the precision needed.

α Fe-γ Fe-*Spinel Equilibrium*

Spinel composition S_2 is the oxide in equilibrium with both ferrite and austenite as demanded by the Fe-Cr binary phase diagram.

In Fe-Cr binary alloys at 1300°C the alpha plus gamma region extends from about 6% Cr to 7% Cr as judged from the curve shown by Hansen's (13) recent review. Hence, there must be a three-phase triangle based on approximately 6% Cr and 7% Cr with the apex lying at some point S_2 on the spinel solid solution. An attempt was made to obtain a lattice parameter from the spinel "equilibrated" with an alloy lying near the critical chromium composition, but the grain size of the oxide was too fine to exhibit a satisfactory diffraction pattern. Hence, point S_2 in Fig. 9 is shown as lying approximately midway between points S_1 and S_3.

Equilibrium Oxygen Pressure as a Function of Composition

Figure 12 shows a pressure-composition diagram based mainly on data available in the literature, but to some extent on information obtained in this investigation. These data are marked with filled circles.

The pressure level of the α Fe-spinel-rhombohedral oxide equilibrium where log $Po_2 = -13$ was calculated from the equation given by Richardson, Jeffes, and Withers (14): $2FeCr_2O_4 = 2Fe + O_2 + 2Cr_2O_3$ $\Delta F = +131{,}600 - 24.2T$ and from the relation $\Delta F = -RT \ln K$. Although Richardson, *et al.*, were apparently not aware of it, this reaction should be written in some manner to indicate that it is not pure iron here, but a solid solution of 13% Cr in Fe.

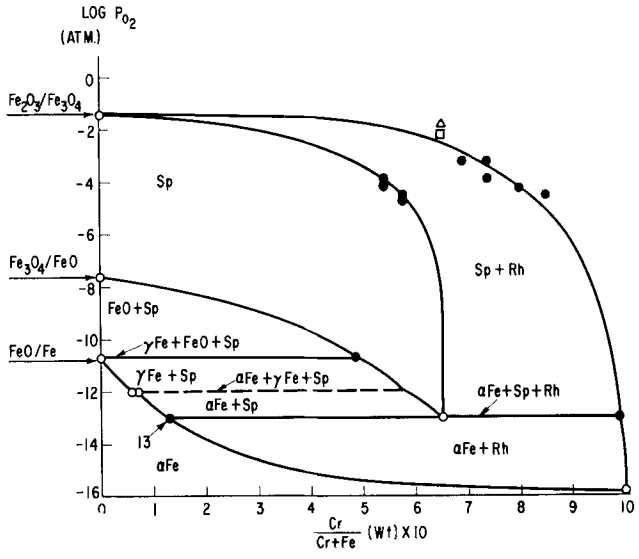

Fig. 12. Oxygen pressure-composition plot for 1300°C. Sp, spinel (based on $FeCr_2O_4$); Rh, rhombohedral (Fe_2O_3-Cr_2O_3) solid solution; αFe, pure bcc Fe or bcc Fe-Cr solid solution; •, this investigation; O, various sources, △, Schmahl; □, calculated from Richardson, et al.

This equilibrium is graphically shown as the lowest reaction horizontal in Fig 12. The left-hand terminus is the 13% Cr-Fe composition as explained above, and at the right-hand end is shown the 0.5% Fe_2O_3 in solution in Cr_2O_3.

It should be mentioned that the composition axis of this figure is the fractional weight chromium X10, referred to the metallic constituents only.

The α Fe, γ Fe, spinel equilibrium pressure has not been determined, but its left-hand terminus is at approximately 6-7% Cr at 1300°C as given by the binary phase diagram.

The top reaction horizontal corresponding to γ Fe, FeO, spinel equilibrium has a pressure level determined by the established Fe/FeO equilibrium pressure, and its right-hand terminus is at a value of 48.5% Cr or a Cr/Cr + Fe × 10 value of 4.85.

In the spinel + rhombohedral solution two-phase region in the top of the drawing, several experimental points are shown which were obtained by controlled pressure oxidation of $FeCr_2O_4$ (see Table IV). Small pellets of $FeCr_2O_4$ powder were heated to 1300°C for various periods of time using oxygen pressures varying from 15 μ to 500 μ, obtained by a variable vacuum leak.

The datum point (open square) near the curve describing stability for the rhombohedral solution

Table IV. Controlled oxidation of $FeCr_2O_4$ at 1300°C

O_2 pressure, microns	Log Po_2, atm	Oxidation time, hr	Lattice parameter (a_o) and Cr wt ratio a_o	$\frac{Cr}{Cr+Fe}$	Rhombohedral oxide Cr/Cr + Fe wt ratio based on high angle line measurements
15	—4.70	24	8.3851 ±.0005	0.575	Too diffuse
25	—4.48	8	8.3848 ±.001	0.575	0.85-0.90
50	—4.18	8	8.3909 ±.002	0.54	0.80-0.83
100	—3.88	8	8.389 ±.002	0.54	0.74
500	—3.18	24	Too weak		0.69
500	—3.18	3	No pattern		0.74

was calculated from the Richardson, *et al.* equation plus the following two:

$$2Fe_2O_3 = 4Fe + 3\ O_2 \text{ and } 2Fe_2O_3 \cdot 4Cr_2O_3 =$$

$$2Fe_2O_3 + 4Cr_2O_3$$

The free energy for this last equation was calculated on the basis of an ideal solution. In view of the fact that there is a complete series of solid solutions between Cr_2O_3 and Fe_2O_3, the assumption of ideality might be approximately correct. In any case, the free energy change involved in the formation of the $Fe_2O_3 \cdot 2Cr_2O_3$ solid solution must be small compared to the other processes involved.

By summing up the above equations of known ΔF, one arrives at the change in free energy for the following equation

$$2Fe_2O_3 \cdot 4Cr_2O_3 = 4FeO \cdot Cr_2O_3 + O_2$$

$$\Delta F = +124{,}250 - 68.7T$$

Solving for ΔF for 1300°C (1573°K) and substituting in $\Delta F = -RT \ln K = -RT \ln Po_2$, one finds $Po_2 = 4.48$ mm and log Po_2 in atmospheres is −2.23. This oxygen pressure is that required to oxidize completely the spinel of composition $FeO \cdot Cr_2O_3$ to the rhombohedral oxide of identical Cr/Fe ratio at 1300°C. In addition, Schmahl (15) has given an oxygen pressure for the dissociation of $Fe_2O_3 \cdot 2Cr_2O_3$ at 1323°C as 1.05×10^{-2} atm or log $Po_2 = -1.79$. This is plotted as an open triangle just above the open square point. Because his data refers to 1323°C, this point should be somewhat too high, as it is. Hence, it appears to be essentially in agreement with the Richardson, *et al.* point as calculated above.

It should be emphasized that the data plotted in this region are not of high accuracy, and in particular, the composition estimates of the rhombohedral solution from x-ray data are of poor accuracy, mainly because of poor x-ray photograms. However, the fact that these points cluster reasonably well to a smooth curve passing close to the other data (open points) offers some assurance that the experimental points may not be too far off.

The course of the curves bounding the two phase spinel + rhombohedral region provides the information necessary for establishing the tie lines between these two phases on the isothermal phase diagram, Fig. 9. However, in view of the questionable accuracy of these curves, it seems hardly worthwhile to attempt to draw in "accurate" tie lines. Anyone interested can do this readily from the information given.

Rate of Internal Oxidation in 5% Cr-Fe and in 10% Cr-Fe Alloys

Some measurements were made in the above two alloys on thick samples (about 0.2 in. thick) at 1000° and 1300°C. Fairly thick samples were chosen so that the diffusion distance would be small compared to the sample thickness. The samples were rectangular in shape and were encapsulated in SiO_2 with iron-saturated FeO as an oxygen source. The depth of penetration of the spinel subscale is shown in Table V.

Table V. Rate of penetration of spinel subscale

1000°C	Hours	Penetration, cm
5% Cr	20	0.0034
	40	0.0045
10% Cr	20	0.0031
	40	0.0048
1300°C		
5% Cr	1	0.0058
	64	0.0250
10% Cr	1	0.0071
	2	0.0071
	4	0.0150
	8	0.0155
	64	0.0451

Results at 1000°C are not very meaningful since the accuracy of measurement was poor. However, in the case of the 10% Cr alloy at 1300°C, it is possible to demonstrate that the data plotted as cm vs. $t^{1/2}$ yield a straight line which passes through the origin. If time is plotted in seconds, the slope is found to be about 7×10^{-8} cm²/sec. Evidently the rate of progress of the subscale layer is diffusion controlled, as would be anticipated. However, there is insufficient knowledge about concentration gradients in the layer to be able to calculate an oxygen diffusion rate.

Discussion

It seems clear that the disparity between various investigators' work in the results of Fe-Cr alloy scaling experiments lies in the nonequilibrium nature of such experiments. Evidently there was not always a full realization that very significant changes in alloy composition occurred during the progress of an oxidation run. These alloy composition changes are reflected in changes in the nature of the scale formed.

Another complication is caused by a tendency for the scale to separate from the alloy. When this can occur, the tendency for nonequilibrium scales is enhanced since there is poor contact between metal and scale. This means that a scale can exist in a higher state of oxidation than would be possible in contact with the alloy.

Thermodynamically, the scales of lowest oxygen pressure lie closest to the metal, and the scale nearest the gas phase must be of highest dissociation pressure. In a nonequilibrium experiment, if Cr_2O_3, "Fe Cr_2O_4," and Fe_2O_3 are all found in the scale, they must be present in the order listed from metal to gas phase. This order can be seen in Fig. 12. It can be seen also from Fig. 12 that during air oxidation one should not observe spinel as the outermost layer of scale for any Fe-Cr alloy because the spinel is only stable at very low oxygen partial pressures.

The actual scales observed will depend in large measure on the severity of the oxidation, which for any chromium level might be measured by the per cent chromium converted to various oxides. Yearian, *et al.* (1) recognized the so-called A and B types of scale representing a difference in the amount of oxidation. Under light oxidation, a 20% Cr alloy will only show the equilibrium Cr_2O_3 scale. With

more drastic conditions; higher temperature, longer time or possibly higher oxygen pressure, the chromium present is not adequate to prevent iron oxides from forming. In this case, one expects an outer layer of nearly pure Fe_2O_3, next a spinel layer, and finally a Cr_2O_3-Fe_2O_3 rhombohedral solid solution of variable composition.

The occurrence of different layers of variable composition will be expected, depending on the parameters just mentioned, plus specimen geometry. Therefore, there is no fundamental significance in reporting a specific series of layers in a scale unless all the variables are very closely specified, and unless the precise thickness and composition of each layer are well documented. This has not often been done in the past. What is needed at present in this and in other systems is a better characterization of the individual layers, including their defect structure and, of particular importance, their mode and rate of growth. This would probably entail controlling oxygen pressure so that the growth characteristics of a single layer could be studied.

From a practical point of view, the appearance of Fe_2O_3, or of iron chromite, during the oxidation of Fe-Cr base alloys is evidence of failure. Either the chromium content was too low, the temperature too high, or the time of exposure too long. There is good evidence that various small additions to the Fe-Cr type alloy can improve their oxidation resistance appreciably, but this will be reported elsewhere.

Finally, one must be cautious about translating results of oxidation behavior in pure oxygen to the behavior in air. The nitrogen content of air appears to play a significant role in the structures observed during the oxidation of Fe-Cr alloys. Chromium nitrides have been observed in Fe-Cr samples heated in air. This effect apparently has been little studied.

Summary and Conclusions

An isothermal section for equilibrium conditions at 1300°C in the Fe-Cr-O system has been presented. With the exception of a minor modification, this section also represents conditions at 1000°C. With the aid of this diagram, one sees that there are two types of equilibrium scale formed on Fe-Cr alloys: spinel or iron chromite below 13% Cr, and Cr_2O_3 containing a little dissolved Fe_2O_3 at higher chromium contents. With the additional information on the gamma iron-FeO equilibrium noted by Birchenall (12), this diagram agrees qualitatively with the one suggested by Woodhouse and White (2).

The oxidation mode for alloys in equilibrium with the spinel is mainly internal oxidation, at least at temperatures over 1000°C, while the oxidation mode for alloys over 13% Cr is formation of a surface oxide. This difference is of prime importance in regard to oxidation resistance. The rate of formation of the internal oxide at 1300°C is very rapid compared to the oxidation rate for surface Cr_2O_3. Since this is the case, alloys low in chromium content fail very rapidly, while the chromium-rich alloys are comparatively resistant to oxidation.

Platinum wire marker experiments seem to show that at 1000° or 1300°C the Cr_2O_3 on 20 or 30% Cr-Fe alloys forms almost entirely by cation diffusion. Oxygen diffusion from the gas phase apparently plays an insignificant role. This indicates that, to improve the oxidation rate of Fe-Cr base alloys, one should alter in some manner the rate of diffusion of Cr^{+3} in Cr_2O_3, such as by altering the nature of the defect structure of Cr_2O_3. The subject of the Cr_2O_3 defect structure cannot be expanded here, but for those interested in this subject the work of Hauffe and Block (10) and Fischer and Lorenz (11) should be mentioned.

Acknowledgments

It is a pleasure to acknowledge the general assistance of Mr. Leo Butler. The rather extensive x-ray data were obtained by Mrs. Rose DiCerbo and Mrs. Dorothy DeCarlo. Miss Eileen Alessandrini prepared many electron diffraction studies of the scales

Manuscript received July 31, 1959.

Any discussion of this paper will appear in a Discussion Section to be published in the December 1960 JOURNAL.

REFERENCES

1. H. J. Yearin, E. C. Randell, and T. A. Longo, *Corrosion*, **12**, 515t (1956).
2. D. Woodhouse and J. White, *Trans. Brit. Ceramic Soc.*, **54**, 365 (1955).
3. R. G. Richards and J. White, *ibid.*, **53**, 422 (1954).
4. R. L. Rickett and W. P. Wood, *Trans. A.S.M.*, **22** 347 (1934).
5. H. M. McCullough, M. A. Fontana, and F. H. Beck, *ibid.*, **43**, 404 (1950).
6. D. Caplan and M. Cohen, *Trans. AIME*, **194**, 1057 (1952).
7. J. Moreau, *Compt. rend.*, **236**, 85 (1953).
8. P. E. Wretblad, *Z. anorg. Chem.*, **189**, 329 (1930).
9. H. J. Yearian, J. M. Kortwright, and R. H. Langenheim, *J. Chem. Phys.*, **22**, 1196 (1954).
10. Karl Hauffe and Jochen Block, *Z. Phys. Chem.*, **198**, 232 (1951).
11. W. A. Fischer and Gert Lorenz, *Arch. Eisenhuttenw.*, **28**, 497 (1957).
12. C. E. Birchenall, Private communication.
13. M. Hansen, "Constitution of Binary Alloys," McGraw-Hill Book Co., New York (1958).
14. F. D. Richardson, J. H. E. Jeffes, and G. Withers, *J. Iron Steel Inst., London*, **166**, 213 (1950).
15. N. G. Schmahl, *Z. Elektrochem.*, **47**, 835 (1951).

A Model of the Mechanism of Electrochemical Conversion from Active to Passive States

W. A. Mueller

Physical Chemistry Division, Pulp and Paper Research Institute of Canada, Montreal, Quebec, Canada

ABSTRACT

A model is developed of the mechanism of passivation of metals by oxide films. It is based on the assumption of the formation of a passivating film caused by the reaction of OH^- ions with the metal surface. With increased potential the film-free area decreases exponentially and with a higher exponent than does the density of the anodic dissolution current. Thus in the conversion from the active to the passive state, the current density is reduced exponentially to the constant and very low value characteristic of the passive state. This mechanism of passivation is explained by equations which describe the density of the anodic dissolution current as a function of the pH and the potential difference between the metal and the electrolyte. Good agreement with the theory is shown by published data for iron, nickel, chromium, gold, and silver. A simple method is given to derive all the constants required for the mathematical formulation of the anodic dissolution current from experimental data. Flade's equation relating to the boundary potential between the active and the passive state of iron is discussed. The principles and formulas, although derived specifically for formation of oxide films, are considered also to be applicable to the electrochemical passivation by other films.

The mechanism of the reactions which cause the formation of a passivating film on metals is of basic interest in studying the nature of passivity. These reactions can be analyzed by means of partial polarization curves, if exact polarization curves in the potential range of the conversion from active to passive states are available. A detailed description of the analysis of polarization curves is being prepared for publication in another paper (1). This paper describes a model which allows an analysis of the density of the anodic dissolution current, particularly during the conversion from active to passive states. Equations are derived for the anodic dissolution current in the active state, for the conversion to the passive state and for the Flade potential (2) and these are used to interpret a series of pertinent empirical data.

The passivity of metals caused by the formation of an oxide film is the most important case of passivity; this is the case for which equations have been derived primarily. However, calculations for other types of passivating films of electrochemical origin may be made by using the same equations. Of primary importance is the inclusion of all known facts concerning the active and passive states.[1] These include the electrochemical properties of the anodic dissolution current from the active state through the Flade potential to the passive state.

Conditions for measuring accurate polarization curves in the potential range of the conversion from active to passive states have been derived before (3,4). Potentiostatic control prevents the state of instability expressed as a "jump of the potential." Accurate polarization curves measured potentiostatically in the potential range of the conversion from the active to the passive state were published previously for iron in a solution of 100 g/l NaOH and 35 g/l Na_2S (4). These curves, which were subsequently corroborated by Kesler (5), and Uusitalo (6), show an exponential increase of the current density with increasing potential in the active state (Fig. 1 and 3a). After reaching the maximum, the current density declines exponentially, thus demonstrating the conversion from active to passive states.

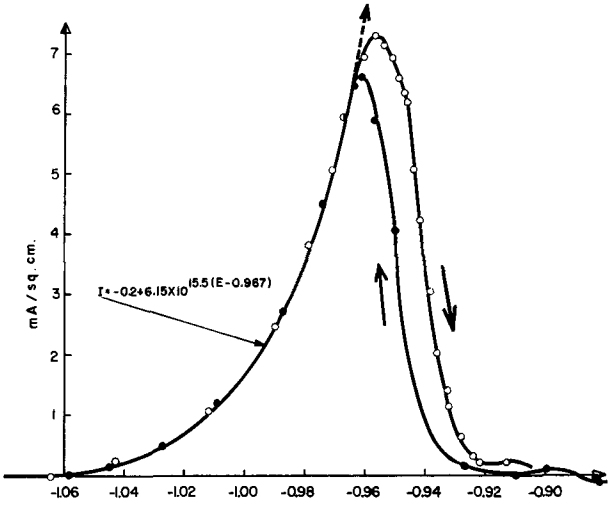

Fig. 1. Density of the anodic dissolution current of iron in a solution of 100 g/l NaOH plus 35 g/l Na_2S measured with reference to a saturated calomel cell. ○ Measured with increasing potential; • measured with decreasing potential.

[1] For a comprehensive survey of the literature on passivity the reader is referred to the symposium in Heiligenberg, 1957 [*Z. Elektrochem.*, 61, No. 6/7 (1958)].

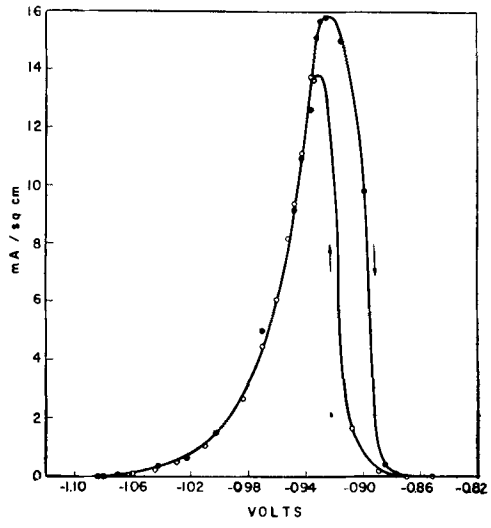

Fig. 2. Density of the anodic dissolution current of iron in a solution of 100 g/l NaOH + 35 g/l Na_2S + 30 g/l pyrogallol with reference to a saturated calomel cell. • Measured with increasing potential; ○ measured with decreasing potential.

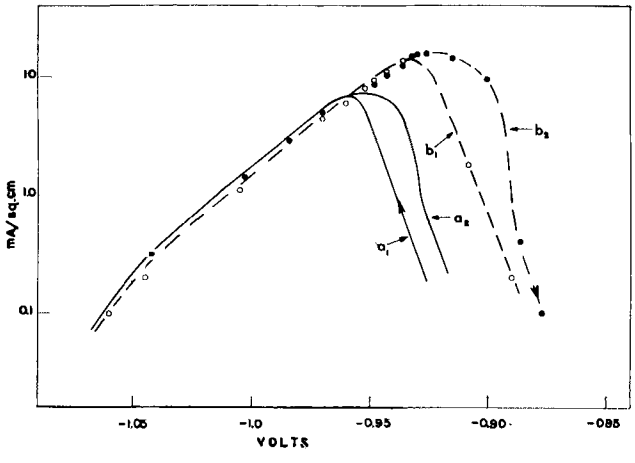

Fig. 3. Semilogarithmic plotting of the curves of Fig. 1a and b showing the exponential relations of both the increasing and decreasing current densities. The extended curves a_1 and a_2 represent the measurement without the addition of pyrogallol. The dotted curves b_1 and b_2 and the plotted points refer to the measurement in liquor containing pyrogallol.

An interesting change is noticed after adding 30 g/l pyrogallol to the above solution (Fig. 2 and 3b). The polarization curves recorded are identical with the previous curves in the range of exponentially increasing current density in the active state. However, the maximum current density is higher and is reached at a less negative potential. The decrease of the current density owing to passivation occurs also at less negative potentials. There are examples of several metals showing the same type of curves in different solutions given in recent publications (7-12).

The general equation of the anodic dissolution current I_a as a function of the measurable potential difference E between the metal and the electrolyte in the active state (1) is

$$I_a = I_o\, f(\mathrm{pH}) \exp \frac{\alpha_a n_a F}{RT} (E - E_o) \qquad [1]$$

where α_a is symmetry factor of the reaction of anodic dissolution amounting to unity or less, n_a is the valency of the determining dissolution reaction, which in the simplest case, but not generally, is the valency of the metal dissolving in the active state, $\alpha_a n_a$ is over-all electrochemical transfer coefficient, I_o and E_o are a couple of interdependent values of current density and potential at pH = 0, and f(pH) is the dependence of the Tafel relation on pH.

This equation is valid only if the rate of the reverse reaction, characterized by electrodeposition of the dissolved metal, is negligible in comparison to the rate of dissolution. In some cases, e.g., chromium in H_2SO_4, f(pH) = 1 (10). However, in the case of iron immersed in perchlorate and sulfate f(pH) $\neq$ 1 according to Heusler (9).

Pourbaix (13) has shown that the relation between equilibrium pressure and potential of iron is independent of the pH value in the pH range from 0 to about 9. Similarly the valency of the iron ions formed is assumed to be 2 (14). There is some evidence, however, that the dissolution of iron in alkaline solutions leads to the formation of Fe_3O_4 as was found in a dilute solution of $NaNO_2$ (15). This reaction also would explain the average valency 2 2/3 found in the dissolution of iron in (NaOH + Na_2S) solutions (4). For this reason; and in agreement with Pourbaix's diagram (13), it is assumed that at pH values higher than 9, Eq. [1] is still valid; however, the exponent $\alpha_a n_a$ might be different.

The Flade potential E_F (2), which represents the boundary potential between the active and the passive states, depends on the pH value. For iron in the range of pH 0 to 4 Flade discovered a relationship which can be expressed by

$$E_F = E_{F_o} - \frac{RT}{F} 2.3(\mathrm{pH}) \qquad [2]$$

where E_F is the Flade potential and E_{F_0} the Flade potential at pH = 0. Equation [2] has been verified by Franck (7).

The partial current density I_p of the anodic dissolution current in the passive state is independent of the potential difference between electrode and electrolyte in a considerable range of this potential (7-10). The iron ions formed in this potential range are trivalent. The anodic current density at high positive potentials (trans-passive range) is accompanied by the formation of FeO_3 and FeO_4^{--} (13).

Under the influence of a constant current density the conversion from the active to the passive state requires a time period which can be approximately expressed by the formula (7)

$$t_p = k/I - I_m \qquad [3]$$

where t_p is time during which the current passivates the metal, k constant, I current density, and I_m minimum current density sufficient for passivation. This relation was found to be valid also for metals other than iron; for gold for instance, in hydrochloric acid (16, 17), and for chromium in sulfuric acid (10). It is widely accepted (18, 8, 19-21) that the passivity of iron in many aqueous solutions is caused by an iron oxide film. The thickness of the film ap-

parently varies considerably between a film strong enough to be stripped from iron by dissolution of the backing metal (22, 23) on the one hand, and a film of molecular dimensions on the other (12, 24-27). In thick films, a layer of Fe_3O_4 adjacent to the iron surface is covered by one of Fe_2O_3 (19). At steady-state conditions the film thickness increases linearly with the potential (19-21). Visible deposits (28), usually of a bulky nature, are not considered typical features of the passive state as passivity is reached without these.

General Theory

Basic Concepts.—Since the formation of the passivating film is an electrochemical phenomenon, its rate on a film-free surface is an exponential function of the metal-electrolyte potential difference. This film originates from the reaction of anions, contained in the electrolyte, with the metal surface [Müller (29)]. For the present model the metal atoms of the film are assumed to maintain their original position in the metal lattice as surface atoms. The film is therefore very strongly bonded to the metal. In the case of iron, the electrostatic field which produces the passivating film is assumed to convert the iron atoms at the surface to the trivalent state. Thus a film is formed consisting of a monolayer of Fe_2O_3.

During the conversion from the active to the passive state, the film covering part of the surface reduces the rate of anodic dissolution because the rate of anodic dissolution is proportional to the ratio of film-free area to total area ("film-free" meaning free of the passivating film.) The corrosion rate of the film-free fraction is assumed to be undiminished.

The anodic current density in the passive state is usually very small and is caused by a very slow corrosion process. Since this current density does not depend on the potential, direct anodic dissolution is out of the question. The only alternative is to assume that a slow dissolution of the passivating film occurs continuously. The damage done to the film is immediately compensated by film reformation, which is basically an anodic process. For this reason, the anodic current-density in the passive state is proportional to the rate of film dissolution and is independent of the potential.

The variation of film thickness found empirically indicates film growth with increased potential from monomolecular dimension, reached initially by passivation at the Flade potential, to about 50 or 100Å. In agreement with Vetter (20) and Weil (21), it is assumed that the increase of the thickness of passivating films is caused by the migration of iron and oxygen ions in opposite directions across the oxide film under the influence of the potential gradient. The film thickness increases with increasing potential until the rate of film growth is reduced by the decreasing gradient of the potential to the value of the rate of film dissolution. Hence, under equilibrium conditions, the film maintains a thickness which increases linearly with the potential.

With decreasing potential, the gradient of the potential in the film is decreased and so is the rate of film formation by migration. The unchanged rate of film dissolution causes a decrease of the film thickness until stable conditions are reached, i.e., when the rate of film formation has become equal to the rate of film dissolution.

The validity of these derivations is limited by the assumption that the rates of possible reverse reactions of the anodic dissolution, i.e., electrode position of the dissolved metal, and of the formation of a passive film, characterized by rebreaking the bonds, are negligible. As the reverse reactions are substantial under certain conditions, their effect has been derived in another paper (30).

Formation of an Fe_2O_3 Film on Iron as an Electrochemical Process

The electrochemical reaction involved in the formation of an Me_2O_n film on a film-free metal surface can be formulated

$$Me + n(OH)^- \rightleftharpoons Me_2O_n + n/2\ H_2O + ne^- \quad [4a]$$

or

$$Me + n(OH)^- \rightleftharpoons Me(OH)_n + ne^- \quad [4b]$$

This reaction supplies n electrons per reacting metal atom to the metal. The rate of this reaction depends on the OH^- concentration and the potential difference between metal and electrolyte. Equation [4b] formulates the reaction in agreement with the chemical analysis of passive films on iron by Neilsen and Rhodin (31). Oxygen-free solutions will now be considered. The effect of dissolved oxygen will be discussed later.

The rate of film formation r_f on a film-free surface follows Tafel's relation and is proportional to $(OH^-)^{n_{OH}}$. As $(OH^-)^{n_{OH}} = \exp 2.3 n_{OH}\ (pH - 14)$, r_f can be formulated

$$r_f = r_{14} \exp\left[2.3\ n_{OH}\ (pH - 14) + \frac{\alpha_p\ n_p\ F}{RT}\ (E - E_{14})\right] \quad [5]$$

where α_p is the symmetry factor, n_{OH} order of the process with respect to (OH^-), n_p valency controlling the rate of Me_2O_3 formation on the metal, r_{14} the rate of film formation on a film-free iron surface at $pH = 14$ and $E = E_{14}$, and E_{14} characteristic value of E at $pH = 14$. Equation [5] takes into consideration only the forward reaction which forms metal oxygen bonds at the interphase. If the backward reaction of rebreaking the bonds is so strong that equilibrium conditions are approached, Eq. [5] is no more strictly valid (30).

For reasons of simplicity the calculation is better referred to $pH = 0$. Thus Eq. [5] is converted to

$$r_f = r_o \exp\left[2.3\ n_{OH}\ (pH) + \frac{\alpha_p\ n_p\ F}{RT}\ (E - E_o)\right] \quad [6]$$

where r_o is the rate of film formation on a film-free metal surface at $pH = 0$ and $E = E_o$.

Equation [6] defines the rate of the film formation on a film-free metal surface. The rate of the film formation in an area partly covered by film is proportional to the ratio of the surface area of film-free metal to the total metal surface. This part of the derivation follows the Langmuir adsorption theory and is similar to that of Franck (7) and of Gerischer

(8). At steady state the rate of film formation is equal to the rate of film dissolution. Hence

$$a_c\, r_c = a_f\, r_f \qquad [7]$$

where a_c is film-covered area, a_f film-free area, and r_c rate of film dissolution of metal oxide or hydroxide from a film-covered area. r_c is assumed to be independent of the potential as the dissolution goes without exchange of charges. It may also be stressed that Eq. [7] does not describe an equilibrium between film formation and dissociation of the film into the original components. The ratio of the film-free area to the total area a_t is given by

$$a_f/a_t = 1/1 + \frac{r_f}{r_c} \qquad [8]$$

Combining Eqs. [6] and [8]

$$\frac{a_f}{a_t} = \frac{1}{1 + \frac{r_o}{r_c} \exp\left[2.3\, n_{OH}\,(pH) + \frac{\alpha_p\, n_p\, F}{RT}(E - E_o)\right]} \qquad (9)$$

Eq. [9] shows the very rapid decrease of the film-free area with increasing potential and pH values.

Anodic dissolution current in the potential range of the conversion from active to passive state.—The density of the anodic dissolution current I_a at totally film-free areas is given by Eq. [1]. Only the film-free area is assumed to contribute to the anodic current in this calculation. The partial coverage of the surface by an insoluble film reduces this current density to an amount which is proportional to the ratio of film-free area to total area. Thus Eqs. [1] and [9] may be combined to calculate the anodic current density I_{af} on a partly film-covered surface

$$I_{af} = I_o \frac{f(pH) \exp \frac{\alpha_a\, n_a\, F}{RT}(E - E_o)}{1 + \frac{r_o}{r_c} \exp\left[2.3 n_{OH}\,(pH) + \frac{\alpha_p\, n_p\, F}{RT}(E - E_o)\right]} \qquad [10]$$

For the application of Eq. [10] the ratio r_o/r_c must be determined. In Eq. [3], t_p gives a reciprocal measure of r_o: however, since the potential changes continuously during the measurement, this must be regarded as approximate only. Accurate measurements of r_o should be made at constant potential in the passive state, e.g., at the Flade potential. There is, however, a clearcut relation between r_o/r_c and I_{po}/I_p ($I_{po} = I_p$ at pH = 0). When 50% of the surface is covered with the protective film, the current density $I_{0.5}$ becomes 50% of the value calculated for a film-free surface, and the potential becomes $E_{0.5}$. When $E = E_{0.5}$ in Eq. [10], I_o f (pH)-$2I_{0.5}$ and the denominator of Eq. [10] becomes 2. Thus

$$\frac{r_o}{r_c} \exp\left[2.3\, n_{OH}\,(pH) + \frac{\alpha_p\, n_p\, F}{RT}(E_{0.5} - E_o)\right] = 1 \qquad [11]$$

For the potential $E_{0.5}$ at pH = 0 the symbol $E_{o-0.5}$ may be used, and for the rate of film formation r_o at pH = 0 and $E_{o-0.5}$ the symbol $r_{o-0.5}$. According to Eq. [11] $r_{o-0.5}$ equals r_c when E_o equals $E_{o-0.5}$. Hence,

$$\frac{r_{o-0.5}}{r_c} \exp\left[2.3\, n_{OH}\,(pH) + \frac{\alpha_p\, n_p\, F}{RT}(E_{0.5} - E_{o-0.5})\right] = 1 \qquad [12]$$

The rate of film dissolution r_c at a completely film-covered area is proportional to I_p, the current density in the passive state, according to the given basic concept. At pH = 0, I_p becomes I_{po}, hence

$$r_{o-0.5}/r_c = I_{po}/I_p \qquad [13]$$

By substituting $r_{o-0.5}/r_c$ from Eq. [13] into Eq. [10] an equation results which contains only measurable quantities or constants as follows

$$I_{af} = \frac{I_o\, f(pH) \exp \frac{\alpha_a\, n_a\, F}{RT}(E - E_o)}{1 + \frac{I_{po}}{I_p} \exp\left[2.3\, n_{OH}\,(pH) + \frac{\alpha_p\, n_p\, F}{RT}(E - E_{o-0.5})\right]} \qquad [14]$$

The current density of the anodic dissolution current on a film-free surface as expressed in the numerator can be described by using any pair of related values of current density and potential to replace $I_o\, f(pH)$ and E_o, for instance, $2I_{0.5}$ and $E_{0.5}$. The second term of the denominator can be formulated

$$\frac{I_{po}}{I_p} \exp\left[2.3\, n_{OH}\,(pH) + \frac{\alpha_p\, n_p\, F}{RT}(E_{0.5} - E_{o-0.5})\right] \exp \frac{\alpha_p\, n_p\, F}{RT}(E - E_{0.5})$$

According to Eq. [12] and [13] this expression equals $\exp \frac{\alpha_p\, n_p\, F}{RT}(E - E_{0.5})$. Thus a simplified formula of the current density in the potential range of the conversion is derived

$$I_{af} = 2I_{0.5} \frac{\exp \frac{\alpha_a\, n_a\, F}{RT}(E - E_{0.5})}{1 + \exp \frac{\alpha_p\, n_p\, F}{RT}(E - E_{0.5})} \qquad [15]$$

The above derivation does not take into account the dissolution of the passivating film in the electrolyte which causes the flow of a small anodic current I_p at a completely covered surface. The partial current I_d which is caused by the film dissolution on a partly covered surface is proportional to the ratio film-covered area to total area. According to Eq. [9] and [11] the ratio film-free to total area amounts to

$$1/1 + \exp \frac{\alpha_p\, n_p\, F}{RT}(E - E_{0.5})$$

and the ratio film-covered to total area is put into Eq. [16] as factor of I_p

$$I_d = I_p \frac{\exp \frac{\alpha_p n_p F}{RT} (E - E_{0.5})}{1 + \exp \frac{\alpha_p n_p F}{RT} (E - E_{0.5})} \qquad [16]$$

In cases of typical passivity this partial current I_a is negligible in comparison with $I_{0.5}$. However, there are conditions under which I_a forms a substantial part of the combined current density I_c; then the calculation of I_c requires the addition of I_a to I_{at} as follows

$$I_c = \frac{2 I_{0.5} \exp \frac{\alpha_a n_a F}{RT} (E - E_{0.5}) + I_p \exp \frac{\alpha_p n_p F}{RT} (E - E_{0.5})}{1 + \exp \frac{\alpha_p n_p F}{RT} (E - E_{0.5})} \qquad [17]$$

Equation [17] covers the curve of the density of the anodic dissolution current as a function of the potential including the active and passive states. It is evident that Eq. [17] can be derived without special assumptions concerning type of metal and reacting ions and it is assumed to be valid if the assumptions about the mechanism of film formation are appropriate.

Comparison with experimental results.—From the above it is clear that the ratio $\beta = \alpha_p n_p : \alpha_a n_a$ determines the form of the curve of the anodic dissolution current. If β is unity the curve forms a polarographic wave, i.e., an S-shaped transition from current density 0 to a constant current density amounting to $2 I_{0.5} + I_p$ (Fig. 4). This is the shape of the curves found with silver (12) in (11M NH_3 + 1M $(NH_4)_2SO_4$), with gold (8) in 4.0*N* HCl, and with iron (8,9) in 1.0*N* H_2SO_4 at 25°C. However, this type of curve might also be caused by a film of salt, as this condition can cause the formation of a constant current density.

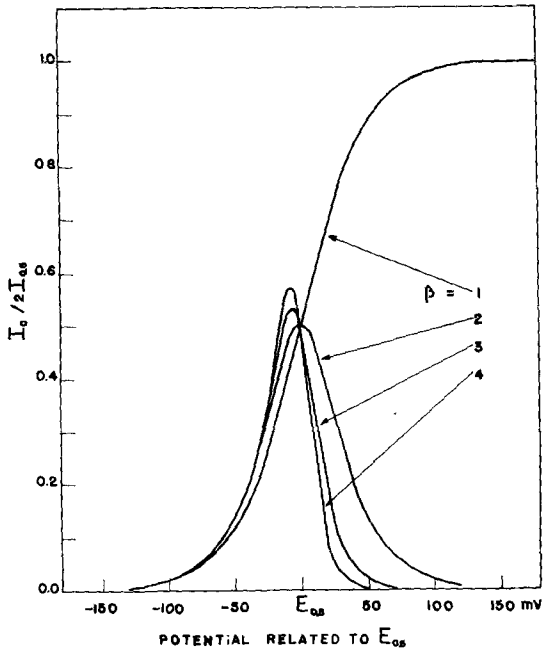

Fig. 4. Calculated curves characteristic of the density of the anodic dissolution current as a function of the potential. The ratio β of the exponent in the formula describing the anodic dissolution reaction to the exponent in the formula of the film forming reaction control the form.

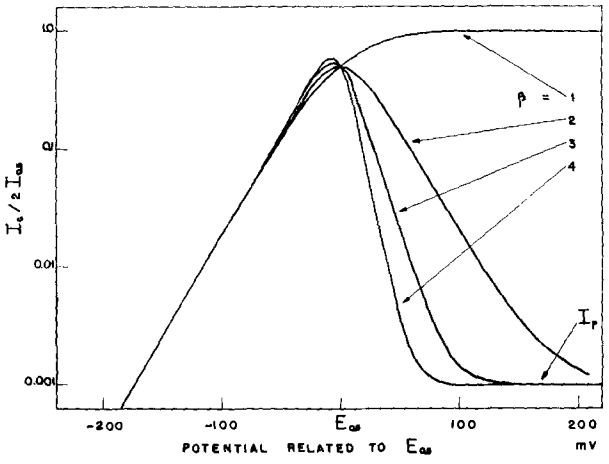

Fig. 5. Semilogarithmic plotting of the curves of Fig. 4 which shows the typical 3 ranges of nearly linear relation.

When $\beta = 2$ the curve is symmetrical, the branch covering the active state being the mirror image of the branch measured in the range of the conversion from the active to the passive state. When $\beta > 2$, the decrease of the current density in the range of the conversion from the active to the passive state becomes increasingly steeper than its increase in the active state. The curves of Fig. 1 and 2 show the typical form derived for $\beta = 3$ to 4.

In semilogarithmic plotting the calculated curve assumes a very simple form. When the second term in each numerator and denominator of Eq. [17] becomes negligible in comparison with the first term, the resulting equation in semilogarithmic plotting gives the straight line (Fig. 5)

$$\left(\frac{d \ln I_c}{dE}\right)_a = \frac{\alpha_a n_a F}{RT} \qquad [18]$$

Equation [18] is valid in the active range (subscript a). When the second term in the numerator and the first term in the denominator become negligible, another straight line is formed in semilogarithmic plotting as follows

$$\left(\frac{d \ln I_c}{dE}\right)_{a \to p} = \frac{(\alpha_a n_a - \alpha_p n_p) F}{RT} \qquad [19]$$

Equation [19] formulates the curve in the potential range of the conversion from active to passive state (subscript $a \to p$). When the first term of each nominator and denominator becomes small in comparison with the second term, I_c equals I_p.

The straight lines given by Eq. [18] and [19] cross at the coordinates $2I_{0.5}$ and $E_{0.5}$ and the second and third straight lines cross at the coordinates I_p and E_F. Thus a simple method of calculating all the characteristic constants of Eq. [17] from measured curves becomes evident. Kolotyrkin's (10) anodic current density potential curves in semilogarithmic plotting demonstrate these features. His curves obtained from chromium and nickel in H_2SO_4 consist of three straight lines representing the active state, the conversion to the passive state, and the passive state.

$E_{0.5}$ and the Flade Potential

For the current density as a function of pH a relation based on Eq. [14] and [16] can be formulated as follows

$$I_c = \frac{I_o f(pH) \exp \frac{\alpha_a n_a F}{RT} (E - E_o) + I_{p_o} \exp \left[2.3 n_{OH} (pH) + \frac{\alpha_p n_p F}{RT} (E - E_{o-0.5}) \right]}{1 + \frac{I_{p_o}}{I_p} \exp \left[2.3 n_{OH} (pH) + \frac{\alpha_p n_p F}{RT} (E - E_{o-0.5}) \right]} \quad [20]$$

Equation [20] shows the influence of pH and of the current density I_p in the passive state on the anodic dissolution current. The characteristic potential $E_{0.5}$ of their cross-point with the line of the active state is given by

$$E_{0.5} = E_{o-0.5} - \frac{RT}{\alpha_p n_p F} \left[2.3 n_{OH} (pH) + \ln \frac{I_{p_o}}{I_p} \right] \quad [21]$$

because at $E_{0.5}$ the second term of the denominator equals unity (Eq. [12] and [13]). $E_{0.5}$ is independent of the function f(pH). This might be expected because the potential at which the film covers 50% of the surface does not depend primarily on the rate of anodic dissolution. Typical features of the calculated curves are the following: in the active state there is one straight line in semilogarithmic plotting if the current density which is independent of pH (f(pH) = 1). The conversion to the passive state is shown by parallel straight lines for a variation of pH as demonstrated in Fig. 6. Kolotyrkin (10) gives a demonstration of these conditions from a study of the current density of the anodic dissolution of chromium in 1.0N, in 0.1N and 0.01N H_2SO_4. His curves in semilogarithmic plotting consist of one straight line of the current in the active state with straight lines of the conversion to the passive state branching off at potentials of 0.05 v difference.

It is also interesting to note that the alteration of the polarization curve found after the addition of pyrogallol (Fig. 1 and 2) might be caused by an increased solubility of the passive film which effects a change of I_p. This assumption agrees with the experimental result of MacLean and Gardner (32) who studied the corrosivity of wood extractives. These

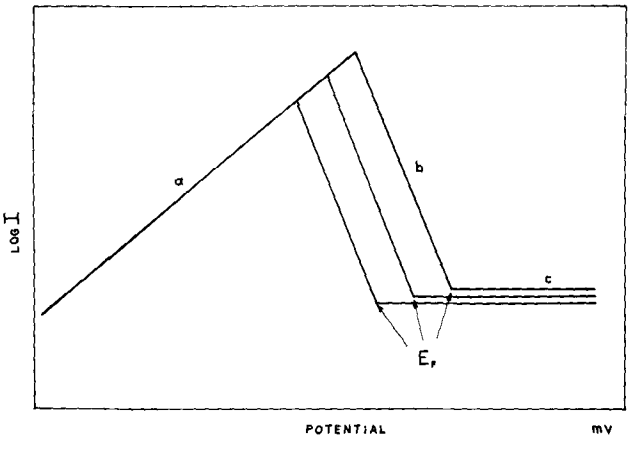

Fig. 6. Schematic semilogarithmic plotting of the density of the anodic dissolution current: (a) film-free active range, (b) conversion to the passive state, and (c) Flade potential E_F and the passive state.

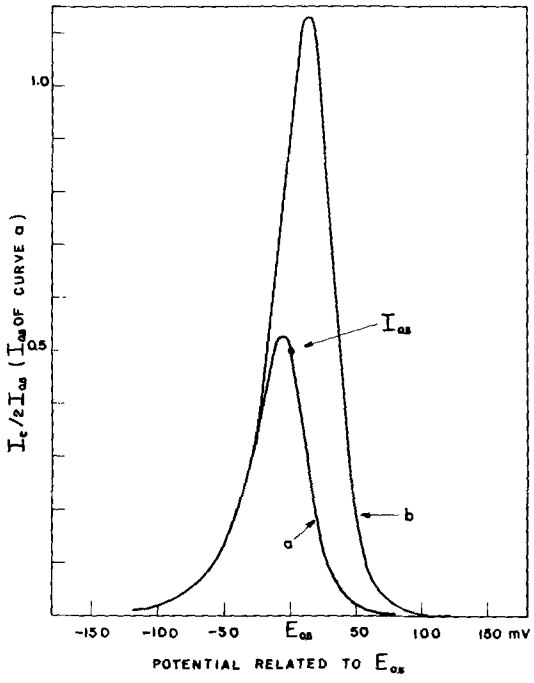

Fig. 7. Density of the anodic dissolution current calculated for a variation of the rates of film dissolution and film formation:

(a) $\frac{I_{p_o}}{I_p} \exp [2.3 n_{OH} (pH)] = 1;$

(b) $\frac{I_{p_o}}{I_p} \exp [2.3 n_{OH} (pH)] = 0.1$

authors suggested that the increased corrosivity of alkaline cooking liquor found by addition of 1,2 dihydroxybenzene and derivatives, such as pyrogallol, was due to increased solubility of ferric iron salts. Figure 7 demonstrates the calculated effect in two curves the shape of which agrees very well with that of Fig. 1 and 2.

Franck (7) on repeating Flade's (2) experiments, uses the expression "critical current density which causes the local activation" to describe the current density at the Flade potential. Franck does not indicate whether this critical value of the current differed at different pH values. Hence the definition of Franck's experimental values of the Flade potential is not exactly known.

In the present work, the Flade potential is defined as the potential at which the density of the anodic dissolution current I_{at} equals I_p, the density of the current in the passive state. It may be stated that this definition does not consider the Flade potential as an equilibrium potential for the formation and disintegration of the protective oxide film (19). According to the definition the two terms in the numerator of Eq. [20] are equal at E_F. Differentiation of the equation calculated for E_F with respect to pH results in the relation

$$E_F = E_{F_o} - (pH) \frac{RT}{F} \frac{2.3 n_{OH} - \frac{d \ln f(pH)}{d (pH)}}{\alpha_p n_p - \alpha_a n_a} \quad [22]$$

The meaning of Eq. [22] may be demonstrated in Fig. 8 which plots the current-potential relation on a semilogarithmic scale. The curve referring to pH = 0 is characterized by the crosspoints E_{F_o}/I_{p_o} and $E_{o-0.5}/2I_{o-0.5}$ ($I_{o-0.5} = I_{0.5}$ at pH = 0). According to Eq.

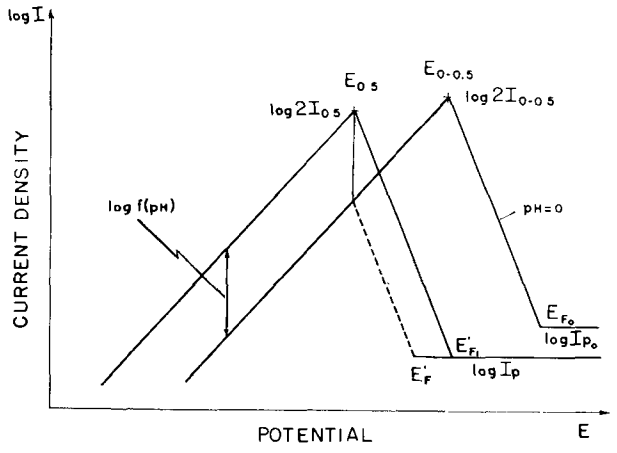

Fig. 8. Schematic semilogarithmic plotting of the anodic dissolution current showing the effect of f(pH) on the Flade potential (Eq. [22]).

[21], $E_{0.5}$ is independent of f(pH). If f(pH) equals unity the Flade potential is E'_F. If f(pH) increases with pH the resulting Flade potential $E'_{F'}$ reaches a value between E_{F_0} and E'_F. Equation [22] gives values of the same order of magnitude as Eq. [2]. However, exact values of the current-density-potential relation at varied pH are required for a definite decision on the validity of Eq. [22].

Comparison with Previously Developed Theories About Passivity

The theory presented is based on the accepted idea of a protective film, consisting of Fe_2O_3 in the case of iron. This theory leads to the conclusion that the electronic state of the metal surface influences the conversion process. A high value of β means a rapid decline from the maximum current density to the passive state, i.e., a typical passivity. An increase of the valency during the conversion from the active to the passive state increases β, because it means $n_p/n_a > 1$. Hence transition elements which increase the valency during the conversion are singled out as elements of typical passive behavior. Thus the original electron configuration theory (33,17,34) is corroborated, and the present theory forms a bridge between Faraday's protective film theory, and Schoenbein's theory (35) that passivation involves an essential alteration of actual metal properties.

The complementary relation between the presented theory and the theory of Vetter (20) and Weil (21) about the passive film is evident. The presented theory leads from an unprotected surface to one which is protected by a monolayer film. The growth of the film thickness is explained by their theory. Thus these two theories cover two neighboring potential ranges.

However, there is disagreement with certain previously published theories. Development of oxygen (7) or of an iron oxide higher in oxygen content than Fe_2O_3 (36) was assumed by some authors to be a necessary or characteristic condition for reaching passivity. This assumption probably has been stimulated by measurements with current controlled experimental arrangements which cause a jump of the potential from the active state over a large range of the passive state (3,4). Depending on the experimental conditions, the potential may reach stable values only in the transpassive state. With an adequate potentiostatic arrangement it is easily shown that the development of oxygen or of high iron oxides is not characteristic of the passive state of iron, but of the transpassive state.

The theory of Müller (28) assumes the deposition of porous metal salts on the rapidly corroding metal surface, particularly in strong acids. On the iron surface below the pores of the deposit, chemical passivity is assumed to be caused by the extremely high current density. Instead of this the present theory assumes that anions can form a salt film on metals. Corrosion rate and current density then are reduced to a value proportional to the solubility of the salt film. Once the potential for the formation of the oxide film is reached, the conversion from the salt-film-covered to the oxide-film-protected metal takes place.

Oxygen and oxidizing agents are well known promoters of passivity. Two different mechanisms were proposed to explain passivation by oxidation. By the first, formation of oxide films occurred by direct reaction between metal and oxygen or oxides. This is the mechanism of the formation of protective films of oxides during the exposure of metals to dry atmospheric oxygen. Dissolved oxidizing reagents, such as chromates, may also promote the formation of a protective film by direct reaction with the metal in the active state (18). By the second proposed mechanism, oxygen or oxides dissolved in water produce an electrochemical reaction between metals and oxidizing agents, consisting of removal of negative charges from the metal surface according to the equation (37)

$$\tfrac{1}{2}\,O_2 + 2e^- \rightleftharpoons O^{2-} \qquad [23]$$

An oxidizing process of this type involves a cathodic current-density according to Faraday's law. If this current density is higher than the maximum anodic current density in the active state, it causes a shift to the passive state. Thus, even though oxygen might contribute to the formation of a passive film, the decisive factors are pH and potential.

An explanation of passivity, and particularly of the Flade potential, has recently been given by Göhr and Lange (19). After a survey of the iron oxides and their properties, the basic chemical reaction involved in the formation of the Flade potential was formulated as follows:

$$Fe_3O_4 + \tfrac{1}{2}H_2O \rightarrow 3/2Fe_2O_3 + \tfrac{1}{2}H_2;\ U_H = +0.58\ v \qquad [24]$$

Even though the present theory assumes an Fe_2O_3 film in agreement with Göhr and Lange, the concept of the mechanism of film formation is different. According to the present derivation the Flade potential is not an equilibrium potential, it is a potential defined by a steady state condition as explained already.

The given derivation reaches from the active state over the range of the conversion from the active to the passive state and over the Flade potential to the passive state. The basic assumptions made and the results derived do not interfere with the theory and the facts known from Vetter (20) and Weil (21) about the neighboring passive state. At the Flade potential the proportion of film free to total area is extremely small and the film coverage almost literally complete. The present derivation studies the formation of a monolayer film. The growth of this film by inner migration which might begin before it covers the complete surface has been described by Vetter (20) and Weil (21).

Manuscript received May 21, 1959.

Any discussion of this paper will appear in a Discussion Section to be published in the December 1960 JOURNAL.

REFERENCES

1. W. A. Mueller, To be published.
2. F. Flade, *Z. physik. Chem.*, **76**, 513 (1911).
3. N. D. Green, Paper presented at N.A.C.E. Conference, March 1959.
4. W. A. Mueller, *Can. J. Tech.*, **34**, 162 (1956); *Tappi*, **40**, 129 (1957).
5. R. B. Kesler and J. F. Bakken, *Tappi*, **41**, 97 (1958).
6. E. Uusitalo, *Papper och Trä*, **8**, 393 (1958).
7. U. F. Franck, *Z. Naturforsch.*, **4a**, 378 (1949); Habilitations Schrift Goettingen (1954).
8. H. Gerischer, *Angew Chem.*, **70**, 285 (1958).
9. K. E. Heusler, *Z. Elektrochem.*, **62**, 582 (1958); K. E. Heusler, K. F. Bonhoeffer, and K. G. Weil, *Z. physik. Chem.*, in preparation.
10. Y. M. Kolotyrkin, *Z. Elektrochem.*, **62**, 664 (1958).
11. R. Olivier, Dissertation, Leiden (1955).
12. R. P. Tischer and H. Gerischer, *Z. Elektrochem.*, **62**, 50 (1958).
13. M. Pourbaix, *Chem. & Ind.*, **1953**, 780.
14. K. F. Bonhoeffer, *Z. Elektrochem.*, **55**, 151 (1951).
15. M. Cohen, Symposium on Charge Transfer Processes, Toronto, Sept. 1958, Paper No. 20; *J. Phys. Chem.*, **56**, 451 (1952).
16. G. Armstrong and J. A. V. Butler, *Trans. Faraday Soc.*, **30**, 1173 (1934).
17. U. Sborgi, *Atti Lincei*, **1**, 315, 388 (1925); *Gazz.*, **56**, 532 (1926).
18. M. Cohen and A. F. Beck, *Z. Elektrochem.*, **62**, 696 (1958).
19. H. Göhr and E. Lange, *ibid.*, **61**, 1291 (1957).
20. K. J. Vetter, *ibid.*, **58**, 230 (1954); **62**, 642 (1958).
21. K. G. Weil, *ibid.*, **59**, 711 (1955); **62**, 638 (1958).
22. U. R. Evans, *Nature*, **126**, 130 (1930); *J. Chem. Soc.*, **1930**, 478.
23. U. R. Evans, *Z. Elektrochem.*, **62**, 619 (1958).
24. P. Berge, *Compt. rend*, **245**, 1239 (1957).
25. K. F. Bonhoeffer, *Z. Elektrochem.*, **47**, 147 (1941).
26. E. S. Snavely and N. Hackerman, Symposium on Charge Transfer Processes, Toronto, Sept. 1958.
27. W. H. Wade and N. Hackerman, *Trans. Faraday Soc.*, **53**, 1636 (1957).
28. W. J. Müller, *Z. Elektrochem.*, **30**, 401 (1924); **36**, 365 (1930); **36**, 379 (1930).
29. E. Müller and K. Schwabe, *ibid.*, **38**, 407 (1932).
30. W. A. Mueller, To be published.
31. N. A. Nielsen and T. N. Rhodin, Jr., *Z. Elektrochem.*, **62**, 707 (1958).
32. H. MacLean and J. A. F. Gardner, *Pulp & Paper Mag. Can.*, **54**, 125 (Nov. 1953).
33. A. S. Russell, *Nature*, **115**, 455 (1925); **117**, 47 (1926); A. S. Russell, D. C. Evans, and S. W. Rowell, *J. Chem. Soc.*, **1926**, 1877.
34. R. Swinne, *Z. Elektrochem.*, **31**, 417 (1925).
35. C. T. Schoenbein and M. Faraday, *Phil. Mag.*, **9**, 53, 65 (1836); C. T. Schoenbein, *Pogg. Ann.*, **37**, 590 (1836).
36. H. H. Uhlig and T. L. O'Connor, *This Journal*, **102**, 562 (1955); H. H. Uhlig, *Z. Elektrochem.*, **62**, 626 (1958).
37. W. Schwartz, *Metallwissenschaft und Technik*, **10**, 513 (1956); **10**, 921 (1956).

Kinetics of the Dissolution of Copper in Aqueous Solutions of Aliphatic Amines

S. C. Sircar[1] and D. R. Wiles[2]

Department of Mining and Metallurgy, University of British Columbia, Vancouver, Canada

ABSTRACT

Studies of the rate of dissolution of copper in aqueous solutions of ammonia, and methyl-, ethyl-, and n-butylamines under a high pressure of oxygen have shown the reaction to occur in two stages: a rapid pre-equilibrium involving the free amine molecule, and a slower reaction step involving either the free amine molecule or its conjugate acid. This mechanism leads to a partial understanding of the passivity of copper surfaces in nearly neutral amine solutions.

Recent studies of the kinetics of the attack of various complexing agents on metallic copper have been extended to include the aliphatic amines. Earlier work on ammonia (1,2) and on some amine-type chelating agents (3) has suggested that the free base and its protonated form act to cause dissolution by independent paths, and that the reaction is first order in each species. Thus

$$\frac{d[Cu^{++}]}{dt} = k_1[A] + k_2[AH^+] \qquad [1]$$

where A represents the free amine, and AH^+ its singly protonated form.

The present study, involving methyl, ethyl, and n-butyl amines, was made with the thought of ob-

[1] Present address: Bakhrabad, Cuttack 2, Orissa, India.

[2] Present address: Department of Chemistry, Carleton University, Ottawa, Canada.

serving possible variation in kinetic behavior among the members of this homologous series, and also of finding out how well ammonia would fit in as a first member of such a series.

Experimental

The apparatus and procedure used were the same as those described earlier (3,1). Briefly, these were as follows.

The reaction took place in a one-gallon autoclave, under a pressure of oxygen kept constant at about 8.0 atm. The solution, about 2 l in volume, was made up by diluting stock solutions of accurately known concentrations and was maintained at an ionic strength of at least 0.1M by addition of reagent-grade sodium perchlorate. The dissolution specimen was made from conductivity grade (99.97%) copper, heat treated to give small grains of nearly random orientation. This specimen, mounted in Bakelite, was supported in the solution with its exposed face tangential to the 8-cm-diameter cylinder swept out by the impeller blades.

The amines, of Kodak White Label grade, were used without further purification. Reaction solutions were made from calculated amounts of stock solutions of the amines and of reagent-grade perchloric acid. Concentrations of the amine stock solutions were determined by titration to a methyl red end point with sulfuric acid. The composition of each solution was checked by titration. During experiments, the reacting solutions were maintained at a temperature of 25.0° ± 0.1°C. Samples, withdrawn at intervals, were analyzed colorimetrically for copper by carbamate method (4).

Results

The amines used in this work are listed in Table I along with the constants for their acid dissociation in aqueous solution:

$$K_a = \frac{[A]\,[H^+]}{[AH^+]}$$

Unfortunately, the complexes formed by these amines with cupric ion (other than the complexes with ammonia) have not been investigated. It is reasonable to assume, however, that the copper is coordinated to four amine groups, which are most likely arranged in a plane square[3] around the central atom.

The rate plots ([Cu^{++}] vs. time) were found, as in the earlier work, to be linear. This once again demonstrates the absence of such effects as autocatalysis and progressive roughening of the copper surface. The observed dependence of the rate on the amine concentration did not support the anticipated first-order behavior, but was rather of the form shown for methylamine in the lower curve of Fig. 1. The same type of behavior was found for all the amines studied.

These data can be described quite well by an expression of the form:

$$R = \frac{d[Cu^{++}]}{dt} = \frac{k_1[A]\,S}{1 + k_1[A]} \cdot k_2[A] \qquad [2]$$

where S represents the exposed surface area of the copper sample. This is shown further in that a plot of $[A]^2/R$ vs. [A] gives a straight line, as would be expected from Eq. [2]. This is shown for methylamine in Fig. 2.

The observed effects of added acid, that is, the "aminium" form of the complexing agent, are such as not to support without qualification the view previously suggested (1) that the reaction of the protonated form follows an independent path. Figure 1 shows a family of curves for different values of the acidity. Some deviation from complete independence of reaction path is shown by the fact that the curves of rate vs. aminium concentration, although linear, have slopes which vary with amine concentration. These data are presented in Fig. 3.

The nature of this dependence suggests that the over-all rate equation may be of the form

$$\frac{d[Cu^{++}]}{dt} = \frac{k_1[A]\,S}{1 + k_1[A]} \{k_2[A] + k_3[AH^+]\} \qquad [3]$$

A careful re-investigation of the rate dependence in the ammonia system revealed that here, too, the reaction is not simply first order as had previously been reported (1) but follows the same pattern as was found for the amines. Since the deviation from

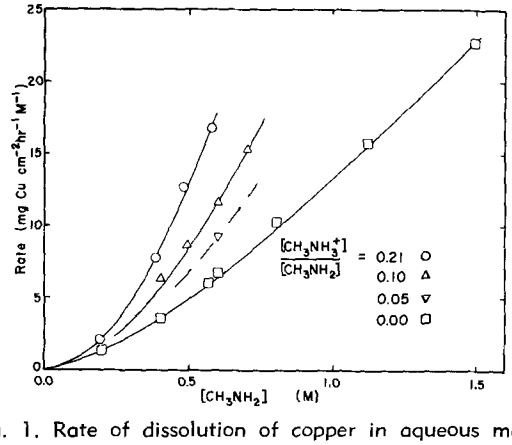

Fig. 1. Rate of dissolution of copper in aqueous methylamine solutions of various acidities.

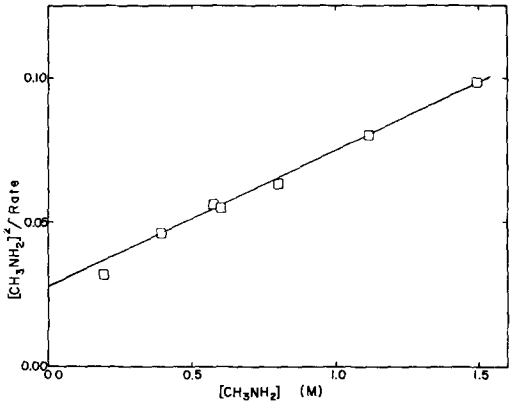

Fig. 2. Plot of $[A]^2/R$ vs. [A] for the dissolution of copper in aqueous solutions of methylamine.

[3] This assumption is based on the fact that most complexes of Cu^{++} which have been studied are square planar. See Ref. (6).

Table I. Amines used in this work

Amine	K_a*
Ammonia	5.68×10^{-9}
Methylamine	2.30×10^{-9}
Ethylamine	1.80×10^{-9}
n-Butylamine	2.46×10^{-9}

* Data adapted from Ref. (5).

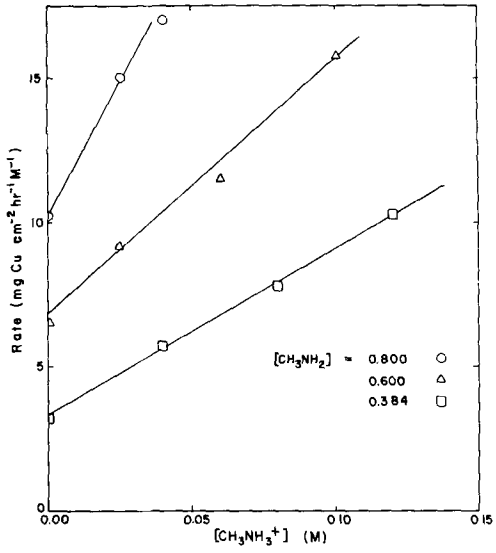

Fig. 3. Rate of copper dissolution in aqueous methylamine solutions as a function of the acidity, at constant concentration of free amine.

linearity is not great, this observation is not in disagreement with Halpern's original work, but is the result rather of a refinement in experimental sensitivity. Experimental data are summarized in Table II.

Values for the constants in Eq. [3] determined for ammonia and the various amines are presented in Table III

The form of Eq. [3] suggests that there is a pre-equilibrium involving adsorption of amine molecules on a saturable surface, producing "active sites." This equilibrium appears to be followed by reaction at the active sites via one of the two previously mentioned independent paths. The adsorption of oxygen on the surface is evidently very fast. The whole process, then, is envisioned as occurring in the following way: (The subscript $_s$ designates a species residing in the surface).

1. $Cu_s + \frac{1}{2} O_2 \xrightarrow{fast} Cu_s - O$

2. $Cu_s - O + A \overset{fast}{\rightleftarrows} Cu_s(A) - O$ $\quad k_1$

3a. $Cu_s(A) - O + A \xrightarrow{slow} Cu_s(A_2) - O$ $\quad k_2$

4a. $Cu_s(A_2) - O + H_2O \xrightarrow{fast} Cu(A)_2^{++} + 2\,OH^-$

3b. $Cu_s(A) - O + AH^+ \xrightarrow{slow}$ $\quad k_3$

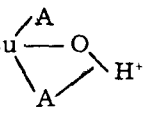

4b.

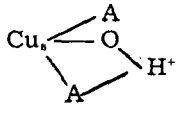

$\xrightarrow{fast} Cu(A)_2^{++} + OH^-$

Table II. Summary of kinetic data†

Complexing agent	Ionic strength	Concentration		Rate of solution, mg Cu cm^{-2} hr^{-1}
		Amine	Aminium	
Methylamine	0.1	0.195	—	1.20
		0.40	—	3.40
		0.57	—	5.80
		0.60	—	6.60
		0.80	—	10.20
		1.12	—	15.60
		1.49	—	22.6
		1.49	—	22.7
Methylamine	0.2	0.80	0.025	15.0
		0.80	0.040	17.0
		0.80	0.050	18.0
		0.80	0.050	18.0
		0.80	0.075	48.8*
		0.80	0.100	55.6*
		0.80	0.125	52.0*
		0.80	0.195	50.0*
Methylamine	0.2	0.192	0.040	2.10
		0.384	0.080	7.80
		0.480	0.100	12.60
		0.576	0.120	16.7
Methylamine	0.2	0.384	0.040	5.70
		0.384	0.080	7.80
		0.384	0.120	10.30
Methylamine	0.1	0.40	0.040	6.2
		0.50	0.050	8.6
		0.60	0.060	11.6
		0.70	0.070	15.2
		0.60	0.03	9.2
		0.60	0.10	15.8
Ethylamine	0.1	0.203	—	1.30
		0.400	—	3.60
		0.535	—	6.40
		0.76	—	9.00
		0.92	—	12.60
		1.04	—	16.6
Ethylamine	0.2	0.210	0.050	2.80
	0.35	0.210	0.100	4.50
	0.2	0.210	0.150	5.80
n-Butylamine	0.1	0.187	—	1.10
		0.326	—	2.80
		0.63	—	7.60
		0.96	—	14.3
		1.29	—	20.7
		1.64	—	32.3
n-Butylamine	0.2	0.202	0.025	1.80
		0.202	0.050	2.60
		0.40	0.025	5.00
Ammonia	0.1	0.086	—	2.10
		0.165	—	5.45
		0.310	—	14.1
		0.66	—	38.0
Ammonia	0.1	0.20	0.0020	10.00
		0.20	0.0040	12.6
		0.30	0.0030	17.8
		0.30	0.0060	22.2
		0.40	0.0040	26.4
		0.40	0.0080	32.8

† Temperature: 25° ± 0.1°C; oxygen partial pressure: 8.2 atm; ionic strength adjusted with $NaClO_4$.

* No explanation has been found for these anomalously high rates.

Table III. Rate constants determined in this work

Amine	k_1*	k_2*	k_3*
Ammonia	4.7	80	2450
Methylamine	1.9	21	140
Ethylamine	2.3	20	90
n-Butylamine	1.9	23	90

* The units are: for k_1 liters per mole, and for k_2 and k_3 mg Cu^{++} cm^{-2} hr^{-1} $mole^{-1}$ liter. While the limits of error could not be determined accurately, it is felt that these values are correct to within about 5% for k_1 and k_2 and about 10% for k_3.

In the above, k_1 is an equilibrium constant, while k_2 and k_3 are the rate constants.

Since, under the conditions of the experiments, variation of the oxygen pressure makes no difference to the reaction rate, it can be assumed that the equilibrium in Step 1 is shifted very far to the right, so that the surface is completely covered with a layer of adsorbed oxygen atoms. It should be pointed out that there is no direct evidence to suggest that the oxygen adsorption precedes the amine adsorption. However, since the order of the first two steps is not at present important, the above arrangement is taken as satisfactory.

The values given in Table III for the rate constants show a marked reduction in reaction rate on going from ammonia to the amines. However, only k_3 shows any significant change as the length of the carbon chain is increased, and even here the change is not evident beyond ethylamine.

The results of the experiments done at constant total amine concentration, seen in Fig.4, in addition to confirming the nature of Eq. [3], may give some insight into the mechanism of passivation of copper in neutral or acid amine solutions. It appears that, as the concentration of free amine decreases, the position of the pre-equilibrium (Step 2) is moved far to the left, and the number of active sites is greatly reduced. Thus the reaction step (3a or 3b), involving either the free amine or its conjugate acid, is able to proceed only at a very slow rate.

The fact that the rates in nearly neutral solutions are much less than are expected from Eq. [3] (solid line in Fig. 4) cannot be accounted for on the basis of erroneous values for the rate constants. It seems possible that the surface may be closed by the adsorption of some inert species, or perhaps by the formation of an electrical double layer involving the aminium ion. Such a mechanism has been proposed (7) to explain the effect of chloride ion on the rate of dissolution of copper in acid chloride solutions.

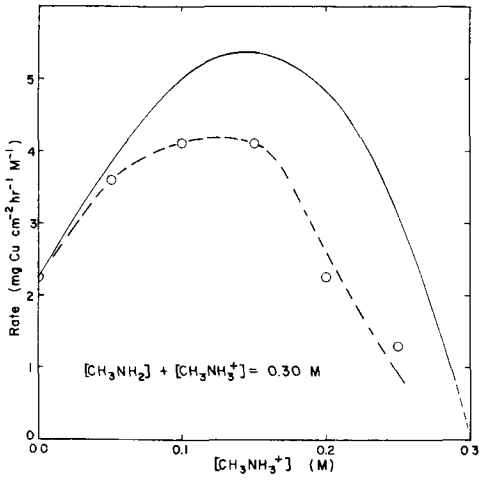

Fig. 4. Rate of copper dissolution in aqueous methylamine solutions as a function of the acidity, at constant concentration of total amine. Solid line calculated from Eq. [3], using the values given in Table III for the constants.

Acknowledgments

The authors express thanks to Dr. J. Halpern for helpful discussions. Financial support by the National Research Council (Canada) is gratefully acknowledged.

Manuscript received June 29, 1959.

Any discussion of this paper will appear in a Discussion Section to be published in the December 1960 JOURNAL.

REFERENCES

1. J. Halpern, *This Journal*, **100**, 421 (1953).
2. J. I. Fisher and J. Halpern, *ibid*, **103**, 282 (1956).
3. J. Halpern, H. Milants, and D. R. Wiles, *ibid.*, **106**, 647 (1959).
4. E. B. Sandell, "Colorimetric Analysis for Traces of Metals," p. 204, Interscience Publishers, Inc., New York (1950).
5. I. M. Kolthoff and V. A. Stenger, "Volumetric Analysis," Interscience Publishers, Inc., New York (1942).
6. J. C. Bailar, "The Chemistry of the Coordination Compounds," p. 371, Reinhold Publishing Corp., New York, (1956).
7. J. R. Weeks and G. R. Hill, *This Journal*, **103**, 203 (1956).

The Attack of Copper-Gold, Silver-Gold, Nickel-Copper, and Silver-Copper Alloys by Sulfur at Elevated Temperatures

Barry D. Lichter[1] and Carl Wagner[2]

Department of Metallurgy, Massachusetts Institute of Technology, Cambridge, Massachusetts

ABSTRACT

Copper-gold alloys involving 10 and 33 mole % Au and Ag-Au alloys involving 12 mole % Au are attacked by liquid or gaseous sulfur above 400°C very rapidly with formation of a composite scale consisting of an outer homogeneous sulfide layer and an inner two-phase layer involving Au-rich alloy and sulfide in accord with theoretical considerations regarding the instability of a plane alloy-sulfide interface. The tendency to form a rugged alloy-sulfide interface decreases with higher Au contents especially at lower temperatures and the rate of attack by sulfur decreases accordingly. Silver-copper alloys involving 40 mole % Cu are also rapidly sulfidized at 400°C and yield a single sulfide layer of uniform thickness. Nickel-copper alloys sulfidized at 400°C yield a scale consisting of an outer layer which is supposedly digenite $Cu_{1.8}S$, and an inner layer which is supposedly a solid solution of Cu_2S in nickel sulfide.

In two previous papers (1,2), diffusion processes during the oxidation of alloys involving noble metals have been considered. In particular, a theoretical analysis of the interplay of diffusion processes in the alloy and the scale shows that a plane alloy-oxide interface is not stable if only one component of a binary alloy is oxidized and diffusion in the alloy is slow in comparison to diffusion in the oxide of the less noble metal (2). Thus a highly rugged alloy-oxide interface may be formed as has been found by various authors cited previously (2). To supplement available observations, the attack of Cu-Au and Ag-Au alloys by sulfur has been investigated. The experimental methods were weight gain measurements and microscopical examination of sectioned samples, supplemented by chemical analysis of detached scales and x-ray investigations. In addition, observations are presented on the attack of Ni-Cu and Ag-Cu alloys by sulfur involving sulfidization of both alloy constituents.

Copper-gold and Ag-Au alloys were chosen because the self-diffusion coefficients of silver and copper in their sulfides stable above 300°C are as high as 10^{-6} to 10^{-5} cm²/sec (3-6), whereas the interdiffusion coefficients in solid solutions Cu-Au and Ag-Au are much lower, e.g., 10^{-12} to 10^{-11} cm²/sec at 500°C (7-12). Moreover, the solubility of sulfur in silver and copper is very low (13). In particular, the solubility of S in Cu (coexisting with Cu_2S) at 600°C has been found to be as low as 10^{-3} a/o (atomic percent) (14). Thus internal sulfidization is not likely to interfere. While this investigation was conducted, however, it was found in accord with previous observations by Maclaurin (15) that solid Ag_2S-Au_2S solutions are formed and thereby certain complications not anticipated in the theoretical analysis (2) do occur. According to Maclaurin (15), Cu_2S also dissolves Au_2S but to a minor extent.

Figure 1 shows schematically a cross section through the scale which one may expect when Cu-Au alloys react with sulfur vapor of atmospheric pressure at 500°C. Under these conditions, only cubic Cu_xS ($1.7 \leqq x \leqq 2$) is formed supposedly, whereas at lower temperatures several sulfide phases may be formed as discussed below. In addition to an outer layer consisting of cuprous sulfide, Fig. 1 shows an inner two-phase layer consisting of penetrating sulfide zones interspersed with metallic trunks rich in gold.

As a limiting case, one may assume that copper diffuses in the metallic trunks only in a direction parallel to the original surface of the alloy, no plastic flow of the metallic trunks takes place, and thus the local gold concentration in the two-phase scale is equal to the initial gold concentration of the alloy.

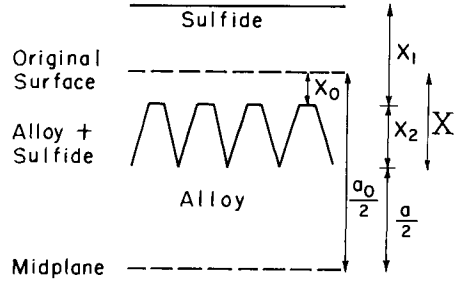

Fig. 1. Schematic section across a Cu-Au sample sulfidized at 500°C with a homogeneous layer of Cu_2S and a two-phase layer consisting of Cu_2S I and gold-rich alloy. (x_0 distance between outer boundary of the two-phase layer and initial surface, x_1 thickness of outer sulfide layer, x_2 thickness of two-phase layer, X distance between alloy-scale boundary and initial surface, a_0 initial thickness of the sample, a thickness of the unattacked core of the sample).

[1] Present address: Air Force Cambridge Research Center, Bedford, Massachusetts.

[2] Present address: Max-Planck-Institut für physikalische Chemie, Göttingen, Germany.

In this case, the outer boundary of the two-phase scale coincides with the original surface, i.e., $x_o = 0$.

In the sulfide phase, copper ions and electrons are supposed to diffuse outward, and plastic flow of the sulfide is supposed to take place so that the transition of copper from the metallic to the sulfide phase does not result in the formation of excessive voids.

Under these conditions, Cu-Au and Ag-Au alloys involving up to about 50 mole % Au are expected to be sulfidized at nearly the same rate as pure Cu and Ag with diffusion in the sulfide phase as rate-determining step.

The actual situation may deviate from the above limiting case in several respects.

1. Since metal ions and electrons move outward and plastic flow of the sulfide is limited, voids at the alloy-sulfide boundary may be formed in accord with observation by Czerski and Patzau (16), Billy and Valensi (17), Moore (18), and Rickert (19) on the sulfidization of pure Cu and Ag. In such voids, sulfur vapor originating from the dissociation of sulfide may diffuse and form sulfide farther inward whereby voids are filled at least in part.

2. Plastic flow of metallic trunks rich in gold may occur. Accordingly, the outer boundary of the two-phase scale is displaced by a distance x_o from the original surface as is shown in Fig. 1.

3. Side-branching of the penetrating sulfide zones may occur and produce a sponge-like network of gold-rich alloy.

4. In the case of excessive side-branching, individual gold-rich alloy particles in a sulfide matrix may be formed and move inward in the same fashion as inert markers move inward when a metal is oxidized and cations rather than anions migrate in the oxide. This also results in a displacement of the outer boundary between one-phase and two-phase scale toward the bulk alloy, i.e., $x_o > 0$.

5. Even under conditions where a plane alloy-sulfide interface is not stable, a nearly plane alloy-sulfide interface may occur on most of the alloy, but there may be pronounced local attack, especially along grain boundaries. Accordingly, the sulfur take-up of the sample is small, but the maximum depth of sulfide penetration may be high.

6. In the case of gold-rich alloys a plane alloy-sulfide interface, although theoretically not stable, may prevail without significant irregularities as, e.g., presumably in the case of the oxidation of Pt-rich Ni-Pt alloys (1,2). Under these conditions, diffusion of the less noble component of the alloy toward the alloy-sulfide interface becomes the rate-determining step.

7. In addition to diffusion, transfer of cations from the alloy to the sulfide may be an important rate-determining step according to recent observations by Rickert (19) on the sulfidization of pure Ag and Cu.

The experimental results reported below show that the systems investigated in this research exhibit considerable deviations from the limiting case conceived for theoretical calculations (2). In view of the complexities which have been found, results have qualitative rather than quantitative significance. No particular efforts have been made to obtain precise weight gain data because at the present stage the structure of the scale and the order of magnitude of reaction rates seem of primary interest. The discussion of the most characteristic features is stressed. Observations of seemingly minor importance are mentioned briefly but are not discussed at length.

Experimental

Materials

Copper.—Commercial Cu (99.94%) was available as 0.2 cm sheet. In addition, high-purity Cu (99.-999%) in rod form was rolled to 0.2 and 0.3 cm sheet.

Silver.—Ag shot (99.95%) was melted under nitrogen and sucked into 7 mm Vycor tubes whereby rods were obtained which were rolled to 0.2 and 0.3 cm sheet.

Nickel.—Commercial Ni (99.5% Ni, 0.32% Co, 0.15% Fe, less than 0.02% Pb) was obtained in the form of 0.1 cm sheet.

Copper-gold and silver-gold alloys.—Cu-Au alloys with mole fractions of gold $N_{Au} = 0.10$, 0.33, 0.61, and 0.74 and Ag-Au alloys ($N_{Au} = 0.12$, 0.35, and 0.56) were obtained from Baker & Co., Newark, New Jersey, where cast alloys were rolled to a thickness of 0.24 cm, annealed in nitrogen at 700°C for 15 min, quenched in water, and cross-rolled to a final thickness of 0.2 cm. These alloys are designated "as received" below. Microscopic examination of etched surfaces revealed the presence of effects of cold work and coring. To eliminate inhomogeneities and promote grain growth, samples of all alloys were annealed in a nitrogen atmosphere saturated with methanol for 100 hr approximately 100°C below the respective liquidus temperatures. The annealing time was sufficient to remove indications of a cored structure. These alloys are designated "annealed" below.

Nickel-copper alloys.—Ni-Cu alloys were prepared by J. D. Harrison. Reagent grade Cu and Ni were melted separately under hydrogen in order to remove oxygen. Alloys were prepared by vacuum melting in an induction furnace, admitting helium, and sucking samples into 9 mm Vycor tubes. The alloys contained 10, 29, and 58 atomic % Cu. Cast rods were rolled to 0.1 cm sheet.

Silver-copper alloys.—An alloy of eutectic composition ($N_{Ag} = 0.60$, $N_{Cu} = 0.40$) was prepared by melting high-purity Ag and Cu under nitrogen, sucking samples into 7 mm Vycor tubes whereby rods were obtained which were rolled to 0.3 cm sheet.

Sulfur.—U. S. P. sulfur powder was used without further purification.

Preparation of Samples

Samples were cut from the prepared sheet with a jeweller's saw, and a small hole was drilled at one end of each sample. The dimensions of samples were as follows: copper and silver, 0.5 x 1.0 x 0.2 or 0.3 cm; copper-gold and silver-gold, 0.5 x 1.0 x 0.2 cm; nickel and nickel-copper, 0.7 x 1.0 x 0.1 cm; silver-copper, 0.9 x 1.5 x 0.3 cm. The cut edges were abraided on emery paper to remove saw marks, and the large surfaces were further polished on emery

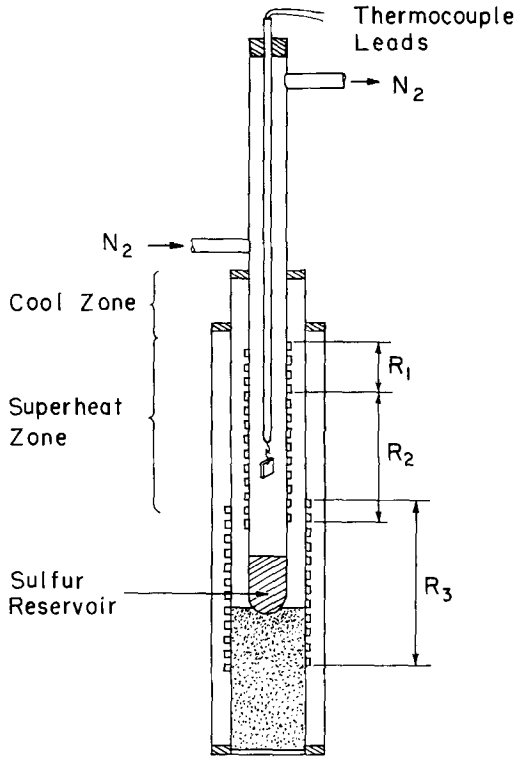

Fig. 2. Set-up for sulfidization in superheated sulfur vapor (500°-700°C) and in liquid sulfur (300°-400°C).

paper to 3/0 grade. Samples were washed with soap and water and rinsed in acetone or methanol. After surface preparation, samples were weighed immediately and inserted in the furnace.

Sulfidization Procedure

Reactions were studied (*a*) in sulfur vapor of atmospheric pressure (700°, 600°, and 500°C) and (*b*) in liquid sulfur (400° and 300°C). Figure 2 shows the set-up designed especially for tests in sulfur vapor. Power is supplied in three stages. The upper two stages ($R_1 = 8$ ohms, $R_2 = 15$ ohms) consisting of a single ribbon winding (1/16 in., "Chromel A", B and S number 28) cemented directly to the inner 25 mm Vycor tube with a common central lead were used to superheat sulfur vapor. The third stage ($R_3 = 5$ ohms) consisting of a ribbon winding ⅛ in., "Chromel A", B and S number 24) cemented to a 38 mm Vycor tube concentric with the inner tube was used to boil sulfur in the lower reservoir. A third concentric Pyrex tube was used as "storm window." Power was supplied from a constant voltage transformer and controlled by means of three variacs connected with the heating resistances R_1, R_2, and R_3. The maximum temperature which could be reached in the superheat zone was 725°C with a total electrical power imput of 1 kw. Temperature fluctuations were about ±5°C.

With the help of this design, it was possible to overcome initial difficulties which were encountered with a conventional two-stage furnace consisting of a ceramic tube surrounded by a thick packing of magnesia. When the conventional furnace was used, sulfur condensed at the upper end of the furnace and ran downward in a rather irregular manner because of the high peak of the viscosity of sulfur at 187°C (20). Applying sufficient power to the upper stage R_1 of the set-up shown in Fig. 2, liquid sulfur flowing downward was vaporized before it reached the superheat zone R_2 used for the sulfidization experiments. Boiling and recycling of sulfur and the location of the sample could be observed readily with this design.

To react samples with liquid sulfur, power was supplied only to the reservoir heated by R_3.

Samples were supported in the furnace by quartz hooks suspended on the sealed end of a Vycor tube which accommodated a thermocouple.

The samples and supporting hooks were weighed separately with a precision of 0.1 mg. At the completion of a run the Vycor tube was removed quickly from the furnace, and the sample was allowed to cool in air before weighing. For runs at 400° and 300°C, molten sulfur occasionally remained on the surface of the samples after withdrawal. The sulfur immediately ignited on contact with air and required from 5 to 10 sec for complete combustion. For most runs the weight gain was recorded as the difference in weight between the sample plus hook before and after reaction. Whenever it was possible to separate sample and hook, the weight gain was recorded as the difference in weight between the sample alone before and after reaction.

Evaluation of Weight Gain Measurements

To obtain results which are independent of the geometry of the samples and determined only by thermodynamic variables, it is necessary to conduct scaling experiments with sufficiently large samples so that the lateral dimensions are much greater than the thickness of the scale. If this condition is not satisfied, edge effects do occur, since the outer area of the sample increases and the area of the boundary between scale and metal decreases during the scaling process. Moreover, in view of local stresses, cracks within the scale and local detachment of the scale from the metallic core may occur as has been found especially in investigations on the oxidation and the sulfidization of iron (21-26).

Because of the high price of gold and the high reaction rates, it was not possible to use samples of sufficient size in order to prevent edge effects. Therefore, a definite rate law cannot be expected and, accordingly, no rate constants are reported. To represent results graphically, however, it was found expedient to plot weight gains per unit nominal area vs. the square root of time. In the calculation of the nominal area, only the large faces of the samples, approximately 0.5 x 1.0 cm, were taken into account; the smaller faces with a width of 0.1 or 0.2 cm were disregarded. Plots of this kind may in general be approximated by straight lines except when the reaction goes to completion.

Metallography

After reaction with sulfur, samples were cast in methylmetacrylate plastic. Powdered polymer was mixed with an equal volume of liquid monomer.[3] Hardening of the plastic occurs at room temperature without application of heat or pressure.

[3] Both supplied under the name "Casto-Mold" by Cosmos Products Inc., New York, N. Y.

Mounted samples were ground on a wet abrasive belt to approximately the center section. Next, samples were abraded lightly on wet silicon-carbide paper. Final polishing was performed on a "gamal" cloth wheel, using levigated gamma-alumina fine abrasive. A few samples were machine polished on lead laps, a standard procedure for preparing mineral specimens. These samples produced scale structures identical with those of manually prepared samples which indicated that the latter were representative. Samples were generally observed unetched except when it was desirable to observe the relation between the structure of the unattacked core and the structure of the scale. Unreacted samples were prepared similarly but were polished on broadcloth wheels with a coarse alumina abrasive before final polishing with "gamal" cloth. For grain size determinations a number of etchants were used. For "annealed" alloys, standard solutions of 10% KCN-2% KI and 5% $(NH_4)_2S_2O_8$ were applied separately with an eyedropper. The strength of the mixture was altered by dilution according to the gold content of the alloy. A 3% iodine solution in methanol, used (27) in studies with Cu_3Au (N_{Au} = 0.25), was found profitable only with a Cu-Au alloy with N_{Au} = 0.33. For as-received samples, the 10% KCN-2% KI and the 5% $(NH_4)_2S_2O_8$ etchant were used. Slightly better structures could be obtained with the help of staining etchants containing $FeCl_3$ or $K_2Cr_2O_7$. The latter revealed concentration gradients in as-received alloys.

Sulfidization of Cu-Au Alloys

Pure copper.—Weight gain curves of Cu samples reacted with sulfur at 300°, 400°, and 500°C are shown in Fig. 3. In view of the high rate of the reaction at 500°C, superheating of the samples may have occurred. Thus values for 500°C are only indicative for a very rapid reaction.

At 300° and 400°C, there may be formed three reaction products, (*a*) hexagonal chalcocite, Cu_2S II, with a variable deficit of copper, (*b*) face-centered cubic digenite with the approximate formula $Cu_{1.8}S$, and (*c*) hexagonal covellite, CuS (28-33).

At 500°C, CuS is unstable as its dissociation pressure exceeds 1 atm (34-36). Moreover, according to Hirohara (5), hexagonal Cu_2S II is unstable above 470°C. Instead, a face-centered cubic modification, Cu_2S I, is found. Its lattice is identical with that of digenite (5, 28, 29, 33). Tentatively, it may be assumed that the homogeneity of the phase Cu_2S I at 500°C extends from a Cu/S ratio of 2.0 to about 1.8. Thus face-centered cubic Cu_2S I is supposedly the only reaction product at 500°C.

Sectioned and polished samples which were sulfidized in part contained only gray sulfide. A thin outer blue layer of CuS becomes visible on samples sulfidized at 400°C only after much longer sulfidization, e.g., 24 hr. The gray sulfide may actually consist of two separate layers corresponding to hexagonal Cu_2S and digenite $Cu_{1.8}S$, or the respective transformation products formed on cooling. So far, however, no experimental evidence of Cu_2S II and digenite as separate reaction products has been obtained.

In accord with observations by Czerski and Patzau (16) and Rickert (19) sections of Cu samples sulfidized at 400°C showed numerous voids in the scale next to the metal whereas no voids were found in the outer scale. The porosity of the inner scale may be due to local detachment of the scale similar to that reported for the oxidation and sulfidization of iron (21-26).

Cu-Au *alloys.*—Weight gain plots for Cu-Au alloys involving 10 and 33 mole % Au are shown in Fig. 4 and 5.

Copper-gold alloys involving 10 mole % Au were sulfidized at about the same rate as pure copper as follows by comparing weight gain curves in Fig. 3 and 4. Microscopical examination of sectioned samples revealed an outer homogeneous sulfide layer and an inner two-phase layer consisting of sulfide

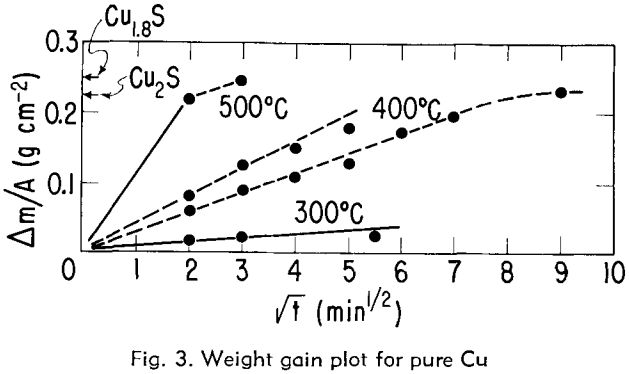

Fig. 3. Weight gain plot for pure Cu

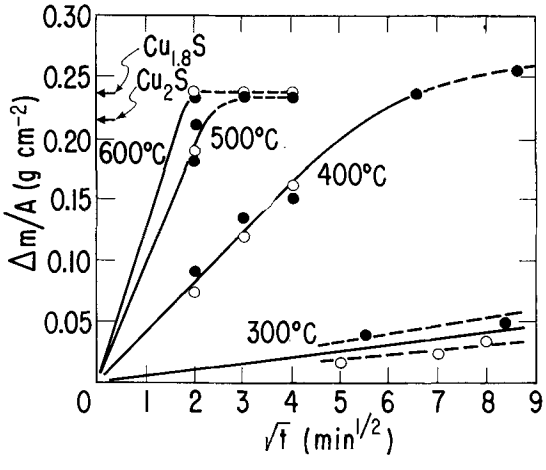

Fig. 4. Weight gain plot for Cu-Au alloy, N_{Au} = 0.10. ○ Annealed; • as-received.

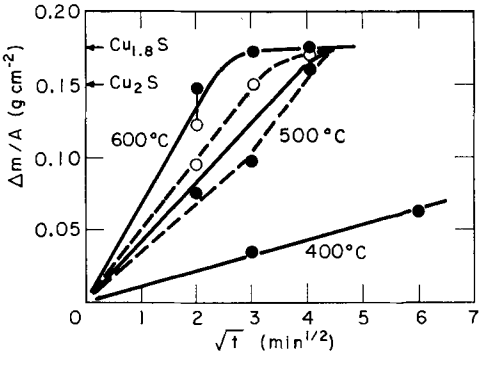

Fig. 5. Weight gain plot for Cu-Au alloy, N_{Au} = 0.33. ○ Annealed; • as-received.

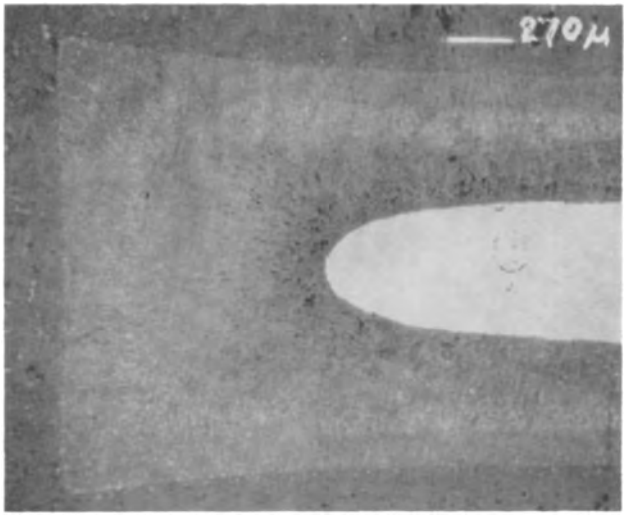

Fig. 6. Section of Cu-Au alloy (N_{Au} = 0.10, annealed) sulfidized at 500°C for 4 min. White region on the right-hand side is unattacked alloy, which is surrounded by a two-phase layer and an outer homogeneous sulfide layer shown only in part. Black spots in the two-phase layer are due to porosity. The width of the two-phase layer at the left-hand side is nearly equal to the original thickness. In the middle of the sample shown at the right-hand side, the two-phase layer has contracted.

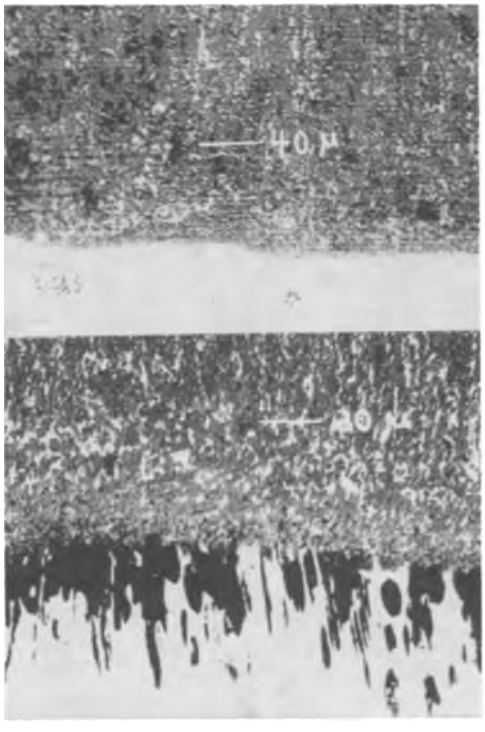

Fig. 7. Details of alloy-scale boundary of Cu-Au alloys (N_{Au} = 0.10) sulfidized at 500°C for 4 min. (a) (top) Annealed sample; (b) (bottom) as-received sample.

and metal. Figures 6 and 7a show that the boundaries between the various layers on annealed samples were remarkably well defined. In contrast, "as received" samples showed pronounced local sulfide penetrations presumably associated with copper-rich regions of the alloy, see Fig. 7b. Even in the outer scale, especially at the outer surface, gold particles were observed. Probably, these gold particles were formed when samples were cooled and solid Cu_2S-Au_2S solid solutions present at elevated temperatures decomposed. This interpretation is supported especially by the observation that the amount of gold in the outer scale increased when samples were stored at room temperature for a longer time.

Table I. Scale measurements for annealed Cu-Au alloys

N_{Au}	Temp, °C	t, min	x_1, mm	x_2, mm	X, mm	x_0, mm
0.10	500	4	1.1	0.6	0.7	0.1
	400	4	0.38	0.18	0.23	0.05
		9	0.60	0.32	0.39	0.07
		16	0.75	0.48	0.54	0.06
	300	25	0.08	0.07	0.07	—
		49	0.10	0.06	0.06	—
		64	0.10	0.06	0.06	—
0.33	500	4	0.3	0.35	0.35	—
		9	0.6	0.5	0.6	0.1
		16	0.65	0.9	1.0	0.1

Scale measurements for annealed alloys are presented in Table I. The thicknesses of the outer one-phase layer and the inner two-phase layer, x_1 and x_2, respectively, were measured approximately at the middle of the large faces of the sample with the help of a movable stage micrometer. In addition, the width a of the unattacked alloy was determined. By subtracting half the thickness of the unattacked alloy from half the initial thickness of the sample $a_o/2$, the distance X between the original surface and the boundary between the scale and the unattacked alloy was obtained, $X = a_o/2 - a/2$, see Fig. 1. Finally, the distance x_o between the original surface and the boundary between the outer one-phase and the inner two-phase scale was calculated as $x_o = X - x_2$. Finite values of x_o indicate either dissolution of gold in the sulfide, or a displacement of gold-rich alloy toward the middle of the sample either by plastic flow of the metallic trunks, or by inward movement of isolated gold-rich particles as has been mentioned above. From the values listed in Table I, one recognizes that the displacement x_o does not exceed 20% of the distance X to which the attack has penetrated.

Copper-gold alloys involving 33 mole % Au were sulfidized more slowly according to weight gain curves shown in Fig. 5. Microscopical examination of sectioned samples sulfidized at 400°, 500°, and 600°C revealed the same general type of scaling as that shown in Fig. 6, but with a rather abrupt change in the width of the single-phase regions in the two-phase scale. The width in the inner part of the two-phase region was much smaller than in the outer part. Scale measurements are listed in Table I.

Copper-gold alloys involving higher gold contents (N_{Au} = 0.61 and 0.74) were sulfidized at much lower rates. Even at 700°C, only minor weight gains were obtained, e.g., $\Delta m/A = 0.002$ g/cm² for $N_{Au} = 0.61$ after 16 min and for $N_{Au} = 0.74$ after 64 min.

Microscopical examination of sectioned samples which had been reacted at 700°C revealed the absence of a typical two-phase scale described above for alloys involving lower gold contents. Instead, there was found a thin uniform sulfide layer containing small amounts of Au which presumably was formed by decomposition of Cu_2S—Au_2S solid solutions present at elevated temperatures. For samples

involving 61 a/o Au, isolated patches of a two-phase scale were observed between the outer sulfide and the inner unattacked core. Comparison of the alloy grain size with the width of the single-phase constituent in the two-phase patches, together with observations at the scale-alloy boundary, suggest that a considerable amount of grain boundary attack is responsible for the appearance of the patches. No patches were observed for alloys involving 74 a/o gold. However, occasional penetration along grain boundaries was observed. At lower temperatures (600° and 500°C) only a uniform sulfide layer was observed.

Additional Observations on the Structure of the Scale.

The occurrence of a sponge-like network of gold-rich alloy within the two-phase scale has been confirmed directly for Cu-Au alloys involving 33 a/o Au. Upon dissolving the sulfide phase in a mixture of equal volumes of HNO_3 and H_2O with a small addition of KNO_2, a sponge-like network of gold-rich alloy could be isolated.

When the two-phase scale from an alloy involving 10 a/o Au was treated in the same way, the details of the structure were lost. This indicates that the two-phase scale of the latter alloy involved islands of gold-rich particles or sponge in a sulfide matrix rather than a coherent network of gold-rich alloy.

The width of the single-phase regions in the two-phase scale of gold-rich alloys ($N_{Au} = 0.10$ and 0.33) was found to depend markedly on temperature. The higher the temperature, the greater was the width. This is due at least in part to coarsening of the disperse structure while the sample was at temperature as follows from microphotographs shown in Fig. 8. Two Cu-Au samples ($N_{Au} = 0.33$) were reacted to completion in sulfur vapor at 500°C. A section of one of these samples is shown in Fig. 8a. A section of the other sample which was heated to 700°C for further 16 min, is shown in Fig. 8b. The width of the single-phase regions in Fig. 8b is considerably greater than that in Fig. 8a and similar to the width in a sample reacted to completion directly at 700°C, see Fig. 8c. This shows that the residual gold-rich alloy in the two-phase layer undergoes considerable structural changes. Au_2S is dissolved in Cu_2S to some extent (15) especially at higher sulfur activities. Thus gold can be transferred between different points of the sulfide-alloy interface involving different curvatures by virtue of local dissolution and redeposition corresponding to a decrease of the area of the gold-sulfide interface and the free energy of the system. In addition, gold atoms may migrate along the gold-sulfide interface.

At all temperatures, the width of the single-phase regions in the two-phase scale was found to be considerably smaller than the grain size of the original alloy. This indicates that transgranular penetrations of sulfide do occur in accord with observations on the attack of solid alloys by liquid metals which dissolve one component of the solid alloy preferentially (37).

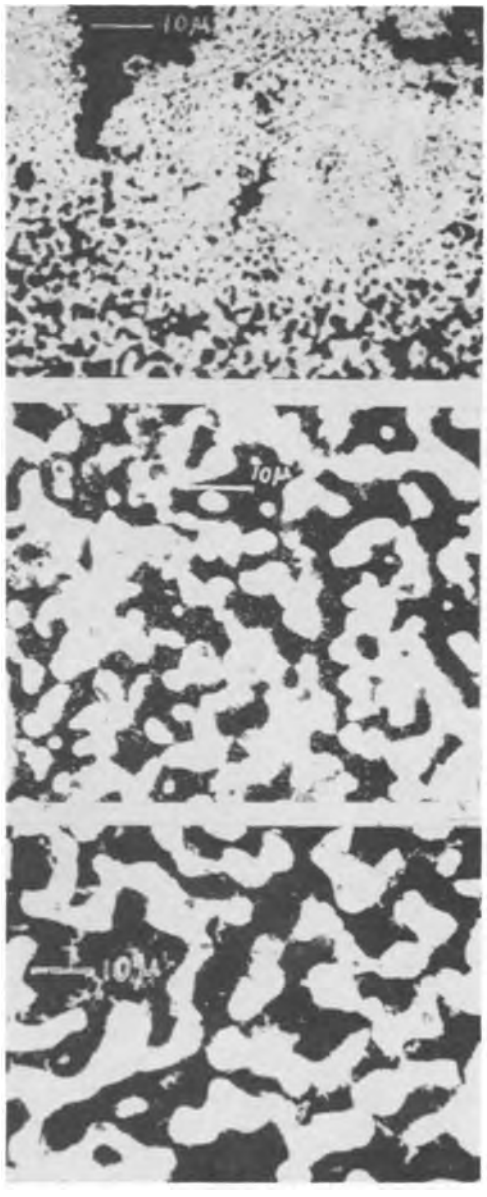

Fig. 8. Structures of two-phase layers obtained on Cu-Au alloys ($N_{Au} = 0.33$, as-received). (a) (top) Sample sulfidized at 500°C for 16 min; (b) (center) sample sulfidized at 500°C for 20 min and annealed in sulfur vapor at 700°C for 16 min; (c) (bottom) sample sulfidized at 700°C for 4 min.

Auxiliary Investigations

Chemical analysis of Cu samples completely sulfidized at temperatures ranging from 400° to 725°C yielded Cu/S atom ratios of 1.77 to 1.84 in accord with weight gain measurements. Somewhat higher Cu/S atom ratios, 1.86 to 1.89, were found in the scale detached from Cu samples which were incompletely sulfidized at 300° to 500°C. Ratios of 1.77 to 1.84 are characteristic of digenite (presumably identical with Cu_9S I) coexisting with sulfur vapor of atmospheric pressure above 500°C, or CuS below 500°C. The same Cu/S ratios were found in the scale detached from sulfidized Cu-Au alloys ($N_{Au} = 0.10$ and 0.33).

The composition of metallic particles in the two-phase scale formed on partially sulfidized Cu-rich alloys ($N_{Au} = 0.10$ and 0.33) was determined by x-ray diffraction investigations. Samples were sectioned parallel to the alloy-scale interface at several

positions in the two-phase scale. The diffraction patterns from the exposed surfaces, obtained with filtered copper radiation on a Norelco diffractometer, showed the spectra of pure gold to within $2\theta = \pm 0.2°$ where θ is the Bragg angle for Cu Kα reflections in the angular region $90° > 2\theta > 35°$. Even at that position in the two-phase scale practically adjacent to the interface between scale and remaining core of the copper-rich alloys, the spectra for virtually pure Au were observed.

Discussion

According to weight gain plots shown in Fig. 4 and 5 the rate of sulfidization of Cu-rich alloys is about the same for as-received samples and annealed samples, but there is a slight tendency for as-received samples to be sulfidized somewhat more rapidly than annealed samples as is indicated especially by results obtained for $N_{Au} = 0.10$ at 300°C shown in Fig. 4. Scale measurements are in accord herewith. In essence, however, the presence of inhomogeneities in as-received samples does not lead to a different type of attack but only modifies some characteristics of the attack found with annealed samples.

Upon extrapolating weight gain data and scale measurements for Cu-rich alloys ($N_{Au} = 0.10$ and 0.33), it follows that the final weight of a sample is reached after about the same time at which the core of unattacked alloy has disappeared. Hence most of the copper originally present in the two-phase layer is converted readily into sulfide, and accordingly the trunks of the remaining alloy consist mostly of gold. This has been confirmed by x-ray diffraction investigations reported above.

In accord with previous theoretical calculations (2), Cu and Cu-Au alloys containing 10 and 33 mole % Cu react very fast. With increasing concentration of Au, the rate of sulfidization of alloys containing up to 33 a/o Au decreases, although not considerably. To make a comparison without using a rate law explicitly, one may compare the times required for penetration of sulfide to a given depth X. For 500°C and $X = 0.05$ cm, one has $t \sim 3$ min if $N_{Au} = 0.10$ and $t \sim 5$ min if $N_{Au} = 0.33$. For 400°C and $X = 0.02$ cm, one has $t \sim 4$ min if $N_{Au} = 0.10$ and $t \sim 12$ min if $N_{Au} = 0.33$.

Gold-rich alloys ($N_{Au} = 0.61$ and 0.74) are sulfidized much more slowly than Cu-rich alloys. This is consistent with the absence of a typical two-phase scale. Thus one has a transition to the other limiting case involving a plane alloy-sulfide interface. Since diffusion in the sulfide phase is much faster than in the alloy, the activity of the sulfur at the alloy-sulfide interface is equal to that at the sulfide surface, the Cu concentration at the sulfide-alloy interface is virtually equal to zero, and diffusion of Cu toward the alloy-sulfide interface is the rate-determining step. According to Eqs. [16] to [20] of a previous, more general calculation (1) the distance x_i between the alloy-sulfide interface and the initial surface of the alloy is

$$x_i = 2u(D't)^{1/2} \qquad [1]$$

where D' is the interdiffusion coefficient of the alloy and the parameter u is determined by

$$\pi^{1/2} e^{u^2} \operatorname{erfc} u = 1 - N_{Au}^{(o)} \qquad [2]$$

The number of moles of metal contained in an alloy layer of thickness x_i *is* x_i/V' where V' is the molar volume of the alloy. Assuming the formula $Cu_{1.8}S$ as representative for the composition of the scale, sulfidization of 1 mole Cu corresponds to a weight increase of $M_S/1.8$ where $M_S = 32$ is the atomic weight of sulfur. Hence the weight increase $\Delta m/A$ per unit area is

$$\Delta m/A = x_i M_S/1.8\,V' = 2uM_S(D't)^{1/2}/1.8\,V' \qquad [3]$$

Equation [3] is evaluated for 500°C and $t = 1$ hr $= 3600$ sec with $D' = 2 \times 10^{-11}$ cm²/sec according to Jost (10), and values are compared with interpolated or extrapolated experimental values,

N_{Au}	0.33	0.61	0.74	
$\Delta m/A$ (calc.)	0.70	0.28	0.16	mg/cm²
$\Delta m/A$ (obs.)	300	2.4	1.2	mg/cm²

The experimental values $\Delta m/A$ are higher than the calculated values inasmuch as the alloy-sulfide interface was not plane under the conditions used in the present investigation. For Cu-rich alloys, the observed attack is especially high as compared to the calculated value. This illustrates the general conclusion that the instability of a plane interface may have a very large effect on the corrosion characteristics of an alloy. On the other hand, for Au-rich Cu-Au alloys for which a well-defined two-phase layer is not found and irregularities of the alloy-sulfide interface are not spectacular, the observed magnitude of attack is comparable to that calculated for a plane alloy-sulfide interface rather than to that of pure Cu or Cu-rich Cu-Au alloys.

Sulfidization of Ag-Au Alloys

Pure silver.—The reaction between pure Ag and sulfur is known to proceed very rapidly above 180°C because of easy migration of both cations and electrons in Ag_2S formed as reaction product above 180°C (38-40). In accord herewith, the time required for complete conversion of 2 mm Ag platelets into Ag_2S was found to be less than 4 min at 400° and 500°C. According to Czerski, Mrovec, Wallisch, and Werber (40) the rate is determined by a phase boundary reaction when the thickness of the Ag_2S layer is less than 0.1 cm, whereas diffusion control prevails with Ag_2S layers which are several centimeters thick according to Rickert (19).

Ag-Au *alloys.*—Weight gain curves for Ag-Au alloys involving 12 mole % Au are shown in Fig. 9. The sulfidization rate is remarkably high, although somewhat lower than for pure Ag. The total weight gain exceeds that for formation of Ag_2S alone and corresponds to the formation of a solid Ag_2S-Au_2S solution in accord with previous observations by Maclaurin (15). Microscopical examination of sectioned samples sulfidized at 400° and 500°C revealed an outer homogeneous sulfide layer and inner two-phase layer consisting of sulfide and Au-rich alloy, see Fig. 10. Scale measurements are shown in Table II. Samples sulfidized at 300°C showed only a homogeneous sulfide layer.

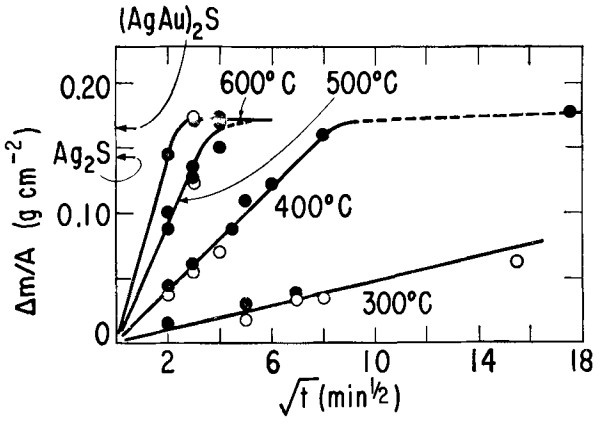

Fig. 9. Weight gain plot for Ag-Au alloy, $N_{Au} = 0.12$. ○ Annealed; • as-received.

Upon comparing microphotographs of sections of the scale in Fig. 10 and the original alloy in Fig. 11, it is clearly seen that the width of the single-phase regions in the two-phase scale is much smaller than the grain size in the original alloy. This illustrates the occurrence of transgranular attack.

According to Fig. 9, weight gain data for annealed alloys agree fairly well with data for as-received alloys. Sections of as-received samples showed a less well-defined boundary between two-phase scale and unattacked alloy, but the observed irregularities were much smaller than in the case of Cu-Au alloys shown in Fig. 7b.

Ag-Au alloys involving 35 mole % Au were found to react much more slowly. Weight gain curves are shown in Fig. 12.

Sectioned samples sulfidized at 700°, 600° and 500°C revealed considerable attack at grain boundaries together with transgranular attack. The resultant scale structure differs from that shown schematically in Fig. 1. Values of x_2 reported in Table II represent the average depth of penetration along grain boundaries. A thin two-phase region resulting from transgranular attack could be observed at the boundary between the outer sulfide scale (containing patches of alloy, presumably due to decomposition of Au_2S-Ag_2S solid solutions) and the core of the alloy. The thin two-phase layer follows the contour of the boundary between the alloy and the outer sulfide. The width of the thin two-phase layer is of the order of $x_2/10$. However, in the vicinity of a grain boundary, considerably more two-phase scale is formed, i.e., attack initiating at grain boundaries spreads into adjacent grains and results in formation of a two-phase scale.

Table II. Scale measurements for annealed Ag-Au alloys

N_{Au}	Temp, °C	t, min	x_1, mm	x_2, mm	X, mm	x_0, mm
0.12	500	9	0.92	0.31	0.65	0.34
	400	4	0.24	0.05	0.14	0.09
		9	0.37	0.06	0.20	0.14
		16	0.51	0.06	0.32	0.26
0.35	600	4	0.22	0.3	0.4	0.12
		16	0.43	0.4	0.6	0.22
	500	4	0.15	0.3	0.4	0.10
		16	0.25	0.4	0.4	0.12

Samples sulfidized at 400°C showed only a homogeneous sulfide layer. In view of the relatively low rate found at 400°C, the activity gradient of sulfur

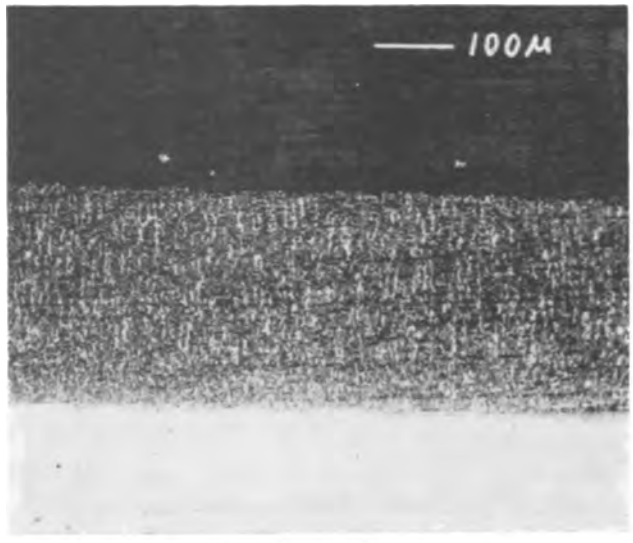

Fig. 10. Section of Ag-Au alloy ($N_{Au} = 0.12$, as-received), sulfidized at 500°C for 9 min with a homogeneous sulfide layer at the top, a two-phase layer in the middle, and unattacked alloy at the bottom.

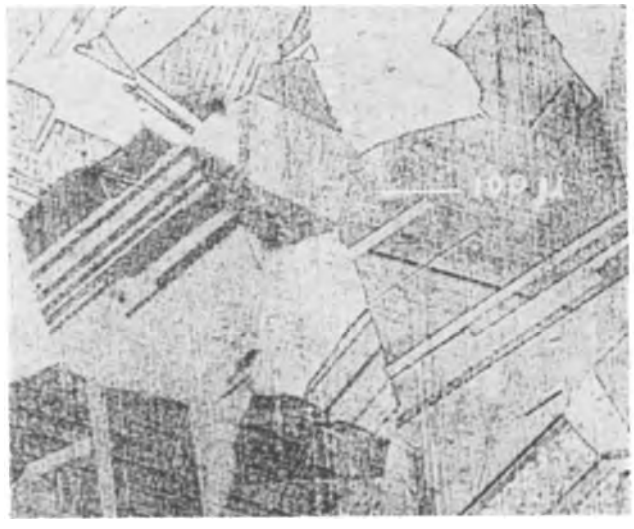

Fig. 11. Section of annealed Ag-Au alloy ($N_{Au} = 0.12$) etched with a mixture of a 10% KCN + 2% KI solution and a 5% $(NH_4)_2S_2O_8$ solution.

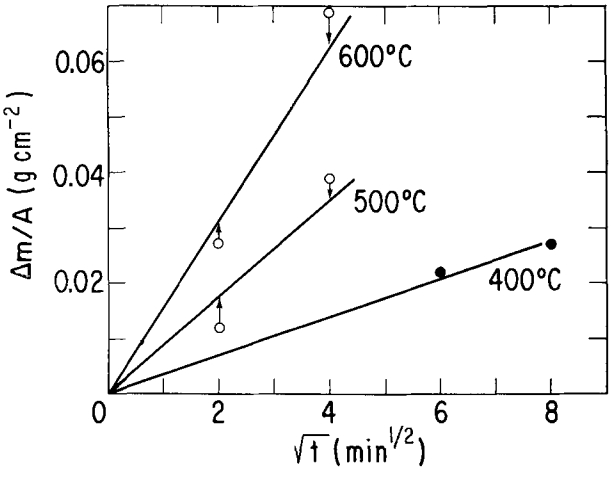

Fig. 12. Weight gain plot for Ag-Au alloy, $N_{Au} = 0.35$. ○ Annealed; • as-received.

in the sulfide must be small. Thus the activity of sulfur at the alloy-sulfide interface is nearly that of pure liquid sulfur, and accordingly a solid Ag_2S-Au_2S solution is formed.

Ag-Au alloys involving 56 a/o Au showed only slight attack. Even at 700°C, $\Delta m/A$ was as low as 0.0015 mg/cm² after 25 min. Microscopical examination of samples sulfidized at 500°, 600°, and 700°C revealed the presence of smooth sulfide layers with plane sulfide-alloy interfaces.

Discussion

In view of the formation of solid Ag_2S-Au_2S solutions (15), the behavior of Ag-Au alloys deviates from the behavior of Cu-Au alloys in several respects.

The structure of the scale may be similar to that found on Cu-rich Cu-Au alloys with an outer homogeneous sulfide layer and an inner two-phase layer consisting of sulfide and Au-rich alloy as shown in Fig. 10 for $N_{Au} = 0.12$. Since the attack is very rapid, there must be a significant gradient of the sulfur activity within the scale. The tendency for dissolution of Au diminishes with decreasing activity of sulfur, i.e., with increasing distance from the outer surface. Therefore, only little Au is dissolved at the boundary between the two-phase scale and unattacked alloy, whereas the outer parts of Au-rich alloy in the two-phase scale are gradually eaten away. Accordingly the outer boundary of the two-phase scale is displaced inward from the initial surface of the sample, i.e., $x_o > 0$, see Table II.

As an alternative, it is conceivable that Ag-rich Ag-Au alloys are sulfidized with formation of a sulfide layer of uniform thickness in which the Ag/Au ratio is virtually equal to that in the alloy. Since, the standard free energy of formation of Ag_2S is considerably more negative than that of Au_2S, the alloy coexisting with a solid solution Ag_2S-Au_2S of given composition has necessarily a much higher Au/Ag ratio than the sulfide phase. Thus there must be a thin zone of Au-rich alloy next to the sulfide phase.

To simplify calculations, it is assumed that the self-diffusion coefficients of Ag^+ and Au^+ ions in the sulfide phase are equal, and accordingly the Au/Ag ratio in the sulfide layer is independent of the distance from the surface. The driving force for outward migration of the cations is essentially a diffusion potential gradient resulting from the electrons which have a high mobility and, therefore, have the tendency to move ahead (41-43). Thus the rational rate constant k_r defined as the rate of metal transport in equivalents per unit area per unit time for unit thickness of the sulfide layer is (42)

$$k_r = (D''/2V_{eq}'') \ln a_S^{\circ}/a_S^{(i)} \qquad [4]$$

where D'' is the self-diffusion coefficient of the cations in the sulfide phase, V_{eq}'' is the volume of one equivalent of sulfide, $1/V_{eq}''$ is the cation concentration in equivalents per unit volume of the sulfide, a_S° is the sulfur activity at the outer surface, and $a_S^{(i)}$ is the sulfur activity at the alloy-sulfide interface.

The rate constant k_{PB} introduced by Pilling and Bedworth (44) is related to k_r as has been shown previously (38),

$$k_{PB} = (\Delta m/A)^2/t = k_r M_S^2/2V_{eq}'' \qquad [5]$$

From Eqs. [4] and [5] it follows that

$$\Delta m/A = (k_{PB}t)^{1/2} = (M_S/2V_{eq}'') [D''t \ln (a_S^{\circ}/a_S^{(i)})]^{1/2} \qquad [6]$$

Tentatively, chemical equilibrium at the alloy-sulfide interface is assumed. In view of the high degree of disorder of the cations in Ag_2S above 180°C (28), the sulfide phase may be supposed to be an ideal solution of $Ag^+ + 0.5\ S^{2-} = AgS_{0.5}$ and $Au^+ + 0.5\ S^{2-} = AuS_{0.5}$ (45). Thus, if the law of mass action is applied to the reactions

$$Ag\ (alloy) + 1/2\ S = AgS_{0.5}\ (sulfide) \qquad [7]$$

$$Au\ (alloy) + 1/2\ S = AuS_{0.5}\ (sulfide) \qquad [8]$$

the activities may be replaced by the respective mole fractions. Hence

$$\frac{1-y}{2_{Ag}^{(i)} [a_S^{(i)}]^{1/2}} = K_1 \qquad [9]$$

$$\frac{y}{a_{Au}^{(i)} [a_S^{(i)}]^{1/2}} = K_2 \qquad [10]$$

where y is the mole fraction of $Au_{0.5}S$, equal to the ratio of the number of Au^+ ions to the sum of the numbers of the cations, $1 - y$ is the mole fraction of $AgS_{0.5}$, $a_{Ag}^{(i)}$ and $a_{Au}^{(i)}$ are the activities of Ag and Au, respectively, which are determined by the composition of the alloy at the interface, and K_1 and K_2 are constants.

Upon subtracting corresponding sides of Eqs. [7] and [8] one has

$$Ag\ (alloy) + AuS_{0.5}\ (sulfide) = Au\ (alloy) + AgS_{0.5}\ (sulfide) \qquad [11]$$

with the equilibrium condition

$$\frac{a_{Au}^{(i)}\ (1-y)}{a_{Ag}^{(i)}\ y} = K_1/K_2 = K_{ex} \qquad [12]$$

where K_{ex} is the equilibrium constant of the exchange reaction in Eq. [11].

The value of K_1 may be calculated from the standard free energy of formation ΔF° for $1/2\ Ag_2S = AgS_{0.5}$ deduced from emf measurements (46). Hence

$$K_1 = \exp(-\Delta F^{\circ}/RT) = 75 \text{ at } 445°C \qquad [13]$$

Formulating Eq. [9] for the three-phase equilibrium alloy + sulfide + sulfur with starred variables and the special values $a_s^* = 1$ and $y^* \cong 0.5$ according to Maclaurin (14), one has

$$a_{Ag}^* = (1 - y^*)/K_1 (a_s^*)^{1/2} = 0.0067 \text{ at } 445°C \qquad [14]$$

corresponding to $N_{Au}^* = 0.95$ as mole fraction of Au in the alloy, according to equations interrelating mole fractions and activities in Ag-Au alloys recommended by White, Orr, and Hultgren (47).

The value of K_{ex} may then be obtained by formulating Eq. [12] for the three-phase equilibrium alloy + sulfide + sulfur,

$$K_{ex} = \frac{a_{Au}^*(1-y^*)}{a_{Ag}^* y^*} = 141 \text{ at } 445°C \quad [15]$$

whereupon in view of Eqs. [12] and [13]

$$K_2 = K_1/K_{ex} = 0.53 \text{ at } 445°C \quad [16]$$

With the help of Eqs. [12] and [15], one may readily calculate y for arbitrarily chosen compositions of the alloy at the interface, using activities according to White, Orr, and Hultgren (47). From a plot y vs. $N_{Au}^{(i)}$ one may read $N_{Au}^{(i)}$ for a given value of y which supposedly equals the bulk mole fraction of Au in the alloy. Finally, one may calculate the value of $a_S^{(i)}$ with the help of Eq. [10]

$$a_S^{(i)} = (y/K_2 a_{Au}^{(i)})^2 \quad [17]$$

For $N_{Au} = 0.35$ in the bulk alloy one has $y = 0.35$ and obtains $N_{Au}^{(i)} = 0.93$ and $a_S^{(i)} = 0.51$ at the alloy-sulfide interface, whereas in a system free of gold according to Eqs. [9] and [13] $a_S^{(i)} = 1.78 \times 10^{-4}$ at 445°C. Hence, in view of Eq. [4], the ratio of the rate constants for a Ag-Au alloy ($N_{Au} = 0.35$) and pure Ag is

$$k_r(N_{Au} = 0.35)/k_r(N_{Au} = 0)$$
$$= \ln 0.51/\ln (1.78 \times 10^{-4}) = 0.077 \quad [18]$$

Extrapolation of data reported by Rickert (19) yields

$$k_r(N_{Au} = 0) = 17 \times 10^{-6} \text{ equiv./cm sec at } 445°C \quad [19]$$

From Eqs. [5], [18], and [19] it follows that

$$\Delta m/A = 0.38 \text{ g/cm}^2$$
$$\text{for } N_{Au} = 0.35,\ t = 3840 \text{ sec at } 445°C \quad [20]$$

which is about 14 times greater than the experimental value obtained at 400°C, $\Delta m/A = 0.027$ g/cm². Since the various values involved in the calculation supposedly depend on temperature only to a minor extent, the divergence between the experimental and the calculated value is an indication that equilibria at the interfaces are not readily established. This is in accord with observations on the sulfidization of pure silver especially at 200° and 300°C (19). Since Ag is sulfidized very rapidly, one may conclude tentatively that the rate of transfer of Au from the alloy to the sulfide phase is the limiting factor.

If the gold content of the alloy exceeds the maximum content of Au_2S in the sulfide phase for a given activity of sulfur, ($N_{Au} > y^*$), it is also possible that a sulfide layer of uniform thickness is formed, but with accumulation of Au in the alloy near the alloy-sulfide interface. Then diffusion in the alloy determines the rate as is shown in what follows.

Fick's second law for diffusion in the alloy reads

$$\partial N_{Au}'/\partial t = D'\partial^2 N_{Au}'/\partial x^2 \text{ at } x > x_i \quad [21]$$

where N_{Au}' is the local mole fraction of gold in the alloy, D' the interdiffusion coefficient of the alloy supposedly independent of composition, x distance from the original surface, x_i distance of the alloy-sulfide interface from the original surface, and t time.

The initial condition is

$$N_{Au}' = N_{Au} \text{ at } x = 0, t = 0 \quad [22]$$

Since $D'' >> D'$, the gradient of the sulfur activity in the sulfide layer is very small, i.e., $a_S^{(i)} \cong a_S^\circ$ and, therefore,

$$y \cong y^* \quad [23]$$

$$N_{Au}'(x = x_i) \cong N_{Au}^* \quad [24]$$

As long as the alloy in the middle of the sample has virtually the original composition, equations for diffusion in a semi-infinite space apply. Thus the displacement of the locus of the alloy-sulfide interface is supposed to be in accord with the parabolic law

$$x_i = 2u(D't)^{1/2} \quad [25]$$

where u is a parameter calculated below.

Equations [21], [22], [24], and [25] are satisfied by

$$N_{Au}' = N_{Au} + [N_{Au}^* - N_{Au}] \frac{\text{erfc}\,[x/2(D't)^{1/2}]}{\text{erfc } u} \quad [26]$$

The molar volume of the alloy is denoted by V' and the surface area of the sample by A. The total number of moles of Ag and Au sulfidized per unit time is $(A/V')\ (dx_i/dt)$. Thus the number of moles of Au entering the sulfide layer per unit time is

$$dn_{Au}'/dt = y^*(A/V')\ (dx_i/dt) \quad [27]$$

According to Eq. [25] the alloy-sulfide interface moves by

$$dx_i = u\,(D'/t)^{1/2}dt \quad [28]$$

within the time dt. The amount of Au in the volume element Adx_i is $N_{Au}^* Adx_i/V'$ and must be equal to the sum of the amount of gold diffusing backward

$$(D'A/V')\ [-(\partial N_{Au}'/\partial x)_{x=x_i}]dt$$

and the amount of gold transferred from the alloy to the sulfide phase within the time dt. Hence, using Eqs. [27] and [28] and regrouping,

$$(N_{Au}^* - y^*)\ u\,(D'/t)^{1/2} = -D'\,(\partial N_{Au}'/\partial x)_{x=x_i} \quad [29]$$

Upon substituting Eqs. [25] and [26] in Eq. [29], it follows that

$$\pi^{1/2} e^{u^2} \text{erfc } u = (N_{Au}^* - N_{Au})/(N_{Au}^* - y^*) \quad [30]$$

whereby the parameter u is determined.

Equation [30] comprises Eq. [2] stated above for Cu-Au alloys with neglect of Au in the sulfide phase. Equation [2] is obtained from Eq. [30] by letting $N_{Au}^* = 1$ and $y^* = 0$.

Sulfidization of 1 mole of Ag (or Au) corresponds to pick-up of 0.5 g-atom of sulfur, with a weight gain of $M_S/2$. The total number n of moles of Ag and Au lost from the alloy is $n = x_i A/V'$. In view of Eq. [25], the weight gain per unit area is found to be

$$\Delta m/A = M_S x_i/2V' = u M_S (D't)^{1/2}/V' \quad [31]$$

Equation [31] involves the diffusion coefficient D' in the alloy, whereas Eq. [6] involves the diffusion

coefficient D'' in the sulfide phase. Since $D' << D''$, one has, therefore, to expect a sharp decrease in the rate of sulfidization when the mole fraction of Au in the alloy exceeds the upper limit of the mole fraction y^* of $AuS_{0.5}$ in the sulfide phase provided that diffusion control prevails.

To evaluate Eq. [31] for $N_{Au} = 0.56$ at 500°, the values $N_{Au}^* = 0.95$ and $y = 0.5$ valid for 445° are used as an approximation. Then Eq. [30] yields $u = 1.6$. Substituting $u = 1.6$, $V' = 10.3$ cm³/mole and $D' = 3.2 \times 10^{-12}$ cm²/sec according to Jost (8), one obtains from Eq. [31]

$$\Delta m/A = 0.6 \times 10^{-3} g/cm^2 \qquad [32]$$

for $N_{Au} = 0.56$ and $t = 3840$ sec at 500°C which is about 3.5 times less than the experimental value, $2.1 \times 10^{-3} g/cm^2$. The divergence between the calculated and the observed value is supposedly due in part to the approximations used in the calculation and in part to the occurrence of minor irregularities of the alloy-sulfide interface.

Sulfidization of Ni-Cu Alloys

At 400°C, Ni-Cu alloys involving 10, 29, and 58 a/o Cu were found to react with sulfur at a rate which is of the same order of magnitude as that for pure Ni, but much more slowly than pure Cu. Weight gain data are shown in Fig. 13. Results obtained with samples involving 58 a/o Cu showed a large scatter.Since local detachment of the scale is suspected as the reason for irregular results, the highest weight gains observed for different samples in runs lasting the same time are reported as representative values. The parabolic rate law is obeyed approximately in contradistinction to the linear rate law reported by Hauffe and Rahmel (48) for the reaction between pure nickel and sulfur vapor at pressures ranging from 10^{-2} to 1 mm Hg and 630°C.

Microscopical examination of sectioned samples revealed the presence of two distinct, essentially homogeneous sulfide layers, see Fig. 14. The alloy-scale interface and the interface between the two sulfide layers were essentially plane. Both sulfide layers, however, showed considerable porosity. According to chemical analysis, the Cu-Ni ratio in the scale was nearly equal to the Cu-Ni ratio in the alloy. The two sulfide layers could not be separated from each other. Therefore, the two layers have not been analyzed separately.

Since the ratio of the thickness of the outer sulfide layer to that of the inner sulfide layer increases with increasing copper content of the alloy, the outer sulfide layer is supposed to be mostly copper sulfide and the inner sulfide layer mostly nickel sulfide.

At 400°C the system Ni-S involves 4 intermediate phases which may be characterized by the approximate formulas Ni_3S_2, Ni_7S_6, NiS, and NiS_2 (13, 49). According to an investigation of the ternary system Cu-Ni-S by Köster and Malfinger (50), the phase Ni_3S_2 dissolves some Cu_2S but probably less than 1 mole % at 400°C.

A tentative schematic representation of the various diffusion processes is shown in Fig. 15 where the occurrence of different sulfides of Ni and Cu is disregarded. Copper and nickel (presumably as ions and electrons) enter the inner sulfide layer I of average composition Ni_yCu_zS and migrate outward. At the interface between the two sulfide layers, most of the arriving nickel ions, some copper ions, and electrons combine with sulfur ions from the outer layer II, Cu_xS, to form Ni_yCu_zS. In the outer Cu_xS layer, copper ions and electrons migrate to the surface and react with sulfur in order to form Cu_xS. In accord with experimental results, it is assumed that Cu and Ni enter the scale and migrate across layer I at the same ratio at which Cu and Ni are present in the alloy. Since the concentration of Cu in layer I is presumably much lower than the concentration of Ni, the mobility of Cu must be sufficiently greater than the mobility of Ni. This is

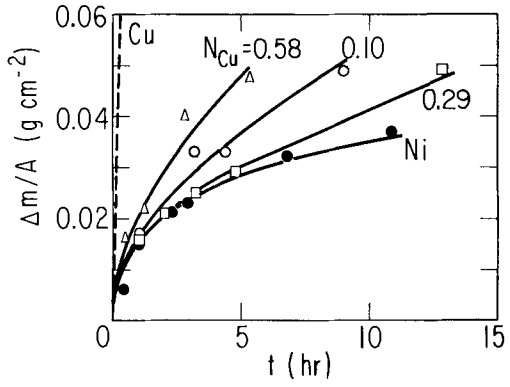

Fig. 13. Weight gain plot for Ni-Cu alloys sulfidized at 400°C.

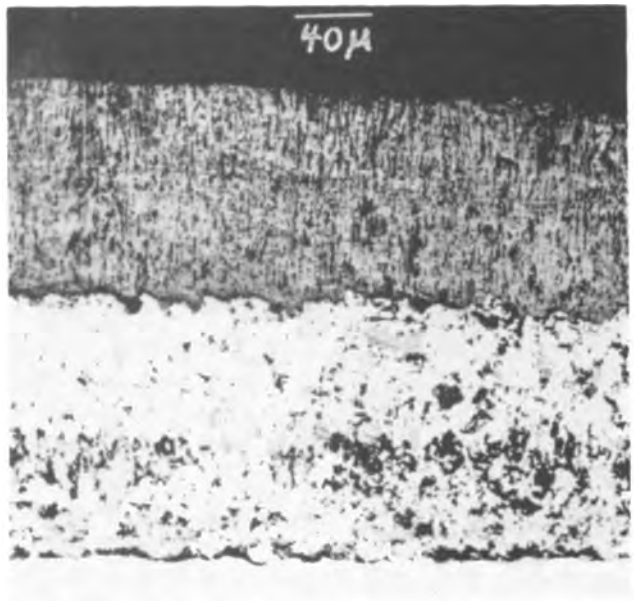

Fig. 14. Section of Ni-Cu alloy ($N_{Cu} = 0.58$) sulfidized at 400°C for 100 hr.

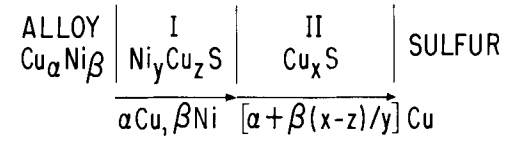

Fig. 15. Schematic representation of diffusion processes in the scale on Ni-Cu alloys exposed to sulfur at 400°C. Reaction at the Ni_yCu_zS-Cu_xS interface: αCu (in Ni_yCu_zS) + βNi in (Ni_yCu_zS) + $(\beta/y)Cu_xS = (\beta/y)\ Ni_yCu_zS + [\alpha + \beta(x-z)/y]$ Cu (in Cu_xS).

in accord with other observations according to which the mobility of monovalent ions is considerably greater than that of ions carrying a higher electrical charge.

Sulfidization of Ag-Cu Alloys

Samples of Ag-Cu alloy of eutectic composition are sulfidized in liquid sulfur at 400°C at about the same rate as the pure components. The size of the samples were 0.9 x 1.5 x 0.3 cm with a total initial surface area of 4 cm^2. The weight gains after 4, 9, 16, and 25 min were 0.369, 0.553, 0.565, and 0.660 g, respectively. The last sample was sulfidized completely. Microscopical examination of sectioned samples revealed a single sulfide layer with only minor irregularities at the alloy-sulfide interface.

Since the standard free energy of formation of Cu_2S is about twice that of Ag_2S, preferential sulfidization of copper may be expected. Actually, however, Ag and Cu enter the scale at the ratio at which they are present in the alloy as has been ascertained by chemical analysis. Presumably, the scale consists of solid solutions of the quasi-binary systems Ag_2S—Cu_2S and Ag_2S—$Cu_{1.8}S$. Various observations suggest considerable mutual solubilities (51, 52). However, complete miscibility is impossible since the terminal phases of these systems have incompatible structures at 400°C. Ag_2S has a body-centered cubic sulfur sublattice (28), Cu_2S II is hexagonal (29), and $Cu_{1.8}S$ has a face-centered cubic sulfur sublattice (28, 29).

Conclusions

High-temperature oxidation of pure metal yields, in general, oxide or sulfide layers of uniform thickness with diffusion in the scale as rate-determining step as an important limiting case. When an alloy rather than a pure metal is oxidized, one component of the alloy may be oxidized preferentially. In view of differential oxidation, diffusion processes take place in both the alloy and the scale. In special cases, the over-all ratio of the components in the scale may be the same as in the alloy, but the local ratio of the components in the scale may vary with distance from the outer surface. In addition to homogenous layers, there may occur two-phase layers either consisting of alloy enriched with respect to the more noble component and an oxide or sulfide of the less noble metal, or consisting of two oxides or sulfides of different metals. In the present research, typical examples from a large variety of possible situations have been found. The exploration of the decisive factors has been stressed. Many details have not yet been fully clarified.

Sulfidization of Cu-Au and Ag-Au alloys involving low Au contents, e.g., 10 a/o Au yields a composite scale consisting of an outer homogeneous sulfide layer and an inner two-phase layer involving Au-rich alloy and sulfide. This is in accord with theoretical considerations according to which a plane alloy-sulfide interface is not stable since the interdiffusion coefficients in the alloy are much lower than the diffusivities in the sulfide phases (2). At higher Au contents the tendency to form a rugged interface decreases especially at lower temperatures. At intermediate Au contents, local sulfide penetrations occur particularly at grain boundaries. Finally, Au-rich alloys may yield a nearly plane alloy-sulfide interface with only minor irregularities. The gradual change in the structure of the scale is reflected by a gradual decrease in the rate of attack. Alloys involving low Au contents are attacked very rapidly at about the same rate as the pure base metals since trunks of Au-rich alloy in the two-phase scale do not change the diffusion resistance of the sulfide to a large extent. In contrast, Au-rich alloys are attacked very slowly presumably with diffusion of Ag or Cu to the alloy-sulfide interface as the rate-determining step.

Silver-copper alloys also yield a sulfide layer of uniform thickness, in which the ratio of the components is the same as in the alloy in spite of the large difference in the standard free energies of formation of Ag_2S and Cu_2S. Thus only diffusion in the sulfide layer is essential and accordingly the rate of attack is about as high as that of pure Ag or Cu.

In contrast, Ni-Cu alloys immersed in liquid sulfur yield two sulfide layers. The outer layer is supposedly digenite $Cu_{1.8}S$, and the inner layer a solid solution involving nickel sulfide as solvent and Cu_2S as solute. The over-all Cu/Ni ratio in the scale is virtually the same as in the alloy. Thus only diffusion in the scale is essential. Both nickel and copper migrate presumably across the inner sulfide layer which grows by a displacement reaction between nickel ions, electrons, and copper sulfide.

Acknowledgment

This paper is based on a thesis submitted by B. D. Lichter in partial fulfillment of requirements for the degree of Sc.D. in metallurgy, Massachusetts Institute of Technology, Cambridge, Mass.

Research has been sponsored by the National Science Foundation and by Office of Ordnance Research, U. S. Army, under Contract DA-19-020-ORD-3661. The authors want to express their thanks to D. L. Guernsey for chemical analyses.

Manuscript received April 3, 1959.

Any discussion of this paper will appear in a Discussion Section to be published in the December 1960 JOURNAL.

REFERENCES

1. C. Wagner, *This Journal*, **99**, 369 (1952).
2. C. Wagner, *ibid.*, **103**, 571 (1956).
3. H. Braune and O. Kahn, *Z. physik. Chem.*, **112**, 270 (1924).
4. C. Tubandt, H. Reinhold, and W. Jost, *Z. anorg. u. allgem. Chem.*, **177**, 253 (1928).
5. E. Hirahara, *J. Phys. Soc. Japan*, **6**, 421, 428 (1951).
6. R. L. Allen and W. J. Moore, *J. Phys. Chem.*, **63**, 223 (1959).
7. H. Braune, *Z. physik Chem.*, **B110**, 147 (1924).
8. W. Jost, *ibid.*, **B9**, 73 (1930).
9. C. Matano, *J. Phys. Soc. Japan*, **9**, 41 (1934).
10. W. Jost, *Z. physik. Chem.*, **B16**, 123 (1932).
11. W. A. Johnson, *Trans. Am. Inst. Mining Met. Engrs.*, **143**, 107 (1941).
12. H. Ebert and E. Trommsdorf, *Z. Elektrochem.*, **54**, 294 (1950).
13. M. Hansen and K. Anderko, "Constitution of Binary Alloys," McGraw-Hill Book Co., Inc., New York (1958).

14. J. S. Smart and A. A. Smith, Jr., *Trans. Am. Inst. Mining Met. Engrs.*, **166**, 144 (1946).
15. J. S. Maclaurin, *J. Chem. Soc. (London)*, **69**, 1269 (1896).
16. L. Czerski and S. Patzau, *Arch Gornictwa i Hutnictwa*, **2**, 354 (1954).
17. M. Billy and G. Valensi, *J. chim. phys.*, **53**, 832, 843 (1956).
18. W. J. Moore, *ibid.*, **53**, 843 (1956).
19. H. Rickert, *Z. physik. Chem. N.F.*, in press.
20. R. F. Bacon and R. Fanelli, *J. Am. Chem. Soc.*, **65**, 639 (1943).
21. L. B. Pfeil, *J. Iron Steel Inst.*, **119**, 501 (1929).
22. B. W. Dunnington, F. H. Beck, and M. G. Fontana, *Corrosion*, **8**, 2 (1952).
23. H. Engell and F. Wever, *Acta Met.*, **5**, 695 (1957).
24. J. D. Mackenzie and C. E. Birchenall, *Corrosion*, **13**, 783t (1957).
25. D. W. Juenker, R. A. Meussner, and C. E. Birchenall, *ibid.*, **14**, 39t (1958).
26. R. A. Meussner and C. E. Birchenall, *ibid.*, **13**, 677t (1957).
27. R. Bakish and W. D. Robertson, *Trans. Am. Inst. Mining Met. Engrs.*, **203**, 424 (1955).
28. P. Rahlfs, *Z. physik. Chem.*, **B31**, 157 (1936).
29. N. W. Buerger, *Econ. Geol.*, **36**, 19 (1941).
30. M. J. Buerger and N. W. Buerger, *Am. Mineralogist*, **29**, 55 (1944).
31. W. Rühl, M. Sc. Thesis, University of Erlangen, 1952, private communication.
32. Gmelins Handbuch der anorganischen Chemie, Kupfer B, pp. 432 ff., Verlag Chemie, Weinheim (1959).
33. S. Djurle, to be published.
34. G. Preuner and I. Brockmüller, *Z. physik Chem.*, **81**, 129 (1913).
35. E. T. Allen and R. H. Lombard, *Am. J. Sci.*, (4) **43**, 175 (1917).
36. W. Biltz and R. Juza, *Z. anorg. u. allgem. Chem.*, **190**, 161 (1930).
37. J. D. Harrison and C. Wagner, to be published.
38. C. Wagner, *Z. physik. Chem.*, **B21**, 25 (1933).
39. H. Reinhold and H. Seidel, *Z. Elektrochem.*, **41**, 499 (1935).
40. L. Czerski, S. Mrowec, K. Wallisch, and T. Werber, *Arch. Hutnictwa*, **3**, 49 (1958).
41. C. Wagner, *Z. physik Chem.*, **B32**, 447 (1936).
42. C. Wagner, "Diffusion and High Temperature Oxidation of Metals" in "Atom Movements," pp. 153-173, American Society for Metals, Cleveland, Ohio (1951).
43. C. Wagner, *J. Chem. Phys.*, **21**, 1819 (1953).
44. N. B. Pilling and R. E. Bedworth, *J. Inst. Metals (London)*, **29**, 529 (1923).
45. C. Wagner, "Thermodynamics of Alloys," pp. 108 ff., Addison-Wesley Press, Cambridge, Mass. (1952).
46. K. Kiukkola and C. Wagner, *This Journal*, **104**, 379 (1957).
47. J. L. White, R. L. Orr, and R. Hultgren, *Acta Met.*, **5**, 747 (1957).
48. K. Hauffe and A. Rahmel, *Z. physik. Chem.*, **199**, 152 (1952).
49. T. Rosenquist, *J. Iron Steel Inst. (London)*, **176**, 37 (1954).
50. W. Köster and W. Malfinger, *Z. Elektrochem.*, **46**, 135 (1940).
51. C. Tubandt and H. Reinhold, *Z. physik. Chem.*, **A140**, 291 (1929).
52. N. G. Schmahl, *Angew. Chem.*, **65**, 447 (1953).

Influence of Electrode Surface Conditions on the Electrical Strength of Liquified Gases

D. W. Swan and T. J. Lewis

Electrical Engineering Department, Queen Mary College, London, England

ABSTRACT

The strengths of liquified argon, oxygen and nitrogen are of the order of 1 mv/cm but are found to depend to a marked degree on the nature of the electrode surfaces. The strength can be changed in a regular manner (sometimes by as much as 50%) by changing both the electrode metal and the degree of surface oxidation. The important discovery is that the *anode* as well as the cathode has a strong influence on the strength. This surprising result has, as yet, no obvious explanation in terms of usual breakdown mechanisms but may be very significant, not only for theories of breakdown in these liquids but for hydrocarbon liquids as well.

Studies of the electric strength of liquid dielectrics have been concerned almost exclusively with organic materials because of their practical importance as electrical insulation. Insulating oils are mixtures of complex hydrocarbons in which trace compounds can have a strong influence and, in an endeavor to simplify the studies, less complex hydrocarbons such as pure n-paraffins have been investigated extensively (1). Even for these liquids, the molecules are complex, purification is complicated, and electrode conditions difficult to assess. In addition, discharges attendant on measurements of the electric strength cause gas evolution, carbon and other deposits, and seriously disturb the electrode surfaces. Because of these difficulties, the major discharge processes cannot be studied accurately in the liquid phase. There are, however, other much simpler dielectric liquids without these disadvantages in which breakdown mechanisms can be more easily understood, and which offer the opportunity for much more precise and controlled measurements. These are liquified gases and, although they are of no importance as practical insulants, much information can be gained from them which helps in understanding the processes occurring in the organic liquids.

Of the possible liquified gases, argon, oxygen, and nitrogen are most suitable for study since they may be easily obtained by condensation. Argon is ideal

because it has a simple atomic structure and is inert; other rare gases are not so convenient since they are more expensive and not easily liquified. Oxygen and nitrogen can also be obtained with reasonable purity and are simple diatomic gases with distinctive properties. All these should produce negligible by-products when electrical breakdown occurs because the discharge merely creates gas which then recondenses. In the case of oxygen, oxidation reactions may be caused on the electrodes and surface reactions may also occur with nitrogen, but the possible processes will be few compared with those in hydrocarbons. These three liquids also possess other advantages for breakdown investigations. Thus argon does not react with the electrode surfaces and electrons will remain free in it. Oxygen readily forms negative ions, thereby trapping electrons, and also encourages surface reactions at the electrodes, especially in the craters formed by previous discharges. Nitrogen is not inert but is only slightly reactive compared with oxygen. Each liquid, therefore, produces different discharge conditions, and there is also the possibility of investigating, for example, argon with a small admixture of oxygen, so reducing the number of free electrons in the argon.

The electric strengths of these liquids have been investigated on a limited scale already by Kronig and Van de Vooren (2) who obtained values between 860 and 1040 kv/cm depending on the electrode material. No other measurements of electric strength have been made, and there is only one measurement of natural conductivity at high electric stress for liquid oxygen by Pao (3). Induced conduction has been fairly well studied, however; the liquids being irradiated with x-rays or α particles (3-9). This work has given data on ion mobilities in these liquids and has clearly demonstrated that oxygen and also nitrogen can quench electron bursts in argon by forming negative ions of low mobility. A concentration of 0.7% oxygen in liquid argon was sufficient to quench all electron pulses, but a 15% concentration of nitrogen was required for the same effect. Clearly, electrons are not likely to remain free in liquid oxygen or nitrogen except, perhaps, at the highest fields approaching the electric strength when electron detachment may occur.

The work reported here represents an initial investigation into the strength of these liquids with the intention of estimating the role of the electrode surfaces in determining the strength. It is more extensive and of greater precision than that of Kronig and Van de Vooren (2). Techniques already used for reliable measurements on hydrocarbons have been employed. It will be shown that electrode effects are dominant in argon, and this may have important implications in the studies of breakdown in hydrocarbons.

Equipment and Procedure

A diagram of the test cell arrangement is shown in Fig. 1. It consists of a long glass tube, A, sealed at the lower end and flanged at the top. The electrode mounting B is rigidly fixed at one end of a stainless steel tube C which, in turn, is sealed to a metal flange D at the top. The vacuum sealed high voltage connection E is led through tube C and terminates in a small bushing at the lower fixed electrode. The other earthed electrode with its connector F is fixed to a stainless steel shaft, G, which can be moved vertically by a micrometer H. A vacuum seal is maintained by a metal bellows J joining G and D. The flanges D and A are then sealed by an o-ring joint which also locates the electrode assembly at the lower end of the cell. Gap adjustment between the 0.5-cm diameter spherical electrodes can be made to within $\pm$ 1 μ, i.e., with $\pm$ 2% error for a 50-μ gap, and is checked several times during an experiment in order to compensate for any temperature changes. Zero gap is obtained by using a sensitive detector as already described (10). Gas is admitted via K and caused to condense by placing liquid oxygen or nitrogen in the outer Dewar vessel L. The test cell is of sufficient length above the Dewar vessel for the top flange D and micrometer to remain at room temperature during experiments. By using liquid oxygen in L when condensing oxygen and liquid nitrogen for nitrogen condensation, it is possible to effect a slow and controlled condensation with adequate temperature control. Liquid argon, which has a small temperature range (84°-87°K) is obtained by boiling liquid oxygen in L at a controlled rate at reduced pressure. Normally the cell is filled with liquid to a level just below the lower edge of B and this requires only 15 cc of liquid, i.e., about 45 liters of gas at N.T.P. In all experiments equilibrium conditions were obtained by allowing 1 hr to elapse after condensation before making measurements.

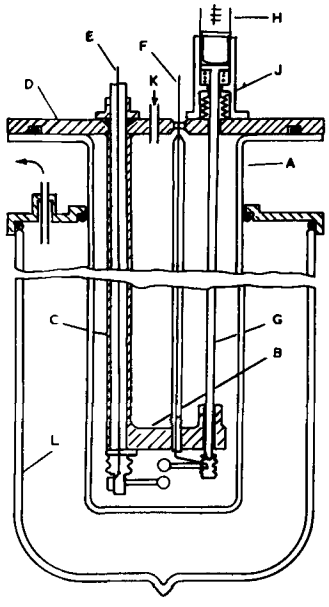

Fig. 1. Diagram of test cell

The temperature and pressure in the cell could be measured but, as Kronig and Van de Vooren have found, small pressure changes do not affect the strength. In the present series of experiments, the liquids were always in contact with their saturated vapors. For reasons given above, the temperatures were sensibly constant and are given in Table I.

The gas to be tested was passed through a P_2O_5 drying tube and a sintered glass filter of 1-μ pore

Table I. Data for gases used

	Argon	Oxygen	Nitrogen
Boiling point at atmospheric pressure, °K	87.3	90.2	77.3
Purity, %	99.95	99.5	99.9
Significant impurities, vpm	N_2 <500 O_2 <20 H_2 <10	H_2 <50 Carbon compounds <15	O_2 <10 Carbon compounds <15

size to remove dust particles. The purity of the gases is given in Table I and it is important to note that argon and nitrogen contained traces of oxygen. Since a slight internal positive pressure was maintained in the system, which was in any case vacuum tight, it is improbable that any further gas contamination occurred.

A 25 kv fully stabilized direct voltage source capable of very fine control was used for the measurements, and the voltage applied to the electrodes was measured by recording the current through a 1000 M ohm high stability resistor connected across the electrodes. The absolute error in voltage measurement was <2% and relative values could be obtained with much less error than this. When breakdown occurred the current flow was limited by using a fast electronic by-pass circuit of a type already described (10). This was capable of discharging the stored energy of the voltage supply within 1 μ sec of breakdown and so limited the energy dissipated in the liquid to the residual associated with the test cell capacitance. There was, therefore, minimum gas evolution and electrode damage. This permitted repeated measurements to be made on the same electrode surfaces without significant deterioration. Operation of the diverter also indicated breakdown without need for visual observation of the spark. Kronig and Van de Vooren report observing occasional very low electric strengths which they attribute to gas bubbles on the electrodes. Since they did not divert the discharge energy and low strengths have not been observed in the present work, their deduction seems correct.

The techniques adopted for electrode preparation were similar to those found to be reliable with hydrocarbons (1, 11). Surface scratches and previous discharge damage were removed by buffing the electrode on a rough mop with polishing compound. This was followed by further polishing on finer mops until the surface was smooth when viewed under a microscope of magnification X150. Polishing material was then removed by washing in hexane; then a soft mop, free of grease, was used to prepare the final surface. At this stage the surface was comparatively free of grease and heated by the polishing process so that initial oxidation occurred rapidly. Further oxidation could then be arrested by washing the electrodes in dust-free hexane (11). For certain measurements to be described, various oxidation thicknesses on oxidizing metals were required; these were obtained by delaying the wash in hexane and allowing the electrodes to remain for predetermined times in dry air in a dessicator. Oxidation times were then taken as measures of oxidation thickness, with zero time and minimum thickness arbitrarily chosen to correspond to that involved in directly transferring the electrodes from the final mop to hexane without delay.

The electrodes were then transferred to the test cell and washed again in dust free hexane. Finally, the whole test cell assembly was evacuated to a pressure of 10^{-5} mm Hg for a period of 18 hr to remove hexane vapors and other volatile impurities. Before condensing the gas to be tested, the cell was flushed with a sample of the same gas and re-evacuated for a short while.

Electric Strength

Electric strengths of the three liquids were measured using both stainless steel of zero oxidation

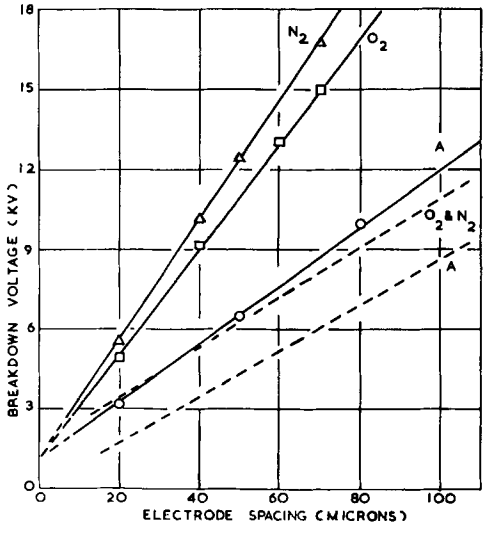

Fig. 2. Breakdown voltage vs. electrode spacing with platinum electrodes. O, Argon; □, oxygen; △, nitrogen. - - - Results from ref. (2).

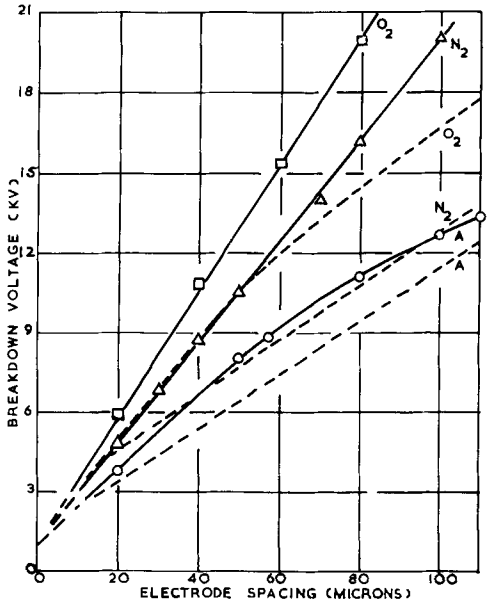

Fig. 3. Breakdown voltage vs. electrode spacing with stainless steel electrodes. O, Argon; □, oxygen; △, nitrogen. - - Results from ref. (2).

Table II. Mean strengths for liquified gases (mv/cm)

	Platinum electrodes		Stainless steel electrodes	
	from Fig. 2	from ref. (2)	from Fig. 3	from ref. (2)
Argon	1.10	0.86	1.42	1.00
Oxygen	2.00	0.93	2.38	1.04
Nitrogen	2.26	0.93	1.88	1.00

time, and platinum electrodes, in order to make direct comparison with the values obtained by Kronig and Van de Vooren. Results for a range of electrode spacings are given in Fig. 2 and 3, together with the earlier results. The coefficient of variation was found to be less than 10%. Mean strengths for the liquids, obtained from the slopes of the plots, are given in Table II. In the case of argon with stainless steel electrodes, which had been subjected to a glow discharge in hydrogen in order to reduce the oxide layer still further, a linear plot is not obtained, and the value shown in Table II is the slope for the smaller electrode spacings. The new values are higher than the previous ones in all cases. This may be due to the use of 0.5-cm diameter spherical electrodes rather than the 1-cm diameter sphere-plane arrangement used by Kronig and Van de Vooren, or to the use of the energy diverter; but, as will be shown below, the difference could be ascribed to electrode surface conditions. Argon has the lowest strength with either electrode material, but nitrogen is either stronger or weaker than oxygen according to whether platinum or stainless steel electrodes are employed (2). Good reproducibility of these results was obtained except for nitrogen with stainless steel electrodes. For this gas, results for different samples could not always be repeated even though the techniques were maintained constant. Values given in Fig. 3 are the most probable ones obtained from a large number of experiments. Similar difficulties have been found with electrical discharge measurements on nitrogen gas on a previous occasion (12), and at the moment there is no explanation of the effect. The nonlinear plot for argon and stainless steel suggests that the strength of argon for really large spacings ($> 100\ \mu$) would be much less than that quoted in Table II, and any increase for smaller spacings may be due to the influence of the electrodes, but more measurements are required to prove this.

In view of the earlier evidence from α-particle and γ-ray induced conductivity (3-9) it is expected that in argon, at least, a small percentage of oxygen (or somewhat greater amounts of nitrogen) should alter the pre-breakdown state by quenching avalanche discharges and causing electrons to attach to form negative ions. These ions would be transported to the anode and an ion concentration built up there. Although the ionization potential of oxygen (12.2 ev) is less than that of argon (15.8 ev), this does not appear to be important in deciding the strength of the liquid since addition of oxygen to argon raises the strength. For instance, addition of 20% oxygen to argon raised the strength from 1.66 to 2.42 mv/cm for a 40-μ gap with stainless steel electrodes. This is an increase of 45% but is still less than the strength of pure oxygen. In order to reveal any electrode effect in this process, stainless steel electrodes were rendered oxide-free by glow discharge and used to measure the strength of liquid argon both before and after a small quantity of oxygen had been added. Measurements of the strength at 1-min intervals showed a gradual increase amounting in all to nearly 30% over a period of 25 min. Addition of a much larger quantity of oxygen at the end of this period caused an immediate further increase of about 10%. These results suggest that the initial gradual increase could be associated with electrode oxidation and the later one with attachment processes in the bulk of the liquid.

Electrode Effects

It is obvious from the experiments described that a strong electrode influence exists. This has been further studied in two ways, both of which are described briefly. In the first, the influence of electrode metal prepared with a zero oxidation time was found for each gas. Plots similar to those of Fig. 2 and 3 were made for a range of electrode spacings and the electric strengths found as before. These strengths, given in Table III, can be changed by almost 100% by a change of electrode material. There is no correlation with work function; in fact, the order of increasing strength for the different metals is not the same for each gas even with electrodes of gold or platinum which should provide stable surfaces. Gold gives a higher strength than platinum for argon but not for oxygen or nitrogen. In any relationship between strength and cathode emission properties, platinum, having a higher work function than gold, might be expected to give a higher strength especially in argon which is inert. It is in this liquid, however, that the lower strength is found.

The next series of experiments, using argon because of its inertness, involved electrodes having various degrees of oxidation obtained by the method already outlined. Figure 4 shows the influence of this oxidation time. Each point is the mean strength found from plots similar to Fig. 2 or 3 and thus represents a large number of measurements. As expected, neither gold nor platinum produce any variation with oxidation time whereas stainless steel and brass, which oxidize readily, cause a large change. For these oxidizing metals the strength reaches a maximum after oxidation times of 15 and 70 min, respectively. Larger oxidation periods than these, i.e., greater thicknesses of oxide, cause a gradual decline in strength, and shorter times giving thinner layers also lower the strength.

The initial rise to the peak could be associated

Table III. Mean strengths as a function of electrode material

Electrodes	Work function, ev	Electric strength, mv/cm		
		Argon	Oxygen	Nitrogen
Stainless steel	—	1.40	2.38	1.88
Brass	—	1.01	1.44	1.62
Copper	4.47	1.40	1.81	—
Gold	4.58	1.16	1.24	1.50
Platinum	5.29	1.10	2.00	2.24

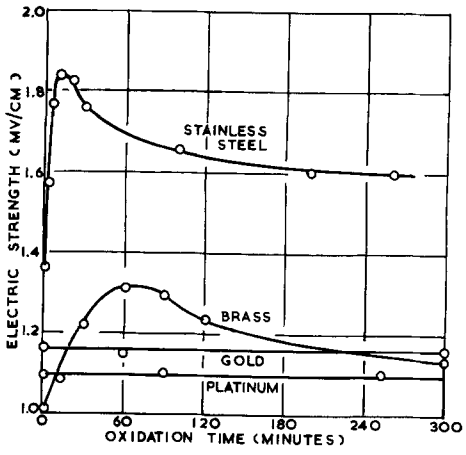

Fig. 4. Effect of electrode oxidation time on mean electric strength of argon.

with a decrease in electron emission resulting from an increase in work function caused by oxide growth. Any increase in work function in this way might be offset by a decrease caused by positive ions produced in the discharge processes coming back to this oxide layer (13). The over-all cathode emission would be determined by these opposing effects and, as the oxide layer thickened beyond a certain value, it is possible for the positive ion layer to increase in effectiveness because of the insulating properties of the oxide which would hinder ion neutralization.

For the whole range of oxidation times, therefore, the emission might initially decrease and then increase again, and if electric strength was directly related to emission, the curves in Fig. 4 are reasonable. This would be a plausible mechanism if the behavior were found to be independent of the anode, but unfortunately this is not the case. By using mixed electrodes, it has been possible to show an anode dependence also. For example, with a stainless steel anode and an aluminum cathode, the strength was practically the same as for two stainless steel electrodes, but reversal of the polarity gave a strength equal to that for aluminum electrodes. In other experiments using gold anodes and stainless steel cathodes, it was possible to change considerably the effect of oxidation time from that shown for stainless steel in Fig. 4. Thus, any mechanism of breakdown in liquid argon must include the role of the anode as being of great importance.

Conclusion

These results and others not reported indicate that the "intrinsic" strengths of the three liquified gases have not, in fact, been measured. It may well be that electrode effects will always prevent this being achieved with any certainty. The breakdown stresses are $\sim 10^6$ v/cm so that electron emission from the cathode might be expected, but it should be borne in mind that at temperatures of $\sim 90°K$ Schottky field-aided thermionic emission, which is considered to be significant for liquid breakdown at room temperature, will be negligible. At the same time the field strength does not seem to be large enough for appreciable cold field emission. Measurements of the natural conductivity of liquid argon at 10^6 v/cm confirms this since no detectable current was found. Nevertheless, individual microscopic sites might emit more freely and would then increase the probability of breakdown in these regions. The number and activity of the sites would depend on cathode material and preparation and on the incidence of positive ions generated by discharge processes as already outlined.

It is very much more difficult to suggest processes by which the anode conditions might influence the electric strength, especially when the emission from the cathode is feeble and probably confined to microscopic sites. The normal concepts of gas breakdown which we may tentatively employ here involve primary electron avalanche or α processes, followed by secondary mechanisms in the gas or at the cathode surface. In particular, positive ions produced by the avalanches may yield secondary electrons at the cathode (γ process). This mechanism does not, however, include the anode at all. If the anode is to be important, it is necessary that positive ions should be generated at the anode at a rate controlled by the conditions there and that the yield of positive ions from the rest of the liquid should be small. Two processes seem possible but there may be others. In both, the presence of oxygen in small amounts in the liquid is required in order that electrons emitted from the cathode have a good chance of forming negative ions. A negative ion approaching the anode creates a strong local field which will act across any oxide layer present, so increasing the probability either of ionization of any adsorbed molecules on the oxide layer (including neutralized oxygen ions), or of direct extraction of positive metal ions through the oxide as in an oxidation process. Ions created in this way then proceed to the cathode and by a γ process yield further electrons with the consequent possibility of a breakdown instability. An alternative process which requires positive ions to be produced by avalanches is as follows. The formation of negative oxygen ions serves to transport oxygen to the anode where the ions are neutralized. A concentration of oxygen will then build up in the immediate anode neighborhood to an equilibrium controlled by the availability of electrons and ease of neutralization of the ions. This oxygen-rich anode layer will now have a marked influence on positive-ion production which, according to avalanche growth, should be greatest in the same region. Both processes require the existence of negative ions which, for argon liquid, means the presence of an oxygen impurity. Further experiments on nitrogen and oxygen liquids need to be made to see whether anode effects are present in these liquids also.

The attachment properties of oxygen may also be responsible for the apparent intercept on the voltage axis found in Fig. 2 and 3. While this may be ascribed to the presence of a Paschen minimum as in gases, occurring for spacings of less than about 1 μ, it could also be due to an oxygen and oxygen ion layer at the anode of, perhaps, the same order of thickness. As the electrode spacing is reduced, so this layer exerts a proportionally greater influence on

the strength. It is significant that similar intercepts are found for hydrocarbon liquids containing oxygen (1).

The role of oxygen, therefore, seems the same for liquified gases and hydrocarbon liquids. The electrode effects found with the former may also exist for the latter. The present investigation is valuable in suggesting effects which may well be present in hydrocarbons, but which are masked by the more numerous side effects. Work is proceeding to discover whether this is so. Measurements in compressed gases similar to that already undertaken (14) would also be very valuable and should yield closely related information to that given here.

Acknowledgment

The authors are grateful for the generous financial assistance from the British Electrical and Allied Industries Research Association enabling equipment to be purchased. Thanks are also due to Professor M. W. Humphrey Davies for the facilities provided and for encouragement, and to the Department of Scientific and Industrial Research for a maintenance grant to one of us (D.W.S.). Dr. A. E. Guile was responsible for much of the early design of the test cell and his considerable help is acknowledged.

Manuscript received Nov. 2, 1959. This paper was prepared for delivery before the Philadelphia Meeting, May 3-7, 1959.

Any discussion of this paper will appear in a Discussion Section to be published in the December 1960 JOURNAL.

REFERENCES

1. T. J. Lewis, *This Journal*, **107**, 185 (1960).
2. R. Kronig and A. I. Van de Vooren, *Physica*, **9**, 139 (1942).
3. C. S. Pao, *Phys. Rev.*, **64**, 60 (1943).
4. G. W. Hutchinson, *Nature*, **162**, 610 (1948).
5. N. Davidson and A. E. Larsh, *Phys. Rev.*, **74**, 220, (1948); *ibid.*, **77**, 706 (1950).
6. A. N. Gerritsen and J. Koolhaas, *Physica*, **10**, 49 (1943).
7. A. N. Gerritsen, *ibid.*, **14**, 381 (1948).
8. R. L. Williams, *Can. J. Phys.*, **35**, 134 (1957).
9. R. L. Williams and F. D. Stacey, *ibid.*, **35**, 928 (1957).
10 T. J. Lewis, *Proc. Inst. Elec. Engrs. (London)*, **100**, Pt. IIa, 141 (1953).
11. R. Hancox, *Brit. J. Appl. Phys.*, **8**, 476 (1957).
12. G. A. Kachickas and L. H. Fisher, *Phys. Rev.*, **88**, 878 (1952).
13. W. B. Green, *J. Appl. Phys.*, **26**, 1259 (1955); *ibid*, **27**, 921 (1956).
14. A. H. Sharbaugh and P. K. Watson, Annual Rep. Conf. on Elec. Insul. 1957 Meeting p. 32, Nat. Acad. Sci., Nat. Res. Council (1958).

Molecular Structure and the Electrical Strength of Liquid Hydrocarbons

T. J. Lewis

Electrical Engineering Department, Queen Mary College, London, England

ABSTRACT

It is suggested that electrons moving through hydrocarbon liquids are able to excite molecular vibrations of infrared frequencies, and that this provides an effective energy loss mechanism. The relative magnitudes of this loss may be estimated for a wide range of hydrocarbons and other liquids and can be used in a criterion of breakdown. Thus the electrical strengths of these liquids measured under standard conditions may then be compared with their molecular structures. A good correlation is found.

In recent years the electric strength of a large number of hydrocarbon liquids has been measured using microsecond pulse and continuous voltages. The results published are reliable in that they are repeatable, but they do not represent the intrinsic strengths because of several influences, such as electrode effects, inherent in the measurements. In spite of this, the experiments have demonstrated that the strength is dependent on the molecular properties of these hydrocarbons and quite small changes such as that from hexane to heptane or to isopentane produce a significant effect. Because of the work of Sletten (1) of this laboratory, who has demonstrated that dissolved oxygen increases the strength of n-hexane considerably, it is now realized that the attainment of the highest strengths may not indicate the closest approach to the intrinsic value. As discussed below, many measurements already made must have been influenced strongly by oxygen in solution and, for this reason alone, it is timely to re-examine the relationship between electric strength and molecular structure. This has been discussed in various ways already (2-6) and in this paper the earlier ideas are re-stated concisely in a criterion which permits the molecular influence to be separated from the other factors. Any simple criterion of this sort is open to detailed criticism but, since the theory of breakdown is by no means clarified, the adoption of a simple criterion is advantageous. Having established the criterion, its validity will be examined using experimental results.

Basic Processes

The electric strength of a simple hydrocarbon liquid is considered to be determined by the onset of an instability initiated by the primary processes of electron emission from the cathode and electron multiplication or associated charge accumulation in the bulk of the liquid (2). These processes are

likely to be inter-related and secondary effects arising from impurities or from the measuring technique (7) may also occur. It is then difficult to separate the primary processes by measurements of the electric strength except under special conditions. Stresses greater than 10^6 v/cm are reached in these liquids before breakdown occurs, and it is commonly accepted that field extraction of electrons from the cathode must be occurring (8, 9): a major component of the infra-breakdown conduction current arising from these emitted electrons. Excluding impurities, the mode of conduction is then either by quasi-free electrons or negative ions formed by attachment and at the highest fields possibly by positive ions produced by collision ionization. The mobilities and energies of these particles depends on the collision characteristics of the liquid so that once an electron is emitted the subsequent processes are governed by the liquid and dependence on molecular properties may be expected.

Cathode Mechanisms

If the strength is to be related to liquid properties, the cathode should either play a consistent or else a negligible part in the breakdown process. Evidence from the literature suggests that the cathode effect may be both erratic and elusive, some authors reporting a dependence on electrode material and others not. The electrode surfaces in all cases is covered by complex and perhaps insulating layers of oxide, gas, and other adsorbed impurities. Charge transported to such surfaces can build up electric double layers strongly influencing the emission and preventing any direct relationship between it and the work function of the pure cathode metal. Green (8) has suggested that positive ions deposited on the cathode from the liquid are responsible for enhanced emission in n-hexane and has found a definite dependence on electrode metal and degree of oxidation.

The strengths achieved when measurements are made with pulse voltages of sufficiently short duration depends on the degree of electron availability, and cathode conditions are then important. This situation is analyzed by Ward and Lewis (7), and Hancox and Tropper (10) have also reported an effect of this kind in which cathode oxidation altered the impulse strength of transformer oil.

The relative importance of the control exercised by the separate cathode and liquid processes also determines the degree of electrode dependence. For breakdown both processes need to be above a certain threshold of activity. If the field strength required to promote the liquid mechanisms is high and at the same time the cathode is a good field-emitter, then the breakdown is liquid-controlled and cathode dependence is masked. On the other hand, a liquid of lower "intrinsic strength" with a poor cathode emitter would be expected to show cathode effects. Normal measurements might give either situation as the literature seems to indicate. In Fig. 1 these two conditions are shown by using a point-plane electrode system (11). When the liquid is relatively highly stressed, i.e., the plane negative, a cathode dependence is present, but this

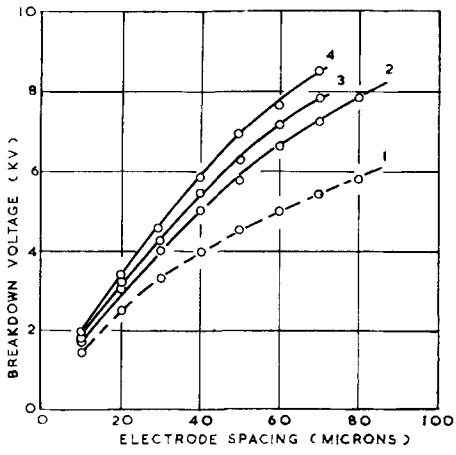

Fig. 1. Breakdown voltage of a point-plane electrode system in n-hexane, Ref. (11). 1. Point cathode, no dependence on electrode material; 2. plane cathode, aluminum electrodes; 3. plane cathode, copper electrodes; 4. plane cathode, chromium electrodes.

disappears when the polarity is reversed. A negative point insures a copious emission and the liquid, being less highly stressed, then controls the breakdown.

Since extensive experiments on various hydrocarbon series have demonstrated already that liquid effects may be observed in some detail it can be concluded that the cathodes were consistent in behavior and able to yield the required emission in these experiments. Any liquid influence on electron emission would remain reasonably constant because of the strong chemical and physical similarities in these hydrocarbon series.

Electronic Processes in the Liquid

As in gaseous or solid phases, an electron gains energy from the applied field and loses it in collisions with molecules. The efficiency of energy transfer in a collision is energy dependent and at low field strengths a stable condition is reached in which only electrons of low energy are accelerated by the field. Although the electron population will contain some electrons of much larger energies, the probability of energies sufficient for ionization will be insignificant. As the field is increased, the distribution will shift to higher energies and ionizing collisions will become more probable. Energy distributions and collision probabilities have long been known for gases (12). In liquids, the complexity of the molecules and the increased density can change the relative importance of various collisions so that these must be reconsidered. The major collision processes are:

(*a*) Elastic. At low field strengths the majority of collisions will be purely elastic involving little energy loss because of the high mass ratio of hydrocarbon molecule and electron.

(*b*) Vibrational. An energy loss, which may not be nearly so important in the gaseous phase unless the molecules are complex, arises from the excitation of molecular vibrations. The vibrations associated with the binding forces are usually in the infrared frequency band and energy quanta in the range 0.1-1 ev are involved. Vibrations excited in this way may couple to other molecules especially when

local order exists. This type of collision is considered to be a major loss process in solid breakdown.

(c) Attachment. Saturated hydrocarbons are not expected to be electronegative, but low-energy electrons could form ionic complexes or clusters by induced polarization of neighboring molecules. These clusters would behave as large ions at low fields, but the electron could be freed by thermal activation or field acceleration at higher fields, leaving the polarized molecular atmosphere behind as in the Wien effect.

(d) Excitation. Excitation transitions in the hydrocarbons requires energy quanta of several electron volts, and the excited molecule can subsequently either emit a photon or for the majority of hydrocarbons stabilize by dissociation (13). Even if photon emission occurred, it would be strongly absorbed by neighboring molecules and would not have the importance found in gas breakdown. The increased density together with the increased number of excitation and ionization levels of the complex molecules will cause the distinct energy gap between excitation and ionization of a gas to be lost in a liquid (14). Consequently, excitation will no longer form such an effective regulating mechanism to limit the ionization process as in gases.

(e) Ionization. Ionization energies are ~10 ev and decrease progressively as any particular hydrocarbon series is ascended. Positive ions of low mobility produced by the collision will disturb the field and cause enhanced emission at the cathode (8). These ions are important in causing a breakdown instability.

Apart from the major processes, electron collisions may also involve impurity molecules and give rise to a variety of effects but for conciseness, only a few of these may be mentioned. Organic impurities such as related hydrocarbons are not likely to upset the breakdown process in the pure liquid; others of a polar nature can induce a low strength. The cleaning techniques adopted reduce the effects of these latter impurities, but their presence in small controlled amounts may be useful in detecting certain breakdown processes. For instance, Darveniza (15) of this laboratory has shown that traces of anthracene cause n-hexane to emit visible light with a photon energy of about 2.5 ev when the breakdown field is approached, thus giving evidence for the presence of electrons of this energy. Water is an important impurity of which most is removed chemically, but some must remain as a trace. In dissociated form it can contribute to the conduction current and is probably regenerated at the electrodes as Plumley has suggested (16). Provided the accepted drying techniques are employed there is no evidence at the moment for it having any strong influence on breakdown.

Another important class of impurity is dissolved gas which introduces additional collision centers having energy levels which may be very different from those of the pure liquid. The excitation and ionization energies of oxygen and nitrogen, which are likely to be dissolved, are greater than the corresponding values for hydrocarbons such as n-hexane so that these transitions in the gases are not likely to occur. The most important effect to be expected is the strong electron attachment of oxygen which is discussed more fully below. The presence of an actual gas phase in the form of bubbles has been considered on many previous occasions especially for oils. Bubbles could easily initiate breakdown, but the majority of evidence suggests that the influence of dissolved gas in simple hydrocarbon liquids is through individual electron-gas molecule collisions rather than bubbles.

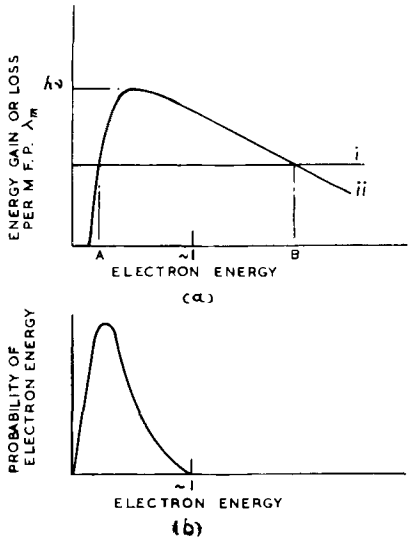

Fig. 2. Energy diagrams for vibrational collisions. (a) Energy balance below breakdown stress (i) energy gain from field E, (ii) energy loss in vibrational collisions of frequency ν; (b) electron energy distribution function corresponding to (a).

Vibrational Collisions

From the assessment above, it is concluded that vibrational collisions account for the major electron energy loss in pure hydrocarbon liquids replacing excitation collisions as the major control of collision ionization. The vibration collision loss can then be used to establish a breakdown criterion similar to that proposed for solids (14, 17). This may be done by reference to Fig. 2a which shows the hypothetical electron energy gain from the field E and loss to molecular vibrations per minimum mean free path λ_m for this collision. It is assumed that the vibration cross section reaches a peak $Q_m = (N\lambda_m)^{-1}$, where N is the number of molecules per cc, for an energy equal to a few multiples of the threshold value. Electrons in the range AB tend to shift in energy toward A, but this is opposed by thermal fluctuations repopulating the higher energy ranges. For a particular applied field below the breakdown value and constant electron emission and absorption at the electrodes, an equilibrium energy distribution is set up characterized by a severe curtailment in the excitation-ionization energy range ~ I(Fig. 2b). As the field is increased, point B moves down and more electrons will be capable of acceleration by the field toward ionization energies, but the increase will be small until the condition B = I is reached. At this field strength, many more electrons are available for acceleration. Thus the condition B = I represents the onset of a significant collision ionization or α process. At still higher fields the condition A = B will be

reached and electrons of any energy are then accelerated towards I.

The α process causes electron avalanches and, by analogy with gas breakdown, we require either that these should grow to a particular size or that an instability through secondary processes such as positive-ion emission enhancement at the cathode should occur. In any of these cases the necessary condition for an instability is that α should reach a minimum value. From Fig. 2, the condition can be expressed as

$$e\,E_m\,\lambda_m = Ch\nu \qquad [1]$$

where E_m is the breakdown field, C ($\leqq 1$) determines the required α value, and $h\nu$ is the energy quantum transferred in a vibration collision of frequency ν. This criterion, or variations, has been utilized by several authors (2-6, 18). It should be noted that C takes account of the experimental conditions (e.g., pulse or continuous voltage measurements) and would be affected by any electrode conditions capable of altering secondary processes and thereby requiring a new α value for an instability. Because of these effects, Eq. [1] is useful for comparing liquids only when C remains reasonably constant throughout the experiments. This seems to have been achieved for the alkanes and alkyl benzenes (2-6). Through Eq. [1] it is possible to relate strength to molecular structure.

Vibration Frequency ν and Minimum Free Path λ_m

Vibration frequencies of the hydrocarbons are restricted to a few bands. Characteristic wave-numbers, determined from infrared spectra, can be associated with the carbon-hydrogen groups and with the skeletal carbon-carbon bonds (Table I). It is well known that these are characteristic of the groups and independent of the rest of the molecules. As the electron energy increases, each mode of oscillation may be excited in turn, but from our concept of the breakdown process and knowledge of the infrared absorption intensities it is expected that the major energy loss will occur in exciting 2960 cm^{-1} vibrations of the CH_1, CH_2, and CH_3 groups. This requires an energy quantum of 0.37 ev. Vibrations of the carbon skeleton in alkanes require a lower energy, and the skeleton is screened by CH bonds so that it is likely to be less effective in causing loss. The same applies to the alkyl radical of the alkyl benzenes. The benzene ring itself is best considered as a single independent group having a highest frequency as in Table I.

The independent behavior of the various groups as shown by their infrared spectra suggests that these hydrocarbon liquids may be considered to a first approximation as dense gas-like phases of the group

Table I. Infrared vibrations of hydrocarbon groups

Group	Wave number, cm^{-1}	Energy quantum, ev
CH_1, CH_2, CH_3	~2960	0.37
CH_3, CH_2	1450	0.18
CH_3	1000	0.12
C-C skeleton	890-1090	0.11-0.14
Benzene ring (CH modes)	~3000	0.37

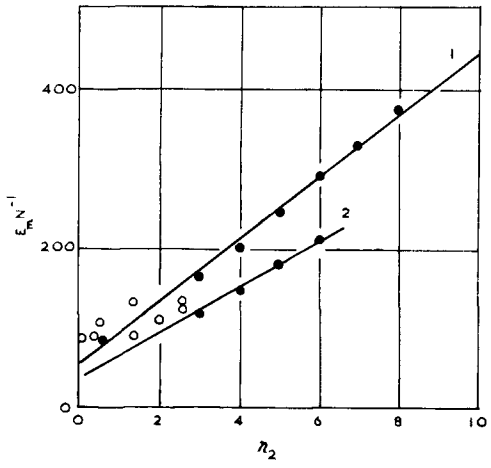

Fig. 3. E_mN^{-1} vs. n_2 for alkanes according to Eq. [4]. Curve 1, from short duration pulse measurements; curve 2, from direct voltage measurements. o Points marked thus are for branched chain alkanes containing the Q_1 cross section.

oscillators, each acting as an independent collision center and having a uniform distribution in the liquid. Thus (2, 4)

$$\lambda_m^{-1} = N\,\Sigma n_i Q_i \qquad [2]$$

where n_i is the number of i^{th} groups per molecule for which the maximum collision cross section for the 2960 cm^{-1} mode is Q_i.

Equation [1] may now be checked against the electric strength determinations reported by Sharbaugh, *et al.* and by Lewis (2-6) in which consistent techniques leading to a constant C were adopted in each series of measurements. Combining Eq. [1] and [2] and writing the constant k to include C and the common frequency of vibration ν then

$$E_mN^{-1} = k\,\Sigma n_i Q_i \qquad [3]$$

If i = 3, 2, 1 refers to CH_3 CH_2 and CH groups, then for n-alkanes C_nH_{2n+2}

$$E_mN^{-1} = k\,(n_2Q_2 + 2Q_3) \qquad [4]$$

i.e., E_mN^{-1} vs. n_2 should give a linear plot of intercept 2 k Q_3 and slope k Q_2 as is indeed confirmed for both sets of measurements in Fig. 3. Results for branched alkanes have been added to Fig. 3 and lie above the linear plot as expected because of the neglect of Q_1 in Eq. [4]. By plotting

$$(E_mN^{-1}n_1^{-1} - k\,n_3Q_3n_1^{-1}) \text{ vs. } n_2n_1^{-1}$$

for the isomers, the expected linear plot is again found which gives an estimate of k Q_1 and a check on k Q_2. It no longer appears necessary to place branched chain isomers on a separate characteristic and to ascribe a new characteristic frequency ν to them as suggested earlier (4). The relative magnitudes of Q_1, Q_2, and Q_3 agree well in the two sets of measurements in spite of the very simplified model.

For n-alkyl benzenes $C_6H_5-C_nH_{2n+1}$ Eq. [3] becomes

$$E_mN^{-1} = k\,(n_2Q_2 + Q_3 + Q_b) \qquad [5]$$

where Q_b is the cross section of the benzene ring. Results obtained by Sharbaugh, Crowe, and Cox (5) fit this law as in Fig. 4a (6, 19). Also in agreement

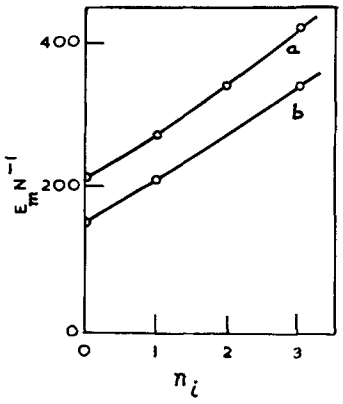

Fig. 4. $E_m N^{-1}$ as a function of molecular structure for alkyl benzenes. (a) n-Alkyl benzenes according to Eq. [5], $n_1 = n_2$; (b) branched-alkyl benzenes according to Eq. [6], $n_1 = n_3$.

with the criterion are the results for benzene, methyl benzene, and t-butyl benzene (Fig. 4b), fitting accurately the relationship

$$E_m N^{-1} = k\ (n_3 Q_3 + Q_b) \qquad [6]$$

Cross sections estimated from Fig. 4, show that Q_b is relatively large as might be expected but also that k Q_2 and k Q_3 are considerably greater (~100%) than estimates from the alkanes. This may be due in the first place to a shift in the breakdown criterion since there is no reason why C (Eq. [1]) should be the same in both series. Changes may also occur in the cross sections because the alkyl benzenes are polar with the ring negative. This would increase the interaction between the alkyl groups and electrons. It is also probable that the liquid structure differs in the two cases with a consequent effect on λ_m (see below).

Equation [1] is also supported by measurements on the dimethyl siloxane (silicone) liquids which have similar chain structures to the alkanes. The main skeleton consists of silicon-oxygen bonds, replacing the carbon-carbon bonds of the alkanes, and methyl side groups are added at the silicon sites to give a general formula $(CH_3)_3Si-[O\ Si(CH_3)_2]_n-O\ Si(CH_3)_3$. An important difference is that the silicone skeleton is relatively exposed at the oxygen sites and the silicon oxygen bonds are polar. Equation [3] becomes

$$E_m N^{-1} = k\ (n_3 Q_3 + n_o Q_o) \qquad [7]$$

where Q_o refers to the oxygen site. The strengths found with direct voltage for the first four members of the series again give a linear characteristic when plotted according to Eq. [7] (6), bearing in mind that the dimer exhibits exceptional behavior in many of its other physical properties (20). The value of k Q_3 so obtained is identical with that from the alkanes. It has been shown already that the CH_3 group in the silicones has a vibration of ~3000 cm^{-1} very close to that found in the hydrocarbons so that the agreement in the estimates of k Q_3 appears significant.

On the whole, therefore, experiments on a large number of simple liquids can be arranged systematically according to Eq. [1] based on individual molecular groups.

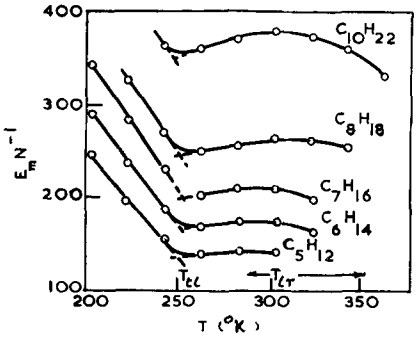

Fig. 5. Variation of E_m/N with temperature for n-alkanes showing transition temperatures.

Liquid Structure

The assumption of a uniform distribution of collision centers implies that the liquid is isotropic along individual electron paths. It is known that local order can exist in n-alkanes, however, and that this is temperature dependent. The liquid phases for pentane to decane are characterized by three states having transition temperatures T_{tl} and T_{lr} in the neighborhoods of 245° and 288°-355°K, respectively (21). Below T_{tl} the state is quasi-crystalline and the molecules pack with their long axes parallel to form crystallites. In the range T_{tl}-T_{lr} libration occurs about the long axes and above T_{lr} complete rotation is possible and local order disappears. Many physical properties change when taken through these transitions; Fig. 5 shows that the electric strength is no exception (22). By plotting $E_m N^{-1}$ against temperature in this figure normal density changes are annulled, structure effects are accentuated, and T_{tl} and T_{lr} become obvious. The change at T_{tl} is particularly abrupt. In a crystallite at low temperature the density of scattering centers due to CH_2 and CH_3 groups will be greater along the chain axis than perpendicular to it, and an electron with a trajectory along the axis will suffer the greater loss. This situation could occur as a result of field-induced orientation of the anisotropic molecule and will lead to a smaller value of λ_m in Eq. [1]. As the temperature is increased, both orientation and the crystallite size will decrease, so increasing λ_m and lowering the strength. In the range T_{tl}-T_{lr}, the onset of libration will increase the effective volume occupied by each molecular group and so increase the cross-section. The two opposing effects of decreasing orientation and increasing cross section would account for the small changes in E_m/N in this range. Normal results quoted in Fig. 3 are in this range. Above T_{lr} complete rotation is possible and the disordering processes already begun at lower temperatures cause a further fall in strength. Since the alkyl benzenes are polar, field orientation is likely to be stronger than in the alkanes and this may help to account for the increased effective cross sections found for the CH_2 and CH_3 groups in these liquids. A similar increase in orienting force would occur for the alkanes if ions attach in any way to the chain molecules.

Oxygen Effects

Account must now be taken of the study recently reported by Sletten (1) in which oxygen was shown

to have a marked influence on the strength of n-hexane (and presumably on other n-alkanes). His conclusion is that the results reported by Lewis, House, Sharbaugh, and others refer to liquids in which dissolved oxygen caused an increase in strength. He demonstrated that the strength of n-hexane may be increased from 0.9 mv/cm to the levels normally reported by dissolving oxygen in the liquid. Nitrogen did not affect the strength at all. It is necessary to determine whether the concepts in this discussion are in any way disturbed by this discovery. Because small changes in molecular structure influence the strength (2-6), even in the presence of oxygen, it is logical to seek a mechanism by which oxygen raises the strength without disturbing the controlling influence of the hydrocarbon vibrations.

Oxygen is electronegative and forms negative ions. According to the latest work (23) attachment in the gaseous phase involves a dissociative process, with the formative of an atomic ion, which has a peak at electron energies of about 6 ev lying between the vibrational and ionization energies of the hydrocarbons. If the same attachment process occurs when oxygen is dissolved, it will remove free electrons of energies above the vibration peak normally capable of contributing to the α process in the liquid. The conversion of electrons to low-mobility negative ions would also reduce the conduction current as observed (1). The attachment cross section (23) is, however, smaller than seems necessary to explain the large influence on the strength, but its effectiveness may be enhanced by transport of the oxygen ions to the anode. A layer of oxygen and oxygen ions will be built up there and brought to an equilibrium as regards oxygen concentration and electrical double-layer strength determined by the applied field. The layer would be strongly electronegative and therefore resistive to electron motion. Strong evidence for the existence of this layer on the anode has been provided recently by Ward of this laboratory who used an electrode with a layer formed in this way as the cathode in a pulse breakdown test on n-hexane. The strength was initially greater than 2.1 mv/cm and declined to the more normal value of 1.5 mv/cm as the layer diffused away and the cathode regained its emission properties. Oxygen will, therefore, tend to reduce α and restrict the volume for avalanche development. This can be accounted for in the present theory by an increase in the constant C of Eq. [1]. Further work on the role of oxygen and other gases is in progress.

The Adamczewski Theory

The theory given by Adamczewski (18) employs the same type of energy loss concept as here, but there are detailed differences which are important, especially as excellent agreement with pulse measurements (4, 5) have been obtained by him.

The major energy loss is ascribed to C—C bond vibrations of wave numbers 890 and 1090 cm^{-1}, either of which ultimately give strengths in close agreement with the pulse measurements. Reasons for not preferring this mode of vibration, which in the author's opinion cannot be overlooked, have been given already. The mean free path λ_m is also calculated differently. In the work of Sharbaugh, *et al.* (4) and Lewis (2) no attempt is made to estimate the absolute cross sections from bond dimensions and only relative magnitudes in terms of k are derived. Adamczewski, however, assumes the collision cross section to be a longitudinal geometrical section of the molecule. The n-alkane molecule is taken to be a cylinder of base radius r and length $l(n-1)$ where $2r$ (=4.9Å) is the mean distance between molecular axes, assuming crystal order as in the solid, l (= 1.23Å) is the C—C bond length projected on the axis and n is the number of carbon atoms. The collision cross section is then $Q = 2r\ l(n-1)$ or $\lambda_m = [2Nr\ l(n-1)]^{-1}$. This calculation neglects thermal motion by which the molecule may be orientated randomly to the electron path. It is also doubtful whether the molecular spacing should be taken as $2r$ in determining the collision cross section. The same cylindrical model is also used for branched-chain alkanes (by adjusting r to compensate for the reduction in l due to the side groups) and for the alkyl benzenes. In the latter case the benzene ring is not considered as an entity but is used to extend the length of the alkyl radical by including two carbon atoms of the ring as part of the radical. The remaining ring bonds and any side groups then influence r. Adherence to a cylindrical model does not seem justified in these cases.

Finally, Eq. [1] is used with C = 1, i.e., no account is taken of other mechanisms vital to the breakdown process. Neither the oxygen effect nor the lower strengths obtained with direct rather than pulse voltages can be accommodated in the criterion. There are, therefore, great difficulties in accepting the Adamczewski theory, but the close agreement with experimental values is intriguing and demands further study.

Conclusion

The discovery of the oxygen effect and the statistical concepts given in another contribution (7) should help greatly in separating cathode from liquid effects and in determining C in Eq. [1]. By employing oxygen and perhaps other additives in controlled amounts the basic processes should be capable of investigation. Further work is also required to clarify the orientation effect over a range of temperatures including the solid state. Permanently orientated molecules in the solid might show strong directional properties and higher strengths. In the meantime the present treatment using a simple model provides a consistent relationship between measured electric strengths and molecular structure of these hydrocarbons. Up to now the reported strengths of insulating oils have been lower than what might be expected by extrapolation from simple hydrocarbons of less complexity. Careful separation of the oil will not only indicate particular molecular species which lower the strength but also provide valuable information on the relationship between electric strength and molecular structure.

Manuscript received Nov. 2, 1959. This paper was prepared for delivery before the Philadelphia Meeting, May 3-7, 1959.

Any discussion of this paper will appear in a Discussion Section to be published in the December 1960 JOURNAL.

REFERENCES

1. A. M. Sletten, *Nature*, **183**, 311 (1959).
2. T. J. Lewis, *J. Appl. Phys.*, **27**, 645 (1956).
3. R. W. Crowe, J. K. Bragg, and A. H. Sharbaugh, *ibid.*, **25**, 392 (1954).
4. R. W. Crowe, A. H. Sharbaugh, and J. K. Bragg, *ibid.*, **25**, 1480 (1954).
5. A. H. Sharbaugh, R. W. Crowe, and E. B. Cox, *ibid.*, **27**, 806 (1956).
6. T. J. Lewis, *Brit. J. Appl. Phys.*, **9**, 30 (1958).
7. B. W. Ward and T. J. Lewis, *This Journal*, **107**, 191 (1960).
8. W. B. Green, *J. Appl. Phys.*, **26**, 1257 (1956); *ibid.*, **27**, 921 (1956).
9. H. House, *Proc. Phys. Soc.*, **B70**, 913 (1957).
10. R. Hancox and H. Tropper, *Proc. Inst. Elec. Engrs. (London)*, Paper No. 2408M, Sept. 1957.
11. T. J. Lewis, *Proc. Phys. Soc.*, **B66**, 425 (1953).
12. L. B. Loeb, "Basic Processes of Gaseous Electronics," Chap. 4, University of California Press, Berkeley (1955).
13. S. A. Korff and R. D. Present, *Phys. Rev.*, **65**, 274 (1944).
14. A. von Hippel, *J. Appl. Phys.*, **8**, 815 (1937).
15. M. Darveniza, *Nature*, **183**, 743, (1959).
16. H. J. Plumley, *Phys. Rev.*, **59**, 200 (1941).
17. H. Frohlich, *Repts. Progr. Phys.*, **6**, 411 (1939).
18. I. Adamczewski, *Zesztyty Naukowe Politechniki Gdanskiej*, **3**, 3 (1957).
19. D. Berg and J. Kraitchman, Annual Report 1956, Conference on Electrical Insulation, National Academy of Sciences, National Research Council, 41 (1957).
20. N. Wright and M. J. Hunter, *J. Am. Chem. Soc.*, **69**, 803 (1947).
21. R. J. Moore, P. Gibbs, and H. Eyring, *J. Phys. Chem.*, **57**, 172 (1953).
22. T. J. Lewis, *J. Appl. Phys.*, **28**, 503 (1957).
23. J. D. Craggs, R. Thorburn, and B. A. Tozer, *Proc. Roy. Soc.*, **A240**, 473 (1957).

A New Statistical Theory for the Breakdown of Liquid Hydrocarbons

B. W. Ward and T. J. Lewis

Electrical Engineering Department, Queen Mary College, London, England

ABSTRACT

Hitherto it has been accepted that breakdown under pulse conditions occurs in liquid hydrocarbons with an insignificant statistical time lag. Theories have been developed in which the whole of any time lag measured has been assigned to a formative time, but these theories are not at all satisfactory. The paper shows that (*a*) that a significant statistical time lag does in fact exist provided the experimental procedure is correctly interpreted and (*b*) that a proper statistical analysis of the previous pulse measurements together with a statistical theory of breakdown shows that these measurements provide clear evidence *for* rather than against, a statistical time lag. Experimental results are given to show how the statistical time lag depends on electric stress and on cathode conditions.

The electric strengths of pure simple hydrocarbons indicate the possible strengths for liquid dielectrics of more commercial interest and also provide data for the determination of the breakdown mechanism in liquids. Alkanes and certain aromatic hydrocarbons have received attention in this way, but, in spite of increasingly reliable experiments, no general theory for the whole breakdown process has emerged and many conflicting ideas exist.The present contribution has the aim of presenting a new statistical model for the breakdown process, and hypotheses, supported by experimental evidence, are advanced which will help to explain many of the apparent discrepancies.

Electric strengths have been measured with both continuous and short duration voltages, but here attention will be concentrated on the latter type of test. The liquids, of which n-hexane has been most frequently tested, are given preliminary chemical purification if necessary and then further cleaned in a closed system to remove water, ionic impurity, dust particles of size $> 1\mu$, and dissolved gas. However, as Sletten has shown recently (1), most results for n-hexane, at least, and probably for other hydrocarbons refer to liquids containing significant amounts of oxygen which raise and stabilize the strength. The oxygen in these cases must have come from the air during a final stage in the cleaning process or while being stored after cleaning. The test cell is frequently integral with the cleaning system and the electrodes are usually 1 cm diameter metal spheres at a spacing of less than $\sim 10^{-2}$ cm. Electrodes are highly polished and degreased beforehand and for the experiments reported here, were stainless steel.

With this preparation, the strength of n-hexane is in excess of 1.5 mv/cm for pulse voltages of 1.5 μ sec or less (2), and at this stress field emission of electrons from the cathode must be taking place and contributing significantly to the conductivity of the liquid. A typical plot of strength vs. pulse duration (3) is shown in Fig. 1. Any point is the mean of a set of measurements having a coefficient of variation of about 5%, and a measurement is made by applying successive pulses of constant duration and increasing amplitude until a breakdown occurs. A distinct change occurs for pulse lengths $< T_0$ and the times $T \leqq T_0$ have been considered to be a measure of the formative time of the breakdown process. If the

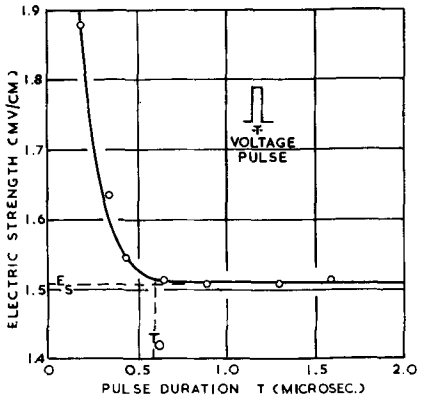

Fig. 1. Typical characteristics for a hydrocarbon liquid n-hexane (3).

pulse time T was greater than T_o, breakdown was considered to occur invariably at a time T_o provided the voltage was sufficient to cause a stress E_s (Fig. 1). This idea has been generally accepted (3, 4) and supported by statements that the statistical time lag was negligible, breakdown being easily initiated by ample electrons from the cathode (3-5). The times $T \leqq T_o$ have been related to the transit times of certain ions of mobility μ across the sphere gap d according to the law $T = d\ (\mu E)^{-1}$ (where E is the applied stress) and so compared with viscosity (4). This theory does not easily explain why the formative time should be influenced by the cathode material as observed, nor does it explain several discrepancies in published results (3-6).

There is also contrary evidence that the statistical time lag is not in fact zero from experiments using "step-function" pulse voltages in which the time lag to breakdown is measured directly for each voltage application. Strigel (7) using oil, and Saxe and Lewis (8) with n-hexane, have reported considerable random variations in the time lags even at stresses of 1.9 mv/cm. The work reported here confirms the existence of a statistical lag and also shows that it was almost certainly present in short-duration pulse experiments such as those leading to Fig. 1. By employing a statistical method, all these measurements become consistent and a physical interpretation is possible in which the roles of the liquid and cathode are clear. We begin by setting up a statistical model for the breakdown condition applicable to measurements with step-function and short duration pulse voltages.

Theory

The necessary assumptions for the model are (*a*) that electrons are ejected randomly from the cathode into the liquid with a mean rate I per second, and (*b*) that each electron has a probability W of initiating a breakdown process having a formative time t_f which is small. Cathode surface conditions will control I and liquid properties will determine W and t_f and all three quantities will be dependent on the field strength (see Fig. 2) and electrode geometry.

Step-function voltages.—If a step-function voltage is applied creating a mean stress E in the liquid, it may be shown [see (8) and references therein] that the probability of breakdown occurring within a

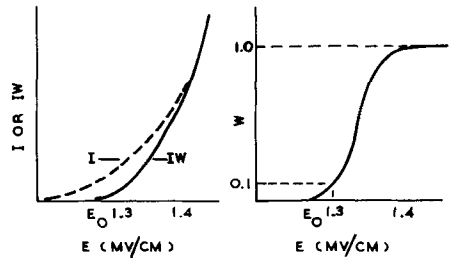

Fig. 2. I, W, and IW as functions of applied stress E. Values given are for a hypothetical liquid.

time interval t to $t + dt$ after the instant of voltage application is

$$P(E)\,dt = WI \exp\left[-WI(t - t_f)\right] dt \qquad [1]$$

From this the mean time lag before breakdown occurs, $\bar{t}$, is given by

$$\bar{t} = t_f + (WI)^{-1}$$

and the probability of a time lag $> t$ is exp $[-WI(t - t_f)]$. These expressions are valid for $t \geqq t_f$. Equation [1] shows that the shorter time lags are most probable and according to Fig. 2 there will be a threshold condition $E = E_o$, $W = 0$ below which P is zero. As the field strength increases, the mean time lag $\bar{t}$ will decrease in accordance with the field dependence of IW. Although the theory indicates that many time lags need to be measured to obtain an accurate estimate of P, experience has shown that reliable indications may be obtained from relatively few measurements.

Short-duration pulses.—The probability of breakdown occurring with a pulse duration T, producing a stress E is

$$p(E) = 1 - \exp\left[-IW(T - t_f)\right] \qquad [2]$$

which will be zero for $E < E_o$ and $T < t_f$ and will tend to unity as E increases. The usual procedure is to apply a succession of pulses of constant T and increasing magnitude in steps ΔE until a breakdown is recorded. If at each level of stress N pulses are applied, the probability of breakdown at a stress E_m is then, assuming $t_f = 0$ for the present,

$$P_m = 1 - (1 - p_m)^N = 1 - \exp\left[-I_m W_m T N\right] \qquad [3]$$

and the probability of a breakdown first occurring at a level E_n in any succession of pulses is

$$Q_n = Pn \prod_{m=0}^{n-1} (1 - P_m) \qquad [4]$$

The initial level corresponds to $m = 0$ and for most applications can be taken as E_o. Using Fig. 2, it is easy to show that Q_n increases from zero at E_o, passes through a maximum and then decreases as E_n becomes large; the exact form depending on IW.

For convenience in calculation it is better to transform to a continuous variable, replacing Q_n by $Q(E)dE$ which is defined as the probability of a first breakdown in the interval E to $E + dE$ and writing λ (instead of N) as the number of pulse applications in a unit interval of stress. It is found that

$$Q = \lambda p \exp\left[-\lambda \int_{E_0}^{E} p\, dE\right] \qquad [5]$$

The distribution Q need not be symmetrical since this depends on the form of IW. It will give a most probable breakdown stress E_p and an average stress E_{av} but unless asymmetry is great $E_p \sim E_{av}$.

The same model has been used for step-function and short duration voltages, but measurements might lead to very different conclusions in the same two cases. In the first, random time lags would be obvious immediately, but with the second Q might have little spread and E_p or E_{av} could be reasonably precise. Any fluctuations in this case might then be ascribed to extraneous influences rather than to the true breakdown process. It should be noted that E_0 will be the breakdown stress with continuous voltage and there will be a negligible chance of breakdown at this stress with pulses of microsecond duration. If the model is correct, measurements with either step-function or short duration voltages should yield information concerning the cathode and liquid function I and W. The most important result is that it gives an entirely different interpretation of the characteristic shown in Fig. 1 as will be demonstrated immediately.

Comparison with Experiment

As already mentioned, with E_p equal to 1.5 mv/cm or greater, the emission I is likely to be a field-aided thermionic process according to a Schottky law (9) which can be written as

$$I = B \exp\left(15\, E^{1/2}\right)$$

E is in mv/cm and B is a constant determined by the temperature and nature of the cathode surface. Other workers have proposed alternative field emission laws, but the exact nature is immaterial for the present argument since we require merely that I should increase rapidly with E. Making an arbitrary choice, $B = 0.01$, gives $I = 10^6$ electrons/sec for $E = 1.5$ mv/cm and using this with W for a hypothetical liquid, as in Fig. 2, in Eq. [2]-[5] it is possible to obtain Fig. 3. The formative time t_f has been neglected for ease in calculation, but it will be reintroduced below.

The agreement between the theoretical characteristic in Fig. 3 and the experimental one in Fig. 1 is striking. The parts AB and BC of the curve mainly depend on I and W, respectively, and the position of the curve on the axis of stress E_{av} may be shifted to conform with any specific liquid by adjustment of these. Adjustment on the T axis is not arbitrary however, and the discrepancy between Fig. 3 and Fig. 1 is due to the assumption $t_f = 0$ which causes the asymptotic value of T for large E_{av} to be zero in the theoretical case but not in the practical one. This can be rectified easily by including a nonzero t_f in the theoretical derivation.

The most significant result of the statistical theory is that the region of maximum curvature at B is not due to a formative time but is produced by the statistical requirements and the shape of the IW curve. Figure 3 also emphasizes that over the small range of T normally employed, the characteristic can appear to be independent of T in the range BC. Extrapolation to large T corresponding in the limit to tests with continuous voltage would yield a breakdown stress equal to E_0. It should be noted that for ethyl alcohol and water, a strong dependence on T has been found even when T was several microseconds (5).

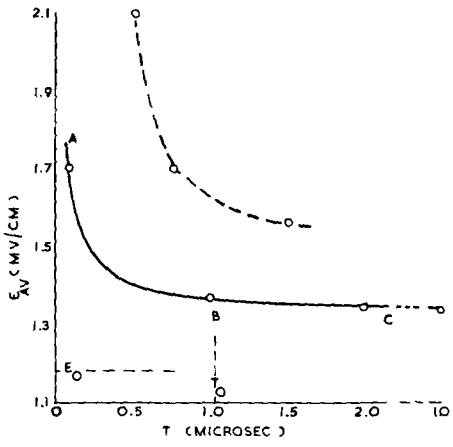

Fig. 3. Calculated breakdown stress E_{av} as a function of pulse duration for a hypothetical liquid. The region of maximum curvature at B is not due to a formative time which has been put equal to zero in the derivation.
- - - curve obtained from experiments on n-hexane similarly prepared to that employed for Fig. 4.

The procedure adopted has been to choose I and W and then derive the breakdown stress vs. pulse duration curve, but there is no reason why the procedure should not be changed and the experimental curve together with I used to determine W and t_f, for instance.

Direct support for the statistical model has recently been obtained in this laboratory. Using n-hexane and stainless steel spherical electrodes at

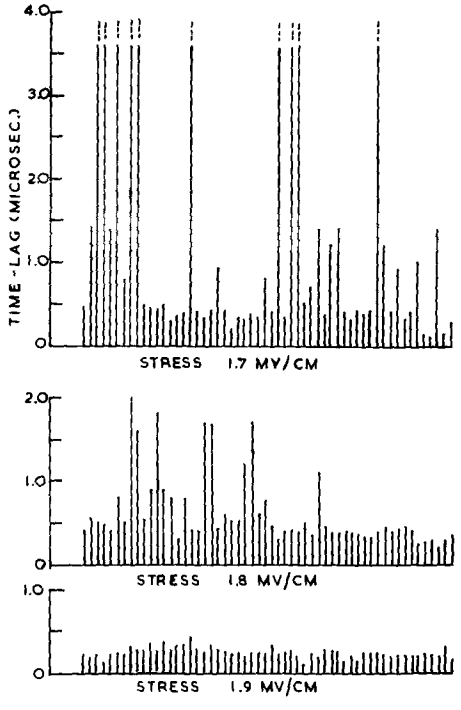

Fig. 4. Statistical time-lag sequences for n-hexane. Each vertical trace indicates the time lag for a particular step-function pulse. Electrodes were stainless steel with $d = 5 \times 10^{-3}$ cm.

a spacing of 5 x 10^{-3}cm, time lags have been measured directly using a "step-function" pulse having a front of 10^{-7} sec and lasting at maximum voltage for a time $> 10^{-4}$ sec. Time lags were recorded automatically using the technique of Saxe and Lewis (8). Figure 4 shows a series of these measurements. There is no doubt that the time lags are random and decrease in mean value as the stress is raised. At 1.7 mv/cm, lags well in excess of 3.5 μsec are recorded and even at 1.8 mv/cm lags greater than 1.5 μsec are not infrequent. These results give quite a different impression from that deduced formerly from short-duration pulses (2-6) under very similar experimental conditions. On the earlier theory, at a stress of 1.8 mv/cm, it would be considered that the time to breakdown could not exceed about 0.25 μsec, being due entirely to a formative process.

In order to confirm that Fig. 3 and 4 represent the same phenomena, measurements have been made on similar samples of n-hexane using short-duration rather than step-function voltages. All other conditions were identical. The pulses were produced by matched line techniques and increased in steps ΔE = 0.05 mv/cm with $N = 1$. Values of E_{av} obtained have been added to Fig. 3. The dependence on pulse duration is in general agreement with the theory and Fig. 1 and with other results (4, 5). The strength increases rapidly when the pulse duration is reduced sufficiently. Further comments concerning cathode influence on these results are given below. According to the theory, the distribution Q_n, (Eq. [4]), should shift to lower stresses when N is increased. To verify this, experiments were repeated with $N = 5$ instead of unity. The predicted shift occurred as the sample results in Table I indicate because if a procedure in which $N = 1$ had been adopted, all except measurement 4 and 5 would have resulted in higher breakdown stresses.

Thus, by comparing the theory with earlier work and by performing both types of test under otherwise identical conditions, it has been demonstrated that breakdown in n-hexane can be consistently described by the statistical model. It is inferred that the model will also be applicable to the other simple liquids tested. A few implications of this are now examined.

Discussion

Cathode effects.—According to the theory, cathode effects should predominate in the range AB (Fig. 3). Figure 5 reproduces measurements made by Crowe (3) with stainless-steel electrodes in n-hexane and other n-alkanes at two electrode spacings. Since all these liquids have common properties and the electrodes received a consistent preparation, it would be expected that the emission properties of the cathodes would be similar in all cases, i.e., that the characteristics would merge in the region AB. This is, in fact, seen to be the case in Fig. 5. Through W, liquid influences cause the curves to separate in the region BC. The differences found between the cathode regions in the experiments here (shown in Fig. 3) and those of Crowe and co-workers (2, 3, 6,) (Fig. 1) and other authors (4, 5) may be ascribed directly to differences in the emissive properties of the cathodes employed.

Table I. Influence of number of pulse applications on breakdown stress

	Breakdown measurement number							
	1	2	3	4	5	6	7	8
Breakdown stress, mv/cm	1.45	1.45	1.55	1.45	1.25	1.35	1.45	1.55
Number of pulse applications at the breakdown stress	4	5	2	1	1	2	4	2

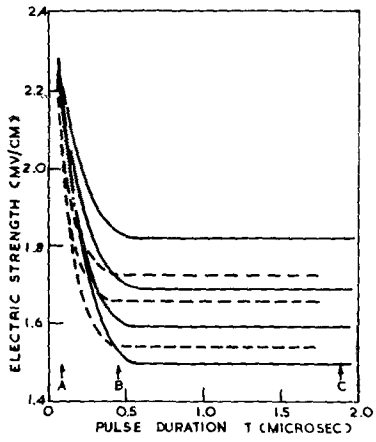

Fig. 5. Electric strength as a function of pulse duration according to Crowe (3). —— d = 6.35 x 10^{-3} cm; - - - d = 5.08 x 10^{-3} cm.

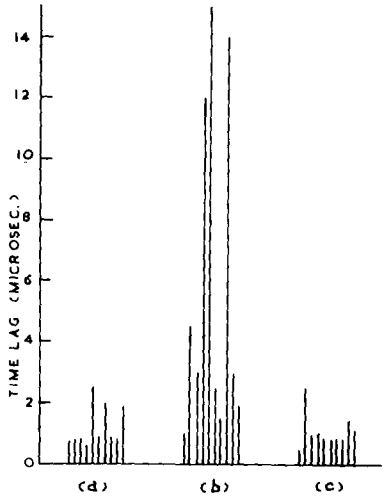

Fig. 6. Statistical time lags for n-hexane at a stress of 1.4 mv/cm, (a) and (c) roughened cathode, (b) polished cathode. Electrodes of stainless steel with d = 5 x 10^{-3} cm.

Conclusive evidence concerning the direct influence of the cathode on breakdown is shown by the time-lag measurements of Fig. 6. It is well known that an abraded metal cathode will exhibit considerably enhanced electron emission (10) and so should yield a much greater value of I than a normally polished one. Consequently, a pair of stainless steel electrodes were prepared, one being highly polished and the other roughened, and used to test n-hexane at a spacing of 5 x 10^{-3}cm. Measurements were made at a stress of 1.4 mv/cm; the polarity being reversed after every ten measurements. When the cathode was rough, time lags were short, but on reversal the

lags normally expected at that stress were obtained. A further reversal recovered the short lags once more. This experiment and others in which the degree of oxidation of the cathode was found to change the mean time lag clearly indicate the role of the cathode.

Liquid effects.—The W dependent region BC (Fig. 3) depends on the properties of the liquid and on the electrode spacing (3, 4) and thus from this region information pertaining to the breakdown mechanisms in the liquid phase may be found. Since formally T may be extended to very long times, liquid influence on pulse and continuous voltage measurements may be unified. These matters, together with the oxygen effect found by Sletten which does not alter the model proposed here, are discussed at length in a subsequent paper (11).

Formative time.—According to the statistical model, times $T < T_0$ are not measures of a true formative time t_f and even when t_f is zero (as assumed in Fig. 3) a finite T_0 exists. T_0 corresponds approximately to the stress at which W becomes unity and cathode conditions predominate but does not apparently have any further significance. The true formative time may be estimated at very high stresses from the experimental results because the statistical lag then tends to zero. Values estimated in this way from the work of Crowe as in Fig. 1 and 5 give t_f not greater than about 1×10^{-7} sec for a 5×10^{-3} cm gap. An estimate of similar magnitude may be made from the work of Edwards (5) and with certain reservations from that of Goodwin and Macfadyen (4). The time-lag measurements at 1.9 mv/cm, Fig. 4, also suggest a formative time not greater than 10^{-7} sec. This estimate is much less than those based on T_0 and helps to explain why certain discrepancies existed in earlier interpretations. For instance, Edwards found T_0 to be practically independent of the liquid but dependent on electrode separation in general agreement with Crowe and co-workers, whereas Goodwin and Macfadyen reported that T_0 increased with molecular chain length and viscosity. Goodwin and Macfadyen also found that the formative time as defined by them was influenced by the cathode material and thus difficult to explain.

If t_f is about 10^{-7} sec at a stress of 1.9 mv/cm and is ascribed to the transit time of a particle, the mobility is $\sim 3 \times 10^{-2}$ cm^2/v sec which is appreciably greater than ion mobilities measured at lower fields in these liquids by Adamczewski (12) although it is possible that the mobility will decrease as the stress decreases. Further investigations are required to determine t_f and ion and electron mobilities directly in the range above 1.5 mv/cm.

A fuller study of the nature of the statistical time lag is now being made which should permit the various cathode and liquid mechanisms to be understood in more detail. If the cathode influence is understood, greater progress can then be made in establishing a theory for breakdown in liquids comparable with that in gases. The statistical hypothesis should help greatly in achieving this.

Acknowledgment

One of the authors (B.W.W.) is grateful to the Department of Scientific and Industrial Research for an award enabling this study to be made, and thanks are also due to Professor M.W. Humphrey Davies for providing facilities in the Department.

Manuscript received November 2, 1959. This paper was prepared for delivery before the Philadelphia Meeting, May 3-7, 1959.

Any discussion of this paper will appear in a Discussion Section to be published in the December 1960 JOURNAL.

REFERENCES

1. A. M. Sletten, *Nature*, **183**, 311 (1959).
2. R. W. Crowe, A. H. Sharbaugh, and J. K. Bragg, *J. Appl. Phys.*, **25**, 1480 (1954).
3. R. W. Crowe, *ibid.*, **27**, 156, (1956).
4. D. W. Goodwin and K. A. Macfadyen, *Proc. Phys. Soc.*, **66**, 85, (1953).
5. W. D. Edwards, *Can. J. Phys.*, **29**, 310 ,(1951).
6. A. H. Sharbaugh, J. K. Bragg, and R. W. Crowe, *J. Appl. Phys.*, **26**, 434 (1955).
7. R. Strigel, "Elektrische Stossfestigkeit," 2nd ed., Springer-Verlag, Berlin (1955).
8. R. F. Saxe and T. J. Lewis, *Brit. J. Appl. Phys.*, **6**, 211, (1955).
9. H. House, *Proc. Phys. Soc.*, **B70**, 913 (1957).
10. F. Llewellyn Jones and C. G. Morgan, *Proc. Roy. Soc.*, **A218**, 88 (1953).
11. T. J. Lewis, *This Journal*, **107**, 185 (1960).
12. I. Adamczewski, *Ann. Phys.*, **8**, 309, (1937).

Kinetics of the Oxidation of Antimony

A. J. Rosenberg A. A. Menna, and T. P. Turnbull

Lincoln Laboratory, Massachusetts Institute of Technology, Lexington, Massachusetts

ABSTRACT

The oxidation of antimony has been studied between 265° and 385°C. The reaction is characterized by an initially parabolic growth rate, which degenerates into a time-independent rate, controlled by the gaseous diffusion of $(Sb_2O_3)_2$ from the surface region to the cold wall outside the sample furnace. The stationary rate decreases with increasing oxygen pressure and with increasing diffusion length. A compact layer of Sb_2O_3 forms on the antimony surface and supports a further overgrowth of Sb_2O_5. Kinetic data have been analyzed to obtain thermochemical parameters for the reaction which yields $(Sb_2O_3)_2(g)$ and agreement is obtained with known data for the equilibrium $2Sb_2O_3(s) \rightleftharpoons (Sb_2O_3)_2(g)$.

Several studies now in progress in these laboratories (1) deal with the oxidation of intermetallic compounds containing antimony as a principal element. To provide a suitable frame of reference, it has been necessary to examine the oxidation of elemental antimony itself. The present article is concerned with the kinetics of this reaction in the temperature range, 265°-385°C.

Experimental

Reaction rates were determined by following the oxygen pressure at constant volume. A thermistor manometer was used, permitting instantaneous pressure measurements in the range, 1-500 μ, with a precision of better than 0.1% (2).

Single crystals of 99.999+% antimony were used. Small wafers were cleaved normal to the (0001) direction, and this plane accounted for more than 75% of the exposed surfaces, which totaled 0.5 cm^2 per sample. The samples were cleaved in air and transferred directly to an 8 mm tube which was then connected to an adsorption apparatus of the type described earlier (2). A movable tube furnace which maintained the sample temperature to ± 1°C was then raised into position. Oxygen of spectroscopic purity was used throughout.

Results

Upon exposure to oxygen at 358°C, antimony reacts readily, but the rate rapidly decreases by two orders of magnitude and becomes constant (Fig. 1). During the reaction a yellow-white crystalline material deposits on the walls of the sample enclosure at the point where it leaves the furnace. The material can be displaced by raising the position of the furnace. It was established by both x-ray and electron diffraction that the entire deposit consists of senarmontite, the cubic form of Sb_2O_3 (3). If the oxygen in the sample chamber is evacuated during the experiment, Sb_2O_3 continues to evaporate from the sample. When this evolution ceases and oxygen is readmitted to the system, the kinetics of Fig. 1 are repeated.

If the sample is quenched during the reaction by removing the furnace, an irregular crystalline overgrowth, identified as Sb_2O_5 by electron diffraction,

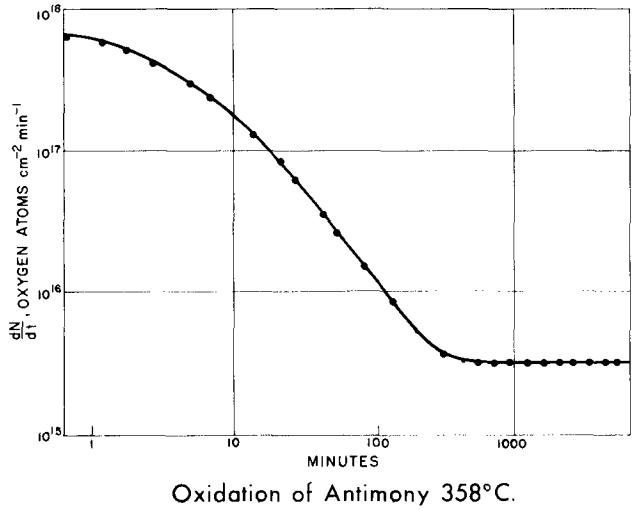

Fig. 1. Oxidation of antimony at 358°C. Oxygen pressure, 0.40-0.45 mm, surface area = 0.5 cm^2.

is observed on the surface of the sample. By sectioning the sample and scanning the exposed surface, it was further established by reflection electron diffraction that a layer of cubic Sb_2O_3 separates the Sb_2O_5 from the antimony substrate (Fig. 2).[1]

[1] Bound and Richards (4) observed the formation of senarmontite on antimony films heated in air above 250°C.

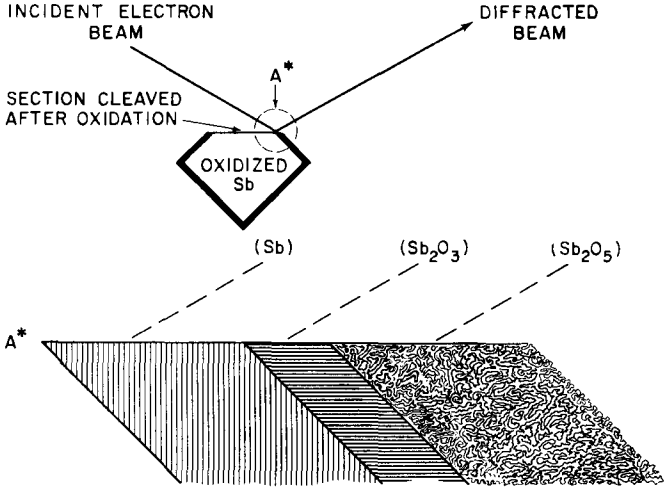

Fig. 2. Reflection electron diffraction by oxidized antimony

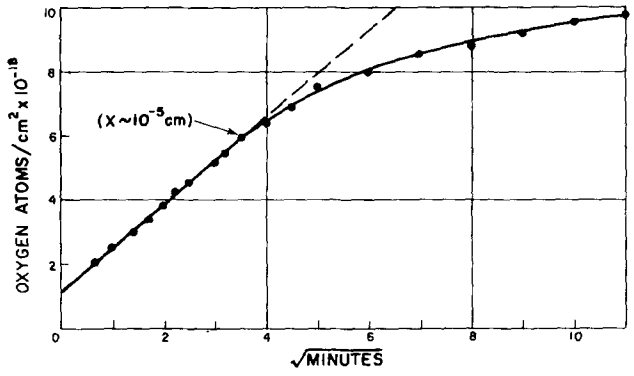

Fig. 3. Oxidation of antimony at 350°C. Oxygen pressure, 0.40-0.45 mm, surface area = 0.5 cm².

Clearly, the oxidation proceeds in at least two stages. The formation of an oxide film presumably controls the initial stage. Growth of the film requires that it be penetrated by either antimony or oxygen, so that the rate diminishes as the film thickens. Ideally, $dX/dt = kX^{-1}$ and $X = (2k)^{1/2} t^{1/2}$ where X is the film thickness, t is the reaction time, and k depends only on temperature and pressure. Figure 3 shows that the oxygen uptake does indeed increase linearly with $t^{1/2}$ during the first 15 min of reaction at 358°C. The rate then drops more rapidly than expected and approaches its stationary value.

When the steady state is attained the reaction rate is controlled by the distillation of Sb_2O_3 from the surface of the sample to the cold wall at the inlet to the sample enclosure. This is shown by two decisive results.

(i) The stationary rate varies inversely with the oxygen pressure, as shown in Table I. Accordingly, neither the primary oxidation reaction, nor the diffusion of oxygen or antimony through the oxide film, nor the diffusion of oxygen through the gas phase control the reaction since the rates of each should increase with pressure.[2] One may conclude, therefore, that oxygen acts by impeding the vapor phase diffusion of Sb_2O_3.

(ii) The stationary rate depends on the position of the sample in the furnace. Figure 4 shows that when the position of the sample relative to the top of the surrounding furnace is changed from 11 cm to 1.5 cm, the rate increases by almost an order of magnitude. Since the only effect of this manipulation is to shorten the gaseous diffusion path, the diffusion of Sb_2O_3 to the cold wall must control the rate.

[2] A chemical reaction of oxygen to inhibit vaporization of Sb_2O_3, e.g., through the equilibrium, $Sb_2O_3 + \frac{1}{2}O_2 = Sb_2O_4$ may also be disallowed since the negative pressure effect increases with increasing temperature in the range, 285°-360°C (Fig. 4). This would require that the inhibiting reaction be endothermic, and, since the entropy of any reaction which fixes gaseous oxygen is negative, the over-all free energy change would be positive.

Table I. Dependence of stationary oxidation rate on oxygen pressure, T = 352°C

Oxygen pressure, μ	Rate (oxygen atoms cm^{-2} min^{-1}) x 10^{-15}
550	1.1
270	1.2
170	1.45
90	3.2
40	7.2
15	7.9

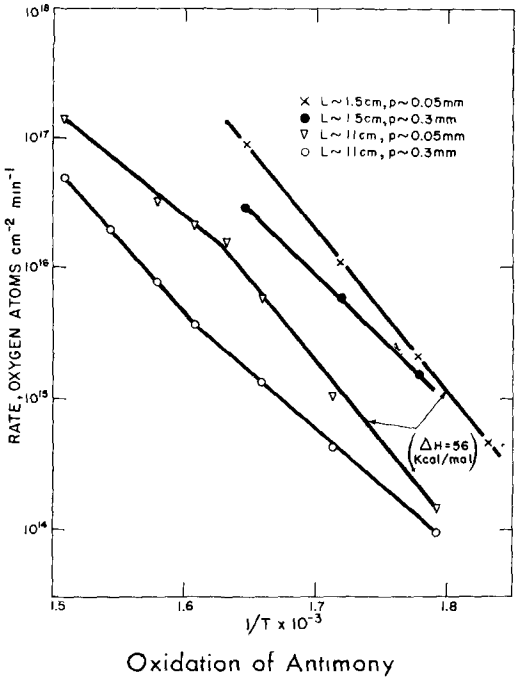

Fig. 4. Effect of temperature, pressure, and furnace level on the stationary oxidation rate. Surface area = 0.5 cm².

Discussion

The high-temperature oxidation of antimony parallels that of germanium (5) in that the diffusion of a volatile oxide through the vapor phase leads to a stationary reaction velocity. In the case of germanium the volatile species is GeO; in the case of antimony, it is $(Sb_2O_3)_2$ (6). The rate at which $(Sb_2O_3)_2$ diffuses from a gas reservoir at concentration, C_o, can be estimated from kinetic theory. We shall follow the treatment given by Law and Meigs (5) for the diffusion of GeO. The rate is given by:

$$V = \frac{\lambda \Gamma C_o A}{\frac{\lambda \Gamma (L - \Delta)}{D} + 1} \qquad [1]$$

λ is the accommodation coefficient of $(Sb_2O_3)_2$ at the surface from which it arises; $\Gamma = (kT/2\pi m)^{1/2}$ where m is the molecular mass of $(Sb_2O_3)_2$; Δ is the mean free path in the vapor; L and A are the length and cross section of the path separating the reservoir from the cold wall where the pressure of $(Sb_2O_3)_2$ is virtually zero; D is the diffusion coefficient of $(Sb_2O_3)_2$ through oxygen. Ideally D should vary as $1/p_{O_2}$; in the present case, the dependence, while inverse, is not linear. For the present qualitative purposes we assume, as an approximation, that

$$D = D_o (T/273)^{1.75} (760/p_{O_2}) \qquad [2]$$

where D_o is estimated to be 0.04 cm^2/sec for $(Sb_2O_3)_2$ (5, 7).

Substituting $C_o = 1.0 \times 10^{18} PT^{-1}$ molecules/cc where P = pressure in mm of $(Sb_2O_3)_2$ in the reservoir, $\Gamma = 150T^{1/2}$ cm/sec, and $D = 1.7 \times 10^{-3} T^{1.75} p_{O_2}^{-1}$ cm^2/sec, Eq. [1] becomes

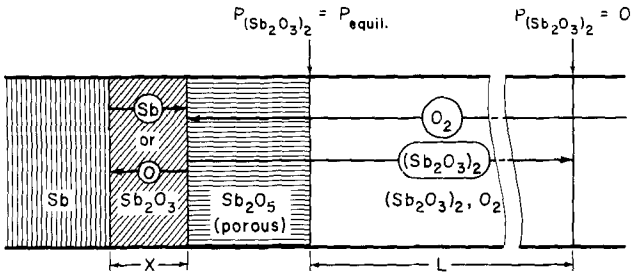

Model for High Temperature Oxidation of Antimony

Fig. 5. Model for the oxidation of antimony

$$V = \frac{1.5 \times 10^{20} \lambda A T^{-1/2} P}{9 \times 10^{4} \lambda (L = \Delta) p_{O_2} T^{-1.25} + 1} \quad [3]$$

$(Sb_2O_3)_2$ molecules/sec

Equation [3] is of the right form to account qualitatively for the negative effects of increasing p_{O_2} and L on the stationary oxidation rate. It is consistent, furthermore, with the fact that the relative effect of P_{O_2} increases with both T and L. Evaluating Eq. [3] at $L - \Delta \sim L = 11$ cm, $A = 0.5$ cm^2, $T = 600$°K, and $p_{O_2} = 0.05$ mm, we obtain

$$V\ (600°K) = \frac{3 \times 10^{15} \lambda P}{17\lambda + 1}\ (Sb_2O_3)_2 \text{ molecules/sec} \quad [4]$$

This is to equated to the rate of oxygen uptake by the sample, hence,

$$V(600°K) = \frac{1.1 \times 10^{21} \lambda P}{17\lambda + 1} \text{ oxygen atoms/min} \quad [5]$$

Since the effects of p_{O_2} and L are contained in the first term of the denominator of the rate expression, this term must be comparable with unity. Consistent with this qualitative calculation, we assume $17\lambda >> 1$ and obtain finally

$$V(600°K) \approx 6 \times 10^{18} P \text{ oxygen atoms/min} \quad [6]$$

The observed rate of oxygen uptake under these conditions (Fig. 5) is 5×10^{15} oxygen atoms/min, whence

$$P(600°K) \approx \frac{5 \times 10^{15}}{6 \times 10^{19}} = 8 \times 10^{-5} \text{ mm} \quad [7]$$

The purpose of this calculation is to decide whether $P = P_{equil.}$, where $P_{equil.}$ is the equilibrium vapor pressure of a plausible surface reaction yielding $(Sb_2O_3)_2(g)$. If this is the case, the standard free energy of the reaction will be given by $\Delta F° = -RT \ln(P/760)$, $= +19$ kcal/mole. The enthalpy of the reaction will be defined through Eq. [3], from which it is seen that

$$V \sim AT^{0.75} \sim BT^{0.75} \exp(-\Delta H/RT) \quad [8]$$
$$\sim C \exp(-\Delta H/RT)$$

where, C is constant for any small range of T. Thus the enthalpy corresponds approximately to the activation energy of the oxidation reaction. From Fig. 4 one obtains $\Delta H \approx +56$ kcal/mole in the range 270°-340°C for $p_{O_2} \sim 0.05$ mm, independent of L.

With the presence of $Sb_2O_3(s)$ and $Sb_2O_5(s)$ at the surface established by electron diffraction, the four reactions given in Table II must be considered as potential sources of $(Sb_2O_3)_2(g)$. The values of ΔH, $\Delta F°$, and $P_{equil.}$ for each reaction have been calculated from the data of Hincke (8), Simon and Thaler (9), and Coughlin (10). Reactions [1],[3], and [4] are inconsistent with the kinetic analysis, giving impossibly high or low values of $P_{equil.}$. Reaction [2], on the other hand, satisfactorily accounts for the predictions of both Eq. [7] and [8].

The results give compelling evidence that the vaporization of Sb_2O_3 goes to equilibrium in the region immediately surrounding the sample, yielding a regulated pressure of $(Sb_2O_3)_2$. Although Sb_2O_5 is the most stable oxide of antimony below 360°C, it does not participate in the equilibrium. Thus, the chemical interactions of $(Sb_2O_3)_2(g)$, $Sb_2O_5(s)$, and O_2 must be very slow compared to the over-all oxidation rate. This is consistent with the observations of many workers that the interconversions of the antimony oxides through the addition or loss of O_2 are extraordinarily slow reactions (9).

A model for the oxidation is illustrated in Fig. 5. The model assumes that the primary reaction of Sb + O_2 yields $Sb_2O_3(s)$ in an isothermal system below 350°C. Continued oxidation to Sb_2O_5 is much slower. A compact film of Sb_2O_3 forms at the surface and continued reaction of Sb requires that either Sb or O_2 diffuse through the film. The rate of oxidation thus decreases with $1/X$, as observed (Fig. 3). Simultaneously $(Sb_2O_3)_2$ evaporates from the surface of the film and escapes through the oxygen atmosphere to condense on the available cold wall. The rate at which it escapes is controlled by the difference between its pressure at the surface of the sample, P, and that at the wall. The latter is virtually zero, while the maximum value that P can have is $P_{equil.}$, the equilibrium vapor pressure above $Sb_2O_3(s)$. The Sb_2O_3 film thus will thicken to a point (about 10^{-5} cm) where the further diffusion of O_2 or Sb through it exactly matches the maximum rate at

Table II. Thermochemical parameters for formation of $(Sb_2O_3)_2$ vapor at 600°K, $p_{O_2} = 0.05$ mm, standard states $p_{O_2} = P_{(Sb_2O_3)_2} = 1$ atm

	Reaction	ΔH, kcal/mole	$\Delta F°$, kcal/mole	$P_{equil.}$, mm
1.	$4Sb(s) + 3\,O_2(g) = (Sb_2O_3)_2(g)$	-291 ± 4	-238 ± 4	$\sim 10^{77}$
2.	$2Sb_2O_3(s) = (Sb_2O_3)_2(g)$	$+47 \pm 2$	$+22 \pm 1$	4×10^{-6}-2×10^{-5}
3.	$\frac{6}{5}Sb_2O_5(s) + \frac{8}{5}Sb(s) = (Sb_2O_3)_2(g)$	-18 ± 7	-44 ± 7	$\sim 10^{19}$
4.	$2Sb_2O_5(s) = (Sb_2O_3)_2(g) + 2\,O_2(g)$	$+165 \pm 10$	$+86 \pm 5$	$\sim 10^{-17}$
	Calculated from kinetics, Eq. [7] and [8]	$+56 \pm 3$	$+19 \pm 0.5$	8×10^{-5}

which oxygen is removed from the sample as $(Sb_2O_3)_2(g)$.

When the rate of gaseous diffusion is altered through changes in $P_{equil.}$, D, or L, the rate of transfer of Sb or oxygen across the Sb_2O_3 film is altered identically by an adjustment of the film thickness. This is best illustrated by the transient effects which are observed when the pressure, hence D, is changed. When the pressure is raised, the rate of oxidation sharply increases before falling to the lower value characteristic of the higher pressure. Conversely, when the pressure is dropped, the rate only slowly rises to the higher stationary value.

While the reaction proceeds, Sb_2O_3 is slowly oxidized to the nonvolatile Sb_2O_5 which crystallizes as a porous overgrowth atop the Sb_2O_3 film. Its rate of formation is so small as to contribute only slightly to the over-all rate of oxygen uptake. Furthermore, it does not significantly impede the escape of $(Sb_2O_3)_2$ by either physical or chemical interaction. When the supply of fresh O_2 to the sample is interrupted, however, the Sb_2O_3 film will continue to evaporate. When it is exhausted the Sb_2O_5 will collapse on the antimony substrate and be dissipated through the reaction, $8Sb + 6Sb_2O_5 \rightarrow 5(Sb_2O_3)_2$.

The model accounts for the principal experimental features of the oxidation of antimony in the temperature range 265°-350°C. The shift in mechanism above this temperature (cf. Fig. 4) is probably related to the fact that the rate of oxidation of Sb_2O_3 to Sb_2O_4 becomes appreciable above 350°C (9).

Manuscript received Oct. 5, 1959. The work reported in this paper was performed by Lincoln Laboratory, a center for research operated by Massachusetts Institute of Technology with the joint support of the U. S. Army, Navy, and Air Force.

Any discussion of this paper will appear in a Discussion Section to be published in the December 1960 JOURNAL.

REFERENCES

1. A. J. Rosenberg, M. C. Lavine, A. A. Menna, and T. P. Turnbull, to be published.
2. A. J. Rosenberg, *J. Am. Chem. Soc.*, **78**, 2929 (1956).
3. R. M. Bozorth, *ibid.*, **45**, 1621 (1923).
4. M. Bound and D. A. Richards, *Proc. Phys. Soc.*, **51**, 256 (1939).
5. J. T. Law and P. S. Meigs, *This Journal*, **104**, 154 (1957).
6. H. Biltz, *Z. Physik. Chem.*, **19**, 385 (1896).
7. A. Lonius, see L. B. Loeb, "The Kinetic Theory of Gases," p. 272, McGraw-Hill Book Co., New York (1934).
8. W. B. Hincke, *J. Am. Chem. Soc.*, **52**, 3869 (1930).
9. A. Simon and E. Thaler, *Z. Anorg. u. Allgem. Chem.*, **154**, 253 (1927).
10. J. P. Coughlin, *Bull. 542, U. S. Bur. of Mines*, 1954.

CaS:Cu,Eu Electroluminescent Phosphors

A. Wachtel

Research Department, Westinghouse Electric Corporation, Bloomfield, New Jersey

ABSTRACT

Introduction of Cu into CaS:Eu does not interfere with the red Eu^{++} emission. Excitation of the blue CaS:Cu emission is more effective by 3650Å than by 2537Å. Firing with excess Cu gives rise to deposits of free Cu_2S which may cause an efficient system of contact electroluminescence. The electroluminescent properties depend on the physical characteristics of the phosphors, including its state of agglomeration. At moderate concentrations of Eu, the blue emission of CaS:Cu is entirely suppressed in electroluminescent excitation.

This investigation was performed as part of a program to study new electroluminescent (EL) phosphors with red emission. CaS:Eu was chosen for the following reasons:

1. The red emission of this phosphor (1-3) can be excited by contact-electroluminescence (4).
2. As in ZnS, Cu is an efficient activator of alkaline earth sulfides. Excess Cu_2S has been proposed as responsible for local field intensification in ZnS EL phosphors (4). Through the use of excess Cu, a system analogous, with respect to energy transfer, to ZnS:Cu,Mn was sought.
3. Other red-emitting alkaline-earth sulfide phosphors such as CaS:Ni (5), MgS:Mn (6, 7), and MgS:Sm (8, 9) were not considered as promising because of the high sensitivity to moisture of MgS and repeated failure on the part of the writer to reproduce the CaS:Ni phosphor. Some preliminary work indicated that BaS:Sb may show a weak red emission, while the orange-red emission of BaS:Cu (10) seemed to depend on the presence of oxygen and is yellow in pure BaS:Cu phosphors.

Experimental Technique

Preparation of Raw Materials

CaS.—Most of the phosphor preparation was performed with CaS prepared by reduction of $CaSO_4$ with H_2 at 1000°C (11, 12), followed by firing in dry H_2S (12). The $CaSO_4$ for this purpose was precipitated with reagent H_2SO_4 from hot $Ca(NO_3)_2$ solution, purified according to a previously reported procedure (13). The CaS thus obtained is very voluminous. Denser materials as obtained by firing of $CaCO_3$ or CaO in H_2S (14), either directly or after reaction with sulfur (15), were investigated only at a later stage of this project.

Fluxes.—The usual fluxes were generally available in sufficiently pure form either directly or in

the form of suitable precursors from which they could be prepared easily. Halides were often added as resublimed ammonium salts which are not hygroscopic and, on thermal decomposition during firing, readily react with CaS to form the corresponding calcium halide, while the NH_3 formed furnished a reducing atmosphere.

Europium.—A convenient dry addition of the necessarily small amounts of Eu consisted of drying a solution of 99.9% Eu_2O_3[1] in dilute HNO_3 slurried with a definite weight proportion of purified sulfur. Usually, a concentration of 5% Eu on S was employed. This form of Eu addition was considered more versatile than the well-known use of a definite flux as carrier of the activator. The presence of free sulfur during the first stages of firing was also considered advantageous from the standpoint of decreasing the reactive O_2 concentration in the interstices of the powder, which is otherwise difficult to replace by N_2.

Mixing.—The usual technique of mixing consisted of directing a gentle current of dry N_2 on the mortar. This enabled the handling of hygroscopic substances such as $CaBr_2$ or CaI_2, as well as minimized decomposition of CaS without resorting to the use of a dry box and its attendant inconveniences. Whenever desirable, the preparation of oxygen-free phosphors was accomplished most reliably by conducting at least the latter part of the firings in a current of dry H_2S.

Firing.—Firing was conducted in transparent silica tubes, 15 mm ID, 17 mm OD, 75 mm long, closed at one end and charged with 2-3 g of the powder such that an empty channel was present throughout the length of the tube. While this resembles the use of boats, it also enabled the simultaneous firing of more than one sample under identical conditions in cases where appreciable interaction through atmospheric convection was not anticipated. Purified N_2 at a flow rate of about 500 ml/min was used as a protective atmosphere. H_2S, where used,[2] was passed through dioctyl phthalate followed by Ba $(OH)_2$ solution, "Drierite" (anh. $CaSO_4$) and P_2O_5. The gas inlet tube for H_2S had an ID of ½ in. and was charged with granular CaS extending into the hot zone of the furnace. Gradual discoloration of this CaS showed that it absorbed residual heavy metal impurities as well as converting to H_2S any residual gaseous impurities (H_2O, HCl) by simple metathesis.

An alternate method of firing consisted of capping the silica tube with another tube also closed at one end, and whose ID is no more than 1-2 mm larger than the OD of the tube containing the phosphor. This arrangement effectively prevents spontaneous convection of the atmosphere over the phosphor with the surrounding N_2 and thereby minimizes losses of volatile components such as ammonium halides. For this reason, however, the atmosphere over the phosphor is not replaced by N_2 during the initial flushing and about 500 mg S is added to the charge to displace this atmosphere during the initial warm-up of the system. This method is hereafter referred to as firing in a sulfur atmosphere.

[1] Obtained from Research Chemicals Inc., Burbank, Calif.

[2] Matheson "halogen-free" H_2S.

Measurements

It will be shown that the highly conducting nature of these phosphors introduced a considerable dependence of EL output on the resistance of the electrodes of the cell used for testing. Similarly, differences in conductivity between different phosphors were reflected in anomalous differences in EL output if such samples were operated simultaneously in a simple cell. It was therefore necessary to test each phosphor individually even at the expense of possibly imperfect reproduction of operating voltage and exact cell spacing. The power input with respect to the lateral dimension of the emitting area (25 mm diameter circle) was equalized by using an aluminized conducting glass of which only the necessary area of tin oxide was left uncovered. A 12 μ sheet of Mylar was laid on the conducting side of the glass by means of a thin film of castor oil. An oil-soaked paper spacer of about 110 μ thickness served to separate this from the solid Al electrode. Most measurements were performed with an applied voltage of 800 v at 10,000 cps.

All measurements were performed by means of a Spectra Brightness Spot Meter[3] which, except on rare occasions, was set on the "red" position to avoid any blue emission contributed by CaS:Cu. However, this was usually negligible.

The phosphor was screened through 200 mesh and mixed with castor oil in 1:1 weight proportion and placed between the cell electrodes. On application of the voltage, the EL output initially obtained tended to change due to simultaneous bridging (16) of the phosphor particles and decay of intrinsic EL. This resulted either in an initial increase followed by a decrease or a continuous decrease. In all cases, the maximum readings obtained were recorded.

General Conditions for Electroluminescence

Firing of CaS with Eu and more Cu than can be incorporated at a given halide concentration[4] results in discoloration due to formation of free Cu_2S and EL. Washing of the phosphor in alcoholic NaCN solution is possible without chemical decomposition other than removal of Cu_2S, but decreases EL.

In order to decrease the halide concentration present with Cu during firing and yet optimize the flux concentration with respect to enhancing the Eu emission, a two-stage procedure was found advantageous. A photoluminescent CaS:Eu phosphor is prepared, using the desired fluxes. The phosphor is slurried subsequently with anhydrous methanol containing the necessary amount of Cu as halide. Boiling causes deposition of the Cu as sulfide on the phosphor which is then washed with methanol until halide-free. After decanting, the phosphor is dried and refired either as is or with further additions. The refired phosphor is preferably again washed with methanol and then dried and screened.

The uniform deposition of Cu effected by this method is shown by almost complete disappearance of photoluminescence due to optical screening. Re-

[3] Photo Research Corp., Hollywood, Calif.

[4] Halide fluxes were usually preferred. As in ZnS, halides were noted to aid the incorporation of Cu in CaS (presumably as Cu^+) although this was not studied on a quantitative basis.

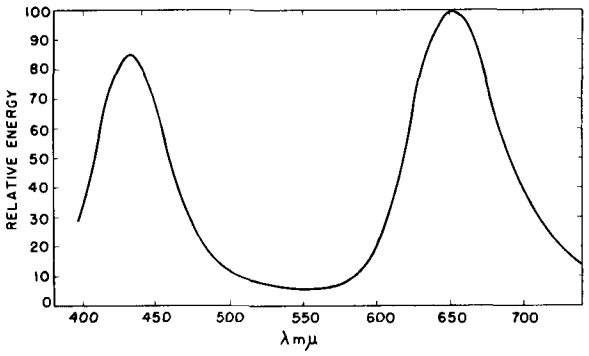

Fig. 1. Spectral distribution of 3650Å—excited emission of CoSi:Cu, Eu(0.01%) phosphor.

firing then causes a shrinkage of the precipitated layer into discrete particles of Cu_2S, and photoluminescence is restored. Electroluminescence shown at this point, when viewed through the magnification afforded by the Spectra-Meter, is seen to originate from discrete separated points which in the case of better specimens do not appear brighter but are more numerous.

Experimental Results

Photoluminescence

Introduction of Cu into CaS:Eu causes the well-known blue emission of CaS:Cu together with the red Eu^{++} emission. The Cu emission is well excited by 3650Å as shown in Fig. 1. The relative heights of the two peaks are incidental and depend on the Eu/Cu ratio and firing conditions. It is noteworthy that under 2537Å excitation, the Cu emission is largely suppressed in favor of stronger Eu emission. At low Eu concentration (0.01%),[5] the introduction of Cu, however, also enhances the otherwise weak 3650Å-excited Eu emission. This phenomenon may be analogous to the sensitized luminescence of CaS:Sm, Bi and CaS:Sm, Pb phosphors (17).

Introduction of Na^+ (and to a lesser extent Li^+) suppresses the red Eu^{++} emission. Because of the almost identical ionic sizes of Ca^{++} and Na^+, this phenomenon may well be regarded as charge compensation of substitutional Na^+ with Eu^{+++} which may thus be stabilized in the lattice. If this is so, then it tends to support Jaffe's (3) conclusion as to the divalent nature of Eu in alkaline earth sulfides. Heavier alkalies, if added as halides, do not have this effect, although the respective carbonates do.

At low Eu concentration, firing in H_2S also causes increased response to 3650Å excitation. Some of these observations are summarized in Table I which

[5] All percentages reported in this paper refer to mole or atom per cent.

Table I. Relative intensities of 6540Å peak of CaS:Eu as a function of phosphor preparation

Phosphor	3650Å	2537Å
1. CaS:Eu(0.01%):$CaCl_2$(5%):MgO(10%), N_2, 1050°C	1.0	29.5
2. No. 1 refired in H_2S at 1050°C	1.5	25.0
3. Like No. 2, but including 0.5% Cu	7.9	11.8
4. CaS:Eu(0.04%):NaBr(5%):Cu(1%), N_2, 1050°C	0.7	1.6

Table II. Effect of 5 mole % flux on CaS:Eu(0.02%) and CaS:Eu(0.02%):Cu(1.0%) fired in N_2 at 1050°C

	CaS:Eu:flux	CaS:Eu:Cu:flux			
		Fluor.	(3650Å exc.)	EL	
	Fluor. color (3650Å exc.)	Output	Color	Output	Color
CaF_2	pink	2.0	pink	1.3	rose
$CaCl_2$	pink	3.0	pink	1.2	rose
$CaBr_2$	pink	3.0	rose	2.5	rose
CaI_2	pink	3.6	white-pink	1.9	rose
$(NH_4)_2HPO_4$	pink	2.0	white-pink	1.3	rose
$NH_4HB_4O_7$	pink	3.0	white-pink	1.6	rose
Li_2CO_3	negl.	1.2*	green	trace	yellow
Na_2CO_3	blue	20*	yel.-green	none	—
K_2CO_3	v-weak	18*	white-green	none	—
Cs_2CO_3	v-weak	10*	white-green	none	—

* Spectra Meter set on "ft-L."

shows measurements of the 6540Å peak height taken on excitation with two sources whose relative output was measured by the fluorescence of sodium salicylate. The figures refer to relative values normalized for equal number of quanta of incident 2537 and 3650Å radiation.[6] It should be mentioned that increased Eu concentration greatly increases the 3650Å-excited fluorescence, so that the low values of sample No. 4 in Table I are due to the effect of Na^+.

Effect of Phosphor Composition and Firing on EL

The effect of fluxes was investigated by firing CaS with 0.01 mole % Eu + 5 mole % flux at 1050°C in N_2 for 1 hr. The second firing was conducted with 1 mole % Cu for 20 min at 1050°C in N_2. Table II shows that $CaBr_2$ resulted in the brightest EL. CaI_2 suffers decomposition but yields similar results if used in larger quantity. The effect of alkali carbonates is the same as discussed in the previous section and, in addition, not even blue or green EL is observed. The brighter fluorescence of the green emission is probably only an effect of color. It appears to consist of a band peaked at 505 mμ as shown in Fig. 2 for a CaS:Cu,Eu,Na phosphor. Because of the halide-gettering effect of Na_2CO_3, this green center might consist of Cu^{++}. It may, however, also be identifiable with the green emission peaked at 495 mμ as obtained by Asano and Kishimoto (18) on 3CaS:$CaSO_4$:Cu,Na_2SO_4 phosphors, which these

[6] Under the simplified assumption of linear dependence of fluorescence on intensity of excitation.

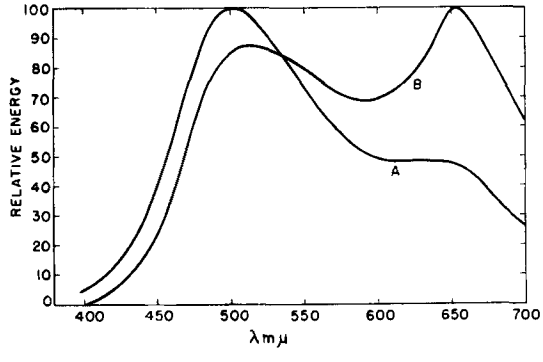

Fig. 2. Spectral distribution of emission of a CaS:Cu:Eu(0.01%):Na phosphor. A, 3650Å excitation; B, 2537Å excitation.

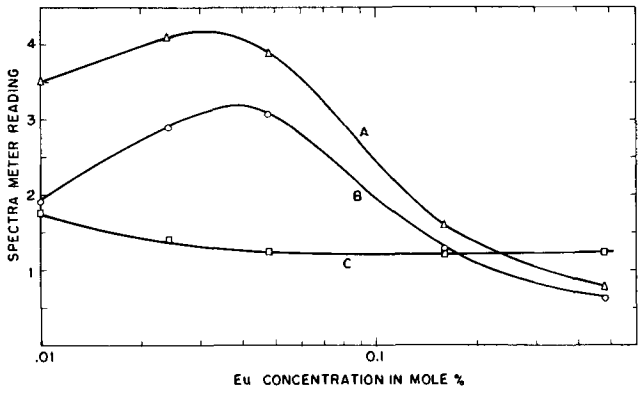

Fig. 3. Effect of Eu concentration on EL of CaS:Cu(1.-0%):Eu(x) phosphors. A, Spectra Meter set on ft-L (brightness; B, spectra Meter set on "red;" C. Ratio of A/B.

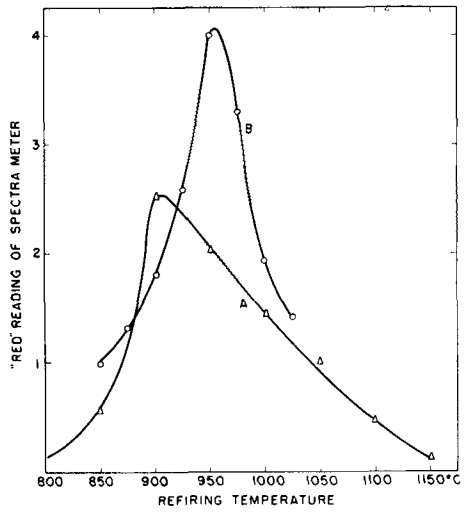

Fig. 4. Effect of refiring temperature in EL of two compositions: A, CaS+0.038% Eu+5% $NH_4HB_4O_7$+10% NH_4Br, 1050°C, N_2—15 min, H_2S—45 min, washed, +1.15CuS+2.-5% NH_4HBO_7, H_2S, 20 min; B, CaS+ 0.038% Eu+5% NH_4-HB_4O_7+10% NH_4Br, 1050°C, N_2—15 min, H_2S—45 min, +1.5% $CuCl_2$, washed, +5% $NH_4HB_4O_7$, H_2S—20 min.

authors ascribe to "CaS". The 10 mμ shift to longer wave lengths obtained here may be due to superposition of a portion of the Eu emission. Here again, 2537Å excitation tends to favor the excitation of the few Eu^{++} centers still present.

Figure 3 shows the result of increasing Eu concentration in similarly prepared phosphors fluxed with $CaBr_2$. The ratios of measurements taken through the different filters of the Spectra Meter show that, at low Eu concentration, there is an appreciable blue contribution of CaS:Cu. Spectral distribution measurements showed that in the neighborhood of maximum red output (0.04 mole % Eu) the blue emission is entirely absent. In Fig. 3, this can also be estimated by the leveling-off of the ratio curve whose residual height thereafter is a function of the response of the particular photometer to the Eu emission only.

The gradual disappearance of the blue CaS:Cu emission which occurs with increasing Eu concentration is analogous to the effect observed on introducing Mn into ZnS:Cu. Inasmuch as the red Eu emission is best excited by wave lengths much shorter than the Cu emission, one is probably not dealing with an optical cascade process. The same conclusion may be drawn from the strong excitability of the blue emission by 3650Å, alongside with the red Eu emission. The mechanism therefore involves sensitization as in ZnS:Cu,Mn (19) as well as many other doubly activated systems.

Inasmuch as the excess Cu_2S is thought to effect local field intensification, its particle size and distribution as well as the surface condition of the phosphor were considered to be critical. Figure 4 shows that this is probably affected by the refiring temperature in the presence of Cu which shows sharp optima with respect to EL output. Similarly, the prefiring temperature and amount of Cu added have a pronounced effect. This is shown in Table III. It will be noted that, with the exceptions of a few points showing what are believed to be accidental variations, the ratios of EL to fluorescence brightness tend to increase with increasing Cu addition and then level off in the neighborhood of maximum observed EL. This indicates that decreasing EL at higher Cu concentrations may be an optical effect due to darker body color.

It was generally noted that the parameters influencing EL output of this system appear to be more numerous than could be investigated within the scope of this study. Table IV gives a summary of some measurements taken on differently prepared phosphors. KBr as a flux was investigated because it resulted in particularly bright photoluminescent Eu emission (first firing), while $NH_4HB_4O_7$ has usually proven advantageous on EL if both firings are conducted in H_2S. It is now shown that either of these fluxes tended to reduce EL output, especially when used together.

An effort was made to shift the emission spectrum to shorter wave lengths and thus increase the visual output of these phosphors. This is known to occur upon partial substitution of Ca by Mg or Sr. In-

Table III. Effect of Cu addition on EL of phosphors prefired at three temperatures

Mole % Cu added	1020°C Prefired			1050°C Prefired			1080°C Prefired		
	EL	Fluorescence	Ratio	EL	Fluorescence	Ratio	EL	Fluorescence	Ratio
0.75	2.7	1.3	2.07	1.8	1.5	1.2	0.65	1.6	0.4
1.0	2.25	0.95	2.38	4.0	1.2	3.3	1.7	1.2	1.4
1.25	3.1	0.72	4.3	5.5	0.85	6.5	4.3	0.9	4.8
1.5	6.8	0.63	10.8	6.0	0.74	8.1	4.0	0.77	5.2
1.75	3.5	0.45	7.8	2.3	0.54	4.3	3.9	0.52	7.5
2.0	5.0	0.40	12.5	5.2	0.48	10.8	4.3	0.39	11.0
2.5	3.5	0.35	10.0	4.0	0.38	10.5	3.6	0.50	7.2
5.0	1.92	0.16	12.0	1.8	0.17	10.5	1.3	0.14	9.3

Table IV. Effect of 5 mole% KBr and 5 mole% $NH_4HB_4O_7$("AB") and firing atmosphere on CaS:Eu(0.038):Cu(1.5) prefired at 1050°C, 1 hr and refired at 950°C, 20 min

Basic composition*	First firing				Second firing				
	Additions		Atmosphere		Additions		Atmosphere, EL obtained at 10 kc, 800 v		
	AB	KBr	S	H_2S	AB	KBr	S	N_2†	H_2S
1	+	—	—	+	+	—	3.7	4.2	3.6
2	+	+	—	+	+	—	—	—	3.0
3	+	—	—	+	+	+	—	—	3.0
4	+	+	—	+	+	+	—	—	0.9
5	+	—	+	—	+	—	1.2	1.3	2.0
6	+	+	+	—	+	—	1.5	—	1.5
7	+	—	+	—	+	+	1.2	—	1.5
8	+	+	+	—	+	+	0.9	—	0.7
9	—	—	—	+	—	—	6.2	4.9	—
10	—	+	—	+	—	—	3.9	5.7	—
11	—	—	+	—	—	—	2.6	6.9	—
12	—	+	+	—	—	—	4.2	5.8	—
13	—	—	+	—	—	+	1.0	0.36	—

* 10 mole % NH_4Br for H_2S (open tube), or 1 mole % NH_4Br for S (capped tube) first firing, added in all cases.
† Open tube, but S added to mix for rapid reduction of entrained oxygen.

creased brightness was achieved, however, only on ultraviolet excitation. The substitutions generally introduced phosphorescence[7] and decreased or completely extinguished EL (20).

Additional attempts were made to optimize the nature of Cu_2S segregations. Of interest may be the effect of $CaBr_2$ or CaO in the second firing. This is shown in Fig. 5 and 6. In the case of $CaBr_2$, the effect was noted to depend on the use of H_2S and the sample size refired. Under optimum conditions, it may be postulated that partial incorporation of Cu^+ at the surface of the phosphor causes enhanced emission, while the particle size of the remaining Cu_2S is somewhat reduced. However, increased $CaBr_2$ retention (as in the case of large additions, N_2 refiring, or larger sample sizes) dissolves too much Cu. A particularly advantageous effect of the $CaBr_2$ at this stage consists of decreasing the fluxing action of the Cu_2S which is also well known in ZnS phosphors. The effect of CaO (Fig. 6) is of interest inasmuch as most if not all of this is converted to CaS during the firing in H_2S. The advantageous effect of low CaO addition, in this case, is therefore probably due to modified surface structure. Otherwise, it may be seen that oxygen in the finished phosphor is probably detrimental.

Effect of Physical Structure of CaS and Finished Phosphors on EL

A number of phosphors were prepared under conditions whereby the only variable consisted of CaS prepared by different methods and therefore differing in particle size and degree of agglomeration. Correlation of the results with microscopic examination of the phosphors showed that the highest brightness values were always obtained on phosphors consisting of thin, uniform, and fairly extended agglomerates, relatively free of fine background. No correlation of EL brightness with degree of crystallinity as obtained by x-ray powder diffraction patterns could be noted. Generally, the differences in EL output obtained here were as great as previously reported on as a result of varying phosphor composition and firing procedures. To illustrate this further, Table V shows four phosphors, each separated into two fractions 45-75 μ and <45 μ. It can be seen that the differences in EL output are considerable. Since the largest single crystals of phosphor rarely exceed 3 μ in size, it appears that the EL output of this system is a function of agglomeration.

Attempts to achieve this artifically were made by preparing phosphors from CaS derived from $CaCO_3$ or CaC_2O_4 of particle size up to 100 μ as obtained by

[7] The phosphorescence of CaS:Eu:$CaBr_2$ is quenched at Eu concentrations as low as 0.024 mole %. Most of the present phosphors were prepared with 0.04 mole % Eu.

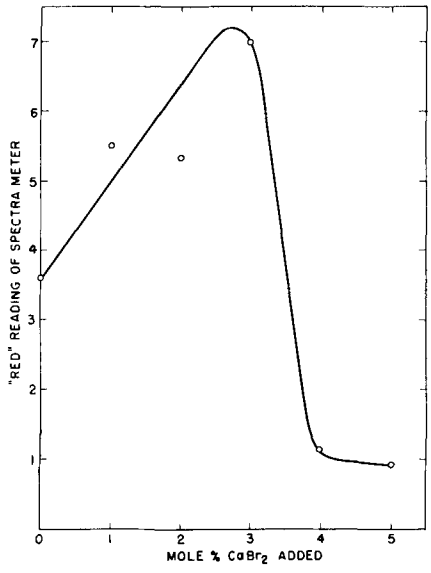

Fig. 5. Effect of $CaBr_2$ added in second firing in H_2S. One gram samples refired at 950°C for 20 min.

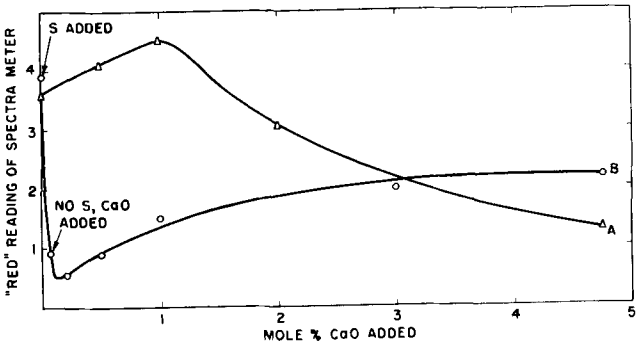

Fig. 6. Effect of CaO added in second firing in two atmospheres: A, procedure No. 1 in Table IV, H_2S refired. B, procedure No. 11 in Table IV, N_2 refired. The true abscissa of the second point is unknown. As drawn, it represents the probable oxide contamination.

Table V. EL output of different particle size fractions of CaS:Cu,Eu phosphors

Phosphor No.	45-75 μ	<45 μ	Ratio
1	3.3	2.2	1.5
2	0.95	0.26	3.6
3	1.2	0.26	4.6
4	1.0	0.33	3.0

homogenous precipitation with urea. These preparations were handled with sufficient care so as to avoid mechanical destruction of agglomerates whose outward shape remained, throughout all stages of preparation, that of the original crystals of $CaCO_3$ or CaC_2O_4. The EL output of these phosphors was, however, low and the dark body color suggested lack of penetration of the Cu beyond the outer surfaces of the agglomerates. Simultaneously prepared control phosphors obtained from finer CaS:Eu in which some agglomeration occurred during the second firing had a lighter body color and better EL performance.

Properties of CaS:Eu,Cu EL Phosphors

Chemical properties.—The chemical properties of the phosphors are essentially those of CaS, i.e., well-known. Slow decomposition as a result of exposure to atmospheric moisture has no noticeable effect on photoluminescence but does affect the EL. In connection with this, the effect of moisture absorbing additives was investigated. Table VI shows that the additives have an immediate detrimental effect. Its nature has not been determined.

EL properties.—Figure 7 and 8 show the voltage and frequency dependence of a typical phosphor. It can be seen that the voltage dependence is quite steep, possibly owing to the small intrinsic particle size of the phosphor (21). On the other hand, the frequency dependence is comparatively slight and better specimens can be excited to be readily visible at 60 cps. The luminous efficiency at 10,000 cps excitation of two phosphors is shown in Fig. 9. Under equal conditions of input (voltage and cell characteristics) the more efficient phosphor also consumed on the average 1.7 times as much power as the less efficient phosphor, i.e., was approximately 2.5 times brighter. The shape of the graphs suggests that maximum efficiency occurs at field strengths which are higher than can be achieved in practice. Somewhat similar but less reproducible results were obtained at 500 cps excitation.

Electrical properties.—As mentioned earlier, the conductivity of the CaS:Eu,Cu phosphor is very high compared to that of normal ZnS:Cu EL phosphors. Table VII shows the effect of electrode resistance on EL output of two phosphors. Under similar experimental conditions, no perceptible difference could be noted for the usual ZnS:Cu EL phosphor. Assuming a similar slope of log L vs. $V^{-1/2}$ as shown in Fig 7 and a voltage drop across the phosphor layer which is proportional to its effective resistance[8] under the particular conditions of cell operation, the respective resistances across the thickness of the 110 μ x 25 mm patch of phosphor suspension

[8] For simplicity, the calculation was made as for an ohmic resistance. Actually, the conductivity is purely an effect of ϕ, since an insulating layer of Mylar is used.

Table VI. Effect of moisture and additives on EL output

Additive	Time of exposure to 100% relative humidity 0	1 hr	20 hr
none	2.0	1.5	0.62
1% CaO	2.0	0.8	0.49
1% MgO	1.4	0.66	0.45

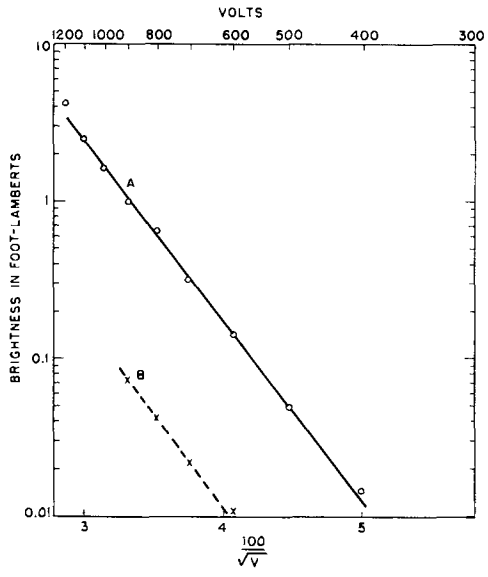

Fig. 7. Voltage dependence of EL of a CaS:Cu, Eu phosphor. Cell spacing 110 μ. A, 10,000 cps; B, 400 cps.

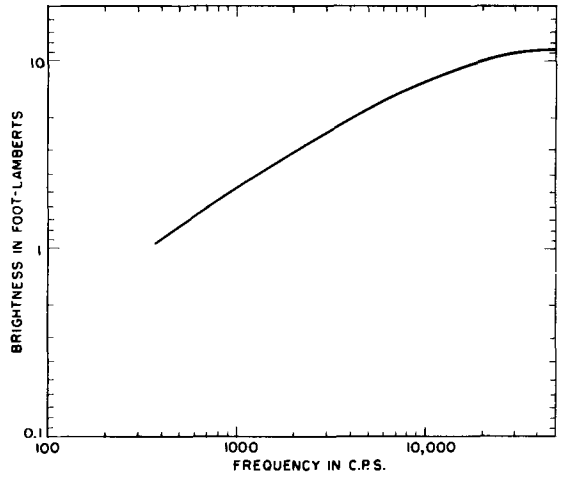

Fig. 8. Frequency dependence of EL of a CaS:Cu, Eu phosphor. Excitation at 800 v.

turn out to be about 1000 and 2000 ohms, respectively, i.e., very low values. Inasmuch as Fig. 9 suggests that a more conducting phosphor may also be more efficient (and much brighter) the difficulties in reproducible phosphor comparison with respect to different cell characteristics can readily be appreciated. It is for this reason that only values appearing within any one table or figure are comparative with each other.

Discussion

The observations made in this investigation suggest a model for the CaS:Eu,Cu EL phosphor consisting of a fine dispersion of Cu_2S particles in con-

Table VII. Effect of electrode resistance on EL output

Resistance from bus bar to phosphor, ohms	EL, 10 kc, 800 v Phosphor a	Phosphor b
50	4.0	2.5
90	—	2.5
145	—	2.0
250	1.8	1.8

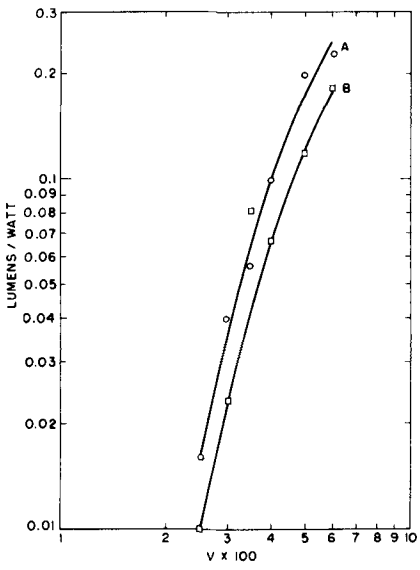

Fig. 9. Luminous efficiency of EL of two CaS:Cu, Eu phosphors excited at 10,000 cps. A, bright phosphor; B, dim phosphor.

tact with the surfaces of a red-emitting CaS:Eu,Cu phosphor. If the coated phosphor particles are agglomerated, there results increased EL output. The reason for this is not clear at present; however, one reason may be proposed on the grounds that penetration of the dielectric embedding material into the interior of the agglomerates may be poor, so that the bulk of the emitting material is subjected to greater than average field strengths. This would also explain the poorer performance of all systems in which the Cu_2S phase may be assumed to be in contact with the dielectric, i.e., either single crystal background or surface coated agglomerates.

The model is in some respects similar to the one proposed by Lehmann for ZnS:Cu EL phosphors (4) except that here one seems to be dealing with a more heterogeneous system. Phosphor formation in ZnS is associated with considerable crystal growth, and the formation of field intensifying disturbances is a process occuring during this growth and subject only to the over-all composition of the system and the firing procedure. In the present phosphor, however, there is little evidence of this, and special efforts must be made to obtain the desired physical structure by means other than relying on the usual (automatic) recrystallization process. It can, at present, only be estimated that at least one parameter responsible for high EL output should be identifiable with the concentration and state of dispersion of the Cu_2S phase on the surface of the CaS:Eu,Cu phosphor. Other parameters may be the crystallographic nature and electrical properties of the Cu_2S-CaS interface. It is probably in this respect that the comparison with ZnS:Cu EL phosphors breaks down, inasmuch as the brightness and efficiency obtainable in ZnS:Cu EL phosphors can only be explained in terms of highly specialized junctions.

The EL properties of CaS:Eu,Cu need not be regarded as an isolated case among alkaline-earth sulfides. Besides the blue-emitting CaS:Cu phosphor, yellow-emitting BaS:Cu EL phosphors were prepared successfully during preliminary phases of this study. Orange-red emitting $BaS:BaSO_4$:Cu (10) prepared with some nonincorporated Cu showed lower EL output, possibly due to presence of appreciable phosphorescence (deep traps). There is reason to believe that, under suitable conditions of preparation, any known semiconductor-type phosphor which may be coactivated by Cu may be amenable to similar treatment, provided that the phosphor tolerates the high activator concentration known to be advantageous for EL emission (22) and that deep traps can be reduced.

Summary

A method of obtaining EL in CaS:Eu has been presented, consisting of the introduction of Cu in concentrations greater than can be accommodated in the phosphor lattice. Among the various procedures tried, definite relationships have been found to exist between EL output and Cu concentration, firing temperatures and atmospheres, fluxes, and the physical nature of the raw material employed. The EL exhibited by this system appears to be a form of contact EL produced at more points than can be achieved by mechanical mixtures, and microscopic examination shows that the best specimens consist entirely of thin agglomerates of uniform size. In addition, it is visualized that the nature of the Cu_2S-CaS:Cu, Eu interface may influence the efficiency of EL produced at individual contact points. The parameters necessary to optimize this effect reproducibly are more numerous than could be investigated at present, and this difficulty is at least partially caused by the conductivity of the phosphor which influences its relative performance under slightly different conditions of excitation.

The absence of blue CaS:Cu emission shows that an energy transfer mechanism possibly analogous to that occurring in ZnS:Cu,Mn may take place. It is felt that the method can be adapted to other phosphors whose activator and trap distribution are such as not to interfere with the EL excitation process.

Acknowledgments

The writer is indebted to Miss I. Walinski for her aid in the performance of much of the experimental work, as well as to Mr. I. Meister and Drs. C. K. Lui-Wei, W. A. Thornton, and W. Lehmann for measurements. He also wishes to thank Professor E. Banks and Dr. W. Lehmann for helpful discussions and Dr. H. F. Ivey for reading and suggesting improvements in the original manuscript.

Manuscript received Aug. 27, 1959.

Any discussion of this paper will appear in a Discussion Section to be published in the December 1960 JOURNAL.

REFERENCES

1. H. M. Fernberger, U. S. Pat. 2,372,071, March 20, 1945.
2. P. Brauer, *Z. Naturforsch.*, **6a**, 561 (1951).
3. P. M. Jaffe and E. Banks, *This Journal*, **102**; 518 (1955).
4. W. Lehmann, *ibid.*, **104**, 45 (1957).
5. P. Lenard, F. Schmidt, and R. Tomaschek, "Handbuch der Experimental-physik," XXIII, 1, p. 331, Akad, Verlagsges. Leipzig (1928).

6. E. Tiede and F. Richter, *Ber. deutsch. chem. Ges.*, **55**, 69 (1922).
7. I. Schaper, *Ann. Physik*, **85**, 942 (1928).
8. R. Tomaschek, *ibid.*, **75**, 109, 561 (1924).
9. M. Travinicek, *ibid.*, **79**, 237 (1926).
10. Reference (5), p. 378.
11. K. F. Stripp and R. Ward, *J. Am. Chem. Soc.*, **70**, 401 (1948).
12. "Inorganic Syntheses," Vol. III, L. J. Audrieth, Editor, p. 20, McGraw Hill Book Co., New York (1950).
13. A. Wachtel, *This Journal*, **105**, 256 (1958).
14. "Preparation and Characteristics of Luminescent Materials," G. R. Fonda and F. Seitz, Editors, p. 30, J. Wiley & Sons, Inc., New York (1948).
15. Reference (5), p. 327.
16. W. Lehmann, *This Journal*, **103**, 24 (1956).
17. S. Rothschild, *Physik. Z.*, **37**, 757 (1936).
18. S. Asano and T. Kishimoto, *Science of Light*, **6**, 101 (1957).
19. H. C. Froelich, *J. Opt. Soc. Am.* **43**; 320 (1953) and U. S. Pat. 2,743,239 (April 24, 1956).
20. C. H. Haake, *J. Opt. Soc. Am.*, **47**, 881 (1957).
21. W. Lehmann, *This Journal*, **105**, 585 (1958).
22. W. Lehmann, *J. Opt. Soc. Am.*, **48**, 647 (1958).

Influence of Crystal Size on the Spectral Response Limit of Evaporated PbTe and PbSe Photoconductive Cells

W. D. Lawson, F. A. Smith[1], and A. S. Young

Royal Radar Establishment, Malvern, England

ABSTRACT

Photoconductive layers of PbTe have been formed by evaporation on substrates at different temperatures. The size of crystals in the layers has been estimated from electron micrographs and x-ray diffraction, and a correspondence has been obtained between crystal size and the limit of spectral response. Sensitivity up to the long wave-length limit set by the energy gap is not achieved unless the crystals are greater than a critical size; for lead telluride this is about a quarter of a micron. A similar effect has been shown to occur with PbSe.

Photoconductive layers of PbTe are commonly prepared by an evaporation technique usually in a low pressure of oxygen, followed by a sensitizing heat treatment either *in vacuo* or in a low pressure of oxygen. PbS and PbSe cells can be made similarly, or the layers can be formed by chemical precipitation from solutions and this may or may not be followed by heat treatment. It is well known that the sensitivity and the spectral response of layers depend very markedly on the preparation process and on the subsequent heat treatment, and, although some very sensitive cells have been prepared, the processes employed are mainly empirical (1) and the precise effect of each stage in the treatment is not always clear. This note shows that the long wave-length limit of the spectral response of a layer is related to the size of the crystals in the layer and that full spectral response is not developed unless the crystals are of adequate size. Thus layers prepared initially with small crystals respond only to the shorter wave lengths and one effect of heat treatment is growth of the crystals with a corresponding extension of the response to longer wave lengths.

Preparation of Layers

The layers used in this investigation were all prepared by the evaporation technique described in detail by Young (2) for PbTe, in Dewar-type cell blanks fitted with sapphire windows. Powder from crushed single crystals was used as starting material and it was first evaporated onto the sapphire window of the cell blank in a good vacuum (10^{-6} mm Hg) and then transferred to the glass substrate which carried the electrode system, through a low pressure of oxygen (10^{-2} to 10^{-3} mm Hg). The thickness of the layers was about one micron and apart from the variables noted in Table I the conditions of preparation were as nearly identical as possible for all layers.

Measurement of Spectral Response

The measurements of spectral response were made using a Leiss double monochromator (3) fitted with sodium chloride prisms. The monochromatic radiation from the output slit was divided into two beams, one of which was deflected to the layer under test, the other to Hilger thermocouple. The path lengths of the two beams were made equal in order to eliminate the effects of atmospheric absorption.

The input radiation to the monochromator, from a Nernst filament source, was chopped at two frequencies by two independent rotating sectored disks. One frequency of 5 cps was suitable for the thermocouple response time, and the other of 800 cps was used in the photoconductive response circuit. The signal from the thermocouple, after amplification at 5 cps, was used in a servosystem to control the aperture of the input slit and so maintain a constant energy output from the monochromator over the wave-length range 1 to 7 microns.

The cell under test was connected through a series load resistor to a constant voltage source and the 800 cps signal developed was amplified in a tuned high-gain amplifier (4) and fed to a pen recorder.

[1] A.E.R.E., Harwell, England.

The wave-length scale on the chart was derived from calibration pips obtained from the monochromator prism drive. The response curves are reproduced as they were drawn by the recorder; the wave-length scale is not linear because the dispersion of the prisms is not linear with either prism drive or chart drive. The response scale is linear but arbitrary as we were not concerned in this study with absolute measurements of sensitivity.

The apparatus was arranged so that spectral responses could be monitored while the cells were being processed on the pumping system and all spectral responses were measured with the cells at 90°K.

Electron Microscope Examination of the Layers

At one micron the layers are too thick to be examined directly in a transmission electron microscope and replicas have to be used. Some photographs were taken in a reflection electron microscope, but they were difficult to interpret and the replica technique was found to be the best way of examining the structure of the layers. Preshadowed aluminum replicas about 250Å thick were used, prepared by first evaporating a layer of boric oxide onto the photoconductive layer, then the shadowing material, uranium or gold-palladium alloy at an angle of ~ 30°, and finally the aluminum layer evaporated from three directions simultaneously to ensure a continuous replica. The replicas were then floated off by immersing the specimen gently in water. The magnification of all the E. M. pictures is about 10,000 times; crystal sizes were measured from these photographs.

X-Ray Photographs

Back reflection x-ray Laue photographs of the layers were taken, with the front window of the cell removed, using radiation which consisted predominantly of the $K\alpha_1$ and $K\alpha_2$ lines of copper. A half-millimeter diameter collimator directed the beam on to the specimen, and the film-specimen spacing was 3 cm. Exposure times of 3-4 hr were required.

The x-ray photographs give an indication of crystal size (5) since the scattered beams from very small crystals are broadened and the broadening from crystals up to 300Å thick is sufficient to prevent resolution of the α doublet. Between 300Å and 1000Å broadening still occurs, but the doublet can be resolved and above 1000Å the doublet is fully resolved. Crystal sizes from 1000Å up to 10,000Å give continuous sharp diffraction rings, but above that there are insufficient orientations present in the irradiated region of the layer to give continuous rings which then begin to appear spotty.

Debye-Scherrer photographs taken on powder scraped from the layers confirmed that the material was PbTe with the same lattice spacing, 6.45Å, as the original crystals.

Results

Lead Telluride.—Figures 1 to 6 show x-ray and electron microscope photographs and measurements of spectral response at 90°K, obtained from a series of lead telluride layers prepared as described in

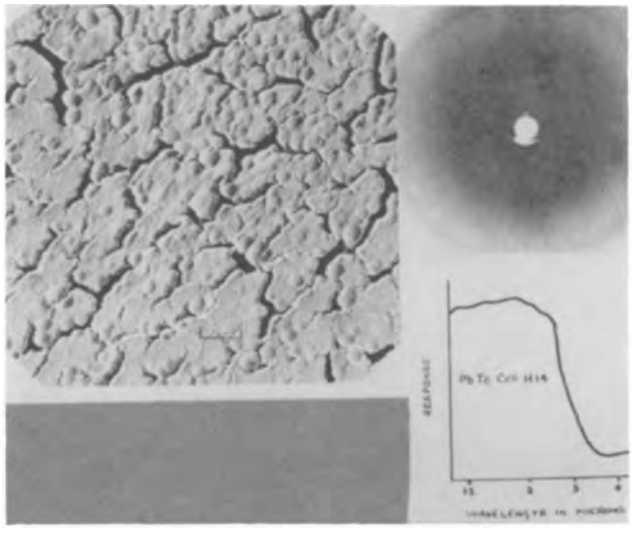

Fig. 1. PbTe cell H14 formed ot 90°K. Electron micrograph, x-ray Laue photograph, and spectral response.

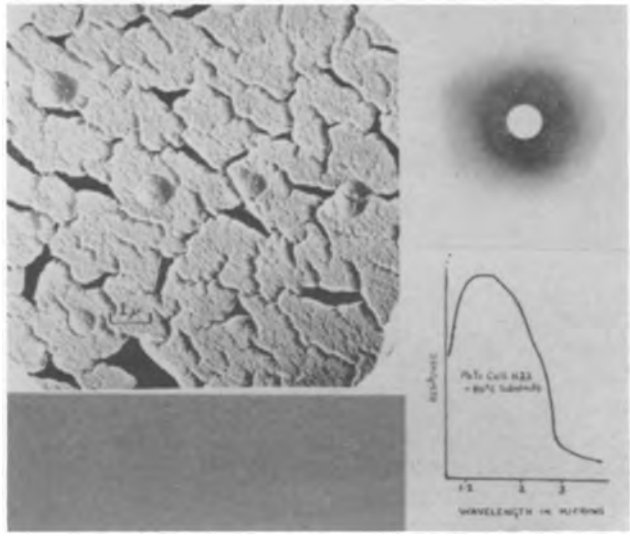

Fig. 2. PbTe cell H22 formed at 193°K. As Fig. 1

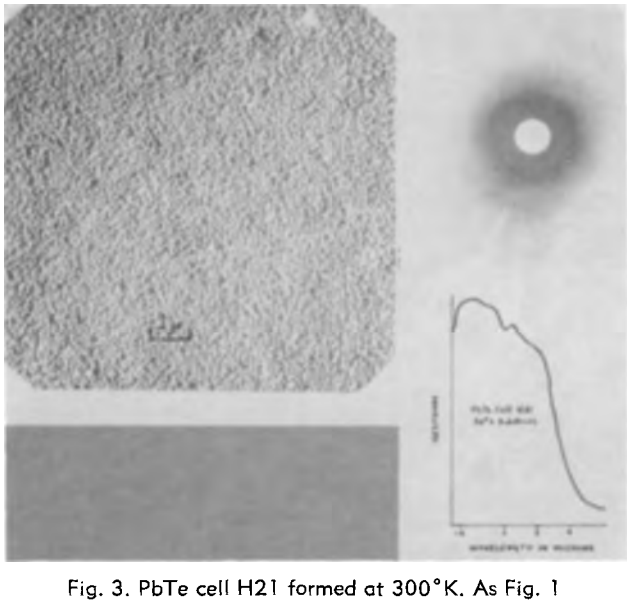

Fig. 3. PbTe cell H21 formed at 300°K. As Fig. 1

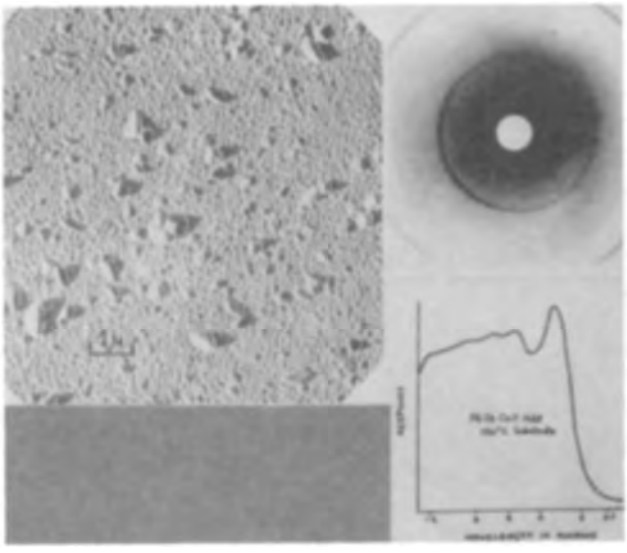

Fig. 4. PbTe cell H20 formed at 420°K. As Fig. 1

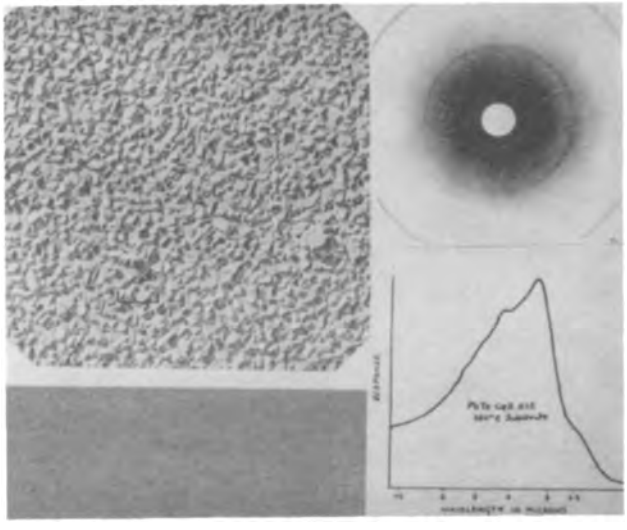

Fig. 5 PbTe cell H18 formed at 650°K. As Fig. 1

(2) but with the glass substrate held at different temperatures while the layers were being formed. Table I gives the substrate temperature at which each cell was formed and also the long wave-length limit of its photoconductive response and an estimate from the x-ray and electron micrographs of the mean size of the crystallites in the layer.

The oxygen pressure at which each layer was formed is also given in Table I, and it will be seen that the pressure has been increased with substrate temperature. This increase was found to be necessary in order to obtain a reasonable sensitivity in each layer, but we found that oxygen pressure by itself had no influence on the limit of response. The precise role of oxygen in the sensitizing process is not discussed in this paper. Jones (6) has shown in experiments on the oxidation of lead selenide that the amount of oxygen taken up in the sensitizing process is small (<2%).

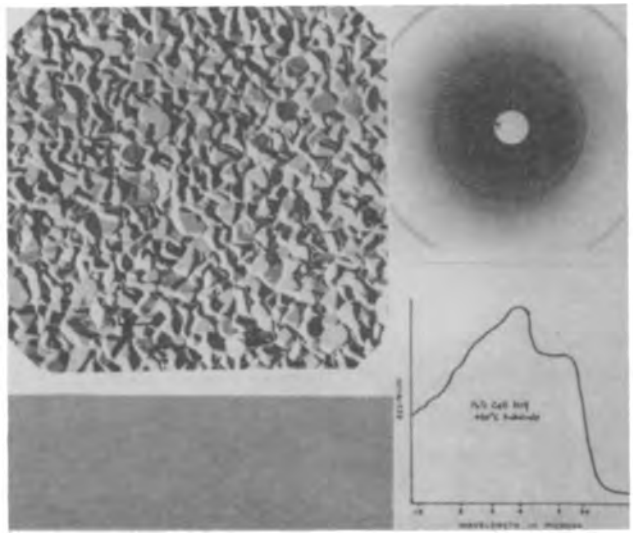

Fig. 6. PbTe cell H19 formed at 720°K. As Fig. 1

From absorption measurements on single crystals (7) lead telluride should give a photoconductive response at 90°K extending to 5.8μ on the long wave-length side, assuming correspondence between absorption and photoconductivity. It will be seen from Fig. 1-6 that the full spectral response is obtained only from layers formed on the hotter substrates and the limit of response in layers formed on the colder substrates occurs at shorter wave lengths. The reason becomes apparent from the electron micrographs. These show a progressive increase in crystallite size with increasing substrate temperature, as might be expected, and it is only those layers which have crystallites of adequate size which exhibit the full spectral response out to 5.8μ. The critical size is between a quarter and a half a micron; crystals smaller than that are apparently unable to absorb the longer wave-length radiation and the spectral response is limited correspondingly. This explanation is confirmed by the discrepancy between the measured absorption of layers (8) and single crystals (7). The layers gave an absorption edge at about 2μ (measured at 290°K), whereas the absorption edge of single crystals at the same temperature occurs at 4.5μ. The absorption edge of single crystals varies very little

Table I

Figure No.	1	2	3	4	5	6	7
Cell No.	H14	H22	H21	H20	H18	H19	H14
Substrate temp, °K	90	193	300	420	650	720	90
Oxygen pressure, mm Hg	5×10^{-4}	10^{-3}	5×10^{-3}	7×10^{-3}	10^{-2}	10^{-2}	5×10^{-4}
Limit of response, microns	3[x]	3[x]	4	5	5.8	5.8	2.5[+]
Crystallite size, microns	<0.03[x]	<0.03[x]	0.06	0.12	0.25	0.5	

[x] After the layer had warmed up to room temperature.
[+] Before the layer had warmed up to room temperature.

with deviations from stoichiometry or with the state of strain of the crystal. The conditions of preparation of the layers in reference (8) are not given, so a comparison of their properties with ours is not possible.

The response of cell H18 formed at 650°K goes out as far as that of cell H19 formed at 720°K, but in the latter cell high sensitivity is maintained right out to 5.5μ whereas in H18 the sensitivity falls rapidly beyond 4.5μ. This again can be attributed to the difference in crystal size. An apparent anomaly occurs in the response of cell H14, prepared at 90°K, which goes to a slightly longer wave length than H22, formed at 193°K. These responses were, however, measured after each cell had been allowed to warm up to room temperature, cell H14 for a longer time than H22. Some increase in crystal size may occur at room temperature so that spectral responses measured after warming up are not truly characteristic of the temperature of formation. This is consistent with the result in Fig. 7 which shows the response curve of cell H14 taken immediately after the layer was formed at 90°K and before it had been allowed to warm up at all; the limit of response occurs at an even shorter wave length, 2.5μ. It was not possible to measure the characteristic crystal size corresponding to 90°K as an x-ray or replica could not be taken without letting the layer come to room temperature, but the result can again be explained in terms of crystal size since it is likely that the layer formed at very low temperature consists of very small crystals.

The response of H14 after a further anneal at 620°K is shown in Fig. 8 together with the x-ray and electron photographs. The doublet in the Laue diagram is now distinctly resolved, c.f. Fig. 1 showing that the crystals have grown and this is confirmed in the electron micrograph. The limit of photoconductive response has now moved out to about 5.8μ and sensitivity is well maintained to nearly 5.5μ.

The physical appearance of the layers in Fig. 1, 2, and 8 is characteristic of layers which are formed on substrates below room temperature. It is likely that the cracks develop through differential expansion during the period of warming up to room temperature.

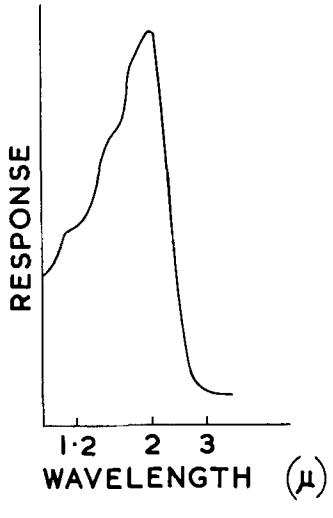

Fig. 7. Spectral response of PbTe cell H14 measured immediately after formation.

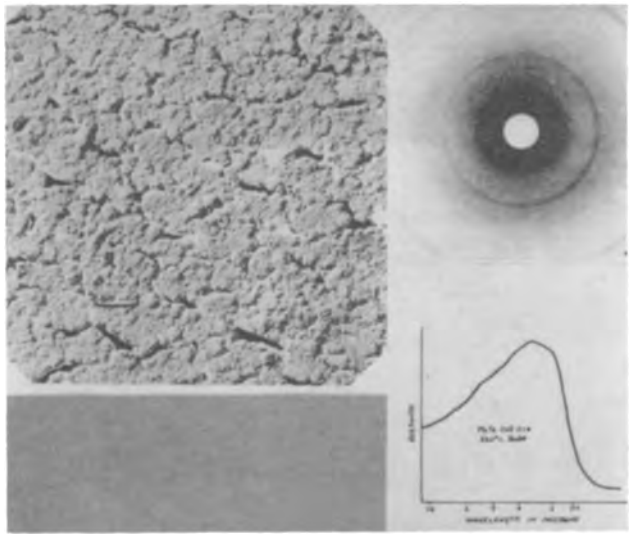

Fig. 8. Electron micrograph, x-ray Laue photograph, and spectral response of PbTe cell H14 after anneal at 620°K.

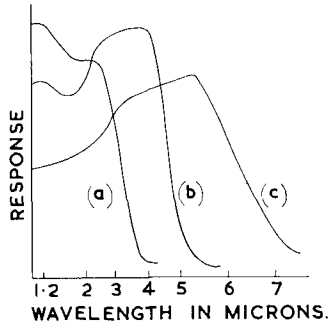

Fig. 9. Spectral responses of PbSe cells baked at different temperatures. (a) Cell H1 left at room temperature; (b) cell H3 baked at 420°K; (c) cell H8 baked at 570°K.

Lead selenide.—Lead selenide layers prepared in the same way by evaporation give similar results, and the dependence of spectral response on crystal size again occurs. The results are not given here in detail but Fig. 9 shows how the limit of response can be moved to longer wave lengths. Cell H1 was formed on a cooled substrate at 90°K through an oxygen pressure of 10^{-2} mm Hg, it was allowed to warm up to room temperature, and its response was measured (at 90°K) some time later. The response ends at about 3.5μ. Cell H3 was prepared similarly and subsequently baked *in vacuo* (10^{-6} mm Hg) at 420°K; its response extends to about 5.2μ. Cell H8 was baked instead to 570°K with a corresponding extension of response to about 7μ, the same as the limit at 90°K in single crystals (9). X-ray and electron micrographs of these layers again showed a gradual increase in crystal size with the temperature of the heat treatment.

Conclusion

The long wave-length limits of photoconductive response and absorption of evaporated layers of PbSe and PbTe are related to the size of the crystallites in the layer. By controlling crystallite size the response or the absorption of a layer can be made to terminate at any wave length up to the

limit fixed by the energy gap of the compound. Thus infrared filters and selective narrow-band filter-detector combinations can be constructed to operate anywhere within the spectral range of the material.

Acknowledgments

The authors are indebted to Miss A. E. Rennie for taking the x-ray photographs, Mr. A. A. Brooker for assistance with the preparation of cells, and Dr. C. S. Lees for helpful discussions on the electron microscope study. The paper is published by permission of the Controller, H. M. Stationery Office.

Manuscript received Sept. 9, 1959.

Any discussion of this paper will appear in a Discussion Section to be published in the December 1960 JOURNAL.

REFERENCES

1. T. S. Moss, *Proc. I.R.E.*, **43**, 1869 (1955).
2. A. S. Young, *J. Sci. Instr.*, **32**, 142 (1955).
3. V. Roberts, *ibid.*, **29**, 134 (1952).
4. D. A. H. Brown, *ibid.*, **29**, 292 (1952).
5. N. F. M. Henry, H. Lipson, and W. A. Wooster, "The Interpretation of X-ray Diffraction Photographs," Macmillan Co., New York (1951).
6. R. H. Jones, *Proc. Phys. Soc.*, **B70**, 1025 (1957).
7. A. F. Gibson, *ibid.*, **B65**, 378 (1952).
8. A. F. Gibson, *ibid.*, **B63**, 756 (1950).
9. A. F. Gibson, W. D. Lawson, and T. S. Moss, *ibid.*, **A64**, 1054 (1951).

Relation of Some Surface Chemical Properties of Zinc Silicate Phosphor to its Behavior in Fluorescent Lamps

D. E. Harrison[1]

Luminescent Materials Laboratories, Lamp Metals and Components Department, General Electric Company, Cleveland, Ohio

ABSTRACT

The importance of the surface properties of zinc silicate phosphor to fluorescent brightness and lumen maintenance has been demonstrated. A phenomenological theory is developed which accounts qualitatively for some of the changes that occur during lamp burning. Inherent in this theory is the concept of a high-temperature surface phase which is a part of the zinc silicate crystal. The surface phase may be retained at room temperature by rapid quenching, but if the phosphor is cooled slowly the surface phase dissociates, probably into its constituent oxides. As a result Mn^{2+} can be oxidized, and Zn^{2+} can be reduced either by vacuum firing or by photolysis by u.v. light. Metallic zinc is produced as a consequence of lamp burning and it amalgamates with mercury. The zinc atoms on the phosphor surface act as vapor traps for mercury and cause it to distribute itself over the surface, probably as tiny droplets. The oxidation of Mn^{2+} and the reduction of Zn^{2+} can be prevented by formation of a protective layer on the phosphor surface, e. g. $ZnSb_2O_6$. It is thought that the surface properties of zinc silicate phosphor, particularly those which affect the extent and perfection of a protective coating, greatly influence the quality of lamps produced by identical procedures.

Zinc orthosilicate activated by manganese is a phosphor which has been the subject of numerous investigations (1-5). In addition to the usual green luminescent form, red and yellow phosphors have been prepared (6-9). The green luminescent form is of value as a lamp phosphor. Unfortunately however, when it is used in fluorescent lamps it exhibits poor maintenance. Lowry (10) showed that the maintenance could be improved substantially by the addition of small amounts of Sb_2O_3 to the phosphor; the best results were observed when the addition was made to the coating suspension. Merrill and Davis (11) demonstrated similar results by incorporation of small amounts of As plus Pb in the phosphor matrix during synthesis.

The practical advantages of Sb_2O_3 additions have been used for many years, but nevertheless seemingly identical phosphor preparations and lamp-making procedures yield different lamp results.

The subject is treated as a summarization of observations which seem pertinent to an understanding of the zinc silicate phosphor. Phase studies are considered to show that under equilibrium conditions phosphor compositions consist essentially of $(Zn, Mn)_2SiO_4$ plus SiO_2. The effects of the ZnO/SiO_2 ratio and phosphor synthesis temperature on lumen output are shown. Some of the surface chemical properties of zinc silicate phosphor are given, and evidence is presented for changes in the crystallographic structure of the surface. Finally a phenomenological mechanism of fluorescent deterioration of zinc silicate phosphors in fluorescent lamps is given.

Experimental Procedure

Raw materials used where silicic acid prepared by hydrolysis of tetraethylorthosilicate, New Jersey Zinc Company USP grade ZnO, Mallinckrodt reagent grade $MnCO_3$, Sb_2O_3, As_2O_5, $(NH_4)_2HPO_4$, SnO_2, TiO_2 H_3BO_3, and Reynolds $Al_2O_3xH_2O$. Compositions were mixed in a mortar with acetone until dry. Calcines were prepared in fused silica crucibles at temperatures ranging from 1200° to 1300°C. Heat treatments were done in silicon carbide electric resistance furnaces and platinum-wound resistance furnaces.

[1] Present address: Metallurgy Department, Research Laboratories, Westinghouse Electric Corp., Pittsburgh, Pa.

The *p*H values of water suspensions of zinc silicate phosphor were measured in the following manner: 60 ml of distilled water were adjusted to a *p*H of 6.0 by absorption of a small amount of CO_2. One gram of phosphor was added to the water and the mixture was stirred sufficiently to maintain the phosphor in suspension. The polyethylene beaker which contained the suspension was covered and a stream of nitrogen was passed over the cover in order to prevent CO_2 from diffusing in around the electrodes and stirrer. Measurements were obtained by means of a Beckman glass electrode *p*H meter. Results were reproducible to ± 0.05 *p*H units.

Lumen data were obtained from 40-w fluorescent lamps using standard lamp-making and photometry procedures.

Results and Discussion

Phase Studies

The system ZnO-SiO_2 was investigated by Bunting (12) who reported that Zn_2SiO_4 is the only compound which exists in the binary system. The absence of a metasilicate is surprising, for this compound is found in other systems of the type RO-SiO_2 where RO = CaO, MgO, SrO, BaO, or MnO. Leverenz (13) postulated the existence of a deficiency structure between the ortho-and meta-silicate compositions. This opinion was based on observations from x-ray studies that no new phases appeared with ZnO/SiO_2 ratios between the ortho-and meta-silicate compositions and that the Zn_2SiO_4 pattern remained unchanged when mixtures were prepared from ZnO and silicic acid.

Re-examination of the system confirmed the earlier results of Bunting that $ZnSiO_3$ does not exist. Microscopic and x-ray examination of compositions between Zn_2SiO_4 and SiO_2 (introduced as silicic acid) revealed that the silica is very reluctant to form a crystalline modification even on prolonged heating and that it does not occur as isolated particles but rather it appears to form a "cocoon" around the Zn_2SiO_4 crystals. X-ray and microscopic data show no evidence of solid solution between Zn_2SiO_4 and SiO_2.

Studies in the system ZnO-MnO-SiO_2 (14) showed that there is a binary join between Zn_2SiO_4 and $MnSiO_3$ and that $MnSiO_3$ is soluble in Zn_2SiO_4 in excess of 10 mole % at 1300°C, which is more than twice the amount of manganese normally used as an activator. Since there appears to be no solubility of SiO_2 in either Zn_2SiO_4 or $(Zn,Mn)_2SiO_4$, phosphor compositions can be regarded as essentially a two-phase system of $(Zn,Mn)_2SiO_4$ plus SiO_2.

In order to investigate the effects of the ZnO/SiO_2 ratio and synthesis temperature of the phosphor on lamp performance, the following synthesis technique was used: over-all compositions with the desired ZnO/SiO_2 ratios were prepared at 1200°-1250°C from ZnO plus silicic acid. The required amount of manganese was introduced as the carbonate in a second firing at either 1200°, 1250°, or 1300°C. This procedure yields a wide range of phosphor compositions which have high powder brightness. If $ZnO + SiO_2 + MnO$ initially are fired together, a firing temperature of 1300°C is required to develop full brightness unless a flux is used.

Zinc silicate phosphor is excited by 2537Å or 3650Å radiation but the response to 3650 develops after firing the phosphor at higher temperatures than are required for good response to 2537. This effect was demonstrated by thermal gradient firings in air. Zinc orthosilicate was prepared at 1200°C/4 hr. To this material was added the necessary amount of $MnCO_3$ and the mixture was fired in a thermal gradient furnace in the temperature range from 600° to 1350°C. At 1200°C the phosphor had 95% of the maximum fluorescent brightness observed when excited by 2537, but it had practically no response to 3650. 1220°C increased the response both to 2537 and 3650. The maximum brightness under 2537 was obtained between 1250° and 1300°, but at 1350°C there was marked sintering and a decrease in brightness. In contrast, the brightness under 3650 increased in a uniform manner from 1250° to 1350°C.

Relation of Phosphor Preparation to Lumen Output

The effect of various ZnO/SiO_2 ratios on lamp performance is given in Fig. 1. Test phosphors were prepared by first forming zinc silicate at 1200°C and then introducing the required amount of manganese in a second firing at 1200°C. A control phosphor was prepared by firing together $ZnO + MnO + SiO_2$ at 1300°C using a ZnO/SiO_2 ratio of 1.7/1.0. In all tests an addition of 0.1 wt % Sb_2O_3 was made to the phosphor coating suspension. A line on the ordinate opposite the ZnO/SiO_2 ratio indicates the spread in lumen values obtained from a seven lamp test at zero hours. The two curves shown per test represent the extremes per variation, as measured during the time of the test. The data show that a phosphor with a mole ratio of 1.9/1.0 is comparable in lumen performance to one with a ratio of 1.5/1.0, whereas a phosphor with a ratio of 1.7/1.0 is substantially better. By some means a certain excess of silica gives an improvement in lumen output, but too large an excess cancels the initial gain. Since silicic acid in contact with $(Zn, Mn)_2SiO_4$ is reluctant to form a crystalline modification even on prolonged heating, too large an excess of silica may have a deleterious effect on lamp performance as a result of carrying water into the lamp. However, the fact that some sort of surface protection is required strongly suggests that the surface properties of zinc silicate itself may be an important factor in phosphor depreciation.

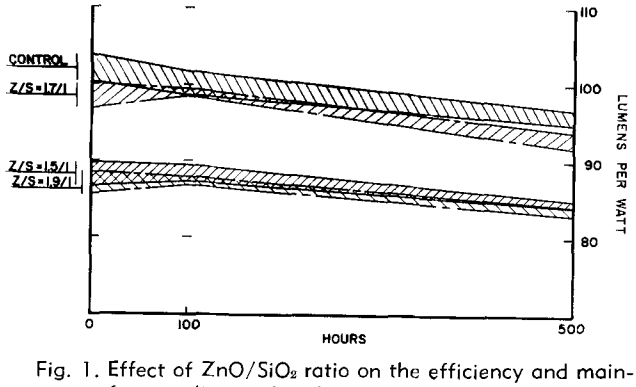

Fig. 1. Effect of ZnO/SiO_2 ratio on the efficiency and maintenance of zinc silicate phosphors.

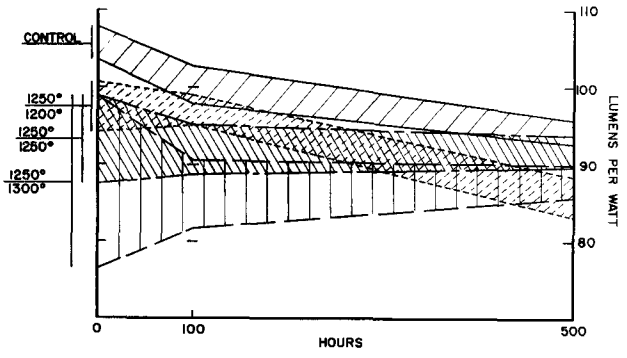

Fig. 2. Effect of firing temperature on the efficiency and maintenance of zinc silicate phosphors.

Further evidence of the possible effect of surface properties was given by the following test: zinc silicate was formed at 1250°C; the required amount of manganese was introduced in a second firing at either 1200°, 1250°, or 1300°C to yield compositions low in free silica, i.e., $(Zn_{0.90}Mn_{0.05})_2SiO_4$. Lamps were prepared from each of the three test lots; results are shown in Fig. 2. The lines on the ordinate opposite the firing temperatures and the two curves per test have the same meaning as in Fig. 1. It is seen that the spread within each group increases as the second firing temperature increases. As lamp burning progresses, changes occur which tend to minimize the differences initially present. Evidently higher firing temperatures produce changes in the phosphor which make it more susceptible to lamp making variables.

Evidence for the Formation of a Surface Phase

The suspicion that a surface alteration does occur in zinc silicate phosphor during synthesis is confirmed by comparison of x-ray and electron diffraction data. These data, which are listed in Table I, were obtained from a sample with a molar composition of $(Zn_{0.90}Mn_{0.05})_2SiO_4$ and fired three times at 1250°C/3 hr. The first column lists "*d*" values obtained from x-ray data which reflect the arrangement of atoms in the interior of the crystal. The fourth column lists "*d*" values calculated from electron diffraction data which gives the arrangement of atoms on the surface. Comparison of the two sets of "*d*" values shows that there is a shift in lattice spacing between the surface and interior of the crystal.

The surface phase cannot be accounted for by an accumulation of either ZnO, MnO, Mn_2O_3, Mn_3O_4, $ZnMn_2O_4$, or any of the crystalline modifications of SiO_2. Therefore, it appears that a distinct new phase develops on the surface of $(Zn,Mn)_2SiO_4$.

Zinc silicate phosphor can fluoresce either green, yellow, or red, or a combination of these colors depending on the method of preparation. As was mentioned earlier, zinc silicate phosphor develops a response to 3650Å excitation when fired at temperatures higher than about 1200°C. Since the green emission under 3650Å is the same as that under 2537Å, it appears that the development of a surface phase serves to introduce new absorption centers but not different types of luminescent centers. Comparison of the x-ray data of yellow luminescent powders studied by Rooksby and McKeag (7) and Pfeiffer and Fonda (8), respectively, and of yellow and yellow-green luminescent films examined by Feldman and O'Hara (9) showed no correlation with the surface phase postulated in the present study. The red fluorescent form is in a vitreous state as shown by Pfeiffer and Fonda.

Closely related to the phenacite structure of zinc orthosilicate is the spinel arrangement. The oxygen atoms in spinel are in a face-centered cubic order. The "*d*" spacings of a face-centered cubic structure were calculated on the basis of the strongest line observed in the electron diffraction data. The last column in Table I lists the calculated "*d*" values. There appears to be a reasonable fit between the calculated values and the "*d*" values obtained from electron diffraction data, particularly with the smaller "*d*" spacings. The data show that a surface rearrangement has occurred and that it seems to be a spinel-like structure.

The phenacite and spinel structures of A_2BO_4 compounds are similar enough that, in some cases, an increase in temperature can cause a phase transition. For example, Li_2SO_4 and Li_2MoO_4 are dimorphic with low-temperature phenacite and high-temperature spinel structures. Since bulk Zn_2SiO_4 does not have a spinel modification, and since, in general, reconstructive inversions show positive volume changes in the direction of increasing temperature, a spinel modification of zinc silicate could be expected to be stable at the surface of the crystal at temperatures nearer the melting point, e.g., 1200°-1300°C. Therefore, at some lower temperature, the postulated surface phase will become unstable and should ideally invert back to the phenacite arrangement. As will be developed later, it appears unlikely that a simple inversion occurs but rather that the surface phase dissociates into its constituent oxides.

Differential thermal analysis data seem to fit this general scheme: DTA curves of previously formed zinc silicate phosphors showed a small but reproducible exothermic effect on heating, beginning at about 1250° and exhibiting a broad maximum in the region of 1320°C. No heat effects were observed during cooling. High-temperature x-ray analysis by Hummel (15) demonstrated that the thermal effect is not the result of a "bulk" crystallographic

Table I. $(Zn_{0.60}Mn_{0.05})_2SiO_4$ thrice fired at 1250°C/3 hr

"Substrate"			"Surface"			F-cubic $a = 9.138$
d	*I/I*	Δd_1*	*d*	*I*	Δd_2*	*d*
4.055	60	+0.181	3.874	M	+0.696	4.572
3.509	90	+0.179	3.330	M	−0.101	3.229
2.850	60	+0.096	2.754	S	0	2.754
2.650	100	+0.108	2.542	M	+0.096	2.638
2.327	70	+0.085	2.242	M	+0.046	2.284
2.017	30	+0.062	1.953	W	−0.101	2.043
1.866	70	+0.060	1.806	M	+0.059	1.865
1.692	20	+0.039	1.653	W	+0.105	1.758
1.602	30	+0.015	1.587	W	+0.028	1.615
1.523	20	+0.020	1.503	W	+0.020	1.523
1.424	60	+0.023	1.401	S	−0.008	1.393
1.340	40	+0.020	1.320	M	−0.001	1.319
1.213	10	+0.022	1.191	W	−0.002	1.189
1.007	20	+0.011	0.996	WM	+0.001	0.997

* Δd_1 and Δd_2 are the differences between the "*d*" values of the "substrate" and the "surface" and the "surface" and the F-cubic spacings, respectively.

inversion. Since the phosphor was originally furnace-cooled from about 1250°C, a stable high-temperature surface phase has had an opportunity to invert to a low-temperature modification or to dissociate. The exothermic effect at 1250°C on reheating suggests a recombination reaction of the dissociated products of the high-temperature surface phase. If there were a simple crystallographic inversion, an endothermic rather than an exothermic effect would be expected. The sluggishness of a dissociation or inversion could prevent the appearance of any distinct thermal effects on cooling.

A rough estimate of the thickness of the surface layer can be made by comparing the patterns obtained by x-ray and electron diffraction techniques. For ionic crystals, the depth of electron penetration is of the order of 10Å (16), whereas, oxide films several hundred angstroms in thickness have insufficient volumes to produce x-ray lines. Since the x-ray pattern did not show even diffuse lines corresponding to the electron diffraction data, the surface phase may be from about ten to several hundred angstroms in thickness. A surface film with this order of volume could conceivably produce the thermal effect detected by DTA.

Some Surface Chemical Properties of Zinc Silicate Phosphor

Differences in the surface properties of the phosphor are reflected in measurements of *p*H and oxidizing potential. The data are shown in Fig. 3. Zinc orthosilicate, free of manganese, has a *p*H of about 6.80 and, of course, no oxidizing potential as evidenced by organic indicators such as benzidine (17). When the previously formed zinc silicate was activated by manganese to yield the composition $(Zn_{0.90}Mn_{0.50})_2SiO_4$, fired at 1250°C/4 hr, and cooled in the furnace, it exhibited marked oxidizing potential and a *p*H of 7.85. When this phosphor was quenched from temperatures above 1000°C, the oxidizing potential was lost and the *p*H dropped to 6.82.

Changes in *p*H and oxidizing potential can be explained on the basis of the properties of a surface structure. A phosphor preparation temperature of 1300°C will favor divalent manganese by the valency isobar effect. Since Mn^{3+} will substitute isomorphously for Zn^{2+}, rapid quenching of the phosphor should freeze in the surface structure in which Mn^{2+} is stable. Therefore, a quenched phosphor would have zero oxidizing potential and a *p*H similar to that of unactivated zinc orthosilicate. On the other hand, if the phosphor is cooled slowly, the surface phase has an opportunity to dissociate and as a result some of the divalent manganese is oxidized. Consequently the phosphor now exhibits high oxidizing potential. The higher *p*H over that of nonactivated zinc silicate is probably a result of the formation of $Mn_2O_3 \times H_2O$ or $MnO_2(OH)_2$ on the surface of the phosphor where it serves as another source of $(OH)^-$ ions.

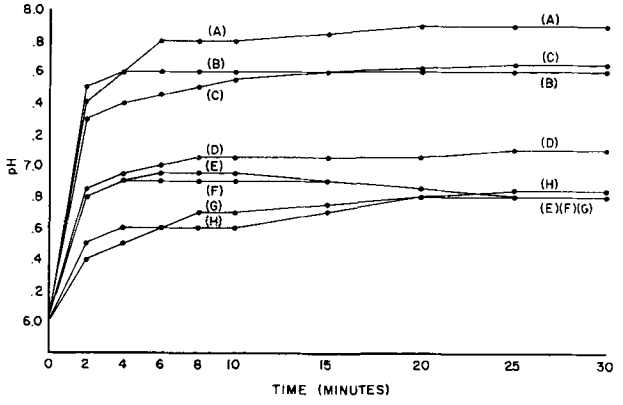

Fig. 3. Effect of surface treatment of zinc silicate phosphors on pH. (A) $(Zn_{0.90}Mn_{0.05})_2SiO_4$; (B) $(Zn_{0.90}Mn_{0.05})_2SiO_4:B_2O_3$; (C) ZnB_2O_4; (D) $(Zn_{0.90}Mn_{0.05})_2SiO_4:Sb_2O_3$; (E) $(Zn_{0.90}Mn_{0.05})_2SiO_4:P_2O_5$; (F) $Zn_3(PO_4)_2$; (G) Zn_2SiO_4; (H) $(Zn_{0.90}Mn_{0.05})_2SiO_4$ air quenched from 1050°C.

Froelich (18) concluded from his studies of Mn-activated silicate phosphors that oxidizing matter, presumably Mn^{3+}, is located at or near the surface of the phosphor crystals. Thus, he observed that Zn-Be silicate, which is isostructural with Zn_2SiO_4, activated by manganese acquired a tan coloration and high oxidizing potential when fired between about 350° and 1000°C. Experiments showed that the higher oxides of manganese did not develop during phosphor synthesis but only after the material was heated in the temperature range of instability previously mentioned. Summarizing, Froelich comments that, "it can be said that manganese-activated silicate phosphors, in particular Zn-Be silicates, have a rather unstable crystal surface which is subject to chemical deterioration and disintegration, depending upon the surrounding atmosphere and temperature. Small amounts of manganese oxide on or immediately below the crystal surface, held more or less loosely in the lattice, are fairly easily attacked by oxygen from the atmosphere or other oxidizing substances. They sever their bonds with the other oxides in the crystal lattice and are oxidized to free, brown manganic oxide, Mn_2O_3, giving rise to a change in the natural color and an apparent loss of fluorescent brightness. . ."

The oxidation of surface manganese can be avoided in other ways than by quenching. Refiring the phosphor with $(NH_4)_2HPO_4$ produces a film of zinc phosphate on the material at temperatures from 300° to 800°C. The oxidizing potential is lost and the *p*H is very nearly that of $Zn_3(PO_4)_2$ as shown in Fig. 3. Similar treatment of the phosphor with H_3BO_3 destroys the oxidizing potential and yields a material with a *p*H nearly that of ZnB_2O_4. However, the firing temperature is limited to 300°-500°C because of the volatility of B_2O_3. Refiring the phosphor with Sb_2O_3 produces a film of $ZnSb_2O_6$ as revealed by x-ray analysis, and again the oxidizing potential is lost.

Changes in the surface properties of zinc silicate phosphor can be produced at moderate temperatures in vacuum. The procedure was to place the phosphor sample in an alumina boat which then was sealed in a Pyrex tube and evacuated to 1μ. The tube was inserted in a furnace so that one end protruded from the furnace. Samples were heated at 600°C for 20 hr. Results obtained from untreated phosphor and phosphors with various surface modifications are shown in Table II. Zinc orthosilicate free of manganese was partially reduced, and metallic zinc collected on the cool portion of the tube. Manganese solid solutions in zinc orthosilicate substantially increased the reduction of zinc as evidenced by a darker gray powder and larger deposits of metallic zinc on the tube.

When zinc silicate phosphor is fired at 1200°-1300°C under neutral or reducing conditions, the powder turns gray in color and the fluorescent brightness is much decreased. Therefore, it appears that Zn_2SiO_4 itself may be subject to reduction quite apart from the effect of a surface phase. However, since the formation of metallic zinc can be prevented by suitable surface treatment, the surface structure of zinc silicate seems to play an important role in the process. Assuming that the surface structure does contribute directly to the formation of metallic zinc, the effect may arise from two causes. Under the same conditions of vacuum heat treatment zinc metal will distill from ZnO. Consequently the occurrence of zinc metal in the phosphor may be the result of the presence of ZnO from the dissociation of the surface at 600°C. Another possible cause may be from an oxidation-reduction reaction which occurs as a result of the instability of the surface phase. Since the coordination number of silicon in inorganic crystalline materials is invariably four, the postulation of a surface-spinel phase suggests the occurrence of a "normal" spinel structure. That is, a structure in which Si^{4+} ions are in fourfold and Zn^{2+} ions are in sixfold coordination positions. When zinc silicate which was prepared at a high temperature is reheated at a moderately low temperature, e.g., 600°C, the surface-spinel phase becomes unstable and attempts to form a phenacite structure. This requires that the Zn^{2+} ions change their coordination number from 6 back to 4 since all cation sites in the phenacite structure are fourfold coordination positions. Although the over-all cation/anion ratio has to be maintained in the structure transition, it may be that local surface conditions give rise to oxidation-reduction reactions between O^{2-} and Zn^{2+} ions. The loss of Zn and O_2 unbalances the stoichiometry so that dissociation of the surface phase results. As shown in Table II, Mn^{2+} substitutions for Zn^{2+} increases the amount of metallic zinc produced. However, consideration of the free energy changes shows that reduction of Zn^{2+} cannot result from the oxidation of Mn^{2+}. Therefore, it appears that manganese plays an indirect role in the reduction of zinc ions and it may serve to increase the instability of the surface phase. Examination of the relative field strengths of Mn^{3+} or Mn^{4+} and Zn^{2+} (where field strength is defined as ionic valence/ionic radius) shows that manganese ions have higher polarizing power than zinc ions. Consequently, oxidation of Mn^{2+} enables it to compete more successfully for oxygen ions than can Zn^{2+}. As a result, another disruptive force is introduced which would tend to cause dissociation of the high-temperature phase.

Table II. Stability of zinc silicate phosphor

Sample	Oxidizing potential	Body color after 600°C for 20 hr at 1μ Hg pressure	Deposit on tube	Fluorescent brightness (2537Å rad.) $(Zn,Mn)_2SiO_4$ at 100%
Zn_2SiO_4	—	Light gray	Zinc	—
$(Zn, Mn)_2SiO_4$	Positive	Dark gray	Zinc	72%
$(Zn, Mn)_2SiO_4: P_2O_5$	Negative	Dark gray	—	72%
$(Zn, Mn)_2SiO_4: As_2O_5$	—	White	—	102%
$(Zn, Mn)_2SiO_4: Sb_2O_5$	—	White	—	97%

The reactivity of zinc silicate phosphor is demonstrated by the ease with which it will react with other oxides to form a second compound on the surface of the phosphor. For example, Al_2O_3 will react with zinc silicate at 1000°C to form a layer of $ZnAl_2O_4$, a spinel. By suitable surface treatment both the oxidation of Mn^{2+} and the reduction of Zn^{2+} ions can be prevented. Re-firing the phosphor with Sb_2O_3 or As_2O_5 forms surface films of $ZnSb_2O_6$ and probably $ZnAs_2O_6$, respectively. As a result the phosphor body color remains white and the fluorescent brightness is maintained. Since $ZnAs_2O_6$ has low u.v. absorption and causes reduction of oxidized manganese present in the untreated phosphor to the divalent state, the powder brightness is somewhat higher than that of the untreated material. A surface film of zinc phosphate prevented zinc metal from volatilizing from the phosphor, but reduction still occurred as evidenced by a gray powder color and loss of fluorescent brightness (see Table II).

A fluorescent lamp provides a low-pressure environment for the phosphor and, during exhaust, temperatures in excess of 500°C. In addition there is the possibility of reducing Zn^{2+} by photolysis from u.v. radiation produced by the mercury arc. Kressin (19a) reports that graying occurs in zinc silicate phosphors on exposure to strong u.v. light. He has attributed the observed graying to the formation of elemental manganese. Two of the experiments on which Kressin (19b) bases his conclusions are the following:

(*a*) A weighed amount of gray irradiated phosphor was placed in a silica bulb and heated in the presence of a measured small amount of oxygen until the white color of the original phosphor was restored. The oxygen then was pumped off, burned with hydrogen to form water, and the latter determined by means of Karl Fischer reagent. The amount of oxygen used up by the phosphor then was found by difference. A blank sample of unactivated zinc silicate without manganese, carried through the entire process as before, showed no oxygen consumption whatever.

(*b*) Zinc silicate with manganese was settled on a quartz plate and irradiated in vacuum with a quartz lamp. During this experiment, the vessel was connected to a mass spectrometer, and the evolution

of oxygen could be detected with this instrument. A blank run with zinc silicate free of manganese did not show the evolution of any oxygen.

Kressin's data can be equally well accounted for by the formation of elemental zinc. Thus, the consumption of oxygen in experiment (*a*) and the evolution of oxygen in experiment (*b*) could be associated with the oxidation and reduction of zinc. The fact that the blank, which contains no manganese, did not show a similar reaction is probably a result of zinc orthosilicate having low absorption for u.v. radiation.

If metallic zinc is produced by photolysis or by the mechanism described earlier, it logically can be expected to react with mercury, probably to form an amalgam. To test this hypothesis phosphor was brushed from lamps after they had burned for 3000 hr. Mercury was separated from the phosphor by shaking a suspension of 5 g of the phosphor in an NH_4OH solution, which caused dispersion of the phosphor, until a ball of mercury collected at the bottom of the tube. The 4 mg of mercury which were recovered were washed with acetic acid to dissolve traces of Zn_2SiO_4. Chemical analysis revealed that the mercury contained 5 wt % Zn but no Mn. Microscopic examination of the zinc amalgam before chemical analysis revealed that it consisted of a mixture of liquid and well defined hexagonal platelets. These platelets are described by Mellor (20) as beta-zinc amalgam. Reference to the phase diagram of the system Zn-Hg (21) shows that Zn is soluble in Hg to 2.15 wt % at 20°C. Therefore, zinc in excess of this limit separates from the liquid as crystals of beta-zinc amalgam.

Relation of Surface Properties to the Accumulation of Mercury on the Phosphor

A mechanism of lumen depreciation is indicated in which zinc metal sites on the phosphor surface act as "vapor traps" which cause the mercury to distribute itself over the phosphor surface. Of the several factors responsible for lumen depreciation, adsorption of mercury is generally regarded as the principal cause (22). The condensation of mercury in tiny droplets on the phosphor surface has been considered by Froelich (22). If it is assumed that the normal 10-20% lumen drop is the result of shadowing by mercury droplets, the size of the droplets required lies between that necessary to cover a certain fraction of the lamp surface to that required to cover the same fraction of the geometric surface of the phosphor powder. Thus, a 40-w lamp with internal surface area of 1320 cm^2 would require spheres of 0.1 to 0.05 μ in diameter to shadow 10-20% of the surface area. A 40-w fluorescent lamp contains about 3.7 g of zinc silicate phosphor which has a surface area of 1.0 to 1.3 m^2/g. Therefore, the geometric surface area is in the order of 10^4 cm^2. Again assuming that the mercury condenses in spheres, droplets with diameters in the order 0.01 to 0.001 μ would be required to cover 10-20% of the geometric phosphor surface area.

Application of the well-known Thomson equation (23) shows that a mercury sphere with a 0.1 μ diameter would have about 10% higher vapor pressure than that over a flat surface. The equation is not valid for spheres with diameters 0.01-0.001 μ since the surface tension is no longer independent of the diameter. Such classical considerations do not take into account the effect of surface forces on the behavior of small droplets of mercury nor do they consider the effect of zinc atoms in "seeding" the condensation of tiny mercury droplets.

The behavior of excess silica with Zn_2SiO_4 suggests that surface forces are appreciable. As was described earlier, excess silicic acid used in the preparation of Zn_2SiO_4 is reluctant to form a crystalline modification and tends to form a cocoon around the zinc silicate crystals. In contrast, excess silicic acid used in the preparation of $CaSiO_3$ readily forms quartz crystals which tend to remain as isolated particles. Thus, it seems possible that small droplets or patches of mercury might be particularly stable on the surface of the zinc silicate phosphor. Unfortunately, electronmicroscopy has not resolved the problem so that the distribution of mercury is still a matter of conjecture.

It is instructive to note that a lamp which has burned for some time and then is reheated to about 300°C will regain substantially all of its lumen drop, but the rate of lumen decrease on re-burning is much greater than it was initially. Evidently the sites which cause deposition of mercury on the surface of the phosphor are not destroyed by heating to 300°C with the result that the lumen drop is much more rapid because of the greater number of sites operating. Such a description is in qualitative agreement with the observation that a gray colored phosphor, which had been removed from a lamp after some hours of burning, could not be bleached by acetic acid until the sample had been reheated to about 300°C. Heating zinc amalgam to this temperature will distill off the mercury and leave a residue of zinc. Since zinc amalgam is insoluble in acetic acid whereas zinc is soluble, it is necessary to decompose the amalgam before the zinc can be dissolved.

Relation of Phosphor Surface Chemistry to Lamp Brightness

The behavior of zinc silicate phosphor during lamp making and lamp burning is complicated. However, the observations discussed serve at least qualitatively to account for the major changes in phosphor brightness. Phosphor removed from a lamp immediately after lamp making is discolored and it has suffered about a 10% loss in brightness. Two factors contribute to this effect. Since the phosphor was furnace cooled, dissociation of the surface phase has led to higher oxidation states of manganese and consequently a tan coloration. The addition of Sb_2O_3 to the coating suspension has led to the formation of $ZnSb_2O_6$ which has high u.v. absorption.

As lamp burning progresses the phosphor suffers further losses in brightness as mercury collects on the surface of the material. The body color changes from a tan coloration to a dark gray color. Metallic zinc atoms are believed to serve as "vapor traps" which cause the mercury to be distributed over the

Table III. Effect of various additives on the lumen performance of zinc silicate phosphors

Sample	0 hr, LPW	100 hr, LPW	500 hr, LPW
$(Zn, Mn)_2SiO_4$	95.7	83.3	70.9
$(Zn, Mn)_2SiO_4$: P_2O_5	110.4	81.6	65.1
$(Zn, Mn)_2SiO_4$: 0.25 wt % As_2O_5	110.3	98.0	85.8
$(Zn, Mn)_2SiO_4$: 0.10 wt % Sb_2O_3	102.6	95.2	84.2
$(Zn, Mn)_2SiO_4$: 0.10 wt % As_2O_5 + 0.10 wt % Sb_2O_3	108.4	98.3	85.1
$(Zn, Mn)_2SiO_4$: special treatment	109.0	104.1	99.0

surface of the phosphor. Two factors can lead to the production of metallic zinc: the decomposition of the surface phase; and reduction of Zn^{2+} by photolysis. Both effects may operate, but it is nevertheless clear that prevention of the oxidation of Mn^{2+} and reduction Zn^{2+} should give substantial improvements in lumen output.

The benefit of a protective coating is demonstrated by the lumen data shown in Table III. The addition of either $(NH_4)_2HPO_4$, Sb_2O_3, or As_2O_5 was made to the coating suspension. As a result the development of a surface film most probably occurs only during lehring. Lamps prepared from untreated zinc silicate gave about 71 lpw (lumens per watt) after 500 hr of burning. The addition of P_2O_5 gave only 65 lpw. This result is consistent with the data given in Table II which show that, although P_2O_5 additions prevented oxidation of Mn^{2+}, reduction of Zn^{2+} did occur. The larger lumen decrease observed than for untreated phosphor may be the deleterious effect of additional H_2O in the lamp from unreacted H_3PO_4. As is well known, the addition of 0.1 wt % Sb_2O_3 to the coating suspension gives substantial improvements both in initial lumens and lumen maintenance so that after 500 hr lamps have about 84 lpw. A mill addition of 0.1 wt % Sb_2O_3 plus 0.1 wt % As_2O_5 was better at 100 hr than either Sb_2O_3 or As_2O_5 alone. The substantial gain in zero hour lumen achieved by adding As_2O_5 alone or in combination with Sb_2O_3 is probably the result of better formed $ZnAs_2O_6$ or $ZnSb_2O_6$ on the surface of the zinc silicate crystals. Evidently the surface layer is not entirely stable since the initial gain in lumens over Sb_2O_3 alone was lost after about 500 hr of burning. By special treatment of the phosphor it is possible to achieve 99 lpw after 500 hr. Thus, appropriate surface treatment of the phosphor improves not only the lumen output but also the lumen maintenance.

Ideally, $(Zn, Mn)_2SiO_4$ stabilized by a suitable surface film should be an optimum phosphor composition. However, a certain excess of silica is required as shown by the data in Fig. 1. A phosphor with a ZnO/SiO_2 ratio of 1.9/1.0 gave lower lumens than one with a ratio of 1.7/1.0. Since Sb_2O_3 was added to the coating suspension, a film of $ZnSb_2O_6$ could form only during lehring, that is, in the minute or two that the phosphor was above about 500°C. It seems likely that any factor which affects the kinetics of formation of $ZnSb_2O_6$ also will affect lamp performance. Similar results are shown by the data in Fig. 2. A particular phosphor composition had varying susceptibility to lamp-making conditions depending on the temperature at which the phosphor was prepared. Since it is shown that surface alterations do occur in zinc silicate, it is likely that different heat treatments will produce various degrees of surface alteration. The change in response to 3650Å excitation appears to be associated with alterations in surface structure which also could conceivably have a marked effect on the kinetics of the formation of $ZnSb_2O_6$. Thus, heat treatments which produce changes in response to 3650Å excitation also yield phosphors which give lamps with different lumen outputs. Consequently, it appears that the surface properties of a phosphor, particularly those which affect the extent and perfection of a protective coating, greatly influence the quality of lamps produced by identical procedures.

The proposed mechanism of zinc silicate phosphor deterioration does not explain why some lamps actually improved in maintenance from 100 to 500 hr (see Fig. 2). Also in need of an explanation is that although zinc-beryllium silicate and zinc silicate are isostructural the former is much more stable in lamps than the latter. However, in the case of zinc-beryllium silicate there is the possibility of forming a surface film of Be_2SiO_4 which may help prevent reduction of Zn^{2+}.These results emphasize that there are many other factors needing research to explain the maintenance of lamps.

Acknowledgments

Grateful acknowledgment is given to Miss Eileen Allessandrini of General Electric Company Research Laboratory for supplying the electron diffraction data, to Miss Mary V. Hoffman for obtaining some of the lamp data, to Mr. J. G. Rabatin for supplying the DTA data, to Mr. J. W. Hunter for analysis of the zinc amalgam, and to Dr. C. A. Brown for his many stimulating discussions.

Manuscript received Sept. 16, 1959.

Any discussion of this paper will appear in a Discussion Section to be published in the December 1960 JOURNAL.

REFERENCES

1. G. R. Fonda, *J. Phys. Chem.*, **43**, 561 (1939).
2. K. H. Butler, *This Journal*, **93**, 143 (1948).
3. E. Nagy, *J. Optical Soc. Am.*, **39**, 42 (1949).
4. H. W. Leverenz, "An Introduction to the Luminescence of Solids," pp. 223-233, John Wiley and Sons, New York (1950).
5. S. Larach and J. Turkevich, *Phys. Rev.*, **89**, 1060 (1953).
6. A. Schleede and A. Gruhl, *Z. Elektrochem.*, **29**, 411 (1923).
7. H. P. Rooksby and A. H. McKeag, *Trans. Faraday Soc.*, **37**, 308 (1941).
8. H. G. Pfeiffer and G. R. Fonda, *This Journal*, **99**, 140 (1952).
9. C. Feldman and Margaret O'Hara, *J. Optical Soc. Am.*, **48**, 816 (1958).
10. E. F. Lowry, *This Journal*, **95**, 242 (1949).
11. J. B. Merrill and A. B. Davis, U.S. Pat. 2,554,999 (May 29, 1951).
12. E. N. Bunting, *J. Research Nat. Bur. Standards*, **4**, 134 (1930); R. P. 136; E. M. Levin, H. F. McMurdie, and F. P. Hall, "Phase Diagrams for Ceramists," The Am. Ceram. Soc. (1956).
13. H. W. Leverenz, *loc cit.*, p. 328.
14. D. E. Harrison, Unpublished data.
15. F. A. Hummel, Private communications.
16. C. E. Hall, "Introduction to Electron Microscopy," p. 252, McGraw-Hill Book Co., Inc., New York (1953).

17. F. Feigl, "Qualitative Analysis by Spot Tests," pp. 55, 242, Elsevier Publishing Co., Inc., Amsterdam (1947).
18. H. C. Froelich, *Trans. Electrochem. Soc.*, **87**, 429 (1945).
19a. G. Kressin, "Technisch-Wissenschaftliche Abhandlungen der Osram Gesellschaft," p. 235, Springer Verlag (1958).
19b. G. Kressin, Private communications.
20. J. W. Mellor, "Inorganic and Theoretical Chemistry," vol. IV, p. 1038, Longmans, Green & Co., London (1946).
21. E. A. Anderson, "Metals Handbook," p. 1222, The American Society for Metals, Cleveland (1948).
22. H. C. Froelich, *J. Applied Phys.*, **17**, 573 (1946).
23. Samuel Glasstone, "Textbook of Physical Chemistry," p. 495, D. van Norstrand Co., Inc., New York (1946).

The System BaO-TiO_2-P_2O_5: Phase Relations, Fluorescence, and Phosphor Preparation

D. E. Harrison[1]

Luminescent Materials Laboratory, Lamp Metals and Components Department, General Electric Company, Cleveland, Ohio

ABSTRACT

The subsolidus phase relations were determined in the system BaO-TiO_2-P_2O_5 by using x-ray and petrographic techniques. Four compounds were isolated and individually prepared: $2BaO:TiO_2:P_2O_5$ melts congruently at 1197° ± 3°C; $BaO:TiO_2:P_2O_5$ has a rapidly reversible dimorphic inversion at 967° ± 5°C and it melts congruently at 1428° ± 3°C; $4BaO:3TiO_2:P_2O_5$ melts incongruently at 1302° ± 3°C; and $BaO:4TiO_2:3P_2O_5$ melts incongruently at 1368° ± 3°C. The only compound in the system which is of the self-activated type is $2BaO:TiO_2:P_2O_5$. It has an emission similar to that of $MgWO_4$. Compositions of maximum fluorescence are restricted to the join $2BaO:P_2O_5$-$2BaO:TiO_2:P_2O_5$ since compositions off this join contain either $BaO:TiO_2:P_2O_5$, $4BaO:3TiO_2:P_2O_5$ or TiO_2 which have high u.v. absorption but are nonfluorescent phases.

Henderson and Randy (1a) developed a phosphor with a composition of $2Ba_2P_2O_7$: 0.5 to 2.5 TiO_2. (In this paper, "activator concentrations" such as 0.5 to 2.5 TiO_2 refer to moles of material per mole of $Ba_2P_2O_7$.) This phosphor, which is excited by 2537Å radiation, has an emission similar to that of $MgWO_4$ and it is of the self-activated type. It is reported that maximum fluorescence occurs with a composition of $2Ba_2P_2O_7$: 1.0 TiO_2 but that relatively large increases in the concentration of titania only slowly decrease the intensity of fluorescence.

The system BaO-TiO_2-P_2O_5 provides an unusual opportunity to relate the ternary phase relations to the fluorescent properties without the uncertainties attending the introduction of small amounts of an activator as the fourth component. The purpose of this study was to determine the subsolidus phase relations and to show how the brightness of phosphor compositions is influenced by small amounts of nonfluorescing phases which necessarily occur as a result of the ternary phase relations. Subsolidus phase relations were determined by examining compatibility triangles and isolating compounds. It is hoped that the phase data and particularly the characterization of the fluorescent compound will prove useful in a fundamental study of this self-activated phosphor.

Experimental Procedure

Reagent grade $BaCO_3$, $BaHPO_4$, TiO_2, $(NH_4)_2HPO_4$, and BaF_2 were used as starting materials. Compositions were prepared by grinding the ingredients in a mortar with acetone until dry. Calcines were prepared in either fused silica or platinum crucibles at temperatures ranging from 700° to 1100°C for periods up to 3 weeks.

X-ray data were obtained from a General Electric, XRD-5, diffractometer using $Cu_{k\alpha}$ radiation (λ = 1.540Å) filtered with nickel.

The immersion technique was used to determine the refractive index of crystals. Indices up to 1.700 were determined to an accuracy of ±0.001, from 1.71 to 1.80 to an accuracy of ±0.005, and 1.84 to 2.00 to an accuracy of ±0.02.

Differential thermal analysis (DTA) data were obtained with an automatically recording apparatus, as described by Rabatin and Card (2).

The melting points of compounds were determined by a quench technique similar to that described by Shepherd, Rankin, and Wright (3). Thermocouples were calibrated using gold (mp, 1063°C), lithium metasilicate (mp, 1201°C), and diopside (mp, 1392°C). Since it was impossible to quench 20-g samples of ternary compound compositions to glasses, calcines were used as starting materials for quench studies.

Ultraviolet absorption was measured by determining the u.v. reflected from a sample. The detector consisted of a Corning 9863 filter, a layer of zinc silicate phosphor, a green filter, and a barrier layer photocell.

Relative fluorescent brightness was measured by a barrier layer photocell corrected to eye sensitivity.

[1] Present address: Metallurgy Department, Research Laboratories, Westinghouse Electric Corp., Pittsburgh, Pa.

Results and Discussion

Phase studies, binary systems.—The system BaO-TiO_2 was examined extensively by Rase and Roy (4). Five compounds exist: $2BaO:TiO_2$, $BaO:TiO_2$, $BaO:2TiO_2$, $BaO:3TiO_2$, and $BaO:4TiO_2$. The compound $BaO:2TiO_2$ has a lower limit of stability at 1210°C; below this temperature the composition is a mixture of $BaO:TiO_2$ and $BaO:3TiO_2$. Jonker and Kwestroo (5) discovered two new compounds which belong to the binary system. These compounds, $2BaO:5TiO_2$ and $2BaO:9TiO_2$, are stabilized by small additions of SnO_2 or ZrO_2. The system TiO_2-P_2O_5 was examined recently by Harrison and Hummel (6) who showed that $5TiO_2:2P_2O_5$ and $TiO_2:P_2O_5$ are the only compounds which occur in this system.

No complete phase diagram of the system BaO-P_2O_5 is reported, but a number of compounds are claimed. Glatzel (7) reports the occurrence of $BaO:P_2O_5$, and Ouvrard (8) shows the existence of $2BaO:P_2O_5$. A cubic form of $3BaO:P_2O_5$ is listed in the ASTM X-ray Diffraction Patterns, and a rhombohedral form is reported by Zachariasen (9). Recently, Langguth, Osterheld, and Karl-Kroupa (10) presented x-ray data for a new compound $3BaO:2P_2O_5$. Re-examination of the system confirmed the existence of the four compounds claimed. Further work was done on the new compound $3BaO:2P_2O_5$. Since it was not possible to quench the entire composition to a glass, conventional quench technique could not be used to determine the melting point. After fusion the quenched product always consisted of $3BaO:2P_2O_5$ plus glass. Therefore, it is concluded tentatively that the 3:2 compound melts congruently. DTA gave an endotherm at 900°C on heating and a second endotherm at 990°C followed by melting. The thermal effect at 900°C is the result of a slowly reversible dimorphic inversion which was found by static methods to occur at 870° ± 10°C. Microscopic examination showed that the low-temperature form has maximum and minimum refractive indices of 1.628 and 1.618, respectively. The high-temperature form is nearly isotropic with a refractive index of about 1.626. Typical x-ray patterns of the high- and low-temperature forms are given in Table II and compared with the data of Langguth, Osterheld, and Karl-Kroupa. Langguth, *et al.* fired their sample of 3:2 at 550°C/12 hr, whereas in the present work the low-temperature form was prepared at 800°C/24 hr. The differences in crystal development obtained at these firing temperatures may account for the discrepancies in the x-ray data.

Phase studies, ternary system.—Compatibility triangles were determined by comparison of x-ray and microscopic data of ternary compositions with data from the binary systems. Compositions investigated are shown in Fig. 1 and listed in Table I.

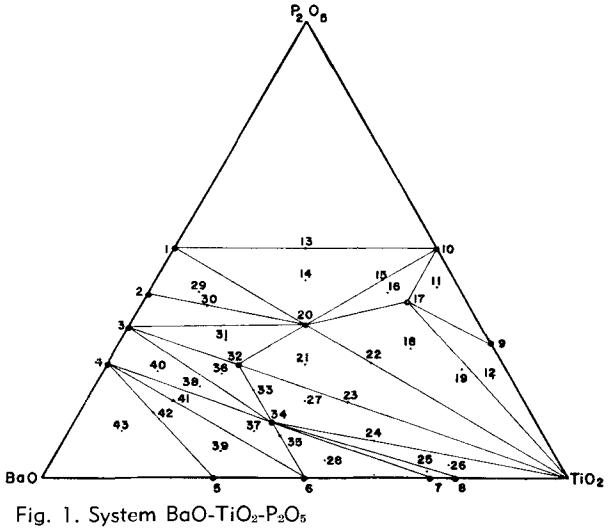

Fig. 1. System BaO-TiO_2-P_2O_5

Comp. No.
1—$BaO:P_2O_5$
2—$3BaO:2P_2O_5$
3—$2BaO:P_2O_5$
4—$3BaO:P_2O_5$
5—$2BaO:TiO_2$
6—$BaO:TiO_2$
7—$BaO:3TiO_2$

Comp. No.
8—$BaO:4TiO_2$
9—$5TiO_2:2P_2O_5$
10—$TiO_2:P_2O_5$
17—$BaO:4TiO_2:3P_2O_5$
20—$BaO:TiO_2:P_2O_5$
32—$2BaO:TiO_2:P_2O_5$
34—$4BaO:3TiO_2:P_2O_5$

Table I. Compositions in the system BaO-TiO_2-P_2O_5

Comp. No.	Mole % composition			Phases present
	BaO	TiO_2	P_2O_5	
1	50.0	—	50.0	BP
2	60.0	—	40.0	B_3P_2
3	67.0	—	33.0	B_2P
4	75.0	—	25.0	B_3P
5	67.0	33.0	—	B_2T
6	50.0	50.0	—	BT
7	25.0	75.0	—	BT_3
8	20.0	80.0	—	BT_4
9	—	71.5	28.5	T_5P_2
10	—	50.0	50.0	TP
11	5.0	55.0	40.0	BTP + BT_4P_3 + T
12	3.0	76.0	21.0	BT_4P_3 + T_5B_2 + T
13	25.0	25.0	50.0	BP + BT
14	28.5	28.0	43.5	BP + BT + BTP
15	14.3	42.8	42.8	TP + BTP
16	15.0	45.0	40.0	TP + BTP + BT_4P_3
17	12.5	50.0	37.5	BT_4P_3
18	16.0	57.0	27.0	BTP + BT_4P_3 + T
19	9.1	63.6	27.3	BTP + BT_4P_3 + T
20	33.3	33.3	33.3	BTP
21	37.5	37.5	25.0	BTP + B_2TP + T
22	25.0	50.0	25.0	BTP + T
23	33.3	50.0	16.7	B_2TP + T
24	30.8	61.5	7.7	B_4T_3P + T
25	25.5	73.5	1.0	?
26	20.0	77.5	2.5	?
27	41.6	41.6	16.8	B_2TP + B_4T_3P + T
28	43.5	53.5	3.0	B_4T_3P + BT + BT_3
29	50.0	10.0	40.0	BP + BTP + B_3P_2
30	50.0	12.5	37.5	B_3P_2 + BTP
31	50.0	20.0	30.0	B_2P + BTP + B_2TP
32	50.0	25.0	25.0	B_2TP
33	50.0	30.0	20.0	B_2TP + B_4T_3P
34	50.0	37.5	12.5	B_4T_3P
35	50.0	40.0	10.0	B_4T_3P + BT
36	55.0	22.5	22.5	B_2P + B_2TP + B_2T_3P
37	55.0	35.0	10.0	B_3P + B_4T_3P + BT
38	60.0	20.0	20.0	B_2P + B_4T_3P + B_3P
39	63.0	31.0	6.0	B_3P + BT + B_2T
40	67.0	10.0	23.0	B_2P + B_4T_3P + B_3P
41	67.0	17.0	16.0	B_3P + BT
42	71.5	14.3	14.3	B_3P + B_2T
43	80.0	10.0	10.0	?

Legend:
BP = $BaO:P_2O_5$
B_3P_2 = $3BaO:2P_2O_5$
B_2P = $2BaO:P_2O_5$
B_3P = $3BaO:P_2O_5$
B_2T = $2BaO:TiO_2$
BT = $BaO:TiO_2$
BT_3 = $BaO:3TiO_2$
BT_4 = $BaO:4TiO_2$
T_5P_2 = $5TiO_2:2P_2O_5$
TP = $TiO_2:P_2O_5$
BT_4P_3 = $BaO:4TiO_2:3P_2O_5$
BTP = $BaO:TiO_2:P_2O_5$
B_2TP = $2BaO:TiO_2:P_2O_5$
B_4T_3P = $4BaO:3TiO_2:P_2O_5$

Table II. Characteristic x-ray patterns

High-temperature $3BaO:2P_2O_5$ (25°C)		(After Langguth, *et al.*) $3BaO:2P_2O_5$		Low-temperature $3BaO:2P_2O_5$ (25°C)	
d	*I/I*	*d*	*I/I*	*d*	*I/I*
6.32	20			7.76	25
4.95	15			5.24	30
3.93	50	5.10	w	5.01	15
3.83	100			4.87	15
3.45	85	4.66	w	4.74	30
3.37	55	4.19	w	4.44	5
3.32	70	3.97	w	3.95	10
3.29	45			3.88	15
3.21	80	3.76	w	3.81	50
3.14	50	3.58	s	3.63	80
3.07	45	3.44	w	3.52	70
3.03	85	3.38	w	3.42	25
2.91	20	3.30	s	3.34	100
2.82	45	2.99	w	3.14	30
2.79	50	2.93	w	3.10	60
2.70	20	2.79	m	2.83	50
2.40	15	2.72	w	2.76	50
2.33	15	2.60	w	2.59	10
2.24	35	2.54	w	2.55	35
2.19	20			2.42	10
2.16	35			2.40	20
2.14	45			2.37	20
2.11	30			2.33	10
2.09	50	2.23	m	2.24	10
2.07	20	2.19	w	2.20	35
2.02	15			2.16	15
1.996	25	2.13	vw	2.14	25
1.951	20	2.10	m	2.09	35
1.916	15			2.07	25
1.717	15			2.05	10
1.646	20			2.04	15
				1.988	10
				1.971	10
				1.940	20
				1.909	25
				1.883	15
				1.843	20
				1.816	20
				1.799	20
				1.742	25
				1.720-1.705	15
				1.668	15
				1.589	15
				1.572	10
				1.567	10
				1.552	10
				1.520	20
				1.432-1.414	10
				1.397	15

$2BaO:TiO_2:P_2O_5$		Low-temperature $BaO:TiO_2:P_2O_5$ (25°C)		High-temperature $BaO:TiO_2:P_2O_5$ (1024°C)	
d	*I/I*	*d*	*I/I*	*d*	*I/I*
8.34	30	7.69	10	4.41	45
4.17	80	4.39	30	4.15	5
3.90	25	4.13	20	3.83	77
3.59	10	3.86	40	3.34	10
2.84	5	3.75	50	3.20	10
2.78	100	2.96	100	2.91	100
2.73	10	2.85	30	2.82	5
2.65	3	2.72	5	2.77	5
2.39	3	2.60	20	2.66	5
2.28	3	2.57	30	2.59	20
2.25	3	2.43	25	2.54	85
2.19	3	2.25	5	2.41	30
2.14	5	2.15	10	2.23	10
1.943	3	2.13	5	2.20	5
1.751	10	2.12	10	2.12	35
1.665	3	1.940	10	1.916	50
1.338	5	1.928	10	1.776	25
		1.875	10	1.663	15
		1.792	15	1.627	15
		1.738	5	1.543	30
		1.557	5	1.529	30
		1.545	5		
		1.476	10		
		1.462	5		
		1.284	5		
		1.246	5		
		1.202	10		
		1.030	10		

$4BaO:3TiO_2:P_2O_5$		$BaO:4TiO_2:3P_2O_5$	
d	*I/I*	*d*	*I/I*
4.74	10	4.19	70
4.69	10	3.67	100
4.44	5	3.45	10
4.27	10	3.07	10
4.06	5	2.83	90
3.57	20	2.71	10
3.41	5	2.66	10
3.25	10	2.41	20
3.18	100	2.25	5
3.04	5	2.19	5
2.93	5	2.18	10
2.86	10	2.04	10
2.80	60	1.984	10
2.66	10	1.920	5
2.41	5	1.833	20
2.37	5	1.760	5
2.34	20	1.711	5
2.20	10	1.646	10
2.18	10	1.576	10
2.10	20	1.529	5
2.02	5	1.513	5
1.928	20	1.502	5
1.854	5	1.498	10
1.792	10	1.460	10
1.732	5	1.409	5
1.682	20		
1.617	5		
1.586	5		
1.432	5		
1.399	5		
1.383	5		
1.379	5		
1.281	5		
1.253	5		
1.201	5		
1.075	5		
1.058	5		

Since the temperature range examined was from 800° to 1100°C, $BaO:2TiO_2$ does not appear as a phase in the ternary system. Composition No. 28 consisted of a mixture of $4BaO:3TiO_2:P_2O_5$ + $BaO:TiO_2$ + $BaO:3TiO_2$ but not $2BaO:5TiO_2$. Therefore, it appears that $2BaO:5TiO_2$ does not occur as a stable phase in the ternary system in the temperature range studied. The sluggishness with which equilibrium is reached in the triangles $3BaO:P_2O_5$ — $2BaO:TiO_2$ — BaO and $4BaO:3TiO_2:P_2O_5$ — $BaO:3TiO_2$ — TiO_2 prevented determination of the phase relations within these triangles. However, the boundaries of the triangles are correct as drawn. No extensive solid solution regions exist in the ternary system. Four ternary compounds were discovered and individually prepared. A diagram of the compatibility triangles is given in Fig. 1 and the phase data are listed in Table I.

The compound $2BaO:TiO_2:P_2O_5$ has maximum and minimum refractive indices of 1.688 and 1.672, respectively. At 1197° ± 3°C, 2:1:1 melts congruently. DTA showed no thermal effects between ca. 100°C and the melting temperature. A characteristic x-ray pattern is listed in Table II.

The compound $BaO:TiO_2:P_2O_5$ has maximum and minimum refractive indices of 1.84 and 1.79, respectively, and it melts congruently at 1428° ± 3°C. DTA exhibits an endotherm at 970°C on heating and a exotherm at 905°C on cooling. The thermal effects are the result of a rapid-reversible-dimorphic inversion. High-temperature x-ray examination showed that the inversion occurs at 967° ±5°C. Characteristic x-ray diffraction data of the high- and low-temperature forms are given in Table II.

The compound $4BaO:3TiO_2:P_2O_5$ has a refractive index of about 1.71, and it melts incongruently at 1302° ± 3°C into a liquid and $3BaO:P_2O_5$. Comparison of the x-ray data of 4:3:1 and 3:1 shows that they are almost identical but differences in optical properties of these two compounds proved that 4:3:1 dissociates into 3:1 and a liquid. DTA shows no thermal effects from about 100°C to the melting temperature. A characteristic x-ray pattern is given in Table II.

The compound $BaO:4TiO_2:3P_2O_5$ has refractive indices between 1.88 and 1.92, and it melts incongruently at 1368° ± 3°C into a liquid and probably 1:1:1. X-ray examination of the dissociated product did not reveal a clearly defined phase but suggests that it might be a transition phase between the high- and low-temperature forms of 1:1:1. DTA showed no thermal effects from about 100°C to the melting temperature.

Fluorescent studies.—Reference to Fig. 1 shows that the composition region, $2Ba_2P_2O_7:0.5\text{-}2.5TiO_2$, of useful phosphors reported by Henderson and Ranby lies on the joins $2BaO:P_2O_5$-$2BaO:TiO_2:P_2O_5$ and $2BaO:TiO_2:P_2O_5$-TiO_2. Observation of the end members reveals that 2:1:1 fluoresces a blue color whereas 2:1 and TiO_2 do not fluoresce at all. The optimum phosphor composition claimed by Henderson and Ranby is $2Ba_2P_2O_7:1.0TiO_2$ or actually 50 mole % $2BaO:P_2O_5$ + 50 mole % $2BaO:TiO_2:P_2O_5$, since there is essentially no solubility between end members. Surprisingly, a composition with 50 mole % dilution by 2:1 fluoresces only slightly less brightly than the 2:1:1 compound. This may be explained by the relatively low u.v. absorption of $2BaO:P_2O_5$ and the method of measuring powder brightness. Powder brightness is measured from a sample which has effectively infinite thickness for u.v. light; therefore low absorbing, nonfluorescing particles behave as voids. In this regard it is interesting to examine the fluorescence of compositions in the compatibility triangles which terminate at the 2:1:1 compound.

Composition No. 31, for example, is a mixture of 35 mole % 2:1:1, 31 mole % 1:1:1, and 34 mole % 2:1. However, this composition has only 52% of the brightness of 2:1:1 or $2Ba_2P_2O_7:1.0TiO_2$ because of the presence of 1:1:1 which has high u.v. absorption but no fluorescence. A similar situation exists in composition No. 36 which is composed of 44 mole % 2:1:1, 28 mole % 4:3:1, and 28 mole % 2:1. Like 1:1:1, the presence of 4:3:1, which is a nonfluorescent, highly u.v. absorbing phase, causes this composition to have only 68% of the brightness of 2:1:1. Compositions Nos. 21 and 27 exhibit only 36 and 25% brightness, respectively, due to the presence of TiO_2 in addition to either 1:1:1 or 4:3:1. Absorption and brightness data are summarized in Table III.

Table III. Ultraviolet absorption and fluorescent brightness of Ba-Ti-phosphate compositions

Comp. No.	Mole % composition in terms of compatible phases					U.V. abs.	% powder brightness in terms of
	2:1:1	1:1:1	4:3:1	2:1	TiO_2	in %	2:1:1
32	100	—	—	—	—	96	100
20	—	100	—	—	—	98	0
34	—	—	100	—	—	97	0
3	—	—	—	100	—	21	0
TiO_2	—	—	—	—	100	96	0
31	35	31	—	34	—	97	52
36	44	—	28	28	—	96	68
21	47	42	—	—	11	97	36
27	57	—	26	—	17	96	25

Effect of phosphor composition on brightness.—Because of the low reactivity of TiO_2, the formation of 2:1:1 can be facilitated by using an excess of $2BaO:P_2O_5$. More satisfactory results can be achieved by employing a flux, such as BaF_2, as was used by Henderson and Ranby. Since chemical analysis shows that fluorine is lost on firing, the BaF_2 appears to be oxidized to BaO, apparently by a mass action effect. In order to remain on the 2:1 — 2:1:1 join or to arrive at the 2:1:1 compound, it is necessary to compensate for the additional BaO with P_2O_5. The use of SrF_2, as claimed in a recent patent by Uehara, Kobuke, and Tomishima (11), probably requires similar treatment, since it is likely that small amounts of Sr will substitute for Ba in the phosphor matrix.

A particularly effective method of introducing extra P_2O_5 is by use of $BaO:P_2O_5$. Conveniently, this compound melts congruently into a stable liquid at 843° ± 3°C. Since phosphor synthesis proceeds rapidly at about 1000°C, the combined effects of a fluoride flux and liquid $BaO:P_2O_5$ yield well-formed phosphor. The liquid initially produced by melting of $BaO:P_2O_5$ does not cause sintering, and a phosphor with small particle size is obtained.

The dramatic effect on phosphor brightness with compositions on either side of the 2:1:1 — 2:1 join is demonstrated by the following experiment: Three compositions were prepared (A) $4BaHPO_4 + 1.3TiO_2 + 0.07BaF_2$; (B) $4BaHPO_4 + 1.3TiO_2 + 0.07BaF_2 + 0.07BaO:P_2O_5$; and (C) $4BaHPO_4 + 1.3TiO_2 + 0.07BaF_2 + 0.14BaO:P_2O_5$. Composition (A) lies just off the join in the compatibility triangle 2:1 — 2:1:1 — 4:3:1. Composition (B) is on the join and composition (C) is again located off the join in the triangle 2:1 — 2:1:1 —1:1:1. All compositions were fired at 900°C for 2 hr, a second time at 930°C for 2 hr, and finally fired at 1000°C for 15 hr. The results of

Table IV. Relative fluorescent brightness of some Ba-Ti-phosphate compositions

Composition	Heat treatments 900°C for 2 hr	930°C for 2 hr	1000°C for 15 hr
A*	96	82	82
B*	92	92	100
C*	74	76	80
	900°C for 2 hr	930°C for 2 hr	980°C for 15 hr
D‡	98	90	69
E‡	96	96	100
F‡	57	59	69

* A: 62.4 mole % 2:1:1 + 36.7 mole % 2:1 + 0.9 mole % 4:3:1
B: 62.8 mole % 2:1:1 + 37.2 mole % 2:1
C: 57.5 mole % 2:1:1 + 39.2 mole % 2:1 + 3.3 mole % 1:1:1

‡ D: 44.5 mole % 2:1:1 + 53.5 mole % 2:1 + 2.0 mole % 4:3:1
E: 46.5 mole % 2:1:1 + 53.5 mole % 2:1
F: 37.0 mole % 2:1:1 + 56.5 mole % 2:1 + 6.5 mole % 1:1:1

powder brightness measurements are given in Table IV. Assuming loss only of water and fluorine, the fired compositions are given in Table IV in mole per cent by compatible phases.

The brightness data show that as equilibrium is attained, composition (A) which contains 0.9 mole % 4:3:1, and composition (C) which contains 3.3 mole % 1:1:1 have only 80% of the brightness of composition (B) on the join 2:1:1 — 2:1. The loss in brightness of compositions (A) and (C) shows that 4:3:1 and 1:1:1 are more effective absorbers for u.v. radiation than their mole percentages would suggest. Examination of the reaction sequence reveals that the first phase to form is $2BaO:P_2O_5$ from the decomposition of $BaHPO_4$. $2BaO:P_2O_5$ reacts with TiO_2 to form $2BaO:TiO_2:P_2O_5$ and depending on composition either 4:3:1 or 1:1:1 form as equilibrium is reached. The reaction sequence is illustrated by composition (A). An initial firing at 900°C gave a product with 96% brightness but successive firings at 930° and 1000°C lowered the brightness to 82%. Composition (C) which has the additional fluxing action of liquid $BaO:P_2O_5$ approached the equilibrium value during the initial firing at 900°C. Thus, it seems likely that the 4:3:1 and 1:1:1 phases occur on the surfaces of the 2:1:1 and 2:1 phases where they can act as more effective absorbers for u.v. light than their mole percentages would indicate.

Three other compositions were selected similar to (A), (B), and (C). The additional compositions were prepared as follows (D) $4.0BaHPO_4 + 1.0TiO_2 + 0.15BaF_2$; (E) $4.0BaHPO_4 + 1.0TiO_2 + 0.15BaF_2 + 0.15BaO:P_2O_5$; and (F) $4.0BaHPO_4 + 1.0TiO_2 + 0.15BaF_2 + 0.30BaO:P_2O_5$. Fluorescent brightness data and compositions by compatible phases are given in Table IV. The results parallel those obtained from compositions (A), (B), and (C). In addition, it is demonstrated that doubling the amount of 4:3:1 from 0.9 mole % in (A) to 2.0 mole % in (D) only further decreases the brightness by about 10%. Thus it appears that doubling the amount of 4:3:1 increases the effective u.v. absorbing area by about 10%, which again suggests that 4:3:1 occurs as patches on the surface of the phosphor.

Conclusions

1. The subsolidus phase relations were determined in the system $BaO-TiO_2-P_2O_5$. Four ternary compounds were isolated: (*a*) $2BaO:TiO_2:P_2O_5$ melts congruently at 1197° ± 3°C, and it has maximum and minimum refractive indices of 1.688 and 1.672, respectively; (*b*) $BaO:TiO_2:P_2O_5$ melts congruently at 1428° ± 3°C, and it has maximum and minimum refractive indices of 1.84 and 1.79, respectively; (*c*) $4BaO:3TiO_2:P_2O_5$ has a refractive index of about 1.71, and it melts incongruently at 1302° ±3°C, and (*d*) $BaO:4TiO_2:3P_2O_5$ melts incongruently at 1368° ± 3°C, and the refractive indices lie between 1.88 and 1.92.
2. $3BaO:2P_2O_5$ exhibits a slowly reversible dimorphic inversion at 870° ± 10°C. The low-temperature modification has maximum and minimum refractive indices of 1.628 and 1.618, respectively. The high-temperature form is nearly isotropic with a refractive index of about 1.626.
3. $2BaO:TiO_2:P_2O_5$ is the only compound in the system which is of the self-activated type. It has an emission similar to that of $MgWO_4$.
4. Compositions with maximum fluorescence are restricted to the join $2BaO:P_2O_5$-$2BaO:TiO_2:P_2O_5$, since compositions off this join contain either $BaO:TiO_2:P_2O_5$, $4BaO:3TiO_2:P_2O_5$, or TiO_2 which have high u.v. absorption but are nonfluorescent phases.

Acknowledgments

The author thanks Professor F. A. Hummel of the Pennsylvania State University for supplying the high-temperature x-ray data, and J. G. Rabatin of the General Electric Company for obtaining the differential thermal analysis data.

Manuscript received Sept. 16, 1959.

Any discussion of this paper will appear in a Discussion Section to be published in the December 1960 JOURNAL.

REFERENCES

1(a) S. T. Henderson and P. W. Ranby, *This Journal*, **98**, 479 (1951).
(b) P. W. Ranby, U.S. Pat. 2,596,509 (May 13, 1952).
2. J. G. Rabatin and C. S. Card, *This Journal*, **104**, 68C [abs. 90] (1957).
3. E. S. Shepherd, G. A. Rankin, and F. E. Wright, *Am. J. Sci.*, 4th Ser., **28**, 293 (1909).
4. D. E. Rase and Rustom Roy, *J. Am. Ceram. Soc.*, **38**, 110 (1955).
5. G. H. Jonker and W. Kwestroo, *J. Am. Ceram. Soc.*, **41**, 390 (1958).
6. D. E. Harrison and F. A. Hummel, *J. Am. Ceram. Soc.*, **42**, 487 (1959).
7. A. Glatzel, Ueber dimetaphosphorsaure and tetrametaphosphorsaure Salze, Diss., Wiirzburg, 1880, *Bull. Nat. Research Council*, **118**, 13 (1949).
8. L. Ouvrard, *Ann. chim Phys.*, **6**, (16) 289 (1889); *Bull. National Res. Council*, (118) 13 (1949).
9. W. H. Zachariasen, *Acta Cryst.*, **1**, 263 (1948); *Bull. Nat. Research Council*, **118**, 13 (1949).
10. R. P. Langguth, R. K. Osterheld, and E. Karl-Kroupa, *J. Phys. Chem.*, **60**, 1335 (1956).
11. Y. Uehara, Y. Kobuke, and H. Tomishima, U.S. Pat. 2,882,238 (April 14, 1959).

An Apparatus for the Preparation of Semiconductor Grade Silicon by Film Boiling

Ray C. Ellis, Jr.

Research Division, Raytheon Company, Waltham, Massachusetts

ABSTRACT

A film boiling technique is used to increase the rate of thermal decomposition of silicon tetraiodide. The silicon is deposited molten on a submerged induction-heated graphite shape and is collected after its departure from the hot zone by flotation. Apparatus is described for the synthesis and purification of large quantities of silicon tetraiodide.

Depending on the semiconductor application, silicon of purity of as little as one part per billion is required. Zone segregation has been of limited use for silicon. Many difficulties have been encountered when melting and solidifying silicon in known crucible materials. The most effective method of zone segregation utilizes a floating zone (1).

Semiconductor grade silicon has been prepared by the reduction of silicon tetrachloride with zinc vapor (2), the reduction of a halogenated silicon compound with hydrogen (3-8), and by the thermal decomposition of silane (9) and of silicon tetraiodide (10, 11).

Recently it was shown that the rate of deposition of titanium from the thermal decomposition of titanium tetraiodide could be increased greatly if the geometry were changed from the Van Arkel-de-Boer (12) method to a film boiling geometry (13). This is the basis of the apparatus described below.

Silicon tetraiodide is a suitable starting material. The free energy change for the decomposition $SiI_4 \rightarrow Si + 2I_2$ at 1 atm becomes zero at about 1770°K. This figure may be in considerable error because of the uncertainty of the data available (14). At this temperature, K of the reaction, $I_2 \rightarrow 2I$, is about 8 $l/mole^{-1}$ with a contribution of −7.32 kcal/mole (15).

The partial pressure of iodine which limits the reaction is supplied by the decomposition. The rate of the decomposition by film boiling is most dependent on the removal of iodine from the reaction zone (11).

Silicon tetraiodide melts at 127°C and boils at 300°C, mp 122°-122.5°C, bp 301.5°C (16). Its density is greater than that of silicon and aids in the removal of the product from the reaction zone by flotation. Silicon tetraiodide can be prepared easily in large quantities (Appendix I) and can be purified in large quantities (Appendix II).

Experimental

Apparatus.—The apparatus for the decomposition consists of a graphite heater, A in Fig. 1, heated with coils, B, driven by a 20 kw rf generator. The heater is held at its base by two molybdenum wires, C, in an inner quartz liner, D. This liner assembly can be changed without disassembling the entire

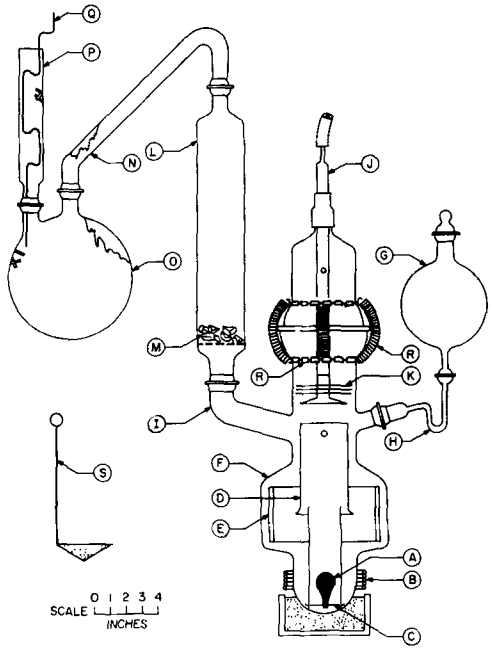

Fig. 1. Apparatus for the decomposition of silicon tetraiodide by film boiling.

apparatus. The inner liner and the outer quartz liner, E, are contained in the reactor, F, which has a total volume of about 10 l and rests in sand. The reactor is fitted with a 2-l feeding flask, G, and feeding tube, H, a sidearm, I, and a large upper joint. The upper joint contains a gas inlet tube, J, on which are hung a series of tantalum baffles, K. Attached to the side arm is the column, L, filled with quartz cullet, M. A condenser, N, leads from the top of the column to a 10-l receiving flask, O. Connected to the receiving flask is a vent or stack, P, in which is placed a cleaning crank, Q. All joints are held together with ball joint clamps except the large joint, which is held together with a chain and spring clamp, R. The chains on each side of the joint are held with springs of suitable number and strength. The chains distribute the pressure evenly.

Operation.—After the graphite heater has been put into place and about 3 l of liquid silicon tetraiodide have been added, the apparatus is flushed with an inert gas such as argon. The graphite then is heated to just below the decomposition temper-

ature (1800°C est.). The flushing gas is adjusted to the point where the heavy vapors of silicon tetraiodide just rise to the baffles. This keeps the large joint between the reactor and the top clean. As the boiling continues the condensing vapors rise in the column and heat it. This prevents clogging of the cold column later by iodine. The power put into the graphite is increased and decomposition begins. Iodine vapors obscure all the inner parts of the apparatus and the decomposition proceeds with iodine distilling out of the column and into the condenser and receiving flask. To prevent clogging, the condenser is heat-cycled periodically to melt the solidified iodine down into the receiver. The crystals in the stack are broken free with the crank.

The molten silicon builds up continuously on the graphite and breaks to the surface of the surrounding liquid in a bright display of molten droplets. The inner quartz liner directs the silicon droplets upward and dumps them out onto the surface of the liquid tetraiodide. The outer quartz liner prevents the molten droplets from floating into the side of the glass container. Very few droplets stick to any surface. Fresh silicon tetraiodide is added as it is needed during the decomposition to keep the liquid level up. This is accomplished by melting the solidified silicon tetraiodide in the feeding flask and through the feeding tube trap.

After several pounds of silicon have collected, the power is turned off, the top is opened, and the inner liner removed. The pellets then can be removed with a tantalum screen ladle (S, Fig. 1). The pellets are soaked in distilled water and then in hydrofluoric acid solution to rid them of any silica. After washing and drying, the pellets are ready for use.

In disassembling the apparatus the joints of the feeding tube and the condenser are loosened by heating and are separated. The top of the reactor is removed and the liquid contents of the reactor poured (usually with filtering) into a flask for storage. The glassware is cleaned by an overnight immersion in hot, 10% sodium hydroxide solution, followed by a scrubbing in Alconox solution and a rinse in demineralized water.

Heater.—Special attention must be paid to the surface on which the silicon deposits since naturally no contamination of the silicon by the surface material or its impurities is desired. The best material found was graphite.

The graphite selected has to be both pure and dense for this application. It was found that commercial graphite with a density of less than about 1.70 was completely disintegrated into silicon carbide by molten silicon. This destructive process was seen less frequently as more dense graphite was used. As silicon starts to form on a graphite surface a protective layer of silicon carbide forms. This prevents further reaction unless the graphite is porous. In this case the silicon runs into the pores, forming some silicon carbide. The volume of the silicon carbide is greater than that which the graphite originally occupied, resulting in a crack which relieves the strain. Silicon runs into this crack and the destructive process continues.

The shape selected for the graphite has smooth contours to encourage the least violent liquid and gas flow around it and to minimize the strains induced on its surface by the thin silicon carbide layer.

Unfortunately there is a finite solubility of carbon in molten silicon. Therefore the graphite (or silicon carbide) dissolves to an appreciable extent in the silicon that has formed. A very small amount of silicon carbide crystallizes out of the silicon pellets as they solidify. This amounts to about 0.1%. Occasionally a graphite heater had to be replaced because of extensive erosion.

Silicon carbide was used in several experiments and found to erode about as rapidly as the dense graphite samples.

Results

Product.—The product is a mass of various sized polycrystalline droplets of silicon ranging from ⅛ to ⅜ in. in diameter. Many of the droplets broke after solidification. The product is pictured in Fig. 2.

Rates as high as 120 g/hr have been observed. This corresponds to 10 g of silicon/hr/cm^2. By suspending the graphite in the vapor, a rate of 1.0 g/hr/cm^2 was obtained at about 1800°C. This tenfold increase in the rate by the introduction of film boiling compares with the factor of 100 found by Petersen (13) using titanium tetraiodide.

The purity of the prqduct was determined by drawing a test crystal from each batch and measuring its resistivity. The average resistivity of about a thousand runs was found to be about 5-10 ohm-cm, p-type. The impurity element was identified as boron by determining the segregation coefficient. The highest resistivities found were in the 300 ohm-cm range, but it is believed this was due to compensation.

Although the small carbon (or carbide) content in the silicon did not affect the resistivity, it interfered in the growth of single crystals by appearing as a dross on the molten product during crystal growing.

Several methods have been used to remove the silicon carbide from the product. The product has

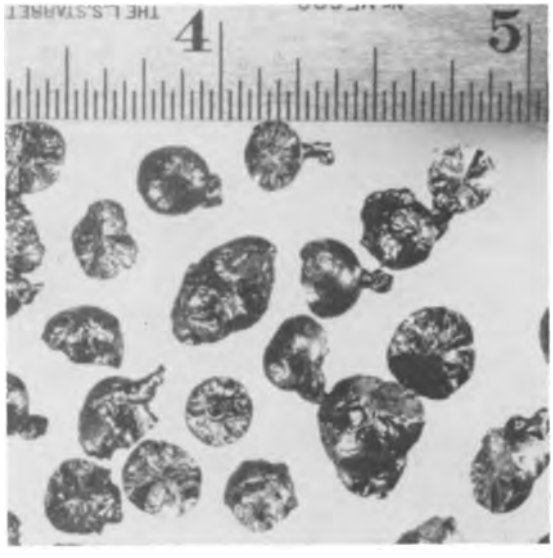

Fig. 2. The product: solidified droplets of silicon

been filtered through quartz wool and fritted quartz disks but these steps, while removing the carbide, introduce oxygen (17).

Temperature of decomposition.—The decomposition in this system starts suddenly because the sudden darkening of the contents of the reactor is seen when the temperature is increased by very small increments. Several methods have been used to estimate this temperature. Direct optical measurement was impossible because of the deep iodine color. Just prior to decomposition, the temperature is about 1700°C. When the graphite was heated in argon with the same power input as above, the temperature was about 150° higher. In one case where silicon tetraiodide was used, hydrogen was introduced just under the heater to obtain better visibility. The deep iodine color was dispelled everywhere except in the immediate neighborhood of the decomposition zone. It is interesting to note that under these conditions small quantities of triiodosilane distilled out of the column.

Placing a thermocouple inside the graphite and free from silicon tetraiodide vapors could not be accomplished without the disintegration of the thermocouple with silicon at temperatures somewhat below where the reaction appears to begin.

A further estimate of the decomposition temperature was attempted by observing the time it took the pellets to solidify. Knowing the heat of fusion and the heat capacity of molten silicon and assuming an emissivity as high as unity, one can calculate the time required for a pellet of a given size to solidify, assuming heat loss by radiation only. The calculated cooling time is still much larger than the observed, showing considerable heat loss by conduction.

Thermodynamics predicts an equilibrium decomposition temperature of 1770°K at 1 atm but this is very dependent on the iodine partial pressure. Reducing the iodine pressure reduces the temperature at which decomposition can take place. A discussion of this equilibrium has been made by Schäfer and Morcher (18, 19) and by Loonam (20). It is interesting to note that, with an adequate supply of iodine at a total pressure of 1 atm, the formation of silicon tetraiodide is self-sustaining, sometimes producing temperatures sufficient to soften quartz (Appendix I).

Summary

An apparatus has been used for the thermal decomposition of silicon tetraiodide by film boiling on a graphite surface to produce semiconductor grade silicon at a rate of 120 g/hr. The estimated decomposition temperature is 1800°C at 1 atm. The small solubility of carbon in silicon at this temperature does not affect the resistivity but does hinder the growth of single crystals from the product.

APPENDIX I

Apparatus for the Production of Large Quantities of Silicon Tetraiodide

Literature on preparation of metal halides by direct combination are too numerous to mention. Much of the preparative work on silicon halides has been done by Schumb, *et al.* (21). The following represents an improvement on Szekely's method (3) in that the apparatus can be run almost continuously and that the rate of the reaction is somewhat higher.

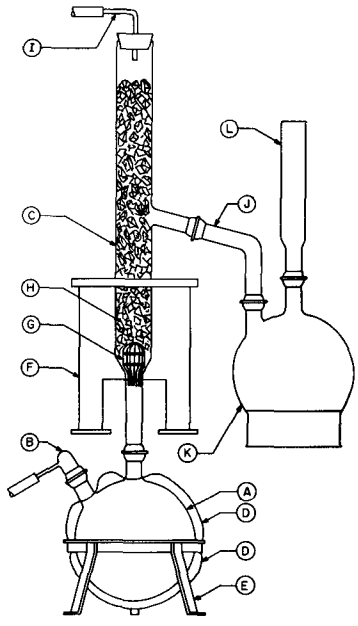

Fig. 3. Apparatus for the preparation of silicon tetraiodide

Experimental.—Resublimed iodine was purchased in 25-lb drums from J. T. Baker Chemical Company, Phillipsburg, New Jersey. The crude silicon (low aluminum grade) was purchased in 100 lb drums from the Electro-Metallurgical Division of Union Carbide and Carbon Corporation. The silicon was crushed to about 1 mesh before use.

The apparatus (Fig. 3) consists of a 5 l boiler flask, A, fitted with an inlet tube, B, and an opaque quartz burning tube, C. A heating mantle, D, surrounds the boiler and supports it. The assembly is supported by a sturdy tripod, E. The lower portion of the burning tube is surrounded by a resistance furnace, F. A tantalum or molybdenum wire plug, G, in the neck of the burning tube supports the silicon charge, H. A one-holed rubber stopper and a glass tube in the top of the burning tube act as a secondary inlet tube, I. The burning tube has a side arm which connects through an elbow, J, to a 5 l receiver, K. The receiver is fitted with an open tube, L, called a stack.

To ready the apparatus for use, the burning tube is filled with crushed silicon and the boiler is loaded with about 4 l (40 lb) of molten iodine. This material is generally iodine recovered from the decomposition of silicon tetraiodide. The system is swept with argon slowly through both inlet tubes.

The furnace is turned on and its temperature increased until the purple vapors appearing in the side arm and elbow change to a white aerosol of silicon tetraiodide. The boiler temperature is increased and the reaction proceeds vigorously as iodine distills up into the burning tube. Usually the furnace is turned off completely to avoid overheating as the reaction is self-sustaining.

As the reaction continues, the flushing gas is decreased to a very low flow rate. The necks of the receiver and the stack are heated periodically with a large soft flame to melt down any solid that has collected. Silicon in the burning tube is knocked down into the reaction zone by tapping the tube gently with a heavy wooden stick. To run the apparatus more or less continuously, the boiler and burning tube can be recharged and the receiver replaced. The washing procedure for the burning apparatus is identical to that used for the decomposition apparatus.

The impure product that distills into the receiver is usually a dark pinkish-brown liquid cooling to a brown waxy solid. The rate of production can be controlled by regulating the boiler temperature and averages 7.5

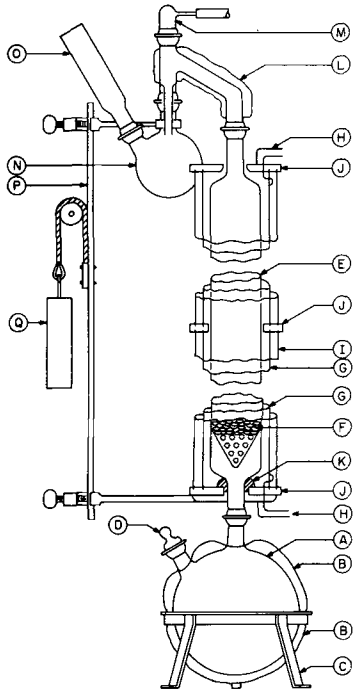

Fig. 4. Still for the distillation of silicon tetraiodide

lb/hr of crude product. The yield is essentially quantitative.

The rate of burning cannot be increased greatly because several times the opaque quartz tube had sagged dangerously because of over-heating. If pure silicon is used as the starting material, the reaction starts with great difficulty and the burning rate is quite slow.

APPENDIX II

Still for the Purification of Large Quantities of Silicon Tetraiodide

The still used for the purification is an easily built laboratory-scale still for handling of large quantities of a dense, high boiling material such as silicon tetraiodide. It is of the usual type with a few innovations for use with silicon tetraiodide. The weight of the column and receiver is counterbalanced so that a redistribution of weight during distillation will not strain the neck of the boiler flask. The thermometer was eliminated from the prototype still head because it was more convenient to take product cuts on an empirical basis.

Experimental.—The apparatus (Fig. 4) consists of a 12-l boiler pot, A, enclosed in a heating mantle, B. The mantle and flask are supported by a sturdy tripod, C. The boiler has a side arm, D, for the introduction of crude silicon tetraiodide. A column, E, 72 in. long and 3 in. in diameter is packed with ⅜ in. glass helices, F, and is connected to the boiler. The column is surrounded by two jackets. The inner jacket, G, is wound with nichrome wire, H, to balance the heat loss of the column. The outer jacket, I, is insulating. To facilitate the construction of the apparatus, the jackets were each made of two parts. The column assembly is held in position by three grooved Transite rings, J. The column rests in glass wool, K. The weight of the column assembly is supported by the bottom Transite retainer. The top of the column connects to an insulated still head, L, which is fitted with a gas inlet tube, M. The receiver, N, is attached to the still head and is fitted with a vent, O, called a stack. An internal extension on the head directs the distillate away from the joint between the head and the receiver. The column and receiver assembly is attached to a movable rack, P. The column, receiver, and rack are counterbalanced by a weight, Q, to prevent strain on the neck of the boiler flask.

Usually the charge of crude silicon tetraiodide is about 85 lb. It is contaminated largely with iodine. The first fraction is deeply colored with iodine, bp 184°C, and somewhat contaminated with boron triiodide. By the time the pure yellow distillate of silicon tetraiodide appears these impurities have been collected. The temperature of the upper part of the column is lowered slightly by decreasing the power in the winding of the upper, inner jacket. The throughput stops and the receiver is quickly changed. Product is similarly taken in batches. Crude silicon tetraiodide can be added as desired.

The distillation was carried out at 1 atm to avoid the use of vacuum equipment. This step did necessitate the introduction of suitable insulation and heating of the apparatus.

The reflux ratio during operation was about 3:1 and it is estimated that there were about seven theoretical plates.

The product is a yellow liquid or a white solid with the melting point found to be 127°C. The throughput of the column could be as large as 7 lb/hr, because there was good separation of impurities. The nearest boiling containment was boron triiodide with a boiling point of 210°C (16), a separation of 90°C from silicon tetraiodide. The product was analyzed spectroscopically and no impurities were found.

Manuscript received June 22, 1959.

Any discussion of this paper will appear in a Discussion Section to be published in the December 1960 JOURNAL.

REFERENCES

1. P. H. Keck, *Physica*, **20**, 1059 (1954).
2. D. W. Lyon, O. M. Olsen, and E. D. Lewis, *J. (and Trans.) Electrochem. Soc.*, **96**, 359 (1949).
3. G. Szekely, *This Journal*, **104**, 663 (1957).
4. H. C. Theuerer, *Bell Labs. Record*, **33**, No. 9, 337 (1955).
5. D. W. Lyon, "Rare Metals Handbook," Ch. 19, Reinhold Publishing Co., New York (1954).
6. A. E. van Arkel, *Metallwirtschaft*, **13**, 405, 511 (1934).
7. Siemens and Halske Ag. Brit. Pat. 809,250 and 795,191.
8. R. C. Sampler, E. F. Maverick, and M. L. Croutch, *This Journal*, **104**, 317 (1957).
9. Progress Reports. Contract No. DA-36-039-SC-72768 to the Lansdale Tube Co. (Philco Corporation), Lansdale, Pennsylvania.
10. F. B. Litton and H. C. Andersen, *This Journal*, **101**, 287 (1954).
11. A. F. Armington, "Some Aspects of the Decomposition of Silicon Tetraiodide," paper presented at the 113th Meeting of the Electrochemical Society, New York, May 1, 1958.
12. A. E. van Arkel and J. H. de Boer, U. S. Pat. 1,671,213 (1928).
13. A. W. Peterson, and L. A. Bromley, *J. Metals*, **8**, 284 (1956).
14. L. L. Quill, "The Chemistry and Metallurgy of Miscellaneous Materials," 1st ed., McGraw-Hill Book Co., Inc., New York (1950).
15. Stark and Bodenstein, *Z. Elektrochem.*, **16**, 961 (1910).
16. H. C. Andersen and L. H. Belz, *J. Am. Chem. Soc.*, **75**, 4828 (1953).
17. W. K. Kaiser and P. H. Keck, *J. Appl. Phys.*, **28**, 882 (1957).
18. Schafer and Morcher, *Angew. Chem.*, **68**, 583 (1956).
19. Schafer and Morcher, *Z. anorg. u. allgem. Chem.*, **29C**, 279 (1957).
20. A. C. Loonam, *This Journal*, **106**, 238 (1959).
21. W. C. Schumb and R. C. Young, *J. Am. Chem. Soc.*, **52**, 1464 (1930).

Imaging-Furnace Developments for High-Temperature Research

Peter E. Glaser

Arthur D. Little, Inc., Cambridge, Massachusetts

ABSTRACT

The principles of imaging furnaces using the sun or a high intensity electric arc are presented. The performance of imaging furnaces with the two energy sources are contrasted and the relative advantages of each source are pointed out. Details on arc performance and construction are given. Advances in instrumentation for measuring and controlling temperature and heat flux are described. The function of a flux distributor to obtain larger uniformly heated area is explained.

The goal of high-temperature research is to obtain a better understanding of the behavior of materials under conditions of extreme temperatures. Therefore, means had to be found to generate high temperatures under controlled conditions in the laboratory. Among the approaches for generating high temperatures are those relying on heat transfer by a gas, induction heating, or resistance heating, and those using only radiant heating by means of an imaging furnace.

The imaging furnace, an optical system to concentrate radiation from a suitable heat source, has been found a useful research tool in studies of high-temperature phenomena. In an imaging furnace, the heat source is far enough from the sample to transmit heat by radiation only and not by conduction or convection. The advantages of this method are freedom from contamination of the sample (both by furnace vapors and a sample container), the possibility of studying the behavior of the material in either air or a controlled atmosphere, and the ease with which instruments can be brought close to the sample without being subjected to excessive heat.

Imaging Systems

During the past few years, solar furnaces, using the sun to provide radiant energy, have created considerable interest (1), although their dependence on the weather has restricted their applications. The substitution of an artificial source to permit the use of an imaging furnace inside a laboratory has been found to offer definite advantages (2). The development of new high-intensity electric arcs (3) has provided radiant-energy-producing capabilities beyond those found in a solar furnace.

Figure 1 shows the possible arrangements by which the source can be imaged onto a sample. A single paraboloidal mirror (4) and a paraboloidal mirror in combination with a flat mirror (5) have been used to image the sun onto the sample. Ellipsoidal-(6) and paraboloidal-mirror combinations (7) have been used in conjunction with electric arcs. An optical system using an ellipsoidal mirror with the source located at the major focal distance (8) produces a reduced image and the highest flux density, while a refractive system (9) is capable of giving a uniform image irradiation. The two-paraboloidal-mirror and two-ellipsoidal-mirror systems have found wide usage; two-ellipsoidal mirrors have some advantage in convenience of controlling the radiation.

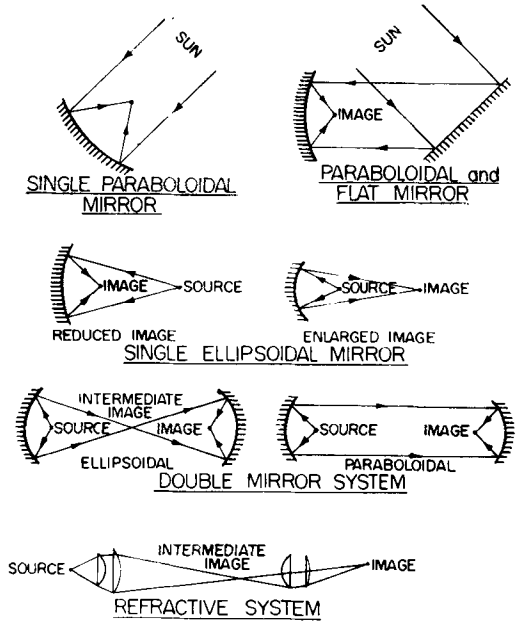

Fig. 1. Optical systems of imaging furnaces

The choice of optical system and imaging source depends on the desired characteristics of the image. A single mirror tends to have the least transmission loss, and, if the location of the source is transposed, either an enlarged or reduced image can be obtained. In addition to the type of image obtained (as determined by the optical system), the radiation flux density, distribution of the flux density at the focal zone, and fluctuation in the source output influence the usefulness of an imaging furnace.

When the sun is used as the radiation source, the flux density at the image is determined by the amount of radiation that reaches the collecting mirror system after absorption by the atmosphere (about 1.3 cal/cm^2/min). Because of the limited output of this radiation source, considerable effort had to be expended in establishing the optimum size and geometry (10) of the collecting mirrors so that a high image flux density could be attained.

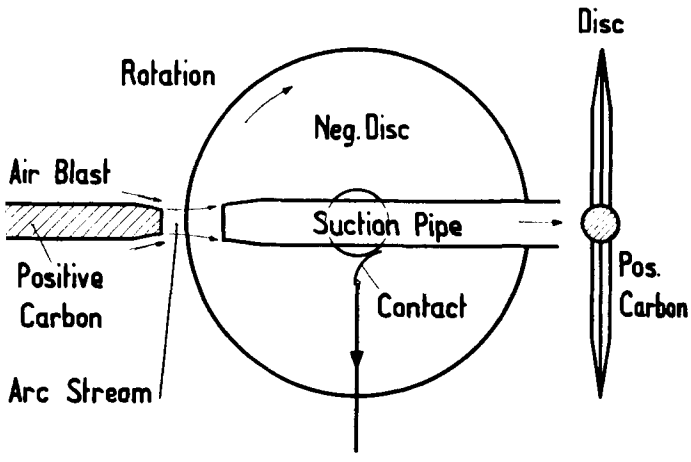

Fig. 2. Blown arc arrangement

Electric-Arc Sources

The electric arcs that have been used in imaging furnaces are of the Beck (11) type. The outstanding visible characteristic of this high-intensity electric arc is a jet of gaseous material ejected from the anode crater in the form of a vertical tail flame. The flow velocity and flow direction of this tail flame are determined by internal electromagnetic fields and thermal effects. These vaporized anode components, comprising atoms, ions, and possibly some diatomic molecules, radiate very strongly; their steady-state behavior depends on the current density. Much of the radiation that emanates from the gaseous materials of the tail flame is lost, since it cannot be concentrated into an image. A considerable improvement over the conventional high-intensity electric arc is represented by the Gretener (12) blown arc. Figure 2 shows the mechanism by which a blown arc is obtained. Tangential air jets surrounding the anode direct a conical stream of air inward toward the arc. In this manner, the gaseous materials are concentrated in the form of a cylinder of brilliantly glowing gases. In addition, the air jets surrounding the anode cool the outside surface thus allowing a higher current density without an increase in carbon consumption.

Operational Requirements

Operational requirements and experimental procedures may determine the type of source and optical system of an imaging furnace. The spatial distribution of the radiant flux density at the focal zone of the collecting mirror must be considered; it has been shown to follow approximately a Gaussian distribution (13). A useful parameter describing it is the radial distance from the optical axis at which the flux density has dropped to 90% of that measured on the axis. The nature of the optical system and the size and type of source determine what this radial distance will be.

Although a maximum image flux density is desirable, a constant flux density at the image plane is necessary. When the sun is used as the radiation source, nearly ideal constant conditions prevail at the image; no other source has been able to produce equivalent conditions.

Constancy of flux density is influenced by nonuniform composition of the arc electrodes, irregular burning of the electrodes (caused by the effects of magnetic fields), variations in the supply of voltage, unsatisfactory electrode feed devices and controls, and an unstable arc (caused by an excessive current density). The positioning of the positive carbon in the focal plane of the source mirror is critical; a movement of ⅛ in. from the electrode focal plane can cause a change of 10% in the flux density at the image.

The duration of an experiment to be performed in an imaging furnace may influence the selection of a source. Theoretically, the sun provides the longest daily operating time for an imaging furnace, but actually, this time depends on the location of the furnace and on the weather. In the northern latitudes, atmospheric conditions may limit the number of uninterrupted operating hours available; the electric arc offers a better alternative when continuous use of the imaging furnace is desired.

Considerable improvements have been made in the structure of electrodes (14) for improving the performance of electric arcs, particularly the blown arc. The improved carbon electrodes have a cored structure designed to prevent disturbing light fluctuations when the arc is being burned. A suitable electrode has a double-cored construction. The inner core contains rare earth compounds that provide a high intensity of light; the proportion of rare earth in the outer core is greater than that in the inner core. Experimentally produced electrodes using this construction allow a far greater current density to be employed and thus make possible a higher flux density.

At lower current densities, electrodes may have to be replaced in about 20 min, while at higher current densities, they may have to be changed in about 5 min. Disk cathodes can operate for several hours.

ADL-Strong Arc-Imaging Furnace

A double-ellipsoidal-mirror system has been designed on the basis of requirements posed by high-temperature research procedures. This system offers an excellent compromise between the requirements of high-radiation flux density, large image size, temperature control, duration of the radiation pulse, and flexibility for experimental measurements. Figure 3 is a diagram of the ADL-Strong arc-

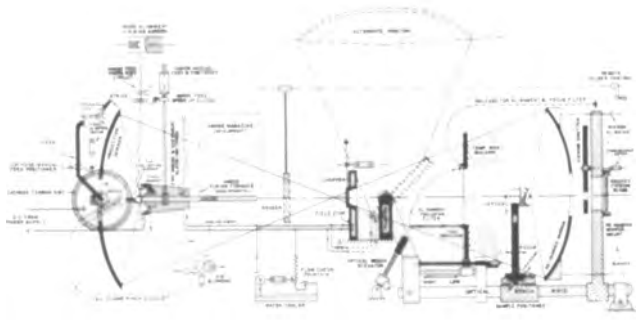

Fig. 3. Diagram of ADL-Strong arc imaging furnace

imaging furnace. The arc source is a Gretener-type arc with a 10-mm rod anode and a carbon-disk cathode. An auxiliary 6-in. diameter collecting mirror located behind the anode reflects a portion of the radiation to the main source mirror. Two ellipsoidal 21-in. diameter mirrors are used; these can be operated with the optical axis in either a horizontal or vertical position by the insertion of a flat diagonal mirror. With the optical axis in the vertical position, it is possible to melt powders and study liquid phases, with the parent materials forming the container.

Temperatures of the sample are controlled by a temperature modulator that consists of a sliding aperture with remote electric controls. An alignment and focusing disk forms part of the modulator and enables the mirrors to be aligned on the optical axis and a sample to be located in the focal plane. The sample is mounted on a positioner that permits tri-axial movement through remote electric drives. Two shutters are used, one located near the intermediate image, and the other just behind the opening in the collecting mirror. The purpose of these shutters is to permit the separation of incident and reflected radiation from the sample as well as to allow a specific radiation pulse to be obtained. The power required by the arc is 180 amp continuous to 300 amp intermittent at 75 v and is supplied by a selenium rectifier.

Measurement Techniques

Once the capability of generating high temperature with an imaging furnace had been developed, the need arose to have instruments available for the measurement of physical parameters, particularly heat flux and temperature.

Heat Flux

Calorimeter.—Figure 4 shows the cross section of the calorimeter (15), designed to meaure heat flux reaching the focal zone of the collecting mirror, where the energy arriving over a 140-degree solid angle is accumulated inside a black-body cavity

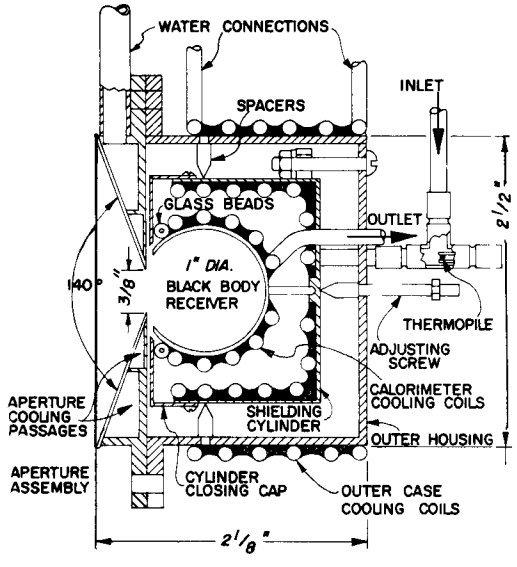

Fig. 4. Cross-section of calorimeter

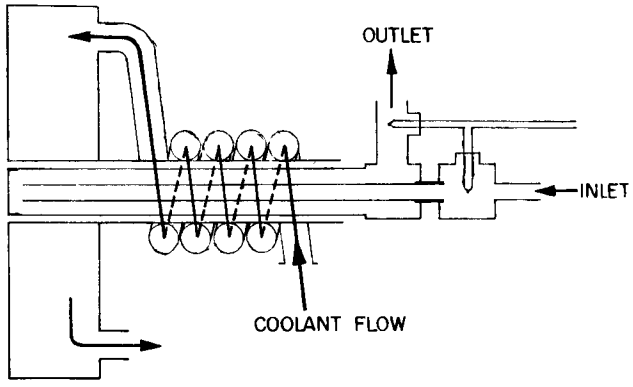

Fig. 5. Cross section of calorimeter

and transferred to the circulating water; this energy is calculated from measurements of the temperature rise and quantity of water flowing. The device is designed with an accuracy of ± 5% and has been used as our basic calibrating calorimeter.

Figure 5 shows a cross section of the water-cooled calorimeter used to measure the radiation over 180-degree solid angle. The measuring area of the calorimeter is blackened and water-cooled, and the temperature rise and quantity of water flowing is measured. This type of calorimeter requires calibration, since some of the incident energy is radiated again at the front surface.

Radiometer.—The two calorimeters described measure the total radiation received over a specific diameter at the focal plane. In some instances, it may be of interest to measure the maximum flux density (rather than the average flux density) as well as the flux distribution across the focal plane.

Figure 6 shows a circular-foil radiometer (16). The receiving area of this water-cooled radiometer is 0.9 mm in diameter. Since it has a very short time constant, the measurement of rapidly varying fluxes or of the continuous traversal of the focal plane can be accomplished. Figure 7 shows the cross section through the radiometer. A blackened, thin circular foil of constantan fastened to a water-cooled copper block absorbs the radiation, and a thin copper wire attached to the center of the circular foil measures the temperature rise at its center.

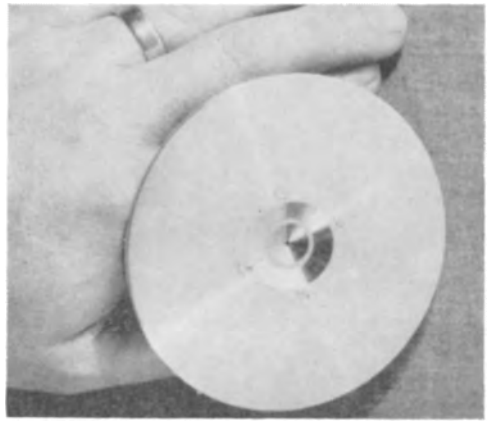

Fig. 6. Circular foil radiometer

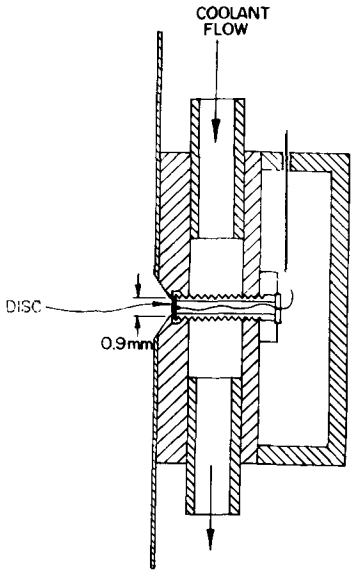

Fig. 7. Cross section of radiometer

The circular-foil radiometer calibrated with the absolute calorimeter can also measure the radiation flux density at the focal zone. Figure 8 shows the flux distribution obtained in both the solar furnace and the arc-imaging furnace with the radiometer. Also shown are the instantaneous flux variations recorded by the radiometer in the arc-imaging furnace; these variations are of the order of ± 5%. Improvements in the electric feeding device, the power supply, and the uniformity of the electrode are expected to further reduce the flux variations.

When a short-time radiation pulse is to be used, conventional calorimeters cannot be applied use-

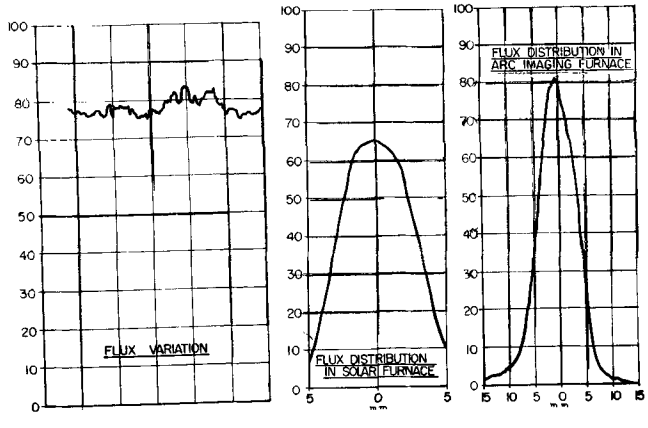

Fig. 8. Flux distribution and variation

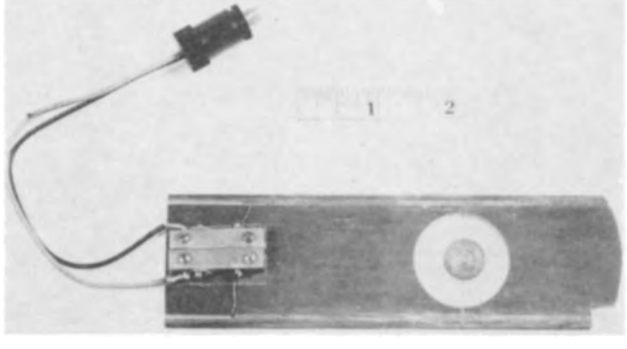

Fig. 9. Copper disk calorimeter

Table I. Performance data ADL-Strong arc imaging furnace

Device	Flux, cal/cm² sec	Equiv. black body temp, °K	Amp @ 75 v d.c.	Anode carbon type
Radiometer				
1 mm diam	265	3750	300	Experimental "Ultrex"
	225	3600	155	Modified "Ultrex"
Calorimeter				
9.5 mm diam	220	3550	300	Experimental "Ultrex"
	145	3240	155	Modified "Ultrex"

fully. Instead, a copper disk is suspended by thin wires, and its temperature is measured by a thermocouple after calibration with the calorimeter (Fig. 9).

Table I shows the performace data of the ADL-Strong arc-imaging furnace. Although in prior work 4000°K (obtained from calorimetry) was reported as the highest value attained, the lower temperatures measured in the ADL-Strong furnace are partially attributed to the use of second surface-collecting mirrors.

Temperature Measurements

Conventional optical pyrometers measure accurately only the temperatures of a black body (17), a condition that few samples are able to satisfy. Although drilling small holes into the sample surface to approximate black body conditions is valid theoretically, this expedient raises questions concerning the uniformity of cavity temperatures and may not be feasible with some of the samples to be tested.

The optical pyrometer can be used for accurate temperature measurements in an imaging furnace if suitable shutters are provided for separating emitted and reflected radiation. Radiation emitted by, or reflected from, the sample is observed with an optical pyrometer sighted through a hole at the center of the collecting mirror (Fig. 3). The shutter located near the intermediate image position rotates about an axis that is slightly displaced from the optical axis of the ellipsoidal mirrors and periodically shields the sample from the arc radiation. An off-axis shutter behind the collecting mirror is provided with a small opening that coincides with the optical axis; it is driven in synchronization with the previous shutter by means of synchronous motors. The field coils of the motors are connected in such a manner that the two shutters can be either in phase or out of phase. In the in-phase position, only radiation emitted by the sample is observed, since all other radiation is prevented from reaching the sample. In the out-of-phase position, both emitted radiation and the arc radiation reflected from the sample are observed.

The apparent surface temperature of the sample is measured with the two shutters rotating in phase. A second temperature is then measured with the shutters out of phase. Kirchhoff's equation relating reflectivity to emissivity can then be used to deter-

mine the approximate spectral emissivity; once this is known, the true temperature can be calculated

$$\frac{1}{e^{C_2/\lambda T_{p1}} - 1} = K \frac{\epsilon(\lambda,T)}{e^{C_2/\lambda T_M} - 1} \qquad [1]$$

$$\frac{1}{e^{C_2/\lambda T_{p2}} - 1} = K \frac{\epsilon(\lambda,T)}{e^{C_2/\lambda T_M} - 1} + \frac{K[1 - \epsilon(\lambda,T)]}{e^{C_2/\lambda T_s} e - 1}$$

$$\epsilon(\lambda,T) = 1 - \frac{1}{K}\left(\frac{1}{e^{C_2/\lambda T_{p2}} - 1} - \frac{1}{e^{C_2/\lambda T_{p1}} - 1}\right)(e^{C_2/\lambda T_s} e - 1)$$

$$T_M = \frac{\lambda}{C_2} \ln^{-1}\left[1 + K\epsilon(\lambda,T)\,(e^{C_2/\lambda T_{p1}} - 1)\right] \qquad [2]$$

The first equation relates the in-phase apparent temperature of the sample to the true sample temperature. The second equation relates the out-of-phase apparent temperature to the sample temperature and to the effective temperature of the arc source. The last term in this equation represents the reflected arc radiation received by the pyrometer.

An effective arc temperature must be used in the equation in place of the arc temperature, because the mirrors of the imaging furnace are not perfect reflectors and do not have perfect geometry. These imperfections reduce the spectral brightness of the arc image. For determination of the effective arc temperature, a plain mirror is placed about 2 in. in front of the focal zone, and the apparent temperature of the arc image is measured with an optical pyrometer provided with suitable filters. These equations can then be solved simultaneously to give a value of the spectral emissivity. The value of the emissivity is then used with the first equation so that a true temperature accurate to 5% is obtained. A comparable measuring procedure has been used to measure cathode temperatures in a cavity (18).

A modified optical pyrometer allows the measurement of temperatures automatically and provides a record of temperature variations occurring as fast as 1/100 of a second.

Flux Uniformity

The optical system used in an imaging furnace determines the spatial distribution of the radiant flux density. With the two-ellipsoidal-mirror system, a high flux density over a limited image size is obtained (Fig. 8). At times it may be desirable to enlarge the image area and, instead of a Gaussian distribution, to obtain a uniform distribution over a larger area. The usefulness of defocusing (19) depends to a large extent on the type of optical system; defocusing is usually accompanied by a decrease in uniformity even as the image size increases. Although optical systems to obtain larger images with a uniform distribution have been developed (20) low flux densities usually result. To meet the requirements for either a high temperature over a small area or a uniform flux distribution over a large area, a flux redistributor was developed. This flux redistributor (Fig. 10) can be placed in front of the focal plane of the imaging furnace; it provides a uniform distribution over a fairly large image area. By using this instrument, we were able to concentrate 20 cal/cm²/sec over a ⅝-in. square area; Figure (11) shows the increased uniformity of burned patterns when the redistributor is used; Fig. 12 shows the pattern without the flux redistributor. This device intercepts the flux by means of four mirrors and redistributes it onto the sample plane in a uniformly illuminated area.

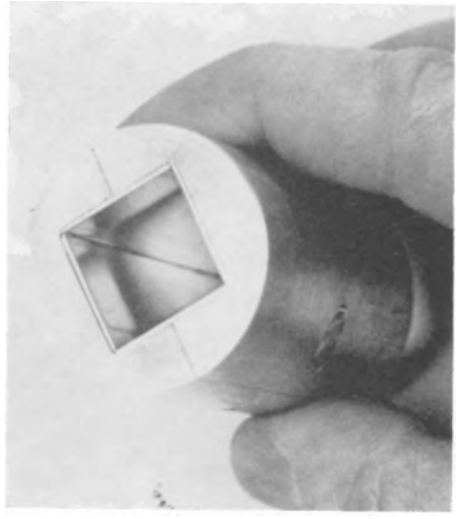

Fig. 10. Flux redistributor

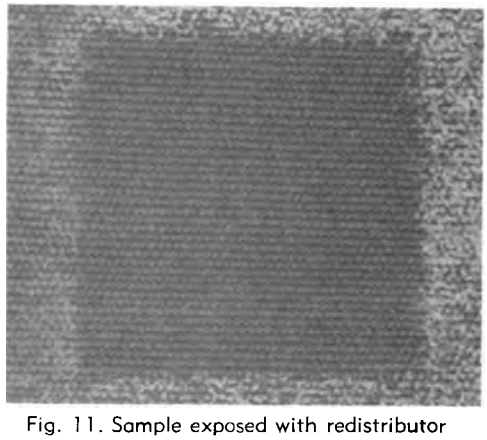

Fig. 11. Sample exposed with redistributor

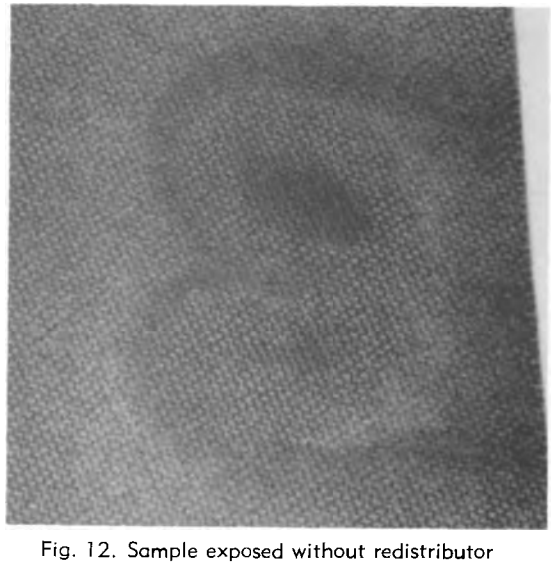

Fig. 12. Sample exposed without redistributor

The effect of a nonuniformity in the energy beam is almost completely eliminated by the use of the flux redistributor. If U_m is the maximum nonuni-

formity expressed as a percentage of the flux distribution without a flux redistributor, then with the redistributor the nonuniformity is given by:

$$U < \frac{S_a}{100} U_m$$

where S_a is a shadow attenuation function depending on the ratio of length to inside dimension and on the reflectivity of the inside surfaces of the flux redistributor.

Conclusions

The use of imaging furnaces for the radiant heating of materials has been of considerable interest to many researchers. Because of the newness of the device, however, the lack of instrumentation, and the nonexistence of well-defined experimental procedures, its applications have not as yet been widespread. As more information accumulates, its advantages and drawbacks will become more fully appreciated and its usefulness demonstrated in a greater number of research projects. As is the case with many new research tools, it cannot be expected to solve all high-temperature-research problems; rather, it will be applicable to those research projects where the ingenuity of the experimenter and experimental requirements make it invaluable.

Acknowledgments

The author would like to thank the members of the staff of Arthur D. Little, Inc., and Strong Electric Company, Toledo, Ohio, for their interest, help, and cooperation in the design, instrumentation, and manufacture of the arc-imaging furnace. Particularly noteworthy were the designs worked out by F. Chellis, the development of the flux redistributor by M. Chen, and the temperature-measurement methods developed by H. Blau. C. Warner, A. Camus, and J. Lund made valuable contributions to the measurements of heat flux and helped make the ADL-Strong arc-imaging furnace a safe and dependable research tool.

Manuscript received July 22, 1959. This paper was prepared for delivery before the Philadelphia Meeting, May 3-7, 1959.

Any discussion of this paper will appear in a Discussion Section to be published in the December 1960 JOURNAL.

REFERENCES

1. Proceedings of the 1957 Solar Furnace Symposium, *J. Solar Energy, Science and Engineering*, **1**, April-July (1957).
2. P. E. Glaser, High Intensity Arc Symposium, p. 71, The Carborundum Co., Niagara Falls, N. Y. (1958).
3. W. Finkelnburg and J. P. Latil, *J. Opt. Soc. Am.*, **44**, 1 (1954).
4. W. M. Conn, *Am. Ceram. Soc. Bull.*, **33**, 69 (1954).
5. F. Trombe, *J. Solar Energy, Science and Engineering*, **1**, 9 (1957).
6. M. R. Null and W. W. Lozier, *Rev. Sci. Instr.*, **29**, 163 (1958).
7. J. Farber, Symposium on High Temperature, Stanford Research Institute, Menlo Park, Calif. p. 1 (1956).
8. M. R. Null and W. W. Lozier, To be published *J. of SMPTE*.
9. T. R. Broida, U. S. Naval Radiological Defense Laboratory Report, USNDRL-417 (1952).
10. N. K. Hiester, *et al., Jet Propulsion*, **27**, 507 (1957).
11. F. Beck, D. R. Pat., 262913, March 1910.
12. E. Gretener, *J. of SMPTE*, **55**, 391 (1955).
13. G. A. Swope and F. C. Henriques, Report TOI 54-8, Technical Operations, Inc., Arlington, Mass. (1954).
14. C. E. Greider, U. S. Pat. 2,797,351, June 25, 1957.
15. P. E. Glaser, *Rev. Sci. Instr.*, **28**, 1084 (1957).
16. R. Gardon, *ibid.*, **24**, 366 (1953).
17. A. G. Emslie and H. H. Blau, *This Journal*, **106**, 877 (1959).
18. C. H. Prescott, "Temperature: Its Measurement and Control," p. 1199, Reinhold Publishing Co., New York (1941).
19. R. de La Rue, *J. Solar Energy, Science and Engineering*, **1**, 94 (1957).
20. R. Gardon, *Rev. Sci. Inst.*, **25**, 459 (1954).

Metal Mists and Aluminum Losses in the Hall Process

Warren E. Haupin

Alcoa Research Laboratories, New Kensington, Pennsylvania

ABSTRACT

Reaction of aluminum with Hall cell electrolyte forms aluminum monofluoride and sodium which dissolve in some form to give the bath a reducing capacity equivalent to a free aluminum content of about one tenth per cent. The so-called "metal mist" forms in the presence of moisture and consists of hydrogen bubbles containing a small partial pressure of aluminum monofluoride, sodium, and sodium tetrafluoroaluminate. Increasing the NaF/AlF_3 ratio of the electrolyte increases the sodium and decreases the aluminum monofluoride partial pressure, but sodium has a much higher partial pressure; hence, a low NaF/AlF_3 ratio is desirable to minimize metal reoxidation. Carbon dioxide is abundant in the anode gas of a smelting cell and is soluble in the bath. It oxidizes the free metal both in and over the bath. The rate of this reoxidation appears to be controlled by the rate of diffusion and convection of dissolved metal away from the metal-bath interface.

Almost any oxygen-containing gas, including water vapor, is reduced when it is bubbled through Hall bath (87% $NaF-AlF_3$ of various NaF/AlF_3 ratios, 8% CaF_2, 5% Al_2O_3) when the electrolyte is contacting aluminum, thereby indirectly oxidizing the aluminum. The mechanism of the aluminum reoxidation, the composition of the "mist" or "fog" that forms, and even the question of whether acid bath (excess AlF_3 over the cryolite composition) or alkaline bath (excess NaF) causes the greater metal loss have, however, been the subject of considerable controversy (1-16).

Various investigators have reported the fog to be sodium (4-9), aluminum (10-13), aluminum monofluoride (16), aluminum carbide (19), hydrogen (14,15), or some combination of these. The apparent composition of the fog was influenced by the method used to identify the fog. Investigators immersing copper strips in bath, held over aluminum, picked up aluminum in the copper, which has a high solubility for aluminum. They interpreted this as indicating the mist was aluminum. However, investigators similarly using lead, which has a high solubility for sodium, found that the lead picked up sodium.

Composition of Mist

A mist must be a separate phase, but bubbles of sodium vapor or aluminum monofluoride vapor were ruled out by thermodynamic considerations, for these vapors cannot exist at 1 atm pressure at the bath temperature in contact with molten cryolite. Thermodynamics did not rule out the presence of these gases at a much lower partial pressure, but this presupposed the presence of some other gas. There was also the possibility of a mist of finely divided aluminum suspended in the cryolite, and mechanisms for obtaining such suspensions have been postulated (12,13).

To start the present investigation, it was thought desirable to extend Grjotheim's investigation (14) of metals which form a mist in Hall baths. At 980°C in a graphite crucible, it was found that a mist formed when magnesium, aluminum, sodium, or zinc was added to the bath. Sodium and zinc caused a violent bubbling when added, but a foggy appearance remained for 15 to 30 min after the bath became still. The bath remained clear when tin, nickel, lead, copper, or silver was added. The metals that made a mist were all metals capable of displacing hydrogen from water. Since sodium and zinc were above their boiling points, it might be claimed that the mist was vapors of these metals. The other mist formers, however, were well below their boiling temperatures.

Operators of the Hoopes-type aluminum refining cells claimed that the bath in their cells did not form a mist. To investigate this and to observe the effect of lowering the sodium ion concentration of the bath, melts were prepared of the following compositions by weight:

Bath 1—30% BaF_2, 21.5% AlF_3, 37.5% Na_3AlF_6, 11% MgF_2
Bath 2—18% BaF_2, 21% AlF_3, 45% Na_3AlF_6, 16% CaF_2
Bath 3—26% AlF_3, 58% Na_3AlF_6, 16% CaF_2
Bath 4—100% Li_3AlF_6

These baths all formed a mist when aluminum was added. The most logical explanation for the bath in commercial refining cells being free from mist is that the bath had a layer of molten aluminum floating on its surface and was thereby protected from absorbing moisture.

Local cell action.—The loss of aluminum when held under fused salts in Pyrex was studied. No loss of metal was found in pure NaCl-KCl eutectic at 750°C. With the addition of 10% Na_3AlF_6 both chemical and electrochemical solution of aluminum occurred. Electrochemical solution was obtained by placing a graphite rod into the bath and contacting the aluminum. The rate of electrochemical solution was controlled by polarization of the carbon and took a carbon area approximately six times the metal area to obtain double the rate of chemical solution. A

tenfold increase in metal loss was obtained with a carbon area roughly 30 times the metal area.

Loss in inert crucibles.—To determine if mist formation in the Hall bath was the result of electrochemical action and rule out the carbide mist theory, neutral Hall bath and bath No. 3 were each melted in crucibles of sintered alumina, silicon nitride, and magnesite, respectively. These baths formed a mist upon the addition of aluminum, regardless of the crucible used.

To eliminate completely any crucible effect or local cell action, a pool of molten bath was melted in a pile of powdered Hall bath using radiant energy from an electric arc in argon between tungsten electrodes. The molten bath held in solid bath was clear. A 0.1 mg piece of aluminum was dropped in the pool. It moved about by convection currents and left a trail of mist reminding one of the tail of a comet. Eventually, the aluminum was consumed. When a 1 mg piece of aluminum was added, it rested on the bottom and a mist rose in streamers. A 1-g piece completely fogged in the bath. Since no carbon was present in the system, these tests ruled out the carbide mist theory. They also indicated that no electrolytic cell action was necessary for mist formation. Based on the foregoing evidence Grjotheim's conclusion was accepted: that a mist of hydrogen forms by the reaction between free metal and moisture that dissolves in the bath.

Howard (18) has shown that a vapor of sodium tetrafluoro aluminate ($NaAlF_4$) exists over molten cryolite. Therefore, one must conclude that the hydrogen bubbles will have a small partial pressure of $NaAlF_4$.

Formation of a Hydrogen Mist

While the tests just described gave indirect evidence of a mist of hydrogen, they did not prove that hydrogen was the only source of mist. Grjotheim (15) suggested that polynuclear metal ions may cause a foggy appearance. A more quantitative test was designed therefore to ascertain if hydrogen was the only source of fog or mist. Baths of the desired composition were mixed as dry powdered reagent grade chemicals and added to a crucible at the bottom of a sealed retort, as shown in Fig. 1. The bath was dried at 200°C for 12 hr, then melted and held at 980°C. Dry argon was flushed continuously through the retort at 100 cc/min. The retort had a replaceable copper sleeve extending from the top of the crucible to the top of the retort, a distance of 12 in. Metallic vapors condensed and partially alloyed with this sleeve. Some metal condensed also on and in the gas inlet and outlet tubes. The top of the retort was water cooled to protect the "O" ring seals and to cool the upper part of the copper sleeve. The escaping gases passed consecutively through an electrostatic precipitator to remove particulate matter, sodium fluoride pellets to remove HF, magnesium perchlorate to remove moisture, ascarite to remove CO_2, hot copper oxide to oxidize CO to CO_2 and hydrogen to water, magnesium perchlorate to absorb the oxidized hydrogen, and finally ascarite to remove CO_2 oxidized from CO. The absorption chambers

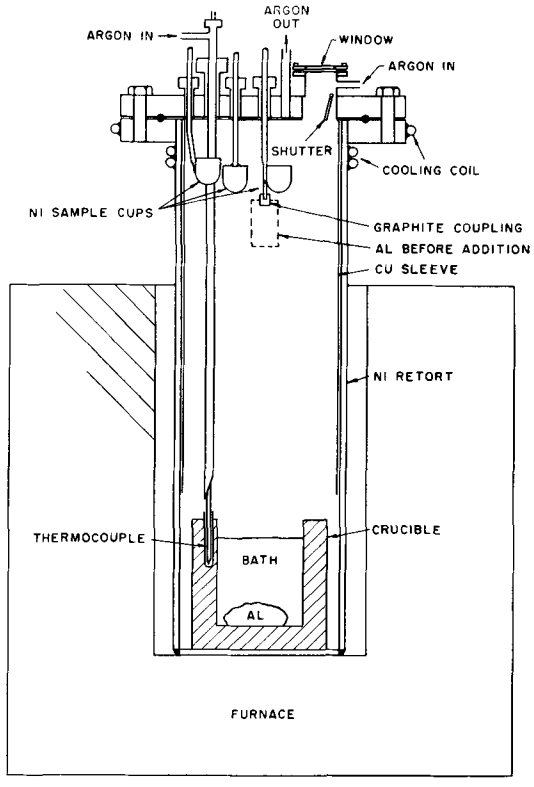

Fig. 1. Sealed system for metal mist tests

were weighed periodically during the test. Also, throughout the run, observations were made of the mist in the bath through a glass window equipped with a shutter and wiper operated through "O" ring seals. Bath samples were taken and metal addition made by control rods operated through "O" ring seals so that the system was never open to the atmosphere.

As soon as the bath became molten, bath sample No. 1 was taken. Then 100 g of aluminum were added to the remaining 750 g of molten bath. As soon as the metal melted, the bath became fogged and the surface was agitated by escaping gas bubbles. After ½ hr, the time of maximum hydrogen evolution determined by weight gain of the absorption bottle, bath sample No. 2 was taken. Since it was difficult to see clearly enough through the window to be sure of the complete absence of mist, duplicate runs were made of the first three tests. The retort was opened after 72 hr, at which time all measurable hydrogen evolution had stopped. The bath, at this time, was in each case found to be mist-free. The taking of bath sample No. 3, therefore, was set at 72 hr. Table I gives the results. The free metal in the frozen bath samples was determined by hydrogen evolution with HCl and is reported in equivalent per cent free aluminum. Both hydrogen and methane were frequently evolved. The methane, assumed to have come from Al_4C_3, represented 0-0.24% Al_4C_3 by weight in the bath. There was no correlation between the evolution of methane and the presence of mist or the NaF/AlF_3 ratio of the bath.

An attempt was made to analyze the frozen bath samples separately for metallic sodium and metallic aluminum by vacuum distillation and by mercury extraction. No free aluminum or sodium was found

Table I. Results of bath sample No. 3

Bath molten (length of time)	10 min	40 min	72 hr
Aluminum present under bath	No	Yes	Yes
Bath appearance	Clear	Fogged	Clear
H_2 evolution	None	0.2-0.25 ml/min	None
Reducing power of bath, as equivalent % free aluminum			
With 3.6%* AlF_3 in bath	0.00%	0.08%	0.09%
With neutral bath	0.00%	0.11	0.10
With 11.5%* NaF in bath	0.00%	0.12	0.11

* Initial composition, by weight.

Table II. Weight loss (in grams) of aluminum

Crucible	C	C	C	BN	SiC
NaF/AlF_3 wt ratio, start	1.34	1.50	1.86	1.50	1.50
NaF/AlF_3 wt ratio, end	1.14	1.34	1.31	1.43	ND[3]
Aluminum losses as					
Na condensate	3.1 g	5.5 g	10.0 g	0.2 g	ND[5]
Al condensate	0.8	0.6	0.4	0.5	ND[5]
Carbide	5.7	2.5	3.7	0	ND[4]
Into crucible	1.1	0.6	0.8	ND[2]	ND[2]
Oxidized by H_2O	0.5	0.4	0.4	1.3	1.6
Na+AlF dissolved in bath	0.6	0.7	0.8	ND[3]	ND[3]
Total Al loss	11.8	10.3	16.1	ND	ND
Weighed loss of Al[1]	11.1	11.3	16.9	5.1	15.9

ND—Not determined.
[1] Weight loss is not accurate because of difficulty in separating adhered bath from aluminum.
[2] Did not want to sacrifice expensive crucible.
[3] Previous data appeared sufficient.
[4] Difficult to obtain in carbide system.
[5] Cu condensing sleeve became detached during run.

by either method, but this was attributed to faulty technique. It is planned some time in the future to make a more detailed study of these techniques.

An apparent separation of the aluminum and sodium was obtained by hydrogen evolution, using first water and then a sodium hydroxide solution. The first evolution was assumed to represent metallic sodium, again correcting for any methane evolution. When all evolution stopped, sufficient NaOH was added to the water to make a 10% NaOH solution. The second evolution was assumed to represent aluminum. Hall bath with a NaF/AlF_3 weight ratio of 1.5 showed 0.16% Na and 0.05% Al by this technique, while bath with a NaF/AlF_3 ratio of 1.3 showed 0.10% Na and 0.05% Al. These results were not exactly consistent with Table I or with theory. Theory would lead one to expect a higher aluminum concentration in the second bath sample, for AlF in the molten bath should decompose to Al and AlF_3 in the frozen bath samples. It was feared that water was giving some evolution from the aluminum. Because of this, no great reliance is placed in this method of separately analyzing for Al and Na.

A mist or fog was present only when hydrogen was being evolved. No second type of mist suspected by Grjotheim was found. No hydrogen was evolved until aluminum was added. Upon addition of aluminum, free metal was found in the bath and a mist formed. After 72 hr, hydrogen evolution had stopped, but the bath still contained free metal. Later we shall see that the free metal in solution creates a vapor pressure of aluminum monofluoride and sodium over the bath. The metal loss through reaction with moisture apparently depended on how dry the bath and crucible were initially.

Metal Losses

Table II gives the weight loss in grams of the aluminum and shows the various ways in which this aluminum was lost. The aluminum loss into the crucible was determined by a chemical analysis of the crucible for calcium, sodium, aluminum, fluorine, and aluminum carbide, all corrected for a blank of the crucible before the test. The aluminum loss into the crucible was taken as the excess of metal ions over the fluoride ion on an equivalent basis. The total carbide figure included both the carbide on the crucible and adhering to the aluminum. The aluminum loss by reaction with moisture dissolved in the bath was determined by the hydrogen evolution from the system. The aluminum loss as a vapor escaping from the bath was determined by chemical analysis of the copper shield and gas inlet and exit tubes and the condensate adhering to them. Both free aluminum and sodium were found. Naturally, much of the sodium condensing did not alloy with the copper and burned when the retort was opened. Care was taken to minimize the loss of sodium oxide fumes and the sodium that burned was determined from the sodium oxide formed.

Aluminum and Sodium Vaporization

Perhaps the manner in which the sodium and aluminum condensate varied with bath ratio, shown in Table II, is even a more significant finding than the composition of the fog. Metallic sodium in the vapor over the bath probably is accounted for by the equilibrium:

$$\underset{\text{(lig)}}{Al} + \underset{\text{(bath)}}{Na_3AlF_6} \rightleftharpoons \underset{\text{(bath)}}{3Na} + \underset{\text{(bath)}}{2AlF_3}$$

$$\downarrow\uparrow\ 3Na$$

$$\text{(p in argon)}$$

The vapor pressure of aluminum is too low to account for the transfer of aluminum. The most plausible explanation for the aluminum transfer is that the aluminum was carried as aluminum monofluoride vapor through the following sequence of reactions:

$$\underset{\text{(lig)}}{2Al} + \underset{\text{(bath)}}{AlF_3} \rightleftharpoons \underset{\text{(bath)}}{3AlF} \rightleftharpoons$$

$$\underset{\text{(p in argon)}}{3AlF} \rightarrow \underset{\text{(Cu alloy)}}{2Al} + \underset{\text{(solid)}}{AlF_3}$$

To check this theory a ⅛ in. diameter copper rod was sealed in a graphite capsule 1 in. OD x 2 in. long with ⅜ in. thick walls. The air in the pores and cavity of the capsule was replaced with argon by placing the capsule in the chamber, evacuating, and then filling with argon. The capsule was then

floated on molten bath for 24 hr. After the test the capsule was broken open. No bath penetrated the capsule, but the surface of the copper rod was covered with a white powder that was found by x-ray diffraction to be AlF_3. The copper rod had assumed the color of yellow brass and qualitative spectrographic analysis showed it to have picked up between 1 and 10% aluminum. This was taken as evidence of a sizable vapor pressure of aluminum monofluoride over the bath.

In the foregoing reasoning it was assumed that aluminum monofluoride and sodium were soluble in some form in the bath, otherwise there appeared to be no mechanism for carrying free metal from the pool of aluminum under the bath to the surface of the bath to generate a vapor pressure of aluminum monofluoride, and sodium. However, the dissolved species need not be aluminum monofluoride and sodium. Either would suffice, or any other appropriate species such as Al, Al^+, Na_2^+, or any combination of these. Through their respective equilibriums with the bath, these constituents would create a vapor pressure of aluminum monofluoride and sodium over the bath and give the bath an activity of aluminum monofluoride and sodium so that it would reduce carbon dioxide or moisture.

Since the argon flow was the same in all the metal holding tests, the ratio of the weights of aluminum and sodium condensed should, on a mole basis, be proportional to the partial pressures of the aluminum monofluoride and sodium over the bath. Even though the partial pressure of AlF was increased by a low NaF/AlF_3 ratio, sodium still had a higher partial pressure over the bath than AlF and apparently a higher activity in the bath. This to a large extent explains why acid baths give higher current efficiencies than neutral or alkaline baths.

The steps in the reoxidation of aluminum appeared to be: (*a*) a reaction at the metal-bath interface to give a solution of free metal or its equivalent in the bath, (*b*) diffusion and convection of the free metal away from this interface, (c) reaction between the free metal from the bath and carbon dioxide from the anode. Reoxidization of free metal by moisture cannot account for more than about 0.6% loss in current efficiency for unburned gas from commercial cells averages less than 1% hydrogen by volume.

Nozaki and Miyanchi (12), investigating industrial cells that were suddenly disconnected due to war action, found that the free metal concentration in the electrolyte varied from none near the anodes to the maximum near the metal pad. Bath samples taken in the static metal holding tests showed the equivalent of about 0.1% free aluminum. A sample of similar electrolyte taken 3 in. from the side of an anode and 3 in. above the metal pad of an operating cell showed only the equivalent of 0.02% free aluminum or about one fifth of the equilibrium value. A similar sample of electrolyte was taken and CO_2 determined as present. It appears from the concentration and distribution of free metal that the slow step in the reoxidation of aluminum in commercial cells is the transport of free metal from the cathode to the vicinity of the anode. This is confirmed further by the observation that greater anode-cathode separation improves current efficiency.

Solubility of CO_2 in Bath

Förland and Associates (17) have reported solubility of CO_2 in molten cryolite. This was confirmed by taking a quickly frozen sample of electrolyte, as described previously, from an operating cell and a similar sample as a blank from the sealed system. Both were heated to approximately 500°C in a vacuum and the gas evolved analyzed by a mass spectrograph. The 10-g sample of the bath from the reduction pot evolved approximately 21 μg of carbon dioxide. The sample from the sealed system evolved two micrograms of carbon dioxide. This was taken as confirmation of Förland's findings.

The fact that both sodium and carbon dioxide were present in the sample of electrolyte from a commercial cell indicates a highly nonequilibrium condition exists within the electrolyte. Apparently there are strata of dispersed and dissolved carbon dioxide and dissolved free metal which are being mixed and reacting.

Numerous other gases also were evolved from the sample of the electrolyte from the reduction pot. They are listed in Table III.

Other Sources of Aluminum Loss

Another major source of aluminum loss in these tests was the formation of aluminum carbide. There was some indication (Table II) that the carbide formation was more severe in acid baths, but the trend was not very distinct. The loss of free metal, probably mostly sodium, penetrating into the crucible accounts for most of the remaining metal loss.

Use of Crucibles Other than Carbon

A test in a boron nitride crucible showed an abnormally small aluminum loss. When the cell was opened and the bath poured, however, the metal pad was covered with a dark film. The test made in a silicon carbide (SiN bonded) crucible showed practically the same metal loss as in a graphite crucible. If the principal cause of metal loss were an electrochemical cell reaction between the aluminum and the carbon, then it would appear that the metal loss would be lower both with the SiC and BN crucibles because of the lower electrical conductivity of the crucibles. The fact that the loss was practically the same in SiC as in the graphite crucible would lead one to believe that, at least under the conditions of these tests, the solution of aluminum was predominantly chemical rather than electrochemical. Previ-

Table III. Gases evolved from a rapidly frozen 10-g sample of electrolyte from a reduction pot when reheated to 500°C in vacuum

Carbon dioxide	21 micrograms
Nitrogen	5
Carbon monoxide	4
Hydrogen	1
Sulfur dioxide	1
Water	1
Silicon tetrafluoride	0.1
Carbon disulfide	0.1

ous tests in Pyrex, using fluorides diluted by chlorides, showed the metal loss was increased by electrolytic cell action. Perhaps in the present case, carbide formation on the graphite crucible inhibited local cell action, or it could be that straight chemical reaction was fast enough to maintain the equilibrium concentration in the bath. Carbon dioxide bubbling through the bath in a commercial cell certainly will remove the free metals from the bath at a much greater rate. Under these conditions cell action to form sodium may become a factor. In the present test, the lower metal loss in the boron nitride crucible appeared to be associated with the presence of a boride film over the surface of the aluminum.

Conclusions

Molten Hall bath in contact with molten aluminum develops a reducing capacity equivalent to about 0.1% free aluminum dissolved in the bath. The presence of sodium and aluminum monofluoride vapors over the bath indicates solution of free metal in some form in the bath. The visible mist, on the other hand, is hydrogen formed by reaction between moisture and free metal dissolved in the bath. Naturally the bubbles contain a small partial pressure of Na, AlF, and $NaAlF_4$. Aluminum monofluoride and sodium vapors are evolved even from a clear, mist-free bath. Increasing the NaF/AlF_3 ratio of the bath increases the sodium loss and decreases the aluminum monofluoride loss. The aluminum monofluoride loss, however, is small compared to the sodium loss even from an acid bath. In an operating reduction cell the free metal concentration in the bath does not reach its equilibrium value in the bulk of the bath but varies from a maximum near metal pad to a minimum near the anode. This indicates that the process of diffusion and convection of free metal in the bath is the rate-controlling step in the reoxidation of aluminum.

Manuscript received July 6, 1959.

Any discussion of this paper will appear in a Discussion Section to be published in the December 1960 JOURNAL.

REFERENCES

1. R. Lorenz, *Z. Elektrochem.*, **13**, 582 (1907).
2. P. P. Fedotieff and Iljensky, *Z. Anorg. Chem.*, **80**, 113 (1913).
3. W. Jander and H. Herrmann, *ibid.*, **239**, 65 (1938).
4. T. G. Pearson and J. Waddington, *Discussion Faraday Soc.*, **1**, 307 (1947).
5. R. Schadlinger, *Alluminio*, **22**, 691 (1953).
6. A. Vajna, *La Matallurgia*, **44**, 585 (1952).
7. A. Vajna, *Alluminio*, **19**, 541 (1950).
8. A. Vajna, *ibid.*, **20**, 29 (1951).
9. E. Grünert, *Z. Elektrochem.*, **48**, 393 (1942).
10. E. Pruvot, *Alluminio*, **22**, 699 (1953).
11. E. Pruvot, *ibid.*, **22**, 721 (1953).
12. H. Nozaki and K. Miyanchi, *J. Chem. Soc. Japan* (Ind. Chem. Sec.), **51**, 3 (1948).
13. E. Vuignier, *Bull Soc. Franc. Electriciens, II*, **13**, 56 (1952).
14. K. Grjotheim, *Alluminio*, **22**, 679 (1953).
15. K. Grjotheim, "Contribution to the Theory of Aluminum Electrolysis," Kg 1. Norske Videnskab, Slelskabs, Skrifter 1956, Nr 5.
16. T. G. Pearson, "Chemical Background of the Aluminum Industry," Roy. Inst. Chem. Lect. Mono. Repts. No. 3 (1955).
17. T. Förland, H. Stroegraues, and S. Urnes, *Alluminio*, **22**, 631 (1953).
18. E. H. Howard, *J. Am. Chem. Soc.*, **76**, 2041 (1954).
19. Unpublished Alcoa Reports.

Anodic Precipitation of Tracer Manganese as Dioxide

Edward A. Heintz[1] **and L. B. Rogers**

Department of Chemistry and Laboratory for Nuclear Science,
Massachusetts Institute of Technology, Cambridge, Massachusetts

ABSTRACT

Quantitative recovery of carrier-free $10^{-9}M$ manganese (II) is possible from weakly acidic solutions. The use of lead dioxide as either a nonisotopic carrier or a chemical displacing agent makes possible high recoveries from more acidic solutions.

Electrolytic procedures for the recovery of radioactive tracers offer the advantages of being easily adaptable to remote control operation as well as being quite selective. The present study aimed to define conditions under which carrier-free manganese could be deposited quantitatively as the dioxide. In addition, the use of lead dioxide as a carrier (1) was examined because it enabled better recoveries to be made from solutions too acidic to permit deposition of tracer manganese dioxide alone.

The choice of lead as a carrier was also based on the ready availability of conditions (2) and mechanism (3) for its anodic deposition. The ability of thallium (III) oxide to carry manganese was investigated only briefly and was found, as expected, to be less satisfactory.

[1] Metals Research Laboratories, Union Carbide Metals Co., Niagara Falls, N. Y.

Results

Anodic behavior of manganese alone.—The only depositable species in solution was manganese (II) either as a radioactive tracer alone, at an estimated concentration of $10^{-9}M$ in $1.0M$ potassium nitrate solutions, or with added nonradioactive manganese up to millimolar. Figure 1 shows that, as the pH was increased, complete deposition of carrier-free manganese dioxide ($10^{-9}M$) was first attained at pH 4.

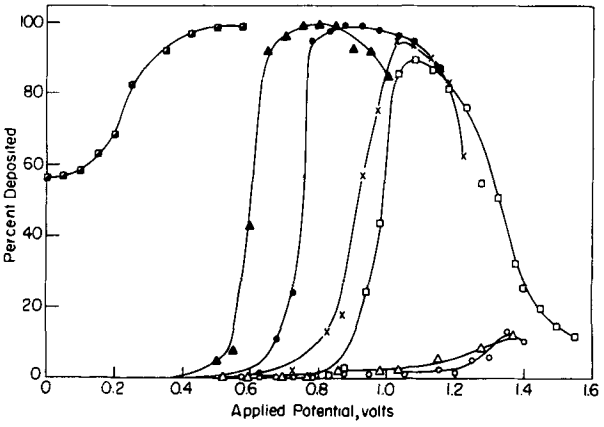

Fig. 1. Effect of initial pH on the deposition of trace manganese-52 from 1.0M potassium nitrate.

	Initial pH	Final pH
Open circle	1.00	1.00
Open triangle	2.10	1.92
Open Square	3.48	3.10
Large X	4.05	3.90
Solid circle	4.92	6.15
Solid triangle	6.02	7.05
Half & half square	9.05	9.00

The decrease found at more anodic potentials has been attributed to formation of a higher valence state having greater solubility (1).

In general, the manganese could be deposited, stripped, and redeposited at will by choosing the proper potential, thereby indicating that removal from solution was primarily an electrochemical process. However, the contribution of adsorption was evaluated by measuring at open circuit the decrease in activity of a tracer solution with time. At *p*H values less than 7.0, adsorption was negligible, i.e., less than 3% in 12 hr. At *p*H 9.0, however, virtually all of the activity was adsorbed within an hour. It was surprising to find most of the radiomanganese on the electrode.

From *p*H 3.5 to 6.0, the curves (at the 50% level) shifted at a rate of 155 mv/*p*H unit. If the reaction were

$$Mn^{++} + 2H_2O \rightarrow MnO_2 + 4H^+ + 2e \qquad [1]$$

this shift should be 120 mv at 25°C. The discrepancy may indicate that some deposited manganese was not in the tetravalent state. However, some of the discrepancy can be attributed to *p*H changes during a run. For example, a series of points were obtained using solutions carefully adjusted to *p*H 6.10 before electrolysis at each potential. These showed a spread of ±0.03 v at the level of 50% deposited whereas a comparable study at *p*H 4.00 showed less than ±0.01 v variation. It is interesting to note that the extent of deposition was usually in agreement with an earlier estimate (4) of 10^{-54} for the apparent solubility product of manganese dioxide.

At a given *p*H, one would expect the completeness of deposition to increase with the concentration of manganese. When more tracer was present, a larger percentage of manganese precipitated under a given set of conditions. Thus, 95% precipitated when three times the normal amount of tracer was used compared to 80% from the normal amount. In addition, the deposition curve proved to be the same as that for the normal amount of radiomanganese plus $10^{-8}M$ of inert manganese (II) nitrate. Decreasing the tracer to one-half the standard amount resulted in only 60% coprecipitation. Inspection of the above data showed that, regardless of the initial amount of tracer present, approximately the same amount of tracer remained in solution at the completion of the deposition. The average concentration of manganese in the tracer calculated from these data was $1 \times 10^{-9}M$, the same as estimated from activity data. Exact agreement was fortuitous but did indicate that contamination of the tracer with nonradioactive manganese was not serious.

Higher concentrations of manganese were examined by adding nonradioactive manganese. Figure 2 shows that near *p*H 2.0 complete deposition was attained at $10^{-4}M$ and higher. From the tracer alone a maximum of 10% was deposited. This curve served as a "blank" for later coprecipitation studies.

Coprecipitation of trace manganese with lead dioxide.—The *p*H region in which carrier-free manganese dioxide precipitated completely was sufficiently high to incur interferences from a number of other elements if attempts were made to apply the method to mixtures. For that reason, coprecipitation from more acidic media (1) was investigated further.

Factors which affect the coprecipitation of radiomanganese with lead are applied potential, *p*H, and the amount of carrier. The lower limit of potential was that at which lead deposited as its dioxide. This limit depended on the initial concentration of lead (II), shifting approximately 30 mv in a cathodic direction with each tenfold increase in concentration. The upper limit was the potential at which oxidation of manganese to a higher, more soluble valence became significant. Both the upper and lower limits were *p*H dependent, shifting approximately 120 mv in a cathodic direction with each tenfold increase in *p*H.

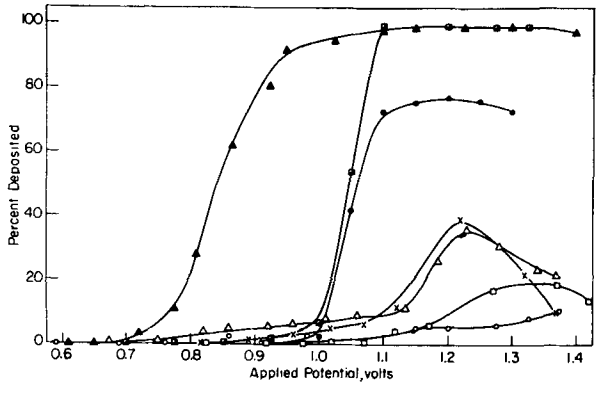

Fig. 2. Effect of total manganese concentration on the deposition of manganese from 1.0M potassium nitrate.

	Initial concentration of total manganese	Initial pH	Final pH
Open circle	Trace	2.10	1.92
Open square	1×10^{-8}M + trace	2.00	1.93
Open triangle	1×10^{-7}M + trace	2.04	1.95
Large X	1×10^{-6}M + trace	2.00	1.90
Solid circle	1×10^{-5}M + trace	2.07	1.95
Half & half square	1×10^{-4}M + trace	2.00	1.88
Solid triangle	2×10^{-3}M + trace	1.90	1.72

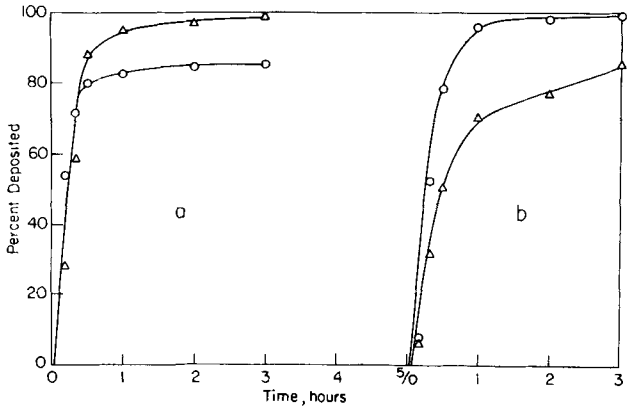

Fig. 3. Coprecipitation of manganese with 50 mg lead (II) carrier as a function of potential in 1.0M potassium nitrate at a pH of 2.0. (a) initial pH 2.00, final pH 1.85, E = +1.320 v vs. SCE; (b) initial pH 2.00, final pH 1.85, E = +1.275 v vs. SCE. Open circle, per cent manganese deposited, open triangle, per cent lead deposited.

Before starting studies of coprecipitation, depositions of lead or manganese alone were made at a number of different potentials using different initial concentrations. The relative rates later proved to be the same when both elements were deposited simultaneously.

Effect of applied potential and amount of carrier.—Figure 3 illustrates the effect of applied potential at a given pH. At the less anodic potential, lead deposited slower and gave a somewhat more adherent deposit. Use of a less anodic potential is analogous in an ordinary precipitation process to a slower rate of addition of reagent, a change which usually leads to larger and more nearly perfect crystals. However, the particles formed at both potentials were sufficiently large (greater than 1 μ) to give sharp lines on x-ray powder diffraction pictures.

At the less anodic potential, there was no reason for the potential to change the rate of deposition of the manganese because the potential was still sufficient to oxidize all of it to the tetravalent state. Hence, the net effect was greater coprecipitation for a given amount of lead. Table I shows that the effect was more striking for smaller amounts of carrier where the final fraction of manganese coprecipitated was usually smaller. The logarithmic distribution coefficient, λ, (5) was noticeably larger when the rate of deposition was slower although neither case gave a constant value during a run. For example, the values obtained for a run at +1.275 v decreased continuously from 6 to 2, whereas at +1.320 v they started at 2 and decreased to 0.3. The homogeneous distribution coefficient, D, (6) also changed during a run but it varied more than λ and in an apparently random fashion.

At potentials more anodic than +1.380 v, the efficiency of coprecipitation decreased markedly. At a potential of +1.425 v, lead was practically completely deposited at the end of 5 hr, while radiomanganese was only about one-third coprecipitated. For a similar deposition at +1.480 v only about 9% of the manganese coprecipitated. At these higher potentials, manganese was probably oxidized more or less to the more soluble heptavalent state in which form its tendency to coprecipitate should be smaller.

Table I. Effect of applied potential on the coprecipitation from 1.0M potassium nitrate of manganese-52 with lead dioxide after four hours

pH		Applied potential, v	Mg. lead present	Per cent lead deposited	Per cent manganese coprecipitated
Initial	Final				
1.00	1.00	+1.350	50	100	81
1.00	1.00	+1.320	50	70	96
2.00	1.85	+1.320	50	100	85
2.00	1.83	+1.275	50	85	98
1.00	0.98	+1.350	25	100	82
1.00	1.00	+1.320	25	44	95
2.03	1.92	+1.320	25	100	80
2.05	1.95	+1.275	25	76	96
1.05	1.05	+1.350	15	100	53
2.00	1.83	+1.350	15	100	69
0.98	0.98	+1.350	10	100	18
1.00	1.00	+1.320	10	50	74
2.08	1.90	+1.320	10	100	58
2.02	1.96	+1.275	10	78	94
1.03	1.00	+1.350	5	100	10
2.05	1.89	+1.350	5	100	24

In order to determine whether the manganese was firmly bound in the deposit or held on the surface, 50 mg of lead (II) at +1.350 v was completely deposited along with 84% of the radiomanganese. The potential was then raised to +1.480 v and the increase in the amount of manganese in the aqueous phase determined. After 4 hr, only 4% of the total manganese had returned to the solution. If the tracer had been distributed equally throughout the deposit, the 4% removed would have come from the top nine layers of lead dioxide. However, since the true area of the electrode was undoubtedly at least ten times the geometrical area, the tracer must have been stripped only from the surface.

Effect of electrode size.—A small gauze anode having a geometrical surface area of 13 cm^2 and a platinum wire anode having a geometrical surface area of 4 cm^2 were substituted, in turn, for the 79 cm^2 gauze electrode. Solutions of 1.0M potassium nitrate with 50 mg lead (II) plus the standard amount of radiomanganese were used after adjustment to a given pH.

At pH 1.0, a greater fraction of radiomanganese deposited than lead. This seemed reasonable because, although the rates of deposition, as measured by depletion of the solution, were considerably slower than observed for the large gauze electrode, the rate at which lead was depositing at the small electrode after the first few minutes was actually higher in terms of millimoles per square centimeter per minute than in the more depleted solution having the larger electrode. The result is comparable to that obtained by using more carrier, or to that in which lead deposition was slowed by a change in the electrolyte (*vide infra*).

At pH 2.0, the situation was reversed, and a greater fraction of lead deposited. A change in the rate of lead deposition was observed consistently between pH 1 and 2, but no satisfactory rationalization can be suggested for its existence. Irregular behavior has also been encountered under other conditions (4).

Table II. Removal at +1.350 v of manganese-52 by successive additions of lead (II)

(A) pH 2.0 Amount lead, mg	Per cent original Mn removed Observed	Calculated*	Amount lead, mg	Per cent original Mn removed Observed	Calculated
10	55	55	5	24	24
10	20	23	5	18	19
10	13	12	5	15	14
10	7	6	5	8	7
10	3	3	5	6	6
	—	—		—	—
Total coprecip.	98	99		75	70
(B) pH 1.0					
10	18		5	11	
10	19		5	8	
10	20		5	10	
10	19		5	8	
	—			—	
Total coprecip.	76			37	

* Calculated on the basis of the first extraction factor being constant during the successive additions.

Table III. Effect of supporting electrolyte on the coprecipitation at +1.350 v of manganese-52 with 50 mg lead (II)

(A) pH 1.0 Supporting electrolyte	γ (9)	Relative % Pb deposited per minute	Relative % Mn coprecip. per minute	% Mn coprecip.
1.0 *M* $NaClO_4$	0.58	3.18	1.13	58
1.0 *M* $LiClO_4$	0.91	1.05	0.65	58
1.0 *M* KNO_3	0.45	1.05	0.89	80
1.0 *M* $NaNO_3$	0.55	0.53	0.53	95
1.0 *M* $LiNO_3$	0.76	0.43	0.38	85
5.0 *M* $NaClO_4$	—	3.80	1.00	26
4.0 *M* $NaClO_4$ plus 1.0 *M* $NaNO_3$	—	3.18	2.00	66
4.9 *M* $NaClO_4$ plus 0.1 *M* $NaNO_3$	—	3.80	1.00	23
(B) pH 2.0				
1.0 *M* $NaClO_4$	0.53	3.18	1.13	60
1.0 *M* $LiClO_4$	0.91	1.59	0.94	56
1.0 *M* KNO_3	0.45	1.59	0.92	84
1.0 *M* $NaNO_3$	0.55	1.59	1.15	94
1.0 *M* $LiNO_3$	0.76	1.05	1.00	90

Successive additions of carrier.—Large amounts of carrier required great care in handling to avoid mechanical losses from the electrode. To decrease the total, a series using small successive additions of carrier was explored as being analogous to cross-current extraction (7). Data for successive 5 and 10 mg additions given in Table II show that, at a pH of 2.0, an approximately constant extraction factor, E, was obtained. Remembering that the extraction factor is defined as the ratio of the amount deposited to the amount remaining in solution of a given level of carrier, the ratio for 10 mg additions was 1:1, while for 5 mg additions it was about 1:3.

In contrast, at a pH of 1.0, E varied with each addition of lead such that for each 10 mg addition of lead about 20% of the *initial* amount of trace was removed; for each 5 mg, about 10% of the *initial* amount of trace present. Gordon (8) has described a type of coprecipitation in which the amount of tracer carried per unit weight of carrier was independent of the amount of tracer present initially. He attributed this to phase saturation. To test this, successive 10 mg portions of lead were added to a solution containing three times the normal amount of tracer. In this case, each 10 mg portion carried 8%, 7% and 8% of the initial tracer present. On a weight basis, the amount of tracer coprecipitated with a given amount of carrier was the same as before. Although it seems unlikely, the lead dioxide formed at pH 1.0 behaved as though it were saturated with manganese dioxide.

Effect of supporting electrolyte.—Table III shows the effect of a change in electrolyte on the deposition rates of lead and manganese. In each case lead was completely deposited, although the time required depended on the supporting electrolyte. Perchlorate generally led to faster depositions of lead than did nitrate, possibly due to inhibition by lead nitrate complexes of the type $PbNO_3^+$ (10), perchlorate having less tendency to form such complexes (11). Nitrite, at a concentration of 0.01*M*, had no effect. For a given anion, it appears that the rate of lead deposition was related inversely to the hydrated cationic radii (12) which decrease on going from lithium to potassium.

In addition to increasing the relative rate of lead deposition, perchlorate media could affect adversely the amount of radiomanganese coprecipitated in another way, especially when very concentrated supporting electrolytes were used. Thermodynamically, the reaction

$$Mn^{++} + ClO_4^- + 2H^+ \rightarrow Mn^{+++} + ClO_3^- + 2H_2O \quad [2]$$

is spontaneous as written, as it has a negative change in free energy of some 20 kcal. This was tested by observing that in a millimolar solution of manganese (II), which was 1.0*M* in sodium perchlorate and at pH 2.0, a brown precipitate formed after two days without noticeable change in the pH. At the trace level, some manganese could react in this way during a run and thus form a radiocolloid that would not deposit on the anode. Such a result was actually observed: in 5.0*M* perchlorate, only 26% of the tracer coprecipitated; in a mixture of perchlorate and nitrate, only 66% of the tracer coprecipitated (compared with 85% in the absence of the perchlorate). Even the deposition of millimolar manganese at a pH of 1.0 from 1.0*M* sodium perchlorate was only 80% complete at a potential of +1.300 v, whereas from 1.0*M* potassium nitrate solution under identical conditions, deposition was more than 99% complete.

Open-circuit studies.—Byrne (4) noted that, when an electrode was disconnected from the potentiostat following an incomplete coprecipitation and was allowed to stand overnight in the solution, almost all of the radiomanganese was found on the electrode in the morning. This phenomenon was easily checked as shown by the data run in Table IV. A similar study at pH 2.0 gave results that were virtually identical. In both cases, the change in potential was similar to that observed by Wynne-Jones and coworkers (13) for pure lead dioxide.

Thermodynamically, the reaction

$$PbO_2 + Mn^{++} \rightarrow Pb^{++} + MnO_2 \quad [3]$$

Table IV. Changes in solution characteristics with time that occurred on disconnecting the external potential (+1.350 v) from an anode in 1.0M potassium nitrate solution at pH 1.0

Time, hr	Potential, v	Per cent Mn deposited	Per cent Pb deposited
0.0	1.350	80	99
0.5	1.325	—	—
1.0	1.305	84	96
2.0	1.293	86	95
5.0	1.273	87	94
10.0	1.255	98	88

has a negative change in free energy of about 2.4 kcal. Postprecipitation of radiomanganese onto the electrode is, therefore, spontaneous and is quite probably due to chemical replacement rather than to adsorption, although some contribution from the latter cannot be entirely discounted.

Farradini and Haissinsky (14) had reported that a trace of protactinium-233 was deposited spontaneously on a freshly prepared lead dioxide electrode but not on one that had been aged overnight in distilled water. The difference between a "fresh" and an "aged" lead dioxide electrode was attributed to a layer of oxygen dissolved in the crystal lattice or held on the surface of the "fresh" oxide. After such an electrode had been stored in distilled water for 12 hr, the oxygen had escaped presumably. A comparable study for manganese-52 was undertaken so as to rule out this possibility. Both platinum and lead dioxide electrodes were examined.

Several lead dioxide electrodes were prepared by anodizing platinum gauze electrodes at +1.350 v in a 1.0*M* potassium nitrate solution containing 50 mg of lead (II) at a *p*H of 1.0. Some electrodes were used immediately ("fresh"); others were stored in distilled water overnight ("aged"). Whether the oxide was "fresh" or "aged" made no difference: about 65% of the trace manganese deposited at open circuit in the first hour; another 25%, in the next hour. The deposits reached 98% after a total of 6 hr indicating that surface oxygen was unimportant.

To rule out the unlikely possibility that oxygen alone on the surface of bare platinum could cause radiomanganese to deposit, a platinum electrode was anodized in the absence of lead. It was then disconnected from the potentiostat and a standard amount of radiomanganese added. After 4 hr, only a little more than 1% of the manganese had deposited on the electrode. To complete the circle, it was shown that if lead dioxide were deposited completely from 1.0*M* potassium nitrate at *p*H 1.0 before adding manganese tracer, further electrolysis at +1.350 v deposited only 8% of the manganese. Clearly, when lead was not depositing, the applied potential strongly deterred the deposition of manganese.

Coprecipitation of trace manganese with thallium (III) oxide.—The carrying ability of thallium (III) oxide was investigated briefly. Thallium was chosen because it provided a different type of oxide with regard to structure and atomic ratio. Also, thallium could be determined easily with a polarograph and its anodic deposition behavior had been noted (15). Coprecipitations were expected to be much less efficient because it presented a change in valence type.

At a *p*H of 1.0, thallium (III) oxide would not deposit on an anode from a solution containing 50 mg of thallium (I) in 1.0*M* potassium nitrate although thallium was oxidized, as evidenced by the high current flow. However, using 50 mg thallium (I) at a *p*H of 2.0, about 90% of the thallium could be deposited, presumably at Tl_2O_3, before the remainder precipitated into the bulk of the solution and ruled out further study. Approximately 6% of the manganese coprecipitated with the thallium (III) oxide that adhered to the electrode. The deposition was rapid, only 20 min being required to deposit 90% of the thallium. Because the time was rather short, it was thought that the tracer might not have had sufficient time to incorporate itself in the crystal, so a smaller electrode of 13 cm^2 geometrical area was used. As in the case of lead, somewhat more tracer deposited, but not enough to make thallium a useful carrier for manganese.

Discussion and Conclusions

The isolation and simultaneous concentration of $10^{-9}M$ carrier-free manganese-52 by anodic electrodeposition as dioxide is quantitative above *p*H 4. The potential must be limited so as to avoid low recovery due to formation of a more soluble higher valence state. A lower *p*H would probably be necessary to decrease the interference from other elements if they were present. In that case, coprecipitation with lead dioxide could be used to effect complete recovery of the manganese. The later separation of manganese from lead could be done in a variety of ways including cathodic deposition of lead into mercury.

Chemical displacement of manganese (II) from aqueous solution by reaction with electrolytic lead dioxide was slower than electrolysis but always quantitative. The use of powdered lead dioxide should make the replacement faster, but it would necessitate a filtration. Other techniques leading to slower but more nearly complete recovery for a given amount of lead dioxide are the use of smaller electrodes and of successive additions of small portions of carrier.

The mechanism for anodic coprecipitation of manganese and lead dioxide appears to be either anomalous mixed-crystal formation or internal adsorption, processes which are difficult to distinguish (16). Although the dioxides of lead and manganese crystallize in the rhombic and tetragonal systems, respectively, anomalous mixed-crystals might form. However, the fact that the logarithmic distribution constant, λ, did not have a constant value indicates internal adsorption to be the more probable mechanism.

Experimental

Chemicals.—Solutions of carrier-free six-day manganese-52 were prepared by dissolving deuteron-bombarded chromium in 10*M* sulfuric acid and distilling permanganic acid (17). Calculations from radioactivity data indicated that these solutions were about $10^{-9}M$ in manganese-52. Evidence has been cited to show that the concentration of total manganese was in the same range. Before use, all manganese-52 stock solutions were precathodized for 2

hr at a potential which insured that all of the tracer was in the divalent state. Other stock solutions, all of them nitrates, were a 0.0103*M* solution of manganese (II) standardized by the bismuthate method (18); a 50 mg/ml solution of lead (II) standardized as the sulfate (19); and a 50 mg/ml solution of thallium (I), standardized against bromate (20).

Apparatus.—Depositions were carried out using a volume of 150 ml in a glass cell 5 cm in diameter and 12.5 cm tall. A platinum gauze anode with a geometrical area of 79 cm^2 was used except in one set of experiments where a 13 cm^2 gauze and a platinum spiral with a geometrical area of 4 cm^2 were substituted. Electrodes were pre-anodized in 1.0*M* sulfuric acid. Nitrate or perchlorate salt bridges were used to connect the saturated calomel reference electrode and the isolated platinum cathode to the electrolytic solution. The solution was stirred by a magnetized Teflon-covered stirring bar. The temperature, unless otherwise specified, was maintained at 25.5° ±0.5°C.

The potential of the anode was controlled to at least ±2 mv using potentiostats (21). The potentials were adjusted at the beginning of each run and checked at intervals thereafter using a Rubicon potentiometer reading to ±0.1 mv. All pH measurements were made with a Beckman Model G pH meter.

A single-channel differential discriminator, coupled through a linear amplifier to a thallium-activated sodium iodide scintillator was used to obtain the gamma-ray spectrum in the characterization of the manganese-52 in the radiochemical studies. The same scintillator-amplifier combination coupled to a binary scaler was used to count samples withdrawn from the deposition cells.

Procedures

Electrolytic.—A typical electrolytic solution was prepared by adding 145 ml of a chosen supporting electrolyte to the deposition cell along with a predetermined volume of carrier solution, usually 0.1 to 1.0 ml from a Kirk micro-pipet. A standard volume of radiomanganese, from 1.0 to 4.0 ml, was then added so as to produce about 10,000 cpm above the average background of 250 cpm. Equilibrium was reached after 1 hr at a given potential whereupon a 500 μl sample was withdrawn for analysis and the potential adjusted for the next electrolysis. To define a curve for per cent deposited vs. potential, the potential was changed anodically in successive 50 mv increments. After reaching the desired limiting potential, the direction of change was reversed until all the deposit had been stripped off the electrode. This procedure tested both reproducibility and reversibility of the system.

Analytical.—The 500 μl sample was placed in a one-dram glass vial and counted for at least 1 min or until 10,000 counts above background had registered in order to minimize the counting error (22). In calculating the amount of tracer or carrier deposited at any given time, corrections were made for the amount of solution previously withdrawn and, in the case of the radiochemical measurements, for the background and the natural decay of the radionuclide.

Manganese was analyzed by the periodate method (23) when present in macro amounts (i.e., 10^{-4} to $10^{-3}M$). Lead and thallium were determined by conventional polarographic procedures (24, 25).

Acknowledgment

The authors are indebted to Dr. Charles F. Morrison, Jr., for assembling and calibrating the counting equipment used in this study and to Dr. A. D. Pearson for x-ray diffraction pictures of deposits.

This work was supported in part by the United States Atomic Energy Commission under Contract AT(30-1)-905.

Manuscript received Aug. 28, 1958.

Any discussion of this paper will appear in a Discussion Section to be published in the December 1960 JOURNAL.

REFERENCES

1. J. T. Byrne and L. B. Rogers, *This Journal*, **103**, 442 (1956).
2. W. T. Schrenk and P. H. Delano, *Ind. Eng. Chem., Anal. Ed.*, **3**, 27 (1931).
3. M. L. Nichols, *ibid.*, **3**, 385 (1931).
4. J. T. Byrne, Ph.D. Thesis, Mass. Institute of Technology, 1951.
5. H. Doerner and W. Hoskins, *J. Am. Chem. Soc.*, **47**, 662 (1925).
6. L. Henderson and J. Kracek, *ibid.*, **49**, 738 (1927).
7. L. Alders, "Liquid-Liquid Extraction," pp. 64-86, Elsevier Publishing Co., Houston, Texas (1955).
8. L. Gordon, J. I. Peterson, and B. P. Burtt, *Anal. Chem.*, **27**, 1770 (1955).
9. W. M. Latimer, "Oxidation Potentials," 2nd Ed., p. 349, Prentice-Hall, Inc., New York (1952).
10. H. M. Hershenson, M. E. Smith, and D. N. Hume, *J. Am. Chem. Soc.*, **75**, 507 (1953).
11. H. Remy, "Treatise on Inorganic Chemistry," Vol. I., p. 809, Elsvier Publishing Co., Houston, Texas (1956).
12. E. W. Washburn, *J. Am. Chem. Soc.*, **31**, 322 (1909).
13. W. Beck, P. Jones, and W. F. K. Wynne-Jones, *Trans. Faraday Soc.*, **50**, 1249 (1954).
14. C. Ferrandini and M. Haissinsky, *J. Chim, Physique*, **1956**, 722.
15. P. Delahay and G. L. Stiehl, *J. Am. Chem. Soc.*, **73**, 1755 (1951).
16. O. Hahn, "Applied Radiochemistry," Chapters 4 and 5, Cornell University Press, Ithaca, N. Y. (1936).
17. J. D. H. Strickland and G. Spicer, *Anal. Chim. Acta*, **3**, 543 (1949).
18. I. M. Kolthoff and E. B. Sandell, "Textbook of Quantitative Inorganic Analysis," 3rd Ed., p. 677, Macmillan Co., New York (1952).
19. *Ibid.*, p. 669.
20. *Ibid.*, p. 606.
21. R. W. Lamphere and L. B. Rogers, *Anal. Chem.*, **22**, 463 (1950).
22. R. J. Rainwater and C. S. Wu, *Nucleonics*, **1**, No. 2, 60 (1947).
23. N. H. Furman, Editor, "Scott's Standard Methods of Chemical Analysis," 5th Ed., p. 573, D. van Nostrand, Inc., New York (1939).
24. I. M. Kolthoff and J. J. Lingane, "Polarography," 2nd Ed., p. 528, Interscience Publishers Inc., New York (1952).
25. *Ibid.*, p. 520.

Mass Transfer and Current Distribution under Free Convection Conditions

Kameo Asada, Fumio Hine, Shiro Yoshizawa, and Shinzo Okada

Department of Industrial Chemistry, Faculty of Engineering, Kyoto University, Kyoto, Japan

ABSTRACT

Correlation of mass transfer with current distribution, for deposition and dissolution of metals, on vertical electrodes, under free convection conditions, is discussed. The equation of mass transfer and the Laplace equation, determining the concentration and potential distributions, respectively, are solved simultaneously. The results explain most features of observed current distributions.

This paper is concerned with current distribution for deposition and dissolution of metals at vertical electrodes. The rate of metal deposition may be controlled mainly or partly by the rate of transfer of ions to the cathode. In the absence of agitation, ions are usually transferred by free convection, a process which has received much theoretical and experimental investigation (1-14). Owing to depletion of reactive ions, the density of the cathodic region becomes lower than that of the bulk of the solution; an upward flow of solution then results. (Circumstances at the anodic region are just reversed.) A diffusion layer formed around a body is generally thicker with increasing distance from the frontal edge of the body. Hence, under limiting current conditions the current density (or the reciprocal of the thickness of the diffusion layer) is inversely proportional to the *fourth* root of the distance from the bottom of the cathode, as confirmed by Wagner (3), Ibl (8), and Wilke (11).

Even at current densities below limiting ones, the same type of current distribution would be expected, if the interface concentration of the reactive species remains uniform. Such uniformity of the interface concentration is, however, not always the case, as discussed by Ibl (5, 10) and Wagner (13). In the case of rectangular cell with vertical electrodes on opposite ends, a reduction of the electrolytic current is accompanied by more uniform current distributions, because of the predominance of ohmic drop and chemical polarization over concentration polarization. Under such circumstances the thickness of the diffusion layer tends to be proportional to the *fifth* root of the distance from the bottom; this suggests that the mass transfer process is not exclusively dependent on hydrodynamic conditions.

This paper describes a theoretical approach to the intermediate domain between the extreme cases: uniform interface concentration and uniform current density. This requires simultaneous consideration of mass transfer and current distribution. These two problems have so far been studied rather separately. Effects of mass transfer on polarization characteristics were interpreted by using the thickness of the diffusion layer calculated from the limiting current, e.g. (14); this is not rigorous unless the polarization is uniform and of the nature of concentration polarization (13). On the other hand, it has been accepted that predominance of polarization over ohmic drop improves current distributions, e.g. (15). But this conclusion is based on the tacit assumption that the relationship between current density and polarization is the same for every point on the electrode. Such a condition applies to chemical polarization but is not always realized when mass transfer plays a part in polarization. It follows from these discussions, that mass transfer, electrode kinetics, and electrical resistance of baths and electrode materials are united through transfer of electric charge or current distribution.

An integration of mass transfer with the other two factors has been treated in related fields of science. Modern theories of polarography have systematically correlated electrode kinetics to diffusion (16); in addition the effect of ohmic drop on polarographic waves has been described (17). Heat transfer from a two-dimensional solid wall to a moving fluid has been analyzed (18). Levich (19) and the present authors (20) discussed current distributions over a flat plate electrode in a longitudinal flow under the condition of uniform polarization. This problem is mathematically identical to simple mass transfer processes such as the dissolution of nonelectrolytes studied by several authors (21-23). Weaver and Parry (24) estimated current distributions at a streaming mercury electrode under nonuniform polarization, by assuming that, in this case, resistance of solution is localized to the vicinity of the electrode surface.

Theoretical

The model to be treated is a cell of rectangular vertical section with vertical electrodes full-end on opposite sides. The x-axis is chosen as the cathode surface and x measures the vertical distance from the bottom of the cell. The y-axis is the bottom of the cell and y measures the horizontal distance from the cathode toward the anode.[1] The height and breadth of the cell are denoted by h, and b, respec-

[1] A glossary of symbols will be found at the end of the paper.

tively. The cathode ($y = 0$) and anode ($y = b$) are distinguished by subscripts c and a, respectively.

Distribution of concentration C is determined by a differential equation of mass transfer. The distribution of potential follows the Laplace equation

$$\partial^2\phi/\partial x^2 + \partial^2\phi/\partial y^2 = 0 \qquad [1]$$

Equation [1] is valid if there is an excess of indifferent electrolyte in the bath so that diffusion potential gradients are negligible in comparison with ohmic ones and the conductivity κ is uniform. The boundary conditions are common to both electrode surfaces and are expressed by

$$\begin{aligned} i &= i_e\{(°C/*C)\exp[-\alpha n\mathbf{F}(E-E_e)/RT] \\ &\quad - \exp[(1-\alpha)n\mathbf{F}(E-E_e)/RT]\} \\ &= n\mathbf{F}D|*C - °C|/\delta \\ &= \kappa(\partial\phi/\partial y) \qquad \text{at } y = 0 \text{ and } y = b \end{aligned} \qquad [2]$$

In Eq. [2], i is the local current density, i_e the exchange current density, α the transfer coefficient, n the number of Faradays per gram-ion reacting, $\mathbf{F}$ the Faraday, E the local electrode potential, E_e the equilibrium electrode potential, R the molal gas content, T the absolute temperature, °C and *C the concentration of the reactive species at the electrode surface and in the bulk, respectively, D the diffusion coefficient of the reactive species, and δ the differential thickness of the diffusion layer. Although not necessary for the problem, it is convenient to assume that the same kinetics operate at the cathode and anode; in other words, common values of E_e, n, i_e, and α are assigned to both electrodes. This problem was solved by means of successive approximation.

If distribution of i is given, the equation of mass transfer may be solved approximately and one obtains

$$\delta^5 = n\mathbf{F}Dki^{-2}\int_0^x i\,dx \qquad [3]$$

where k is a constant specific to the system. The derivation of Eq. [3] and an evaluation of k is described in the following section. When the anode is concerned, x should be replaced by $h - x$ in Eq. [3].

On the other hand, Eq. [1] was solved by expansion into a Fourier series. The origin of the potential ϕ was chosen to satisfy

$$\begin{aligned} \phi_{y=0} \equiv \phi_c &= -(E_c - E_e) \\ \phi_{y=b} \equiv \phi_a &= V - (E_a - E_e) \end{aligned} \qquad [4]$$

V being the terminal voltage (constant along any current flux). Equation [4] is self-consistent, if the potential drop within electrode material is negligible and if the equilibrium emf of the cell is zero. Equation [1], the last member of Eq. [2], and the additional boundary condition at the bottom and top of the electrolyte

$$\partial\phi/\partial x = 0 \quad \text{at } x = 0 \text{ and } x = h \qquad [5]$$

are satisfied by

$$\begin{aligned} \phi &= \bar{\phi}_c + \bar{i}y/\kappa \\ &\quad - (2/\kappa h)\sum_{s=1}^{\infty}\{\cos(s\pi x/h)[\sinh(s\pi b/h)]^{-1} \\ &\quad \cdot[\cosh(s\pi[b-y]/h)\int_0^h I_c \sin(s\pi x/h)\,dx \\ &\quad - \cosh(s\pi y/h)\int_0^h I_a \sin(s\pi x/h)\,dx]\} \end{aligned} \qquad [6]$$

where I_a, I_c are defined by

$$I_j = \int_0^x (i_j - \bar{i})\,dx \quad (\text{for } j = a, c) \qquad [6']$$

and where $\bar{\phi}_c$ is the mean cathode potential and $\bar{i}$ the mean current density.

A cycle of successive approximation is composed of: (i) specification of $\bar{\phi}_c$ as the given condition (instead of V), (ii) assumption of i_c and i_a, followed by calculation of $\bar{i}$, (iii) evaluation of ϕ_c and ϕ_a by means of Eq. [6], (iv) determination of i_c consistent with ϕ_c through Eqs. [2]-[4], and (v) simultaneous determination of i_a and V consistent with ϕ_a through Eqs. [2]-[4] and satisfying the condition: $\bar{i}_c = \bar{i}_a$. As the integration of i and the calculation of the resulting Fourier coefficients were done repeatedly, i_c and i_a were approximated by definite numbers of exponential and polynominal terms of (x/h), respectively. This led to no serious error except in the neighborhood of the lower edge of the cathode, where $|\partial i/\partial x|$ is very large. Such an analysis could be extended to more complicated geometry, if a prior application of conformal mapping is possible.

Thickness of Diffusion Layer

One of the special features of ionic mass transfer processes by free convection as compared with the corresponding heat transfer processes and those by forced convection is the behavior of species indifferent to electrode reactions. Those species contribute to the density difference to an extent nearly as large as the reactive ones; in this respect analysis by Wagner (3) appeared to be rigorous, and his treatment was followed. Cathodic deposition of copper from $CuSO_4 - H_2SO_4$ baths was taken as an example, with the same coordinates as in the preceding section. Wagner's analysis was modified in the following three ways. (*A*) The interface concentration °*C* was regarded as a variable with x instead of a constant. (*B*) Since the velocity profile used by Wagner gives values of the limiting current which are too high, the profile of Wilke (12) was employed,[2] and the thicknesses of the hydrodynamic boundary layer and the diffusion layers of all species present were assumed equal and denoted by δ'. (*C*) In order to take migration of H^+ into account Wagner differentiated the thickness of the H^+ diffusion layer from that of Cu^{++}. In the present paper, the concentration profile of Cu^{++} will be given by

$$(C - °C)/(*C - °C) = 2y/\delta' - 2(y/\delta')^3 + (y/\delta')^4 \qquad [7]$$

and a parameter ϵ will be introduced in the profile of H^+, *i.e.*, the latter profile will be given by a power series in y/δ' with the coefficients of the first, second, third and fourth power terms taken as $(2 + \epsilon/3)$, $-\epsilon$, $-(2 - \epsilon)$ and $(1 - \epsilon/3)$, respectively.

[2] Although the observation of boundary layers (uniform current density) by Ibl (10), published during the present study, is in favor of the former profile, discussion of the profile itself is outside the limits of this paper.

This gives a differential equation:

$$(1/8k) \cdot d\,[\delta^3\,(^*C - {}^\circ C)^2]/dx = 2(^*C - {}^\circ C)/\delta' = i/n\mathbf{F}D$$

where

$$k = 126\,(\nu D/g)/[9\beta_1 - \beta_2\,(18 - \epsilon)/(6 + \epsilon)]$$

$$\epsilon = -\,(90\,t - 30)/(15\,t + 2) \qquad [8]$$

In Eq. [8], ν is the kinematic viscosity, g the acceleration of gravity, t the transference number of H^+, β_1 and β_2 the density coefficients (*i.e.*, the relative increase in density caused by unit increase in the concentrations of $CuSO_4$ and H_2SO_4, respectively), and °C, *C and D refer to Cu^{++}. Equation [8] was solved for the following three cases, with the boundary condition for δ':

$$\delta' = 0, \text{ at } x = 0 \qquad [9]$$

(i) Provided the *interface concentration °C is independent of x*, the differential thickness of the diffusion layer δ and the limiting current density i_d are expressed by

$$\delta^4 = 4kx/3(^*C - {}^\circ C)$$

and

$$i_d = n\mathbf{F}D\ ^*C(3\ ^*C/4kx)^{1/4} \qquad [10]$$

respectively. Equation [10] is different from those presented by other authors (1-4, 12) only in the detail of the constant k and gives estimates of limiting currents in accordance with those observed by Wilke (11).

(ii) If the *functional dependence of i on x is known*, Eq. [8] leads to Eq. [3]. In the special case of uniform current density, it follows from Eq. [3] that

$$\delta^5 = n\mathbf{F}Dkx/\bar{i} \qquad [11]$$

which is similar to those presented by Sparrow and others (10, 13, 25).

(iii) When the *electrode potential E is uniform over the electrode*, one obtains from Eqs. [2], [7], and [8]

$$d\xi/d\mu = \mu^4\,(3\mu + 5)/(\mu + 1)^2$$

where

$$\mu = k_f\delta'/2D,$$

$$\xi = k \cdot k_f{}^5\,x/^*C\,D^4\,(k_f - k_b),$$

$$k_f = (i_e/n\mathbf{F}\ ^*C)\ \exp\,[-\alpha n\mathbf{F}(E - E_e)/RT]$$

$$k_b = (i_e/n\mathbf{F}\ ^*C)\ \exp\,[(1 - \alpha)n\mathbf{F}(E - E_e)/RT] \qquad [12]$$

which is solved as

$$\xi = \frac{3}{4}\mu^4 - \frac{1}{3}\mu^3 - \frac{1}{2}\mu^2 + 3\mu - 5\ln(1 + \mu) + 2\mu/(1 + \mu). \qquad [13]$$

At $\xi = 0$ and $\xi \to \infty$ Eq. [13] reduces to Eqs. [11] and [10], respectively. Current distributions calculated from Eq. [13] were used as the first approximation for the procedure described in the preceding section.

Experimental and Results

A methacrylate cell (5 cm width, 32 cm breadth and 15 cm depth ID) was filled with solution up to a level $x = 10$ cm from the bottom, and immersed in a bath controlled at 25°C. Copper electrodes (0.1 mm in thickness) were covered with polyvinyl chloride paint except for the electrode surfaces, which were 5 cm in width and 10 cm in depth. The cathode was placed in contact with one of the end walls. The anode was supported by grooves cut into the sides and bottom of the cell, at different distances y from the cathode. Local current densities were measured by weighing what deposited or dissolved. Since introduction of a Luggin capillary might disturb hydrodynamic conditions, local electrode potentials were measured in the following way: five holes (1 mm in diameter) were drilled on one of the side walls at different depths for each electrode position, and each hole was connected with rubber tubing to a glass vessel in which a saturated calomel electrode was inserted in turn.

As noted by Ibl (8), excess of indifferent electrolytes retards the establishment of diffusion layers typical for free convection, while shortage of indifferent electrolytes may invalidate the assumptions on which the theory is based. From these considerations a system, $0.1M$ $CuSO_4 - 1.5M$ H_2SO_4, was chosen. For this system theoretical and experimental values of current densities and electrode potentials were obtained. Typical results are represented in Fig. 1-4. The following physical properties are used in the calculation: $\kappa = 0.543$ mho/cm, $D = 5.99 \times 10^{-6}$ cm²/sec, $\nu = 1.15 \times 10^{-2}$ cm²/sec, $\beta_1 = 120.6$ cm³/mole, $\beta_2 = 53.5$ cm³/mole, and $t = 0.81$ (26-28, and International Critical Tables); kinetic data were estimated at $i_e = 10^{-1}$ ma/cm² and $\alpha = 0.5$ (20).

Figures 1 and 2 refer to the case of infinite distance between electrodes ($b = \infty$ in Fig. 1, calculated, and $b = 32$ cm in Fig. 2, experimental). Cathodic current distributions shift from an inverse fourth root dependence on x (Eq. [10]) to a virtually uniform shape, with decreasing mean current density. As already mentioned, this is attributable to the competition of concentration polarization with chemical polarization and the resistance of the bath.

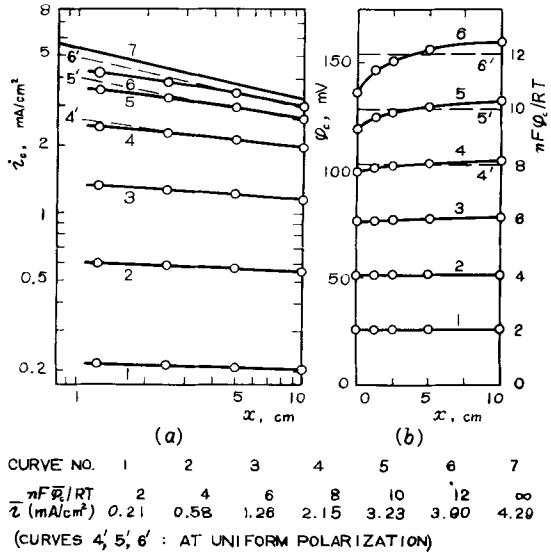

Fig. 1. Calculated distributions of (a) cathodic current density and (b) cathode potential, for b = ∞; x is the vertical distance from the bottom.

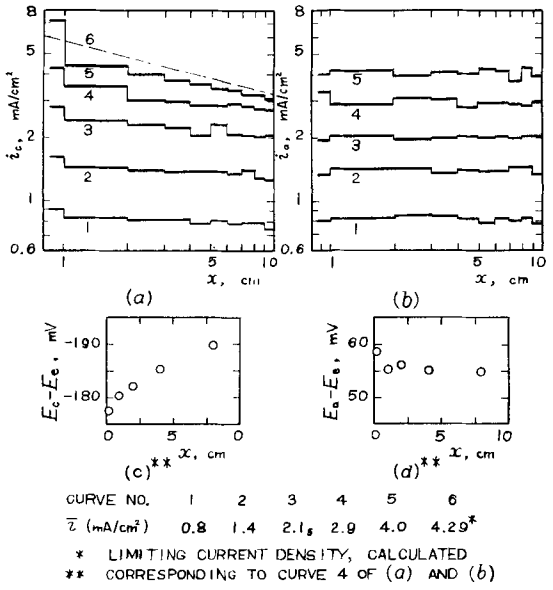

Fig. 2. Observed distributions of (a) cathodic current density, (b) anodic current density, (c) cathode potential, and (d) anode potentiol, for b = 32 cm.

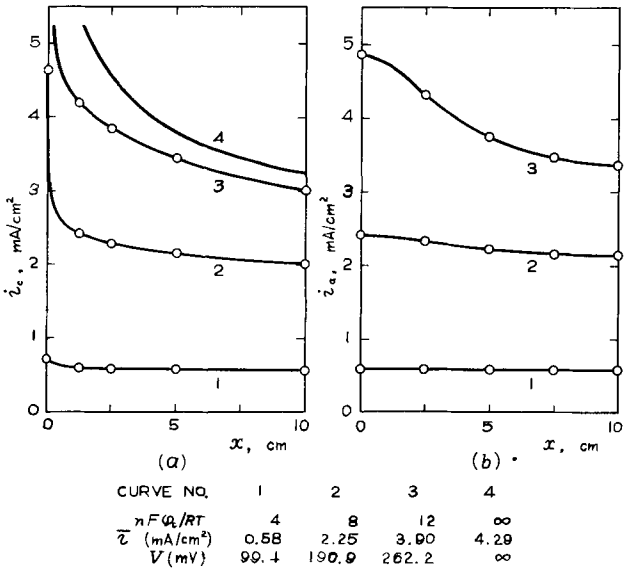

Fig. 3. Calculated distributions of (a) cathodic current density and (b) anodic current density, for b = 2 cm.

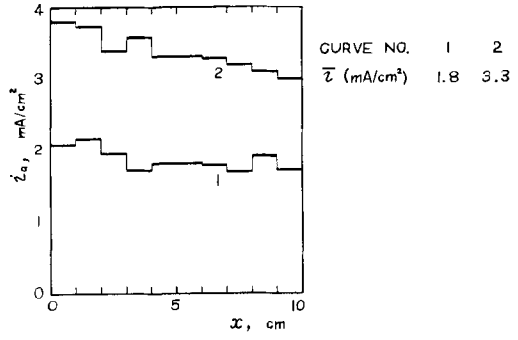

Fig. 4. Observed anodic current distributions, for b = 2 cm

The effect of the first two factors is seen separately in the dashed curves of Fig. 1, representing the case of uniform polarization [refer to (iii) of the preceding section]. The last factor results in much more uniform current distributions and nonuniform electrode potentials [see Fig. 1 (b) and Fig. 2 (c)].[3] Relatively low polarization around the lower portion of the cathode in association with relatively high current density shows plainly the peculiar effect of mass transfer on current distributions. This situation was observed also by Ibl (5). On the other hand, anodic current densities and potentials are virtually uniform (see Fig. 2), because anodic polarization is almost exclusively a chemical one as expected from Eq. [2].

Figures 3 and 4 refer to the case of finite distance between electrodes ($b = 2$ cm). The mutual influence of the cathode and the anode, whose current distributions were originally nonuniform and uniform, respectively, would cause better uniformity of current distribution at the cathode and worse uniformity at the anode. Distributions of cathodic current densities and potentials were, however, practically unaltered from the previous case ($b = \infty$) while marked change results at the anode; current densities at the anode, like those at the cathode, now become relatively high at near the bottom. This may be understood from the difference in polarization characteristics. Owing to the inclusion of concentration polarization, the slope $|\partial E/\partial i|$ of cathodic polarization curves is larger than that of anodic ones at the same current density. The larger the slope and the conductivity of the bath, the stronger is the buffering action against change in current densities (15).

Extension to Practical Conditions

The above discussions are concerned exclusively with 0.1*M* $CuSO_4$ — 1.5*M* H_2SO_4 solution at 25°C. In this system the effect of mass transfer on current distributions was remarkable, because the conductivity is high for the concentration of reacting ions. On the other hand, typical working conditions in industry are as follows: for electroplating, 0.8*M* $CuSO_4$ — 0.5*M* H_2SO_4, 20-30°C and 5-15 ma/cm²; for electrorefining, 0.6*M* $CuSO_4$ — 1.5*M* H_2SO_4, 50°C and 20 ma/cm² (29). The conductivities of these baths are not much different from those of the present study, and current densities may be less than one half of the limiting values. Such conditions would correspond to the curves on Fig. 1 numbered 4 or less. Hence failure in uniformity of current distributions due to mass transfer may be tolerable, and it would be overlooked because of probable predominance or superposition of geometrical effects.

Next, cells for testing plating conditions (such as Haring and Hull cells) are mentioned. The principle on which their use is based is such that current distributions in the vertical direction due to mass transfer are left out of consideration, and effects of polarization are interpreted in a unified way in terms of the throwing power. Such a cell is, however, operated by nature under more severe conditions than in practical plating. Indeed Ibl (5) reported that deposits appeared in a triangular form on the corner nearer to the anode and the bottom of a Hull cell. Moreover, Shreir and Smith (30) found that

[3] Except for the present case of a rectangular geometry, the resistance of the bath does not help the establishment of uniform current distributions, while chemical polarization always does.

quality of deposits was worse at the upper half of cathodes even under ordinary conditions.

Acknowledgment

The authors wish to express their appreciation to Asahi-kagaku-kogyo-shoreikai (The Asahi Association for Development of Chemical Engineering) for its support of the present study. They are grateful to Dr. R. W. Parry of the University of Michigan who read the manuscript and offered helpful suggestions.

GLOSSARY OF SYMBOLS

b — distance between electrodes (cm)
C — concentration of reactive species (mole/cm^3)
$^\circ C$ — concentration of reactive species at the electrode surface (mole/cm^3)
$^* C$ — concentration of reactive species at the bulk (mole/cm^3)
D — diffusion coefficient of reactive species (cm^2/sec)
E — electrode potential (volt)
E_e — equilibrium electrode potential (volt)
$\mathbf{F}$ — the Faraday (amp sec/eq)
g — acceleration of gravity (cm/sec^2)
h — height of electrodes (cm)
i — current density (amp/cm^2)
i_d — limiting current density (amp/cm^2)
i_e — exchange current density (amp/cm^2)
k — defined by Eq. [8] (mole)
k_f, k_b — apparent rate constants of the forward and backward reactions, respectively, defined by Eq. [12] (cm/sec)
n — number of Faradays per gram-ion reacting (eq/mole)
R — molal gas constant (joules/deg K mole)
t — transference number of H^+ (dimensionless)
T — absolute temperature (deg K)
V — terminal voltage (volt)
x — vertical coordinate parallel to electrodes measured from the bottom of the cell (cm)
y — horizontal coordinate perpendicular to electrodes measured from the cathode towards the anode (cm)
α — transfer coefficient (dimensionless)
β_1, β_2 — density coefficients (see text) (cm^3/mole)
δ — differential thickness of diffusion layer (cm)
δ' — integral thickness of diffusion layer (cm)
ϵ — parameter of migration for H^+ (dimensionless)
κ — conductivity (mho/cm)
μ — defined by Eq. [12] (dimensionless)
ν — kinematic viscosity (cm^2/sec)
ξ — defined by Eq. [12] (dimensionless)
ϕ — potential (volt)

subscripts

$_c$ — cathode
$_a$ — anode

Manuscript received Oct. 27, 1958. This paper was abstracted from the Dissertation of K. Akada, Kyoto University and was presented before the fall meeting of the Electrochemical Society of Japan, November 28 and 29, 1957.

Any discussion of this paper will appear in a Discussion Section to be published in the December 1960 JOURNAL.

REFERENCES

1. B. Levich, *Acta Physicochim.*, **19**, 125 (1944).
2. J. N. Agar, *Discussions Faraday Soc.*, **1**, 26 (1947).
3. C. Wagner, *This Journal*, **95**, 161 (1949).
4. C. H. Keulegan, *J. Research Nat. Bur. Standards*, **47**, 156 (1951).
5. N. Ibl, W. Ruegg, and G. Trümpler, *Helv. Chim. Acta*, **36**, 1624 (1953).
6. N. Ibl, Y. Barrada, and G. Trümpler, *ibid.*, **37**, 583 (1954).
7. N. Ibl, *ibid.*, **37**, 1149 (1954).
8. N. Ibl, K. Buob, and G. Trümpler, *ibid.*, **37**, 2251 (1954).
9. N. Ibl and R. Müller, *Z. Elektrochem.*, **59**, 671 (1955).
10. N. Ibl and R. H. Müller, *This Journal*, **105**, 346 (1958).
11. C. R. Wilke, M. Eisenberg, and C. W. Tobias, *ibid.*, **100**, 513 (1953).
12. C. R. Wilke, M. Eisenberg, and C. W. Tobias, *Chem. Engr. Progr.*, **49**, 663 (1953).
13. C. Wagner, *This Journal*, **104**, 129 (1957).
14. T. Pavlopoulos and J. D. H. Strickland, *ibid.*, **104**, 116 (1957).
15. C. Wagner, *ibid.*, **98**, 116 (1951).
16. P. Delahay, "New Instrumental Methods in Electrochemistry," Interscience Publishing Co., New York (1954).
17. W. Vielstich and P. Delahay, *J. Am. Chem. Soc.*, **79**, 1874 (1957).
18. S. Sugawara and T. Sato, *Trans. Japan. Soc. Mech. Engrs.*, **19**, 13 (1953).
19. V. G. Levich and N. N. Meiman, *Chem. Abstr.*, **46**, 4892h (1952).
20. S. Okada, S. Yoshizawa, F. Hine, and K. Asada, *J. Electrochem. Soc., Japan*, **25**, 562 (1957).
21. F. Paneth and K. Ferzfeld, *Z. Elektrochem.*, **37**, 577 (1931).
22. D. A. Frank-Kamenetskii (translated by N. Thon), "Diffusion and Heat Exchange in Chemical Kinetics," Princeton University Press, Princeton (1957).
23. P. L. Chambré and A. Acrivos, *J. Appl. Phys.*, **27**, 1322 (1956); *Ind. Eng. Chem.*, **49**, 1025 (1957).
24. J. R. Weaver and R. W. Parry, *J. Am. Chem. Soc.*, **78**, 5542 (1956).
25. E. M. Sparrow and J. L. Oregg, *Trans. Am. Soc. Mech. Engrs.*, **78**, 435 (1956).
26. A. R. Gordon and A. Cole, *J. Phys. Chem.*, **40**, 73 (1936).
27. R. K. Richardson and F. D. Taylor, *This Journal*, **20**, 179 (1911).
28. M. Eisenberg, C. W. Tobias, and C. R. Wilke, *ibid.*, **103**, 413 (1956).
29. Electrochem. Soc., Japan (editor), "Denki-kagaku-binran (Handbook of Electrochemistry)", Maruzen Book Co., Tokyo, rev. ed. (1953).
30. L. L. Shreir and J. W. Smith, *This Journal*, **99**, 64, 450 (1952).

Technical Notes

On the Influence of Combinations of Impurities on the Electrolysis of Zinc

Georg Steintveit and Hans Holtan, Jr.

Det Norske Zinkkompani A/S, Eitrheim, Odda, Norway, and Metallurgy Department, Norways Institute of Technology, Trondheim, Norway, respectively

It is a well established fact that the electrolysis of zinc sulfate solutions is very sensitive to impurities present in the electrolyte, and results of experimental investigations have been reported both in textbooks (1) and in the literature (2). In recent years the subject seems to have gained increased interest (3-12). Some investigators have also applied radioactive tracers in their studies (13-15).

Metallic impurities of known poisonous action are Ge, Sb, As, Sn, Co, Ni, Se, Te, etc. Further it is also assumed that organic materials affect zinc deposition. Of particular interest in this respect is beta naphthol or alpha-nitroso-beta-naphthol (16), as this reagent is found in some technical electrolytes. Combinations of the impurities mentioned are particularly harmful. Especially is the combined effect of Co and Sb known to be very dangerous (17, 18). Nevertheless, there seems to exist some confusion regarding the subject as at least one zinc producer (19, 20) keeps a high level of Co in solution and in addition adds amounts of Sb and beta naphthol to improve zinc deposition.

Our investigations comprised the *combined action of several of said impurities* in concentrations which may occur in actual plant operation.

The influence of as much as four impurities present simultaneously was investigated. It was found that there is no law of additivity for the influence of impurities. Thus the presence of only one of two impurities may not harm the electrolysis at all, but when they are present simultaneously they may be harmful. Similar findings were reported later by Turoshima and Stender (6). Angel and co-workers (21) have performed similar experiments on chlorine-caustic electrolysis. One of our results was the observation of the very bad influence of the combination Co,Sb and beta naphthol. Below are shown the results of a series of experiments performed under identical conditions in cells fed with the following solutions:

	Pure zinc sulfate solution	% current efficiency
1.	0.003 g Co/l	90.3
2.	0.050 mg Sb/l	91.7
3.	0.030 g beta naphthol/l	91.1
4.	0.003 g Co/l + 0.050 mg Sb/l	76.8
5.	0.03 g beta naphthol/l + 0.050 mg Sb/l	91.4
6.	Co precipitated from 10 mg/l to 4 mg/l by means of beta naphthol	81.6
7.	As 6 + 0.050 mg Sb/l	25.1

Conditions during electrolysis were: current density, 4.2 amp/dm^2; cell temperature, 30°C; zinc content, 130 g/l; cell acidity, approximately 90 g H_2SO_4/l; time between stripping cathodes, 48 hr.

We see that the influence of the combinations Co,Sb, and Co,beta naphthol are harmful and that the combination Co,Sb,beta naphthol is extremely unfavorable. In the latter case the deposits were heavily corroded and showed a characteristic appearance of pinholes and of spheres under which there were voids.

There is no doubt that a real corrosion takes place even if there is present a "cathodic protection" current of 4.2 amp/dm^2. This is clearly seen also in the simple case where Co is added as the only impurity. It then formed holes in the deposits, and these holes grow as the electrolysis is continued. When a good deposit is formed from a pure solution, it is possible to start corrosion of the deposit by adding the proper combinations of impurities to the solution. When beta naphthol was present as the only impurity, we observed tiny holes in the deposits. Lashkorev and Krynkova (22) have shown that the discharge of zinc and other ions is inhibited by beta naphthol. During electrolysis, hydrogen bubbles are probably attached to the beta naphthol, thus making the holes visible.

A theoretical investigation of the phenomenon is planned.

Acknowledgment

The authors are indebted to the management of Det Norske Zinkkompani A/S for inspiring encouragement during this work and for kind permission to publish this work which was performed at the Company's Research Laboratory in 1954.

Manuscript received Sept. 25, 1959.

Any discussion of this paper will appear in a Discussion Section to be published in the December 1960 JOURNAL.

REFERENCES

1. R. Müller, "Allgemeine und Technische Electrometallurgi," Springer, Wien (1932).
2. U. C. Tainton and E. T. Clayton, *Trans. Am. Electrochem. Soc.*, **57**, 279 (1930); *Metal Ind. (London)*, **37**, 229 (1930).
3. G. Sacciati, *Ind. mineraria*, **4**, 511 (1953).
4. A. G. Pecherskaya and V. V. Stender, *Zhur. Priklad. Khim.*, **23**, (9), 920 (1950).

5. U. F. Turoshina and V. V. Stender, *J. Appl. Chem. U.S.S.R.*, **28**, 155 (1955).
6. *Ibid.*, **28**, 447 (1955).
7. *Ibid.*, **27**, 1019 (1954).
8. A. I. Levin, A. V. Pomosov, V. S. Koletova, I. E. Gurevich, E. A. Ukshe, and N. T. Rogatkina, *Korroziya i Metallopokrytiya, sbornik Stalei*, **1953**, No. 43, 5.
9. A. A. Salin, *Vestnik. Akad. Nauk. Kazakh. S. S. R.*, **12**, 73 (1956).
10. N. T. Kudryatsev and A. G. Atanasyants, *Trudy Moskow Kim. Technol. Inst. im D. I. Mendeleva*, **1956**, 143.
11. N. Matsuura, *J. Chem. Soc. Japan*, Pure Chem. Sec., **74**, 24 (1953).
12. G. T. Wever, *J. Metals*, **11**, 130 (1959).
13. N. Matsuura, *J. Chem. Soc. Japan*, Pure Chem. Sec., **74**, 239 (1953).
14. Z. A. Sheka, *Ukrain. Khim. Zhur.*, **22**, 387 (1956); **22**, 394 (1956).
15. A. I. Levin and V. S. Kolevatova, *Tswetny-Metal*, **29**, 28 (1956).
16. W. C. Snow, *Trans. Am. Inst. Mining Met. Engrs.*, **121**, 502 (1936).
17. *Can. Mining J.*, **75**, 271 (1954).
18. D. R. Zosimovich and N. F. Bogatova, *Zhur. Fiz. Khim.*, **33**, 1324 (1959).
19. W. C. Snow, *Trans. Am. Inst. Mining Met. Engrs.*, **121**, 516 (1936).
20. "Extractive Metallurgy in Australia," Frank A. Green, Editor, Australasian Institute of Mining and Metallurgy, Melbourne (1953).
21. G. Angel, T. Linden, S. Dahlerus, and R. Brännland, *This Journal*, **102**, 246 (1955).
22. M. Lashkorev and A. Krynkova, *Doklady Akad. Nauk. S.S.S.R.*, **62**, 47 (1948).

Dendritic Inclusions in AlSb Grown-Junction Diodes

H. C. Gorton

Battelle Memorial Institute, Columbus, Ohio

One of the disturbing factors in the development of solid-state devices is the anomalous behavior of individual units fabricated from material with seemingly homogeneous characteristics. One of the causes for such anomalies, found in grown-junction diodes of aluminum antimonide, has been the inclusion of impurities in the form of long filaments, which in some cases pass through the junction. The possibility of a similar mechanism for such anomalous behavior in other semiconductor devices also is suggested.

The peak inverse voltage of grown-junction AlSb diodes generally has been consistent with values expected for material of a given carrier concentration, and general uniformity has been observed in the electrical properties of different diodes cut from the same ingot.

In several AlSb crystals, p-n junctions were grown by adding tellurium or selenium to the melt after pulling had commenced. In each of the cases of interest, 0.5 a/o (atomic per cent) tantalum had been added to the melt prior to pulling the crystal (1). In one such crystal, the mobility and carrier concentration of the p-type material were 420 $cm^2\ v^{-1}\ sec^{-1}$ and $1 \times 10^{16}\ cm^{-3}$, respectively. Consequently, peak inverse voltages in excess of 150 v were expected. However, of seven diodes fabricated from single-crystal sections of the grown junction, five were linear and two broke down at about 5 v reverse potential.

Microscopic examination of the diodes, after having been etched in 1:1 $HCl:HNO_3$, revealed the presence of long, thin fibers about 1 to 5 μ in diameter oriented parallel with the direction of growth of the crystal and penetrating the junction. A powder Debye-Sherrer pattern of the filaments showed them to be Al_3Ta. The fortuitous fact that Al_3Ta happens to be insoluble in the etchant used to prepare the diodes made observation of the inclusions possible. Figure 1 shows a sectioned slice of an AlSb ingot containing a p-n junction. The increase in the density of the filaments toward the center of the crystals

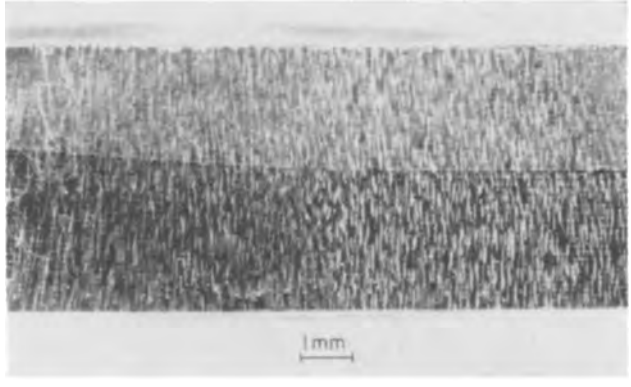

Fig. 1. Section of AlSb ingot with Al_3Ta inclusions showing p-n junction.

may be seen in the figure. Each of the two diodes mentioned above that showed some rectification was taken from near the edge of the crystal. The effect of the fibrous inclusions on the electrical properties of a p-n junction is readily apparent. The fibers appear to be shorter on the right than on the left, because they intersect the surface on the right at a slightly steeper angle.

As may be seen in Fig. 1, the growth of the filaments is inhibited at the p-n junction near the periphery of the crystal, evidently resulting from a physical disturbance due to the addition of the impurity. This discontinuity in the growth of the filaments is indicative of the fact that they are formed as the crystal is being grown and are not associated with solid-state diffusion processes subsequent to the formation of the crystal, such as the decoration of dislocations.

Figure 2 is a photomacrograph of the top side of the same specimen shown in Fig. 1. The bright spots on the dark background are the ends of the filaments protruding from the etched surface. Areas of higher and lower density of the filaments may be seen to have radial symmetry. The radial symmetry of the

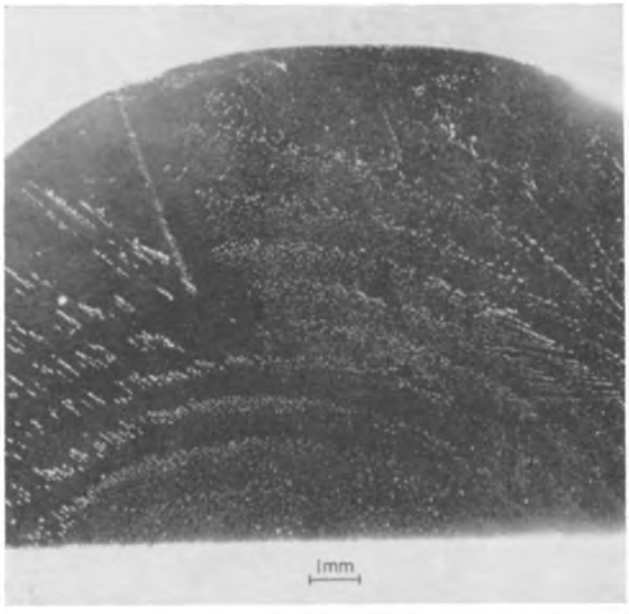

Fig. 2. Section of AlSb ingot showing filaments protruding from etched surface.

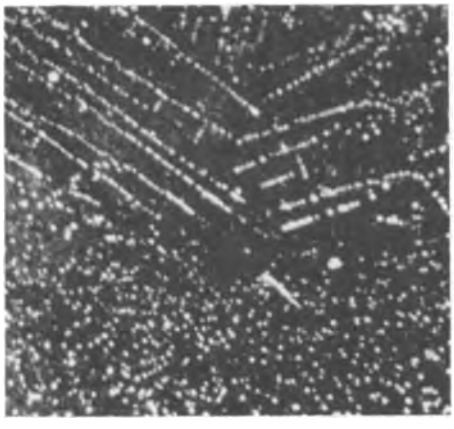

Fig. 3. Exploded view of section of Fig. 2 showing linear array of inclusions. Scale, 1⅜ in. = 1 mm.

grouping of the filaments apparently is associated with diffusion of the impurity to preferred sites at the solid-liquid interface. A detailed study of this phenomenon may lead to a greater understanding of the structure of the solid-liquid interface under various growth conditions. It is also interesting to note that such fibrous inclusions may grow in a single-crystal matrix, without themselves acting as nucleation centers for new crystallites.

A closer examination of Fig. 2 shows several areas of parallel linear arrays of the fibrous inclusions, which are superimposed on the annular areas of high and low density of impurities. These parallel linear arrays are localized to single crystal sections of the ingot. Figure 3 is an exploded view of a small section of the crystal shown in Fig. 2. Here the linear array of the inclusions is quite apparent. Such an array immediately suggests its similarity to dislocation etch pits in other semiconducting materials.

Billig (2) showed that crystals possessing the zinc blende structure solidify dendritically when freezing takes place at a rapid rate. It is here suggested that even with the relatively slow pulling rates associated with normal crystal-growing techniques, incipient dendritic growth takes place at the solid-liquid interface. Crystal growth therefore would initiate along preferred crystal planes from which it would extend dendritically in the plane of the solid-liquid interface. An incipient dendritic lattice at the solid-liquid interface therefore would be built up whose structure would be characteristic of the crystallographic plane presenting itself to the melt. Impurities in the melt with segregation coefficients less than one therefore would tend to be trapped in the interstices of the incipient dendritic lattice. Since the different crystallographic surfaces would propagate themselves into the interstices of the dendritic lattice, any imperfections in the crystal growth would tend to form dislocations in these areas also. In either case, if the dislocations were made visible as etch pits or if the impurities were made visible either as etch pits or as insoluble inclusions, they would show ordered arrays characteristic of the dendritic growth of the matrix.

It is further suggested that certain impurities, such as Al_3Ta, segregating to the interstices of the dendritic lattice would tend to propagate themselves along the direction of growth of the crystal. Visual observation of such inclusions would be rendered impossible, except as etch pits where they would intersect a surface, if they happened to be soluble in the etchants used to process the semiconductors. Such a situation may be a factor in accounting for the disturbing fact that some crystals whose bulk properties show acceptable electrical characteristics nevertheless are unsuitable for device application.

Acknowledgment

The author wishes to thank the members of the Compound Semiconductor Research Group for their permission to publish this work.

Manuscript received June 19, 1959.

Any discussion of this paper will appear in a Discussion Section to be published in the December 1960 JOURNAL.

REFERENCES

1. M. Genser and W. P. Allred, U.S. Pat. 2,816,023.
2. E. Billig, *Proc. Roy. Soc., London*, **A235**, 37 (1956).

Ohmic Contacts to Semiconducting Ceramics

D. R. Turner and H. A. Sauer

Bell Telephone Laboratories, Incorporated, Murray Hill, New Jersey

Flaschen and Van Uitert (1) made a low-resistance ohmic contact to ferrite and semiconducting titanate ceramics with indium wetted with mercury or gallium rubbed on the surface. For investigative purposes and perhaps for some applications the low melting indium-gallium alloy is satisfactory. The difficulty of attaching terminals to indium-gallium, due to its susceptibility to physical deterioration by mechanical abuse and changes in its wetting properties, has spurred the search for a more practical contact material. This paper describes a method of preparing stable low-resistance ohmic contacts to titanate ceramics to which terminals can be soldered. The process can be used to make ohmic contacts to intermetallic compounds such as gallium-arsenide and thermoelectric semiconductors such as bismuth-telluride. The method consists of depositing metal contacts such as nickel on appropriate surfaces of the material and subsequently heat treating the contacts. Nickel is deposited most conveniently by chemical reduction, the "electroless" process (2). Electroless nickel deposition was used by Sullivan and Eigler (3) to make ohmic contacts to silicon, where a heat treatment may not be required.

Experimental

Most of the experimental work to be described here was done on lanthanum-doped barium titanate ceramics ($Ba_{0.998}La_{0.002}TiO_3$) which are n-type semiconductors. These materials exhibit large positive temperature coefficients of resistance (4). Two stable low-resistance ohmic contacts are required on devices for thermistor applications. The test specimens were wafers 1 cm in diameter and about 2 mm thick. The adhesion and surface coverage of the electroless nickel deposit on the titanate ceramic is improved if the surface is prepared by lapping, for example with No. 600 silicon carbide. The area to be coated with nickel is "activated" by dipping in stannous and palladium chloride solutions (5). This procedure deposits a thin layer of palladium on the surface which catalyzes the start of nickel deposition by chemical reduction in the "electroless" solution. Three minutes in the electroless nickel solution (solution temperature ~95°C) deposits a layer of nickel about 0.001 mm thick which is adequate for contact purposes.

Results and Discussion

The electroless nickel contact on the titanate ceramic is nonohmic as deposited. A low-resistance ohmic contact is obtained when the specimen is heat treated to at least 170°C for about 10 min. This is illustrated in Fig. 1 which gives the voltage-current curves obtained at room temperature on a typical titanate ceramic disk with electroless nickel contacts. The initial V-I curve is nonlinear, and at 0.7 v the

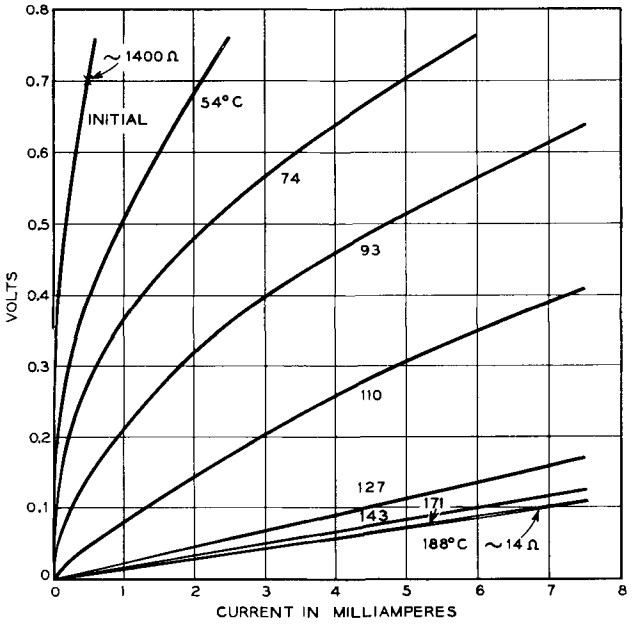

Fig. 1. Effect of heat treatment temperature on the voltage-current relation of a disk of lanthanum-doped barium titanate ceramic with electroless nickel contacts. Specimens measured at room temperature.

total resistance[1] is about 1400 ohms. After the ceramic has been heat treated for 10 min at 54°C, the contact resistance is decreased but it is still nonohmic. Higher heat treatment temperatures decrease the contact resistance still further. The contact resistance continues to decrease with increasing heat treatment temperature up to about 170°C where it approaches a minimum value. This may be considered a minimum processing temperature for obtaining low-resistance ohmic contacts. The total sample resistance of 14 ohms at this point is essentially the body resistance of the ceramic as determined by the four point probe method.

The resistance of the ohmic contact increases with time after heat treatment. This aging effect decreases if longer heat treatment times are used or the temperature of heat treatment is raised. It was found that, with heat treatment temperatures up to about 250°C, the time of heat treatment was an important factor. Longer heat treatment times decreased the rate at which the contact resistance increased with time. The time factor became less important as the heat treatment temperature approached 250°C. Above 250°C, heat treatments longer than 5 or 10 min did not change the aging characteristics of the ohmic contact. The most stable ohmic contacts were obtained when the specimen was heated to the highest temperature tried, 400°C.

[1] The total resistance includes the resistance of two contacts plus the body resistance of the sample.

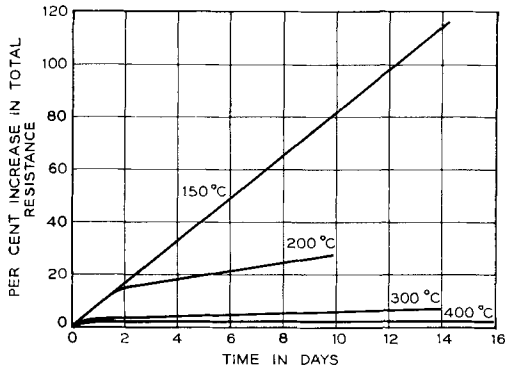

Fig. 2. Effect of heat treatment temperature on power aging of electroless nickel contacts on lanthanum-doped barium titanate disks. Samples measured at room temperature.

The effect of heat treatment temperature on contact resistance aging is shown in Fig. 2. For this experiment, electroless nickel contacts were applied to a series of 20-ohm ceramic disks and each group was heat treated at a different temperature. The heat treatment time was 30 min for 150° and 200°C and 10 min for 300° and 400°C. Those heated to 300° and 400°C were tinned with lead-tin solder to protect the electroless nickel from excessive oxidation. These aging tests were carried out at an elevated temperature of about 80°C since it was found that some heating accelerated the aging effect. The samples were heated electrically by passing either a.c. or d.c. current through the ceramics. Plotted in Fig. 2 is the per cent increase in total resistance as a function of aging time in days. The total resistance measurements were always made at room temperature. When heat treated at 150°C, the total resistance of the test pieces increased linearly with time and the resistance doubled in about 12 days. The contact resistance stability improved with higher heat treatment temperatures. At 400°C, there was a slight change during the first day after which no further resistance change was detected up to 16 days.

Long-time shelf aging tests indicate that electroless nickel contacts heat treated even at 400°C are not perfectly stabilized against increases in the contact resistance. If the contact resistance becomes too large, however, the low contact resistance obtained after the initial heat treatment can be renewed with another brief heat treatment.

The results obtained with titanate ceramics can be explained if it is assumed that the initial nonohmic behavior of electroless nickel is due to an adsorbed layer of oxygen between the ceramic and the nickel (6). The heat treatment removes the adsorbed oxygen presumably by reaction with the nickel. The deterioration of the ohmic contact is attributed to the re-formation of the insulating oxygen layer as the result of oxygen diffusion to the ceramic-nickel interface.

Electroplated nickel, copper, gold, indium, and silver have also been used to make ohmic contacts to titanate ceramics. Electroplated nickel gives the same results as electroless nickel, however, the latter is preferred over plated nickel since it is more convenient to use in this application. Indium provides an ohmic contact as plated but the adhesion is poor. Silver contacts must be heat treated in a vacuum or in an oxygen-free system to produce the ohmic contact. Oxygen diffuses through silver rapidly at elevated temperatures thus the oxygen layer at the semiconductor-silver interface is removed by chemical reaction on heating only in an oxygen-free ambient. Electroless nickel contacts on gallium-arsenide single crystals are made ohmic by tinning the nickel with a lead-tin solder. The heat treatment alone does not make the contact ohmic. Sharpless (7) has shown that tin is important in producing ohmic contacts to gallium-arsenide.

Manuscript received July 22, 1959. This paper was prepared for delivery before the Ottawa Meeting, Sept. 28-Oct. 2, 1958.

Any discussion of this paper will appear in a Discussion Section to be published in the December 1960 JOURNAL.

REFERENCES

1. S. S. Flaschen and L. G. Van Uitert, *J. Appl. Phys.*, **27**, 190 (1956).
2. A. Brenner and G. E. Riddell, U. S. Pat. 2,532,283 and 2,532,284.
3. M. V. Sullivan and J. H. Eigler, *This Journal*, **104**, 226 (1957).
4. H. A. Sauer and S. S. Flaschen, Proc. 1956 Electronic Components Symposium, pp. 41-46, May (1956).
5. F. Pearlstein, *Metal Finishing*, **53**, 59 (1955).
6. H. A. Sauer and S. S. Flaschen, *Bull. Amer. Ceram. Soc.*, to be published.
7. W. H. Sharpless, *Bell System Tech. J.*, **38**, 259 (1959).

Preparation of InAs, InP, GaAs, and GaP by Chemical Methods

D. Effer and G. R. Antell

Research Department, Metropolitan-Vickers Electrical Company Limited, Trafford Park, Manchester, England

The formation of crystals of the arsenides and phosphides of indium or gallium by a vapor phase reaction between the lower valency halides of these metals and arsenic or phosphorus has been previously reported (1). This work has now been extended to show that these basic reactions may also be used to prepare the compounds by the following methods: (*a*) continuous flow vapor phase reaction in the presence of an unreactive carrier gas; (*b*) direct reaction in the liquid phase; (*c*) by passing AsH_3 or PH_3 into the molten chlorides; and (*d*) by a replacement reaction starting with $AsCl_3$ or PCl_3 and the metal.

The following equations illustrate the over-all reactions involved.

$$2\,MCl + Y \rightarrow MCl_2 + MY \qquad [1]$$

$$3\,MCl_2 + Y \rightarrow 2\,MCl_3 + MY \qquad [2]$$

where M corresponds to In or Ga and Y to As or P.

Of the possible reactions under each heading only those involving indium monochloride and gallium dichloride were investigated. Some of the reactions resulted in the formation of colored, solid complexes which decomposed at higher temperatures to give the appropriate III-V compound. Reference is made to the possible structure of these intermediates in the discussion section.

X-ray diffraction measurements were used to establish the identity of all the III-V compounds produced.

The various methods offer alternative routes to the ultimate purification of the compounds. In this respect it has been established that chlorine has little or no effect on the electrical properties of InAs, but we have not carried out any experiments to determine the effect of this element on the other three compounds under discussion.

Experimental

Examples of the reactions given under (*a*), (*b*), (*c*) and (*d*) above are as follows:

(*a*) A continuous flow vapor phase method was carried out by passing gallium dichloride and As vapor in pure nitrogen as a carrier gas through a heated quartz tube. The reactants were introduced into the main tube from separately heated compartments such that the composition of the final mixture was in the proportions given in Eq. [2]. After mixing, the vapors passed through a furnace set at approximately 800°C followed by another at 600°C. The latter furnace served to remove any unchanged reactants and volatile products. GaAs was deposited in powdery form in this furnace, and a 75% yield was obtained by a single passage through the heaters.

(*b*) Direct reaction in the liquid phase was carried out by heating gallium dichloride with arsenic powder under a pure nitrogen gas atmosphere, at approximately 500°C for 24 hr. The gallium arsenide formed was separated mechanically from the small amount of free gallium which resulted from the heating and finally baked out under vacuum at 600°C.

To prepare the phosphides of the metals, liquid yellow phosphorus was reacted with gallium dichloride or indium monochloride at substantially 300°C in a pure nitrogen gas atmosphere for 1 hr. Normally only a temperature sufficient to keep the chloride in a molten condition was necessary to produce the reaction. Colored complexes varying from yellow to red were obtained. On heating slowly to approximately 500°C, these decomposed to give InP or GaP.

(c) AsH_3 and PH_3 are relatively unstable gases, AsH_3 decomposing into its elements at about 230°C and PH_3 at 440°C. Passage of AsH_3, in a carrier gas of pure hydrogen, through gallium dichloride at approximately 300°C produced an orange-colored complex which decomposed on heating slowly to 600°C to give GaAs powder. GaP was similarly prepared by passing PH_3 in a nitrogen carrier gas through gallium dichloride at approximately 300°C, the yellow complex formed being slowly heated to 500°C under vacuum to give GaP powder.

Passage of PH_3, in a pure nitrogen carrier gas, through InCl at approximately 300°C produced a red complex which yielded InP on heating slowly to 500°C under vacuum.

(*d*) A variation of the basic reactions was carried out by employing $AsCl_3$ or PCl_3 and the appropriate metal. Using the reaction between $AsCl_3$ and In as an example, when these are heated in molecular proportions an exchange reaction occurs

$$AsCl_3 + In \rightarrow InCl_3 + As$$

If the reaction takes place using an excess of In, InAs is finally produced. It is assumed that a lower halide of In is formed at one stage by the reaction between $InCl_3$ and In and that this reacts with arsenic to form indium arsenide as in the basic Eq. [1] and [2].

All of the four compounds were produced in this way by heating the chlorides to their boiling point ($AsCl_3$ 130°C; PCl_3 76°C) with the metal in sealed evacuated quartz tubes arranged vertically. As the reaction progressed, the temperature was gradually increased to approximately 350°C. Finally, the tubes were placed horizontally in a furnace and heated

slowly to 600°C with what was originally the top end of the tube protruding in order to free the III-V compound from volatile products. The tubes were sealed off in the middle and drawn off. In the case of InAs and GaAs the powders produced were melted by dropping the tubes vertically at 4 cm/hr through a furnace. In all cases except InP the compounds were produced with efficiencies greater than 95% the single experiment with *InP* yielding 65%.

Of the reactions described under the four headings, reaction (*d*) is considered to be most worthy of further investigation with regard to the preparation of the semiconducting compounds in the state of high purity. The $AsCl_3$ or PCl_3 may be purified by careful fractional distillation and finally distilled into reaction capsules containing highly purified In or Ga which are then sealed off. On completion of the reaction as detailed above InAs and GaAs may be melted directly or injected into a "floating zone" or "hanging drop" of the molten compound.

InP and GaP powders produced from the reaction are more difficult to melt due to the high pressures of phosphorus produced at the melting points of these materials. Melting of InP may be attempted in ampoules of extra thick wall or by using an autoclave pumped up to a pressure equal to the dissociation vapor pressures produced by the molten compound. Alternatively the InP powder may be used as charge material for a crystal pulling apparatus.

Discussion

The composition of the colored complexes observed during some of the reactions was not elucidated. Gallium dichloride has been denoted as $GaCl_2$ but is actually dimorphic similar to indium dichloride. Evidence for the formulation of $Ga^{I}(Ga^{III}Cl_4)$ has been given by x-ray diffraction studies with crystalline gallium dichloride (2) and by Raman spectra of the fused compound (3). Further evidence for the formulation which may have a considerable bearing on the structure of the observed complexes has been obtained by passing H_2S through gallium dichloride (4). A solid complex containing Ga, Cl, and S was obtained of variable composition, the reaction occurring with the Ga^{I} ion. It seems possible that the reactions between gallium dichloride and AsH_3, PH_3, and liquid phosphorus behave in an analogous manner.

Acknowledgment

The authors wish to thank Mr. R. W. McEvan for assistance in the experimental work and Mr. R. P. Chasmar for helpful criticisms of the manuscript. They also wish to thank Sir Willis Jackson, F.R.S., Director of Research and Education, Metropolitan-Vickers Electrical Co. Ltd., for permission to publish.

Manuscript received Sept. 8, 1959.

Any discussion of this paper will appear in a Discussion Section to be published in the December 1960 JOURNAL.

REFERENCES

1. G. R. Antell and D. Effer, *This Journal*, **106**, 509 (1959).
2. G. Garton and H. M. Powell, *J. Inorg. Nucl. Chem.*, **4**, 84 (1957).
3. L. A. Woodward, G. Garton, and H. L. Roberts, *J. Chem. Soc.*, **1956**, 3723.
4. R. C. Carlston, E. Griswold, and J. Kleinberg, *ibid.*, **80**, 1532 (1958).

The Change in Open-Circuit Potential of the Manganese Dioxide Electrode on Discharge and the Discharge Mechanism

W. C. Vosburgh and James H. DeLap

Department of Chemistry, Duke University, Durham, North Carolina

ABSTRACT

Discharge of electrodeposited MnO_2 electrodes for successive short periods at *p*H 8, with time for reattainment of equilibrium, shows that the potential of partially discharged MnO_2 is a linear function of the amount of lower oxide formed over part of the discharge. With this relationship, some previous data on the overpotential of MnO_2 in acid electrolytes are interpreted more simply than before in terms of the discharge mechanism previously proposed. The overpotential is shown to be a linear function of the square root of the current density.

In previous attempts to measure the change in open-circuit potential of the MnO_2 electrode as the result of discharge, the time allowed for recovery from polarization was insufficient (1, 2). This was suspected at the time, but a compensating slow decrease in potential made longer times of doubtful value. The metal anode used in the discharge was probably responsible for much of the decrease (3), and in the present investigation this source of error was avoided. After a small discharge the potential increased for 4 to 40 days, depending on how much the electrode had been discharged previously. The final, nearly constant potential was an approximately linear function of the amount of discharge over the first quarter of the total capacity. The interpretation of some overpotential measurements with acid electrolytes (4) has been reconsidered in the light of this result.

Experimental

Electrodes.—MnO_2 was electrodeposited on graphite rods from a bath of 0.33M $MnSO_4$ and 0.67M H_2SO_4, or from a similar bath containing also 0.3M $(NH_4)_2SO_4$ at 90°C (1, 2, 5). The graphite rods were of 0.48 cm diameter and were covered for a length of 5.1 to 5.2 cm, and on one end, with MnO_2, giving an apparent area of 8 cm^2. Much of the bare portion of the rod was covered with glass sealed to the graphite by glyptal cement for protection from the electrolyte. The current in the electrodeposition was 25 ma (3.13 ma/cm^2) and the time 30 min, giving about 0.2 millimole of MnO_2. The MnO_2 formed in the bath without $(NH_4)_2SO_4$ was probably γ-MnO_2 (6). That deposited in the presence of $(NH_4)_2SO_4$ has been shown to differ in discharge characteristics from γ-MnO_2 (5) and was probably largely α-MnO_2.

After electrodeposition, the electrodes were washed by allowing them to stand in test tubes of 0.01M $(NH_4)_2SO_4$ acidified to *p*H 4.5, this solution being changed daily. Washing was continued until a test for Mn^{++} in the wash solution by oxidation to MnO_4^- with KIO_4 was negative. This usually required 2 to 3 weeks. Each electrode was then immersed in an electrolyte of 1M $(NH_4)_2SO_4$ buffered at *p*H 8 by NH_3. This portion of electrolyte was contained in a 125-ml bottle fitted with a rubber stopper bearing the electrode. By means of a ground-glass joint the electrode was mounted in the stopper in such a way that it could be transferred easily to and from a discharge cell. The stopper also had a hole for the salt-bridge of a saturated calomel electrode, and all of the important potential measurements were made with the electrode in the bottle. Measurements in the discharge cell were used for control only. New electrodes were kept in the bottles with frequent measurements until the potential was decreasing only very slowly; this period was about two weeks usually. The final potential attained was taken as the initial potential of the discharge curve.

Electrodes standing in electrolyte decreased more or less rapidly for a few days and then attained a steady rate of decrease of about 0.1 mv a day which was the same for all electrodes. Although γ- and α-MnO_2 electrodes had nearly the same potential at first, the α-MnO_2 electrodes decreased more rapidly initially and for a longer time, about 10 days. Thereafter the potential was around 70 mv lower than the γ-MnO_2 electrodes, but the slow decrease was at the same rate.

Discharge and subsequent potential measurements.—Tests showed that an electrode could be transferred from one bottle of electrolyte to another of the same electrolyte with no appreciable change in potential. It was concluded that removal of an electrode for discharge and returning it to the same bottle would have no effect other than that of the discharge. It was observed that removal to a discharge cell equipped with 8 graphite rods to act as the anode usually caused a small decrease in potential. The change indicated was considered negligible in comparison with the discharge.

The discharge cell contained about 250 ml of the 1M $(NH_4)_2SO_4$ electrolyte, *p*H 8. The electrode was placed centrally in the cell and was surrounded by 8 graphite electrodes connected together, which formed the anode. A calomel electrode allowed measurement of the changing potential during discharge by a recording potentiometer. A current of 2

Table I. Temperature coefficients of electrodeposited MnO_2 electrodes measured against S.C.E. at 10° to 35°C

Electrode	$\Delta E/\Delta t$, mv/deg C	
	pH 5	pH 8
γ-MnO_2 undischarged	0.07	0.50
γ-MnO_2 discharged 60 ma-min	0.15	0.58
α-MnO_2 undischarged	0.14	0.61
α-MnO_2 discharged 60 ma-min	0.16	0.58

ma from an outside source was passed for the discharge and was regulated by hand.

For discharge an electrode was given a final measurement in the storage bottle and transferred to the discharge cell. A current of 2 ma was passed for a measured time, usually 5 or 10 min. Then the electrode was transferred back to the storage bottle and measured occasionally against a saturated calomel electrode until the potential was increasing less than 1 mv a day. After the first discharge of a new electrode about 4 days was required. In later discharges the times required increased with the amount of total discharge to as much as 40 days. Electrodes of α-MnO_2 required more time than those of γ-MnO_2. All measurements were made at room temperature (in the vicinity of 25°C), and corrections made when necessary for both temperature and pH changes.

Temperature and pH corrections.—For the temperature corrections electrodes in bottles were measured at intervals from 10° to 35°C against a calomel electrode, with about 48 hr allowed at each temperature for the attainment of constancy. In addition to the pH 8 measurements some were made with a 1M $(NH_4)_2SO_4$ electrolyte buffered at pH 5 with pyridine and pyridinium sulfate. The changes in potential per degree are shown in Table I. These are averages for two electrodes which agreed within 0.03 mv/degree at pH 5 and 0.05 mv/degree at pH 8.

The change of potential with pH was determined by transfer of a number of electrodes from one electrolyte to another and measuring after equilibrium was attained. The average change was close to the theoretical 59 mv/pH unit at 25°C.

Test for Mn^{++}.—The solutions in the bottles were tested for Mn^{++} when the electrodes had come to equilibrium. The solution tested was replaced by a fresh portion of electrolyte in the bottle for the next discharge.

Results

The discharge curves determined as above are shown in Fig. 1. The more important are the curves for γ-MnO_2. The solid straight lines are shown to represent the discharges from 10 to 60 ma-min for three electrodes quite well. For a fourth electrode (not shown) which required longer preliminary washing than the others, the first 40 ma-min of discharge was straight. The dashed lines indicate deviations from the straight lines in the first discharge period and after 60 ma-min. No Mn^{++} was found in the electrolytes in which these electrodes were stored for recovery during the first 100 ma-min of discharge. After that an average of 0.12 mg/20 ma-min of discharge was found. Previously (7) in continuous discharges at pH 8 no Mn^{++} was found in the discharge cell until after 150 ma-min.

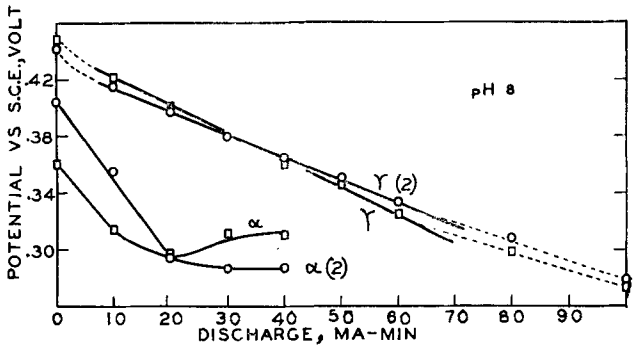

Fig. 1. Variation of equilibrium open-circuit potential with amount of discharge in electrolyte of pH 8; α- and γ-MnO_2. Circles represent averages for two electrodes.

The straight lines for γ-MnO_2 at pH 8 indicate that over a certain portion of the discharge the electrode potential decreases linearly with the increase in lower oxide formed. Deviations from linearity are found at the beginning and below a potential of 0.34 v against the saturated calomel electrode. Within the linear range no Mn^{++} is found in solution, and the entire reduction product remains on the electrode. During the recovery process the product, which is probably formed mainly in the outer portion of the MnO_2 (8, 9), appears to become distributed more uniformly. Even though this process may not have been entirely complete at the time of the final measurements, the amount of product in the surface layer must have been approximately proportional to the total product formed. It has been assumed previously that the electrode potential is determined in part by the composition of the surface layer, but it was thought that the relationship was logarithmic and similar to the Nernst equation (4). The present results indicate a linear relationship over a limited range of compositions. A similar linear relationship is apparent in the data of Kozawa (10) especially in his Fig. 7 showing the decrease in electrode potential when MnO_2 is reduced with varying amounts of Mn^{++}. Ruetschi, Angstadt, and Cahan (11) showed that there is a linear relationship between the potential of a PbO_2 electrode and the surface concentration of adsorbed oxygen.

The formation of Mn^{++} in solution during the later recovery periods (beyond 100 ma-min) after removal of the electrode to another container, does not seem to be in accord with the discharge mechanism proposed by Cahoon and co-workers (12, 13).

In the discharge of α-MnO_2 at pH 8 no Mn^{++} was found for the first 20 ma-min and the potential decreased more rapidly than for γ-MnO_2. The discharge reaction evidently does not penetrate as deeply in α-MnO_2 as in γ-MnO_2, giving a more rapid change in surface composition.

Discussion

The recovery curve.—The straight-line relation between electrode potential and discharge time over a limited range, as shown in Fig. 1, suggests a revision in the interpretation of some previous data (4). It was assumed previously that the electrode

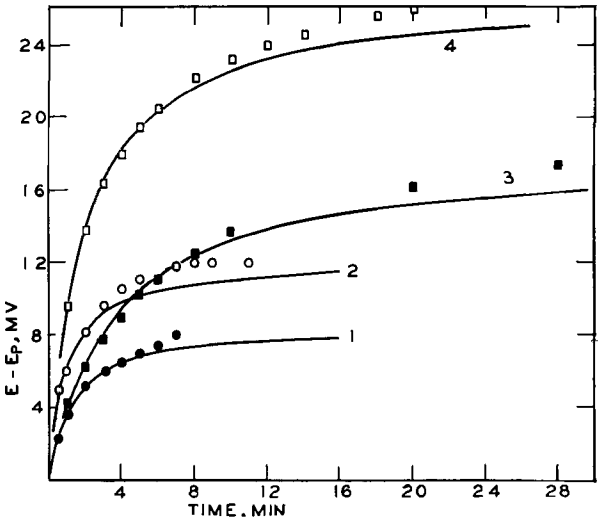

Fig. 2. Decay of polarization in acid electrolytes.

potential is related to the composition of the MnO_2 surface by a logarithmic relation of the form of the Nernst equation (4, 10).

In the discharge of electrolytic MnO_2 electrodes in H_2SO_4 solution containing $MnSO_4$ (4) the potential first decreases, then passes through a minimum and rises to a constant value, indicating a steady state of polarization. The steady state was ascribed to a balance between the lower oxide formed and that dissolved by the electrolyte per time unit. On breaking the circuit a relatively slow rise to a constant open-circuit potential takes place, as shown in Fig. 2.

The amount of polarization shown in Table II of the previous paper (4) was in all cases less than 60 mv, whereas the straight line portions of the γ curves in Fig. 1 extend over about 100 mv. Therefore, a linear relationship between the composition of the surface and the electrode potential may be expected to hold for the polarization in acid electrolytes.

Let E be the variable electrode potential during recovery from polarization, E_e the constant open-circuit potential after recovery, and E_p the closed-circuit potential in the steady state of polarization. If the iR drop and solution concentration polarization are negligible, E_p is also the open-circuit potential at the instant of breaking the circuit. Following the suggestion of Fig. 1, we may write

$$\Delta E = -k' \Delta L \qquad [1]$$

with L defined as a measure of the amount of discharge of product in the electrode surface. It may be somewhat approximate to apply this to the recovery process since the linear relationship may not hold all the way to E_e. However, we shall assume its validity and consider that $L = 0$ when $E = E_e$ which also is an approximation when the solution contains Mn^{++}. Then for the recovery process,

$$E_e - E = k' L \qquad [2]$$

The assumptions made previously that the primary discharge product is a Mn(III) oxide or hydroxide (for which we shall use the formula MnOOH), that the recovery reaction is a disproportionation as in Eq. [3] and that this reaction is rate-controlling are retained. We may add the newer concept that the lower oxide is formed both on and below the surface of the MnO_2 (8).

$$2MnOOH + 2H^+ = Mn^{++} + MnO_2 + 2H_2O \qquad [3]$$

For the velocity of this reaction at constant H^+ concentration we may write

$$-dL/dt = k'' L^2 \qquad [4]$$

This may be somewhat too simple because of the neglect of a reverse reaction, but it seems sufficient for testing the theory. Integration and evaluation of the constant for the condition $L = L_p$ when $t = 0$ gives

$$1/L - 1/L_p = k'' t \qquad [5]$$

with L_p standing for the concentration of product in the surface in the steady state of polarization. Combination of Eq. [2] and [5] gives

$$1/(E_e - E) - 1/(E_e - E_p) = k_1 t \qquad [6]$$

in which $k_1 = k''/k'$.

Equation [6] can be tested by recalculation of the data presented in Fig. 4 and 5 of Yoshiza and Vosburgh (4). Figure 2 gives the results of such a calculation. Curves 1, 2, and 4 represent the same data as the two lower curves of (4): Fig. 4 and the higher of Fig. 5, respectively. Curve 3 represents a different experiment from the lower curve of (4): Fig. 5, but carried out under the same conditions. The lines in Fig. 2 were calculated by Eq. [6] using the experimental values for E_e and E_p and an arbitrary value of k_1 determined for each curve from some of the experimental points. The experimental points shown were taken from recorder curves for the recovery process.

The agreement of the earlier experimental points with the calculated curves is good. The later points deviate from the curves in the direction of too rapid increase in E. It was pointed out above that the equation might not be exact when $E_e - E$ is small. The agreement of the calculated lines and the experimental points is better in curves 3 and 4 than in the corresponding curves of (4): Fig. 5. Curve 2 is not as good as the corresponding one in (4): Fig. 4, but curve 1 may be considered about equal to the lowest (4): Fig. 4 curve, since the earlier points in the latter are not on the curve.

Relation between overpotential and current.—A better test of the above theory is in the relation between overpotential and current in discharges in acid solution. The steady state of polarization in acid electrolytes is enough different from the equilibrium state of the electrode so that Eq. [2] should be a better approximation than for the recovery process.

For the MnO_2 electrode the overpotential has been defined as the difference between the equilibrium open-circuit potential after a discharge and the potential of the steady state of polarization (14). In acid electrolytes the overpotential is not a linear function of the logarithm of the current density (4).

In the steady state of polarization the rate at which lower oxide is formed, $i/\mathbf{F}$ equivalents/sec, can be set equal to the rate at which it is removed

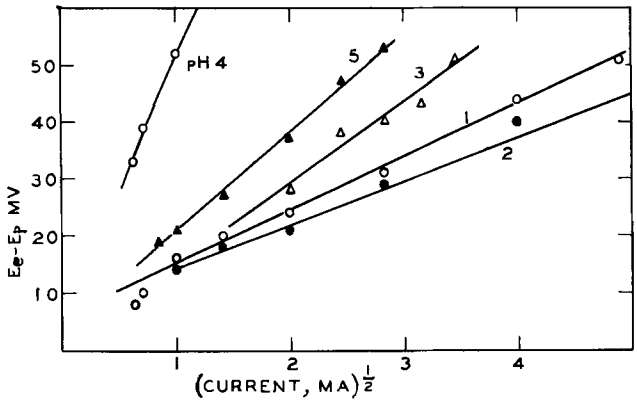

Fig. 3. Overpotential, E_e-E_p, plotted against the square root of the current. Numbers refer to electrolyte compositions (Ref. 4); 1, 1M H_2SO_4; 2, 0.5M; 3, 0.1M; 5, 0.01M; all 0.1M $MnSO_4$. Electrolyte pH 4, acetate buffer and no $MnSO_4$.

from the surface. According to Eq. [4] and the definition of L_p the rate of removal should be equal to $k''L_p^2$. Then

$$i = \mathbf{F}\, k''\, L_p^2 \qquad [7]$$

Combining with Eq. 2 when $E = E_p$ and $L = L_p$

$$i = \mathbf{F}\, k''(E_e - E_p)^2/(k')^2$$

$$E_e - E_p = k_2\, i^{1/2} \qquad [8]$$

Equation [8] predicts a linear relationship between overpotential, $E_e - E_p$, and $i^{1/2}$. Figure 3 shows that this is true over the entire range of currents tried by Yoshizawa and Vosburgh (4). Four different electrolytes, Nos. 1, 2, 3, and 5, give satisfactory straight lines within the limits of error. There was insufficient data for electrolyte 4. An electrolyte of pH 4 gave a slightly curved line. Some of the overpotentials for this electrolyte (not shown in Fig. 3) were so large that the validity of Eq. [1] might be questioned. The data plotted are from (4): Tables II and III.

According to Eq. [8] the lines of Fig. 3 should pass through the origin. However, most of them would pass above the origin, if extended. A constant term in Eq. [8] would be needed to express them. The points of lowest overpotential for the most acid solution in Fig. 3 deviate from the line in the direction to approach $\Delta E_e = 0$ at $i = 0$. This may be connected with the breakdown of the linear relationship between E and oxide composition when the lower oxide component is small.

The data on the growth of polarization of the previous paper have not been recalculated, since these involve the little understood phenomenon of the passage of the electrode potential through a minimum. A recalculation would not be likely to add materially to the older interpretation.

The experimental data and calculations of this paper are in agreement with the assumption made previously that the primary product of the reduction of MnO_2 is a Mn(III) compound formed within the MnO_2 structure, and that its formation is followed by a disproportionation. The assumption of primary reduction to Mn(II) would lead to a linear relationship between overpotential and current, which is not found. However, recent work has shown a linear relation to hold for PbO_2 and TiO_2 electrodes, for which no disproportionation reaction is possible. This work will be reported later.

Acknowledgment

This work was supported in part by a James B. Duke Fellowship and in part by the Office of Ordnance Research. The authors are indebted to Mr. Bruce C. Tyson, Jr., for measurement of the change of potential with pH.

Manuscript received Aug. 14, 1959. This paper was prepared for delivery before the Columbus Meeting, Oct. 18-22, 1959.

Any discussion of this paper will appear in a Discussion Section to be published in the December 1960 JOURNAL.

REFERENCES

1. D. T. Ferrell, Jr., and W. C. Vosburgh, *This Journal*, **98**, 334 (1951).
2. A. M. Chreitzberg, Jr., and W. C. Vosburgh, *ibid.*, **104**, 1 (1957).
3. W. C. Vosburgh, D. R. Allenson, and Stanley Hills, *ibid.*, **103**, 91 (1956).
4. S. Yoshizawa and W. C. Vosburgh, *ibid.*, **104**, 399 (1957).
5. A. Kozawa and W. C. Vosburgh, *ibid.*, **105**, 59 (1958).
6. W. F. Cole, A. D. Wadsley, and A. Walkley, *Trans. Electrochem. Soc.*, **92**, 133 (1947).
7. W. C. Vosburgh, M. J. Pribble, A. Kozawa, and A. Sam, *This Journal*, **105**, 1 (1958).
8. J. Brenet, *Proc. Intern. Comm. Electrochem. Thermodynam. and Kinetics*, 8th Meeting, Madrid, 1956, p. 394.
9. W. C. Vosburgh, *This Journal*, **106**, 839 (1959).
10. A. Kozawa, *ibid.*, **106**, 79 (1959).
11. P. Ruetschi, R. T. Angstadt, and B. D. Cahan, *ibid.*, **106**, 547 (1959).
12. N. C. Cahoon, *ibid.*, **99**, 343 (1952).
13. N. C. Cahoon, R. S. Johnson, and M. P. Korver, *ibid.*, **105**, 296 (1958).
14. A. M. Chreitzberg, Jr., and W. C. Vosburgh, *ibid.*, **104**, 1 (1957).

Effect of Adsorption of Polar Organic Compounds on the Reactivity of Steel

Howard F. Finley[1] and Norman Hackerman

Department of Chemistry, The University of Texas, Austin, Texas

ABSTRACT

Rate studies were made for the oxygen-free reaction between steel powder and 1*N* H_2SO_4, both uninhibited and inhibited. In particular, it was shown that the retardation of the reaction by organic polar compounds was influenced more markedly by molecular structure than by molecular weight or area.

This study is a continuation of the work reported by Hackerman and Cook (1) on the adsorption of polar organic compounds on steel and their effect on its reactivity in acid solution. A comprehensive theory of the general adsorption of organic inhibitors and subsequent inhibition of acid dissolution by polarization of the anodic reaction was given by Hackerman and Makrides (2). The investigations undertaken here were for the purpose of obtaining additional information as a basis for confirming or denying the theory as stated.

Experimental

The essential features of the experimental approach have been described (1). The principle used was to determine gravimetrically the increase in weight of a sample of steel powder on being exposed to a solution of benzene containing the organic inhibitor. The metal used was SAE 1010 steel powder purchased from the Vanadium-Alloys Steel Company. It had a composition of 0.10 C, 0.10 Si, 0.24 Mn, 0.012 P, 0.012 S, and test Fe. It was purchased as powder which passed No. 100 sieve mesh and further sieved, the 140 to 200 range being used.

The benzene was thiophene-free, C.P. grade and was free also from H_2S, CS_2, and SO_2. The polar organic compounds were obtained from several sources. Hexamethylenimine and heptamethylenimine were obtained from Dr. P. D. Gardner, The University of Texas. Diallylamine, 1,4,4, trimethylpiperdine, and 1-benzylpiperdine were obtained from Dr. N. J. Leonard, The University of Illinois; tetrahydrothiophene from Delta Chemical Works, and four alkyl aryl sulfonate salts from Dr. A. H. Roebuck, Continental Oil Company. The remainder of the compounds were of the best grade of Eastman chemicals. In all cases, except for the sulfonate salts, the compounds were liquids and were redistilled. The sulfonate salts were 99.5% pure as received.

In making solutions of the inhibitors, two liters of 0.0100M solution were made and then solutions of 0.005, 0.0025, 0.00125, 0.00063, 0.00031M prepared by dilution of the proper aliquotes.

The relative inhibitor efficiency was determined by measuring the reaction rates in 1*N* H_2SO_4 of the steel powder either untreated or previously exposed to the benzene solutions of the inhibitors. The acid was prepared in 4-liter quantities from stock concentrated C.P. H_2SO_4.

The data are good in general to 5%.

Procedure.—The procedure for determining the amount of polar organic compound adsorbed on the steel has been described (1). There were, however, some modifications made in the method of determining relative inhibitor efficiencies. The apparatus used was essentially the same, with one or two minor alterations, but the technique of treating the data was completely different. Previously the results were compiled as a relative activity based on the time required to liberate 36, 81, and 126 ml of hydrogen gas or the time for the dissolution of 1.6, 3.4, and 5.2% of the metal. Basis time for reaction on clean steel was taken as an average from a number of different runs made on different samples. There are two objections to this procedure. The first is that there is only a relatively small amount of inhibitor on the surface of the steel, and after a short time of reaction it can be expected to be swept away or undermined so that it no longer protects the metal. The second is that unreduced steel powder already has a considerable surface oxide layer, and reaction rates with acid are both low and erratic from sample to sample.

It was believed that the following procedure would eliminate these objections. The powder was reduced in 150-g sample lots under hydrogen for 24 hr at 600° ± 25°C, both inhibited and uninhibited samples being treated alike. Individual curves were run for each sample lot and the inhibited samples were compared with these. Plots were made of volume of hydrogen evolved against time of reaction. The slope of the curve at zero time was obtained by extrapolation and a graphical method. The procedure used was to stand a small mirror on edge on the curve in such a way that the curve was continuous with its reflection. The base of the mirror was then normal to the curve at point of contact. Check values obtained with curves of known slope were never in error more than 2 or 3%. This approach is versatile and readily provides volume vs. time, rate vs. time, and rate vs. volume curves.

[1] Present address: Creole Petroleum Corporation, Cabimas, Edo. Zulia, Venezuela.

The relative inhibitor efficiency, y, was calculated from the equation

$$y = \frac{R_p - R_I}{R_p} \qquad [1]$$

where R_p is the reaction rate at zero time for the plain steel and R_I that for the inhibited steel.

Reaction rate data.—Typical hydrogen evolution data from uninhibited steel samples are shown in Fig. 1. These curves were not immediately amenable to analysis. The data were first plotted as volume vs. square root of the time and seemed to give a fair fit. However, the upper and lower ends of the curves deviated somewhat (Fig. 2). A better fit was obtained by plotting hydrogen volume against the square of the natural logarithm of the time. This is shown for the same data in Fig. 3. The equation for the curves is then

$$V = k_o \ln^2 t + k_1 \qquad [2]$$

The rate equation becomes

$$\frac{dV}{dt} = 2k_o \frac{\ln t}{t} \qquad [3]$$

Figure 4 shows the data of the 30°C curve from Fig. 1 plotted as reaction rate vs. time and compared with the function $(k\ln t/t)$ normalized to $(k\ln t/t) = 3.5$ at $t = 2.5$, one of the actual data points.

This time dependence of the hydrogen volume is somewhat difficult to interpret. There was a slight increase in pH as the reaction proceeded but nothing of magnitude sufficient to explain the great decrease in reaction rate. Various investigators (3-5) have solved the square root dependence curve in the case of dry oxidation of metals, basing their solution on the diffusion of reactants through the oxide layer formed on the surface of the metal. Figure 5 shows that there is a general similarity between the shape of a $t^{1/2}$ and a $\ln^2 t$ curve. From this the tentative conclusion concerning the latter curve is that it is due to barrier layer formation.

The hydrogen volume-time dependence of the inhibited samples failed to show the same relationship. A typical curve is shown in Fig. 6 compared with a rate curve for plain steel. The rate increases slowly at first, reaches a peak at about 10 min, and then begins to decrease. The final rate is somewhat lower than that for plain steel, but its rate of change with time is about the same.

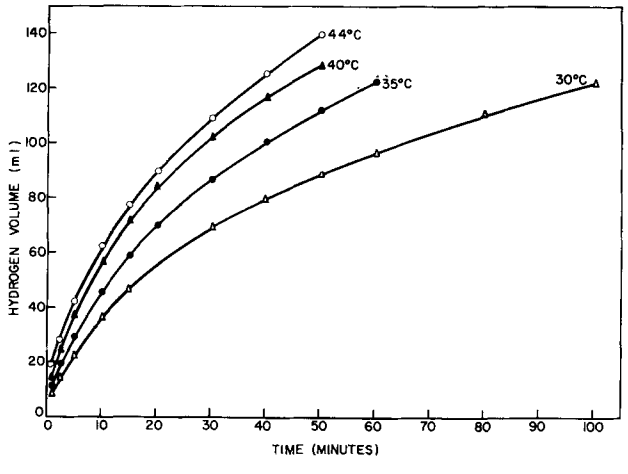

Fig. 1. Hydrogen evolution from steel in 1N H_2SO_4.

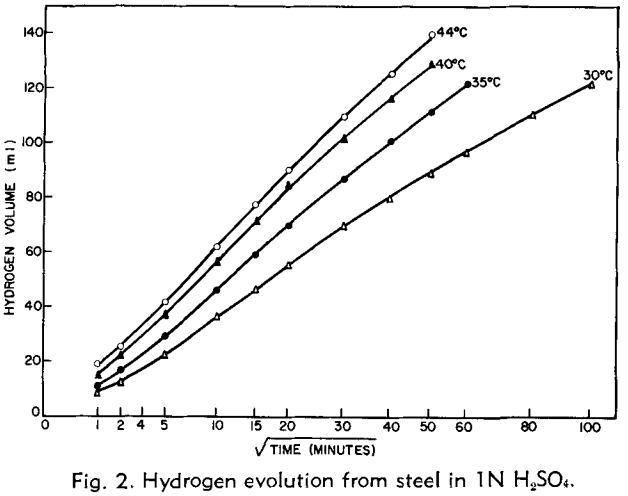

Fig. 2. Hydrogen evolution from steel in 1N H_2SO_4.

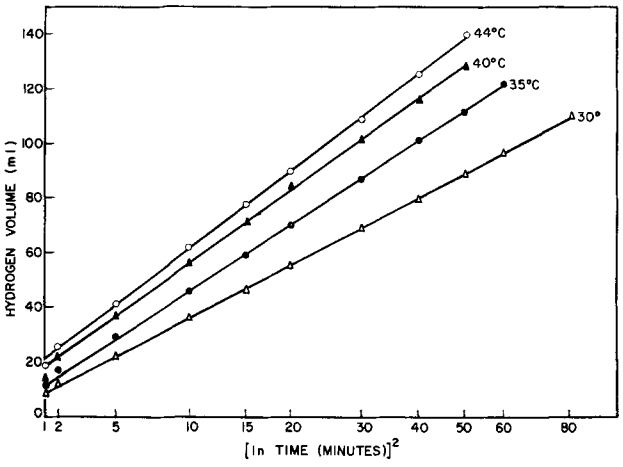

Fig. 3. Hydrogen evolution from steel in 1N H_2SO_4.

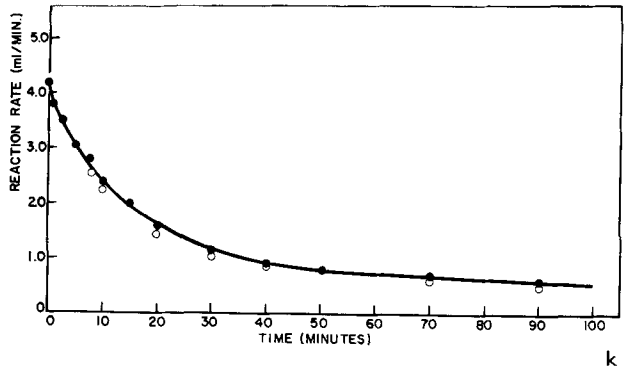

Fig. 4. Hydrogen evolution from steel in 1N H_2SO_4. ○, $\frac{k}{t}$ ln t normalized to $\frac{k}{t}$ ln t = 3.5 at t = 2.5; ●, experimental.

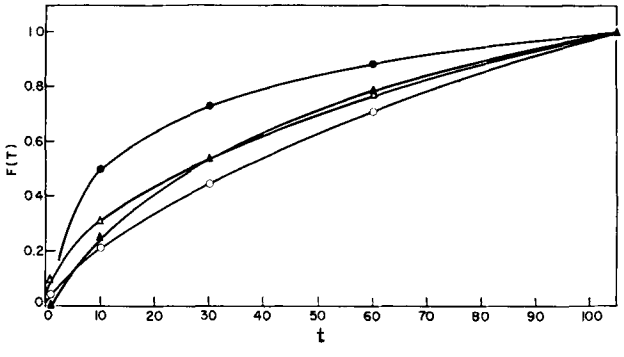

Fig. 5. ▲, $\ln^2 t$; △, $t^{1/2}$; o, $t^{2/3}$; ●, ln t.

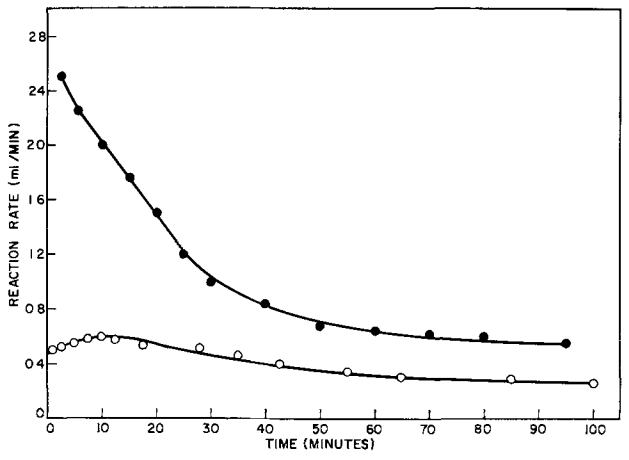

Fig. 6. Hydrogen evolution from steel in 1N H_2SO_4. •, Unhibited; o, inhibited.

The first 10 min the preadsorbed inhibitor is being removed from the surface by undermining, and fresh surface is being continuously exposed. At the same time a barrier layer is forming over the surface of the steel. After about 10 min of reaction the effect becomes predominant and the reaction rate begins to decrease. Thus protection of the steel functions simultaneously through two mechanisms: adsorbed inhibitor and barrier layer formation.

Adsorption and inhibitor efficiency data.—The data for the adsorption of the polar organic compounds are shown in Table I and that for the relative inhibitor efficiencies in Table II. The sulfonate salts were found to be extremely insoluble not only in benzene and water but also in all the usual solvents. For this reason adsorption curves could not be obtained for these compounds. However, they were slightly soluble in 1N H_2SO_4 so that relative inhibitor efficiency curves could be obtained with the inhibitor *in situ*. These data are also given in Table II.

A typical adsorption isotherm and a relative inhibitor efficiency curve are shown in Fig. 7.

The adsorption of the heterocyclic amines, pyrrolidine, piperdine, hexamethlenimine, and heptamethylenimine was not dependent on the number of carbon atoms in the molecule and only slightly on the molecular cross-sectional area. The approximate cross-sectional areas of all compounds studied were determined from Stuart and Briegleb atom models (obtained from Arthur S. LaPine and Company, Chicago), and are given in Table III. Photographs were made of each model with the camera lens in the position of a metal surface atom onto which the polar molecule had adsorbed. Line drawings were made from the photographs and the cross-sectional area calculated assuming that the molecule was free to rotate about the center of its electron density. A plot of the amount of imine adsorbed vs. area is shown in Fig. 8. It is seen that the large molecule adsorbs less but only slightly so. From the areas per molecule and the nitrogen adsorption area of the metal, it was calculated that approximately two layers of inhibitor adsorbed in each case.

There is a marked difference between the adsorption behaviors of these cyclic imines and the high molecular weight aliphatic amines studied earlier (1). Both adsorption data and relative inhibitor efficiency data show that all the imine is irreversibly adsorbed (note the plateaus in Fig. 7). The aliphatic amines adsorbed in every case about the same

Table I. Amount of inhibitor adsorbed (μM/g)

Concentration (molar × 10^3)	10	5	2.5	1.25	0.63	0.31
Pyrrolidine	0.99	0.68	0.61	0.58	0.78	0.80
Piperidine	0.65	0.80	—	0.71	0.68	0.63
Hexamethylenimine	0.68	0.59	0.64	0.61	0.68	0.45
Heptamethylenimine	0.45	0.46	0.49	0.38	0.47	0.41
1, 4, 4 Trimethylpiperidine	0.61	0.60	0.65	0.61	0.52	0.34
1-Benzylpiperidine	0.27	0.25	0.23	0.22	0.19	0.15
Diallylamine	0.97	0.54	0.56	0.44	0.31	—
Tetrahydrofuran	1.42	1.16	1.14	1.11	1.17	1.35
Tetrahydropyran	0.17	0.30	0.34	0.35	—	0.61
Tetrahydrothiophene	0.34	0.56	0.43	0.38	0.21	0.20

Table II. Relative inhibitor efficiency

Concentration (molar × 10^3)	10	5	2.5	1.25	0.63	0.31	0.16
Pyrrolidine	0.43	0.27	0.21	0.14	0.16	0.03	—
Piperidine	0.31	0.42	0.37	0.38	0.27	0.31	—
Hexamethylenimine	0.61	0.57	0.62	0.62	0.55	0.50	—
Heptamethylenimine	0.83	0.61	0.72	0.81	—	0.04	—
1, 4, 4 Trimethylpiperidine	0.51	0.44	0.40	0.46	0.49	0.36	—
1-Benzylpiperidine	0.65	0.66	0.58	0.54	0.45	0.37	—
Diallylamine	0.55	0.32	0.36	0.15	0.06	0.00	—
Tetrahydrofuran	0.37	—	0.38	0.20	0.24	0.03	—
Tetrahydropyran	0.11	0.15	0.16	0.12	—	0.15	—
Tetrahydrothiophene	0.27	0.37	0.40	0.32	0.27	0.11	—
Tetradecyl-benzene Sodium Sulfonate	—	—	—	0.42	0.40	0.41	0.41
Dodecyl	—	—	0.43	0.34	0.31	0.22	0.06
Decyl	—	0.55	0.40	0.37	0.34	0.12	—
Octyl	—	0.61	0.35	0.20	0.04	0.02	—

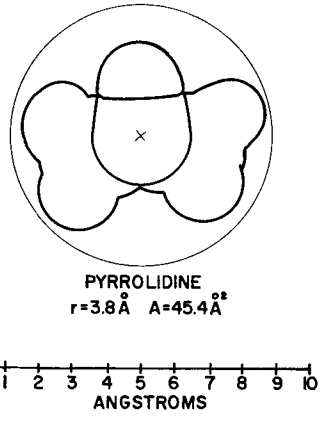

Table III. Molecular areas obtained from maximum radii using atom models

	r (Å)	A (Å²)
Piperidine	4.3	58.1
Hexamethylenimine	4.0	50.3
Heptamethylenimine	5.3	88.2
Tetrahydrofuran	3.4	36.3
1-Benzylpiperidine (Extended)	6.8	145.3
Tetrahydropyran	4.2	55.4
1-Benzylpiperidine (Close-Packed)	5.3	88.2
1, 4, 4 Trimethylpiperidine	4.4	60.8
Tetrahydrothiophene	4.0	50.3
Diallylamine — I = 11.3Å, h = 5.2Å, A = 58.8Å²		

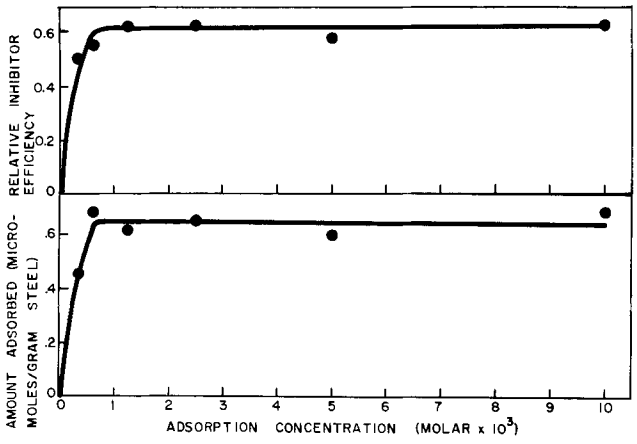

Fig. 7. Inhibitor efficiency of hexamethylenimine (upper); adsorption of hexamethylenimine (lower).

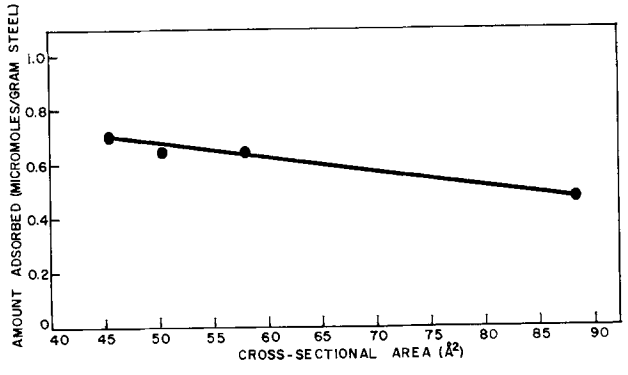

Fig. 8. Point 1-4, pyrrolidine; hexamethylenimine; piperidine; heptamethylenimine.

amount irreversibly and an additional amount, easily desorbed, that increased with the molecular weight of the amine. This difference can be attributed to two things: (*a*) the secondary nitrogen atom of the imines has a greater electron density for coordinating with metal surface atoms, and (*b*) the short, rigid, nearly planar hydrocarbon tails of the imines do not intertwine and lead to physical adsorption. The amines chemisorb less to begin with and their longer, less rigid hydrocarbon tails probably form a loose, haphazard arrangement on top of the chemisorbed layers.

The small amount of adsorption of the 1-benzyl piperdine is due to its large cross-sectional area. In addition the electrophylic phenyl group tends to reduce the electron density on the nitrogen atom. The high degree of adsorption of the tetrahydrofuran is due to its small cross-sectional area. There were evidently areas on the surface available to it that were not available to the other molecules.

Tetrahydrothiophene exhibited a surprisingly small degree of adsorption. However, the compound is extremely volatile. The simple adsorption equipment used in these experiments was not designed for use with volatile compounds.

The relative inhibitor efficiency of the heterocyclic imines is a function of the number of carbon atoms in the ring. This is shown in Fig. 9 and for comparison the data for the n-aliphatic amines taken from Hackerman and Cook's data. The amines also show a linear dependence on the number of carbon atoms for octylamine through tetradecylamine but decidedly less protection for hexadecylamine and octa-

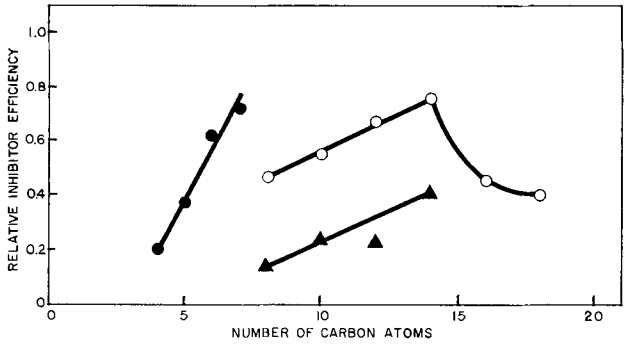

Fig. 9. ●, Heterocyclic imines; ○, aliphatic amines; ▲ alkyl aryl sodium sulfonates.

decylamine. Levine and Zisman (6) found similar behavior for n-aliphatic acids, alcohols, and amines. They noted a marked change in the kinetic coefficient of friction and contact angle for those of 14 or more carbon atoms and attributed this to a transition between monolayers which were liquid condensed and those which were solid.[2] It is seen that the imines increase in efficiency about 20% on the addition of a methyl group, while the amines below hexadecylamine increase by only about 5%.

The imines are relatively good inhibitors. This is in consonance with the fact that secondary amines inhibit better than primary amines. An additional increase in efficiency in going to the tertiary compound can be seen by comparing 1,4,4-trimethylpiperdine with piperdine. It should be noted that there is a greater increase on adding a methyl group to the ring than to the nitrogen atom. Thus,

$$\text{piperdine} < \text{1,4,4-trimethylpiperdine} < \text{hexamethylenimine}$$

The data for the two oxygen compounds is not straightforward. The high relative protection of the tetrahydrofuran is because of the high degree of adsorption observed. The relative inhibitor efficiency of the tetrahydrothiophene was very good even without considering the reduced adsorption of the compound due to its volatility. If the ratio of efficiency to amount adsorbed is considered, the order is

$$\text{tetrahydrofuran} < \text{pyrrolidine} < \text{tetrahydrothiophene}$$

In analyzing the data for the alkyl aryl sodium sulfonates two things must be considered: (*a*) the inhibitor is in the solution and not preadsorbed, and (*b*) the sulfonate salts are very insoluble compared to the other compounds studied. A plot of relative inhibitor efficiency against the number of carbon atoms in the alkyl chain is shown in Fig. 9. Like the amines, the increase is about 5% per methyl group.

Thus we see that homologous series of three types of compounds: heterocyclic imines, aliphatic amines, and alkyl aryl sulfonates exhibit a linear dependence of relative inhibitor efficiency on the number of carbon atoms in the molecule. This cannot be attributed

[2] At first glance, it seems that the sharp drop for hexadecylamine and octadecylamine amine could be ascribed to micelle formation in the solution or to reduced solubility. However, it should be noted that the adsorption increased regularly with molecular weight and what is shown in Fig. 9 is a reduction in effect. Similarly, Levin and Zisman (6) describe a reduction in effect, as did Marsh (7), in connection with a discontinuous change in oil wetting properties. Therefore, the reason could just as well lie in a two-dimensional phase change for instance. In any event, this is a problem which is outside the scope of the present work.

to an increase in barrier layer resistance due to longer chain length on ascending the homologous series, since the amines would then be expected to show a greater effect than the imines. The explanation lies in a more fundamental property of the molecule.

One possible explanation lies in the charge-transfer-no-bond adsorption complex theory advanced by Matsen, Makrides, and Hackerman (8). This postulates that on chemical adsorption a surface complex is formed between adsorbate and adsorbent whose ground state is characterized by a linear combination of wave functions for a no-bond state and a dative state. The dative state lies above the no-bond state by an amount equal to $I_B - (E_A + E_C)$ where I_B is the ionization energy of the adsorbate, a Lewis base, E_A the electron affinity of the metal, a Lewis acid, and E_C the coulombic interaction energy. For a given metal with a series of polar inhibitors, the value of $(E_A + E_C)$ should be constant, but the value of I_B will vary from inhibitor to inhibitor. A lower value of I_B results in a lower value of the energy of the dative state and consequently a lower value of the energy of the ground state. A lower ground state energy is reflected in a stronger bond of chemisorption and a greater relative inhibitor efficiency.

A nucleophylic methyl group tends to increase the electron density on the polar group of organic inhibitors. This is observed as a decrease in ionization potential of each higher member of a homologous series. Data for the compounds studied here are not available, but values of the ionization potentials of some low molecular weight amines were made available by Matsen (9). These values are:

Group	Mono	Di	Tri
Methyl	8.97±0.02	8.24±0.02	7.82±0.02
Ethyl	8.86±0.02	8.01±0.01	7.50±0.02
Propyl	8.78±0.02	7.84±0.02	7.23±?
Butyl	8.71±0.03	7.69±0.03	

A plot of these is shown in Fig. 10. Thus it is seen that the change in ionization energy in ascending a homologous series of amines is about the same per methyl group but that the value of the ionization energy is dependent on whether the amine is primary, secondary, or tertiary.

The inductive effect of a methyl group, with its attendent decrease in ionization potential of the polar group, is thus a possible explanation of the linear dependence of relative inhibitor efficiency on the number of carbon atoms in the molecule. In the heterocyclic imines the change in relative inhibitor efficiency per methyl group is almost 20% reflecting the fact that each carbon in a ring compound is able to exert an inductive effect along both sides of the chain back to the terminal group. The value of 5% for the amines results from the decrease in inductive effect as additional carbon atoms are interspersed in the chain. The same is true for the alkyl aryl sulfonates. The para polarized benzene nucleus.

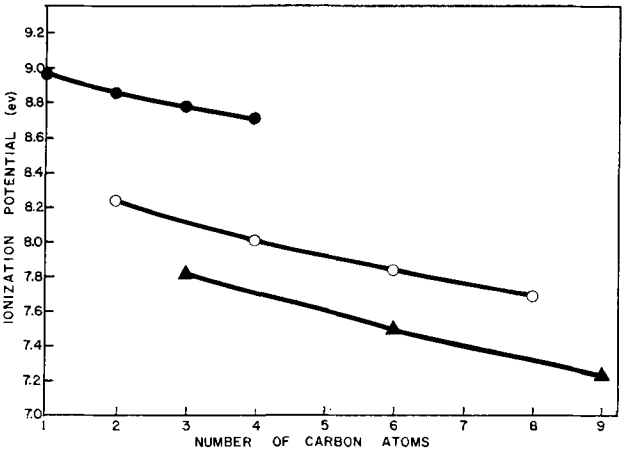

Fig. 10. •, Primary amines; ○, secondary amines; △, tertiary amines.

hydrocarbon chain + 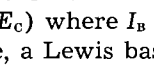 – polar group

is such that the inductive effect is transmitted across it, even though the benzene ring is an electrophylic group.

Conclusions

1. In these experiments the rate of hydrogen evolution from reduced plain steel powder in 1*N* H_2SO_4 is a function of $(\ln t/t)$. Also, the steel was protected by barrier layer formation and by adsorbed inhibitor simultaneously, when the latter was present.

2. The heterocyclic nitrogen, oxygen, and sulfur compounds investigated here exhibit chemisorption under the experimental conditions imposed.

3. Over a range of molecular weights in an homologous series of heterocyclic imines, aliphatic amines, and alkyl aryl sulfonates, the relative inhibitor efficiency is a linear function of the number of carbon atoms in the molecule.

4. A possible explanation of this is the inductive effect of a methyl group with its attendent decrease in ionization potential of the polar group.

Acknowledgment

This research was sponsored in part by the Robert A. Welch Foundation and in part by the Office of Naval Research (Contract Nonr-375(02)). The authors are happy to express their appreciation for this support.

Manuscript received May 29, 1959.

Any discussion of this paper will appear in a Discussion Section to be published in the December 1960 JOURNAL.

REFERENCES

1. N. Hackerman and E. L. Cook, *J. Phys. Chem.*, **56**, 524 (1952); *This Journal*, **97**, 1 (1950).
2. N. Hackerman and A. C. Makrides, *Ind. Eng. Chem.*, **46**, 523 (1954).
3. C. Wagner, *Z. physik. Chem.*, **21B**, 25 (1933).
4. T. P. Hoar and L. E. Price, *Trans. Faraday Soc.*, **34**, 867 (1938).
5. N. F. Mott, *ibid.*, **36**, 472 (1940).
6. O. Levine and W. A. Zisman, *J. Phys. Chem.*, **61**, 1068 (1957).
7. B. E. Marsh, "Corrosion Control with Fatty Nitrogen Derivatives," Paper No. 44, 15th NACE Conference, Chicago, March (1959); Abstract in Corrosion, **15**, 82, January (1959).
8. F. A. Matsen, A. C. Makrides, and N. Hackerman, *J. Chem. Phys.*, **22**, 1800 (1954).
9. From a private communication to Professor F. A. Matsen, University of Texas from K. Watanabe, 1951.

Mechanism of the Iron-Hydrogen Sulfide Reaction at Elevated Temperatures

Hans Arm,[1] Paul Delahay, Charles Hudgins,[2] Fritz Hügli,[3] Lester Hulett,[4] and Mohsin Qureshi[5]

Coates Chemical Laboratory, Louisiana State University, Baton Rouge, Louisiana

ABSTRACT

The mechanism of the iron-hydrogen sulfide reaction was studied in the 500°-760°C temperature range for a total gas pressure of 1 atm. The rate of attack was essentially constant (linear law), and the corrosion scale was composed of two layers: a thin dense layer adjacent to the metal and a porous layer with a coarse crystalline structure. These two features which differentiate this reaction from the iron-sulfur vapor reaction are interpreted on the basis of two main effects: (*a*) partial blocking of reaction sites by hydrogen produced during attack, and occurrence of a reaction at a constant number of reaction sites; and (*b*) continuous recrystallization of the dense scale into a porous scale offering no barrier to transport of reactants. This mechanism is self-regulating.

The following evidence is presented: (*a*) linear Arrhenius plots were obtained; (*b*) essentially the same rate of attack was observed for hydrogen-hydrogen sulfide and helium-hydrogen sulfide mixtures having the same partial pressure of hydrogen sulfide; and the dependence of rate on hydrogen sulfide pressure was accounted for; (*c*) the attack rate was not affected by the coating of specimens with a dense layer of varying thickness obtained by preliminary attack in sulfur vapor; (*d*) the iron-sulfur reaction, which obeys the parabolic law of attack, was inhibited by hydrogen diffusing from the back of the specimen surface; (*e*) recrystallization of the dense layer into the porous one was observed for specimens aged in helium; and (*f*) aging of iron sulfide with a fine crystalline structure (prepared by sulfur attack) in the corresponding hydrogen-hydrogen sulfide equilibrium mixture caused the scale structure to become somewhat coarse.

Discussion of experimental methods covers the following points: (*a*) measurements of the rate of attack with a quartz spring balance in hydrogen-hydrogen sulfide and helium-hydrogen sulfide mixtures; (*b*) techniques for attack in sulfur vapor followed by hydrogen sulfide attack; (*c*) use of a mild steel cartridge containing lithium aluminum hydride in the hydrogen diffusion studies; and (*d*) scale thickness studies.

The iron-hydrogen sulfide reaction at elevated temperatures has two unusual features which distinguish it from most other metal-gas reactions with solid scale formation: (*a*) the rate of attack becomes constant after a short time (a few minutes above 500°C), i.e., the attack follows a linear law; and (*b*) a scale composed of two layers is formed, the layer adjacent to the metal having a fine crystalline structure and the outer layer being of a porous and coarse structure. [See review of previous work in the recent paper of Dravnieks and Samans (1).] In contrast, the iron-sulfur reaction, according to Hauffe and Rahmel (2), follows the normal parabolic law of attack (corresponding to a diffusion controlled process) with formation of a single homogeneous scale having a fine crystalline structure. The same product of attack, iron sulfide, is obtained in both reactions, and yet the kinetics are very different. An interpretation for these differences is given here.

Recent kinetic investigations of this problem were made by Dravnieks and Samans (1) and by Haycock (3). The manuscript of the former authors was available at the onset of our work while Haycock's manuscript became available in the fall of 1958. Dravnieks and Samans postulate a mechanism controlled by a surface reaction which they assume to be the dissociation of hydrogen sulfide at the scale surface. They account for the two-layer scale by assuming two different processes, namely diffusion of sulfide ions in the dense layer and diffusion of ferrous ions in the coarse layer. Haycock postulates mixed control by diffusion of sulfide ions across the dense layer and recrystallization of the dense layer into the porous layer. A linear law is observed when the dense layer reaches a constant thickness. Continuous recrystallization is greatly accelerated by hydrogen produced in the iron-hydrogen sulfide reaction. Haycock concludes from marker experiments that sulfide ion is the diffusing species. This is accounted for by the assumption that the diffusion rate

[1] Postdoctoral fellow, 1957-1958. Present address: Laboratory for Organic Chemistry, University of Bern, Bern, Switzerland.

[2] Predoctoral fellow, 1956-1957. Present address: Development and Research Department, Continental Oil Co., Ponca City, Oklahoma.

[3] Postdoctoral fellow, 1956-1957. Present address: Technical High-school, Winterthur, Switzerland.

[4] Predoctoral fellow, 1956-1958 (part-time) and 1958-1959.

[5] Postdoctoral fellow, 1958-1959. Present address: Department of Chemistry, Muslim University, Aligarh, India.

for ferrous ions is decreased because of the formation of "E-centers." By analogy with other cases (4), Haycock assumes that E-centers are formed by trapping of hydrogen in cation vacancies of the lattice.

Our purpose was to design experiments to discriminate as unambiguously as possible between control by a surface reaction and that by a diffusion process and to determine whether hydrogen plays a role in recrystallization of the dense layer into a coarse layer (not observed when hydrogen is not present). The following studies were made: (*a*) confirmation of the linear law at different temperatures and determination of the heat of activation; (*b*) attack in mixtures of hydrogen sulfide and hydrogen or helium; (*c*) attack of iron in sulfur vapor followed by hydrogen sulfide attack; (*d*) study of the effect of hydrogen on the iron-sulfur vapor reaction, hydrogen being supplied by diffusion through the iron from the unexposed face of the corroding specimen; and (*e*) determination of the scale thicknesses and effect of aging on the two-layer scale.

Experiment (*a*) would give an indication of mixed control by two processes having different heats of activation if a nonlinear Arrhenius plot were obtained. The combination of experiments (*b*), (*c*), and (*d*) should allow discrimination between control by a surface reaction and by diffusion. Experiment (*e*) should provide direct evidence of recrystallization.

Experimental Methods

Attack in Hydrogen Sulfide and Hydrogen Sulfide-Hydrogen or Hydrogen Sulfide-Helium Mixtures

Rates of attack were determined from the increase in specimen weight. The specimen in the lower Vycor reaction chamber (Fig. 1A) was suspended on a fine Vycor fiber attached to a quartz spring (obtained from Worden Laboratories, Houston, Texas). The quartz spring extended only in the upper Pyrex chamber and was essentially at room temperature; i.e., no temperature correction in the calibration was necessary. The elongation of the spring was measured with a cathetometer (Gaertner, Chicago) with an error not exceeding 0.05 mg for specimens weighing approximately 0.5 g.

The chamber with its gas preheater coil was connected to a gas mixing system which could supply hydrogen and mixtures of hydrogen sulfide with either hydrogen or helium. Traces of oxygen in the electrolytic grade hydrogen (Matheson) were removed by passing the gas through a "Deoxo" catalyst cartridge (obtained from Engelhard Industries, Inc., Newark, N. J.). Hydrogen sulfide and helium were used as supplied in tanks (Matheson). The composition of the gas mixtures was constantly controlled (*a*) from the individual flow rates, as measured with differential pressure manometers, in the determination of the heat of activation, and (*b*) by a sensitive thermal conductivity cell in the comparison of attack rates for hydrogen-hydrogen sulfide and helium-hydrogen sulfide mixtures. A gas reservoir with twice the capacity of the reaction chamber was inserted between the chamber and the mixing system. The gas reservoir was used in the initiation of the reaction. The reaction chamber was bypassed during the adjustment of the gas mixture composition.

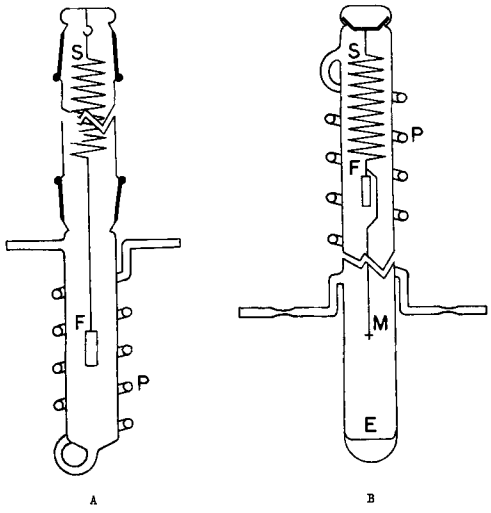

Fig. 1(A). Apparatus for the study of the reaction of iron with hydrogen sulfide and mixtures of hydrogen sulfide and hydrogen or hydrogen sulfide and helium. F, specimen; S, quartz spring; P, gas preheater coil. Fig. 1(B). Apparatus for mixed attack experiments and for hydrogen diffusion experiments. F, iron cartridge or other specimen; S, quartz spring; E, sulfur pool; P, gas preheater coil; M, platinum wire marker.

Specimens were made of spectroscopically pure iron sheets, for which the suppliers (Jarrell Ash Co., Newtonville, Massachusetts) gave the following analysis: 4 ppm Mn; 2 ppm Ni, Si, Mg; 1 ppm Cu, Ag, Na, Li; other metals were not detected spectroscopically. The specimen dimensions of approximately 0.05 x 0.7 x 1.4 cm were determined accurately with a micrometer. Specimens were washed in petroleum ether and acetone before use.

After introduction of the specimen in the reaction chamber the entire flow system was evacuated to a pressure below 1 mm. The absence of leaks was ascertained, and the system was flushed repeatedly with hydrogen and finally evacuated again. Hydrogen then was passed through at a rate of approximately 200 ml/min (linear velocity of approximately 1 cm sec^{-1}), and the furnace was brought to the desired temperature. Reduction of traces of oxide on the specimen followed for 2 hr at 500°C or a higher temperature. After removal of hydrogen by evacuation, the gas mixture was passed through the chamber at the rate of 200 ml/min, and the attack was followed as described above.

Mixed Attack

Experiments in which attack by sulfur vapor was followed by hydrogen sulfide attack involved one difficulty, namely, that to avoid condensation, no part of the apparatus could be colder than the vessel in which sulfur was vaporized. The Pyrex chamber of Fig. 1B was constructed with the upper end open. Sulfur was introduced, and the specimen, suspended on a quartz spring, was hung on an inverted U-rod. The top of the chamber then was sealed. Procedures

for the purging and reduction were the same as for the hydrogen sulfide attack. After reduction of the specimen, the chamber was filled with helium and sealed at the constricted sections of the side arms, the upper part of the chamber being maintained all the time at 575°C. The lower furnace was raised around the sulfur reservoir and heated to 230°C. Vaporized sulfur condensed in the section of the chamber (between the two furnaces), approximately 2 in. in length, which remained cool during the warm-up of the lower furnace. Heater sleeves were slipped over the side arms to avoid sulfur condensation. After the lower furnace reached 230°C, a heater clamp was placed around the exposed midsection, and attack of the specimen was initiated. This method reduced the uncertainty of the zero time to a few minutes.

After the desired increase in weight, as followed by the cathetometer, had been reached, sulfur attack was stopped by removal of the lower furnace, the upper furnace remaining at 575°C. The heater sleeves were removed and the gas flow system, discussed above, was connected to the sidearms with thick-walled Tygon tubing. The system then was evacuated and purged with hydrogen. The hydrogen-hydrogen sulfide mixture of previously adjusted composition was introduced in the chamber by the snapping of the sidearm tips inside the Tygon tubing at the inlet and outlet. Rates of attack were determined from cathetometer readings at a gas flow rate of 200 ml/min.

Influence of Diffusing Hydrogen on the Iron-Sulfur and Iron-Hydrogen Sulfide Reactions

The effect of hydrogen diffusing from the back of the specimen surface during attack in sulfur vapor was studied. The specimen was a mild carbon steel cartridge, 4 x 20 mm with a bore of 2 mm diameter, containing 20 mg of lithium aluminum hydride. The air in the cartridge was flushed with helium while the mouth was crimped together. The cartridge was immediately sealed with an acetylene torch, the lower part of the cartridge being kept cold in water. A platinum wire was attached to the top of the cartridge for suspension purposes, and the wire and sealed portion of the cartridge were masked with a porcelain cement (Saureisen). The cement was allowed to harden in air for at least 24 hr before the cartridge was used. Immediately before use, the cartridge was polished with Behr-Manning 400A sandpaper and jeweler's rouge cloth and then washed with acetone and petroleum ether.

The cartridge and a long platinum wire were suspended on a quartz spring inside a Pyrex tube whose bottom had been filled previously with sulfur (Fig. 1B). This Pyrex tube was provided with an inlet and outlet for hydrogen. The tube then was sealed at the top and placed in a furnace. The cartridge was reduced for 2 hr in a stream of hydrogen, the lower part of the reaction tube remaining at room temperature. After reduction, the furnace was cooled and the tube was removed. The hydrogen remaining in the tube was replaced with helium, and the gas inlet and outlet were sealed off and shortened so that they would not protrude outside the furnace.

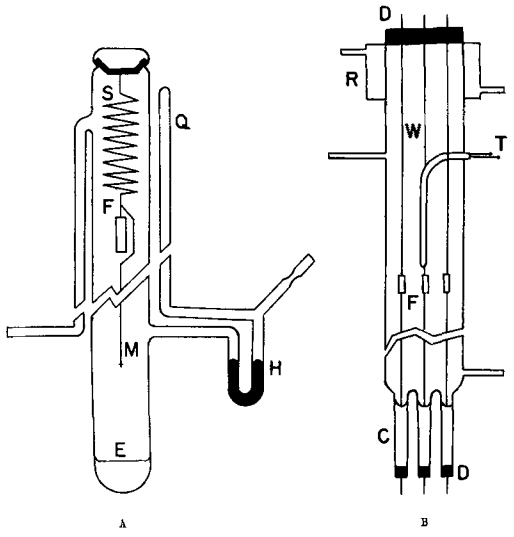

Fig. 2(A). Apparatus for measuring rates of hydrogen diffusion through iron and iron sulfide. S, quartz spring; F, cartridge; E, sulfur pool; M, platinum wire marker; H, differential pressure manometer; Q, tube containing the reference volume of gas at the same temperature as the cartridge. Fig. 2(B). Apparatus for scale studies. F, specimens; W, chromel wires; T, thermocouple; C, detachable casting tubes containing sulfur; D, rubber stoppers; R, cooler.

Sulfur attack followed according to the procedure described in the previous section.

In some experiments with blank cartridges, i.e., without lithium aluminum hydride, the reaction tube was evacuated after hydrogen reduction and kept at a pressure of 0.02 mm for 8 hr to remove the hydrogen which had diffused into the metal.

Experiments on the effect of hydrogen diffusion on hydrogen sulfide attack involved the same procedure as described above for spectroscopically pure specimens except that cartridges were utilized.

Diffusion of Hydrogen in Iron and Iron Sulfide Scale

Rates of hydrogen diffusion through iron with or without ferrous sulfide scale were obtained with the chamber of Fig. 2A. The initial steps were the same as in the preceding section. After reduction, hydrogen was replaced by helium in the chamber. The side arm on the left was sealed off close to the wall of the chamber, and the small sidearm protruding from the U-tube was sealed off at the constriction. Condensation of sulfur was prevented by a specially shaped heater. Sulfur vapor attack was carried out at 500°C all the time. The U-tube was connected, after removal of its heater, to a vacuum system with a thick wall Tygon tube. A small glass bulb containing 5 ml of mercury was also connected near the U-tube and in parallel with the vacuum system. The tip of the sidearm in the Tygon tube was snapped and the reaction chamber was evacuated with the forepump. The sulfur reservoir was sealed off to eliminate subsequent errors in pressure measurements as a result of gas release from the sulfur. Evacuation to 1 μ was continued with an oil diffusion pump. Mercury from the small reservoir was poured through the sidearm and into the U-tube, and the sidearm was sealed. An all glass, completely sealed system with a built-in differential pressure mano-

meter thus was obtained. Pressure variations in the reaction chamber resulting from hydrogen diffusion through the cartridge wall were measured with a cathetometer.

Scale Thickness Studies

A special reaction vessel was designed for scale thickness studies to allow rapid casting of specimens in molten sulfur. Five specimens (only three shown in Fig. 2B) were suspended on chromel wire by means of insulating glass hooks. The wires were strung through rubber stoppers. The casting tubes were filled with sulfur chips which were melted with a clamp heater just before the casting of a specimen. After attack in a hydrogen sulfide-hydrogen mixture, the specimen was lowered into the molten sulfur, and the casting tube was allowed to cool. The five specimens could be cast at different times. The reduction in hydrogen before attack and the attack were conducted as above.

The tendency of the scale to peel off as a result of the temperature change was minimized by the use of curved specimens as suggested by Haycock (3). The scale remained quite adherent on the concave side.

Mounted specimens were cut with a high-speed, glass-cutter's saw. The cross section was polished with graded emery cloths and levigated alumina on a metallographic polishing wheel. A Bausch and Lomb metallographic microscope was used for examination and photography.

Specimens obtained in mixed attack and aging experiments and cartridges from experiments with hydrogen diffusion were mounted in an EPON resin.[6] The procedure was as follows: Add 9 parts EPON 828 to 1 part curing agent (DTA); mix well; pour into mold around the specimen; allow the EPON to cure for 24 hr at room temperature.

Aging of Scale in Hydrogen-Hydrogen Sulfide Mixture

Specimens were attacked in sulfur vapor as in the mixed attack experiments. After attack, hydrogen was introduced in the chamber much in the same way as hydrogen sulfide was introduced in the mixed attack studies, and the pressure in the chamber was adjusted slightly above atmospheric pressure. The equilibrium partial pressure of hydrogen sulfide, in the conditions of this experiment, was quite insignificant in comparison with the hydrogen pressure (see below, influence of diffusing hydrogen on sulfur vapor attack), and this allowed the use of pure hydrogen rather than the equilibrated mixture hydrogen-hydrogen sulfide. After aging, the chamber was allowed to cool slowly to room temperature before the specimens were removed. Specimens then were mounted in the EPON resin.

Mechanism of the Iron-Hydrogen Sulfide Reaction

Postulated Mechanism

The results of attack in helium-hydrogen sulfide mixtures and mixed attack experiments led us to postulate a mechanism for the iron-hydrogen sulfide reaction which was further confirmed by experiments on sulfur attack with hydrogen diffusion and experiments on aging of the scale. The mechanism is as follows:

Hydrogen produced by the iron-hydrogen sulfide reaction remains in large part adsorbed (or associated in some other fashion) with iron sulfide. The number of reaction sites available for attack by hydrogen sulfide is considerably decreased as a result of hydrogen adsorption, and attack occurs at an essentially constant number of reaction sites, i.e., a linear law of attack is observed. Furthermore, diffusion is not rate controlling (at least at sufficiently high temperatures, i.e., above 500°C approximately) because of continuous recrystallization of the scale into a coarse layer which offers no diffusion barrier. The thickness of the thin layer is not sufficient to cause diffusion control.

This mechanism is self-regulating in that a decrease (or increase) in rate would result in a decrease (or increase) in the rate of hydrogen production and, consequently, in an increase (or decrease) in the number of reaction sites. The latter effect then would compensate the initial decrease (or increase) in rate that caused it.

Supporting evidence will now be presented.

General Characteristics and Effect of Temperature[7]

The two essential characteristics of the iron-hydrogen sulfide reaction, linear law of attack and formation of a two-layer scale, are apparent from Fig. 3 and 4. The slope of the log-log plot in Fig. 3 is quite close to unity, i.e., the law of attack is linear. In the early stage of attack (5-15 min) the rate is somewhat larger than the constant rate observed afterwards. This effect causes the slope of the log-log plot in Fig. 3 to be somewhat smaller than unity. The initial high rate possibly results from the difference in the metal and scale areas.

At temperatures below 500°C, plots of the increase in specimen weight vs. time exhibit a marked

[6] Courtesy of Dr. E. W. Haycock, Shell Development Co., Emeryville, California. Information about EPON resins can be obtained from the Shell Development Co.

[7] This section based on the work of L. Hulett, C. Hudgins, F. Hügli, and M. Qureshi.

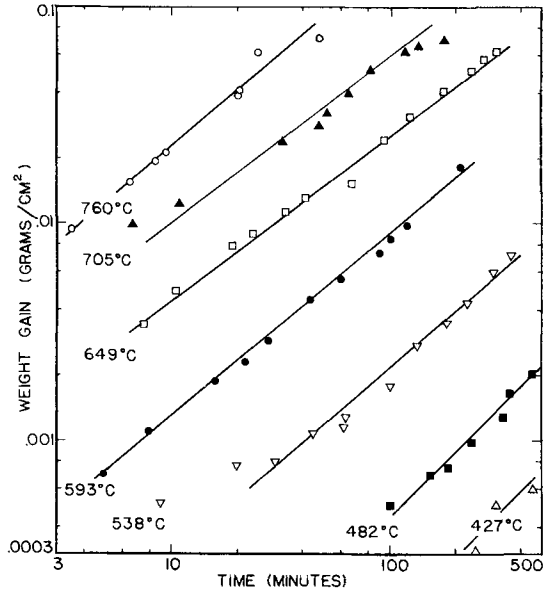

Fig. 3. Weight gain of iron against time for reaction in hydrogen sulfide at 1 atm at different temperatures.

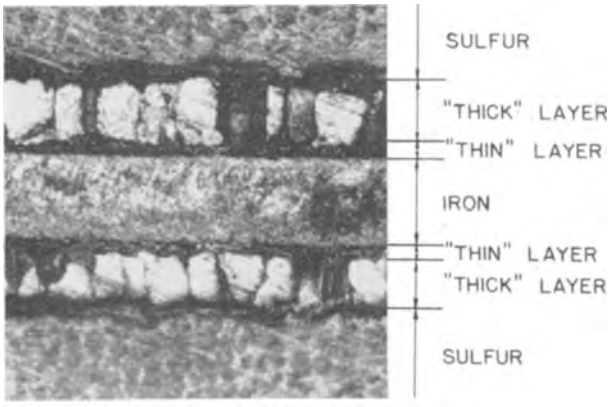

Fig. 4. Photomicrograph of section of specimen after 60 min exposure to hydrogen sulfide at 1 atm and 649°C. Magnification, 200× before reduction for publication.

curvature [cf. Dravnieks and Samans (1) and Haycock (3)] which is probably due to partial diffusion control.

Arrhenius plots for the data on Fig. 3 and similar data for a 4:1 hydrogen-hydrogen sulfide mixture are linear (Fig. 5). Mixed control of kinetics by two processes having rather different heats of activation is ruled out by the linear plot of Fig. 5. The corresponding heat of activation is 30 kcal/mole, as compared to 20 kcal/mole according to Dravnieks and Samans (1) and 12 kcal/mole according to Haycock (3). The variation from 30 to 12 kcal/mole is possibly due to differences in hydrogen coverage. (This point was suggested to us by Dr. Haycock.) Indeed, the values of 30, 20, and 12 kcal/mole were obtained, respectively, in pure hydrogen sulfide at 1 atm, in hydrogen at 1 atm with a relatively low partial pressure of hydrogen sulfide, and in hydrogen at 600 p.s.c. with hydrogen sulfide at 0.6 p.s.c. If one assumes that hydrogen desorption is the rate-determining step, the foregoing heats of activation correspond to the heats for hydrogen adsorption. The values of 30 to 12 kcal/mole then are of the right order of magnitude, and their variation with coverage is in the right direction. Compare for instance with the heat for hydrogen adsorption on nickel which, according to Beeck (5), decreases from approximately 30 kcal/mole near zero coverage to 17 kcal/mole near full coverage. The iron sulfide scale probably behaves as a metal for hydrogen adsorption because of the high density of free electrons (high conductivity of scale).

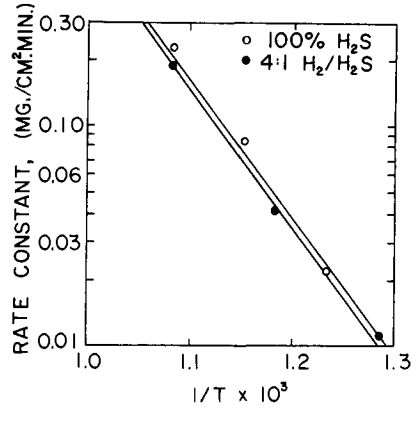

Fig. 5. Arrhenius plots of the rate constant for attack in hydrogen sulfide and in hydrogen-hydrogen sulfide mixture.

Attack in Hydrogen Sulfide-Hydrogen and Hydrogen Sulfide-Helium Mixtures[3]

It is well established that the rate of attack of iron in hydrogen-hydrogen sulfide mixtures depends on the partial pressure of the gases [cf. Dravnieks and Samans (1) and references therein]. The effect can be accounted for by thermodynamics, and there is little doubt that near equilibrium a thermodynamic interpretation holds. Hydrogen, however, might act primarily as a diluting agent in the attack of iron in hydrogen-hydrogen sulfide mixtures not near equilibrium. Essentially the same rate of attack then should be obtained with hydrogen-hydrogen sulfide and helium-hydrogen sulfide mixtures having the same partial pressures of hydrogen sulfide, if variations in hydrogen coverage did not complicate matters. Figure 6 shows that the same rates are indeed observed with mixtures having the same partial pressure of hydrogen sulfide. (Incidentally, the decrease in rate at low partial pressures of hydrogen sulfide is not caused by depletion of reactant.)

These observations preclude interpretation based on a Wagner model for the kinetics of attack, since such a model presupposes equilibrium attainment at the metal-scale and gas-scale interfaces. Very different rates of attack would be obtained for a reaction obeying a Wagner model when hydrogen is replaced by helium, especially for low partial pressures of hydrogen sulfide. The data of Fig. 6 do not eliminate diffusion as a partial or total rate-controlling factor, but it can be concluded from them that equilibrium is not reached at the metal-scale and/or scale-gas interfaces. Of course, departure from equilibrium does not necessarily imply control by a surface reaction since the surface reaction might be too fast to be rate-controlling.

Since, according to our interpretation, the rate of attack depends on hydrogen coverage, Fig. 6 im-

[3] This section based on the work of C. Hudgins, F. Hügli, and L. Hulett.

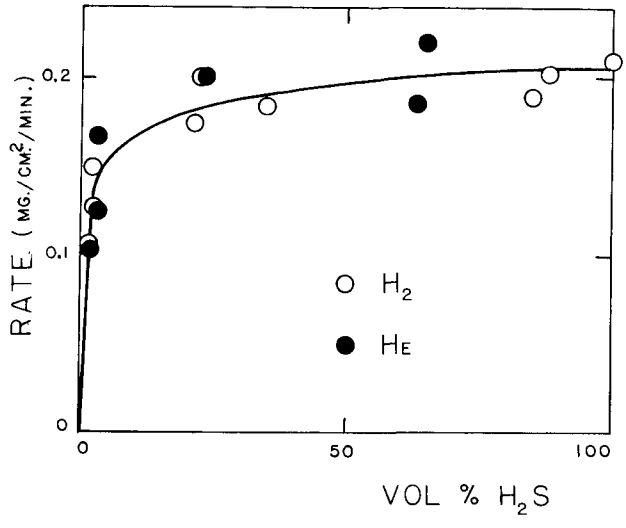

Fig. 6. Rate of attack at 649°C against volume per cent of hydrogen sulfide for mixtures of hydrogen sulfide with hydrogen or helium.

plies that this coverage remains essentially the same when helium is substituted for hydrogen. Of course, coverage by hydrogen for adsorption equilibrium would be affected by such a substitution unless full coverage were achieved for the lowest partial hydrogen pressure. One then must assume that adsorption equilibrium is not reached for hydrogen.

The data of Fig. 6 can be interpreted on the basis of the postulated mechanism. It is assumed (*a*) that the attack rate is proportional to the partial pressure of hydrogen sulfide and (*b*) that the rate is proportional to the number of reaction sites, i.e., the "free area." Thus

$$v = kp(1-\theta) \qquad [1]$$

where v is the attack rate, k a proportionality constant, θ the "coverage" by hydrogen, and p the partial pressure of hydrogen sulfide. The coverage by hydrogen increases with the rate of production of hydrogen, i.e., with v. A rigorous relationship between v and θ would be complicated because it would include the adsorption isotherms for hydrogen and hydrogen sulfide, or kinetic terms corresponding to these isotherms, and possibly other considerations for the interaction between hydrogen and the scale [Haycock's E-centers (3)]. Furthermore, the dependence of θ on p should be considered. This dependence is quite minor for the data of Fig. 6, if the foregoing analysis is accepted. It will suffice for the present purpose to assume without any claim to rigor that

$$\theta = k'v \qquad [2]$$

By elimination of θ from Eq. [1] and [2] there follows an equation in the form of a Langmuir isotherm (but the similarity ends with the form of the equation)

$$v = \frac{kp}{1 + kk'p} \qquad [3]$$

It follows from Eq. [3] that a plot of p/v against p should be linear. This is the case (Fig. 7) for the data of Fig. 6.

Dravnieks and Samans (1) also noted that the dependence of attack on pressure obeys a Langmuir isotherm type of equation, and, in fact, they reported linear plots of p/v against p. Their explanation, however, is different from the one offered here.

Mixed Attack[6]

Rather conclusive proof of the absence of diffusion control was obtained from mixed attack experiments. Data for attack in hydrogen-hydrogen sulfide mixtures (4:1) are given in Fig. 8 for specimens with different initial thicknesses of iron sulfide scale (as obtained by preliminary attack in sulfur vapor). After an initial period, which is interpreted below, the same rate of attack prevails regardless of the thickness of the initial scale of iron sulfide. This conclusion holds even for the experiment in which the initial scale was approximately twice as thick as the scale formed during hydrogen sulfide attack. An interpretation of the iron-hydrogen sulfide reaction based on control by diffusion in the scale is inconsistent with these observations.

[6] This section based on the work of H. Arm, L. Hulett, and M. Qureshi.

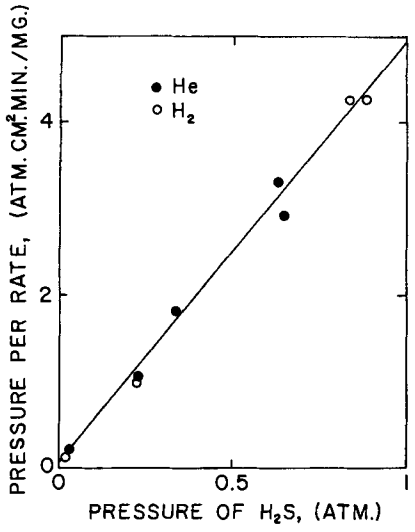

Fig. 7. A verification of Eq. [3] for the data in Fig. 6

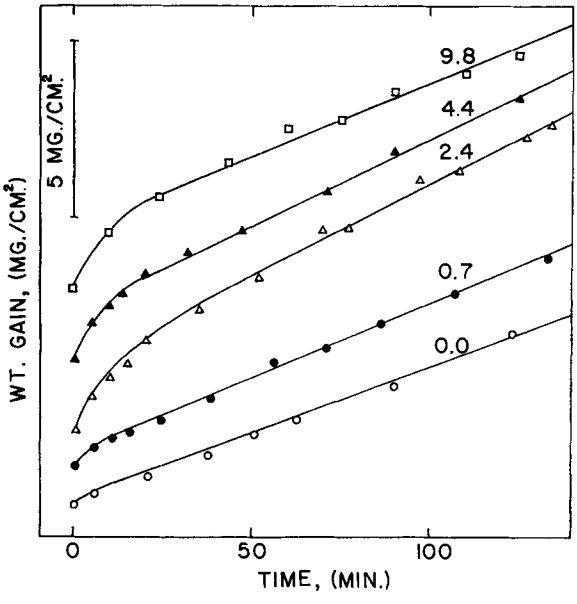

Fig. 8. Increase of weight against time for specimens previously attacked in sulfur vapor. Number on each curve is weight of iron sulfide in mg/cm² formed during sulfur vapor attack. Temperotures: molten sulfur during sulfur vapor attack, 230°C; specimen during sulfur vapor and hydrogen sulfide attacks 575°C; curves are shifted for clarity.

It could be argued that the scale underwent some transformation during the initial hydrogen sulfide attack and that the rate became constant when the thin dense layer obtained in the usual hydrogen sulfide attack was formed. Examination of the scale (Fig. 9) did not confirm this view. The outer scale exposed to hydrogen sulfide was composed of large crystals, but the bulk of the scale had remained quite compact and homogeneous. Furthermore, the initial rate of attack in hydrogen sulfide was higher than the constant value reached at a later stage, and yet the initial scale (formed in sulfur vapor) had a fine crystalline structure.

The initial rapid attack can be interpreted in terms of the postulated mechanism. Thus, the area at the gas-iron sulfide interface before hydrogen

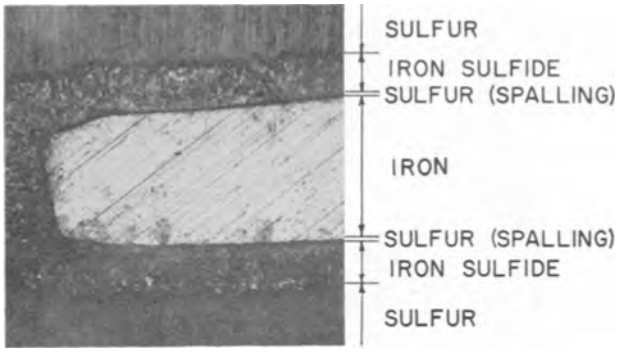

Fig. 9. Photomicrograph of section of specimen after attack by sulfur vapor followed by hydrogen sulfide attack. Temperature: 575°C. Magnification, 200× before reduction for publication.

sulfide attack was larger than for the metallic surface corresponding to the same projected area. Hence, rates of attack by hydrogen sulfide were initially larger than for a metallic specimen without prior sulfur attack. However, the self-regulating mechanism soon brought the rate to a constant value. Note that the curves of Fig. 8 for the three thicker scales appear to be the same, i.e., the initial process was independent of the scale thickness once a sufficiently thick scale had been produced.

Influence of Diffusing Hydrogen on Sulfur Vapor Attack[10]

Since hydrogen, in our interpretation, is supposed to block in part the surface for attack in the iron-hydrogen sulfide reaction, it was thought that a similar effect might be observed in the iron-sulfur vapor reaction if hydrogen were allowed to diffuse from the back of the specimen surface. The data of Fig. 10, obtained by the cartridge technique, confirm this inference. The parabolic law was confirmed for the blank cartridges which had been left in vacuum for 8 hr after hydrogen reduction. An induction period was observed for blank cartridges which had not been vacuum treated, and an even longer induction period was observed for cartridges containing lithium aluminum hydride. In all cases, sulfur attack resumed its normal course after a sufficiently long time. The interpretation is as follows:

Hydrogen produced in the lithium aluminum hydride cartridge diffused toward the outside surface of the cartridge and greatly reduced the attack by sulfur vapor. Nevertheless, an iron sulfide scale slowly built up. The diffusion rate for hydrogen through the compact scale (no leaks!) was lower than through iron, as shown[11] in Fig. 11, and consequently, coverage of the scale by hydrogen decreased as the scale became thicker. This resulted in a progressive increase in rate of attack until the film had become so thick that diffusion was practically stopped. Attack then resumed its normal course. Complete decomposition of lithium aluminum hydride cannot be invoked for resumption of normal attack because of the respective amounts of this substance and diffused hydrogen that were involved.

[10] This section based on work of L. Hulett and M. Qureshi.

[11] One calculates from the rate of diffusion of hydrogen for the cartridge without scale the approximate inner pressure of hydrogen of 2 atm on the basis of the permeability data of Jost (7).

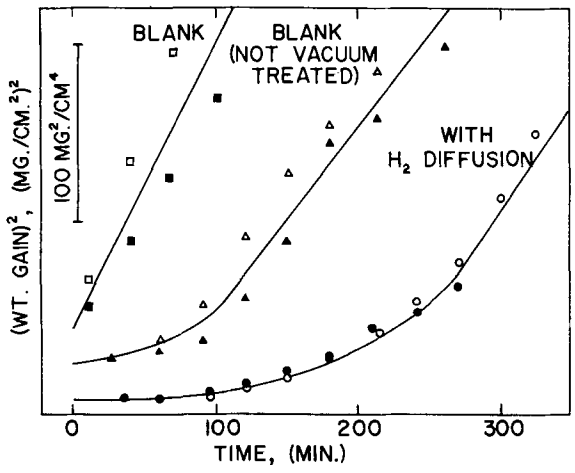

Fig. 10. Plots of the square of the weight gain against time for iron cartridge during attack by sulfur vapor. Temperatures during attack: molten sulfur, 230°C; cartridge, 500°C. Curves are equally shifted at the origin by 20 mg^2/cm^4.

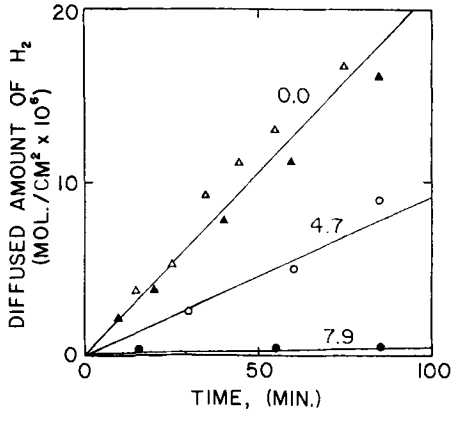

Fig. 11. Data for hydrogen diffusion through iron or iron coated with iron sulfide scale. Number on each line is the weight of iron sulfide in mg/cm^2. Temperature: 500°C.

The same interpretation holds for the blank cartridges which had not been vacuum treated. Hydrogen which had diffused in the metal during reduction then hindered attack in sulfur vapor until it could no longer appreciably cover the scale surface.

Further confirmation of the above interpretation was obtained by similar experiments in which the blank cartridge and a lithium aluminum hydride filled cartridge were attacked in hydrogen-hydrogen sulfide mixture (4:1). The same rate of attack was observed in both cases, and no induction period due to the presence of hydrogen was observed.

An alternative explanation, based on thermodynamic considerations, namely that iron attack by sulfur did not proceed in the presence of hydrogen, is ruled out. Thus, one calculates from the data of Rosenqvist (6) that the equilibrium constant for the reaction $FeS + H_2 \rightleftharpoons Fe + H_2S$ at 500°C is 2×10^{-4}. The amount of hydrogen sulfide formed in one of the experiments was in fact determined by passing the gas through a detection tube used in air pollution studies.[12] A maximum amount of 6×10^{-6} moles of hydrogen sulfide was formed in the reaction chamber. Since the amount of hydrogen sulfide produced is so small, the retarded sulfur attack is

[12] Courtesy of Professor P. W. West, Louisiana State University.

Table I. Thicknesses of the dense layer of iron sulfide produced by attack by a 4:1 hydrogen-hydrogen sulfide mixture at 575°C

Reaction time, min	Thickness, mm × 10^3	Number of determinations
30	1.6	2
140	6.5	1
180	8.0	4
480	7.7	1
540	8.9	1
550	7.7	1
660	7.7	1
720	8.9	1

definitely not due to reduction of iron sulfide by diffusing hydrogen.

Another possible interpretation according to which Haycock's E-centers (3), resulting from the presence of hydrogen in the film, decrease diffusion by cation vacancy does not account for the resumption of attack. Thus, the scale, at least in its inner layer, retained a relatively high concentration of E-centers because of the vicinity of hydrogen supply. This layer would have offered a permanent barrier to vacancy diffusion, i.e., attack would never have resumed unless the film had cracked. The latter explanation, however is invalidated by the very low diffusion rate of hydrogen through the scale (Fig. 11). Of course, one could say that sulfide ion is the diffusing species, but the role of hydrogen then remains unexplained.

Recrystallization of the Scale[18]

It is well established [see Dravnieks and Samans (1) for review of literature] that the thin dense layer reaches an essentially constant thickness. The data on Table I confirm this, but it should be noted that initially (30 min) the thin layer had not reached its constant thickness although a linear law was already observed. This seems to preclude, with other arguments discussed above, control by diffusion through the thin layer.

Since the thin layer reaches a constant thickness, there must be a continuous transformation of the thin dense layer into the porous one (Fig. 4). We observed that aging of the two layer scale in a helium atmosphere causes a progressive disappearance of the dense layer. Since such a transformation is not observed for iron sulfide produced by the iron-sulfur vapor reaction, hydrogen or hydrogen sulfide must be responsible for recrystallization. Haycock (3) suggested a tentative mechanism for the recrystallization process, and he showed that hydrogen greatly enhanced the sintering rate of powdered iron sulfide. Powdered ferrous sulfide with a large initial surface area did not appreciably sinter when left in a vacuum for 5 hr at 500°C. In the presence of hydrogen at the same temperature the surface area was reduced by half after only 2 hr, and the powder had visibly sintered to a porous plug.

Haycock's experiments were corroborated by studies on aging of iron sulfide, prepared by sulfur attack, in the equilibrium hydrogen-hydrogen sulfide mixture (see Experimental Methods). The outer crystalline structure of the scale became somewhat more coarse upon aging (Fig. 12).

[18] This section based on the work of L. Hulett and M. Qureshi.

Fig. 12. Photomicrograph of section of specimen, attacked in sulfur vapor at 500°C (vessel with liquid sulfur at 230°C), after a 48-hr aging in hydrogen at a pressure slightly above 1 atm. Note EPON resin around metal contour as a result of scale spalling. Magnification, 200× before reduction for publication.

Conclusion

It is concluded that the linear law of attack for the iron-hydrogen sulfide reaction at elevated temperatures (above 500°C approximately) results from two main effects: (*a*) partial blocking at reaction sites by hydrogen produced during attack, and (*b*) continuous recrystallization prevents the formation of a thick dense scale that would become a real diffusion barrier for sufficient thicknesses. The blocking of reaction sites is self-regulating and the linear law is thus obeyed.

Acknowledgment

The support of the American Petroleum Institute is gratefully acknowledged. The authors are indebted to the following members of the Subcommittee on Corrosion, Division of Refining, of the American Petroleum Institute for helpful discussions: Messrs. E. B. Backensto, E. A. Camp, and R. J. Hafsten. Discussions with Drs. A. Dravnieks and E. W. Haycock were most fruitful. Messrs. E. G. Smith and G. F. Mathes of the Mechanical Engineering Department, Louisiana State University, kindly provided equipment for the photomicrographic studies.

X-ray equipment used in some structure studies was purchased in part with a grant from the National Science Foundation.

Manuscript received July 30, 1959.

Any discussion of this paper will appear in a Discussion Section to be published in the December 1960 JOURNAL.

REFERENCES

1. A. Dravnieks and C. H. Samans, *This Journal*, **105**, 183 (1958).
2. K. Hauffe and A. Rahmel, *Z. physik. Chem.*, **199**, 152 (1952).
3. E. W. Haycock, *This Journal*, **106**, 764, 771 (1959).
4. D. Caplan and M. Cohen, *J. Metals*, **4**, 1057 (1952).
5. O. Beeck, *Advances in Catalysis*, **2**, 151 (1950).
6. T. Rosenqvist, *J. Iron Steel Institute*, **176**, 37 (1954).
7. W. Jost, "Diffusion in Solids, Liquids, and Gases," p. 305, Academic Press, New York (1952).

Nickel-Aluminum Alloy Coatings Produced by Electrodeposition and Diffusion

Dwight E. Couch and Jean H. Connor

National Bureau of Standards, Washington, D. C.

ABSTRACT

Nickel-aluminum alloy coatings were produced by diffusion of aluminum electrodeposited over nickel. The aluminum was plated from baths operated at 25°-1000°C. The alloys were much harder than nickel and were superior to nickel coatings in salt spray, atmospheric exposure, and air oxidation tests. Attempts to codeposit the two metals were not successful.

Nickel-aluminum alloys are very resistant to oxidation in air at temperatures of 500°-1100°C. They are hard and resistant to corrosion at normal temperatures. Alloys of this type have been prepared by metallurgical methods (1, 2) but, because the alloys are brittle, they are difficult to use in the manufacture of intricately shaped objects. Electrodeposited coatings of these alloys should provide valuable protection to other metals. In previous studies (3) coatings of nickel-aluminum alloys were formed by the electrodeposition of aluminum, from a fused cryolite bath, on nickel. Beck (4) used a cryolite bath to form nickel aluminide coatings on nickel-plated molybdenum and identified the various phases of the alloy diffusion layer. Many objects that require coating cannot withstand a temperature of 1000°C at which the cryolite bath is operated; therefore, other baths that may be used at lower temperatures were investigated. Fink and Solonki (5) studied several aluminum chloride alkali chloride baths with a 1 to 1 mole ratio. Collins (6) used a higher aluminum chloride content and obtained smooth deposits. A review of aluminum coating processes was given by Murphy (7).

Electrodeposition of Nickel and Aluminum from Organic Type Baths

All of the known organic-type baths (8-13) for plating aluminum were investigated to see if nickel could be codeposited with aluminum. In general, nickel salts were only slightly soluble in the organic solvents used to prepare the baths and no alloy deposits were produced. Electrodeposition of nickel from other organic solvents also was investigated, since the desired alloy would be predominantly nickel. Ductile nickel deposits could not be obtained from any of the organic baths. Thin, coherent, highly stressed, lustrous deposits were obtained sometimes. These contained only 85% nickel, the remaining 15% probably was occluded organic material. Table I lists organic solvents and nickel salts used in the experiments. Since pure nickel could not be electrodeposited from organic solvents, this approach was abandoned.

The ether-hydride bath (8) was used successfully to produce coatings of aluminum that could be alloyed with nickel. However, an intermediate coating of zinc or copper was required to give necessary adhesion and to prevent blistering of the aluminum

Table I. Organic baths used in the electrodeposition of nickel

Solute:	$NiCl_2$		$NiBr_2$		NiI_2		$Ni(CF_3COO)_2$		$Ni(C_3F_7COO)_2$		$Ni(SCN)_2$	
Solvent	Solubility*	Nature of deposit	Solubility	Nature of deposit	Solubility	Nature of deposit	Solubility	Nature of deposit	Solubility	Nature of deposit	Solubility	Nature of deposit
Formamide	S	Coherent	T	Coherent	T	Black coherent	S	Coherent	T	Coherent	T	Fair
Acetamide	T	Fair	T	Fair	T	Fair	—	—	—	—	—	—
Dimethylformamide	i	None	i	None	T	None	S	Poor	T	Poor	T	Poor
Acetonitrile	T	Poor	S	None	T	None	S	Coherent	S	Fair	i	None
Ethyleneglycol dimethyl ether	T	None	T	Black powder	S	Black powder	S	Black	S	Powder	T	None
Tetrahydrofuran	T	None	T	Black powder	S	Black powder	S	Poor	S	None	T	None
Ethyl ether	i	None	i	None	i	None	—	—	T	Powder	i	None
Tetraethyleneglycol dimethyl ether	T	None	S	Black powder	S	Black powder	S	None	S	Coherent	T	Powder
Xylene	i	None	i	None	T	None	i	None	i	None	T	None
Toluene	i	None	i	None	T	None	i	None	i	None	T	None
Benzene	i	None	T	None	T	None	T	None	i	None	T	None
N-butylamine	T	None	T	None	T	None	S	Black	S	Black	S	Black

* i, Insoluble; T, Trace; S, Soluble.

deposit during the heat treatment at 550°C required to alloy the aluminum with the nickel.

Fused Salt Baths and Conditions of Operation

Several fused-salt baths for the electrodeposition of aluminum were studied, and the following were found to be the most satisfactory: potassium chloride-sodium chloride-cryolite, aluminum chloride-sodium chloride.

The composition and optimum operating conditions for these baths are as follows:

Potassium chloride-sodium chloride-cryolite: sodium chloride, 440 g; potassium chloride, 560 g; cryolite, 150 g; temperature, 700°-800°C; current density, 2-10 amp/dm^2; anodes, graphite; container, graphite.

Aluminum chloride-sodium chloride: aluminum chloride (anhydrous), 900 g; sodium chloride, 200 g; temperature, 160°-180°C; current density, 1-4 amp/dm^2; anodes, tungsten or graphite; covered container, glass (Pyrex or equivalent).

Potassium chloride-sodium chloride-cryolite bath.—This bath was contained in a graphite crucible and operated at temperatures from 650° to 900°C. At the higher temperature the graphite crucible oxidized rather rapidly, and at 650°C the aluminum diffused into nickel rather slowly. Therefore, most of the deposits were made at 700°-750°C. At this temperature the aluminum deposit was liquid and alloyed with the nickel.

Samples (0.1 x 3 x 6 cm) to be plated were placed in the bath and allowed to heat up to bath temperature before electrolysis. Excellent adhesion was obtained on nickel, iron, and previously prepared Ni-Al alloys. No precleaning of the specimen was necessary. At 700°C an aluminum deposit 6 μ thick could be produced by using a current density of 7 amp/dm^2 for 5 min. When the electrolysis was continued under these conditions for more than 5 min, the aluminum was electrodeposited faster than it could diffuse into the nickel, and free aluminum was produced on the surface of the sample. Thicker deposits could be produced by using a lower current density for a longer time, or by operating at a higher temperature. Deposits 25 μ thick were prepared at 700°C by the following schedule: 7 amp/dm^2 for 5 min, 4 amp/dm^2 for 20 min, and 2 amp/dm^2 for 90 min.

The cathode current efficiency for plating aluminum on nickel cathodes is shown in Fig. 1. The efficiency was about 90% at 15 amp/dm^2, but decreased, as the current density decreased. At 0.5 amp/dm^2 the solution rate of the alloy equaled the deposition rate, thus giving an efficiency of zero. The efficiency at current densities greater than 15 amp/dm^2 could not be determined because the aluminum deposited more rapidly than it could diffuse into the nickel and was lost as molten aluminum into the bath. Nickel and Ni-Al alloy slowly dissolved in the bath. Nickel dissolved at a rate of about 0.6 mg/cm^2/hr, and the Ni-Al alloy dissolved at approximately 1.6 mg/cm^2/hr.

Alloy deposits 25 to 75 μ thick[1] produced from the

[1] The thickness referred to here and at all later places in this paper is the thickness of the electrodeposited aluminum as determined by the increase in weight of the sample as a result of the aluminum deposit. Therefore it is not a measure of the actual thickness of the alloy layer formed.

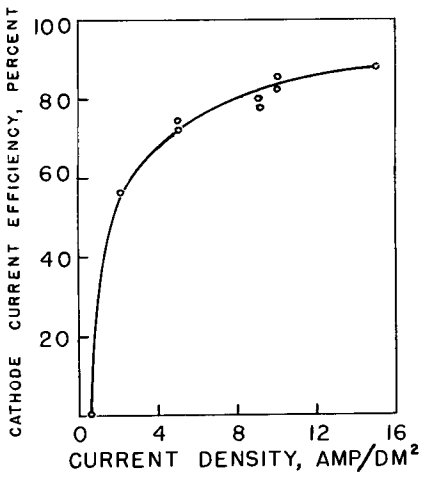

Fig. 1. Cathode current efficiency of aluminum electrodeposited from potassium chloride-sodium chloride-cryolite bath at 700°C.

potassium chloride-sodium chloride-cryolite bath contained from 43 to 52% Al. This represents an average composition of 1 mole Ni to 2 moles Al. No attempts were made to identify the separate phases of this alloy system.

Occasionally, deposits produced at the higher current densities showed traces of free aluminum on the surface. Excess aluminum was removed with 2.5M aqueous sodium hydroxide. This solution dissolved the alloy at a rate of about 0.005 mg/cm^2/hr.

Aluminum chloride-sodium chloride baths.—This bath was operated at a temperature where very little diffusion of aluminum into nickel took place. Therefore, it was necessary to heat the samples after plating to form the alloy. Temperatures of 700°C could be used for thin coatings 5 μ thick, but coatings 25 μ thick melted, and only a small fraction of aluminum diffused into nickel, the remainder formed a metallic bead at the edge. The approximate time required for various thicknesses of aluminum to diffuse into nickel at 700° and 550°C are shown in Fig. 2. Values for 700°C were obtained on flat specimens that were held horizontally to prevent run off of molten aluminum.

If the aluminum chloride-sodium chloride mole ratio was less than 1.5, as in the baths described by Fink and Salonki (5), and operated at 160°-180°C,

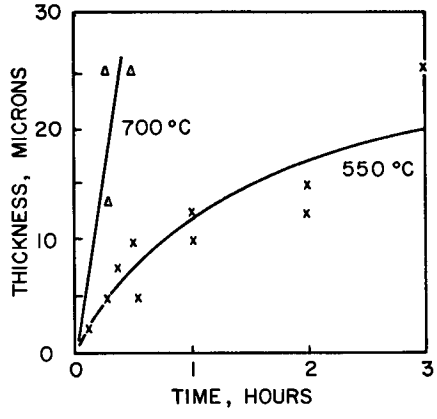

Fig. 2. Time required to completely alloy aluminum with nickel at various temperatures. Aluminum was plated from $AlCl_3$-NaCl bath, or ether-hydride bath.

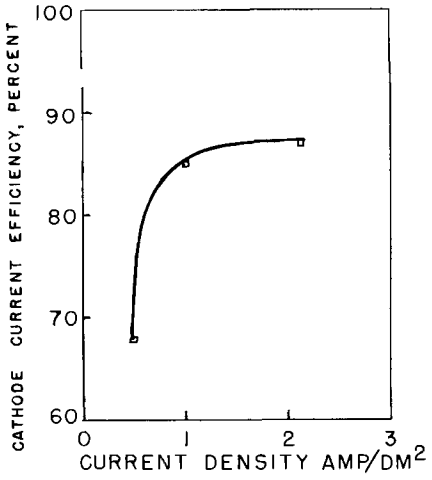

Fig. 3. Cathode current efficiency for electrodeposition of aluminum from on $AlCl_3$-NaCl bath at 170°C.

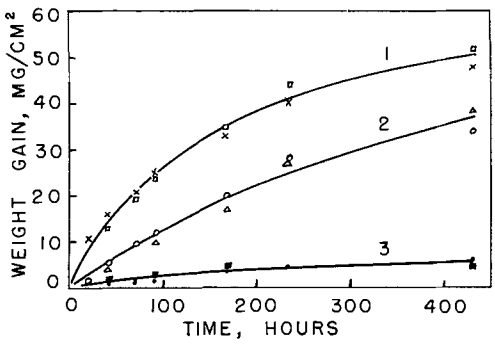

Fig. 4. Oxidation of nickel and nickel-aluminum alloy at 1000°C. Curve 1. □, x, pure nickel, duplicate samples; 2. o, △, alloy coating, approximately 8 μ, duplicate samples; 3. ●, ■, alloy coating, approximately 25 μ, duplicate samples.

the maximum thickness of satisfactory deposits was about 5 μ. Thicker deposits were rough and powdery. Electrodeposits up to 25 μ thick were obtained from a bath similar to that given by Collins (6). However tungsten was used for anodes instead of aluminum.

Figure 3 shows the cathode current efficiency of aluminum chloride-sodium chloride bath. Chlorine liberated at the insoluble anode apparently dissolved in the bath in sufficient amounts to slowly dissolve aluminum deposit, thus accounting for the decrease in cathode efficiency at the lower current densities. Moisture that reacted with aluminum chloride produced some hydrogen chloride that attacked the aluminum deposit.

When aluminum electrodeposited from this bath was overplated with a second layer of aluminum, the adhesion was very poor. Aluminum deposits that were allowed to stand in the bath showed surface attack and formation of a thin black film. This film prevented adhesion of the second deposit. Anodic treatment of the panel in the bath caused a similar condition regardless of current density (1-15 amp/dm^2). If the sample was heated to alloy the first aluminum deposit with nickel, a second layer could be deposited with sufficient adhesion to allow heat treatment to alloy it with the first layer.

Codeposition of nickel and aluminum from fused salt baths.—Aluminum and nickel can be codeposited from a bath containing sodium chloride, potassium chloride, cryolite, and nickel chloride at current densities of 100 amp/dm^2 or greater. These deposits contained 30 to 50% Al. Unfortunately, they were produced only as very thin deposits, and attempts to form deposits 25 μ thick resulted in thin coherent layers covered with a black noncoherent material. At current densities of less than 100 amp/dm^2, the deposits contained no aluminum. Nickel anodes were insoluble and were coated with a tan-colored material that was also insoluble in the bath. This was presumably an oxide or oxychloride of nickel. Other fused-salt systems studied are listed in Table II. No alloy deposits were obtained from these baths. Although aluminum could be electrodeposited from most of them, nickel only could be electrodeposited after the addition of nickel salts.

Evaluation of Deposits

Oxidation.—In air at 550°C, Ni-Al alloy coatings on steel oxidized at a slower rate than nickel-coated steel. Similar results were obtained at 1000°C using nickel panels as a basis metal. Nickel panels, 6 x 3 x 0.1 cm, were cut from rolled sheet nickel. Two of these panels were used as controls while five others were plated in the fused aluminum chloride-sodium chloride bath to the following average thicknesses: 8, 8, 10, 25, and 25 μ. Two panels (8 and 10 μ aluminum) were heated in air at 750°C for 30 min and others were heated in helium for 15 hr at 550°C to alloy the aluminum; all panels showed a slight gain in weight of about 3 x 10^{-5} g/cm^2. Oxidation curves are shown in Fig. 4. The oxide of one panel spalled in large flakes when cooled after heating for 20 and 44 hr. This oxide was weighed and added to the total weight gain of the panel. This panel had oxidized at about the same rate as the pure nickel. A coating of

Table II. Fused salt baths used in deposition of nickel and aluminum

Bath composition	Temp, °C	Deposit obtained	Type deposit	Anode used	Anode effect
NaCl-$AlCl_3$	160	Aluminum	Coherent	Nickel	Insoluble
KCl-NaCl-NaCN	600	Nickel	Dendrites	Nickel	Soluble
KCl-NaCl-NaCN-$NiCl_2$	600	Ni^{++} chemically reduced to Ni	—	—	—
NaCl-KCl-Na_3AlF_6-$NiCl_2$	700-800	Nickel	Dendrites	Graphite	Insoluble
NaCl-KCl-Na_3AlF_6-$NiCl_2$	700-800	Nickel	Dendrites	Nickel	Passivated
NaCl-$AlCl_3$-$NiCl_2$	600	Nickel	Dendrites	Nickel	Soluble
KBr-$AlBr_3$-$NiBr_2$	200	Black powder	Powder	Nickel	Soluble
KBr-$AlBr_3$-$NiBr_2$	200	Black powder	Powder	Tungsten	Insoluble
$NaPO_3$-$NiCl_2$-Na_3AlF_6	700-800	Nickel	Dendrites	Nickel	Soluble
KCl-NaCl-$Ni_3(PO_4)_2$-Na_3AlF_6	600	Nickel	Dendrites	Nickel	Soluble

8 μ Al reduced the amount of oxidation at 1000°C about 40%, curve 2, while a coating of 25 μ Al reduced the oxidation by about 80%, curve 3. Heating samples in an inert atmosphere to alloy aluminum with nickel did not affect the rate of oxidation.

The oxide layer that formed on the Ni-Al alloy was gray, while that formed on the nickel was vitreous and black in color. A gray oxide formed on specimens with a coating of 8 μ Al, but after heating about 100 hr at 1000°C, the surfaces of the panels were black. Those specimens with 25 μ Al retained their gray color for 300 to 400 hr before the black nickel oxide covered a significant amount of the surface.

Figure 5 shows that alloy coatings 25 μ thick do not give satisfactory protection to steel at 900°C. The iron diffused through the coating, resulting in rapid oxidation. Thicker coatings are required to protect steel at these temperatures.

Salt spray test.—Salt spray tests were made on steel (6 x 3 x 0.1 cm) coated with Ni-Al alloy. Samples were first nickel plated, then separated into groups in random fashion. One group was used as a control, while the alloy was formed on the other group. In this way the influence of the nickel plating process was minimized. The most corrosion-resistant coatings were produced by plating aluminum from the sodium chloride-potassium chloride-cryolite bath and subjecting these coatings to oxidation at 500°-600°C prior to testing. Rapid temperature cycling of these panels did not affect their corrosion resistance. The coatings were more resistant if the aluminum thickness was less than 50% of the total thickness of the coatings (see Table III). In the salt spray tests, 5 or more samples were used for each thickness tested and the average time required for the first rust to form on the surface is given in Table III.

Evaporated aluminum coatings[2] 0.1 μ thick, which were alloyed with nickel by heating in air, caused a decrease in the corrosion of nickel-plated steel. Although they showed the first rusting at the same time as the control panels (5 hr), the surface area was 7% rusted after 75 hr as compared to 30% on the control panels.

[2] Panel size in these tests were 10 x 15 x 0.1 cm.

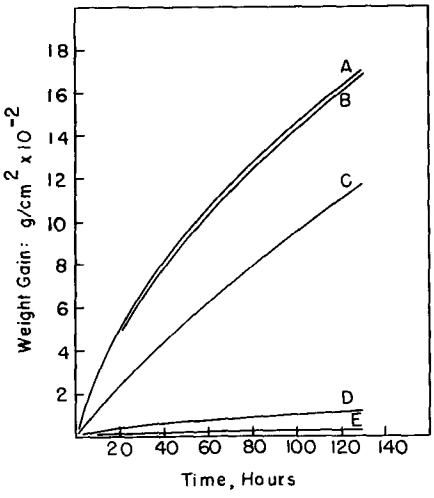

Fig. 5. Oxidation at 900°C in air of alloy-coated steel and nickel. Coatings were prepared in cryolite bath at 1000°C. Curve A, steel; B, 25 μ of nickel on steel; C, 25 μ of nickel plus 25 μ of aluminum on steel; D, wrought nickel; E, 25 μ of aluminum on wrought nickel.

Sprayed aluminum coatings[2] were also effective in reducing corrosion by salt spray. Although small areas of uncoated nickel could be seen through the sprayed coating, these areas could not be detected after the sample was heated. The sprayed coating was initially about 20-30 μ thick, but after heating for 30-45 min at 550°C, which was sufficient time to produce an alloy layer about 10 μ thick, the samples were treated with 2.5M aqueous sodium hydroxide to remove the excess aluminum. They then were subjected to salt spray tests. These samples showed rust after 30 hr and were 2% rusted after 75 hr. The control[2] samples showed the first rusting after 5 hr and were 30% rusted after 75 hr.

Corrosion studies conducted on atmospheric exposure racks at Washington, D. C., correlated well with the salt spray tests. Steel panels coated with 25 μ Ni and 5 μ Al did not show rust at the end of one year of exposure, while coatings with 12 μ Ni plus 4 μ Al showed traces of rust after eight months of exposure. Nickel-plated control panels tested simul-

Table III. Salt spray tests (20% solution) on 3 x 6 cm steel samples coated with Ni-Al alloy or nickel. The time shown is an average time for 5 or more samples

Thickness, μ Nickel	Thickness, μ Aluminum	Type bath used to deposit Al	Other treatments	Time in salt spray to first rust,* hr
50	8	$NaCl$-KCl-Na_3AlF_6	Oxidized 90 hr 550°C in air	400
50	8	$NaCl$-KCl-Na_3AlF_6	None	300
25	25	$NaCl$-KCl-Na_3AlF_6	None	100
12	5	$NaCl$-KCl-Na_3AlF_6	None	40
12	5	$NaCl$-KCl-Na_3AlF_6	Oxidation cycled†	60
12	5	$NaCl$-KCl-Na_3AlF_6	Oxidized 90 hr 550°C	70
5	35	$NaCl$-KCl-Na_3AlF_6	None	20
12	5	$AlCl_3$-$NaCl$	Heated to form alloy	30
50	None	—	None	20
25	None	—	None	10
12	None	—	None	5

* Samples were inspected after 5 hr, 20 hr, and every day thereafter.
† Samples were heated at 550°C for 10 min, then cooled to room temperature 10 min, then reheated to 550°C. This cycling was repeated for 24 hr, then they were salt spray tested 24 hr, then oxidation cycled 24 hr, etc.

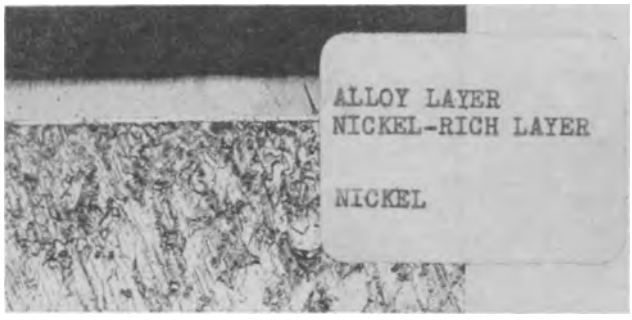

Fig. 6. Nickel-aluminum alloy formed by plating 25 μ of aluminum over nickel and heating at 550°C to alloy aluminum with nickel. Magnification 200X before reduction for publication.

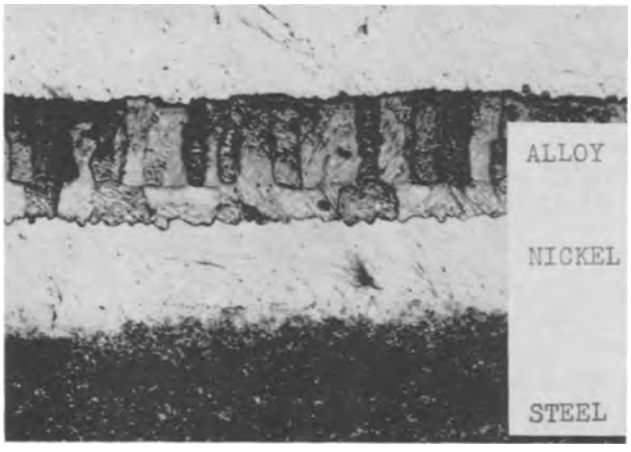

Fig. 7. Nickel-aluminum alloy produced in sodium chloride-potassium chloride-cryolite bath at 700°C. This deposit was heated 2 hr at 1000°C after plating. Magnification 500X before reduction for publication.

taneously with the above samples showed rust after four months and one month, respectively.

Metallographic examinations.—Figure 6 shows a deposit prepared from low-temperature fused aluminum chloride-sodium chloride bath at 160°C, then alloyed with nickel by heating at 500°-600°C for a few hours. Figure 7 shows a deposit produced from potassium chloride-sodium chloride-cryolite bath, after heating for 2 hr at 1000°C. No structure could be developed on the alloy in the as-plated condition.

The Knoop hardness of the Ni-Al alloy produced from the chloride-cryolite bath was 620 for thin films and 700-725 for thicker coatings (50 μ). The hardness of deposits produced from the all-cryolite (3) bath varied from 611 to 788.

The coatings were brittle, and, if 25 μ thick, they could be separated from the basis metal by repeated bending. Thin coatings 5 μ thick fractured when bent, but did not separate from the basis metal. Results of bending samples of two different thicknesses around a 0.6 cm diameter rod are shown in Fig. 8.

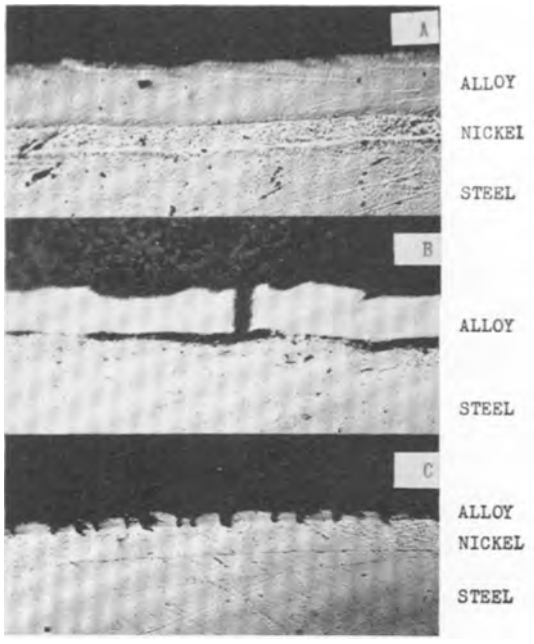

Fig. 8. Nickel-aluminum alloy over steel. A, 50 μ nickel and 40 μ aluminum formed by plating 3 separate deposits of aluminum; B, effect of bending deposit "A" 90 degrees over a 0.6 cm diameter rod; C, effect of bending a deposit of 12 μ nickel and 5 μ aluminum to 90 degrees over a 0.6 cm diameter rod. Magnification 200X before reduction for publication.

Acknowledgment

This research was supported by the United States Air Force under Contract No. DO 33(616)-57-10, monitored by the Materials Laboratory, Wright Air Development Center, Wright-Patterson Air Force Base, Ohio.

Manuscript received Sept. 3, 1959. This paper was prepared for presentation at the Ottawa Meeting, Sept. 28-Oct. 2, 1958.

Any discussion of this paper will appear in a Discussion Section to be published in the December 1960 JOURNAL.

REFERENCES

1. J. H. Westbrook, *This Journal*, **103**, 54 (1956).
2. E. M. Grala, NACA Tech. Note 3660 (1956), Lewis Flight Prop. Lab., Cleveland, Ohio.
3. D. E. Couch, H. Shapiro, and A. Brenner, *This Journal*, **105**, 485 (1958).
4. W. Beck, *ibid.*, **106**, 783 (1959).
5. C. G. Fink and D. N. Solonki, *Trans. Electrochem. Soc.*, **91**, 203 (1947).
6. F. R. Collins, *Iron Age*, January 17, **169**, 100 (1952).
7. N. F. Murphy, *Metal Finishing*, **50**, 76 (1952).
8. D. E. Couch and A. Brenner, *This Journal*, **99**, 234 (1952).
9. J. H. Connor and A. Brenner, *ibid.*, **103**, 657 (1956).
10. F. H. Hurley and T. P. Weir, *ibid.*, **98**, 203 (1951).
11. A. C. Doumas and N. F. Murphy, *Tech. Proc. Am. Electroplaters' Soc.*, **43**, 162 (1956).
12. M. A. Miller and C. D. Baker, U.S. Pat. 2,763,605, Sept. 18, 1956.
13. K. Ziegler and H. Lehmkuhl, *Angew. Chem.*, **67**, 424 (1955).

Effect of Addition Agents on Tungsten Codeposition

J. S. Sallo[1] and R. D. Fisher

Magnetic Research Department, The National Cash Register Company, Dayton, Ohio

ABSTRACT

Small quantities of certain addition agents will prevent the codeposition of tungsten with iron, nickel, or cobalt. Data are presented comparing addition agent concentration with the amount of tungsten in a nickel-tungsten codeposit. Polarographic data indicate that addition agents which prevent tungsten codeposition are capable of being adsorbed at a Hg cathode and form complexes with the codepositing metal ion. These complexes are more readily reduced than is the original codepositing species. The cathode potential of the deposition process is lowered to a more positive potential by the addition agent. Structural studies show that the deposit does not consist of alternate layers of tungsten and codeposited metal as is required by the catalytic reduction mechanism. It is shown that the addition agent effect can be explained by a mechanism of codeposition involving complex formation.

Many claims have been made for the deposition of pure tungsten from aqueous tungstate solution (1-3). Subsequent investigation of these processes has shown that the deposits always contain iron, nickel, or cobalt (codepositing metal ion) (4), and that deposition ceases when these impurities are exhausted from the plating solution. When no such impurities are present in the plating solution, oxides of tungsten may be deposited at the cathode; however, under these conditions reduction of tungstate to tungsten has not been observed.

Many baths have been developed for the codeposition of tungsten with iron, nickel, or cobalt. The most successful of these are the complex ammoniacal baths which have been developed by Brenner (5) and by Holt (6). Brenner's baths allow the codeposition of sound Ni-W deposits containing 20% tungsten. Iron-tungsten deposits containing 50% tungsten can be plated from such baths. Two mechanisms have been proposed to explain the codeposition process. These are the catalytic reduction mechanism and the complex formation mechanism.

The catalytic reduction mechanism proposes that laminations observed in the codeposits are alternate layers of tungsten and the codeposited metal (iron, nickel, or cobalt) (7). The codeposited metal acts as a catalytic surface on which, in the presence of hydrogen, the tungstate anion is reduced chemically and electrochemically to metallic tungsten. When a layer of tungsten has covered this catalytic surface, the deposition ceases and the formation of a fresh layer of catalytic codeposited metal begins.

The complex formation mechanism describes the codeposition as taking place from some complex of tungstate and the codepositing metal ion (7). The function of the codepositing metal ion is to provide a reducible tungstate complex. The major disadvantage of the complex formation mechanism is that no complex of tungstate with ions of iron, nickel, or cobalt has been observed.

The effect of addition agents on tungsten codeposition and data indicating that the codeposits are solid solutions are discussed in this paper.

[1] Present address: Minneapolis-Honeywell Regulator Company, Research Center, Hopkins, Minnesota.

Experimental

Deposition studies.—All chemicals used were C.P. reagent grade and were not further purified.

The plating bath used for the nickel tungsten deposition was as follows: $NiCl_2 \cdot 6H_2O$, 28 g/l (0.12 mole/l); $Na_2WO_4 \cdot 2H_2O$, 32 g/l (0.036 mole/l); NH_4Cl, 50 g/l (0.94 mole/l); sodium citrate, 100 g/l (0.39 mole/l); H_2O and NH_4OH to 1 liter at a *p*H of 8.5. For the iron-tungsten and cobalt tungsten codeposits 0.12 mole/l of $FeCl_3 \cdot 4H_2O$ or $CoCl_2 \cdot 6H_2O$, respectively, were used in place of $NiCl_2 \cdot 6H_2O$.

The cathodes for deposition were 0.003 in. thick sheets (2 x 2 in.) of phosphor bronze to which were welded copper wires for electrical contact. The copper contacts were kept well above the solution level. The cathodes were cleaned cathodically in an alkaline medium, followed by an acid dip (1:1 HCl), and a distilled water rinse. Sheets or rods of pure tungsten were used as anodes. The temperature of the bath was controlled at 90° ± 0.5°C by means of a glascol heating mantel. The current density was 2 amp/dm^2. The volume and *p*H of the solution were maintained by continuous addition of a NH_4OH, H_2O solution through a peristaltic action pump.

In the studies leading to the determination of the minimum concentration of addition agent required to prevent tungsten codeposition completely, a fresh plating system was used for each addition agent concentration. In the studies showing the decrease of tungsten content in the nickel-tungsten deposit with increasing addition agent concentration, successive additions of the addition agent were made to a single plating system.

Cathode potential studies.—Cathode potentials were determined at varying current densities on the following three baths:

1. $NiCl_2 \cdot 6H_2O$, 28 g/l (0.12 mole/l; NH_4Cl, 50 g/l (0.94 mole/l); and sodium citrate, 100 g/l (0.39 mole/l) H_2O and NH_4OH to a *p*H of 8.5.

2. Same as 1 except 32 g/l $Na_2WO_4 \cdot 2H_2O$ (0.036 mole/l) added.
3. Same as 2 except 0.1 g/l (0.0013 mole/l) thiourea added.

Cathode potentials during deposition from the above baths were determined by the direct method.

The cell consisted of a 2-liter beaker with a heating mantle and contained a platinum cathode (0.95 x 1.01 x 0.022 cm) and two platinum anodes (2.2 x 2.2 x 0.022 cm). The distance between the anodes and cathode was 4.75 cm. The flat platinum cathode was coupled with an external Beckman saturated calomel electrode by means of a bridge made from 6.3 mm Pyrex tubing with one end drawn out to a capillary tip 1 mm in diameter and 1 cm long. The tip was bent at 90° and placed near the face of the cathode. To measure the potential, a L&N type K-3 potentiometer supplied a balancing emf, and a Kintel Microvoltammeter served as a Null detector. The potentials were measured commencing with the initial static potential emf. The readings of the emf were taken at various current densities. The current was measured with a Simpson milliammeter (Model 373). Sufficient time (2-3 min) was allowed for each measurement to enable the potentials to reach a steady value. Individual determinations were reproducible within ± 5 mv. No correction was made for the *IR* drop between the capillary tip and the surface of the cathode. Also, a nonuniform current density results with a parallel electrode system since the current density is highest at the edges. These factors and others make the absolute cathode potential measurements somewhat uncertain. The *p*H and volume of each bath were maintained by continuous additions of NH_4OH and H_2O, and temperature was controlled at 90° ± 1°C.

X-ray diffraction.—X-ray diffraction was performed on a North American Phillips type diffractometer. In all cases copper K α radiation was used, the potential was 35 kv, the current was 20 ma, the scanning rate was 2°/min, and the Geiger counter voltage was 1385. The time constants were 8, 2, and 16 sec for nickel, tungsten, and nickel-tungsten, respectively.

X-ray fluorescence.—The plated samples were analyzed for Ni, Co, Fe, and W, respectively on a Norelco x-ray spectrograph. The unit was operated with a W x-ray tube at 50 kv and 50 ma. Fixed count operation was employed, i.e., the times were recorded to obtain 512,000 counts for Ni; 256,000 counts for Co; 128,000 counts for Fe; and 32,000 counts for W. These readings were converted to counts/second for each element. A LiF crystal was used and first-order peaks of the elements were used as follows: Ni $K\alpha_1$ at 48.61° 2θ, Co $K\alpha_1$ at 52.74° 2θ, Fe $K\alpha_1$ at 57.45° 2θ, and W $L\alpha_1$ at 42.99° 2θ.

Since the use of a W x-ray tube means that a W count will be produced even if the sample is free of W (background), the point at which no W appears in the deposit for each series of samples was double-checked using a Norelco x-ray spectrograph employing a Mo x-ray tube, operating at 50 kv and 40 ma. In this case a NaCl crystal was used and a scan was made over the W $L\alpha_1$ peak in the second order (at 63.13° 2θ). The absence of W in the end-point samples was confirmed for all series.

Several nickel-tungsten samples were prepared in accordance with the instructions of previous workers (5). These were used as standards for the x-ray spectrometer. The graph of % W in the deposit vs. addition agent concentration is shown in Fig. 1.

Since the composition of the standard was not checked by chemical analysis, the accuracy of the values given is doubtful. However, the relative values of the concentrations in different specimens are probably valid.

Polarographic studies.—The polarographic studies were carried out using a L&N "polarotron" and a type-E electrochemograph. Polarograms were determined in a 1M NH_4OH, 0.2M NH_4Cl supporting electrolyte with 0.005% gelatin. Chemicals were C.P. grade.

Results

Many of the addition agents which were studied in this program were found to prevent the codeposition of tungsten with iron, nickel, or cobalt. These are thiourea, thiosulfate ion, thiocyanate ion, thioacetamide, and water soluble substituted thioureas. Among the addition agents which have no effect on the composition of tungsten codeposits are gelatin, saccharine, and urea. No criteria for the structure required of an addition agent for the prevention of tungsten codeposition can be established at this time; however, all successful addition agents investigated contained sulfur.

The effect of varying quantities of sodium thiosulfate, potassium thiocyanide, and thiourea on the approximate composition of the nickel-tungsten codeposit is shown in Fig. 1. The cut-off concentrations of other addition agents which prevent tungsten codeposition are shown in Table I. These cut-off concentrations were determined by an x-ray fluorescence unit with a molybdenum source.

It has been observed that the concentration of thiourea necessary to prevent tungsten deposition increases with increasing current density. That is, increasing the current density decreases the effectiveness of the thiourea. This decrease in effectiveness with increasing current density may be explained by the desorption of the thiourea with increased negative potential, or it may be due to in-

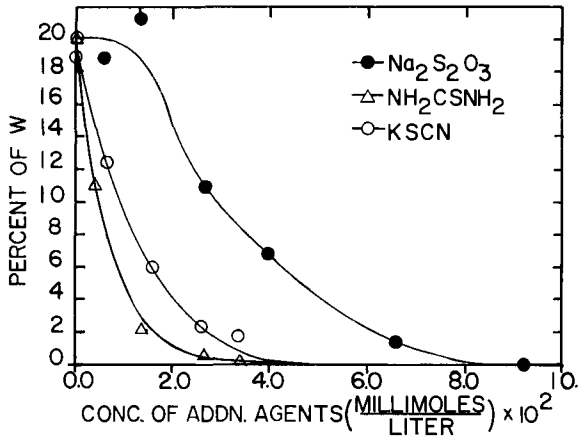

Table I. Effect of addition agents on W codeposition

Addition agent	Deposition of W ceases,* mg/l	Bath
$Na_2S_2O_3$	9.24	Ni-WO_4
KSCN	5.12	Ni-WO_4
NH_2CSNH_2	3.0	Ni-WO_4
NH_2CSNH_2	9.0	Co-WO_4
$Na_2S_2O_3$	29.5	Co-WO_4
KSCN	5.76	Co-WO_4
NH_2CSNH_2	20.0	Fe-WO_4

* Results were obtained by x-ray fluorescence using an x-ray unit containing a molybdenum tube.

creased decomposition of the thiourea with increased negative potential. The latter seems more likely since depletion of thiourea has also been observed. For example, a deposit was made from a bath containing the minimum quantity of thiourea (3 mg/l) required to prevent tungsten codeposition with nickel for a period of 4 hr at 2 amp/dm^2. After this period, a fresh deposit was then made from this bath and tungsten was found in the deposit. The thiourea concentration necessary to prevent W codeposition increases with Ni, Co, and Fe, respectively. In all cases investigated the concentration of addition agent necessary to prevent tungsten codeposition is larger when cobalt is the codepositing metal rather than nickel.

The potential required for the deposition of the tungsten alloys is more noble than the potential required for the deposition of the metal (Fe, Ni, or Co) by itself (8-10). According to data published by Markwell and Holt (11), a criterion for tungsten deposition is that the dynamic cathode potentials of the codepositing ion (Ni, Co, Fe) solutions, with and without tungsten ion, must be within 85 mv of each other. Therefore, it was of interest to determine the effect of thiourea on the cathode potentials of nickel and nickel tungstate solutions. The cathode potential, E_c (vs. SCE) at 2 amp/dm^2 of pure nickel solution was −1100 mv, while the solution containing nickel and tungstate ions had a cathode potential of −970 mv. When 0.1 g/l of thiourea was added to the nickel-tungstate solution, the cathode potential was −880 mv. This value is 90 mv below the cathode potential of the nickel-tungstate solution and 200 mv below the cathode potential of the nickel solution (Table II).

The polarographic method was employed to study the addition agent effect. The half-wave potential ($E_{1/2}$) of the cathodic nickel waves was determined in 1M NH_4OH, 0.2M NH_4Cl, supporting electrolyte and using 0.05 g/l of gelatin as a maxima suppressor. The results of these polarographic measurements are given in Table III. All effective addition agents cause a shift in the half-wave potential of the Ni wave. This is attributed to complex formation between the addition agent and the nickel species.

Except for the thiosulfate, the effective addition agents are seen to form complexes which are more easily reduced than is the original nickel species. This conclusion was also confirmed for thiourea by cathode potential studies.

Since, in general, complex formation makes an ion more difficult to reduce and shifts $E_{1/2}$ to a less

Table II. Cathode potential measurements

Plating bath	E_c*
Nickel	1.1
Nickel-tungstate	0.970
Nickel-tungstate-thiourea	0.880

* Potentials are given vs. a saturated calomel electrode at 2 amp/dm^2.

Table III. Polarographic half-wave potential

Metal ion and complexing agent	$E_{1/2}$ volts
Ni	1.04
Ni + thiourea	1.017
Ni + thioacetamide	0.987
Ni + allylthiourea	1.015
Ni + urea	1.033
Ni + sodium thiosulfate	1.075
Ni + thiosemicarbazide	0.897
Ni + KSCN	1.030

Test solution contained 4.2 × 10^{-5}M Ni^{++}, 2½ cc of 0.2% gelatin solution, 20 cc 5M NH_4OH, 20 cc 5M NH_4Cl, and 0.5 g of each complexing agent per 100 cc solution. $E_{1/2}$ vs. saturated calomel electrode.

noble potential, the observed behavior in this case probably results from the high overvoltage normally associated with the reduction of $Ni(H_2O)_x^{++}$ or $Ni(NH_3)_x^{++}$.

The suppression of the polarographic maximum, as by gelatin, occurs by adsorption of a surface active species at the cathodic mercury drop. Table IV indicates the effectiveness of addition agents as suppressors of the maximum of the cathodic nickel wave. All results are in the absence of gelatin or any other known surface active material. Therefore, it is concluded that all effective addition agents are adsorbed at the cathode. However, there is no quantitative correlation between their effectiveness as maxima suppressors and as tungsten deposition inhibitors.

The catalytic reduction mechanism states that the structure of the deposit consists of alternate layers of tungsten and the codeposited metal. If this is the case, x-ray diffraction should show a phase of nickel and a phase of tungsten, and the diffraction pattern obtained should consist of the superimposed diffraction patterns of pure nickel and pure tungsten. It has been reported that the diffraction pattern of the codeposit is that of a solid solution (5); however, the x-ray data which led to this conclusion was not published. Results obtained in the present investigation are shown in Table V. It is clear from the table that no tungsten phase is present. Instead the codeposit contains only nickel peaks shifted in the direction expected for a solid solution of tungsten in nickel. That the codeposit is a solid solution of tungsten in nickel, and not alternate layers of nickel and tungsten, is thereby confirmed.

Discussion

The addition agents which were found to prevent tungsten codeposition with nickel have several features in common. They all contain at least one sulfur atom, lower the cathode potential of the deposition process, can form bulk complexes with the co-

Table IV. Polarographic adsorption data

Complexing agent	Molar conc. × 10^3	Approximate % adsorption[a]
1-allyl-2-thiourea	5.17	100
Thiosemicarbazide	5.50	96
Thioacetamide	6.77	67
Thiourea	6.60	25
Sodium thiosulfate	4.02	31
Potassium thiocyanate	6.20	22
Urea	8.30	0
Gelatin	—	100[b]

[a] $\%\ \text{Adsorption} = \dfrac{(H_n - I_d) - (H_a - I_d)}{H_n - I_d} \times 100$

H_n is height of the maximum of Ni wave without the complexing agent; H_a is height of the maximum of Ni wave in the presence of the complexing agent; I_d is height of the Ni wave in the presence of gelatin.

[b] Arbitrarily set at 100% adsorption.

Table V. X-ray diffraction data

Ni (f.c.c.)		Ni-W (f.c.c.)		W (b.c.c.)	
d-spacings[a]	Relative intensity[b]	d-spacings	Relative intensity	d-spacings	Relative intensity
2.034(111)	100	2.047(111)	100	2.235(110)	100
1.763(200)	68	1.779(200)	20		
1.245(220)	11	1.252(220)	12	1.580(200)	15
1.0628(311)	17	1.0726(311)	12	1.291(211)	9.5
1.0168(222)	4.8	1.0292(222)	7.6	1.1190(220)	9.5
0.8824(400)	2.4	0.8837(400)	4.5	1.0004(310)	7.4
0.80808(331)	4.8	0.81712(331)	9.1	0.8461(321)	5.3
		0.79990(421)	9.1	0.7918(400)	1.1

[a] Distance between lattice planes in angstrom units.

[b] Obtained by subtracting background and setting most intense peak at 100.

depositing metal ion, and are adsorbed at a dropping mercury cathode. The addition agents which were found to have no effect on the composition of the codeposit were either not adsorbed (i.e., urea) or formed no complexes (i.e., gelatin) with the codepositing metal ion.

It is likely that the formation of a complex between the codepositing species and the addition agent is essential for the prevention of tungsten codeposition. All such complexes are more easily reduced than is the original nickel species, as is shown by the shift to more noble values of the half-wave potentials and of the dynamic cathode potentials. It has also been shown that all addition agents which prevent tungsten codeposition are capable of being adsorbed at the mercury cathode. The fact that very small quantities of addition agent prevent the codeposition and the observed depletion of the addition agent supports the hypothesis that this adsorption is also essential for the prevention of codeposition. As further evidence for this, it has been observed that tungsten will deposit normally from a solution containing 3 mg/l of thiourea (enough to completely prevent codeposition) provided an excess (0.8 g/l) of gelatin is added. This indicates a competition for adsorption between gelatin and thiourea and further demonstrates that adsorption of the addition agent is essential for the prevention of tungsten codeposition.

If one may assume that the behavior of the plating solution at a tungsten alloy electrode is not grossly different from that of the polarographic solution at a mercury cathode, then a plating mechanism consistent with these observations can be formulated. It would involve the adsorption of the addition agent at the cathode and its formation of complexes with the codeposition metal ion[2] as it approaches the cathode. During the formation of this new complex, the original complex between the codepositing ion and the tungstate ion dissociates, and tungsten deposition is prevented.

The x-ray diffraction data negate the mechanism involving alternate layers of the two metals, as does the lack of any periodicity in the plating voltages (12).

Acknowledgments

The authors wish to thank Dr. D. A. Norton, Dr. W. E. Keiser, and Mr. M. Fornoff of The National Cash Register Company and Mr. G. Rappaport, Inland Manufacturing Company, for performing the x-ray diffraction and x-ray fluorescence studies. They are also indebted to Dr. H. J. Modi for many stimulating discussions.

Manuscript received Feb. 2, 1959. This paper was prepared for delivery before the New York Meeting, April 27-May 1, 1958.

Any discussion of this paper will appear in a Discussion Section to be published in the December 1960 JOURNAL.

REFERENCES

1. M. L. Holt and L. Kahlenberg, *Metal Ind.*, **31**, 94 (1933).
2. L. F. Yntema, *J. Am. Chem. Soc.*, **54**, 3775 (1932).
3. C. G. Fink and F. L. Jones, *Trans. Electrochem. Soc.*, **59**, 461 (1931).
4. M. L. Holt, *ibid.*, **66**, 453 (1934).
5. A. Brenner, P. Burkhead, E. Seegmiller, *J. Research Nat. Bur. Standards*, **39**, 351 (1947).
6. M. H. Lietzke and M. L. Holt, *J. (and Trans.) Electrochem. Soc.*, **94**, 252 (1948).
7. M. L. Holt and L. E. Vaaler, *ibid.*, **94**, 50 (1948).
8. W. E. Clark and M. H. Lietzke, *This Journal*, **99**, 245 (1952).
9. L. N. Goltz and V. N. Kharlamov, *J. Appl. Chem., USSR*, **9**, 640 (1936).
10. H. Offermanns and M. V. Stackelberg, *Metalloberfläche*, **1**, 142 (1947).
11. D. R. Markwell and M. L. Holt, *J. Electrochem. Soc.*, **104**, 488 (1957).
12. Z. A. Solovyerva and A. T. Vagramyan, Reports of the Academy Science of USSR, Division of Chemical Science 1954, No. 2, 230-235.
13. T. P. Hoar and I. A. Bucklow, *Trans. Inst. Met. Finishing*, **32**, 186 (1955).

[2] This is, at present, not distinguishable from complex formation followed by selective adsorption of the addition agent codepositing metal ion complex.

Correction

In the article by R. Weil and R. Paquin entitled "The Relationship between Brightness and Structure in Electroplated Nickel" which appeared in the February 1960 JOURNAL, on page 88 in Table II the data for the quantity of reflection light and the eye evaluation brightness group for Specimen 3006a belong to Specimen 3006b and vice versa.

The Mechanism and Efficiency of Electroluminescence in ZnS Phosphors

F. F. Morehead, Jr.[1]

Lamp Research Laboratory, General Electric Company, Nela Park, Cleveland, Ohio

ABSTRACT

This work describes the application of a model of the electroluminescent process to the photon emission and power consumption of insulated electroluminescent phosphors as a function of voltage and frequency. The model represents an extension of one described earlier. The model leads to a convenient summary of such data and an increased understanding of their significance. An upper limit to the efficiency of impact electroluminescence in insulated particles is proposed on the basis of the implications of the model.

One of the difficulties encountered in correlating data for electroluminescence in ZnS phosphors is that there does not exist an adequate model of the process. The lack of such a model makes impossible a convenient summary of the variation of brightness and power dissipation with voltage, frequency, and temperature. Comparisons of the properties of the electroluminescence of different phosphors are difficult to describe in meaningful terms and even more difficult to relate to differences in the fundamental properties of the phosphors. The purpose of this work is to present as complete an approach to an adequate model based on the collision excitation mechanism as is possible at present.

This model, to be described in the following section, is consistent with the relevant experimental data reported in the literature (1-6) although not in entire agreement with their interpretation [cf. (2, 3)]. The major premise is that of delayed recombination, which, despite alternative suggestions (7) remains unambiguously demonstrated (1, 2, 6). Further, the model is a straightforward extension of work by the present writer (1) with some changes suggested by consideration of efficiency. It is similar in concept but more detailed and more accurate than one described by Lehmann (5).

Finally, the model yields a phenomenological approach toward estimating maximum efficiencies that can be achieved with electroluminescence produced by impact ionization. The primary consideration is the relation between the way in which light emission and power consumption increase with voltage in insulated particles.

A Model of the Electroluminescence Process

The principal features of this model have been described previously (1); the same notation will be retained. The electrons participating in the electroluminescence process in a given particle are divided into two populations: n_e "mobile" electrons, which emerge from and return to a "high-field region" in each voltage cycle and N_T "trapped" electrons in the particle bulk which do not succeed in returning to this region. The origin of the high-field region in which carrier acceleration and impact ionization occur is discussed in a following section. It is assumed that all of the participating electrons have been ionized from the lattice and that the resultant holes are localized in the high-field region at N_+ recombination centers, so that

$$n_e + N_T = N_+ \qquad [1]$$

Of the n_e mobile electrons a fraction α recombine at the emission (recombination) centers and a much larger fraction β are trapped. These βn_e electrons are field-ionized by the succeeding voltage half-cycle and accelerated such that $F\beta n_e$ ionizing collisions occur, where $F \sim e^{-\frac{const}{E}}$ and E is the effective field in the high-field region. We have then

$$\alpha + \beta = 1 \qquad [2]$$

and

$$\alpha n_e = F\beta n_e \qquad [3]$$

to maintain a steady-state condition with respect to ionization and subsequent recombination. We further define Ψ as the fraction of the total number of electrons, $n_e + N_T$, which are in the particle bulk at the beginning of a voltage half-cycle, and which fraction returns to the high-field region

$$\Psi = n_e/(n_e + N_t) = n_e/N_+ \qquad [4]$$

The fraction α is of course proportional to the number of ionized recombination centers, which, as mentioned above, are localized in the high-field region

$$\alpha = N_+X \qquad [5]$$

where X is a capture cross section for these centers relative to trapping.

With the assumption $\alpha << \beta$, algebraic combination of Eq. [1], [2], [3], [4], and [5] gives the following

$$\alpha \sim F$$
$$n_e \sim \Psi F/X$$
$$B/f \propto \alpha n_e \sim \Psi F^2/X \qquad [6]$$

where B/f is the light emission/voltage cycle.

[1] Present address: Research Laboratory, International Business Machines Corp., Poughkeepsie, N. Y.

Trapping and retrapping in the phosphor bulk delays the return of the ionized electrons to the recombination region, which return is facilitated by a field opposite in direction to the ionizing field. Ψ is then a function of the frequency and amplitude of the voltage and of the temperature. The form of this function has been given in previous work (1) for a sinusoidal voltage V of frequency f

$$\Psi = 1 - e^{-\mu}$$
$$\mu = k_\mu \frac{V}{f^{0.6}} e^{-E_0/kT} \quad [7]$$

For a distribution rather than a single trap depth E_0, a weighted sum of terms of the form $e^{-E_{0i}/kT}$ applies.

Application of the above model to the electroluminescence brightness (time-averaged for photons) yields

$$B = B_\infty f \Psi F^2 \quad [8]$$

where B_∞ is a constant.

The motion of the n_e mobile electrons as well as that of the N_T trapped electrons under the influence of the applied field leads to an increase in both the real and imaginary capacitance of the cell C′ and C″ over the value of these constants in the absence of a carrier-producing process in the insulated phosphor particles C'_0 and C''_0. The power dissipated by the cell W, the stored power VAR, and the cell current i are given by

$$W = \omega C'' V^2$$
$$VAR = \omega C' V^2$$
$$i = \omega \mid C \mid V \quad [9]$$

where

$$C = C' + iC''$$

The increase in C′ and C″ arising from the electroluminescence process is proportional to the increase in the two populations of electrons, n_e and N_T, so that we can write

$$C' = C'_0 + \bar{C}'_1 n_e + \bar{C}'_2 N_T$$
$$C'' = C''_0 + \bar{C}''_1 n_e + \bar{C}''_2 N_T \quad [10]$$

where $\bar{C}'_1$ and $\bar{C}''_1$ are constants containing geometric and mobility or polarizability factors and $\bar{C}'_2$ and $\bar{C}''_2$ are similar constants of lower magnitudes representing the more limited excursions of the trapped electrons. One should emphasize here that the lossy motion of a trapped electron is conduction between traps rather than displacement within a trap. The designation "trapped" simply indicates electrons which do not succeed in returning to the recombination region within a half-cycle. Substituting in Eq. [10] from [6] gives

$$C' = C'_0 + C'_1 \Psi F + C'_2 (1 - \Psi) F$$
$$C'' = C''_0 + C''_1 \Psi F + C''_2 (1 - \Psi) F \quad [11]$$

The model thus leads to the expectation of a fairly direct correlation between photon brightness B and power consumption W.

Experimental Technique

A demountable cell was used for most experiments consisting of a circular copper block for one electrode and a circular conducting glass plate for the other. The latter makes contact at its periphery with a metal ring attached through an insulator to the copper electrode, providing a fixed separation of the electrodes. The phosphor powders were mixed with a viscous liquid, #1254 Aroclor (a chlorinated biphenyl, Monsanto Chemical Company), to give a desired volume loading. The mix first was deposited on the conducting glass plate, freed of admixed air in a vacuum chamber, and then pressed against the copper electrode, which was covered with a ¼ mil Mylar film to elminate electrolytic processes that might otherwise occur in the liquid medium. The experimental results reported below are not corrected for the effect of the Mylar film, since this correction does not significantly alter the results relative to the purposes of this work.

The cells were operated by means of a wide range oscillator, a 60 w audio amplifier, and a transformer. This combination of units provides up to 450 v rms above 100 cps to beyond the 5 kc frequency to which the measurements were limited to avoid a significant contribution of the resistance of the conducting glass to the power absorption. For measurements at lower frequencies a d-c amplifier which was limited to below 250 v rms was used.

The power consumption and current were measured with a Model 102 electronic wattmeter (John Fluke Engineering Co.) which was checked periodically against known resistances and capacitances.

Cell brightnesses were measured with a 1P21 photomultiplier tube whose output current was read with an electrometer. In each case the output of the photomultiplier was compared with the cell brightness in footlamberts as measured with a Photo Research Corporation "Spectra" brightness spot meter (Model UB) at each of the frequencies employed.

To obtain the cell output in lumens, the brightness in footlamberts was multiplied by the cell area in square feet. To convert the photomultiplier output to a relative photon count in those cases in which the wave-length distribution of the electroluminescence shifts with frequency, several procedures were used. The emission spectra of a ZnS,ZnO:Cu,Cl phosphor were measured at 100 cps and 5 kc, and plotted as relative amount of radiant power (for equal frequency intervals) $dW/d\nu$ vs. photon energy $h\nu$. The S-4 response of the 1P21 photomultiplier was obtained in response for equal radiant power at each photon frequency R_ν. The following integral gives the relative photomultiplier response/photon/second for the particular emission spectrum characteristic of the frequency f

$$(PMR)^{h\nu}_f = \frac{\int \left(\frac{dW}{d\nu}\right)_f R_\nu \, d\nu}{\int \left(\frac{dW}{d\nu}\right)_f \frac{d\nu}{\nu}}$$

For the phosphor described above we had from numerical integration of the above

$$\frac{(PMR)^{h\nu}_{5\text{ kc}}}{(PMR)^{h\nu}_{100\text{ cps}}} = 1.44$$

which is the correction factor by which the photo-

multiplier readings at 5 kc must be divided to obtain the number of photons emitted relative to 100 cps.

Similar calculations give the relative photomultiplier response/watt for each frequency

$$(\mathrm{PMR})^{w}_{f} = \int\left(\frac{dW}{d\nu}\right)_{f} \mathrm{R}\nu\, d\nu \;\Big/\; \int\left(\frac{dW}{d\nu}\right)_{f} d\nu$$

such that for the ZnS,ZnO: Cu,Cl

$$\frac{(\mathrm{PMR})^{w}_{5\ \mathrm{kc}}}{(\mathrm{PMR})^{w}_{100\ \mathrm{cps}}} = 1.42$$

The luminous equivalent of the emission at each frequency can be calculated in similar fashion with the use of the standard eye response curve, which equivalents are 296 lpw for 5 kc and 395 at 100 cps. The ratio of the sensitivity of the photomultiplier in lumens/unit deflection at 100 cps to that at 5 kc will therefore be

$$\mathrm{SR}(100\ \mathrm{cps},\ 5\ \mathrm{kc}) = 1.42\,\frac{395}{296} \sim 1.9$$

This value compares reasonably well with the sensitivity ratios for this phosphor (ZnS,ZnO: Cu,Cl) measured directly as described above with the brightness spot meter, about 1.75 ±0.2. Thus as a rough rule of thumb, one can estimate the correction necessary to convert photomultiplier outputs to relative photon counts as being approximately

$$[\mathrm{SR}(f_1,f_2)]^{0.6}$$

As a final procedure a set of filters were arranged to cover the electroluminescent cell in such a fashion as to give a linear photon count response (when combined with the S-4 1P21 response) in the wavelength range of 4400 to 5600Å. Calculations of the relative cell area assigned to each filter were based on their measured transmission curves. Satisfactory agreement with the results of the above procedures was obtained.

Experimental Results

Figure 1 shows the agreement of the measured photon emission of an electroluminescent cell of a

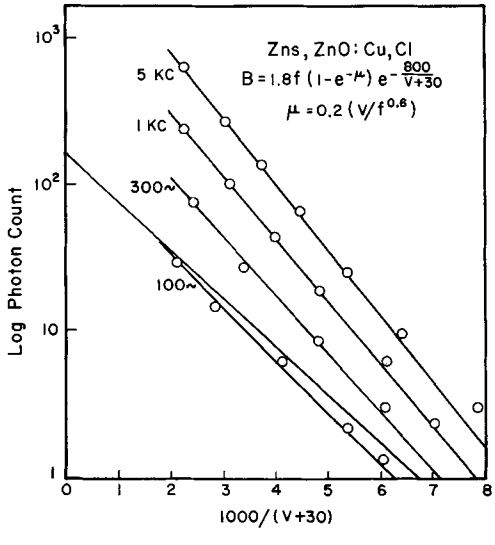

Fig. 1. Log photon count vs. $\dfrac{1000}{V + V_0}$ for ZnS, ZnO:Cu, Cl

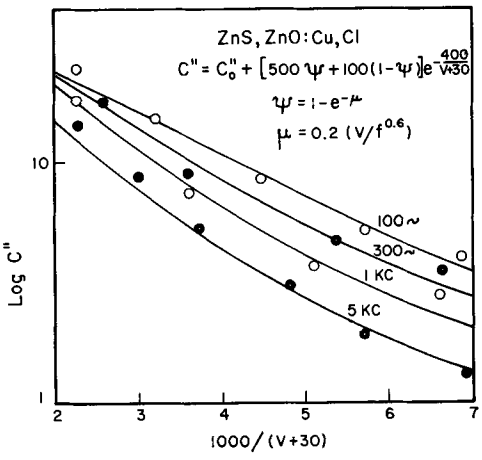

Fig. 2. Log imaginary cell capacitance vs. $\dfrac{1000}{V + V_0}$ for ZnS, ZnO:Cu, Cl.

ZnS,ZnO: Cu,Cl phosphor as a function of voltage and frequency with the form dictated by the model, Eq. [8]. The ionization efficiency F has been given the form

$$\mathrm{F} = e^{-\frac{\hat{c}}{V+V_0}} \qquad [12]$$

The reasons for choosing this form are given in the following section. The straight lines are not exactly the theoretical curves but are drawn through calculated points at $\dfrac{1000}{V + 30} = 2$ and $\dfrac{1000}{V + 30} = 6$ for each frequency. The heavy line is the relation between emission and voltage that would obtain at 100 cps for $\Psi = 1$. Figure 2 shows the agreement of the measured values of the imaginary cell capacitance in $\mu\mu$f with the form predicted by the model, Eq. [11]. Ψ and F are taken from the light measurements (Fig. 1) and C''_0, C''_1, and C''_2 then chosen to give a good fit of the solid (calculated) lines with the experimental points. (C''_0 is about 15 $\mu\mu$f in most cases.) Higher losses than those expected invariably are experienced at the highest voltages. This extra consumption is believed due to nonelectroluminescent processes, possibly associated with the presence of moisture (5).

Variation of cell thickness d and phosphor volume loading N_p give within experimental error the expected changes in the various parameters, viz.

$$B_2 = fB_{\infty 1}\frac{d_2}{d_1}\frac{N_{p2}}{N_{p1}}(\Psi)e^{-\frac{2c_1(d_2/d_1)}{V+V_{01}(d_2/d_1)}}$$

$$\frac{d_2}{d_1}C''_2 = C''_0(N_{p2}) + \left(\frac{N_{p2}}{N_{p1}}\right)\left[C''_{11}\Psi + C''_{21}(1-\Psi)\right]e^{\frac{c_1(d_2/d_1)}{V+V_0(d_2/d_1)}}$$

$$\Psi = 1 - e^{-\mu}$$

$$\mu = k_{\mu 1}\frac{d_1}{d_2}\frac{V}{f^{0.6}}$$

where the subscripts 1 and 2 refer to the parameters appropriate to cells of thicknesses d_1 and d_2 and phosphor volume loadings N_{p1} and N_{p2}.

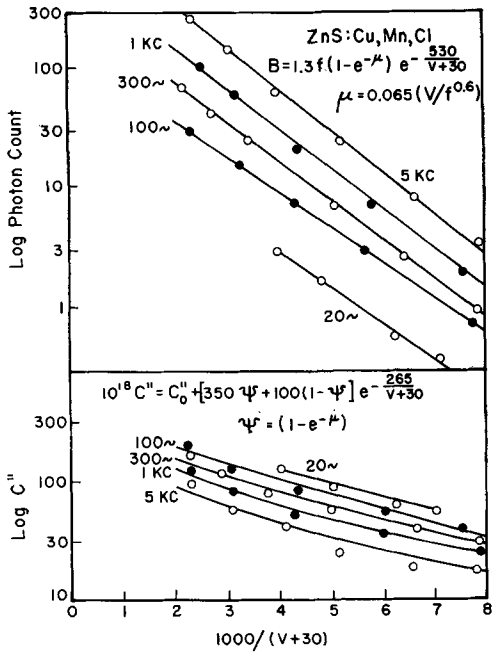

Fig. 3. Log photon count and log imaginary cell capacitance vs. $\frac{1000}{V + V_o}$ for ZnS:Cu, Mn, Cl.

Figure 3 shows the agreement of the model with the brightness and power data for a yellow-emitting ZnS:Cu,Mn,Cl phosphor. There is, of course, no shift in the emission spectrum with frequency. The green- and blue-emitting centers are impact ionized as in the previously described phosphor, but on recombination, the excitation energy is transferred to the yellow-emitting Mn-center, by means of a quantum mechanical resonance process (8, 9). The ground state and excited state of the Mn center are both thought to be below the top of the valence band, so that direct collision excitation rather than ionization of this center can occur (2). This latter mode of excitation of this center occurs significantly only at much higher currents than those characteristic of "normal" ionization electroluminescence and dominates only in cells that allow continuous current flow at very low frequencies or for d-c voltages.

A further distinction of the Mn-phosphor is the very low value obtained for k_μ in the expression for Ψ. This difference results in a much larger contribution of the N_T trapped electrons (a lower value of Ψ) to the power consumption of the cell, which increases rapidly with frequency. Thus if one measures a maximum phosphor efficiency (neglecting C''_o) of 6.0 lpw at 100 cps and 100 v, the equations shown in Fig. 3 predict a maximum efficiency of 8.4 lpw at 20 cps and 80 v. The solid lines shown in Fig. 3 for photon emission and C" at 20 cps were plotted on the basis of measurements made between 100 cps and 5 kc. The agreement with the experimental points shows that one may accurately extrapolate on the basis of the model outside of the actual range of measurements. By contrast, if one measures a maximum phosphor efficiency of 6.0 lpw at 100 cps and 140 v for the ZnS,ZnO:Cu,Cl phosphor, one can expect a maximum efficiency of only about 6.2 lpw at 20 cps and 100 v on the basis of the model and the experimentally determined parameters.

The reason for the low value of k_μ for the Mn-phosphor is not wholly understood. There is no evidence for the presence of deep traps, which would give a lower value at room temperature to $k_\mu = k_{\mu} e^{-E_0/kT}$, in either the thermoluminescence or the temperature dependence of the electroluminescence. The answer perhaps lies in a greater concentration of traps with consequently greatly increased retrapping and a slower rate of return at a given applied voltage and frequency. Similar consideration may also apply to the Ni-quenched phosphor discussed below.

ZnS:Cu, Al phosphor have even higher values of k_μ at room temperature than those coactivated with chlorine. A value as high as $k_\mu = 0.66$ has been measured, giving a very nearly linear frequency response to the phosphor at the higher voltages. A further advantage of the phosphor is the absence of color shift with frequency (2).

Interesting variations in the model parameters are produced by firing longer at higher temperatures to yield a higher mean particle size. One such ZnS,ZnO:Cu,Cl phosphor gives the following results (a correction for the greater cell thickness required to accommodate this phosphor has been made)

$$B = 0.32 f \Psi \left[e^{-\frac{255}{V+20}} \right]^2$$

$$C'' = C''_o + [500\Psi + 250\ (1 - \Psi)]\ e^{-\frac{255}{V+20}}$$

$$\Psi = 1 - e^{-\mu}$$

$$\mu = 0.18 \left(\frac{V}{f^{0.6}} \right)$$

A comparison of this phosphor with the usual ZnS,ZnO:Cu,Cl under a microscope shows the former to have roughly twice the average particle size of the latter The change in the parameters contained in the expression for photon emission (cf. Fig. 1) as a result of the increased particle size correlates reasonably well on the basis of Lehmann's work (10). He found that B_∞ (Eq. [8]) varied inversely as the square of the mean particle size. The present results correlated on this basis with a size ratio of 2.3.[2] His experiments also show that the equivalent of the threshold voltage c (Eq. [12]) varied inversely with the 0.7 power of the mean particle size. Lehmann's analysis of the latter constant is in terms of the 1.0 power rather than 0.7, but the former value cannot explain phenomenologically the decrease in maximum efficiency with increasing particle size which he observed, and 0.7 is in better agreement with his data than 1.0. From the ratio of the c-values then, one obtains a particle size ratio of $\left(\frac{400}{255} \right)^{\frac{1}{0.7}} = 1.9$, in reasonable agreement with the above figure.

Lehmann's analysis was based on the following relation between brightness, voltage, and frequency

$$B = A f \exp\ (-\sqrt{G/V}$$

while we have been using an expression which, at sufficiently low frequencies, reduces to

$$B = B_\infty f \exp\,(-2c/(V + V_0))$$

Although no attempt at a rigorous mathematical analysis has been made, it has been the experience of the present author that, at low frequencies, a set of data which fits the equation used by Lehmann above will also be consistent with the second expression above, with the following approximate relations between the constants

$$B_\infty = 0.10\ A;\ 2c = 0.12\ G;\ V_0 = 0.05\ (2c) = 0.006\ G.$$

Therefore any functional relationship between the constants A and G and parameters such as particle size, cell thickness, etc., will also apply, within a constant factor, to the constants B_∞ and c.

The coarse phosphor is also considerably less efficient than the normally sized phosphor, by a factor of about 1.6. On the basis of the model discussed above one would predict this for at least two reasons. First, the variation of c inversely as the 0.7 power rather than 1.0 power of the mean particle size indicates that a smaller fraction of the total voltage appearing across the particle is concentrated in the high field for large particles than for small. Hence proportionally more useless energy is dissipated in the low field volume by the "mobile" electrons. Second, the relative value of C''_2 to that of C''_1 is greater for the larger particles, indicating, quite reasonably, that in large particles the trapped electrons are subjected to displacements over larger distances within the high-field region in their unproductive agitation by the applied field.

The invariance of C''_1 with particle size suggests that the polarizability per available conduction electron at $V = \infty$ (the number of which is proportional to B_∞) varies directly as the square of the particle size. k_μ is also relatively invariant with particle size, which tends to confirm its association with the average field in the phosphor particles rather than the high-field region. It should be realized, however, that the above analysis is based mostly on data from a single phosphor sample.

The introduction of a killer such as Ni into a phosphor of the ZnS,ZnO:Cu,Cl type produces a quenching of the emission which depends on frequency alone (11). To determine the value of k_μ associated with such a phosphor one can use the change in slope at a particular voltage of ln B vs. $\frac{1}{V + V_0}$ (Fig. 1, 3) as a function of voltage, viz.

$$\frac{d \ln B}{d\left(\frac{1}{V + V_0}\right)} = \frac{d \ln \Psi}{d\left(\frac{1}{V + V_0}\right)} - C$$

$$= \frac{(V + V_0)^2}{V} \frac{\mu}{e^\mu - 1} - C \qquad [14]$$

$$\mu = k_\mu \frac{V}{f^{0.6}}$$

[2] That exact agreement is not to be expected is shown by the somewhat different particle size correlations reported by Goldberg (11).

The results of such an analysis on a ZnS,ZnO:Cu,Cl, Ni phosphor are

$$B = \frac{B_\infty}{Q} (\Psi)\, e^{\frac{710}{V+30}}$$

$$C'' = C''_0 + [500\,\Psi + 150\,(1 - \Psi)]\, e^{-\frac{355}{V+30}}$$

$$\mu = 0.1 \frac{V}{f^{0.6}}$$

f:	100	300	1000	5000 cps
$1/Q$:	1.0	1.17	1.60	2.0

The value of $1/Q$ has arbitrarily been set at 1.0 for 100 cps. The addition of the Ni has also had the effect of reducing the value of k_μ (more traps?) as well as quenching the emission at the lower frequencies, compared to the ZnS,ZnO:Cu,Cl phosphor (Fig. 1, 2). Thus a Ni-quenched phosphor can be sublinear, as well as superlinear or linear with frequency at a fixed voltage.

The analyses of the phosphors described above, other than the Ni-quenched material, have been made on the assumption of the absence of quenching. Using Eq. [14] to determine k_μ for ZnS,ZnO:Cu,Cl yields a value of 0.16, compared with 0.2 (Fig. 1), suggesting a small but significant amount of quenching. Trace amounts of Fe, Ni, or Co are undoubtedly present in this phosphor.

It should be mentioned also in this section that for all the phosphors examined, the dependence of the real part of the cell capacitance on voltage and frequency was such that, within experimental error, $C'_1 \sim C''_1$ and $C'_2 \sim C''_2$. Thus of the total energy absorbed by a conduction electron falling through a given potential, roughly half is stored as potential energy and returned to the field on field reversal.

Efficiency of Electroluminescence in Insulated Particles

The efficiency η with which the insulated electroluminescent phosphor converts the electrical power it absorbs from the applied field into luminous flux is proportional to (Eq. 8, 9, 11)

$$\eta \propto \frac{B}{W} = \frac{B f \Psi F^2}{\omega V^2 F[C_1'' \Psi + C''_2(1 - \Psi)]} \qquad [15]$$

The power absorbed by the cell dielectric and phosphor in the absence of electroluminescence, $\omega C''_0 V^2$, has been neglected, since we wish here to estimate the limiting efficiency of the electroluminescence process alone.

For most phosphors, at sufficiently low frequencies, $C'' \Psi >> C''_2 (1 - \Psi)$ so that

$$\eta \propto \frac{F}{V^2} \qquad [16]$$

Maximum efficiency then occurs at that voltage V_m for which

$$\frac{d \log F}{d \log V} = 2 \qquad [17]$$

The form of the maximum phosphor efficiency obtainable from insulated particles can be written

$$\eta_m = \frac{n_e\,(2.5\epsilon) F_m}{n_e (V_e\,\epsilon)} \qquad 400 \text{ lpw} \qquad [18]$$

2.5ϵ is the energy of a typical visible photon; V_e the voltage through which a typical "mobile" electron falls; $F_m = F(V_m)$. (Acceptable "white" luminescence with a luminous equivalent greater than 400 would be difficult to achieve.) One-third is a reasonable guess for the value of $2.5/V_e$ at η_m. V_e is the product of two factors: the average field over the path of the electrons and the mean path of the electrons. Both factors are assumed proportional to the applied field V, so that Eq. [18] is in fact dimensionally consistent with [15] and [16]. For most phosphors the average field across the cell, and hence across the phosphor in a liquid dielectric (5), is about 1.5 v/μ peak at the voltage of maximum efficiency. For $V_e = 3 \times 2.5 = 7.5$ v, the mean path of the electrons in this field is 5 μ, which is not unreasonable. If, as indicated above, half the absorbed energy is stored and later returned to the field, and in the absence of competing, nonradiative recombinations, an upper limit to the maximum phosphor efficiency may be set at

$$\eta_m = \frac{2}{3} F_m \qquad 400 = 267\, F_m \qquad [19]$$

The value of F_m depends on the form of the voltage dependence of $F(V)$. If we apply the usual form $F = \exp(-\text{const}/\sqrt{V})$, which is presumed to arise from the formation of an exhaustion layer (Eq. [2]), we have $F_m = e^{-4} \sim \frac{1}{50}$, which, substituted in Eq. [19], gives $\eta_m < 5.3$ lpw. Measurements have been published which exceed this by approximately a factor of three (10). If these are correct, then the expression $F = \exp(-\text{const}/\sqrt{V})$ does not give a reasonable characterization of the voltage dependence of F. Furthermore, the formation of an exhaustion layer requires the movement of a considerable quantity of charge before an ionization field is obtained, so that the maximum efficiency of such a process would have an even lower limit than 5.3 lpw. For these reasons, consideration of the formation of an exhaustion layer was eliminated from the model description.

Application of the form $F = \exp(-\text{const}/V)$ yields $F_m = e^{-2} \sim \frac{1}{7}$ or $\eta_m < 38$ lpw, a value high enough to explain efficiency obtained experimentally thus far. Such a voltage dependence can arise from, among other possibilities, the intrusion of elongated "spikes" of a conducting phase, such as Cu_2S, into the ZnS phosphor particle interior (13). The field at the tip of such an intrusion can easily be an order of magnitude greater than the average field. The ratio of the high field at the tip of the spike to the average field is given roughly by the ratio of the length of the spike to its cross-sectional diameter (14). This ratio undoubtedly increases with particle size. In such a case the value of the exponential constant c in the expression for $F = \exp -(c/V)$ is a monotonically decreasing function of particle diameter a, $c = c(a)$, and the effective value of F that applies to the rather wide particle size distribution encountered with electroluminescent phosphors is an integral or summation of the form

$$F = \sum_i f_i e^{-\frac{\bar{c}(a_i)}{V}} \qquad [20]$$

where the subscript i applies to a narrow range of particle sizes of mean diameter a_i and relative frequency f_i. The form $\exp(-\text{const}/\sqrt{V})$ has been shown to approximate the behavior of Eq. [2] except at the highest applied voltage (15), which makes it possible to use $\exp(-\text{const}/\sqrt{V})$ to describe the dependence of electroluminescence brightness on voltage. A more suggestive approximation to Eq. [20] is (16-18).

$$F = e^{-\frac{c}{V+V_0}} \qquad [21]$$

where the relative value of the constant V_0 is considered as simply a measure of the dispersion of a_i, particularly in the direction of larger than average particles. (Much smaller than average particles do not contribute much to brightness or power absorption at voltages in the neighborhood of maximum phosphor efficiency; only a small fraction of the particles that are absorbing power will be operating at the voltage of maximum efficiency for that fraction, so that the effective value of F_m will be less than e^{-2}. In fact, application of Eq. [17] to Eq. [21] for $V_0 \cong 0.10c$, true for the phosphors described above, yields

$$F_m = e^{-2.7} \sim \frac{1}{15}$$

Therefore to test the "limit" of about 38 lpw, one would have to use a phosphor of both uniform and small particle size since, as indicated in the discussion of the coarse phosphor, smaller particles concentrate a larger fraction of their total voltage across the high-field region, and on the basis of this model would be expected to operate more efficiently.

Finally, it should be mentioned that for the relations developed earlier in this paper between photon emission and power consumption to apply accurately to the assembly of particle sizes present in a typical electroluminescent phosphor, one must hope, applying Eq. [20] to [8] and [11], that the following is a good approximation

$$\frac{\sum_i f_i e^{-\frac{2\bar{c}(a_i)}{V_1}}}{\sum_i f_i e^{-\frac{2\bar{c}(a_i)}{V_2}}} \sim \left[\frac{\sum_i f_i e^{-\frac{\bar{c}(a_i)}{V_1}}}{\sum_i f_i e^{-\frac{c(a_i)}{V_2}}} \right]^2$$

for any values of V_1 or V_2 within the range of interest.

Acknowledgment

The writer wishes to thank the following persons for many helpful suggestions as well as the preparation of most of the phosphors: Dr. I. L. Smith, Dr. M. Aven, Dr. R. M. Potter, and Mrs. M. S. Jaffe.

Manuscript received Oct. 15, 1959.

Any discussion of this paper will appear in a Discussion Section to be published in the December 1960 JOURNAL.

REFERENCES

1. F. F. Morehead, Jr., *This Journal*, **105**, 461 (1958).
2. P. Zalm, *Philips Research Repts.*, **11**, 353, 417 (1956).
3. W. A. Thornton, *Phys. Rev.*, **102**, 38 (1956).
4. G. F. Alfrey and J. B. Taylor, *Proc. Phys. Soc.*, **B68**, 775 (1956).
5. W. Lehmann, *J. Optical Soc. Am.*, **48**, 647 (1958); *This Journal*, **103**, 24 (1956).
6. J. F. Waymouth and F. Bitter, *Phys. Rev.*, **95**, 941 (1954).
7. E. E. Loebner and I. J. Hegyi, Enlarged Abstracts, Electronics Division, The Electrochemical Society, Philadelphia Meeting, p. 45 (1959), not published.
8. H. C. Froelich, *J. Optical Soc. Am.*, **43**, 320 (1953).
9. D. L. Dexter, *J. Chem. Phys.*, **21**, 836 (1953).
10. W. Lehmann, *This Journal*, **105**, 585 (1958).
11. P. Goldberg, *ibid.*, **106**, 34 (1959).
12. W. Lehmann, *Phys. Rev.*, **101**, 489 (1956).
13. W. Lehmann, *This Journal*, **104**, 45 (1957).
14. K. Maeda, *J. Phys. Soc., Japan*, **13**, 1352 (1958).
15. W. Lehmann, Enlarged Abstracts, Electronics Division, The Electrochemical Society, Philadelphia Meeting, p. 18 (1959), not published.
16. W. Lehmann, *This Journal*, **103**, 667 (1956).
17. B. T. Howard, H. F. Ivey, and W. Lehmann, *Phys. Rev.*, **96**, 799 (1954).
18. G. Destriau and H. F. Ivey, *Proc. IRE*, **43**, 1911 (1955).

SYMBOLS

α — Fraction of n_e "mobile" electrons that recombine with emission each half-cycle.

β — Fraction of n_e "mobile" electrons that are trapped in high-field regions each half-cycle.

ϵ — Electron charge.

η — Electroluminescence efficiency.

μ — A constant in expression for Ψ: $\mu = k_\mu \dfrac{V}{f^{0.6}}$

Ψ — $\dfrac{n_e}{n_e + N_T} = (1 - e^{-\mu}) = \Psi$

ω — $2\pi f$

a — Effective particle diameter

B — Photon emission/cycle, arbitrary units.

B_∞ — Photon emission/cycle extrapolated to $V = \infty$.

$c, \bar{c}$ — A constant in one expression for $F = e^{-\frac{c}{V+V_0}}$ for the cell; $F = e^{-\bar{c}/(V+V_0)}$ for particles of a given diameter.

C_0', C_0'' — The real and imaginary parts of the cell capacitance in absence of electroluminescence.

C'_1, C''_1 — Constant coefficients in expression for real and imaginary capacitance contributed by "mobile" electrons.

C'_2, C''_2 — The same for "trapped" electrons.

d — Cell thickness.

$\mathbf{E}$ — Effective ionizing field.

E_0 — Trap depth.

F — Probability of impact ionization of a secondary electron by a primary electron in high-field region.

f — Frequency in cps.

f_i — Relative frequency of occurrence of particles of mean diameter a_i.

i — Cell current

k_μ — A constant in expression for μ.

n_e — Number of electrons that return to the high-field region each half-cycle.

N_+ — Steady-state number of ionized centers in high-field region.

N_T — Steady-state number of electrons that remain trapped in phosphor bulk.

$(PMR)_f^{h\nu}$ — The 1P21 photomultiplier response to a given number of photons/second distributed according to emission spectrum of a given phosphor at frequency f.

$(PMR)_f^{w}$ — Same for a given radiant power.

Q — Quenching factor by which the emission expected in the absence of quenching is divided.

R_ν — Relative response of the 1P21 photomultiplier for equal radiant power at each photon frequency.

$SR(f_1,f_2)$ — Response of the 1P21 photomultiplier to a given number of lumens emitted by a phosphor at a frequency f_2 relative to that at a frequency f_1.

T — Absolute temperature.

V — The rms voltage.

V_0 — A constant in the expression for F.

V_e — Potential through which a typical electron falls in the electroluminescence process.

N_p — Fraction of cell volume occupied by phosphor.

VAR — Stored power, $VAR = \omega C' V^2$.

W — Consumed power, $W = \omega C'' V^2$.

X — A constant proportional to capture cross section of the ionized activators.

Electroluminescence under Pulsed Square Wave Excitation

R. Zallen,[1] W. T. Eriksen, and H. Ahlburg

Research Division, Raytheon Company, Waltham, Massachusetts

ABSTRACT

The slow return of an electroluminescent cell to its equilibrium state following a field excitation has been studied for a blue-green emitting Zn(S,O): Cu,Cl phosphor and for a yellow-emitting ZnS: Mn,Cu phosphor. The light pulse emitted upon the rise of a square voltage pulse was measured as a function of repetition rate and of temperature between —130° and 150°C. Relaxation times encountered varied between 10^{-2} sec and 10^{5} sec. The temperature dependence of the relaxation rate exhibits effective activation energies of about 0.4, 0.7, and 0.6 ev, respectively, for the blue, green, and yellow emission bands. The results do not seem to favor the mechanism of delayed recombination. An alternative mechanism is suggested whereby the number of filled deep donors is assumed to control the electroluminescence emission via the number of field-ionizable electrons available for collision-excitation of centers. Observations were also made on some other effects associated with square wave excitation.

A complete picture of the microscopic processes involved in the light emission from insulated zinc sulfide crystals under high electric fields (1) has not yet been established firmly, although various models have been more or less successful in accounting for different aspects of the phenomenon. The present work was undertaken to obtain further insight into the nature of electroluminescence.

This paper describes some observations on the electroluminescence of two zinc sulfide phosphors under pulsed d-c voltage excitation and their interpretation in the light of proposed mechanisms. Square wave voltage excitation is in some ways simpler than the extensively studied sine wave excitation and yields information not readily obtainable from studies of brightness wave forms under sinusoidal voltages.

When a square wave pulse is applied to an electroluminescent cell two pulses of light emission are generally observed (2-5), one upon application of the external field and the other upon removal of that field. The first light pulse reaches its maximum shortly after the voltage rise is completed, then decays in roughly exponential fashion until the inception of the second light pulse at the removal of the voltage. A typical time dependence of luminescence and applied voltage is shown in Fig. 1.

[1] Present address: Gordon McKay Laboratory, Harvard University, Cambridge, Mass.

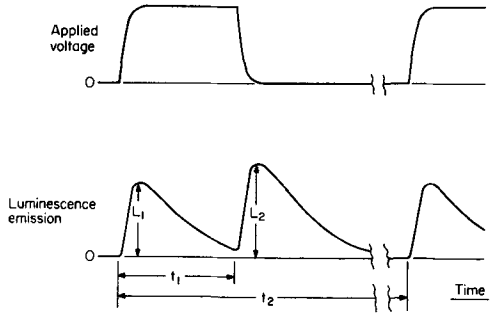

Fig. 1. Typical brightness waveform under square wave voltage excitation: t_1 = pulse width; t_2 = repetition interval; L_1, L_2 = peak intensities of the two light pulses.

In this work measurements were made of the emitted light pulses and their decay characteristics as a function of the two time parameters of the pulsed square wave voltage excitation: pulse width and repetition interval. These effects were studied in the temperature range of —130° to 150°C. The yellow emission band of a manganese-activated phosphor and the blue and green emission bands of a copper-activated phosphor (isolated by means of optical interference filters) were studied. The voltage dependence of emission intensity was checked and found to fit closely to exp $[-b/V^{1/2}]$ as has been widely observed for sine wave excitation (2).

Experimental

The preparation of the phosphors is shown in Table I and the panel construction in Fig. 2. Chlorine was included as a charge compensating coactivator in the copper-activated phosphor. Monovalent copper ions substitutionally replacing zinc ions in the crystal are more easily incorporated if chlorine is present simultaneously to substitute for sulfur (6). It has also been proposed (7) that chlorine promotes the formation of sulfur vacancies thought to be necessary for luminescence in ZnS. Preparation of the manganese-activated phosphor did not require

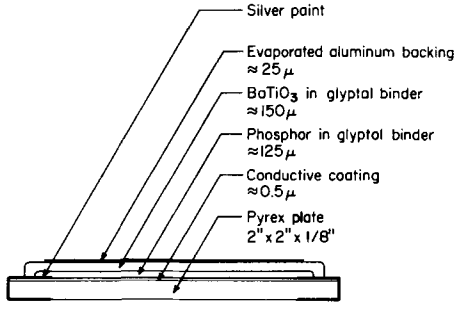

Fig. 2. Construction of the electroluminescent cells

Table I. Phosphor preparation

Phosphor	Zn(S, O): (Cu, Cl)	ZnS: (Mn, Cu)
Activation	0.005 g atom Cu/mole ZnS 0.02 g atom Cl/mole ZnS 0.4 mole ZnO/mole ZnS	0.0025 g atom Cu/mole ZnS 0.0125 g atom Mn/mole ZnS
Firing Temp., Time, Atmosphere	900°C 24 hr air	1100°C 1 hr dry H_2S
Post-Firing Washing Procedure	1. hot acetic acid (20%) 2. water 3. NaCN solution (3%) 4. water 5. methanol	1. NaCN solution (3%) 2. water 3. methanol
Drying Temp., Time, Atmosphere	125°C 16 hr air	125°C 16 hr air

a coactivating halide flux since manganese replaces zinc as a divalent ion in the lattice so that charge compensation is unnecessary (8). Some copper was also included in this phosphor since it has been found to promote electroluminescence (9). The numbers given for the thickness of the various layers are representative. A rough check on the measured phosphor layer thickness was given by the capacitance of the panels which was about 10^{-9} farads in each case. The phosphor powder was mixed with a binder and sprayed onto the conductive surface of a Pyrex plate serving as the transparent electrode. A second layer of binder containing powdered barium titanate was applied to the back of the phosphor layer. This insulating layer was found to be useful in preventing breakdown across thinner portions of the phosphor layer without sacrificing much of the voltage drop across the latter due to the large dielectric constant of barium titanate. An aluminum backing evaporated onto the barium titanate layer served as the rear electrode. Silver paint around the edges of the glass plate allowed contact to be made between the conductive coating electrode and a copper strip pressed against the front of the plate. The aluminum electrode was held against the surface of a copper block kept at ground potential, which also served as the thermal reservoir used in controlling the temperature of the phosphor.

The experimental arrangement is shown schematically in Fig. 3. Tektronix units of the 160 series provided the square wave signals which were fed into an amplifier capable of delivering outputs up to 2000 v with a rise time in the vicinity of 10 μ sec. An RCA 6199 photomultiplier was used to monitor the luminescence. The time dependence of the exciting voltage and of the emitted light were displayed on a Tektronix 545 oscilloscope equipped with a dual trace preamplifier.

The panel was enclosed in a stainless steel chamber fitted with a quartz window for viewing the luminescence. A copper rod connected to the copper block in contact with the panel's aluminum backing led outside the housing through a Teflon insulator. This rod could be immersed in a refrigerant or in a heating coil to vary the temperature of the electroluminescent cell. Temperature was measured by an iron-constantan thermocouple with one junction located on the surface of the copper block next to the panel.

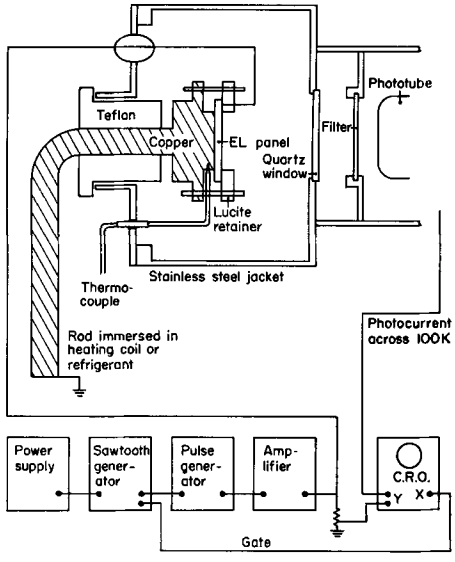

Fig. 3. Schematic diagram of the experimental arrangement.

Procedure and Measurements Performed

The aluminum backing electrode was kept at ground potential while the transparent electrode was driven back and forth between ground and a high negative potential. By means of a Balzers graduated interference filter serving as a crude spectrometer in the visible it was determined that the yellow-orange emission of the manganese panel consisted of the characteristic single broad band peaked around 5800Å. The copper-activated panel exhibited the well-known blue-green emission which changes in spectral content with varying operating conditions, e.g., becomes bluer with increasing frequency. The overlapping emission bands of this phosphor were separated by two Balzers interference filters transmitting 4610Å and 5300Å with peak transmissions of 30% and half widths of 100Å. Because of the reduction in intensity in selecting such narrow spectral ranges for investigation, the measurements on the Zn (S,O): Cu,Cl panel were made at higher exciting voltages and greater phototube sensitivity than were used in the measurements on the ZnS: Mn, Cu panel.

Detailed measurements were made on the variation of the two peak intensities, L_1 and L_2, with the repetition interval t_2, and with temperature. 400-v pulses of 10 msec duration were used in the ZnS: Mn, Cu studies, 700-v pulses of 1 msec duration for

the Zn (S,O):Cu, Cl. The pulse widths chosen were the smallest times needed to allow the first light pulse to decay to a value small relative to L_2. The output photocurrent of the photomultiplier was passed through a 10^5 ohm resistor and displayed on the oscilloscope. When L_1 and L_2 were widely different ($L_1 << L_2$), the signal was fed into both channels of a dual trace preamplifier with each channel set at a scale convenient for measuring one of the peak heights. For long repetition intervals the peak heights were taken from a photograph of the scope trace.

Measurements were made of the decay of the second light pulse after removal of the applied field (L vs. t from L_2 on). For the ZnS: Mn, Cu panel, 400-v pulses of 10 msec duration and 10 cps repetition rate were used in making these measurements. For the Zn (S,O): Cu, Cl panel, 700-v pulses of 1 msec duration and 10 cps repetition rate were used. The delaying sweep circuit of the oscilloscope was employed for these measurements. This decay characteristic was studied at various temperatures.

Qualitative observations were made on the brightness wave forms of the luminescence emission with very small pulse widths. This turned up some interesting effects which will be discussed.

Results

Luminescence emission occurs on the rise and on the fall of the applied voltage, giving the two light pulses L_1 and L_2. For a given voltage amplitude and for the low duty cycles normally employed ($t_1 << t_2$), it was found that L_1 depends on t_2 and L_2 on t_1. This is to be expected if the dominant factor in determining the state of a phosphor at a particular temperature is the time elapsed from the last preceding excitation, i.e., the last preceding voltage shift (3). Thus it is not surprising that the second light pulse is insensitive to the repetition interval and that the first light pulse is unaffected by the duration of the applied voltage following it.

Figures 4 and 5 are log-log plots of the variation in peak intensity of the first light pulse with repetition interval for the two phosphors at several temperatures. Figure 5 consists of the two sets of curves for the green and the blue emission of the copper-activated phosphor. Any small drift in either the applied voltage amplitude or the phototube sensitivity would be expected to change both L_1 and L_2 by the same factor. In order to compensate for such variations the data are normalized by plotting the peak height ratio, L_1/L_2, as the dependent variable.

In all cases the peak height ratio is of the order of unity for small t_2 and falls off as t_2 increases. At low temperatures the drop-off is slower than at high temperatures. At —125°C this variation is well frozen out, with very little change in L_1/L_2 occurring in times less than an hour. For the manganese-activated panel the ratio falls until a terminal value of the order of 10^{-1} to 10^{-2} is attained at a particular value of t_2, and then remains constant. For the copper-activated panel the ratio falls to 10^{-3}, the limit of measurement, without exhibiting any saturation effect. The blue emission of this panel possesses a faster decrease of L_1 with t_2 than does the green emission, al-

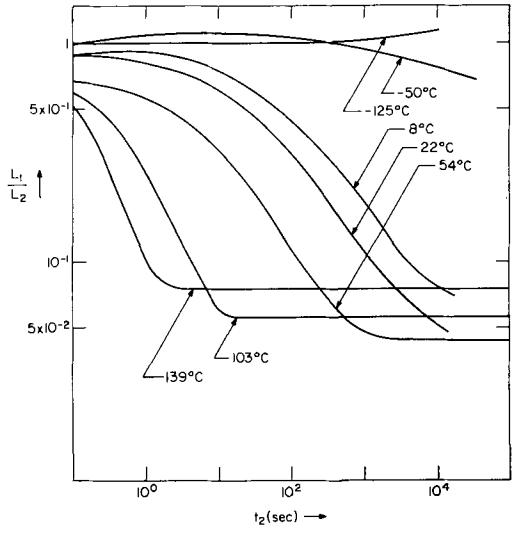

Fig. 4. Peak intensity of the first light pulse vs. repetition interval for the ZnS:Mn,Cu panel.

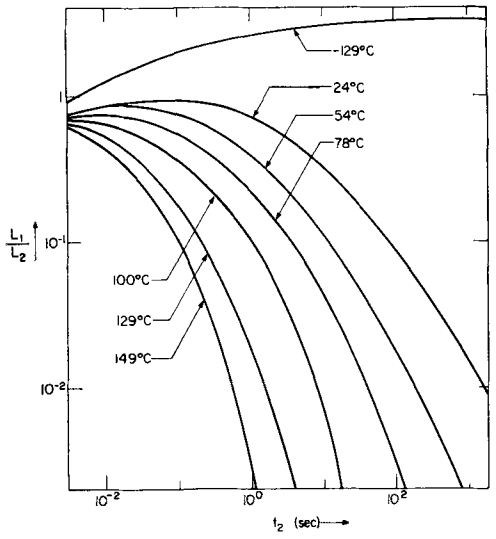

Fig. 5a. Peak intensity of the first light pulse vs. repetition interval for the Zn(S,O):Cu,Cl panel; green emission.

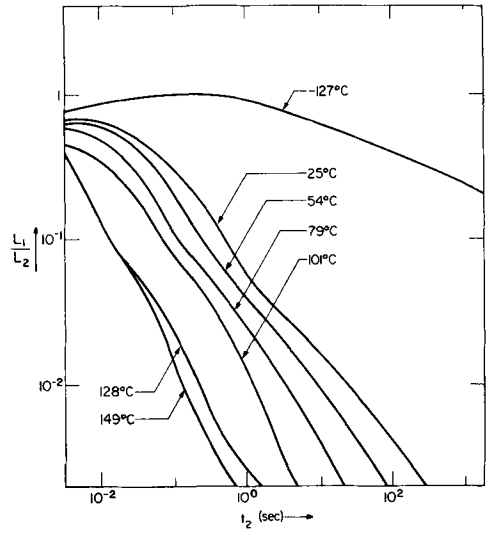

Fig. 5b. Peak intensity of the first light pulse vs. repetition interval for the Zn(S,O):Cu,Cl panel; blue emission.

though the latter decay seems to catch up with the former at very long repetition times. Waymouth and Bitter (4) measured the integrated light output of a blue-green phosphor upon removal of an applied voltage of long duration. They observed a slow decay with increasing duration time similar to that reported here for increasing repetition time, with the blue decay occurring more quickly than the green decay. Their results are compared to ours in the following section.

The temperature dependence of L_1 (t_2) is interesting since such a thermally controlled process can yield information on energy levels of electrons involved in the excitation or recombination processes taking place in electroluminescence. An analysis and interpretation of this temperature dependence is discussed in the next section.

Figures 6 and 7 show the time decay of the second light pulse upon removal of the applied field for the two phosphors at three of the temperatures studied, the latter figure giving both the blue and the green decays of the Zn (S,O): Cu,Cl panel. The ZnS: Mn, Cu data do not exhibit any appreciable systematic temperature shift whereas the Zn (S,O): Cu,Cl curves exhibit a minor systematic change with temperature. The initial slope of the decay at −125°, 25°, and 150°C gives decay rates of 17, 14, and 8×10^3 sec^{-1}, respectively, for the blue and 11, 8, and 5×10^3 sec^{-1} for the green emission. In addition to this decrease of the initial rate of decay, these curves also become more exponential in shape (linear on a semi-log plot) with increasing temperature so that after long times the emission is lower and the decay rate greater for high temperatures than for low. This produces the cross-over of the decay curves shown in Fig. 7. The initial decay rate of the ZnS: Mn,Cu data is 0.9×10^3 sec^{-1} and the shape of this decay does not change with temperature.

Figure 8 shows some brightness waveforms obtained by application of voltage pulses of short duration. For the manganese-activated phosphor, equal increments of emission occur at the rise and fall of the applied voltage except with pulse widths less than about 0.5 msec for which the second increment becomes smaller than the first. Nudelman and Matossi (5) report a very similar behavior for the blue component of a ZnS: Cu,Pb phosphor with a critical pulse width of 0.7 msec. The blue emission of our copper-activated phosphor also exhibits equal increments of emission, but at pulse widths down to 0.2 msec. For the green emission of their phosphor, Nudelman and Matossi report equal peak heights at the voltage rise and fall for pulse widths greater than 0.7 msec. Our observations are similar, except that the critical time observed is about 0.2 msec.

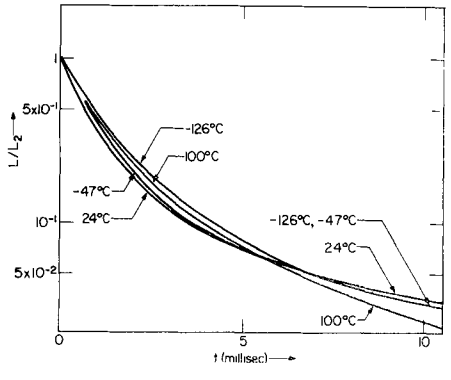

Fig. 6. Decay of light emission L on removal of the applied voltage for the ZnS:Mn,Cu panel.

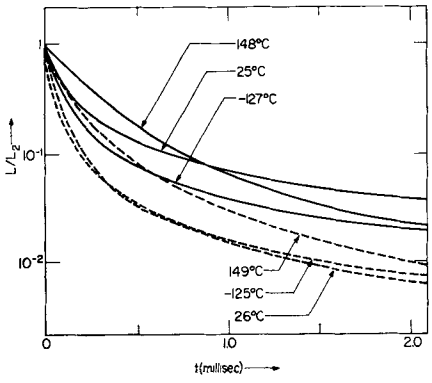

Fig. 7. Decay of light emission L on removal of the applied voltage for the Zn(S,O):Cu,Cl panel. Green emission: solid lines; blue emission: dashed lines.

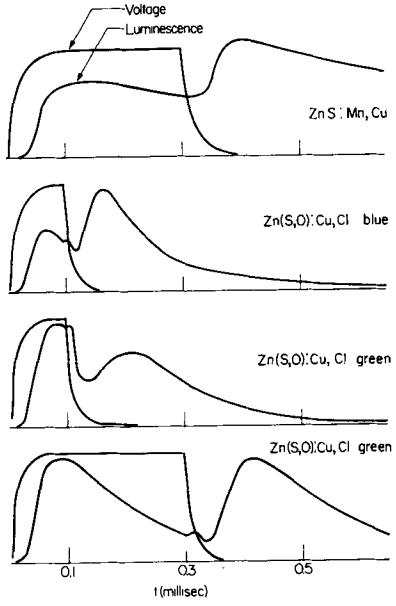

Fig. 8. Brightness waveforms using short pulses

Some interesting effects were observed in the Zn (S,O): Cu,Cl panel. The blue emission exhibits a very small peak preceding the build-up of the second light pulse. This stimulation peak appears at small repetition intervals and is insensitive to pulse width. The green emission also reveals this effect. In addition, however, at short pulse widths this emission shows a sharp dip upon the start of the voltage drop. This quenching dip precedes the build-up of the second light peak but follows the stimulation peak. Some representative brightness waveforms are shown in Fig. 8. The two effects are independent. The stimulation peak is most noticeable at short repetition times and long pulse widths, but as the pulse width is reduced the quenching dip becomes dominant. Nudelman and Matossi observed stimulation peaks, but for the green emission only. They did not find quenching dips in their phosphor.

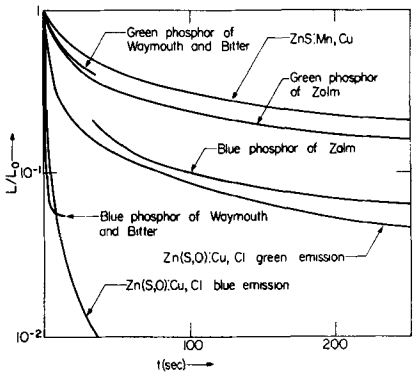

Fig. 9. Room temperature data on the dependence of the emitted light L after an elapsed time t from the preceding voltage shift. L_0 is the value of L for t = 0.

Both of these effects were absent in our manganese-activated phosphor.

Discussion

In Fig. 9 the room temperature curves of Fig. 4 and 5 are replotted on semi-log paper along with some data of Waymouth and Bitter (4), and of Zalm (2), who also noticed this slow return of an electroluminescent cell to its original state following a field excitation. These curves demonstrate that this decay does not follow an exponential law. Rather, the log-log plots are suggestive of the power-law decays encountered in phosphorescence (10). Such decays may be accounted for in terms of the emptying of a collection of filled traps of various depths. For example, it has been shown (11) that a uniform trap distribution, that is, an equal number of traps of all depths, gives a decay with a t^{-1} dependence at long times. It is interesting that the blue emission decay approximates this hyperbolic relationship at the higher temperatures. A trap distribution varying exponentially with trap depth, that is, $dN_E/dE = A \exp[-\alpha E]$, gives a decay going as t^{-n} for long times (11), where $n = \alpha kT + 1$. If a t^{-n} law is assumed and compared with the steepest slopes encountered in Fig. 4 and 5, n is found to vary linearly with temperature from 0° to 150°C, going from 0.7 to 1.8 for the green emission, from 0.5 to 1.2 for the blue emission, and from 0.4 to 0.8 for the yellow emission. These observations suggest that the mechanism responsible for the behavior of L_1 with time and temperature is the thermal release of trapped electrons (or holes). The existence of traps in zinc sulfide phosphors has been widely demonstrated by means of glow curves and other methods (12).

The above reasoning may be summarized by the following syllogistic argument: (*a*) temperature dependent phosphorescence has been accounted for in terms of electrons thermally ejected from traps; (*b*) the decay curves of L_1 vs. t_2 resemble reported temperature dependent power-law phosphorescence decays; (*c*) therefore, the present measurements may reasonably be explained by the thermal release of trapped electrons.

In order to characterize the temperature dependence of the data, the following method has been employed. A particular value of L_1/L_2 is first selected, and then the value of t_2 corresponding to this level of the peak height ratio is noted for each of the various temperatures studied. The reciprocal of this arbitrarily defined relaxation time is plotted against reciprocal temperature on semi-log paper (hoping, of course, to obtain a straight line). This calculation is repeated for several choices of peak height ratio. The rationale for this procedure is the assumption that the extent to which the phosphor has retrogressed toward its equilibrium condition at a particular time following a field excitation is more or less defined by the value of L_1/L_2 at that time. The reciprocal of the time needed for the relaxation to proceed to a given stage is then taken as a measure of the rate of the relaxation process.

The results are shown in Fig. 10 and 11. Despite the crudeness of the approach and the expected complexity of the actual trap distributions, reasonably good straight lines were obtained. The activation energies corresponding to the slopes of the lines are listed in Table II. The effective trap depths obtained fall in the range of 0.3-0.5 ev for the blue emission, 0.5-0.8 ev for the green emission, and 0.6 ev for the yellow emission. For each emission band the effective trap depths increase with decreasing choices of L_1/L_2. Thus the deeper traps control the later stages in the relaxation process, which is reasonable as it is to be expected that the shallow traps empty first.

Before resuming this discussion of the role of traps in this phenomenon, a brief digression on the nature of the electronic states of the luminescence centers involved may be useful. It is generally agreed that the manganese centers give rise to perturbed ionic states lying well below the top of the valence band (13). Accepting the collision-excitation hypothesis, a ground-state electron interacts with a conduction electron accelerated to optical energies by the electric field in a localized high-field region of the crystal and is raised to a bound excited state from which it drops back to the ground state after a characteristic time, giving off a photon

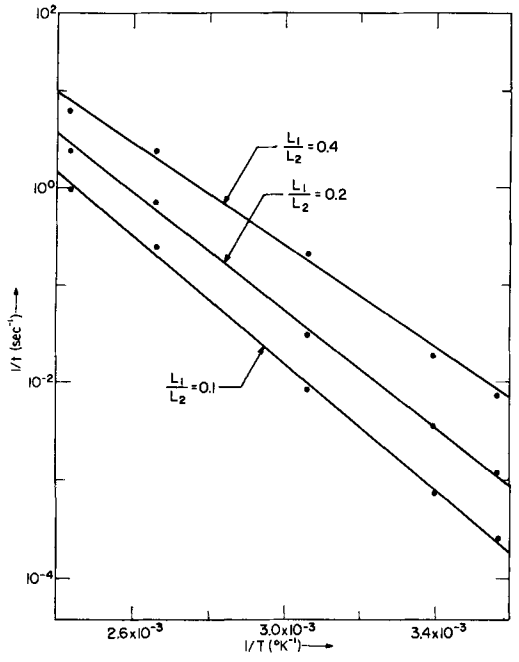

Fig. 10. Temperature dependence of the ZnS:Mn,Cu relaxation time.

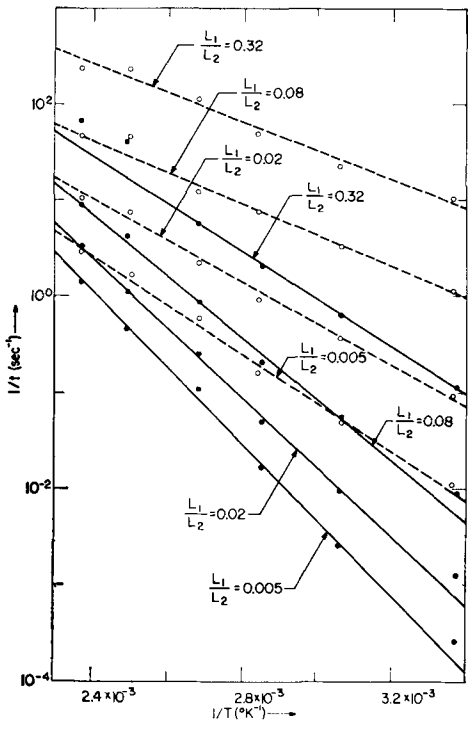

Fig. 11. Temperature dependence of the Zn(S,O):Cu,Cl relaxation time ———— green emission; - - - - -, blue emission.

Table II

Phosphor	Emission band	L_1/L_2	Activation slope in ev
ZnS: Mn, Cu	Yellow	0.4	0.52
		0.2	0.60
		0.1	0.64
Zn(S, O): Cu, Cl	Blue	0.32	0.30
		0.08	0.33
		0.02	0.43
		0.005	0.51
Zn(S, O): Cu, Cl	Green	0.32	0.49
		0.08	0.64
		0.02	0.71
		0.005	0.78

in the process. Ionization does not occur. This picture is consistent with our observations on the yellow emission band. The temperature independence of the decay of the light pulse (Fig. 6), as well as the absence of stimulation or quenching effects, indicates that bound states are involved. The equal increments of emission on the rise and fall of the external field may be understood on the basis of equal effective fields [the field at the voltage fall is due to polarization charges (3-5) to be discussed later] exciting equal numbers of centers which are simply added to the excited centers left over from previous excitations. This latter statement contains the assumption that the number of centers excited at any time is a small fraction of the total so that the number available for excitation remains essentially constant.

In copper-activated zinc sulfide, it is generally assumed that the emission process for both green and blue bands involves transitions between perturbed crystal states lying within the forbidden gap, and either conduction electrons (14) (Schön-Klasens model) or valence band holes (15) (Lambe-Klick model). The green emission exhibits equal peak heights with rise and fall of voltage, as well as sharp quenching dips upon field removal which may be due to charge carriers being swept out of a region in which they had been participating in radiative recombination with ionized activators. In addition, the shape of the light pulse decay is temperature dependent (Fig. 7). These observations favor the belief that excitation of the green centers involves ionization and production of mobile charge carriers. The situation is ambiguous for the blue band since this emission resembles that of the manganese in giving equal increments upon field application and removal, while it possesses a temperature dependence of the light pulse decay similar to that of the green band.

It has been reported (3) that an internal polarization is present which develops upon application of an external field and which decays upon removal of that field with a time dependence similar to that observed for L_1 vs. t_2. This polarization may result from the trapping of charge carriers in regions removed from their place of origin due to migration under the action of the field. It shall be assumed that both this internal polarization and the L_1 dependence arise from the same trapping mechanism within the phosphor.

Waymouth and Bitter (4) propose the trapping scheme shown in Fig. 12 in terms of the Schön-Klasens model. Upon application of the field, electrons are collision-ionized from activator centers into the conduction band whence they are swept by the field to another part of the crystal. Here they are held until field removal, whereupon they return and recombine radiatively with the empty activator centers. During the interim, however, the ionized centers may thermally release their trapped holes to the valence band where they may subsequently be retrapped by deeper quenching centers. Electron-hole recombination occurring at these quenching centers is assumed to be nonradiative at high temperatures, while at low temperatures light of longer wave length is emitted. This process reduces the light pulses emitted in the blue and green bands upon removal of the field, and also accounts for the temperature quenching of the photoluminescence.

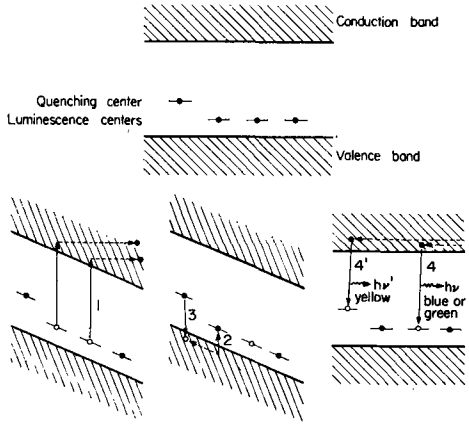

Fig. 12. Schon-Klasens model applied to electroluminescence (after Waymouth and Bitter).

Waymouth and Bitter, from temperature dependence measurements of L_2 vs. t_1, obtained activation energies of 0.29 and 0.21 ev for the green and blue bands, respectively, which they interpret as giving the separation between the vacant activator levels and the top of the filled band. Garlick and Gibson (16), from measurements of temperature quenching, obtained 0.95 ev for green-emitting ZnS:Cu and 0.59 ev for yellow-emitting ZnS:Mn. Activation energies observed here are about 0.7 ev, 0.4 ev, and 0.6 ev for the green, blue, and yellow bands, respectively.

Although this model is consistent with observations on the decrease of the burst of light emitted on removal of an applied field with increasing time of application of that field, there remain some objections to it. It does not appear to account for the decay of the light pulse emitted on aplication of the field with increasing time elapsed from the previous field excitation (our measurements of L_1 vs. t_2). As mentioned above, it seems likely that excitation of the green luminescence band, with emitted radiation (transition 4 in Fig. 12) of about 2.4 ev photon energy, involves ionization of an electron into the conduction band (or a hole into the valence band). Since the band gap of zinc sulfide is about 3.8 ev (17), the depth of the traps involved (transition 2 in Fig. 12) should be about 1.4 ev, much greater than observed values. This failure of the measured activation energies to give the band gap when added to the energy of the emitted radiation contradicts the picture shown in Fig. 12. It is tempting, but doubtful, to explain this discrepancy by invoking Schön's hypothesis of widely different energy levels for thermal and optical processes (18).

In connection with Fig. 12, it may be worthwhile to mention the related concept of delayed recombination proposed by several workers (2, 3). According to this model, electrons removed from ionizable activators by collision excitation on application of a high field are quickly swept to the positive side of the crystal where they are held until removal of the field releases them for radiative recombination with empty centers. Thus excitation of luminescence centers is thought to occur only on the rise of an applied d-c voltage pulse while luminescence emission occurs primarily at the fall of the voltage as only then may electrons return to recombine with ionized centers. Frequently quoted evidence for this theory is the observation that $L_1 << L_2$. However, Fig. 4 and 5 reveal that $L_1 << L_2$ only for long repetition intervals and high temperatures. Over wide ranges of operating conditions, e.g., for t_2 up to an hour at $-125°C$, L_1 and L_2 are approximately equal. These measurements do not favor delayed recombination. In addition the delayed recombination mechanism is not applicable to activators for which the excited state is a bound perturbed ion state and the electron is never physically removed from the center, e.g., manganese.

In view of the difficulties with this model, we will propose a mechanism by which we hope to account for, among others, these experimental findings: (*a*) the light pulse emitted on application or removal of voltage decays with the time elapsed from the preceding field excitation (voltage shift); (*b*) temperature dependence of (*a*) resembles the emptying of trap distributions of depths between 0.3 and 0.8 ev; (c) there is a component of internal polarization which builds up and decays in synchronism with the above effect.

When an external field is applied to a phosphor, there is evidence (3) that large voltage drops are concentrated across small regions of the phosphor due to the existence of barrier layers or rectifying junctions. It is in these high field regions that electroluminescence takes place. Electrons are field-ionized from deep traps and then accelerated to optical energies by the field. Some of these "hot" electrons collide with activator centers and lose all or part of their kinetic energy in raising electrons to excited states from which radiative transitions back to the ground state may later occur. It is natural to assume that the number of luminescence centers excited will be proportional to the concentration of energetic free electrons which, in turn, should strongly depend upon the number of "loose" electrons (electrons thermally excited to or injected into the conduction band, or electrons in traps shallow enough to be directly ionized by the field) originally present to initiate the process. It is hypothesized here that the experimental facts listed above are due to time variations in this population of loose electrons. Thus we consider changes in the number of centers excited rather than changes in the efficiency of the radiative recombination to be the dominant factor.

It is proposed here that the light emissions L_1 and L_2 are independent luminescence events produced by separate excitations at the rise and fall of applied voltage, and that a difference in their intensities reflects a difference in the number of centers excited in each case. Application of the external field establishes a space charge as electrons are swept out of the high field region. The time required for the development of this polarization is of the order of the critical pulse width mentioned earlier (5). Some of the free electrons produced by the applied field are trapped in a normally unoccupied trap distribution. When the external field is removed, part of the polarization charge decays quickly in a time similar to the build-up time. However, that portion of the space charge consisting of electrons in deep traps decays very slowly at a rate determined by the thermal release of trapped electrons. This accounts for the last of the experimental facts listed above, viz., the "frozen-in" component of polarization observed by Waymouth and Bitter.

Consider an electroluminescent phosphor in an equilibrium condition ($t_2 \rightarrow \infty$) at a certain temperature. Application of a field finds a certain number of loose electrons available for acceleration and collision-excitation of luminescence emission L_1. Let us denote this value of L_1 for a first voltage application, i.e., L_1 for $t_2 \rightarrow \infty$, as $L_1°$. Removal of the external field momentarily leaves an unopposed polarization field which causes a second excitation of luminescence, L_2. However, this field finds a larger number of field-ionizable electrons as traps were

filled on the voltage rise. This increases the resultant number of hot electrons to take part in collision-excitation. Thus we may understand the situation whereby $L_1 << L_2$ without recourse to delayed recombination.

A second similar voltage pulse applied after a short time finds the same nonequilibrium concentration of loose electrons so that for short repetition intervals we find $L_1 \approx L_2$. A voltage pulse applied after a considerable elapsed time ($t_2 >> t_1$) will find the phosphor partially relaxed towards thermal equilibrium so that $L_1^\circ < L_1(t_2) < L_2$. From Fig. 4 and 5 we note that L_1° is about one-twentieth of L_2 for the manganese-activated phosphor, while for the copper-activated phosphor L_1° is below the limit of measurement, i.e., less than one-thousandth of L_2. Thus we may interpret (*a*) in terms of a return to thermal equilibrium of the number of field-ionizable electrons via the thermal emptying of an overpopulated trap distribution. The temperature dependence mentioned in (*b*) then follows naturally from Boltzmann statistics. These trapped electrons comprise the slowly decaying component of polarization mentioned above so that this polarization decays in synchronism with L_1, as stated in (*c*).

Although this mechanism accounts for the above experimental behavior it is not without its difficulties, a normal situation among electroluminescence theories. Since L_1 is assumed to vary with the number of occupied deep donors in the crystal, the effect should be largely independent of the particular luminescence center involved for a given host phosphor. However, we obtained different activation energies for the green and blue emissions of the copper-activated phosphor. Further assumptions may be needed to explain these observations in terms of our model. Another objection might be that filling of traps does not seem to occur to any great extent during electroluminescence as evidenced by the very weak glow curves following voltage excitation (9). This result may be due to the fact that electroluminescence is confined to just a small fraction of the phosphor volume. Also, other observations re-emphasize the importance of traps (19).

Summary

Measurements of the temperature-dependent decay of L_1 with t_2 suggest a process involving the thermal emptying of donors of depths between 0.3 and 0.8 ev. This phenomenon has been reported to be correlated with a polarization charge. We therefore attribute the traps to the host crystal rather than to the luminescence centers. The mechanism of delayed recombination does not appear to account satisfactorily for the data. An alternative suggestion is proposed whereby the number of filled deep donors is assumed to control the electroluminescence emission via the number of field-ionizable electrons available for collision excitation of centers.

Manuscript received Oct. 12, 1959.

Any discussion of this paper will appear in a Discussion Section to be published in the December 1960 JOURNAL.

REFERENCES

1. G. Destriau, *Phil. Mag.*, **38**, 700 (1947).
2. P. Zalm, *Philips Res. Repts.*, **11**, 353 (1956).
3. J. F. Waymouth and F. Bitter, *Phys. Rev.*, **95**, 941 (1954).
4. J. F. Waymouth and F. Bitter, *ibid.*, **102**, 686 (1956).
5. S. Nudelman and F. Matossi, *This Journal*, **101**, 546 (1954).
6. F. A. Kröger, *Ergebn. exakt. Naturw.*, **29**, 104 (1956).
7. N. Riehl and H. Ortmann, "Zinksulfid-Luminophore," p. 31, Verlag Chemie, Weinheim, 1957.
8. C. C. Klick and J. H. Schulman, *Solid State Physics*, **5**, 148 (1957).
9. G. F. J. Garlick, *Handb. d. Phys.*, **26**, 99 (1958).
10. H. W. Leverenz, "An Introduction to Luminescence of Solids," p. 254, John Wiley & Sons, Inc., New York (1950).
11. J. T. Randall and M. H. F. Wilkins, *Proc. Roy. Soc. (London)*, **A184**, 390 (1945).
12. W. Hoogenstraaten, *Philips Res. Repts.*, **13**, 515 (1958).
13. W. W. Piper and F. E. Williams, *Solid State Physics*, **6**, 129 (1958).
14. M. Schön, *Z. Physik*, **119**, 463 (1942); H. A. Klasens, *Nature*, **158**, 306 (1946); H. A. Klasens, *This Journal*, **100**, 72 (1953).
15. J. Lambe and C. C. Klick, *Phys. Rev.*, **98**, 909 (1955).
16. G. F. J. Garlick and A. F. Gibson, *J. Opt. Soc. Amer.*, **39**, 935 (1949).
17. W. W. Piper, *Phys. Rev.*, **92**, 23 (1953).
18. M. Schön, Halbleiter-Probleme, **4**, 285 (1958).
19. C. H. Haake, *J. Opt. Soc. Amer.*, **47**, 881 (1957).

Anodization of InSb

J. D. Venables and R. M. Broudy

Research Laboratories, National Carbon Company, Division of Union Carbide Corporation, Cleveland, Ohio

ABSTRACT

The dependence of the constant current anodization curve on crystallographic face and illumination is reported for monocrystalline InSb. It is shown that illumination changes the film formation rate, either increasing or decreasing it depending on certain experimental conditions. Photovoltages similar to those reported for other anodic films have been observed.

The work of Dewald (1) on anodization of InSb indicates that this material is in some ways particularly suited to a study of the general oxidation process. InSb forms in the zincblende structure which, although cubic, does not possess a center of inversion; therefore, opposite directions are not necessarily equivalent. This geometrical polarity, which also can be revealed by etching (2,3), is an important factor in the experiments of Dewald (1) in that he finds that (111) faces anodize at a faster rate than the $(\bar{1}\bar{1}\bar{1})$ faces.[1] In the present account we show the crystallographic dependence of the constant current anodization curves.

In the previous literature, several authors have reported a photodependence of the oxidation process for various materials such as Ta (4-6), Si (7), Cu (8), and Al (6). We have found that photoeffects also exist in the InSb system; several associated phenomena are reported here.

Apparatus

The experimental arrangement is shown in Fig. 1. An appropriately masked sample[2] with either the (111) or $(\bar{1}\bar{1}\bar{1})$ face exposed is made the anode in a 0.1*N* KOH solution held at constant temperature. An electronic constant current source serves as a power supply to provide current densities in the neighborhood of 200 μa/cm^2. Voltages which represent the drop across the anode film are monitored using a reference electrode of InSb connected to a recording voltmeter with a high input impedance.

The samples are x-ray oriented, cut, and then mechanically polished with various grades of alumina down to 0.1 μ which produces a mirror-like finish on the selected face. After masking, they are pre-anodized to 10-20 v and then immersed in concentrated HF which removes the oxide film but does not attack the InSb substrate. This process (pre-anodizing and film removal) is repeated until the anodization curves are completely reproducible.

[1] Allen (2) has made the correlation between anodization rates and etch pits. Pits appear on the $(\bar{1}\bar{1}\bar{1})$ face.

[2] The masking agent used was either polystyrene in toluene (1) or G.E. 1202 baking varnish. The latter is more durable.

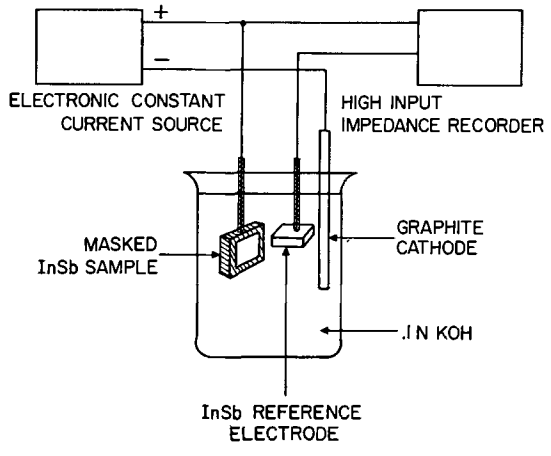

Fig. 1. Experimental arrangement for constant current anodization studies on InSb.

Anodization Curves

In Fig. 2 typical recorder curves of the voltage drop across the film on the (111) and $(\bar{1}\bar{1}\bar{1})$ faces are shown as a function of time at constant current. There are several features of the curves which are of interest: (*a*) the initial region of the two curves is similar and nonlinear, tending to curve upward until the turnover point is reached. The nonlinearity is perhaps a consequence of the formation of space charge in the oxide layers during anodization (9); (*b*) the turnover voltage is different for the two faces and is always greater for the $(\bar{1}\bar{1}\bar{1})$ face than for the (111) face, under identical experimental conditions. This unusual crystallographic dependence indicates that the turnover probably is not a

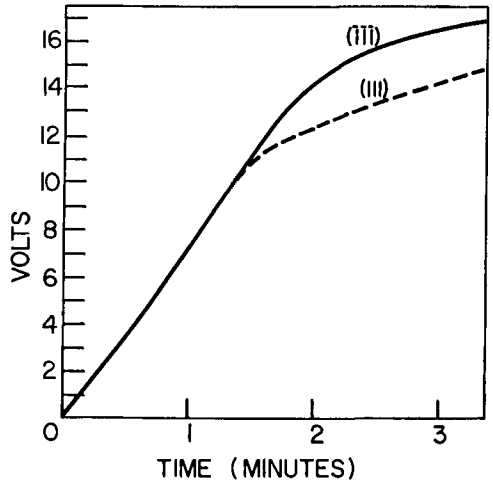

Fig. 2. Constant current anodization curves for (111) and $(\bar{1}\bar{1}\bar{1})$ faces of InSb.

consequence of the structure of the oxide film (porosity, cracks, etc.) but that the metal-oxide interface plays some role in the process.

When a piece of InSb is anodized with both the (111) and ($\bar{1}\bar{1}\bar{1}$) faces exposed, it is observed by means of interference colors that the film thickness is the same on both faces until the turnover region is reached. As anodization continues beyond this point, the interference colors indicate that a thicker film forms on the (111) face than on the ($\bar{1}\bar{1}\bar{1}$). By means of the following experiment we have shown that this is due to a redistribution of current density which takes place when the (111) face reaches its turnover point. The experimental arrangement is shown in Fig. 3. Two InSb samples with {111} faces of equal area but of opposite crystallographic sign are connected to a common constant current supply through separate ammeters. Since the voltage drop across the solution and cathodes is negligible, this is equivalent to anodizing a single sample having both crystallographic faces exposed, except that now the current through each face can be monitored separately. Initially both meter readings are the same; however, as soon as the (111) face reaches its turnover voltage for the currents involved, its resistance ceases to increase. Eventually most of the current flows through the (111) face producing a thicker film on it than on the ($\bar{1}\bar{1}\bar{1}$) face. Apparently this redistribution occurs because the electric field required for ion flow cannot be maintained across the film on the ($\bar{1}\bar{1}\bar{1}$) face after the (111) face attains the turnover voltage.

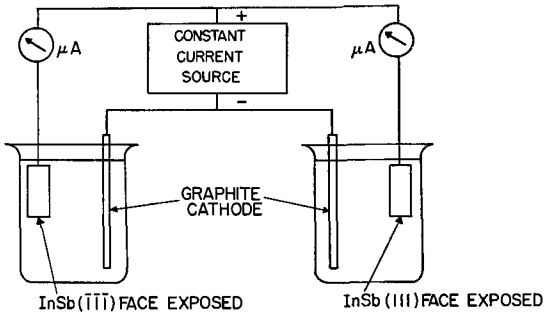

Fig. 3. Experimental arrangement to monitor current through (111) and ($\bar{1}\bar{1}\bar{1}$) faces separately.

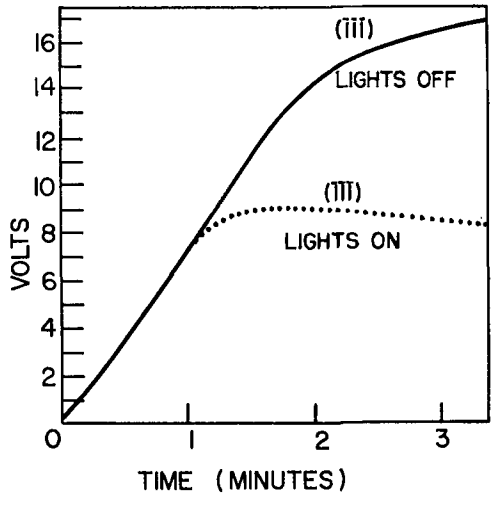

Fig. 4. Effect of illumination on constant current anodization curves.

Photoanodization

When a sample undergoing anodization is irradiated with visible light of wave length shorter than approximately 5200Å, it is observed that the initial part of the anodization curve remains unaffected but that the turnover voltage is decreased. The illumination from a 300-w slide projector produces the effect shown in Fig. 4. Accompanying this reduction in turnover voltage under the two sets of experimental conditions described below, there occurs a change in the film formation rate.

Condition No. 1.—The exposed face of an InSb sample is illuminated evenly and anodized under constant current conditions beyond the turnover point. The relative thickness of the film formed is measured using the step gauge method described by Dewald (1). The film is removed with HF and the sample, now in total darkness, is anodized again using the same value of current for the same length of time. Step gauge measurements show that the illuminated film is thinner than the one formed in darkness, indicating that the efficiency of film formation is lowered when the sample is illuminated.

Condition No. 2.—In this experiment, only half of the exposed InSb face is illuminated during anodization. The process is carried out past the turnover point and it is observed that the above situation is reversed. At first glance it appears that here the light increases the efficiency of film formation since the illuminated section is now thicker than the dark section. We have shown, in an experiment similar to the one discussed in the previous section, that this is actually due to a redistribution of current density which takes place when the illuminated section reaches the turnover. Figure 5 depicts the experimental arrangement. Two identical faces are anodized, one with illumination and the other without. The two samples are connected to a common constant current supply through separate meters.

Again it is observed that initially both meter readings are the same; however, as soon as the illuminated face reaches the light-induced turnover voltage its resistance ceases to increase with time and most of the current flows through that face. This produces a film on the illuminated face which is considerably thicker than the one which is formed

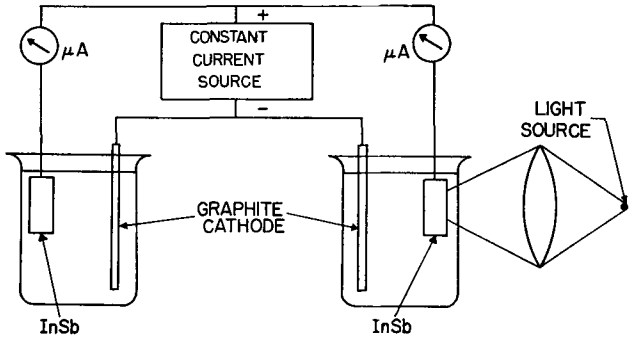

Fig. 5. Experimental arrangement to monitor current through illuminated and nonilluminated faces of InSb separately.

in darkness. A device which utilizes this photoanodization effect to record an image projected on the face undergoing anodization has been described elsewhere (10).

Photovoltages

When InSb of any orientation is anodized beyond the turnover point (it makes no difference whether the turnover is light-induced or not) and then removed from the circuit, it is found that a voltage appears across the film when illuminated. This photovoltage, which incidentally has the same polarity as the anodizing voltage, saturates at approximately 1.5 v and is similar in many respects (time constants, decay, internal impedance, etc.) to photovoltages found in Ta_2O_5 films by van Geel, Pistorius, and Winkel (8). Because of this similarity, no further description is given here. We do wish to point out, however, that the photovoltage demonstrates the existence of light-induced carriers (electrons or holes) in the system. We speculate that perhaps it is these carriers which serve to lower the film forming efficiency during photoanodization by providing electronic (or hole) conduction in addition to the ionic current.

Summary

The phenomena observed during our preliminary studies on the InSb anodic system have been presented at this time because of their unique character. No attempt has been made to interpret the data theoretically since several questions which are raised by this initial work remain to be clarified. For example, we do not know whether the crystallographic dependence of anodization rate as observed by Dewald (1) exists during the initial stages of the anodic process or occurs only near the turnover point as our initial experiments seem to indicate. In addition it is not known why the turnover occurs at all or why illumination changes the turnover point; it is possible that space charge effects which have been discussed by Dewald (9) and light-induced space charge effects which were hypothesized by Vermilyea (11) may be responsible for the observation phenomena.

Acknowledgments

The authors wish to thank Dr. R. G. Lye, Dr. W. Ware, and Dr. S. Senderoff for many helpful discussions of this work. They are also indebted to R. E. Hart, Jr. for his help in sample preparation.

Manuscript received Aug. 13, 1959.

Any discussion of this paper will appear in a Discussion Section to be published in the December 1960 JOURNAL.

REFERENCES

1. J. F. Dewald, *This Journal*, **104**, 244 (1957).
2. J. W. Allen, *Phil. Mag.*, **2**, 1475 (1957).
3. J. D. Venables and R. M. Broudy, *J. Appl. Phys.*, **29**, 1025 (1958).
4. D. A. Vermilyea, *J. Appl. Phys.*, **26**, 489 (1955).
5. D. A. Vermilyea, *This Journal*, **104**, 212 (1957).
6. W. Ch. van Geel, C. A. Pistorius, and P. Winkel, *Philips Research Repts.*, **13**, 265 (1958).
7. P. F. Schmidt and W. Michel, *This Journal*, **104**, 230 (1957).
8. J. Kruger, *Nat. Bur. Standards (U.S.) Tech. News Bull.*, **47** (March 1958).
9. J. F. Dewald, *This Journal*, **102**, 1 (1955).
10. J. D. Venables and R. M. Broudy, *J. Appl. Phys.*, **30**, 1110 (1959).
11. D. A. Vermilyea, *This Journal*, **104**, 216 (1957).

Lifetime Preservation in Diffused Silicon

M. Waldner[1] and L. Sivo

Semiconductor Products Department, General Electric Company, Electronics Park, Syracuse, New York

ABSTRACT

Minority carrier lifetime in silicon which has been diffused in BCl_3 plus nitrogen at 1100°C may be in excess of 100 μsec. Diffusion at 1200°C may give lifetimes in excess of 25 μsec. The lifetimes are significantly higher than the values obtained by heat treatment without the BCl_3. A similar effect is observed if chlorine or PCl_5 is added to the nitrogen ambient. Some lifetime preservation after extended heat treatment following the BCl_3 treatment indicates that the glassy layer deposited during the treatment plays a significant role in the process.

Several methods for lifetime preservation during the heat treatment of silicon, such as is incurred during a diffusion process, have been reported. These include slow cooling (1), vacuum heat treatment (2), and gettering by a metal-silicon liquid phase on the silicon surface (3). The purpose of this paper is to show that relatively high lifetime may be maintained in silicon that has been diffused with boron, even with fairly rapid cooling, and that the diffusion process, using BCl_3 gas, plays a significant role in this lifetime preservation; furthermore, that chlorine gas or PCl_5 as well as the BCl_3 also give the effect of lifetime preservation.

The use of BCl_3 as a carrier for boron during diffusion has been noted by Fuller and Ditzenberger (4). Moreover, Prince (5) has noted that during the diffusion of boron in such a process lifetime regeneration of previously diffused silicon may be observed on thin samples.

Experimental Procedure

The diffusion and heat treatment were carried out in a dual tube furnace with 1⅛ in. ID quartz tubes. The silicon was in a 5-15 ohm-cm resistivity

[1] Present address: Hughes Products, Semiconductor Division, Newport Beach, California.

range with initial lifetimes in excess of 100 μsec. The silicon wafers were supported either horizontally in a separate quartz half tube or vertically in a slotted quartz holder. The wafers were from 35 to 60 mils thick. One of the quartz tubes was used to run control samples in a nitrogen gas flow of 10 ft³/hr.[2]

Three programs were used during the introduction of the BCl_3. They were as follows: Program A—The samples were introduced into the furnace, with only a nitrogen flow, followed by a BCl_3 flow of 0.04 ft³/hr with 18 ft³/hr of nitrogen, for 30 sec, 0.04 ft³/hr of BCl_3 and 10 ft³/hr of nitrogen for 30 sec, 0.04 ft³/hr of BCl_3 and 4 ft³/hr of nitrogen for 4 min, and 10 ft³/hr of nitrogen only for the rest of the run; Program B—The samples were introduced into the furnace, with only a nitrogen flow, followed by a BCl_3 flow of 0.04 ft³/hr with 10 ft³/hr of nitrogen for 30 sec, 0.04 ft³/hr of BCl_3 with 4 ft³/hr of nitrogen for 4 min, and 10 ft³/hr of nitrogen only for the rest of the run; Program C—A BCl_3 flow of 0.04 ft³/hr with 4 ft³/hr of nitrogen was established before introduction of the samples, which were then held at approximately a 500°C zone of the furnace for 1 min, a 900°C zone for 1 min, and at 1100°C for 4 min, followed again by a 10 ft³/hr flow of nitrogen only for the rest of the run.

The first of these programs, with the high initial nitrogen flow, was chosen to minimize back diffusion of air into the furnace. However, the programs which allowed higher initial BCl_3 concentrations, especially at low temperatures as in program C, gave the best results.

The PCl_5 was introduced by placing several grams of PCl_5 in the quartz tube at a point where the temperature was about 180°C. The PCl_5 gradually sublimed in the nitrogen carrier gas.

The chlorine heat treatment involved a chlorine flow rate of 0.04 ft³/hr for 4 min, mixed with 4 ft³/hr of nitrogen, followed by a chlorine flow rate of 0.01 ft³/hr, mixed with 10 ft³/hr of nitrogen, for the remainder of the run.

In most of the experiments the sample was cooled by turning the furnace off after the heat treatment. The resulting cooling cycle ("slow cool") is shown in Fig. 1. Two other cooling cycles were used. One involved cooling the sample by withdrawing it from the furnace during a 15-min period ("fast cool"); the other was a rapid withdrawal from the furnace ("air quench").

The pellets were prepared for diffusion by soaking in 48% nitric acid (to remove a nickel plate used in preliminary lifetime measurements), followed by three successive etches in "white" etch (4 parts HNO_3, 1 part HF), followed by a soak in HNO_3 and final rinses in deionized water and distilled water.

[2] All flow rates are given in air equivalent at 14.7 psi and 70°F.

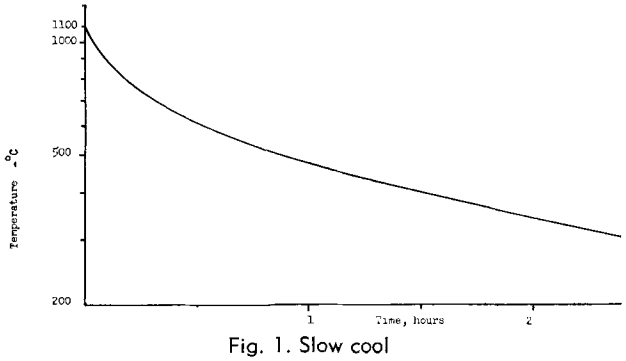

Fig. 1. Slow cool

The lifetime of the samples were determined by a measurement of the photoconductivity decay following excitation of excess carriers by a sparked light source (6). For all but the very short lifetimes, the illumination was through a 1.6 mm thick silicon filter. For measurements on the short lifetime samples either a 0.2 mm filter or no filter were used. Because trapping may have been present in the very low lifetime samples, the true lifetime may in some cases be less than the measured decay times which are given here. On the higher lifetime samples, with junctions, photovoltaic measurements (7) on several samples confirmed the spark data. For two samples an attempt was made to estimate the lifetime from the amplitude of the collected signal in the usual drift mobility experiment (8). These checks indicated that the measured lifetime in the n-type control samples was correct, but that the lifetimes measured on p-type control samples was much too high.

In many of the samples the minority carrier diffusion distance was so great that a very large correction, due to surface recombination, needed to be applied to the measured values. For this reason both the measured decay times and the corrected values are given.

Experimental Results

Lifetime Preservation

Below are listed the results for a number of experiments with the boron trichloride process, at 1100° for ½ hr, with "slow cooling." The boron diffused junction depth was about 0.04 mil. The control runs listed were run simultaneously with the listed boron diffusion of the same run number.

BCl_3 diffusion, 1100°C for ½ hr, n-type silicon

Run	Program	Material	Measured t, μsec	Corrected t
24	A	M2455	48	125
27	A	M2455	43	80
34	A	M2455	37	60
38	A	M2455	50	120
45	B	M2455	53	150
45	B	FZK59	68	120
47	B	M2455	54	170
47	B	FZK59	65	110
48	B	M2455	240*	240
48	B	FZK59	180*	180
50	B	FZK59	33	42
50	B	M2474	49	95
50	B	M2474	47	100
51	C	M2474	39	80
51	C	M2474	65	200
	Control (vs. BCl_3), 1100°C for ½ hr, n-type silicon†			
34		M2455	4.2	4.2
48		M2455	3	3
48		FZK59	2.6	2.6
50		M2474	3.6	3.6
50		M2474	3.9	3.9
51		M2474	3.7	3.7
51		M2474	4‡	4‡

* Photovoltaic measurement.
‡ Estimated as 5 μsec from drift mobility experiment.
† All but the first measurement were obtained with the 63 mil silicon filter.

Run	Program	Material	Measured t, μsec	Corrected t
BCl_3 diffusion, 1100°C for ½ hr, p-type silicon				
34	A	XP3223	7.8	7.8
38	A	M2592	6	6
48	B	M2592	17	32
50	B	XP3223	10	14
50	B	XP3223	5.6	5.6
50	B	M2592	14.5	22
50	B	M2592	15	31
51	C	XP3223	11.7	16
51	C	XP3223	9	9
51	C	M2592	27	72
51	C	M2592	26.5	70
Control (vs. BCl_3), 1100°C for ½ hr, p-type silicon†				
34		XP3223	3	3
48		M2592	3.7	3.7
50		XP3223	3	3
50		XP3223	2.5	2.5
50		M2592	4	4
50		M2592	3	3
51		XP3223	2.1	2.1
51		XP3223	2.1	2.1
51		M2592	3*	3
51		M2592	2.8	2.8

M2455: n-type Czochralski, 9-13 ohm-cm, approximately 20 dislocations/cm²
FZK59: n-type floating zone, 10-11 ohm-cm, approximately 10^4 dislocations/cm²
M2474: n-type Czochralski, 5-8 ohm-cm
XP3223: p-type floating zone, 5-10 ohm-cm, approximately 2×10^4 dislocations/cm²
M2592: p-type Czochralski, 5-8 ohm-cm, approximately 7×10^3 dislocations/cm²
* No observable lifetime from drift mobility measurement.
† These measurements were made with no filter or a thin filter. At least half of the samples showed evidence of trapping in the shape of the decay curve.

Both high dislocation density floating zone and low dislocation density Czochralski n-type material gave consistently high lifetimes well above those obtained with the control samples. Control sample lifetimes were usually about 4 μsec, although one exceptional value of 14 μsec was observed during the experiment. Some variation would be expected in the control results because of the expected dependence upon cleanliness.

The results with p-type material have been somewhat more erratic. However, use of the program C has resulted in lifetime values comparable to those observed in n-type material. Furthermore, although the listed values for the control lifetimes are similar to those reported for the n-type material, many of these samples showed evidence of trapping. An effort to correlate the results with those of a drift mobility measurement, which was successful with one n-type sample, failed with the p-type sample. Consequently, it is likely that the measured decay times for these control samples are not characteristic of the recombination process but are dominated by trapping effects.

The lifetime in a larger number [36] of diffused junctions on lower resistivity, 0.5 to 1 ohm-cm, n-type silicon was measured by means of the photovoltaic effect. The median lifetime on these samples was in excess of 10 μsec.

The results with chlorine and PCl_5 added to the nitrogen are tabulated below. Slow cooling was used.

Run	Material	Measured t, μsec	Corrected t
11	M2455 (n-type)	45	74
11	M2455 (n-type)	22.5	76
33	M2455 (n-type)	21	26
16	M2455 (n-type)	16.5	20
32	M2455 (n-type)	21	26
31	XP3223 (p-type)	2.9	2.9
32	XP3223 (p-type)	7.1	7.1
41	M2455 (n-type)	5	5
(Chlorine for 4 min only)			
Control (vs. chlorine) 1100°C for ½ hr			
11	M2455 (n-type)	7	7
11	M2455 (n-type)	12.5	14
16	M2455 (n-type)	5	5
31	XP3223 (p-type)	2.5	2.5
PCl_5 at 1100°C for ½ hr			
37	M2455 (n-type)	29	58
37	XP3223 (p-type)	3.1	3.1

For both the chlorine and PCl_5 ambient the lifetimes, at least in n-type material, were higher than those of the control samples. When the chlorine was run only for a few minutes at the beginning of a run, as in run 41 above, no marked lifetime retention was observed. This is in contrast to the results with BCl_3.

In the case of the chlorine treatment, a significant difference in lifetime in several samples run together was noticed. For instance, for three samples placed vertically and directly behind each other in the gas flow at 1100°C the corrected values were 74, 52, and 29 μsec in order from the upstream end. This effect, if present, was much less pronounced with the BCl_3 process. The values in a corresponding experiment with the BCl_3 were 90, 90, and 72 μsec.

The tabulation below shows the results obtained when the diffusion time at 1100°C was extended, or the temperature raised to 1200°C. N-Type material was used.

Time and temperature	Measured t, μsec	Corrected t
2 hr at 1100°C	43	80
2 hr at 1100°C	37	60
21 hr at 1100°C	11.5	13
21 hr at 1100°C	19	24
21 hr at 1100°C Control	3.4	3.4
½ hr at 1200°C	26	38

Lifetimes in excess of those resulting from the heat treatment alone may be obtained during extended diffusion, or at 1200°C. In order to obtain the results quoted at 1200°C it was necessary to apply the boron from the BCl_3 at 1100°C and then raise the temperature to 1200°C. If the BCl_3 is introduced at 1200°C, the adherent glassy deposit otherwise obtained on the silicon surface is not observed. Instead, layers which were cracked and chipped were found.

The effect on the final lifetime of the three cooling cycles which were tried is shown below. N-type silicon diffused for ½ hr at 1100°C, with program A, was used. The fast, 15-min cooling was without

Cooling	t Measured, μsec	t Corrected
Slow cool	48	125
Fast cool	37	90
Air quench	7.5	7.5

serious effect, although the air quench did give much lower lifetime.

Lifetime Regeneration

An experiment was performed on several diffused silicon p-n junctions (provided by F. E. Gentry) to determine the feasibility of lifetime regeneration with the BCl_3 process. These samples had been diffused with gallium to a junction depth of about 3 mils. These samples were run through program C with slow cooling. The low-temperature step changed to 700°C for 1 min. Two samples were subjected to a control cycle with nitrogen ambient only. The photovoltaic method was used to measure the lifetime before and after the processing. Values quoted below may be taken only as relative values for this particular experiment because the boundary conditions imposed by the deeply diffused junctions are not those for which the photo-voltaic equipment was calibrated. Results are tabulated below.

Process		Initial t, μsec	Final t
Program C		1	6.8
		2.7	24.3
		3.6	11.9
		3.0	6.1
	Average	2.6	12.3
Control		3.4	2.3
		2.7	2.0

These results substantiate Prince's observation (5) that lifetime regeneration may be obtained in this way.

Discussion

The above data show that lifetimes of 20 to over 100 μsec may be obtained in diffused p-n junctions formed by the diffusion of boron from a BCl_3 carrier. The similar results obtained with PCl_5 and chlorine suggest that the chlorine liberated by the decomposition of the boron trichloride and phosphorus pentachloride plays a part in the process. However, good results can be obtained with BCl_3 even though the gas flows only a few minutes, while with chlorine a continuous flow is necessary. This suggests that the adherent glassy deposit formed on the silicon surface during the BCl_3 flow also plays a part.

Chlorine is known to attack many metals at elevated temperatures. Indeed, during the PCl_5 and chlorine experiments there was some attack even on the silicon. It may be that the chlorine provides an effective in-site etching and cleaning of the presumably contaminated silicon surfaces. Moreover, because of such an etching action, the chlorine may act as an impurity getter at the silicon surface during the diffusion. The results with BCl_3, despite the short application of the gas, suggest that the glassy surface layer may act as an impurity getter, or at least mask the silicon against the in-diffusion of impurities coming from the carrier gas or the walls of the furnace.

As has been described, a BCl_3 program that had beneficial effects on the n-type material did not work as well on the p-type material. It was necessary to modify the process to obtain markedly improved results on p-type material. This suggests that, at least under the conditions of these experiments, an impurity (not necessarily the only one) was present which was particularly effective in reducing the lifetime in the p-type material, and was particularly difficult to remove from the system.

Acknowledgments

The writers wish to thank R. E. Hysell for his assistance and instruction in the lifetime measurements, J. P. Dietz for making the dislocation density estimates, J. E. Greever and D. C. Jillison for supplying the silicon crystals, and J. F. Elliott for discussions of his related work which initially suggested this study.

Manuscript received Sept. 18, 1959.

Any discussion of this paper will appear in a Discussion Section to be published in the December 1960 JOURNAL.

REFERENCES

1. B. Ross and J. R. Madigan, *Phys. Rev.*, **108**, 1428 (1957).
2. A. N. Baker and G. Bemski, paper presented at I.R.E.-A.I.E.E. Semiconductor Device Research Conference, Boulder, Colorado, July, 1957.
3. S. J. Silverman and J. B. Singleton, *This Journal*, **105**, 591 (1958).
4. C. S. Fuller and J. A. Ditzenberger, *J. Appl. Phys.*, **25**, 1439 (1954).
5. M. B. Prince, U. S. Pat. 2,790,940, April 30, 1957.
6. D. T. Stevenson and R. J. Keys, *J. Appl. Phys.*, **26**, 190 (1955).
7. M. Waldner, *Proc. I.R.E.*, **47**, 1004 (1959).
8. J. R. Haynes and W. Shockley, *Phys. Rev.*, **81**, 835 (1951).

Electrolytic Reduction of Nitro- and Dinitrotetralins

R. N. Boyd, A. A. Reidlinger, and M. J. Sher

Department of Chemistry, Washington Square College, New York University, New York, New York

ABSTRACT

The polarographic reduction of mono- and dinitrotetralins was studied in buffered solutions at four different *p*H values. The reduction became more difficult and was less complete with increase in *p*H. The relative heights of the multiple waves were interpreted in terms of certain electron changes, and these were checked by coulometric measurements at controlled potentials. The first stage in reduction in the tetralin series appears generally to be a four-electron change as it is in the benzene series.

In the course of other work in this laboratory it was found necessary to prepare most of the isomeric dinitrotetralins. From a search of the literature it became evident that a study of the polarographic behavior of the dinitrotetralins would be a logical extension of the work carried out by Pearson (1) on various dinitro compounds in the benzene series.

For the sake of completeness all four possible dinitrotetralins as well as the two known mononitrotetralins were prepared; 5 x 10^{-4}M solutions of the nitro compounds in 80% ethanol were studied in four buffered solutions. The compounds were also studied by constant potential coulometry to determine the number of electrons associated with each polarographic wave.

Experimental

6-Nitrotetralin (2), 5-nitrotetralin (3,4), 5,6-dinitrotetralin (2), and 5,7-dinitrotetralin (2) were prepared by methods given in the literature.

5,8-Dinitrotetralin.— 5-Aminotetralin (5) was nitrated (2) to give a low yield of 8-nitro-5-aminotetralin. One gram of the nitroamine was stirred into a mixture of 4 ml trifluoracetic acid and 0.5 ml 90% hydrogen peroxide (6); the solution was kept below 50° for 1 hr. At the end of this time the reaction mixture was poured over ice. The solid dinitro product was filtered off and recrystallized from ethanol. Yield, 0.1 g, mp 88.0°-88.1° [Literature: 87-88° (7)].

6,7-Dinitrotetralin.—6-Aminotetralin (3, 4) was transformed by nitration (2) to give 7-nitro-6-aminotetralin. One gram of the nitroamine was oxidized by trifluoroacetic acid and 90% hydrogen peroxide as described previously. The dinitro product was recrystallized from methanol. Yield, 0.3 g, mp 109.0°-109.2° [Literature: 108° (2)].

Polarographic procedure.—The polarograph employed was a Fisher Elecdropode which had been calibrated against a Type K L&N potentiometer. The electrolysis cell was a modified H-type cell. At a drop time of 4.0 sec with an open circuit and using an alcohol solution buffered by acetic acid and sodium acetate, the drop weight was 6.5 mg. The electrolysis cell was immersed in a thermostat maintained at 25°± 0.2°, and a saturated calomel electrode was used as the anode. Dissolved oxygen was removed by bubbling prepurified nitrogen through the solution for 20 min; the gas was previously passed through another sample of the solution under test. The polarographic curves were plotted as the experimentally determined currents minus the blanks. The half-wave potentials were corrected for *IR* drop.

The solutions were made by adding 10.0 ml of the proper buffer solution to 40.0 ml of 95% ethanol which was 6.25 x 10^{-4}M in nitro compound and then adding sufficient 95% ethanol to give a total volume of 50.0 ml. The apparent *p*H values of the solutions were measured using a Beckman *p*H meter Model G.

The buffer solutions were the following: for *p*H 2.1, 0.800M potassium chloride, 0.100M hydrochloric acid; *p*H 6.4, 4.00M sodium acetate, 3.00M acetic acid; *p*H 9.4, 1.00M triethylamine, 0.500M hydrochloric acid; *p*H 11.0, 1.00M phenol, 0.500M sodium hydroxide. All buffers were also made 0.050% in methyl cellulose. C.p. chemicals were used in each case.

Coulometric procedures.—Electrolyses were performed on 2-5 x 10^{-4} solutions of the nitro compounds in 80% ethanol. Initial currents were low due to low solubility of the nitro compounds and were generally of the order of 20 to 50 ma. The reductions were usually allowed to proceed to zero current (or at most 0.1-0.5 ma) and they generally lasted for 2-4 hr.

Electrolyses were carried out at a stirred mercury cathode at *p*H 2.1. Potentials (vs. SCE) were maintained constant (±15 mv) by means of a Lingane-Jones potentiostat (8) at values which were read from the polarographic curves. Those values were selected which appeared to offer the best chances for step-wise reductions.

The electrolytic cell consisted in the main of a standard three-neck one-liter round-bottom flask to which an extra neck had been added. One neck was fitted with a nitrogen bubbler which extended to the bottom of the flask and a 4-ft length of 6-mm tubing which served as an outlet. The center neck was fitted with the portion of the cell that served as the anode compartment; it consisted of a piece of an 8-in Pyrex test tube to which an 18-mm fritted-glass filter of medium porosity was fused. The anode was a silver gauze in contact with nearly saturated aqueous potassium chloride. A third neck

Table I. Constant potential reduction of nitro- and dinitrotetralins

Compound	pH	E (vs. SCE)	n (coulom.)	n (polarog.)[a]
5-Nitro	2.1	−0.80	6.03	6
6-Nitro	2.1	−0.75	6.21	6
5, 6-Dinitro	2.1	−0.30	3.82	4
		−0.75	11.72	12
6, 7-Dinitro	2.1	−0.22	3.98	4
		−0.80	12.11	12
5, 7-Dinitro	2.1	−0.23	3.91	4
		−0.40	8.11	8
		−0.90	12.21	12
5, 8-Dinitro	2.1	−0.25	3.71	4
		−0.80	11.72	12

[a] Estimated to nearest integral number of electrons from wave heights of the polarographic curves.

was fitted with a glass-sealed platinum wire through which contact was made to the 50 ml of triply distilled mercury which served as the cathode. The remaining neck was fitted with a saturated potassium chloride salt bridge (9) that was in contact with the cathode and led to the same calomel electrode that was used in determining the polarographic curves. Stirring was done by a magnetic stirring motor and a Teflon-covered stirring bar.

A silver coulometer of the usual design (10) was placed in series with the electrolysis cell.

In operation, 500 ml of buffer solution were introduced into the flask and deaerated for 30 min with prepurified nitrogen. The electrolysis of the buffer solution was carried out at −1.03 v (vs. SCE) until the current dropped to approximately 0.2 ma, and then the circuit was opened. Twenty to thirty milligrams of nitro compound were introduced, deaeration was resumed, and stirring was maintained for ½ hr to insure complete dissolution. The coulometer was then placed in series with the cell, and the circuit was closed. The electrolysis was allowed to proceed at the desired potential until the current dropped to a negligible value. It was found necessary to have a vigorous stream of nitrogen bubbling through the cell at all times during an electrolysis in order to prevent atmospheric oxygen from diffusing into the system.

Coulometric values obtained from the nitro- and dinitrotetralins are listed in Table I.

Large-scale reduction of 1,3-dinitrobenzene.—The anode compartment was a 150-ml porous cup, the anolyte was 20% sulfuric acid, and the anode was a carbon rod. The entire assembly was suspended in a 400-ml beaker which served as the cathode compartment. A pool of mercury covering the bottom of the beaker was used as the cathode. Its potential was controlled by a Lingane-Jones potentiostat (8) just as in the coulometric procedure. The cathode compartment was fitted with a nitrogen bubbler. The catholyte was stirred with a Teflon-covered stirring bar and a magnetic stirring motor.

Dissolved oxygen was removed from the catholyte by bubbling nitrogen through the solution for 20 min. Pre-electrolysis of the catholyte, consisting of 250 ml of the buffer solution (pH 6.4), was carried out at −0.60 v (vs. SCE) until the current dropped to a negligible value (2 ma). This took about 20 min. The circuit was opened and 1,3-dinitrobenzene (1.5 g) was introduced, and nitrogen was bubbled through the cell for 30 min. At the end of this time, the circuit was closed again, and the electrolysis was allowed to proceed at −0.50 v vs. SCE (value chosen from the polarogram). The initial current was 0.150 amp, and the electrolysis was allowed to continue until the current dropped to 2 ma.

The solvent was removed at reduced pressure, and the orange-yellow residue was recrystallized twice from benzene. The yield was 0.8 g of N-(3-nitrophenyl)hydroxylamine, mp 119°-119.5° [Literature: 118°-119° (11)].

The same product was obtained from a reduction at −0.55 v (vs. SCE) in which a nickel gauze cathode and a platinum anode were used.

Discussion

Pearson (1) has claimed that the first of the multiple waves obtained from the polarographic reductions of dinitro compounds is usually that corresponding to a four-electron change, the transformation of a nitro group to a hydroxylamino group. Present coulometric data amply confirm this conclusion for the nitro- and dinitrotetralins.

The polarogram obtained by Pearson (1) from *m*-dinitrobenzene is very similar to the one that he obtained from 2,4-dinitrotoluene and to the one obtained in the present work from 5,7-dinitrotetralin. Large-scale electrolytic reductions of *m*-dinitrobenzene at controlled potentials and at pH 6.4 show that N-(3-nitrophenyl)hydroxylamine is indeed the first reduction product, the result of a four-electron change. *m*-Dinitrobenzene rather than a dinitrotetralin was chosen for a test of the coulometric procedure at controlled potentials because it gives an intermediate that is stable enough to be isolated and identified.

It is shown conclusively by coulometry that reductions in acid lead to complete reduction with the formation of polyamines (for a dinitro compound this requires twelve electrons). At pH 9.4 complete reduction becomes more difficult, and the final product may be a bis-hydroxylamine (an eight-electron change) or an aminohydroxylamine (a ten-electron change). At pH 11 the curves are rather diffuse and difficult to interpret simply. The diffuseness may be due to secondary electrode processes involving reduction of condensation products.

It can be seen from Table II that as the pH increases the separation between the component waves also increases. Pearson (1) suggested for the dinitrobenzenes that this was due to a decrease in salt formation in alkaline media, and the same seems to hold in the present case.

It can also be seen that 5-nitrotetralin is more difficult to reduce than 6-nitrotetralin. This is in good agreement with the findings of Pearson (1) that o-nitrotoluene is more difficult to reduce than either *m*- or *p*-nitrotoluene. It may also be mentioned that when a mixture of 5-nitrotetralin and 6-nitrotetralin is allowed to react with a limited amount of sodium hydrogen sulfide, only 6-nitrotetralin will be reduced.

Table II. Polarographic reduction of nitro- and dinitrotetralins[a]

Compound	pH 2.1 $E_{1/2}$	2.1 i_d/C	6.4 $E_{1/2}$	6.4 i_d/C	9.4 $E_{1/2}$	9.4 i_d/C	11.0 $E_{1/2}$	11.0 i_d/C
5-Nitro	—0.36	11.6	—0.60	10.9	—0.81	9.1	?	8.9
	—0.56	16.2	?	15.6				
6-Nitro	—0.35	11.3	—0.56	11.3	—0.76	9.7	?	9.2
	—0.55	14.8	?	15.1				
5, 6-Dinitro	—0.21	9.2	—0.42	8.4	—0.55	8.5	—0.62	8.2
	—0.38	25.4	—0.64	25.2	—0.86	20.9	?	23.5
6, 7-Dinitro	—0.18	8.8	—0.39	8.7	—0.50	8.8	—0.56	8.4
	—0.34	25.1	—0.62	22.8	—0.83	21.8	—0.97	?
			?	25.2				
5, 8-Dinitro	—0.19	7.4	—0.37	8.4	—0.49	7.2	—0.55	7.2
	—0.40	23.6	—0.69	24.8	—0.92	21.2	—1.01	20.8
5, 7-Dinitro	—0.20	9.0	—0.41	9.5	—0.58	9.0	—0.72	7.8
	—0.34	18.6	—0.62	18.8	—0.83	17.8	—0.96	16.5
	—0.72	26.9	—1.37	27.5				

[a] The values of $E_{1/2}$ are in volts vs. SCE, and those of i_d/C are in μa/mmole/l. A question mark indicates that the wave is too indefinite to assign values with any degree of certainty.

An examination of Fisher-Hirschfelder molecular models showed that the three atoms of the nitro group in *o*-nitrotoluene or 5-nitrotetralin cannot so easily lie in the plane of the aromatic ring as in the other isomers. As a result of the probable steric inhibition of resonance, the hindered nitro group should be expected to be more like an aliphatic nitro group which, in general, is the more difficult to reduce (12).

Finally, as might be expected, present results with the dinitrotetralins present a striking concordance with the work of Pearson (1) on *ortho-*, *meta-*, and *para*-dinitro compounds in the benzene series.

Acknowledgment

The authors wish to thank Dr. R. T. Schenck for his suggestions concerning some of the apparatus used in this work. They are also grateful to the Minnesota Mining and Manufacturing Company for the gift of trifluoroacetic acid, and to the Becco Chemical Division of the Food Machinery and Chemical Corporation for the gift of 90% hydrogen peroxide.

Manuscript received Aug. 20, 1959.

Any discussion of this paper will appear in a Discussion Section to be published in the December 1960 JOURNAL.

REFERENCES

1. J. Pearson, *Trans. Faraday Soc.*, **44**, 683 (1948).
2. G. Schroeter, *Ann.*, **426**, 17 (1922).
3. L. K. Chudozilov and V. Vesely, *Rec. trav. chim.*, **44**, 123 (1925).
4. W. M. Cumming and G. Howie, *J. Chem. Soc.*, **1931**, 3176.
5. W. E. Bachmann and R. D. Morin, *J. Am. Chem. Soc.*, **66**, 553 (1944).
6. W. D. Emmons and A. F. Ferris, *ibid.*, **75**, 4623 (1953).
7. L. K. Chudozilov, *Collection Czech. Chem. Communs.*, **1**, 302 (1929).
8. J. J. Lingane and S. L. Jones, *Anal. Chem.*, **22**, 1169 (1950).
9. H. A. Laitinen, *Ind. Eng. Chem., Anal. Ed.*, **13**, 393 (1941).
10. O. F. Steinbach and C. V. King, "Experiments in Physical Chemistry," p. 159, American Book Co., New York (1950).
11. K. Brand, *J. prakt. Chem.*, **74**, 464 (1906).
12. I. M. Kolthoff and J. J. Lingane, "Polarography," 2nd ed., Vol. II, p. 750, Interscience Publishers, New York (1952).

Decomposition of Uranyl Fluoride between 700° and 950°C

L. M. Ferris and F. G. Baird[1]

Chemical Technology Division, Oak Ridge National Laboratory, Oak Ridge, Tennessee[2]

ABSTRACT

The thermal decomposition of uranyl fluoride was studied by a thermogravimetric technique between 700° and 950°C. At temperatures below 900°C, the main decomposition reaction is

$$3\ UO_2F_2 \rightarrow 2/3\ U_3O_8 + UF_6 + 1/3\ O_2$$

In an atmosphere of dry helium, the rate of decomposition was first order with respect to uranyl fluoride. The rate constants, determined with a constant helium flow rate of 270 cc (STP)/min, were $k = 3.72 \times 10^{11} \exp(-71{,}800/RT)$. Sublimation of uranyl fluoride, as a parallel, first order process, occurred at temperatures above 825°C.

Previous investigators (1) have reported that uranyl fluoride undergoes thermal decomposition at temperatures as low as 300°C. Several decomposition products, which include the uranium oxides U_3O_8 and UO_2, and uranium tetrafluoride were found under various conditions, but the data were insufficient to determine the exact stoichiometry. In contrast, preliminary data obtained in this laboratory (2) indicated that uranyl fluoride was quite stable in a dry atmosphere below 700°C. Above this temperature slow decomposition occurred, apparently according to the reaction $3\ UO_2F_2 \rightarrow UF_6 + 2/3\ U_3O_8 + 1/3\ O_2$. Further work performed in this laboratory, which supports the preliminary data, is presented in this paper.

Experimental

Materials.— High-purity uranyl fluoride was prepared by the ion exchange method of Higgins, Roberts, Hancher, and Marinsky (3). Details of the method are given in Fig. 3 of their article. The product was quite hygroscopic and initially contained 4.5 w/o (weight per cent) water. During the course of the investigation, the water content increased to about 6.2 w/o. It was demonstrated, however, that complete dehydration could be achieved at 150°-250°C without causing pyrohydrolysis. The purity of the dehydrated uranyl fluoride was 99.4 ± 0.3%. The major impurities were uranium dioxide and uranium tetrafluoride.

All gases used in the study were of high purity. Before use they were dried carefully by passage through ta charcoal bed, held at −196°C, and two Drierite bulbs.

Apparatus.—Weight loss data, used in determining the stoichiometry and rates of decomposition, were obtained with a semi-automatic, recording thermobalance. The thermobalance provided a continuous plot of the sample weight vs. time. Details of this instrument and its operation may be found elsewhere (4).

Procedure.—At the start of each experiment, a 2-g sample of the hydrated uranyl fluoride was weighed accurately into a small platinum basket. This sample was then transferred to the thermobalance reaction chamber where it was dehydrated by heating to about 230°C in a stream of dry helium. Reaction rates were obtained by continuously recording the isothermal weight loss due to decomposition at several predetermined temperatures. A gas flow rate of 270 cc (STP)/min was used in each experiment.

Determination of the Stoichiometry

Prior to initiation of the experimental work, estimates were made of the standard free energy changes of the following reactions which include all the decomposition products reported by other workers (1):

$$UO_2F_2 \rightarrow UO_2 + F_2 \qquad [1]$$

$$2\ UO_2F_2 \rightarrow UO_2 + UF_4 + O_2 \qquad [2]$$

$$3\ UO_2F_2 \rightarrow UF_6 + 2/3\ U_3O_8 + 1/3\ O_2 \qquad [3]$$

$$4\ UO_2F_2 \rightarrow UF_4 + U_3O_8 + 2\ F_2 \qquad [4]$$

$$3\ UO_2F_2 \rightarrow 2\ UO_2 + UF_6 + O_2 \qquad [5]$$

A plot of $\Delta F°$ vs. temperature for reactions [1]-[4] is found as Fig. 2, Ref. (2). For reaction [5], $\Delta F°$, in kcal, can be computed from the equation $\Delta F° = 109\text{-}0.085\ t$ where t is °C. The free energy change is positive for all the reactions; however, that for reaction [3] is the least positive of the others and could be expected to be the main reaction in a dry system.

In accordance with the thermodynamics, uranouranic oxide (U_3O_8) was the only decomposition product which could be identified by x-ray analysis at temperatures below 880°C. At 900°C, a small amount of uranium dioxide was present in the product.

Reaction [3] was shown to be the main decomposition reaction by comparison of the calculated weight losses and chemical analyses expected from reactions [1]-[5] with those obtained by decomposing uranyl fluoride at 880°-900°C until constant

[1] Present address: Department of Chemistry, University of Wisconsin, Madison, Wisconsin.

[2] Operated by Union Carbide Corporation for the U. S. Atomic Energy Commission.

Table I. Comparison of calculated[a] weight losses and chemical analyses for reactions [1]-[5] with those determined experimentally

Exp. No.	Temp, °C	Reaction	Weight loss, %	U in residue, %	U(IV) in residue, %	F in residue, %
		[1]	12.34	88.15	88.15	0.0
		[2]	5.19	81.51	81.51	13.01
		[3]	39.25	84.80	28.27	0.0
		[4]	6.17	82.38	41.19	6.57
		[5]	41.56	88.15	88.15	0.0
3[b]	900		40.1	82.1	38.4	2.0
4	900		42.7	79.4	43.5	1.7
5	900		41.8	84.3	32.5	1.6
10	900		43.3	85.3	34.6	0.16
18	880		44.5	70.7[c]	31.6	0.14
19	880		41.4	83.6	38.7	0.10

[a] Weight losses and composition of the residues were calculated for complete decomposition according to reactions [1]-[5].
[b] In each case the decomposition was essentially complete, i.e., the residue had attained a constant weight.
[c] Analysis is obviously low.

weight was obtained (Table I). Reactions [1], [2], and [4] may be eliminated from consideration at the outset on the basis of weight loss alone. Comparison of the uranium (IV) analysis of the residue with that expected from reactions [3] and [5] leaves no doubt that reaction [3] is the main decomposition reaction.

A rapid loss in weight, corresponding to complete dehydration, occurred at temperatures below 250°C. Any further weight loss was attributed to the decomposition of uranyl fluoride. In all cases, the per cent weight loss due to decomposition was slightly greater than expected from reaction [3]. As indicated by the uranium (IV), fluoride, and x-ray analyses, reaction [2] may also have occurred to a slight extent. In most cases the residue was found to be virtually pure U_3O_8; therefore, it was concluded that the excess weight loss was due primarily to simultaneous sublimation of uranyl fluoride. It is important to note that if reaction [2] occurred to a significant extent the weight loss would be less than expected from reaction [3] alone.

Rates of Decomposition in Dry Helium

If it is assumed that the following parallel, first order reactions

$$UO_2F_{2(s)} \xrightarrow{k} 2/9\ U_3O_{8(s)} + 1/3\ UF_{6(g)} + 1/9\ O_{2(g)} \quad [3]$$

$$UO_2F_{2(s)} \xrightarrow{k_v} UO_2F_{2(g)} \quad [6]$$

account for the total loss in weight when a sample of uranyl fluoride undergoes decomposition, the following equation is easily derived

$$\frac{-dw_s}{dt} = (fk + k_v)\ w \quad [7]$$

In Eq. [7], w_s is the sum of the weights of uranyl fluoride and urano-uranic oxide, i.e., the weight of the sample at any time, w is the weight of uranyl fluoride at any time, and f is a stoichiometry factor defined by

$$f = \left[1 - \frac{2/9 M_{U_3O_8}}{M_{UO_2F_2}} \right] = 0.3925 \quad [8]$$

in which M is the molecular weight of the respective compound. Since

$$w = w^\circ \exp\left[-(k + k_v)t\right] \quad [9]$$

Eq. [7] may also be expressed as

$$\frac{-dw_s}{dt} = (fk + k_v)\ w^\circ \exp\left[-(k + k_v)t\right] \quad [10]$$

For convenience, define

$$X = fk + k_v \quad [11]$$

$$Y = k + k_v \quad [12]$$

Then, integration of Eq. [10] with the boundary condition that $w_s = w_s^\circ$ at $t = 0$ yields

$$w_s - w_s^\circ = \frac{Xw^\circ}{Y}\left[\exp\left(-Y\,t\right) - 1\right] \quad [13]$$

Rearrangement of Eq. [13] and conversion to common logarithms gives

$$\log\left[\frac{Y(w_s - w_s^\circ)}{Xw^\circ} + 1 \right] = \frac{-Yt}{2.303} \quad [14]$$

Equation [14] contains the two desired quantities, k and k_v, in terms of experimentally measurable quantities, but it cannot be used directly. However, the rate constants may be evaluated by the following method, if the assumptions made above are valid. The quantity X may be computed from the initial slope of a plot of sample weight vs. time, i.e., at $t = 0$, Eq. [10] reduces to

$$\frac{-dw_s}{dt} = Xw^\circ \quad [15]$$

Once X is known, Y may be evaluated from Eq. [14] by successive approximations using the experimentally determined weight-time data. Arbitrary values for Y are used in the calculation of the logarithmic portion of Eq. [14]. This logarithmic quantity is then plotted vs. time. If the value chosen for Y is not the correct one, a curved plot will result. Successive approximations are continued until the plot becomes linear. Then, as required by Eq. [14], the value of Y used in the calculation of the logarithmic term will equal that calculated from the slope of the line. The rate constants k and k_v can then be obtained by solving Eq. [11] and [12] simultaneously.

For the special case where no sublimation occurs, Eq. [14] reduces to

$$\log\left[\frac{w_s - w_s^\circ}{f w^\circ} + 1 \right] = \frac{-kt}{2.303} \quad [16]$$

Here a plot of the logarithmic term vs. time should be linear with k evaluable from the slope.

Figure 1 contains several examples of the type of first order plot which results when the rate of sublimation is negligible, i.e., k_v is approximately zero. The lower curve in Fig. 1 illustrates the marked deviation from linearity which results if

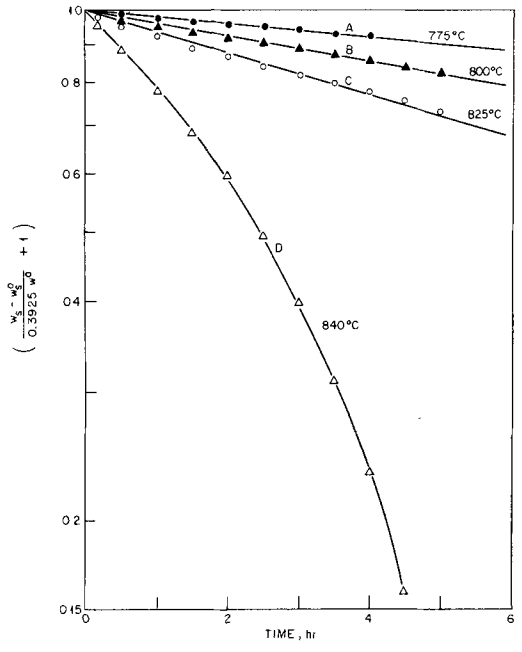

Fig. 1. Decomposition of UO_2F_2, showing a single first-order process below 825°C.

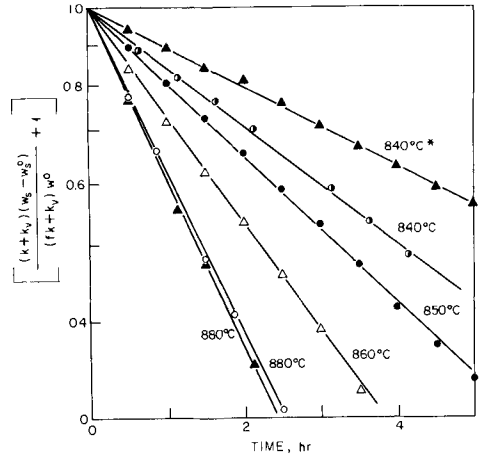

Fig. 2. Representative plots obtained when decomposition and sublimation of UO_2F_2 are considered parallel, first-order processes at temperatures above 825°C.
* Curve plotted from same weight-loss data as the lower curve in Fig. 1.

sublimation is ignored at temperatures above 825°C. Use of Eq. [14] to show that decomposition and sublimation are parallel, first order reactions is illustrated by Fig. 2. It should be noted that the upper curve in Fig. 2 was plotted from the same data used to plot the lower curve in Fig. 1. Table II contains the rate constants obtained over the temperature range of 750°-880°C., while a least squares plot of log k vs. $1/T$ is found in Fig. 3. The temperature dependence of the rate constant for the decomposition reaction is $k = 3.72 \times 10^{11} \exp(-71{,}800/RT)$.

Discussion of Results

Consideration of several other variables would be necessary before a detailed rate expression could be determined. Among the important variables omitted in this study were the effects of oxygen partial pressure, gas velocity, and gas density on the rate of decomposition. The results of preliminary

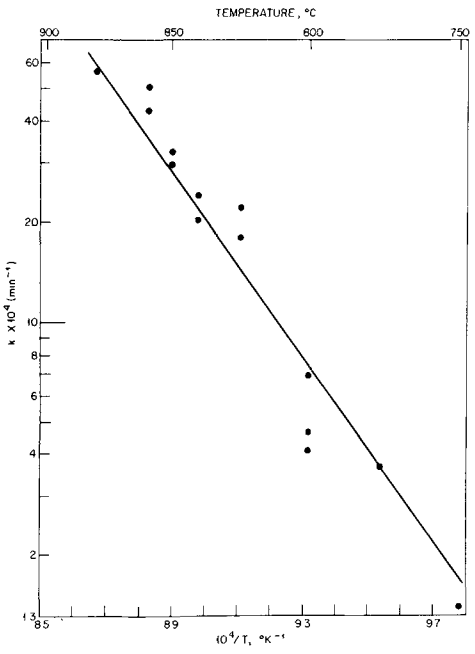

Fig. 3. Rate constants for the reaction 3 $UO_2F_2 \rightarrow$ 2/3 U_3O_8 + UF_6 + 1/3 O_2.

experiments (Table III) indicated that the rate of decomposition decreased with increasing oxygen partial pressure.

An attempt was made to estimate the heat of

Table II. Rate constants[a] for the decomposition and sublimation of UO_2F_2

Exp. No.	Temp,[b] °C	$10^4/T$, °K^{-1}	$10^4\,k$, min^{-1}	$t_{1/2}$, hr	$10^4\,k_v$, min^{-1}	$k_v/(k+k_v)$
8	750	9.78	1.4	82	—	0.0
7	775	9.54	3.6	32	—	0.0
15	800	9.32	6.9	17	—	0.0
1	800	9.32	4.1	28	—	0.0
2	800	9.32	4.7	25	—	0.0
6	825	9.11	18	6.3	0.1	0.005
20	825	9.11	22	5.3	—	0.0
1	840	8.98	20	5.7	9.3	0.32
14	840	8.98	24	4.8	—	0.0
21	850	8.90	32	3.6	11	0.26
22	850	8.90	30	3.8	5.1	0.14
16	860	8.83	43	2.7	7	0.14
17	860	8.83	51	2.2	6.3	0.11
18	880	8.67	56	2.1	27	0.33
19	880	8.67	56.5	2.0	26	0.31

[a] Rates measured in dry helium flowing at 270 cc (STP)/min.
[b] Temperatures were maintained within 5°C of the recorded temperature with a Pyr-O-Vane proportional controller.

Table III. Effect of oxygen partial pressure on the rate of decomposition of UO_2F_2

Initial weight of sample: 2 g; gas flow rate: 270 cc (STP)/min

Gas	Weight loss after 3 hr at 840°C, mg
Helium	320
	320
Air	43
	25
Oxygen	23
	20

sublimation of uranyl fluoride by assuming that the slope of a plot of log k_v vs. $1/T$ was equal to the heat of sublimation. However, the scatter in the values of k_v precluded any such estimation.

Acknowledgment

The authors are pleased to acknowledge Mr. I. R. Higgins for the preparation of the uranyl fluoride, and Mr. J. F. Land for his assistance in performing the experiments. Chemical and x-ray analyses were provided by the groups of Mr. G. R. Wilson, Mr. W. R. Laing, and Mr. R. L. Sherman, of the ORNL Analytical Chemistry Division.

Manuscript received Aug. 13, 1959. This paper was presented before the Nuclear Technology Subdivision, American Chemical Society, Boston, Mass., April, 1959.

Any discussion of this paper will appear in a Discussion Section to be published in the December 1960 JOURNAL.

REFERENCES

1. J. J. Katz and E. Rabinowitch, "The Chemistry of Uranium," Div. VIII, Vol. 5, p. 570, National Nuclear Energy Series, McGraw-Hill, New York (1951).
2. L. M. Ferris, *J. Am. Chem. Soc.*, **79**, 5419 (1957).
3. I. R. Higgins, J. T. Roberts, C. W. Hancher, and J. A. Marinsky, *Ind. Eng. Chem.*, **50**, 285 (1958).
4. L. M. Ferris, *ibid.*, **51**, 200 (1959).

Some Properties of Aluminum Nitride

K. M. Taylor and Camille Lenie

Research and Development Division, The Carborundum Company, Niagara Falls, New York

ABSTRACT

Aluminum nitride crystals in the form of six-sided prismatic needles, up to 0.5 mm in diameter by 30 mm long, and thin plates, 2-3 mm in diameter, have been prepared by vaporization of aluminum in a nitrogen atmosphere at temperatures ranging from about 1800° to 2000°C, and the properties of the crystals determined. Also, an aluminum nitride body, having a density of 98% of theoretical, has been prepared by hot pressing the fine powder, and a study made of its properties.

Aluminum nitride, AlN, consists of 65.81% aluminum and 34.19% nitrogen. Although aluminum nitride was prepared many years ago, its properties have not been well known. Early investigators considered it too unstable, especially with respect to moisture and oxidizing conditions, to be useful as a refractory. More recent work, however, has indicated that aluminum nitride, prepared at high temperature, is relatively inert and, therefore, may have applications as a refractory.

Reconsideration of the potentialities of aluminum nitride as a refractory appears to have started with a publication (1) in 1956 by Kohn and associates of the U. S. Bureau of Mines. These investigators incidentally obtained small crystals of aluminum nitride while working at high temperatures on another project and reported that the crystals were inert to hot and cold mineral acids and alkali solutions. Other recent workers who found aluminum nitride a relatively stable material include Rey (2), Renner (3), and Long and Foster (4). Notwithstanding the considerable recent work on aluminum nitride prepared at high temperature, there is still disagreement on many of its properties such as melting point, hardness, color, and oxidation resistance.

Refractories based on aluminum nitride are not now commercially available, although Rey (2) has prepared aluminum nitride brick by a sintering process and Long and Foster (4) have made laboratory-size crucibles, also by a sintering method. In addition, Johnson (5) has prepared a composite aluminum nitride-cryolite body, and Taylor (6) has used aluminum nitride as a bond for other refractory materials. High density, impervious, essentially pure aluminum nitride ware, however, has not previously been made.

The objects of the present work were to study crystalline aluminum nitride further, especially those properties which are still in dispute, and to prepare and determine the properties of a high-density aluminum nitride body. In the latter instance, hot pressing was chosen as a method of fabrication because preliminary experiments indicated that it would yield ware of maximum density, and, therefore, of optimum physical properties.

Crystalline Aluminum Nitride

Formation of Crystals.—Two methods of forming the crystals were tried: (*a*) heating aluminum nitride powder in a nitrogen atmosphere at high temperatures to induce crystal growth by recrystallization, and (*b*) heating aluminum metal powder in a nitrogen atmosphere to sufficiently high temperatures to vaporize the aluminum and thus form crystals by a vapor phase reaction. The second method was more effective and was used to prepare most of the crystals described in this report.

Sintered aluminum nitride boats and crucibles were used as containers in vaporizing the metal. The reaction was carried out in a horizontal graphite tube resistance furnace or in a vertical induction furnace having a graphite susceptor. In the horizontal resistance furnace, it was possible, using an optical pyrometer with telescope, to follow the origin, growth, and development of the crystals and to measure the corresponding temperatures at the same time.

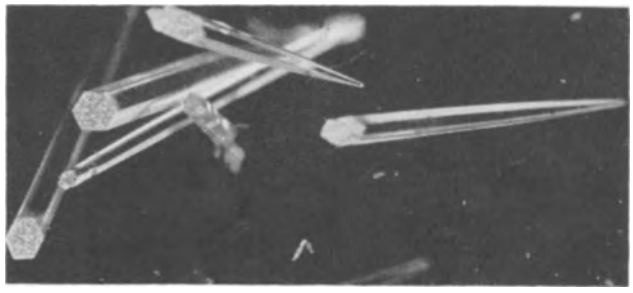

Fig. 1. Aluminum nitride crystals in the form of six-sided prismatic needles, obtained by nitriding aluminum vapors at 1850°C.

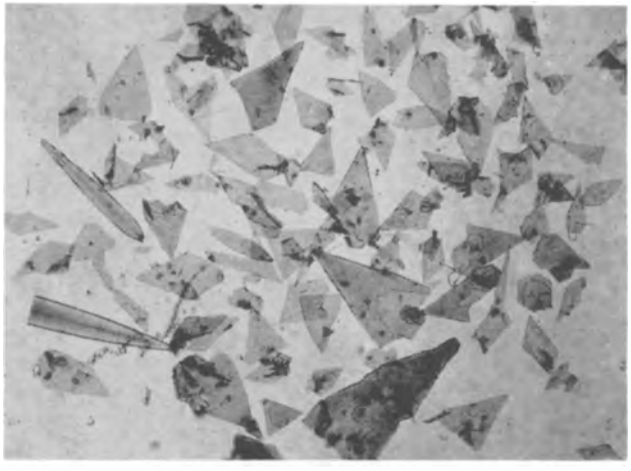

Fig. 2. Plate-like crystals of aluminum nitride formed by heating aluminum nitride powder in nitrogen at temperatures in excess of 1900°C.

It was observed that short, extremely fine filaments of aluminum nitride formed in the range of 1450°-1750°C, while at 1800°-1900°C the crystals were predominantly well-defined six-sided prismatic needles, some of which were about 0.5 mm in diameter and 30 mm long (Fig. 1). Some elongated plates also formed in this temperature range. At 1900°-2050°C, new growth appeared mainly as plates (Fig. 2), while above about 2050°C, previously formed crystals began decreasing in size very slowly due to vaporization. In the case of the prismatic needles shown in Fig. 1, the tapered end was the free end.

Color.—The color of the crystals varied from white to various shades of blue. Rey (2) states that pure aluminum nitride forms blue hexagonal crystals. Long and Foster (4) claim that pure aluminum nitride is water white and that the blue coloration results from the presence of about 7% aluminum oxycarbide (Al_2OC) in the crystals. They report that aluminum oxycarbide is isomorphous with aluminum nitride and that formation of solid solution between the two compounds is very likely. They suggest that Al_2OC results from a reaction between carbon monoxide, incidentally formed in the graphite lined furnace, and aluminum in the sample. In order to test these theories, aluminum nitride crystals were formed in carefully controlled atmospheres of (*a*) nitrogen only, (*b*) in nitrogen containing 0.5-2% of carbon monoxide, and (c) in nitrogen containing 1% of methane. Blue crystals formed only when carbon monoxide was present, the shade of blue becoming deeper with increasing amount of carbon monoxide in the nitriding atmosphere; 0.5% carbon monoxide resulted in light blue crystals, while 2% carbon monoxide produced dark blue crystals. Chemical analysis of the crystals showed the presence of carbon and oxygen in an approximately equimolecular ratio. The percentage of carbon varied from a few tenths of a per cent in the light blue crystals to about 2% in the deeper colored crystals. If carbon and oxygen are combined as aluminum oxycarbide, Al_2OC, as stated by Long and Foster (4), then the amount of this compound in the crystals prepared in the present study ranged up to about 14%.

Crystal structure and density.—Both the white and blue crystals have the hexagonal wurtzite structure. Other investigators have reported cell dimensions as follows:

Investigator	Type of material	Cell dimensions a_0	Cell dimensions c_0
Ott (7)	Powder	3.113	4.981
Stackelberg and Spiess (8)	Light gray powder	3.104±0.005	4.96±0.008
Kohn, Cotter, and Potter (1)	Blue crystals	3.10±0.01	4.965±0.01
Paretzkin (9)	Powder	3.114	4.986

In the present investigation, unit cell dimensions were determined by x-ray diffractometer back reflection techniques. Each sample was standardized independently with a spectrographically pure silicon sample. The National Bureau of Standards value of $a = 5.4301$Å for silicon was used.

The following values were obtained for light colored aluminum nitride: $a = 3.111$Å; $c = 4.980$Å.

A sample of the dark blue crystals containing approximately 2% carbon and 2.7% oxygen produced an x-ray diffraction pattern with broader reflections, some of which showed three distinct peaks. Most of these were shifted from the peaks of the light material. Values of 3.11-3.13Å for the *a* dimension and 4.93-4.98Å for the c dimension were obtained, depending on which peak was evaluated. Differences in reflections of the white and blue crystals were not detected when the usual film techniques were used. Possibly the blue samples contained enough pure AlN to overshadow the less prominent shifted reflections. Also, the general broadening would tend to produce the same geometrical center for the reflections of both the white and blue crystals.

The density of aluminum nitride, calculated from the cell dimensions $a = 3.111$Å and $c = 4.980$Å, is 3.26 g/cc.

Melting point.—The literature reports melting points in the range of 2000°-2400°C. Renner (3) observed strong vaporization of aluminum nitride at 2450°C, but no melting. The present investigation confirms Renner's conclusions. The experiments were carried out in a microfurnace (10) at atmospheric pressure in argon. Well-formed prismatic crystals, about 0.2-0.5 mm thick by about 2-5 mm long, were heated in a V-shaped tungsten crucible,

making observations with an optical pyrometer. The crystals were heated to 1800°C in 2-3 min, after which the temperature was increased at the rate of about 200°C/min. Some vaporization could be observed at 2300°C; at 2450°C vaporization was rapid, and after 1 min at 2500°C the crystals had completely disappeared without evidence of melting. In some experiments, crystals were heated to 2450°-2500°C in about 3 min and then immediately allowed to cool. The crystals had partially vaporized, but no evidence of melting was observed.

Hardness.—Hardness values on the Mohs scale ranging from 5 to between 9 and 10 are found in the literature. No accurate microhardness indentations have been reported. However, crystals obtained in the present research were sufficiently large that Knoop indentations could be made readily. All indentations were made with a load of 100 g, the force being applied perpendicular to the c or long axis of the crystal. Some indentations were made with the long diagonal of the indenter parallel to, and some perpendicular to the c axis of the crystal. Results varied somewhat with the direction, probably because of the anisotropic nature of the crystals. The over-all hardness of aluminum nitride appears to be approximately 1200. This is equivalent to a hardness of slightly higher than 7 on the Mohs scale. Detailed hardness data are seen in Table I.

Oxidation resistance.—Aluminum nitride crystals appear to begin to oxidize in air at about 700°C. This was investigated by heating colorless and blue crystals on a platinum lid in flowing air to various temperatures for 24 hr, and then carefully examining the crystals microscopically after each test. At between 700° and 800°C, the surface of clear transparent crystals became slightly foggy, indicating the beginning of oxidation. The oxidation rate of well-formed crystals, however, was slow even at much higher temperature, because of the formation of a dense adherent aluminum oxide film. Thus, after 24 hr at 1400°C, the cross section of crystals of about 1 mm diameter and 7 mm long showed an oxide surface film estimated to be 40 μ thick. The inside core of the crystal, however, was still clear and transparent.

Tendency to oxidize also was determined by heating 2-3 g samples of the finely milled powder, having an average particle size of about 5 μ, in a flowing stream of air. The weight gain, after 24 hr at 700°C, was 3.2%, corresponding to a conversion of 13% of the compound to aluminum oxide. When a new sample of the same powder was heated 24 hr in air at 800°C, the increase in weight was 9%, corresponding to a conversion of about 36% of the compound to aluminum oxide. In the latter case, x-ray diffraction clearly showed the presence of gamma alumina.

Corrosion resistance.—Crystals of aluminum nitride have been immersed in water at room temperature for several months with no apparent effect on the crystals. Some recent investigators (1, 3, 4) state that aluminum nitride is essentially unaffected by mineral acids. In the present research, it was observed that aluminum nitride crystals were dissolved slowly in a boiling mixture of one part concentrated hydrochloric and one part water. Thus, prismatic needles having a diameter of about 80 μ were dissolved completely in 80 hr. The corrosion rate, based on these experiments, is approximately 170 mils per year.

Table I. Hardness of aluminum nitride crystals

Indentation* No.	Knoop hardness, K_{100} White crystals	Blue crystals
1	1010	920
2	1075	970
3	1010	980
4	1115	1030
5	1000	1050
* Average	1042	990
6	1453	1415
7	1426	1510
8	1454	1450
9	1356	1445
10	1348	1530
* Average	1407	1470
Over-all average	1225	1230

* Indentations 1 through 5 were made with the long diagonal of the indenter parallel to the c axis of the crystal, 6 through 10 were made with the long diagonal of the indenter perpendicular to the c axis.

Hot Pressed Aluminum Nitride

Preparation of hot pressed aluminum nitride.—Aluminum nitride powder was prepared by direct combination of aluminum and nitrogen. Alcoa's No. 101 atomized aluminum powder was mixed with 1% sodium fluoride, which catalyzes the nitriding at low temperatures (11), and heated in purified nitrogen in a refractory crucible. The temperature was raised rapidly to 650°C and then increased slowly over a period of 40 hr to a maximum of 1800°C. In this way a porous sintered agglomerate was obtained. It was reduced readily by dry ball milling in a stainless steel mill with stainless steel balls to a light gray powder with an average particle size of about 5 μ. Chemical analysis of the milled aluminum nitride powder and also the calculated composition, based on this analysis, are shown in Table II. It will be noted that the aluminum nitride content is approximately 96%, and that the chief impurity is alumina. The density of the powder was 3.23 g/cc, compared with a density of 3.26 g/cc as calculated from the cell dimensions of the crystals.

Table II. Aluminum nitride powder
(Pure AlN: 65.81% Al; 34.19% N)

Chemical analysis		Calculated composition	
Al	64.8%	AlN	96.0%
N	32.8%	Al_2O_3	2.1%
C	0.2%	Other compounds	1.9%
Si	0.4%		
Fe	0.1%		
O	1.0%		

Particle size: 0.5 to 25μ
Density: 3.23 g/cc

Table III. Strength and elasticity properties of hot pressed aluminum nitride

Temp, °C	Modulus of rupture, psi	Modulus of elasticity, psi
25	38,500	50×10^6
1000	27,000	46×10^6
1400	18,100	40×10^6

Test specimens, 3 in. in diameter and 3 in. long, were fabricated by hot pressing the milled powder at 2000°C in graphite dies, applying pressures of about 5000 psi. Test bars, 3 x 0.5 x 0.25 in., were cut from the hot pressed pieces with a diamond wheel and then ground to produce smooth parallel surfaces. The test specimens were light gray in color and had a bulk density of 3.20 g/cc or about 98% of the theoretical for pure aluminum nitride. Using a load of 100 g, 10 Knoop hardness indentations gave values ranging from 1005 to 1240, with an average of 1130.

Strength and elasticity.—Data for modulus of rupture and modulus of elasticity at room temperature, 1000° and 1400°C, are presented in Table III. Four specimens, 3 x 0.5 x 0.25 in. were tested at each temperature, pressure being applied perpendicular to the direction in which the bars were hot pressed. These values compare favorably with those for other high-density ceramic materials, especially at high temperatures. For instance, hot pressed alumina is stronger at room temperature, but weaker at 1400°C. The modulus of elasticity of hot pressed aluminum nitride is about the same as that of hot pressed alumina at room temperature, but is higher than that of hot pressed alumina at 1400°C.

Long and Foster (4) reported a modulus of rupture of sintered aluminum nitride at room temperature of 11,500 psi. The exact density of the test specimens was not given but presumably was appreciably lower than that of the hot pressed material reported herein. Rey (2) reported the compressive strength of sintered aluminum nitride brick to be about 3000-4000 psi. Preliminary tests on the hot pressed material indicate a compressive strength of about 300,000 psi.

Thermal conductivity.—The thermal conductivity was measured by a linear flow comparative method, parallel to the direction of pressing, in an atmosphere of stagnant nitrogen, using Inconel as a standard. Values obtained over a temperature range of 200°-800°C are shown in Table IV. These results indicate that aluminum nitride is a good conductor of heat, being intermediate between dense silicon carbide, which is an excellent conductor, and alumina, which is a fair conductor. This is illustrated by the following comparative values for thermal conductivity expressed in cal/cm²/cm/sec/°C obtained by the same method:

Material	At 200°C	At 800°C
Dense SiC	0.24	0.10
Hot pressed AlN	0.072	0.048
Dense Al_2O_3	0.054	0.017

The present data are in sharp contrast to those of Long and Foster (4), who recently reported the thermal conductivity of sintered aluminum nitride at 25°C as 0.0042 cal/cm²/cm/sec/°C. The density of the specimens used by Long and Foster was not disclosed, but the density of some of their test specimens used for determination of electrical resistivity was as high as 2.66 g/cc. It seems probable, therefore, that the difference in density alone is not responsible for the great dissimilarity of the thermal conductivity values, but rather the difference in methods is mainly responsible. According to Kingery and co-workers (12) thermal conductivity at zero porosity can be calculated employing the following simplified relationship of Loeb:

$$k_s = \frac{km}{(1 - P_v)}$$

where k_s is the solid thermal conductivity (zero porosity); k_m, measured thermal conductivity; P_v, volume pore fraction.

Even if it is assumed that the thermal conductivity, $k_m = 0.0042$ cal/cm²/cm/sec/°C, measured at 25°C by Long and Foster, is for a specimen with 40% porosity, the thermal conductivity at zero porosity calculated according to above equation, will be only 0.007 cal/cm²/cm/sec/°C.

The accuracy of the present method has been checked by comparing the results obtained on some standard materials with data from other laboratories as illustrated in the following examples:

Laboratory	Material	Thermal conductivity, cal/cm²/cm/sec/°C 400°C	600°C
Carborundum	Inconel	0.049	0.057
National Bureau of Standards (13)	Inconel	0.049	0.058
Carborundum	Nickel	0.119	0.130
International Nickel Company (14)	Nickel	0.112	0.136

Thermal expansion.—The determination of thermal expansion was made by the dilatometer method, using a silicon carbide dilatometer assembly (15). Thermal expansion was measured parallel to the direction of pressing, on a bar 3 in. long and 0.5 in. in diameter. Values are given in Table V. These

Table IV. Thermal conductivity of hot pressed aluminum nitride

Temp, °C	Cal/cm²/cm/sec/°C	Btu/ft²/in./hr/°F
200	0.072	209
400	0.060	173
600	0.053	153
800	0.048	139

Table V. Thermal expansion of hot pressed aluminum nitride

Temperature interval, °C	Linear expansion, cm/cm/°C
25-200	4.03×10^{-6}
25-600	4.84×10^{-6}
25-1000	5.64×10^{-6}
25-1350	6.09×10^{-6}

check closely the results reported by Long and Foster (4) (4.8 x 10^{-6} cm/cm/°C in the range 20°-500°C) for the sintered aluminum nitride. The thermal expansion of hot pressed aluminum nitride is in the moderate range for a ceramic, being only slightly higher than that of silicon carbide.

Thermal shock resistance.—The high thermal conductivity and low thermal expansion of hot pressed aluminum nitride are conducive to good thermal shock resistance. Bars, 3 x 0.5 x 0.25 in., heated rapidly to 2200°C in an oxygen-acetylene torch and cooled rapidly, did not crack or spall when the test was repeated consecutively several times. The thermal shock resistance was evaluated also by measuring the loss in strength of hot pressed aluminum nitride bars after 30 cycles of heating in 2.5 min to 1400°C and rapidly cooling to room temperature in an air blast. The modulus of rupture before thermal cycling was 38,500 psi and after thermal cycling, 33,700 psi, or a loss of 12% of the original strength.

Stability in various atmospheres at elevated temperatures.—Test specimens, 0.25 x 0.5 x 0.5 in., were exposed to flowing air, oxygen, dry steam, chlorine, and hydrogen at elevated temperatures. Results are reported in Table VI. The last column shows the percentage of aluminum nitride converted to aluminum oxide or aluminum chloride according to the different conditions of the experiments. As can be seen from these data, the effect of air or oxygen at temperatures up to 1400°C or of steam at 1000°C after 30 hr is slight. At 1700°C in air, however, the rate of oxidation becomes rather rapid. It will be recalled from the discussion of the crystalline material that it was found that oxidation of aluminum nitride in air starts at about 700°C, but that the rate of oxidation is slow even at temperatures as high as 1400°C, because of the formation of a protective oxide coating. This coating also accounts for the slow rate of oxidation of the dense hot pressed material. Figure 3 shows a 0.25 x 0.5 in. cross section of a bar after exposure to air at 1400°C for 24 hr. The oxide layer is approximately 60 μ or 2-3 mils thick. At 1700°C, however, it was noted that the oxide coating tended to crack and no longer protected effectively the aluminum nitride against oxidation. The cracking of the coating at this temperature may be due to the appreciable difference in the thermal expansion of aluminum oxide and aluminum nitride.

Table VI. Stability of hot pressed aluminum nitride in various atmospheres of elevated temperatures (Test specimens, 0.25x0.5x0.5 in.)

Atmosphere	Temp, °C	Time, hr	Conversion to other compounds, %
Air	1000	30	0.3 Al_2O_3
Air	1400	30	1.3 Al_2O_3
Air	1700	4	10.6 Al_2O_3
Oxygen	1400	30	0.9 Al_2O_3
Dry steam	1000	30	0.3 Al_2O_3
Chlorine	500	30	<0.1 $AlCl_3$
Chlorine	700	30	19.2 $AlCl_3$
Hydrogen	1700	4	nil

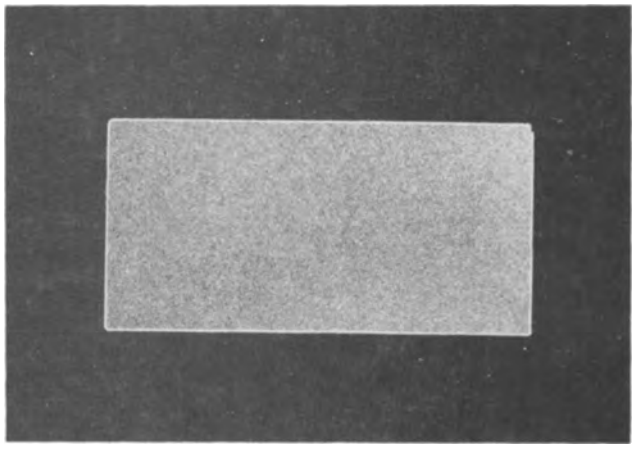

Fig. 3. Cross section of a hot-pressed aluminum nitride specimen showing the protective oxide coating after heating in air 24 hr at 1400°C.

It is of interest to note the difference in the oxidation rate of hot pressed aluminum nitride and the sintered material as reported by Long and Foster (4). Exposure to air for 1 hr at 1200°C of 1-cm cubes of sintered material resulted in a conversion of about 11% of the sample to aluminum oxide, whereas exposure to air for 30 hr at 1400°C of dense hot pressed aluminum nitride specimens of comparable size resulted in a conversion of only about 1% to aluminum oxide.

Table VI also shows that hot pressed aluminum nitride is not appreciably attacked by chlorine at 500°C, but that the reaction rate at 700°C is rapid. Furthermore, hot pressed aluminum nitride is practically unaffected by hydrogen at 1700°C for 4 hr.

Corrosion in water and mineral acids.—As in the case of the crystalline material, hot pressed aluminum nitride is slowly dissolved by hot mineral acids. The results of the corrosion tests are shown in Table VII. Specimens 0.25 x 0.5 x 0.5 in. were heated in a 600 ml volume of water and in the several mineral acids for 72 hr. With the exception of hydrofluoric acid, the tests were made at the boiling temperatures of the liquids. The corrosion rate in boiling water can be considered as low. Although dissolution in the mineral acids is slow, the rate is too great to classify hot pressed aluminum nitride as a corrosion resistant material in these acids. It will be recalled that

Table VII. Corrosion of hot pressed aluminum nitride in water and mineral acids (0.25x0.5x0.5 in. specimens in 600 ml liquid, 72 hr)

Corrosive liquid	Temp, °C	Corrosion rate, mils/year
Water	100	14
Conc. HCl acid	72	320
1 Conc. HCl acid: 1 H_2O	110	570
Conc. H_2SO_4 acid	305	180
1 Conc. H_2SO_4 acid: 1 H_2O	145	550
Conc. HNO_3 acid	120	150
1 Conc. HNO_3 acid: 1 water	111	200
1 HF: 1 HNO_3 conc. acids	57	160
1 Conc. HF acid: 1 water	57	215

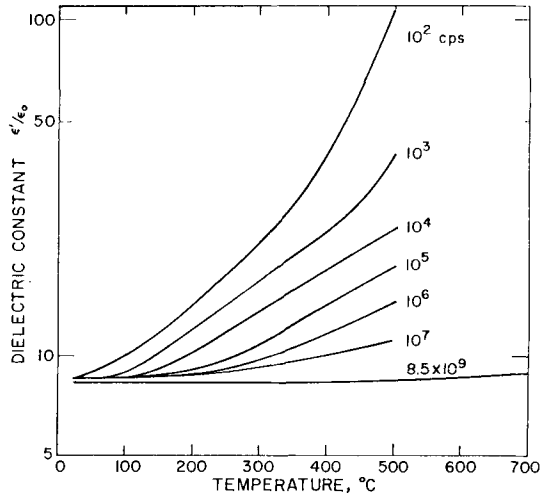

Fig. 4. Effect of temperature on dielectric constant of hot pressed aluminum nitride at several frequencies.

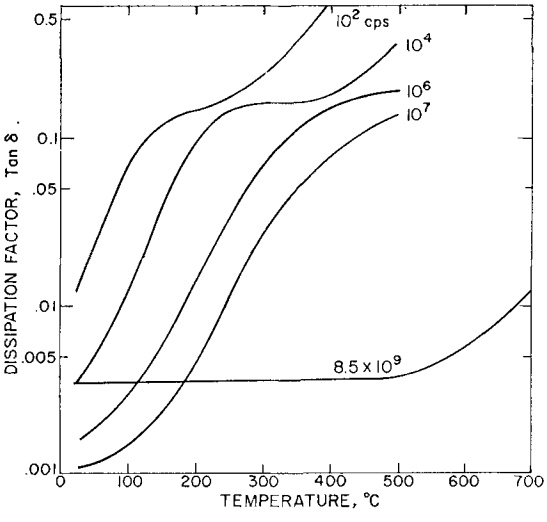

Fig. 5. Effect of temperature on dissipation factor of hot pressed aluminum nitride at several frequencies.

the corrosion rate of single crystals in a boiling mixture of 1 part concentrated hydrochloric and 1 part water was estimated to be about 170 mils per year.

Corrosion in cryolite and aluminum and in boric oxide.—Hot pressed aluminum nitride was heated in an inert atmosphere in a bath consisting of a mixture of molten cryolite and aluminum for 66 hr at 1200°C without visual evidence of corrosion. A piece of hot pressed aluminum nitride, 0.25 x 0.5 x 0.5 in., immersed in molten boric oxide for 4 hr at 1000°C, showed only very slight evidence of attack in the form of faint surface marking and a weight loss of 0.02%. This is equivalent to a corrosion rate of about 25 to 30 mils per year.

Electrical properties.—The electrical properties of hot pressed aluminum nitride appear to be similar to those of alumina, and especially to some of the high density hot pressed aluminas. Dielectric constant and dissipation factor were determined by the Laboratory for Insulation Research at Massachusetts Institute of Technology and also by our own laboratories, the results agreeing fairly closely. Data on dielectric constant are shown in Fig. 4. At room temperature the dielectric constant, over a wide range of frequencies, is about 8.5 compared with between 9 and 10 for many aluminas. The dielectric constant increases rapidly with temperature at low frequencies, less rapidly at high frequencies. At a frequency of 8.5 x 10^9 cps, the change with temperature is only slight. This behavior is also typical of the aluminas.

The dissipation factor at various frequencies and temperatures is shown in Fig. 5. At low frequencies, the dissipation factor increases rapidly with temperature. However, at the frequency of 8.5 x 10^9 cps, the change with temperature up to 500°C is slow. At room temperature the dissipation factor at the various frequencies is between about 0.01 and 0.001, while for the aluminas, the dissipation factor at this temperature is about 0.001 to 0.0001. At high temperatures (400°-500°C) and low frequencies (10^2-10^3 cps) the dissipation factor of hot pressed aluminum nitride and alumina are comparable, while at high temperatures and high frequencies the dissipation factor of the aluminas is appreciably lower.

The volume resistivity of hot pressed aluminum nitride as calculated from the dielectric constant and dissipation factor is shown in Fig. 6. Data for a hot pressed alumina at two frequencies are also shown in Fig. 6 for comparison. At a frequency of 100 cps, the resistivity of hot pressed aluminum nitride is about 2 x 10^{11} ohm-cm at room temperature and 7 x 10^7 ohm-cm at 500°C. Resistivity decreases with frequency; this is also typical for the aluminas and other ceramic insulators.

Summary

Pure aluminum nitride is white. Blue crystals are formed when the metal is heated above 1750°C in nitrogen containing small amounts of carbon monoxide.

Aluminum nitride does not melt under atmospheric pressure in argon, but vaporizes rapidly at about 2400°C. Its Knoop hardness, with a load of

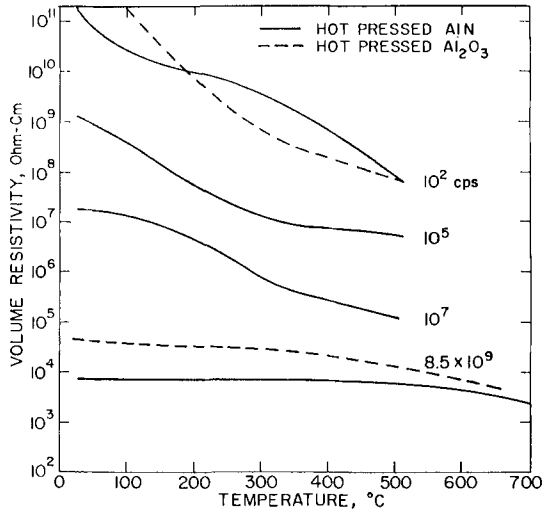

Fig. 6. Effect of temperature on volume resistivity of hot pressed aluminum nitride at several frequencies. Data for a hot pressed alumina at two frequencies are shown for comparison. (Data obtained from Tables of Dielectric Materials Volume V- Laboratory for Insulation Research, Massachusetts Institute of Technology.)

100 g, is approximately 1200, which is equivalent to seven plus on the Mohs scale.

Aluminum nitride starts to oxidize in air at between 700° and 800°C, but in the case of large crystals and the dense hot pressed material, oxidation is slow up to 1400°C because of the protective oxide surface layer formed. It is inert to hydrogen at 1700°C but is attacked by chlorine between 500° and 700°C.

Although aluminum nitride in the crystalline or hot pressed form does not dissolve readily in boiling mineral acids, it is not highly corrosion resistant to these acids. However, it has relatively good corrosion resistance to molten boric oxide and to a mixture of molten aluminum and cryolite in inert atmospheres.

Strength of hot pressed aluminum nitride is lower than that of high-density aluminum oxide at room temperature, but is higher at 1400°C. Compared with most ceramics, it has high thermal conductivity, low thermal expansion, and good thermal shock resistance. Its electrical properties, in many respects, are similar to those of aluminum oxide.

Acknowledgments

The authors are indebted to various members of the Research and Development Division of The Carborundum Company for help in obtaining data and also to Mr. W. B. Westphal of the Laboratory for Insulation Research, Massachusetts Institute of Technology, for measurements of electrical properties.

Manuscript received August 10, 1959. This paper was prepared for delivery before the Philadelphia Meeting, May 1-5, 1960.

Any discussion of this paper will appear in a Discussion Section to be published in the December 1960 JOURNAL.

REFERENCES

1. J. A. Kohn, Perry G. Cotter, and R. A. Potter, *Am. Mineral.*, **41**, 355 (1956).
2. M. Rey, *Silicates Industries*, **22**, 453 (1958).
3. Von Th. Renner, *Z anorg. u. Allgem. Chem.*, **298**, [1-2] 22 (Jan. 1959).
4. George Long and L. M. Foster, *J. Am. Ceram. Soc.*, **42**, No. 2, 53 (1959).
5. A. F. Johnson; U. S. Pat. 2,480,473 (1949).
6. K. M. Taylor, U. S. Pat. 2,839,413 (1958).
7. H. Ott, *Z. Physic*, **22**, 201 (1924).
8. M. v. Stackelberg and K. F. Spiess, *Z. Phys. Chem.*, **A175**, 140 (1935).
9. A.S.T.M. X-ray Powder Data File No. 8-262.
10. W. A. Lambertson and G. Lewis, *This Journal*, **106**, 124 (1959).
11. J. C. Charlton and Ch. C. Evans, British Pat. 784,126 (1957).
12. W. D. Kingery, J. Francl, R. L. Coble, and T. Vasilos, *J. Am. Ceram. Soc.*, **37**, No. 2, 107 (1954).
13. National Bureau of Standards, private correspondence, 1951.
14. Development and Research Division, International Nickel Co., Technical Bulletin T-15, 1949.
15. S. D. Mark. Jr., and R. C. Emanuelson, *Am. Ceram. Soc. Bull.*, **37**, No. 4, 193 (1958).

Relative Rates of Electromigration of Different Ions of the Same Charge across Permselective Membranes

Ruth McClintock, Rex Neihof,[1] and Karl Sollner

Laboratory of Physical Biology, National Institute of Arthritis and Metabolic Diseases, National Institutes of Health, Public Health Service, Bethesda, Maryland

ABSTRACT

A theory is developed which correlates the ratio of the rates of electromigration across permselective membranes of two species of critical exchangeable ions coexisting in solution with the ratio of the rates of spontaneous exchange across the same membrane of the same two species of ions for a third ion in the other solution, and with the bi-ionic potential arising across the same membrane between solutions each containing one of the ions under investigation, at the same activity. The numerous factors which must be considered in electromigration experiments, particularly polarization, are outlined. With solutions in the range of 0.02-0.2*N* and with current densities of about 0.3-1.0 ma/cm², the agreement between the ratios predicted by the theory is closely approached, in many instances within the limits of the experimental errors. At lower current densities, the experimental flux ratios are markedly lower than postulated by the theory, for unknown reasons. At higher current densities, with increasing polarization, there is a gradual decline of these flux ratios, as predicted by theoretical considerations.

In a previous paper we demonstrated the occurrence of greatly different rates of exchange of ions of the same charge across porous membranes of extreme ionic selectivity (permselective membranes) (1). This effect was studied in systems such as System 1 which, in the case of exclusively cation-permeable, anion-impermeable membranes of ionic character, ←⊕→, are represented by:

Solution 1	←⊕→	Solution 2
A^+X^- B^+X^-	Membrane of extreme cationic selectivity	L^+X^-

[System 1]

Here A^+, B^+, and L^+ represent the exchangeable (critical) cations, X^- the nonexchanging, nonpermeating anions. Anionic systems with exclusively anion permeable membranes, ←⊖→, are analogous. Depending on the nature of the membranes, the ratio of the initial rates of simultaneous exchange of univalent ions, A^+ for L^+ and B^+ for L^+, can be as high as 1:100 and more.

These ratios of the rates of exchange, that is, the ratios of the net fluxes of any two species of critical univalent ions coexisting in Solution 1, $(\phi_{A^+}/\phi_{B^+})_{exch.}$, were shown to be correlated to the potentials arising with the same membrane in cells of the type:

Solution 1			←⊕→	Solution 2		
Calomel electrode	KCl conc.	c_1 A^+X^-	c_1 B^+X^-	KCl conc.	Calomel electrode

[Cell 1]

(and analogous cells with exclusively anion permeable membranes) (1). The sign and the magnitude of the potential arising in such cells, the so-called "bi-ionic" potential, $E_{bip.}$, as was pointed out by Michaelis (2), are determined by the relative ease with which the two critical ions penetrate the membrane: if in Cell 1 the cations A^+ of Solution 1 penetrate the membrane with greater ease than do the cations B^+ of Solution 2, then Solution 2 will be charged positive; if the converse is true, Solution 2 will be negative.

Expressing this concept quantitatively one may write

$$E_{bip.} = \frac{RT}{\mathbf{F}} \ln \frac{\tau^\circ_{A^+}}{\tau^\circ_{B^+}} \qquad [1]$$

where $\tau^\circ_{A^+}$ and $\tau^\circ_{B^+}$ represent the transference numbers of A^+ and B^+ within the membrane (the superscript ° being used throughout to indicate equality of activities) (3-6). The ratio of these transference numbers is considered to be a quantitative measure of the relative intrinsic abilities of the A^+ and B^+ ions to penetrate across the particular membrane.

If this holds true, the ratio of the transference numbers can be used to predict the ratio of fluxes of A^+ and B^+ ions across the membrane when present at equal activities in Solution 1, and exchanging for a third ion in Solution 2, as in System 1 (1). If this predicted ratio of fluxes derived from the bi-ionic potential is designated $(\phi^\circ_{A^+}/\phi^\circ_{B^+})_{bip.}$, we may write:

$$\left(\frac{\phi^\circ_{A^+}}{\phi^\circ_{B^+}}\right)_{bip.} = \frac{\tau^\circ_{A^+}}{\tau^\circ_{B^+}} \qquad [2]$$

Experimentally it was shown that in most instances these ratios, $(\phi^\circ_{A^+}/\phi^\circ_{B^+})_{bip.}$, agree within the limits of experimental error with the experimentally established ratios of exchange, $(\phi^\circ_{A^+}/\phi^\circ_{B^+})_{exch.}$ (1):

[1] Present address: Chemistry Division, Naval Research Laboratory, Washington 25, D. C.

$$\left(\frac{\phi^\circ_{A^+}}{\phi^\circ_{B^+}}\right)_{bip.} = \left(\frac{\phi^\circ_{A^+}}{\phi^\circ_{B^+}}\right)_{exch.} \quad [3]$$

If, in systems such as System 1, the ratio of the activities of any two species of exchangeable ions in Solution 1 was not 1:1, the ratios of their initial net fluxes across the membrane, $(\phi_{A^+}/\phi_{B^+})_{exch.}$, were shown to agree satisfactorily, usually within the limits of the experimental error, with the corresponding ratios derived from the bi-ionic potentials, $(\phi^\circ_{A^+}/\phi^\circ_{B^+})_{bip.}$, times the ratios of the activities of the two ions under consideration, $a_{A^+}{}^{[1]}/a_{B^+}{}^{[1]}$, according to the equation:

$$\left(\frac{\phi_{A^+}}{\phi_{B^+}}\right)_{exch.} = \frac{a_{A^+}{}^{[1]}}{a_{B^+}{}^{[1]}}\left(\frac{\phi^\circ_{A^+}}{\phi^\circ_{B^+}}\right)_{bip.} \quad [4a]$$

Combining Eq. [3] and [4a], we may write the expanded equation:

$$\left(\frac{\phi_{A^+}}{\phi_{B^+}}\right)_{exch.} = \frac{a_{A^+}{}^{[1]}}{a_{B^+}{}^{[1]}}\left(\frac{\phi^\circ_{A^+}}{\phi^\circ_{B^+}}\right)_{bip.} = \frac{a_{A^+}{}^{[1]}}{a_{B^+}{}^{[1]}}\left(\frac{\phi^\circ_{A^+}}{\phi^\circ_{B^+}}\right)_{exch.} \quad [4b]$$

Analogous considerations were shown to apply to systems with more than two species of critical ions in Solution 1.

After the ratios of the rates of spontaneous exchange across permselective membranes of coexisting species of ions of the same charge were thus correlated satisfactorily with the bi-ionic potentials arising with these ions across the same membranes, the next obvious step was to test whether analogous correlations exist with the ratios of the migration in an electric field of ions of the same charge across permselective membranes. This electromigration could be studied in cells such as Cell 2, which is essentially System 1 provided with electrodes:

	Solution 1		Solution 2	
		$\leftarrow\oplus\rightarrow$		
Anode	c_1 A^+X^- c_1 B^+X^-		c_2 L^+X^-	Cathode

Cell [2]

This matter, mentioned briefly at an earlier occasion (7), is the subject of the present communication.

When a positive current is passed through Cell 2 from left to right, A^+ and B^+ ions are transported simultaneously from Solution 1 through the membrane into Solution 2, the total number of equivalents of ions moved being identical with the number of faradays passed through the cell.

If the ratio $(\phi^\circ_{A^+}/\phi^\circ_{B^+})_{bip.}$ and the closely similar ratio $(\phi^\circ_{A^+}/\phi^\circ_{B^+})_{exch.}$ represent a measure of the ratio of the intrinsic competitive propensities of these two ions to penetrate across the membrane, the ratio in which the current is transported by the A^+ and B^+ ions across the membrane in Cell 2 may be expected to be the same, provided $a_{A^+}{}^{[1]}$ equals $a_{B^+}{}^{[1]}$. Denoting the ratio of these net fluxes of the A^+ and B^+ ions, which may also be considered as the ratio of their transport numbers in the membranes, as $(\phi^\circ_{A^+}/\phi^\circ_{B^+})_{elect.}$ we may write:

$$\left(\frac{\phi^\circ_{A^+}}{\phi^\circ_{B^+}}\right)_{elect.} = \left(\frac{\phi^\circ_{A^+}}{\phi^\circ_{B^+}}\right)_{bip.} = \left(\frac{\phi^\circ_{A^+}}{\phi^\circ_{B^+}}\right)_{exch.} \quad [5]$$

If the concentrations of A^+ and B^+ in Cell 2 are not identical, this is taken into account in the same manner as in the case of exchange studies (1) by the use of the more general equation

$$\left(\frac{\phi_{A^+}}{\phi_{B^+}}\right)_{elect.} = \left(\frac{a_{A^+}{}^{[1]}}{a_{B^+}{}^{[1]}}\right)\left(\frac{\phi^\circ_{A^+}}{\phi^\circ_{B^+}}\right)_{bip.} = \left(\frac{a_{A^+}{}^{[1]}}{a_{B^+}{}^{[1]}}\right)\left(\frac{\phi^\circ_{A^+}}{\phi^\circ_{B^+}}\right)_{exch.} \quad [6]$$

or its analogue for anionic cells.

The foregoing derivation of the flux ratio $(\phi_{A^+}/\phi_{B^+})_{elect.}$ implicitly makes the assumption that potentially complicating effects do not arise to a significant extent. Specifically it is based on the assumptions that:

1. the membranes are of ideal ionic selectivity;
2. equilibrium conditions at the membrane-solution interfaces are maintained;
3. the distribution of ions in the membrane has reached a stationary state;
4. polarization does not arise;
5. electrophoretic effects, particularly a coupling of the movements of different ionic species, are absent;
6. spontaneous net exchange of ions across the membranes is absent; and
7. osmosis, due to differences in the activity of the solvent at the two sides of the membrane does not occur.

Assumption 1 means that no significant quantity of noncritical ions penetrates across the membrane, a condition which is readily fulfilled by permselective collodion matrix membranes (8-10).

Assumption 2 implies that the distribution of ions at the membrane-solution interfaces during electromigration corresponds to the equilibrium distribution of ions which would exist without the flow of current, in the absence of any spontaneous net exchange of ions across the membrane. This assumption is closely linked to the problem of membrane polarization which is treated below, Assumption 4.

Assumption 3 states that the distribution of the ions in the membranes under the influence of the electric field has reached a stationary state. This condition would be fulfilled either if such a stationary state is the same as that with no current flowing, or if a current has been passed through the cell prior to the experiment proper for a period long enough to achieve the stationary state. Membranes having ion exchange capacities which are low compared with the total ionic content of Solution 2 would be expected to cause the least error even if Assumption 3, which is not readily tested by an independent method, should not be strictly fulfilled.

Assumption 4, that polarization at the membrane-solution interfaces does not arise, can be true only with infinitely weak currents, quite as in the case of metallic electrodes.

While polarization at metallic electrodes has been treated widely in the literature, membrane polarization has not been studied extensively. Polarization at

metallic electrodes is thus a useful starting point in discussing membrane polarization.

Electrode polarization is best known for nominally reversible electrodes in contact with single electrolyte solutions such as $CuSO_4/Cu$. Ordinarily one distinguishes (*a*) *chemical polarization* due to a slow step or steps involved in the discharge of the ions, such as their dehydration, and the deposition of the discharged material in a stable form at the cathode, or to the inverse processes in the anodic dissolution of a metal electrode; and (*b*) *concentration polarization* which is due to the slowness of the diffusion of ions in the solution. There is a decrease of the concentration in the solution in the immediate neighborhood of the cathode where ions are being discharged, and an increase near the anode from which metal dissolves and goes into solution in the form of ions. In a thin layer of solution there is always a concentration gradient from that of the bulk of the solution to the smaller or larger (for cathode and anode, respectively) value at the electrode; diffusion into or from the bulk solution tends to reduce these concentration differences near the electrodes. The layer in which this occurs is commonly referred to as the *diffusion layer*. The thickness of this layer can be reduced by stirring, but it cannot be eliminated entirely. With solutions at room temperature that are stirred thoroughly by ordinary mechanical devices a diffusion layer with an apparent thickness of 20 to 30 μ remains.

Before the ions can reach the cathode they must traverse the diffusion layer from the bulk solution; the rate at which ions reach the cathode is proportional to their concentration in the solution. Concentration polarization at a given current density can be reduced by the use of solutions of higher concentrations and by stirring, or by raising the temperature, but it cannot be eliminated entirely. Concentration polarization is less at lower current densities.

At the phase boundaries between two electrolytic conductors, such as an electrolytic solution and an ionic membrane, *chemical polarization* which involves the discharge of ions obviously does not occur except under the most extreme conditions (11).

Concentration polarization, however, does occur when a current passes across the phase boundary between two ionic conductors if the ratios of the transference numbers of cations and anions in the two phases are not the same, as pointed out first by Nernst and Riesenfeld (12) for the simple case of a uni-univalent electrolyte distributed between two liquid phases. Such polarization consists of an increase in concentration of electrolyte at the one side of the phase boundary and a corresponding decrease at the other. The ratios of the transference numbers, $t^{+[1]}/t^{-[1]}$ and $t^{+[2]}/t^{-[2]}$, are obviously not the same if Phase 1 is an electrolytic solution and Phase 2 an ionic membrane equilibrated with it (12-14).

With permselective membranes the situation is much simpler. In such membranes of practically ideal ionic selectivity either the cations or the anions have a transference number of zero. Only the counter ions of the fixed wall charges, the critical ions of the adjacent solution, move into the membrane phase or are released by it.[2] Thus, with permselective membranes the concentration polarization in a solution containing a single electrolyte is quantitatively the same as if the membrane were a reversible electrode on which the ion under consideration is deposited, or from which it is released by dissolution.

The cells investigated in this paper, such as Cell 2, contain two species of critical ions of the same charge in Solution 1, thus being analogous to electrolytic cells in which an alloy is deposited from a mixed solution. In the two solutions of such cells concentration polarization will arise with respect to all ions according to their respective transport numbers in the solutions and the membrane. Therefore, the degrees of concentration polarization of two ions of the same charge will, in general, be different. In other words, the ratio of the concentration of the two critical species of ions in the solution layers immediately adjacent to the membranes will be different from that in the bulk solution. In cells such as Cell 2, this effect would be disturbing particularly at the phase boundary between Solution 1 and the membrane, where the critical ions move from the solution into the membrane, thereby changing profoundly the most important parameter of the cell. If concentration polarization did not change the ratio of the concentrations of the two permeable ions but only their absolute concentrations, concentration polarization would be of little consequence in the present situation.

Assume, for instance, that the A^+ ions in Cell 2 represent potassium ions and B^+, lithium ions. The former have in free solution about twice the diffusion velocity and ionic mobility of the latter. In ordinary permselective membranes the ratios $(\phi^\circ_{K^+}/\phi^\circ_{Li^+})_{exch.}$ or $(\tau^\circ_{K^+}/\tau^\circ_{Li^+})_{bip.}$ are in most instances about six (1). Although the K^+ ions reach the interface about twice as fast as the Li^+ ions, they are removed by the current into the membrane about six times as fast as the Li^+ ions; thus a relatively stronger depletion of the K^+ ions than of the Li^+ ions would arise in Solution 1 at the membrane-solution interface.

The concentration polarization which we have considered so far is the polarization which arises in the solutions. On the membrane side of the interface, concentration polarization in the classical sense, a decrease or increase in total concentration of electrolyte, cannot occur with membranes of extreme ionic selectivity in which all movable ions are of the same charge. However, another type of concentration polarization may conceivably arise. In our discussion up to now the assumption was made (Assumption 2) that equilibrium with respect to the distribution of ions is always maintained between the surfaces of the membrane and the layers of solution immediately adjacent to it. The question arises whether or not the assumed ion exchange equilibrium on the surface of the membrane is maintained when two competing species of ions of the

[2] This is not true if the degree of polarization is extreme, and the concentration of the electrolyte in the diffusion layer immediately adjacent to the membrane becomes so low that the ions of the water, H^+ or OH^- ions, contribute significantly to the transportation of electricity across the membrane (14). Conditions under which this effect arises are not considered in this paper.

same charge are forced by the electric field into the surface of the membrane. There might be some processes associated with the transition of the ions from the solution into the membrane, such as partial dehydration, which are slow and occur at different speeds with the two species of critical ions under consideration. No information fully pertinent to this point seems to be available. It must be assumed that this type of polarization, if it should exist, would, like all other polarization effects, be more pronounced the higher the current density.

Assumption 5 states that there is no electrophoretic coupling of the movement of the A^+ and the B^+ ions in the membrane. Such a coupling may be visualized as being due to an electro-osmotic movement of liquid in the pores which is caused by the friction between the electromigrating ions and the solvent. With the two species of ions electromigrating in the same stream of liquid, the electrophoretic effect would always tend to equalize the experimentally observable fluxes, thus bringing the flux ratios, $(\phi_{A^+}/\phi_{B^+})_{elect.}$ nearer to unity than those predicted on the basis of the bi-ionic potentials or from exchange studies.

Assumption 6, that there is no significant spontaneous net exchange of ions by diffusion across the membrane, can be realized by the use of membranes of high resistance; the rate of exchange of ions across a membrane, *ceteris paribus,* being inversely proportional to its resistance.

Assumption 7 stipulates that movement of water caused by an inequality of the solvent activities at the two sides of the membrane is absent or negligibly small. The direction of this movement of water would depend on the composition of the two solutions or more correctly on the concentrations in the two layers of solution immediately adjacent to the membrane. If polarization occurs, this would result in a reduced concentration of this layer in Solution 1 and in an increased concentration on the side of the more dilute Solution 2. This effect would tend to alter the osmotically active concentration difference across the tested membrane. The use of fairly dense membranes of low water permeability, such as the permselective collodion matrix membranes, tends to minimize the errors due to osmotic solvent movement (8-10).

The conditions postulated by the various assumptions discussed above, except the absence of electrophoretic effects may be realized experimentally to an adequate extent, primarily by the use of low current densities and solutions which are not too dilute in cells with dense, high resistance membranes. The absence of electrophoretic effects, however, cannot be achieved as a matter of principle, except in the unique and trivial instance of equal mobilities within the membrane of the two competing species of critical ions. The mutual interactions between the two types of electromigrating critical ions, the charged pore walls, and the solvent are inherent in the electromigration experiments, independent of the current density. Only the experiments can show whether the simple theoretical approach which has led to Eq. [5] and [6] is justified by the facts.

A study somewhat similar to the present has been published by Bergsma and Staverman (15). Using technical membranes of fairly high water content, they found rather unsatisfactory agreement between theory and experiment. Gregor and Wetstone (16) and Bilberg and Brun (17) have briefly touched the same subject. From a more practical point of view some phases of the problem of the simultaneous electromigration of ions across membranes were taken up by Di Benedetto and Lightfoot (18) and by Partridge and Peers (19).

Design of the Experiments

The experiments were designed not only to fulfill adequately the requirements of the assumptions outlined above, but also to permit ease and accuracy of analysis. Pairs of ions were chosen which do not interfere analytically with each other. Further, to facilitate accurate measurement of concentration changes in the solution into which the ions were transported, Solution 2, the initial concentrations in that solution of the ions under study were made low. Various possible types of cells satisfy these conditions. We chose cells which fulfill the condition described by the Donnan membrane equilibrium:

$$\frac{a_{A^+}{}^{[1]}}{a_{B^+}{}^{[1]}} = \frac{a_{A^+}{}^{[2]}}{a_{B^+}{}^{[2]}} \qquad [7]$$

In cells with only strong uni-univalent inorganic electrolytes, it is adequate and more convenient to operate with normalities instead of activities, the ratios of which are for practical purposes identical with those of the corresponding activities, for example:

	Solution 1		Solution 2	
		$\leftarrow\oplus\rightarrow$		
Anode	$0.1N$ A^+X^- $0.1N$ B^+X^-	|	$0.001N$ A^+X^- $0.001N$ B^+X^-	Cathode

[Cell 3]

Before the passage of current, such cells are in equilibrium with respect to the distribution of the critical ions. No spontaneous net exchange of ions between the two solutions can occur until the flow of current has shifted the ratios of their concentrations away from the Donnan distribution.

Although Cell 3 is in equilibrium with respect to the distribution of the ions, it is not in equilibrium with respect to the solvent; there is an osmotic flow of water from Solution 2 into Solution 1. Such an osmotic flow would decrease by the same absolute value the speed of electromigration of the two critical ions across the membrane, and thus would increase the experimental flux ratios above the calculated ones. The influence of osmosis would be most noticeable in long duration, low current density experiments. The osmotic and the electro-osmotic effects in Cell 3 operate in opposite directions and thus tend to cancel.

The following considerations were applied in the detailed planning of the experiments. In order that the concentrations of the ions under study in Solution 1 and therefore also the ratio of their concentrations remain practically unchanged, the volume of this solution should be large and its concen-

tration high compared with that of Solution 2. The volume of Solution 2 should be small, so that a given small amount of electricity passed through the cell would bring about changes in concentration which are large enough to permit accurate analyses. To obtain a large concentration change in a short time with a given current density, it is desirable to have a high ratio of the membrane area to the volume of Solution 2.

To fulfill as far as possible Assumptions 1, 6, and 7 listed in the preceding section, the membranes chosen should be of virtually ideal ionic selectivity, of sufficiently high resistance to prevent significant spontaneous exchange of ions between the two solutions, and dense enough to prevent appreciable osmotic water movement. Further, the membranes should have low ion exchange capacities so that exchange of ions between them and the solutions cannot affect significantly the ratio of the ionic concentration of the solutions.

Permselective membranes except those with very low resistances have satisfactory ionic selectivities in solutions up to about 0.2*N*, they also have low ion exchange capacities (8-10). In general, membranes of higher resistance yield a lower rate of osmotic water movement. However, the resistance must not be so high as to make the exchange studies for the determinations of the $(\phi^\circ_{A^+}/\phi^\circ_{B^+})_{exch.}$ ratios too tedious, or to cause a significant amount of heat to be generated by the flow of the maximum current used. Although the concentrations of both species of critical ions in Solution 1 should be high, the total concentration of Solution 1 can be raised safely only to a certain extent (which depends on the membrane) because the ionic selectivities of the membranes are lower at higher concentrations (8-10).

Also, the current densities used should be low to minimize polarization. However, a certain total quantity of electricity must flow through the cell before analytical data of sufficient accuracy can be obtained. Low current densities therefore necessitate long experimental periods. Under these conditions the danger of a significant spontaneous exchange of ions is increased, due not only to the time factor but also to the less pronounced unidirectional flux of ions in the membrane. The range of current densities used must represent a compromise between these antagonistic requirements.

When a current is passed through Cell 3, the products of electrolysis developed at metallic electrodes, particularly H^+ and OH^- ions, would seriously affect the essential membrane processes. In cells with cation selective membranes and solutions of the halides, the use of silver-silver halide electrodes would considerably ameliorate this situation; however, disturbing electrode processes would still occur with the current densities used in many of our experiments. The difficulties due to electrode processes can be eliminated by using guard membranes of extreme ionic selectivity which separate the electrodes from Solutions 1 and 2 (15, 20). If the tested membrane is cation permeable the guard membranes must be anion permeable, and *vice versa,* as shown in Cells 4a and 4b.

It is evident which ions are transported by the current to and from the different compartments of Cell 4, how contamination of Solutions 1 and 2 from the adjacent electrode compartments is suppressed, and how electroneutrality is maintained in each compartment.

Apparatus and Procedure

The experimental cell, shown schematically in Fig. 1a, consisted of four Lucite sections clamped together by means of four bolts. The compartments so formed, A, B, C, and D, were separated from each other by the tested membrane and two guard membranes, mounted flat between Parafilm gaskets. The exposed area of each membrane was 23.7 cm^2.

The two end sections forming the electrode compartments A and D each had an air hole at the top and a tube at the bottom for introducing or draining

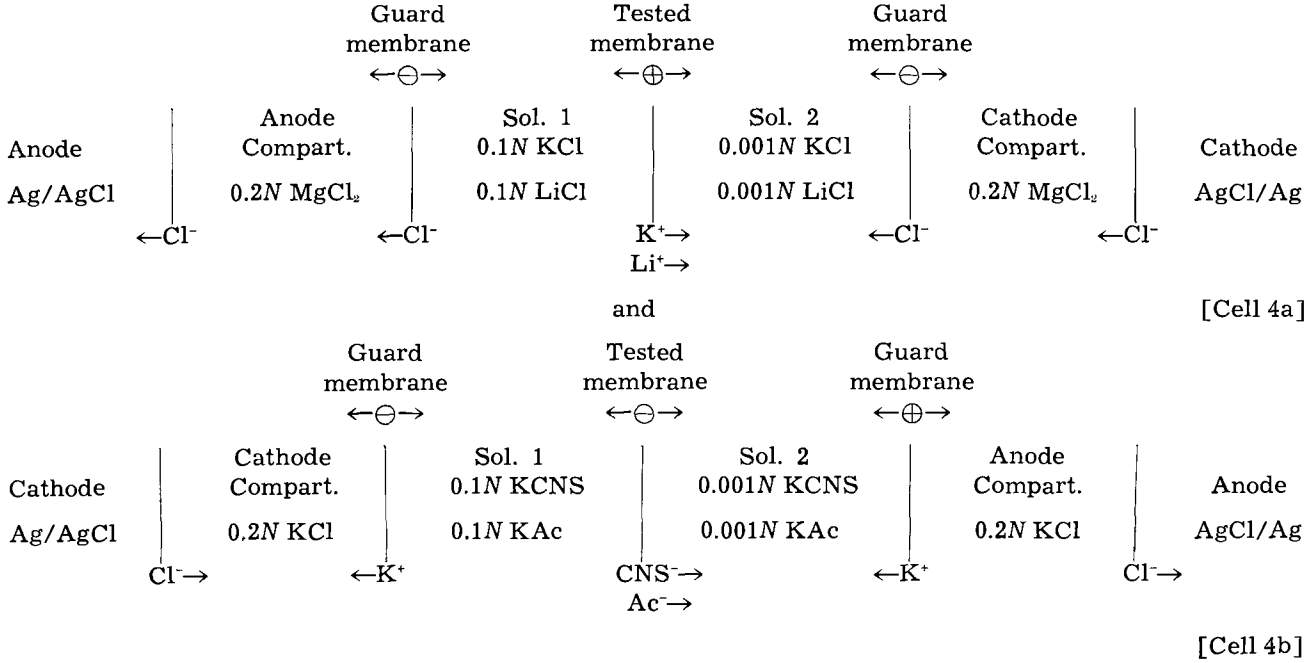

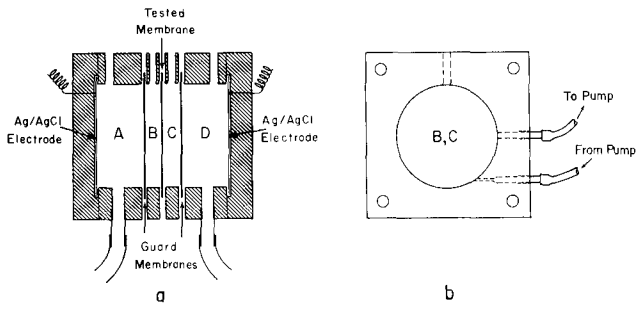

Fig. 1. Cell for the study of the electromigration of ions across membranes (schematic). (a) Cross section through the cell; (b) plastic section forming compartment B or C.

solutions, and contained an electrode, a silver disk on which silver chloride had been deposited by electrolysis from a chloride solution.

The two sections forming compartments B and C on either side of the tested membrane were machined as shown in Fig. 1b. Each had a hole at the top and was provided with a closed loop of polyvinyl chloride (Tygon) tubing. These loops passed through a peristaltic pump which circulated the solutions at a rate of about 100 ml/min. This stirring was vigorous enough that further increases in the rate of circulation made no significant difference in the experimental results. The volume of solution required for filling completely either compartment B or C including the loop of tubing was about 20 ml which, when necessary, was increased to about 200 ml by placing a reservoir in the pumping circuit.

The membranes were cut from the cylindrical parts of test tube-shaped permselective collodion matrix membranes, the preparation and properties of which have been described in detail (8-10). The cation selective membranes contained acidic polyelectrolytes as activating agents, polyacrylic acid (PAA) in the case of weak acid membranes and polystyrene sulfonic acid (PSSA) in the case of strong acid membranes (8). The anion selective membranes were made with basic polyelectrolytes, poly-2-vinyl-N-methyl-pyridinium halide (PVMP) or protamine chloride (9, 10).

The tested membranes had unit area resistances in 0.1*N* KCl, ρ^*, from 125 to 300 ohm-cm^2, the guard membranes from 250 to 900 ohm-cm^2. Membranes in these ranges of resistance are known to be of high ionic selectivity as determined from the measurement of concentration potentials or from leak studies, their permeabilities to the critical ions at 0.1*N* being about 400 to 2000 times that of the noncritical ions (8-10). They have ion exchange capacities of 0.4 to 2.0 μeq/cm^2, water contents of 6-13%, and are about 30 μ thick.

For measurement of the *bi-ionic potentials*, $E_{bip.}$, the compartments B and C on opposite sides of the tested membrane were filled with 0.1*N* electrolyte solutions, each containing one of the critical ions to be studied; the electrode compartments were left empty. The solutions, which were stirred continuously, were renewed repeatedly over a period of several hours to establish a stationary state across the membrane (4). Immediately after renewing both solutions again, the potential was measured using saturated calomel half-cells with saturated KCl-agar bridges, and the temperature recorded. This was repeated until successive readings agreed within ± 2%. These potentials were not corrected for the asymmetry of the two liquid-junction potentials at the tips of the bridges. The flux ratio, $(\phi^\circ_{A^+}/\phi^\circ_{B^+})_{bip.}$ was obtained using Eq. [1] and [2].

For the determination of the ratios of the *rates of exchange*, a reservoir was placed in the pumping circuit of one of the compartments adjacent to the tested membrane, B or C, and filled with Solution 1, a 0.2*N* solution containing equal concentrations of the two critical ions under study. The other compartment, without reservoir, was filled with Solution 2, 0.2*N* NH_4Cl if the tested membrane was cation permeable or 0.2*N* KNO_3 if it was anion permeable. Both solutions were circulated for stirring. A stationary state across the membrane was obtained, as described above, before starting the experiment proper with fresh solutions. The duration of the exchange experiments was chosen so that the concentrations of the critical ions in Solution 2 became sufficient for accurate analysis. The ratio of their concentrations gives the ratio of the exchange fluxes, $(\phi^\circ_{A^+}/\phi^\circ_{B^+})_{exch.}$. These experimental runs were repeated until two or more runs agreed within 5-10%.

To measure the *electrical fluxes*, the electrode compartments A and D were filled with about 50 ml of 0.2*N* $MgCl_2$ if the tested membrane was cation permeable, or 0.2*N* KCl if the tested membrane was anion permeable. One of the compartments adjacent to the tested membrane, B or C, was provided with a reservoir and filled with the more concentrated solution, Solution 1 [Cell 4]. The compartment on the other side of the tested membrane, without reservoir, was filled with the more dilute solution, Solution 2. Both solutions were circulated for stirring. The membrane was equilibrated with the solutions as described above. Before an experimental run, both solutions were changed, the more dilute solution three times. Finally, a measured volume of the dilute solution was placed in the compartment of Solution 2 and the flow of a direct current of the chosen intensity, 0.042-4.2 ma/cm^2, started. The duration of the experiments, 3-480 min, was adjusted so that the concentrations of the critical ions in the dilute solution increased sufficiently for accurate determination of the concentration changes. The currents passed were 1-100 ma; the total quantity of electricity in the individual runs was 0.2-0.6 x 10^{-3} faraday. The experimental runs at any given current density were repeated, usually two or three times with about 100% variation in their duration. The electrical flux ratios, $(\phi_{A^+}/\phi_{B^+})_{elect.}$, for each experimental run were obtained from the ratios of the increases in concentration of the two critical ions. These ratios were ordinarily reproducible within 15%.

As a routine check for satisfactory performance of the cell, the number of equivalents of critical ions transported was compared with the number of faradays of electricity passed, as determined by an iodine coulometer or as calculated from the magnitude and duration of the current. It also should be mentioned that the membranes did not change significantly during a series of experiments, as indicated

by the constancy of the exchange flux ratios and of the bi-ionic potentials. The sequence in which the experiments were carried out did not influence the results.

In numerous instances the positions of the solutions and the direction of the current were reversed with respect to the tested membrane; with the electrolytes used in the experiments reported below in detail, no significant effect was found.

The analytical determinations of anions were carried out by standard micromethods (21), ordinarily with an estimated error of ±1%. The cations were determined by means of a flame spectrophotometer, the error in analysis being in most cases less than ± 3%, never more than ± 5%.

Before presenting the results of the experiments which were carried out by the methods just outlined, several preliminary tests are described which were made to explore to what extent certain of the conditions assumed in the theoretical development are fulfilled in our experimental cells.

During the course of the electromigration experiments the ratio of the A^+ and B^+ ions in Solution 2 is changed from the Donnan equilibrium distribution shown in Cell 4, and spontaneous back exchange of ions tends to occur, contrary to our assumption.

Back exchange is not readily measured in the presence of the electric field applied in the electromigration experiments. We therefore have tested whether such an exchange of ions might occur in the absence of an impressed electric field. The membranes were of the same types employed in the electromigration experiments, with ρ^* of 175-275 ohm-cm^2. Solutions similar to the final solutions obtained in the electromigration studies were placed in the compartment of Solution 2 and allowed to exchange against Solution 1 while both solutions were stirred. At the end of the exchange periods, 2-16 hr, little or no change in the concentrations of the ions was found. There would have been even less back exchange during the electromigration runs: first, with current flowing, the back exchanging ions would have had to move against an electrical gradient; second, the concentration difference which would cause back exchange is initially zero and would be built up only in course of time. Thus it is certain that back exchange was quantitatively unimportant during the electromigration experiments.

To test whether osmosis due to differences in the activities of the solvent at the two sides of the membrane occurs, the rate of osmotic water movement was measured, as described previously (8-10), with 1.0*N* KCl against water. The same membranes were used as in the back exchange experiments. The rates of osmotic water movement were 2 to 6 mm^3/hr-cm^2. Since the rate of water movement is proportional to the difference in osmolar concentrations, the greatest rate to be expected with the solutions used in our electromigration experiments is approximately one-fourth as much.

The water transported per equivalent of ions moved was also determined for the same membranes. The experimental arrangement was similar to that for the measurement of osmosis, but with the addition of Ag/AgCl screen electrodes on either side of the membrane. The quantity of water transported per faraday depended on the critical ion and the resistance of the membrane. It was independent of the current density and essentially independent of the concentration, in the range of interest here. The values with acidic membranes were 3-4 moles of water per equivalent of K^+ and 6-8 per equivalent of Li^+; for the basic membranes, 4-5 moles per equivalent of Cl^- and 8-10 for Ac^-. The lower figures were obtained with the higher resistance membranes.

The difference in the number of moles of water transported by ions of the same charge may be taken as an indication that an electrophoretic coupling of the movement of such ions exists when they electromigrate simultaneously across a membrane. However, at present it does not seem possible to evaluate this effect quantitatively.

Another aspect of the electro-osmotic transportation of water of interest here is its correlation to the osmotic water movement, the two being opposed in direction to each other in the electromigration experiments. The electro-osmotic effects are proportional to the number of equivalents of ions transported, independent of the duration of the experiment. The osmotic effects, however, are proportional to the time and are thus proportionately less for the shorter experiments at higher current densities. The data indicate that the osmotic and electro-osmotic effects were of the same order of magnitude at the lowest current densities used in our electromigration experiments, 0.042-0.127 ma/cm^2; at the highest current density employed (4.2 ma/cm^2) the electro-osmotic effect was an order of magnitude greater than the osmotic effect.

The effect of the electro-osmotic and osmotic movement of water on the volume and therefore the concentration of Solution 2 must also be considered. At low current densities the two effects, being of about the same magnitude and opposite in direction, tend to cancel and produce little change in the volume of Solution 2. At high current densities where electro-osmosis predominates, a maximum of approximately 6 mM or about 0.1 ml of water is moved into Solution 2 during a single run. This is only about 0.5% of the initial volume of Solution 2, so that the volume change which results from the water movement and the concomitant effect on the concentration of ions in Solution 2 may be neglected.

Results and Discussion

Figures 2-4 summarize our experimental results. In the coordinate graphs the mean values of the ratios of the electrical fluxes for each current density studied are plotted and connected by straight lines. The length of the vertical line at each plotted point indicates the average deviation of the electrical flux ratio from the mean value of replicate experiments. This alternative is used to give an indication of the reproducibility of the experiments, since many more data would be necessary to make possible a meaningful statistical analysis.

To the right of each coordinate graph are two bar graphs, one showing the ratios calculated from

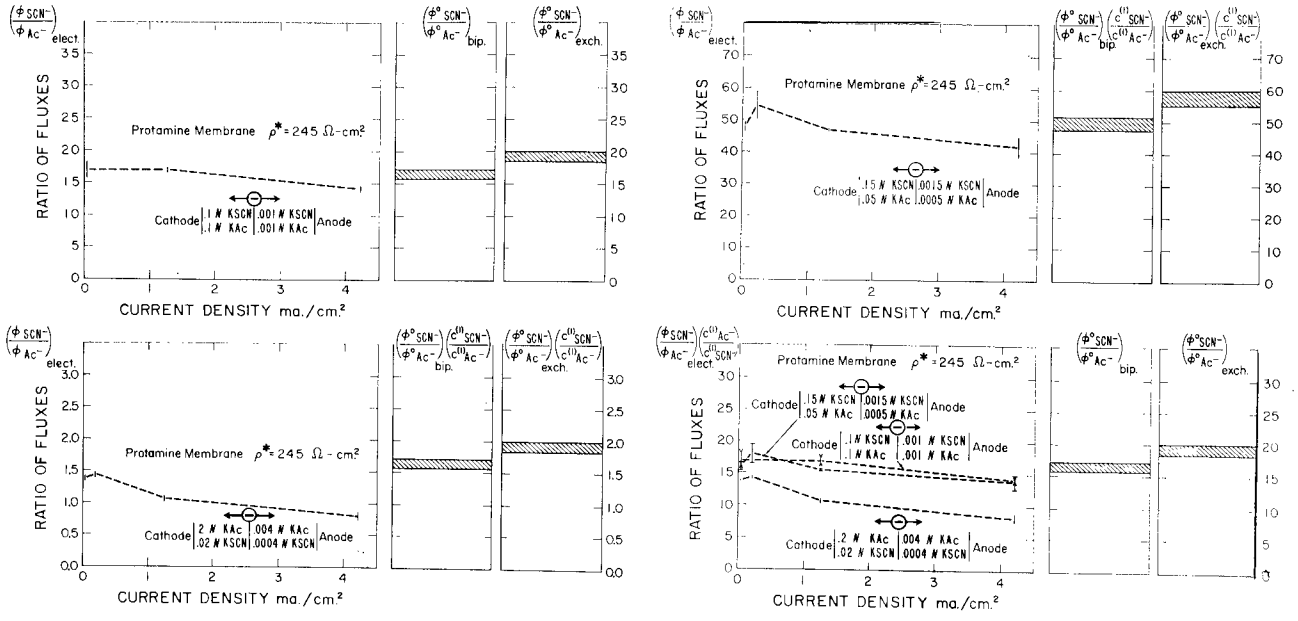

Fig. 2. A comparison of the ratios of fluxes of SCN^- and Ac^- ions (i) as transported by an electric current across an exclusively anion permeable permselective protamine collodion matrix membrane, $(\phi_{SCN^-}/\phi_{Ac^-})_{elect.}$, (ii) as calculated from the bi-ionic potential with the two ions separated by the same membrane, $(\phi^\circ_{SCN^-}/\phi^\circ_{Ac^-})_{bip.}$, and (iii) as measured in the simultaneous exchange of the two ions across the same membrane, $(\phi^\circ_{SCN^-}/\phi^\circ_{Ac^-})_{exch.}$.

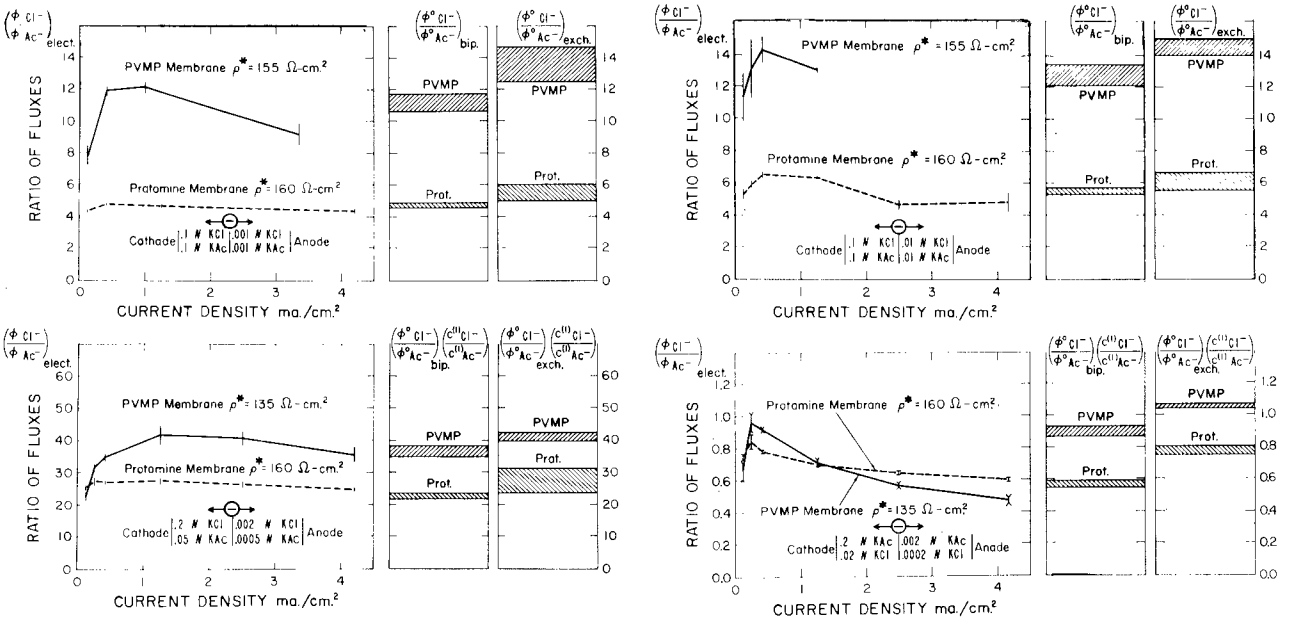

Fig. 3. A comparison of the ratios of the fluxes of Cl^- and Ac^- ions (i) as transported by an electric current across exclusively anion permeable permselective poly-2-vinyl-N-methyl-pyridinium (PVMP) and protamine collodion matrix membranes, $(\phi_{Cl^-}/\phi_{Ac^-})_{elect.}$, (ii) as calculated from the bi-ionic potential with the two ions separated by the same membranes, $(\phi^\circ_{Cl^-}/\phi^\circ_{Ac^-})_{bip.}$, and (iii) as measured in the simultaneous exchange of the two ions across the same membranes, $(\phi^\circ_{Cl^-}/\phi^\circ_{Ac^-})_{exch.}$.

the bi-ionic potentials, and the other, the exchange flux ratios. These graphs have the same vertical scale as the coordinate graphs. In the bar graph of the ratios derived from the bi-ionic potentials, the width of the shaded areas represents the estimated uncertainty in these ratios assuming the measurement of the bi-ionic potential to be accurate within ± 2%. Because the ratio is a logarithmic function of the bi-ionic potential, the width of the shaded areas increases exponentially with the heights on these bar graphs. In the case of the exchange ratios, the width of the shaded areas represents the average deviation from the means of replicate experiments.

Figures 2 and 3 show results obtained with exclusively anion permeable membranes, ←⊖→: Fig. 2 with a protamine membrane and SCN^- and Ac^- as critical ions; Fig. 3 with protamine and poly-2-vinyl-N-methyl-pyridinium (PVMP) membranes Cl^- and Ac^- ions. Figure 4 gives the results with exclusively cation permeable membranes, ←⊕→, polystyrene sulfonic acid (PSSA) and polyacrylic acid (PAA) membranes, with K^+ and Li^+ as critical ions.

A comparison of each pair of bar graphs shows that the flux ratios calculated from the bi-ionic potentials and from the exchange measurements agree

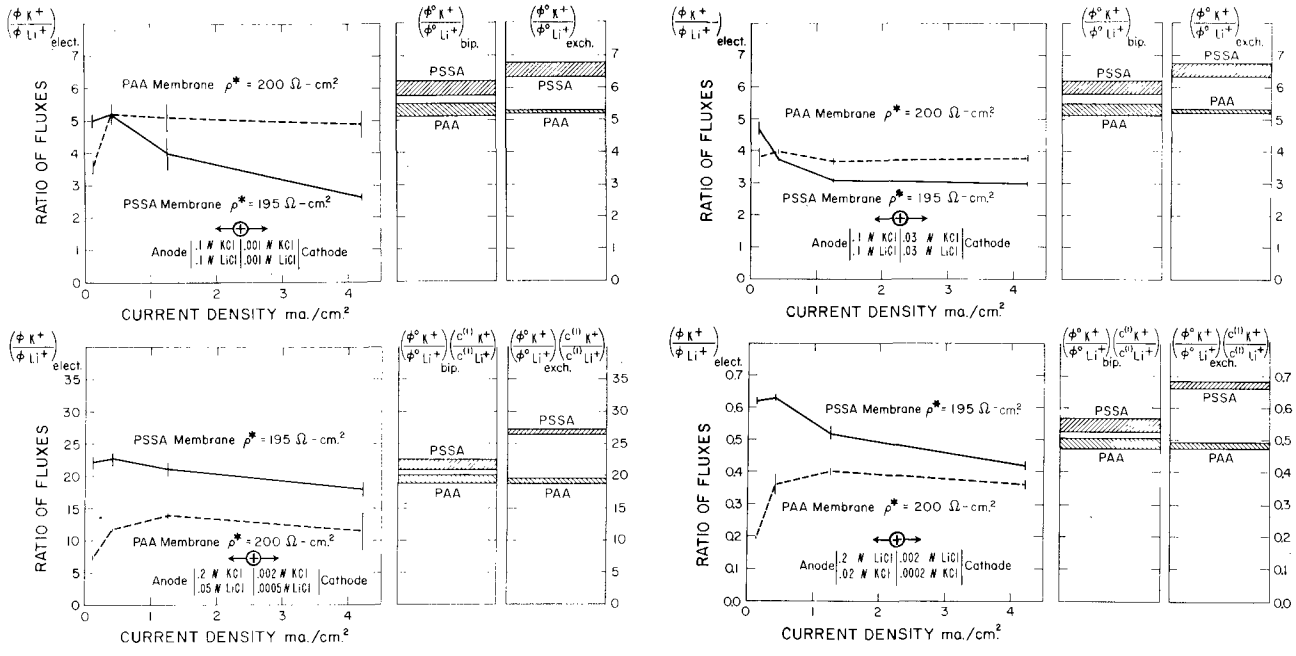

Fig. 4. A comparison of the ratios of the fluxes of K^+ and Li^+ ions (i) as transported by an electric current across exclusively cation selective permselective polystyrene sulfonic acid (PSSA) and polyacrylic acid (PAA) collodion matrix membranes, $(\phi_{K^+}/\phi_{Li^+})_{elect.}$, (ii) as calculated from the bi-ionic potentials with the two ions separated by the same membranes, $(\phi^\circ_{K^+}/\phi^\circ_{Li^+})_{bip.}$, and (iii) as measured in the simultaneous exchange of the two ions across the same membranes, $(\phi^\circ_{K^+}/\phi^\circ_{Li^+})_{exch.}$.

reasonably well with each other, the exchange flux ratios being somewhat higher than the ratios calculated from the bi-ionic potential. The agreement between the two ratios is similar to that reported by Neihof and Sollner (1).

The curves of the ratios of electrical fluxes versus current density in the coordinate graphs of Fig. 2-4 show in the majority of the investigated cells a maximum in the range of current densities of about 0.3-1.0 ma/cm². At higher current densities the ratios of the fluxes are lower, being lower the greater the current density. At current densities less than about 0.3 ma/cm² there is in nearly every cell a significant, in several instances a very marked, drop in the electrical flux ratio. The slope may in many cases be steeper than indicated by the graphs, since the experimental points at low current densities are not close enough together to define exactly the maximum of the curves.

This general shape of the curves is not to be anticipated on the basis of the theoretical treatment. The latter predicts only the observed lowering of the electrical flux ratios as the current density increases, primarily due to polarization and, secondarily, to an increasing preponderance of the electroosmotic over the osmotic liquid movement.

A comparison of the electrical flux ratios at the maxima of the curves with the ratios given by the corresponding bar graphs shows a fairly good quantitative agreement with most of the cells. An extrapolation to zero current of the parts of the curves between about 0.5 ma/cm² and 4.0 ma/cm² would yield an intercept which would show an even better agreement with the bar graphs. This extrapolation, however, seems questionable in view of the drop of the curves at the lower current densities.

The downward slope of the curves toward the side of the lower current densities is contrary to the theoretical expectation. Since this effect occurs quite regularly and is in magnitude far outside the limits of the experimental errors, it must be considered as real. The experiments on spontaneous back exchange reported above preclude an explanation on this basis of the low flux ratios obtained at low current densities. In some instances a spontaneous back exchange with no current passing was not detectable. The greatest back exchange with no current would correspond to less than one-third of the observed decrease in ratios. However, as mentioned previously, any back exchange during the electromigration runs must have been less. Attempts based on the conventional electrochemistry of permselective membranes to explain the lower electrical flux ratios at the lowest current densities have not yet been successful.

That the electrical flux ratios at the maxima of the curves, where polarization is still small, show satisfactory agreement with the theory, seems to indicate that the electrophoretic coupling of the electromigration across the membrane of two species of critical ions is not very marked—the available data are inadequate for any quantitative statement.

Thus the outlined theory seems justified in principle as a first approximation, although it is not adequate to describe the phenomena over more than a very limited area of current densities. Proof is lacking that such agreement between theory and experimental results would be found with membranes of higher porosity, in which each electromigrating ion transports a much greater number of water molecules (22) than in the rather dense membranes used in the present study.

Any more comprehensive and rigorous approach to the problem of the ratios of the electromigration across permselective membranes of two or more species of critical ions coexisting in solution will be confronted not only with the complexity of the membrane processes themselves, but also with the

problem of polarization. Polarization, as indicated by our experimental results, is a most important factor, at all but rather low current densities. The general approach to the theory of irreversible processes given by de Groot (23) and the more specific treatment of membrane processes along analogous lines by Staverman, Kirkwood, Schmid, Schlögl, Spiegler and others yield a useful conceptual framework (24-28). However, the practical obstacles to the use of this approach with experimental cells are formidable. Disregarding polarization in the solutions and assuming no complications such as slow reactions at the membrane-solution interfaces, the situation even with membranes of ideal ionic selectivity is highly complex. With three species of particles, A^+, B^+, and H_2O, which are movable with respect to the membrane, it would be necessary to determine six independent flux constants, which describe the interactions between these particles, in order to know their flux equations (28). However, a given set of constants applies only to a given ratio of A^+ and B^+ in the membrane and additional data, or permissible assumptions, are needed to describe any different A^+/B^+ ratio. Moreover all such constants apply only to the particular membrane under study; different constants pertain to each different membrane.

An approach along these lines to the problem of the ratios of the electromigration across permselective membranes of co-existing species of critical ions is an undertaking of a major magnitude. This prompts us, for the time being, to stop further work in this direction.

Manuscript received Aug. 13, 1959. This paper was prepared for delivery before the New York Meeting, April 27-May 1, 1958.

Any discussion of this paper will appear in a Discussion Section to be published in the December 1960 JOURNAL.

REFERENCES

1. R. Neihof and K. Sollner, *Discussion Faraday Soc.*, **21**, 94 (1956).
2. L. Michaelis and A. Fujita, *Biochem. Z.*, **161**, 47 (1925); L. Michaelis, *Bull. Natl. Research Council (U.S.), No. 69* (1929); *Kolloid Z.*, **62**, 2 (1933).
3. K. Sollner, *J. Phys. Chem.*, **53**, 1211, 1226 (1949).
4. S. Dray and K. Sollner, *Biochim. Biophys. Acta*, **18**, 341 (1955).
5. S. Dray and K. Sollner, *ibid.*, **21**, 126 (1956); **22**, 213, 220 (1956).
6. R. Neihof and K. Sollner, *J. Phys. Chem.*, **61**, 159 (1957).
7. K. Sollner, *Discussion Faraday Soc.*, **21**, 120 (1956).
8. R. Neihof, *J. Phys. Chem.*, **58**, 916 (1954).
9. M. H. Gottlieb, R. Neihof, and K. Sollner, *J. Phys. Chem.*, **61**, 154 (1957).
10. M. Lewis and K. Sollner, *This Journal*, **106**, 347 (1959).
11. K. Sollner, *Z. Elektrochem.*, **35**, 789 (1929).
12. W. Nernst and E. H. Riesenfeld, *Ann. Physik*, (4), **8**, 600 (1902).
13. L. Michaelis, "Die Wasserstoff-ionenkonzentration," Berlin, Springer (1922); English Edition, Translated by W. Perlzweig, "Hydrogen Ion Concentration," Williams and Wilkins Co., Baltimore (1926).
14. A. Bethe and T. Toropoff, *Z. Physik Chem.*, **88**, 686, (1914); **89**, 597 (1915).
15. F. Bergsma and A. J. Staverman, *Discussion Faraday Soc.*, **21**, 61 (1956).
16. H. P. Gregor and D. M. Wetstone, *ibid.*, **21**, 162 (1956).
17. E. Bilberg and T. S. Brun, Universitetet I Bergen, Årbok 1956, Naturvitenskapelig rekke Nr. 11., Bergen 1956.
18. A. T. Di Benedetto and E. N. Lightfoot, *Ind. Eng. Chem.*, **50**, 691 (1958).
19. S. M. Partridge and A. M. Peers, *J. Appl. Chem.*, **8**, 49 (1958); A. M. Peers, *ibid.*, **8**, 59 (1958).
20. T. R. E. Kressman and F. L. Tye, *Discussion Faraday Soc.*, **21**, 185 (1956).
21. Kolthoff and Furman, "Potentiometric Titrations," 2nd ed., John Wiley & Sons, Inc., New York (1931); Kolthoff and Stenger, "Volumetric Analysis," Vol. II, 2nd ed., Interscience Publishers, Inc., New York (1947); Snell and Snell, "Colorimetric Methods of Analysis," Vol. II, 3rd ed., D. Van Nostrand Co., Toronto, New York, and London (1949).
22. C. W. Carr, R. McClintock, and K. Sollner, in preparation.
23. S. R. de Groot, "Thermodynamics of Irreversible Processes," North Holland Publishing Co., Amsterdam (1951).
24. A. J. Staverman, *Trans. Faraday Soc.*, **48**, 176 (1952).
25. T. G. Kirkwood, "Ion Transport across Membranes," H. Clarke, Editor, pp. 119-127, Academic Press, New York (1954).
26. G. Schmid, *Z. Elektrochem.*, **56**, 181 (1952).
27. R. Schlögl, *Z. Physik. Chem.*, N. F. **3**, 73 (1955); R. Schlögl and U. Schödel, *ibid.*, **5**, 372 (1955).
28. K. S. Spiegler, *Trans. Faraday Soc.*, **54**, 1408 (1958).

Surface Coverage during Hydrogen and Oxygen Evolution

P. Rüetschi, J. B. Ockerman, and R. Amlie

Research Center, The Electric Storage Battery Company, Yardley, Pennsylvania

ABSTRACT

The relation between surface coverage and electrode potential during hydrogen and oxygen evolution was studied with inert electrodes of very large surface area. Desorption of gas after interruption of current was followed with micro-volumetric techniques and overvoltage decay was measured simultaneously. The steady-state overvoltage varied linearly with the total amount of hydrogen or oxygen evolved after interruption of current. The true surface area of the electrodes was determined by the BET method, and the capacity was obtained from charging curves. Average effective charges in the double layer per desorbed reacting particle were calculated from these data.

A given (experimentally measurable) over-all Volta potential difference at an electrochemical interface may be established by an infinite number of different charge distributions in the electrode double layer. For the interpretation of transient electrode phenomena (experiments with voltage or current step functions, or a-c techniques) the time-dependence of the charge distribution along the coordinate vertical to the electrode surface, or of the double layer capacity, must be taken into account. Adsorption processes on electrodes are often relatively slow, and it is shown below that considerable time periods may be required to establish steady-state conditions.

Build-up of overvoltage at constant current is generally linear with time over voltage regions extending in some cases over several hundred millivolts if the double layer capacity remains constant during the time period involved (1-6). This is the case if the build-up of the double layer charge is due to accumulation of the same (reacting) species in the same average state (constant distance from electrode interface, constant dipole for adsorption bond) throughout. Changes in the electrode capacity during the charging period (nonlinear charging curves) could result from a variation in specific capacity of a particular species with total Volta potential difference (adsorption state, particularly average distance from the electrode surface varying with potential) or from adsorption of several different species with different specific capacities in such a way that the number of each species in the interface does not vary linearly with over-all Volta potential difference.

The decay of overvoltage after interruption of current becomes, after an initial time period, generally linear with the logarithm of time (1, 4, 6-11). This again can generally be expected only in potential regions where the double layer capacity is constant. This is the case if the number of each species contributing to the charge of the double layer decreases linearly with electrode potential, and if the specific average capacity (adsorption state, distance from electrode surface) is independent of the total Volta potential difference.

Overvoltage in general decays more slowly than expected for an ionic double layer without strong adsorption. The reacting species, maintaining the overvoltage, must be strongly (specifically) adsorbed. Electrodes have the characteristic of maintaining a nonequilibrium concentration of reacting species at the interface over considerable time periods (12). The persistence of nonequilibrium electrode potentials is manifested convincingly by experiments with reversed pulse technique (6). Speculations about the actual configuration of the intermediates (protons, hydrogen molecule ions, atomic hydrogen, surface metal hydrides, molecular hydrogen, for H_2 evolution; and oxygen ions, hydroxyl ions, hydrogen peroxide ions, atomic oxygen, surface oxides, molecular oxygen, for O_2 evolution) on the basis of current-voltage relations only, are not conclusive in view of the fact that (mixtures of) these species might be present in the interface together with foreign inert species, not taking part directly in the reaction. In this connection it is important to point out that there is no such thing as a neutral particle (atom, molecule) in an electrochemical interface. All the surface bonds must have substantial ionic components. This becomes particularly evident from the work function effects of adsorption on solid-gas interfaces (13). The differentiation between atomic and ionic species in the interface is therefore only one of degree and not clear-cut at all. It is the purpose of the present investigation to shed more light on the actual configuration in the electrode interface during hydrogen and oxygen evolution, to study the number and state of adsorbed (activated) species, and to determine the relation between surface coverage and overvoltage. Particular consideration is given to time effects due to slow adsorption phenomena.

Theory

The electrode reaction of gas evolution can be described approximately by the rate equation (13)

$$i = A \exp \{-\alpha Z_i e\, V/kT + \alpha Z_i e\, V_f/kT - (\epsilon^* - \epsilon^\circ)/kT\} \quad [1]$$

where i is the current density, A a factor independent of potential, α the transfer coefficient, $Z_i e$ the

charge of the reacting species in the interface, $V = \psi_I - \psi_{II}$ the Volta potential difference between electrode I and solution II, $V_f = (\psi_I - \psi_{II})_f$ the Volta potential difference at which the number of the reacting species in the interface becomes zero,[1] and $\epsilon^* - \epsilon^\circ$ the covalent adsorption energy of the reacting species.[2] The transfer coefficient α is given by $\alpha = (1/2)(1 - \gamma) = 1/2 - \gamma/2$, where γ is the fraction of the variation of electrode polarization due to inert foreign species according to the theory of Rüetschi (21). The factor A is given by $A = \nu Z_i e \delta n_i$, where ν is a jump frequency and δ the thickness of the reaction zone, and n_i the concentration of the reacting ions in the bulk of the solution (number per cm^3). The instantaneous current, during build-up or decay of overvoltage, is given by

$$i = C\, dV/dt = C\, d(\psi_I - \psi_{II})/dt \qquad [2]$$

where C is the double layer capacity. Combining [1] and [2] and integrating at constant C, one obtains

$$V = \frac{kT}{\alpha Z_i e} \ln \left\{ \frac{tA\alpha Z_i e}{CkT} \exp \left[\frac{\alpha Z_i e V_f}{kT} - \frac{\epsilon^* - \epsilon^\circ}{kT} \right] + \exp \left[\frac{\alpha Z_i e V_o}{kT} \right] \right\} \qquad [3]$$

where $V_o = (\psi_I - \psi_{II})_o$ is the Volta potential difference of the electrode at zero time (beginning of build-up or decay).

If the time t is sufficiently long, the second term in braces can be neglected, and the potential decays on open circuit linearly with logarithm of time.

$$dV/d \ln t = \pm kT/\alpha Z_i e \qquad [4]$$

During constant current charge, the potential increases linearly with time, if C is constant, according to Eq. [2].

$$V = it/C + V_o \qquad [5]$$

In the present paper Eq. [1] to [5] were tested experimentally for hydrogen and oxygen evolution. Deviations from these equations demonstrate the influence of voltage and time effects on the capacity C. Experiments on overvoltage decay were coupled with gas desorption measurements. Such measurements give information about the amount of partially or completely discharged reacting species in the interface.

It should be pointed out here that the behavior of an electrode interface can be described quite accurately with the simple model of a condenser. Each species on the electrolyte side of the interface contributes a characteristic charge to the double layer, and contributes through its specific average capacity in a characteristic way to the total Volta electrode potential difference of the electrode. The total charge is compensated on the electrode side of the interface by an excess or deficiency of electrons, depending on whether the electrode is on the negative or positive side of the zero charge potential. The double layer capacity remains constant only if each species has a constant specific capacity, independent of the total Volta potential difference, and if the number of each species varies linearly with total Volta potential difference.

Equations [1] to [5] imply a reacting species, with charge $Z_i e$, whose energy in the double layer can be compared with its energy in the bulk of the electrolyte. For hydrogen evolution in acid solution, it is convenient to define the proton as reacting species. The charge of the double layer on the solution side in sulfuric acid, e.g., is due to reacting protons, SO_4^{--} ions and overlapping electrons (partially discharged hydrogen ions, or polarized hydrogen atoms). Then $Z_i = 1$, and α is determined by the relative contribution of SO_4^{--} ions and electrons (and conceivably other charged species) to the variation of the electrode potential (21). After having defined the reacting species, Eq. [1] and [4] allow calculation of $\alpha = (1/2)(1 - \gamma)$ from experimental data. A priori, only the product αZ_i can be determined experimentally, but not the individual components γ and Z_i. Only after definition of the reacting species is γ determined. If, in the case of H_2 evolution, the variation in polarization is due to accumulation of reacting protons only, $\gamma = 0$ and $\alpha = \frac{1}{2}$.

For oxygen evolution in acid solution one can define the reacting species as the hypothetical O^{--} ion. On the solution side of the double layer, this ion can be associated with protons (producing OH^- or H_2O), or with overlapping electron holes (producing partially discharged species like O^-, O, O_2^{--}, O_2^-, O_2) or both, producing HO_2^-, and H_2O_2. The charge on the solution side is therefore due to O^{--} and associated foreign species (including SO_4^{--} and ions of the metal). If the variation in polarization due to foreign species were zero, then $\gamma = 0$ and $\alpha = \frac{1}{2}$. If the variation in polarization were due entirely to OH^- ions, each O^{--} is associated with *one* proton and $\gamma = -1$. Since $Z_i = 2$, $(\frac{1}{2})(1 - \gamma)Z_i = 2$ and $\alpha = 1$. To demonstrate that the choice of the reacting species is not arbitrary, one could assume OH^- as the reacting species and variation of polarization due to accumulation of OH^- ions only. Then $Z_i = 1$, $\gamma = 0$, $\alpha = \frac{1}{2}$, and thus $(\frac{1}{2})(1 - \gamma)Z_i = \frac{1}{2}$. This shows that α depends on the choice of the reacting species.

In the following discussion we shall adopt $Z_i = 1$ for hydrogen and 2 for oxygen, since these are the charges actually required to liberate one atom of the gases from their state in the bulk of the solution. The experimental results then yield values for γ, which is a measure of the contribution of foreign species (other than H^+ or O^{--}, respectively) to the variation of polarization for H_2 and O_2 evolution. The factor γ can theoretically assume any value between $-\infty$ and $+1$ (21).

Measurements of build-up of overvoltage at constant current give information about the total capacity of the double layer. Capacity is measured here by the voltage change produced by an external known current. During overvoltage decay, the instantaneous internal current cannot be measured directly, but it is reasonable to assume that it is adequately described by [1].

[1] The potential V_f was denoted V_{if_o} in an earlier theoretical paper (21).

[2] Only changes in $V = \psi_I - \psi_{II}$ are measured in overvoltage studies: $\Delta V = \Delta(\psi I - \psi II) = \Delta\eta$, where η is the overvoltage. In this paper the reference electrodes to which overvoltages are referred are the reversible $Pb/PbSO_4$ and $PbO_2/PbSO_4$ electrodes.

It is necessary to define the term capacity as the charge transferred per unit voltage change. During fast charging, an outer layer of ions is built up at the interface. As time proceeds, part of these ions are brought closer to the interface and are partially discharged. This results in an apparent increase in capacity. Only the gas actually leaving the interface does not contribute anything to the charge of the double layer. In the present paper, the capacities were determined from relatively slow charging curves, which means that they are essentially the capacities for an average adsorption state. On open-circuit decay, an ionic, outer double layer would require theoretically 2 or 4 electronic charges to produce one molecule of H_2 or O_2. Actually, less charge may be required for species already partially discharged in the interface. The amount of gas desorbed in excess of the amount expected for an ionic type double layer is a measure of the number and state of adsorbed and partially discharged reacting species. Thus, even for constant capacity (voltage changing linearly with current-time product) the amount of gas desorbed need not be linear with the amount of electricity passed, nor with the voltage change.

Experimental

To obtain measurable amounts of gas during overvoltage decay, inert electrodes of large surface are required. In the present study, the electrodes were sections of storage battery plates. The electrode for the hydrogen evolution studies consisted of pure metallic sponge lead, with a grid of a lead-calcium alloy (0.075% Ca by weight) and was 7.5 cm high, 3.6 cm wide, and 0.55 cm thick. The total weight of the electrode was 70.00 g. The electrode for the oxygen evolution studies was a PbO_2 sponge plate with a lead-calcium grid alloy (0.075% Ca by weight) and 4.0 cm high, 2.0 cm wide and 0.60 cm thick, weighing 44.02 g. It should be pointed out that PbO_2 is an excellent material for the study of oxygen overvoltage since it cannot be oxidized to a higher oxide and since it has a low electronic resistivity (*ca.* 10^{-4} ohm-cm).

The large-area electrode is shown in Fig. 1 at B. The electrolyte was 5*M* H_2SO_4 prepared from triply distilled water and purified acid. The electrolyte level (E) was adjusted to allow a minimum amount of dead space. Electrode potentials were measured against a sealed mercurous sulfate reference electrode in 5*M* H_2SO_4. The large-area electrodes were polarized by means of a polarizing electrode of pure lead (A). During polarization at constant current, both stopcocks in Fig. 1 were kept open. The electrodes were polarized at small current densities over prolonged time periods prior to the actual experiments on decay and build-up of overvoltage, to remove $PbSO_4$ from the surfaces.

Build-up of overvoltage at constant current and decay of overvoltage on open circuit were followed with an electrometer amplifier (General Radio Voltmeter Amplifier 1230-A) driving a high-speed recorder [Brown-Honeywell Model Y 153 X (19) VX 156] with a precision of 1 mv, current drains of less than 10^{-13} amp, and with a response of 1 mv in 20 msec. Constant current was obtained from an

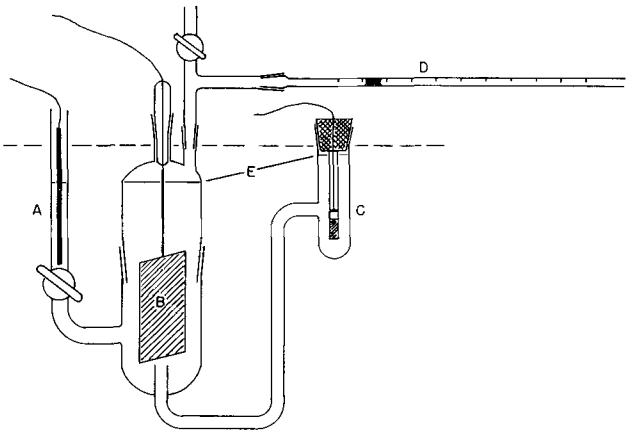

Fig. 1. Cell for overvoltage and gas desorption measurements. A, polarizing electrode; B, large area electrode under study; C, reference electrode; D, capillary; E, electrolyte level.

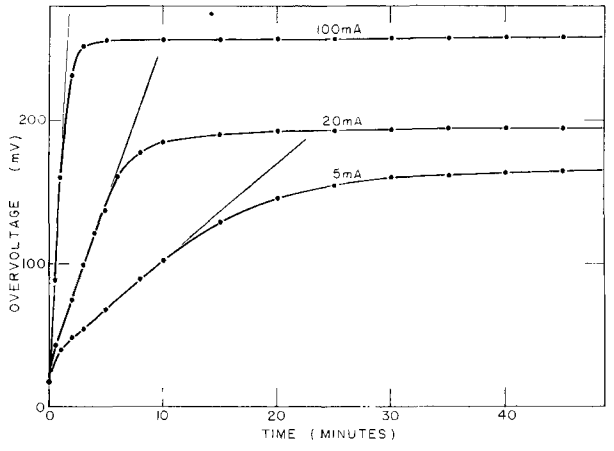

Fig. 2. Build-up of oxygen overvoltage on PbO_2 at constant currents, in 5.0M H_2SO_4 at 30°C.

electronic circuit described earlier (14). To minimize any changes in electrode surface, the electrode potentials were never allowed to reach reversible values. The reversible potential of the $PbO_2/PbSO_4$ electrode in 5*M* H_2SO_4 is 1.704 v vs. H_2 (or 1.111 v *vs.* Hg/Hg_2SO_4) in the same solution. During oxygen overvoltage decay the potential was allowed to reach a value of 1.717 v vs. H_2 (13 mv above the reversible $PbO_2/PbSO_4$ potential). At this point the charging current was switched on again and the constant current charging curves were obtained (Fig. 2). In this manner, specific adsorption effects due to SO_4^{--} ions were minimized. It is known that SO_4^{--} ions are adsorbed on PbO_2 between 1.70 and 2.0 v vs. H_2, and that above this potential adsorption does not change much (15). A similar procedure was followed during hydrogen overvoltage studies on metallic lead. The reversible potential of the $Pb/PbSO_4$ electrode −0.372 v vs. H_2 (or −0.965 v vs. Hg/Hg_2SO_4) in 5*M* H_2SO_4. During decay of overvoltage the potential was allowed to reach a value of −0.392 v vs. H_2 (20 mv more negative than the reversible potential). This decreased the effects of SO_4^{--} adsorption; however, these effects were nevertheless pronounced, which is understandable since the zero charge potential of metallic lead is at about −0.7 v vs. H_2 (16). Only at potentials negative to this value can the polarization be expected to be due predominantly

to accumulation of H^+ ions. In the case of the $PbO_2/PbSO_4$ electrode the zero charge potential in $5M$ H_2SO_4 is at +1.70 to +1.75 v vs. H_2 (17, 18). This indicates that SO_4^{--} adsorption is less noticeable for the oxygen overvoltage experiments. This was confirmed experimentally. Gas desorption from the electrodes was measured from the displacement of a dibutylphthalate drop in a 1 cm^3 Pyrex capillary, calibrated in units of 1/100 cm^3. After interruption of the polarizing current, the stopcocks were closed instantaneously and the position of the dibutylphthalate drop followed with time. Volume corrections for atmospheric pressure changes were made by simultaneously following a drop in a second capillary attached to a cell with the same dead-space, but without electrodes. The whole system was carefully thermostated to ± 0.05°C.

At the end of the measurements the electrodes were washed carefully with distilled water and ethyl alcohol and dried quickly in a vacuum desiccator containing $CaCl_2$. The surface areas of the electrodes were determined by standard BET techniques and yielded 35.2 m^2 for the PbO_2 electrode and 15.9 m^2 for the Pb electrode.

Overvoltage studies on porous electrodes can lead to different results from smooth electrodes due to the nonuniform current distribution over the true surface area (19). If the ohmic drop due to current flow in the pores cannot be neglected in comparison with the polarization at the interface, the porous electrode will show different polarization characteristics. According to Ksenzhek and Stender (20) the overvoltage η varies with distance x from the surface of the porous electrode toward the interior according to

$$\eta = 4b \tanh^{-1} [\exp (-x/\sqrt{b/2Si_o\rho}) \tan (\eta_o/4b)] \quad [6]$$

where i_o is the exchange current density, ρ the electrolyte resistivity, S the specific surface area of the porous electrode in cm^2/cm^3, and $b = RT/\alpha ZF$ (Tafel slope/2.303); η_o is the apparent overvoltage at the surface of the porous electrode, and η the true overvoltage at the reaction interface. The penetration depth x_e, where the true current density has fallen to $1/e$ of the apparent value, is $x_e = \sqrt{b/2Si_o\rho}$. For our experiments, with $b = 0.05$, $S = 50{,}000$ cm^2/cm^3, $i_o = 10^{-9}$ amp/cm^2, $\rho = 1$ ohm-cm, the penetration depth becomes 22.4 cm. This is 100 times the value of the half-thickness of our porous plates. This shows that pore-structure effects should be negligible in our experiments.

Results

The electrodes were polarized at constant current to a steady-state overvoltage. The corresponding Tafel plots are shown in Fig. 3. Here overvoltage is referred to the reversible $Pb/PbSO_4$ potential for hydrogen evolution, and to the reversible $PbO_2/PbSO_4$ potential for oxygen evolution. These are the stable electrode potentials the electrodes would actually reach on prolonged open circuit. The current densities refer to the total BET electrode surface. Hydrogen overvoltage increases slowly over many hours. If overvoltages are measured over short time intervals, the Tafel slope is 0.120 v i.e.,

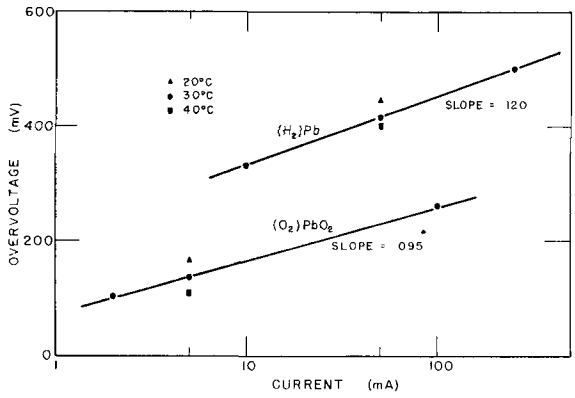

Fig. 3. Tafel curves for hydrogen overvoltage on lead and oxygen overvoltage on PbO_2. Overvoltage measured against reversible $Pb/PbSO_4$ and $PbO_2/PbSO_4$ electrodes, respectively, in 5.0M H_2SO_4 at 20°, 30°, and 40°C.

with $Z_i = 1$, $\gamma = 0$, and $\alpha = \frac{1}{2}$ (Fig. 3). The change in overvoltage from one current density to another is then simply due to accumulation of reacting species only, according to the theory of Rüetschi (21). If, on the other hand, the Tafel curve is taken slowly, allowing longer time periods for each current, the slope increases to 0.160 v in the voltage region of Fig. 3. This means that now slowly adsorbing or desorbing foreign species are contributing to changes in the charge of the double layer (desorption of SO_4^{--} ions), or that the reacting species have a smaller specific capacity (larger distance to the electrode surface) such that for a given number of reacting species in the interface, the electrode potential is higher than before. From the slope 0.160 v one obtains $\alpha = 0.37$ and $\gamma = 0.25$. The latter is the fraction of variation of polarization attributable to desorption of SO_4^{--} or changes in specific capacities of reacting protons (21).

In Fig. 3, oxygen overvoltage has a Tafel slope of about 0.095 v, depending again somewhat on the rate of taking the curve. However, adsorption effects are smaller than for hydrogen on lead, which can be explained on the basis of the relative position of the zero charge potentials. With $Z_i = 2$ one obtains from the Tafel slope $\alpha = 0.32$ and $\gamma = 0.37$. The latter fraction of voltage change from one current to another, is attributable to adsorption or association of foreign species, such as SO_i^{--} (along with the reacting species O^{--}), or changes in specific capacity of reacting species (21). Considering the large surface areas of the electrodes the true current densities are extremely low, in the order of 10^{-9} to 10^{-8} amp/cm^2. However, the exchange currents for hydrogen and oxygen evolution on these electrodes are in the order of 10^{-12} and 10^{-10} amp/cm^2, and therefore the experiments fall into the Tafel region. Measurements of the gas evolved at steady state showed that 97% or better of the current went into gas production, and therefore, no other charging reactions interfered.

Figure 2 shows oxygen overvoltage build-up at constant current. From the slopes of the linear portions one obtains a capacity of 44 farads for the double layer. With a BET surface of 35.2 m^2, this is 125 $\mu F/cm^2$, a relatively high value, which would be even higher if only part of the surface were elec-

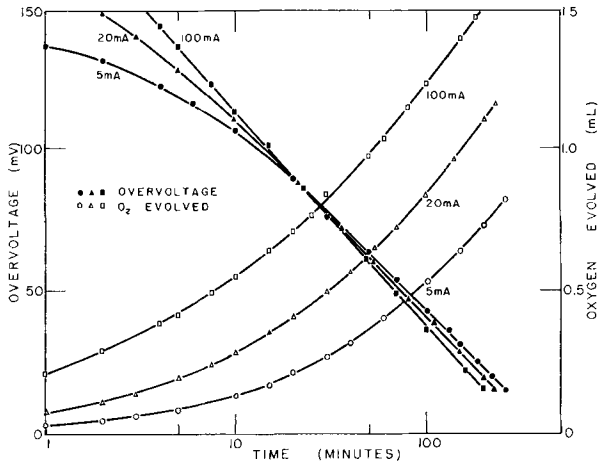

Fig. 4. Decay of oxygen overvoltage on PbO_2 for various prepolarizing currents and oxygen gas desorbed; temperature 30°C.

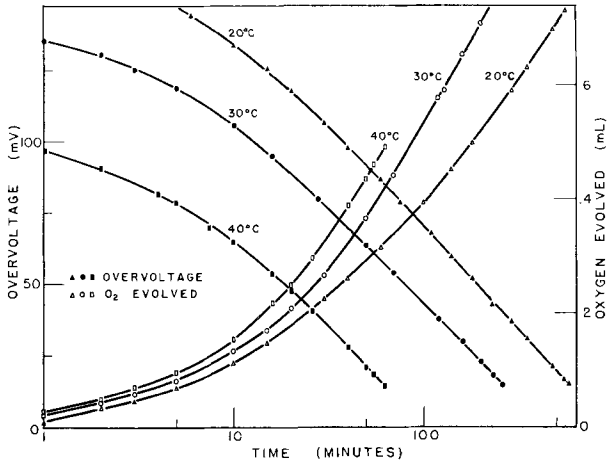

Fig. 5. Decay of oxygen overvoltage on PbO_2 at various temperatures and oxygen gas desorbed. Prepolarizing current 5 ma.

trochemically active. The high value for the capacity indicates strong adsorption of the reacting species. There is a slight bend in the initial portion of the charging curve indicating a small variation in capacity due to a different initial charge distribution.

Figures 4 and 5 show oxygen overvoltage decay on open circuit, and simultaneous gas desorption. Oxygen overvoltage decreases linearly with the logarithm of time, indicating a fairly constant capacity during decay. The decay slope is almost independent of temperature and of prepolarizing current. Figure 4 indicates that at the same temperature (30°C) a given voltage is reached in the same time, independently of prepolarizing current. According to Fig. 5 the desorption rate increases with temperature. In Fig. 6 the logarithm of the gas evolution rate in cm^3/min is plotted against $1/T$ for given overvoltage values. The slopes of the straight lines tend to become less steep with increasing overvoltage. If the rate of O_2 evolution could be set equal to the instantaneous internal current, then the slopes would be, according to Eq. [1], a measure for the term $-\{\alpha Z_i eV - \alpha Z_i eV_f + \epsilon^* - \epsilon^\circ\}/2.303\ k$. A plot of this term against overvoltage should then yield a straight line with a slope of $-\alpha Z_i e/2.303\ k$ $= 5010\ \alpha Z_i$. One could then determine the value of αZ_i by this method, but the accuracy of the measurements is not sufficient to obtain an exact value, although one obtains the correct order of magnitude ($\alpha Z_i = 1 \pm 2$). However, the instantaneous internal current cannot be set equal to the instantaneous gas evolution rate, at 2 electrons per H_2 and 4 electrons per O_2. The slope of the oxygen overvoltage decay curves in Fig. 4 and 5 is about 0.078 v, which is fairly close to the value of the Tafel slope. With $Z_i = 2$ this gives $\alpha = 0.38$ and $\gamma = 0.23$.

In Fig. 7 the results of Fig. 4 have been correlated in such a manner that the total oxygen evolved has been plotted against overvoltage. A voltage of +13 mv above the reversible $PbO_2/PbSO_4$ potential has been chosen arbitrarily for the endpoint of decay. It seems reasonable to assume that at this low value the same state of the electrode surface is reached, independently of prepolarizing current.

Since 1 cm^3 of O_2 at 700 mm Hg and 30°C corresponds to 15.5 amp sec, one can calculate how the voltage should decay, at 2 electrons per oxygen atom, if only a discharge of the double layer capacity of 44 farads were involved. One cm^3 of O_2 evolved should then decrease the potential by 350 mv. In Fig. 7, this theoretical slope has been plotted, marked with 2*e*. Other slopes, corresponding to 1*e* and 0.5*e* per oxygen atom are also indicated. It is

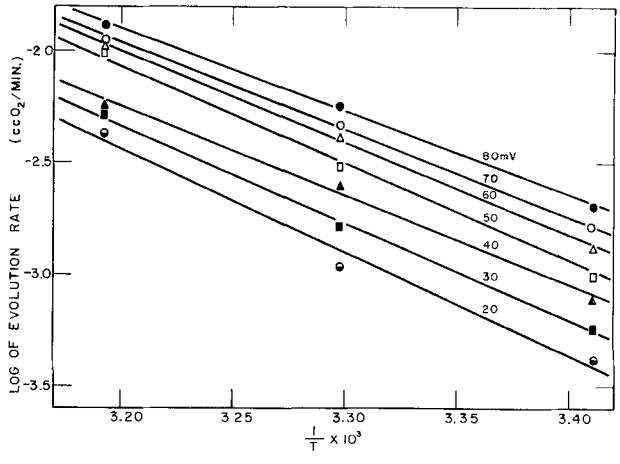

Fig. 6. Logarithm of oxygen gas evolution rates on PbO_2 on open circuit (in cm^3/min) as a function of $1/T$ for various fixed values of overvoltage.

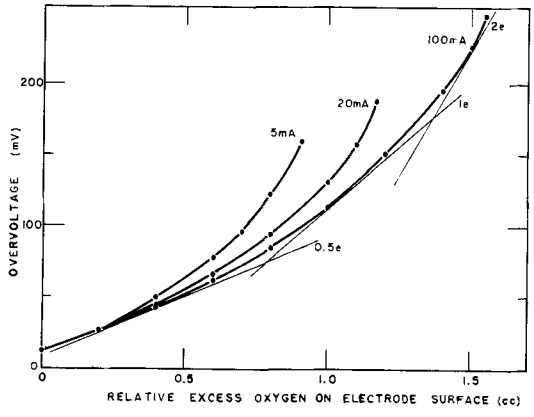

Fig. 7. Oxygen overvoltage decay on PbO_2 as a function of oxygen gas desorbed from the electrode at 30°C.

Table I. Observations on PbO_2 anode

Prepolarizing current, ma	Overvoltage, mv vs. $PbO_2/PbSO_4$	Oxygen atoms desorbed per BET cm^2
100	242	2.12×10^{14}
20	190	1.61×10^{14}
5	158	0.91×10^{14}

interesting to note that for the initial portions of overvoltage decay, the slope approaches the value for 2*e*. However, for later portions, the voltage decay is much smaller, the difference being a measure for the amount of oxygen already partially discharged. A slope of 2*e* could indicate the discharge of 2 OH^- or O^{--} in the outer double layer.

There is another important result in Fig 7. The slope of the plot of the steady-state overvoltage against the total amount of oxygen desorbed gives a straight line. The slope of this line could be interpreted theoretically by postulating the presence of oxygen species with an average charge of about 1*e* per atom in the double layer, although such an interpretation is not rigorous. If the total amount of oxygen desorbed is related to the BET surface of the electrode, one obtains the figures of Table I (1 cm^3 O_2 at 760 mm Hg, 30°C contains 4.84 x 10^{19} atoms).

Build-up of hydrogen overvoltage on lead at constant current is shown in Fig. 8. From the slope of the linear portion one obtains a capacity of 1.67 farad. With a BET surface of 15.9 m^2, this is 10.5 $\mu F/cm^2$, a small value, indicating that the charges are at considerable distance from the surface. Since the charging was done at relatively low rates, this capacity does probably include some changes in SO_4^{--} adsorption and adsorption capacities due to partially discharged protons.

Figures 9 and 10 give hydrogen overvoltage decay curves and gas evolution curves. Decay of hydrogen overvoltage is nearly linear with the logarithm of time, indicating a nearly constant capacity. The decay slope is almost independent of temperature and prepolarizing current. The temperature has a smaller effect on the rate of desorption than for oxygen. In Fig. 11, the logarithm of the hydrogen evolution rate (cm^3/min) is plotted against 1/*T*. The

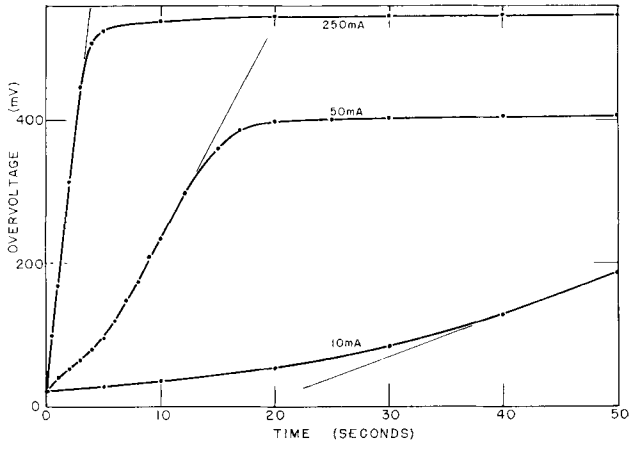

Fig. 8. Build-up of hydrogen overvoltage on Pb at constant currents. Electrolyte 5.00M H_2SO_4 at 30°C.

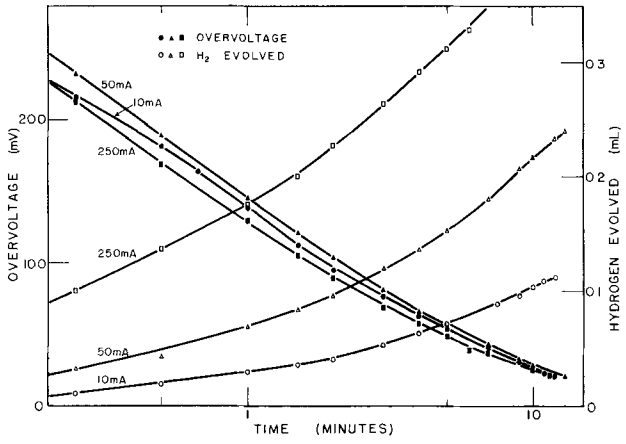

Fig. 9. Decay of hydrogen overvoltage on Pb and hydrogen gas desorbed, for various prepolarizing currents at 30°C.

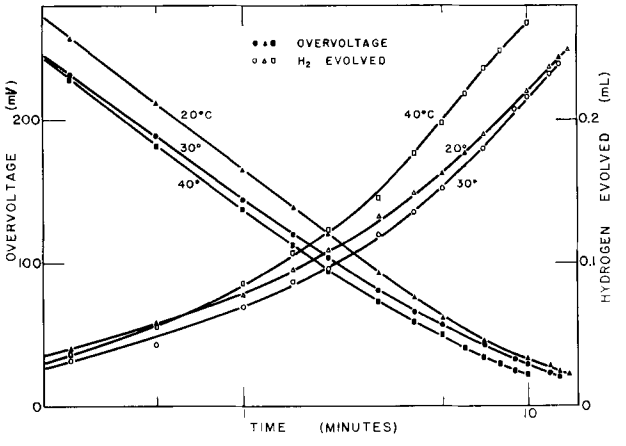

Fig. 10. Decay of hydrogen overvoltage on Pb and hydrogen gas desorbed at various temperatures; prepolarizing current 50 ma.

slopes of the lines are nearly equal but tend to decrease with increasing overvoltage. The variation in the slopes would be a measure for αZ_i if the instantaneous current were equal the rate of gas evolution, which is not exactly the case. One can derive however the right order of magnitude ($\alpha Z_i = 0.5 \pm 1$), although the method is not precise.

The slope of the hydrogen overvoltage decay curves in Fig. 9 and 10 averages 0.145, which is close to the slope of the Tafel curve, when it is taken slowly. The value 0.145 gives with $Z_i = 1$ values for $\alpha = 0.41$ and $\gamma = 0.17$. This shows that the variation in polarization due to foreign species (e.g., adsorption of SO_4^{--} during decay) or the influence of partially discharged hydrogen is not excessive, according to Rüetschi's theory (21).

In Fig. 12 the total amount of H_2 desorbed after interruption of current (to a potential 20 mv more negative than the $Pb/PbSO_4$ electrode) was plotted against overvoltage decay. At the end of decay, the same state of the electrode is reached, independently of prepolarizing current. Since 1 cm^3 of H_2 at 760 mm Hg and 30°C corresponds to 7.75 amp sec at 1*e* per H, one can calculate that 1 cm^3 of H_2 should discharge 1.67 farad by 4.65 v. This theoretical slope between the hydrogen evolved and overvoltage decay is shown in Fig. 12 as a line marked with 1*e*. This is the theoretical decay of the voltage if each

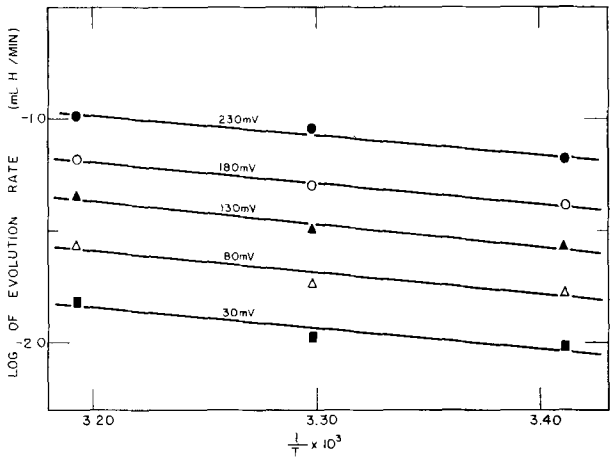

Fig. 11. Logarithm of gas evolution rates on Pb on open circuit (in cm^3/min) as a function of 1/T for various fixed values of overvoltage.

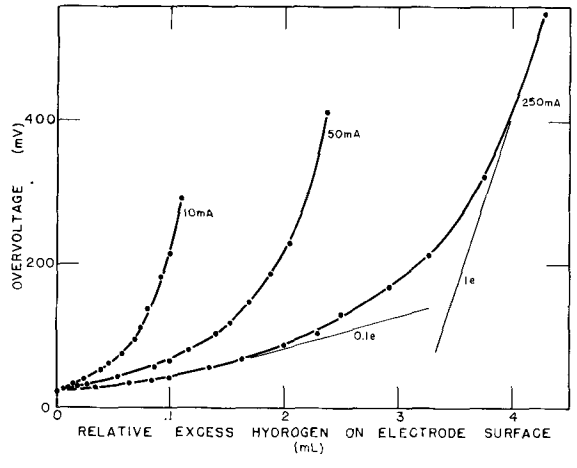

Fig. 12. Hydrogen overvoltage decay on Pb as a function of hydrogen gas desorbed from the electrode at 30°C.

hydrogen atom desorbed were to originate from a proton in a double layer with a capacity of 10.5 $\mu F/cm^2$. For the initial portion of the decay, the voltage decreases according to this theoretical slope. However, for later portions, the potential decreases much less. The difference between the theoretical slope of 1*e* and the experimental values is a measure of the already partially discharged hydrogen in the surface (overlap of H^+ and electron cloud). This hydrogen contributes to the charge of the double layer only by the heteropolarity of the adsorption bonds. Toward the end of the decay, the potential is determined largely by the adsorption of SO_4^{--} ions, as in the case of the oxygen overvoltage SO_4^{--} become the potential determining species at the reversible potential.[3]

During decay of H_2 and O_2 overvoltages, the potentials approach asymptotically the reversible $Pb/PbSO_4$ and $PbO_2/PbSO_4$ potentials, respectively, while H_2 and O_2 evolution are continuing at a small but steady rate since the $Pb/PbSO_4$ potential is negative to the potential of the hydrogen electrode and the $PbO_2/PbSO_4$ potential positive to the oxygen electrode (self-discharge).

[3] Note that the diffusion of adsorbed gas along the grain surfaces of the porous electrodes to the locations of bubble formation might be interfering with the simple interpretation of the results given in this paper.

Table II. Observations on Pb cathode

Current, ma	Overvoltage, mv, vs. $Pb/PbSO_4$	Hydrogen atoms desorbed per BET cm^2
250	553	13.0×10^{13}
50	410	7.2×10^{13}
10	293	3.3×10^{13}

The steady-state overvoltage prior to interruption of current varies, according to Fig. 12, linearly with the total amount of hydrogen evolved. The slope of this line corresponds roughly with the slope of a line calculated for a theoretical discharge of a double layer of 10.5 $\mu F/cm^2$ at 0.5 electron for each hydrogen atom desorbed. This could be interpreted as resulting from a mixture of adsorbed H atoms and protons in the double layer, or the presence of H_2^+. The significant fact is that more hydrogen is desorbed than one could expect from the discharge of a purely ionic type double layer, indicating the presence of partially discharged reacting species.

The total amount of H_2 evolved from the electrode during hydrogen overvoltage decay, down to a potential 20 mv more negative than the $Pb/PbSO_4$ potential, has been correlated to the BET surface. Since 1 cm^3 of H_2 at 760 mm Hg at 30°C contains 4.84 x 10^{19} atoms, the figures of Table II were obtained.

Basically, the same laws apply both to hydrogen and oxygen overvoltage. In either case, the electrode potential (overvoltage) seems to be determined essentially by the number of adsorbed activated species at the interface, these species being present in various states of discharge, and by adsorbed foreign inert species, not taking part directly in the electrode reaction (21). Desorption follows a Becker-Zeldovich equation, which is coherent with a Temkin isotherm (13).

Acknowledgments

The authors are indebted to W. J. Burgess and M. L. Block of the Physical Chemistry Division for assistance in BET measurements, and to C. G. Grimes, Director of Research of the Electric Storage Battery Company, for permission to publish this investigation.

Manuscript received June 8, 1959. This paper was prepared for delivery before the Philadelphia Meeting, May 3-7, 1959.

Any discussion of this paper will appear in a Discussion Section to be published in the December 1960 JOURNAL.

REFERENCES

1. E. Baars, *Marburger Sitzungsberichte*, **63**, 214 (1928).
2. A. Frumkin and S. Slygin, *Acta Physicochim., URSS*, **5**, 819 (1936).
3. F. P. Bowden and K. E. W. Grew, *Discussion Faraday Soc.*, **1**, 91 (1947).
4. L. M. Elina, T. I. Borisova, and T. I. Zalkind, *Zhur. Fiz. Khim.*, **28**, 785 (1954).
5. M. Breiter, C. A. Knorr, and W. Volkl, *Z. Elektrochem.*, **59**, 681 (1955).
6. P. Rüetschi, R. T. Angstadt, and B. D. Cahan, *This Journal*, **106**, 547 (1959).
7. G. Armstrong and J. A. Butler, *Trans. Faraday Soc.*, **29**, 1261 (1933).
8. A. Frumkin, *Acta Physicochim. URSS*, **18**, 23 (1943).

9. W. R. Busing and W. Kauzmann, *J. Chem. Phys.*, **20**, 1129 (1952).
10. J. O'M. Bockris and A. K. M. Shamshul Huq, *Proc. Roy. Soc.*, **A237**, 277 (1956).
11. A. L. Pitman and G. W. Work, NRL Reports No. 4844, 4845, 4852, 5031 (1956-1957), Naval Research Laboratory, Washington, D. C.
12. W. Gutt, and D. J. G. Ives, *Proc. Chem. Soc.*, p. 344, Dec. 1957.
13. P. Rüetschi, *This Journal*, **106**, 819 (1959).
14. P. Rüetschi and B. D. Cahan, *ibid.*, **104**, 406 (1957).
15. I. G. Kiseleva and B. N. Kabanov, *Doklady Akad. Nauk SSSR*, **108**, 864 (1956).
16. Y. M. Kolotyrkin and N. Y. Bune, *Zhur. Fiz. Khim.*, **29**, 435 (1955).
17. B. N. Kabanov, I. G. Kiseleva, and D. I. Leikis, *Doklady Akad. Nauk, SSSR*, **99**, 805 (1954).
18. D. I. Leikis and E. K. Venstrem, *ibid.*, **112**, 97 (1957).
19. A. N. Frumkin, *Zhur. Fiz. Khim*, **23**, 1477 (1949).
20. O. S. Ksenzhek and V. V. Stender, *Doklady Akad. Nauk SSSR*, **107**, 280 (1956).
21. P. Rüetschi, *This Journal*, Under consideration.

A Study of the Factors Affecting the Electrical Characteristics of Sintered Tantalum Anodes

G. L. Martin,[1] C. J. B. Fincham, and E. E. Chadsey, Jr.

National Research Corporation, Cambridge, Massachusetts

ABSTRACT

Measurements were made of the electrical characteristics (d-c leakage, capacitance, and equivalent series resistance) of anodically oxidized sintered tantalum pellets, which were made from three tantalum powders of different purities, particle shapes, and particle size distributions. The apparent densities of the pellets after sintering were also measured. The effects of varying the pressed density of the pellets and the time and temperature of sintering were studied systematically, and the results were correlated in the form of empirical relationships.

A tantalum electrolytic capacitor is composed of three basic parts: the tantalum anode, the tantalum oxide dielectric, and the electrolyte which acts as the cathode.

The tantalum anode may be foil, wire, or a sintered porous pellet made from powder. The sintered pellet can give the highest surface area per unit volume and hence the highest capacitance per unit volume of the three types. The tantalum oxide dielectric is formed by anodic oxidation of the tantalum anode. The cathode is an electrolyte, which may be either liquid (e.g., aqueous solutions of sulfuric or phosphoric acids) or solid (e.g., manganese dioxide). References (1-3), for example, give more detailed descriptions of the construction and operation of tantalum capacitors.

This paper reports a study of some of the factors, especially sintering conditions, which affect the electrical properties of porous sintered tantalum anodes and their oxide films. The electrical properties studied were d-c leakage, which is defined as the current which flows when a specified d-c voltage is impressed across the anode and its oxide film; the capacitance, which varies with the surface area and thickness of the oxide film; and the equivalent series resistance (*ESR*), which was calculated from the measured dissipation factor (*D*) using the relationship

$$ESR = \frac{D}{2\pi f C}$$

where C is the capacitance (in farads), f is the frequency of the a-c signal (in cps), and *ESR* is given in ohms.

[1] Present address: Department of Chemistry, University of Alabama, University, Alabama.

Experimental Techniques

Pressing.—The tantalum powder was pressed into cylindrical pellets of 0.25 in. diameter in a floating-body steel die. No lubricant or binder was used. The pellets all weighed 1.8 g. Annealed 10-mil tantalum lead wires were pressed into the pellets.

Sintering.—The pressed pellets were sintered inside a closed tantalum can, in a modified NRC 2904 resistance-heated vacuum furnace. Temperature was measured with a tungsten-molybdenum thermocouple with the hot junction resting on top of the tantalum can. Temperatures measured in this way were probably lower than the true temperatures of the pellets in the can. The furnace was pumped, through a cold trap, to a pressure of about 5×10^{-6} mm Hg (and a leak rate of less than 10^{-3} mm Hg/min into a volume of about 40 liters) before the power was turned on. At the end of a run, the charge was allowed to cool to about 200°C under vacuum; then argon was admitted. The furnace was not opened to air until the charge temperature was less than 100°C.

Electrical testing.—The sintered pellets were anodized at a constant current of 35 ma/g up to 200 v, in an 0.01% phosphoric acid solution at 92°C. They were held at 200 v for 2 hr. The maximum voltage determined the thickness of the oxide film and hence its capacitance per unit area. At 200 v the thickness of the oxide film is about 0.3 μ (4).

The anodized pellets were washed for ½ hr in de-ionized water and dried in air overnight at room temperature.

Measurements of d-c leakage, capacitance, and dissipation factor were done using 10% phosphoric acid at room temperature as electrolyte.

Direct current leakage was measured after 2 min at 140 v. Capacitance and dissipation factor were measured at 120 cps with a 0.5 v a-c signal, using a modified General Radio 650-A impedance bridge. The signal source was a Hewlett Packard 205 AG audio signal generator, and a Hewlett Packard 400D vacuum tube voltmeter was used as the null detector.

Sinter densities.—The apparent densities of the pellets after sintering were determined by measuring the diameters and lengths of the pellet at several places on the pellet with a pointed end micrometer.

This method was found to give results agreeing well (within 1%) with measurements made by coating the pellets with nail polish and weighing them in air and water.

Materials

Three different tantalum powders were selected for study, and were given the designations E-11, SG-73R, and L-533. As discussed below, there were considerable differences between these powders in chemical purity, particle size distribution, and particle shape.

Chemical purity.—The analyses of the three powders are given in Table I. The impurities showing the widest differences in levels between the powders are O, C, N, Fe, Cr, Si, and Na. In general, SG-73R was the most pure, and L-533 the least pure, of the three powders.

Table I. Analyses of tantalum powders

Impurity	Impurity content, ppm		
	E-11	SG-73R	L-533
O	720	480	930
H	10	10	50
C	25	25	120
N	25	30	750
Fe	100	87	460
Ni	<100	52	25
Cr	61	110	<10
Si	560	81	780
Al	<50	<50	<50
Nb	220	120	140
Na	1500	30	—
Cu	<50	<50	<50
Ti	<50	<10	40
Zr	<50	<50	<50
Mo	<100	<25	<25

< Means below the limit of detection by method used.

Table II. Particle size distribution

Screen mesh	Particle size, μ	Weight per cent in fraction		
		E-11	SG-73R	L-533
+60	>250	—	—	8.6
−60+100	250-150	—	—	8.0
−100+200	100-74	—	—	16.5
−200+325	74-44	12.7	2.5	13.2
−325				
	44-36	1.7	1.0	0.5
	36-30	6.1	4.1	0.3
	30-25	10.5	10.4	1.9
	25-20	14.0	15.7	4.2
	20-15	17.4	24.5	7.4
	15-10	19.7	27.6	18.6
	10-5	13.7	10.6	17.4
	5-0	0.6	0.9	2.0
	Totals	96.4	97.3	98.6

Particle size measurements below 44μ were done using a Roller subsieve particle size analyzer.

Particle size distributions.—These are shown in Table II. Measurements of particle size above 44 μ were done by screen analysis, and below 44 μ by using a Roller subsieve particle size analyzer (5). L-533 differed from the other two powders in having a considerable amount of material in the greater than 74 μ range. In general SG-73R had the lowest average particle size, and L-533 the highest, of the three powders. However, in view of the particle shapes (see below) of L-533, the measurements of particle size for this material are of doubtful significance.

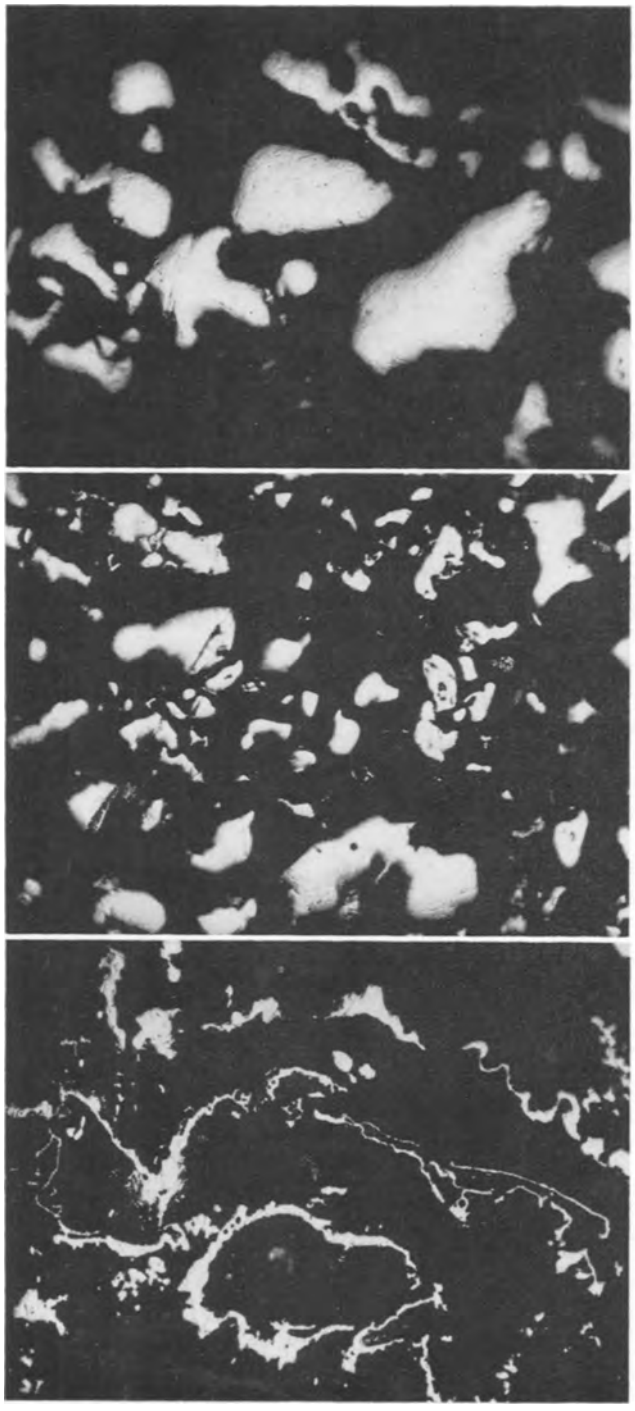

Fig. 1. Particle shape. Photomicrographs of powder particles mounted in plastic, sectioned, and polished. Top, E-11; middle, SG-73R; bottom, L-533.

Table III. Electrical results, sample E-11

Temp, °C	Time, min	D_g = 8.5				D_g = 9.5				D_g = 10.5				D_g = 11.5			
		L	*C*	*ESR*	*L/C*	*L*	*C*	*ESR*	*L/C*	*L*	*C*	*ESR*	*L/C*	*L*	*C*	*ESR*	*L/C*
	30	1.0*	12.41*	6*	0.08	0.9	11.75	10	0.08	0.8	10.72	12	0.07	0.8	9.82	15	0.08
1750	90	1.0*	10.99*	8*	0.09	1.0	10.41	17	0.10	0.8	9.60	21	0.08	0.9	8.51	30	0.11
	180	—	—	—	—	0.7	9.57	20	0.07	0.6	8.43	22	0.07	0.6	7.50	30	0.08
	30	1.0**	10.80**	8**	0.09	0.8	10.28	13	0.08	0.8	9.62	13	0.08	0.9	8.63	21	0.10
1900	90	1.0	10.16	9	0.10	0.7	8.95	12	0.08	0.8	8.13	18	0.10	0.7	7.15	24	0.10
	180	—	—	—	—	0.6	8.03	14	0.08	0.8	7.27	19	0.11	0.7	6.24	31	0.11
	30	1.1	9.84	9	0.11	0.8	9.67	12	0.08	0.7	8.86	13	0.08	0.7	7.85	23	0.09
2050	90	1.0	8.13	10	0.12	0.8	7.62	15	0.11	0.7	6.91	22	0.10	0.6	6.01	31	0.10
	180	—	—	—	—	0.5	6.68	26	0.07	0.5	6.07	32	0.08	0.4	5.03	45	0.08

L is d-c leakage at 140 v, in μa/g; *C*, capacitance at 120 cps, in microfarad/g (200 v formation); *ESR*, equivalent series resistance, in ohm/pellet; D_g, green density, in g/cc.
* Indicates one "wild" pellet out of six.
** Indicates two "wild" pellets out of six.

$$C = 3.75 \times 10^4/T - 3.50 \log (t + 6) - 32.47/(16.6\text{-}D_g) + 3.20 \qquad (T \text{ in } °K)$$

$$L/C = 0.09 \pm 0.02$$

Particle shape.—Samples of each of the powders were mounted in plastic, sectioned, and polished. Figure 1 shows photomicrographs of the sectioned particles, at a magnification of 500 x before reproduction. The particle shapes of E-11 and SG-73R were somewhat similar, in that the particles tended to be solid and regular in shape. L-533 had several different particle shapes, including hollow hemispheres and "strings." The particle size of such irregular shapes is not measured accurately by screening or by air elutriation in the Roller apparatus.

Results

The results of this study were obtained using the experimental techniques described above. In particular, the electrolyte used for measurement of leakage, capacitance, and equivalent series resistance was always 10% phosphoric acid. However, other work done in these laboratories has shown that, when liquid electrolytes are used, to a first approximation leakage and capacitance are independent of electrolyte. Equivalent series resistance is markedly dependent on the electrolyte, since part of the series resistance is due to the ohmic resistance of the electrolyte in the pores of the anode. Equivalent series resistance therefore varies with the specific resistivity of the electrolyte. The specific resistivity of 10% phosphoric acid at room temperature is about 15 ohm-cm (6, 7).

E-11.—Pellets pressed to three different green densities (9.5, 10.5, and 11.5 g/cc) were sintered at three different temperatures (1750°, 1900°, and 2050°C) for three different times (30, 90, and 180 min).

The electrical results obtained on these pellets are shown in Table III, together with results for a green density of 8.5 g/cc (see below). Each result is the average from four pellets, two from one sinter run and the other two from a second sinter run. The table shows the leakage per gram (*L*, in microamperes), the capacitance per gram (*C*, in microfarads), the equivalent series resistance per 1.8 g pellet (ESR, in ohms), and the leakage divided by the capacitance (*L/C*, in microamperes per microfarad).

It can be seen that both leakage and capacitance decreased as the green density and time and temperature of sintering increased, the over-all change for the range of conditions studied being about a factor of two. As the values of *L/C* show, *L* and *C* changed at the same rate, so that *L/C* was constant at 0.09 ± 0.02 μa/microfarad over the range of conditions.

It was found that the relationship between capacitance and sintering conditions could be expressed in the form of an empirical equation, with independent terms in green density, time, and temperature. This equation is

$$C = 3.75 \times 10^4/T - 3.50 \log (t+6) - 32.47/(16.6\text{-}D_g) + 3.20$$

where *T* is temperature, in °K, *t*, time, in minutes, D_g green density, in g/cc, and *C*, capacitance, in microfarads/g. The average difference between the value of *C* given by this equation and the measured value of C is 1.5%. The maximum difference is 4.9%. These differences are well within experimental error. The expression $(t+6)$ occurs in the term for time because *t* was measured as time at the designated temperature. The additional 6 min is an estimate of the extra effective time due to heating and cooling periods. The density of tantalum metal is 16.6 g/cc, and this number appears in the term for green density.

The equivalent series resistance results showed some scatter which tends to obscure the trends. However, it is clear that *ESR* increased markedly with increasing green density, and also to some extent with time. The effect of temperature is uncertain.

After the results described above were obtained and the capacitance equation derived, the study of E-11 was extended to a lower green density of 8.5 g/cc, at the same temperatures, but for two times only (30 and 90 min). The results are shown in Table III. The agreement between the measured capacitance and the capacitance predicted by the previously derived equation is excellent, the largest difference being 6%. Values of *L/C* also agree with

Table IV. Sinter densities and capacitance per unit volume, sample E-11

Temp, °C	Time, min	Green density, g/cc: 8.5 D_s	8.5 Cvol.	9.5 D_s	9.5 Cvol.	10.5 D_s	10.5 Cvol.	11.5 D_s	11.5 Cvol.
	30	8.98	111	9.72	114	10.54	113	11.41	112
1750	90	9.60	106	10.06	105	10.70	103	11.69	99
	180	—	—	10.34	99	11.04	93	11.93	89
	30	9.53	103	10.05	103	10.80	104	11.54	100
1900	90	—	—	10.59	95	11.34	92	12.03	86
	180	—	—	10.77	86	11.46	83	12.27	77
	30	9.75	96	10.28	99	10.96	97	11.78	92
2050	90	10.46	85	11.05	84	11.73	81	12.20	73
	180	—	—	11.50	77	11.92	72	12.77	64

D_s is sinter density (g/cc) and Cvol. is capacitance per unit volume (microfarads/cc).

those previously found; however, a different kind of result was obtained with a few pellets sintered at the less severe sintering conditions. One, or at most two, of six pellets sintered under the same conditions started to "gas" violently during anodization, and on measurement were found to have leakages of the order of 400 μa/g. These values were termed "wild" leakages and are not included in the averages in the table. The reasons for this phenomenon are not clear, but it is associated with lower green densities and lower times and temperatures of sintering (see also the results for L-533 below).

The results for equivalent series resistance appeared to follow the same trends as those previously obtained.

The apparent densities of the pellets after sintering were measured for the pellets studied electrically. Results are shown in Table IV, together with the values for capacitance per unit volume, which were obtained by multiplying the capacitance per gram by the sinter density in g/cc. For practical purposes, in the manufacture of capacitors, the capacitance per unit volume is the important parameter, rather than the capacitance per unit weight.

The sinter density increased with time and temperature of sintering and also with green density, but the difference between green density and sinter density became less as the green density increased. The capacitance per unit volume was almost independent of green density, except at the highest green density (11.5), where there was some decrease. The capacitance per unit volume decreased with increasing time and temperature of sintering.

SG-73R.—A similar study to that made on E-11 was made with SG-73R, except that the data were not as complete and sinter densities were not measured.

The electrical results are shown in Table V, where the values are the averages from six pellets.

The trends of leakage and capacitance were very similar to those for E-11, and L/C was again found to be constant, although the value of 0.07 ± 0.01 μa/microfarad for SG-73R was slightly lower than that for E-11 (0.09 ± 0.02). The capacitance values could be expressed by an equation, in terms of green density, time, and temperature, of the same form as that used for E-11. The average difference between the values of capacitance given by this equation and the measured values was 2%. The maximum difference was 5.1%. The equation is $C = 4.83 \times 10^4/T - 3.72 \log (t + 6) - 46.56/(16.6\text{-}D_g) + 1.19$.

The measurements of equivalent series resistance showed less scatter than that found for E-11, partly because experimental technique had been improved. The equivalent series resistance increased with increasing green density and time, and slightly with increasing temperature.

L-533.—The study of L-533 was made over a range of green densities (7.0 to 10.5 g/cc) extending lower than that used for E-11. Only times of 30

Table V. Electrical results, sample SG-73R

Temp, °C	Time, min	D_g = 8.5 L	C	ESR	L/C	D_g = 9.5 L	C	ESR	L/C	D_g = 10.5 L	C	ESR	L/C	D_g = 11.5 L	C	ESR	L/C
1750	90	1.0	12.05	8.3	0.08	0.9	11.17	8.7	0.08	0.7	10.02	12.1	0.07	—	—	—	—
	30	0.9	11.47	7.6	0.08	0.85	10.75	9.1	0.08	—	—	—	—	—	—	—	—
1900	90	0.8	10.59	8.2	0.08	0.7	9.37	10.2	0.07	0.6	8.45	14.1	0.07	0.5	7.12	23.8	0.07
	180	0.6	9.24	9.6	0.07	0.55	8.38	12.3	0.07	—	—	—	—	—	—	—	—
	30	0.8	10.67	9.1	0.08	0.7	10.18	11.0	0.07	0.6	8.96	12.5	0.07	—	—	—	—
2050	90	0.6	8.60	9.4	0.07	0.55	8.02	12.0	0.07	—	—	—	—	—	—	—	—
	180	0.5	7.96	10.1	0.06	0.4	6.89	15.0	0.06	—	—	—	—	—	—	—	—

L is d-c leakage at 140 v, in μa/g; C, measured capacitance at 120 c ps, in microfarad/g (200-v formation); ESR, equivalent series resistance, in ohm/pellet; D_g, green density, in g/cc.

$$C = 4.83 \times 10^4/T - 3.72 \log (t + 6) - 46.56/(16.6D_g) + 1.19 \quad (T \text{ in } °K)$$

$$L/C = 0.07 \pm 0.01$$

Table VI. Electrical results, sample L-533

Temp, °C	Time, min	D_g = 7.0				D_g = 8.0				D_g = 9.5				D_g = 10.5			
		L	*C*	*ESR*	*L/C*	*L*	*C*	*ESR*	*L/C*	*L*	*C*	*ESR*	*L/G*	*L*	*C*	*ESR*	*L/C*
1750	90	—	—	—	—	1.7*	14.78	10	0.12	1.3	11.88	17	0.11	1.2	9.54	29	0.13
1900	30	—	—	—	—	1.6*	15.66	11	0.10	—	—	—	—	—	—	—	—
	90	—	—	—	—	1.4	11.59	13	0.12	1.3	9.53	24	0.14	3.1	7.77	41	0.40
2050	30	2.5*	14.02	12	0.18	1.7	12.36	12	0.14	1.5	10.36	25	0.14	—	—	—	—
	90	—	—	—	—	1.2	9.75	15	0.12	1.0	7.66	35	0.13	6.4	5.66	63	1.13

L is d-c leakage at 140 v, in μa/g; *C*, capacitance at 120 cps, in microfarad/g (200-v formation); *ESR*, equivalent series resistance, in ohm/pellet; D_g, green density, in g/cc.
* One or more pellets had "wild" leakages.
$C = 8.04 \times 10^4/T - 7.34 \log (t + 6) - 94.0/(16.6\text{-}D_g) + 0.40$ (T in° K)
L/C not constant.

and 90 min were used. Electrical results are shown in Table VI, each number being the average from four pellets.

As with E-11 and SG-73R, the capacitance decreased with increasing green density, time, and temperature. However, leakage did not follow the same trend over the whole range of conditions, so that while *L/C* was essentially constant at 0.12 ± 0.02 μa/microfarad for green densities of 8.0 and 9.5, there was a definite increase in *L/C* at a green density of 10.5 and higher temperatures. There were also pellets showing "wild" leakage at the lower green densities and times and temperatures. These were not included in the averages.

The capacitance measurements fitted the same form of equation relating them with green density, time, and temperature as that found to apply for E-11 and SG-73R. The equation is

$$C = 8.04 \times 10^4/T - 7.34 \log (t+6) - 94.0/(16.6\text{-}D_g) + 0.40$$

This equation does not fit the data quite as well as did the equations for E-11 and SG-73R, the average and maximum differences between the measured and calculated capacitances being 3.4% and 9.2%, respectively. This may be due in part to the less complete data used in deriving it.

The equivalent series resistance increased with increasing green density, temperature, and time.

The results of sinter density measurements and the values of capacitance per unit volume derived from them and the capacitances per unit weight are shown in Table VII. Unlike E-11, the capacitance per unit volume of L-533 changed markedly with green density, decreasing with increasing green density. Capacitance per unit volume also decreased with increasing time and temperature.

Comparison of Results

Leakage.—The most significant differences between the leakage results for the three powders were, first, the constancy of *L/C* for E-11 and SG-73R compared with the increase in *L/C* for L-533 at higher green densities and temperatures, and second, the conditions at which the phenomenon of "wild" leakage occurred. Some pellets of E-11 had "wild" leakages at a green density of 8.5 and lower temperatures and times, whereas, under the same conditions, no pellets of SG-73R showed "wild" leakage. L-533 gave "wild" leakages only at green densities below those studied for the other two powders.

Capacitance.—For all three powders the relationship between capacitance and sintering conditions could be expressed by an empirical equation of the form

$$C = A \times 10^4/T + B \log (t + 6) + C'/16.6\text{-}D_g + D$$

There were, however, considerable differences in the values of the coefficients A, B, C′, and D for the three powders. These coefficients (shown in Table VIII) are a measure of the sensitivity of the capacitance to changes in sintering conditions. It can be seen that the capacitance of E-11 is the least sensitive to changes in conditions, and that of L-533 is the most sensitive. SG-73R is much closer in sensitivity to E-11 than to L-533, but is more sensitive

Table VII. Sinter densities and capacitance per unit volume, sample L-533

Temp, °C	Time, min	Green density, g/cc: 7.0		8.0		9.5		10.5	
		D_s	Cvol.	D_s	Cvol.	D_s	Cvol.	D_s	Cvol.
1750	90	—	—	10.00	148	11.41	136	12.15	116
1900	30	—	—	9.50	149	—	—	—	—
	90	—	—	9.91	115	11.18	107	11.86	92
2050	30	8.76	123	9.89	122	11.17	116	—	—
	90	—	—	10.47	102	11.78	90	12.45	70

D_s is sinter density (g/cc) and Cvol. is capacitance per unit volume (microfarad/cc).

Table VIII. Comparison of capacitance equations

General form of equation:
$$C = A \times 10^4/T + B \log (t + 6) + C/(16.6\text{-}D_g) + D$$

Sample	A	B	C'	D
E-11	3.75	−3.50	−32.47	+3.20
SG-73R	4.83	−3.72	−46.56	+1.19
L-533	8.04	−7.34	−94.0	+0.40

C is capacitance, in microfarad/g (200-v formation); T, temperature, in °K; t, time, in minutes; D_g, green density, in g/cc.

to changes in temperature and green density than is E-11.

Figures 2, 3, and 4 show the changes in capacitance of the three powders with changing temperature (at constant time and green density), time (at constant temperature and green density), and green density (at constant time and temperature), respectively. Those graphs show not only the relative sensitivities of the capacitance of the powders to changes in conditions as described above, but also the effects of each of the separate variables

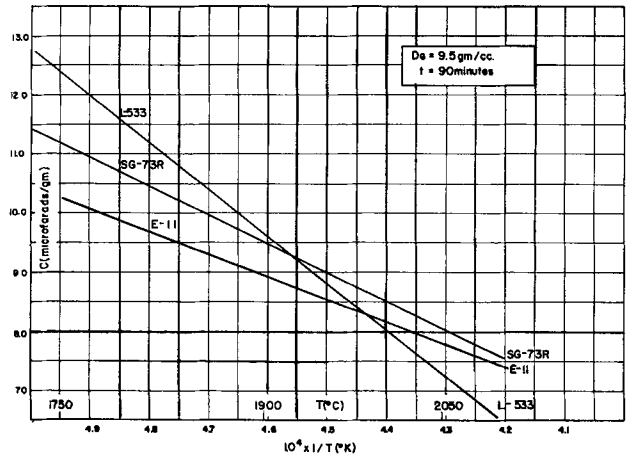

Fig. 2. Capacitance vs. temperature at constant time and green density.

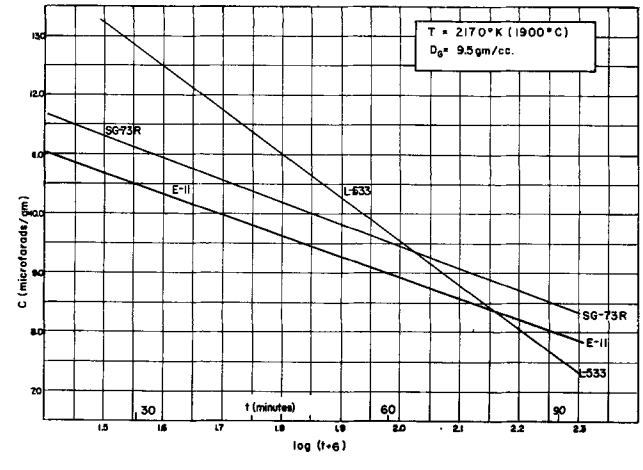

Fig. 3. Capacitance vs. time at constant temperature and green density.

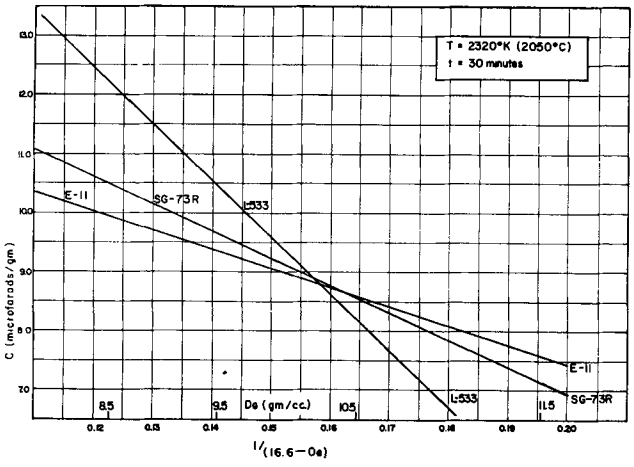

Fig. 4. Capacitance vs. green density at constant time and temperature.

(time, temperature, and green density) relative to each other. The changes in capacitance due to the separate effects of the over-all changes in each variable were approximately equal, over the ranges studied.

Equivalent series resistance.—The equivalent series resistance increased with green density and time for all three powders. It increased with temperature for SG-73R and L-533, but the effect of temperature for E-11 is uncertain. The *ESR* of L-533 was the most sensitive of the three powders to changes in sintering conditions, and also the highest in magnitude for a given set of conditions.

Conclusions

No attempt has been made to give speculative interpretations of the observed results, since it is thought that speculation could be more misleading than helpful when discussing such complex systems. Much more experimental work is needed in this field before, for example, any meaningful physical interpretation could be given for the form of the general capacitance equation, or the phenomenon of "wild" leakage could be explained. It is hoped that such work will be forthcoming.

Manuscript received June 22, 1959. This paper was prepared for delivery before the Philadelphia Meeting, May 1-5, 1959.

Any discussion of this paper will appear in a Discussion Section to be published in the December 1960 JOURNAL.

REFERENCES

1. M. Whitehead, *Bell Lab. Record*, **28**, 448 (1950).
2. R. L. Taylor and H. E. Haring, *This Journal*, **103**, 611 (1956).
3. D. A. McLean and F. S. Power, *Proc. IRE*, **44**, 872 (1956).
4. L. Young, *Proc. Roy. Soc.*, **244A**, 41 (1958).
5. P. S. Roller, *J. Am. Ceram. Soc.*, **20**, 167 (1937).
6. H. E. W. Phillips, *J. Chem. Soc.*, **95**, 59 (1909).
7. C. M. Mason and J. B. Culvern, *J. Am. Chem. Soc.*, **71**, 2387 (1949).

The Growth of Anodic Oxide Films on Germanium

Solomon Zwerdling and Sumner Sheff[1]

Lincoln Laboratory, Massachusetts Institute of Technology, Lexington, Massachusetts

ABSTRACT

Thick uniform germanium dioxide films of controlled thickness have been grown anodically on both n- and p-type germanium. The electrolyte used was a 0.25*N* solution of anhydrous sodium acetate in glacial acetic acid. The composition of the films was established by gravimetric and spectrometric methods. From the current efficiencies and the other parameters of the electrolysis, certain significant properties of the oxide films were calculated, i.e. differential formation field during growth, resistivity, and thickness. Furthermore, it was possible to determine changes in these quantities by evaluating them for different intervals of the electrolysis.

The presence of a thick oxide film on a germanium substrate is considered of importance in understanding the surface properties of semiconductors. Such specimens could be used for physical measurements involving electronic interactions between the oxide layer and the substrate, e.g., the influence of various gaseous ambients on the surface conductivity. Anodic electrolysis was selected to produce these films, since it readily permits obtaining pertinent electrochemical data for the films including differential formation field during growth, resistivity, and thickness. Furthermore, the oxidation rate may be controlled readily, and the films may be formed at room temperature, so that the electrical characteristics of the substrate are unaltered.

Anodic oxide film growth on electrodes has been studied rather extensively for metals in aqueous electrolytes (1-8), and several theories (4, 9-11) have been proposed according to which the formation current density should be dependent exponentially on the electric field across the oxide film. The data obtained for these systems have been essentially in agreement with theory. In recent years, the experiments have been extended to semiconductors, including germanium (12), indium antimonide (13), and silicon (14). In this paper, we will present the detailed results obtained for the electrochemical parameters of the anodic oxide film formation on germanium in a nonaqueous electrolyte.

Experimental

Apparatus.—The experiments for producing the oxide films were performed at room temperature in a three compartment electrolytic cell with the same electrolyte in all three compartments. The experimental arrangement is shown schematically in Fig. 1. Current was obtained from an electronically stabilized current supply having an equivalent source voltage of 100 kv. The anode was grounded and its voltage relative to a reference platinum electrode in the same electrolyte was measured and recorded continuously by a very high input impedance electronic potentiometer. The circuit was designed so that the current could be monitored on the same apparatus without interrupting the circuit.

Samples.—The samples were Ge wafers (approximately 2 × 1 × 0.1 cm) carefully lapped with No. 600 and No. 800 silicon carbide followed by a 1.5 min CP-4 etch.[2] Surfaces were examined in intense oblique light and were reprocessed if not satisfactory. For repeated anodic oxidations with the same electrode, only a 0.5 min CP-4 etch was used. Tygon paint (air-dried, then baked at 70°C overnight) was used to protect the lead soldered to the anode which was only partially immersed in the electrolyte.

The geometrical areas of the electrodes were determined to ± 1% by means of an optical comparator capable of reading dimensions to within 0.005 cm. A surface roughness factor of 1.3 was assumed based on measurements reported by Law (15). The depth of immersion of the Ge anode was determined from the boundary line of the oxidized portion of the electrode observed after the removal of the oxide film by immersion in 0.01*N* sodium hydroxide (aq.).

Electrolyte.—A large number of experiments showed that it was apparently impossible to grow oxide films on germanium using aqueous electrolytes, due to the appreciable solubility of the formed

[2] CP-4 consists of concentrated HNO_3 (5 parts by volume), glacial CH_3COOH (3 parts), 48% HF (3 parts) and Br_2 (0.06 part).

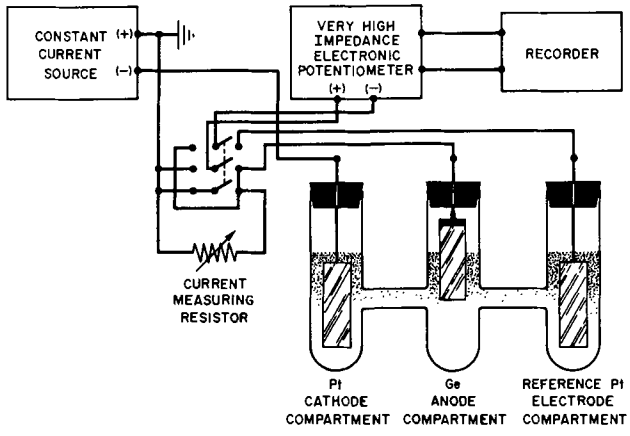

Fig. 1. Schematic diagram of electrolysis apparatus

[1] Present address: Semiconductor Division, Raytheon Manufacturing Company, Newton, Mass.

GeO_2 in water. Among many electrolyte systems tried a solution of anhydrous sodium acetate in glacial acetic acid (A.R.) was found suitable and it was employed in the present study. The optimum composition for producing satisfactory oxide films over the current density range from 50-400 $\mu a/cm^2$ was found to be 0.25*N* and it was employed throughout.

Anodically formed GeO_2 is essentially insoluble in the electrolyte (less than 0.2 γ/ml) as shown by a colorimetric procedure described below. The electrolyte had a specific conductivity of 43.7 $\mu mho\text{-}cm^{-1}$ at 24.3°C.[3]

Analytical.—A method for the determination of the amount of oxidized Ge in the anodic films was developed by a modification of the oxidized hematoxylin photometric procedure described by Newcombe, *et al.* (16). The modifications involved (*a*) dissolving the oxide film on the electrode by a 10-sec immersion with stirring in 0.01*N* aqueous sodium hydroxide, neutralizing with 0.04*N* aqueous sulfuric acid, and making up to standard volume with phthalate buffer of pH = 3.2, (*b*) using 10 ml aliquots of this solution to determine the Ge concentration, and (*c*) allowing 60 min for the reaction time between the Ge and the hematoxylin. The 10-sec immersion time was experimentally found sufficient to remove completely even the thickest film grown and make negligible any contribution due to further oxidation and dissolution of the electrode. A calibration curve was obtained by using β-GeO_2 standard solutions prepared by dissolving a weighed quantity of the oxide in 0.01*N* aqueous sodium hydroxide, neutralizing, and diluting to volume with the same reagents as above. Optical density measurements were made on a Beckman Model DU Spectrophotometer to a precision of ± 0.002 unit standard deviation.

Determination of Oxide Composition

A study was made in order to determine the composition of the anodic films. Since the electrolysis was performed in glacial acetic acid, the possibility that the films were germanium tetraacetate was investigated. This compound had been synthesized by Schmidt, *et al.* (17) and was reported to be soluble in benzene and acetone. These anodic films were found to be insoluble in those reagents.

To test the assumption that the films were GeO_2, experiments were performed to determine the stoichiometric ratio of germanium to oxygen. The ratio was calculated from the weight loss of germanium anodes after the film had been removed by dissolution in aqueous sodium hydroxide and from the amount of germanium found in the resulting solution. The films were grown on p-type germanium at 100 $\mu a/cm^2$ for 10 hr. They were freed of sodium acetate by ten 5-min rinsings in fresh portions of glacial acetic acid, and of acetic acid by pumping in a vacuum desiccator for several hours. Radiotracer experiments using Na^{22} tagged electrolyte indicated that this rinsing procedure was sufficient to remove completely all sodium ions possibly adsorbed on the film. By counting the aqueous sodium hydroxide solutions containing the dissolved film grown in the tagged electrolyte, it was found that no significant amount of sodium was incorporated in the film. Prior to weighing, the films were equilibrated at atmospheric pressure in a desiccator for 30 min. Weighings were made on a microbalance to a precision of $\pm 2\gamma$. A stoichiometric ratio of 1:2 corresponding to the empirical formula GeO_2 was found.

X-ray diffraction patterns were taken of the powder obtained by mechanically removing the film material grown on Ge anodes. A diffuse pattern was obtained indicative of an amorphous powder. After recrystallization from redistilled water, the diffraction pattern contained only the lines associated with the hexagonal form of GeO_2.

The composition of the anodically formed film was investigated further by determining its infrared absorption spectrum. Transmission measurements were made using two oxidized electrodes in series, corresponding to four film thicknesses, in the radiation beam. The spectral region from 2-20 μ was scanned. This was possible since bulk germanium is transparent in this region. Only the absorption bands of GeO_2 (18) were found and are shown in Fig. 2(a) and (b), thus confirming that the films were germanium dioxide.

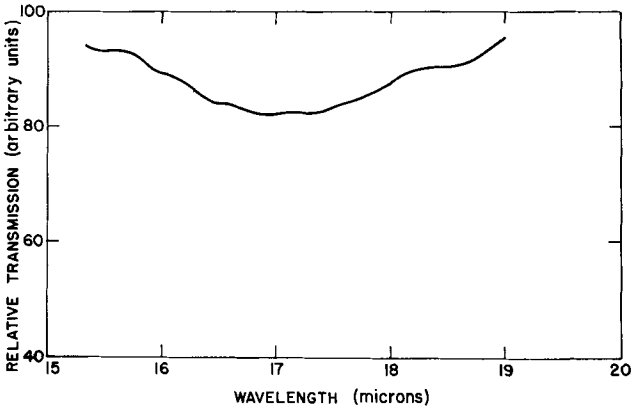

Fig. 2(a). Infrared transmission of GeO_2 films produced anodically on germanium (16 to 18μ band).

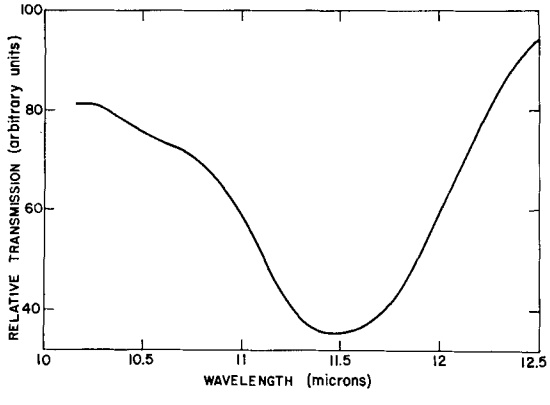

Fig. 2(b). Infrared transmission of GeO_2 films produced anodically on germanium (11.5μ band).

[3] A small quantity of the electrolyte was refluxed at 120°C for 1 hr with 0.6% of its weight of acetic anhydride to dehydrate it further. The resulting solution had a specific conductivity of 42.4 $\mu mho\text{-}cm^{-1}$ at 27.5°C as contrasted to a value of 49.5 $\mu mho\text{-}cm^{-1}$ for the original solution. Attempts to grow uniform oxide films on Ge anodically with the refluxed electrolyte were unsuccessful. Further investigations with this electrolyte may elucidate the reaction mechanism of the anodic oxidation.

Electrochemical Considerations of Film Growth

Certain pertinent properties of the oxide films were calculated from the parameters of the electrolysis, i.e., the total current, the anode area, and the increase of voltage across the oxide with time as the film grew thicker.

The differential oxide formation field at any thickness is defined as

$$E_d = dV/dx = dV/\beta dq_f \quad [1]$$

where E_d is the differential oxide formation field, v/cm; V the potential across the film, v; x the film thickness, cm; and β the centimeters of film thickness formed per amp-sec/cm^2 of charge q_f passed leading to oxide formation.

The thickness of the oxide film at any time t is given by

$$x_t = x_o + \beta q_f \quad [2]$$

where β is taken to be a constant, and x_o is the thickness prior to electrolysis. The density of the oxide formed on the Ge anode was assumed to be that of bulk hexagonal GeO_2 (4.28 g/cm^3) (19), so that a calculation for β yielded 6.35 x 10^{-5} cm^3(amp-sec)$^{-1}$, and for the average thickness of a GeO_2 layer 3.4Å. The current efficiency for oxide formation ϵ is defined as

$$\epsilon = i_f/I \quad [3]$$

where i_f is the oxide formation current density and I the total current density. If the current efficiency is a constant during a given electrolysis interval in the anodic oxidation of Ge to GeO_2, then

$$\epsilon = 4\mathbf{F}M_{Ge}/Q \quad [4]$$

where **F** is the Faraday constant, M_{Ge} is the number of moles of Ge anodically oxidized, and Q is the total charge passed during that interval. If the electrical resistivity of the oxide ρ_{ox} is a constant during the same interval, from Ohm's law,

$$\rho_{ox} = E_d/I \quad [5]$$

Since $i_f = dq_f/dt$, Eq. [3] may be combined with Eq. [1] to give

$$E_d = dV/\beta i_f dt = (1/\beta\epsilon I)\, dV/dt \quad [6]$$

and with Eq. [2] to give

$$x_t = x_o + \beta\epsilon It \quad [7]$$

Alternatively, the thickness of the film may be determined from

$$x_t = W_{Ge}\, G/D \quad [8]$$

where W_{Ge} is the quantity of oxidized Ge on the surface in g/cm^2, G is the gravimetric factor for GeO_2/Ge, and D is the density of GeO_2 in g/cm^3.

Because of the experimental method used, the current efficiency could be obtained only as an average over an interval of electrolysis. Therefore, it was only possible to evaluate the differential field for those intervals during which the current efficiency was constant. Since the electrolyses were performed at constant current density, such intervals would be expected to exhibit a linear rise of voltage with time. As the potential across the oxide was the only component of the measured anode potential that was expected to contribute primarily to its increase with time as the oxide grew thicker, the rate of increase of the latter was taken equal to the rate of increase of potential across the oxide dV/dt. This increase was assumed to be due only to the increase in the film thickness and not to any changes in the oxide already formed.

It was necessary to consider the possibility of the formation of a p-type "inversion" layer at the surface of n-type Ge when anodized in the sodium acetate-glacial acetic acid electrolyte. The effect was not observed in the electrolyses performed except at the highest current density used. For this case, the anode voltage rose abruptly to abnormally high values when the current was turned on, and within 1 min had fallen to the value normally obtained with p-type germanium under the same conditions. During further electrolysis, the behavior of the anode voltage with time remained normal. Evidently, the oxide film formed within 1 min of electrolysis was sufficiently thick to destroy the "inversion" layer by preventing the electrolytic double layer from affecting the normal electron and hole densities at the surface of the germanium substrate. Furthermore, an accumulation of electrolytic oxidation products near the anode might also have contributed to the rise of anode potential with time. It is likely, however, that this did not occur since the potential of a platinum anode substituted for the germanium was found to remain constant during prolonged electrolysis.

Results and Discussion

As a consequence of the above considerations, the criteria adopted for a successful anodic oxide film growth experiment were: (*a*) the film grown should be of uniform thickness as evidenced by the uniformity of the color it produced by optical interference in white light, and (*b*) for all intervals following the initial shorter one, the anode voltage should increase uniformly with time at constant current density.

For current densities between 66 and 240 μa/cm^2, uniform films appearing blue and yellow, respectively, in white light were obtained. The anode voltage vs. time curves satisfied criterion (*b*), although the onset and duration of the intervals varied with the current density. Plots of corrected anode potential vs. electrolysis time for both n- and p-type germanium are shown in Fig. 3.

The correction was chiefly due to the *IR* drop in the anolyte included in the measured voltage and depended on the geometry of the experimental cell. By substituting a platinum anode for the germanium and electrolyzing at various current densities in the range studied, these corrections were evaluated, the largest being about 4.5 v at the highest current density. The curves show the different linear intervals for the different current densities. The values of dV/dt which were used in calculating E_d from Eq. [6] for the different linear intervals were obtained from these curves. The current efficiencies for the different linear intervals were calculated from the charge passed during each interval

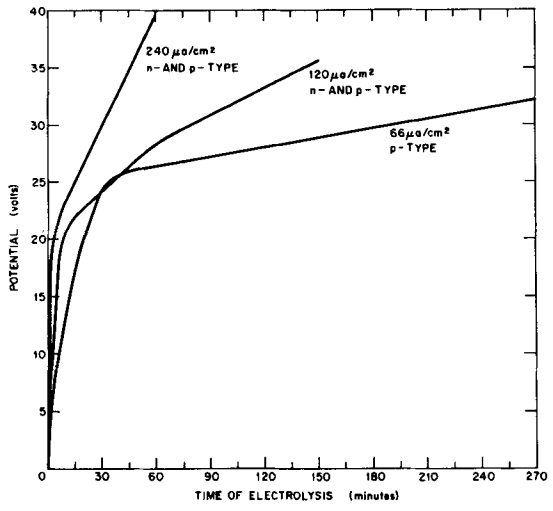

Fig. 3. Potential of Ge anodes vs. a reference Pt electrode during growth of anodic oxide films in 0.25N sodium acetate in glacial acetic acid (corrected for IR drop in electrolyte).

and from differences in the amounts of oxidized germanium found in films grown at the same current density for times equal to those at the beginning and end of each interval. From such differences, the values for M_{Ge} in Eq. [4] were obtained. It was established that the current efficiency actually was constant throughout a linear interval, by dividing each of two such intervals into two parts and obtaining the current efficiency for these parts. The results for two samples of both n- and p-type germanium are shown in Table I. The uncertainty of the efficiency determinations for the total interval in each case was ± 5%. Since the determinations for the intermediate intervals involve smaller differences between relatively large quantities of oxidized germanium than in the case of the corresponding total intervals, the uncertainty for the former was ± 10%. Consequently, within this experimental error the current efficiency was constant throughout a linear interval.

A comparison was made between the anodic oxidation parameters of the (111), (110), and (100) faces of p-type Ge with resistivities of approximately 30 ohm-cm. Experiments were performed for periods of 6 hr at various current densities in the range of interest. The results indicated that, within experimental error, there were no differences between the anodic oxidations of the various crystallographic planes.

Table I. Current efficiency for anodic oxidation of germanium

Material	Total current density, μa/cm²	Specimen	Interval, min	Current efficiency, %
n-type Ge (30 ohm-cm)	120	1	60-105	11
			105-150	11
			60-150	11
		2	60-105	12
			105-150	11
			60-150	11
p-type Ge (30 ohm-cm)	66	3	60-150	17
			150-270	16
			60-270	16
		4	60-150	17
			150-270	16
			60-270	17

The results of a series of determinations of the anodic oxide growth parameters for n- and p-type Ge of 30 ohm-cm resistivity, electrolyzed at the indicated current densities are shown in Table II. For the p-type Ge, the (111) face was used, and for the n-type Ge, the (111) and (100) faces were used. The values reported are the averages of determinations with each electrode as well as with different samples cut from adjacent sections of the same ingot. The current densities for repeated experiments could be reproduced only to within ± 3% on account of the partial immersion technique used for the Ge anodes. The reproducibility of the determinations of dV/dt was ± 5%, so that the values for E_d, ρ_{ox}, and i_f are reported with an uncertainty of ± 8%. Within this experimental error, both n- and p-type Ge showed the same behavior during anodic oxide film growth.

The average current efficiency values obtained for the oxidations during the initial nonlinear intervals at the various current densities were all approximately the same, about 24-26%. The duration of these nonlinear intervals was shorter the greater the corresponding current density. However, for the later intervals, there is a tendency for the efficiency to decrease with increasing current density. It is interesting to note that in all cases, the first pronounced change in slope occurred at a potential between 20 and 24 v (see Fig. 3). This might indicate a change in the anodic process which could arise from the onset of increased electron and/or "hole" conductivity in the oxide due to the field across it, or to a heating effect by the current passing. Since the current efficiency of oxide formation for any current density, following the change of slope, is less than during the initial interval as is evident from Table II, it follows that the electronic conductivity increases at this point probably accompanied by a decrease in ionic conductivity in the oxide since the total current density remains constant.

For the measurements taken at a current density of about 120 μa/cm², the values of the current efficiency and dV/dt are smaller for the third interval than they are for the second interval, but in approximately the same proportion. Consequently, the related values for E_d and ρ_{ox} are about the same for these intervals.Furthermore, the three different current densities employed resulted in E_d values for the later intervals that were approximately proportional to the respective current densities. Therefore, the corresponding resistivities, ρ_{ox} are again about the same. This indicates that the oxide films grown were alike.

Using the assumption for the oxide density stated earlier, the thicknesses of the oxide films were found to range from 220 to 1240Å. The amounts grown for specific intervals are shown separately in Table II.

Table II. Anodic oxide growth parameters for n- and p-type germanium in 0.25N sodium acetate in glacial acetic acid

Interval, min	Area, cm^2	Total current density, $\mu a/cm^2$	Oxidized Ge, micro-mole/cm^2	Current efficiency, %	$10^3\ dV/dt$, v/sec	$10^{-6}\ E_d$, v/cm	$10^{-10}\ \rho_{ox}$, ohm-cm	Thickness x_t, Å
			p-type Ge, (30 ohm-cm)					
0-60	2.12	66	0.16	26	—	—	—	390
60-270	2.12	66	0.35	16	0.47	0.70	1.1	850
								1240
0-20	2.09	120	0.10	25	—	—	—	230
20-60	2.09	120	0.14	19	2.3	1.6	1.3	340
60-150	2.19	120	0.19	11	1.4	1.7	1.4	460
								1030
0-10	2.17	240	0.09	25	—	—	—	220
10-60	2.17	240	0.22	10	5.5	3.5	1.4	530
								750
			n-type Ge, (30 ohm-cm)					
0-20	2.42	120	0.10	26	—	—	—	240
20-60	2.42	120	0.15	19	2.1	1.4	1.2	360
60-150	2.56	120	0.19	11	1.3	1.6	1.3	460
								1060
0-10	2.41	240	0.09	24	—	—	—	220
10-60	2.41	240	0.21	11	5.5	3.3	1.4	510
								730

In conclusion, we have shown that relatively thick oxide films may be grown on germanium by anodic electrolysis in the nonaqueous electrolyte system: sodium acetate-glacial acetic acid. It was not possible to deduce a simple relationship between the formation current density and the differential formation field in this case, as is usually found for metal-aqueous electrolyte systems. Likewise, no definite relationship between these parameters was reported for an analogous semiconductor nonaqueous electrolyte system by Schmidt and Michel (14) who studied the anodic formation of oxide films on silicon in a solution of 0.04*N* potassium nitrate in N-methyl acetamide. Similar curves for the increase in anode potential with time were obtained in their study and ours. Anodic oxide films on indium antimonide have been grown in the aqueous electrolyte 0.1*N* potassium hydroxide by Dewald (13) where, although the potential vs. time curves were similar to those found for Ge and Si, the data obtained could be fitted empirically to the relationship $i_f \propto \exp(E_f)$. In this work on InSb, it was indicated that the interpretation of the kinetic parameters derived from the experimental data was difficult, since the necessary mathematical formulations of the detailed theory of the oxidation of such a binary intermetallic electrode have not yet been developed. The interpretation of the data for the more complex system of a semiconductor electrode in a nonaqueous electrolyte must also await further theoretical and mathematical developments.

Acknowledgment

The authors wish to thank Dr. Harry C. Gatos of this Laboratory for many helpful discussions and assistance with the preparation of the manuscript. The x-ray measurements and crystallographic orientations were performed by Mr. Joseph W. Sanchez. The radiotracer experiments were performed with Mr. J. A. Kafalas, to whom the authors express their thanks.

Manuscript received July 2, 1959. The work reported in this paper was performed by Lincoln Laboratory, a center for research operated by Massachusetts Institute of Technology with the joint support of the U.S. Army, Navy, and Air Force.

Any discussion of this paper will appear in a Discussion Section to be published in the December 1960 JOURNAL.

REFERENCES

1. J. J. Polling and A. Charlesby, *Proc. Phys. Soc.*, **67**, 3-B, 201 (1954).
2. H. A. Johansen, G. B. Adams, Jr., and P. Van Rysselberghe, *This Journal*, **104**, 339 (1957).
3. L. Young, *Trans. Faraday Soc.*, **50**, 153 (1954).
4. A. Guntherschultze and H. Betz, *Z. Physik*, **92**, 367 (1934).
5. A. Charlesby, *Proc. Phys. Soc.*, **66**, 317 (1953).
6. R. D. Misch and E. S. Fisher, *This Journal*, **103**, 153 (1956).
7. P. E. Lake and E. J. Casey, *ibid.*, **105**, 52 (1958).
8. G. B. Adams, Jr., P. Van Rysselberghe, and M. Maraghini, *ibid.*, **102**, 502 (1955).
9. N. F. Mott, *Trans. Faraday Soc.*, **43**, 429 (1947).
10. N. Cabrera and N. F. Mott, *Repts. Progr. in Physics*, **12**, 163 (1948-1949).
11. J. F. Dewald, *This Journal*, **102**, 1, (1955).
12. S. Zwerdling and S. Sheff, *ibid.*, **103**, 61C (1956).
13. J. F. Dewald, *ibid.*, **104**, 244 (1957).
14. P. F. Schmidt and W. Michel, *ibid.*, **104**, 230 (1957).
15. J. T. Law, *J. Phys. Chem.*, **59**, 543 (1955).
16. H. Newcombe, W. A. E. McBryde, J. Bartlett, and F. E. Beamish, *Anal. Chem.*, **23**, 1023 (1951).
17. H. Schmidt, C. Blolm, and G. Jander, *Angew. Chem.*, **A59**, 233 (1947).
18. W. Kaiser, P. H. Keck, and C. F. Lange, *Phys. Rev.*, **101**, 1264 (1956).
19. W. Zachariasen, *Z. Kryst.*, **67**, 226 (1928).

Interpretation of Measurements of Potential Decay on Open Circuit

Paul C. Milner

Bell Telephone Laboratories, Incorporated, Murray Hill, New Jersey

ABSTRACT

Observations of the change in electrode potential as a function of time on open circuit have proved a useful method for the study of electrode kinetics and double-layer capacitances. The interpretation of such observations may be complicated by capacitative effects resulting from competing faradaic processes. Consideration of these effects is included in a theory of open-circuit decay. In certain cases such effects are virtually indistinguishable from double-layer capacitances and they may be of surprising importance. The analysis of decay measurements is also considered, and a new method is described.

In view of recent interest in the decay of overpotential on open circuit in studies of electrode kinetics and of double-layer capacitances, it is pertinent to re-examine the theoretical basis for interpretation of observations. The simplicity of the measurement and its applicability to large electrodes should be recognized. Former interpretations of potential-decay data have depended on very simple theories. This has, in a number of cases, proved inadequate or led to erroneous results.

Early observations of hydrogen overpotential decay made by Baars (1) and Bowden and Rideal (2) were simply explained by Butler and Armstrong (3, 4) in terms of the discharge of a capacitor (electrical double layer) by a faradaic current which is an exponential function of the potential (Tafel current). On this basis, explicit potential-time relations are readily derivable and have been given by a number of authors (5-11). Where the faradaic reaction has equal anodic and cathodic Tafel slopes, expressions valid throughout the whole potential range have been derived (11, 12), and the situation near the equilibrium potential has also been considered (9, 13). When diffusion is a factor in the faradaic process, Grahame (10) and Scott (14) have shown the extreme complexity to be expected in any analysis of decay measurements.

The more general situation, in which more than one faradaic process occurs, is treated here. It has been approached only by Lukovtsev and Temerin (15) in their treatment of the discharge of the nickel oxide electrode by oxygen evolution without consideration of the electrical double layer.

General Equations

For any electrode

$$i_{ext} - \Sigma i_f = dq_{dl}/dt = C_{dl}\, dE/dt \qquad [1]$$

where i_{ext} is the external current, Σi_f is the sum of the currents for faradaic processes at the electrode, q_{dl} is the charge on the electrode side of the electrical double layer, t is the time, C_{dl} is the differential capacitance of the electrical double layer, and E is the potential of the electrode, measured with respect to an unpolarized reference electrode (Gibbs-Stockholm sign convention). In any given electrode system, C_{dl} is a function of potential, but its variation over short ranges of potential is generally small, and it may be treated as a constant to a good approximation. By analogy with mercury (16), C_{dl} may be expected to be of the order of 20 μf/cm^2 of true electrode surface.

The potential-time relation to be observed for any electrode can therefore be determined if the current-potential relations for the faradaic processes are known. Although the rates of many faradaic processes are influenced strongly by mass transport phenomena, such complex effects will be neglected here and all phases will be assumed homogeneous. The resulting simplification will be only an approximation to the state of affairs in a system where mass transport is important. Since sufficient homogeneity of a phase can be assured by adequate mixing, and since the extent of inhomogeneity in a real system depends markedly on geometrical as well as electrochemical considerations, the treatment given here will omit any specific discussion of these factors. The current-potential relation for a faradaic process is then determined entirely by activation control.

Close to the equilibrium potential E_e, the faradaic current intensity is given by

$$i_f = i_0 n\mathbf{F}(E - E_e)/RT \qquad [2]$$

where i_0 is the exchange current intensity (17) and n the number of electrons passed when the rate-determining reaction occurs once. Both i_0 and E_e are dependent on the concentrations of reacting species.

At potentials considerably removed from E_e, the current intensity is given by the Tafel equation

$$i_f = \pm\, i_0 \exp[\pm\alpha\mathbf{F}(E - E_e)/RT] \qquad [3]$$

where α is the anodic or cathodic transfer coefficient (17) and the upper signs are used for anodic processes, the lower for cathodic. The Tafel slope is $\pm 2.303\, RT/\alpha\mathbf{F}$.

Normally, investigations of electrode kinetics are made in systems which are buffered in an electro-

chemical sense. Hydrogen and oxygen evolution are usually studied in fairly acidic or basic electrolytes to prevent significant changes in pH during the course of an experiment. Problems associated with mass transport and ohmic solution effects are also reduced by this procedure. The faradaic current for a reaction in a system which is electrochemically well-buffered with respect to that reaction is then given by [2] or [3] with both i_0 and E_e constant.

However, the electrochemical buffering of a system with respect to one reaction often precludes the buffering of the system with respect to competing reactions which may occur. For example, it is possible to examine the kinetics of silver deposition in solutions containing both silver and hydrogen ions in large quantity, but the process of hydrogen evolution at silver electrodes cannot be studied in solutions containing appreciable quantities of silver ion without great difficulty.

In such a case, it is customary to buffer the system with respect to the reaction of interest and to eliminate as far as possible all other reactants. Even then, the measured steady-state current-potential relations will not refer to the desired reaction unless all the remaining possible reactions are either at equilibrium or so slow for kinetic reasons that they may be disregarded. Very slow reactions may be neglected in general, but it is necessary to consider the possibility of remaining unbuffered reactions which are at equilibrium under steady-state conditions.

For example, during hydrogen evolution at any metal electrode in an acid solution, there exists a finite equilibrium quantity of metal ion in solution at any given steady-state hydrogen overpotential. A change in potential changes the amount of metal ion required for equilibrium and results in a faradaic current corresponding to oxidation of, or reduction to, the metal. Current-potential relations for such an unbuffered reaction are complex, depending on the potential, the exchange current for the reaction, and the concentration of metal ion, all of which are interrelated and time dependent. However, if the unbuffered reaction is characterized by an inherently large rate constant, the process may be considered to take place under conditions close to thermodynamic reversibility, and a considerable simplification becomes possible.

In this case, the faradaic current may be related to the potential by

$$i_f = dq_f/dt = (dq_f/dE_e)\,(dE_e/dt) \qquad [4]$$

where dq_f is the positive charge carried by the faradaic process from electrode to electrolyte in time dt. Two classes of faradaic processes are of interest.

The equilibrium potential for the metal-metal ion couple $M = M^{z+} + ze^-$ is given by

$$E_e = E^\circ + (RT/z\mathbf{F}) \ln a \qquad [5]$$

where a is the activity of M^{z+} and E° is the standard electrode potential. If the activity can be approximated by the molarity c, the activity change resulting from a faradaic process is

$$da = dc = dq_f/z\mathbf{F}V \qquad [6]$$

where V is the volume of the solution in liters. With the assumption that E is not significantly different from E_e, i.e., that the electrode substantially maintains thermodynamic reversibility with respect to the metal-metal ion reaction, the faradaic current is given by

$$i_f = (z^2\mathbf{F}^2V/RT) \exp [z\mathbf{F}(E - E^\circ)/RT](dE/dt) \qquad [7]$$

For the reaction: reduced species = oxidized species + ze^-,

$$E_e = E^\circ + (RT/z\mathbf{F}) \ln a_o/a_r \qquad [8]$$

where a_o and a_r are the activities of oxidized and reduced species. Approximating activities by molarities c_o and c_r,

$$i_f = [z^2\mathbf{F}^2V(c_o + c_r)/4RT] \operatorname{sech}^2 [z\mathbf{F}(E - E^\circ)/2RT](dE/dt) \qquad [9]$$

As long as $E - E^\circ \leq -0.078/z$ volt, so that $c_o/(c_o + c_r) \leq 0.05$, Eq. [9] may be approximated within 10% by the simpler expression

$$i_f = [z^2\mathbf{F}^2V(c_o + c_r)/RT] \exp [z\mathbf{F}(E - E^\circ)/RT](dE/dt) \qquad [10]$$

which has the same potential dependence as the current for the metal-metal ion reaction. A similar approximation is valid when E is sufficiently greater than E°.

It will be noted that no kinetic parameters appear in these expressions for i_f since these unbuffered faradaic processes are assumed in effect to be infinitely fast. If, as is often the case, i_0 is large and dE/dt is not, the limitations introduced by such an assumption are probably less serious than those brought about by the neglect of mass transport phenomena. Quantitative considerations including diffusion and forced convection are prohibitively complex, but qualitatively it is apparent that inhomogeneity in the electrolyte may have a considerable effect, since then only the volume of electrolyte nearest the electrode remains in virtual equilibrium with it during a change in potential.

Potential-Time Relations

With an appropriate choice of current-potential relations, potential-time relations during open-circuit decay may be determined for any electrode. As a specific example, the decay of hydrogen overpotential at a metal electrode in a well-stirred acid electrolyte free from oxygen and other reducible material will be considered, so that the reactions which take place during the decay are $2H^+ + 2e^- \rightarrow H_2$ and $M \rightarrow M^{z+} + ze^-$. The unbuffered metal-metal ion reaction is assumed to be at equilibrium at all times.

Near the equilibrium hydrogen potential.—For this metal electrode in a potential region such that hydrogen evolution is occurring at a rate given by Eq. [2], Eq. [1], [2], and [7] give

$$i_{ext} - i_0 n\mathbf{F}(E - E_e^h)/RT - (z^2\mathbf{F}^2V/RT) \exp [z\mathbf{F}(E - E^\circ)/RT](dE/dt) = C_{dl}(dE/dt) \qquad [11]$$

where E_e^h is the equilibrium hydrogen potential. It is apparent that in a steady-state condition ($dE/dt = 0$), no current is carried by the metal-

metal ion reaction and only the first two terms are finite.

On opening the circuit, $i_{ext} = 0$ and integration yields

$$C_{dl} \ln [(E - E_e^h)/(E_0 - E_e^h)] + (z^2\mathbf{F}^2V/RT) \exp [z\mathbf{F}(E_e^h - E^\circ)/RT] \times \{Ei[z\mathbf{F}(E - E_e^h)/RT] - Ei[z\mathbf{F}(E_0 - E_e^h)/RT]\} = -(i_0 n\mathbf{F}/RT)t \quad [12]$$

where $Ei[x]$ is the exponential integral of x, t is the time on open circuit, and E_0 is the potential at the moment of opening the circuit ($t = 0$). If the circuit is opened from a steady-state condition in which the external current is i_i, Eq. [11] shows that $i_0 n\mathbf{F}/RT$ may be replaced by $i_i/(E_0 - E_e^h)$.

If $E^\circ >> E_e^h$, the second term in [12] may be neglected and ln $(E - E_e^h)$ becomes a linear function of time during the decay with a slope of $-i_0 n\mathbf{F}/C_{dl}RT$. Under this condition, the fraction of the current from the hydrogen evolution reaction used during the decay in forming metal ions is negligible, and a plot of $\ln(E - E_e^h)$ vs. t may be used in the determination of C_{dl}. If the measured potential at the moment of interruption of current is in error because of an ohmic potential drop in the solution between the electrode and the reference electrode, such a plot also provides a means of determining E_0. This type of behavior, which corresponds to the discharge of a capacitor through an ohmic resistance, has been predicted (9), observed experimentally (18), and used in the determination of capacitance (13).

On the other hand, when a negligible fraction of the current from the hydrogen evolution reaction is used in changing the charge in the electrical double layer, the first term of [12] may be neglected, and $Ei[z\mathbf{F}(E - E_e^h)/RT]$ is a linear function of t. When $z\mathbf{F}(E_0 - E_e^h)/RT$ is small, the difference between exponential integrals may be approximated by $\ln [(E - E_e^h)/(E_0 - E_e^h)]$, so that the relation between $\ln(E - E_e^h)$ and t is again linear. However, the slope is now $-(i_0 n/z^2\mathbf{F}V) \exp [z\mathbf{F}(E^\circ - E_e^h)/RT]$ and is unrelated to the capacitance of the electrical double layer.

In Fig. 1, log $(E_e^h - E)$ is plotted against t during the open-circuit decay of hydrogen overpotential at a 1 cm² metal electrode whose ions are divalent. As parameters typical of such a system, $i_0 = 10^{-8}$ amp, $n = 1$, and $C_{dl} = 20$ μf were chosen, and the volume of solution was taken to be 10^{-3} liter. Three cases are shown, each originating at the same value of $E_e^h - E_0 = 0.026$ v, but with different values of $E^\circ - E_e^h$.

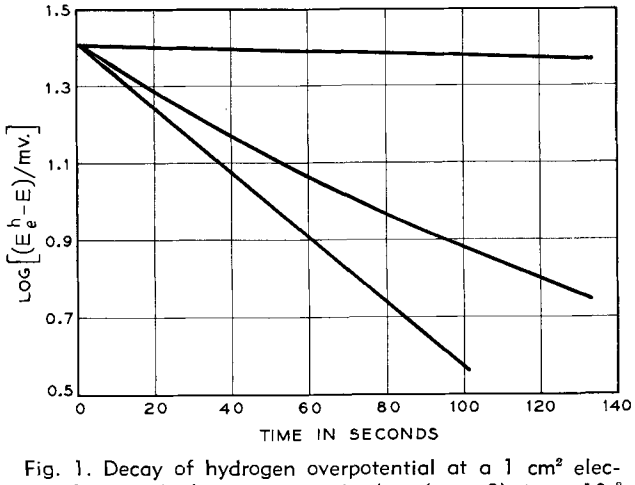

Fig. 1. Decay of hydrogen overpotential at a 1 cm² electrode of a metal whose ions are divolent (z = 2). $i_0 = 10^{-8}$ amp, n, = 1, $C_{dl} = 20\mu f$, V = 10^{-3} liter, E_e^h-E_0 = 0.026 v. Lower curve, E°-$E_e^h \geqq 0.313$ v; middle curve, E°-E_e^h = 0.254 v; upper curve, E°-E_e^h = 0.195 v.

The most rapid decay corresponds to $E^\circ - E_e^h \geqq 0.313$ v. In this case, the second term of Eq. [12] is less than 1% of the first term so that the slope of log $(E_e^h - E)$ vs. t is a measure of C_{dl}. The least rapid decay corresponds to $E^\circ - E_e^h = 0.195$ v. For this and any smaller values, the second term of [12] is at least 100 times the size of the first term so that the fraction of the current from the hydrogen evolution reaction changing the charge in the electrical double layer is negligible. The middle curve corresponds to $E^\circ - E_e^h = 0.254$ v, an intermediate case.

While the theory on which these plots are based is limited by the approximations made in its derivation, the large capacitative effect shown by faradaic process involving the metal-metal ion couple should be strongly emphasized. It can be shown readily that the oxidation of a metal in contact with a solution containing m moles of divalent metal ion corresponds to an apparent capacitance of the order of $1.5 \times 10^{13}\, m$ μf, and even in extremely dilute solutions this may easily exceed the capacitance of the electrical double layer.

In the Tafel region.—For the same metal electrode in a potential region where the current for hydrogen evolution is given by Eq. [3],

$$i_{ext} + i_0 \exp [\alpha\mathbf{F}(E_e^h - E)/RT] - (z^2\mathbf{F}^2V/RT) \exp [z\mathbf{F}(E - E^\circ)/RT](dE/dt) = C_{dl}(dE/dt) \quad [13]$$

On opening the circuit, $i_{ext} = 0$, and integration yields

$$C_{dl}\{\exp [\alpha\mathbf{F}(E - E_e^h)/RT] - \exp [\alpha\mathbf{F}(E_0 - E_e^h)/RT]\} + [\alpha z^2\mathbf{F}^2V/(\alpha + z)RT] \exp [z\mathbf{F}(E_e^h - E^\circ)/RT]\{\exp [(\alpha + z)\mathbf{F}(E - E_e^h)/RT] - \exp [(\alpha + z)\mathbf{F}(E_0 - E_e^h)/RT]\} = (i_0\alpha\mathbf{F}/RT)t \quad [14]$$

If $E^\circ >> E_e^h$, the second term in [14] may be neglected because a negligible fraction of the current from hydrogen evolution is used in forming metal ions. In this case, the equation may be rewritten

$$E = E_0 + (RT/\alpha\mathbf{F}) \ln \{1 + (\alpha\mathbf{F}i_0 t/RTC_{dl}) \exp [\alpha\mathbf{F}(E_e^h - E_0)/RT]\} \quad [15]$$

If the circuit is opened from a steady state in which the external current is i_i, Eq. [13] indicates that [15] may be simplified by replacing $i_0 \exp [\alpha\mathbf{F}(E_e^h - E_0)/RT]$ by $-i_i$.

If C_{dl} is independent of potential, the ratio i_0/C_{dl} is determined solely by the composition of the system, and Eq. [15] shows then that, at sufficiently large values of t, all decays in a system of constant composition become coincident, regardless of E_0 and electrode area. Furthermore, when t is large, the potential is a linear function of ln t with a slope of $RT/\alpha\mathbf{F}$.

Since Baars (1) and Bowden and Rideal (2) in 1928, many workers have observed such behavior. The experiments of Fedotov (19) are of particular interest, for the values of C_{dl} which he determined from measurements of the decay of hydrogen over-

potential on mercury agree well with the a-c determinations of capacitance at the same potentials. In certain cases, successive potential-time curves starting from different values of E_0 have been observed to cross by Hickling and Salt (20) and Kolotyrkin (21). This has been ascribed by the latter to changes in surface area, but this explanation is clearly inapplicable under the conditions in which Eq. [15] applies.

If a negligible fraction of the current from the hydrogen evolution reaction is used in changing the charge in the electrical double layer, the first term in Eq. [14] may be neglected and the equation may be rewritten

$$E = E_0 + [RT/(\alpha + z)\mathbf{F}]\ln\{1 + [i_0 t(\alpha + z)/z^2\mathbf{F}V] \times \exp[\alpha\mathbf{F}(E_e^h - E_0)/RT] \exp[z\mathbf{F}(E^\circ - E_0)/RT]\} \quad [16]$$

which corresponds to the result obtained by Lukovtsev and Temerin (15).

The similarity in form between Eq. [15] and [16] is striking and clearly indicates that in the Tafel region capacitative effects resulting from faradaic processes may well be indistinguishable from the capacitance of the electrical double layer. The essential difference is that the slope exhibited by a plot of E vs. ln t at large values of t is $RT/(\alpha + z)\mathbf{F}$ rather than $RT/\alpha\mathbf{F}$. It is interesting to note that in this case, a crossing of decay curves can be ascribed to changes in surface area, since the resulting change in i_0 is uncompensated by a corresponding change in V. The discrepancies observed by Hickling and Salt (20) between decay slopes and the negatives of the Tafel slopes measured by a direct method lend additional weight to this explanation of such behavior.

In Fig. 2, $E_e^h - E$ is plotted against log t during the open-circuit decay of hydrogen overpotential at the same 1 cm² metal electrode illustrated in Fig. 1. Again, typical parameters for such a system were chosen: $i_0 = 10^{-8}$ amp, $C_{dl} = 20$ μf, and the volume of solution containing divalent metal ions in equilibrium with the electrode was taken to be 10^{-3} liter. The transfer coefficient α was chosen to be ½, so that the Tafel slope is −0.118 v/tenfold change in current. Three decays are shown, each from the same value of $E_e^h - E_0 = 0.592$ v, but with different values of $E^\circ - E_e^h$.

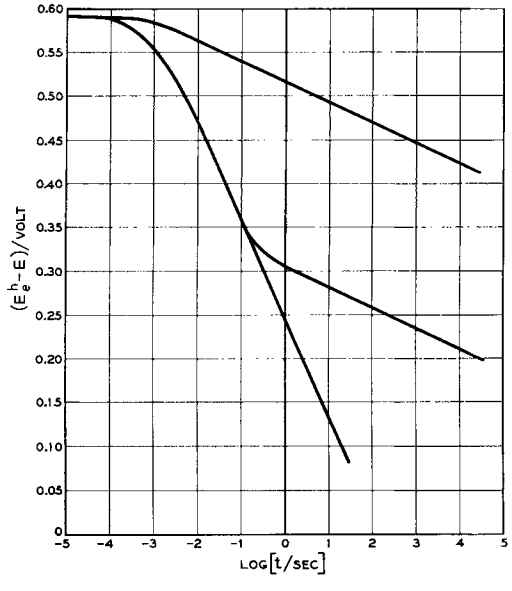

Fig. 2. Decay of hydrogen overpotential at a 1 cm² electrode of a metal whose ions are divalent (z = 2). $i_0 = 10^{-8}$ amp, $\alpha = ½$, $C_{dl} = 20$ μf, V = 10^{-3} liter, E_e^h-E_0 = 0.592 v. Lower curve, E°-E_e^h = 0.183 v; middle curve, E°-E_e^h = −0.080 v; upper curve, E°-E_e^h = −0.344 v.

The most rapid decay corresponds to $E^\circ - E_e^h = 0.183$ v, in which case Eq. [15] is applicable, since the second term of Eq. [14] is no more than about 1% of the first term and may be neglected. The least rapid decay corresponds to $E^\circ - E_e^h = -0.344$ v, and in this case the relative magnitudes of the terms are reversed. The middle curve is for $E^\circ - E_e^h = -0.080$ v, an intermediate case, and is of particular interest because of the relatively sharp transition it exhibits. In the initial portion essentially all the current from the hydrogen evolution reaction goes to change the charge in the electrical double layer and the decay coincides with the decay curve for $E^\circ - E_e^h = 0.183$ v. The later part of the decay is parallel to the decay for $E^\circ - E_e^h = -0.344$ v and like it, results from the capacitative effect shown by the metal-metal ion couple. It is apparent that in this intermediate case, observations of the potential at times greater than 1 sec or of decays from values of $E_e^h - E_0$ of less than about 0.31 v will not include any capacitative effects due to the electrical double layer.

While it is doubtful that experimental conditions corresponding exactly to the approximations introduced in the derivation of Eq. [14] are ever attained in practice, it may be noted that Salkind (22) and Conway and Bourgault (23) have observed two-stage decays of potential analogous to that illustrated in Fig. 2 in studies of the decay of oxygen overpotential on nickel oxide electrodes. Similar considerations may well account for some of the anomalously large slopes observed during open-circuit decay measurements on oxygen-evolving platinum electrodes (8).

Analysis of Decay Measurements in the Tafel Region

From the discussion of the previous section and a comparison of Eq. [15] and [16], it is clear that any decay from a steady-state condition can be represented at least approximately by an equation of the form

$$E = E_0 - b_t \ln(1 + t/t_0) \quad [17]$$

where b_t and t_0 are parameters characteristic of the decay. Where a transition occurs, as illustrated in Fig. 2, values of b_t and t_0 may be associated with each portion of the curve. In the simple case of the discharge of the electrical double layer illustrated in Eq. [15], t_0 may be identified with the quantity $b_t C_{dl}/i_t$, and similar identifications may be made in more complex cases. Although numerical values of b_t and t_0 can be determined by the analysis of measured decay curves, further information is necessary before physical meanings can be assigned to these parameters.

Where t_0 can be identified with $b_t C_{dl}/i_t$, the determinations of the ratio b_t/t_0 is sufficient to determine C_{dl}, and from Eq. [17] this is given by the negative of the initial slope. A similar situation obtains when a faradaic process exhibits a capacitative effect. An

expansion of the logarithmic term of Eq. [17] shows that for small values of t the potential is a linear function of t, but in practice this linear region is sufficiently small that measurements of considerable sensitivity are required if the ratio b_t/t_0 is to be found with any degree of accuracy.

This becomes apparent if the initial slope is considered to be approximated by a line drawn between E_0 and a later value of E. It can be shown that this will differ from the true value $-b_t/t_0$ by more than 10% if the later value of E is more than $0.2b_t$ away. Since values of b_t of greater than ± 0.051 v are seldom observed, it is apparent that precise measurements of the decay must be made within about 0.010 v of E_0 to give b_t/t_0 to 10%.

It is worth noting that in the interrupter method developed by Hickling (24) and others for measuring overpotential when ohmic potential drops exist in the solution between the electrode and the reference electrode, use is made of this linear potential-time region to extrapolate open-circuit measurements of potential to $t = 0$ and thus to determine E_0. Although the values of E_0 are less sensitive than the values of b_t/t_0 to an erroneous assumption as to the range over which the linear region extends, it is clear that care must be exercised when such a linear extrapolation is made.

There are several methods by which b_t and t_0 may be separately determined from experimental data. Most obviously, an empirical choice of t_0 can be made such that E is a linear function of $\ln (1 + t/t_0)$. The slope of such a line is $-b_t$. This procedure is, however, likely to be somewhat more tedious and less accurate than a method not involving trial and error.

When t is much larger than t_0, the potential becomes a linear function of $\ln t$ with a slope of $-b_t$ as shown in Fig. 2. The equation of this linear function is

$$E = E_0 - b_t \ln (t/t_0) \qquad [18]$$

from which it is apparent that the function passes through the value $E = E_0$ at $t = t_0$. Thus a linear extrapolation of the latter part of the E vs. $\log t$ plot to E_0 gives t_0 directly. Since it has been noted that all decay curves for a given electrode coincide at large values of t regardless of the value of E_0, the quantity $E_0 + b_t \ln t_0$ is constant and t_0 has therefore been termed the time required for the potential to decay to E_0 from infinite potential (11).

Two considerations make this method of determining t_0 and b_t less attractive than it at first appears. If it is assumed possible to take an exact tangent to the E vs. $\ln t$ curve at any point and to use this tangent for the determination of b_t and t_0, it can be shown that the value of t_0 obtained will be in error by more than 10% unless the tangent is taken at a time greater than 46 t_0, which corresponds to a potential decay of more than 3.8 b_t. Consequently, the method cannot be used with accuracy unless the potential decay is observed over a sizable range. This requirement eliminates its use in that part of the Tafel region nearest the equilibrium potential because the decay must then be followed into a potential region in which Eq. [17] is no longer applicable.

A second important consideration in the application of this method arises from the assumptions made during the derivations leading to Eq. [17]. For small changes in potential, b_t and t_0 may be taken as constants to a good approximation; but over larger ranges such constancy may be seriously questioned, throwing doubt on the extrapolation to E_0.

The following method of analysis overcomes to a considerable extent the objections raised to the procedures described above. The inverse of dE/dt is, from Eq. [17],

$$\left(\frac{dE}{dt}\right)^{-1} = -\frac{t_0 + t}{b_t} \qquad [19]$$

so that dt/dE is a linear function of t with a zero intercept of $-t_0/b_t$ and a slope of $-1/b_t$. In practice, dt/dE may be approximated by $(t_{n+1} - t_n)/(E_{n+1} - E_n)$ and plotted against $(t_n + t_{n+1})/2$ without introducing significant errors, for it can be shown that the computed derivative is within 5% of the true value as long as $t_{n+1} - t_n$ is less than $1.2(t_n + t_0)$. This procedure is particularly attractive in that it can be used to determine t_0 and b_t from measurements over any small range in potential and is limited only by the accuracy with which E and t can be measured.

Acknowledgment

The author is indebted to J. F. Dewald and U. B. Thomas for many helpful discussions during the course of this work.

Manuscript received July 28, 1959. This paper was prepared for delivery before the Chicago Meeting, May 1-5, 1960.

Any discussion of this paper will appear in a Discussion Section to be published in the December 1960 JOURNAL.

REFERENCES

1. E. Baars, *Sitzber. Ges. Beford. ges. Naturw. Marburg*, **63**, 2.3 (1928).
2. F. P. Bowden and E. K. Rideal, *Proc. Roy. Soc.* **A120**, 59 (1928).
3. J. A. V. Butler, *Trans. Far. Soc.*, **28**, 379 (1932).
4. G. Armstrong, J. A. V. Butler, *Trans. Faraday Soc.*, **29**, 1261 (1933).
5. A. N. Frumkin, *Acta Physicochim. USSR*, **18**, 23 (1943).
6. A. N. Frumkin, *Discussions Faraday Soc.*, **1**, 57 (1947).
7. A. Hickling and F. W. Salt, *Trans. Faraday Soc.*, **38**, 474 (1942).
8. W. R. Busing and W. J. Kauzmann, *J. Chem. Phys.*, **20**, 1129 (1952).
9. J. O'M. Bockris and E. C. Potter, *This Journal*, **99**, 169 (1952).
10. D. C. Grahame, *J. Phys. Chem.*, **57**, 257 (1953).
11. H. B. Morley and F. E. W. Wetmore, *Can. J. Chem.*, **34**, 359 (1956).
12. W. A. Roiter, W. A. Juza, and E. S. Polujan, *Acta Physicochim. USSR*, **10**, 389 (1939).
13. S. Schuldiner and R. E. White, *This Journal*, **97**, 433 (1950).
14. W. T. Scott, *J. Chem. Phys.*, **23**, 1936 (1955).
15. P. D. Lukovtsev and S. A. Temerin, *Trudy Soveshchaniya Elecktrokhim. Akad. Nauk SSSR, Otdel. Khim. Nauk*, **1950**, 494 (1953).
16. D. C. Grahame, *J. Am. Chem. Soc.*, **63**, 1207 (1941).
17. J. O'M. Bockris, "Modern Aspects of Electrochemistry," Chap. 4, Academic Press, New York (1954).
18. J. O'M. Bockris and E. C. Potter, *J. Chem. Phys.*, **20**, 614 (1952).
19. N. A. Fedotov, *Zhur. Fiz. Khim.*, **25**, 3 (1951).

20. A. Hickling and F. W. Salt, *Trans. Faraday Soc.*, **37**, 450 (1941).
21. Ya. M. Kolotyrkin, *Zhur. Fiz. Khim.*, **20**, 667 (1946).
22. A. J. Salkind, "Investigation of the Sintered Plate Nickel-Cadmium Battery." Thesis, Polytechnic Institute of Brooklyn (1958).
23. B. E. Conway and P. L. Bourgault, *Can. J. Chem.*, **37**, 292 (1959).
24. A. Hickling, *Trans. Faraday Soc.*, **33**, 1540 (1937).

Glossary of Symbols

C_{dl} — Capacitance of the electrical double layer, dq_{dl}/dE, farads.
E — Potential measured with respect to an unpolarized reference electrode, v (Gibbs-Stockholm sign convention).
E_e — Equilibrium potential of a faradaic process, e.g., a metal-metal ion process ($i_f = 0$), v.
E_e^h — Equilibrium potential of the hydrogen gas electrode, v.
E° — Standard potential of the faradaic process, v.
E_0 — Potential at beginning of decay ($t = 0$), v.
dq_f — Amount of positive charge entering electrolyte from electrode by means of the faradaic process, coulombs.
q_{dl} — Amount of positive charge on electrode side of the electrical double layer, coulombs.
i_{ext} — Current intensity in external circuit, amp.
i_f — Current intensity corresponding to the faradaic process, dq_f/dt, amp.
i_i — Steady-state current intensity in external circuit at the moment of opening the circuit, amp.
i_0 — Exchange current intensity for an activation-controlled electrode reaction, amp.
t — Time, also time on open circuit, sec.
t_0 — Parameter of decay, sec.
n — Number of electrons passed in an activation-controlled reaction when the rate-determining step occurs once.
α — Transfer coefficient for an activation-controlled reaction.
z — Number of electrons passed by the faradaic process in one occurrence of the over-all reaction.
b_t — Parameter of decay, change in potential for an e-fold change in time when $t >> t_0$, v.
a — Activity.
a_o — Activity of oxidized species.
a_r — Activity of reduced species.
c_o — Molarity of oxidized species.
c_r — Molarity of reduced species.
V — Liters of electrolyte in equilibrium with the electrode.

Arsine Evolution and Water Reduction at an Arsenic Cathode

H. W. Salzberg and Bernard Goldschmidt[1]

Chemistry Department, City College, New York, New York

ABSTRACT

The effects of current density, temperature, acidity, and salt concentration on the evolution of arsine have been studied at arsenic and lead-arsenic cathodes. Analysis of the data indicates that the surface of the electrode is largely covered with chemisorbed hydrogen at current densities as low as 5-10 ma/cm^2, that arsine is formed by reduction of water molecules on the chemisorbed layer of hydrogen, that the rate-determining step is the disproportionation between adjacent surface hydrides, and that water molecule reduction takes place at the electrode even in 1M sulfuric acid at current densities at least as low as 1 ma/cm^2.

Previous work (1-4) on tin, lead, and antimony cathodes has shown that on these cathodes, when cathodic disintegration or hydride formation occurs, the water molecule, rather than the hydronium ion, is the immediate source of the hydrogen present in the hydride molecule. This water molecule reduction is observed at current densities at least as low as 20-30 ma/cm^2 in solutions of pH 2.5 or higher. To see if water molecules are reduced at lower current densities and in more acid solution, it was decided to investigate the arsenic-arsine system, since arsine is known to form at low current densities and because micro methods for its determination are known.

Apparatus, Method, and Materials

The apparatus was that of the previous work, with only minor changes (1). The arsine was absorbed in $HgCl_2$-$KMnO_4$-H_2SO_4 solution and determined colorimetrically by the standard molybdenum blue method (5).

The electrolytic solutions were made of C. P. materials dissolved in distilled water and usually pre-electrolyzed at c.d.'s between 10 and 500 ma/cm^2 for periods up to 24 hr. Check runs using different batches of solution made from different lots of material were in good agreement with each other.

Arsenic cathodes were prepared by plating arsenic out of concentrated solutions of $AsCl_3$ in glacial acetic acid, using the method of Audrieth (6). It is felt that the surfaces were pure arsenic since any zinc that leached out of the brass before plating started would not replate, due to the large differences in both potential and concentration between the zinc and the arsenic. In any event, each cathode immediately before use was cleaned in fresh concentrated HCl and then replated from fresh plating solution for about 10 min at about 3-6 ma/cm^2 to remove impurities and/or oxide film. The lead-arsenic surface was prepared simply by dipping a lead washer of appropriate size into an arsenic plating solution. No conclusions can be drawn concerning this surface except that it was a mixture of arsenic and lead.

Current densities were calculated on the basis of geometric area, which means that real current densities and real rates of arsine formation were lower than the figures given here. Also, due to different

[1] Present address: Department of Chemistry, University of Wisconsin, Madison, Wis.

histories, each cathode must have had a roughness factor at least slightly different from the others.

40°C runs were controlled to within 0.2°C, 25°C runs were controlled to within 1°C.

Potentials were not measured while arsine formation was being determined. Separate cells with a calomel reference were used. First the potential was measured directly at the desired apparent current density. Then the *IR* drop was measured, using a current interrupter technique, and subtracted from the total reading to give the potential of the cathode vs. the calomel. The interrupter was a mercury capillary relay activated by 60-cycle half-wave rectified house current. The make-break times were of the order of microseconds. The *IR* drop was obtained from the calibrated oscilloscopic trace of the potential.

The temperature coefficient was obtained by averaging temperature coefficients for several different cathodes. This procedure was followed because differences in roughness caused different apparent rates at each temperature for the various cathodes whose temperature coefficients, however, were in agreement.

In order to guard against false rates due to changes in surface, each cathode was run first at 25°C, then at 40°C, at 25°C again, at 40°C again, etc, and the temperature coefficients were calculated from values in agreement with each other. Results were then averaged among all other cathodes used in the temperature coefficient experiments. Also, different batches of solution were used with the same cathodes, and the same solutions were used with different cathodes. Whenever results were not self-consistent they were discarded.

As an additional check, after 2 years had elapsed, temperature coefficients were re-run with different materials, different cells, and a different cathode system. The cathode was a 10 cm^2 cone of silver-plated brass which had been plated with arsenic to a thickness of several millimeters. Solutions were made with conductivity water. Solids were CP materials recrystallized from conductance water. The scouring gas was electrolytic hydrogen passed over a palladium catalyst to remove oxygen and then passed over activated carbon at solid CO_2-acetone temperature. Pre-electrolysis was carried out for periods of time up to 5 days. Although apparent c.d. and rates differed from those of the original work, temperature coefficients were in substantial agreement with the original.

In spite of the elaborate precautions discussed above, the results were often dishearteningly irreproducible. To a great extent this was due to differences in surface. Each cathode had a slightly different shape, area, position in the cell, arsenic thickness, arsenic roughness, a different time lapse between the original plating and use, and a different plating current. Results therefore varied from cathode to cathode. Curves obtained with different cathodes were shifted slightly along the axis, although the shapes of the curves were the same. However, differences between curves for different cathodes were minor compared to differences resulting from changes in *p*H. Also, by the nature of the reaction,

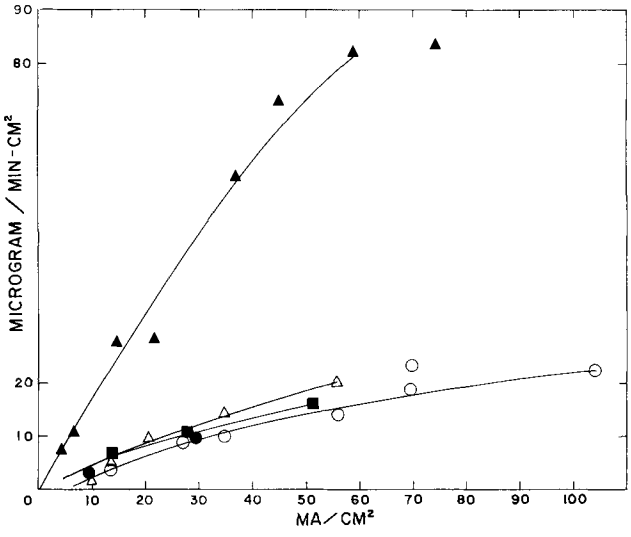

Fig. 1. Rate of arsine evolution vs. current density, ▲, 1M Na_2SO_4, △, 0.1M H_2SO_4; ○, 1M H_2SO_4; •, 1M H_2SO_4-Grube's data; ■, 1M H_2SO_4 on Pb-As cathode.

the surface of any cathode must have changed during each run, thus giving rise to further irreproducibility.

Nevertheless by discarding the results of those cathodes that gave erratic results and by purifying and re-purifying solutions, results were finally obtained that were self-consistent and valid.

Experimental Results

Figure 1 shows the rate of arsine production plotted against apparent current density. The efficiency of arsine formation is low, only about 10% of the current going into arsine in neutral solution and about 1-2% in acid. Increased acidity lowers the rate of arsine formation. Arsine is formed at current densities less than 1 ma/cm^2. At high current densities, the rate falls off, probably due to a high *p*H around the cathode. The rate of arsine production at an arsenic-lead surface in molar acid is definitely higher than at an arsenic surface in the same solution. The fact that the two points taken from Grube's work (7) fit so well is fortuitous, since there would have been a slightly different curve using another cathode. Nevertheless, the agreement is good. Curves obtained, but not plotted here, for mixtures of acid and salt, would fall between those for pure acid and pure salt solutions. Curves obtained, but not plotted here, using cathodes that had accumulated a layer of surface oxide by standing in the laboratory for varying periods of time, gave results that were both higher and more erratic. Results using cathodes that had been deliberately given an oxide coating were also higher.

Figure 2 shows the overvoltage curves for arsenic and arsenic-lead surfaces in acid solution and the *voltage* curve for arsenic in neutral solution. Potentials are higher in neutral solution. Lead-arsenic potentials in acid are more than with arsenic in acid but less than for arsenic in neutral solution. The 25° and 40°C curves in neutral solution correspond at low current densities but diverge above current densities of about 30 ma/cm^2, with the 25°C curve being slightly higher. Each curve has two regions

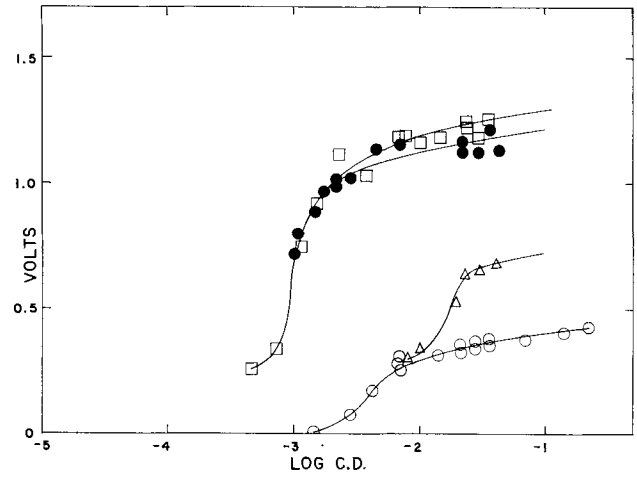

Fig. 2. Potential vs. current density curves. ○, overvoltage on arsenic in H_2SO_4 at 25°C; △, overvoltage on lead-arsenic in acid at 25°C; □, voltage on arsenic in neutral solution at 25°C; ●, overvoltage on arsenic in neutral solution at 40°C.

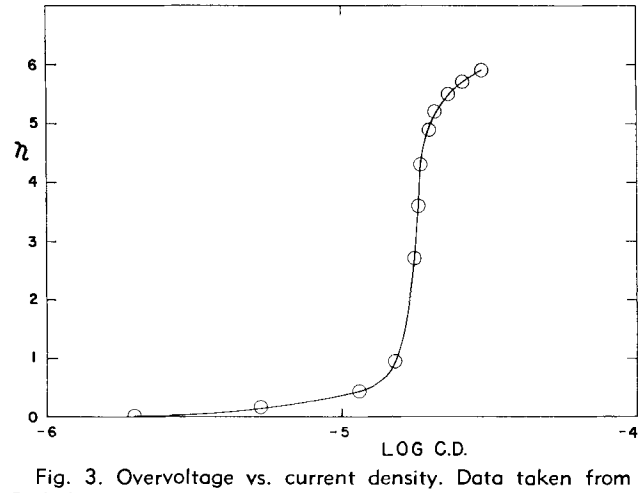

Fig. 3. Overvoltage vs. current density. Data taken from Grube's work on arsenic in acid solution.

corresponding to a build-up of potential at low current densities and a leveling off at higher current densities. The slopes observed at higher current densities are about those values generally observed at high hydrogen overvoltage, but in view of the crudeness of the apparatus, with a rather large experimental error. The leveling off at high current densities is in agreement with the results reported by Lloyd (8) and the general shape of the curve is that reported by Grube (7) as shown in Fig. 3. This graph shows that Grube's values differ from ours but that his curve has the same shape. Noteworthy also is the fact that at very low current densities his slope is about 0.03.

Table I gives some temperature coefficients. Within experimental error, they are all the same.

Discussion

Coverage of the surface by hydrogen.—The overall mechanism must proceed by way of a disproportionation between two adjacent arsenic-hydrogen groups. The probability of a simultaneous reaction between three adjacent As-H groups and of three consecutive electrochemical reductions at one site for each arsine molecule is negligible. This disproportionation would then occur between an arsenic-monohydrogen and an arsenic-dihydrogen group.

Table I. Temperature coefficients at constant current

Solution	Cathode	Rate at 40°C/ rate at 25°C
1M H_2SO_4	As	1.3 ± 0.2
1M H_2SO_4	As-Pb	1.2 ± 0.3
1M Na_2SO_4	As	1.2 ± 0.2

Since, in neutral solution, about 10% of the current goes into arsine production via adjacent arsenic hydrogen groups, at least 20% of the surface is covered by hydrogen atoms, even at 1 ma/cm² (Fig. 1). Yet the combination of surface hydrogen atoms in the unadsorbed or physically adsorbed state is extremely rapid (9). For such a large fraction of the surface as 20% to be covered by hydrogen, the heat of adsorption would be at least 23 kcal/mole, using the calculations of Salzberg and Schuldiner (9). This means that the hydrogen would be chemisorbed in the form of a surface hydride. Actually, arsenic and hydrogen do form a strong covalent bond whose energy is estimated by Pauling (10) to be 47 kcal/mole.

The arsenic-dihydrogen group mentioned above is either an adsorbed molecule or a surface dihydride. The latter would have to be extremely unstable since no such substance has been reported. On the other hand, since the bond energy of the hydrogen molecule is about 104 kcal/mole and that of two As-H bonds would be about 94 kcal/mole, an adsorbed hydrogen molecule would not be likely to break down into two hydrogen atoms which then form covalent bonds with an arsenic atom, i.e., disproportionate into an arsine molecule. Rather, the process would go the other way. Two hydrogen atoms held by covalent bonds to the same arsenic atom would combine to form a molecule of hydrogen. Since the radius of an arsenic atom is 1.25Å and that of the hydrogen atom is 0.37Å there would be plenty of room for two hydrogen atoms to be bound to one surface arsenic atom. The dihydrogen group would therefore be AsH_2, a surface hydride, formed either by a second hydrogen atom being produced at a site which already has a hydrogen atom [(a) in Fig. 4] or by a disproportionation between two adjacent AsH groups [(b) in Fig. 4]

In Fig. 4, the large circles represent arsenic atoms, the small ones hydrogen atoms. Step (a) is an electrochemical reaction; step (b) is also an electrochemical reaction; step (c) is a disproportiona-

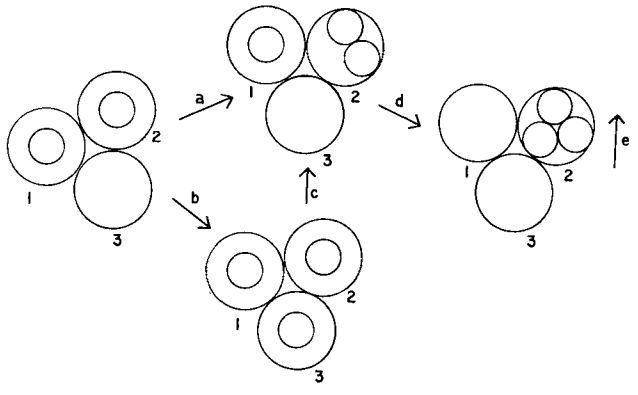

Fig. 4. Diagram of possible reaction paths. Large circles are arsenic atoms, small circles are hydrogen atoms.

tion between two adjacent monohydride molecules forming a dihydrogen molecule; step (d) is a disproportionation forming an arsine molecule; and step (e) is the desorption of the arsine from the surface.

In either event, whether the dihydride is formed electrochemically as in (a) or by disproportionation as in (c) arsine formation must be preceded by the formation of adjacent As-H groups. Since the dihydrogen molecule must be unstable, breaking down rapidly into molecular hydrogen and arsenic, most of the dihydride formed would go directly into molecular hydrogen. An over-all 10% yield of arsine implies that much more than 10% of the current goes into the formation of the unstable dihydrogen hydride and therefore that the surface would be largely saturated with monohydrogen hydride.

The rate-determining process.—The rate-determining step in arsine formation in both neutral and acid solution is (d) in Fig. 4, the disproportionation between As-H and AsH_2. Also, the water molecule, rather than the hydronium ion is the immediate source of the hydrogen found in arsine. These ideas follow from the facts that : (*a*) arsine production falls off as acidity is increased and in acid solution increases as sodium sulfate is added; (*b*) even in acid solutions, the potential at current densities where arsine is produced is high enough to reduce water molecules; (*c*) the temperature coefficient of arsine production at constant current is positive and the same in both acid and neutral solution. The import of this last statement may not be immediately obvious and so some elaboration is required.

The rate of a reaction is directly proportional to the number of reactant particles which possess a total energy equal to that of an activated complex. The energy of the activated complex is relatively independent of temperature. (For example, if the activated complex in this case is a molecule consisting of a surface arsenic atom and two adsorbed hydrogen atoms, there are no degrees of translational freedom, one degree of rotational freedom, and one degree of vibrational freedom less than the normal $3N$-6. The heat capacity at constant volume, according to classical theory, is at most 10 cal/mole-degree. Over a 15 degree range at constant pressure, the energy of the activated complex would change by about 170 cal at most.) Consequently, the reaction products at the moment of formation all have about the same energy regardless of the temperature at which the reaction occurs. After formation, inelastic collisions result in thermal equilibrium and so at higher temperatures the reaction products will have a greater energy. Nevertheless, at the moment of formation, the products have an energy independent of temperature.

One exception to this, however, is the case of electrochemical reactions involving an overvoltage. To speed up these reactions, electrical energy is supplied to the reacting particles, thus increasing the number that have the required energy. If the overvoltage is α, the electrical energy added per equivalent is $\alpha n\mathbf{F}$, where α is a fraction whose value is usually about ½ and **F** is the faraday. The rest of the electrical energy supplied to the system $(1-\alpha)n\mathbf{F}$ goes to the products of the rate-determining step. (This is obvious since this fraction of the expended energy does not influence the rate of reaction.) So, for these reactions, the energy of the reaction products is greater than that of the activated complex by $(1-\alpha)n\mathbf{F}$ until thermal equilibrium is reached. This means that the higher the overvoltage, the greater the energy of the products, since more electrical energy must be supplied. The products of water molecule reduction, which occurs at a higher voltage, will have a greater energy than the products of hydronium ion reduction. The higher the current, the greater the energy of the products, since the voltage is greater. Finally, the higher the temperature, the lower the overvoltage of the reaction and the less the energy of the reaction products at the moment of formation. With this in mind we can get down to cases.

The positive temperature coefficient, at constant current, eliminates an electrochemical, rate-determining step (RDS) since at constant current an electrochemically formed activated complex would be produced at a rate independent of temperature. The RDS then involves neutral products of electrochemical steps, i.e., the RDS is either (c), or (d) or (e) in Fig. 4.

The positive temperature coefficient also eliminates an RDS between electrochemical reaction products that react immediately, before they undergo collisions with solvent molecules and reach thermal equilibrium. The energy of newly formed products of an electrochemical step would decrease, if anything, with increased temperature and decreased overvoltage and hence the temperature coefficient of an RDS involving newly formed reactants would not be positive.

On the other hand, if all of the participants in the RDS had reached equilibrium, there would be no difference in the rates in neutral and in acid solution, since the energies of the reactants would depend only on temperature and not on *p*H. This eliminates the desorption of arsine [reaction (e)] as the RDS.

The only possibilities left are the two disproportionation reactions which could occur between one newly formed hydrogen atom and either one or two previously formed atoms that had already reached thermal equilibrium, that is either (c) or (d) in Fig. 4. Of these the formation of dihydrogen hydride (c) can be dismissed as the RDS. If the movement of the newly formed high-energy hydrogen atom from position 3 to position 2 is slow, the movement of the previously formed, and therefore lower energy, hydrogen atom from position 1 to position 2 should be even slower. But this would make (d) slower than (c) and so (c) could not be the RDS.

By elimination, therefore, the RDS is the disproportionation between the AsH and a newly formed electrochemically produced AsH_2 group, step (d).

The rate of this reaction obviously depends on the energy of the AsH_2. If this is formed by reduction of a water molecule at a high overvoltage, its energy would be higher than if it were formed from a hydronium ion at a lower overvoltage. But, since

the temperature coefficient is the same in both acid and neutral solution, the dihydrogen hydride must be formed with the same energy in both cases. This means that the hydride would be formed by reduction of water molecules, since presumably neutral solutions would not have sufficient hydronium ion present at the surface to maintain the reaction. The difference in rates between the acid and neutral solutions is the result of fewer water molecules being reduced in acid solutions.

The dihydrogen hydride formed from hydronium ion reduction would not have enough energy to form arsine but would break down to molecular hydrogen. Since the ion is more easily reduced than the water molecule, in acid before water molecule reduction can start, a critical current density must be reached at which the surface hydronium ion concentration is too small to support the current. The shape of the curve supports this idea. The greater the acidity, the more hydronium ion initially present, and the higher the neutral salt concentration the fewer hydronium ions initially present at the surface. The data show that increased acidity and decreased neutral salt concentration lowers the rate of arsine formation.

The production of arsine at a lead-arsenic cathode would follow the same mechanism as at an arsenic cathode, since in acid solution the temperature coefficient is the same, the shape of the overvoltage curve is the same, the shape of the rate curve is the same, and the rates and potentials both fall between those of arsenic in neutral solution and in acid solution.

The evolution of hydrogen, as distinct from the formation of arsine, has several different rate-determining steps, depending on the current density. At very low current densities, the surface is not saturated with hydrogen and the RDS is the combination of atoms to form molecules. The initial slope of Fig. 3 is about 0.03, within experimental error, and the overvoltage is less than about 40 mv.

Above about 10^{-5} ma/cm^2, Grube's results indicate that the surface starts to become saturated and the potential increases to that required for production of hydrogen on an arsenic hydride surface. This steep rise also shows up in the first portion of the curves in Fig. 2.

At about 5-10 ma/cm^2, the surface is saturated with monohydrogen hydride and the slope of the overvoltage curve levels off to about the 0.12 value expected for the reduction of a water molecule or the slow or retarded discharge of a hydronium ion. The fluctuations at higher values, especially in neutral solution, are either due to changes in the surface produced by arsine formation or to increase in *p*H.

The same mechanism of hydrogen production applies to the case of the lead-arsenic cathode except that here water reduction probably occurs at a lower current density than on pure arsenic.

Conclusions

It must be re-emphasized that uncertainty as to the true surface area makes the rate and current density data valid only as an upper limit. Also, use of tank hydrogen and ordinary distilled water in the earlier work could have lead to serious errors. However, the checks run with conductance water and a hydrogen purification train were in good enough agreement to indicate that the results were valid.

These conclusions stem from an analysis of the present work and from consideration of the data of Grube (Fig. 3).

1. Arsine is formed by reduction of water molecules on an arsenic surface covered with chemisorbed hydrogen in the form of a covalent hydride.
2. The rate-determining step in arsine formation is the disproportionation between an AsH and an adjacent AsH_2 group or molecule.
3. Water reduction takes place even in lM acid at current densities at least as low a 1 ma/cm^2.
4. The reactions at a lead-arsenic surface are the same as at an arsenic surface except that in acid solution water reduction starts at lower current densities on the arsenic-lead cathode. Consequently, at a given current density, the voltage and therefore the amount of arsine formed is greater at the lead-arsenic surface.
5. At current densities below 1-2 x 10^{-5} amp/cm^2 in acid solution, the formation of hydrogen atoms is reversible. The rate-determining step in hydrogen evolution at this low current density is the combination of hydrogen atoms. The heat of activation is at least about 23 kcal/mole.
6. The saturation of the surface with chemisorbed hydrogen is virtually complete at current densities of about 10^{-2} amp/cm^2.

This work has implications for the general problem of hydrogen overvoltage. It shows, we believe, that water molecules are reduced at cathodes in acid solution at current densities well below those required for cathode disintegration. This is in agreement with the work of Schuldiner (11) and Schuldiner and Hoare (12) who showed that on palladium and platinum water molecules are reduced at low current densities at *p*H 0.8 and 1.4, respectively. In both cases the voltage required for water reduction was less than that which is commonly observed at high overvoltage cathodes, such as mercury and lead.

Perhaps the best summary of the position is that concentration polarization at the surface occurs at current densities much lower than that previously expected and that therefore water molecule reduction occurs.

Acknowledgment

This work was made possible only by the aid of the Office of Naval Research. The authors wish to thank Sr. Sigmund Schuldiner for advice and encouragement and Dr. Saul Berman for administrative assistance.

Manuscript received Jan. 31, 1958.

Any discussion of this paper will appear in a Discussion Section to be published in the December 1960 JOURNAL.

REFERENCES

1. F. Mies and H. W. Salzberg, *This Journal*, **105**, 64 (1958).

2. H. W. Salzberg, *ibid.*, **100**, 146 (1953).
3. L. W. Gastwirt and H. W. Salzberg, *ibid.*, **104**, 701, (1957).
4. H. W. Salzberg and A. J. Andreatch, *ibid.*, **101**, 528 (1954).
5. Sandel, "Colorimetric Determination of Traces of Metals," Interscience Publishers, New York (1950).
6. L. F. Audrieth and C. W. Stilwell, *J. Am. Chem. Soc.*, **54**, 472 (1932).
7. G. Grube and H. Kleber, *Z. Elektrochem.*, **30**, 517 (1924).
8. W. Lloyd, *Trans. Faraday Soc.*, **26**, 15 (1930).
9. H. W. Salzberg and S. Schuldiner, *This Journal*, **104**, 319 (1957).
10. L. Pauling, "Nature of Chemical Bond," Cornell University Press (1940).
11. S. Schuldiner, *This Journal*, **101**, 426 (1954).
12. S. Schuldiner and J. P. Hoare, *ibid.*, **102**, 488 (1955).

Technical Notes

Creeping Silver Sulfide

T. F. Egan and A. Mendizza

Bell Telephone Laboratories, Incorporated, Murray Hill, New Jersey

An effect was observed when a silver specimen coated with a porous gold electroplate was exposed to sulfur vapor. Silver sulfide formed at the pore sites as would be expected, but in addition it spread radially and rapidly on the gold surface, to which it was strongly adherent.

For a preliminary investigation of this effect, a silver panel was prepared, one half of which was heavily gold plated to produce a silver-gold junction. The cleaned specimen was suspended in air saturated with sulfur vapor at 60°C at which temperature the vapor pressure of sulfur is 0.0001 mm (1). After an overnight exposure (17 hr) silver sulfide had crept over the gold surface along the entire bimetallic boundary.

Figure 1 depicts the appearance of the sulfided surfaces at the conclusion of the test (165 hr). Periodic measurements were made at a point of maximum creepage and are shown in Fig. 2. A cross section of the specimen at the gold-silver junction is shown in Fig. 3. It is apparent that the cavity was produced by migration of silver ions needed for the formation of the sulfide on the gold. It is also evident that the sulfide coating on the gold is of the same order of thickness as that on the silver. However, it tapers rather abruptly to a thin film which at the leading edge exhibits interference colors (Fig. 1).

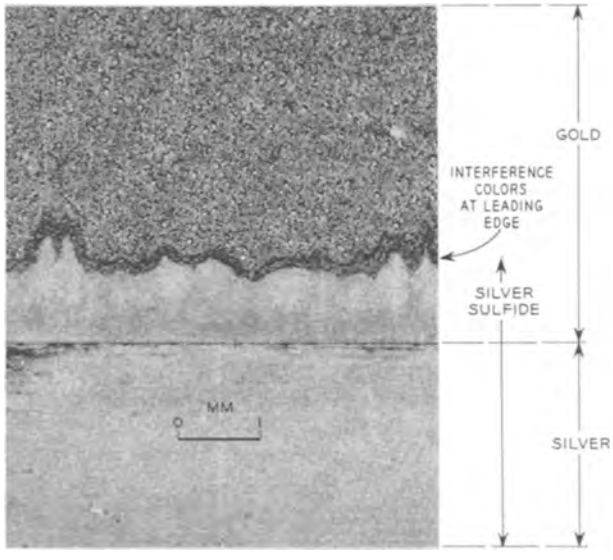

Fig. 1. Advance of silver sulfide on gold after 165 hr in sulfur vapor at 60°C. Leading edge very thin, exhibits interference colors.

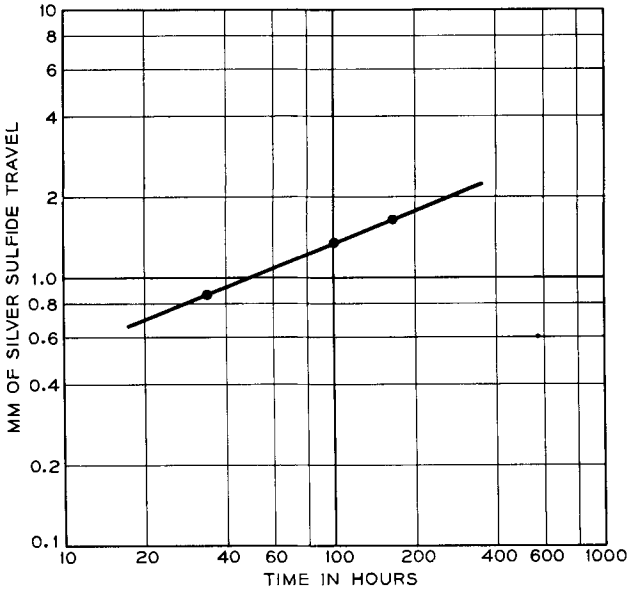

Fig. 2. Creepage silver sulfide on gold-sulfur vapor at 60°C.

The same experiment was performed using rhodium and silver. Direct microscopic examination revealed needles of silver sulfide at the bimetallic juncture but no creepage of silver sulfide on the rhodium surface. Figure 4 is a photomicrograph of a

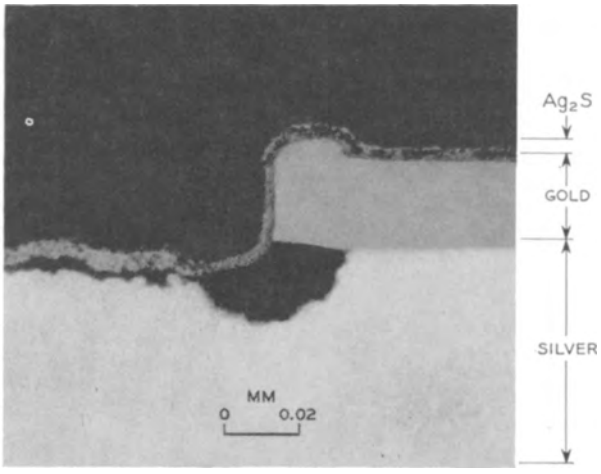

Fig. 3. Cross section of specimen showing cavity in silver and sulfide film on silver and on gold plate.

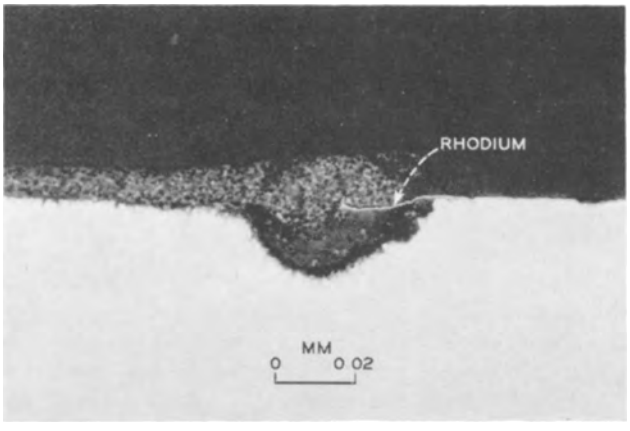

Fig. 4. Cross section of rhodium plated silver showing cavity resulting from silver sulfide needle growth.

cross section of this specimen. It shows what might appear to be a slight amount of creeping of the silver sulfide on the rhodium. This, however, is unlikely since the relatively thick sulfide coating ends abruptly. If creeping had occurred, one would expect the sulfide on the rhodium to taper out to an extremely thin film as had occurred in the case of the gold. The silver sulfide on the rhodium probably resulted from a collapse of the needles during the molding operation. The cavity, which undercuts the rhodium, indicates the quantity of silver required to form the silver sulfide needles. A similar experiment with silver and palladium also failed to produce spreading of silver sulfide.

At the present time there is no completely adequate explanation for the behavior of silver sulfide on the metals studied.

A recent (2) paper discusses a similar effect involving tantalum partly coated with silver and exposed to iodine vapors at 174°C. Silver iodide formed not only on the silver but spread rapidly over the uncoated tantalum surface. The spreading mechanism postulated for this effect assumes local cell action, enhanced by relative ease of flow of ions and electrons in different phases. In this instance spreading of the corrosion product is favored by the ease of flow of silver ions in the iodide and the ease of flow of electrons in tantalum. The same effect was obtained with silver on platinum and on graphite. While this theory appears to be operative in the case of the spreading of silver sulfide on the gold, it is not clear why the same phenomenon does not occur when rhodium or palladium is substituted for the gold, at least at the temperature employed (60°C).

From the practical point of view this phenomenon is of considerable importance. Silver-gold combinations are fairly common in electrical contact design. Some of the usual fabrication methods are electroplating, overlays, and inlays. Silver solder is also used to attach gold to other metals. In all cases, it should be realized that whenever a junction of silver and gold exists in a sulfiding atmosphere, the gold surface will be contaminated with silver sulfide. In these experiments, silver sulfide was more adherent to gold than to silver (Fig. 3) which would indicate that it would be more difficult to remove by contact wipe. Therefore, while silver sulfide is always undesirable on electrical contacts, it may be even more detrimental on gold.

Acknowledgment

The authors are indebted to Mr. E. E. Thomas for the photomicrographs.

Manuscript received Oct. 14, 1959.

Any discussion of this paper will appear in a Discussion Section to be published in the December 1960 JOURNAL.

REFERENCES

1. K. Neumann, *Z. Phys. Chem.*, **A171**, 416 (1934).
2. Christa Ilschner-Gensch and C. Wagner, *This Journal*, **105**, 198 (1958).

A New Method for Preparing Hydroxide-Free Alkali Chloride Melts

Donald L. Maricle[1] and David N. Hume

Department of Chemistry and Laboratory for Nuclear Science, Massachusetts Institute of Technology, Cambridge, Massachusetts

Molten salts have been used extensively in recent years as solvents for electrochemical processes and investigations. Alkali metal chlorides in particular offer excellent thermal stability, good solvent properties, and a wide potential span between anodic and cathodic decomposition limits. However, the difficulty of removing the last traces of residual moisture from the salts has often necessitated rather arduous drying procedures (1-3). If the moisture is not removed, hydrolysis occurs upon fusion as indicated by Eq. [1]

[1] American Cyanamid Co. Fellow 1958-1959. Present address: American Cyanamid Co., Stamford, Conn.

$$Cl^- + H_2O \rightarrow HCl\uparrow + OH^- \quad [1]$$

The hydroxide ion thus produced precipitates metal ions, attacks glass, and is reduced more easily than the alkali metals, thus diminishing the usable potential range of the solvent.

Laitinen, *et al.* (4) have studied the preparation of a hydroxide-free, 59-41 mole % lithium chloride-potassium chloride eutectic by measuring the hydroxide ion concentration polarographically in the melt. Lithium salts are particularly difficult to dry, and polarography is sensitive to low concentrations of hydroxide ions. As a result they found it necessary to use a procedure involving vacuum treatments and fusion under hydrogen chloride which, until it was developed into a routine operation, required several days to complete. By such means they were able to obtain melts with low polarographic residual currents and with little tendency to etch glass apparatus.

The authors have made a polarographic study of drying procedures for the equimolar sodium chloride-potassium chloride melt 740°C, using a tungsten micro-electrode 0.8 mm in diameter and 5 mm long and a platinum-platinum (II) reference electrode. It was found that if the ordinary dry salts were fused and flushed with pure argon for 20 min to remove dissolved oxygen, only a small hydroxide reduction wave was found. Using a standard addition method for calibration, the hydroxide concentration of such a melt was estimated to be 0.17 millimolal, or 3 x 10^{-4}% expressed as water. If rigorously dried hydrogen chloride is bubbled through the melt for 20 min before the argon flush, even this small hydroxide ion impurity is removed. Typical polarograms with and without hydrogen chloride treatment are shown in Fig. 1. This is in considerable contrast to the lithium chloride-potassium chloride eutectic which will contain gross amounts of hydroxide ions if fused without special drying procedures and in which dry hydrogen chloride is not effective for removing hydroxide ions.

A new and better method of removing hydroxide impurities from both melts has been developed in

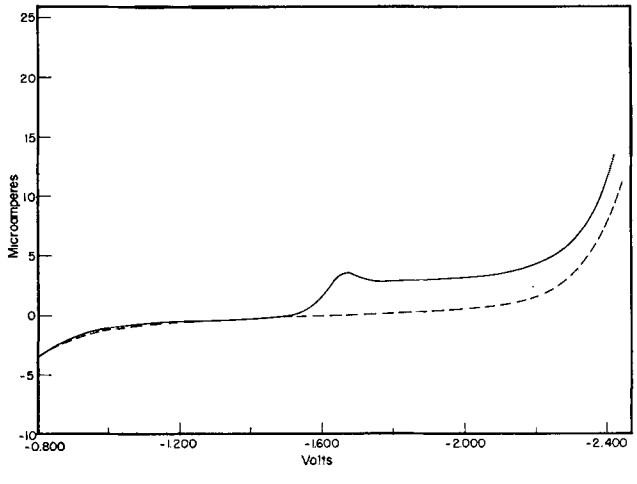

Figure 1. Residual polarographic currents in the NaCl-KCl melt before (solid line) and after (dotted line) removal of hydroxide ion impurity.

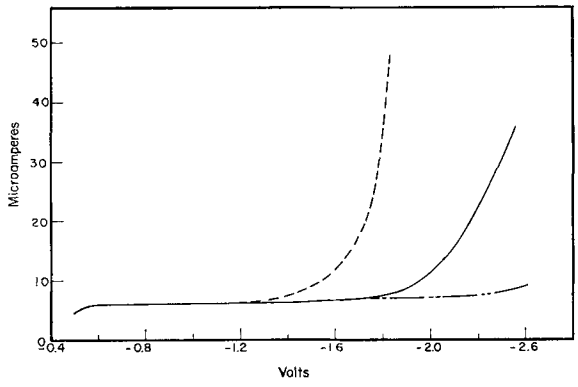

Figure 2. Residual polarographic currents during the purification of the LiCl-KCl eutectic. - - - - - Before treatment; ——— after 20 min chlorine and 20 min argon; ——— - - ——— after 40 min chlorine and 20 min argon.

the present investigation. This method eliminates the need for pre-drying any salts and can be carried out easily and rapidly. It consists simply of passing chlorine through the melt immediately after fusion of the undried salts. The reaction, presumably, is that of Eq. [2].

$$2OH^- + 2Cl_2 \rightarrow O_2\uparrow + 2HCl\uparrow + 2Cl^- \quad [2]$$

The hydroxide ion is thus removed without contamination of the melt with any extraneous nonvolatile species. The oxygen and hydrogen chloride gases are swept out by the chlorine, and the chlorine is easily removed by flushing argon through the melt. After 20 min of treatment with chlorine followed by a 20 min argon flush, the hydroxide ion concentration in a sodium chloride-potassium chloride melt was reduced below the level detectable polarographically. Polarograms recorded before and after the chlorine treatment are shown in Fig. 1. For treating this melt, chlorine has the advantage of being much easier to dry than hydrogen chloride. An additional drawback to the use of hydrogen chloride is its characteristic of altering the fluid characteristics of the melt in such a way that splashing and spattering occurs with consequent deposition of melt at unwanted places in the apparatus.

The use of chlorine is extremely advantageous for drying lithium-ion-containing melts. Figure 2 shows polarograms obtained before and after chlorine treatments in the 59-41 mole % lithium chloride-potassium chloride eutectic at 450°C with a tungsten micro-electrode and a platinum foil used as an anode and reference electrode. It is apparent that after 40 min of chlorine treatment, the hydroxide ion concentration has been reduced below the level detectable polarographically. This was found to be true even if the salts were taken directly out of the bottle, with no pre-drying. A 20-min flush with argon was sufficient to remove the chlorine from this melt also. Therefore, if chlorine is used to purify the melt, the procedure takes only about 1 hr, in contrast with previously used procedures requiring up to several days.

While this method has been used by the authors to purify only the two melts mentioned above, it is

presumed that chlorine could be used to remove hydroxide impurities from other alkali metal and alkaline earth chlorides. However, it is interesting to note that if the temperature of the lithium-chloride-potassium chloride eutectic was raised from 450° to 740°C, reaction [2] did not occur to any appreciable extent, and the color of the chlorine solution changed from nearly colorless to red-brown. The sodium chloride potassium chloride melt exhibits a deep red-brown color when saturated with chlorine at 740°C. It appears as if higher temperatures favor the formation of a chlorine species which has a sufficiently diminished oxidizing power that it cannot oxidize the hydroxide ion in lithium-ion-containing melts.

Acknowledgment

This work was supported in part by the United States Atomic Energy Commission under Contract AT(30-1)-905.

Manuscript received Nov. 18, 1959.

Any discussion of this paper will appear in a Discussion Section to be published in the December 1960 JOURNAL.

REFERENCES

1. S. Senderoff and A. Brenner, *This Journal*, **101**, 16 (1954).
2. H. J. Gardner, C. T. Brown, and G. J. Janz, *J. Phys. Chem.*, **60**, 1458 (1946).
3. G. J. Hills, O. Inman, and L. Young, Proc. Intern. Comm. Electrochem. Thermodynam. and Kinet. 8th meeting, **90** (1958).
4. H. A. Laitinen, W. S. Ferguson, and R. A. Osteryoung, *This Journal*, **104**, 516 (1957).

Brief Communications

Location of Diffused pn-Junctions on Germanium by Electrodeposition of Copper

Reinhard Glang

Diamond Ordnance Fuze Laboratories, Washington, D. C.

The delineation of diffused junctions on silicon by chemical deposition or electroplating of metals has been described frequently in recent publications and can be achieved in various ways. Germanium, however, offers difficulties. It seems to be impossible to sharply define a junction on germanium by chemical displacement reactions (1). Electroplating methods of locating grown junctions on germanium crystals have been reported occasionally (2, 3), but apparently no procedure has been published for defining *diffused* junctions on germanium with metals. The technique described below makes it possible to delineate the junction between p-type germanium and thin diffused n-type layers.

A small piece of a diffused germanium wafer is angle lapped (4) as shown in Fig. 1 in order to expose the junction. The lapping is done against a glass plate, using an alumina abrasive 0.3μ in particle size, in order to avoid deep scratches on the beveled region. The surface is cleaned carefully with organic solvents and distilled water.

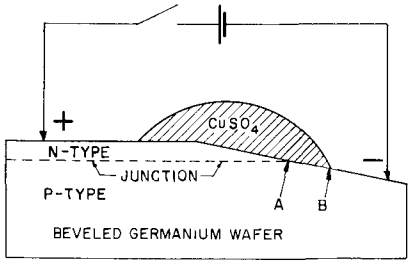

Fig. 1. Copper plating of diffused germanium wafer for delineation of junction.

The plating solution is prepared by dissolving approximately 20 g of $CuSO_4 \cdot 5H_2O$ in 80 ml of water and adding about 1 ml of concentrated (49%)HF. The hydrofluoric acid is intended to keep the germanium surface free from oxide. A small drop of this solution is placed on that part of the beveled surface where the junction is believed to be located. This is done carefully with a capillary pipette, so that the droplet does not flow over the edges of the germanium sample. Two adjustable metal probes are then brought into contact with the surface, one on the beveled p-region and the other on the non-beveled n-region. A small d-c voltage is applied between the probes, and the p-type region serves as the cathode. During these operations, the surface of the sample must be protected from strong light in order to avoid a photovoltage across the junction and consequent deposition of a thin film of copper on the n-region of the wafer. The circuit supplying the voltage is closed at 20-sec intervals for periods of only about 1 sec. After the first pulse, a deposit of copper is usually visible over the whole area between point A and point B in Fig. 1. This layer of copper adheres firmly to the germanium surface.

As indicated above, the voltage is applied continuously for only about 1 sec. Longer applications yield anode reactions which result in an electrolytic etch of the n-region, dulling its surface, and thus interfering with subsequent junction depth meas-

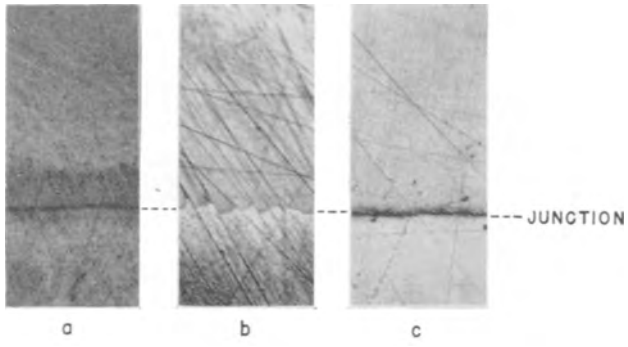

Fig. 2. Diffused pn-junctions in germanium. The lower thirds of the photographs show the copper-plated p-type region of the bevel. Lapping angles and junction depths: (a) 2°, 2μ; (b) ¾°, 2μ; (c) ¾°, 6.5μ. Magnification 300X before reduction for publication.

urements made with an interference microscope (4). The value of the voltage is critical and depends on the dimensions of the sample as well as on the sheet resistivity. On rectangular samples of width 2 mm, length 5-10 mm, junction depth 1-2μ, and sheet resistivity about 150 ohm, a voltage of 15 to 20 v and a current of about 30 to 50 ma adequately define the junction. Too high a voltage causes the copper to begin to spread over the n- as well as the p-region. A more common failure results from a voltage which is too low. In this case, copper tends to deposit from the edge of the drop nearest to the negative probe (i.e., point B, Fig. 1) while the region near the junction (i.e., point A Fig. 1) remains uncovered.

On samples having the previously specified dimensions, but sheet resistivities of 30 ohm or less and junction depths of 8 to 10μ, conditions are less critical; voltages as low a 5 v and currents of about 20 ma have proved effective.

Figure 2 shows samples of diffused germanium the lower thirds of which are the copper-plated p-type regions and the upper two thirds of which are the n-type regions. In Fig. 2a, the upper portion of the sample is not beveled, while in Fig. 2b and 2c the beveled n-region extends all the way to the upper edges of the photographs. Lapping angles and junction depths for these samples are as follows: (a) 2°, 2μ; (b) ¾°, 2μ; (c) ¾°, 6.5μ. As a consequence of the angle lapping procedure, the beveled surface areas are scratched. The surface damage accounts for minor irregularities in the junction delineation as clearly shown in Fig. 2b. On samples having a junction depth of only 1 or 2μ, irregularities in the copper-plated edge larger than those shown in Fig. 2b are occasionally observed, and these irregularities follow the surface profile. For example, when a scratch 1μ in depth was present on the sample's surface prior to diffusion, the junction depth was increased in this particular region.

For junction depths in the order of only 1μ it is advisable to use a lapping angle of 1° or smaller. A steeper bevel tends to permit extension of the copper plated area beyond the junction line, as occurred in Fig. 2a where the lapping angle was 2°. The surface damage which is done in the angle lapping procedure undoubtedly distorts the junction region and causes an apparent inaccuracy in its delineation. The larger the lapping angle the more serious this effect will be.

Considering the fact that the plating voltage biases the junction in the reverse direction, the currents between the probes are surprisingly high. Even in the absence of copper sulfate solution, these currents are of the same order of magnitude. Consequently, there must be a high leakage current, either through or by-passing the junction, but not through the drop. By etching 1 to 2μ deep into the beveled part of the surface, the leakage current can be reduced greatly. This is another indication of the disturbing influence of a damaged surface layer and explains why the voltage is so critical for effective plating. The voltage has to be sufficiently high to force through the droplet and into the diffused n-layer that fraction of the total current which is required to produce a visible deposit of copper. The main fraction of the current, however, will go from the p-type to the n-type region through the damaged surface layer, which offers a path of lower resistance across the junction.

Manuscript received Nov. 16, 1959.

Any discussion of this paper will appear in a Discussion Section to be published in the December 1960 JOURNAL.

REFERENCES

1. D. R. Turner, *This Journal*, **106**, 701 (1959).
2. H. E. Bridges, J. H. Scaff and J. N. Shive, "Transistor Technology," Vol. I, p. 288, D. van Nostrand Co., Inc., Princeton, N. J. (1958).
3. R. C. A. Laboratories, "Transistors" I, p. 130 (1956).
4. W. L. Bond and F. M. Suits, *Bell System Tech. J.*, **35**, 1209 (1956).

Magnetic Gradient at the Surface of Ferromagnetic Substances

S. Yamaguchi

The Institute of Physical & Chemical Research, Tokyo, Japan

The gradient of the magnetic field found at the surface of a magnet body has been measured by means of electron diffraction. This magnetic gradient was taken into consideration for elucidation of the Hedvall effect in catalysis and corrosion (1).

Experimental.— A flux of electrons spreads in passing through a magnetic field with a gradient. This phenomenon is observable in a diffraction pattern obtained from a ferromagnetic substance (Fig. 1).

A reduced iron catalyst[1] for practical ammonia synthesis and the sharp edge of a razor blade of

[1] This catalyst was produced by reducing blocks of iron oxide (Fe_3O_4) with hydrogen. The iron catalyst thus prepared kept the initial form of the oxide block.

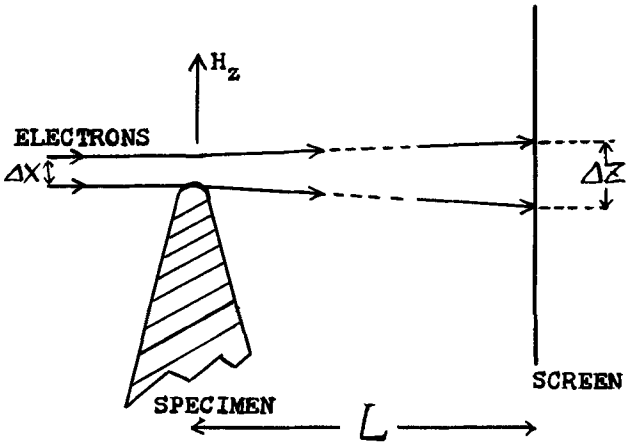

Fig. 1. Experimental arrangement

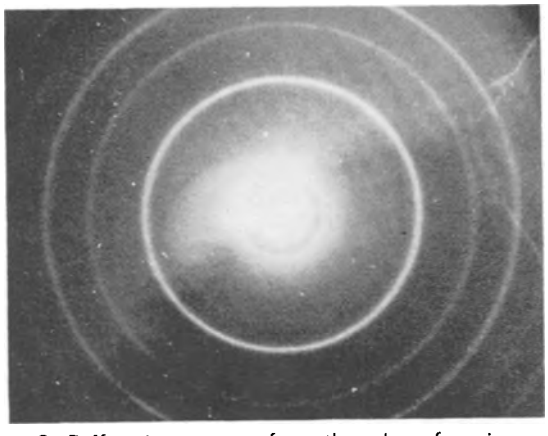

Fig. 2. Diffraction pattern from the edge of an iron catalyst. Wave length: 0.0308Å; camera length: 495 mm; positive enlarged 2.3 times.

hard steel were employed as objects for the experiment. The remanence of the former specimen was about 5000 gausses and that of the latter was about 10000 gausses. The surface (area: about 5 mm^2) of the catalyst was scanned with the electron beam (diameter: about 0.05 mm) in order to locate the maximum gradient of the magnetic field found at the catalyst surface. The electron beam grazed the sharp edge of the razor blade. Diffraction patterns obtained from the iron catalyst (size: 5 x 5 x 1 mm) and that from the razor edge (5 x 5 mm) are shown in Fig. 2 and 3. In these figures it is noticeable that the diffraction rings show a preferred orientation regarding the diffraction width, being diffuse in the direction of the magnetic field, but sharp in the direction perpendicular to the field. The relation between the field (H_z)and the spreading of the diffraction width of the (110) ring is illustrated in Fig. 4.

The central spot found in the diffraction pattern of Fig. 2 is enlarged 35 times in Fig. 5(a). It is noticeable here that the incident beam spreads along the direction of the magnetic field of the specimen. The cross section of the undistorted incident beam is shown in Fig. 5(b) with the same magnification as in Fig. 5(a). The amount of the magnetic spreading of the incident beam is measurable at the diffraction ring as well as at the central spot.

Measurement of the magnetic gradient.—The spreading ΔZ of the incident beam resulting from

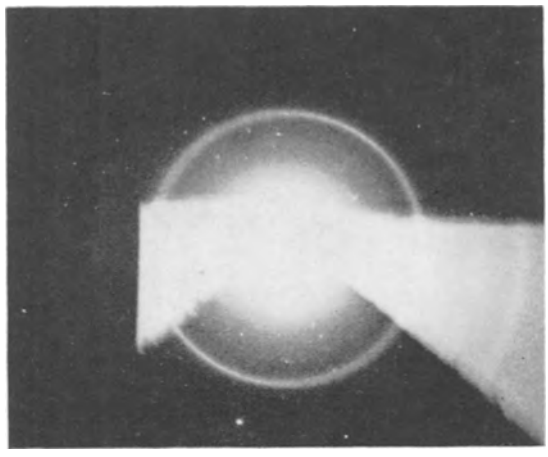

Fig. 3. Diffraction pattern from sharp edge of a razor blade. Wove length: 0.0309Å.

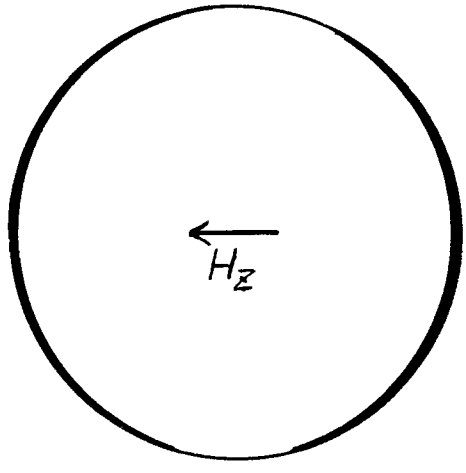

Fig. 4. Oriented spreading of the (110) ring in Fig. 2 and 3. H_z: the direction of the field.

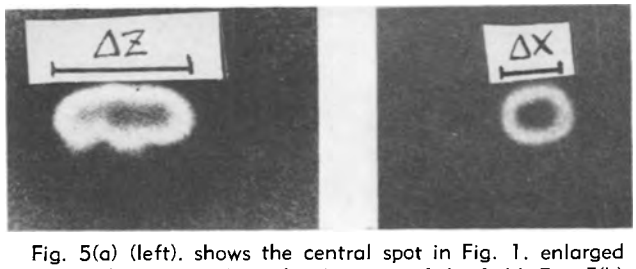

Fig. 5(a) (left). shows the central spot in Fig. 1. enlarged 35 times. It spreads along the direction of the field. Fig. 5(b) (right). shows the cross section of the undistorted incident beam; it is nearly circular.

the action of the magnetic gradient ($\partial H_z/\partial Z$) in the present conditions (Fig. 1) is given by

$$\frac{\Delta Z}{\Delta X} = e \left|\frac{\partial H_z}{\partial Z}\right| \cdot \frac{\lambda L l}{h} \qquad [1]$$

where e is the electron charge (1.6 x 10^{-20} emu), ΔX is the diameter of the flux of the undistorted incident beam, λ is the wave length of the electrons, h is Planck's constant (6.6 x 10^{-27} erg sec), L is the camera length (495 mm), and l is the magnetic path traveled by the electrons. In Fig. 2 or in Fig. 5(a) and (b) we measure $\Delta Z/\Delta X \cong 2.3$, and $\lambda = 0.0308$Å. If the magnetic path l is assumed tentatively to be 1μ we obtain

$$\frac{\partial H_z}{\partial Z} \cong 6 \times 10^5 \text{ gauss/cm}$$

as the maximum gradient according to Eq. [1]. This value of the magnetic gradient is not absolute because of the uncertainty in l.

In Fig. 3 we measure $\Delta Z/\Delta X \cong 3{,}4$, and $\lambda = 0.0309$Å. Therefore, we obtain

$$\frac{\partial H_z}{\partial Z} \cong 9 \times 10^5 \text{ gauss/cm}$$

as the maximum gradient on the razor edge. This value is rather absolute, because the l-value here assumed is approximately equal to the minimum thickness of the truncated wedge of the razor blade (1μ).

Conclusion.—The maximum magnetic gradient is related to the lattice distortion or the magnetostriction found at the surface of the specimen. It is known that catalysis and corrosion of metals depend frequently on this lattice distortion. The magnetic Hedvall effect in catalysis and corrosion should be studied by scanning the magnet surface with a fine electron beam according to the present process.

Manuscript received Sept. 30, 1959.

Any discussion of this paper will appear in a Discussion Section to be published in the December 1960 JOURNAL.

REFERENCES

1. J. A. Hedvall, "Einführung in die Festkörperchemie," pp. 196-202, Fried. Vieweg & Sohn, Braunschweig (1952); H. H. Uhlig and A.de S. Brasunas, *This Journal*, **97**, 448 (1950).

Overtemperature in Metal Scaling

D. Caplan

National Research Council, Ottawa, Canada

Overtemperature resulting from the heat of reaction can affect the reaction kinetics of gases with metal surfaces. This has been discussed recently in the high-temperature oxidation of iron (1), iron-nickel (2), uranium (3), and molybdenum (4), and by the writer as a possible explanation for large differences in scaling rates of iron-chromium alloys with different surface preparations (5). To investigate the latter and because other measurements of overheating had been indirect, it was decided to determine the overtemperature directly with a thermocouple welded to the surface of the specimen.

The metals tested were high-purity vacuum melted iron, a pure Fe-26 Cr alloy, and a commercial Fe-30 Ni alloy (kindly supplied by R. T. Foley from material used in reference 2). Specimens in sheet form were used to provide an adequate surface/mass ratio. A chromel/alumel thermocouple was spot welded to the prepared metal surface. The assembly was lowered into the open top of a vertical tube furnace (on-off control) and the thermocouple output recorded on a strip chart potentiometer (L&N Speedomax G, full scale 50 mv pen travel in one second). Relevant details of six runs are listed in Table I.

The temperature/time curves are reproduced in Fig. 1. Runs 1 and 2 demonstrate that large overtemperatures can develop when iron is oxidized. A similar conclusion was reached by Schmahl, *et al.* (1), but quantitative comparison of the results is not possible because of the more positive attachment of the thermocouple and differences in the experimental conditions: overheating will be less if these conditions are such as to decrease the reaction

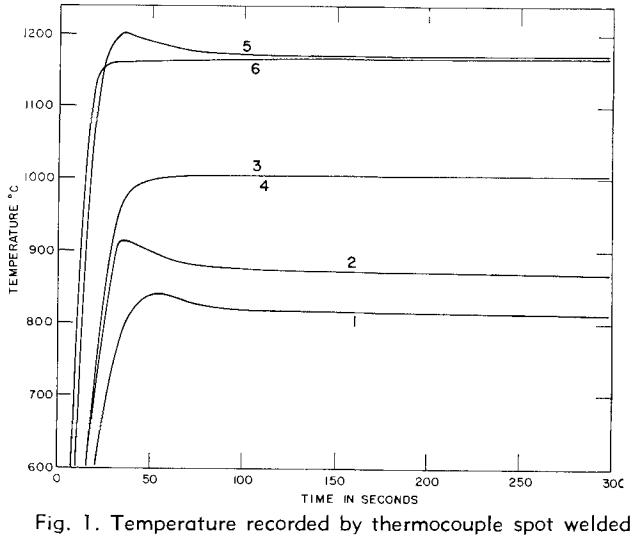

Fig. 1. Temperature recorded by thermocouple spot welded to surface of specimen.

Table I

Run	Alloy	Size, cm	Weight, g	Surface prep.	Temp, °C	Atmosphere	Overtemp, °C
1	Fe	1 × 5 × 0.04	1.3	Electropolished	812	O_2, 200 ml/min	27
2	Fe	1 × 5 × 0.04	1.3	Electropolished	866	O_2, 200 ml/min	47
3	Fe-30 Ni	2 × 3.8 × 0.06	3.4	Etched as in ref. (2)	1005	still air	nil
4	Fe-30 Ni	2 × 3.8 × 0.06	3.4	Etched as in ref. (2)	1005	O_2, 100 ml/min	nil
5	Fe-30 Ni	2 × 3.8 × 0.06	3.4	Etched as in ref. (2)	1170	O_2, 100 ml/min	29
6	Fe-26 Cr	1 × 5 × 0.04	1.3	Electropolished	1165	O_2, 200 ml/min	nil

$$\frac{\partial H_z}{\partial Z} \cong 6 \times 10^5 \text{ gauss/cm}$$

as the maximum gradient according to Eq. [1]. This value of the magnetic gradient is not absolute because of the uncertainty in l.

In Fig. 3 we measure $\Delta Z/\Delta X \cong 3{,}4$, and $\lambda = 0.0309$Å. Therefore, we obtain

$$\frac{\partial H_z}{\partial Z} \cong 9 \times 10^5 \text{ gauss/cm}$$

as the maximum gradient on the razor edge. This value is rather absolute, because the l-value here assumed is approximately equal to the minimum thickness of the truncated wedge of the razor blade (1μ).

Conclusion.—The maximum magnetic gradient is related to the lattice distortion or the magnetostriction found at the surface of the specimen. It is known that catalysis and corrosion of metals depend frequently on this lattice distortion. The magnetic Hedvall effect in catalysis and corrosion should be studied by scanning the magnet surface with a fine electron beam according to the present process.

Manuscript received Sept. 30, 1959.

Any discussion of this paper will appear in a Discussion Section to be published in the December 1960 JOURNAL.

REFERENCES

1. J. A. Hedvall, "Einführung in die Festkörperchemie," pp. 196-202, Fried. Vieweg & Sohn, Braunschweig (1952); H. H. Uhlig and A.de S. Brasunas, *This Journal*, **97**, 448 (1950).

Overtemperature in Metal Scaling

D. Caplan

National Research Council, Ottawa, Canada

Overtemperature resulting from the heat of reaction can affect the reaction kinetics of gases with metal surfaces. This has been discussed recently in the high-temperature oxidation of iron (1), iron-nickel (2), uranium (3), and molybdenum (4), and by the writer as a possible explanation for large differences in scaling rates of iron-chromium alloys with different surface preparations (5). To investigate the latter and because other measurements of overheating had been indirect, it was decided to determine the overtemperature directly with a thermocouple welded to the surface of the specimen.

The metals tested were high-purity vacuum melted iron, a pure Fe-26 Cr alloy, and a commercial Fe-30 Ni alloy (kindly supplied by R. T. Foley from material used in reference 2). Specimens in sheet form were used to provide an adequate surface/mass ratio. A chromel/alumel thermocouple was spot welded to the prepared metal surface. The assembly was lowered into the open top of a vertical tube furnace (on-off control) and the thermocouple output recorded on a strip chart potentiometer (L&N Speedomax G, full scale 50 mv pen travel in one second). Relevant details of six runs are listed in Table I.

The temperature/time curves are reproduced in Fig. 1. Runs 1 and 2 demonstrate that large overtemperatures can develop when iron is oxidized. A similar conclusion was reached by Schmahl, *et al.* (1), but quantitative comparison of the results is not possible because of the more positive attachment of the thermocouple and differences in the experimental conditions: overheating will be less if these conditions are such as to decrease the reaction

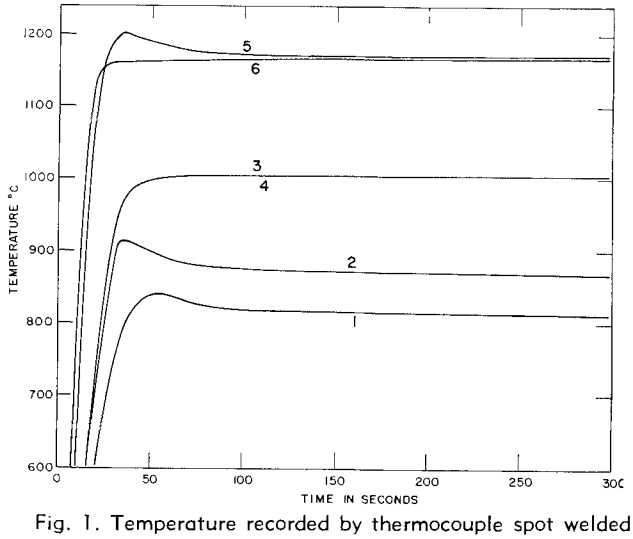

Fig. 1. Temperature recorded by thermocouple spot welded to surface of specimen.

Table I

Run	Alloy	Size, cm	Weight, g	Surface prep.	Temp, °C	Atmosphere	Overtemp, °C
1	Fe	1 × 5 × 0.04	1.3	Electropolished	812	O_2, 200 ml/min	27
2	Fe	1 × 5 × 0.04	1.3	Electropolished	866	O_2, 200 ml/min	47
3	Fe-30 Ni	2 × 3.8 × 0.06	3.4	Etched as in ref. (2)	1005	still air	nil
4	Fe-30 Ni	2 × 3.8 × 0.06	3.4	Etched as in ref. (2)	1005	O_2, 100 ml/min	nil
5	Fe-30 Ni	2 × 3.8 × 0.06	3.4	Etched as in ref. (2)	1170	O_2, 100 ml/min	29
6	Fe-26 Cr	1 × 5 × 0.04	1.3	Electropolished	1165	O_2, 200 ml/min	nil

rate, increase the heat capacity of the specimen, or remove heat more efficiently from it.

The negative result in runs 3 and 4 with Fe-30 Ni at 1000° indicates that the deviation in the Arrhenius plot observed by Foley (2) was not due to overheating but rather to his alternative suggestion, that of a change in scaling mechanism. At 1170° the scaling rate is large enough to give sensible overheating (run 5).

No overtemperature in run 6 demonstrates that the relatively rapid initial scaling obtained with Fe-26 Cr alloys in the electropolished condition (5) is due to some cause other than overheating.

Manuscript received Dec. 21, 1959.

Any discussion of this paper will appear in a Discussion Section to be published in the December 1960 JOURNAL.

REFERENCES

1. N. G. Schmahl, H. Baumann, and H. Schenk, *Arch. Eisenhüttenw.*, **27**, 707 (1956).
2. R. T. Foley and C. J. Guare, *This Journal*, **106**, 936 (1959).
3. B. E. Hopkinson, *ibid.*, **106**, 102 (1959).
4. E. S. Bartlett and D. N. Williams, *Trans. Met. Soc. AIME*, **212**, 280 (1958).
5. D. Caplan, A. Harvey, and M. Cohen, to be communicated (presented at E.C.S. Columbus Meeting, 1959).

An Investigation of the Discharge Characteristics of Groups VI-VIII Oxides in an Alkaline Electrolyte

C. K. Morehouse and R. Glicksman

Semiconductor and Materials Division, Radio Corporation of America, Somerville, New Jersey

ABSTRACT

Experimental half-cell potential discharge data are given for a number of Groups VI-VIII oxides in strongly alkaline NaOH solution, along with comparisons between these data and their theoretical potentials. In general, the reduction of these oxides at a carbon electrode in alkaline electrolyte is irreversible.

Many of the desirable features of a battery cathode material, such as a high reversible electrode potential and coulombic capacity, stability, and compatibility with other cell components, are found among the metallic oxides. In a previous paper (1) experimental half-cell discharge data were given for a number of Groups Ib-Vb oxides in strongly alkaline NaOH solution along with comparisons between these data and their theoretical potentials. As an extension of this work, half-cell potential discharge data for various Group VI-VIII oxides in NaOH electrolyte are presented in this paper.

Experimental Procedure

Discharge data on the various oxides were obtained by use of a technique previously described by the authors (2). In this technique, a 0.5 g sample of the cathode material mixed with 10% Shawinigan acetylene black was discharged at constant current in a large volume of electrolyte. The change in the cathode potential with time was measured with a L&N Type K potentiometer using a saturated calomel reference electrode. Discharge data were corrected for the *IR* drop associated with the apparatus and electrolyte by means of an oscillographic technique.

The half-cell potentials are all referred to the normal hydrogen electrode and represent the average of two or three measurements. The reproducibility of the data is ±0.01-0.03 v.

In this study, a zinc anode was used with an alkaline electrolyte of 30% by weight NaOH solution which was saturated with ZnO. The solution was 10.7*M* prior to the addition of ZnO. The purpose of the ZnO is to reduce the corrosion of the Zn anode in the strongly alkaline electrolyte. During the discharge, hydroxide ions are formed, but as the solution is strongly alkaline initially, the change in hydroxide ion activity of the solution is negligible.

Potential measurements of the HgO electrode in this electrolyte vs. a S.C.E. give a value of +0.043 v for the HgO half-cell referred to the normal hydrogen electrode. The deviation from the standard potential of the HgO electrode ($E^\circ - E = +0.055$ v) is due to the greater hydroxide ion activity of the electrolyte, as well as to the existence of a liquid junction potential at the alkaline-saturated KCl interface. As these factors are constant for all measurements of the half-cell potentials, +0.055 v can be added to the experimentally determined discharge potentials of the various oxides in order to compare these values with their standard electrode potentials.

Experimental Data and Discussion of Results

Group VIb oxides.—Figure 1 shows half-cell potential discharge curves of CrO_3, Cr_2O_3, MoO_3, and WO_3 obtained when these compounds are discharged at a rate of 0.005 amp/g in the strongly alkaline NaOH electrolyte. As would be expected from standard potential data (3), Cr_2O_3, MoO_3, and WO_3 are reduced with great difficulty and have discharge potentials of −1.10 v or lower. The −1.10 v value is the potential characteristic of the discharge of hydrogen on the carbon electrode in this alkaline solution at that current density. In agreement with these results, Von Stackelberg, *et al.* (4) found that molybdate and tungstate do not produce polarographic waves in neutral or alkaline solution.

Chromic trioxide, which is discharged as a chromate ion in alkaline electrolyte, undergoes a one-step reduction at a potential from −0.35 to −0.40 v in this electrolyte. This value is about 0.2 v more negative than its reversible potential. Hence, the reduction of chromate ion under these conditions of discharge is irreversible. This fact is in general agreement with the polarographic data of Lingane and Kolthoff (5) for the reduction of chromate ion at the dropping mercury electrode. However, their half-wave potential values are from 0.25 to 0.30 v more negative than the cathode potential of CrO_3 given in Fig. 1.

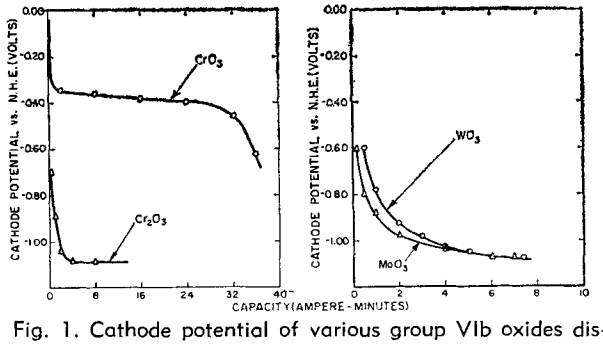

Fig. 1. Cathode potential of various group VIb oxides discharged in 30% NaOH-70% H_2O, saturated with ZnO electrolyte at a rate of 0.005 amp/g.

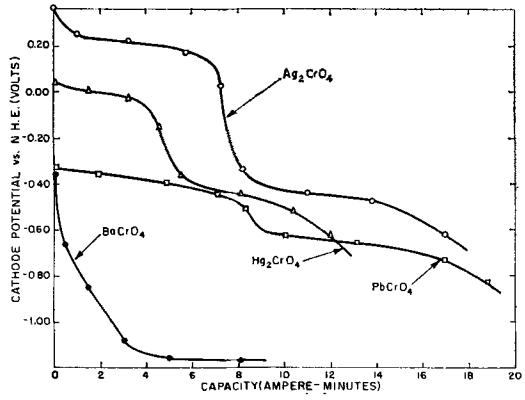

Fig. 2. Cathode potential of various chromates discharged in 30% NaOH-70% H_2O, saturated with ZnO electrolyte at a rate of 0.005 amp/g.

Under the present conditions of discharge, the reduction of $CrO_4^=$ does not proceed farther than the +3 oxidation state because the discharge of hydrogen ions at the carbon cathode takes place at a less negative potential than that required for the reduction of $Cr(OH)_3$ or CrO_2^-. Thus, the reduction of $CrO_4^=$ in alkaline solution can be expressed by the following equation

$$CrO_4^= + 4H_2O + 3e^- = Cr(OH)_3 + 5\ OH^-,\ E^\circ_B = -0.13\ v \quad [1]$$

If a 3 electron change and a −0.60 v end potential are assumed, the CrO_3 electrode operates at an electrode efficiency of 73.5%.

Figure 2 shows half-cell potential discharge curves of $BaCrO_4$ and the metal chromates, Ag_2CrO_4, Hg_2CrO_4, and $PbCrO_4$, all of which contain a reducible cation. The latter three compounds exhibit a two-step potential-time discharge curve with potential steps characteristic of their respective oxides (1), and of the chromate ion. For $PbCrO_4$, the chromate ion is discharged first because its cathode potential is less negative than that of the plumbite ion. With a −0.60 v end potential for Ag_2CrO_4 and Hg_2CrO_4 and an −0.80 v end potential for $PbCrO_4$, and if a 5 electron change is assumed, electrode efficiencies of 69, 74, and 73%, respectively, are obtained from these compounds.

The rapid decrease in cathode potential of the highly insoluble $BaCrO_4$ compound during discharge is believed due to the resultant low concentration of chromate ion available for the electrochemical reaction.

Group VIIb oxides.—Work by Walkley (6-8) on the Mn-Mn^{++} and Mn^{++}-MnO_2 couples has done much to clarify the thermodynamics of the various oxidation states of manganese. According to Latimer (3), it now appears definite that cell measurements on the Mn^{++}-MnO_2 and MnO_2-MnO_4^- couples are reliable and reproducible when the manganese dioxide is in the form of pyrolusite, prepared by heating manganous nitrate. He lists the following alkaline cell reactions which involve manganese dioxide, manganate, and permanganate

$$MnO_4^- + 2H_2O + 3e^- = MnO_2\ (\text{pyrolusite}) + 4\ OH^-,\ E^\circ_B = +0.588\ v \quad [2]$$

$$MnO_4^- + e^- = MnO_4^=,\ E^\circ = +0.564\ v \quad [3]$$

$$MnO_4^= + 2H_2O + 2e^- = MnO_2 + 4\ OH^-,\ E^\circ_B = +0.60\ v \quad [4]$$

The MnO_4^--MnO_2 potential was obtained from direct cell measurements (9), and values for the MnO_4^--$MnO_4^=$ and $MnO_4^=$-MnO_2 couples were obtained by recalculations of the equilibrium measurements of Schlesinger and Siems (10).

The half-cell potential discharge curves presented in Fig. 3 show that $KMnO_4$ initially operates at a potential from 0.06 to 0.08 v lower than the theoretical potentials of the MnO_4^--$MnO_4^=$ and $MnO_4^=$-MnO_2 couples, after corrections are made for the *p*H of the solution and for the liquid junction potential. The two-step potential-time discharge curve of this compound in alkaline electrolyte can be interpreted in terms of a 3 electron reduction to MnO_2, with subsequent reduction to the +3 and +2 oxidation states of manganese. No analytical data, however, are available to confirm this reasoning.

In contrast to $KMnO_4$, $BaMnO_4$ operates at a cathode potential 0.9 v lower than the theoretical potential of the $MnO_4^=$-MnO_2 couple and gives little capacity in the alkaline electrolyte.

$KReO_4$ also operates at a considerably lower cathode potential than $KMnO_4$ in alkaline electrolyte, as would be expected from the following standard potential data given by Latimer (3):

$$ReO_4^- + 2H_2O + 3e^- = ReO_2 + 4\ OH^-,\ E^\circ_B = -0.594\ v \quad [5]$$

$$ReO_4^- + 4H_2O + 7e^- = Re + 8\ OH^-,\ E^\circ_B = -0.584\ v \quad [6]$$

$KReO_4$ operates at a potential of from 0.15 to 0.20 v below its theoretical value, although it is uncertain whether the reduction of $KReO_4$ proceeds by Eq. [5] or [6]. On the basis of a 3 electron reduction step (Eq. [5]), it is calculated that this electrode would operate at an efficiency of 95%, if a −1.0 v end potential is assumed.

It is of interest to discuss the manganese dioxide electrode, which has long been used as a cathode material in primary cells because of its high theoretical electrode potential and coulombic capacity. Although the reduction of manganese dioxide is often represented by a simple equation such as the one calculated by Walkley (11) from thermal data,

$$MnO_2 + H_2O + e^- = MnOOH + OH^-,E^\circ_B = +0.17\ v \quad [7]$$

the half-cell potential discharge curve of this cathode exhibits a sloping characteristic as shown by the data in Fig 3. This suggests a complex reaction mechanism.

Recent studies of the alkaline reduction of manganese dioxide in dry cells by Cahoon and Korver (12) showed both divalent manganese, presumably formed as $Mn(OH)_2$ in the cathode, and an insoluble manganese oxide residue as the reduction products. That divalent manganese is an end product in the alkaline reduction of MnO_2 is evident from the half-cell potential discharge curves in Fig. 3 of electro-

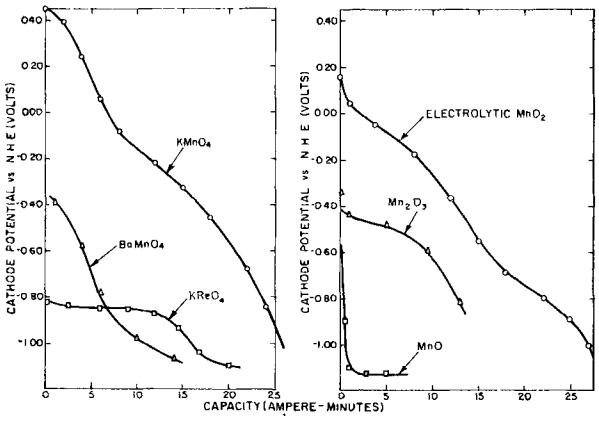

Fig. 3. Cathode potential of various group VIIb oxides discharged in 30% NaOH-70% H_2O, saturated with ZnO electrolyte at a rate of 0.005 amp/g.

lytic MnO_2 (85% MnO_2 content) and Mn_2O_3. For example, if end potentials of −0.40 v and −0.80 v are assumed for a one and two electron reduction, respectively, electrode efficiencies of 80 and 71% are obtained for MnO_2. For Mn_2O_3, an electrode efficiency of 62% is obtained if an 0.80 v end potential and a one electron change are assumed. However, the reduction of Mn_2O_3 may also take place according to the following idealized equations of Walkley (11):

$$3Mn_2O_3 + H_2O + 2e^- = 2Mn_3O_4 + 2\,OH^-, E^\circ_B = -0.18\text{ v} \quad [8]$$

$$2Mn_3O_4 + 2H_2O + 4e^- = 6MnO + 4\,OH^-, E^\circ_B = -0.39\text{ v} \quad [9]$$

Reduction ceases at the divalent manganese state, as evidenced by the discharge data for MnO. This effect is to be expected on the basis of the high negative potential of the $Mn(OH)_2$-Mn couple.

The slightly higher initial cathode potential of electrolytic manganese dioxide as compared to the potential given in Eq. [7] is thought to be due to the difference in the thermodynamic properties of the various oxides which differ chiefly in their E° values (11). These values for γ −MnO_2 are about 150 mv higher than those for pyrolusite.

Measurements conducted in acid solution (6) have shown that the E° values of the following reaction

$$MnO_2 + 4H^+ + 2e^- = Mn^{++} + 2H_2O, E^\circ_A = +1.23\text{ v} \quad [10]$$

depend on both the structural type of oxide and the value of n in the formula MnO_n. The variation in potential of various manganese dioxides in acid solution is illustrated by the half-cell potential discharge data in Fig. 4 for naturally occurring African MnO_2 and a synthetic electrolytic MnO_2. The discharge curves were obtained by discharging these compounds at a rate of 0.005 amp/g in 480 g/l $AlCl_3 \cdot 6H_2O$ electrolyte. A similar relationship between the two dioxides also exists in strongly alkaline solution (13).

The discharge curves for the two manganese dioxides in this acidic electrolyte are considerably flatter than those obtained for these compounds in solutions of higher pH. In addition, if an end potential of zero volt is assumed, both these compounds

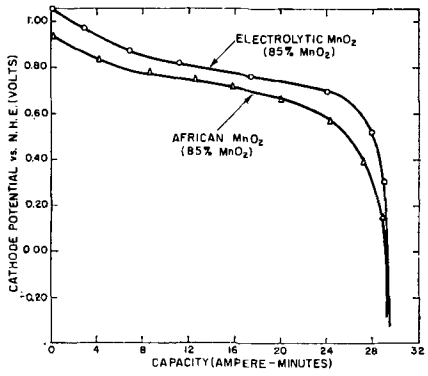

Fig. 4. Cathode potential of synthetic and naturally occurring manganese dioxide discharged in 480 g/l $AlCl_3 \cdot 6H_2O$ electrolyte at a rate of 0.005 amp/g.

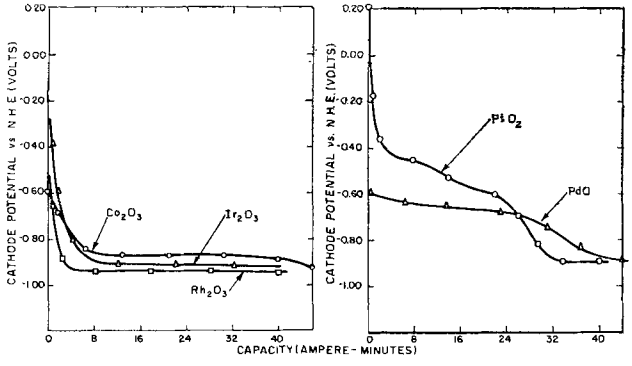

Fig. 5. Cathode potential of various group VIII oxides discharged in 30% NaOH-70% H_2O, saturated with ZnO electrolyte at a rate of 0.005 amp/g.

are reduced to the divalent manganese state with electrode efficiencies of 94%.

Group VIII oxides.—Figure 5 presents a comparison of the half-cell potential discharge curves of the oxides of the +3 valence state of cobalt, rhodium, and iridium, along with the discharge curves of PtO_2 and PdO_2 in alkaline electrolyte. Co_2O_3, Ir_2O_3, and Rh_2O_3 are reduced with difficulty in this electrolyte, and the flat potential-time discharge curve around −0.90 v probably represents the potential at which hydrogen ion is discharged. The discharge of hydrogen ion at the carbon electrode in this electrolyte occurs at a potential approximately 0.2 v less negative than usual (see Fig. 1), probably because of the presence of small amounts of these low hydrogen overpotential metals in the carbon mix. The low cathode potentials of these oxides would not be expected on the basis of Latimer's standard potential data.

Similarly, PtO_2 and PdO operate at potentials considerably below the theoretical values given by Latimer

$$Pt(OH)_6^= + 2e^- = Pt(OH)_2 + 4\,OH^-, E^\circ_B = +0.1 \text{ to } +0.4\text{ v} \quad [11]$$

$$Pt(OH)_2 + 2e^- = Pt + 2\,OH^-, E^\circ_B = +0.15\text{ v} \quad [12]$$

$$Pd(OH)_2 + 2e^- = Pd + 2\,OH^-, E^\circ_B = +0.07\text{ v} \quad [13]$$

Figure 5 indicates that the reduction of PtO_2 to Pt appears to take place in two steps, whereas PdO exhibits a flat potential-time discharge curve in the alkaline electrolyte. For these oxides, electrode effi-

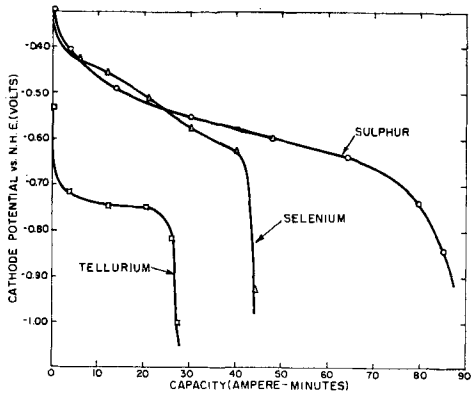

Fig. 6. Cathode potential of various group VIo elements discharged in 30% NaOH-70% H_2O, saturated with ZnO electrolyte at a rate of 0.005 amp/g.

ciencies of 100% are obtained to a −0.90 v end potential.

Group VIa oxides.—One of the most striking characteristics of the Group VIa potentials is the decrease in oxidizing power of the free elements with increasing atomic weight, as indicated by the following standard potential data (3)

$$S + 2e^- = S^=, E^\circ = -0.48 \text{ v} \quad [14]$$

$$Se + 2e^- = Se^=, E^\circ = -0.92 \text{ v} \quad [15]$$

$$Te + 2e^- = Te^=, E^\circ = -1.14 \text{ v} \quad [16]$$

The half-cell potential discharge data of Fig. 6 show that Se and Te in an alkaline electrolyte operate at cathode potentials considerably more positive than the values given by Latimer. The latter values are in doubt, however, because of the difficulty encountered in obtaining accurate thermodynamic data with which to calculate these potentials. S and Se, which have comparable sloping half-cell potential-time discharge curves, operate at approximately the same cathode potentials during the course of the discharge. This is in disagreement with the expected results based on the chemical reactivity of S and Se. If an −0.80 v end potential is assumed, electrode efficiencies of 82,100 and 100% are obtained from S, Se, and Te, respectively.

Figure 7 gives half-cell potential discharge data for various oxides of the +4 and +6 states of these elements. The oxides of Se and Te operate at cathode potentials of from −0.50 to −0.60 v in this alkaline electrolyte, although the corresponding sulfur compounds, Na_2SO_3 and Na_2SO_4, cannot be reduced under the present conditions of discharge.

It is apparent from the data that both the selenate and tellurate compounds are reduced with a corresponding eight electron change to the selenide and telluride ion, respectively. With an −0.80 v end-potential, electrode efficiencies of 93% and 80% are obtained for $NaTeO_4$ and $NaSeO_4 \cdot 10\,H_2O$. Recent work (14) on the controlled potential electrolysis of telluric acid at a mercury cathode further indicates that the reduction of +6 tellurium proceeds to −2 tellurium.

Similarly Lingane and Niedrach (15) showed by a coulometric technique that the reduction of +4 tellurium in alkaline medium proceeds to −2 tellurium according to the following equation:

$$TeO_3^= + 3H_2O + 6e^- = Te^= + 6\,OH^- \quad [17]$$

On the basis of a six electron change, electrode efficiencies of 57% and 65% have been calculated from the data in Fig. 7 for SeO_2 and TeO_2.

Group VIIa oxides.—The free halogens as well as the oxygen acids and their salts are powerful oxidizing agents with respect to their reduction to the halide. Oxides of the +5 and +7 oxidation states, because of their high theoretical capacity, are of principal interest for use as cathode materials in primary cells.

Figure 8 presents half-cell potential discharge curves of $KClO_3$, $KBrO_3$, and KIO_3 obtained when these compounds are discharged at a rate of 0.005 amp/g in strongly alkaline NaOH solution. In agreement with polarographic data (16), the reduction of bromate and iodate ions to the corresponding halide ions takes place in a single step. If an −0.80 v end potential and a 6 electron change are assumed for the reduction of $KBrO_3$ and KIO_3, these compounds operate at efficiencies of 92 and 91%, respectively.

The data in Fig. 8 and Latimer's standard potential data

$$IO_3^- + 3H_2O + 6e^- = I^- + 6\,OH^-, E^\circ_B = +0.274 \text{ v} \quad [18]$$

$$BrO_3^- + 3H_2O + 6e^- = Br^- + 6\,OH^-, E^\circ_B = +0.61 \text{ v} \quad [19]$$

show clearly that the reduction of both ions is irreversible. Despite the more positive standard potential of BrO_3^- as compared with IO_3^-, KIO_3, and $KBrO_3$

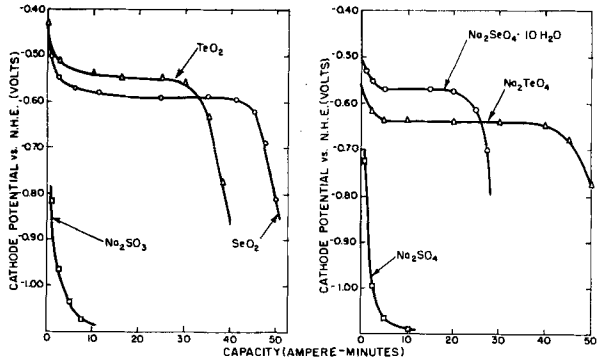

Fig. 7. Cathode potential of various group VIa oxides discharged in 30% NaOH-70% H_2O, saturated with ZnO electrolyte at a rate of 0.005 amp/g.

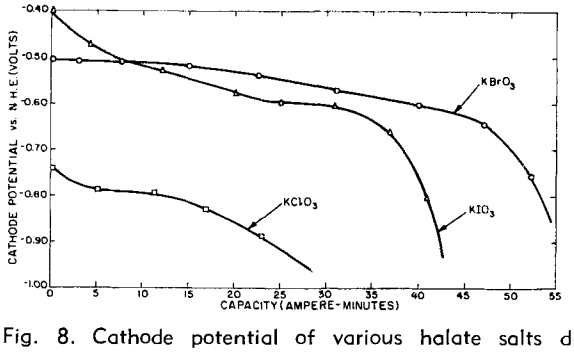

Fig. 8. Cathode potential of various halate salts discharged in 30% NaOH-70% H_2O, saturated with ZnO electrolyte at a rate of 0.005 amp/g.

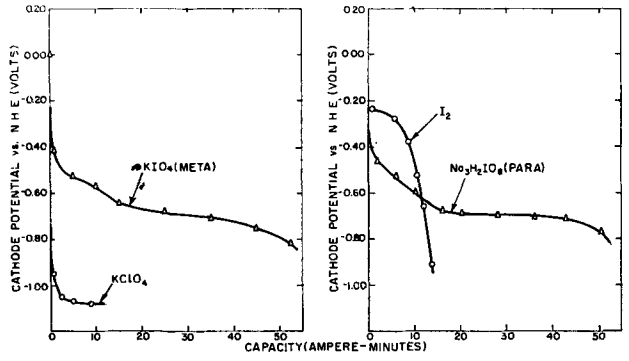

Fig. 9. Cathode potential of various perhalote compounds discharged in 30% NaOH-70% H_2O, saturated with ZnO electrolyte at a rate of 0.005 amp/g.

operate at comparable cathode potentials in the alkaline electrolyte. This is attributed to a higher overpotential for the reduction of BrO_3^- as compared with the reduction of IO_3^-. For example, at the dropping mercury electrode in acid medium, it has been found that the overpotential amounts to about 0.7 v for iodate and about 1.3 v for bromate (16).

The low cathode potential of $KClO_3$, as compared with $KBrO_3$ and KIO_3, is in agreement with observations that chlorate is not readily reduced at a cathode on electrolysis of a chlorate solution, nor is chlorate ion reduced at a dropping mercury electrode.

Figure 9 compares the half-cell potential discharge curves of sodium paraperiodate ($Na_3H_2IO_6$) and potassium metaperiodate (KIO_4) with that of potassium perchlorate. As expected from the highly negative cathode potential of $KClO_3$ given in Fig. 8 and from the fact that the oxidizing power of the oxy acids of chlorine (and their salts) decreases with increase in oxidation number of chlorine, $KClO_4$ cannot be reduced under the present conditions of discharge. The reduction of periodate, however, appears to take place with a two electron change to iodate, as follows:

$$H_3IO_6^{=} + 2e^- = IO_3^- + 3\ OH^-,\ E^\circ_B = \text{ca.} + 0.7\ \text{v} \quad [20]$$

The iodate ion subsequently is reduced to the iodide in accordance with Eq. [18]. If a −0.60 v end potential and a 2 electron change are assumed, both KIO_4 and $Na_3H_2IO_6$ are reduced to the iodate with electrode efficiencies of 86%. For reduction to the halides, KIO_4 and $Na_3H_2IO_6$ give electrode efficiencies of 90 and 100%, respectively, if an 8 electron change and an end potential of −0.80 v are assumed. Similarly, the electroreduction of periodate at the dropping mercury electrode in acid solution (17) shows two general waves corresponding to a reduction to the iodate and then to the iodide.

The high cathode potential of iodine shown in Fig. 9 further indicates that reduction of the iodate proceeds directly to the halide rather than through the halogen stage.

Manuscript received Oct. 8, 1959. This paper was prepared for delivery before the Ottawa Meeting, Sept. 28-Oct. 2, 1958.

Any discussion of this paper will appear in a Discussion Section to be published in the December 1960 JOURNAL.

REFERENCES

1. R. Glicksman and C. K. Morehouse, *This Journal*, **104**, 589 (1957).
2. C. K. Morehouse and R. Glicksman, *ibid.*, **103**, 94 (1956).
3. W. M. Latimer, "Oxidation Potentials," 2nd ed., Prentice-Hall, Inc., Englewood Cliffs, N. J. (1952).
4. M. von Stackelberg, P. Klinger, W. Koch, and E. Krath, *Tech. Mitt. Krupp Forschungsber*, **2**, 59 (1939).
5. J. J. Lingane and I. M. Kolthoff, *J. Am. Chem. Soc.*, **62**, 852 (1940).
6. A. D. Wadsley and A. Walkley, *J. (and Trans.) Electrochem. Soc.*, **95**, 11 (1949).
7. A. Walkley, *ibid.*, **93**, 316 (1948).
8. A. Walkley, *ibid*, **94**, 41 (1948).
9. L. V. Andrews and D. J. Brown, *J. Am. Chem. Soc.*, **57**, 254 (1935).
10. H. I. Schlesinger and H. B. Siems, *ibid.*, **46**, 1965 (1924).
11. A. Walkley, *This Journal*, **99**, 209C (1952).
12. N. C. Cahoon and M. P. Korver, *ibid.*, **106**, 745 (1959).
13. C. K. Morehouse and R. Glicksman, *ibid.*, **103**, 94 (1956).
14. E. Norton, R. W. Stoenner, and A. I. Medalia, *J. Am. Chem. Soc.*, **75**, 1827 (1953).
15. J. J. Lingane and L. W. Niedrach, *ibid.*, **71**, 196 (1949).
16. I. M. Kolthoff and J. J. Lingane, "Polarography," Vol. II, Chapt. XXXIV, Interscience Publishers, New York (1952).
17. R. H. Coe and L. B. Rogers, *J. Am. Chem. Soc.*, **70**, 3276 (1948).

Kinetics of the Dissolution of Copper in Aqueous Solutions of Aliphatic Diamines

S. C. Sircar[1] and D. R. Wiles[2]

Department of Mining and Metallurgy, University of British Columbia, Vancouver, Canada

ABSTRACT

The recent work on the mechanisms of the dissolution of copper in aqueous solutions of amines has been extended to the diamines. The chelating agents used were ethylenediamine, 1,3 propanediamine, and 1,4 butanediamine. The dissolution reaction is shown to involve two distinct steps. The first step is found to be an adsorption pre-equilibrium. In the second step, two types of reaction compete: chelation and attack by a second ligand. Desorption of the complex follows these steps. In 1,4 butanediamine, the chelation step is not observable, while in ethylenediamine the chelation appears to be so fast as to obscure the bimolecular reaction. In propanediamine, both are evident. The reactions of the singly protonated species have been found to be solely by bimolecular attack.

Recent studies (1-4) have done much to elucidate the mechanism of the dissolution of metallic copper in oxygen-containing solutions of various complexing agents. The work of Halpern (1) demonstrated that it is necessary to define two kinetic regions: the "low oxygen pressure" region, in which diffusion of reactants limits the rate, and the "high pressure region," in which the reaction rate is chemically controlled at the surface. Halpern also showed that the rates of dissolution by ammonia molecules and by ammonium ions were essentially independent, although some free ammonia must be present for any dissolution to occur.

Our recent study (4), involving dissolution of copper in solutions of ammonia, and methyl-, ethyl-, and n-butylamines, and their conjugate acids, led to a fairly clear picture of the reactions involved. It was concluded that the reactions take place in the following stages (where A represents the amine, and the subscript s designates species residing in the surface).

$$Cu_s + \tfrac{1}{2}\,O_2 \rightleftharpoons Cu_s{-}O \qquad \text{fast, } K \text{ large}$$

$$Cu_s{-}O + A \rightleftharpoons Cu_s{-}O(A) \qquad \text{fast, } K_1$$

$$Cu_s{-}O(A) + A \rightarrow Cu_s{-}O(A)_2 \qquad \text{slow, } k_2$$

$$Cu_s{-}O(A)_2 + H_2O \rightarrow Cu(A_2)^{++} + 2\,OH^- \qquad \text{fast}$$

Competitive with the attack by the second amine molecule is attack by a molecule of the conjugate acid, or "aminium" ion. Thus, the last two steps could occur in the following way:

$$Cu_s{-}O(A) + AH^+ \rightarrow Cu_s{-}O(A)(A\text{-}H^+) \qquad \text{slow, } k_3$$

$$Cu_s{-}O(A)(A\text{-}H^+) \rightarrow Cu(A)_2^{++} + OH^- \qquad \text{fast}$$

The pre-equilibrium appeared not to involve the aminium ion, a fact which accounts, at least in part, for the observed passivity of copper in ammonia-free solutions of ammonium salts (2, 4).

The rate of a reaction which proceeds according to the above mechanism can be expressed by the following equation:

$$\text{Rate} = \frac{d[Cu^{++}]}{dt} = \frac{K_1[A]S}{1 + K_1[A]} \cdot \{k_2[A] + k_3[AH^+]\} \qquad [1]$$

This equation was found to describe the observed rates very well for ammonia and the aliphatic amines studied. S represents the total surface area.

The observation of the bimolecular nature of the dissolution reaction led to the speculation that ethylenediamine may behave similarly. In this last case, however, the reaction would be monomolecular, because both attacking groups are attached to the same molecule. It seemed to be of interest, in view of this, to study the dissolution kinetics in solutions of longer chained diamines. In such case, one would expect the chelation step to become slower as the number of atoms in the chain increases.

It was with this in view that the present work was undertaken. The reagents used were ethylenediamine (en), 1,3 propanediamine (pn), and 1,4 butanediamine (bn), which form, on chelation, rings with five, six, and seven atoms, respectively. Data on the acid-base equilibria and the copper complexing equilibrium for these diamines are shown in Table I.

Experimental

The experimental methods used were the same as those of the previous work (3, 4). The experiments were performed in a 1-gal stainless steel autoclave fitted with a titanium liner. The oxygen pressure and stirring rate were maintained high enough to in-

[1] Present address: Bakhrabad, Cuttack 2, Orissa, India.
[2] Present address: Department of Chemistry, Carleton University, Ottawa, Ont., Canada.

Table I. Some equilibrium data for the diamines used in this work (5)

Equilibrium	Log K
Ethylenediamine (en)	
$Cu^{++} + en \rightleftharpoons Cuen^{++}$	10.73
$Cuen^{++} + en \rightleftharpoons Cuen_2^{++}$	9.30
1, 3 Propanediamine (pn)	
$Cu^{++} + pn \rightleftharpoons Cupn^{++}$	10.58
$Cupn^{++} + pn \rightleftharpoons Cupn_2^{++}$	9.08
1, 4 Butanediamine (bn)	
$Cu^{++} + bn$	No chelate*

* We have found only negative references to chelates involving 1, 4 butanediamine (6, 7). Pfeiffer (8) has made the $Cu(1, 4\ bn)_2^{++}$ chelate, but only in alcohol and ether solutions.

sure that the transport of reactants to the surface was not a factor in rate control. Samples withdrawn periodically from the autoclave were analyzed spectrophotometrically for copper by the carbamate method (9). As in our previous work, solutions were maintained at an ionic strength of 0.1 by adjustment with $NaClO_4$. All experiments were done at a temperature of 25.0° ± 0.1°C and at an oxygen pressure of 7.8 atm.

The 1,3 propanediamine and 1,4 butanediamine were obtained from K and K Chemicals Inc., and were used without further purification. On long standing the stock solutions of these reagents tended to become yellowish and were replaced. The ethylenediamine was obtained as 99% pure material from Carbide and Carbon Chemicals Corporation and was used without further purification. It had been found earlier (3) that fractional distillation of the ethylenediamine had no effect on the rate of dissolution.

Acid effects were studied after addition of measured amounts of reagent grade perchloric acid to the diamine solution.

Reproducibility of analyses and of rate measurements was very good, generally to within ±2%. At very high rates, there seemed to be greater scatter in the results. It is not understood why this is so, but it may be that transport control is becoming important.

Results

The experimental measurements made were on the systems under three different sets of conditions involving, respectively, the free diamines, the monoprotonated species (the first conjugate acids), and the free diamines with excess acid added.

Free diamines.—The results of rate measurements on the free diamines are summarized in Table II and shown graphically in Fig. 1, 2, and 3.

The forms of the curves for the three diamines are very different from each other, but can nevertheless be described quantitatively in terms of a single set of competing mechanisms, based on our earlier conclusion (4) that two amine groups coordinate with a copper atom before it enters the solution. If one suppose a surface, covered with adsorbed oxygen atoms, to engage in a fast equilibrium adsorption (K_1) of the diamine molecule, then the desorption of the complexed copper atom may follow after either chelation (k_1) by the diamine molecule al-

Table II. Rates of dissolution of copper in diamine solutions

Ethylenediamine		1, 3 Propanediamine		1, 4 Butanediamine	
[en]	Rate (mg Cu cm^{-2} hr^{-1})	[pn]	Rate (mg Cu cm^{-2} hr^{-1})	[bn]	Rate (mg Cu cm^{-2} hr^{-1})
0.047	11.7*	0.0215	3.4	0.052	0.60
0.070	16.5	0.048	6.6	0.101	1.35
0.071	17.2*	0.091	10.8	0.229	4.05
0.095	22.8*	0.111	12.6	0.44	8.50
0.104	22.8	0.123	12.8	0.502	9.70
0.128	34.4	0.135	14.7		
0.143	31.3*	0.163	16.7		
		0.183	18.9		
		0.196	20.0		
		0.215	21.6		

* From Ref. 3.

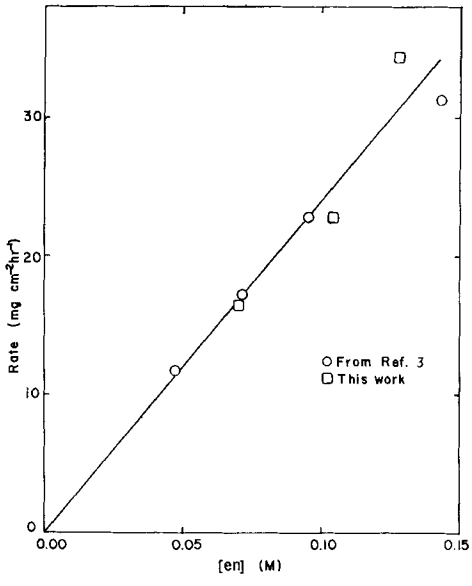

Fig. 1. Rate of dissolution of copper in free ethylenediamine (en) solution as a function of concentration.

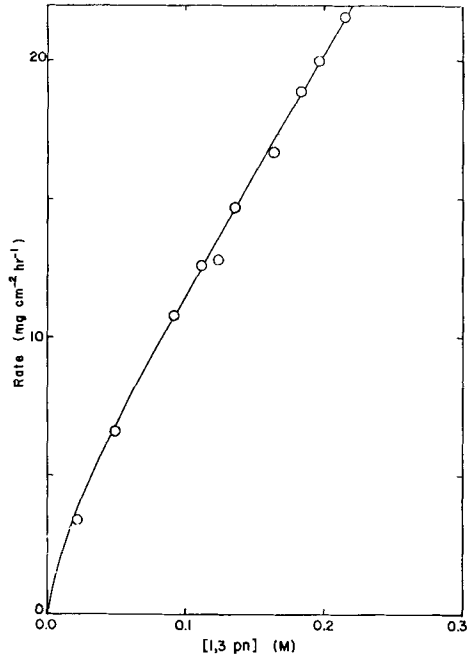

Fig. 2. Rate of dissolution of copper in 1,3 propanediamine (pn) solutions as a function of concentration. Solid line calculated using Eq. [2].

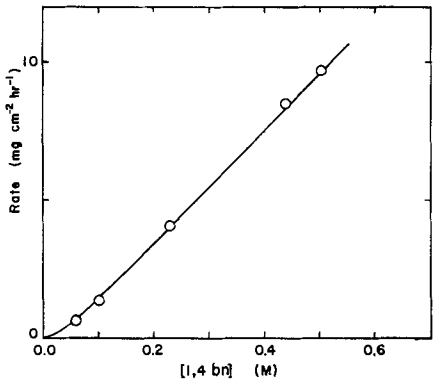

Fig. 3. Rate of dissolution of copper in 1,4 butanediamine (bn) solutions as a function of concentration. Solid line computed using Eq. [3].

ready attached, or attack (k_3) by a second molecule, such that each is coordinated at only one position. The over-all rate of dissolution is then given by Eq. [2]

$$\text{Rate} = \frac{d[Cu^{++}]}{dt} = \frac{K_1[X]S}{1 + K_1[X]}(k_1 + k_3[X]) \quad [2]$$

It is seen that where k_1 is very small, i.e., when chelation does not occur measurably, Eq. [2] reduces to:

$$\text{Rate} = \frac{K_1[X]S}{1 + K_1[X]} \cdot k_3[X] \quad [3]$$

Equation [3] is analogous to that used (4) to describe the bimolecular attack of the mono-amines on copper. It is found (Fig. 3) that this equation very well describes the observed effect of 1,4 butanediamine concentration on the dissolution rate.

If, on the other hand, k_1 is very large, (i.e., much larger than $k_3[X]$) for low values of $K_1[X]$, Eq. [2] reduces to

$$\text{Rate} = K_1k_1[X]S \quad [4]$$

This is equivalent to the expression used in earlier work (3) to describe the effect of ethylenediamine concentration on the rate of dissolution.

In the event that neither the chelation reaction nor the bimolecular attack can be ignored, then Eq. [2] must be used in full. This equation is seen in Fig. 2 to describe rather well the observed rates of dissolution of copper in 1,3 propanediamine.

The values found for the constants are given in Table III. The limits of error quoted are estimated by varying the constant enough to give a clearly bad fit of the data. It is these values for the constants which give the curves drawn in Fig. 1, 2, and 3.

Pure acid species.—Dissolution rates obtained in solutions of the mono-protonated species, ethylenediaminium and 1,3 propanediaminium, are given in Table IV.

The results can be interpreted satisfactorily by Eq. [5]

$$\text{Rate} = \frac{K_2[X]S}{1 + K_2[X]}(k_2 + k_4[X]) \quad [5]$$

where k_2 is found to be zero. It is evident from the form of Eq. [5] that dissolution in these solutions

Table III. Values found for the constants in Eq. [2] for the pure diamines

	en	1, 3 pn	1, 4 bn
K_1	$K_1k_1 = 240 \pm 10$	60 ± 5	22 ± 2
k_1	$K_1k_1 = 240 \pm 10$	5.0 ± 0.5	<0.1
k_3	$<<k_1$	85 ± 2	21 ± 0.5

Table IV. Rates of dissolution of copper in aqueous solutions of ethylenediaminium (enH^+) perchlorate and 1, 3 propanediaminium (pnH^+) perchlorate. These data are plotted in Fig. 4.

[enH⁺] (M)	Rate (mg cm⁻² hr⁻¹)	[pnH⁺] (M)	Rate (mg cm⁻² hr⁻¹)
0.022	4.8	0.17	2.40
0.039	8.6	0.040	6.40
0.061	16.2	0.060	9.8
0.071	19.6		
0.084	28.0		

occurs by bimolecular attack. The chelation step, corresponding to the constant k_2, evidently does not occur in the pure acid systems. The mechanism proposed for this dissolution is closely analogous to that described for the free amines.

The values for the constants for the above reactions are given in Table V. The curves shown in Fig. 4 were calculated using these values.

Mixed acid and basic species.—The "acid effect"–the change in rate on addition of acid to an excess of the free diamine–was studied only for 1,3 propanediamine. The results are given in Table VI.

It seems likely that the nature of the processes occurring in this mixed system are the same as those occurring in the pure systems, with two additional "cross-reactions" leading to the same reacting species

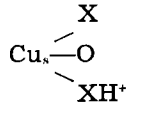

Since it is not possible kinetically to distinguish between the two paths by which this species can be formed, the observed cross-reaction rate will be best considered as the linear sum of the two independent

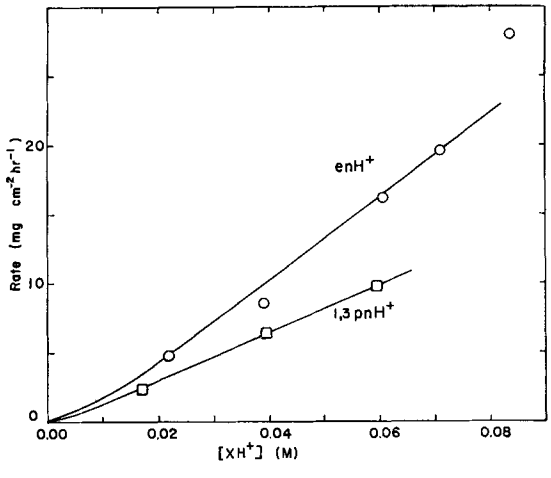

Fig. 4. Rate of dissolution of copper in solutions of ethylenediaminium (enH^+) and 1,3 propanediaminium (pnH^+) perchlorates. Solid lines calculated using Eq. [5].

Table V. Values for the constants in Eq. [5] for the pure mono-protonated diamines

	enH+	pnH+
K_2	120 ± 20	275 ± 25
k_2	0	0
k_4	310 ± 10	175 ± 10

Table VI. Rates of dissolution of copper in solutions containing both the acidic and basic forms of 1,3 propanediamine

[pn](M)	[pnH+](M)	Rate (mg cm^{-2} hr^{-1})
0.025	0.005	4.7
0.025	0.010	5.3
0.025	0.020	6.5
0.045	0.010	8.7
0.045	0.020	10.5
0.045	0.030	12.3
0.10	0.020	18.0
0.10	0.040	24.0
0.10	0.060	28.0

rates. Values were determined for the apparent rate constants by considering each reaction, in turn, to account for the whole of the cross reaction. Values are given in Table VII. This procedure necessarily will involve several sources of error. It is not surprising, then, that the values of the constants computed from the results of individual experiments showed a trend rather than a random scatter. The total range of the trend was only 40%, for reaction rates varying by as much as a factor of six, so it seems justifiable to give a 20% "confidence limit" on the mean values. The total experimental rates and computed rates are compared in Fig. 5.

Summary and Discussion

The dissolution of metallic copper in aqueous solutions of aliphatic diamines has been found to occur as the sum of a complex array of competing processes. These processes all give the same final product, that is, dissolved cupric ion, appropriately complexed, and the competing steps can be isolated only by studying extremes of pH, such that a small number of reactions are overwhelmingly predominant.

The reaction involves an oxygen-adsorption pre-equilibrium step

$$Cu_s + \tfrac{1}{2} O_2 \overset{fast}{\rightleftharpoons} Cu_s{-}O$$

followed by one of two competing pre-equilibria:

$$Cu_s{-}O + X \overset{fast}{\rightleftharpoons} Cu_s{-}O{-}X \qquad K_1$$

$$Cu_s{-}O + XH^+ \overset{fast}{\rightleftharpoons} Cu_s{-}O{-}XH^+ \qquad K_2$$

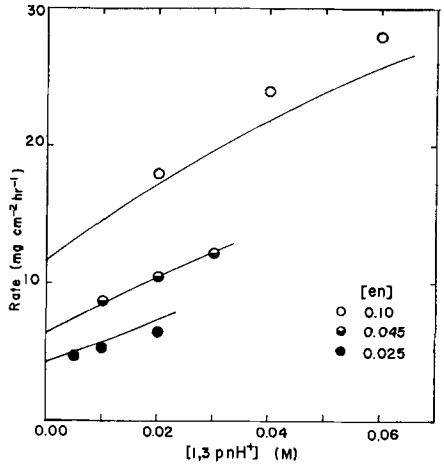

Fig. 5. Rate of dissolution of copper in mixed solutions of ethylenediamine (en) and ethylenediaminium (enH+) perchlorate: Comparison of experimental and calculated values.

The first of these two adsorbed species can form a chelate complex and desorb:

$$Cu_s{-}O{-}X \overset{slow}{\rightarrow} Cu_s{-}O{=}X \rightarrow \qquad k_1$$

$$Cu_s{-}O{=}X + H_2O \overset{fast}{\rightarrow} CuX^{++} + 2\,OH^-$$

The competing step involving the acid species:

$$Cu_s{-}O{-}XH^+ \rightarrow Cu_s{-}O{=}XH^+ \qquad k_2$$

$$Cu_s{-}O{=}XH^+ \rightarrow CuX^{++} + OH^-$$

appears not to occur to a detectable extent. There is also a bimolecular attack, very much the same as that occurring with the mono-amines (4):

$$Cu_s{-}O{-}X + X \overset{slow}{\rightarrow} Cu_s{-}O{-}X \qquad k_3$$

$$Cu_s{-}O{-}XH^+ + XH^+ \overset{slow}{\rightarrow} Cu_s{-}O{-}XH^+ \qquad k_4$$

and the corresponding cross reactions:

$$Cu_s{-}O{-}X + XH^+ \overset{slow}{\rightarrow} Cu_s{-}O{-}XH^+ \qquad k_5$$

$$Cu_s{-}O^+ + X \overset{slow}{\rightarrow} Cu_s{-}O{-}XH^+ \qquad k_6$$

Table VII. Summary of the equilibrium and rate constants

	K_1	K_2	k_1	k_2	k_3	k_4	k_5	k_6
en (K_1k_1 = 240 ± 10)	60 ± 5	120 ± 20	—	0	$<<k_1$	310 ± 10	—	—
pn	22 ± 2	275 ± 25	5.0 ± 0.5	0	85 ± 2	175 ± 10	975 ± 200	210 ± 40
bn		—	<0.1	—	21 ± 0.5	—	—	—

Each of these last steps is, of course, followed by hydration and desorption. The general equation to describe the rate gives the sum of all the six competing reactions.

$$\text{Rate} = \frac{d[Cu^{++}]}{dt} = \frac{S}{1 + K_1[X] + K_2[XH^+]}$$

$$\{K_1[X](k_1 + k_3[X] + ck_5[XH^+])$$

$$+ K_2[XH^+](k_2 + k_4[XH^+] + (1 - c)k_6[X])\} \quad [6]$$

where c and $(1 - c)$ are normalizing constants. The values of the constants in Eq. [6] are summarized in Table VII.

A comparison of constants is very instructive in some respects, although it must be emphasized that because of the complex nature of the system, quantitative comparison of the constants may not be justified.

Of foremost importance is the relation between the competitive reactions of chelation and bimolecular attack, as shown by the constants k_1 and k_3 for the free diamines and by k_2 and k_4 for the first conjugate acids. It is found that ethylenediamine dissolves copper almost wholly by chelation, 1,4 butanediamine almost wholly by means of bimolecular attack, and 1,3 propanediamine by a combination of both. This trend is in agreement with what one would expect from a consideration of the length of the carbon chains involved.

The value 240 obtained for the product K_1k_1 for ethylenediamine is much smaller than one would expect from an extrapolation of the values of K_1 and k_1 obtained for 1,3 propanediamine and 1,4 butanediamine. It seems possible that the chelation may occur so rapidly that the preliminary adsorption cannot attain equilibrium, that is, the term $K_1[X]/(1 + K_1[X])$ of Eq. [2] and [6] does not give the true concentration of the species $Cu_s\overset{en}{\diagup}O$. If this is so, then this system should properly be studied by use of a steady-state treatment. Unfortunately not sufficient data are available to make this distinction meaningful.

In the acid system, it is found that neither ethylenediamine nor 1,3 propanediamine dissolves by the chelation mechanism. This is perhaps surprising in view of the effect of acid on promoting the bimolecular dissolution of copper in the aliphatic monoamines.

It seems significant that in all cases the attack of the surface by a protonated species is more rapid than by the free amine. This is true in the pre-equilibria, in the bimolecular attack and in the cross reactions. This generalization does not, however, hold for the chelation reaction, which does not occur in the acid system.

Keelen and Anderson (10), studying the dissolution of nickel in diamines, suggested that there is competitive adsorption involving the diamine and the solvent where both are necessary in the dissolving species. Thus, they concluded, the chelation can have an interfering effect. This situation is clearly different from the present one, in which contact at two points seems to be required for dissolution.

Acknowledgment

The financial support of the National Research Council (Canada) is gratefully acknowledged.

Manuscript received Aug. 10, 1959.

Any discussion of this paper will appear in a Discussion Section to be published in the December 1960 JOURNAL.

REFERENCES

1. J. Halpern, *This Journal*, **100**, 421 (1953).
2. J. I. Fisher and J. Halpern, *ibid.*, **103**, 282 (1956).
3. J. Halpern, H. Milants, and D. R. Wiles, *ibid.*, **106**, 647 (1959).
4. S. C. Sircar and D. R. Wiles, *ibid.*, **107**, 164 (1960).
5. H. Irving, R. J. P. Williams, D. J. Ferrett, and A. E. Williams, *J. Chem. Soc.*, **1954**, 3494.
6. A. E. Martell and M. Calvin, "Chemistry of the Metal Chelate Compounds," p. 138f, Prentice-Hall, New York (1952).
7. F. Basolo and R. G. Pearson, "Mechanisms of Inorganic Reactions," p. 20f, John Wiley & Sons, Inc., New York (1958).
8. P. Pfeiffer, *Naturwiss.*, **35**, 190 (1948).
9. E. B. Sandell, "Colorimetric Determination of Traces of Metals," p. 204, Interscience Publishers, New York (1950).
10. T. L. Keelen and R. C. Anderson, *J. Phys. Chem.*, **59**, 881 (1955).

Brief Communications

The JOURNAL accepts short technical reports having unusual importance or timely interest, where speed of publication is a consideration. The communication may summarize results of important research justifying announcement before such time as a more detailed manuscript can be published. Consideration also will be given to reports of significant unfinished research which the author cannot pursue further, but the results of which are of potential use to others. Comments on papers already published in the JOURNAL should be reserved for the Discussion Section published biannually.

Submit communications in triplicate, typewritten double-spaced, to the Editor, Journal of The Electrochemical Society, 1860 Broadway, New York 23, N. Y.

Dissolution of Single Crystals of Copper in Aqueous Ethylenediamine

Leslie H. Jenkins

Solid State Division, Oak Ridge National Laboratory,[1] Oak Ridge, Tennessee

ABSTRACT

The kinetics of the dissolution of preferentially oriented single crystal plates of 99.999% copper in stirred aqueous solutions of 10^{-2}M ethylenediamine containing oxygen have been studied. The dissolution rates, which were controlled by a transport process in solution, were a function of the temperature and stirring rate of the solution, but were independent of the crystallographic orientation of the exposed metal surface. From the examination of the facets developed during the course of the reaction on crystals with low index faces, it was concluded that the order of stability of the crystal faces was (100) > (110) > (111) in this particular system. Other than anomalous faceting observed in regions thought to correspond to grain boundaries, no correlation between chemical reactivity and crystal imperfections was observed.

The kinetics of the dissolution of polycrystalline copper in aqueous solutions which contain oxygen and a reagent capable of dissolving copper oxides have been studied extensively (1-3). These and other data show that by suitably varying the conditions under which the reaction is carried out, the type of kinetic control operative in any given system may be altered.

Halpern (1) rigorously defined such conditions for the oxidation of copper in aqueous ammonia solutions containing oxygen. More recently data have been obtained on the dissolution of copper in oxygen-containing solutions by several complexing agents, including ethylenediamine (3); however, the kinetic data reported is restricted to regions of high oxygen pressures where the rate is zero-order in oxygen and first-order in the complexing agent.

If single crystals of copper are exposed to environments such as these, facets and/or pits are developed on the surface of the metal. The geometrical symmetry of these facets or pits is a function of, among other things, the crystallographic orientation of the exposed face of the metal crystals. Also, it is generally believed that some of the pits and facets on the surface should bear a relationship to points where dislocations in the single crystals intersect the surface, since these are points at which the chemical potential is greater than that of an idealized atomically smooth surface. Kinks, steps, and other points of departure from the theoretically ideal surface should also be more favorable energetically as sites where reactions are initiated (4). Therefore, it appeared worthwhile to observe the changes in surfaces of single crystals of copper of various crystallographic orientations undergoing dissolution while gathering kinetic data on the system. The reaction of copper with oxygen in dilute aqueous ethylenediamine which is described by the following equation, was chosen for investigation:

$$Cu + 1/2\,O_2 + H_2O + 2\,en \rightarrow Cu(en)_2^{++} + 2\,OH^- \quad [1]$$

[1] Oak Ridge National Laboratory is operated by Union Carbide Corporation for the U. S. Atomic Energy Commission.

Conditions were such that a transport process in solution was rate-controlling. Future work will include observations on this and other aqueous systems under various types of kinetic control.

Experimental

Material.—American Smelting and Refining Company 99.999% material was used to grow copper single crystals of specific orientation by seeding from the melt in graphite crucibles. Specimens produced were parallelepipeds approximately 0.1 x 1 x 7 cm having the desired surface orientation on the 7 x 1 cm area. From these slugs three samples 0.1 x 1 x 2 cm were cut carefully with a jeweler's saw. Each crystal used was within three degrees of the desired surface orientation, and all data reported here were gathered on single crystalline material. A 1/16 in. diameter hole was drilled at one end of the crystal so that it could be suspended in the reaction vessel. The large sides of the crystal were lightly polished on a polishing wheel with 10μ Al_2O_3 to remove gross surface roughness. The sample was then cleaned by washing first in acetone, then in 2:1 HNO_3. A smooth, mirror-like surface was produced on the crystal by electropolishing, washing, and drying in the manner recommended by Young and Gwathmey (5). It was possible to use samples for more than one kinetic determination, if the surface was electropolished before each use; specimens whose surfaces were replicated for electron-micrograph studies were discarded after replication. It was felt that the process of stripping the replica film could introduce defects in the crystals by unknowingly bending or damaging in some other way.

Other than the exceptions noted below, all solutions were made from either CP or reagent grade chemicals and water which had been demineralized, distilled through a tin lined still, and stored in a seasoned polyethylene reservoir. Copper sulfate solutions were made by dissolving a weighed sample of AS&R 99.999% copper in excess, reagent grade

nitric acid. A 10% excess of standard sulfuric acid solution was added, and the mixture evaporated to dryness but not to SO_3 fumes. The residue was dissolved and diluted to volume in a volumetric flask. Portions of this solution were mixed with 10% excess ethylenediamine to prepare solutions of bis-ethylenediamine copper (II) sulfate. Hydrazine solutions were prepared from technical grade 85% hydrazine hydrate in water supplied by The Mathison Company. Since preliminary studies showed that identical results were obtained, both from the standpoint of kinetics and metal surface changes, whether solutions were prepared from triply distilled ethylenediamine or the 95-100% material supplied by Eastman Kodak Company, the latter material was used.

Hydrogen was purified by passing commercial grade tank gas first over hot copper and then through drying towers packed with magnesium perchlorate.

Oxygen-free solutions were prepared by bubbling about 100 ft^3 of purified hydrogen saturated with water vapor through a fine fritted disk in the solution reservoir shown in Fig. 1 at a rate of 10 ft^3 per day.

Apparatus.—The glass reaction vessel shown in Fig. 1 was designed to be used with solutions either free of oxygen or saturated with air. After placing a magnetic stirring bar sealed in glass in the bottom of the chamber, the polished copper crystal was suspended from the glass hook in the barrel of the vessel. The standard taper joint with bright platinum electrodes was placed in position and the entire apparatus attached to the filling rack.

If solutions free of oxygen were to be used, the system, exclusive of the solution reservoir, was alternately evacuated and filled with hydrogen. Twenty cycles were sufficient to remove all detectable traces of oxygen from the system. The volumetric bulb was then filled with about 82 ml

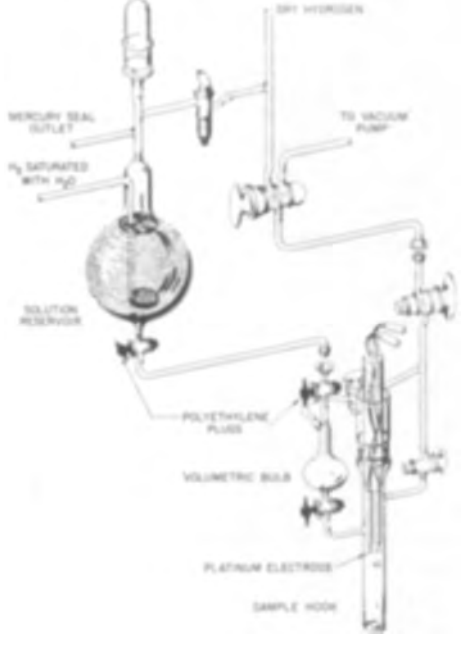

Fig. 1. Portion of filling rack with reaction chamber

of oxygen-free solution under its atmosphere of hydrogen from the storage reservoir, and the stopcocks sealing the bulb from the remainder of the system were closed. The system was again alternately evacuated and filled with hydrogen for a total of ten cycles. At the completion of these operations the solution and the sample were both at atmospheric pressure under hydrogen. A clamshell heater was placed about the reaction chamber, and the copper sample annealed at 450°C for 16 hr. The heater was then removed and the apparatus cooled to room temperature, removed from the rack, and placed in a water bath controlled to ± 0.02°C. After allowing 1 hr for temperature equilibrium to be established, the magnetic stirrer was engaged and all the solution allowed to flow from the volumetric bulb into the reaction chamber. The stopcocks isolating the reaction chamber were then closed.

When solutions saturated with air were desired the volumetric bulb was filled with 82 ml of solution and isolated from the rest of the system. The apparatus was attached to the rack and flushed with hydrogen for 20 cycles. The remainder of the procedure was repeated as on solutions containing no oxygen. By this method the copper sample did not have access to oxygen until contacted by the solution.

Progress of reactions was followed by observing conductivity changes in the solutions with time. Conductivity values were obtained with a Wheatstone bridge arrangement using an oscilloscope as a null detector. Maximum sensitivity of the system was such that the change in resistance produced by the dissolution of one atom layer of copper could be observed; however, in most cases the data were gathered under conditions in which the dissolution of 3-5 atom layers were required to produce an observable change in conductivity. Measurements were taken with the slide wire position held constant during the reaction. The null point was determined by adjusting a five decade standard resistance box.

Surface replicas.—Samples whose surfaces were to be replicated for observation with the electron microscope were removed from the reaction vessel after the desired amount of copper had been removed. They were washed quickly in a stream of distilled water for 1 min, then dried in a jet of oxygen. Surfaces were preshadowed with platinum at a 4:1 shadow angle and replicated with carbon.

Treatment of data.—At time t, the relative concentration of a component which determines the extent of a reaction may be expressed as a function of the observed conductivity values of the solution:

$$\% \text{ material unreacted} = \left(1 - \frac{\Delta\sigma_t}{\Delta\sigma_f}\right) 100 \quad [2]$$

where $\Delta\sigma_t$ is conductivity change from time zero to time t and $\Delta\sigma_f$ is conductivity change from time zero to time reaction completed.

The first-order rate equation expressed in terms of conductivity is:

$$\log \frac{C_i}{C_i - C_i\left(\frac{\sigma_i - \sigma_t}{\sigma_i - \sigma_f}\right)} = kt/2.303 \qquad [3]$$

where C_i is initial concentration of reactant which controls extent of reaction, σ is the conductivity of the solution. The subscripts i, t, and f refer to the initial value before reaction has commenced, the value at time t, and the final value at completion of the reaction, respectively. If resistance values are substituted for conductivity terms, the equation becomes

$$\log \frac{R_f - R_i}{R_i} + \log \frac{R_t}{R_f - R_t} = kt/2.303 \qquad [4]$$

where R is the resistance of the solutions. Subscripts indicate values at times as above.

A plot of log $R_t/R_f - R_t$ vs. time should give a straight line, the slope of which is equal to $k/2.303$, if first-order kinetics are obeyed by the reactant controlling the extent of the reaction. It must be emphasized that Eq. [3] and [4] apply only to the component which governs the extent of the reaction. The denominator of the logarithmic term in Eq. [3] expresses the concentration of such a component at time t. Obviously, the expression is incorrect for a reactant present in excess of that demanded by the stoichiometry of the chemical reaction involved.

Experimental Results

Analytical data.—It is not necessary that the concentrations of the components be known for a kinetic treatment based on conductivity data, but at the completion of the reactions the solutions were analyzed for copper with a Beckman Model DU spectrophotometer using both the ethylenediamine method of Jonassen and Dexter (6) and the neocuproine method of Smith and McCurdy (7). The latter method is two orders of magnitude more sensitive. Data on the solubility of air in water (8) agreed with the copper analysis and showed that the extent of the reaction was limited by the amount of oxygen dissolved in the solutions when an excess of reagent capable of dissolving copper oxide was present.

These two methods of analysis offer sensitive means for determining the concentration of mono- and divalent copper in solutions of ethylenediamine. Tests proved that the cuprous complex of ethylenediamine does not adsorb light of 540 mμ, the wave length for maximum adsorption by the cupric complex (6). Any significant difference in copper concentration detected by the two methods can be attributed to the presence of monovalent copper in the ethylenediamine solution. No such differences were found.

Oxygen-Free Solutions

At 25°C the following solutions, each 10^{-2}M in the reagent listed, which had been deaerated in the manner described, were exposed to copper single crystals which had been annealed and maintained in an atmosphere of hydrogen: ethylenediamine; hydrazine sulfate; hydroxylamine sulfate; hydroxylamine; potassium cyanide (adjusted to pH 9 with KOH); HCl; H_2SO_4. Although it has been reported that in concentrated solutions KCN (9) will react with copper and water to liberate hydrogen, no copper was found in any of the solutions (limit of detection was 0.2 μg total Cu), and examination of the metal surface also showed no detectable changes.

The chemical reaction of major interest in this study was that shown in Eq. [1]. However, when all dissolved oxygen in the system had reacted, the solution contained copper ions in contact with copper metal. Since it represented a potential source of further reaction, the following equilibrium was investigated

$$2Cu^+ \leftrightharpoons Cu^{++} + Cu^0 \qquad [5]$$

To study this reaction, two solutions which had been freed of dissolved O_2 in the manner previously described were prepared; one 10^{-4}M $CuSO_4$ in 10^{-3}M H_2SO_4, the other 10^{-4}M $CuCl_2$ in 10^{-3}M HCl. Each solution, under a H_2 atmosphere in the solution reservoir, was introduced into the reaction vessel shown in Fig. 1 and exposed to a copper single crystal which had been annealed and maintained in a H_2 atmosphere. The apparatus was placed in a constant temperature bath at 25.00° ± 0.02°C. While in the bath the solutions were stirred continuously at a stirring speed of 500 rpm. After four days the solutions were analyzed for total copper by the method of Smith and McCurdy (7), and no change in copper concentration could be detected. In order to observe effects of complex species, an oxygen-free 10^{-4}M solution of a $Cu(en)_2SO_4$ in 10^{-3}M ethylenediamine was also exposed to a copper crystal under the conditions described above. Again, after four days no change in copper concentration could be detected. If the value of 10^6 (see below) for the equilibrium constant of reaction [5] is correct, a change ~ 5 x 10^{-6}M in copper would be expected in the sulfate and chloride solutions. Such a concentration change would be detected easily by the analytical method used.

Bodlander and Storbeck (10) derived a value of 10^4 for the equilibrium constant for reaction [5] from data on the solubility of copper (I) halides in solutions of alkali halides. Although they attempted to interpret the data to account for complex ion formation, it can be shown that in a 0.2M alkali halide solution containing 10^{-4}M copper (II) halide (these concentrations are typical of those studied by Bodlander and Storbeck), the equilibrium constant cannot be less than about 10^6, if no complex ions are formed and the solubility requirements of copper (I) halides are satisfied. Therefore, their interpretation of the data must not correct completely for copper (I) present as a complex ion.

Fenwick (11) avoided the problem of complex ions by determining the copper (I) present in solutions of $Cu(ClO_4)_2$ and $HClO_4$ exposed to metallic copper. The equilibrium constant was determined to be about 10^6. This value agreed, within the limits of experimental error, with that of Luther (12) which had been determined from solutions of $CuSO_4$ and H_2SO_4 exposed to metallic copper. It should be

pointed out, however, that sources of copper (I) other than that shown by Eq. [5] were available in these systems. Air-saturated solutions such as were used in both experiments contain dissolved oxygen capable of reacting with metallic copper to form Cu_2O which would dissolve in the concomitant acids. Also, a film of Cu_2O was surely present on the metallic samples before exposure to the solutions. And finally, the work of Kruger (13) and Miller and Lawless (14) on oxide films formed on copper in various solutions raises the question whether the solutions of Fenwick and Luther were at equilibrium with the metal or an oxide covered metal.

Although there is no proof that the results reported by the authors were obtained on systems at equilibrium, the four days allowed for equilibrium to be established was the same as that allowed by Fenwick. Also, it would appear that some doubt of the validity of previously reported equilibrium constants for the reaction in question is justifiable. It is clear that at the concentrations studied either equilibrium is established so slowly or the extent of reaction is so small that reaction [5] can be disregarded as a means of removing copper from the metal surface in a reasonable time.

Solution Saturated with Air

When saturated with air all the solutions previously mentioned did react with copper. Since it afforded an easy means of analysis for copper the ethylenediamine system was studied extensively. All data were gathered on solutions initially air-saturated which were 10^{-2}M in ethylenediamine. This concentration of complexing agent represents a tenfold excess over that necessary to react with all the copper oxide which could be formed by dissolved oxygen at 25°C.

Rate data were gathered at three different stirring speeds—200, 500, and 650 rpm, at temperatures of 7.50°, 25.00°, 34.47°, 47.04°, and 56.57° all ± 0.02°C. Since the sample was suspended about 2 in. above the impeller and due to the small cross section of the reaction chamber, the stirring efficiency was much less than that in the system described by Halpern (1). Dissolution rates were determined for crystals with surface orientations of (111), (100), (110), (611), and (210). The high index faces gave kinetic results identical to those obtained from the three close-packed faces; therefore, only results from the latter are reported here.

Figure 2 shows the percentage of the original oxygen remaining in solution as a function of time at a stirring speed of 500 rpm at various temperatures. It is obvious that the reaction rate was not affected by the different crystal faces exposed. This was true at all the temperatures which were investigated. Figure 3 demonstrates that an increased stirring rate increased the rate of dissolution but that the rate was not affected by crystal orientation. Again, this was true for the three stirring rates at all temperatures. Typical rate data from conductivity values are shown in Fig. 4. As previously stated, analysis for copper content at the completion of the reactions showed that the extent of the reaction was

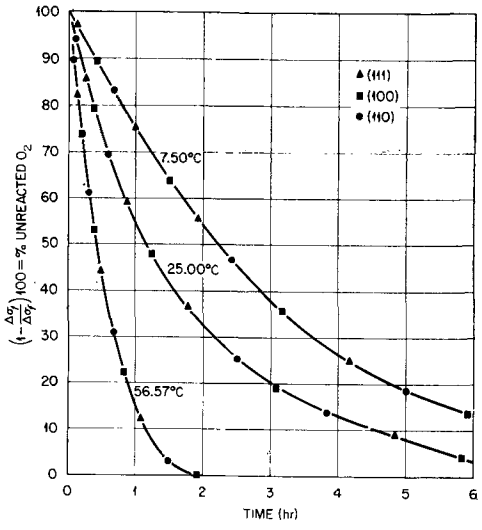

Fig. 2. Effect of temperature and crystallographic orientation on dissolution rate in 10^{-2} M ethylenediamine at a stirring velocity of 500 rpm.

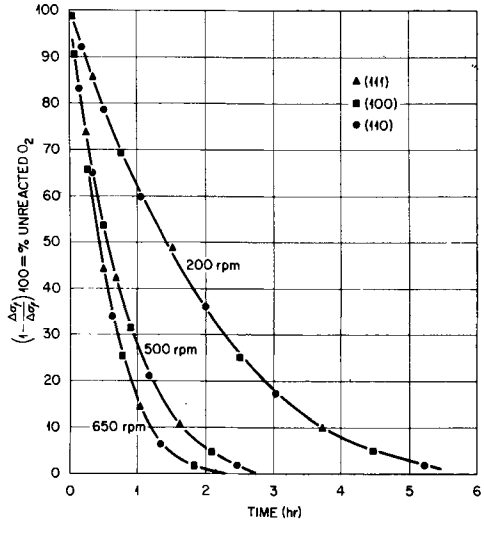

Fig. 3. Effect of crystallographic orientation and stirring velocity on dissolution rate in 10^{-2} M ethylenediamine at 47.04°C.

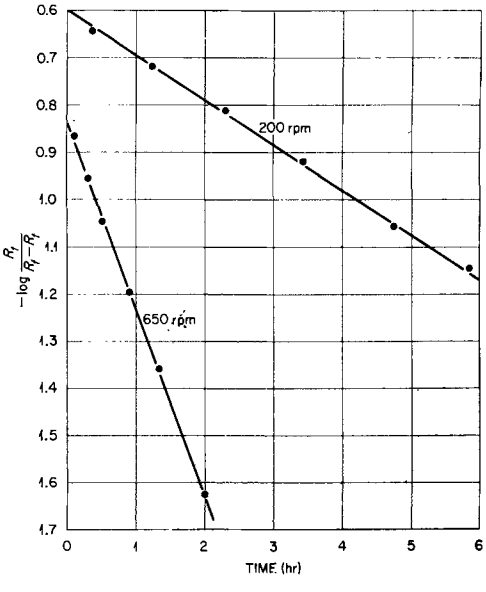

Fig. 4. Effect of stirring velocity on specific reaction rate at 25°C in 10^{-2} M ethylenediamine.

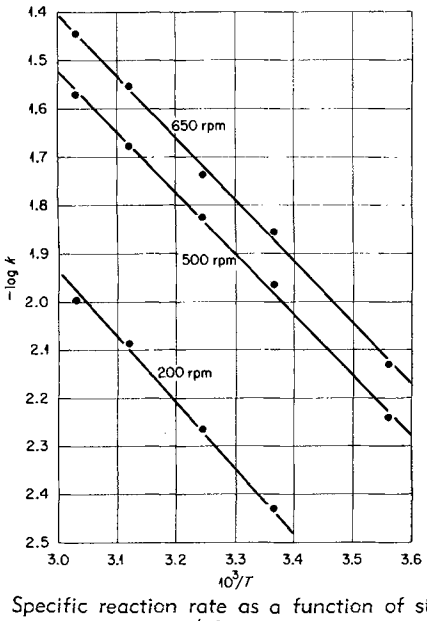

Fig. 5. Specific reaction rate as a function of stirring velocity and temperature in 10^{-2} M ethylenediamine.

determined by the amount of oxygen dissolved in the solutions. Therefore, the applicability of conductivity data to Eq. [2] and [4] demonstrates that the process was kinetically first-order with respect to oxygen and independent of the ethylenediamine concentration in these systems. A plot of log rate constants for the three stirring speeds is shown in Fig. 5 as a function of temperature. From the slopes of the lines, which are identical for the three stirring speeds, the apparent activation energy for the process was determined to be about 5800 cal $mole^{-1}$.

If air-saturated solutions were not stirred and thermal fluctuations in the temperature bath were very small, no reaction occurred at 25° and 35°C. Apparently a protective layer which prevents further reaction is formed over the reacting surface. Not only was no copper detected in the solution after 24 hr, but also there was no evidence of growth of a visible oxide film on the sample. The protective film is very unstable, for normal thermal agitation of unstirred solutions on the laboratory bench at room temperature is sufficient to cause reaction at a reasonable rate.

Experiments in which the stirred solutions were open to the atmosphere were also conducted. Under these conditions, conductivities of the solutions initially changed linearly with time. This is not unexpected if the rate of adsorption of oxygen from the air by the solution was at least as great as the rate at which oxygen reacted with copper. After a period of a few hours, depending on the temperature and the stirring rate, the reaction rate decreased, probably due to the decrease in concentration of free ethylenediamine. This point was not investigated further.

Oxide Film

In systems such as these the presence and possible role of oxide films is always open to question. In order to compare the behavior of these systems with one containing a film, a (110) crystal was oxidized in pure oxygen at 250°C until the sample was covered with a single-crystalline film of Cu_2O 700Å thick. The crystal was placed in the reaction chamber and the system flushed repeatedly with hydrogen. Obviously, it was impossible to anneal the specimen. The dissolution rate of the film in oxygen-free 10^{-2}M ethylenediamine, at a stirring speed of 500 rpm at 25°C, was determined from conductivity changes in the solution. Initially, there was an induction period of 30 min in which no conductivity change could be observed. (The reasons for the existence of an induction period in the dissolution of oxide films are not well understood, but such an observation is not unusual.) Dissolution then started and the conductivity changes were a linear function of time for a 2-hr period, at which time the rate decreased rapidly. About 80 min later the reaction was complete, and no further change with time was observed. The solution was analyzed for copper and the result was in excellent agreement with the amount of copper in an oxide film of this thickness. The decrease in rate at the end of the reaction could possibly be due to a slower dissolution rate of thinner oxide films which lie near the metal substrate; however, it seems more reasonable to assume that other factors, which are not understood at this time, caused the decreased rate.

Conductivity data indicated that at the completion of the 2-hr reaction period, the time at which the reaction rate started to decrease, about 630Å had been dissolved from the film. The copper required to form an oxide film of this thickness is equivalent to a dissolution of 375Å of metal. Air-saturated solutions of ethylenediamine under identical stirring and temperature conditions remove a corresponding amount of copper in about 15 min. While it is certain that the final reaction product in the air-saturated solutions studied is divalent copper, it is problematical whether the reaction proceeds through a Cu_2O or CuO mechanism. Although it is perhaps not permissible to compare the dissolution of Cu_2O films in oxygen-free solutions with other dissolution rates, it would appear that, if an oxide film is present on the crystals studied in air-saturated solutions, it must be an extremely thin one lacking the characteristics usually associated with a thick film.

Surface Effects

The (110) surface showed no substructural effects. At the very earliest point observed in the reaction no etch pits or subgrain boundaries could be seen; only faceting was observed. Figure 6 demonstrates the orderly progression of facet development on this surface. After an amount of copper corresponding to an average of 3000 atomic layers had been removed, the surface was no longer (110) but rather a series of facets thought to be (100) composed of long sharp-topped ridges separated by relatively deep valleys. It is difficult to obtain precise data about the depth of the valleys or the angle at which their sides intersect the base (110) surface from electron micrograph studies; however, it is certain that the facets lie in the (110)-(100) zone, and it is highly probable that the surfaces of the facets are (100) since the "subfaceting" on the

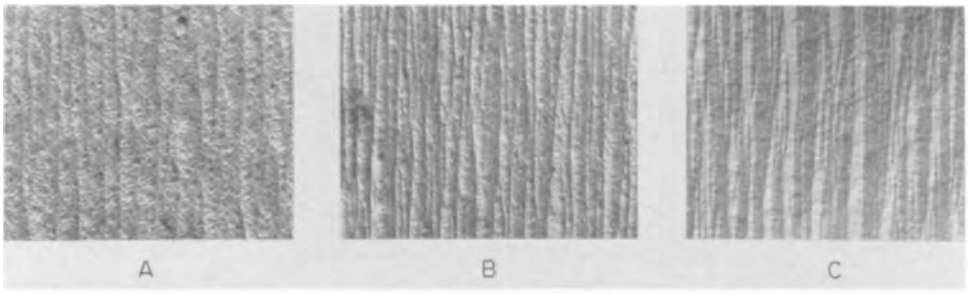

Fig. 6. Facet development on (110) surface. Average atomic layers of copper removed: A, 900; B, 1800; C, 3000. Magnification before reduction for publication: A, 50000X; B, 25000X; C, 8500X.

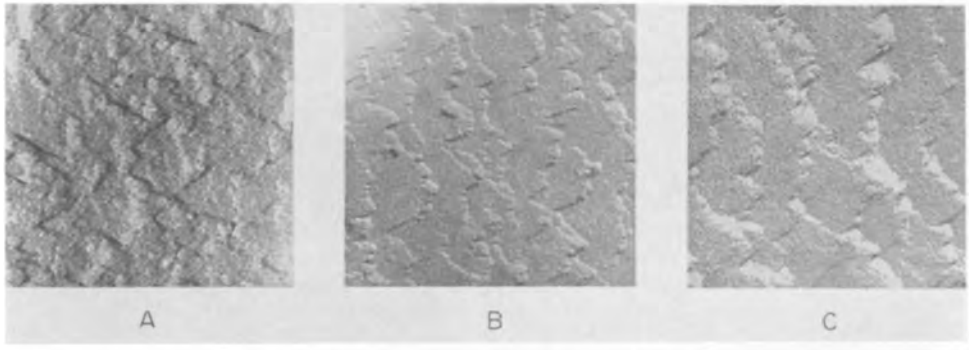

Fig. 7. Facet development on (111) surface. Average atomic layers of copper removed: A, 900; B, 1800; C, 3000. Magnification of A, B, C 17000X before reduction for publication.

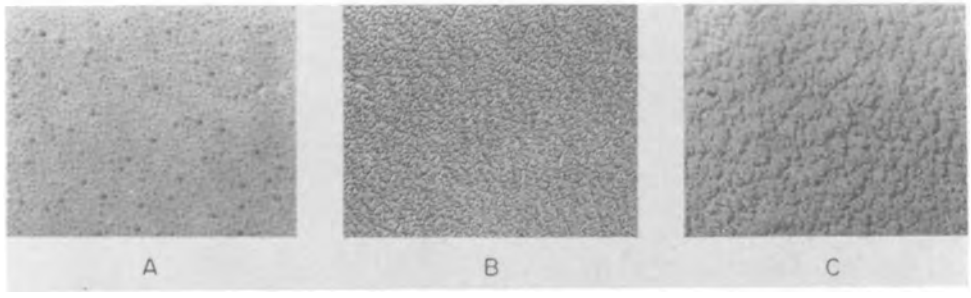

Fig. 8. Hillocks formed on (100) surface. Average atomic layers of copper removed: A, 900; B, 1800; C, 3000. Magnification before reduction for publication: A, 25000X; B, 12500X; C, 17000X.

sides of the valleys is identical with that of a (100) surface. If the fully developed facets are assumed to be (100), calculations of the amount of copper removed prove that the tops of the ridges certainly lie below the original (110) surface; however, the faceting process does start very early, and most of the material removed came from the valley areas.

Pitting is seen on the (111) surface at the earliest observable stages. Figure 7 illustrates how these pits grow and coalesce as the reaction proceeds to produce stepped facets which are oriented in two principal directions. From the orientation of the crystal and the shadows produced in the replication process, it is possible to prove that the facets are principally (110) faces. Furthermore, these facets start developing from pits very early in the dissolution process. Again, data on the total copper removed show that, at stages of the reaction where the facets are well developed, even the tops of the facets are well below the original surface. Also, at early stages of the reaction prior to extensive facet development it is possible to see pits which may have some relationship to the substructure of the crystal. A few of the pits are arranged in lines which apparently have some relationship to subgrain boundaries in the crystal.

Neither pitting nor oriented faceting is observed on the (100) surface even after the removal of copper corresponding to an average of 3000 atomic layers. From the beginning of the reaction rounded hillocks are seen on the surface. The development of these hillocks as the reaction proceeds is shown in Fig. 8. Arrangements of some of the hillocks in lines which may have some correspondence to subgrain boundaries are observed throughout the reaction.

Discussion

Kinetic Results

To prevent the formation of oxide films on a specimen before contact with the solutions it was desirable to anneal and maintain the copper crystal in an atmosphere of hydrogen. Therefore, it was not possible to mask the crystal edges of undesirable orientation from the solution. These edges of various orientations constituted 5-10% of the total exposed surface area. Also, electropolishing rounded off the edges of the crystal to produce other departures from the desired orientation. It seems clear then that if conditions had been such that the rate of oxidation at the crystal face was rate-controlling, no rate difference due to crystallographic orientation would have been observed since such differences would not be expected to be very large. However, the kinetic data at different stirring rates and temperatures demonstrate that conditions were such that a transport process in solution was rate-controlling. The activation energy determined for the reaction is of the magnitude anticipated for a process under transport control but certainly lower than expected for a system in which the rate-determining step is chemical in nature.

During the course of the reaction, the concentration of hydroxyl ion was constantly increasing in accordance with the requirements of Eq. [1]. This resulted in a corresponding decrease in the concen-

tration of the protonated form of ethylenediamine due to the equilibrium requirements of the reaction of ethylenediamine with water

$$en + H_2O \leftrightharpoons enH^+ + OH^- \quad [6]$$

Over-all, the concentration of hydroxyl ion increased about 10% while that of the ethylenediaminium ion decreased the same amount. No change in reaction rate due to these concentration changes was observed. Since initially both concentrations were only about 10% of that of the total ethylenediamine present, the changes in concentrations probably were not large enough to produce the effects observed in systems more concentrated in oxygen, ethylenediamine, and ethylenediaminium ion (3).

Experimental observation established that the reaction rate was directly proportional to the gross surface area of the sample, confirming the repeated observations of others; however, it is interesting that as the reaction proceeded there was no departure from first-order kinetics. Figure 6C shows the (110) surface at a time when the reaction was about 75% complete. At this time the surface area was approximately twice that of the original crystal before reaction started due to the troughs formed by removal of copper. As previously stated, the sides of the valleys show substructural developments like the (100) and certainly are not atomically smooth and, therefore, the roughness factors of this and the original surface can reasonably be assumed to be about the same. Since the average distance between crests of the troughs is about 7000Å these features cannot be considered negligible. Logically, it would be reasonable to expect deviations from first-order kinetics on all major faces of the crystals due to the increase in surface area, especially in the latter stages of the reaction when the change in surface area has reached a maximum. The observed structural effects would lead one to expect the greatest difference on the (110) and the least on the (111) in this particular system. These differences were, of course, not observed.

For such a system under kinetic control by a transport process, the critical area must be approximately that area of the solution which is circumscribed by the boundaries of the sample. Only macroscopic topographical deviations from a flat surface can alter this boundary area and, consequently, the reaction rates. Changes in surface area are effective only to the extent to which they contribute to such macroscopic fluctuations. Since the facets developed on the (110) were approximately 3500Å high, this suggests that the transport dependence observed is related to volume diffusion within the solution rather than diffusion across an interfacial barrier, for it seems clear that the area of such a barrier should be proportional to the microscopic surface area of the crystal.

Surface Orientations

In the system studied the (100) surface appears to be the stable orientation. At no time during the normal reaction is oriented faceting observed on surfaces of this type. However, if crystals of this orientation are reacted in systems with larger volumes so that more copper can be removed, faceting is observed as is demonstrated by the surface replica shown in Fig. 9. These facets consist of pits of various sizes, some of which have grown into each other to form large facets of random orientation. Over-all, there is clearly a tendency to maintain the (100) orientation. At higher magnifications the flat areas of this surface were seen to have a structure similar to that shown in Fig. 8A. It should be noted that casual observations would lead to the conclusion that the pits seen in Fig. 9 are associated with sites which are more reactive than the remainder of the surface. This cannot be the case, for Fig. 8 illustrates that the attack is a general one. The occurrence of pits under these conditions must be largely statistical and results from the propensity of the surface to maintain the more stable (100) orientation. The rapid development of (100) facets on the (110) surface supports the argument that the (100) is the stable orientation under these conditions. The development of facets, largely (110), on the (111) surfaces may represent a metastable condition. Since the (100) orientation is about 55° from the (111) and the (110) only 35°, the faceting observed may represent a progression to a surface state of lower energy as quickly as possible. These observations are complicated by the fact that the original surfaces of these specimens were about 2° removed from the (111). It is difficult to understand why original faceting of threefold symmetry illustrated in Fig. 7A should degenerate to twofold symmetry and why so much of the surface should maintain (111) orientation. It is reasonable to assume that if the surface were permitted to react to the point that it was covered with (110) facets, then the development of (100) facets on (110) facets would be observed; however, such arguments are questionable for the relationships between surface energies and surface area vs. total energy in systems of this type are not obvious. If no external forces are applied to the crystal, the relative stability of copper faces is (111)>(100)>(110). Since this relationship was not observed, it is possible that faceting is dependent on both the reagents in solution and their concentration.

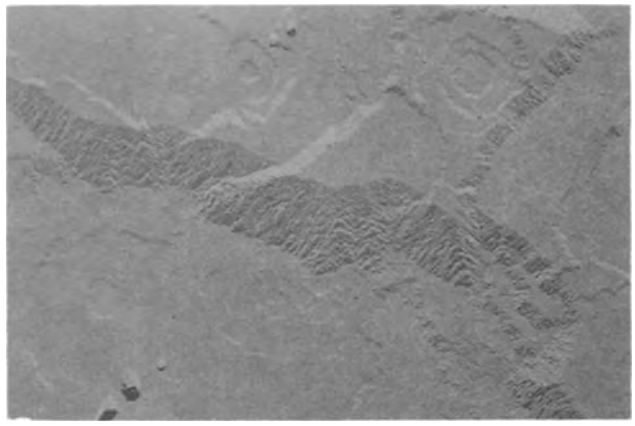

Fig. 9. Facets on (100) surface after dissolution of an average of 30,000 atomic layers. Magnification 6500X before reduction for publication.

Fig. 10. Optical photograph of (100) surface shown in Fig. 8B. Magnification 200X before reduction for publication.

Only from replicas of the (111) surface in the early stages of reaction is it possible to obtain any information about the number of reaction sites. It is seen in Fig. 7A that the initial attack on the surface results in small triangular pits enclosed in larger ones. If each small pit is considered a nucleation point for reaction, then there are about 10^{11} such points per square centimeter of surface area. This number is much too large to be related solely to line defects in the crystal, and it is not certain that the number represents more than a limit to the means of observation.

On all (100) surfaces there are structural details like those shown in Fig. 10 which are thought to be related to subgrain boundaries within the crystal and which persist throughout the normal reaction. Similar patterns are observed on the (111) until faceting becomes so pronounced that they no longer are visible. No substructural effects of this type are observed on the (110). On the (100) these areas are hillocks raised above the rest of the surface indicating a decreased reactivity at these points, while on the (111) the lines are rows of pits which lie below the remainder of the surface, and the reactivity must be greater at such points. Whether or not such areas are representative of subgrain boundaries, their contradictory behavior is difficult to understand.

Conclusions

1. In the dilute, oxygen-free solutions studied, there is no measurable reaction between copper metal and divalent copper in solution. Either values quoted for the equilibrium constants are wrong or equilibrium is extremely slow in being established in these solutions.

2. The rate of dissolution of single crystalline copper in a closed system of air-saturated, 10^{-2}M solutions of ethylenediamine is controlled by a transport process in the solution. The rate is a function of the temperature and rate of stirring of the solution but is independent of the crystallographic orientation of the exposed metal surface. The activation energy determined is of the magnitude expected for a process under transport control.

3. While the dissolution rate appears to be directly proportional to the gross surface area of the sample, it seems likely that this is an oversimplification of a more complex relationship.

4. The dissolution rate of a Cu_2O film of predetermined thickness proved to be much slower than the removal of a corresponding amount of copper under similar conditions. If an oxide film was present on the crystals studied, it was an extremely thin one lacking the usual properties of a true film several angstroms thick.

5. The crystallographic orientation of facets developed on the metal surfaces during dissolution shows that the most stable face is not the close-packed (111). The relative stability of crystal faces in this particular system apparently is (100)>(110)>(111).

6. Nucleation of reaction sites appears to be a random process on all surfaces, and the number of such sites on the (111) face is much larger than would be permitted if reaction sites were limited to points where dislocations intersected the crystal surface.

7. The difference in reactivity of the areas thought to be subgrain boundaries on the (100) and (111) does not support the assumption generally made that these are regions of greater reactivity. At this time, no explanation of the lack of correlation between crystal imperfections and reactivity can be made.

Acknowledgment

J.O. Stiegler prepared all the surface replicas and electron micrographs, and R. M. Wallace is responsible for much of the supporting photographic work in this study. The oxide film on the (110) surface was prepared by the group headed by J. V. Cathcart in the Oak Ridge National Laboratory Metallurgy Division. The author is also indebted to F. W. Young, Jr., for many valuable discussions during the research and in the preparation of this paper. The contributions of all are gratefully acknowledged.

Manuscript received Nov. 4, 1959. This paper was prepared for delivery before the Columbus Meeting, Oct. 18-22, 1959.

Any discussion of this paper will appear in a Discussion Section to be published in the December 1960 JOURNAL.

REFERENCES

1. J. Halpern, *This Journal*, **100**, 421 (1953).
2. W. D. Robertson, V. F. Nole, W. H. Davenport, and F. P. Talboom, Jr., *ibid.*, **105**, 569 (1958).
3. J. Halpern, H. Milants, and D. R. Wiles, *ibid.*, **106**, 647 (1959).
4. N. Cabrera, "The Oxidation of Metals," "Semiconductor Surface Physics," R. H. Kingston, Editor, pp. 327-348, University of Pennsylvania Press (1956).
5. F. W. Young, Jr., and A. T. Gwathmey, *Acta Met.*, **4**, 145 (1956).
6. H. B. Jonassen and T. H. Dexter, *J. Am. Chem. Soc.*, **71**, 1553 (1949).
7. G. F. Smith and W. H. McCurdy, Jr., *Anal. Chem.*, **24**, 371 (1952).
8. N. A. Lange, Ed., "Handbook of Chemistry," 8th ed., p. 1082, Handbook Publishers, Inc., Sandusky, Ohio (1952).
9. N. V. Sidgwick, "The Chemical Elements and Their Compounds," Vol. I, p. 133, Oxford University Press, London (1950).
10. G. Bodlander and O. Storbeck, *Z. anorg. Chem.*, **31**, 458 (1902).
11. F. Fenwick, *J. Am. Chem. Soc.*, **48**, 860 (1926).
12. R. Luther, *Z. physik. Chem.*, **36**, 385 (1901).
13. J. Kruger, *This Journal*, **106**, 847 (1959).
14. G. T. Miller, Jr., and K. R. Lawless, *ibid.*, **106**, 854 (1959).

Studies on Cathodic Protection Using the Hull Cell

I. Action of Corrosion Inhibitors

K. S. Rajagopalan and Y. V. P. Ramachandra Row

Central Electrochemical Research Institute, Karaikudi, India

ABSTRACT

A new method of studying inhibitor action is proposed. It is shown that the action of acid inhibitors is changed profoundly under impressed current conditions. The study also reveals that the potential of the cathodically protected metal is not a fixed value as is usually believed but changes in the presence of inhibitor.

Cathodic protection is used in combination with another well-known method of corrosion prevention, viz., addition of corrosion inhibitor, in electrolytic derusting with acid solutions to prevent basis metal attack. It is, therefore, of considerable interest to know how the two methods function in conjunction with each other, in particular, how the current requirement for cathodic protection is influenced by inhibitor action. This aspect has apparently not received adequate attention so far. Preliminary experiments (1) carried out in this Institute have shown that the current requirement for cathodic protection can be conveniently studied by the Hull Cell technique (2, 3) which is so widely used in the study of electrodeposition and that precise information on inhibitor action under impressed current conditions can be obtained by this method. The application of this technique to the study of inhibitor action in sulfuric acid medium is considered here with reference to four commonly used acid inhibitors.

Experimental

Metal.—Mild steel having the following composition was used: C — 0.1 to 0.2%, Mn — 0.4 to 0.5%, P — 0.07 to 0.08%, S — 0.02 to 0.03%. Specimens of 18 gauge sheet steel cut to the size of Hull cathode and provided with a handle at the center were used in the Hull Cell experiments. Specimens of the same mild steel sheet 3 x 1 in. were used in independent experiments to determine weight loss at protection current. The specimens were initially freed of rust and scale, abraded with 120 emery, and degreased with methanol, hot benzene and hot acetone.

Set-up.—The Hull Cell used here (Fig. 1) is a small box of trapezoidal plan in which the cathode is placed at a fixed angle with respect to the anode (3). Both electrodes occupy the full cross section of the cell and the distribution of current density on the cathode for a 267 ml cell is given by the equation C. D. at any point. Amp/dm^2 = I (2.98-5.24 log L/2.54), where I is cell current in amperes and L is distance in centimeters of the point from the high current density end of the cell. The equation applies between the limits 1.3 and 6.4 cm. The dimensions of the Hull Cell are given in Fig. 1.

The cell was fabricated from ¼ in. thick perspex (trade product made from acrylic resin). To facilitate experimentation at elevated temperatures, the cell was placed inside a lead-lined brass bath of slightly greater height than the Hull Cell and both brass bath and the perspex Hull Cell filled with acid solution till acid level was nearly flush with the top of the cell. A lead anode was used.

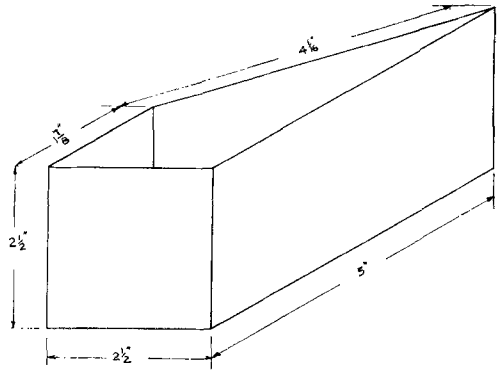

Fig. 1. Hull Cell

Procedure.—Experiments were made at various cell currents. The specimen was introduced into the cell after adjusting the current using a dummy specimen so that current started flowing to the specimen simultaneously with the immersion of the specimen. Immediately after test, the specimen was taken out and quickly reimmersed in a 0.5% NaOH solution followed by rinsing with cold water and drying to prevent attack by the acid after it was disconnected from the cell. The dried specimen was completely etched when the maximum current density obtained on the specimen was insufficient to give protection. An etched as well as a bright, unattacked region was observed when current densities required for complete cathodic protection were obtained in the Hull Cell. The line dividing these two regions were usually quite sharp and reproducible to the extent of less than 3 mm. All the results reported in the paper were obtained under conditions of uniform stirring with a mechanically driven glass stirrer rotating at an approximate speed of 750 rpm.

Results

Effects of temperature and acid concentration on the protection current.[1]—The effects of bath temper-

[1] The current density at which the dividing line is obtained.

Table I. Effects of some experimental variables on protection current.
Duration of test = 30 min

Protection line,** cm	Concentration of acid solution, moles/l	Temp, °C
—	0.5	60
—	0.5	60
6.1	0.5	60
6.1	0.5	60
6.1	0.5	60
5.8	0.5	60
5.8	0.5	60
NE	0.5	30
NE	0.5	40
NE	0.5	50
4.8	0.5	70
NE	0.05	60
E	21	60

** Distance of dividing line from high current density end.
NE, no part of the surface got etched. E, completely etched.

ature and acid concentration on the current required for cathodic protection in 0.5 mole/l H_2SO_4 solution were studied in the first instance. The results obtained in replicate experiments for a cell current of 1.5 amp are given in Table I.

The metal remained practically unattacked at lower temperatures than 60°C as shown in Table I. As the temperature was increased beyond 50°C, etched and unattacked regions appeared. The dividing line shifted to higher current density values at 70°C as compared to 60°C. Apparently, at temperatures lower than 60°C the rate of corrosion is so low and the effect of even the lowest cathodic current obtainable on the plate are sufficiently marked to make the etching of the metal surface insignificant; while at 60°C and 70°C the corrosion rate is sufficiently high for etching to appear on unprotected regions within the duration of the test (30 min) for a cell current of 1.5 amp. At 2 M acid concentration the metal was practically completely etched

Table II. Protection currents obtained for different cell currents.
Duration of test = 30 min

No.	Electrolyte	Cell current, amp	Protection line, cm	Current corresponding to protection line (calculated from Eq. [1]) ma/dm²
1	5% H_2SO_4	1.5	6.1	1500
		0.75	3.8	1400
2	5% H_2SO_4 + 0.01% Thiourea	0.75	NE	—
		0.5	6.4	450
		0.25	3.8	550
3	5% H_2SO_4 + 0.01% Gelatine	0.75	4.6	1300
		0.5	2.8	1400

and at 0.5 mole/liter the etched surface was not seen at all. The two regions became visible on the plate only at the intermediate concentrations of 0.5 mole/liter. The values obtained in 0.5 M acid solution at 60°C (see Table I) show that the position of the dividing line between the etched and the unattacked regions is quite reproducible. All the subsequent experiments were carried out at this temperature (60°±2°C).

Applicability of the Hull Cell equation.—The applicability of the equation given earlier, which gives the distribution of current density on the cathode, has been studied in several ways. First, the current densities for cathodic protection when different cell currents are employed have been compared. Results are given in Table II.

It is seen from Table II that a fairly good correspondence is observed between the protection currents obtained at different cell currents.

Losses in weight at the protection currents determined by means of independent experiments at similar current densities are given in Table III. It is seen that the corrosion rate is quite high in the absence of current and becomes negligible at the protection current. The protection currents themselves were calculated on the basis of the Hull Cell

Table III. Weight losses in the presence and absence of protection current, electrode potentials, and inhibitor efficiencies of four inhibitors
Duration of test = 30 min

			When protection current is not applied			When protection current is applied		
No.	Inhibitor	Concentration of inhibitor, %	Weight loss, g/dm²	Inhibition* efficiency, %	Electrode potential vs. SCE, v	Protection current, ma/dm²	Weight loss, g/dm²	Potential
1	Nil	—	2.8	—	—0.520	1500	0.017	—0.740
2	Quinoline	0.01	2.6	7	—0.500	800	0.011	—0.500
3	Quinoline	0.05	2.4	14	—0.490	700	—	—0.560
4	Quinoline	0.1	2.2	21	—0.480	500	—	—0.560
5	B-naphthol	0.01	2.6	7	—0.480	1100	0.014	—0.740
6	B-naphthol	0.025	2.3	18	—0.470	700	—	—0.740
7	B-naphthol	0.05	2.5	11	—0.460	500	—	—0.740
8	B-naphthol	0.1	2.3	18	—0.450	400	—	—0.740
9	Thiourea	0.01	0.15	95	—0.500	500	0.020	—0.720
10	Thiourea	0.025	0.07	98	—0.480	500	—	—0.720
11	Thiourea	0.05	0.05	98	—0.460	500	—	—0.720
12	Thiourea	0.1	0.05	98	—0.450	500	—	—0.720
13	Gelatine	0.01	1.2	57	—0.460	1400	0.007	—0.680
14	Gelatine	0.025	0.4	86	—0.440	1300	—	—0.680
15	Gelatine	0.05	0.3	89	—0.430	1000	—	—0.680
16	Gelatine	0.1	0.15	95	—0.430	800	—	—0.680

* Inhibition efficiency is calculated by the formula: $\left\{\frac{\text{Wt loss in the absence of inhibitor—Wt loss in the presence of inhibitor}}{\text{Wt loss in the absence of inhibitor}}\right\} \times 100$

equation. The results, therefore, suggest that the protection current can be predicted on the basis of the equation with a fair amount of accuracy. It may, however, be argued that a weight loss of 0.007 to 0.02 g/dm²/30 min cannot be strictly considered as representing complete cathodic protection. It is to be noted, however, that the present work relates to conditions which are connected with processes such as pickling operations which normally do not extend beyond 30 min. For this duration, the rate of loss as obtained should be considered very satisfactory. It may be pointed out in this connection that the maximum inhibition by the most efficient inhibitor used corresponds to a weight loss of 0.05 g/dm²/30 min with an inhibition efficiency of 95%. The combined effect of the two methods is appropriately studied keeping in view the highest order of protection obtainable with either method.

The Hull equation was derived from weight of metal deposited in different regions in various plating baths as well as by the direct determination of current distribution on the Hull plate. Measurement of current distribution on the cathode in Hull Cell under the conditions employed in the present study is of interest. This has been carried out using the strip method described by Hull (2). In this method a ¼ in. steel strip with a perspex back and edges painted with several coats of an acid resistant bituminous paint was used as the auxiliary electrode. It has been observed that current densities obtained by this method show fairly good correspondence with those calculated from the equation mentioned earlier in the region 1.3 to 6.4 cm from the high current density end of the cathode. At greater distances the measured values fall much more slowly than the equation would give. It may be noted in this connection that most of the measurements reported are confined to the region of 6.4 cm.

Protection current in relation to concentration of inhibitor.—The protection current at four concentrations of each of the four inhibitors considered, viz., B-napthol, quinoline, gelatine, and thiourea, are plotted against concentration in Fig. 2. It is seen from the figure that valuable information regarding the behavior of the inhibitors is given by this method. The effect of gelatine increases with concentration and does not reach a maximum value even at 0.1%. As compared to this, quinoline and thiourea make themselves more or less completely felt at the lowest concentration (0.01%), and further changes in concentration do not increase their effectiveness. These are also more effective than gelatine at all concentrations. In the case of B-naphthol, increase in concentration of inhibitor has a profound effect on the requirement of current and it reduces the current requirement more than quinoline and thiourea at 0.1%, although it is less effective than quinoline or thiourea at 0.01%.

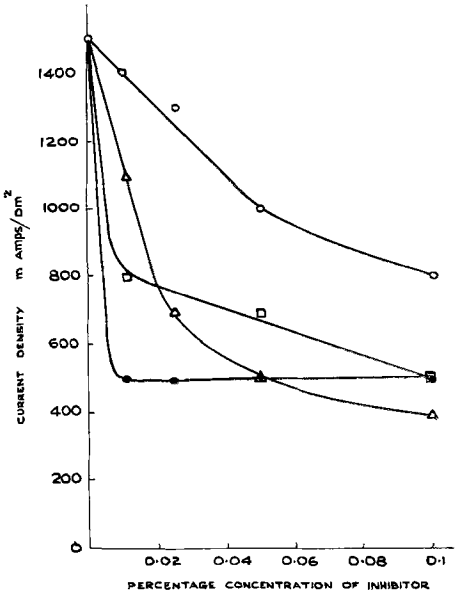

Fig. 2. Protection current vs. concentration of inhibitor. □ quinoline; △ B-napthol; • thiourea; ○ gelatine.

Inhibition efficiences of the 4 inhibitors.—The inhibition efficiency of the four inhibitors are given in Table III in terms of weight loss data with and without inhibitor when no cathodic current is applied. It is seen from Table III that the efficiency of inhibition of the different inhibitors is in the order thiourea > gelatine > B-naphthol, quinoline. The inhibition efficiency of gelatine increases with concentration, and it becomes nearly as efficient as thiourea at 0.1%. Both B-naphthol and quinoline inhibit poorly at all concentrations. As compared to this, the effectiveness of the different inhibitors in reducing the current required for cathodic protection is in the order thiourea > quinoline > B-naphthol > gelatine at 0.01%. It may be mentioned in this connection that, although quinoline and B-naphthol inhibit poorly at 60°C (the temperature at which all the present experiments have been carried out), they inhibit to a greater extent of 25°C.[2] The loss in the inhibitive action of quinoline at elevated temperatures has been noticed by other workers also (4).

Electrode potentials at currents corresponding to protection currents.—The potentials were measured using an electronic millivoltmeter and saturated calomel electrode as the reference electrode. All the potential measurements were made in independent experiments at the protection current densities found by Hull Cell experiments. Potential data are given in Table III. It is seen that the potential corresponding to the protection current is not a constant value and varies with each system, but it remains the same for the same system at all concentrations though the protection current varies. The potentials before current is applied, however, vary with concentration of inhibitor.

The mechanism of cathodic protection as well as inhibitor action has been very satisfactorily interpreted in terms of the Evans diagram (5, 6). In the former case, cathodic protection is believed to have been attained when the metal is cathodically polarized to the open-circuit potential of the local anodes. In the latter case, the inhibitor increases either the anodic or cathodic polarization behavior

[2] It is necessary to draw the reader's attention here to the inhibition efficiency value given in ref. (1). This was obtained in experiment at room temperature as it was not expected that the extent of inhibition would change markedly with temperature. Our main interest at that stage was to bring out the reversal of the order under impressed current conditions.

of the local cells and brings about reduction in the corrosion rate. Both anodic and cathodic polarization behavior can also be influenced simultaneously. The direction in which the over-all potential will shift as a result of inhibitor action has been succinctly dealt with by Mears (7) as well as Hoar (8). In the present case, when no current is applied, the potential shift in all cases is in the nobler direction. Maximum shift is given by gelatine at 0.1% when the metal is 90 mv more positive than in uninhibited solution. This should indicate that all the inhibitors polarize the metal surface anodically and that this effect increases with concentration of inhibitor. On the other hand, the fact that all the inhibitors considered here reduce the current required for cathodic protection suggests that in the presence of inhibitor the metal is more cathodically polarized. It is further noticed that in the case of gelatine and quinoline the potential at which complete cathodic protection is obtained differs from that of uninhibited acid solution. It is reduced by 180 mv in the case of quinoline and 60 mv in the case of gelatine. Thus, it would appear that the action of corrosion inhibitors is a complex phenomenon in which not only increased anodic and cathodic polarization are involved but also a reduction in the potential requirement. Let us now consider the inhibition efficiencies of the different inhibitors given in Table III. Thiourea shows very high inhibition efficiency in the absence of current. This is observed even at the lowest concentration of the inhibitor employed.

The protection current is minimum in this case at 0.01% and there is no change of the protection current with concentration of inhibitor. The potential corresponding to satisfactory cathodic protection is the same as that of acid solution without inhibitor. It would, therefore, appear that thiourea increases the anodic and cathodic polarization characteristics of the metal surface considerably on addition and that this brings about the high inhibition efficiency in the absence of current as well as the lowering of the protection current in the experiments on cathodic protection. In the case of gelatine, the inhibition efficiency increases with concentration; so also the lowering of the protection current increases with concentration. The potential data indicate that the potential at which cathodic protection is obtained is lowered. So gelatine may be said to give cathodic protection and inhibition by lowering the potential requirement and by increasing the anodic and cathodic polarization characteristics of the metal surface and that these are a function of inhibitor concentration. B-naphthol and quinoline cause considerable lowering of the protection current at all concentrations although they give very poor inhibition in the absence of current. This suggests that these inhibitors become effective only in the presence of cathodic current. The conclusions drawn by Mann (9) and others (10) based on over voltage measurements and the theory put forward by Warner (11) that N-type inhibitors which can form quaternary ammonium ions can be adsorbed at cathodic areas when the metal is operating as cathode appears to have some validity in the light of the results obtained with quinoline and B-naphthol. The action of the inhibitors is seen only when cathodic current is applied. This should mean that these two inhibitors are adsorbed on the metal surface only at more negative potentials than the corrosion potential of steel in sulfuric acid [cf. (13)]. Quinoline apparently reduces the current requirement by lowering the potential requirement and B-naphthol by increasing cathodic polarization.

The factors determining the current required for complete cathodic protection have been the subject of a number of important studies. On the basis of practical experience it is believed that, if a steel structure is maintained at a potential of −0.77 v vs. saturated calomel electrode, it will be completely protected. This criterion has been widely used. Our study shows that even in the same electrolyte the presence of small quantities of inhibitors can bring about very substantial changes in the potential at which protection is obtained and that this change takes place to different extents in the case of the different inhibitors. It is, however, a constant value for each system. The theoretical studies of Wagner (12) appear to show that under certain conditions assumed by him the criterion for cathodic protection can be stated without recourse to Evans' diagram and that the current required for cathodic protection can be worked out on the basis of lowering the metal potential to a value 0.2 v more negative than the standard single electrode potential of the metal. The present work indicates that from a practical point of view much greater caution has to be exercised in using particular potential values as criteria for cathodic protection.

Acknowledgment

The authors gladly acknowledge the kind help and encouragement given by Professor K. S. G. Doss, Director, Central Electrochemical Research Institute.

Manuscript received Aug. 14, 1959.

Any discussion of this paper will appear in a Discussion Section to be published in the December 1960 JOURNAL.

REFERENCES

1. K. S. Rajagopalan and Y. V. P. Ramachandra Row, *Naturwissenschaften*, **46**, 319 (1959).
2. R. O. Hull, *Proc. Am. Electroplaters' Soc.*, **1939**, 52.
3. J. W. Cuthbertson, *Metal Ind.*, **79**, 87 (1951).
4. N. D. Rusyanova and N. V. Hoftmann, *J. Appl. Chem., USSR* (English Translation) **30**, 1630 (1957).
5. R. B. Mears and R. H. Brown, *Trans. Electrochem. Soc.*, **74**, 519 (1938).
6. T. P. Hoar, *J. Electrodepositor's Tech. Soc.*, **14**, 33 (1937).
7. R. B. Mears and R. H. Brown, *This Journal*, **97**, 75 (1950).
8. T. P. Hoar, Proc. International Cong. Surface Activity, Part III, Butterworths Scientific Publications, 81 (1957).
9. C. A. Mann, *Trans. Electrochem. Soc.*, **69**, 115 (1936).
10. J. O. M. Bockris and B. E. Conway, *J. Phys. Chem.*, **53**, 527 (1949).
11. J. C. Warner, *Trans. Electrochem. Soc.*, **55**, 287 (1929).
12. C. Wagner, *This Journal*, **99** (1952); **104**, 631 (1957).
13. L. I. Antropo, *J. Indian Chem. Soc.*, **35**, 309 (1958).

Particle Separations by Nonuniform Electric Fields in Liquid Dielectrics, Batch Methods

Herbert A. Pohl and James P. Schwar[1]

Plastics Laboratory, Princeton University, Princeton, New Jersey

ABSTRACT

The motion of suspended solids in nonuniform electric fields in liquid dielectrics is called dielectrophoresis. Some of the quantitative aspects of dielectrophoretic behavior of solids is reported herein. The yield of precipitated solids is seen to rise with applied voltage in cells of cylindrical geometry, until a critical or "sluff-off" voltage is reached. The yield is seen to decrease with increase of volume fraction of suspended solids in the range of 1 to 50% v/v. The yield depends on voltage gradient, applied potential, cell dimensions, and relative dielectric constants of solid and liquid. In particles of given size, yield is observed to be directly dependent on the dielectric constant. Moisture is shown to have a small but demonstrable effect. As expected, the amount and character of dielectrophoretic behavior is observed to be independent of the direction of the field applied.

Current flow during the process was observed to range up to about 20 $\mu\mu$a, and to indicate that a new method of conduction takes place with the particles present. It is suggested that this is due to ionic charging of the particles by usual current flow in the liquid dielectric, with the particles then aiding current flow and energy consumption (dielectric loss) by rotating.

The motion of suspended solids caused by nonuniform electric fields is called "dielectrophoresis" (1-3). The most polar material moves toward the place of greatest field intensity. Unlike electrophoresis, this does not require charged particles. Instead, it depends on the force felt by all polar material when in a nonuniform field. It may be described as arising from the unequal pulls exerted by the forward and backward direction of the electric field on the dipole produced in the particle by the field. Reversal of the field produces no change in the direction of the pull on isotropically polarizable particles.

Prior work on the more quantitative experimental aspects has shown that the field strength, electrode size, cell size, and particle size are important parameters affecting the yield of material held by the central electrode in a cell of cylindrical geometry. Field strength, electrode size, and particle size show criticality. At certain upper limiting voltages, small central electrode diameters, and small particle sizes, all precipitation appears to be prohibited. The work described here is a continued study of other such factors. The effects of varied dielectric constant of the powder, of the dryness of the system, of the polarity, and of the powder concentration are reported.

The apparatus and handling methods used in this study are essentially those as reported earlier.

Effect of Dielectric Constant of the Powder

As shown in the simplified theory (1, 2), the effect should be proportional to the difference in the dielectric constants of the liquid dielectric and the solid.

The following experiment was done in the apparatus previously described (3) with three powdered substances of differing polarizabilities. The dielectric constants of solid ammonium chloride, polyvinyl chloride (PVC), and sulfur are: 7.0, 4.6, and 3.67. The dielectric constant of the liquid dielectric, composed of carbon tetrachloride-benzene mixtures chosen to be equal in density to the solid in use, is approximately 2.26. In agreement with expectation, the amount of ammonium chloride precipitated in a given time at voltages below the critical voltage is found to well exceed that of the polyvinyl chloride or the sulfur. The amount of PVC pulled out in turn exceeds that of the sulfur. Data were obtained on particles of the same average particle size, namely, 163 μ (see Fig. 1 for details).

The critical voltage, i.e., the voltage at which the particles appeared to be no longer held by the central electrode, was observed to increase with increasing dielectric constant of the powder. That for NH_4Cl was 7.6 kv, that for PVC was 7.0 kv, that for sulfur was 5.2 kv under the following experi-

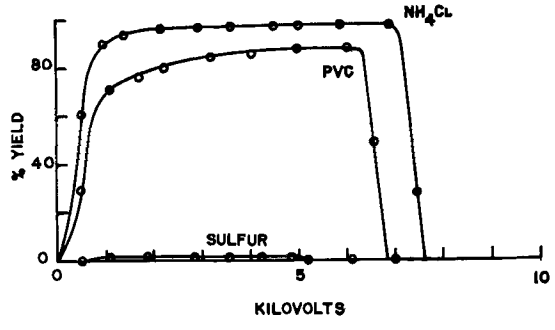

Fig. 1. Effect of varied dielectric constant of the solid powder on the precipitation yield during dielectrophoresis.

[1] Present address: Division of Engineering, Texas College of Arts and Industries, Kingsville, Texas.

mental conditions: powder suspended in CCl_4-benzene mixtures; alternating voltage used, reported as RMS: 60 cps; central wire diameter, 0.794 mm, Teflon coated to a thickness of 5 mils; test duration, 180 sec of flow at 12.5 ml/sec of feed liquid suspension: outer cell electrode diameter, 9.8 mm, ID.

Effect of Electrode Polarity

Data were obtained for the yield of PVC precipitated vs. the applied voltage in static fields, in which the polarity of the electrodes were reversed. The data of Table I show that while the central electrode is positive and the outer electrode negative the precipitation yield is identical to within experimental error with the condition of having the same but inverse voltage on the electrodes. This is in conformity with the view that the phenomenon is not electrophoresis, but is dielectrophoresis. Corona effects about the central electrode are thought to be present, especially at higher applied voltages, for when the field is suddenly reversed at very high voltages, the particles clinging to the central electrode suddenly are rapidly repelled to the cell wall. They will remain there for a time until the charge accumulated on the particles by their imbedment in the "corona region" about the central electrode leaks away. The particles then eventually migrate back toward the central electrode if the reverse voltage is maintained.

Effects of the Presence of Moisture

In an effort to find a factor effective in the behavior of the dielectrophoretic precipitations, the effect of careful drying was studied. The powdered material, in this case, polyvinyl chloride seived to pass 100 mesh, and stop on 140 U.S. mesh screen (nominal 127 μ average particle diameter), was used "as is" after long storage at room humidity, and after drying 24 hr at 105°C. The liquid dielectric, a mixture of CCl_4 and benzene, both of reagent grade, having the same density as the freshly wet powder, was used as received from the supplier, and also after drying over anhydrous $CaCl_2$ for one week. The precipitation yield was observed to be slightly higher (about 2% change in relative values) for the less dry materials. Perhaps this can be attributed to the slight changes in the dielectric constant of the liquid due to the water (see Fig. 2 for details). The critical cut-off voltage for the precipitation was rather higher in the case of the dry materials. This is probably due in part at least to the decreased conductivity of the liquid dielectric. Increased conductivity permits a higher rate of conductive counter-polarization of the particles, thus accelerating sluff-off. Numerically the critical voltages observed were: dry-8.6 kv; wet-7.9 kv.

Table I. Effect of field direction on the yield during dielectrophoresis

Data on particles of polyvinyl chloride of 126μ average particle diameter, suspended in CCl_4:C_6H_6 mixture of closely equivalent density between cylindrical electrodes, outer electrode, inner electrode, liquid velocity and test duration were as in the previous experiment.

Voltage	% Yield (central electrode positive)
500	20.4
1100	64.5
1900	70.1
2700	75.2
3400	78.6
3900	80.6
4600	82.6
5500	83.8
6400	83.8
6900	85.0
7800	24.7

Voltage	% Yield (central electrode negative)
500	19.6
1150	62.8
1900	69.4
2800	73.8
3600	77.2
4600	82.2
5500	83.5
6600	83.5
7800	23.9

Effects of Varied Particle Concentration

It is observed that, as the concentration of the solid suspended in the liquid dielectric increased, the yield of solid precipitated in a given time decreases. The experiments showing this were carried out in a cylindrical electrode cell of 9.8 mm ID, using a central wire electrode of 0.794 mm wire that was coated with 5 mil thick layer of Teflon. Polyvinyl chloride powder of spherical shapes, of nominal 127 μ average diameter, as in the above experiment, was used, at various concentrations in mixtures of CCl_4 and benzene adjusted to have similar density. The liquid velocity during the flow period of filling and draining was 12.5 ml/sec; the potential across the cell fixed at 2000 v. The test duration was 180 sec. The yield of powder collected at very low volume fraction (0.047) was 79% and fell smoothly with increase of volume fraction of powder to zero % yield at an extrapolated 51% volume fraction of powder, as the data in Fig. 3 show.

Current Flow during Dielectrophoresis

Preliminary measurements of the current flow taking place during the dielectrophoresis showed that breaks in the current vs. voltage curve occurred at points corresponding to obvious changes in the yield per cent vs. voltage curve. The current flow was observed to be greater with increased concentrations of powder, and to be greater with increase of particle size. Typical results obtained are shown in Table II and in Fig. 4. The data selected

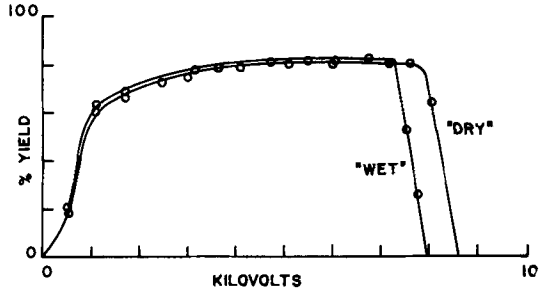

Fig. 2. Effects of moisture on the precipitation yield of polyvinyl chloride spheres during electrophoresis.

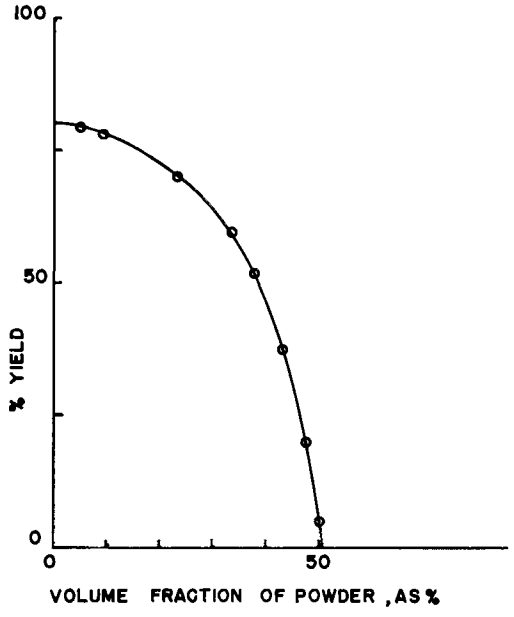

Fig. 3. Effects of powder concentrations on precipitation yield during dielectrophoresis.

Table II. Preliminary data on current flow as affected by concentration and particle size during dielectrophoresis

Particle size Mesh range	Nominal average particle diameter, μ	Current, $\mu\mu$a	Precipitate collected, as % of total	Volume fraction of powder in original suspension
−60, +80	213	2.0	60	0.091
−100, +140	127	1.06	81	0.091
−100, +140	127	2.7	68	0.250

for 2000-v potential across the cell in Table II do not show the break in the current-voltage curves observed but indicate the magnitudes of the currents and the relative changes observed on changing the particle size or concentration.

The data in Table II was obtained using a Kiethley electrometer across a high resistance in series with the cell and voltage supply circuit.

The greater conductivity of powder suspensions of larger particle size coincides with the observed lower critical voltage for sluff-off of the precipitated powder in those cases. The latter phenomenon is believed to be related to the current flow during dielectrophoresis, that current viewed as producing counter-polarization on the particles opposing the dielectrophoretic action. This effect—of current increasing with the particle size—and the observed direct dependence of the current on the

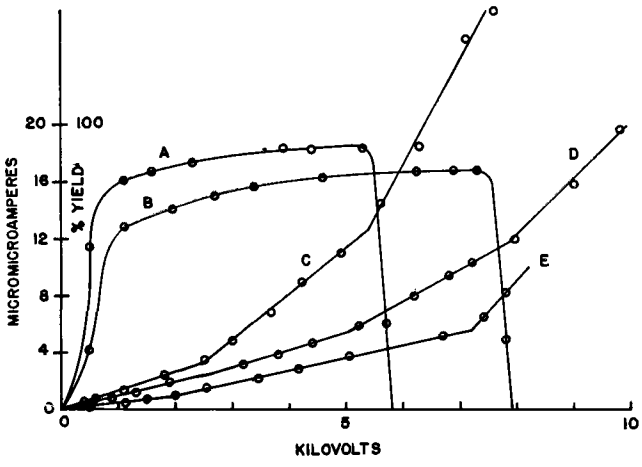

Fig. 4. Deposition and electric current characteristics during dielectrophoresis. Curve A: precipitation yield for PVC of 213 μ average particle diameter at 0.091 volume fraction in liquid dielectric. Curve B: precipitation yield for PVC of 127 μ average particle diameter at 0.091 volume fraction in liquid dielectric. Curve C: current flow during dielectrophoresis of 127 μ average particle diameter PVC at 0.25 volume fraction in liquid dielectric. Curve D: current flow during dielectrophoresis of 213 μ average particle diameter PVC at 0.091 volume fraction in liquid dielectric. Curve E: current flow during dielectrophoresis of 127 μ average particle diameter PVC at 0.091 volume fraction in liquid dielectric. Conditions: PVC powder suspended in CCl_4-benzene mixture of closely similar density; liquid velocity 12.5 ml/min; cell ID, 9.8 mm; wire electrode 0.794 mm and coated with 5 mils of Teflon; ***static field.***

particle concentration lend support to the view that a new method of current carrying is taking place. As suggested in an earlier paper (3), current flow through the liquid dielectric deposits ions on the suspended particles. A rotation of the particles, started, say, by Brownian motion, now acts to carry current across the volume occupied by the particles. This additional current carrying ability of the suspension is believed to be contributing here.

Manuscript received Sept. 23, 1959. This paper was prepared for delivery before the Philadelphia Meeting, May 3-7, 1959. A portion of the research reported in this paper was sponsored jointly by the Army Signal Corps and Office of Naval Research under Signal Corps Contract No. DA-039 sc-70154 and O.N.R. 356-375.

Any discussion of this paper will appear in a Discussion Section to be published in the December 1960 JOURNAL.

REFERENCES

1. H. A. Pohl, *J. Appl. Phys.*, **22**, 869 (1951).
2. H. A. Pohl, *ibid.*, **29**, 1182 (1958).
3. H. A. Pohl and J. P. Schwar, *ibid.*, **30**, 69 (1959).

Nonuniform Field Effects in Poorly Conducting Media

Herbert A. Pohl

Plastics Laboratory, School of Engineering, Princeton University, Princeton, New Jersey

ABSTRACT

A simplified theory of the behavior of suspended polymer particles in a real liquid dielectric is presented. It is becoming well known that nonuniform fields exert an attractive force of interesting magnitude on particles of high dielectric constant suspended in a liquid medium of lower dielectric constant. In a real dielectric there is an appreciable effect due to the very small currents (10^{-3} amp at kilovolts applied) which even good liquid insulators support.

It is shown that, in a real dielectric, the initial attraction to the central electrode felt by all particles due to the nonuniform field and its polarizing induction is gradually overcome by the repulsive effects of charge accumulated on the particles due to ionic conduction in the liquid. The "reversal time" for the particle motion is calculated and shown to be reasonable.

The ability of nonuniform electric fields to produce desirable separations of materials of differing dielectric constant is now well recognized. It is the purpose of this paper to help establish some of the more quantitative features of the phenomenon. Mueller (1), Pohl (2-4), and Loesche and Hultschig (5) independently examined the theory of the size and direction of the action of nonuniform fields on mixed dielectrics. Mueller concluded from his excellent analysis that the effects would not be appreciable for particles of molecular size. Loesche and Hultschig also concluded this from their theoretical and experimental study. However, it has been shown (2-4) that the action of nonuniform fields on macroscopic particles is indeed appreciable and can be used for certain separations. Debye (6-9) concluded from theoretical considerations that grading of macromolecules, such as high polymers, should be possible by this technique.

As defined earlier (2) "dielectrophoresis" is the motion of matter caused by polarization effects in a nonuniform electric field. Other effects interfere, such as conduction, thermal convection, diffusion, and the over-all effect of the sequence: charging (whether by electrode, particle, or ion contact) and followed by electrostatic repulsion. As expected, in dielectrophoresis the most polar material moves toward the region of greatest field intensity. However, all materials conduct. In this sense a theory developed on the assumption of no current flow in the electrical system, although helpful, is too simple. As a first step in considering the effects of conduction, the following rather elementary considerations are presented with no guarantee of having more than suggestive merit.

We may assume the particle to be in equilibrium with the various forces on it in a real dielectric

$$F_e + F_j + F_d + F_\eta = 0$$

where F_e is the dielectrophoretic force, F_j the force due to conduction-produced charge, F_d diffusional or osmotic force, and F_η = viscous drag force.

Dielectrophoretic force, F_e.—As shown in a prior paper (3), the dielectrophoretic force on a spherical particle in an electric field with uniform properties (i.e., "corona" effects absent) and cylindrical symmetry is

$$F_e = -4\pi a^3 \epsilon_0 K_1' \cdot \frac{(K_2'-K_1')\ V_1^2}{(K_2'+2K_1')r^3\left(\ln\frac{r_1}{r_2}\right)^2} \cdot r^0$$

$$= -4\pi \frac{a^3 \epsilon_0 K_1' (K_2'-K_1')}{r^3\ (K_2'+2K_1')} \cdot E_1^2 r_1^2 r^0$$

where ϵ_0 is permitivity of free space, r_2 the radius of outer, grounded cylinder, r_1 the radius of inner cylinder at potential V_1, r the distance of particle center from the axis, a the radius of particle, K_1' the relative dielectric constant of liquid medium, K_2' the relative dielectric constant of particles, r^0 the unit radius vector, V, V_1 the potential at r and r_1, respectively, and E, E_1 the field at r and r_1, respectively.

The negative sign indicates that the motion due to this force will be toward the axis. The motion will be strictly radial.

For present purposes we may gather all terms except those of immediate interest into a single constant, k_e,

$$F_e = \frac{-k_e a^3 V_1^2}{r^3\left(\ln\frac{r_1}{r_2}\right)^2} r^0$$

where

$$k_e = 4\pi\epsilon_0 K_1' \frac{(K_2'-K_1')}{K_2' + 2K_1'}$$

Electrostatic force, F_j, on current-induced dipoles.—The force on a particle carrying free electric charges in an electric field, E, is

$$F_j = Q \cdot E$$

where Q is the free charge.

In a field of cylindrical symmetry it may be shown that

$$V = V_1 \ln\left(\frac{r}{r_2}\right) \Big/ \ln\left(\frac{r_1}{r_2}\right)$$

and

$$E = -\nabla V = -r^0 V_1 \Big/ \ln\left(\frac{r_1}{r_2}\right) \cdot \frac{1}{r} = E_1 \frac{r_1}{r}$$

The charge Q, accumulated by the particles during their life in the liquid and between discharging contacts with the outer electrode will be assumed to be proportional to their cross-sectional area and to the current density. The current in the real dielectric will be assumed due to ionic conduction in the liquid and to charge transfer between particles. It is assumed that voltage gradients sufficient to strip off electrons from the particles by field effects do not act here.

Consider the forces which arise on a particle sitting at rest in a field in which an ionic current flows. Let the particle be an insulator similar (but not necessarily identical) in dielectric constant and conductivity to the liquid medium. The motions of the ions in solution due to thermal motion and electrical forces cause them to diffuse through the liquid and, in particular, to collide with the particles of interest here. These ions generally adhere to the particles because of attractive electrical image forces. These forces arise as soon as the ion comes rather close to the particle. We may expect a high fraction of approaching ions to adhere until such time as the accumulated electric charge on the particle gives rise to a repelling field. The presence of the initial polarization on the particle gives rise to an initially attractive field for the approaching ions. This *induced* "surface" charge will make the surface field on the particle attractive to the ions until neutralized. Only then will the surface charge begin to be repellent to the oncoming ions. Our calculations from this point on largely concern themselves only with the period of ion-carried surface charging of the particle up to the point of neutralizing the induced surface charge, i.e., where no repulsion exists. Hence, we may assume for the present that all oncoming ions are picked up and held by the particle. Ionic current will then deposit equal numbers of positive and negative charge on opposite faces of the particle.

The charge density, q, will be proportional to the current density, j, to the time, t, of deposition; and to the projected area, $d\sigma$, of the area segment dA under consideration at P.

$$q = jt \frac{d\sigma}{dA}$$

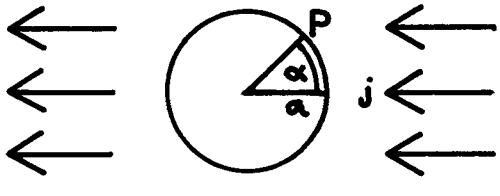

Now $\frac{d\sigma}{dA} = \cos\alpha$

therefore

$$q = j_1 t \cos\alpha - j_2 t \cos\alpha$$

where j_1 is the current in the liquid dielectric, j_2 is the current in the particle itself; therefore, $q_{net} = (j_1 - j_2) t \cos\alpha$.

the moment, $d\mu$, of that charge at P is

$$d\mu = 1 \cdot q \cdot dA$$

where $1 = a \cos\alpha$ = lever arm of moment. The total moment of the charged sphere is

$$\mu = \int_A lqdA$$

$$= \int_0^\pi (a\cos\alpha)(jt\cos\alpha)(2\pi a^2 \sin\alpha\, d\alpha)$$

$$= \frac{4\pi}{3} a^3 jt = jt \cdot (\text{volume})$$

Note that the moment turns out to be the volume of the particle times the total positive charge deposited.

This is also true for particles of other shapes. For example, consider a particle of nearly cubic shape, actually a particle of the shape of a sector of a cylindrical annulus sitting at an average distance, r, from the axis of the cylindrical electrode system. Let it have a length of side $2a$ in the radial direction, a length $2a$ in the cylindrical axis direction, and a median arc length also of $2a$ along the circumference of the imaginary cylinder axial to the electrode axis and passing through r. It may be shown that the moment is

$$\mu = 8a^3 jt = jt \cdot (\text{volume})$$

where $8a^3$ is the volume of the nearly cubical particle if $a << r$.

The translational force on a dipole in a nonuniform field is

$$F_j = \mu \cos\theta \cdot \nabla|E|$$

where θ is the angle the dipole makes with the impressed field. Here, $\theta = \pi$ $\cos\theta = -1$.

$$\nabla|E| = \nabla \left| \frac{E_1 r_1}{r} \right|$$

in a field of radial symmetry for

$$E = \frac{E_1 r_1}{r}$$

where E_1 is the field intensity at a distance r_1 hence

$$\nabla|E| = \frac{\partial}{\partial r} \frac{E_1 r_1}{r} = \frac{-E_1 r_1}{r^2}$$

and

$$F_j = \mu \frac{E_1 r_1}{r^2}$$

For a spherical particle laden with charge due to the current flow

$$F_j = \frac{4\pi}{3} a^3 jt \frac{E_1 r_1}{r^2}$$

As the current density, j_0, in an ohmic cylindrically symmetrical field is

$$(j_1 - j_2)_{r=r_0} = j_0 = \frac{E_0}{\rho_1} - \frac{E_0}{\rho_2} = \frac{E_1 r_1}{r_0} \cdot \frac{\rho_2 - \rho_1}{\rho_1 \cdot \rho_2}$$

where ρ_1 and ρ_2 are the specific resistivities of the liquid and the particle, respectively.

At the surface of a spherical particle of dielectric constant K_2' in a medium of dielectric constant K_1' the field E_{1z}, is

$$E_{1z} = \frac{3K_1'}{K_2'+2K_1'} \cdot E_0$$

where E_0 is the field strength in the liquid, far from the particle.

The above relation, strictly speaking, applies only at the onset of current arrival. As the net polarization of the surface drops to zero (the conductance delivered charge equals the field induced polarization charge)

$$E_{1z} = E_0$$

However for $K_2' = 5$, $K_1' = 2$, as for representative pairs of materials,

$$\frac{3K_1'}{K_2'+2K_1'} = \frac{2}{3}$$

hence the variation of field at the surface during charging is not great in such cases. For later mathematical simplicity we choose to set

$$j = \frac{E_{1z}}{\rho} = \frac{3K_1'}{K_2'+2K_1'}\frac{E_0}{\rho}$$

where ρ is the specific resistivity. Hence

$$F_j = 4\pi a^3 t \cdot \frac{E_1^2 r_1^2}{r^3} \cdot \frac{K_1'}{K_2'+2K_1'} \cdot \left(\frac{\rho_2-\rho_1}{\rho_1\rho_2}\right)$$

Diffusional or osmotic force, F_d.—The osmotic pressure, Π, due to a set of suspended particles of concentration, n, per cc is

$\Pi = nkT$ [Van't Hoff equation (10)]

where k is Boltzmann constant and T is absolute temperature.

The pressure gradient along the r direction among the particles of varied concentration is

$\frac{\partial \Pi}{\partial r} = kT\frac{\partial n}{\partial r}$ = force per unit volume of particles.

This pressure gradient or directed force per particle due to concentration gradient is then F_d, where

$$F_d = \frac{1}{n}\frac{\partial \Pi}{\partial r} = \frac{kT}{n} \cdot \frac{\partial n}{\partial r}$$

We may compare the magnitudes of the two forces as follows:

$$F_d = kT\,\Delta n/n \cdot 1/\Delta r$$

Now $\Delta n/n$ is the fractional change in concentration along r for any volume under consideration. The maximum relative change possible is unity (presence vs. absence of particles). The minimum change in radial distance having meaning can be considered to be equal to the diameter, $2a$, of the particle. Then

$$F_{d(max)} = \frac{kT}{2a}$$

For $a = 1\ \mu$, $T = 300°K$, $k = 1.38 \times 10^{-16}$ $\frac{\text{erg}}{(\text{deg.})(\text{molec.})}$

$F_{d(max)} = 2.07 \times 10^{-10}$ dynes per particle

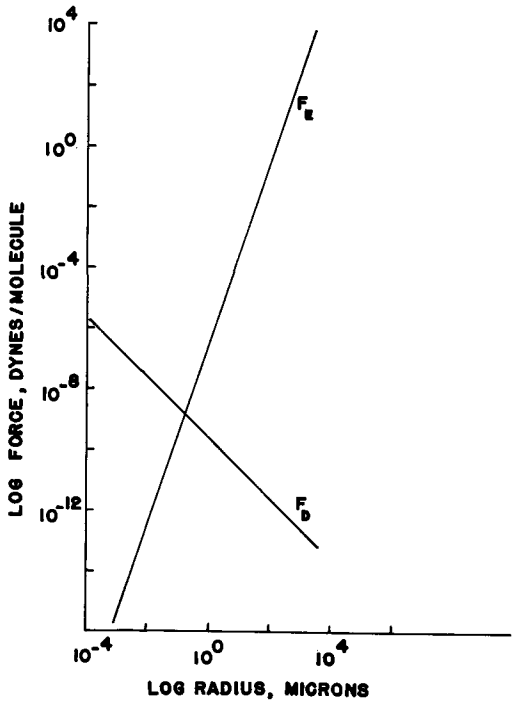

Fig. 1. Comparison of diffusional (osmotic) and dielectrophoretic forces for particles of various radii.

Values for other radii can be ascertained from Fig. 1.

An example of the magnitude of the force on a particle due to a cylindrically symmetrical electric field follows:

$$F_e = \frac{-4\pi a^3 \epsilon_0 K_1'(K_2'-K_1')E_1^2 r_1^2}{r^3(K_2'+2K_1')}$$

For

r = 1 mm = 10^{-3}m = distance from axis

r_1 = 0.5 mm = 5 x 10^{-4}m = radius of central electrode

r_2 = 5 mm = 5 x 10^{-3}m = radius of outer electrode

V_1 = 3000 v (outer electrode grounded)

$|E| = \frac{-V_1}{r\ln(r_1/r_2)}$ = 1.30 x 10^6 v/meter

ϵ_0 = 8.85 x 10^{-12} coul/(volt)(meter) = permittivity of space

a = 1μ = 10^{-6}m

K_2' = 5

K_1' = 2

F_e = 3.15 x $10^{-12}\left[\frac{\text{coulomb volts}}{\text{meter}} = \text{newtons}\right]$

= 3.15 x 10^{-7} dynes

which is much larger than the maximum osmotic force on this particle (2.07 x 10^{-10} dynes).

Values for other particle radii under these electrical conditions can be ascertained from Fig. 1.

For particles of over 1μ diameter this force may be shown to be negligible in comparison with the electrical ones.

Viscous drag.—For spherical particles one may use Stokes' law to find the force, $F\eta$, required to keep spherical particles moving at a velocity, v, in a medium of viscosity, η.

$$F\eta = 6\pi a\eta v = 6\pi a\eta \, dr/dt$$

Particle path in nonuniform fields in real dielectrics.—It is reasonable, as said earlier, to assume that the particle is in effective equilibrium with the various forces on it, i.e.

$$F_e + F_j + F_d + F_\eta = 0$$

Combining equations for these values as given earlier, we find

$$\frac{-k_e a^3 V_1^2 r^0}{r^3\left(\ln\frac{r_1}{r_2}\right)^2}\,\frac{-V_1 r^0 \frac{j_1 a^2 r_1}{r}\int_0^t \frac{dt}{r(t)}}{\ln\left(\frac{r_1}{r_2}\right)}$$

$$+ \frac{kT}{n}\cdot\frac{\partial n}{\partial r} + 6\pi a\eta\frac{dr}{dt} = 0$$

Deposition and dispersion of spherical particles in a cylindrical electrode cell in which ionic current flows.—For purpose of the present simplified calculations we neglect osmotic forces for particles of over 1 μ size. We return then to our assumption of equilibrium among the dielectrophoretic, electrostatic, and viscous drag forces.

$$F_e + F_j = F_\eta = 6\pi a\eta v$$

or

$$6\pi a\eta v = -4\pi\epsilon_0 K_1'\frac{(K_2'-K_1')a^3}{(K_2'+2K_1')r^3}(E_1 r_1)^2 +$$

$$\frac{4\pi a^3 t(E_1 r_1)^2(K_1')}{r^3(K_2'+2K_1')}\cdot\frac{\rho_2-\rho_1}{\rho_1\rho_2}$$

solving for $v = \frac{dr}{dt}$

$$\frac{dr}{dt} = v = \frac{(E_1 r_1)^2 a^2 K_1'\cdot 2}{3\eta(K_2'+2K_1')r^3}$$

$$\left[-\epsilon_0(K_2'-K_1') + \frac{t(\rho_2-\rho_1)}{\rho_1\rho_2}\right]$$

collecting terms in r and t and integrating gives

$$v = \frac{-a^2 A}{r^3} + \frac{a^2 Bt}{r^3}\cdot\frac{\rho_2-\rho_1}{\rho_1\rho_2}$$

$$r^4 - r_0^4 = -4a^2 At + \frac{2a^2 Bt^2}{\rho_1\rho_2}(\rho_2-\rho_1)$$

where r_0 is initial radial distance of particle from axis of cylindrical electrodes, r the "final" radial distance after time, t,

$$A = \frac{2}{3}\frac{(E_1 r_1)^2 K_1'\epsilon_0(K_2'-K_1')}{\eta(K_2'+2K_1')}$$

$$B = \frac{2}{3}\frac{(E_1 r_1)^2 K_1'}{\eta(K_2'+2K_1')}$$

The variation of $r^4 - r_0^4$, a measure of the particle excursion, is seen to be parabolic with time. The furthest inward excursion for a particle is $r_0 - r_1$, which occurs, say, at $t = t_1$.

At $t = t_2 = 2t_1$, the particle originally at r_0 will have drifted out again to r_0. This is because of the eventual overcoming of the attractive dielectrophoretic force, F_e, by the growing repulsive force F_j due to ionic charging of the particle.

After $t = t_2$, the particles will be further out than at the start of the experiment.

At $t = t_1$, the velocity of the particles due to all forces is zero. We may term this "sluff-off time."

$$t_1 = \frac{A}{B}\frac{\rho_1\rho_2}{(\rho_2-\rho_1)} = \epsilon_0\frac{\rho_1\rho_2}{\rho_2-\rho_1}(K_2'-K_1')$$

(therefore the sluff-off time, t_1, is independent of voltage but is directly dependent on the resistance of solution)

$$t_2 = \frac{2A\rho\rho'}{B(\rho'-\rho)}$$

and

$$r_{0\,max}^4 = r_1^4 + \frac{2a^2A^2}{B}\left(\frac{\rho_1\rho_2}{\rho_2-\rho_1}\right)$$

good up to $r_{0max} = r_2$ for conducting particles

In the absence of corona-type effects, the sluff-off time, t_1 is of course expected to be independent of the applied voltage for the dielectrophoretic forces due to initial polarization and current-induced polarization depend in the same way on the voltage.

The maximum "yield" or fraction of the tube contents swept out is

$$y_{max} = \frac{\text{volume swept out}}{\text{total volume available}}$$

$$= \frac{\text{amount of powder deposited}}{\text{total amount of powder available}}$$

$$= \frac{\pi(r_{0\,max}^2 - r_1^2)L}{\pi(r_2^2-r_1^2)L}$$

$$= \frac{\left(r_1^4 + \frac{2a^2A^2\rho_1\rho_2}{B(\rho_2-\rho_1)}\right)^{1/2} - r_1^2}{r_2^2-r_1^2} \text{ for } r_1 \leqq r_0 \leqq r_2$$

and if

$$r_1 << r_2$$

$$y_{max} \cong \left(\frac{2\rho_1\rho_2}{B(\rho_2-\rho_1)}\right)^{1/2}\frac{aA}{r_2^2}$$

At any time,

$$y = \frac{\left(r_{1_r}^4 + 4a^2At - 2a^2Bt^2\frac{\rho_2-\rho_1}{\rho_1\rho_2}\right)^{1/2} - r_1^2}{r_2^2-r_1^2}$$

and for

$$r_1 << r_2$$

$$y \cong \frac{a}{r_2^2}\left(4At - \frac{2Bt^2(\rho_2-\rho_1)}{\rho_2\rho_1}\right)^{1/2}$$

$$\cong \text{const.}\frac{V_1 a}{r_2^2}\left(\text{const. } xt - \text{const. } xt^2\frac{(\rho_2-\rho_1)}{\rho_2\rho_1}\right)^{1/2}$$

The above equations, then, suggest (*a*) that the sluff-off time, t_1, is relatively independent of voltage, (*b*) the sluff-off time, t_1, is directly proportional to the resistivity factor $(\rho_1\rho_2/\rho_1 - \rho_2)$, (c) the deposit will first form, then suddenly unform, (*d*) the amount of deposition should be proportional to (i) particle size, (ii) voltage, (iii) inverse area of cell, (iv) time at short times, and (v) should be of

short life if the system resistivity is low and the resistivities are rather different; or long, if the conductivity of the particles matches or is greater than that of the liquid.

It need hardly be said that the simple theory mentioned can be expected to apply only roughly to systems in which there is superimposed annular fluid flow. Unfortunately, for experimental convenience, the experimental data available are on systems with appreciable annular flow. Only rough analogy may be made with the theory which is for a system with no liquid flow. Experiments designed to test the hypotheses above are under way.

As one check of the theory we can calculate a sluff-off time, t_1, using reasonable values for the indicated constants

$$t_1 = \frac{A}{B}\rho = \epsilon_0\rho\ (K_2'-K_1')$$

Let

$$\rho = 1.3 \times 10^{15} \text{ ohm meter}$$

$$\epsilon_0 = 8.85 \times 10^{-12} \text{ farad/meter}$$

$$K_2' - K_1' = 5 - 2 = 3$$

$$t_1 = 8.85 \times 10^{-12} \frac{\text{coul}}{(\text{volt})\,(\text{m})} \times 1.3 \times 10^{15} \frac{(\text{volt})\,(\text{sec})\,(\text{meter})}{\text{coul}} \times 3$$

$$= 1.15 \times 10^4 \text{ sec, or about 3 hr.}$$

This value of 10^4 sec for an assumed specific resistance of 1.3×10^{15} ohm meters based on that measured for hexane in a similar system (11) turns out to be an entirely reasonable one and lends a measure of confidence to the theoretical results.

Manuscript received Sept. 23, 1959. This paper was prepared for delivery before the Philadelphia Meeting, May 3-7, 1960. A portion of the research reported in this paper was sponsored jointly by the Army Signal Corps and Office of Naval Research under Signal Corps Contract No. DA-36-039 sc-70154 and O.N.R. 356-375.

Any discussion of this paper will appear in a Discussion Section to be published in the December 1960 JOURNAL.

REFERENCES

1. F. H. Meuller, *Wiss. Veröffentl. Siemens-Werken*, **17**, 20 (1938).
2. H. A. Pohl, *J. Appl. Phys.*, **22**, 869 (1951).
3. H. A. Pohl, *ibid.*, **29**, 1182 (1958).
4. H. A. Pohl and J. P. Schwar, *ibid.*, **30**, 69 (1959).
5 A. Loesche and H. Hultschig, *Kolloid-Z.*, **141**, 177 (1955).
6. P. J. W. Debye, *Phys. Rev.*, **91**, 210 (1953).
7. P. Debye, P. P. Debye, B. H. Eckstein, W. A. Barber, and G. J. Arquette, *J. Chem. Phys.*, **22**, 152 (1954).
8. P. Debye, P. P. Debye, and B. H. Eckstein, *Phys. Rev.*, **94**, 1412 (1954).
9. W. A. Barber, P. Debye, and B. H. Eckstein, *ibid.*, **94**, 1412 (1954).
10. S. Glasstone, "Textbook of Physical Chemistry," p. 671, D. Van Nostrand, Inc., New York (1946).
11. Progress Report XXII, Laboratory for Insulation Research, M.I.T., December 1957.

Continuous Separations of Suspensions by Nonuniform Electric Fields in Liquid Dielectrics

Herbert A. Pohl and Charles E. Plymale

Plastics Laboratory, Princeton University, Princeton, New Jersey

ABSTRACT

Suspensions of various solids in organic dielectric liquids can be separated continuously into their components by pulsating direct or alternating current electric fields of modest strength. The method and its important variables are described, together with the results observed for several systems. It is found, for example, that there exists a critical lower voltage and a critical upper voltage between which the operation must take place if appreciable separation is to take place. Best results are obtained if the dielectric constant exceeds that of the liquid. Among other separations possible, it is shown that zircon-rutile particle mixtures readily separate under conditions of dielectrophoresis. These materials cannot be separated by density or magnetic methods. A simple theory for the forces exerted on the particles sitting in combined gravitational and nonuniform electric fields is given.

Suspensions of various solids in organic dielectric liquids can be treated continuously by pulsating direct or alternating current nonuniform electric fields of modest strength to clarify or enrich the suspensions. Materials of differing polarizability can be separated. The methods and some of the important variables are described in this paper. It is found, for example, that there exists a critical lower voltage and a critical upper voltage between which operations must take place if appreciable separation is to occur. Best results are obtained if the dielectric constant of the suspended solids exceeds that of the liquid dielectric. An increase in conductivity of both liquid dielectric and of suspension is observed to occur in the voltage range where dielectrophoresis changes. The results are analogous in many respects to those obtained in earlier batch studies (1-4).

Experiments were, speaking broadly, carried out under two types of conditions. In one set, cylindrically symmetrical electrodes were used while close match of densities of powder and liquid was main-

tained. In such an electrode system, the force exerted on the particles depends strongly ($1/r^3$) on the distance from the central electrode axis. In the other set of experiments, an attempt was made to operate between electrodes of such design that the force on the particles did not depend on geometrical position in the channel in which they moved ("isomotive" cell), while the particles fell freely through a liquid of rather lower density than themselves.

Experiments in the Cylindrical Electrode Geometry

As outlined above, particles of various materials were suspended in liquid dielectrics of closely matching density. These suspensions were then subjected to the action of the nonuniform field existing between cylindrically symmetrical electrodes. Flow was continuous and axial in the cell. The feed was at the top. The liquid was withdrawn simultaneously at the bottom from two outlets, one drawing material from the region close to the central electrode and the other drawing material from the periphery (see Fig. 1). The concentration of suspended solids in the two existing streams was compared optically using an electrophotometer. A plot of the observed concentration ratios showed that little effect was to be noted until at least a somewhat critical value of voltage was applied across the electrodes. Beyond this region, a sharp increase in pullout of material was noted at the axial region of the cell as the applied voltage was increased. This increase continued with increase of voltage until a rather sharp maximum was observed, following which a rapid decrease in pullout was displayed until, at a high and rather critical voltage, a return to equality of concentrations of the two exciting streams was observed.

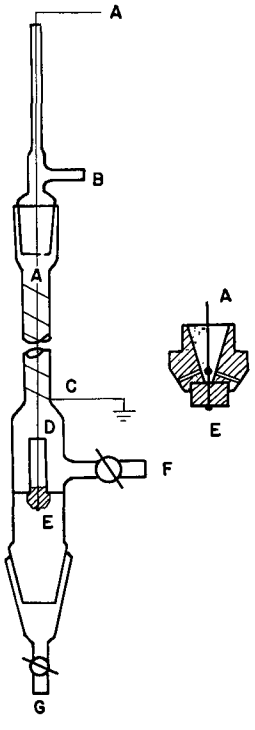

Fig. 1. Schematic diagram of cell used for continuous dielectrophoresis (cylindrical geometry). A, high potential (central) electrode; B, feed inlet; C, grounded outer electrode, consisting of bare wire wrapped onto glass tube; D, central takeoff tube; E, insulating (Teflon) central electrode support, perforated to pass suspension of particles; F, peripheral product vent; G, central product vent.

The suspensions examined were (*a*) spherical particles of selected size ranges, e.g., 100-140 U.S. mesh, of polyvinyl chloride suspended in CCl_4-benzene mixture (see Fig. 2), and (*b*) powdered ammonium chloride particles of selected size range suspended in CCl_4-benzene mixture of similar density (see Fig. 3).

Current measurements made on the above systems showed the d-c current to be very small, about

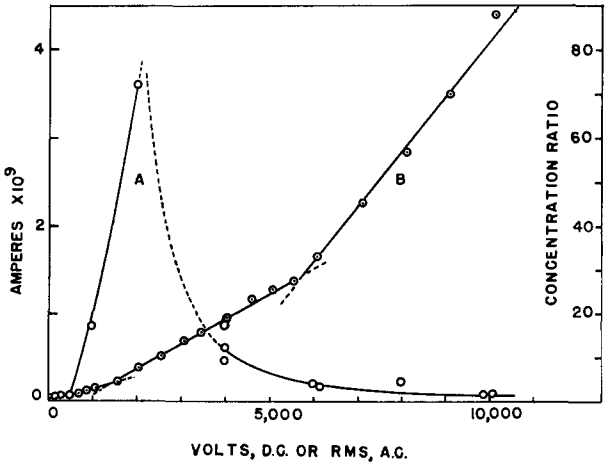

Fig. 2. Deposition and direct current flow during continuous dielectrophoresis of polyvinyl chloride. Curve A, Concentration ratio, central to peripheral, of exiting streams versus 60 cps, a-c rms voltage. Determined with swollen PVC; 90 μ average particle size; suspended in 1:1 v/v CCl_4-benzene mixture; space velocity of liquid, 10.5 cm/min: Teflon-coated central wire electrode, wire 0.74 mm diameter, 0.3 mm coating: Cell ID, 11 mm, powder concentration, 6% as volume fraction of suspension. Curve B, current vs. voltage for above system, but using static voltage.

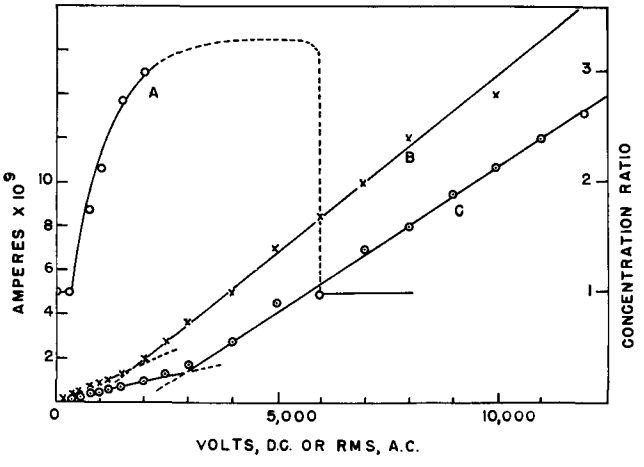

Fig. 3. Deposition and direct current flow during continuous dielectrophoresis of ammonium chloride. Curve A, concentration ratio, central to peripheral, of exiting streams vs. 60 cps, a-c rms voltage. Determined with NH_4Cl; 90 μ average particle size; suspended in 94:6 v/v CCl_4-benzene mixture; space velocity of liquid, 10.5 cm/min: Teflon coated central wire electrode, wire 0.74 mm diameter, 0.3 coating; cell ID, 11 mm; powder concentration, 2% as volume fraction of suspension. Curve B, current vs. voltage for above system, but using static voltage. Curve C, current vs. voltage in above geometry, using static voltage, and only flowing CCl_4 liquid in cell.

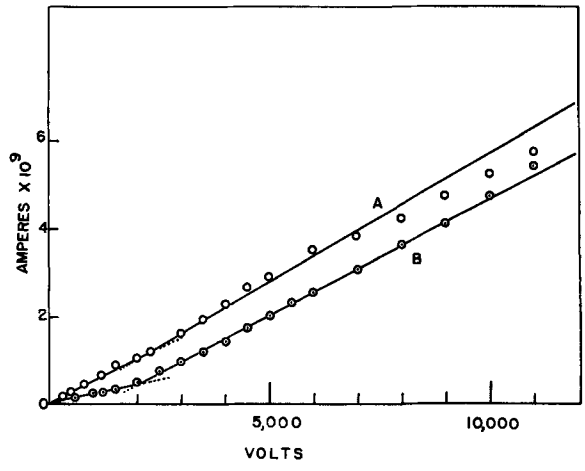

Fig. 4. Direct current flow in the liquid dielectric, 1:1 v/v CCl_4-benzene. Cylindrical cell geometry; liquid having space velocity of 10.5 cm/min, cell inside diameter, 11 mm. Curve A, data for bare 1.630 mm diameter wire. Curve B, data for bare 0.645 mm diameter wire.

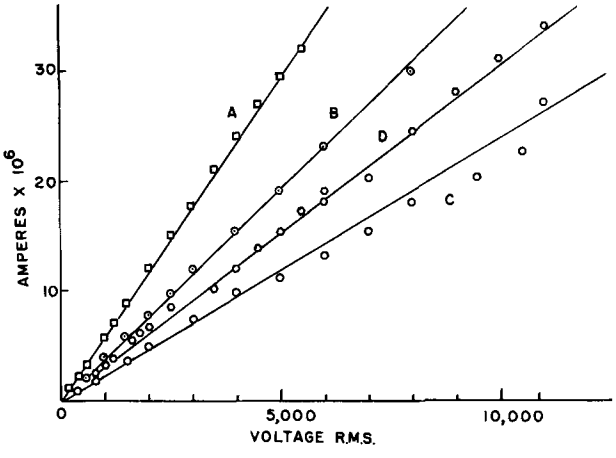

Fig. 5. Total current in electrode systems of cylindrical geometry containing a liquid dielectric. Alternating voltage applied; liquid having space velocity of 10.5 cm/mm, cell inside diameter, 11 mm, liquid dielectric, 1:1 v/v CCl_4-benzene; total current includes charging and loss currents. Curve A, data for bare 1.630 mm diameter wire. Curve B, data for bare 0.645 mm diameter wire, Curve C, data for bare 0.202 mm diameter wire. Curve D, data for Teflon covered wire; wire diameter, 0.74 mm, coating 0.3 mm thick.

1.0 to 100 $\mu\mu$a or slightly higher. The d-c current was measured using a Kiethley electrometer and appropriate shunts. The current was observed to be ohmic up to about the voltage at which the particles began to respond vigorously to the field. At this point a marked rise in current flow was observed, indicating a second mechanism of conduction had appeared (see Fig. 2-4). The data of Fig. 4 were made for comparison and were obtained on the pure liquid dielectric. The observed slight discontinuity in the current vs. voltage curves in the case of the pure liquid has not been elucidated. The discontinuities for the cases of solids present are rather larger. Alternating current measurements made on the above systems showed, as expected, that the dielectric loss current (10^{-9} amp) was too small to be detected easily in the presence of the relatively large charging current due to capacitance and stray inductances in the system (about 10^{-5}). Figure 5

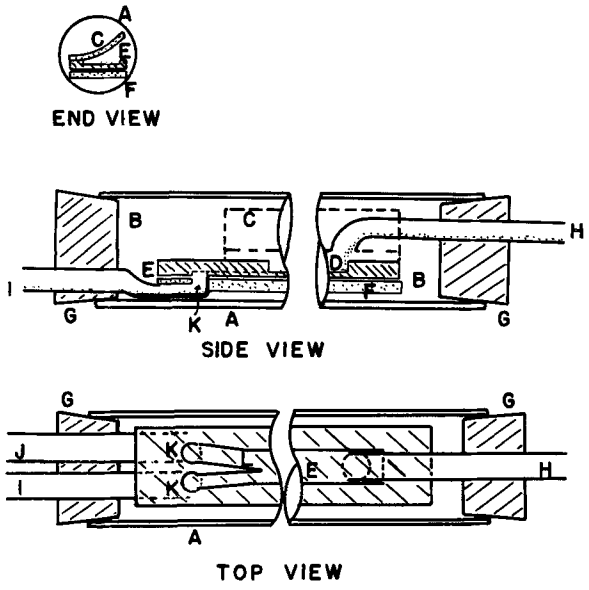

Fig. 6. Schematic diagram, isomotive cell for continuous dielectrophoretic separations. A, glass outer cell wall; B, dielectric liquid; C, curved upper brass electrode; D, solid particles lying in flat groove of Teflon insulator plate; E, Teflon plate, grooved; F, lower flat brass electrode; G, Neoprene stopper; H, Feed inlet, copper; I, lower exit tube, copper; J, upper exit tube, copper; K, exit holes; L, groove divider cut in Teflon.

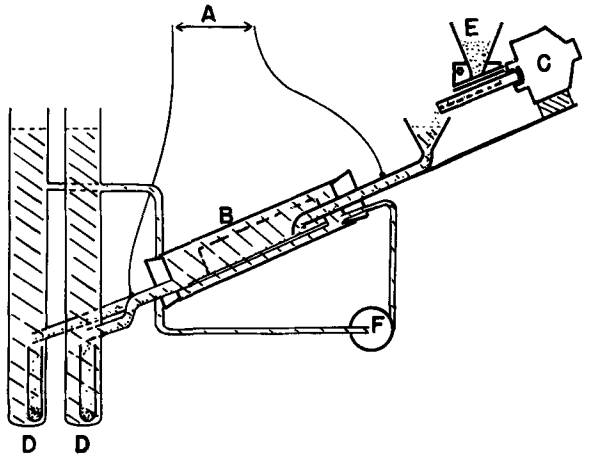

Fig. 7. Schematic diagram of isomotive cell operation. A, high voltage source; B, isomotive cell; C, vibrator; D, powder collectors; E, supply hopper for powder mixture; F, pump.

shows this for 60 cps current vs. voltage for several inner electrode sizes.

Experiments in "Isomotive" Cell Geometry

In these experiments, an attempt was made to have the solid particles pass through the nonuniform field cell in a long narrow tray in between electrodes of such a shape as to produce a force which was constant electrically and directed in opposition to that of gravity. Materials in powder form were then shaken down along this long narrow tray. The tray was given a slight tilt across its narrow dimension and a large inclination along its length (see Fig. 6 and 7). The dielectrophoretic force tended to hold particles up against the slight gravity pull exerted due to the tilt. Those particles most strongly pulled electrically would exit from

the lower end of the tray at one (uppermost) edge of the channel; those pulled least by the electrical force would tend to exit from the lower end of the tray at the other slightly lower edge of the channel. The angle of tilt was roughly estimated as 3° in experiments *A*, *B*, and *C* below. In experiments *D-H*, the tilt angle was more carefully measured by protracting.

The whole tray and electrode system was kept immersed in a low viscosity liquid dielectric (benzene or cyclohexane for experiments *A*, *B*, *C*; carbon tetrachloride for experiments *D-H*). Powders were fed in at the upper end and removed continually by sampling tubes at the lower end. After testing a number of cell designs to at least partially optimize performance, the following results on powders were obtained.

(*A*) Polyvinyl chloride powder was observed to be collectable at will in either of the exits from the cell, depending on the voltage applied. At very low or nil voltages, all of the powder collected in the lower exit. At medium voltages higher and higher fractions of the powder could be collected in the upper exit until, at about 1300 v, about 90% of the existing powder was observed to pass out the upper exit. As the voltage was increased beyond this range, the process was observed to become less selective, the powder behavior more erratic, and the proportion collected in the lower exit increased until the cell acted with very low selectivity (see Fig. 8).

(*B*) A powdered mixture of $Na_2Cr_2O_7 \cdot 2H2O$ and TiO_2, both of mesh size less than 80 was fed into the hopper and cell. At nil voltage very little of either kind of particle was observed to pass into the upper exit. As the voltage was increased a larger and larger fraction of TiO_2 was collected at the upper exit, until at about 300 v a maximum was observed. The proportion of the dichromate passing into the upper exit remained low until about 1000 v. At voltages higher than this (up to 2000 v a.c. rms) a lack of selectivity of the cell was observed, and a mixture of both solids was observed to go into the lower and upper exits (see Fig. 9).

(*C*) A mixture of 60-100 mesh rutile mineral (gray-black form of TiO_2) with 60-80 mesh polyvinyl chloride was passed through the cell. At nil voltage, neither type of particle passed out the upper exit. As the voltage was increased, a greater and greater fraction of the rutile passed into the upper exit, until at a voltage of about 750 v a.c., rms, slight quantities of PVC powder were observed to accompany it out the upper electrode. At higher voltage, as before, less selectivity in the separation was observed (see Fig. 10).

(*D*) The "operating curves" for the pure single components were determined by measuring the volume fraction of feed material which left by the high exit at various applied voltages. Samples of powders passing 100 U. S. mesh and resting on 140 U. S. mesh (nominal 127 μ average particle diameter) were used throughout the following experiments (see Fig. 11-14, e.g.). Following these determinations of the behaviors of the single components, the ability of the isomotive cell to separate 1:1 v/v mixtures of these powders was then determined. Compositions of the materials exiting from the low and high exits were determined by counting under a microscope. The following results (*E-H*) were obtained.

(*E*) *Silicon carbide-aluminum oxide*: Alumina and carborundum obtained from the Bay State Abrasives Company was screened and graded. Separation by dielectrophoresis of the carborundum from the alumina was found to be relatively easy. Figure 15 shows the percentage composition of the streams of powder coming from the high and low exits as a function of applied voltage. It may be seen that the carbide is readily pulled over to the high exit in preference to the alumina. At very

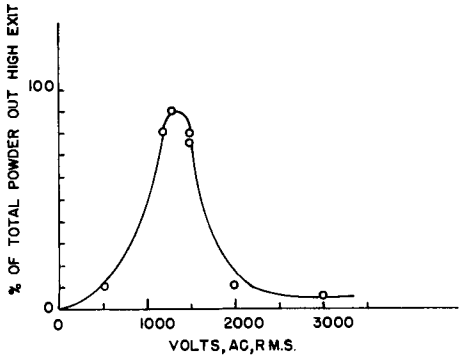

Fig. 8. Behavior of polyvinyl chloride spheres in isomotive cell.

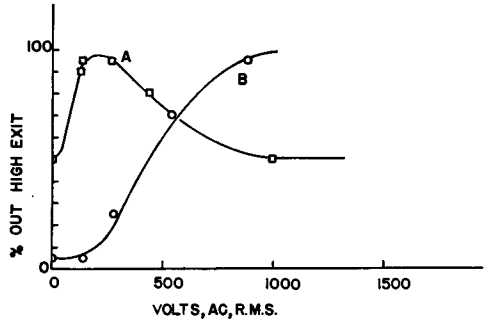

Fig. 9. Behavior of sodium dichromate-titanium dioxide particle mixtures in isomotive cell. Curve A, per cent of rutile in powder coming out high exit. Curve B, per cent of total powder coming out high exit.

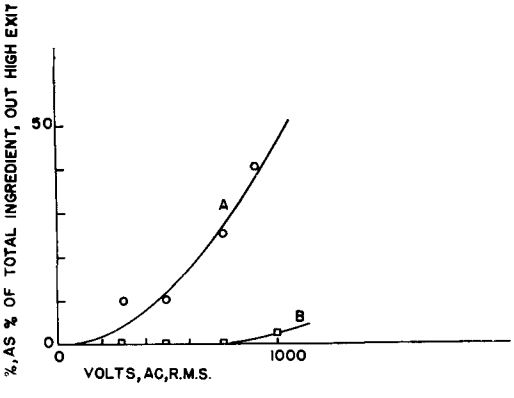

Fig. 10. Behavior of polyvinyl chloride-rutile mixtures in isomotive cell. Curve A, per cent of total rutile coming out high exit. Curve B, Per cent of total polyvinyl chloride coming out high exit.

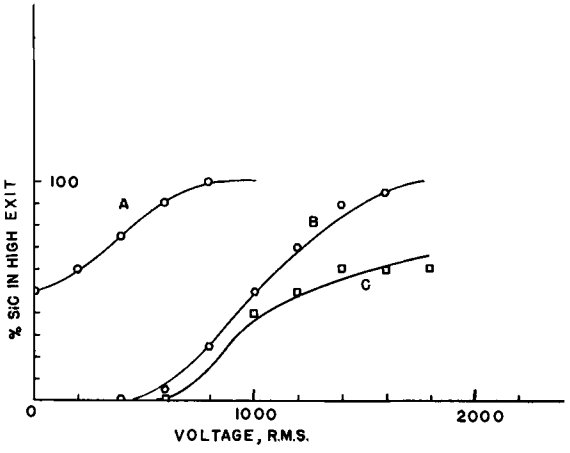

Fig. 11. Behavior of silicon carbide particles in isomotive cell. Curve A, 0° tilt. Curve B, 3° tilt. Curve C. 6° tilt.

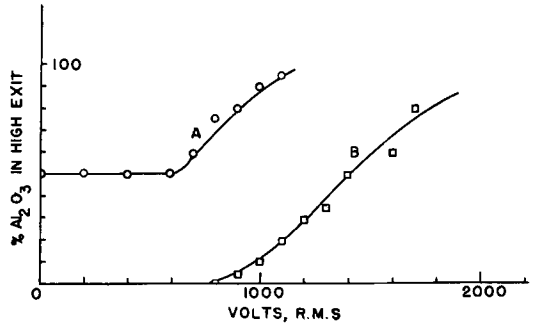

Fig. 12. Behavior of aluminum oxide particles in isomotive cell. Curve A, 0° tilt. Curve B, 3° tilt.

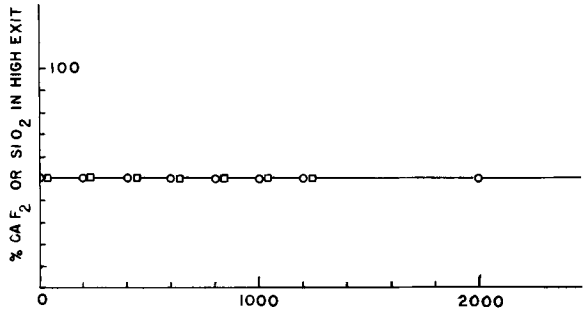

Fig. 13. Behavior of calcium fluoride (fluorite) and SiO_2 particles in isomotive cell. Circles, SiO_2; squares, CaF_2.

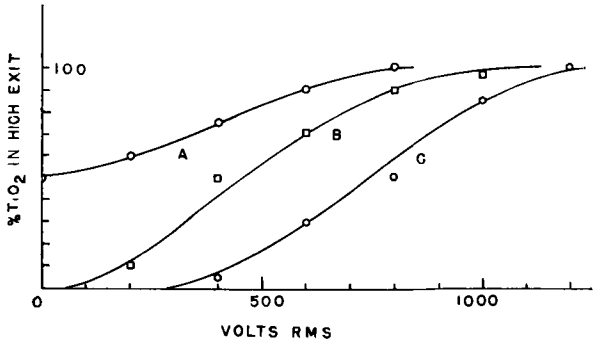

Fig. 14. Behavior of rutile (TiO_2) particles in isomotive cell. Curve A, 0° tilt. Curve B, 3° tilt. Curve C, 6° tilt.

low voltages, neither kind of particle succeeds in reaching the high exit. At low voltage the carbide in pure form succeeds in coming out the high exit. As the voltage increases beyond this point, a larger and larger fraction of it goes out the high exit, until as the lower critical voltage for the alumina is

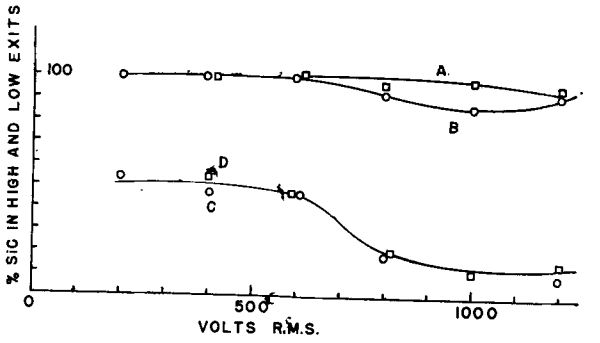

Fig. 15. Behavior of silicon carbide-aluminum oxide particle mixtures in isomotive cell. Composition at (A) high exit, 6° tilt; at (B) high exit, 3° tilt; at (C) low exit, 3° tilt; and at (D) low exit, 6° tilt.

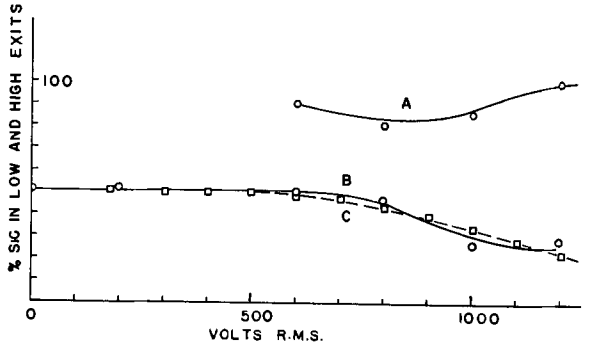

Fig. 16. Behavior of silicon carbide-silica mixtures is isomotive cell, cell at 3° tilt. Curve A, composition out high exit. Curve B, composition out low exit. Curve C, composition calculated from operating curves of pure components.

reached, a trace of alumina appears in it. As the voltage applied is increased still further almost all of the carbide and more and more of the alumina goes out the high exit, making the high exit stream steadily richer in alumina. The lower exit now delivers nearly pure alumina.

(*F*) *Silicon carbide-silicon dioxide*: Silicon carbide, as above, and purified "glass grade" sand, "Berkeley Fine Dry Special" from the Pennsylvania Glass Sand Corporation, seived and graded to pass 100 U. S. mesh and rest on 140 mesh (nominal 127 μ average particle diameter) were found to be easily separable by dielectrophoresis. Determination of the "operating curve" for the pure SiO_2 showed that in the present design of isomotive cell it would not come out of the high exit at any voltage applied if the tilt angle was as large as 3°. The curve for pure SiC is shown in Fig. 11. Separation curves are shown in Fig. 16. The behavior over-all resembled that for the Al_2O_3-SiC mixtures except for the nearly complete absence of SiO_2 in the upper exit. Some carry-over was experienced at the higher voltages, however. Experiments showed that SiO_2 particles alone did not move out the higher exit under any conditions of voltage applied at 3° tilt or greater.

(*G*) *Silicon carbide-calcium fluoride*: This mixture was studied because it formed an interesting example of an otherwise difficult separation. The closeness of the densities (SiC) $d_{20} = 3.17$; CaF_2, $d_{20} = 3.18$) and the absence of particularly outstanding magnetic properties precludes density or mag-

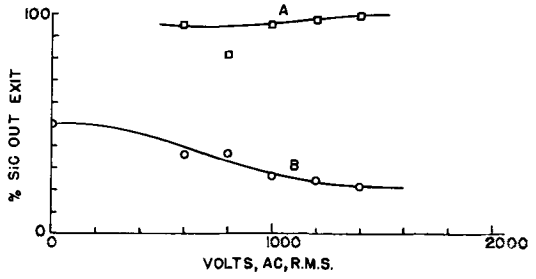

Fig. 17. Behavior of calcium fluoride (fluorite)-silicon carbide particle mixtures in isomotive cell. Curve A, high exit 3° tilt. Curve B, low exit 6° tilt.

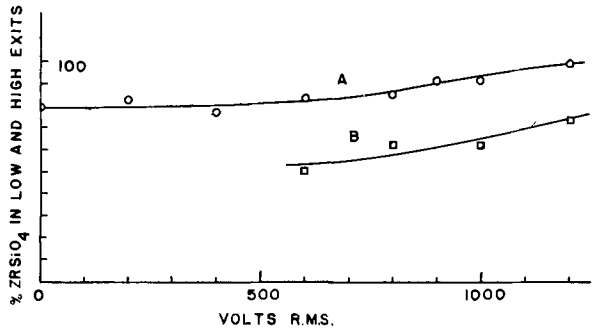

Fig. 18. Behavior of zircon-rutile particle mixtures in isomotive cell. Curve A, product in lower exit. Curve B, product in high exit, 3° tilt.

netic separations. As can be seen from Fig. 17, these two solids are readily separable by dielectrophoresis in the isomotive cell. CaF_2 like SiO_2 does not move out the high exit if alone at tilts of 3° or more.

(*H*) *Zircon-rutile*: This mixture of minerals which cannot be separated by density or magnetic methods proved readily separable by dielectrophoresis in the isomotive cell. Results are shown on Fig. 18. The separations were done on zircon sand from Yamba Beach, Australia. As received, it contained about 21% rutile from which it was readily separated by a preparatory cleanup run. Rutile, mineral, crushed and graded was used in making 1:1 v/v mixtures for this study. Zircon, like SiO_2, does not move out the high exit if alone in the cell at tilts of 3° or more.

Discussion of Results

It may be considered that forces on the particles in the tray come from at least five causes:

1. Osmotic.
2. Gravitational (corrected for bouyancy).
3. Dielectrophoretic, arising from the effect of the nonuniform electric field on the field polarized neutral particles.
4. Dielectrophoretic, arising from the effect of the nonuniform electric field on the current-induced (or produced) dipoles on the particle surface.
5. Electrophoretic, arising from the effect of the electric field on *excess* charges on the particles. Excess charges, may arise from several possible causes. A charge unbalance may arise from current-induced charging accumulating initially by image force adsorption in equal numbers, followed by local discharge due to "corona" effects at sharp edges on the particle. A charge unbalance may also arise from other causes such as contact or near contact with electrodes or other particles bearing an unbalance of charges. Still other mechanisms are possible. The nature of conduction in these organic liquid dielectrics is not completely clear, although ionic mechanisms appear to be prominent (6). The appearance of a break in the current-voltage curve of the liquid dielectric alone (Fig. 2-4) indicates that there may be some change in type of conduction even in the liquid without large amounts of suspended particles. This opens the question as to the cause of the several breaks observed in the curves for suspensions. It may be that in the present experiments that traces of powder impurity were present in the liquid dielectric studied. It may also be that the effect observed is due entirely to phenomena characteristic of particle-free liquid. Further studies of this intriguing problem are under way.

A simplified theory of the net force at any time after arrival in the field is given below for spherical particles, excluding the more difficult calculable electrophoretic forces arising from more or less random charging, and also excluding osmotic or concentration gradient forces which are generally negligible for particles above about 0.2 μ diameter.

The gravitational force, F_g, effective along the bottom of the tilted tray is

$$F_g = -i\frac{4}{3}(d_2-d_1)a^3 g \sin\alpha \qquad [1]$$

where a is the particle radius, d_2, d_1 the densities of particle and liquid dielectric, respectively, g the gravitational constant, and α the angle of tilt from horizontal.

As shown in earlier work (2) the dielectrophoretic force, F_e, arising from induction in a nonuniform field on neutral particles is

$$F_e = 2\,a^3 K_1'\epsilon_0\left(\frac{K_2'-K_1'}{K_2'+2K_1'}\right)\nabla|E|^2 \qquad [2]$$

where K_1', K_2' are the relative dielectric constants of the liquid and solid, ϵ_0 is the permittivity of free space, and E the electric field at the particle.

In accord with results described elsewhere (5) it can be shown that the dielectrophoretic force, F_j, arising from the effect of a nonuniform field on current-induced dipoles on the surface of spherical particles is

$$F_j = i(\mu\cdot\nabla|E|) \qquad [3]$$

where

$$\mu = 4\pi/3\; a^3 j\, t \qquad [4]$$

μ is electric moment due to current-produced charge accumulation, and j is the net current arriving at surface of particle.

$$j = j_1 - j_2 \qquad [5]$$

j_1, j_2 is the current in medium and particle, respectively, i the unit vector in horizontal direction (unity if $\nabla|E|$ coincides with tray bottom direction), and t the time of flow of current.

By Ohm's law

$$j_1 = E_{1z}/\rho_1 \quad [6]$$

$$j_2 = E_{1z}/\rho_2 \quad [7]$$

where E_{1z} is the electric field at particle-liquid interface

$$E_{1z} \cong E\left(\frac{3K_1'}{K_2'+2K_1'}\right) \quad [8]$$

during most of the charging period and ρ_1, ρ_2 are the specific resistivities of the liquid and particles, respectively.

Combining equations

$$F_j = 2\pi a^3 t\left(\frac{K_1'}{K_2'+2K_1'}\right)\left(\frac{\rho_2-\rho_1}{\rho_1\rho_2}\right)\nabla|E|^2 \quad [9]$$

The net force on the particle in the direction along the tray bottom is then, F_{net}

$$F_{net} = F_e + F_j + F_g \quad [10]$$

$$F_{net} = 2\pi a^2\nabla|E|^2\left(\frac{K_1'}{K_2'+2K_1'}\right)\left[\epsilon_0(K_2'-K_1') + t\frac{(\rho_2-\rho_1)}{\rho_2\rho_1}\right] - i\frac{4\pi}{3}a^3 g(d_2-d_1)\sin\alpha \quad [11]$$

As a test of the above equations, we may examine a comparison of the calculated and observed forces. The electrical and gravitational forces are observed to be in balance, for example, when the voltage is just large enough to cause the particles to begin to go out the upper exit at a given tilt. Table I contains data relevant to this comparison. The voltage values, listed as "V critical" were found from use of data in Fig. 11, 12, 14, and 18, and were chosen at the point where the first particles could be detected in the higher exit during a 3° tilt. The value for the dielectric constant of silicon carbide is estimated from its behavior. The values of $\nabla|E|^2_{max}$ are those[1] calculated for a cylindrical electrode of radius 0.60 cm spaced 0.241 cm from a flat plate. The values of the calculated electrical and gravitational forces, F_e and F_g, were obtained using the given equations.

Table I. Comparison of the calculated electrical (dielectrophoretic) force and gravitional force on particles in a tilted tray (3° tilt) in a nonuniform electrical field due to combined flat and cylindrical plates

Substance	Density, g/cc	Dielectric constant	$V_{critical}$, v(rms)	$\nabla\|E\|^2$, v/m² ×10⁻¹²	F_e, newtons/m³/unit vol.	F_g, newton/m³/unit vol.
SiC	3.17	(10)	500	2.40	(38.2)	810
Al_2O_3	4.0	8.6	800	6.12	87.6	1230
TiO_2	4.26	70	150	0.216	5.8	1370
$ZrSiO_4$	4.7	12.5	600	3.44	61.8	1590

That the calculated values for the electrical force are less than those calculated for the gravitational at balance is believed to be due to what may be termed the "bunching effect." The electrical force is that calculated for lone spherical particles which are so small as to leave the acting electrical field unaffected. The experimental observations of the critical voltages were obtained instead using rather concentrated streams of particles. It is believed that considerable particle-particle and particle-field interactions exist in such circumstances which greatly accentuate the nonuniform field force on the aggregates. This is evidenced, for example, by the bridging effects already noted. This problem is under further study and it is hoped that further light can be shed on this phenomenon.

REFERENCES

1. H. A. Pohl, *J. Appl. Phys.*, **22**, 869 (1951).
2. H. A. Pohl, *ibid.*, **29**, 1182 (1958).
3. H. A. Pohl and J. P. Schwar, *ibid.*, **30**, 69 (1959).
4. H. A. Pohl and J. P. Schwar, "Particle Separations by Nonuniform Electric Fields in Liquid Dielectric, Batch Methods," Paper presented at The Electrochemical Society, May 6, 1959, Philadelphia, Pa.
5. H. A. Pohl, "Non-Uniform Field Effects in Poorly Conducting Media," *ibid.*
6. Progress Report XXII, Laboratory for Insulation Research, M.I.T., December 1957.

[1] For a cylindrical electrode above and parallel to a flat plate,

$$\nabla|E|^2_{max} = \frac{25}{54}\sqrt{5}\,\frac{V^2}{y_1^3\left[\ln\left|\frac{y_1-y_0}{y_1+y_0}\right|\right]^2}$$

where V is the voltage between electrodes, y_0 the least distance between cylinder and flat electrodes, $y_1 = \sqrt{(y_0+R)^2 - R^2}$, and R is the radius of curvature of the cylindrical electrode, and the field quantity is measured at the surface of the flat plate.

December 1960 Discussion Section

A Discussion Section, covering papers published in the January-June 1960 JOURNALS, is scheduled for publication in the December 1960 issue. Any discussion which did not reach the Editor in time for the June 1960 Discussion Section will be included in the December 1960 issue.

Those who plan to contribute remarks for this Discussion Section should submit their comments or questions in triplicate to the Managing Editor of the JOURNAL, 1860 Broadway, New York 23, N. Y., *not later than September 1, 1960.* All discussion will be forwarded to the author(s) for reply before being printed in the JOURNAL.

Electrodeposition of High-Purity Chromium from Electrolytes Containing Fluoride or Fluosilicate

N. Ryan

Aeronautical Research Laboratories, Australian Defence Scientific Service, Department of Supply, Melbourne, Australia

ABSTRACT

Investigation of the variables affecting the laboratory scale deposition of chromium from chromic acid electrolytes containing fluoride or fluosilicate has enabled the optimum conditions for the production of high-purity chromium (0.03-0.04 wt % oxygen, 0.0008-0.002 wt % nitrogen) at the highest current efficiency (38-45%) to be determined. This current efficiency is much higher than the 8-10% in the chromic acid-sulfate electrolyte in which chromium of a similar grade can be produced.

Continuous electrodeposition in a larger cell showed that the current efficiency in fluoride-containing electrolytes decreased progressively with time to a steady 25-30%. No explanation has been found for this decrease. After steady conditions have been achieved, the advantages in current efficiency of the fluoride over the sulfate bath remains substantial.

It has been known for several years that fluorides and fluosilicates are effective catalysts in chromium plating solutions. Electrolytes containing these anions have been used commercially, particularly in Germany, but they have not yet been used for the purpose of producing high-purity chromium.

In these laboratories the pure chromium (0.02 wt % O_2, 0.002 wt % N_2, 0.001 wt % max. metallic elements including C, S, Si) required for experimental work on the development of chromium-base alloys is produced from chromic acid electrolytes containing sulfate (1) at current efficiencies of 8-10%. It is known that improved current efficiencies are obtained when using electrolytes containing either fluoride or fluosilicate, and it was therefore decided to investigate solutions containing these anions to determine whether or not they could be used to produce a high-grade chromium deposit.

Work by Bilfinger (2) (reviewed by Hood) (3) on baths containing fluoride and fluosilicate resulted in a series of curves and tables which revealed the optimum deposition conditions necessary to maintain the highest current efficiencies at 55°C. In the present study, an electrolyte temperature of 100°C was chosen for the preliminary investigations, after a consideration of the results of work carried out by Brenner, *et al* (4). These workers showed that the relationship between electrolyte temperature and oxygen content of chromium deposited from chromic acid solutions containing fluoride was similar to that associated with the chromic acid-sulfate electrolytes, i.e., increasing electrolyte temperature resulted in a decrease in the oxygen content of the chromium deposit. The experimental program was therefore designed to yield, for a bath temperature of 100°C, information of a similar character to that previously obtained by Bilfinger at 55°C. This was done by studying independently each variable affecting the efficiency of deposition and purity of the product.

For ease of reading and brevity in this report the expressions "fluoride-containing electrolyte" and "chromium deposited from an electrolyte containing fluoride" will in general be replaced by the terms "fluoride electrolyte" and "fluoride chromium," respectively. The terms "fluosilicate electrolyte," "sulfate electrolyte," "fluosilicate chromium," and "sulfate chromium" have corresponding meanings.

Apparatus

The apparatus, holding 250-300 ml of solution, consisted of a glass vessel with inlet and outlet arms which were used for the electrode connections and for the introduction of the electrolyte. Gases evolved during electrolysis escaped via a reflux condenser, which assisted in maintaining a stable electrolyte concentration by eliminating fume and evaporation losses. Since fresh electrolyte was used for each experiment and deposition runs were limited to 1 hr, no precautions were necessary to counter fluosilicate contamination arising from the glass container. Chemical analysis of the deposited chromium confirmed the absence of silicon. The use of fresh electrolyte also helped to reduce the build-up of trivalent chromium, which would have introduced a further significant variable.

The electrolytes were prepared from high-grade chromic acid containing the following nominal impurities: 0.02% SO_4, 0.004% NO_3, 0.01% Fe, and 0.1% Na. Fluoride was added as hydrofluoric acid and fluosilicate as the potassium salt.

Chromium was deposited on ½ in. diameter copper tubes which were subsequently dissolved by digestion in nitric acid. High-purity lead was first used as the anode material, but this was found to become inactive within a very short period. It was therefore replaced by a 7% tin-lead anode, as used in some commercial fluoride baths. A heavy scale formed on this anode, and in the early test runs this was removed. However this practice was found to

Table I. Variables affecting the deposition of chromium in fluoride electrolytes

Run No.	Electrolyte composition		F/CrO_3, %	Temp, °C	Current density, amp/ft²	Current efficiency, %	Oxygen, wt %	Nitrogen, wt %
	CrO_3, g/l	F, g/l						
F1	315	3.0	0.96	101	1100	8	0.4	0.002
F2	310	10.0	3.20	102	1050	15	0.35	0.003
F3	300	5.65	1.81	102	1150	39	0.04	0.0012
F4	295	4.4	1.50	100	1150	40	0.04	0.003
F5	300	16.0	5.35	102	1100	No deposit	—	—
F6	200	2.5	1.25	102	1000	19.5	0.068	0.0016
F7	300	7.46	2.5	101	964	32.3	0.14	0.002
C1	100	1.75	1.75	101	950	33	0.037	0.005
C2	200	3.5	1.75	102	910	38.5	0.04	0.005
C3	300	5.25	1.75		910	45	0.04	0.005
C4	400	7.00	1.75		910	35	0.044	0.003
T1	300	5.14	1.71	55	1010	28.5	0.4	0.008
T2	300	5.14	1.71	70	1010	23.5	0.15	—
T3	300	5.14	1.71	82	1010	24	0.09	0.007
T4	300	5.14	1.71	92	1010	38	0.08	0.006
T5	300	5.14	1.71	30	1010	Black powdery deposit	—	—
CD1	300	5.25	1.75	101	1360	44	0.028	0.003
CD2	300	5.25	1.75	102	1125	48.5	0.035	0.003
CD3	300	5.25	1.75	102	670	39	0.035	0.003
CD4	300	5.25	1.75	102	1200	48	0.033	0.003

be unnecessary as the scale did not in any way affect the activity of the anode.

For a preliminary study of larger scale production, a plating cell consisting basically of an 8 in. diameter round bottomed "Hysil" glass vessel holding up to 10 l was constructed. A lid of laminated fiber board, coated with a heavy layer of polyvinyl chloride, served as a covering for the cell and held four 12 in. double-surface reflux condensers, the copper cathode (1 in. tube) and electrical connections to the annular anode made from a 7% tin-lead alloy (6 in. diameter, 3/8 in. thick). The volume of electrolyte normally used was 8 l, and as in the case of the small cell no precautions were taken to protect the glass from the action of the fluoride.

Power to this cell was supplied by a 250 amp capacity selenium rectifier. No heating of the electrolyte was necessary, other than bringing up to temperature prior to the commencement of a run, as the power input (200 amp at 5-6 v) was sufficient to maintain a boiling solution. Arrangements for continuous operation were not developed and plating times were limited to 6-7 hr runs.

Analysis

Oxygen analysis of the deposited chromium was carried out by the Adcock method and nitrogen was determined using the semi-micro Kjeldahl method. Fluoride and fluosilicate concentrations in the bath were determined by a modification of the steam distillation process used by Reynolds and Hill (5).

Conditions of Operation

The current efficiency-catalyst acid curves obtained by Bilfinger (2) at 55°C gave strong indications of the sensitivity of current efficiency to

Table II. Variables affecting the deposition of chromium in fluosilicate electrolytes

Run No.	Electrolyte composition		SiF_6/CrO_3, %	Temp, °C	Current density, amp/ft²	Current efficiency, %	Oxygen, wt %	Nitrogen, wt %
	CrO_3, g/l	SiF_6, g/l						
S1	300	3.4	1.14	101	900	26.5	0.12	0.0008
S2	300	6	2.00	101	900	39	0.04	0.0008
S3	300	4.50	1.50	101	870	35	0.06	0.0008
S4	300	7.50	2.50	101	730	22	0.12	0.0008
S5	300	5.25	1.75	101	915	36	0.054	0.0014
S6	300	6.75	2.25	101	900	33	0.10	0.0014
S7	300	5.62	1.87	101	880	38.5	0.04	0.0012
CS1	500	10	2	101	900	29.5	0.05	0.0008
CS2	400	8	2	101	875	35	0.06	0.0012
CS3	200	4	2	100	910	32	0.06	0.0016
CS4	100	2	2	100	906	19	0.04	0.0008
CS5	350	7	2	101	920	36.5	0.04	0.0008
TS1	300	6	2	70	900	26.5	0.2	0.004
TS2	300	6	2	85	940	37.0	0.08	0.0012
TS3	300	6	2	63	924	15*	0.25	—
TS4	300	6	2	92	885	38.5	0.06	0.001
DS1	300	6	2	102	1300	39.5	0.06	0.0008
DS2	300	6	2	101	610	28.4	0.084	0.001
DS3	300	6	2	101	1606	36.8	0.09	0.0012
DS4	300	6	2	101	1160	40.0	0.036	0.0008

* Powdery deposit, current efficiency value doubtful.

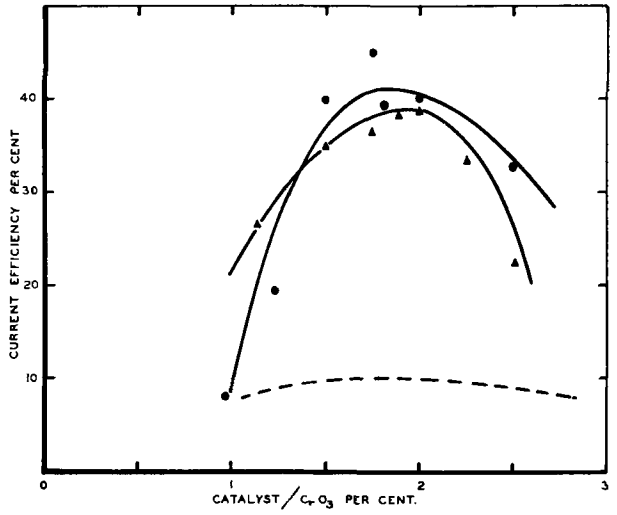

Fig. 1. Effect of catalyst-chromic acid ratio on current efficiency. •, Fluoride electrolyte; ▲, fluosilicate electrolyte; - - - -, sulfate electrolyte.

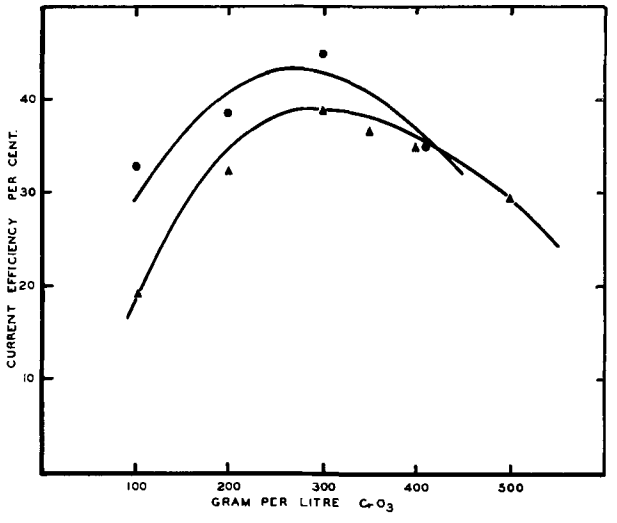

Fig. 2. Effect of chromic acid concentration on current efficiency. •, Fluoride electrolyte; ▲, fluosilicate electrolyte.

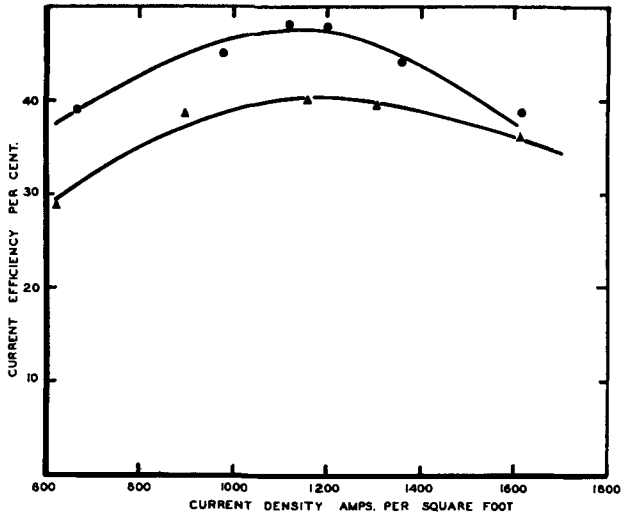

Fig. 3. Influence of current density on current efficiency. •, Fluoride electrolyte; ▲, fluosilicate electrolyte.

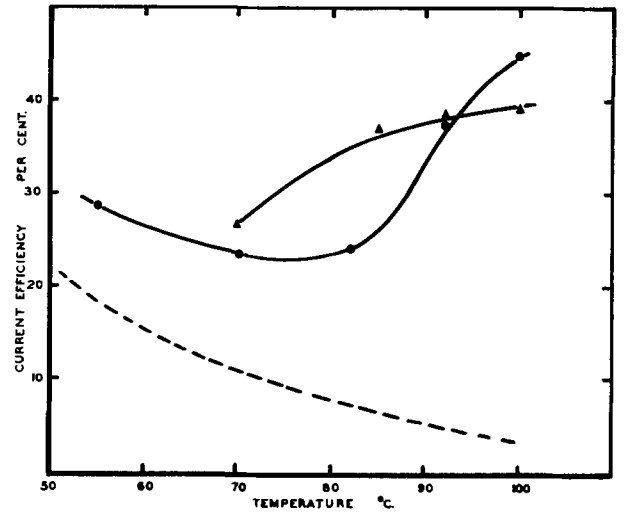

Fig. 4. Change in current efficiency with electrolyte temperature. •, Fluoride electrolyte; ▲, fluosilicate electrolyte; - - - -, sulfate electrolyte.

both fluoride and fluosilicate concentration in chromic acid electrolytes. For tests at 100°C, a chromic acid concentration of 300 g/l was selected, this being the standard concentration used in the production of sulfate chromium. Results are recorded in Tables I and II. The efficiency values are plotted against catalyst concentration in Fig. 1. The curve for sulfate electrolytes at 82°C is incorporated in Fig. 1 for comparison.

The results of the above test runs established the catalyst-chromic acid ratio at 1.75% for the fluoride electrolyte and 2% for the fluosilicate electrolyte. Several chromic acid solutions were prepared at concentrations ranging between 100 and 500 g/l CrO_3 each containing the required catalyst addition at the ratio cited above. These solutions were then electrolyzed at current densities of 880-950 amp/ft^2. The electrolyte temperature was maintained at 100°-102°C. The current efficiency data obtained are recorded in Tables I and II and illustrated graphically in Fig. 2.

From a study of the results obtained during this test series, chromic acid solutions of the following composition were prepared: (*a*) 300 g/l CrO_3, 5.25 g/l F; and (*b*) 300 g/l CrO_3, 6 g/l SiF_6. These solutions were electrolyzed at 100°-102°C using current densities ranging from 600 to 1600 amp/ft^2. Results are recorded in Tables I and II and shown in Fig. 3.

All of the above experiments were carried out in boiling electrolytes and the high current efficiencies obtained were particularly interesting. The association of high current efficiency with high temperature differed markedly from the behavior of sulfate electrolytes, i.e., decreasing efficiency with increasing temperature, and warranted further investigation. Hence electrolytes were prepared from 300 g/l solutions of chromic acid containing either 5 g/l fluoride or 6 g/l fluosilicate, and these were electrolyzed at various temperatures using current densities between 850 and 1010 amp/ft^2, as detailed in Tables I and II. The temperatures given in Tables I and II were measured by a thermometer attached to the cathode. It is possible however that the actual temperature at the cathode surface was slightly higher than those registered. The results of these experiments are given in Fig. 4, together with sul-

fate-electrolyte data (6). In the fluosilicate electrolyte, deposits at temperatures below 65°C were powdery, and the calculated current efficiency was thus doubtful. This may have been due to too high a current density which could result in some hydrolysis at the electrode surface.

The information obtained from these tests was both unexpected and interesting in that for both the fluoride and fluosilicate electrolytes current efficiency increased to a maximum value toward 100°C.

Gas Content of Electrodeposits (Oxygen and Nitrogen)

Oxygen.—Analysis of chromium deposited from the fluoride and fluosilicate baths at various temperatures showed that the oxygen content varied with temperature in much the same way as for sulfate chromium, i.e., as the electrolyte temperature was increased the oxygen content decreased rapidly between 50° and 80°C and then more gradually toward 100°C.

Results are recorded in Tables I and II and plotted in Fig. 5 together with the corresponding oxygen-temperature curve for a sulfate electrolyte. From these curves it is seen that while fluoride and fluosilicate chromium can be deposited with low oxygen content (0.03-0.05 wt %) they are unlikely to have as low an oxygen content as sulfate chromium produced under the optimum conditions. Against this, however, are the remarkably high current efficiencies of the fluoride and fluosilicate baths. At 100°C the efficiency of the sulfate electrolyte is 3% as compared with 40-45% for the fluoride and fluosilicate electrolytes.

Nitrogen.—The results suggest that the nitrogen content tends to decrease with increasing electrolyte temperature. However, this effect is doubtful, and other work (7) has shown that when higher nitrate impurity (0.1%) is present in the bath, the nitrogen content of the chromium is unaffected by electrolyte temperature.

Analysis of the chromium deposits from electrolytes of varying catalyst concentrations showed that the oxide impurity was particularly susceptible to changes in fluoride and fluosilicate concentrations. Low oxygen values occurred within the same catalyst concentration ranges which gave highest current efficiency. These values are recorded in Tables I and II and plotted against catalyst-chromic acid ratio in Fig. 6. Similar effects have been noted for the oxygen content of sulfate chromium, as is also indicated in Fig. 6. The nitrogen content was not affected.

Results recorded in Tables I and II show that variation in chromic acid concentration and current density have little or no influence on either the oxygen or nitrogen content in fluoride or fluosilicate chromium.

Electrodeposition from Fluoride Electrolytes in a 10-l Glass Cell

Using the information obtained from the preceding part of this investigation it was decided to carry out some preliminary tests in a larger scale apparatus as a step toward regular chromium production

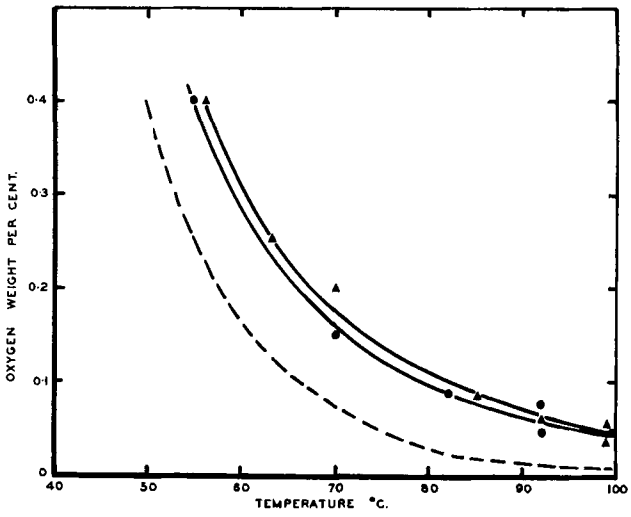

Fig. 5. Decrease in oxygen content with increasing electrolyte temperature. •, Fluoride chromium; ▲, fluosilicate chromium; - - - - -, sulfate chromium.

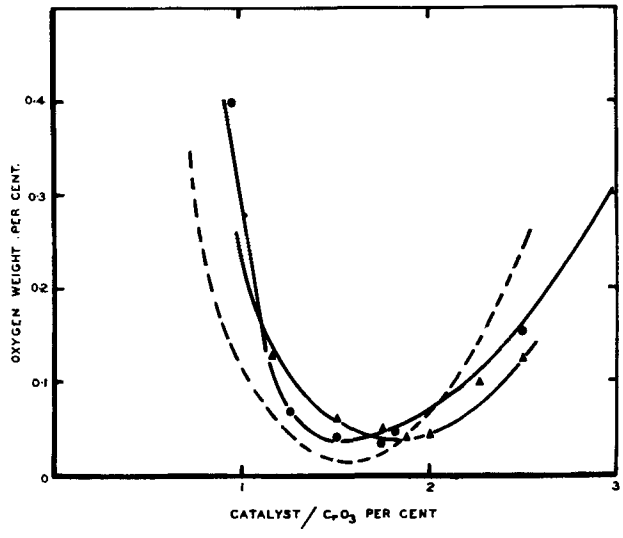

Fig. 6. Changes in oxygen content with various catalyst-chromic acid ratios. •, Fluoride chromium; ▲, fluosilicate chromium; - - - - -, sulfate chromium.

from fluoride containing electrolytes. Table III which lists details of some of these preliminary runs shows that the current efficiency falls successively as the bath ages.

Factors which could have some influence on this current efficiency decrease are:

1. Trivalent chromium concentration which showed increasing values corresponding to the decreasing current efficiency results (see Table III).
2. The considerable build-up of nodules and the treeing of the deposits which upsets the effective current density by increasing the over-all cathode surface area and which produces a nonuniform distribution of current density over the cathode surface. In addition some loss of chromium results from the detachment of nodules from the cathode.
3. The possible formation of fluosilicate contamination by the chemical action of the fluoride electrolyte on the glass vessel.

Influence of trivalent chromium concentration.—In order to study the effect of this variable on the current efficiency a solution of known trivalent chro-

Table III. Electrodeposition in the 10-l glass cell

Run No.	L1	L2	L4	L6	L7
Electrolyte composition					
CrO_3 g/l	290	309	300	300	310
F g/l, start	4.5	5	5	5.6	5.4
F g/l, finish	4		5	5	5.25
Cr, g/l	1.2	1.32	2.32	5.14	5.2
Active age of bath, hr	7	11	25	40	47
Temperature, °C	102	102	102	102	102
Current density, amp/ft²	1150	1150	1150	1100	1150
Current efficiency, %	40	35	32	25	24
Oxygen, wt %	0.04	0.04	0.04	0.035	0.03
Nitrogen, wt %	0.0028	0.003	0.003	0.002	0.0012

mium concentration was prepared by adding a known amount of Cr_2O_3. This solution was electrolyzed in the small experimental cell. As indicated in Table IV, a current efficiency of 42% was recorded, which apparently indicated that the trivalent chromium concentration did not influence the current efficiency. However, reconsidering this factor it was thought possible that by introducing trivalent chromium into solution as Cr_2O_3, the trivalent chromium complex formed might not be the same as that which exists in the electrolyte as a result of natural aging. Hence a further solution was prepared in which the trivalent chromium was increased by artificially aging the electrolyte using a large cathode surface area separated from a small anode surface by means of a porous porcelain pot. In this way solutions containing 15 and 27 g/l trivalent Cr were prepared for electrolysis in the small cell. The results, recorded in Table IV again show that trivalent chromium added to the bath does not affect the current efficiency significantly.

Current density and nodule formation.—The above tests suggested the possibility that in the large cell much more chromium was being lost as nodules than had been expected. Work with sulfate electrolytes (1,6) has shown that nodule formation is influenced by current density, lower densities yielding smoother deposits. Tests were therefore carried out with the fluoride electrolyte at lower current densities in the large cell for 6- and 7-hr runs. It was noticed that treeing and nodule formation were reduced. In this way the effective current efficiency was increased to some extent as shown in Table V, but it did not return to the high values obtained (40-45%) in the survey investigation.

Fluosilicate contamination in fluoride electrolyte.—As stated previously no precautions were taken to protect the glassware from etching by the fluoride in the electrolytes used. In the 1-hr experimental runs this factor was considered negligible since the time was short and fresh electrolyte was used for each test. An analysis of the electrolyte which had been in the larger 10 l glass cell for a period of approximately 3 months showed a fluosilicate content of the order 0.6-0.7 g/l SiF_6. This represents a tie-up of 0.5 g/l fluoride which would upset the effective fluoride-chromic acid ratio. This fluosilicate contamination may have contributed to the continual decrease in current efficiency but only to a minor extent, by producing a slight variation in the chromic acid catalyst ratio which could be eliminated by using an inert cell lining.

Table IV. Effect of trivalent chromium concentration

Electrolyte composition				Time of electrolysis, hr	Temp, °C	Current efficiency, %
CrO_3, g/l	F, g/l	Cr, g/l				
295	4.74	1.45 as Cr_2O_3		1	102	42
		Artificially aged				
		Start	Finish			
292	5.2	15	3	1	102	42
280	5.0	27	2.94	1	102	39.5

Table V. Effect of reduced current density on chromium recovery

Electrolyte composition		Current density, amp/ft²	Current efficiency, %
CrO_3, g/l	F, g/l		
300	5.24	1000	32
310	5.46	910	34.5
305	5.62	800	33.5
306	5.60	660	34.8

Effects of Impurities in the Electrolyte

Sulfate.—Since high-purity chromic acid would be uneconomical for full-scale chromium production, some tests were carried out using a commercial grade of chromic acid having the following impurity levels: 0.5-0.8% SO_4, 0.003% NO_3, and less than 0.5% metallics. This was found to produce chromium at much lower current efficiencies than those obtained when pure chromic acid was used. It has been reported (2,8) that sulfate additions in fluoride and fluosilicate electrolytes are associated with a decrease in current efficiency. This led to a series of experiments in which sulfate was (*a*) purposely added to a pure chromic acid electrolyte and (*b*) completely removed from a commercial chromic acid electrolyte by precipitation with barium hydroxide, but without introducing excess barium as a further variable. Results are given in Table VI and show that the sulfate impurity in commercial chromic acid appreciably reduces the current efficiency of the fluoride electrolyte.

Tin.—The use of a 7% tin-lead alloy as an anode in the electrodeposition of fluoride chromium introduced the possibility of tin traces being entrapped in the chromium. Using spectrographic and polarographic analysis, 0.005 wt % tin was detected in the chromium. This was not considered of a sufficiently high value to influence the properties of the metal. Further tests were carried out using a pure tin

Table VI. Influence of electrolyte sulfate impurity

Electrolyte	Nominal composition CrO_3, g/l	F, g/l	SO_4, g/l	Current efficiency, %
Commercial CrO_3	300	5	0.65	26
	300	5	0.24	31
Commercial CrO_3 SO_4 pptd. with $Ba(OH)_2$	300	5	Trace	42
Pure CrO_3 with added SO_4	300	5	0.56	29

anode, but even in this extreme case the deposited chromium showed only 0.08% tin. These results are given in Table VII, which also shows that plating ceased during the run with the tin anode. This suggested that while tin might not cause serious contamination of the electrodeposit, it could have a deleterious effect on the performance of the electrolyte. This was confirmed by tests in electrolytes deliberately contaminated with tin, where the current efficiency decreased with increasing tin content, as indicated in Table VII. This factor is discussed further in the following section.

Alternative Anode Materials

As demonstrated above tin contamination of the electrolyte resulted in an efficiency decrease and may arise when using 7% tin-lead anodes continuously. Therefore several alternative anode materials were studied, the primary requirements being an alloy which would remain active and not contaminate either the electrolyte or the deposit. Alloys examined were Pb-7% Sn, -4% Sn, -1% Sn, and 0.5% Sn; Pb-2% Ag; Pb-2% Zn; Pb-2% Ag -2% Zn; Pb-1% Na, and Pb-0.5% Te. The alloys which proved to be most resistant to the fluoride solutions were the Pb-Sn alloys (0.5-4% Sn), Pb-Te, Pb-Ag, Pb-Na. The Pb-Na alloy was particularly brittle and for this reason was not selected. Using the Pb-2% Ag anode, silver was detected in the chromium. It was found that the concentration of tin in the lead anode could be reduced to 0.5% and still maintain an active anode. The probable level of contamination using this anode composition was considered negligible, and it was used in all further tests.

Chromium Deposition in a Polyethylene Lined Plating Cell

Because of the danger of fluosilicate contamination, inert lining materials were investigated. Polyethylene was found to be resistant to the highly active solution but it softened at the high temperatures. However, providing the lining was well supported this was not a major problem.

A polyethylene-lined vessel was designed which consisted essentially of a steel tank (10-12 l capacity) lined first with lead and then with polyethylene. To a lid, which was similarly lined, were attached the electrode inlets and the outlet for waste gases which included a polyethylene-tube spiral condenser. During electrolysis the lid was sealed to the cell with a polyethylene gasket.

The electrolyte, containing 300 g/l CrO_3-5.4 g/l F, was prepared from commercial grade chromic acid, the sulfate impurity being precipitated with barium hydroxide. The results of deposition in this bath are listed in Table VIII; all runs are of 6-7 hr duration. Simultaneous tests, using sample electrolytes from the large bath, were carried out in the small experimental cell and showed higher efficiency values (see Table VIII). These tend to show that the time for deposition or thickness of deposit is the main factor in the low efficiencies recorded in the larger scale cells. The chromium produced in the large cell was of a high order of purity and the current efficiency, although lower than anticipated, remained relatively constant during the tests.

Properties of "Fluoride" Chromium

Chromium deposited from the fluoride electrolyte has been arc-cast, extruded, swaged, and rolled using procedures similar to that already reported (9,10) for chromium deposited from the chromic acid-sulfate electrolyte. Thus it was possible to compare the properties of cold-worked and recrys-

Table VII. Effect of tin contamination in the electrolyte

Electrolyte composition CrO_3	F, g/l	Sn, g/l	Anode material	Tin in chromium, wt %	Current efficiency, %
300	5.4	—*	Pb — 7% Sn	0.005	42
300	5.4	—*	Pure Sn	0.08	Plating ceased during run
300	5.32	0.0	Pb — 0.5% Te	—*	38
300	5.32	4.6	Pb — 0.5% Te	Tin detected spectrographically	15.0
300	5.32	7.4	Pb — 0.5% Te		9.6

* Not determined.

Table VIII. Deposition of chromium in polyethylene-lined cell

Electrolyte composition CrO_3, g/l	F, g/l	Temp, °C	Current density, amp/ft²	Current efficiency, %	Current efficiency in test cell, %	Oxygen, wt %	Nitrogen, wt %
310	5.4	100-102	880	34	38	0.008	0.001
306	5.32	100-102	800	26	34	Not detected	Not detected
300	5.36	100-102	640	25	36	Not detected	Not detected
300	5.2	100-102	880	24.5	32	Not detected	Not detected
300	5.3	100-102	760	25	34	Not detected	0.0005

Table IX. Transition temperatures of rolled "sulfate" and "fluoride" chromium

Material	Composition, wt %		Ductile/brittle transition in bending °C		Hardness (V.P.N.)	
	O_2	N_2	As rolled	Recrystallized	As rolled	Recrystallized
Sulfate Chromium	—	0.002	−60	380	—	—
Fluoride Chromium	0.012	0.001		195	185	130
	0.025	0.002	−87	121	219	115

Table X. Room-temperature tensile properties of rolled "sulfate" and "fluoride" chromium

Material	Tensile strength, psi	Elongation on $4\sqrt{\text{area}}$, %	Reduction in area, %
Sulfate Chromium	100,000	40	50
Fluoride Chromium	88,000	57	55

tallized fluoride chromium with those of the sulfate material. The ductile-brittle transition temperatures and tensile properties of these materials in the form rolled strip are listed in Tables IX and X, and show that the fluoride chromium can be fabricated equally as well as chromium deposited from the chromic acid-sulfate electrolyte and has superior ductility values.

Discussion

The most puzzling feature of this investigation is the decrease in current efficiency on changing from the small test cell experiments to the pilot plant stage. At first sight it would appear that this current efficiency decrease was excessive and that some simple explanation might be found in that variables such as trivalent chromium concentration, fluosilicate contamination, or tin impurity could have a deleterious influence. However as has been shown above none of these factors had any appreciable influence on the current efficiency. It was demonstrated that the trivalent ion concentration did not have any influence. The source of the fluosilicate contamination was removed by using a polyethylene lined vessel, and tin contamination was greatly reduced by replacing the 7% tin-lead anode by one containing 0.5% tin.

In view of the above it was considered that the major effect might be due to the nodule growth, treeing, and the general roughness associated with the deposition of thicker coatings than those obtained in the small cell. By comparison with the sulfate bath (1, 6) where efficiencies of the order 14% are obtained for runs of 1 hr but drops to 6-7% for periods up to 72 hr, it may well be anticipated that a current efficiency of 42% in the small fluoride bath for hourly runs could drop to 20% for plating times of say 20 hr giving an equivalent thickness of chromium to that obtained in the sulfate bath. This current efficiency is in fact very close to the one obtained in this investigation which was 25% for 8-hr runs in the pilot plant equipment. By analogy with the operation of the sulfate bath where it is possible, by improved control of the operating variables (10) and also continual purification of the electrolyte by ion exchange, to obtain current efficiencies of 9-10% it should be possible to achieve current efficiencies of 27-30% in the fluoride bath.

It is true that this comparison does not in any way explain why treeing and general surface roughness occurs in aged baths, but it does help to put the drop in efficiency found in the fluoride bath in perspective. An explanation of the phenomenon must wait on a more fundamental attack on the more basic factors operating in the electrodeposition of chromium for considerable periods of time.

In the fluoride electrolyte a minimum current efficiency at electrolyte temperatures between 70° and 80°C was noted. The latter temperature is the maximum at which previous investigators had worked when examining plating conditions for fluoride electrolytes. Because up to this temperature the current efficiency in fluoride electrolytes shows the same downward trend as in sulfate electrolytes it has presumably been concluded that the current efficiency in the former would continue to decrease as the temperature is raised. No explanation for the minimum in the current efficiency-temperature curve can be given on the basis of the present results.

Conclusions

1. The optimum conditions for the deposition of high-purity chromium were (*a*) for the chromic acid-fluoride electrolyte: electrolyte composition, 300 g/l CrO_3, 5.25 g/l F; current density, 1150 amp/ft^2; electrolyte temperature, 100°-102°C; giving a current efficiency of 40-45% in 1-hr runs. (*b*) for the chromic acid-fluosilicate electrolyte: electrolyte composition, 300 g/l CrO_3, 6 g/l SiF_6; current density, 1150 amp/ft^2; electrolyte temperature, 100°-102°C; giving a current efficiency of 38-40% in 1-hr runs. These conditions yielded chromium containing 0.03-0.04 wt % oxygen and 0.0008-0.002 wt % nitrogen.

2. The oxygen content of the chromium was sensitive to changes in catalyst concentration. The catalyst concentration which gave the maximum current efficiency also gave the minimum oxygen concentration. This impurity concentration decreased with increasing electrolyte temperature in the same manner as found in the sulfate electrolytes, but the average minimum value was higher (0.03 wt %) than for the sulfate product (0.01 wt %). This minimum value was not influenced by changes in current density or chromic acid concentration.

3. The nitrogen impurity level was not changed in any consistent manner by any of the variables investigated.

4. Deposition of chromium from the chromic acid-fluoride electrolyte under semi-production conditions was accompanied by a progressive decrease in current efficiency with time to a steady value of 25-30%. The following are the conclusions from the investigation of some of the variables which could effect current efficiency: (*A*) The trivalent chromium concentration did not influence current efficiency. (*B*) A decrease in the current density for large-scale tests produced a slight increase in cur-

rent efficiency due apparently to a decrease in nodule formation (*C*) Tin was detected in both the chromium deposit and the electrolyte, and it was shown that tin contamination could reduce the current efficiency. (*D*) Any sulfate impurity in the chromic acid used must first be removed since sulfate contamination was shown to be associated with a reduction in current efficiency. However, the decrease in current efficiency with time was greater than could be explained by any combination of these factors.

5. "Fluoride" chromium fabricated by arc-casting, extrusion, swaging, and rolling at 700°C possessed mechanical properties which compared favorably with those of "sulfate" chromium prepared by similar means.

Acknowledgments

The author would like to thank Mr. E. J. Lumley for all nitrogen analysis and Messrs. J. B. Dance and A. R. Edwards for continued encouragement and helpful discussion in the preparation of this report. For permission to publish this paper acknowledgment is also made to the Chief Scientist, Australian Defence Scientific Service, Department of Supply, Melbourne, Australia.

Manuscript received Nov. 16, 1959.

Any discussion of this paper will appear in a Discussion Section to be published in the December 1960 JOURNAL.

REFERENCES

1. H. T. Greenaway, *J. Inst. Metals*, **83**, 121 (1954-1955).
2. R. Bilfinger, *Metallwirtschaft*, **22**, 466 (1943).
3. T. A. Hood, *Metal Finishing*, **50**, 103 (1952).
4. A. Brenner, Polly Burkhead, and C. Jennings, *J. Research, Nat. Bur. Standards*, **40**, 31 (1948).
5. D. S. Reynolds and W. L. Hills, "Applied Inorganic Analysis," Hillebrand, Lundel, Bright and Hoffman, John Wiley & Sons, New York.
6. H. T. Greenaway, Unpublished work.
7. N. Ryan and E. J. Lumley, *This Journal*, **106**, 388 (1959).
8. R. MacNair, *Metal Ind.*, **73**, 448 (1948).
9. H. L. Wain, S. T. M. Johnstone, F. Henderson, and N. Louat, *J. Inst. Metals*, **86**, 281 (1957-1958).
10. J. J. Dale, Private communication.

Polarization of Luminescence in ZnS and CdS Single Crystals

A. Lempicki

General Telephone and Electronics Laboratories Inc., Bayside, New York

ABSTRACT

The fluorescent emission from hexagonal ZnS and CdS single crystals is found to be polarized preferentially perpendicular to the c axis for both polarized and unpolarized excitation. Cubic ZnS crystals emit unpolarized radiation. The results are analyzed in terms of a simple dipole theory which is shown to be inadequate for the description of luminescent centers in these materials. Preliminary observations on the polarization of fluorescence of ZnO crystals are reported.

The so-called Weigert effect (1) or polarization of fluorescence has been known for many years. A large amount of work has been done on the properties of organic molecules in various media (1, 2). The method has not been applied extensively to the inorganic luminescent materials. A notable exception is found in the work of Lambe, Compton, West, and Klick (4-7) in this country and Feofilof (3) in Russia. The substances investigated by these authors were mostly halides.

Recent successes in the growth of single crystals of the sulfides (8, 9) made it possible to apply the polarization techniques to the study of the luminescent centers in these materials.

The simplest physical model of a luminescent center can be conceived as an atomic or molecular aggregate giving rise to a classical electric oscillator. If this is the case, the polarization studies should enable us to determine the components of the polarizability tensor and the orientation of the oscillator in the lattice.

Usually the measurement of polarization is made in the longitudinal direction as illustrated on Fig. 1. The fluorescent medium is at the origin of the coordinates O and is excited by an electromagnetic wave propagated along the $-x$ axis. The electric vector E is parallel to z. Observations are made through an analyzer A which can be rotated either parallel or perpendicular to E. One introduces a quantity p:

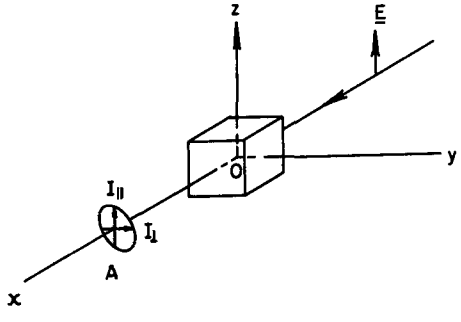

Fig. 1. Measurement of polarization-longitudinal experiments.

$$p = \frac{I_{\parallel} - I_{\perp}}{I_{\parallel} + I_{\perp}} \; ; \; -1 \leq p \leq 1 \qquad [1]$$

where $I_{||}$ and $I_{\perp}$ are the observed intensities of fluorescence for the two directions. The theories of the effect aim at calculating p from a suitable model of the fluorescent center. There are various degrees of sophistication in these theories which are briefly described.

The Rayleigh-Tyndall model.—For monochromatic excitation one assumes that the fluorescence is essentially a scattering process without change of wave length. As in Rayleigh scattering the intensity in any given direction is proportional to the square of the dipole moment μ. This moment is determined by the polarizability tensor α through the equation

$$\mu = \alpha \underline{E}$$

In crystals it is assumed normally that the principal axes of this tensor are oriented along main crystallographic directions. In spite of the usually large Stokes shift ($\lambda_{absorption} < \lambda_{emission}$). This simple model has been used successfully in determining the symmetries of some luminescent centers in halides (4) and in diamond (10).

Separate absorption and emission oscillators.—It has been first pointed out by Perrin (11) in connection with work on fluorescent solutions that sometimes it may be necessary to postulate two different kinds of oscillators. The exciting energy is first absorbed by an absorption oscillator and then transferred to an emission oscillator. This formally allows for a shift in energy between absorption and emission and accounts for negative values of p sometimes observed in solutions. Feofilof has used essentially the same model in determining the symmetry of luminescent centers in CaF_2 and NaF (3). In this case the sign and magnitude of p change with the exciting wave length, and it is necessary to introduce two separate oscillators.

The models (a) and (b) are essentially classical although Jablonski (12) and Lafitte (13) have used quantum mechanical methods in describing the energy transfer between the two sets of oscillators.

Quantum mechanical treatment.—If the symmetry of the crystal and luminescent center are known, it is possible to write down selection rules for dipole transition (14). In a still more refined treatment the matrix elements could be computed, and from these one should be able to estimate p.

Experimental Methods

The experimental arrangement is represented schematically in Fig. 2. A mercury arc source is placed at S. The 3650Å radiation is isolated by means of filter 1 and passes through a Glen-Thompson polarizer which can be rotated about the x axis (θ). The fluorescence generated in specimen C passes through a polaroid analyzer and is detected by a photomultiplier Ph. Filter 2 has a sharp cut-off for the exciting radiation. The optical system of a Zeiss polarizing microscope was adapted for the measurements.

There are several important precautions which must be taken in order to obtain reliable results. Most important is that no polarized excitation reaches the detector. This is achieved by suitable

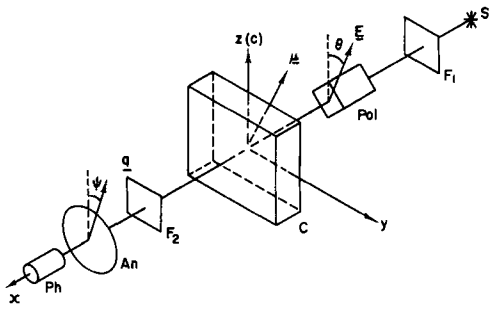

Fig. 2. Experimental arrangement for the measurement of polarization. S, radiation source; F_1, filter; Pol, polarizer; C, crystal; R_2, filter; An, analyzer; Ph, photomultiplier.

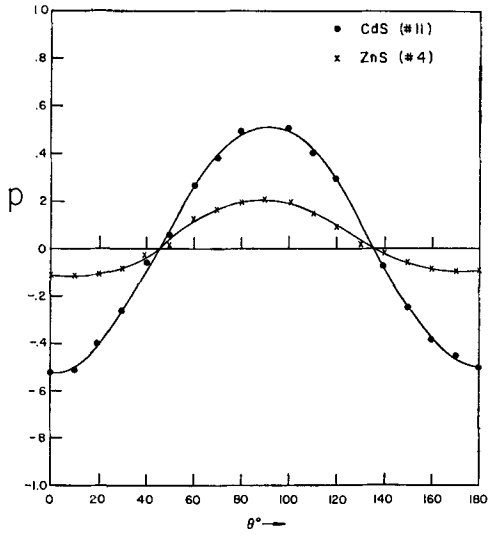

Fig. 3. Polarization factor p vs. the azymuth θ for a CdS and ZnS:Cu crystal. For $\theta = 0$ the exciting electric vector is parallel to the c axis.

combinations of filters 1 and 2. The specimens in form of plates are mounted over a diaphragm. The exciting beam is made nearly parallel by removing the microscope condenser and using suitable stops. It is important that the numerical aperture of the objective gathering the fluorescence be as small as possible. The reason for this is given in the appendix.

Since the angles θ and Ψ can be set independently we can generalize Eq. [1] and define p as

$$p(\theta) = \frac{I(\Psi = \theta) - I\left(\Psi = \theta + \frac{\pi}{2}\right)}{I(\Psi = \theta) + I\left(\Psi = \theta + \frac{\pi}{2}\right)} \qquad [2]$$

In our measurements we have chosen the z axis to coincide with the c axis of the crystals. In case of excitation with natural (unpolarized) light the angle θ is, of course, not specified. We define then for this case

$$p_n = \frac{I(\Psi = 0) - I\left(\Psi = \frac{\pi}{2}\right)}{I(\Psi = 0) + I\left(\Psi = \frac{\pi}{2}\right)} \qquad [3]$$

It should be noted that measurements with natural light are much more sensitive than with polarized light. The reason for this is that, if the filter system

Table I. Polarization data

Type	Impurity, mole %	Fluorescence peak, Å	Structure	$p(0°)$	$p(90°)$	p_n
1. ZnS	Cu $2x10^{-4}$		Hex.			—0.24
2. ZnS	Cu 2.10^{-4}		Hex.			—0.24
3. ZnS:Cu	0.02	4500	Hex.	—0.03	0.20	—0.12
4. ZnS:Cu	0.02	4500	Hex.	—0.11	0.20	—0.16
5. ZnS:Cu	0.02	4500	Hex. (cub)	—0.07	0.16	—0.09
6. ZnS	Cu $2x10^{-4}$		Hex. (cub)	—0.08	0.12	—0.11
7. ZnS	Cu 0.01	4500	Cub.	0.00	0.00	0.00
8. ZnS:Mn	0.1	5750	Cub.	0.00	0.00	0.00
9. ZnS:Mn	1.0	5750	Cub. (hex)	—0.03	0.07	—0.05
10. ZnS:Mn	1.0	5750	Cub. (hex)	—0.06	0.02	—0.02
11. CdS		6800	Hex.	—0.52	0.51	—0.50
12. ZnO	Clear	5180	Hex.	0.00	0.00	0.00
13. ZnO	Clear	5180	Hex.	0.00	0.00	0.00
14. ZnO	Red	5130	Hex.	0.27	—0.25	0.28
15. ZnO	Red	5130	Hex.	0.48	—0.48	0.45

(1 and 2) is not ideal and the fluorescence weak, then an appreciable fraction of the excitation can reach the photomultipler. If it is polarized, it will affect the value of p. With natural light this leaking excitation can produce only a constant background independent of the setting of the analyzer.

Results

The ZnS crystals (Table I) used in this investigation were grown by a vapor phase method by Kremheller and Samelson of our Laboratories. Some of them were deliberately activated (by doping the starting powder) with Cu and Mn. Others were used as grown. The impurity concentration is given in the second column of Table I.

Specimens designated by ZnS:Cu and ZnS:Mn were doped intentionally during growth. Those designated by ZnS had only accidental impurities. The concentration of impurities was determined on a random selection of crystals from the same growth batch.

The requirements of bright fluorescence and platelike geometry with the c axis in the plane of the plate seriously limit the number of suitable specimens. A fluorescent spectrum (under 3650Å excitation) was obtained on crystals which were sufficiently bright and the peak is given in the third column. X-ray analysis was obtained for all specimens. Crystals 1 and 2 are essentially free of stacking disorder and birefringence banding. All other ZnS specimens show varying amounts of both. Some, like 5, 6, 9 and 10, show, besides the main structure, diffraction spots due to the other phase. This is indicated in brackets. The remaining three columns of Table I give the values of p for excitation polarized parallel to c, perpendicular to c and natural light.

All the ZnS and CdS crystals, except 7 and 8, which are cubic, show a fluorescence preferentially polarized perpendicular to the c axis. The intensity was too weak for crystals 1 and 2 to measure $p(0°)$ and p (90°), but these crystals have the highest values of p_n observed on any specimen of ZnS. The presence of disorder which is equivalent to the introduction of the cubic phase is seen to decrease the magnitude of p. Table I does not include numerous results obtained on cubic crystals many of which were electroluminescent. No polarization of fluorescence or electroluminescence was found in these. Unfortunately, no hexagonal ZnS:Mn crystals comparable in perfection with specimens 1 and 2 were available. This makes it difficult to distinguish between the property of the luminescent centers (Mn and Cu) and the lattice. It is impossible to compare ZnS:Cu an ZnS:Mn crystals which show different amounts of disorder.

Specimen 11 is a hexagonal CdS crystal with an emission peak near 6800Å.[1] Its fluorescence is also polarized perpendicular to c with a value of $|p| = 0.5$ considerably higher than in ZnS crystals.

Figure 2 gives the variation of p (θ) as a function of the azymuth θ for crystals 4 and 11. The CdS curve is symmetrical about the x axis and can be represented by an equation of the form $p(\theta) = -\frac{1}{2} \cos 2\theta$. If we make measurements with natural light excitation and plot p_n as a function of the angle Ψ we obtain a similar result $p_n = -\frac{1}{2} \cos 2\Psi$. This means that the polarization is quite independent of the mode of excitation. For ZnS the results are somewhat different. As seen from Table I and Fig. 2 we have in general

$$|p| \ (0°) \ | < |p_n| < |p \ (90°)$$

It should be stressed that quantitative measurements of polarization require a rather high degree of external crystal perfection. This is demonstrated by the following observations. One specimen of CdS consisted of a very clear plate joined to a thicker heavily striated part. Measurements of polarization were made in the two regions. In the clear portion p_n was about —0.3, whereas it decreased to almost zero in the less perfect part. To further check the effect of surface we have etched crystal 11 in HNO_3. The previously shiny surface turned rough and the polarization decreased from $p_n = 0.5$ to $p_n = -0.18$.[2] We believe that in specimens 1, 2, and 11 no surface depolarization effects were present.

Miscellaneous Observations

We have observed a polarization of the green electroluminescence in pure (nonphotoluminescent)

[1] The crystal was obtained from Dr. I. Broser of the Fritz Haber Institut der Max Planck Gesellschaft, Berlin. Beyond the presence of silver its exact impurity content is unknown.

[2] That a rough surface produces depolarization can be demonstrated by placing a ground glass plate between the crossed polarizers of a microscope. The field of view will not extinguish.

CdS. The crystals had Ga electrodes which had to be "formed" (15). These measurements were rather difficult because of the instability of emission. Values of p up to -0.3 were observed. The electroluminescence is thus also preferentially polarized perpendicular to c.

Some measurements were also made on ZnO crystals of two distinct types. Clear and transparent crystals (12, 13) obtained from vapor phase reaction show a weak *body* photoluminescence peaking at 5180A. No polarization effects were observed on these. The second category (14, 15) obtained from zinc refineries have a deep red color and an intense fluorescence confined to a *surface* layer. The peak of the fluorescence confined to the surface layer is only slightly lower (5130Å) than that of the clear crystals. However, polarization is quite marked and in this case polarized preferentially parallel to c. A tentative explanation of this effect in terms of surface and volume properties has been proposed by Birman (16).

Discussion

One important question which must be settled before we draw conclusions from our results is the possible effect of dichroism. In ZnS, according to data of Piper, *et al.* (17) and Balkanski and Waldron (18), α ($\|$ c) $<$ α ($\perp$ c), where α ($\|$ c) and α ($\perp$ c) are the absorption constants for light polarized parallel and perpendicular to c. Hence, if fluorescence emission was initially unpolarized, it would become preferentially polarized parallel to c as it travels from the luminescent center to the surface of the crystal. This is contrary to our observations and thus dichroism cannot be responsible for the results. The situation is more complicated in the case of CdS for which α ($\|$ c) becomes larger than α ($\perp$ c) at wave lengths larger than 5350Å (12). Here dichroism could in principle produce the observed polarization at 6800Å. This point was checked directly by illuminating the crystal with unpolarized radiation approximating in wave length the fluorescent emission. The amount of polarization introduced by dichroism in both CdS and ZnS crystals was found to be below the experimental error and thus of no importance for our measurements.

In order to see whether the Rayleigh-Tyndall theory of scattering can account for the observed polarization we shall consider a very general model for the luminescent centers. Let us assume that there are n of them in the volume of the crystal under observation. Each center will be characterized by a certain polarizability tensor α^n_{ij}. The x, y, z coordinate system of Fig. 2 may or may not coincide with the principal axes system of some centers. The polarizability tensors of some centers may be identical.

The exciting radiation produces a dipole moment μ^n in each center. The direction of this moment is determined by the α^n_{ij} — s and the exciting electric field intensity E. Since observations are made along the x axis, only the components μ^n_y and μ^n_z will contribute to the observed intensity. These are given by

$$\mu^n_y = \alpha^n_{yy}\, E \sin\theta + \alpha^n_{yz}\, E \cos\theta$$
$$\mu^n_z = \alpha^n_{yz}\, E \sin\theta + \alpha^n_{zz}\, E \cos\theta \qquad [4]$$

Where θ is the angle between E and the z axis (Fig. 2). Since the polarizability tensor is symmetrical (19) only three components for each center (α^n_{yy}, α^n_{zz}, α^n_{yz}) determine the intensity.

The magnitude of the scattered (photoluminescent) intensity depends on the coherency of scattering from the various dipoles. In the absence of definite information about this we compute the intensity for both complete coherency (I_c) and complete incoherency (I_i). We have

$$I_c(\theta,\Psi) \sim \sum_n (\mu^n_y \sin\Psi + \mu^n_z \cos\Psi)^2$$
$$I_i(\theta,\Psi) \sim [(\sum_n \mu^n_y)\sin\Psi + (\sum_n \mu^n_z)\cos\Psi]^2 \qquad [5]$$

From Eqs. [5], [4], and [2] we can compute the polarization factors for both cases (Eq. [6] and [7]). The corresponding equations for natural light excitation are obtained by averaging Eq. [5] over θ and substituting in Eq. [3] (Eq. [8] and [9]).

$$p_c(\theta) = \frac{[2C\,(B^2\cos^2\theta + A^2\sin^2\theta) + AB\sin 2\theta]\sin 2\theta + [(B^2\cos^2\theta - A^2\sin^2\theta) - \cdots}{(B^2\cos^2\theta + A^2\sin^2\theta) + 2C\,(B\cos^2\theta + A\sin^2\theta)\sin 2\theta + \cdots\cdots}$$
$$\cdots\cdots \frac{-(A-B)\sin 2\theta - C^2\cos 2\theta]\cos 2\theta}{+[(A-B)\sin 2\theta + C^2\cos 2\theta]} \qquad [6]$$

and

$$p_i(\theta) = \frac{(A'\cos^2\theta - B'\sin^2\theta)\cos 2\theta - C' + (2C' + F')\sin^2 2\theta + 2(D'\sin^2\theta + \cdots}{(A'\cos^2\theta + B'\sin^2\theta) + C' + 2(D'\sin^2\theta + E'\cos^2\theta)\sin 2\theta + \cdots\cdots}$$
$$\cdots\cdots \frac{+E'\cos^2\theta)\sin 2\theta + \frac{1}{2}(E' - D')\sin 4\theta}{+\frac{1}{2}(D' - E')\sin 4\theta} \qquad [7]$$

$$p_{rc}(\Psi) = \frac{B^2 - A^2}{A^2 + B^2 + 2C^2}\cos 2\Psi + \frac{2(A+B)C}{A^2 + B^2 + 2C^2}\sin 2\Psi \qquad [8]$$

$$p_{ri}(\Psi) = \frac{B' - A'}{A' + B + 2C'}\cos 2\Psi + \frac{2(D' + E')}{A' + B' + 2'C}\sin 2\Psi \qquad [9]$$

The constants are

$$A = \sum_n \alpha^n_{yy} \qquad A' = \sum_n (\alpha^n_{yy})^2$$
$$B = \sum_n \alpha^n_{zz} \qquad B' = \sum_n (\alpha^n_{zz})^2$$
$$C = \sum_n \alpha^n_{yz} \qquad C' = \sum_n (\alpha^n_{yz})^2$$
$$D' = \sum_n \alpha^n_{yy}\alpha^n_{yz}$$
$$E' = \sum_n \alpha^n_{zz}\alpha^n_{yz}$$
$$F' = \sum_n \alpha^n_{yy}\alpha^n_{zz} \qquad [10]$$

Although the formulas are rather complicated, we can draw from them certain general conclusions, at least in the case of CdS. First, let us remark that for natural light excitation the polarization factors have the form $p_n \sim R \cos(2\theta + \phi)$, where R is an amplitude and ϕ a phase. Any partially polarized radiation must give rise to such a dependence. The important fact is that experimentally we find $R = -\frac{1}{2}$ and $\phi = 0$ (for CdS). This eliminates the sin 2Ψ term in Eq. [8] or [9]. Thus we must have $C = D' = E' = 0$. We now have to consider the coherent and incoherent case separately.

For the coherent case, the requirement $R = -\frac{1}{2}$ yields $A^2 = 3B^2$. If we substitute this into Eq. [6] we see that there is no way of reducing it to $-\frac{1}{2} \cos 2\theta$, which the experiment indicates.

For the incoherent case. we have from Eq. [9]:

$$\frac{B' - A'}{A' + B' + 2C'} = -\frac{1}{2}$$

Again, Eq. [7] cannot be reduced to the form $-\frac{1}{2} \cos 2\theta$ with the three arbitrary constants A', B', C' and the condition $A' \neq B'$.

Before we form our conclusions, let us dispose of a certain approximation which we have not mentioned explicitly. We have assumed that the exciting electric field components are $E \sin\theta$ and $E \cos\theta$ (see Eq. [4]). In fact, for ZnS at the excitation wave length of 3650Å the absorption constant α ($\perp$c) is larger than α (||c). For CdS no measurements are available. If the same is true for CdS as for ZnS, we should use for the y component $E\sigma \sin\theta$ where σ represents an attenuation factor ($\sigma < 1$) as compared with the z component. If we recalculate the polarization factors Eqs. [6], [7], [8], and [9] in terms of σ we still cannot reduce simultaneously [6] and [8] or [7] and [9] to the experimentally observed form of $-\frac{1}{2} \cos 2$ (angle).

Thus, in the case of CdS, and in contrast to diamond and the halides, a model involving arbitrarily oriented anisotropic dipoles cannot account for the results.

The case of ZnS is more complicated because the $p(\theta)$ curves show an asymmetry (Fig. 2) and, therefore, a dependence of polarization of emission on the mode of excitation. It should be stressed that it is very important to obtain measurements of p as a function of θ over a whole period and not only at isolated points. Only then can one draw meaningful conclusions as to the adequacy of the dipole model of a luminescent center.

Finally, even in the case of CdS, it may be possible to construct a model involving two oscillators per center and account for the observations. In such a center an energy transfer would take place. This possibility has been discussed by Dexter (22) and lately by Malemed (23). On the other hand, it is possible to account for the polarization measurements qualitatively in terms of the symmetry of the valence bands in these materials rather than the center itself. A fuller discussion of the various possibilities is given in the accompanying paper by Birman (16).

Acknowledgments

The author is indebted to Drs. A. Kremheller and H. Samelson for the ZnS crystals, to I. Broser for the CdS crystal, to Dr. R. W. Smith, of RCA, for the electroluminescent CdS crystals and to Dr. A. R. Hutson, of B.T.L., for the ZnO crystals. Mr. V. A. Brophy and S. Kellner performed the x-ray analysis and Dr. J. L. Birman has contributed by his discussions and criticism.

Manuscript received Nov. 9, 1959. This paper was prepared for delivery before the Philadelphia Meeting, May 3-7, 1959.

Any discussion of this paper will appear in a Discussion Section to be published in the December 1960 JOURNAL.

REFERENCES

1. P. Pringshein, "Fluorescence and Phosphorescence," Interscience Publishers Inc., New York (1949).
2. T. Forster, "Fluorescenz Organischer Ferbindungen," Vandenloeck and Ruprecht, Gottingen (1951).
3. P. P. Feofilof, *J. Phys. Rad.*, **17**, 656 (1956).
4. J. Lambe and W. D. Compton, *Phys. Rev.*, **106**, 684 (1957).
5. W. D. Compton and C. C. Klick, *ibid.*, **110**, 349 (1958).
6. J. Lambe and E. J. West, *ibid.*, **108**, 634 (1957).
7. C. C. Klick and W. D. Compton, *J. Phys. Chem. Soc.*, **7**. 170 (1958).
8. A. Kremheller, *Sylvania Technologist*, **3**, 11 (1955).
9. L. C. Green, *et al.*, *J. Chem. Phys.*, **29**, 1375 (1958).
10. R. J. Eliott, I. G. Matthews, and E. W. J. Mitchell, *Phil. Mag.*, **3**, 360 (1958).
11. F. Perrin, *Ann Phys. Paris*, **12**, 169 (1929).
12. A. Jablonski, *Acta Phys. Pol.*, **10**, 33 (1950), **10**, 194 (1950).
13. E. Laffitte, *Ann. Phys. Paris*, **10**, 71 (1955).
14. J. L. Birman, *Phys. Rev. Let.*, **2**, 157 (1959).
15. R. W. Smith, *Phys. Rev.*, **105**, 900 (1957).
16. J. L. Birman, *This Journal*, **107**, 409 (1960).
17. W. W. Piper, *et al.*, *Phys. Rev.*, **110**, 323 (1958).
18. M. Balkanski and W. Waldron, *ibid.*, **112**, 123 (1958).
19. M. Born, "Optik," p. 308, Springer, Berlin (1933).
20. J. F. Nye, "Physical Properties of Crystals," p. 300, Clarendon Press, Oxford (1957).
21. C. W. Bunn, "Chemical Crystallography," Oxford (1946).
22. D. L. Dexter, *Phys. Rev.*, **108**, 630 (1957).
23. N. T. Malemed, *J. Phys. Chem. Soc.*, **7**, 146 (1958).

APPENDIX

Imagine the dipole moment μ (Fig. 2) of an oscillator to be decomposed into three components μ_x, μ_y, μ_z. By making $\psi = 0°$ or $90°$ we would like to obtain a signal due only to the components μ_z or μ_y, respectively. The intensity of radiation is zero along the axis of a dipole but increases as the square of the sine of the colatitude angle away from the axis. Thus, if the aperture is large, part of the radiation due to μ_x will also be intercepted by the objective. The ratio of the intensities due to the components μ_x, μ_y, μ_z is given by

$$\frac{I(\mu_z)}{I(\mu_x)} = f(\gamma)\frac{\mu_z^2}{\mu_x}; \frac{I(\mu_y)}{I(\mu_x)} = f(\gamma)\frac{\mu_y^2}{\mu_x}$$

where sin γ is the numerical aperture of the objective. f (γ) can be obtained by computing the ratio of the fluxes through the objective from the dipole radiation intensity formula $I \sim \sin^2\theta\mu^2/r^2$. In Table II we give a few values of f (γ) for different objectives. If all the components of μ are equal the last column gives the percentage admixture of the unwanted $I(\mu_x)$ component. In most of our work we used the first objective.

Table II. Effect of numerical aperture

Sin γ	f(γ)	%I(μ_x)
0.08	332	0.30
0.22	48.4	2.06
0.45	11.2	8.92

Polarization of Fluorescence in CdS and ZnS Single Crystals

Joseph L. Birman

General Telephone and Electronics Research Laboratories Inc., Bayside, New York

ABSTRACT

The polarization of fluorescence in hexagonal (wurtzite) crystals of CdS and ZnS gives a clue to the symmetry of the states between which the luminescent transition occurred. Unfortunately this clue is at present equivocal; there are many models for the center which would be consistent with the observed polarization.

Various symmetry properties of the wurtzite structure are discussed; the band structure of CdS and ZnS at k = 000 is discussed. These symmetry and band structure considerations are used to set up and consider various models, Lambe-Klick, Schoen-Klasens, etc., which would be in accord with observation of polarization. It is concluded that the Lambe-Klick model is the simplest which is in accord with the presently available observations. Some experimental tests are proposed which should help the descision among the various models. In conjunction with other single crystal optical, electrical, and magnetic measurements, polarization studies may prove decisive in obtaining quantitative knowledge about the centers in sulfides.

Although the sulfide phosphors have been studied for many years and a great deal of progress has been made in rationalizing their luminescent, photoconductive, and electroluminescent properties by means of particular theoretical models, basic uncertainty remains concerning the chemical nature and energy level structure of the luminescent center in these materials. It was with the hope of contributing to the clarification of the energy level structure of certain important phosphors that the work reported by Lempicki (1) was undertaken. The problem of the chemical nature of the center (the local atomic constituents and configurations) is not discussed in this paper: rather we shall focus on the energy level structure of centers, in the simplest phosphors, which would be consistent with the polarization observations. Because of its simplicity we shall emphasize the Lambe-Klick model, without losing sight of the fact that at the present time no definitive choice of model can be made. Certain experiments will be suggested on the basis of which a decision may be made between the different models.

In Table I a summary is given of the major aspects of the experimental situation presented in Lempicki's paper. We note that the polarization of luminescence at room temperature (3650Å excited) in hexagonal CdS:Ag and ZnS:Cu is considerable but not complete. For CdS:Ag the degree of polarization of fluorescence is constant and independent of polarization of the exciting radiation. For ZnS:Cu we note structure sensitivity, as well as a slight dependence on the polarization of the exciting radiation (1). Some problems which the model should answer are: (*a*) origin of polarization; (*b*) the fact that polarization is not 100% at room temperature; (*c*) polarization of fluorescence is (in CdS:Ag) independent of polarization of exciting radiation; and (*d*) the sensitivity of the ZnS polarization results on the underlying crystal structure.

Table I. Summary of polarization experiments

Material	Radiation	Temp	$I_\perp/I_\parallel$
CdS:	EL	>300°C	1.5
	edge‡	liq N_2	6.3
CdS:Ag	6200	RT**	3
ZnS:Cu			
(hex)	4300	RT	~1.25
(cubic)	4500	RT	1*
ZnO			
(surface)	5130	RT	0.33†
(volume)	5180	RT	1*

* Unpolarized emission.
† Preferentially polarized || to crystal c axis.
‡ D. Dutton, *J. Phys. Chem. Solids*, 6, 101 (1958).
** RT signifies room temperature measurement.

No discussion of the ZnS:Mn results is given. Some possible models for the ZnO results are put forward in the Appendix.

Band Models for the Sulfide Centers

One common model which was introduced for the centers in the sulfides was the so-called Schoen-

$$\frac{I(\mu_z)}{I(\mu_x)} = f(\gamma)\frac{\mu_z^2}{\mu_x}; \frac{I(\mu_y)}{I(\mu_x)} = f(\gamma)\frac{\mu_y^2}{\mu_x}$$

where sin γ is the numerical aperture of the objective. f (γ) can be obtained by computing the ratio of the fluxes through the objective from the dipole radiation intensity formula $I \sim \sin^2\theta\mu^2/r^2$. In Table II we give a few values of f (γ) for different objectives. If all the components of μ are equal the last column gives the percentage admixture of the unwanted $I(\mu_x)$ component. In most of our work we used the first objective.

Table II. Effect of numerical aperture

Sin γ	f(γ)	%I(μ_x)
0.08	332	0.30
0.22	48.4	2.06
0.45	11.2	8.92

Polarization of Fluorescence in CdS and ZnS Single Crystals

Joseph L. Birman

General Telephone and Electronics Research Laboratories Inc., Bayside, New York

ABSTRACT

The polarization of fluorescence in hexagonal (wurtzite) crystals of CdS and ZnS gives a clue to the symmetry of the states between which the luminescent transition occurred. Unfortunately this clue is at present equivocal; there are many models for the center which would be consistent with the observed polarization.

Various symmetry properties of the wurtzite structure are discussed; the band structure of CdS and ZnS at k = 000 is discussed. These symmetry and band structure considerations are used to set up and consider various models, Lambe-Klick, Schoen-Klasens, etc., which would be in accord with observation of polarization. It is concluded that the Lambe-Klick model is the simplest which is in accord with the presently available observations. Some experimental tests are proposed which should help the descision among the various models. In conjunction with other single crystal optical, electrical, and magnetic measurements, polarization studies may prove decisive in obtaining quantitative knowledge about the centers in sulfides.

Although the sulfide phosphors have been studied for many years and a great deal of progress has been made in rationalizing their luminescent, photoconductive, and electroluminescent properties by means of particular theoretical models, basic uncertainty remains concerning the chemical nature and energy level structure of the luminescent center in these materials. It was with the hope of contributing to the clarification of the energy level structure of certain important phosphors that the work reported by Lempicki (1) was undertaken. The problem of the chemical nature of the center (the local atomic constituents and configurations) is not discussed in this paper: rather we shall focus on the energy level structure of centers, in the simplest phosphors, which would be consistent with the polarization observations. Because of its simplicity we shall emphasize the Lambe-Klick model, without losing sight of the fact that at the present time no definitive choice of model can be made. Certain experiments will be suggested on the basis of which a decision may be made between the different models.

In Table I a summary is given of the major aspects of the experimental situation presented in Lempicki's paper. We note that the polarization of luminescence at room temperature (3650Å excited) in hexagonal CdS:Ag and ZnS:Cu is considerable but not complete. For CdS:Ag the degree of polarization of fluorescence is constant and independent of polarization of the exciting radiation. For ZnS:Cu we note structure sensitivity, as well as a slight dependence on the polarization of the exciting radiation (1). Some problems which the model should answer are: (*a*) origin of polarization; (*b*) the fact that polarization is not 100% at room temperature; (*c*) polarization of fluorescence is (in CdS:Ag) independent of polarization of exciting radiation; and (*d*) the sensitivity of the ZnS polarization results on the underlying crystal structure.

Table I. Summary of polarization experiments

Material	Radiation	Temp	$I_\perp/I_\parallel$
CdS:	EL	>300°C	1.5
	edge‡	liq N_2	6.3
CdS:Ag	6200	RT**	3
ZnS:Cu			
(hex)	4300	RT	~1.25
(cubic)	4500	RT	1*
ZnO			
(surface)	5130	RT	0.33†
(volume)	5180	RT	1*

* Unpolarized emission.
† Preferentially polarized || to crystal c axis.
‡ D. Dutton, *J. Phys. Chem. Solids*, 6, 101 (1958).
** RT signifies room temperature measurement.

No discussion of the ZnS:Mn results is given. Some possible models for the ZnO results are put forward in the Appendix.

Band Models for the Sulfide Centers

One common model which was introduced for the centers in the sulfides was the so-called Schoen-

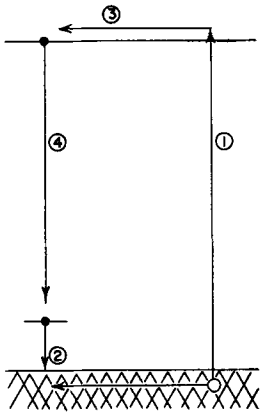

Fig. 1. Schoen-Klasens model for luminescent cycle in the sulfides.

Klasens band model (2). This model is illustrated in Fig. 1. According to the Schoen-Klasens model, the process of luminescence occurs as follows: If an incident photon is absorbed, with energy within the fundamental absorption edge, a free electron and a hole are created. The hole is captured by the center, which thus loses its electron. Since the energy level of the ground state of the center is assumed close to the valence band of the crystal, little energy is released when the hole is captured. (This energy is degraded in the form of infrared emission or thermal energy given up to the lattice.) The center, with a hole localized in it, at an energy level close to the valence band, is now in position to participate in the process of luminescence. Luminescence occurs when a free electron, which has been created by an incident photon, is captured by the hole localized at the center.

More recently, Lambe and Klick (3) have proposed an alternate model, which is shown in Fig. 2. In this model, the ground state of the center consists of an electron bound in an energy level close to the conduction band. As before, the process of luminescence may occur when an incident photon creates an electron and a hole in the crystal. However, if the center is filled initially, the first step, i.e., capture of a hole by the center, is the luminescent process. Subsequent capture of an electron by the empty center serves only to prepare the center again for later participation in further luminescent cycles. In this model, we see that in a certain sense it is the free hole which dominates the process of luminescence.

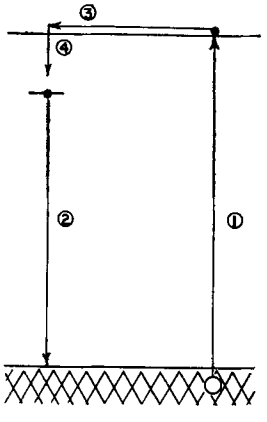

Fig. 2. Lambe-Klick model for luminescent cycle in the sulfides.

In both the Schoen-Klasens and Lambe-Klick models, luminescence and photoconductivity are intimately connected by means of the energy bands in the phosphor—the luminescent process involving the transition of a "free" carrier in an energy band to a bound state (4). If this type of model is correct, it is understandable that the polarization results (1) could not fit into a simple classical oscillator picture: the band scheme is quantum mechanical, with no strict classical analogue. However, without further modification neither Schoen-Klasens nor Lambe-Klick models indicate how polarization may arise. While the weight of experimental evidence in the sulfides seems to favor either Schoen-Klasens or Lambe-Klick "band" models for the centers (5), other possible models cannot be ruled out. In particular, a "two oscillator" model—separate absorption and emission oscillators—may be at least mentioned. For example, in ZnS the absorbed 3650Å radiation may create excitons which then decompose at the center, emitting the characteristic fluorescence. (Even more general kinds of mechanisms might be envisioned for separate absorption and emission processes.) Such processes, within the two oscillator framework, would focus attention on the details of the recombination processes within a more or less isolated center, rather than upon band-center processes (within the context of such models the apparent connection between photoconductivity and luminescence would be more complex to explain than for the band models).

In any event to know how to get the necessary anisotropy to yield polarization requires study of the symmetry of the wurtzite lattice, both for examination of band-center processes and recombination processes within a center located at a particular site. In the next section, certain results pertaining to the effect of the symmetry of hexagonal (wurtzite) lattice on optical selection rules are summarized. An understanding of the effects associated with the symmetry of the hexagonal structure is necessary for us to proceed with further consideration of models.

Symmetry of Wurtzite and Zinc Blende Structures

All of the descriptive information about wurtzite or zinc blende structures is contained in their space group designations: C^4_{6v} for wurtzite, T^2_d for zinc blende (6). Actual experimental CdS crystals seem almost invariably to be of pure wurtzite structure; the ZnS crystals almost invariably are mixed structures, whether or not predominantly wurtzite or zinc blende. The symmetry groups of interest to us in each structure are: the point group of the space group, various site groups.

For zinc blende, the point group of the space group is T_d, for wurtzite it is C_{6v}. Now, in zinc blende there are sites with full symmetry T_d, while in wurtzite no site (occupied) has symmetry C_{6v}. Major interest in these particular symmetry groups arises from the energy band picture, since at k = 000 in the zone, the wave functions of the crystal must belong to

an irreducible representation of the point group of the space group (7). (If a function belongs to a particular irreducible representation of a group, its symmetry properties are specified when the operations [rotations, reflections, etc.] of the group are applied to it. Conversely, knowing the irreducible representations of a group it is possible to indicate the type of functions which may belong to it, that is 's', 'p_x', 'p_y', 'p_z', etc. In what follows we find both approaches helpful.) We also need to consider the spin orbit effect, particularly in sulfides, since this introduces certain effects of interest in the analysis. Formally, the procedure involved is a consideration of the irreducible representations of the "double group" of the particular group (7). The relationship between single and double group representations is easily obtained from the theory and physically corresponds to "turning on" (consideration of) the spin-orbit effect. After wave functions have been classified into symmetry types, the analysis may be carried one step further to a discussion of the allowed optical (electric dipole) selection rules. These rules tell us the states which may be connected by an allowed optical transition, and we shall indicate that a transition between states Γ_i and Γ_j is allowed optically by writing $\Gamma_i \leftrightarrow \Gamma_j$. If a limitation occurs, insofar as the optical transition is only allowed for particular polarization of the electric vector of the exciting radiation with respect to a crystal axis (e.g., the unique [c] or [00.1] of the wurtzite structure) it will be so indicated in the tables. If wave functions and selection rules were known, matrix elements and oscillator strengths of various optically allowed transitions could be computed. This degree of refinement does not seem warranted at the moment.

Since the cubic zinc blende does not possess a unique axis, no polarization effects arise; those states between which optical transitions can occur for point group T_d are so connected without any regard to polarization of excitation or emission. Results are given in Table II. For wurtzite, there exists a unique axis so that polarization effects may arise in addition to straightforward selection rules. Results are given in Table III for group C_{6v}. While at this time we present only the formal results of the group theory analysis, restricting ourselves to labeling the states by means of their symmetry designations, we shall later give a more physical picture of the states (in the band structure section). In any event, if we are given the information that radiation (absorbed or emitted) is, or is not, polarized, and that the "center" which (absorbs/emits) has effective net symmetry T_d, or C_{6v} in zinc blende or wurtzite, respectively, we may, by using Tables II and III, determine all the possible states for these symmetries between which optical transitions are allowed, and then further which states can give rise to polarization effects.

In Table IV similar information is given for the group C_{2v}, a subgroup of both T_d and C_{6v}. No point in crystal space in a wurtzite structure has this symmetry. In zinc blende, this group is a site group (see below).

The site symmetries (8) in zinc blende or wurtzite (that is, the point symmetry of the particular substitutional or interstitial site) are the following: in zinc blende, T_d, C_{3v}, C_{2v}, C_s; in wurtzite, C_{3v}, C_s. The main interest from the point of view of polarization effects would be in the site group C_{3v} in wurtzite structure, as this is the site for both substitutional and interstitial impurities. In addition, C_{3v} is the effective site symmetry in faulted zinc blende structures. In Table V selection rules are given.

Clearly, we are faced with formidable difficulties in attempting to interpret the observed polarization results in terms of the states between which optical transitions have occurred. There is a many-to-one correspondence between the observation of polarization and the pairs of states which might be involved, if these are the states of various "natural" groups in wurtzite. In zinc blende we expect no polarization, except perhaps in the case of faulted

Table II. Symmetry group Td*†

Single group representations: Γ_1, Γ_2, Γ_3, Γ_4, Γ_5
Double group representations: Γ_6, Γ_7, Γ_8
Optically allowed transitions:

$\Gamma_1 \leftrightarrow \Gamma_4$	$\Gamma_6 \leftrightarrow \Gamma_7$
$\Gamma_2 \leftrightarrow \Gamma_5$	$\Gamma_6 \leftrightarrow \Gamma_8$
$\Gamma_3 \leftrightarrow \Gamma_4$	$\Gamma_7 \leftrightarrow \Gamma_8$
$\Gamma_4 \leftrightarrow \Gamma_4$	$\Gamma_8 \leftrightarrow \Gamma_8$
$\Gamma_5 \leftrightarrow \Gamma_5$	
$\Gamma_3 \leftrightarrow \Gamma_5$	

* *See* G. Dresselhaus, *Phys. Rev.*, **100**, 581 (1955).
† In the text of the present paper, and in Fig. 4, Γ_4 is referred to as Γ_4'.

Table III Symmetry group C_{6v}*†

Single group representation: Γ_1, Γ_2, Γ_3, Γ_4, Γ_5, Γ_6
Double group representation: Γ_7, Γ_8, Γ_9
Optically allowed transitions:

$\Gamma_1 \leftrightarrow \Gamma_1$ ||c	$\Gamma_7 \leftrightarrow \Gamma_7$ $\perp$ and ||c
$\Gamma_1 \leftrightarrow \Gamma_5$ $\perp$c	$\Gamma_8 \leftrightarrow \Gamma_8$ $\perp$ and ||c
$\Gamma_2 \leftrightarrow \Gamma_2$ ||c	$\Gamma_7 \leftrightarrow \Gamma_9$ $\perp$c
$\Gamma_2 \leftrightarrow \Gamma_5$ $\perp$c	$\Gamma_8 \leftrightarrow \Gamma_9$ $\perp$c
$\Gamma_3 \leftrightarrow \Gamma_3$ ||c	$\Gamma_9 \leftrightarrow \Gamma_9$ ||c
$\Gamma_3 \leftrightarrow \Gamma_6$ $\perp$c	
$\Gamma_4 \leftrightarrow \Gamma_4$ ||c	
$\Gamma_4 \leftrightarrow \Gamma_6$ $\perp$c	
$\Gamma_5 \leftrightarrow \Gamma_5$ ||c	
$\Gamma_5 \leftrightarrow \Gamma_6$ $\perp$c	
$\Gamma_6 \leftrightarrow \Gamma_6$ ||c	

* The unique axis of this group is taken || to c.
† *See* J. Birman, *Phys. Rev.*, **114**, 1490 (1959).

Table IV. Symmetry group C_{2v}*

Single group representations: Γ_1, Γ_2, Γ_3, Γ_4
Double group representations: Γ_5
Optically allowed transitions:

$\Gamma_1 \leftrightarrow \Gamma_1$ ||x	$\Gamma_5 \leftrightarrow \Gamma_5$ $\perp$, and ||x
$\Gamma_1 \leftrightarrow \Gamma_3$ $\perp x$	
$\Gamma_1 \leftrightarrow \Gamma_4$ $\perp x$	
$\Gamma_2 \leftrightarrow \Gamma_2$ ||x	
$\Gamma_2 \leftrightarrow \Gamma_3$ $\perp x$	
$\Gamma_2 \leftrightarrow \Gamma_4$ $\perp x$	
$\Gamma_3 \leftrightarrow \Gamma_3$ ||x	
$\Gamma_4 \leftrightarrow \Gamma_4$ ||x	

* The unique axis of this group is taken || to x.
† G. Dresselhaus, *Phys. Rev.*, **100**, 581 (1955).

Table V. Symmetry group C_{3v}*

Single group representations: Γ_1, Γ_2, Γ_3

Double group representations: Γ_4, Γ_5, Γ_6

Optically allowed transitions:

$\Gamma_1 \leftrightarrow \Gamma_1 \,\|\|\, c$	$\Gamma_4 \leftrightarrow \Gamma_4 \,\|\|\, c$
$\Gamma_1 \leftrightarrow \Gamma_3 \perp c$	$\Gamma_4 \leftrightarrow \Gamma_6 \perp c$
$\Gamma_2 \leftrightarrow \Gamma_2 \,\|\|\, c$	$\Gamma_5 \leftrightarrow \Gamma_5 \,\|\|\, c$
$\Gamma_2 \leftrightarrow \Gamma_3 \perp c$	$\Gamma_5 \leftrightarrow \Gamma_6 \perp c$
$\Gamma_3 \leftrightarrow \Gamma_3 \,\|\|\, c, \perp c$	$\Gamma_6 \leftrightarrow \Gamma_6 \,\|\|\, c, \perp c$

* The unique axis of this group is taken || to c.

zinc blende crystal structure when the net site symmetry is reduced from T_d to effectively C_{3v}, and a unique axis has been introduced into the crystal structure. While polarization may arise in either wurtzite or faulted zinc blende structures, the values of the polarization must depend on the detailed energy level scheme. For example, it may be not observable if a cluster of closely lying states with different selection rules is optically accessible from a given initial state. In particular, while faulting formally reduces the site symmetry of a zinc blende structure to that of the wurtzite structure: e.g., from T_d to C_{3v}, the states split off by the lower symmetry may remain sufficiently close (if the perturbation is small) to be optically accessible, so that no observable polarization may result.

Conversely even though a particular optical transition may be allowed for both polarizations ($\perp$ and $\|$), the matrix elements whose values relate to the oscillator strength of the transitions for the two polarizations may be sufficiently different in magnitude so as to give an apparent polarization effect. These remarks are intended to emphasize the lack of uniqueness which obtains in assigning particular transitions as those involved in an observation of polarization.

We next discuss band structure of CdS and ZnS.

Energy Bands in the Sulfides

The complexity of the energy bands in some monatomic semiconductors (9) is indicative of what may be true also in the sulfides. On the other hand, we have not yet been driven by the weight of experimental evidence in the sulfides into the need for consideration of comparable complexity. In fact the simplest picture: tight binding (LCAO), extrema at k = 000, seems for the moment adequate, as well as simple, and we restrict our attention to this picture.

Since the outer valence electrons of both Zn (or Cd) and S are 's' and 'p' the states in the crystal are considered at k = 000 which can arise from these atomic orbitals. This means that we need to determine the crystal states (irreducible representations of T_d in zinc blende or C_{6v} in wurtzite) at k = 000 which can be obtained by combining 's' and 'p' orbitals. The states which are important from this point of view are illustrated in Fig. 3. The left side of the figure refers to zinc blende, the right to wurtzite. In Table VI the wave functions which are appropriate to the differently labeled states are indicated. From the figure we see a correlation between zinc blende states and the corresponding wurtzite states. In particular, we note the effect of the different wurtzite crystal symmetry, in causing a splitting of previously degenerate zinc blende states. The additional splitting due to spin orbit effect is also indicated for wurtzite.

Table VI. Wave function at a site

Basic set of s and p functions

$$\phi_{01} = s|\alpha\rangle \qquad \phi_{13} = y|\alpha\rangle$$
$$\phi_{02} = s|\beta\rangle \qquad \phi_{14} = y|\beta\rangle$$
$$\phi_{11} = x|\alpha\rangle \qquad \phi_{15} = z|\alpha\rangle$$
$$\phi_{12} = x|\beta\rangle \qquad \phi_{16} = z|\beta\rangle$$

Group T_d*:

Γ_1: ϕ_{01}; ϕ_{02}.

Γ'_4: ϕ_{11}; ϕ_{12}; ϕ_{13}; ϕ_{14}; ϕ_{15}; ϕ_{16}.

Γ_6: ϕ_{01}; ϕ_{02}.

Γ_7: $\left\{ \begin{array}{l} (1/\sqrt{3})\,[-i\phi_{11} - \phi_{13} + \phi_{16}]: \\ (1/\sqrt{3})\,[i\phi_{12} - \phi_{14} - \phi_{15}]. \end{array} \right\}$

Γ_8: $\left\{ \begin{array}{l} (i/\sqrt{2})\,[\phi_{12} - i\phi_{14}]; \\ (i/\sqrt{6})\,[i(\phi_{11} - i\phi_{13}) + 2\phi_{16}]; \\ (i/\sqrt{6})\,[i(\phi_{12} + i\phi_{14}) + 2\phi_{15}]; \\ (i/\sqrt{2})\,[\phi_{11} + i\phi_{13}]. \end{array} \right\}$

Group C_{6v}†:

Γ_1: $\left\{ \begin{array}{l} a\phi_{01} + b\phi_{15}; \\ a\phi_{02} + b\phi_{16}. \end{array} \right\}$

Γ_5: ϕ_{11}; ϕ_{12}; ϕ_{13}; ϕ_{14}.

Γ_7: $\left\{ \begin{array}{l} a\phi_{01} + b\phi_{15} + c/2(\phi_{11} + i\phi_{13}); \\ a\phi_{02} + b\phi_{16} + c/2(-\phi_{12} + i\phi_{14}). \end{array} \right\}$

Γ_9: $\left\{ \begin{array}{l} (1\sqrt{2})\,(\phi_{11} - i\phi_{13}); \\ (-1\sqrt{2})\,(\phi_{12} + i\phi_{14}). \end{array} \right\}$

* For T_d, x, y, z are along the usual cartesian coordinate axes.

† For C_{6v}, x, y are perpendicular to z, and z is taken parallel to "C", the unique axis.

Table VII. Crystal wave functions

Zinc blende states at $\Gamma(k = 000)$; group T_d:

States with symmetry properties $\Gamma_1 - \Gamma_8$ may be formed (see Tables II and VI) by adding a function centered on one base site to that centered on the other, for example, for Γ_1 crystal function:

$$\Gamma_1: \left\{ \begin{array}{l} a\phi_{01}(Zn) + b\phi_{01}(S) \\ a\phi_{02}(Zn) + b\phi_{02}(S) \end{array} \right\}$$

see Table VI for definition of ϕ.

Wurtzite states at $\Gamma(k = 000)$ — group C_{6v}:

States with symmetry Γ_1, Γ_5, Γ_7, Γ_9 may be simply formed by adding functions centered at the site: Zn1, Zn2, S1, S2, where Zn1, etc., indicates the type of, and number of, the particular site. For a Γ_1 function

$$\Gamma_1: [a\phi_{01}(Zn1) + b\phi_{15}(Zn1)] + [a\phi_{01}(Zn2) + b\phi_{15}(Zn2)] + [a'\phi_{01}(S1) + b'\phi_{15}(S1)] + [a'\phi_{01}(S2) + b'\phi_{15}(S2)]$$

Wurtzite states at $\Gamma'(k = 0, 0, (2\pi)/c)$ — group C_{6v}:

Although $\Gamma' = \Gamma$ in the reduced zone, it is helpful to consider it as distinct in the Jones or Energy zone. States Γ_2, Γ_6, Γ_8, at k = 0, $0(2\pi)/c$ are simply related to Γ_1, Γ_5, Γ_7, at k = 0, 0, 0 respectively. For example:

$$\Gamma_2: [a\phi_{01}(Zn1) + b\phi_{15}(Zn1)] - [a\phi_{01}(Zn2) + b\phi_{15}(Zn2)] + [a'\phi_{01}(S1) + b'\phi_{15}(S1)] - [a'\phi_{01}(S2) + b'\phi_{15}(S2)]$$

(cf. Γ_1 preceding.)

a, b, c, d are constants.

Physically, as earlier writers have indicated, the valence band consists mainly of electronic states localized about S while the conduction band has the states about Zn; this is, of course, an oversimplified picture. Table VI may be helpful in obtaining a physical picture of different wave functions associated with various states. In particular, we note that the zinc blende p-like (x, y, z) valence state Γ'_4 is split by the lower wurtzite potential into $\Gamma_5 + \Gamma_1$ which are, respectively, (x,y) and (s + z) orbital types. The spin-orbit effect in wurtzite causes $\Gamma_5 \rightarrow \Gamma_9 + \Gamma_7$ and it can be seen that Γ_9 remains (x,y) in orbital character, while Γ_7 contains a mixture of (x, y, s + z) states. Other changes caused by symmetry and spin-orbit effects can be easily obtained from Fig. 3 and Table VI.

The order of states, and separations, shown in Fig. 4 seem to be in accord with a variety of experiments in hexagonal CdS, including, absorption and reflection spectra, excitation spectrum of edge emission and of photoconductivity, and the exciton absorption spectrum (10). (On the other hand, preliminary cyclotron resonance results seems to indicate a more complex band structure for CdS, without agreeing or disagreeing with the separations shown in Fig. 4.) Again, the many-one correspondence between these experiments and band models needs emphasis, as some other band level schemes also consistent with the data could be proposed.

Figure 3 also reviews the polarization selection rules between certain states, which were already given in the various tables, and are now to be understood as restricting band-band optical transitions.

The band structure and order of states shown in Fig. 3 may be assumed also to apply to ZnS although there is at this time no comparably complete experimental evidence for ZnS. Numerical calculation, by the cellular method, of the band structure of ZnS in zinc blende and wurtzite structures (neglecting spin-orbit effect) gives an order of states in agreement with that illustrated in Fig. 3. In addition, the problem of crystal faulting is very significant in actual ZnS crystals, the faults causing barriers (11), changes in effective band gap (11) and, perhaps, changes in the order of states in the barrier (this seems unlikely although possible!). Hence, our major concern is with CdS center energy levels, even though actual major interest is in the ZnS luminescent systems.

It is now evident that the band models of Fig. 1 and Fig. 2 must be modified to take account of the actual band structures in the sulfides and that, in addition, if a symmetry designation is applied to the luminescent center state, polarization effects may be expected. While we work within the framework of the band scheme of Fig. 3 and 4 for the sulfides it is necessary to emphasize that the order of states and separations which have been assigned are provisional (although supported by the present weight of evidence).

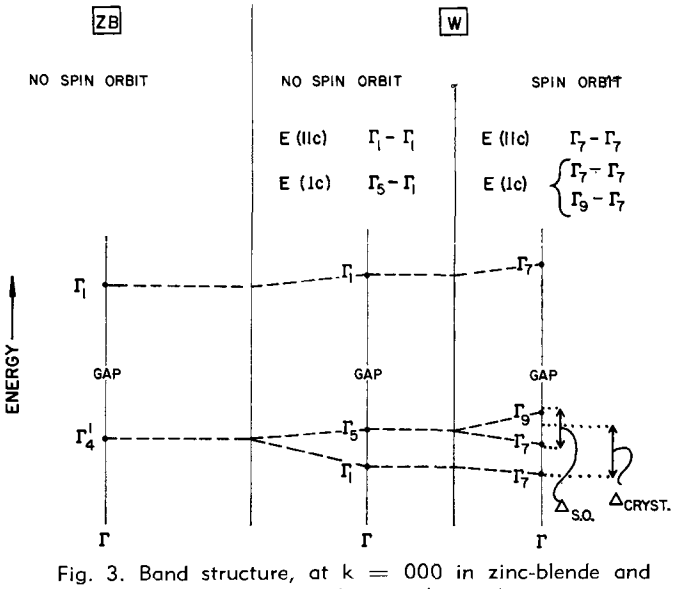

Fig. 3. Band structure, at k = 000 in zinc-blende and wurtzite structures showing the correlation between corresponding states. (This applies to the sulfides.)

Modified Band Models for Sulfide Centers

With the preceding development in mind, we are now in a position to formulate band models which, although still quasi-descriptive, are more refined than the simple S-K and L-K models. It will be possible then to evaluate alternate models and formulate (albeit tentatively) some opinion as to which model more simply accounts for polarization data.

It is evident from Fig. 4 that the valence and conduction band energy levels for a sulfide (particularly CdS) in hexagonal crystal structure, have particular symmetry properties (belong to particular irreducible representations). Similarly, the "center" state wave function must belong to some symmetry type. The simplest assumption one may make would seem to be: *the center has the maximum symmetry allowed for the crystal.* This would call for a center with Γ_7 symmetry, if we include the spin-orbit effect. Since the symmetry of the bands has been fixed (tentatively) by previous arguments we may rule out an S-K model for the moment, as the $\Gamma_7 - \Gamma_7$ transition is allowed for both $\perp$ and $\parallel$ polarizations. (S-K models are discussed below.) We are thus led to the L-K model modified for complex band structure: Fig. 5 in which a center with Γ_7 symmetry is placed near the conduction band. The process of luminescence then involves: (*a*) creation of free electrons and holes, by absorption of radiation whose energy is within the fundamental absorption edge, (b) attainment of thermal equilibrium by the holes, which populate the several

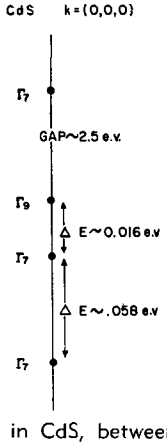

Fig. 4. Separations, in CdS, between states at k = 000. (Not to scale.)

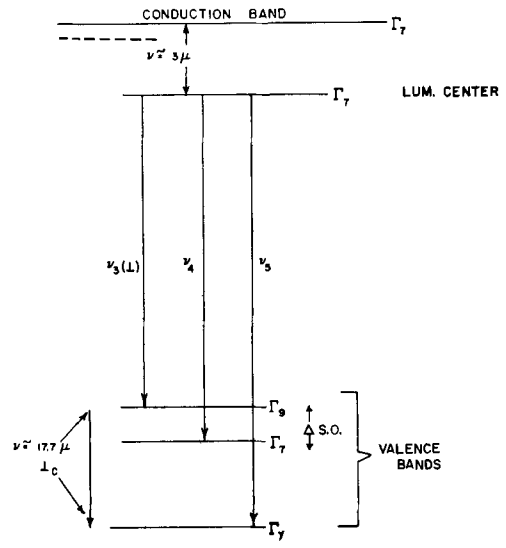

Fig. 5. Modified Lambe-Klick model for luminescent center and cycle. The 3 μ infrared luminescence quench, as well as the 17.7 μ absorption which should quench polarization are shown. Polarization of transitions can be obtained from Table III. The dotted line near the conduction band indicates the level from which edge emission is believed to occur.

valence bands as given by a Boltzmann factor, (c) recombination of the electron in Γ_7 center with a hole, and emission of characteristic radiation ($\nu_3 + \nu_4 + \nu_5$) depending on the state of the hole at the moment of recombination, and finally, (*d*) capture of another electron by the center which is then returned to its initial state. If these are the steps involved in the production of preferentially polarized luminescence, then the L-K model leads to the following predictions for the luminescence (neglecting the lowest Γ_7 valence band):

(I) Both CdS edge emission (from a state closer to the band) and the 6200Å (CdS) emission should be polarized, and both should obey the law for the temperature dependence of polarization

$$I_{\perp}/I_{||} = a \exp(\Delta_{s.o.}/kT) + b \qquad [1]$$

where $\Delta_{s.o.} = 0.016$ ev for CdS if the previous assignments are correct. Note that the significant feature is not that a and b (or $I_{\perp}/I_{||}$) be identical for the edge and 6200Å emission, but that $\Delta_{s.o.}$ be the same. Constants a and b depend on details of edge-center (trap) and luminescent center wave functions and would be only accidentally the same for the different emissions, as would the actual numerical values of polarization at any temperature. However, Δ which arises from the hole distribution between valence bands, must be the same if the L-K model of luminescence as we have presented it, and the accepted model of edge emission (12) are both correct in the approximation used.

(II) The excitation spectrum of luminescence and edge emission should be identical, since all that is involved in excitation is the creation of free electrons and holes (the latter being thermally distributed among the valence bands) and this is an intrinsic (host) property.

(III) The luminescence should be resolvable into several bands (centered on ν_3, ν_4, ν_5) of which ν_3 would be totally polarized $\perp$ to c, as given by selection rules.

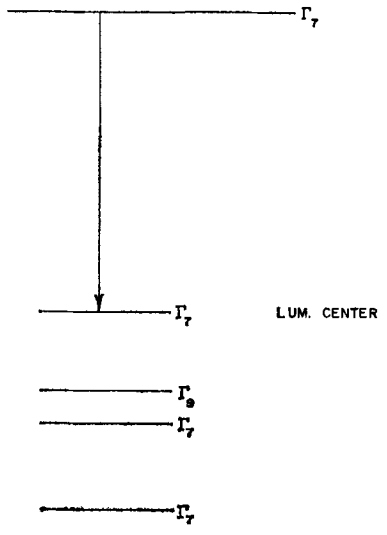

Fig. 6. Schoen-Klasens model with Γ_7 symmetry luminescent center.

(IV) The 6200Å emission should be polarized independently of the polarization of exciting radiation since excitation only creates free carriers.

(V) Polarized infrared radiation (17.7μ) should quench the polarization of fluorescence by promoting the holes in the Γ_9 valence state to the lowest Γ_7 valence band: a hole in the latter does not give rise to polarized radiation.

(VI) The 3μ *IR* quench band, which promotes electrons from the "center" level to the conduction band should be operative for both polarizations.

As will be seen, these predictions should be helpful indeed to the decision among competing models.

While the polarization of the 4500Å ZnS emission would be generally understandable in the identical type of L-K framework, the entire ZnS problem is complicated by the structure faulting which exists, and which contributes considerable complexity to the "band" structure of an actual specimen (11). A true test of (I)-(VI) above for ZnS should be made

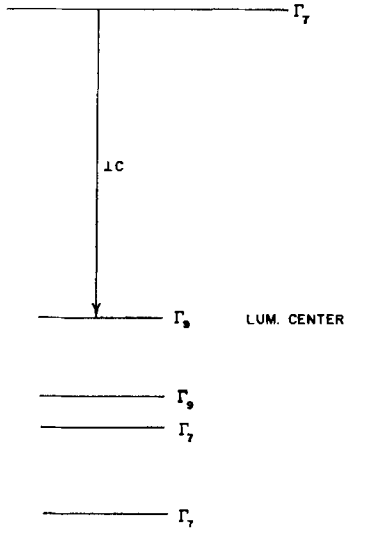

Fig. 7. Schoen-Klasens model with Γ_9 symmetry luminescent center.

on perfect hexagonal crystals, [cubic ZnS (zinc blende) shows no polarization (Table I)]. The structure sensitivity of the ZnS results, then, resides in the lack of polarization of emission in the "cubic" regions of a mixed crystal, as well as in the unknown effect which occurs for an activator within a fault plane region.

We now turn to some alternate models which would be consistent with polarization findings. The first class of alternate models we consider are S-K "band" models. Immediately we are led to several S-K models: one with ground state Γ_7, Fig. 6, one with ground state Γ_9, Fig. 7, and finally types whose ground "state" is actually a complex of several states, Fig. 8a, b. We shall, in the interest of brevity, only focus on salient features of each of these models, in particular emphasizing important differences which may be observed between each of these models and the L-K model which was discussed in some detail.

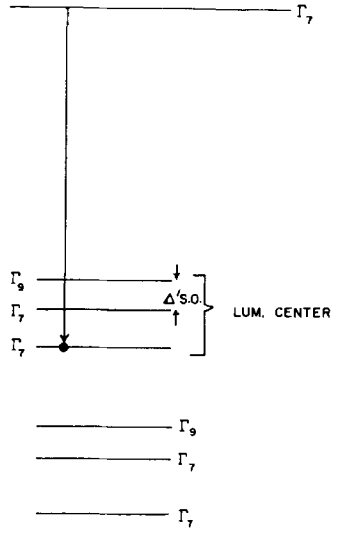

Fig. 8a. Schoen-Klasens model with three ground states. One electron is assumed in the center, normally, and the polarization should not be temperature dependent.

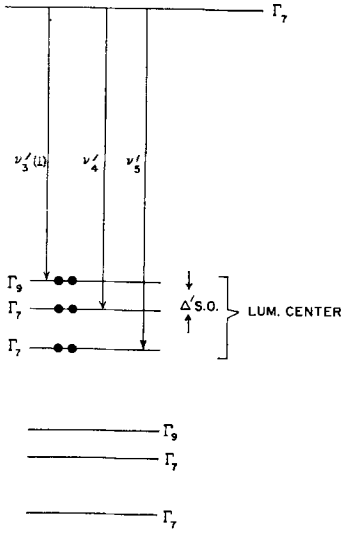

Fig. 8b. Schoen-Klasens model with three ground states. Six electrons are assumed in the "unexcited" ground state. Polarization may then be temperature dependent, if a single hole is captured by the center and reaches equilibrium among the three states.

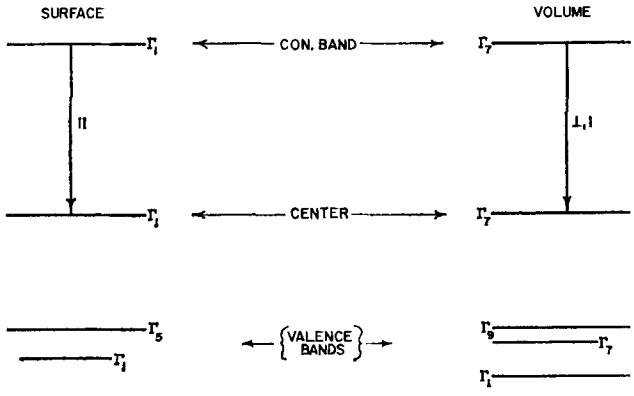

Fig. 9. Possible model for the ZnO polarization results. Assuming greater ionicity on the surface, we may classify states neglecting spin-orbit effect, while in volume the spin-orbit splitting is assumed necessary. This yields different selection rules on surface and volume.

The model in Fig. 6 requires that the transition $\Gamma_7 - \Gamma_7$, allowed for both polarizations by selection rules, shall have different strength for $\perp$ than for $||$. (In particular $I_{\perp} > I_{||}$). This model would predict a temperature independent polarization of luminescence.

The model of Fig. 7 would produce polarization ($\Gamma_7 - \Gamma_9$ transition) perpendicular to c, but to explain the lack of complete polarization some alternate mode of recombination with the center must be provided. As in the previous case, the polarization should be temperature independent.

A model more in the actual S-K spirit is that of Fig. 8a, b in which the ground "state" of the center consists of several levels, duplicating the valence band structure at k = 000, so a ground state trio of states is shown for the center. Now we may assume either that one, or six, electrons normally populate the ground states of the center. In the one electron in center case, Fig. 8a, according to the sequence which is assumed to apply for a S-K type model, at the instant of recombination, the free electron which will recombine to yield light sees the empty trio and recombines with any of the three available levels with some probability which is *a priori* fixed. If the center has only one electron in its normal ground state, it is clear that there will not be a temperature dependence for the polarization, since at the instant of recombination the entire ground state trio is empty. Temperature can only affect the state which the electron occupies after recombination, or before the valence band hole captures this electron to prepare the center for recombination. Neither of these will affect the polarization of emitted fluorescence. If in the unexcited state, the center is filled (13), i.e., consists of six electrons, Fig. 8b, (two in each doubly degenerate state of the trio) we have the possibility of temperature dependence of the polarization. This follows from the fact that the center will capture one hole, if the irradiation produces free holes and electrons, and this hole will reach thermal equilibrium between the various ground levels of the center. The particular state with the hole in it is the only state available for recombination; hence, the possibility of a tem-

perature dependence. If there is a temperature dependence, it should follow an equation formally identical to Eq. [1] as would the L-K model since the controlling factor is the Boltzmann distribution of hole occupancy of the center ground states. In fact, if the ground states of the center are replicas of the valence band k = 000 states, the only possibility for distinguishing this Schoen-Klasens model and the Lambe-Klick model would be in the *numerical values* of the constant Δ' arising in Eq. [1] for edge and 6200Å emission, and in the IR quench frequency. It is unlikely that the center states' spacings and that of the valence bands at k = 000 should be identical, even though the various splittings arise, in the center as in the bands, from crystal symmetry and spin-orbit effects. Consequently, the decisive factors here will be the numerical values obtained if the fluorescence should prove temperature dependent. Note that the last three "S-K" models dispense with the assumption of a highly symmetric Γ_7 state for the "ground" state of the center, and may therefore be considered more "complicated" than the L-K model.

This concludes our consideration of simple "band" models which are in the spirit of L-K and S-K models and which would account for polarization. These band models are based on the k = 000 band order of states of Fig. 4, and would perhaps require revision if the band edges in particular sulfides were not at k = 000; certainly revision would be required if the order of band states were determined to be different from that we have taken. Rather than pretend to completeness by considering models based on these contingencies, we feel it preferable to consider the various possibilities already discussed (particularly, the simple L-K model) as working hypotheses and await the results of experiments—among them those proposed in (I-VI) above to help with the decision.

Two-Oscillator Models

As indicated in Lempicki's paper, models which involve separate absorption and emission oscillators have been successfully employed in accounting for fairly complicated data on polarization of fluorescence in solutions, and in certain ionic phosphors. In a certain (non-classical) sense the band models discussed above are two-oscillator models, since absorption in the lattice and emission at the center are distinct processes. However, more usual models of this class would be of a type where one "atom-like" center (polarizable dipole) absorbs the radiation and then either suffers some internal rearrangement (radiationless transition to another excited electronic state) and then emits, or actually transfers the excitation energy to another center where it is degraded by photon emission (14). A more recent variant of two-oscillator models would involve exciton creation (absorption step), migration, and then decomposition at the center (emission step) (15). Perhaps, even a single-triplet exciton conversion step may account for the needed stability of an exciton which would undertake such a process.

Assuming an absorption (excitation) process which would (for 3650Å irradiation) not leave a memory (i.e., polarization of fluorescence is seen to be independent of the polarization of the exciting radiation) the polarization of fluorescence then gives us information about the states involved in the emission. For processes of this kind, it is natural to assume that the emitting center will be located at a site and, therefore, possesses the site symmetry which, in wurtzite crystals, is C_{3v}. The wave functions of the emission center would then belong to irreducible representations of this site group (see Table V) and the optical selection rules would also then be appropriate. It would be then natural to construct as a model of the electronic states of the emitting center one derived from "s" and "p" type wave functions split in the appropriate manner in the existing crystal field. Such a model can easily be constructed from the information in Table V: depending on whether spin-orbit effect should be included will depend on the particular symmetry assignments of center states. Again, with respect to the L-K model more fully discussed above, it is evident that temperature and IR quench effects on the polarization, if they exist, should be quite different for the emission center-site model than for the L-K band model.

Discussion

It should be clear that the presently available polarization data alone are insufficient for the purpose of coming to an unequivocal conclusion about the nature of the centers, and in particular, even for deciding among the various band models or even between band models and "two-oscillator" models. We are led by a chain of plausibility arguments involving all the known properties of centers in the sulfides, to prefer band models, and within the class of band models to prefer the L-K model because of its relative simplicity. Many assumptions have been made in the process of formulating this chain including assumptions about the band structure (which seems supported by the evidence now available) and the symmetry of the center. Detailed theoretical analysis of the validity of the L-K model would be most fruitful if the model had been better established by virtue of additional experimental results.

In this context, then, we anticipate that the polarization studies can be most helpful in delineating properties of the various models which could be used to differentiate them, for example, by means of symmetry designations of the states of the center. In addition, one may make use of correlations by studying a simple sulfide system and then correlating the results and model obtained on such a system with that which would be appropriate for a more difficult system. For example, one may study polarization in hexagonal crystals and extrapolate the results to cubic systems since it is likely that a continuous correlation between hexagonal and cubic systems exists. In addition, the knowledge obtained for the 6200Å CdS emission by studying polarization may be carried over to the corresponding ZnS emission band (17): the former system being a "cleaner" one structurally and, hence, less ambiguous to interpret.

Acknowledgments

It is a pleasure to thank A. Lempicki for much discussion of his work. Dr. G. Neumark has also participated actively in discussions of the various models and her comments have been helpful, particularly in regard to S-K models. The author also wishes to thank Mrs. A. White for carefully typing the entire manuscript.

Manuscript received Nov. 9, 1959. This paper was prepared for delivery before the Philadelphia Meeting, May 3-7, 1959.

Any discussion of this paper will appear in a Discussion Section to be published in the December 1960 JOURNAL.

REFERENCES

1. A. Lempicki, *This Journal*, **107**, 404 (1960).
2. H. A. Klasens, *ibid.*, **100**, 72 (1953).
3. J. Lambe and C. C. Klick, *Phys. Rev.*, **100**, 573 (1955).
4. M. Schoen, *Physica*, **20**, 930 (1954).
5. C. C. Klick and J. H. Schulman, "Luminescence in Solids," in "Solid State Physics," Editors F. Seitz and D. Turnball, **5** (1957).
6. R. W. G. Wyckoff, "Crystal Structures,"**I**, Interscience Publishers, New York.
7. G. F. Koster, "Space Groups and their Representations," in "Solid State Physics," edited by F. Seitz and D. Turnball, **5** (1957).
8. R. S. Halford, *J. Chem. Phys.*, **14**, 8 (1946).
9. F. Herman, *Rev. Mod. Physics*, **30**, 102 (1958); B. Lax, *ibid.*, **30**, 122 (1958).
10. D. Dutton, *Phys. Rev.*, **112**, 785 (1958); D. Dutton, *J. Phys. Chem. Solids*, **6**, 101 (1958); A. Lempicki, *Proc. Phys. Soc.* (in press); R. L. Kelly and W. J. Fredericks, *Phys. Rev. Ltrs.*, **2**, 389 (1959); R. G. Wheeler, *ibid.*, **2**, 463 (1959); also D. Thomas and J. Hopfield, *Phys. Rev.*, **116**, 573 (1959) and other references cited therein.
11. J. L. Birman, *Phys. Rev.*, **115**, 1492 (1959).
12. J. Lambe, C. C. Klick, and D. L. Dexter, *ibid.*, **103**, 1715 (1956).
13. Suggested by G. Neumark, and independently by W. Hoogenstraten, Private communication.
14. N. T. Melamed, *J. Phys. Chem. Solids*, **7**, 146 (1958).
15. S. Keller and G. Pettit, *Phys. Rev.*, **115**, 526 (1959).
16. W. Choyke, D. Hamilton, and L. Patrick, "Polarized Edge Emission of SiC," Scientific Paper #6-41003-1-P1, Westinghouse Research Labs., Pittsburgh, Pa., July 27, 1959; L. Patrick, "Polarization of Luminescence of Donor-Acceptor Pairs," Scientific Paper #6-40603-1-P1, Westinghouse Res. Labs., Pittsburgh, Pa., July 28, 1959. The author is indebted to Dr. Choyke for his kindness in providing him with preprints of these papers.
17. W. Van Gool, *Philips Research Repts.*, **13**, 157 (1958).

APPENDIX I

Temperature dependence of polarization.—Consider the conduction state Γ_{7c} and only the two uppermost valence states Γ_9 and Γ_{7v} (see Fig. 5). Let the number density of holes in either valence state be given by p_9 and p_7 and neglect the lowest Γ_7 valence band. Then the intensity of emission polarized perpendicular to c is given by

$$I_{\perp} \cong p_9[M(\nu_3)]^2 + p_7[M^{\perp}(\nu_4)]^2$$

where $M(\nu_3)^2$ involves some constants (effective mass, etc.) and the square of the matrix element for the optical transition Γ_7-Γ_9 from the center state to the valence band, and $(M^{\perp}(\nu_4)^2$ involves the square of the matrix element for the Γ_7-Γ_7 transition for light polarized to c. For the intensity emitted || c we obtain

$$I_{||} \sim p_7[M^{||}(\nu_4)]^2$$

where $M^{||}(\nu_4)$ is similarly defined. Hence

$$I_{\perp}/I_{||} = \frac{p_9}{p_7}a + b$$

where a and b are ratios of constants. Assuming a Boltzmann distribution of holes between the upper two valence states, which are separated by the spin-orbit splitting energy $\Delta_{s.o.}$, we obtain

$$I_{\perp}/I_{||} = ae^{\Delta_{s.o.}/kT} + b$$

for the temperature dependence of fluorescence polarization.

APPENDIX II

Polarization in ZnO.—The zinc oxide results (Table I) are, of course, even more fragmentary and less capable of unique explanation than the corresponding results for the sulfides. However, some intriguing possibilities suggest themselves if we examine the selection rules for group C_{6v} (Table III). Again, we note that the measured polarization of room temperature surface luminescence (mainly *parallel* to c) is only partial, which suggests either a cluster of final (or initial) states or a transition between only two discrete states, allowed for *both* polarizations with different strengths depending on polarization.

It is possible to argue that the ZnO surface and volume luminescence are connected in the sense that they originate from the same center (atomic surroundings) but perturbed, with a wave function changed due to location on the surface or in the volume. Thus, we may imagine that

$$\Psi \text{ surface} = \Psi \text{ volume} + \lambda\Psi^{(1)}$$

for the center wave function depending on its location. Since a change in wave function in the first order (of a perturbation) will produce a second order change in energy, the luminescence may have approximately the same wave length, but considerably changed polarization properties, since polarization will involve the perturbation of the wave functions, through their optical matrix element, in the first order.

Suppose the surface of the crystal, due to distortions, is more ionic than the volume so that at the surface the net oxygen charge is nearly —2 while in the volume it is $-2 + \delta$ due to an overlap of charge density on the zinc ion, the latter having charge $(+2 - \delta)$. Since the net spin-orbit splittings will be a resultant of splittings on both Zn and O, with the latter's contribution small, we might expect to consider states on the surface nearly neglecting the spin-orbit effect while those in the volume include this. We are led to a model shown in Fig. 9 Physically, we are arguing that the surface Γ_7 state is more nearly Γ_1-like than the volume state and, hence, that $I_{||}/I_{\perp} > 1$ at the surface.

Other speculations involving L-K models and the same argument about wave function distortion would make use of the Γ_5-Γ_6 selection rule (surface) and the change of $\Gamma_5 \rightarrow \Gamma_9 + \Gamma_7$ in volume, with a corresponding change of selection rules to allow both polarizations in emitted light.

Evidently, for ZnO, as well as for the sulfides, studies of the temperature and IR effects on the polarization are required.

Effect of CdS Addition in ZnS:Cu, In and ZnS:Ag, In Phosphors

Eugene F. Apple

Research Laboratory, General Electric Company, Schenectady, New York

ABSTRACT

ZnS:Cu,In and ZnS:Ag,In phosphors each can show two emission bands under 3650Å excitation, namely, in the green (short) and orange (long) with Cu and in the blue and yellow with Ag activator. Addition of CdS causes the ratio of intensities of the short to long wave-length emission to increase. This observation is interpreted using the donor-acceptor associated pair model proposed recently for the long wave-length emission process.

ZnS phosphors coactivated with Ga or In and activated with Cu or Ag exhibit long wave-length emission bands (under u.v. excitation) in addition to the short wave-length emissions which peak at 5200Å with Cu and 4450Å with Ag. Kroger and Dikhoff first reported the former emissions with peaks at 5700Å and 6800Å in samples containing Ga and In coactivators, respectively. According to these authors (1) the spectral distributions of the bands were relatively independent of the particular activators involved.

More recently, Apple and Williams again studied the ZnS: (Cu or Ag), (Ga or In) phosphors and found that the spectral distribution of the long wave-length emission depends on the identity of the activator, as shown in Fig. 1, and the coactivator, as shown in Fig. 2. In most phosphors studied, both the long and short wave-length emission bands were observed. However, by changing the concentration of activator and coactivator, or the identity of the coactivator, or the temperature at which the phosphor was excited, the ratio of intensities of the short to long wave-length emissions, I_s/I_l, could be varied over a wide range (2).

The study reported in this paper concerns the effect of CdS addition on the ratio of emission intensities, I_s/I_l, in ZnS:Cu, In and ZnS:Ag, In phosphors. In ZnS phosphors exhibiting both the short and long wave-length emissions or the long wave-length emission only, addition of CdS causes an increase in I_s/I_l. Above 25-30 mole % CdS the long wave-length emission band is not observed at temperatures as low as −195°C. Effects of activator-coactivator concentration and temperature on the ratio I_s/I_l are included as well as typical glow curve measurements. These effects are interpreted using the model for the long wave-length emission proposed by Apple and Williams.

Experimental Results

Preparation of phosphors.—Mixtures of prefired ZnS and CdS (both from General Electric Company, luminescent grade) containing from 0 to 50 mole % CdS were ground and ballmilled until uniform. These mixtures were used in preparation of all the phosphors. The impurities, Cu, Ag, and In, were added to the mixtures as aqueous solutions. After slurrying with water the phosphor preparations were dried at 100°C, ground in a mortar, and fired at 1100°C in a stream of H_2S[1] for 2 hr. The phosphors were air-cooled to room temperature in the

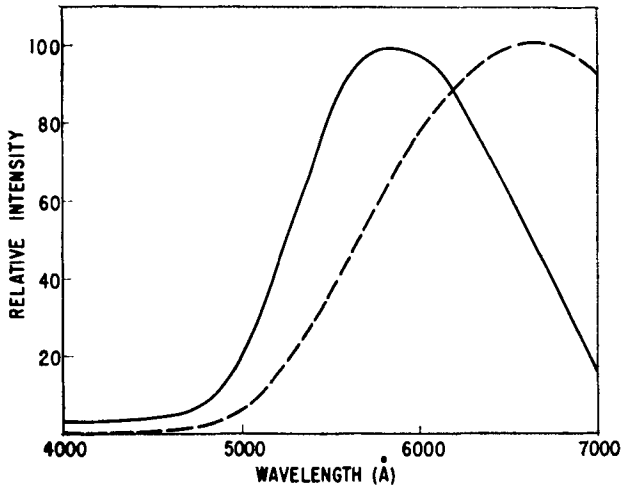

Fig. 1. Long wave-length emission spectra of hex. ZnS:10^{-4} Cu, Ga and hex. ZnS:10^{-4} Ag, Ga under 3650Å excitation at −196°C. Phosphors were fired in H_2S at 1150°C. ——— ZnS:10^{-4} Ag, Ga; - - - - - ZnS:10^{-4} Cu, Ga.

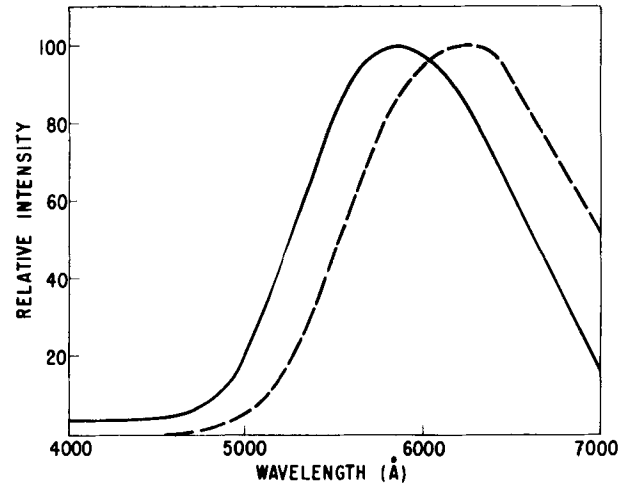

Fig. 2. Long wave-length emission spectra of hex. ZnS:10^{-4} Ag, Ga and hex. ZnS:10^{-4} Ag, In under 3650Å excitation at −196°C. Phosphors were fired in H_2S at 1150°C. ——— ZnS:10^{-4} Ag, Ga; - - - - - ZnS:10^{-4} Ag, In.

[1] The H_2S (Matheson Co.) was bubbled through Ba(OH)$_2$ solution, then passed through columns containing silica gel and P_2O_5, and finally passed through a −50°C trap before coming in contact with the sample.

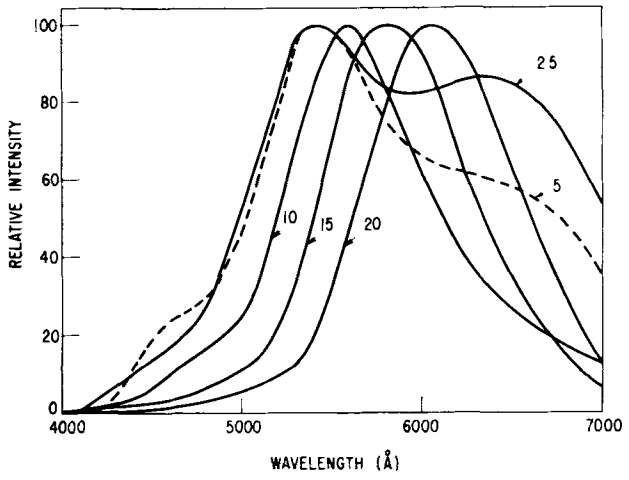

Fig. 3. Emission spectra for hex. (Zn,Cd)S:10^{-5} Cu, In under 3650Å excitation at room temperature. Mole per cent CdS is indicated. Phosphors were fired in H_2S at 1100°C.

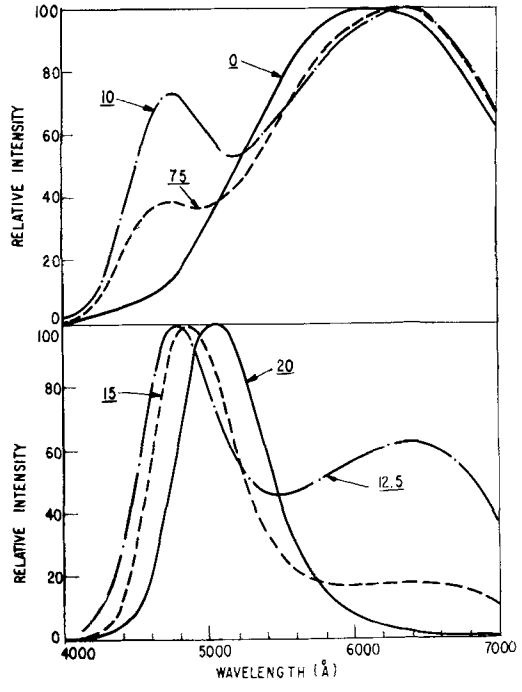

Fig. 4. Emission spectra of hex. (Zn,Cd)S:10^{-4} Ag, In under 3650Å excitation at room temperature. Mole per cent CdS is indicated. Phosphors were fired in H_2S at 1100°C.

H_2S stream. The mole % CdS and the gram-atom fraction of impurities identified with the samples throughout this paper correspond to the amounts present before firing.

Emission spectra at room temperature.—Emission spectra, under 3650Å excitation obtained from a G. E. mercury lamp, #H100-FL4, with Corning No. 5860 and Kopp No. 41 filters, were recorded on an automatic spectroradiometer which plots radiant energy flux vs. wave-length. Room temperature spectra of a typical series, hex. (Zn, Cd)S: 10^{-5} Cu, In are shown in Fig. 3. The spectra have been normalized so that the intensity of the predominant peak is 100. The ratio of relative intensities, I_s/I_l, which is about 1.16 in the 2.5% CdS sample, goes up with increasing CdS content until, with 20% CdS and above, the emission is entirely in the short wave-length band.

The emission spectra for hex. (Zn, Cd)S: 10^{-4} Ag, In at room temperature are shown in Fig. 4. In this series the phosphor with no CdS shows predominantly the long wave-length emission. As the CdS content is increased the relative intensity ratio, I_s/I_l, increases until at 20% virtually all the emission occurs in the short wave-length band. Hexagonal (Zn, Cd)S: 10^{-4} Cu, In gives similar results.

In both groups of phosphors the spectral distribution of the short wave-length emission as measured at the peak intensity moves to longer wave-lengths, i.e., lower energy, at the rate of about 0.017 ev/mole % CdS whereas the rate with the long wave-length emission is only about 0.003 ev/mole % CdS. The long wave-length spectra were measured at —195°C where the other emission does not interfere as much, as will be shown in the next section. However, because of the broadness of the spectra at the emission peak, the latter rate is only very approximate. Above 25% CdS, no long wave-length emission is observed even at —195°C in any of the samples measured. All the emission spectra were very reproducible on repeat samples prepared under the same conditions.

T dependence of emission.—The *T* dependence of emission was measured by recording spectra as the sample contained on a large Cu block was cooled slowly from about 250° to —195°C. Spectra for hex. (0.95 Zn 0.05 Cd)S: 10^{-5} Cu, In at temperatures from 245° to —80°C are shown in Fig. 5. This phosphor achieves its maximum brightness at about 210°C. The ratio of I_s/I_l increases with increasing temperature. Above about 0°C, a plot of log I_l/I_s vs. $1/T°K$ on any (Zn,Cd)S:Cu, In phosphor gives a linear relationship as is shown in Fig. 6. From the slope of this line, the difference in energies of the two types of centers is obtained (2). This energy decreases with increasing CdS content; for example, in (Zn, Cd)S: 10^{-5} Cu, In, it decreases from 0.34 ev to 0.24 ev in the range 0 — 10% CdS. Measurements were limited to samples containing 10% or less CdS because of the increased overlap of the short and long wave-length bands at higher CdS concentrations. In addition, the measurements were limited to Cu-activated phosphors because of the marked temperature quenching above 80°C observed in Ag-activated samples.

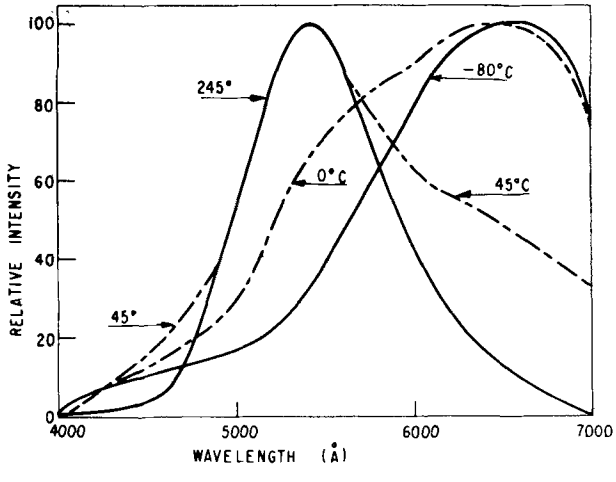

Fig. 5. Emission spectra of hex. (0.95 Zn, 0.05 Cd) S:10^{-5} Cu, In measured at the indicated temperatures.

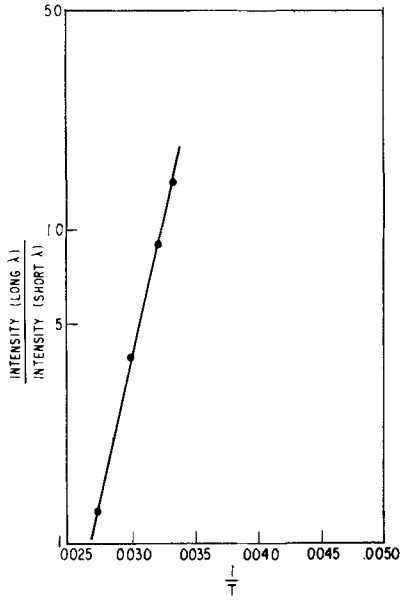

Fig. 6. T(°K) dependence of emission in (0.97 Zn, 0.03 Cd) S:10^{-5} Cu, In under u.v. excitation.

Effect of activator-coactivator concentration.—In a particular series with constant Cd content, increase in the concentration of activator (and coactivator) over the range 10^{-6} to 5 x 10^{-4} g-atoms/mole (Zn, Cd)S results in a decrease in the ratio of relative intensities, I_s/I_l, when excited at a given temperature. This data on the effect of concentrations is consistent with that already reported for ZnS:Cu,In or ZnS:Ag, In phosphors (2).

Glow curve measurements.—Glow curve measurements were made on the hex. (Zn, Cd)S: 10^{-4} Cu, In series. The phosphors were excited for 5 min with a BH-4 lamp at —195°C after which they were warmed in the dark at a rate of 10°/min. An RCA 5819 PM tube was used as detector. The glow peaks shown in Fig. 7 move to lower temperatures with increasing CdS content. This effect of CdS is consistent with the results obtained by Hoogenstraaten with Al, Ga, and Cl donors (3).

Discussion

(Zn, Cd)S phosphors showing only what in this paper is called the short wave-length emission band have been studied extensively by many people. It has been shown that ZnS and CdS form solid solutions over the entire range and that in the 0-30 mole % CdS range, the absorption edge, as deduced from reflectance spectra, moves at the rate of about 0.020 ev/mole % CdS to lower energies (4). In turn, in (Zn, Cd)S:(Cu or Ag), (Al or Cl) phosphors the spectral distribution of the short wave-length emission moves to longer wave lengths, i.e., lower energies, at the rate of about 0.018 ev/mole % CdS (5). The donor levels assumed to be introduced by the coactivator become shallower with increase in CdS concentration as indicated by the thermal glow measurements. The rate in this case in the 0-30% region is about 0.012 ev/mole % CdS (3).

In the present study both the shift in the short wave-length emission to longer wave lengths and the shift in glow curve maxima to lower temperatures with increase in CdS content are qualitatively consistent with the data already reported by other

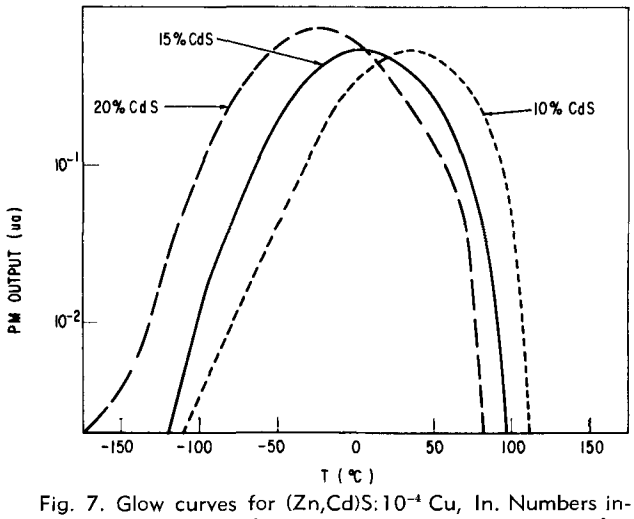

Fig. 7. Glow curves for (Zn,Cd)S:10^{-4} Cu, In. Numbers indicate mole per cent CdS. Excitation: BH-4 lamp at —195°C; heating rate 10°/min.

authors. Because of the very broad glow curves in evidence in (Zn, Cd)S:Cu, In phosphors it is probable that the ground states of the donor levels are distributed over a range of energies so that a unique value for a trap depth is not too meaningful. (In this paper, trap depth and ground state of the donor level are synonymous.) Johnson has obtained evidence that such a distribution exists in the several ZnS:Cu,Al and ZnS:Cu,In phosphors he has analyzed (6). The glow curves indicate, however, that the distribution of traps becomes shallower (with respect to the conduction band) with increasing CdS content. The temperature dependence of emission data for (Zn,Cd)S: 10^{-5} Cu,In also shows that the ground state of the donor level becomes shallower with CdS addition. The spectral distribution of the long wave-length emission in ZnS:Cu,In or ZnS:Ag,In changes at the rate of about 0.003 ev/mole % CdS in the 0-25% range.

In a phosphor showing both the long and short wave-length emission bands it would be expected that the bands should gradually merge with increasing CdS content because of their different rates of displacement. Beyond the point of mergence only one emission band should be observed since the donor levels are then shallow. As a result, transitions involving the ground state of the donor (between highly associated pairs) or an excited state of the donor (between loosely associated pairs) or the conduction band (between unassociated pairs) to the ground state of the activator would be virtually indistinguishable. In the (Zn,Cd)S:Cu,In or (Zn,Cd)S:Ag,In phosphors studied the bands are not observed to merge completely because the CdS, in addition to causing the bands to move as stated, also effects a change in their relative intensities. Increase in CdS content causes an increase in the ratio I_s/I_l so that (Zn,Cd)S phosphors showing both the short and long wave-length emissions or the long wave-length emission only, will, with substitution of 25-30% CdS for ZnS, show only the short wavelength emission even at —195°C. Perhaps the long wave-length emission could be observed at still lower temperatures. This newly observed effect of CdS on I_s/I_l is thought to be directly connected with the

decrease in donor (coactivator) depth attending the increase in CdS content.

Two models have been proposed for the long wave-length emission process in ZnS. Using the data of Kroger and Dikhoff, Klasens proposed that the long wave-length emission was due to the radiative recombination of a free hole with an electron trapped at a coactivator. As an alternative he suggested (7) that the radiative transition may involve recombination of a hole in a "waiting state" located above the filled band with an electron trapped at a coactivator. The nature of the waiting state was not clearly defined, but the idea was probably invoked to minimize the large difference in energies between the observed thermal and optical trap depths. The optical depth on the Klasens model, which would be approximately the difference between the band gap energy and the energy at the peak of the long wave-length emission, is about 1.3 ev greater than the thermal trap depth reported by Hoogenstraaten (3). Klasens also reported that the addition of 20% CdS in ZnS:Ag,In caused the peak of the long wave-length emission measured at −183°C to shift from 6100 to 6200Å or only 0.03 ev. This shift is considerably less energywise than the corresponding shift with CdS addition in the short wave-length emission.

More recently, Apple and Williams suggested another model for the long wave-length emission process which is based on the fact that the spectral distribution of this emission depends on the identity of both activator (Cu or Ag) and coactivator (Ga or In). They suggested that both species are involved in the luminescent center and concluded that the radiative transition giving rise to the long wave-length emission is between a coactivator-activator pair sufficiently close to each other in the lattice so that the ground state wave functions of the two overlap. This luminescent transition is shown on the band model in Figure 8a. In most of the phosphors they prepared, both the long and short wave-length emission bands were observed. By changing the concentration of activator and coactivator, or the coactivator identity, or the temperature at which the phosphor was excited, the ratio of intensities of the short to long wave-length emissions, I_s/I_l, could be varied over a wide range. Using an analysis based on the new model for the long wave-length center and on the Prener-Williams model for the short wave-length center (8) (shown in Fig. 8b) the authors were able to account qualitatively for the effects of the foregoing parameters on the ratio of intensities of the two emission bands. In the latter model, luminescence is attributed to transitions between coactivator-activator pairs which are not so highly associated as those giving the long wave-length emission.

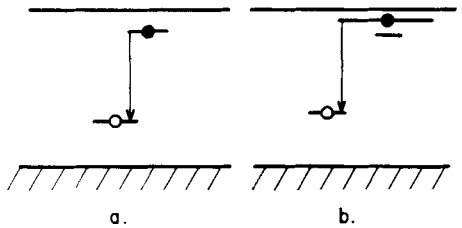

a. b.

Fig. 8. Band theory models for the (a) long and (b) short wave-length (8) luminescent centers.

Apple and Williams suggested that the ratio of intensities of the short to long wave-length emission in ZnS: (Cu or Ag), (Ga or In) was dependent on at least two factors, the ratio of occupational probabilities of the emitting states of the short and long wave-length centers and the ratio of fractions of coactivator-activator (or donor-acceptor) pairs involved in each of the two types of centers. They said that the difference in the peaks of the emission spectra of the two bands is a measure of the difference in energies of the emitting states of the two types of centers and that the ratio of occupational probabilities, $P_{(\epsilon_s)}/P_{(\epsilon_l)}$, of the emitting states is given approximately by:

$$P_{(\epsilon_s)}/P_{(\epsilon_l)} \approx e^{\frac{-he}{kT}\left(\frac{1}{\lambda_s}-\frac{1}{\lambda_l}\right)} \quad [1]$$

where λ_s and λ_l are the wave lengths at the emission peaks of the respective bands. In ZnS phosphors this factor greatly favors the long wave-length emission; it is dependent on the depth of the ground state of the donor (which is the emitting state of the long wave-length emission). For example, at temperatures where thermal equilibrium applies, the ratio of intensities of the short to long wave-length emission is greater in ZnS:Ag,Ga than in ZnS:Ag,In because the ground state of Ga is 0.08 ev shallower than that of In (according to thermal glow measurements) (3). The value for $(1/\lambda_s - 1/\lambda_l)$ is smaller in the former case which leads to a more positive value of $P_{(\epsilon_s)}/P_{(\epsilon_l)}$. Also, at room temperature I_s/I_l is much larger in cubic than in hexagonal ZnS:Cu,In, due presumably to the fact that the donor ground state due to In is shallower in cubic than in the hexagonal phase (9).

The model suggested by Apple and Williams will be used to interpret the results of the effect of CdS addition on the emission in ZnS:Cu or Ag, In phosphor since this model is most consistent with the experimental results thus far obtained.

The increase in the ratio of intensities of the short to long wave-length emissions with increase in CdS content may be due to the change in the ratio of occupational probabilities of the emitting states, which change is a direct consequence of the gradual decrease in the depth of the ground state of the In level with CdS increase. From Eq. [1], I_s/I_l would increase with increasing CdS because the term $(1/\lambda_s - 1/\lambda_l)$ becomes smaller. As the short wave length approaches the long wave-length emission peak, $(1/\lambda_s - 1/\lambda_l)$ becomes so small that the actual mergence of the two peaks is not observed since before this point, the ratio of occupational probabilities has increased to such an extent that the short wave-length emission is overwhelmingly favored.

As was pointed out by Apple and Williams, the ratio of fractions of pairs contributing to the two emissions greatly favors the short wave-length emission and tends to balance out the occupational probability effect except where this ratio becomes large as with increasing CdS. In a series containing

a constant amount of Cd, the decrease in the ratio of intensities, I_s/I_l, with increasing concentration of activator and coactivator is due to the increase in the fraction of pairs contributing to the long wave-length emission. These results are consistent with those found previously for ZnS: (Cu or Ag), (Ga or In) phosphors.

In summary, CdS addition in ZnS:Cu,In or ZnS: Ag,In causes an increase in the ratio of short to long wave-length emission intensities. This increase is due to the increase in the ratio of the occupational probabilities of the emitting states of the two centers. Although other models could possibly be used to interpret these results, the fact that the spectral distribution of emission of the long wave-length center is dependent on the identity of both donor and acceptor is taken as evidence that the long wave-length luminescent transition is between associated donor-acceptor pairs as already pointed out (2).

Preliminary measurements show that CdS has the same general effect in ZnS:Cu,Ga or ZnS:Ag, Ga as in ZnS:Cu,In or ZnS:Ag,In.

Acknowledgments

The author wishes to thank the following people: Mrs. D. J. Weil for preparation of samples; Dr. F. J. Studer and Miss G. Lloyd for measurement of spectra; Dr. P. D. Johnson and Mr. F. C. Mostek for measurement of thermal glow curves; and Dr. J. S. Prener and Dr. F. E. Williams for review.

Manuscript received Nov. 16, 1959. This paper was prepared for delivery before the Philadelphia Meeting, May 1-5, 1959.

Any discussion of this paper will appear in a Discussion Section to be published in the December 1960 JOURNAL.

REFERENCES

1. F. A. Kroger and J. Dikhoff, *Physica*, **16**, 297 (1950).
2. E. F. Apple and F. E. Williams, *This Journal*, **106**, 224 (1959).
3. W. Hoogenstraaten, *ibid.*, **100**, 356 (1953); Thesis, University of Amsterdam, February 1958.
4. F. A. Kroger, *Physica*, **7**, 1 (1940).
5. S. Lasof, R. Shrader, and H. Leverenz, "Preparation and Characteristics of Solid Luminescent Materials," p. 224, John Wiley & Sons, Inc., New York (1946).
6. P. D. Johnson, Private communication.
7. H. A. Klasens, *This Journal*, **100**, 72 (1953).
8. J. S. Prener and F. E. Williams, *Phys. Rev.*, **101**, 1427 (1956); F. E. Williams, *J. Opt. Soc. Amer.*, **47**, 869 (1957).
9. E. F. Apple and D. J. Weil, Electrochem. Soc. Enlarged Abstracts, Electronics Div., Spring Meeting, Philadelphia, May 1959, p. 52.

Growth and Heat Treatment of Zinc Sulfide Single Crystals

A. Kremheller

General Telephone and Electronics Laboratories Inc., Bayside, New York

ABSTRACT

Zinc sulfide crystals grow readily from the vapor phase if small traces of certain impurities, such as zinc oxide and copper, are present. The decrease of ambient impurity concentration leads first to very thin, flexible, ribbon-like crystals which are hexagonal, and finally to nucleation with little growth. The purity of crystals depends not only on the composition of the starting material but also on the purity of the combustion tube employed; contamination during growth leads to an impurity gradient in crystals and to impurity variations among crystals. Crystals usually exhibit disorder of the crystal structure, although pure cubic or hexagonal structure can be achieved by annealing or quenching. Heat treatment also changes the impurity content and attendant properties, such as physical color, luminescence behavior, electrical properties, and disorder of the crystal structure.

There has been considerable interest in the growth of zinc sulfide single crystals during the past decade (1-3) because it is expected that the mechanisms of photoluminescence, photoconductivity, and electroluminescence will be better understood by studying single crystals. Natural zinc sulfide crystals are available in large size; however, they contain comparatively high impurity concentrations, usually of the order of 1% by weight. Since commercial applications of zinc sulfide phosphors require small quantities of additives, such as a few parts per million of activator and coactivator, natural crystals have been of but little importance in such researches.

Another requirement in preparing crystals for research purposes appears to be the proper control of the crystal structure (4). Synthetic crystals grown by the conventional vapor phase methods (3) exhibit one-dimensional disorder (3, 5-7, 8) consisting of randomness, mixed hexagonal-cubic structure in the same crystal, and the presence of polytypes which are intermediate between the hexagonal and cubic crystal systems.

Alfrey and Taylor (9) came to the conclusion that "unfortunately, single crystals (of zinc sulfide—the author) are difficult to grow and the amount and nature of the activators cannot be controlled, so that crystals grown by different experimenters will differ in constitution." The present paper shows how some of these difficulties have been overcome. It describes some experiments dealing with the preparation of zinc sulfide single crystals of controlled chemical composition and crystal structure. Previously reported observations (3, 8) are extended and, in many cases quantitatively corroborated;

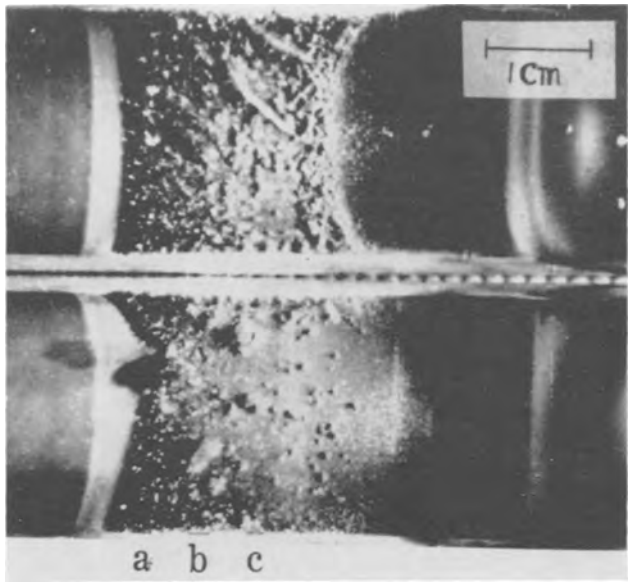

Fig. 1. Longitudinally split tube with crystals; regions a, b, c, as indicated in Table VII.

some new results are presented which appear to have experimental and theoretical implications as to the preparation of single crystals.

Experimental

The single crystals of zinc sulfide which have been investigated in the course of these studies were prepared from the vapor phase by sublimation. The growth method employing a U-shaped transparent quartz cooling finger which permits the control of nucleation, crystal structure, and morphology of crystals has been described previously (3). This technique is not described in any detail because the main experimental results are generally available (10). Recently Matsumura, *et al.* (11) have confirmed our observations (3, 8) in the course of investigating very thoroughly the growth and morphology of zinc sulfide single crystals obtained by the cooling-finger technique. Their observations are in essential agreement with many of our unpublished results; however, we were led by experimental circumstances to some additional investigations which are discussed here.

In another variation of vapor phase sublimation, a longitudinally split mullite tube is placed inside the mullite combustion tube (Fig. 1). This method leads to the growth of large voluminous crystals, which can be sampled readily and accurately from the various growth regions in the split tube. These large, oblong crystals were used mostly in the diffusion experiments described below.

Growth of pure single crystals.—The crystal growth on a cooling finger has been conducted as part of an attempt to prepare large crystals of high purity. Since the quartz combustion tube tends to break when cooled to room temperature after every experiment,[1] it was decided to keep the quartz tube continuously above 1000°C. In this way it was possible to conduct up to 30 growth experiments without loss of the quartz combustion tube. Consequently the cooling finger arrangement became a necessity for removing the crystals after growth was completed. In addition, since the cooling device can be removed rapidly from the hot zone, completely hexagonal crystals are obtained readily by temperature quenching.

[1] Quartz crystallizes in the tridymite form with an attendant volume increase of 15% when cooled to 900°C.

Table I. Decrease in impurity content,* in per cent by weight, of crystals grown on the cooling finger during consecutive growth experiments. (— not detected.)

Experiment No.	1	2	4	8
Cu	0.0005	0.0003	0.0002	<0.00001
Fe	0.0004	0.0002	0.0001	—
Pb	0.0003	0.00006	0.00002	<0.00001

* Quantitative spectrographic analysis by T. Veleker, Sylvania Electric Products Inc., Towanda, Pennsylvania.

Activated crystals are grown readily by this technique, with the desired level of activation depending on the additives physically admixed to the zinc sulfide powder or kept in a separate quartz boat; however, difficulties were met in preparing very pure crystals by the cooling-finger technique.

It was observed that the yield of crystals decreased with successive growth experiments. There was a trend to very thin, plate-like crystals with consecutive experiments. These thin tissue-like crystals were very flexible and exhibited interference colors in reflected light. After several experiments, nucleation still took place on the cooling finger, but the nuclei no longer grew into visible crystallites.

A correlation between the decrease in the rate of crystal growth and the increase in the purity of the crystals has been observed. Table I indicates that a gradual decrease of contamination occurs with successive growth experiments. It appears that the quartz tubes and boat are gradually cleaned, and the incorporation of impurities through the vapor phase and from the quartz substrate decreases accordingly.

There is additional proof that impurities are instrumental in the growth of zinc sulfide single crystals. The growth of crystals could again be brought about by using a quartz cooling finger which had not been used previously. The introduction of copper metal or zinc oxide powder into the boat was similarly effective in stimulating crystal growth.

Influence of tubing material.—The physical appearance, growth habit, and impurity content of crystals depend markedly on the tube material employed for crystal growth. As indicated above, there is a decrease in impurity levels with the successive use of a given transparent quartz tube. This purification effect occurs also with opaque quartz, while the increase in purity of crystals grown in consecutive experiments in mullite tubing has not been studied; however, crystals of successive batches became gradually light-yellowish to colorless in color and greenish-blue photoluminescent, while the first batch was dark-brown and nonphotoluminescent. Table II indicates average values of the tube composition and starting zinc sulfide powder which are based on several quantitative spectrographic analyses. The zinc sulfide powder is essentially spectrographically pure, while the tube ma-

Table II. Chemical composition of tube materials and original zinc sulfide powder, in per cent by weight

Element	Mullite	Opaque quartz	Transparent quartz	Zinc sulfide
Al	10-100	0.01-0.1	0.01-0.1	—
Ca	0.001	0.001	0.001	—
Cu	0.001-0.01	0.0001-0.001	0.0001	<0.00001
Fe	0.01-0.1	0.0001-0.001	<0.0001	<0.0001
Mg	0.01-0.1	0.0001-0.001	0.0001-0.001	0.0001
Mn	0.0001	0.0001	0.0001	0.00001
Ni	0.0001-0.001	—	—	<0.0001
Pb	0.0001	0.0001	<0.0001	<0.00005
Si	10-100	10-100	10-100	0.0001

Table III. Impurities in crystals grown in different tubes, in per cent by weight

Element	Crystals grown in tubes of Mullite	Opaque quartz	Transparent quartz
Al	0.0012	0.00025	0.00012
Ca	0.0004	0.0002	—
Cu	0.01	0.0013	0.0003
Fe	0.0007	0.0002	0.00015
Mg	0.0005	0.0002	0.0002
Mn	0.0001	0.00002	0.00002
Ni	0.00035	0.0001	<0.0001
Pb	—	—	—
Si	0.001-0.01	0.001-0.01	<0.001

terial is obviously the main source of contamination during growth.

The impurities are given as an average from several spectrographic determinations on randomly sampled crystals, Table III. One finds, as expected, that crystals grown in combustion tubes containing many impurities are contaminated accordingly. However, even the appearance and physical properties of the crystals depend on the kind of tubing material employed (Table IV).

One finds many crystals grown on the cooling finger that are not photoluminescent because they are very pure, while some crystals grown on the wall of the mullite tube are not photoluminescent because they contain too many impurities.

In general one observes also that the volume-to-surface ratio of crystals increases markedly with the impurity content. Some indication was found that traces of Ni, Co, and Fe in conjunction with Cu are very instrumental in introducing a brown to dark-brown physical color.

Nonuniformity in impurity content.—There has been considerable mention of the fact that the crystals of a specific batch differ widely with respect to purity and perfection of the crystal structure (9, 12, 13). While a partial analysis of these problems has already been presented (3, 8) in previous communications, additional evidence on the origin and elimination of these difficulties is given in the present paper. In this section three problems will be dealt with: (*a*) a comparison between the impurity level of the crystals and the material remaining in the boat, (*b*) spectrographic determination of impurities in the crystals grown in contact with the combustion tube wall and of the crystal fraction not in contact with the wall, and (*c*) the change of impurity level with location in longitudinally split tubes. The data are again averages of several experiments and show the typical features that cause the nonuniformity in purity from crystal-to-crystal and within single crystals grown by vapor phase methods.

Table V. Impurities, in per cent by weight, in single crystals and starting material after growth is completed

Element	Crystals on cooling finger	Powder in quartz boat
Al	0.001	0.0005
Ca	0.0002	0.0001
Cu	0.005	0.002
Fe	0.0007	0.0003
Ni	0.0005	0.0002

Table VI. Impurities, in per cent by weight, incorporated from the vapor phase and by solid-state diffusion

Element	Crystal fraction from wall	Crystal fraction not in contact with wall
Al	0.005	0.0005
Cu	0.015	0.003
Fe	0.001	0.0005

Table V shows that some impurities are incorporated preferentially in the single crystals on the quartz cooling finger in a mullite combustion tube. This becomes apparent when one compares the analyses of crystals with those of the contaminated residual starting material which was kept in a transparent quartz boat.

The powder in the boat also increased in particle size, but since the single crystals are much larger, one may assume that the impurities that are preferentially accumulated may cause the rapid growth, i.e., they may act as mineralizers.

In the second investigation, about half of every single crystal grown on the wall of the longitudinally split tube was broken off, and spectrographic analyses were run on both these and on the parts remaining in contact with the tube wall.

It was found, as indicated in Table VI, that the crystal fraction in contact with the wall contains a higher impurity level than crystals into which impurities were preferentially incorporated by vapor phase diffusion. This result confirms previous observations (14) which indicated an impurity gra-

Table IV. Properties of crystals grown in different combustion tubes

	Mullite	Opaque quartz	Transparent quartz
Physical color	Brown to dark brown	Yellow to whitish	Colorless
Transparency	Opaque or transparent	Some transparent	Most transparent
Electrical resistivity	Near 10^7 ohm-cm	10^9-10^{11} ohm-cm	$>10^{11}$ ohm-cm
Luminescence color	Green, orange, or none	Light green to blue	None or bluish

Table VII. Dependence of impurity content, in per cent by weight, of crystals on growth location in longitudinally split combustion tube, (regions a, b, and c of Fig. 1)

Element	Region a	Region b	Region c
Al	0.01	0.005	0.0005
Cu	0.012	0.006	0.002
Fe	0.002	0.001	0.0002
Ni	0.001	0.0006	0.0001

Table VIII. Purification of zinc sulfide single crystals by diffusion

Temperature, °C	before	800	1000	1100	1100
Time of annealing, hr	anneal	7	7	2	16
Per cent by weight of copper found	0.008	0.005	0.003	0.0025	0.00092

dient in cadmium sulfide crystals grown by a similar method.

The local impurity distribution from crystal-to-crystal can be studied when a longitudinally split tube is used, which also facilitates the sampling of crystals. Crystal growth starts at a sharp boundary which is near 1080°C (region a in Table VII and Fig. 1); the largest crystals grow in this region; they are brown to dark-brown in physical color. As the color lightens with the location farther from this dark region, the crystals become gradually smaller, the particle size following about an exponential dependence with the distance. Table VII shows the impurities found, and the photograph (Fig. 1) shows the split tube with crystals.

Control of impurity content and crystal structure by heat treatment.—It has been indicated above that the growth of very pure and large crystals in a reasonable reaction time leads to intrinsic difficulties. Therefore, it did not appear desirable to grow crystals of high purity, but instead an attempt was made to achieve this objective (i.e., the preparation of single crystals of controlled crystal structure and chemical composition) by heat treatment after crystal growth was completed.

Copper is considered to be the most important impurity because of its role as an activator and its relatively high concentration (Table III) in the large crystals which were grown in mullite tubing. The observation of Riehl and Ortmann (15) that copper diffuses readily into the zinc sulfide lattice suggested a method for purification. The purification method depends on impurity diffusion from the crystal into pure zinc sulfide powder in which the crystal is embedded. A variation of this method may also be used to activate crystals by diffusion in the opposite direction. The times and temperatures involved in purification by this process are indicated in Table VIII; some additional results are given in Fig. 2.

A large number of crystals have been heat treated in this way, and one observes that the purification process leads to various attendant changes. The brown physical color diminishes and the transparency increases; the electrical resistivity increases by

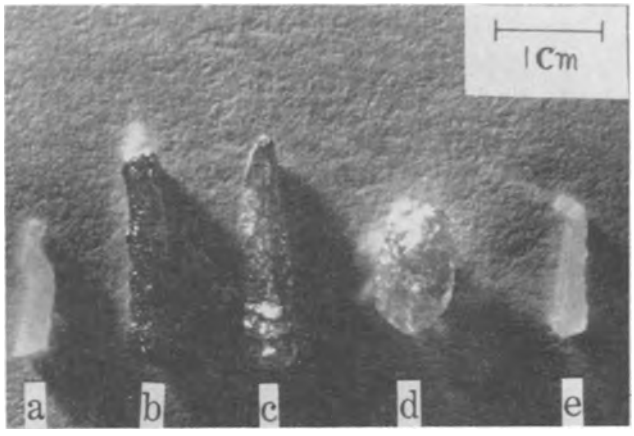

Fig. 2. Zinc sulfide crystals before and after annealing at 1000°C: (a) Piece of crystal b, annealed for 100 hr, pure embedding powder changed 3 times, (b) original, not annealed crystal, (c) crystal annealed for 32 hr in pure powder, (d) crystal annealed for 50 hr, and (e) crystal annealed for 200 hr, embedding powder changed 5 times. Crystals a-e were made cubic by a second annealing of 5 hours at 900°C in pure zinc sulfide powder.

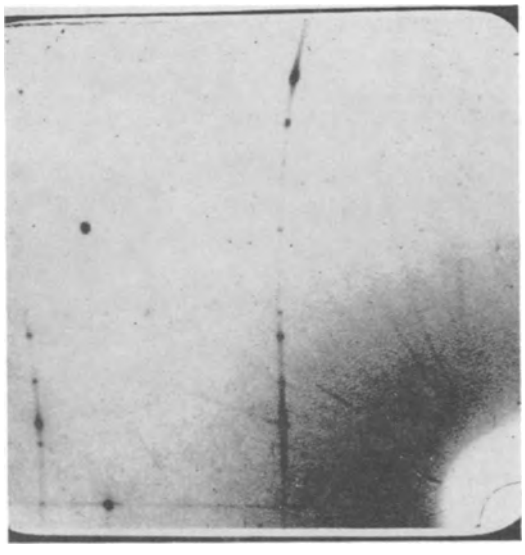

Fig. 3. X-ray diagram of a mixed hexagonal-cubic zinc sulfide crystal rotated about the c-axis; randomness, and 4- and 6-layer polytypes are observed.

several orders of magnitude; crystals turn photo- and electroluminescent or frequently change their emission color; changes in crystal structure also take place in many cases.

The crystal structure is usually quite disordered if zinc sulfide single crystals are grown on the wall of the combustion tube. The disorder consists of randomness, mixed hexagonal-cubic structure in the same crystal, and the presence of polytypes. An x-ray diffraction pattern of such a disordered crystal is shown in Fig. 3; the crystal has been rotated about the c-axis. The photograph shows the presence of mixed hexagonal-cubic structure, randomness as indicated by the blackening between the distinct spots, and the presence of 4- and 6-layer polytypes.

These disordered crystals are usually observed if one permits the furnace to cool at the rate governed by its heat capacity. If completely cubic crystals (Fig. 4) are desired, it is usually sufficient to keep

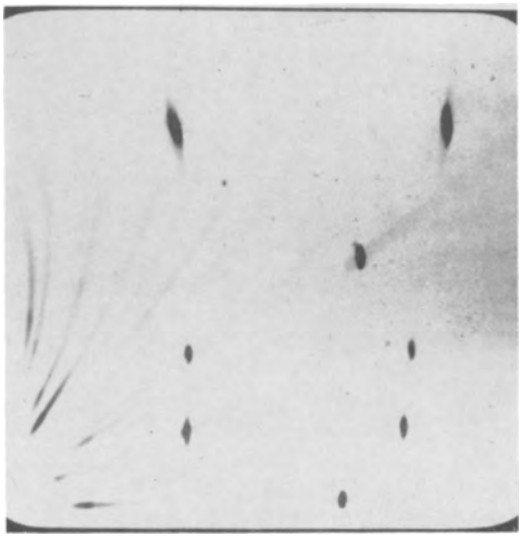

Fig. 4. X-ray diagram of cubic zinc sulfide single crystal rotated about the 111-direction.

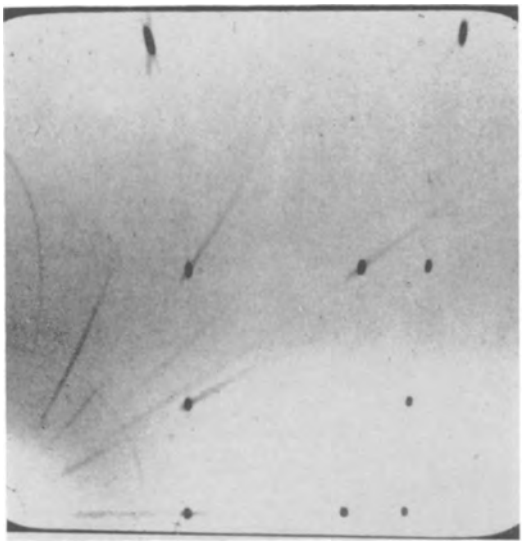

Fig. 5. X-ray diagram of hexagonal zinc sulfide single crystal rotated about the c-axis.

the crystals for 5 to 10 hr near 900°C. In this way one can combine the purification or activation of the crystal with the alteration of the crystal structure, so that a cubic crystal of controlled activator content is obtained.

The method employing the cooling finger also permits the preparation of completely hexagonal crystals (Fig. 5). The U-shaped cooling finger with crystals on the tip can be removed easily and rapidly from the hot condensation zone, so that the crystals are quenched after growth is completed (Fig. 6). It has been observed in all these cases that hexagonal crystals are formed, and therefore one may assume that crystals grew in this form under the growth conditions employed. This result is readily obtained when the cooling finger is used, while growth on the wall of the combustion tube does not permit rapid temperature quenching.

Hexagonal crystals can also be activated or purified by heat treatment after growth, although it is necessary to keep the annealing temperature below 800°C so that no transformation of the crystal structure (3) occurs while diffusion of foreign atoms

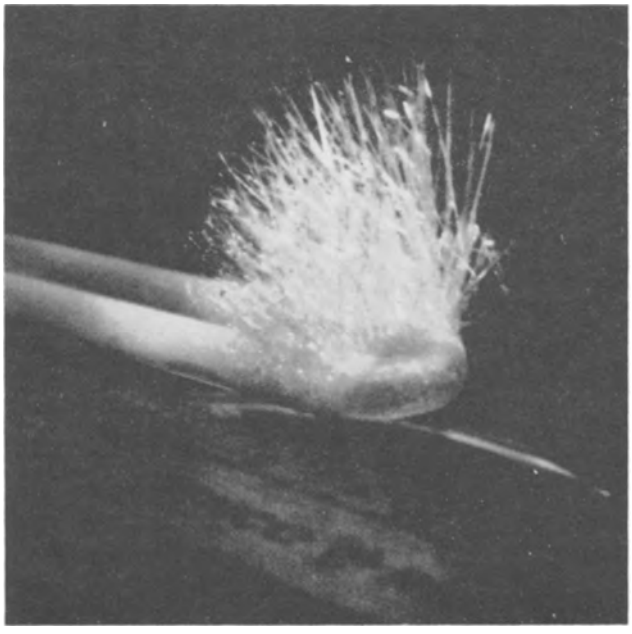

Fig. 6. Hexagonal crystals grown on the tip of the U-shaped quartz cooling finger.

(15) is taking place. In this way it has been possible to obtain pure or activated crystals belonging to the hexagonal system.

Conclusion

Certain impurities appear to be necessary when zinc sulfide single crystal growth is to proceed from nuclei. One may speculate that such mineralizers may facilitate the formation of screw dislocations, so that no need for the formation of a "two-dimensional nucleus" exists.

This behavior leads to inherent difficulties when an attempt is made to grow large pure crystals. Therefore, heat treatment with attendant diffusion has been employed in preparing large single crystals of controlled chemical composition. This annealing technique also eliminates the impurity gradient within a given crystal and impurity variations among crystals that depend on the growth site within the combustion tube.

Heat treatment also permits the deliberate control of the crystal structure, so that pure cubic or hexagonal crystals with or without a desired degree of randomness can be obtained, although the latter and the occurrence of polytypes appear to be markedly dependent on the presence of small amounts of foreign elements (3).

As a next step in investigating some pertinent problems, a detailed study of the impurity dependence of the crystal structure and disorder and their correlation with the appropriate free energy changes appears to be indicated. Such investigations should finally permit one to overcome the difficulties still remaining to be solved in the preparation of zinc sulfide single crystals of controlled chemical composition and crystal structure.

Acknowledgment

The author is greatly indebted for valuable contributions of D. J. Bracco, T. Veleker, R. Bastian, D. T. Palumbo, L. W. Strock, and V. A. Brophy. The

assistance of J. T. Ragusin and S. Faria with the experimental work is gratefully appreciated.

Manuscript received Dec. 16, 1959. This paper was prepared in part for presentation before the Chicago Meeting, May 2-6, 1954.

Any discussion of this paper will appear in a Discussion Section to be published in the December 1960 JOURNAL.

REFERENCES

1. D. C. Reynolds and S. J. Czyzak, *Phys. Rev.*, **79**, 543 (1950); S. J. Czyzak, D. C. Reynolds, R. C. Allen, and C. C. Reynolds, *J. Opt. Soc. Amer.*, **44**, 864 (1954); L. C. Greene, D. C. Reynolds, S. J. Czyzak, and W. M. Baker, *J. Chem. Phys.*, **29**, 1375 (1958).
2. Wm. W. Piper, *J. Chem. Phys.*, **20**, 1343 (1952).
3. A. Kremheller, *Sylvania Technologist*, **8**, 11 (1955).
4. A. H. McKeag and E. G. Steward, *This Journal*, **104**, 41 (1957).
5. C. Frondel and C. Palache, *Amer. Min.*, **35**, 29 (1950).
6. M. A. Short and E. G. Steward, *Acta Cryst.*, **8**, 733 (1955).
7. H. Mueller, *Neues Jb. Mineral. Abh.*, **84**, 43 (1952).
8. A. Kremheller, Heat Treatment of Zinc Sulfide Single Crystals, paper presented at the Spring Meeting of The Electrochemical Society at Chicago, May 1954.
9. G. F. Alfrey and J. B. Taylor, *Proc. Phys. Soc. (London)*, **68B**, 775 (1955).
10. "Methods of Experimental Physics," Vol. 6, Solid State Physics, edited by K. Lark-Horovitz and Vivian A. Johnson, Academic Press, New York, 1959, part B, p. 297.
11. T. Matsumura, H. Fujisaki, and Y. Tanabe, *Sci. Rep. Ritu*, **A10**, No. 6, 459 (1958).
12. D. R. Frankl, *Phys. Rev.*, **100**, 1105 (1955).
13. T. B. Tomlinson, J. Electronics, **2**, 293 (1956).
14. A. Kremheller, Ph.D. Thesis, Munich University, Munich, January 1952.
15. N. Riehl and H. Ortmann, *Z. Physik. Chem.*, **A188**, 109 (1941).

Characteristics of the {111} Surfaces of the III-V Intermetallic Compounds

Harry C. Gatos and Mary C. Lavine

Lincoln Laboratory, Massachusetts Institute of Technology, Lexington, Massachusetts

ABSTRACT

Surface characteristics of the {111} crystallographic planes of the III-V intermetallic compounds (zinc-blende structure), and in particular those of InSb, are discussed. The polarity of these compounds along the <111> directions leads to pronounced physical chemical differences between the {111} surfaces terminating with group III atoms and those terminating with group V atoms. Differences in etching, dislocation etch pit formation, and electrode potential are presented. Dislocation etch pits form on the group III surfaces and not on the group V surfaces of the six compounds investigated (InSb, GaSb, AlSb, InAs, GaAs, and InP). A proposed interpretation is based on the relative reactivity of the group III and group V atoms as affected by their bond configuration and the polarity of the zinc-blende structure.

A number of investigators have reported on the etching characteristics (1-5) and other surface properties of the III-V compounds (4, 6). InSb has been principally employed because of its availability.

Among the various crystallographic planes, the {111} are of special interest because the III-V compounds (zinc-blende structure) exhibit polarity along the <111>directions. Thus, there is significant difference between parallel {111} surfaces, arbitrarily designated as {111} and $\{\bar{1}\bar{1}\bar{1}\}$ as shown in Fig. 1. The outermost atom layer in each surface consists of either group III or group V atoms which are triply bonded to the lattice. This results from the fact that the {111} surfaces can be created only by cuts between planes such as AA and BB (Fig. 1) where atoms are singly bonded to one another. A surface configuration containing atoms singly bonded to the lattice, resulting, for instance, from a cut AB'B' is not stable (4, 5, 8). Furthermore, slip on the {111} planes occurs between AA and BB rather than AA and B'B'.

Dislocation etch pits are found only on the {111} and not on the $\{\bar{1}\bar{1}\bar{1}\}$ surface (1, 2, 5, 6). The identification of the two types of surfaces in InAs and GaSb was achieved recently by Warekois and Metz-

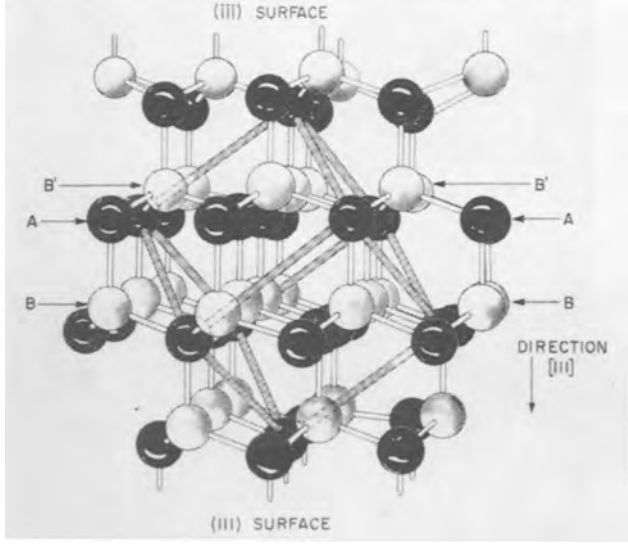

Fig. 1. Crystal structure (zinc-blende) of the III-V intermetallic compounds; the unit cell is indicated. •, group III atoms; ○, group V atoms.

ger (9). They showed by x-ray techniques that in InAs and GaSb the {111} planes developing dislocation etch pits terminate with the group III atoms. This has been also shown for GaAs (10), and for InSb and other III-V compounds (11).

In the present paper, the etching characteristics and the formation of dislocation etch pits in III-V compounds are discussed, and an interpretation is advanced for the observed differences between the two types of {111} planes and the formation of dislocation etch pits on the {111}and not on the $\{\bar{1}\bar{1}\bar{1}\}$ surfaces.

Experimental

Reactivity of the {111} Surfaces

Quantitative differences in reactivity between the A[1] and B surfaces were determined by measuring their etching rates. For this purpose, high-purity InSb samples were employed having exclusively A or exclusively B surfaces. They were actually tetrahedrons having as all four sides either only A or only B surfaces. Each set of A and B tetrahedrons was prepared from the same single crystal of InSb by grinding the surfaces to the proper orientation as determined by x-ray diffraction. The geometric relationship between an A and a B tetrahedron is shown in Fig. 2 and can be conveniently related to the diagram of Fig. 1.

At room temperature and above, the etching rates of both types of surfaces in a number of oxidizing media are controlled by the diffusion of the oxidizing species in solution to the surface of the sample as has been shown for InSb and for other III-V compounds (12). Consequently, no difference in rates is observed at these temperatures. However, the etch patterns of the two types of tetrahedrons are different since the nature of the attack is not necessarily a function of the dissolution rate. On the A tetrahedron dislocation etch pits appeared on all four sides whereas no dislocation etch pits appeared on the B tetrahedron. This experiment certainly eliminates the possibility that the etching behavior of the crystallographic surface under study is affected by adjacent surfaces of different orientation and chemical reactivity.

[1] For convenience, group III atoms will be designated as A atoms and group V atoms as B atoms; {111} surfaces terminating with A or B atoms will be designated as A or B surfaces, respectively.

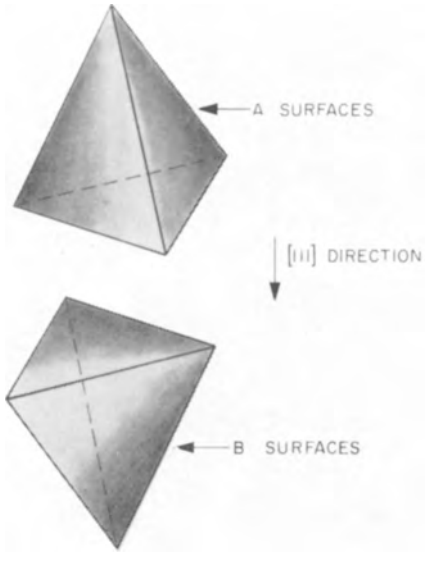

Fig. 2. Geometric relationship between tetrahedron A having exclusively group III atom surfaces, i.e., (111), $(1\bar{1}\bar{1})$, $(\bar{1}\bar{1}1)$, $(\bar{1}1\bar{1})$ and tetrahedron B having exclusively group V atom surfaces, i.e., $(\bar{1}\bar{1}\bar{1})$, $(\bar{1}11)$, $(1\bar{1}1)$, $(11\bar{1})$. Compare with Fig. 1.

The etching of both tetrahedrons proceeds at the same rate at 25°C with an activation energy of approximately 5 kcal, which is characteristic of diffusion-controlled dissolution processes (13, 14). At lower temperatures, however, the rates diverge, that of the A surfaces falling to one-tenth the rate of the B surfaces at 4°C. The activation energy associated with the etching of the A surfaces rises to approximately 25 kcal, which is characteristic of chemical activation-controlled processes, whereas the etching of the B surfaces remains diffusion-controlled. Clearly then, in the case of InSb, surfaces terminating with Sb atoms have a far greater tendency to react than those terminating with In atoms. This undoubtedly prevails at room temperature but cannot be detected by etching rate measurements since diffusion of the oxidizing species to the surface is the rate-determining step.

The above difference in reactivity was also confirmed by electrode potential measurements. InSb electrodes, one exposing an A surface and one exposing a B surface, were prepared from one single InSb crystal. In various etching media in the vicinity of 0°C, they exhibited significant differences in electrode potential (75 mv or greater). The electrode with the In surface was always more noble than that with the Sb surface, consistent with the rate measurements.[2] Electrodes prepared from different InSb ingots also showed the same potential difference as those prepared from the same ingot. On the other hand, electrodes with the same type of surface (either In or Sb) exhibited no potential difference within experimental error (5-10 mv).

Etching Characteristics

General Remarks.—Surface heterogeneities usually serve as centers for the initiation of preferential etching and etch pits. Such heterogeneities can result from cold work and from dislocations intersecting the surface. The morphological growth of etch pits or etch patterns, however, depends strongly on the nature of the chemical etchant. More often than not, slow acting etchants reveal surface heterogeneities (16). Fast etchants tend to dwarf local differences in surface reactivity and lead to chemical polishing.

In some instances virtually all of the dislocations can be revealed individually by employing slow etchants. The etch pit count can then serve for dislocation density determinations (17). In general, however, an etching agent which develops dislocation etch pits does not necessarily reveal all of the

[2] The dissolution rate of a metal in acid oxidizing media is usually determined by the reduction rate of the oxidizing agent (15), and the dissolution potential of the metal approaches its reversible value. This also applies to the present case, regardless of temperature. Thus, the more noble dissolution potential of the A surfaces clearly indicates that they have a lesser tendency to react than the B surfaces.

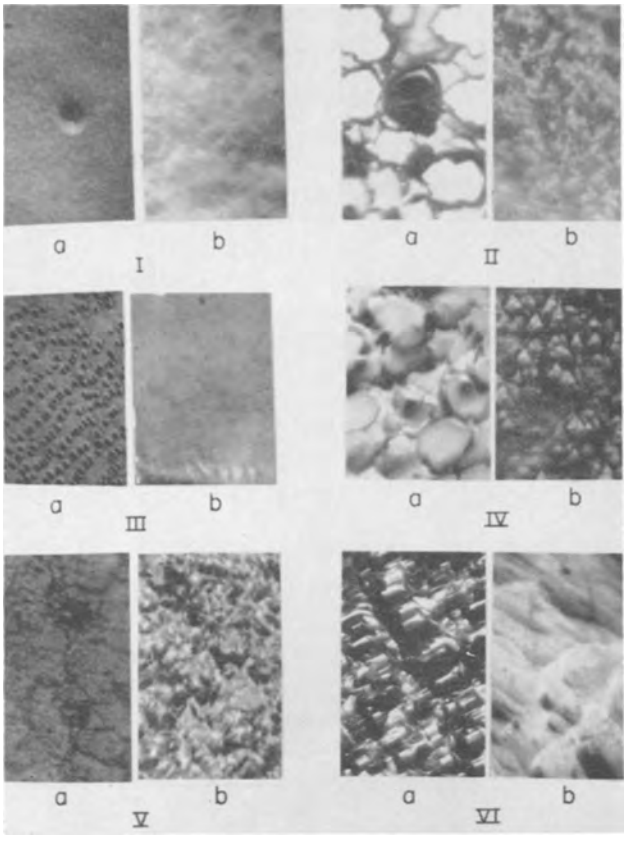

Fig. 3. {111} surfaces (a) terminating with group III atoms and $\{\bar{1}\bar{1}\bar{1}\}$ surfaces (b) terminating with group V atoms of III-V compounds. The compounds, the composition of the etchants in parts by volume, the etching time and temperoture are: I, InSb; 2 conc. HNO_3:1 conc. HF:1 glacial CH_3COOH; 4 sec; 25°C.(315X). II, InAs; 0.4N Fe^{+++} in conc. HCl; 30 min; 25°C (525X). III, GaSb; 2 conc. HNO_3:1 conc. HF:1 glacial CH_3COOH; 15 sec; 25°C (315X). IV, GaAs; 0.2N Fe^{+++} in 6N HCl; 10 min; 82°C (1500X). V, AlSb; 1 30% H_2O_2:1 conc. HF:1 H_2O; 1 min; 25°C, followed by 1 conc. HCl:1 conc. HNO_3; 2 sec; 25°C (525X). VI, InP; 0.4N Fe^{+++} in conc. HCl; 1.5 min; 25°C (525X). (All magnifications are before reduction for publication.)

dislocations terminating at a given surface. The fact that distinct dislocation etch pits have not been observed on the $\{\bar{1}\bar{1}\bar{1}\}$ planes certainly does not imply that these surfaces are not intersected by dislocations.

Dislocation etch pits.—In order to establish whether or not the appearance of dislocation etch pits on the A surfaces alone is a general phenomenon, several III-V compounds were studied under varied experimental conditions. InSb, GaSb, AlSb, InAs, GaAs, and InP in single crystal form and of relatively high purity were employed. The surfaces were ground to within 1 degree of the desired orientation as determined by x-ray diffraction. A variety of etching media (inorganic and organic acids) were employed, containing different oxidizing agents such as HNO_3, H_2O_2, Fe^{+++}, MnO_4^-, $Cr_2O_7^=$, Ce^{++++}, and $V(OH)_4^+$ at various concentrations. Etching experiments were performed for periods ranging from a few seconds to 2 hr and at temperatures up to 82°C. Under such varying conditions, a multitude of etch figures were obtained. In no instance, however, were dislocation etch pits observed on the B surfaces of any of the compounds. Dislocation etch pits were developed on the A surfaces of all six compounds. This occurred in many preferential etchants (leading to etch figures) as well as in nonpreferential etchants (leading primarily to chemical polishing). Representative examples for the compounds employed are shown in Fig. 3. It should be noted that etchants acting preferentially on the A surfaces showed preferential action on the B surfaces also, but did not reveal dislocation etch pits on the latter.

Etch figures on the {111} surfaces of InSb.—In some instances, the same etchant can act both preferentially and nonpreferentially depending on the reaction time and surface pretreatment. Figure 4 shows A surfaces of InSb etched in Fe^{+++} etchant for various times. It is noted that the dislocation etch pits grow with time. Although not shown, the dislocation etch pits for the cases corresponding to Fig. 4-VI and 4-VII were larger than those in Fig. 4-V. Simultaneously the etch figures grow in size and merge into each other. They are shallow at all times with relatively flat {111} bottoms and grow sidewise. It is believed that in this case, heterogeneities originally present in the abraded surface contribute greatly to the initiation of the patterns shown in Fig. 4-I. As the cold worked layer is removed, etching proceeds rather uniformly and eventually leads to a chemical polish except for the areas immediately adjacent to the dislocations. For the same etchant, the cold-worked layer is removed in shorter times by increasing the temperature and therefore the etching rate. Figure 5-I shows that a

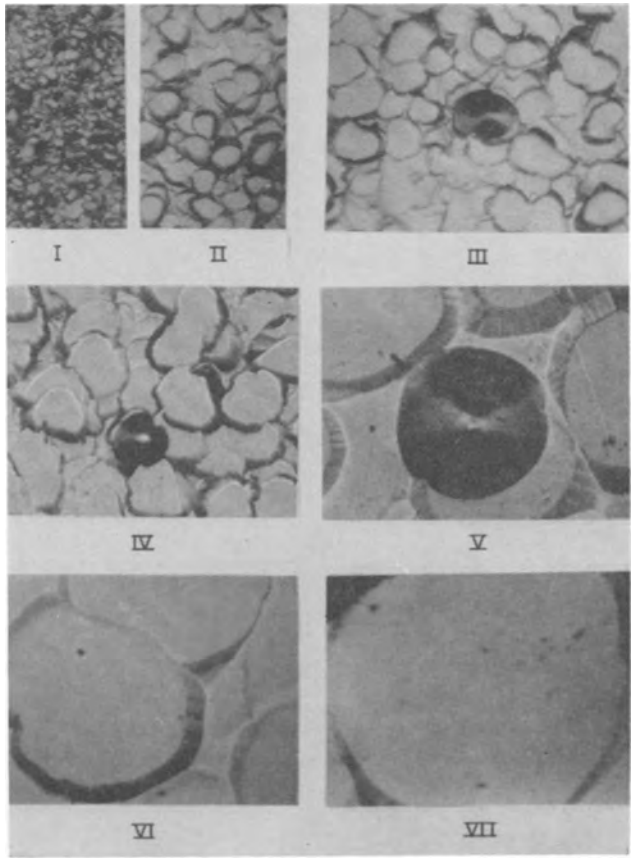

Fig. 4. {111} A surfaces of InSb etched in 0.4N Fe^{+++}—conc. HCl (515X) for various times. I, 5 min; II, 10 min; III, 15 min; IV, 20 min; V, 30 min; VI, 60 min; VII, 90 min.

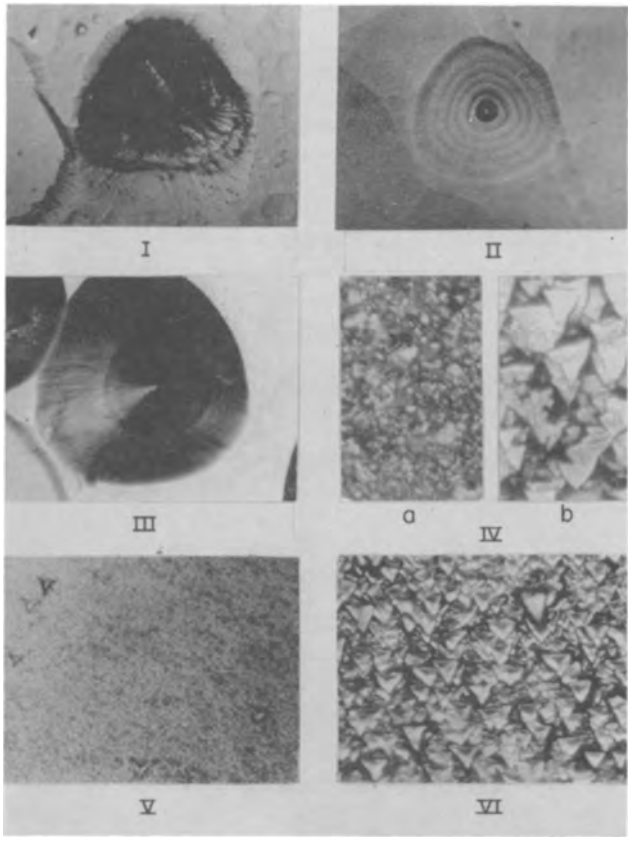

Fig. 5. {111} surfaces of InSb. I, Surface A etched for 5 min at 82°C in 0.4N Fe^{+++}— conc. HCl (515X). II and III, surface A etched for 4 sec in 2 conc. HNO_3:1 conc. HF:1 glacial CH_3COOH at 25°C, subsequently etched for 30 min in 0.4N Fe^{+++}—conc. HCl at 25°C (515X). IV, Surface B, etched for 5 min (a) and 90 min (b) at 25°C in 0.4N Fe^{+++}— conc. HCl (515X). V, Surface B of cases II and III (515X). VI, Surface B of case I (515X).

surface etched at 82°C for 5 min resembles that obtained at room temperature in 30 min. Consistent with this, essentially no preferential etch patterns appear if the surface is pretreated in a fast non-preferential etchant and subsequently etched by Fe^{+++}. Some dislocation etch pits, as the one shown in Fig. 4-II, did not form during the pretreatment with the fast etchant. Those developed during pretreatment (Fig. 5-II) grew further in the Fe^{+++} etchant (Fig. 5-III).

The etch patterns of the B surfaces persist longer than those of the A surfaces. It can be seen in Fig. 5-IV that in 90 min (Fig. 5-IVb) the growth of the etch figures on the B surface is appreciably less than the corresponding etch figures on the A surface of Fig. 4-VII. Figures 4-I and 5-IVa represent opposite sides of an {111} wafer; the same is true for Fig. 4-VII and 5-IVb for 5-II and 5-V, and finally for 5-I and 5-VI. Actually, in many cases, etch figures are revealed on the B surfaces while the A surfaces appear chemically polished.

Each side of the triangular patterns on the {111} surfaces is parallel to an <110> and perpendicular to a <211> direction. It is not uncommon for the A surfaces to develop hexagonal-type patterns with each of their sides again parallel to an <110> direction (Fig. 6-I). On occasion, the {110} planes develop intersecting the surface at an angle of 60°

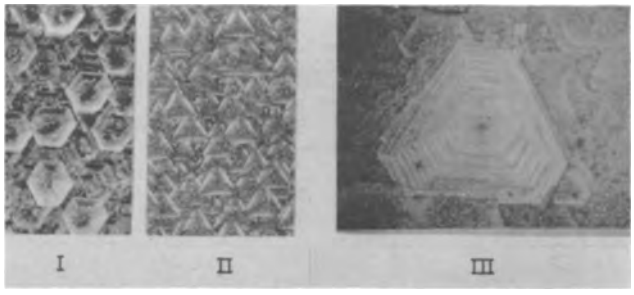

Fig. 6. {111} InSb surfaces etched for 30 min at 82°C in 0.2N Fe^{+++}—6N HCl. I, surface A (145X), II, surface B (145X), III, surface A (315X).

along the sides of the triangular or hexagonal patterns and lead to inverted pyramid-like etch patterns as can be seen in Fig. 6-I and to some extent in Fig. 6-II. An etch figure with a distinct terrace-like structure surrounding a dislocation etch pit is shown in Fig. 6-III.

Apparently, it is through the advancement of their sides that etch patterns grow. It will be recalled that at the temperature under consideration the over-all dissolution rate is the same for both A and B surfaces. The flat {111} bottoms of the etch figures on the A surfaces are not attacked as fast as the {110} planes mentioned above or any planes intersecting the surface at a steep angle along the sides of the etch figures. The chemical reactivity of the B surfaces on the other hand is much greater than that of the A surfaces. Consequently, the bottoms of the etch figures on the B surfaces are attacked appreciably, and their growth sidewise does not proceed as fast as on the A surfaces. This accounts for the fact that the etch figures of the A surfaces become rounded and grow faster than those of the B surfaces under the same experimental conditions. It is for the same reason that the etch figures of the B surfaces persist even under conditions under which the A surfaces appear chemically polished.

Discussion

Atomic Model for the A and B {111} Surfaces

Regarding the differences in behavior between A and B surfaces, it is proposed that the B surface atoms are very reactive chemically, since they are only triply bonded to the lattice, whereas their normal valence is five. Surface A atoms, also triply bonded to the lattice, must be appreciably less reactive since they are normally trivalent. The bond configuration of the zinc-blende structure (sp^3 tetrahedral hybrid orbitals) is illustrated schematically for the {111} direction (I). The formation of an A and a B surface (by a cut between planes AA

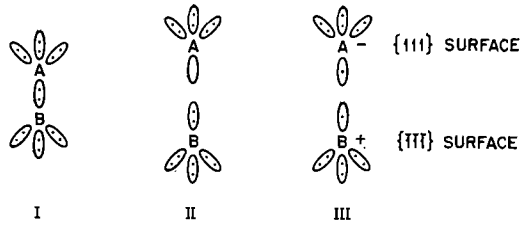

and BB of Fig. 1) can be represented as in II or III where both A and B atoms retain their tetrahedral

bond configuration. In II, atom B acquires both electrons; in III, atoms A and B acquire one electron each from the pair of electrons corresponding to the bond being broken. Case III is thermodynamically improbable since the ionization potential associated with the formation of B^+ is much greater than the electron affinity associated with the formation of A^-. Case II is considered as the most likely to occur as it leads to electrically neutral surfaces. In considering case II it is not possible to decide unambiguously whether or not A or B atoms are more reactive on the basis of the hybrid orbitals involved. However, it is reasonable to state that in etching processes where oxidizing (electrophilic) agents are involved, B atoms are more reactive than A because they have an unshared pair of electrons available for oxidation. Similarly, A atoms could possibly have a greater tendency to react with nucleophilic agents (unshared pair of electrons), but this case does not concern us at present.

The above valency or hybrid orbital model shows that B surface atoms should be more reactive than A in electrophilic ambients. Thus the model accounts for the observed differences between the A and B surfaces. It also accounts for the formation of dislocation etch pits on the A surfaces as shown below. The presence of the filled unshared electron orbitals on the B surfaces and the unfilled orbitals on the A surfaces points to pronounced differences in electronic phenomena between the two surfaces. These phenomena include surface conductivity, photoconductivity, surface recombination velocity, and others.

Obviously the model does not take into consideration possible surface states nor does it involve quantum mechanical aspects. However, it does account for the experimental results. A quantum mechanical verification should prove of considerable interest.

Edge dislocations in the zinc-blende structure.—It has been shown that in the zinc-blende structure, slip occurs on the {111} planes and along the <110> directions (5). The dislocation axis in this structure is parallel to the <110> direction and forms a 60° angle with the Burgers' vector (18). Considering the polarity of the zinc-blende structure it is apparent that α[3] and β dislocations can intersect both the A and the B surfaces. Venables and Broudy (5) showed that for InSb, only one type of dislocations leads to the formation of dislocation etch pits on the {110} and probably on the {111} surfaces. If their work is viewed in the light of Warekois' (11) identification of the crystallographic polarity of InSb the observed dislocations are α (In) dislocations. Atom models of 60° edge dislocations intersecting an {111} surface are shown in Fig. 7 and 8.

Since dislocation etch pits result from only one type of dislocations and since these pits do not develop on both the A and the B surfaces, it appears that elastic strains associated with edge dislocations in the III-V compounds do not play a significant role in etch pit formation. Rather, the formation of dislocation etch pits is controlled primarily by the specific chemical differences between the A and the B atoms on the {111} surfaces and at the dislocations as affected by their bonding characteristics along the polar <111> direction and the dislocation axis.

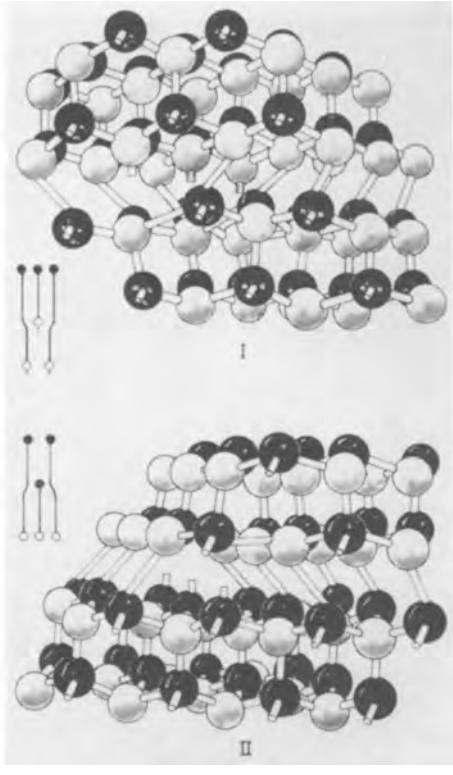

Fig. 7. Atom models showing a 60° edge dislocation intersecting the A surface. Surface of interest is defined by the atoms with protruding bonds. I, Dislocation terminating in a row of B atoms; II, dislocation terminating in a row of A atoms.

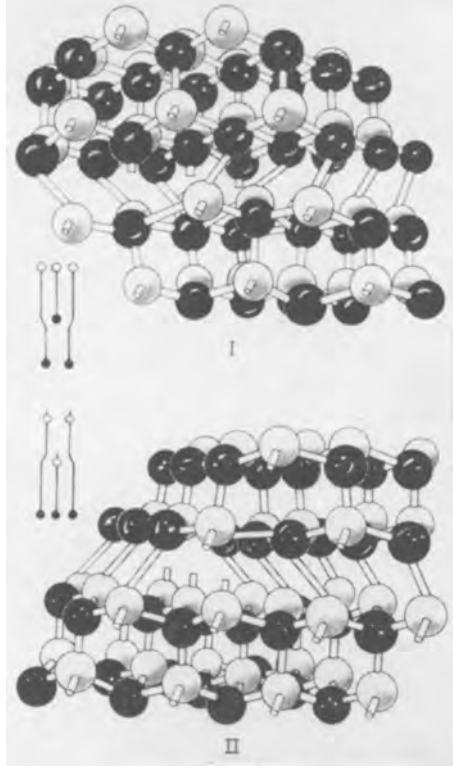

Fig. 8.Atom models of a 60° edge dislocation intersecting the B surface. Surface of interest is defined by the protruding bonds. I, Dislocation terminating in a row of A atoms; II, dislocation terminating in a row of B atoms.

[3] Dislocations with a row of triply bonded A atoms will be designated as α dislocations, and those with B atoms will be designated as β.

Etching and dislocation etch pit formation on the {111} surfaces.—Since both α and β dislocations intersect the A and the B surfaces, there are four possibilities: Aα, Aβ, Bα, and Bβ. As shown in Fig. 7 and 8 the α dislocations terminate with a divalent A atom (A_2) on the A surfaces and the β dislocations terminate with a divalent B atom (B_2) on the B surfaces. In the cases Aβ and Bα the terminal dislocation atom is trivalent (B_3 and A_3, respectively) and actually it does not lie in the outermost surface layer. Regarding the relative reactivities of the triply and doubly bonded surface atoms it is reasonable to state that $B_2 > B_3$ and $A_2 > A_3$ (it will be recalled that $B_3 > A_3$). Singly bonded A or B surface atoms are not being considered since such a surface configuration is unstable, as pointed out above. If it were stable, no difference in behavior would be expected between the A and the B surfaces. Finally, the quadruply bonded atoms immediately below the outermost surface layer are considered stable when compared with the triply bonded surface atoms.[4]

Etching and etch pit formation will be considered from an atomistic point of view. Although simplified, such an approach seems desirable at this time, particularly in dealing with covalent crystals.

Considering first {111} surfaces not intersected by edge dislocations (Fig. 1), it appears that the removal of triply bonded surface atoms (A atoms in the case of A surfaces and B atoms in the case of B surfaces) must be associated with the rate-determining step of the etching process. The atoms immediately below the outer surface atoms become singly bonded and, therefore, extremely unstable, as the outer surface atoms to which they are bonded are removed. It is because the outer surface atoms play such a significant role in the behavior of the {111} surfaces that major differences are observed between the A and the B surfaces.

The A and B surfaces intersected by edge dislocations are now considered:

Case Aα (Fig. 7-II).—The terminal A_2 atom of the dislocation is the first one to react. Then two B_3 adjacent atoms, which will react faster than any A_3 surface atoms, are exposed. As these B_3 atoms react, four A_2 surface atoms are exposed as well as an A_2 atom of the dislocation. Thus, it is apparent that the attack proceeds faster along the dislocation than over the rest of the surface leading to the formation of a dislocation etch pit.

Case Aβ (Fig. 7-I).—Strictly speaking the terminal B_3 atom of the dislocation does not belong to the outermost surface atom layer, and its role in the etching process is not expected to be of primary importance. Even if this B_3 atom is attacked before the A_3 surface atoms, then two A_2 surface atoms are exposed but the next atom of the dislocation remains bonded to three A_3 atoms. It is apparent from the diagram that in such a case the attack does not necessarily proceed preferentially along the dislocation, but rather in a layer-like fashion over the surface.

Case Bα (Fig. 8-I).—This case is in many respects similar to the Aβ case. Actually, the formation of dislocation etch pits is even less favorable here. The terminal atom of the dislocation is A_3 which is less reactive than the surface B_3 atoms.

Case Bβ (Fig. 8-II).—Although this case is analogous to Aα, it does not lead to the formation of dislocation etch pits. As the terminal dislocation atom B_2 is attacked, two A_3 atoms are exposed which will not react as fast as the B_3 surface atoms. These A_3 atoms delay the exposure of the next B_2 dislocation atom until the surrounding B_3 surface atoms are attacked. Hence, no preferential attack along the dislocation axis takes place.

[4] Surface configurations with "steps" and "kinks" will not be considered at this time. They will be treated in a future communication.

Summary

Dislocation etch pits were observed on the {111} surfaces terminating with group III atoms in six III-V intermetallic compounds (InSb, GaSb, AlSb, InAs, GaAs, and InP) in a number of etching solutions. In all six compounds no dislocation etch pits were observed on the {111} surfaces terminating with group V atoms. In addition to this difference, at low temperature the group III {111} surfaces exhibit appreciably smaller etching rates and more noble electrode potentials than the group V surfaces. Furthermore, etch figures develop on the group V surfaces in etchants which chemically polish the group III surfaces. This applies even under conditions in which both types of {111} surfaces exhibit the same etching rates.

An atomic model is proposed with unshared filled tetrahedral orbitals in the case of B surfaces and unfilled orbitals in the case of A surfaces. The model accounts for the observed differences between the two types of surfaces and points to further differences in electronic properties.

Acknowledgment

The authors are indebted to Mrs. M. J. Button for assisting with the experiments, to E. P. Warekois for identifying the surfaces by x-ray diffraction, and to Dr. A. J. Rosenberg for suggesting the use of tetrahedrons in determining the etching rates of the A and B surfaces.

Manuscript received Oct. 8, 1959. This paper was prepared for delivery before the Columbus Meeting, Oct. 18-22, 1959. The work reported in this paper was performed by Lincoln Laboratory, a center for research operated by Massachusetts Institute of Technology with the joint support of the U. S. Army, Navy, and Air Force.

Any discussion of this paper will appear in a Discussion Section to be published in the December 1960 JOURNAL.

REFERENCES

1. H. A. Schell, *Z. Metallkunde*, **48**, 158 (1957).
2. J. W. Allen, *Phil. Mag.*, **2**, 1475 (1957).
3. W. Bardsley and R. L. Bell, *J. Electron*, **3**, 103 (1957).
4. M. C. Lavine, A. J. Rosenberg, and H. C. Gatos, *J. Appl. Phys.*, **29**, 1131 (1958).
5. J. D. Venables and R. M. Broudy, *ibid.*, **29**, 1025 (1958).
6. R. E. Maringer, *ibid.*, **29**, 1261 (1958).
7. J. F. Dewald, *This Journal*, **104**, 244 (1957).
8. P. Haasen, *Acta Met.*, **5**, 598 (1957).
9. E. P. Warekois and P. H. Metzger, Pittsburgh Diffraction Conference Abstracts, p. 48, November 1958; *J. Appl. Phys.*, **30**, 960 (1959).
10. J. G. White and W. C. Roth, *J. Appl. Phys.*, **30**, 946 (1959).
11. E. P. Warekois, Unpublished results.

12. M. C. Lavine, A. J. Rosenberg, and H. C. Gatos, To be published.
13. M. B. Abramson and C. V. King, *J. Am. Chem. Soc.*, **61**, 2290 (1939).
14. W. W. Harvey and H. C. Gatos, *This Journal*, **105**, 654 (1958).
15. H. C. Gatos, *Corrosion*, **12**, 322 (1956).
16. H. C. Gatos, W. W. Harvey, and M. C. Lavine, *Rev. Met.*, **55**, 1149 (1958).
17. S. A. Kulin and A. D. Kurtz, *Acta Met.*, **2**, 354 (1954).
18. W. T. Read, Jr., *Phil Mag.*, **45**, 775 (1954).

Etching Behavior of the {110} and {100} Surfaces of InSb

Harry C. Gatos and Mary C. Lavine

Lincoln Laboratory, Massachusetts Institute of Technology, Lexington, Massachusetts

ABSTRACT

Preferential and nonpreferential etching characteristics of the {110} and {100} surfaces of InSb were investigated. Since {111} facets develop in the etch figures of these surfaces, the morphology of the etch figures reflects the crystallographic polarity of InSb along the <111> directions. Dislocation etch pits were found both on the {110} and on the {100} surfaces. The role of the relative reactivities of the various crystallographic planes in the over-all etching behavior of InSb and the effect of cold work are discussed.

InSb and other III-V intermetallic compounds with the zinc-blende structure have two types of {111} surfaces, i.e., one type terminating with group III atoms (A surfaces) and one terminating with group V atoms (B surfaces). The two types of surfaces, resulting from the crystallographic polarity of the <111> directions, exhibit markedly different physical chemical properties (1). Thus, it was found that the B surfaces of InSb are far more reactive than the A surfaces in oxidizing (electrophilic) agents. It is expected that the same applies to the {111} surfaces of the other III-V intermetallic compounds. This difference in reactivity was shown responsible for the fact that dislocation etch pits appear on the A surfaces and not on B surfaces of six III-V compounds investigated (InSb, GaSb, AlSb, GaAs, InAs, InP).

Since the zinc-blende structure exhibits no polarity in the <110> and <100> directions, no differences in behavior are expected among the various {110} surfaces or the various {100} surfaces. It will be shown, however, that in certain etchants {111} facets develop on the {110} and {100} surfaces, and consequently the <111> polarity of zinc-blende structure is reflected in the etching behavior of these surfaces.

It is the purpose of the present paper to demonstrate the role of the <111> crystallographic polarity on the etching behavior of the {110} and {100} surfaces of InSb and show that this behavior is consistent with the atomic model proposed to explain the relative reactivities of the A and B surfaces of the III-V intermetallic compounds (1). The effects of surface heterogeneities introduced by cold work are also discussed.

{110} Surfaces

In the present study wafers used were cut from high-purity InSb single crystals. The parallel sides of the wafers were ground to within 1° from the {110} orientation as determined by x-ray diffraction. Before etching they were ground with 1600 mesh garnet powder.

Two types of etchants were employed: (*a*) preferential etchants leading to the formation of etch figures, and (b) fast nonpreferential etchants resulting in the formation of dislocation etch pits on an otherwise chemically polished surface. A number of nonpreferential etchants can be employed successfully; among various preferential etchants studied the one consisting of 0.2*N* Fe^{+++} ions in 6*N* HCl was found the most suitable.

Typical results obtained with the preferential etchant are shown in Fig. 1-I. Upon cursory exami-

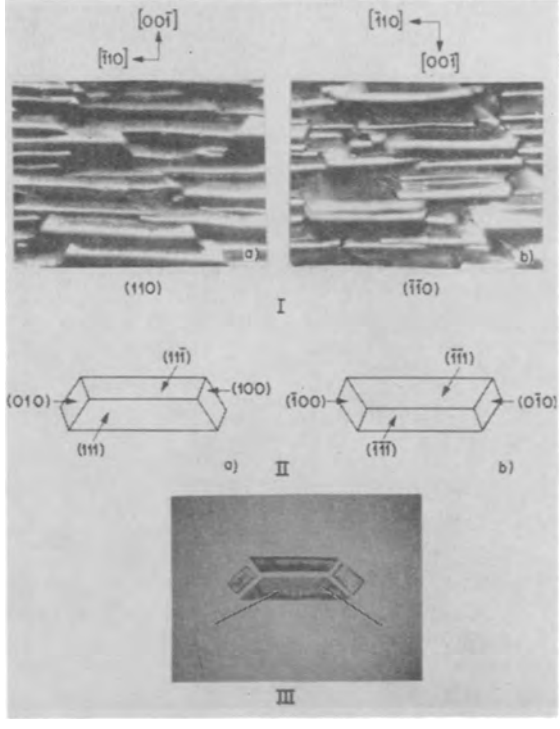

Fig. 1. Etch figures on {110} surfaces of InSb developed with 0.2N Fe^{+++} in 6N HCl at 82°C. I, opposite faces of an {110} wafer, 1500 X. II, schematic diagram of individual etch figures. III, exploded view of an etch figure; each facet was photographed individually while positioned parallel to the field of observation; arrows point to dislocation etch pits (approx. 800 X). (All magnifications are before reduction for publication.)

nation no difference is apparent between the two etched sides (Ia and Ib) of these wafers. Goniometric analysis of the etch figures shows that their elongated facets are {111} planes bounded by {100} planes as illustrated schematically in Fig. 1-II. The planes designated as (111) and $(\bar{1}\bar{1}1)$ are A planes whereas those designated as $(11\bar{1})$ and $(\bar{1}1\bar{1})$ are B planes. It can be seen that in an etch figure the A planes develop to a greater extent being less reactive than the B planes. As a result of this, and by considering the geometry of the zinc-blende structure and the relative position of the A and B planes (1), the trapezoid-like figures on the opposite {110} faces should appear inverted when the wafer is rotated about the $[\bar{1}10]$ direction as it can be seen clearly in Fig. 1-II.

The difference in size between the A and B facets of the etch figures varies according to the etching conditions. If the {110} surfaces are exposed to the preferential Fe^{+++} etchant without first removing the cold worked layer introduced by abrasion, the difference in over-all size between the A and B planes is not very pronounced. However, if the cold worked layer is removed by a fast nonpreferential etchant and then the surface is etched with the Fe^{+++} etchant, the A planes essentially predominate over the B planes and the {110} surfaces acquire a scale-like (shingle-like) appearance.

It was considered of interest to find out whether or not the etching behavior of the microscopic A and B facets of the etch figures resembles that of the A and B surfaces of InSb. It was possible to develop dislocation etch pits on the A facets of the etch figures but not on B facets, in accord with the behavior of ordinary A and B surfaces. Furthermore, the A and B facets of the etch figures were unambiguously distinguishable by their over-all appearance which was typical of the A and B surfaces, respectively, etched in the Fe^{+++} etchant. It should be pointed out that the A and B facets are best examined microscopically when positioned parallel to the field of observation. They form a 35° angle with the {110} surface. In the present case an ordinary metallograph was employed and the {110} wafers were positioned at the appropriate angles by means of suitable platforms. An exploded view of an etch figure is shown in Fig. 1-III. The arrows in the A facet point to dislocation etch pits.

Nonpreferential etching revealed distinct dislocation etch pits in a background of chemically polished

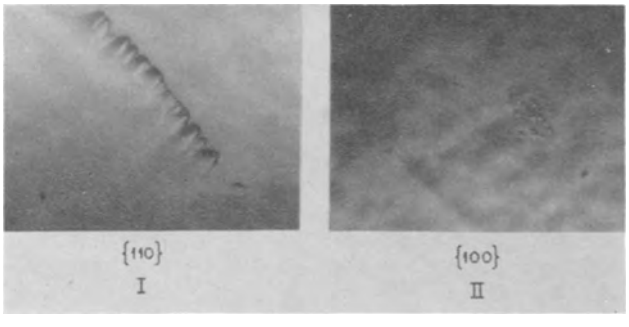

Fig. 2. Dislocation etch pits on the {110} and {100} surfaces (540 X). Etchant (in parts by volume): 5 conc. HNO_3; 5 conc HF; $2H_2O$.

Table I. Etching rates of various crystallographic planes of InSb

Plane	Etching rate	
	Etchant 1, mg/cm²/min	Etchant 2, mg/cm²/sec
{111}—B	0.2_5	7.8
{100}	0.2_2	7.8
{110}	0.2_6	2.5
{111}—A	0.2_3	0.5

Etchant 1: 0.2*N* Fe^{+++} in 6*N* HCl; 10°C; Etchant 2: in parts by volume, 2 conc. HNO_3; 1 conc. HF; 1 glacial CH_3COOH; 4°C.

{110} surface as shown in Fig. 2-I. The over-all etching rate of the {110} surfaces was determined by employing samples bounded entirely by {110} surfaces. Results are shown in Table I together with rates of the A, B, and {100} surfaces. It is seen that in the Fe^{+++} etchant the various surfaces exhibit essentially the same etching rate since, in this case, the over-all etching process is controlled by the transport of oxidizing species of the etchant to the InSb surface. Consequently, no conclusions can be drawn about the relative reactivity of the various surfaces. In the nonpreferential etchant, at 4°C, the A surfaces exhibit the lowest rate. Under these conditions etching of the A and the {110} surfaces is under chemical activation control (activation energy approximately 25 kcal/mole) whereas etching of the B and the {100} surfaces is under diffusion control (activation energy approximately 5 kcal/mole). These results are discussed further below.

{100} Surfaces

The {100} wafers employed in these experiments were prepared as the {110} wafers. As shown in Fig. 2-II, dislocation etch pits are revealed by nonpreferential etching, but they are appreciably smaller than the etch pits developing on the A or even the {110} surfaces under similar experimental conditions. Dislocation etch pits on the {100} surfaces of InSb or other III-V intermetallic compounds have not been reported in the literature. Yet, {100} surfaces like the {111} and {110} surfaces are intersected by the 60° edge dislocations of the zinc-blende structure.

On the {100} surfaces of InSb preferential etchants develop etch figures which are similar to those reported for GaAs (2). Figures 3-Ia and 3-Ib show the preferentially etched parallel surfaces of an {100} wafer. It is seen that the longer dimension of the rectangular etch figures on the one side of the {100} wafer is at a right angle to the longer dimension of the etch figures on the opposite side of the wafer. The etch figures are bounded by <110> directions.

Goniometric examination revealed that the etch figures are truncated tetragonal pyramid structures, the four sides being {111} planes. The top plane of the truncated pyramid is either flat {100} or has higher order planes (usually {411}) forming a shallow angle (approximately 19°) with the <100> direction. Between individual truncated pyramids occasionally pits are observed which are inverted pyramid-like depressions with flat {100} bottoms. The geometry of the etch figures is shown in Fig.

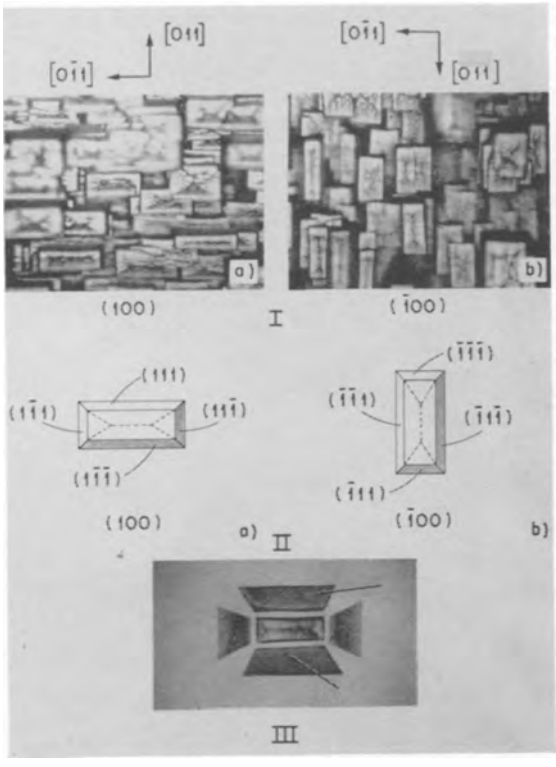

Fig. 3. Etch figures on {100} surfaces of InSb developed in 0.2N Fe^{+++} 6N HCl at 82°C. I, opposite faces of an {100} wafer, 1500 X. II, schematic diagram of individual etch figures; higher order planes occasionally present are indicated with dotted lines. III, exploded view of an etch figure; each facet was photographed individually while positioned parallel to the field of observation; arrows point to dislocation etch pits (approx. 800 X).

3-II. Here also the A facets [(111), ($\bar{1}$1$\bar{1}$), (1$\bar{1}\bar{1}$), and ($\bar{1}\bar{1}$1)] of the etch figures develop to a greater extent than the B facets [($\bar{1}$11), (1$\bar{1}$1), (11$\bar{1}$), and ($\bar{1}\bar{1}\bar{1}$)] and the etch figures appear as rectangular parallelograms rather than squares when viewed parallel to the <100> direction.

With techniques similar to those employed in the case of the {110} surfaces it was possible to develop and record conical dislocation etch pits on the A facets of the etch figures and to reveal on the individual facets the typical appearance of preferentially etched A and B surfaces. An exploded view of an etch figure is shown in Fig. 3-III. The arrows in the A facets point to dislocation etch pits.

If the cold-worked layer of the {100} surfaces is removed by chemical polishing prior to preferential etching the A facets develop to a much greater extent than the B facets. In addition the flat {100} facets are not developed and the etch figures become elongated structures as shown in Fig. 4.

The over-all etching rates of the {100} surfaces shown in Table I were obtained with samples bounded entirely by {100} surfaces.

Discussion

The development of certain crystallographic planes during crystal growth, as well as the distribution and morphology of etch figures, is associated with mechanisms which constitute a complex and controversial problem. The present results contribute to the elucidation of one of the aspects of

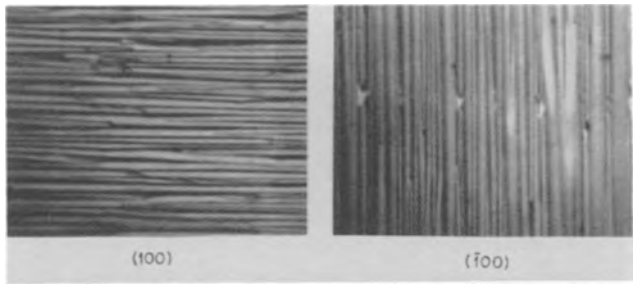

Fig. 4. Opposite faces of an {100} wafer of InSb etched with 0.2N Fe^{+++} in 6N HCl at 82°C following removal of the abraded surface in a nonpreferential etchant (1500 X).

this problem, i.e., the role of relative reactivity of the various crystallographic planes in the formation of dislocation etch pits and the morphology of etch figures. Of particular interest in the present case is the fact that two types of crystallographically equivalent {111} planes are involved.

In the case of InSb it was shown conclusively that in oxidizing etchants the A surfaces are far less reactive than the B surfaces [see Table I and also ref. (1)]. This difference in reactivity was considered the controlling factor for the observed differences in etching behavior between these two types of surfaces and in particular for the formation of dislocation etch pits on the A surfaces and not on the B surfaces. In the present study it was possible to confirm these differences in behavior on microscopic A and B facets of individual etch figures.

Differences in etching rates among the various surfaces of InSb are masked in many oxidizing media, as in the case of the Fe^{+++} etchant (Table I), since the etching rates are controlled primarily by transport processes in the etchant, even at low temperatures. However, as evidenced by the results of Table I for the nonpreferential etchant, it is believed that the reactivity of the principal crystallographic planes of InSb decreases in the following order (3)

$$B\ \{111\} \gtrsim \{100\} > \{110\} > A\ \{111\}$$

The {110} surfaces have both A and B atoms triply bonded to the lattice and, therefore, are more reactive than the A surfaces but less reactive than the B surfaces. Ideally {100} surfaces can consist of either A or B atoms; however, real {100} surfaces consist of both A and B atoms which are only doubly bonded to the lattice. Consequently the {100} surfaces are more reactive than the {110} surfaces. This reasoning does not show clearly whether or not the {100} surfaces are less reactive than the B surfaces. Doubly bonded B atoms are more reactive than triply bonded B atoms but doubly bonded A atoms are most likely less reactive than triply bonded B atoms (1). As will be pointed out below, however, the reactivity of the {100} surfaces is probably somewhat smaller than that of B surfaces.

For a dislocation etch pit to develop (or an etch pit in general) it is necessary that etching proceeds faster in the direction of the pit than on the surface surrounding it. It was shown (1) that this condition is met in oxidizing media only when dislocations consisting of a row of triply bonded A

atoms (α dislocations) intersect the A surfaces of III-V compounds. Apparently, in the zinc-blende structure, the elastic strains present in the direction of the dislocations do not enhance the reactivity to an appreciable extent under the present etching conditions. The conical etch pits presently observed on the {100} surfaces are attributed to dislocations on the basis of their morphology, which is typical of dislocation etch pits in the diamond and zinc-blende structure, and because rows of such etch pits were observed along low angle boundaries on the {100} surfaces. Like the etch pits of the A and {110} surfaces, the etch pits of the {100} surfaces are also believed to be due to α and not due to β dislocations [cf. ref. (4)].

By employing suitable InSb cylinders Venables and Broudy (4) found that dislocation etch pits become smaller in going from the {111} to the {110} surfaces. They reported no dislocation etch pits on the {100} surfaces. The conditions for dislocation etch pit formation on the {110} surfaces are not as favorable as on the A surfaces where the relatively low reactivity of the A surface atoms is essentially responsible for the formation of pits. The high reactivity of the atoms of the {110} surfaces and especially of the {100} surfaces prevents pronounced preferential attack along the dislocation axis.

The etch figures appearing during preferential etching of InSb surfaces consist of low indexed crystallographic facets and represent limiting etch forms. The elongated shape of the etch figures of the {100} surfaces (Fig. 4) is the result of the very high reactivity of the B planes. On both the {110} and {100} surfaces the more reactive B {111} facets develop to a lesser extent than the A facets. Since slow reacting planes predominate during etching of concave surfaces, the development of the etch figures is probably preceded by the formation of concave etch pits. No effort was made to follow the growth steps of the etch figures under the present, very rapid etching rates.

As in the case of {111} surfaces of InSb (1) here also cold work modified the preferential etching behavior. Cold-worked surfaces develop better defined etch figures than the surfaces from which the cold work has been removed (compare for example Fig. 3-I and 4). Actually in the case of {111} surfaces it was found that certain etchants act preferentially when cold work is present and lead to chemical polishing in the absence of cold work. Cold-worked surfaces are heavily populated with imperfections such as complex networks of dislocations, presenting numerous high energy centers which react appreciably faster than the rest of the surface and lead to the formation of etch pits.

Since the thickness of the cold-worked surface layer is estimated to be of the order of a few microns, these pits do not propagate to any great extent but rather develop into the steady-state shape of the etch figures. The observed excessive overlapping of the etch figures (Fig. 1 and 2) is suggestive of the multitude of centers for the initiation of etch pits. The varying size of these primary etch pits is very likely responsible for the varying dimensions of the etch figures. High reactivity centers for pit nucleation are present in all real surfaces but obviously to a much lesser extent than in those with a damaged layer. If active centers are assumed as necessary for the initiation of etch pits which develop into etch figures, then no etch figures should be expected to form on a flat, imperfection-free surface [cf. ref. (5)]. Such surfaces are not encountered in reality.

Cold work usually results in enhanced reactivity. In the case of the {100} surfaces the enhanced reactivity of the A and B planes decreases the difference in their reactivities and, thus, the etch figures of the {100} surfaces become rectangular as shown in Fig. 3 rather than elongated shapes as shown in Fig. 4.

From the experimental results and the preceding discussion it is apparent that the formation of dislocation etch pits and the over-all morphology of the etch figures is strongly affected by the relative reactivity of the principal crystallographic planes.

Manuscript received Oct. 8, 1959. This paper was prepared for delivery before the Columbus Meeting, Oct. 18-22, 1959. The work reported in this paper was performed by Lincoln Laboratory, a center for research operated by Massachusetts Institute of Technology with the joint support of the U. S. Army, Navy, and Air Force.

Any discussion of this paper will appear in a Discussion Section to be published in the December 1960 JOURNAL.

REFERENCES

1. H. C. Gatos and M. C. Lavine, *This Journal*, **107**, 427 (1960).
2. H. A. Schell, *Z. Metallkunde*, **48**, 158 (1957).
3. See also M. C. Lavine, A. J. Rosenberg, and H. C. Gatos, *J. Appl. Phys.*, **29**, 1131 (1958).
4. J. D. Venables and R. M. Broudy, *ibid.*, **29**, 1025 (1958).
5. A. P. Honess, "The Nature, Origin and Interpretation of the Etch Figures on Crystals," pp. 33-37, John Wiley & Sons, Inc., New York (1927).

Polarographic Reductions of Benzyl Halides

Leland W. Marple, Leif E. I. Hummelstedt,[1] and L. B. Rogers

Department of Chemistry and Laboratory for Nuclear Science, Massachusetts Institute of Technology, Cambridge, Massachusetts

ABSTRACT

A polarogram for benzyl chloride in a supporting electrolyte of lithium chloride has a dip in the limiting current due to electrostatic repulsion from the interface of the monovalent anion produced by transfer of the first electron. The dip is decreased by the presence of electronegative substituents on the ring and is eliminated by a moderate concentration of surface-active tetramethylammonium ions in the solution.

Benzyl bromide and iodide each undergo two widely separated one-electron reduction steps at concentrations less than $10^{-4}M$. At higher concentrations, adsorption phenomena are encountered in the region of potential between the two waves due to the presence of bibenzyl, a by-product of the first reduction step.

The exploratory work of von Stackelberg and Stracke (1) showed that reductions of organic halogen compounds became easier on going from chloride to bromide to iodide. The over-all reaction usually involved replacement of the halogen atom with a hydrogen atom. The half-wave potentials were independent of *p*H, showing that addition of hydrogen did not occur in the rate-determining step, but after the transfer of electrons.

The steps in the polarographic reduction of an organic halogen compound, RX, can be represented by the following reactions (1, 2):

$$RX + e^- \rightarrow RX^- \quad [1]$$

$$RX^- \rightarrow R\cdot + X^- \quad [2]$$

$$R\cdot + e^- \rightarrow R^- \quad [3]$$

$$R^- + H_2O \rightarrow RH + OH^- \quad [4]$$

In some cases, side reactions (1),

$$2\,R\cdot \rightarrow R:R \quad [5]$$

or (3)

$$RX + Hg \rightarrow RHgX \quad [6]$$

are known to occur. It is generally assumed that addition of the first electron is the slow step and that reactions [2], [3], and [4] are relatively rapid because only one wave is usually observed for each halogen atom replaced.

Most aliphatic halogen compounds appear to reduce like carbon tetrachloride, for which no stable intermediates (ions or radicals) are believed to exist. Although the over-all reaction usually involves replacement of the halogen with a hydrogen atom, in the reduction of 1,2-dibromoethane, the principal product is reported to be ethylene (1). This reduction must involve virtually simultaneous transfer of two electrons, followed by elimination of two bromide ions and formation of a double bond. Normally, formation of a divalent negative intermediate must be considered improbable.

We felt that the addition of an aromatic ring to the carbon having the halogen atom, or the presence of a double bond in the 2-position should tend to increase the stability of intermediates in the reduction process. This was indeed found to be so. The first intermediate formed by benzyl chloride, the monovalent negative ion, $[C_6H_5CH_2Cl]^-$, appears to have a relatively long life-time. The chief evidence for the existence of such a long-lived intermediate is the appearance of a dip in the limiting current plateau. (Ring-substituted derivatives of benzyl chloride also have dips in their polarograms.) Similar dips in the polarograms for inorganic anions have been studied extensively by Frumkin and his coworkers (3, 5). It is generally agreed that the phenomenon is the result of electrostatic repulsion of a reducible anion from the negative electrode surface.

Current dips were not observed for either benzyl bromide or iodide. Instead, the present study indicates that a long-lived neutral species, either a stable free-radical or a dimer is formed. Mass-spectrometric evidence has confirmed the latter. The only other case where a stable product of a one-electron transfer has been reported is that for reductions of allyl mercury halides (3).

Results

Benzyl Chloride

The polarogram for this compound conformed to the general description of the process for the removal of a halide insofar as a single wave was obtained and its position was relatively independent of *p*H (see Fig. 1). Unlike most organic halides, its polarogram had a marked dip in the limiting-current plateau, a phenomenon that was observed under a variety of conditions. The dip was eliminated by the presence of $0.07M$ tetramethylammonium ion. Because dips in the limiting currents of anions are similarly affected, a negatively charged species of relatively long lifetime must be involved.

The polarograms can be explained by assuming that the limiting current prior to the onset of the

[1] Present address: Eastern Laboratory, E. I. du Pont de Nemours & Co., Inc., Gibbstown, N. J.

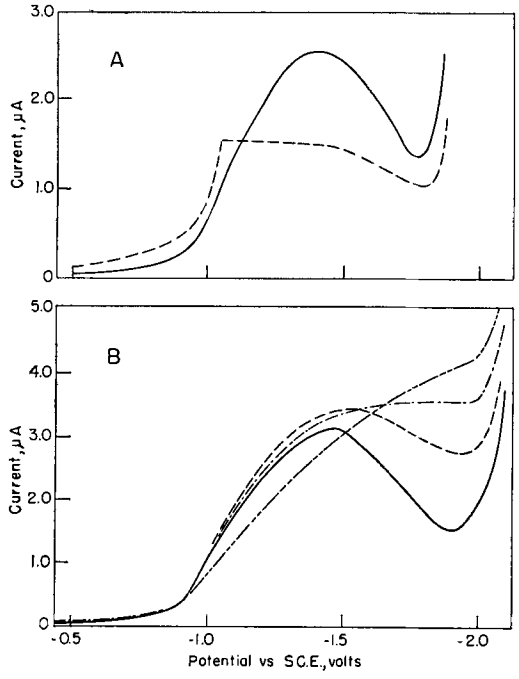

Fig. 1A. Polarograms of 1.17 x 10^{-3} M benzyl chloride in 0.092M NaOH. - - - - in 2.0% methanol; ——— in 51.0% methanol. Fig. 1B. Effect of $(CH_3)_4$ NCl on polarograms of 1.04 x 10^{-3} M benzyl chloride in 51.0% CH_3OH and 1.0M LiCl. ——— No $(CH_3)_4$ NCl added; - - - - - 0.030M $(CH_3)_4$ NCl; — · — · — · 0.070 M $(CH_3)_4$ NCl; — · · — · · — 0.47M $(CH_3)_4$ NCl.

dip corresponds to a two-electron transfer. As the potential of the electrode becomes more cathodic, progressively more of the product formed by reaction [1] is repelled from the surface of the electrode before reaction [2] (followed by [3] and [4]) can take place. In the presence of tetramethylammonium ion, however, repulsion of the ion is not as significant so that reaction [2], and those that follow, can proceed to completion. In that connection, it is interesting to note that the presence of calcium ion (0.49*M*) had no effect on the current dip. According to Reinmuth (6), this indicates that ion-pair formation is not the primary effect, but instead the structure of the double-layer. In addition, a temperature increase to 35°C, which would favor more rapid dissociation of the intermediate ion, did eliminate the dip.

There are two additional points of interest in connection with the effect of tetraalkylammonium salts. First, von Stackelberg and Stracke, in their broad survey of the polarography of organic halides, used 0.1*M* tetraethylammonium bromide as a background electrolyte. As a result, they observed no dips in their limiting currents. Second, in the present investigation it was found that large amounts of tetraalkylammonium salts produced a cathodic shift in the wave (Fig. 1) which was attributed to blocking of the electrode surface (7-9). Hence, the use of tetraalkylammonium salts to eliminate such current dips may result in shifts of the half-wave potential in either direction (2, 10).

In the case of benzyl chloride, the dip in the limiting current reached a value approximately one-half the maximum, indicating complete repulsion

Table I. Compounds exhibiting dips in the limiting current plateau in 1.0M LiCl and 51.0% CH_3OH

Compound	Conc, moles/liter	"$E_{1/2}$" v vs. S.C.E.	$\frac{i_{min}}{i_{max}}$
Benzyl chloride	1.04×10^{-3}	—1.066	0.45
α-Chloro-p-xylene	1.44×10^{-3}	—1.071	0.47
α, o-Dichlorotoluene	1.57×10^{-3}	—0.923	0.75
α, p-Dichlorotoluene	1.40×10^{-3}	—1.011	0.64
α, 2, 4-Trichlorotoluene	1.40×10^{-3}	—0.898	0.94
α, 3, 4-Trichlorotoluene	1.40×10^{-3}	—0.908	0.87
1-(Chloromethyl) naphthalene	8.3×10^{-4}	—0.953	0.85

of the organic ion. The fact that the value for limiting current was not corrected for a change in $m^{2/3}t^{1/6}$ with potential probably accounts for a ratio slightly smaller than 0.5. At potentials of —1.3, —1.5, and —1.7 v, the current proved to be diffusion controlled. Furthermore, the relative size of the dip appeared to be independent of concentration as low as $10^{-5}M$ where the correction for residual current was larger than the reduction current.

In Table I are listed the results on other related compounds which showed current dips. Note that the compound having two chlorine atoms in the ring gave the smallest dip, the compound with one chlorine in the ring, next. There may be many contributing factors but, in this case, the chief factor appears to be the greater distribution of charge which decreases the repulsion of the anion by the electrode. This hypothesis is supported by the smaller dip found on going from a benzene ring to a naphthalene ring. Furthermore, the presence of only 0.01*M* tetramethylammonium ion was sufficient to eliminate the small dip obtained with α-chloromethyl naphthalene.

Substitution in the ortho position appears particularly efficient in decreasing the dip. This suggests that there is a steric factor that aids the elimination of chloride ion.

Finally, Table I indicates that the presence of a larger number of chlorine atoms on the ring appears to produce a less cathodic half-wave potential. However, it should be pointed out that the locations of the waves are strongly influenced by adsorption.

The presence of adsorption effects is clearly evidenced in the original polarograms for benzyl chloride, particularly in low percentages of methanol. The dashed curve in Fig. 1A was obtained in 2% methanol. During the drawn-out initial portion of the wave, the individual drop shapes were quite characteristic of adsorption. Following the gradual rise at the beginning of the polarographicwave, the current increased rapidly to the limiting-current plateau. Much the same behavior was found in 20% methanol, but at 51% methanol adsorption behavior had almost disappeared. At 80% there was no evidence for adsorption either in the individual drop shapes or in the polarograms as a whole. All of the compounds in Table I showed similar adsorption behavior although most of them showed more evidence of it in 51% methanol than did benzyl chloride. Adsorption effects will be discussed later in more detail.

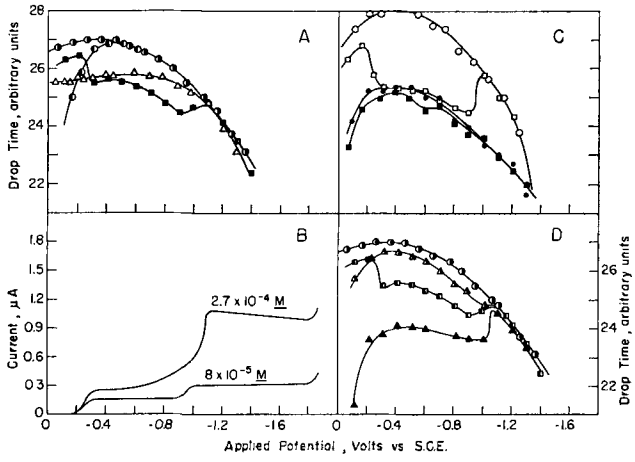

Fig. 2. Effects on electrocapillary curves of supporting electrolyte, solvent composition, and reducible species. Supporting electrolyte only.
Open circle, 2% MeOH-0.092 N NaOH; circle, solid right half, 51% MeOH-0.092 N NaOH; circle, solid left half, 51% MeOH-0.100 N KBr; solid circle, 80% MeOH-0.092 N NaOH.
Benzyl bromide ,1.13 x 10^{-3}M. open square, 2% MeOH-0.092 N NaOH; square, solid left half, 51% MeOH-0.092 N NaOH; solid square, 80% MeOH-0.092 N NaOH.
Open triangle, Bibenzyl, 2.83 x 10^{-4}M in 51% MeOH-0.092N NaOH; triangle, solid right half, benzyl chloride, 1.40 x 10^{-3}M in 51% MeOH-0.092N NaOH; solid triangle, benzyl iodide, 0.85 x 10^{-3}M in 51% MeOH-0.092N NaOH.

Benzyl Bromide and Benzyl Iodide

While polarograms for benzyl bromide had no current dips, they did show two distinct reduction steps at concentrations from 1 x 10^{-5} to about 1 x $10^{-4}M$. Only below 1 x $10^{-4}M$ were two diffusion-controlled waves of equal height obtained. A typical polarogram is shown in Fig. 2B.

It is clear that each wave must correspond to a one-electron reduction. The first wave must be due to formation of the monovalent ion. The large separation of the first and second waves indicates that the radical produced by decomposition of the monovalent ion is not easily reduced further, probably because of a rapid conversion to bibenzyl according to Reaction 5. The absence of a current dip in the plateau of the second wave indicates that decomposition of the monovalent ion is, as expected, much faster in the case of the bromine compound than for chlorine.

The behavior of benzyl iodide, at concentrations between 1 x 10^{-5} and 2 x $10^{-4}M$, was virtually identical with that of benzyl bromide. Not only were two diffusion-controlled waves of equal height obtained but, in addition, the half-wave potentials for the first and second waves agreed, within experimental error, with the values obtained for benzyl bromide. Again, no dip in the limiting current was observed.

At concentrations higher than about $10^{-4}M$, the first waves of both benzyl bromide and benzyl iodide did not increase with concentration as fast as the second. Although the limiting current for the second wave had normal drop shapes and continued to be diffusion controlled, the shapes of the tracings for individual drops became increasingly characteristic of strong adsorption in the range of potential covered by the first wave. Changes in limiting current with mercury height gave plots falling between diffusion and adsorption control. The limiting current had a temperature coefficient of 2% per degree which did not differentiate between the two but did rule out kinetic control. Furthermore, the foot of the second wave acquired the desorption characteristics reported previously for the benzyl chloride wave (Fig. 2B). At concentrations greater than millimolar, behavior was quite erratic and two additional poorly shaped waves appeared between the usual first and second waves.

The electrocapillary curves shown in Fig. 2 not only confirm the presence of adsorption but give further insight with respect to the differences that were observed. A comparison of Fig. 2A and 2B shows that a marked decrease in drop time occurred in the region of the first wave and continued to the second wave. Upon passing through the second reduction the drop time returned to that of the background electrolyte. The decrease in the region of the plateau of the first wave is not attributable to bromide ion produced in the reduction or by the slow hydrolysis of benzyl bromide. (Note the negative slope of the limiting-current plateau in Fig. 2B. However, the presence of 0.1*M* bromide ion did affect the electrocapillary curve on the positive side of the maximum.) In the limiting-current region of the first wave, bibenzyl is strongly adsorbed whereas toluene, the final reduction product, and benzyl alcohol, the hydrolysis product, are not adsorbed at the millimolar level. This indicates that the product of Reaction 5, bibenzyl, was the main source of the adsorption effects.

Adsorption of the reduction product of the first wave is less pronounced at higher concentrations of alcohol. Figure 2C shows that there is little adsorption in 80% methanol probably due to greater competition for the surface from methanol as well as to greater solubility of the product. The somewhat greater adsorption found in the case of benzyl iodide in alkaline solutions of 51% methanol may reflect the faster decomposition in this medium of its monovalent ion compared to that formed by benzyl bromide (see Fig. 2D). As a result, a somewhat higher concentration of bibenzyl would be produced at the surface.

Other aspects of adsorption were examined briefly. First, it was possible to show that, at low concentrations of benzyl bromide, the half-wave potential for the first reduction was sensitive to the presence of surface-active anions and hydroxide; in the presence of 0.092*M* sodium hydroxide or 0.10*M* potassium bromide the wave appeared at more cathodic potentials than in the presence of chloride, in which the wave was, in turn, more cathodic than that in nitrate. There was also a corresponding shift in the electrocapillary curve.

The effect of the presence of bromide ion was studied originally because of its presence due to decomposition of benzyl bromide in alkaline solutions. Hydrolysis led to erratic results for half-wave potentials, particularly in the case of benzyl iodide, which decomposed even faster. Decomposition was slower in higher concentrations of methanol and at the same time, the half-wave potentials were shifted

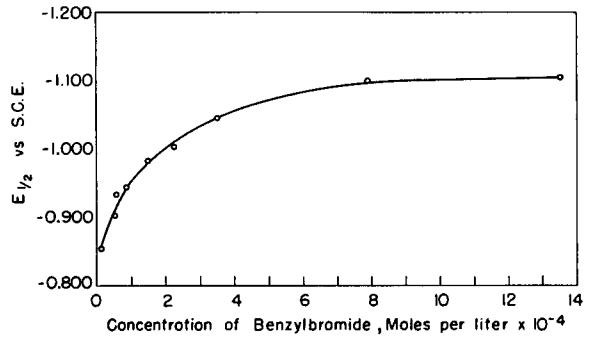

Fig. 3. Effect of concentration of benzyl bromide on its half-wave potential in 51% methanol that is 0.092M in sodium hydroxide.

to more cathodic values. These shifts indicated that a charged species was being produced by the reaction and ruled out the possibility that the neutral halide was undergoing ionization prior to reduction.

The position of the second wave for benzyl bromide was a function of concentration. Thus, there was approximately a 250 mv cathodic shift on going up from 1 x 10^{-5} to 1 x $10^{-3}M$. At higher concentrations the wave remained constant, probably due to attainment of maximum sorption (see Fig. 3). Benzyl chloride showed a similar but much smaller dependence on concentration.

It is important to note that the half-wave potential for each wave of benzyl bromide agreed with the corresponding one for benzyl iodide within experimental error. Agreement of the first waves, which involve different reducible species, was surprising but can be rationalized in terms of virtually simultaneous electron transfer and halide elimination. On the other hand, agreement of the half-wave potentials for the second waves is to be expected because the same intermediate, the benzyl radical, is undergoing further reduction in each case. The resulting carbanion undoubtedly reacts with the solvent to form toluene.

From the electrocapillary curves in Fig. 2, it was quite clear that bibenzyl, or a closely related compound, must have been formed in the first reduction steps of the bromide and iodide derivatives. However, the presence of bibenzyl was later confirmed by making mass-spectrometric studies of products isolated from extracts of large-scale electrolyses. A $10^{-4}M$ solution of benzyl bromide in 50% methanol containing 0.1M potassium bromide was electrolyzed at −0.5 v vs. S.C.E. using a mercury-pool cathode until the current had decreased to a negligible value. The solution was again made $10^{-4}M$ in benzyl bromide and electrolysis continued. A white solid precipitated before the end of the electrolysis, and it gave the typical mass-spectrometric pattern of bibenzyl. Masses of 182 and 91 were particularly prominent. The original benzyl bromide showed no trace of mass 182.

Another electrolysis was carried out in which droplets of excess benzyl bromide were present at all times. A mass spectrogram of an ether extract, from which the more volatile materials had been pumped off, clearly indicated the presence of large amounts of $C_6H_5CH_2C_6H_4CH_2Br$ (masses 260 and 262), or one of its isomers, and $C_6H_5CH_2C_6H_4CH_2$ (mass 181) and the corresponding metastable peak at 126. The presence of relatively small amounts of bibenzyl was indicated by the small peak at mass 91 and the fact that mass 182 was somewhat higher than that expected from the isotopic ratio of carbon in a fourteen-carbon species. The formation of such a halide can be explained easily by the presence of the large excess of benzyl bromide in the solution. A reaction product of this type might well lead to the appearance of the additional polarographic waves which appeared in millimolar solutions of benzyl bromide (and iodide). Large peaks at masses 165 and 166 were also found in this extract but could not be explained satisfactorily.

Neither of the above electrolysis products gave any indication of masses for $C_6H_5CH_2HgBr$ or $C_6H_5CH_2Hg$. Generally, the peaks for HgBr and $HgBr_2$ were roughly equivalent and were found to the same extent in blank electrolyses. However, as one might expect small amounts of benzylmethyl ether (mass 122) formed by solvolysis were present but there was no benzyl alcohol (mass 108).

A similar experiment, in which an air-free suspension of benzyl bromide (in 50% methanol containing 0.1M potassium bromide) was shaken with mercury (no potential applied), showed no evidence of a spontaneous reaction leading to an organo-mercury compound. The small amounts of mercury present were also found in the blank. Therefore, there is no basis for suggesting that the electrochemical reduction of benzyl bromide (and probably the iodide) is preceded by a reaction with mercury or that the benzyl radical attacks mercury after being formed. In the case of the corresponding allyl halides, prior chemical reaction may indeed occur (3), but the proposed dissociation to form RHg^+ prior to reduction seems unlikely, except for one of the compounds, because of the reported cathodic shift in reduction potential as the dielectric constant of the medium was lowered.

Experimental Details

Polarograms and electrocapillary curves were obtained as before (10). The organic halides were the purest obtainable from Eastman Kodak Company and were used as received. Stock solutions were prepared in pure methanol from which aliquots were taken to prepare polarographic solutions. Polarograms were run at 25°C and a line drawn through the maximum currents for use in the figures. Limiting currents were tested for diffusion control by plotting reduction current vs. square root of the mercury height; a straight line was interpreted as an indication of diffusion control. Temperature coefficients of the limiting currents were also studied between 2° and 35°C and, except for the dip of benzyl chloride, were found to be close to 2%/C°.

Mass spectrometric studies were made on a CEC Model 21-103C. In every case, masses were scanned to at least 400.

Acknowledgment

The authors are very much indebted to Professor Klaus Biemann and his associates for running the mass spectrometric analyses and providing vital de-

tails for interpretation of those results. This work was supported in part by the United States Atomic Energy Commission under Contract AT(30-1)905.

Manuscript received June 26, 1959. This paper was prepared for delivery before the Columbus Meeting, Oct. 18-22, 1959.

Any discussion of this paper will appear in a Discussion Section to be published in the December 1960 JOURNAL.

REFERENCES

1. M. von Stackelberg and W. Stracke, *Z. Elektrochem.*, **53**, 118 (1949).
2. J. L. Lothe and L. B. Rogers, *This Journal*, **101**, 258 (1954).
3. A. Kirrmann and M. Kleine-Peter, *Bull. Soc. Chim., France, 1957*, 894; see also, G. Costa, *Ricerca Sci.*, **22**, S133 (1952).
4. A. Frumkin, "Adsorption of Organic Substances at the Metal-Electrolyte Solution Interface and Its Influence on Electrochemical Processes" in "Electrical Phenomena and Solid-Liquid Interface," p. 58, Academic Press, New York (1957).
5. A. Frumkin, N. Nikolajeva-Fedorovich, and R. Ivanova, *Can. J. Chem.*, **37**, 253 (1959).
6. W. H. Reinmuth, Paper presented at the 134th Meeting of the American Chemical Society, Chicago, Illinois, September 1958.
7. A. A. Kryukova and M. A. Loshkarev, *Zhur. Fiz. Khim.*, **30**, 2236 (1956).
8. M. A. Loshkarev and M. G. Dikova, *Ukrain. Khim. Zhur.*, **22**, 457 (1956).
9. M. A. Loshkarev and A. A. Kryukova, *Zhur. Fiz. Khim.*, **31**, 452 (1957).
10. L. E. I. Hummelstedt and L. B. Rogers, *This Journal*, **106**, 248 (1959).

Preparation of Boron from Boron Carbide

David R. Stern

American Potash & Chemical Corporation, Whittier, California

ABSTRACT

A process to prepare elemental boron from boron carbide is presented. Included is evidence that the process is one of anodic transfer. Boron of at least 99.8% purity can be made directly from technical grade materials. Purity is a function of electrolysis voltages and boron carbide purity. Current efficiencies in excess of 95% are obtained and preferred electrolysis conditions are stated.

Preparation of elemental boron has been discussed by a large number of investigators (1-19). Not all processes give sufficient purity. Filament and arc discharge techniques have generally been regarded as the preferred methods of securing a high-purity crystalline boron (2, 3, 5-8, 11, 12, 17, 19). New interest in elemental boron as thermistors and possible semiconductor devices has reemphasized the problem of attaining higher purities. McCarty and coworkers (18) have discovered new low-temperature crystalline modifications of elemental boron.

Vapor phase deposition techniques are generally limited by metallic filament contamination. Impurities are generally tantalum, tungsten, molybdenum, carbon, and titanium (2, 3, 7, 11, 12, 17, 19). Another disadvantage with these contaminants is that they are not removed with secondary upgrading techniques. Deposition on a filament of elemental boron and lower decomposition temperatures are significant contributions (7, 19).

Desire for a potentially higher purity product without heavy metal contamination focused attention on an electrolytic approach. Andrieux, Cooper, and others have developed electrolytic reductions (4, 9, 10, 14-16).

This research effort has resulted in an electrolytic process for boron, which is an anode transfer technique (13). This transfer technique has been applied both to elemental boron and boron carbide. Feasibility studies were conducted on a laboratory exploratory basis in small cells. The scope of this paper is limited to the bench scale preparation of elemental boron from boron carbide.

Experimental Procedure

Cell.—A cross section of the cell used in this investigation is presented in Fig. 1. The unit consisted of a porous carbon basket with a porous carbon diaphragm. Carbide was packed between the diaphragm and porous basket. This cartridge unit was lowered into a dense graphite crucible by steel rods. Removal and recharging with boron carbide could be accomplished without a complete cell shutdown.

External heating was accomplished using graphite resistors. Cell temperatures were measured with Chromel-Alumel thermocouples inserted into the recesses in the centering post and the hollow cathode which was also a thermowell.

An argon blanket could be maintained over the entire cell.

Electrolyte.—The electrolyte consisted of sodium chloride, potassium chloride, and potassium fluoborate with an initial composition of 40-40-20 wt %, respectively. During the course of electrolysis, cathode deposits are withdrawn periodically. Occluded electrolyte is water leached and can be recovered and recycled.

Electrolysis.—After the anode compartment was packed with boron carbide, sufficient predried salt is added to cover the carbide. This cartridge charge was then placed in the heating furnace and melted under argon. Whenever fresh salts, a new diaphragm, or new crucible were used, pre-electrolysis was performed at 2.5 v from ½ to 1 hr before actual electrolysis. The pre-electrolysis deposit acted as a scavenger of impurities and was a direct means of purifying the electrolytic system. A cathode was

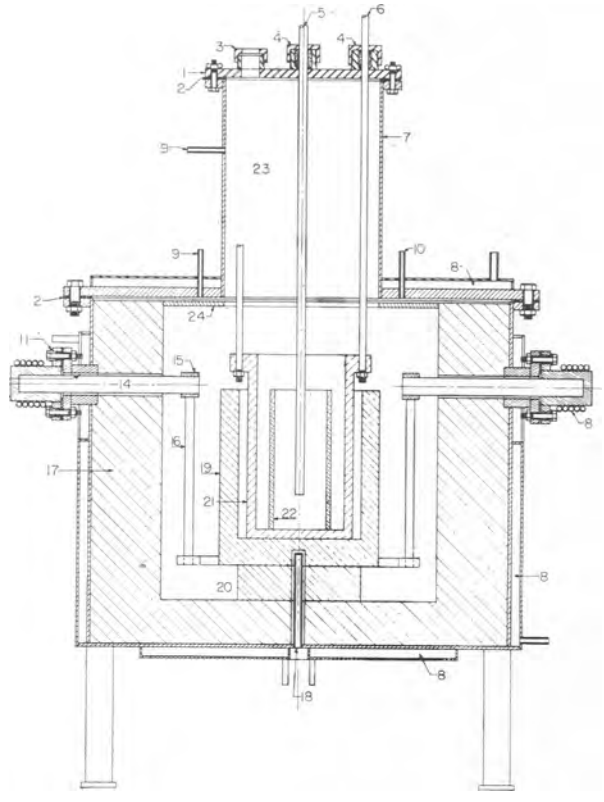

Fig. 1. Bench scale boron carbide cell: 1, stainless (316) lid; 2, Neoprene gasket; 3, sight glass; 4, packing glands; 5, cathode; 6, anode tie rods; 7, mild steel shell; 8, water jackets; 9, argon inlet; 10, argon outlet; 11, insulating bushing; 12, Vycor tube; 13, copper a-c electrode connector assembly; 14, main graphite electrode lead; 15, graphite a-c electrode connector; 16, a-c graphite resistor rod; 17, magnesia insulating bricks; 18, centering post; 19, dense carbon cup; 20, carbon pedestal; 21, porous carbon basket; 22, porous carbon diaphrogm; 23, cooling chamber; 24, heat baffle.

then inserted to a known depth so that a given cathodic current density could be set initially.

At completion of electrolysis the cathode was raised and allowed to cool. To recharge the boron carbide, the cartridge unit was raised, salt allowed to drain, and a new unit inserted.

Processing.—Figure 2 is a photograph of a typical cathode deposit. This deposit was placed in a polyethylene beaker of distilled water on removal. Upon standing in the water the deposit would break off the rod and was wet ground in an iron mortar and leached twice with 10% hydrochloric acid. It was then washed free of acid, rinsed with acetone, and vacuum dried under argon.

The final sample was then weighed and analyzed. Most samples were analyzed for total boron content, sodium, iron potassium, silicon, nitric acid insolubles, and water soluble boron.

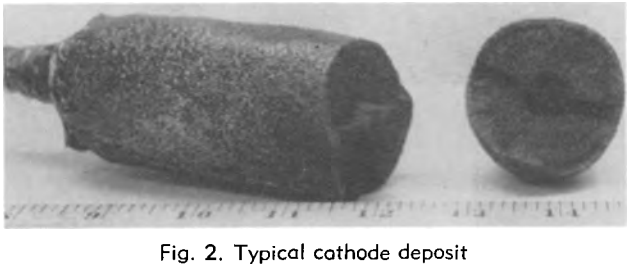

Fig. 2. Typical cathode deposit

Experimental Results

Product purity.—The purest elemental boron resulting from this investigation was 99.8%. This purity was obtained using commercial reagents without any prior purification or recrystallization. Control of the electrolysis and atmosphere were the only precautions taken. Major impurities were sodium, silicon, iron, and carbon. These generally could be limited to less than a total of 0.2%. Lower levels of impurities were sodium 0.05%, silicon 0.07%, iron 0.05%, and carbon (as B_4C) 0.06%. These lower levels, however, were not obtained simultaneously in one sample.

Effect of cell voltage.—An important factor contributing to product purity is cell voltage. A typical relationship between sodium impurity and cell voltage is presented in Figure 3. At voltages between 0.9-1.0 v sodium contents were as low as 0.05%, but no smooth correlation was obtained. It must be pointed out that anodic current density is not constant in this system.

A similar relationship can be shown for the silicon and iron impurities, but the final level of these impurities are also dependent on the processing technique.

These results indicate that the concentration of major impurities in the product is a direct function of cell voltage, the higher the cell voltages the higher the impurities.

Electrolytic decomposition of the fluoborate and alkali halides occur at higher voltages. These reactions are indicated by the liberation of chlorine and adversely affect the current efficiency of the process as well as product purity.

As long as sodium is a component of the electrolyte, there will be some sodium contamination, but by maintaining voltage below 1.2 v, sodium content may be kept below 0.2%.

Origin of other contaminants.—Table I lists the typical spectrographic analyses of the new raw materials entering the process and the materials of con-

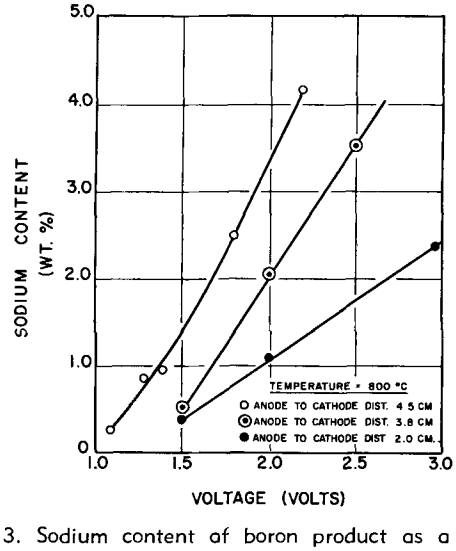

Fig. 3. Sodium content of boron product as a function of cell voltage.

Table I. Semi-Quantitative spectrographic analyses

Constituent	Weight per cent			
	B_4C*	KBF_4*	Carbon†	Graphite‡
Boron	Major	Major	—	0.0008
Silicon	0.17	0.02	0.017	0.012
Iron	1.2	0.015	0.045	0.032
Magnesium	0.26	0.00092	0.0068	0.0016
Titanium	0.10	nil	0.0018	0.0036
Copper	0.0072	0.0011	0.0013	0.00044
Manganese	0.16	nil	—	—
Calcium	0.026	0.26	0.038	0.018
Zirconium	0.20	nil	—	—
Aluminum	0.3	0.0034	0.012	0.030

* Technical grades.
† Grade 20 porous carbon.
‡ C. S. Graphite.

struction. Boron carbide contains the major contaminants except for the calcium in the fluoborate. Thus, purity of the elemental boron is closely allied to the purity of boron carbide. Silicon and iron are anodically transferred in this process.

Pre-electrolysis yields a deposit containing approximately 14% iron, 12% silicon, and only 16% boron.

Figure 4 presents product purity as a function of cumulative electrolysis. These results indicate that whenever a new charge is electrolyzed the purity is low probably due to moisture and the impurities in the boron carbide and the salts.

After an initial conditioning period the purity increases and remains high during most of the remaining electrolysis. Drop off in purity is attributed to higher transfer voltages resulting from the build-up of carbon in the anode compartment as boron is depleted. If the product covering 90% of the electrolysis time were combined into a single sample, an average product purity of 98% would result. The maximum purity attained was 99.8% boron.

Effect of temperature.—High-purity product is obtained at good current efficiencies within a temperature range of 700°-850°C. No definite relationship between temperature and product purity has been noticed within this range. Although a detailed study of the phase relationship of the KCl-NaCl-KBF_4 mixture has not been made, operation above the KCl-NaCl eutectic 660°C must be employed. Above 850°C loss of the fluoborate increases

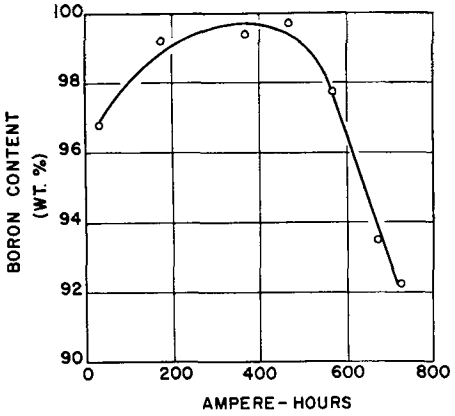

Fig. 4. Product purity as a function of cumulative ampere-hours.

and deposits tend to fall from the cathode. A compromise temperature of 800°C was adopted for the major part of this investigation.

Current density.—Cathodic current density has been varied between 12 to 75.0 amp/dm^2. High current efficiencies are obtained throughout this range. No significant correlation was found between initial current density and boron purity.

Boron material balance.—It has been stated that boron was derived from the carbide and that fluoborate was only a carrier salt. Previous electrolysis systems (4, 9, 10, 13-16) have operated at higher voltages and consequently have not been anodic transfer processes.

Table II lists some experiments, which offer some proof that in this system boron is derived from the anodic boron carbide.

The following points should be noticed: (*a*) experiments conducted without boron carbide (regardless of a carrier) gave no product below 1.3 v; (*b*) experiments conducted without fluoborate (with B_4C) also gave no product even up to 2.2 v; (*c*) the solvent for the carrier salt may be pure KCl, NaCl, or halide mixtures; (*d*) at voltages higher than 3 v boron trichloride is formed.

Analyses of the boron carbide also give evidence of the boron being extracted. These data are presented in Table III.

Final proof of boron transfer is presented in Table IV. Examination indicates that a total of 61 g of elemental boron was extracted on the cathode deposit during electrolysis, whereas only 12 g of boron was available initially in the fluoborate and 11 g of this were accounted for at the completion of electrolysis.

Cell electrolyte.—Cell electrolyte analyses have indicated that concentrations of sodium, potassium,

Table II. Electrolytic systems

Electrolyte	Anode	Voltage	Yield
KCl-KBF_4-NaCl	None	<1.0	None
KCl-KBF_4-NaCl	None	>1.3	Some
KCl-KBF_4	None	<1.0	None
KCl-NaCl	Boron carbide	2.2	None
KCl-NaCl	Boron carbide	3.2	None*
KCl-NaCl-NaF	Boron carbide	1.2	None
KCl-KBF_4	Boron carbide	<1.0	Yes
KCl-KBF_4-NaCl	Boron carbide	<1.0	Yes
LiCl-KF-KBF_4	Boron carbide	2.8	Some
KCl-KF-KBF_4	Boron carbide	<1.1	Yes

* BCl_3 fumes.

Table III. Anodic transfer of boron from boron carbide

	Weight per cent	
	Before electrolysis*	After electrolysis†
Total B	75.4	18.8
H_2O Sol. B	0.05	—
HNO_3 Ins.	98.2	83.58
Fe	0.11	0.04
Si	0.16	—
B in HNO_3 Ins.	76.58	19.61

* Technical grade powder B_4C.
† Analysis after 1063 amp-hr of electrolysis.

Table IV. Boron balance in boron carbide cell

	g	g
Total boron in cell initially:		
As B_4C	74	
As KBF_4 (electrolyte)	12	
		86
Total boron remaining in cell after electrolysis:		
In anode charge	13	
In electrolyte	8	
		21
Total boron removed from cell during electrolysis:		
By deposition	61	
By salt drag out and sampling	3	
		64
Total boron accounted for		85
Boron unaccounted for		1

and chloride ions do not change appreciably during electrolysis. Concentrations as a function of cumulative ampere-hours are presented in Fig. 5. All concentrations are relatively constant except that of the fluoride ion. This is contrary to what is expected in the electrolysis of a halide-fluoborate system where the potassium fluoride concentration increases as boron fluoride is reduced to boron. The boron concentration at the start increases for a short period of time. This probably represents the solution of boron from the carbide. This observation is illustrated vividly in Fig. 6 when the fluoride to boron mol ratios are plotted as a function of electrolysis time. The ratio in fluoborate is four, while an inspection of the curve shows a decrease to a ratio of two. Chemical analyses of the purge gas indicate that some fluoride is lost from the system as boron trifluoride, but the rate of solution of boron from the carbide more than compensates for that volatized from the system. Material balance data indicate that the physical quantity of fluoborate lost is relatively small and can be made up by fluoborate additions.

Electrolysis data.—Current efficiency for this system is based on the following electrode reaction:

$$B^{+3} + 3e \rightarrow B^{\circ} \qquad [1]$$

Some data on electrolysis are presented in Table V. High current efficiencies are obtained and energy consumption is low. A pound of 94-99% boron requires from 3-4 kwhr of electrical energy.

Summary and Conclusions

An electrolytic anode transfer process for the preparation of high-purity elemental boron from boron carbide has been presented. Evidence that the process is one of anodic transfer is included.

The following conclusions concerning this method of preparing elemental boron can be set forth:

1. Boron of at least 99.8% purity can be made directly from technical grade materials without prior purification treatment.
2. Elemental boron can be prepared in purities at least equal to that attained via vapor deposition processes without the corresponding heavy metal contamination.
3. Major impurities are sodium, silicon, iron, and carbon. The total of these impurities can be reduced to 0.2% or less.
4. Impurity levels in the boron are a function of the electrolysis voltage and purity of the boron carbide.

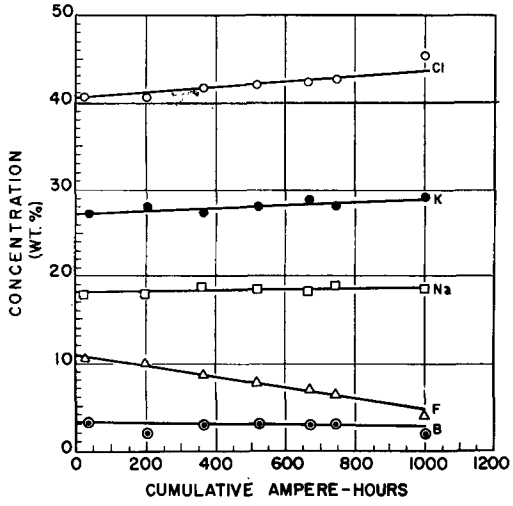

Fig. 5. Electrolyte composition as function of cumulative ampere-hours.

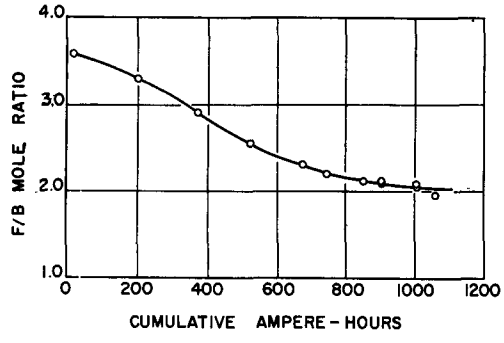

Fig. 6. Fluoride boron mole ratio as a function of cumulative ampere-hours.

Table V. Electrolysis data

Temp, °C	Voltage, v	Current, amp	Time, hr	Final deposit weight, g	Cathodic current density, amp/dm²	Current efficiency, %	kwhr/lb Boron
735	1.1	6.9	24	21	16.6	92.0	3.9
740	1.1	6.5	23	18.8	14.4	90	4.0
725	1.1	3.5	29.5	12.0	11.9	81	4.3
790	1.0	7.9	19.0	17.4	13.5	96	3.9
800	1.0	6.9	19.0	17.5	14.0	98	3.4
800	1.0	4.2	24.0	12.7	9.0	90	3.6
795	1.0	5.3	23	17.1	11.3	97	3.2
800	1.0	3.7	23	12.9	8.4	101	3.0
810	0.9	5.8	52.5	39.6	10.7	90	3.1
810	1.0	4.1	66	35.7	8.2	94	3.4
800	1.0	5.7	30	21.7	5.1	92	3.6

5. Voltages less than 1.2 v, cathodic current densities between 12.0 and 75.0 amp/dm^2, and 800°C are the preferred conditions of electrolysis.

6. Current efficiencies for this anodic transfer process are high. Efficiencies in excess of 95% are easily obtained. Energy consumption is 3-4 kwhr/lb boron.

7. The application of this technique as a secondary upgrading technique for higher purity borons has been postulated.

Acknowledgment

The author would like to express his appreciation to Mr. Aiji Uchiyama and Mr. Quentin H. McKenna who conducted both the laboratory and bench scale work on this project.

Manuscript received Oct. 12, 1959. This paper was prepared for delivery before the Chicago Meeting, May 1-5, 1960.

Any discussion of this paper will appear in a Discussion Section to be published in the December 1960 JOURNAL.

REFERENCES

1. H. Moissan, *Ann. chim. et. phys.*, **6**, 296 (1895).
2. E. Weintraub, *Trans. Am. Electrochem. Soc.*, **16**, 165 (1909).
3. A. E. Van Arkel, U.S. Pat. 1,774,410, Aug. 26, 1930.
4. J. L. Andrieux, *Ann. chim.*, **12**, 423 (1929).
5. L. Hackspill, A. Stieber, and R. Hocart, *Compt. rend.*, **193**, 776 (1931).
6. D. P. Mellor, S. B. Cohen, and E. B. Underwood, *Australian Chem. Inst. J. & Proc.*, **3**, 329 (1936).
7. A. J. Laubengayer, D. T. Hurd, A. E. Newkirk, and J. L. Hoard, *J. Am. Chem. Soc.*, **65**, 124 (1943).
8. M. Formstecher and E. Ryskevic, *Compt. rend.*, **221**, 747 (1945).
9. H. S. Cooper, U.S. Pat. 2,572,248, Oct. 23, 1951.
10. H. S. Cooper, U.S. Pat. 2,572,249, Oct. 23, 1951.
11. G. H. Fetterley, U.S. Pat. 2,542,916, Feb 20, 1951.
12. G. M. Murphy, "Separation of Boron Isotopes," National Nuclear Energy Series, Vol. 3, U.S. Atomic Energy Commission, Oak Ridge, Tennessee (1952).
13. Norton Co., Australian Pat. 164,170, July 18, 1955.
14. J. L. Andrieux and W. J. Deiss, *Bull. soc. chim., France*, 838 (1955).
15. N. P. Nies, E. W. Fajans, L. L. Thomas, L. E. Hiebert, and V. Morgan, U.S. Pat. 2,832,730, Apr. 29,1958.
16. N. F. Murphy and R. S. Tinsley, U. S. Pat. 2,848,396, Aug. 19, 1958.
17. D. R. Stern and L. Lynds, *This Journal*, **105**, (11) 676 (1958).
18. L. V. McCarty, J. S. Kasper, F. H. Horn, B. F. Decker, and A. E. Newkirk, *J. Am. Chem. Soc.*, **80**, 2592 (1958)
19. K. E. Bean and R. J. Sparks, "Research Investigation of Physical Chemistry and Metallurgy of Semiconductor Materials," 2nd Quarterly Report, Mar. 1, 1959-June 1, 1959, Signal Corp, Contract DA-36-039-SC-78246.

Contribution to the Theory of Current Distribution in Local Cells

Carl Wagner

Max-Planck-Institut für physikalische Chemie, Göttingen, Germany

ABSTRACT

The distribution of the anodic current density in local cells involving anodic dissolution of a metal and reduction of oxygen as the cathodic reaction is calculated for a diffusion controlled limiting cathodic current density.

Statement of the Problem

Corrosion of metals in aqueous solutions may in general be accounted for by the superposition of anodic and cathodic reactions. The anodic reaction which is the dissolution of a specified metal is inherently confined to the surface of that metal. Cathodic reactions involve reduction of oxidizers, e.g., reduction of elemental oxygen to water, or evolution of hydrogen from hydrogen ions. If only one metal without inhomogeneities is present, anodic and cathodic reactions occur randomly at its surface (1), and the net current density vanishes everywhere. In the presence of chemically inert inclusions, conducting oxide layers, or other electronic conductors which are in electrical contact with the metal, cathodic reactions may also occur at the surface of these materials. In the latter case referred to as local cell action, there is a net current flowing inside the electrolyte from the metal which is dissolved as anode to the other material as cathode. The occurrence of cathodic reactions at the other materials increases inherently the rate of dissolution of metal as the anodic reaction and thus aggravates corrosion. If the dissolving metal is directly adjacent to cathodic areas, the rate of attack is especially high at the boundary. Thus conditions favoring local cell action are to be avoided if possible in order to minimize corrosion. This, however, is not always easy to accomplish. Therefore, it is desirable to formulate rules of thumb in order to estimate the potential dangers resulting from local cell action.

Current distributions in local cells have been calculated by Waber and his associates (2-7). For coplanar adjacent cathodes and anodes shown in Fig. 1, the current density next to an anode-cathode boundary becomes infinite if polarization is disregarded (2). Thus for a realistic approach, polar-

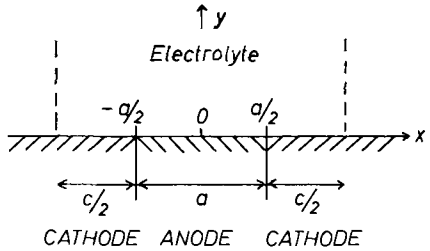

Fig. 1. Anode with adjacent cathodes

ization must be taken in account in estimating the maximum local corrosion rate at an anode-cathode boundary. If both the anodic and the cathodic polarization curve can be approximated by straight lines involving the same slope, the potential distribution in the electrolyte can be obtained in terms of a Fourier series or integral and therefrom the local current density can be calculated (3,4). Calculations for other conditions seem desirable. In what follows calculations are presented for a diffusion controlled limiting cathodic current density in solutions containing oxygen.

In accord with Waber it is assumed that there are no solid corrosion products which impede diffusion and conduction in the electrolyte.

General Presuppositions

The electrical potential ϕ in an electrolyte involving a constant electrical conductivity obeys the Laplace equation

$$\text{div grad } \phi = 0 \qquad [1]$$

For a single cathodic and a single anodic reaction and for a constant electrical potential in the metallic conductors, the boundary conditions can be formulated as (8)

$$\phi \text{ (anode)} + \eta_a(J_a) = \Phi_a \qquad [2]$$

$$\phi \text{ (cathode)} - \eta_c(J_c) = \Phi_c \qquad [3]$$

where ϕ (anode) and ϕ (cathode) are the electrical potentials in the electrolyte next to the anode and the cathode, respectively, Φ_a and Φ_c are constants, and η_a and η_c, respectively, are the absolute values of the overpotentials of the anodic and the cathodic reaction corresponding to the absolute local current densities J_a and J_c. Since cations are supposed to migrate from the anode toward the cathode, ϕ (anode) is more positive than ϕ (cathode).

At the anode, metal is dissolved and simultaneously the oxidizer, e.g., oxygen, is reduced cathodically. The net current density at the anode, $J_a - J_c$, is equal to the product of the specific conductivity σ of the electrolyte and the absolute value of the local potential gradient, $\partial\phi/\partial n$, normal to the surface of the electrode according to Ohm's law,

$$[J_a - J_c = \sigma|\partial\phi/\partial n|] \text{ anode} \qquad [4]$$

At the cathode, reduction of oxidizer, e.g., oxygen, is supposed to be the only electrode reaction. Thus

$$[J_c = \sigma|\partial\phi/\partial n|] \text{ cathode} \qquad [5]$$

To obtain solutions for the potential and the current distribution from Eq. [1] to [5], the polarization curves must be known for both the anodic and the cathodic reaction. In particular, it is possible to calculate the local current densities at both the cathode and the anode as the intensities of sources and sinks with the help of an integral equation (8). This method has been found to be profitable for calculating the current density distribution in cells used for the deposition of metals. So far, linear polarization curves have been assumed. It is possible, however, to formulate and to solve the integral equation also for other types of cathodic or anodic polarization curves with the help of numerical methods.

Under most practical conditions, the polarization curves are not known and not easy to determine. Consequently, for practical purposes one has to rely on direct observations of corrosion rates rather than on calculations based on polarization curves. Direct observations always refer to a special set of conditions. To predict corrosion rates under somewhat different conditions, it is, therefore, necessary to make conjectures and extrapolations. To this end, this paper presents calculations for conditions which are idealized yet characteristic of practical situations.

In most practical cases, corrosion involves reduction of oxygen as the cathodic reaction. The current density J_c at the cathode as a function of the negative value of the local single electrode potential rises first exponentially owing to activation control and finally tends to a limiting value $J_{c(max)}$ corresponding to diffusion control. The value $J_{c(max)}$ is proportional to the concentration of oxygen in the bulk electrolyte and moreover depends on the convection of the electrolyte. This type of polarization curve is well known from polarographic investigations. The behavior of the cathode may, therefore, be approximated by

$$J_c \cong 0 \text{ if } -E_c < -E_{c(1/2)} \qquad [6]$$

$$J_c \cong J_{c(max)} \text{ if } -E_c > -E_{c(1/2)} \qquad [7]$$

where $E_{c(1/2)}$ denotes the half-wave potential at which $J_c = J_{c(max)}/2$.

According to Delahay (9), the value of $J_{c(max)}$ may not be single-valued because oxygen is reduced either to H_2O_2, or to H_2O especially at lower single electrode potentials. In the latter case the maximum current density is twice as much as for reduction to H_2O_2. This, however, is irrelevant for the calculation of the order of magnitude of local cell action.

The equilibrium single electrode potential $E_{a(eq)}$ of the dissolving metal is assumed to be more negative than the half-wave potential $E_{c(1/2)}$ of oxygen where signs of potentials are chosen in accord with the Stockholm convention. The difference

$$\Delta E = E_{c(1/2)} - E_{a(eq)} \qquad [8]$$

is, therefore, assumed to be positive.

In a solution containing oxygen and under conditions precluding local cell action, a metal exhibiting a high activation polarization on dissolving may assume essentially the half-wave potential of oxygen. Under these conditions ΔE is balanced mainly by the overpotential of the dissolving metal,

$$\Delta E \cong \eta_a(J_a = J_{c(max)}) \qquad [9]$$

Thus neither increase of oxygen supply nor local cell action affects the rate of metal dissolution to a significant extent.

The following considerations refer, therefore, to more reactive metals such as zinc which exhibit a relatively low activation polarization on dissolution. It is assumed that without local cell action the corrosion rate is controlled by diffusion of oxygen, i.e.,

$$J_a \cong J_{c(max)} \quad [10]$$

Moreover it is assumed that the anodic polarization curve may be approximated by a straight line over a sufficiently wide range corresponding to the relation

$$E_a - E_{a(eq)} = \eta_a = J_a h_a \quad [11]$$

where E_a is the electrode potential of the anode with a current density J_a and $h_a = dE/dJ_a$ is a constant.

In the case of local cell action, the maximum corrosion rate is attained if the dissolving metal is polarized to the half-wave potential $E_{c(1/2)}$ of the cathodic reaction. The corresponding potential shift is $\eta_a = \Delta E$ and the current density J_a is equal to $\Delta E/h_a$ according to Eq. [11]. For a significant rise of the anodic dissolution rate of a metal due to local cell action it is, therefore, necessary that $\Delta E/h_a >> J_{c(max)}$, or

$$\Delta E/h_a J_{c(max)} >> 1 \quad [12]$$

Coplanar Cathodes and Anodes

Coplanar cathodes and anodes are considered as one of the most important practical cases involving local cell action. The two-dimensional geometry of the electrodes is shown in Fig. 1 and is identical with the geometry considered by Waber and Rosenbluth (3). The anode is supposed to have a finite width a. The cathodes at either side of the anode are supposed to consist of another chemically inert material involving a high electrical conductivity. The width of the cathodes and the depth of the electrolyte are assumed to be infinite.

According to previous calculations for similar situations (3, 4, 8), one may anticipate two different limiting cases determined by the magnitude of the dimensionless ratio a/k_a where a is the width of the anode and $k_a = \sigma h_a$ is the so-called polarization parameter.

I. If $a << \sigma h_a$, polarization enforces a nearly uniform anodic current density, the potential drop in the electrolyte becomes insignificant, and $E_a \cong E_{c(1/2)}$. Hence, in view of Eq. [8] and [11]

$$J_a = \Delta E/h_a \quad [13]$$

II. If $a >> \sigma h_a$, the potential in the electrolyte along the anode is nearly constant whereas the anodic current density varies greatly and is especially high at the anode-cathode boundary. Under these conditions, an approximate solution of the current distribution may be obtained by calculating first the potential and current distribution in the electrolyte for vanishing polarization of the anode and introducing subsequently the effect of anodic polarization as a perturbation.

In view of Eq. [6] and [7], the Laplace equation for the electrical potential ϕ in the electrolyte as a function of the coordinates x and y is to be solved for the boundary condition

$$\phi = 0 \text{ at } |x| \leqq a/2,\ y = 0 \quad [14]$$

$$\partial\phi/\partial y = J_{c(max)}/\sigma \text{ at } a/2 \leqq |x| \leqq (a+c)/2,\ y = 0 \quad [15]$$

$$\partial\phi/\partial y = 0 \text{ at } |x| > (a+c)/2,\ y = 0 \quad [16]$$

Equation [14] refers to the anode of width a at which the potential ϕ is supposedly constant and equal to zero by definition. Equation [15] refers to those sections of the cathodes where the single electrode potential is more negative than the half-wave potential. Equation [16] refers to farther sections of the cathode.

The distance (a+c)/2 at which the local single electrode potential is equal to the half-wave potential $E_{c(1/2)}$ of the cathodic reaction is not explicitly given but implicitly by the condition that the electrical potential ϕ at $|x| = (a+c)/2$, $y = 0$ must be equal to the negative value of the difference ΔE between the half-wave potential $E_{c(1/2)}$ of the cathodic reaction and the equilibrium single electrode potential $E_{a(eq)}$ of the anode,

$$\phi[|x| = (a+c)/2, y = 0] = -[E_{a(eq)} - E_{c(1/2)}] = -\Delta E \quad [17]$$

An approximate solution may be obtained by disregarding the occurrence of current lines beyond the broken lines in Fig. 1 corresponding to the boundary condition

$$\partial\phi/\partial x = 0 \text{ at } |x| = (a+c)/2,\ y > 0 \quad [18]$$

An analogous problem has been considered in conjunction with cathodic protection (10). Using Eq. [36] of a previous paper (10) with the notation of the present paper, one has

$$\phi = \frac{J_{c(max)}}{\sigma}\left\{ y + \frac{a+c}{\pi}\,\mathrm{Re}\left[i \sin^{-1}\frac{\sin \pi z/(a+c)}{\sin \pi a/2(a+c)} \right] \right\} \quad [19]$$

where $z = x + i\,y$ is the complex variable used in conformal mapping. Equation [19] satisfies the Laplace equation and the boundary conditions stated in Eq. [14], [15], and [18].

Substitution of Eq. [19] in Eq. [17] yields

$$\frac{\sigma\,\Delta E}{J_{c(max)}} = c\left\{ \frac{1 + c/a}{\pi\, c/a} \cosh^{-1}\frac{1}{\sin[\pi/2(1+c/a)]} \right\} \quad [20]$$

The expression in braces is equal to ½ if $c/a << 1$, and equal to 2.28 if $c/a = 1000$. Thus, for most practical situations, the expression in braces may be assumed to be equal to unity in order to obtain the order of magnitude of c. Hence

$$c \sim \sigma\,\Delta E/J_{c(max)} \quad [21]$$

The value of c may be considered as the effective width of the cathodic areas which determines the magnitude of the amount of oxygen reacting at the cathode.

The potential at the anode is equal to zero by definition according to Eq. [14]. The potential at the cathode is given by Eq. [19],

$$\phi(|x| > a/2, y = 0) = -\frac{(a+c)\,J_{c(max)}}{\pi\,\sigma} \cosh^{-1}\frac{\sin[\pi x/(a+c)]}{\sin[\pi a/2(a+c)]} \quad [22]$$

From Eq. [19] and Ohm's law the net current density $J_a - J_{c(max)}$ at the anode is obtained as

$$J_a - J_{c(max)} = -\sigma \left(\frac{\partial \phi}{\partial y}\right)_{|x| < a/2,\, y = 0}$$

$$= J_{c(max)} \left\{ \frac{\cos\left(\frac{\pi x}{a+c}\right)}{\left[\sin^2\left(\frac{\pi a/2}{a+c}\right) - \sin^2\left(\frac{\pi x}{a+c}\right)\right]^{1/2}} - 1 \right\} \quad [23]$$

The validity of Eq. [19] to [23] is restricted because of the underlying approximations. First, it must be recalled that the cathodic current density is a continuous function of the electrode potential in contrast to the step function suggested in Eq. [6] and [7] on which Eq. [15] and [16] are based. Second, current lines spread beyond $|x| = (a+c)/2$ in contradistinction to the boundary condition in Eq. [18] used instead of Eq. [16]. Third, anodic polarization has been ignored but must be considered.

If $c >> a$, i.e., according to Eq. [21], if

$$\sigma \Delta E/a J_{c(max)} >> 1 \quad [24]$$

most of the potential drop in the electrolyte occurs in front of the anode where current lines are crowded. Approximations used for the calculation of the potential ϕ far away from the anode, especially at $x \geqq (a+c)/2$, are, therefore, virtually irrelevant for the validity of Eq. [23]. Deviations from Eq. [23] are mainly due to anodic polarization. Pertinent calculations are presented below.

If conversely $c << a$, i.e., if

$$\sigma \Delta E/a J_{c(max)} << 1 \quad [25]$$

most of the potential drop in the electrolyte occurs in front of the cathodes where current lines are crowded. Consequently, if $c << a$, use of approximations at the outer boundary of the cathodes, i.e., $|x| \geqq (a+c)/2$ causes a much greater error than in the former case where $c >> a$. Even if $c << a$, however, Eq. [22] and [23] yield the correct order of magnitude of ϕ and J_a next to the anode-cathode boundary if anodic polarization is negligible.

Since current lines ending at the cathode at $|x| < (a+c)/2$ spread beyond $|x| = (a+c)/2$, the decrease of the potential along the cathode with increasing distance x is less steep than has been calculated from Eq. [19] based on Eq. [18] according to which current lines beyond $|x| = (a+c)/2$ are precluded. The magnitude of this error may be estimated by comparing the variation of the potential at the surface of a galvanic couple involving constant current densities J at the cathode and the anode of equal width b/2 for conditions indicated in Fig. 2a and 2b. The potential distribution in the electrolyte can be calculated readily by superimposing the potentials resulting from line sources and sinks (11). In this way the change in the potential along the cathode of Fig. 2a without current lines beyond the boundaries of the electrodes is found to be

$$\phi(x = b/2) - \phi(x = b)$$

$$= \frac{bJ}{\pi^2 \sigma}\left[\int_{\pi/4}^{3\pi/4} \ln \sin \eta \, d\eta - \int_{0}^{\pi/2} \ln \sin \eta \, d\eta \right] \quad [26]$$

$$= 0.74 \; (bJ/\sigma)$$

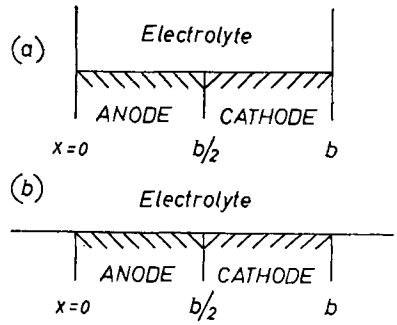

Fig. 2. Galvanic couples for estimating the effect of sidewise spreading of current lines on the potential drop along the cathode according to Eq. [26] and [27].

whereas for conditions shown in Fig. 2b with current lines expanding sidewise,

$$\phi(x = b/2) - \phi(x = b)$$

$$= [(2 \ln 2)/\pi] \; (bJ/\sigma) = 0.44(bJ/\sigma) \quad [27]$$

The ratio of the values calculated in Eq. [25] and [26] is 1.7. Thus cutting off the space for the spreading of current lines beyond $|x| = (a+c)/2$ in Fig. 1 by using Eq. [18] instead of Eq. [16] does not affect the order of magnitude of the above calculations even if $c << a$ as far as the vicinity of the anode-cathode boundary is concerned.

According to Eq. [23], the anodic current density at the anode-cathode boundary $x = a/2$ tends to infinity as in other problems where polarization at a boundary is disregarded (2, 3, 8). Thus polarization must be taken in account in order to obtain a realistic result. To this end, an approximate method indicated in Fig. 6 of a previous paper (8) may be employed as is shown in what follows.

Equations [22] and [23] have been derived for vanishing anodic polarization. If anodic polarization is considered to be a minor perturbation, Eq. [22] and [23] may still be used as first-order approximations except for the immediate vicinity of the anode-cathode boundary.

For each of the limiting cases $c >> a$ and $c << a$, one obtains from Eq. [22] and [23]

$$J_a(x \leqq a/2) = A(a/2 - x)^{1/2} \quad [28]$$

$$\phi(x \geqq a/2) = -B(x - a/2)^{1/2} \quad [29]$$

The symbols $\leqq$ and $\geqq$ mean "slightly smaller than" and "slightly greater than," respectively. The constants A and B are calculated below in Eq. [39] and [42] for $c >> a$ and in Eq. [48] and [52] for $c << a$.

Since anodic polarization does occur, the potential at the anode is lowered by $h_a J_a$. In view of Eq. [14]

$$\phi = -h_a J_a \text{ if } x < a/2 \quad [30]$$

Substitution of Eq. [28] in Eq. [30] yields

$$\phi(x \leqq a/2) \cong -h_a A/(a/2 - x)^{1/2} \quad [31]$$

In Fig. 3 the potential in the vicinity of the anode-cathode boundary is shown as curve I and curve II calculated from Eq. [31] and [29], respectively. Two divergent branches are obtained. This divergence is due to the fact that the anodic current density tends

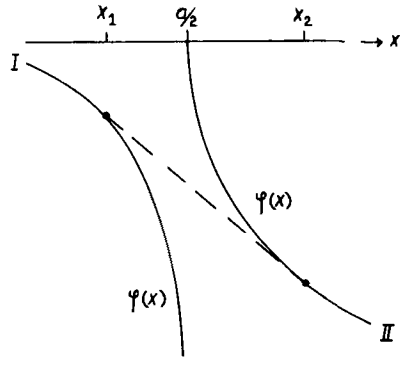

Fig. 3. Potential ϕ (x, y = 0) near the anode-cathode boundary at x = a/2.

to infinity at x = a/2, y = 0 if anodic polarization is disregarded. Actually, the potential must be represented by a smooth curve. To obtain an approximation, one may draw the common tangent line pertaining to curves I and II, which is indicated by the broken line between the coordinates x_1 and x_2 in Fig. 3.

Equating the slopes of the tangent lines at $x = x_1$ and $x = x_2$ and the slope of the broken line in Fig. 3, one obtains with the help of Eq. [29] and [31]

$$-\frac{h_a A}{2(a/2-x_1)^{3/2}} = -\frac{B}{2(x_2-a/2)^{1/2}} = \frac{-B(x_2-a/2)^{1/2} + h_a A/(a/2-x_1)^{1/2}}{x_2-x_1} \quad [32]$$

Upon solving Eq. [32] for $(a/2 - x_1)$ and $(x_2 - a/2)$, it follows that

$$a/2 - x_1 = 3^{1/2} h_a A/B \quad [33]$$

$$x_2 - a/2 = 3^{3/2} h_a A/B \quad [34]$$

With the help of Eq. [31] and [33] the potential at the cathode boundary is obtained as

$$\phi(x = a/2, y = 0) = \phi(x = x_1, y = 0) + (a/2 - x_1)(\partial\phi/\partial x)_{x=x_1, y=0} \cong -(3^{3/4}/2)(h_a AB)^{1/2} \quad [35]$$

Hence the anodic current density at the anode-cathode boundary (x = a/2) is found to be

$$J_a = -\phi(x = a/2)/h_a \cong (3^{3/4}/2)(AB/h_a)^{1/2} \quad [36]$$

Next the values of A and B for the two limiting cases c >> a and c << a are calculated.

1. If c >> a, the cosine in Eq. [23] is nearly equal to unity and the sine functions may be approximated by their arguments. Hence Eq. [23] becomes

$$J_a \cong \frac{(a+c)}{\pi(a^2/4 - x^2)^{1/2}} J_{c(max)} \text{ if } c >> a \quad [37]$$

For the vicinity of the anode-cathode boundary at $x \lesssim a/2$, it follows from Eq. [37] that

$$J_a \cong \frac{a+c}{\pi[a(a/2-x)]^{1/2}} J_{c(max)} \cong \frac{c}{\pi[a(a/2-x)]^{1/2}} J_{c(max)} \quad [38]$$

Upon comparing Eq. [28] and [38] it follows that

$$A \cong \frac{J_{c(max)}\, c}{\pi a^{1/2}} \text{ if } c >> a \quad [39]$$

If c >> a and $x \lesssim a/2$, the sine functions in Eq. [22] may be approximated by their arguments. Thus

$$\phi(x \lesssim a/2, y = 0) \cong -\frac{a+c}{\pi\sigma} J_{c(max)} \cosh^{-1}(2x/a) \quad [40]$$

For $x \cong a/2$, the inverse hyperbolic cosine function has an argument close to unity and therefore may be approximated by

$$\cosh^{-1}(2x/a) = \cosh^{-1}[1 + 2(x - a/2)/a] \cong 2[(x - a/2)/a]^{1/2} \quad [41]$$

Substitution of Eq. [41] in Eq. [40] yields Eq. [29] with

$$B \cong \frac{2}{\pi} \frac{(a+c) J_{c(max)}}{\sigma a^{1/2}} \cong \frac{2}{\pi} \frac{c\, J_{c(max)}}{\sigma a^{1/2}} \text{ if } c >> a \quad [42]$$

Upon substituting Eq. [39] and [42] in Eq. [36], using Eq. [21], and omitting numerical factors of the order of unity, the anodic current density at the anode-cathode boundary is found to be

$$J_a(x = a/2) \sim \left(\frac{\sigma}{a h_a}\right)^{1/2} \Delta E \text{ if } c >> a \quad [43]$$

2. If c << a and $x \sim a/2$, the trigonometric functions in Eq. [22] and [23] may be approximated by the following expressions

$$\sin\frac{\pi x}{a+c} = \cos\left[\frac{\pi}{2}\left(\frac{a+c-2x}{a+c}\right)\right] \cong 1 - \frac{1}{2}\left(\frac{\pi}{2}\frac{a+c-2x}{a+c}\right)^2 \quad [44]$$

$$\sin\frac{\pi a/2}{a+c} = \cos\left(\frac{\pi}{2}\frac{c}{a+c}\right) \cong 1 - \frac{1}{2}\left(\frac{\pi}{2}\frac{c}{a+c}\right)^2 \quad [45]$$

$$\cos\frac{\pi x}{a+c} \cong \cos\frac{\pi}{2}\frac{a}{a+c} = \sin\frac{\pi}{2}\frac{c}{a+c} \cong \frac{\pi}{2}\frac{c}{a+c} \quad [46]$$

Upon substituting Eq. [44] to [46] in Eq. [23] and omitting terms of higher order, it follows that the current density J_a next to the anode-cathode boundary $(a/2 - x << c)$ is

$$J_a \cong \frac{c}{2[c(a/2-x)]^{1/2}} J_{c(max)} \quad [47]$$

Upon comparing Eq. [28] and [47], it follows that

$$A = (c^{1/2}/2)\, J_{c(max)} \text{ if } c << a \quad [48]$$

Substitution of Eq. [44] and [45] in Eq. [22] yields the potential at the cathode next to the cathode-anode boundary,

$$\phi(x \gtrsim a/2, y = 0) = \frac{(a+c) J_{c(max)}}{\pi\sigma} \cosh^{-1} f(x) \quad [49]$$

where

$$f(x) = \frac{1 - \frac{1}{2}\left[\frac{\pi}{2}\frac{a+c-2x}{a+c}\right]^2}{1 - \frac{1}{2}\left[\frac{\pi}{2}\frac{c}{a+c}\right]^2} \quad [50]$$

If $c << a$ and $(x - a/2) << c$, $f(x)$ may be approximated by

$$f(x) \cong 1 - \frac{1}{2}\left[\frac{\pi}{2}\frac{a+c-2x}{a+c}\right]^2 + \frac{1}{2}\left[\frac{\pi}{2}\frac{c}{a+c}\right]^2 \cong 1 - \frac{1}{2}\left[\frac{\pi^2 c(a/2-x)}{(a+c)^2}\right] \quad [51]$$

Substituting Eq. [51] in Eq. [49] and using the first term of a series expansion for the inverse hyperbolic cosine function involving an argument close to unity, one obtains Eq. [29] with

$$B \cong \frac{c^{1/2} J_{c(max)}}{\sigma} \quad \text{if } c << a \quad [52]$$

Upon substituting Eq. [48] and [52] in Eq. [36], using Eq. [21], and omitting factors of the order of unity, the anodic current density at the anode-cathode boundary is found to be

$$J_a(x = a/2) \cong \left[\frac{\Delta E\, J_{c(max)}}{h_a}\right]^{1/2} \quad \text{if } c << a \quad [53]$$

For the current density J_a at the center of the anode the following relations are obtained.

1. If $c >> a$, it follows from Eq. [37] for $x = 0$ with the help of Eq. [21] and omission of factors of the order of unity that

$$J_a(x = 0) = \frac{2(a+c)}{\pi a} J_{c(max)} \cong \frac{\sigma \Delta E}{a} \quad [54]$$

2. If $c << a$, it follows from Eq. [23] and [46] that

$$J_a(x = 0) \cong J_{c(max)} \quad [55]$$

i.e., local cell action at the center of a sufficiently large anode is insignificant since J_a tends to the value determined by the local rate of oxygen supply.

Discussion and Conclusions

According to the foregoing considerations the local current density J_a for dissolution of a metal may be determined

1. by the rate of oxygen diffusion

$$J_a \cong J_{c(max)} \quad [56]$$

in accord with Eq. [10], or

2. by the potential drop in the electrolyte (resistance control) corresponding to the relation

$$J_a \sim \sigma\, \Delta E/a \quad [57]$$

which is deduced in Eq. [54] for the center of an anode of width a with adjacent cathodes if $c >> a$, or

3. by anodic polarization control corresponding to the relation

$$J_a = \Delta E/h_a \quad [58]$$

which has been obtained above as Eq. [13] for sufficiently narrow anodes ($a << \sigma\, h_a$).

The current density J_a at an anode-cathode boundary may be given by Eq. [43] if $c >> a$ and thus be equal to the geometrical mean of the right-hand members of Eq. [57] and [58] corresponding to a combination of resistance and anodic polarization control.

Alternatively, J_a at an anode-cathode boundary may be given by Eq. [53] if $c << a$ and thus be equal to the geometrical mean of the right-hand members of Eq. [56] and [58] corresponding to a combination of oxygen diffusion and anodic polarization control.

The validity range of the various approximations is determined mainly by the values of two dimensionless groups, N_1 and N_2,

$$N_1 = a/k_a = a/\sigma h_a \quad [59]$$

$$N_2 = \Delta E/h_a J_{c(max)} \quad [60]$$

The group N_1 is the ratio of the width a of the anode and the corrosion parameter k_a which in turn is defined as the product of the conductivity σ and the slope h_a of the potential-current density curve of the anodic reaction. The corrosion parameter $k_a = \sigma h_a$ is equal to the thickness of the electrolyte which yields a potential drop equal to the overpotential η_a of the anodic reaction at a given current density. The value of $N_1 = a/\sigma h_a$ is decisive for the uniformity of the current density at the anode. If $N_1 << 1$, the anodic current density is virtually uniform. Conversely, if $N_1 >> 1$, the anodic current density is much higher at the edges of the anode than at the center.

The group N_2 is the ratio of the potential difference ΔE defined in Eq. [8] to the overpotential $\eta_a = h_a J_{c(max)}$ pertaining to an anodic current density which is equal to the cathodic current density $J_{c(max)}$. The corrosion rate is significantly increased by local cell action only if $N_2 >> 1$,

The increase in corrosion rate due to local cell action may be represented by the ratio Q of the current density of metal dissolution with local cell action to that without local cell action. If the latter value is equal to the maximum current density of oxygen reduction in accord with Eq. [10], the value of Q becomes

$$Q = J_a/J_{c(max)} \quad [61]$$

So far, limiting cases have been considered, and it has been assumed that either $N_1 << 1$, or $N_1 >> 1$, etc. Since the approximate formulas for $N_1 << 1$ and $N_1 >> 1$ become identical if $N_1 = 1$, etc., it is not necessary to state $N_1 << 1$ or $N_1 >> 1$ but simply $N_1 < 1$ or $N_1 > 1$. Thus one has four principal cases listed in Table I whose occurrence is determined by the values of the dimensionless groups N_1 and N_2. Figure 4 shows the ranges of these cases graphically.

The summary presented in Table I involves considerable simplifications since factors of the order of unity have been omitted. Such a simplified rep-

Table I. Limiting cases of local cell action for conditions shown in Fig. 1

($N_1 = a/\sigma h_a$; $N_2 = \Delta E/h_a J_{c(max)}$; $Q = J_a/J_{c(max)}$)

Case	I	II	III	IV
Range	$N_2 < 1$	$N_1 < 1; N_2 > 1$	$N_1 > 1; N_2 > N_1$	$N_1 > 1; N_2 < N_1$
c/a	—	$c > a$	$c > a$	$c < a$
J_a (center)	$J_{c(max)}$	$\frac{\Delta E}{h_a}$	$\frac{\sigma \Delta E}{a}$	$J_{c(max)}$
J_a (edge)	$J_{c(max)}$	$\frac{\Delta E}{h_a}$	$\left(\frac{\sigma}{a h_a}\right)^{1/2} \Delta E$	$\left(\frac{J_{c(max)} \Delta E}{h_a}\right)^{1/2}$
Q (center)	1	N_2	N_2/N_1	1
Q (edge)	1	N_2	$N_2/N_1^{1/2}$	$N_2^{1/2}$

resentation seems to be adequate for most purposes because in practice the basic data for a rational analysis such as the rate of oxygen supply and the slope of the anodic polarization curve are, in general, estimated rather than precisely known.

To illustrate the significance of the various cases, representative values of N_1 and N_2 are calculated. The value of ΔE is of the order of 1 v. The value of $J_{c(max)}$ depending on convection of the electrolyte can be expected to lie between 10^{-5} and 10^{-3} amp/cm^2. The electrical conductivity σ ranges in most cases between 5 x 10^{-4} for fresh water and 5 x 10^{-2} ohm^{-1}cm^{-1} for sea water. The slope $h_a = dE/dJ_a$ of the anodic polarization curve of a fairly reactive metal such as zinc in a 10^{-4}M Zn^{2+} ion solution is estimated to be of the order of 10^2 v/amp cm^{-2} corresponding to an exchange current density of 10^{-4} amp/cm^2, whereas less reactive metals such as iron or nickel exhibit higher values depending on the value of J_a.

For reactive metals, $N_2 = \Delta E/h_a J_{c(max)}$ lies, therefore between 10 and 10^2, i.e., is greater than unity. Consequently, cases II, III, and IV are expected to occur. According to Table I, Q(edge) $= J_a$(edge)/$J_{c(max)}$ is equal to N_2, $N_2/N_1^{1/2}$ and $N_2^{1/2}$ for cases II, III, and IV, respectively. For $\Delta E = 1$ v, $h_a = 10^2$ v/amp cm^{-2}, and $J_{c(max)} \cong 10^{-4}$ amp/cm^2 one obtains, therefore, values of Q(edge) between 10 and 100.

To have a value of $N_1 = a/\sigma h_a < 1$ corresponding to case II with uniform corrosion, the width a of the anode must be less than 5 x 10^{-2} cm in fresh water and less than 5 cm in sea water. Otherwise, case III or IV involving a higher corrosion rate at the edge of the anode than at the center occurs. If $N_2/N_1 = \sigma \Delta E/aJ_{c(max)} > 1$, case III occurs. If conversely $N_2/N_1 < 1$, case IV occurs. For $\Delta E = 1$ v, and $J_{c(max)} = 10^{-4}$ amp/cm^2, the width of the anode for a transition from case III to case IV is $a \cong 5$ cm

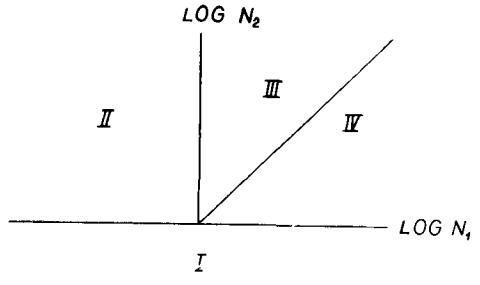

Fig. 4. Ranges of the dimensionless group $N_1 = a/\sigma h_a$ and $N_2 = \Delta E/h_a J_{c(max)}$ for the limiting coses I, II, III, and IV listed in Table I.

in fresh water and $a \cong 500$ cm in sea water. If the width of the anode is less, i.e., case III prevails, the current density J_a decreases with increasing width a of the anode at both the center and the edge. If conversely the width of the anode exceeds 5 cm in fresh water, or 500 cm in sea water, i.e., case IV prevails, J_a (center) tends to $J_{c(max)} = 10^{-4}$ amp cm^{-2} and J_a(edge) is found to be 10^{-3} amp cm^{-2} independent of the width of the anode and the conductivity of the electrolyte if $h_a = 10^2$ v/amp cm^{-2}.

The foregoing calculations refer to a value of $J_{c(max)} = 10^{-4}$ amp/cm^2 as an average representative value. In view of a rather large variability of $J_{c(max)}$ with the oxygen concentration in the bulk electrolyte and the intensity of convection, the dependence of the various phenomena on the magnitude of $J_{c(max)}$ is of special interest. If $N_1 > 1$ and $N_2 > N_1$, i.e., $J_{c(max)} < \sigma \Delta E/a$, case III is realized. The values of J_a at both the center and the edge of the anode are independent of $J_{c(max)}$, i.e., the rate of oxygen supply. On increasing the oxygen supply, N_2 becomes less than N_1 and, accordingly, case IV is realized. Then J_a(edge) is proportional to the square root of $J_{c(max)}$ and J_a(center) $\cong J_{c(max)}$. It is noteworthy that J_a is found to be virtually independent of the rate of oxygen supply if the supply is low, in particular if the oxygen concentration in the electrolyte is low. This is an important characteristic of local cell action contrary to usual rules of kinetics. The lower the oxygen concentration in the electrolyte, the greater is the effective area of the cathodes to which oxygen diffuses. In view of this compensation the rate of corrosion for cases II and III is controlled not by oxygen diffusion but by the resistance of the electrolyte and by anodic polarization.

The scheme in Table I and Fig. 4 is not strictly applicable to less reactive metals such as iron or nickel involving higher values of $h_a = dE/dJ_a$ which are not constant but depend on J_a. Under these conditions, only certain trends can be stated. First, in the case of metals exhibiting a large activation overpotential on dissolving, case I corresponding to a value of $N_2 < 1$ is favored, i.e., local cell action is not likely to enhance corrosion of a metal such as nickel. Second, if $N_2 > 1$, case II involving uniform attack is expected to occur with anodes of greater width than has been calculated above for a more reactive metal such as zinc since $N_1 = a/\sigma h_a$ is inversely proportional to h_a. The lower the reactivity of a metal, the lower is the rate of attack since J_a for case II is inversely proportional to h_a. Third, the less reactive a metal, the lower is the effect of

local cell action at edges since J_a(edge) is inversely proportional to $h_a^{1/2}$ for cases III and IV according to Eq. [43] and [53], respectively, if $h_a = dE/dJ_a$ is constant.

Although local cell action aggravates corrosion, the potential danger is not unlimited as is shown by the foregoing discussion. In many practical cases, the effect of local cell action is even less severe, if in contradistinction to an important presupposition introduced above, solid corrosion products are formed and constitute some kind of protective layer especially at locations involving a high initial attack.

The foregoing considerations refer to reduction of oxygen as the cathodic reaction. It is important to recall that evolution of hydrogen is another cathodic reaction which does occur in parallel and may prevail under certain conditions. The characteristics of local cell action due to oxygen reduction and to hydrogen evolution differ in some respects. In particular, in the case of hydrogen evolution as the predominant cathodic reaction the corrosion rate is increased considerably by small areas of a material involving a low hydrogen overpotential in a matrix of a less noble metal such as zinc at which the hydrogen overpotential is high. In contrast, in most practical cases where corrosion is due to reduction of oxygen, the cathodic current density is independent of the nature of the solid conductor because J_c is close to the limiting value $J_{c(max)}$. Under these conditions, inclusions of foreign materials affect the corrosion rate only to a minor extent. For this reason, only large cathodic areas have been considered above.

The conclusions drawn in this paper differ in some respect from those drawn by Waber and his associates (2-7, 12) because the analysis in the present paper presupposes a limiting current density of the cathodic reaction, whereas Waber, *et al.* assume linear polarization curves for both the cathodic and the anodic reaction. Both approaches supplement each other. In particular, if hydrogen evolution rather than oxygen reduction takes place as the cathodic reaction, and local depletion of hydrogen ions is not a decisive factor, Waber's analysis may be considered to be more relevant.

Manuscript received Sept. 1, 1959.

Any discussion of this paper will appear in a Discussion Section to be published in the December 1960 JOURNAL.

REFERENCES

1. C. Wagner and W. Traud, *Z. Elektrochem.*, **44**, 391 (1938).
2. J. T. Waber, *This Journal*, **101**, 271 (1954).
3. J. T. Waber and M. Rosenbluth, *ibid.*, **102**, 344 (1955).
4. J. T. Waber, *ibid.*, **102**, 420 (1955).
5. J. T. Waber and B. Fagan, *ibid.*, **103**, 64 (1956).
6. J. T. Waber, J. Morrissey, and J. Ruth, *ibid.*, **103**, 138 (1956).
7. J. T. Waber, *ibid.*, **103**, 567 (1956).
8. C. Wagner, *ibid.*, **98**, 116 (1951).
9. P. Delahay, *ibid.*, **97**, 198, 205 (1950).
10. C. Wagner, *ibid.*, **99**, 1 (1952).
11. C. Wagner, *ibid.*, **104**, 631 (1957).
12. J. T. Waber, *Corrosion*, **13**, 95t (1957).

Effect of Hydrogen Pressure on the Hydrogen Overvoltage on Bright Rhodium

Sigmund Schuldiner

U. S. Naval Research Laboratory, Washington, D. C.

ABSTRACT

The effect of hydrogen pressure on the hydrogen overvoltage on bright, active rhodium was determined. The data indicated that the overvoltage mechanism was controlled by the $2H_{ads} = H_2$ step. Kinetic parameters for the mechanism were quantitatively determined including the surface coverage with adsorbed atomic hydrogen. A Langmuir adsorption isotherm resulted from the relationship between surface coverage with atomic hydrogen at equilibrium and the partial pressure of molecular hydrogen above the solution.

It has been shown in a previous study of the effect of hydrogen pressure on the overvoltage on bright platinum (1) that pressure effects can be used to determine kinetic parameters and to establish a reasonable reaction mechanism. In the investigation reported here pressure effects on hydrogen formation and ionization reactions on bright rhodium were studied. By using this metal in rapidly stirred, strong acid solution, diffusion effects were virtually eliminated, and it was possible to make a quantitative determination of the kinetic parameters.

Experimental

Breiter, Kammermaier, and Knorr (2) showed that the properties of an "aged" rhodium electrode are different from those of a "new" electrode. This was confirmed by this investigation. On a new rhodium electrode it was found that at first the overvoltage was relatively high, but that on repeated anodic and cathodic cycling to high polarization values (−0.4 v cathodic and > 1 v anodic) a reproducible electrode of high activity was obtained.

The general experimental techniques were the same as those previously used (3, 4). The cell was constructed of Teflon and is shown in Fig. 1. The rhodium (99.5 + %) cathode was prepared by melting the tip of a 0.025 in. thick rhodium wire with a hydrogen/oxygen flame and forming a small sphere. The wire was then inserted into the 0.02 in. hole

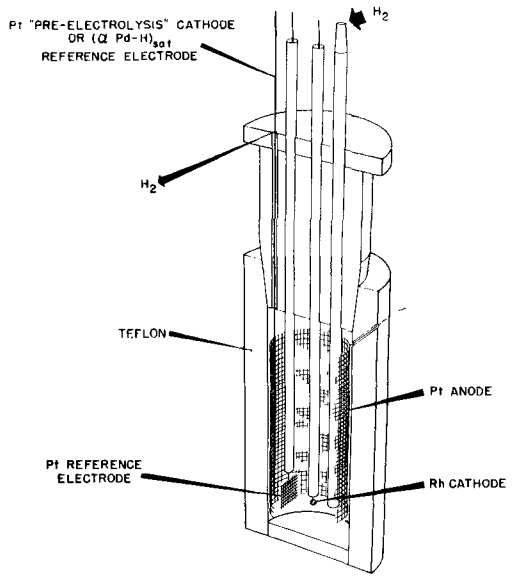

Fig. 1. Electrolytic cell

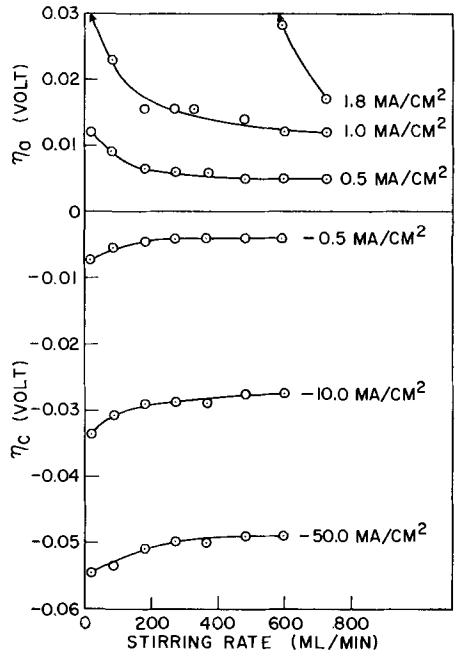

Fig. 2. Effect of stirring rate (P_{H_2} = 1 atm) on η_c and η_a

in the Teflon rod shown in Fig. 1. A molten polyethylene seal was made between the bottom of the Teflon rod and the rhodium wire. The resulting rhodium electrode then consisted of a bead at the end of a 2 mm exposed length of wire. The total apparent area of exposed rhodium was 0.10 cm². The solution was in all cases 1M H_2SO_4. Purified gases consisting of either pure hydrogen or mixtures of hydrogen and helium were bubbled through the acid solution in the cell. The method of preparation of the gas mixtures and the determination of the hydrogen partial pressure are described in a previous paper (1).

After the solution was pre-electrolyzed and the rhodium electrode was activated by repeated anodic and cathodic polarization, repeated measurements were taken at each partial pressure of hydrogen under both anodic and cathodic polarization. Overvoltages at each current density were time independent. The reference electrode to cathode interface *IR* drop was determined by interrupter measurements (3). The data given are average values of individual runs. The precision of an individual reading was better than 0.5 mv. The maximum deviation of the average values was ±0.5 mv at low overvoltages and ±2 mv at high overvoltages. The temperature was 27° ±1°C.

Experimental Results

Concentration polarization effects were minimized by rapid stirring with gas. Figure 2 shows the effect of stirring rate on overvoltage for pure hydrogen. The data show that a value is reached after which the overvoltage is independent of stirring rate. Stirring rates in excess of these values were used for all measurements.

Cathodic overvoltage, η_c, vs. log apparent current density curves at different hydrogen pressures are shown in Fig. 3. Figure 4 shows the anodic overvoltage, η_a, vs. log apparent current density curves. At low current densities a linear relationship between the anodic and cathodic overvoltages and apparent current density was found and these results are shown in Fig. 5.

From the experimental data shown in Fig. 3-5, kinetic parameters and a reaction mechanism can be determined.

Calculation of Kinetic Parameters

The Tafel slopes of ~0.0295 shown in Fig. 3 indicate that the reaction mechanism is a fast discharge of hydronium ions followed by a slow combination of hydrogen atoms, H_{ads}, to molecules;

$$H_3O^+ + e^- = H_{ads} + H_2O \qquad [1]$$

$$2H_{ads} \xrightarrow{\text{slow}} H_2 \qquad [2]$$

This mechanism is confirmed by the limiting anodic current densities found in Fig. 4. These limiting current densities would be caused by the coverage of adsorbed hydrogen atoms on the rhodium surface dropping to zero. It will be shown later that the limiting current densities shown in Fig. 4 are not due to a diffusion process.

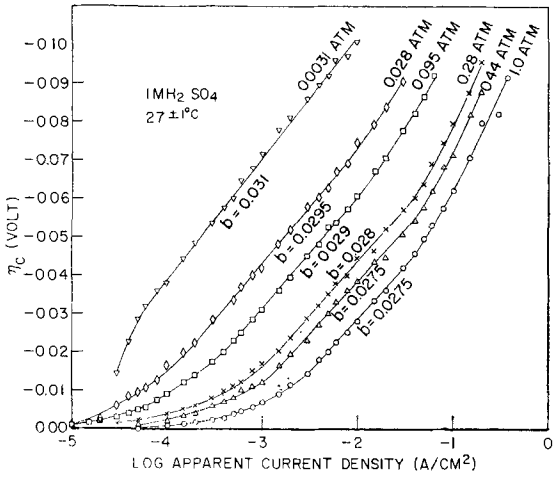

Fig. 3. Relations for η_c vs. log ($-i_c$)

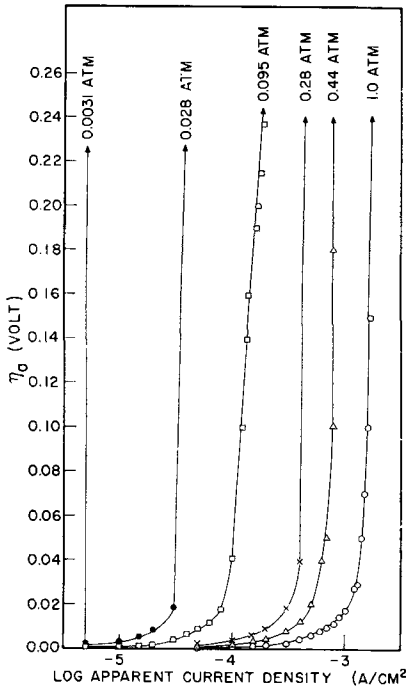

Fig. 4. Relations for η_a vs. log i_a

The equations (1) for this mechanism are:

$$i_c = i_{o,c}\frac{(1-\theta)^2}{(1-\theta_0)^2}[\exp(-2\eta_c\mathbf{F}/RT)-1] \qquad [3]$$

$$i_a = i_{o,a}\frac{(1-\theta)^2}{(1-\theta_0)^2}[1-\exp(-2\eta_a\mathbf{F}/RT)] \qquad [4]$$

where i_c, i_a are the applied cathodic and anodic current densities respectively; $i_{o,c}$, $i_{o,a}$ are the cathodic and anodic exchange current densities, respectively; η_c, η_a are the cathodic and anodic overvoltage, respectively; θ is the fraction of available surface covered with atomic hydrogen; θ_0 is the fraction of available surface covered with atomic hydrogen at zero current density, (equilibrium); and R, T, and $\mathbf{F}$ are the gas constant, absolute temperature and the Faraday, respectively.

At overvoltages near equilibrium $\theta \approx \theta_0$ and Eq. [3] and [4] can be simplified to:

$$i_c = i_{o,c}[\exp(-2\eta_c\mathbf{F}/RT)-1] \qquad [3a]$$

$$i_a = i_{o,a}[1-\exp(-2\eta_a\mathbf{F}/RT)] \qquad [4a]$$

The values of $i_{o,c} = -i_{o,a}$ can therefore be determined for various values of hydrogen partial pressure, P_{H_2}, by plotting i_c vs. $[\exp(-2\eta_c\mathbf{F}/RT)-1]$ and i_a vs. $[1-\exp(-2\eta_a\mathbf{F}/RT)]$. These plots are shown in Fig. 6.

The values of θ_0 and θ can be determined in the following way. If one plots i_c vs. $[\exp(-2\eta_c\mathbf{F}/RT)-1]$ throughout the entire range of values determined, the curves shown in Fig. 7 are obtained. The deviation at higher current densities, where θ is significantly greater than θ_0, from the straight line fit found

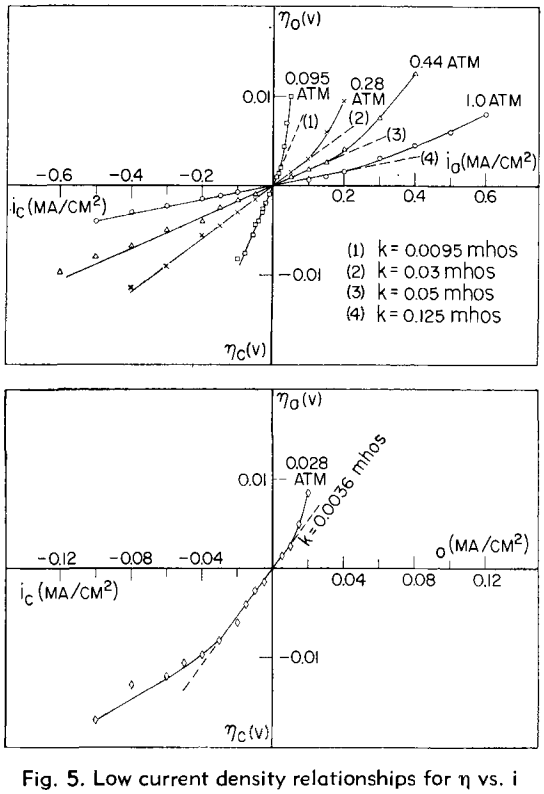

Fig. 5. Low current density relationships for η vs. i

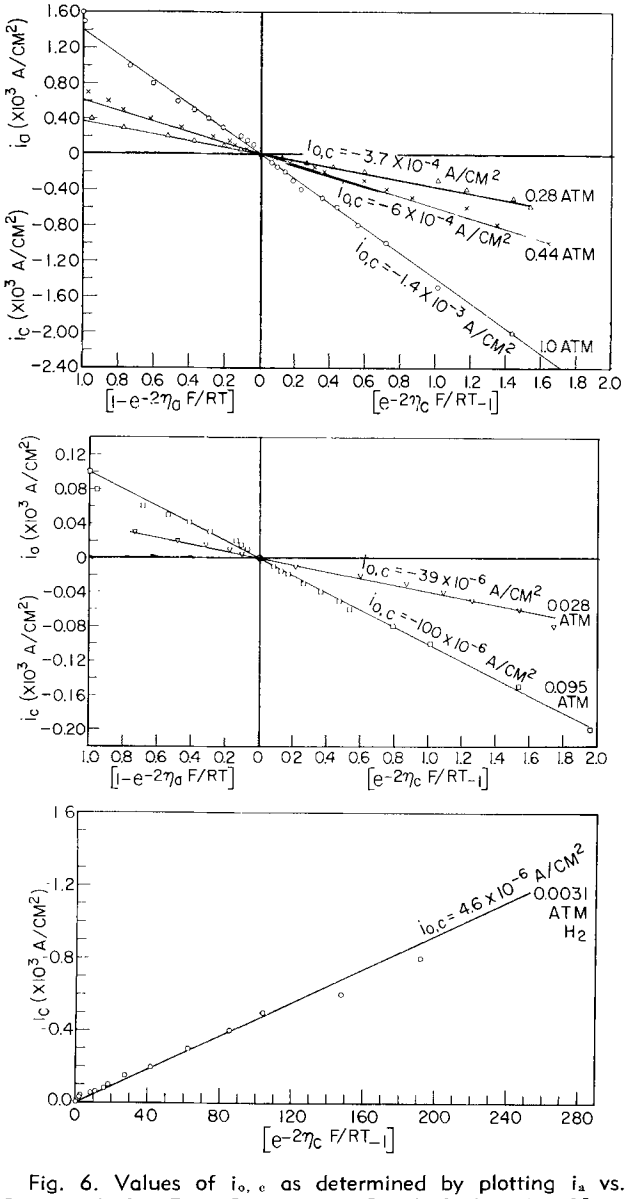

Fig. 6. Values of $i_{o,c}$ as determined by plotting i_a vs. $[1-\exp(-2\eta_a F/RT)]$ and i_c vs. $[\exp(-2\eta_c F/RT)-1]$.

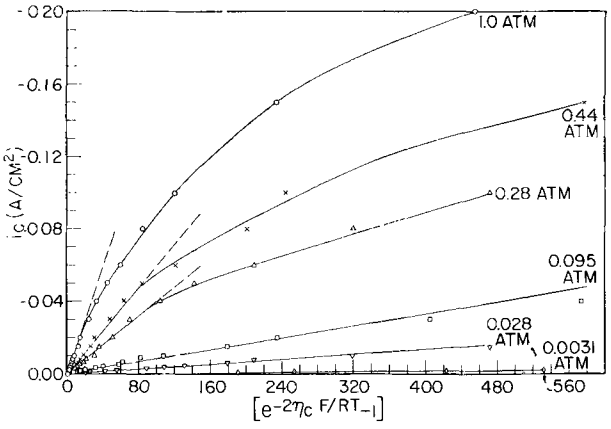

Fig. 7. i_c vs. $[\exp(-2\eta_c F/RT) - 1]$

at low current densities is a function of the ratio $(1-\theta)^2/(1-\theta_0)^2$. Hence in order to linearize these curves one would have to plot i_c vs. $(1-\theta)^2/(1-\theta_0)^2$ $[\exp(-2\eta_c \mathbf{F}/RT)-1]$. One can then solve for $(1-\theta)^2/(1-\theta_0)^2$ using Eq. [3]. Since the slow combination step, Eq. [2], of the reaction mechanism in the absence of a back reaction can be written as follows

$$i_c = \vec{k}_2 \theta^2$$

and since

$$i_{o,c} = \vec{k}_2 \theta_0^2$$
$$i_c/i_{o,c} = \theta^2/\theta_0^2 \qquad [5]$$

By simultaneous use of Eq. [3] and [5] one can solve for θ_0 and θ when $\eta_c > 0.03$ v, then

$$\theta_0 = \frac{[\exp(-2\eta_c \mathbf{F}/RT)-1]^{1/2} - (i_c/i_{o,c})^{1/2}}{(i_c/i_{o,c})^{1/2}\{[\exp(-2\eta_c \mathbf{F}/RT)-1]^{1/2}-1\}} \qquad [6]$$

and

$$\theta = (i_c/i_{o,c})^{1/2}\,\theta_0 \qquad [7]$$

The limiting cathodic current densities, $i_{c,L}$, were determined from Eq. [5]. When $i_c = i_{c,L}$, $\theta = 1$, hence

$$i_{c,L} = i_{o,c}/\theta_0^2 \qquad [8]$$

The limiting anodic current densities, $i_{a,L}$, were determined from Eq. [4]. When $i_a = i_{a,L}$, $\theta = 0$ and since η_a is a large positive number, $\exp(-2\eta_a \mathbf{F}/RT) \approx 0$, hence

$$i_{a,L} = i_{o,a}/(1-\theta_0)^2 \qquad [9]$$

The rate constants for the over-all reaction, $k = \pm(di/d\eta)_{\eta\to 0}$ (the sign is negative for the cathodic and positive for the anodic directions) near equilibrium where there is a linear relation between η and i were determined from Fig. 5. The stoichiometric numbers, μ, were calculated from the Horiuti (5) relationship

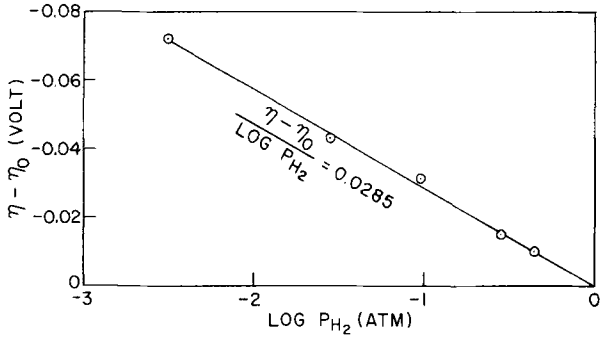

Fig. 8. η-η_0 vs. log P_{H_2}

$$\mu = 2i_{o,c}\mathbf{F}/kRT \qquad [10]$$

Table I lists the kinetic parameters which were determined as indicated above. In addition the experimentally determined values of $i_{a,L}$ are shown for comparison with the calculated values.

Discussion

Several investigators have established (1, 6-11) that at a given current density in the linear Tafel region the hydrogen overvoltage on a cathode is related to the hydrogen pressure by the expression

$$\eta = \eta_0 + (RT/2\mathbf{F}) \ln P_{H_2} \qquad [11]$$

where η, the overvoltage, is defined as the potential difference between the working electrode and a reversible hydrogen electrode in the same solution, η_0 is the overvoltage at 1 atm of hydrogen and P_{H_2} is the partial pressure of hydrogen above the solution. A plot of $\eta - \eta_0$ vs. log P_{H_2} for the data which was taken at 27°C should therefore give a straight line with a slope of 0.0295 v. Figure 8 shows such an experimental plot with a slope of 0.0285 v. The agreement is very good which not only confirms Eq. [11] but also serves as a verification of the hydrogen partial pressure values.

The effects of current density on surface coverage with atomic hydrogen, θ, for various P_{H_2} values are shown in Fig. 9. Here i_c is plotted vs. θ^2. According to Eq. [5], when the back reaction is negligible there should be a linear relation between i_c and θ^2 with a slope of $i_{o,c}/\theta_0^2$. As shown by Eq. [8], when $i_c = i_{c,L}$ the slope is simply $i_{c,L}$. Since, when the back reaction is negligible, the surface coverage should be only a function of current density independent of P_{H_2}, a slope of $i_{c,L}$ should apply for all the data shown in Fig. 9. The average $i_{c,L}$ values of −1.49 amp/cm^2 given in Table I has been drawn through each set of points shown in Fig. 9. As can be seen the fit of this

Table I. Kinetic parameters

P_{H_2}, atm	$i_{o,a} = -i_{o,c}$, amp/cm^2	θ_0, average values	Calc. $i_{a,L}$, amp/cm^2	Expt. $i_{a,L}$, amp/cm^2	$i_{c,L}$, amp/cm^2	k, mhos/cm^2	μ
1.0	1.4×10^{-3}	0.029	1.48×10^{-3}	1.87×10^{-3}	−1.66	0.125	0.87
0.44	6.0×10^{-4}	0.020	6.24×10^{-4}	8.5×10^{-4}	−1.50	0.050	0.93
0.28	3.7×10^{-4}	0.015	3.81×10^{-4}	4.5×10^{-4}	−1.64	0.030	0.96
0.095	1.0×10^{-4}	0.008	1.02×10^{-4}	1.9×10^{-4}	−1.56	0.0095	0.82
0.028	39×10^{-6}	0.0053	39.4×10^{-6}	35×10^{-6}	−1.40	0.0036	0.84
0.0031	4.6×10^{-6}	0.0020	4.62×10^{-6}	$\sim 5 \times 10^{-6}$	−1.15	—	—
				Avg	−1.49		0.88

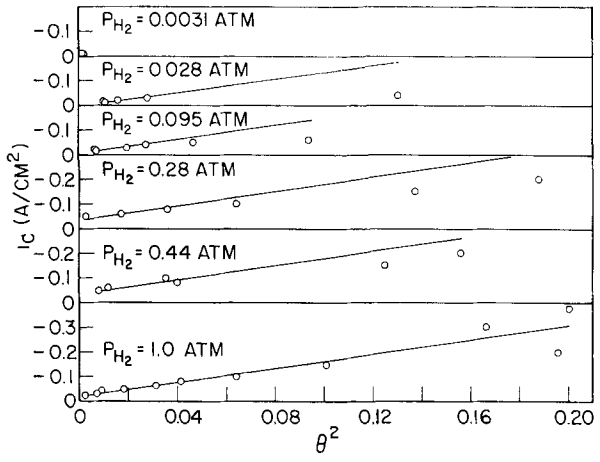

Fig. 9. Relations between i_c and θ^2

slope through the points at θ^2 values below 0.06, which corresponds to a θ value of 0.245, is good. The poorer fit at higher θ^2 values is undoubtedly due to the assumption of a Langmuir isotherm (12) in the derivation of Eq. [3] and [4]. A better fit would probably be obtained by use of a Temkin (13) isotherm at coverages above 0.2. However, the use of the Langmuir isotherm for the calculation of kinetic parameters in the present paper is valid since θ_0, and $i_{a,L}$ represent low and zero coverage, respectively, whereas $i_{c,L}$ represents full coverage. The Langmuir isotherm does apply to these conditions.

The Langmuir isotherm is

$$\theta_0^2/(1-\theta_0)^2 = KP_{H_2} \qquad [12]$$

The data for this isotherm is plotted in Fig. 10 and an excellent fit to a straight line intersecting the zero point is obtained. The calculated K value is 0.0009. The Langmuir isotherm shown in Fig. 10 confirms the fact that the atomic hydrogen coverage of the rhodium surface at equilibrium is low. It also confirms the electrode mechanism postulated and the method of calculating the kinetic parameters. In addition, since the anodic part of the curves shown in Fig. 6 show a good linear fit from zero overvoltage to about the point where the limiting anodic current density is reached, one can conclude that $\theta_0 << 1$. This is because during anodic polarization the value of θ must range from θ_0 at equilibrium to zero at the limiting current density. If this range of values was a significant fraction of unity then one could not obtain a linear fit using Eq. [4a].

A further confirmation of the applicability of the calculations used is the stoichiometric number, μ,

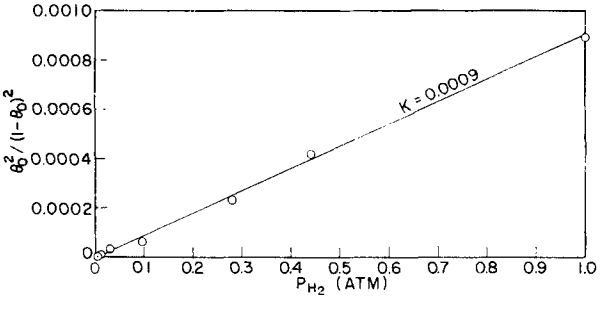

Fig. 10. Langmuir adsorption isotherm, $\theta_0^2/(1-\theta_0)^2$ vs. P_{H_2}

being close to unity and the agreement between the experimental and calculated anodic limiting current densities shown in Table I. There is always a possibility that some hydrogen is dissolved in the metal near the surface, and this would tend to result in making the experimental error in the direction of higher $i_{a,L}$ values. This is generally observed in Table I comparing the experimental $i_{a,L}$ values with the calculated values.

Ershler (14) by use of charging curves, Eucken and Weblus, and Breiter, Knorr, and Völkl (15) from a-c impedance measurements have concluded that the surface of a platinum metal is covered largely with atomic hydrogen at the hydrogen equilibrium potential. The results given here and in previous papers from this laboratory (1, 16) have shown that the surface of platinum metals is covered only sparsely with atomic hydrogen at equilibrium. It is conceivable that both results may be correct. For example, a layer of atomic hydrogen may exist just beneath the metal surface or is so incorporated in the metal surface that it is in effect a part of the metal. If this atomic hydrogen is not in equilibrium with the molecular hydrogen in solution, then it may be detected by charging curves, or by a-c methods but would not play a part, except possibly as a catalyst, in the hydrogen surface potential-determining reaction at equilibrium. It could be that such a layer is formed by the activation procedures used with platinum metals which generally consist of alternate anodic and cathodic treatment. Such a layer may also exist even at very low hydrogen partial pressures. It is noteworthy that the a-c impedance measurements of Breiter, Knorr, and Völkl (15) gave virtually the same high surface coverage for Pt metals in both hydrogen and nitrogen saturated solutions. The transitory nature of highly activated platinum (17-19) in highly purified solutions may be due to such a layer of atomic hydrogen being decreased in time rather than to the accumulation of impurities on the surface.

Diffusion effects in this investigation must be negligible under the experimental conditions used. The reason for this can be seen from the fact that $i_{a,L}$ values are always greater than $i_{o,a}$ values. If diffusion were important, when $\theta_0 << 1$, $i_{a,L}$ values must always be smaller. This can be seen from the relation

$$1/i_{a,L} = (1-\theta_0)^2/i_{o,a} + 1/i_{o,d} \qquad [13]$$

where $i_{o,d}$ is the so-called diffusion exchange current density. This means that for the system reported here $i_{o,d}$ must be much larger than $i_{o,a}$.

Another verification of the kinetic analysis used in this paper would be an experimental determination of $i_{c,L}$. This was impossible to achieve with the technique used in this investigation. This is due primarily to the large coverage of the metal surface with hydrogen bubbles at current densities approaching 0.5 amp/cm^2. New techniques are being considered with which it is hoped that this difficulty may be overcome and a determination of $i_{c,L}$ may be possible.

Manuscript received Aug. 27, 1959.

Any discussion of this paper will appear in a Dis-

cussion Section to be published in the December 1960 JOURNAL.

REFERENCES

1. S. Schuldiner, *This Journal*, **106**, 891 (1959).
2. M. Breiter, H. Kammermaier, and C. A. Knorr, *Z. Elektrochem.*, **60**, 119 (1956).
3. S. Schuldiner, *This Journal*, **99**, 488 (1952).
4. S. Schuldiner, *ibid.*, **101**, 426 (1954).
5. J. Horiuti, *J. Research Inst. Catalysis, Hokkaido*, **1**, 8 (1948).
6. S. J. Bircher and W. D. Harkins, *J. Am. Chem. Soc.*, **45**, 2890 (1923).
7. M. Knoble, *ibid.*, **46**, 2751 (1924).
8. H. M. Cassel and E. Krumbein, *Z. physik. Chem.*, **A171**, 70 (1934).
9. G. Schmid and E. K. Stoll, *Z. Elektrochem.*, **47**, 360 (1941).
10. J. O'M. Bockris and R. Parsons, *Trans. Faraday Soc.*, **45**, 916 (1949).
11. K. J. Vetter and D. Otto, *Z. Elektrochem.*, **60**, 1072 (1956).
12. I. Langmuir, *J. Am. Chem. Soc.*, **54**, 2798 (1932).
13. M. I. Temkin, *Z. Fiz. Khim.*, **15**, 296 (1941).
14. B. Ershler, *Acta Physicochim.*, **7**, 327 (1937).
15. A. Eucken and B. Weblus, *Z. Elektrochem.*, **55**, 114 (1951); M. Breiter, C. A. Knorr, and W. Völkl, *ibid.*, **59**, 681 (1955).
16. S. Schuldiner, *This Journal*, **106**, 440 (1959).
17. A. N. Frumkin, *Z. Physik. Chem.*, **207**, 321 (1957).
18. A. N. Frumkin and E. Aikasjan, *Dokl. Akad. Nauk SSSR*, **100**, 315 (1955).
19. M. Breiter, H. Kammermaier, and C. A. Knorr, *Z. Elektrochem.*, **60**, 37 (1956).

Technical Notes

Effect of Oxygen on the Active-Passive Behavior of Stainless Steel

Norbert D. Greene[1]

M tals Research Laboratories, Union Carbide Metals Company, Division of Union Carbide Corporation, Niagara Falls, New York

The usefulness of potentiostatic polarization methods for studying passivity of metals has been demonstrated (1-7). These techniques are used here to determine whether dissolved oxygen has any effect on the active-passive behavior of stainless steel. The passivating inhibitor mechanism proposed by Stern (8) assumes that the presence of small quantities of oxidizing agents (or passivators) does not affect appreciably the anodic dissolution kinetics of a metal. This study is a direct test of this assumption. Further, it is also useful in testing the validity of theories which attribute passivity to the retardation of anodic dissolution by adsorbed oxygen from solution (9-11).

Type 430 stainless steel in sulfuric acid was chosen for this study because its active-passive transition is reproducible and does not vary with time, and the critical anodic current density is sufficiently high so that spontaneous passivation does not occur in oxygen-saturated solutions.

Experimental

Potentiostatic anodic polarization measurements were conducted with apparatus and techniques described in detail elsewhere (7, 12). Electrodes were machined from Type 430 stainless steel (15.90% chromium, 0.30% manganese, 0.054% carbon, 0.31% silicon, 0.005% phosphorus, and 0.011% sulfur) furnace-cooled after 1 hr at 780°C. Polarization measurements were conducted in hydrogen- and oxygen-saturated sulfuric acid solutions.

[1] Present address: Department of Metallurgical Engineering, Rennselaer Polytechnic Institute, Troy, New York.

Electrodes were pre-exposed to the test solutions for 15 to 20 hr prior to polarization measurements. All tests were performed at 24° to 26°C.

Results

Figure 1 shows anodic polarization data for Type 430 stainless steel in hydrogen-saturated normal sulfuric acid. The active corrosion potential is indicated on the ordinate. This curve is typical of most active-passive metals (1-7). As the potential is increased, current density increases to a maximum, here called critical anodic current density, I_c. The corresponding potential is called the primary passive potential, *Epp*. At potentials more noble than *Epp*, current decreases, eventually to very small values, and becomes time-dependent. Above approximately 0.900 v, current again increases with potential and oxygen evolution occurs. The current maximum at 0.050 v is not significant in the passivation process and is not considered further here.

Although Fig. 1 is an applied current polarization curve, other studies, to be reported later, demonstrate that it closely approximates actual anodic dissolution rate over a wide range of potentials. At potentials above reversible oxygen potential (0.900 v) and within approximately 50 mv of the active corrosion potential, significant distortion occurs because of contributions from oxygen and hydrogen evolution, respectively.

Figure 2 shows the polarization of Type 430 stainless steel in oxygen-saturated normal sulfuric acid. In contrast to the behavior in hydrogen-satu-

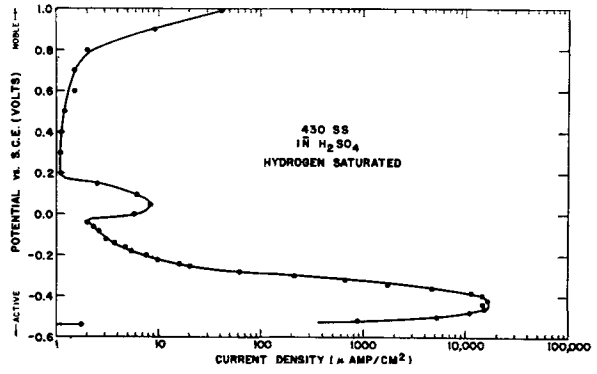

Fig. 1. Anodic polarization of Type 430 stainless steel in hydrogen-saturated 1N sulfuric acid.

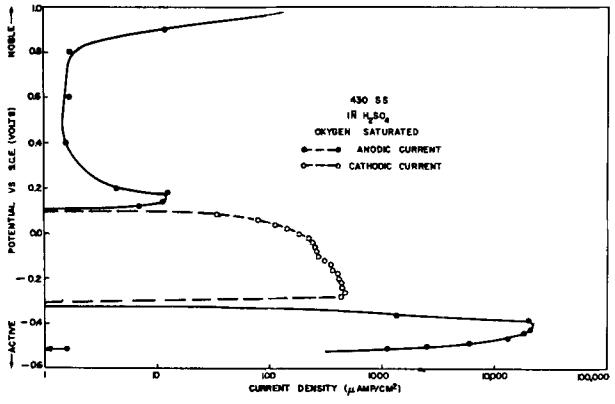

Fig. 2. Anodic polarization of Type 430 stainless steel in oxygen-saturated 1N sulfuric acid.

rated acid, this system demonstrates two stable mixed potentials as evidence by the appearance of the cathodic loop between −0.300 and 0.100 v. In this environment, Type 430 stainless alloy can exist in either the active state at −0.517 v or the passive state at 0.100 v.[2] Since both active and passive states are stable, the system does not spontaneously transform from one to the other. However, the alloy can be repeatedly transformed from one state to the other by application of suitable anodic or cathodic currents. Thus, the limiting diffusion current of oxygen in an oxygen-saturated solution is sufficient to maintain stable passivity but insufficient to cause spontaneous passivation. For descriptions of cathodic loops, spontaneous passivation, and other phenomenological features of active-passive metals, see (2, 5, 8, 14).

Similar experiments were performed in 5 and 10*N* sulfuric acid and are summarized in Table I.

[2] Although the initial passive potential of this system was 0.100 v, the time-dependency of passive dissolution (4, 7, 13) produced a slow shift in the noble direction. After 48 hr in the passive condition, this potential increased to 0.345 v.

Table I. Primary passive potentials (Epp) and critical anodic current densities (I_c) of Type 430 stainless steel in sulfuric acid

Potentials = v vs. SCE; current = ma/cm²

Acid concentration	Hydrogen saturated		Oxygen saturated	
	Epp	I_c	*Epp*	I_c
1*N*	−0.420	17	−0.420	21
5*N*	−0.340	26	−0.340	29
10*N*	−0.260	40	−0.280	43

All oxygen-saturated solutions exhibited cathodic loops during anodic polarization. Differences between hydrogen-saturated and oxygen-saturated solutions shown in Table I are within the limits of experimental accuracy.

Discussion

Figures 1 and 2 and Table I demonstrate that oxygen, in sufficient concentration to maintain passivity of Type 430 stainless steel, does not affect anodic dissolution of this alloy. Thus, passivity cannot be attributed to the retardation of anodic dissolution by the adsorption of oxygen from solution as proposed by several investigators (9-11). Although oxygen adsorption undoubtedly occurs on stainless steel surfaces, it does not retard dissolution. The fact that stable passivity has been observed in the absence of oxygen (5) offers additional evidence that passivity is not caused by adsorbed oxygen.

The presence of oxygen does not measurably affect dissolution kinetics of Type 430 stainless steel in sulfuric acid. Therefore, for this system, the assumption that anodic and cathodic partial processes are mutually independent (4, 8) is correct. For predicting both the effectiveness of passivating agents and the relative passivating tendencies of alloys, this assumption can probably be generally applied, as shown by the success of recent studies of this nature (2, 7, 8).

Although a mechanism for passivity cannot be deduced from the measurements performed here, this study further confirms the phenomenological description of passivity proposed by Stern (8). Simply, any oxidizer capable of producing a mixed potential within the passive potential region can produce stable passivity. In this sense, oxygen demonstates no specific property; its behavior is typical of any strong oxidizing agent.

Summary

1. It is shown that the presence of oxygen has no apparent effect on the anodic dissolution kinetics of Type 430 stainless steel. The primary passive potential and the critical anodic current density are essentially the same in the presence or absence of dissolved oxygen.

2. The passivating inhibitor theory described by Stern is supported by this study.

3. Results of this study are not consistent with adsorbed oxygen theories of passivity.

Acknowledgment

The author acknowledges the capable assistance of E. A. Tomes who performed the experimental measurements presented here. Discussions with Dr. A. C. Makrides and Dr. M. Stern are greatly appreciated.

Manuscript received Jan. 20, 1960.

Any discussion of this paper will appear in a Discussion Section to be published in the December 1960 JOURNAL.

REFERENCES

1. W. A. Mueller, *Can J. Technol.*, **34**, 162 (1956).

2. C. Edeleanu, *J. Iron Steel Inst.*, **188**, 122 (1958).
3. M. Prazák and V. Cihál, *Z. Elektrochem.*, **62**, 739 (1958).
4. Y. M. Kolotyrkin, *ibid.*, **62**, 664 (1958).
5. M. Stern and H. Wissenberg, *This Journal*, **106**, 755 (1959).
6. R. Otsuka, *J. Electrochem. Soc. Japan*, (Overseas Ed.), **27**, E41 (1959).
7. N. D. Greene, To be published.
8. M. Stern, *This Journal*, **105**, 638 (1958).
9. M. G. Fontana and F. H. Beck, *Metal Progress*, **51**, 939 (1947).
10. T. P. Hoar and U. R. Evans, *This Journal*, **99**, 212 (1952).
11. H. H. Uhlig and S. S. Lord, Jr., *ibid.*, **100**, 216 (1953).
12. N. D. Greene, *Corrosion*, **15**, 369t (1959).
13. M. Stern, *This Journal*, **106**, 376 (1959).
14. G. Okamoto and M. Nagayama, *Corrosion Engineers* (Japan), **7**, 1 (1958).

A Controlled Diffusion Process for Indium in N-Type Germanium

F. Barson, M. J. Dyett, C. Karan, and W. E. Mutter

Product Development Laboratory, International Business Machines Corporation, Poughkeepsie, New York

In the fabrication of NPN diffused base transistors, one conventional process starts with N-type germanium and diffuses a P-type skin into its surface. An N-type emitter dot is then alloyed into the diffused skin to complete the NPN structure.

One complication which arises, particularly during the diffusion process, is that of thermal conversion; that is, when germanium is heated above about 500°C and cooled fairly rapidly, additional acceptor levels appear in the bulk of the crystal (1). The density of these thermal acceptors is often great enough that N-type germanium is completely converted to P-type.

The cause of this thermal conversion in germanium is associated primarily with the introduction of copper into the material. Copper is apparently usually present in trace amounts on the surface and, due to its very high diffusivity at elevated temperatures, spreads rapidly throughout the bulk of the germanium where it acts as an acceptor center (2, 3). In addition, quenches from high temperatures may introduce acceptor levels of another kind, which are apparently due to quenched-in lattice defects (4, 5). Except with very rapid cooling rates, however, this latter type of thermal acceptor is not too troublesome.

Several investigators have suggested means of minimizing thermal conversion due to copper contamination. Annealing the germanium at 500°C precipitates the copper in clusters which are electrically inactive (2, 6); however, since the copper is not actually removed from the sample by this method, further heating cycles may cause conversion to occur once more. A vacuum heat treatment, on the other hand, removes the possibility of conversion by actually evaporating the copper from the sample, maintaining its resistivity (7). Another method is to clean the germanium in potassium cyanide prior to any proposed heat treatment (8, 9). The cyanide forms soluble complexes with copper, removing it before it can diffuse in and be troublesome. Finally, it has been shown that certain molten metals in contact with germanium, due to their high solubility for copper, act as getters which extract the copper from the germanium (10-12).

It is this last method which has been employed in the present work to develop a practical process for diffusion into N-type germanium. By a proper choice of the getter metal, it has been found possible not only to retain the original resistivity of the N-type germanium wafer, but also to use this metal as a source of acceptor impurities for the diffusion itself.

Method and Results

Approximately 0.1 mil thickness of indium metal was evaporated onto one side of the N-type germanium wafers to be diffused. The wafers were then placed, indium side down, on a graphite slab and heated in a wire-wound furnace under an atmosphere of slowly flowing forming gas. The temperature used for the diffusion was 875°C. At this temperature, the molten indium film under the germanium provided enough indium vapor in the furnace so that a P-type skin formed by diffusion on the upper sides of the wafer.

In this way, the indium served both as a getter to remove copper from the sample and also as a source of the acceptor impurity for diffusion as well. The thickness of the P-type skin so formed could be controlled by the length of time that the sample was held at high temperature. Following the diffusion, the samples were cooled and the indium film, presumably now containing any copper originally present in the germanium, was removed from the bottom of the wafers by lapping.

The resistivities of the wafers were measured by the four-point probe method prior to the evaporation, and again after the diffusion (on the lapped, N-type surface). Seldom was the density of thermal acceptors introduced by the process found to exceed 1×10^{14} cm^{-3}. This means that germanium in the range of 3-6 ohm-cm suffered an increase in resistivity of less than 0.5 ohm-cm.

The junction depth X_j for a diffusion was measured by beveling a portion of the surface at a low angle and locating the junction with a thermal probe mounted on a sensitive depth gauge. To estimate C_o, the surface concentration for the indium diffusion, the familiar error function distribution was evaluated at the junction:

$$C_j = C_o \operatorname{erfc} X_j/2\sqrt{Dt}$$

Assuming a diffusion coefficient of 1.5×10^{-12} cm^2/sec at 875°C, C_o was calculated to be about 5×10^{18}

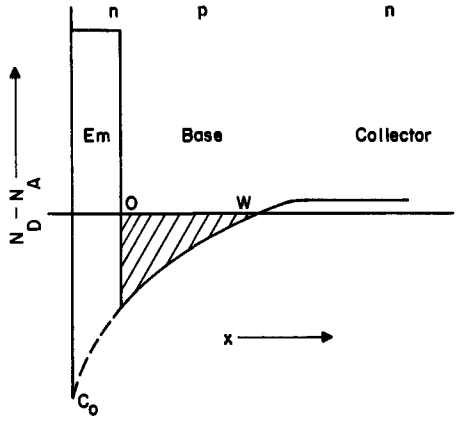

Fig. 1. Impurity distribution in a transistor made by the process described. Shaded area represents $\int_o^w P\,dx$.

cm^{-3}. The assumed diffusion coefficient is in good agreement with that determined by several earlier investigators (13-15); furthermore, the resulting C_o was consistent with sheet resistance measurements made in a manner similar to that of Backenstoss (16) for silicon diffusions.

In order to point out a practical difficulty in making transistors of the indium-diffused material described above, we recall that the fabrication process is now to alloy an N-type emitter into the P-type skin. This results in an impurity distribution somewhat as shown in Fig. 1. The emitter efficiency for this structure can be shown to be (17):

$$\gamma = \frac{1}{1 + \frac{\mu_p}{\mu_n} \frac{\int_o^w P\,dx}{L_{pe} N_o}}$$

Notice that the integral, which represents the shaded area in Fig. 1, should have a small value to give a high emitter efficiency. This means that if C_o is large, the emitter must be alloyed very close to the collector junction (that is, the base must be very narrow) to preserve a high emitter efficiency. This calls for very precise control of alloying; for placing the emitter junction at too shallow a depth results in low emitter efficiency, while placing it at too great a depth results in alloying completely through to the collector junction. There are several ways to lower C_o in the indium diffusion process so as to decrease the slope of the impurity distribution and thus allow more leeway in the emitter alloying process. A method which was both simple and effective was to use an evaporated film of both indium and tin together as a getter-source and then to perform the diffusion exactly as described in the original process, a single-zone furnace sufficing.

We recall that, for an ideal solution, the vapor pressure of the solute is proportional to its mole fraction in the solution (Raoult's law). Hence, we would expect that as the concentration of indium in the evaporated tin-indium film was decreased, the vapor pressure of the indium at diffusion temperatures would similarly decrease, and with it the C_o of the diffusion process. That this is actually the case is illustrated in Fig. 2 which shows the C_o for several diffusions using indium and tin-indium films on the germanium wafers. The values of C_o are based once more on junction depth measurements and an assumed diffusivity of $D = 1.5 \times 10^{-12}$ cm^2/sec at 875°C. The limits of probable error shown are largely due to uncertainty in the junction depth measurement, which was about ± 0.02-0.03 mil. The trend, however, is clear, demonstrating the variation of C_o which is possible with the method described.

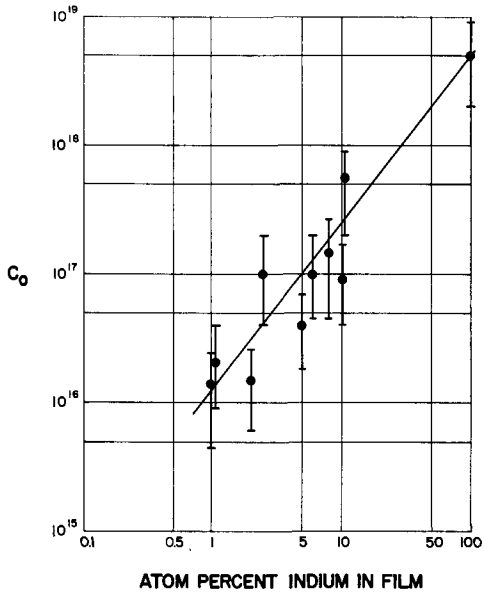

Fig. 2. Surface concentration C_o as a function of the evaporated film composition.

Tin was selected as the second metal to dilute the indium, partly because it is reportedly inert electrically in germanium (18) and partly because, due to its low vapor pressure, it did not itself evaporate appreciably during the longer diffusion runs. It should perhaps be pointed out that, although it is the atom percent of indium in the evaporated film which is plotted in Fig. 2, the actual molten film during diffusion was a ternary solution of indium, tin, and also germanium dissolved at the diffusion temperature. Thus the data presented apply only to the case described, in which the film is in physical contact with the germanium during diffusion.

Conclusion

The experimental results presented show that molten indium metal in contact with germanium can be used not only as a getter to prevent thermal conversion, but also as a simultaneous source of indium vapor for diffusion into the germanium. Furthermore, by diluting the indium with tin, the surface concentration of indium in the diffused skin can be reduced controllably. This, plus the fact that only a simple, one-zone diffusion furnace is required, makes the process an easy and practical one for producing diffused skins on germanium for diffused base transistor manufacture.

Acknowledgments

The authors are indebted to Mr. P. Ostapkovich for his advice and assistance in arranging the ex-

perimental work, and to Mr. B. Szabo for sheet resistance measurements.

Manuscript received Sept. 21, 1959. This paper was prepared for delivery before the Ottawa Meeting, Sept. 28-Oct. 2, 1958.

Any discussion of this paper will appear in a Discussion Section to be published in the December 1960 JOURNAL.

REFERENCES

1. H. C. Theuerer and J. H. Scaff, *J. Metals*, **4**, 59 (1951).
2. C. S. Fuller and J. D. Struthers, *Phys. Rev.*, **87**, 526 (1952).
3. W. P. Slichter and E. D. Kolb, *ibid.*, **87**, 527 (1952).
4. S. Mayburg, *ibid.*, **95**, 38 (1954).
5. H. Letaw, *J. Phys. and Chem. of Solids*, **1**, 100 (1956).
6. R. A. Logan, *Phys. Rev.*, **100**, 615 (1955).
7. G. Finn, *ibid.*, **91**, 754 (1953).
8. R. A. Logan, *ibid.*, **91**, 757 (1953).
9. P. Wang, *J. Phys. Chem.*, **60**, 45 (1956).
10. R. A. Logan and M. Schwartz, *J. Appl. Phys.*, **26**, 1287 (1955).
11. H. Kroemer, "Transistors I," p. 132, RCA Laboratories, Princeton, N. J. (1956).
12. C. D. Thurmond and R. A. Logan, *J. Phys. Chem.*, **60**, 591 (1956).
13. C. S. Fuller, *Phys. Rev.*, **86**, 136 (1952).
14. W. C. Dunlap, *ibid.*, **94**, 1531 (1954).
15. W. Boesenberg, *Z. Naturforsch.*, **10A**, 285 (1955).
16. G. Backenstoss, *Bell System Tech. J.*, **37**, 699 (1958).
17. J. L. Moll and I. M. Ross, *Proc. I. R. E.*, **44**, 72 (1956).
18. F. A. Trumbore, *This Journal*, **103**, 597 (1956).

Technical Feature

The Double Layer in Electrochemistry[1]

A. N. Frumkin

Institute of Electrochemistry of the Academy of Sciences of the U.S.S.R., Moscow, U.S.S.R.

In every group of phenomena there is some specific feature which leaves its mark on the science dealing with these phenomena. As it seems to me, a specific feature of this kind in the case of electrochemical processes is the existence of the electric double layer at the metal-solution interface. Perhaps I am not quite impartial in this statement, as I, if I may say so, stood at the cradle of the double layer theory, but still I think that there are many elements of truth in it.

There is nothing exceptional in the fact that when two phases come into contact there appears a double layer at the interface. The ions, as any other solute, tend to be distributed between the phases in accordance with the difference in their standard chemical potentials. But, as their large electric charges inhibit the separation of ions in considerable quantities, the distribution equilibrium is secured by attaining a certain difference of electric potentials with a simultaneous formation of a double layer at the interface, which necessitates the transfer of but small quantities of ions from one phase to the other, provided the area of the interface is not very great. The laws governing the value of this equilibrium potential difference were established long ago by Gibbs and Helmholtz; for the form of these laws which is familiar to chemists we are indebted to Nernst and Lewis. The importance of these relationships cannot be overemphasized; however, one must keep in mind that they tell us nothing about the mechanism of the establishment of the potential difference or about the structure of the double layer being formed.

[1] Palladium Medal Address delivered at the Chicago Meeting, May 3, 1960.

At the present time we get our knowledge about the structure of the double layer in the first place from a-c measurements of electrode capacities or by other similar methods. Earlier data which I had to consider when I began to study this problem (more than 40 years ago) were based on measurements of electrocapillary curves, i.e., of the relation between interfacial tension σ and potential difference ϕ. In order to determine from these data the electric properties of the interface, one must use the Lippmann-Helmholtz equation

$$\frac{\partial \sigma}{\partial \phi} = -\epsilon \qquad [1]$$

where ϵ is the charge density on the metal surface.

The application of Eq. [1] to experimental data showed in a number of cases a rather complex relationship between σ and ϕ. The majority of scientists of that time thought that the double layer should behave as a flat condenser, i.e., that ϵ should be proportional to ϕ. They explained the deviations observed by the inaccuracy of Eq. [1], although the latter is strictly deduced from the principles of thermodynamics. Even such an authority in the field of chemical thermodynamics as van Laar held this view. Only the French physicist Gouy found a better approach to the theory of electrocapillarity. But Gouy worked at a provincial university at Nancy which he left but seldom, and his works were little known to scientists interested in physicochemical problems. In any case, when I presented a paper with the experimental confirmation of the correctness of Eq. [1] and some critical remarks on the

theory of van Laar to the "Zeitschrift für physikalische Chemie," it was at first rejected by the Editor.

In this paper the electric charges were determined from the current strength necessary for charging a growing mercury drop, just in the same way as it is often done at the present time, and $\partial\sigma/\partial\phi$ was calculated from electrocapillary curves (1). There still remained a contradiction which could not be removed for a long period of time: the double layer capacities as directly measured by Krüger, Bowden and Rideal, Erdey-Gruz and Kromrey always proved to be much smaller than the capacities calculated from electrocapillary data using Eq. [1] or found from experimental values of ϵ. This discrepancy seemed to be so firmly established that even attempts to give it a theoretical explanation were made. Thus a hypothesis was suggested according to which the capacity measured by means of an alternating current must be exactly equal to one-half the capacity obtained from electrocapillary data (2). However Proskurnin and Frumkin showed in 1935 (3) that the discrepancies observed were caused by a different and much more trivial circumstance, viz., the presence of organic impurities which penetrate the capillary of the capillary electrometer slowly, but easily reach the unprotected surface of a mercury electrode used in capacity measurements. It was found that when such impurities are carefully eliminated both methods of capacity determination give identical results. Overcoming the difficulties connected with capacity measurements in dilute solutions enabled us to find a capacity minimum at the point of zero charge, which was a strong confirmation of the theory of the diffuse double layer (4).

Somewhat later Grahame adapted the a-c method to capacity measurements on a growing mercury drop (5), which permitted the requirements to be lowered in respect to solution purity and to increase the precision of the method.

The demonstration of the correctness of the Lippmann-Helmholtz equation and the development of methods of direct capacity measurements formed a sound basis for the investigation of the structure of the double layer and for the verification of the theory of the double layer on the metal-solution interface. I shall not dwell here on the well-known history of the development of this theory which is associated with the names of Helmholtz, Gouy, and Stern. Considerable advances were made in the postwar period by David Grahame, whose untimely death was a great blow to all his friends and colleagues. By introducing the concept of a difference in the distances of closest approach of anions and cations to the metal surface, Grahame succeeded in giving a satisfactory picture of the relationship between the double layer structure and the concentration of the electrolyte for the case when ions are attracted by coulombic forces only, i.e., when the phenomenon commonly called specific adsorption is absent (6).

Such an agreement between theory and experiment is somewhat surprising, as the fact that the solution side of the double layer is composed of individual ions was not taken into consideration in the development of the theory, or in other words, the ionic charges were, so to say, smeared parallel to the metal-solution interface. Indeed, the theory developed on this basis cannot account for the experimentally observed dependence of the double layer structure on the concentration in the presence of a marked specific adsorption of anions. On my suggestion Esin and his collaborators (7) and later Ershler (8) attempted to work out a theory of a discrete double layer and to remove these discrepancies. Ershler's concepts recently were developed further by Grahame (9); several papers by Parsons (10) also are concerned with this problem. However, despite the efforts exerted, in my opinion we are not yet in possession of a fairly satisfactory quantitative theory of the double layer in which this discrete structure would be taken into account. Some success in this direction was achieved recently by Levich and Kiryanov (11).

Grahame supposed, following Gouy in this, that inorganic cations, unlike anions, do not display any specific adsorbability on the metal-solution interface; in the case of cations such an adsorbability was ascribed only to large organic cations. The investigations carried out in the past years at the Moscow University showed, however, that this assumption is not quite justified (12). Thus, the adsorbability of the Tl^+ ion on the mercury surface, as seen from Fig. 1, in which the electrocapillary curves for solutions of H_2SO_4 with additions of Tl_2SO_4 are shown, can be compared with that of the Br^- ion. A certain adsorbability also is displayed by the lead ions and a very small, although a clearly detectable one, even by the ions of the alkali metal Cs^+ (13). These phenomena are much more pronounced in the case of cation adsorption on the surface of the solid metal platinum (14). Proving the existence of a specific cation adsorption is, in my opinion, important in connection with the role that the adsorbed atoms (or adions) are supposed to play in the electrodeposition of metals (15-17).

The presence of a double layer at the mercury-solution interface affects a number of its properties, for instance interfacial tension, adhesion between metal and solution, and others. I shall discuss here only one of these properties, viz., mobility in an

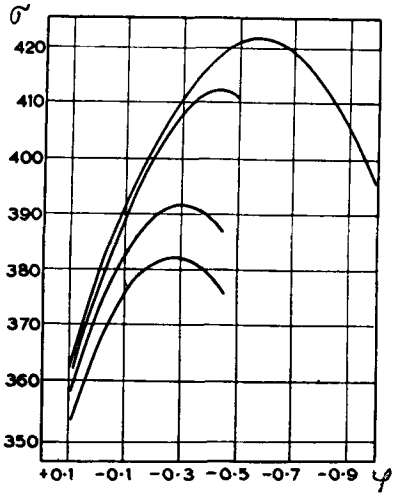

Fig. 1. Electrocapillary curves in N KNO_3 + 0.01N HNO_3 + x N $TlNO_3$ solutions. Curves from top to bottom: x = 0; 0.01; 0.1 and 0.2 (NCE).

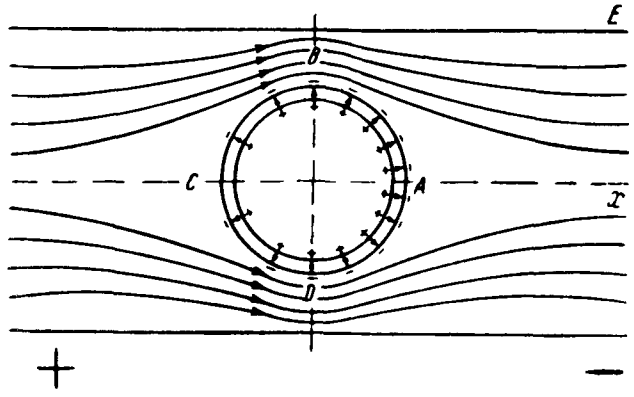

Fig. 2. Schematic picture of the double layer of an ideal polarized positively charged metal drop placed in an external electric field. The arrows show the direction of the lines of force of the field.

electric field. When an electric field is applied, the mercury drop in the electrolyte solution comes into motion. The mechanism of this motion, first observed by Christiansen (18), essentially differs from that of the well-known electrokinetic motion. Its velocity, in the case of identical field tension and solution viscosity for drops having a radius a of the order of 1 mm, may exceed that of electrokinetic motion by five orders of magnitude. The mechanism of these movements is best illustrated by the simple example of an ideal polarized positively charged drop with a Helmholtz double layer. In this case, the distribution of the lines of force of the external electric field in the vicinity of the drop (Fig. 2) is similar to their distribution in the vicinity of an insulator, in other words they are tangential to the drop. Under these conditions the electric field acts on the outer sheet of the double layer, but not on the inner one, as the field tension within the metal is equal to zero due to its high electric conductivity. Thus, the effect of the field on the outer sheet of the double layer is not compensated for (to be more precise, it is compensated by the forces applied at a considerable distance from points B and D to the poles of the drop A and C). Under the influence of these forces the mercury in the drop comes into a vortical motion, as is shown in Fig. 3, and the reactive repulsion from the surrounding medium causes the drop to move along the field lines. The mathematical theory of this motion developed by Levich and myself (19) gives the following expression for the drop velocity v, the field tension at a sufficient distance from the drop being equal to E

$$v = \frac{a\epsilon E}{2\mu+3\mu^1+\epsilon^2/\kappa} \qquad [2]$$

where μ and κ denote the viscosity and the electric conductivity of the solution and μ^1 the viscosity of mercury.

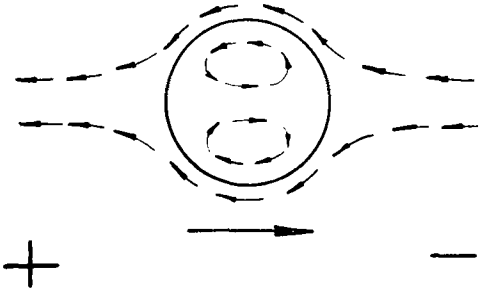

Fig. 3. Motion of a positively charged mercury drop in an electrolyte solution under the action of the electric field. The small arrows show the direction of the motion of the solution and mercury at any point, the big arrow, the direction of the motion of the drop as a whole.

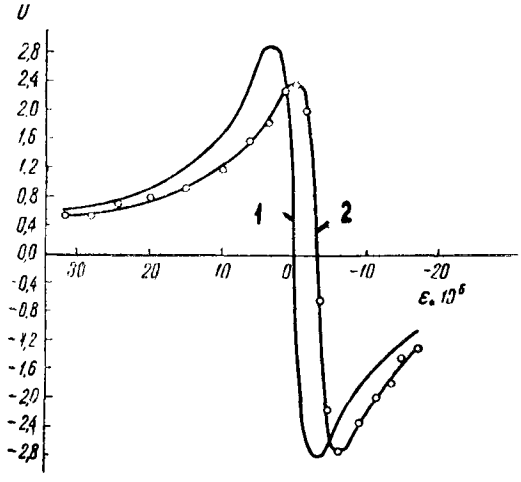

Fig. 4. Relationship between the mobility of mercury drops in a 0.02N KBr solution in glycerol and the charge density ϵ; $\kappa = 1.9 \times 10^{-5}$; $\mu = 2.8$. 1, Computed from Eq. [2]; 2, experimental data. μ in cm/sec v; ϵ in coulomb/cm^2.

Equation [2] was verified on mercury drops falling in a viscous glycerol solution and deflected by a horizontal electric field; definite electric charges were imparted to the drops before they broke off from the capillary (20). As seen from Fig. 4, the theoretical calculations are confirmed by experiments; the slight shift of the experimental curve is caused by the presence of oxygen traces which gradually made ϵ somewhat more positive (it is very difficult to remove oxygen completely from the viscous solution). For small values of ϵ, Eq. [2] gives mobility values of the same order as those which would be found in the case of a sphere having a free charge with the density ϵ. At first sight, this seems surprising, as the charge of the metal side of the double layer is completely compensated by the charges with an opposite sign which are located in the ionic sheet of the double layer. However, as I have already mentioned, a compensation of charges does not lead to a compensation of forces. With increase of ϵ, v increases, reaching a maximum at

$$\epsilon = \kappa^{1/2}(2\mu + 3\mu^1)^{1/2} \qquad [3]$$

and then decreases. This can be accounted for by the fact that the transfer of charges by the moving mercury surface results in an electric field directed opposite to the impressed field and diminishing its effect (this has not been taken into account in plotting Fig. 4, which therefore holds true only for small values of ϵ). A similar inhibiting effect is also observed in the case of a drop moving under the action of forces of a different nature, e.g., gravity, which results in a somewhat unexpected relationship between the velocity of the falling drop and its

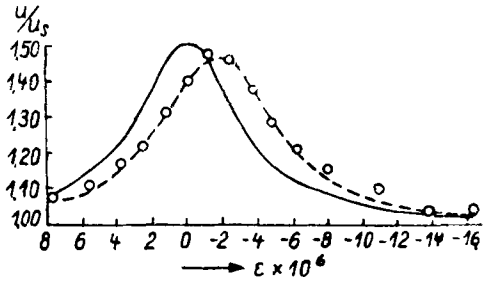

Fig. 5. Ratio of the rate of fall of a mercury drop in a glycerol solution saturated with Na_2SO_4 to that calculated by Stokes formula as a function of the charge density ϵ; $\kappa = 8.1 \times 10^{-6}$, $\mu = 7.2$. Solid curve, calculated values; circles, experimental data.

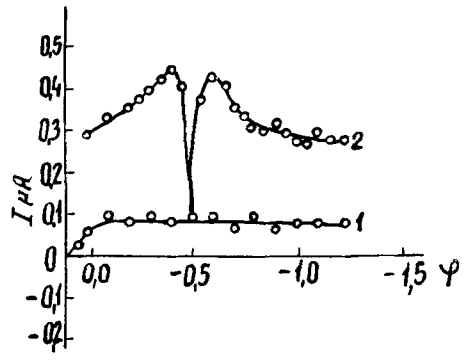

Fig. 6. C.v. curves in 0.28×10^{-4} N $Hg_2(ClO_4)_2$ + 0.002N $KClO_4$ corrected for charging current (NCE). 1, In the absence of an external field, 2, with the external field applied, E = 0.47 v/cm.

charge (21). A more detailed analysis permits us to conclude that in a viscous medium an uncharged drop must fall one and a half times faster than a charged one. The relationship between the velocity of the fall and the charge observed experimentally is compared in Fig. 5 with the theoretical dependence; the velocities of the fall are referred to that of a strongly charged drop, which is in accordance with Stokes law. The slight shift of the experimental curve with respect to the theoretical one can be accounted for quantitatively, if the depolarizing effect of the oxygen traces is taken into consideration.

The electrocapillary motion of droplets with metallic conductivity may arise in any electrolyte. A method was proposed recently to make use of this motion in extracting sulfide inclusions from molten slags (22).

Electrocapillary movements underlie the so-called polarographic maxima. The tangential movement of the drop surface calls forth an extra supply of the depolarizer which, according to Levich (23), is proportional to the square root of the tangential velocity. This fact makes it possible for currents in excess of the normal limiting diffusion current, which can be computed with the help of Ilkovic's equation, to pass through the cell. However, under the usual working conditions of a dropping electrode, the electric field causing the movement of the drop surface depends on complex geometrical conditions at the capillary tip; it is also influenced by the effect of convective diffusion of the depolarizer on the concentration polarization. Moreover the polarization curves are distorted by ohmic potential drops in the solution. Therefore the development of a quantitative theory of polarographic maxima presents great difficulties, which account for the chaotic state of this problem in modern polarographic literature. I shall not dwell here on the attempt made in this direction by myself and Levich, although, as it seems to me, we succeeded in explaining the basic features of the phenomena observed (24). I prefer to confine myself to the consideration of a case, when the polarographic maxima of the first kind may, so to say, be observed in an idealized form. To achieve this in the place of the mechanism of self-generation of motion, which is operative in the case of polarographic maxima of the first kind, we must provide a possibility to generate motion by means of an electric field which would be independent of the current on the drop. For this purpose a dropping mercury electrode was placed in an electrolyte solution and an electric field was applied to the latter by means of two subsidiary electrodes, the ratio of the supporting electrolyte and of the depolarizer concentrations being chosen in such a way that no polarographic maximum of the first kind should occur under normal conditions (25). The results obtained with 0.28*N* $Hg_2(ClO_4)_2$ + 0.002*N* $KClO_4$ are given in Fig. 6. Current-voltage curve 1 was obtained without the application of an external electric field, curve 2 with the application of a field having a gradient of 0.47 v/cm. This curve, which is of an unusual shape, is in close agreement with Eq. [2]. Its left-hand branch, corresponding to positive values of ϵ, greatly resembles the positive polarographic maxima of the first kind, as they are observed when the concentration of the supporting electrolyte is not too low. Polarograms obtained under normal conditions, however, show no second maximum at negative values of ϵ. I cannot discuss here the causes of this discrepancy, which, however, may be explained on the basis of the theory mentioned above (24).

The theoretical interpretation of the so-called maxima of the second kind, which depend on the flow of mercury out of the capillary, is much simpler than the interpretation of the maxima of the first kind. In this case, it is of fundamental importance to take into consideration the same inhibition of the surface motion by the double layer charges, which results in the decrease of the velocity of a falling charged drop. The maxima of the second kind play an important role in the theory of the rotating mercury drop electrode of Kolthoff and Okinaka (26).

Of special interest is the question about the relationship between the double layer structure and the nature of the metal. The latter may have an effect on the capacity of the Helmholtz layer as well as on the potential of zero charge. At the present time we are in possession of sufficient experimental data only on the second point. Let us consider first liquid metals. The information which we can obtain on this subject from measurements in

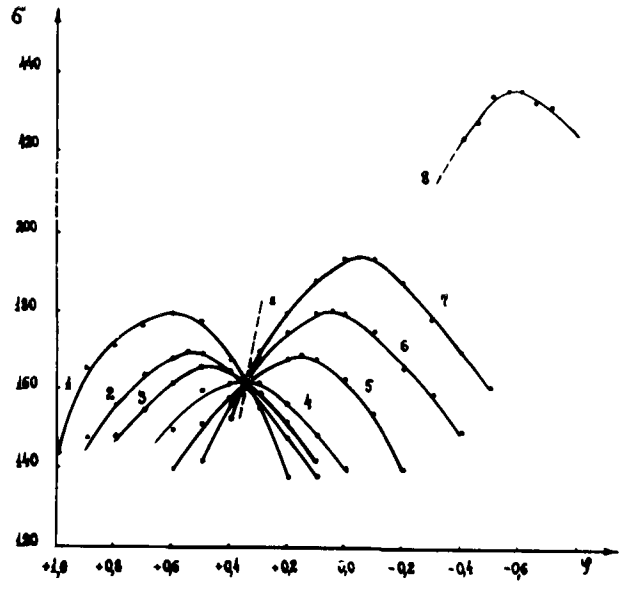

Fig. 7. Electrocapillary curves of Te-Tl alloys in LiCl + KCl. 1, Te; 2, 3.83 at. % Tl; 3, 10.9%; 4, 22.1%; 5, 42.3%; 6, 53.7%; 7, 65.2%; 8, Tl. Reference electrode Pb, LiCl + KCl, 0.1% $PbCl_2$.

aqueous solutions is naturally limited; we get more data with molten electrolytes. Electrocapillary phenomena in melts have been particularly investigated at the Sverdlovsk University (27). Electrocapillary curves for the Te-Tl system, plotted from measurements made by Kusnezov, *et al.*, are shown in Fig. 7. This system is characterized by an exceptionally great difference in the positions of the electrocapillary maxima, i.e., of the points of zero charge, which is as large as 1.25 v. The double layers at the metal-electrolyte interface at the point of zero charge being eliminated, the value given is similar in many respects to the Volta potential between the respective metals measured in vacuum (28). If the orientation of molecules of the solvent and the specific adsorption of ions are not taken into consideration, this value can be regarded as a kind of Volta potential in a material medium. I have already dealt with this problem in a paper which I presented at the 7th Annual Symposium on Colloid Chemistry at Baltimore about 30 years ago. At the present time a similar point of view is held by many electrochemists, e.g., Temkin (29), Rüetschi and Delahay (30). In my opinion, the determination of zero charge potentials gives the most direct answer to the question about the relationship between the difference of potentials between the poles of a galvanic cell with electrodes from different metals and the corresponding Volta potential, which has greatly attracted the attention of electrochemists since the beginning of the 19th century.

However, the similarity between the differences of zero charge potentials and Volta potentials does not necessarily result in a complete coincidence of these values, as the zero charge potentials may be influenced in a varying degree on the two electrodes by the preferential adsorption of one of the ions of the melt or by the orientation of the molecules of the solvent; the presence of a material medium may also have some effect on the distribution of the electronic cloud in the surface layer of the metal.

As a result of these complications the potential difference between water and mercury at the zero charge point of mercury is not equal to the sum of the galvani-potentials at the water-gas and vacuum-mercury interfaces, but exceeds it by an amount which was found by me to be equal to 0.30 v (31). Using more recent values of the Volta-potential between mercury and aqueous solutions (32), and of the zero charge potential of mercury (6) we get the value 0.26 v for this quantity. The assumption that the difference between the potentials of zero charge of two metals coincides with the Volta-potential between them is equivalent to the assumption that there exists a relationship between the zero charge potential and the electronic work function w, which can be expressed by the equation (33)

$$\phi_N - w = \text{constant} \qquad [4]$$

In accordance with the foregoing this relationship can only be approximate; it is not likely that one can make it more exact by introducing a certain coefficient before w, as has sometimes been suggested (34). The problem of the relationship between ϕ_N and w was recently discussed also in American literature (30, 35, 36). In the author's opinion, in order to verify these relationships at the present time, first it is necessary to be in possession of more exact experimental data both on the electronic work function and especially on the zero charge potentials.

The problem of investigating the double layer structure becomes more complicated when dealing with solid metals, although in the place of interfacial tension measurements, which cannot be carried out in this case, there appears an opportunity to study the effect of the double layer on such properties of metals as hardness (37-39), friction (40, 41), electrokinetic potential (42), stability of suspensions or sols. Unfortunately, the interpretation of results obtained from such measurements is not always as unambiguous as it is in the case of electrocapillary measurements. Very much was expected from capacity measurements on solid electrodes, in particular from the determination of zero charge potentials by means of the location of the capacity minimum in dilute solutions of electrolytes (43). However, the investigations carried out hitherto have only partly justified these expectations, as it is not always possible to obtain with solid metals capacity-potential (C,ϕ) curves comparable with those for mercury. Such a curve for the surface of a Zn monocrystal in 0.1N KCl (44), together with curves for Hg and liquid Ga (45) in the same electrolyte, is shown in Fig. 8. The capacity of the Zn monocrystalline surface within the frequency range of 1-10 kilocycles changes but little with frequency (by 5-8%) in contrast to what is observed in the case of polycrystalline zinc. This makes us suppose that the dispersion of the capacity, which interferes with capacity measurements on solid metals, is at least partially accounted for by the unevenness of the surface and the presence of micro-

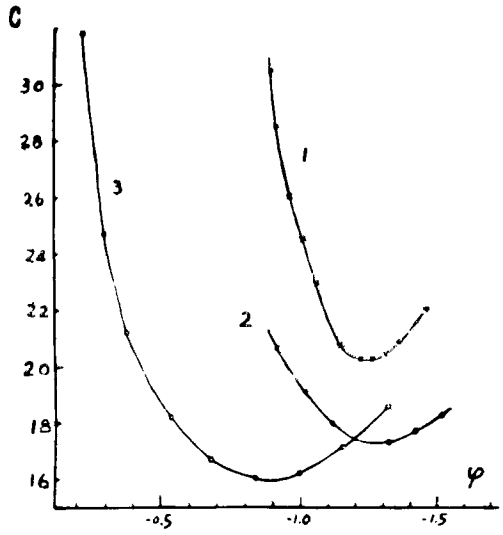

Fig. 8. Relationship between the differential capacity C and the potential ϕ in 0.1N KCl (NHE). 1, Zn monocrystal; 2, liquid Ga (according to Grahame); 3, Hg.

scopic cracks, although other explanations have been given to this phenomenon as well (46).

A curious inference can be made from determinations of zero charge potentials by means of the capacity minimum in dilute solutions (as well as from the hardness maximum) in the case of Pb and PbO_2 electrodes (47). The zero charge potential ϕ_N of PbO_2 is located at 1.8 v vs. NHE, the zero charge potential of Pb at —0.7; the difference between these two values is 2.5 v, which is even greater than the difference of potential between the poles of a lead storage cell.

With the help of capacity measurements Leikis has studied in detail the behavior of a silver electrode. As shown in Fig. 9, a pronounced minimum is observed in a dilute solution of Na_2SO_4 on the C,ϕ curve of silver; the silver wire had been subjected to cleaning with moist glass powder and boiling in an alkaline solution. This minimum disappears with an increase in solution concentration. The zero charge potential found in this way is equal to —0.7 v vs. NHE which coincides approximately with the results of electrocapillary measurments on molten silver

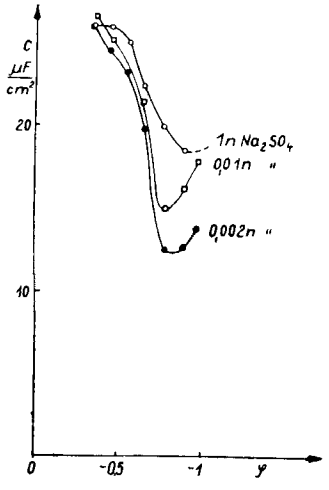

Fig. 9. Differential capacity of an Ag electrode in Na_2SO_4 solutions (NHE).

($\phi_N = -0.6$), but not with other data in the literature. The investigation of the effect of the solution concentration and of the presence of surface active anions and organic substances confirms the correctness of this ϕ_N value.

Leikis's experiments produced a noteworthy result. In electrochemical measurements wide use is made of a technique for cleaning electrode surfaces by means of vigorous cathodic polarization. But if a silver electrode is subjected to cathodic polarization in N Na_2SO_4 up to $\phi = -1.25$ v vs. NHE, the conditions of the surface, as it can be inferred from capacity measurements, change markedly, and at $\phi = -1.35$ v this change becomes irreversible. C,ϕ curves obtained with such an electrode differ widely from normal curves.

There exists still another reason why care must be exercised in interpreting the results of the measurements of C,ϕ curves when solid electrodes are used. In the presence of adsorbed hydrogen or oxygen on the electrode surface along with the double layer capacity a pseudocapacity is measured, the value of which depends on the exchange current between the adsorbed layer and the solution (48). In these cases the minima observed on C,ϕ curves may represent pseudocapacity minima and therefore tell us nothing about the zero charge potential. Apparently, such is the case with active platinum electrodes (49), and this accounts for the relationship observed between the location of the minimum on C,ϕ curves of Pt and the pH of the solution (50). While making measurements in dilute solutions at high frequencies Kabanov and Birinzeva could find no capacity minimum on platinum which could be interpreted as corresponding to the most diffuse state of the double layer at the point of zero charge (51). This is possibly due to a marked heterogeneity of the surface of an activated platinum electrode.

It is evident that in the case of an extremely heterogeneous surface the measurable potential of zero charge represents a certain mean value at which occurs the transition from a preferential anion adsorption to a preferential cation adsorption. Such a potential of zero charge does not necessarily correspond to the most diffuse structure of the double layer.

In the case of solid electrodes with a large surface, the formation of the double layer causes marked changes in the composition of the solution, which are known to produce errors in pH measurements with the help of platinized platinum electrodes if the system is insufficiently buffered. The determination of these changes in the composition can serve as a method for the investigation of the double layer structure. This method was applied successfully to such substances as platinum and activated carbon. Two results obtained recently may be mentioned in this connection. As the zero charge potential for platinum is more positive than the normal hydrogen potential, this metal is negatively charged when placed in a hydrogen atmosphere in acid solutions. The formation of the double layer, for instance in an acidified N Na_2SO_4 solution, is accompanied therefore by a transfer of hydrogen ions to the solution and by an increase in solution acidity, which can be

measured if platinized electrodes are used. However, in the presence of surface active halogen anions, the mechanism of the establishment of the equilibrium potential difference is changed; with the increase of the anion adsorbability the double layer formed by negative charges on the metal surface and cations attracted by them is replaced by a double layer with a negative sheet formed by adsorbed anions. In the case of a *N* NaI-solution acidified up to *p*H ~ 3, as has been found by Balashova and Kasarinov (52), the potential difference due to the adsorption of anions becomes so great that at the equilibrium hydrogen potential the sign of the charge of the platinum is reversed. Under these conditions the formation of the double layer is accompanied by a decrease in the solution acidity, and not by an increase in the latter.

A hydrogen electrode with a still better developed surface can be made by depositing some platinum on the surface of activated carbon. Such platinized carbon in a hydrogen atmosphere adsorbs from neutral solutions of salts considerable amounts of cations, which are replaced by hydrogen ions. The magnitude of the adsorption effect depends on the final *p*H of the solution just as would be expected from the theory outlined, if one assumes that ϕ_N for "hydrogen" carbon is equal to 0.03 v (53).

The idea according to which the electrolyte adsorption on activated carbon is a process connected with the establishment of the equilibrium potential difference was met with opposition. A number of scientists preferred to interpret these phenomena on the same lines, as is done in the case of adsorption on ion exchange resins, i.e., without taking into account the electronic conductivity of carbon. However, the "electrochemical" theory of electrolyte adsorption on carbon received recently a conclusive corroboration in the investigations carried out by Strazhesko at the Ukrainian Academy of Sciences in Kiev (54). Strazhesko found that the acidification caused by cation adsorption from solution increases markedly (2-3 times), when solutions in nonaqueous solvents, e.g., acetone, are used instead of aqueous ones. Such a phenomenon, quite inexplicable on the basis of the "chemical" theory of electrolyte adsorption on carbon, can be interpreted, if one assumes that the zero charge potential of carbon, as well as that of mercury, is shifted toward more positive values when molecules of acetone are substituted for those of water. In this case at the reversible hydrogen potential the carbon surface must really carry a more negative charge in a nonaqueous solvent.

An original method for the determination of the zero charge point of platinum was proposed recently (42, 55). The presence of the diffuse double layer causes two metallic surfaces in an electrolyte solution to repel and prevents them from drawing together. Voropaeva, Derjaguin, and Kabanov measured the force necessary for establishing at different potentials a conducting contact between two crossed platinum wires immersed in a dilute KCl solution. As seen in Fig. 10, there is a pronounced minimum on the curve showing the relationship

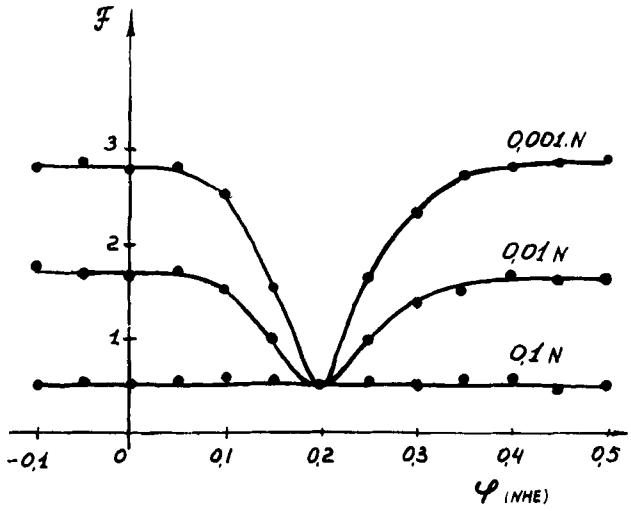

Fig. 10. Relationship between the potential and the force F, which must be applied in order to establish a contact between two platinum wires in KCl solutions.

between the force and the potential, at the zero charge potential. The value of ϕ_N found in this way is in good agreement with the results of adsorption measurements. It is not quite clear why in this case we do not meet with the difficulties, which were encountered during the attempts to determine the location of the zero charge potential of platinum from the capacity minimum in dilute solutions.

When dealing with the problem of points of zero charge, the supposed existence of an essential difference between the case of a reversible electrode and that of an ideal polarized one has been sometimes mentioned in the literature (30, 56). It seems to me however that there are no theoretical grounds for such a differentiation (39). Although the mechanism of the formation of the double layer in these two cases is, generally speaking, different, its structure and, consequently, the physical meaning of the zero charge potential must be similar. In accordance with this it was possible to show that the change in the double layer capacity with electrolyte concentration at the zero charge potential of thallium amalgams in dilute solutions of electrolytes proceeds in conformity with the same laws as those for mercury, although the equilibrium concentration of Tl^+ ions in the solution at the zero charge potential reaches in this case a measurable value (57).

The concept about the existence of the electric double layer was not made use of in the first investigations of the kinetics of electrochemical processes. This could not have been expected, since at the time the net velocity of electrochemical processes was associated with purely chemical or diffusion steps. Only after the idea of the finite velocity of electrochemical steps proper and of their dependence on the interfacial potential difference had been introduced in the theory of electrode processes (Audubert, Butler, Erdey-Gruz, and Volmer), did it become possible to combine the double layer theory and the principles of electrochemical kinetics. The first attempt in this direction was seemingly made by the author (58); it was supposed

that the reacting particles follow the Boltzmann distribution law and that only a part of the potential difference is effective in determining the rate of the process. The original conclusions referred to the case of the hydrogen ion discharge. If we generalize the expression obtained for the case when an electron is transferred to a particle carrying n charges, where n can be either positive or negative, the result assumes the following form (59)

$$i = \mathrm{K} \exp\left[-\alpha(\phi-\phi_1) - n\phi_1\right] F/RT \qquad [5]$$

where i is the current density, c the bulk concentration of the reacting particle, if necessary corrected for concentration polarization, and α a constant satisfying the condition $0<\alpha<1$. The problem of the physical interpretation of the value α is yet open to discussion and in practical use of the equations of electrochemical kinetics α must be considered as an empirical constant. An accurate determination of the meaning of ϕ_1 is of great importance. The value ϕ_1 was regarded primarily as the potential in the center of the charge of the reacting particle at its equilibrium location in the Helmholtz layer, although the possibility to refer it to the location of the charge center in the transition state of the reaction should be considered too.[2] As was shown by the experiments of Bagozky (62) and others, Eq. [5] expresses exactly the relationship between the H_3O^+ ion discharge rate in KCl + HCl solutions and the concentrations of the components, if the value ϕ_1 is considered as the potential in the plane of the closest approach of cations to the electrode surface and this potential is computed on the basis of the classical theory of the diffuse double layer. Thus, neglecting the details of the double layer structure involves no great errors in the case when the reacting particle is an H_3O^+ cation, repelled by K^+ or H_3O^+ cations which form the ionic sheet of the double layer. However, much greater difficulties were encountered, when a different group of reactions was considered, i.e., the electroreduction processes of multivalent anions, during which the reacting particles are attracted by the ions present in the ionic sheet of the double layer. These reactions, which have been studied in detail in Moscow since 1949, are characterized by an anomalous form of c.v. curves (59, 63). Namely, the usual increase in the current, which occurs when the cathodic polarization is increased, is followed by a sharp falling off, taking place at potentials in the vicinity of the zero charge potential or more negative than the latter. When the potentials become still more negative, the current rises again. In many but not in all cases (64) these anomalies disappear with an increase in the concentration of the supporting electrolyte. As an example of these anomalous c.v. curves, a curve for the reduction of the $S_2O_8^{2-}$ ion on an amalgamated rotating disk electrode in the presence of $0.01N$ Na_2SO_4 is shown in Fig. 11.

The pecularities of the electroreduction of multivalent anions are explained by the repulsion between the reacting particle and the negatively

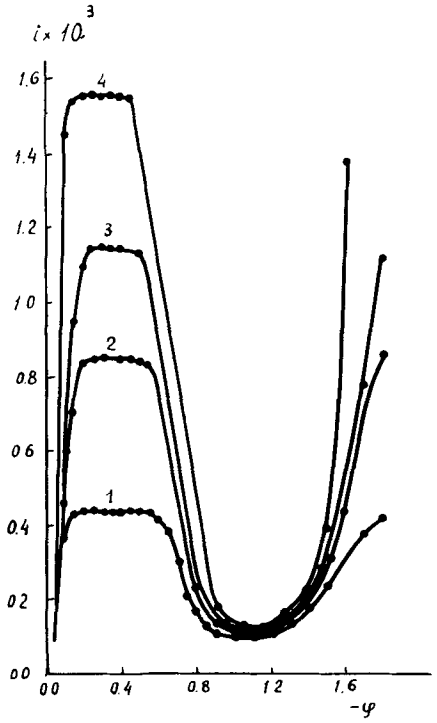

Fig. 11. C.v. curves for the reduction of 10^{-3} N $K_2S_2O_8$ in the presence of 10^{-2} N Na_2SO_4 on a rotating amalgamated disk electrode. Rates of rotation: 1, 650; 2, 2800; 3,5000; 4, 9000 rpm.

charged electrode surface. In Eq. [5] this effect is accounted for by the term containing ϕ_1; in fact, it is easy to show, that at $n = -2$ or $n = -3$ and with a reasonable value assumed for α, Eq. [4] represents a c.v. curve with a minimum in the region of potentials corresponding to negative surface charges. Although in some cases the experimental c.v. curves, corrected for concentration polarization, can be expressed even quantitatively by means of Eq. [5], a more detailed study of this problem shows that the concepts used as a basis in the derivation of this equation in this case are insufficient. As it is beyond the scope of this paper to discuss all the aspects of the problem, which, moreover, have been dealt with lately in a number of reviews (65), I intend to mention only the following point. Equation [5] is derived on the assumption that within the double layer the reacting particles follow the Boltzmann distribution law. As Levich's calculations have shown (66), this distribution cannot be realized at sufficiently high current densities in the case when the sign of the charge of a reacting multivalent particle is opposite to that of the charge of the electrode surface, if the distribution of potentials is in accordance with the classical theory of the double layer. In fact the rate of the penetration of such particles through the double layer and therefore the rate of their transfer from the bulk to the electrode surface under the conditions stated would be insufficient. Moreover the theoretical rate values obtained under these assumptions are several orders of magnitude lower than those observed.

It seems to me that the only way to overcome this difficulty is to take into consideration the discrete

[2] An equation similar to Eq. [5] and differing from the latter only in that 1/2 is substituted for α, was recently deduced on a different basis, that of a theory developed by Marcus (60, 61).

structure of the ionic sheet of the double layer and the interaction between the reacting anions and the neighboring cations. Another solution of this problem would be to assume that not those anions which are predominant in the bulk of the solution react on the cathode, but ionic pairs with a smaller charge, as, for instance, the $MeS_2O_8^-$ ions in the case of a $Me_2S_2O_8$ solution (66, 67) and $Me_2Fe(CN)_6^-$ ions in the case of a $Me_3Fe(CN)_6$ solution. But difficulties are encountered if we are to follow this hypothesis consistently, i.e., improbably low values must be ascribed to α. Furthermore the thickness of the reaction layer in the case of reactions of the type

$$Me^+ + S_2O_8^= \rightleftharpoons MeS_2O_8^- \qquad [6]$$

in all probability is so small that the formation of those ionic pairs which react on the electrode must take place within the double layer. Thus, if we accept this assumption, we still must make an allowance for the interaction between oppositely charged ions within the double layer.

It appears that in that range of potentials for which reliable determinations of the c.v. curves can be made, it is possible to account for the phenomena observed during the reduction of multivalent anions by means of the theory of slow discharge, taking into account the formation of cationic bridges in the double layer. But involuntarily one is led to think that at sufficiently negative potentials a different mechanism of the electrode process is possible, consisting of a transfer of electrons from the electrode to particles located at distances comparable with the thickness of the diffuse double layer. As such a transfer would remove the difficulties connected with the repulsion of anions by the electrode surface, it would seem that in the case of anion reduction the most favorable conditions for such a mechanism are realized. Gurney was the first to point out the possible role of such electronic transfers in discharge processes (68), although the example chosen by him–the hydrogen ion discharge–was undoubtedly not suitable, as the high value of the adsorption energy of the product of the reaction–the hydrogen atom–makes the discharge at a distance from the metal surface energetically unfavorable. We must admit however that the feasibility of such transfers even in the case of anion reduction has not hitherto been corroborated by experiment, although we do not have sufficient reasons to deny their reality in the case when the cations of the electrolyte, as for example Li^+ cations, have a relatively low tendency to form ionic pairs. The research work in this direction must be continued, particularly taking into account what is known about the existence of solvated electrons in many solvents. Generally speaking, it may be said that the state of our knowledge about the transfer of electrons over long distances in the case of electrode processes is about the same as in the case of redox reactions occurring in the bulk of the solution.

The idea of the importance of the structure of the double layer for the kinetics of electrode processes has gradually become firmly established in electrochemistry, as for instance is shown by the review of Breiter, Kleinerman, and Delahay (69). However, one must mention the progress made in research in another, at first sight opposite, direction. Investigations carried out after the war, in particular in Czechoslovakia, have shown that the net rate of a great number of electrode processes is determined by chemical reactions resulting in the formation of an electroactive substance from inactive components in the bulk of the solution and therefore, as it would seem, independent of the double layer structure. At present it appears, however, that such a contraposition of these two concepts would be incorrect, as in a number of cases the thickness of the reaction layer becomes comparable with that of the diffuse double layer (70). Under these conditions it is necessary to take into consideration the effect of the electric field of the double layer upon the kinetics of the process, although it is a chemical and not an electrochemical one. Unfortunately we know as yet very little how this is to be done.

I have dealt hitherto only with the direct effect of the double layer on the reactions on the electrode. But its indirect effects are perhaps of still greater importance. The adsorption of surface active ions and of neutral molecules depends on the electric field of the double layer and these ions and molecules, in their turn, may act as catalyzers or inhibitors in electrochemical processes. It would be beyond the scope of the present paper to dwell on this problem, the study of which has given us many conclusive proofs of the existence of a close connection between the structure of the interface and the kinetics of the electrode processes (71, 65). However, I want to consider at least one particular case, that of the adsorption of anions which do not take a direct part in the electrode process. I have chosen this case because its consideration brings us, in a sense, to the limits within which we may use those very elementary concepts on whose basis Eq. [5] and some other similar relationships were deduced. In accordance with Eq. [5] the specific adsorption of anions must shift the ϕ_1 — potential toward more negative values and consequently increase the velocity of the processes of cation reduction. As might be easily proved, this conclusion holds for anodic processes of cation formation as well. It was first confirmed in the work of Jofa, Kabanov, *et al.*, for the case of the discharge of hydrogen ions on a Hg cathode (72) and later for a number of other reactions, many of which are well known from polarographic literature (73). However, at present, we know that in some cases the adsorption of anions on solid electrodes results not in an acceleration, but in a retardation of reactions of discharge and of formation of cations (74, 75). Thus, the adsorption of the Br^- ion and particularly of the I^- ion greatly retards the ionization of H_2 on a Pt electrode (76, 77), as well as the ionization of the hydrogen on the β phase of the Pd-H system (78). Apparently, the bond between the adsorbed anion and the metal surface becomes so firm in these cases that it is the modification of the properties of the electrode surface by the adsorbed

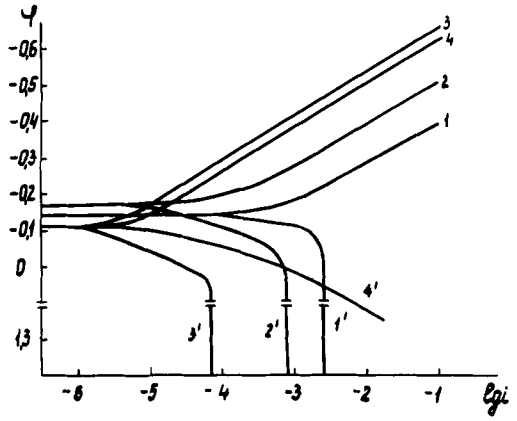

Fig. 12. Cathodic and anodic c.v. curves for stainless steel. 1, 1^1 10N H_2SO_4; 2, 2^1 10N H_2SO_4 + 0.01N KBr; 3, 3^1 10N H_2SO_4 + 0.001N KI; 4, 4^1 10N H_2SO_4 + 0.2N KI. The potentials are referred to a hydrogen electrode in 10N H_2SO_4.

anions, which results in a kind of passivity, that is of principal importance and not the change in the distribution of the potential in the double layer. This passivity probably is caused by the saturation of the free valencies of the electrode surface by chemisorbed anions and is accompanied by a decrease in the double layer capacity (79). The fact that this phenomenon is observed with solid electrodes only suggests that it is connected somehow with the presence on the electrode surface of active centers with high values of adsorption energies which strongly influence the kinetics of the process. An interesting example of this kind of action of anions is seen in the behavior of a stainless steel with 17% Cr and 9% Ni in the presence of I^- ions (80). As shown in Fig. 12, the addition of I^- ions to 10*N* H_2SO_4 increases the hydrogen overvoltage and facilitates the anodic passivation of steel. The inhibition of the cathodic and anodic processes results in a great diminution (4000 times) in the rate of the spontaneous dissolution of this steel in 10*N* H_2SO_4. The dissolution rate passes through a minimum at a I^- ion concentration of about 0.01% and increases again with further increase in the latter, not attaining, however, its original value. As it appears to me, these results show conclusively that metal passivation does not necessarily involve the covering of the surface with a protective layer forming a phase.

The investigation of the effect of anions on the kinetics of electrode processes permits us to draw the conclusion that the development of the theory of the double layer on the basis of purely electrostatic concepts must be considered as only a step in the building up of a surface chemistry of metals on a wider scale.

My address was concerned with the double layer on the metal-solution interface, but in order to understand their electrical properties it is essential to compare phenomena occurring on different kinds of interfaces. In a paper presented at the 7th Symposium on Colloid Chemistry I gave particular consideration to the comparison between the orientation of organic molecules on the metal-solution and solution-gas interfaces. It is very instructive as well to compare the results of electrocapillary measurements in solutions containing aromatic compounds (71, 81) with the results of determinations of the electron work function in the presence of adsorbed layers of molecules of this kind (82). Great attention has been paid lately to the problems of the semiconductor-vacuum and the semiconductor-electrolyte interfaces. The application of ideas developed in the investigation of the metal-electrolyte interface to the study of these interfaces has already given important results and undoubtedly will be still more fruitful in the future.

REFERENCES

1. A. Frumkin, *Z. physik. Chem.*, **103**, 43 (1923).
2. F. Krüger and G. Krumreich, *Z. Elektrochem.*, **19**, 617 (1913).
3. M. Proskurnin and A. Frumkin, *Trans. Faraday Soc.*, **31**, 110 (1935).
4. M. Vorsina and A. Frumkin, *Compt. rend. acad. sci. U.R.S.S.*, **24**, 918 (1939).
5. D. C. Grahame, *J. Am. Chem. Soc.*, **63**, 1207 (1941); **68**, 301 (1946); *Chem. Revs.*, **41**, 441 (1947).
6. D. C. Grahame, *This Journal*, **98**, 343 (1951); *J. Am. Chem. Soc.*, **76**, 4819 (1954); **79**, 2093 (1957); *Z. Elektrochem.*, **59**, 773 (1955); D. C. Grahame and B. Soderberg, *J. Chem. Phys.*, **22**, 449 (1954); D. C. Grahame, M. Poth, and J. Cummings, *J. Am. Chem. Soc.*, **74**, 4422 (1952).
7. O. Esin and B. Markov, *Acta Physiochim. U.R.S.S.*, **10**, 353 (1939); O. Esin and V. Shikov, *J. Phys. Chem. (U.S.S.R.)*, **17**, 236 (1943).
8. B. Ershler, *J. Phys. Chem. (U.S.S.R.)*, **20**, 679 (1946).
9. D. C. Grahame, *Z. Elektrochem.*, **62**, 264 (1958); *J. Am. Chem. Soc.*, **80**, 4201 (1958).
10. R. Parsons, *Trans. Faraday Soc.*, **51**, 1518 (1955); **55**, 999 (1959); Proc. 2nd Congr. Surface Activity, Electrical Phenomena, p. 38 (1957); Proc. of the 4th Electrochemical Meeting, Academic Press, p. 42, Moscow (1959).
11. B. Levich and V. Kirjanov, *Compt. rend acad. sci. U.R.S.S.*, In press.
12. A. Frumkin and A. Titievskaja, *J. Phys. Chem. (U.S.S.R.)*, **31**, 485 (1957); A Frumkin and N. Poljanovskaja, *ibid.*, **32**, 157 (1958); A. Frumkin, in "Surface Phenomena in Chemistry and Biology," p. 189 (1958).
13. B. Damaskin, N. Nikolajeva-Fedorovich, and A. Frumkin, *Compt. rend. acad. sci. U.R.S.S.*, **121**, 129 (1958); F. Deane, A. Higinbotham, D. C. Grahame, Abstracts Theoretical Division, Electrochemical Society, Philadelphia Meeting, 1959, p. 39.
14. A. Obrucheva, *J. Phys. Chem. (U.S.S.R.)*, **32**, 2155 (1958); *Compt. rend. acad. sci. U.R.S.S.*,**120**, 1072 (1958).
15. E. Mattson and J. O'M. Bockris, *Trans. Faraday Soc.*, **55**, 1586 (1959); B. E. Conway and J. O'M. Bockris, *Proc. Roy. Soc. (A)*, **248**, 394 (1958); W. Mehl and J. O'M. Bockris, *Can. J. Chem.*, **37**, 190 (1959).
16. H. Gerischer and R. Tischer, *Z. Elektrochem.*, **61**, 1159 (1957); H. Gerischer, *ibid.*, **62**, 256 (1958).
17. W. Lorenz, *Z. physikal. Ch. N. F.*, **19**, 25 (1959).
18. Christiansen, *Ann. Phys.*, (4), **12**, 1072 (1903).
19. A. Frumkin and B. Levich, *Acta Physicochim. U.R.S.S.*, **19**, 573 (1945); A. Frumkin, *J. Colloid. Sci. I* 277 (1946); B. Levich, *J. Phys. Chem. (U.S.S.R.)*, **21**, 689 (1947).
20. I. Bagozkaja, *J. Phys. Chem. (U.S.S.R.)*, **23**, 123 (1949).
21. I. Bagozkaja and A. Frumkin, *Compt. rend. acad. sci. U.R.S.S.*, **55**, 135 (1947); *J. Phys. Chem. (U.S.S.R.)*, **21**, 1033 (1947); *J. Phys. Colloid Chem.*, **52**, 1 (1948); A. Frumkin and B. Levich, *Acta Physicochim. U.R.S.S.*, **21**, 193 (1946).

22. V. Chlynov and O. Esin, *Compt. rend. acad. sci. U.R.S.S.*, **123**, 320 (1958); **120**, 134 (1958).
23. B. Levich, *J. Physic. Chem. (U.S.S.R.)*, **22**, 721 (1948); Physico-chemical hydrodynamics, 2nd ed., p. 406, Moscow (1959).
24. A. Frumkin and B. Levich, *J. Phys. Chem. (U.S.S.R.)*, **21**, 1335 (1947); A. Frumkin, *ibid.*, **29**, 1318 (1955); T. Krjukova, S. Sinjakova, and T. Arefjeva, "Polarographic Analysis," p. 94, 617, Moscow (1959); T. Krjukova, *Z. Physik. Chem.*, **212**, 247 (1959).
25. T. Popova and T. Krjukova, *J. Phys. Chem. (U.S.S.R.)*, **25**, 283 (1951).
26. J. Kolthoff and Y. Okinaka, *J. Am. Chem. Soc.*, **79**, 3326 (1957).
27. S. Karpachev and A. Stromberg, *J. Phys. Chem. (U.S.S.R.)*, **7**, 755 (1936); **10**, 739 (1937); **13**, 1831 (1939); **18**, 47 (1944); *Acta Physicochim. U.R.S.S.*, **12**, 523 (1940); V. Kusnezov, V. Kocherguin, M. Tishchenko, and E. Posdnysheva, *Compt. rend. acad. sci. U.R.S.S.*, **92**, 1197 (1953); V. Kusnezov, V. Ashpur, and G. Poroshina, *ibid.*, **101**, 301 (1955); V. Kusnezov, V. Axenov, and M. Klevzova, *ibid.*, **128**, 763 (1959); V. Kusnezov, T. Djakova, and V. Malzeva, *J. Phys. Chem. (U.S.S.R.)*, **33**, 1551 (1959).
28. A. Frumkin and A. Gorodetzkaja, *Z. physik. Chem.*, **136**, 451 (1928); A. Frumkin, *Coll. Symp. Ann.*, **7**, 89 (1930).
29. M. Temkin, *Bull. acad. sci. U.R.S.S. (Izvestiya), Chem. Ser.*, 235 (1946).
30. P. Rüetschi and P. Delahay, *J. Chem. Phys.*, **23**, 697 (1955).
31. A. Frumkin, *ibid.*, **7**, 552 (1939).
32. J. B. Randles, *Trans. Faraday Soc.*, **52**, 1573 (1956).
33. V. Novakovsky, E. Ukshe, and A. Levin, *J. Physic. Chem. (U.S.S.R.)*, **29**, 1847 (1955).
34. B. Vasenin, *ibid.*, **27**, 878 (1953); **28**, 1672, 1872 (1954).
35. B. Jakuszewski, *Bull. soc. sci. lettres Lódz*, Cl.III, N4 (1957); *J. Chem. Phys.*, **31**, 846 (1959).
36. A. de Bethune, *ibid.*, **31**, 847 (1959).
37. P. Rehbinder and E. Venstrem, *J. Phys. Chem. (U.S.S.R.)*, **19**, 1 (1945); **26**, 12 (1952); *Compt. rend. acad. sci. U.R.S.S.*, **68**, 329 (1949); P. Rehbinder and V. Lichtman, Proc. 2nd Congress Surface Activity, Electrical Phenomena, 1957, p. 563.
38. W. Klinkenberg, K. Lucke, and S. Masing, *Z. Metallkunde*, **42**, 361 (1951).
39. A. Frumkin, *Uspekhi Khim.*, **24**, 933 (1955); *Z. Elektrochem.*, **59**, 807 (1955).
40. F. Bowden and Young, *Research*, **3**, 235 (1950); F. Bowden and D. Tabor, Properties of the Metallic Surfaces, Inst. Metals, 1953.
41. J. O'M. Bockris and Parry-Jones, *Nature*, **171**, 930 (1953).
42. N. Balashova and A. Frumkin, *Compt. rend acad. sci. U.R.S.S.*, **20**, 449 (1938).
43. T. Borisova, B. Ershler, and A. Frumkin, *J. Phys. Chem. (U.S.S.R.)*, **22**, 925 (1948); T. Borisova and B. Ershler, *ibid.*, **24**, 337 (1950).
44. Tsa Chuan-sin and S. Jofa, *Compt. rend. acad. sci. U.R.S.S.*, **131**, 137 (1960).
45. D. Grahame, Proc. of the 4th Electrochemical Meeting, p. 27, Academic Press, Moscow (1959).
46. J. O'M. Bockris, W. Mehl, and B. Conway, Proc. of the 4th Electrochemical Meeting, p. 380, Academic Press, Moscow (1959); J. O'M. Bockris and B. Conway, *J. Chem. Phys.*, **28**, 707 (1958).
47. B. Kabanov, I. Kiseleva, and D. Leikis, *Compt. rend. acad. sci. U.R.S.S.*, **99**, 805 (1954); D. Leikis and B. Kabanov, *Trans. Inst. Phys. Chem.* (New Methods of Physicochemical Investigations) Moscow (1957), **6**, p. 5; D. Leikis and E. Venstrem, *Compt. rend. acad. sci. U.R.S.S.*, **112**, 97 (1957).
48. D. Leikis, *ibid.*, In press.
49. P. Dolin and B. Ershler, *J. Phys. Chem. (U.S.S.R.)*, **14**, 886 (1940); *Acta Physicochim. U.R.S.S.*, **13**, 747 (1940); P. Dolin, B. Ershler, and A. Frumkin, *J. Phys. Chem. (U.S.S.R.)*, **14**, 907 (1940); *Acta Physicochim. U.R.S.S.*, **13**, 779 (1940).
50. B. Kabanov and T. Birinzeva, *Compt. rend. acad. sci. U.R.S.S.*, **131**, 132 (1960).
51. V. Cheifetz and B. Krasikov, *ibid.*, **109**, 586 (1956).
52. N. Balashova and V. Kasarinov, *ibid.*, In press.
53. E. Kuchinsky, R. Burstein, and A. Frumkin, *J. Phys. Chem. (U.S.S.R.)*, **14**, 441 (1940); *Acta Physicochim. U.R.S.S.*, **12**, 795 (1940); B. Bruns, R. Burstein, N. Fedotov, and M. Livshitz, *ibid.*, **8**, 47 (1938).
54. D. Strazhesko, *Compt. rend. acad. sci. U.R.S.S.*, **102**, 885 (1955).
55. T. Voropajeva, B. Derjaguin, and B. Kabanov, *ibid.*, **128**, 981 (1959).
56. H. Oehl and H. Strehlov, *Z. physik. Chem. N. F.*, **1**, 241 (1954); **4**, 89 (1955); *Z. Elektrochem.*, **58**, 665 (1954); **59**, 818 (1955).
57. L. Boguslavsky, *J. Phys. Chem. (U.S.S.R.)*, In press.
58. A. Frumkin, *Z. physik. Chem. (A)*, **164**, 121 (1933).
59. A. Frumkin and G. Florianovich, *Compt. rend. acad. sci. U.R.S.S.*, **80**, 907 (1952).
60. W. Reinmuth, L. Rogers, and L. Hummelstedt, *J. Am. Chem. Soc.*, **81**, 2947 (1959).
61. R. A. Marcus, *Can. J. Chem.*, **37**, 155 (1959); *J. Chem. Phys.*, **24**, 979 (1956).
62. V. Bagozky, *Compt. rend acad. sci. U.R.S.S.*, **58**, 1387 (1947); *J. Phys. Chem. (U.S.S.R.)*, **22**, 1466 (1948); V. Bagozky and I. Jablokova, *J. Phys. Chem. (U.S.S.R.)*, **23**, 413 (1949).
63. T. Krjukova, *Compt. rend acad. sci. U.R.S.S.*, **65**, 517 (1949); T. Kalish and A. Frumkin, *J. Phys. Chem. (U.S.S.R.)*, **28**, 473 (1954); G. Florianovich and A. Frumkin, *ibid.*, **29**, 1827 (1955); A. Frumkin and N. Nikolajeva, *Chem. Phys.*, **26**, 1552 (1957); A. Frumkin, N. Nikolajeva-Fedorovich, and R. Ivanova, *Can J. Chem.*, **37**, 253 (1959); N. Nikolajeva-Fedorovich, L. Fokina, and O. Petrij, *Compt. rend. acad. sci. U.R.S.S.*, **122**, 639 (1958); N. Nikolajeva-Fedorovich and B. Damaskin, Proc. of the 4th Electrochemical Meeting, Academic Press, Moscow, 1959, p. 150; A. Frumkin, O. Petrij, and N. Nikolajeva-Fedorovich, *Compt. rend. acad. sci. U.R.S.S.*, **128**, 1006 (1959).
64. H. Laitinen and E. Onstott, *J. Am. Chem. Soc.*, **72**, 4565 (1950).
65. A. Frumkin, *Trans. Faraday Soc.*, **55**, 156 (1959); *Bull. acad. sci. U.R.S.S. (Izvestiya) Chem. Ser.*, 1429 (1957); Abstracts Theoretical Division, Philadelphia Meeting, 1959, p. 1; A. Frumkin and N. Nikolajeva-Fedorovich, *Bull. Moscow Univ. (Vestnik)*, N4, 169 (1957).
66. B. Levich, *Compt. rend. acad. sci. U.R.S.S.*, **67**, 309 (1949); **124**, 869 (1959).
67. L. Gierst, "Cinétique d'approche et réactions d'électrodes irréversibles," Bruxelles (1958).
68. R. Gurney, *Proc. Roy. Soc.*, **A134**, 137 (1932).
69. M. Breiter, M. Kleinerman, and P. Delahay, *J. Am. Chem Soc.*, **80**, 5111 (1958).
70. J. Koryta, Abstracts of Papers 2nd Int. Congr. Polarography, p. 29 (1959).
71. A. Frumkin, Proc. Sec. Int. Congr. Surface Activity, Electrical Phenomena, p. 58 (1957); *Nova Acta Leopoldina, N.F.*, **19**, N132, (1957); *Compt. rend. acad. sci. U.R.S.S.*, **85**, 373 (1940).
72. S. Jofa, B. Kabanov, E. Kuchinsky, and F. Chisjakov, *J. Phys. Chem. (U.S.S.R.)*, **13**, 1105 (1939).
73. Y. Heyrovsky, *Disc. Faraday Soc.*, **1**, 212 (1947); R. Piontelli, *Compt. rend. 2-ème Réunion CITCE, Milano*, 1951, p. 3; J. Randles and K. Somerton, *Trans. Faraday Soc.*, **48**, 937, 951 (1952); K. Schwabe, *Z. Elektrochem.*, **59**, 663 (1955); L. Antropov, *Uspekhi Khim.*, **25**, 1043 (1956).
74. J. Kolotyrkin and N. Bune, *J. Phys. Chem. (U.S.S.R.)*, **21**, 581 (1947); **29**, 435 (1955); *Compt. rend. acad. sci. U.R.S.S.*, **100**, 295 (1955); J. Kolotyrkin and L. Medvedjeva, *J. Phys. Chem. (U.S.S.R.)*, **25**, 1355 (1951); **29**, 1477 (1955); L.

Medvedjeva and J. Kolotyrkin, *ibid.*, **31**, 2668 (1957); J. Kolotyrkin, Proc. 9th Meeting CITCE, London, 1959, p. 406; *Trans. Faraday Soc.*, **55**, 455 (1959).
75. S. Jofa and L. Medvedjeva, *Compt. rend acad. sci. U.R.S.S.*, **69**, 213 (1949); S. Jofa, E. Ljachovezkaya, and K. Sharifov, **84**, 543 (1952); S. Jofa and G. Roshdestvenskaja, **91**, 1159 (1953); S. Jofa, *Bull. Moscow Univ. (Vestnik)*, **N2**, 139 (1956).
76. E. Wicke and B. Weblus, *Z. Elektrochem.*, **56**, 169 (1952).
77. A. Frumkin and E. Ajkasjan, *Compt. rend acad. sci. U.R.S.S.*, **100**, 315 (1955); *Bull acad. sci. U.R.S.S. (Izvestiya) Chem. Ser.*, 202 (1959); E. Ajkasjan, *J. Phys. Chem. (U.S.S.R.)* **33**, 1016 (1959).
78. L. Shanina, *Compt. rend. acad. sci. U.R.S.S.*, In press.
79. V. Losev, *ibid.*, **88**, 499 (1953); T. Birinzeva and B. Kabanov, *J. Phys. Chem. (U.S.S.R.)*, **33**, 844 (1959); A. Rakov, T. Borisova, and B. Ershler, *ibid.*, **22**, 1930 (1948).
80. Chua Bao-din, Shen Sin-su, S. Jofa, and E. Michailova, *Compt. rend. acad. sci. U.R.S.S.*, **130**, 129 (1960).
81. M. Gerovich *ibid.*, **86**, 543 (1954); **105**, 1278 (1955); M. Gerovich and G. Rybalchenko, *J. Phys. Chem. (U.S.S.R.)*, **32**, 109 (1958); M. Gerovich and N. Poljanovskaja, *Nauch. Doklady Wisschei Shkoly, Chimia*, 651 (1958).
82. M. Suhrmann, *Z. Metallkunde*, **46**, 780 (1955).

Brief Communications

Preparation of Solid Electrodes for Hydrogen Overpotential Studies

A. C. Makrides and M. T. Coltharp[1]

Metals Research Laboratories, Union Carbide Metals Company, Division of Union Carbide Corporation, Niagara Falls, New York

The importance of minimizing the amount of impurities in solution in hydrogen overpotential measurements has been stressed repeatedly (1). Following the example of Frumkin and his co-workers (2), pre-electrolysis is used extensively to this end. In purified solutions, hydrogen overpotential on mercury follows the Tafel equation with closely reproducible exchange current and Tafel slope (3). Results with solid electrodes vary widely, however. Deviations from Tafel behavior and time dependence of the overpotential at any given current density have been reported frequently (4, 5).

We have measured hydrogen overpotential on nickel ("spectroscopic" purity) by the direct method. Unlike previous work with this system (6), results were time independent and coincident curves were obtained with increasing and decreasing current densities. This study will be reported in detail later. The method used to prepare electrodes, which we believe applicable to similar studies with other metals, is presented here.

Nickel electrodes were cleaned by immersion in a chromic-sulfuric acid solution ("cleaning solution"), followed by washing with boiling conductivity water. Upon immersion in alkaline (0.1*N* NaOH) test solutions, electrodes exhibited passive potentials (>0.200 v vs. hydrogen in the same solution). They were activated by cathodic polarization at 2 ma/cm^2 for about 5 min. Rest potentials were within 2-3 mv of the reversible hydrogen potential. After a run, which generally required about 100 min, the electrode was passivated by anodic polarization at about 40 μa/cm^2 and left in this condition until the next run whereupon the electrode was again activated by cathodic polarization as described above. Reproducible results were obtained over a period of about two days. For longer times, the rest potentials became increasingly positive and overpotentials became time dependent, particularly at higher current densities. It is probable that for the longer times adsorbed impurities, probably dissolved glass, were not removed by passivation (anodic polarization to 1.0 v).

The Tafel slope was 0.110 v at 30°C, not much different from that reported by Bockris and Potter in their study of hydrogen overpotential on nickel (6). However, the exchange current in 0.1*N* NaOH was 1.5 x 10^{-5} amp/cm^2, i.e., about 30 times larger than 5 x 10^{-7} amp/cm^2 given in (6).

The possibility that these results can be attributed to a film of high specific area formed by reduction of the passive layer was ruled out by runs in 0.1*N* HCl. In this solution nickel activates spontaneously, the oxide apparently dissolving. The electrode was in solution for about 4 hr. It corroded at a rate of about 4 x 10^{-5} amp/cm^2 with a rest potential of —0.014 v against hydrogen. The equivalent of about 300 surface layers (~ 180 x 10^{16} atoms) dissolved during this time. Results were entirely analogous to those in alkaline solutions, i.e., overpotentials were time independent and ascending and descending curves agreed closely. The Tafel slope, 0.100 v, was essentially that reported in (6) while the exchange current was 5 x 10^{-5} amp/cm^2, or about 40 x the value 1.2 x 10^{-6} given in reference (6)

The time dependence of the overpotential, the inability to retrace a polarization curve with the same electrode, the deviation from the Tafel relation of the steady-state curves, and the low exchange currents reported in (5) and (6) must therefore be attributed to impurities adsorbed on the electrode,

[1] Present address: Department of Chemistry, University of Texas, Austin, Texas.

probably prior to its exposure to solution. Electrodes were pretreated in (6) by heating in hydrogen at about 350°C.

Common methods of preparing solid electrodes involve either etching or heating in hydrogen at temperatures below the softening point of borosilicate glass (6). Etching does not remove all impurities, a fact demonstrated by the existence of a variety of compounds which inhibit dissolution. Heating in vacuum or in hydrogen apparently is not effective unless temperatures approaching the melting point of the metal are used ("flashing") (7). In the method presented here the electrode is exposed to highly oxidizing conditions. Impurities are probably displaced by negative ions at the large positive potentials (> 1.0 v) attained. Further, it is generally found that organic impurities are adsorbed to a smaller extent on oxides than on metals; at the same time, they are adsorbed less strongly in the oxidized than in the reduced form (8). It is expected, therefore, that on reducing or dissolving the passive layer a "clean" electrode surface is produced.

"Active," reproducible platinum electrodes have been obtained by anodic polarization (9). Recently, Walker and Adams (10) cleaned platinum electrodes for polarographic studies in a manner similar to that presented here. This method can be employed with all metals which do not dissolve markedly under highly oxidizing conditions and which can be activated by a cathodic current. The surface can be regenerated after one or more runs if the metal passivates in the test solution at small anodic current densities (for example, nickel in *0.1N* NaOH).

Manuscript received Dec. 7, 1959.

Any discussion of this paper will appear in a Discussion Section to be published in the December 1960 JOURNAL.

REFERENCES

1. J. O'M. Bockris and E. B. Conway, *Trans. Faraday Soc.*, **45**, 989 (1949); J. O'M. Bockris, "Modern Aspects of Electrochemistry," p. 260, Butterworths, London (1954).
2. A. Frumkin, *Acta Physicochim.*, **18**, 23 (1943).
3. Jofa, *ibid.*, **10**, 903 (1939). Jofa and A. Frumkin, *ibid.*, **18**, 183 (1943); J. O'M. Bockris and A. M. Azzam, *Trans. Faraday Soc.*, **48**, 145 (1952).
4. P. Lukowzew, S. Lewina, and A. Frumkin, *Acta Physicochim.*, **11**, 21 (1939).
5. A. M. Azzam, J. O'M. Bockris, B. E. Conway, and H. Rosenberg, *Trans. Faraday Soc.*, **46**, 918 (1950).
6. J. O'M. Bockris and E. C. Potter, *J. Chem. Phys.*, **20**, 614 (1952).
7. J. K. Roberts, *Proc. Roy. Soc. (London)*, **A152**, 445 (1935).
8. E. B. Maxted, "Advances in Catalysis," Vol. III, p. 129, Academic Press, New York (1951).
9. S. Schuldiner, *This Journal*, **106**, 891 (1959).
10. D. E. Walker and R. N. Adams, 136th Meeting of Am. Chem. Soc., Atlantic City, 1959.

Periodic Phenomena at a Nickel Electrode in Sulfuric Acid

Jörg Osterwald[1] and Heinz-Gerhard Feller[2]

Corrosion Laboratory, Department of Metallurgy,
Massachusetts Institute of Technology, Cambridge, Massachusetts

In connection with electrochemical investigations of nickel-copper and chromium-nickel-iron alloys we observed positively and negatively damped oscillations occurring at the nickel electrode in sulfuric acid. This type has not yet been described in the literature, although periodic phenomena at a nickel electrode are known (1, 2). Although investigations of this new type could not be completed during our stay in the United States, we should like to summarize the most important experimental results obtained so far.

The polarization curve for transpassive nickel in *1N* sulfuric acid at 25°C obtained potentiostatically is shown in Fig. 1. If one tries to measure the same curve galvanostatically, this is only possible for current densities below A. Above A the electrode potential does not become stable, but oscillations occur. Near A these oscillations are almost sinoidal (see right part of Fig. 2b), while they become more and more deformed with higher current densities. If one increases the current density beyond B, the potential jumps to a value lying above C on the other branch of the polarization curve. This phenomenon is remarkable, because usually the other

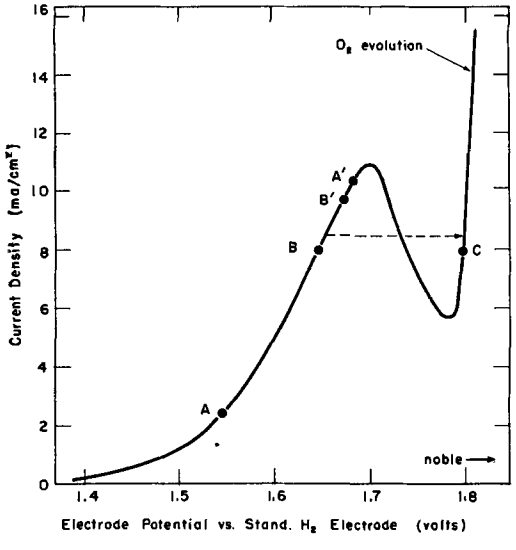

Fig. 1. Polarization curve of nickel in the transpassive region at 25°C obtained potentiostatically.

branch of a polarization curve can only be reached by applying a current density greater than the value related to the maximum.

As already mentioned, a constant potential is obtained below A under galvanostatic conditions, but

[1] Present address: Max-Planck-Institut für physikalische Chemie, Göttingen, Germany.
[2] Present address: Institut für Metallkunde der Technischen Universität, Berlin, Germany.

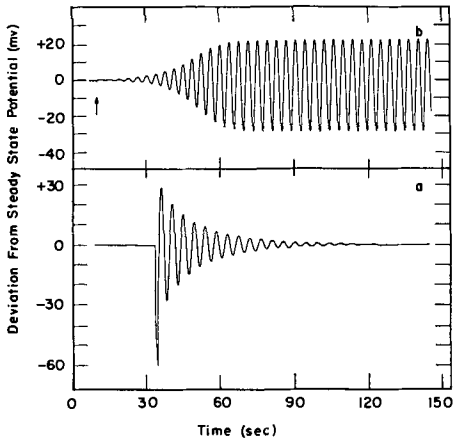

Fig. 2. Oscillations of potential under galvanostatic conditions (original oscillograms); T = 25°C. a, Damped oscillations, c.d. = 2.26 ma/cm²; b, negatively damped and steady oscillations, c.d. = 2.87 ma/cm².

a small positive or negative additional current pulse stimulates damped oscillations (Fig. 2a). With the exception of the first oscillations after the stimulating pulse the deviation ΔU from the steady-state potential may be described by the following equation:

$$\Delta U = \Delta U_0 e^{-\lambda t} \cos (2\pi\nu t + \delta)$$

ΔU_0 depends on the height of the pulse, while the damping constant λ and the frequency ν are only functions of the current density applied continuously. The phase angle δ depends on the zero point of the time scale.

In the region above A, oscillations occurring with increasing amplitude or, in other words, with negative values of λ can be observed by means of a special technique. A potential of the region above A is applied potentiostatically to the electrode. Then the galvanostatic circuit is adjusted to a current density equal to that which corresponds to the potentiostatically applied potential. If one now applies this current density to the cell immediately after having disconnected it from the potentiostatic circuit, one observes sinoidal potential oscillations, which eventually turn to steady oscillations. Figure 2b gives an example. The arrow marks the point at which the cell was switched from the potentiostatic to the galvanostatic circuit.

Using the same technique we found that above B' in Fig. 1 again steady oscillations occur under galvanostatic conditions, while above A' damped oscillations can be observed.

With decreasing acid concentration the whole region between A and A' becomes smaller, until first the region between B and B' disappears and finally at approximately 0.3*N* sulfuric acid only damped oscillations occur. The damping constant λ, however, has a minimum at a certain current density, to which a maximum of the frequency corresponds approximately.

A more quantitative description of the phenomena and an attempt at a theoretical explanation will be given after further information has been obtained, especially for the dynamic behavior of the nickel electrode under potentiostatic or other than galvanostatic conditions.

Acknowledgment

The authors are indebted to Professor H. H. Uhlig for his aid and encouragement. They wish to express their gratitude to the International Nickel Company and to the Shell Companies Foundation, Inc. for fellowship grants.

Manuscript received Jan. 19, 1960.

Any discussion of this paper will appear in a Discussion Section to be published in the December 1960 JOURNAL.

REFERENCES

1. R. Piontelli and G. Sarravalle, *Z. Elektrochem.*, **62**, 759 (1958).
2. U. F. Franck, Private communication.

Conductivity of Silver Iodide Pellets for Solid-Electrolyte Batteries

J. N. Mrgudich[1]

Laboratory for Insulation Research, Massachusetts Institute of Technology, Cambridge, Massachusetts

ABSTRACT

Silver amalgam electrodes were found to provide polarization-free contacts for the measurement of the conductivity of compressed AgI powder pellets. Correlation of the conductivity data with x-ray diffraction studies established the presence of a deformed hexagonal phase as an important factor in determining pellet conductivity. Deformation can be induced by compression, but care must be taken to avoid transformation into the face-centered cubic phase with some resultant decrease in conductivity. Preliminary evidence is presented that hexagonal deformation can be induced by suitable thermal or mechanical pretreatment of the AgI powder.

Lehovec and Broder (1) showed that thin sections of certain solid ionic conductors can serve as electrolytes of electrochemical battery systems. Such "solid-electrolyte" batteries, because of inherently easier control and confinement of the electrolyte, promise significant improvement over conventional batteries using liquid electrolytes.

Some of the advantages are illustrated by a cell made by the author in December 1952. Its active components were a sheet of Ag foil as anode, a pellet of compressed AgI powder as electrolyte, and a pellet of 50% AgI and 50% African MnO_2 as cathode. Cross-section diameter was 1.27 cm and overall volume was about 0.15 cc. Despite this small volume the open-circuit voltage, after nearly six years of unsealed storage at ambient room temperature, dropped by only 4% (from 0.56 to 0.54 v) since February 1953. The short-circuit flash current remained substantially constant at 17 μamp. The Ag electrode, except at its periphery where atmospheric oxygen resulted in tarnishing, remained uncorroded.

The most serious shortcoming of such solid-electrolyte systems is their very low flash current, usually measured in μamp/cm^2 of electrode area. This manifestation of high internal resistance follows directly from the fact that the room-temperature conductivity of even the best solid ionic conductors lies six to eight orders of magnitude below that of conventional battery electrolytes. In consequence, unless the room-temperature conductivity of suitable solid ionic conductors can be increased by at least four orders of magnitude, the practical use of the otherwise eminently promising solid-electrolyte batteries will be limited to microwatt power applications.

The purpose of this investigation was to study and develop methods for increasing the room-temperature ionic conductivity of AgI. Silver iodide was chosen because of its reported relatively high room-temperature ionic conductivity, its apparently simple conduction process which involves only Ag^+ ions moving through a fixed I^--ion lattice, and the substantial absence of interfering electronic conduction.

[1] Present address: U.S. Army Signal Research and Development Laboratory, Fort Monmouth, N. J.

Unfortunately AgI is not easily prepared in the form of single crystals stable at room temperature, and there is today little theoretical interest in conductivity measurements on compressed powders. Nevertheless, in view of eventual applications which will of necessity resort to the use of multicrystalline electrolyte in the form of compressed powders, evaporated films, chemical deposits, or painted layers, measurements on such powders and efforts to increase their ionic conductivity are meaningful in a practical sense. Furthermore, multicrystalline electrolytes profit from increased ionic mobility along interfacial surfaces so that, even if single crystals were available, there would be a need for study of the conductivity of compressed powders.

Polarization Phenomena in Measurements of Ionic Conductivity

It is well known that if a d-c voltage is applied across an ionic conductor, the resultant flow of current decreases with time (2, 3). To avoid such polarization effects, a-c voltage (usually 1000 cps), four-probe sample holders, pulse techniques, or combinations thereof are applied. These measures may be adequate when sample temperature is high or when sample conductivity is low. However, blocking layer effects become more pronounced as the temperature drops or as conductivity increases. Brennecke (4), for example, confirming earlier work by Lehfeldt (5), found that d-c conduction through various alkali halides obeys Ohm's law at high temperatures but begins to deviate as temperature decreases. Johnston (6), studying AgBr at room temperature, reported that the a-c conductivity was a function of frequency (even up to 10,000 cps) and that this dependence increased with samples of higher conductivity (about 10^{-7} ohm^{-1} cm^{-1}). There is thus no certainty that conventional methods for minimizing polarization are adequate for a study whose objective is the synthesis of materials exhibiting extraordinarily high ionic conductivities (about 10^{-8} or better) at room temperatures.

Use of Amalgamated Silver Electrodes

In the course of some preliminary studies it was found that application of quite small d-c voltages

across an AgI pellet between identically amalgamated Ag electrodes yielded a remarkably stable current flow. This constancy led to efforts to use such amalgamated electrodes in the development of an apparently polarization-free d-c method for the measurement of the conductivity of AgI pellets.

The amalgamated electrodes were prepared by rubbing Hg onto disks of clean and polished Ag sheet (1.525 cm diameter, approximately 0.15 cm thick). Just before use the electrodes were wiped clean and residual scum removed by rinsing the surface with clean, distilled Hg dropping from a burette.

Pellets of AgI (1.525 cm diameter) were made by compression in a hand-actuated laboratory press (capacity 1120 kg/cm², 16,000 psi). Since the objective was to carry out extensive tests of the reproducibility of a new method, we required ready availability of a relatively large amount of uniform AgI. Most of this work used two different grades of powdered, commercial AgI made homogeneous by thorough mixing after passing through a 35-mesh screen. After compression, the pellets were gently smoothed with 3/0 emery paper to remove peripheral feathering and surface glaze. Then they were placed between identically amalgamated Ag electrodes backed by Pt electrodes to prevent solder contamination of the amalgamated electrodes (Fig. 1).

The voltage across the array could be changed by adjusting the value of the decade-box resistance R_2. Three voltage ranges (0.0001, 0.001, and 0.01 v) sufficed for most of the work. The galvanometer (Leeds and Northrup, D'Arsonval, 0.008 μa/mm deflection at 1 meter) was calibrated for each voltage range by use of a standard calibrated decade resistance replacing the array. Switch S served as an easy means for reversal of current direction to check for the presence of polarization.

Figure 2 compares the results of conductivity measurements on a given pellet of AgI between clean, polished Ag electrodes before and after electrode amalgamation. The slight upward trend of the

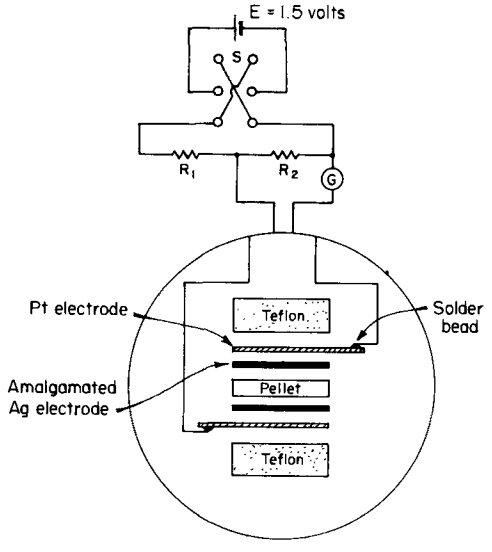

Fig. 1. Exploded view of conducting array, with circuit used to permit easy reversal of applied d-c voltage.

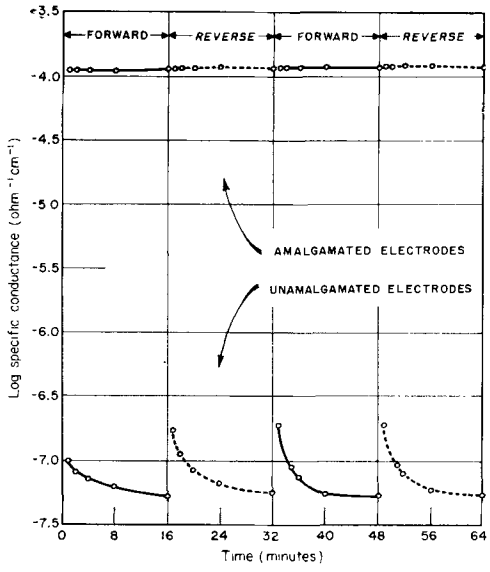

Fig. 2. Elimination of polarization through use of amalgamated silver electrodes.

amalgamated-electrode curve is undoubtedly due to an observed 1°C rise in room temperature during the 64-min run. The lesser fluctuations within each 16-min run fall easily within the errors induced by small random variations of the galvanometer zero. These fluctuations, however, are trivial when viewed in the perspective of Fig. 2 and its very strong evidence of absence of polarization with amalgamated electrodes.

Considerable time and effort were spent in demonstrating that this method allows for the reproducible determination of the conductivity of AgI at room temperatures. Repeated assembly, measurement, disassembly, electrode reamalgamation, and remeasurement on the same pellet, and variations of pellet dimensions showed that the conductivity is both reproducible and independent of pellet thickness, i.e., that it complies with Ohm's law (Table I).

In a further evaluation of the method, Westphal[2] carried out some a-c measurements of conductivity as a function of frequency. He showed (Table II)

[2] W. B. Westphal, Laboratory for Insulation Research, Massachusetts Institute of Technology, Cambridge, Mass.

Table I. Conductivity of silver iodide—test of reproducibility and compliance with Ohm's law

Material	Pellet No.	Compression pressure (kg/cm²)	Thickness (cm)	Conductivity ($ohm^{-1}cm^{-1}$) x 10^{+4}	Average value	Deviation from mean %
AgI*	68	281	0.1068	1.28, 1.31, 1.28 1.27, 1.28	1.28	1.0
AgI*	58	702	0.0986	1.50, 1.48, 1.48	1.51	1.9
	59	702	0.1944	1.47		
	60	702	0.3834	1.54, 1.57		
	61	702	0.7675	1.50		
AgI†	54	702	0.0969	0.98	1.00	1.7
	55	702	0.1894	1.02		
	56	702	0.3813	0.99		
	57	702	0.7692	1.02		

* Mallinckrodt Chemical Works.
† Allied Chemical and Dye Corporation.

Table II. Comparison of conductivities at various frequencies

Electrodes	Ag amalgam		Ag paint		Evap. Ag	
Pellet thickness (cm)	0.384	0.763	0.385	0.762	0.383	0.763
Frequency (cps)						
100	1.54	1.53	1.00	1.29	1.43	1.46
300	—	—	1.35	1.51	1.45	1.52
1,000	1.54	1.53	1.46	1.58	1.44	1.56
3,000	—	—	1.50	1.60	—	1.58
10,000	1.54	1.53	1.52	1.60	1.48	1.59
100,000	1.54	1.54	1.54	1.58	1.48	1.62
300,000	—	—	1.55	1.61	1.49	1.62
1,000,000	1.55	1.52	1.58	1.62	1.50	1.63

All conductivities are given in $(ohm^{-1}cm^{-1}) \times 10^{+4}$. Pellets were made of Mallinckrodt silver iodide powder compressed at 702 kg/cm² and were approximately 16 days old at the time of measurement.

that with Ag paint or evaporated Ag electrodes the a-c conductivities approached constancy only above 10,000 cps and even then yielded values that varied with sample thickness. It will be noted that similar a-c measurements using amalgamated electrodes gave conductivities independent of both frequency and sample thickness.

The major precaution that must be taken with amalgamated electrodes is avoidance of scum. When this is realized, the results are readily reproducible and the pellet, even after week-end contact with the electrodes, shows no discoloration or evidence of reaction with Hg (formation of HgI_2 or Ag_2HgI_4). Addition of weights to the assembled vertical array is of no significant effect up to 100 g. Beyond this point the conductivity decreases by about 6% at 200, 13% at 500, and 19% at 1000 g. This effect seems to be due to squeezing out of a mobile amalgam interface.

When an amalgamated array is first assembled, it exhibits a variable transient voltage that dies away to a fraction of a microvolt within about 10 min. Although this may be due to a slight difference in the temperature of the two electrodes [Reinhold (7) has shown that a difference of 1°C in the relative temperatures of the electrodes of an Ag-AgI-Ag array near room temperature can result in a voltage difference of about 1000 μv], it is more likely that amalgam redistribution is involved since the top electrode is always initially negative with respect to the bottom. Careful conductivity measurements, of course, must await practical disappearance of these transients.

Effect of Compression Pressure on Pellet Conductivity

Although description of a d-c method for measurement of the conductivity of AgI is the major objective of this paper, a few very preliminary applications have been made.

Table III gives the room temperature conductivities of pellets of Mallinckrodt AgI compressed at various pressures and temperatures. The low-temperature compressions were made by quick compression of pre-assembled cavity, plug, sample, and plunger after chilling the pressure chamber and sample overnight at —10°C. Likewise, the high-

Table III. Conductivities of pellets as function of compression pressure at different temperatures

Compression pressures		Compression temperatures, °C		
kg/cm²	psi	−10°	27°	95°
140	2,000	0.43	0.65	0.96
281	4,000	1.08	1.23	1.17
421	6,000	1.38	1.36	1.31
562	8,000	1.43	1.37	1.31
702	10,000	1.56	1.48	1.27
843	12,000	1.58	1.55	2.30
983	14,000	1.61	0.89	—
1220	16,000	1.80	0.74	2.66

All conductivities are given in $(ohm^{-1}cm^{-1}) \times 10^{+4}$. Pellets compressed at −10°C and 27°C were 24 days old at the time of measurement; those at 95°C were 4 days old.

temperature compressions were made on preheated assemblages.

The most interesting feature of Table III is the conductivity "break" observed beyond 843 kg/cm² in the room-temperature series. This break was confirmed with a second run of Mallinckrodt AgI and was also observed using the Allied Chemical material.

Suspecting that a phase change was associated with the conductivity break, x-ray diffraction techniques (Norelco diffractometer, filtered Cu radiation, scanning speed of 1°/min, chart speed of 1.27 cm/min) were applied to a study of the second room-temperature pressure series using *unpolished* Mallinckrodt pellets. It is known that there exist at least three modifications of AgI (8). The γ phase, yellow, stable up to about 137°, is face-centered cubic with $a_o = 6.502$Å. The β phase, orange, stable from 137° to about 146°C, but apparently metastable at room temperature, is hexagonal with $a_o = 4.59$ and $c_o = 7.49$Å. The α phase, brown, stable only above 146°C, is body-centered cubic with $a_o = 5.044$Å. It is particularly interesting to note that the axial ratio for the hexagonal phase is very close to the 1.633 value characteristic of ideal close packing. As Manson (9) pointed out, this means that all strong γ-cubic lines will face at nearly the same positions as strong hexagonal lines although there

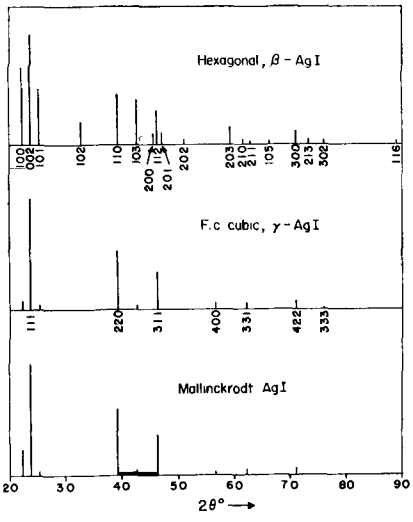

Fig. 3. X-ray diffraction angles and relative intensities of β and γ silver iodide.

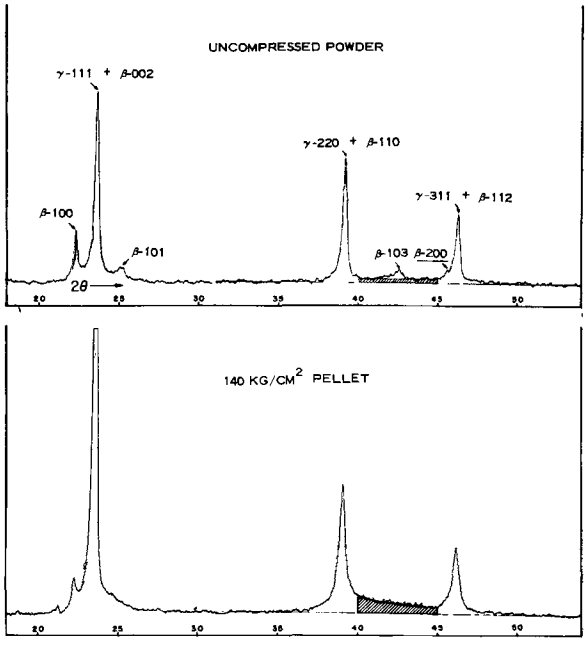

Fig. 4. Structural changes associated with initial compression of AgI powder.

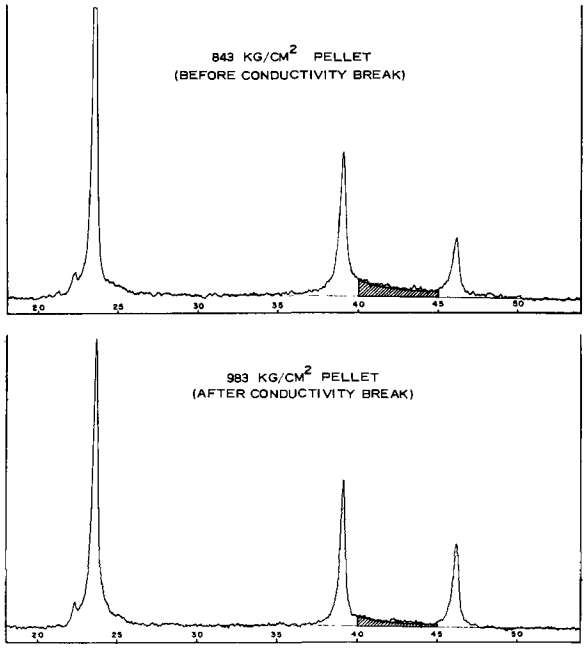

Fig. 5. Diffraction traces of pellets before and after conductivity break.

will be lines in the hexagonal pattern not present in the γ-cubic. The two upper charts of Fig. 3 (practically pure γ and β materials obtained from Mr. Manson[3]) illustrate these line coincidences. The bottom chart shows that the Mallinckrodt material is essentially γ-cubic with easily detectable amounts of β-hexagonal.

Figure 4 illustrates diffraction differences between uncompressed Mallinckrodt powder and a pellet compressed at room temperature at 140 kg/cm² (2000 psi). There is a sharp increase in the $\gamma(111) + \beta(002)$ intensity, all β lines tend to disappear, the entire region between 2θ values of 39-46° becomes abnormally fogged (shaded area), and all cubic lines tend to broaden with asymmetric tailing of the base.

The sharp increase in $\gamma(111) + \beta(002)$ intensity indicates a pressure-induced orientation of grains of one or both phases. The other three effects can be explained on the basis that pressure broadens all hexagonal lines. Such line broadening is indicative of strong deformation of hexagonal crystallites and/or pronounced grain fragmentation. The fact that line broadening occurs at relatively low pressure (even at 35 kg/cm², 500 psi) and the logical assumption that grain deformation precedes grain fragmentation favor acceptance of the lattice-deformation viewpoint.

X-ray traces of pellets compressed at pressures up to 843 kg/cm² (12,000 psi) were essentially the same as for the 140 kg/cm² (2000 psi) pellet. Relatively marked changes took place, however, in the pressure range corresponding to the conductivity break (Fig. 5). There was a decrease in the $\gamma(111) + \beta(002)$ intensity, a decrease in shaded-area fogging, and an increase in line symmetry with some indications of line sharpening. These changes in the diffraction patterns may be due to a pressure-induced tendency for the disappearance of deformed hexagonal phase, probably by conversion to γ-cubic. The associated drop in conductivity is strong evidence of the importance of the deformed hexagonal phase as a conductivity-imparting ionic "solder."

At higher pressure (1,220 kg/cm², 16,000 psi), shaded-area fogging, while still present, diminishes in a manner consistent with the slightly lowered conductivity (cf. Table III).

Some Exploratory Measurements

It has been found that the conductivity of pellets decreases slowly with time. There is a linear relationship between log specific conductance and log time. This is reminiscent of the linear relationship known to exist in metal deformation where per cent recovery of yield stress varies linearly with log time and can be construed as evidence supporting the lattice-deformation concept.

Using a special sample holder (Fig. 6) which employed pools of liquid silver amalgam, it was possible to make a preliminary study of the effect of increasing temperature on the conductivity of a pellet compressed at 702 kg/cm² (10,000 psi) at

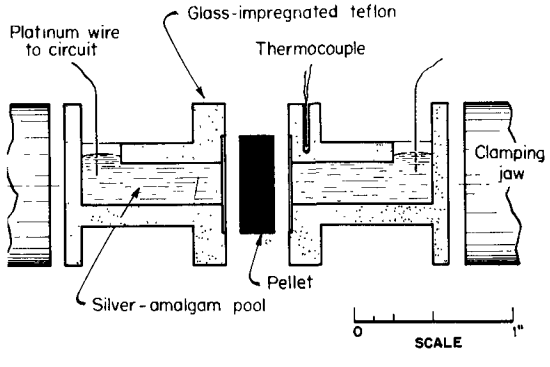

Fig. 6. Conductivity cell using liquid amalgam pools

[3] Air Force Cambridge Research Center, Bedford, Mass.

room temperature. Evidence of a temperature-accelerated relief of hexagonal deformation was noted during an overnight stand at about 75°C. Further temperature increase resulted in a tremendous increase in conductivity, from 7.2 x 10^{-4} ohm^{-1} cm^{-1} at 132°C to 9 ohm^{-1} cm^{-1} at 138°C. Pellet color changed from greenish yellow to speckled orange with little, if any, change in pellet dimensions. It seems probable that a phase transition from essentially γ-cubic to essentially equally dense β-hexagonal took place. Overnight standby at 138°-139°C resulted in a drop in conductivity to 1.2 ohm^{-1} cm^{-1}. Further increase in temperature resulted in a *drop* to about 1.0 x 10^{-1} ohm^{-1} cm^{-1} at 146°C beyond which temperature the pellet color changed from speckled orange to solid tan-brown (probably a transformation of β-hexagonal to α-cubic) with no significant increase in conductivity. The pellet underwent sharp expansion. For all practical purposes this expansion concluded the temperature run. Cooling to room temperature gave a canary-yellow pellet (compared to the original greenish-yellow) and a conductivity estimated at 1 x 10^{-7} ohm^{-1} cm^{-1}. Repeated temperature cycling (room temperature to 180°C) with the expanded pellet showed that pellet-color changes were remarkably consistent; invariably canary yellow below 137°, speckled orange between 137°-146° and tan-brown above 146°C. Furthermore, the conductivity changed sharply only at about 137°C, indicating that the transition from γ-cubic to β-hexagonal is probably more important with respect to conductivity than that from the β-hexagonal to α-cubic.

Time was not available for the preparation of the large quantities of pure γ and β AgI needed for a careful study of the effect of compression temperature and pressure on structurally homogeneous phases. It has been shown, however, that pellets of Manson's purest γ and β materials, at room-temperature compression pressures of 281 kg/cm^2 (4000 psi), gave conductivities of 1.9 and 3.5 x 10^{-5} ohm^{-1} cm^{-1}, respectively. Both of these are significantly lower than the 281 kg/cm^2 pellet of the Mallinckrodt γ-β mixture at 12.3 x 10^{-5} ohm^{-1} cm^{-1}. A possible explanation of this anomaly of a mixture having a conductivity higher than either of its two components may lie in the residual deformation present in the uncompressed Mallinckrodt powder (cf. shaded area, top trace of Fig. 4) and absent in the Manson pure-hexagonal material.

X-ray examination of Allied Chemical AgI showed it to be (like the Mallinckrodt material) a mixture of γ and β phases. Grinding in a mechanical mortar for 2 hr resulted in the line tailing, abnormal fogging, and line broadening characteristic of hexagonal deformation. The conductivities of 281 kg/cm^2 pellets of ground and unground materials were 22.4 and 8.0 x 10^{-5} ohm^{-1} cm^{-1}, respectively, indicating the possibility of inducing hexagonal deformation by mechanical pretreatment of the starting material.

In a quick and incomplete study of the effect of heating and cooling of Allied Chemical AgI it was found that heating the powder in air to 140°, 165°, and 200°C, followed by slow cooling to room temperature, resulted in no significant change in the x-ray traces. However, a sample heated to 200°C for 2 hr and then quenched by sprinkling into a pool of liquid air did show deformation of the hexagonal phase. No conductivity measurements have been made thus far, but thermal shock treatment of powders seems promising.

Prognosis

The work here reported demonstrates that the conductivity of a pellet of compressed AgI can be increased substantially. It does not appear premature to prognosticate conductivities at least one order of magnitude higher (i.e., ca. 10^{-3} ohm^{-1} cm^{-1}) than any yet observed. At this value the conductance of a pellet of 1 cm^2 area and 0.01 cm thickness would correspond to an "electrolyte" resistance of about 10 ohm. Ignoring other resistance sources within the cell, this electrolyte resistance would permit a flash current of about 50 mamp with a cell of 0.5 v open-circuit voltage. Such current outputs would definitely widen the applicability of solid-electrolyte batteries.

However, availability of a highly conductive solid electrolyte, although necessary, is not a sufficient condition for satisfactory battery operation. For example, the conductivity of the cathodic depolarizer must also be high, both from the standpoint of ions entering through the electrolyte from the anode and of electrons entering through the external circuit. Furthermore, volumetric changes associated with discharge (anode consumption and depolarizer expansion) require some compensating physical mobility of the electrolyte or suitable design characteristics. These problems need further study.

Acknowledgment

The author is indebted to Professor A. R. von Hippel and Dr. A. Smakula for many hours of helpful discussion, and to Dr. D. S. Tannhauser and Mr. A. D. Bedrosian for continuing counsel and guidance. Furthermore, he acknowledges the effective co-operation of many members of the Fort Monmouth organization and of the staff and graduate students of Massachusetts Institute of Technology. He is grateful, also, to Professor G. S. Brown, Head, Department of Electrical Engineering, for status as a member of the School for Advanced Study.

Manuscript received Sept. 16, 1959. This work was made possible by a one-year Secretary of the Army Research and Study Fellowship award.

Any discussion of this paper will appear in a Discussion Section to be published in the December 1960 JOURNAL.

REFERENCES

1. K. Lehovec and J. Broder, *This Journal*, **101**, 208 (1954).
2. J. and P. Curie, *Ann. chim. phys.*, **17**, 385 (1889); **18**, 203 (1889).
3. A. R. von Hippel, "Dielectrics and Waves," pp. 228-234, John Wiley & Sons, Inc., New York (1954).
4. C. G. Brennecke, *J. Appl. Phys.*, **11**, 202 (1940).
5. W. Lehfeldt, *Z. Physik*, **85**, 717 (1933).
6. W. G. Johnston, *Phys. Rev.*, **98**, 1777 (1955).
7. H. Reinhold, *Z. anorg. u. allgem. Chem.*, **171**, 181 (1928).
8. J. D. H. Donnay and W. Nowacki, "Crystal Data," p. 497, Geological Society of America, New York (1954).
9. J. E. Manson, *J. Appl. Phys.*, **26**, 423 (1955).

Sine Wave Pulse Current Tester for Batteries

K. Kordesch and A. Marko[1]

Research Laboratory, Union Carbide Consumer Products Company, Division of Union Carbide Corporation, Cleveland, Ohio

ABSTRACT

An instrument has been developed which measures the voltage of a battery during discharge, eliminating its ohmic component. The instrument is portable operated on 60 cycle alternating current and features direct meter readings (instead of an oscilloscope). Its simplicity and ruggedness make it especially suited for development and production control tasks. Results of measurements on different types of cells are presented to illustrate the wide applicability of the instrument.

The intention of the authors was to develop a simple and reliable instrument for the evaluation of battery performance under load conditions. The method of measuring polarization and internal resistance values by means of periodic current interruption was chosen because these parameters are very characteristic for a battery system.

Square wave generators have been used frequently to study the characteristics of electrodes of galvanic systems. The literature reports many of these devices, some of them quite useful in research and development laboratories. However, most of these instruments are complex, use an oscilloscope, and are not suitable for rugged performance conditions. Furthermore, they require highly skilled personnel for interpretation of the measurements (1-3).

The principle of a circuit which enables us to subject a cell to a periodically interrupted discharge (pulse current load) and measure the voltage of the cell between the discharge periods is shown in Fig. 1 (4). In position one, 1, the double pole vibrator switch, S, connects the cell on test to a discharge circuit consisting of a variable resistor, R, and an ammeter, A. In position two, 2, of the switch, the cell is charging a capacitor, C, to the potential existing during the current off-time. A high resistance voltmeter, V_1, indicates this voltage. If the vibrator switch operates at a frequency of at least 50 cycles, the polarization of the cell reaches a steady-state value corresponding to the load current indicated by the ammeter. A booster battery prevents the discharge current from changing too much when the cell voltage changes. The voltmeter, V_2, indicates the terminal voltage of the cell being tested.

[1] Present address: Wright Air Development Center, Dayton, Ohio.

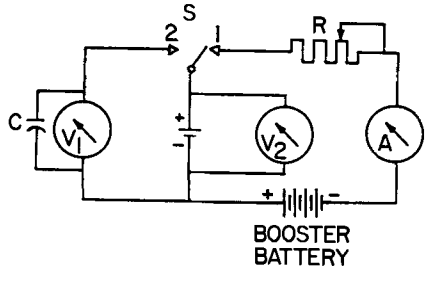

Fig. 1. Vibrator circuit

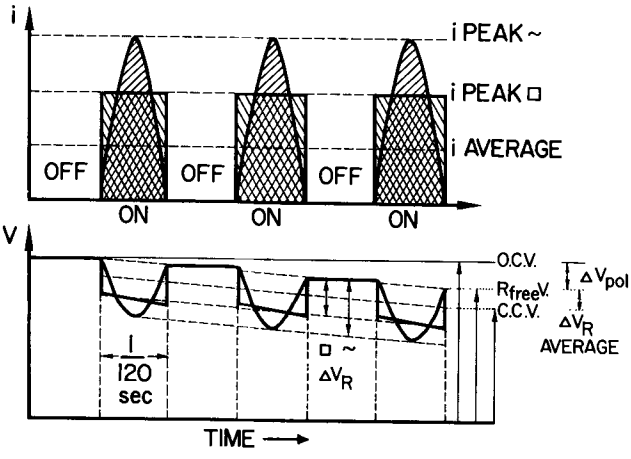

Fig. 2. Effect of square or sine wave pulses on a battery system.

Figure 2 shows in an artist's sketch the oscillographic curves obtained from a battery system subjected to a pulse current. First, only square wave pulses shall be discussed in connection with the just mentioned vibrator switch circuit. The current pulses are pictured in the upper section of the sketch. With an equal "off" and "on" time (1/120 sec) the average current is one half of the peak current. The galvanic cell responds to this average current indicated by a moving coil instrument of the common d-c ammeter-type. In the lower part of the sketch, the effect of the current pulse on the voltage of the cell is shown. Only a few pulses are shown in the drawing, but it should be understood that the system will reach a certain steady state, e.g., after 1 min of closing the circuit, the readings may be taken. The voltage of the cell without the resistance component, R_{free} V, is represented by the top level of the pulse curves. The terminal voltage, CCV, is represented by the average value of the pulses (½ of the square pulse). The difference between the OCV and the R_{free} voltage indicates the sum of all slow polarization effects in the cell system (ΔV_{Pol}), the difference between the highest points and the lowest points of the pulse curves represents the resistance

voltage drop caused by the corresponding peak current. The resistance value in ohms is calculated by dividing $\Delta V_{R\square}$ by the current i peak □. It is important to note that the same value is obtained by dividing the difference between the R_{free} voltage and the CCV (ΔV_R average) by the average current. The circuit shown in Fig. 1 provided meter indications of $i_{Average}$, R_{free} Voltage, the initial OCV and the later CCV. From these figures one can calculate the polarization and resistance components of the voltage drop caused by the load condition (ΔV_{Pol} and R). The pulse frequency can be chosen from a range between 30 and 400/sec in which no differences have been found in practical cell testing. Mechanical vibrators operate in the 50-100 cycle range, the later discussed electronic switch circuit uses the line frequency of 60 cycles. A too low pulse frequency causes deviation due to recuperation effects during the "off" time; too high frequencies introduce capacitance errors. However, if we consider that the accuracy of common good meters is not better than one half of a per cent, we do not need a better reproducibility of our measurements than ±5 mv (for a 1-v cell). This is the case with all depolarizers tested (manganese dioxide, nickel oxides, lead dioxide, silver oxides) and with most of the available anodes (zinc, cadmium, lead).

The vibrator circuit of Fig. 1 has been used in battery testing circuits with the main objective of studying the polarization characteristics of cells under heavy load conditions. Powerful depolarizers such as silver or nickel oxides polarize to such a small extent that resistance variations obscured the measurements of polarization effects (5).

Mechanical switching proved to be inadequate for high currents; contact bouncing sometimes caused erroneous meter indications. The production of exact square waves by means of mercury switches or electronic circuits could not be solved with a simple apparatus. The inherent capacitance-rounding of square waves and the "cable ring" effects with longer leads were additional reasons for investigating a circuit employing rectified sine wave pulses for test purposes.

The sine wave pulses needed for the polarization of the cell are conveniently taken from the 60-cycle a-c line. Figure 2 shows the effect of half-wave sine pulses of the same mean current value as the square wave pulses. The actual discharge current is one-third of the peak current in accordance with calculations of the mean values of rectified waves. The factor for the ideal, non-truncated half-sine wave for the period 0-360° is $1/\pi$. In a moving coil instrument with D'Arsonval movement the torque on the coil is proportional to the current; therefore the meter reads the average value, which corresponds to the coulometric value of the current. A hot wire, dynamometer or other square law (RMS) instrument cannot be used in this case because its deflection represents I^2R, in our case about 1.45 times larger than the average current (6).

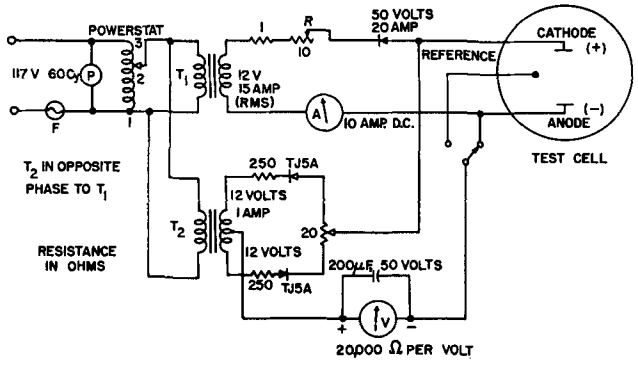

Fig. 3. Sine wave pulse current tester

Figure 3 shows the circuit diagram of one of the most versatile versions of the test instrument. A powerstat transformer circuit, T_1, produces a 12-v alternating current which is rectified and used as a single-phase pulse current to discharge the test cell. The current is regulated at the input of the powerstat and also by means of a variable resistor R. The a-c voltage should be at least six times the cell voltage to assure a clean sine wave shape. The average value of the current is indicated by the ammeter A. In order to connect the voltmeter, V, to the cell between the current pulses (same principle as the vibrator circuit in Fig. 1) a gating circuit is employed represented by a second small transformer T_2 and a double diode bridge. This gating circuit has the purpose of producing alternatingly a very low resistance path and an extremely high resistance connection between the (+) terminal of the voltmeter and the cathode of the test cell. The (−) terminal of the voltmeter is continuously connected to the anode of the cell (or a reference electrode, if desired). The proper timing of the gating circuit is enforced by an alternating current introduced into the bridge by means of transformer T_2. This alternating current does not add or subtract any potential between the center tap of the transformer and the tap of the balancing potentiometer, but it "opens" or "closes" the two diodes in the bridge circuit in opposite phase to the current pulses of the transformer circuit T_1. The voltmeter V indicates the voltage of the capacitor which is charged only during "off current" periods. The proper value of the capacitor is dependent on the resistance of the voltmeter, but not critically. The gating diodes should be of a very high forward/backward current ratio, preferably over 1000:1. Transformer T_2 may be replaced by an additional winding on T_1, but in practice it turned out to be far more convenient to use a separate small transformer for the gating unit, which can be separated completely from the power section in cases where it is desired to subject many cells in series to the pulse current but measure the R_{free} voltages of individual cells.

A reference electrode can be used for the independent measurement of the polarization of cathodes or anodes. The position of the reference electrode is not critical because electrolyte resistance effects are also eliminated.

In some cases where an extension to higher pulse frequencies was desired (e.g., in studies of magnesium electrodes showing passivation effects) we used an audio generator to produce the pulse currents. For work on high resistance batteries (organic depolarizers, solid electrolyte cells) we changed the

silicon diodes of the gating circuit to vacuum tubes and the 20,000 Ω/v meter to a vacuum tube meter (the capacitor across the voltmeter should then be in the range of 1-10 μF).

The principal circuit has been used by the authors for eliminating the disturbing ohmic resistance component in oxygen sensing elements operating on the air-depolarized cell principle, and in connection with fuel cell studies a similar circuit was described at the Electrochemical Society Meeting in October, 1956 (7). Variations of it have been employed for experimental state of charge determination of Ni-Cd batteries (8).

The data obtained with our interrupter have been checked many times against a precision square wave (electronically) switching instrument,[2] and as far as any useful battery system was concerned, no deviation could be detected. With modern rectifier and transistors, the whole instrument can be made small-sized, the largest components being the transformer, the ammeter, and voltmeter. There is no limitation to the current or voltage range of the batteries to be tested; the circuit can be adapted easily to any test requirement.

In order to demonstrate the versatility of the instrument examples of test results with different battery systems are given in the following figures. Differences in depolarizer mix formulation (Fig. 4), influence of geometrical construction (Fig. 5), and system variations (Fig. 6) express themselves in characteristic polarization and resistance curves.

In Fig. 4 (Leclanché cells) Cell A is a regular D-size cell and cell B is a D-size photoflash cell. Both cells have been discharged with a 500 ma pulse current and the R_{free} voltage and the *CCV* are shown as obtained on a simultaneous recording. The ohmic resistance values are calculated from the differences. The cathode of cell A is manufactured mainly from natural ore, the bobbin of cell B contains a large percentage of artificial MnO_2 and more graphite. The gradual loss of depolarizing power or the increase of cell resistance on light intermittent duty or after long storage periods shows up in a similar way if periodic checks (e.g., 1-min tests) are made during the life time of the cells (5, 8).

Figure 5 shows the characteristics of two D-size alkaline MnO_2 cells with powder zinc anodes. Cell

[2] Constructed by Professor E. Yeager, Western Reserve University, for the Research Laboratory of Union Carbide Consumer Products Company.

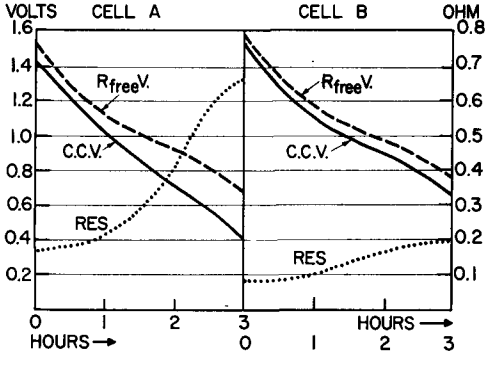

Fig. 4. Discharge characteristics of a standard D-size cell (A) and a photoflash cell (B) 500 ma.

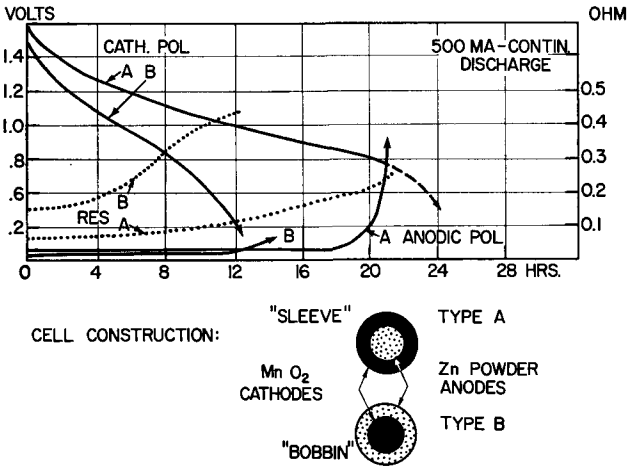

Fig. 5. D-size alkaline MnO_2 cells on 500 ma. Discharge (constr. A and B).

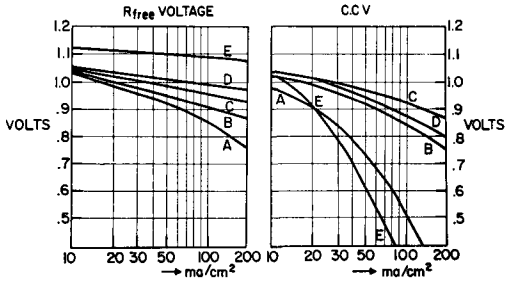

Fig. 6. Terminal voltage and ΔV_{Res} free voltage of hydrogen-oxygen fuel cells. Geometry: A, parallel tube electrodes; B, concentric tube electrodes; C, D, E, parallel plate construction. Electrolytes: A, B, C, 30% KOH at 60°C; D, molten caustic at 200°C; E, fused carbonates, 500°C.

A contains a sleeve type cathode, cell B is made with a bobbin type cathode. In these diagrams only the R_{free} voltages and the resistance values are plotted vs. time. The average discharge current is 500 ma. Here the R_{free} voltage curves are named "polarization curves;" they are measured against a zinc reference electrode positioned between cathode and anode. This gave the possibility to record the anodic polarization curve also.

Figure 6 shows a collection of performance data characteristic for different types of hydrogen-oxygen fuel cells. R_{free} voltage curves are shown on the left side of the figure and *CCV* curves are shown on the right side of the figure. The current density is on a logarithmic scale to cover a wider range. It demonstrates how important it is to know the R_{free} voltage curves to judge performance characteristics. From the terminal voltages (right side) one would say that cell C is the best, cell D the worst; but a look at the corresponding curves on the left side indicates that E has the lowest polarization drop, A the highest. The observed differences are partially due to geometry factors and partially caused by different operating conditions. The R_{free} voltage curves of Fig. 6 agree very well with the values calculated from independent a-c bridge measurement of cell resistances. The advantage of using a pulse current instrument for such studies is the freedom of variation caused by uncontrolled resistance changes during the duration of the test. Lead wire

and contact resistance errors are eliminated. The "true" voltage of the chemical system is directly indicated on the voltmeter.

The pulse current tester described has also been used for charge control purposes. The R_{free} voltage reading is a better indication of the state of charge than the *CCV* because it is not influenced by conductivity changes in the electrolyte or gas film phenomena in the gassing period of the charging procedure. The use as a sensing circuit for automatic constant voltage charging units has been proposed (5). The gating circuit can be used in connection with thyratrons and magnetic current regulators (8). Adaptation to full wave rectifier circuits is achieved by a C-R phase shift arrangement in the gating bridge, "connecting" the voltmeter only during the very short current off period between the two rectified half-waves (the counter voltage of the cell causes truncated sine pulses).

Manuscript received Nov. 4, 1959. This paper was prepared for delivery before the Columbus Meeting, Oct. 18-22, 1959.

Any discussion of this paper will appear in a Discussion Section to be published in the December 1960 JOURNAL.

REFERENCES

1. D. Staicopoulos, E. Yeager, and F. Hovorka, *This Journal*, **98**, 68 (1951); see also R. R. Witherspoon, H. Urbach, E. Yeager, and F. Hovorka, Tech. Rep. Western Reserve University, ONR, Proj. NR 359-277, No. Nonr 581 (00).
2. E. Newberry, *Trans. Faraday Soc.*, **43**, 127 (1947).
3. A. Hickling and F. W. Salt, *ibid.*, **37**, 450, (1941).
4. A. Marko and K. Kordesch, U.S. Pat. 2,662,211, Dec. 8, 1953.
5. K. Kordesch and F. Kornfeil, U.S. Pat. 2,864,055, Dec. 9, 1958, Rep. of SCEL Proj. No. 3-99-09-021 (1954). K. Kordesch, Technical Memorandum, M-1664, June 9, 1955, U.S. Army Signal Research and Development Laboratory.
6. L. B. W. Jolley, "Alternating Current Rectifications," p. 47, J. Wiley & Sons, Inc., New York (1926).
7. K. Kordesch, Battery Symposium, Electrochemical Society, Oct. 1956, Abstract No. 27.
8. A. W. Speyers, 13th Annual Power Sources Conference, U.S. Army Signal Res. & Dev. Lab., Ft. Monmouth, N. J. Contract rep. by Vitro Laboratories.

An Investigation of the Reaction between Aluminum and Water

Walter J. Bernard and John J. Randall, Jr.

Sprague Electric Company, North Adams, Massachusetts

ABSTRACT

It was found that the film formed on aluminum by the action of water between 80° and 100°C consists of a hydrate of aluminum oxide containing as much as 32% water, rather than stoichiometric $Al_2O_3 \cdot H_2O$, as previously reported in the literature. The reaction is not instantaneous but is delayed by the presence of the natural oxide film on the metal. It was also concluded that hydrated oxide growth does not depend on the movement of aluminum ions through the film.

When pure aluminum is immersed in boiling water, there is an initial period during which no visible reaction occurs, followed by hydrogen evolution and the production of an adherent layer of hydrated oxide. The discharge of gas occurs at first at several widely separated points and then quickly spreads over the entire surface of the metal. The rate of hydrogen evolution soon decreases and is barely perceptible after 10 min or so, although weight measurements show that oxidation of the metal continues beyond this point. Considerable literature exists on the subject of this oxidation, but we are unaware of any previous mention of the existence of the inhibition period. In this paper we are suggesting an explanation for this inhibition period and present some new evidence for the composition of the oxide film which is formed, as well as some observations on the mechanism of film formation.

Experimental

The metal used was 0.003 in. thick high-purity Alcoa aluminum foil, with a guaranteed minimum Al content of 99.986%. Representative samples of this material (Alcoa analysis) gave the following concentration of impurities: 10 ppm Cu, 10 ppm Fe, 10 ppm Si, and 40 ppm Zn. Specimens used had a surface area of 100 cm^2.

Degreased specimens were prepared by soaking in trichloroethylene, rinsing in benzene, and then drying under vacuum.

Foil specimens were electropolished in a bath recommended by Jaquet (1) for a period of 2 min at a current density of 9 ma/cm^2. The solution was cooled in an ice bath and constantly stirred with a magnetically driven stirring bar during polishing. The foil was washed thoroughly with distilled water in order to remove the last traces of the electropolishing solution, since the presence of minute impurities may affect the subsequent reaction with water (2).

Hydrations at 100°C were carried out in Pyrex beakers which were cleaned scrupulously before each run. Specimens were suspended in the water from Pyrex rods. The presence of glass had no noticeable effect on the reaction even after a reaction time of 1 hr, as shown by the fact that a few parallel experiments in Teflon beakers gave essentially the same results. The reaction water had a conductivity of about 1.2×10^{-6} ohm^{-1} cm^{-1} and was preboiled for 15 min before using in order to expel

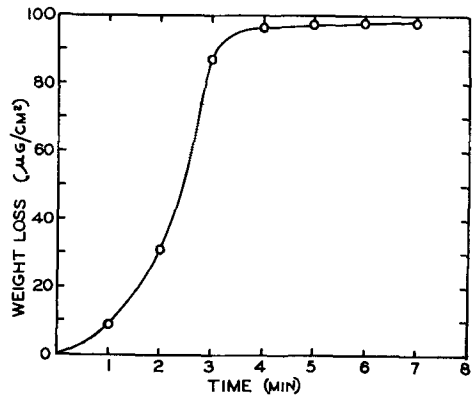

Fig. 1. Rate of removal of hydrated aluminum oxide from the surface of aluminum by CrO_3-H_3PO_4 stripping solution at 85°C. Reaction time with water was 1 hr at 100°C.

dissolved gasses. Reactions at lower temperatures were made in flasks kept in a thermostatted bath. The water was not maintained in an inert atmosphere. For these runs the foil was held in a perforated glass cup which was joined to an extension of a 45/50 $\overline{\$}$ joint. The assembly could be removed easily and quickly at the end of the reaction to be quenched in room-temperature water.

The extent of the reaction was determined by weight changes involving the dissolution of the hydrated oxide film in a solution of 2% CrO_3 and 5% H_3PO_4 at 85°C; the attack of this solution on the underlying metal is reported to be extremely slow (3). The behavior of the stripping solution for a typical hydrated specimen is shown in Fig. 1. After all the oxide is removed the rate of attack on the base metal is only 0.2 $\mu g/cm^2/min$ which is sufficiently slow for our purposes. The method was calibrated by checking the weight loss of anodic films of known weight.

A source of error in this method would result if the hydrated oxide were not completely stable during reaction and if part were lost by dissolution or through mechanical action. However, we were unable to detect the presence of aluminum in the water after a reaction time of 60 min. On the other hand, we observed that, if the water had been used for reaction for a period of some hours, a subsequent oxidation gave slightly higher results than were obtained in freshly prepared water. The reason for this is not clear.

Hydrated oxide was obtained free of metal by dissolving the aluminum in a hot solution of bromine in methanol. It was necessary to wash the oxide thoroughly in order to remove the products of the reaction. This was accomplished by refluxing the oxide in several changes of methanol. The final product was dried at 80°C for 2 hr.

Thermogravimetric analysis was carried out on a Chevenard Recording Balance which was used with a maximum sensitivity of 0.5 mg/mm of chart. The maximum temperature attainable was 1000°C and the heating rate was 2.5°C/min.

Density measurements were made hydrostatically in toluene.

The measurement of the hydrogen evolved in the reaction of the hydrate and the underlying metal was made in an all-glass apparatus. A 10 ml gas burette was connected by capillary tubing to a 12 mm reaction tube containing the sample. The tube was sealed and the entire system was flushed with argon before reaction. The sample was heated quickly to 600°C and held at that temperature for an hour before removing the furnace; Pyrex glass was satisfactory under these conditions. Water from the hydrate was absorbed in a P_2O_5 trap at the exit of the furnace and, therefore, did not contribute to the volume change in the system. This was verified by decomposing $NiSO_4 \cdot 6H_2O$ under the same conditions, whereby the water was absorbed quantitatively. A sample of the isolated hydrate of alumina was also decomposed in this manner and gave no volume increase in the apparatus.

Debye-Scherrer powder patterns were made with samples mounted in a 57.3 mm Phillips powder camera, using CuKα radiation. Exposure times were of the order of 16 hr.

All weighings were made on a Brinkmann-Sartorius Microbalance to the nearest 10 μg.

Results and Discussion

Composition of the film.—It is generally accepted that the product of the reaction above 80°C is boehmite, α-$Al_2O_3 \cdot H_2O$; the characteristic electron diffraction pattern of this compound has been observed by Harrington and Nelson (4), Hart (5), and Kerr (6). Some of the characteristic lines of the boehmite pattern have also been obtained by us by x-ray diffraction. The very diffuse patterns obtained by us and others indicate a poor degree of crystallinity. This evidence is not sufficient to establish the reaction product as pure boehmite, although further support for this composition is given by Bryan (7), whose gravimetric analysis led to the conclusion that the surface product consists of nearly stoichiometric $Al_2O_3 \cdot H_2O$. Bryan's analytical method is subject to criticism, however, on the basis of some of our findings and there is evidence to show that the reaction product contains water considerably in excess of that required for the monohydrate. Bryan reported the water content of the film to be 15.5%, as compared to 15.0% for the theoretical value for the monohydrate. This was determined by heating the metal to 600°C after reaction and measuring the weight loss. However, we have found that this leads to low results because part of the water in the film reacts with the base metal during heating to produce more oxide. If, instead, the hydrated product is separated from the metal by dissolving the aluminum in methanol-bromine solution (8) and then dehydrated, we find that the water content may be as high as 32%. The same results may be obtained by weighing the foil before and after reaction and then removing the reaction products by dissolving in a chromic acid-phosphoric acid solution and reweighing. By the use of the appropriate calculations the three measurements lead to the total weight of hydrated oxide and the amount of water present. This latter procedure is a more convenient method and has been used for the measurements of the rates of reaction discussed below.

We have also shown that the hydrated surface oxide reacts with the base metal during heating by measuring the volume of hydrogen evolved under these conditions. In a typical experiment, a sample of aluminum with an area of 100 cm^2, which had been treated with boiling water for 60 min, produced 1.5 ml of hydrogen when heated to 600°C for 1 hr in an inert atmosphere. This corresponds to 1.2 mg of water, which would not have been detected by Bryan's method, out of a total hydrated oxide weight of 10.9 mg and a water content of 3.0 mg. A more pronounced effect was obtained by the use of etched foil, for which the true surface area is not precisely known but is several times greater than for smooth foil. With this material, volume increases of 5-6 ml were observed under the same conditions.

Finally, the measured density of the oxide was found to be 2.4 ±0.1 g/cm^3, as compared to 3.0 for pure boehmite (9).

The form in which the excess water is combined in the surface product is not known. The composition of the film most frequently approximates that of a dihydrate, but this probably has no significance. It could be postulated that the contribution of an appreciable quantity of trihydrate would give the observed composition but there is no physical evidence to show the presence of either of the two known trihydrates. Thermogravimetric analysis shows that a large fraction of the water is loosely bound and is lost before the expected range of decomposition of boehmite. This is shown by the comparison of the thermograms of the hydrated oxide and pure boehmite[1] in Fig. 2. The thermogram shown here was obtained from the oxide formed at 100°C. Nearly identical traces were observed for the products formed at 80° and 90°C.

Reaction mechanism.—Hart (5) has suggested that the growth of the hydrated oxide occurs by outward migration of aluminum from the metal and offers as evidence the observation that anodic films which have been stripped from the metal and then treated with boiling water do not give the electron diffraction pattern of boehmite. Kerr (6) has modified this experiment so that part of the underlying metal was allowed to remain in contact with the anodic film and then carried out the hydration reaction. Electron diffraction then indicated the presence of boehmite only in the vicinity of the islands of metal. According to these observations, the mechanism of boehmite formation must involve the movement of aluminum to the oxide-water interface, since the anodic oxide itself does not appear to become hydrated.

[1] Obtained from Alcoa Research Laboratories.

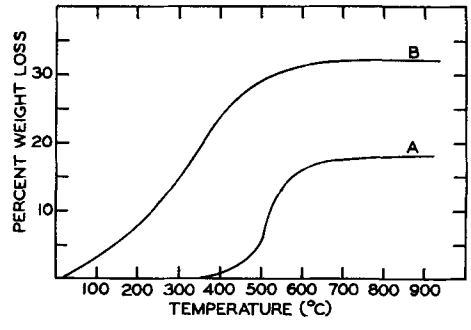

Fig. 2. Thermograms of: A. boehmite; B. reaction product of aluminum and water at 100°C.

Table I. Comparison of x-ray diffraction data of boehmite (ASTM) and hydrated anodic films*

ASTM		Hydrated anodic films	
d	Relative intensity	d	Relative intensity
6.11	100	6.28	Strong (very diffuse)
3.16	65	3.18	Strong (diffuse)
2.35	53	2.35	Strong (diffuse)
1.98	6	1.97	Weak
1.86	32	1.86	Strong (diffuse)
1.77	6		
1.66	13		
1.53	6	1.54	Weak
1.45	16	1.43	Weak
1.43	9	1.40	Weak
1.38	6	1.36	Weak
1.31	15	1.31	Weak

* Only the 12 strongest diffraction lines of boehmite are listed.

On the other hand, Spooner (10) has shown by x-ray diffraction patterns that boiling water transforms isolated oxide to boehmite, and MacLennan (11) has reported that there is no essential difference in the impedance characteristics between isolated and nonisolated oxide films which have been exposed to boiling water. Both of these observations have been made with nonbarrier films (formed in sulfuric acid), but we have also confirmed Spooner's results using barrier films formed to 100 v in ammonium borate solution, taking great care to remove the underlying metal completely, and hydrating for 20 min at 100°. This has also been confirmed by Hinde, Kellet, and Harris (12). A comparison of our x-ray diffraction data for a hydrated anodic film and ASTM data for boehmite is given in Table I. Furthermore, thermogravimetric analysis of this substance gave results which are identical to those obtained from the hydrate in Fig. 2. These observations are in direct contradiction to those of Kerr and Hart, but repeated and careful study leaves no doubt that the presence of metallic aluminum is not necessary for the conversion of anodic oxide to "boehmite."

In the attempt to determine the kinetics of the direct reaction between aluminum and water, we have made the assumption that the formation of oxide occurs at the metal-oxide interface. This is based on the discussion in the preceding paragraph, the physical nature of the final product and the rate at which the consecutive reaction—the hydration of the oxide-occurs.

The final hydrated oxide is completely unlike the coherent film formed by anodic oxidation, consisting of loosely connected particles. This is shown by examination of the oxide after removal of the underlying metal. When in contact with the metal this oxide is probably of a highly porous nature and could be penetrated easily by water, thus making it unnecessary to consider an ionic mechanism for oxide growth.

A further condition which must be met for the reaction to occur at the metal-oxide interface is that

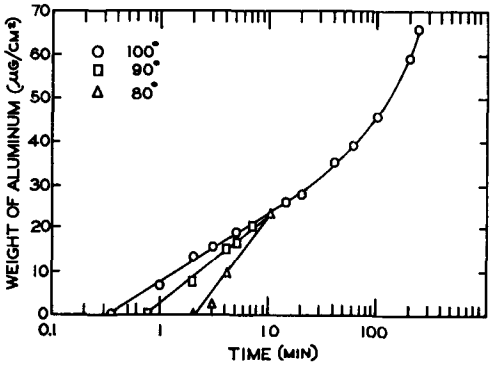

Fig. 3. Weight of aluminum reacted vs. time of immersion in water at 80°, 90°, and 100°C. Data corrected for amount of pre-existing oxide on degreased foil.

the hydration step take place as soon as the oxide is formed. There is some justification for this belief, since, as shown in the following section, anodically formed films are hydrated at a very rapid rate. Calculations show that the rate is greater than the rate of hydrated oxide formation on the metal. There is, of course, no evidence to show that the transitory oxide formed in the water reaction is identical to the anodically formed oxide, but the physical similarities of the final hydrated product of each would lead one to believe that this is the case.

In view of these considerations it would be expected that the rate-determining process would be the diffusion of water through the film, although the kinetics may be complicated to an unknown extent by the rate at which evolved hydrogen is transported from the reaction surface. It should also be recognized that the rate of oxide growth is also strongly influenced by the specific impurities present in the metal; the absolute data presented here, therefore, apply only to aluminum of the composition described earlier.

If the process occurs uniformly over the surface of the metal and if the rate of diffusion of water is dependent on the thickness of the film, a parabolic law would be expected to govern the growth; independence of film thickness would result in a linear rate law. In the cited paper by Hart a constant growth rate is reported, but this is open to question since the change in thickness was followed for only 2 min. The initial rate is extremely rapid and could probably be fitted to a linear plot, but it soon decreases, as shown in Fig. 3. However, a parabolic law also fails to fit the observed data over a reasonable period of time. In Fig. 3 the weight of aluminum reacted at 100°C is plotted as a logarithmic function of time. In this plot the weight of aluminum reacted, rather than the weight of the oxide or the total weight of product formed, is used in order to avoid the assumption of a constant composition of product, since the calculated amount of water in the surface film was found to vary from 23% to 32%.

We have also plotted some of the data obtained from experiments at 80° and 90°C. Results for longer reaction times are not included because of the failure to obtain satisfactorily reproducible results. The observations are anomalous in some respects. There is a marked increase in the inhibition period with decreasing temperature, but about 10 min after reaction starts there is little difference in rates for the first 2 hr. After that time the rate at 100° is significantly greater than at the lower temperatures.

At 100°C an apparent logarithmic rate law is observed for the first 30 min or so, followed by a reasonable fit to a parabolic law up to about 250 min. The nature of the hydration process would not lead us to believe that a true logarithmic law of the type discussed by Uhlig (13) is operating here, but rather that the apparent logarithmic dependence is fortuitous. The fact that a simple parabolic dependence is not observed over the entire time interval studied suggests that a uniform, homogenous reaction layer is not formed, at least in the beginning, or that the evolution of hydrogen complicates the kinetics to a greater extent than was assumed. It is also possible that a form of lateral growth, postulated by Evans (14), may explain this behavior.

The thicknesses of the films are greater than reported by Hart from his electron diffraction measurements. After 1.5 min (on electropolished specimens) he observed a film thickness of 100Å, whereas our calculated thickness under the same conditions, based on the weight of the film and the measured density, is 1500Å.

Inhibition period.—The previously unreported inhibition period is believed to be due to the presence of the existing oxide film on the metal; foil which has been electropolished shows a much smaller inhibition period. The time required for hydrogen to be evolved on degreased foil at 100°C is about 20-22 sec, on foil cleaned in cold H_2SO_4-$K_2Cr_2O_7$ solution it is 15-18 sec, and on electropolished foil 5-11 sec. The fact that the electropolished specimens do not show an inhibition time of zero is a result of the very thin film which is formed on the foil during the washing period after removal from the electropolishing bath. Thin films of aluminum, vacuum-deposited on glass, show an apparent inhibition period of 1-2 sec if transferred rapidly from the vacuum apparatus to boiling water, but it is difficult to observe the effect because the boiling water tends to rupture the thin metal film. However, what appears to be an instantaneous reaction with boiling water is observed with aluminum which has been freshly abraded with a stainless steel point.

The properties of the natural oxide film on aluminum have not yet been elucidated completely. The thickness of the film is dependent on the history of the metal and its environment; a summary of the many investigations of this subject has been given by Hart (15). It is generally agreed that after an initial rapid growth of oxide on the pure metal further growth occurs at a very slow rate at room temperature, and that the thickness of the film probably never exceeds 100Å. In the course of our work we have made direct measurements of the film weight (on acid-cleaned foil) by the stripping method and have found it to be 4.0 $\pm$0.4 $\mu g/cm^2$. If the film were to consist of α-Al_2O_3, the densest form of alumina, the oxide film would be 100Å thick. Since there is little doubt that the film does not consist of α-Al_2O_3, but of some less dense form of alumina, it must be considerably thicker than 100Å.

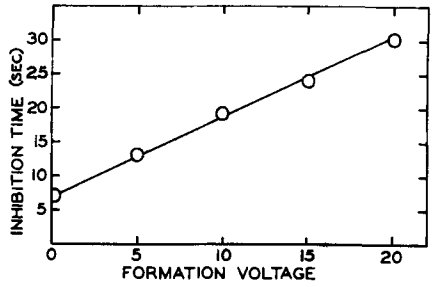

Fig. 4. Inhibition time for the reaction of electropolished aluminum foil with water vs. the thickness of anodic oxide on the foil.

Hunter and Fowle (16) consider the film to consist of a barrier layer about 10Å thick on the metal surface, with a porous layer above the barrier, but it is difficult to reconcile this model with our observations of the inhibition period. If electropolished aluminum foil is anodically oxidized to a specific voltage, up to 25 v, and then subjected to the action of boiling water, the entire oxide film is eventually penetrated and visible hydrogen evolution occurs. The time required to penetrate the film, in addition to the inhibition period characteristic of the foil pretreatment, is approximately proportional to the thickness of the anodically formed layer. This is shown in Fig. 4. At the current density used (0.1 ma/cm^2) the thickness of the anodic oxide is 11.9Å/v (17), and the penetration (or hydration) rate of the oxide is, therefore, about 12Å/sec. The pre-existing film on acid-cleaned foil, on the other hand, is penetrated only at the rate of 0.7Å/sec if the barrier portion alone of the film is responsible for the inhibition period. If this is true, then the naturally formed barrier film must be physically quite different from the anodically formed amorphous films. On the other hand, if the porous portion of the film also contributes to the inhibition period, it would be expected to become hydrated during the process. This would result in an easily detectable weight change. No such weight change occurs, and we have concluded that the pre-existing film is probably penetrated without hydration during the inhibition period.

In connection with the hydration of anodically formed aluminum, an interesting observation was made concerning the spatial relationship of the two oxides. Degreased foil shows no weight gain during the first 18-sec immersion in boiling water, but the same foil which has been anodically formed to 25 v before reacting with water shows a weight gain of 1.5 μg/cm^2 during the first 18 sec. Electropolished foil, which has been similarly formed, showed the same weight gain under these conditions. This indicates that anodic formation occurs on the solution side of the pre-existing oxide film, and that anodic growth takes place by aluminum ion movement through the film. This is in agreement with the conclusion of Lewis and Plumb (18) and is analogous to experiments made by Young (19) on tantalum.

Acknowledgment

The authors wish to acknowledge the assistance of Mrs. Concetta Duval and the Analytical Laboratory of this Company.

Manuscript received Nov. 30, 1959.

Any discussion of this paper will appear in a Discussion Section to be published in the December 1960 JOURNAL.

REFERENCES

1. P. A. Jaquet, *Met. Revs.*, **1**, 157 (1956).
2. D. Altenpohl, *Aluminium*, **33**, 78 (1957).
3. J. E. Lewis and R. C. Plumb, *Intern. J. of Appl. Radiation and Isotopes*, **1**, 33 (1956).
4. R. A. Harrington and H. R. Nelson, Am. Inst. Mining Met. Engrs., Inst. Metals Div., Tech. Publ. No. *1158*, 14 pp. (1940).
5. R. K. Hart, *Trans. Faraday Soc.*, **50**, 269 (1954).
6. I. S. Kerr, *Proc. Phys. Soc.*, **69B**, 1055 (1956).
7. J. M. Bryan, *J. Soc. Chem. Ind.*, **69**, 169 (1950).
8. T. J. Nurse and F. Wormwell, *J. Appl. Chem. (London)*, **2**, 550 (1952).
9. R. Fricke and H. Severin, *Z. anorg. u. allgem. Chem.*, **205**, 127 (1932).
10. R. C. Spooner, *Nature*, **178**, 1113 (1956).
11. D. F. MacLennan, *Corrosion*, **15**, 283t (1959).
12. R. M. Hinde, E. A. Kellet, and P. H. Harris, *Nature*, **183**, 39 (1959).
13. H. H. Uhlig, *Acta Met.*, **4**, 541 (1956).
14. U. R. Evans, *Trans. Faraday Soc.*, **41**, 365 (1945).
15. R. K. Hart, *Proc. Roy. Soc. (London)*, **A236**, 68 (1956).
16. M. S. Hunter and P. Fowle, *This Journal*, **103**, 482 (1956).
17. W. J. Bernard and J. W. Cook, *ibid.*, **106**, 643 (1959).
18. J. E. Lewis and R. C. Plumb, *ibid.*, **105**, 496 (1958).
19. L. Young, *Trans. Faraday Soc.*, **53**, 841 (1957).

Corrosion Behavior and Passivity of Nickel-Chromium and Cobalt-Chromium Alloys

A. Paul Bond[1] and H. H. Uhlig

Corrosion Laboratory, Department of Metallurgy,
Massachusetts Institute of Technology, Cambridge, Massachusetts

ABSTRACT

Pure Ni-Cr alloys containing up to 29% Cr and Co-Cr alloys containing up to 23% Cr were prepared in vacuum. Corrosion rates in sulfuric and nitric acids, corrosion potentials, and critical current densities for passivity were determined at 25°C. It is concluded that specific alloying proportions of passive compositions are better evaluated in relation to electron configuration of the alloy system by critical current densities than by potential or corrosion rate measurements.

Much work on the corrosion behavior of iron-chromium alloys has been published and is useful to an understanding of conditions favoring passivity in alloy systems. Similar data for the cobalt-chromium system have not been reported. For nickel-chromium alloys most of the previous work involved rather impure metals and often ill-defined experimental conditions. Data reported by Rohn (1) and Pilling and Ackerman (2) indicate that as Cr content is increased, corrosion rates of the Ni-Cr alloys in oxidizing media are decreased. Grube (3) showed that in 1*N* HNO_3, the alloys become passive and their corrosion rates reach a minimum at about 10% Cr.

In the present work, relatively pure Ni-Cr and Co-Cr alloys were investigated for the low Cr solid solution range. Particular attention was paid to the quantitative alloying proportions required to achieve passivity.

Experimental Procedure

Alloys were prepared from high-purity Cr purchased from the Electro Metallurgical Company, carbonyl Ni (99.93% Ni) furnished by courtesy of the International Nickel Company, and high-purity Co (99.97% Co) supplied by courtesy of the Cobalt Information Center at Battelle Memorial Institute. Induction melting was carried out under a vacuum of 10^{-5} mm Hg, with the melt contained in a "Morganite" high-purity aluminum oxide crucible. No deoxidizers were added. Samples were cast in a helium atmosphere by drawing the melt into 8 mm diameter "Vycor" tubes and plunging the ingots into water. The helium was purified by passage over Mg chips at 640°C and, in later experiments, over Ti sponge at 800°C. In both cases the helium was passed through a trap surrounded by liquid nitrogen before entering the furnace.

Homogenization of castings was carried out at 1100°C for 12 hr in silica tubes using a helium atmosphere followed by a water quench. The Co-Cr alloys, which were hard and rather brittle, were used in the as-homogenized condition, while the Ni-Cr ingots were cold rolled to a thickness of 2.5 mm, given a 15-min anneal at 1000°C, and water quenched. Composition of each alloy was determined by chemical analysis.

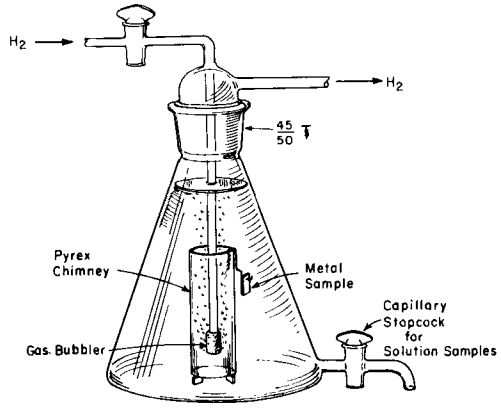

Fig. 1. Cell for measuring corrosion rates by weight loss and solution analysis.

Corrosion rate measurements were carried out in an air thermostat maintained at 25° ±0.5°C, using 2000 ml cells of the type shown in Fig. 1. Laboratory compressed air, filtered by means of glass wool and charcoal, was bubbled through the cells at the rate of 40 ml/min as determined by a flow-meter provided for each cell. Solutions were prepared from laboratory distilled water and reagent grade chemicals.

Specimens of Ni-Cr alloys for corrosion rate determinations were cut as rectangular coupons measuring approximately 3 cm long, 0.5-1 cm wide, and 0.2 cm thick. A hole 0.3-0.4 cm in diameter was drilled near one end so that the sample could be hung from a glass hook. These specimens were abraded smooth, finishing with 600 grit silicon carbide wet polishing paper. After washing with distilled water and wiping dry, specimens were immersed in boiling benzene for 5 min. This was followed by pickling in hot 6*N* H_2SO_4. Pickling was continued until the surface was sufficiently etched to reveal the microstructure of the metal. After pickling, samples were thoroughly washed with distilled water and dried in a desiccator.

[1] Present address: Diamond Fuze Laboratory, Washington, D. C.

Corrosion rates were measured by colorimetric analysis of aliquots of the test solution in which specimens were immersed. By periodic sampling, corresponding weight loss was calculated as a function of time. For Ni the dimethylglyoxime method (4) was used, and for Co the thiocyanate method (4). Conventional gravimetric weight loss measurements were also made and checked with weight losses calculated from analysis of the solution. All runs were continued for sufficient time to reach a constant corrosion rate.

Electrodes for polarization measurements were similar in size and shape to the corrosion rate specimens. Nickel wire was silver soldered to a stem which was machined on the electrode. A Teflon gasket between the electrode and a Pyrex tube was compressed by means of a nut and machine screw silver soldered to the nickel wire, in order to exclude the electrolyte from contact with any metal other than the electrode proper.

Potential measurements were made using a portable potentiometer in series with an electronic pH meter employed as a high resistance galvanometer. An Ag-AgCl, 0.1*N* KCl electrode was the reference electrode. Constant polarization current was supplied by 30 dry cells in series with an adjustable resistance.

Critical current densities for passivity were determined in a cell fitted with two auxiliary Pt electrodes and arranged so that the alloy electrodes could be pickled within the cell with 1:1 H_2SO_4, washed, and the test electrolyte introduced without exposure to air. Test solution and distilled water for washing were contained in 5-gal carboys connected to the cell by glass tubing. Deaeration was accomplished by prepurified grade nitrogen which had been passed over copper turnings at 450°C. The Luggin capillary of the salt bridge filled with the test solution was placed adjacent to the alloy electrode.

Critical current densities for passivity were measured by two methods. For Ni-Cr alloys, the "indirect" method was used. This consisted of applying a series of constant anodic currents slightly above the critical current density and measuring the times required to reach the passive potential. Current density i was then plotted against the reciprocal of time t for passivity in accord with the relation $i - i_c = K/t$, where i_c is the critical current density (5, 6). This relation is linear for currents not exceeding the critical current density by more than a factor of 2 or 3, and can thus be extrapolated to reciprocal time = 0 to obtain i_c. The value K represents the number of coulombs per unit area required to achieve passivity.

For the Co-Cr alloys, the "direct" method was used (7). This consisted of applying a given current and observing the potential. The lowest current which passivated the electrode was taken as the critical current density. At currents below the critical, polarization was continued until the potential changed at a rate less than 2 mv/min. The two methods give comparable values for i_c, as was demonstrated by similar measurements for the Fe-Cr alloys (8).

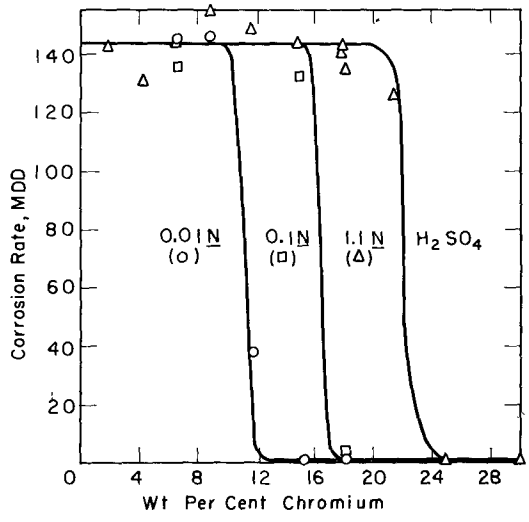

Fig. 2. Corrosion rates of Ni-Cr alloys in aerated H_2SO_4, 25°C, 4-day runs.

Corrosion potentials were also measured in the above cell. The electrodes were prepared in the same way as specimens for the corrosion rate determinations.

Experimental Results

Nickel-chromium.—Corrosion rates were measured in several media. In deaerated 1.1*N* (5%) H_2SO_4, 25°C, 10 day runs, corrosion rates were low, being of the order of 1 mdd, and showed little variation with chromium content.

In Fig. 2 the results of 4-day runs in aerated 1.1, 0.1, and 0.01*N* H_2SO_4 are shown. It can be seen that the corrosion rates of the active alloys are all the same within experimental error, the standard deviation being 6.3 mdd as determined from replicates. However, alloys containing more than a critical amount of Cr show a corrosion rate of practically zero, corresponding to the passive condition. These passive alloys sometimes showed an initial weight

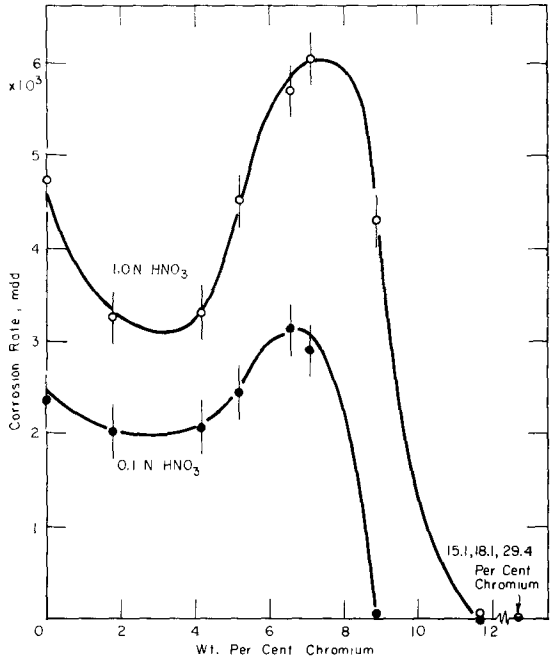

Fig. 3. Corrosion rates of Ni-Cr alloys in HNO_3, 25°C, 1-day runs.

loss as determined by colorimetric analysis, after which any further change was very slight. It should be noted that higher acid concentration shifts the passivity limit to higher chromium contents.

Figure 3 shows corrosion rates of these alloys in 1.0 and 0.1*N* HNO_3 as determined by one-day runs. Confidence limits (95%) were calculated by standard statistical methods (9). It can be seen that the initial Cr additions had little effect on the corrosion rate, causing only a slight decrease. Further additions caused a marked increase, with a peak occurring around 7% Cr. This type of behavior was also observed by Rohn (1) and Pilling and Ackerman (2), while Grube (3) found only a horizontal arrest but not a peak. The transition from activity to passivity is quite abrupt, coming between 7.1 and 8.9% Cr in 0.1*N* HNO_3, and between 8.9 and 11.7% Cr in 1.0*N* HNO_3.

Corrosion rates were also determined in 1*N* H_2SO_4 to which was added 25 g of hydrated ferric sulfate per liter. In this case only one run was made, all samples being placed in the same cell. The data of Table I show that this solution is much more strongly corrosive toward the two alloys which remained active than is 1.0*N* HNO_3. The initial major critical passive composition is shifted to lower Cr content, now lying between 4.2 and 6.6% Cr. These corrosion rates were determined by the conventional weight loss method only, since the high concentration of iron in the solution interferes with the colorimetric determination of nickel. However, since in other oxidizing media studied, these alloys, when in the active condition, exhibited a constant corrosion rate from the beginning of the run, it seems reasonable that this was also true in this case. The active alloys were left in the solution 6 hr, the others for 2 days.

Corrosion potentials of Ni-Cr alloys in deaerated (H_2-saturated) 1.1*N* H_2SO_4 showed no systematic variation with chromium content and, in fact, the potentials of these alloys were not far removed from the potential of the reversible hydrogen electrode. Corrosion potentials in 0.1 and 1.0*N* HNO_3 are shown in Fig. 4. There is a more or less continuous ennobling of the corrosion potential with increasing chromium content with a slight peak being observed in the region of 4-6% Cr.

Critical current densities for passivity were determined for these alloys in N_2-saturated 1.1*N* H_2SO_4 by the indirect method. The results are shown in Fig. 5 and 6. These curves have similar shape, but with the absolute values of critical currents considerably larger in 1.1*N* than in 0.01*N* H_2SO_4. It appears that in both cases the critical current density decreases sharply as Cr is increased to the vicinity of 14%, after which the decrease in critical current density becomes much less steep. Coulombs per square centimeter for passivity in 1.1*N* H_2SO_4 range from 0.3 for high Cr alloys to 2.0 for low Cr alloys.

Table I. Corrosion rates of Ni-Cr alloys in 1.0*N* H_2SO_4 plus 25 g $Fe_2(SO_4)_3 \cdot 9H_2O$/liter, aerated, 25°C

% Cr	1.8	4.2	6.6	8.9	11.7	15.1	18.1
mdd	8259	6950	6	9	0	0	0

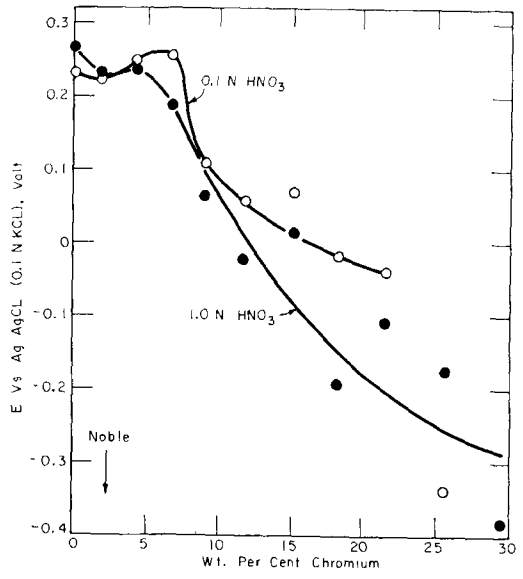

Fig. 4. Corrosion potentials of Ni-Cr alloys in HNO_3, 25°C

Cobalt-chromium.—In contrast to the Ni-Cr system, the Co-Cr alloys do not have a single phase structure. Pure cobalt itself in the annealed condition is a mixture of hexagonal close-packed and face-centered cubic phases, and this behavior is reflected in that of the alloys. There is some disagreement as to the Co-Cr phase diagram (10, 11), but there is agreement that at the annealing temperature of 1100°C all alloys used in this work would be in a single phase field. Also, Wever (10) reported that x-ray data revealed only the face-centered cubic and hexagonal close-packed phases in alloys of 20 and 30% Cr quenched from 1000°C. Since the

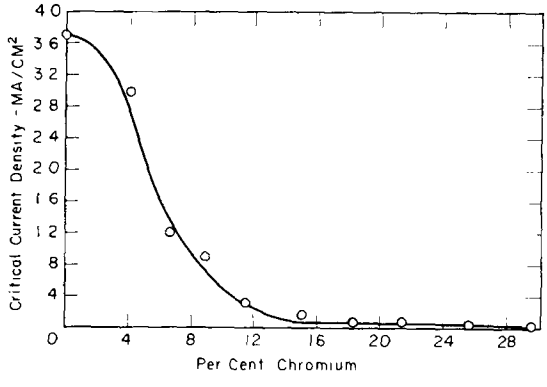

Fig. 5. Critical current densities for passivity of Ni-Cr alloys in N_2-saturated 1.1N H_2SO_4, 25°C.

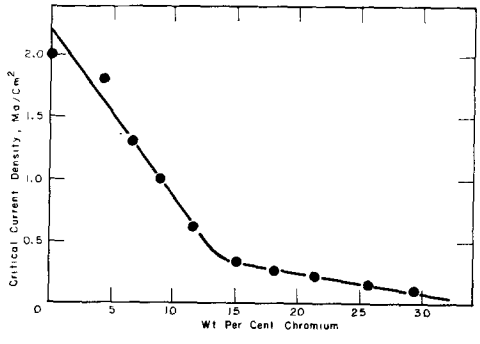

Fig. 6. Critical current densities for passivity of Ni-Cr alloys in N_2-saturated 0.01N H_2SO_4, 25°C.

temperature of the transformation is relatively low (500°-850°C), and the equilibrium two-phase field between the high- and low-temperature modifications is narrow, it appears that very little diffusion would take place during quenching. Therefore, it is probable that the two phases present in the alloys as tested had the same chemical composition.

Kröhnke and Masing (12) studied the corrosion potential and anodic and cathodic polarization behavior of face-centered cubic and hexagonal close-packed Co in 0.1 and 2.0*N* HCl. They found the two crystalline modifications to behave identically. One of us also found that body-centered and face-centered cubic 18-8 stainless steels corrode at essentially the same rates in several media (13). From this it appears reasonable to conclude that the behavior of the Co-Cr alloys was not greatly affected by the presence of two different crystalline forms. Metallographic examination showed that the microstructures of all these alloys are similar and that the observed changes in electrochemical behavior do not correspond to any change in microstructure.

Corrosion rates of the Co-Cr alloys in 0.1 and 1.0*N* HNO_3 are shown in Fig. 7. Time of test ranged from hours to days depending on whether the corrosion rate was high or low. Uniform corrosion was observed in all cases. Pure Co has a corrosion rate about 10 times higher than pure Ni, and the active alloys also show higher rates than do the Ni-Cr alloys. The shapes of the corrosion rate-composition curves also differ for the two alloy systems in that the initial Cr addition causes a marked decrease in corrosion of the Co alloys and no maximum is found. There is, however, a discontinuity in slope in the region from 2 to 4% Cr, similar to the more pronounced change in the Ni-Cr system. The onset of passivity in HNO_3 begins at about 12% Cr, since alloys containing more Cr corroded at a rate of 0 mdd in 0.1 *N* HNO_3 and 0 to 7 mdd in 1.0*N* HNO_3.

Corrosion potentials of these alloys in 1.0*N* HNO_3 are shown in Fig. 8. A pronounced shift toward more noble potentials is observed as Cr content is increased, but it is not possible on the basis of these data alone to draw any conclusions regarding critical composition limits for passivity.

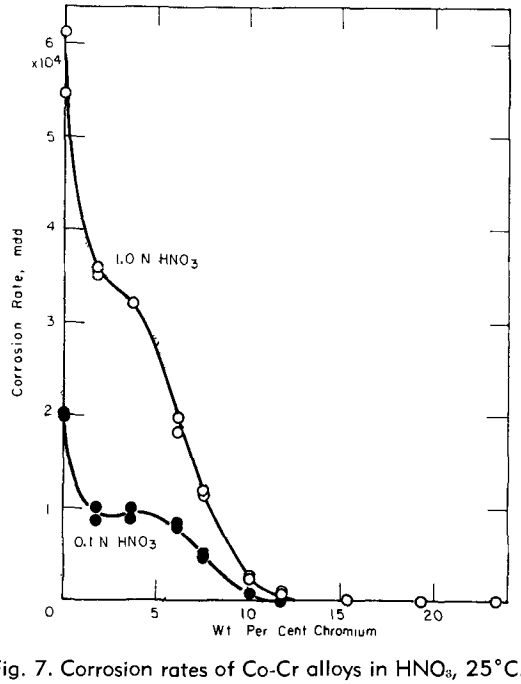

Fig. 7. Corrosion rates of Co-Cr alloys in HNO_3, 25°C.

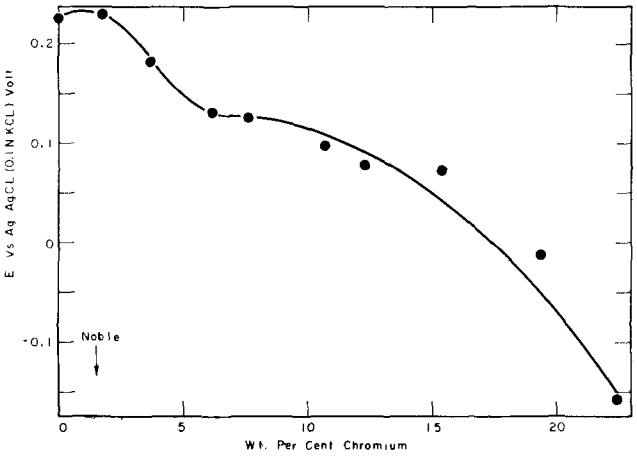

Fig. 8. Corrosion potentials of Co-Cr alloys in 1.0N HNO_3, 25°C.

Figure 9 is a plot of critical current densities with composition, obtained by the direct method. Pure Co, as well as alloys containing up to 6.2% Cr, have very high critical currents, while a sharp drop occurs in the vicinity of 8% Cr, followed by a levelling off again. These data give a clear indication of a critical composition in the vicinity of 8% Cr, as well as indicating that for alloys of this or higher Cr content the critical current density (~1 ma/cm²) is low enough for self-passivation of the alloys to be possible in strongly oxidizing media.

Discussion

Nickel-chromium alloys.—In deaerated 1.1*N* H_2SO_4 the corrosion of Ni and Ni-Cr alloys appears

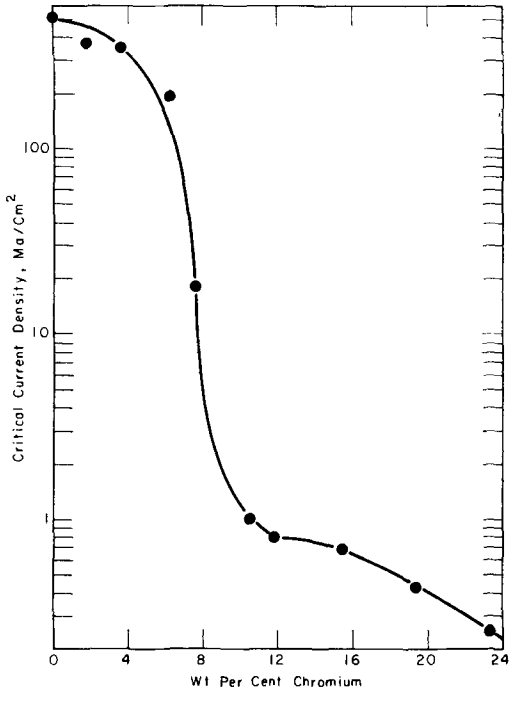

Fig. 9. Critical current densities for passivity of Co-Cr alloys in N_2-saturated 1.0N H_2SO_4, 25°C.

to be largely under anodic control. This is suggested by the fact that the corrosion potentials are not far removed from potentials of the reversible hydrogen electrode. This means that the local cathodes are only slightly polarized.

On the other hand, in aerated sulfuric acid the corrosion rates of the active alloys appear to be controlled by diffusion of dissolved oxygen to the metal surface. This is indicated by the fact that the corrosion rates of the active specimens are essentially independent both of alloy composition and acid concentration. It is also indicated by correspondence of the corrosion rate (140 mdd = 5.3 x 10^{-5} amp/cm^2) to the limiting diffusion current density for oxygen, i.e., in accord with the equation $i = (DnFc/\delta)$, where $D = 2 \times 10^{-5}$ cm^2/sec, $n = 4$, $F = 96{,}500$ coulombs/equiv., $c = 2.5 \times 10^{-7}$ moles dissolved O_2/cc, and δ the thickness of the stagnant diffusion layer is assumed equal to 0.035 cm. The latter value of δ is consistent with observed values.

That the corrosion rates of the active alloys should be anodically controlled in deaerated acid and cathodically controlled in aerated acid is in no way self-contradictory. In deaerated acid, the cathodic process is reduction of hydrogen ions to gaseous hydrogen, while in aerated acid the cathodic reaction involves reduction of dissolved oxygen by hydrogen ions to form water. The standard free energy change for the latter reaction is much greater than that of the former, so that in aerated solution the difference between the open circuit anode and cathode potentials is much greater than in deaerated solution. Thus a very large current would be necessary to polarize the local anodes to the open circuit cathode potentials, and long before this happens the limiting diffusion current for oxygen is reached and becomes the rate-determining step.

In all the oxidizing media used in this work the Ni-Cr alloys exhibited a critical composition, that is, alloys containing less than the critical amount of chromium for passivity corroded relatively rapidly compared to those containing more than the critical percent. The term passive, as used in this discussion, is limited to the case of a metal which is polarized to a potential more noble than its Flade potential in the given environment and has an accompanying comparatively low corrosion rate. In the case of those alloys which are passive under a given set of conditions, it can be assumed from previous discussions (7, 14-16) that the local anodic current produced by corrosion of the active alloy exceeded the critical current density for passivity. In this way the low corrosion rate of the passive state follows in sequence the higher corrosion rate of the active state.

It appears to be a general rule that whenever the current density equivalent to the corrosion rate approaches the critical current density passivity is established. The present data bear out this relationship. The corrosion current densities are always less than the critical current densities to an extent dictated by the anode-cathode area ratio, a low ratio accounting for a greater observed difference between the two values than a high ratio.

Based on the fact that the passive film on Fe, Cr, and Cr-Fe alloys is equivalent to about 0.01 coulomb/cm^2 (8) or less, the value of 0.3 to 2 coulomb/cm^2 for Ni-Cr alloys indicates that anodic dissolution of the alloy precedes passivity. The same is true of iron the value for which is about 1 coulomb/cm^2, and as Franck (6) showed, an insulating film of perhaps $FeSO_4$ forms first, favoring high current densities within pores of this film necessary to achieve the passive state. This situation is also borne out by a relatively low initial slope of potential vs. time at constant applied current density for Ni-Cr alloys preceding a rapid fall of potential to the noble passive value, whereas for stainless steels which passivate without initial salt film formation, the potential fall is immediate, and coulombs for passivity are a direct measure of the amount of passive film substance on the surface.

The rather wide variation in the amount of Cr needed to passivate these alloys in different media is a result of the different corrosion rates, anode-cathode area ratios, and critical current densities which prevail in these media. In the case of aerated sulfuric acid, only the critical currents and not the corrosion rates of the active alloys were reduced as the acid concentration was reduced. Decreases in acid concentration correspondingly lowered the critical amount of Cr required for passivity because critical current density decreases with increasing Cr. Since the critical Cr compositions fall in a region where critical current density is changed only slowly with Cr content, small changes in the critical current density for passivity by means of decreasing acid concentration shifted the critical Cr content markedly.

In nitric acid, corrosion rates as well as critical currents were raised as acid concentration was increased. The increase in corrosion rate is probably due to increase in concentration of nitrate ion, which is reduced at the local cathodes, while increase in hydrogen ion concentration increases observed critical current densities. The observed increase in Cr necessary to produce passivity in these alloys on increasing acid concentration indicates that the higher critical current density brought about by increased acid concentration outweighs the effect of increased corrosion current. By adding ferric ions to 1*N* H_2SO_4, a corrosion rate higher than that in 1*N* HNO_3 was obtained at approximately the same hydrogen ion concentration, so that the critical amount of Cr was decreased from about 12 to 6.6% Cr as is seen from data of Table I and Fig. 3.

In retrospect, all the data show that passivity limits for these alloys as obtained from corrosion data reflect not only the basic properties of the alloy system, but also depend strongly on the environment. Important are the nature of the anion, depolarizer concentration, surface *p*H, degree of stirring, etc. This is especially true of a system such as Ni-Cr, because critical current densities do not vary as sharply with composition as they do in the Cr-Fe alloys as shown, for example, by data of King and Uhlig (8).

The variation of critical current density with alloy composition appears to be the important funda-

mental property of alloys capable of becoming passive. The shape of the critical current-composition curve is found to be nearly the same in 1.1 and 0.01*N* H_2SO_4 (Fig. 5 and 6) even though the critical currents are much smaller for the lower acid concentration. In both cases a change in slope occurs or a practical minimum is reached in the vicinity of 14% Cr. This is the figure which it would probably be most profitable to compare with the prediction of a critical composition at 8.2% Cr made by one of us (17) based on electron configuration in the alloy system. Other than the simplified assumptions made in the theoretical calculation, difference between theory and observation may also be a result of experimental factors, such as a possible difference between surface composition from bulk composition of the alloys caused by preferential corrosion of one of the alloy components.

Cobalt-chromium alloys.—The behavior of the Co-Cr system was similar to the Ni-Cr system, as might be expected. Differences in shape of the corrosion-composition curves in nitric acid indicate that Cr alloyed with Co, even in small amounts, decreases the corrosion rate (Fig. 7), while in the Ni-Cr system, Cr markedly increases the corrosion rate just short of the passive composition (Fig. 3). This may be related to the possibility that Co is a better catalyst than Ni for reduction of NO_3^-, which in turn is consistent with a much higher corrosion rate of pure Co than pure Ni in HNO_3. This being the case, if Cr is an intermediate catalyst, an addition of Cr to Co will increase cathodic polarization of Co-Cr alloys while decreasing it for Ni-Cr alloys.

The effect of Cr on the critical current densities of the Co-Cr alloys (Fig. 9) was much more pronounced than in the Ni-Cr system (Fig. 5, 6). In this respect, behavior of Co-Cr alloys is similar to the behavior reported for Fe-Cr alloys (8). The critical current densities for the Co alloys containing more than 10% Cr were about the same or somewhat lower than those of the corresponding Ni-Cr alloys, but the low Co-Cr alloys and pure Co had much higher critical current densities. For this reason, the critical composition is clearly indicated as close to 8% Cr. This is in reasonable agreement with the 6.2% Cr predicted by the electron configuration theory (17).

Acknowledgment

The authors are grateful for support of this research by the Office of Naval Research.

Manuscript received Dec. 3, 1959. This paper was prepared for delivery before the Houston Meeting, Oct. 9-13, 1960.

Any discussion of this paper will appear in a Discussion Section to be published in the December 1960 JOURNAL.

REFERENCES

1. W. Rohn, *Z. Metallkunde*, **18**, 387 (1926).
2. N. B. Pilling and D. E. Ackerman, *Trans. Am. Inst. Mining Met. Engrs.*, **83**, 248 (1929).
3. G. Grube, *Z. Metallkunde*, **19**, 438 (1927).
4. E. B. Sandell, "Colorimetric Determinations of Traces of Metals," Interscience Publishers, Inc., New York (1944).
5. W. Shutt and A. Walton, *Trans. Faraday Soc.*, **30**, 914 (1934).
6. U. F. Franck, *Z. Naturforsch.*, **4A**, 378 (1949).
7. H. H. Uhlig and G. Woodside, *J. Phys. Chem.*, **57**, 280 (1953).
8. P. F. King and H. H. Uhlig, *J. Phys. Chem.*, **63**, 2026 (1959).
9. W. J. Youden, "Statistical Methods for Chemists," John Wiley & Sons, Inc., New York (1951).
10. F. Wever and V. Hashimato, *Mitt. Kaiser Wilhelm Inst., Eisenforsch. Düsseldorf*, **11**, 293 (1929).
11. A. R. Elsea, A. B. Westerman, and G. K. Manning, *Trans. Am. Inst. Mining Met. Engrs.*, **180**, 579 (1949).
12. G. Kröhnke and G. Masing, *Werkstoffe und Korrosion*, **4**, 86 (1953).
13. H. H. Uhlig, *Trans. ASM*, **30**, 947 (1942).
14. H. H. Uhlig and P. F. King, *This Journal*, **106**, 1 (1959).
15. M. Stern, *ibid.*, **105**, 638 (1958).
16. N. Tomashov, *Corrosion*, **14**, 229t (1958).
17. H. H. Uhlig, *Z. Elektrochem.*, **62**, 700 (1958).

Dissolution of Nickel in Acid Ferric and Ceric Solutions

Phoebus M. Christopher and Cecil V. King

Department of Chemistry, New York University, New York, New York

ABSTRACT

Dissolution rates of nickel cylinders rotated in acidified solutions of $FeCl_3$ and $Ce(SO_4)_2$ have been measured. The rates are transport-controlled, but the Ni surface becomes extremely rough, and first-order constants are obtained only if a uniform degree of roughness is maintained during runs. The values of the rate constants then depend on the structure of the metal, e.g., whether it has been annealed, mechanically worked, etc.

The rate of dissolution of nickel in ferric alum solutions was measured by Van Name and his coworkers (1), who found it to be approximately the same as that of several other metals in the same reagent. The authors regarded the dissolution to be controlled by diffusion, or by convective-diffusive transport, of ferric ion to the metal surface.

The present study shows that a polished nickel surface becomes very rough in acidified ferric and ceric solutions, more so in the former than in the latter. This is at least partly due to preferential dissolution at grain boundaries and at flaws in the mechanically worked metal. It indicates that, while the cathodic reaction (reduction of ferric or ceric

ions) probably occurs equally well at any point on the surface, the anodic reaction (formation of aqueous Ni^{++}) is not uniformly distributed. The rough surface of a rotating cylinder increases turbulence in the solution, at least near the interface, which results in larger dissolution rates than are found with smooth cylinders. The effect of roughness has been studied by Makrides and Hackerman in the dissolution of steel (2). These authors decided that roughness may increase the effective surface area at high rotational speeds, where the effective thickness of the boundary layer is small.

Experimental

Cylinders were cut from a nickel anode bar (99.6% Ni, supplied by International Nickel Co.) which had been rolled to an elliptical cross section. They were 2.52 cm long and 1.9-1.7 cm in diameter when in use. They were mounted on a shaft with only the peripheral surfaces exposed to the solutions. Some specimens were annealed by heating at 850°C for 2 hr in argon and cooling over a period of 4-5 hr in the same gas.

The reaction vessel was a square bottle (which has the effect of baffles in the solution), equipped with a tube passing through a hole in one side to admit nitrogen. The solution volume was 400 ml in all cases. Solutions were deaerated since preliminary runs showed that oxygen is reduced freely. All experiments were carried out at 18°-21°C. C.P. $FeCl_3$ was used directly while U.S.P. $Ce(SO_4)_2$ was recrystallized twice. All ferric solutions were made up with 1M HCl and all ceric solutions with 1M H_2SO_4. Dissolution was followed by weighing the cylinders after 2- to 10-min runs.

Results and Discussion

The first experiments were carried out with specimens which were polished with 2/0 emery paper initially, but not repolished when they were removed and weighed. At 3000 rpm the surface very quickly became rough, and the weight loss increased in successive equal time intervals in the same solution; for example in 0.05M $FeCl_3$ (initially) the dissolution rate had doubled after half the ferric ion had been reduced. Figure 1 is a plot of log (a-x) for two unannealed cylinders run in this manner. In 0.02M $Ce(SO_4)_2$ the rate became first-order after

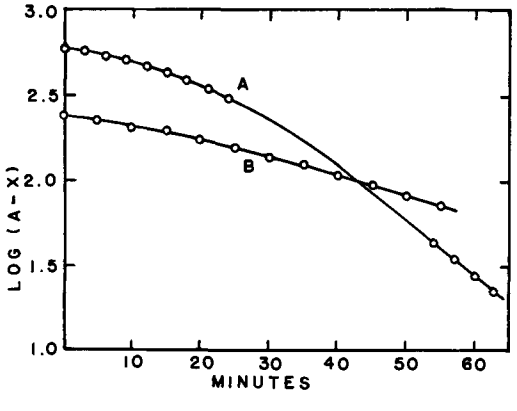

Fig. 1. Unannealed cylinders, polished initially and allowed to roughen with time. A, 0.05M $FeCl_3$ + 1M HCl. B, 0.02M $Ce(SO_4)_2$ + 1M H_2SO_4.

25 min, while in 0.05M $FeCl_3$ a somewhat longer time was required. Values of k (from the slopes, see Eq. [1] below) varied from 0.39 to 1.9 cm/min in the ferric solution, and from 0.34 to 0.71 cm/min in the ceric solution. Examination showed that the surface became rougher in the $FeCl_3$.

Thereafter runs were made in two ways: (a) the cylinder was polished initially and after each short immersion, to keep it as smooth as possible; or (b) the specimen was etched before use until there was no further effect on the rate. In both cases consistent rate constants k were obtained with the first-order equation:

$$k = \frac{2.3\,V}{A\,t} \log \frac{a}{a-x} \qquad [1]$$

where V is in cm^3, A in cm^2 (the apparent or projected area), and the other symbols have their usual meanings. Since the metal cylinders dissolved at a steady rate of 0.5 mg/10 min in the 1M HCl solution after all ferric ion had been reduced, a corresponding correction was applied to all weight losses. Dissolution in 1M H_2SO_4 after ceric ion was reduced was negligible.

Table I gives mean values of k for several runs of 60- or 70-min duration with unannealed cylinders. It is evident that the exact values of k obtained with polished samples depend on the time period chosen for immersion between polishings; the value 0.78 for $FeCl_3$ is twice that found from the initial slope of the log $(a - x)$ plot in Fig. 1 This does not, however, apply to the ceric solution.

In addition to the uncertainty of reproducibility with polished cylinders, it became evident that different unannealed cylinders reached different maximum rates after etching. This was probably due to lack of uniformity of structure of the anode bar from which they were cut. Part of the roughness took the form of irregular grooves along the length of the cylinders, in the direction in which the bar had been rolled, and the appearance varied from one cylinder to another. For these reasons some of the cylinders were annealed in order to obtain more uniform structure. On etching, the surface appeared much rougher than that of unannealed specimens, and dissolution rates were higher in most cases. Table II gives some values of k from single short runs designed to test the effect of solution concentration.

The rate constant in $FeCl_3$ apparently can vary from about 1.0 to a maximum of 2.2 cm/min under these conditions, depending on the past history of the metal, but for any one specimen it is reproducible and is independent of reagent concentration. In $Ce(SO_4)_2$ it is possible that the degree of roughness reached depends somewhat on concentration. The dissolution in 0.05M $FeCl_3$ of an annealed specimen,

Table I. Mean values of k in cm/min. Peripheral speed of cylinders, 17,000 cm/min.

	0.05M $FeCl_3$ + 1M HCl	0.02M $Ce(SO_4)_2$ + 1M H_2SO_4
Polished	0.78	0.33
Etched	1.83	0.78

Table II. Values of k in cm/min for etched cylinders in $FeCl_3$ (+HCl) at 17,000 cm/min and $Ce(SO_4)_2$ (+H_2SO_4) at 18,000 cm/min

Conc, M	$FeCl_3$ unannealed	$FeCl_3$ annealed	$Ce(SO_4)_2$ unannealed
0.02	1.08	2.16	0.82
0.04	1.10	2.21	0.87
0.06	1.06	2.22	1.01
0.08	1.14	2.17	1.00
0.10	1.06	2.11	1.05

polished initially, was similar to that shown in Fig. 1, but maximum roughness had not been reached after 55 min in the same solution.

A few runs were made in 0.02M $FeCl_3$ at other rotational speeds, and values of k are plotted in Fig. 2. While the values are consistent among themselves, it will be seen that these cylinders had their own characteristic rates.

The following empirical equation represents dissolution rates for smooth cylinders in a number of cases (3):

$$k = 0.010\ U\ (D/\nu)^{0.8} \qquad [2]$$

where U is peripheral speed, D, diffusion coefficient, and ν, kinematic viscosity. The lower dashed line of Fig. 2 represents this equation, using $D = 7 \times 10^{-6}$ cm²/sec for $FeCl_3$ (4) and $\nu = 9.36$ cm²/sec (the value for 1M HCl). The equation is of course inadequate in this case. At 17,000 cm/min it gives $k = 0.54$; for a smooth copper cylinder in $FeCl_3$ King and Weidenhammer (4) found 0.56 cm/min.

For roughened cylinders Makrides and Hackerman (2) proposed the equation:

$$k = (1.25 + 5.76 \log d/h)^{-2}\ U\ (D/\nu)^{0.644} \qquad [3]$$

where d is the cylinder diameter and h is the average height of surface irregularities. Microscopic examination of annealed Ni cylinders, etched in $FeCl_3$ to maximum dissolution rate, showed a fairly uniform groove depth at grain boundaries of about 0.05 cm. The upper dashed line of Fig. 2 represents Eq. [3] using this value of h and with D and ν as before. It obviously gives a much better prediction of the magnitude of the experimental values. The exponent 0.644 on the inverse of the Prandtl number D/ν has not been verified, and the function is quite sensitive to this exponent; e.g., with a value of 0.8, Eq. [3] gives almost the same slope as the lower dashed line of Fig. 2. Also, Eq. [3] predicts that k should vary with cylinder diameter, but this has not been tested.

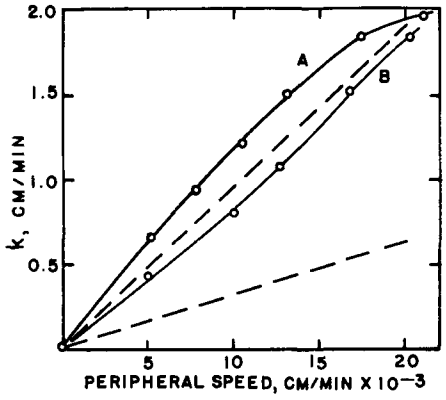

Fig. 2. Rate constant vs peripheral speed in 0.02M $FeCl_3$ + 1M HCl. A, annealed cylinder. B, unannealed. Lower dashed line, Eq. [2]. Upper dashed line, Eq. [3].

Manuscript received Dec. 31, 1959.

Any discussion of this paper will appear in a Discussion Section to be published in the December 1960 JOURNAL.

REFERENCES

1. R. G. Van Name and D. U. Hill, *Am. J. Sci.*, (4) **42**, 301 (1916).
2. A. C. Makrides and N. Hackerman, *This Journal*, **105**, 156 (1958).
3. C. V. King and N. Mayer, *ibid.*, **100**, 473 (1953).
4. C. V. King and L. Weidenhammer, *J. Am. Chem. Soc.*, **58**, 602 (1936).

Oxidation of Niobium in the Temperature Range 350°-750°C

D. W. Aylmore, S. J. Gregg, and W. B. Jepson

Department of Chemistry, University of Exeter, Exeter, England

ABSTRACT

The kinetics of the oxidation of niobium in dry oxygen at 1 atm pressure have been measured at temperatures in the range 350°-750°C with some additional measurements at 0.1 atm. At 350°C, in tests lasting 270 hr, the oxidation is protective, but at 400°C and above the metal oxidizes, apart from an initial period, at a constant rate with a second breakaway reaction (rate transition) at 450° and 500°C but not at higher temperatures. The anomalous temperature coefficient of the linear rate has been confirmed. The specific surface of the oxide scale has been measured and, apart from an anomaly at 400°C, is shown to decrease with increasing temperature of oxidation and this is ascribed to sintering. The oxidation kinetics of a purer batch of niobium were also investigated. The effect of moisture is to decrease the rate at 400° and 450°C, whereas at 600°C the rate is unchanged.

There have been a number of kinetic studies of the oxidation of niobium both in air and in oxygen. Inouye (1) has investigated the oxidation in dry and in moist air at atmospheric pressure at temperatures in the range 400°-1200°C and has found that the effect of moisture was to increase the linear rate

at 400°C and to decrease it at 600°C. Klopp, Sims, and Jaffee (2) have measured the rate of oxidation in both dry oxygen and ordinary air at temperatures in the range 600°-1200°C and have investigated the penetration of oxygen into the metal. The comprehensive study by Bridges and Fassell (3) has dealt with the oxidation in oxygen at pressures from 1 to 41 atm at temperatures over the range 400°-800°C; the linear rate of oxidation was found to be pressure dependent and the temperature coefficient of the reaction was shown to be negative from 550° to 650°C. Gulbransen and Andrew have dealt with the kinetics at 0.1 atm of oxygen in two separate investigations (4, 5) covering the temperature ranges 250°-375°C and 375°-700°C, respectively; at temperatures up to 375°C the metal oxidized according to a parabolic rate law over the first 2 hr, the period of the studies, but at higher temperatures the reaction, after an initial protective stage, underwent a breakaway [Gulbransen and Andrew (5) use "rate transition"] and the rate of oxidation increased up to the constant value, that of the linear rate. The linear rate was found to be almost independent of temperature between 550° and 625°C. More recently, Cathcart, Campbell, and Smith (6) have confirmed the breakaway and shown it to be associated with the development of small, blister-like cracks in the oxide film. Goldschmidt (7), following earlier work by Brauer (8), has re-investigated the polymorphic forms of the oxide product, niobium pentoxide, and shown that there are in fact two, and not three, such forms, viz., the α- or "low-temperature" modification which transforms spontaneously to the β- or "high-temperature" modification even at room temperature.

The present work constitutes an investigation of the oxidation kinetics at temperatures in the range 350°-750°C in oxygen at pressures of 1 atm with some additional measurements at 0.1 atm. The anomalous temperature coefficient of the reaction has been confirmed, and a second breakaway has been found to occur both at 450° and at 500°C but not at higher temperatures; this absence of second breakaway is believed to be due to a sintering of the oxide, which is confirmed to some extent by measurements of the specific surface of the oxide scale. Approximate calculations from these measurements lead to a value for the average crystallite size which is in good agreement with that found by Goldschmidt (7) using x-ray methods. The results for the kinetics in moist oxygen are in disagreement with those of Inouye (1) for moist air; the course of the oxidation differs little from that in dry oxygen.

Experimental

The main kinetic study was carried out by gravimetric determination of the weight gain of the sample on a thermal balance in an oxygen pressure of 1 atm. The niobium sample was contained in a basket of platinum gauze (to hold any fragments of oxide spalling from the metal) which was suspended in the reaction chamber by a length of platinum wire hooked to the underside of the balance pan; at the start of the run the furnace, pre-set to reaction temperature, was raised into position round the reaction chamber and thermal equilibrium was reached within about 10 min. The arrangement was similar to that previously described (9), except that the oxygen was additionally dried by passing it over "Linde" molecular sieves (10).

In addition, several runs were carried out at 0.1 atm using a quartz spring balance of conventional design, while the early stages of the oxidation at two temperatures were examined using a low sensitivity quartz microbalance (11, 12) (precision: 4 μg); with both these techniques, oxygen was admitted to the outgassed sample at reaction temperature.

The bulk of the work was carried out with material (niobium A) obtained from Murex Ltd. in the form of 1/16 in. thick sheet (analysis: C, 0.1%; Al, 0.03%; Si, 0.02%; Fe, 0.03%; Cr < 0.01%; Mn < 0.01%; Cl < 0.01%; Pb < 0.01% and Ta 0.3 to 0.4%). Samples in the form of a rectangle (4 x 1.5 cm) were cut from the sheet and abraded down to Grade 00 emery under petroleum ether and finally degreased in benzene vapor. Some additional runs were also carried out with a purer material (niobium B) in the form of 0.010 in. thick sheet (analysis: C, 0.0162%; Ta, 0.143%; Fe, 0.008%; Zr, 0.65%; Ti, 0.013%; N, 0.028%; O, 0.107%). This latter was kindly donated by Dr. K. F. Andrew and was of the same batch as that used in his study (5) with Dr. E. A. Gulbransen.

Results

Oxidation of Niobium A in Dry Oxygen

At 350°C, the first temperature studied, the weight gain of a sample exposed for 265 hr was only 0.5 mg cm^{-2}, and as far as could be judged, the rate of oxidation decreased with time.

Curves for the increase in weight (mg/cm^2 of geometric surface) against time were obtained for temperatures at 50° intervals in the range 400°-750°C, and the runs were continued at all temperatures, except 400°, until the sample had been oxidized to completion.

The course of the oxidation at 400°C is shown in Fig. 1; the rate increases over the branch OA becoming constant after about 8 hr in agreement with earlier work (3). Runs at this temperature were continued for 230 hr, after which time about 25% of the metal was oxidized, and the rate of oxidation was constant over this period. At 450°, however, the rate increased only for the first 30 min, after which it decreased (AB of Fig. 2), becoming constant after

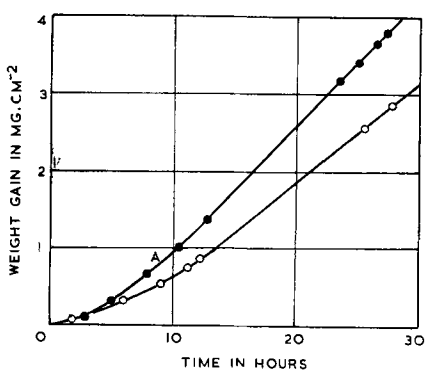

Fig. 1. Oxidation of niobium in dry and in moist oxygen at 400°c. (○, dry oxygen; ●, moist oxygen).

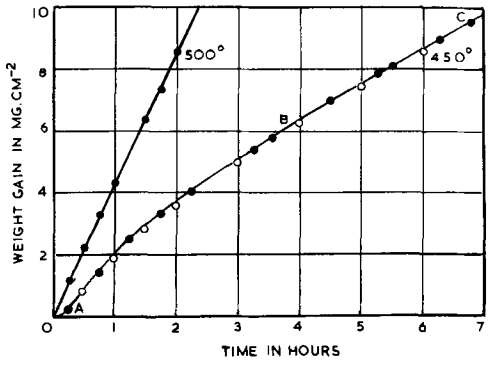

Fig. 2. Oxidation of niobium at 450°C in dry and in moist oxygen and at 500°C in dry oxygen. (●, dry oxygen; ○, moist oxygen).

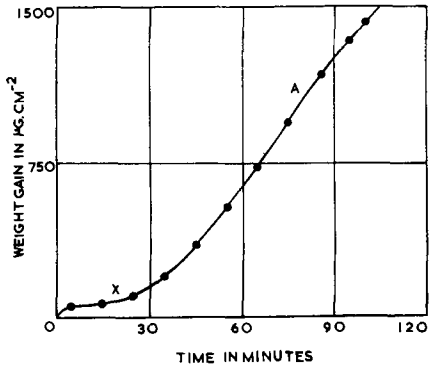

Fig. 3. Oxidation of niobium at 450°C and 0.1 atm oxygen showing the first breakaway at X.

4 hr; the early stages of the oxidation at this temperature were investigated in more detail on the microbalance at 7.6 cm oxygen pressure. From the curve of Fig. 3 which is typical, it is seen that after breakaway at X the rate increases to a maximum value (1.4 mg cm^{-2} hr^{-1}) at A and then decreases. Presumably if the run could have been carried out for a longer period, the rate would ultimately have become constant as in Fig. 2. The weight gain of 70 μg cm^{-2} at which breakaway occurred is in agreement with earlier work (5). The curve corresponding to complete oxidation of the metal is shown in Fig. 4, and it can be seen that the linear branch BC persists for only about 20 hr; at C the rate of oxidation increases, so that a second breakaway can be said to have occurred, and then decreases until at D a further section of the metal undergoes a second breakaway reaction and the metal oxidizes to completion.

At 500°C the material oxidized at a constant rate from the start of the run (Fig. 2) for a period of about 6 hr, after which it began to increase (Fig. 5); toward the end of the run there was a second breakaway reaction and the metal then oxidized to completion at a much higher rate. At 550° and 600°C the kinetics again conformed to the linear rate law from the start of the run; now there was no second breakaway and the linear rate was maintained until about 75% of the metal had been consumed, after which the rate began to fall off (Fig. 5). This was probably due to a decrease in the area of metal undergoing oxidation. The behavior at 650°C was rather similar, except that the decrease in rate occurred after only 25% of the metal had been oxi-

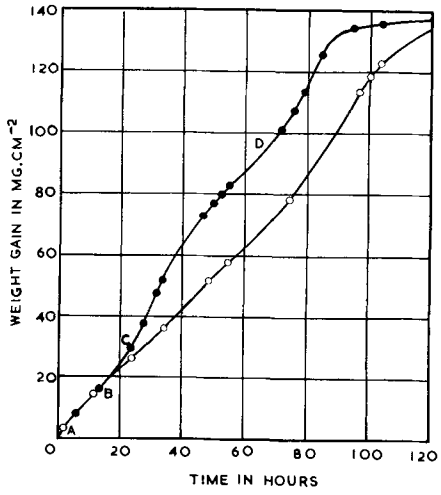

Fig. 4. Oxidation of niobium at 450°C in dry and in moist oxygen. (●, dry oxygen; ○, moist oxygen).

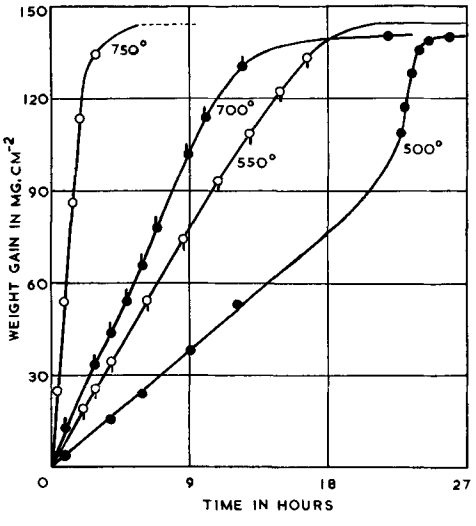

Fig. 5. Oxidation of niobium at 500°, 550°, 700°, and 750°C in dry oxygen.

dized, and cannot therefore be due to a decrease of sample area.

At 700°C the oxidation curve showed no clear linear branch (Fig. 5); after decreasing for the first 5 hr, the rate increased and then slowly decreased again. At temperatures of 550°C and above, no second breakaway was obtained in any of the runs.

At least three runs were carried out at each temperature, and the linear rates at 400°C and at temperatures from 500° to 650°C were in good agreement, often within 2-3% of the mean; at 450°C the spread in values of the rate was wider (about 15%). The times for which second breakaway occurred (450° and 500°C) agreed within about 10% of the mean. The average linear rates for each temperature are given in Table I and are plotted in Fig. 6

Table I. Oxidation rates of niobium in dry oxygen

Temp, °C	Rate, mg $cm^{-2}h.^{-1}$	Temp, °C	Rate, mg $cm^{-2}h.^{-1}$
400	0.163	600	35.7
450	1.31	650	8.72
500	4.0	700	16.9*
550	8.52	750	64*

* Approximate values only.

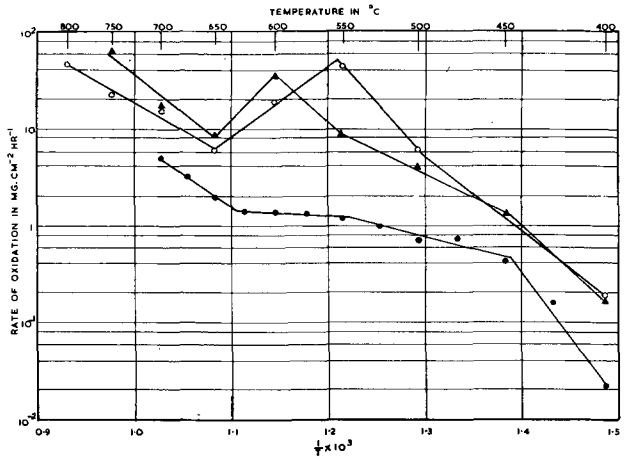

Fig. 6. Summary graph showing the change of linear rate with temperature, the data are plotted in the Arrhenius form [triangles, this work. ○, Bridges and Fassell (3); ●, Gulbransen and Andrew (5)].

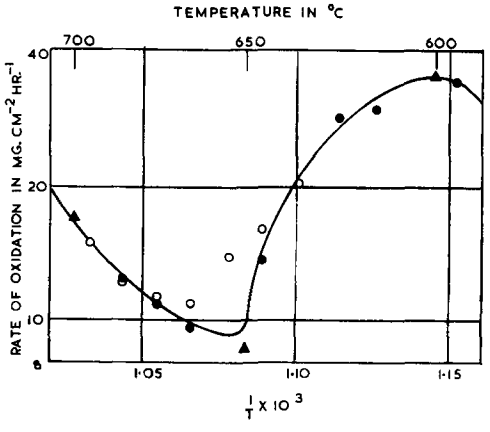

Fig. 7. Negative temperature coefficient of the reaction from 600° to 650°C. ○, ascending temperatures; ●, descending temperatures; ▲, data from Table I.

in the Arrhenius form; values from the literature (1, 5) are included for comparison.

As will be seen, the rate at 650°C is less than that at 600°C, and in order to confirm the apparent negative temperature coefficient of the reaction between these two temperatures, two additional experiments were carried out. In the first, a sample was oxidized for 10 min at 635°C and the linear rate measured, the temperature was then raised in steps of 10° up to 695°C and the linear rate measured at each temperature; in the second, the linear rate was measured at a number of temperatures in the range 685°-595°C, the temperature being lowered stepwise. The results, which are given in Fig. 7, show that over the range 600°-650°C the linear rate does in fact decrease with increasing temperature of oxidation.

The Oxide Product

The weight gain corresponding to complete oxidation of the metal agreed to within 0.01%, after making due allowance for oxidation of the impurity elements, with that calculated for niobium pentoxide (1).

The product obtained on oxidizing the metal to completion at 450°C consisted of a mixture containing approximately equal weights of scale and of fine powder, the latter being composed of particles with diameters up to 50μ, with the majority in the 5-10μ range. Since the product obtained on oxidizing a sample to a weight gain corresponding to a point on branch BC (Fig. 4) was composed only of scale, it may be concluded that the powdered oxide only forms after the second breakaway (point C). Microscopic examination of the metal surface after second breakaway revealed the presence of deep craters which in some cases extended to the opposite face (Fig. 8).

The percentage by weight of scale in the product resulting from complete oxidation of the metal increased with increasing temperature of oxidation, and at 550°C, the lowest temperature at which second breakaway did not take place, the product contained 90% scale. The oxide obtained at each temperature was carefully sieved through platinum gauze (80 mesh/linear in.) to separate the powder from the scale, and the specific surface of the latter was then measured by the method of krypton sorption (13); for the 400°C sample, which was only partially oxidized, a fragment of scale was detached from the metal for the specific surface measurement. Previous work (13) has shown that repeat determinations of the specific surface agree within ±1%. As can be seen from Fig. 9, the specific surface S of the oxide scale varies over a comparatively wide range, from 0.9 $m^2\ g^{-1}$ to 19.8 $m^2\ g^{-1}$ for the oxides formed at 750° and 450°C, respectively.

An approximate estimate of the size of the individual crystallites making up the scale can be obtained by arbitrarily assuming the latter to be made up of equal-sized cubelets of edge-length 1. Using the expression (14)

$$l = \frac{6}{S\rho}$$

where ρ is the density of the oxide, the 450° and 750°C products then correspond to crystallite sizes of 0.061μ and 0.68μ, respectively. These values are in reasonable agreement with those found by Goldschmidt (7) using x-ray analysis. The decrease of specific surface with increasing temperature of oxidation from 450°C upwards (Fig. 9) points to the scale having sintered after it has been formed. This is substantiated by an experiment where the scale

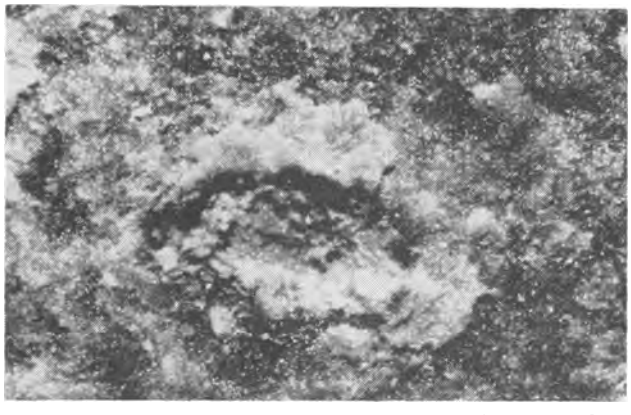

Fig. 8. Characteristic appearance of the metal surface after second breakaway, oxidized at 450°C for 47 hr. Magnification 200X before reduction for publication.

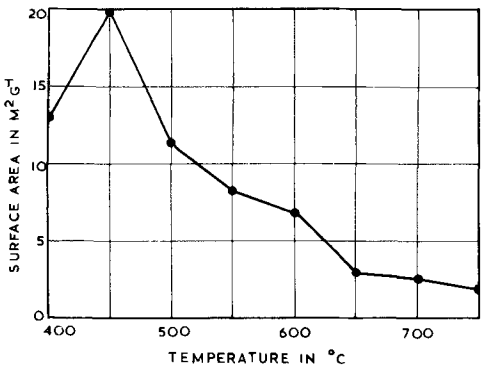

Fig. 9. Specific surface of the oxide scale as a function of oxidation temperature. The times of oxidation were 247 hr (400°), 122 hr (450°), 29 hr (500°), 24 hr (550°), 5 hr (600°), 20 hr (650°), 11 hr (700°), 4.5 hr (750°C).

formed at 500°C was heated for a period of 5 hr in oxygen at 700°C, when the specific surface fell from 11.3 to 5.9 $m^2 g^{-1}$. The rate of sintering of the scale will depend both on the time and temperature of heating, and since the rate of oxidation is not a single-valued function of temperature (see Fig. 6), the fact that a smooth curve cannot be drawn through the experimental points of Fig. 9 is readily understood. Thus, the specific surface of the 600°C product is apparently too large with respect to the 550° and 650°C products, but the oxidation time was only 5 hr for the first, as compared with 24 and 20 hr, respectively, for the last two products.

That sintering should occur is hardly surprising, for the temperature of oxidation expressed as fraction of the melting point (7) of the oxide (1733°K) ranges from 0.39 to 0.59, and, as is well known (15), solid-state processes are greatly accelerated at temperatures above a critical value T_c, characteristic of the solid but lying within the range $0.39T_f$ to $0.53T_f$, where T_f is the melting point of the solid.

Oxidation of Niobium A in Moist Oxygen

Samples of niobium were oxidized in moist oxygen saturated at 25°C (1.8 wt %), at 400°, 450°, and 600°C. At each temperature the course of the oxidation was very similar to that in dry oxygen (Fig. 1 and 2) although at 400°C (Fig. 1) 13 hr elapsed before the rate of oxidation became constant, while at 450°C (Fig. 4) the second breakaway was retarded. The linear rates at 400° and 450°C, viz., 0.133 and 0.97 mg cm^{-2} hr^{-1}, are somewhat less than the corresponding values for dry oxygen (0.163 and 1.31 mg cm^{-2} hr^{-1}, respectively), while at 600°C the linear rate in the moist gas was the same, within experimental error, as that in the dry.

The present results are in marked disagreement with those of Inouye (1) for moist air (1.39 wt %) who found that the rate at 400°C was increased by a factor of about 30 and the rate decreased at 600°C by some 40%.

Oxidation of Niobium B in Dry Oxygen

Samples of the purer material, niobium B, were oxidized at a number of selected temperatures in order to compare both the shape of the oxidation curve and the linear rate with those of niobium A. The oxidation behavior of the two batches of metal differed markedly in that second breakaway and the associated formation of powdery oxide occurred much more readily with niobium B. Thus at 600°C, second breakaway occurred with niobium B after oxidation for 1 hr and the oxide product was largely made up of powder (84%) whereas with niobium A no second breakaway was detected; the two products also differed in appearance (Fig. 10); moreover the linear rate for B (30 mg cm^{-2} hr^{-1}) is significantly less than for niobium A (35.7 mg cm^{-2} hr^{-1}). At 650°C second breakaway occurred (Fig. 11) after about 10 minutes' oxidation and the linear rate could not be measured.

At 550°C and 0.1 atm of oxygen the linear rate of oxidation of niobium B was again less than that of niobium A (1.9 compared with 2.2 mg cm^{-2} hr^{-1}), and second breakaway occurred (Fig. 12) after about 45 minutes' oxidation. A comparison of the linear rate for niobium A at 550°C and 0.1 atm oxygen pressure with that for 1 atm oxygen pressure shows that the rate is pressure dependent.

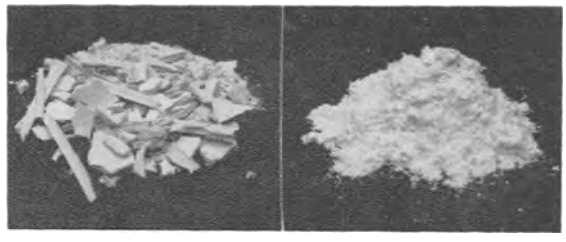

Fig. 10. Comparison of the products obtained on oxidizing niobium to completion at 600°C. left, niobium A; right, niobium B.

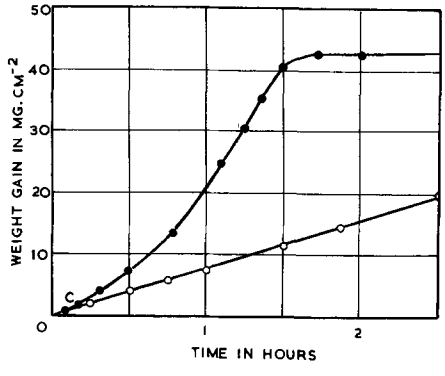

Fig. 11. Comparison of the oxidation of niobium A (○) with that of niobium B (●) at 650°C and 1 atm oxygen. Second breakaway has occurred at C with niobium B.

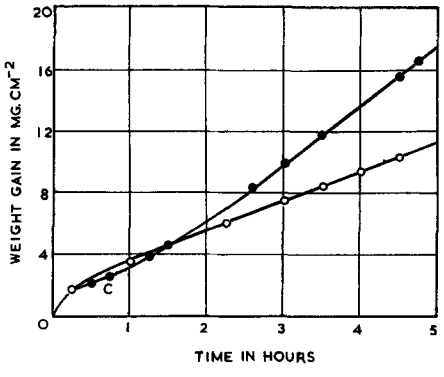

Fig. 12. Comparison of the oxidation of niobium A (○) with that of niobium B (●) at 550°C and 0.1 atm oxygen. Second breakaway has occurred at C with niobium B.

Discussion

It would appear that at 350°C the oxidation of niobium is protective although experiments of much longer duration are needed to settle this point conclusively in view of the fact that the weight gain of the sample after 270 hr (500 μg cm^{-2}) is considerably larger than that for which breakaway occurs at the higher temperatures. At 400°C and above, the oxidation is nonprotective and the metal oxidizes until it is all consumed. Gulbransen and Andrew (5) were unable to detect a first breakaway (cf. Fig. 3) at 525°C and above; similarly in the present work a run on the microbalance at 550°C and 7.6 cm oxygen pressure failed to show a breakaway. This is probably because the rate of oxidation is so large that breakaway occurs before the first reading can be taken on the microbalance; thus after 90 sec the weight gain was 150 μg cm^{-2}, a value which is considerably greater than the 70 μg cm^{-2} for which breakaway occurred at 450°C.

In a recent electron microscope study, Cathcart, Campbell, and Smith (6) have shown that breakaway, and therefore the onset of nonprotective oxidation, is associated with the formation of blister-like cracks in the oxide film. They suggested that the oxide layer thickened by anionic diffusion and that the volume expansion resulting from the build-up of new oxides at the metal/oxide interface produced compressive stresses which ultimately caused the oxide to fracture. Presumably oxygen gas then is able to enter the newly formed crack and allow a new continuous oxide layer to form and to thicken until the compressive stresses reach the fracture strength of the oxide, when a further crack appears. This process will be occurring at points all over the metal surface, and although the thickness of uncracked oxide will never be uniform, it can be regarded as statistically maintaining a constant thickness and so acting as a barrier film.

The specific surface measurements, together with earlier measurements of pore volume (14), show the oxide scale to be porous to oxygen, so that the rate of oxidation must be controlled either by the rate of diffusion of reactant across the barrier film or else by the rate of solution of reactant in the latter. Since the oxidation rate is pressure dependent the barrier film model would (on the basis of the Wagner theory of parabolic oxidation) require the oxidation to proceed either by diffusion of oxygen ions between interstitial positions or by diffusion of Nb^{5+} ions between vacant cation sites. Because of the large positive charge of the Nb^{5+} ion, anionic diffusion seems the more likely. However, either possibility would require a metal-deficient oxide, whereas niobium pentoxide itself is in fact oxygen deficient, although niobium containing comparatively large amounts of tantalum (~1.4%) gives an oxide product which contains greater than the stoichiometric content of oxygen at temperatures near to 450°C (16) (niobium A contains 0.3-0.4% tantalum). It must however be remembered that the structure and composition of the barrier film may differ greatly from that of the scale; the former may in fact be the adherent black substrate found by Klopp, Sims, and Jaffee (2) and shown to contain both NbO and Nb_2O_5.

It is also important to realize that the marker experiment of Cathcart, Campbell, and Smith (6) does not provide evidence for anionic diffusion, in that the conditions (4 hr oxidation at 450°C) were such that breakaway had occurred so that the sample was presumably covered with a layer of porous oxide; and the marker would be expected to remain on the outer surface of the scale irrespective of the type of diffusion through the barrier film. In other words, a marker experiment will not distinguish between the passage of oxygen gas and the diffusion of oxygen ions. Marker experiments on the oxide layer before breakaway would be useful in establishing the type of diffusion, although the experimental difficulties would be considerable (17,18) in view of the small thickness of film involved.

Concerning the shape of the oxidation curves, the initial increase in rate at 400°C (branch OA, Fig. 1) is consistent with the model discussed above, and almost certainly corresponds to a progressive extension of the area of metal undergoing nonprotective oxidation, the point A denoting the completion of this process. Similarly, the increase at 450°C (from X to A of Fig. 3) probably arises from the same cause but the marked decrease along AB (Fig. 2) indicates that the barrier film is increasing in thickness; possibly the development of cracks in the barrier film is influenced by the thickness of scale above it. That the rate of oxidation at temperatures of 500°C and above is constant from the start is clearly because the rate had become constant before the weight gain of the sample was sufficient to be detected on the thermal balance. Certainly the results of Gulbransen and Andrew (5), and also the present results at 550°C and 0.1 atm, clearly show that the rate does in fact decrease to a constant value.

The fact that the linear rates of oxidation, when plotted in the Arrhenius form, do not fall on a straight line (Fig. 6) is probably the most striking feature of the oxidation of niobium. Neither niobium (19) nor niobium pentoxide (7) shows any phase changes in the temperature range of the present investigation, so that any explanation along these lines can be discounted. The reason why the linear rate decreases from 600° to 650°C is not clear, though this effect could come about as the result of a change in the type of diffusion through the barrier film from, say, anionic to cationic. The temperature coefficient of either process will be positive, but from 600° to 650°C the type of diffusion could be mixed, the proportion of the one increasing at the expense of the other with increasing temperature. Simultaneous cationic and anionic diffusion has recently been put forward, for example, to interpret data for the oxidation of zirconium (20).

It is known that the oxidation of niobium is accompanied by diffusion of oxygen into the underlying metal and that the penetration increases with time (2). Second breakaway could thus come about along the lines suggested by Pemsler (21) for zirconium oxidation: namely by detachment of the barrier film from the metal in consequence of the

changing stresses produced in it by the embrittlement of the metal; some evidence for this is provided by the observation that with niobium B the black film is found adhering to the oxide scale after breakaway has taken place. This model is consistent with the absence of second breakaway at 550°C and above; indeed, the ready sintering of the oxide scale at these temperatures points to a high degree of plasticity, which might be expected to be present in the barrier film itself.

The reaction mechanism after the second breakaway is not clear, but the powdery form of the oxide suggests that individual grains of metal have become separated, possibly because of penetration of oxygen down the grain boundaries. Certainly the saturated vapor pressure of niobium at 450°C is so small (22) (an extrapolation from 2000° gives 10^{-42} mm) as to exclude completely any possible reaction between niobium vapor and oxygen, a mechanism which has been suggested (9) to explain the reaction following the second breakaway of magnesium in oxygen.

The fact that the course of the oxidation of niobium in moist oxygen is essentially the same as in the dry gas (except for small changes in the linear rate) is consistent with the fact that niobium pentoxide does not form any hydrates so that only a small fraction of the sites at the oxide/gas interface is likely to be occupied by chemically adsorbed water, and as a consequence the amount of "water" entering the barrier film will be small. With magnesium (9), on the other hand, the effect of water is to increase the linear rate over that in the dry gas by as much as tenfold and to suppress second breakaway, facts consistent with the existence of the hydroxide $Mg(OH)_2$ and the consequent strong adsorption of water on magnesium oxide.

A question, which has already attracted some interest (7), is whether oxidation for a short period at a much higher temperature will anneal out the compressive stresses in the oxide film, and so prevent first breakaway. This point has been tested by Goldschmidt, who found that breakaway still occurred; presumably the rate at which the stressed oxide is formed is greater than the rate at which the stresses are alleviated. This view is supported by the fact that breakaway occurs after a smaller weight gain the higher the oxidation temperature. If the oxide film were annealed in the absence of thickening, that is to say in vacuo, it is conceivable that breakaway could not take place. However, in an experiment where a sample was oxidized at 450°C for 10 min, annealed *in vacuo* for 170 hr at 900°C, and then re-exposed to oxygen at 450°C, breakaway still occurred, the curve of oxidation being the same in shape as that for the un-annealed specimen, with the linear rate actually greater by some 50%.

Acknowledgments

The authors are grateful to Dr. K. F. Andrew for the gift of the niobium sheet, to Mr. E. R. Braithwaite for carrying out the particle size determination of the oxide powder, and to Professor G. K. T. Conn for allowing them the use of the Vickers projection microscope. They are also grateful to the U. K. Atomic Energy Authority for the financial support which they have given to this work.

REFERENCES

1. H. Inouye, U.S. Atomic Energy Commission Publ., 1953 [ORNL-1565].
2. W. D. Klopp, C. T. Sims, and R. L. Jaffee, U. S. Atomic Energy Commission Publ. 1957 [BMI-1170].
3. D. W. Bridges and W. M. Fassell, Jr., *This Journal*, **103**, 326 (1956).
4. E. A. Gulbransen and K. F. Andrew, *Trans. Am. Inst. Mining Met. Engrs.*, **188**, 586 (1950).
5. E. A. Gulbransen and K. F. Andrew, *This Journal*, **105**, 4 (1958).
6. J. V. Cathcart, J. J. Campbell, and G. P. Smith, *ibid.*, **105**, 442 (1958).
7. H. J. Goldschmidt, *J. Inst. Metals*, **87**, 235 (1958-1959).
8. G. Brauer, *Z. anorg. u. allgem. Chem.*, **248**, 1 (1941).
9. S. J. Gregg and W. B. Jepson, *J. Inst. Metals*, **87**, 187 (1958-1959).
10. C. C. Addison, E. Iberson, and J. B. Raynor, *Chem. and Ind.*, **1958**, 96.
11. E. A. Gulbransen, *Rev. Sci. Inst.*, **15**, 201 (1944).
12. D. W. Aylmore, S. J. Gregg, and W. B. Jepson, To be published in J. Inst. Metals.
13. D. G. Smith, Thesis, University of Exeter (1958).
14. D. W. Aylmore, S. J. Gregg, and W. B. Jepson, To be published.
15. G. I. Finch and K. P. Sinha, *Proc. Royal Soc.*, **239A**, 145 (1951).
16. B. B. Argent, Private communication.
17. S. Mrowec and T. Werber, *This Journal*, **6**, 363 (1958).
18. E. A. Gulbransen and K. F. Andrew, *ibid.*, **6**, 363 (1958).
19. C. R. Tottle, *J. Inst. Metals*, **85**, 375 (1956-1957).
20. O. Flint and J. H. O. Varley, *J. Phys. Chem. Solids*, **6**, 213 (1958).
21. J. P. Pemsler, *This Journal*, **105**, 315 (1958).
22. R. Speiser, P. Blackburn, and H. L. Johnston, *ibid.*, **106**, 52 (1959).

The Difference Effect and Anodic Behavior of Zirconium Dissolving in Hydrofluoric Acid

M. E. Straumanis, W. J. James, and W. C. Custead

Departments of Metallurgical and Chemical Engineering, University of Missouri, School of Mines and Metallurgy, Rolla, Missouri

ABSTRACT

Zirconium dissolving in hydrofluoric acid exhibited a positive difference effect of such an efficiency that the hydrogen volume developed by the internal polarization current was completely overbalanced by the effect. As with other metals the effect was independent of the concentration of the acid and was accompanied by a strong shift in potential of the Zr electrode toward noble values (passivation). Similar potential changes were also recorded in presence of salts or more noble metals while they were displaced by the Zr. Simultaneously, the rate of dissolution of Zr dropped (nearly to zero with Pt^{4+} additions). In the latter case the black hydride film on the surface disappeared and the Zr turned bright and shiny (passive Zr). A decrease in formation of the hydride film was observed in other cases of anodic polarization. The activity of Zr returned when the anodic current was cut off. As the effect of local currents, due to anodic polarization is reduced to a minimum, the high rate of dissolution of Zr is explained by direct chemical action of Zr with molecular HF.

Only three metals have been investigated in the authors' laboratories for the difference effect exhibited in acids: zinc, titanium, and aluminum. The results obtained with a fourth metal, zirconium, are summarized in the present article.

As discussed previously (1) the difference effect provides information about the polarizability of a metal, without making potential measurements. It reveals the true passivation ability of the metal in a certain solvent being under an anodic current.

Zirconium in HF exhibits a positive effect, meaning that the rate of dissolution V_1 of zirconium, as measured by the rate of hydrogen development, is decreased to V_2, while an anodic current is passing the surface of the zirconium electrode (Eq. [1]):

$$\Delta = V_1 - V_2 \qquad [1]$$

Thus, the difference effect, Δ, expressed in $mm^3\ cm^{-2}\ min^{-1}$, having the dimensions of a rate, is in this case positive. Actually the effect indicates the decrease in rate of dissolution of the metal while under an anodic current.

Procedure and Materials

The measurement of the difference effect was carried out as previously described (2). However, a larger three-necked boiling flask of 500 cm^3 capacity, holding 300 cm^3 of acid, was used instead of the smaller flask, and a stirrer rotating about 200 rpm was added. The stirring rate had little influence on the difference effect itself. A zirconium electrode (3) of 1 cm^2 area exposed to the acid, was always placed 5 mm from a platinized platinum electrode (3). The reactor flask was immersed in a thermo regulated water bath of 25° ±0.1°C. The hydrogen evolved was collected in a gas burette.

The rate of dissolution V_1 in $mm^3\ cm^{-2}\ min^{-1}$ of the zirconium electrode was determined; then the circuit from this electrode to that of platinum was closed (through a milliammeter and a resistance), the current I flowing through the cell was registered, and the rate V_2 was determined from the total rate V_t: $V_2 = V_t - 6.97I$, where 6.97 is the volume of H_2 in mm^3 produced by 1 ma/min. Substituting in Eq. [1] the values for V_2, Δ can be calculated:

$$\Delta = V_1 - (V_t - 6.97I) \qquad [2]$$

High-purity zirconium[1] was used for the anodes. It contained O_2-0.11, N_2-0.05, Fe-0.04, and Hf-0.01% by weight. After rolling the metal the stress was relieved by annealing in vacuum for 30 min at 700°C. From this sheet, approximately 1.6 mm thick, square anodes of 1 and 3.8 cm^2 area were cut. Reagent grade HF (48%) was used for the preparation of solutions of seven normalities. All operations with the acid were performed in polyethylene, polystirole, or wax lined glass vessels.

The Difference Effect

Unlike titanium the reaction of zirconium with HF (neglecting fluoride complexes) proceeds according to Eq. [3] (4):

$$Zr + 4HF \rightarrow ZrF_4 + 2H_2 \qquad [3]$$

This reaction was rechecked several times for Zr/H_2 ratio and was found to be quite accurate (5, 6). One gram Zr develops 491.43 cm^3 of hydrogen at standard conditions, or 1 mm^3 of the gas corresponds to 0.002035 mg Zr.

Although the rates of self-dissolution of Zr in HF are well reproducible (within a few per cent) (5),

[1] Obtained from U. S. Bureau of Mines, Albany, Oregon.

Table I. Positive difference effect on Zr in 0.3*N* HF at 25°C; surface area 3.8 cm². H_2 volumes reduced to STP

Time, min	V_1, mm³/cm² min	I, ma/cm²	6.97I, mm³/cm² min	V_t, mm³/cm² min	Δ, mm³/cm² min	K, mm³/ma min
0	—	—	—	—	—	—
5	410	0	—	—	—	—
10	419	0	—	—	—	—
15	—	16.8 *	118.8	375	158.3	9.28
20	—	17.3		366		
25	401	0	—	—	—	—
30	397	0	—	—	—	—
35	—	5.30	36.9	392	43.9	8.28
40	—	5.30		397		
45	388	0	—	—	—	—
50	375	0	—	—	—	—
55	375	0	—	—	—	—
60	370	0	—	—	—	—
65	—	7.90	55.1	366	72.6	9.19
70	—	7.90		361		
75	392	0	—	—	—	—
80	370	0	—	—	—	—
85	366	0	—	—	—	—
90	—	17.6 *	124	343	146.5	8.23
95	—	17.9		335		
100	357	0	—	—	—	—
105	366	0	—	—	—	—
						Average 8.75 ± 0.53†

* Maximum current (no external resistance).
† Largest deviation.

this is not at all essential in determining the difference effect. The independence of the effect from the rate follows from the fact that the same value for the effect is obtained in various concentrations of the acid, in which the rates of self-dissolution vary vastly. However, to obtain conformable results, a constant rate of dissolution is of importance. Therefore, the measurements of the effect were started only then when, after the irregular initial period, the rate of self-dissolution became fairly constant, reaching the maximum. Furthermore, rate determinations were made before and after application of the anodic current; the adjacent rates were taken as an average for the self-dissolution. To show the magnitude of the figures involved and the procedure of calculations, data obtained in 0.3*N* HF are summarized in Table I. The constant K, which shows the reproducibility of Δ-measurements, was calculated from (8)

$$\Delta = KI \qquad [4]$$

by substituting KI for the Δ in Eq. [2]:

$$K = 6.97 + \frac{V_1 - V_t}{I} \qquad [5]$$

As shown in Table I all measurements resulted in a positive Δ-effect, but unlike previous studies V_1 was always larger than V_t (Eq. [5]) resulting in K values appreciably larger than 6.97 mm³/ma min, the differences exceeding the limit of error of the determinations. To eliminate the possibility of a systematic error, additional runs in the same apparatus were made using a Ti electrode instead of Zr. However, the average value of K, which was smaller than 6.97 (V_t was larger than V_1) agreed within 2% with that previously obtained (2). This was an indication that no systematic errors were involved in the determinations, and measurements were continued with Zr in 6 other concentrations of HF. As a result, the Δ-effect, calculated from Eq. [2] and plotted against the anodic current density, gave a straight line (Fig. 1), the inclination of which was independent of the concentration of the acid exactly as observed for Ti (2), Al [in acid (1) and in base (7)] and Zn (8). The variation of the electrode area (3.8 cm² anodes were used for runs in 0.2 and 0.3*N* HF) had no apparent effect on the result. Figure 1 also shows that the Δ-effect is proportional

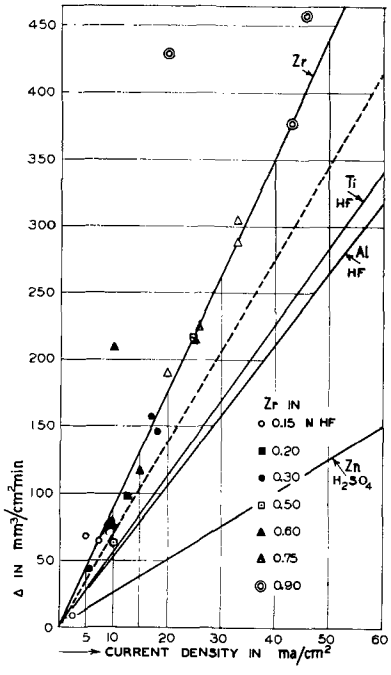

Fig. 1. Difference effect on Zr vs. current density in 7 different concentrations of HF at 25°C. Effects on Zn, Al, and Ti are given for comparison. The dashed line shows the rate of H_2 (= 6.97I) evolution at the cathode by the current.

to current density (Eq. [4]). The K-values calculated were as follows. In 0.15N HF: 8.09, 13.8, 3.56, and 9.17; in 0.2N HF: 7.72 and 8.07; in 0.3N—see Table I; in 0.5N: 8.68 and 6.17; in 0.6N: 8.68, 21.0, 7.73, and 8.65; in 0.75N: 9.21, 9.50, and 8.73; in 0.9N: 9.93, 22.9, and 8.74 $mm^3\ ma^{-1}\ min^{-1}$. Despite the relatively large fluctuations in the K-values, which may be attributed to sudden changes in the rates of self-dissolution while the Zr electrode was under the anodic current, there are only two constants less than 6.97. The mean from all measurements is 9.8; disregarding the less probable values (3.56, 13.8, 21.0, and 22.9), $K = 8.6$ with an average deviation of ± 0.7 is obtained. If the difference from 6.97 had resulted from errors of experimental nature one would expect a random distribution of K values below 6.97.

The average value of $K = 8.6 \pm 0.7$ $mm^3\ ma^{-1}\ min^{-1}$ for Zr dissolving in HF means that the rate of self-dissolution of Zr is reduced by 8.6 mm^3 by each milliampere minute flowing anodically through 1 cm^2 of the electrode. As 1 ma min produces (on the cathode) only 6.97 mm^3 H_2, then the current (developed by the Zr electrode itself), not only annihilates this volume, but even decreases the rate of self-dissolution by an additional 1.6 mm^3. This is a behavior not anticipated previously (1). Nevertheless the just mentioned 23% difference is real; it results from a large number of measurements, which in the average were reproducible within 10%, as could be shown by parallel experiments in 0.15N HF. Thus, an anodic current strongly passivates the Zr electrode, and any means (see below) which cause currents should passivate such an electrode.

Potentials and Rates

Potential of zirconium in pure HF.—Before making a study of the influence of an anodic current on the potential of a Zr electrode, the behavior of the electrode in pure HF was explored by measuring the emf of the cell

Zr|HF, salt bridge (sat. KCl sol.), 1N KCl, Hg_2Cl_2|Hg

and reducing the measured potential of the Zr electrode to the hydrogen scale by adding +0.242 v. The HF solution was always stirred (300 rpm).

The general trend is that the dissolution potential (ϵ') of the Zr electrode is very negative (around −0.90 v in 0.5N HF) right after the immersion, but quickly becomes more positive with time, approaching a steady potential in about 1 hr or more. It becomes more negative with increasing concentration of the acid (5). The potential-acid concentration curve is very similar to that obtained with Ti or Al in HF (1). However, the potential is sensitive to any change occurring on the surface of the electrode, like film formation or breakdown. Thus, the separate measurements made in the same concentration of acid at different times do not agree too well. Nevertheless, the effect of additions of ions of more noble salts to the acid upon the dissolution potential of Zr is so pronounced that there is no doubt about the reality of such measurements.

Potentials in presence of more noble metal salts.—Salt additions of $PtCl_4$, $AgNO_3$, and $AuCl_3$ to the 0.1N HF (300 cm^3) were made to give 0.001M solutions for each salt. As shown in Fig. 2 the potential of the Zr electrode shifts considerably toward more noble values immediately after the addition of the salts, as with Al (9). This shift was considerably higher in the case of Pt and Ag (Fig. 2; A, C). Direct observations of the Zr electrode showed that after the addition of noble metal salts the initially black surface (Zr hydride film) (10) turned shiny, the rate of dissolution (H_2-evolution) dropped, and the black (white in the case of $AgNO_3$) loose deposit of the displaced metal started to appear on the zirconium surface. The potential of the metal remained noble as long as there were noble metal ions (Pt^{4+}, Au^{3+}, Ag^+) in the solution. However, the loose deposit did not adhere well to the shiny zirconium surface and gradually broke off. When there was no longer any replacement of the deposit from the solution, the potential of the Zr started to drop (Fig. 2, D) and the rate of dissolution increased again. Thus, the behavior of Zr is just opposite to that of other active metals (Zn, Cd, Fe, Al in HCl): as long as there is a deposit on its surface, the metal is passive; its activity (in HF) returns when the deposit is gone. Aluminum in HF behaves somewhat similarly as its rate of dissolution is retarded by Ag^+, Pt^{4+} and other ions, but is increased by Au^{3+} and Ni^{2+} ions (9).

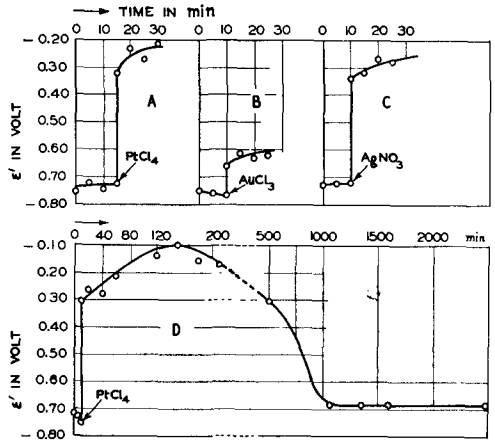

Fig. 2. Effect of salt additions on the potential of Zr dissolving in 0.1N HF, hydrogen scale.

Dissolution rates in presence of noble metal salts.—The change in rate of dissolution was followed from pressure measurements of the evolved hydrogen. A typical curve is shown in Fig. 3. After start-

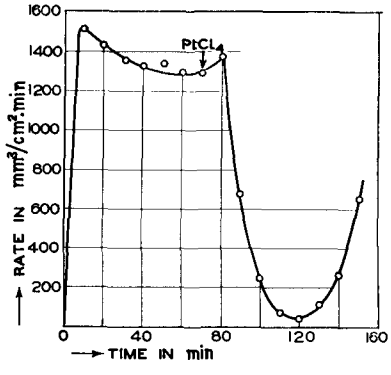

Fig. 3. Effect of $PtCl_4$ addition (0.001M) on the rate of dissolution of Zr in 0.5N HF.

ing the run, the rate of dissolution first increases, (short induction period), then slowly decreases. Upon the addition of the $PtCl_4$ solution the rate increased about 6% in the first 10 min and then decreased in 50 min by 96% resulting in an almost complete passivation of the Zr. However, the Pt deposit adhered loosely, and as before during the potential measurements, began to drop off. Simultaneously the rate of dissolution increased sharply. In the case of $AgNO_3$ and $AuCl_3$ additions, the rate dropped by 18 and 38% respectively and was still decreasing at the termination of the experiments.

In all three cases the zirconium surface under the loose deposit was bright, shiny, and heavily pitted, unlike that observed during the dissolution in pure acid.

The deposits in all three cases were identified by x-rays as the pure respective metals. Thus, there was a definite parallelism between potential and rate measurements.

Anodic Polarization of Zirconium

The anodic polarization of zirconium was investigated by Hackerman and Cecil (12), by van Ryssel-berghe and associates (13, 14) and others (15). The experiments were made in sodium chloride, carbonate, borate, and other aqueous solutions. In view of the peculiar behavior of zirconium in HF, it seemed worthwhile to make anodic potential measurements of the metal in this acid.

To avoid contamination of the Zr-Pt cell by other than hydrogen gases, no external emf was used at first, but only the current produced by the Zr itself (3). Its potential was measured, as usual, using a capillary touching the dissolving Zr surface. The results obtained are shown in Fig. 4. The strong influence of the anodic current on the dissolution potential of Zr is evident. The increase in potential is stronger the more dilute the acid. This effect is much more pronounced than in the case of Al (1) and already resembles a true anodic passivation. Thus, the internal anodic current (produced by the Zr electrode itself, and used in the Δ-effect measurements) as well as the external strongly shifts the potential of the electrode toward nobler values; simultaneously the rate of self-dissolution of the Zr drops. This is in agreement with the passivation of Zr observed in the presence of ions of more noble salts. However, no shiny surface was observed in absence of these salts.

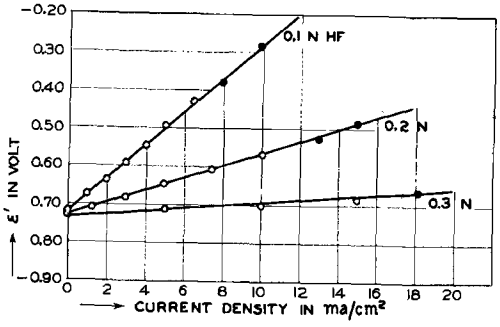

Fig. 4. Potential-current density curves of Zr dissolving anodically in HF (hydrogen scale). Each point is an average of at least two measurements. Solid points are obtained from measurements using an external current.

Discussion

It follows from these experiments that the dissolution of Zr in HF is strongly influenced by the action of local currents. However, this effect is opposite to that of other common metals, where the rate of dissolution is greatly increased by the presence of impurities. When noble metals are deposited on Zr, they cause a slight increase in the rate of dissolution (see Fig. 3) followed by a rapid decrease to nearly total passivation. The explanation is that the current produced by the deposited noble metal after an initial increase in dissolution shifts the anodic potential so far to noble values (see Fig. 2, A,B,C) that the local cathodes on Zr become inactive, i.e., their emf becomes too small to work effectively (1), and the dissolution ceases.

The positive difference effect, the direct potential measurements under anodic polarization, and the dissolution rates with noble metal salt additions testify to the strong passivating action of the anodic current. The difference effect is so strong that the work of the polarizing current is not only completely neutralized, but even overbalanced so that the action of the internal polarization current becomes more than 100% effective (K is 8.6 $mm^3\ ma^{-1}\ min^{-1}$ instead of 6.97– the hydrogen value of the current). Conversely the falling off of noble metal particles from the Zr surface causes the potential to become more negative and causes an increase in rate of dissolution (Fig. 2, D). The reasons for passivation by the anodic current are not yet known. However, it was observed that the initially dark surface (hydride film) of the active metal turned shiny upon passivation (e.g., when noble metal particles were deposited on Zr). Thus, the anodic current prevents hydride film formation by reducing the formation of hydrogen at the anode and apparently promotes the formation of a new film of unknown composition (oxide?). The effect observed by Stern on Ti (16) may be explained similarly. Formation of such passivating layers would reduce the rate of diffusion of molecular HF to the active surface and would account for a higher activation energy, as observed by Vander Wall and Whitener (17), while dissolving Zr in HF-HNO_3 mixtures, rather than in pure HF alone (11).

If now an anodic current passivates the surface of dissolving Zr (and Ti) (2), the fast dissolution rate of Zr in HF (with the anodic current off) can be explained by a chemical reaction of Zr metal with HF, outside the action of local currents, by collision of HF molecules with Zr atoms on the surface of the metal. An anodic current which makes the potential of the metal much more noble then acts as mentioned above. Our own rate measurements (11) as well as those of Smith and Hill (18) and of Vander Wall and Whitener (17) also suggest in the main a chemical action of HF. Some attempts have been made to explain the mechanism and rates of such action by the velocity of dissolution of corrosion products formed on the surface of the metal in the acid; e.g., an attempt was made to show that the dissolution of Fe in HCl is controlled by the rate of hydrolysis of $FeCl_3$ formed on the surface of the metal, or the rate of Al dissolution by the velocity

of dissolution of $Al(OH)_3$ in the acid (19). However, our experimental and theoretical attempts to explain similarly the process of dissolution of Zr in HF with ZrO_2 as an intermediate product failed.

Acknowledgment

The authors are grateful to the Atomic Energy Commission for its support of this investigation (AT-11-1-73 Project 5).

Manuscript received July 6, 1959.

Any discussion of this paper will appear in a Discussion Section to be published in the December 1960 JOURNAL.

REFERENCES

1. M. E. Straumanis and Y. N. Wang, *This Journal*, **102**, 304 (1955).
2. M. E. Straumanis and P. C. Chen, *ibid.*, **98**, 351 (1951).
3. M. E. Straumanis and P. C. Chen, *Corrosion*, **7**, 229, Fig. 13A and 13B (1951).
4. M. E. Straumanis and J. T. Ballass, *Z. anorg. Chem.*, **278**, 36 (1955).
5. M. E. Straumanis, W. J. James, and A. S. Neiman, *Corrosion*, **15**, 286t (1959).
6. M. E. Straumanis, C. S. Lin, and W. J. James, AEC AT (11-1)-73, Project 5, (1959).
7. M. A. Streicher, *J. (and Trans.) Electrochem. Soc.*, **96**, 170 (1949).
8. A. Thiel and J. Eckell, *Z. Elektrochem.*, **33**, 370 (1927); M. E. Straumanis, *Z. physik. Chem.*, **A148**, 349, 356 (1930).
9. M. E. Straumanis and Y. N. Wang, *This Journal*, **102**, 382 (1955).
10. W. J. James and M. E. Straumanis, *ibid.*, **106**, 631 (1959).
11. W. J. James, W. G. Custead, and M. E. Straumanis, AEC AT (11-1)-73, Project 5, (1959); *J. Phys. Chem.*, **64**, 286 (1960).
12. N. Hackerman and O. B. Cecil, *This Journal*, **101**, 419 (1954).
13. M. Maraghini, G. B. Adams, and P. van Ryssel-berghe, *ibid.*, **101**, 400 (1954); **102**, 502 (1955).
14. H. A. Johansen, G. B. Adams, and P. van Ryssel-berghe, *ibid.*, **104**, 339 (1957).
15. Literature see ref. (13) and (14).
16. M. Stern, *Chem. Eng. News*, April 13, p. 26 (1959); M. Stern and H. Wissenberg, *This Journal*, **106**, 759, 755 (1959).
17. E. M. Vander Wall and E. M. Whitener, *Ind. Eng. Chem.*, **51**, 51 (1959).
18. T. Smith and G. R. Hill, *This Journal*, **105**, 117 (1958).
19. See, e.g., T. G. O. Berg. *J. Chim. Phys.*, **51**, 141 (1954); *Z. anorg. u. allgem. Chem.*, **273**, 96, 101 (1953).

Oxidation of Zirconium and Zirconium Alloys

H. A. Porte, J. G. Schnizlein, R. C. Vogel, and D. F. Fischer

Chemical Engineering Division, Argonne National Laboratory, Lemont, Illinois

ABSTRACT

The rate of oxidation of zirconium followed a cubic rate law in the temperature range 400°-900°C at oxygen pressures of 50, 200, and 800 mm. At 200 mm the activation energy was calculated to be 42.7 ± 0.7 kcal/mole.

The oxidation of zirconium binary alloys containing 1, 2, and 4 atom % of aluminum, beryllium, carbon, chromium, cobalt, copper, hafnium, iron, lead, molybdenum, nickel, niobium, platinum, silicon, tantalum, tin, titanium, tungsten, uranium, and vanadium was studied at 700°C and 200 mm oxygen. For those additives which are soluble in zirconium the initial oxidation rates are explained by a valency effect; the breakaway phenomenon is explained in terms of a 15% deviation of the ionic radius from that of zirconium. X-ray and electron diffraction studies indicate that for some alloys the breakaway coincides with a polymorphic transformation in the zirconium dioxide film.

The reaction of zirconium with oxygen at high temperatures has been studied by several investigators (1-8). A comparison of the results shows discrepancies concerning which rate law, cubic or parabolic, best describes the oxidation kinetics. For example, Gulbransen and Andrew (1) studied the reaction on foil specimens between 200° and 425°C and reported that the parabolic rate law fit their data. But Belle and Mallett (2) showed by replotting the same data in a different fashion that the cubic rate law was obeyed, implying that the interpretation of data can be somewhat arbitrary in some cases.

In another study (3) Gulbransen and Andrew found that between 400° and 600°C the method of surface preparation influenced the reaction kinetics. Mechanically polished foils obeyed the cubic rate law and reacted faster than chemically polished foils which obeyed the parabolic rate law. A later study by Charles, Barnartt, and Gulbransen (8) on the prolonged (up to 500 hr) oxidation of zirconium foils at 350° and 450°C confirmed the cubic rate law for mechanically polished specimens.

There is some reason to suspect that the size and shape of samples may influence the reaction kinetics. Belle and Mallett (2) studied the oxidation reaction on rod specimens between 575° and 950°C and found that the cubic rate law fit the data. On foil specimens in approximately the same temperature range, Cubicciotti (4), Fassell (5), and Garibotti, Green, and Baldwin (6) observed the parabolic rate law.

There is even some evidence that the particular rate law which is followed depends on the temperature range. In a recent study by Kofstad (7), zirconium was oxidized under conditions of linearly increasing temperature. It was shown that between 650° and 950°C the cubic rate law was obeyed and

between 950° and 1100°C the parabolic rate law fit the data.

Some investigators (1, 4, 5) have studied the effect of pressure. The concensus was that pressure has little or no effect on the reaction of zirconium with oxygen.

The reported work on the reaction of zirconium alloys with oxygen has been confined previously to zirconium-tin alloys for which important uses have been found in the field of nuclear reactor engineering. Mallett and Albrecht (9) have studied the oxidation of 1.5 and 2.5 weight % tin alloys at high temperatures. Gulbransen and Andrew (10) studied the reaction of Zircaloy-2 and -3a with oxygen. In both investigations tin was found to increase the rate of oxidation.

Nitrogen also reacts with zirconium, but at a much slower rate than has been found for the reaction with oxygen. Several studies (1, 6, 11-13) have been made, and most investigators agree that the parabolic rate law is obeyed. The product of the reaction at all temperatures has been identified as golden-yellow zirconium nitride. There is some evidence (1) that the presence of small traces of oxygen in the nitrogen noticeably accelerates the rate of the reaction.

Some work has also been done on the reaction of zirconium (11, 14, 15) and zirconium alloys (14, 16-18) with air. In general, the reaction rate is higher in air than in either nitrogen or oxygen alone. Both zirconium dioxide and zirconium nitride have been identified as products of the air reaction. The data on alloy oxidation indicate that in most cases additives to the metal do not improve the resistance of zirconium to oxidation in air.

The purpose of this study was to investigate the fundamental processes involved in the oxidation mechanism. The experimental approach was as follows. First, the influence of such variables as surface preparation and sample form was determined. Next, temperature and pressure dependence studies covering the temperature range 400°-900°C at three pressures, 50, 200, and 800 mm, were made. However, the major effort was devoted to studying the kinetics of the reaction of numerous zirconium alloys with oxygen at 700°C. Simultaneously, an investigation was made of the structure of the oxide films produced.

Experimental

Method.—The reaction of zirconium and zirconium alloys with oxygen was measured by a volumetric method. Essentially, the apparatus consisted of a reaction chamber which was connected through stopcocks to a pressure regulator, a gas buret, and a vacuum system. With the exception of the reaction tube, which was made of quartz, the apparatus was made entirely of Pyrex. The system was evacuated by a two-stage glass mercury-diffusion pump backed by a mechanical pump.

The reaction tube, which was supported in a vertically mounted resistance furnace, consisted of two parts which were joined by a means of a greased ball joint (below the furnace and cooled by a jet of air). Sealed to the lower section was an evacuated inner tube which extended well into the furnace hot zone and filled most of the cross-sectional area of the reactor, thus minimizing the volume of gas exposed to the temperature gradient at the lower end of the furnace. The metal sample rested on top of a long thermocouple well which passed through the center of the inner tube of the reactor.

The reactor was joined by a greased, ground glass joint to a 2-mm capillary line leading to the pressure regulator and the gas buret. The water jacketed gas buret was connected with a flexible tube to a similar buret which served as a mercury reservoir. As the sample consumed oxygen, the pressure in the reactor decreased slightly, causing mercury in the pressure regulator to make contact with a sealed-in tungsten wire. A zero current relay closed the power circuit to a motorized rod runner which raised the mercury reservoir. Mercury flowed into the gas buret, increased the pressure in the system, and the electrical contact in the pressure regulator was opened.

Coupled with the rod runner was a precision helically wound potentiometer (Helipot) which translated the position of the reservoir into an electrical potential. Changes of this potential, recorded on a strip chart potentiometer-recorder, were proportional to the movement of the reservoir and, thus, were proportional to the volume of oxygen consumed by the sample. By application of the gas laws and the measured sample area the consumption could be expressed in micrograms of oxygen per square centimeter of surface. After calibration, sensitivities from 0.05 to 12 $\mu g/cm^2$ were determined, depending on oxygen pressure and the choice of buret diameter.

A hinged-type Hevi-duty combustion tube furnace was used for runs at 700°C and below while a platinum-wound Marshall furnace was used for runs above 700°C. The furnace temperature was controlled to ±3°C by a proportional controller operated by the output from a thermocouple located at sample level outside, but near the reactor.

Before the start of the run the specimen and reaction tube were evacuated at room temperature for 16 hr at pressures of less than 10^{-5} mm to minimize the reaction of zirconium with gases present in the vacuum system during the heat-up period. After establishing thermal equilibrium at the desired temperature, the run was started by closing off the high vacuum line and admitting oxygen to the reaction chamber.

Unless otherwise specifically indicated, all runs were made on specimens which were machined parallelepipeds, 1 x 1½ x 2 cm. Freshly polished specimens were used for each run.

X-ray diffraction investigations of the oxide films were carried out by means of a Norelco X-ray diffraction powder camera (114.59 mm diameter). For electron diffraction investigations, an RCA electron diffraction unit Model EMU-2 was used.

Materials.—Table I shows the principal impurities in the arc-melted Grade I crystal bar zirconium used in the oxidation studies on pure zirconium.

To study the effect of impurities on the oxidation properties of zirconium a series of binary alloys with

Table I. Analysis of zirconium. Chemical analyses for C, H, N, O; all other elements determined by spectrograph analyses

Element	Zirconium used in oxidation studies, amount, ppm	Zirconium used as base metal for alloys, amount, ppm
Ag	<1	1
Al	10	<10
B	<0.1	0.5
C	79	19
Cr	1	5
Cu	5	100
Fe	800	80
H	—	0.6
Hf	<1000	<500
Mg	<1	15
Mn	1	<1
N	23	11
Ni	100	<50
O	185	77
Pb	4	15
Si	50	50

additives at three nominal concentration levels, 1, 2, and 4 atom %, was obtained.[1] The actual analyzed alloy compositions are given in Table IV. Arc-melted Grade I crystal bar zirconium having the analysis also given in Table I was used in the preparation of these alloys.

The oxygen used in these experiments was taken directly from the tank without further purification. Mass spectrographic and dew point analyses showed the following typical impurities (in volume per cent): argon 0.1; carbon dioxide 0.06; nitrogen 0.2; and water 0.005.

Effect of surface preparation.—To determine whether massive parallelepiped samples would show an effect similar to that reported by Gulbransen and Andrew (3) on foils a study was made in the range 400°-700°C. Table II presents a summary of the data. At least two runs were performed for each method of polishing at every temperature and average results are listed.

Mechanically polished specimens reacted somewhat faster at 400° and 500°C than chemically polished specimens, but at 600° and 700°C there was no significant difference in reaction rates. This is essentially the same conclusion reached by Gulbransen and Andrew.

The cubic rate law best expressed the data from all methods of polishing, although in the range 400°-600°C the log-log slopes obtained from chemically polished samples were slightly higher than those obtained from mechanically polished samples. At 700°C the log-log slopes were insensitive to sample pretreatment. Thus, the rate law obeyed by parallelepiped samples was independent of surface preparation.

The reproducibility was good for all methods of polishing. Therefore, since the 600-grit mechanical polish was found to be the quickest and simplest, it was used in all of the pure zirconium and alloy studies.

Effect of sample shape.—In going from massive metal to foil the surface area per unit weight is increased. At the same time several other factors which may possibly influence the rate are affected. Metallurgical condition of the metal, i.e., grain size, crystal orientation, strains, etc., are changed. Also, certain impurities may be introduced during the rolling operations. It would be necessary to separate and study each of these variables to investigate thoroughly the effect of foil samples on reaction rate. Such a study was beyond the scope of this investigation. However, two runs were made on 0.25-mm (10-mil) foils which had been cold rolled from sponge zirconium. The foil samples were polished through 600 grit and run at 700°C and 200 mm oxygen pressure. The slopes of the log-log plots were 0.35 in both cases, in good agreement with the parallelepiped samples. The cubic rate constants were found to be 2.3 x 10^7 and 2.8 x 10^7 $(\mu g/cm^2)^3$/min, somewhat larger than values obtained from parallelepiped samples. The more rapid reaction on foil specimens may be explained in part by a higher heat of reaction caused by the increased surface area to mass ratio. Examination of the product immediately after one of the foil runs revealed an adherent black oxide film similar to those formed on the parallelepiped samples.

Effect of temperature.—Oxidation rates were measured at various temperatures in the range 400°-900°C at an oxygen pressure of 200 mm. Plots of the log of the weight gain vs. the log of time for typical runs at these temperatures are given in Fig. 1. The straight lines indicate agreement with the general rate expression $W^n = kt$. The values of n can readily be obtained since the slope of the line on this type of plot is $1/n$.

From the values of $1/n$ listed in Table III it is seen that the reaction rate is best expressed by the cubic rate law, $W^3 = kt$. The value of $1/n$ increased slightly from 400° to 800°C and then dropped a

Table II. Effect of surface preparation on the reaction of zirconium with oxygen (Oxygen pressure, 200 mm)

Temp, °C	Surface preparation	Slope of log-log plot, $1/n$	Cubic rate constant, k, $(\mu g/cm^2)^3$/min
400	Mechanical polish—600 grit[a]	0.29±0.00	(11±5.2) × 10^2
400	Chemical polish[b]	0.36±0.01	(5.9±2.0) × 10^2
500	Mechanical polish—600 grit	0.31±0.01	(3.5±0.1) × 10^4
500	Chemical polish	0.33±0.01	(2.1±0.3) × 10^4
600	Mechanical polish—600 grit	0.33±0.01	(1.2±0.4) × 10^6
600	Chemical polish	0.37±0.01	(1.1±0.3) × 10^6
700	Mechanical polish—600 grit	0.34±0.02	(1.6±0.2) × 10^7
700	Mechanical polish—0.5μ[c]	0.36±0.01	(1.5±0.1) × 10^7
700	Attack polish[d]	0.36±0.02	(1.3±0.1) × 10^7
700	Chemical polish	0.35±0.01	(1.5±0.2) × 10^7

[a] Specimens ground down with successively finer grades of silicon carbide paper to 600-grit paper. Water used as lubricant.
[b] Composition of chemical polish solution: 45 parts H_2O, 45 parts HNO_3 (conc), and 10 parts HF (48%).
[c] Extension of the 600-grit polish with Linde A abrasive on Miracloth lap.
[d] Mechanical polish through 0.5μ in which 1 ml HF (48%) and 0.5 ml HNO_3 (conc) are added to 98.5 ml of Linde A abrasive.

[1] Zirconium binary alloys were prepared by Oregon Metallurgical Corporation, Albany, Oregon.

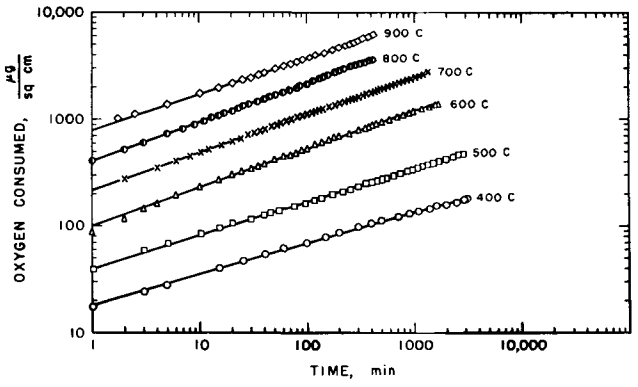

Fig. 1. Effect of temperature on the reaction of zirconium with oxygen.

bit at 900°C. There is no apparent reason for the increasing trend in the value of $1/n$; however, the drop from 800° to 900°C may be attributed to the transformation from α to β zirconium which occurs at 862°C. The cubic rate law constants listed in Table III were obtained from plots of W vs. $t^{1/3}$.

A plot was made of the log of the cubic rate constants vs. $1/T$ for the temperature range 400°-900°C. The equation of the best straight line through the points was determined by the method of least squares and the activation energy was calculated to be 42, 700 ± 700 cal/mole by the Arrhenius-type equation, $k = Ae^{-E/RT}$. The corresponding rate constant for the reaction in $(\mu g/cm^2)^3$/min was

$$k = (5.94 \times 10^{16})e^{-42,700/RT}$$

In comparison, Belle and Mallet (2) obtained an activation energy of 47.2 kcal/mole and Charles, Barnartt, and Gulbransen (8) calculated a value of 38 kcal/mole.

The length of the runs, as indicated in Table III, varied from a minimum of 400 min to several thousand minutes in some cases; however, the run length had no effect on either the log-log slopes or the cubic rate constants. No breakaway phenomena were observed in any of the runs, even at the higher temperatures. One run at 800°C was carried out for longer than 5600 min without giving any sign of a breakaway.

Table III. Cubic rate constants for the reaction of zirconium with oxygen

(Oxygen pressure, 200 mm)

Temp, °C	Length of run, min	Slope of log-log plot, $1/n$	Cubic rate constant, k, $(\mu g/cm^2)^3$/min
400	3235	0.29	1.6×10^8
400	4275	0.29	5.6×10^2
500	4238	0.30	3.5×10^4
500	2860	0.32	3.6×10^4
600	1660	0.33	1.6×10^6
600	4250	0.34	8.9×10^5
700	1415	0.29	1.5×10^7
700	1400	0.31	1.8×10^7
700	1400	0.33	1.5×10^7
700	1400	0.33	2.0×10^7
700	1323	0.35	1.7×10^7
700	400	0.36	1.6×10^7
700	1345	0.36	1.3×10^7
700	1408	0.36	1.4×10^7
800	5645	0.36	1.3×10^8
800	400	0.37	1.3×10^8
800	413	0.38	1.3×10^8
800	415	0.39	1.3×10^8
900	400	0.32	5.3×10^8
900	418	0.34	5.3×10^8

The reaction produced a shiny blue-black oxide at all temperatures. A few white specks were observed on the surface of the oxide at 900°C.

Because of the high solubility of oxygen in zirconium (29 atom %), the reaction is somewhat complicated. A sample which had been run at 900°C was mounted in Bakelite, polished, and then a photomicrograph was taken. The thickness of zirconium dioxide, as measured from the photomicrograph, was found to be 22 μ; the thickness calculated from the amount of oxygen consumed was 41 μ, based on the assumptions that (*a*) the ratio of the real to measured surface area was one and (*b*) the only product formed was zirconium dioxide having a density of 5.73 g/cc. Evidently, an appreciable solution of zirconium dioxide in zirconium takes place at 900°C.

Effect of pressure.—The effect of variation in pressure on the reaction rate kinetics was determined. Runs were made at oxygen pressures of 50, 200, and 800 mm in the temperature range from 400° to 900°C. The data showed that the oxidation rate was relatively insensitive to pressure. The values of the log-log slopes indicated the cubic rate law at all pressures. The cubic rate constants agreed very well at the different pressures, and no apparent trend could be seen at any temperature. These results confirm the work of other investigators who found no pressure effect.

Effect of additives to zirconium.—The study of the effect of small amounts of impurities on the oxidation kinetics of zirconium was carried out using a series of binary zirconium alloys. These were alloys of zirconium with aluminum, beryllium, carbon, chromium, cobalt, copper, hafnium, iron, lead, molybdenum, nickel, niobium, platinum, silicon, tantalum, tin, titanium, tungsten, uranium, and vanadium. Each binary system included three nominal compositions, 1, 2, and 4 atom %, except that the 4 atom % tungsten alloy was impossible to fabricate.

The experimental conditions used were 700°C and 200 mm of oxygen. The choice of a particular temperature and pressure was somewhat arbitrary, but was dictated by certain important considerations. It was desirable to work at some high temperature in the alpha zirconium region, so that the oxidation would take place at a conveniently measurable rate at reasonable pressures. This limited the temperature range from approximately 600°C to the alpha to beta transformation temperature, 862°C. Certain metals, e.g., cobalt, copper, chromium, iron, molybdenum, nickel, niobium, platinum, tantalum, titanium, tungsten, uranium, and vanadium, could be expected to lower the transformation temperature (19). Therefore, it was decided to work at 700°C, which was far enough below 862 to be sure that beta zirconium was not present in any of the alloys. Another factor in favor of choosing 700°C as the

Table IV. Oxidation of zirconium alloys
(700°C and 200 mm oxygen)

Alloy composition, atom %	Slope of log-log plot[a] $1/n$		Rate constant[b]	Break-away time, min	Break-away weight, $\mu g/cm^2$	Break-away rate, $\mu g/(cm^2)$ (min)	Length of run, min	Total weight gain, $\mu g/cm^2$	Color and character of oxide film
Pure Zr	0.33		1.6	No breakaway			1400	2845	Blue-gray; adherent
1.42 Al	0.36		14.0	25	1467	58.9	280	14100	Ivory with raised edges; adherent
2.15 Al	0.33		12.0	24	1401	49.3	280	13683	Ivory with raised edges; adherent
3.62 Al	0.29		8.0	7	948	84.2	198	16232	Black; adherent
0.90 Be	0.29		1.2	No breakaway			1400	2513	Blue (gold tinge); adherent
2.09 Be	0.34		1.3	No breakaway			1400	2542	Black (blue tinge); adherent
4.23 Be	0.30		1.1	No breakaway			1400	2400	Black with white raised edges; adherent
0.65 C	0.36		2.5	No breakaway			1400	3256	Silver-gold with white edges and spots; adherent
1.64 C	0.41	p	2.7	48	1225	15.3	600	7400	Gold with rough surface; flakes off
3.72 C	0.46	p	4.8	23	1076	25.4	600	17500	Gray cinder-like oxide; some flakes off
0.86 Co	0.34		1.6	No breakaway			1285	2725	Gray-black; adherent
2.49 Co	0.34		1.7	No breakaway			1400	2884	Gray; adherent
3.72 Co	0.33		2.2	No breakaway			1400	3118	Gray (gold tinge); adherent
0.77 Cr	0.33		1.7	No breakaway			1400	2850	Black; adherent
1.63 Cr	0.34		1.9	No breakaway			1400	2987	Blue-gray; adherent
3.61 Cr	0.33		1.7	No breakaway			1400	2923	Black; adherent
1.08 Cu	0.34		1.1	No breakaway			1400	2458	Black; adherent
1.84 Cu	0.33		0.90	No breakaway			1400	2347	Black; adherent
3.60 Cu	0.33		0.78	No breakaway			1400	2385	Black; adherent
1.09 Fe	0.34		3.0	No breakaway			1300	3400	Gold-gray; adherent
1.98 Fe	0.35		2.7	No breakaway			1400	3335	Blue-gray; adherent
3.95 Fe	0.33		2.4	No breakaway			1400	3200	Gray; adherent
1.03 Hf	0.34		1.4	No breakaway			1400	2673	Black with raised edges; adherent
2.22 Hf	0.34		1.4	No breakaway			1400	2648	Gray-black with raised edges; adherent
4.08 Hf	0.35		1.4	No breakaway			1400	2529	Black with raised edges; adherent
1.03 Mo	0.36		2.5	No breakaway			1400	3492	Black with raised edges and white spots; adherent
2.34 Mo	0.35		7.0	40	1368	13.1	850	10300	Silver-gray with raised edges; adherent
3.65 Mo	0.36		7.5	64	1248	11.9	850	10200	Silver-gray with raised edges; adherent
0.91 Ni	0.35		1.5	No breakaway			1400	2715	Black; adherent
2.48 Ni	0.34		1.1	No breakaway			1400	2484	Black; adherent
4.22 Ni	0.32		1.0	No breakaway			1400	2436	Gray (gold tinge); adherent
0.60 Nb	0.36		5.9	365	2680	5.0	875	5717	Black with raised edges; adherent
1.82 Nb	0.46	p	6.2	500	5625	7.7	875	8500	Silver with raised edges; adherent
3.82 Nb	0.35		6.7	49	1550	16.3	680	10519	Silver-black with raised edges; adherent
0.58 Pb	0.28		1.1	273	1465	9.7	890	5938	Black with raised edges; adherent
1.62 Pb	0.30		1.6	34	835	15.9	580	9123	Black with raised edges; adherent
4.00 Pb	0.28		0.85	7	460	9.7	895	11165	Silver-gray with raised edges; adherent
1.08 Pt	0.34		1.5	No breakaway			1400	2684	Black; adherent
2.04 Pt	0.32		0.91	630	1815	2.9	1400	3225	Black with blisters; adherent
4.22 Pt	0.31		0.81	655	1763	1.8	1400	2980	Black with raised edges; adherent
0.80 Si	0.40		3.4	No breakaway			1400	3396	Gray with white specks on faces; adherent
1.94 Si	0.43	p	2.2	115	1650	12.7	600	5921	Tan with rough surface; flakes off
3.60 Si	0.39		1.7	6	439	97.0	165	12046	Tan with rough surface; flakes off
0.96 Sn	0.28		0.92	235	1345	12.8	650	4450	Tan with black spots; adherent
1.68 Sn	0.32		1.1	111	1098	12.9	650	7100	Coral; adherent
3.60 Sn	0.31		2.2	20	521	292.0	117	13071	White; flakes off

Table IV. Oxidation of zirconium alloys (cont'd)

Alloy composition, atom %	Slope of log-log plot[a] 1/n	Rate constant[b]	Break-away time, min	Break-away weight, μg/cm²	Break-away rate, μg/(cm²) (min)	Length of run, min	Total weight gain, μg/cm²	Color and character of oxide film
1.04 Ta	0.60	p 39.5	No breakaway			500	13200	Blue-black with raised edges; adherent
1.78 Ta	0.66	p 30.5	No breakaway			500	11600	Black with raised edges; adherent
3.54 Ta	0.60	p 26.9	270	7830	26.1	500	13000	Silver-white with raised edges; adherent
1.08 Ti	0.37	69.7	370	6215	9.3	930	11134	Black with raised edges and blisters; adherent
2.12 Ti	0.39	251	385	9468	13.0	790	14770	Black with raised edges and blisters; adherent
4.16 Ti	0.43	p 90.8	275	15975	33.1	590	24917	Black (gold tinge) with raised edges; edges flake off; faces adherent
0.89 U	0.36	3.2	No breakaway			1400	3535	Black with raised edges; 2 faces gold flaky oxide
1.76 U	0.36	4.1	No breakaway			1400	3938	Black with raised yellow edges; adherent
3.52 U	0.35	3.5	530	2645	1.7	1400	4078	Black with raised yellow edges; adherent
1.01 V	0.35	4.5	530	2810	3.9	1285	5292	1 face black and 5 faces yellow and black; adherent
1.84 V	0.41	p 4.3	120	2363	6.8	1175	9195	Black with raised edges and yellow-green spots; adherent
3.88 V	0.42	p 29.0	No breakaway			615	14272	Dark yellow with raised edges; flakes off
0.68 W	0.35	1.9	No breakaway			1400	2980	Black; adherent
1.96 W	0.32	3.5	No breakaway			1400	3700	Black with yellow adherent oxide at flaws in metal; adherent

[a] The log-log slope applies only to the portion of the run before breakaway.
[b] Cubic rate law constants [10^7 (μg/cm²)³/min] unless preceded by p which signifies parabolic rate law constant [10^4 (μg/cm²)²/min]. Both apply only to the portion before breakaway.

temperature at which to make the study was that in a recent study (9) on the high-temperature oxidation of two zirconium-tin alloys it was reported that the minimum times for breakdown of the protective properties of the films occurred at 700°C.

The kinetic data for the oxidation of the alloys are presented in Table IV. In most cases duplicate 1400-min runs were made with each alloy composition and the results averaged.

A number of alloys oxidized similar to pure zirconium. Many others, however, exhibited the oxidation phenomenon usually referred to as "breakaway." In these cases the oxidation kinetics changed from an initially cubic or parabolic rate to a faster essentially linear rate of oxidation. When the data were plotted in the usual fashion, log oxygen consumed vs. log time, it was found that, after the initial straight line portion of the plot, an upward curvature took place which eventually leveled off into another straight line portion. The "breakaway time" and "breakaway weight" were defined as the time and oxygen consumed at the last point on the initial straight line portion of the oxidation curve. Within a given system the breakaway weights and breakaway times usually decreased with increasing additive concentration as illustrated in Fig. 2 for the tin alloys.

An examination of the results revealed that the alloys could be grouped conveniently according to four types of reaction behavior as indicated in Fig. 3.

Many of the alloys and pure zirconium (Group I, Fig. 3) oxidized according to the cubic rate law and did not exhibit breakaway phenomena. Slopes of log weight gain vs. log time plots were in the range 0.28 to 0.40. The cubic rate constants ranged from 0.78 x 10^7 to 3.5 x 10^7 (μg/cm²)³/min.

The 1 and 2 atom % tantalum and the 4 atom % vanadium alloys (Group II, Fig. 3) oxidized according to the parabolic rate law and did not exhibit

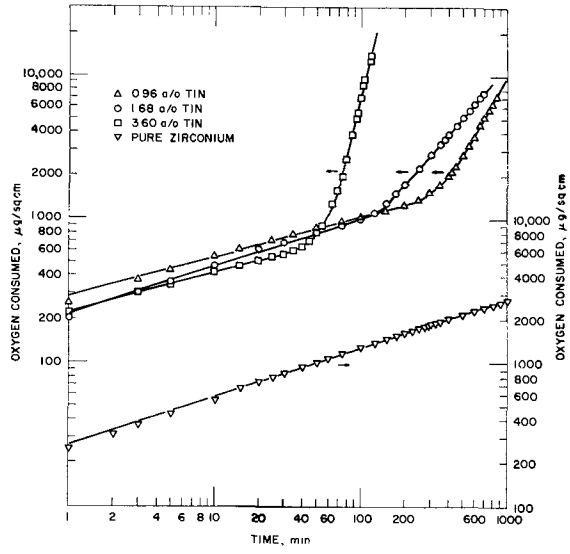

Fig. 2. Reaction of zirconium-tin alloys with oxygen at 700°C and 200 mm oxygen pressure.

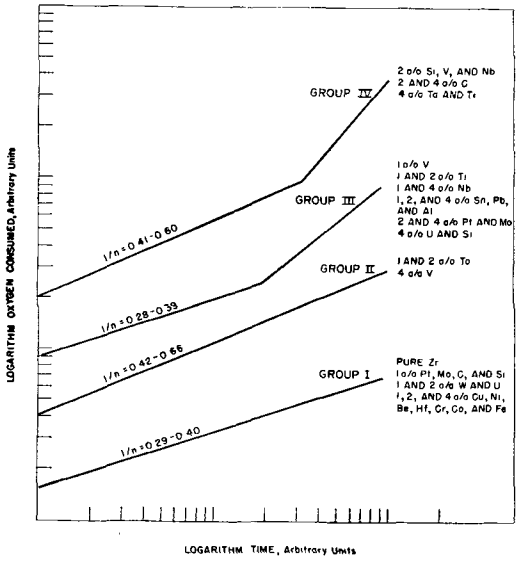

Fig. 3. Oxidation of various zirconium alloys at 700°C and 200 mm oxygen pressure, general oxidation characteristics.

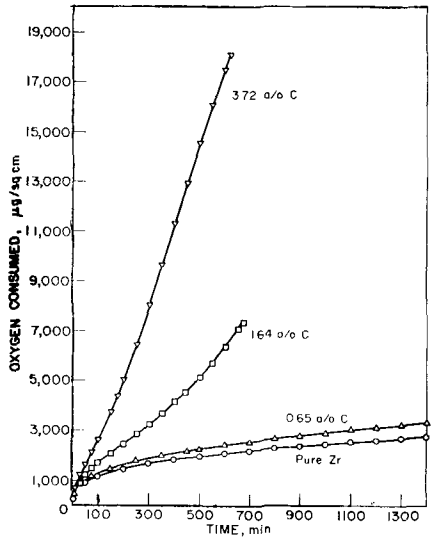

Fig. 5. Oxidation of zirconium-carbon alloys at 700°C in 200 mm oxygen.

breakaway phenomena. They had log-log slopes in the range 0.41-0.66. The parabolic rate constants were 39.5 x 10^4, 30.5 x 10^4, and 29.0 x 10^4 $(\mu g/cm^2)^2/min$, respectively.

Another large group of alloys (Group III, Fig. 3) oxidized initially according to the cubic rate law but later exhibited breakaway phenomena. The cubic rate constants ranged from 0.81 x 10^7 to 251 x 10^7 $(\mu g/cm^2)^3/min$. Breakaway times ranged from 6 to 655 min, and breakaway weights ranged from 439 to 9468 $\mu g/cm^2$. After the breakaways, faster linear rates, ranging from 1.7 to 292 $\mu g/cm^2/min$, were followed for the duration of the runs.

The last group of alloys (Group IV, Fig. 3) oxidized initially according to the parabolic rate law but later exhibited breakaway phenomena. The parabolic rate constants ranged from 2.2 x 10^4 to 90.8 x 10^4 $(\mu g/cm^2)^2/min$. Breakaway times ranged from 23 to 500 min, and breakaway weights varied from 1076 to 15,975 $\mu g/cm^2$. The faster linear rates after breakaways ranged from 6.8 to 33.1 $\mu g/cm^2/min$.

Of the 20 binary alloy systems investigated only the copper, nickel, beryllium, and hafnium alloys showed any increased resistance to oxidation as compared with pure zirconium. The oxidation behavior of the copper alloys is illustrated in Fig. 4.

In some alloy systems, as typified by the carbon system (Fig. 5), the lower concentration alloys oxidized at slow initial rates without a breakaway while the high concentration alloys oxidized at faster initial rates (sometimes even following a different rate law) and then exhibited breakaway.

Widely different types of breakaway phenomena were observed. For instance, in the tin system (Fig. 2) the breakaways were distinct and obvious, while in the titanium system (Fig. 6) the breakaways represent little more than a gradual increase of an already fast rate.

A description of the films formed during the oxidations has been included in Table IV. For the alloys where no breakaway occurred, the oxide films were

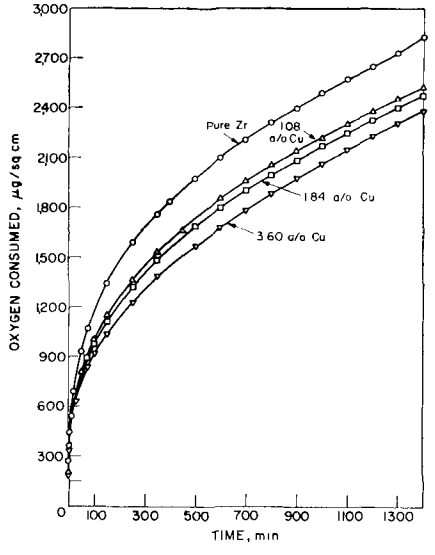

Fig. 4. Oxidation of zirconium-copper alloys at 700°C in 200 mm oxygen.

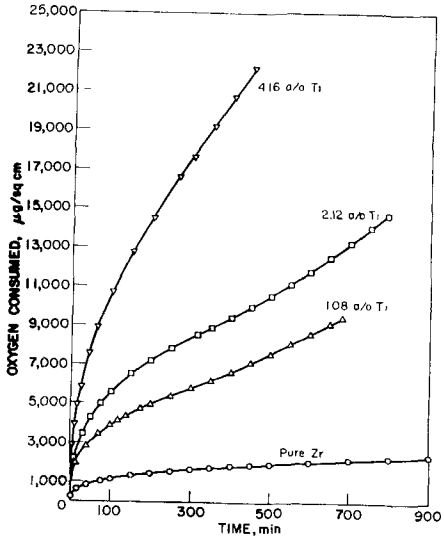

Fig. 6. Oxidation of zirconium-titanium alloys at 700°C in 200 mm oxygen.

usually black or gray and very adherent. In contrast, the films observed after the breakaway occurred still may have been adherent but were generally light-colored and cracked or porous.

Discussion

Mechanisms.—Several studies have been made to determine the mechanism of formation of the oxide film on zirconium. By employing inert markers it has been observed (9, 21) that the oxidation proceeds by oxygen (anion) migration through the oxide film toward the metal-metal oxide boundary. In another study (22) it was reported that anodic oxidation of zirconium at room temperature under low electric fields also proceeds by anion migration through the zirconium dioxide.

Consideration of the size of oxygen ions shows that they are too large to occupy interstitial positions in the zirconium oxide lattice. Therefore, it may be concluded, at least in thin films without cracks, that anion diffusion takes place by lattice defects or holes.

Measurements of thermoelectric power[2] on films of pure zirconium and zirconium-tin alloys gave negative values (9). Thus, it may further be concluded that these films were anion deficit semiconductors (n-type).

A few attempts have been made to provide a theoretical basis for the cubic rate equation. Mott (23, 24) derived a cubic rate equation based on the premise that diffusion of cation vacancies is rate controlling, where the number of vacancies is proportional to the number of negative ions per unit surface area and to a linear field set up by the ions. Engell, Hauffe, and Ilschner (25) derived a similar equation based on migration of positive holes and diffusion of lattice vacancies. Both of these derivations were based on p-type oxide films. A different approach has been taken by Uhlig (26) who recently derived a cubic rate equation based on electron flow from the metal as the controlling step in the oxidation process. This equation would be applicable for films of thickness up to several thousand angstrom units in which case the space charge in the oxide is important.

An attempt to explain the cubic oxidation of titanium has been made by Kofstad and Hauffe (27). They suggested that, in view of the high solubility of oxygen in titanium, the cubic rate law could be interpreted in terms of diffusion of oxygen through the outer layer of oxygen-enriched titanium. Since zirconium also has a high oxygen solubility, it is probable that the cubic oxidations of zirconium and titanium follow a similar mechanism.

Thus, it is not altogether surprising that the oxidation of zirconium, which ostensibly proceeds by inward oxygen diffusion, does not obey the simple parabolic rate law because the oxidation kinetics are complicated by oxygen dissolution in the outer layer of zirconium metal.

Correlation of isothermal rate data with Wagner-Hauffe theory.—According to the Wagner-Hauffe (28) semiconductor approach to alloy oxidation, foreign ions of lower valency than zirconium should increase the rate of oxidation, since they create more lattice defects. Conversely, ions of valency higher than zirconium should reduce the concentration of oxygen ion defects and thus decrease the oxidation rate. Although this theory was derived for oxidation obeying the parabolic rate law, it is not necessarily limited to this, since it has been found to apply to the case of zinc, which followed a logarithmic rate law (29).

A condition which must be met for the Wagner-Hauffe theory to apply is that the metal which is added to zirconium must share in the film formation but must not give rise to the formation of a new phase. Examination of the oxide films formed on several alloys was attempted by x-ray and electron diffraction, but because the alloys were so dilute it was impossible to determine whether or not a new phase was formed since neither additive metal oxides nor unoxidized additive metals could be detected. Thus, it is necessary to predict the composition of the films from available solubility data.

Since solubility equilibrium does not have an opportunity to be established in the oxide phase in experiments with the conditions of this study, it is believed that solubility data for the oxide systems are not germane. A more appropriate way of predicting the composition of the oxide film is in terms of the solubility of added metal in zirconium before oxidation. Thus, if the added metal is in true solution in the metallic state, it is assumed that segregation into two distinct oxide phases will not occur on oxidation, even if the oxide of the added metal is insoluble in zirconium dioxide. This statement should be true for reasonably dilute alloys and for temperatures sufficiently low that the mobilities of the metal ions in the oxide phase are low. For the problem under immediate consideration both of these conditions are true.

In the case of a metal insoluble in zirconium, the alloy probably consists of agglomerates of the second metal randomly situated throughout the zirconium. Then, when oxidation occurs, these islands of additive metal produce additive metal oxide which remains as a separate oxide phase.

In Table V data are presented for the alloy systems which were studied in this program and which are in the category of the additive metal being reasonably soluble (greater than 1 atom %). The Wagner-Hauffe theory should be applicable to these systems. Only for the case of lead does the prediction of the theory disagree with the experimental data. Lead is an exceptional additive in that its Goldschmidt ionic radius is 52% greater than that of zirconium. All of the other additives considered in this table have ionic radii less than that of zirconium. The oxide of lead most likely formed, PbO, is also thermodynamically the least stable additive oxide of the series by many kilocalories. Therefore, for these two reasons lead can be considered unique. As predicted by theory, none of the additives which were soluble in zirconium increased the oxidation

[2] To determine the type of conduction (electrical) in a semiconductor it is necessary to make measurements of thermoelectric power. If the current is carried exclusively by electrons then the thermoelectric power will be negative, whereas the thermoelectric power must be positive if the current is carried by the positive holes.

Table V. Prediction of initial oxidation behavior and breakaway phenomena of some zirconium alloys

Initial oxidation rate predicted to increase if oxidation number of additive is less than 4. Breakaway predicted to occur if ionic radius of additive differs from Zr^{4+} by 15% or more.
Consideration restricted to zirconium alloys whose additive solubility in alpha zirconium is greater than 1 atom % (a/o).

Alloy additive	Solubility in Zr at 700°C,[a] a/o	Most likely oxidation No. in oxide[b]	% Difference of additive ionic radius from Zr^{4+} radius[c]	Observed breakaway phenomena[d] and ratio[e] of initial rate constants 1 a/o[f]	2 a/o[f]	4 a/o[f]
Al	1.6	3	—34	8.8 B	7.5 B	5.0 B
Hf	Miscible	4	—3.5	0.88	0.88	0.88
Nb	3	2	—21	3.7 B	P B	4.3 B
Pb	3	2	+52	0.69B	1.0 B	0.50B
Sn	2	4	—15	0.58B	0.69B	0.75B
Ta	5	2[g]	—22	P	P	P B
Ti	Miscible	2	—21	4.4 B	157 B	P B

[a] From data compiled by G. L. Miller, "*Zirconium*," Academic Press. Inc., New York (1957), Chap. 13.
[b] Predicted from free energy of formation at 973°K/g atom of oxygen from data compiled by A. Glassner, ANL-5750 (1957).
[c] Goldschmidt ionic radii used. Ionic radius of zirconium as 0.87A.
[d] Breakaway phenomenon indicated by letter "B".
[e] Ratio of cubic rate constant of alloy to that for pure zirconium at 700°C; rate considered to be increased if ratio greater than 1.5. Symbol "P" indicates oxidation followed parabolic rate law in which case the oxygen consumed per unit time was greater than that for pure zirconium.
[f] Nominal concentrations. For exact concentrations see Table IV.
[g] Experimentally demonstrated that TaO formed when Ta reacts with ZrO_2 at 1700°C [W. A. Chupka, J. Berkowitz, and M. G. Ingram, *J. Phys. Chem.*, **26**, 207 (1957)].

resistance because none had oxidation numbers greater than four.

The agreement of experimental results with predicted results is actually better than indicated by six metals out of seven. The phase diagrams in the literature indicate that beryllium, carbon, chromium, cobalt, copper, iron, molybdenum, nickel, platinum, silicon, tungsten, uranium, and vanadium are relatively insoluble in zirconium at 700°C. These additives, therefore, should not follow the predictions of the valence effect of Wagner-Hauffe theory. In the 13 cases cited, 11 do not follow the prediction and only 2 (vanadium and iron) follow the prediction. However, the oxide of vanadium, V_2O_5, has a low melting point (675°C) and thus is not typical. The other additive (iron) shows a slightly increased rate of oxidation which follows the prediction despite the very low solubility in zirconium. It is felt that no single theory is adequate to explain the oxidation rate effects of additives which are not soluble in zirconium, for which the Wagner-Hauffe theory does not apply . In these cases it is necessary to consider the properties of the individual oxides concerned such as preferential oxidation relative to zirconium, protective nature of the oxides, diffusion rates of ions in the oxides, and electrical conductivities of the oxides.

Breakaway phenomenon and ionic radius.—The breakaway phenomenon is a general characteristic of high-temperature zirconium corrosion and oxidation. It has been observed to occur in high-temperature water (20), in air (6, 14, 15, 30) and in oxygen (6, 9, 10). The interpretation given to the breakaway has been that, since the volume ratio of zirconium dioxide to zirconium is 1.5, the oxide grows under compressive strain and, at a certain film thickness, cracks to release the compression, thus leading to the breakaway. According to the assumed model, when zirconium alloys containing soluble additives are oxidized the film produced consists of additive metal dispersed in zirconium dioxide. If the ionic radius of the additive ion is sufficiently different from the ionic radius of zirconium, it is reasonable to expect that the lattice of zirconium dioxide will become distorted and breakaway will occur at a lower film thickness than is the case with pure zirconium.

As an extension of this reasoning a general rule, which appears useful in predicting the occurrence of the breakaway phenomenon, was formulated. This rule is that a breakaway will occur when the Goldschmidt ionic radius of the soluble additive element differs by 15% or more from the ionic radius of zirconium.

Reference to Table V shows that all 7 soluble additives (aluminum, hafnium, lead, niobium, tantalum, tin, and titanium) follow the rule. Actually, 19 out of 21 alloy compositions obeyed the rule, the only exceptions being the lower concentration tantalum alloys.

For insoluble additives the oxide film consists of zirconium dioxide and separate agglomerates of additive metal oxide. In the low concentrations encountered in this study these additives should not have any effect on the breakaway. This was borne out experimentally since out of 38 alloys containing insoluble metals, 27 did not show breakaways during the period of observation. In the 11 cases where breakaway did occur the additive metal oxide may have interfered with the adherency of zirconium dioxide to zirconium, but there are probably several causes for this effect, and any relationship between breakaway and ionic radius of insoluble metals is undoubtedly coincidental.

Structure of zirconium dioxide film.—In one study (31) concerned with the growth of oxide films on zirconium in high-temperature water, it was reported that an initial film of tetragonal zirconium dioxide transformed to the monoclinic oxide after which the corrosion proceeded at an accelerated rate.

In a recent electron-diffraction and kinetic study (30) of the oxidation of zirconium and some of its alloys with aluminum, tin, and titanium in air it was proposed that the breakaway is associated with a phase transformation in the film of zirconium dioxide. According to the theory advanced, the initial film formed on zirconium is the cubic polymorph of zirconium dioxide. As the oxidation progresses the film transforms to the tetragonal and finally to the monoclinic (stable) form of zirconium dioxide. The breakaway, it was reported, coincides with the last transformation.

To test this hypothesis and to obtain a better understanding of the mechanism of oxide film growth on zirconium alloys, electron and x-ray diffraction analyses have been obtained on oxidized zirconium alloy samples.

The oxide structures observed on 16 different alloys after oxidation to selected extents are presented with the oxidation data in Table VI.

Of the 13 samples (pure zirconium and 12 alloys) examined after less oxidation than the breakaway

Table VI. Oxide phases on oxidized zirconium alloys (Oxidized at 700°C in 200 mm oxygen; evacuated cooled and examined)

Alloy, a/o	Breakaway weight,[a] $\mu g/cm^2$	Observed oxide phase[b] Before breakaway	After breakaway
Pure Zr	(None)	fcc	—
1.42 Al	1467	fcc	Monoclinic[c]
1.64 C	1225		Monoclinic[c]
3.72 C	1076 p	fcc	
3.60 Cu	(None)	fcc plus unknown	—
4.08 Hf	(None)	Monoclinic	—
1.82 Nb	5625 p	Unknown bcc plus unknown	
4.22 Pt	1763	fcc	fcc
3.60 Sn	521		Monoclinic[c]
1.94 Si	1650 p		Monoclinic[c]
1.78 Ta	(None) p	fcc plus unknown	—
3.54 Ta	7830		Monoclinic[c]
2.12 Ti	9468	fcc	fcc plus unknown
4.16 Ti	15975 p	fcc plus unknown	fcc plus unknown
3.52 U	2645	Unknown bcc	Monoclinic[c]
3.88 V	(None) p	Monoclinic	—
1.96 W	None	fcc	—

[a] Initial oxidation follows cubic rate law unless indicated as parabolic by letter p.
[b] Electron diffraction by glancing from oxidized parallelepiped surface; interpretation by H. Knott and M. Mueller, Metallurgy Division. It was not possible to distinguish the cubic from the tetragonal modification of ZrO_2.
[c] Determined by x-ray diffraction of powder removed from surface. Interpretation by D. S. Flikkema, Chemical Engineering Division.

weight, 9 showed the face-centered cubic structure (3 of which had another unknown phase), 2 showed an unknown body-centered cubic structure, and 2 showed the monoclinic structure.

Of the 9 alloys oxidized beyond breakaway, 3 showed the face-centered cubic structure (2 of which had another unknown phase), and 6 showed the monoclinic structure.

Some of the unidentified phases found may be binary or ternary compounds with the alloying element. To identify the unknown phases would involve an extended research program beyond the scope of this investigation.

Although a majority of the alloys showed a relationship between the oxidation kinetics and the change of structure of the oxide film, careful consideration of the data show enough exceptions to the predicted sequence of polymorphic transformations to make it clear that there is no rule which is applicable *a priori* to all zirconium alloy systems.

The predicted sequence of phase transformations in the zirconium dioxide film and the relationship to the oxidation kinetics as outlined above is probably an oversimplified explanation which may be applicable for pure zirconium and some zirconium alloys but cannot be extended to include all zirconium alloys.

In order to understand better the mechanism of oxide film growth on zirconium, more information concerning the nature of the film must be obtained. The most promising way of accomplishing this appears to be through further electron diffraction studies of oxide films.

Acknowledgment

The assistance in the laboratory of A. Porter and of student aides, V. Sidhu and P. Tonne, is gratefully acknowledged. The authors are indebted to V. H. Munnecke for assistance in procurement of the alloys, D. S. Flikkema for x-ray diffraction analyses, and H. Knott and M. Mueller for electron diffraction studies.

Manuscript received Sept. 8, 1959. Work on this paper was performed under Contract No. W-31-109-Eng-38, U. S. Atomic Energy Commission.

Any discussion of this paper will appear in a Discussion Section to be published in the December 1960 JOURNAL.

REFERENCES

1. E. A. Gulbransen and K. F. Andrew, *J. Metals*, **1**, 515 (1949).
2. J. Belle and M. W. Mallett, *This Journal*, **101**, 229 (1954).
3. E. A. Gulbransen and K. F. Andrew, *J. Metals*, **9**, 394 (1957).
4. D. Cubicciotti, *J. Am. Chem. Soc.*, **72**, 4138 (1950).
5. M. W. Fassell, NP-4246 (1952).
6. D. J. Garibotti, H. M. Green, and W. M. Baldwin, Jr., AECU-3013 (1955).
7. P. Kofstad, *Acta Chem. Scand.*, **12**, 701 (1958).
8. R. G. Charles, S. Barnartt, and E. A. Gulbransen, *Trans. Am. Inst. Mining Met. Engrs.*, **212**, 101 (1958).
9. M. W. Mallett and W. M. Albrecht, *This Journal*, **102**, 407 (1955).
10. E. A. Gulbransen and K. F. Andrew, *Trans. Am. Inst. Mining Met. Engrs.*, **212**, 281 (1958).
11. E. T. Hayes and A. H. Roberson, *J. (and Trans.) Electrochem. Soc.*, **96**, 142 (1949).
12. A. Dravnieks, *J. Am. Chem. Soc.*, **72**, 3568 (1950).
13. M. W. Mallett, J. Belle, and B. B. Cleland, *This Journal*, **101**, 1 (1954).
14. L. F. Kendall, R. B. Wheeler, and S. H. Bush, *Nucl. Sci. Eng.*, **3**, 171 (1958).
15. C. A. Phalnikar and W. M. Baldwin, Jr., *Proc. Am. Soc. Testing Materials*, **51**, 1038 (1951).
16. F. B. Litton and S. L. Ogburn, AF-TR-5943 (1959).
17. C. T. Anderson, E. T. Hayes, A. H. Roberson, and W. T. Kroll, BM-RI-4568 (1950).
18. J. A. Burka, C. S. Crouse, and R. E. Swift, AECU-3661 (1957).
19. ASM Symposium, "Zirconium and Zirconium Alloys," Cleveland (1953).
20. B. Lustman and F. Kerze, Jr., "Metallurgy of Zirconium," pp. 610, 625, McGraw-Hill Book Co., Inc., New York (1955).
21. J. Chirigos and D. E. Thomas, WAPD-53 (1952).
22. O. Flint and J. H. O. Varley, *Nature Lond.*, **179**, 145 (1957).
23. N. Mott, *Trans. Faraday Soc.*, **36**, 472 (1940).
24. N. Cabrera and N. F. Mott, *Rept. Prog. Phys.*, **12**, 162 (1949).
25. H. Engell, K. Hauffe, and B. Ilschner, *Z. Electrochem.*, **58**, 478 (1954).
26. H. H. Uhlig, *Acta Met.*, **4**, 541 (1956).
27. P. Kofstad and K. Hauffe, *Werkstoffe und Korrosion*, **7**, 642 (1956).
28. O. Kubaschewski and B. E. Hopkins, "Oxidation of Metals and Alloys," pp. 120-130, Butterworths Scientific Publications, London (1953).
29. W. H. J. Vernon, E. I. Akeroyd, and E. G. Stroud, *J. Inst. Met.*, **65**, 301 (1939).
30. I. I. Korobkov, D. V. Ignatov, A. I. Yevstyukhin, and V. S. Yemelyanov, A/Conf. 15/P/2054, Proceedings of the Second International Conference on Peaceful Uses of Atomic Energy, Geneva (1958).
31. C. M. Schwartz, D. A. Vaughan, and G. C. Cocks, BMI-793 (1952).

High-Field Conduction Currents in Liquid n-Hexane under Microsecond Pulse Conditions

P. Keith Watson and A. Harry Sharbaugh

Research Laboratory, General Electric Company, Schenectady, New York

ABSTRACT

A novel pulse technique has been developed for measuring conduction currents due to millisecond, microsecond, and submicrosecond pulses of voltage. Using this method, a study has been made of conduction currents in liquid n-hexane at fields from 0.1 to 1.4 Mv/cm and at gap spacings from 2.5 to 25 mils. No evidence for electron multiplication was obtained at fields below 1.25 mv/cm, but there are marginal indications of the beginning of an α-process above 1.3 Mv/cm.

At fields near breakdown extremely large values of current have been measured; the authors' calculations indicate that these currents originate at microscopic points on the cathode surface. Because of the large current density and the high local field, the energy input to the liquid at the tips of these asperities is possibly as large as 10^7 watts/cm^3. This could lead to local vaporization of the liquid to form a bubble even in times as short as a few microseconds. If a bubble is so formed, then breakdown of the liquid could readily proceed by subsequent growth of the bubble across the gap to form a spark channel.

Considerable progress has been made in the measurement of electric breakdown strength in the liquid phase through the use of rectangular pulse techniques (1-3), and such methods of measurement are now widely used. On the other hand, measurements of conduction currents in insulating liquids have continued to rely on d.c. (2, 4, 5), presumably because of the experimental difficulties inherent in making reliable measurements of currents under short pulse conditions.

With the advances that have taken place in electrometer design and in pulse techniques during the past few years, it has become possible to surmount these difficulties, and we have developed a method for measuring conduction currents at high fields due to millisecond, microsecond, and submicrosecond pulses of voltage.

In a series of preliminary experiments, a comparison was made between the d-c and pulse methods (6). The measurements were made under virtually identical chemical and physical conditions, the only differences being in the methods used for applying the voltage and for measuring the resulting conduction currents in the liquid.

The present paper describes the extension of the pulse measurements to the high-field region, stresses of the order of 1.5 Mv/cm having been attained in some of the experiments. Thus the current measurements have been extended to include field strengths which approach the highest breakdown fields reported for hexane.

Experimental Technique

Equipment.—The hexane used in the experiments was first purified, using previously described techniques (7). It was then passed through silica gel, refluxed over sodium, and distilled into an electrolyzer, in which it was subject to a field of 10 kv/cm for 24 hr to remove the last traces of polar impurities. Finally, it was allowed to pass into the test cell via an ultra-fine fritted glass filter (average pore size, 1 μ). From the test cell, the hexane could be returned to the still for recycling.

The test cell was an integral part of the purification system; it was made of glass, with optical windows to allow microscopic examination of the test gap. A number of electrode sizes were used, ranging from 3/16 to 1 in. diameter across the flat portions; these surfaces were flat to within 0.05 mils, and their edges were provided with Rogowski profiles. The electrode material was stainless steel. An electrical contact method was used for determining the gap zero, and a micrometer was used for setting the gap length. A capacitance test was developed for determining the degree of parallelism of the electrodes.

D-C measurements.—Our d-c measurements were carried out over a range of gap lengths from 2.5 to 25 mils and up to field strengths of 300 kv/cm. When voltage was applied to the liquid, there was a pronounced initial current decay, which lasted some minutes, until the current settled down to its steady-state value, which was often several orders of magnitude smaller than the initial value. These findings are in agreement with those of Whitehead (8), Nikuradse (9), and others, but little attention appears to have been paid to this disturbing phenomenon by recent workers (2, 4, 5).

This fall in current is probably due to the build up of polarization charges in the vicinity of the electrodes, thus resulting in a distortion of the field in the liquid as a whole. On the basis of these and other results there seems to be good evidence for

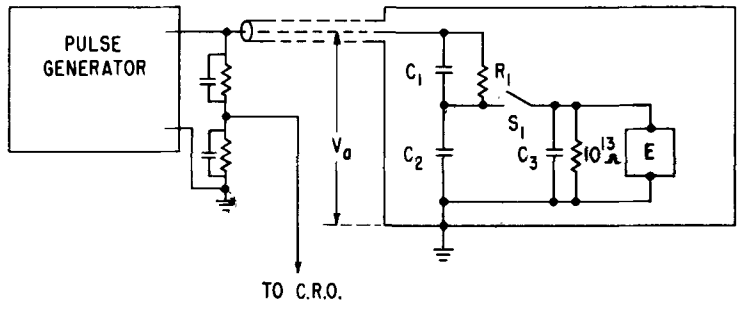

Fig. 1. Circuit used for pulse measurements of conduction currents. V_a is the applied voltage; C_1, capacitance of conduction cell; C_2, storage capacitor; C_3, input capacitance of the electrometer circuit; R_1, resistance of the liquid; S_1, switch; E, electrometer.

suspecting that d-c conduction current measurements in liquids are of an extremely complex nature and are unreliable as a guide to pre-breakdown phenomena.

Pulse measurements.—The pulse measurement technique which we have developed is to be described in detail elsewhere; briefly it is based on the fact that a voltage pulse, V_a, applied to a series circuit consisting of a resistance, R, and capacitance, C, leaves behind on the capacitor a charge proportional to $(V_a/R)\tau$. Here τ is the pulse duration, which must be short compared to the time constant CR.

In the present circuit, shown schematically in Fig. 1, a rectangular voltage pulse is applied to the series combination C_1R_1 and C_2, where C_1 is the capacitance of the conduction cell, R_1 is the resistance of the liquid, and C_2 is the capacitance of the high quality storage capacitor.

After the voltage pulse has passed, the charge remaining on C_2 is measured by closing the switch, S_1, and reading the voltage V_3 on the electrometer. The resistance R_1 is then given by,

$$R_1 = \frac{V_a C_2 \tau}{V_3(C_1 + C_2)(C_2 + C_3)}$$

The limit of sensitivity of the method is governed by background noise. A charge of 10^{-12} coulombs on C_2 can be measured with an accuracy of about 5%, and this error decreases with increasing charge magnitude. This charge sensitivity corresponds to a current of 1 μa for a pulse of 1 μsec duration; obviously, the current sensitivity increases linearly with pulse width. Moreover, by integrating the charge over a train of pulses, the sensitivity may be increased.

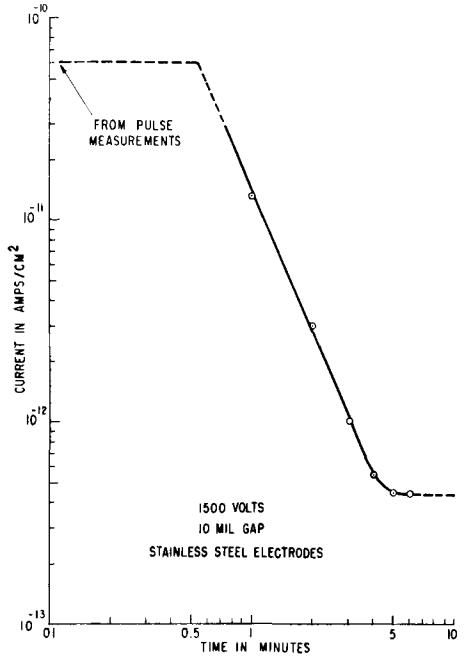

Fig. 2. Time dependence of typical d-c current measurements in n-hexane.

Experimental Results

Comparison between d-c and pulse measurements.—The results obtained using the pulse method are quite different from d-c results. The main differences are as follows: first, the absolute magnitudes of the currents obtained are orders of magnitude greater than for d.c.; and second, in the range 10 msec to 1 μsec the magnitudes of the pulse currents are independent of the duration of the applied field, whereas, in the d-c case, the currents decrease with time.

The d-c decay has been analyzed in the light of the pulse measurements, and a typical series of d-c measurements is shown in Fig. 2. These currents were measured at 1-min intervals during the first six minutes after the application of voltage to the liquid. It will be seen that the initial value of the d-c sequence is, in fact, of the same order as the corresponding pulse measurement, whereas the final d-c value is a factor of 10^{-2} smaller.

Pulse measurements at high fields.—We have used the techniques described above to make current measurements in hexane as a function of magnitude and duration of applied voltage, and also of gap width.

The results obtained fall naturally into two ranges of field strengths: the first covers the sub-breakdown range, from 100 v/mil (40 kv/cm) up to 1200 v/mil (500 kv/cm), and the second includes the range from 1500 v/mil up to fields in excess of 3700 v/mil (1.5 mv/cm). Breakdown of hexane can occur throughout the latter range, although the actual value of breakdown voltage depends on a number of other variables such as pulse width, gap width, and electrode surface.

Our results in the sub-breakdown range are plotted in Fig. 3, which shows the current density as a function of applied voltage for gap widths of 5 through 20 mils. These results were obtained using 10 msec pulses of voltage, but virtually identical results were obtained with pulse widths as short as 100 μsec. The dashed lines in the figure are curves of constant field strength. These are virtually horizontal throughout the range, that is, the currents

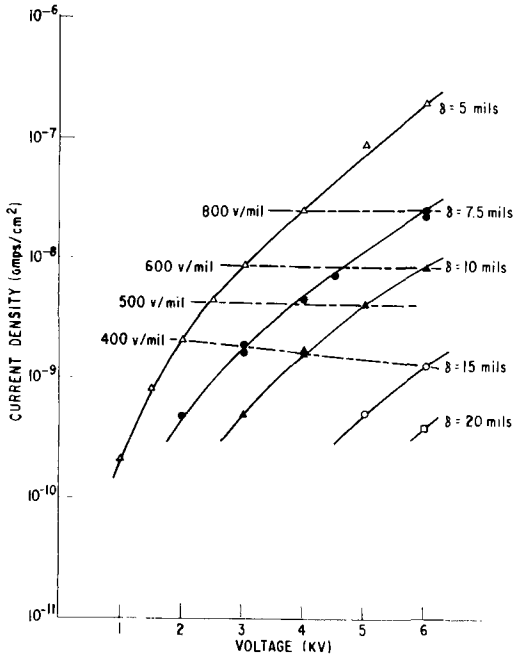

Fig. 3. Dependence of current density on voltage, n-hexane, stainless steel electrodes, 10 msec pulse width.

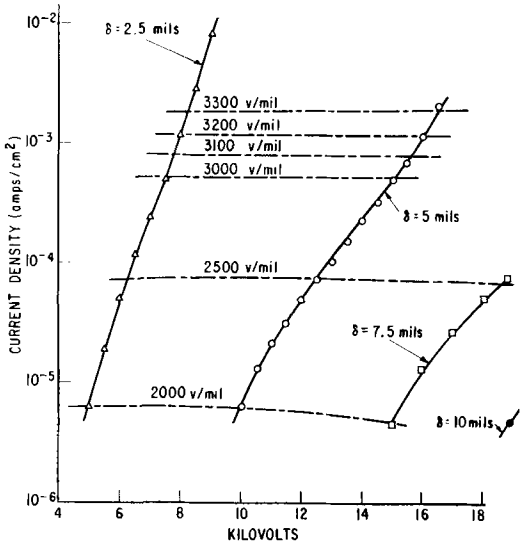

Fig. 4. Dependence of current density on voltage, n-hexane, stainless steel electrodes, 5, 3, 1.5 μsec pulse widths.

are essentially independent of gap width at all field strengths shown in the figure.

At field strengths of the order of 1200 v/mil (0.5 Mv/cm) breakdown occasionally occurred; after only one such breakdown, the current magnitude increased very markedly. This effect was attributed to decomposition products arising from breakdown in the liquid. These spuriously high currents continued to be obtained even after changing the sample, and in order to restore the former low value of conductivity, it was necessary to remove the electrodes and clean them. In order to make current measurements at higher values of field, it was necessary to use single pulses of voltage rather than trains of pulses. It was also necessary to resort to shorter pulse widths and so make use of the well-known increase of breakdown strength with decrease in pulse width.

Despite the use of short pulses, occasional breakdowns still occurred. Fortunately, at fields above about 1 Mv/cm, the electronic conduction currents are usually so much larger than the ionic currents that one can continue to use a sample, even after several breakdowns have taken place. After each breakdown, the sample conductivity was checked at a lower field in order to determine if any increase in current had occurred as a result of the breakdown. If a measurable increase was found, it was compensated for in the subsequent analysis.

The test then proceeded at a shorter pulse width until breakdown occurred again, at which point the pulse was shortened further. This procedure was followed, down to a pulse width of 0.5 μsec (the shortest pulse which the generator would deliver).

By means of this technique we have been able to make current measurements at fields as large as 1.4 Mv/cm; the results obtained are shown in Fig. 4.

Wherever possible, the measurements have been made at a number of gap spacings, and from this data we have plotted the constant field lines shown in Fig. 4.

As in the lower field region, we see that the constant field lines are essentially horizontal up to fields of 3100 v/mil (1.2 Mv/cm); this indicates that the measured currents are independent of gap width up to this field. At fields of 3200 and 3300 v/mil there may be evidence of a slight increase of current with gap width.

In concluding this description of the results we may summarize as follows: The currents are independent of pulse width, within the limits of experimental accuracy over the range from 10 msec to 1 μsec. The currents are proportional to electrode area and are independent of gap width up to fields of 3100 v/mil (1.2 Mv/cm).

Finally, it may be noted that the accuracy of the method of measurement is well indicated by the constant field lines; errors in the setting of voltage, gap width, and pulse width would lead to erratic constant field lines. However, as may be seen in Fig. 3 and 4, even a fourfold change in gap width does not appear to incur any appreciable deviation from a smooth curve.

Discussion of Results

Evidence for Electron Multiplication

One of the most controversial points in the interpretation of conduction and breakdown measurements in liquids concerns the presence (or absence) of an electron multiplication process in the liquid. Those who interpret behavior at high fields by means of a Townsend model are prone to favor the existence of an electron multiplication, or "α-process," and some have published d-c conduction data which are consistent with this model (2, 5, 9).

On the other hand, there are others who doubt the existence of an α-process in liquids and have d-c measurements to support their point of view (4, 10). The possibility of resolving this problem is regarded as one of the most important aspects of the present work.

The only satisfactory method for detecting and measuring a multiplication process involves the determination of the gap width dependence of conduction currents at constant field strength. In the presence of multiplication, currents will increase with gap width in accordance with the equation $I = I_0 \exp \alpha\delta$; that is, at constant field, the current should increase exponentially with gap width. I_0 is the current emitted at the cathode and will be field dependent. In the present work we have measured the current over a wide range of fields and at a limited number of gap widths in an attempt to determine whether or not such a multiplication process exists in liquid hexane.

The current obtained at fields up to 1 Mv/cm show no sign of increasing with gap width, indeed, at the lowest fields there is some evidence of a decrease of current with increasing gap, although this effect may not be real.

On the other hand, the currents at the very highest fields do show a slight increase with gap width, which might be indicative of an incipient α-process. We have therefore carried out a statistical analysis of the data at fields above 1 Mv/cm in order to determine whether this rise is significant.

The ratio of currents at gaps of 5 mil and 2.5 mil was taken as our statistic. The mean of these ratios at the eleven highest field strengths was 0.993, with a standard deviation of 0.075. Applying Bessel's correction to obtain the best estimate of the standard deviation, σ, of the parent population, we obtain $\sigma = 0.079$. Obviously, the mean ratio does not differ significantly from unity, so that there is no evidence for an α-process in the bulk of the data above 1 Mv/cm.

The ratios of the currents at the two highest fields were then examined: Their mean is 1.08, and the standard error of the mean for a sample of two is $S_2 = 0.079/\sqrt{2} = 0.056$, so that the mean ratio differs from unity by $1.43 \times S_2$. Now, the probability that a normally distributed statistic will differ from the mean by +1.43 standard deviations by chance alone is 7.6%, so that the observed results are possibly significant, but further evidence is required before the existence of a multiplication process can be established.

Thus we conclude that there is no evidence for an α-process at fields up to 1.2 Mv/cm, but that there are marginal indications of the beginning of such a process at 1.3 Mv/cm.

Electron Emission Processes at the Cathode

We have presented, above, the observations that lead us to conclude that electron multiplication in the gap is relatively unimportant. Therefore it is assumed that the observed field dependence of the current is explicable in terms of electron emission from the cathode, and the various possible emission mechanisms are examined below.

One possible source of current is field emission as described by the Fowler-Nordheim equation

$$I = 6.2 \times 10^{-6} \frac{\mu^{1/2} S}{(\mu + \phi)\, \phi^{1/2}} E^2 \exp (-6.8 \times 10^7 \phi^{3/2}/E)$$

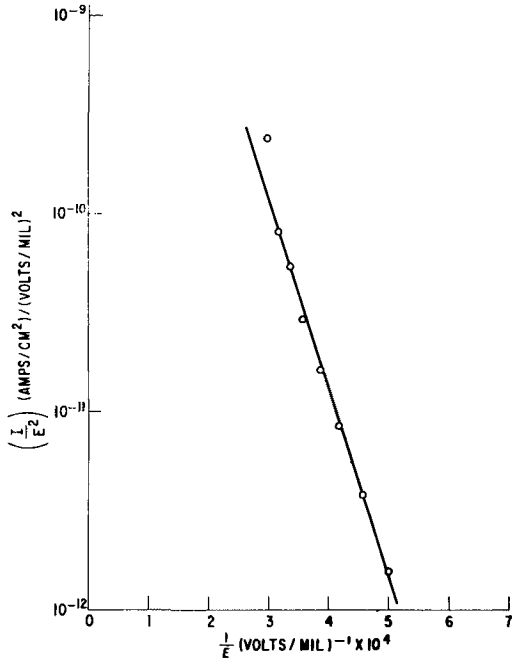

Fig. 5. Field emission plot, n-hexane, stainless steel electrodes.

Here μ is the Fermi level of electrons in the metal, and is usually taken as 5 e.v., ϕ is the work function in e.v., S is the emitting area in cm^2, and I is the current in amps. Figure 5 shows that our data give a good fit to this equation although this in itself does not constitute sufficient evidence for its validity. From the slope and intercept of the straight line in the figure, we calculate a value of $\phi = 0.25$ e.v. and an emitting area $S = 8 \times 10^{-8}$ cm. These values are lower than one might expect.

More realistic values for the work function ϕ are obtained if one takes into account the roughness of the metallic surface. As is well known, although a surface may be highly polished, it is still microscopically rough and local fields at the tips of asperities may exceed the applied field by orders of magnitude. We have taken this into account by introducing a field multiplication factor M and have recalculated ϕ and S as a function of M. The results are given in Table I. The work function becomes more reasonable at a field multiplication of ten, but our largest observed currents (greater than 10^{-3} amp) would then lead to local current densities of 10^6 amp/cm^2 for an emitting area of 10^{-9} cm^2; this is obviously unreasonable.

However, it has been shown by Jones and Morgan (11) and Goodwin (12) that the difficulties with the Fowler-Nordheim equation can be resolved by invoking the presence of an oxide layer on the cathode; this is obviously present in the case of our stainless steel electrodes.

Table I. Dependence of field emission parameters on M

M	ϕ (e.v.)	S (cm^2)
1	0.25	8×10^{-8}
10	1.2	2×10^{-9}
100	5.4	8×10^{-11}

Table II. Dependence of field emission parameters upon M for surface with oxide layer

M	ϕ_1	S
1	0.25	8×10^{-2}
10	1.2	2×10^{-3}
100	5.4	8×10^{-5}

The emission of electrons through such a barrier has been examined by Jones and Morgan on the basis of an analysis by Stern, Gossling, and Fowler (13). The equation derived by the latter shows that the theoretical current is given by

$$I = 6.2 \times 10^{-6} \frac{\mu^{1/2} S}{(\mu + \phi_1)\ \phi_1^{1/2}}\ E^2 \times \left[\exp\ (-6.8 \times 10^7\ \phi_2^{3/2}/E)\ \frac{\phi_1}{\phi_2} \right] B$$

where ϕ_1 is the work function of the metal, ϕ_2 is the work function of the oxide layer, and B is the barrier term

$$B = \exp \left\{ -6.8 \times 10^7 \left[\frac{\phi_1 + \phi_2 + (\phi_1 \phi_2)^{1/2}}{\phi_1^{1/2} + \phi_2^{1/2}} \right] a \right\}$$

where a is the film thickness. It will be seen that the only major difference between the Stern-Gossling-Fowler equation and the Fowler-Nordheim equation lies in the barrier term.

Inserting typical values for ϕ_1 and ϕ_2, and assuming an oxide film thickness of 10^{-7} cm, we obtain $B = 10^{-6}$. Using this factor we have recalculated Table I to yield the values shown in Table II. As before, S is the total emitting area per unit of electrode surface; it arises from the combined effects of many individual surface irregularities. These values for the emitting area are much more reasonable than those calculated on the basis of the Fowler-Nordheim equation. Taking $M = 10$ as representative, we obtain current densities of the order of 1 amp/cm^2 at the tips of the asperities.

We note, however, that a current density of this magnitude may lead to appreciable space charge distortion of the applied field. This results in a decrease of the field at the cathode and ultimately to space charge limitation of the current.

A calculation of this effect is complicated by the nonuniformity of emission from the cathode. Nevertheless, we may make a rough estimate as follows: assume that the local current density at the points is 1 amp/cm^2, and that this current density decreases with the square of the distance from the center of the asperity, tending toward the measured current density of 10 ma/cm^2 at the anode. For a hemispherical boss of radius 10^{-4} cm and an electron velocity of 10^4-10^5 cm/sec (14), we obtain a reduction of 10-100 kv/cm in the cathode field. This suggests that some space charge limitation of the cathode currents may occur at slightly higher fields. For the moment, however, we have chosen to ignore the effect, and to assume that the field in the gap is determined solely by the applied voltage and the electrode geometry.

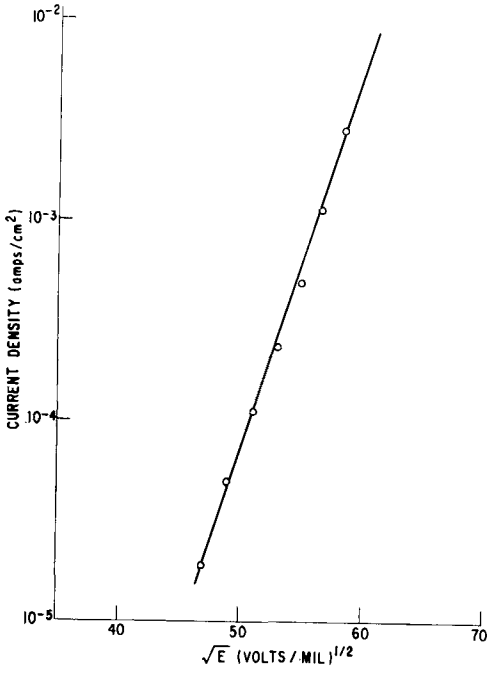

Fig. 6. Schottky plot, n-hexane, stainless steel electrodes

Another possible source of current which should be considered is field-enhanced thermionic emission of electrons, as described by the Schottky equation:

$$I = I_0 \exp\ [4.4\sqrt{E}/\sqrt{\epsilon T}]$$

Here I_0 is the thermionic current density at an absolute temperature T, and ϵ is the dielectric constant of the medium adjacent to the emitting surface. Figure 6 shows that our data from 0.2 Mv/cm to 1.4 Mv/cm give a good fit to this equation although, as observed in the case of the Fowler-Nordheim equation, this in itself does not prove that the equation is applicable. From the slope of the straight line in Fig. 6 and a knowledge of T and ϵ, we compute a value of five for the field enhancement factor M. From the zero field intercept of this line we obtain a value of 10^{-14} amp/cm^2 for I_0; in order to account for a thermionic emission current of this order at room temperature, one needs to postulate a work function of the order of 1.25 e.v.

It should be pointed out that the computed value of ϕ is very insensitive to the value of I_0; a change of 10^5 in I_0 changes the work function by 25% in the opposite direction. However, taking into account the uncertainty with which we know the value of the work function for emission into a liquid, we conclude that the magnitude of the observed current is consistent with that to be expected from field-enhanced thermionic emission.

In order to distinguish between Schottky emission and field emission, it is proposed to repeat our conduction measurements as a function of temperature.

Conclusions

On the basis of our measurements we arrive at the following conclusions:

1. An electron multiplication process does not play a significant role in conduction and, therefore, in breakdown in hexane.

2. Currents originate either by Schottky emission, or by field emission, from asperities on the cathode; in the latter case, their magnitude would be influenced strongly by an oxide layer on the cathode.

3. The average energy input to the liquid near breakdown is unexpectedly large (about 10^4 watts/cm^3). At the tips of the asperities the energy input may be as large as 10^7 watts/cm^3, and this could lead to local vaporization of the liquid in times as short as a few microseconds.

4. Thus we conclude that liquid breakdown involves the formation of a vapor bubble at the cathode and its subsequent growth toward the anode, bridging the gap with a vapor channel of low electric strength.

It has long been recognized that cavitation may play a role in the breakdown of liquid dielectrics, bubbles being formed either from dissolved gas (15, 16) or by the local vaporization of the liquid itself (17). Indeed, the fact that the breakdown strength of a liquid is pressure dependent is direct evidence that a change of phase is involved in the breakdown mechanism (18-20).

We believe, however, that until the present work was carried out, the mechanism of formation of these bubbles was unknown; we anticipate that this knowledge will enable us to extend our understanding of the breakdown mechanism.

Manuscript received Nov. 2, 1959. This paper was prepared for delivery before the Philadelphia Meeting, May 3-7, 1959.

Any discussion of this paper will appear in a Discussion Section to be published in the December 1960 JOURNAL.

REFERENCES

1. K. A. Macfadyen and W. D. Edwards, *Nature*, **163**, 171 (1949).
2. D. W. Goodwin and K. A. Macfadyen, *Proc. Phys. Soc.*, **66**, 85 (1953).
3. A. H. Sharbaugh, J. K. Bragg, and R. W. Crowe, *J. Appl. Phys.*, **24**, 814 (1953).
4. W. B. Green, *ibid.*, **26**, 1257 (1955).
5. H. House, *Proc. Phys. Soc.*, **70**, 913 (1957).
6. P. K. Watson and A. H. Sharbaugh, Ann. Rep., 1957 Conf. on Elec. Ins., p. 1.
7. A. H. Sharbaugh, R. W. Crowe, and E. B. Cox, *J. Appl. Phys.*, **27**, 806 (1956).
8. J. B. Whitehead and R. Marvin, *Trans. AIEE*, **45**, 299 (1929).
9. A. Nikuradse, "Das flussige Dielektrikum," pp. 83 and 133, Springer, Berlin (1934).
10. L. Inge and A. Walther, *Tech. Phys. U.S.S.R.*, **1**, 539 (1935).
11. F. Llewellyn Jones and C. G. Morgan, *Proc. Roy. Soc.*, **A218**, 88 (1953).
12. D. W. Goodwin, *Proc. Phys. Soc.*, **B69**, 61 (1956).
13. Stern, Gossling, and Fowler, *Proc. Roy. Soc.*, **A124**, 699 (1929).
14. O. H. LeBlanc, *J. Chem. Phys.*, **30**, 1443 (1959).
15. F. Koppelmann, *ETZ*, **46**, 1413 (1931).
16. F. M. Clark, *J. Franklin Inst.*, **215**, 39 (1933).
17. A. Gunther-Schulze, *J. Radioaktivität u. Elektrotechnik*, **19**, 92 (1922).
18. W. D. Edwards, *Can. J. Phys.*, **29**, 310 (1951).
19. P. K. Watson and J. B. Higham, *Proc. I.E.E.*, Pt. IIA, **100**, 168 (1953).
20. K. C. Kao and J. B. Higham, *This Journal*, being reviewed.

On the Physical Characteristics and Chemical Composition of Electroluminescent Phosphors

Paul Goldberg and S. Faria

General Telephone and Electronics Laboratories Inc., Bayside, New York

ABSTRACT

Through controlled removal of surface layers, it was found that surface chemical barriers are not responsible for electroluminescence in zinc sulfide phosphors. Polycrystalline phosphors are shown to be almost uniform with respect to chemical, physical, and electroluminescent properties as one passes from the surface into the crystallite bulk. Electron micrographs show the character of the particles as successive layers of phosphor surfaces are removed by acid etching. The experimental results at progressive stages of etching are interpreted in terms of an inefficient surface layer and of decreased particle size after etching. Regions capable of serving as the site of field intensification are held to exist throughout the volume of the particles.

If a phosphor is to emit visible light on exposure to an electric field, the phosphor must first accept energy from that field. The mechanism by which this is done is a major problem of electroluminescence research. Only a few phosphor types are known to absorb electrical energy and emit light. It is important to elucidate the nature of the physical and chemical differences between these phosphors and similar but nonelectroluminescent materials. At least one difference in zinc sulfide phosphors is held to be the presence of a barrier region in the electroluminescent particles which leads to impact ionization of luminescent centers (1, 2). Throughout the literature one finds emphasis placed on a chemical inhomogeneity in the crystal which is held to serve as the barrier site (3-6). Presumably no electroluminescence would be found were this inhomogeneity removed. It is the aim of the present work to explore the surface and volume of electroluminescent zinc sulfide to ascertain the degree of physical and chemical uniformity and to relate the results to current concepts.

It has been stated that the barriers responsible for electroluminescent excitation reside on the phosphor surface. Supporting this view are the following two experiments: (i) Zalm has deposited copper sulfide on a nonelectroluminescent zinc sulfide phosphor, and, by this simple process, converted a nonelectroluminescent phosphor into one which is electroluminescent. Cyanide washing removed the copper sulfide and destroyed the phosphor's ability to be field-excited (5); (ii) Destriau performed etching experiments to remove phosphor surfaces and found that this caused an initial improvement followed by ever diminishing sensitivity of the electroluminescent materials (7). In contrast, barriers inside powder particles have been proposed from observations on the spatial distribution of emission from individual grains (8). In single crystals both surface and volume barriers were reported, again from observations on location of light emission (5, 9-12).

Regarding the barrier composition some qualitative ideas have been formulated by various workers (4-6). The preparation of electroluminescent phosphors usually involves copper concentrations above that which yields maximum photoluminescent intensity. The barrier may thus be related to this copper excess. Zalm associates the barriers with conducting particles of copper sulfide on the phosphor surface (5).

In the work reported here, the principal experimental approach was the step-by-step removal of portions of the phosphor mass by chemical etching. At each successive etching stage the properties of the phosphor were studied. These properties include the phosphor cell emittance and electrical loss as functions of voltage. Electron microscopy and x-ray diffraction of the powders were employed as auxiliary analytical tools. Chemical analyses for copper were also performed. To the extent that phosphor material is removed uniformly from the surfaces, these measurements reflect properties of the phosphor as a function of depth into the crystal. In etching experiments of this type it is clear that account must be taken of changes in particle size and possibly in particle shape.

Experimental Technique

Phosphors and analytical methods.—The phosphors studied were mainly of the ZnS:Cu,Cl type. They contained 0.08% Cu by weight and were green-emitting below 1 kc. In most of the work the electroluminescent phosphor was first fractionated by elutriation to yield specimens with improved uniformity of particle size distribution. A potassium silicate solution was employed as a dispersing agent for the settling from aqueous solution. The phosphors were etched with solutions of 6*N* HCl by agitation of the mixtures at 60°-80°C. The progress of the etching was monitored by weight loss due to H_2S evolution. Specimens etched to various extents were obtained by either of two methods: (i) etching of a large mass of phosphor with periodic sampling, and (ii) etching of individual samples to the desired mass reduction. The two methods led to roughly comparable results. The electron micrographs were recorded of representative samples with a minimum of nine photographs per sample. Direct platinum-shadowed carbon replicas were employed throughout.

X-ray diffraction patterns were obtained with a recording diffractometer. Quantitative spectrographic analyses for copper for each stage of etching were also tabulated. In a few instances, particle size distribution data were obtained with a Coulter particle size apparatus (13).

Optical and electrical measurements.—The brightness data were taken with a demountable electroluminescent cell 25 x 25 x 0.150 mm in size with a castor oil dielectric at a phosphor volume fraction of 0.33. Brass and conductive glass (500 ohms per square) served as electrode materials. The detector was an RCA 1P21 photomultiplier corrected by a Wratten No. 106 filter to yield an approximate eye response. The brightness was recorded with a Photovolt Model 520 photometer calibrated with a Spectra 100 ft-L standard brightness source.

The measurement of electrical losses was achieved with a bridge circuit which measured the capacitance and the equivalent parallel resistance of the test cell.

Experimental Results

Electroluminescent properties of etched phosphors.—The brightness L and electrical loss of the etched phosphors were measured as a function of voltage V. In Fig. 1 the brightness data are shown plotted as log L vs. $V^{-1/2}$ for a constant frequency of 1 kc. Two effects should be noted: (i) after initial etching the brightness is improved at all voltages, and (ii) subsequent stages of etching give increased slopes as would be expected from decreases in particle size (14, 15).

The efficiency, η, of this group changes with extreme etching according to the trend established by Lehmann for efficiency variation with particle size

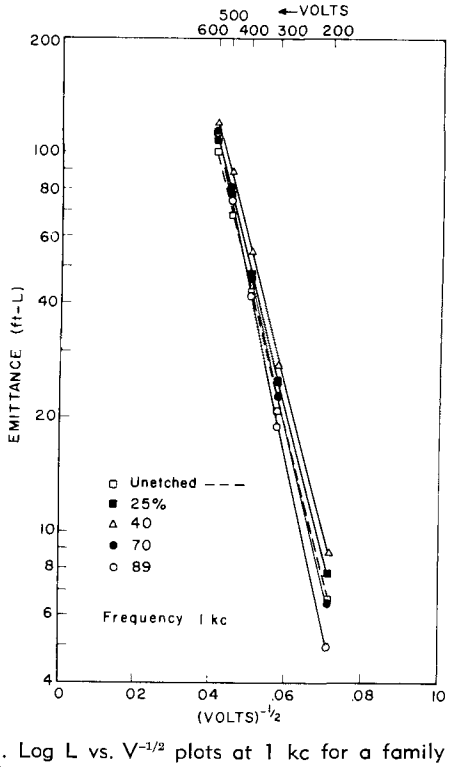

Fig. 1. Log L vs. $V^{-1/2}$ plots at 1 kc for a family of phosphors subjected to various amounts of etching.

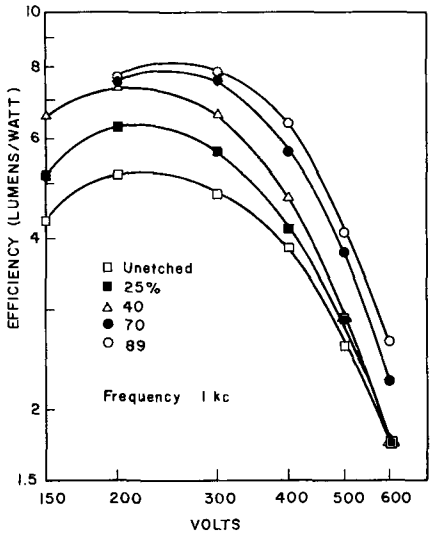

Fig. 2. Log η vs. Log V for phosphors in Fig. 1, frequency is 1 kc.

(14). Figure 2 contains data of log η vs. log V at a constant frequency of 1 kc with the degree of etching as a parameter. The voltage at which maximum efficiency occurs remains fixed for the initial stages of etching. Heavy etching occasions a shift in this voltage which is probably a consequence of smaller particle size. The maximum efficiency depends only slightly on frequency with the optimum range falling near 300 to 400 cps.

The improved brightness and higher efficiency resulting from extensive etching of these phosphors do not appear to be a consequence of the particular phosphor synthesis employed. Thus in addition to the ZnS:Cu, Cl already mentioned, the following phosphors, etched to remove between 60% and 90% of the phosphor mass, all show as high or higher levels of brightness and efficiency as before etching: ZnS:Cu,Cl-Pb (16); ZnS:Cu,Al (4); Zn(S,Se):Cu,Br (17); and ZnS:Cu,Cl-Mn.

Chemical analyses for activator inhomogeneity.—The aim of these chemical analyses was to probe the chemical homogeneity of the phosphor on the assumption that the particle mass was removed uniformly.[1] Table Ia gives results of spectrographic analyses for copper in the remaining solids as a function of degree of etching. The relative particle size is specified in Table I with the diameter of the unetched material designated as unity. The mean diameter of the unetched phosphor is 8.3μ as measured by the gas adsorption (BET) method and 22μ as determined with the Fisher Sub-Sieve Sizer. Table Ib gives similar data for another phosphor of different average copper content. Before analyzing for copper, the powders were washed with 1% potassium cyanide solution to remove any loosely bound Cu_2S which forms by precipitation on exposed surfaces subsequent to destructive etching.

The values in Table Ia show that the samples possess gradients in Cu concentration of less than 5×10^{-6} g at Cu/mole per micron of crystal. This value is determined by the precision of the analyses.

[1] The absence of specific etch geometry in most of the etched phosphors suggests that all surfaces experience about the same degree of dissolution.

Table Ia

Wt. % removed by etching	Fraction of initial size (calculated) [a]	Wt % Cu found (±a.d.)	No. of samples analyzed
0	1.00	0.065 ± 0.002	4
25	0.91	0.066 ± 0.002	3
33[b]	0.87	0.065 ± 0.002	2
70	0.67	0.067 ± 0.003	3
89	0.48	0.069 ± 0.002	4

Table Ib

Wt. % removed by etching	Fraction of initial size (calculated)	Wt % Cu found (±a.d.)	No. of samples analyzed
0	1.00	0.15 ± 0.015	2
50	0.79	0.16 ± 0.015	2
90	0.46	0.15 ± 0.015	2

[a] Calculated from weight loss assuming spherical geometry.
[b] This sample is not included in the measurements shown in Fig. 1 and 2.

The results do not rule out the existence of an inhomogeneous impurity distribution. Significant activator concentration gradients may be too small to be detectible by methods described above. It appears, however, that there is no bulk activator phase residing on the surface of these phosphors which is of critical importance to electroluminescence.

Electron Microscope Studies

Unetched electroluminescent phosphors.—The appearance of the grains is mainly globoid. The surfaces are on the whole mottled by tiny protuberances or crater-like depressions with dimensions of a half micron or less. Terracing, characterizing the original crystal growth, is found in localized regions. Striations are also evident in restricted parts of most grains. The terracing and striations are the only surface features indicating a high degree of crystallinity. Prismatic faces are conspicuously absent. A typical particle is shown in Fig. 3.

Etched electroluminescent phosphors.—Materials at the initial stages of etching show little of the

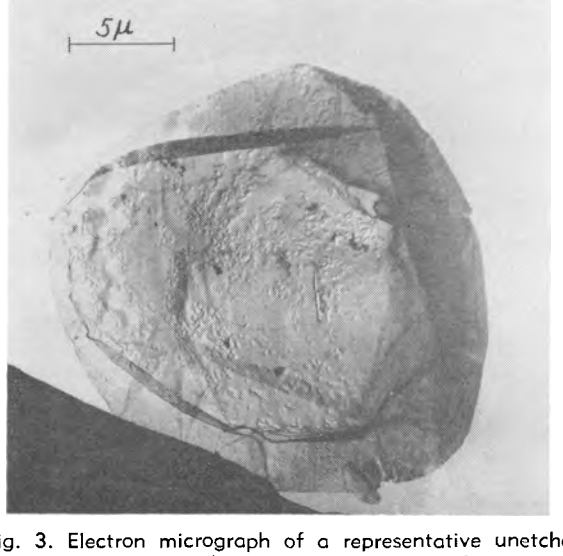

Fig. 3. Electron micrograph of a representative unetched electroluminescent particle showing a mottled surface.

Fig. 4. Electron micrograph of an etched electroluminescent particle, about 40% mass removed. This general appearance is preserved at higher degrees of acid etching.

mottled surface character and are apparently chemically polished. Here the geometry is more characteristic of a crystalline substance. Crystal faces can be discerned in a representative particle shown in Fig. 4. These are disturbed by small bumps, regions of striae, and irregular depressions. Only rarely is an etch pit of regular geometry found. This character persists through all stages of etching. From this information (and the x-ray data) a picture of fragmented crystal order emerges for the electroluminescent particles.

After about 90% of the phosphor mass is removed, the photographs show a distinct reduction in particle size. If a spherical geometry is assumed, a reduction in mass by 90% is equal to a reduction in diameter of about 50% which is on the average the order of the observed decrease in size. Some particle size distribution measurements were made which show that mass removal was achieved by attacking particles of all sizes rather than the fine ones preferentially. Figure 5 shows the histogram of size distribution by volume (or weight) of an unetched phosphor. Figure 6 is the distribution of this phosphor after etching away 80% of the mass. The significant feature is the shift in the apparent mean size from approximately 35-40μ to about 25-30μ showing extensive etching of the larger grains. The electroluminescent properties of these two phosphors are related in the same way as already described in Fig. 1 and 2 for the unetched and the heavily etched phosphors.

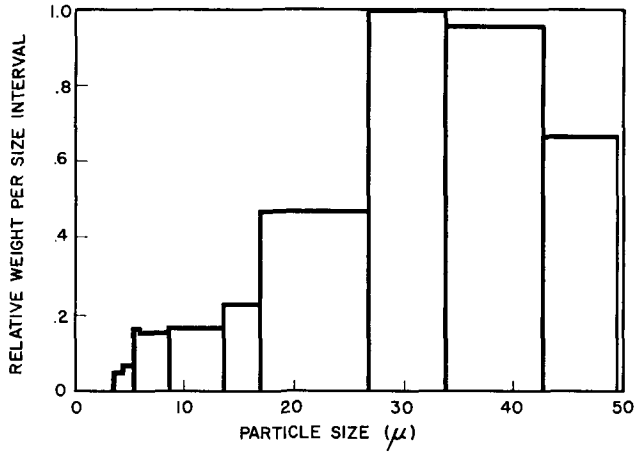

Fig. 5. Distribution of particle size by volume (or weight) of a representative unetched electroluminescent phosphor; measurement range is 3.4-49 μ.

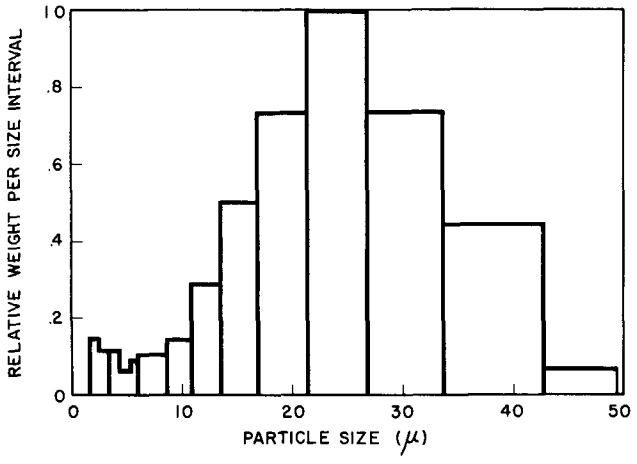

Fig. 6. Distribution of particle size by volume (or weight) of the phosphor shown in Fig. 5 after etching away 80% of the mass; measurement range is 1.7-49 μ.

Nonelectroluminescent phosphor particles of the ZnS:Cu,Cl type show qualitatively about the same degree of structural discontinuity as do their electroluminescent counterparts. There are, however, in these materials none of the striations seen in the electroluminescent phosphors.

Specific etch patterns.—In one specimen an etch geometry of an unusual character was found. The specimen was etched to 93% mass removed.[2] Two representative particles are shown in Fig. 7. The char-

[2] The etching procedure was different here. First 80% of the mass was etched away; the phosphor was dried and etched again with fresh acid.

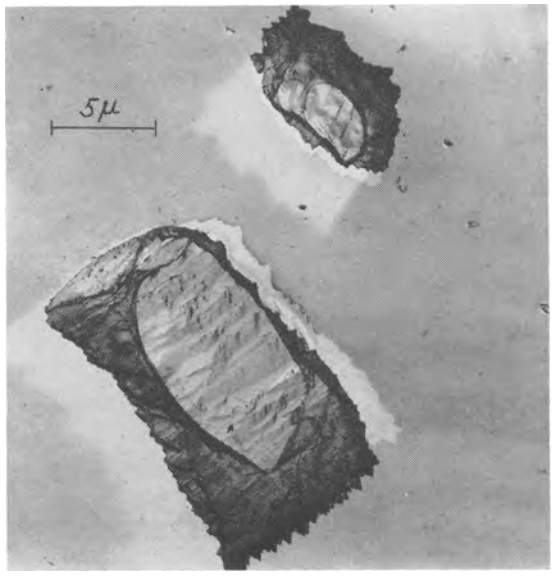

Fig. 7. Uncommon geometry in a highly etched electroluminescent specimen (93% mass removed) showing pyramids on one end. The crystal structure of the powder, of which this particle is representative, is cubic with little or no hexagonal content.

acteristic shape is oblong with one end showing well-defined pyramidal peaks. The peaks fall mainly into two groups whose average angles are 62° 51′ (±1° 40′) and 70° 45′ (±2° 10′), respectively. These particles show cubic structure in the x-ray diffraction pattern with a small hexagonal content and some birefringence. They possess ridges running normal to the direction in which the peaks point. Peaks within one particle are found which point in directions which are out of parallel with others by about 5° of arc. Also, the lateral ridges are, in some particles, out of parallel by as much as 13°. These facts point to structural units whose boundary divides the particle parallel to the direction of the pyramids.

It is possible that the occurrence of peaks only on one side of each particle is a consequence of the absence in the sphalerite lattice of a structural center of symmetry. Recently White and Roth (18) have shown how asymmetric etch patterns in GaAs wafers (sphalerite structure) etched in (111) planes correlate with the noncentrosymmetric structure. We may thus postulate that the peaks in Fig. 7 point in the <111> direction. This contention is supported by x-ray diffraction patterns obtained from individual particles in the etched specimen. Wolff has reported that in ZnS crystals the rates of dissolution by HCl of (111) faces and $(\bar{1}\bar{1}\bar{1})$ faces are different. He suggests that this is a consequence of structural asymmetry along the <111> direction and that the face made up primarily of sulfur atoms is attacked at the greatest rate (19). Thus we postulate that the pyramids in Fig. 7 appear on the "sulfur" face.

The light output from a sampling of fifteen particles from this material was followed visually with a microscope arrangement similar to that of Waymouth and Bitter (20). In all but one case the particles were distinctly more luminous with the elongated axis parallel to the applied field rather than perpendicular.

Crystal structure.—The structure of the family of phosphors which have undergone successive etching is, to a first approximation, uniform throughout the lattice. The dominant form is cubic in most of the electroluminescent materials reported upon here. The nature of the phosphor synthesis is such that the cubic structure may have occurred as a consequence of either low-temperature annealing or of milling the hexagonal form at a stage following crystallization. The diffraction patterns show some subtle qualitative changes at various stages of etching. A small residual hexagonal component existing in the unetched phosphor is reduced in the more heavily etched phosphors. Also, from observations on line breadth in the back reflection region, the highly etched grains are found to have a greater degree of order than the unetched phosphor. Assuming that strong etching exposes the particle cores, the ordering effect may arise from a slower cooling rate in the inner layers after the synthesis. In support of this the interiors are found to have a stronger blue component in the photoluminescence than the unetched parent phosphor. Leverenz states that the shorter wave lengths are favored by slower cooling (21).

Discussion

The results show that the polycrystalline phosphors are nearly homogeneous in chemical, physical, and electroluminescent properties as one passes from the surface and penetrates deeply into the crystallite bulk. One exception to this is the existence of a thin inefficient surface layer much like that found in cathode ray phosphors (22).[3] Following the removal of this layer, the electroluminescent properties vary with the extent of etching in a fashion like that previously described for particle size reduction (14, 15). The results are at odds with the concept that a surface chemical phase is responsible for the potential barrier and thus for the source of electroluminescence excitation, since strong electroluminescence persists following the removal of substantial amounts of surface material. It would appear that the phosphor particle's surface modifies its electroluminescent capability, but does not serve as a site of intrinsic electroluminescent properties. Such modification of a solid's bulk properties by its surface is often encountered in other areas of semiconductor studies.

The most acceptable physical description of electroluminescent particles is one in which regions capable of serving as the location of field intensification are to be found throughout the electroluminescent particle. The location within the particle of the site which finally serves as the active barrier is not certain. The following, however, does appear well founded on the basis of the above experiments: if the site of field intensification exists on or near the particle surface, removal of this surface brings new barrier sites into play with equal capabilities for the generation of electroluminescence. The particular site which serves as a barrier may depend on particle orientation, shape, and contact with other particles. It appears likely as a consequence of arguments based on particle size effects that only one or two barriers are operative in a particle at any one time (15).

The concepts proposed here are in disagreement with Zalm's model (5) of a conducting surface phase. The source of the diagreement lies in the fact that electroluminescence which is produced by impurity activation at high temperatures and that arising from the deposition of conducting phases on nonelectroluminescent phosphors are different in two important ways. First, the field-excited emission from an otherwise nonelectroluminescent phosphor with a copper sulfide surface phase is orders of magnitude below that of products synthesized by conventional methods. Second, conventional electroluminescent phosphors cannot be deactivated by washing with a cyanide solution. Thus, we find that a phosphor which was refluxed with a 50% KCN solution loses little if any of its sensitivity.

The experiments of Larach and Shrader (6) do not offer convincing evidence for a region near the

[3] Kremheller proposes that etching, and therefore roughening, of the surface of some phosphors improves light output owing to decreases in multiple internal reflections (23).

particle surface which is richly interdiffused with copper, as they maintain. They have performed no chemical analyses as a function of penetration into the crystal volume. It would be of interest to know if their phosphors experience the same type of changes described in this report or if the materials lose sensitivity following destructive etching.

Destriau's work on etching of electroluminescent phosphors (7) may, on the basis of this report, be thrown into different perspective. His measurements were of the minimum voltage required for visibility as a function of the extent of etching. The course of his curve shows an initial decrease (sensitivity increase) followed by a monotonic increase (sensitivity decrease). This is the same pattern followed by the data in Fig. 1 in the low voltage region. Initial etching increases sensitivity; heavier etching produces an apparent sensitivity decrease which is more precisely a consequence of particle size change.

One finds subtle effects on penetrating the grains which, in the second approximation, show the grains to be inhomogeneous. These are the bluer photoluminescence and more ordered structure of the internal regions. The relation, if any exists, of these effects to electroluminescence cannot be made on the basis of the above experiments.

Acknowledgments

It is a pleasure to acknowledge many helpful discussions with Drs. D. H. Baird, A. K. Levine, R. N. Summergrad, and Mr. C. F. Tufts. Also thanks are due J. T. Ragusin for aid in phosphor preparation, S. Weisberger for chemical analyses, Mr. Tufts for the electron micrographs and the Crystallography Staff for x-ray work.

Manuscript received Feb. 1, 1960. This paper was prepared for delivery before the Chicago Meeting, May 1-5, 1960.

Any discussion of this paper will appear in a Discussion Section to be published in the December 1960 JOURNAL.

REFERENCES

1. D. Curie, *J. Phys. Rad.*, **13**, 317 (1952).
2. W. W. Piper and F. E. Williams, *Phys. Rev.*, **87**, 151 (1952).
3. G. Destriau and H. F. Ivey, *Proc. IRE*, **43**, 1911 (1955).
4. H. C. Froelich, *This Journal*, **100**, 496 (1953).
5. P. Zalm, *Philips Res. Repts.*, **11**, 353, 417 (1956).
6. S. Larach and R. E. Shrader, *J. Phys. Chem. Solids*, **3**, 159 (1957).
7. G. Destriau, Symp. Brooklyn Polytech. Inst., Brooklyn, N. Y. (Sept. 1955).
8. A. H. McKeag and E. G. Steward, *This Journal*, **104**, 41 (1957).
9. E. E. Loebner, Symp. Brooklyn Polytech. Inst., Brooklyn, N. Y. (Sept. 1955).
10. E. E. Loebner and H. Freund, *Phys. Rev.*, **98**, 1545 (1955).
11. G. Diemer, *Philips Res. Repts.*, **10**, 194 (1955).
12. D. R. Frankl, *Phys. Rev.*, **100**, 1105 (1955); *ibid.*, **3**, 1540 (1958).
13. The particle size measurement is an electrical one in which pulses are counted the heights of which are proportional to particle volume; R. H. Berg, ASTM Special Technical Publication *No. 234*, 245 (1958).
14. W. Lehmann, *This Journal*, **105**, 585 (1958).
15. P. Goldberg, *ibid.*, **106**, 34 (1959).
16. H. H. Homer, R. W. Reulon, and K. H. Butler, *ibid.*, **100**, 566 (1953).
17. I. J. Hegyi, S. Larach, and R. E. Shrader, *ibid.*, **104**, 717 (1957).
18. J. G. White and W. C. Roth, *J. Appl. Phys.*, **30**, 946 (1959).
19. G. A. Wolff, Information presented at the 1959, Fall Meeting of the Electrochemical Society, Columbus, Ohio.
20. J. F. Waymouth and F. Bitter, *Phys. Rev.*, **95**, 941 (1954).
21. H. W. Leverenz, "An Introduction to Luminescence of Solids," p. 217, J. Wiley & Sons, Inc., New York (1950).
22. G. F. J. Garlick, *Handb. der Physik* (Light and Matter II), **26**, 1 (1958).
23. A. Kremheller, *This Journal*, **107**, 8 (1960).

December 1960 Discussion Section

A Discussion Section, covering papers published in the January-June 1960 JOURNALS, is scheduled for publication in the December 1960 issue. Any discussion which did not reach the Editor in time for the June 1960 Discussion Section will be included in the December 1960 issue.

Those who plan to contribute remarks for this Discussion Section should submit their comments or questions in triplicate to the Managing Editor of the JOURNAL, 1860 Broadway, New York 23, N. Y., *not later than September 1, 1960*. All discussion will be forwarded to the author(s) for reply before being printed in the JOURNAL.

Preparation and Properties of AlSb-GaSb Solid Solution Alloys

J. F. Miller, H. L. Goering, and R. C. Himes

Battelle Memorial Institute, Columbus, Ohio

ABSTRACT

Ingots of the quasi-binary GaSb-AlSb alloy were prepared by progressive casting and zone casting at various rates of crystallization. Results of x-ray diffraction studies, metallographic studies, hardness determinations, and chemical analyses indicate that, with the possible exception of a narrow composition range between 10 and 30 mole % AlSb which was not investigated, solid solution prevails in the system. Bulk specimens of single phase, solid solution alloy were obtained by use of low linear rates of crystallization (0.05 in./hr), while at higher rates of crystallization (¼ to 1¼ in./hr) two intermingled solid phases were characteristically obtained.

Vegard's law was found to be at least roughly applicable; with lattice constants for the alloys ranging between values of 6.0963Å for pure GaSb and 6.1361Å for pure AlSb. Optical energy gaps determined for alloy specimens increased regularly with cell size from a value of 0.68 ev for GaSb to a value of 1.74 ev for AlSb. Values of electrical resistivity and hole mobility for the relatively impure alloy specimens were also intermediate between those for the compounds in a like state of purity.

Liquidus data are also presented for the system.

In recent years, there has been considerable interest in systems composed of two intermetallic compounds of the A^{III} B^{V} type (e.g., GaSb-InSb, InAs-InSb, etc.). This interest arises because of the possibility of obtaining semiconducting materials, the properties of which can be varied over a continuous range of values. Since regular variation of the structure-sensitive properties with composition can be expected only for those systems or composition ranges in which solid solution occurs, the majority of previous investigations (1-8) in this area have been concerned chiefly with the existence of such ranges in the various systems.

In a number of instances, however, apparently conflicting results have been reported. In the case of the system GaSb-InSb, for example, Koster and Thoma (1) report a degenerate eutectic diagram with no appreciable terminal solid solution, while Kolm, Kulin, and Averbach (2) report approximately 10% solid solution at each end of the diagram. On the other hand, results reported by Goryunova and Fedorova (3), Woolley, Smith, and Lees (4), Woolley and Smith (5) indicate that a complete range of solid solution exists in this system. Similarly conflicting conclusions have been reached regarding the systems InAs-InSb (3, 5, 6), AlSb-InSb (1, 5), and AlSb-GaSb (1, 5). Woolley and Smith (5) suggest that the discrepancies exist because, in some instances, the samples were in a metastable state. Results of those investigations for which adequate information is given regarding thermal history of the materials (e.g., cooling rate during crystallization, or time and temperature used for heat treatment) appear to be consistent with this observation. Satisfactory evaluation of all previous work is not possible, however, since in some cases no details are given concerning heat treatment of specimens. Firm conclusions regarding the precise nature of these systems therefore must be based to a large extent on the results of additional investigations.

This investigation was concerned with temperature-composition relationships for the system AlSb-GaSb and with pertinent physical properties of the alloys obtained. The study is incomplete in the sense that full characterization of the system and full development of certain of the analytical and preparative techniques have not yet been realized. Data presented do, however, furnish much new or confirmatory evidence regarding the nature of this particular system, and it is believed that certain of the techniques which are discussed may be applicable to other alloy systems of this type.

Experimental Procedures

All samples studied were prepared by direct reaction at elevated temperatures, of proper proportions of highly purified elements[1] sealed in quartz or Vycor under an atmosphere of pure argon. Atmospheres of hydrogen, used in some early experiments to suppress oxidation, were not considered to be satisfactory. Numerous small voids, which apparently were formed by precipitation of the gas from solution on freezing, were always present in alloy specimens solidified under hydrogen. In work with compositions other than pure GaSb, temperature of each sample was initially held in the range 1060°-1080°C (just above the melting point of AlSb) for a period of one-quarter hour to react the elements and homogenize the melt before proceeding with the experiment. Since the glasses (quartz, Vycor, etc.) are attacked rapidly by molten samples containing Al or AlSb, internal crucibles or boats of pure graphite[2] were used for such compositions.

[1] Gallium, 99.995 + %; aluminum, 99.992 + %; antimony, 99.996 + %.

[2] National Carbon Co., AUC grade.

Differential thermal analysis was employed in making the phase-diagram study. Samples were contained in graphite cells which had a graphite thermocouple well extending into the center of the sample chamber. Graphite was used as a reference material. Both temperatures and temperature differential were recorded continuously by means of a dual-unit Brown Electronik Potentiometer-Recorder. At cooling rates of 3°C/min, well-defined thermal arrest points were obtained. Thermometry of the apparatus was calibrated by measuring the freezing points of high-purity lead, antimony, and germanium. The measured freezing point of GaSb, 702°C, which is in good agreement with values of 703°C and 706°C reported by others (1, 6), served as a check on the calibration.

Alloy ingots were prepared by two techniques: progressive casting and zone casting. Progressive casting, in which crystallization is caused to progress at a controlled rate along an initially wholly molten ingot, maintained in a horizontal position, was used for exploratory purpose. [This method of crystallization has been termed normal freezing by Pfann (10).] Because of the variation of composition with distance along a progressively cast ingot (except at an invariant point or in the case of an ideal solution), a number of specimens having different compositions usually can be obtained from a single ingot.

Relatively large specimens of uniform composition are, however, required for certain physical studies (e.g., solidus determinations, chemical analyses, etc.). Zone casting, which is essentially single-pass zone melting, was investigated as a potential means of obtaining such specimens. Theoretically, for a system or composition range in which the components form solid solutions, this method of casting should yield ingots which are of uniform composition over a considerable portion of their length. If a macroscopically homogeneous charge is used, composition of the recrystallized ingot should change appreciably in only the first several and the final zone lengths. When material of a given composition (representing some point on the solidus of the system) is used as the main charge, and material of the corresponding liquidus composition is used as a charge in the first zone length, then composition of the recrystallized ingot should vary only in the final zone length. Solid charges consisting of either air-quenched ingots or thoroughly blended lots of the alloy material in powder form were recrystallized in this way. Induction heating was employed for all casting experiments, and the rate of movement of the ingot through the induction coil was considered to be rate of crystallization. Molten zone-length to ingot-length ratios of 0.2 to 0.25 were used for the zone casting. Alloy ingots were cast progressively under a number of conditions, and specimens from selected locations in these ingots were examined by use of x-ray diffraction, metallographic techniques, and hardness tests.

In preparing specimens for metallographic examination, a staining etch of 10 g $FeCl_3$, 1000 ml H_2O, and 100 ml concentrated HCl was used. In Knoop hardness determinations, 100 and 500 g indenter loads were used. Except for Sample PC-1-4, which spanned a range of progressions, all samples taken for x-ray, optical, electrical, and chemical analyses were from thin slab-like sections which were cut along planes normal to the longitudinal axes of the ingots so as to minimize the effect of variations in composition.

X-ray diffraction studies were made on powder samples prepared by grinding the bulk specimens under anhydrous benzene. The diffraction patterns were obtained by use of Ni K radiation and a 114.6 mm diameter Debye-Scherrer camera. In determining precision lattice constants, results were corrected for film shrinkage and other errors (11) by extrapolating the plots of apparent lattice parameters against the function $\frac{1}{2}[(\cos^2\theta/\theta) + (\cos^2\theta/\sin\theta)]$, where θ is the Bragg angle.

Infrared transmission spectra were obtained at room temperature for polished platelets of the compounds and alloys ranging in thickness from 0.003 to 0.010 in. The Beckman D U, Beckman Model IR-2, and Perkin-Elmer Model 21 spectrometers were used for the wave-length ranges, 0.4 to 1.5, 0.65 to 2.0, and 2.0 to 15 μ, respectively, as was required. In determining optical energy gap, cutoff wave length was taken as that wave-length at which value of the Beer-Lambert absorption coefficient reached a value of 200 cm^{-1}. Use of this convention has yielded values for a number of other semiconducting compounds (12) which are generally in good agreement with other published values (e.g., room temperature values of 0.16 ev for pure InSb, 0.35 ev for InAs, 1.32 ev for InP, and 1.39 ev for GaAs).

In making the electrical measurements, both antimony films and solder contacts were used to eliminate the very high contact resistance exhibited by the alloys, especially by those rich in AlSb. The antimony films were formed *in situ* by use of hot concentrated KOH as a reducing agent. Tungsten probes then were held in contact with the films by spring tension. The solder contacts, made with Sn-Pb solder and aluminum solder flux, appeared to be more reliable for low temperature measurements. All Hall data were taken at a field strength of 5000 gauss.

For chemical analyses, the samples were dissolved in alkali. The total amount of antimony present was determined by titration with potassium bromate. Aluminum and gallium were converted to the mixed oxides and the total amount present was determined gravimetrically. The fraction of each present in the mixture was calculated then by the classical method.

Experimental Results and Discussion

Physical properties of GaSb *and* AlSb.—As a first step toward characterization of the system, pertinent physical properties of the compounds GaSb and AlSb were measured. The values obtained, which are summarized in Table I, were determined for specimens prepared from high-purity elements as has been described. Purity of the specimens studied, as deduced from electrical measurements, was about 2×10^{17} impurity atoms/cm^3.

The lattice constants, 6.0963Å for GaSb and 6.1361Å for AlSb, are roughly equal in magnitude to those reported by Blunt, *et al.* (13, 14), but are

Table I. Physical constants of GaSb and AlSb

	Melting point, °C	Lattice constant (a_0), A	Optical energy gap (ΔE at 300°K), ev	Knoop hardness
GaSb	702	6.0963 ± 0.0003	0.68	309
AlSb	1050(25)	6.1361 ± 0.0003	1.74	304

reversed in order of assignment, i.e., Blunt assigns the larger value to GaSb. The cell size for GaSb is slightly higher than that obtained by Kolm, *et al.* (2). However, values reported here, which represent the results of a number of determinations, are in good agreement with other reported values (5, 15), are consistent with expected interatomic distances for these compounds calculated according to Pauling (16), and are consistent with the cell size-composition relationship observed in our studies of the alloys.

The optical energy gap for GaSb, 0.68 ev, agrees reasonably well with other published values (17-20), which all fall in the narrow range between 0.67 and 0.71 ev. On the other hand, published values for the optically determined band-gap width of AlSb at 300°K (18, 20-22) range from 1.52 to 1.7 ev, while that obtained in this work is 1.74 ev. Some disagreement is to be expected because of the different methods used to select the cutoff wave length, but the wide divergence of reported values indicates that other factors such as sample purity and surface condition probably are involved also. For example, AlSb is slowly attacked by atmospheric water vapor. As is indicated in Fig. 1, presence of the products of this reaction on the surface of the specimen drastically alters the spectrum, and may be responsible for some of the low gap values reported.

The difference between Knoop hardness values, 309 for GaSb and 304 for AlSb, is insignificant. However, for systems in which the components form solid solutions, hardness passes through a maximum at some intermediate composition because of the effects of lattice distortion (23, 24). It is possible, therefore, to use hardness measurements as an analytical tool.

Temperature-composition data. — Differential thermal analysis of selected alloy compositions

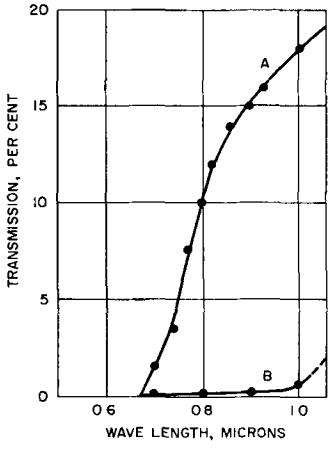

Fig. 1. Transmission for Specimen of AlSb. A, Protected from atmosphere; B, after 20-hr exposure to atmosphere.

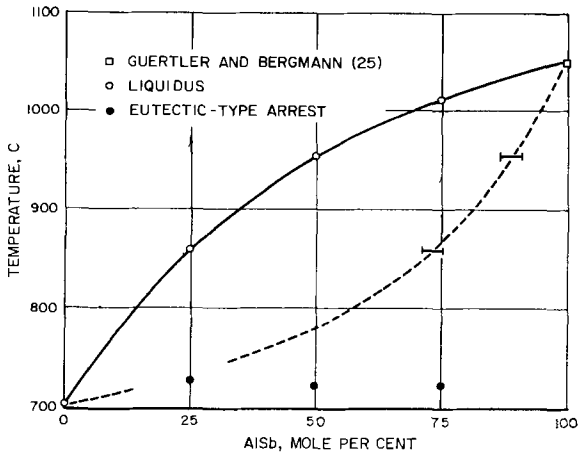

Fig. 2. Thermal data for GaSb-AlSb system

yielded accurately reproducible data on the liquidus of the system. These data are plotted in Fig. 2. Cooling curves were obtained for four compositions, at 0, 25, 50, and 75 mole % AlSb. Each liquidus point plotted represents the average of three determinations for which precision and accuracy were within the range indicated by the circle about the point. The AlSb point is that of Guertler and Bergmann (25). In each of the alloy samples, freezing took place over a wide temperature range, and near the end of freezing a "eutectic-type" arrest was noted which consistently occurred slightly above the freezing point of GaSb. The shaded circles on the plot show these latter halts.

The data are consistent with those to be expected for a system with a miscibility gap in the solid, but could also result from nonequilibrium conditions. Stohr and Klemm (26), for example, initially obtained similar data for the Si-Ge system but were able, after annealing samples for extremely long periods at temperatures slightly below the expected solidus, to demonstrate the existence of an uninterrupted range of solid solutions in that system.

Since sizeable, homogeneous alloy specimens were not available, solidus studies were not undertaken on the AlSb-GaSb system. Results of other types of studies to be discussed, however, show that wide ranges of solid solution exist in this system also and, further, strongly suggest that complete solid solution can be obtained as has been reported (27). Location of the dotted solidus curve was approximated from the results of x-ray diffraction studies (Table II) on recrystallized alloy ingots, PC-1, PC-2, ZC-1, ZC-2. As is indicated in the Fig. 2, these results suggest that if a miscibility gap exists, it is restricted to a relatively narrow composition range between about 10 and 30 mole % AlSb.

Casting.—Data for Ingot PC-1, which was progressively cast from a melt containing 75 mole % GaSb at a rate of ¼ in./hr, are typical of results obtained for ingots cast at relatively high linear crystallization rates (i.e., ¼ to 1¼ in./hr). Results of the x-ray analysis (Table II) show that two crystalline phases were present in the ingot. The minor[3] phase was very similar to pure GaSb and

[3] Major and minor are arbitrary designations used to show qualitatively the extent to which each exists.

Table II. X-ray analysis of cast ingots

Sample	Progression, %*	Phase†	Lattice constant, a_o, A	Mole % AlSb (by Vegard's law)
Progressively cast, ¼ in./hr; melt 75 mole % GaSb, 25 mole % AlSb				
PC-1-1	5	Major	6.1260 ± 0.0005	75
		Minor	6.0970 ± 0.0005	
PC-1-2	16	Major	6.1250 ± 0.0005	72
		Minor	6.0966 ± 0.0005	
PC-1-3	29	Major	6.1201 ± 0.0003	60
		Minor	6.0965 ± 0.0005	
PC-1-4	32-42	(Annealed)	6.114 ± 0.001	45
PC-1-5	55	Major	6.1077 ± 0.0003	29
		Minor	6.0962 ± 0.0005	
PC-1-6	76	(Single)	0.0963 ± 0.0003	
Progressively cast, 0.05 in./hr; melt 50 mole % GaSb, 50 mole % AlSb				
PC-2-1	20		6.1327 ± 0.0003	92
Zone cast, 0.05 in./hr; charge 50 mole % GaSb, 50 mole % AlSb				
ZC-1-1	8		6.1310 ± 0.0003	87
ZC-1-2	17		6.1288 ± 0.0003	82
ZC-1-3	47		6.1266 ± 0.0003	76
ZC-1-4	64		6.1176 ± 0.0005	54
Zone cast, 0.05 in./hr; first zone 75 mole % GaSb, 25 mole % AlSb; remainder of charge 50 mole % GaSb, 50 mole % AlSb				
ZC-2-1	9		6.1237 ± 0.0003	69
ZC-2-2	33		6.1200 ± 0.0006	60
ZC-2-3	54		6.1201 ± 0.0003	60
ZC-2-4	74		6.1007 ± 0.0006	11

* Fraction of the ingot crystallized in advance of sample location.
† Major and minor are arbitrary designations.

persisted throughout the ingot.[4] The major phase appeared to be a concentrated solid solution of the two compounds, the composition of which varied in a regular manner with progression along the ingot (Fig. 3a). Lattice parameters indicate that near the head (first to freeze) of the ingot this phase contained high concentrations of AlSb, and that the concentration of AlSb present in this solid phase decreased with progression of the solid-liquid interface along the ingot as concentration of AlSb in the melt was lowered. Beyond a point between 55 and 76% progression, where the supply of AlSb in the melt apparently was exhausted, this phase was no longer precipitated. Lattice parameters for this major phase correspond to those for solid solutions containing 75 to 29 mole % AlSb, as calculated by Vegard's law.[5]

While the polyphase nature of the AlSb-rich portion of the ingot suggests a broad miscibility gap, results of a single annealing experiment, which was carried out with a specimen from this progressively cast ingot, indicate that the polyphase material does not represent an equilibrium precipitate. Sample PC-1-4 was ground to a fine powder and was annealed for 96 hr at 650°C in an evacuated ampoule prior to examination. This anneal treatment appeared to have homogenized the polyphase material, converting it to a single-phase powder with a somewhat diffuse x-ray pattern.

Results of metallographic studies agreed with those of the x-ray analysis. In the first portions of

[4] Due to the slow evolution of antimony from the melt during recrystallization, the last portions of the ingots to be frozen were metallic (gallium) and therefore were not analyzed.

[5] Vegard's law has been found to hold for the systems, GaSb-InSb, GaAs-InAs, and InAs-InP [see ref. (6) and (9)] and has been shown at least roughly applicable in this research (see Table IV).

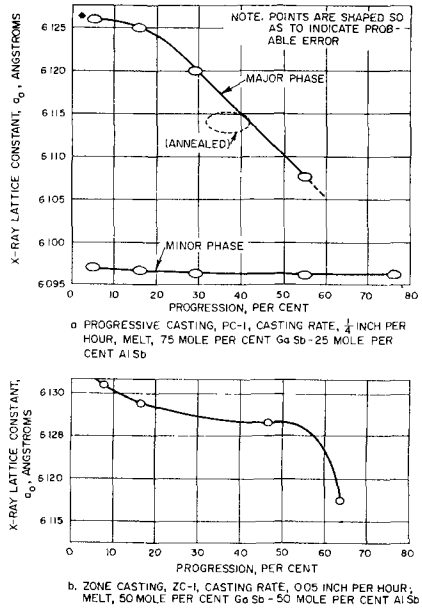

Fig. 3. Cell size as a function of progression along cast ingots.

ingots cast at relatively high linear crystallization rates (≧¼ in./hr) two distinct phases were present, while only a single GaSb-rich phase was present in the last portions. Knoop hardness values were determined for the two phases by carefully placing the indenter on selected crystallites. Values for the minor phase were consistently low, averaging about 310, which is close to the KHN for pure GaSb. Values for the major phase, however, were significantly higher, ranging up to 348, as would be expected for concentrated solid solutions.

It was possible, by use of a very low rate of crystallization, to prepare single-phase ingots of the solid-solution alloy. This is shown by the results of x-ray diffraction analyses (Table II) of samples from the ingots which were cast at a rate of 0.05 in./hr. Lattice parameters for the single-phase solid solutions thus obtained indicate that concentrations of AlSb present in the solutions ranged from 11 to 92 mole %, assuming Vegard's law to apply throughout the range.[6] Results of metallographic studies also

[6] Note the precipitous drop in cell size between progressions 54 and 74 in Ingot ZC-2. Further note that in these ingots, no cell sizes corresponding to AlSb contents between 11 and 29 mole % have been observed. If, as these results suggest, a miscibility gap exists, Vegard's law should not be expected to hold near the solubility limit.

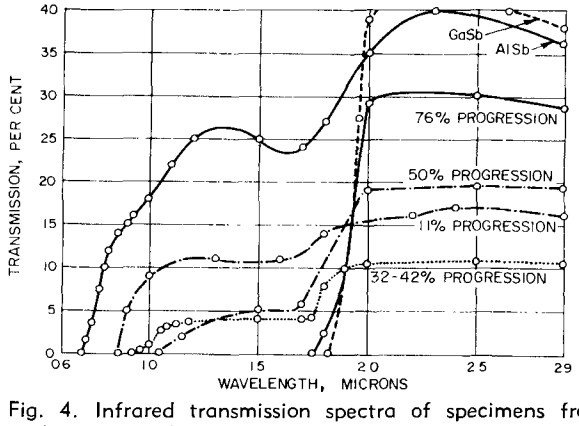

Fig. 4. Infrared transmission spectra of specimens from typical progressively cast ingot PC-1 and of the compounds GaSb and AlSb. Ingot PC-1: Casting rate, ¼ in./ hr; melt, 75 mole % GaSb-25 mole % AlSb.

indicated that these ingots were single phase, solid-solution alloys. Knoop hardness, determined at random locations on a section from the center of Ingot PC-2, progressively cast from a melt containing 50 mole % GaSb was 335 ±7.

The plot of lattice constant vs. progression for Ingot ZC-1 (Fig. 3b), which was prepared by zone casting a charge containing 50 mole % GaSb, follows the relationship expected for a system, or range of compositions, in which the components form solid solutions. Extent of the nearly flat portion of the curve indicates that this technique offers promise as a method for producing sizeable homogeneous specimens of the alloy.

Ingot ZC-2 was formed by zone casting a charge made up of two alloy compositions (an alloy containing 75 mole % GaSb in the first zone length, and an alloy containing 50 mole % GaSb in the remaining length) in an attempt to produce an ingot of more uniform composition. Variation of lattice constants, however, indicates that the estimated location of the solidus, which was used to select the compositions and was based on knowledge of the system at that time, was in error. Composition varied near the head of the ingot, but was again nearly constant over a considerable range of progression in the central regions.

Optical data.—Infrared transmission spectra of specimens from the polyphase Ingot PC-1 are shown in Fig. 4 along with those of the compounds GaSb and AlSb. Energy gap values, summarized in Table III, were computed from these spectra according to the convention described above, which yields gap values generally consistent with other physical parameters for the respective specimens. The spectrum of the specimen taken at 76% progression is seen to be nearly identical with that of GaSb, and shows an absorption edge which corresponds to an energy gap of 0.69 ev. Reading from short to long wave lengths, spectra of the other three specimens each shows a sharp rise in transmission followed by a plateau which is in turn followed by a second sharp rise to peak transmission and then gradual decline to the long wave tail. This is the type of spectrum one might expect for a specimen composed of individual crystallites of two different phases with unequal energy gaps, providing that the crystallites were so disposed that those of one phase do not interfere with transmission through those of the second. (Such disposition of crystallites is quite probable in the polyphase specimens studied.) If such were the case, the threshold of transmission should correspond to that of the second phase.

Applying this interpretation, and normalizing to equal peak transmission for the two phases, energy gaps calculated for specimens at 11, 32, and 50% progression are 1.43 and 0.72 ev, 1.28 and 0.70 ev, and 1.12 and 0.70 ev, respectively. Note that the smaller gap in each case is very nearly equal to that measured for GaSb, as are x-ray lattice constants for the minor phase in each of the specimens from this ingot. It is also possible that manifestation of the absorption band attributed to spin orbit splitting (28), which is present in the spectra of p-type AlSb (and which can also be seen in the spectra of AlSb and of the single phase samples presented here), is responsible for the behavior observed in the vicinity of 1.7μ. However, the plateau and second rise in transmission are very sharply defined, particularly for the samples at 32-42 and 50% progression, whereas gradual changes are characteristic of the absorption due to the spin orbit splitting.

Table III. Optical data for cast ingot*

Sample	Progression along ingot, %	Mole % AlSb (by Vegard's law)	Absorption edge, mμ	Energy gap, electron-volts
PC-1-1a	11	—	865	1.43
PC-1-4	32-42	45	965	1.28
PC-1-4a	50	—	1110	1.12
PC-1-6	76	1	1790	0.69
PC-2-1	20	92	758	1.63
ZC-1-1	9	87	800	1.55
ZC-1-2	16	82	815	1.52
ZC-1-3	31	—	830	1.49
ZC-1-4	53	—	842	1.47
ZC-2-1	9	69	845	1.46
ZC-2-2	33	60	865	1.43
ZC-2-3	54	60	900	1.38
ZC-2-4	74	11	1670	0.74

*Ingot	Casting rate	Charge (mole %)
PC-1	0.25 in./hr	75 GaSb—25 AlSb
PC-2	0.05 in./hr	50 GaSb—50 AlSb
ZC-1	0.05 in./hr	50 GaSb—50 AlSb
ZC-2	0.05 in./hr	75 GaSb—25 AlSb in first zone 50 GaSb—50 AlSb, remainder

Regardless of the phenomena responsible for the 1.7μ absorption, there is little doubt that the spectra show, by the different wave lengths for threshold transmission for the various specimens, the presence of materials with various energy gaps, which decrease from about 1.4 to 0.7 ev with progression along the ingot. It seems clear that these are the energy gaps of solid solutions that increase in GaSb content with progression along the ingot.

Spectra for single phase specimens from the zone cast ingots (Fig. 5 and 6) show well-defined absorption edges, the locations of which indicate that energy gaps for these single phase alloys ranged from 1.55 to 0.74 ev. The relatively small changes in energy gap over rather wide ranges of progression for the zone-cast ingots (Fig. 7), again indicate that this technique offers promise as a method for producing single-phase alloy of uniform composition.

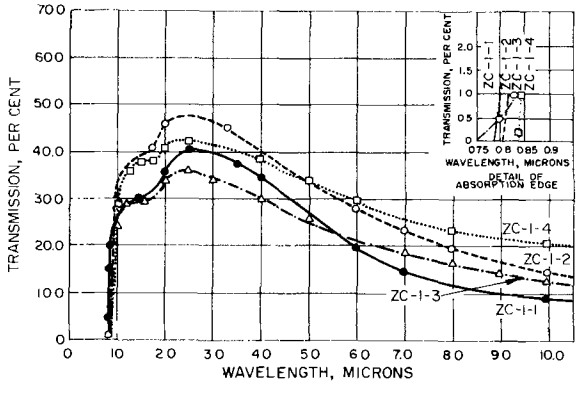

Fig. 5. Infrared-transmission spectra of specimens from zone-cast ingot ZC-1. Casting rate, 0.05 in./hr; charge, 50 mole % GaSb-50 mole % AlSb.

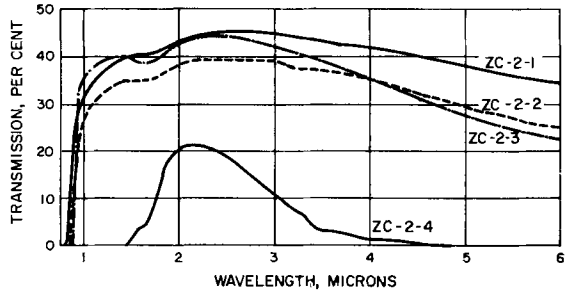

Fig. 6. Infrared transmission spectra of specimens from zone-cast ingot, ZC2. Casting rate, 0.05 in./hr; charge in first zone, 75 mole % GaSb-25 mole % AlSb; remainder of charge, 50 mole % GaSb-50 mole % AlSb.

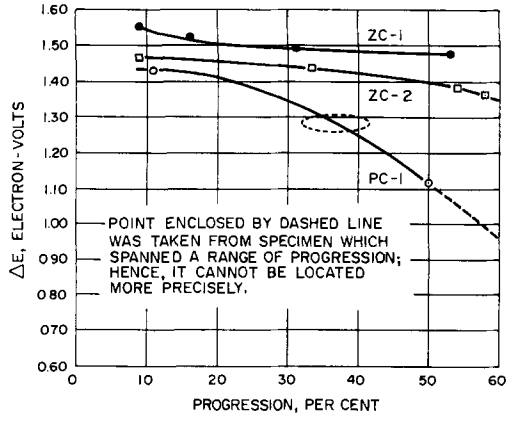

Fig. 7. Optical energy gap vs. progression for cast ingots. ZC-1: Zone cast at 0.05 in./hr; charge, 50 mole % GaSb-50 mole % AlSb. ZC-2: Zone cast at 0.05 in./hr; charge, 75 mole % GaSb-25 mole % AlSb in first zone, 50 mole % GaSb-50 mole % AlSb in remainder. PC-1: Progressively cast at ¼ in./hr; charge, 75 mole % GaSb-25 mole % AlSb.

Electrical data.—Electrical measurements have been made both at room temperature and over a range of temperatures for a number of the alloy specimens, but to date, these studies have not progressed far enough to permit the drawing of accurate conclusions. Data for single-phase specimens from Ingot ZC-2, which are presented in Table IV, show a regular variation of resistivity with composition. Figures 8 and 9 show variation of resistivity, Hall coefficient, and mobility as a function of temperature for Sample ZC-2-2. The curves appear to be typical of those generally obtained in the extrinsic region for an impure, high energy gap semiconductor. Mobility for the alloy (Fig. 9) appears to exhibit an approximate $T^{-3/2}$ temperature dependence above 700°K, suggesting that lattice scattering predominates here.

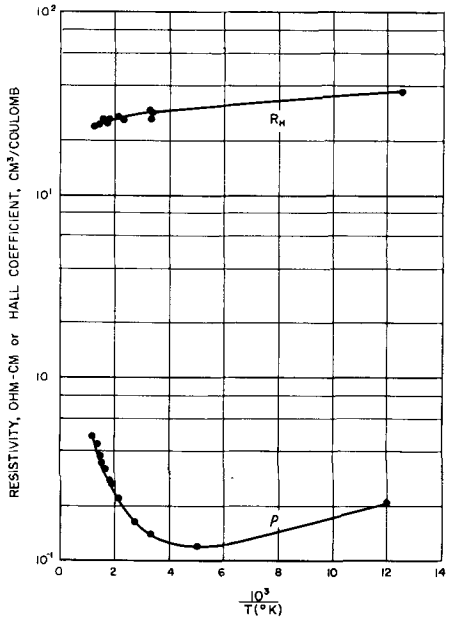

Fig. 8. Hall coefficient and resistivity vs. temperature for single-phase GaSb-AlSb alloy specimen ZC-2-2 (40 mole % GaSb-60 mole % AlSb by Vegard's law).

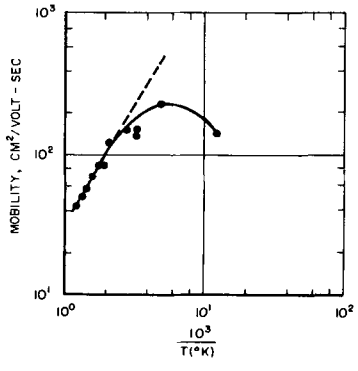

Fig. 9. Mobility as a function of reciprocal temperature for single-phase GaSb-AlSb alloy (40 mole % GaSb-60 mole % AlSb by Vegard's law).

Correlation of Data

More comprehensive analysis was made of material present in zone cast Ingot ZC-2 than of any other material treated in this study. Results of chemical, x-ray, optical, and electrical analyses for four single-phase specimens from this ingot have been summarized in Table IV. The chemical anal-

Table IV. Analysis of zone cast ingot, ZC2*

Sample	Progression along ingot, %	Chemical: Mole %, GaSb	X-ray: Lattice constant, a_o (Å)	X-ray: Mole % GaSb (by Vegard's law)	Optical: Energy gap, ΔE (ev)	Electrical: Hall coefficient, R_H (cm^3/coulomb)	Electrical: Resistivity, ρ (ohm-cm)	Electrical: Mobility, μ (cm^2/volt-sec)	Electrical: Density of carriers, n_p (cm^{-3})
ZC2-1	9	26 ± 4	6.1237 ± 0.0003	31 ± 1	1.46	+58	0.22	264	1.3×10^{17}
ZC2-2	33	38 ± 2	6.1200 ± 0.0006	40 ± 2	1.43	+29	0.11	264	2.6×10^{17}
ZC2-3	54	45 ± 3	6.1201 ± 0.0003	40 ± 1	1.38	+20	0.075	264	3.7×10^{17}
ZC2-4	75	96 ± 3	6.1007 ± 0.0006	89 ± 2	0.74	+5	0.014	357	1.5×10^{18}

* Casting rate, 0.05 in./hr; charge, 75 mole % GaSb—25 mole % AlSb in first zone, 50 mole % GaSb—50 mole % AlSb in remainder.

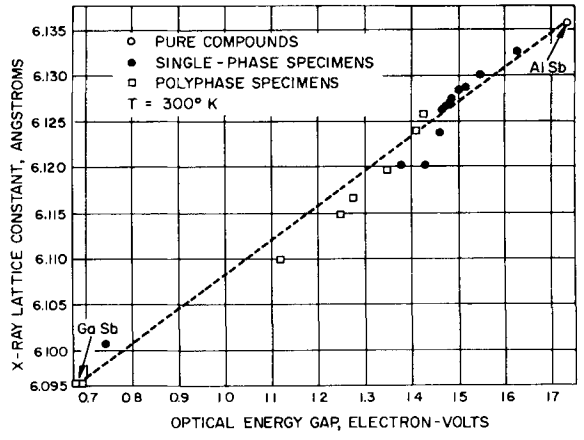

Fig. 10. Energy gap vs. cell size for solid solutions of GaSb-AlSb.

yses were run on very small samples and therefore must be assigned rather wide error limits. Nevertheless, the results constitute direct evidence that concentrated solid solution alloy was obtained. Compositions determined by chemical and x-ray analyses agree reasonably well, differing by only about 2 mole % (beyond stated limits of error) at maximum, thus confirming the applicability of Vegard's law in this system, at least for rough composition determination. The increase in carrier concentration with progression along the ingot probably results from the segregation of an impurity (or impurities) during recrystallization, but could also rise from loss of antimony.

Figures 3 and 7 show variation in lattice constant and energy gap with progression along typical ingots. These two sets of data were combined by eliminating the common variable, percentage progression, where this could accurately be done (i.e., where both parameters had been determined for a single specimen, or in regions of regular variation for the parameters). The combined data have been plotted in Fig. 10. Although there is some scattering of the points, an approximately linear relationship between energy gap and cell size is indicated.

Summary

Ingots of GaSb-AlSb alloy were crystallized from melts (cast) under various conditions. Results of x-ray and metallographic studies, hardness tests, optical transmission studies, and chemical analyses of alloy specimens indicate that:

1. Solid solution prevails in the system, with possible exception of a narrow composition range between 10 and 30 mole % AlSb, which was not investigated.

2. Bulk specimens of single phase, solid solution alloy can be prepared by use of low linear rates of crystallization (0.05 in./hr).

3. At higher linear rates of crystallization (¼ to 1¼ in./hr), two intermingled solid phases are characteristically obtained.

4. The zone casting technique offers promise as a method for producing single phase alloy of uniform composition.

5. An approximately linear relationship exists between lattice parameter and composition of the single phase GaSb-AlSb alloys.

6. An approximately linear relationship exists between lattice parameter and energy gap of the single phase GaSb-AlSb alloys.

Acknowledgment

This work was supported by Union Switch and Signal, Division of Westinghouse Air Brake Company. The authors are also indebted to A. E. Austin for the x-ray work, R. D. Bucheit, who made the metallographic studies, C. D. Smith and R. W. Koch for assistance with optical studies, and J. W. Moody, who made the electrical measurements.

Manuscript received Aug. 11, 1959. This paper was prepared for presentation at the Chicago Meeting, May 1-5, 1960.

Any discussion of this paper will appear in a Discussion Section to be published in the December 1960 JOURNAL.

REFERENCES

1. W. Koster and B. Thoma, *Z. Metallkunde*, **46**, 293 (1955).
2. C. Kolm, S. A. Kulin, and B. L. Averbach, *Phys. Rev.*, **108**, 965 (1957).
3. N. A. Goryunova and N. N. Fedorova, *J. Tech. Phys. (U.S.S.R.)*, **24**, 1339 (1955).
4. J. C. Woolley, B. A. Smith, and D. G. Lees, *Proc. Phys. Soc. (London)*, **B69**, 1339 (1956).
5. J. C. Woolley and B. A. Smith, *ibid.*, **72**, 214 (1958).
6. I. G. Greenfield and R. L. Smith, *Trans. Am. Inst. Mining Met. Engrs.*, **203**, 351 (1955).
7. C. Shih and E. A. Peretti, *J. Am. Chem. Soc.*, **74**, 608 (1953).
8. J. S. Blakemore, *Can. J. Phys.*, **35**, 91 (1957).
9. O. G. Folberth, *Z. Naturforsch.*, **10a**, 502 (1955).
10. W. G. Pfann, *J. Metals*, **4**, 747 (1952).
11. J. B. Nelson and D. P. Riley, *Proc. Phys. Soc. (London)*, **57**, 160 (1945).
12. R. W. Koch, J. F. Miller, and H. L. Goering, "Band Separations of a Number of Semiconducting Compounds From Optical Data," paper presented before The Electrochemical Society, May 5, 1954.
13. R. F. Blunt, W. R. Hosler, and H. P. R. Frederikse, *Phys. Rev.*, **96**, 576 (1954).
14. R. F. Blunt, H. P. R. Frederikse, J. H. Becker, and W. R. Hosler, *ibid.*, **96**, 578 (1954).
15. R. K. Willardson, A. C. Beer, and A. E. Middleton, *This Journal*, **101**, 354 (1954).
16. L. Pauling, *J. Am. Chem. Soc.*, **69**, 542 (1947).
17. H. Leifer and W. Dunlap, *Phys. Rev.*, **95**, 51 (1954).
18. R. G. Breckenridge, R. F. Blunt, W. R. Hosler, H. P. R. Frederikse, J. H. Becker, and W. Oshinsky, *Physica*, **20**, 1073 (1954).
19. V. Roberts and J. E. Quarrington, *J. Electronics*, **1**, 152 (1955).
20. F. Oswald and R. Schade, *Z. Naturforsch.*, **9a**, 611 (1954).
21. H. J. Hrostowski and M. Tannenbaum, *Physica*, **20**, 1065 (1954).
22. R. F. Blunt, H. P. R. Frederikse, and J. H. Becker, *Phys. Rev.*, **94**, 1431 (1954).
23. J. H. Frye and W. Hume-Rothery, *Proc. Roy. Soc.*, **A181**, 1 (1942).
24. J. H. Frye and J. W. Camm, *Trans. Am. Inst. Mining Met. Engrs.*, **152**, 75:83 (1943).
25. W. Guertler and A. Bergmann, *Z. Metallkunde*, **25**, 81 (1933).
26. H. Stohr and W. Klemm, *Z. anorg. u. allgem. Chem.*, **241**, 314 (1939).
27. U. S. Pat. No. 2,710,253, R. K. Willardson, H. L. Goering, and A. E. Middleton to Battelle Development Corporation.
28. R. Braunstein, "Intervalence Band Transitions in GaAs," paper presented before International Conference on Semiconductors, August 18, 1958, Rochester, New York. See also R. Braunstein, *Phys. Rev.*, **111**, 480 (1958).

The Diffused Shot-melting Technique for Making Germanium and Silicon p-n Junction Devices

I. A. Lesk

Semiconductor Products Department, General Electric Company, Syracuse, New York

ABSTRACT

The diffused shot-melting technique involves the melting and resolidifying of a piece (conveniently obtained in the form of shot) of semiconductor on a wafer of the same material (having essentially the same melting point) to form a single crystal boundary region, and the subsequent diffusion of impurities across the interface. Shot-melting may be done so quickly that the interface coincides with the original surface of the wafer. Impurity contents of the shot and wafer may be chosen so that a variety of p-n junction devices results after diffusion, and several junctions may be made on the same wafer by this process to form more complex structures. Although lifetime and resistivity changes generally occur, they can often be minimized by subsequent treatment such as alloy gettering or annealing. Simplicity and flexibility of diffused shot-melting have made it a convenient laboratory technique for making many semiconductor devices.

It is often necessary in the study and design of solid state structures to make a fairly large number of devices having different impurity concentrations and geometries in order to test theories and ideas as they are generated. For greatest versatility, the processes used should be simple and flexible. Although many excellent device fabrication techniques already exist and are used in manufacturing, development, and research, diffused shot-melting has some unique advantages that make its application particularly inviting in some cases.

Shot Melting

The shot melting technique involves the melting and resolidifying of a piece [conveniently obtained in the form of shot (1)] of semiconductor on a wafer of the same material (having essentially the same melting point) to form a single crystal boundary region. Melting of the wafer is prevented by providing a large vertical thermal gradient. Figure 1 illustrates this process, the example chosen being a p-type region on an n-type base. In Fig. 1(a), the shot is placed on top of the n-type wafer. The shot is generally polycrystalline, containing an impurity concentration up to 1% or so. When the heat source, located above the semiconductor pieces, is turned on, the shot starts to melt from the top. The liquid surface contour forms a section of a sphere, so that by the time the shot is all molten it has only a very small area of contact with the n-type pellet, Fig. 1(b). The pellet will not start to melt at this point because of the large vertical temperature gradient, provided by placing the heater above the work and by resting the n-type wafer on a large thermal capacity support. The shot is completely melted because heat is entering it from the top, and very little heat is leaving the bottom by conduction due to the small area of contact with the wafer. This condition lasts but a very short period of time (of the order of a second), following which the molten sphere suddenly spreads at an extremely rapid rate and immediately freezes back part way into a pyramidal shape, Fig. 1(c). At this time the heat source may be removed so the structure freezes the rest of the way, Fig. 1(d). If the heat source were not turned off, the pyramid and then the wafer would subsequently melt.

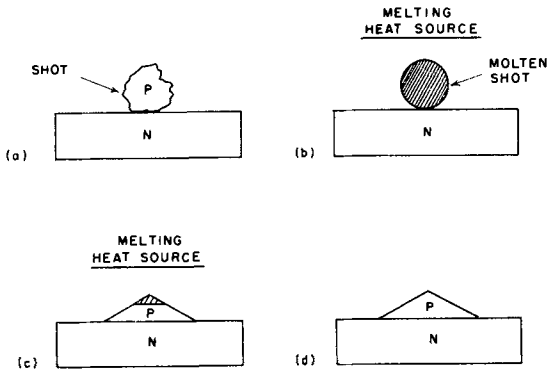

Fig. 1. Steps in the shot-melt process. (a) Shot (p-type) placed on wafer (n-type); (b) heat source turned on, shot just finished melting; (c) heat source unchanged, shot suddenly spreads on wafer and partly refreezes; and (d) heat source turned off, remaining part of shot frozen.

The shot-melt process would be of limited general use in semiconductor device technology were it not for the following two properties.

1. The p-type semiconductor region that forms adjacent to the n-type pellet is single crystal growing epitaxially on the pellet. After a short distance (of the order of a mil) it becomes polycrystalline. However, a single crystal region this thick is more than adequate for most devices. Figure 2 is a photomicrograph of a silicon shot-melt structure section, showing the p-n junction, the n-type pellet, and the grown p-type single crystal region which ends in polycrystalline p-type silicon. The pattern brought

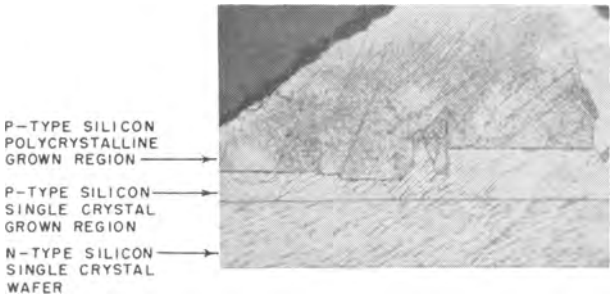

Fig. 2. Photomicrograph of silicon shot-melt p-n junction structure showing single crystal grown region. X190.

out in the single regions by the etch (10% sodium hydroxide, 15% sodium nitrite in water at about 100°C) shows that they have the same orientation.

2. If a very large thermal gradient is maintained, the boundary between pellet and shot-melt regions will coincide very closely with the original surface of the pellet. That is, the penetration of the molten shot into the pellet surface is exceedingly small. Figure 3 is a photomicrograph of a germanium pellet with shot melt regions on both sides (pnp structure) showing that the planes of the p-n junctions are flat and coincide closely with the original surfaces of the pellet. As sometimes occurs with large shot-melt regions, two small voids may be seen in the bottom (p-type) grown region.

The following explanation is proposed to account for the lack of penetration of the molten region into the pellet surface. When the shot first becomes entirely molten, it does not make intimate contact with the pellet. Surface oxide on the pellet may be at least partially responsible for this, since silicon appears to remain at this stage longer than germanium. When intimate contact between the molten and solid semiconductor regions is established at the point of contact between the sphere and plane, lateral wetting is greatly enhanced, and the area of intimate contact quickly increases. As each new incremental area of contact forms, thermal flow to the cooler substrate quickly freezes a small volume of the molten material onto the substrate. As spreading proceeds, the heat content of the shot becomes depleted, so the already deposited regions get thicker. Hence, crystal growth takes place radially as well as upward, the final diameter of the pyramid being determined by the heat content of the molten sphere as well as the temperature, thermal capacity and surface condition of the pellet. If larger shot are used, the spreading will proceed until limited by the edges of the pellet (c. f. bottom region, Fig. 3).

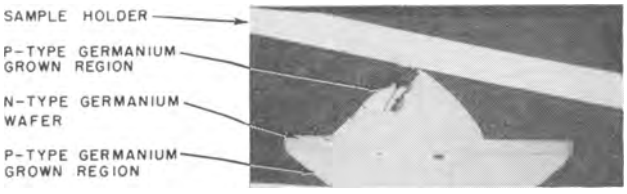

Fig. 3. Photomicrograph of germanium double shot-melt p-n-p junction structure showing how original surface of n-type wafer is preserved. X40.

Diffused Shot-Melting

Because of the short heat cycle during shot melting, little diffusion of the common donor and acceptor impurities takes place even though the temperature is high. Hence, an abrupt boundary exists between the two regions. If graded junctions are required, a diffusion cycle (most conveniently done in a separate furnace) may be subsequently used. When a diffusion cycle follows shot-melting, the complete process will be referred to as diffused shot-melting.

The shot may be made to contain two (or more) impurities. If the ratios of majority to minority impurity concentrations and diffusion coefficients are chosen in the right ranges, then the minority impurity will diffuse ahead and become the majority impurity in a narrow region of the pellet adjacent to the shot-pellet interface. Figure 4 illustrates this process to make a germanium pnp transistor structure.

The impurity concentrations in the grown shot region adjacent to the pellet may be calculated from those in the (uniformly doped) molten shot by taking into account their distribution coefficients. However, since the growth rate is variable, so will be the distribution coefficients (2, 3). The impurity concentration in the shot melt region probably is that governed by the equilibrium distribution coefficient, in a thin plane adjacent to the pellet, and increases with distance into the pyramid because the growth rate increased with distance into the pyramid. For diffused bases, the impurity concentration is critically dependent on that in the source region in a layer approximately as thick as the diffused base itself. For very thin diffused bases, therefore, a first approximation (4) is to assume diffusion from a region of high uniform impurity concentration (determined by the equilibrium distribution coefficients) into a region of low uniform impurity concentration (that of the original pellet). In practice, this approximation has worked well.

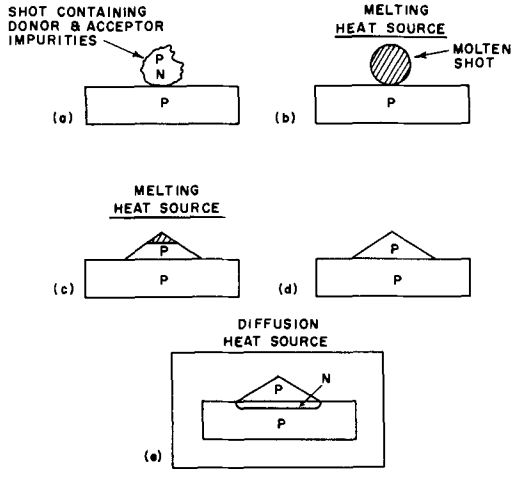

Fig. 4. Steps in the diffused shot-melt process. (a) Shot (containing donor and acceptor impurities) placed on wafer (p-type); (b), (c), (d) same as in Fig. 1; and (e) structure heated, n-type layer formed in wafer by diffusion.

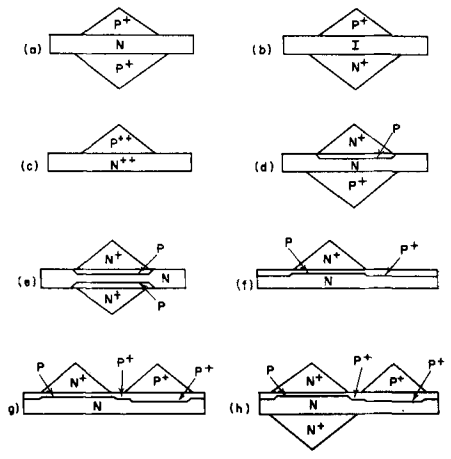

Fig. 5. Some example of shot-melt and diffused shot-melt structures. (a) pnp transistor; (b) pin diode; (c) tunnel diode; (d) pnpn switch; (e) npnpn symmetrical switch; (f) npn transistor; (g) npn transistor with 2 shot-melt contacts; and (h) npn transistor with 3 shot-melt contacts.

Application to Some Semiconductor Devices

Some examples of shot-melt and diffused shot-melt devices, all of which have been made and tested, are shown in Fig. 5. Figure 5(a) illustrates a pnp transistor made by melting shot on either side of a wafer. A similar structure, made to yield a pin diode, is shown in Fig. 5(b). A shot melt structure in which both p-type and n-type regions are degenerate, Fig. 5(c), has a tunnel diode characteristic. This requires a p-n barrier width of at most a few hundred angstroms, giving proof of the abrupt nature of the impurity transition at the boundary between shot and wafer. Figure 5(d) illustrates a pnpn switch, made by diffused shot-melting with double doped shot on one side of the wafer, singly doped shot on the other. This may be extended somewhat to make a symmetrical npnpn switch, as shown in Fig. 5(e).

Surface diffusion can be done at the same time as the bulk diffusion. A structure made in this way is depicted in Fig. 5(f), in which the surface diffused layer is left on only the top side of the wafer. The surface concentration of the vapor diffused layer must be less than that in the shot if a p-n junction is not to form over the surface of the pyramid. In Fig. 5(g) a singly doped p-type shot is placed beside the doubly doped shot (left), and the device diffused in an atmosphere containing an acceptor impurity. The result is a transistor structure, the left pyramid serving as the emitter, the right one as the base. This device is made somewhat more complex in Fig. 5(h), where an n-type impurity doped shot, to serve as a collector contact (bottom) is made before (or after) the diffusion cycle. In this figure, the surface diffused layer is removed from all wafer surfaces except the top one.

Devices made by the diffused shot-melting technique often did not have electrical characteristics as good as those made by other techniques. This is because there is a severe lifetime degradation during the shot-melt cycle, junction size is hard to control, lateral junction spacing [i.e., Fig. 5(h)] is not easy to reproduce, and resistivity often changes when the starting value is high. Nevertheless the ease and versatility with which semiconductor p-n junction structures may be made by diffused shot-melting make its use particularly attractive in some cases. The structures have no low melting components to limit fabrication and assembly techniques. Diffusion is from a volume source, so, except in structures where surface diffused layers are also required, no precise atmospheric control during diffusion is needed. Also, some or all of the lifetime and resistivity degradation produced during the shot-melt cycle can be removed by processes such as surface alloy gettering or annealing during or subsequent to the diffusion cycle.

Acknowledgment

The help of Mrs. L. Roehrig and N. E. Collins in fabricating the structures, and of C. V. Bielan and F. A. Carranti in making the metallographic sections and photomicrographs, is greatly appreciated.

Manuscript received Nov. 18, 1959. This paper was prepared for delivery before the Columbus Meeting, Oct. 18-22, 1959.

Any discussion of this paper will appear in a Discussion Section to be published in the December 1960 JOURNAL.

REFERENCES

1. I. A. Lesk, *This Journal*, **103**, 601 (1956).
2. R. N. Hall, *J. Phys. Chem.*, **57**, 836 (1953).
3. J. A. Burton, R. C. Prim, and W. P. Slichter, *J. Chem. Phys.*, **21**, 1987 (1953).
4. I. A. Lesk and R. E. Coffman, *J. Appl. Phys.*, **29**, 1493 (1958).

Polarographic Studies in Acetonitrile and Dimethylformamide

V. Behavior of Aromatic Ketones and Aldehydes

S. Wawzonek and A. Gundersen

Department of Chemistry, State University of Iowa, Iowa City, Iowa

ABSTRACT

Benzophenone, acetophenone, p-methoxyacetophenone, benzaldehyde, and anisaldehyde are reduced stepwise polarographically in anhydrous dimethylformamide. Large-scale electrolytic reduction of benzophenone indicates that the ketyl anion is formed as a stable intermediate since, in the presence of carbon dioxide and ethyl iodide, benzilic acid and diphenylethylcarbinol are formed, respectively. Acetophenone, benzaldehyde, and anisaldehyde form principally pinacols under these conditions. The reduction of p-methoxyacetophenone is complicated by tar formation.

Previous polarographic studies in acetonitrile and dimethylformamide have shown that this method is capable of furnishing evidence for the existence of stable anion-free radicals in the reduction of aromatic hydrocarbons (1, 2) and semiquinone anions in the reduction of quinones(3).

In the present study the polarographic behavior and electrolytic reduction of aromatic ketones and aldehydes has been investigated to determine whether ketyl anions are produced in dimethylformamide.

Experimental

The solutions were studied in a cylindrically shaped cell with a mercury pool anode and fitted with side arms for the anode connection and for admission of nitrogen. All measurements were made in a water thermostat at 25° ± 0.1°.

The current-voltage curves were obtained with a Sargent Model XII polarograph having a current scale calibration of 0.00497 μa/mm at a sensitivity of one.

The dropping mercury electrode was operated at 60 cm pressure and had a drop time of 3.42 sec in dimethylformamide (open circuit). The $m^{2/3}t^{1/6}$ value was 1.96 $mg^{2/3}$ $sec^{1/2}$.

The dimethylformamide was purified in a manner similar to that reported previously (1). The compounds were obtained from stock and purified by crystallization or distillation.

Electrolytic Reductions

The electrolytic reductions of the various carbonyl compounds were carried out at a platinum anode and mercury cathode in a similar manner to that described earlier (1). The area of the cathode was 65 cm^2 and the line voltage was 80 v. Typical procedures are illustrated below. The results are given in Table II.

Benzophenone.—A solution of 5 g of benzophenone and 7.72 g of potassium iodide in 300 ml of dimethylformamide was deoxygenated with nitrogen for 1 hr. Direct current was allowed to pass through the cell for 20 hr and gave a blue solution.

The catholyte and anolyte were poured into 50 ml of 10% acetic acid solution and the solvent was removed under reduced pressure at 100°. Extraction with ether followed by removal of the solvent gave an oil which was soluble in isopropyl alcohol and in hot petroleum ether. Benzopinacol, if present, would be insoluble in these solvents. When the petroleum ether was cooled, 2.8 g of benzohydrol melting at 66°-68° was obtained. A mixture with an authentic sample melted at the same point. The benzophenone which remained in the petroleum ether was determined in some of the experiments as the oxime.

Benzophenone and carbon dioxide.—A solution of dimethylformamide (300 ml) containing potassium iodide (7.72 g) and benzophenone (5 g) was deoxygenated with carbon dioxide for 1 hr. Electrolysis was carried out for 20 hr while a stream of carbon dioxide was passed through the solution. The cathode compartment remained colorless during the electrolysis. Removal of the solvent under reduced pressure gave a residue which was extracted with ether. The ether insoluble portion was found to be water soluble. Upon acidification of the aqueous solution benzilic acid (3.1 g) melting at 149°-152° precipitated. A mixture with an authentic sample melted at the same point.

Benzophenone and ethyl iodide.—A solution of potassium iodide (7.72 g) and benzophenone (20 g) in dimethylformamide (300 ml) was deoxygenated with nitrogen for 1 hr and then electrolyzed for 15 hr. During the electrolysis, oxygen-free ethyl iodide was dropped into the cathode compartment. Removal of the solvent under reduced pressure was followed by extraction with ether. The yellow oil (17.5 ml) obtained was freed of benzophenone by refluxing with hydroxylamine hydrochloride (9 g) and potassium hydroxide (15 g) in ethanol (30 ml) and water (6 ml) for 5 min. The solution was poured into 1*N* potassium hydroxide (200 ml) and extracted with hexane. After concentration and cooling of the hexane solution 3.2 g of diphenylethylcarbinol melting at 93°-95° was recovered. A

mixture with an authentic sample melted at the same point.

Acetophenone.—A solution of dimethylformamide (300 ml) containing 17 g of tetrabutylammonium iodide and 20 g of acetophenone, was deoxygenated with nitrogen for 1 hr and then electrolyzed for 14 hr. The resulting solution was poured into 600 ml of water containing 20 ml of acetic acid. Extraction with ether was followed by concentration to 100 ml. The resulting solution on mixing with 200 ml of hexane, concentrating, and cooling gave 6.0 g of meso-acetophenone pinacol melting at 117°-120°. A mixture with an authentic sample melted at the same point.

Results

The polarographic data obtained for the various aromatic ketones and aldehydes in various solutions are given in Table I. The waves in all cases were well defined. The addition of water shifted both waves to more positive potentials.

The half-wave potentials of the second wave for benzophenone, acetophenone, and benzaldehyde are more negative than those reported by Given (4). Since the addition of water shifts the second wave to more positive potentials, the latter study was probably carried out in dimethylformamide which was not completely anhydrous.

To help formulate electrode reactions and identify intermediate species large-scale electrolytic reductions were carried out with benzophenone, acetophenone, benzaldehyde, *p*-methoxybenzaldehyde, and *p*-methoxyacetophenone in the presence and absence of carbon dioxide. An electrolysis also was performed with benzophenone in the presence of ethyl iodide. Complete analysis of the products from compounds other than benzophenone was prevented by the formation of tars and oils. Results are summarized in Table II.

Table I. Polarographic behavior of aromatic ketones and aldehydes in dimethylformamide containing 0.175*M* tetrabutylammonium iodide and varying amounts of water

Compound	Conc.[a]	% Water by volume	$E_{1/2}$ (v) vs. Hg pool 1st Wave	$E_{1/2}$ (v) vs. Hg pool 2nd Wave	I_d[b] 1st Wave	I_d[b] 2nd Wave
Benzophenone	2.34	0	—1.21	—1.78	1.32	0.88
		0.99	—1.19	—1.69	1.33[c]	0.88[c]
		4.76	—1.17	—1.62	1.34[c]	0.70[c]
		9.09	—1.14	—1.57	1.39[c]	0.68[c]
Acetophenone	0.985	0	—1.46	—2.15	1.41	0.55
		0.99	—1.42	—2.05	1.35[c]	1.46[c]
		4.76	—1.37	—1.99	1.34[c]	0.98[c]
		9.09	—1.33	—1.96	1.29[c]	0.95[c]
Benzaldehyde	1.93	0	—1.28	—2.17	2.11	1.18
		0.99	—1.24	—2.09	2.10[c]	1.57[c]
		4.76	—1.20	—2.05	2.00[c]	1.49[c]
		9.09	—1.19	—2.02	1.82[c]	1.48[c]
p-Methoxyacetophenone	1.03	0	—1.50	—1.99	1.88[d]	0.81[d]
p-Methoxybenzaldehyde	0.993	0	—1.48		1.86[e]	

[a] Millimoles per liter.
[b] $I_d = i_d/Cm^{2/3}t^{1/6}$.
[c] Corrected for change in concentration of compound.
[d] Capillary with $m^{2/3}t^{1/6}$ of $mg^{2/3}sec^{-1/2}$ and a droptime of 3.60 sec (open circuit) at 45 cm pressure.
[e] Capillary with $m^{2/3}t^{1/6}$ of 1.56 $mg^{2/3}sec^{-1/2}$ and a droptime of 3.91 sec (open circuit) at 50 cm pressure.

Discussion of Results

Examination of the results in Table I indicates that aromatic ketones and aldehydes are reduced stepwise at the dropping mercury electrode in anhydrous dimethylformamide. In contrast to its effect on the waves of hydrocarbons and quinones addition of water caused little change in the first wave, but caused a shift of the second to more positive potentials and an increase of the diffusion current in some examples. The double waves found are similar to those reported in aqueous alkali by Ashworth (5) and would suggest the following general mechanism of reduction for these compounds.

$$R_2C{=}O + e \rightarrow R_2C{-}O^- \text{ (1st wave)}$$

$$R_2C{=}O + 2e \rightarrow R_2C{-}O^- \text{ (2nd wave)}$$

Evidence for these electrode reactions is the observation made in the large-scale electrolytic reduction of benzophenone. In solutions in dimethylformamide containing potassium iodide, in which only the first polarographic wave is obtained, a blue coloration is produced. A similar color is reported for the monosodium derivatives of benzophenone in liquid ammonia (6).

The presence of the intermediate ketyl anion for benzophenone was further demonstrated by the electrolysis of benzophenone in the presence of carbon dioxide and ethyl iodide with potassium iodide as a supporting electrolyte; benzilic acid and diphenylethylcarbinol were formed, respectively. If the reduction is carried out in the absence of these reagents or in the presence of water, the blue color is discharged, slowly in the first case, and benzophenone and benzohydrol are obtained. Changing the supporting electrolyte to lithium iodide produced similar results.

Treatment of metal ketyls in hydrocarbon solvents or ether with ethyl bromide and carbon dioxide produces similar products together with benzophenone (7, 8). The reaction with water likewise results in the formation of benzophenone and benzohydrol (9).

The formation of the ketyl anion also has been demonstrated with electron resonance studies by Austen, *et al.* (10) of solutions of benzophenone reduced electrolytically at controlled potentials in dimethylformamide.

Determination of n for the waves of benzophenone using a micro cell (11) with 0.5 ml of a solution of benzophenone ($2 \times 10^{-3} M$) containing tetrabutylammonium iodide as a supporting electrolyte gave values of 1.54 and 1.82 respectively for the two waves. When the electrolysis was limited to the first wave by using potassium iodide as the supporting electrolyte, no appreciable decrease in the concentration of benzophenone occurred. The latter behavior indicates that the ketyl anion formed is reoxidized at the anode to benzophenone.

Table II. Large-scale electrolytic reductions of aromatic ketones and aldehydes in dimethylformamide

Compound	Amperes: Start	Amperes: Finish	Time of electrolysis	Products formed
HCON$(CH_3)_2$—0.155*M* $(C_4H_9)_4NI$ (300 ml)				
5.0 g $(C_6H_5)_2CO$	0.70	0.10	23 (hr)	Benzohydrol (2.7 g)
20 g $C_6H_5COCH_3$	0.60	0.05	14	Acetophenone pinacol (5.1 g)
20 g $C_6H_5COCH_3$ + excess CO_2	0.60	0.05	14	Atrolactic acid (1.0 g)
20 g C_6H_5CHO	0.60	0.05	19	Hydrobenzoin (7.3 g) Benzaldehyde (5 ml)
20 g C_6H_5CHO + CO_2	0.60	0.05	24	Hydrobenzoin (6.1 g)
20 g p-$CH_3OC_6H_5COCH_3$	0.60	0.05	27	2, 3-Dianisylbutadiene-1, 3 (traces)
20 g p-$CH_3OC_6H_5COCH_3$ + CO_2	0.60	0.05	20	p-Methoxyatrolactic acid (traces)
20 g p-$CH_3OC_6H_5CHO$	0.45	0.15	20	Hydroanisoin (1.9 g)
20 g p-$CH_3OC_6H_5CHO$ + CO_2	0.40	0.10	24	Hydroanisoin (1.3 g)
HCON$(CH_3)_2$—0.155*M* KI (300 ml)				
5.0 g $(C_6H_5)_2CO$	0.50	0.10	20	Benzohydrol (2.8 g)
5.0 g $(C_6H_5)_2CO$ + CO_2	0.60	0.10	20	Benzilic acid (3.1 g)
20 g $(C_6H_5)_2CO$ + 20% H_2O	2.5	1.0	12	Benzohydrol (17.1 g) Benzophenone (1.5 g)
20 g $(C_6H_5)_2CO$ + C_2H_5I	0.70	0.05	15	Diphenylethylcarbinol (3.2 g) Benzophenone (16.6 g)
HCON$(CH_3)_2$—0.155*M* LiI (300 ml)				
20 g $(C_6H_7)_2CO$	0.50	0.05	14	Benzohydrol (2.76 g) Benzophenone (14.75 g)

Logarithmic analysis of the reduction wave for benzophenone in potassium iodide solution showed a slope of 0.051. A similar analysis in the presence of tetrabutylammonium iodide showed a slope of 0.070 for the first wave and a slope of 0.080 for the second. Both waves show some kinetic character and are irreversible.

Since the ketyl anion is stable in dimethylformamide it is possible that the second wave may represent a

$$(C_6H_5)_2\dot{C}—O^- + e \rightarrow (C_6H_5)_2\ddot{C}—O^-$$

direct reduction of this ion to the dianion. The latter would react more readily with the solvent or water than the ketyl anion and give benzohydrol. The smaller diffusion current observed for this wave may be caused by the repulsion of the ketyl anion from the electrode.

The dianion is a much stronger base than the ketyl anion and would react irreversibly with water to form the carbinol anion.

$$(C_6H_5)_2\dot{C}—O^- + H_2O \rightarrow (C_6H_5)_2\underset{H}{C}—O^- + OH^-$$

Further reaction of the latter with water would be reversible. The second wave therefore should be influenced more by the addition of water and this behavior was observed.

Acetophenone when reduced electrolytically in the presence of carbon dioxide gives only a 4% yield of atrolactic acid. In the absence of carbon dioxide acetophenone pinacol was obtained.

Under similar circumstances, p-methoxyacetophenone gave only traces of acidic material and considerable amounts of tar. Distillation of the tar gave a small amount of 2, 3-di-p-anisylbutadiene-1, 3. This compound without doubt resulted from the pinacol.

Benzaldehyde on reduction alone gave a 43% yield of hydrobenzoin. In the presence of carbon dioxide the yield of hydrobenzoin was reduced to 30%, but no mandelic acid was formed.

The reduction of anisaldehyde resulted in considerable amounts of tar and a 5% yield of hydroanisoin.

The different behavior observed for the acetophenones and benzaldehydes in these large-scale electrolyses from that of benzophenone is apparently dependent on the stability of the intermediate ketyl anion

$$2R_2—\dot{C}—O^- \rightleftarrows R_2C(O^-)—CR_2(O^-)$$

or the extent of its dimerization to the pinacolate anion.

The results obtained with benzophenone would point to a stable ketyl anion since carbonation produces a high yield of benzilic acid. Under the same conditions the ketyl anions from acetophenone and benzaldehyde and their methoxy derivatives are less stable and either dimerize or undergo reactions which form tars.

The actual mechanism for the reaction of the benzophenone ketyl anion with various reagents is still not known. This anion is no doubt a resonance hydrid and

$$(C_6H_5)_2C{-}O^- \leftrightarrow (C_6H_5)_2\underline{C}{-}O\cdot$$

could undergo a direct reaction with the reagents involved.

$$(C_6H_5)_2\underline{C}{-}O\cdot + CO_2 \rightarrow (C_6H_5)_2C(COO^-){-}O\cdot$$

The resulting product from the reaction with carbon dioxide would take up an electron in the electrolytic reduction and form the benzilate anion.

$$(C_6H_5)_2C(COO^-){-}O\cdot + e \rightarrow (C_6H_5)_2C(COO^-){-}O^-$$

In the same reaction of metal ketyls in hydrocarbon solvents another ketyl anion would furnish the electron necessary.

$$(C_6H_5)_2C(COO^-){-}O\cdot + (C_6H_5)_2C{-}O^- \rightarrow$$

$$(C_6H_5)_2C(O^-)COO^- + (C_6H_5)_2C{=}O$$

A similar mechanism is implied for the formation of benzohydrol in the electrolytic reduction of benzophenone in dimethylformamide by Austen, *et al.* (10).

Disproportionation of the ketyl anion to benzophenone and the dianion, which could undergo similar reactions, is considered not to be feasible energetically (12).

$$2(C_6H_5)_2C{-}O^- \rightarrow (C_6H_5)_2\bar{C}{-}\bar{O} + (C_6H_5)_2CO$$

The possibility of the formation of the pinacolate anion followed by its dissociation into benzophenone and its dianion as

$$2(C_6H_5)_2\underline{C}{-}O^- \rightleftarrows (C_6H_5)_2C(O^-){-}C(O^-)(C_6H_5)_2 \rightleftarrows$$

$$(C_6H_5)_2C{=}O + (C_6H_5)_2\underline{C}{-}O^-$$

proposed by Acree (13) cannot be completely eliminated as a basis for the reactions of the ketyls.

Manuscript received Aug. 12, 1959. This paper was prepared for presentation at the Buffalo Meeting, Oct. 6-10, 1957 and is based on the Ph.D. thesis of A. Gundersen (June 1960). The research was supported by the Office of Ordnance Research under Contract DA-11-022-ORD-1868.

Any discussion of this paper will appear in a Discussion Section to be published in the December 1960 JOURNAL.

REFERENCES

1. S. Wawzonek, E. W. Blaha, R. Berkey, and M. E. Runner, *This Journal*, **102**, 235 (1955).
2. S. Wawzonek and D. Wearring, *J. Am. Chem. Soc.*, **81**, 2067 (1959).
3. S. Wawzonek, R. Berkey, E. W. Blaha, and M. E. Runner, *This Journal*, **103**, 456 (1956).
4. P. H. Given, M. E. Peover, and J. Schoen, *J. Chem. Soc.*, **1958**, 2074.
5. M. Ashworth, *Collection Czechoslov. Chem. Communun.*, **13**, 229 (1948).
6. C. B. Wooster, *J. Am. Chem. Soc.*, **50**, 1388 (1928).
7. W. Schlenk, J. Appenrodt, A. Michael, and A. Thal, *Ber.*, **47**, 473 (1914).
8. C. B. Wooster and W. E. Holland, *J. Am. Chem. Soc.*, **56**, 2438 (1934).
9. W. E. Bachmann, *ibid.*, **55**, 1179 (1933).
10. D. E. G. Austen, P. H. Given, D. J. E. Ingram, and M. E. Peover, *Nature*, **182**, 1784 (1958).
11. G. A. Gilbert and E. K. Rideal, *Trans. Faraday Soc.*, **47**, 396 (1951).
12. N. S. Hush and J. Blackledge, *J. Chem. Phys.*, **23**, 514 (1955).
13. S. F. Acree, *Am. Chem. J.*, **29**, 588 (1903).

Preparation and Refining of Yttrium Metal by Y-Mg Alloy Process

O. N. Carlson, J. A. Haefling, F. A. Schmidt, and F. H. Spedding

Institute for Atomic Research and Department of Chemistry, Iowa State University, Ames, Iowa

ABSTRACT

Yttrium metal was prepared by the reduction of YF_3 with calcium forming a low melting Y-Mg intermediate alloy. Magnesium was removed by sublimation to produce yttrium metal sponge. A method is described for removing oxygen and fluorine from the alloy by extraction with fused yttrium salts. The results of electron beam melting and zone refining are also presented. Some properties of yttrium metal of 99.9% purity obtained by the extraction refining process are discussed.

Recent interest in the possible uses of various rare earth metals as reactor materials led to this investigation of the preparation of high-purity yttrium metal. An acceptable absorption cross section for thermal neutron (1.31 barns), relatively high melting point (1500°-1550°C), resistance to attack by liquid uranium and uranium alloys (1), and its potential as a new alloying element in high-temperature materials are some of the properties that are responsible for the increasing interest in the metallurgy of yttrium.

Thompson (2), Trombe (3), and Daane and Spedding (4) have previously prepared experimental quantities of yttrium metal. The principal objective of this investigation was the preparation of yttrium metal in higher purity and larger quantities for use in the development of fabrication procedures and in the investigation of the properties of yttrium and its alloys.

The basic process described in this paper is the reduction of YF_3 with calcium in the presence of magnesium to form a low melting Y-Mg alloy. The reaction was carried out at 950°C in a refractory metal crucible under an inert gas atmosphere. Anhydrous $CaCl_2$ was added to the charge to flux the high melting CaF_2 produced by the reaction. A refining step in the process consisted of a fused salt extraction in which some of the interstitial impurities were extracted from the molten Y-Mg alloy. The magnesium was sublimed out of the alloy by heating *in vacuo*, yielding a metallic sponge which was subsequently arc melted into a massive yttrium ingot. The resulting yttrium metal was evaluated by spectroscopic and chemical analyses and by metallographic examination. The hardness, fabricability, and other properties of the metal were also determined.

Materials

In the preparation of high-purity yttrium it is essential that all reactants be of the highest possible purity since most of the impurities in these materials end up in the metal product.

It was recognized from the outset that high-purity YF_3, with a minimum of oxide contamination, was a prerequisite if that material were to be used as the starting salt. The details of the preparation of the YF_3 employed in these studies are given in an Ames Laboratory report (5).

A few pounds of YCl_3 were prepared for use in refining experiments. Yttrium metal sponge was converted to the chloride by reacting it with anhydrous HCl gas at 700°C. The crude product was purified by redistillation *in vacuo* at 950°C. The purity of the best YCl_3 and YF_3 that were obtained is estimated as 99.9%.

Anhydrous $CaCl_2$ of analytical grade purity (greater than 99%) was obtained from the J. T. Baker Co. Since this material contained small amounts of water, it was further dehydrated by heating to 450°C in a stainless steel vessel under a dynamic vacuum. When high-purity $CaCl_2$ was required, as in the extraction experiments, the chloride was given an additional treatment by passing anhydrous HCl over the vacuum-dried salt at 500°C.

Commercially pure calcium metal obtained from the New England Lime Company was vacuum redistilled at 900°C as described by Smith, *et al.* (6). Table I gives the analysis of the calcium after distillation.

Magnesium metal was distilled in the same apparatus at a temperature of 850°C. The carbon content was reduced to 0.02 wt % by this procedure, nitrogen to 0.005 wt %, and oxygen to less than 0.01 wt %.

Reduction of YF_3

Yttrium fluoride can be reduced by calcium in the presence of $CaCl_2$ and magnesium metal to form an Y-24 wt % Mg intermediate alloy. The alloy and slag produced in the reaction are both molten at 950°C, thus making it possible to carry out the reduction in a refractory metal crucible under an inert gas atmosphere. Calcium chloride was selected as the fluxing agent since it forms a low melting eutectic with CaF_2. It also decreases the density of the slag which is an important factor if complete separation from the alloy phase is to be achieved. Removal of the magnesium from the alloy and melting of the yttrium sponge are discussed in a later section of this paper.

Table I. Analysis of redistilled calcium metal

Element	Wt %
Magnesium	0.300
Carbon	0.020
Nitrogen	0.005
Aluminum	0.003
Iron	0.003
Manganese	0.002
Nickel	0.002

Apparatus and procedure.—A sketch of the apparatus used in the reduction process is shown in Fig. 1. The temperature of the retort was measured by a thermocouple placed on the exterior wall surface.

Several refractory metals and oxides were tested as crucible materials and tantalum was found to be the most inert. Most of the small-scale, high-purity experiments were carried out in tantalum; however titanium crucibles were used in the large reductions and in the more routine experiments.

The reductions were carried out in the following manner. Massive pieces of magnesium and calcium were transferred to the reduction crucible, and a mixture of YF_3 and $CaCl_2$ was loaded into the charging hopper. A typical charge consisted of 1500 g YF_3, 1350 g $CaCl_2$, 680 g calcium, and 290 g Mg. The unit was evacuated by means of a mechanical pump prior to placing the retort in the gas furnace.

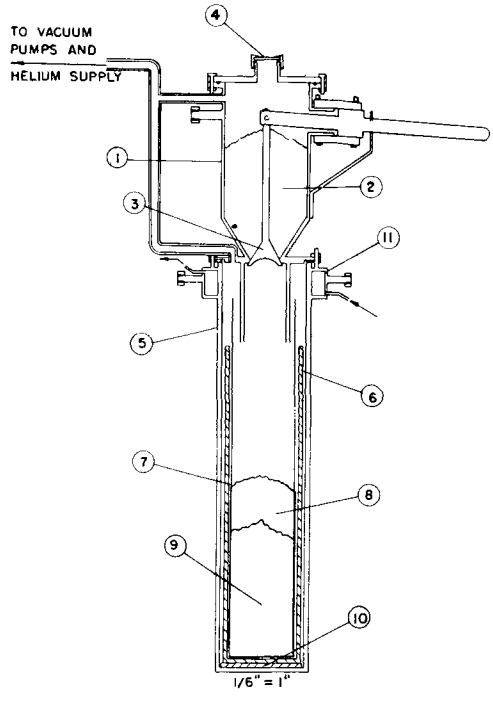

Fig. 1. Schematic drawing of reduction retort and charging hopper; 1, charging hopper; 2, $CaCl_2$ and YF_3; 3, control valve; 4, sight glass; 5, steel retort; 6, Ti or Fe retaining crucible; 7, Ti crucible; 8, Mg; 9, Ca; 10, graphite disk; 11, water jacket.

When the temperature of the retort had reached 800°C, helium gas was admitted and a pressure of 1-5 psi (gauge) was maintained in the system throughout the remainder of the run. When a temperature of approximately 900°C was attained as indicated by a thermocouple immersed in the molten calcium-magnesium phase, the YF_3-$CaCl_2$ mixture was added slowly from the hopper into the heated zone of the reaction crucible. The absence of a sharp temperature rise during the reduction process indicates that the reaction is either endothermic or only slightly exothermic.

At the completion of the run the hot retort was raised from the furnace, placed in a rack, and tilted to a few degrees from the horizontal. By allowing solidification to occur in this position, the slag and alloy could be removed more easily thus avoiding damage to the reduction crucible.

Experimental results.—A comprehensive investigation was made of the effects of reaction conditions, physical state and purity of the ingredients, proportion of the reactants, and handling procedures on the quality and yields of the yttrium metal obtained.

From experiments in which various oxides were added to the reduction charge, it was concluded that any oxides present in the reactants are transferred quantitatively to the Y-Mg phase during the reduction. Comparisons between granular and massive calcium revealed that yttrium prepared from granular calcium contained an average of 0.1 wt % more oxygen than that prepared from massive metal. This differential was observed with calcium on which the grinding and screening operations were carried out in a specially designed dry room. For this reason, the use of freshly distilled calcium and magnesium in massive form is strongly advocated if the oxygen content is to be kept as low as possible.

The composition of the intermediate alloy was set at 24 wt % magnesium, a composition that lies close to the intermediate phase, Y-Mg (7). This alloy possesses the properties of brittleness, low melting point, and relatively high density that are essential to the success of this process. The proper proportions of the other reactants were determined experimentally. A 10 wt % excess of calcium reductant gives a metal recovery of greater than 99% of theoretical; a smaller excess results in some decrease in yield. The critical slag composition was also determined by adjusting the YF_3-$CaCl_2$ ratio in the charge. A slag composition of 52 wt % $CaCl_2$ gave best slag-metal separations and highest metal yields.

Tests showed that the alloy picks up significant amounts of oxygen after a brief exposure to air saturated with water vapor but not from oxygen of the air. Therefore the crushing and transferring of the alloy were handled in a dry box filled with helium.

In spite of these precautions the oxygen content of the best yttrium prepared by this method was in the range of 0.1-0.2 wt %. This is shown along with other analytical data in Table II. The values represented are averages from a large number of reductions made in titanium crucibles. Statistical treatment of these data indicate that the standard deviation for the larger values reported is ± 0.01% or less.

Table II. Major impurities in yttrium metal prepared by the calcium reduction of yttrium fluoride

Impurity	Wt %	Impurity	Wt %
Oxygen	0.170	Nitrogen	0.015
Titanium	0.150	Silicon	<0.015
Fluorine	0.080	Copper	0.004
Nickel	0.035	Magnesium	0.003
Iron	0.030	Calcium	0.001
Carbon	0.020	Total rare earths	<0.050

Magnesium Removal and Arc Melting

The volatile components of the alloy must be removed almost completely before the resulting sponge can be arc melted. At the same time care must be exercised to avoid melting and spattering during the initial stages of the magnesium and calcium removal. As a first step the alloy was crushed into pieces approximately ½ in. in diameter in a jaw crusher enclosed in the dry box.

The sublimation was carried out in a 6-in. diameter stainless steel retort equipped with a condenser. The alloy was placed in a titanium vessel inside the vertical retort. The system was evacuated to a pressure of 10^{-4} mm Hg at the outset, and this pressure was maintained throughout the run. The retort and its contents were heated to 900°C in an electric furnace, held at this point for 4 hr, and then increased to 950°C and held for a period of 20 hr. The magnesium vapors were collected on the condenser which was cooled by a flow of air. The yttrium obtained in this manner was a bright, porous sponge containing approximately 0.01 wt % magnesium and calcium.

The yttrium sponge was consolidated into ingot form by arc melting. The sponge was compacted into electrodes, and these were generally arc melted into 1-lb evaluation ingots in an inert gas atmosphere. In processing larger amounts of yttrium, the sponge was consummably arc melted twice with the second melting being carried out under a dynamic vacuum. The steps in this melting operation are represented by the three forms of the metal shown in Fig. 2. About 90 lb of metal are shown in each processing step.

Refining of Yttrium

In an effort to remove some of the impurities from yttrium, particularly oxygen and fluorine, several

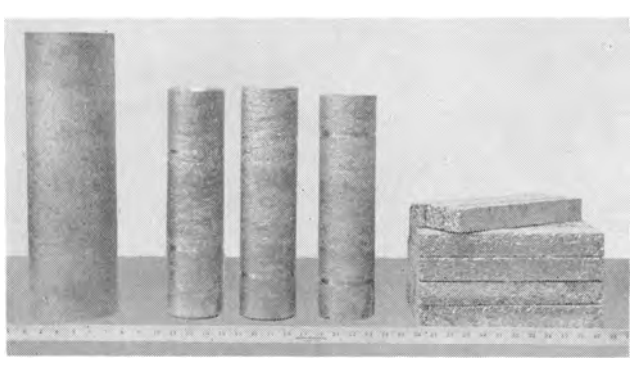

Fig. 2. Six-inch diameter ingot (left); 4-in. diameter ingots (center); and 27 sponge compacts or electrodes.

refining techniques were tried. The more successful methods are discussed in this section.

Refining of Y-Mg alloy with a fused salt.—It was observed that the oxygen content of the Y-Mg alloy was reduced significantly after being in contact with a fused salt containing YF_3 or YCl_3. Several experiments were run in an attempt to gain some understanding of this phenomenon.

The same apparatus that was used in the reduction of YF_3 was employed in these experiments, but with one modification. The charging hopper was replaced by a vacuum head through which the shaft of a stirring rod was inserted. A titanium or tantalum paddle was attached to this shaft and was rotated inside an "O" ring seal. Approximately 0.5 wt % titanium was dissolved by the yttrium alloy when both the reduction and extraction steps were carried out in a titanium crucible with a titanium stirrer. No detectable contamination from the crucible was encountered when a tantalum system was used.

The slag from a regular reduction was removed and the extractant, such as YF_3 and $CaCl_2$, was added to the alloy in the crucible. The alloy and salt phases were brought to the molten state (950°C), the stirrer was lowered to the fused salt-alloy interface and rotated slowly for approximately 30 min to insure adequate mixing during the extraction.

A mixture of YF_3 and $CaCl_2$ was investigated extensively as the extractant salt. Extractions with mixtures of varying composition were run on 1200-g portions of Y-Mg alloy of uniform composition. In one series a fixed quantity of YF_3 was used and the amount of $CaCl_2$ was varied. From this it was observed that the $CaCl_2$ concentration is not critical as long as enough is present to flux the YF_3 properly.

In another series the amount of $CaCl_2$ was held constant and the amount of YF_3 was varied. As is seen from the data in the upper half of Table III, 650 g of fluoride in the extractant produces the maximum purification and increased amounts have no additional effect. Since the alloy contains a sufficient amount of residual calcium to reduce approximately 150 g of YF_3, no decrease in the oxygen content was observed when this amount of fluoride was used in the extractant mixtures.

Further understanding of the extraction process was gained from experiments using two different grades of YF_3 and Y-Mg alloy. The data in Table III show the effect of the oxygen concentration in the alloy and in the YF_3 on the amount of extractant required to produce the maximum decrease in oxygen content. For alloy containing 0.20 wt % oxygen, only 650 g of high-purity YF_3 (0.04 wt % oxygen) was required to decrease the oxygen content of the yttrium to 0.05 wt %, whereas a greater quantity of the lower grade fluoride was required to produce the same purification. For alloy containing 0.5 wt % oxygen, the 650-g quantity of high-purity fluoride did not give metal of maximum purity, although the oxygen content was lowered appreciably. A greater amount of this quality of YF_3 was required to decrease the oxygen content of the alloy from 0.50 to 0.06 wt %.

In an attempt to determine if the form of the oxide influences the distribution of oxygen between the two phases, 0.1 wt % of oxygen was added as MgO, CaO, Y_2O_3, and YOF to successive reductions. As was indicated earlier in this paper, oxygen from all of these compounds is transferred to the alloy phase in the reduction step. The results of this series of experiments indicated that the form of the oxide in the reduction charge does not appear to have any effect on the degree of purification obtained by the fused salt treatment.

Other salt mixtures were investigated as possible extractants of oxygen and fluorine from the Y-Mg alloy. The results of a series of tests using various extractants on alloy initially containing 0.20 wt % oxygen and 0.12 wt % fluorine are summarized in Table IV. The data in the table show that both oxygen and fluorine are extracted by fused YCl_3 and that the fluoride content can be lowered substantially by a contact with $CaCl_2$.

As can be seen from Table IV the purest metal was obtained by extraction with YF_3-$CaCl_2$ followed by a second extraction with YCl_3. This two-stage extraction was performed several times to ascertain the reproducibility of the method. Yttrium metal of the purity shown in Table V was obtained on repeated experiments. The metal prepared in this way was used for metal evaluation, determination of physical constants, and microscopic examination.

The extractant salts are readily recoverable and can be reduced to the metal or used again in refining experiments. The $CaCl_2$ is leached from the salt mixture and anhydrous HF gas is passed over the residual fluoride at 750°C. This results in a quality of YF_3 equivalent to that of the original material. The YCl_3 likewise can be reclaimed by vacuum sublimation.

Table III. Results of experiments using YF_3-$CaCl_2$ extraction mixtures on 1200-g portion of Y-Mg alloy

Oxygen content of* initial alloy, wt %	Wt % O† in YF_3	Grams of YF_3 in extractant mixture	Wt % O in Y† after extrac.
0.20	0.04	1650	0.052
0.20	0.04	1150	0.053
0.20	0.04	650	0.060
0.20	0.04	150	0.210
0.20	0.22	1150	0.063
0.20	0.22	650	0.112
0.50	0.04	1150	0.065
0.50	0.04	650	0.137

* Based on yttrium metal content.
† Spectroscopic values (8).

Table IV. Experiments with various fused salts as extractants for Y-Mg alloy

Extractant salt	Analysis of yttrium after extraction	
	Wt % O	Wt % F
$CaCl_2$	0.170	0.045
YF_3-$CaCl_2$	0.050	0.070
YCl_3	0.060	0.035
Double extraction with YF_3-$CaCl_2$	0.030	0.070
YF_3-$CaCl_2$ followed by YCl_3	0.018	0.007

Table V. Analyses of yttrium metal refined by double extraction method

Impurity	Wt %	Impurity	Wt %
Iron	0.030	Copper	0.004
Nickel	0.020	Nitrogen	0.002
Oxygen	0.015	Calcium	0.001
Silicon	<0.015	Hydrogen	0.001
Tantalum	<0.010	Magnesium	0.001
Carbon	0.009	Titanium	0.001
Fluorine	0.006	Total rare earths	<0.050

Electron beam melting and zone refining.—Several pounds of yttrium sponge containing 0.045 wt % oxygen and 0.060 wt % fluorine were electron-beam melted by the Temescal Metallurgical Corporation. Analysis of the ingot after two melting operations gave 0.045 wt % oxygen and 0.004 wt % fluorine.

An yttrium rod containing 0.052 wt % oxygen and 0.065 wt % fluorine was zone refined at a rate of 6 in./hr. After two zone passes, segments of the bar were again analyzed. The oxygen content showed no significant change, but the fluorine content decreased to 0.002 wt %. No differences were observed in the oxygen or fluorine concentrations at either end of the zone-melted region.

Thus, it appears that fluorine can be removed from yttrium metal by electron beam melting and by zone refining, *in vacuo,* but oxygen is not affected. The major portion of the fluorine is removed as a volatile compound in both methods although the exact species has not been determined.

Properties of Yttrium Metal

Although many of the physical properties of yttrium have been measured previously, a few properties of the higher purity yttrium obtained from this investigation were determined for purposes of comparison. Melting points have been observed from as low as 1450°C to as high as 1550°C for metal of differing purity. Eash (9) reported a value of 1515°C on metal that contained 0.2 wt % oxygen as the major impurity. Since the lattice parameters and melting point of a metal are often sensitive to oxygen content, it appeared desirable to determine these constants for the purer metal. The melting point of 99.9% purity yttrium prepared in this investigation was determined to be 1495° ± 5°C. This determination was made using an optical pyrometer method (10) in which a small hole was drilled into an yttrium rod. The specimen was heated by passing a high current through it, and the temperature within the hole was continuously observed until melting was evident.

Likewise, there are differences in the reported lattice parameters of yttrium. Spedding, Daane, and Hermann (11) reported values of $a = 3.6474$Å and $c = 5.7306$ for the metal that was available to them while parameters of $a = 3.662$Å and $c = 5.752$Å were obtained for the metal prepared in this investigation. The theoretical density of this material was 4.46 g/cc as compared with a measured density of 4.45 g/cc.

Yttrium metal of this quality has a hardness of 35-45 Brinell (500 kg load) and can be worked extensively at room temperature. A specimen was rolled from an original thickness of 0.250 in. to a final thickness of 0.012 in. with no intermediate anneal. This represents a reduction in thickness of greater than 90%. A photograph of the original coupon and of a section of the 18-in. ribbon obtained by cold rolling is shown in Fig. 3. A cylinder, 0.25 in. in diameter before swaging, is shown in the photograph; another cylinder, 0.125 in. diameter after cold swaging, is also shown.

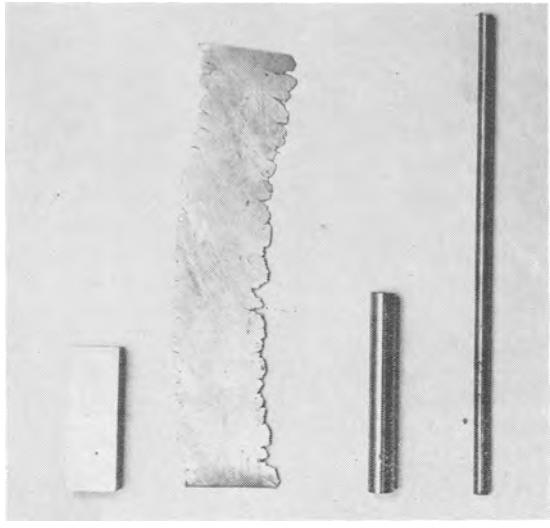

Fig. 3. Yttrium specimen before and after cold rolling to 90% reduction in thickness (left) and before and after swaging (right).

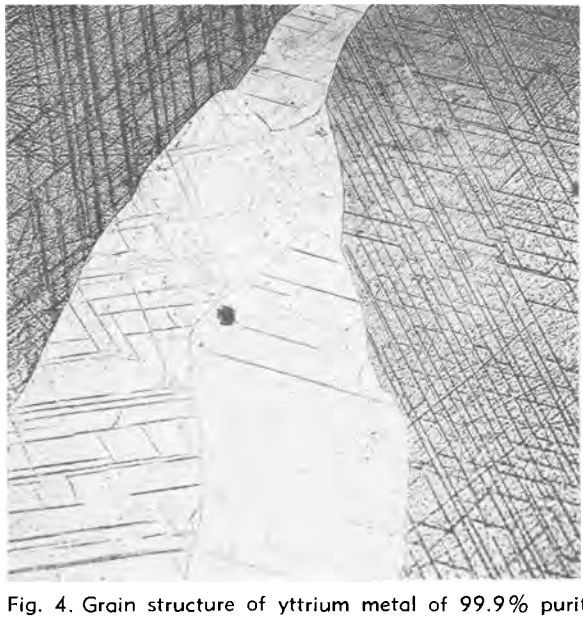

Fig. 4. Grain structure of yttrium metal of 99.9% purity. Etchant: conc. HNO_3. Magnification 250X.

Photomicrographs of yttrium metal of 99.9% purity are shown in Fig. 4 and 5. The coarse grain structure of the arc cast metal can be seen from Fig. 5. The lines that extend across the grains are characteristic of high-purity yttrium. These appear to be deformation bands believed to have been introduced by strains during solidification.

Summary

A process for preparing yttrium metal is described. The basic process consists of the formation of a low-melting intermediate Y-Mg alloy which is subsequently converted to yttrium sponge metal.

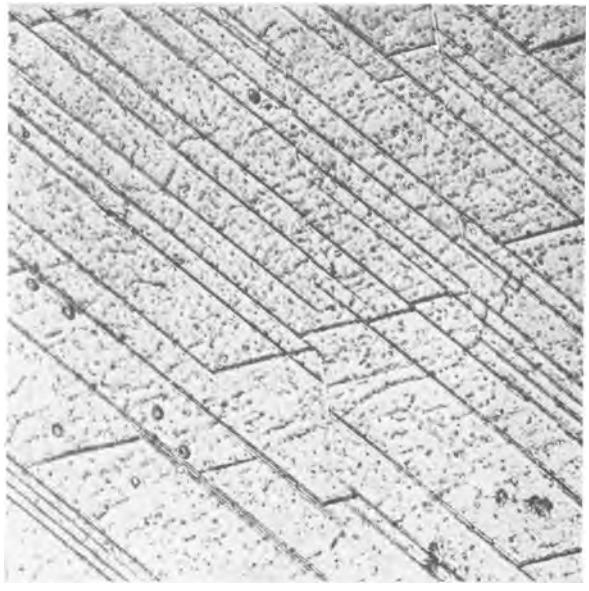

Fig. 5. Enlargement of same area as Fig. 4 showing deformation bands and small inclusions. Magnification 500X.

Several refining procedures are described. One of these involves the extraction of oxygen from the molten Y-Mg alloy by a fused salt containing YF_3 or YCl_3. Fluorine can be removed by an extraction treatment on the alloy or by electron beam melting or zone refining of yttrium metal.

Yttrium metal of 99.9% purity was prepared by methods described in this paper. The melting point, lattice parameters, and hardness were determined on metal of this purity and the cold working characteristics and microstructure were studied.

Acknowledgments

The authors would like to express their gratitude to Dr. V. A. Fassel and members of the spectroscopic group of the Ames Laboratory and to Dr. C. V. Banks and his associates for performing the multitude of chemical analyses. They would like to acknowledge the assistance of C. Moore, I. Jensen, M. Hedberg, R. Griffith, E. Ritland, and M. Thompson in performing these experiments.

Manuscript received Nov. 20, 1959. This paper was prepared for delivery before the Chicago Meeting, May 1-5, 1960. Paper is Contribution No. 815; work was performed in the Ames Laboratory of the U. S. Atomic Energy Commission.

Any discussion of this paper will appear in a Discussion Section to be published in the December 1960 JOURNAL.

REFERENCES

1. R. W. Fisher and C. B. Fullhart, *2nd International Conf. on Peaceful Uses of Atomic Energy*, **7**, 216 (1958).
2. A. P. Thompson, W. B. Holton, and H. C. Kremers, *Trans. Am. Electrochem. Soc.*, **49**, 442 (1926).
3. M. F. Trombe and M. F. Mahn, *Compt. rend.*, **220**, 778 (1945).
4. A. H. Daane and F. H. Spedding, *This Journal*, **100**, 442 (1953).
5. C. V. Banks, O. N. Carlson, A. H. Daane, V. A. Fassel, R. W. Fisher, E. H. Olson, J. E. Powell, and F. H. Spedding, "Studies on the Preparation, Properties and Analysis of High Purity Yttrium Oxide and Yttrium Metal," Report IS-1, p. 13, (July 1959).
6. J. F. Smith, O. N. Carlson, and R. W. Vest, *This Journal*, **103**, 409 (1956).
7. E. D. Gibson aond O. N. Carlson, ASM Preprint No. 146; to be published in *Trans. Am. Soc. Metals*, **52**.
8. C. V. Banks, *et al.*, *op. cit.*, p. 125.
9. D. T. Eash and O. N. Carlson, ASM Preprint No. 142; to be published in *Trans. Am. Soc. Metals*, **52**.
10. H. A. Wilhelm and P. Chiotti, *Trans. Am. Soc. Metals*, **42**, 1295 (1950).
11. F. H. Spedding, A. H. Daane, and K. W. Hermann, *Acta Cryst.*, **9**, 559 (1956).

Exchange Current Measurements in KCl-LiCl Eutectic Melt

H. A. Laitinen, R. P. Tischer,[1] and D. K. Roe[2]

Department of Chemistry and Chemical Engineering, University of Illinois, Urbana, Illinois

ABSTRACT

Exchange currents have been measured of some liquid and solid metal electrodes (Cd, Zn, Pb, Bi, Ag, Ni, Pt) and one redox system (V^{3+}/V^{2+}) in a KCl-LiCl eutectic melt at 450°C. Measurements over a hundredfold concentration range permitted calculation of the heterogeneous rate constant and of the transfer coefficient. Two relaxation methods were used: the double pulse method as developed by Gerischer and Krause and the voltage step method as described by Vielstich and Delahay. In cases where both methods were applied independently to the same system the results were in good agreement. The purity of the eutectic melt was improved considerably by filtration and by displacement of heavy metal ion impurities with metallic magnesium. The evaluation of voltage step measurements was revised by allowing for the effect of the finite charging time of the double layer. Agreement was not found with the theory of the double pulse method given by Matsuda, Oka, and Delahay, perhaps because of some additional process, other than diffusion, taking place in a period of time comparable to the duration of the first pulse. On the basis of the reaction of platinum with cadmium at 450°C it is possible to account for the observations made earlier in this laboratory by C. H. Liu and H. C. Gaur on the emf and polarization behavior of cadmium-plated platinum electrodes.

In recent years the increasing importance of fused salts in many fields of science and technology has incited a considerable number of investigations of their properties. Molten salts have found much interest as media for electrochemical processes in connection with their applications in metallurgy, analytical and synthetic chemistry and, more recently, in high-temperature galvanic cells. Relatively few studies, however, have been made of the rates of electrode processes in molten salts, because such electrode processes can be expected to be very fast and their study would therefore require elaborate techniques. The relaxation methods developed recently for the study of fast reactions in aqueous solutions are most suitable for fused salt studies. Doubts have sometimes been expressed as to whether these methods would be able to avoid the interference of diffusion as a rate-determining process, since diffusion in molten salts (1) is often not faster than in aqueous solutions at room temperature. It is possible, however, to distinguish between diffusion-controlled and charge transfer controlled reactions even in fused salts, and diffusion effects can be eliminated under the proper experimental conditions.

The first successful application of a relaxation method to electrode reactions in fused salts was made by Randles and White (2). In a low melting nitrate eutectic the rate of the reaction $Ni^{2+} + 2e^- + Hg = Ni\ (Hg)$ was evaluated from a-c impedance measurements. Measurements were attempted on several other metal ion-metal amalgam reactions, but they were found to be too rapid for the method.

Laitinen and Osteryoung (3), about the same time, sought to use the same a-c technique with platinum electrodes in the KCl-LiCl eutectic. Direct interpretation of the measurements was not possible because of complicating experimental conditions which caused a very large frequency dispersion of the resistance and capacitance measurements.

Under more amenable experimental conditions, primarily with a melt prepared from dry salts, Laitinen and Gaur (4) were able to make more refined measurements of the same type. Although the frequency dispersion of the measurements on platinum microelectrodes was still present, the data were interpretable by the introduction of a correction for adsorption of the reducible ion (5). The correction was necessary to remove the "inverted" character of the reaction impedance, in which the resistive component is smaller than the capacitative component. While there is no direct evidence that this is a valid correction, the resulting exchange currents for the cadmium and zinc couples appear to have reasonable values, as will be confirmed in this paper.

Hill (6) measured the impedance behavior of silver electrodes using $AgNO_3$ as the solute in a ternary nitrate melt, of silver-plated tungsten electrodes in LiCl-KCl eutectic containing dissolved AgCl, and of tungsten electrodes in Ti(III)—Ti(II) systems in the LiCl-KCl eutectic. In all cases the residual capacity and resistance of the solvent were markedly frequency dependent Many of the faradaic impedance plots were "inverted."

Interpretation of a-c impedance measurements requires the elimination of the double layer capacity. The residual capacity has, in general, been found to be a function of frequency in fused salts. The other relaxation methods, potential step and current step, are made at relatively very short times, which corresponds to high frequencies in the a-c method,

[1] Present address: Gebr. Böhler and Co. AG, Düsseldorf-Oberkassel, Germany.
[2] Present address: Shell Development Co., Emeryville, California.

and should be less ambiguous since the measured resistance and capacitance show less frequency dispersion at high frequencies.

The double pulse method developed by Gerischer and Krause (7) is potentially capable of measuring extremely rapid electrode reactions. The problem of charging the double layer is dealt with directly by the use of two current pulses. The first pulse is as short as possible (1 μsec) and is adjusted in height to just charge the double layer. The second pulse is much smaller and of longer duration. The overvoltage resulting from the second pulse is measured directly with an oscilloscope.

A theoretical analysis of the double pulse method has been given by Matsuda, Oka, and Delahay (8). They show that the concentration change at the electrode surface during the charging pulse cannot always be neglected and that the true reaction resistance can be obtained by extrapolation to zero duration of the first pulse.

The other method used in this investigation is the voltage step method (9). In principle, it is a potential step method, but a reference electrode provided with a Luggin capillary is not used. The voltage applied to the cell is constant, but the potential of the indicator electrode is not constant during the passage of current because of the changing iR drop in the cell. The actual potential can, however, be obtained by subtracting the product of the measurable current and resistance from the known voltage step. The charging current, of course, obscures the oscilloscopic observation of the kinetically controlled current during the initial period of electrolysis, so an extrapolation procedure is used. The method is well suited to fused salt measurements because of the low cell resistance; the charging current duration is thereby shortened. It has the obvious limitation that, with very rapid reactions, diffusion may become the rate-controlling process before the charging is completed. It is possible, however to distinguish between kinetic and diffusion control from the current-time behavior.

Theoretical

Relaxation methods which employ pulse techniques depend on current or voltage measurements at very short times, before diffusion becomes the rate-determining process. During the first moment of electrolysis a large fraction of the current charges the double layer and prevents direct observation of the faradaic process.

In the double pulse method (7) this problem is overcome by charging the double layer with a very short current pulse. The electrolyte resistance is compensated for by a bridge circuit as shown in Fig. 5 in the experimental section. The height of the first pulse is adjusted so that the potential transient, after the charging pulse, starts out with a horizontal tangent, the idea being that the potential for a short moment is constant and therefore the entire current is faradaic because no portion of the current is used for charging. From the potential measured at this moment and from the magnitude of the second pulse measured by the potential drop across the compensating resistor it is then possible to calculate the transfer resistance X, from which the exchange current density is obtained by

$$i_o = \frac{RT}{n\mathbf{F}XA} \qquad [1]$$

where A is the electrode area and the other symbols have their usual significance. One of the limits of this method is encountered with high rates corresponding to very low transfer resistances that are less than 1% of the electrolytic resistance. There are two reasons for this limitation: (a) It is not possible to adjust the compensating resistor for the electrolyte resistance accurately enough by the available procedure. (b) For a ratio of electrolytic resistance to transfer resistance equal to 100, the differential input of the amplifier must be balanced to within 0.1%, even if an accuracy of only 10% is required in measurement of the transfer resistance. This difficulty can be overcome to a certain extent by using lower concentrations. Unfortunately there then arises the other difficulty, mentioned in the original paper by Gerischer and Krause (7) and analyzed quantitatively by Delahay and co-workers (8), that diffusion becomes rate determining after a time comparable to the duration of the charging pulse. Thus the range of concentration that can be investigated successfully with this method becomes smaller and smaller with increasing reaction rate.

In the voltage step method (9) the faradaic current, observed after the charging current has become negligible, is extrapolated back to zero time. The calculation of the exchange current density is immediate from the measured "zero time" current $i_{t=0}$, the known voltage step V and the total resistance of the system R_T. Similar to the above equation

$$i_o = \frac{RT}{n\mathbf{F}A} \frac{i_{t=0}}{(-V - i_{t=0}R_T)} \qquad [2]$$

The sign of V is given by the European convention; when negative, the current is cathodic (positive). Therefore the quantity on the left is always positive, as it should be.

The definition of the exchange current density is

$$i_o = n\mathbf{F}k_h^\circ C_{Ox}^{1-\alpha} C_R^{\alpha} \qquad [3]$$

where k_h° is the standard heterogeneous rate constant at the standard (formal) potential of the couple, C_{Ox} and C_R are the concentrations (in mole cm^{-3}) of the oxidized and reduced forms of the couple and α is the transfer coefficient. From a series of measurements at different concentrations the transfer coefficient is obtained from the slope of a plot of log i_o vs. log C_{Ox} (C_R is constant in the case of a metal/metal ion system using pure metal electrodes). The value of k_h° can then be calculated from Eq. [3]. In the case of a redox system, such as V^{3+}/V^{2+}, it was more convenient experimentally to vary the ratio by oxidizing V^{2+} to V^{3+} with a constant current. The transfer coefficient was calculated by plotting i_o/C_O vs. C_R/C_O, since

$$i_o/C_{Ox} = n\mathbf{F}k^\circ_h(C_R/C_{Ox})^{\alpha} \qquad [4]$$

The current which charges the double layer obeys the relation

$$i_{ch} = \frac{V}{R_T} \exp\ (-t/R_T C_{dl})$$

where C_{dl} is the differential double layer capacity. In the essential absence of any reducible or oxidizable species, only the charging current will be observed. A semilogarithmic plot of current vs. time has an intercept of V/R_T and a slope of $1/(2.303R_TC_{dl})$. In this way the solution resistances were measured. Also a series of measurements was made over 1.8 v potential range, from which a differential double layer capacity/potential curve was calculated (see Fig. 14).

In the voltage step method, it is assumed that the kinetically controlled current rises instantaneously to a maximum after the application of the voltage step and then decreases linearly with the square root of time until diffusion becomes rate determining. During the charging of the double layer, the potential of the electrode is given by

$$V_t = V[1-\exp(-t/R_TC_{dl})]$$

assuming that the faradaic current is much smaller than the charging current. From this equation it is obvious that the potential is zero at the instant the voltage step is applied. Therefore the kinetic current is not at a maximum, but is zero. During the next several microseconds, the kinetic current should increase as the potential increases and finally reach a maximum when the charging current becomes negligible. Therefore the extrapolated value of the kinetically controlled current at zero time is larger than it should be because the observed current is higher than the current theoretically derived for the condition of infinitely rapid charging of the double layer.

In Fig. 1 is shown the experimental current-time curve of the reduction of V^{3+} to V^{2+}. The charging current is also shown, as measured at the same potential with the same platinum microelectrode. The difference between the two curves is the faradaic current and the figure shows that it corresponds with the general shape described above. In the bottom half of the figure is plotted the current against the square root of time; the linear portion has been extrapolated to zero time. This extrapolation was then transferred to the top graph.

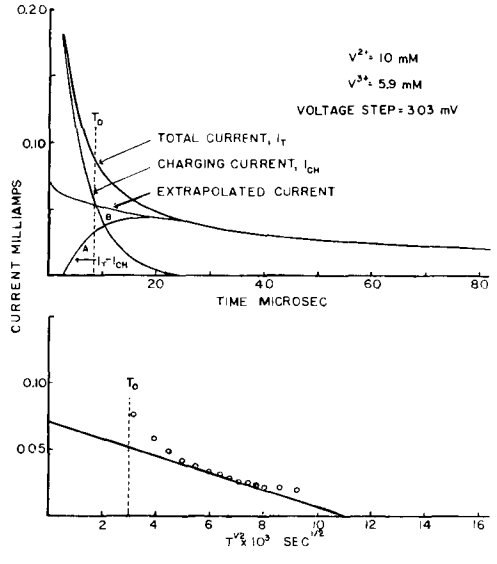

Fig. 1. Current-time curve of V^{3+}/V^{2+} and charging curve

If the charging current were not finite in duration, the faradaic current would have a value at zero time which would be somewhat lower than that shown in the lower graph of Fig. 1. Therefore at one point, which may be called the "effective zero time," the extrapolated faradaic current is equal to the hypothetical current at zero time. This point has been chosen in a way which is only a first approximation, but is nevertheless intuitively satisfying. A vertical line is drawn on the current time graph at such a point, t_o, on the time axis, that the area A under the faradaic current-time curve to the left of the line is equal to the area B between the extrapolated and the observed curves. The current value on the extrapolated line at t_o is then called the "effective zero time" current, i_{t_o}, and is used to calculate the exchange current. The potential across the cell at the same time is equal to the applied voltage, V, minus the product of the total current, i_T, and the total resistance, R_T. The current i_{t_o} is smaller than the extrapolated current at $t = 0$, but the total current, faradaic plus charging, is larger so that the iR correction is larger. Since the exchange current is proportional to the quotient of the current and the corrected voltage step, $(-V - iRT)$, the two effects tend to cancel.

In the treatment of the experimental data, the above method of calculating the exchange current resulted in a significant improvement in the case of the slower reactions. The values for zinc and cadmium, calculated by both methods were within 4% of each other, which is less than the experimental error. However if the circuit resistance was increased, so that the charging time was longer, great deviations in the calculated exchange current resulted unless the modified procedure was applied.

Experimental

Preparation and purification of the KCl-LiCl *eutectic melt.*—Reagent grade KCl and LiCl require extensive drying as well as purification before the resulting eutectic melt is suitable for electrochemical studies. Prolonged vacuum drying and the use of HCl gas during the fusion of the salts has been shown to remove all of the water and reverse the hydrolysis of LiCl (10, 11). Further purification is necessary to remove the heavy metal ion impurities and the decomposition products of what is presumably an organic solvent residue.

The most convenient and expedient method for the removal of heavy metal ions, which are present to the extent of 0.0005% or about 0.4 mM in the molten eutectic (calculated as lead), was found to be simple displacement with a more active metal. Magnesium is ideally suited in this medium because of its very negative standard potential (−2.58 v vs. 1M platinum reference electrode) (12). It is expected that the small concentration of Mg^{2+} will have a negligible effect on the electrode processes of interest here; the most active metal used was zinc, with a standard potential of −1.56 v (12).

The index of melt purity used in this laboratory is the residual current (10), measured with a 26-

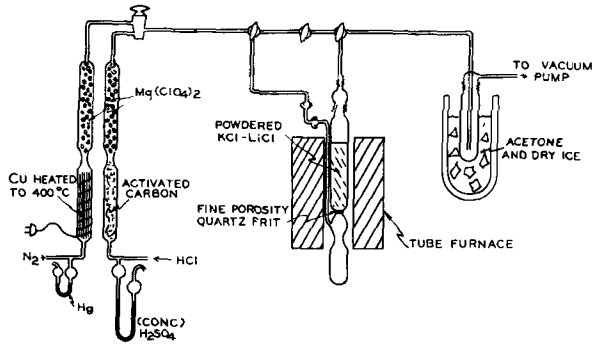

Fig. 2. Apparatus for purifying the melt

gauge platinum microelectrode, ground flat to expose only the cross section of the platinum wire, with an apparent area of 0.13 mm^2. In melts treated with magnesium, the residual current was in the range of 0.08 to 0.4 μa at a potential of −2.0 v vs. a platinum reference electrode. Up to a potential of about −1.5 v, the residual current was anodic by a few hundreths of a microampere. Without treatment with magnesium, the residual current was cathodic over the entire potential range, reaching about 1 to 2 μa at −2.0 v.

Individual batches of the eutectic melt were prepared in the apparatus shown in Fig. 2. Approximately 150 g of KCl-LiCl eutectic mixture, previously powdered in a ball mill, was placed in the vertical Vycor tube. A few tenths of a gram of magnesium turnings or powder was added to the salts. The pressure was reduced to 0.01 mm Hg by a Cenco vacuum pump. After about 12 hr of vacuum drying at room temperature, the furnace was turned on and the temperature was increased slowly over a 36-hr period. Before the temperature increased to the melting point of the eutectic (352°C), the system was vented to dry HCl gas, which had been passed over activated carbon to remove possible hydrocarbon impurities. When the salts were molten, additional HCl was admitted through the small side tube and up through the fine porosity quartz frit. Treatment with HCl for 1 hr is more than enough to drive out the last traces of water. The apparatus was then evacuated with a water aspirator, connected to the system through the dry ice-acetone trap, to remove the HCl gas. Three evacuations, each followed by a nitrogen flush through the quartz frit, removed nearly all of the HCl. Then the molten eutectic was filtered by evacuation below the quartz frit. The ampoule was heated with a gas burner during the filtration. When the process was completed, the tube furnace was raised to expose the constriction in the tube, just below the Vycor-Pyrex graded seal, and the ampoule was sealed off with a torch. When the eutectic mixture is cool, it will not stick to the walls of the ampoule if it is completely dry. "Wetting" of the glass is indicative of the presence of oxide (13).

Fused salt apparatus.—The major part of the apparatus is similar to that previously used in this laboratory (10, 12). The melt was contained in a 6-cm diameter Pyrex tube, about 35 cm long. After thorough cleaning with boiling 70% $HClO_4$, the tube was dried and the ampoule was placed inside. The tube was then heated under vacuum for a time, to remove surface water from the glass. Before the melting point of the eutectic was reached, the system was vented to dry, oxygen-free argon, and the ampoule tip was broken. When the eutectic became molten, the ampoule was raised to allow the melt to drain out and then removed. The cell compartments were then added. In these kinetic studies, simple 20 x 100 mm test tubes were used as cells. The resistance of the cells was reduced somewhat by slightly blowing out the side of the tube, or by sealing in a fritted glass disk. The other electrodes, platinum reference and carbon rod, were contained in the usual fritted glass tubes. The microelectrode was positioned just above the counter electrode in the same compartment. Cell resistances were of the order of 2-3 ohms. Silicone stoppers, because of their superior heat resistance, were used to cover the opening of the cell.

The furnaces were of the vertical tube type and had small windows or peepholes in the side to facilitate the adjustment of the electrodes. Temperature control was provided by proportional or on-off controllers. Short time variations were less than 1°C.

A flowing atmosphere of argon, dried with $Mg(ClO_4)_2$ and deoxygenated over hot copper, was maintained at all times to prevent the entrance of air and moisture.

Electrodes.—Two basic microelectrodes were used in all the kinetic measurements: tungsten sealed in Pyrex or uranium glass and platinum sealed in "soft" glass. Although lead glass (Corning 0120) makes a very good seal with platinum, the lead ions in the immediate vicinity of the seal are reduced when the electrode is used in fused salts at 450°C. This reduction is evidenced by a hump in the polarographic current voltage curve, starting at about −0.9 v vs. a platinum reference electrode. The shape of the hump depends on the polarization rate, but the area under the curve is the same for a given electrode. After a cathodic polarization, the metal-glass seal is black; anodization restores the original appearance of the seal. Several other "soft" glasses were tried, but they either failed to maintain a tight seal with the platinum or were quickly etched by the molten salts. Upon request, the Corning Glass Works kindly prepared a special batch of glass (Corning 010, G-164-EC) which was no longer available. This glass contains no lead oxide, has a very low conductivity and a coefficient of thermal expansion close to that of platinum. Although this glass is slightly etched after several hours in the melt at 450°C, in all other respects it is very satisfactory.

It was found that platinum does not serve as a suitable indicator electrode when coated with a liquid film of low melting metal such as cadmium, zinc, or bismuth. To illustrate the effect, the results of a brief study of the alloying of platinum with cadmium at 450°C will be given. A piece of platinum foil of 1 cm^2 area was plated with 10 mg of Cd from aqueous solution. Upon heating in an evacuated tube for 1 hr at 450°C, the weight of the specimen was unchanged. Upon dissolving the cadmium with

aqueous HCl, a spongy layer of platinum was left on the surface. The total weight of platinum was unchanged; the weight of the spongy layer which was presumed to have been alloyed was determined by carefully scraping it off and weighing it by difference. From the weight of the cadmium and spongy platinum, the composition of the alloy was calculated to be 64 mole % Cd and 36 mole % Pt. This corresponds closely to a compound Cd_2Pt, which has long been known (14) and which has a melting point of 745°C (15). Platinum dissolves readily in liquid Cd at 450°, but with a limited film of Cd, the solid alloy Cd_2Pt is formed and its further diffusion into Pt is very slow. The standard potential of a liquid Cd pool, measured with a tungsten contact, calculated from several series of potential-concentration measurements, differed only 6 mv, in the negative direction, from the value reported by Laitinen and Liu (12). The latter values had been obtained by measurements with a platinum microelectrode soon after plating it during the course of recording a cathodic polarogram. Similarly, the potential of a freshly zinc plated platinum electrode agreed with that of a pure zinc pool. The only potential which was found to be significantly different was that of bismuth, as reported elsewhere in this paper. It is probable that the surface alloy formation of cadmium and zinc may be responsible for the very different results reported (4) from a-c and steady-state current-voltage measurements for the kinetics of the cadmium and zinc couples at plated platinum surfaces.

Tungsten electrodes were prepared from 0.7 to 1 mm diameter rods sealed into Pyrex or uranium glass. The cross-sectional surface was polished to a mirror bright finish with 4/0 emery paper. Prior to use, the surface was cleaned in alkaline hydrogen peroxide, rinsed, and dried. Tungsten was not used as the active electrode material. When a clean tungsten microelectrode was inserted into a pool of liquid cadmium or zinc, a small droplet of the metal would adhere to the surface. This type of microelectrode has many of the advantages of a hanging mercury drop, but the area is not reproducible. Since no evidence of surface contamination with time has been found, the practice was to use the same droplet for a series of measurements at different concentrations. The area was determined by measuring the dimensions of the solidified metal with an ocular micrometer. The geometry of the drop corresponded satisfactorily to a segment of a sphere.

The other liquid metals, i.e., bismuth and lead, used in the kinetic studies would not adhere to a clean tungsten surface. Consequently, bismuth was plated onto the same type of electrode from a concentrated solution of Bi^{3+} in the melt. A layer of about 10^{-3} mm thickness exhibited the same potential as a bismuth pool; the activity of the deposit was therefore unity. Visual inspection showed that the entire surface was covered with bismuth. An alternate method was used to make a lead electrode. The cross section of a tungsten-Pyrex seal was ground out to a small cup and the end of the electrode was bent 180°. The reproducibility of the size of the lead drop in the cup was not satisfactory, and there was a variation of the cell resistance and measured data with changes of the position of the drop in the cup.

Microelectrodes of the metals which are solids at 450°C were made by plating platinum electrodes of the type described with the desired metal from aqueous solutions. The deposit was lightly polished with emery paper and washed with water. The apparent surface area was used in the calculation of the exchange current density.

In the kinetic measurements of the V^{3+}/V^{2+} couple, a platinum ball electrode was used. The end of a 26-gauge platinum wire was heated just to the melting point in a hydrogen-oxygen flame. If the wire was then removed slowly from the flame, a very smooth sphere resulted. This was sealed into Corning G-164-EC glass so that only a hemisphere of platinum was exposed. From differential capacity measurements, with an a-c bridge, at a frequency of 1000 cycles sec^{-1}, in 1M $HClO_4$ solution, it was shown that the roughness factor of this type of electrode is about half the roughness factor of a platinum microelectrode polished with 4/0 emery paper. Comparisons were also made with a piece of platinum foil which had a known roughness factor[3] of 1.12. At a potential of +0.6 v vs. SCE, the capacity/cm^2 (apparent) of the "fire polished" ball was nearly the same as the capacity/cm^2 (true) of the platinum foil.

The low melting metals were added to the test tube compartments as liquids. The cleaned and dried pieces of metal were melted above the compartment in an argon filled Pyrex tube, ending in a small capillary. If any metal oxide was present, it tended to cling to the walls of the tube above the capillary. Electrical contact with the pool counter electrode was made with a tungsten rod sealed in Pyrex; the end of the rod protruded a few millimeters beyond the seal.

Counter electrodes of the metals which are not liquids at 450°C were made from foils of the metal under investigation. A large piece of about 12 cm^2 area was fashioned into a right cylinder. Electrical contact was made with a platinum wire spot welded to the foil.

After the counter-electrode was in the filled cell, the potential was measured against a platinum reference electrode. Even in the most carefully purified melts, the potential corresponded to a low concentration, 0.3 to 0.4 mM, of metal ions. With noble metals, such as platinum and bismuth, the spontaneous concentration was much lower (0.01 to 0.05 mM), as might be expected. If magnesium had not been used in the purification of the melt, the spontaneous concentration was several millimolar. The potential also became more positive with time, indicating an increase in the concentration. It is suspected that silica, leached from the glass, is responsible for the slow oxidation of most of the metals studied.

The concentration of the metal ion was changed by anodizing the counter electrode with a constant current for a known time. From the potential meas-

[3] The roughness factor of a 100-cm^2 area foil was evaluated by the krypton adsorption (B.E.T.) method through the kind cooperation of Professor Norman Hackerman, of the University of Texas.

urements at each concentration, it is possible to calculate the initial concentration. Analysis of the contents of several cells after the experiments confirmed the reliability of this procedure.

Vanadous solutions were prepared by anodizing vanadium metal. It was then necessary to filter the solution into another compartment, because finely divided vanadium metal appeared in the solution. A platinum foil cylinder was placed in the solution to oxidize a fraction of the vanadous ions to the vanadic state with a constant current. The solution was vigorously stirred to avoid concentration polarization. The platinum foil also served as the unpolarizable counter electrode during the kinetic measurements.

Platinum reference electrodes were constructed and used exactly as previously reported (16). The same is true of the carbon rods used as working electrodes for the anodization and cathodization of metals and solutions. The volume of the eutectic in the cells was determined by argentometric titration of the chloride.

Electronic equipment-double pulse method.—A block diagram of the electronic circuit for application of the double pulse is shown in Fig. 3. The Tektronix Oscilloscope 535/S2 was used for triggering the pulses. (The delaying sweep of this scope can be released by a push button, which in turn triggers the main sweep.) The gate from the main sweep was fed into the pulse generators, Tektronix 161 and 163, through a capacitor and a resistor. The relative position of the pulses could be adjusted by the input

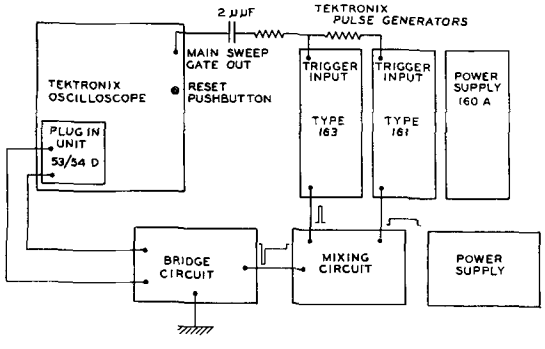

Fig. 3. Block diagram of the electronic circuit for the double pulse method.

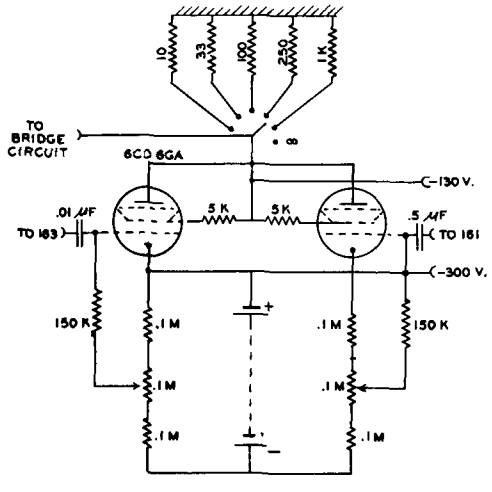

Fig. 4. Circuit for mixing the two pulses

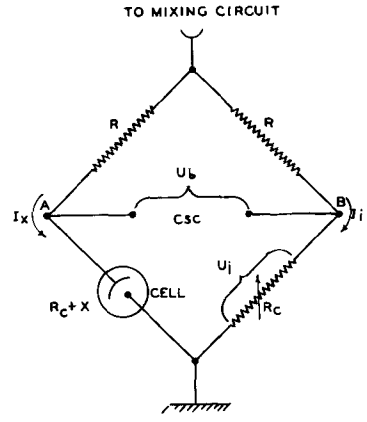

Fig. 5. Bridge circuit for compensating electrolyte resistance.

controls of the generator. The two pulses were mixed in the circuit shown in Fig. 4. The beam power tubes of this circuit are able to pass pulses up to 200 ma. The actual limitation in our measurements was given by the output voltage of the 163 generator which furnished the charging pulse. The grid bias of the beam power tubes was adjusted to a residual current of about 1 μa, which is considered to be negligible. The resistors in the plate circuit were built in for testing purposes. The bridge circuit shown in Fig. 5 was applied as outlined in the introduction. A little slug tuned coil in series with the resistor R_c was used to compensate for the higher inductivity of the cell circuit. In some later experiments two Tektronix 121 preamplifiers were added to improve the frequency response of the system. The rise time was then limited by the pulse generators (0.2 μsec.). The preamplifiers are linear up to an output of 1 v. This limited the current applicable to the cell to

$$\frac{1 \text{ volt}}{\mu(R_c + R_x)}$$

where μ is the amplification of the preamplifiers, R_c is the electrolyte resistance, and R_x is the transfer resistance.

The two pulses used in this method need not be constant current pulses, as has been the usual practice. Using small resistors in the upper branches of the bridge may cause the current to vary somewhat with time, but at the same time improve the frequency response of the equipment. The current I_x, the polarization U_x, and the corresponding transfer resistance X can be calculated from the voltages measured across the bridge U_b and across the compensating resistor U_i with the following formulas:

$$I_x = \frac{U_i R - U_b R_c}{R\ R_c} \cong \frac{U_i}{R_c}$$

$$U_x = \frac{U_b(R + R_c)}{R} \cong U_b$$

$$X = \frac{U_b(R + R_c)R_c}{U_i R - U_b R_c} \cong \frac{U_b R_c}{U_i}$$

The resistors in the upper branches of the bridge are R and the compensating resistor is R_c. The ap-

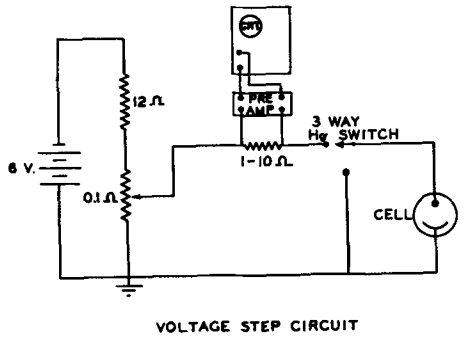

Fig. 6. Circuit for the voltage step method

proximations hold for $R>R_c$. In these measurements U_b was always of the order of magnitude of U_t, or smaller. The above equations, which have been derived for a d-c bridge, should provide a good approximation for the conditions under which the values are measured. From these formulas, an estimate can be made of the necessary value of the resistors in the upper branches of the bridge which will avoid the necessity of corrections in the evaluation. For most of the measurements, resistors R of 10 ohms were used. In checking the effect of the duration of the first pulse, where a constant current is essential, 100-ohm resistors R were substituted without, however, any appreciable difference in results.

Voltage step equipment.—The circuit diagram of the voltage step apparatus is shown in Fig. 6. Its design and function are quite simple. The desired voltage step (usually 2-7 mv) is set by moving the contact on the voltage divider. The exact value was measured to within 0.01 mv with a Student-type potentiometer. The current through the voltage divider was about 0.5 amp, so the resistance across which the voltage step was developed was only 0.005-0.016 ohms. The microelectrode was short-circuited to the counter electrode through the three-way mercury switch. When the switch was moved to the other position, the break occurring before the make, the voltage step was applied between the two electrodes. The current was measured as an iR drop across the precision resistor R_m. The signal was amplified through a video preamplifier (17), modified to operate differentially, and was observed on the screen of a Tektronix 535/S2 oscilloscope equipped with a 53/54 D plug-in preamplifier. The maximum usable sensitivity of the equipment was 0.2 mv/cm and the upper limit of the bandwidth was 0.45 mc. With a 5-ohm measuring resistor, currents could be measured to an estimated ± 2 μa The accuracy of the electronic equipment was periodically checked with a potentiometer and was always within 1%. Sweep rates of 10 or 20 μsec/cm were generally used.

The current time curves were photographed on 35-mm Kodak Plus-X film. The beam intensity and grid line illumination were adjusted to give only a minimum exposure. The image on the negative was very fine and when enlarged to twice the size of the oscilloscope screen, the lines were less than a millimeter wide. The enlarged curves were traced on graph paper with the aid of a french curve. Current-time points from the traced lines were then plotted as current vs. the square root of time.

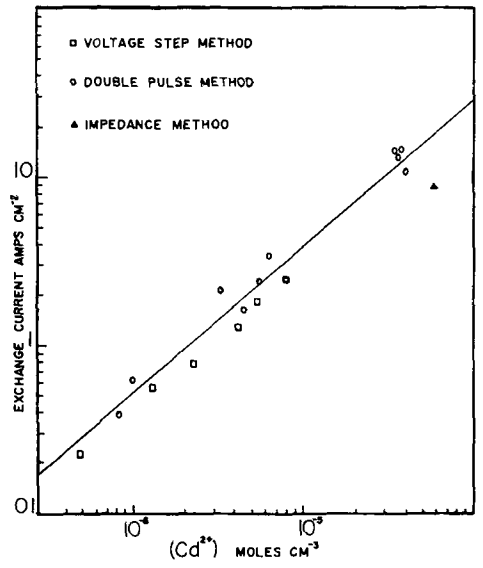

Fig. 7. Exchange currents measured on cadmium

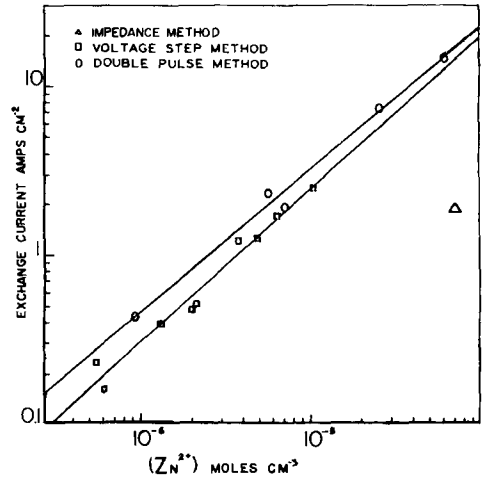

Fig. 8. Exchange currents measured on zinc

Results

Cadmium and zinc.—The cadmium and zinc couples were the first ones studied in this investigation. They were known to be fast reactions, not only from polarographic behavior, but from the a-c impedance measurements (4) described earlier. The earlier impedance measurements were conducted with a polished platinum electrode in melts of a lesser purity. Therefore some difference might be expected between these results and those of Laitinen and Gaur (4).

The exchange currents corresponding to a wide range of Cd^{2+} and Zn^{2+} concentrations are shown graphically in Fig. 7 and 8. On these log-log plots, a linear relation is expected from Eq. [3], with a slope equal to $1-\alpha$. The results of both methods are included on the graphs, as well as the point determined earlier by Laitinen and Gaur. Considering the assumptions that were necessary in the evaluation of the latter experiments and the fact that platinum was used as an electrode, the agreement is surprisingly good.

Each point on the graphs is the average of a series of measurements taken with polarizations between 1 and 10 mv. There was no systematic difference between the results obtained with anodic and cathodic polarizations. The majority of the voltage step measurements were taken in the cathodic direction.

The influence of temperature was investigated in the case of cadmium by measuring the exchange current at 400°, 450°, and 500°C. The activation energy calculated by the Arrhenius equation and was found to be 3 ± 1 kcal mole^{-1}.

Since zinc has a melting point within the range of temperatures investigated, measurements were taken on liquid as well as on solid zinc. Within the limits of accuracy, no difference was observed. This result is similar to the observation of Gerischer and Krause (7) on mercury in a perchloric acid/water eutectic.

Additional experiments were performed with zinc and thallium; no quantitative results can be given for the latter metal because the electrode area was not known. The purpose was to test the influence of the rise time of the double pulse equipment and the extent of the correction obtained when the reaction resistance was extrapolated to zero length of the first pulse. The results for zinc are shown in Fig. 9. Similar behavior was observed with thallium. These results are not in accord with the theory presented by Matsuda, Oka, and Delahay. The dependence of the reaction resistance upon the length of the first pulse was much greater than required by the theory, but still within the over-all limits of accuracy of these measurements (±10%). Calculation of diffusion coefficients from the experimental dependence led to ridiculously low values.

The improvement of the frequency response by using two preamplifiers as mentioned above, enhanced the discrepancies, showing that the poorer rise time of the original equipment was not responsible. Data obtained with and without high rise time equipment differed by 20% when the first pulse was 3 μsec long. But when the values were extrapolated to zero length of the first pulse the results differed by a factor of 2 or more. The shorter the first pulse the bigger was the difference between the two sets of measurements. To explain these results one has to assume some additional process interfering at very short times. The frequency dispersion of the residual capacitance (4) in this melt might be present at these short times. However it does not seem likely that a dispersion which is caused by the establishment of a new steady state on the metal surface with adsorbed ions can occur so rapidly. A quantitative explanation for this effect is still pending and so for the sake of consistency the results listed in Table I are those obtained without taking into account the dependence on the length of the first pulse.

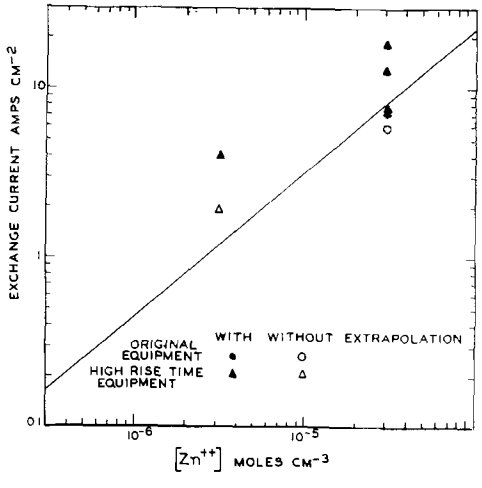

Fig. 9. Exchange currents measured on zinc to test the influence of rise time and extrapolation to zero length of the first pulse.

Lead.—With lead, as also with bismuth and thallium, the hanging drop electrode could not be used because the metal did not adhere to the tungsten surface. Double pulse measurements were taken with a lead drop in the cup-type electrode. Results are shown in Fig. 10. The large variation is due to the difficulties encountered with the cup electrode and because of the uncertainty in the surface area measurements. The best results were obtained with a very small drop which did not fill the cup.

Bismuth.—Although the kinetic data for the reaction $Bi^{3+} + 3e^- = Bi(lq)$ lack precision, primarily because of the volatilization of $BiCl_3$ from the melt, there is no doubt that it is the slowest reaction of all those investigated. The transfer coefficient is larger than that of any of the other metal ion-metal couples. Figure 11 illustrates the dependence of the exchange current on the Bi^{3+} concentration as determined by the voltage step method. The "effective zero time" currents were used to calculate the

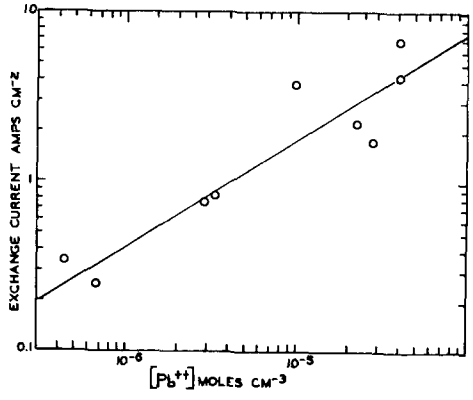

Fig. 10. Exchange currents measured on leod

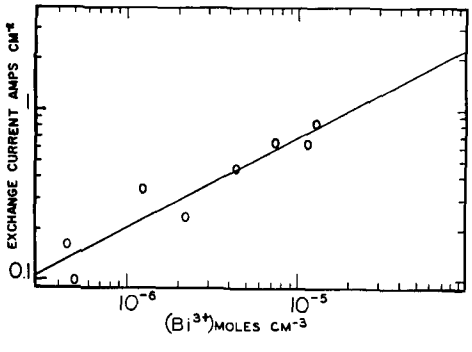

Fig. 11. Exchange currents measured on bismuth

exchange currents according to the method presented in the beginning of the article.

The standard potential of the bismuth couple was calculated from five separate series of measurements of the bismuth potential as a function of concentration. To minimize the error caused by the volatilization of $BiCl_3$, the contents of the compartment were analyzed for bismuth. The average value of $E°$ was -0.640 ± 0.010 v compared to the molar platinum electrode. This is the only case where the potential measured with a tungsten electrode in contact with a metal pool differed appreciably with the potential measured with a plated platinum electrode, as reported by Laitinen and Liu (12). When a platinum electrode was inserted into the same compartment with the tungsten electrode and then plated, the potential corresponded to the one given before, but differed from the potential of the tungsten electrode by nearly 0.1 v. If the platinum electrode was inserted into the bismuth pool, it quickly dissolved. The thermal emf between platinum and tungsten is negligible.

Platinum,[4] *nickel, and silver.*—For solid electrodes there was no difficulty in determining the apparent surface area, which was used in the calculation of the exchange current density. Silver sometimes recrystallized in the melt forming fine whisker-like fibers, causing an increase in exchange current. In such cases, after polishing and cleaning the electrode the measured values were the same as before.

Figure 12 shows the results obtained with these solid metals by the double pulse method without the high rise time preamplifiers. Some of the exchange currents of the silver couple have been calculated by extrapolation to zero length of the first pulse. As can be seen, such points are within the limits of precision of the measurements.

Vanadium(III)-vanadium(II). — This electrode couple is distinctly different from the above examples because both forms of the couple are solvated ions. The exchange current is then a function of two concentrations. The data cannot be compared with the metal ion/metal couples because of the lack of a common reference concentration. The plot of $i_o/(V^{3+})$ vs. $(V^{2+})/(V^{3+})$ shown in Fig. 13 results in a straight line, as expected from Eq. [4].

From measurements at 400°, 450°, and 500°C, the activation energy was found to be 2.8 ±0.4 kcal mole^{-1}; a value which is surprisingly close to that of the cadmium couple.

Evaluation and compilation of the measured data. —Table I contains the kinetic data calculated from the measurements with the two methods. The rate constant $k_h°$ is listed as well as the molar exchange current, $°i_o$. Since the calculation of the rate constant required an extrapolation of over four orders of magnitude to an imaginary concentration of 1 mole cm^{-3}, no limits of error are given. The molar exchange current, i.e., the exchange current at a concentration of 1 mole liter^{-1}, is considered to be a more suitable measure of the rate of an electrode reaction.

[4] Qualitative observations were made of the anodic behavior of platinum in a melt containing about 0.1 mole liter^{-1} Pt^{++}. At positive polarizations of about 100 mv, the current-voltage curve has an unstable region. The anodic current suddenly drops to less than 100 μa cm^{-2}. A layer of $PtCl_2$ is formed at the electrode surface. The slow dissolution of this layer is now the rate determining process. It was possible to apply cell voltages up to 5 v without much increase in current, because of the ohmic drop in the layer. Some chlorine is evolved, but only at much higher polarizations, due to the iR drop in the layer, than at a carbon surface. The amount of current required for the formation of the layer shows that it is a thick salt layer and not a passive layer. After switching off the current, the cell voltage immediately drops to 1 v and then, within milliseconds to seconds depending on the time of anodization, decreases to its equilibrium value. The quantitative investigation of these phenomena requires the application of an electronic potentiostat because of the unstable region in the current voltage curve. This observation may prove useful in developing a method for electrolytically polishing platinum.

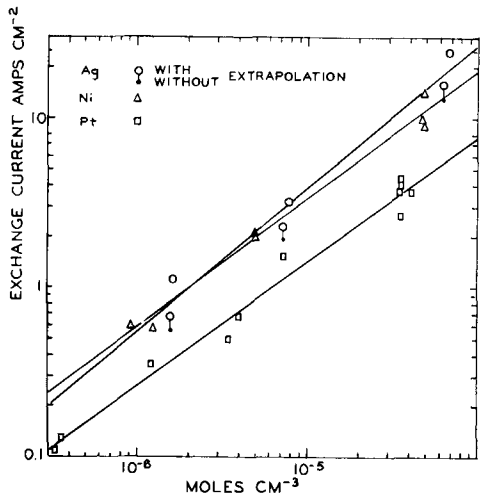

Fig. 12. Exchange currents measured on platinum, silver and nickel.

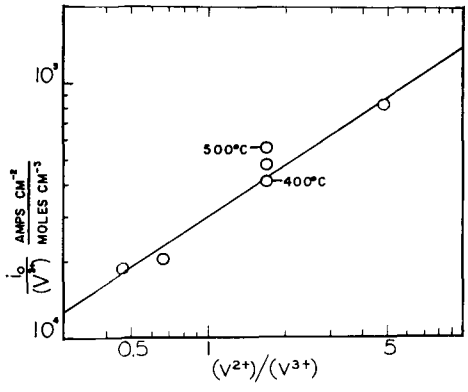

Fig. 13. Exchange currents measured for the V^{3+}/V^{2+} couple

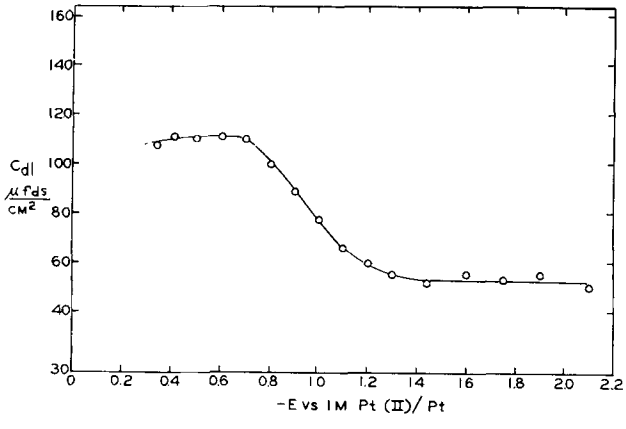

Fig. 14. Differentiol double layer capacity of platinum in the eutectic as a function of potential.

Discussion

In general, the exchange currents of the electrode reactions in this melt at 450°C are not much

Table I

	Molar exchange current amp cm^{-2}	α	k_h^0, cm sec^{-1}
Both methods			
Cd^{2+}/Cd	210 (±50)	0.13 (±0.05)	0.4
Double pulse			
Zn^{2+}/Zn	150 (±30)	0.16 (±0.05)	0.3
Pb^{2+}/Pb	30 (±15)	0.38 (±0.06)	0.01
Ag^{+}/Ag	190 (±50)	0.16 (±0.05)	0.65
Ni^{2+}/Ni	110 (±20)	0.25 (±0.06)	0.1
Pt^{2+}/Pt	40 (±10)	0.27 (±0.06)	0.03
Voltage step			
Zn^{2+}/Zn	150 (±20)	0.10 (±0.05)	0.4
Bi^{3+}/Bi	8 (±3)	0.5 (±0.1)	0.0009
V^{3+}/V^{2+}	30 (±2)	0.67 (±0.05)	0.3

higher than those of the fastest reaction so far investigated in aqueous solutions. The transfer coefficient was somewhat lower, except in the case of bismuth, lead, and vanadium(III)/vanadium(II), which were the three slowest reactions found. The obvious similarity in the behavior of several systems with otherwise differing chemical properties suggests a common discharge mechanism which presumably involves the exchange of metal ions between the electrode and chlorocomplex species in solution.

In the previous work on impedance measurements (3, 4) and in the double pulse method employed here, certain features of the observations do not behave in accordance with the simplest reaction model of a one-step charge transfer mechanism involving diffusing species. In particular, the "inverted" capacitance-resistance behavior, which can be caused by specific adsorption of the electroactive species (5), was explained on this basis by Laitinen and Gaur. A similar "inverted" behavior of capacitative and resistive components of impedance can be predicted, at least over a limited frequency range, for a dissociation reaction preceding the charge transfer reaction if the rate of dissociation reaction is less than or comparable to the rate of the charge transfer reaction (18).

It is therefore instructive to consider qualitatively the effects of adsorption and of prior dissociation on the double pulse and voltage step methods. The effect of adsorption of electroactive species would depend on whether the adsorbed layer represents an *additional* reaction path (parallel admittance) as assumed in the treatment of impedance measurements (4, 5) or whether prior adsorption is a step in the main reaction path (series admittance). In the former case, both the double pulse and voltage step methods would respond (for rapid charge transfer to the adsorbed phase) by showing an abnormally large double layer capacity. Indeed, a purely capacitative correction for adsorption was found adequate in several cases of impedance measurements (5), and in any case the resistive component of this correction is very small. For a slow charge transfer reaction to the adsorbed phase, a large time constant would be introduced into the reaction of the adsorbed phase, but in this case the main charge transfer reaction would also be expected to be slow. In the voltage step method the time constant for the charging process was found to be normal even in the presence of an electrode reaction. In the double pulse method, the charging is forced to happen in the short time interval of the first pulse. As has been already mentioned, the detailed behavior of the double pulse method does not comply with the simple charge transfer reaction model.

For prior adsorption as a step in the main reaction (the series admittance model), the effect would be similar to, although not identical with, that of a prior dissociation. All methods of measurement would be affected by the rate of the prior step if its rate were comparable to or slower than the transfer of charge.

Independent proof of the reality of specific adsorption or dissociation is needed before definite conclusions as to reaction mechanism can be reached. The irregularities in the a-c impedance measurements and the unexpectedly large dependence of the measured reaction resistance on the duration of the first pulse in the double pulse indicate, however, that simple charge transfer control does not prevail.

Manuscript received Dec. 9, 1959. This paper was prepared for delivery before the Philadelphia Meeting, May 3-7, 1959.

Any discussion of this paper will appear in a Discussion Section to be published in the December 1960 JOURNAL.

REFERENCES

1. H. A. Laitinen and H. C. Gaur, *Anal. Chim. Acta*, **18**, 1 (1958).
2. J. E. B. Randles and W. White, *Z. Elektrochem.*, **59**, 666 (1955).
3. H. A. Laitinen and R. A. Osteryoung, *This Journal*, **102**, 598 (1955).
4. H. A. Laitinen and H. C. Gaur, *ibid.*, **104**, 730 (1957).
5. H. A. Laitinen and J. E. B. Randles, *Trans. Faraday Soc.*, **51**, 54 (1955).
6. D. L. Hill, G. J. Hills, L. Young, and J. O'M. Bockris, *J. Electroanalytical Chem.*, **1**, 79 (1959).
7. H. Gerischer and M. O. Krause, *Z. phys. Chem. N. F.*, **10**, 264 (1957); **14**, 184 (1958).
8. H. Matsuda, S. Oka, P. Delahay, *J. Am. Chem. Soc.*, **81**, 5077 (1959).
9. W. Vielstich and P. Delahay, *ibid.*, **79**, 1874 (1957).
10. H. A. Laitinen, R. A. Osteryoung, and W. S. Ferguson, *This Journal*, **104**, 516 (1957).
11. W. G. Burkhard and J. D. Corbett, *J. Am. Chem. Soc.*, **79**, 6361 (1957).
12. H. A. Laitinen and C. H. Liu, *ibid.*, **80**, 1015 (1958).
13. H. von Wartenberg, *Z. angew. Chem.*, **69**, 258 (1957); *Z. anorg. u. allgem. Chem.*, **273**, 257 (1953).
14. Strohmeyer, *Schw. J.*, **22**, 376 (1818); W. R. E. Hodkinson, R. Waring, and A. P. H. Desborough, *Chem. N.*, **80**, 185 (1899); A. Pospielow, *Ber. phys. Ges.*, **5**, 346 (1907).
15. K. Rav, *Proc. Iowa Acad. Sci.*, **38**, 166 (1931).
16. H. A. Laitinen and W. S. Ferguson, *Anal. Chem.*, **29**, 4 (1957).
17. Preferred Circuits, Naval Aeronautical Electronic Equipment, NAVAER 16-1-519, p. 26-2, Superintendent of Documents, U.S. Gov't Printing Office, Washington 25, D. C. (1955).
18. Cf. J. E. B. Randles, *Discussions Faraday Soc.*, **1**, 11 (1947); H. Gerischer, *Z. physik Chem.*, **202**, 292, 302 (1953); *Z. Elektrochem.*, **57**, 604 (1953).

A Study of the Oxidation of Hydrogen at Platinized Platinum Electrodes

Thomas C. Franklin and Samuel L. Cooke, Jr.[1]

Chemistry Department, Baylor University, Waco, Texas

ABSTRACT

A coulometric technique using a polarograph was used to study the oxidation of hydrogen at platinized platinum electrodes. The results obtained by this technique are in agreement with results obtained by charging curve and a-c bridge techniques. This technique showed the presence of two forms of hydrogen adsorbed at the surface of the platinum, and it also showed the presence of hydrogen absorbed in the platinum. A study of the effect of pH on the current voltage curves suggested that absorbed hydrogen migrated as a charged species, probably H_3^+.

The oxidation of hydrogen at platinum electrodes has been investigated by a number of workers. Bowden (1) and Butler (2-4) and co-workers studied the process using charging curve techniques. Frumkin and other Russian workers (5-13) followed this with a detailed study of the oxidation of hydrogen on platinum electrodes using similar charging curve techniques. A group of German workers (14-19) have studied the same problem using both alternating current bridge and charging curve techniques.

In Frumkin's work three arrests can be noted in the curves between the potential of the hydrogen electrode and the oxygen region in sulfuric acid solutions. The first two were grouped together as being caused by the process of removing adsorbed hydrogen. The third was attributed, along with another possibility, as being due to the process of removing hydrogen from the interior of the platinum.

Two maxima were obtained in capacitance of the electrode vs. polarizing potential curves plotted from data obtained in the bridge experiments. Eucken and Weblus (14, 15) attributed these effects to the presence of two different forms of adsorbed hydrogen on the surface of the platinum.

In a study of the competition between hydrogen and organic molecules for sites on the platinum electrode (20) the amount of hydrogen was measured by electrooxidation of the hydrogen using a polarograph and by measurement of the number of coulombs used in the oxidation. In conjunction with this study of poisoning, a study was made of the oxidation of hydrogen using this coulometric technique. It was felt that this technique was more rapid than the charging curve experiments of Frumkin and that it did not involve the special equipment needed for the bridge method or the high speed charging curves obtained by workers such as Breiter.

Experimental Materials and Method

The hydrogen electrodes used in this work were made by plating a 1 to 2 cm length of 20-gauge bright platinum wire with platinum black after the manner of Clark (21). A 3% solution of chloroplatinic acid with 0.06% lead acetate present was used as the plating bath. The electrode was washed with distilled water, cleaned of old platinum black with *aqua regia*, checked for surface cleanness by observing the uniformity of hydrogen evolution in 6*N* HCl, and then plated for a prescribed length of time at 2-10 ma. Since no visible evolution of hydrogen occurred at the current densities used, it was presumed that the discharge of platinum was the only significant process occurring. The number of coulombs passed could thus be used as an estimate of the thickness of the platinum black. To obtain a reproducible electrode, the thickness of the platinum black was controlled by the number of coulombs passed (22). Electrodes identical within 1% could be prepared under very carefully controlled conditions.

After plating, the electrodes were washed in a vigorous stream of redistilled water, charged with hydrogen in the electrolyte to be used, and placed in the hydrogen-saturated electrolyte in the apparatus for study. Equilibrium occurred almost immediately as indicated by the cell maintaining a constant potential, which was measured with a L&N K-2 potentiometer.

The apparatus is pictured in Fig. 1. The physical arrangement of the apparatus is shown in the inset.

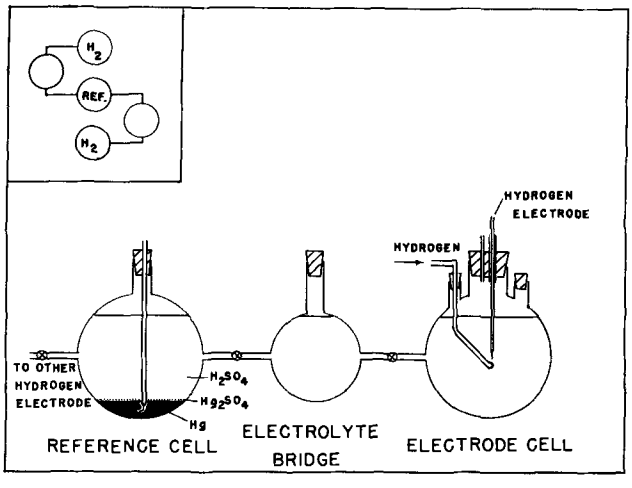

Fig. 1. Apparatus. Inset: physical arrangement

[1] Present address: Interscience, Inc., Richmond, Virginia.

The S-shaped arrangement permitted study of two electrodes with only one reference electrode. The complete apparatus was maintained at 25.0°C. The reference half-cell was Hg, Hg_2SO_4 in sulfuric acid and Hg, HgO, NaOH in basic solutions. The sodium hydroxide and sulfuric acid were of the same concentration as the electrolyte in the hydrogen electrode cell.

A series of runs were made in the *p*H range between 2*N* sulfuric acid and 2*N* sodium hydroxide. This was done by adding sulfuric acid to sodium hydroxide and *vice versa*. The *p*H was determined from the hydrogen electrode.

The hydrogen was prepared in a zinc-sulfuric acid Kipp generator and was bubbled through two wash bottles containing electrolyte. In the neutral and basic runs, the gas was first bubbled through strong sodium hydroxide to remove any acid carried over from the generator. Contact between hydrogen and rubber tubing was minimized, and all rubber was digested for two days in hot, concentrated sodium hydroxide and washed with distilled water before use.

In the early phases of the problem an investigation was made of the effect of various purification techniques on the results of the experiments. Several sources of hydrogen were used, including commercial tank hydrogen, Kipp generator hydrogen (using two different sources of zinc and two different sources of sulfuric acid), and electrolytically generated hydrogen. The hydrogen was purified in several different types of trains. Some runs were made in an all-glass apparatus and others were made in which the rubber connections were replaced with Tygon. The apparatus was in all cases soaked for 24 hr or longer, in some cases with distilled water and in others with the solution to be studied. Some experiments were carried out in sulfuric acid solutions that had been pre-electrolyzed overnight according to the procedure of Schuldiner (23). In all of these experiments the results were essentially the same. The presence of a poison decreased the amount of hydrogen at the electrode surface but did not change the general shape of the curves.

Hydrogen was bubbled into the cell for at least twice as long as necessary for potentiometric equilibrium. The cell was then permitted to stand for at least an equal amount of time. Then the hydrogen at the electrode was electrolytically oxidized using a Sargent Model XXI polarograph to record the current-voltage curve for the oxidation. When the cell resistance was greater than 500 ohms it was necessary to insert a compensation circuit. This circuit differed in design but not in principle from that of Nicholson (24). A lathe wound compensating slidewire was placed adjacent to the balancing slidewire of the recorder and an extra contact was constructed on the regular contact mount of the recorder. The current-voltage curves were also current-time curves for the oxidation process, and the area under the curves was proportional to the number of coulombs needed for the oxidation. The compounds used were all of reagent grade. The water was triply distilled.

Data and Results—Sulfuric Acid Solutions

A typical current-voltage curve for the oxidation of the hydrogen present at platinized platinum in 2*N* sulfuric acid is shown in Fig. 2. Three very distinct maxima are observed and are indicated by Roman numerals. A fourth maximum is observed when the voltage is allowed to sweep beyond the region where hydrogen is oxidized. Previous workers (25, 26) have shown the fourth maximum to be due to the formation of a surface oxide of platinum. These maxima are not experimental artifacts as is shown by the fact that they were obtained under a wide

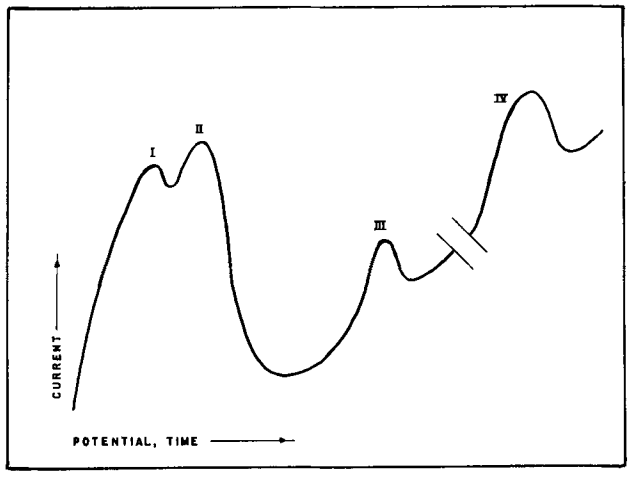

Fig. 2. Typical current-voltage curve for hydrogen oxidation on a platinized platinum anode in 2N sulfuric acid.

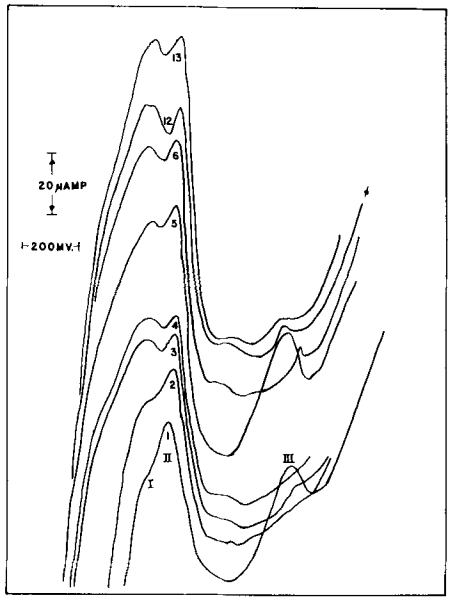

Fig. 3. Effect of oxidations, time, and formation of oxide on the shape of the current-voltage curve.

Number of the Oxidation	Conditions
1	New electrode after hydrogen bubbling.
2	10 min after oxidation No. 1.
3	10 min after oxidation No. 2.
4	10 min after oxidation No. 3.
5	510 min after oxidation No. 4.
6	10 min after oxidation No. 5.
12	10 min after oxidation No. 11, the potential was allowed to sweep through the point of formation of the oxide of platinum.
13	10 min after oxidation No. 12.

Roman numerals denote the maxima. Origin of curves shifted along current axis.

variety of conditions including variations in the voltage sweep rate, the temperature, and the electrode plating conditions. Rotating the electrodes made the curves irregular but did not essentially change the area under the three maxima caused by the oxidation of hydrogen.

Figure 3 shows the effects of (*a*) time since the previous oxidation, (*b*) formation of the first surface oxide of platinum, and (*c*) successive oxidations on the shape of current-voltage curves in sulfuric acid. To prevent the curves from overlapping, the origin is shifted along the current axis. The first and second maxima are observed to develop with successive oxidations and after formation of the oxide. The third maximum is prominent in oxidations No. 1 and 5 and poorly defined in the other oxidations. The third maximum grows slowly as compared to the first two maxima. This is shown by Fig. 4 which represents the relation between area under the third maximum and time since the previous oxidation. The difference in rate of growth of this maximum and of the other two maxima can be appreciated when it is realized that in less than 3 min a similar plot for maxima I or II would go beyond the range of Fig. 4, and equilibrium would be reached in 10 min.

From these data it can be concluded that the first two maxima are a result of the oxidation of two forms of hydrogen adsorbed on the surface of the platinum. This is shown by the fact that the area under these maxima increases with repeated oxidations (Fig. 5) (the expansion and contraction of the crystal lattice on oxidation and then reduction increased the surface area) and by the fact that the area under these maxima decreased following a Freundlich adsorption isotherm in the presence of poisons (20). The third maximum presumably corresponds to the oxidation of hydrogen absorbed in platinum. It is a well-known fact that hydrogen absorbs in metals more slowly than it adsorbs on metals (27).

The above interpretation agrees with the interpretations of the Russian workers (5-13) in that they observed the slow forming absorbed hydrogen. It agrees with the German workers (14-19) in that they distinguished between the two forms of adsorbed hydrogen. Breiter (16-19) observes a third form of surface hydrogen to which this technique is insensitive. However, the interpretation of the two forms of adsorbed hydrogen as hydrogen adsorbed on oxygen, and on platinum (14), might just as well be interpreted as chemically and physically adsorbed hydrogen, respectively.

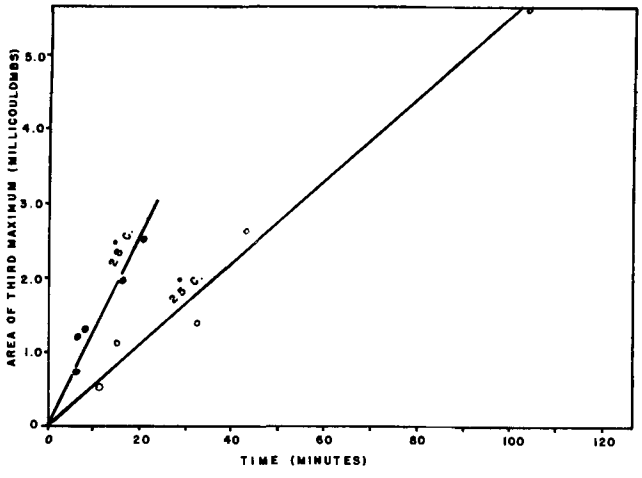

Fig. 4. Effect of time on the area under third maximum in acid solutions.

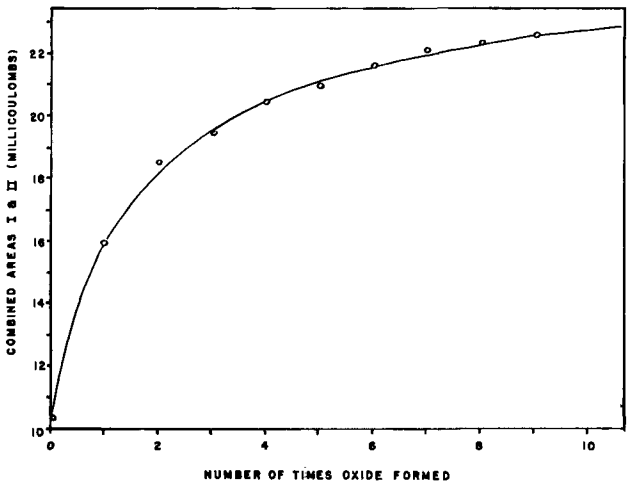

Fig. 5. Effect of oxide formation on combined areas I & II in acid solutions.

Basic and Neutral Solutions

The three maxima were still observed in 2N sodium hydroxide. However, two things made the hydrogen electrode in basic solutions more difficult to study: (*a*) The three maxima are very close together and thus there is a tendency for one or more of them to become ill-defined; (*b*) all three forms of hydrogen were completely replenished in the 10 min normally allowed between oxidations (in acid solutions it took over 3 hr for the absorbed hydrogen to reach equilibrium). Some experiments indicate that this difference in rate was due to poisoning of the electrode by sulfate ion.

Although no quantitative studies, such as those in sulfuric acid, could be made, a qualitative comparison was made of the effects of (*a*) time since the previous oxidation, (*b*) formation of the first oxide of platinum, (c) successive oxidations, and (*d*) hydrogen evolution, on the area under the curves in the neighborhood of each maximum in 2*N* sulfuric acid and 2*N* sodium hydroxide. This comparison is shown in Table I.

Table I. Summary of results in acidic and basic solutions

Effect on the area under the curve in the region of each maximum.

Maximum	Successive oxidations	Time since previous oxidation	Oxide formation	Hydrogen evolution
		Basic Solutions		
I(A)	Increase	No effect	Increase	Increase
II(B)	No effect	Increase	No effect	No effect
III(C)	No effect	No effect	Increase	No effect
		Acidic Solutions		
I	Increase	No effect	Increase	Increase
II	No effect	No effect	Increase	No effect
III	No effect	Increase	No effect	No effect

From these results it was concluded that the last two maxima had shifted their relative positions and the I, II, and III maxima in basic solutions correspond in acidic solutions to I, III, and II, respectively. This was further indicated by the fact that if one momentarily generates hydrogen on the electrode in basic solutions and then oxidizes it, one obtains the current-voltage curve shown in Fig. 6 containing only the two peaks I(A) and III(C) corresponding to the two surface forms of hydrogen (I and II in acid solutions). To study further this shift, the behavior of the current-voltage curves was investigated at intermediate *p*H values.

The potentials of the maxima relative to the normal hydrogen electrode are plotted as a function of *p*H in Fig. 7. The data for each maximum are on straight lines, except for a deviation in the *p*H range from 6 to 10. This deviation is attributable to a decrease in the *p*H at the electrode surface in the unbuffered solutions due to the generation of hydrogen ions during the oxidation. There was a definite shift in the relative positions of maxima II and III (acidic) as one goes from acidic to basic solutions. The potentials at which the two surface forms (maxima I and II in acid) are oxidized shift by 0.054 and 0.044 v in the negative direction for each unit rise in *p*H. It is expected that a reversible oxidation producing one hydronium ion for each electron will shift the potential by 0.059 v per *p*H unit. The deviation of these two slopes from the expected value may be due to a voltage drop caused by the resistance of the solution. The effect was more pronounced for the second surface form since the current was much higher. The potential for the maximum corresponding to the oxidation of the absorbed hydrogen (III in acid) shifts by 0.094 v per *p*H unit. This high slope shows that the absorbed hydrogen migrates as a charged species to the surface where it is oxidized. This slope corresponds most nearly to the reaction $H_3^+ = 3\ H^+ + 2e^-$, whose potential should shift by 0.089 v per *p*H unit. Because of the uncertainty of the resistance correction, the formula of the charged species could be different, but this experiment suggests that absorbed hydrogen must be a charged species. The presence of H_3^+ absorbed in platinum has been indicated by a number of workers (28), and Pearson (29) has concluded that in the absence of water the hydrogen ion prefers to associate with the hydrogen molecule.

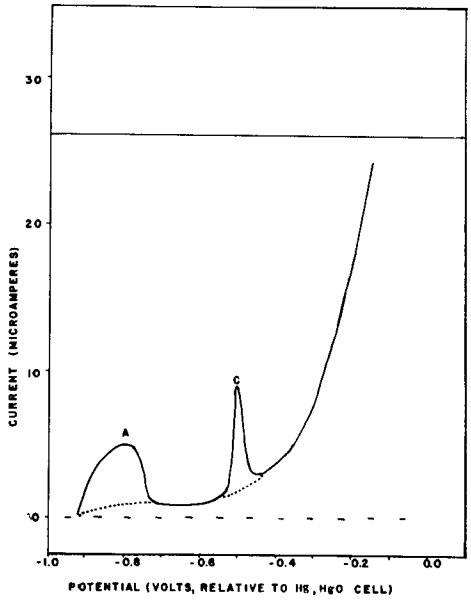

Fig. 6. Current-voltage curve for a hydrogen electrode in basic solution.

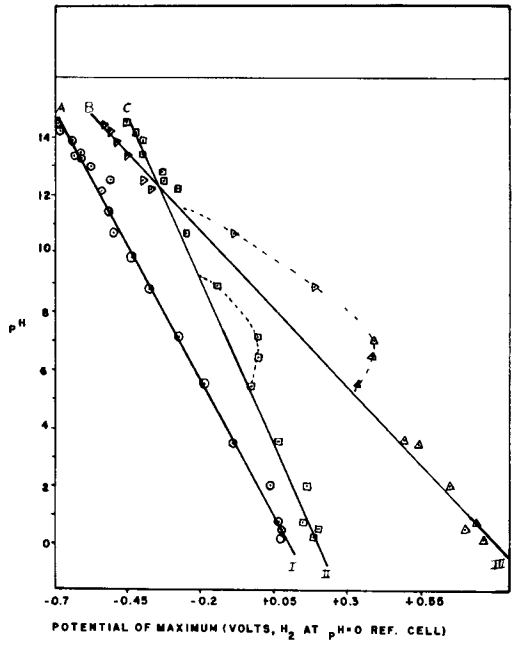

Fig. 7. pH dependence of the potentials of the maxima referred to the normal hydrogen electrode. Circle with dot, maximum I in acid and I(A) in basic solutions; square with dot, maximum II in acid—III(C) in basic solutions; triangle with dot, maximum III in acid—II(B) in basic solutions.

Summary

From current-voltage curves for the oxidation of hydrogen at platinized platinum electrodes in aqueous sulfuric acid, it was concluded that three forms of hydrogen are involved. These three forms, in order of ease of electrolytic oxidation, are postulated to be two forms of adsorbed hydrogen and one form of absorbed hydrogen, in agreement with the conclusions of other workers. Hydrogen is absorbed into platinum much more rapidly from sodium hydroxide solutions than from sulfuric acid solutions. The effect of *p*H on the current-voltage curves suggests that absorbed hydrogen is present as a charged species, probably H_3^+.

From these experiments, it can be concluded that the present technique, the use of current-voltage curves (with a constant voltage sweep rate) can be used for a study of the behavior of hydrogen on metal electrodes. This technique is faster than the slow charging curve technique and not as difficult experimentally as the a-c bridge or fast charging curve techniques. In agreement with the work of Frumkin (7, 12) and Eucken and Weblus (14) it showed the presence of two forms of hydrogen adsorbed on the surface of platinum differing in ease of oxidation, and the presence of hydrogen absorbed in the metal.

One of the major disadvantages of this technique is the presence of a residual current that must be subtracted. A residual current is present because of

the oxidation of molecular hydrogen in solution diffusing to the surface. For some reason the absorption of hydrogen in platinum from basic solutions is much more rapid than in acid. The reverse process, the diffusion of hydrogen from the interior of the metal to the surface, causes a high residual current in basic solutions. However, in sulfuric acid solutions especially, one can obtain a measure of the amount of hydrogen present at the electrode surface in the different forms by taking the area under each maximum and subtracting the area due to the residual current.

Acknowledgment

The authors take this opportunity to thank the Research Corporation for the financial assistance they gave to this research.

Manuscript received June 8, 1959.

Any discussion of this paper will appear in a Discussion Section to be published in the December 1960 JOURNAL.

REFERENCES

1. F. P. Bowden, *Proc. Roy. Soc. (London)*, **125A**, 446 (1929).
2. J. A. V. Butler and G. Armstrong, *ibid.*, **137A**, 604 (1932).
3. G. Armstrong, F. R. Himsworth, and J. A. V. Butler, *ibid.*, **143A**, 89 (1933).
4. J. A. V. Butler and G. Drever, *Trans. Faraday Soc.*, **32**, 427 (1936).
5. A. Slygin and A. Frumkin, *Acta Physicochem, U.R.S.S.*, **3**, 791 (1935).
6. A. Slygin, A. Frumkin, and W. Medwedowsky, *ibid.*, **4**, 911 (1936).
7. A. Frumkin and A. Slygin, *ibid.*, **5**, 819 (1936).
8. B. V. Ershler and M. Proskurnin, *ibid.*, **6**, 195 (1937).
9. B. Ershler, *ibid.*, **7**, 327 (1937).
10. B. Ershler, G. Deborin, and A. Frumkin, *ibid.*, **8**, 565 (1938).
11. A. Slygin and B. Ershler, *ibid.*, **11**, 45 (1939).
12. A. Frumkin and E. E. Aikasyan, *Doklady Akad. Nauk*, **100**, 35 (1955).
13. E. E. Aikasyan and A. I. Fedorova, *ibid.*, **86**, 1137 (1952).
14. A. Eucken and B. Weblus, *Z. Elektrochem.*, **55**, 114 (1951).
15. E. Wicke and B. Weblus, *ibid.*, **56**, 169 (1952).
16. M. Breiter, C. A. Knorr, and R. Meggle, *ibid.*, **59**, 153 (1955).
17. M. Breiter, C. A. Knorr, and W. Volkl, *ibid.*, **59**, 681 (1955).
18. M. Breiter, H. Kammermaier, and C. A. Knorr, *ibid.*, **60**, 37 (1956).
19. M. Becker and M. Breiter, *ibid.*, **60**, 1080 (1956).
20. T. C. Franklin and R. D. Sothern, *J. Phys. Chem.*, **58**, 951 (1954).
21. W. M. Clark, "The Determination of Hydrogen Ions," Williams and Wilkins, Baltimore, Md. (1932).
22. W. M. MacNevin and M. Levitsky, *Anal. Chem.*, **24**, 973 (1952).
23. S. Schuldiner, *This Journal*, **99**, 488 (1952).
24. M. M. Nicholson, *Anal. Chem.*, **27**, 1364 (1955).
25. S. E. S. El Wakkad and S. H. Emara, *J. Chem. Soc.*, **1953**, 461.
26. W. Nestorova and A. Frumkin, *Zhur. Fiz. Kim.*, **26**, 1178 (1952).
27. D. P. Smith, "Hydrogen in Metals," University of Chicago Press, Chicago, Ill. (1948).
28. D. T. Hurd, "An Introduction to the Chemistry of the Hydrides," p. 59, John Wiley & Sons, Inc., New York (1952).
29. R. G. Pearson, *J. Chem. Phys.*, **16**, 502 (1948).

Technical Notes

Charging Curves for Germanium Electrodes

W. W. Harvey, S. Sheff, and H. C. Gatos

Lincoln Laboratory, Massachusetts Institute of Technology, Lexington, Massachusetts

The assertion has been repeatedly made in the literature [e.g., ref. (1-3)] that germanium surfaces in aqueous solution are covered with an oxidic layer. This assertion seems to be based on thermodynamic considerations and on the observation by Turner (4) that, during anodic dissolution, approximately a monolayer of surface oxide or hydroxide is present. However, direct experimental evidence for the existence of an oxidic layer on a germanium electrode not polarized anodically has been lacking. Accordingly, the chemical state of the surface was re-investigated using the method of charging curves, i.e., plots of electrode potential vs. time at constant current density.

Results and Discussion

Figure 1 shows the changing character of the charging curves obtained in 1.0*N* H_2SO_4 on progressive removal of dissolved oxygen [cf. ref. (2, 4)].

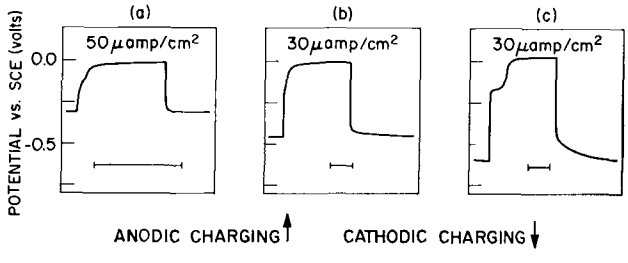

Fig. 1. Changing character of charging curves for germanium on displacing dissolved O_2; horizontal markers represent 10 sec on the abscissa; (a), 1.0N H_2SO_4, as made up; (b) and (c), following N_2 bubbling.

After the concentration of oxygen has been reduced to a low value by prolonged bubbling of purified inert gas, a charging curve such as illustrated in Fig. 2(a) can be obtained. Further removal of oxygen by cathodic reduction results in increased

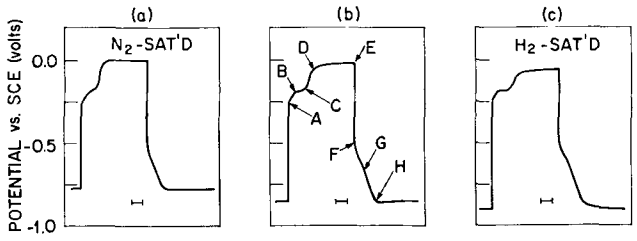

Fig. 2. Charging curves obtained in 0.1N H_2SO_4 after prolonged bubbling of purified N_2; markers represent 150 μcoulomb/cm^2(5 sec) on the abscissa. (a), Initial charging behavior at 30 μa/cm^2; (b), behavior after repeated cycling; (c), same, except solution H_2-satd.

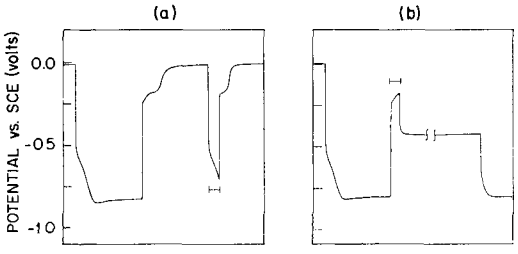

Fig. 3. Examples of charging curve analysis (actual tracings) in 0.1N H_2SO_4; width of markers is equivalent to 150 μcoulomb/cm^2.

polarization during the cathodic step, as shown in Fig. 2(b) and (c). A second consequence is the development of the segment $\overline{BC}$ of the anodic curve. Charging curves similar to those of Fig. 2 but with the cathodic portion extending in a third stage to a more negative potential have also been obtained, particularly at somewhat higher current densities than reported here.

The charging curves have been analyzed in several ways (see below and also Fig. 3); the main features are interpreted as follows: the change in potential along $\overline{AB}$ results from the anodic oxidation of hydrogen atoms chemisorbed during $\overline{GH}$ (by cathodic reduction of hydrogen ions); along the horizontal portion of $\overline{BC}$, hydrogen molecules on the solution side of the interface are oxidized (to hydrogen ions); following this, germanium surface atoms are oxidized. Reversing the current after the final anodic potential has been reached brings about the reduction of the anodically formed surface oxide in the interval $\overline{FG}$.

It is of interest to note that the sequence of processes during charging is different for germanium and platinum, whose charging behavior has been studied most extensively. The first stage of the anodic polarization curve for platinum (5) corresponds to the ionization of cathodically formed hydrogen (6) and consists of an initial horizontal portion (ionization of free hydrogen in the solution), followed by a linear increase of potential (ionization of chemisorbed hydrogen). The second stage for platinum is a rapid increase of potential, corresponding to charging of a double layer. For a polarized germanium electrode, on the other hand, it is evident that an appreciable change in the total semiconductor-electrolyte potential difference must occur before the electric field at the interface has been altered sufficiently to bring about the oxidation of cathodically formed hydrogen or the reduction of anodically formed surface oxide.

In a separate experiment, it was shown that the steady-state anodic reaction in hydrogen-saturated solution is the same (viz., germanium dissolution) as in nitrogen-saturated solution, and so it was established that molecular hydrogen is not oxidized during the anodic dissolution of germanium. In addition, it was shown by chemical tests that metagermanic acid (the product of anodic dissolution) is not reduced to a lower valence state at the germanium cathode.

The charging curves of Fig. 2 and 3 were obtained with hemispherical electrodes (p-type) to insure uniform current distribution at the semiconductor surface. (Similar curves were obtained using disk-shaped n- and p-type electrodes with {111} orientation.) Taking 7.5 x 10^{14}/cm^2 as the average density of atoms at the real surface and using the value 1.3 as the roughness factor of chemically polished germanium (7,8), it is readily calculated that one electron per surface atom is equivalent to 1.56 x 10^{-4} coulomb/cm^2. By analyzing spectrochemically for germanium entering the solution during repeated anodic-cathodic charging, it was possible to obtain essential information relevant to the oxidation of germanium surface atoms in the initial stages of the anodic process. Thus, it was found that at 30 μa/cm^2, germanium dissolved is equivalent to 18 sec of the 30-sec anodic stage of Fig. 2(b); i.e., a charge equivalent to 12 sec (3.6 x 10^{-4} coul/cm^2, or 2.3 electrons per surface Ge atom) at the stated current density is consumed in the oxidation of chemisorbed hydrogen, free hydrogen, and germanium surface atoms. Further, by successively decreasing the cycle duration, it was found that anodic dissolution begins at the inflection in $\overline{CD}$ (i.e., roughly midway between C and D in the figure); however, oxidation of surface atoms is not completed until the steady-state anodic dissolution potential is reached (beyond D). For the specimens employed, the surface coverage by chemisorbed hydrogen during steady-state cathodic charging was equivalent to approximately 0.6 atom layer.

It is evident from the data presented that the anodic formation of surface oxide or hydroxide requires less than two electrons per surface germanium atom. In fact, as indicated by the coulomb equivalent of $\overline{FG}$ [(Fig. 3(a)], not more than one electron per surface atom is required in this process. Time-lapse studies have shown further that in the absence of dissolved oxygen (and other oxidizing substances which attack germanium), chemical species chemisorbed onto, and presumable covalently bonded to germanium as a result of electrolytic processes remain chemisorbed indefinitely.

If a properly prepared germanium surface is polarized cathodically without prior anodic treatment, only the hydrogen reduction portion [beginning at G in Fig. 2(b)] of the charging curve is observed. The same result is obtained if, following a series of charging cycles, the electrode is polarized anodically only to B [see Fig. 3(b)]. These observa-

tions constitute the most direct evidence available at present for the absence of an appreciable oxidic layer on germanium surfaces in nonoxidizing aqueous environments.

Conclusions

It was shown that in dilute H_2SO_4 not more than one electron per germanium surface atom is required during the anodic formation of a surface oxide or hydroxide layer and that the equivalent coverage by chemisorbed hydrogen during cathodic charging is closer to 0.5 than to 1.0. It was further shown that virtually oxide-free germanium surfaces can be obtained in aqueous electrolytes.

Acknowledgment

The authors wish to acknowledge the assistance of Mrs. M. J. Button with some of the experiments.

Manuscript received Jan. 15, 1960. The work reported in this paper was performed by Lincoln Laboratory, a center for research operated by Massachusetts Institute of Technology with the joint support of the U. S. Army, Navy, and Air Force.

Any discussion of this paper will appear in a Discussion Section to be published in the December 1960 JOURNAL.

REFERENCES

1. H. Gerischer, *Bull. soc. chim. Belges*, **67**, 437 (1958).
2. J. Bardeleben, *Z. physik. Chem. (Frankfurt)*, **17**, 39 (1958).
3. J. F. Dewald, "Semiconductors," N. B. Hannay, Editor, p. 727, Reinhold Publishing Corp., New York (1959).
4. D. R. Turner, *This Journal*, **103**, 253 (1956).
5. A. Hickling, *Trans. Faraday Soc.*, **41**, 333 (1945).
6. J. D. Pearson and J. A. V. Butler, *ibid.*, **34**, 1163 (1938).
7. J. T. Law, *J. Phys. Chem.*, **59**, 543 (1955).
8. S. P. Wolsky, *Phys. and Chem. Solids*, **8**, 114 (1959).

A Comparison of Etching and Fracturing Techniques for Studying Twin Structures in Ge, Si, and III-V Intermetallic Compounds

J. W. Faust, Jr. and H. F. John

Research Laboratories, Westinghouse Electric Corporation, Pittsburgh, Pennsylvania

In many cases the detection or location of twins is accomplished most easily by etching. If the etchant is judiciously chosen, one can locate the twin boundary and also determine the orientation of the material on either side of the boundary (1). Three methods of revealing twins by etching and a new method of revealing twins by fracturing are discussed below.

Techniques for Revealing Twins by Etching

1. Preferentially etch a lapped surface. The twin boundary is revealed by the change in the characteristic etch pits as a result of the orientation difference across the boundary. If the orientations of the faces across the twin plane are not equivalent, then a step will also be produced at the boundary as a result of the etch rate being a function of the orientation.

2. Chemically or electrolytically polish a lapped surface. The twin will be revealed as a groove (if the orientations of the faces across the twin plane are equivalent) or as a step (if the orientations are not equivalent).

3. Immerse a mechanically polished surface in a chemical polish or a preferential etch for a very short time. The twin line will be revealed as a groove.

Any of these methods can be applied to the study of twin structures in semiconducting materials; however, difficulties in interpretation can arise if the twins are very closely spaced, and particularly if the etched surface is perpendicular to one of the <211> directions. Billig (2) in his study of twin structures in "dendritic" Ge does not give any details of his experimental technique; however, examination of his photomicrographs indicates that he must have used method 3, i.e., the dendrite cut perpendicular to its length, polished, and etched in a preferential etch. Since his technique reveals not only the twin lamella but also dislocations, a complete analysis of the cross section is impossible in many cases.

Of the three etching techniques, method 3 (employing a chemical polish on a mechanically polished surface) is particularly useful when properly

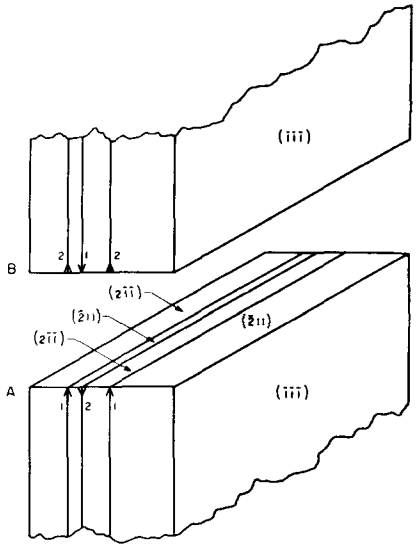

Fig. 1. Diagram of a cut section containing three twin boundaries. The "arrows" on the twin planes are traces of {111} planes.

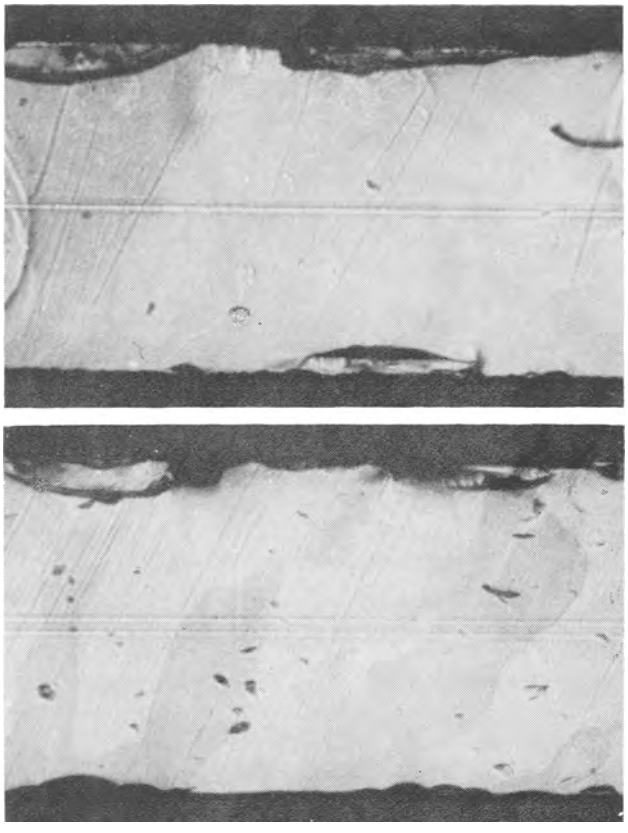

Fig. 2. Side A; Side B. Polished and etched {112} surfaces of germanium containing 3 twin planes. Sides A and B have the crystallographic significance shown in Fig. 1. Magnification 200X before reduction for publication.

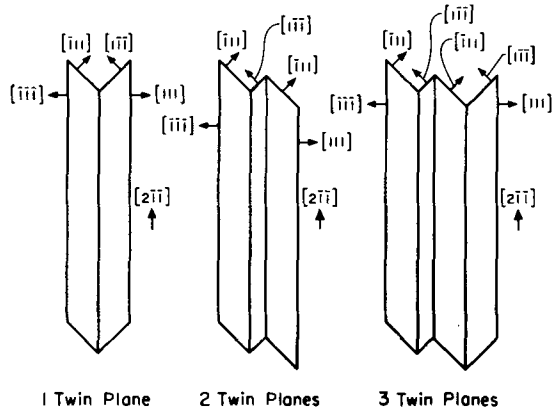

Fig. 3. Diagrams of thin sections fractured at both ends. Indices of twinned segments are referred to parent crystal.

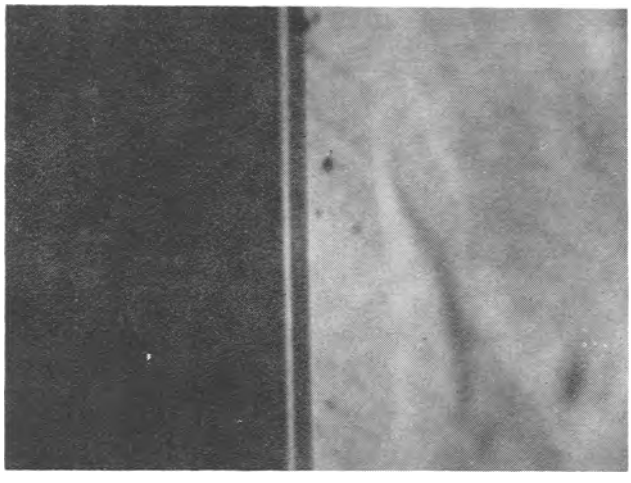

Fig. 4. Photomicrograph of a fractured germanium dendrite showing the 3 twin boundaries. Magnification 500X before reduction for publication.

interpreted; however, our new technique of fracturing thin sections of Ge, Si, or III-V compounds is more rapid and more easily interpreted.

Interpretation of Etch Patterns

As an illustration of the problem involved in interpreting etch patterns obtained according to method 3, let us choose a section of Ge containing three closely spaced twins and cut this section into two pieces, A and B, such that the cut is perpendicular to the <211> directions, as shown in Fig. 1. If sections A and B are mechanically polished and then given a 10-sec CP4 etch,[1] it is found that side A has a definite groove and two faint lines, while side B has two definite grooves and a faint line. In many cases the twins are spaced so close together that one or both of the faint lines will be "lost" in the definite etch groove. Figure 2 shows this apparent etching anomaly for sides A and B. This apparent anomaly is merely the result of the action of the etch on the {111} planes and the effect of the energy of the twin plane on the etch rate. The CP4 is slightly preferential to the {111} planes; however, it is not preferential enough to keep the etch from acting as a chemical polish. Because of the twin boundary energy, the etch attacks more rapidly at the twin boundary starting a groove. If {111} planes converge on the twin plane from the surface, as shown by twin planes marked 2 in Fig. 1, atoms can be removed along these exposed planes also; the result will be a definite groove. If, however, the {111} planes diverge from the surface at a twin boundary, as shown by twin planes marked 1 in Fig. 1, atoms cannot be removed from these unexposed {111} planes, and the result will be a faint groove caused only by the attack of the etch as a result of the energy associated with the twin plane. The number of definite grooves, n, can be found

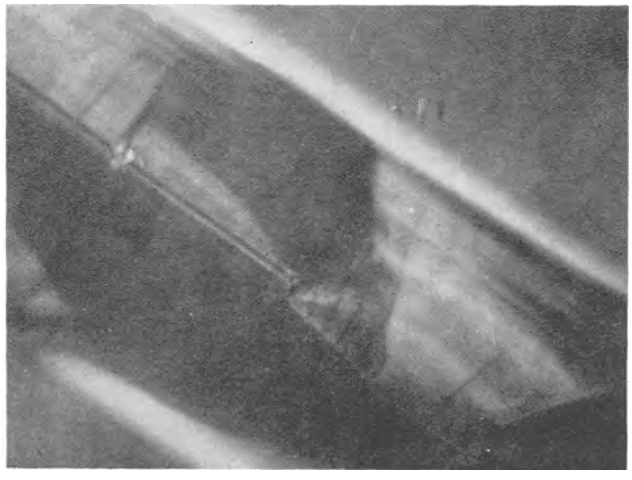

Fig. 5. Photomicrograph of a fractured germanium dendrite showing 3 twin boundaries, a grain boundary and a single twin boundary at the edge. Magnification 200X before reduction for publication.

[1] Composition, 25 parts HNO_3; 15 parts glacial acetic acid; 15 parts HF; and 0.3 parts bromine.

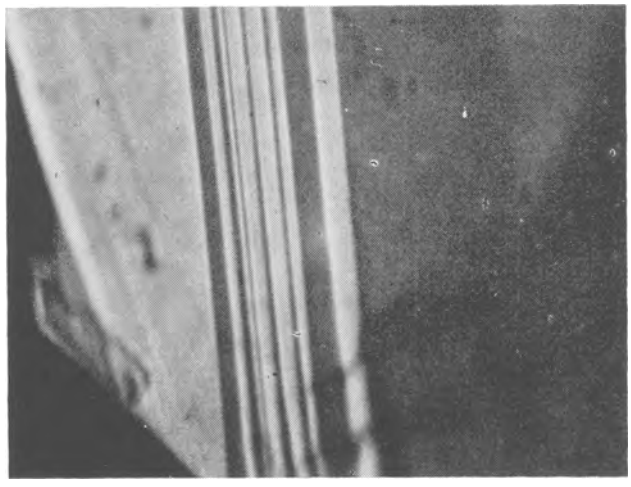

Fig. 6. A fractured germanium dendrite showing 13 twin boundaries. Magnification 1000X before reduction for publication.

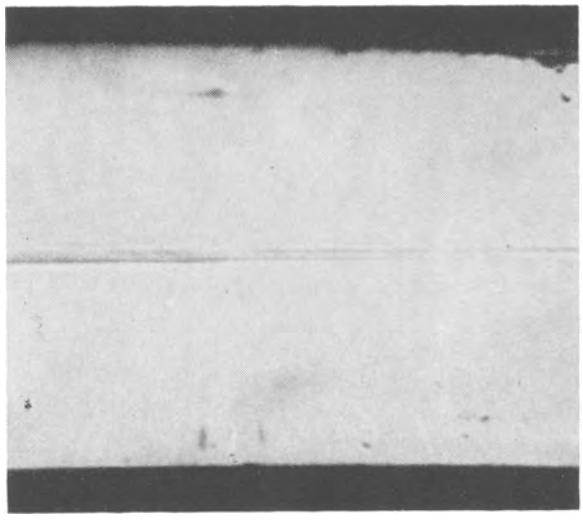

Fig. 7. A fractured germanium dendrite illustrating {112} cleavage: compare uniform focus with Fig. 5. Magnification 200X before reduction for publication.

from the number of twin planes, t, by the following formulas:

For an odd number of twin planes, where A and B have the significance shown in Fig. 1,

side A $\quad n = (t-1)/2$
side B $\quad n = (t+1)/2$

For an even number of twin planes

side A or B $\quad n = t/2$

Interpretation of Fracture Surfaces

The cleavage planes for germanium and silicon are the {111} planes. Upon careful fracturing, these materials break on their cleavage planes. This technique is suitable for use on thin sections cut from grown crystals or on dendritic crystals which grow naturally in the <112> direction. In this technique a line is scribed across the {111} face parallel to the [110] direction to control where the fracturing is to occur; fracturing is accomplished by bending. Each twin plane changes the direction of the {111} cleavage planes as shown in the diagram in Fig. 3; thus each line represents a twin boundary. Figure 4 is a photomicrograph of a fractured Ge dendrite that contained 3 twin boundaries. Electron micrographic examination of such a twinned structure showed no additional twins. The cleavage surfaces show some fracture steps but are, for the most part, excellent. In some cases where the twin lamella ends before reaching the edge of the section, a single twin or grain boundary can extend to the edge; even the grain boundaries are faithfully revealed by this technique, as shown in Fig. 5. This technique has revealed as many as 13 twins in a distance of 20μ as shown in Fig. 6. In a few cases we have observed that cleavage takes place on {112} planes; this is illustrated in Fig. 7 by the fact that the edges of the fracture are in focus with the middle of the Ge section. This method also works well for dendrites of silicon and the III-V intermetallic compounds, although for the latter, the interpretation is somewhat difficult because of the secondary cleavage plane (3).

Acknowledgments

The authors wish to express their thanks to Dr. R. Stickler for the electron microscopic examination.

This work was performed on Contract No. AF33 (600)-39378 BPSN 9-(8-4608)-42019–Wright Air Development Center.

Manuscript received Nov. 19, 1959.

Any discussion of this paper will appear in a Discussion Section to be published in the December 1960 JOURNAL.

REFERENCES

1. J. W. Faust, Jr., I.R.E.-A.I.E.E. Devices Conference, State College, Pa., June 1953 (unpublished); J. W. Faust, Jr., Electrochemical Society, Enlarged Abstracts No. 90, Cincinnati, Ohio, May 1955.
2. E. Billig, *Acta Met.*, **5**, 53 (1957).
3. J. F. DeWalt, *This Journal*, **104**, 244 (1957).

Bonding and Semiconductivity Relationships in Bi_2Te_3 and CdI_2 Type Structures

C. H. L. Goodman

Research Laboratories, The General Electric Company Limited, Wembley, England

It appears of interest to point out a possible relationship between layer structures of Bi_2Te_3 and CdI_2 types.

In a previous paper (1) a simple bonding scheme was put forward for Bi_2Te_3 which satisfactorily accounted for the 28 valence electrons in a manner consistent with the observed semiconductivity of this compound. A related bonding scheme seems possible for the 3-layer CdI_2 structure: I atoms, with the same coordination as the outer Te atoms in

5-layered Bi_2Te_3, would employ p^3 (plus s^2, lone pair) bonding orbitals while the metal atom, with 6-coordination like Bi in Bi_2Te_3, would employ sp^3d^2 hybridized bonding orbitals.[1] The 16 valence electrons of CdI_2 form 2-electron covalent-ionic bonds within the triple I-Cd-I layer structure, I-I inter-layer bonding being of van der Waals' type in agreement with Hartman's calculations (4).

Following (5) this scheme indicates that $A^{II}X_2^{VII}$ and $A^{IV}X_2^{VI}$ compounds with CdI_2 structure (e.g., CdI_2,$ZrSe_2$) should be semiconductors or insulators [in agreement with the findings in ref. (6) and (7) for example] while compounds such as $NiTe_2$ should be metallic [in agreement with the findings in ref. (8)]. Furthermore, ignoring bond-length effects, the greater electronegativity differences for $A^{II}X_2^{VII}$ compared with $A^{IV}X_2^{VI}$ compounds should lead to considerably lower energy gaps for the latter, which, by the same argument, should have higher energy gaps than related $A_2^{V}X_3^{VI}$ compounds with Bi_2Te_3 type structure.

Not all CdI_2 type compounds can be described in this way. Thus Ag_2F requires a scheme with resonating p^3 bonds, (which give rise to Ag-Ag interlayer bonding and accommodate all 9 valence electrons), and, following (5), should also be a semiconductor.

[1] This would appear to require d-orbital contraction; see for example ref. (2). Promotional energies for such bonding orbitals would in any case be much less than those suggested from spectroscopic data for free atoms, as has been pointed out by Wilmshurst (3).

The nature of the bonding in $A^{IV}X_2^{VII}$ compounds such as PbI_2 is less clear. Eighteen valence electrons must be accommodated in closed sub-shells or bonds for the criteria for semiconductivity given in ref. (5) to be satisfied. This might be achieved by p^3d^3 (+lone pair) bonding orbitals for A^{IV} atoms, although coordination symmetry argues somewhat against this view. More detailed bond studies along these lines would appear of interest.

Acknowledgment

It is a pleasure to acknowledge stimulating correspondence with J. Suchet.

Manuscript received Feb. 15, 1960.

Any discussion of this paper will appear in a Discussion Section to be published in the December 1960 JOURNAL.

REFERENCES

1. J. R. Drabble and C. H. L. Goodman, *J. Phys. Chem. Solids*, **5**, 142 (1958).
2. D. P. Craig and E. A. Magnusson, *J. Chem. Soc.*, **1956**, 4895; D. P. Craig, "The Inorganic Chemistry of Sulphur," p. 343, The Chemical Society, London (1958).
3. J. K. Wilmshurst, *J. Chem. Phys.*, **30**, 889 (1959).
4. P. Hartman, *Acta Cryst.*, **11**, 365 (1958).
5. C. H. L. Goodman, *J. Phys. Chem. Solids*, **6**, 305 (1958).
6. E. Putseiko, *Dokl. Akad. Nauk S.S.S.R.*, **67**, 1009 (1949).
7. F. K. McTaggart, *et al.*, *Australian J. Chem.*, **2**, 445 (1958).
8. V. P. Zhuze and A. R. Regel, *Zh. Tekh. Fiz.*, **25**, 978 (1955).

The Adhesion of Vapor-Deposited Molybdenum Coatings

S. T. Wlodek[1] and J. Wulff

Department of Metallurgy, Massachusetts Institute of Technology, Cambridge, Massachusetts

The reduction of molybdenum pentachloride with hydrogen has often been proposed as a method of producing a dense molybdenum coating (1, 2). The exploitation of this process has been advanced recently by a theoretical treatment of the plating kinetics (3) and the development of a technique capable of plating large articles (4) with vapor deposited molybdenum.

The purpose of this note is to report on the factors which control the adhesion of the molybdenum coating, restricting the discussion to the formation of the plate on a metallic base. The most important variables which affected the adherence of the molybdenum plate studied in this investigation were: purity of raw materials, sample preparation, and the chemical composition of the material being coated.

Experimental

The plating technique used in this study was basically the same as that described by Spacil and Wulff (3). High-purity molybdenum pentachloride was prepared by the chlorination of molybdenum powder followed by the redistillation of the resultant product to prepare a fraction free of oxychloride contamination. After purification by passing over copper gauze (500°C), followed by a dry ice trap and a magnesium getter (500°C), hydrogen (36 l/hr) was passed over solid molybdenum pentachloride and saturated with the pentachloride vapor. The degree of saturation was kept constant by adjusting the temperature (100-120°C) of the pentachloride so that the color of the resultant gas mixture compared to an empirically arrived at standard (saturated solution of methyl orange in water diluted 1:400 in alcohol). The H_2-$MoCl_5$ gas mixture was then introduced into the reaction chamber where the plate was deposited on the inside of 0.5-in. diameter, 4.0-in. long tubes of the material to be plated. The reduction conditions in the actual plating chamber were 900°C and a pressure of 2.0 cm Hg. The whole system was constructed of Pyrex or Vycor.

After plating, the relative room temperature adherence of the base metal-molybdenum plate assembly was determined by compressing the sections of the as-plated tubing to 50% of the initial diameter and by completely flattening sections taken parallel to the length axis of the original as-plated tube. As shown in Fig. 1, these tests allowed an empirical characterization of five classes of adhesion; the first representing a bond strength which

[1] Union Carbide Metals Company, Niagara Falls, N. Y.

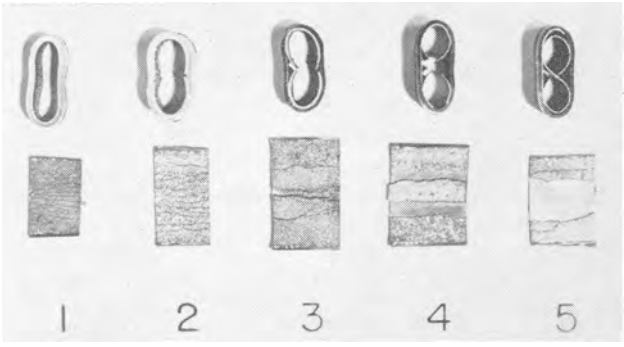

Fig. 1. Typical results of adhesion tests showing examples of the five main classes of adhesion.

exceeded the tensile strength of as-plated molybdenum; the fifth a bond weak enough to result in the complete exfoliation of the coating after testing.

In regard to the role of plating conditions on adherence, the effect of sample preparation and accidental contamination of the pentachloride with oxychlorides were found to be critical. Surfaces cleaned by chemical etching were found preferable to those prepared by mechanical cleaning. The presence of oxychlorides in the plating system, which were subsequently reduced to produce layers of MoO_2 in the plate, destroyed any adherence, even if the oxide films were less than 10^{-4} in. thick. In addition, if an oxide-contaminated molybdenum plate was deposited on iron or nickel, bulging or blistering of the plate would occur often (Fig. 2). Since this structural defect was observed only when MoO_2 was present at an interface highly permeable to hydrogen, the blistering could have been produced by entrapment of steam due to the reduction of the molybdenum oxides by the hydrogen that can diffuse through the nickel or iron base.

The effect of sample composition on the adherence of the as-plated molybdenum was studied by plating specimens of pure iron, 1020 and 1030 plain carbon steel, 18-8 stainless steel, pure copper and nickel, and Inconel. In addition, pure iron, and in some cases low carbon steels, electroplated with

Table I. Effect of base material on adherence

Base material	Thickness of molybdenum plate, in. × 10^3	Adhesion rating*
Pure copper	28.0	2
Pure nickel	7.0	1
Inconel	3.0	1
Pure iron	2.0	4
1020 steel	3.0	5
1030 steel	2.0	4
18-8 stainless steel	7.0	3
Chromium (0.001-in.) plated iron	8.0	3
Copper (0.001-in.) plated iron	6.0	1
Cobalt (0.001-in.) plated iron	8.0	1
Nickel (0.002-in.) plated iron	8.0	1
Nickel (0.0008-in.) plated iron**	6.0	1
Rhodium (0.0006-in.) plated iron	8.0	1
Chromized 1020 steel	3.0	5
Nickel plated (0.0003-in.) 1030 steel**	2.0	1

* See Fig. 1 for classification of adhesion ratings.
** Replacement nickel phosphide coating, all other electrolytic.

nickel, cobalt, copper, chromium, and rhodium were also evaluated. As indicated in Table I, satisfactory as-plated adhesion of the molybdenum plate could not be obtained on pure iron, stainless, low-carbon steel, or on chrome-plated surfaces. Nickel, copper, and Inconel, or any of the iron or steel samples which had been electroplated with nickel, cobalt, copper, or rhodium before vapor plating with molybdenum exhibited excellent as-plated adherence.

Metallographic examination of samples of pure iron, 18-8 stainless steel, or chromium-electroplated iron, vapor plated with molybdenum did not indicate that surface oxide films on these materials were responsible for the poor adherence. Since appreciable amounts of iron and especially chromium chlorides were produced during plating experiments on iron- and chromium-rich surfaces, reaction with chlorides must have occurred during the plating of these materials. The degree of reaction was strong enough to remove any oxide films originally present.

Fig. 2. Vapor deposit of molybdenum (top) on iron (bottom). Note the thick band of MoO_2 and the associated "blister." Etched with alkaline ferricyanide. Magnification 250X before reduction for publication.

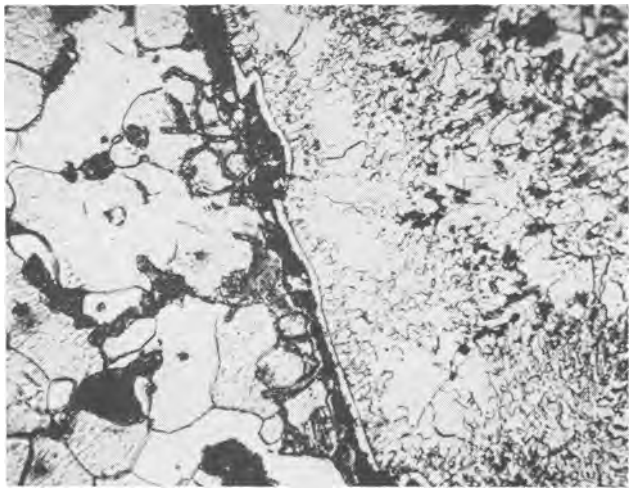

Fig. 3. S.A.E. 1030 steel (left side) coated with molybdenum (right side). Note the thin band of Mo_2C at the interface and Mo_2C inclusions in the plate. Etched with alkaline ferricyanide. Magnification 750X before reduction for publication.

Table II. Hardness and width of the intermetallic phases formed in the interface between molybdenum coating and material on which it is deposited

System	Characteristic adherence	Phase	Hardness* V.P.N. 16-g load	Width,* in. × 10^{-5}
Mo-Cu	1 to 2	immiscible	—	—
Mo-Co	1	Mo_6Co_7	1700	18
		$MoCo_3$	1050	15
Mo-Fe	4	Mo_6Fe_7	750	20
Mo-Ni	1	MoNi	1200	28
		$MoNi_3$	1600	17
Mo-Rh	1	Epsilon	1500	18

* As measured on samples annealed 100 hr at 900°C after plating. Identification of phases after Hansen and Anderko (6).

Evidence of grain-boundary attack of chromium-rich surfaces but not of chromium-free steels was often noted.

Although the carburization (Fig. 3) of the molybdenum plate deposited directly on a steel was believed to be the main reason for the poor adhesion always found with carbon steel specimens, the poor bonding exhibited by stainless steel, pure iron, or chromium-plated specimens was not found to be related to the formation of brittle films of intermetallic compounds at the molybdenum-base metal interface. Indeed, no correlation was found between the hardness (Table II) or width of the intermetallic phases that form on prolonged annealing (100 hr at 900°C) in the iron-molybdenum, nickel-molybdenum, copper-molybdenum, cobalt-molybdenum, or rhodium-molybdenum systems and the as-plated adherence. It should be stressed that these observations were made on specimens whose integrity on metallographic examination was excellent (Fig. 4 and 5).

In addition, the excellent relative bond strength of vapor-deposited molybdenum to pure iron electroplated with nickel, copper, cobalt, or rhodium

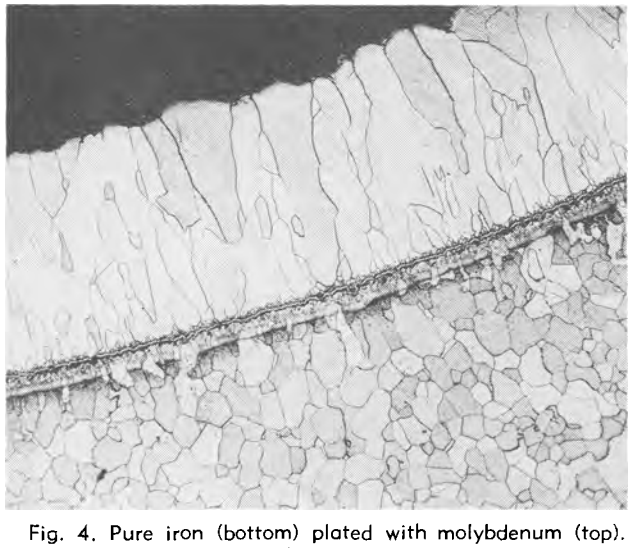

Fig. 4. Pure iron (bottom) plated with molybdenum (top). Note the Mo_6Fe_7 band. Etched with nital and alkaline ferricyanide. Magnification 75X before reduction for publication.

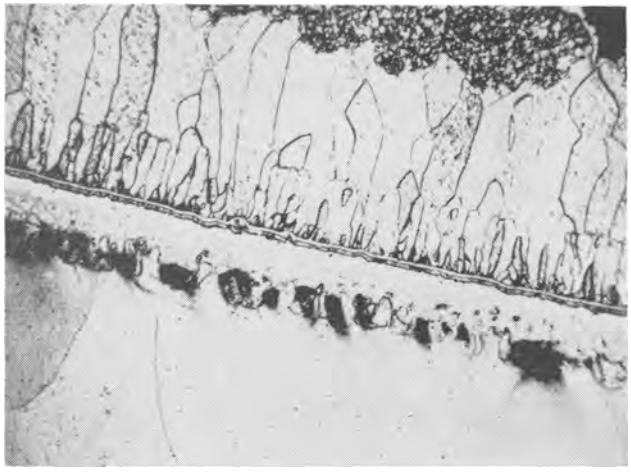

Fig. 5. Rhodium (0.0006 in.) electroplated pure iron (bottom) and vapor plated with molybdenum (top). Note thin gray band of the molybdenum-rhodium epsilon phase. Etched with nital and alkaline ferricyanide. Magnification 200X before reduction for publication.

remained completely unaffected by the 100-hr anneal at 900°C as long as the electroplate was thicker than 0.001 in. The poor bond strength of pure iron to pentachloride molybdenum was not improved by the same anneal.

Discussion

These results indicate that if carburization or oxide contamination of the molybdenum plate is prevented, the nature of the intermetallic phases that form at the molybdenum-base metal interface does not govern the as-plated adherence. In addition, the adherence of the plate after prolonged annealing is also only slightly affected by the growth of brittle intermetallic bands. The only correlation between the adherence of pentachloride molybdenum and the nature of the surface on which it is deposited seems to be a chemical one. In brief, metals such as iron or chromium which form chlorides more readily than molybdenum (5) were always found to be unsatisfactory surfaces for vapor deposition. Conversely, surfaces rich in copper, nickel, cobalt, or rhodium, all of which form less stable chlorides than molybdenum (5), consistently provided an excellent bond to pentachloride reduced molybdenum. Since appreciable amounts of chromic chloride or ferric chloride were always found in the exhaust system following plating experiments on iron- or chromium-rich surfaces, some experimental justification for associating poor adherence with chloride reactivity exists. It is suggested that the formation of chlorides involving the constituents of the metal being plated on, destroys the adherence by contaminating the surface. Also, since this reactivity occurs only with surfaces that form more stable chlorides than molybdenum, a replacement reaction could occur between the molybdenum chloride gas and the constituents of the surface. Since any reduction of the molybdenum chlorides by such elements as iron or chromium will produce a plate of higher chlorine, iron, or chromium content than that obtained by hydrogen reduction, a lower purity material of lower ductility, and thus poorer adherence, could form.

It is not possible to associate the poor adherence of vapor-deposited molybdenum to iron- or chromium-rich surfaces with the presence of oxide films on the steel or chromium surface. Any films of iron oxide present on the sample would be reduced by the hydrogen and chloride plating environment, while the chromic oxide films would be etched off by the chloride attack. The contention that affinity for oxygen does not characterize a strata to which poor adherence is to be expected is borne out by the excellent adherence found in deposits formed on rhodium-plated steels or pure Inconel, surfaces that possess a high affinity for oxygen but good resistance to chloride formation.

From these studies, it is possible to conclude that adherent coatings of molybdenum can be vapor plated onto surfaces which are free of carbon or constituents that form more stable chlorides than molybdenum. The coating system must, of course, be so designed as to eliminate oxygen contamination of the plate. By pre-treating samples containing carbon, iron, or chromium with an electroplate of copper, cobalt, nickel, or rhodium, adherent coatings can be applied to almost any material stable at the plating temperature. In closing, it is possible to suggest that similar criteria may govern the adherence of chromium, tantalum, or tungsten coatings when they are produced by chloride reduction.

Acknowledgment

This research program was supported by the Department of the Army, Boston Ordnance District, Watertown Arsenal.

Manuscript received Nov. 2, 1959.

Any discussion of this paper will appear in a Discussion Section to be published in the December 1960 JOURNAL.

REFERENCES

1. C. F. Powell, I. E. Campbell, and B. W. Gonser, *J. (and Trans.) Electrochem. Soc.*, **93**, 258 (1948).
2. W. J. Childs, J. E. Clive, W. M. Kisner, and J. Wulff, *Trans. A.S.M.* (1950).
3. H. S. Spacil and J. Wulff, Submitted to *Journal of Metals, A.I.M.E.* (1959).
4. P. L. Raymond, *This Journal*, **106**, 444 (1959).
5. L. L. Quill, "The Chemistry and Metallurgy of Miscellaneous Materials-Thermodynamics," McGraw-Hill Book Co., New York (1950).
6. M. Hansen and K. Anderko, "Constitution of Binary Alloys," 2nd ed., McGraw-Hill Book Co., New York (1958).

Brief Communication

Growth of Single Crystal Silicon Overgrowths on Silicon Substrates

Albert Mark

U. S. Army Signal Research and Development Laboratory, Fort Monmouth, New Jersey

A single crystal silicon overgrowth has been produced on a silicon substrate. This phenomenon confirms a fundamental principle for silicon showing that it is possible to have a vapor phase chemical reaction between the solid and vapor of one of its compounds. The silicon monolayers grow by accretion of atoms from the generating medium and assimilate as a single crystal overgrowth to the (100) orientation of the silicon substrate.

The reaction is based on the reduction of silicon tetrachloride by hydrogen, $SiCl_4 + 2H_2 \rightleftharpoons Si + 4HCl$, using a slow growth process. The deposited silicon layer or film has an orderly atomic lattice and continues the internal lattice structure of the substrate crystal without boundary layers at the interfaces. In this respect, the silicon layer is synonymous with and is an extension in three dimensions (growth in volume) of the original substrate surface over its entire periphery.

The deposit growth imitates and assumes the same growth pattern as initially exposed after an acid etch of the substrate face prior to a run. Rosette-like formations found in loosely masked areas continue their geometry in extending out and embracing the limits of their original boundary area. These appear to grow more prominently along their outer boundaries with the internal areas gradually filling in as the growth continues. The mechanical quality of the grown surface therefore is dependent to a great extent on the initial substrate geometrical configuration.

The deposit growth eventually assumes a dense jet black glassy surface which is difficult to distinguish from the original substrate face. Fully developed, this characterizes the ideal mechanical overgrowth surface. If the entire substrate face is loosely masked with a cover crystal, a denser, more uniform quality overgrowth results. This is apparently due to reduced heat losses at the crystal interfaces.

Electron diffraction studies of the overgrowths described were made at Purdue University by H. J. Yearian, Professor of Physics. His summation statement of his report follows: "From these results it may be concluded that all of the regions studied were single crystals of at least fair quality. On those

specimens for which a mask had been used, the deposits were thick enough to insure that the results represent the deposit and not the substrate."

The significance of an overgrowth layer of silicon can best be realized by enumeration of some of the probable electronic applications.

1. Application for fabricating surface devices (silicon deposited and growing out from a surface). —(*a*) An overgrowth of single crystal silicon of an opposite conductivity type to that of the silicon substrate crystal on which it is grown will act as a "surface junction." This implies a diode structure form. (*b*) An overgrowth of single crystal silicon acting as a surface junction can be processed to high or low resistivity values. (*c*) An overgrowth of single crystal silicon can be of the same conductivity type as the silicon substrate forming intrinsic pp^+ or nn^+ regions. (*d*) An overgrowth of single crystal silicon as a wide area film will act as a matrix with its surface containing innumerable junction points through proper masking techniques. (*e*) An overgrowth of a single crystal silicon film with a large area junction structure could be made sensitive to various forms of radiation, for example, for use in solar cells.

2. Multilayered devices.—(*a*) Alternate overgrowths of single crystal silicon films on parent or foreign substrates, each with its own discrete resistivity or conductivity type, will alternately act as high resistance I regions, pn and np junctions, and pp^+, nn^+ regions. (*b*) An overgrowth of single crystal silicon can be an active or passive element when used or incorporated into micromodule circuits.

3. Miscellaneous uses.—(*a*) An overgrowth of single crystal silicon allowed to grow to only an extremely thin film will act as a base region permitting the fabrication of very high frequency devices. (*b*) As an overgrowth of single crystal silicon on a foreign substrate with a lattice distance closely matching that of silicon. In this type of device, the substrate, if a metal, would act as the support media and as one pole of an electrical contact.

The perfection and extended use of this process in all its variations will permit the utilization of silicon in presently unexplored device areas thereby broadly increasing its usefulness as a semiconductor material.

Acknowledgment

The author wishes to express his thanks and gratitude to Professor H. J. Yearian and associates of Purdue University for the efforts expended in making the electron diffraction studies and evaluation of the samples.

Manuscript received Jan. 29, 1960.

Any discussion of this paper will appear in a Discussion Section to be published in the December 1960 JOURNAL.

Brief Communications

The JOURNAL accepts short technical reports having unusual importance or timely interest, where speed of publication is a consideration. The communication may summarize results of important research justifying announcement before such time as a more detailed manuscript can be published. Consideration also will be given to reports of significant unfinished research which the author cannot pursue further, but the results of which are of potential use to others. Comments on papers already published in the JOURNAL should be reserved for the Discussion Section published biannually.

Submit communications in triplicate, typewritten double-spaced, to the Editor, Journal of The Electrochemical Society, 1860 Broadway, New York 23, N. Y.

Discussion Section

This Discussion Section includes discussion of papers appearing in the JOURNAL of The Electrochemical Society, Vol. 105, No. 1 (January 1958) and Vol. 106, No. 4, 6, 7, 8, 10, and 11 (April, June, July, August, October, and November 1959). Discussion not available for this issue will appear in the Discussion Section of the December 1960 JOURNAL.

The Anodic Oxidation of Zinc and Zinc-Tin Alloys at Very Low Current Density

S. E. S. El Wakkad,[1] A. M. Shams El Din, and H. Kotb
(pp. 47-51, Vol. 105, No. 1)

(NOTE: The following is Dr. Shams El Din's reply to the discussion by M. Prazák which appeared in the December 1959 Discussion Section, p. 1072. These comments reached the Editorial Office too late to be included in December.)

A. M. Shams El Din: Tin and zinc form a simple eutectic system containing about 8% zinc, so that the electrodeposited alloy containing 20-25% zinc consists of the eutectic plus some free zinc.[2] Because zinc is the more electronegative of the two components, the electrode behavior of the alloy is to a great extent determined by the zinc and not by the tin. Thus, for example, in aerated 3% potassium chloride solution at room temperature, the electrode potential of the alloy vs. the saturated calomel electrode is approximately −1.0 v. The corresponding values of pure tin and pure zinc are −0.45 v and −1.02 v, respectively.[2]

Despite this fact, the tin of the alloy still manifests itself and exerts some of its properties on the general behavior of the alloy. The final behavior of the alloy need not, therefore, be the algebraic sum of its constituents. In the curves given in our original paper and also in the curve accompanying the comments of Dr. Prazák, it is clearly shown that the tin of the alloy oxidizes after the zinc. How much the tin oxide(s) film will affect the behavior of the zinc is difficult to tell, but the main fact is that it does affect it. This is also observed from other corrosion experiments employing techniques such as salt spraying and humidity tests. Thus, for example, salt spraying experiments (20% salt solution) with pure zinc result in the formation of dense white corrosion products which are not observed in the case of the alloy despite its free zinc content.[2] Humidity tests also reveal the superiority of the alloy to the zinc. Apparently, such difference in behavior between the alloy and zinc is to be attributed to the presence of tin.

The interesting finding of Dr. Prazák, that the behavior of the alloy is not the sum of its components, might be due to the fact that after the initial dissolution of the zinc the concentration of the tin at the surface of the alloy becomes higher than the corresponding value in the bulk of the alloy.

The occurrence of two current humps in the polarization curve of zinc in Dr. Prazák's Fig. 1 does not necessarily mean, in our opinion, a building of a new oxide of zinc. If zinc is able to form two oxides, then it should reveal this property also in the galvanostatic curves as do the other metals.[3] The first current hump in Fig. 1 starts at a potential of about −1.2 v which is in good agreement with the potential of the system Zn/ZnO at this *p*H value. A corresponding step is also reported in our paper. The second, smaller, oxidation step starts at about −0.6 v, and a similar step is not observed in our polarization curves. In our opinion, the second step observed in the potentiostatic experiments of Dr. Prazák corresponds to the thickening of the already present oxide film. Simultaneous dissolution in the form of zincate is also to be expected. The constancy of the current associated with this process over an increasing potential range of about 1.8 v suggests a corresponding increase in the resistance of the system electrode/electrolyte. The solution side of the system cannot be the cause of an increase in the resistance, first, because it is a good conductor, and, second, because in the polarization curve of zinc given in Fig. 1 there occur two different constant currents, a fact which reflects the conclusion that the solution side of the system cannot be the cause of resistance increase. The constancy of the current is, therefore, to be ascribed to the increase in the resistance of the oxide film. This can occur through an increase in the thickness of the film and/or the closing of the pores of the oxide. Such processes will have the ultimate result of decreasing the conductivity of the surface film.

Probably, if the effect of variables such as the alkali concentration and the presaturation of the solution with zinc oxide on the limiting current of the second step were to be studied, a clearer insight could be gained concerning the nature of the process(es) taking place at the electrode surface.

Before such understanding of these processes at the surface of both the zinc and the alloy electrodes is achieved, the suggestion of a homogenous passive layer growing on the surface of the nonhomogenous Sn-Zn alloy is to be considered as *ad hoc*.

Other than this point, the interesting observations of Dr. Prazák are in full agreement with ours. Thus, the polarization curve of the alloy shows clearly the oxidation of both the zinc and tin at their respective potentials. The quantities of electricity consumed in the building up of zinc and tin hydroxides on the alloy are less than those for pure zinc and tin alone.

[1] Deceased.

[2] Tin Research Institute, "Tin-Zinc Alloy Plating," Technical Publication, March 1952.

[3] S. E. S. El Wakkad and S. H. Emara, *J. Chem. Soc.*, 1952, 461, *ibid.*, 1953, 3504, 3508; S. E. S. El Wakkad and A. M. Shams El Din, *ibid.*, 1954, 3094, 3098; S. E. S. El Wakkad, A. M. Shams El Din, and J. A. El Sayed, *ibid.*, 1954, 3103; S. E. S. El Wakkad, T. M. Salem, A.M. Shams El Din, and Z. Hanafi, *ibid.*, 1956, 2857.

Controlled Potential Reactions of Cadmium and Silver in Alkaline Solution

G. T. Croft (pp. 278-284, Vol. 106, No. 4)

Indra Sanghi[4]: We have reported some galvanostatic and potentiostatic experiments with zinc[5, 6] and have similar work with cadmium in progress. While the experimental procedure is different from that used by Dr. Croft, some of the basic inferences from the data are very similar. For this reason, I offer the following comments.

In his paper, Dr. Croft has measured currents, at constant overpotential, as a function of time. He found that, after sufficient time had elapsed, current and time were related by an equation of the type $I = F(\phi)\ t^{-1/2}$. From this, he took the oxide to obey the parabolic growth law and interpreted $F(\phi)$ as a function relating the rate of reaction to the overpotential. His basic assumption that the application of the above equation to the currents, *measured after sufficient time,* implies that the oxide grows from the beginning to the end in a parabolic manner is not quite clear, particularly as Charlesby[7] had shown that the rate equation would depend on the time range during which the growth is studied. In fact, he has defined the various thickness ranges in which the logarithmic, the cubic, and the parabolic laws can successively define the oxide layer growth under the same conditions and on the same electrode, the parabolic law taking over when the films have thickened to a definite extent. Moreover, Delahay[8] and Bieri[9] have shown that for the study of the $It^{1/2}$ relationship the first few minutes are very crucial in order to derive any theoretical conclusions as, later on, convection and other effects interfere. Further, Dr. Croft found that currents at equivalent times after application of the same anodic potentials were not generally reproducible. There is then some doubt about the significance of the so-called constancy of $It^{1/2}$ at large values of time.

Our own galvanostatic and potentiostatic studies[10] on Cd, similar to those on Zn,[5, 6] do not lead to a constant I^2t in all cases where the passivation was reached within a few minutes (10 min).

Dr. Croft found that for Cd electrodes $F(\phi)$ has at least one maximum and often two, most probably between 18 and 40 mv overpotential. The significance of this observation is not clear. It is doubtful as to how far these represent actual layer growth. Our potentiostatic measurements reveal that, in KOH concentrations ranging between 1 and 3.5 N, active dissolution occurs during the first 50 mv overpotential. Only when the overpotential is raised beyond 50 mv, a uniform coherent oxide layer starts to thicken, with decrease of current rate. According to our ideas, the predominant layer growth occurs in the current plateau region, clearly revealed by our potentiostatic measurements, at a nearly constant rate over a wide overvoltage range (ca 1400 mv) before oxygen evolution commences. This wide range of study has, perhaps, been overlooked by Dr. Croft.

Essentially, this layer grows as oxide, and only at the oxide/electrolyte interface is it partially converted into $Cd(OH)_2$. The electrode, may, therefore, be pictured as $Cd/CdO/Cd(OH)_2/KOH$ solution.

Dr. Croft's observation that a higher current is required to force the electrode to oxidize at 30 mv than at 97 mv is clearly explained by our potentiostatic measurements which show that in the active dissolution region a higher current is sustainable at a lower overpotential than the smaller currents that can be sustained at high overpotentials in the "pseudo passivation region" of 1400 mv extending from ca -0.7 to $+0.7$ v vs. the Hg/HgO/N KOH half-cell.

For the triangular wave transients, Dr. Croft prepolarized Cd anodically at 1 ma/cm^2 till ϕ rose to 30 mv anodic when the current was turned off and later subjected to triangular waves. Our constant current polarization curves indicate that in 5N KOH (as used by Croft) 1 ma/cm^2 would increase the overpotential by 30 mv in less than a minute; surely it would not suffice to render the electrode truly passive. Moreover, the effect of this very short anodic polarization would be mostly lost during the prolonged period in which the current is turned off and the electrode is allowed to come to the equilibrium potential. Thus, the exact significance of this procedure is not quite clear.

Perhaps it was this factor of observing the Cd surface in the active region and/or after leaving it in the electrolyte on open circuit for sufficient time that was responsible for Croft's observation of only $Cd(OH)_2$ on the electrode surface. On the other hand, x-ray and electron optical observations of Huber and Lake and Casey have clearly shown the presence of CdO.

Similarly, Croft's observation of the change of oxidation rate, from the initial logarithmic rate to a parabolic rate later, may be explained on the basis of Charlesby's theories as indicated above.

Our detailed results are under publication separately.

George T. Croft: Dr. Sanghi is quite correct in the statement that the $F(\phi)t^{-1/2}$ relationship[11] *implies* that the hydroxide grows from the beginning to the end in a parabolic manner. On the other hand, it is clear from Fig. 2 of the discussed paper that the entire growth process is not described by a parabolic law and, in fact, most of the oxide growth does not follow the parabolic law. However, the *current* (rate of growth) does fit a parabolic relation for a time equal to about 70% of the total time of observation.

[4] Central Electro Chemical Research Institute, Karaikudi, India. (Present address: Gannon Dunkerley & Co., Ltd., P. O. Box 1547, Fort, Bombay 1, India.)

[5] I. Sanghi and M. Fleischmann, *Electrochimica Acta*, 1, 161 (1959.)

[6] I. Sanghi and W. F. K. Wynne-Jones, *Proc. Indian Acad. Sci.*, 47A, 49 (1958).

[7] A. Charlesby, *Proc. Phys. Soc. (London)*, 66, B317 (1953).

[8] P. Delahay, *Anal. Chem.*, 27, 478 (1955).

[9] B. Bieri, Ph.D. Thesis, Berne University, Berne, Switzerland (1949).

[10] I. Sanghi, *This Journal*, Discussion Section, 106, 532 (1959).

[11] G. T. Croft, *This Journal*, 106, 278 (1959).

During this time, the electrode is in such a state that, if it were suddenly forced to oxidize at a constant current density of about 1 ma/cm^2, the electrode potential would go immediately to the oxygen overpotential for the electrode. An electrode in such a state will, for purposes of this discussion, be considered passive or pseudopassive. It is for electrodes in the passive or pseudopassive state that the parabolic law appears best to fit the data. Fixed and sweeping potential measurements of $F(\phi)$ were made, using electrodes in the passive state.

It would, therefore, be more accurate (and perhaps less confusing) to say that Eq. [1] describes the current for a time greater than t_p where t_p is the time required for passivity to set in.

As regards the influence of convection currents in the electrolyte, we found that the current through the electrode (fixed potential) in the passive state was unchanged if the electrolyte was stirred. If one is studying a reaction whose electrode potential is determined by the concentration in solution of the ion undergoing electron exchange at the electrode-solution interface, the true electrode potential can be observed for only short periods of time because, as the reaction proceeds, local concentration changes cause convection currents which give rise to anomalous results.[12] Evidently, we are not studying a phenomenon related to convection because of the long time involved and the failure to observe convection effects directly.

A controversy exists over the products of the electrochemical reaction of cadmium in alkaline solution. Immediate analysis (by x-ray techniques) of reaction products formed prior to onset of passivity and after passivity sets in shows consistently no signs of CdO. $Cd(OH)_2$ is the only reaction product we detected in our laboratory by x-ray techniques. This result is confirmed by the work of Uno Falk,[13] who made a specific search for CdO in an x-ray diffractometer study of cadmium oxidation and reduction *in situ*. He found only Cd and $Cd(OH)_2$. By weighing experiments, he also verified the reaction as $Cd + 2OH^- \rightarrow Cd(OH)_2 + 2e$. Salkind[14] has also shown that only $Cd(OH)_2$ forms during oxidation of cadmium in alkaline electrolytes.

Oxide Nucleation and the Substructure of Iron

E. A. Gulbransen and K. F. Andrew (pp. 511-515, Vol. 106, No. 6)

J. L. Walter and C. G. Dunn[15]: The authors state that the growth of oxide nuclei may be related to the number and arrangement of dislocations in the underlying metal crystal. They also state that the nucleation centers become ordered along definite crystallographic directions when the iron is annealed in impure hydrogen. They conclude that water vapor in the hydrogen is responsible for ordering of the nucleation sites.

Our studies of grain growth in high-purity iron and silicon iron annealed under slightly oxidizing conditions indicate that the nonrandom oxide patterns correlate with the patterns of thermal etch that exist at the surface of grains of certain orientations.

It is known that iron[16] and silicon iron[17] will thermally etch when annealed in atmospheres containing a small amount of water vapor or oxygen. Thermal etching will not occur if the atmosphere is sufficiently pure. Grains having orientations near (100) and (111) at the gas-metal interface thermally etch to striations. The thermal etch steps become curved when the low index planes (100) and (111) are within 1-2 degrees of the plane of a slightly uneven surface.

Fig. 1. 1000 X before reduction for publication

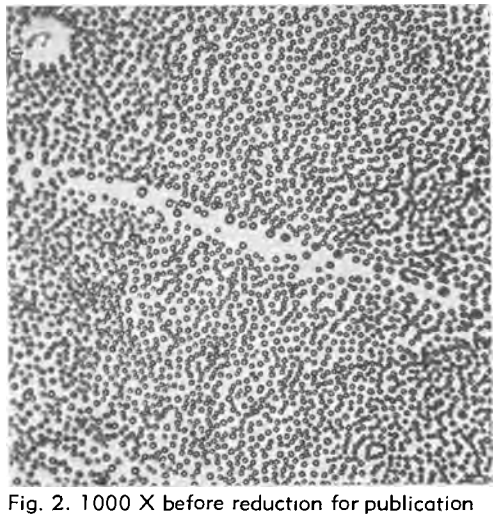

Fig. 2. 1000 X before reduction for publication

The interaction between the thermal etch steps and oxides is clearly seen in Fig. 1 of this discussion. This is a photograph of a sample of high-purity iron annealed for 24 hr at 875°C in tank argon. The oxides formed circular patterns similar to those shown by the authors' Fig. 5. A nearly random distribution of oxides on a grain near (112) is shown in Fig. 2 of this discussion. This was a sample

[12] P. Delahay *Anal. Chem.*, 27, 478 (1955).

[13] Uno Falk, Battery Division Abstract No. 27, Electrochemical Society Meeting, Columbus, Ohio, Oct. 1959.

[14] A. J. Salkind, Battery Division Abstract No. 26, Electrochemical Society Meeting, Columbus, Ohio, Oct. 1959.

[15] Metallurgy and Ceramics Research Dept., Research Lab., General Electric Co., P. O. Box 1088, Schenectady, N. Y.

[16] J. Benard, J. Moreau, and F. Gronlund, *Compt. rend.*, 246, 756 (1958).

[17] C. G. Dunn and J. L. Walter, "On the Thermal Etching of Silicon Iron," Letter to the Editor, *Acta Met.*, In press.

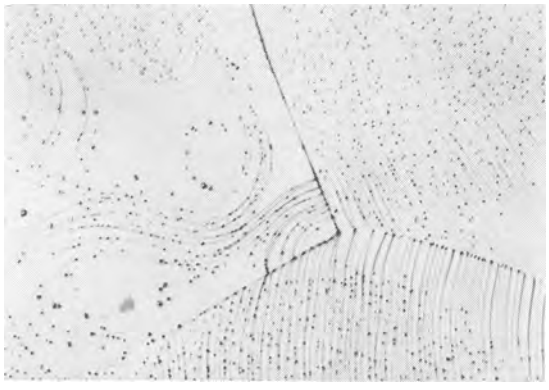

Fig. 3. 500 X

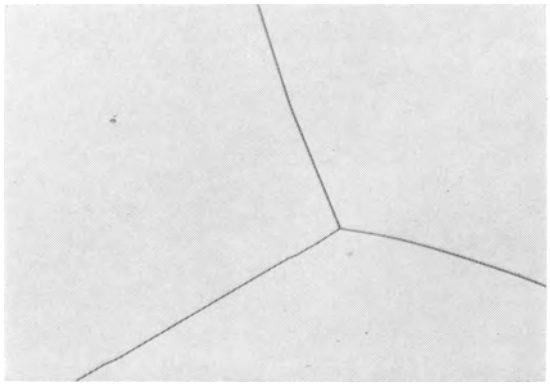

Fig. 4. 500 X

of high-purity silicon iron annealed at 1200°C for ½ hr in tank argon. Grains of this orientation do not show strong thermal etch patterns.

Fig. 3 of this discussion shows a variety of oxide patterns. This sample of high-purity silicon iron was annealed for 1 hr at 1300°C in purified argon. The dew point of the argon was −98°F. All three grains had (100) planes within 3° of the plane of the sample. It can be seen that the oxides, in general, form in rows along the thermal etch steps. Bending of the thermal etch steps at the groove formed by the intersection of the grain boundary with the sample surface is clearly visible. The average number of oxides, measured at the area shown in the photograph, was 9.1 x 10^6/cm^2. After photographing the above area, carbon was added to the sample and it was then electropolished and electroetched in chrome-acetic acid to produce etch pits at dislocation sites. Figure 4 of this discussion shows the same area as is shown in Fig. 3 after the treatment to reveal dislocations. A separate test showed that the amount of carbon added was sufficient to decorate the dislocations introduced by deformation. It is evident that there is no relationship between the oxides at the surface and the dislocations present in the metal since the number of dislocations in the sample was estimated to be approximately 10^4/cm^2.

It is concluded that the pattern of the oxides at the surface of high-purity iron and silicon iron is determined by the nature of the surface discontinuities rather than by the arrangement of dislocations in the underlying metal crystal.

E. A. Gulbransen: The resemblance of thermal etching patterns to oxide nucleation patterns has been pointed out to us by Hoar [18] and by Fraser [19] as early as 1953. We feel that there may be a resemblance between the two phenomena, but we disagree with the conclusions of Walter and Dunn.

Unfortunately, the experiments of Walter and Dunn given here are inconclusive. The spots on their Fig. 3 were assumed to be oxide but were not proven, while the value of 10^4/cm^2 for the number of dislocations in Fig. 4 appear to us to be absurd. Silicon iron is a poor material to use to demonstrate the relationship between dislocations and oxide nuclei. At 1300°C, selective evaporation occurs and a film of silica probably is formed on the surface. Solid phase reactions could occur which would leave residual material on the surface.

Since writing our paper, we now feel even stronger that nucleation centers exist in metals. These centers are involved not only in the formation of initial oxide nuclei but in the formation of oxide whiskers and platelets[20]. These nucleation centers can be oriented by stress, [21] impurities in the metal, and by the nature of the reaction environment.[22] Studies are now being made in our laboratory to elucidate these problems. Whether these nucleation centers can be related to the present concepts of dislocations is problematical at the moment. Most of the present concepts of dislocations have been developed on the basis of mechanical properties and the very complicated phenomena of etch pits.

Rectification by Zircaloy 2 in High-Temperature Water

J. N. Wanklyn and R. Aldred (pp. 529, Vol. 106, No. 6)

P. Cohen[23]: In 1950, the writer experienced the same difficulties reported by the authors, namely electrolytic corrosion of zirconium at 600°F, using 60-cycle current at about 6 v, in heating a zirconium specimen in a heat transfer corrosion test. Failure of the test specimen occurred in 200 hr.

The problem is a general one where electrical heating of zirconium in high-temperature water is required for prolonged periods. In seeking a solution to the problem, the effect of frequency on the electrolytic corrosion of zirconium in NaCl solutions was investigated at room temperature. The corrosion efficiency decreased rapidly and monotonically with increasing frequency, reaching very low values in frequency range 400 to 1000 cycles. Since it could be most readily procured, a 400-cycle 50-kva aircraft type generator was obtained. Coupled with an available 3000-amp 100-kva transformer, the 400-cycle generator was used in subsequent tests of the same type.[24] Actually, 1000-cycle motor generator sets of the size required for this type of work are also available and may be more satisfactory.

[18] T. P. Hoar, Private communication.

[19] M. Fraser, Private communication.

[20] E. A. Gulbransen and T. P. Copan, General Discussion of the Faraday Society on Crystal Imperfections and the Chemical Reactivity of Solids, Kingston, Ont., Sept. 1959.

[21] E. A. Gulbransen and T. P. Copan, "Proceedings of the Symposium on Internal Stresses and Fatigue in Metals," p. 397, Elsevier Publishing Co., New York (1959).

[22] E. A. Gulbransen and T. P. Copan, "Physical Metallurgy of Stress Corrosion Fracture," p. 155, "Metallurgical Society Conferences Vol. 4," Interscience Publishers, Inc., New York (1950).

[23] Atomic Power Dept., Westinghouse Electric Corp., P. O. Box 355, Pittsburgh 30, Pa.

[24] "Out-of-Pile Dynamic Loop Tests of Irradiated Fuel Materials," L. A. Waldman and W. T. Lindsay, Jr., WAPD-PWR-CP-2945, p. 26. Obtainable from Technical Information Service, USAEC.

On an Ion-Exchange Property of Manganese Dioxide

A. Kozawa (pp. 552-556, Vol. 106, No. 7)

Alfons Krause[25]: In his investigation, Kozawa found an exchange between zinc ions and H+ ions on the surface of MnO_2, which he explained as occurring through hydration of the surface; however, not every MnO_2 is suitable for the exchange. It is well known, and also mentioned by Kozawa, that MnO_2 cannot be hydrated when annealed at an excessively high temperature, whereas less annealed samples do add water, in spite of being practically water free. We are dealing here with active and inactive MnO_2, and differences in structure have not been considered by Kozawa in his exchange-scheme. According to this over-simplified scheme, each oxide theoretically should be able to add water, regardless of whether or not this is possible in practice.

In my opinion, these differences can be accounted for by the radical structure[26] which accounts for the active state, i.e., the active sites of a metal oxide. The actual model of the normal structure of MnO_2 is not so important, but rather that only two types of radicals may be found in active MnO_2, namely, R≡Mn- and R≡Mn-O-.[27] The latter is an electron acceptor and a potential anion. It also can be considered as a Lewis acid. The radical R=Mn-, however, is an electron donator and a possible cation. The radicals disappear only by strong annealing due to a "healing" of the MnO_2 lattice, thus making the oxide practically inactive:

R≡Mn- -O-Mn≡R → R≡Mn-O-Mn≡R (schematic)
(active) (inactive)

The radical MnO_2 is enabled to add H_2O molecules as expressed in the following equation:

$$R{=}Mn- + H_2O + -O{+}Mn{\equiv}R \rightarrow 2R{\equiv}Mn\text{-}OH$$

The resulting hydroxide reacts further with ammoniacal zinc oxide solution which is, in fact, an exchange of hydrogen for zinc:

$$2\,R{\equiv}Mn\text{-}OH + [Zn(NH_3)_2Cl_2] \rightarrow$$

$$2\,R \equiv Mn\text{-}O\frac{Zn}{2} + 2\,NH_4Cl \qquad [1]$$

For nonradical, i.e., inactive MnO_2, the equations cannot be applied.

The exchange process, incidentally, may be considered in another way, namely that the MnO_2 assumes the function of a chromatographic column. Here, also, the radical structure of MnO_2 is essential as was shown previously for Al_2O_3.[28] Through the action of ammonia, the chromatographic column (MnO_2) assumes a negative charge, whereupon zinc ions can be taken up. This is, in fact, an inhibited coagulation of the chromatographic MnO_2[28]:

$$(R{\equiv}Mn\text{-})_2 + (-O\text{-}Mn{\equiv}R)_2 + [Zn(NH_3)_2Cl_2] + 2H_2O \rightarrow 2\,R{\equiv}Mn\text{-}OH + 2NH_4^+ + 2\,(O\text{-}Mn{\equiv}R)^- + Zn^{++} + 2\,Cl^- \rightarrow Zn(O\text{-}Mn{\equiv}R)_2 + 2\,R{\equiv}Mn\text{-}OH + 2NH_4^+ + 2Cl^- \qquad [2]$$

[25] Institute of Inorganic Chemistry, University of Poznan, Poznan, Poland.

[26] A. Krause and H. Krach, *Ber. deut. chem. Ges.*, **69**, 2709 (1936); A. Krause, *Przemysl Chem.*, **28**, 267, 558 (1949); A. Krause in J. Alexander's "Colloid Chemistry," Vol. VII, p. 175, New York (1950).

[27] A. Krause, *Z. anorg. u. allgem. Chem.*, **301**, 294 (1959).

[28] A. Krause, *Bull. soc. des amis sci. et lettres de Poznan*, **Ser. B. XIII**, 111 (1956).

Akiya Kozawa: It seems reasonable to assume that the ion-exchange reaction mostly takes place only on the surface of MnO_2, since the ion-exchange reaction attains at a equilibrium in a short time and it is reversible on *p*H change of the solution (Fig. 9 of the paper). On the surface of MnO_2, there exist unsatisfied chemical bonds which might correspond to "Radicals," R≡M- and R≡M-O- mentioned by Professor Krause. The final surface structure of the MnO_2 with the adsorbed zinc ion, $(R{\equiv}Mn\text{-}O)_2Zn$, proposed by Professor Krause [*See* Eq [1] and [2]; I think there is a mistake in Eq. [1], which should be $2R{\equiv}Mn\text{-}OH + Zn(NH_3)_2Cl_2 \rightarrow (R{\equiv}Mn\text{-}O)_2Zn + 2NH_4Cl$], is quite similar to that shown in Fig. 10. Difference between the two mechanisms is as follows: as the surface of MnO_2 before zinc adsorption, he is considering R≡Mn-OH resulting from radicals R≡Mn-O- and R≡Mn- by adding H_2O molecules, and I am considering $R{\equiv}Mn\text{-}OH_2$ by a simple hydration. I do not have experimental results to distinguish between the two. It is, however, well known that metal ions hydrate in aqueous solutions, and so it would be permissible to consider a hydration of manganese ions on the surface of ionic crystal of MnO_2 in an aqueous solution.

Professor Krause considers that the active sites of MnO_2 surface, namely the radical structures, are essential for the ion-exchange adsorption. However Fig. 6 shows that the amount of the ion-exchange (zinc adsorption) is proportional simply to the surface area measured by gas adsorption (B.E.T. method), regardless of those samples, active MnO_2 or inactive MnO_2, which were prepared by annealing the active MnO_2 below 450°C. According to my experimental results, the saturate adsorption of zinc ion in Fig. 8 corresponds nearly to the monolayer coverage, that is, every two manganese atoms on the surface of MnO_2 adsorb one zinc ion as shown in Fig. 10. From these facts only active sites would not be essential, but rather all the surface of MnO_2 may be responsible for this zinc adsorption.

The Significance of the Flade Potential

M. J. Pryor (pp. 557-562, Vol. 106, No. 7)

H. H. Uhlig[29]: Dr. Pryor's model for the passive film on iron introduces another assumed structure additional to structures he quotes assumed previously by others. Unfortunately, for the present state of knowledge in this field, any of these models is not readily proved or disproved. There are only fragments of circumstantial evidence which support one model over the other, but as yet no critical experiment has been performed or offered.

We have come to accept an adsorbed film model of the passive film over all others because it appears to fit in with the greatest number of observations. These observations have been summarized in a previous paper.[30] Among the important lines of evidence are that those metals and alloys (transition group) best able to chemisorb their environment are also those that tend to be passive. Furthermore, the alloying relations leading to optimum catalytic

[29] Corrosion Lab., Dept. of Metallurgy, Massachusetts Institute of Technology, Cambridge 39, Mass.

[30] H. H. Uhlig, *Z. Elektrochem.*, **62**, 626 (1958).

properties which depend on chemisorption are similar to those leading to optimum passivity. In addition, the calculated free energy of formation of the chemisorbed passive film on iron is close to the observed value based on measured heat of adsorption.

On the other hand, Dr. Pryor's model suggests that all metals on which semiconducting oxides form should exhibit passive properties. This is not the case. Copper on which a p-type Cu_2O film forms, or zinc on which an n-type ZnO film forms, are not passive in nitric acid or in any aqueous environment in the same sense as are iron and chromium.

The formation of ferric ions on corrosion of passive iron in sulfuric acid is readily explained by local action cells of which the adsorbed passive film represents a large cathodic area in contact with exposed iron at very small pores, in accord with measurements of porosity in the passive film by Vetter.[31] High current densities established at the small anode sites account for corrosion products of valence 3 rather than, 2, an effect which is readily observed during anodic polarization of iron in sulfuric acid employing increasing current densities.

M. J. Pryor: Professor Uhlig's comments are representative of an entirely different view as to the cause of passivity of metals (i.e., adsorption as opposed to three-dimensional film formation). These different views on the nature of passive surfaces must, of necessity, lead to different interpretations of the meaning of the Flade potential. Since these opposed views on the mechanism of passivation are well known, it appears idle to reiterate them in detail at this time.

In order to explain the Flade potential, it previously has been deemed necessary to assume the initial existence of either a two-phase passivating oxide film or an adsorbed passivating layer of some type. Neither concept has received any significant experimental support from structural studies of passive iron surfaces. Accordingly, it appears to be more logical to develop an explanation of the Flade potential based on the breakdown of a crystallographically single-phase passivating γ-Fe_2O_3 film. The present work shows that such a model adequately can explain the Flade potential, provided that a change in defect structure with thickness is assumed. Such changes in defect structure with thickness have been suggested previously for sulfide films on silver.[32]

Professor Uhlig believes that our paper implies that all metals which carry semiconducting oxides should develop passivity as, for instance, by immersion in concentrated nitric acid. Such a hypothesis is nowhere claimed in the article nor is such an implication intended. Instead, we have pointed out that the Flade potential observed on iron can be related well to electrochemical reactions involving protective γ-Fe_2O_3 films having a p-n defect structure. We further have pointed out how such a film structure may develop during the passivation of iron.

In order for a semiconductive surface film to confer passivity to a metal, it is necessary for the film to have either a high electronic resistance, a high ionic resistance, or both. Furthermore, the surface film must be nonporous and compact. If such is not the case, as for instance with copper which forms low-resistance semiconductive films, then passivation in the normal sense will not occur. It is also significant to note that such metals do not normally exhibit a Flade potential.

It appears that one of the advantages of the present model lies in its ability to cover aspects of the Flade potential which have received only cursory attention in the past. For example, most previous investigators have been concerned primarily with measurement of the potential itself. Rather less attention has been directed to the duration of the potential arrest. It is of interest to note that repeated anodic passivation and activation of an iron specimen in sulfuric acid results in a steady and quite spectacular increase in the duration of the Flade potential arrest. This increase in the duration of the potential arrest does not appear to be particularly sensitive to the time for which the specimen is permitted to remain in the active state. Furthermore, differing means of interrupting the polarizing current appear greatly to influence the length of the Flade potential arrest. These observations are difficult to rationalize on the basis of electrochemical reactions unrelated to the defect state of the surface oxide films. They also tend to confirm the general validity of the approach contained in our article.

Peter F. King[33]**:** Dr. Pryor is to be congratulated for his valuable attempt to explain the Flade potential. His explanation is more satisfying than some of those which have been attempted in the past. The semiconductive oxide approach has some things in its favor, but there are also some shortcomings. One of these is the small amount of reaction necessary to bring about passivity, which is not sufficient to produce an oxide film 50Å thick. It is true that the argument may be made, and may be valid, that the onset of passivity has never been studied on an absolutely clean metal surface and that the small amount of reaction usually measured may, indeed, be only the growth of the excess oxide ion concentration necessary in Dr. Pryor's theory. Even if oxide is not present initially, oxidation of iron and its alloys in passivating media occurs in an apparently logarithmic fashion with time, as shown by the recent work of Brasher[34] and Stern.[35] It is likely that this oxidation results in defect oxides of the type postulated by Dr. Pryor. However, we do not feel that this oxide determines the Flade potential, as it is only the result, not the cause, of passivity.

We contend that the cause of passivity is a layer of chemisorbed oxygen produced on initial immersion of the metal into the passivating medium. One would expect, from (*a*) the approximate equivalence of the Flade potential obtained on iron after anodic passivation with the passivation potential,[36] and (*b*) the equivalence of the thickness of the film

[31] K. Vetter, *Z. Elektrochem.*, 55, 274 (1951).

[32] F. S. Stone, *Proc. 3rd Int. Congr. Reactivity of Solids, Madrid*, 1956, p. 641.

[33] Metallurgical Lab., Dow Metal Products Co., Midland, Mich.

[34] O. Kubaschewski and D. M. Brasher, *Trans. Faraday Soc.*, 55, 1200 (1959); D. M. Brasher and D. H. Kingsbury, *ibid.*, 54, 1214 (1958).

[35] M. Stern, *This Journal*, 106, 376 (1959).

[36] K. F. Bonhoeffer, *Z. Metallk.*, 44, 77 (1953).

on passive iron at the Flade potential[37] to the amount of reaction which occurs during the passivation process,[38] that the superior oxide decays first during activation. The result (just before activation occurs) is a film which is almost equivalent to the film formed during the passivation process.[39]

The major argument in favor of the conclusion that chemisorbed oxygen is the cause of passivity in the case of iron and the iron-chromium alloys in aqueous environments, apparently overlooked by Dr. Pryor, is the equivalence of the experimentally observed Flade potential with that calculated, albeit roughly, from the heat of adsorption of oxygen on iron.[40] It is hoped that similar comparisons can be extended to other cases, such as the alloys of iron and chromium, where the Flade potentials have been measured but the heats of adsorption are not yet available.

M. J. Pryor: Dr. King's discussion is appreciated and raises several important points. It is first worth while to point out that the interpretation of the Flade potential advanced by Professor Uhlig and Dr. King[41] and that advanced by the writer have one important feature in common. Both interpretations involve the reduction of oxygen association in some manner with the passive iron surface. The main disagreement centers around the manner in which this oxygen is disposed on the passive surface (i.e., as an adsorbed layer or as part of a nonstoichiometric oxide film) and whether this oxygen per se is responsible for passivity.

Several factors, as pointed out in the reply to Professor Uhlig's discussion, favor the view that the oxygen is associated with a nonstoichiometric oxide film. These include the sensitivity of the length of the Flade potential arrest to the manner in which the passivating potential is interrupted. If, for instance, passivation of iron is achieved anodically in 1.0*N* sulfuric acid at a potential of +0.8 v (hydrogen scale) and the polarizing voltage is interrupted, then a characteristic length of Flade potential arrest may be determined. This duration depends on the time of anodic polarization, the voltage applied, and the specimen history. If the specimen is polarized for the same time at 0.8 v and the polarizing potential is then reduced smoothly and quickly to 0.6 v after which the polarizing voltage is again interrupted, the length of the Flade potential arrest is greatly shortened. In extreme conditions, the arrest may be virtually eliminated. Such an observation fits well with the concept of a p-n layer of γ-Fe_2O_3 in which the distribution of p-type defects is field stabilized. It is also a difficult observation to explain on purely electrochemical grounds unrelated to the defect structure of a three-dimensional surface film.

While the agreement between the calculated "heats of absorption" for the $O \cdot O_2$ layer referred to by Dr. King and the Flade potential[41] is impressive, it should be realized that there is a very broad assumption involved in these calculations. In the absence of supporting data, application of results of Tompkin[42] on chemisorption of dry gaseous oxygen to the rather specialized $O \cdot O_2$ layer, believed by Uhlig and King to exist under passivating conditions, appears to be of uncertain technical validity. Unless this extrapolation can be experimentally justified, it should be realized that the agreement between the calculated heats of adsorption and the Flade potential is speculative in nature.

[37] K. G. Weil, *Z. Elektrochem.* **59**, 711 (1955).

[38] P. F. King and H. H. Uhlig, *J. Phys. Chem.*

[39] H. H. Uhlig and P. F. King, *This Journal*, **106**, 1076 (1959).

[40] H. H. Uhlig and P. F. King. *This Journal*, **106**, 1 (1959).

[41] H. H. Uhlig and P. F. King, *This Journal*, **106**, 1 (1959).

Surface to Volume Considerations in the Palladium-Hydrogen-Acid System

J. P. Hoare (pp. 640-643, Vol. 106, No. 8)

Gilbert W. Castellan[43] and Robert J. Fallon[44]: We believe that the results obtained in this investigation can be given a simpler interpretation than the one proposed in the article. We have made an extensive investigation [45] of the rate of entrance of hydrogen into palladium in sulfuric acid solution. This investigation shows quite clearly that the rate-determining step is transport of molecular hydrogen through the diffusion layer of aqueous solution at the surface of the metal. The subsequent steps, dissociation at the surface, penetration of the metal skin, and diffusion in the bulk metal, are comparatively fast. We also noticed that the length of the 0.050-v plateau is inversely proportional to the rate of increase of H/Pd with time. We developed the rate equation. It turns out that the rate is a function of area-to-volume ratio, the geometry of the specimen, and the rate constants for the several steps. The author finds that the length of the 0.050-v plateau is a linear function of volume-to-area ratio. This is at best only qualitatively in agreement with the rate equation. There are two important reasons for this: the author used three different geometries, bead, foil, wire; and we believe that he did not give sufficient attention to the stirring in the solution.

Three points in the author's interpretation need further discussion: (*A*) slowness of penetration of the metal skin; (*B*) the irregular "step" type of curve reported for the relative resistance vs. time; (*C*) the "overshoot" of the α-plateau.

(*A*) Skin penetration: If penetration of the metal skin were the slow step, slow compared to transport to the surface, and compared to dissociation, then a layer of H atoms should accumulate on the surface. This surface concentration of H atoms should approach that which is appropriate to the β-alloy and the potential of the electrode should be zero and not 0.050 v.

(*B*) In over 400 experiments on the measurement of relative resistance vs. time, we never observed the step-wise behavior reported by the author. We believe that the reason for this is that in our experiments the cell was small, the wire was a simple loop or helix, the hydrogen flow produced good stirring and established a definite diffusion layer at the wire surface. In the author's experiments the

[42] Quoted by B. Trapnell, "Chemisorption," p. 215, Academic Press Inc., New York (1955).

[43] Dept. of Chemistry, Catholic University of America, Washington, D. C.

[44] Institute of Molecular Physics, University of Maryland, Baltimore, Md.

[45] R. J. Fallon and G. W. Castellan, *J. Phys. Chem.*, **64**, 4 (1960).

cell is long, 19 cm, and the wire is stretched diagonally across the cell. He says that the flow rate of hydrogen was approximately constant but gives no clue as to where the hydrogen was introduced, or how fast or steady the flow rate was. We have not observed the plateau at about $R/R_0 = 1.065$ reported by Flanagan and Lewis[46] and by the author; however, in our experiments the rates of absorption were usually much faster and our resistance vs. time curves do show a change in slope in this region. The typical dependence of R/R_0 which we observe[45] is quite similar to that reported in Fig. 2 of Flanagan and Lewis.[46]

If the flow rate of the hydrogen is constant as the author claims, and stirs the solution well enough to establish a definite diffusion layer at the metal surface, then we can see no reason for the step type of curve which he observes in the relative resistance vs. time.[45] On the other hand, if the stirring is erratic, such an irregular curve should be observed.

(C) The "supersaturation" or "overshoot" of the α-potential: If, as the α-alloy reaches the saturation limit, the supply of hydrogen is restricted (due to poor stirring), then the hydrogen enters very slowly and the β-phase has a longer time in which to nucleate. The supersaturation which occurs before the β-alloy forms is small and no overshoot is observed. If, on the other hand, an ample supply of H_2 is maintained as the α-limit is reached, the H_2 enters quickly and the supersaturation reaches a noticeable value before the β-phase nucleates. This is exactly analogous to supercooling. If the melt is cooled very slowly, supercooling is less likely to occur; if it is chilled rapidly, it may well supercool. We observe that the overshoot is consistently more pronounced for smaller wires. This supports the above explanation. The author observes the overshoot in the exact circumstances where the stirring is likely to have been very good—the open helix of wire. We do not believe that an extraordinary surface film is responsible for this behavior. Also, we have observed the overshoot too consistently for it to be an accident in preparation.

J. P. Hoare: Although Castellan and Fallon have done very fine work, a few comments may be in order. As one knows, when a palladium sample is immersed in a water solution of sulfuric acid, the surface will be covered with adsorbed water molecules. When molecular hydrogen is bubbled through the solution, some of these molecules will enter the outer Helmholtz plane[47] which is the closest approach of a particle to the surface without being physically adsorbed. Then, the hydrogen will be adsorbed, probably by complexing with the adsorbed water to give hydrogen atoms adsorbed on the surface. These will then be dissolved in the metal. The concentration of particles on the surface will contribute to the magnitude of the potential. Castellan and Fallon suggest that, if the solution of hydrogen by palladium is the slow process, one must have a build-up of adsorbed hydrogen atoms on the surface and a potential of 50 mv would not be observed. This may not be the case since the build-up of hydrogen concentration may take place in the double layer as molecular hydrogen, if such a build-up of hydrogen exists. It may be possible that the H_2 in the double layer will not be adsorbed until certain surface conditions are met which are controlled by the solution process of hydrogen entering the palladium metal.

Castellan worked with very small diameter wires. The reported work by Hoare indicated that the step-wise form of the charging curves was most pronounced on wires of larger diameters. The plateau at $R/R_0 = 1.065$ is very short on curves taken from wires of small diameter and might well be missed. A step-wise curve can occur if the resistance is a function of the distortion in the palladium lattice which is a function of the way in which the β-phase nucleates. If the β-phase nucleates by the sudden merging of domains of the β-phase, a series of steps may be reflected in the resistance-time curves. Fedorova and Frumkin[48] have arrived at similar conclusions.

As far as the supersaturation effect is concerned, it has been this author's experience that the overshoot only occurs on electrodes which have been cleaned and activated without additional mechanical stress being applied in the mounting of the electrode. This is the case for Castellan's work. If, however, as was done here, the wire, after being prepared, is wound about a polyethylene form or stretched in mounting, the overshoot on the charging curve is not found. This suggests that a film similar to that proposed in the author's paper has been broken up by the mechanical stress and the palladium surface is exposed. Only if the film is intact, as with Castellan's work, will the overshoot be observed since then the palladium surface will not be exposed until the film has been dissolved. It is the solution process of the film that causes the overshoot in the charging curve.

The Relation of Gas Composition to Current Efficiency in an Aluminum Reduction Cell

T. R. Beck (pp. 710-713, Vol. 106, No. 8)

Jack D. Hamlin[49]**:** I have read with great interest the development presented by Dr. Beck. Endeavoring to understand fully his development, independent calculations have been made, and a development results which leads to somewhat different conclusions.

Allow me to attempt to make my point by considering the electric current as two components. First, there is that fraction of the total current which is the current that is a part of the electrochemical reaction. The second part of the current is that fraction of the total current which is not taking part in the electrochemical reaction. This part is electronic conduction, or in an analogous way, it is current that is shunted around the electrochemical path.

Now consider only the fraction of the current that takes part in the electrochemical reaction. In

[46] T. B. Flanagan and F. A. Lewis, *Trans. Faraday Soc.*, 55, 1409 (1959).

[47] D. C. Grahame, *Chem. Rev.*, 41, 441 (1947).

[48] A. Fedorova and A. Frumkin, *Zhur. Fiz. Khim. USSR*, To be published.

[49] Development Engineering, Reynolds Metals Co., P. O. Box 191, Sheffield, Ala.

terms of the author's Eq. [1], this amount of current produces 4 moles of aluminum and n moles of carbon dioxide. Subsequentially, $\left[\frac{2x}{3}\right]$ moles of aluminum are reoxidized by reaction with CO_2—from Eq. [2]. A point I wish to emphasize is that if n moles of CO_2 are produced initially then 4 moles of aluminum are also produced initially.

Now consider the fraction of the current that did not take part in the electrochemical reaction. Let us assign a value to this fraction of $\frac{Z}{100}$. We can now ask the question: If all of the current had taken part in the electrochemical reaction, how much aluminum would have been produced initially? The answer is:

$$4 \div \left(1 - \frac{Z}{100}\right), \text{ moles}$$

I, therefore, offer that if n moles of CO_2 actually are produced initially as expressed in Eq. [1] and used in Eq. [6b] then, likewise, 4 moles of aluminum are initially produced and, consequently, Eq. [6a] becomes,

$$\% \text{ CE} = 100\left[\frac{4 - 2/3x}{4}\right]\left[1 - \frac{Z}{100}\right]$$

If x is then solved for in this equation and equated to x as solved for in Eq. [6b], an equation for current efficiency results that is different from that presented in the paper.

$$\% \text{ CE} = \left(\frac{y - n + 6}{3}\right)\left(\tfrac{1}{2}\% \text{ CO}_2 + 50\right)\left(1 - \frac{Z}{100}\right)$$

or

$$\% \text{ CE} = k(\tfrac{1}{2}\% \text{ CO}_2 + 50)$$

Using the data presented by Dr. Beck, the corresponding values of k are as follows:

Anode bake temp, °C	k
959	1.01
1,070	0.98
1,150	0.96

T. R. Beck: I am grateful to Mr. Hamlin for pointing out that my derivation does not properly account for electronic conduction. My assumption that electronic conduction and loss of aluminum or other reduced species to the lining or atmosphere were exactly equivalent was incorrect. I wish to amend my derivation to properly include electronic conduction.

Assume that Z is the per cent loss of equivalent aluminum by the mechanisms presented in the paper: (a) escape of sodium from cell; (d) formation of sodium and/or aluminum carbide with lining; (e) oxidation of aluminum during tapping. Assume Z' is percentage of current carried by mechanisms: (b) direct oxidation of reduced species at anode; (c) electronic conduction. In Eq. [4a]:

$$\frac{A}{A + B} = \left(1 - \frac{Z'}{100}\right)$$

$$A = 4$$
$$C = 2/3\,x$$
$$D = 4\frac{Z}{100}$$

Eq. [6a] therefore becomes:

$$\% \text{ CE} = 100\left[\frac{4 - (2/3)x - 4\,Z/100}{4}\right]\left(1 - \frac{Z'}{100}\right)$$

Eq. [6c] becomes:

$$\% \text{ CE} = \left[\frac{6 - n + y}{3}(50 + \tfrac{1}{2}\% \text{ CO}_2) - Z\right]\left(1 - \frac{Z'}{100}\right) \text{ and}$$

Eq. [10] becomes:

$$\% \text{ CE} = [g(50 + \tfrac{1}{2}\% \text{ CO}_2) - Z]\left(1 - \frac{Z'}{100}\right)$$

Although not necessarily true for all aluminum cells, there are good reasons for believing that electronic conduction was not significant in the 10,000-amp experimental cell. Electronic shunt losses can be divided into several types: 1. losses through faulty insulation exterior to the bath; 2. electronic conduction through the bath; 3. short circuits between anode and cathode by metal splashing; 4. electronic conduction between anode and cathode through accumulated carbon "dust," sloughed from the anodes, floating on the bath surface.

It is certain that there were no significant shunt losses exterior to the bath for the experimental cell, although these have been known to occur in commercial cell lines. The work of Frank and Foster[50] indicates that electronic conduction is not significant through cryolite melts. There were no indications of short circuits by metal splashing in the experimental cell. This, however, can occur in large, high amperage, commercial cells in which large electromagnetic forces acting on the metal pad are developed. It is doubtful that there was significant shunt loss through carbon dust because there was only a small amount in the cell, its conductivity was poor because it was loosely packed, and the carbon lining was insulated from it by a layer of frozen cryolite or "ledge." There was noticeably more "dust" in the cell when using the low-bake temperature anodes. If electronic conduction through the dust were significant, then Z' would have been larger for the low-bake temperature and the value of k calculated by Mr. Hamlin would be smaller, whereas the reverse was true.

It should be pointed out that error in metering of cell current also would be reflected in the value of Z', making it either plus or minus. The shunt and ammeter for the experimental cell were calibrated and known to be accurate to $\pm\frac{1}{2}\%$.

Whether direct oxidation of reduced species at the anode occurs is not known, so it is not certain that Z' was zero. On the other hand, there was considerable direct evidence that Z was not zero. As was stated in the paper, pockets of sodium metal were frequently found condensed in the cell "crust."

[50] W. B. Frank and L. M. Foster, *J. Phys. Chem.* **61**, 1531 (1957).

Metallic sodium was also found in the carbon lining, and it has been observed in linings of commercial cells. It is well known that sodium and/or aluminum carbide is found in used cell linings.

Since there was direct evidence that Z was greater than zero and there was no evidence that Z' was not zero, I believe that my analysis of the data is correct as it stands.

Influence of Silicon on the High-Temperature Oxidation of Copper and Iron

J. W. Evans and S. K. Chatterji (pp. 860-866, Vol. 106, No. 10)

J. L. Meijering[51]: The authors conclude that the diffusivity of oxygen in Fe is much greater than is commonly supposed. However, their results agree satisfactorily with subscale measurements[52] on iron containing Al, and only the large discrepancy with respect to the measurements of Bramley, *et al.*,[53] is apparent. The latter authors treated their deoxidizing experiments with Fe containing 0.09% oxygen by weight as if the oxygen was homogeneously dissolved, which led to a far too small value of the diffusion coefficient D_o. It now is certain that the solubility c_o is quite small, and then the experiment in footnote 53 can be shown to lead to a value of about 1.5×10^{-11} cm²/sec for c_oD_o at 1000°C,[52] if c_o is expressed as atomic fraction. This is a third of the value deduced from the internal oxidation experiments with Fe containing 1% Al and, in view of the various uncertainties, this must be considered as satisfactory.

For comparison, we roughly calculated c_oD_o from the 998°-run of the authors, using the equation

$$c_oD_o = x\,(x + x_s)\,c_{Si}/t,$$

where x_s is the thickness of the metal layer converted into scale. This equation is valid only for small values of c_{Si}, the atomic fraction of silicon in the alloy. It is readily deduced from section 3 of footnote 54 (see below), if one assumes that each Si atom captures only 2 oxygen atoms in the subscale. This is not certain, and the proportionality of x_s with $\sqrt{t}$ (assumed in deriving the equation) is also not well fulfilled. Nevertheless, the value 3×10^{-11} cm²/sec found from the subscale thickness x and the weight increase after 5 hr at 998°C can be said to be in agreement with the results of footnotes 52 and 53.

J. W. Evans and S. K. Chatterji: We are grateful to Dr. Meijering for pointing out that our results relating to the diffusivity of oxygen in iron confirm his own experiments with aluminum in iron, and those of Bramley, *et al.*, which he has corrected, and sincerely regret not referring to his work.

Although we were aware that the oxygen solubility assumed by Bramley was probably too high (*see* Kitchener, Bockris, Gleiser, and Evans[55]) and, therefore, led to a too low value for the diffusivity, we see that our original remarks did not imply this.

We would like at this time to correct an error in the orignal paper. In the list of References, Ref. 18 should read: J. W. Evans and S. K. Chatterji, *J. Phys. Chem.*, **62**, 1064 (1958).

[51] Philips Research Labs., N. V. Philips' Gloeilampenfabrieken, Eindhoven, The Netherlands.

[52] J. L. Meijering, *Acta Met.*, **3**, 157 (1955).

[53] A. Bramley, F. W. Haywood, A. T. Cooper, and J. T. Watts, *Trans. Faraday Soc.*, **31**, 707 (1935).

[54] J. L. Meijering and M. J. Druyvesteijn, *Philips Research Repts.*, **2**, 81 (1947).

[55] J. A. Kitchener, J. O'M. Bockris, M. Gleiser, and J. W. Evans, *Acta Met.*, **1**, 93 (1953); *Trans Faraday Soc.*, **48**, 995 (1952).

On the Measurement of the Temperatures of Unenclosed Objects by Radiation Methods

A. G. Emslie and H. H. Blau, Jr. (pp. 877-880, Vol. 106, No. 10)

Tibor S. Laszlo[56]: This paper is a valuable contribution to an old and still controversial problem. There is complete agreement on the fact that the dual color pyrometer operates on the assumption that the emissivity does not change with the change in wave length. The controversy begins where the validity of this assumption is considered. There are several reported data on dual color pyrometry with remarkably good accuracy (± ¼% at 1700°K). It is possible that in these cases the experimental conditions were such that the fundamental assumption was valid. The value of the present work lies in the fact that it furnishes information on the magnitude of error when the emissivity does change with wave length.

This writer cannot but completely agree with the authors' conclusion that the emissivity has to be *measured* at the temperature where the optical pyrometer is to be used. The paper quotes an emissivity measurement method (Ref. 5) at high temperatures, using the solar furnace, which was suggested by the writer. In the frame of the paper, however, the procedure appears too difficult to perform. The method, as described briefly in the following, is really rather simple.

For each solar furnace there is a fixed concentration factor, i.e., the ratio between normal incident solar radiation intensity and heat flux at the focal zone. This factor can be determined by the method presented in the reference. Once this factor is known, the emissivity determination consists of a normal incident solar flux measurement using a pyrheliometer and of a simultaneous brightness temperature measurement at the sample in the focal zone using an optical pyrometer. From the incident solar flux, the flux at the focal zone can be calculated and, from this, the black body temperature of the sample. Knowing both the black body and brightness temperature, the emissivity can be calculated.

A. G. Emslie and H. H. Blau, Jr.: A number of methods have been suggested for temperature measurement in imaging furnaces. The method[57] which we have found most suitable involves direct measurement of the spectral reflectance of the hot specimen. Both the absolute temperature of the specimen and the spectral reflectance (and hence spectral emittance) can be determined from measurements of three intensities: the monochromatic intensities emitted and reflected by the hot speci-

[56] Research and Advanced Development Div., Avco Manufacturing Corp., Wilmington, Mass.

[57] H. H. Blau, Jr., "Measurement of Flux Emittance and Related Properties," *Proc. Int. Symposium on High Temperature Technology, Stanford Research Institute, 1960.*

men, and the monochromatic intensity incident on the hot specimen. The measurements can be performed with an optical pyrometer or other suitable instrument. This method requires no assumptions of equality of spectral and total emittance or of absence of conductive and convective heat losses by the sample as would seem to be the case with Laszlo's method.

Herbert W. Newkirk[58] and **B. B. Brenden**[59]: We have the following remarks regarding Emslie and Blau's article.

The basic principle of the two-color pyrometer is that, when the ratio of the radiant intensities from the sample at two wave lengths is determined, the unknown emissivity is eliminated. Eq. [6] assumes at least gray-body conditions, that is, the emissivities at the chosen wave lengths are equal. In general, the gray-body assumption over a wide spectral interval is not valid. However, narrower spectral intervals can usually be found for incandescent solids for which the gray-body assumption is valid. The choice of the wave-length interval will be determined by the amount of radiant energy available and the sensitivity of the ratio to temperature changes.[60] It is considered good practice in two-color pyrometry to make measurements of spectral emissivity for the material in question in order to select the optimum spectral interval.[61]

It is highly unlikely that the ratio of the emissivities for any incandescent solid at the two wave lengths can be greater than 1.2. In the case of tungsten, for example, the ratio of emissivities is 1.1 at 3600°K with $\lambda_1 = 0.47\ \mu$ and $\lambda_2 = 0.65\ \mu$. Thus, the error in the determination of the true temperature using a two-color pyrometer cannot be greater than 2% at this temperature. This accuracy is equal to or considerably better than that attained with conventional pyrometers. Furthermore, two-color pyrometers offer the advantage of providing an electrical output which can be used to drive a recorder, operate control instruments, etc.

Finally, two-color pyrometers are much less affected by smoke, fumes, and emissivity changes during experiments than single-color pyrometers or total radiation pyrometers. Work in this laboratory[62-64] has indicated that the increased accuracy, automation, freedom from emissivity effect, and a temperature limit above 4000°K are features of two-color pyrometers which can be used advantageously in many areas of high temperature research.

[58] RCA Labs., Radio Corp. of America, Princeton, N. J.

[59] General Electric Co., Richland, Wash.

[60] A. I. Dahl and W. E. Hill, "Temperature Measurements—High Temperature Physics," General Electric Co., Schenectady, N. Y., Report No. 58GL6, Jan 24, 1958.

[61] W. E. Hill, "Temperature Measurements—Applications of Two-Color Pyrometry," General Electric Co., Schenectady, N. Y., Report No. 58GL257, Sept. 15, 1958.

[62] B. B. Brenden and H. W. Newkirk, Jr., "Multicolor Pyrometry," General Electric Co., Richland, Wash., HW-56506, Sept. 1, 1958.

[63] B. B. Brenden and H. W. Newkirk, Jr., "A Multicolor Pyrometer," General Electric Co., Richland, Wash., HW-57162 Rev., Nov. 11, 1958.

[64] B. B. Brenden and H. W. Newkirk, Jr., "An Improved Recording Multi-Color Pyrometer," General Electric Co., Richland, Wash., HW-60678, May 27, 1959.

A. G. Emslie and H. H. Blau, Jr.: Experience shows that the two-color pyrometer can be used for accurate temperature measurement in special cases such as those quoted by Newkirk and Brenden. The conclusions given in our paper are nevertheless strictly true and serious errors are often introduced if equal emittance at the two wave lengths is assumed. For example, the ratio of emittances at 0.46 and 0.65 μ is 1.97 for pure copper. This difference would lead to a temperature error of 5% at 1000°K. In fact, gray-body behavior has been observed to be the exception rather than the rule.[65]

The Action of Nickel and Cobalt in Electroluminescent Zinc Sulfide Phosphors

P. Goldberg (pp. 948-954, Vol. 106, No. 11)

W. Lehmann[66]: (*A*) What do you know about the mean particle sizes and the particle size distributions of your samples? We know now that they may have marked influence on the voltage dependence of electroluminescence.

(*B*) If the measurements of the voltage dependence of electroluminescence of your samples had been extended to more decades of the brightness, could not a deviation from either equation [i.e., $n = 0$ and $n = 1$ in $L = AV^n \exp(-b/V^{1/2})$] be expected?

Paul Goldberg: (*A*) It is unlikely that particle size effects or size distribution effects exert any influence (in these experiments) over the changes in voltage dependence of electroluminescence occasioned by the incorporation of nickel or cobalt. All of the specimens in Fig. 4 and 5 of the paper under discussion, including the control, were prepared under identical thermal conditions from separate portions of a single, previously crystallized phosphor. The modifier was incorporated by solid state-diffusion. No data exist as to size or distribution of sizes of the materials in question. It is improbable, however, that the diffusion process, which occurred at 800°C, changed the size or distribution within the family of phosphors. From previous experience with similar preparations, the mean particle size probably lies between 20 and 30 μ. The distribution of sizes is most likely log-normal.

(*B*) It is possible that the voltage dependence of electroluminescence could change were the measurements extended outside the reported range. The burden of the data in Fig. 4 and 5 is to show that phosphors with varying modifier concentrations, when measured in the same range of applied field, exhibit a change in functionality within the group. We have not tested whether this change in functionality occurs in ranges of applied field not covered in the original publication.

[65] G. G. Gubareff, Shao-yen Ko, and P. E. McMall, Jr., Honeywell Research Center Report, GR 2462-R3 (1956).

[66] Lamp Div., Westinghouse Electric Corp., Bloomfield, N. J.

Oxygen Overpotential in Molten Carbonates

George J. Janz, Francisco Colom, and Fumihiko Saegusa

Department of Chemistry, Rensselaer Polytechnic Institute, Troy, New York

ABSTRACT

The overvoltage of the oxygen evolution reaction on Pt electrodes has been measured in a ternary mixture of molten Na_2CO_3-Li_2CO_3-K_2CO_3 with current densities up to 50 ma/cm^2 and temperatures up to 1000°C. Two well distinguished regions in the overvoltage-log current density relation are observed. At current densities less than 1 ma/cm^2 the marked dependence of the oxygen overpotential on the composition of the gas flow and on temperature are characteristic of a concentration-type overpotential most probably due to the build-up of oxide-ion in the melt. In the range of about 1-50 ma/cm^2, the oxygen overpotential seems activation controlled. From the temperature coefficient of the overpotential, a value for the energy of activation for oxygen evolution of 10.4 ± 1.1 kcal mole^{-1} is obtained. The role of the platinum electrode as an oxygen ion electrode in the over-all process corresponding to the oxygen evolution reaction:

$$CO_3^{-2} \rightarrow CO_2 + O + 2\bar{e}$$

is discussed.

Studies of the oxygen overpotential in molten salts have been quite limited. Agar and Bowden (1) have investigated oxygen evolution on Ni and Pt electrodes in fused NaOH up to 340°C, whereas in molten nitrates a study of this process at temperatures up to 250°C has been reported by Karpatscheff and Patzug (2). Some measurements on the oxygen overpotential for sulfates, silicates, phosphates, and carbonates dissolved in fluorides, and for a Na,K/CO_3 mixture at 700°-900°C have been reported by Flood and Forland (3). The present communication describes the results of further measurements of the oxygen overpotential in molten carbonates. A ternary mixture, Li, Na, K/CO_3 (m. 403°C) was used to extend the temperature range for the studies over a much wider range. Platinum was selected for this study since results of emf measurements of oxygen ion activity in Na,K/CO_3 (4) and Na/SO_4,CO_3 (5) mixtures had confirmed that the CO_2-O_2, Pt electrode behaves as an oxygen-ion electrode in these melts.

Experimental

Chemicals.—Sodium, potassium, and lithium carbonates (Reagent Grade) were recrystallized, and dried at 500°C under CO_2 atmosphere. The purified carbonates were stored in a desiccator over P_2O_5 until required for use. In order to extend the measurements to the widest possible temperature range, the ternary mixture (6): 22.8% Li_2CO_3, 27.4% K_2CO_3, and 49.8% Na_2CO_3, m. 403°C was selected for the present investigation. The homogeneous melt of this composition was prepared preliminary to the measurements in a small auxiliary furnace using a CO_2 atmosphere and platinum crucible.

Apparatus.—The experimental assembly, illustrated schematically in Fig. 1, consisted of an electrically heated furnace, B, closed by a water-cooled brass top, A, supporting the ceramic tubes of the thermocouple well, gas delivery tube, and electrode leads, C, E, F, G, respectively, leading to a 20 ml capacity platinum crucible, D, which contained the melt and also served as the cathodic electrode. The latter was supported, as shown, on an alundum base. The anode was a platinum foil of 2 to 4 cm^2, and the reference electrode was a fine Pt wire placed nearby. A series of alundum disks above the crucible served as baffles to minimize heat losses. Two thermocouples, a Pt-Pt 10% Rh couple observed on a recording controller (L&N Speedomax H) and a chromel-alumel couple observed manually with a potentiometer were placed at the same level close to the cell in the furnace. The electrical circuit was the conventional arrangement for the direct measurement of electrode polarization. The d-c current source consisted of four 45-v batteries in series and

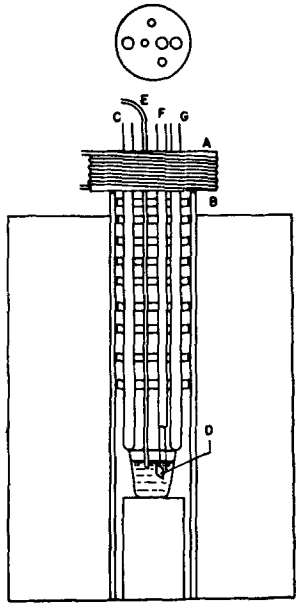

Fig. 1. Experimental assembly for oxygen overpotential measurements in molten carbonates.

Table I. Variation of oxygen overvoltage (η) on platinum with current density (I) in molten Li_2CO_3-Na_2CO_3-K_2CO_3 Mixtures

I, ma/cm²		25	20	15	10	5	3	1	0.5	0.2	0.1	0.05	0.01
mv	A (i)	T, 420°C;		gas flows: (cc/min)		CO_2, 1.5; O; 1.3							
$\eta(i\uparrow)$		420	391	368	333	286	257	226	206	195	177	173	84
$\eta(i\downarrow)$		429	396	368	332	279	245	198	173	154	169	173	—
	A (ii, a, b)	T, 420°C				CO_2, 50; O_2, 42.8							
$\eta\ (i\uparrow)$	a	487	458	430	399	339	304	250	224	190	176	162	—
$\eta\ (i\downarrow)$	a	540	472	472	458	400	358	301	256	212	190	169	143
$\eta\ (i\uparrow)$	b	580	540	475	459	415	368	293	260	230	208	190	—
$\eta\ (i\downarrow)$	b	550	547	534	502	469	440	370	334	285	271	249	155
	B (i)	T, 480°C				CO_2, 4.4; O_2, 3.7							
$\eta(i\uparrow)$		504	484	437	397	327	282	204	168	129	101	83	48
$\eta(i\downarrow)$		445	430	419	382	315	273	197	163	134	108	84	—
	B (ii)	T, 480°C				CO_2, 50; O_2, 42.8							
$\eta(i\uparrow)$		573	540	433	374	321	256	191	162	132	100	70	12
	B (iii)	T, 480°C				O_2, 42.8 alone							
$\eta(i\uparrow)$		—	468	436	394	323	273	189	155	131	119	105	65
	C (i)	T, 515°C				CO_2, 4.4; O_2, 3.7							
$\eta(i\downarrow)$		407	395	376	337	284	238	168	131	105	86	72	45
$\eta(i\uparrow)$		495	473	434	384	308	252	181	144	109	88	72	—
	C (ii)	T, 515°C				CO_2, 50; O_2, 42.8							
$\eta(i\downarrow)$		540	545	497	482	307	254	180	148	115	98	84	49
$\eta(i\uparrow)$		509	462	385	336	287	244	183	156	123	108	88	
	C (iii)	T, 515°C				O_2, 42.8 alone							
$\eta(i\downarrow)$		479	454	408	354	280	221	139	99	69	55	38	10
	C (iv)	T, 515°C				CO_2, 50; O_2, 42.8							
$\eta(i\downarrow)$		484	454	415	348	266	221	160	137	114	98	86	63
$\eta(i\uparrow)$		405	377	354	323	252	210	156	130	107	114	100	—
	D (i)	T, 600°C				CO_2, 4.4; O_2, 3.7							
$\eta(i\downarrow)$		378	348	319	281	240	210	167	150	130	102	72	18
$\eta(i\uparrow)$		346	318	296	262	231	209	193	178	122	93	58	—
	D (ii)	T, 600°C				CO_2, 43; O_2, 37							
$\eta(i\downarrow)$		348	324	298	271	231	201	155	134	111	94	74	32
$\eta(i\uparrow)$		358	335	312	282	238	212	175	152	116	92	69	—
	D (iii)	T, 600°C				CO_2, 50; O_2, 42.8							
$\eta(i\downarrow)$		325	302	274	240	194	167	123	103	81	68	53	22
$\eta(i\uparrow)$		326	310	289	262	219	196	155	125	91	70	53	
	D (iv)	T, 600°C				O_2, 42.8 alone							
$\eta(i\downarrow)$		354	318	288	247	183	148	90	62	30	15	4	—4

Table I (Cont'd)

mv	D (v)	T, 600°C				CO_2, 50; O_2, 42.8							
$\eta(i\downarrow)$		350	329	304	270	213	177	130	108	87	71	52	35
$\eta(i\uparrow)$		361	342	307	276	225	187	136	112	85	65	56	
	E (i)	T, 700°C				CO_2, 43; O_2, 37							
$\eta(i\downarrow)$		304	285	267	235	201	153	107	82	57	41	30	20
$\eta(i\uparrow)$		339	315	289	269	218	173	113	83	54	39	29	
	E (ii, a, b)	T, 700°C				CO_2, 50; O_2, 42.8							
$\eta(i\downarrow)$	a	284	262	240	208	163	142	98	73	49	32	22	11
$\eta(i\uparrow)$		279	259	238	214	184	158	101	74	45	30	21	—
$\eta(i\downarrow)$	b	290	266	240	210	170	143	100	79	52	35	28	18
$\eta(i\uparrow)$		294	270	247	218	181	152	96	70	47	33	26	—
	E (iii)	T, 700°C				O_2, 42.8 alone							
$\eta(i\downarrow)$		313	286	259	234	182	142	71	38	8	—8	—12	—16
	F (i, a, b)	T, 800°C				CO_2, 50; O_2, 42.8							
$\eta(i\downarrow)$	a	257	233	206	173	137	113	65	42	30	21	13	10
$\eta(i\uparrow)$		300	275	233	206	157	120	63	39	23	16	11	
$\eta(i\downarrow)$	b	333	316	283	220	159	120	68	48	34	28	25	22
$\eta(i\uparrow)$		352	308	260	220	152	113	63	45	32	27	25	
	F (ii)	T, 800°C				O_2, 42.8 alone							
$\eta(i\downarrow)$		315	294	259	220	152	101	25	16	—6	—9	—10	—10
	G (i)	T, 900°C				CO_2, 16; O_2, 13.6							
$\eta(i\downarrow)$		246	232	206	164	103	69	33	22	18	15	14	14
$\eta(i\uparrow)$		—	224	178	146	87	56	—	—	—	16	14	—
	G (ii, a, b, c)	T, 900°C				CO_2, 50; O_2, 42.8							
$\eta(i\downarrow)$	a	233	224	206	162	101	70	35	26	21	19	17	15
$\eta(i\uparrow)$		245	222	196	151	92	63	33	25	18	17	16	—
$\eta(i\downarrow)$	b	230	212	188	154	98	69	30	19	13	11	9	9
$\eta(i\uparrow)$		230	215	187	149	97	64	29	18	13	13	11	9
$\eta(i\downarrow)$	c	278	248	218	173	115	76	35	27	18	15	13	13
$\eta(i\uparrow)$		256	241	216	170	107	74	33	25	18	15	13	—
	G (iii)	T, 900°C				O_2, 42.8 alone							
$\eta(i\downarrow)$		286	252	180	134	52	26	7	3	1	0	0	—
	H (i)	T, 1000°C				CO_2, 50; O_2, 42.8							
$\eta(i\downarrow)$		217	200	176	121	68	39	8	0	—4	—9.7	—7	—8
$\eta(i\uparrow)$		255	220	170	120	64	35	7	—1	—5	—7	—7	—
	H (ii)	T, 1000°C				No gas flow							
$\eta(i\downarrow)$		264	243	230	202	156	120	64	41	25	19	14	11
$\eta(i\uparrow)$		265	250	235	222	156	125	55	34	18	15	13	—

a cascade of variable resistors through which the current was drawn.

The gases, CO_2 and O_2, were bubbled through the melt when measurements were in progress using a gold tube extension on the alundum gas inlet, E. The gases were passed through drying trains containing successively silica gel, P_2O_5, and silica gel, monitored on flowmeters, and mixed before entering the melt.

Measurements.—Exploratory measurements with relatively high current densities, 200 ma/cm^2 showed platinum present in the melts after the ex-

periments (due to attack of the crucible). Small coherent gray particles, presumably platinum, were noted after dissolution of the melt in water after the measurement and the crucible showed attack. Using current densities of 50 ma/cm^2 and less, no insolubles were noted in the above test after an experiment, and no visible corrosion of the crucible was noticeable. While these observations qualitatively showed that corrosion did not occur to a great extent in the duration of the experiments, the possible formation of surface oxides electrochemically on the platinum anode is not ruled out. To condition the anode, and thus obtain higher reproducibility in measurements, the first measurements in each experiment were made at relatively high temperatures (700°-900°C). Current densities were restricted to an upper limit of 50 ma/cm^2 in all measurements in view of the above observations relative to corrosion effects.

The results of the measurements for the range 420°-1000°C in the ternary carbonate mixture are summarized in Table I. The resistive potential drop for an electrode separation of 0.1 cm may be estimated as 6 mv maximum at c.d. of 20 ma/cm^2 from the specific conductivity of molten carbonates at 800°-900°C. The correction may be neglected since the value is less than the limits of accuracy of the measurements. The composition and rate of the gas bubbling through the melt, and the overpotential measurements for the run-up ($i\uparrow$) and run-down ($i\downarrow$) are given, with several checks to illustrate the reproducibility of the results at various current densities. The procedure in general was to apply a high c.d. to the anode initially and subsequently decrease the polarization current gradually to a low value. After the first run-down, the current was increased to its initial value for a check run. Overpotential measurements were made immediately after each current change; a minimum of approximately 10 min was required in each case for the potential to reach constancy. At the temperature limits, 420° and 1000°C, only a few measurements were made.

Results

Analyses of the data summarized in Table I gave a series of curves, of which three are illustrated in Fig. 2 to show the relation between the overpotential, η, and logarithm of current density, log i, in molten carbonates for oxygen evolution. The curves in Fig. 2 were selected to illustrate the results at the three temperatures, 480°, 600°, and 900°C, with the same gas mixture and flow rate in each case. Inspection shows that these curves exhibit two well distinguished regions in each case. At low c.d. (<1 ma/cm^2) the overpotential changes with increasing temperatures until the η — log i relation is very nearly parallel to the abscissas (Fig. 2) at the higher temperatures (near 1000°C). In the c.d. range of 1-50 ma/cm^2 the slope of the η — log i relation is very nearly constant at any one temperature, and shows a smaller temperature dependence in contrast to the preceding region. Temperature coefficients of the overpotential at constant current density $(\partial\eta/\partial T)_i$ from these data are summarized

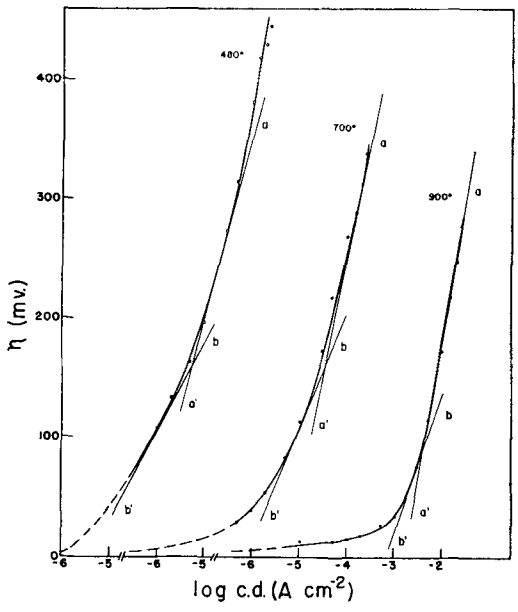

Fig. 2. Oxygen overpotential-current density relations in molten carbonates as a function of temperature. Data are for: A, 480°C; B, 600°C; C, 900°C; and a gas flow in each case of: CO_2, 50 cc/min; O_2, 42.8 cc/min. The lines a-a' and b-b' are theoretical.

in Table II. Inspection of the results shows that for the two temperature ranges, $(\partial\eta/\partial T)_i$ is much less at lower c.d. than at higher c.d., the difference being approximately an order of magnitude.

Since molten carbonates are not chemically inert to O_2 and CO_2, the variations in the rates of flow for the gas mixture bubbling through the melt cannot be interpreted simply as a stirring effect on overpotential. The dependence of η on the gas composition could be checked readily by variation of the CO_2/O_2 ratio in the feed gas. The results at 515°C are illustrated in Fig. 3. It is readily noted that the overpotential is markedly less when the concentration of O_2 in the gas mixture is increased at low c.d. (<1 ma/cm^2) whereas it is essentially independent of this variable at higher c.d. (>1 ma/cm^2).

At constant overpotential, the temperature dependence of current density may be expressed by:

$$\left(\frac{\partial \ln i}{\partial T}\right)_\eta = \Delta H/RT^2 \qquad [1]$$

The results analyzed accordingly for values of η equal to 0, 200, and 300 mv, where the data for the former were gained by extrapolation, are illustrated in Fig. 4. The slopes of the lines were calculated by the least-squares method. The values for ΔH thus found were 10.4 ±1.1 kcal/mole for $\eta = 0$, and 9.1 ±1.1 kcal/mole for $\eta = 200$ and 300, respectively. The variation in ΔH is less than the probable error and may be taken as constant, i.e., 9-10 kcal/mole in molten carbonates.

Table II. Temperature coefficient of oxygen overpotential in molten carbonates

Temperature range	420°-600°C		600°-1000°C	
c.d. (ma/cm^2)	0.05	20	0.05	20
$(\partial\eta/\partial T)_i \times 10^3$ (v/°C)	—0.5	—1.05	—0.06	—0.25

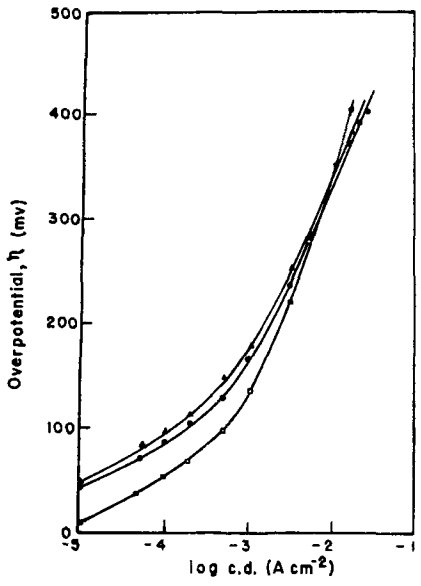

Fig. 3. Oxygen overpotential-current density relation in molten carbonates as a function of gas composition. Composition and flow rates of gas; upper curve, CO_2, 50 cc/min; O_2, 42 cc/min; middle curve, CO_2, 4.4 cc/min; O_2, 3.7 cc/min; lower curve, O_2 only, 42.8 cc/min (measurements at 515°C).

Whereas the melts were white after the experiments in the present investigation, some attack on the Pt with the formation of platinum oxide on the electrode seems not improbable. The data from related experiments having Pt in contact with molten carbonates (6-8) confirm some chemical attack in these basic melts, most probably an oxidation of Pt with simultaneous reduction of the alkali metal oxide species from the thermal dissociation of the molten carbonates.

Discussion

Reference has already been made to the emf studies of the $Pt(O_2)$ electrode in molten Na, K/CO_3 (4) and Na/CO_3, SO_4 (5) mixtures in which measurements confirmed that this electrode really behaves as an oxygen (oxide ion) electrode in such basic melts. In the present investigation the reproducibility of the measurements in the $\eta - i$ cycles, and the reproducible zero overpotential at zero c.d. in each experiment are most readily understood in the function of the $Pt(O_2)$ electrode as an oxygen-ion electrode in carbonate melts.

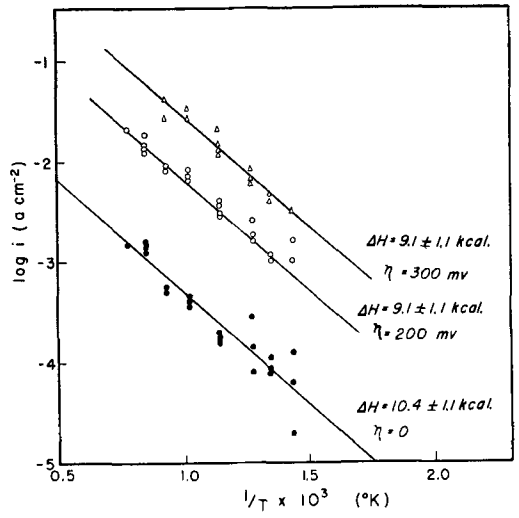

Fig. 4. Temperature dependence of the current density at constant oxygen overpotential in molten carbonates.

Relative to this point, the thermal dissociation of the alkali metal carbonates to the corresponding oxide and CO_2 is well established; the most recent investigation in this field being that of Motzfeld (6) for Na_2CO_3 up to 1050°C using the Knudsen effusion technique. While no such measurements have been reported for the ternary carbonate melt, there is little doubt that the carbonates in the mixture dissociate into the oxide ion and CO_2. In the present study it seems most likely that the activity of the oxide ion is given by the expression:

$$a_{O^{-2}} = K \frac{a_{CO_3^{-2}}}{p_{CO_2}} \qquad [2]$$

in accord with the dissociation equilibrium for the carbonates:

$$CO_3^{-2} \leftrightarrows CO_2 + O^{-2} \qquad [3]$$

for which both the rate of dissociation and the equilibrium will be functions of the temperature in the conventional manner.

Some information on the nature of the electrode processes contributing to the over-all reaction:

$$CO_3^{-2} \rightarrow CO_2 + O + 2\bar{e} \qquad [4]$$

at the anode can be gained from the dependence of the overpotential on current density and temperature.

In general the overpotential is expressed in terms of the logarithm of current density by the following equations:

$$\eta_c = \frac{RT}{n\mathbf{F}} \ln\left(1 - \frac{i}{i_o}\right) \qquad [5]$$

and

$$\eta_a = a - \frac{RT}{n\alpha\mathbf{F}} \ln i \qquad [6]$$

where η_c and η_a are the overpotentials for concentration and activation controlled electrode processes, respectively, and where the latter equation is the well-known Tafel equation. Both types may arise in the present system for, if the carbonate dissociates to form the oxide ion, both (*a*) the transfer of the oxide ion from the bulk of the solution to the layer of the melt in contact with the anode by migration or diffusion, and (*b*) the discharge of the oxide ion directly to form atomic oxygen

$$O^{-2} \rightarrow O + 2\bar{e} \qquad [7]$$

or, in view of the probable formation of oxides on the anode surface

$$O^{-2} + M \rightarrow M{-}O + 2\bar{e} \qquad [8]$$

followed by processes such as

$$M{-}O + M{-}O \rightarrow M + O_2 \qquad [9]$$

leading to oxygen evolution, undoubtedly are steps in the over-all process.

In the case of activation control [i.e., (*b*) above] with $\alpha = 0.5$, the slope of the $\eta - \log i$ equation is

equal to 2.303 $RT/\mathbf{F}$ for a two electron transfer in the electrode process (i.e., $n = 2$). For concentration polarization with $n = 2$ in this system, a slope of 2.303 $RT/2\mathbf{F}$ is to be predicted. The theoretical slopes for activation and concentration type overpotential, a-a' and b-b', respectively, are shown in Fig. 2.

The temperature coefficient of η at constant current density, from the preceding equations, is given by

$$\left(\frac{\partial \eta_c}{\partial T}\right)_i = \frac{\eta_c}{T} - \frac{RT}{\mathbf{F}}\left(\frac{i}{i - i_o}\right)\left(\frac{\partial \ln i_o}{\partial T}\right) \qquad [10]$$

and

$$\left(\frac{\partial \eta_a}{\partial T}\right)_i = -\frac{E}{RT^2} \Big/ \left(\frac{\partial \ln i}{\partial \eta}\right)_T = -\frac{E}{\alpha \mathbf{F} T} \qquad [11]$$

Using the value of 9-10 kcal/mole found in the present investigation as the activation energy for anodic oxygen evolution, $(\partial \eta_a/\partial T)_i$ is predicted as approximately equal to -1.0×10^{-3} v/°C in the range 500°-600°C, and -0.6×10^{-3} v in the neighborhood of 1000°C. On the other hand, it has been found for a number of cases that $(\partial \eta_c/\partial T)_i$ is generally less than $(\partial \eta_a/\partial T)_i$ by approximately one order of magnitude. Comparison with the experimental results (Table II) shows that the temperature dependence of η found is consistent with the above concepts in the first approximation.

Some additional support for the above interpretation of the $\eta - \log i$ relations is seen in the effect of the composition of the gas flow on η. The change in the composition of the gas ($CO_2 + O_2$), i.e., the change in p_{O_2}, is related to the oxygen ion activity (refer Eq. [2]). The decrease in η (see Fig. 3) in the region of low c.d. when oxygen only is bubbled through the melt is thus as predicted for concentration rather than activation overpotential in this range. As indicated earlier the present experiments do not lend themselves to check the effect of stirring (by changes in the gas flow rate) since the melt is not chemically inert to the gas used for this purpose. A decreasing importance of the region of concentration polarization at low c.d. would be predicted with increasing temperatures, i.e., enhanced thermal decomposition of the carbonates and thus increased oxide ion activity at more elevated temperatures, in light of the above. This effect is clearly illustrated by the present results (e.g., see Fig. 2).

In summary, the preceding considerations show that the experimental results are more readily understood in accord with the carbonate dissociation-oxide ion scheme rather than through the direct electrochemical oxidation of the carbonate ion, and that the overpotential is in large part the concentration type in the region of low c.d. (<1 ma/cm^2) and the activation type at higher c.d. (1-50 ma/cm^2).

A point that frequently arises in the field of high-temperature chemistry is the need for an estimate or "forecast" of the behavior of systems at higher temperatures, largely owing to the lack of the necessary data for the high-temperature systems. A comparison of the results of the present study with the values found for oxygen evolution on Pt in aqueous electrolytes is thus instructive. In molten carbonates, the value of ΔH, the activation energy for the over-all process in the region of higher current densities from the present results is in the range 9-10 kcal mole^{-1}. In 0.1N NaOH, 0.1N HNO_3, and 0.2N H_2SO_4, the values for the parameter are (9) 13.8 ± 0.6, 18, and 22.1 kcal mole^{-1}, respectively.

Acknowledgments

The authors wish to acknowledge with thanks stimulating suggestions by Dr. T. Forland (Norway), Dr. D. E. Douglas (General Electric Co.) and Dr. N. D. Greene (R.P.I.) in the course of this investigation.

Manuscript received Sept. 28, 1959. Research for this work was supported by the Office of Naval Research, Chemistry Branch, under ONR Contract Nonr 591-(10).

Any discussion of this paper will appear in a Discussion Section to be published in the June 1961 JOURNAL.

REFERENCES

1. N. N. Agar and F. P. Bowden, *Proc. Roy. Soc.*, **A169**, 206 (1939).
2. S. Karpatscheff and S. Patzug, *Z. physik. Chem.*, **173**, 383 (1935).
3. H. Flood and T. Forland, *Discussions Faraday Soc.*, **1**, 302 (1947).
4. E. Baur and R. Brunner, *Z. Elektrochem.*, **41**, 794 (1935).
5. H. Flood, T. Forland, and K. Motzfeld, *Acta Chem. Scandinav.*, **6**, 252 (1952).
6. K. Motzfeld, *J. Phys. Chem.*, **59**, 139 (1955).
7. D. L. Douglas, Private communication.
8. G. J. Janz and M. R. Lorenz, Unpublished work.
9. J. O'M. Bockris, "Modern Aspects of Electrochemistry," p. 266, Academic Press, Inc., New York (1954.)

Study of the Recuperation Reaction in the Leclanche Dry Cell

M. P. Korver, R. S. Johnson,[1] and N. C. Cahoon[2]

Research Laboratory, Union Carbide Consumer Products Company, Division of Union Carbide Corporation, Cleveland, Ohio

ABSTRACT

The cathodic reaction in the Leclanché dry cell has been described previously as consisting of two steps. The first of these steps is the electrochemical reduction Mn^{IV} to Mn^{II}. The second step is the chemical reaction of Mn^{II} produced in the first step with unreacted Mn^{IV} to form an insoluble Mn^{III} compound. Two chemical reactions can occur producing MnOOH and $ZnO \cdot Mn_2O_3$, manganite and hetaerolite, respectively. The latter reactions, termed recuperation reactions, have been subjected to analysis and rate studies to determine the effects of factors such as *p*H, concentration, and temperature. These reactions are found to be slow enough to limit dry cell operation under certain conditions. The more active depolarizers, such as electrolytic MnO_2, show more rapid recuperation reaction than the natural MnO_2 ore. The basic concepts of heterogeneous chemical kinetics have been applied to this problem, and a simple mathematical equation was found which was applicable to all the data. These findings, correlated with previous results, support the cathodic reaction mechanism theory previously presented.

Progress in dry cell technology for many years was based largely on empirical efforts since only meager fundamental data were available. The reaction,

$$Zn + 2NH_4Cl + 2MnO_2 = ZnCl_2 \cdot 2NH_3 + Mn_2O_3 + H_2O \quad [1]$$

was accepted as representative of the operation of a battery. Early experimental work in this laboratory (1) by French and MacKenzie resolved the cathodic portion of reaction [1] into two separate reactions. The first of these is the electrochemical reduction of Mn^{IV} to Mn^{II}, reaction [2]; the second is the chemical removal of Mn^{II} by further reaction with unused Mn^{IV} to form the Mn^{III} reduction product. From more recent findings (2), it appears that the chemical reactions at the cathode can be represented by two distinct types of chemical processes. Reactions [3] and [4], the "recuperation reactions," involve removal of the Mn^{++} produced by the primary reaction. These can be shown as follows:

$$MnO_2 + 4H^+ + 2e = Mn^{++} + 2H_2O \quad [2]$$

$$MnO_2 + Mn^{++} + 2(OH)^- = 2MnOOH \quad [3]$$

$$MnO_2 + Mn^{++} + 4(OH)^- + Zn^{++} = ZnO \cdot Mn_2O_3 + 2H_2O \quad [4]$$

Reaction [2] found an important application in the utilization test (3), a rapid means of evaluating manganese dioxide depolarizers on the laboratory bench. However, certain samples of depolarizers did not perform as well in experimental cells as results of the utilization test had indicated. It was obvious that some other factor limited the service of these particular depolarizers. An important example was synthetic pyrolusite prepared by the thermal decomposition of manganese nitrate (4). This material gave efficient depolarization in the utilization test, but its effectiveness in experimental cells was substandard. It seemed probable that the rates of the recuperation reactions might be critical for the group of samples. This paper presents the results obtained from a study of several depolarizer samples.

Experimental

To study the reactions between MnO_2 and Mn^{++}, a solution containing manganous chloride is reacted with solid manganese dioxide. The progress of the reaction is followed by observing the decrease in Mn^{++} concentration.

In first attempts to establish a satisfactory method of studying the rate of the recuperation reaction, it was found that an increase in temperature increased the rate of the reaction to such an extent that accurate temperature control in a thermostat became necessary. For example, one depolarizer sample studied at pH 7 was completely reduced to MnOOH at 35°C in about 8% of the time required at 21°C. This finding is in accord with the well-known observation that the electrical output of a dry cell on a standard flashlight test, such as 4 ohm HIF, is increased a considerable amount by an increase in temperature, such as given above, when other factors do not interfere with cell operation. Thus, cell performance at practical temperatures can well be limited by the recuperation reaction rate. Similarly, other factors, such as depolarizer type, electrolyte pH, etc., were found to be as important as the temperature in influencing the reaction rate. From this work, both technique and apparatus were finally selected for precise control of the variables.

[1] Present address: Riegel Textile Corporation, Ware Shoals, S. C.
[2] Battery Development Laboratory, Union Carbide Consumer Products Company, Division of Union Carbide Corporation, Cleveland, Ohio.

In conducting an experiment, approximately one mole of MnO_2 along with one-half liter of 2M NH_4Cl solution is introduced into the reaction vessel, a six-necked, three-liter flask. This mixture is stirred, and high-purity nitrogen is bubbled in for at least an hour. A second flask (serving as a reservoir) in the water bath contains a liter of solution 2M in NH_4Cl and 1.5M in $MnCl_2$. This also has nitrogen bubbled through it to purge the solution of dissolved atmospheric oxygen. The contents of the reservoir flask are allowed to equilibrate with the bath held constant within 0.5° and the *p*H is adjusted with concentrated NH_4OH to the proper value. The liter of solution is then pumped from the reservoir into the reaction flask by using a small pressure of nitrogen. A calomel half-cell and a glass electrode are suspended in the reaction mixture. These electrodes are connected to a L&N Speedomax recorder-controller which in turn controls an automatic pump. Since in the recuperation reactions hydroxyl ions are consumed, the pump injects a standardized quantity of NH_4OH into the reaction mixture when the *p*H falls below a predetermined value. By this method, the solution *p*H is automatically maintained within 0.3 of a *p*H unit.

During the course of the reaction, small samples of slurry are extracted and immediately centrifuged. The supernatant liquid is then put through a sintered glass filter. A 5 ml portion is retained for analysis. The quantity of Mn^{++} is determined by the method of Lingane and Karplus (5). From these values of concentration and the total volume of solution, the uptake of Mn^{++} can be obtained.

Discussion

It is well known that Mn^{++} reacts with manganese dioxide (6). It is also recognized by others that this reaction is important in the functioning of the dry cell (7). However, physicochemically the reaction has not been too well characterized and there appears to have been no work done on the kinetics of the reaction. Cowley and Walkley (8) have reported some work on this reaction in connection with the cause of the potential drift of manganese dioxide electrodes.

A study (9) has been conducted on the isotopic exchange in the MnO_2-Mn^{II} system. Although it is not definitely stated by Pullman and Haissinsky, the work in this laboratory suggests that they used acid solutions. They concluded that the exchange reactions occur much faster with precipitated oxides than with those prepared by the ignition of $Mn(NO_3)_2$. The latter were of the pyrolusite type.

The recuperation reactions are of a heterogeneous type in which a solid reacts with a solution to form an insoluble product on the surface of the original solid phase. As with all heterogeneous reactions, the problem of diffusion—or mass transfer—of the reactants to the reacting surface—or interface—imposes an additional limitation to the over-all reaction rate. Under certain circumstances, this diffusion may become rate controlling. As the reaction progresses at the solid surface, the surface area of the MnO_2 is diminished progressively. The new solid phase formed on the surface of the original solid can further significantly retard the diffusion of the reactants toward the reaction zone.

Interpretation of Results

Let Z define the total moles of divalent manganese consumed at any time t (in minutes) per mole of MnO_2 initially present. The moles of MnO_2 present at time $t = 0$ are readily calculated from the weight of the starting material and its "free MnO_2" [3] content, which is obtained by the usual methods of ore analysis. From Eq. [3] and [4], it is obvious that $Z = 1$ when the reaction is completed, provided the process is stoichiometric.

Representative data for electrolytic MnO_2 are shown in Fig. 1. Here Z is plotted as a function of time t (in minutes). During this experiment, the temperature was maintained at 43.95° ±0.05°C and solution *p*H held at 5.40 ±0.15. The experimental data may be represented quite well by the relation:

$$\frac{t}{Z} = \frac{t}{b} + \frac{1}{k} \qquad [5]$$

where b and k are constants selected by the conventional method of least squares.

By taking the limit as t approaches zero, it is seen that Z also approaches zero. At the other limit, as t becomes infinitely large, Z approaches b. Thus, b represents the maximum value of Z. If the reaction was stoichiometric and it went to completion, then b would be unity.

By differentiating once and with the proper substitutions, one obtains

$$\frac{dZ}{dt} = k\left(1 - \frac{Z}{b}\right)^2 \qquad [6]$$

Clearly, this is the rate expression for the process under conditions of constant temperature and *p*H, and with a given starting material. The constant k is the specific rate constant and dZ/dt is the instantaneous rate in terms of moles uptake of Mn^{++} per

[3] Free MnO_2 is the amount of MnO_2 in the depolarizer which is available to react electrochemically.

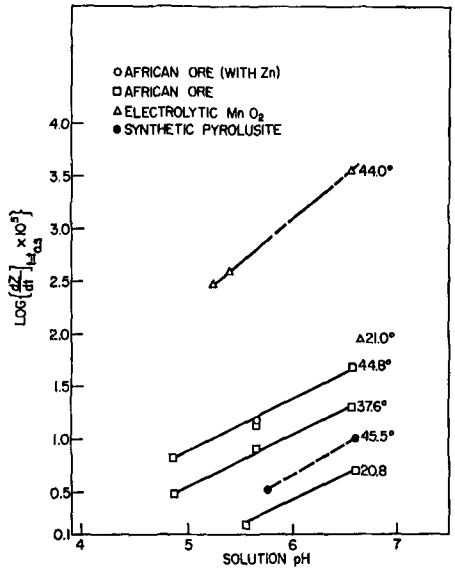

Fig. 1. Relationship of recuperation rate with time for electrolytic MnO_2.

Table I. Reaction rate constants and half-life values for several types of MnO_2

Type of oxide	Temp, °C	Solution pH	b	k	$\text{Log}\left\{\left[\frac{dZ}{dt}\right]_{t=t_{0.5}} \times 10^5\right\}$
African ore	44.80	6.56	0.755	0.00220	1.679
African ore	37.55	6.56	0.760	0.000926	1.310
African ore	20.90	6.60	0.510	0.000225	0.708
African ore	44.74	5.65	0.702	0.000556	1.140
African ore	37.55	5.65	0.625	0.000333	0.920
African ore	20.65	5.55	0.588	0.0000625	0.188
African ore	44.70	4.85	0.552	0.000272	0.826
African ore	37.55	4.85	0.395	0.000122	0.491
Electrolytic MnO_2	43.95	6.55	1.272	0.142	3.553
Electrolytic MnO_2	43.95	5.40	1.056	0.01613	2.605
Electrolytic MnO_2	43.95	5.25	1.007	0.01163	2.471
Electrolytic MnO_2	20.93	6.65	0.940	0.00741	2.268
Synthetic pyrolusite	45.32	6.60	0.996	0.000426	1.026
Synthetic pyrolusite	45.31	5.75	0.158	0.000133	0.522
Activated MnO_2	38.09	6.60	1.362	0.0263	3.410
Activated MnO_2	20.75	6.55	1.056	0.00400	2.294
Activated MnO_2	37.60	5.73	1.013	0.00833	2.342
Activated MnO_2	20.94	5.68	0.833	0.00120	1.398
Activated MnO_2	45.20	4.90	0.732	0.00152	1.522
Activated MnO_2	38.09	4.86	0.761	0.000435	1.082

mole of MnO_2 initially present per minute. When the reaction is half completed, that is, at the half-life ($t = t_{0.5}$), the instantaneous rate is one-fourth of k. For reasons pointed out later, the half-life rate $\left[\frac{dZ}{dt}\right]_{t=t_{0.5}}$ is a useful quantity in this study.

In Fig. 1, the t/Z values obtained in this experiment are plotted as a function of t. It is seen that, except for the initial readings, the data conform to a straight line well within the range of the experimental error. From Eq. [6], one sees that for any given finite time there is a finite, single value for the rate. At time zero, the rate is numerically equal to k and as time increases the rate becomes slower. As the time becomes infinitely large, the reaction approaches completion and the reaction rate tends toward zero. Thus, it is seen that Eq. [5] and [6] not only fit the experimental data but also possess the necessary qualities of a rate expression.

Equation [6] shows that the rate is proportional to the square of the fraction of unreacted MnO_2 that is present. The reaction might be considered to be second order with respect to this unreacted portion; however, the order of reaction is of little significance in a system as complex as that of MnO_2.

A number of manganese dioxide samples from different sources has been studied. These have been tested in the temperature range of 21°-45°C and within the solution pH interval of about 4.8-6.6. The values of temperature and pH are those which appear to be comparable to the ones found in actual dry cell testing. Further work showed that Eq. [5] served as the best mathematical representation of the data from experiments using all types of manganese dioxides studied. Thus, the equation has a general application to this kinetics problem.

Reaction rate as a function of temperature.—In Fig. 2, the logarithm of the rate at the half-life is plotted as a function of pH. The lines are isotherms. Starting materials were electrolytic MnO_2, synthetic pyrolusite, and African ore. Values of k, b, and the reaction rates at the half-life for electrolytic MnO_2, African ore, activated MnO_2 (10), and synthetic pyrolusite appear in Table I. For a given oxide, the vertical distance between the lines gives the change in the logarithm of the rate at the half-life with the change in temperature. Using the well-known Arrhenius equation, $k = se^{-\Delta H_a/RT}$, and the change in the rate with temperature variation, one can evaluate ΔH_a, the apparent energy of activation.

For three of the oxides studied, the values in kilocalories are:

Electrolytic MnO_2	26. ± ? kcal/mole
African ore	17. ± 4 kcal/mole
Activated ore	22. ± 4 kcal/mole

Although only one set of values was available for calculation of the apparent energy of activation of electrolytic MnO_2, the value is presented so that a general order of magnitude for the calculation is available for comparative purposes. The average value of about 20 kcal for the apparent energy of

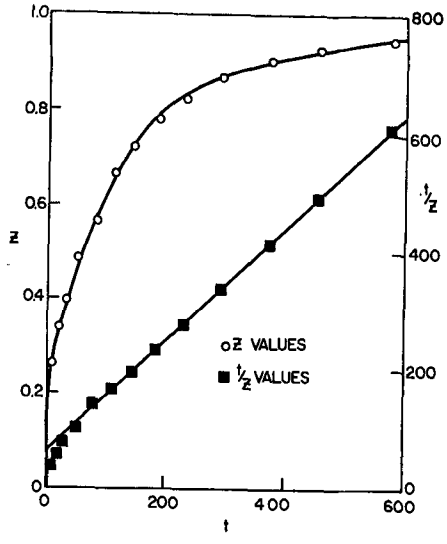

Fig. 2. Logarithm of the reaction rate as a function of temperature and solution pH.

activation confirms that the fundamental reaction involved is not under diffusion control (11).

It is likely that the lower the energy of activation, the more rapid is the reaction. On this basis, African ore, for which the lowest value is presented, should be the most active depolarizer. However, actual test and battery performance show African ore to possess the lowest recuperation reaction rate of this group of depolarizers. Therefore, we must conclude that the value of s in the Arrhenius equation, concerned with such factors as depolarizer surface area, crystal type and structure, particle size, etc., is important in influencing the recuperation reaction rates.

Reaction rate as a function of solution pH.—If one assumes a linear relationship and the fact that pH involves the logarithm of the hydrogen ion activity, one can show that

$$\left.\frac{dZ}{dt}\right]_{t=t_{0.5}} = K(OH^-)^m \qquad [7]$$

where K is a constant, m is the slope of the straight lines in Fig. 2 and (OH^-) is the hydroxyl ion concentration. Theoretically, the above would be correct for only one temperature and at constant mean ion activity coefficient. However, with the narrow temperature and pH ranges, Eq. [7] is no doubt a close approximation. The slopes of the lines for African ore are 0.49 ±0.01.

If the hydroxyl ion concentration in the bulk of the solution were the important factor, then from the chemical reaction, Eq. [3], one could suggest that the rate should be proportional to the square of the hydroxyl ion concentration. The data show that this is not the case. What is important is the concentration of the hydroxyl ions in the immediate vicinity—no doubt sorbed on the surface—of the MnO_2 particles. The concentration on the surface is, of course, influenced by the concentration in the bulk of the solution. This phenomenon of preferential ion adsorption is well recognized.

Reaction rate as a function of stirring speed.—With the particular experimental setup, it was found that changing the stirring speed from 480 to 390 rpm had no appreciable effect on the reaction rate. These values represent the useful range with the present apparatus. At stirring speeds below 390 rpm, the solid phase tends to form a mass in the bottom of the reaction vessel and hence is removed from the reaction system. With the plastic stirrer and the all-glass reaction vessel, it seemed unwise to increase the stirring speed much above 480 rpm. With this limited range of stirring speeds, however, it is doubtful whether the boundary regions of the particle would be changed and the diffusion varied to any extent.

Reaction rate as a function of oxide type.—A comparison of the reaction rates for the different oxides and the logarithm of the rate of recuperation reaction at the half-life (under conditions of 21°C and a solution pH of 6.5) are shown in Table II. As would be expected, a correlation exists between reaction rate and the general order of dry cell performance. In spite of the fact that there is a correlation, the true relationship between "rate" and "service" is no doubt complicated. On this account, it is considered unwise to attempt to predict the battery quality of manganese dioxide from recuperation rate measurements alone.

Table II. Reaction rate of representative MnO_2 samples at the half-life

Type of MnO_2	$\mathrm{Log}\left\{\left.\frac{dZ}{dt}\right]_{t=t_{0.5}} \times 10^5\right\}$
Activated ore	2.38
African ore	0.660
Synthetic pyrolusite	0.013
Electrolytic MnO_2	2.13

Reaction Mechanism

A plausible mechanism for this topochemical process has been proposed. In the absence of zinc, the chemical reaction is described by Eq. [3]. Before the reaction can occur, the reducing agent (Mn^{++}) and hydroxyl ions must first be adsorbed on the surface. After adsorption, the reduction of the MnO_2 occurs. At the site of reaction, a layer of Mn^{+++} oxide is formed. The x-ray diffraction pattern shows that this product is isostructural with the mineral manganite, MnOOH. Half of the mass of the material is formed by the reduction of the MnO_2 and the other half is produced by oxidation of the adsorbed Mn^{++}. A microscopic examination of the particles taking part in the reaction shows that the particles have actually increased in size. All four samples studied had approximately the same particle surface area of 0.20-0.50 m^2/g, even though the screen analysis showed differences in the per cent through the 200 mesh screen. Particle surface area is the term given to the total external area of all of the particles in a 1-gram sample and is calculated from settling rate curves.

At first, the MnO_2 particles are adjacent to the solution phase and the reaction goes fairly rapidly. Once the reaction has been initiated, the MnO_2 is separated from the adsorbed reactants by a layer, or film, of MnOOH. This layer offers a resistance to the reaction and the rate is slowed down. It has been shown that the rate is proportional to the second power of the fraction of remaining, unreacted MnO_2.

The reduction of the MnO_2 could be accomplished by the migration of hydrogen ions and electrons across the manganite barrier, going from the outermost surface toward the unreacted MnO_2. This process of an ion migration in manganese oxides has been recognized previously (12). These adsorbed divalent manganese ions lose an electron. They are thus oxidized to the trivalent state and are immediately precipitated as MnOOH. Under most conditions, the trivalent manganese ion is unstable.

The various oxides obey the same rate equation and they have the same characteristics, such as apparent energy of activation, of the same order of magnitude. It is thus concluded that all of these manganese dioxides react through the same mechanism. The slowest rate was that displayed by syn-

thetic pyrolusite. This can be attributed to the fact that pyrolusite has a lower oxidation potential than a more reactive form, such as electrolytic MnO_2. This so-called recuperation reaction is an oxidation-reduction process. The MnO_2 is the oxidizing agent and the divalent manganese is the reducing agent.

When zinc is present in solution as dissolved zinc chloride, the resultant reaction product is hetaerolite ($ZnO \cdot Mn_2O_3$) rather than manganite. It is probable that the zinc occurs in the solid phase by virtue of a coprecipitation process along with the Mn^{++} that becomes oxidized and precipitated. When the reaction product is hetaerolite, the reaction rate is about the same as in the absence of zinc. An example of this is shown in Fig. 2. It is highly possible that the hydrogen ions and electrons migrate more rapidly through a hetaerolite layer than through a barrier of manganite. It is conceivable that this by-product layer on the surface of the manganese dioxide particle could constitute a barrier to prevent the completion of the recuperation reaction. If this were true, it should result in a change in the slope of the observed reaction rate. At this time, we have seen no evidence for such interference.

Manuscript received Oct. 30, 1959. This paper was prepared for delivery before the Columbus Meeting, Oct. 18-22, 1959.

Any discussion of this paper will appear in a Discussion Section to be published in the June 1961 JOURNAL.

REFERENCES

1. H. F. French and A. A. MacKenzie, Unpublished work.
2. N. C. Cahoon, R. S. Johnson, and M. P. Korver, *This Journal*, **105**, 296 (1958).
3. N. C. Cahoon, *ibid.*, **99**, 343 (1952).
4. M. L. Kaplan, U. S. Pat. 1,287,041 (1917).
5. J. J. Lingane and R. Karplus, *Anal. Chem.*, **18**, 191 (1946).
6. W. Feitknecht and W. Marti, *Helv. Chim. Acta*, **28**, 129 (1945); O. T. Christensen, *Z. Anorg. Chem.*, **27**, 321 (1901).
7. H. F. McMurdie, P. N. Craig, and G. W. Vinal, *Trans. Electrochem. Soc.*, **90**, 509 (1946).
8. J. M. Cowley and A. Walkley, *Nature*, **161**, 173 (1948).
9. B. Pullman and M. Haissinsky, *J. Phys. Radium*, **8**, 36 (1947).
10. C. F. Burgess, U. S. Pat. 1,305, 250, June 3, 1919.
11. S.Glasstone, K. J. Laidler, and H. Eyring, "The Theory of Rate Processes" McGraw-Hill Book Co., Inc., New York and London (1941).
12. H. Strung, *Naturwiss.*, **78**, 89 (1943).

The Nitric-Hydrofluoric Acid Pickling of Zircaloy-2

M. A. DeCrescente,[1] P. F. Santoro, A. S. Powell, and R. H. Gale

Materials Development Laboratory, Nuclear Division, Combustion Engineering, Inc., Windsor, Connecticut

ABSTRACT

The dissolution of Zircaloy-2 has been studied in the temperature range 15.6°-37.8°C in unagitated and agitated hydrofluoric-nitric acid solutions. The dissolution rate was found to increase with HF concentration and agitation. The energy of activation for the Zircaloy-2 pickling process compares very well with the value for the unalloyed zirconium pickling process, 3.3 kcal/mole. The energy of activation does not depend on agitation.

Smith and Hill (1) studied the rate of dissolution of unalloyed zirconium in hydrofluoric-nitric acid mixtures using Zr^{95} as a radioactive tracer. They reported an energy of activation of 3.3 kcal/mole for the process. The pickling of Zircaloy-2 (1.45 w/o Sn, 0.133 w/o Fe, 0.044 w/o Ni, 0.08 w/o Cr) was studied by Friedl, *et al.* (2) in order to determine the safe limits of pickling bath operation. A value of 5.0 kcal/mole for the energy of activation was calculated from a temperature-dissolution rate study. Friedl postulated that (*a*) the differences in agitation used in the two studies may account for the observed differences in the temperature dependency of the dissolution rate, or (*b*) a real difference in the energy of activation existed. In the study carried out by Hill and Smith, the pickling rate of zirconium increased with stirring rate up to a point beyond which the rate remained constant. Their experiments were carried out on the "flat" part of the pickling rate-stirring rate curve. The pickling investigation by Friedl on Zircaloy-2 was carried out at a constant stirring rate, 100 rpm, presumably on the sloping part of the pickling rate-stirring rate curve. Both investigators agree that un-ionized hydrofluoric acid is the active etchant.

The work of Smith and Hill has established that the dissolution of zirconium is HF diffusion controlled and not adsorption or reaction controlled. The high energy of activation obtained by Friedl, if real and independent of agitation, would indicate that the alloying elements have provided a diffusion barrier less permeable to the HF. The work reported here was initiated (*a*) to resolve the effect of alloying constituents in the pickling of Zircaloy-2 and (*b*) to explain the variable results encountered in production pickling. The effect of hydrofluoric acid concentration, temperature, and agitation on the pickling of Zircaloy-2 in $HF-HNO_3$ mixture would be determined for this purpose.

Experimental

Vapor blasted reactor grade Zircaloy-2 specimens were degreased with ethyl alcohol, washed with a synthetic detergent, rinsed with demineralized water, and stored in a vacuum desiccator. The pickling was carried out in a 1-liter polyethylene beaker immersed in a constant temperature water bath

[1] Present address: CANEL, Middletown, Connecticut.

Table I. Pickling rates of Zircaloy-2 in unagitated solutions

Run*	°C	$\frac{1}{T°K} \times 10^3$	Vol % HF	Molarity[HF]	Pickling rate, mils/min	Pickling rate/[HF], mils/min
1	15.6	3.46	2.5	0.69	0.280	0.404
2	15.6	3.46	3.0	0.83	0.325	0.398
3	15.6	3.46	3.5	0.97	0.400	0.408
4	15.6	3.46	4.0	1.11	0.451	0.405
5	21.1	3.40	2.5	0.69	0.304	0.447
6	21.1	3.40	3.0	0.83	0.364	0.446
7	21.1	3.40	3.5	0.97	0.451	0.452
8	21.1	3.40	4.0	1.11	0.493	0.450
9	26.7	3.34	2.5	0.69	0.307	0.491
10	26.7	3.34	3.0	0.83	0.367	0.494
11	26.7	3.34	3.5	0.97	0.469	0.496
12	26.7	3.34	4.0	1.11	0.544	0.495
13	32.2	3.28	2.5	0.69	0.349	0.534
14	32.2	3.28	3.0	0.83	0.445	0.543
15	32.2	3.28	3.5	0.97	0.532	0.542
16	32.2	3.28	4.0	1.11	0.574	0.541
17	37.8	3.22	2.5	0.69	0.400	0.577
18	37.8	3.22	3.0	0.83	0.490	0.590
19	37.8	3.22	3.5	0.97	0.514	0.583
20	37.8	3.22	4.0	1.11	0.643	0.585

* Area = 0.0975 dm^2.

(±0.1°C). A preliminary study showed that the pickling rate was independent of area and vapor blast pretreatment (3). The temperature of the pickling solution was measured with a paraffin-coated thermometer. All specimens were pickled for 2 min in 700 ml of fresh solution prepared from C.P. reagents and deionized water just prior to use, rinsed 4 min, dried and stored in a vacuum desiccator until weight changes were determined.

Initially, the pickling was carried out in unagitated solutions (runs 1-20). In order to minimize local concentration and temperature effects, subsequent tests were carried out in solution, agitated by means of a polyethylene stirrer (Runs 27-32). Dissolution rates were measured over the hydrofluoric acid (Baker and Adamson reagent grade, 40 w/o) concentration range, 2.5 to 4.0 v/o. Forty v/o nitric acid (Baker Analyzed reagent grade, 70 w/o) was used in each case. These concentrations represent the composition of standard zirconium production pickling solution (2).

Results

Dissolution of Zircaloy-2 in unagitated solution.—Pickling rates were determined by measuring the change in weight of a Zircaloy-2 specimen after 2-min exposures to pickling solutions freshly prepared for each determination. Table I contains the pickling rates of Zircaloy-2 in unagitated HF-HNO_3 solutions.

The observed rates plotted against HF concentrations (40 v/o HNO_3) at 15.6°, 21.1°, 26.7°, 32.2°, and 37.8°C gave straight lines through the data.

Effect of agitation on pickling.—The dissolution of Zircaloy-2 in 3.5% HF-40% HNO_3 was studied at 21.7°C (71°F) at a series of stirring rates. A plot of these data appears in Fig. 1. The increase in pickling rate with stirring is characteristic of a diffusion-controlled mechanism.

A series of experiments were carried out in 3.5% HF-40% HNO_3 at a stirring rate of 500 rpm in order to determine if local temperature and concentration effects have any influence on the temperature dependence of the pickling rate.

The influence of agitation on the observed pickling rates can be explained as follows:

As the dissolution reaction proceeds, the concentration of reactants immediately surrounding the specimen in an unstirred solution may decrease below the bulk concentration, especially if the rate of diffusion of reactants to the specimen's surface is low. An apparent decrease in pickling rate results. Mixing serves to remove any concentration gradients which may be found. Also the temperature of the solution at the metal surface may increase above the bulk temperature if the heat of reaction is not effectively dissipated. An apparent increase in the pickling rate results. Although the two effects, diffusion and temperature, counterbalance each other it can be seen by comparison of the pickling rates in unagitated solution (Table I) to the rates in agitated solution that the temperature effect is the more important of the two. Mixing facilitates dis-

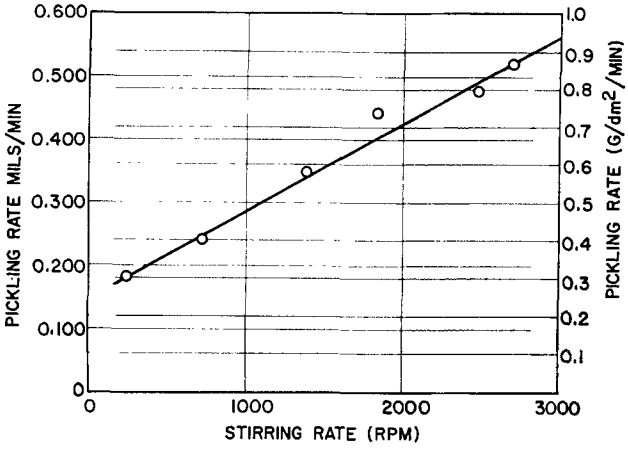

Fig. 1. Effect of agitation on pickling rate at 21.7°C

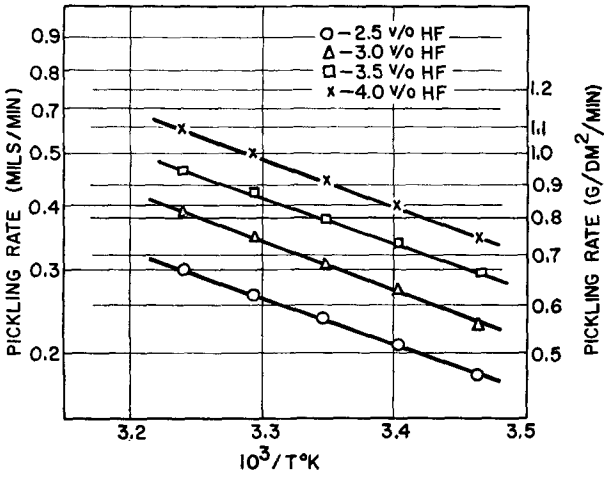

Fig. 2. Log of pickling rate vs. 1/T°K at 2.5, 3.0, 3.5, and 4.0 v/o HF, unagitated. ⊖ = 2.5 v/o HF; △ = 3.0 v/o HF; ⊡ = 3.5 v/o HF; X = 4.0 v/o HF.

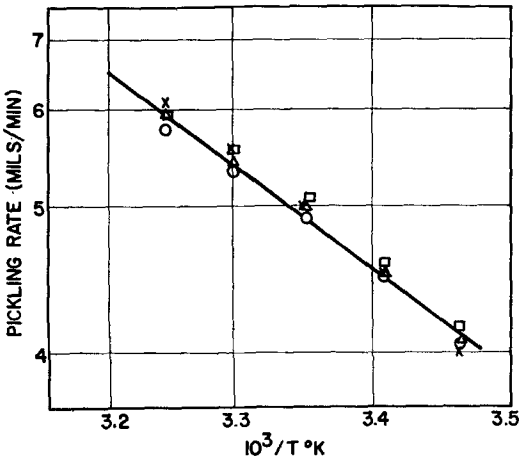

Fig. 3. Pickling rate per mole of HF, [pickling rate]/[HF] vs. 1/T°K, unagitated.

sipation of the heat of reaction and provides a uniform temperature throughout the bath.

Kinetic treatment.—A plot of pickling rate (mils/min) at 2.5, 3.0, 3.5, and 4.0% (unagitated solution) vs. reciprocal absolute temperature yielded straight lines (Fig. 2). Very close agreement of the slopes was observed and a value of 3.3 kcal/mole for the energy of activation of the pickling process resulted.

v/o HF	2.5	3.0	3.5	4.0
E_{act} (kcal/mole)	3.2	3.4	3.2	3.4

Under conditions of high acidity (HNO_3), all of the fluoride present exists as undissociated HF. The rate data obtained, therefore, were recalculated on the basis of HF concentrations, i.e., rate/[HF], and log rate/[HF] plotted against $1/T°K$ (Fig. 3). The four lines in Fig. 2 are resolved into one straight line. This behavior indicates that the rate of pickling of Zircaloy-2 is dependent only on the concentration of undissociated HF at constant tempera-

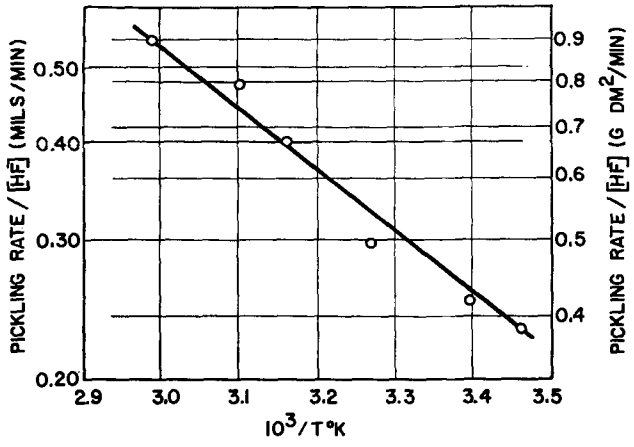

Fig. 4. Pickling rate vs. 1/T°K agitated

tures. Nitric acid does not directly take part in the pickling reaction but its presence insures complete association of HF.

When an Arrhenius plot was prepared from the pickling data obtained using agitated baths (500 rpm), an energy of activation of 3.6 kcal/mole resulted (Fig. 4). The agreement between the activation energies in the agitated and unagitated solutions is well within experimental error. It is evident from this agreement that the heat of reaction and the thermal properties, e.g., heat capacity, of the solution remain constant within experimental error in the temperature range studied.

The experimental energy of activation for the Zircaloy-2 pickling process, 3.2-3.6 kcal/mole, agrees quite favorably with the results of Smith and Hill (3.3 kcal/mole) obtained with pure Hf-free zirconium. A diffusion process identical to the one described for unalloyed zirconium must be postulated as the rate-controlling step.

It is apparent therefore that alloying zirconium with Sn, Fe, Cr, Ni does not alter the zirconium pickling mechanism. The permeability of the diffusion layer to HF is not affected by alloying. Neither can the high energy of activation observed by Friedl be attributed to the effect of stirring. It is interesting to note that the Zircaloy-2 used by Friedl had been rejected for pressurized water-reactor application because of stringer-like corrosion. The discrepancy in the energy of activation observed by Friedl *et al.* may be related to the stringer corrosion susceptibility of the material.

Manuscript received May 27, 1959.

Any discussion of this paper will appear in a Discussion Section to be published in the June 1961 JOURNAL.

REFERENCES

1. T. Smith and G. R. Hill, *This Journal*, **105**, 117 (1958).
2. E. B. Friedl, W. E. Berry, P. D. Miller, and F. W. Fink, BMI-1270, June 1958.
3. A. S. Powell and M. A. DeCrescente, Unpublished results.

Hydrogen Pickup in Various Zirconium Alloys during Corrosion Exposure in High-Temperature Water and Steam

Stanley Kass

Bettis Atomic Power Laboratory, Westinghouse Electric Corporation, Pittsburgh, Pennsylvania

ABSTRACT

The hydrogen pickup during corrosion in high-temperature water and steam of various binary and ternary alloys of zirconium with iron and tin has been studied. The total hydrogen content of specimens exposed to 400°C steam was found to be greater than that of specimens exposed to 360°C water. Furthermore, the per cent of theoretical hydrogen absorbed in the various alloys was markedly affected by the binary or ternary alloy addition. The per cent theoretical hydrogen absorbed by binary zirconium-iron alloys increased as the iron content was increased from 0.3 to 1.5 weight per cent (w/o) and the value for zirconium-tin alloys increased slightly as tin was increased from 0.5 to 0.9 w/o. The hydrogen pickup behavior of ternary zirconium-tin-iron alloys reflected the behavior of zirconium-iron binary alloys.

Several facts relating to the hydrogen pickup of zirconium alloys during corrosion in high-temperature water are known. Goldman and Thomas observed the amount of hydrogen pickup by zirconium exposed to degassed water is proportional to the amount of corrosion, and when corrosion testing is carried out in hydrogenated water, more hydrogen is picked up than when the corrosion medium is degassed water (1). The latter is believed to occur because more hydrogen is available for reaction in the hydrogenated water than is available only from the stoichiometric amount produced during the corrosion processes. Goldman and Thomas also noted that higher corrosion rates and higher hydrogen pickup rates occur in Zircaloy-2 as the initial hydrogen content of the metal is increased. Recently, workers at Battelle Memorial Institute, Columbus, Ohio, confirmed the observation that the amount of hydrogen pickup is proportional to the amount of corrosion (2). Previously reported experiments by Thomas and Kass showed that pre-oxidation of Zircaloy-2 in dry oxygen at 400°C has no effect on the 400°C steam corrosion kinetics (3). The interchangeability of the corrosion data obtained in both dry oxygen and steam indicates that the corrosion of Zircaloy-2 in 400°C steam is not associated with corrosion product hydrogen. On the other hand, it was observed that crystal bar zirconium exhibits spalling (breakaway) in high-temperature steam but not in dry oxygen, suggesting that hydrogen is in some way related to "breakaway" in the corrosion of zirconium.

Recent studies have determined the hydrogen pickup in Zircaloy-2 during corrosion for extended periods in high-temperature water and steam (4). These studies show there is a definite increase in the hydrogen content of Zircaloy-2 during corrosion testing and this hydrogen increase is independent of the initial hydrogen content, up to about 1000 ppm, after which the rate of hydrogen uptake rises sharply with increasing initial hydrogen content.

The studies described below were undertaken to determine hydrogen pickup in various binary and ternary alloys of zirconium with iron and tin during corrosion exposure in 360°C (680°F) water and 400°C (750°F) steam.

Experimental Procedures

Materials.—Fifteen-pound ingots were double arc-melted from high-purity tin, iron, and reactor-grade sponge zirconium[1] at the Bureau of Mines, Albany, Oregon. The ingots were forged and rolled at 788°C (1450°F) to 0.190-in. strip and then cold rolled with intermittent vacuum anneals at 788°C to 0.017-in. strip.

Experimental techniques.—Foils 1.5 x 4 x 0.017 in. were bright etched in an aqueous solution containing 39% HNO_3 and 3.5% HF at 100°F for sufficient time to remove 0.001 in. per surface. After washing and soaking in tap water for 6 to 8 hr to remove all residual etchant, the foils were rinsed in alcohol and air dried. Four foils from each ingot were degassed at 800°C for 48 to 72 hr in vacuum (less than 10^{-6} mm Hg). After degassing, the 1.5 x 4 x 0.015-in. foils were sheared into 0.5 x 0.5 x 0.015-in. specimens and submitted to corrosion tests in 360°C water at saturation pressure and in 400°C steam at 100 atm using methods and precautions outlined previously (5, 6). Weight gain measurements were made periodically. A minimum of two specimens per alloy were removed periodically from the corrosion test and were analyzed for hydrogen using the hot vacuum extraction method.

Experimental Results and Discussion

Tables I and II show the corrosion weight gains and total hydrogen contents of the various alloys after each of the exposure periods. (The contribution of the hydrogen uptake to the weight gain has been regarded as negligible; thus the weight gain

[1] Arc-melted reactor grade zirconium contains approximately 300 ppm iron, 20 ppm chromium, 20 ppm nickel, <10 ppm tin, <40 ppm nitrogen.

Table I. 360°C water test results

Alloy		Days of test 28	56	84	112	140	169	197
Zr	Weight gain, mg/dm²	10	23	64	121	165	210	277
	Hydrogen content, ppm	16	25	151	264	416	735	970
	% Theoretical H_2	19	21	23	31	50	40	47
Zr + 0.29% Fe	Weight gain, mg/dm²	15	25	24	42	42	52	76
	Hydrogen content, ppm	70	79	89	191	227	264	322
	% Theoretical H_2	32	26	34	50	55	53	49
Zr + 0.51% Sn	Weight gain, mg/dm²	10	19	24	36	61	80	158
	Hydrogen content, ppm	14	13	16	28	194	247	368
	% Theoretical H_2	8	5	5	7	20	21	21
Zr + 0.88% Sn	Weight gain, mg/dm²	9	21	81	139	188	234	298
	Hydrogen content, ppm	17	19	177	505	537		738
	% Theoretical H_2	30	9	21	28	22		26
Zr + 0.93% Sn 0.25% Fe	Weight gain, mg/dm²	11	21	18	28	38	47	55
	Hydrogen content, ppm	50	69	67	98	139	161	203
	% Theoretical H_2	32	25	46	34	39	39	38
Zr + 1.54% Fe	Weight gain, mg/dm²	20	37	36	61	68	74	87
	Hydrogen content, ppm	233	173	310	393	502	509	833
	% Theoretical H_2	80	54	88	69	72	71	101
Zr + 0.50% Sn 1.54% Fe	Weight gain, mg/dm²	21	42	42	58	70	78	91
	Hydrogen content, ppm	249	266	341	544	570	583	740
	% Theoretical H_2	96	65	74	84	79	63	74

value is considered being due solely to oxide film formation.) The tables contain an additional entry, per cent theoretical hydrogen which is defined as the ratio of hydrogen pickup in the sample to the stoichiometric amount of hydrogen produced by the corrosion reaction, $Zr + 2H_2O = ZrO_2 + 4H$.

Corrosion behavior.—Maximum corrosion resistance in 360°C water was shown only by the alloys which contain iron as binary or ternary additions. The unalloyed zirconium samples gained weight throughout the test and exhibited adherent oxide films. The addition of 0.5% tin to zirconium resulted in lower weight gains, but the 0.88% tin alloy yielded weight gains higher than unalloyed zirconium. The two iron binary alloys demonstrated an improvement in corrosion resistance. Furthermore, iron additions greatly improved the corrosion properties of zirconium-tin alloys.

The steam data further verified the noncorrosion resistant nature of unalloyed zirconium and zirconium-tin alloys. The addition of 0.5% tin delayed spalling from 42 to 56 days, but the 0.88% tin alloy

Table II. 400°C steam test results

Alloy		Days of test 14	28	42	56	70	84	98	112
Zr	Weight gain, mg/dm²	58	80	Spalled					
	Hydrogen content, ppm	186	630						
	% Theoretical H_2	46	87						
Zr + 0.29% Fe	Weight gain, mg/dm²	19	25	34	43	67	72	67	71
	Hydrogen content, ppm	92	133	125	128	209	181	194	
	% Theoretical H_2	54	51	38	29	28	22	28	
Zr + 0.51% Sn	Weight gain, mg/dm²	43	125	129	Spalled				
	Hydrogen content, ppm	184	547	747					
	% Theoretical H_2	36	45	38					
Zr + 0.88% Sn	Weight gain, mg/dm²	346	Spalled						
	Hydrogen content, ppm	760							
	% Theoretical H_2	24							
Zr + 0.93% Zn 0.25% Fe	Weight gain, mg/dm²	18	29	44	53	82	83	84	86
	Hydrogen content, ppm	85	151	151	178	204	205	205	
	% Theoretical H_2	47	43	32	34	25	25	26	
Zr + 1.54% Fe	Weight gain, mg/dm²	33	43	58	79	Spalled			
	Hydrogen content, ppm	258	354	402	418				
	% Theoretical H_2	82	79	80	57				
Zr + 0.50% Sn 1.54% Fe	Weight gain, mg/dm²	32	40	63	78	114	Spalled		
	Hydrogen content, ppm	320	433	460	504	758			
	% Theoretical H_2	82	92	70	56	50			

spalled between 14 and 28 days exposure. Small additions of iron were again observed to produce corrosion resistant material; however, the 1.5% iron alloy failed by spalling after 56 days of exposure. Beneficial effects on the properties of zirconium-tin alloys were also observed to occur with iron additions. The 0.25% iron alloy, with or without tin, exhibited the best corrosion resistance.

Hydrogen contents.—The total hydrogen contents of the various alloys are noted to increase with increasing corrosion exposure, and higher hydrogen uptakes are obtained at 400°C than at 360°C. (It should be noted that all specimens were initially degassed to approximately 2 ppm hydrogen.) In water, the unalloyed zirconium is seen to pick up the largest amount of hydrogen while the 0.93% tin-0.25% iron alloy exhibited the lowest total hydrogen content. In steam, very high hydrogen uptakes are noted. The addition of 0.5% tin produced essentially no change in the hydrogen pickup of unalloyed zirconium, but the 0.88% tin alloy showed a higher hydrogen uptake. Small additions of iron to zirconium or zirconium-tin alloys produced markedly lower total hydrogen contents. It is also noted that the hydrogen uptake of zirconium-iron alloys increases with increasing iron content.

Relationship between corrosion and hydrogen uptake.—Examination of the hydrogen pickup of the zirconium alloys during aqueous corrosion shows that there is an initial period in which the rate of hydrogen pickup decreases with time, followed by a period in which a new rate operates. This behavior is consistent with the corrosion reaction of zirconium and its alloys (hence, with the rate at which the hydrogen is produced) which is characterized by the relationship $W = kt^n$. It does not necessarily follow, however, that the hydrogen should be picked up at an identical rate because the hydrogen pickup process depends on many other variables including nature of the original film, alloy content and distribution, concentration gradient of hydrogen from the metal oxide interface to the center, rate of hydrogen diffusion at testing temperature.

If the 360°C weight change and hydrogen content data are plotted as functions of time on logarithmic scales, reasonably straight lines with the following slopes are obtained:

Alloy	Weight gain slope	Hydrogen slope
Unalloyed Zr	1.76	2.10
0.51% Sn	0.85 then 2.32	0.22 then 3.92
0.88% Sn	1.63	1.89
0.29% Fe	0.40 then 1.32	0.20 then 0.88
1.54% Fe	0.77	1.19
0.93% Sn + 0.25% Fe	0.45 then 0.55	0.35 then 1.34
0.50% Sn + 1.54% Fe	0.78	0.84

The corrosion slopes represent the exponent "n" in the equation relating weight gain and time. Thus, only the iron bearing alloys are seen to be corrosion resistant in 360°C water. High hydrogen slopes are associated with high corrosion slopes, indicating a relationship between corrosion and hydrogen pickup. If the hydrogen uptake behavior follows an exponential rate law, then equations of the form $H = Kt^{n'}$, where n' is the hydrogen slope, are to be expected. Remarkable similarity between the values of n and n' for each of the alloys is observed.

If it is assumed that the diffusion of hydrogen is a controlling step in hydrogen buildup, then parabolic relationship between hydrogen content and time is to be expected. A slope of 0.5, which indicates parabolic behavior, does not appear in these instances.

When the hydrogen data of the corrosion resistant alloys (those containing iron) are reviewed, it is apparent that the increase during the initial exposure period is great, then the hydrogen increase becomes smaller. The fact that hydrogen pickup decreases after the first exposure period requires an explanation. One possible mechanism is that the oxide film acts, in some way, as a barrier to the diffusion of hydrogen ions, protons, hydroxyl ions, to the metal-oxide interface. This suggests that the hydrogen pickup of samples oxidized in a nonhydrogenating medium subsequently transferred to a hydrogen producing medium should not show large increases in hydrogen content.

Factors influencing the behavior of ternary alloys.—The following analysis and comparisons were made in an attempt to observe whether the behavior in water and steam with respect to hydrogen pickup of the ternary alloys is directly influenced by the behavior of the component binary alloys. A more convenient way of examining the hydrogen absorption phenomenon during aqueous corrosion exposure is to express the amount of hydrogen picked up by the specimens as a function of the amount of hydrogen liberated by the specimens during corrosion. In this manner differences in the corrosion resistance of the alloys under study can be normalized.

Figures 1 and 2 summarize the behavior of the per cent theoretical hydrogen of the zirconium-tin and zirconium-iron binary alloys in 360°C water. The curve pertaining to the tin alloys initially shows a minimal value at approximately 0.5% tin. After prolonged exposure (greater than 112 days), no differences are observed between the 0.5 and 0.9% alloy. Different behavior is noted for the effect of iron. The per cent theoretical hydrogen increases with increasing iron concentration. It is thus apparent that iron contributes to the pickup of hydro-

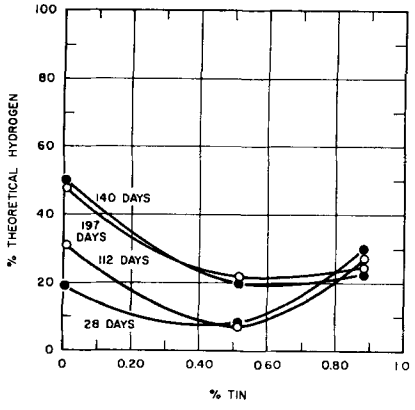

Fig. 1. Hydrogen pickup of zirconium-tin alloys in 360°C water.

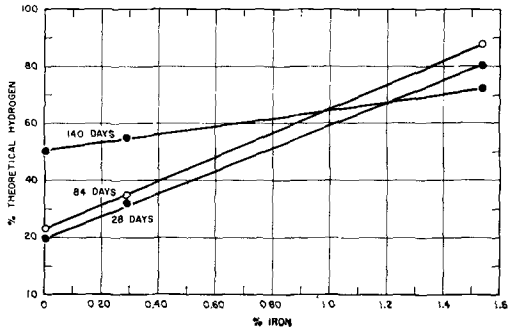

Fig. 2. Hydrogen pickup of zirconium-iron alloys in 360°C water.

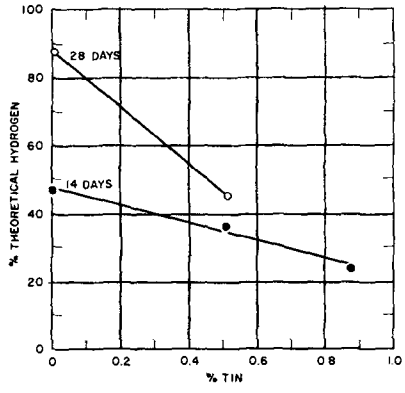

Fig. 3. Hydrogen pickup of zirconium-tin alloys in 400°C steam.

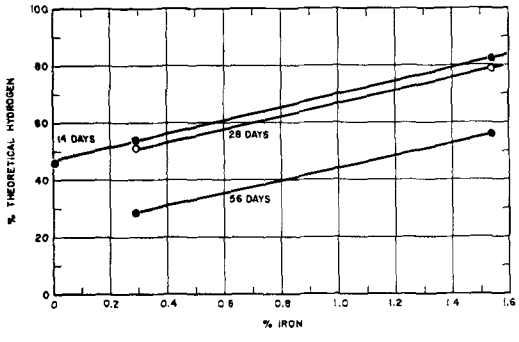

Fig. 4. Hydrogen pickup of zirconium-iron alloys in 400°C steam.

gen during water corrosion while the influence of tin is slight.

Figures 3 and 4 show the same alloys after exposure to 400°C steam. Although the data are very limited because of the low corrosion resistance of binary tin alloys, the per cent theoretical hydrogen is indicated to decrease with increasing tin content. The iron containing alloys show an increase in per cent theoretical hydrogen as the iron content is increased from 0.29 to 1.5 w/o. The higher iron concentration reproducibility exhibited higher per cent theoretical hydrogen after all test periods than the low iron alloy.

The manner in which the per cent of theoretical hydrogen varies with time for simultaneous tin and iron additions in 360°C water is shown in Fig. 5. It

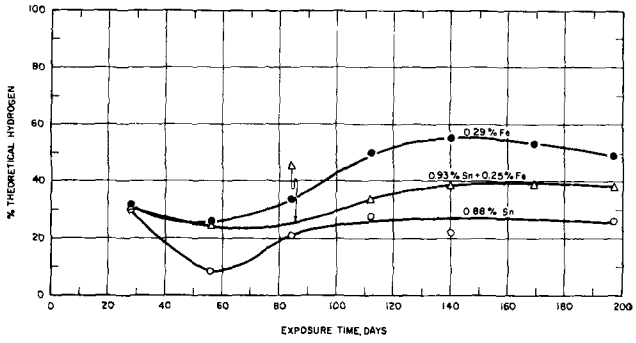

Fig. 5. Hydrogen pickup of zirconium—1% tin—0.25% iron alloy in 360°C water.

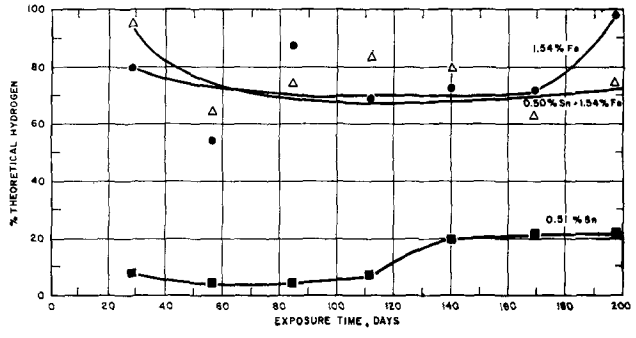

Fig. 6. Hydrogen pickup of zirconium—0.5% tin—1.5% iron alloy in 360°C water.

is observed that the ternary alloy shows per cent theoretical hydrogen between the values obtained for the tin and iron binary alloys. The tin binary alloy exhibits the lower value while the iron binary alloy exhibits a higher value.

Figure 6 shows similar summary plot of the alloys representing the 0.5% tin-1.5% iron alloy in 360°C water. Here it is noted that the ternary alloy clearly reflects the behavior of the binary iron alloy with respect to the pickup of hydrogen during corrosion exposure.

Acknowledgment

This work was performed and reported as part of Contract AT-11-1-GEN-14 granted by the United States Atomic Energy Commission.

Manuscript received Nov. 9, 1959.

Any discussion of this paper will appear in a Discussion Section to be published in the June 1961 JOURNAL.

REFERENCES

1. K. M. Goldman and D. E. Thomas, USAEC Report, WAPD-MM-184, 1953.
2. C. M. Schwartz and D. A. Vaugh, USAEC Report, BMI-1120, Aug. 1, 1956.
3. D. E. Thomas and S. Kass, *This Journal*, **104**, 261 (1957).
4. K. M. Goldman, S. Kass, W. W. Kirk, and D. E. Thomas, Unpublished Work, Bettis Laboratory.
5. B. Lustman and F. Kerze, "Metallurgy of Zirconium", Chap. 6, McGraw-Hill Book Co., New York (1955).
6. S. Kass, *Corrosion*, **106**, 2, (1960).

A New Explanation of Gas Evolution in Electrically Stressed Oil-Impregnated Paper Insulation

Z. Krasucki, H. F. Church, and C. G. Garton

British Electrical and Allied Industries Research Association, Leatherhead, Surrey, England

ABSTRACT

In void-free oil-impregnated paper, gas evolution starts at a critical stress which is markedly dependent on the degree of dryness of the paper. The gas first formed arises from decomposition of water in the cellulose, the nature of the impregnant having little effect. Subsequent more rapid gassing resulting from decomposition of the oil is a secondary process depending on ionization within gas bubbles previously formed. Study of the fundamental primary process suggests that water absorbed by the cellulose is ionized by electron bombardment in regions of high stress and is then decomposed electrochemically.

Although alternative materials are available, paper impregnated with an insulating liquid is still widely used as the insulation for high voltage cables and inductive windings or as the dielectric for capacitors where reliability under moderate temperature conditions and low cost are of importance.

If gas pockets within the stressed insulation are avoided, life under a-c stress is usually long. It is known however that in oil-impregnated paper, electrical discharges occur above a certain critical value of applied stress, E_i, even if the paper is so well impregnated that no voids are present initially. If the voltage be maintained at the discharge inception level, the discharges increase rapidly in magnitude, sometimes to several times the initial value within the first minute, and life may be very limited. E_i is directly dependent on the hydrostatic pressure on the oil, but when different makes of oil-impregnated paper capacitors were compared at the same internal pressure (normal atmospheric) mean values of E_i covering a range of 5:1 were observed. The cause of these large differences was not known. The effects of such factors as the density and type (rag or kraft) of paper, and the viscosity and iodine number of the oil, on discharge inception stress are relatively very small (1).

When observations on electrically stressed oil-impregnated paper are made under the microscope, the onset of discharges coincides with the sudden appearance of a gas bubble in the oil. A systematic study has been made to determine which part of an oil-paper dielectric gives rise to gas formation in the absence of initial gas bubbles, and to elucidate the mechanism of the process.

When electrical discharges take place within a gas bubble already present, they generate further gas through decomposition of the oil, and the bubble increases in size. This paper, however, is not concerned with the rate of gas production in oil once gaseous ionization has started; the latter phenomenon has been investigated extensively, is known to be dependent on the nature of the oil and the presence of additives, and gassing tests have been developed to assist in the selection of oils where they are required to withstand discharges.

The novel feature of the present work is the attempt to investigate the primary process of the formation of the first gas bubble.

The conditions under which gas could be evolved when oil alone was stressed were first investigated; afterwards a number of solid dielectrics, including capacitor paper, cellophane, polyethylene, polystyrene, polyethylene terephthalate, glass, and mica, were studied immersed in oil or other liquids.

Tests in Oil Alone

When oil is filtered completely free from particles and fibers and is not supersaturated with dissolved gas, gassing cannot normally be induced to take place by the application of electric stress using immersed metal electrodes without breakdown occurring simultaneously. The following exceptions to this are known.

(i) Gas evolution under stress has been reported at very low pressures even from degassed oil (2), but the origin of the initial gas phase is not known.

(ii) With one electrode in the form of an extremely sharp needle (radius 1 μ or less) and several millimeters spacing between the electrodes, localized intrinsic breakdown of the oil at the needle point, with gas evolution, is possible without general breakdown ensuing. With normal transformer and capacitor oils under these conditions, the gas bubbles produced move away from the point at such high velocity that they are difficult to observe. If, however, an extremely viscous liquid is used so that the products of the localized breakdown (carbon and gas bubbles) remain where they are formed, breakdown channels may gradually grow from the point and lead eventually to general breakdown. Tree-like conducting channels formed in this way in hexachlordiphenyl are illustrated in Fig. 1.

These exceptional methods of initiation of gassing are not believed to occur in normal oil-impregnated paper dielectrics, e.g., in capacitors and cables. First, these systems normally operate at near atmospheric

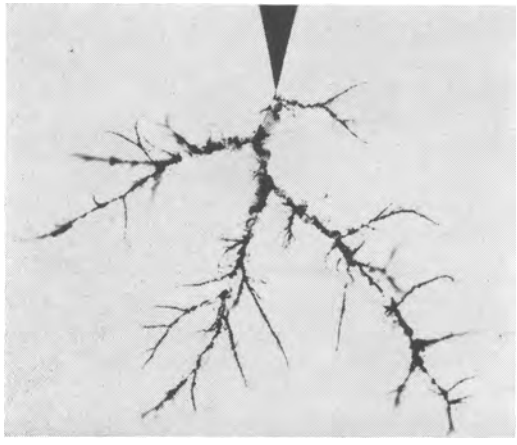

Fig. 1. Breakdown channels in hexachlordiphenyl

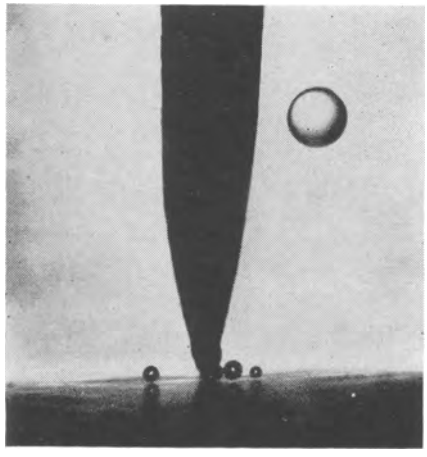

Fig. 3. Evolution of gas at the point of contact between a needle electrode and solid dielectric (cellophane).

or higher pressure. Second, the applied stress is usually insufficiently high for local intrinsic breakdown to take place except perhaps in the case of dielectrics containing abnormal conducting inclusions or other localized faults which would lead to failure on proof test. Gassing by the mechanism discussed later in this paper and consequent failure by the action of discharges usually occur at much lower electric stresses than those required for intrinsic failure. The observations reported here do however suggest how manufacturers can raise discharge inception stress of liquid-impregnated paper insulation and increase working stress.

Effects of Stress on Liquid-Solid Mixed Dielectrics

When moist cellulosic fibers bridge the gap between electrodes in oil, they give rise to gas formation at relatively low electric stress. Gas bubbles are formed only when the fibers form a continuous bridge between the electrodes, and evolution is then observed at points of contact between the fibers and the electrodes. Evolution of gas has also been observed at points where fibers touch one another in the electrode gap provided bridging occurred.

In an effort to understand the cause of this, various solid-liquid mixed dielectrics were studied, using thin sheet solid material and simple electrode forms.

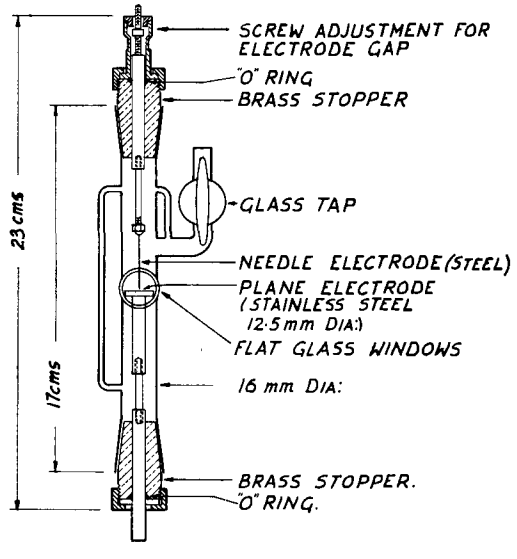

Fig. 2. Test cell

In the first experiments the sheet dielectric material to be tested was attached to the plane electrode of the test cell shown in Fig. 2. The other electrode was a needle of about 40 μ radius at the tip which could be moved relative to the plane electrode. The electrode gap could be observed with a microscope through optically flat windows. The cell was designed so that vacuum impregnation of the system with dielectric liquids could be effected, and tests if required could be carried out at reduced pressure. The following observations were made at atmospheric pressure:

(i) With the cell filled with filtered mineral oil no gassing was observed below the breakdown voltage so long as a gap existed between the needle and the solid dielectric attached to the plane electrode, whatever the nature of the solid.

(ii) With the solid insulation in the form of undried cellulose (cellophane or paper in equilibrium with ordinary room atmosphere) and the needle touching the solid, small gas bubbles were evolved continuously at the point of contact above a critical applied stress. Figure 3 shows gas evolution at the point of contact between the needle electrode and sheet cellophane immersed in mineral oil. The gas bubbles moved rapidly away from the needle and, in degassed oil, dissolved in a few minutes. The phenomenon was observed with both a-c and d-c applied stress but not necessarily at the same magnitude of stress. The onset of gassing coincided with "discharge inception" when the system was connected to a discharge detector.

(iii) The critical gassing stress increased with the state of dryness of the cellulose. With cellulose (paper or cellophane) which had been in equilibrium with air almost saturated with water vapor, gassing commenced at a stress of 6-7 v (peak) per micron. For cellulose exposed to ordinary room air (relative humidity say 65%), the critical stress was considerably higher (about 70 v/μ for two thicknesses of 10 μ capacitor paper) and this rose several times with further drying until with very dry paper or cellophane no gassing was observed below the breakdown stress (280 v/μ for two thicknesses of

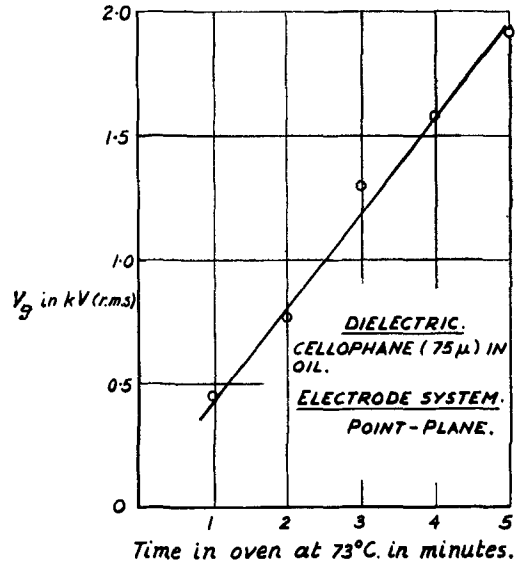

Fig. 4. Dependence of minimum voltage for gas evolution (V_g) on dryness of oil-immersed cellophane.

10 μ paper). The rather lower critical stresses observed in actual capacitors with moisture free paper dielectric are presumably due to the occurrence of sites with an enhanced local stress from conducting particles or thin places in the much larger area involved.

The effect of progressive oven drying on the voltage V_g at which gas evolution commenced at the needle electrode for cellophane of 75 μ thickness, previously exposed to atmospheric humidity, is shown in Fig. 4.

(iv) With solid dielectrics of relatively low water absorption, e.g., polyethylene, polystyrene, polyethylene terephthalate, polytetrafluorethylene, mica, and glass, no gassing was observed up to stresses approaching breakdown [in most cases 400-600 v (peak) per micron] even after long exposure to high humidity. Stresses which could be applied to these materials without gassing or breakdown occurring after exposure to almost 100% R.H. for periods of ½-1 hr are shown in Table I, which also includes gassing stresses for cellulosic materials which had been exposed to the damp atmosphere before immersion in the oil.

(v) Other materials of high water absorption, e.g., cellulose triacetate and gelatine, behaved like cellophane and paper, i.e., when damp gassing occurred at low stress, but the gassing stress increased with drying. Results for cellulose triacetate and gelatine in the damp condition are included in Table I.

(vi) Evolution of gas under electric stress from incompletely dried cellulose occurred when a silicone fluid, carbon tetrachloride, pentachlordiphenyl, or carbon disulfide was substituted for mineral oil, the minimum gassing stress being substantially unaffected by the change of immersion medium. Carbon disulfide is especially interesting in that it is not expected to yield gaseous decomposition products. The gas bubbles must therefore arise from the solid or its contained moisture.

Since the voltage at which gas is evolved from oil-impregnated cellulose increases with increasing dryness of the cellulose, it should be possible to increase the discharge inception voltage of an oil-impregnated paper capacitor by special attention to the drying of the dielectric. Measurements were therefore made of resistivity and discharge inception voltage on samples of rag paper (40 μ thickness) dried to different degrees. Vacuum dried paper was allowed to regain moisture to the required degree and immediately immersed in oil and assembled into a small capacitor with aluminum electrodes under the oil. The electrodes were flat foils 6 μ thick, pressed on to the dielectric the area of which was 4 cm^2. A-C discharge inception voltages were measured with a detector sensitive to 0.5 p coulomb. The results are shown in Fig. 5 where discharge inception stress E_i is plotted as a function of resistivity of the impregnated paper. E_i increased with increasing resistivity by a factor of 4 between paper in equilibrium with room atmosphere and "dry." The resistivities shown in Fig. 5 are considerably lower than corresponding resistivities for ordinary rolled paper capacitors. This is due to the tight clamping employed in the present tests which gave a more intimate contact with the paper.

Table I. Evolution of gas from solid dielectrics which had been exposed to damp atmosphere

Substance	Thickness, μ	Behavior under electric stress	Gassing stress, v (peak)/μ
Polyethylene	45	No evolution of gas bubbles at voltages up to the breakdown voltage 3.4 kv (peak)	>76
Polystyrene	12	No evolution of gas bubbles at voltages up to 7 kv (peak)	>580
Polyethylene terephthalate	12	No evolution of gas bubbles at voltages up to 4.7 kv (peak)	>390
Polytetrafluorethylene	17	No evolution of gas bubbles at voltages up to 7 kv (peak)	>410
Mica	10	No evolution of gas bubbles at voltages up to the breakdown voltage 5.4 kv (peak)	>540
Glass	150	No evolution of gas bubbles at voltages up to the breakdown voltage 10 kv (peak)	>67
Capacitor paper	10	Evolution of gas bubbles at about 70 v (peak)	7
Cellophane	75	Evolution of gas bubbles at 420 v (peak)	6
Cellulose triacetate	30	Evolution of gas bubbles at about 570 v (peak) (BDV = 2.46 kv (peak))	19
Gelatine	33	Evolution of gas bubbles at 280 v (peak)	7

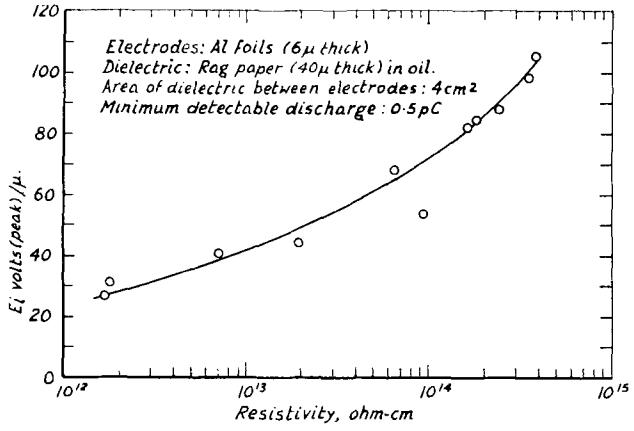

Fig. 5. Variation of discharge inception stress (E_i) with resistivity of oil immersed paper.

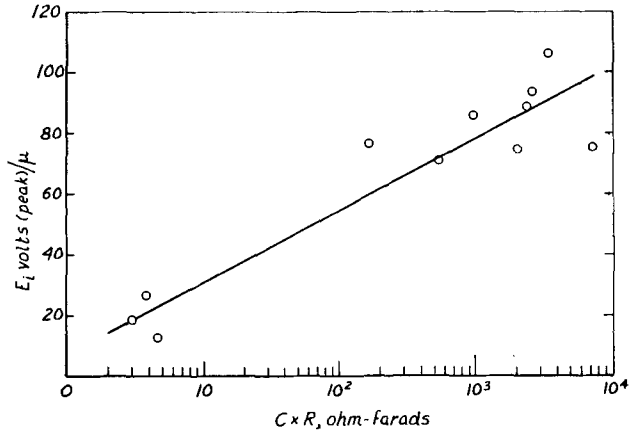

Fig. 6. Dependence of discharge inception stress (E_i) of kraft paper capacitors (C = 0.02μ F) on C x R.

In addition to the above tests on clamped plate capacitors, some normally wound 0.02 μF kraft paper units (4 paper layers x 10 μ) were impregnated in the laboratory with capacitor oil. The insulation resistance was varied by vacuum drying the units to different degrees before impregnation. Only a few tests have been made so far, but the results shown in Fig. 6 indicate that the more thorough the drying process the greater is the E_i value of the capacitor. Although precise measurements of moisture content of the paper dielectric of these capacitors were not made, these results and others suggest that E_i increases from 15 to more than 100 v (peak) per μ as moisture content decreases from a few per cent to to less than 0.1%.

Discussion of Results

The observations reported here strongly suggest that the gas initially generated in electrically stressed paper impregnated with a dielectric liquid is derived from water contained in the cellulose. Provided gas bubbles are not present initially, the threshold value of stress for gassing at normal pressures is low only with impregnated materials containing an appreciable amount of absorbed moisture, and is increased by drying. The gas observed is not water in the vapor phase formed, say, through local heating at points of contact between the electrodes or conducting inclusions and the cellulose; bubbles of steam produced in this way would condense in a small fraction of a second, contrary to the observed life of the bubbles of several minutes.

Water in liquid form can be electrolyzed readily into its constituent gases at a frequency of 50 cps at suitable current density. Experiments, in which the gas evolved from moist electrically stressed paper under an insulating liquid was collected, also showed that an explosive mixture of hydrogen and oxygen was formed from the water with both d-c and a-c (50~) voltages, although under mineral oil some of the oxygen may be absorbed immediately by oxidation of the oil. The average leakage current density through an oil-impregnated paper capacitor, however, is insufficient to account for the observed rate of gas evolution at the discharge inception stress on the basis of electrolysis of the water (3), unless some mechanism exists to cause a great increase in current in a few very small areas where abnormal stresses are present. Such a local enhancement of conductivity cannot be explained by moisture movement toward high stress regions; theoretical considerations based on energy of sorption of water in cellulose rule this out as a major effect even at stresses of the same order of magnitude as the intrinsic strength of cellulose. Experimental results have confirmed this.

Tests performed on paper in various states of dryness show however that its conductivity increases very greatly as the breakdown stress is approached especially when it is moist. Figure 7 shows the effect of varying the d-c measuring voltage on the resistivity of 28 cm² areas of kraft capacitor paper 20 μ thick (2 x 10 μ layers) after conditioning in various atmospheres. The observed great increase in conductivity of cellulose containing moisture at high stresses may be a consequence of electron emission from the electrodes, the electron bombardment of

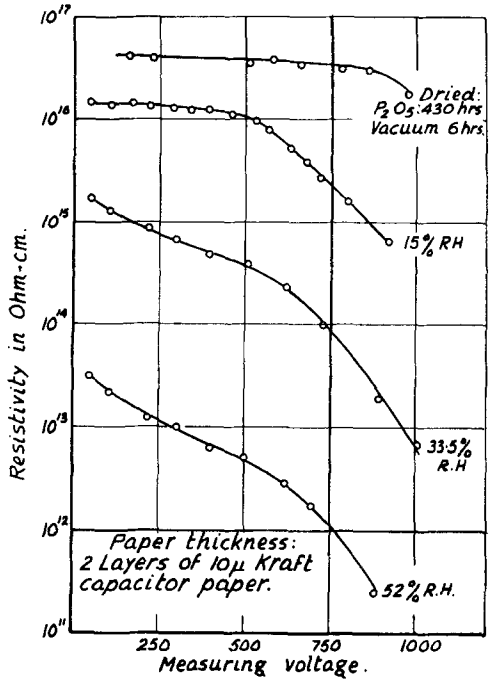

Fig. 7. Effect of measuring voltage on resistivity of paper in various states of dryness.

the cellulose causing dissociation of the bound water molecules. Although the maximum applied stress in Fig. 7 is only 0.5 mv/cm, locally it may be several times higher due to stress concentration at the edges or at any microscopic irregularities on the electrodes, and because of variations of thickness of the paper and the presence of conducting inclusions. Stresses of more than 1 mv/cm would certainly be sufficient for electron emission.

It is possible therefore that gas evolution in a capacitor commences at local points of stress concentration, say near the site of a conducting inclusion in the paper or at electrode edges, where the resultant high degree of dissociation of the water would lead to rapid electrolysis.

Such a mechanism would explain why discharge inception stress in oil-impregnated paper capacitors is not greatly affected by time of application of d-c stress or frequency of a-c stress and is little dependent on temperature which has a very considerable effect on leakage current at working stress. In a well sealed capacitor, temperature may have an indirect effect on discharge inception stress by causing a change of pressure, but at constant pressure the effect of temperature is small. It is clear therefore that a simple electrochemical mechanism based on average currents at working stress is inadequate, but that an explanation involving electron emission at high stress is in agreement with experimental observations.

The practical value of this work is that it demonstrates the importance of very thorough drying of oil-impregnated paper insulation if the highest possible working stress is required.

Acknowledgment

The authors wish to thank the Director (Dr. H. G. Taylor) and the Council of the British Electrical and Allied Industries Research Association for permission to publish this paper.

Manuscript received Feb. 15, 1960. This paper was prepared for delivery before the Philadelphia Meeting, May 3-7, 1959.

Any discussion of this paper will appear in a Discussion Section to be published in the June 1961 JOURNAL.

REFERENCES

1. P. Cucka, Electrical Research Association Technical Report Ref. L/T356, 1957.
2. H. Basseches and M. W. Barnes, *Ind. Eng. Chem.*, **50**, 959 (1958).
3. H. F. Church and C. G. Garton, *Proc. I.E.E.*, **100**, IIA, 111 (1953).

ZnS:Cu, Cl and (Zn, Cd)S:Cu, Cl Electroluminescent Phosphors

A. Wachtel

Research Department, Westinghouse Electric Corporation, Bloomfield, New Jersey

ABSTRACT

Procedures for the preparation of ZnS:Cu,Cl and (Zn,Cd)S:Cu,Cl EL[1] phosphors are based on firing in an atmosphere containing elementary S. Cl-incorporation is controlled by firing in capped silica tubes or in open boats in a current of $N_2 + S_2Cl_2$. Dependence of brightness on activator concentration is established on the basis of presumably constant excess Cu as Cu_2S. The use of Pb was found to be disadvantageous. Introduction of Cd causes formation of the hexagonal phase and a (Cu,Cd)S compound and simultaneous decrease of electroluminescence brightness as well as dependence of electroluminescence emission color on Cd concentration. A two-step firing procedure is given by means of which this effect may be partially avoided.

This paper deals with efforts to improve the brightness and maintenance of blue and green emitting EL phosphors, as well as attempts to prepare phosphors emitting at longer wave lengths by means of partial substitution of Zn by Cd. While a considerable amount of data on the preparation of ZnS:Cu, Cl EL phosphors has appeared in the literature (1), the experimental procedures used in the present study are based on those developed by Lehmann (2). These may be summarized as follows:

1. The highest EL output is obtained for compositions prepared with only ZnS, Cu, and Cl and preferably excluding other cations such as Pb.

2. A considerable improvement of the phosphor is obtained by firing in an atmosphere containing elementary S. It is believed that this improvement is due to reduction of the number of S-vacancies and consequently deep traps which otherwise tend to form.

The second point necessarily implies that the addition, or presence after firing, of ZnO is detrimental. This is contrary to data first obtained by Destriau (3) and then by a number of workers in the field [a review as well as original data have been published by Wendel (4)]. An explanation may be offered in terms of a model for the EL excitation mechanism as proposed by Lehmann (5) according to which electrically conducting inclusions in ZnS crystallites similar to the Cu-rich surface layers proposed by Zalm, Diemer, and Klasens (6) and by Zalm (7) provide sufficient local intensification of the applied field. Accordingly, either ZnO or Cu_2S may play such a role. Lehmann, has shown experimentally that Cu_2S is preferable.

[1] Electroluminescence or electroluminescent is hereafter abbreviated EL.

Experimental Techniques

Unfired mixes were prepared by slurrying pure ZnS (RCA No. 33Z19) with aqueous solutions of $Cu(C_2H_3O_2)_2 \cdot H_2O$ and NH_4Cl, followed by drying, addition of S and remixing. Firing was usually done in 10 g quantity of material filled into transparent silica tubes, 75 mm long, 15 mm ID, and 17 mm OD, closed at one end and capped with similar tubes 18 mm ID and 20 mm OD. Several such tubes could be arranged in a larger silica tube near its closed end and protected with an atmosphere of purified N_2 in the usual manner. All fired phosphors were washed in NaCN solution followed by H_2O and alcohol, and were then dried and screened.

EL-brightness readings were performed with a Spectra Brightness Spot Meter,[2] using a demountable cell filled with 40% (by volume) suspensions of phosphor in castor oil. Since small geometrical deviations of the cell assembled at different times could not always be avoided, the effective field strength across the phosphor layer was standardized by operating the cell at a voltage such that a standard phosphor (also included) had a predetermined brightness.

ZnS:Cu, Cl Phosphors

Mechanism of Cl incorporation.—The amount of Cl incorporated at a given concentration of Cu was estimated in a relative but sensitive manner by visual comparison of the blue-green hue of emission of the fired phosphor. Preliminary investigations indicated that the Cl content decreases with increasing batch size and increases slightly with firing time and the volume of the firing container used, so long as this volume is small enough to permit the phosphor mix to be surrounded by a saturated atmosphere of its own thermal decomposition products. For larger sample sizes fired, an empirical relationship

$$\%\mathrm{Cl} = x(0.97 + 0.003 \text{ g ZnS})$$

was found to result in equal emission color, where x is the amount of Cl added to a 10-g sample.

The observations suggested that, during the initial stages of firing, thermal decomposition releases substantially all of the added Cl to the atmosphere. As the firing proceeds this Cl is subsequently absorbed at a slower rate. The sulfur added appears to decrease strongly the Cl incorporation inasmuch as it causes a shift in emission to shorter wavelengths (8), i.e., in favor of the blue emission band. This may be compensated for by higher Cl additions such as presently described.

The EL brightness was found to reach a broad maximum for firing temperatures in the neighborhood of 950°C. Singly fired phosphors were usually characterized by nonhomogeneous Cl content, i.e., a mixture of more bluish and more greenish emitting portions. Grinding and refiring with no additions other than S always resulted in homogeneous, brighter, and more reproducible phosphors. During the refiring, about 30% of the incorporated Cl is lost, which must be compensated for in the initial unfired composition, since after firing the rate of Cl incorporation is strongly reduced. Firing times of 1.5 hr were found to result in equilibrium conditions.

Activator concentration.—An EL ZnS:Cu, Cl phosphor is known to require the presence of a high concentration of activator sites (9, 10) whose formation is, for present purposes, assumed to be a function of coactivator (Cl) incorporated, so long as the molar concentration of Cu appreciably exceeds that of Cl. The performance of an EL phosphor depends, however, not only on the amount of incorporated (at least partially charge-compensated) Cu, but also on the conducting phase of Cu_2S whose formation depends on, and is a function of, the presence of excess Cu during the firing process.[3] Conditions for keeping this constant and at a near-optimum value were empirically determined for 10-g quantities fired to obey the relationship

$$\text{mole \% Cu} = 0.55 + 0.45 \text{ mole \% Cl}$$

Under present conditions, the sintering of the phosphor appears to be determined entirely by the amount of excess Cu_2S formed, so that a rapid, although approximate and only relative, estimate of excess Cu concentration could be made in this manner.

Phosphors prepared with Cl additions up to 30 mole % and corresponding additions of Cu showed approximately equal sintering. Figure 1 shows the EL brightness obtained at two frequencies over a portion of this range of compositions. The fact that an EL output appreciably higher than zero is noted for no Cl addition may be explained by a small Cl content of the raw materials, and the brightness found at this point was noted to be quite variable, depending on the particular lot of ZnS used. The similarity of the curves to the dependence of brightness on Al addition as noted by Froelich (11) is quite evident. It is also interesting to note that compositions resulting in maximum EL brightness are such that about 25% of the added Cu is retained after NaCN washing, which is the same figure reported by Froelich (12) for ZnS:Cu, Mn phosphors fired at 1100°C in H_2S. The practical aspects of these results are presented in more detail in a recent

[2] Photo Research Corp., Hollywood, Cal.

[3] NaCN-washed EL phosphors show an increase in green/blue ratio of emission and lose most of the EL when refired at the original firing temperature (950°C).

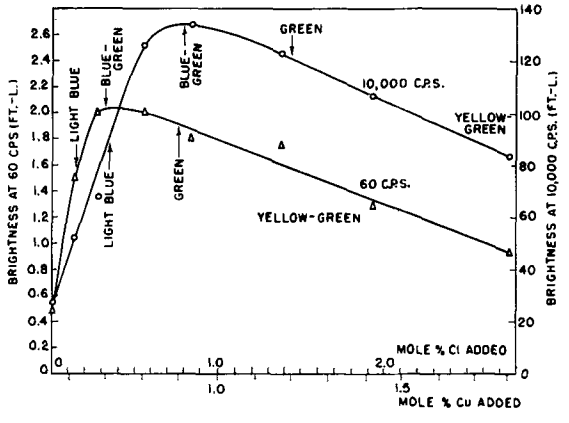

Fig. 1. Brightness of ZnS:Cu, Cl phosphors fired with 5 wt % S at 950°C, 2 x 90 min, as a function of activator addition. The Cl additions specifically refer to 10-g quantities fired in silica tubes of 13.5 ml volume.

Table I. Typical activator additions and retained concentrations (in mole %) for 10-g batches of ZnS, fired at 950°C—2 x 90 min

	Light blue	60 cps green	10,000 cps green
Cu added	0.62	0.71	0.89
Cu retained after NaCN washing	0.033	0.105	0.50
Cl added	0.14	0.34	0.75
Cl retained	0.095	0.16	0.32

patent (13). Table I shows typical values of Cu and Cl found by chemical analysis of NaCN-washed phosphors designed for light blue emission, as well as maximum brightness at 60 and at 10,000 cps excitation, respectively.

Effect of Pb.—Because of the frequent use of Pb (15) in the preparation of EL phosphors, its effect was also investigated. Table II shows the results obtained, where the first three samples (except for S) represent a composition obtained by averaging a number of representative formulations described in the patent literature. Samples 4, 5, and 6 differ only in the use of extra NH_4Cl, so as to compensate for the effect of Pb which consists of volatilizing excess Cl as $PbCl_2$.

In samples 7, 8, and 9, an attempt was made to duplicate present compositions, except that Pb was also used which, in turn, required higher Cl additions so as to maintain a blue/green hue of emission color similar to that presently representing optimum activation incorporation. Sample 10 is a normal control phosphor prepared without Pb.

It can be seen that in all cases the use of Pb resulted in a strong reduction of EL as compared to the control. Since the use of 5 mole % Cl alone would result in a nearly 100% coactivated and almost non-EL phosphor, any advantages of the use of Pb, as observed by others, is probably restricted to cases where raw materials with high Cl content were employed.

Effect of ZnO.—Figure 2 shows the effect of increasing additions of ZnO to compositions designed either for 60 cps or for 10,000 cps excitation. The initial slight increase in brightness lies within the reproducibility of phosphor preparation and measurements.

The presence of ZnO results in an effect similar to an increase in Cl addition. Most of the S added

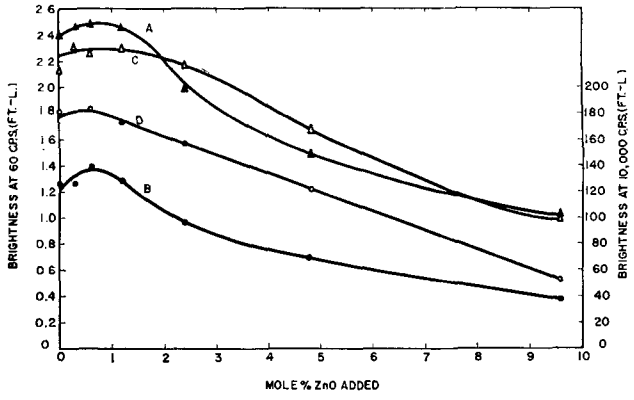

Fig. 2. Brightness of ZnS:Cu, Cl phosphors with activator additions designed for 60 cps and for 10,000 cps excitation, respectively, as a function of ZnO added before firing. A, 60 cps phosphor excited at 60 cps; B, 60 cps phosphor excited at 10,000 cps; C, 10,000 cps phosphor excited at 60 cps; D, 10,000 cps phosphor excited at 10,000 cps.

evaporates before reaction with ZnO can occur; the remainder, however, may react with ZnO and can no longer decrease incorporation of Cl. Moreover, Kröger and Dikhoff (14) have shown that oxygen itself causes preferential association with Cu and has a definite solubilizing effect. Since the decreased brightness observed may therefore be interpreted as merely a departure from optimum final activator and Cu_2S concentrations, a number of phosphors were prepared with about a tenth of the usual additions of Cl so as to match the green/blue ratio of emission of normal phosphors. The best results obtained were, however, only about one-third of the output normally obtained at 60 cps, while at 10,000 cps the EL was comparatively negligible. Similarly poor results were obtained by firing phosphors without free S, even in the absence of ZnO.

Effect of alkali chlorides.—The incorporation of Cl, although subject to the parameters described above, appeared to be independent of its form of addition, so long as no extraneous cation is included. On the other hand, the addition of Cl in the form of alkali chlorides as originally reported by Beutler and Prener (16) results in a shift in emission color to the blue.[4] With increasing atomic weight of the cation, the shift becomes more pronounced. The

[4] On the basis of enough Cl to result in green emission color if introduced as NH_4Cl, $ZnCl_2$, or HCl. Otherwise, there is, of course, no color shift.

Table II. EL response obtained with various compositions containing Pb

Sample No.	Composition in mole % before firing: ZnO	$1/3\{\frac{Pb(OH)_2}{2PbCO_3}$	$PbCl_2$	$Cu(C_2H_3O_2)_2 \cdot H_2O$	NH_4Cl	S	Fluorescence emission color	EL brightness: 60 cps	10,000 cps
1*	7.2	0.28	—	0.085	—	—	Green-blue	0.15	2.0
2	7.2	0.28	—	0.085	—	15	Blue	0.05	2.5
3	7.2	0.28	—	0.085	—	15	Blue-green	0.10	3.4
4	7.2	0.28	—	0.085	0.84	15	Blue	0.30	5.6
5	7.2	0.28	—	0.085	5.5	—	Green-blue	0.20	5.8
6	7.2	0.28	—	0.085	5.5	15	Green-blue	0.30	6.4
7	—	—	0.28	0.77	5.0	—	Yellow-green	0.60	20.0
8	—	—	0.28	0.77	5.0	15	Green	0.20	25.0
9	Sample No. 8 refired with 15 mole % S only						Green	0.80	45.0
10	—	—	—	0.77	0.75	15	Blue-green	3.0	180.0

* Fired in open boat in current of N_2. All other samples are fired in capped tubes.

Table III. Effective Cl retention in mole % estimated by emission color of ZnS fired with 0.75 mole % Cu and 2.75 mole % Cl added as alkali chlorides

HCl	LiCl	NaCl	KCl	RbCl	CsCl
1.25*	0.32	0.12	0.10	0.07	0.055

* On the basis that about 45% of the added Cl is incorporated. Actually, this would require at least 1.25 mole % Cu addition.

mechanism whereby this occurs has not been ascertained but seems to resemble the Cl-gettering action of K_2CO_3 as described by Ranby (17) and could be interpreted either as decreasing incorporation of the chloride due to decreasing solubility of the K-salt in the ZnS lattice, or decreasing association of chloride with Cu activation sites (18, 19) due to increasing association of the Cl with the alkali metal ions. The effect is, of course, noticeable only at Cu concentrations well above those normally employed in photoluminescent phosphors. Table III shows the results of adding 2.75 mole % Cl as alkali chlorides to ZnS with 0.75 mole % Cu, where the effective Cl concentration of the fired phosphors was estimated on the basis of emission color. With the exception of the values for Rb and Cs which are very uncertain due to the difficulty of comparing deep hues, the points may be plotted as a straight line of log Cl vs. log atomic weight of the cation.

The EL output of the blue-emitting phosphors (such as those fired with KCl) does not differ significantly from normal blue-emitting ZnS:Cu, Cl prepared without KCl but with a sufficiently low addition of NH_4Cl. The output of the greener-emitting phosphors fired with NaCl and LiCl is, however, considerably poorer. It may be noted that the emission color of the phosphor fired with LiCl matches that of a normal EL phosphor fired with 0.75 mole % NH_4Cl (optimum for 10,000 cps excitation) while the EL brightness is only about 60% of such a control sample.

It was interesting to observe that high concentrations of KCl also inhibit the effective incorporation of additional Cl added in an "available" form (i.e., as NH_4Cl, $ZnCl_2$, etc.) to the extent that for each mole per cent KCl present, about 0.5-0.75 mole % NH_4Cl is required to shift the emission color from blue to green. Here again, however, green-emitting phosphors prepared in this manner are characterized by very poor output.

The effect of KCl on maintenance of output during operation is particularly pronounced. Table IV shows the result of measurements in PVCA (polyvinyl chloride acetate copolymer) dielectric taken at 4000 cps on phosphors fired with variable additions of KCl and NH_4Cl. The last two rows represent normal control phosphors. It can be seen that the maintenance of the blue-emitting control phosphor is quite poor, but can be improved by a factor of 5 by the use of KCl. Inasmuch as the maintenance of ZnS:Cu, Cl phosphors increases with activator concentration (20), it seems not too far fetched to visualize that the very high Cl additions made in the present manner somehow become available with respect to their influence on maintenance, although without corresponding formation of green-emitting centers.

Use of S_2Cl_2.—The firing technique as described earlier in this paper was developed mainly because the composition of the atmosphere surrounding the phosphor during firing is a function of the composition of the unfired mix, so that the Cl incorporation could be controlled in a simple manner. Incorporation of Cl from a continuous supply such as HCl, introduced from the outside, would presumably continue until all of the Cu has been transformed into

Table IV. Properties of KCl-fluxed ZnS:Cu, Cl phosphors fired with 0.2 mole % Cu, as a function of additional Cl added as NH_4Cl. Brightness measurements at 400 cps in castor oil; maintenance measurements at 4,000 cps in PVCA dielectric

KCl, mole %	NH_4Cl, mole %	Particle size, μ	Brightness, ft-L	Emission Color	Spectra meter ratios* r	g	b	% Maintenance after 20 hr	Brightness x maintenance
10	0	2-6	3.95	Blue	0.025	0.257	0.718	11.7	0.46
10	1	2-10	3.6	Green-blue	0.030	0.335	0.635	35.0	1.26
10	2	2-10	3.9	Green-blue	0.043	0.390	0.567	—	—
10	5	3-12	3.25	Blue-green	0.053	0.497	0.450	—	—
10	10	3-20	2.3	Green	0.060	0.570	0.370	84.0	1.93
20	0	2-10	2.35	Blue	0.020	0.200	0.780	27.6	0.93
20	2	2-10	4.65	Light blue	0.033	0.307	0.660	42.5	1.98
20	4	2-10	3.3	Green-blue	0.040	0.333	0.627	—	—
20	10	3-15	2.5	Blue-green	0.052	0.402	0.546	—	—
20	20	6-25	2.85	Green	0.058	0.507	0.435	80.3	2.3
30	0	2-3	3.2	Blue	0.023	0.181	0.796	46.0	1.47
30	3	1-3	3.95	Light blue	0.035	0.275	0.690	58.8	2.32
30	6	2-6	1.95	Green-blue	0.040	0.290	0.670	—	—
30	15	3-20	1.9	Green-blue	0.042	0.350	0.608	—	—
30	30	6-40	4.1	Blue-green	0.047	0.393	0.560	66.6	2.74
50	0	2-4	2.3	Blue	0.017	0.193	0.790	35.8	0.83
50	5	1-2	3.65	Green-blue	0.034	0.322	0.644	55.6	2.03
50	10	1-4	1.7	Green-blue	0.035	0.345	0.620	—	—
50	20	3-50	3.45	Blue-green	0.030	0.333	0.637	—	—
50	50	8-50	3.55	Blue-green	0.033	0.365	0.602	80.0	2.83
0	0.35	5-15	20.0	Green	0.070	0.630	0.300	37.0	7.4
0	0.08	3-10	4.7	Light blue	0.025	0.260	0.715	8.7	0.41

* Ratios of the response at the Spectra Meter settings "red", "ft-L" (green), and "blue," respectively, divided by the sum.

green-emitting Cu-Cl centers. followed by eventual conversion of the ZnS into $ZnCl_2$. In order to limit this reaction, mixtures of HCl + H_2S are generally employed, and investigations of a quantitative nature pertaining to such reactions have been published by Kröger, Hellingman, and Smit (9) and by Kröger and Smit (21).

As mentioned before, the role of S in similarly limiting the incorporation of Cl has been verified experimentally, although only in a qualitative manner. However, unlike H_2S, the S constitutes an oxidizing environment during firing which is advantageous for the formation of good EL phosphors. In order to carry this one step further, the addition of Cl in elementary form was considered. The most convenient manner of accomplishing this was in the form of S_2Cl_2 added to the N_2 by aeration in a gas scrubbing bottle. For this purpose, no S or halide was added to the unfired mix, which was placed in an open boat near the closed end of the firing tube. It turned out that the equimolecular addition of S and Cl effected in this manner resulted in Cl incorporation to the extent normally obtained for phosphors designed for high-frequency excitation. The phosphors were characterized by a lighter (less yellow-green) body color after NaCN washing, and a stronger dependence of brightness on applied voltage. Details pertaining to the preparation of this type of phosphor have also been described (22).

(Zn, Cd)S:Cu, Cl Phosphors

The same firing technique, using capped silica tubes as described, was used throughout this phase of the investigation. The CdS raw material was RCA33C291. The Cu and Cl additions were generally maintained at those suitable for high-frequency excitation, so as to favor the long wavelength emission band.

Figure 3 shows the results of substituting an increasing molar percentage of CdS for ZnS. A small addition (3.3%) results in the expected shift in emission color to yellow-green and somewhat improved brightness. Increasing additions of Cd, however, rapidly decrease the output of the phosphors. While this may be caused partly by the introduction of deep traps associated with Cd as proposed by Zalm (7), three additional phenomena were noted, particularly in the region of rapid decreasing EL:

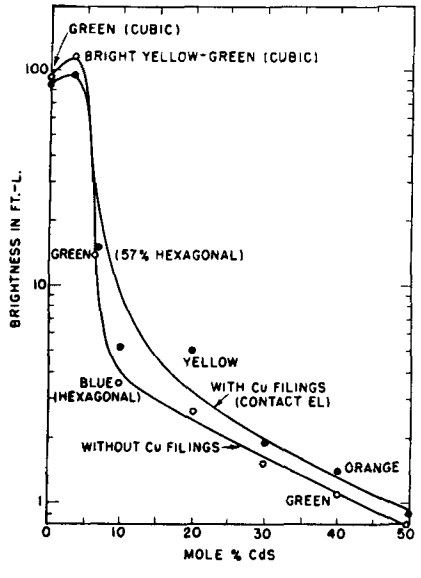

Fig. 3. Effect of Cd concentration on EL and contact-EL of (Zn, Cd)S:Cu, Cl phosphors. Measurements taken at 1000 v, 8,000 cps in 200 μ castor oil cell with 25 μ Mylar protection.

1. Formation of hexagonal phase. The first two points in Fig. 3 represent samples which are 100% cubic, the third sample is 57% hexagonal, and the rest are 100% hexagonal. It should be mentioned that Zalm (7) also considered the cubic phase of ZnS to be more suitable from the standpoint of EL, while Jaffe (23) noted a corresponding decrease of EL on introduction of Mg into ZnS, occurring simultaneously with formation of hexagonal material.

2. A shift in EL excited emission color back to shorter wave lengths. The emission color of (0.9Zn, 0.1Cd)S was greenish blue, although its photoluminescence was green-yellow as expected for this composition. No explanation of this phenomenon can be given at present.

3. Formation of a dark-colored separate phase, insoluble in NaCN solution. When prepared in pure form, this material is black and shows a hexagonal x-ray diffraction pattern very similar to that of CdS. Chemical analysis shows 18.5% Cu. Its exact identity has not as yet been established, although it appears to be some type of (Cd, Cu)S.

The decreasing EL output caused by the introduction of Cd into ZnS:Cu, Cl phosphors appears to occur simultaneously with the formation of hexagonal material and is associated with the formation of the (Cd,Cu)S phase. Phosphorescence observed in such phosphors strongly indicates that the mechanism in which high activator concentrations normally quench phosphorescence in ZnS:Cu, Cl phosphors is disturbed. Since, on the other hand, the characteristic ultraviolet-excited fluorescence is not so strongly influenced, the following mechanism may be proposed. The Cu_2S inclusions tend to be associated primarily with the cubic modification of the base material. Introduction of more than a few per cent of Cd causes formation of a hexagonal phase which allows the excess Cu to combine with CdS to form a separate compound which is not capable of fulfilling the same role of field intensification as Cu_2S. At the same time, depletion of this excess Cu disturbs the Cu-equilibrium of the system during firing and lowers the activator concentration of the phosphor to the point whereby persistent phosphorescence may be observed. Removal of the Cu_2S effectively destroys the EL-excitation mechanism.

The hypothesis was tested by mixing the phosphors with Cu-filings and subjecting them to contact-EL (24). Because of this comparatively inefficient manner of EL excitation, as well as the lower activator concentration of the (Zn, Cd)S:Cu, Cl phosphors, the increase in brightness obtained was small. On the other hand, the normal shift in EL-excited emission color was now observed. This

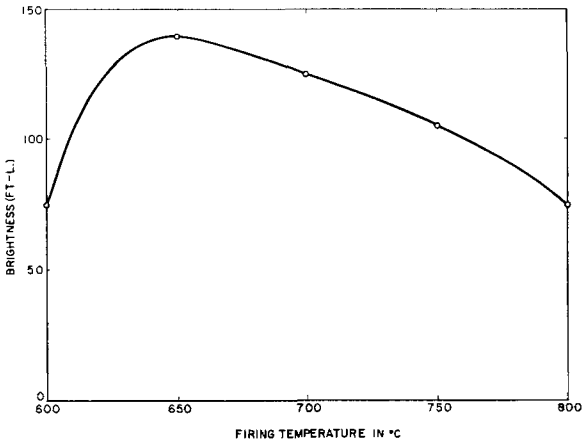

Fig. 4. Brightness at 600 v, 10,000 cps excitation of (9Zn:1Cd)S:Cu, Cl prepared from ZnS:Cu, Cl phosphor + CdS as a function of firing temperature. Firing times, 1 hr.

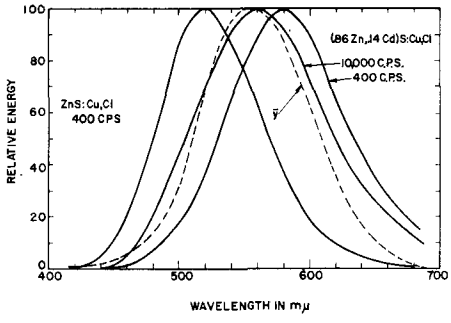

Fig. 5. Spectral distribution of (0.86 Zn, 0.14 Cd)S:Cu, Cl in comparison with that of green-emitting ZnS:Cu, Cl and sensitivity of human eye.

means that, at high Cd concentration, the slightly brighter orange contact EL represented a considerably higher emittance than the slightly less bright green, normally excited EL. It should also be mentioned that cubic or hexagonal photoluminescent ZnS:Cu(0.01%), Cl performed about equally well when subjected to contact EL.

Among several methods tried to overcome this interference, only one was at least partially successful: A normally prepared, but not NaCN-washed, green-emitting ZnS:Cu, Cl EL phosphor is mixed with unfired CdS and S and refired at a lower temperature. Figure 4 shows the effect of refiring temperature on 0.9 ZnS:Cu, Cl + 0.1 CdS which can be seen to be quite critical. At the present stage of development, the procedure is, however, not very reproducible and apparently subject to the particle size and technique of mixing of the two components to be refired. At best, 14 mole % CdS have been incorporated into ZnS:Cu,Cl without formation of the separate (Cd, Cu)S phase and formation of hexagonal structure. Figure 5 shows the emission spectra obtained at two frequencies of excitation of a (0.86Zn, 0.14Cd)S:Cu,Cl phosphor prepared in this manner. Although the spectral distribution at 10,000 cps resembles the eye-sensitivity distribution more closely, the brightness obtained was only about one-third that of the green-emitting ZnS:Cu,Cl phosphor prior to refiring with CdS. However, it should be mentioned that even refiring at 650°C of ZnS:Cu, Cl without CdS addition resulted in decreased brightness, generally to the extent of about 25%. The method is therefore a compromise designed to effect maximum incorporation of CdS with a minimum of chemical interference. Etching of such phosphors in HCl revealed that they are not homogeneous, inasmuch as the emission color continuously shifted to shorter wave lengths with increasing time of etching. This type of phosphor may therefore represent an optically filtered system of little practical importance.

Summary

Procedures for the preparation of lead-free ZnS:Cu,Cl and (Zn, Cd)S:Cu,Cl have been presented, based on firing of the raw materials in an oxidizing atmosphere containing sulfur vapor. The dependence of EL output on activator concentration is meaningful only for phosphors fired with additions of Cu such as to result in presumably similar concentrations of excess Cu_2S and consequently similarly efficient excitation processes. Control of incorporated Cl may be effected by firing in capped silica tubes or by firing in N_2 + S_2Cl_2. Alkali chlorides decrease the incorporation of Cl, more so with increasing atomic weight of the cation. Experiments with KCl have resulted in blue-emitting phosphors with greatly improved maintenance.

Substitution of Zn by Cd decreases the emittance as well as the dependence of EL-excited emission color on Cd concentration which is normally observed with ultraviolet excitation. This effect occurs simultaneously with formation of hexagonal (Zn, Cd)S and a (Cd,Cu)S compound which is insoluble in NaCN solution. A two-step firing procedure may be employed by means of which this interference is partially avoided through formation of a non-homogeneous optically filtered system. The brightness of such phosphors, however, is low.

Acknowledgments

The writer wishes to thank Mr. G. Scanlon and Miss I. Walinski for preparation and brightness measurements of phosphor samples, as well as Dr. W. A. Thornton and Dr. C. K. Lui-Wei for data on maintenance and crystal structure, respectively. He also wishes to thank Dr. H. F. Ivey for reading and suggesting improvements in the original manuscript.

Manuscript received March 11, 1960. This paper was prepared for delivery before the Chicago Meeting, May 1-5, 1960.

Any discussion of this paper will appear in a Discussion Section to be published in the June 1961 JOURNAL.

REFERENCES

1. *See* H. F. Ivey, Bibliography on Electroluminescence and related Topics, I.R.E. Trans. Electron Devices, *ED-6*, 203 (1959).
2. W. Lehmann, Canadian Pat. 579,685, July 14, 1959.
3. G. Destriau, *Phil. Mag.*, **38**; 700, 774, 800, 885 (1947).
4. G. Wendel, *Z. Phys. Chem.*, **206**, 169 (1956).
5. W. Lehmann, *This Journal*, **104**, 45 (1957).
6. P. Zalm, G. Diener, and H. A. Klasens, *Philips Research Repts.*, **9**, 81 (1954).
7. P. Zalm, *ibid.*, **11**, 353 (1956).
8. S. Rothchild, U.S. Pat. 2,541,384, Feb. 13, 1951.
9. F. A. Kroger, J. E. Hellingman, and N. W. Smit, *Physica*, **15**, 990 (1949).
10. R. Bowers and N. T. Melamed, *Phys. Rev.*, **99**, 1781 (1955).

11. H. C. Froelich, *This Journal*, **100**, 496 (1953).
12. H. C. Froelich, U. S. Pat. 2,743,239, April 24, 1956.
13. A. Wachtel, U. S. Pat. 2,874,128, Feb. 17, 1959.
14. F. A. Kröger and J. A. M. Dikhoff, *This Journal*, **99**, 144 (1952).
15. H. H. Homer, R. W. Rulon, and K. H. Butler, *ibid.*, **100**, 566 (1953).
16. C. C. Bentler and J. S. Prener, U. S. Pat. 2,755,255, July 17, 1956.
17. P. W. Ranby, U. S. Pat. 2,866,116, Dec. 23, 1958.
18. J. S. Prener and F. E. Williams, *Phys. Rev.*, **101**, 1427 (1956).
19. J. S. Prener and F. E. Williams, *This Journal*, **103**, 342 (1956).
20. W. A. Thornton, in press.
21. F. A. Kröger and N. W. Smit, *Physica*, **16**, 317 (1950).
22. A. Wachtel, Canadian Pat. 579,687, July 14, 1959.
23. P. M. Jaffe, in press.
24. W. Lehmann, *This Journal*, **104**, 45 (1957).

Gold-Activated (Zn,Cd)S Phosphors

M. Avinor[1]

Philips Research Laboratories, N.V. Philips' Gloeilampenfabrieken, Eindhoven, Netherlands

ABSTRACT

Gold is shown to produce three emission bands in CdS at 640, 800 and 1150 mμ. The long wave band appears only when a coactivator is used while the short wave bands are observed with activation by gold alone. The 1150 mμ band in CdS is shown to correspond to the 530 mμ gold band in ZnS.

The greenish fluorescence of gold-activated zinc sulfide is well known (1-3), but the properties of the luminescent centers have been investigated only limitedly. It was generally assumed in earlier work that they differed considerably in character from the centers of copper and silver in zinc sulfide. This was attributed to the theoretical possibility of gold being incorporated in the trivalent as well as the monovalent state. By using trivalent metals as coactivators instead of halogens, Kröger and Dikhoff (4) showed that the gold band was composed of two bands at 470 and 530 mμ, and that the latter became predominant by coactivation.

There is some likelihood of confusing the short wave band of gold at 470 mμ with the self-activated band of zinc sulfide at 460 mμ. However, the short wave band seems to be really due to gold because the two gold bands remain distinct even when the activator concentration is increased to 1 mole % (5). At such high activator concentration the self-activated band is usually completely suppressed. The two gold bands were assumed (4) to correspond to the "blue" and "green" bands of copper, although the order of the coactivated bands of silver (435 mμ), copper (516 mμ) and gold (530 mμ) does not correspond to their order in the periodic system.

Recently a further attempt was made by Henderson, Ranby, and Halstead (6) to find a correlation between the luminescent properties of Cu, Ag, and Au in ZnS and in (Zn,Cd)S phosphors. These authors did not control the atmosphere in which they fired their phosphors and they used chlorine coactivation through the addition of fluxes. No systematic correlation between the bands of the various activators could be found, although the authors claimed to have demonstrated three emission bands for copper and gold and two bands for silver.

The short wave silver band in ZnS was shown by Van Gool (7) to be situated at 388 mμ, by starting from CdS and tracing the shift of the emission bands in a series of mixed (Zn, Cd)S crystals up to ZnS. The short and the long wave bands are rather well resolved in CdS. In the present work we investigated the emission bands of gold by starting from CdS and following the bands as more and more of the cadmium was replaced by zinc.

[1] On leave of absence from the Scientific Department, Ministry of Defense, Israel.

Experimental

The aluminum coactivator was added to the pure base material as a solution of the ammonium alum, and the gold was added as a solution of the chloride. The powders were dried at 120°C overnight and then fired in small quartz test tubes at 950°C for 2 hr in a stream of pure hydrogen sulfide. After withdrawal from the furnace the tubes were allowed to cool, again in a stream of hydrogen sulfide. The products were ground and refired in hydrogen sulfide at 1100°C for 1 hr. An activator concentration of 2.10^{-4} atom per mole was used, which is about the optimum concentration for these sulfide phosphors. No fluxes were used.

The present experiments were limited to activation by gold alone or gold balanced by an equal molar concentration of a trivalent coactivator. Phosphors with activator to coactivator ratio different from unity were not investigated. It is known, however, that in the case of copper and silver additional emission bands may appear (4, 7).

The emission was measured by a recording spectrophotometer with photomultiplier or lead sulfide detector, and the usual corrections were applied for obtaining equal energy spectra. Excitation was by the ultraviolet, blue, and green lines of a high-pressure mercury lamp for phosphors containing a high proportion of CdS. Filters were used to remove progressively the longer wave lines as the emission bands shifted towards the ultraviolet. For 20 mole % or less of CdS the 313 mμ line of mercury was used, unless otherwise indicated. In this way the excitation was mostly fundamental for the various compositions and allowed detection of both the impurity and the edge emission.

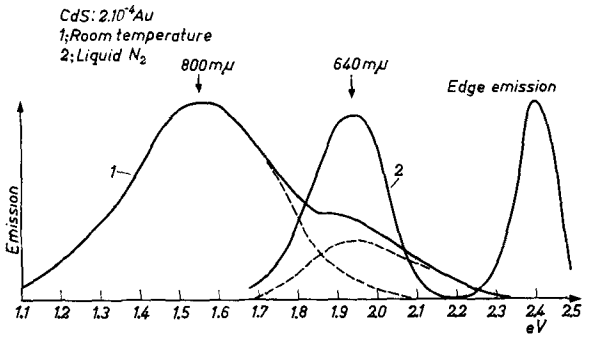

Fig. 1. Emission spectrum of gold-activated CdS at room and liquid nitrogen temperature.

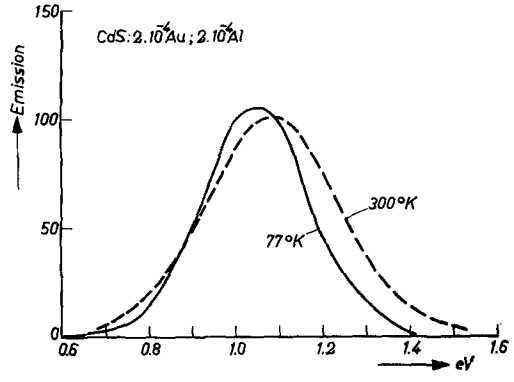

Fig. 2. Emission spectrum of CdS activated by equal amounts of Au and Al at room and liquid nitrogen temperature.

Results

We find that whereas copper (8) and silver (7) are known to give two emission bands each in CdS, gold produces three distinct bands. Two bands are found at 640 mμ and 800 mμ when gold alone is used as an activator (Fig. 1). The third band appears as the only band at 1150 mμ when the gold activator is balanced by a trivalent coactivator such as aluminum (Fig. 2). The same emission band is also found when indium is used instead of aluminum. On cooling to liquid nitrogen temperature it shows only a slight shift toward longer wave lengths (Fig. 2), and no other emission bands appear. When zinc is substituted for cadmium in the host lattice this band is displaced in a regular manner toward shorter wave lengths (Fig. 3, 4) and appears at 530 mμ in zinc sulfide. Thus the 1150 mμ coactivated gold emission in CdS corresponds very well to the emission bands of coactivated silver and copper at 730 and 1020 mμ, respectively (Fig. 4).

The optical absorption of the coactivated gold centers in CdS extends beyond the fundamental absorption edge (Fig. 5) and gives the powder a reddish brown body color. In this respect, too, the coactivated gold centers resemble closely the coactivated centers of copper and silver.

Omission of the coactivator shows important differences between gold and the other activators. The short wave emissions of copper and silver appear in CdS when the activator concentration exceeds the coactivator concentration. With no coactivator at all gray products are obtained on firing in

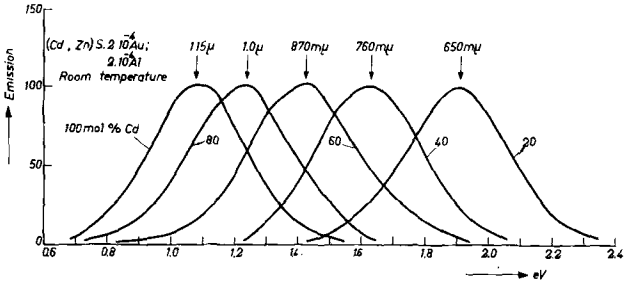

Fig. 3. Emission spectra of (Zn,Cd)S phosphors activated by gold and aluminum at room temperature.

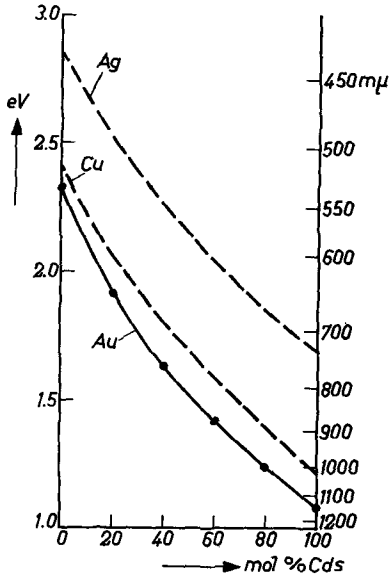

Fig. 4. Shift of emission peak of coactivated (Zn,Cd)S phosphors activated by Au, Cu, and Ag. Room temperature.

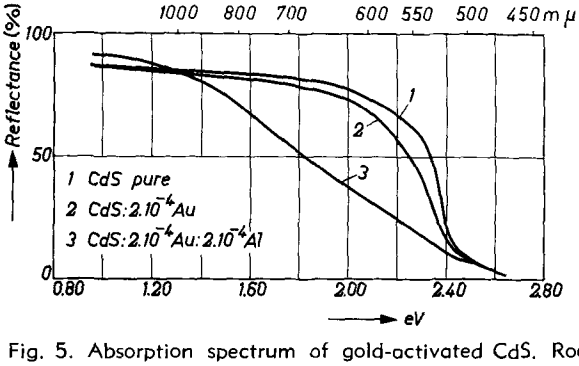

Fig. 5. Absorption spectrum of gold-activated CdS. Room temperature.

an atmosphere of hydrogen sulfide, indicating that much of the activator remains unincorporated as the free sulfide. Gold alone as an activator, however, is well incorporated in CdS with only a small change in the absorption spectrum (Fig. 5). Two emission bands have been found in this case (Fig. 1) at 640 and 800 mμ. The small amount of chlorine introduced with the gold (which was added as gold chloride) is probably driven out by the current of hydrogen sulfide on firing, and its effect as a coactivator is not felt. This is supported by the observation that the two bands are both different from the coactivated band, that these bands do not appear in a coactivated phosphor, and also by the slight effect on the

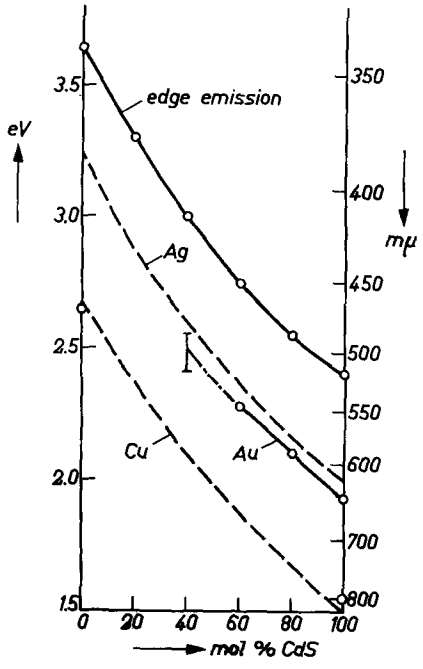

Fig. 6. Shift of emission peak of the short wave bands of (Zn,Cd)S phosphors activated by Au, Cu, and Ag. Liquid nitrogen temperature.

absorption spectrum. The coactivated band appears, together with other bands, when high chloride concentrations are used, as in the experiments of Henderson, *et al.* (6).

The 640 mμ band predominates at low temperatures in CdS activated by gold alone, but in contrast to coactivated phosphors the edge emission is not suppressed (Fig. 1) so that the visible emission looks yellow. Indeed, it is remarkable that for high zinc content and fundamental excitation the edge emission surpasses in intensity the activator emission (Fig. 7).

On introducing zinc into the lattice the 640 mμ band is displaced towards shorter wave lengths, but its intensity falls quickly so that the band cannot be traced into the zinc-rich region (Fig. 7). Further interference arises from the strong edge emission and from the coactivated band which comes up even without addition of coactivator as the zinc content is increased. However, if normal displacement of the band with zinc content is assumed (Fig. 6), this band should appear at about 400 mμ in zinc sulfide. No such emission has been reported to date.

The 800 mμ band which appears at room temperature in CdS activated by gold alone (Fig. 1) is rather wide and of weak intensity. Its intensity is about 10% of the intensity of the 640 mμ band at low temperatures. The displacement of this band with zinc content also could not be followed because of interference from other bands as the zinc content was increased. If we assume normal displacement with zinc content, we see (Fig. 6) that this band should correspond to the 470 mμ gold band in ZnS.

It is interesting to note that in gold-activated ZnS with higher gold concentration the coactivated band at 530 mμ appears even when no coactivator is added. In Fig. 8 is given the emission of ZnS(Au) for long wave u.v. excitation so that interference from the

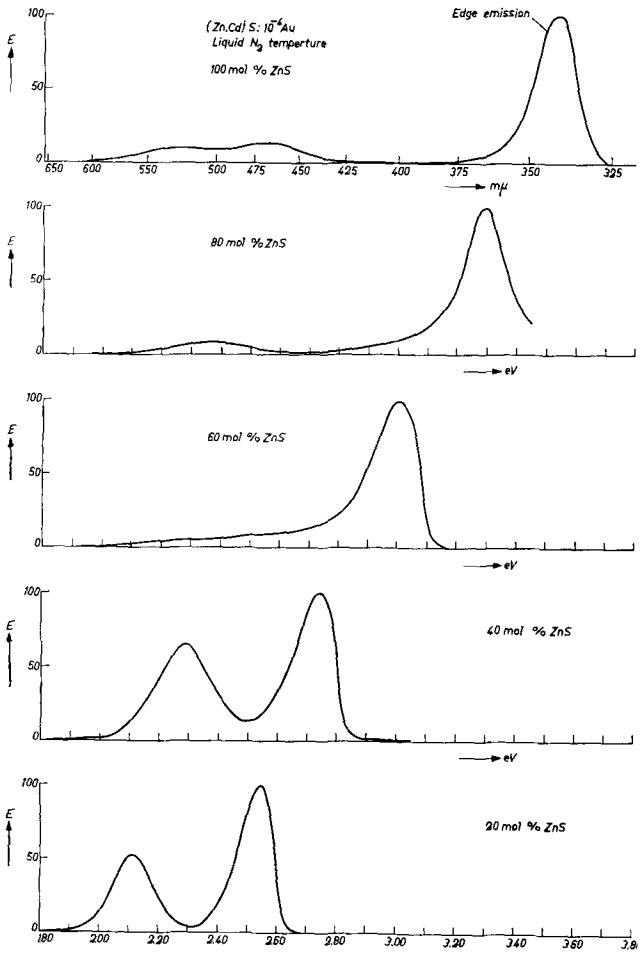

Fig. 7. Emission spectra of gold-activated (Zn,Cd)S phosphors at liquid nitrogen temperature. Fundamental excitation was used for each composition. Intensities were normalized with respect to the "edge emission."

edge emission is eliminated. We see that both the coactivated band at 530 mμ and the short wave band at 470 mμ appear in comparable intensities. The emission can be well accounted for by assuming

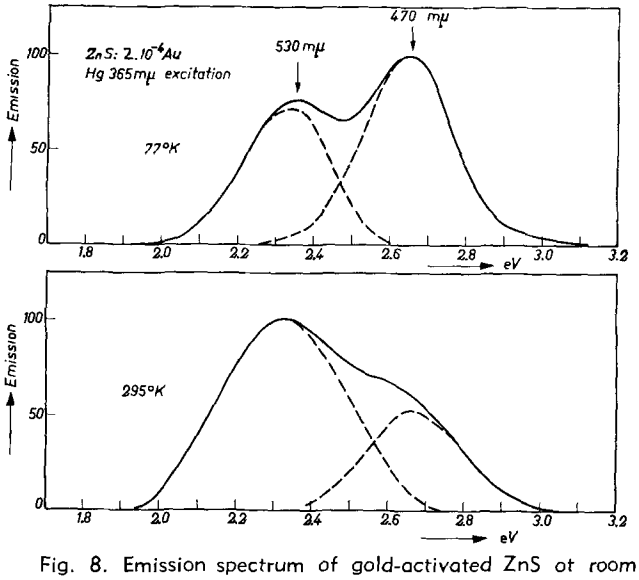

Fig. 8. Emission spectrum of gold-activated ZnS at room and liquid nitrogen temperatures. Resolution into sub-bands was done assuming that these change only in intensity, and not in position, with temperature.

these two bands to change only their relative intensities and not their position with temperature.

Discussion

The emissions of coactivated gold phosphors were found to correspond closely to coactivated copper and silver emissions over the whole range from CdS to ZnS, and it may be concluded that in this case gold is incorporated in the same state as the other activators. In view of the work of Henderson, *et al.* (6) it is interesting to note that chlorine, and presumably also other halogens, do not fully coactivate gold in (Zn,Cd)S phosphors. Such a marked difference between the halogens and the trivalent metals has not been observed for activation by copper and silver.

On the other hand, the short wave emission bands of gold show notable differences from the short wave bands of copper and silver. The nature of these centers is still unknown.

Acknowledgment

The author wishes to express his thanks to Dr. G. Diemer for helpful discussions and to Dr. A. Bril for measurement of the emission spectra.

Manuscript received Nov. 16, 1959. This paper was prepared for delivery before the Chicago Meeting, May 1-5, 1960.

Any discussion of this paper will appear in a Discussion Section to be published in the June 1961 JOURNAL.

REFERENCES

1. C. J. Milner, *Trans. Faraday Soc.*, **4**, 101 (1938).
2. S. T. Henderson, *Proc. Roy. Soc.*, **A173**, 323 (1939).
3. H. W. Leverenz, "An Introduction to the Luminescence of Solids," John Wiley & Sons, Inc., p. 211, New York (1950).
4. F. A. Kröger and J. Dikhoff, *Physica*, **16**, 297 (1950).
5. W. van Gool, Private communication.
6. S. T. Henderson, P. W. Ranby, and M. B. Halstead, *This Journal*, **106**, 27 (1959).
7. W. van Gool, *Philips Res. Repts.*, **13**, 157 (1958).
8. E. Grillot and P. Guintini, *Comp. Rend. Paris*, **239**, 418 (1954).

Electrolytic Reduction of Nitro- and Dinitronaphthalenes

R. N. Boyd and A. A. Reidlinger

Department of Chemistry, Washington Square College, New York University, New York, New York

ABSTRACT

The polarographic reduction of mono- and dinitronaphthalenes was studied in buffered solutions at four different *p*H values. The relative wave heights of the multiple waves could be reasonably interpreted in terms of certain electron changes, and these were also checked by coulometric measurements on electrolyses run at controlled potentials. The first stage in reduction appeared to be a four-electron change. At *p*H 2.1 reduction often proceeded to completion, but there was polarographic evidence of intermediate stages for the homonuclear dinitro compounds. At *p*H 11, 1,4-dinitronaphthalene shows a two-electron change which may be due to a quinoid intermediate, as may a ten-electron change at *p*H 9.4 for the same compound.

The polarographic behavior of numerous dinitro derivatives of benzene has been investigated by Pearson (1), Bergman and James (2), and others, but very little has been done (3-5) with nitro compounds in the naphthalene series. Therefore, all ten possible dinitronaphthalenes were prepared, and the polarographic reduction of 5 x 10^{-4}M solutions of the nitro compounds in 80% ethanol was studied in four buffered solutions.

Electrolytic reductions at constant potentials of 2 — 5 x 10^{-4}M solutions of the nitro compounds in 80% ethanol were carried out at *p*H 2.1 using a stirred mercury cathode. The amount of current passed in each reduction was measured by a silver coulometer, and these coulometric values were compared with the relative wave heights of the polarographic curves in order to determine the particular reduction processes associated with each wave.

Experimental

Nitro compounds.—The nitro- and dinitronaphthalenes were prepared by previously published procedures, and the melting points of the products agreed with the literature values.

In particular, 2,3-dinitronaphthalene was prepared by the method of Chudozilov (6), m.p. 170-170.5° (Lit.: 170.5-171°), since the procedure given by Hodgson and Turner (7) led to a product which, although claimed to be the 2,3-isomer, melted at 159° and was found in the present work and by Ward (8) to be 1,7-dinitronaphthalene (mixed m.p. of alleged 2,3-isomer and authentic 1,7-isomer gave no depression).

Polarographic and coulometric procedure.—The polarographic and constant-potential coulometric studies were carried out with the same equipment, in the same manner and in the same buffers, as described for the work with the nitrotetralins (9), except that 2,6-dinitronaphthalene was run at a concentration of 1.0 x 10^{-4}M because of its extremely low solubility in 80% ethanol.

Polarographic data are given in Table I and constant-potential coulometric data in Table II.

Discussion

In Table II there is a comparison of the n values estimated from the relative wave heights of the polarographic curves and those obtained by coulo-

Table I. Polarographic reduction of the nitro- and dinitronaphthalenes[a]

	2.1		6.4		9.4		11.0	
	$E_{1/2}$	i_d/C	$E_{1/2}$	i_d/C	$E_{1/2}$	i_d/C	$E_{1/2}$	i_d/C
1-Nitro	—0.30	11.0	—0.51	10.4	—0.73	10.8	—0.83	10.3
	—0.65	15.8	?	?				
2-Nitro	—0.30	10.3	—0.49	11.1	—0.70	11.0	—0.82	10.9
	—0.72	15.7	?	?				
1, 2-Dinitro	—0.12	10.4	—0.30	10.1	—0.42	10.1	—0.44	?
	—0.38	30.1	—0.62	29.8	—1.06	31.4	—0.83	?
							—1.09	?
1, 3-Dinitro	—0.16	10.4	—0.33	10.2	—0.52	10.7	—0.62	9.8
	—0.27	21.1	—0.50	20.2	—0.76	21.2	—0.86	20.6
	—0.93	30.7	—1.45	?				
1, 4-Dinitro	—0.06	9.3	—0.29	9.7	—0.36	9.5	—0.39	5.6
	—0.36	29.1	—0.62	28.6	—0.93	25.5	—1.49	28.4
					—1.32	29.0		
1, 5-Dinitro	—0.22	22.9	—0.37	10.6	—0.57	10.3	—0.63	10.4
	—0.78	29.6	—0.50	19.7	—0.74	20.4	—0.84	20.2
			—1.48	26.9				
1, 6-Dinitro	—0.22	23.6	—0.38	10.1	—0.58	10.2	—0.64	10.5
	—0.82	31.1	—0.51	20.7	—0.74	21.2	—0.85	21.6
			—1.43	26.7				
1, 7-Dinitro	—0.22	24.1	—0.35	9.3	—0.50	10.5	—0.58	10.7
	—0.86	29.9	—0.51	19.7	—0.76	20.3	—0.85	21.4
			—1.36	26.5				
1, 8-Dinitro	—0.26	24.7	—0.48	19.8	—0.64	20.2	—0.72	20.7
	—0.69	29.9	—1.23	28.1	?	?	?	?
2, 3-Dinitro	—0.20	21.7	—0.34	9.9	—0.51	10.1	—0.60	10.4
	—0.67	28.3	—0.45	19.0	—0.68	18.9	—0.77	19.9
			—1.39	24.0				
2, 6-Dinitro	—0.14	5.2	—0.34	5.5	—0.49	5.6	—0.55	5.5
	—0.28	12.5	—0.55	10.9	—0.78	11.2	?	?
	—0.90	16.7	—1.36	14.6				
2, 7-Dinitro	—0.23	21.2	—0.37	10.3	—0.55	10.4	—0.63	10.6
	—0.81	29.3	—0.52	20.2	—0.73	19.7	—0.82	21.4
			?	?				

[a] The values of $E_{1/2}$ are in volts vs. S.C.E., and those of i_d/C are in μa/mmole/l. A question mark indicates that the wave is too indefinite to assign values with any degree of certainty. The pH values listed are the apparent values for the ethanolic solutions used in the electrolyses. The values of i_d/C are the sums of the individual wave heights.

metric analyses. It is evident that there is fairly good agreement between the two sets; and there is excellent agreement between them in the cases where the polarographic waves are well defined. It appears likely that for these compounds the electrolytic processes are the same at a stirred mercury cathode as at a dropping mercury electrode.

As has been found with derivatives of benzene (1, 2) and tetralin (9), the first of the multiple waves obtained from the polarographic reductions of nitro derivatives of naphthalene is usually one corresponding to a four-electron change, the transformation of a nitro group to a hydroxylamino group. This is especially true when the reductions are carried out at the higher pH's.

Kasagi (3) reported a single wave for "mononitronaphthalene" (presumably the 1-isomer) at about —0.9 v. Apparently the electrolytic medium he used, benzene-ethyl alcohol-lithium chloride, was alkaline (comparable to pH 11 in the present work). Thus his report of two waves of equal height for "dinitronaphthalene" (probably the 1,5-isomer) at potentials below —1.0 v agrees with the present results for 1,5-dinitronaphthalene at pH 11 or even at pH 9.4, and the two waves (as well as that for the mononitro compound) represent four-electron changes.

The constancy of wave height reported by Bezuglyi and Ogdanets (5) for "mononitronaphthalene" over a pH range of 2 to 12, and the variation of $E_{1/2}$ with pH for 1- and 2-nitronaphthalene reported by Imoto (4), also agree with the present findings.

Figure 1 shows two polarographic curves; curve A is a polarogram (uncorrected for residual current) that was obtained from a solution of 1,2-dinitronaphthalene at apparent pH 2.1; curve B is a polarogram (uncorrected for residual current) that was obtained from the same solution after an electrolysis in which a quantity of electricity equivalent to 3.9 electrons per molecule of dinitro compound had been passed through the cell. It can be seen that curve B is approximately two-thirds the height of curve A, and that it has the same half-wave potential as the second wave in A. The conclusion that can be drawn from these facts are the

Table II. Constant potential reduction of the nitro- and dinitronaphthalenes[a]

Compound	E_r	n (coulom.)	n (polarog.)[b]
1-Nitro	—0.35	3.97	4
	—0.80	5.83	6
2-Nitro	—0.35	4.00	4
	raised to —0.95	5.93	6
1, 2-Dinitro	—0.20	3.90	4
	—0.70	11.75	12
1, 3-Dinitro	—0.17	4.31	4
	raised to —0.40	8.28	8
	—0.90	12.48	12
1, 4-Dinitro	—0.13	4.07	4
	—0.65	11.93	12
1, 5-Dinitro	—0.50	7.59	(9)
	—0.85	11.64	12
1, 6-Dinitro	—0.40	8.65	(9)
	—0.90	11.91	12
1, 7-Dinitro	—0.35	10.00	(10)
	raised to —0.92	11.91	12
1, 8-Dinitro[c]	—0.50	8.85	10
	—0.85	11.58	12
2, 3-Dinitro	—0.40	8.15	(9)
	—0.90	12.15	12
2,6-Dinitro	—0.17	4.19	4
	—0.85	12.03	12
2, 7-Dinitro	—0.37	8.09	8
	—0.95	11.55	12

[a] E_r is the potential of the cathode (vs. S.C.E.) at which the reduction was carried out; n is the number of electrons involved in the reduction. The apparent pH was 2.1.
[b] Estimated to nearest integral number of electrons from wave heights of the polarographic curves.
[c] At pH 6.4 and —0.80 v, n was 8.17. When E_r was raised to —1.30 v, n was 12.47.

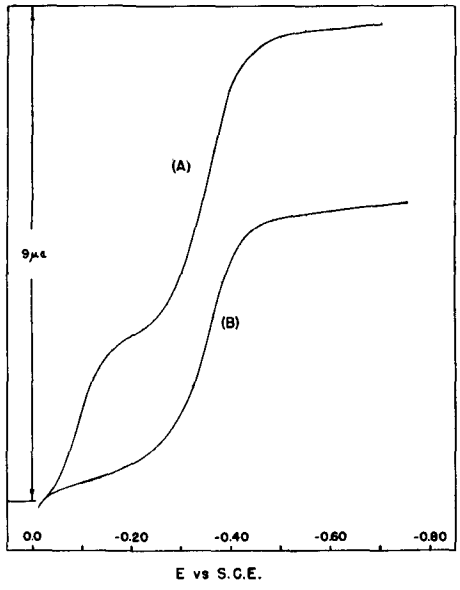

Fig. 1. Polarograms of 1,2-dinitronaphthalene at pH 2.1. A, Original nitro compound; B, after reduction equal to 3.9 electrons per molecule.

following: (*a*) the first wave of curve A corresponds to a four-electron change; (*b*) the second wave, which is twice the height of the first, undoubtedly represents an eight-electron change; (*c*) the intermediate reduction product, most likely an hydroxylamine, was stable enough in the acidic solution to yield a satisfactory polarogram.

The chemical (and electrolytic) reduction of nitro compounds in acid solution leads to the formation of amines, and it is highly probable that those polarographic reductions of dinitro compounds which require twelve electrons lead in acid to complete reduction with the formation of diamines. As the *p*H increases, reduction becomes more difficult and the polarographic curves show that eight- and ten-electron changes are commonly found. At *p*H 11 the curves are too diffuse in some cases to permit interpretation. At this *p*H the rate of condensation of intermediate products can be appreciable, and the diffuseness is probably due to secondary processes involving these condensation products.

It can be seen from Table I that, as the *p*H increases, the separation between the component waves for the dinitro compounds also generally increases. Pearson (1) found this to be true for dinitrobenzenes and dinitrotoluenes [as the present authors did for the tetralin series (9)] and it is attributed to a decrease in salt formation as the medium becomes more alkaline. For if $-NR_2$ or —NHOH is an electron-releasing group but $-NR_3^+$ (and presumably $-NH_2OH^+$, too) is electron-attracting, one should expect that the nitro group in an N-arylhydroxylamine would accept electrons (be reduced) less readily than a nitro group in an N-arylhydroxylammonium salt.

The difference in the relative ease of reduction between 1-nitronaphthalene and 2-nitronaphthalene is smaller than that found for the corresponding 5- and 6-nitrotetralins (9). An examination of molecular models showed that if there were any interference between the 1-nitro group and the hydrogen atom of the 8-position, it was much less than the interference at corresponding positions in 5-nitrotetralin (9). Hence it is reasonable that 1- and 2-nitronaphthalene resemble each other more closely than do 5- and 6-nitrotetralin [or o- and m-nitrotoluene (1)].

The polarograms obtained in the present work for 1,3-dinitronaphthalene bear a striking similarity to the curves obtained previously for compounds of similar "meta" structure, namely m-dinitrobenzene (1, 2), 2,4-dinitrotoluene (1) and 5,7-dinitrotetralin (9). In general, present results for the homonuclear dinitronaphthalenes (except for the 2,3-isomer which as a β,β-isomer is unique in structure) agree with the findings for *ortho-*, *meta-*, and *para*-dinitro groups in the benzene (1, 2) and tetralin series (9).

Where two nitro groups are "ortho" or "para" with respect to each other in the homonuclear dinitronaphthalenes, the greater separation of the component waves can be attributed to a lessening of the positivity (and hence reducibility) of the nitro group in the initially formed nitrohydroxylamine. For example, resonance should play a greater part in the stabilization of the 1,2- and 1,4-deriva-

tives (I and II, respectively) than it does in the case of the 1,3- or 2,3-derivative (III).

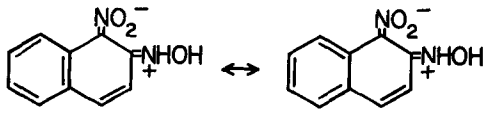

I

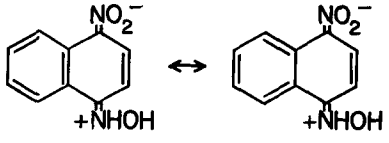

II

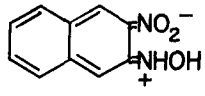

III

No important extra structures can reasonably be drawn for the 1,3-isomer; in the instance of 2,3-dinitronaphthalene only one quinoid structure (III) can be drawn, and it can make only a small contribution to the resonance energy. This may account for the anomalous behavior of the 2,3-isomer, which was not unexpected. The decrease in the positivity of the nitro group in the nitrohydroxylamine derived from 2,3-dinitronaphthalene certainly would not be so great as that in the 1,2- and 1,4-isomers, and hence the separation of the component polarographic waves should be less marked.

At *p*H 6.4, and in alkaline solutions, all the heteronuclear dinitronaphthalenes except the 1,8-isomer are reduced in much the same manner. The first wave corresponds to a four-electron change, and the second wave to an eight-electron change.

From Table I it can be seen that the separation of the component waves is distinctly greater in the curves obtained from 1,7-dinitronaphthalene than in the curves obtained from 1,5-, 1,6-, and 2,7-dinitronaphthalene, and is greatest of all in the curve for 2,6-dinitronaphthalene. Of the heteronuclear nitrohydroxylamines, quinoid structures can be drawn only for the 1,5-, 2,6-, and 1,7-isomers (IV, V, and VI, respectively).

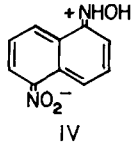

IV

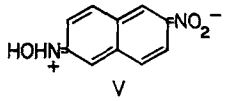

V

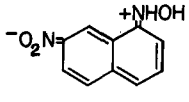

VI

The quinoid structure for the 2,6-isomer (V) is undoubtedly the most important of these (2,6-naphthoquinone, for example, is the only known heteronuclear naphthoquinone); and, therefore, the reducibility of the remaining nitro group should be most affected. It is notable that 2,6-dinitronaphthalene also shows a four-electron wave in acid solution (as well as at *p*H 6.4 and in alkaline media). The occurrence of a four-electron step in acid solution indicates an unusual stability for the hydroxylamine stage (V), since reduction in acid generally leads to a diamine (or some other highly reduced product).

The separation of waves for the 1,7-isomer is less (only one p-benzoquinoid ring, VI) than for the 2,6-isomer, and it is in accord with conjecture that the separation for the 1,5-isomer (no p-benzoquinoid ring, IV) is not appreciably greater than for the 1,6- and 2,7-isomers, for which one can write no quinoid structures at all.

1,8-Dinitronaphthalene is the only dinitronaphthalene that does not show an initial four-electron wave in any of the buffered solutions studied. It has been reported (10) that 2,2'-dinitrobiphenyl also does not give a four-electron wave at any of the *p*H values studied; instead, its first wave at *p*H 6.4 corresponds to an eight-electron change. Large-scale reduction (11) at a controlled potential and at *p*H 6.4 showed benzo(c)cinnoline (VII) to be the major reduction product obtained from 2,2'-dinitrobiphenyl.

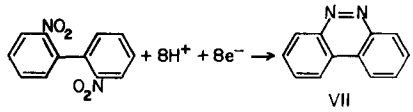

VII

It is possible that the polarographic reduction product from 1,8-dinitronaphthalene at *p*H 6.4 (and at higher *p*H values) is correspondingly 1,8-naphthopyrazole (VIII).

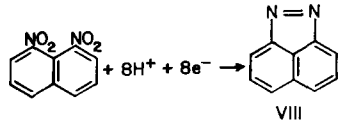

VIII

At *p*H 2.1 the probable ten-electron reduction could be interpreted as the formation of the dihydro derivative of the pyrazole (corresponding to the formation of a hydrazo compound). Under acidic conditions, where a low coulometric value was obtained for 1,8-dinitronaphthalene, the electrolyzed solution became deep purple in color. When the electrolysis was carried out at *p*H 6.4 the final solution was orange-yellow in color; yet it, too, turned to purple on standing in contact with air. It has been shown (10) that the dihydro derivative of benzo(c)-cinnoline undergoes dismutation to give a mix-

ture of benzo(c)cinnoline and 2,2'-diaminobiphenyl. Perhaps the dihydro derivative of the pyrazole also is similarly unstable.

A nine-electron change, such as found for 1,5- and 1,6-dinitronaphthalene, may be the result of two concurrent electrode processes (1); it would be awkward to account for an odd-electron change in any other way.

The polarographic curve for 1,4-dinitronaphthalene at *p*H 11 displays an unusual wave that appears to be associated with a two-electron step. This curve is very similar to the one that Holleck and Exner (12) obtained from 1,4-dinitrobenzene in alkaline solution. Holleck and Exner studied the reduction of the three isomeric dinitrobenzenes at the dropping mercury electrode over a wider range of *p*H values than is found in the work of Pearson (1). They stated that 1,4-dinitrobenzene gave very peculiar multi-stage curves that were caused by two concurrent processes. They claimed that in alkaline solution a two-electron change produced a stable quinone-like intermediate (IX) which was then reduced to N-(4-aminophenyl)hydroxylamine.

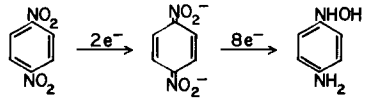

IX

It would be expected that the double bonds between the nitrogen atoms and the ring would be similar in stereochemical requirements to carbon-to-carbon double bonds, and therefore all the atoms must be in the plane of the ring. It is indeed interesting that 1,4-dinitronaphthalene and 1,4-dinitrobenzene can satisfy the steric demands and do exhibit a two-electron change at *p*H 11; whereas 5,8-dinitrotetralin, in which neither nitro group can ever be coplanar with the aromatic ring (9), gives a first wave at *p*H 11 which corresponds to a typical four-electron change, and there is no evidence of a two-electron step.

If one accepts the proposal of a quinoid intermediate for a two-electron step, one might reasonably extend the general idea and suggest that polarographic waves which appear to represent ten-electron reductions can be interpreted by means of quinoid structures, too, rather than as N-(aminoaryl)hydroxylamines (12). This would mean that the reduction product would be a quinone diimine. It is therefore possibly more than merely coincidence that at *p*H 9.4 the only compounds that show waves indicating ten-electron changes, 1,4-dinitronaphthalene, 5,6-dinitrotetralin (9), and 6,7-dinitrotetralin (9), are those for which diimines appear to be quite reasonable (X, XI, and XII, respectively).

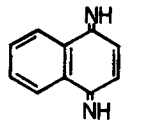

X

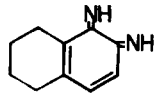

XI

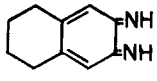

XII

However, it should be pointed out that the potential of −1.32 v (Table I) for reduction of the alleged 1,4-diimine to a 1,4-diamine does seem high for an analog of 1,4-naphthoquinone.

Acknowledgments

The authors wish to thank Dr. R. T. Schenck for his suggestions about apparatus, Morton Meadow for gifts of chemicals and time in the preparation of 1,7-dinitronaphthalene, and the DuPont Corporation for a generous gift of 1,5-dinitronaphthalene.

Manuscript received Dec. 8, 1959.

Any discussion of this paper will appear in a Discussion Section to be published in the June 1961 JOURNAL.

REFERENCES

1. J. Pearson, *Trans. Faraday Soc.*, **44**, 683 (1948).
2. I. Bergman and J. C. James, *ibid.*, **50**, 60 (1954).
3. M. Kasagi, *Kogyo Kagaku Zasshi*, **54**, 745 (1951); *C. A.*, **47**, 7950 (1953).
4. E. Imoto, R. Motoyama, and H. Kakiuchi, *Bull. Naniwa Univ.*, **A3**, 203 (1955); *C. A.*, **49**, 15557 (1955).
5. V. D. Bezuglyi and N. D. Ogdanets, *Trudy Komissii Anal. Khim., Akad. Nauk S.S.S.R., Inst. Geokhim i Anal. Khim.*, **7**, 149 (1956); *C. A.*, **50**, 15345 (1956).
6. L. K. Chudozilov, *Coll. Czech. Chem. Comm.*, **1**, 302 (1929).
7. H. H. Hodgson and H. S. Turner, *J. Chem. Soc.*, **1943**, 635.
8. E. R. Ward, T. M. Coulson, and J. G. Hawkins, *ibid.*, **1954**, 4541.
9. R. N. Boyd, A. A. Reidlinger, and M. J. Sher, *This Journal*, **107**, 302 (1960).
10. S. D. Ross, G. J. Kahan, and W. A. Leach, *J. Am. Chem. Soc.*, **74**, 4126 (1952).
11. M. J. Sher, Ph.D. Dissertation, New York University, 1955.
12. L. Holleck and H. J. Exner, *Z. Elektrochem.*, **56**, 677 (1952).

Polarography of Some Aromatic Nitro and Carbonyl Compounds

Julia T. Gary and R. A. Day, Jr.

Department of Chemistry, Emory University, Atlanta, Georgia

ABSTRACT

The polarographic reduction of the nitro and carbonyl groups in 2-nitrofluorenone, 2,7-dinitrofluorenone, and 2,5-dinitrofluorenone has been studied in buffered solutions over a pH range of about 1-13. To aid in interpreting the electrode reactions, additional polarographic studies were made with several compounds containing only the nitro or carbonyl group. These compounds were fluorenone, 4-nitrobiphenyl, 4,4′-dinitrobiphenyl, 2.4′-dinitrobiphenyl, 2,5-dinitrofluorene, and 2-aminofluorenone, and the polarography was carried out under the same solution conditions. The number of electrons involved in the reduction steps of several of these compounds was measured using the controlled cathode potential technique. It was found that the characteristic double waves of the carbonyl group in fluorenone are merged into a single two-electron wave in the dinitrofluorenones. This effect is apparently a general one, caused by the decrease in stability of the intermediate free radical brought about by the hydroxylamine groups in the aromatic nucleus.

The polarographic reduction of relatively few compounds containing both nitro and carbonyl groups has been reported in the literature. The nitrobenzaldehydes have been most thoroughly studied (1-4), and it has been possible to assign the various waves to the different steps in the reduction of the nitro and carbonyl groups.

We were particularly interested in the effect that an amino (or hydroxylamino) group has on the carbonyl waves in compounds where both groups are attached to a single aromatic nucleus. An aromatic nitro group is normally reduced at a lower potential than a carbonyl group; hence, when the carbonyl group is undergoing reduction the other substituent in the aromatic nucleus is the amino or hydroxylamino, not the nitro group. It has been observed that, whereas an aromatic aldehyde is normally reduced in two well-separated one-electron steps in sodium hydroxide solutions, the waves are apparently merged into a single two-electron step in meta-nitrobenzaldehyde (2). In the case of ortho and para-nitrobenzaldehydes the waves remain separate (2).

The ketone fluorenone is well known for its tendency to reduce in two well-separated one-electron steps in both acid, neutral, and basic media. It was therefore, of interest to study the behavior of the carbonyl group in fluorenone in cases where a nitro group was substituted in the 2 or 7 position of the fluorene nucleus. As the work progressed some dinitrofluorenones were studied and to aid in the interpretation of their behavior of the following compounds is described herein: fluorenone, 2-nitrofluorenone, 2,7-dinitrofluorenone, 2,5-dinitrofluorenone, 2-aminofluorenone, 4-nitrobiphenyl, 4,4′-dinitrobiphenyl, 2,4′-dinitrobiphenyl, and 2,5-dinitrofluorene.

Experimental

Polarographic data were obtained with a L&N Electrochemograph Type E. Half-wave potentials were corrected for *IR* drop and for lag caused by galvanometer damping. The electrolysis cell, experimental procedure, and buffer solutions were the same as described previously (5). However, because of the low solubility of several of the compounds in ethanol-water mixtures, a mixture of water and acetone was employed. The compound of interest was dissolved in acetone, and the cell solution was made by mixing equal volumes of this solution with the appropriate aqueous buffer. A single capillary of Corning marine barometer tubing was used. Its characteristics were: droptime 5.0 sec, $m = 1.34$ mg sec^{-1}, determined in a water-acetone mixture, buffered with citrate-phosphate (apparent pH 5.0) with an open circuit. The calculated value of $m^{2/3}\ t^{1/6}$ was 1.59 $mg^{2/3}\ sec^{-1/2}$.

The coulometric measurements were carried out using a potentiostat of the Lingane-Jones type (6) and a hydrogen-oxygen coulometer. The cell, electrodes, and experimental procedures were essentially those recommended by Lingane (7).

Samples of 2-nitrofluorenone, 2-aminofluorenone, 2,5-dinitrofluorene, 2,5-dinitrofluorenone, and 2,7-dinitrofluorenone were kindly furnished us by the late Professor C. W. Bennett of Western Illinois State College (8). All other compounds studied were Eastman Kodak White Label chemicals. Reagent grade acetone was found to give no polarographic waves in the potential range normally employed.

Results

The half-wave potentials of the several compounds at different pH values are listed in Table I, along with measured and estimated values of the number of electrons consumed in the reduction process.[1] The behavior of the compounds will be discussed individually.

[1] A more complete list is available and may be obtained by writing to the authors.

Table I. Half-wave potentials of nitro and carbonyl compounds

Substance	pH (aq.)	Wave 1 $-E_{1/2}$	n	Wave 2 $-E_{1/2}$	n	Wave 3 $-E_{1/2}$	n
Fluorenone	1.5	0.61	[1]*	0.86	[1]*		
	3.4	0.74	[1]	0.99	[1]		
	5.0	0.85	[1]	1.02	[1]		
	7.4	1.05	[2]				
	9.8	1.13	—	1.53	—		
	12.0	1.15	[1]	1.49	[1]		
2-Aminofluorenone	1.3	0.62	[2]				
	3.7	0.77	[2]				
	5.0	0.86	[2]				
	7.0	1.02	[2]				
	9.6	1.13	[2]				
	12.0	1.18	[1]	1.45	[1]		
2-Nitrofluorenone	1.4	0.20	4	0.68	2	0.98	2
	4.0	0.38	[4]	0.84	[2]		
	6.5	0.54	[4]	1.03	[2]		
	9.6	0.74	[4]	1.16	[2]		
	11.0	0.85	[4]	1.21	—		
4-Nitrobiphenyl	1.4	0.20	[4]	0.74	[2]		
	3.8	0.38	[4]	0.87	[2]		
	6.8	0.63	[4]				
	9.2	0.76	[4]	1.06	—		
	11.2	0.79	—	1.00	—		
4, 4'-Dinitrobiphenyl	1.4	0.15	8	0.78	2		
	3.6	0.35	[8]	0.91	[2]		
	7.0	0.54	[4]				
		0.68	[4]				
	8.5	0.63	[4]	1.20	[2]		
		0.76	[4]				
	11.7	0.70	—	1.18	—		
2, 4'-Dinitrobiphenyl	1.3	0.24	8	0.82	2		
	3.0	0.33	[8]	0.87	[2]		
	4.0	0.40	[4]				
		0.62	[4]				
	7.9	0.67	[4]				
		0.82	[4]				
	11.7	0.65	—	1.09	—		
2, 5-Dinitrofluorene	1.4	0.20	?				
	4.1	0.39	[8]				
	8.5	0.71	[8]				
	10.9	0.72	—	1.07	—		
	11.6	0.72	—	1.10	—		
2, 5-Dinitrofluorenone	1.5	0.20	8	0.61	2	1.01	2
	4.0	0.36	[8]	0.88	[2]		
	6.3	0.42	4	1.04	2		
		0.56	4				
	8.5	0.55	[4]	1.15	[2]		
		0.71	[4]				
	10.2	0.73	—	1.16	[2]		
	11.5	0.72	—	1.16	[2]		
2, 7-Dinitrofluorenone	1.4	0.25	8	0.68	4	1.00	2
	4.3	0.36	[8]	0.89	[4]		
	6.6	0.42	4	1.07	2		
		0.56	4				
	7.7	0.49	—	1.12	[2]		
		0.65	—				
	10.4	0.73	—	1.20	[2]	1.72	—
	11.3	0.74	—	1.20	[2]	1.75	—

Values of n given in brackets were estimated from the diffusion currents. Values not in brackets were measured coulometrically and rounded off to the nearest whole number.

Fluorenone gives two well-defined one-electron waves in both acid and basic media. In the pH range of about 7-9 the waves are merged. In ethanol-water solutions of low alcohol content these waves are usually separate over the entire pH range; however, they are merged in the pH range of 6-8 in solutions which contain a high percentage of alcohol (9) and it is not surprising to find them merged here in a medium which is fairly high in acetone concentration. The 2-amino derivative is reduced in a single 2-electron step throughout the acid range; separation into two waves was not observed until the pH was raised to about 11. At pH 12 the waves were well separated into two one-electron steps. This behavior is in accord with that previously observed for meta-nitrobenzaldehyde (2) except at the highest pH studied.

In the case of 2-nitrofluorenone it is apparent that wave 1 corresponds to the reduction of the nitro group to hydroxylamine, this being a 4-electron step. Wave 2 is obviously due to reduction of the carbonyl, and here too the wave is a 2-electron step. There was no evidence of separation of the carbonyl wave into two steps at any pH although the wave-height did decrease appreciably at high pH values. A third wave was observed at pH 1.4, and the coulometric n-value corresponded to a 2-electron step. This probably corresponds to reduction of the hydroxylamino group to the amine. The wave was not observed at higher pH values.

The behavior of 4-nitrobiphenyl was similar to that of nitrobenzene (10, 11) in the low pH region, two waves of four and two electrons, respectively, being formed. The second wave was not observed in neutral media but did reappear in solutions of pH greater than 8.6. This behavior is not observed with nitrobenzene and may result from the fact that the unsubstituted benzene ring can supply electrons to the substituted ring, thereby facilitating the release of the hydroxyl group and the formation of a reducible quinoid structure (12). A macroelectrolysis was carried out in 0.1M HCl at a potential of −0.50 v. The reduction product was isolated and recrystallized. The melting point (152°-154°C) indicated that the product was 4-hydroxylaminobiphenyl. The product gave a characteristic red color with concentrated sulfuric acid.

At low pH values the compound 4,4'-dinitrobiphenyl gave reduction waves of eight and two electrons, respectively. This contrasts to the behavior shown by p-dinitrobenzene (10) in giving two waves of four and eight electrons. Apparently both nitro groups in the diphenyl compound are reduced to hydroxylamine simultaneously, whereas the two groups in the benzene ring are reduced in separate steps. In the pH range of about 7-10, however, the 8-electron wave of dinitrobiphenyl does split into two 4-electron steps. It is probable that each 4-electron wave corresponds to reduction of a single nitro group to the hydroxylamine, rather than to reduction of the two groups simultaneously to the nitroso stage. At low pH the hydroxylamine can add a proton, and the resulting positively charged group makes easier the reduction of the second nitro group. At higher pH the free hydroxylamine can act as an electron-releasing group, thereby making the reduction of the second nitro group more difficult. This would account for the splitting of the 8-electron wave as the pH is increased. The 2-electron step mentioned above was not present in solution of

about pH 7, but did reappear about pH 8.5. Hence, from pH 8.5 to 10 there were three waves of 4, 4, and 2 electrons, respectively. About pH 10 the first two waves were merged again. Complete reduction of both nitro groups to amines (12 electrons) was not observed at any pH, whereas p-dinitrobenzene did show complete reduction up to pH 4.1 (10).

The behavior of 2,4'-dinitrobiphenyl was very similar to that of the 4,4'-isomer. The initial 8-electron wave split into two 4-electron steps at a lower pH (about 4) and the two did not merge again until about pH 11. This behavior more nearly corresponds to that of m-dinitrobenzene (10) which gives two initial 4-electron waves up to pH 9.2. Again, however, no more than 10 electrons were taken up by the biphenyl compound whereas Pearson found complete reduction of m-dinitrobenzene at low pH values (10).

The behavior of 2,5-dinitrofluorene was different from that of both the dinitrobenzenes and the dinitrobiphenyls. Only one wave, corresponding to an 8-electron reduction, was observed over the pH range of about 1-10. Apparently both nitro groups are reduced simultaneously even though they are in different rings, and rotation of the two rings with respect to one another is not possible. This remained the case even at higher pH values where the 8-electron wave of the dinitrobiphenyls split into two 4-electron steps. Two waves were observed around pH 11 and 12, but in such basic solutions side reactions of the reduction products complicate the picture and the mechanism is complex.

The behavior of the nitro groups of both dinitrofluorenones resembled that of the dinitrobiphenyls more than that of dinitrofluorene. At low pH there was an initial 8-electron wave which split above pH 4 into two 4-electron waves. The waves were merged again at high pH. With both compounds wave 2 is obviously produced by reduction of the carbonyl group. The half-wave potentials are very near the values of those of 2-aminofluorenone and those of the second wave of 2-nitrofluorenone. At all pH values the current corresponded to the uptake of two electrons, there being no indication of a separation into two one-electron steps, nor a significant decrease in current at high pH. Apparently the two hydroxylamino groups in the fluorene nucleus (meta to the carbonyl) greatly decrease the stability of the intermediate free radical formed by addition of one electron to the carbonyl group. The free radical is then reduced at its formation potential and dimerization does not occur. This effect is the same as that previously observed with m-nitrobenzaldehyde.

Both dinitrofluorenones give a 2-electron wave around −1.00 v at pH 1.4. This corresponds to the reduction of one hydroxylamine group to the amine. Wave 2 of 2,7-dinitrofluorenone in solutions of low pH corresponded to an uptake of four electrons. This is probably caused by over-lapping of the waves corresponding to the reduction of the carbonyl group and one of the hydroxylamino groups. In other words at pH 1.4 the 2,7 compound took up 14 electrons, corresponding to complete reduction of both nitro groups to amines, and the carbonyl group to the secondary alcohol. At pH values greater than 4 the reduction of the nitro groups stopped at the hydroxylamine stage, as is normally found for aromatic nitro compounds.

Manuscript received Jan. 18, 1960.

Any discussion of this paper will appear in a Discussion Section to be published in the June 1961 JOURNAL.

REFERENCES

1. A. Korshunov and L. N. Sazanova, *Zhur. Fiz. Khim.*, **23**, 1299 (1949).
2. R. A. Day, Jr. and R. M. Powers, *J. Am. Chem. Soc.*, **76**, 3085 (1954).
3. E. Gergeley and T. Iredale, *J. Chem. Soc.*, **1953**, 3226.
4. R. Portillo and G. Varela, *Anales fis. y quim.*, **40**, 839 (1944); *Anales bromatol*, **2**, 147 (1950).
5. R. M. Powers and R. A. Day, Jr., *J. Am. Chem. Soc.*, **80**, 808 (1958).
6. J. J. Lingane and S. L. Jones, *Anal. Chem.*, **22**, 1169 (1950).
7. J. J. Lingane, "Electroanalytical Chemistry," p. 251, Interscience Publishers, Inc., New York (1953).
8. C. W. Bennett, W. G. Jewsbury, and J. P. Dupuis, *J. Am. Chem. Soc.*, **68**, 2489 (1946); C. W. Bennett and W. W. Muelder, *ibid.*, **75**, 6039 (1953).
9. R. A. Day, Jr., S. R. Milliken, and W. D. Shults, *J. Am. Chem. Soc.*, **74**, 2741 (1952).
10. J. Pearson, *Trans. Faraday Soc.*, **44**, 683 (1948).
11. J. E. Page, J. W. Smith, and J. G. Waller, *J. Phys. Colloid Chem.*, **53**, 545 (1949).
12. I. M. Kolthoff and J. J. Lingane, "Polarography," Vol. II, p. 748, Interscience Publishers, New York (1952).

Kinetics of the Oxidation of Pure Tungsten from 500° to 1300°C

E. A. Gulbransen and K. F. Andrew

Chemistry Department, Westinghouse Electric Corporation, Pittsburgh, Pennsylvania

ABSTRACT

Kinetic studies were made on the oxidation of tungsten from 500° to 1300°C for time periods up to 6 hr, and for oxygen pressures from 0.1 atm to 0.00132 atm. The rate data were fitted to the parabolic rate law. A number of deviations and transitions were observed. For all of the experiments the initial slopes of the parabolic rate law plots were smaller than the final values found for thick films. A transition in the rate of oxidation was observed for weight gains of 2500-4000 $\mu g/cm^2$ at temperatures of 650°-800°C. Photographs of the oxidized surface above 650°C show that oxidation occurs in a preferential manner at the edges. Pressure had a strong effect on the rate of oxidation for the experiments above 950°C. At 1200°C weight loss curves were observed for pressures as high as 0.1 atm. Above 1200°C the oxidation reaction is similar to the combustion of graphite. The rate of oxidation is limited by the volatility of WO_3, the diffusion of oxygen to the surface, and the diffusion of W_3O_9 away from the surface.

The behavior of tungsten and its surface oxides in oxidizing and neutral atmospheres and in vacuum at high temperature is an interesting scientific problem. This paper presents results of an extensive study of the following problems: (*a*) the effect of time and temperature on the rate of oxidation of tungsten from 500° to 1300°C, (*b*) the effect of pressure on the time course of oxidation at four temperatures, (c) physical structure and crystal structure of the oxide scale, and (*d*) mechanism of reaction.

The oxidation of tungsten below 500°C has been studied by Gulbransen and Wysong (1) and by Gorbounova and Arslambékov (2). Gulbransen and Wysong (1) found the oxidation to follow the parabolic rate law between 400° and 500°C. Deviations were found to occur at 550° and below 400°C. A heat of activation of 45,650 cal/mole was calculated from the parabolic rate law constant. Tungsten oxides were found to volatilize at temperatures as low as 800°C for thick oxide films. Thin oxide films were found to require a higher temperature for volatilization of WO_3. Gorbounova and Arslambékov (2) found that the heat of activation for the temperature range of 390°-487°C was dependent on the surface preparation. Oxidation experiments on electrolytically polished samples gave a heat of activation of 46,500 cal/mole from the parabolic rate law constant while studies on mechanically polished samples gave a heat of activation of 41,000 cal/mole.

Dunn (3) studied the oxidation of tungsten from 700° to 1000°C and found the parabolic rate law was followed. The temperature variation of the parabolic rate law constant was found to follow an exponential law of the Arrhenius type. An inflection was noticed at 850°-900°C and was attributed to a phase change in the oxides.

Scheil (4) studied the oxidation rate at 500° and 700°C over long periods of time and found a linear rate law. This was interpreted as evidence for the presence of a nonprotective film.

An intermediate type of rate law was suggested by Nachtigall (5) and Kieffer and Kolbl (6).

Webb, Norton, and Wagner (7) studied the oxidation of tungsten between 700° and 1000°C. The oxidation reaction was found to follow the parabolic rate law initially but transformed to a linear rate law for thick films. Two oxide layers appeared to form. In the outer layer a porous powdery yellow tungstic oxide WO_3 was formed, while in the inner layer a thin film of adherent oxide of uncertain composition was formed. Two rate processes were combined to give the over-all rate law. These were the parabolic rate law for the inner oxide layer and the linear rate law for the outer layer.

Baur, Bridges, and Fassell (8) studied the oxidation of tungsten rod and sheet from 600° to 850°C as a function of oxygen pressures from 20 to 500 psia. A linear rate law was found. Oxygen pressure increased the rate of oxidation. An equilibrium adsorption process was proposed to occur prior to the rate determining step.

Arkharov and Kozmanov (9) studied the composition of the oxide scale on tungsten between 500°-1350°C and the mechanism of reaction. They concluded that diffusion of oxygen was the rate-controlling process.

Semmel (10) studied the oxidation of tungsten in flowing air from 982° to 1371°C. The oxidation of tungsten was found to change from a linear to a parabolic rate law as the temperature was increased. Oxide melting was proposed to account for the decrease in oxidation rate above 1150°C.

Experimental

Kinetic studies were made using the vacuum microbalance method (11). Small strips of 5 mil tungsten sheet or small lengths of 9 mil wire were

suspended from a sensitive quartz beam microbalance operating inside an all glass and ceramic vacuum system (12). A 1-in. I. D. gas tight mullite furnace tube was used to enclose the sample. This tube was sealed directly to the all-glass vacuum system. No metal, rubber, grease joints or stopcocks were used in the reaction system. Pressures of less than 10^{-8} mm Hg could be attained after 24 hr of pumping (12).

To minimize the reaction of tungsten with the residual gases present in the vacuum system on heating to temperature the sample and furnace tube were pumped for several hours at a pressure of 10^{-6} mm Hg or lower. Purified oxygen was added after the furnace was raised and thermal equilibrium established. The time course of the reaction was followed semicontinuously by reading the balance position relative to a fixed point.

The furnace temperature was maintained constant to ±1.5°C by the use of a calibrated high sensitivity recorder controller and a calibrated Pt-Pt + 10% Rh thermocouple.

Two microbalances of different sensitivities were used. For rapid reactions a specially constructed low sensitivity microbalance was used having a sensitivity of 0.234 x 10^{-3} cm/μg. The high sensitivity balance had a sensitivity of about 0.9 x 10^{-3} cm/μg. Four sample sizes were used corresponding to surface areas of 2.69 cm^2, 1.34 cm^2, 0.61 cm^2, and 0.32 cm^2. The specimens weighed 0.3770 g, 0.1533 g, 0.07019 g, and 0.0315 g, respectively. The wire samples were 1 cm long, weighed 0.0078 g, and had surface areas of about 0.0743 cm^2.

Weight gains of 8 mg could be measured on specimens having a surface area of 0.32 cm^2 and weighing 0.0315 g. This weight gain was equivalent to 94% of the metal reacting with oxygen to form WO_3.

Specimens were prepared from Westinghouse high-purity 5 mil cold rolled tungsten sheet or 9 mil wire. The spectrographic analysis of the sheet was as follows: Al, 0.0001-0.001; Mn, not detected; Fe, 0.001-0.01; Si, 0.001-0.01; Mg, 0.0001-0.001; Mo, 0.001-0.01; Cu, < 0.001; Ag, 0.0001-0.001; Ni, 0.0001-0.001; and Ca, 0.0001-0.001.

Spectroscopic analyses of the tungsten wire were as follows: Al, 0.0004; Mn, < 0.0005; Fe, 0.0020; Si, 0.003; Mg, < 0.0005; Ni, < 0.0005; K, 0.0035; Mo, 0.0015; C, 0.005; O, 0.0024; N, 0.0005; H, 0.0007; Cd, 0.002.

Specimens were cut to shape by a small shearing machine with the specimen hot or cold. The hole for the supporting wire was drilled by a high velocity jet of Al_2O_3. A tungsten etch containing NaOH and $K_3Fe(CN)_6$ was used to remove the scale formed by heating during the shearing operation. Samples were next washed with distilled water.

The surface was polished with emery paper through 4/0 and finally cleaned with petroleum ether and absolute alcohol.

Each oxidation experiment was made with a new specimen. The experimental results were reproducible to 10% except for the temperature ranges where transition effects were observed.

Initially, cold sheared specimens were used. However, the oxidation curves were not reproducible due to excessive splitting of the metal during oxidation. This splitting effect opened up new areas of metal for reaction. Most of the results reported in this study were for hot sheared tungsten samples. Splitting also occurred for hot sheared samples but to a much lesser degree.

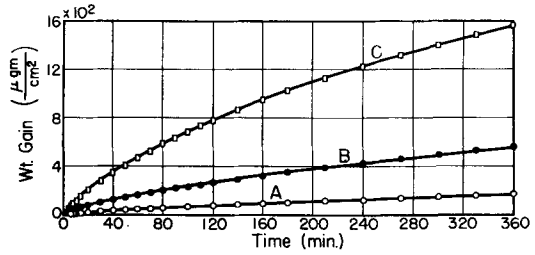

Fig. 1. Oxidation of tungsten, 500°-600°C, 0.1 atm. O_2, abraded, A—500°C, B—550°C, C—600°C.

Results

Effect of temperature.—Abraded hot sheared tungsten strip specimens were oxidized over the temperature range of 500°-1150°C at a pressure of 0.1 atm of purified oxygen. For the 500°-650°C temperature range the time period was 6 hr. At 1150°C, a time period of 6 min was sufficient for nearly complete reaction of the tungsten sample. Figures 1 to 4 show weight gain versus time plots of the experimental measurements. Weight gain is given in micrograms per square centimeter and time in minutes. No correction was made for surface area changes during reaction.

To relate the weight gain in micrograms per square centimeter to oxide thickness in Angstroms a factor of 67.5 could be used. This factor was calculated from a density of 7.16 for the oxide WO_3 and a surface roughness ratio of unity. However, thickness calculations based on this factor were subjected to three limitations for heavily oxidized specimens. Reaction occurs more rapidly at the edges, cracking introduces porosity in the oxide layer, and surface area for reaction decreases. The factor 67.5 is significant only for the early stages of the oxidation reaction.

Figure 1 shows the weight gain curves for the 500°, 550°, and 600°C runs. The rate of oxidation decreases as the oxide thickens which indicates that the oxide scale was limiting the rate of oxidation. Calculations based on Fig. 1 show an average oxide film of about 100,000Å thick was formed on tungsten at 600°C in 6 hr. For the same oxidation conditions a 2120Å thick oxide film was formed on nickel and a 32,600Å thick oxide film was formed on zirconium.

Table I shows a summary of the oxide weight gains after 5, 10, 60, 180, 360 min of oxidation for the complete set of experiments. The color of the oxide at the surface and edges and the stability of the oxide scale to cracking and splitting were also tabulated.

Figure 2 shows oxidation curves for the 600°-750°C runs. S-shaped oxidation curves were observed in some of the experiments. Rapid changes in rate of oxidation occurred in the weight gain vs. time curves for weight gains of about 2,500 to 3,000 μg/cm^2. Small yellow crystals of oxide were formed on the 650°C oxidized surface while green oxide

Table I. Weight gain vs. time, tungsten oxidized at temperatures of 500°-1150°C, 7.6 cm of O_2 pressure, also color and adherence of oxide film

T, °C	Wt. gain at time, min ($\mu g/cm^2$) 5	10	60	180	360	Color	Adherence of oxide Surface	Edge
500	8.72	12.2	49	104	171	Blue black	Stable	Stable
500	19.5	31.0	91	180	283			
550	36.3	54.0	169	353	564	Blue black	Stable	Stable
600	67.4	119	473	1,020	1,560	Blue black with green edges	Stable	Stable
600†	93.5	143	523	1,080	1,620	Blue black	Stable	Split
600*	84.8	136	496	1,020	1,520	Blue black	Stable	Stable
612.5	90.0	149	569	1,270	1,710	Blue black	Stable	Stable
625	130	211	776	1,620	3,160	Black with yellow spots	Spalled	Split
625	140	263	1,340	2,880	4,660			
637.5	152	255	930	1,820	3,680	Black with yellow spots	Spalled	Split
650.0	228	330	1,130	2,930	8,020	Blue black with yellow covering	Spalled	Split
650.0	230	390	1,300	2,310	4,300	Blue black with yellow covering	Spalled	Stable
700	550	930	2,420	—	—	Black with green edges	Stable	Stable
750	1,050	1,600	3,380	—	—	Black with green edges	Stable	Stable
750	1,180	1,790	4,130	11,800	—	Black with green edges	Stable	Stable
750	1,340	1,740	3,740	—	—	Black with green edges	Stable	Split
775	1,470	2,000	4,980	—	—	Black with green edges	Stable	Split
800	1,590	2,140	8,780	—	—	Black with green edges	Stable	Split
800	1,730	2,310	9,300	—	—	Black with green edges	Stable	Split
825	1,830	2,760	—	—	—	Black with green edges	Stable	Split
850	2,980	4,940	16,100	—	—	Blue black, greenish yellowish edges	Stable	Split
900	2,510	4,060	17,600	—	—	Blue black, greenish yellowish edges	Stable	Split
950	3,620	5,940	—	—	—	Black with green edges	Stable	Split
950	3,950	6,140	—	—	—			
950	4,320	6,540	—	—	—			
1000	7,110	14,500	—	—	—	Black with greenish edges	Stable	Split
1050	13,800	21,900	—	—	—			
1100	16,000	25,000	—	—	—	Yellow-black	Stable	Split
1150	14,700	—	—	—	—			

† Heat treated at 1000°C overnight.
* H_2 reduced overnight at 600°C.

crystals formed on the edge of the samples oxidized at 700° and 750°C.

At 750°C a weight gain of 11,800 $\mu g/cm^2$ was found after 3 hr of reaction. Visual observations of the oxidized surface and the kinetic data show that tungsten has poor resistance to oxidation at 750°C. Rapid oxidation occurs in a preferential manner at the edges. Spalling occurred in some of the experiments. If cracking or spalling occurs so that oxygen can react more rapidly with the metal, a rapid change will occur in the rate of oxidation. Due to stresses at the sample edges, cracking occurs first at the edges.

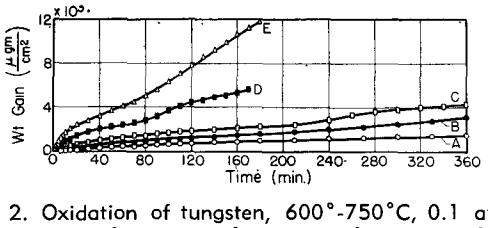

Fig. 2. Oxidation of tungsten, 600°-750°C, 0.1 atm. O_2, abraded, A—600°C, B—625°C, C—650°C, D—700°C, E—750°C.

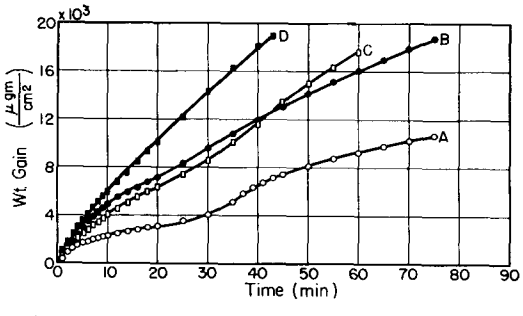

Fig. 3. Oxidation of tungsten, 800° to 950°C, 0.1 atm. abraded, A-800°C, B—850°C, C—900°C, D—950°C.

Figure 3 shows oxidation curves for the 800°-950°C oxidation runs. Again S-shaped curves were found at 800° and 850°C. A weight gain of 16,090 $\mu g/cm^2$ was observed at 850°C in 1 hr. Examination of the sample showed splitting had occurred at the edges. Calculations based on Fig. 1-3 shows that the increase in rate of oxidation with temperature becomes smaller above 800°C.

Figure 4 shows oxidation curves for the 950° to 1150° range of temperature. Reaction times of 6-45 min gave nearly complete reaction of the tungsten to form WO_3.

The 1100°C oxidation showed an initial reaction rate of 83.0 $\mu g/cm^2/sec$ and an average rate of 41.5 $\mu g/cm^2/sec$ for the 10-min run. Assuming a WO_3 scale is formed, the heat of formation of WO_3 contributes 0.34 $cal/cm^2/sec$ to the sample. Without radiation and convection losses this heat would raise the sample temperature 82°C/sec. Assuming black body conditions, radiation losses alone would limit the total temperature rise to 24°C. After the first minute of reaction the sample would assume a temperature rise of 12°C. However, convection currents in the gas would also transfer heat from the specimen and limit the temperature rise to less than 12°C.

If reaction occurs locally at the edges, local heating can occur which would lead to a higher temperature and a more rapid reaction at the edges. This factor combined with stress conditions at the edges leads to breakdown conditions for oxidation.

Figure 5 shows oxidation curves for the 1100° to 1200°C range of temperature using 9-mil wire specimens. The 1100° and 1150°C runs show initial weight gains. After 2-5 min of oxidation the specimens start to lose weight at a nearly constant rate. The 1200°C curve shows a weight loss immediately after adding oxygen. As fast as oxide is formed evaporation occurs.

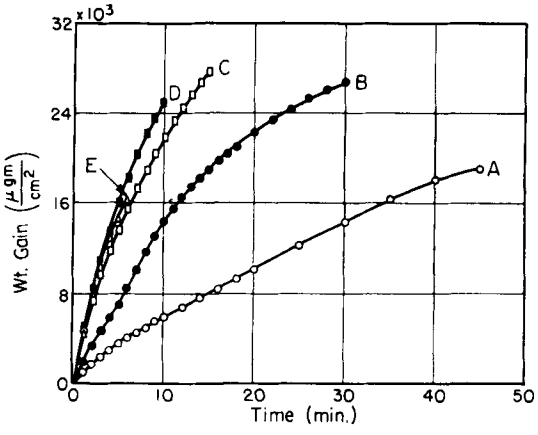

Fig. 4. Oxidation of tungsten, 950°C to 1150°C, 0.1 atm. O_2, abraded A—950°C, B—1000°C, C—1050°C, D—1100°C, E—1150°C.

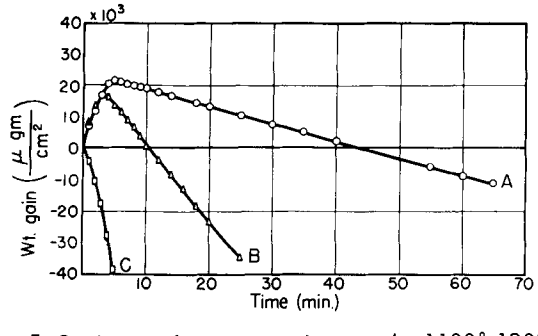

Fig. 5. Oxidation of tungsten, wire sample, 1100°-1200°C, 0.1 atm. O_2, abraded, A—1100°C, B—1150°C, C—1200°C.

The 1100°C run showed an average reaction rate of 85.5 $\mu g/cm^2/sec$ for the first 4 min of reaction. This compares to a value of 83.0 $\mu g/cm^2/sec$ for the initial reaction rate of a strip specimen of tungsten. The wire specimens were oxidized over a fairly long time period to show the effect of evaporation on the oxidation process. At 1200°C the theoretical rate of evaporation of WO_3 was faster than the rate of oxidation. The net result is a weight loss curve.

Above 1200°C the rate of oxidation at 0.1 atm of oxygen pressure was too rapid to measure on our microbalance apparatus. Oxidation and evaporation of the 9-mil tungsten wire specimen was complete in 1 or 2 min of reaction time. To extend our results to 1300°C the oxidation reaction was studied at a pressure of 0.0013 atm. Figure 6 shows the results. Weight loss in $\mu g/cm^2$ was plotted against time in minutes. S-shaped weight loss vs. time curves were found.

Figures 5 and 6 suggest that for temperatures of 1200°C and higher evaporation of WO_3 occurred as fast as the oxide was formed. The form of the oxidation curve was governed by diffusion of oxygen to the surface and geometrical considerations of the decreasing surface available for reaction. As oxide volatilizes the surface area of metal decreased and a slower rate of reaction resulted.

Effect of pressure.—For many metals the effect of pressure on the kinetics of the oxidation reaction is less important than time and temperature. For tungsten which forms a volatile oxide oxygen pressure and the pressure of inert gases are very important.

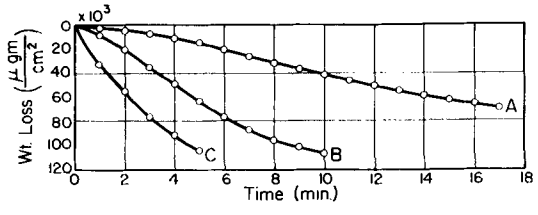

Fig. 6. Oxidation of tungsten, wire sample, 1200°-1300°C, 0.0013 atm. O_2, abraded, A—1200°C, B—1250°C, C—1300°C.

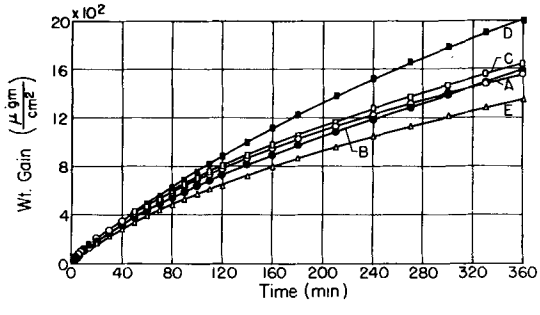

Fig. 7. Oxidation of tungsten at 600°C, effect of O_2 pressure, A—0.1 atm., B—0.068 atm., C—0.0355 atm., D—0.0132 atm., E—0.0079 atm.

Three temperatures were chosen for the studies on the pressure effect using strip specimens, 600°, 950°, and 1050°C. Additional experiments were made at 1000° and 1100°C. Figure 7 shows oxidation curves at 600°C for five pressures between 0.1 atm and 0.0079 atm. Each curve shows a slowly decreasing rate of reaction as the oxide thickens. Decreasing the oxygen pressure from 0.1 atm to 0.0132 atm slightly increased the rate of oxidation. The effect of pressure is small on the rate of oxidation. At 600°C the volatility of WO_3 was unimportant in the dry oxidation of pure tungsten. Figure 8 shows the effect of oxygen pressure on the rate of oxidation at 950°C together with the volatility curve of WO_3 (13, 14). Decreasing the oxygen pressure lowers the rate and extent of oxidation. The volatility of WO_3 and diffusion of WO_3 away from the surface has affected the time course of oxidation.

Figure 9 shows the effect of oxygen pressure on the time course of oxidation at 1050°C together with the volatility curve for WO_3 (14). At this temperature the oxygen pressure has a major effect on the time course of the reaction. For oxygen pressures of

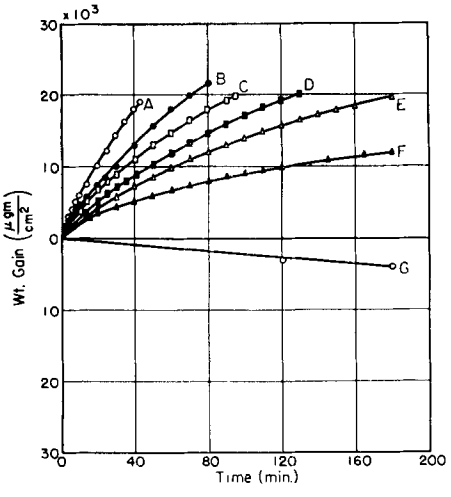

Fig. 8. Oxidation of tungsten, at 950°C, effect of pressure, A—0.1 atm., B—0.047 atm., C—0.0118 atm., D—0.00528 atm., E—0.0033 atm., F—0.00132 atm., G—volatility WO_3.

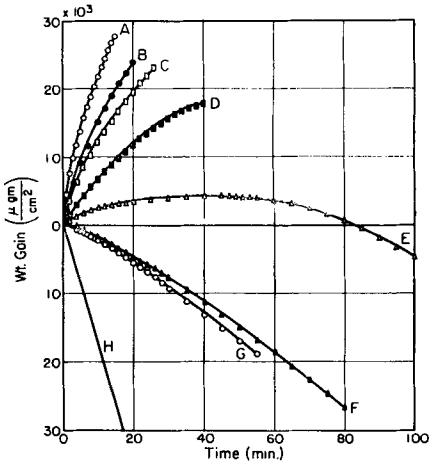

Fig. 9. Oxidation of tungsten at 1050°C, effect of pressure, A—0.1 atm., B—0.0512 atm., C—0.0263 atm., D—0.0112 atm., E—0.0066 atm., F— 0.0033 atm., G—0.00131 atm., H—volatility WO_3.

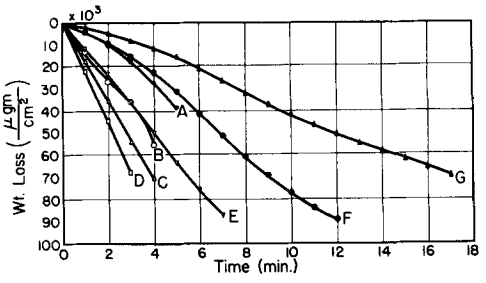

Fig. 10. Oxidation of tungsten, wire sample, at 1200°C, effect of pressure, abraded, A—0.1 atm., B—0.047 atm., C—0.025 atm., D—0.012 atm., E—0.0066 atm., F—0.0033 atm., G—0.0013 atm.

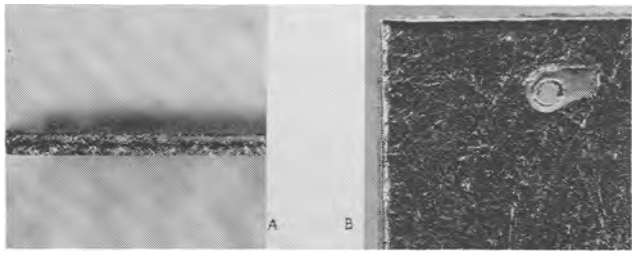

Fig. 11. Photograph Oxidized Tungsten Sample 750°C., 0.1 atm. of O_2, 2 Hours, Hot Sheared, 20x, A. Edge, B. Surface.

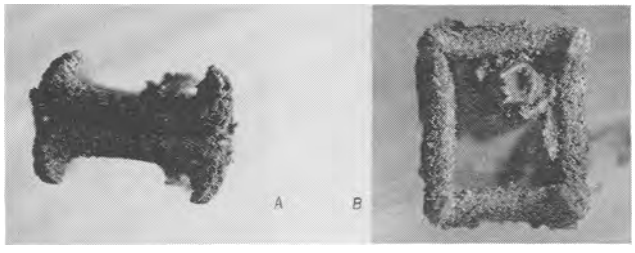

Fig. 12. Photograph Oxidized Tungsten Sample 950°C., 0.1 atm. O_2, 54 minutes, 20x, Hot Sheared, A. Edge, B. Surface.

0.0033 atm and lower, curves F and G, a weight loss is observed. This plot demonstrates the fact that two processes control the weight gain vs. time curves at 1050°C. The first process is the formation of the oxide scale and the second process is the volatility of WO_3 and its diffusion into the gas phase. The latter process is a function of the density of the oxygen atmosphere surrounding the specimen. Curve H shows the volatility curve of WO_3 in vacuum (14).

Table II summarizes the studies on the pressure effect at the temperatures of 600°-1100°C.

Figure 10 shows a study of the effect of oxygen pressure on the oxidation of wire specimens of tungsten at 1200°C for 7 pressures. Table III summarizes the data. Weight loss curves were obtained for all pressures at 1200°C. The maximum weight loss curve occurs at an oxygen pressure of 0.012 atm. The decrease in the rate of weight loss below 0.012 atm oxygen pressure is probably due to the lower rate of oxidation. Again S-shaped curves were obtained for the lower oxygen pressures. The S-shaped curve is due to the decrease in surface area.

Photographic studies.—To show the localized nature of the oxidation reaction at the edges a number of the oxidized samples were photographed at 20 X magnification. Figures 11-12 show photographs of both the edge and surface of the oxidized metal

Table II. Weight gain vs. time, tungsten oxidized at temperatures of 600°-1100°C, varying O_2 pressure, also color and adherence of oxide film

T, °C	O_2 pressure, cm Hg	($\mu g/cm^2$) Wt. gain at time, min 5	10	60	180	360	Color	Adherence of oxide Surface	Edge
							Green edges		
600	7.6	67.4	119.0	473	1,030	1,560	Blue black	Stable	Stable
600	5.2	57.5	104	438	970	1,570	Black	Stable	Stable
600	2.7	71.0	119	480	1,060	1,640	Black	Stable	Spilt
600	1.0	74.8	125	492	1,380	2,000	Black	Stable	Spilt
600	0.50	67.4	109	393	860	1,350	Black	Stable	Stable
950	7.6	3,950	6,140	—	—	—			
950	3.6	2,970	4,660	18,800	—	—			Spilt
950	1.9	2,360	3,790	—	—	—			Spilt
							Green edges		
950	0.9	2,300	3,980	14,800	—	—	Grey black	Stable	Spilt
							Green edges		
950	0.4	1,550	2,850	11,900	—	—	Grey black	Stable	Spilt
							Green edges		
950	0.25	1,070	2,100	9,700	19,600	—	Black	Stable	Spilt
							Green edges		
950	0.10	1,370	2,230	6,600	11,900	44,700	Grey black	Stable	Spilt
							Green edges		
1000	7.6	7,100	14,500	—	—	—	Black	Stable	Spilt
1000	0.90	4,000	6,930	22,500	—	—			Stable
1000	0.25	1,330	2,380	8,500	10,700	—			Stable
1050	10.0	14,100	—	—	—	—			Stable
1050	7.6	13,800	21,900	—	—	—			Stable
							Yellow edges		
							Yellow grey		
1050	5.3	10,100	15,800	23,100	—	—	Surface	Stable	Spilt
1050	3.9	9,200	15,000	—	—	—			Stable
1050	2.0	7,500	12,200	—	—	—			Stable
1050	0.86	3,820	6,850	—	—	—			Stable
1050	0.50	1,560	2,520	3,700	—	—			Stable
1050	0.25	—535	—1,820	18,800	—	—	Grey black	Stable	Stable
1050	0.10	—907	—2,180	—	—	—	Grey black	Stable	Stable
1100	7.6	16,000	25,000	—	—	—	Yellow black	Stable	Spilt
1100	3.9	11,600	19,100	—	—	—			
1100	0.25	—4,730	—10,700	—	—	—	Grey black	Stable	Stable

samples for experiments at 750°C and 950°C. Table IV shows a summary of the oxidation conditions, weight gains, and photographic observations on these samples. Initial breakdown of the oxide-metal interface occurs at the edges during oxidation for both hot and cold sheared samples. However, breakdown occurs on the cold sheared surfaces at an earlier stage of the reaction.

Rate law correlation.—Both the linear and parabolic rate laws have been used to explain the oxidation rate of metals. The linear rate states

$$W = At + C$$

A surface or interface reaction may control the rate of oxidation. In the above equation W is the weight gain, t is the time, and A and C are constants. The parabolic rate law states

$$W^2 = At + C$$

Here the symbols have the same meaning as before. This equation has been derived from fundamental principles of diffusion (15, 16).

To test the application of the parabolic rate law and to show the existence of rapid changes in the rate of oxidation, plots were made of the square of the weight gain versus time over the temperature range. Because of the complex nature of the oxidation reaction of tungsten it is not expected that the parabolic rate law will hold over the complete time, temperature, and pressure conditions. Initial values of the constants probably represent diffusion controlled reactions. Changes from these conditions can be seen by the use of the parabolic rate law plots.

Figure 13 shows the parabolic rate law plot for the 500°C run. The plot shows a steady increase in the value of the rate law constant. An initial value of 4.18×10^{-13} $(g/cm^2)^2$ sec^{-1} was calculated for A. The value for the 5-6 hr time period was 1.75×10^{-12} $(g/cm^2)^2$ sec^{-1}. At temperatures as low as 500°C the protecting properties of the oxide decrease as the oxide thickens.

Similar plots for the oxidation runs at 550° and 600°C show curves like those of Fig. 13. At 625°C a

Table III. Weight gain vs. time, 9-mil tungsten wire, oxidized at 1200°C, varying O_2 pressure

O_2 pressure, Cm of Hg	($\mu g/cm^2$) Wt. gain at time, min 1	2	4
7.6	—4,000	—10,500	—27,500
3.57	—12,000	—27,000	—55,000
1.9	—17,000	—35,500	—70,500
0.91	—22,000	—44,500	—
0.502	—12,500	—23,000	—36,000
0.251	—4,000	—9,500	—22,500
0.099	—2,500	—5,000	—11,500

Table IV. Summary photographic studies oxidation of tungsten 600°-950°C

Temp, °C	Oxidation conditions Pressure, atm	Time	Type of Shearing	Weight gain $\mu g/cm^2$	Results
600	0.0343	6 hrs	Cold	2,850	Shows initial breakdown of oxide at edges
725	0.10	75 min	Cold	5,460	Reaction at edges with cracking
750	0.10	2 hrs	Hot	5,350	Reaction at edges and scratches on surface
850	0.10	75 min	Hot	18,700	Strong edge reaction with cracking
950	0.10	54 min	Hot	20,000	Strong edge reaction extending over surface

transition was noted from parabolic plots of the rate of oxidation data. Figure 14 shows the parabolic rate law plot of the 650°C run. A transition was found after 200 min of reaction or at an oxide thickness of 2400 $\mu g/cm^2$. After 300 min of reaction, Fig. 14 shows the parabolic rate law was again obeyed.

Transitions were found also for the oxidation runs at 650°, 700°, 750°, and 800°C. However, the weight gain for transition was larger. Table V shows the initial and final parabolic rate law constants.

Figure 15 shows a parabolic rate law plot of the 900°C oxidation run. The slope of the plot increased during the first 45 min of reaction to a nearly constant value. The initial value of A was 1.725×10^{-8} $(g/cm^2)^2$ sec^{-1} and the final value 1.45×10^{-7} $(g/cm^2)^2$ sec^{-1}. Similar parabolic rate law plots were found for the 950°, 1000°, 1050°, 1100°, and 1150°C runs.

This analysis suggests that the rate of oxidation of tungsten is not a simple function of the time of reaction. Adhesion of the oxide scale to the metal is very important. Localized cracking of the oxide scale may account for the rapid changes observed in the rate of oxidation.

Figure 16 shows a logarithmic plot of the parabolic rate law constants A vs. $1/T$. Three values from our earlier work (1) at 400°, 450°, and 500°C were included. In addition the data obtained by Dunn (3) and by Webb, Norton, and Wagner (7) were included in the plots. Since the parabolic rate law constants were time dependent, both the initial and final values of the constants from our data were plotted.

Three straight lines were drawn to represent the data. The dashed line in Fig. 16 was drawn to present the initial values of the parabolic rate law constants and the earlier values of Gulbransen and Wysong (1). The slope of the dashed line gave a heat of activation of 44,500 cal/mole. This value was found also by Gulbransen and Wysong (1) to explain the oxidation of tungsten for temperature of 400° to 500°C. Gorbounova and Arslambékov (2)

Table V. Parabolic rate law constants hot sheared tungsten, abraded, 500°-1150°C

Temp, °C	$A\ (g/cm^2)^2\ sec^{-1}$ initial value	$A\ (g/cm^2)^2\ sec^{-1}$ final value
500	1.59×10^{-12}	4.72×10^{-12}
550	5.56×10^{-12}	1.97×10^{-11}
600	3.34×10^{-11}	1.168×10^{-10}
600	3.34×10^{-11}	1.36×10^{-10}
625	1.39×10^{-10}	1.667×10^{-9}
650	2.78×10^{-10}	6.75×10^{-9}
700	8.33×10^{-10}	4.03×10^{-9}
750	3.17×10^{-9}	8.22×10^{-9}
750	5.00×10^{-9}	2.21×10^{-8}
750	3.67×10^{-9}	2.10×10^{-8}
775	5.56×10^{-9}	2.87×10^{-8}
800	8.05×10^{-9}	3.13×10^{-8}
800	6.67×10^{-9}	3.00×10^{-8}
850	3.22×10^{-8}	1.017×10^{-7}
900	1.725×10^{-8}	1.45×10^{-7}
950	4.13×10^{-8}	2.01×10^{-7}
1000	1.4×10^{-7}	3.33×10^{-7}
1050	4.7×10^{-7}	9.34×10^{-7}
1100		6.7×10^{-7}
		1.08×10^{-6}
1150		8.1×10^{-7}

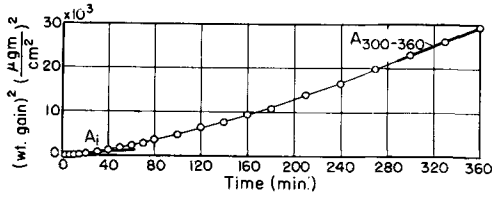

Fig. 13. Oxidation of W, parabolic plot, abraded through 4/0, 500°C, 0.1 atm. of O_2, $A_{initial} = 4.18 \times 10^{-13}$, $A_{300-360} = 1.75 \times 10^{-12}$ $(g/cm^2)^2$ sec^{-1}.

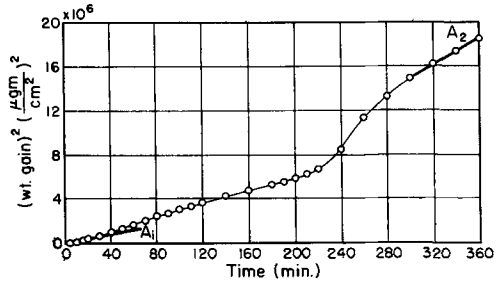

Fig. 14. Oxidation of W parabolic plot, abraded through 4/0, 650°C, 0.1 atm. of O_2, $A_{initial} = 3.33 \times 10^{-10}$, $A_{300-360} = 1.03 \times 10^{-9}$ $(g/cm^2)^2$ sec^{-1}.

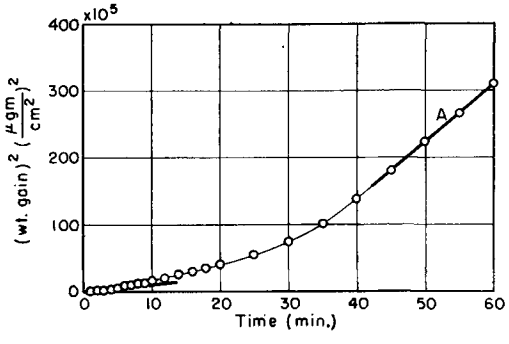

Fig. 15. Oxidation of W, parabolic plot, abraded through 4/0, 900°C, 0.1 atm. of O_2, $A_{45-60} = 1.45 \times 10^{-7}$ $(g/cm^2)^2$ sec^{-1}.

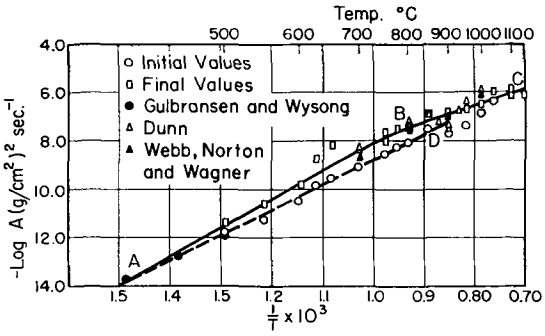

Fig. 16. Log A vs $\frac{1}{T}$, ΔH_{AB} = 54,500 cals per mole, ΔH_{BC} = 32,500 cals per mole, ΔH_{AD} = 44,500 cals per mole.

obtained values of the heat of activation for the low-temperature range of 300°-487°C of 41,000-46,500 cal/mole.

44,500 calories per mole probably represents the heat of formation of defects and the heat of activation of diffusion of metal atoms for the early stage of oxidation when the oxide film is protecting the metal. The final values for the parabolic rate law constants could be fitted by two straight lines. The values below 750°C were fitted by a straight line which gave a heat of activation of 54,500 cal/mole. The high final values for A found between 600° and 700°C were due to the transition stage in the oxidation process. Above 750°C the parabolic rate law constants were fitted to a line having a heat of activation of 32,500 cal/mole. No interpretation can be given to the final values of the parabolic rate law constants.

The parabolic rate data of the several groups of investigators were in fair agreement with our data.

Effect of surface treatment and sample pretreatment.—Three sample pretreatments are compared: no pretreatment, reduced in H_2 at 600°C, and preheated to 1000°C in vacuum of less than 10^{-6} mm Hg. The results show that the as-received and abraded sample oxidized a little slower than abraded samples given a hydrogen or vacuum pretreatment. For practical purposes the rate of oxidation at 600°C is nearly independent of atmospheric pretreatments.

Two surface pretreatments are compared: electropolishing and abrasion. Electropolishing was carried out in a KOH solution. The results show that the electropolished sample reacted at a little slower rate than the abraded sample.

Crystal structure studies of oxide scales.—An extensive study was made of the crystal structure of the oxide scales formed after oxidizing tungsten from 600° to 1100°C. A Guinier-Hägg (17-21) type of focusing x-ray camera was used to bring out the presence of minor phases in the oxide scale. Monochromatic NiK_α radiation was used.

Monoclinic WO_3 was the principal oxide found in the scale for the complete temperature range. Studies on a sectioned oxide scale showed the outer layer to be WO_3 and the inner layer adjacent to the metal WO_3 and W_4O_{11}. The crystal structures of the oxygen compounds of tungsten have been reviewed by Hägg and Magnéli (21). The x-ray diffraction method is not sensitive enough to show the oxide in contact with the metal.

Discussion of Mechanism of Oxidation

Experimental studies show that the time course of the oxidation curves depends strongly on the temperature, pressure, and the stress pattern of the metal at the edges. Eleven or more physical and chemical phenomena must be considered in developing a complete picture of the oxidation of tungsten. These are: (*a*) normal diffusion processes involving the formation of defects and the diffusion of metal or oxygen atoms through the oxide scale, (*b*) the adhesion of the oxide scale to the metal at the surface and at the specimen edges, (*c*) heat effects associated with the high rates of oxidation at the surface, (*d*) solid phase chemical reactions occurring in the oxide scale, (*e*) decrease in surface area as a result of scale formation, (*f*) diffusion of oxygen through the gas phase to the surface for reaction, (*h*) chemisorption of oxygen at the oxide or at the clean metal surface, (*i*) chemical reaction of oxygen at a clean metal surface, (*j*) desorption or evaporation of WO_3, (*k*) diffusion of WO_3 away from the surface into the gas phase, (*l*) decrease in surface area as a result of volatility of WO_3.

No one rate process can be used to explain the complex oxidation reaction of tungsten. At low temperatures the kinetics may be interpreted in terms of a simple diffusion process. However, at high temperature, the oxidation of tungsten closely resembles the combustion of graphite. It is useful to consider the reaction for three temperature ranges (*a*) 500°-600°C, (*b*) 650°-950°C and (*c*) 1000°-1300°C.

Mechanism of oxidation 500°-600°C.—For this temperature range and for lower temperatures the oxidation reaction is probably diffusion controlled. No evidence was found for local cracking at the specimen edges at 500°C after 6 hr of reaction. At 600°C some localized cracking was observed. A parabolic rate law plot of the 500°C data shows the rate law constant to increase with time. We conclude that the protective properties of the oxide scale are steadily becoming poorer. This may be a result of compositional changes in the oxide scale or to microscopic cracking of the oxide scale at the oxide-metal interface. These small cracks although not resulting in spalling give a short circuit for oxygen to reach the metal for reaction.

Composition changes are thermodynamically feasible and have been observed by Hickman and Gulbransen (22) in an earlier electron diffraction study. WO_3 is formed first and appears in the outer part of the scale. Solid phase reactions of tungsten with the higher oxide lead to the formation of WO_2 or other oxides of tungsten.

X-ray diffraction studies on the 600°C oxidized sample show no evidence for an oxide other than WO_3. This appears to conflict with the earlier studies of Hickman and Gulbransen (22). We interpret this discrepancy as due to the difficulties in sampling for our x-ray diffraction method and to the fact that Hickman and Gulbransen (22) worked at lower pressure and shorter oxidation times.

Pressure has only a minor influence on the time course of oxidation for this temperature range.

Mechanism of oxidation 650°-950°.—For this temperature range several new factors must be used to explain deviations from diffusion controlled oxidation. Residual stresses and strains in the metal at the edges give a highly localized oxidation reaction. Pressure also plays an active role at 950°C.

A rapid change is found in the oxidation curves at a scale thickness of 2000-4000 $\mu g/cm^2$. The change is one which leads to a more rapid oxidation. Localized edge type of oxidation develops and adhesion of the oxide scale becomes poor. Crystal structure studies show WO_3 to be the oxide formed.

We interpret the oxidation reaction in this temperature range as follows: A thin layer of oxide scale is formed according to the general laws of diffusion. After reaching a certain thickness the oxide cracks away from the metal at local areas. The cracked areas give access to oxygen and healing occurs until the critical thickness of oxide is again formed. This cracking process is a continuous one over the surface as a function of time. Since only the thin oxide film is formed under diffusion controlled conditions the major part of the oxide scale has little influence on the kinetics of the reaction.

Due to the intimate contact of oxygen with most of the oxide scale the highest oxygen containing oxide is formed, namely WO_3. This is observed in all of the x-ray diffraction studies. For thick oxide scales the only place where WO_2 could form would be in the thin oxide film at the metal-oxide interface.

Since oxygen pressure has a major influence on the time course of oxidation at 950°C the volatility of WO_3 in low oxygen atmospheres is beginning to influence the reaction.

Mechanism of oxidation 1000°-1300°C.—For this temperature range the mechanism of oxidation changes greatly with temperature and pressure. At 1000°C and 0.1 atm oxygen pressure an oxide scale is formed while at 1200°C and higher at 0.01 atm pressure no measurable oxide pickup is noted. However, a thin oxide scale may still be present on the metal. The oxide evaporates as fast as it is formed. We conclude the time course of oxidation is determined by the rate at which oxygen arrives at the surface, by diffusion of the volatilized oxide away from the surface, and by geometrical considerations of the sample surface area. At some temperature in this temperature range the theoretical rate of evaporation is greater than the rate of oxidation. This temperature depends on the oxygen pressure.

The mechanism of oxidation of tungsten at 1200°C and higher is similar to that observed in the combustion of carbon. Gulbransen (23) has derived rate equations for the combustion of artificial graphite under idealized conditions of low-temperature combustion at 425°-575°C and for small amounts of burning.

The combustion reaction of tungsten in oxygen is more difficult to study than the combustion of carbon since reaction variables are different. Oxide scales are formed on tungsten below 1200°C at 0.1 atm pressure. Therefore, studies must be made at temperatures above 1200°C where rapid reaction occurs. Sample area considerations are important and the time period of reaction is very short. Our present methods are not sufficiently accurate for us to apply the absolute reaction rate theory (24) and to analyze the rate-limiting processes.

Other interpretations.—Semmel (10) suggests that the change in the oxidation curves above 1150°C is due to melting of the oxide. No evidence was presented except that the high-temperature runs showed the specimen to have rounded edges. Volatilization of WO_3 could also account for the rounding of the edges. We have seen no evidence for melting in our studies.

Arkharov and Kozmanov (9) interpret the change in the rate of oxidation above 1150°C as due to a structural transformation in the oxide. We suggest from our studies on the effect of pressure that volatility of the oxide is the major factor controlling the oxidation reaction in the temperature range of 1100°-1200°C.

Summary

1. Rate measurements were made on the oxidation of tungsten from 500° to 1300°C, for times up to 6 hr, and for oxygen pressures from 0.1 to 0.00132 atm.

2. The effect of surface preparation and sample pretreatment was also studied.

3. The kinetic data were fitted to the parabolic rate law. However, a number of deviations were observed. For all experiments the initial parabolic rate law constants were smaller than the final values found for thicker films. A transition was observed in the rate of oxidation for weight gains of 2500 to 4000 $\mu g/cm^2$ at temperatures of 650°-800°C.

4. The parabolic rate law data plotted on a logarithmic plot as a function of $1/T$ showed three straight lines. The initial values of the rate law constants were fitted to a line which gave a heat of activation of 44,500 cal/mole. The final values were fitted to another line which gave a heat of activation of 54,500 cal/mole. Above 800°C the final values could be fitted to a straight line which gave a heat of activation of 32,500 cal/mole.

5. Pressure had a strong effect on the rate of oxidation for the experiments at 950°, 1050°, and 1200°C. For these temperatures the volatility of WO_3 must be considered. At 1200°C weight loss curves were observed for pressures as high as 0.1 atm. At this temperature, diffusion of oxygen to the specimen limits the rate of oxidation.

6. Photographs of the oxidized specimens for temperatures of 600°-950°C show that the oxidation of tungsten occurs in a preferential manner at the edges. This causes localized heating and further reaction.

7. The poor protective properties of the oxide scale on tungsten is attributed to three factors: (*a*) the rapid oxidation reaction, (*b*) the poor adherence of the oxide to the metal, and (*c*) the volatility of the tungsten oxides.

Acknowledgment

The authors also wish to acknowledge the careful work of Mr. A. Merlin.

Manuscript received Nov. 5, 1959. This paper was prepared for delivery before the Chicago Meeting, May 1-5, 1960. This research was supported in part by the U.S. Air Force under Contract No. AF33-(616)-5770, Wright Air Development Center, Wright-Patterson Air Force Base, Ohio.

Any discussion of this paper will appear in a Discussion Section to be published in the June 1961 JOURNAL.

REFERENCES

1. E. A. Gulbransen and W. S. Wysong, *Am. Inst. Mining Met. Engrs.*, **175**, 611 (1948).
2. K. M. Gorbounova and V. A. Arslambékov, *Proc. Acad. Sci.* U.S.S.R., Phys. Chem. Section (English Translation) **119**, 151 (1958).
3. J. S. Dunn, *J. Chem. Soc.*, **1929**, 1149.
4. E. Scheil, *Z. Metallkunde*, **29**, 209 (1937).
5. E. Nachtigall, *ibid.*, **43**, 23 (1952).
6. R. Kieffer and F. Kolbl, *Z. anorg. u. allgem. Chem.*, **262**, 229 (1950).
7. W. W. Webb, J. T. Norton, and C. Wagner, *This Journal*, **103**, 107 (1956).
8. J. B. Baur, D. W. Bridges, and W. M. Fassel, Jr., *ibid.*, **103**, 226 (1956).
9. V. I. Arkharov and Yu. D. Kozmanov, *Fiz. Metal. i Metalloved, Akad Nauk S.S.S.R. Ural Filial*, **2**, 361 (1956). Henry Brutcher Translation No. 4104.
10. J. W. Semmel, "High Temperature Materials," p. 510-519, John Wiley & Sons, Inc., New York (1959).
11. E. A. Gulbransen, "Advances in Catalysis," Vol. V, p. 119-175, Academic Press, Inc., New York (1953).
12. E. A. Gulbransen and K. F. Andrew, *Ind. Eng. Chem.*, **41**, 2762 (1949).
13. J. Berkowitz, W. A. Chupa, and M. G. Inghram, *J. Chem. Phys.*, **27**, 85 (1957).
14. P. E. Blackburn, M. Hoch, and H. Johnston, *J. Phys. Chem.*, **62**, 769 (1958).
15. C. Wagner, *Z. Physik. Chem.*, **21B**, 25 (1933).
16. C. Wagner, "Atom Movements," p. 153-73, American Society for Metals, Cleveland, Ohio, (1951).
17. A. Guinier, "X-Ray Crystallographic Technology," Hilger and Watts Ltd., London (1952).
18. A. Guinier, *Ann. Phys.*, **12**, 161 (1939).
19. R. M. M. D'Eye, A.E.R.E. Report, Harwell, Berks., England (1954).
20. R. Ruka nd K. F. Andrew, Westinghouse Research Report 6-40807-11-R3, May 1959.
21. G. Hägg and A. Magnéli, *Rev. Pure and Appl. Phys., Australia*, **4**, 235 (1954).
22. J. W. Hickman and E. A. Gulbransen, *Trans. Am. Inst. Mining Met. Engrs.*, **171**, 371 (1947).
23. E. A. Gulbransen, *Ind. and Eng. Chem.*, **44**, 1045 (1952).
24. K. J. Laidler, S. Glasstone, and H. Eyring, *J. Chem. Phys.*, **8**, 659 (1940).

Thermodynamic Properties of the Aluminum-Silver System

Thomas C. Wilder and John F. Elliott

Department of Metallurgy, Massachusetts Institute of Technology, Cambridge, Massachusetts

ABSTRACT

An electrode potential study of the liquid aluminum-silver system has been conducted with the cell

$$\mathrm{Al(1)} \mid \mathrm{Al^{+++}\ (in\ KCl + NaCl)} \mid \mathrm{Al\ in\ Ag(1)}$$

in the temperature range 700°-980°C. The activities of both components, F_i^M, F_i^E, F^E, and TS^E were determined for 700° and 900°C, and H_i^M and H^M for the temperature range of 700°-980°C. The activity curves are found to be similar in shape to those estimated by Chou and Elliott, but they are more ideal in the vicinity of pure Al. Values for log γ_{Al} in the liquid systems Al-Fe, Al-Fe-C, and Al-Fe-Si-C at 1600°C have been redetermined using the distribution data of Chipman and Floridis, and Chipman and Langenberg.

The reversible concentration cell has proven in many cases to be a valuable and reliable method for determining the thermodynamic properties of an alloy system. When properly arranged and operated reversibly, this type of cell can be used to measure the potential between a pure metal, usually the selected reference state, and its alloy with another metal or metals. This paper reports the results of an experimental study of the liquid aluminum-silver system between 700° and 980°C with the cell:

$$\mathrm{Al(liq)} \mid \mathrm{Al^{+++}(in\ molten\ KCl) + NaCl} \mid$$

$$\mathrm{[Al\ in\ Ag](liq)}$$

The driving force is the net transfer of aluminum from the pure state on the left to the alloy on the right. In this paper, the standard state for aluminum is the pure liquid metal. Several exceptions to this are noted as they arise.

The virtual cell reaction is

$$\mathrm{Al(pure\ liquid)} \rightarrow \mathrm{[Al\ in\ Ag](liquid)} \qquad (I)$$

with three Faradays being transferred per gram atom of aluminum. The several thermodynamic relationships based on the reversible potential E of the cell are:

$$\overline{F}_{Al} - F^{\circ}_{Al} = F^{M}_{Al} = -3\mathbf{F}E \qquad [1]$$

$$\overline{S}_{Al} - S^{\circ}_{Al} = S^{M}_{Al} = 3\mathbf{F}\left(\frac{\partial E}{\partial T}\right)_{X_{Al},\,P} \qquad [2]$$

Also from [1]

$$-3\mathbf{F}E = RT \ln a_{Al} \qquad [3]$$

In these equations **F** is Faraday's constant, 23,063 cal/v eq. It is assumed that the valence of the aluminum ion in the electrolyte is 3. Experimental considerations justifying this assumption are discussed later.

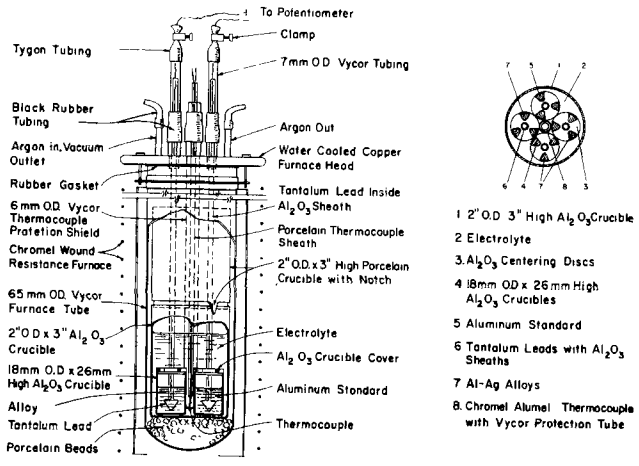

Fig. 1. Cell design. Left, 1A, cell apparatus (only 2 of 4 leads are shown; right, 1B, top view of cell.

The Experiments

Cell design.—Figures 1a and 1b show that each cell contained four electrodes, one of pure aluminum and the other three of aluminum-silver alloys. The metal electrodes were contained in doubly recrystallized pure alumina crucibles (Morganite). The large containing crucible and the sheathing for the tantalum lead wires were of 97% pure vitreous alumina. The small spiders which centered the leads in the electrode crucibles also were of high-purity alumina. The large upper porcelain crucible served as a thermal shield, and by means of holes in the bottom, it helped to guide and locate the cell leads. The chromel-alumel thermocouple was protected by a 6 mm Vycor tube. The lower end of this tube fitted into the central opening between the four electrode crucibles. The whole cell assembly was contained in a 65 mm Vycor tube that was fitted with a water-cooled brass top. Suitable fittings in the top permitted entry of leads, thermocouple sheath, and gas and vacuum connections so that the cell could be evacuated or pressurized as desired.

Cell preparation.—The initial step in making a cell was the preparation of the electrolyte. A sufficient quantity of an equimolar (azeotropic) mixture of KCl and NaCl (C.P.) was purified under vacuum produced by a mechanical pump. The mixture was slowly brought to fusion temperature and then held for 20 hr at 750°C. Several batches were purified by bubbling hydrogen chloride through the fused salt for approximately 10 hr which was followed by vacuum treatment. Cells containing electrolytes prepared in this manner produced potentials which were not as stable as with the straight vacuum treated electrolyte; hence, the simple vacuum treatment was used for all cells. Because of its high volatility, aluminum chloride was purified by subliming it at approximately 190°C under a vacuum of a few mm of Hg. The purified crystals were collected on a water-cooled Pyrex glass cold finger suspended 1 in. above the crude (C.P.) material.

The electrodes were prepared by weighing to the nearest 0.1 mg pieces of the appropriate pure metals. The three high-silver electrodes were prefused. All others were prepared by inserting bits of the pure metals in the electrode crucibles, and fusion occurred as the cell was brought to temperature. Analyses of the pure metals used are shown in Table I.

Table I. Lot analyses of pure metals

Metal	Impurity, wt %	
Aluminum*	Cu	0.002
	Fe	0.002
	Si	0.001
	Other	0.000
	(Al	99.995)
Silver**	Bi	<0.0001
	Cu	0.003
	Fe	<0.0001
	Pb	<0.0001
	(Ag	99.997)

* Gift of the Aluminum Company of America.
** Supplied by the American Smelting and Refining Company.

Tungsten, molybdenum, and tantalum wires were tried as leads initially. Only tantalum resisted attack by the aluminum alloys, and only slight attack was noted up to 900°C with exposure of 20 to 30 hr. Prolonged exposure at above 1000°C resulted in the wire splitting as a result of the formation of a solid brittle product. The temperature excursions used during the experiment were designed to avoid interference from this effect. The leads embrittled severely when exposed to the chloride vapors in the upper portion of the cell but not when in contact with the molten salt. Consequently, each lead was protected with an unbroken sheath of alumina from the electrode surface to the water-cooled head.

The clean cell crucible, alloys, electrode leads, etc., were completely assembled outside the large Vycor tube. With the thermal shield raised slightly above its normal position, the fused KCl-NaCl solution was transferred by a Vycor pipette from the purification tube to the cell. On solidification, the salt held the components of the cell securely in position so that the whole assembly could be handled as a single unit. This technique exposed the salt mixture to the air for a few seconds when it was liquid, and the upper surface after solidification was exposed for approximately ½ hr. In recognition that this was undesirable, a technique was devised for transferring the salt by syphon so it did not contact the air. This method greatly increased the difficulties of assembly and had no apparent effect on the performance of the cells, so it was abandoned in favor of the easier method.

After the salt had cooled sufficiently, pieces of purified $AlCl_3$ (about 5 g) were transferred quickly from a sealed container to the cell. Then the cell was placed in the large Vycor tube and the system was evacuated. This exposed the $AlCl_3$ to the air for no more than 30 sec. Subsequently, the cell tube was pressurized with purified argon and placed in the furnace. All cells were operated with an argon pressure of about 25 mm Hg above atmospheric pressure. Because of the very small pressure co-

efficient of the potential of this type cell, no corrections for the relatively small variations in atmospheric pressure were applied to the potentials read.

Operation of the cell.—A cell was run for approximately 30 hr. During this time potentials were steady and reproducible. A longer time at temperature was possible, but some of the electrolyte volatilized and condensed on the cooler portions of the system. Runs were discontinued before the level of the electrolyte was lowered sufficiently to interfere with the performance of the cell. The concentration of $AlCl_3$ did not change materially from the initial analysis, and repeated checks on the original and final weights of the electrodes showed virtually no change, within a few milligrams, in their weights from that charged. The electrolyte volatilized essentially without changing its concentration which indicated that the $AlCl_3$ had little effect on the azeotropic character of the base composition. At all times the electrolyte was colorless, transparent, and without sediment.

A cell was allowed to remain at 680°-700°C for 12 hr prior to the time measurements were taken. This permitted the cell to "stabilize" and fitted the work schedule. After this period, the potentials differed somewhat from the values obtained immediately after the new cell was brought to temperature. Several typical examples are shown in Table II. This stabilization procedure was followed because it resulted in the potentials being much less sensitive to the flow of small currents incident to taking measurements, and it has been found generally that the initial readings were not reproducible and apparently not reversible.

The temperature sequence followed in a run were usually approximated as follows: (*a*) 700°C, (*b*) 750°C, (*c*) 800°C, (*d*) 720°C, (*e*) 780°C, and (*f*) 850°C. On the high-silver side of the diagram, a similar pattern was followed with 9 or 10 readings being taken, and the final reading was at 983°C. Because of the volatilization problem, temperatures above 900°C were avoided if possible, but it appeared that satisfactory readings could be obtained at 1000°C. Slight attack of the leads and the thermocouple sheath and no attack of the alumina ware were observed in the high-temperature runs.

Sources of Error

Reversibility.—The major problems faced in the operation of a cell for establishing the thermodynamic relationships for a reaction such as Reaction I is that the cell function essentially in a reversible manner, and that the reaction occurring in the cell is actually the one ascribed to it. Several tests performed on the cells studied and a number of observations indicated that the cell used was reversible for the time and temperatures employed. The more significant of the observations were:

1. In seeking the null point at which the potentiometer potential balanced the potential of the cell, a small current from the potentiometer could be passed in either direction through the cell without disrupting the null point. In all cases the null point could be approached with assurance. The readings were not "soft" or vague.

2. Consistent readings were obtained for different cells which had alloy compositions that were the same. A potential reading at a given temperature could be reproduced again after the cell temperature had been raised or lowered. Also, there was no perceptible drift of the potentials with time.

3. The very slight attack on the ceramics and lead wires, the constancy of the $AlCl_3$ concentration in the electrolyte, the constancy of weight of the electrodes, and the absence of silver in the electrolyte indicated that side reactions or the replacement of aluminum by silver were of no consequence. Also, there was no sign of reaction with the other components of the electrolyte. Table III shows that the standard free energies of formation of the other components of the electrolyte were sufficiently low (negative) relative to that of $AlCl_3$ to avoid an exchange reaction.

4. Separate reference electrodes of pure aluminum agreed between themselves within an average of 0.1 mv. Potentials of duplicate alloy electrodes in different runs usually agreed within 0.15 mv at a given temperature. Duplicates were run on all but two of the alloys reported. (Rather than average readings, it was considered to be more suitable to use results from the one of a pair that showed the more stable readings.)

5. Results of a recent study (1) of the behavior of a number of metallic ions in the azeotropic composition of fuzed NaCl-KCl at 738°C indicated strongly that electrical conduction in the salt is essentially ionic. The presence of $AlCl_3$ in small concentrations and contact with liquid Al should not alter this.

Writing the virtual Reaction I and Eq. [1] through [3], as shown, assumes that only trivalent aluminum is present in the electrolyte. An indication that the concentration of monovalent aluminum must be very low can be obtained from the data in Table III and the reaction

$$AlCl_3 + 2Al = 3AlCl \qquad (II)$$

Assuming that the activity coefficient of $AlCl_3$ and AlCl are similar at low concentrations in the electro-

Table II. Effect of 12-hr "stabilization" on the potentials of new cells

Electrode No.	Temp, °C	X_{Al}	Potential in mv		Change, mv
			Initial	After 12 hr	
21-3	686	0.922	1.96	2.03	+0.07
21-4	686	0.571	11.54	12.33	+0.78
18-3	700	0.363	36.06	36.85	+0.79
22-2	696	0.174	105.0	103.9	−1.1
22-4	696	0.039	175.5	178.9	+3.4

Table III. Free energy of formation of chlorides at 800°C.

Reaction	$\Delta F°_f$, cal/g mole
$Na(l) + 1/2Cl_2(g) = NaCl(l)$	−75,900[2]
$K(l) + 1/2Cl_2(g) = KCl(l)$	−78,800[2]
$1/3Al(l) + 1/2Cl_2(g) = 1/3AlCl_3(g)$	−42,400[2]
$Al(l) + 1/2Cl_2(g) = AlCl(g)$	−32,380 ± 3 kcal[3]
$Ag(s) + 1/2Cl_2(g) = AgCl(l)$	−18,500[2]

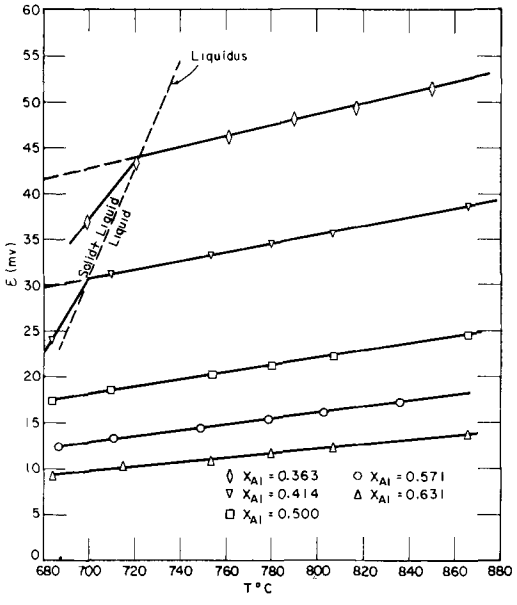

Fig. 2. Examples of emf vs. temperature plots for five liquid Ag-Al alloys.

lyte, and with N_{AlCl_3} equal to 0.01, N_{AlCl} is approximately 10^{-4}. This, with the clarity of the electrolyte and the constancy of the weight of the electrodes, was considered sufficient justification to conclude that Reaction II was of no significance in this work.

Other sources of error.—Temperatures were measured with chromel-alumel thermocouples made from a lot of wire that had been standardized against the melting points of Ag, Cu, Pb, Sn, and Al. No temperature gradients could be detected in the cell when the thermocouple was moved from the bottom of the crucible to the top of the electrolyte. Considering the uncertainty in the thermocouple calibration and uncertainties in the potentiometer circuit, it is estimated that the temperatures recorded were within ± 1°C of the true temperature.

A plot of E vs. °C yielded straight lines for all alloys at temperatures above the liquidus (Fig. 2). From these lines, potentials at several temperatures were obtained for subsequent calculations. Based on the scatter of experimental points about the line, it is estimated that a potential taken at 700° or 900°C (Table IV) for the subsequent calculations were within ±0.15 mv of the true value for cells in the composition range of $0.093 < X_{Al} < 0.857$. The uncertainty is greater for the electrodes which were very high in silver because it was necessary to extrapolate the potentials from the liquid region down to the temperatures of which calculations were made.

Experimental Results

The potentials for the various alloy electrodes at 700° and 900°C and the temperature coefficients of the potentials are shown in Table IV. These results have been converted into alpha and beta functions (4) for correlation and to facilitate subsequent calculations. The defining equations are:

$$\alpha_{Al} = \frac{\ln \gamma_{Al}}{(1-X_{Al})^2} = \frac{-3\mathbf{F}\,E/RT - \ln X_{Al}}{(1-X_{Al})^2} \qquad [4]$$

Table IV. Potentials of experimental cells for liquid Al-Ag solutions

Electrode composition, X_{Al}	E, v 700°C	E, v 900°C	$\partial E/\partial T_{X_{Al}P}$ v/°C × 10^6
0.973	0.00080	0.00108	1.56
0.922	0.00207	0.00265	3.00
0.857	0.00352	0.00470	6.50
0.799	0.00472	0.00678	10.5
0.727	0.00665	0.0098	16.2
0.631	0.00961	0.0145	24.4
0.571	0.01276	0.0192	32.2
0.500	0.0180	0.0263	41.1
0.414	(0.0307) *	0.0404	48.2
0.363	(0.0428)	0.0539	56.3
0.308	(0.0623)	0.0730	53.1
0.245	(0.0919)	0.0998	40.5
0.174	(0.1260)	0.1348	43.6
0.093	(0.1635)	0.1764	65.4
0.039	(0.1851)	(0.2124) *	137

* Parentheses indicate that the liquid is metastable and potentials are extrapolated from results at higher temperatures.

and

$$\beta_{Al} = \frac{H_{Al}^{M}}{(1-X_{Al})^2} = \frac{-3\mathbf{F}\left[E - T\left(\frac{\partial E}{\partial T}\right)_{P,X}\right]}{(1-X_{Al})^2} \qquad [5]$$

Figure 3 shows the alpha function for aluminum at 700° and 900°C, and Fig. 4 shows the beta function which is applicable in the temperature range of 700°-950°C.

As X_{Al} approaches unity, the alpha and beta functions become very sensitive even to very small errors. In the limit, the functions must be finite and the extrapolation to this limit is based on the curve below $X_{Al} = 0.9$ rather than the points above this composition. At the other end of the composition

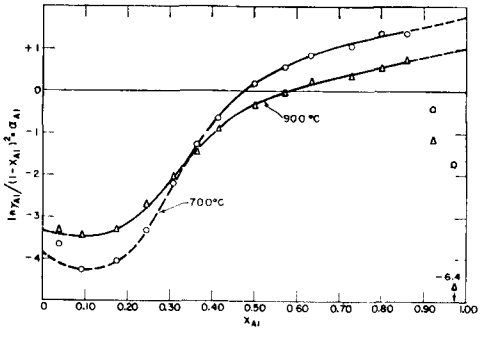

Fig. 3. Alpha function (α_{Al}) for liquid Al-Ag system. Dashed lines show extrapolation from higher temperatures.

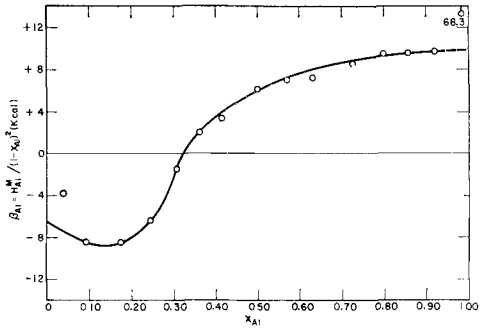

Fig. 4. Beta function (β_{Al}) for liquid Al-Ag alloys

Table V. Limiting activity coefficient of aluminum in liquid silver (γ°_{Al})

Temp, °C	$-\log \gamma^\circ_{Al}$	γ°_{Al}
950	1.36	0.044*
900	1.41	0.039*
800	1.52	0.030*
700	1.66	0.022*

* Liquid phase is metastable (mp pure Ag = 961°C).

scale, the point at $X_{Al} = 0.039$ has considerable uncertainty because the alloy was liquid only above 943°C. Thus it was necessary to extrapolate this point to the lower temperature by means of the value of dE/dT for this cell. This value had considerable uncertainty because the potential for the liquid phase could be measured only in the range of 943°-983°C. Figure 5 shows the alpha function at 950°C for which the limiting activity coefficient of aluminum in silver (γ°_{Al}) is 0.044. By the Gibbs-Helmholtz relationship and the limiting value of H^M_{Al} of −6460 cal/g atom the limiting value of the activity coefficient of aluminum can be obtained at various temperatures. The results given in Table V and the termini of the alpha function at pure silver in Fig. 4 are drawn accordingly.

Calculations

The alpha and beta functions for aluminum can be used to calculate the corresponding properties of silver by an application of the Gibbs-Duhem integration (4).

$$\ln \gamma_{Ag} = -\alpha_{Al} X_{Al} X_{Ag} + \int_{X_{Al}=0}^{X_{Al}} \alpha_{Al} dX_{Al} \qquad [6]$$

$$H^M_{Ag} = -\beta_{Al} X_{Al} X_{Ag} + \int_{X_{Al}=0}^{X_{Al}} \beta_{Al} dX_{Al} \qquad [7]$$

The molar excess mixing properties are

$$F^E = X_{Ag} RT \int_{X_{Al}=0}^{X_{Al}} \alpha_{Al} dX_{Al} \qquad [8]$$

$$H^M = X_{Ag} \int_{X_{Al}=0}^{X_{Al}} \beta_{Al} dX_{Al} \qquad [9]$$

The value of each integral on the right of Eq. [6] to [9] is obtained by determining the area under the appropriate curve in Fig. 3 or 4. From the results, the values of activities, activity coefficients and entropies can be found by usual thermodynamic formulas. The results of the calculations are included in Table VI.

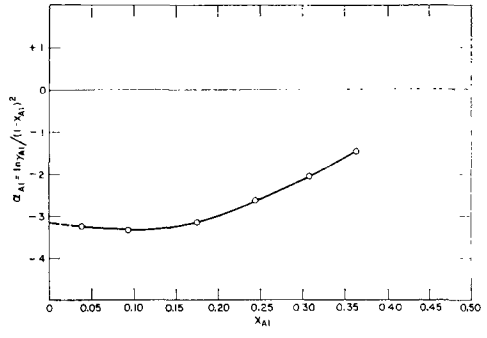

Fig. 5. Alpha function (α_{Al}) for silver-rich Ag-Al alloys at 950°C.

$$\left(\frac{\ln \gamma_{Al}}{(1X_{Al})^2}\right)_{X_{Al}=0} = \ln \gamma^\circ_{Al} = -3.16$$

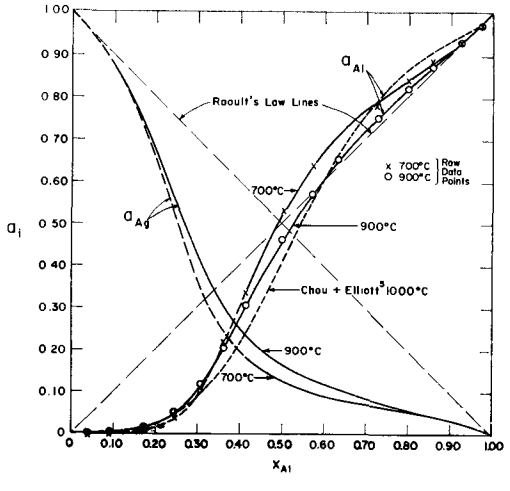

Fig. 6. Activity curves of Ag and Al in their binary system. a_{Ag} calculated by Gibbs-Duhem Equation.

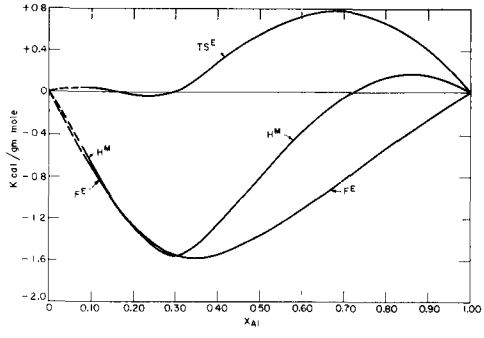

Fig. 7. Molar properties of mixing for Al-Ag system at 900°C.

Plots of the important functions are shown in Fig. 6 and 7.

Discussion of Results

The activity values obtained in this work are to be preferred over those calculated by Chou and Elliott (5) (Fig. 6), who obtained them by combining activities calculated from the phase diagram of the Pb-Ag system with data on the distribution of silver between liquid lead and liquid aluminum which was determined by Lorenz and Erbe (6). Hultgren and co-worker's (7) recalculation of Chou and Elliott's work using Kleppa's (8) calorimetrically determined heats of solution for the Pb-Ag system gives values of F^E for the Al-Ag system which are in reasonably good agreement with the present work. However, recent results by the present authors show a narrower solubility gap in the Ag-Al-Pb system than that reported by Lorenz and Erbe. These results will be reported in the near future, and a recalculation of the old Chou-Elliott results may be attempted in the light of the data now available. It is sufficient to say at this point that there is reasonable agreement between activities in the liquid phase obtained from the phase diagram calculations and those from the direct experimental results.

Activities in the Solid Phases

The results reported here have been used to estimate the activities in the solid phases in the Al-Ag system. This permits a comparison with the earlier

Table VI. Properties of the liquid aluminum-silver system
All values are computed from the curves in Fig. 3 and 4

Part A 700°C

X_{Al}	a_{Al}	a_{Ag}	γ_{Al}	γ_{Ag}	F^{M}_{Al} cal/g mole	F^{M}_{Ag} cal/g mole	F^{E}_{Al} cal/g mole	F^{E}_{Ag} cal/g mole	F^{E} cal/g mole
0.0*	0.00	1.000	0.0217	1.000	$-\infty$	0	−7410	0	0
0.05*	0.00118	0.946	0.0236	0.996	−13000	−110	−7240	−10	−370
0.10*	0.00320	0.873	0.0320	0.970	−11100	−260	−6660	−60	−720
0.20*	0.0168	0.651	0.0838	0.814	−7910	−830	−4800	−400	−1280
0.30*	0.0939	0.365	0.313	0.522	−4570	−1950	−2250	−1260	−1560
0.40*	0.304	0.197	0.759	0.328	−2300	−3140	−530	−2160	−1510
0.50	0.523	0.128	1.05	0.255	−1250	−3980	+90	−2640	−1280
0.60	0.674	0.094	1.12	0.235	−760	−4570	+220	−2800	−990
0.70	0.772	0.073	1.10	0.244	−500	−5060	+190	−2730	−690
0.80	0.843	0.056	1.05	0.280	−330	−5575	+100	−2460	−410
0.90	0.914	0.035	1.02	0.347	−175	−6480	+30	−2050	−180
0.95	0.954	0.020	1.00	0.399	−90	−7570	+10	−1780	−80
1.00	1.00	0.00	1.00	0.471	0	$-\infty$	0	−1460	0

Part B 900°C

X_{Al}	a_{Al}	a_{Ag}	γ_{Al}	γ_{Ag}	F^{M}_{Al} cal/g mole	F^{M}_{Ag} cal/g mole	F^{E}_{Al} cal/g mole	F^{E}_{Ag} cal/g mole	F^{E} cal/g mole	TS^{E} cal/g mole
0.0*	0.00	1.000	0.0390	1.000	$-\infty$	0	−7570	0	0	0
0.05*	0.00221	0.944	0.0443	0.994	−14200	−135	−7270	−15	−380	+50
0.10	0.00598	0.872	0.0578	0.969	−11900	−320	−6570	−75	−720	+40
0.20	0.0263	0.671	0.131	0.838	−8480	−930	−4730	−410	−1270	−20
0.30	0.1036	0.426	0.345	0.608	−5280	−1990	−2480	−1160	−1560	+10
0.40	0.275	0.254	0.687	0.424	−3010	−3190	−880	−2000	−1550	+290
0.50	0.460	0.168	0.921	0.336	−1810	−4150	−190	−2540	−1360	+550
0.60	0.607	0.120	1.01	0.300	−1160	−4940	+30	−2810	−1110	+730
0.70	0.722	0.087	1.03	0.290	−760	−5680	+70	−2880	−820	+780
0.80	0.819	0.060	1.02	0.298	−470	−6550	+50	−2820	−520	+670
0.90	0.907	0.033	1.01	0.326	−230	−7940	+20	−2620	−240	+410
0.95	0.952	0.018	1.00	0.350	−115	−9350	+5	−2450	−120	+230
1.00	1.00	0.00	1.00	0.384	0	$-\infty$	0	−2230	0	0

Part C 700°-900°C

X_{Al}	H^{M}_{Al} cal/g mole	H^{M}_{Ag} cal/g mole	H^{M} cal/g mole
0	−6460	0	0
0.05	−6900	+20	−330
0.10	−6900	+10	−680
0.20	−5100	−340	−1290
0.30	−1210	−1700	−1550
0.40	+1210	−2900	−1260
0.50	+1480	−3100	−810
0.60	+1210	−2760	−380
0.70	+770	−1940	−40
0.80	+370	−720	+150
0.90	+100	+840	+170
0.95	+20	+1720	+100
1.00	0	+2670	0

* For compositions below $X_{Al} = 0.42$ at 700°C and below $X_{Al} = 0.085$ at 900°C the liquid is metastable.

results of Hillert, Averbach, and Cohen's (9) measurements on solid alloys in this system.

A few potentials were obtained for alloys in the alpha phase (high Ag) as shown in Fig. 8. These potentials were extrapolated to 820°K (547°C) and corrected for the change of reference state of solid Al. The potentials obtained are in reasonable agreement with those of Hillert and co-workers.

In the composition range above $X_{Al} = 0.35$, the potentials of the liquid alloys were extrapolated to the liquidus temperatures to give the potentials at the corresponding solidus temperatures. When these potentials are then extrapolated to 820°K and corrected for the change in reference state, they result in an activity curve for aluminum having a very strong positive departure from ideality in the delta phase. Although the general character of the phase diagram and some uncertainty as to the position of the solidus line of the δ phase (9, 10) makes this calculation somewhat uncertain, there is a remarkably good agreement between the earlier results of Hillert, Averbach, and Cohen (9) (their Fig. 2) and those obtained here. It is to be noted that Wittig (11) recently has reported values of H^{M} for the ζ phase which are a little more exothermic than Hillert's values.

Activity Coefficients of Aluminum in Iron Alloys

The experimentally determined activities of aluminum in silver alloys and the enthalpies of solu-

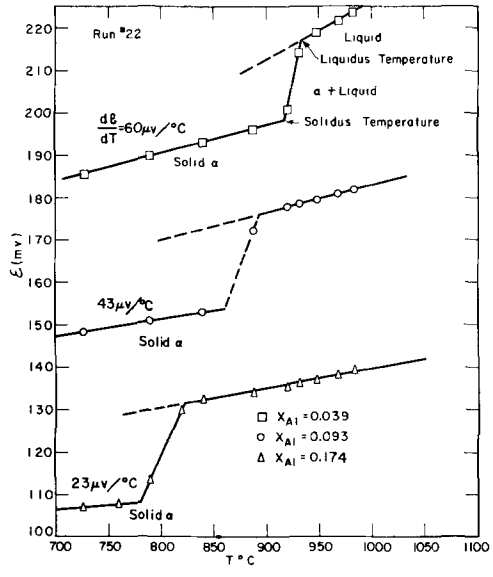

Fig. 8. Potentials for high melting Al-Ag alloys

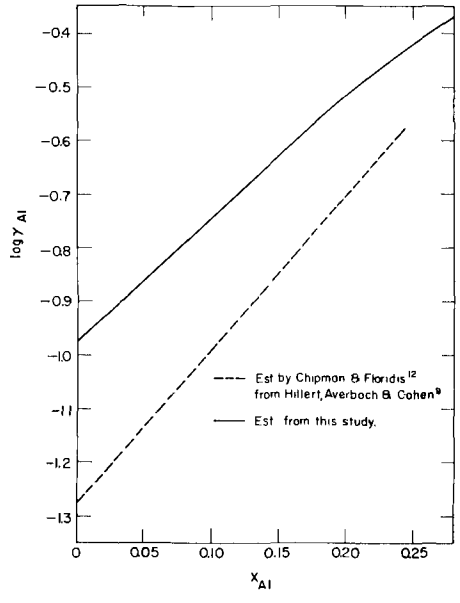

Fig. 9. Log γ_{Al} in liquid Al-Ag alloys at 1600°C. $\epsilon_{Al}^{(Al)} = 5.3$

tion reported here differ somewhat from those reported by Hillert, Averbach, and Cohen (9) which Chipman and Floridis (12) used to determine the activity coefficients of aluminum in iron alloys from the distribution of aluminum between liquid silver and iron alloys. In addition, Chipman and Floridis assumed that log γ_{Al} in liquid Al-Ag alloys was inversely proportional to the absolute temperature.

By use of the experimental results reported here, the values for the activity coefficients of aluminum in the Fe-Al, Fe-Al-C, and Fe-Al-Si-C systems at 1600°C have been recalculated from the data reported by Chipman and Floridis (12) on the distribution of Al between layers of Fe and Ag. The results are shown in Fig. 9, 10, and 11 and in Table VII. It is to be noted that $\epsilon_{Al}^{i} = (\partial \ln \gamma_{Al})/\partial X_i$ for the infinitely dilute solution of i in Al-Fe alloys. The correction applied by Chipman and Langenberg

Table VII. Activity of aluminum in Al-Ag alloys at 1600°C

X_{Al}	Estimated by Chipman and Floridis (12) a_{Al}	Estimated from this work a_{Al}	Estimated from this work log γ_{Al}
0.00	0.00	0.00	—0.972
0.05	0.00363	0.0072	—0.854
0.10	0.0104	0.0184	—0.744
0.15	0.0215	0.035	—0.633
0.20	0.0400	0.061	—0.514

(13) for the silicon in the silver layer has been included in Fig. 11.

The recalculated results in Fig. 9, 10, and 11 can be used to redetermine the aluminum deoxidation constant for steelmaking by the same treatment

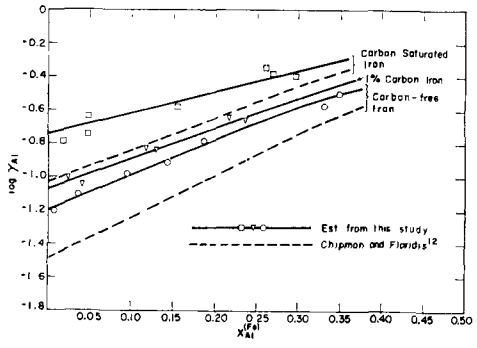

Fig. 10. Log γ_{Al} in Al-Fe alloys at 1600°C using Chipman and Floridis' distribution data (12). $\epsilon_{Al}^{(Al)} = +5.3$ (carbon free.)

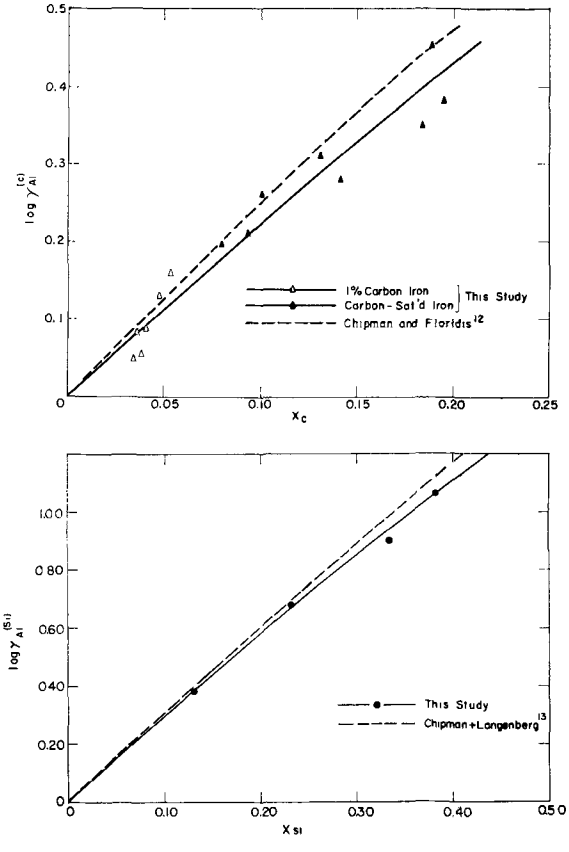

Fig. 11. Effect of carbon and silicon on log γ_{Al} in iron alloys at 1600°C using Chipman and Floridis' distribution data (12) $\epsilon_{Al}^{(C)} = +5.3$ $\epsilon_{Al}^{(Si)} = +7.0$

devised by Chipman and Langenberg (13). However, the results obtained differ very little from those of the earlier authors and consequently retreatment of the data here is not warranted. The essential reasons for the agreement in spite of different values of $\log \gamma_{Al}^{(Fe)}$ being used is that the calculation uses the infinitely dilute solution of Al in Fe as the reference state. This virtually cancels the effect of the change in values of $\log \gamma_{Al}$. Also, the uncertainties inherent in the calculation are probably greater than the change which would arise from the new calculation.

Conclusion

The thermodynamic properties of the liquid Al-Ag system have been determined by means of a high-temperature reversible concentration cell. The results may best be summarized by referring to Fig. 6 and 7 and to Table VI.

Values for $\log \gamma_{Al}$ in the liquid systems Al-Fe, Al-Fe-C, and Al-Fe-Si-C at 1600°C have been recalculated using the distribution data of Chipman and Floridis (12) and Chipman and Langenberg (13).

Acknowledgments

The authors wish to express their sincere appreciation to the United States Atomic Energy Commission for their financial support of this study under Contract No. AT(30-1)-1888, and to Donald L. Guernsey and William T. Martin, Jr. for their analyses of the electrodes and electrolytes.

Manuscript received Dec. 3, 1959. This paper was prepared for delivery before the Philadelphia Meeting, May 3-7, 1959. It was submitted in partial fulfillment for the M.Sc. degree to the Department of Metallurgy, Massachusetts Institute of Technology.

Any discussion of this paper will appear in a Discussion Section to be published in the December 1960 JOURNAL.

REFERENCES

1. D. L. Maricle, Ph.D. Thesis, Massachusetts Institute of Technology, September, 1959.
2. O. Kubaschewski and E. Ll. Evans, "Metallurgical Thermodynamics," 3rd. ed., p. 139, 336, Pergamon Press, Ltd., London (1958).
3. H. Villa, *J. Soc. Chem. Ind.*, **69**, S9 (1950).
4. C. Wagner, "Thermodynamics of Alloys," Addison-Wesley Press, Inc., North Reading, Mass. (1952).
5. Y. H. Chou and J. F. Elliott, (Unpublished, 1957).
6. R. Lorenz and F. Erbe, *Z. anorg. u. allgem. Chem.*, **183**, 311 (1929).
7. R. Hultgren and co-workers, "Compilation of Thermochemical Properties of Metals and Alloys," Published by the Metals Research Laboratory, The University of California, Berkeley, Calif.
8. O. J. Kleppa, *J. Phys. Chem.*, **60**, 446 (1956).
9. M. Hillert, B. L. Averbach, and M. Cohen, *Acta Met.*, **4**, 31 (1956).
10. M. Hansen and K. Anderko, "Constitution of Binary Alloys," McGraw-Hill Book Co., New York (1958).
11. F. E. Wittig, Paper 3H, *Proceedings*, The Symposium on the Physical Chemistry of Metallic Solutions and Intermetallic Compounds, Vol. I, (Symposium No. 9) National Physical Laboratory, H.M.S.O., London, 1959.
12. J. Chipman and T. P. Floridis, *Acta Met.*, **3**, 456 (1955).
13. J. Chipman and F. C. Langenberg, *The Physical Chemistry of Steelmaking*, (Proceedings of M.I.T. Conference on the Physical Chemistry of Iron and Steelmaking, 1956), Technology Press, M.I.T. (1958).

Gas Phase Charged and Electrolytically Charged Beta-Pd-H Alloys

James P. Hoare

Scientific Laboratory, Ford Motor Company, Dearborn, Michigan

ABSTRACT

Open-circuit potential vs. time curves were obtained on various palladium electrodes in hydrogen-stirred sulfuric acid solutions. Evidence is presented to show that the electrochemical properties of electrolytically charged β-Pd-H alloys are different from those of the gas charged alloys. Mechanisms for the charging processes involved are discussed.

Renewed interest in the mechanisms of the occlusion of hydrogen gas in palladium metal has prompted a re-evaluation of the earlier work with more modern techniques. It had been shown that β-Pd-H alloys formed by placing pure palladium metal in pure hydrogen gas under 1 atm are indefinitely stable (1) provided all oxidizing agents such as air or oxygen are excluded. Hoare, *et al.* (2) found that the gas charged β-Pd-H alloy had somewhat different electrochemical properties than the electrolytically charged β-Pd-H alloy; i.e., hydrogen is lost spontaneously from the electrolytically charged β-Pd-H alloy and its hydrogen overvoltage is lower. Flanagan and Lewis (3) made potential and relative resistance measurements on a thin (0.027 cm diameter) palladium wire in acid solutions. Although they were not able to reproduce the finding of Hoare and Schuldiner (4), they did confirm certain results reported by Ratchford and Castellan (5). However, recently (6) the results of Ratchford and Castellan have been shown to be compatible with those of Hoare and Schuldiner.

Contrary to what was found by Hoare and Schuldiner are the data reported by Flanagan and Lewis which show that, once the β-Pd-H alloy is formed electrolytically, hydrogen is not lost and the potential does not return to a positive value of 50 mv after the cathodic current is removed. This investigation is concerned with showing evidence for the existence of two kinds of β-Pd-H alloys and with a confirmation of the results reported by Flanagan and Lewis.

Experimental

In one series of experiments, potential measurements were taken on pure (99.5 + %) palladium cathodes made from 3 cm of 5-mil wire, 1 cm^2 plate of 2-mil foil, 1 cm^2 plate of 4-mil foil, 1 cm^2 plate of 4-mil foil whose surface was about 80% covered with polyethylene, and a bead melted from a strip of foil. In another series, both potential and relative resistance measurements were taken on a 15-mil palladium wire, 11 cm long and wound in the form of a toroid on a polyethylene ring. All experiments were carried out in 2*N* H_2SO_4 solution in a Teflon cell similar to that used before (7). The preparation of the triply distilled water, sulfuric acid solutions, palladium cathodes, and cell has been described elsewhere (4, 7). The hydrogen and helium gases were purified in standard multistage purification trains; the temperature of all experiments was 23° ±1°C. Relative resistance measurements were carried out as before (6). The hydrogen content of the Pd-H alloys was determined using ceric sulfate solutions (4). Electrical contacts to the cathodes were Pt wires imbedded in polyethylene to prevent any solution contact with the Pt or the weld area; the reference electrode is a Pt/H_2 electrode in the same solution.

Results and Discussion

Each palladium cathode was strongly anodized (about 0.1 to 0.5 amp/cm^2) for about 30 min and then cathodized for about 2 hr at a current density of such a magnitude that the electrode was polarized to at least −100 mv against a Pt/H_2 electrode in the same solution. Finally, the circuit was opened and the potential vs. the Pt/H_2 electrode was recorded as a function of time. During this entire procedure, the sulfuric acid solution was stirred constantly by a steady flow of purified hydrogen. These results are presented in Fig. 1, zero time being taken at the moment when the cathodizing current is broken.

From Fig. 1, it is seen that the potential-time curves show a definite dependence on the ratio of the exposed area to the total volume of the cathode. As the value of this ratio decreases, the time required to reach a steady value of zero volt increases. Also, a point is reached at which the potential vs. Pt/H_2

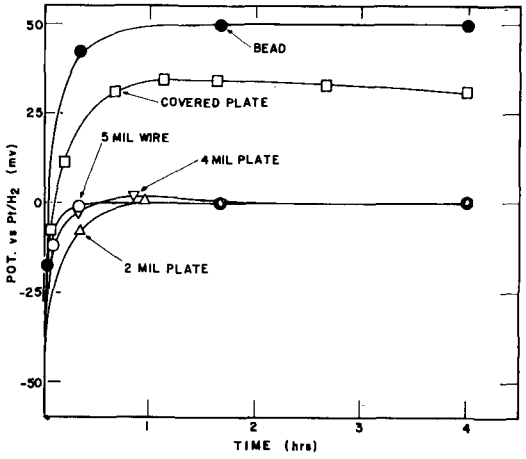

Fig. 1. Open-circuit potential vs. time curves obtained from previously cathodized palladium electrodes in H_2-stirred 2N H_2SO_4 solutions at T = 23° ± 1°C.

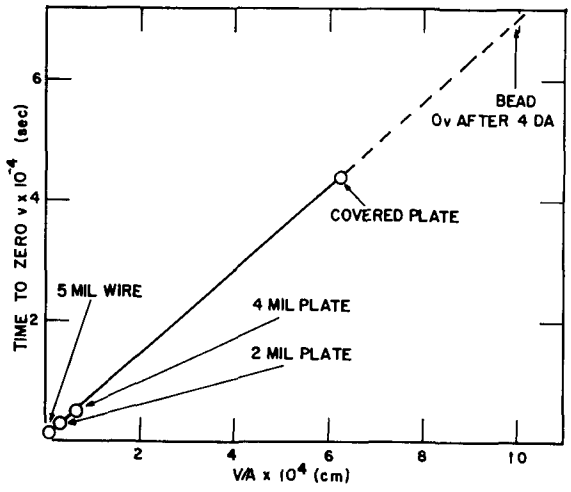

Fig. 2. Curves showing the length of time required for cathodized palladium electrodes to reach a steady value of zero volt vs. Pt/H_2 on open-circuit conditions as a function of the volume-to-surface ratio (V/A) of the electrode.

reverses sign and the curve passes through a maximum value. In fact, a cathode may be designed with a surface-to-volume ratio of such a value that the maximum value becomes a plateau at +50 mv. The palladium bead is such an example and this 50 mv potential was maintained for more than 30 hr before the drift to zero volt began. It was found that the exact shape of the curves was a function of the electrochemical history of the cathode, but the general form of the curves is that shown in Fig. 1. It is for this reason that all the cathodes, on which the curves in Fig. 1 were determined, were anodized and cathodized at approximately the same intensity and for the same duration with approximately the same hydrogen flow.

The volume-to-surface ratio (V/A) was determined (6); Fig. 2 shows that the time to reach zero volt after breaking the cathodizing circuit is a linear function of V/A. It is interesting to note that again (6) the bead falls to the left of this curve. Fallon (8) has also found that palladium beads after cathodization will return to the +50 mv value for a certain length of time.

In another series of experiments, the 15-mil palladium wire toroid was anodized and cathodized in the same manner as described above and the open-circuit potential after cathodization was recorded. The potential went to zero volt without going positive as shown in Fig. 3. However, if about 5-10% of the wire was covered with polyethylene near the weld area, the potential changed sign and, after passing through a maximum in a positive potential region, drifted back to a steady zero value. As long as the rapid flow of hydrogen was maintained, the potential would remain at zero volt indefinitely. Flanagan and Lewis (3) found that in certain cases the potential on their wires also went through a maximum value in a positive potential region.

After the wire had reached a steady value of zero volt, the hydrogen flow was reduced to a point where about one bubble passed through the solution per minute. When a potential reading was to be taken, the H_2 flow was returned to the original rate and the

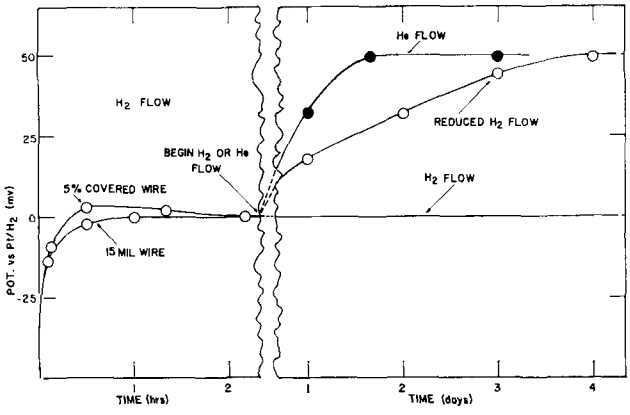

Fig. 3. Open-circuit potential curves obtained on a 15-mil Pd wire toroid after cathodization as a function of time. On the left side a rapid flow of H_2 is maintained at all times. On the right is shown the behavior when the H_2 flow is maintained, reduced to very low flow rates and replaced by He flow.

potential value recorded after the potential had remained steady for about 5 min; then the hydrogen flow was reduced again to the 1 bubble/min rate. The potential-time curve obtained is shown in Fig. 3. It is seen that a value of +50 mv was obtained after about four days.

It seemed possible that, with such a very low hydrogen flow rate, air could have entered the cell through the H_2-outlet tube and could have caused the rise to the positive values. To determine whether this was the case or not, purified helium gas was used to stir the solution rapidly at a steady rate. The potential-time curve obtained by repeating the experiment using He-stirring is shown in Fig. 3. Not only does the potential rise to a steady value of +50 mv, but also it rises faster, reaching the 50 mv value in less than two days. Potential measurements were taken by stopping the He flow and using an H_2 flow until the potential remained steady for about 5 min. The maximum total time for a reading required about 15 min.

The hydrogen content of the palladium wire toroids was determined by placing them in a known quantity of ceric sulfate solution (9), samples of which were titrated for ceric ion (4). These values for the hydrogen content were compared with those determined from Fischer's relationship (6, 10) by using relative resistance measurements which were taken concurrently with the potential measurements.

A palladium wire toroid which had been cathodized and which had come to a steady value of zero volt vs. a Pt/H_2 electrode was found to have an H/Pd atomic ratio of 0.63 using ceric sulfate solution and 0.67 from relative resistance measurements. This is in agreement with that found by other investigators, e.g. (3), and with that reported for a Pd electrode which had been anodized only and then permitted to reach a steady zero volt potential vs. Pt/H_2 (3,5,6). After a previously cathodized Pd wire toroid on open-circuit conditions had come to a steady value of zero volt vs. Pt/H_2 in H_2-stirred 2*N* H_2SO_4 solution, the H_2-stirring was replaced by He for about 72 hr. Then the toroid electrode was removed from the acid solution and placed in ceric sulfate solution in order to determine the hydrogen content of the electrode. Duplicate runs showed that the H/Pd atomic ratio was equal to 0.34 even though relative resistance measurements had given a value of 0.63. This agrees with the data reported in Fig. 4 of ref. (4).

These results may explain the conflicting findings reported by Hoare and Schuldiner and by Flanagan and Lewis concerning the open-circuit potential vs. Pt/H_2 of a previously cathodized palladium electrode in acid solution. As pointed out by Fallon (8), Hoare and Schuldiner reduced the flow of hydrogen to extremely low rates overnight (at least 16 hr/day). Under these conditions, as shown by Fig. 3 of this investigation, the potential eventually does return to +50 mv. It was also found in this investigation that the potential of those electrodes which exhibited positive potentials, such as those presented in Fig. 3, would drift slowly to zero if the very low H_2 flow or the He flow was replaced by a rapid stream of hydrogen gas.

In another experiment, a Pd wire was cleaned (7) and wound as a toroid on a polyethylene ring with Pt leads. This electrode was soaked in triply distilled water in a Teflon cell for about 48 hr. The cell was emptied and the Pd wire toroid sealed inside. Purified dry hydrogen was passed through the cell until the relative resistance reached a value of 1.61. This corresponds to the value for β-Pd-H. In another Teflon cell, 2*N* H_2SO_4 solution was prepared (7) and saturated with purified hydrogen for about 20 min. The gas-charged β-Pd-H toroid was then placed in this H_2-saturated acid solution. A potential of zero volt vs. Pt/H_2 was observed. Next, the hydrogen flow was replaced by helium and these conditions were maintained for about 72 hr. The relative resistance still had a value of 1.61. Finally, the toroid was removed from the acid solution and placed in ceric sulfate solution in order to determine the hydrogen content. In duplicate runs, it was found that the H/Pd atomic ratio was 0.57.

It is interesting to note that gas-phase charged β-Pd-H does not lose hydrogen in He-stirred H_2SO_4 solution while electrolytically charged β-Pd-H does. As reported before (2) these two types of β-Pd-H have very different hydrogen overvoltage characteristics. However, once gas-charged β-Pd-H is anodized in acid solution, the hydrogen overvoltage characteristics become identical to the electrolytically charged β-Pd-H. It was suggested that a film of molecular H_2 gas lies over the layer of adsorbed atomic -H and that, while cathodization does not break up this film, anodization does.

When an anodized palladium electrode in hydrogen-stirred acid solution is put on open-circuit conditions, atoms of hydrogen are transported from the double layer to the electrode surface through an adsorbed water molecule (2). These remove any oxides present thus exposing a pure palladium surface. Adsorbed hydrogen atoms then penetrate the metal skin and are dissolved into the body of the metal as protons. Since the penetration of the metal skin is assumed to be the slow process (6), hydrogen accumulates just inside the metal surface to the

maximum α-Pd concentration (H/Pd $\sim$ 0.03) and a potential of 50 mv more noble than Pt/H_2 is observed owing to the atomic hydrogen electrode reaction (11). As more hydrogen is dissolved, more Pd is converted to the α-Pd-H alloy. Only when the entire body of Pd is converted to the α-phase, will the β-phase nucleate and it is the length of the so-called α-plateau (6), observed in the potential-time curves, that represents the time required to charge the Pd to α-Pd.[1] The β-phase then grows from nucleation centers throughout the α-phase until an H/Pd atomic ratio of about 0.6 is reached when the solution process ceases and a potential of zero volt vs. Pt/H_2 is observed.

This same charging procedure is assumed to occur on pure dry Pd metal placed in a pure dry hydrogen atmosphere, except that hydrogen molecules do not have to displace adsorbed water molecules and the surface of the final β-Pd-H alloy obtained is covered with an adsorbed film of molecular hydrogen. In both cases, hydrogen ceases to be dissolved at an H/Pd atomic ratio of about 0.6.

If a palladium electrode is cathodized in H_2-stirred acid solution, the solvated hydrogen ions are discharged from the double layer to adsorbed atoms on the surface. As described above, the same charging processes from Pd to α-Pd-H to β-Pd-H also occur here. However, the solution process does not stop at H/Pd $\sim$ 0.6, but additional hydrogen may be forced into the Pd electrochemically at high current densities. It has been suggested (13) that this additional hydrogen enters the Pd lattice as atomic hydrogen since it may be possible that there is, at this concentration, enough dissolved hydrogen to form an H1-s impurity band. As a result, the electron is more closely associated with this band than with the Pd 4-*d* band (14). Hydrogen concentrations approaching H/Pd $\sim$ 1 may be obtained (15). Supersaturated β-Pd-H alloys are quite unstable and the additional hydrogen is lost rapidly after the cathodizing circuit is removed. Then if the H_2-flow is replaced by He-flow, more hydrogen will be lost till an H/Pd atomic ratio $\sim$0.35 is reached. However, an anodized Pd wire toroid which had never been cathodized previously and which had come to a steady value of zero volt vs. Pt/H_2 was placed in ceric sulfate solution after the H_2-flow had been replaced by He for about 72 hr. The hydrogen content so determined was equal to an H/Pd atomic ratio of 0.56. Yet, when an anodized electrode such as this is cathodized, the β-Pd-H obtained has all the characteristics of electrolytically charged β-Pd-H.

It appears from the above work that β-Pd-H alloys obtained by cathodization possess different stability properties than those obtained in other ways. It is suggested here that the β-Pd-H lattice formed electrolytically is much more distorted than

[1] It may be pointed out that Lacher (17) and Moon (18) have shown that α-Pd alloys are homogeneous solid solutions while these data suggest that such alloys are nonhomogeneous solutions. This discrepancy is only apparent since Lacher and Moon considered α-Pd alloys in a hydrogen environment where the partial pressure of the hydrogen was low enough (0-0.026 atm) that α-Pd was the stable phase with respect to the β-phase. In this investigation, the partial pressure of hydrogen was 1 atm and in this region the β-phase is the stable phase but cannot nucleate until the mass of Pd has been converted to the α-phase. Equilibrium is never achieved between the α-phase and the external hydrogen atmosphere and the α-phase exists only during the nonequilibrium charging processes.

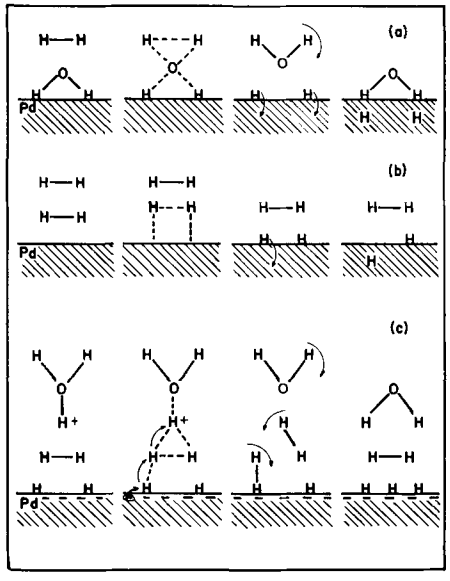

Fig. 4. Suggested possible mechanisms for the solution of hydrogen by palladium. Full lines represent stable bonds; dotted, bonds being formed or being broken. Water is adsorbed with H's next to Pd atoms since the potential at zero charge is positive to Pt/H_2 (2) and therefore a pure Pd surface has a negative charge. The hydrogen symbol, H, in step 4 of (a) and (b) inside the Pd metal represents a proton; the electron has been donated to the metal d-band. (a) Adsorption of hydrogen by previously anodized Pd from H_2-stirred acid solution by complexing with an adsorbed water, an open circuit. (b) Dry gaseous H_2 is adsorbed on dry Pd giving a Pd-H alloy whose surface is covered with an adsorbed layer of molecular hydrogen. (c) Discharge of a solvated proton on a gas charged β-Pd-H cathode; the adsorbed H_2 in step 3 can be desorbed as a free H_2-molecule or adsorbed as two H-atoms shown in step 4.

that formed from gas phase charging due to the formation of the super saturated β-phase. It may be possible that this extra distortion could modify the relative positions and widths of the *s*- and *d*-bands in such a way that the free energy is lowered by loss of hydrogen to an H/Pd atomic ratio of about 0.35 only for the case of the electrolytically charge β-Pd-H in acid solution in the absence of hydrogen or oxidizing agents.

Gas-phase charged β-Pd-H alloys cannot be converted to electrolytically charged β-Pd-H by cathodization alone because the adsorbed molecular hydrogen film prevents supersaturation of the alloy as shown by hydrogen overvoltage measurements (2). If, however, this film is destroyed by preanodization, then subsequent cathodization will result in a β-Pd-H alloy possessing all the properties of the electrolytically charged alloy (Fig. 4).

After the cathodizing current has been removed from certain palladium cathodes, the potential vs. Pt/H_2 swings to positive values before returning to the steady value of zero volt. Conceivably, this might be explained as follows. When the cathodizing circuit is broken, hydrogen above an H/Pd $\sim$ 0.6 is lost rapidly by the supersaturated β-phase. Since the lattice is highly distorted and since there is, without doubt, a readjustment of the partial pressure of hydrogen at points on the surface and within the metal itself, further hydrogen may be lost by inertia which is slowly restored afterward, giving

the observed swing to positive potentials with a subsequent drift to zero. The behavior of such electrodes has been explained by Fallon (8) in terms of the thickness of the diffusion layer at the electrode surface as a function of the stirring rate.

It may be mentioned here that the so-called α-Pd reference electrode, (Pd-H)α/H_3O^+, used by Schuldiner (14, 16) is a good reference electrode. This is true since such an electrode is prepared from an anodized Pd wire placed in a hydrogen atmosphere and it has been shown (6) that such an electrode will maintain a steady-state potential of 50 mv vs. Pt/H_2 for periods of time up to 48 hr or more. If the wire had been cathodized, this would not have been true. Also, Schuldiner's measurements were made within 8 hr so that this reference electrode system acted as though it were at equilibrium.

Summary

1. β-Pd-H alloys may be obtained by allowing a pure sample of palladium to absorb hydrogen either in a dry state from a gaseous hydrogen atmosphere or in hydrogen-stirred acid solutions after the palladium had been anodized. These alloys are stable (do not lose hydrogen) as long as all oxidizing agents are absent, even if the hydrogen atmosphere is removed.

2. β-Pd-H alloys may also be obtained electrolytically by cathodizing the palladium in H_2-stirred acid solutions. These alloys are stable only in a hydrogen atmosphere provided oxidizing agents are absent. If the hydrogen atmosphere is removed these alloys lose hydrogen until an H/Pd atomic ratio of about 0.35 is reached. If the hydrogen atmosphere is returned, the alloy will regain hydrogen till the H/Pd atomic ratio again reaches about 0.6. It is suggested that this behavior is due to the highly distorted lattice caused by the electrochemically produced supersaturated β-Pd-H alloys during cathodization.

3. β-Pd-H alloys obtained from anodized Pd in H_2-stirred acid solutions can be converted to the electrolytically charged alloy by cathodization since the supersaturated alloy is formed in the process. Unlike β-Pd-H obtained from anodized Pd, that obtained by dry gas phase charging possesses a protective hydrogen film which prevents the formation of the supersaturated lattice during cathodization and thereby prevents the conversion to the electrolytically charged alloy. However if this protective film is destroyed by pre-anodization, then cathodization does convert gas charged β-Pd-H to electrolytically charged β-Pd-H.

Acknowledgments

The author is indebted to Sigmund Shuldiner of the Electrochemistry Branch of the U. S. Naval Research Laboratory for his interest and advice.

Manuscript received Dec. 18, 1959. This paper was prepared for delivery before the Chicago Meeting, May 1-5, 1960.

Any discussion of this paper will appear in a Discussion Section to be published in the June 1961 JOURNAL.

REFERENCES

1. D. P. Smith, "Hydrogen in Metals," p. 102, University of Chicago Press, Chicago (1948); L. J. Gillespie and F. P. Hall, *J. Am. Chem. Soc.*, **48**, 1207 (1926); H. Bruening and A. Sieverts, *Z. physik. Chem.*, **A163**, 409 (1932); E. A. Owen and I. J. Jones, *Proc. Phys. Soc.*, **49**, 587, 603 (1937).
2. J. P. Hoare, S. Schuldiner, and G. W. Castellan, *J. Chem. Phys.*, **28**, 22 (1958).
3. T. B. Flanagan and F. A. Lewis, *ibid.*, **29**, 1417 (1958).
4. J. P. Hoare and S. Schuldiner, *J. Phys. Chem.*, **61**, 399 (1957).
5. R. J. Ratchford and G. W. Castellan, *ibid.*, **62**, 1123 (1958).
6. J. P. Hoare, *This Journal*, **106**, 640 (1959).
7. J. P. Hoare and S. Schuldiner, *ibid.*, **102**, 485 (1955).
8. R. J. Fallon, Thesis, Catholic University of America Press, Washington, D.C. (1959).
9. F. A. Lewis and A. R. Ubbelohde, *J. Chem. Soc.*, **1954**, 1710.
10. F. Fischer, *Ann. phys.*, **20**, 503 (1906).
11. S. Schuldiner, G. W. Castellan, and J. P. Hoare, *J. Chem. Phys.*, **28**, 16 (1958).
12. B. Lambert and S. F. Gates, *Proc. Roy. Soc., London*, **108A**, 456 (1925).
13. S. Schuldiner and J. P. Hoare, *This Journal*, **103**, 178 (1956).
14. S. Schuldiner and J. P. Hoare, *Can. J. Chem.*, **37**, 228 (1959).
15. F. Krueger and G. Gehm, *Ann. Phys.*, **78**, 72 (1925).
16. S. Schuldiner, *This Journal*, **106**, 440 (1959).
17. J. R. Lacher, *Proc. Roy. Soc.*, **161A**, 525 (1937).
18. K. A. Moon, *J. Phys. Chem.*, **60**, 502 (1956).

Brief Communications

The JOURNAL accepts short technical reports having unusual importance or timely interest, where speed of publication is a consideration. The communication may summarize results of important research justifying announcement before such time as a more detailed manuscript can be published. Consideration also will be given to reports of significant unfinished research which the author cannot pursue further, but the results of which are of potential use to others. Comments on papers already published in the JOURNAL should be reserved for the Discussion Section published biannually.

Submit communications in triplicate, typewritten double-spaced, to the Editor, Journal of The Electrochemical Society, 1860 Broadway, New York 23, N. Y.

Temperature Dependence of Tafel Slope in the Formation of Very Thin Anodic Oxide Films on Niobium

George B. Adams, Jr., and Timothy Kao[1]

Department of Chemistry, University of Oregon, Eugene, Oregon

ABSTRACT

A kinetic study was made of the formation of very thin anodic oxide films on niobium at constant current over the temperature range −10° to 70°C. Formation voltages were limited to the range below the oxygen evolution potential to eliminate possible interaction of an electronic component of the current with the measured formation field. It was found that the measured temperature dependence of Tafel slope agreed with that predicted by the theory of Mott and Cabrera. Using this theory, a zero field interfacial barrier height of 1.19 ev and barrier half-width of 2.40Å were obtained. Values of the differential formation field are reported at current densities of 1000, 100, 10, and 1 μa/cm^2 at ten degree intervals over the temperature range studied.

Several investigators (1-3), working with tantalum, niobium, and zirconium, respectively, have reported an essentially temperature-independent Tafel slope in the kinetics of formation of anodic oxide films on these metals.

Their results are therefore not in agreement with the simple single-barrier theory of Mott and Cabrera (4, 5), but Dewald's theory (6) which incorporates the assumption of ionic space charge formation in the oxide film is capable of explaining the anomalous temperature dependence.[2]

These investigators worked with oxide films ranging in thickness from several hundreds to several thousands of angstroms. Under these conditions it is probable that a space charge is established in the steady state; some experimental evidence for the presence of space charge has been obtained by Young (7).

The Mott-Cabrera theory for formation of very thin oxide films on metals contains the assumption that no space charge is established in very thin films (<100Å). With the additional assumptions that the rate-determining step in the formation of the oxide is the high-field migration of metal ions from active surface sites on the metal across a metal-oxide interfacial potential energy barrier of height, ϕ, and barrier half-width, b, into interstitial positions in the insulating oxide film, the following equation is derived:

$$F = \frac{\phi}{bq} + \frac{kT}{bq} \ln (I/Ao) \qquad [1]$$

where F is the electrostatic field acting across the oxide film, q is the charge per metal ion, I is the ionic current density, m_s is the surface concentration of metal ions at active surface sites on the metal. V_s is the vibrational frequency of a surface metal ion, and $Ao = qm_s\nu_s$.

The aim of the present work was to test this theory with an applicable system, namely, for the growth of very thin anodic oxide films in which the metal ion is the mobile species in an otherwise insulating film.[3]

Experimental

The experimental techniques employed in this work have been described previously (8, 9).

Electrodes were made up from ½-in. annealed niobium rod (Fansteel research grade) cut into ½-in. lengths, each fitted with a vertical brass rod for handling and electrical contact. This assembly was then masked with six individual coatings of baked Formvar enamel. The plane circular face of each electrode was exposed by abrasion, to give a nominal area of 1.265 cm^2.

Electrode surfaces were prepared initially on a metallographic polishing wheel with No. 280 and No. 600 grit aluminum oxide abrasive slurries and finished with Linde B polishing alumina, to a highly reflecting surface. Electrodes were repolished after each run with polishing alumina.

The electrolyte was made up of 0.1N H_2SO_4 in 35% ethyl alcohol. This electrolyte was also used in the mercury-mercurous sulfate reference electrode. The solution was stirred mechanically during each run and renewed every 8 hr. Temperature was regulated to within ±0.1°C over the range −10° to 70°C with a Wilkens-Anderson refrigerated constant temperature bath.

Current densities from 1 to 100 μa/cm^2 were regulated to within ±0.5% with an electronic current regulator described previously (10). Current density of 1000 μa/cm^2 was regulated electronically with a regulator described by Teeter (11). Current was measured to within 0.5% with a Weston precision low resistance microammeter, model 627. Voltage was recorded on a L&N AZAR recorder using their

[1] Present address: Department of Pediatrics, University of Oregon Medical School, Portland, Oregon.

[2] This theory cannot, however, account for certain characteristics of transients which have been observed with these oxide films.

[3] It is assumed that the niobium ion, because of its small size, is the mobile species in the oxide film (2). The glassy film has an extremely low electronic conductivity (2).

model 7664-N electronic millivoltmeter as a high-input-impedance preamplifier.

Runs made at 1.0 μa/cm^2 were obtained by first polarizing at 100 μa/cm^2 and then dropping back to 1.0 μa/cm^2 on the same electrode surface. It was observed that there was considerably more scatter among the individual formation rates for these runs than for runs made at higher current densities.[4]

All voltage measurements were limited to the range below the potential for reversible evolution of oxygen. By restricting voltage measurements to this range, possible complications involving the action of electronic current on the observed field are avoided, since the ionic current efficiency is then unity.

Results

If Eq. [1] is obeyed, a plot of field vs. absolute temperature should be linear for constant current runs, and the slopes of the regression lines should increase with increasing current density. In addition the lines should extrapolate to a common intercept, ϕ/bq, at the absolute zero of temperature.

Equivalent statements are that the Tafel slope, $[\partial F/\partial \ln I]_T$, should vary in direct proportion to the absolute temperature, or that the barrier half-width, b, should remain constant with temperature.

The results of this investigation are presented in Table I and in Fig. 1.

Each point is the average of at least five individual runs. The lines shown are the least square regression lines. Equations for these lines, with standard deviations of slopes and intercepts are as follows:

$$F_{1000} = (9.88 \pm 0.16 \times 10^6) - (1.65 \pm 0.06 \times 10^4)T$$
$$F_{100} = (9.91 \pm 0.27 \times 10^6) - (1.80 \pm 0.09 \times 10^4)T$$
$$F_{10} = (10.00 \pm 0.26 \times 10^6) - (2.02 \pm 0.09 \times 10^4)T$$
$$F_1 = (11.15 \pm 0.44 \times 10^6) - (2.59 \pm 0.15 \times 10^4)T$$

The barrier half-width, b, was calculated from Tafel slopes [obtained from the regression lines as $(F_{1000} - F_{10})/4.606$], assuming a pentavalent niobium ion. Values of b so obtained ranged from 2.44 to 2.36Å, with a mean of 2.40Å.

[4] When making a 1.0 μa/cm^2 run the electrode is immersed continuously for an interval of more than an hour. At the higher temperatures it became necessary to recoat the electrode on one occasion because gross leakage had developed between the enamel mask and the rim of the electrode face. Slight leakage of this sort would give field values that were too low at the higher temperatures. The 1.0 μa/cm^2 runs would be affected to the greatest extent, because of the protracted immersion times required and the greater percentage effect for a given leakage.

Table I. Variation of field with current and temperature in the formation of very thin anodic oxide films on niobium

T, °K	$F_1 \times 10^{-6}$, v cm^{-1}	$F_{10} \times 10^{-6}$, v cm^{-1}	$F_{100} \times 10^{-6}$, v cm^{-1}	$F_{1000} \times 10^{-6}$, v cm^{-1}
263	4.19±0.05	4.62±0.03	5.09±0.03	5.53±0.03
273	4.06±0.05	4.47±0.01	4.97±0.04	5.41±0.05
283	3.92±0.03	4.32±0.02	4.89±0.01	5.17±0.02
293	3.67±0.02	4.09±0.03	4.73±0.02	4.97±0.01
303	3.23±0.04	3.97±0.02	4.46±0.01	4.88±0.01
313	3.03±0.06	3.78±0.01	4.17±0.01	4.75±0.04
323	2.90±0.07	3.51±0.01	4.07±0.01	4.59±0.01
333	2.51±0.09	3.23±0.01	3.87±0.01	4.38±0.01
343	2.12±0.06	3.01±0.02	3.75±0.02	4.17±0.01

Oxide density, 5 g cm^{-3} (2).

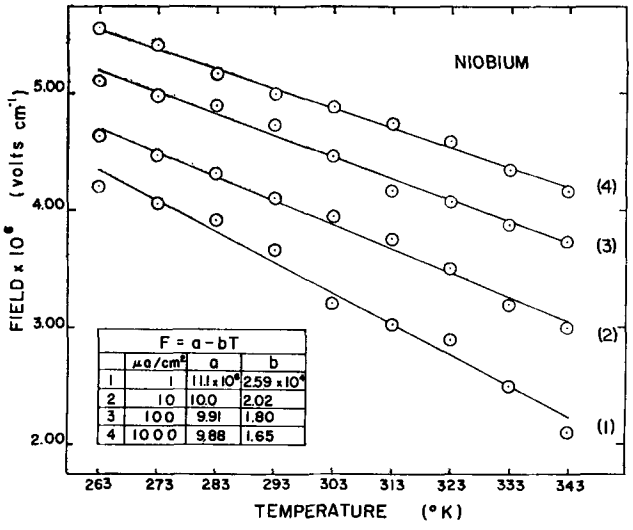

Fig. 1. Temperature dependence of field at 1000, 100, 10, and 1 μa/cm^2.

Using the mean half-jump distance, 2.40Å, and the mean intercept of the field-temperature regression lines for the three highest currents, 9.91 x 10^6 v cm^{-1}, the interfacial barrier height, ϕ, is 1.19 ev.

From the slopes of the regression lines at each current density, Ao can be determined. The resulting values are 1.0, 0.9, 1.9, and 500 x 10^7 amp cm^{-2}, in order of decreasing current density.

Taking $m_s \leq 8 \times 10^{14}$ atoms cm^{-2} and $V_s = 10^{13}$ sec^{-1} (2), one computes $Ao \leq 6 \times 10^9$ amp cm^{-2}, which is satisfactory, since m_s may be considerably less than the value estimated from the density of the metal.

Discussion

The present investigation indicates that the observed temperature dependence of Tafel slope for growth of *very thin* anodic oxide films on niobium is interpretable on the Mott-Cabrera theory for formation kinetics of such anodic films. Previous studies on niobium, reported by Young (11) were made with thicker, high voltage films. Those results are anomalous on the Mott-Cabrera theory in that the barrier half-width, b, was found to be temperature dependent. The present results are not contradictory, however, since that investigation was made with high-voltage films.

Values of differential formation field given in Table I are in general agreement (except for small differences in temperature coefficients) with those of Young (11) whose work was done with chemically polished electrode surfaces and thick films. A barrier half-width, b, of 2.40Å obtained in the present work is smaller than either of the values $a \geq 4.2$Å, $b \geq 3.1$Å reported by Young on the Dewald theory but is in good agreement with the 2.42Å reported by Vermilyea (12) for steady-state measurements.

Runs taken at the lowest current density were not used in the evaluation of ϕ and b. Considerably less precision was obtained with these runs, both individually and in the fit to the regression line.

For the remaining data, variation in Tafel slope with current density is of the same magnitude as the

standard deviations of slope. The trend with temperature, however, is unidirectional. Also the three intercepts agree within their respective limits of error.

The precision obtained in this investigation is less than that for similar measurements on high-voltage films (2). Nevertheless it is felt that the results obtained are significant and adequately explained by the Mott-Cabrera theory.

The general agreement between formation fields for both low- and high-voltage anodic oxide films obtained in the present work is contrary to what was observed previously with zirconium (8). This agreement with niobium is probably due to the fact that the ionic current efficiency is essentially 100% for polished niobium over the complete voltage range (2). There is therefore no depression of field due to electronic leakage, as reported for zirconium (8).

The agreement obtained between low- and high-voltage parameters again confirms the assumption (7) that oxide film formation occurs at unit current efficiency over the low-potential range below oxygen evolution.

Acknowledgment

The work reported here was carried out under contract AT(45-1)-535 between the University of Oregon and the U.S. Atomic Energy Commission.

Manuscript received July 7, 1958.
Any discussion of this paper will appear in a Discussion Section to be published in the June 1961 JOURNAL.

REFERENCES

1. D. A. Vermilyea, *Acta Met.*, **1**, 282 (1953).
2. L. Young, *Trans. Faraday Soc.*, **50**, 159 (1954).
3. G. C. Willis, Jr., Ph.D. Dissertation, University of Oregon (1958).
4. N. F. Mott, *Trans. Faraday Soc.*, **43**, 429 (1947).
5. N. Cabrera and N. F. Mott, *Repts. Prog. Phys.*, **12**, 163 (1948-49).
6. J. F. Dewald, *This Journal*, **102**, 1 (1955).
7. G. B. Adams, Jr., M. Maraghini, and P. Van Rysselberghe, *ibid.*, **102**, 502 (1955).
8. G. B. Adams, Jr., T. S. Lee, S. M. Dragonov, and P. Van Rysselberghe, *ibid.*, **105**, 660 (1958).
9. G. B. Adams, Jr., M. Maraghini, T. S. Lee, and P. Van Rysselberghe, U. S. Atomic Energy Commission Report AECU-3058 (July 1955).
10. T. Teeter, Ph.D. Dissertation, University of Oregon (1954).
11. L. Young, *Trans. Faraday Soc.*, **52**, 14 (1956).
12. D. A. Vermilyea, *This Journal*, **104**, 427 (1957).

High Current Electronic Interrupter for the Study of Electrode Processes

W. E. Richeson[1] and M. Eisenberg[2]

Stanford Research Institute, Menlo Park, California

ABSTRACT

The design of a fast, high current interrupter capable of handling up to 5 amp is presented. Through small modifications even larger currents can be handled. The electronic interrupter is exceptionally versatile, has a short rise time, a variable output current, and a switching rate from 500 cycles per second to any longer period desired. Interruption periods as short as 1.6 microseconds were found to be quite practical. The high speeds, short rise times, and sizable currents make this interrupter an outstanding device compared to past efforts in this field. The applications of the interrupter in the field of electrochemical kinetics are illustrated through experimental work. Potential-time traces for anodic dissolution of titanium were studied.

Polarization can be measured fundamentally in two different ways. In addition to the direct method involving many forms of liquid junction to a reference electrode and in which the current is maintained constant during the measurement, methods are available to measure the potential of a working electrode against a suitable reference electrode during a short interval following interruption of the electrolyzing current. The chief advantage of a pulse interrupter method is that it allows elimination of the *IR*-drop involved between the working electrode and the reference electrode. This becomes particularly important when the geometry of the cell or changes in the electrolytic conductivity in the boundary layer at the electrode are such that corrections and predictions of *IR* drops are not very certain. In addition to offering a method for the elimination of the *IR* drop corrections, the interrupter gives several other types of information about the reaction process. For instance, from the decay curve of the polarization potential of the working electrode, deductions about the nature of the process (whether it is under activation control or under mass transfer control) can be made. From the initial slope of such decay curves one can also calculate the pseudo-capacity of the electrode. The latter offers a basic tool for studying the double layer and diffused double layer [according to Stern's theory (1)]. Thus, interrupters are very important research tools yielding important information about electrode processes from both the equilibrium and the kinetic point of view.

The first modern electronic interrupter was described by Hickling (2) in 1937. This device, how-

[1] Present address: Farnsworth Electronics, Fort Wayne, Indiana.
[2] Present address: Lockheed Missiles and Space Division, Sunnyvale, California.

ever, was still comparatively slow and limited to currents of the order of 10-50 ma. Schuldiner and White (3) obtained current interruptions by applying a disabling pulse to one side of a diode which was in series with the electrolytic cell and a current source. The current capability was in the order of a few milliamperes. More recently, Drossbach (4) used thyratrons to interrupt the current in a circuit containing an electrolytic cell and a current source.

Breiter and Volkl (5) found, however, systematic errors in both thyratron interrupter devices of Hickling and Drossbach. Through the use of calibrated input pulses they found that the error in amplitude of the applied pulse as shown by the measuring thyratron increases as the width of the applied pulse near the peak decreases. The relationship is almost linear. For this reason the thyratron device was found to be more reliable for rectangular input pulses than for sinusoidal or other transient forms. The systematic error is particularly large at low values of potentials. A slight decrease in the systematic error can be achieved by increasing the anode grid potential above 300 v. However, this introduces additional difficulties in fluctuations of the firing point of the thyratron. In addition to these difficulties resulting from the use of thyratrons, the 3 circuits described above were limited by the type of current interruptions which could be obtained, as well as by the level of current that can be handled.

The electronic interrupter described in this paper avoids the use of thyratron tubes and employs an electronic switch consisting essentially of a number of type 6AS7 vacuum tubes operating in parallel. As described here, the interrupter is capable of handling up to 5 amp and performing many different types of interruptions. The "on" and "off" times and switching frequency can be varied practically at will. Furthermore, by addition of more tubes in parallel the current capacity of the interrupter can be increased without involving other major changes.

Design Considerations

The interrupter must act like a near perfect switch which can open and close rapidly without extraneous transients. The device must have a variable conduction level and must be capable of imposing a current function upon some specified steady-state current level. The level of operation must be from a few microamperes to large values, e.g., 5 amp. The period of conduction or no conduction, the ratio between conduction and nonconduction periods, and the frequency of operation of the interrupter should be variable over very wide limits.

The method selected was one in which an electron tube or a group of parallel electron tubes is placed in series with an electrolytic cell and a battery. This electronic switch is controlled by a pulse generator which has a very low output impedance (30 ohms) and a d-c coupling. The pulse generator has a function generator input. This portion of the circuit acts like a power amplifier which controls the electronic switch so that special pulse functions can be used. Provision is made for a potential source and a mercury switch so that the electronic switch will have a step function applied to it which is controlled by a push button. A third provision is for a time standard to be connected to the pulse generator. This standard drives a pulse generating circuit so as to generate symmetrical or asymmetrical pulses to control the electronic switch over very wide limits (1 μsec to a few tenths of a second intervals). Also on this chassis is the provision to vary the amplitude of the signal and the level of the d.c. to the electronic switch.

The effect of stray pickup would be to introduce noise and extraneous signals into the data. When a current is interrupted the circuit impedance becomes large and it may often become difficult to reduce stray pickup. Due to the fact that the input impedance of the measuring apparatus is large (10 megohms in this case), so as to prevent loading, the noise pickup picture becomes worse. The solution is to make leads short and keep all active portions of the circuit well shielded. Special precautions must be taken in order to prevent capacitively loading high impedance portions of the circuit by shielding these portions too tightly. Special precautions must be taken to prevent grounding loops and to hold stray inductance to a minimum. Large diameter, low resistance, low inductance leads were used when possible. In some cases coaxial and twisted leads to carry currents hence and forth were used in order to reduce the inductance of the system and to reduce radiation or stray pickup. Some portions of the circuit were by-passed with capacitors to reduce their inductive effects. Power line variations and noise were reduced by using voltage-regulated transformers and filters.

Design of Mode of Operation

Power supply.—Figure 1 shows the circuit of the power supply which feeds d-c power to the voltage regulation circuit of Fig. 2. The power supply is designed to supply 400 v d.c. at 1,000 ma. The voltage regulator (Fig. 2) has tubes V_{15}, V_{16}, V_{17}, and V_{18} in parallel which gives a total of 8 triode sections of the 6AS7 variety and can individually pass 125 ma. The maximum output of the regulator is about 1 amp at 100 v drop across these tubes. The tubes V_{19}, V_{20}, T_1, T_2, and T_3 form the error-detecting amplifier which drives the above series of regulator tubes. The voltage regulator tube T_4 produces a 150-v supply whose output current cannot vary by more than ± 12 ma about the steady-state current drawn from its 150-v output terminal.

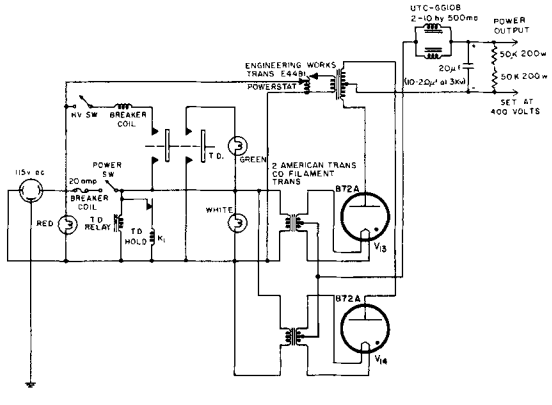

Fig. 1. Power supply

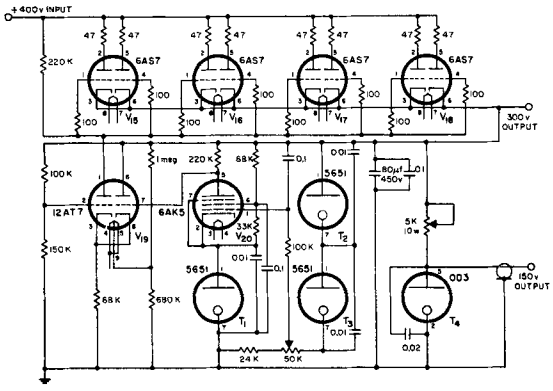

Fig. 2. Voltage regulation circuit. Capacity in $\mu\mu$f and resistance in ohms unless specified.

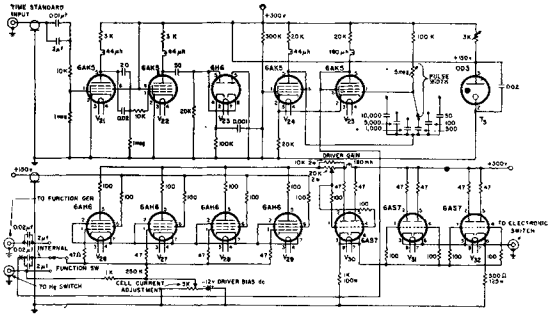

Fig. 3. Pulse generator. Capacity in $\mu\mu$f and resistance in ohms unless specified.

Pulse generator.—The pulse generator (Fig. 3) is the signal source for the electronic switch chassis. The output of the pulse generator is directly coupled to the electronic switch through a coupling box.

Starting with the time standard input jack, signals from the Time Standard (e.g., Hewlett-Packard model 202A) pass through tubes V_{21} and V_{22} which are overdriven amplifiers. When the signal leaves V_{22} it has a squared wave form. This square wave passes to V_{23} which is part of a differentiating and limiting circuit which is responsible for driving V_{24} with sharp positive pips. Tubes V_{24} and V_{25} with associated circuitry form a monostable multivibrator which forms a positive pulse of variable period for each positive pulse coming from V_{23} which is repetitive at the rate prescribed by the time standard. The periods of the positive pulses produced can vary from 2 μsec to 0.15 sec. This positive pulse is fed to point x which is a contact on a selector switch whose other contacts are "To Function Gen" and "Hg Switch." The wiper arms of this switch feed the grids of the parallel combination V_{26}, V_{27}, V_{28}, and V_{29}. This series of tubes forms an amplifier-inverter which feeds a signal to V_{30} which is a cathode follower. V_{30} feeds V_{31} and V_{32} in parallel which is another cathode follower which drives the "electronic switch." Because of the rise time desired and the impedance levels V_{26} to V_{32} were required. The potentiometer, "cell current adjustment," controls the bias on the combination V_{26}, V_{27}, V_{28}, and V_{29}. This controls the d-c level of the output to the electronic switch and therefore its current level. The driver gain control adjusts the magnitude as well as the d-c level of the signal to the electronic switch.

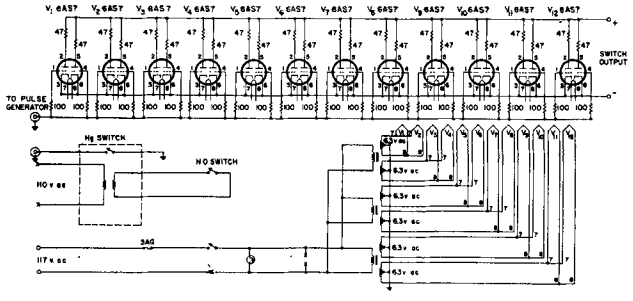

Fig. 4. Electronic switch. Capacity in $\mu\mu$f and resistance in ohms unless specified.

The "function switch" determines the derivation of the "electronic switch" control. The "function generator" position of input at this terminal will be amplified and will control the "electronic switch." Such a function generator might be the Hewlett-Packard low frequency function generator. When the selector switch is on "Hg switch" the pushbutton mercury switch (vide infra) will control the "electronic switch." If the pushbutton is pushed the mercury switch closes and shorts this position to ground. This removes the bias on V_{28} to V_{29} and causes their plate voltage to drop greatly. This step function cuts off the "electronic switch."

Electronic switch.—Tubes V_1 to V_{12} comprise the electronic switch in Fig. 4. With a 50 v drop across the switch, and the grid to cathode voltage equal to zero, the current can be about 5 amp. If the drop across the switch is 60 v, the current can be 6 amp, with a zero grid to cathode voltage. The total dissipation of the present set should not exceed 312 w for any long period of time such as days and weeks. The use of resistors in the plate and grid circuits were for the purpose of avoiding parasitic oscillations. The switch output terminals are in series with the electrolytic cell and the d-c power source.

There is a pushbutton on the panel which actuates a mercury switch. The closure of this switch is grounded. The contact of this switch is brought out to the panel, which allows cabling to one of the inputs to the pulse generator. This input on the pulse generator chassis is labeled "to Hg switch" (left side of Fig. 3).

Coupling box.—Figure 5 shows the coupling circuit between the pulse generator and the electronic switch. The function of this box is to couple the output of the pulse generator to the electronic switch, to set the level of current flowing in the electronic switch, and to assure against grid current being drawn by the electronic switch. The electronic switch current level adjustment should be so adjusted as not to give an indication on the meter M.

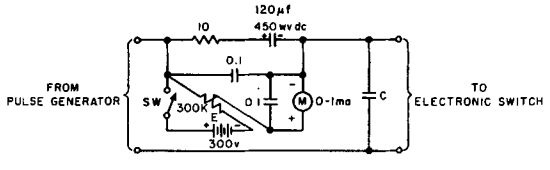

Fig. 5. Coupling box. C, determined the rise time desired; E, 200 v (tapped 300-v miniature battery); M, adjust driver bias control so that this current is always zero; R, electronic switch current level adjust.

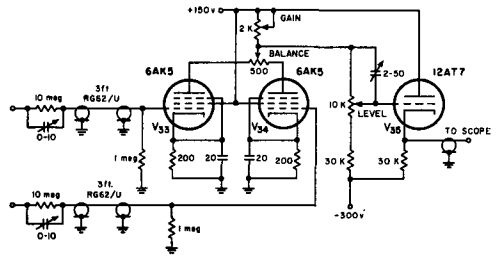

Fig. 6. Difference amplifier. Unless specified, R in ohms, C > 1 in $\mu\mu f$.

The capacitor C (1-50 μf) is included so that the rise time or decay time of the electronic switch may be adjusted.

Difference amplifier.—Tubes V_{33} and V_{34} form the difference amplifier in Fig. 6. The "balance control" is to make adjustments in the event that V_{33} and V_{34} may not have exactly the same characteristics. The gain control adjusts the gain of the difference amplifier. The level control adjusts the d-c level of the output of V_{35} which is a cathode follower. A variable capacitor, C, (2-50 μf) adjusts the shape of the leading edge of fast pulses so as to minimize distortion.

Possible modes of operation.—Figures 7, 8, and 9 present operational block diagrams of Interrupter Circuits No. 1, 2, and 3. The dotted-in capacitors present some of the more important distributed capacitances. Figure 7 shows the circuit which is possible without the use of a difference amplifier and

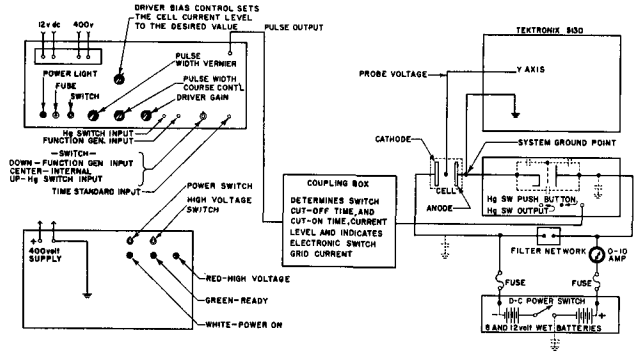

Fig. 7. Interrupter circuit No. 1

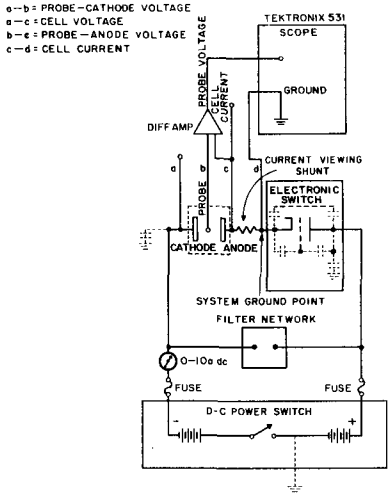

Fig. 8. Interrupter Circuit No. 2

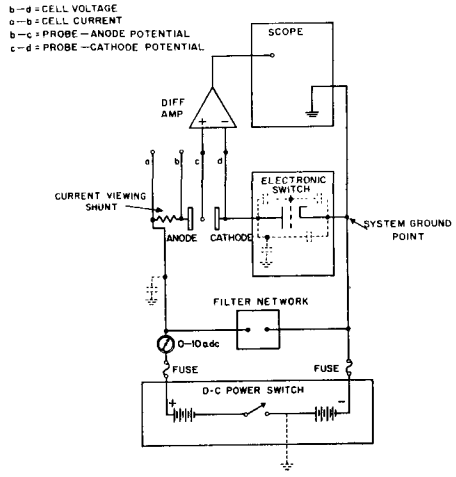

Fig. 9. Interrupter Circuit No. 3

Fig. 8 and 9 show what can be done with the use of difference amplifiers. Due to the existence of distributed inductances in the Interrupter Circuit No. 3 (Fig. 9) is the most desirable circuit since it would have the least ringing.

The method of coupling the electrolytic circuit with the interrupter device is illustrated in Fig. 7. On the right-hand side a bank of lead acid batteries is shown as the source of the electrolytic current. This current passes through an electronic switch (shown directly above the batteries) to the cell and is measured by an ammeter connected in series. The potential developed between the anode in the cell and the reference electrode (probe voltage) is viewed by means of a suitable oscilloscope (in this case Tektronix 513D or 531 was used). After suitable calibration of the oscilloscope in respect to the time as well as voltage axis, visual observations were followed out by photographic records taken with a Polaroid camera. Details of the individual components of the interrupter are shown in Fig. 2, 3, and 4. The voltage regulation circuit as shown in Fig. 2, has an input of +400 v (from the supply unit shown in the lower left-hand corner of Fig. 7) and gives a closely controlled output of either 150 or 300 v. This power is fed into the pulse generator (left upper corner of Fig. 7) whose details are shown in Fig. 3. As a time standard a Hewlett-Packard oscillator is used. Square waves of an adjustable frequency are employed. Whenever a single interruption is desirable a manual switch can be used instead of the time standard. The output of the pulse generator is fed into an electronic switch as shown in Fig. 4. This switch employs a bank of 12 type 6AS7 vacuum tubes. This bank of tubes is necessary to enable the switch to carry and interrupt electrolyzing currents up to 5 amp. The electronic switch is shown in the middle right-hand side of Fig. 7, representing the over-all interrupter circuit arrangement.

Application and Experimental Results

As one method of application of the electronic interrupter a study was made of anodic polarization of titanium. Other possibilities of employing the interrupter were not explored at this time. The main objectives were interruption studies employing elec-

trolyzing currents up to 5 amp for period durations as short as 1 μsec.

The experimental procedure consisted of electrolyzing the cell at a constant current for a sufficient time (usually 5-10 min) to achieve a constant polarization of the anode. Following the calibration of the oscilloscope the electrolytic current was interrupted and a simultaneous photographic recording of the trace on the face of the oscilloscope was taken. This technique was used whenever a full decay of the polarization was wanted. In cases in which the current had to be restored after a desired preset "off" period, this was usually done by employing the time standard as an input to the pulse generator. Usually 1 or 10 cps was used as a frequency for the interruption. In some cases for a given current density interruptions were made for varying (gradually increasing) periods of time. These ranged usually from as little as 1.5 μsec to as long as 4000 μsec. The rise time was found to be about 0.1 μsec.

Results were subsequently evaluated from the photographs of the oscilloscopic traces.

One of the typical experimental situations in studies of electrode kinetics is the inherent involvement of some unknown *IR* drop in the cell. Even under conditions where efforts have been made to reduce or eliminate such an *IR* drop, some small *IR* drops may still exist between the Luggin capillary leading to a reference electrode and the polarized working electrode under study. It is in situations of this type that the use of an interrupter is particularly advantageous.

One of the direct methods for the determination of single electrode polarization which avoids the use of the Luggin capillary with its complicated distortions of the equipotential surfaces and of the hydrodynamic conditions is the so-called "extrapolative method" (6).

This technique is based on the use of two reference electrodes connected to the cell at precisely known distances from the equipotential surface of the electrode itself. The *IR* drop between the electrode and the nearest reference is then calculated by extrapolating from three measurements, as indicated in Fig. 10. It is obvious that the validity of this method depends primarily on two factors; the first requires a uniform current distribution and the second is based on the assumption that the electrode process does not greatly affect the electrolyte conductivity in its immediate vicinity. The use of an electrolytic trough with well-matched electrodes at the end generally provides a uniform primary current distribution. In most solutions where an excess of supporting electrolyte is employed, the net change in electrolyte conductivity in the vicinity of an electrode at which no new ionic species is created, the conductivity changes are usually sufficiently small to make the extrapolative method useful. However, in the case of an anodic dissolution in an electrolyte which does not contain ionic forms of the metal, sizable changes in the conductivity in the immediate vicinity of the anode occur, and the comparison between the interruption technique and the extrapolation method would then definitely be revealing.

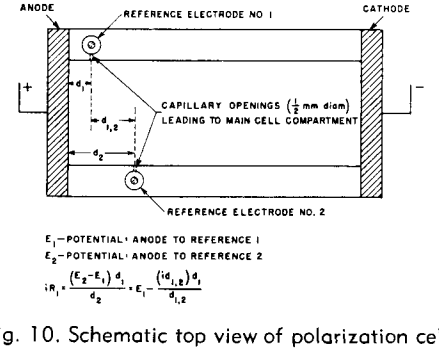

Fig. 10. Schematic top view of polarization cell

To test this point, as well as to evaluate the overall performance of the interrupter, the anodic polarization of a titanium sheet anode (Ti 75A) was studied in a solution (K-2) of the following composition: 11.5% (wt) HF; 6.2% H_2O; 15.0% tetrahydrofuran; 67.3% ethylene glycol at temperatures from 30° to 55°C. Vigorous stirring was employed in the bulk of the cell Table I shows the analysis of the data obtained from such interruption experiments. In addition, the last column shows *IR* drop calculations made by the direct extrapolative method. Bright nickel reference electrodes immersed in the same solution in a separate compartment were employed as shown schematically in Fig. 10. At the open circuit the titanium anode potential was negative in respect to the nickel reference electrode by 0.62 v. However, when polarized at a total current of 0.30 amp (i.e., a current density of 6 ma/cm^2) its potential shifted considerably into the positive direction to a value of +105 v. Upon interruption for a period of 2 μsec an instantaneous vertical drop of 0.4 v was recorded. This drop can obviously be assigned to the *IR* drop component of the potential difference involved between the nearest reference electrode and the polarized titanium anode. Following this rapid *IR* drop a somewhat slower decay of the actual net polarization of the anode began. Thus, as shown for an interruption period of 48 μsec, the potential decreased from 0.65 to 0.54 v during the period from 2 to 5 μsec (following the current break). This value decayed further to 0.40 v within the subsequent 43 μsec (see line 3, Table I).

In experiments employing a total current of 0.70 amp the *IR* drop component estimated from the decay curve was 0.7 v. This was lower than the 0.95 to 0.90 value estimated by means of an extrapolative method employed in the direct polarization measurements (last column of Table I). At this current level longer interruption periods were employed and it can be noticed that a decay of about 1.5 v occurred within 1000 to 2000 μsec. This generally is quite rapid compared with the decay one might expect from a pure diffusion mechanism (7). Similarly, it can be observed that at a total current of 2 amp (current density of 40 ma/cm^2) the anode polarization drops from 2.8 v to 0.30 v within 4000 μsec. This, compared with the zero current potential of −0.62 v, amounts to a decay of 72.7% of the total anode polarization within 0.004 sec. On the basis of these observations it may thus be concluded (8) that the anode polarization of titanium consists essentially (if not completely) of chemical polarization associated with

Table I. Analysis of potential-time traces for titanium anode (Ti75A)[a]
Solution: K-2 — Anode Area = 50 cm²

Total current, amp	Temp, °C	Interruption period, μsec	IR drop[b] estim. from decay, v	Anode potential vs. Ni-ref electrode, volts: Just prior to interruption	5 μsec after interr.	Minimum at end of interr. period	0.5 μsec after closing circuit	Final closed circuit value	IR drop[c] estim. in the direct method, v
0	30			−0.62					
0.30	30	2	—	+1.05	—	0.65	1.05	1.05 (at once)	0.44
0.30	30	48	0.4	1.05	0.54	0.40	0.90	1.05 (40 μsec later)	0.44
0.30	31	70	0.4	0.95	0.45	0.32	0.83	0.95	0.44
0.70	36	1.6	0.7	1.55	—	0.85	1.50	1.55 (3 μsec later)	0.95
0.70	36	25	0.7	1.55	0.65	0.48	1.10	1.55 (75 μsec later)	0.95
0.70	37	60	—	1.55	0.65	0.40	1.05	1.45 (40 μsec later)	0.93
0.70	37	200	—	1.52	—	0.25	0.90	1.47 (300 μsec later)	0.93
0.70	38	1020	—	1.50	—	0.05	1.00	1.50 (1000 μsec later)	0.90
0.70	38	2000	—	1.48	—	0	—	1.48 (3000 μsec later)	0.90
2.00	40	2.6	1.2	3.30	—	1.90	3.00	3.2 (7 μsec later)	2.48
2.00	40	22	1.4	3.30	1.55	1.30	2.75	3.2 (80 μsec later)	2.48
2.00	55	200	—	2.80	—	0.60	—	2.8 (300 μsec later)	—
2.00	55	4000	—	2.80	—	0.30	—	2.8 (3000 μsec later)	—

[a] All experiments were carried out with a repeat rate of 1 or 10 cps.
[b] The IR drop in the electrolytic cell between the anode and the nickel reference electrode.
[c] These values were estimated by extrapolating the bulk electrolyte conductivity to the solution layer adjacent to the electrode.

the activation energy required for the titanium dissolution reaction.

Another interesting conclusion from this work is that the IR drop values obtained from conductivities in the direct method of polarization measurements (last column Table I) are usually larger than the values obtained from the initial rapid drop in the potential-time trace obtained by the interrupter method. These differences become larger and more significant the larger the current densities employed. This, of course, is to be expected since sizable amounts of titanium ions are going into the solution in the immediate vicinity of the anode. The differences, especially at the higher current densities, are sufficiently large to demonstrate the importance of interruption techniques as a research tool in electrode kinetics.

Manuscript received Oct. 26, 1959. This paper was prepared for delivery before the San Francisco Meeting, April 29-May 3, 1956.

Any discussion of this paper will appear in a Discussion Section to be published in the June 1961 JOURNAL.

REFERENCES

1. O. Stern, *Z. Elektrochem.*, **30**, 508 (1924).
2. A. Hickling, *Trans. Faraday Soc.*, **33**, 1540 (1937).
3. S. Schuldiner and R. E. White, *This Journal*, **97**, 433 (1950).
4. P. Drossbach, *Z. Elektrochem.*, **57**, 548 (1953).
5. M. Breiter and W. Volkl, *ibid.*, **58**, 899 (1954).
6. M. Eisenberg, M. S. Thesis, Univ. of California (1951).
7. C. W. Tobias, M. Eisenberg, and C. R. Wilke, *This Journal*, **99**, 359C (1952).
8. A. Hickling and F. W. Salt, *Trans. Faraday Soc.*, **37**, 450 (1941).

The A-C Resistance of a Stainless Steel Electrode and Specific Adsorption

G. M. Schmid and Norman Hackerman

Department of Chemistry, University of Texas, Austin, Texas

ABSTRACT

The a-c resistance of a stainless steel wire electrode was measured in dependence of the type of electrolyte, the polarizing current density, and frequency of the measuring current. It is shown that K^+ is more adsorbed than Na^+ during cathodic polarization, and Cl^- more than F^- during anodic polarization. This method seems to be especially useful in testing the adsorbability of neutral surface active substances during d-c flow.

A wire electrode in contact with an electrolyte represents, with respect to passage of current along the length of the wire, a system similar to two resistors connected in parallel. Thus, when two contacts are made to the same electrode and an a-c or d-c potential is applied, a certain fraction of the total current flow chooses a path through the electrical double layer (edl) and the solution (1). The extent of this leakage can be found by measuring the impedance of the system and comparing it with the impedance of the electrode in air. In doing so, it must be remembered that the impedance of a metal

can vary with the uptake of gas, especially hydrogen (2).

The conduction phenomena of the electrode/electrolyte interface are determined by the structure and composition of the edl. The composition of the edl depends on the kind of electrolyte solution used and on the presence or absence of specifically adsorbed ions and neutral surface active substances. The structure of the edl depends on the potential of the electrode (3). It was found previously that the magnitude of leakage current in the system stainless steel/1.0M Na_2SO_4 depends on the polarizing d-c current density (p.c.d.), or alternatively on the potential of the electrode (4).

The leakage current, besides being governed by the edl, is limited by the conductivity of the solution. It was found to be negligible in the system stainless steel/0.001M Na_2SO_4. Furthermore, when using an electrolytic cell, the current, leaking from the test electrode into solution may also pass from the solution into the auxiliary electrode, comparable to a circuit with three resistors in parallel.

Measurements of the leakage current, i.e., the impedance of the system, between two contacts on the same electrode should permit conclusions to be drawn regarding specific adsorption. The leakage current will have to be compared with a system, the components of which are not specifically adsorbed.

Experimental

Essentially the same experimental setup was used as in previous work (4). Unless otherwise stated, the impedance of the test electrode was measured with 60 cps a.c. in a Wheatstone Bridge, using a Brown-Honeywell Recorder for continuous measurements, with a precision of 0.005 ohms. In order to obtain data on the frequency dependence of the leakage current, a General Radio Co. (GRC) Type 650-A Impedance Bridge was used between 100 cps and 16 kcps, with a Hewlett-Packard (HP) Widerange Oscillator Model 200 DC as power supply. The signal drawn from the bridge was preamplified in a HP Model 450-A Amplifier, filtered and amplified in a HP Model 300-A Harmonic Wave Analyser and observed on an oscilloscope, thus giving an accuracy of 0.01 ohms. Measurements between 550 kcps and 2 mcps were made with a GRC Type 821-A Twin-T Impedance Bridge combined with a GRC Type 1001-A Standard Signal Generator. Here the null-detector was a radio receiver.

Reproducible results, especially at the intermediate frequency range, were obtained only after pretreating the electrodes alternatively, anodically, and cathodically for about 1 hr (5).

In all cases, the test electrode was a type 302 stainless steel wire of 0.038 cm diameter and approximately 90 cm long. The auxiliary electrode was made of the same material and length. The two electrodes were arranged in a glass tube and kept apart 2 cm throughout. The polarizing d-c current was supplied by a Lambda Regulated Power Supply Model 32 M operated at 200 v d.c. or by a 180 v battery and controlled by a set of resistors. The power supply was connected to the upper end of the anode and the lower end of the cathode, thus preventing a d-c potential drop along the wires. All contacts were made outside the electrolyte. Interference of the two circuits was carefully minimized by the use of capacitors and chokes as filters. The potential of the test electrode was measured against a saturated calomel electrode (SCE).

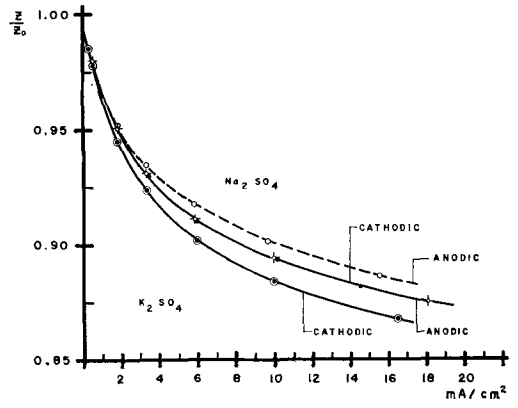

Fig. 1. Relative impedance vs. current density in 0.1M K_2SO_4 and 0.1M Na_2SO_4. (Curves for Na_2SO_4 cathodic and K_2SO_4 anodic coincide. Electrode: Type 302 stainless steel wire, 0.038 cm diameter, surface area 10.6 cm^2, Z_o = 6.556 ohms.

Results

Effect of cations.—The difference between impedance measurements with low-frequency a.c. in air and in solution is very small, either because the coupling capacity of the edl is too small and/or the coupling resistance is too large to allow a significant fraction of the measuring current to leak into solution. When the electrode is sufficiently polarized to make an electrochemical reaction possible, the capacity becomes appreciably higher and/or the resistance drops to low values (6). This causes an a-c leakage as shown in Fig. 1, where the impedance of a stainless steel wire is plotted against the p.c.d. for 0.1M Na_2SO_4 and 0.1M K_2SO_4. Since the anion is the same in both cases, one would expect the curves for anodic polarization to coincide. As stated above however, the leakage current is limited also by the conductivity of the electrolyte (Table I). The better conducting system, K_2SO_4, should in any case show a lower impedance at a given p.c.d., as was found experimentally. The distance between the anodic and cathodic curves is slightly bigger in the case of K_2SO_4, pointing to a more densily packed edl. It was concluded, therefore, that during cathodic polarization K^+ is somewhat more adsorbed than Na^+. This has been reported also on Hg (7) and Pt electrodes (8). In both solutions, the impedance curves for cathodic polarization run lower than those for anodic polarization. This means a larger capacity and/or smaller resistance of the edl on cathodic polarization (6).

Table I. Conductivity in $10^{-4}ohm^{-1}cm^{-1}$ (9)

t°C	Molarity	Na_2SO_4	K_2SO_4	KF	KCl	KBr	KI
25°	0.1	163.08	202.52	107+	128.62	131.4	130.5

+ Interpolated.

Effect of anions.—In solutions of the more common cations, the cathodic electrode reaction is H_2 evolution, and it is reasonable to assume that, at a given current density, differences in the behavior of the edl can be attributed to differences in the adsorbability of ions or neutral substances. An electrochemically inert species, like SO_4^{--}, can be taken as common anion. In varying the anion, however, frequently the anodic electrode reaction changes from anion to anion and with it the composition of the edl. Thus, with KF up to 1.0M and 0.1M KCl (at current densities > 3 ma/cm², see next paragraph) O_2 is evolved at the anode, with KBr up to 1.0M the electrode does not become passive in the current density region investigated and iron dissolution occurs, and with KI the anion is oxidized. The above assumption no longer holds and we can reasonably compare only the curves for 0.1M KF and 0.1M KCl with each other. An additional complication derives from the fact that the auxiliary electrode, only 2 cm away, may participate in the over-all conduction phenomena (4). This interference forces the impedance drops on both sides of the polarization curves to be of the same order of magnitude. So, in judging the effect of different ions on the leakage current, both cathodic and anodic impedance curves have to be considered together. With 0.1M KF and 0.1M KCl the impedance curves for cathodic polarization are also lower than the anodic impedance curves (Fig. 2). It seems to be a general rule that the conductivity of the edl at H_2 evolution is higher than at O_2 evolution potentials. The difference between cathodic and anodic curves is more pronounced on comparing F^- and Cl^- than on comparing K^+ and Na^+, showing a larger effect of anion adsorption. The gap is bigger in the case of Cl^-, which apparently can dehydrate more easily than F^- ions (8, 10). The generally smaller impedance changes in KF can be explained by its smaller conductivity.

It is interesting to note that the curve for 0.1M KI and 0.1M KBr differ remarkably, despite the fact that the solutions have about the same conductivity. This could be attributed to stronger adsorption of I^- combined with a higher edl capacity due to adsorbed I_2.

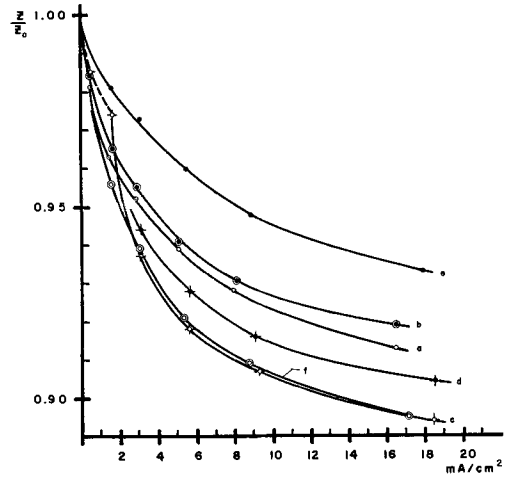

Fig. 2. Relative impedance vs. current density: curve a, 0.1M KF cathodic; curve b, 0.1M KF anodic; curve c, 0.1M KCl cathodic; curve d, 0.1M KCl anodic; curve e, 0.1M KBr anodic; curve f, 0.1M KI anodic. Electrode: Type 302 stainless steel wire, 0.038 cm diameter, surface area 10.5 cm², Z_0 = 6.520 ohms.

Effect of chloride.—Figure 3 gives recorder graphs of measurements in 0.1M K_2SO_4 and 1.0M KCl. In K_2SO_4 the impedance reaches its steady-state value for the corresponding polarizing current density or open-circuit conditions practically instantaneous. During current flow O_2 evolution takes place. In KCl however a sharp impedance drop occurs, followed by a slow increase to a maximum and a final steady-state value. The electrode exhibits a passive potential shortly after the first sharp drop, and gas evolution was observed. During the following increase a slow potential decay with a sudden breakdown at the impedance maximum was experienced. Gas evolution stops and the bright electrode begins to show dark pits. After the polarizing current is cut off, it takes roughly 1 to 2 min for the impedance to reach its steady-state value for open-circuit conditions. The time during which passivity is maintained is a function of temperature, current density, and KCl concentration. At room temperature stainless steel can be held passive in 0.1M KCl with current densities > 3 ma/cm². Current densities < 20 ma/cm² are not enough to maintain passivity in 1.0M KCl. Increase in temperature shortens the time of passivity. At an anodic current density of 20 ma/cm² in 1.0M KCl, the electrode is passive at 39°C for 38 sec only, whereas at 1°C passivity is maintained "permanently" even at considerably smaller current densities. The time during which passivity is maintained is not reproducible because of the large changes in surface involved (pitting, Fe dissolution). For these phenomena the following explanation is proposed. In the first moments of anodic polarization an adsorbed sheet of water dipoles is converted to chemisorbed oxygen (11). The strongly positive potential facilitates the subsequent adsorption of Cl^- ions. Gradually, adsorbed oxygen is partially replaced by adsorbed Cl^-, passivity breaks down, and the potential falls back to Fe dissolution values.

A passive stainless steel electrode provides for a large amount of leakage current (e.g., KF, Fig. 2, a and b). A fairly rapidly dissolving electrode shows less leakage current (e.g., KBr, Fig. 2, e), despite the fact that the adjacent layer of solution should be crowded with iron ions and have good conductivity. At a dissolving electrode, however, continuous regeneration of the surface prevents a high coverage with chemisorbed species, provided the surface changes fast enough. The importance of the inner edl for the contact between metal and solution is again emphasized. The peak in the impedance/time curve (Fig. 3) represents a maximum coupling impedance, the point, where the coverage with adsorbed oxygen is defective so that the passivity breaks down and iron dissolution begins. Chloride ion adsorption blocks the surface for the leakage current. In order to pass into solution by resistive coupling, the measuring a-c current would have to react with Cl^- or Cl_2 alternatively, which is not pos-

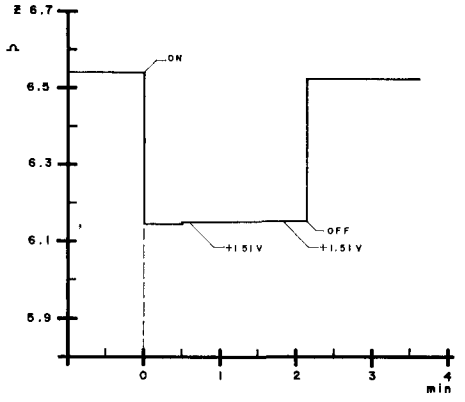

Fig. 3a. Impedance vs. time (recorder traces), 0.1M K_2SO_4, 5.8 ma/cm^2 anodic.

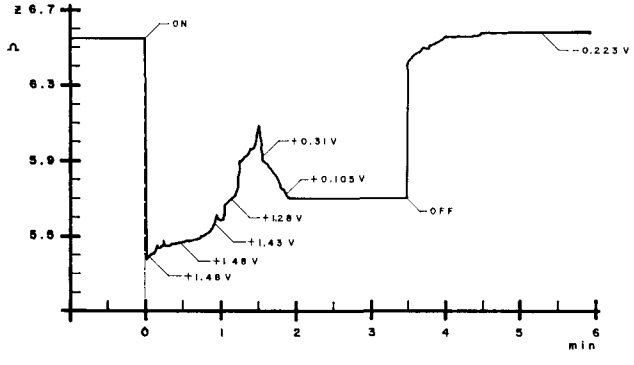

Fig. 3b. Impedance vs. time (recorder traces), 1.0M KCl, 9.3 ma/cm^2 anodic. Potential values with respect to SCE.

sible because of the high overvoltage for this step, thus leaving a capacitive coupling only.

To get further proof for this point of view the potential time pattern of the electrode during cathodic and anodic polarization in 0.5M KCl with a current density of 5 ma/cm^2 was observed on an oscilloscope. The electrode was made passive and the potential was allowed to decay under current flow. Immediately afterward short cathodic pulses (5-10 sec) were applied, and an attempt was made to passivate the electrode again between each cathodic pulse. The potential however never went beyond +1.0 v, showed a flat maximum, and dropped to about +0.2 v in a total elapsed time of 0.5 sec. Only prolonged cathodic polarization (>1.5 min) restored the ability of the electrode to become passive at once when anodically polarized. The negative potential of the electrode during cathodic polarization probably causes desorption of Cl^-. This process however requires some time. After short cathodic pulses there is still enough Cl^- left adsorbed on the surface to prevent the metal from becoming passive again. Prolonged cathodic polarization provides sufficient time for the Cl^- to be desorbed, thus enabling the electrode to achieve passivity when polarized anodically.

Frequency dependence of the leakage current.—The impedance of the electrode in air and in 1.0M Na_2SO_4 without polarizing current is practically the same at low frequencies. Up to about 100 cps the impedance in solution is independent of frequency (Fig. 4,a). The parallel resistance of the edl is high,

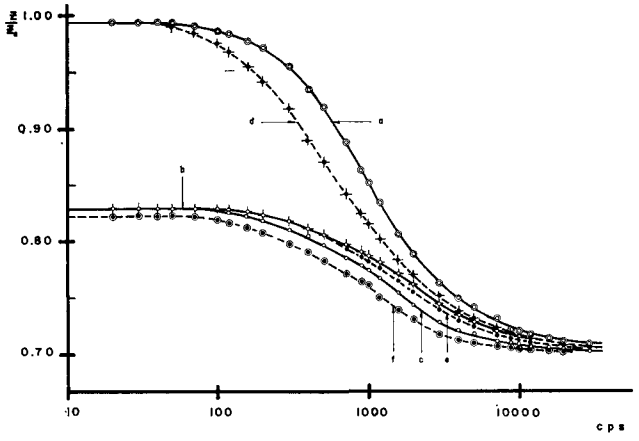

Fig. 4. Relative impedance vs. frequency: 1.0M Na_2SO_4: curve a, open polarizing circuit; curve b, 7 ma/cm^2 anodic; curve c, 7 ma/cm^2 cathodic. 1.0M Na_2SO_4 + 0.2M $(CH_3)_3N$: curve d, open polarizing circuit; curve e, 7 ma/cm^2 anodic; curve f, 7 ma/cm^2 cathodic. Electrode: Type 302 stainless steel wire, 0.038 cm diameter, surface oreo 10.8 cm^2, Z_o = 6.98 ohms.

the capacity small under these conditions. This causes the coupling to be negligible. At higher frequencies the impedance of the edl becomes smaller, permitting a larger part of the a.c. to leak into solution. Above 10 kcps this impedance becomes too small to control the leakage current. The coupling becomes "perfect" and the impedance of the system is governed by the constant impedance of the electrolyte. At about 1 mcps the skin effect (12) begins to show, causing the impedance to increase again.

The polarized electrode shows a considerably lower impedance at low frequencies, the parallel resistance of the edl being much smaller. Above 10 kcps the impedance coincides with the values obtained under open-circuit conditions, the coupling being "perfect" again.

Effect of surface active substances.—The frequency dependence of the leakage current was measured in 0.2M $(CH_3)_3N$ with 1.0M Na_2SO_4 as carrier and compared with a pure 1.0M Na_2SO_4 solution (Fig. 4). Under open polarizing circuit conditions, the greater capacity of $(CH_3)_3N$ becomes clearly visible in the intermediate frequency range, the maximum difference being about 0.3 ohms. Here the conductivity of the solutions and the reactions at the electrodes are the same in either case; the difference therefore can be due only to adsorption of the surface active substance on the electrode.

The capacity remains bigger with $(CH_3)_3N$ under polarizing conditions. The effect is larger on the cathodic side. It has been suggested that organic amines are purely cathodic inhibitors (13). One should expect therefore a stronger adsorption during cathodic polarization. Even in the low-frequency range, the impedance of the edl is lower in $(CH_3)_3N$ during cathodic polarization. It has been pointed out however that organic amines are anodic inhibitors as well (14). The curves for anodic polarization with and without $(CH_3)_3N$ coincide for low frequencies, the difference being small in the intermediate frequency range. This shows that the effect of anodic inhibition is probably smaller in this case.

Summary

It has been shown that measurements of the leakage current can be useful to test adsorption of ions and surface active substances, especially under polarizing current flow, where other methods, e.g., measurements of the edl capacity, do not give satisfactory results. The method is at its best where the leakage current in solutions with neutral surface active substances can be compared with a pure carrier solution. This can be done either by separate impedance measurements, as shown above, or by using two identical cells with the solutions to be compared as two arms in a Wheatstone Bridge and observing the error signal. The optimum frequency for the a-c measuring current is around 1000 cps. Difficulties have been met and are explained in cases, where changes in electrode reaction occurred, especially in potassium halide solutions. Nevertheless it has been possible to show that K^+ is more adsorbed than Na^+ and Cl^- more than F^- on stainless steel. An attempt has been made to explain the peculiar effect of Cl^-, which makes it impossible to maintain passivity even under anodic polarization with a current density high enough to passivate the metal initially.

Acknowledgment

This work was supported in part by the Office of Naval Research under Contract Nonr 375(02) and in part by the Welch Foundation, Houston, Texas. The authors wish to express their appreciation for this help.

Manuscript received Jan. 20, 1960.

Any discussion of this paper will appear in a Discussion Section to be published in the June 1961 JOURNAL.

REFERENCES

1. C. A. Knorr and E. Schwartz, *Z. Elektrochem.*, **39**, 281 (1933).
2. See for example: F. Fischer, *Ann Physik*, [4] **20**, 503 (1906); A. Coehn and H. Juergens, *Z. Physik*, **71**, 179 (1931); J. P. Hoare and Sigmund Schuldiner, *J. Phys. Chem.*, **61**, 399 (1957).
3. A. Frumkin, *Z. Physik*, **35**, 792 (1926); *Ergebn. Exakt. Naturwiss.*, **7**, 235 (1928); J. A. V. Butler, *Proc. Roy. Soc.* [*London*], **A122**, 399 (1929); Electrical Phenomena at Interfaces, London (1951), 63.
4. G. M. Schmid and Norman Hackerman, *This Journal*, **107**, 142 (1960).
5. G. Okamoto, M. Nagayama, and N. Sato, C.I.T.C.E., Proceedings of the Eighth Meeting, Madrid 1956 (London 1958).
6. K. Franke, C. A. Knorr, and M. Breiter, *Z. Elektrochem.*, **63**, 226 (1959).
7. A. N. Frumkin, B. B. Damaskin, and N. V. Nikolaeva-Fedorovich, *Proc. Acad. Sciences, USSR*, **115**, 751 (1957); J. Palacios and A. M. Baptista, *Rev. fac. Cienc, Univ. Lisboa*, 2a, Ser. B, **2**, 137 (1952/53).
8. P. V. Popat and Norman Hackerman, *J. Phys. Chem.*, **62**, 1198 (1958).
9. International Critical Tables, Vol. VI.
10. D. C. Grahame and B. A. Soderberg, *J. Chem. Phys.*, **22**, 449 (1954).
11. Kabanow, Burstein, and Frumkin, *Discussions Faraday Soc.*, **1**, 259 (1947).
12. Radio Engineer's Handbook, New York, (1943) 30.
13. Shih-Jeh Ch'iao and C. A. Mann, *Ind. Eng. Chem.*, **39**, 910 (1947); L. E. Swearingen and A. F. Schram, *J. Phys. Chem.*, **55**, 180 (1951).
14. Norman Hackerman and J. D. Sudbury, *This Journal*, **97**, 109 (1950); Helmut Kaesche and Norman Hackerman, *ibid.*, **105**, 191 (1958).

Technical Notes

Magnesium-Sulfur Dry Cells

C. K. Morehouse and R. Glicksman

Semiconductor and Materials Division, Radio Corporation of America, Somerville, New Jersey

A study of the electrochemical characteristics of the various compounds and elements of the periodic system showed that sulfur has several characteristics which make it worthy of consideration for use as a cathode material in primary batteries. It has a greater ampere-minute capacity per unit of weight (100.3 amp-min/g) and volume (207.6 amp-min/cc) than the cathode materials used in conventional batteries. Although it has a lower reversible potential than the other cathodes, it does have a flat voltage-time discharge curve as measured by the half-cell technique previously described by the authors (1). By the use of this technique, the sulfur cathode has been found to operate at a potential of about —0.4 v (vs. N.H.E.) when discharged at a rate of 0.030 amp/g in a $MgBr_2$ electrolyte. The efficiency of this electrode, which was computed on the assumption that the reaction involves a two-electron change per sulfur atom, was in excess of 80%. In addition to its favorable electrochemical properties, sulfur has a low solubility in aqueous solutions and is readily available at low cost in this country.

The use of sulfur as a cathode material coupled with a zinc anode in a Leclanché-type cell was first described by Walker (2) in 1887. Other patents have been reported which deal with the addition of small amounts of sulfur to the cupric oxide cathode of the Lalande cell in order to raise the cell voltage

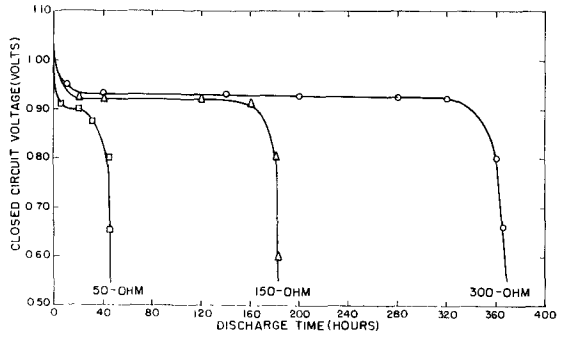

Fig. 1. AA-size $Mg/MgBr_2$/sulfur dry cells discharged continuously through 50-, 150-, and 300-ohm resistances at 21.1°±1.1°C (50% R.H.).

(3-8). These references refer to coupling sulfur with a zinc anode. Such cells have a low operating voltage and thus have practical limitations.

If a sulfur cathode is coupled with a magnesium anode, the reversible potential of the system calculated from free energy data is 2.2 v, assuming the following reaction occurs when energy is withdrawn from the cell:

$$Mg + 2\,OH^- + S = Mg(OH)_2 + S^= \qquad [1]$$

It is well known, however, that magnesium does not operate at its reversible potential in aqueous solutions. For example, in an aqueous *2N* $MgBr_2$ solution, saturated with $Mg(OH)_2$, AZ10A magnesium alloy has a potential (vs. N.H.E.) of 1.42 v under open-circuit conditions and operates at a potential of 1.29-1.32 v over a current density range of 0.5-4.0 ma/cm^2. Thus the operating potential of a magnesium-sulfur primary cell should be about 0.8-0.9 v.

Experimental

Magnesium-sulfur dry cells were assembled using an impact extruded AZ10A magnesium alloy AA-size can (height 4.62 cm, OD 1.32 cm, ID 1.12 cm). The magnesium cans were lined with a piece of salt-free kraft paper (5.72 x 5.72 x 0.005 cm thick), and an extruded slug of cathode mix was inserted in the lined can and consolidated. A carbon rod (height 4.54 cm, diameter 0.404 cm) containing a brass cap, was then inserted in the center of the cathode mix, and the cells sealed in the conventional manner with a rosin base wax. Each cell weighed approximately 10 g and contained about 5 g of cathode mix. The cathode mix, which consisted of equal parts by weight of Shawinigan acetylene black and sulfur mixed with 3% $BaCrO_4$, was wet to the proper consistency with an aqueous $MgBr_2 \cdot 6H_2O$ (500 g/l) solution containing 0.2 g/l $Na_2Cr_2O_7$.

The performance characteristics of the magnesium-sulfur AA-size dry cells of the above formulation and construction are shown in Fig. 1. These data were obtained by discharging the cells continuously through fixed resistances at 21.1° ± 1.1°C (70° ± 2°F) and 50 ±5% R.H.

The open-circuit voltage of the magnesium-sulfur dry cells ranges between 1.60 and 1.65 v; this high voltage is due to either adsorbed air in the cathode mix, or to the small amount of chromate which is added to inhibit the corrosion of the magnesium

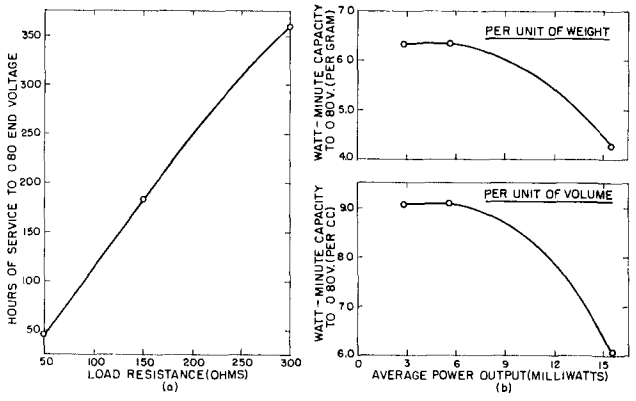

Fig. 2. Capacity data for AA-size $Mg/MgBr_2$/sulfur cells showing (a) hours of service to 0.80 v end voltage vs. load resistance; (b) watt-minutes per unit of volume and weight vs. average power output (capacity and average power computed to 0.80 end voltages from continuous discharge data).

anode. When current is withdrawn from the cells, the voltage falls to between 0.90 and 0.95 v, the operating voltage level of this system. Although these cells operate at a considerably lower voltage than the Leclanché and magnesium-manganese dioxide cells (9), they have a flat discharge curve and give considerably more hours of service to end voltages of 0.9 and 0.8 v than the two manganese dioxide dry cells.

The performance data in terms of continuous service to a 0.80 v end voltage vs. load resistance are presented in Fig. 2. Curves are also given showing the watt-minute capacity per unit of weight and volume as functions of the average continuous power output in milliwatts.

The magnesium-sulfur cell operates at about 0.90 v and offers promise for low drain applications. Its attractive features are high theoretical capacity, constancy of voltage during cell discharge, and the low cost of sulfur. It has problems similar to other magnesium cells. These are: delayed action, high impedance, and loss in capacity on light intermittent tests. The fact that hydrogen sulfide gas is liberated during cell discharge limits its broad applications.

Manuscript received Feb. 11, 1960. This paper was prepared for delivery before the Ottawa Meeting, Sept. 28-Oct. 2, 1958.

Any discussion of this paper will appear in a Discussion Section to be published in the June 1961 JOURNAL.

REFERENCES

1. C. K. Morehouse and R. Glicksman, *This Journal*, **103**, 94 (1956).
2. S. F. Walker, U. S. Pat. 361, 794, April 26, 1887.
3. R. C. Benner and H. F. French, U. S. Pat. 1,255,283, Feb. 5, 1918.
4. R. C. Benner and H. F. French, U. S. Pat. 1,316,761, Sept. 23, 1919.
5. R. C. Benner and H. F. French, U. S. Pat. 1,375,647, April 19, 1921.
6. R. C. Benner and H. F. French, Can. Pat. 215,676, Feb. 7, 1922.
7. R. C. Benner and H. F. French, U. S. Pat. 1,415, 860, May 16, 1922.
8. G. W. Armstrong, U. S. Pat. 1,624,460, April 12, 1927.
9. R. C. Kirk, P. F. George, and A. B. Fry, *This Journal*, **99**, 323 (1952).

On the Anodic Oxidation of Columbium

Robert Bakish

The Alloyd Corporation, Cambridge, Massachusetts

Except for the work of Johansen, *et al.* (1), Young (2, 3), and Adams (4), the author knows of no work on the anodic oxidation of columbium. This communication discusses in brief some aspects of the anodic oxidation of this metal.

The work was done on columbium sheet supplied by Murex Ltd., Rainham, Essex, England, which analyzed as follows: Ta 0.58%, C 0.1%, Ni 0.03%, Si 0.013%, Fe 0.015%, Ti 0.081%, Al and Mg 0.01%, B, W, V traces ($\leqq$ 0.01%). The specimen were thoroughly degreased and etched in a 5:2:2 solution of H_2SO_4 (95%), HNO_3 (70%), and HF (48%) prior to formation which was carried out at constant current of 5.5 ma/cm^2 in 0.1% H_3PO_4 solution. Constant current and constant voltage power supplies capable of maintaining voltages and currents within 1% of output were utilized, and all measurements were carried out in constant temperature bath controlled to $\pm 0.5°$ of the working temperatures and with 1% instruments.

The oxide and its state of crystallinity were identified by standard x-ray diffraction powder techniques supplemented by electron diffraction in transmission. For the electron microscopy triafol replicas shadowed at 30° and 90° incidence with SiO were used.

The voltage current characteristics of columbium and their dependence on temperature as recorded with a two channel recorder are given in Fig. 1, which shows typical data for 1°, 25°, 60°, and 80°C. In these experiments formation at constant current to 300 v was followed by constant voltage once the 300-v value was reached. After the well-known exponential decay of the current to a relatively low value "leakage current plateau," depending on the formation temperature, this value is kept for some time and then rather abruptly increases. The time to current reversal is inversely dependent on temperature with the current hardly reaching a "plateau" value at higher formation temperatures but rapidly getting outside the range of the instrumentation used.

This voltage current behavior is the consequence of crystallization of the amorphous oxide film. The leakage current for samples formed to lower voltages and held under these respective voltages remains at the "plateau" value for considerably longer times, and for a 50-v formation at room temperature no reversal was observed for as long as 24 hr under voltage, which was the duration of the measurements.

The oxide itself is identified with the T-Cb_2O_5 oxide form as determined by Brauer (5).

The influence of the potential on the oxide topography is shown by the composite electron micrograph (Fig. 2) showing representative areas identi-

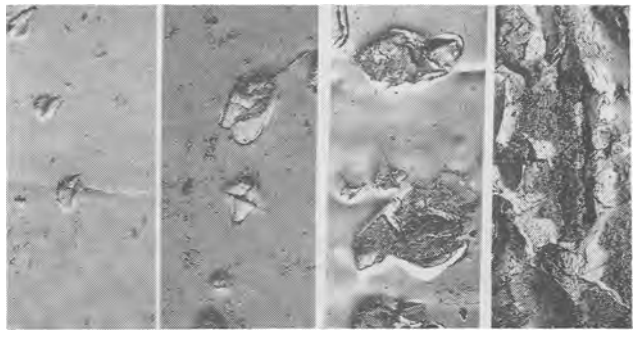

Fig. 2. Dependence of topography on formation voltage. Constant voltage formation to 100, 150, 175, 250. Magnification 5000X before reduction for publication.

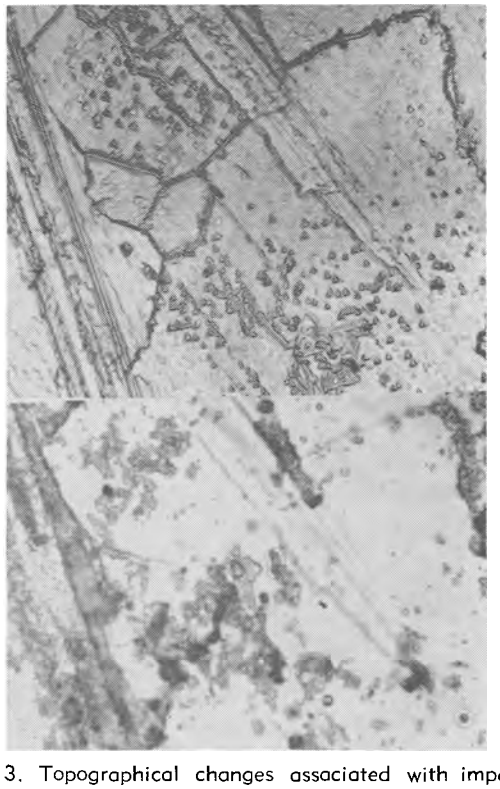

Fig. 3. Topographical changes assaciated with imperfections. Surface as etched and after formation to 320 v. Magnification 1000X before reduction for publication.

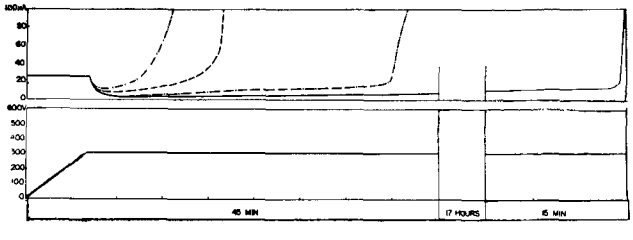

Fig. 1. Voltage-current characteristics of columbium formation. ——— 1°C 1/10% H_3PO_4; —.—. 25°C; — — — 60°C; —..—.. 80°C.

fied with the respective voltages. These observations were made after constant current formations to the voltages indicated. Above 250 v no replicating and, in turn, no electron microscopy are possible due to the disintegration of the oxide. The topographic changes of columbium on crystallization are both different and similar to these changes in tantalum. They are different in that none of the crystalline polygonal areas seen in tantalum (6) are observed here, and similar because here, as well as in tantalum, the crystalline oxide nucleates underneath and grows at the expense of the amorphous oxide, displacing it in the process.

An attempt to evaluate the possible role of cold work and imperfections was also made in this study, with Fig. 3 showing a representative specimen area containing a fine scratch before and after formation to 320 v. Observe the bulk of the crystallization taking place in the area delineated by the scratch and also in the vicinity of the dislocation etch pits (7), indicating, even though not conclusively, the possible catalytic role of imperfections in this crystallization process. It has already been shown that in tantalum crystallization takes place at preferred sites (8).

Results reported here show both similarities and differences between columbium and tantalum. The formation characteristics and the crystallization phenomena are common to both metals, but the greater ease of crystallization of columbium of this purity, as well as some details of the topographic changes brought about with the process, appear different. On the basis of this data, it cannot be asserted whether the observed differences are due to inherent differences between the two metals or to impurities in the columbium acting as crystallization nuclei.

Acknowledgments

The author wishes to thank Dr. M. Brönniman for the electron micrographs, and Dr. H. Müller for identifying the oxides. Mr. E. Muntner's and Mr. R. Cavaleri's assistance in the experimental work is acknowledged. The author is indebted to CIBA for permission to publish this work.

Manuscript received Nov. 2, 1959.

Any discussion of this paper will appear in a Discussion Section to be published in the June 1961 JOURNAL.

REFERENCES

1. H. Johansen, G. B. Adams, Jr., and P. van Rysselberghe, *This Journal*, **104**, 339 (1957).
2. L. Young, *Trans. Faraday Soc.*, **51**, 502 (1955).
3. L. Young, *ibid.*, **51**, 515 (1958).
4. G. B. Adams, Jr. and T. Kao, AECU 3769 (1957).
5. G. Brauer, *Z. anorg. u. allgem. Chem.*, **248**, 1 (1941).
6. D. Vermilyea, *This Journal*, **102**, 207 (1955).
7. R. Bakish, *Trans. Am. Inst. Mining Met. Engrs.*, **212**, 818 (1958).
8. D. Vermilyea, *This Journal*, **104**, 542 (1957).

The Reaction of Zirconium-Oxygen Alloys with Hydrofluoric Acid

M. E. Straumanis and T. Ejima

Department of Metallurgy, the University of Missouri School of Mines and Metallurgy, Rolla, Missouri

Metallic zirconium dissolves readily in hydrofluoric acid according to the equation (1, 2)

$$Zr + 4HF = ZrF_4 + 2H_2 \qquad [1]$$

However, the influence of oxygen in the metal on the amount of hydrogen developed is not yet known. There should be a difference in the behavior of such alloys as compared with similar ones of titanium: whereas the oxides of the latter up to Ti_2O_3, inclusively, dissolve in HF (2), no other oxides are known in the Zr-O system (3) except ZrO_2 which practically does not dissolve in the acid, as found by testing. Thus, the α homogeneous solid solutions up to 29 at. % oxygen and those of the two-phase region up to ZrO_2 (with 66.67 at. % oxygen) should differ in their reaction with HF. It is expected that the homogeneous solid solutions similar to Ti-O alloys (4), will react with the acid as follows

$$ZrO_x + 4HF = ZrF_4 + xH_2O + (2-x)H_2 \qquad [2]$$

By calculating the volume of H_2, Eq. [2], and comparing it with the experimental one the validity of [2] was checked.

ZrO_x Alloys and Experimental Procedure

Dried Zr powder[1] was used as a starting material. According to the manufacturer the composition of the powder was as follows: Zr-96.6, including about 2% of Hf, Al-0.1, Ca-0.1, Fe-0.5, and Mg-0.13 wt %, or altogether for the metallic part, 97.4%, the remainder being oxygen. However, the present investigation shows that the oxygen is dissolved in the metal not as such but is combined with ZrO_2, which forms a solid solution with the metallic Zr. This is in accordance with the results obtained by de Boer and Fast (5). Therefore, only 87.27% Zr is in the metallic state, and the total of metals present is thus 90.1%, the balance (9.9%) being ZrO_2. The amount of free metals found by this calculation was checked by analyzing the Zr powder by the combustion method (6). Weighed amounts of the dry powder were heated in air up to 1000°C so that complete oxidation occurred (it lasted up to 8 hr). From the composition of the sample given above it was calculated that each gram of the metallic part, which alone is capable of burning to ZrO_2, HfO_2, etc.,

[1] Metal Hydrides Incorporated.

Table I. Hydrogen volumes (reduced to normal conditions) developed by Zr powder (sample II) in HF and compared with the volume calculated from combustion analysis

ZrO_2, wt %	Combustion analysis: Zr metal and admixt., wt %	Combustion analysis: H_2 vol calc, ml/g of alloy	H_2 evolution method; H_2 found, ml/g of alloy
9.51	90.49	440.8	434.9
10.44	89.56	436.2	438.5
8.97	91.03	443.4	436.0
8.34	91.66	446.5	
Avg 9.31	90.68	441.7 ±5.0	436.5 ±2.0

Table II. Hydrogen volumes obtained from ZrO_x samples dissolved in HF. Comparison with the volumes calculated per gram of the alloy from the combustion data

Sample	Combustion method: O_2 (in ZrO_2), wt %	Combustion method: Metal (Zr, etc.), wt %**	Combustion method: H_2 vol calc, ml/g	H_2 evolution method: Vol found, ml/g	H_2 evolution method: Δ, %	H_2 evolution method: x in ZrO_x†
I*	0.37	98.58	484.5	488.6	−0.84	0.01
II	2.42	90.69	441.7	436.5	+1.2	0.15
III	3.60	86.13	419.5	419.7	−0.05	0.24
IV	3.99	84.65	412.3	404.6	+1.9	0.27
V	4.30	83.44	406.4	402.4	+1.0	0.29
VI	4.84	81.34	396.2	390.3	+1.5	0.34
VII	4.98	80.86	393.9	386.9	+1.8	0.35
VIII	5.05	80.56	392.4	383.5	+2.3	0.36

* Metallic turnings Hf-free (possibly incomplete combustion).
** Rest—ZrO_2 (source of O_2).
† x—from combustion analyses.

absorbs during the combustion 0.3484 g of oxygen. Hence from the increase in weight and the original weight of the samples the amount of free metal and of ZrO_2 could be calculated. Results are shown in Table I: the Zr powder (sample II) contained 9.31% ZrO_2 or 2.42% oxygen (see Table II) instead of 2.57%, as it follows from the analysis of the manufacturer. This was regarded as a good agreement and, therefore, the Zr powder was used for the preparation of the ZrO_x alloys.

These were prepared by mixing weighed amounts of the dry Zr powder and ZrO_2, and by compressing them in a die under 1500 psi to make a briquette. The latter was heated at 1400°C for 4 hr under a vacuum (2 μ), then quenched in air of room temperature. The color of the samples was silvery gray. They were crushed, pulverized, and parts of the powder were analyzed by burning them in a porcelain crucible to the oxides. From the increase of the sample weight the amount of the metallic part (containing 96.86% Zr) was calculated; the remainder was then the weight of ZrO_2 in the sample before combustion. The volume of hydrogen (STP) which 1 g of samples should develop in HF was computed (487.1 cm^3 for the metallic part of them instead of 491.43 ml H_2, Eq. [1] for 100% Zr) and compared with the volume actually obtained in the dissolution experiments. Or, knowing from the combustion analysis the amount of oxygen present in the sample, the volume of hydrogen was also calculated from Eq. [2]. Both methods lead to the same result.

The volume of hydrogen developed by the samples was determined as described previously (4). However, the procedure is simpler than for Ti, because according to Eq. [1] no lower valency Zr salts are formed and hence no oxidation can occur. Therefore, the air of the apparatus does not have to be replaced by an inert gas or hydrogen. Besides, no side reactions occur and the final volume of hydrogen developed by the sample can be read easily from the gas burette.

Results

Qualitative experiments showed that the homogeneous Zr samples containing up to 29 at. % oxygen dissolve completely in dilute HF (0.3-*1N*). Sometimes a grayish residue is obtained, but it dissolves slowly and completely in water without gas evolution. It is probably $ZrOF_2$, formed because of hydrolysis ($ZrF_4 + H_2O \rightleftharpoons ZrOF_2 + 2HF$) which is a secondary reaction not affecting Eq. [2]. Samples of the two-phase region always leave a white residue identified as ZrO_2 by x-ray diffraction. However, ZrO_2 always remains behind if the homogeneous ZrO_x samples are heated at about 600°C in a hydrogen atmosphere: they absorb hydrogen which is then released upon dissolution in HF, but a residue of ZrO_2 is obtained. Evidently the dissolving hydrogen forces the ZrO_2 to aggregate to larger particles insoluble in HF.

For checking the validity of reaction [2] only samples from the homogeneous region containing up to 22% ZrO_2 (or 27 at. % oxygen) were used. As samples with a still higher oxygen content were difficult to prepare and to handle, no quantitative studies were made with them. From each sample of the homogeneous region, 3-4 combustion and 2-3 hydrogen evolution analyses were made. How good the separate analyses of one sample are and how the averages obtained by the two methods of analysis agree is shown in Table I on the example of Zr powder, used as starting material.

In the case of sample II the difference between the two methods is about 1.2%. However, the analyses by hydrogen evolution can be reproduced much better than those by the combustion method. The reason may be that ZrO_2 may absorb oxygen similarly as it happens with commercial TiO_2 (7) thus increasing the calculated free Zr amount in the samples; the difference of 1.2% may result in this way. This is evident further when one examines the analyses of 6 more samples of ZrO_x as shown in Table II.

Table II shows that the volumes of hydrogen observed and those calculated from the combustion method agree within 2%, whereby the hydrogen evolution method usually gives smaller volumes. If the x-values of the last column are used to make the calculations according to Eq. [2], an agreement within 0.9% with the volumes observed is obtained. In conclusion, although the results of the combustion and the hydrogen evolution method differ in a systematic fashion, the difference can be attributed to the further absorption of oxygen during the long heating period in the former. Therefore the validity of Eq. [2] is clearly established.

The homogeneous ZrO_x alloys behave as if they would consist of a solid solution of ZrO_2 in metallic Zr. This agrees with the statement of de Boer and

and Fast (5) that oxygen in ZrO_x is in form of O^{2-}. As in case of TiO_x (8) the volumes of H_2 developed by ZrO_x in HF can be used for a rapid determination of oxygen and free metal in those alloys.

Acknowledgment

This investigation was supported by the U. S. Atomic Energy Commission (AT (11-1)-73, Project 5). The authors are grateful to Dr. W. J. James, Professor at the Chemical Engineering Department of the School of Mines, for his interest in this work.

Manuscript received Dec. 28, 1959.

Any discussion of this paper will appear in a Discussion Section to be published in the June 1961 JOURNAL.

REFERENCES

1. M. E. Straumanis and J. I. Ballass, *Z. anorg. u. allgem. Chem.*, **278**, 33 (1955).
2. M. E. Straumanis, W. J. James, and A. S. Neiman, *Corrosion*, **15**, 286t (1959).
3. M. Hansen, D. J. McPherson, and R. F. Domagala, Report COO-123, 1953.
4. M. E. Straumanis, C. H. Cheng, and A. W. Schlechten, *This Journal*, **103**, 439 (1956).
5. J. H. Boer and J. D. Fast, *Rec. trav. chim. P. B.*, **59**, 161 (1940).
6. W. F. Hillerbrand and G. E. F. Lundell, "Applied Inorganic Analysis," p. 449, John Wiley & Sons, Inc., New York (1929).
7. A. W. Czanderna and J. M. Honig, *J. Phys. Chem.*, **63**, 620 (1959).
8. M. E. Straumanis, C. H. Cheng, and A. W. Schlechten, *Analyt. Chem.*, **28**, 1883 (1956).

Gelatin Effects on Polarographic Half-Wave Potentials

A. J. Diefenderfer and L. B. Rogers

Department of Chemistry and Laboratory for Nuclear Science, Massachusetts Institute of Technology, Cambridge, Massachusetts

It is well recognized that the presence of relatively large concentrations of gelatin may lead to cathodic shifts of the half-wave potentials for irreversible reactions. A recent publication from our laboratory (1) reported that the irreversible second reduction of p-dinitrobenzene in weakly acidic solutions was shifted toward *less* cathodic potentials by the addition of small amounts of gelatin. This behavior has since been examined in greater detail because of its theoretical implications with respect to the role of gelatin in the electrical double layer.

Our most recent studies have confirmed the anodic shift using two other samples of gelatin. However, the effect has been shown to be due to an unexpected decrease in *p*H caused by impurities in the gelatin.[1] It was found that solutions of 0.50% gelatin prepared from warm (60°C) distilled water, which has just been boiled, reached *p*H values of 4.20 and 4.10 within an hour when stored at 25°C and 2°C, respectively, Several hours later, the *p*H values were 4.07 and 4.00. When approximately a 1-ml portion of such a solution was added to 50 ml of the weakly buffered alcoholic supporting electrolyte, an anodic shift was indeed found. However, when the original *p*H of the supporting electrolyte was restored by adding potassium hydroxide (which had been dissolved in an alcoholic solvent of the same composition), the half-wave potential returned to the value observed before the addition of gelatin. Thus, the reported anodic shift was not a property of the gelatin *per se*.

The nature of the impurities in our commercial gelatin, which produced the abnormally low *p*H value, are unknown and are of no further interest to us.

[1] According to G. Scatchard and O. L. Keller (private communication) pure gelatin would be stable under both the preparative and polarographic conditions employed in our study.

Manuscript received March 28, 1960.

Any discussion of this paper will appear in a Discussion Section to be published in the June 1961 JOURNAL.

REFERENCE

1. L. E. I. Hummelstedt and L. B. Rogers, *This Journal*, **106**, 248 (1959).

December 1960 Discussion Section

A Discussion Section, covering papers published in the January-June 1960 JOURNALS, is scheduled for publication in the December 1960 issue. Any discussion which did not reach the Editor in time for the June 1960 Discussion Section will be included in the December 1960 issue.

Those who plan to contribute remarks for this Discussion Section should submit their comments or questions in triplicate to the Managing Editor of the JOURNAL, 1860 Broadway, New York 23, N. Y., *not later than September 1, 1960*. All discussion will be forwarded to the author(s) for reply before being printed in the JOURNAL.

Brief Communications

Microscopic Observations on Electroluminescent ZnS:Cu Phosphors

Willi Lehmann

Research Department, Westinghouse Electric Corporation, Bloomfield, New Jersey

It is known that the emission of electroluminescence in ZnS:Cu phosphors is concentrated in randomly distributed small spots (1-4). It has also been assumed that electroluminescent ZnS:Cu phosphors contain copper sulfide (probably Cu_2S) as a separate phase segregated in cavities, etc., inside the phosphor particles (Cu_2S on the surface of the particles can be removed by suitable washing procedures) and that these segregations create localized regions of enhanced electric field strength near their edges (5,6). These segregations have now been observed microscopically. The experimental arrangement is shown in Fig. 1. The phosphor particles were stuck on a thin plastic layer between two aluminum electrodes evaporated onto a microscope slide. The space between the particles was filled with a highly refracting liquid [solution of phosphorus and sulfur in methylene iodide (7), $n = 2.06$] in order to obtain a clearer view into the ZnS particles. Even so, some refraction still remained and caused each particle to appear opaque near its edge if illuminated by white light from the rear. The limit of resolution of details inside the particles is estimated to be about 1 μ or somewhat lower.

Because of the smallness of the objects and their three-dimensional extension, the investigation was limited to visual observations. Dark segregations inside of many phosphor particles could be observed. They are frequently, but by far not always, thin and elongated, almost needle-like. They seem to be larger, on the average, in large particles, and *vice versa*. The emission spots of electroluminescence are visibly located directly at the ends of the segregations in many, but not in all cases. Some typical examples are shown in Fig. 2. Some emission spots cannot visibly be correlated to dark segregations; perhaps they are actually present but too small to be observed or are hidden by surface irregularities. In other cases, segregations are present without accompanying emission. It may be that these segregations do not have sufficiently sharp edges (submicroscopically) to create localized regions of high field strength. In agreement with old observations (1, 2), the light emission per spot occurs only once per cycle of the exciting voltage. The question whether the emission occurs when the end of the segregation is cathode or anode could not be decided.

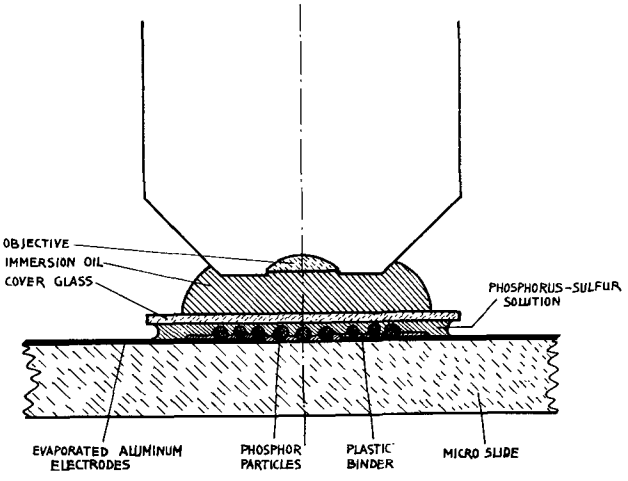

Fig. 1. Arrangement used in microscopic investigations

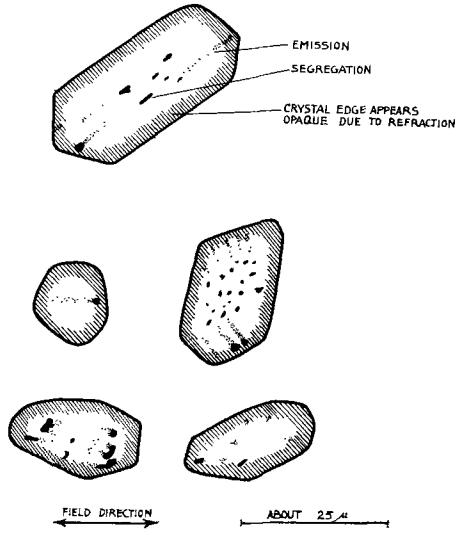

Fig. 2. Phosphor particles containing dark segregations and emitting spots.

The linear dimensions of the segregations approach 5 or 10% of the particle diameter in ordinary phosphor powders. Also the dimensions of the emitting spots range in this order which means that the emission intensity within an average spot is roughly 1000 times higher than the average over the whole phosphor. The brightness of a single spot does not steadily decrease with time (as the integrated emission of an entire electroluminescent cell does) but may undergo all sorts of irregular fluctuations including sudden disappearance after some time of operation or irregular oscillations with time. Even

a movement of two neighboring spots toward each other and complete union within about one or two minutes could be observed. These observations were made on phosphor particles excited by 20 kcps; the particles did not move under the influence of the electric field.

Manuscript received March 22, 1960.

Any discussion of this paper will appear in a Discussion Section to be published in the June 1961 JOURNAL.

REFERENCES

1. J. F. Waymouth and F. Bitter, *Phys. Rev.*, **95**, 941 (1954).
2. P. Zalm, G. Diemer, and H. A. Klasens, *Philips Res. Rept.*, **10**, 205 (1955).
3. A. Kremheller, *This Journal*, **107**, 8 (1960).
4. W. Lehmann, *ibid.*, **107**, 20 (1960).
5. W. Lehmann, *ibid.*, **104**, 45 (1957).
6. K. Maeda, *J. Phys. Soc. Japan*, **13**, 1352 (1958).
7. "Handbook of Chemistry and Physics," 39th ed., p. 2726, Chemical Rubber Publishing Co., Cleveland, Ohio.

Purification of Tantalum Anodes during Sintering

C. J. B. Fincham and G. L. Martin[1]

Metals Division, National Research Corporation, Cambridge, Massachusetts

It is generally believed that the d-c leakage of a sintered-anode tantalum electrolytic capacitor is affected markedly by the chemical purity of the tantalum metal from which it is made. To substantiate this belief it would be necessary to correlate the d-c leakage of the capacitor with the impurity content of the sintered anode rather than with that of the original tantalum powder, since impurity levels change during sintering to an extent dependent on sintering conditions.

Houtz and Karlik (1) have studied the changes in impurity levels of carbon, oxygen, nitrogen, and general metallic contaminants during the sintering of tantalum anodes and correlated their results with the d-c leakage and life of the finished solid-electrolyte capacitors. However, other than their data on carbon, oxygen, and nitrogen, there is no published information on the quantitative changes in the levels of specific impurities during sintering.

The work reported here is a preliminary study of these quantitative changes during various sintering treatments and of the d-c leakages of the resulting anodes.

Sintered anodes were made from five different tantalum powders (three high-capacitance and two low-capacitance) by pressing pellets of known densities and heating the pellets under vacuum at several different conditions of time and temperature, as shown in Table I. The pelleting and sintering techniques used have been described in detail previously (2). The anodes were all cylindrical, 1.8 g in weight, and had an 'as-pressed' diameter of 0.25 in. Each sinter run was made with anodes of only one powder.

The powders and representative anodes from five batches were analyzed quantitatively for the following elements: O, C, N, Na, Al, Cr, Cu, Fe, Mo, Nb, Ni, Si, and Ti, with the results shown in Table I. The remaining anodes were not analyzed for O, C, N, or Na. Oxygen was determined by vacuum fusion,

[1] Present address: Department of Chemistry, University of Alabama, University, Alabama.

Table I. Changes in impurity levels during sintering of anodes and corresponding d-c leakages

Material	Form	Sintering Conditions: Green density, g/cc	Measured temp, °C	Time, hr	L/C* μamp/μfd	Chemical analysis (ppm): O	C	N	Na	Al	Cr	Cu	Fe	Nb	Ni	Si	Ti	
SG-73R (High capacitance)	Powder	—	—	—	—	480	25	30	30	<50	110	<50	87	120	52	81	<10	
	Anode 1	8.5	1750	1.5	0.082	—	—	—	—	<50	<15	<50	20	115	24	29	<10	
	Anode 2	9.5	2050	0.5	0.067	—	—	—	—	<50	<15	<50	18	115	19	25	<10	
	Anode 3	9.0	2050	1.5	0.087	340	8	50	20	<50	<10	<50	<20	110	10	62	<10	
	Anode 4	9.5	2050	3.0	0.062	—	—	—	—	<50	<15	<50	<10	115	<15	26	<10	
L-533 (High capacitance)	Powder	—	—	—	—	930	120	750	—	<50	<10	<50	460	140	25	780	40	
	Anode 1	10.5	1750	1.5	>30.0	—	—	—	—	<50	<15	<50	190	135	<15	64	<10	
	Anode 2	9.0	2050	1.5	0.12	350	10	285	25	<50	<10	<50	47	120	11	78	12	Mg 27
ET-76 (High capacitance)	Powder	—	—	—	—	850	50	25	100	190	130	100-250	190	92	120	160	<10	
	Anode 1	9.0	2050	0.5	24.5	—	—	—	—	<50	<15	<50	20	105	17	<25	<10	
	Anode 2	9.0	2050	1.5	28.0	460	7	40	10	<50	<10	<50	36	110	31	44	<10	
SGL-103R (Low capacitance)	Powder	—	—	—	—	370	25	35	15	<50	170	50	61	150	151	55	<10	
	Anode 1	10.0	2050	0 5	0.07	—	—	—	—	<50	<15	<50	19	145	34	25	<10	
	Anode 2	9.0	2050	1.5	0.074	360	6	60	10	<50	<10	<50	<20	150	16	40	<10	
L-450 (Low capacitance)	Powder	—	—	—	—	770	180	30	<10	200	20	50	250	230	40	450	<10	
	Anode 1	10.5	1750	1.5	27.0	—	—	—	—	70	<15	<50	62	230	<15	98	<10	
	Anode 2	9.0	2050	1.5	27.0	180	58	40	<5	<50	<10	<50	<20	210	<10	40	<10	

Sn, Co, and Mn were <10 in all anodes.
Mg was <10 in all anodes except one (see table).
Pb was <20 in all anodes.
Mo was <25 in all powders and anodes.
< means below limit of detection by method used.
* L/C = d-c leakage at 140 v/unit capacitance for 200-v formation (microamperes per microfarad).

a movement of two neighboring spots toward each other and complete union within about one or two minutes could be observed. These observations were made on phosphor particles excited by 20 kcps; the particles did not move under the influence of the electric field.

Manuscript received March 22, 1960.

Any discussion of this paper will appear in a Discussion Section to be published in the June 1961 JOURNAL.

REFERENCES

1. J. F. Waymouth and F. Bitter, *Phys. Rev.*, **95**, 941 (1954).
2. P. Zalm, G. Diemer, and H. A. Klasens, *Philips Res. Rept.*, **10**, 205 (1955).
3. A. Kremheller, *This Journal*, **107**, 8 (1960).
4. W. Lehmann, *ibid.*, **107**, 20 (1960).
5. W. Lehmann, *ibid.*, **104**, 45 (1957).
6. K. Maeda, *J. Phys. Soc. Japan*, **13**, 1352 (1958).
7. "Handbook of Chemistry and Physics," 39th ed., p. 2726, Chemical Rubber Publishing Co., Cleveland, Ohio.

Purification of Tantalum Anodes during Sintering

C. J. B. Fincham and G. L. Martin[1]

Metals Division, National Research Corporation, Cambridge, Massachusetts

It is generally believed that the d-c leakage of a sintered-anode tantalum electrolytic capacitor is affected markedly by the chemical purity of the tantalum metal from which it is made. To substantiate this belief it would be necessary to correlate the d-c leakage of the capacitor with the impurity content of the sintered anode rather than with that of the original tantalum powder, since impurity levels change during sintering to an extent dependent on sintering conditions.

Houtz and Karlik (1) have studied the changes in impurity levels of carbon, oxygen, nitrogen, and general metallic contaminants during the sintering of tantalum anodes and correlated their results with the d-c leakage and life of the finished solid-electrolyte capacitors. However, other than their data on carbon, oxygen, and nitrogen, there is no published information on the quantitative changes in the levels of specific impurities during sintering.

The work reported here is a preliminary study of these quantitative changes during various sintering treatments and of the d-c leakages of the resulting anodes.

Sintered anodes were made from five different tantalum powders (three high-capacitance and two low-capacitance) by pressing pellets of known densities and heating the pellets under vacuum at several different conditions of time and temperature, as shown in Table I. The pelleting and sintering techniques used have been described in detail previously (2). The anodes were all cylindrical, 1.8 g in weight, and had an 'as-pressed' diameter of 0.25 in. Each sinter run was made with anodes of only one powder.

The powders and representative anodes from five batches were analyzed quantitatively for the following elements: O, C, N, Na, Al, Cr, Cu, Fe, Mo, Nb, Ni, Si, and Ti, with the results shown in Table I. The remaining anodes were not analyzed for O, C, N, or Na. Oxygen was determined by vacuum fusion,

[1] Present address: Department of Chemistry, University of Alabama, University, Alabama.

Table I. Changes in impurity levels during sintering of anodes and corresponding d-c leakages

Material	Form	Sintering Conditions: Green density, g/cc	Measured temp, °C	Time, hr	L/C* μamp/μfd	Chemical analysis (ppm): O	C	N	Na	Al	Cr	Cu	Fe	Nb	Ni	Si	Ti	
SG-73R (High capacitance)	Powder	—	—	—	—	480	25	30	30	<50	110	<50	87	120	52	81	<10	
	Anode 1	8.5	1750	1.5	0.082	—	—	—	—	<50	<15	<50	20	115	24	29	<10	
	Anode 2	9.5	2050	0.5	0.067	—	—	—	—	<50	<15	<50	18	115	19	25	<10	
	Anode 3	9.0	2050	1.5	0.087	340	8	50	20	<50	<10	<50	<20	110	10	62	<10	
	Anode 4	9.5	2050	3.0	0.062	—	—	—	—	<50	<15	<50	<10	115	<15	26	<10	
L-533 (High capacitance)	Powder	—	—	—	—	930	120	750	—	<50	<10	<50	460	140	25	780	40	
	Anode 1	10.5	1750	1.5	>30.0	—	—	—	—	<50	<15	<50	190	135	<15	64	<10	
	Anode 2	9.0	2050	1.5	0.12	350	10	285	25	<50	<10	<50	47	120	11	78	12	Mg 27
ET-76 (High capacitance)	Powder	—	—	—	—	850	50	25	100	190	130	100-250	190	92	120	160	<10	
	Anode 1	9.0	2050	0.5	24.5	—	—	—	—	<50	<15	<50	20	105	17	<25	<10	
	Anode 2	9.0	2050	1.5	28.0	460	7	40	10	<50	<10	<50	36	110	31	44	<10	
SGL-103R (Low capacitance)	Powder	—	—	—	—	370	25	35	15	<50	170	50	61	150	151	55	<10	
	Anode 1	10.0	2050	0 5	0.07	—	—	—	—	<50	<15	<50	19	145	34	25	<10	
	Anode 2	9.0	2050	1.5	0.074	360	6	60	10	<50	<10	<50	<20	150	16	40	<10	
L-450 (Low capacitance)	Powder	—	—	—	—	770	180	30	<10	200	20	50	250	230	40	450	<10	
	Anode 1	10.5	1750	1.5	27.0	—	—	—	—	70	<15	<50	62	230	<15	98	<10	
	Anode 2	9.0	2050	1.5	27.0	180	58	40	<5	<50	<10	<50	<20	210	<10	40	<10	

Sn, Co, and Mn were <10 in all anodes.
Mg was <10 in all anodes except one (see table).
Pb was <20 in all anodes.
Mo was <25 in all powders and anodes.
< means below limit of detection by method used.
* L/C = d-c leakage at 140 v/unit capacitance for 200-v formation (microamperes per microfarad).

carbon by combustion, nitrogen by micro-Kjeldahl, and sodium by flame-photometry. The remaining elements were determined spectrographically using the carrier technique, calibrated by synthetic standards, and, in the cases of Fe, Ni, and Cr, cross-checked by wet-chemical methods. During the spectrographic analyses of the anodes, the additional elements Co, Mg, Mn, Pb, and Sn were looked for but not detected (except Mg in one anode). The estimated limits of detection are given in Table I.

Anodes from the same batches as those analyzed were tested electrically for d-c leakage and capacitance by the following wet-cell method described in detail previously (2).

The anodes were formed at constant current (35 ma/g), in 0.01% phosphoric acid solution at 92°C, to 200 v, held at voltage for 2 hr, washed and dried. DC leakage was measured at 140 v after 2 min at voltage in 10% phosphoric acid solution at room temperature. Capacitance was measured in the same solution at 120 cycles/sec.

The measured ratios of d-c leakage (L) at 140 v (in microamps), to capacitance (C) (in microfarads), for a 200-v formation are given in Table I. In addition, for those batches of anodes for which complete analyses were obtained, measurements of leakage at 70 v for a 100-v formation and leakage at 35 v for a 50-v formation were made. These results are discussed below.

The analytical and electrical results for each set of powder and anodes are listed in Table I in increasing order of severity of sintering conditions. It can be seen that different impurities behaved differently during sintering. Iron and nickel decreased slowly with increasingly severe sintering conditions. Niobium was unchanged from the level in the powder under any sintering conditions tried, and chromium decreased to below the limit of detection under all sintering conditions tried. Silicon decreased on sintering in every case, but the results were erratic and the final levels did not correlate with severity of sintering conditions. Oxygen, carbon, and sodium decreased on sintering, although the extent of the decrease of oxygen was variable. In the powders where the initial nitrogen content was low, a slight increase in nitrogen level during sintering was observed (presumably due to "pick up" from outgassing or small leaks in the vacuum furnace). However, in the one high nitrogen powder (L-533), there was a marked decrease in nitrogen during sintering. Sodium, aluminum, copper, and titanium, when present in detectable amounts in the powder, all decreased during sintering.

Similar qualitative trends were found by Torti (3) in a study of the purification of tantalum during vacuum arc-melting, which takes place at much higher temperatures (> 3000°C). The main difference was in the relatively large loss of niobium observed during arc melting, compared with essentially no loss during sintering.

The correlation of purity of anode with d-c leakage is not so easily seen. However, one generalization perhaps can be made from these data, namely, that with the exceptions of niobium and oxygen none of the anodes with low leakage had any specific impurity at a high level relative to the group of data, whereas the high leakage anodes each had one or more impurities at a relatively high level. The anodes made from ET-76 appear to be an exception to this generalization, but the reason for this may be in the high copper level in the original powder which was introduced by accidental contamination in the course of handling. The copper was therefore essentially a surface contaminant, so that bulk analyses have little meaning with regard to the effective concentration of copper at the surface of the powder and anodes. High leakage due to copper contamination has occasionally been observed in other powders.

It is tempting to speculate that the high leakage of anode 1 of L-533 is due either to a high iron content (which was reduced by the more severe sintering conditions used for the low leakage anode 2) or to a high nitrogen level, presumably somewhere between 750 ppm in the powder and 285 ppm in anode 2.

To speculate further, the high leakages of both anodes made from L-450 might be attributed to high carbon contents, 58 ppm in anode 2, and presumably higher in anode 1. This would agree with the conclusions of Houtz and Karlik (1) that to obtain a satisfactory anode the carbon content must be less than 20 ppm.

However, attempts to place an exact limit on an acceptable impurity level must be tempered by the realization that the concentration of impurities at the surface can be either lower or higher than the impurity levels measured on the bulk of the metal.

Surface contamination of the powder (as in ET-76) or of the sintered anode (e.g., during the processing of the anode to make the finished capacitor) can give higher impurity levels on the surface than in the bulk.

Alternatively, the surface can be purer than the bulk if, during sintering, the rate of removal of impurities is limited by diffusion in the metal rather than by vaporization from the surface.

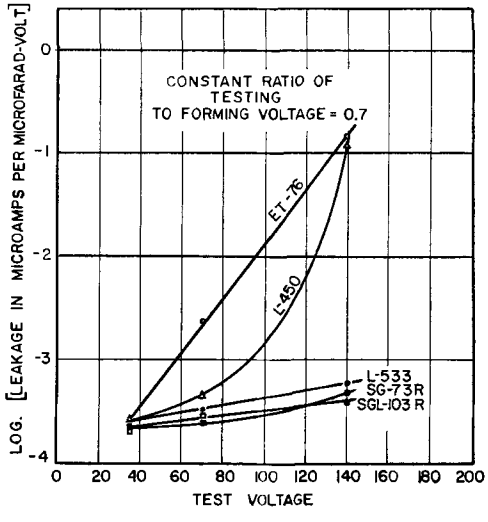

Fig. 1. Variation of d-c leakage per microfarad-volt with test voltage, for a constant ratio of testing to forming voltage and constant sintering conditions.

In discussing the effects of impurities on leakage, results shown in Fig. 1 are of great interest, where the logarithm of the d-c leakage (in microamperes per microfarad-volt) is plotted against test voltage, for a constant ratio of testing to forming voltage. As mentioned above, these measurements were made on anodes from the same batches as anode 4 of SG-73R and anodes 2 of each of the other powders. The results were plotted as leakage per microfarad-volt, since this gives a measure of leakage per unit surface area, irrespective of forming voltage. The points shown at a test voltage of 140 v are those shown as leakage per microfarad (for a 200-v formation) in Table I.

It can be seen from Fig. 1 that the rate of change of leakage with test voltage varies markedly between the different sets of anodes and that whereas at 140 v there is a difference of almost a factor of 400 between the highest and lowest leakage anodes, at 35 v the difference is about 30% and is approaching the limits of experimental error Therefore, it would appear that in any study of leakage vs. purity the maximum sensitivity of results can be obtained by working at the highest voltages.

Acknowledgment

Grateful acknowledgment is made to Dr. F. C. Benner and his analytical group who developed many of the analytical methods used and performed the analyses.

Manuscript received Feb. 18, 1960.

Any discussion of this paper will appear in a Discussion Section to be published in the June 1961 JOURNAL.

REFERENCES

1. C. C. Houtz and S. Karlik, Bell Telephone System Technical Publication, Monograph 3305. (Also published in Proceedings 1959 Electronic Components Conference, p. 116.)
2. G. L. Martin, C. J. B. Fincham, and E. E. Chadsey, Jr., *This Journal*, **107**, 332 (1960).
3. M. L. Torti, *ibid.*, **107**, 33 (1960).

Investigations on the Reaction Mechanism of the Nickel-Cadmium Cell

S. Uno Falk

Svenska Ackumulator AB Jungner, Stockholm, Sweden

ABSTRACT

X-ray diffraction patterns from electrodes submerged in electrolyte have been obtained during charge and discharge by means of a special test cell, and the composition of the active materials has been determined. The question whether CdO or $Cd(OH)_2$ is formed during discharge has been subject to special attention. The low potential reaction of the positive plate has been studied. The emf and the dE/dT have been determined between —40° and +50°C at various states of charge.

The nickel-cadmium cell, the principle of which was patented by Jungner (1) in 1899, has provoked the interest of several investigators ever since, and many theories have been put forward concerning the reactions and thermodynamics of this system. However, opinions still differ in many essentials and this has caused us to publish the results of some investigations carried out to establish the reaction formulas of the nickel-cadmium cell and to elucidate the reaction mechanism.

The Reactants

It is generally agreed that the nickel-cadmium cell works according to the oxygen-lift system, i.e., oxygen (or hydroxyl ion) is transferred from one electrode to the other. This transfer is carried out by the electrolyte.

Opinions have differed appreciably as far as the composition of the compounds constituting the active substances is concerned. Thus, the following formulas have been suggested for the charged material of the positive electrode: $Ni(OH)_4$ (2), NiO_2 (3), $NiO_2 \cdot H_2O$ (4), $NiO_2 \cdot xH_2O$ (5), $Ni(OH)_3$ (6), $2Ni(OH)_3 \cdot 5H_2O$ (7), Ni_2O_3 (8), $Ni_2O_3 \cdot 1.2\ H_2O$ (9), $Ni_2O_3 \cdot 6H_2O$ (10), and β-NiOOH (5) and mixtures or solid solutions of these compounds.

Some of these substances have been referred to in investigations carried out on positive plates of nickel-iron cells, which, however, is of no importance, since the same positive active material is present in these cells.

For the discharged state the following formulas have been suggested: Ni (11), NiO (3), $NiO \cdot 4H_2O$ (4), $2NiO \cdot 9H_2O$ (10), $Ni(OH)_2$ (9), $Ni(OH)_2 \cdot 2H_2O$ (6), $2Ni(OH)_2 \cdot 6H_2O$ (7), Ni_3O_4 (12), and Ni_2O_3 (13).

Cd and CdH_2 (4) have been mentioned as constituents in the charged negative electrode, while CdO (14), Cd_2O (15), $CdO \cdot xH_2O$ (10), and $Cd(OH)_2$ (16) have been suggested for the discharged state.

The first part of these investigations was directed to establishment of the components present in the electrodes at various states of charge. For this purpose x-ray diffraction methods were used primarily.

Several other workers (17-24) used such methods to study different nickel and cadmium compounds. In the cases, however, where electrodes have been investigated, the x-ray exposures have been made on washed and dried samples which obviously may introduce sources of error. Removing the electrolyte may cause hydration changes and, moreover, oxygen may affect the active materials. Therefore, x-ray investigation of an active material in a nickel-cadmium cell should be carried out on a sample completely submerged in the electrolyte and subjected to charge or discharge. Only in that case the spectra obtained may be claimed to represent the true active substances. Application of a charge or a discharge eliminates the risk of decomposition of unstable substances that possibly could be formed when a current is passing, and accordingly otherwise escape detection. These points of view have, as far as we know, been duly taken into account only by Salkind and Bruins (25), who, in an extensive and meritorious investigation of the nickel-cadmium cell have, x-rayed parts of wet electrodes stored in sealed plastic bags and also worked with a Lucite cell, permitting charge and discharge of the electrodes during exposure. Thus, in the first case washing and drying have been avoided and, in the latter, a current is passing. Apparently, the position of the plates in the Lucite cell has permitted free access of the air.

A specially constructed cell was used. It contained one sintered electrode of the kind to be investigated, and one sintered electrode of opposite polarity. Sintered electrodes are used in these investigations, first, because steel ribbons do not screen the active materials and second, because the active materials are not mixed with other substances. Figure 1 shows the set-up. When the desired state of charge has been attained by charge or discharge, the test electrode is pulled sidewise from the counter electrode and is pressed against one of the walls of the plastic bag, making the electrolyte film as thin as possible. The plate is now inserted in the sample holder of the x-ray spectrometer, the part of the bag containing the counter electrode being placed at the side of

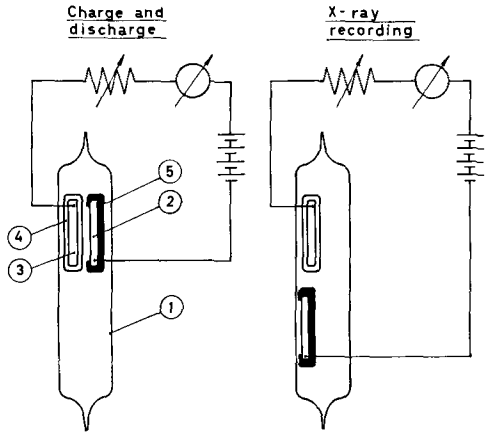

Fig. 1. Polyethylene cell allowing x-ray examination of electrodes without removal from electrolyte and without interruption of current. 1, U-bent very thin polyethylene sheet, welded at the ends and filled with electrolyte; 2, electrode under test; 3, counter electrode; 4, filter paper separator covering the counter electrode; 5, layer of epoxy plastic directing the current exclusively to the plate front.

the holder. The current is not interrupted during these manipulations, nor during the subsequent x-ray exposure. However, the current is sufficiently decreased during the exposure to permit recording the entire diffraction pattern without any appreciable change of the state of charge of the electrode. In this manner, positive as well as negative electrodes have been investigated at various states of charge. For the exposure Ni-filtered Cu K_α-radiation was used. The reflections were registered by means of a Geiger counter and a potentiometer recorder.

The Positive Active Material

Figure 2 shows x-ray patterns of fully charged, 1/3 discharged, 2/3 discharged, and fully discharged positive electrodes. The polyethylene peaks have been omitted from this figure.

The discharged positive material has proved to be $Ni(OH)_2$ of small grain size. This is indicated by the

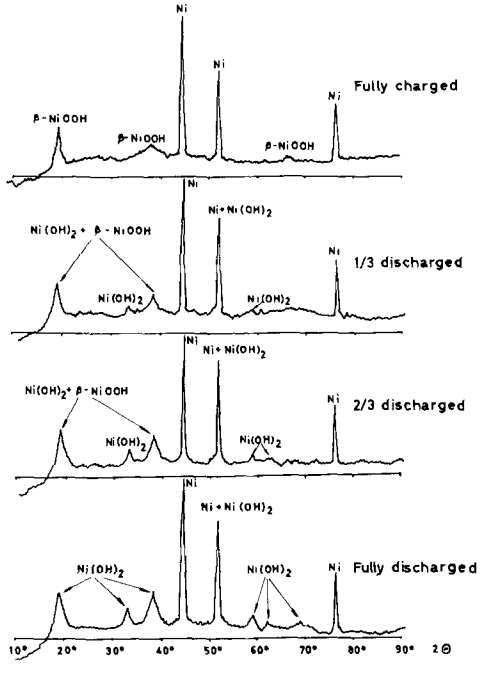

Fig. 2. X-ray diffraction patterns from positive electrode

conspicuous broadening of the $Ni(OH)_2$ lines as compared to, for instance, the Ni reflections. Broadening of the reflections may be due to several other causes, such as irregular lattice, mechanical crystal deformation or lacking chemical equilibrium. However, we have found by means of Hahn's emanation method (26, 27) that the broadening in this case is caused by very small crystals. The approximate crystal size may be calculated from this broadening. During charge this $Ni(OH)_2$ is successively transferred into a still more finely divided compound having a spectrum agreeing well with that of β-NiOOH. No traces of higher nickel oxides have been discovered even at strong overcharge. At discharge β-NiOOH is again transferred into $Ni(OH)_2$. These transformations do not imply a decrease of $Ni(OH)_2$ and an appearance of β-NiOOH reflections but instead some $Ni(OH)_2$ peaks decrease while others gradually are displaced toward β-NiOOH. This indicates the presence of a solid solution of β-NiOOH and $Ni(OH)_2$, further supported by the fact that the emf curve varies with the state of charge. This observation will be discussed later.

In our x-ray investigations of the charged positive material β-NiOOH was the highest nickel compound encountered, this being the case also after heavy overcharge. Naturally, this does not necessarily mean that higher compounds like NiO_2 are not present, as these may be amorphous to x-rays. At any rate, a freshly charged positive plate contains more active oxygen than corresponds to the formula founded on trivalent nickel. This was found by Foerster (9), who stated that the charged material consisted of a solid solution of NiO_2 and $Ni_2O_3 \cdot 1.2H_2O$. The opinion has been shared by several others, but Pitman and Work (28) recently considered it to be more likely that the excess of active oxygen is adsorbed by β-NiOOH. This theory is based on an investigation of the concentration of active oxygen in the electrode as related to the open-circuit potential after charge. If Foerster's theory were correct, the potential would vary linearly with the logarithm of the active oxygen concentration. However, Pitman and Work have observed that the potential decreases directly as a straight line with the oxygen concentration, indicating an oxygen adsorption, thus, as far as we can understand, disproving Foerster's theory. The freshly charged state should, according to Pitman and Work, be represented by the formulas $Ni_2O_3(O)_{ads}$ or $(\beta\text{-NiOOH})_2(O)_{ads}$. As we have found that β-NiOOH is present in the charged active material, the latter formula is considered correct.

The capacity available from the adsorbed oxygen is comparatively small: a freshly charged positive plate will yield 10-15% more capacity than a plate having rested some 24 hr after charge.

The secondary discharge reaction frequently appearing at a voltage of about 0.7 v was an object of interest as early as 1905-1910, when Foerster and Zedner performed some experiments. It has been established that the potential step in question originates from the positive electrode. The causes of the reaction have been widely discussed, but the source accepted nowadays seems to be the oxygen adsorbed

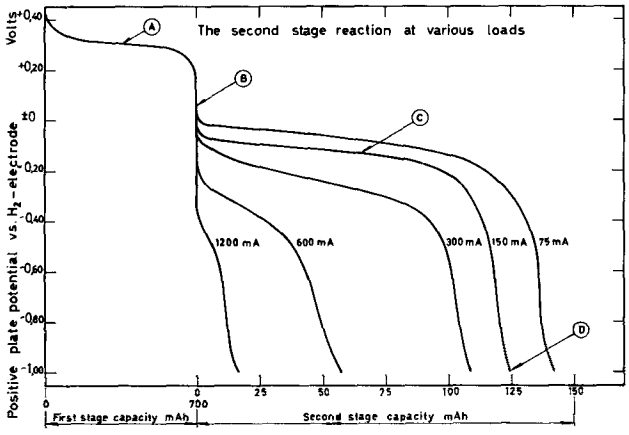

Fig. 3. Second stage reaction at various loads

by the graphite present in positive pocket electrodes, the step not appearing in plates without graphite. This explanation is not correct, as we have been able to find the potential step also in sintered positive electrodes, completely lacking graphite. The duration of the stage can be increased by repeated reversals. The reaction occurring at an anode voltage of about —0.15 v as measured against the hydrogen electrode may correspond to 20% of the total capacity. The step is dependent on the load; its shape at different loads is shown in Fig. 3.

X-ray diffraction patterns have been recorded of sintered positive electrodes, discharged in the polyethylene cell previously described to the points (A), (B), (C), and (D) according to Fig. 3. It was intended to obtain, if possible, the structure of the compounds causing the second stage reaction. However, no new compounds appeared in these patterns, nor were any significant changes of position or intensities of the $Ni(OH)_2$ reflections observed.

The opinion of Glemser and Einerhand (5) that $Ni_3O_2(OH)_4$ is the active compound in this case is not supported by any x-ray investigations carried out by these research workers. The presence of $Ni_3O_2(OH)_4$ should certainly be established by x-rays, but we have found neither this compound nor any other. We believe, therefore, that the step is caused by oxygen adsorbed by the nickel hydroxide. In order to obtain further proof of this theory the relationship between the secondary discharge stage and the ambient air pressure was studied. These investigations, carried out on sintered electrodes, corroborated the statement by Zedner (6) that evacuation will decrease the capacity of this stage. Oxygen is generally liberated with substantially less difficulty in the adsorbed state than when attached chemically to nickel, particularly as the possible nickel compound cannot be very highly oxidized. This circumstance in connection with the negative results of the x-ray diffraction tests substantiates our opinion that the secondary discharge reaction is caused by oxygen adsorbed by $Ni(OH)_2$.

Negative Active Material

Figure 4 shows x-ray diffraction patterns of negative electrodes in fully charged, 1/3 discharged, 2/3 discharged, and completely discharged states.

The discharged material consists mainly of $Cd(OH)_2$. However, a small amount of Cd is always

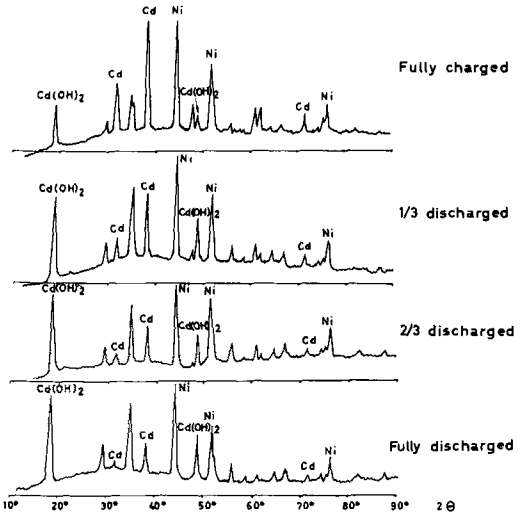

Fig. 4. X-ray diffraction patterns from negative electrode

present. During charge $Cd(OH)_2$ is successively transformed into Cd metal. In this case no solid solution is formed: Cd and $Cd(OH)_2$ spectra may appear simultaneously. This agrees also with the open-circuit voltage measurements carried out at different states of charge. The transformation of $Cd(OH)_2$ into Cd is not complete even after strong overcharge, as indicated by the x-ray pattern at this stage.

According to Troilius (4) a fully charged electrode probably contains a certain amount of CdH_2, which decomposes relatively rapidly after the end of the charge into Cd and H_2. If a discharge is carried out immediately after charge a potential drop appears that might be attributed to CdH_2. However, our x-ray investigations have not revealed any compound corresponding to CdH_2. Comparative tests on negative electrodes and unimpregnated nickel sinter have shown also that the pure nickel sinter after cathodic polarization exhibits a potential "tail" similar to the one noticed on negative electrodes. The value of the potential makes it likely that a pure oxidation of hydrogen adsorbed by the nickel sinter is the cause of this tail. These investigations show that hydrogen may be adsorbed by porous metals, thus giving some extra capacity on discharge. This observation makes it very probable also that the reaction at the negative plate is caused by adsorbed hydrogen. This theory is further corroborated by the fact that evacuation of a negative electrode after a complete charge is accompanied by a substantially less pronounced potential tail when discharged. The capacity excess caused by the adsorbed hydrogen is, however, very slight and in general quite negligible.

The investigations presented here show clearly that $Cd(OH)_2$ is the end product of discharge. However, several writers claim that CdO is formed, this opinion being recently conveyed by Lake and Casey (20) and Winkler (29) among others. According to Lake and Casey, CdO is formed as primary product on anodic oxidation, this oxide subsequently being transformed into $Cd(OH)_2$ in the presence of the alkaline electrolyte. These writers have themselves not been able to establish the presence of CdO, but make this assumption because a dark-colored compound is formed.

Experiments were carried out on charged negative plates, subsequently discharged with various, in some cases very high, currents in the previously described x-ray test cell. The cell has been adjusted on the strongest CdO line, and careful measurements have been made with maximum sensitivity to ascertain the recording of any intensity increase during discharge. All these tests have yielded negative results: in no case has CdO been traced.

Furthermore, plates have been used, the active material of which has been transferred into CdO by heating. After insertion in the sample holder of the x-ray apparatus KOH (sp gr 1.25) was added. The x-ray lines of $Cd(OH)_2$ increase instantaneously from zero to high values, while the CdO reflections weaken. These changes occur within a few seconds. As soon as the plate is touched by the electrolyte, the yellowish brown color changes into grayish white. Thus, it is obvious, that *if* CdO is the primary product of the discharge, which we by no means have been able to prove, this oxide is immediately transformed by the OH^--ions into $Cd(OH)_2$. Potential measurements indicate, however, as will be discussed later, that Cd is transferred directly into $Cd(OH)_2$.

Winkler's claim that CdO is the end product on discharge is supported by weighing negative plates of different states of charge immersed in the electrolyte, which apparently is a simple and reliable method incidentally used as early as 1904 by Schoop (30). The weight increase on discharge indicates, according to Winkler, the formation of CdO. He found an increase of 0.334 g/amp-hr, adjusted to the dry state, against the theoretical value 0.298 g/amp-hr for CdO. Winkler's paper does not indicate the electrolyte concentration used. If his cells were filled with KOH, sp gr 1.20, calculation shows that the weight increase obtained by Winkler and claimed to agree with formation of CdO, indicates $Cd(OH)_2$ just as well. This coincidence is simply due to the different densities of the two materials. In order to elucidate these matters Winkler's measurements have been supplemented by weighings in KOH of sp gr 1.05 and 1.42, these solutions giving larger differences between the theoretical weight increments. If KOH, sp gr 1.05, is used, the weight increase of the immersed electrode should be 0.245 g/amp-hr for CdO and 0.290 g/amp-hr for $Cd(OH)_2$. For KOH, sp gr 1.42, the corresponding values would be 0.227 and 0.169 g/amp-hr respectively.

Results are shown on Fig. 5.

It was found essential during these measurements that all concentration gradients of the electrolyte across the electrode surface were eliminated before taking the reading. It was also found necessary to remove gas bubbles remaining after the charge. Therefore, the electrolyte was stirred and the container was evacuated after every charge. Weighings were performed at equal intervals of time until constant weight was obtained. The values found on discharge were, in general, more reproducible than those obtained on charge. The diagrams indicated clearly that $Cd(OH)_2$ is the product of discharge. Thus, we consider it established beyond doubt that

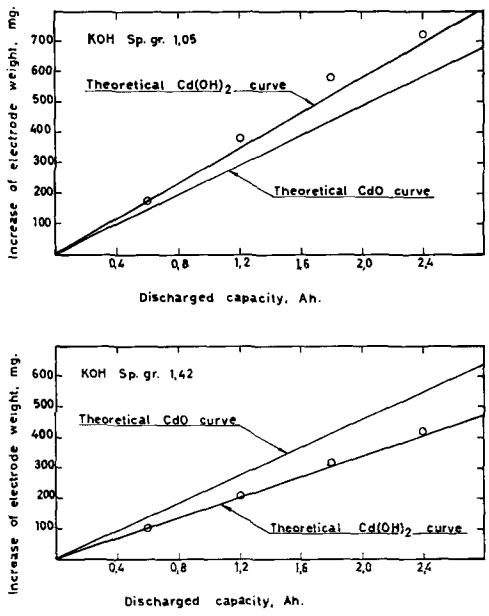

Fig. 5. Weighing of negative electrodes immersed in electrolyte.

$Cd(OH)_2$, not CdO, is the reaction product on discharge of the negative electrode.

The Electrolyte

Opinions on the participation of the electrolyte in the cell reaction have been and still are diverging. Frequently the reaction formula is written in a manner showing that the total concentration of the electrolyte does not change between charge and discharge (7, 31, 32). Condon and Odishaw (2) give a reaction formula according to which the electrolyte is diluted during discharge in a manner similar to the lead cell. According to Troilius (4) and Salkind (25) the total concentration of the electrolyte decreases on charge to regain its original value on discharge.

To clarify this point, potential measurements have been carried out on half charged sintered cells, previously filled with electrolytes of different concentrations. If the over-all concentration does not change in the working cell, then the emf obviously is independent of the electrolyte concentration. The cells were constructed without isolation between the electrodes which, furthermore, were widely separated from each other. Thus the ratio electrolyte/electrodes was substantially higher than is the case in normal cells. These steps were taken, first, to prevent diffusion phenomena on charge and discharge from affecting the measurements, second, to minimize the concentration variations on charge and discharge. Emf and plate potentials were measured. As is shown in Fig. 6, the cell emf increases with decreasing electrolyte concentration. A concentration increase from 5 to 45% causes an emf decrease of about 0.07 v. Consequently, the over-all concentration of the electrolyte is changing in a working cell.

The plate potentials have been measured against a Hg/HgO electrode and the values were corrected for the liquid potentials.

In the negative plate diagram a theoretical curve has been plotted that is based on the equation

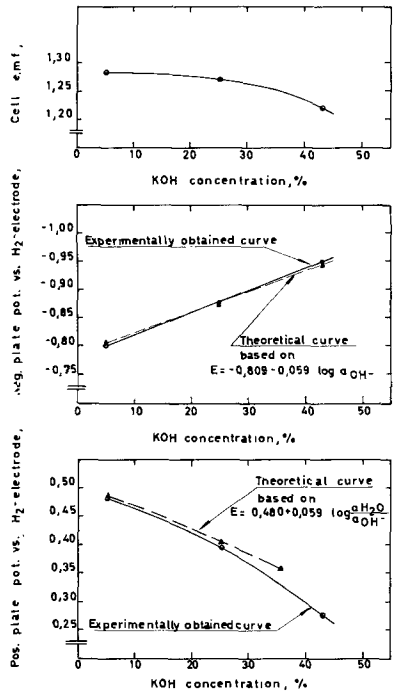

Fig. 6. Electrolyte concentration vs. open-circuit potentials

$$E = -0.809 - 0.059 \log a_{OH^-} \quad [1]$$

This curve is referring to the electrode reaction

$$Cd + 2OH^- \rightleftharpoons Cd(OH)_2 + 2e \quad [2]$$

and agrees evidently very satisfactorily with the experimental curve. Thus, this reaction may be considered as definitely established. As indicated by the formula no water participates in the reaction.

The positive electrode is more sensitive to variations of the electrolyte than the negative one, increasing its potential fairly rapidly when the electrolyte concentration is lowered. The formula indicated by the x-ray investigations is as follows:

$$Ni(OH)_2 + OH^- \rightleftharpoons \beta\text{-NiOOH} + H_2O + e \quad [3]$$

This formula gives the following relationship between electrode potential and electrolyte activities.

$$E = E_0 + 0.059 \log \frac{a_{H_2O}}{a_{OH^-}} \quad [4]$$

If we asume $E_0 = +0.480$ v and insert the activities of H_2O and OH^- for different electrolyte concentrations, the theoretical curve as shown in Fig. 6 is obtained. The agreement between this curve and the experimental one is clearly not very good. It is obvious, however, that the water activity enters into the equation for the electrode reaction. Water is thus formed on charging the nickel electrode.

Reaction Formulas

The main reaction of the positive electrode may, on basis of the previously given results, be written as follows:

$$2\beta\text{-NiOOH} + 2H_2O + 2e \rightleftharpoons 2Ni(OH)_2 + 2\,OH^- \quad [5]$$

This equation may, for better understanding, be split up in the following partial reactions:

$$2\beta\text{-NiOOH} + 2H_2O \rightleftharpoons 2Ni^{3+} + 6OH^- \quad [6]$$

$$2Ni^{3+} + 2e \rightleftharpoons 2Ni^{2+} \quad [7]$$

$$2Ni^{2+} + 4\,OH^- \rightleftharpoons 2Ni(OH)_2 \quad [8]$$

Thus, we can make the formal assumption that trivalent nickel ions are formed by dissolution and dissociation of β-NiOOH. On discharge they are transformed into bivalent nickel ions, which rapidly react with the hydroxyl ions of the electrolyte, forming nickel (II)-hydroxide.

However, it is also possible that the reactions take place directly in the interface between the active material and the electrolyte without dissolution and dissociation of β-NiOOH. Therefore, the given reaction steps are not to be considered as definite.

The main reaction at the negative electrode may be written

$$Cd + 2\,OH^- \rightleftharpoons Cd(OH)_2 + 2e \quad [9]$$

being the summation effect of

$$Cd \rightleftharpoons Cd^{2+} + 2e \quad [10]$$

$$Cd^{2+} + 2\,OH^- \rightleftharpoons Cd(OH)_2 \quad [11]$$

Thus, on discharge the cadmium metal is emitting bivalent ions, immediately reacting with the hydroxyl ions of the electrolyte to form cadmium hydroxide. A summation of Eq. [5] and [9] gives the formula of the total cell reaction

$$2\beta\text{-NiOOH} + Cd + 2H_2O \rightleftharpoons 2Ni(OH)_2 + Cd(OH)_2 \quad [12]$$

In the formulas given above purposely no regard has been paid to the roles of the adsorbed oxygen and hydrogen in the reactions, nor to the secondary discharge stage since all these reactions are of minor importance. The reactions may, however, be written as follows.

$$(\beta\text{-NiOOH})_2(O)_{ads} + H_2O + 2e \rightleftharpoons 2\beta\text{-NiOOH} + 2\,OH^- \quad [13]$$

$$Cd(H_2)_{ads} + 2\,OH^- \rightleftharpoons Cd + 2H_2O + 2e \quad [14]$$

$$Ni(OH)_2(O)_{ads} + H_2O + 2e \rightleftharpoons Ni(OH)_2 + 2\,OH^- \quad [15]$$

Formula [12] for the total cell reaction agrees with the one given by Salkind and Bruins (25).

The EMF and Its Temperature Coefficient

We may assume the emf of the nickel-cadmium cell to be affected primarily by three factors: state of charge, temperature, and electrolyte concentration. The influence of the third factor has been discussed previously.

The emf of the nickel-cadmium cell vs. the state of charge has previously not been subjected to any extensive studies. The relationship between the potential conditions of the nickel electrode and generally rather brief rest periods has on the other hand been investigated by several persons (9, 28, 33, 34).

The results of our x-ray investigations seem to indicate a continuous decrease of the emf with the falling state of charge, because the potential of the positive electrode would fall gradually due to the existence of a solid solution between β-NiOOH and $Ni(OH)_2$, while the negative potential would be

totally independent of the state of charge. In order to obtain a confirmation, measurements were carried out on pocket-type as well as sintered-type cells, which were discharged to different states of charge after previous charging and 5 days of rest. This latter period was introduced to diminish the influence of $(\beta\text{-NiOOH})_2(O)_{ads}$. Emf and electrode potentials were measured after a storage time of 0, 2, 4, and 8 weeks.

These experiments showed that the variations of the electrolyte concentration at various states of charge affected the potentials. The potential of the cadmium electrode, for instance, grew linearly more positive with higher state of charge. Independently of the storage time the potential difference between the 0 and 100% states of charge of the sintered cells amounted to about 11 mv. A check proved this value to agree with the potential change appearing in this type of cell due to the concentration variation of the electrolyte, when formula [12] is applied. Evidently, the magnitude of this difference depends on the ratio volume of active material to electrolyte volume. Naturally, the positive electrode was also similarly affected by the electrolyte variations.

In order to obtain more unaffected values of the relationship between potential and state of charge, tests were carried out as before but on special cells, having a high ratio between electrolyte volume and electrode volume. The specific gravity of the electrolyte in these cells was 1.25. Typical values of emf and electrode potentials as related to the state of charge after 2 weeks' storage at these measurements are shown in Fig. 7.

The curves indicate that the negative electrode potential of the sintered cells is totally independent of the state of charge. This implies the nonexistence of solid solutions of the active compounds. The pocket-type cells have a negative electrode potential which is slightly more negative at higher states of charge. This effect is probably caused by the addition of iron to the negative active material.

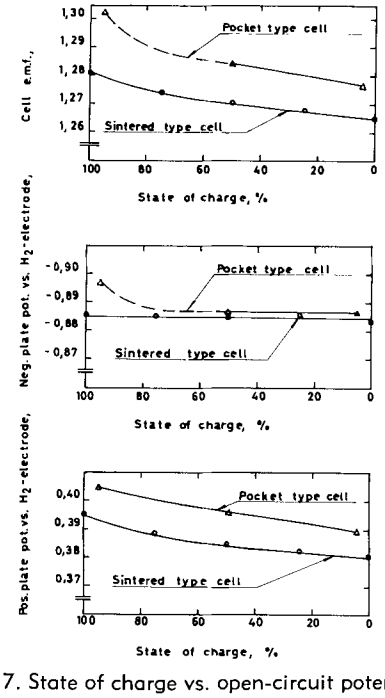

Fig. 7. State of charge vs. open-circuit potentials

The potential of the positive electrode of sintered as well as pocket-type cells is dependent on the state of charge and gradually falling with decreasing state of charge, thus indicating a solid solution of β-NiOOH and $Ni(OH)_2$.

Thus, emf is continuously decreasing with the falling state of charge. In agreement with the collected x-ray data this lowering is caused by the positive electrode.

It is a remarkable fact that the pocket cells consistently display slightly higher emf than corresponding sintered cells. The main part of this effect originates from the nickel electrode, although the cadmium electrode also contributes at higher states of charge.

The relationship between emf and temperature has not yet been subjected to quantitative investigations as far as the nickel-cadmium cell is concerned. This factor has, however, been investigated on the nickel-iron cell, the most extensive work carried out by Hosono and Watanabe (35).

In our investigation cells were tested with pocket as well as sintered electrodes, all discharged to 5, 50, and 95%, respectively, of the capacity after previous full charge. The electrolyte (sp gr 1.25) was covered by paraffine oil in all cells as protection against evaporation. After the discharge the cells were put at rest until the potentials varied only slightly from one day to another. Subsequently, emf and electrode potentials were measured at cell temperatures between about −40° and +50°C. The electrode potentials were all measured with Hg/HgO electrode filled with KOH, sp gr 1.25.

Values for the pocket cells proved to be reproducible at states of charge corresponding to 50 and 95% discharge, while the reproducibility at 5% discharge was less satisfactory and, furthermore, had dE/dT values deviating from the others. This effect indicates an instability and difference in character of the active material at 5% discharge. It is curious in this case that this instability is not dependent on the positive electrode but entirely due to the negative side. It would otherwise have been expected that the positive material would behave differently due to oxygen adsorption. These diverging values of the negative electrode might be due to influence from the iron powder present in the active material.

The sintered cells yielded reproducible values independent of the state of charge. Figure 8 shows typical emf values as related to the temperature on sintered as well as pocket cells. The figures show that all dE/dT values are negative, being more negative for pocket cells than sintered ones at all states of charge. Approximate values of the temperature coefficients of the emf and the electrode potentials are:

dE/dT	dE_a/dT	dE_k/dT
Pocket cells	Sintered cells	Pocket cells
−0.00030	−0.00018	−0.00006
Sintered cells	Pocket cells	Sintered cells
−0.00014	−0.00024	−0.00004 v/°K

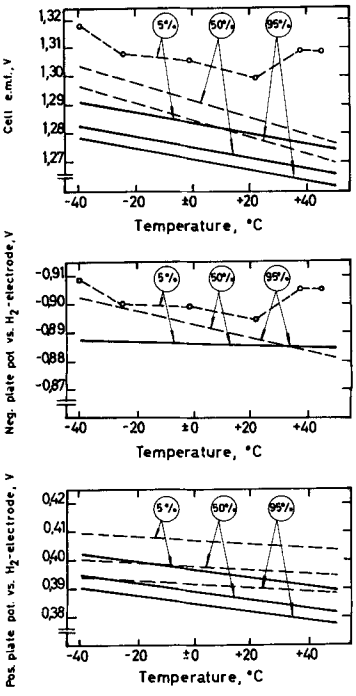

Fig. 8. Emf and electrode potentials vs. temperature. Dashed line, pocket type; solid line, sintered type.

dE/dT is somewhat dependent on the state of charge for pocket cells, of which a 5% discharge yields values disagreeing from the other ones. Otherwise the state of charge does not seem to have any greater influence on the temperature coefficient.

Salkind and Bruins (25) have found that the temperature coefficient of the nickel electrode of sintered cells is negative and decisive in agreement with the values given here.

The differences appearing between sintered and pocket cells as far as emf and dE/dT are concerned are supposed to be due to the presence of graphite in the positive and of iron in the negative pocket electrode.

Summary of Results

1. The main reaction of the nickel-cadmium cell on charge and discharge is
$$2\beta\text{-NiOOH} + \text{Cd} + 2\text{H}_2\text{O} \rightleftharpoons 2\text{Ni(OH)}_2 + \text{Cd(OH)}_2$$
2. The secondary discharge stage of the positive electrode is probably caused by oxygen adsorbed by $Ni(OH)_2$.
3. The high initial potential of the negative electrode after charge is caused by hydrogen adsorbed by Cd.
4. The emf of the nickel-cadmium cell is dependent on the activity of water in the electrolyte and consequently on the hydroxyl ion activity. An increase of the KOH concentration from 5 to 45% results in an emf decrease of about 0.07 v.
5. The emf of the nickel-cadmium cell depends on the state of charge, falling continuously with lower state of charge. This effect can be attributed to the existence of a solid solution between β-NiOOH and $Ni(OH)_2$ in the positive electrode.
6. The dE/dT value of the nickel-cadmium cell is negative. The magnitude is -0.00018 v/°K for sintered cells and -0.00030 v/°K for pocket cells.

Manuscript received Dec. 10, 1959. This paper was prepared for delivery before the Columbus Meeting, Oct. 18-22, 1959.

Any discussion of this paper will appear in a Discussion Section to be published in the June 1961 JOURNAL.

REFERENCES

1. W. Jungner, Swedish Pat. 10,177, March 11, 1899, and 11,487; Oct. 23, 1899.
2. E. V. Condon and H. Odishaw, "Handbook of Physics," McGraw-Hill Book Co., New York (1958)
3. W. Jungner, Swedish Pat. 15,567, Jan. 22, 1901.
4. C. Troilius, Unpublished paper.
5. O. Glemser and J. Einerhand, *Z. Elektrochem.*, **54**, 302 (1950).
6. J. Zedner, *ibid.*, **12**, 463 (1906).
7. G. W. Vinal, "Storage Batteries," 4th ed., p. 203, J. Wiley & Sons, Inc., New York and London (1955).
8. Allmand and Ellingham, "Appl. Electrochemistry," 2nd ed., p. 256, Longmans, Green and Co., New York (1924).
9. F. Foerster, *Z. Elektrochem.*, **13**, 414 (1907).
10. J. T. Crennell and F. M. Lea, "Alkaline Accumulators," p. 94, Longmans, Green and Co., London (1928).
11. M. DeKay Thompson and H. K. Richardson, *Trans. Electrochem. Soc.*, **7**, 95 (1905).
12. National Educational Association monograph.
13. H. Pender, "Handbook for Electrical Engineers," p. 77, John Wiley & Sons, Inc., New York (1917).
14. A. Hauel, *Trans. Electrochem. Soc.*, **76**, 435 (1939).
15. T. A. Edison, British Pat. 20960, 1900.
16. D. W. T. Kirkman and F. Watson Mann, "Alkaline Accumulators," p. 10, (1932).
17. O. Glemser and J. Einerhand, *Z. Anorg. Chem.*, **261**, 26 (1950).
18. G. W. D. Briggs and W. P. K. Wynne-Jones, *Trans. Faraday Soc.*, **405**, 1272 (1956).
19. K. Huber, *Z. Elektrochem.*, **62**, 675 (1958).
20. P. E. Lake and E. J. Casey, *This Journal*, **105**, 52 (1958).
21. D. P. Bogatskii, *Zhur. Obshchei Khim.*, **21**, 3 (1951).
22. R. A. Baker, Bell Labs Memorandum, Oct. 26, 1955.
23. R. W. Cairns and E. Ott, *J. Am. Chem. Soc.*, **55**, 527 (1933); **56**, 1094 (1934).
24. G. L. Clark, W. C. Asbury, and R. M. Wick, *ibid.*, **47**, 2661 (1925).
25. A. J. Salkind and P. F. Bruins "Investigation of the Sintered Plate Nickel-Cadmium Battery," Final Report: Nov. 1, 1955-Feb. 28, 1958, Polytechnic Institute of Brooklyn.
26. O. Hahn, *Naturwissenschaften*, **17**, 295 (1929).
27. S. Lindroth, *J. Am. Ceram. Soc.*, **32**, 198 (1949).
28. A. L. Pitman and G. W. Work, NRL Report 4845 (1956).
29. H. Winkler, *Dtsch. Elektrotech.*, **11**, 223 (1957).
30. M. U. Schoop, *Electrochem. Ind.*, **2**, 272, 310 (1904).
31. M. Stanimirovitch, *La Revue du Nickel*, April-May-June, 1958.
32. A. B. Mundel, *Direct Current*, Sept. 1954.
33. L. M. Elina, T. I. Borisova, and Ts. I. Zalkind, *Zhur. Fiz. Khim.*, **28**, 785 (1954).
34. E. Jones and W. F. K. Wynne-Jones, *Trans. Faraday Soc.*, **405**, 1260 (1956).
35. T. Hosono and K. Watanabe, *J. Electrochem. Soc. Japan*, **19**, 14 (1951).

Oxidation Properties of Tantalum Between 400° and 530°C

J. V. Cathcart, R. Bakish, and D. R. Norton

Metallurgy Division, Oak Ridge National Laboratory, Oak Ridge, Tennessee; Alloyd Corporation, Cambridge, Massachusetts; and Sprague Electric Corporation, North Adams, Massachusetts, respectively

ABSTRACT

The rate of oxidation of tantalum in 1 atm of purified oxygen was measured at three temperatures between 475° and 530°C. The oxide was initially protective but became nonprotective as oxidation progressed. This kinetic behavior was correlated with metallographic and electron optical studies of oxidized Ta specimens, and it was shown that the oxide films became nonprotective through the formation of microscopic blister-like cracks in the oxide. A comparison between the oxidation characteristics of Ta and Nb is given.

In the course of an investigation of the factors which control the degree of protectiveness of oxide films, a study of the oxidation of tantalum in the range 400°-530°C was undertaken. An attempt was made to correlate the results of kinetic, metallographic, and electron optical studies in order to elucidate the oxidation mechanism for tantalum.

Previous investigations of the gaseous oxidation of tantalum have been limited either to rather low temperatures or to short times at higher temperatures. Thus Waber, *et al.* (1) determined the rate of oxidation of tantalum spectrophotometrically and reported a logarithmic form for the rate equation for temperatures from 320° to 450°C. Gulbransen and Andrew (2) observed rate curves of a parabolic type for the 120-min examination period which they employed at temperatures ranging from 250° to 450°C. Vermilyea (3) studied the oxidation rate of tantalum in the temperature range 50°-300°C, and Fassel and co-workers (4) investigated the effect of high oxygen pressure on the oxidation of tantalum at temperatures from 500°-900°C.

Procedure and Results

In the present research, rates of oxidation of tantalum were determined at 475°, 515°, and 530°C. Oxidation specimens were in the form of coupons 1 x 2 x 0.3 cm. Specimens were carefully mechanically polished and prior to oxidation were annealed overnight at a pressure of 10^{-6} mm Hg at the oxidation temperature.

Oxidation rates were determined from the decrease in oxygen pressure in a closed system as oxidation proceeded. Pressure changes were measured with a sensitive differential manometer similar in design to that previously used in a study of the oxidation rates of the alkali metals (5). Oxidations were performed in purified oxygen at approximately atmospheric pressure. The sensitivity of the manometer was such as to permit the detection of a 5Å change in oxide thickness on the tantalum specimens.

The results of these experiments are illustrated in Fig. 1 and 2 where data from representative experiments are given. The quantity of oxygen consumed per square centimeter is plotted against the time of oxidation. A protective film was formed during the early stages of oxidation, but with increasing time a transition period was reached in which the rate of oxidation increased. Finally, the film became virtually nonprotective, and the oxidation rate curve tended toward linearity. The length of the protec-

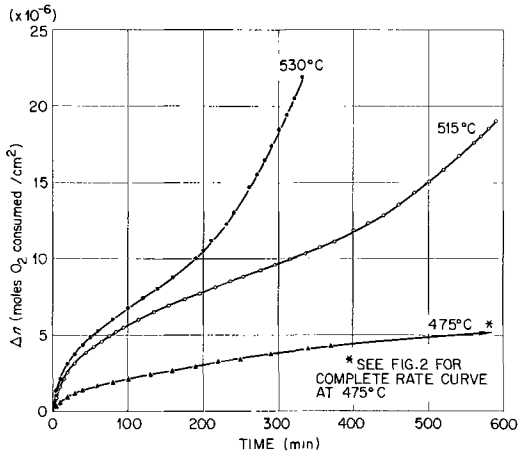

Fig. 1. Oxidation rate curves for Ta at 475°, 515°, and 530°C.

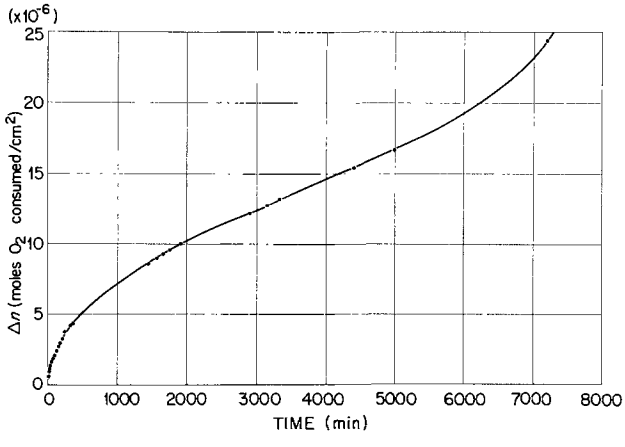

Fig. 2. Oxidation rate curve for Ta at 475°C

tive stage of oxidation varied inversely with temperature. Qualitatively the kinetic behavior of tantalum was very similar to that previously reported for niobium (6).

As a corollary to the rate measurements, the microtopography of the surfaces of oxidized tantalum specimens was examined. Tantalum coupons were prepared in the same manner as described above and oxidized for varying periods of time at temperatures ranging from 400° to 525°C. The oxidized specimens were then preshadowed with gold-manganin and replicated with carbon, and the replicas examined in an electron microscope.

The surfaces of freshly prepared specimens, either chemically or electrolytically polished, exhibited a texture suggestive of bubble-raft dislocation models (see Fig. 3). The origin of this texture is not understood, but it was obtained with a very high degree of reproducibility and persisted during the earliest stages of oxidation. Continued reactions resulted in the superposition on this texture of a pattern of acicular features. As may be seen in Fig. 4, these needle-like structures formed very regular arrays whose orientation varied from grain-to-grain of the substrate metal. This pattern was observed on oxidized specimens which previously had been annealed thoroughly and either chemically or electrolytically polished. On specimens which had been subjected to mechanical polishing only, no such pattern was formed, the oxide film produced under these circumstances exhibiting instead a slight, rather nondescript surface roughening. These results emphasize the relationship between the state of perfection of a metal surface and its oxidation characteristics. Prominent surface features of the oxide film formed on Ta are clearly related to the crystallography of the substrate metal.

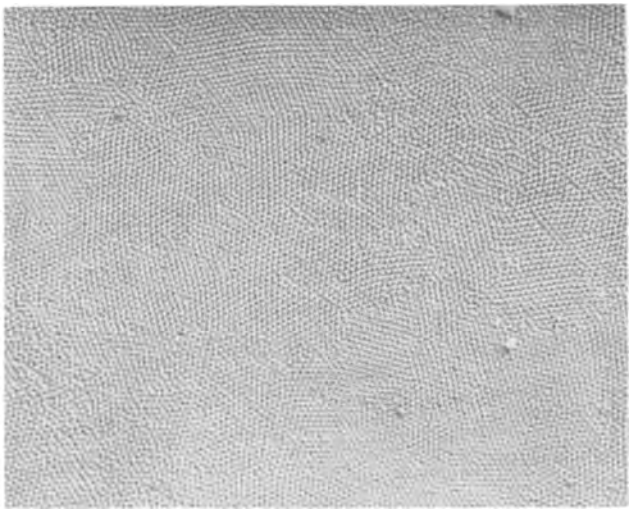

Fig. 3. Electron micrograph of the surface of an electropolished, unoxidized Ta specimen. Indirect carbon replica, Pd shadowed. 33,000 X (All magnifications are before reduction for publication.)

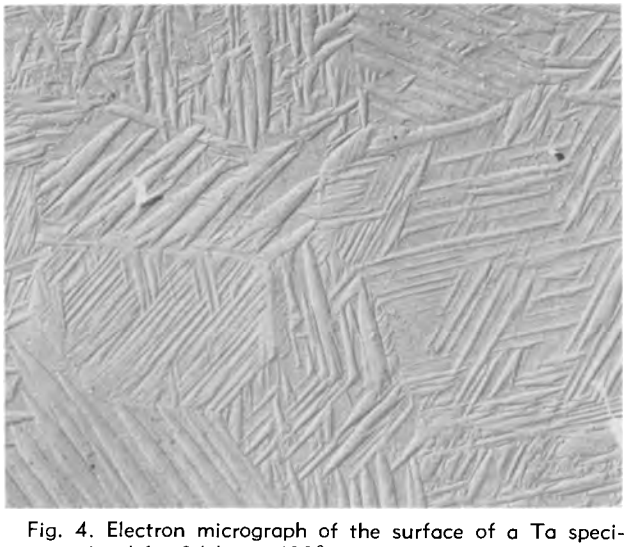

Fig. 4. Electron micrograph of the surface of a Ta specimen oxidized for 24 hr at 400°C. Direct carbon replica, preshadowed with gold-manganin. 7,500X.

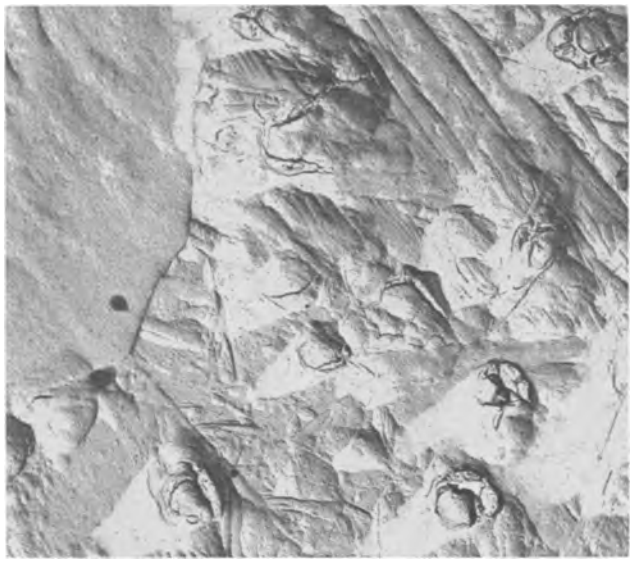

Fig. 5. Electron micrograph of the surface of a Ta specimen oxidized for 10 hr at 515°C. Direct carbon replica, preshadowed with gold-manganin. 12,500 X

At temperatures of 450°C and above, still further oxidation resulted in the formation of numerous cracks and blister-like ruptures in the oxide (see Fig. 5). Such cracks were found after 72, 48, and 4 hr of oxidation at 450°, 475°, and 500°C, respectively.

It was noted that the bubble-raft texture was visible on electropolished Ta specimens before oxidation and that it remained unchanged during subsequent oxidation. Thus the oxidizing of a Ta sample automatically constituted a marker experiment. Since the "markers" receded from the oxide/metal interface, it was concluded that anion diffusion occurred across the Ta_2O_5 film.

Further insight into the oxidation mechanism of Ta was obtained through a metallographic study of taper and cross sections through oxidized Ta specimens. Taper sections such as that shown in Fig. 6 indicated that the oxide film, rather than being confined to a layer parallel to the metal surface, extended into the metal in the form of slightly lenticular platelets parallel to {100} planes of the metal (7). The platelets of oxide appeared to be associated with the needle array observed on the surface of the oxide, and it was thought that the needles represented traces of the platelets on the surface. The formation of similar platelet-like sheets of oxide in

Fig. 6. Low-angle taper section through a Ta specimen oxidized 4 hr at 500°C showing traces of oxide platelets. Depth of cut into specimen increases from left to right. Specimen cathodically etched after polishing. 500 X

Ta was also observed at much higher temperatures and lower pressures of Gebhardt and Seghezzi (8).

Electron- and x-ray diffraction patterns of oxidized tantalum specimens revealed the presence of Ta_2O_5 only. The oxide was crystalline both before and after cracking of the films occurred.

Discussion

The oxidation of Ta proceeded through the formation of a very thin, relatively smooth surface oxide film followed by the production of small platelets of oxide extending into the metal parallel to {100} planes of the metal. The traces of these platelets were visible as acicular forms in the surface oxide. Continued oxidation eventually caused a rupturing of the covering oxide film.

This picture is consistent with the results obtained in the kinetic studies of the oxidation of Ta which indicated an initial protective stage of oxidation followed by a marked increase in the oxidation rate and the on-set of nonprotective oxidation. The increase in oxidation rate was related to the cracking of the oxide film.

It is of interest to compare the oxidation characteristics of Nb and Ta. Important differences exist between the oxidation of the two metals. Two of the major features of oxide films on Ta—the formation of platelets of oxide extending into the metal and the related array of needle-like structures observed on the surface of the oxide—have not been detected in Nb oxide films. On the other hand, striking analogies also have been found in the oxidation properties of the two metals. The oxidation kinetics of both are similar in that at low temperatures both form protective oxide films, for both there is a temperature range in which an initially protective film becomes nonprotective as the time of oxidation increases, and at high temperatures both metals exhibit linear oxidation rate curves. The transition from protective to nonprotective oxidation in both cases is accompanied by similar crack formation in the oxides. Both form analogous series of oxides, and Ta_2O_5 and Nb_2O_5 are crystallographically isomorphous with almost identical lattice parameters (9). Both Ta_2O_5 (10) and Nb_2O_5 (11) are metal-excess semiconductors. These data together with the results of marker experiments indicate that this departure from stoichiometry is due to the presence of anion vacancies in the oxide.

The mechanism of the formation of the oxide platelets is still under investigation; however, the production of the acicular features on the surface of the oxide and the eventual cracking of the oxide films appear to be related at least in part to the mode of diffusion in Ta_2O_5 and to the ratio of the volumes of equivalent amounts of oxide and metal. The model proposed to account for these phenomena is similar to that previously discussed for the oxidation of niobium (6).

If it is assumed, as suggested above, that the oxidation of Ta proceeds via an anion diffusion mechanism, it follows that the new oxide is formed at the oxide/metal interface (or at least that the bottom of the Ta_2O_5 layer if small amounts of the lower oxides are present). A volume increase of approximately 250% is required when Ta is converted to Ta_2O_5. This expansion, however, will be resisted by the already overlying layer of oxide, and the formation of new oxide will be accompanied by the plastic deformation of the existing oxide film. Thus the oxidation process itself continuously produces stresses in the oxide film. In terms of this hypothesis, the stresses resulting from the formation of platelets of oxide in the metal during the oxidation of Ta tend to cause the platelets to press against the layer of covering oxide, deforming this surface film and producing the acicular array already described. Continued oxidation leads to the build up of severe, localized stresses which eventually cause the rupturing of the oxide film.

Manuscript received Dec. 31, 1959.
Any discussion of this paper will appear in a Discussion Section to be published in the June 1961 JOURNAL.

REFERENCES

1. J. T. Waber, G. E. Sturdy, E. M. Wise, and C. R. Tipton, AECU-1355, (1951).
2. E. A. Gulbransen and K. F. Andrew, *J. Metals*, **188**, 586 (1950).
3. D. Vermilyea, *Acta Met.*, **6**, 166 (1958).
4. R. C. Petersen, W. M. Fassell, and M. E. Wadsworth, *J. Metals*, **6**, 1038 (1954).
5. J. V. Cathcart, L. L. Hall, and G. P. Smith, *Acta Met.*, **5**, 245 (1957).
6. J. V. Cathcart, J. J. Campbell, and G. P. Smith, *This Journal*, **105**, 442 (1958).
7. R. Bakish, *ibid.*, **105**, 71 (1958).
8. E. Gebhardt and H. D. Seghezzi, *Z. Metallkde.*, **5**, 248 (1959).
9. N. Schönberg, *Acta Chem. Scand.*, **8**, 240 (1954); S. Lagergren and A. Magneli, *ibid.*, **6**, 444 (1952).
10. W. Hartmann, *J. Physik.*, **102**, 709 (1936).
11. O. Kubaschewski and B. E. Hopkins, "Oxidation of Metals and Alloys," Academic Press, New York (1953).

Equilibrium Space Charge at the Contact of a Metal and a Pure Highly Insulating Liquid and Its Influence on High-Field Conductivity

M. J. Morant

Queen Mary College, University of London, London, England

ABSTRACT

The high-field conduction of a highly purified insulating liquid such as hexane may be largely influenced by electron emission from the cathode. Theoretical interpretations have so far neglected the fact that in equilibrium a space charge layer will probably exist at the contact of a metal and such a liquid, similar to that at a metal-semiconductor contact. The effect of this cannot be calculated without more information, but it does explain the observations that the conduction currents are relatively insensitive to cathode work function. A novel electrostatic method is described which, it is believed, can directly measure the potential of such an electronic double layer at the contact of a metal and a dielectric.

Conduction processes in highly purified insulating liquids are of fundamental interest apart from their value in helping to explain electrical breakdown under extremely high applied fields. A study of the electrical properties of such liquids would ideally give information on the types of charge carrier, their mobilities, trapping and recombination times, etc., and their relationships in determining the actual current and field distribution in a liquid with a given electrode configuration. The variation of the current with the controllable conditions of time, temperature, purity, electrode surface, etc., would follow, electrode processes being particularly important for possible electronic devices. However, little fundamental information is so far available because most of the methods used for investigating gases and solids cannot be used for insulating liquids. In spite of this, the correct interpretation of conductivity measurements alone should be able to provide much information if carried out over a wide enough range of experimental conditions, and particularly as a function of applied field strength. It has recently been shown (1) that with careful technique it is possible to measure the d-c conductivity of a highly purified simple hydrocarbon such as hexane right up to breakdown fields, and this can provide indications of the origins of the current-carrying charges. As field strengths of hundreds of kv/cm are required to obtain currents of about 10^{-10} amp in such liquids, it is not surprising that there have been inconsistencies in the findings of different investigators arising from differences of technique, purity of the liquid, and electrode preparation. Supplementary measurements, not involving conductivity, may therefore be of value in elucidating the critical factors. It is the purpose of this paper to introduce a new type of measurement that can be made on the interface of a highly insulating liquid (or solid) and a metal electrode without applying an external field of any kind. It is believed that this new effect gives the potential difference across an intrinsic space charge layer at the contact of a metal and an insulator.

Before describing the experimental method a brief review is given of the ways in which the electrodes could influence the conductivity, and it is shown that the effects of a double layer between the metal and the liquid must always be included.

Electrode Effects in Liquid Conductivity

Charge transfer in dielectric liquids is more complicated than in either gases or solids. Low energy electrons in a liquid may move in two ways, (i) transferring from molecule to molecule in the field direction, or (ii) trapped permanently to a single molecule which moves as a whole through the liquid. Within each molecule the electron can probably move comparatively freely, but the over-all mobility in the liquid is low whether the electron moves with the whole molecular ion or in a series of jumps between molecules. Charge is probably transferred in both the above ways simultaneously, an electron moving as a large molecular ion until a suitable molecular configuration occurs for the electron to transfer to a neighboring molecule. It may not be possible to distinguish, even theoretically, between the two transport mechanisms. In gases, electron transfer between an ion and a molecule is unlikely because of the low density; also, electrons can move freely between the molecules. In a solid the periodicity leads to a high electron mobility through the lattice, but a trapped electron (i.e., ion) has zero mobility. In both cases it is possible to distinguish between a free electron and an ion. This is not so in a liquid, and a new theoretical background may have to be developed.

Similar reasoning may hold for the transport of positive charge in a liquid. A positive ion may move in the same way as in a gas, but there is the additional possibility that the ion may be neutralized by the transfer of an electron from a neighboring molecule. In this way a positively charged electron vacancy could move through the liquid, corresponding to the movement of positive holes in a semiconducting solid. As for electron transfer it is probably impossible to distinguish between electron vacancies and ion movement. The proportion of the current carried by electrons or electron vacancies as compared with negative or positive ions will depend on the ease with which an electron can be transferred *between* molecules rather than for the whole molecular ion to move.

Any theory of the conduction of dielectrics has, in addition, to account for the origin of the current-carrying charges, and to explain how they are transferred between the insulator and the electrodes. Two distinct types of electrode process exist: (*a*) the electrodes may *emit* all the charged particles required to carry the current; or (*b*) the electrodes may *neutralize* charges which are produced naturally within the dielectric.

The first case includes electron emission from the cathode which is considered further below. Similarly, electron vacancies could be emitted from the anode by the extraction there of an electron, as in a semiconductor. Case (*b*) includes the normal electrolytic effects where the charge originates in the bulk of the liquid due to the dissociation of impurities, absorption of radiation, etc. Both positive and negative ions may be neutralized at the electrodes. When charges originate at the electrodes the conductivity will probably depend greatly on the electrode material, etc., but this is not so if the charge is produced within the liquid.

In general, electrodes can simultaneously perform both functions (*a*) and (*b*) above, e.g., as in a gas discharge where electrons are emitted from the cathode and positive ions neutralize there. Again, in a semiconductor there is a certain naturally occurring charge density (electrons, holes, and charged impurities) and additional charges (minority carriers) may be injected from a contact so that both types of process are operative.

In liquids, as in the other examples, the proportion of the charge carriers originating in the bulk and from the electrodes probably depends on the experimental conditions and on the applied field strength. For example, bulk impurities may account for the low-field conductivity and the emitted charges for the increase of the current with field strength. House (1) has produced evidence for collision ionization in hexane at the highest fields in certain conditions, this being another mechanism by which free charge can originate in the bulk. Whichever source of charge predominates, however, it is important to consider the equilibrium between the charges emitted from the electrodes and those produced within the liquid. It will be shown that one consequence of this is that a space charge layer will always exist in a dielectric liquid close to the electrodes, in the same way as at the contact of a metal and a semiconductor. This layer should greatly influence the charge transfer to the liquid even in cases where the electrode effects predominate.

Theories of the conduction of highly purified liquids have usually either entirely neglected the electrode effects or the presence of charges occurring naturally in the bulk of the liquid. Several authors (1-6) have attempted to explain the high-field conduction in terms of field-aided electron emission from the cathode, but it will be shown that this model must be seriously modified to allow for the production of free charge within the liquid also. The emission theories usually neglect the liquid apart from its dielectric constant, K, and its possible effect in lowering the work function of the metal, so that the conduction current is limited only by the cathode emission, and the electrons are implicitly regarded as being free within the liquid. At the high fields concerned, 10^4-10^6 v/cm, electron emission from the metal may occur by the Schottky process of field-aided thermionic emission, or by Fowler-Nordheim cold emission depending on the conditions. As in the case of electron emission into gases, the former is more likely to give agreement between experimental values and reasonable theoretical estimates of work function, field intensification, and emitting area (7, 8). Even so, the agreement is not perfect, and more elaborate models have been proposed to explain the emission (6, 9).

A serious objection to emission-limited theories of liquid conduction was first raised in 1937 by Plumley (4). Emission should depend on the work function of the cathode, possibly modified from its vacuum value by the presence of the liquid. Plumley showed that, within experimental error, brass and gold cathodes gave the same current in iso-octane up to 175 kv/cm. Thermionic emission (with the vacuum values of the work function) would have given currents in the ratio of 3.10^4:1. More recently, Green (6) has investigated the dependance of conduction currents in hexane on the cathode conditions and has found a variation over a range of about 100:1, but dependant more on the surface layer, as affected by heat treatment, than by the material of the cathode. House (1) found a maximum difference of only 3:1 between silver and chromium electrodes in hexane. Zaki (10), also working in this laboratory, has obtained similar results, and has also shown that differences of up to 100:1 in the high-field currents in hexane may result from the state of oxidation of the cathode. All these results suggest that the conduction is influenced by the cathode, but that it is unlikely to depend simply on the work function. It will be shown that this may be explained by considering the complete surface barrier when some of the free charge is produced within the liquid. But first it is necessary to consider the charge density at the interface of a metal and a dielectric liquid.

Equilibrium Space Charge

The electron density outside the range of image forces of a metal surface of work function ϕ is

$$n_0 = 2\left(\frac{2\Pi mkT}{h^2}\right)^{3/2} e^{-\phi/kT} \text{ cm}^{-3} \qquad [1]$$

Away from such a metal surface in a vacuum the electron density, $n(x)$, decreases indefinitely, and the electrostatic potential, V, rises as required by the Boltzmann distribution and Poisson's equation

$$n(x) = n_0 e^{-eV/kT} \quad [2]$$

and

$$\frac{d^2V}{dx^2} = -4\Pi ne \quad [3]$$

in the one-dimensional case. This is the "electron atmosphere" that always exists in equilibrium with a metal surface in a vacuum. It is distinct from the denser space charge that occurs when current is drawn. At the contact of a metal and an idealized dielectric, there is a similar electron atmosphere except that the dielectric constant, K, has to be included as a denominator in [3], and the electron density, n_0, may be very much greater than at the vacuum interface due to the lowering of the work function of the metal by the dielectric to a value ϕ^*. The difference $(\phi - \phi^*)$ may be regarded as the potential energy of the lowest electronic conducting level in the dielectric (Fig. 1a and b).

The potential rise in the electron atmosphere outside a plane metal surface is easily calculated from [2] and [3] (11). At room temperature the electron density is very low and in vacuum, for example, the potential rises to only 35 mv at a distance of 32 cm from a metal having a work function of 1 ev. The potential rise is even slower for practical values of ϕ. However, the result is very sensitive to *lower* values of ϕ as may be encountered at the contact with a dielectric. For instance if $\phi^* = 0.5$ ev the same potential rise occurs in $3 \cdot 2.10^{-3}$ cm. For two plane electrodes, solutions of [2] and [3] may also be found giving the potential in the enclosed electron space charge. Von Laue (12) and Fowler (13) have shown that the potential close to each electrode is scarcely affected by the presence of the other. In equilibrium the normal contact p.d. occurs between the electrodes and the potential in the gap reaches a peak at a position determined by the work functions. Skinner (14) has considered the current that would flow in an idealized dielectric, containing an electron atmosphere of this form, on applying an additional potential difference.

There are two respects in which a real dielectric may be expected to differ from this idealized case, and both affect the form of the potential variation. In the idealized dielectric the electron density can decrease continuously toward zero (limited only by the applicability of [2] and [3]), but in any real dielectric a lower limit is set by the naturally occurring charge density which, as explained above, will be formed in a liquid by the dissociation of impurities, absorption of stray radiation, and possibly by thermal excitation. For neutrality equal positive and negative charge densities must be produced in the bulk of the liquid. If an electron density n_1 cm^{-3} is formed the potential rise in the space charge between the metal and the bulk of the dielectric must be limited to

$$V_m = \frac{kT}{e} \log_e \frac{n_0}{n_1} \quad [4]$$

as shown in Fig. 1c. This potential difference can be regarded as a first approximation to the contact potential between the metal and the interior of the liquid due to the naturally occurring charge density in the latter. A space charge barrier setting up this potential is required for equilibrium at the interface in the same way as at the contact of a metal and a semiconductor. Equation [4] may in fact be derived from the true equilibrium condition which is the equality of the electrochemical potentials in each phase. Similarly the electron atmosphere in a vacuum is required to try to bring it into equilibrium with the metal.

The second specific effect of the dielectric is to concentrate this "equilibrium space charge" much closer to the interface than in a vacuum. In a real liquid dielectric, the electrons will not be distributed as a perfectly free gas, they will not diffuse far into the liquid, and Eq. [2] will no longer be valid. Any tendency for electrons to become trapped in or between molecules will concentrate the space charge layer even closer to the metal surface as shown in Fig. 1d. With a low effective work function an appreciable part of the equilibrium space charge could be within 10^{-4} cm of the metal.

When considering the emission of electrons into a vacuum the potential of the electron atmosphere is extremely small compared with other surface forces. In liquids, the theories of field-aided electron emission have also neglected the equilibrium space charge, although it now seems probable that it could give appreciable potential changes even within the range of image forces. For this reason the conductivity of liquids is unlikely to be explained by models for the emission of electrons into a vacuum. The above description of the equilibrium space charge applies strictly only when there is no applied field. Much more information about charge carriers, their mobilities, trapping effects, etc., will be required before it is possible to predict the influence of contact space charge on current flow in liquids even with low fields: the methods would be expected to be similar to those developed for metal-semiconductor contacts. The difficulties are even greater for high applied fields. The conductivity increases by anything up to six orders of magnitude between low fields and breakdown. Assuming that this is due to increasing current-carrying charge density in the bulk, the potential across the space charge in the contact region would fall by only 0.6 v (from Eq.

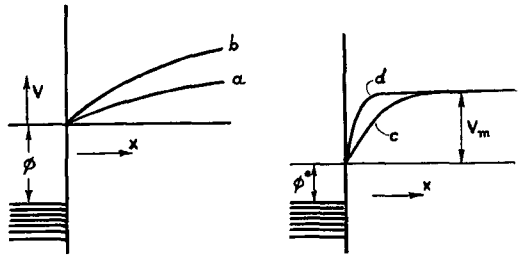

Fig. 1. Potential energy of an electron at the contact of a metal and a dielectric. (a) Vacuum; (b) idealized dielectric; (c) dielectric with bulk charge; (d) dielectric with bulk charge and trapping.

[4]). This emphasizes that the contact space charge rather than straightforward electron emission from the cathode is important up to the highest applied fields.

Although the current flow through the complete surface barrier cannot yet be calculated, the equilibrium space charge has one important consequence which is confirmed experimentally. Electron emission from a cathode to the surface region of a liquid is controlled by the modified work function, ϕ^*, of the metal. The space charge imposes the additional potential barrier, V_m, which from [4] and [1] is

$$V_m = \frac{kT}{e}\left\{\log_e 2\left(\frac{2\Pi mkT}{h^2}\right)^{3/2} - \frac{\phi^*}{kT}\right\} - \frac{kT}{e}\log_e n_1$$

or substituting numerical values, with $T \sim 300°K$, the total barrier height is

$$\left(V_m + \frac{\phi^*}{e}\right) = 1\cdot115 - \frac{1}{40}\log_e n_1 \text{ v} \qquad [5]$$

That is, the total potential barrier between the Fermi level of the metal and a conducting level in the liquid is independent of the work function of the metal, but it does depend on the liquid charge density. A low work function gives a high electron density at the interface and so a large space charge potential, and vice versa (Fig. 2). Thus the relative insensitivity of conduction currents in simple liquids to the cathode material is not incompatible with emission-limited conduction modified by the equilibrium space charge barrier. This removes the major objection to emission theories first stressed by Plumley and confirmed since. Although the barrier height is constant, a relatively small cathode dependence would still be expected due to differences of the barrier shape with ϕ^* and V_m.

It must be stressed that this model is highly simplified and that it assumes electronic equilibrium between the metal and the liquid. The presence of either positive or negative ions alters the double layer potential V_m, but whatever the details, some sort of space charge layer must exist at the interface for equilibrium. The experimental work described below also directly demonstrates the existence of such a space charge layer. At first sight the above model cannot account for the considerable effect of the state of oxidation of the cathode on the conductivity of dielectric liquids. The equilibrium space charge is unaffected by replacing a clean metal surface by an oxide of the same work function so the conduction currents should also be independent

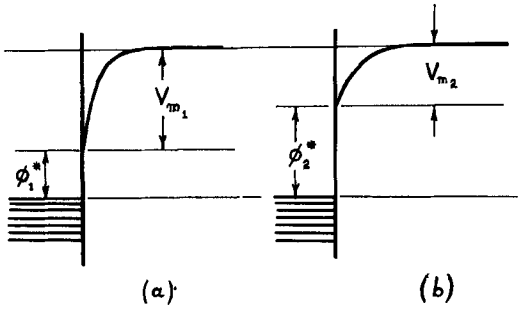

Fig. 2. Potential energy at the contact of a dielectric and electrodes of (a) low, and (b) high work function.

of the oxide work function. However, with current flow across an insulating oxide layer the equilibrium between the solid and the liquid may be seriously disturbed. Electrons may not be able to pass through the oxide layer quickly enough to maintain the equilibrium concentration, n_0, or the space charge potential V_m. The emission current would then be partly limited by the potential across the oxide layer. On the other hand, an unoxidized metal surface could always provide sufficient electrons to maintain the contact space charge in equilibrium right up to the maximum currents found in very pure liquids. Much more information is required before it is possible to differentiate between several possible mechanisms at the oxidized cathode.

Experimental Determination of the Space Charge Potential

It is not possible to detect the equilibrium space charge at the contact of a metal and a very highly insulating liquid by any of the classical methods of electrochemistry. However, a new type of electrostatic effect is described below which is believed to measure directly the potential of the double layer formed by the negative space charge and the positive charge induced on the electrode.

The measurement has similarities to the Kelvin method of measuring the contact or Volta potential between dissimilar metals. Plumley (4) and Macfadyen and Holbeche (15) have shown that the contact potential, measured in this way, is changed only slightly by totally immersing both electrodes in an insulating liquid. This would be expected unless the liquid reacted in different ways with each electrode. If there are contact potentials between each metal and the liquid, they cancel out around the circuit, and they cannot be detected by changing the total capacitance between the electrodes as in the Kelvin method. It is believed that this is overcome in the new method by measuring the change of potential of one of the electrodes when its *contact area* with the liquid is changed. The opposite electrode, usually earthed, remains totally immersed. A suitable arrangement is shown in Fig. 3a. An insulated conical electrode just pierces the surface of the liquid held in a metal cup. It is found that the potential of the cone changes reversibly as it is moved in and out of the liquid. Part of this change is due to the contact potential between the metal surfaces detected by the change in the total capacitance as in the Kelvin method, but this may be measured separately, and there is an additional potential change thought to be due to the charge transfer from the metal to the contact region in the liquid. Owing to the high insulation of both the metal and the liquid at the contact, the contact potentials round the whole circuit (including the liquid) cancel out extremely slowly, so that the contact potential across a single interface (where the contact area changes) may be detected. In this way it is a unique type of measurement.

A simplified theory by which the measured potential can be related to the double layer potential will be given. Figure 4 shows the charge distribution on the whole system arising from a double layer at

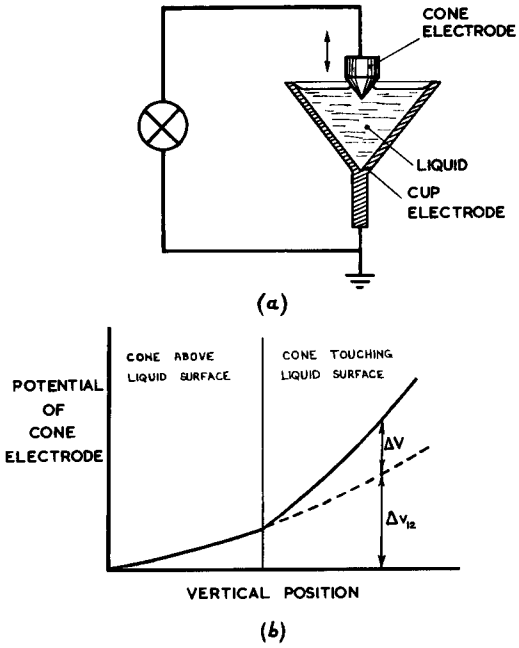

Fig. 3(a). Experimental arrangement for measuring the equilibrium space charge potential at the contact of a metal and an insulating liquid. Fig. 3(b). Form of the potential variation as the cone electrode touches the liquid surface.

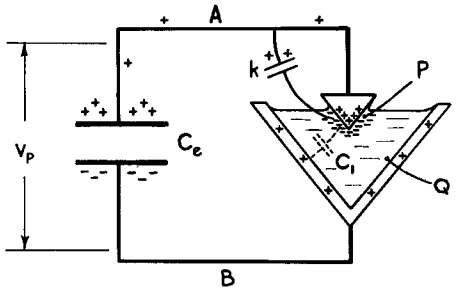

$$V_P = V_1 \frac{C_i}{C_i + C_e}$$

Fig. 4. Charge distribution due to double layer of potential v_1 at contact P.

the conical electrode, P. The charge at this contact is assumed to be positive on the metal and negative just inside the liquid, the potential difference being v_1. The metal A has lost negative charge as a whole to form this double layer. All this charge is concentrated just inside the liquid at P. Every element of capacitance, such as k, between the contact region of the liquid and the metal A must be charged to the double layer potential. Thus not quite all of the induced positive charge is on the contact surface of the metal. If the insulation of the system (including the liquid) is perfect, there are also induced charges on the electrometer (represented by the capacitance C_e, Fig. 4) and on the opposite metal electrode B. In the external circuit the double layer potential v_1 is divided capacitively by C_e and C_i, where C_i is the capacitance between the whole of the cup electrode B and the negative charge layer just inside the liquid at P. Therefore, due to the double layer at P, there exists a potential

$$v_p = \frac{v_1 C_1}{C_1 + C_e}$$

across the electrometer.

By similar reasoning, a double layer of the same polarity but of potential v_2 at the opposite interface of the metal and the liquid gives rise to a potential v_q across the electrometer. The two charge distributions are independent and the electrometer potentials may be added to give the net potential, v, due to the two double layers.

$$v = v_p + v_q = \frac{v_1 C_1}{C_1 + C_e} - \frac{v_2 C_2}{C_2 + C_e} \qquad [6]$$

where C_2 is the capacitance between the negative charge layer just inside the liquid at Q and the whole of the metal A.

In practice it is not possible to measure the steady potential v as it is swamped by stray charges left by contact potentials, etc., on setting up the system, so a difference method must be used. By slightly moving the cone electrode, the contact area with the liquid at P is changed without greatly changing the total capacitance between the electrodes. Therefore the potential of the spurious charges remains practically constant. However, the electrometer potential, v, due to the double layers is much more sensitive to contact area as the capacitance C_1 is due to the field between the negative charge at the contact and the whole of the opposite metal. The corresponding term C_2 associated with the opposite double layer of fixed area, at Q, is unaffected, to a first approximation, by the area change at P. Therefore for a small change of contact area at P, the change of the potential across the electrometer is given simply by

$$\Delta v = \frac{v_1 \Delta C_1}{C_1 + C_e} \qquad [7]$$

and if the capacitances of the system are known, v_1, the potential of a single double layer, may be directly measured.

The above treatment is very simplified, and the full analysis is not given here. The only basic assumptions that have to be made are that the negatively charged layers are thin compared with the dimensions of the apparatus, and that the equilibrium space charge at the contact is set up rapidly, i.e., within a second or two of changing the contact area. The full expression for Δv includes terms due to *both* the metal-liquid interfaces, and for the normal contact potentials between the electrodes (16). The partial and total capacitances of the system have to be examined in detail. Each one is of a few $\mu\mu$farad and of a distributed nature, so that the associated field has to be defined. A measuring technique must be devised for each partial capacitance without deforming the field by the introduction of probes. The analysis eventually gives the potential change, Δv, as a function of the penetration of the liquid surface by the conical electrode, in terms of the potentials v_1 and v_2. By initially preparing both electrodes in the same way, the double layers may be assumed to be the same, and they can be found from measurements of Δv by setting $v_1 = v_2$. Subsequently the double layer of the single contact between the conical electrode and the liquid may be investigated by keeping constant the surface treat-

ment of the opposing cup electrode. The effect of the preparation and material of the conical electrode may be found in this way.

In practice, measurements of electrostatic potentials of a few millivolts in systems of extremely high resistance and very low capacitance are confused by several spurious effects which may be difficult to eliminate or separate, and the present measurement is one of considerable difficulty. It is hoped to describe experimental details in full elsewhere (17). Our first work on this topic followed the discovery of the effect in solid insulation. In that case, the electrodes in contact with a block of the dielectric consisted of an earthed flat plate and a conical or spherical indenter connected to the grid of an electrometer valve (18, 16). Potentials of up to about 60 mv were obtained for a small change of the spherical contact area, but it is now known that these were largely due to the sensitivity of electrometer valves to the precise value of the external resistance: this varies with the contact area in the same way as the expected electrostatic charging (19). The effect is important for all measurements of small charges. It must be allowed for also in measuring the change of potential associated with the change of area of a metal-liquid contact. Comparatively large indicated potentials may also be due to contact potentials between metals. When the total capacitance, C_{12} between the electrodes is changed by slightly moving one of them, the potential changes instantaneously by

$$\Delta v_{12} = v_{12} \frac{\Delta C_{12}}{C_{12}}$$

where v_{12} is the contact potential. The contact p.d. plus the potential due to stray charges is measured independently by moving the conical electrode just above the liquid surface before making actual contact. The double layer effect, Δv, must then be absent. Figure 3b shows how Δv_{12} is extrapolated by independent measurements of the total capacitance, C_{12}, to separate the spurious and true double layer components of the measured change of potential after contact is made. It can be shown that this extrapolation is justified for nonpolar liquids as the change of C_{12} due to the dielectric constant of the liquid is negligible.

When allowance is made for these and other spurious effects, the reversible change of potential, Δv, is of the order of 1 mV/mm of penetration of a conical stainless steel electrode into hexane. The form of the potential variation agrees with that expected from the full expression for Δv in terms of the partial capacitances. Several other possible side effects that could account for the change in the electrode potential have been eliminated either by features of the experimental results or by experimental precautions, and no alternative can be found to the explanation of the measurements in terms of the interfacial double layer. Most of the work has been concerned with proving that this is so, and tests have so far only been made with stainless steel electrodes and highly purified n-hexane. Results show that the interfacial double layer always has the negative side toward the liquid as required for an electron space charge. The double layer potential, derived from Δv, is found to vary between 0.3 and 0.6 v depending on the electrode surface treatment, but an average value of about 0.42 v is obtained by leaving the electrode immersed in hexane for several days.

This result may be compared with the simple theory of the equilibrium space charge. The conductivity of hexane can be as low as 10^{-16} mho/cm. Assuming, for lack of precise information, that there are no bulk space charge effects, this corresponds to about 10^8 charge carriers per cm^3 for a mobility of 10^{-3} cm^2/v sec [LeBlanc (20)]. As such a low conductivity is found only in highly purified liquids, this may be the order of magnitude of the electron density formed in the liquid by stray radiation, etc. If this is so, Eq. [5] shows that the total height $(V_m + \phi^*/e)$ of the potential barrier between the metal and the liquid must be about 0.94 v, so that, if the double layer potential is 0.42 v, the average work function, ϕ^*, of the metal in contact with the liquid is only 0.52 ev. It is difficult to see how the work function of a normal metal surface could be lowered by more than about 0.5 ev by the purely electrostatic effects of a nonpolar liquid (16). The very low value found here for ϕ^* may indicate that there are weakly conducting levels for electrons in the liquid at a depth of about 4 ev, corresponding to the electron affinity of an insulating crystal.

Work on this new electrostatic method of detecting the equilibrium space charge at the contact of a metal and an insulating liquid is continuing, and it is hoped that it will be possible to correlate it with measurements of conductivity carried out on the purest possible samples up to breakdown field strengths.

Acknowledgments

Much of the work described above was carried out in 1951-1954 and was made possible by a maintenance grant from the Department of Scientific and Industrial Research. The current award of the Henley Research Fellowship to the author is also gratefully acknowledged.

Manuscript received March 1, 1960. This paper was prepared for delivery before the Philadelphia Meeting, May 3-7, 1959.

Any discussion of this paper will appear in a Discussion Section to be published in the June 1961 JOURNAL.

REFERENCES

1. H. House, *Proc. Phys. Soc.*, **B70**, 913 (1957).
2. E. B. Baker and H. A. Boltz, *Phys. Rev.*, **51**, 275 (1937).
3. W. R. Le Page and L. A. Du Bridge, *ibid.*, **58**, 61 (1940).
4. H. J. Plumley, *ibid.*, **52**, 140 (1937).
5. D. W. Goodwin and K. A. Macfadyen, *Proc. Phys. Soc.*, **B66**, 85 (1953).
6. W. B. Green, *J. Appl. Phys.*, **26**, 1257 (1955).
7. M. J. Morant, *Proc. Phys. Soc.*, **B68**, 513 (1955).
8. K. Kerner and H. Raether, *Z. Angew. Phys.*, **6**, 212 (1954); also K. Kerner, *ibid.*, **8**, 1 (1956).
9. T. J. Lewis, *Proc. Phys. Soc.*, **B68**, 504 (1955).
10. A. A. Zaki, PhD. Thesis, University of London, (1959).

11. N. F. Mott and R. W. Gurney, "Electronic Processes in Ionic Crystals," p. 171, 2nd ed., Oxford University Press, London (1948).
12. M. von Laue, "Handbuch der Radiologie," 6, p. 460, Leipzig (1925).
13. R. H. Fowler, "Statistical Mechanics," 2nd ed., p. 367, Cambridge University Press, Cambridge (1936); see also M. J. Morant, *J. Appl. Phys.*, **25**, 1053 (1954).
14. S. M. Skinner, *J. Appl. Phys.*, **26**, 509 (1955).
15. K. A. Macfadyen and T. A. Holbeche, *J. Sci. Inst.*, **34**, 101 (1957).
16. M. J. Morant, Ph.D. Thesis, University of London (1955).
17. M. J. Morant, To be published.
18. M. J. Morant and W. K. Mansfield, *Nature* (London), **169**, 499 (1952).
19. M. J. Morant, *J. Sci. Inst.*, **31**, 391 (1954).
20. O. H. Le Blanc, *Bull. Amer. Phys. Soc.*, (II), **4**, 45 (1959).

The Incorporation of Sulfur in Electrodeposited Nickel, Using Thiourea as a Brightener and Leveler

G. T. Rogers[1] and M. J. Ware

Atomic Energy Research Establishment, Harwell, England

and R. V. Fellows

Wilmot Breeden Laboratories, Solihull, Warwickshire, England

ABSTRACT

The amount of sulfur incorporated into nickel electrodeposited from a Watts plating solution containing thiourea as a brightener and leveler has been investigated by radiotracer techniques and autoradiography. The nickel deposit contains sulfur, and the amount of sulfur increases with decreasing current density when the current density is determined by the external electrical circuit or by the geometry of the plating cell. Autoradiographs taken from oblique sections cut through the nickel deposit show the distribution of the sulfur within the deposit. When the nickel is deposited on a surface having a roughness comparable to that encountered technologically incorporation occurs on the peaks of the surface. Thiourea causes leveling which requires the peaks to be regions of lower current density. Therefore the incorporation of sulfur is higher in regions of lower current density when the current density distribution is determined by the behavior of thiourea on a rough surface. Incorporation probably occurs in layers in regions of the deposit which show a laminar structure.

The addition of small quantities of certain organic compounds to solutions used for the electrodeposition of nickel modifies the plating in two ways, brightening and leveling. The mechanisms of brightening and leveling present problems which are relevant to the study of the electrodeposition of metals and which have considerable technological importance. Any investigation of these mechanisms requires data on the extent to which an additive, or compounds derived from it, become incorporated in the nickel plate under various plating conditions. It is also important to know the extent to which anions are incorporated in the plating. Since the amounts of incorporation are too small to be determined conveniently by conventional methods of analysis, radiotracer techniques are very appropriate to these studies because their high analytical sensitivity may be combined with autoradiography to show in detail the distribution of the additive over the area of plating. Recently Beacom and Riley (1) have investigated the incorporation of sulfur compounds from sodium allyl sulfonate using an elegant counting technique and autoradiography to measure the differences between incorporation on the peaks and valleys of grooved cathodes. They found a greater incorporation of sulfur on the peaks than in the valleys, but the scale of their "simulated roughness" was more than two orders of magnitude greater than that which is encountered in practice.

Thiourea is an additive which produces both brightening and leveling, and this paper describes an investigation of the incorporation of sulfur into nickel plating from thiourea labeled with sulfur-35. A study has been made of the distribution of incorporated sulfur within nickel plated on a surface whose roughness is comparable with that of technological interest.

Experimental

The effect of current density on the incorporation of sulfur from thiourea has been studied by plating test cathodes in a Hull cell. The plating baths were supplied with S^{35}—labeled thiourea from a high specific activity stock solution. Plating solutions were prepared by adding labeled thiourea diluted with inactive carrier to a standard Watts' nickel plating solution. A volume of 300 ml of plating solution was used for each cathode which was plated

[1] Present address: United Kingdom Atomic Energy Authority, Wantage Radiation Labs., Wantage, Berks., England.

for 15 min at a total current of 3 amp at 55°C and pH = 4.0. The total concentration of thiourea was 10^{-3} g mole/l and the activity was 517 μc/l. The bath was agitated by a stream of nitrogen introduced along the bottom of the cathode. After plating, the cathodes were washed with cold water and boiled with two changes of distilled water. Autoradiographs were taken from these cathodes by pressing them in close contact with an appropriate photographic emulsion.

Further experiments to determine the effect of current density and thiourea concentration on incorporation were carried out using 1½ in. diameter mild steel disks plated in a cell consisting of an 800-ml beaker with a 1 in. paddle stirrer rotating at 120 rpm between the anode and cathode which were 2¼ in. apart. Four disks were plated at different current densities and thiourea concentrations using 500 ml of fresh plating solution containing 414 μc of S^{35} thiourea for each. All disks were plated at 55°C and pH = 4.0 with a copper coulometer in series with the plating cell. After plating, each disk was washed in the same manner as the Hull cell cathodes. Further boiling of the disks with distilled water caused no change in the incorporated activity.

The β activity of a circle, radius 0.406 cm, at the center of each disk was determined by counting with an end-window Geiger-Muller counter, the geometry of counting being controlled so that the activities of the four samples and a standard source could be compared.

The absorption coefficient for sulfur 35 β particles for the counting conditions used to determine the activities of the disks was determined using one of the disks as a source and nickel absorbers. The absorbers were placed close to the plated disk so that the counting geometry for the external absorbers was as similar as possible to that of the self-absorber. The value of the absorption coefficient in aluminum, the half life, and the absence of any gamma radiation detectable with a scintillation counter showed that all the activity on the disks was due to sulfur 35.

The thickness of the nickel plate at the center of each disk was measured by sectioning. The outside profile of the plating was supported by gluing to it a piece of soft copper sheet with Araldite. The disk was sectioned perpendicular to the plane of the plating, and the section face was polished and etched. The thickness of the plating was measured with a microscope fitted with a reticule eyepiece.

The plating conditions, the plating thicknesses at the centers of the disks, and the activities of the disks are shown in the first six columns of Table II.

To investigate the incorporation of sulfur from sulfate, two brass disks, E and F, were plated in a Watts' solution containing labeled sulfate but not thiourea. 500 ml of the solution contained 16 mc of $(S^{35}O_4)^{2-}$ and the disks were plated for 45 min at a current density of 3.97 amp/dm². The activity of a circle, radius 1.15 cm at the center of each disk, was compared with that of a standard by counting. These activities were very much lower than the activities of the disks plated in the presence of thiourea. Therefore to obtain reasonable counting rates, the counting efficiency was increased by mounting the disks much closer to the counter window. A standard was prepared by diluting 0.1 ml of the plating solution to 100 ml and evaporating 1 ml of the diluted solution onto a counting tray.

Table I

Disk	Surface finish center line avg roughness,* microns	Total conc. thiourea gmole/l	Total act. in bath, μc	Apparent current density, amp/dm²
G mild steel	1.12	10^{-3}	493	4.85
H mild steel	0.19	10^{-3}	493	4.85
K brass	1.17	10^{-3}	407	3.97

* Center line average roughness of length L of the surface equals $\frac{1}{L}\int_0^L |Y1|\, dl$ where y is the distance of the surface from the mean center line.

The distribution of the sulfur in nickel plated on a rough surface in the presence of thiourea has been studied by taking autoradiographs of sections cut obliquely through the plating. Disks were prepared on emery to give surfaces with scratches in one direction and various surface roughnesses. 500 ml of solution were used to plate each disk. Details of the surface and the plating conditions are summarized in Table I.

All disks were carefully cleaned before plating. The adhesion of the plating on disk K, which was used for taper sectioning, was further improved by cleaning it cathodically immediately before plating. The plating was sectioned at 5° to the plane of the plating. The outside profile of the nickel plate was supported by gluing to it a piece of soft copper sheet with Araldite. A 5° cut was then made in the brass, the section mounted in Perspex with the brass side outwards, and rubbed down on emery until a suitable profile appeared. The section was polished using normal metallographic techniques and etched with ammoniacal hydrogen peroxide. Autoradiographs were taken on Kodak A. R. 10 emulsion.

Results

Figure 1 shows autoradiographs of a Hull cell cathode (*a*) plated in a nitrogen-agitated bath and (*b*) in a bath without agitation, but in a nitrogen atmosphere. In Fig. 1, the current density increases along the cathode from left to right, and in all the autoradiographs, radioactive areas appear black.

Ratios of sulfur to nickel atoms in the plating can be calculated from the measured count rates. Suppose C counts/min, corrected for background and counter dead time, are obtained from 1 cm² of plating using a given counting geometry. Assume that the plating is of uniform thickness t cm and that it contains a uniform distribution P atoms of sulfur per atom of nickel. The specific activity of the thiourea in the plating bath S millicuries/g mole is equal to the specific activity of the sulfur in the plating in millicuries/g atom, assuming that there is no exchange of sulfur between thiourea, or sulfur in the plating, and sulfate ions during the deposition. A thin layer of plating thickness dx distance x from the free surface contains $(PSp/W)\ dx$ mc S^{35}/cm²

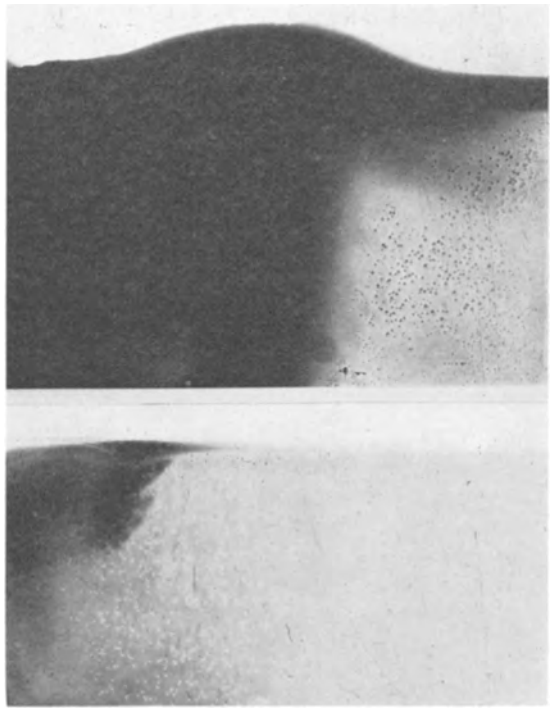

Fig. 1. Autoradiographs of Hull cell cathodes (full size before reduction for publication) (a) (top) plated in a nitrogen agitated bath, (b) (bottom) in a bath without agitation, but in a nitrogen atmosphere. The current density increases along the cathode from left to right and radioactive areas appear black.

where p, W are the density and atomic weight of nickel, respectively. The reduction of the count rate by absorption of $S^{35}\beta$ particles in thickness x of plating can be calculated approximately by assuming an exponential absorption with an absorption coefficient μ (2).

The thin layer at x contributes $(kPSp/W)e^{-\mu x}\,dx$ counts/min/cm^2 to the measured count rate where k is a constant depending on the geometry of the counting arrangement. Since the distance between the counter and the plating is large compared with the total thickness of the plating, k is independent of x.

Integration over the total thickness of the plating t and rearrangement gives

$$P = \frac{W}{kS}\,\frac{\mu}{p}\,\frac{C}{(1-e^{-\mu t})} \qquad [1]$$

A standard containing m millicuries of S^{35} gave C_m counts/min with the same geometry. This standard was sufficiently thin that the neglect of self-absorption does not introduce a significant error. Then $C_m = km$ and

$$P = \frac{mW}{S}\,\frac{\mu}{p}\,\frac{1}{(1-e^{-\mu t})}\,\frac{C}{C_m} \qquad [2]$$

The results of the nickel absorption measurements; $\log_{10}$ (count rate) plotted against absorber thickness (mg/cm^2) gave a line which was slightly convex away from the axes for a range of absorbers up to 10.7 mg/cm^2. A mean mass absorption coefficient was calculated from the gradient of the best straight line through the experimental points using the method of least squares. This gave μ/P = 2.303 x 0.132 = 0.304 cm^2/mg. For disks A, B, C, Table II, S = 0.414/0.5 x 10^{-3} = 0.828 x 10^3 mc/mole and for disk D 0.828 x 10^4 mc/mole. For disk A $(1-e^{-\mu t})$ = 0.986. The standard source of 0.104 microcuries of S^{35} gave 1012 counts/min.

$$P = \frac{0.104 \times 10^{-3} \times 58.7 \times 0.304 \times 10^3}{0.828 \times 10^3 \times 0.986}\,\frac{8612}{1012}$$

$$= 19.4 \times 10^{-3} \text{ atoms S/atom Ni}$$

Results for the other disks, Table II, column 7, have been calculated similarly.

The plating on disk H, Table I, was removed from the mild steel disk and the same area of plating counted from both sides. The activities measured from the two sides differed by 5.5%. The error introduced by the assumption that the sulfur is uniformly distributed in the plating is likely to be of similar magnitude.

The activities of disks E, F plated using labeled sulfate were E, 71.5, and F, 53.8 counts/min/cm^2. 16 mc of labeled sulfate were added to 500 ml of plating solution. The plating thickness at the centers of the disks was 27.7 μ and the activity of a standard which contained 0.032 μc of S^{35} was 3865 counts/min. The weight of this standard (0.1 mg/cm^2) showed that the neglect of self-absorption did not introduce a significant error.

These results give sulfur/nickel atom ratios, calculated using Eq. [2], of 0.33 and 0.25 atoms S/10^3 atoms Ni, respectively, taking the total concentration of sulfate in the plating bath as 1M. A nickel deposit plated under the same conditions was analyzed chemically for sulfur and gave a value of 0.37 atoms S/10^3 atoms Ni.

The autoradiographs, Fig. 2 and 4, show the distribution of sulfur incorporated in nickel plated on a rough surface. The plating on disks G and H was bright, and the original scratch lines still showed on G but did not show on H. Figure 2 shows an enlargement of an autoradiograph of disk G.

Table II

Disk	Current density, amp/dm^2	Total thiourea conc., gmole/l	Total wt. of nickel deposited, g	Plating thickness at center of disk, μ	Plating thickness at center of disk, mg/cm^2	Count rate, c/min/cm^2	Atoms S per 10^3 atoms Ni
A	8.6	10^{-3}	0.321	15.8	14.16	8612	19
B	4.3	10^{-3}	0.474	(24.8) *	22.17	16080	35
C	0.86	10^{-3}	0.488	34.7	30.9	30630	68
D	4.3	10^{-4}	0.482	24.3	21.6	18850	4

* Estimated by comparing the thicknesses on disks C, D and the total weights of nickel deposited on disks B, C, D.

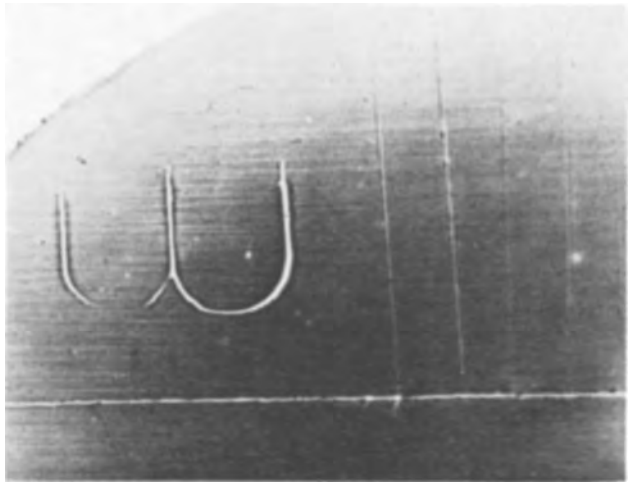

Fig. 2. Autoradiograph (5X before reduction for publication) of nickel plated on disk G which had parallel scratches in one direction. Center line average roughness of fine scratches 1.17 μ.

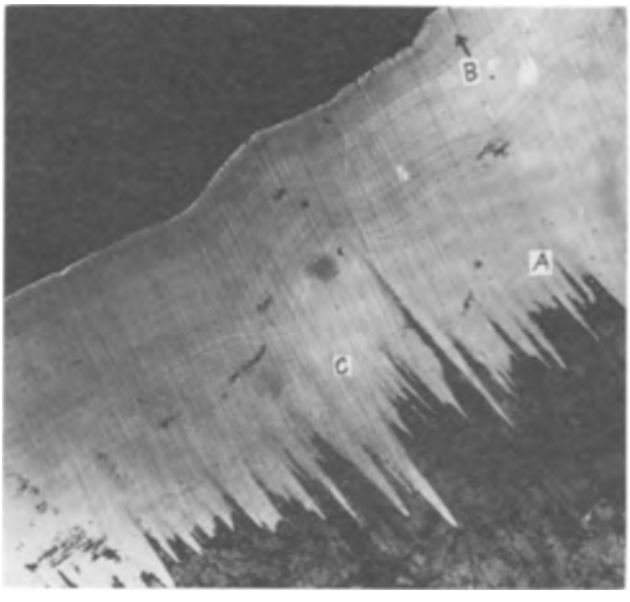

Fig. 3. Micrograph (150X over-all before reduction for publication) of a 5° taper section through nickel plated on a rough surface.

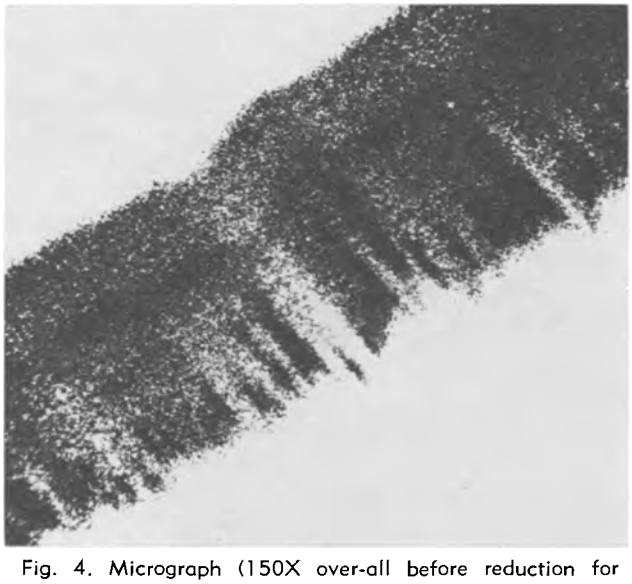

Fig. 4. Micrograph (150X over-all before reduction for publication) taken from an autoradiograph of the taper section shown in Fig. 3.

The taper section was cut from disk K which was plated at an apparent current density of 3.97 amp/dm^2 and its activity corresponded to an incorporation of 44 atoms S/10^3 atoms Ni, in agreement with earlier results (Table II). Figure 3 shows a micrograph of a taper section from disk K, and Fig. 4 is a micrograph at the same magnification taken from an autoradiograph of the section. In Fig. 3 and 4, sectioning at 5° increases the magnification perpendicular to the plane of the plating approximately eleven times. Figure 5 shows the principal features of part of the profile shown in Fig. 3 from which the extra magnification perpendicular to the plane of plating has been removed.

Discussion

Incorporation of sulfur–effect of current density.— The autoradiographs of the Hull cell cathodes show that considerable amounts of sulfur activity are associated with the nickel plated surface, and the cathode plated in the agitated bath shows clearly that the most active areas are those where the current density is lowest. A similar variation of incorporation with current density occurs on the cathode plated in the unagitated bath. High sulfur activity on plated specimens might arise from a uniform thin layer of sulfur-rich metal deposited in the initial stages of plating, which is subsequently covered by nickel containing less sulfur. Then, since the plating is thinner in regions of lower current density, less sulfur β-radiation would be absorbed in these regions, and they would appear to be regions of higher sulfur activity. This possibility was eliminated by plating another Hull cell cathode for 1 min, with the result that very little activity was found on the plate.

Errors in the measurement of the count rate, the volume of stock solution of S^{35} thiourea, and the weight of inactive thiourea added to the bath will introduce errors in the relative values of the sulfur/nickel atom ratios, Table II column 6. These errors are probably less than 10%. The radiochemical

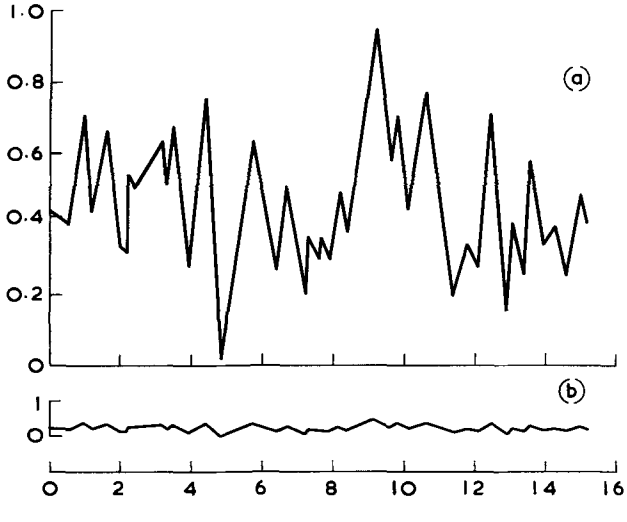

Fig. 5. Scale diagrams of the profile of the surface before plating (a) as seen in the taper section (b) when the additional 11X magnification introduced by the 5° angle of sectioning has been removed. 1 unit = 28 μ.

analysis gives results for a small area at the center of each disk. The plating thickness and therefore the current density decrease from the edge toward the center of a disk, and autoradiographs of the disks show more activity toward their centers. All the results reported in this paper show that incorporation of sulfur varies with current density so differences in current density distribution between disks can affect the relative values of the S/Ni ratios determined at the centers of the disks. The variations in plating thickness, Table II, show that there are appreciable differences in current density distribution between disks, and these differences will introduce errors in the relative values of the S/Ni ratios. The results on the Hull cell cathodes, Fig. 1, show that the amount of incorporation depends on agitation. The conditions of agitation for plating the disks were standardized as far as possible, but differences in agitation between different disks will also introduce errors in the relative values of the S/Ni ratios. It is difficult to assess the total error in the relative values of the S/Ni ratios introduced by differences in current density distribution and agitation, but the error is unlikely to be comparable with the differences in the ratios found for the disks, Table II. Therefore a comparison of the S/Ni ratios provides further qualitative evidence that incorporation of sulfur increases with decreasing current density.

The Hull cell cathodes show that incorporation varies greatly with agitation. Therefore the absolute magnitude of a S/Ni ratio is appropriate only to the particular plating conditions used for the disks.

The results for the incorporation of sulfur from sulfate are less accurate because of the much smaller quantities of sulfur involved.

The S/Ni ratios obtained from the disks show an increase in incorporation with decreasing current density, and autoradiographs of the disks show more activity toward their centers where the thickness of plating shows that the current density was lower than near the edges.

Since in all experiments incorporation was measured by the sulfur^{35} activity, no conclusions may be drawn concerning the chemical form in which sulfur is incorporated.

The deposit on the Hull cell cathode plated in the unagitated bath was much less bright and the general level of incorporation of sulfur much lower than on the cathode plated in the agitated bath. This suggests that brightening and incorporation may both be strongly controlled by the diffusion of thiourea through the solution boundary layer at the metal-solution interface.

Th results obtained using plating solutions containing labeled sulfate anions but no thiourea show that the incorporation of sulfur from sulfate is very much less than from thiourea.

Distribution of incorporation on a rough surface.— The nickel plating on disks G and H showed that thiourea was acting as a brightener and leveler. The scratches on disk G were not completely leveled by the plating, and the corresponding autoradiograph, Fig. 2, shows that, under these conditions, the incorporation of sulfur does not occur uniformly. The finer scratches on disk H were leveled completely, and the incorporation of sulfur showed no fine structure. This suggests that the incorporation depends on the surface profile and is higher either on the peaks or in the valleys. Now leveling requires the time averaged current density to be lower on the peaks than in the valleys, and a comparison of the micrograph and autoradiograph of the taper section (Fig. 3 and 4) shows that incorporation is much higher on the peaks than in the valleys. Therefore high incorporation is again associated with low current density. The dark "tails" to the peaks which show in the micrograph, Fig. 3, may result from the high incorporation of sulfur at these points.

As plating proceeds, the incorporation on peaks becomes weaker and is replaced by a more uniform incorporation which may be layered parallel to the plane of the plating.

Figure 4 suggests a layer of high incorporation immediately above the incorporation on the peaks and one, or possibly two, faint layers above it which appear more clearly when the autoradiograph is examined at a lower magnification. The depth of nickel perpendicular to the autoradiographed surface of the taper section increases linearly from zero at the outside edge of the section to a maximum of ca. 30 μ at the brass-nickel interface. Since the maximum range of S^{35} β-particles in nickel is 35 μ the intensity of radiation per unit area of this surface, and hence the photographic density would decrease monotonically across the autoradiograph of the section for a uniform distribution of sulfur in the plating. Therefore the dark bands which are apparent in the autoradiograph suggest that there are layers of higher sulfur incorporation in the plating. No incorporation of sulfur occurs in the initial filling of the valleys, and at C, where the outside profile of the plating shows that the two large valleys have not been completely leveled, incorporation is lower than at points where leveling is complete. Considerable incorporation of sulfur, showing some layering, occurs in the banded region of the plating. Although the resolution of the autoradiograph is not sufficient in general to show a detailed correlation between incorporation and the banding shown in the micrograph, the three short dark bands at A appear as regions of higher incorporation. At B, curvatures of successive bands and the outside profile of the plating show that local deleveling occurred a short time before the plating was stopped. There is a suggestion in the autoradiograph that the onset of deleveling may have been associated with a local reduction of incorporation.

The results and autoradiographs discussed above show that considerable incorporation of sulfur occurs when nickel is electrodeposited in the presence of thiourea, and that the incorporation increases with decreasing current density in systems where the current density distribution is determined either by the external electrical circuit, or the geometry of the system, as in the Hull cell, or the behavior of thiourea on a rough surface.

When the nickel is deposited on a surface having a roughness comparable to that encountered technologically, the incorporation occurs on the peaks of

the surface, in agreement with Beacom and Riley (1) whose results were obtained on a much larger scale of surface roughness. The layering of incorporated sulfur in regions of the plating where the micrograph shows a laminar structure supports the suggestion by Vanderkooi (3) that layering of the deposit may be associated with the incorporation of additive or compounds derived from it.

Acknowledgments

The authors wish to thank Dr. G. B. Cook and Mr. U. F. Marx for their help and encouragement, and Messrs. Wilmot-Breeden for the provision of experimental facilities and permission to publish this paper.

Manuscript received Aug. 31, 1959.

Any discussion of this paper will appear in a Discussion Section to be published in the June 1961 JOURNAL.

REFERENCES

1. S. E. Beacom and B. J. Riley, *This Journal*, **106**, 309 (1959).
2. E. Bleuler and G. J. Goldsmith, "Experimental Nucleonics," p. 84, Rinehart Publishing Co. (1952).
3. N. Vanderkooi, Doctoral Dissertation, Wayne State University (1958).

(Zn,Hg)S and (Zn,Cd,Hg)S Electroluminescent Phosphors

A. Wachtel

Research Department, Westinghouse Electric Corporation, Bloomfield, New Jersey

ABSTRACT

Solid solutions of (Zn,Hg)S prepared by firing in sealed silica tubes are cubic in structure. With suitable additions of Cu and a coactivator, photoluminescence and electroluminescence are obtained. The coactivators used were halides, Ga, or In. The electroluminescence in the red consists of two emission bands which do not appear to be analogous to the blue and green emission bands of Cu, Cl in ZnS. The quantum efficiency is of the same order of magnitude as that of ZnS:Cu, Cl, but the emission bandwidth is about twice as large and the red electroluminescence consists of emission located to a large extent in the infrared. HgS tends to retain the cubic structure of ternary (Zn, Cd, Hg)S systems provided that the Cd/Hg ratio does not exceed certain limits; until this is so, the introduction of Cd causes increased electroluminescence.

Efforts to prepare EL[1] phosphors emitting at longer wave lengths are usually based on substitution of lattice constituents so as to effect lattice expansion. In ZnS:Cu EL phosphors of Se for S has been investigated by Prener (1) and by Hegyi, Larach, and Shrader (2). Zn(S, Se) and ZnSe constitute good EL phosphors, although the frequency dependence of ZnSe:Cu is large compared to that of ZnS:Cu, so that the low-frequency response is unusually poor.

On the other hand, substitution of Cd for Zn has been shown to result in hexagonal systems with exceptionally poor EL response (3). It is therefore obvious that the effect of substitution of Zn by the next heavier member of the group IIB elements, namely Hg, was of interest. Due to the low sublimation temperature of HgS, its retention in ordinary firing at atmospheric pressure is known to be impossible at temperatures sufficient to cause activator incorporation. Wesch (4) has described a high-pressure furnace by means of which the preparation of pure HgS phosphors was mentioned. Kremheller and Levine (5) prepared (Zn, Hg)S and (Cd, Hg)S solid solutions by aqueous recrystallization under pressure and at temperatures well above the normal boiling point of water, and in a recent publication Kremheller, Levine, and Gashurov (6) describe some of the photoluminescent properties of activated (Zn, Hg)S and (Cd, Hg)S prepared by this method. In the present investigation, the mixed sulfides were prepared by firing in evacuated and sealed silica tubes. Although the pressure developed in the tubes is unknown, the application of hydrostatic pressure from the outside was not found to be necessary.

[1] Electroluminescence or electroluminescent is hereafter abbreviated EL.

Experimental Technique

In addition to the raw materials already described (3), HgS, Ga_2S_3, and In_2S_3 were used. HgS was prepared by reaction of the elements. Ga_2S_3 was prepared by slurrying ZnS with $Ga(NO_3)_3$ solution, drying, and firing in an atmosphere of H_2S. In_2S_3 was precipitated from aqueous solution in the presence of a ZnS carrier, filtered, and dried.

In order to avoid the development of excessive pressure in the sealed tubes, as well as to avoid the influence of gases not normally retained in firings at atmospheric pressure, it was necessary to accomplish complete thermal degassing and decomposition of volatile matter (NH_4-salts, acetate radical) prior to sealing the final mixture into the tubes. All firings were therefore conducted in two stages:

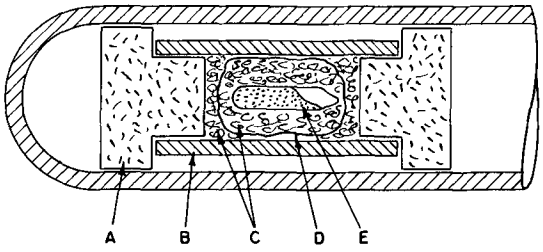

Fig. 1. Technique for firing phosphors with HgS. A, Fire brick; B, mullite tube; C, silica wool; D, silica cloth; E, firing tube.

1. A normal blue or green emitting ZnS:Cu EL phosphor is prepared at atmospheric pressure by known methods (3). The Cu-acetate and NH_4-halides (if any) decompose, and activator incorporation takes place. Traces of H_2O and air are expelled and particle growth of the ZnS facilitates subsequent degassing. The fired phosphor is, however, not washed in NaCN solution since the total amount of Cu added (now partially present as free Cu_2S) is required for the final synthesis of the mixed (Zn, Hg)S EL system.

2. The above product, hereafter referred to as the singly fired phosphor, is mixed with HgS as well as a small amount of S calculated to produce only a few atmospheres of pressure at the subsequent firing. This sulfur addition is necessary since traces of residual air would cause oxidation of S^{2-} and give rise to S-vacancies[2] and poor EL performance of the finished product. The mixture is transferred to a silica tube of 7 mm ID, 9 mm OD, and 40 mm length, closed at one end and provided with a constricted neck at the other end. The tube is evacuated by means of a mechanical oil pump for about 30 min and then sealed at the constriction. The sealed tube is fired at 900°C as shown in Fig. 1.

The thermal insulation afforded by the silica wool packing, as shown in the figure, is necessary to prevent separation of part of the HgS during cooling. The presence of CdS greatly diminishes this effect, and still more homogeneous products may be obtained by allowing the entire assembly to cool in the furnace, although this was rarely done because of obvious considerations of time limitation. Refiring times of 2 hr were found to be sufficient.

The washing procedure in NaCN solution is the same as used for normal green-emitting ZnS:Cu EL phosphors. Because of the small samples (about 2 g) usually prepared, simple grinding in a mortar and pestle was preferred. All figures for Cu and halide in phosphors specifically refer to amounts added before firing, and not to final compositions.

Measurements were performed with a Spectra Brightness Spot Meter,[3] using a demountable castor oil cell. In order to meet the contract requirements as to color, additional measurements were also taken with a red (NBS #3215) filter inserted in the optical path. The ratio between the respective readings served as a sensitive indication of emission color, and it was noted that small differences in this ratio caused large differences in brightness. To enable a valid interpretation of the relative performance of phosphors emitting with different colors, it was therefore necessary to compensate for this effect. The method used consisted of preparing phosphors that differed only in base lattice composition and plotting their relative brightness (based on 100% for the specified color) as a function of the filter ratio. Data on experimental phosphors could then be corrected to yield values hereafter referred to as "normalized brightness."

[2] In the presence of HgS, such reducing conditions result in the formation of metallic Hg, visible as a separate phase.

[3] Photo Research Corp., Hollywood, Calif.

Table I. Unit cell dimensions of cubic (Zn,Hg)S:Cu,NaCl phosphors

Mole % HgS	a (Å)
0	5.406
5	5.429
10	5.443
15	5.469
20	5.486
25	5.516
30	5.532
40	5.569
60	5.665
80	5.745

Results

Photoluminescence of (Zn:Hg)S phosphors.—Some basic information was obtained by firing photoluminescent ZnS:Cu (0.01%):NaCl phosphors with increasing additions of HgS at 750°C. Table 1 shows the unit cell dimensions obtained by x-ray powder diffraction. All phosphors (up to 80% HgS) were cubic, although the HgS used was hexagonal. HgS alone similarly fired was also hexagonal. The values can be plotted to give a reasonably good fit to a straight line. Figure 2 shows the emission spectra (3650Å excitation) as obtained on a Perkin-Elmer Universal Spectrometer. Figure 3 shows the diffuse reflection spectra in the near ultraviolet and visible regions obtained by illuminating through a Farrand monochromator and measuring the reflected radiation with a Bausch and Lomb monochromator adjusted to the same wave lengths. It may be noted that the regular manner in which the spectra shift to longer wave lengths is very similar to the effect of Cd substitution. The shift in emission caused by Hg is about four times greater than that caused by similar concentrations (in mole %) of Cd. It was noted that at low Hg concentration (5 mole %) the fluorescence was unusually weak.

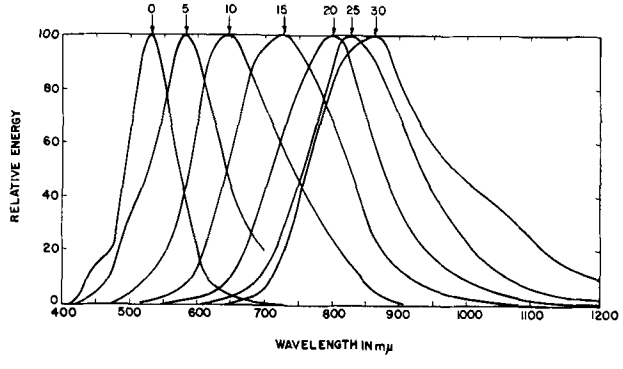

Fig. 2. Emission spectra of (Zn, Hg)S:Cu, NaCl phosphors. Numbers denote mole % HgS in phosphors. Excitation = 3650Å.

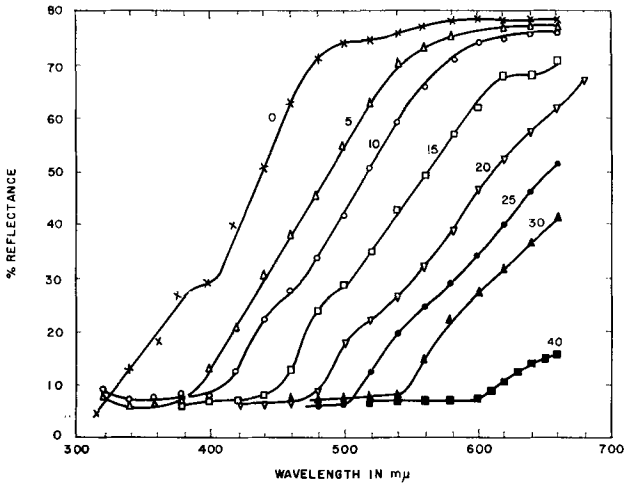

Fig. 3. Diffuse reflection spectra of (Zn, Hg)S:Cu, NaCl phosphors. Numbers denote mole % HgS in phosphors.

The decreasing concentrations of Cu and Cl resulting from increasing additions of HgS were not considered to appreciably influence the shape of the emission and reflection spectra, because Cl was present in excess and only the long wave-length emission band was developed.

Electroluminescent phosphors.—The activator requirements for EL are known to be greater than for photoluminescence. For the systems under investigation, they were also noted to vary with the type of coactivator used. In the case of Cl, additions of the order such as to produce optimum green-emitting singly fired ZnS:Cu, Cl phosphors proved to be too high not only for Cl, but also for Cu. Figure 4 shows the emission spectra of a series of (Zn, Hg)S:Cu(0.2%), Cl(0.075%) phosphors excited at 10,000 cps. The activator additions are such that the ZnS:Cu, Cl phosphor emits predominantly the blue Cu band and are optimum with respect to the orange or red emitting compositions. The emission band gradually shifts to longer wave lengths and broadens until above about 20 mole % Hg, a long wave length emission band increases quite suddenly in relative intensity. It will be shown that this cannot necessarily be identified with the "Cu-green" band emitted in more highly coactivate ZnS-Cu phosphors.

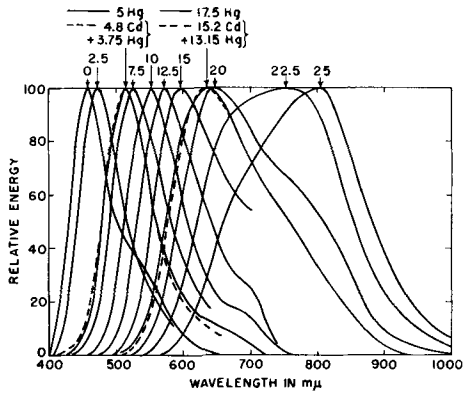

Fig. 4. Emission spectra of (Zn, Hg)S:Cu (0.2%): Cl(0.075%) and two (Zn, Cd, Hg)S:Cu (0.2%:Cl (0.075%) EL phosphors. Numbers denote mole % HgS in samples. Excitation = 10,000 cps.

The effect of Cd on the emission color was determined empirically for orange to deep red emitting (Zn, Hg)S. It was noted that the emission color of [(1 − x)Zn, xHg] S:Cu may be duplicated approximately by firing [(1 − 4n)Zn, 4nCd] S:Cu and refiring this with (x − n)HgS. However, substitutions of more than half of the original concentration of Hg by Cd result in a shift to longer wave lengths. Table II shows the effect on EL brightness of a series of orange-red emitting phosphors based on the original composition (0.8Zn, 0.2Hg)S:Cu (0.2%):Cl(0.075%). The table includes brightness readings of NaCN-washed aliquots of the singly fired (Zn, Cd)S:Cu, Cl phosphors. It also shows measurements by x-ray powder diffraction, so as to illustrate how in both cases the breakpoint in brightness coincides with the appearance of an appreciable percentage of hexagonal phase. These measurements also include values of interlattice spacings (d/n) of the 311 plane. Very similar results are shown in Fig. 5 on deep red emitting phosphors coactivated with Br + I or Ga and excited at 400 cps. This is in agreement with the observation made by Zalm (7), than in ZnS:Cu EL phosphors the cubic phase is preferable.

It can be seen that in all cases Cd increases the emittance of the system until interference by formation of hexagonal material occurs. It can also be

Table II. Effect of Cd/Hg ratio on structure and electroluminescence

First firing					Second firing					
							Brightness			
Mole % Cd used	Brightness 10,000 cps	Emission color	% Hex. phase	d/n, (311)	Mole % HgS added	Mole % Cd in phosphor	400 cps	10,000 cps	% Hex. phase	d/n, (311)
0	6.2	Blue	0	1.630	20	0	0.77	2.4	0	1.653
2	6.8	White-blue	0	1.633	19.5	1.7	0.68	3.5	0	1.653
4	3.5	Green-blue	4	1.634	19	3.2	0.89	3.95	0	1.656
8	1.8	Blue-green	27	1.638	18	6.6	1.10	3.8	0	1.660
16	0.055	Green-blue	100	1.649	16	13.4	1.49	4.9	0	1.665
20	0.024	Green-blue	100	1.654	15	17.0	2.01	5.55	7	1.668
24	0.014	Green-blue	100	1.660	14	20.6	1.16	3.3	43	1.671
28	0.008	Blue-green	100	1.664	13	24.4	0.22	0.17	100	1.677
32	0.006	Green	100	1.668	11*	28.8	0.12	0.25	100	1.679
64	—	—	100	1.707	0	64	—	0.15	100	1.710
72	Faint	Red	100	1.719						
80	Very faint	Red	100	1.728						

* Relationship of 1 Hg = 4 Cd begins to break down. Therefore, only 11 instead of 12 mole % HgS used.

seen that in the presence of HgS a much higher concentration of Cd is permissible before this occurs. The optimum substitution of Hg by Cd appears to be in the neighborhood of 20-25% of the original Hg concentration. Most of the ensuing investigations were therefore performed on such (Zn, Cd, Hg)S:Cu phosphors. The two dashed curves in Fig. 4 represent the emission spectra of (Zn, Cd, Hg)S:Cu, Cl phosphors in which 25% of the Hg was replaced by Cd in the manner outlined above. The compositions are based on original Hg concentrations of 5 mole % (green emission) and 15 mole % (orange emission) and are seen to coincide closely with the emission spectra of the respective (Zn, Hg)S:Cu, Cl phosphors, but the brightness was appreciably higher.

It has been mentioned that optimum additions of Cu and Cl were smaller than those found useful in green-emitting ZnS:Cu, Cl phosphors(3). It was therefore interesting to note that the optimum addition of Br + I [4] was higher, namely similar to that for ZnS:Cu phosphors, although the estimated excess Cu_2S concentration still had to remain smaller than about 0.2 mole %. Such Br + I coactivated phosphors were about two to three times brighter than Cl-coactivated phosphors. In the case of Ga or In coactivation, phosphors were prepared with additions of Cu equal to 0.6 mole % more than the concentration of Ga or In added. Their normalized brightness, excited at 400 cps, increased linearly with coactivator concentration up to 0.125 mole % and then decreased. On the other hand, phosphors coactivated with 0.125 mole % Ga or In showed two brightness maxima with respect to Cu addition, as shown in Fig. 6. It can be seen that the first maximum is very sharp and more pronounced in the case of In coactivation. Prefiring at 1100°C [5] decreases the low Cu maximum. Ga-coactivated phosphors prefired at 1100°C show only a gradual increase in brightness, leveling off at about 1 mole % Cu.

Figure 7 shows the brightness of Br + I and of Ga coactivated (Zn, Cd, Hg)S:Cu phosphors as a function of Cd + Hg concentration. The activator concentrations are not optimized for either system but chosen so that the total Cu addition as well as the green emission color of the ZnS:Cu phosphors are the same. It is interesting to note that in the case of Br + I coactivation there occurs the same initial drop in output at low Hg concentrations as has been observed in the photoluminescent as well as the Cl-coactivated EL phosphors, while, on the other hand, the Ga-coactivated ZnS:Cu is characterized by comparatively poor output, presumably because of the greater trap depth caused by Ga (8, 9). Introduction of Cd + Hg [6] causes an increase in brightness well beyond the point of maximum luminosity (yellow green). This means that, except for the initial drop noted with halide coactivation, the radiant output of the phosphors increases at least up to the point of maximum observed brightness and possibly beyond that. In the case of Ga-coactivation, this might be explained by decreasing trap depth due to lowering of the conduction band, assuming that a similar effect occurs as noted by Klasens for Cd substitution (10). Unfortunately, the

[4] Equimolar mixtures of NH_4Br and NH_4I yielded slightly better results than NH_4Br alone. However, only a very small fraction of the added I^- is retained, so that additions were based on Br^- alone.

[5] To compensate for decreased particle growth in the absence of halides.

[6] The same relationship was noted in the absence of Cd.

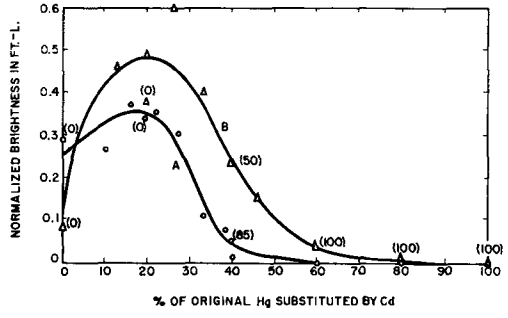

Fig. 5. Normalized brightness of (Zn, Cd, Hg)S:Cu phosphors as a function of Cd/Hg ratio. A, Compositions based on (0.81 Zn, 0.19 Hg)S:Cu(0.4%), (Br + I)(0.46%); B, compositions based on (0.85 Zn, 0.15 Hg)S:Cu(0.9%), Ga(0.13%) Numbers in parentheses denote % hexagonal phase present. Excitation = 400 cps. Groups A and B approximately match in emission color.

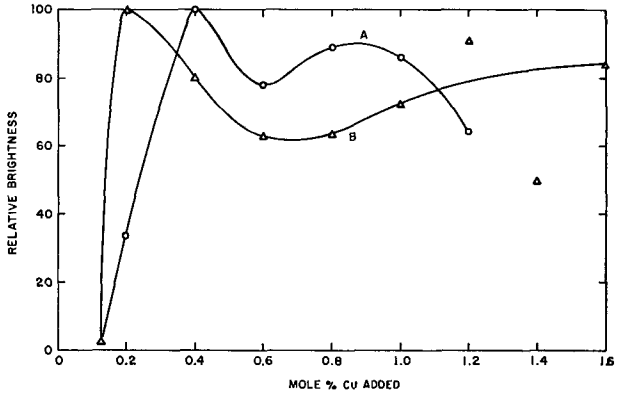

Fig. 6. Normalized relative brightness of red-emitting A:(Zn, Cd, Hg)S: x Cu: 0.125 mole % Ga and B: (Zn, Cd, Hg)S x Cu: 0.125% In phosphors as a function of Cu addition. Excitation = 400 cps.

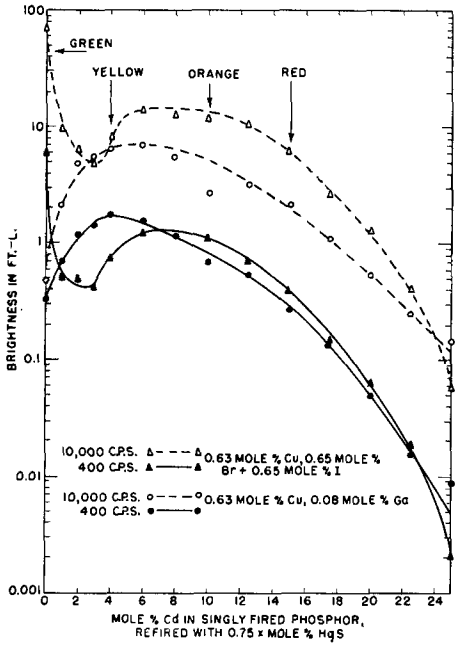

Fig. 7. Brightness and emission colors of (Zn, Cd, Hg)S:Cu phosphors as a function of base lattice composition.

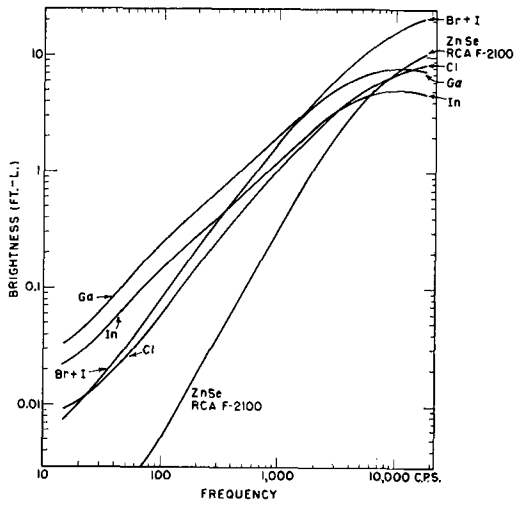

Fig. 8. Brightness of orange-red emitting (Zn, Cd, Hg)S:Cu phosphors with different coactivators and of ZnSe:Cu as a function of frequency.

scope of the present investigation did not permit independent measurements of radiance (such as by thermopile) or glow curves for these samples.

An indication of decreasing trap depth with increasing Cd + Hg concentration was noted, however, by visual observation of thermoluminescence. Similarly, a comparison of the frequency dependence of typical red-emitting phosphors as shown in Fig. 8 indicates decreased output of Ga and In coactivated phosphors at frequencies where no such decrease is evident with halide coactivated phosphors. It should be mentioned that at the red end of the spectrum, the usual variation in emission color with frequency represents variations in brightness which may be more pronounced than in the case of green-emitting phosphors, and that this effect therefore increases the slope of the frequency dependence curves. The phosphors were selected so that at intermediate frequencies their emission color approximately matches that of the ZnSe:Cu phosphor also shown in Fig. 8 for comparison. Therefore they do not necessarily represent specimens suitable for comparison of brightness as a result of optimum conditions of preparation.

It was of obvious interest to determine the actual quantum yield and efficiency of the red phosphor in comparison to a standard green-emitting ZnS:Cu, Cl EL phosphor. The following samples were selected for this purpose:

1. (0.754Zn, 0.133Cd, 0.113Hg)S:Cu, Ga prepared from (0.85Zn, 0.15Cd)S:Cu(0.9%), Ga (0.13%) by refiring with 11.25% HgS. Emission color, red.
2. (0.6945Zn, 0.163Cd, 0.1425Hg)S:Cu, Ga prepared from (0.81Zn, 0.19Cd)S:Cu(0.9%), Ga (0.13%) by refiring with 14.25% HgS. Emission color, deep red.
3. A normal ZnS:Cu, Cl green emitting phosphor.

Each phosphor was operated at 400 cps in the same castor oil cell and the brightness and power consumption measured as a function of applied voltage. In addition, each phosphor while in the same cell was operated at 400 cps and 600 v and the spectral distribution determined, using the same slit width and amplification of the spectrometer. The absolute heights of the resultant curves were therefore comparable. These were corrected for energy, quanta, and luminosity, but not normalized to equal peak heights. Table III gives the integrated values. It is apparent that under similar conditions of excitation the output in energy or quanta for the red phosphors is considerably smaller than for the green phosphor. Nevertheless, the differences in luminosity are much greater and are the main reason for the low brightness presently obtainable with the red-emitting phosphor.

The actual quantum yield was determined according to[7]

$$K = \frac{B\,A\,Q \times 10^{17}}{1.26L}$$

where K is the number of quanta emitted per second, A is the area of the cell in cm², Q is the integrated quantum output, L is the luminosity factor of the spectrum, and B is the brightness in foot-lamberts. Table IV shows the data calculated for each phosphor operating at the voltage where maximum luminous efficiency was observed. It can be seen that the quantum efficiency of the red-emitting phosphor is comparable to that of ZnS:Cu, Cl.

Efforts to increase the brightness without change in emission color appeared to require a narrowing of the spectral distribution with particular emphasis on increasing its slope on the short wave length side. It is well known that in ZnS:Cu phosphors either the blue or the green emission band can be

[7] Let the number of quanta emitted/cm²-sec $= K = \int \frac{C}{h\nu}\cdot\frac{dE}{d\lambda}\,d\lambda$, where C is a constant introduced to correct the arbitrary units in which the spectrum is measured to watts/cm². Then,

$$K = \frac{C}{hc}\int \lambda \frac{dE}{d\lambda}\,d\lambda = \frac{C\,Q}{hc}$$

The constant C may be determined from the measured brightness B (in foot-lamberts) and the spectral distribution as follows:

$$B(\text{ft-L}) = \frac{680\ \text{lpw}}{A\ (\text{ft}^2)}\int Cy\frac{dE}{d\lambda}d\lambda = \frac{680\times 929C}{A\ (\text{cm}^2)}\int y\frac{dE}{d\lambda}d\lambda = \frac{680\times 929CL}{A}$$

Therefore,

$$C = \frac{AB}{680\times 929L}$$

Since $hc = 1.99 \times 10^{-16}$ erg $= 1.99 \times 10^{-23}$ watt-sec,

$$\frac{Q}{1.99\times 10^{-23}}\cdot\frac{AB}{680\times 929L} = \frac{B\,A\,Q\times 10^{17}}{1.26L}$$

Table III. Integrated emission spectra of three phosphors excited in 60μ castor oil cell at 400 cps and 400 v

	Energy $E = \int \frac{dE}{d\lambda}d\lambda$	Quanta $Q = \int \lambda\frac{dE}{d\lambda}d\lambda$	Luminosity $L = \int y\frac{dE}{d\lambda}d\lambda$
Sample No. 1 (red emission)	102.9	77.6	1.36
Sample No. 2 (deep red emission)	166.6	134.8	0.28
ZnS:Cu, Cl (green emission)	472.1	257.0	290.7

Table IV. Output and efficiency of three phosphors excited in 60μ castor oil cell at 400 cps and optimum voltage. Area of cell = 10.8 cm^2

	Voltage, v	Brightness, ft-L	Watts	Lumens/watt	Quanta/sec	Quanta/sec watt
Sample No. 1 (red emission)	350	1.1×10^{-1}	6.4×10^{-4}	2.0×10^{-2}	4.3×10^{18}	6.7×10^{21}
Sample No. 2 (deep red emission)	300	7.2×10^{-3}	1.51×10^{-4}	5.6×10^{-3}	2.35×10^{18}	1.55×10^{22}
ZnS:Cu, Cl (green emission)	350	3.66	1.63×10^{-4}	2.6	2.3×10^{18}	1.4×10^{22}

isolated by employing very low or sufficiently high ratios of coactivator to activator. If the broad spectral distribution of the red-emitting phosphors is the result of superimposed emission bands shifted to longer wave lengths but arising from the same centers, then similar variations in activator proportions should also influence the spectral distribution of the red-emitting phosphor in the same manner. Figure 9 shows, however, that this was not observed. The phosphors represented in the figure were prepared in an effort to maintain approximately the same emission color as measured by means of the filter ratio discussed above. This was reasonably successful but required that with increasing coactivator addition, the concentration of Cd+Hg had to be lowered. Nevertheless, the short wave-length emission band increases with such decreasing Cd+Hg concentration and is quite pronounced at a high coactivator concentration such as to result in only the green-emission band in ZnS:Cu phosphors. The increased brightness obtained at higher Br+I addition may now be explained at least partially by the increased slope of the short wave-length side of the emission spectrum.

Discussion

Perhaps the most important question concerning this study is why substitution of Zn by Hg results in good EL at emission colors similar to the photoluminescence emission colors of the respective phosphors, while substitution of Zn by Cd does not. For (Zn, Cd, Hg)S phosphors with a sufficiently high ratio of Cd/Hg so as to effect a decrease in EL, no evidence of a separate (Cu, Cd)S phase (3) could be observed. Therefore, the only clue in this direction is offered by the difference in crystal structure of the two systems.

It has been noted that hexagonal and cubic ZnS:Cu, Cl phosphors prepared with low Cu concentration (such as 0.01 mole %) perform about

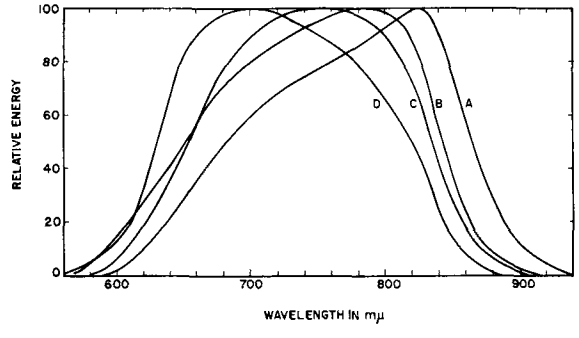

Fig. 9. Emission spectra of (Zn, Cd, Hg)S:Cu phosphors as o function of composition. Excitation = 400 cps. (A), 20.3% Cd, 18.7% Hg, 0.01% Br + 0.01% I; (B), 15.9% Cd, 13.8% Hg, 0.1% Br + 0.1% I; (C), 14.8% Cd, 11.1% Hg, 0.3% Br + 0.3% I; (D), 11.1% Cd, 9.3% Hg, 0.7% Br + 0.7% I.

equally well under artificially induced contact-EL (11). It must therefore be concluded that the better EL performance of cubic (Zn, Hg)S or cubic (Zn, Cd, Hg)S, as compared to the poorer performance of hexagonal (Zn, Cd)S or (Zn, Cd, Hg)S phosphors, results from differences in the means of EL excitation only. In the former case, the field intensifying Cu_2S inclusions are present and active. If in the latter case they are also present, then they are not active, possibly as a result of the different electrical nature of the barrier represented by the nonisomorphic junctions.

The sharp minimum in EL noted at low concentration of Hg is accompanied by a similar minimum of photoluminescence. At present, its appearance can not be explained. Inspection of Fig. 3 shows, however, that the weakly emitting (0.95 Zn, 0.05 Hg)S:Cu, Cl phosphor lacks the secondary hump in reflectivity near the absorption edge. According to an investigation by Froelich (12) the introduction of small amounts of Cu causes just such a hump in the diffuse reflection spectrum of ZnS. This suggests the possibility that at such critically low concentration of Hg, the incorporation of Cu is somehow hindered.

The identity of the long wave-length emission band is questionable since it is favored not by high coactivator concentration (as in ZnS:Cu) but by high Hg concentrations. Bowers and Melamed (13) proposed that the blue emission in ZnS:Cu, Cl may be identified with the "self-activated" blue caused by Zn-vacancies. It now appears that introduction of a sufficient concentration of Hg results in increasing probability that the vacancy becomes a Hg-vacancy. The decreased population of Zn-vacancies would result in the disappearance of the short wave-length band in favor of a different emission band as shown to occur quite abruptly in Fig. 4 and 9. Figure 2 shows that there is also slight evidence that a similar phenomenon occurs with low-Cu photoluminescent phosphors which are sufficiently coactivated so as to give rise to predominantly green (long wave-length band) emission in ZnS.

According to this mechanism, a similar phenomenon should occur on substitution of Zn by Cd. This, however, has not been reported. Instead, Van Gool (14) noted the opposite, namely, a relative increase in the short wave-length emission band of (Zn, Cd)S:Ag phosphors occurring with increasing Cd concentration. These measurements, however, were taken at 77°K while, with increasing temperature, the short wave-length emission band was more rapidly quenched. It is therefore also possible that the increase of relative intensity of the long wavelength emission band with increasing concentration of Hg is caused by increasing thermal quenching of

the short wave-length emission band. The characteristics of the two emission bands in red-emitting (Zn, Hg)S:Cu phosphors are such that at present, no definite conclusions can be drawn as to their origin.

Summary

Introduction of Hg into ZnS:Cu phosphors causes a shift in emission to longer wave lengths which, for moderate substitutions, is about four times as high as that caused by similar molar concentrations of Cd. At sufficient activator concentrations, EL is observed. For compositions emitting in the red end of the spectrum, the quantum efficiency of the EL was found to be of the same order of magnitude as that of green-emitting ZnS:Cu, Cl. This is attributed to the cubic modification of the system, as favored by the presence of HgS, even in ternary (Zn, Cd, Hg)S composition whose concentration of Cd would, in the absence of Hg, result in hexagonal and non-EL systems.

Procedures for the preparation of (Zn, Hg)S and (Zn, Cd, Hg)S EL phosphors have been described. All procedures involve firings with HgS in sealed tubes, using only prefired raw materials. Especially for low-frequency excitation, the substitution of Hg for Zn enables the use of Ga or In as coactivators, presumably due to a decrease in trap depth caused by lowering of the conduction band. For phosphors emitting in the red end of the spectrum, the relative heights of the two emission bands are primarily dependent on Hg concentration. Their identity cannot necessarily be assumed in terms of an analogy with the blue- and green-emission bands in ZnS:Cu phosphors.

From a practical point of view, the (Zn, Hg)S:Cu and (Zn Cd, Hg)S:Cu EL phosphors are preferable to the ZnSe:Cu EL phosphors, mainly because of their better response at low frequencies of excitation, the extent of which can be estimated roughly from Fig. 8. At higher HgS concentrations, EL emission occurring entirely in the infrared has been obtained; the writer does not know to what extent this can be accomplished with (Zn, Cd)Se:Cu EL phosphors. A serious disadvantage is, however, the high volatility of HgS which necessitates special techniques of phosphor preparation.

Acknowledgments

The writer wishes to thank Miss I. Walinski for preparation and brightness measurements of the phosphors, Mr. I. Meister for determinations of spectral distributions, Dr. C. K. Lui-Wei for x-ray diffraction measurements, and Dr. W. Lehmann for determinations of luminous efficiencies. Thanks are also due to Dr. H. F. Ivey for reading and suggesting improvements of the original manuscript.

Manuscript received March 11, 1960. This paper was prepared for delivery before the Chicago Meeting, May 1-5, 1960. This work was supported by Contract AF33(616)-5811 from the Wright Air Development Center.

Any discussion of this paper will appear in a Discussion Section to be published in the June 1961 JOURNAL.

REFERENCES

1. J. S. Prener, U. S. Pat. 2,731,423, Jan. 17, 1956.
2. I. J. Hegyi, S. Larach, and R. E. Shrader, *This Journal*, **104**, 717 (1957).
3. A. Wachtel, *ibid.*, **107**, 602 (1960).
4. L. Wesch, Reichsamt Wirtschaftsausbau Chem. Ber. Investigation No. 15 (PB 52016) pp 487-501 (1942).
5. A. Kremheller and A. K. Levine, *Sylvania Technologist*, **10**, No. 3 (1957).
6. A. Kremheller, A. K. Levine, and G. Gashurov, *This Journal*, **107**, 12 (1960).
7. P. Zalm, *Philips Research Repts.*, **11**, 353 (1956).
8. W. Hoogenstraaten, *This Journal*, **100**, 356 (1953).
9. C. Haake, *J. Opt. Soc. Am.*, **47**, 881 (1953).
10. H. A. Klasens, *This Journal*, **100**, 72 (1953).
11. W. Lehmann, *ibid.*, **104**, 45 (1957).
12. H. C. Froelich, *ibid.*, **100**, 496 (1953).
13. R. Bowers and N. T. Melamed, *Phys. Rev.*, **99**, 1781 (1958).
14. W. Van Gool, *Philips Research Repts.*, **13**, 157 (1958).

Crater Resistance of Submerged Arc Smelting Furnaces Simulated by a Simple Model

Oluf Chr. Bockman

Elektrokemisk A/S, Oslo, Norway

ABSTRACT

An electrolytic trough technique has been used to study the effect of size and shape of the smelting crater on the ohmic resistance of the crater of submerged arc smelting furnaces. The ohm-inch rule is demonstrated, and the correct use of this rule is discussed.

In designing submerged arc smelting furnaces, the anticipated ohmic crater resistance of the projected furnace is the key to the specification of the electrical circuit. Naturally, many workers have devoted themselves to the study of this problem. In 1933, Andrea pointed (1) out that the product of electrode diameter D and crater resistance R of electric smelting furnaces is fairly independent of furnace size. He defined a "peripheral ohm inch factor" r by

$$r = \pi DR \qquad [1]$$

Values of r for different smelting processes have been given by Udy [2] and by Kelly [3]. This factor has proved useful for calculating operating data in designing new furnaces and in scaling up results obtained by pilot tests.

Andrea apparently arrived at this rule empirically. He referred the crater resistance to the electrode periphery by introducing π in Eq. [1], presumably assuming that 1 in. of electrode periphery makes the same contribution to the conductance of the crater in small as well as in large furnaces.

Recently Morkramer (4) derived Eq. [1] by making the following simplifications. The current radiates hemispherically from the tip of the electrode; the charge has a uniform electrical resistivity; the distance from the tip of the electrode to the furnace bottom is very large. On making these assumptions, he demonstrates the r of Eq. [1] actually is the electrical resistivity of the charge.

The simplifications made by Morkramer are drastic. Equation [1] may, however, be derived by making quite a few much more realistic assumptions. This derivation is based on dimensional analysis as applied in the theory of models. Such a derivation may be of value in pointing out the limitations of Eq. [1].

Dimensional Analysis

The conditions prevailing in the smelting zone of an electric furnace are very complex. Actually, the physical properties of the zone and the variation of these properties within the zone are but little known. Probably, temperature and electrical resistivity vary within wide limits. Any calculation of crater resistance by classical methods therefore is bound to fail.

If it is assumed, however, that differently sized furnaces working on the same raw materials form geometrically and electrically similar systems, the theory of models may be used. These assumptions imply that the smelting craters of the furnaces compared have the same shape and the same size relative to electrode diameter and that corresponding points in the two furnaces show the same electric resistivity. Since electric resistivity depends on temperature and composition, corresponding points must also agree in these respects.

The electric current, on passing from the electrode to the charge, may form arcs. Even in submerged arc smelting furnaces the arcs may consume a part of the tip to hearth voltage. The arcs do not obey Ohm's law, the voltage varying in a complex manner which it is difficult to include in the dimensional analysis. The present derivation, therefore, is restricted to the cases where arcing is insignificant. It must also be assumed that the contact resistance between electrode and the charge is negligible. By the passage of the electric current through the charge, Ohm's law may safely be considered valid.

On these assumptions the ohmic voltage drop from the tip of the electrode to the furnace bottom may in principle be found by integrating along a current path according to

$$E = \int \rho i ds$$

where ρ is electric resistivity and i is current density at the increment ds of the path. The variation of ρ and i along the path is however not known. Similarly the electrode current may be found by integrating over any equipotential surface

$$J = \int i dA$$

where i is current density at the surface increment dA. The ohmic crater resistance then is

$$R = E/J = (\int \rho i ds)/(\int i dA)$$

On increasing the size of the system at constant electric resistivity and current density in the various parts of the system, it is seen that E increases with first power and J with second power of linear dimensions. The R therefore is inversely proportional to linear dimensions, which is the basic content of Eq. [1]. The assumption of equal current density in the two sizes of the system is not necessary, however, because E and J are affected in the same way by a change in the level of current density.

The same result may be obtained by a formal dimensional analysis. Since the systems in question are considered as geometrically similar, with corresponding points having equal electrical resistivity, the problem of the shape of the smelting zone and of the variation of resistivity within the zone drop out of the analysis. The only quantities entering the analysis, then, is ohmic crater resistance R, a representative value ρ for the electric resistivity of the charge in the smelting zone, and electrode diameter D representing the size of the system. By the theory of dimensional analysis (5) these quantities have to be arranged in dimensionless groups, which are arguments in the causal relationship. It turns out that only the group RD/ρ is formed. The relationship sought, therefore, is

$$F(RD/\rho) = 0$$

or

$$RD/\rho = \text{constant} \qquad [2]$$

which is equivalent to [1]

A different form of [2] has been reported previously (6).

$$P\rho/DE^2 = \text{constant} \qquad [3]$$

where E is ohmic voltage and P is power input. By the relation

$$E^2/P = R \qquad [4]$$

it is seen that [3] is equivalent to [2]. Solving [3] for E gives

$$E = \text{const.} \sqrt{P/D} \qquad [5]$$

Similarly, the electrode current J is found to be

$$J = \text{const.} \sqrt{PD} \qquad [6]$$

Different formulas have been proposed for relating power input to electrode diameter (1, 7, 8). Whatever relation is used, [5] and [6] are valid within the same range as [2].

Model Experiments

The validity of [2] may be demonstrated for the case of a simple model, where the smelting crater

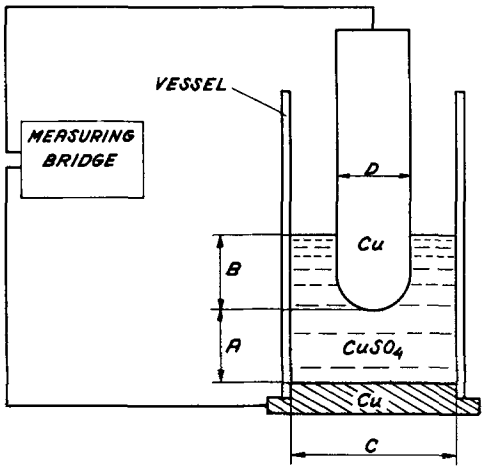

Fig. 1. Model arrangement

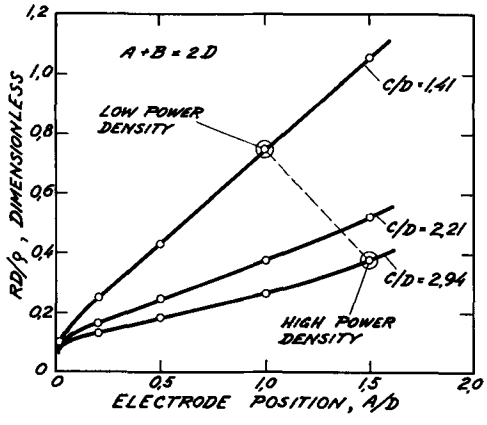

Fig. 2. Effect of electrode position and of size of smelting zone.

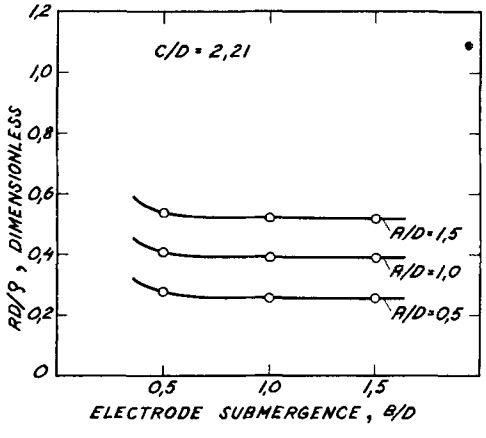

Fig. 3. Effect of electrode submergence

has been simulated by an electrolytic trough as shown in Fig. 1. Between the bottom plate and the electrode, both of copper, is filled an aqueous solution approximately 0.4M $CuSO_4$ and 0.1*N* H_2SO_4. The resistance is measured by a Philips conductivity measuring bridge PR 9500 at a frequency of 1000 cps. The system is made in two sizes, with 1 in. and 2 in. diameter of the electrode, respectively.

In Fig. 2 is shown results obtained for different values of the distance between bottom plate and electrode and for different ratios of vessel to electrode diameters, both at constant liquid level. In Fig. 3 the effect of electrode submergence into the liquid is shown. Corresponding measurements on the two sizes of the system are shown in Table I.

Table I. Values of RD/ρ for 1- and 2-in. electrodes

A/D	B/D	C/D	RD/ρ D = 1 in.	RD/ρ D = 2 in.
0.5	0.5	2.21	0.289	0.278
0.5	1.0	2.21	0.260	0.256
0.5	1.5	2.21	0.256	0.254
1.0	0.5	2.21	0.408	0.414
1.0	1.0	2.21	0.383	0.392
1.0	1.5	2.21	0.380	0.390
1.5	0.5	2.21	0.550	0.543
1.5	1.0	2.21	0.525	0.522
1.5	1.5	2.21	0.522	0.520

Discussion

The model used for simulating the smelting crater is simple and do not reflect all the complexities encountered in actual furnaces. The results, therefore, must be used with caution in interpreting actual furnace behavior. It is seen, however, that within the precision of the measurements Eq. [2] is verified for this simple system.

Within the assumptions made, however, the derivation of Eq. [2] by dimensional analysis is valid also for the complex system of actual furnaces. It is equally valid for three-phase furnaces as for the single electrode furnace simulated by the simple model, as the derivation is not restricted to any definite pattern of electric current. The basic requirement for the derivation is that the smelting zones of the furnaces compared are geometrically and electrically similar. Geometrical similarity implies equal relative electrode position and equal shape and relative size of the smelting zone. Electrical similarity implies that corresponding points of the two smelting zones have equal electric resistivity. The furnaces compared, then, will obtain identical patterns of electric current. This is a less restricting requirement than specifying any definite pattern of electric current and seems to allow a more realistic comparison of different-sized furnaces.

The general trend of measurements on the simple model agrees with everyday experience with smelting furnaces. The resistance increases when electrodes are raised. The shape of the curves on Fig. 2 may indicate the extent to which the voltage drop is concentrated at the tip of the electrode. The slopes of the straight parts of the curves of Fig. 2 correspond exactly to uniform current distribution in the cylindrical vessel. The resistance decreases with increasing diameter of the smelting zone. Most interesting, it is seen from Fig. 3 that the current is found by the model experiments to flow mainly from the very tip of the electrode to the charge. In actual furnaces, the high temperature and good electric conductivity of the smelting zone, as compared with the top of the charge, probably will make this effect still more pronounced.

The derivation of Eq. [2] assumes that the furnaces compared operate at the same relative electrode position and with the same relative size of the

smelting zone. For this to be true, the power input to the furnace must be related to electrode size in a definite manner. Actually, according to Kelly (3), the ohm-inch factor varies with the power density of the electrode. According to his data, furnaces operating at the same power density will show the same value of the ohm-inch factor. By increasing the power density, however, this factor will decrease markedly. By increasing the power input to a given furnace, however, the electrode has to be raised to maintain proper temperature of the metal pool. The size of the smelting zone will in turn increase, which more than offsets the increased distance between electrode and metal. The net result then will be a reduction in the crater resistance. These considerations are illustrated in Fig. 2 by the operating points for low and high power density of the furnace.

For the proper use of the ohm-inch factor, it is important to note that the conditions of the smelting zone may also be affected by the method of attending the furnace. The furnaces to be compared, therefore, must be charged, stoked, and tapped in the same way as far as these operations will influence the furnace performance. When the furnaces operate with substantial arcing of the electrodes, the derivation of Eq. [2] is not valid and the ohm-inch rule should be used with caution.

Most important, the resistivity of the charge depends on the nature of the raw materials used, especially on the nature of the reducing agent. The furnaces to be compared, therefore, must operate on the same raw materials, or at least on the same type of raw materials, if the ohm-inch rule shall apply.

Furnace operation practice differs widely between different works, and the raw materials quality may be highly different in different parts of the world. Two furnaces, operating the same process, picked out at random from different parts of the world most probably will not agree by the ohm-inch rule. In order to use the rule profitably, one has to see that the furnace operations agree with the assumptions underlying the rule. Most profitably the rule may be used internally within the works, when bigger furnaces have to be built, or when scaling up pilot plant results.

Acknowledgment

The author is grateful to Mr. H. Natvig and to Mr. T. Baasen for their helpful comments and discussion of the work. The experimental part has been done by Mr. B. Hogdahl.

Manuscript received Nov. 6, 1958. This paper was prepared for delivery before the Ottawa Meeting, Sept. 28-Oct. 2, 1958.

Any discussion of this paper will appear in a Discussion Section to be published in the June 1961 JOURNAL.

REFERENCES

1. A. Weynarth, *Trans Electrochem. Soc.*, **63**, 309 (1933). F. V. Andrea, *ibid.*, (discussion) 345-347.
2. M. J. Udy, *Can. Chem. Processing*, **35**, 626 (1951).
3. W. M. Kelly, *Metal Progr.*, nr. **5**, 73 (1958).
4. M. Morkramer, Paper presented at convention in Stresa, May (1959).
5. R. E. Johnstone and M. W. Thring, "Pilot Plants, Models, and Scale-up Methods in Chemical Engineering," McGraw-Hill Book Co., Inc., New York (1957).
6. O. C. Bockman, *This Journal*, **101**, 493 (1954).
7. F. V. Andrea, *Trans. AIEE*, **69**, 557 (1950), *J. Four Electr.*, **46**, 92 (1937).
8. N. A. Curtis, *This Journal*, **100**, 81*C* (1953).

Graphite Anodes in Brine Electrolysis

IV. Effect of Anolyte pH on Corrosion Rate in Chlor-Alkali Cells

L. E. Vaaler

Research Laboratories, National Carbon Company, Division of Union Carbide Corporation, Cleveland, Ohio

ABSTRACT

The effect of anolyte *p*H on cell efficiency and anode corrosion rate was studied in an experimental chlorine cell. With increasing *p*H, the expected decrease in current efficiency was observed with a resultant increase in the amounts of oxygen and carbon dioxide evolved. The relative increase in oxygen evolution is far greater than the carbon dioxide evolution. The results can be explained by a mechanism whereby the oxygen is formed from physically adsorbed oxygen, while carbon monoxide is formed from chemisorbed oxygen and oxidized to carbon dioxide by oxygen or dissolved chlorine. The increased corrosion resistance of impregnated graphite as compared to plain graphite may be due to the fact that filling of the voids decreases the effective area to one-third of the initial value.

A study of the behavior of graphite anodes in brine electrolysis, and in particular a determination of the rate at which they corrode, requires that the *p*H of the anolyte be well defined. In some cases *p*H is well defined by close control of such conditions of electrolysis as current density, temperature, and flux of electrolyte through the cell, and need be measured only occasionally. This is often true in cells without diaphragms. Janes (1) found that *p*H in an experimental chlorate cell was reproducible

under controlled conditions of electrolysis and proper adjustment of the acidity of the feed brine.

The situation is less satisfactory with diaphragm cells. Part of the hydroxide ion formed in the catholyte leaks through the diaphragm into the anolyte, and the amount of leakage is a function of the method of preparation and age of the diaphragm. It is difficult to obtain negligible leakage or even a reproducible leakage, with the result that *p*H is not closely maintained. Johnson (2) designed a very useful chlor-alkali diaphragm cell for the laboratory, and it has been used to evaluate various anode materials for many years. However, it has some limits as to precision, and variations in *p*H from cell to cell probably have an important bearing on this. This relates back to the difficulty in preparing the wrapped asbestos diaphragms used in these cells so that reproducible properties are obtained. This problem is also present in commercial cells with deposited diaphragms.

A mercury cathode cell contains no diaphragm but may act in an analogous manner because of hydrogen discharge at the cathode. The discharge produces sodium hydroxide, and it is difficult to maintain this constant, due to the many variables affecting it.

Chlorine cells operate in the *p*H range of 3 to slightly over 4 with current efficiencies of 90% or better. The *p*H is maintained in this range by the buffering action of the anode, which on discharge of oxygen and/or carbon dioxide forms sufficient acid to neutralize sodium hydroxide leaking through the diaphragm. The rate of graphite corrosion is determined to a large extent by the formation of carbon dioxide. The cell efficiency is determined largely by the formation of carbon dioxide plus oxygen. Thus, both the corrosion rate and current efficiency are sensitive functions of the *p*H.

The excellent and comprehensive work of Foerster (3) and others in the early 1900's was, nevertheless, limited because there were no suitable methods of measuring *p*H in the desired range. Some attempts to titrate the very dilute acid in the anolyte gave only approximate answers. The work most closely allied to the present study is that of Murray and Kircher (4), who measured the effect of several variables in a commercial Hooker Cell. Chloride concentrations were not the same at the various *p*H levels tried, but an empirical correction was made to relate directly current efficiency and *p*H. However, corrosion rate and *p*H were not similarly studied and only commercial oil-impregnated graphite anodes were used. Barr (5), using existing fundamental and practical data, developed useful relationships relating cell performance to *p*H and obtained good agreement with the results of Murray and Kircher. However, no prediction could be made of corrosion rate. Okada, Yashida, and Shiragami (6) studied *p*H in a Krebs-type mercury cell under production conditions, but close control was not possible. When the *p*H deviated upward to a significant degree from a statistical average, a drop in current efficiency was noted. Lacheisserie (7) plotted his experimental data on a *p*H-potential diagram showing stability regions for chloride, chlorine, and the various chlorine-oxygen compounds. One-molar solutions were electrolyzed at ambient temperature and an anode current density of 1 ma/cm^2. Thus, conditions were far different from those in a commercial cell.

The purpose of the work reported here was to determine the behavior of three anode materials in anolytes of known *p*H. The materials were plain graphite, impregnated graphite, and platinum; *p*H values ranged from 3.0 to 4.2. The porosity of a graphite anode increases as it is corroded, and the extent of porosity can influence the results of electrolysis. To eliminate variables due to porosity, anodes were used for only a few hours during which time corrosion was slight. The corrosion rate was calculated from the composition of the anodically formed gas rather than from weight loss, since the latter was very small over the period of an experiment. Rates calculated in this manner do not take into account loss of graphite due to the formation of sludge.

Experimental

Electrolysis cell.—Figure 1 is a diagram of the experimental cell. It is of the Wheeler type, with diaphragm and wire-screen cathode in the center, and is a modification of the laboratory cell described by Johnson (2). The anolyte was contained in a 6-in. diameter x 12-in. high glass jar. A polymethylmethacrylate cover sealed the cell and held all of the electrolysis and control apparatus. This included the cathode-diaphragm assembly, two opposed anodes, a resistance heater sealed into glass, thermometer, thermistor temperature-control bead, glass and calomel electrodes, brine inlet, a funnel containing acid or alkali for *p*H control, and orifices for sampling anolyte and anodic gas. These units were pushed through rubber stoppers that fitted in turn into the cell cover. The cover was sealed to the glass jar with a fluorinated paraffin.

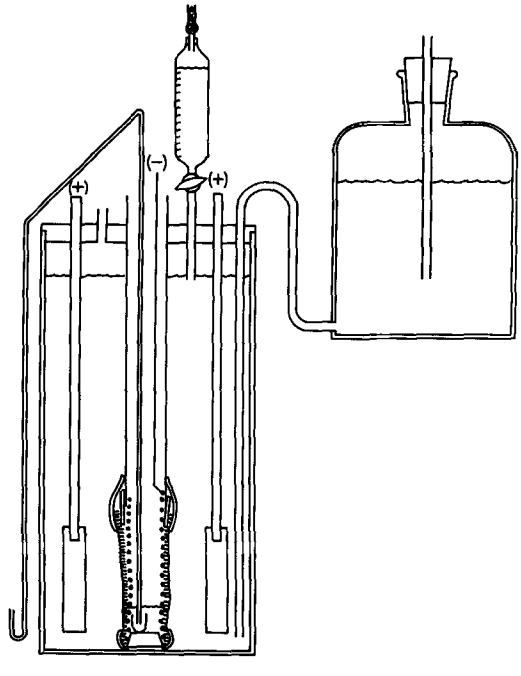

Fig. 1. Experimental chlorine cell

The cathode-diaphragm unit was assembled by partially inserting the end of a 1-in. diameter circular wire-gauze cathode into a glass tube. A rubber sleeve held the two units together and sealed the bottom of the glass tube from anolyte. A 3-in. length of the cathode projecting out of the tube was wrapped with a single layer of asbestos paper, held on with a further wrapping of permeable asbestos tape. Several turns of electrician's rubber tape held the ends of the asbestos tape in place, and a rubber stopper sealed the bottom of the cylindrical cathode. Catholyte was siphoned out of the cathode compartment through a glass tube of sufficiently small diameter to entrain gas bubbles and prevent their collection at the upper bend. A constant head was maintained in the electrolytic cell by means of the feed bottle design shown in Fig. 1.

Platinum sheet anodes 3 x 1¼-in. were bent lengthwise at right angles and positioned so that the bend projected toward the cathode. Graphite anodes were solid specimens ⅝ x ⅝ x 3-in.[1] The average current density for a cell current of 7.2 amp was 0.4 amp/in.^{2}. Independent experiments with an electrode whose front and back halves were separated by a thin strip of insulation showed that about 60% of the current is carried by the front half and 40% by the back half.

For the purpose of experiments at controlled *p*H, a simple diaphragm or partition to separate cathodic hydrogen from the anode gas may have been sufficient. However, the degree of manual control that can be obtained is much improved by use of an efficient diaphragm, since the frequency and amounts of additions that must be made are reduced. The diaphragm in the experimental cell was submerged under an anolyte head of several inches to minimize back-migration of hydroxide. In a Wheeler cell the diaphragm extends to the surface of the anolyte, at which point there is no flow of anolyte into the cathode chamber. Therefore, back migration is extensive at the anolyte surface and is most noticeable in small cells of limited depth.

Analysis.—Anode gas was collected and analyzed by a method used for production control (8). This involves absorption of chlorine and carbon dioxide into alkaline-arsenite solution and analysis of the unabsorbed gas for oxygen, carbon monoxide, hydrogen, and nitrogen in an Orsat apparatus.

A portion of the arsenite solution is acidified and carbon dioxide distilled over into 0.1*N* caustic solution. Barium chloride is added to precipitate the carbonate, and the amount of carbonate present is determined from the amount of acid needed to decompose it. Carbonate in brine was determined by the same distillation procedure, and carbonate in the caustic used for adjusting *p*H was analyzed by adding barium chloride and proceeding as above.

Chlorine (as chloride) in the absorbing mixture was determined by the Volhard procedure, but the simpler Mohr method was suitable for chloride in the anolyte after reducing dissolved chlorine with hydrogen peroxide. Active, or dissolved chlorine in the anolyte was determined by pipetting a sample directly out of the cell into a known amount of acidified ferrous ammonium sulfate, boiling for 7 min and titrating with permanganate. The analysis included chlorine, hypochlorite, chlorate, and any other oxidized chlorine compounds.

Experimental procedure.—The cell was operated continuously at 80°C and 7.2 amp, using platinum anodes. The feed rate was about 100 ml/hr. Under these conditions the anolyte *p*H approximated 3.8, and the catholyte caustic concentration was 110-120 g/l. When graphite anodes were to be studied, they were substituted for platinum at the beginning of an experiment. The *p*H was immediately adjusted to and held at the desired value for 1 hr. Analysis was made for chloride and dissolved chlorine in the anolyte and anode gas was collected for 1-2 hr. Dissolved chlorine was determined again after gas collection. The rate of flow of catholyte out of the cell was generally determined during gas collection.

Calculations.—The amount of dissolved chlorine generated per hour was calculated from a materials balance:

$$\text{Net chlorine dissolved: } = \left[\begin{matrix}\text{Anolyte through}\\ \text{diaphragm}\end{matrix}\right] \times \left[\begin{matrix}\text{Average dissolved}\\ \text{chlorine concentration}\end{matrix}\right] + \left[\begin{matrix}\text{Anolyte}\\ \text{volume}\end{matrix}\right] \times \left[\begin{matrix}\text{Change in dissolved}\\ \text{chlorine concentration}\end{matrix}\right] + \left[\begin{matrix}\text{Dissolved chlorine}\\ \text{removed by sampling}\end{matrix}\right]$$

This amount was expressed as the per cent of the current required to produce it or in cc of STP gas/hr. The flow of anolyte through the diaphragm was estimated to be 10% greater than the flow of catholyte out of the cell. The reduction in volume is due mainly to the decomposition of water into hydrogen and alkali. At *p*H 3.0, the amount of chlorine dissolved was found to be less than the experimental error in the above material balance and was neglected. An experiment at this *p*H was carried out using platinum anodes and stopping the flow of feed brine so that generation of dissolved chlorine could be detected simply by a change in concentration in the anolyte. No change in concentration could be detected over a period of 2 hr.

The amount of air in the sample was determined from the nitrogen present, and the total oxygen corrected for the amount in the air. The evolved Cl_2, CO_2, CO, and corrected O_2 were expressed as volume percent, assuming ideal gases. Further corrections were required for the CO_2 fed into the cell by the brine and by the alkali used for adjusting *p*H. The evolution of about 3 cc of CO_2 per hour could not be accounted for when platinum anodes were used, and a correction for this amount was made when graphite anodes were employed.

Since the corrections are on a volume per hour basis, it is convenient to know the volumes of gases generated per hour. Due to interruptions during gas sampling, leaks, etc., the gas sample could not be considered the total generated during the collection period.

[1] The two grades of graphite used were National Carbon Co. grades AGLR (unimpregnated) and AGLR-58 (linseed oil impregnated). The unimpregnated graphite had a bulk density of about 1.55 g/cc, corresponding to a porosity of about 30%.

The following calculation yielded the corrections, knowing the relative composition of the gas and amount of dissolved chlorine, including hypochlorite and chlorate. The symbols Cl_2, CO_2, CO, and O_2 denote volume per cent values in the sample and Cl_2' CO_2', CO', and O_2' gas produced by electrolysis in cc/hr. The gases requiring 2 and 4 Faradays per mole, respectively, are added so that:

$$x = Cl_2' + CO' \quad [1]$$

$$y = CO_2' + O_2' \quad [2]$$

then

$$\frac{2x + 4y}{1000} = 22.4 \times \mathbf{F} \times E/100 \quad [3]$$

where **F** is Faradays per hour and
E is nonchlorine current efficiency.

$$x + 2y = 112\,\mathbf{F}E = K_1 \quad [4]$$

A second equation in x and y is the following:

$$\frac{CO_2 + O_2}{100} = \frac{y + K_2}{x + y + K_2} = K_3 \quad [5]$$

where K_2 is the carbon dioxide corrected for in cc/hr and is a positive value.

All of the K's are experimental quantities, so [4] and [5] may be solved simultaneously for x and y.

$$y = \frac{K_3(K_1 + K_2) - K_2}{1 + K_3} \quad [6]$$

since:

$$\frac{CO_2' + K_2}{O_2'} = \frac{CO_2}{O_2} \quad [7]$$

substitution from [2] gives

$$CO_2' = \frac{y - K_2(O^2/CO_2)}{1 + (O^2/CO_2)} \quad [8]$$

Therefore, CO_2' can be determined from the value of y calculated from [6] and the ratio of O_2/CO_2 in the gas evolved. O_2' is then calculated from [2].

x can be determined from Eq. [4], and CO' related to it by a derivation similar to the above:

$$CO' = (CO/Cl_2 + CO)\,x \quad [9]$$

Cl_2' is then determined from [1].

Results

Data and calculations for the experiments are summarized in Table I. Each *p*H value represents an average of many readings taken during an experiment, most of which did not vary more than 0.1 unit from the mean. The change in dissolved chlorine during an experiment was not always determined, and values in parentheses are estimated. Regardless of the values shown for dissolved chlorine generated at *p*H 3, this was assumed to be zero. The gas composition shown is that after correction for CO_2 as described above and after inclusion of dissolved chlorine. The small values for carbon dioxide listed for platinum at *p*H 4.2 indicate a reasonably good materials balance for this gas, when none is generated at the anode. The value of 100 minus the chlorine current efficiency is that due to generation of CO_2, CO, and O_2.

Figure 2 is a plot of the nonchlorine current efficiency for the three anode materials which indicate the following order for *p*H 3 to 4:

Plain AGR > Impregnated Graphite > Platinum

At *p*H 4.2 the nonchlorine efficiency with the impregnated graphite is the same as or higher than that with plain graphite. According to the result the *p*H should drop when graphite anodes are substituted for platinum, since the chlorine current efficiency, controlled mainly by the diaphragm leakage, will remain approximately constant. A slight drop has been observed.

Table I. Effect of anode material and anolyte *p*H on cell performance

Anode	*p*H	Anolyte sodium chloride, g/l	Average dissolved chlorine, meq/l	Dissolved chlorine, generated, % of current	Composition of gas generated				100-Cl_2 current efficiency, %	Calculated anode wt loss, g/1000 amp hr
					Cl_2, %	CO_2, %	CO, %	O_2, %		
Plain graphite	3.01	248	40.2	—0.2	99.09	0.82	0.02	0.06	1.76	1.86
	2.98	251	56.7	1.49	98.99	0.84	0.04	0.11	1.92	1.95
	3.82	270	111	(5)	97.86	1.46	0.08	0.62	4.15	3.38
	3.79	271	80.5	4.9	97.68	1.29	0.09	0.91	4.39	3.02
	4.20	252	120.7	7.4	94.90	2.02	0.12	2.97	9.62	4.56
	4.19	259	144.1	11.8	95.74	1.85	0.11	2.30	8.07	4.21
Impregnated graphite	2.99	252	120	2.4	99.19	0.41	0.03	0.35	1.54	0.98
	3.00	254	113	—	99.36	0.33	0.02	0.30	1.27	0.78
	3.80	258	128	(7)	98.31	0.65	0.06	1.00	3.30	1.56
	3.80	262	135	7.2	98.03	0.66	0.06	1.27	3.85	1.58
	4.18	259	141	26.1	95.16	1.03	0.07	3.74	9.17	2.41
	4.23	243	249	38.4	96.05	0.69	0.07	3.17	7.50	1.63
	4.20	262	276	21.0	95.45	1.05	0.07	3.43	8.64	2.39
Platinum	2.99	275	204	(0)	99.72			0.28	0.56	
	3.00	260	20	(0)	99.71			0.29	0.58	
	3.85	268	76	(5)	98.54			1.46	2.88	
	3.97	260	169	(5)	98.79			1.21	2.39	
	4.19	270	144	13.4	97.54	—0.04		2.52	4.91	
	4.19	244	279	11.5	97.05	—0.06		2.98	5.79	

Temperature 80°C. 7.2 Amp on two ⅝ × ⅝ × 3 in. blocks or 1¼ × 3 in. sheets.

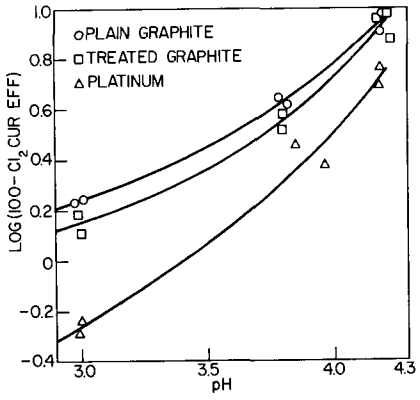

Fig. 2. Effect of pH on current efficiency

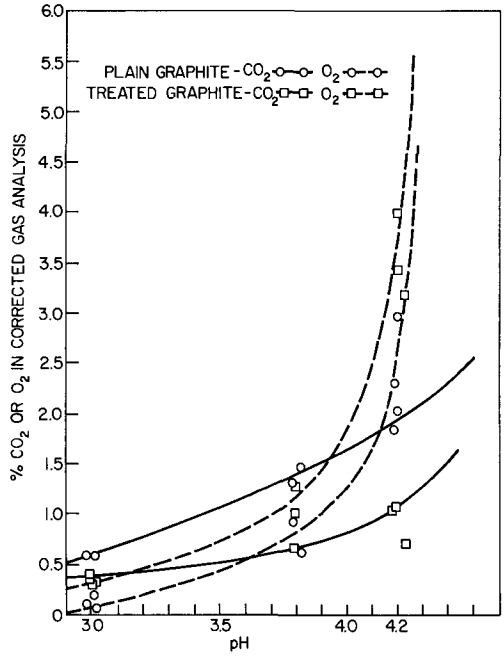

Fig. 3. Effect of pH on per cent O_2 and per cent CO_2

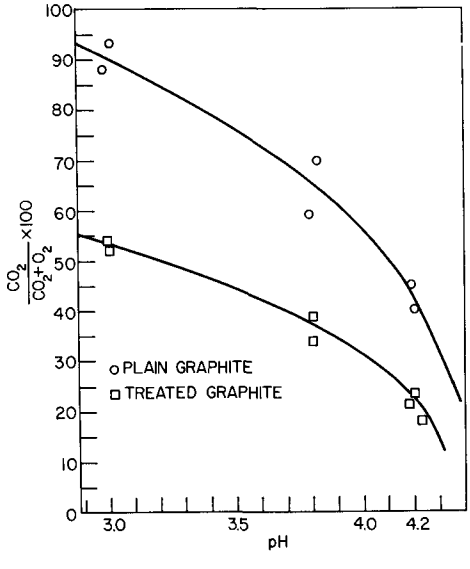

Fig. 4. Effect of pH on ratio $CO_2/CO_2 + O_2$

Figure 3 shows the marked contrast between oxygen and carbon dioxide variations with pH. The oxygen curves undergo a much larger change in slope over the pH range than do the carbon dioxide curves. This means that the slope of a CO_2/O_2 vs. pH plot becomes more negative with increasing pH, as shown in Fig. 4.

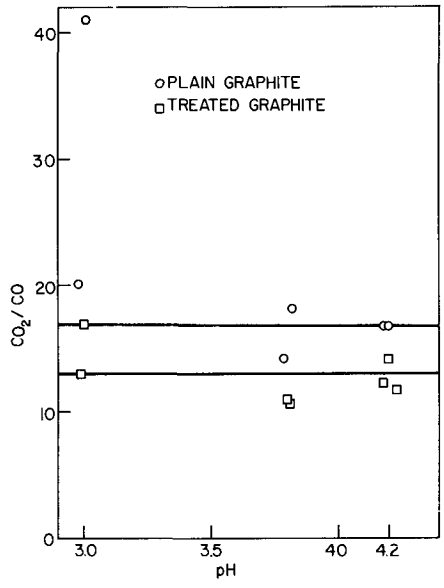

Fig. 5. Effect of pH on ratio CO_2/O_2

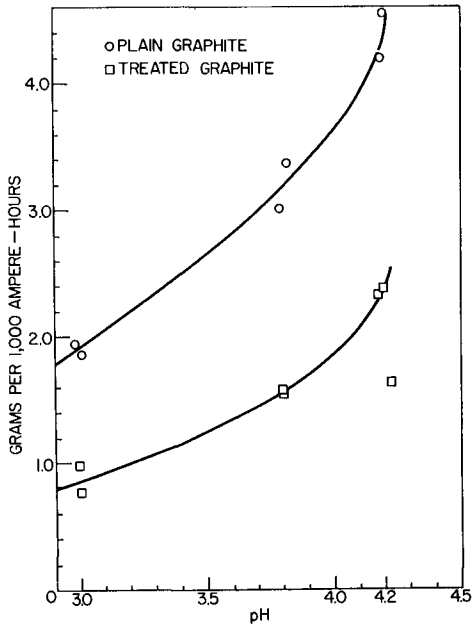

Fig. 6. Effect of pH on anode consumption

On the other hand, the ratio CO_2/CO is probably constant over the pH range. The ratios at pH 3.0 are uncertain, because the amounts of CO in the gas were too small to more than approximate. Figure 5 is a plot of the data and indicates a higher ratio for plain graphite than for impregnated graphite.

Figure 6 shows the variation in carbon consumption as calculated from the gas composition. The curve has the same trend as that for nonchlorine current efficiency, but is less steep because of the compensating effect of the decreasing CO_2/O_2 ratio.

The ratios of consumption for plain graphite compared to impregnated graphite for the three pH values are shown in Table II. The ratio of 2 is unaffected by pH.

Table II. Ratio of consumption of plain graphite relative to impregnated graphite

pH	Weight ratio
3.0	2.2
3.8	2.0
4.2	2.1

Discussion

The amounts of dissolved chlorine in the laboratory cell are much higher than in a commercial cell. With the latter, the amount corresponds to less than 5% of the current under normal operating conditions. This low value may be due to the higher temperature and greater degree of agitation used commercially. The agitation minimizes the formation of an alkaline layer in the anolyte in the vicinity of the diaphragm and thus reduces the amount of chlorate formation. The chemical formation of chlorate is the most reasonable explanation for high chlorine solubility in the laboratory cell, since it is favored by the large ratio of anolyte volume/anode surface. A large anolyte volume means a long hold time for chemical chlorate formation to take place. Electrochemical chlorate formation appears to be no more than expected as evidenced by the amounts of carbon dioxide and oxygen evolved. The very high dissolved chlorine values for impregnated graphite anodes at pH 4.2 appear to involve a further mechanism for solution beyond those operable for the other conditions.

When chlorine current efficiency is based on evolved plus dissolved chlorine, the laboratory and commercial cells compare favorably. This method of comparison is justified in studying anode performance, since the chlorine is formed at the anode regardless of whether it is evolved or dissolved. Results with impregnated graphite anodes in the experimental cell and the Hooker Cell investigated by Murray and Kircher (4) are compared in Table III. Their values are picked off of a curve of hydroxyl ion discharge, which does not include dissolved chlorine. These authors found that chemical chlorate formation was insignificant up to pH 4.2.

The higher chlorine current efficiencies indicated for platinum as compared to graphite reflect a higher overvoltage of oxygen relative to chlorine for the metal. The slightly higher chlorine current efficiency for impregnated as compared to plain graphite is probably related to the less extensive chemical attack by hypochlorite as a result of filling the pores.

The decrease in chlorine current efficiency with increasing pH is expected from the increase in concentration of substances that form oxygen (or CO and CO_2) by anodic oxidation or chemical decomposition. The equilibria and kinetics involved have been discussed in detail by Barr (5) and Murray and Kircher (4). The laboratory data, in confirming the effect of pH on current efficiency, point up the practical attractiveness of using an acid feed to keep anolyte pH low. The decrease in anode consumption is an added advantage. The practical considerations of providing corrosion-proof-containers and conduits for the acid brine as well as a possible decrease in diaphragm life must be balanced against the benefits of operating at lower pH.

Table III. Comparison of current efficiency losses in Laboratory and Hooker Cell

pH	Current efficiency loss	
	Lab. cell	Hooker cell*
3.0	1.4	1.0
3.8	3.6	3.2
4.2	9	6.0

* Values estimated from hydroxyl discharge curve in Ref. (4).

The change in CO_2/O_2 ratio with pH could be due to heterogeneous reactions taking place on the surface of the anode, with or without homogeneous reactions taking place in the vicinity of the anode or in the bulk of the solution. Any of the possible discharge mechanisms could result in adsorption of oxygen directly onto the anode, as could chemical attack of the graphite by hypochlorite. The over-all reaction for discharge of hypochlorite ion, postulated by Foerster (3) from experimental evidence in alkaline solution is:

$$6(OCl)^- + 3H_2O + 6e \rightarrow 6H^+ + 2ClO_3^- + 4Cl^- + \frac{3}{2}O_2$$

Since several steps are probably involved in this over-all reaction, there is the possibility of some intermediate product diffusing away from the anode and homogeneously decomposing to give molecular oxygen. Hypochlorous acid decomposes homogeneously to oxygen and hydrochloric acid. Lister (9) has found the rate to be insignificant except in the presence of a catalyst. Hydrogen peroxide can be formed anodically and decompose to oxygen and water. The question that arises when oxygen is formed from homogeneous reactions is whether such oxygen is available either to attack the anode or to oxidize carbon monoxide formed at the anode or whether it escapes as molecular oxygen and is unavailable as an oxidizing agent. Nevertheless, a mechanism can be proposed, based on the physical and chemical adsorption of all the oxygen supposedly formed, that agrees fairly well with the data.

If, by analogy to mechanisms proposed for air oxidation (10-12), oxygen is adsorbed as a first step, desorption-combination can take place to form oxygen, or a carbon bond can break to form a carbon-oxygen compound. Eyring and Blyholder (10) found that CO was the primary product of air oxidation and ascribed this to its low energy of desorption. Sihvonen (11) proposed that CO comes from desorption of keto or ketene groups formed as a result of oxygen adsorption. He also maintained that α keto acids are obtained during electrolysis, which give rise to a mixture of CO and CO_2. In electrolysis, the presence of adsorbed oxygen need not be the direct result of adsorption of the element, but more probably is the result of oxidation of hydroxyl or hypochlorite ions already present on the surface which then dehydrate or dehydrohalogenate to leave adsorbed oxygen behind. Furthermore, hydroxyl radicals could desorb directly to form hydrogen peroxide which then decomposes to oxygen. This

mechanism is suggested by the fact that Sihvonen found that practically no oxygen was formed at a graphite anode in sulfuric acid solution where peroxide decomposition is slow, while in strong alkali, which readily decomposes peroxide, oxygen was the preponderant anodic gas.

The process for electrolytic oxidation will be assumed to involve the rapid physical adsorption of oxygen on the anode surface, a conversion of a part of this oxygen to desorbed molecular oxygen by a second order reaction and a conversion of the rest to chemisorbed oxygen by a first order reaction followed by rapid desorption of carbon monoxide. The monoxide is then oxidized almost completely to carbon dioxide either by the oxygen desorbed or by dissolved chlorine. The desorption of hydroxyl radicals to form hydrogen peroxide and then oxygen is also a second order reaction, provided the peroxide formation is the rate-determining step.

The following scheme represents the mechanism:

Oxygen source (OH^-, OCl^-, etc)

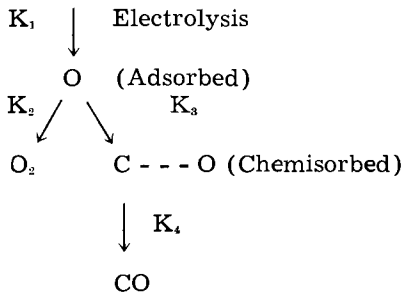

Volume percentages of oxygen and carbon dioxide in the evolved gases are proportional to their rates of formation. In accordance with the assumed mechanism, the volume percentage of carbon monoxide, which is the primary anodic product, is calculated from the volume percentage of carbon dioxide. These rates are proportional to the fraction of active surface sites covered by physically adsorbed and chemisorbed sites, respectively, so that by proper choice of units for the rate constants the following equations hold for the steady state:

$$C_{O_2} = K_2 \theta^2 \qquad [10]$$

$$C_{CO} = K_1 \phi = K_3 \theta \qquad [11]$$

where C_{CO} is volume per cent CO, C_{O_2} is volume per cent O_2, θ is fraction of active sites covered by physically adsorbed oxygen, and ϕ is fraction of active sites covered by chemisorbed oxygen.

$$C_{CO} = K_3 \sqrt{C_{O_2}}/K_2 \qquad [12]$$

which is the obvious relation for competing first and second order reactions leading to carbon monoxide and oxygen, respectively.

To test these assumptions it is necessary to recalculate the data to give CO and O_2 concentrations prior to oxidation of the CO and CO_2. Either oxygen or dissolved chlorine has been assumed to be the oxidizing agent. The results are plotted in Fig. 7, which shows C_{CO} vs. $\sqrt{C_{O_2}}$. Reasonable linearity within the accuracy of the data was obtained for all of the plots. Where it was assumed that oxygen oxidizes carbon monoxide, the lines came closer to the origin. A straight line through the origin indicates rate constants independent of the amount of surface covered with adsorbed atoms, a situation that is not apt to be strictly true. The rate of chemisorption (K_3) when θ and ϕ are very small would probably be higher than when the fractions covered are larger, because only the most active sites on the graphite would be reacting. More exactly, the curves should start at the origin with a slope that decreases with increasing C_{CO} due to a continual decrease in K_3. The Elovich equation [12], or other function with changing slope can be fitted to the data in such a manner that the line passes through the origin, but adds little to a further understanding of the reaction mechanism.

The difference in the results with plain and treated graphite can be explained on the basis of the decrease in area available for electrolysis resulting from the impregnation with oil. The curves in Fig. 7 may be represented as:

$$C_{CO} = A \sqrt{C_{O_2}} + B \qquad [13]$$

A similar equation can be written in which the amount of gas evolved per unit area is used rather than the total

$$C_{CO}/a = A' \sqrt{C_{O_2}}/a + B' \qquad [14]$$

where

$$A' = A/\sqrt{a} \qquad B' = B/a$$

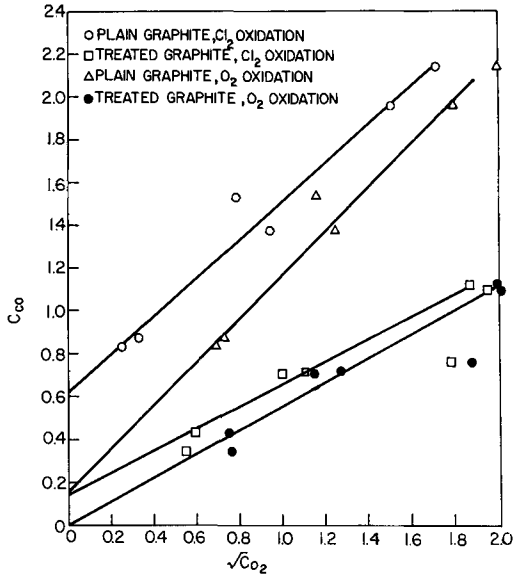

Fig. 7. Plot according to Eq. [12]

Table IV. Relative areas of plain and treated graphite

Graphite	Oxidizing agent	A	B	A_p^2/A_t^2	B_p/B_t
Plain	HOCl	0.89	0.62	3.0	4.1
Treated	HOCl	0.51	0.15		
Plain	O_2	1.02	0.15	3.5	
Treated	O_2	0.55	0		

Thus, in comparing two curves obtained in the same manner:

$$a_1/a_2 = A_p^2/A_T^2 = B_p/B_T \quad [15]$$

where subscripts p and T refer to plain and treated graphite, respectively. Results are shown in Table IV. The area ratio based on the squares of the slopes is probably much more accurate than that based on the intercept ratio, since the intercept is more uncertain, particularly when it is in the vicinity of the origin. Treatment appears to reduce the effective anode area 3 to 4-fold. This seems reasonable, although the possibility that additional oxygen is formed with treated graphite by the catalyzed decomposition of HOCl cannot be discounted. Cobalt is a suitable catalyst and is contained in the impregnating oil. Joost (13) considered that chemical attack by hypochlorite was an important factor in graphite corrosion, since the addition of cobalt was effective in inhibiting corrosion.

The proposed adsorption mechanism, while giving a reasonable explanation of events in the brine solution, would probably need to be modified to account for results in other media. However, Sihvonen's (14) results, in which he obtained more oxygen than CO_2 in strongly alkaline solution and much more CO_2 than oxygen in strong sulfuric acid solution, exhibit the same trend as the brine data.

In commercial cells the corrosion rate of plain graphite is about double that of impregnated graphite, in agreement with the experimental results in which the corrosion was not allowed to proceed to any extent. It remains to be determined whether such a short test is useful in determining practical corrosion resistances of various anode materials.

Acknowledgment

The author acknowledges the help of Nick Zacharias and Paul Lennon in carrying out the experimental work, and helpful discussions with Charles Lowe, N. J. Johnson, M. Janes, M. S. Kircher, and H. Eyring.

Manuscript received Feb. 4, 1960. This paper was prepared for delivery before the Chicago Meeting, May 1-5, 1960.

Any discussion of this paper will appear in a Discussion Section to be published in the June 1961 JOURNAL.

REFERENCES

1. Milton James, *Trans. Electrochem. Soc.*, **92**, 23 (1947).
2. N. J. Johnson, *ibid.*, **86**, 127 (1944).
3. Fritz Foerster, "Electrochemie Wassriger Lösungen," 4th ed., Barth (1923).
4. R. L. Murray and M. S. Kircher, *Trans. Electrochem. Soc.*, **86**, 83 (1944).
5. Lars Barr, *This Journal*, **101**, 497 (1954).
6. S. Okado, S. Yashida, and O. Shiragami, *J. Electrochem. Soc. Japan*, **22**, 672 (1954).
7. H. de Lacheisserie, *Bull. Soc. Franc. Electriciens*, **7**, 499 ((1957).
8. M. S. Kircher, H. R. Engle, B. H. Ritter, and A. H. Bartlett, *This Journal*, **100**, 448 (1953).
9. M. W. Lister, *Can. J. Chem.*, **34**, 465 (1956).
10. G. Blyholder and H. Eyring, *J. Phys. Chem.*, **61**, 682, (1957).
11. V. Sihvonen, *Trans. Faraday Soc.*, **34**, 1062 (1938).
12. L. Bonnetain, X. Duval, and M. Letart, *Compt. rend.*, **246**, 105 (1958).
13. Joost, Dissertation, Dresden (1910). In A. J. Allmand, "The Principles of Applied Electrochemistry," p. 152, 2nd Impression, Longmans Green, New York (1920).
14. V. Sihvonen, *Acta Chemica Fennica*, **7A**, 25 (1934). Also: Uber Die Oxydation Des Graphits, Suomalainen Tiedeakatemia, Helsinki, 1934.

An Electrochemical Study of Uranium in Fused Chlorides

Derek L. Hill, Jeanne Perano, and Robert A. Osteryoung

Department of Chemistry, Rensselaer Polytechnic Institute, Troy, New York

ABSTRACT

The U(III)-U(O) and U(IV)-U(III) standard potentials in $MgCl_2$-NaCl-KCl eutectic, and the U(IV)-U(III) and UO_2(VI)-UO_2(IV) standard potentials in LiCl-KCl eutectic have been measured at 450°C. The values found are respectively, —2.25, —1.30, —1.25, and —0.285 v vs. the standard Pt(II)-Pt(O) reference electrode on the mole-fraction scale. Polarographic studies of the behavior of U(III), U(IV), and UO_2(VI) in LiCl-KCl eutectic at 450°C have been performed. The significance of the results with respect to certain industrially important processes is briefly noted. A coulometric titration procedure utilizing electrogenerated Pt(II) has been developed for an *in situ* determination of U(III) in LiCl-KCl and $MgCl_2$-NaCl-KCl eutectics.

Recent activity in the use of fused salt baths for the electrodeposition of pure uranium (1, 2) and for the extraction of fission products from a liquid metal fuel reactor (3) and other studies (4, 5) involving this metal suggested that an investigation of certain aspects of the electrochemical behavior of uranium in such solvents would be of interest.

Two chloride eutectic solvents were chosen for for study: (*a*) the binary LiCl (59 mole %)-KCl (41 mole %), mp 355°C, because it has been widely used in electrochemical investigations and would enable direct comparison of uranium electrode potentials to be made with those of other metals, and (*b*) the ternary $MgCl_2$ (50 mole %)-NaCl (30 mole

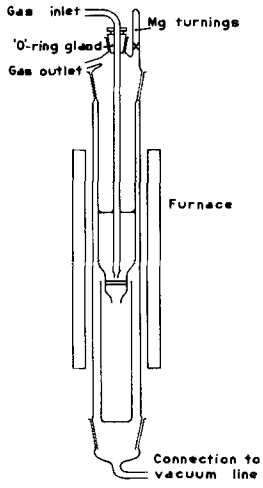

Fig. 1. Pyrex cell for melt purification

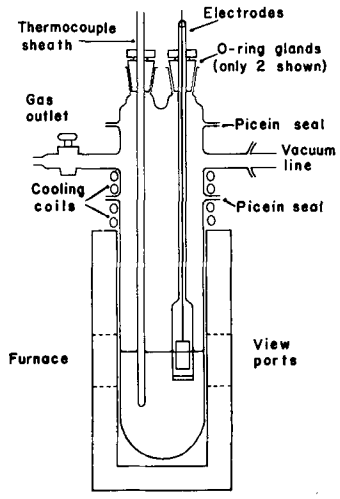

Fig. 2. Pyrex cell assembly

%)-KCl (20 mole %), mp 396°C, because of its suitability for the fission product extraction process.

Experimental and Results

Melt Purification

The apparatus for the dehydration and filtration of the eutectic solvents is shown in Fig. 1. Eutectic components of reagent grade and anhydrous magnesium chloride were mixed in the appropriate ratios and placed in the tube above the fine porosity frit, with the opening of the gas bubbler tube at the lower end, just above the frit. Anhydrous HCl gas was passed through the mixture for 30 min to displace air, and the nichrome-wound tubular furnace was then slowly heated over a period of about 3 hr, HCl passing all the while, until the mixture melted. After HCl had been passed through the melt for a further 30 min, it was replaced by a pure argon stream for 20 min, to remove dissolved HCl. At this point, clean magnesium turnings of Grignard quality were added from the side-tube, and stirred by the argon stream to react with residual impurities. The lower portion of the apparatus was then evacuated, and the melt was filtered into the crucible where it solidified. Finally the apparatus was filled with argon, the crucible was removed, quickly stoppered and transferred to a dry-box by way of a vacuum tunnel, and stored. As required, the weighed solid eutectic, usually about 160 g, was slipped out of the crucible and into the cell assembly, which fitted into a nichrome-wound Vycor tube furnace packed in an insulated container provided with a rear-lighted view-port at the melt level.

Cell Assembly and Related Apparatus

The cell assembly is shown in Fig. 2, the reference electrode and auxiliary cathode fritted compartments, and the titration electrode in Fig. 3 (a) and (b), respectively.

After the solidified eutectic had been placed in the cell and the flanged head carrying the electrodes, etc., had been placed in position, the whole assembly was evacuated overnight at about 10^{-5} mm Hg. It was then slowly warmed until the salt melted under vacuum, after which the temperature was controlled at 450°C by a chromel-alumel thermocouple contained in an immersed glass sheath, acting through a Barber-Coleman Wheelco furnace regulator.

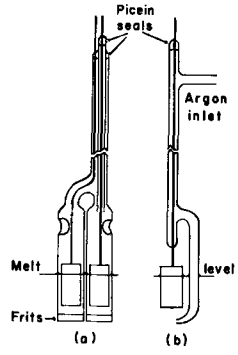

Fig. 3(a). Reference electrode and auxiliary cathode. Fig. 3(b). Argon-stirred titration electrode.

The fritted compartments were then lowered till the frits were just above the surface of the melt, where they were kept for 30 min to aid their outgassing. They were then immersed in the melt to a depth of about 2 cm, the cell was filled with pure argon which was then maintained at a steady flow through the cell; the melt filtered up into the compartments and reached its equilibrium level. The compartments each had a small hole above the melt level to avoid pressure differentials and to facilitate the insertion of the electrodes during the assembly of the cell. The reference electrode was then prepared coulometrically by the anodization at ~5 ma cm^{-2} of the Pt foil or Ag wire in one compartment, using the Pt foil in the other as cathode. The generation of Pt(II) and Ag(I) at 100% current efficiency under these conditions has been well established (6). Anodization was generally continued for a time sufficient to bring the mole fraction of Pt(II) or Ag(I) in the compartment to about $1 - 2 \times 10^{-3}$. The exact concentration was determined at the end of each experiment by the weight of eutectic contained in the compartment and the number of coulombs passed. The Nernst relation was then used to refer the potential of the reference electrode to the standard state of unit mole fraction.

Cylinder argon (99.995%) was passed through P_2O_5 and over titanium sponge at 900°-1000°C. Po-

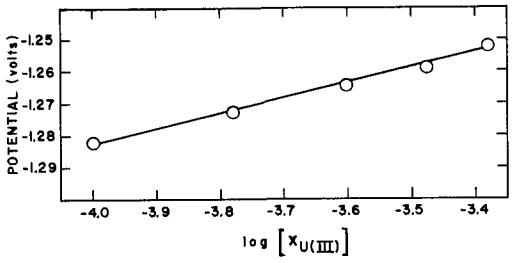

Fig. 4. U(III)-U(O) potential in $MgCl_2$-NaCl-KCl at 450°C. Ag(I)-Ag(O) reference electrode, 3.02 × 10^{-4} mole fraction of Ag(I).

larograms were recorded with a Sargent XXI recording polarograph. A Rubicon Model 2700 precision potentiometer was used to measure cell potentials. A Sargent coulometric current source was used in all constant current anodization or titration procedures.

U(III)-U(O) *Potential In* $MgCl_2$-NaCl-KCl

To a known weight of ternary eutectic, successive quantities of U(III) were introduced coulometrically by the anodization at about 10 ma cm^{-2} of a carefully outgassed pure uranium rod (analysis: Fe 0.003%, Mg 0.0008-0.003%, Si 0.0008%, Cu 0.0008%, Al 0.0005%). Current efficiency of 100% for this process is demonstrated in the present work and is discussed later. The potential of the uranium rod was measured against a Ag(I)-Ag(O) reference electrode after each addition, insuring uniform concentration in the deep red solution by argon stirring.

A plot of this potential against log [U(III)] at 450°C is shown in Fig. 4 and indicates that the Nernst relation is obeyed, the slope of the line (0.0470 v) being in close agreement with that calculated (0.0478 v) for a 3-electron transfer. Extrapolation to unit mole fraction of U(III) yields a value of −1.61 ± 0.01 v against a standard Ag(I)-Ag(O) reference electrode. Using the data of Laitinen and Liu (6) this value becomes −2.25 ± 0.01 v against a standard Pt(II)-Pt(O) reference electrode.

Polarography of U(III) *and* U(IV) *in* LiCl-KCl

The polarographic behavior of U(III) and U(IV) in the binary eutectic was studied using a Pt needle microelectrode prepared by sealing a length of 14 mil diameter Pt wire into 6 mm Pyrex tubing so that about 1.5 mm^2 projected from the seal. Measurements were made with respect to a Pt(II)-Pt(O) reference electrode. Again, U(III) was added coulometrically by the anodization of a pure uranium rod, which was raised out of the melt after each period of anodization. Current efficiency of 100% was found for this process also, and is discussed later.

By restricting the potential range in which the microelectrode was used to less than 1.5 v negative to the reference electrode, reproducible and well-defined waves for the oxidation of U(III) to U(IV) were observed. Figure 5 illustrates the polarograms obtained after successive additions of U(III). As the U(III) concentration was increased, the potential at which the polarographic current attained the residual value became increasingly negative, but, although the magnitude of the shift was of the right order, exact quantitative agreement with that calculated from the Nernst relation was not obtained. At a fixed potential, the polarographic currents due to successive additions of U(III) showed a linear relation to concentration, as illustrated in Fig. 6.

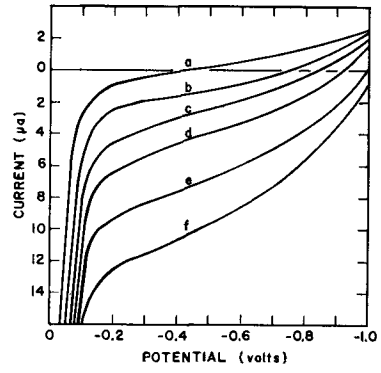

Fig. 5. Polarogroms for the oxidation of U(III) to U(IV) in LiCl-KCl at 450°C. Pt(II)-Pt(O) reference electrode, 1.14 × 10^{-3} mole fraction of Pt(II); microelectrode area 1.65 mm^2; melt weight 160 g; additions of U(III): a:0; b:12; c:28; d:44; e:68; f:92 mg. The current below the zero-axis is anodic.

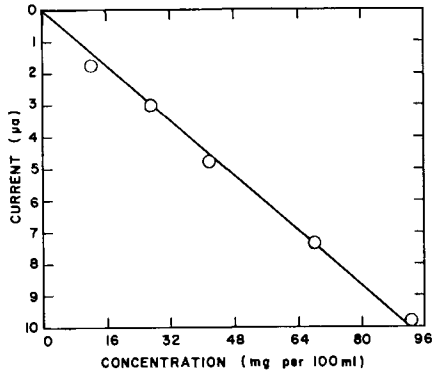

Fig. 6. Relation between U(III)—oxidation polarographic current and U(III) concentration in LiCl-KCl at 450°C (from Fig. 5, at −0.43 v).

Starting with a given concentration of U(III) in the melt, U(IV) could be added to the system by the reaction

$$2U(III) + Pt(II) \rightarrow 2U(IV) + Pt \qquad [1]$$

using Pt(II) generated coulometrically from an immersed Pt foil anode. On making successive additions of U(IV) in this manner, accompanied of course by the equivalent successive removals of U(III), the potential at which the polarographic current attained the residual value became less negative again, and the steady development of the U(IV) reduction wave was observed along with the simultaneous steady disappearance of the U(III) oxidation wave. With equal concentrations of U(III) and U(IV) in the melt, the point of zero current occurred at a potential very close to that found in the potentiometric titration procedure for the determination of the U(IV)-U(III) redox potential described below. The development of the combined U(IV)-U(III) polarograms is shown in Fig. 7.

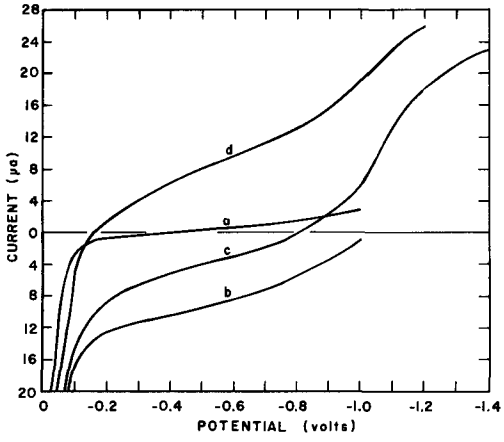

Fig. 7. Development of combined U(III) and U(IV) polarograms in LiCl-KCl at 450°C. Pt(II)-Pt(O) reference electrode, 1.14 × 10^{-3} mole fraction of Pt(II); microelectrode area 1.65 mm^2; a, residual current; b, U(III) oxidation (92 mg U(III) per 100 ml melt); c, U(III) oxidation, U(IV) reduction; d, Pt(II) reduction, U(IV) reduction. Current below the zero-axis is anodic.

Only indistinct waves for the reduction of U(III) to uranium metal were observed, at about —2.2 v, and it appeared that alloying occurred, both from the subsequent appearance of the microelectrode, and also because it was not found possible to obtain unequivocal anodic stripping curves corresponding to the dissolution of the uranium metal which should have been electrodeposited on the microelectrode. The use of a Pt microelectrode at such a negative potential, which is close to that corresponding to the deposition of lithium on Pt (~ —2.4 v), was detrimental to the reproducibility of subsequent polarograms, due to the difficulty of completely dissolving out the electropositive alloying elements from the Pt. The problem was accentuated by the decrease in the separation of the deposition potentials of the two metals by the alloy formation. Attempts to avoid this difficulty by the use of a tungsten or graphite microelectrode were not successful. Immersed, finely polished, flush-ground tungsten microelectrodes were attacked at the glass-metal seal and also gave irreproducible results, while a finely pointed, spectroscopic grade graphite rod immersed just in the surface of the melt gave very unsteady waves and appeared to disintegrate slowly.

A similarly surface-immersed graphite microelectrode was used to examine the behavior of approximately equal concentrations of U(III) and U(IV) at potentials more positive than can be reached with a Pt microelectrode. The U(IV)-U(III) combined wave was clearly shown, but no further waves were found between the potential at which this occurred and that at which chlorine was evolved.

Determination of the U(IV)-U(III) *Redox Potential*

In both the binary and ternary eutectics, when Pt(II) was electrolytically generated from an immersed Pt foil, reaction [1] occurred, and it was found that the potential of the Pt foil, measured against a Pt(II)-Pt(O) reference electrode at intervals between successive periods of anodization, followed typical potentiometric titration curves such as that shown in Fig. 8.

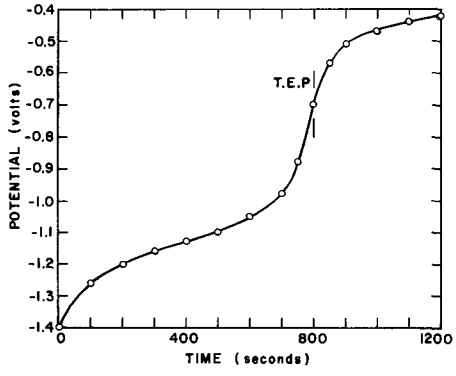

Fig. 8. Coulometric titration of U(III) with Pt(II) in $MgCl_2$-NaCl-KCl at 450°C. Pt(II)-Pt(O) reference electrode, 1.83 × 10^{-3} mole fraction of Pt(II); constant current, 48.25 ma, 1.2 × 10^{-3} equivalents U(III). T.E.P., theoretical end-point.

Titrations were performed with the argon-stirred Pt foil electrode shown in Fig. 3(b). During the course of the titration the initially dark red color of the melts due to U(III) gradually lightened, and just before the end points became light green in color, due to U(IV). Black, finely divided Pt was also seen in the melts. At the end of a titration the immersion of a uranium rod caused the melt to become red again due to the reaction

$$U + 3U(IV) \rightarrow 4U(III) \qquad [2]$$

Since both U(III) and Pt(II) were generated coulometrically, a theoretical end point could be calculated. In experiments with melts having very low residual impurity concentrations, as demonstrated by polarographic residual currents of considerably less than 1 $\mu a\ mm^{-2}$ at —1.0 v against the Pt(II)-Pt(O) reference electrode, the agreement between the amount of U(III) taken and the amount found was very close, as in Fig. 8. In many other experiments, the titration end points fell somewhat short of those calculated. As the initial concentration of U(III) in the melts was less than 600 ppm, it can readily be seen that in the case of a low molecular weight impurity such as oxygen, which reacts very readily with U(III) as described below, less than 10 ppm would be required to oxidize more than 10% of the initial U(III) concentration, and so the occurrence of low titration values is easily understood. Fortunately, this did not interfere too seriously with the determination of the U(IV)-U(III) redox potential which was taken from the relatively flat midportion of the lower branch of the curve. On the mole fraction scale the standard redox potentials found were —1.30 ± 0.01 v in $MgCl_2$-NaCl-KCl eutectic, and —1.25 ± 0.01 v in LiCl-KCl eutectic, with respect to the Pt(II)-Pt(O) couple at 450°C.

For a given experiment the shape of the lower branch of the curve can be calculated from the redox potential by means of the Nernst relation, and in general, good agreement was found with the shape obtained experimentally. Usually the initial potential, before any addition of Pt(II), corresponded to a U(IV) to U(III) ratio of ½% or less.

In view of the polarographic behavior of U(III), U(IV), and Pt(II) it was to be expected that amperometric end-point detection, using a Pt microelectrode at about —0.5 v vs. the working Pt(II)-

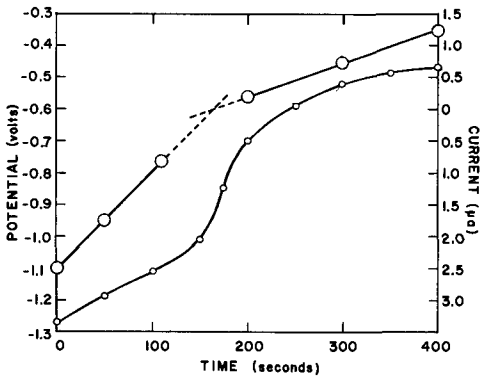

Fig. 9. Coulometric titration of U(III) with Pt(II) in $MgCl_2$-NaCl-KCl at 450°C, with amperometric end-point detection. Pt(II)-Pt(O) reference electrode, 1.75×10^{-3} mole fraction of Pt(II); constant current, 48.25 ma, 2.5×10^{-4} equivalents U(III). Microelectrode area 1.35 mm^2.

Pt(O) reference electrode, would be a convenient adjunct to the titration. In practice however, it usually presented difficulties, due in part to the necessity of waiting a considerable period of time after argon-stirring the melts for the current to become sufficiently steady to enable a reading to be taken, and in part due to the formation during the titration of finely divided Pt, which tended to become attached to the Pt microelectrode, and which was difficult to dislodge. A successful attempt to use this method of end-point detection is shown in Fig. 9 which also demonstrates that the polarographic behavior in the two eutectics was similar.

Preparation, Polarography, and Potentiometry of Uranyl Species

Solutions of the uranyl species were prepared in both eutectics at 450°C by bubbling dry oxygen (7) through the green solutions obtained by the addition of pure anhydrous uranium tetrachloride. The resulting solutions were clear yellow in color at low concentrations, and reddish-orange at high concentrations. The absorption spectrum in LiCl-KCl eutectic at 400°C was very similar to that observed for uranyl species in this solvent at the same temperature by Gruen (8), showing no evidence of the presence of U(IV), and x-ray patterns of the powdered yellow solid, obtained by grinding this solidified eutectic, showed lines characteristic of uranyl chloride. The reaction appeared to proceed smoothly and rapidly to completion with the evolution of chlorine. It was not possible to determine whether it proceeded directly, or through intermediate stages.

In other experiments it was observed that U(III) in solution in these melts also yielded clear yellow solutions rapidly when dry oxygen was bubbled in, but if moist air were used instead, partial precipitation, probably of oxides, also occurred.

To prepare for the polarographic and potentiometric work on the uranyl species, samples of a known weight of LiCl-KCl eutectic containing UO_2(VI) prepared directly in the melt from a known weight of UCl_4 were drawn up into several lengths of 6 mm glass tubing, quickly cooled to prevent the formation of concentration gradients, and sealed off to exclude moisture. Weighed samples of this solidified salt were later tapped out and added to LiCl-KCl solvent for study. This procedure provided a more convenient method for the introduction of known amounts of UO_2(VI) to the melt than does the direct addition of pure anhydrous UO_2Cl_2 powder prepared by the standard method of the reaction of UCl_4 with dry O_2 at 350°C.

Solutions of UO_2(VI) in LiCl-KCl at 450°C prepared in this way gave well-defined polarographic reduction waves at a Pt microelectrode with a Pt(II)-Pt(O) reference electrode; these are shown in Fig. 10.

If the process occurring were the reduction of UO_2(VI) to uranium dioxide, then by holding the potential of the microelectrode at a suitable value along the plateau, solid UO_2 should have been plated onto the electrode. At this point the microelectrode could be disconnected from the polarograph and its potential determined with the potentiometer. By repeating this procedure at various UO_2(VI) concentrations, a Nernst plot should have been obtained if a true equilibrium existed between the oxide and the uranyl species.

This postulate was tested and verified experimentally, and such a Nernst plot is shown in Fig. 11. The slope of the line (0.07166 v) is in good agreement with that calculated for a 2-electron process (0.07174 v). By extrapolation, the standard potential on the mole fraction scale for the UO_2(VI)-UO_2(IV) couple was found to be -0.285 ± 0.005 v against the standard Pt(II)-Pt(O) reference electrode.

Furthermore, a UO_2-plated Pt microelectrode should have produced a large anodic stripping current at potentials more positive than that for the

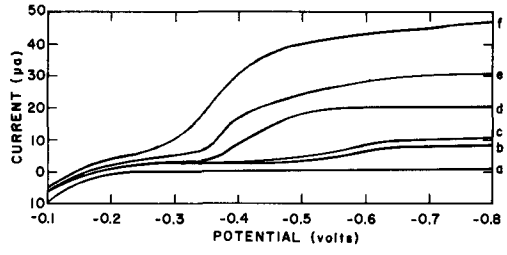

Fig. 10. Polarograms of UO_2(VI) reduction in LiCl-KCl at 450°C. Pt(II)-Pt(O) reference electrode, 1.05×10^{-3} mole fraction; microelectrode area, 1.35 mm^2; mole fractions UO_2(VI) $\times 10^{-4}$: a, 0; b, 0.23; c, 0.63; d, 2.42; e, 3.60; f, 4.80

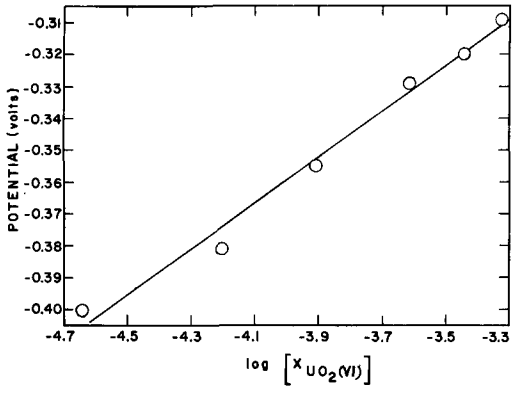

Fig. 11. UO_2(VI)-UO_2(IV) potential in LiCl-KCl at 450°C. Pt(II)-Pt(O) reference electrode, 1.05×10^{-3} mole fraction of Pt(II).

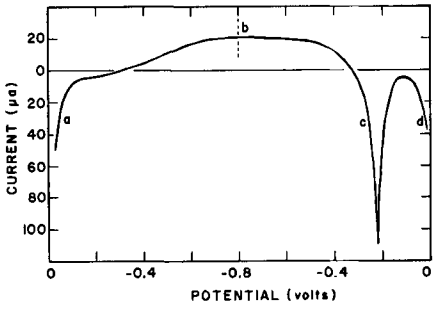

Fig. 12. Combined deposition and anodic dissolution waves for UO_2 in LiCl-KCl at 450°C. Pt(II)-Pt(O) reference electrode, 1.05×10^{-3} mole fraction of Pt(II); mole fraction $UO_2(VI)$, 2.42×10^{-4}; a, Pt dissolution; b, UO_2 deposition, reversal of direction of change in polarization; c, UO_2 dissolution; d, Pt dissolution. Microelectrode area 1.35 mm^2. Current below zero-axis is anodic.

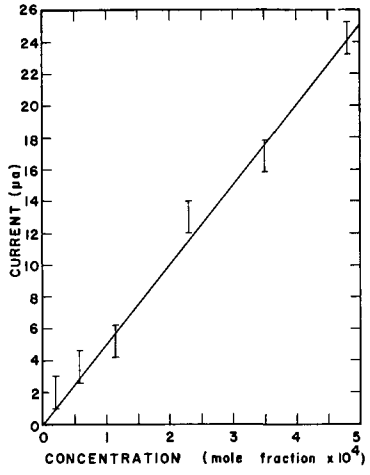

Fig. 13. Relation between wave height for $UO_2(VI)$ reduction and $UO_2(VI)$ concentration in LiCl-KCl at 450°C (from Fig. 10, at −0.7 v).

$UO_2(VI)$-$UO_2(IV)$ equilibrium if its potential were slowly shifted from a value on the plateau toward less negative values. This effect also was observed, and a typical combined deposition and stripping curve is shown in Fig. 12. The relation between wave height and $UO_2(VI)$ concentration is shown in Fig. 13.

Discussion

Results of the coulometric titration establish that U(III) was electrogenerated at 100% current efficiency in both eutectics. The value of the U(III)-U(O) potential in $MgCl_2$-NaCl-KCl eutectic is virtually identical to that found by Gruen and Osteryoung (9) in LiCl-KCl eutectic at the same temperature. Close correspondence of electrode potentials in different melts is not uncommon (10). The U(IV)-U(III) redox potentials observed in the present work provide a similar example. This correspondence of electrode potentials in different melts suggests that in many cases the behavior of the potential determining solute species is not dependent primarily on the nature of the solvent cationic species.

For the cell

$$(-)\mathrm{U}\left\{\begin{array}{l}\mathrm{U(III)}\\ \text{binary or ternary}\\ \text{chloride eutectic}\end{array}\right\}\left\{\begin{array}{l}\mathrm{Ag(I)}\\ \text{binary or ternary}\\ \text{chloride eutectic}\end{array}\right\}\mathrm{Ag}(+) \qquad \text{(I)}$$

the measured emf is in close agreement with that calculated from the established thermodynamic data for the pure compounds. This indicates that the free energies of solution of U(III) and Ag(I) are not very different, and are much smaller than the free energy change for the overall cell reaction, so that only the difference between two minor quantities is included in the calculation. For the cell

$$(-)\mathrm{Pt}\left\{\begin{array}{l}\mathrm{U(IV),U(III)}\\ \text{binary or ternary}\\ \text{chloride eutectic}\end{array}\right\}\left\{\begin{array}{l}\mathrm{Pt(II)}\\ \text{binary or ternary}\\ \text{chloride eutectic}\end{array}\right\}\mathrm{Pt}(+) \qquad \text{(II)}$$

a difference considerably greater than can be attributed to experimental error is found on making a similar comparison between measurement and calculation. Since for the cell

$$(-)\mathrm{Ag}\mid \mathrm{Ag(I)\ LiCl\text{-}KCl} \parallel \mathrm{Pt(II)\ LiCl\text{-}KCl}\mid \mathrm{Pt}(+) \qquad \text{(III)}$$

the same comparison leads to good agreement, it would appear that the difference between the measured and calculated values for the emf of cell (II) may be due to a comparatively large term involving the free energy of solution of U(IV). A possible interpretation of this is that U(IV) forms a chloro-

Table I. Comparison of measured cell potentials with those calculated from thermodynamic data[a] for the pure compounds at 450°C

Cell	Solvent eutectic	Potential measured	Potential calculated
(−)U|U(III)||Ag(I)|Ag(+)	Binary	+1.61[b]	+1.619
(−)U|U(III)||Ag(I)|Ag(+)	Ternary	+1.61	+1.619
(−)Ag|Ag(I)||Pt(II)|Pt(+)	Binary	+0.637[c]	+0.612
(−)U|U(III)||Pt(II)|Pt(+)	Binary	+2.25	+2.231
(−)U|U(III)||Pt(II)|Pt(+)	Ternary	+2.25	+2.231
(−)Pt|U(IV), U(III)||Pt(II)|Pt(+)	Binary	+1.25	+0.835
(−)Pt|U(IV), U(III)||Pt(II)|Pt(+)	Ternary	+1.30	+0.835
(−)U|U(IV)||Pt(II)|Pt(+)	Binary	+2.00[d]	+1.882
(−)U|U(IV)||Pt(II)|Pt(+)	Ternary	+2.01[d]	+1.882

[a] W. Hamer, M. Malmberg, and B. Rubin (16).
[b] D. M. Gruen and R. A. Osteryoung (9).
[c] H. A. Laitinen and C. H. Liu (6).
[d] Calculated from present measurements.

complex of sufficient stability in the chloride melts to shift the measured U(IV)-U(III) potential to a value more negative than that calculated from the thermodynamic formation data.[1] Similar considerations have been used by Flengas and Ingraham (11-15) to explain such differences between experimental and calculated values. Table I lists the comparisons made in the present work.

The U(III) oxidation waves are somewhat drawn out and do not conform quantitatively in respect of either log $[i/(i_d - i)]$ vs. potential plots, or potential at the intersection with the residual current vs. log [U(III)] plots, probably due to the difficulties inherent in recording polarograms at a stationary solid microelectrode. Nevertheless, the polarographic behavior otherwise and the potentiometric titration of U(III) demonstrate clearly that the reaction

$$U(IV) + e^- \rightleftharpoons U(III) \qquad [3]$$

behaves in a electrochemically reversible manner in both melts. In addition, the linear relation between wave height and concentration of U(III), and especially the coulometric titration, provide useful *in situ* analytical procedures. This titration is unique in that it uses an oxidant electrogenerated directly from a metal. Coulometric titration with amperometric end-point detection in fused LiCl-KCl using electrogenerated Fe(III) as oxidant has been the subject of a recent paper (17).

The absence of further oxidation waves at a graphite microelectrode in the potential range between U(III) oxidation and chlorine evolution indicates that U(V) and U(VI) are unstable in the melt, and confirms the observation by Gruen (7) that no reaction occurs when chlorine is bubbled into a solution of UCl_4 in the binary eutectic.

It has long been known (18) that pure molten uranyl chloride can be electrolyzed to produce UO_2 at the cathode and Cl_2 at the anode. The present work with the uranyl species clearly demonstrates that the equilibrium

$$UO_2(VI) + 2e^- \rightleftharpoons UO_2(IV) \qquad [4]$$

can be established in the melt LiCl-KCl, and the movement of the UO_2 deposition potential toward less negative values as the $UO_2(VI)$ concentration is increased is readily understood. This work also confirms and extends the observation by Smirnov and Ivanovsky (19) that anodes of compacted UO_2 could be dissolved anodically in LiCl-KCl eutectic at 650°C, with the production of uranyl ions, and that it was possible to obtain weakly adherent electroplates of UO_2 on molybdenum cathodes. In the present work it was noticed that argon stirring of the melt drastically altered the potential of the UO_2-plated microelectrode in the direction consistent with the physical removal of the plate. Smirnov and Ivanovsky also studied the potential of a UO_2 anode at various current densities, and by extrapolation to zero current density obtained a potential of −0.57 v against a chlorine-chloride reference electrode at 550°C in a dilute but undefined concentration of $UO_2(VI)$. Using the value (20) of −0.216 v for the difference between the standard potentials of the Pt(II)-Pt(O) and Cl_2-Cl^- couples, the present work yields a value of −0.501 v for the $UO_2(VI)$-$UO_2(IV)$ standard potential against the standard Cl_2-Cl^- reference electrode on the mole fraction scale. That this is less negative than the value found by Smirnov and Ivanovsky is to be expected in view of the lower temperature and the use of unit mole fraction as the standard state.

The heights of the $UO_2(VI)$ reduction waves are seen to be an approximately linear function of concentration, but it is difficult to determine them accurately because they are not too steady, and the plateaus are not smooth lines. In this case the difficulties associated with the use of stationary solid microelectrodes are probably accentuated by uneven or rough growth and poor adherence of the oxide plate, and straight line plots of log $[(i_d - i)]$ vs. potential do not have the slope expected for a 2-electron process.

With regard to the electrodeposition of pure uranium from fused salt baths, the present work shows clearly that, in the preparation of uranium by the reduction of U(IV) in a chloride melt, the primary process proceeds stepwise, first to U(III), then to the metal. In view of the measured value of the U(IV)-U(III) redox potential, the majority of metal ion impurities in the melt can oxidize U(III) to U(IV), and this is the probable cause of the presence of U(IV) in the melts deduced from the initial potential of the indicator electrode in the coulometric titrations. Further, since both U(III) and U(IV) react rapidly with oxygen to form $UO_2(VI)$, the reduction of either U(III) or U(IV) from a melt contaminated by oxygen must result in the inclusion of UO_2 with the uranium deposit, and from the measured potentials, both U(III) and uranium metal should be capable of reducing $UO_2(VI)$ to $UO_2(IV)$. For the same reasons, the reversible redox equilibrium between uranium dissolved in a liquid metal and U(III) in a molten chloride solvent will be upset by oxygen impurities in the melt.

Acknowledgment

This work was performed under Contract No. AT 30-2-GEN-16 Subcontract No. S-348 with the U. S. Atomic Energy Commission through Brookhaven National Laboratory.

Manuscript received Jan. 6, 1960. This paper was presented, in part, at the 136th Meeting of the American Chemical Society.

Any discussion of this paper will appear in a Discussion Section to be published in the June 1961 JOURNAL.

REFERENCES

1. L. W. Niedrach and A. C. Glamm, *This Journal*, **103**, 521 (1956).
2. L. W. Niedrach and B. E. Dearing, *ibid.*, **105**, 353 (1958).
3. W. S. Ginell, *Ind. Eng. Chem.*, **51**, 185 (1959).
4. G. Meister, *Metal Progr.*, **53**, 515 (1948).
5. D. Inman, G. J. Hills, L. Young, and J. O'M. Bockris, *Trans. Faraday Soc.*, **55**, 1904 (1959); *Ann. N. Y. Acad. Sci.*, **79**, 803 (1960).

[1] This conclusion is in contrast to that of Inman, *et al.* (5) who conclude that complexing of U(III) occurs. However, it appears that the calculations from which this conclusion was drawn are in error, and that their data do not show significant evidence of complexing of U(III), a result in accord with the present work and with that of Gruen and Osteryoung (9).

6. H. A. Laitinen and C. H. Liu, *J. Am. Chem. Soc.*, **80**, 1015 (1958).
7. D. M. Gruen, *Private communication.*
8. D. M. Gruen, S. Fried, P. Graf, and R. L. McBeth, *Proc. Intern. Conf. Peaceful Uses Atomic Energy, 2nd Conf., Geneva, 1958*, **28**, 112 (1958).
9. D. M. Gruen and R. A. Osteryoung, *Ann. N. Y. Acad. Sci.*, **79**, 897 (1960).
10. S. N. Flengas and T. R. Ingraham, *This Journal*, **106**, 714 (1959).
11. S. N. Flengas and T. R. Ingraham, *Can. J. Chem.*, **35**, 1139 (1957).
12. S. N. Flengas and T. R. Ingraham, *ibid.*, **35**, 1254 (1957).
13. S. N. Flengas and T. R. Ingraham, *ibid.*, **36**, 780 (1958).
14. S. N. Flengas and T. R. Ingraham, *ibid.*, **36**, 1103 (1958).
15. S. N. Flengas and T. R. Ingraham, *ibid.*, **36**, 1063 (1958).
16. W. Hamer, M. Malmberg, and B. Rubin, *This Journal*, **103**, 8 (1956).
17. H. A. Laitinen and B. B. Bhatia, *Anal. Chem.*, **30**, 1995 (1958).
18. W. Hampe, *Chem. Ztg.*, **12**, 106 (1888).
19. M. V. Smirnov and L. E. Ivanovsky, *J. Gen. Chem. U.S.S.R.*, **27**, 329 (1957).
20. H. A. Laitinen and J. W. Pankey, *J. Am. Chem. Soc.*, **81**, 1053 (1959).

Electrochemical Study of Metallic Oxides in Fused Lithium Chloride-Potassium Chloride Eutectic

H. A. Laitinen and B. B. Bhatia

Noyes Chemical Laboratory, University of Illinois, Urbana, Illinois

ABSTRACT

The oxygen electrode does not behave reversibly in LiCl-KCl at temperatures of 400°-500°C, and at oxide ion concentrations of 0.1-0.2M. The following electrode systems behave reversibly as electrodes of the second kind: Cu/$Cu_2O,O^=$; Pt/PtO,$O^=$; Pd/PdO,$O^=$; Bi/BiOCl,$O^=$. The Ni/NiO,$O^=$ and Bi/Bi_2O_3,$O^=$ electrodes did not show reversible behavior. Because of the relatively high solubilities of the metal oxides, the applicability of the metal oxide electrodes to the measurement of oxide ion activity is limited to solutions containing oxide ion in concentrations comparable with, or greater than, that contributed by dissolution of the oxides. This limit is 10^{-3}M or higher, depending on the system. The relatively high solubility of heavy metal oxides in this solvent is attributed to the great complexing tendency of chloride ion. It is probable that these oxides would be much less soluble in nitrate and sulfate melts and thus their utility as acidity electrodes could be extended to lower oxide concentrations.

A molten alkali metal chloride solvent may be said to be "buffered" with respect to the addition of Lewis acids such as $AlCl_3$ because of the presence of a large excess of the weakly basic chloride ion. On the other hand, such a solvent can be rendered basic by the addition of substances such as oxide ion which are more strongly basic than chloride ion.

The purpose of the present investigation was to determine the feasibility of using the oxygen-oxide ion electrode or metal-metal oxide-oxide ion electrodes for the electrochemical measurement of oxide ion activity in molten lithium chloride-potassium chloride eutectic at 450°. A secondary objective was to determine the solubilities of metal oxides from emf measurements.

There is considerable evidence for the reversibility of the oxygen-oxide ion electrode at temperatures of the order of 1000°C in various melts containing oxyanions. The early work of Baur and Ehrenberg (1) on borates, silicates, etc., and of Treadwell (2) on metal oxides, using quartz or porcelain as an electrolyte and silver as the indicator electrode, had indicated that the oxygen-oxide ion was exhibiting reversible behavior.

Csáki and Dietzel (3) reported on emf measurements in cells involving platinum indicator electrodes in borate melts, but their interpretation of the results has been criticized by Flood, Forland, and Motzfeld (4). Antipin (5) used a graphite electrode, which had been anodized to make it behave as an oxygen electrode, as a reference electrode in cryolite at 1050°C. The investigations of Lux (6) largely in sulfate and phosphate systems at 950°C were the first which clearly showed the feasibility of oxide ion activity measurements using a platinum electrode with oxygen gas. Similar measurements were made by Flood and co-workers (4, 7, 8) who demonstrated that the dependence of the potential on oxide ion activity obeyed the Nernst equation.

Work at lower temperatures has been much more limited in scope. Rose, Davis, and Ellingham (9) made measurements involving oxygen electrodes in molten NaOH containing small concentrations of tin or lead at 400°-700° and found that the cells behaved reversibly. Hill and co-workers (10) measured emfs of cells of the type

M/MO/CaO in Li_2SO_4-K_2SO_4/Pt,O_2 [A]

at 550°-750°C and concluded that for iron, copper, and (at temperatures below 658°C) nickel, the cell emf agreed with that calculated from the free energy of formation of the metal oxide. Since both of the electrodes used by Hill, *et al.* theoretically responded equally to oxide ion activity, the cell emf data did not show whether the potentials of the two types of oxide ion electrodes individually varied properly with oxide ion activity. Selis and co-workers (11) in interpreting the galvanic behavior of a Mg-Ni cell in moist lithium chloride-potassium chloride eutectic, considered that the potential-determining systems were $Mg/MgO,O^=$ and either $Ni/NiO,O^=$ (at temperatures of 445°-535°C) or H_2, $Ni/OH^-,O^=$ (at temperatures of 390°-440°C). Once again, the individual electrode behavior against a reference electrode that was invariant with oxide ion activity was not determined.

In the present investigation, a platinum(II)-platinum electrode (12) was used as a reference for the measurement of the potentials of the oxygen-oxide ion electrode and of various metal-metal oxide-oxide ion electrodes as a function of the concentration of oxide ion.

Previous attempts to measure reversible oxygen potentials, using a platinum foil or graphite rod as an indicator electrode, had been unsuccessful (13). In the present study, a porous graphite electrode was used, again with unsuccessful results, as will be seen below.

For an electrode of the second kind, composed of a metal M, its sparingly soluble oxide $MO_{n/2}$, and free oxide ion, the Nernst equation is given by

$$E = E^\circ_{M^{n+},M} + RT/n\mathbf{F} \ln a_{M^{n+}} \quad [1]$$

$$= E^\circ_{M^{n+},M} + RT/n\mathbf{F} \ln (K_{ap}/a_{O^=})^{n/2} \quad [2]$$

$$= E^\circ_{M^{n+},M} + RT/2\mathbf{F} \ln K_{ap} - RT/2\mathbf{F} \ln a_{O^=} \quad [3]$$

where $E^\circ_{M^{n+},M}$ is the standard electrode potential[1] for the metal ion-metal electrode, and $K_{ap} = a_{M^{n+}}{}^{2/n} a_{O^=}$, is the activity product of the sparingly soluble oxide. The first two terms on the right hand side of Eq. [3] can be combined to give the standard potential of the electrode of the second kind, or

$$E = E^\circ_{oxide} - RT/2\mathbf{F} \ln a_{O^=} \quad [4]$$

which is the Nernst equation for the electrode reaction

$$MO_{n/2} \text{ (solid)} + ne^- \rightleftharpoons M + \frac{n}{2} O^= \quad [5]$$

From previous work on the electromotive force series in LiCl-KCl (12) it may be inferred that activities may be replaced by concentrations in Eq. [1]-[4] if a very dilute solution is chosen as the standard state, at least if the mole fraction of added solute is in the range 10^{-2} to 10^{-4}. For analytical purposes it will be convenient to adopt the molarity scale of concentration, although simple conversion factors to molality or mole fraction may be applied if desired. The formal potential $E^{\circ\prime}$, written to describe the electrode with soluble reactants at a concentration of 1M, will therefore be written as E°, the standard potential. At 450°C the Nernst factor $2.303RT/\mathbf{F}$ becomes 0.1434 v, so that the theoretical slope of the plot of potential against log C, the logarithm of molar concentration of oxide ion, becomes 71.7 mv if a solid uncharged oxide is formed, regardless of the valence of the metal. Deviation from this slope implies a different course of the reaction.

The metals in this study were chosen to have stable oxides at the operating temperature and to be comparatively noble, in order that the electrode potentials would not become excessively negative and therefore subject to interference by traces of reducible impurities in the presence of excess oxide.

Experimental

The eutectic mixture of 41 mole % potassium chloride and 59 mole % lithium chloride (melting point 352°C) was used as a solvent system at 450°C, the working temperature in this investigation. The technique of preparation and purification as described in a detailed form earlier (15, 27) was followed. The reference electrode was a platinum plate immersed in a platinum(II) solution prepared in a fritted glass compartment by anodic dissolution with a known quantity of electricity. After each experiment the reference electrode compartment was analyzed by titration for chloride to determine the amount of solvent, and the potential was corrected to a Pt(II) concentration of 1M by calculation using the Nernst equation.

The associated apparatus and equipment used in fused salt methodology has been described elsewhere (16-19).

The oxygen electrode was a porous graphite electrode, of a type described by Senderoff and Mellors (20), which was held in an oxygen atmosphere at 400°C for 5 hr before use.

In the study of metal oxides the solvent was compartmented into medium porosity fused alumina or zirconia tubes. Prior to their actual use the tubes were soaked in hydrochloric acid for a few days in order to remove any basic oxides incorporated as binding agents in the tubes. After this treatment, the tubes were washed thoroughly with distilled water and dried at 500°C before they were inserted in the melt. There was no evidence for the presence of any objectionable species in the melt due to the use of these tubes. The residual current was found to be the same whether alumina or zirconia tubes or fritted glass compartments were used. Glass frits were used only when the study was purely qualitative in nature, for instance, when it was desired to observe color changes in the system. The solutes, generally anhydrous metallic salts, were added to the compartmentation tubes with the aid of a small platinum scoop which was mounted on a glass handle. At times, coulometric generation of metal ions by anodic oxidation of pure metal foils or wires was employed. At the conclusion of each experiment, the chloride content of each compartment was determined by an argentometric titration as described elsewhere (12). Thus, knowing the volume of the solution in the compartment, the concentration of solute at the time of measurement could be calculated.

[1] The IUPAC sign convention (14), in which half-reactions are written as reductions and the sign refers to the sign of the charge on the metal, is used.

The anhydrous metallic oxides were prepared as follows: Calcium oxide, platinum(II) oxide, and bismuth(III) oxide were made by vacuum desiccation of commercially available anhydrous samples. Lithium oxide was prepared from an analytical grade sample of lithium hydroxide monohydrate according to a procedure outlined by Brauer (21). Nickel(II) oxide (22), copper(I) oxide (21), palladium(II) oxide (23), and bismuth(III) oxychloride (21) were prepared according to available procedures.

Results and Discussion

The oxygen electrode, when dipped into solutions 0.09M to 0.21M in lithium oxide, was found very slow to reach equilibrium at temperatures of 400°-500°C. After 6-7 hr, the potential usually had reached a constant value, the final potentials at 450°C being −0.212, −0.328, and −0.407 v against a 1M Pt(II) reference electrode, at oxide ion concentrations of 0.094, 0.167, and 0.21M, respectively. These data do not yield a linear semi-logarithmic plot, and the rate of change of potential with concentration is much greater than predicted by the Nernst equation. The slope of the "best" straight line is about 0.6 v rather than the theoretical 0.0717 v. Similar behavior was observed at 400° and 500°C. It is concluded that reversible behavior could not be achieved under the conditions of the present study. It is likely that carbon takes part in the potential-determining reaction, in view of the finding by Smirnov, *et al.* (24) that at 800°C in KCl-NaCl saturated with CaO, the potential-determining reaction of a carbon electrode is

$$2Ca^{++} + CO_2 + 4e^- \rightleftharpoons C + 2CaO$$

Consequently, the drifting potentials and nonequilibrium character in the present study are probably due to mixed electrode processes.

The following metal oxides were studied in this investigation: copper(I) oxide, nickel(II) oxide, platinum(II) oxide, palladium(II) oxide, bismuth(III) oxide. In addition, bismuth oxychloride was compared with bismuth(III) oxide. The general procedure was to add a weighed amount of an anhydrous metal oxide to the melt collected in a zirconia tube and to measure the potential after each addition, a metal rod or foil serving as the indicator electrode. A different procedure was followed with bismuth oxide and bismuth oxychloride since metallic bismuth is a liquid at the operating temperature in this investigation (450°C). A tungsten rod in contact with a bismuth pool was used as a bismuth electrode. After each addition of metal oxide, the solution was well stirred and left for 15-20 min before a potential measurement was made. In almost all cases studied, the melt was saturated with the first addition of oxide and no change in potential was observed on subsequent additions of oxide. For following the reversibility of these electrode systems, varying amounts of lithium or calcium oxide were added to establish the oxide ion concentration. These oxides are known to be fairly soluble in lithium chloride-potassium chloride eutectic.

To calculate the equilibrium concentration of oxide ion, it was necessary to take into account the contribution from the solubility of the metal oxide. To illustrate the procedure, the measurements on the Pd-PdO system are given in Table I. The measured emfs of cells of the type

Pt|Pt(II), (A molar)||CaO (B molar), PdO (solid)|Pd [B]

were first calculated to a platinum(II) concentration of 1M, to give the figures in the last column. From the standard potential of the Pd(II),Pd electrode (−0.214 v vs. 1M Pt(II)), estimates of the solubility product of PdO were made, using the stoichiometric concentrations of calcium oxide added (column 2). The two values (6.63 and 6.49 × 10^{-5}, respectively) estimated from the higher added oxide concentrations were averaged to give 6.56 × 10^{-5}. From the solubility product, using a quadratic solution, the corrected oxide ion concentrations were calculated. The oxide ion concentration of a saturated solution of PdO without added CaO would be expected to be equal to the square root of the solubility product, or 8.1 × 10^{-3}M. From the standard potential of palladium and the measured emf, a Pd(II) concentration of 9.38 × 10^{-3}M is calculated. This suggests that some initial oxidation of Pd, promoted by the presence of oxide ion, had occurred before the oxygen had been completely flushed from the system. A better estimate of initial oxide concentration is given by $K_{sp}/9.38 \times 10^{-3} = 7.0 \times 10^{-3}$M.

Table I. Potential of Pd, PdO Electrode at Various Concentrations of Added Oxide Ion

Total CaO added, mg to 8.3 ml cell	CaO added, stoichiometric molar conc.	[O=] corr, molar	*E* (Cell[B]), volt measured	*E*, volt, *versus* 1*M* Pt reference
0	0	7.0×10^{-3}	−0.2371	−0.3594
7.8	0.0168	2.06×10^{-2}	−0.2700	−0.3923
15.9	0.0342	3.60×10^{-2}	−0.2862	−0.4058
23.0	0.0494	5.07×10^{-2}	−0.2992	−0.4215

The solubility of each metal oxide was estimated by three procedures: (*a*) from the measured potential of the metal in a solution saturated with its oxide, (*b*) from measurements of the voltammetric (polarographic) diffusion current of a solution saturated with the oxide, and (*c*) from E°_{oxide}, defined as the standard potential of the metal, metal oxide electrode obtained from the experimental curve of electrode potential against logarithm of oxide ion concentration extrapolated to a concentration of 1M (Eq. [4]).

Two alternate procedures were used to prepare half-cells. In the first, a metal was dissolved anodically in the melt and lithium or calcium oxide was subsequently added. In the second, a weighed amount of anhydrous metal chloride was added to the melt containing the soluble calcium or lithium oxide. A brief discussion of each metal-metal oxide system studied will now be given. For each electrode system, a plot of logarithm of molarity of oxide vs. potential against 1M platinum reference electrode has been made. These plots are depicted in Fig. 1, 2, and 3. In each figure the points are connected

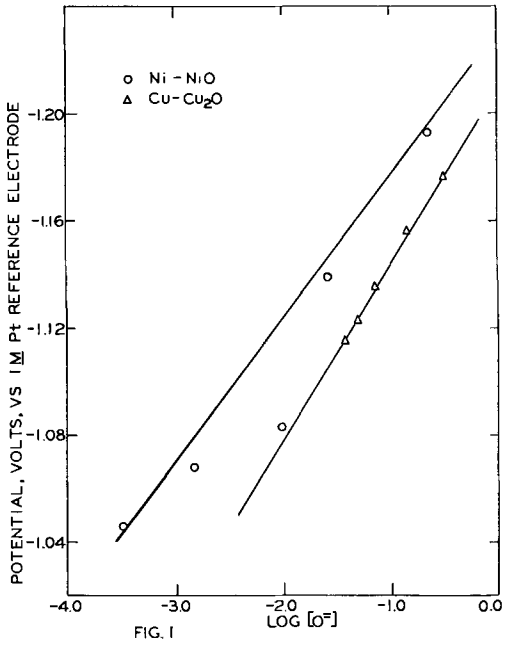

Fig. 1. Experimental behavior of Ni/NiO,$O^=$ and Cu/Cu_2O,$O^=$ electrodes. For comparison with theory, see text.

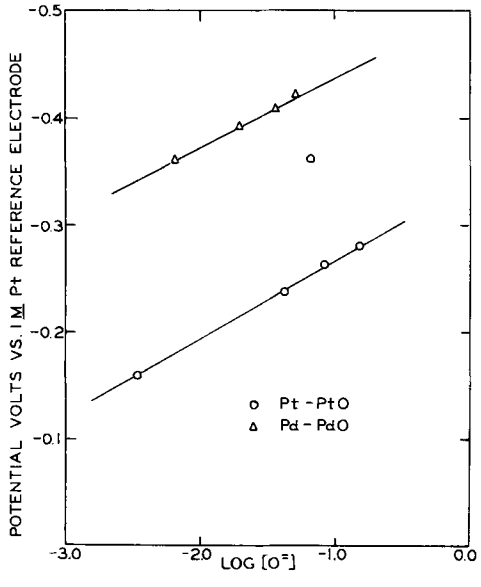

Fig. 2. Experimental behavior of Pt/PtO,$O^=$ and Pd/Pd,O,$O^=$ electrodes. For comparison with theory, see text.

by the best straight line. The experimental and theoretical slopes are compared in the text.

Nickel(II) oxide.—The nickel-nickel oxide couple, $NiO + 2e^- = Ni + O^=$, was the first to be studied. Nickel is known to form NiO as a stable oxide and no oxychloride of this metal is known. The concentration of nickel calculated from the potentials is 3.3×10^{-4} mole liter^{-1}. The concentration found from a polarogram taken of a saturated solution of NiO in the melt was 3.2×10^{-4} mole liter^{-1}. A plot of log [$O^=$] vs. E, shown in Fig. 1, showed a considerable departure from the theoretical slope and therefore indicated irreversibility of the system. The slope calculated by the least squares method is 53 mv as compared to a theoretical slope of 71.7 mv for a reversible half reaction. The E°_{oxide} value can approximately be quoted as —1.23 v which corresponds to

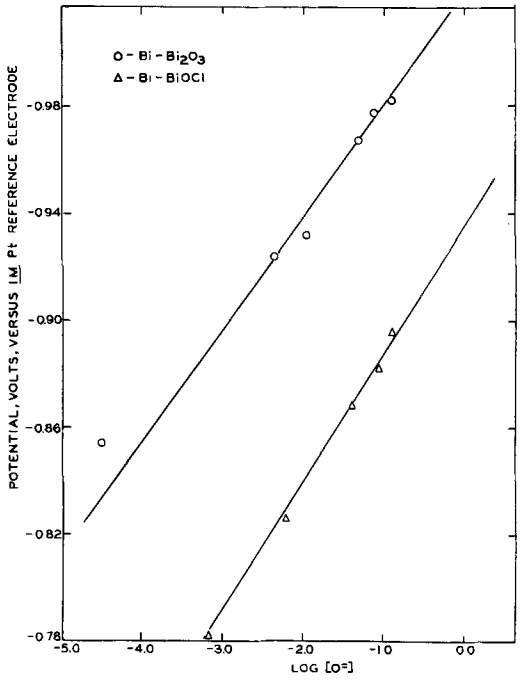

Fig. 3. Experimental behavior of Bi/Bi_2O_3,$O^=$ and Bi/BiOCl, $O^=$ electrodes. For comparison with theory, see text.

solubility of *ca.* 10^{-3} moles/liter, calculated from the theoretical slope. The experimental points on the figure are scattered and thus very little theoretical significance can be attached to the E°_{oxide} value. The value —1.23 v is more positive than expected from $E^\circ_{Ni^{++}-Ni}$ and solubility of NiO estimated polarographically (—1.297 v).

Two reasons may be advanced for the discrepancy between theory and experiment. First, the Ni(II)-Ni system may act irreversibly in the presence of excess oxide ion. This explanation is implausible because of the high exchange current of the Ni(II)-Ni electrode (24) and the moderate solubility of NiO in LiCl-KCl. Second, a higher nickel oxide, e.g., Ni_2O_3, may be formed. In this instance the measured potentials would be mixed potentials due to the presence of NiO and Ni_2O_3. This explanation appears to be more plausible, particularly because the formation of the latter oxide has been shown to be promoted by the presence of lithium oxide (25). Evidence for the existence of Ni_2O_3 at temperatures of 660°C and higher in molten lithium sulfate-potassium sulfate eutectic has also been published recently by Hill and co-workers (10).

Copper(I) oxide.—The solubility of Cu_2O, as determined from potential measurements and from a current-voltage curve, was 3.8×10^{-2} moles liter^{-1} and 5.8×10^{-2} moles liter^{-1}, respectively. A plot of log [$O^=$] vs. E shown on Fig. 1 gave a slope of 66.2 mv and the E°_{oxide} value, —1.207 v. The solubility calculated from the E°_{oxide} value was 6.95×10^{-2} moles liter^{-1} which is in agreement with the values obtained directly. Corresponding to the electrode reaction $Cu_2O + 2e^- \rightleftharpoons 2Cu + O^=$, the system Cu/$Cu_2O$,$O^=$ acts as an electrode of the second kind, but the application of this electrode as an indicator electrode for oxide ion is limited by the high solubility of Cu_2O.

Platinum(II) oxide.—A saturated solution of PtO in equilibrium with solid oxide when brought in contact with the platinum foil electrode registered a potential of −0.0546 v vs. a 3.28×10^{-2} M Pt(II) reference. This potential was stable over a long period (4-5 hr). From the potential the solubility of PtO was calculated to be 3.32×10^{-3} moles liter^{-1}. The effect of additional increasing amounts of CaO on the potential was also followed. A plot of log $[O^=]$ vs. E is shown in Fig. 2. The slope of the plot is 72.5 mv and E°_{oxide} is −0.3385 v. The solubility calculated from the E°_{oxide} value is 4.36×10^{-3} moles liter^{-1} which is in good agreement with the measured value.

In some experiments PtO was generated internally by anodizing platinum foil in the melt in the presence of an excess of CaO. Although the measurements agreed with those obtained by direct addition of PtO, the establishment of equilibrium was so slow that it took almost 24 hr to make four measurements. Stirring of the solution or passing of small current (*ca.* 1 μa), while the measurements were made, did not speed the attainment of equilibrium appreciably

Palladium(II) oxide.—Following the procedure explained above, the solubility of PdO from potential measurements was calculated as 9.4×10^{-3} moles liter^{-1}. The plot of log $[O^=]$ vs. E shown on Fig. 2 gives a slope of 74.2 mv and E°_{oxide}, −0.514 v. The solubility calculated from E°_{oxide} is 8.1×10^{-3} moles liter^{-1}. The attainment of equilibrium in this system was also extremely slow. From the experimental data, however, the electrode system appears to behave as a reversible electrode of the second kind.

Bismuth (III) oxide.—In studying the $Bi/Bi_2O_3,O^=$ system, a re-evaluation of the standard potential of the Bi(III)/Bi electrode was made. Using a tungsten electrode in contact with a molten Bi pool, a value of −0.63 v vs. 1M Pt(II)/Pt on the molarity scale was found. This value is in agreement with the value of −0.64 ± 0.01 v reported elsewhere (24), using a tungsten contact, rather than the previous value of −0.553 v originally reported (12), using a platinum contact. The disagreement may be attributed to alloy formation between platinum and liquid bismuth.

Experimental values of the potential of a bismuth electrode in the presence of sufficient solid Bi_2O_3 to form a solid phase, and with varying concentrations of oxide ion, added as CaO, are given in Fig. 3. The electrode potential followed the empirical equation

$$E = -1.023 - 0.042 \log [O^=] \qquad [6]$$

from which $K_{sp} = 3.2 \times 10^{-6}$ using Eq. [3]. The slope of the logarithmic plot (42 mv), however, does not agree with the theoretical value of 71.7 mv given in Eq. [4]. The value of K_{sp} can also be estimated from the potential of the bismuth pool in the presence of Bi_2O_3 but in the absence of added CaO (−0.8543 v vs. 1M Pt), from which $[Bi^{+3}] = 2.06 \times 10^{-3}$M. If it is assumed that $[O^=] = 3/2\ [Bi^{+3}] = 3.09 \times 10^{-3}$, a value of $K_{sp} = [Bi^{+3}]^{2/3}[O^=] = 5.0 \times 10^{-5}$ is estimated, differing by almost an order of magnitude from the estimate made from the intercept.

From the fact that the theoretical Nernst slope is not observed, however, it can be inferred that the simple solubility equilibrium of Bi_2O_3 is not reached. If Bi_2O_3 dissolves through the intermediate formation of BiO^+, the theoretical Nernst slope would not be affected as long as solid Bi_2O_3 were present at equilibrium. If Bi_2O_3 interacts to form a new solid phase of BiOCl and is present in excess so that both solid phases exist, then the equilibrium

$$Bi_2O_3(\text{solid}) + 2Cl^- \rightleftharpoons 2BiOCl(\text{solid}) + O^= \qquad [7]$$

would correspond to a fixed oxide ion (and therefore bismuth ion) activity. Addition of excess oxide would merely change the relative amounts of the two solid phases. On the other hand, if *all* the Bi_2O_3 were converted to a new solid phase of BiOCl, then, in accordance with the half reaction

$$BiOCl\ (\text{solid}) + 3e^- \rightleftharpoons Bi + O^= + Cl^- \qquad [8]$$

a Nernst slope of 2.3 $RT/3\mathbf{F}$ (47.8 mv) would be expected. The concentration of oxide ion, however, would depend on the amount of Bi_2O_3 as well as CaO which had been added. To clarify this point, a separate study of the $Bi/BiOCl,O^=$ electrode was made.

Bi(III) *oxychloride.*—The bismuth electrode in the presence of solid BiOCl and added CaO was found to obey the equation

$$E = -0.935 - 0.045 \log [O^=] \qquad [9]$$

in good agreement with the theoretical equation

$$E = E^\circ_{Bi^{+3},Bi} + RT/3\mathbf{F} \ln K_{sp} - 0.0478 \log [O^=] \qquad [10]$$

where $K_{sp} = [Bi^{+3}][O^=]$.

From the intercept, $K_{sp} = 4.2 \times 10^{-7}$. From the potential in the absence of added oxide (−0.782 v vs. 1M Pt), a bismuth ion concentration $[Bi^{+3}] = 6.6 \times 10^{-4}$ and $K_{sp} = 4.4 \times 10^{-7}$ are calculated, in good agreement with the value calculated from the intercept. Moreover, from the polarographic wave height for saturated BiOCl, a solubility of 6.9×10^{-4}, corresponding to $K_{sp} = 4.8 \times 10^{-7}$, was estimated.

It may be concluded that the electrode $Bi/BiOCl,O^=$ is behaving reversibly and that the above estimates of the solubility are therefore valid. It is interesting to note that these data indicate no appreciable interaction between Bi^{+3} and $O^=$ to form a complex such as BiO^+.

Returning now to the behavior of Bi_2O_3, it is clear from a comparison of Eq. [6] and [9] that, at the same added oxide ion concentration, the Bi_2O_3 electrode showed a more negative potential than the corresponding BiOCl electrode. If Bi_2O_3 were to interact according to Eq. [7] to produce BiOCl and oxide ion, the oxide ion concentration would be increased and qualitatively the electrode potential would be shifted in the negative direction as actually observed. The slope, however, would be affected because the oxide appearing from reaction [7] would exert more influence at low concentrations than at high concentration of added oxide ion. It appears probable that some interaction occurs between solid Bi_2O_3 and the melt, but that either the reaction is not as simple as represented by Eq. [7] or the system is slow to come to equilibrium, or

both. In an event, the $Bi/Bi_2O_3,O^=$ electrode cannot be regarded as a reversible oxide ion electrode.

Acknowledgment

The porous graphite used in the fabrication of the oxygen electrode was kindly provided by Dr. Seymour Senderoff, of the National Carbon Company. The authors extend their appreciation to the Office of Ordnance Research and the Diamond Ordnance Fuze Laboratory for the financial support of this project and for the research assistantship held by one of them (B. B. Bhatia).

Manuscript received Dec. 17, 1959. This paper was prepared for delivery before the Chicago Meeting, May 1-5, 1960.

Any discussion of this paper will appear in a Discussion Section to be published in the June 1961 JOURNAL.

REFERENCES

1. E. Baur and H. Ehrenberg, *Z. Elektrochem.*, **18**, 1002 (1912).
2. W. D. Treadwell, *ibid.*, **22**, 414 (1916).
3. P. Csáki and A. Dietzel, *Glastechn. Ber.*, **18**, 33, 65 (1940).
4. H. Flood, T. Forland, and K. Motzfeldt, *Acta Chem. Scand.*, **6**, 257 (1952).
5. L. N. Antipin, *Zhur. Fiz. Khim.*, **29**, 1668 (1955).
6. H. Lux, *Z. Elektrochem.*, **45**, 303 (1939); **52**, 220 (1948); **53**, 41 (1949).
7. H. Flood and T. Forland, *Acta Chem. Scand.*, **1**, 592 (1947).
8. H. Flood and T. Forland, *Faraday Soc. Discussions*, No. 1, 302 (1947).
9. B. A. Rose, G. J. Davis, and H. J. T. Ellingham, *ibid.*, No. 4, 154 (1948).
10. D. G. Hill, B. Porter, and A. S. Gillespie, Jr., *This Journal*, **105**, 408 (1958).
11. S. M. Selis, G. R. B. Elliott, and L. P. McGinnis, *ibid.*, **106**, 134 (1959).
12. H. A. Laitinen and C. H. Liu, *J. Am. Chem. Soc.*, **80**, 1015 (1958).
13. H. A. Laitinen and J. W. Pankey, Unpublished investigations.
14. T. S. Licht and A. J. de Bethune, *J. Chem. Education*, **34**, 433 (1957).
15. D. K. Roe, Ph.D. Thesis, University of Illinois (1959).
16. W. S. Ferguson, Ph.D. Thesis, University of Illinois (1956).
17. H. A. Laitinen and W. S. Ferguson, *Anal. Chem.*, **29**, 4 (1957).
18. H. A. Laitinen, R. A. Osteryoung, and W. S. Ferguson, *This Journal*, **104**, 516 (1957).
19. B. B. Bhatia, Ph.D. Thesis, University of Illinois (1959).
20. S. Senderoff and G. W. Mellors, *Rev. Sci. Inst.*, **29**, 151 (1958).
21. G. Brauer, "Handbuch der präparativen anorganischen Chemie," Ferdinand Enke Verlag, Stuttgart (1954).
22. J. R. Tomlinson, *et al.*, *J. Am. Chem. Soc.*, **77**, 909 (1955).
23. R. L. Shriner and R. Adams, *J. Am. Chem. Soc.*, **46**, 1683 (1924).
24. H. A. Laitinen, R. P. Tischer, and D. K. Roe, *This Journal*, **107**, 546 (1960).
25. M. V. Smirnov, S. F. Pal'guev, Y. N. Krasnov, and L. A. Lyapina, *Zhur. Priklad. Khim.*, **30**, 1687 (1957).
26. R. L. Tichenor, *Ind. Eng. Chem.*, **44**, 973 (1952).

Solutions of Some Alkali Halides in the Pure Liquids and in Mixtures of N-Methylacetamide and Dimethylformamide

Lyle R. Dawson and Walter W. Wharton

Department of Chemistry, University of Kentucky, Lexington, Kentucky

ABSTRACT

Dielectric constants, densities, and viscosities of N-methylacetamide, dimethylformamide, and of mixtures of these liquids have been determined at five temperatures. Conductances, densities, and viscosities of solutions of sodium and potassium bromides and potassium iodide in various mixtures of these solvents have been measured at ten-degree intervals from 20° to 50°C. Variations in the dielectric constant of the solvent over the range 35-165 showed no influence on the degree of dissociation of these salts; they are essentially completely dissociated in all of the solvent mixtures studied. Differences in mobilities of the ions are explained in terms of various specific types of solute-solvent interactions.

During the past few years Dawson and co-workers have published from This Laboratory several papers describing the properties of solutions of electrolytes in solvents having high dielectric constants. Very large degrees of dissociation and correspondence with the theoretical Onsager (1) conductance relationships to concentrations much greater in these solutions than in water are attributable to a considerable extent to the high dielectric constants.

The investigation reported in this paper was designed to study the influence of large changes in dielectric constant on the degree of electrolytic dissociation and the mobilities of the ions of some univalent bromides and iodides. It was expected that

some insight into the comparative solute-solvent effects might be obtained also from the results of these studies.

Experimental

Apparatus and procedure.—The bridge assembly and procedures for conductance measurements as well as viscosity and density determinations have been described adequately in earlier papers (2-4). No significant change in the cell constants of the conductance cells could be detected over the temperature range for which they were used. The cells were held in a thermostated oil-bath maintained at a constant temperature to within ±0.1°.

Solvents.—The preparation and purification of N-methylacetamide (NMA) and dimethylformamide (DMF) has been described previously (5, 6). The solvents used in this work had specific conductances in the range 1 to 4×10^{-7} ohm^{-1} cm^{-1} at 30°.

Electrolytes.—The best obtainable commercial grades of sodium and potassium bromides were recrystallized twice from water and alcohol mixtures, fused, then stored in a desiccator over magnesium perchlorate.

Analytical grade potassium iodide was recrystallized twice, dried at 60° in a vacuum oven, then stored over magnesium perchlorate.

Solutions.—Solutions were prepared and dilutions made on a weight basis. All transfers were made in a dry atmosphere.

Dielectric constants of the solvents were measured (7) at 20°, 25°, 30°, and 40°. Extrapolated values were used for 50°.

Results and Discussion

All conductances were corrected by subtracting the conductance of the solvent from that of the solution. Limiting equivalent conductances were obtained by empirical extrapolation of plots of Λ vs. $\sqrt{C}$. Although there is some uncertainty in the Λ_0 values, they are believed to be accurate generally to well within 1%.

In the mixed solvent dimethylformamide (DMF)-N-methylacetamide (NMA) there are brought together isomeric components having approximately equal densities but widely differing viscosities and dielectric constants (Fig. 1). At 40°, the range of dielectric constants from 35 to 165 is spanned. Viscosities vary from 0.67 for DMF to 3.02 centipoises for NMA. Earlier work (4) has shown that sodium and potassium bromides and iodides are completely dissociated in pure NMA.

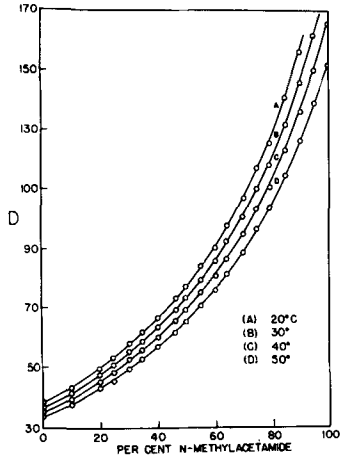

Fig. 1. Dielectric constants of the mixed solvents N-methylacetamide-dimethylformamide.

Table I. Summary of data for solutions of NaBr, KBr, and KI in DMF, NMA, and in the mixed solvent DMF-NMA

% NMA	% DMF	Salt	Temp	Λ_0	η_0	$\Lambda_0\eta_0$
0.0	100.0	KBr	20	78.2	0.00845	0.6604
			30	90.1	0.00746	0.6723
			40	99.8	0.00664	0.6626
			50	111.5	0.00598	0.6670
		NaBr	20	78.6	0.00845	0.6640
			30	89.2	0.00746	0.6654
			40	100.6	0.00664	0.6679
			50	111.8	0.00598	0.6688
90.0	10.0	KBr	20	16.7	0.03765	0.6269
			30	21.3	0.02924	0.6214
			40	26.4	0.02336	0.6172
			50	32.0	0.01907	0.6095
		NaBr	20	16.4	0.03765	0.6186
			30	20.9	0.02924	0.6105
			40	25.9	0.02336	0.6060
			50	31.4	0.01907	0.5988
0.0	100.0	KI	20	77.6	0.00845	0.6552
			30	88.3	0.00746	0.6586
			40	99.4	0.00664	0.6596
			50	110.4	0.00598	0.6604
48.67	51.33	KI	20	39.9	0.01564	0.6234
			30	47.2	0.01314	0.6201
			40	54.9	0.01125	0.6177
			50	63.1	0.00976	0.6159
90.0	10.0	KI	20	18.0	0.03765	0.6777
			30	23.0	0.02924	0.6728
			40	28.5	0.02336	0.6653
			50	34.4	0.01907	0.6575
95.13	4.87	KI	30	20.4	0.03310	0.6759
			40	25.5	0.02635	0.6730
			50	31.3	0.02120	0.6631
98.0	2.0	KI	30	19.1	0.03615	0.6905
			40	24.1	0.02830	0.6823
			50	29.7	0.02274	0.6754
100.0	0.0	KI	30	18.1	0.03888	0.7053
			40	23.0	0.03021	0.6945
			50	28.5	0.02413	0.6875

A summary of pertinent data for the solutions studied is presented in Table I.

Raman spectra and infrared studies (8) have shown that in NMA there exists a trans disposition of the oxygen atom and the amino hydrogen. Hydrogen bonding at these two points produces long chains of molecules leading to extremely high dielectric constants. In an unsubstituted amide such as formamide random associated forms occur which partially cancel contributions made by additional molecules and the dielectric constant is lower. If both amino hydrogens are replaced by alkyl groups, as in DMF, hydrogen bonding is not possible and the dielectric constant is relatively low.

Addition of a small amount of DMF to NMA greatly reduces both the dielectric constant and the viscosity by disrupting the long chains of molecules.

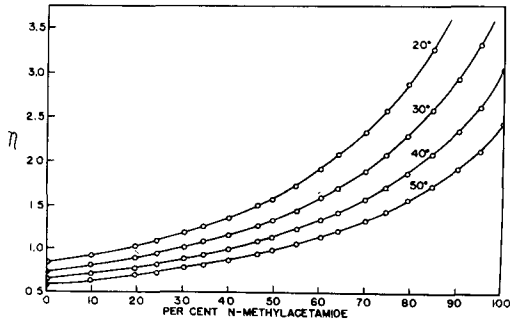

Fig. 2. Absolute viscosities of the mixed solvents N-methylacetamide-dimethylformamide.

Since the densities of the two pure components are so nearly equal, the degree of molecular association has little influence on the density of the mixture.

In all of the solutions studied the viscosity increases as the concentration of added electrolyte becomes greater (Fig. 2). This effect is more pronounced in mixtures richer in NMA. Increased viscosity may result from solvation of the ions by attachment of separate solvent molecules which are available in DMF or which may be produced in NMA by disruption of molecular chains. In addition, the viscosity of NMA solutions may become greater because of other changes in the solvent structure around the ions. In pure NMA the molecules are arranged in long chainlike groups. These linearly disposed molecular chains move past one another without great interference as the liquid flows. Nonelectrolyte solute particles which exert little influence on the solvent molecules encounter resistance which is not abnormally great as they move through the medium. Ionic solute particles at lower concentrations exert pronounced electrostatic attractive forces on various points along the solvent molecular chain but probably disrupt extensively relatively few of the solvent molecular groups. Under the influence of the electrostatic fields of these ions most of the molecular chains around them are only distorted so that they become serrated and curved. Then movement of the solvent units past one another or of solute particles through this medium is greatly hindered. It seems logical that this effect may be largely responsible for the unusual increase in viscosity with increasing concentration of added electrolyte which is observed in NMA solutions.

The absence of a maximum or minimum in the densities, viscosities, or dielectric constants of the solvent mixtures is an indication that compound formation between the components does not occur. The fact that on cooling a solvent mixture, essentially pure NMA crystallizes out, lends additional evidence that interaction between the solvent components is comparatively slight and primarily physical in nature.

Solutions of sodium and potassium bromide.—Plots of the equivalent conductance as a function of the square root of the concentration for sodium and potassium bromides (typical plots shown in Fig. 3-5) at ten degree intervals from 20° to 50° in both the pure components and in the 90-10 NMA-DMF mixtures are typical of highly dissociated electrolytes. Slopes of the KBr plots are slightly less

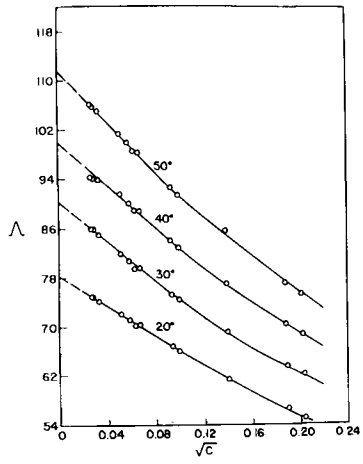

Fig. 3. Kohlrausch plots for solutions of potassium bromide in dimethylformamide.

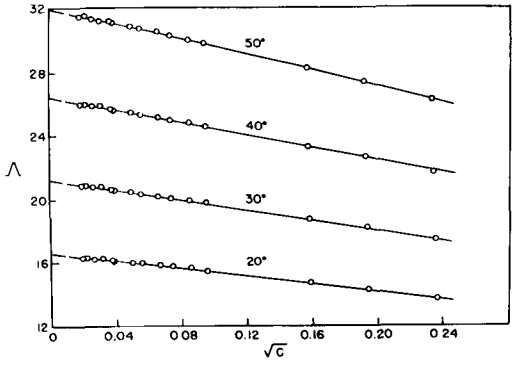

Fig. 4. Kohlrausch plots for solutions of potassium bromide in 90% NMA-10% DMF.

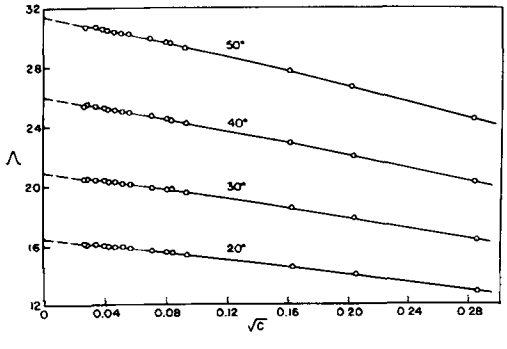

Fig. 5. Kohlrausch plots for solutions of sodium bromide in 90% NMA-10% DMF.

negative while those for NaBr are slightly more negative than the theoretical (Onsager) slopes. The higher charge density on the sodium ion would produce greater ion-solvent interaction than in the case of the potassium ion. This leads to a greater effective viscosity in the immediate environment of the sodium ion although the two alkali ion solvodynamic units may be of nearly equal sizes with equal limiting conductances. The greater solubility of the sodium compound lends support to this supposition.

Solutions of potassium iodide.—Potassium iodide is essentially completely dissociated in both of the pure constituents and in the various solvent mixtures (Fig. 6 and 7). In pure DMF the Λ_0 value for KI is about 1% less than for sodium and potassium bromides (Table I); in the 90-10 DMF-NMA mix-

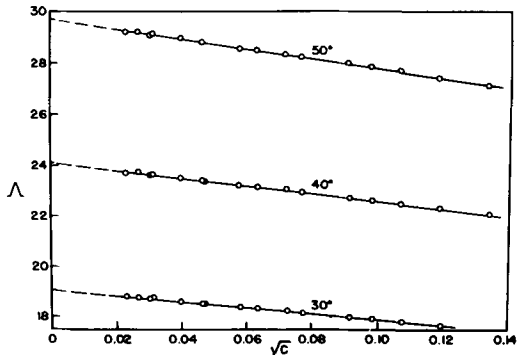

Fig. 6. Kohlrausch plots for solutions of potassium iodide in 98% NMA-2% DMF.

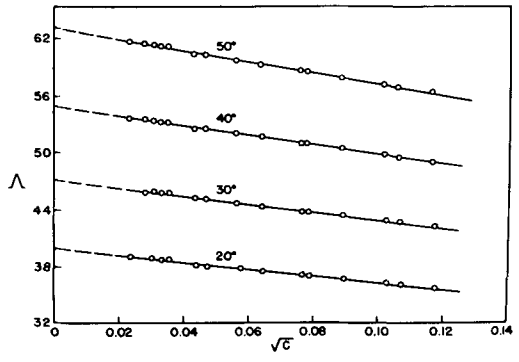

Fig. 7. Kohlrausch plots for solutions of potassium iodide in 48.67% NMA-51.33% DMF.

ture Λ_0 for KI is several per cent greater than for the other two salts.

Speculation concerning the possible mechanisms of solvation of bromide and iodide ions in NMA and DMF may be useful. Because of its smaller size and greater electronegativity, the bromide ion would be more likely to undergo hydrogen bonding through the amino hydrogen of NMA. Hydrogen bonding with DMF would not occur. In DMF solvation of an electron-donor ion could proceed through the electrophilic nature of the carbon atom in the carbonyl group (9). Solvation through electrostatic phenomena as ion-dipole or ion-induced dipole effects would be greater with the bromide ion because of its greater charge density. However, the more easily deformable electron atmosphere of the iodide ion makes it more susceptible to dipole-induced dipole attraction.

A comparison at 40°C of 22.99 for the limiting equivalent conductance of potassium iodide in NMA with the value of 21.04 for potassium bromide obtained by Dawson, Sears, and Graves (11) shows the bromide less conducting by about 10%. At 40°, the Λ_0 value for potassium iodide in NMA is less by a factor of 4.32 than it is in DMF. Λ_0 for potassium bromide, on the other hand, has been reduced by a factor of 4.74 at the same temperature. At this temperature NMA is 4.55 times as viscous as DMF. Thus it is seen that potassium iodide is about 5% more conducting and potassium bromide is about 5% less conducting than would be expected from viscosity effects alone. These data, in addition to the fact that the greater crystallographic diameter of the iodide ion would tend to make it less mobile than the bromide ion, constitute strong evidence that in NMA the bromide ion is solvated to a greater extent than the iodide ion. Similar results are obtained by comparing sodium bromide and potassium iodide.

The results of this investigation emphasize the differences in the behavior of the two halide ions in DMF and in NMA.

Acknowledgments

The authors are indebted to Dr. H. C. Eckstrom for valuable suggestions and to Mr. Murrell Pruitt for some confirmatory experimental work.

Financial support for part of this work was received from the National Science Foundation.

Manuscript received Dec. 31, 1959.

Any discussion of this paper will appear in a Discussion Section to be published in the June 1961 JOURNAL.

REFERENCES

1. L. Onsager, *Physik. Z.*, **28**, 277 (1928).
2. L. R. Dawson, A. Tockman, H. K. Zimmerman, Jr., and G. R. Leader, *J. Am. Chem. Soc.*, **73**, 4327 (1951).
3. C. Berger and L. R. Dawson, *Anal. Chem.*, **24**, 994 (1952).
4. L. R. Dawson, P. G. Sears, and R. H. Graves, *J. Am. Chem. Soc.*, **77**, 1986 (1955).
5. L. R. Dawson, E. D. Wilhoit, and P. G. Sears, *ibid.*, **78**, 1569 (1956).
6. P. G. Sears, E. D. Wilhoit, and L. R. Dawson, *J. Chem. Phys.*, **23**, 1274 (1955).
7. G. R. Leader, *J. Am. Chem. Soc.*, **73**, 856 (1951).
8. S. Mizushima, *et al.*, *ibid.*, **72**, 3490 (1950).
9. A. E. Remick, "Electronic Interpretations of Organic Chemistry," John Wiley & Sons, Inc., New York (1949).

December 1960 Discussion Section

A Discussion Section, covering papers published in the January-June 1960 JOURNALS, is scheduled for publication in the December 1960 issue. Any discussion which did not reach the Editor in time for the June 1960 Discussion Section will be included in the December 1960 issue.

Those who plan to contribute remarks for this Discussion Section should submit their comments or questions in triplicate to the Managing Editor of the JOURNAL, 1860 Broadway, New York 23, N. Y., *not later than September 1, 1960.* All discussion will be forwarded to the author(s) for reply before being printed in the JOURNAL.

Brief Communications

Electronic Magnetoanalysis of an Iron Single Crystal

S. Yamaguchi

The Institute of Physical and Chemical Research, Tokyo, Japan

A piece of iron single crystal about 2 mm in diameter and 10 mm long was used for the experiments described below. One end of this rod was sharpened to a truncated wedge by grinding and then etching with hydrochloric acid. A small permanent magnet (coercive force about 300 Oersted) was attached to the other end of the specimen as indicated in Fig. 1. In this way the magnetic induction of the sample was kept saturated.

To study electron diffraction, an electron beam about 0.05 mm in cross section was allowed to graze the edge of the specimen (Fig. 1). The magnetic deflection of the incident beam can be measured by observing the shift in position of the diffraction pattern. The pattern from the iron crystal was measured with respect to the invariant position of the pattern from a nonferromagnetic gold foil. The patterns from the crystal and the foil were superimposed by means of a double exposure technique (1).

The pattern obtained from an unmagnetized sample (the same iron crystal with the permanent magnet removed) is shown in Fig. 2. The spots from the iron crystal fall on rings which are concentric with rings due to the gold foil. Most of the spots are actually located on rings produced by the gold, due to the near coincidence of the interplanar spacings of iron and gold; this indicates that the specimen contains no major internal stresses.

Figure 3 shows the pattern obtained from the magnetized sample. The spots due to the iron have shifted relative to the reference gold pattern; the shift shows the magnetic Lorentz effect.

Orientation—Figures 2 and 3 show that the incident beam was perpendicular to the (111) plane of the iron single crystal as well as to the magnetic induction $B_{0\bar{1}1}$ perpendicular to the $(0\bar{1}1)$ plane. The relations existing between the incident beam, the

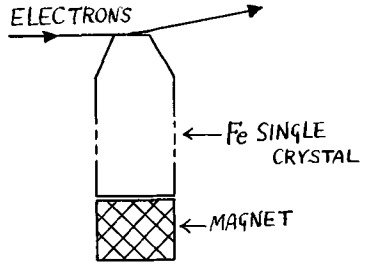

Fig. 1. Arrangement of the specimen relative to the incident beam.

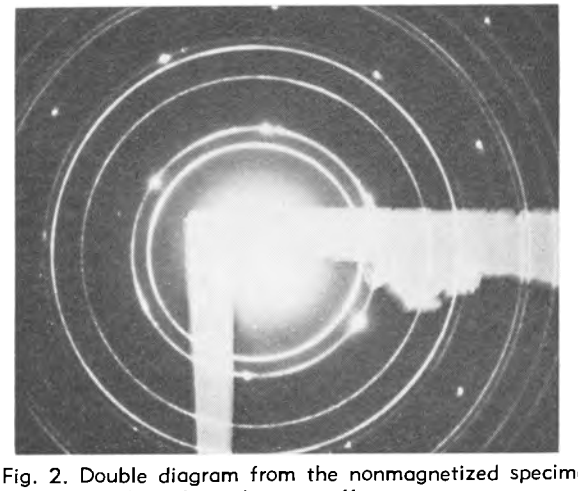

Fig. 2. Double diagram from the nonmagnetized specimen and from a gold foil; no Lorentz effect.

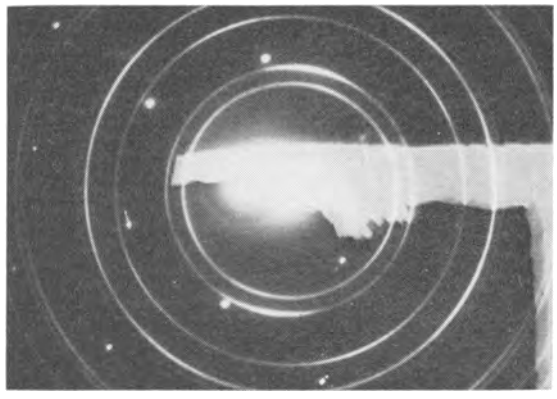

Fig. 3. Double diagram from the magnetized specimen and from a gold foil, showing the Lorentz effect. Wave length, 0.0288Å; camera length; 495 mm; positive enlarged 2.3 times.

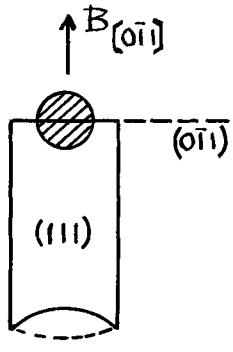

Fig. 4. Relation between the orientation of the specimen and the incident beam.

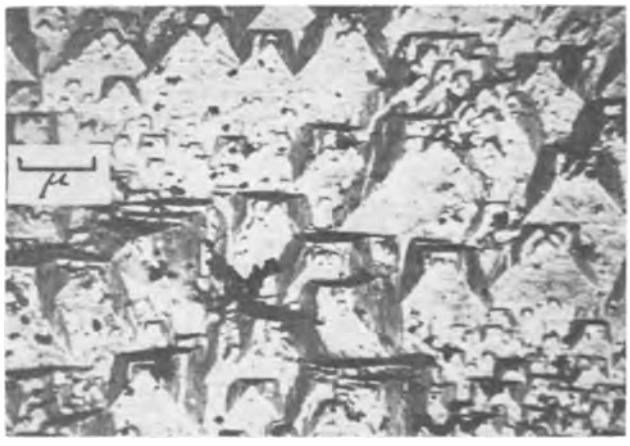

Fig. 5. Electron micrograph of the oxide film on and separated from the specimen.

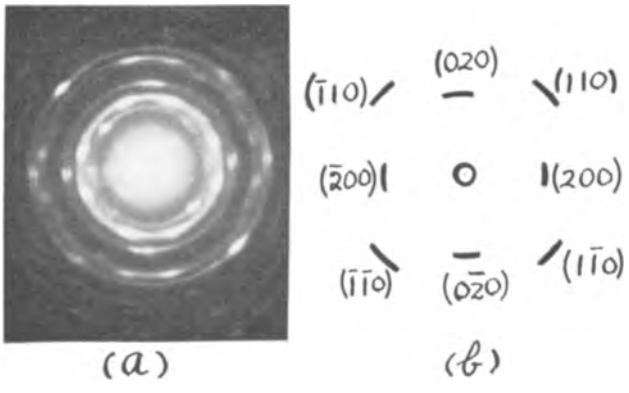

Fig. 6. (a) Diffraction pattern from the oxide film of Fig. 5 (Fe_3O_4). In (b) the Miller indices are assigned to the corresponding oriented diffraction arcs.

orientation of the specimen, and the direction of induction are illustrated in Fig. 4. Here the shadowed circle represents the cross section of the incident beam.

Electron microscopy.—An oxide replica film (thickness: about 200Å) formed on the stem surface of the specimen and then separated from it was enlarged by means of electron microscopy (Fig. 5).[1] Figure 5 pictures the octahedral (111) figures with regular orientation. This confirms the orientation of the specimen as determined by the diffraction process.

An electron beam running perpendicular to the oxide film face of Fig. 5 gave the diffraction pattern shown in Fig. 6(a). This pattern is characteristic of Fe_3O_4 crystals (magnetite, spinel type) oriented as illustrated in Fig. 6(b). In the case of Fig. 6 the incident beam was parallel to the (110) planes of the Fe_3O_4 crystals. It is therefore concluded that the (111) plane of the iron substrate is oriented perpendicular to the (110) planes of the Fe_3O_4 crystals. It is known empirically that there is a regular crystallographic orientation between a ferromagnetic substrate and the ferromagnetic oxide formed on it (2). The result obtained in the present experiment, $(111)_{Fe} \perp (110)_{Fe_3O_4}$, could serve for estimating the position of the iron crystal axis by means of the oxide replica process.

Magnetoanalysis.—The double diagram of Fig. 3 makes it possible to calculate the magnetic induction B of the specimen as a function of its crystal axis. We have a relation between the magnetic deflection of the incident beam readily measurable in Fig. 3 (ΔZ), and B. That is

$$\Delta Z = \frac{eL\lambda}{h} \int_0^l B\, dl \qquad [1]$$

where e is the electron charge (1.6×10^{-20} emu), L is the camera length (495 mm), λ is the wave length of the electrons, h is Planck's constant (6.6×10^{-27} erg sec), and l is the magnetic field traversed by the electron beam.

It is difficult to estimate the magnetic path l in the present experiment. The following process was employed to estimate the value of l. Since the magnetic induction of the specimen under the conditions in Fig. 3 is at saturation induction [B = 20000 gauss (3)], we can calculate the mean value of l according to Eq. [1]. Here it is assumed that B is homogeneous. We thus obtain $\bar{l} = 4\ \mu$, where $\lambda = 0.0288$ A and $\Delta Z = 0.27$ cm. This $\bar{l}$ —value can then be used for the further measurement of the B-H curve of the iron single crystal.

Manuscript received March 16, 1960.

Any discussion of this paper will appear in a Discussion Section to be published in the June 1961 JOURNAL.

[1] This oxidation was carried out in an eutectic bath of KNO_3-$NaNO_3$ at about 300°C. The oxide film was isolated from the substrate with a CH_3OH-Br solution [cf. (3)].

REFERENCES

1. S. Yamaguchi, *This Journal*, **106**, 268 (1959); **107**, 55 (1960).
2. R. D. Heidenreich and E. A. Nesbitt, *J. Appl. Phys.*, **23**, 352, 366 (1952).
3. E. M. Mahla and N. E. Nielsen, *ibid.*, **19**, 378 (1948).
4. R. M. Bozorth, "Ferromagnetism," p. 870, D. Van Nostrand Co., Princeton, N. J. (1956).

Stress Corrosion Cracking

D. van Rooyen

Research Laboratories, Westinghouse Electric Corporation, Pittsburgh, Pennsylvania

A mechanism in which stress corrosion cracks initiate and propagate in austenitic stainless steel in purely electrochemical stages was postulated by Hoar and Hines (1-5). Such a mechanism is supported by recent work (6) which demonstrated that no steps of mechanical fracture could be detected at any stage of the cracking process of 18-8 type stainless steel in boiling magnesium chloride solutions.

In order to account for observed rates of crack propagation, it was calculated that selective dissolution of the highly stressed advancing edge of a crack takes place at current densities of the order of 1 amp/cm^2. Hoar and West (7) demonstrated that 18-8 stainless steels can dissolve at such high current densities without much polarization, provided that the surface is yielding rapidly and provided that concentration polarization is avoided. They concluded that anodic dissolution is highly stimulated by the mechanically induced movement of the surface metal atoms. They further reported that similar tests on pure nickel gave no indication of such a mechanical effect in hot aqueous magnesium chloride.

While it is known that nickel and high nickel alloys do not suffer chloride stress corrosion cracking (8-13), it is uncertain whether their immunity arises in the initiation or in the propagation stage. It is important to know this, since the whole correlation made by Hoar and West between stainless steel and nickel is based on the assumption that cracks actually would not propagate into nickel under their conditions.

Studies on this mechanism of cracking are under way. Attempts are being made to compare the resistance of various alloys to crack propagation with their electrochemical behavior while corroding at high current densities in boiling magnesium chloride solutions. Specimens are prepared by arc depositing a layer of a susceptible material, such as 304 stainless steel, onto a strip of the material to be tested. The compound sample is then alternately rolled and vacuum annealed at 1065°C until the final thickness of about 0.045 in. is reached. The sample is given a final annealing treatment after machining the edges and is placed under direct load while in contact with the test solution which is contained in a glass cell. The load is high enough to cause cracks to start in the susceptible alloy, and their behavior is then studied at the boundary by subsequent metallographic examination. Parallel tests are next carried out in the way described by Hoar and West (7).

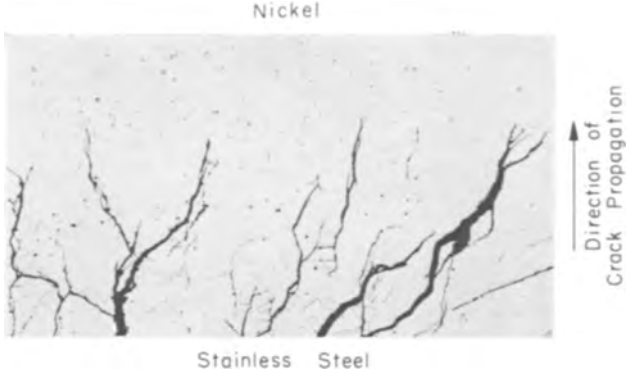

Fig. 1. Cracks stopping at steel-nickel boundary. Magnification 150X before reduction for publication.

Results so far on nickel have confirmed the absence of mechanical stimulation of its anodic dissolution. Furthermore, stress corrosion cracks, which start in the 304 type stainless steel of a bonded specimen, proceed to the nickel boundary where they stop, Fig. 1. It can be seen that the cracks penetrate a short distance into the thin intermediate layer that exists between the sensitive alloy and the nickel. After crack information and penetration in this particular experiment, the stress on the nickel was 43,000 psi, not allowing for any stress-raising effect at the tips of the cracks. Results to be reported later show that it is unlikely that a galvanic effect between the metals could account for the stopping of cracks at the boundary.

The results are in agreement with the electrochemical mechanism of cracking (1-5), although they do not directly constitute further proof.

Acknowledgment

The work reported was partly supported by the Navy Department, administered under the direction of the Office of Naval Research, Washington, D. C.

Manuscript received April 8, 1960.
Any discussion of this paper will appear in a Discussion Section to be published in the June 1961 JOURNAL.

REFERENCES

1. T. P. Hoar and J. G. Hines, *J. Iron Steel Inst.*, **182**, 124 (1956).
2. J. G. Hines and T. P. Hoar, *ibid.*, **184**, 166 (1956).
3. T. P. Hoar and J. G. Hines, Symposium on Stress Corrosion Cracking and Embrittlement, p. 107, John Wiley & Sons, Inc., New York (1956).
4. T. P. Hoar and J. G. Hines, International Committee for Electrochemical Thermodynamics and Kinetics (CITCE), 8th Meeting (Butterworths, London).
5. J. G. Hines and T. P. Hoar, *J. Appl. Chem.*, **8**, 764 (1958).
6. D. van Rooyen, To be published in *Corrosion*.
7. T. P. Hoar and J. M. West, *Nature*, **181**, 835 (1958).
8. C. Edeleanu, "Stress Corrosion Cracking and Embrittlement," p. 129, W. D. Robertson, Editor, John Wiley & Sons, Inc. (1956).
9. O. B. J. Fraser, Symposium on Stress Corrosion Cracking of Metals, A.S.T.M., A.I.M.E. (1945).
10 H. R. Copson, *Corrosion*, **10**, 124 (1954).
11. H. R. Copson, *Welding J.*, **32**, 75S (1953).
12. M. G. Fontana, *Ind. Eng. Chem.*, **46**, 99A (March, 1954).
13. J. T. Waber and S. Waber, U. S. A. E. C. Report LA1313, Los Alamos Scientific Laboratory, Los Alamos, N. M. (1950).

Investigation of the Electrochemical Characteristics of Organic Compounds

V. Heterocyclic Nitro Compounds

R. Glicksman and C. K. Morehouse

Semiconductor and Materials Division, Radio Corporation of America, Somerville, New Jersey

ABSTRACT

A study of the electrochemical characteristics of nitropyridine and other heterocyclic nitro compounds shows that the cathode potential of these compounds during current flow is dependent on the aromaticity of the compound, as well as the type and position of substituent groups on the aromatic ring. The effect of these factors on the cathode potential is interpreted in terms of the electron density distribution in the molecule. Performance characteristics of magnesium dry cells containing 2,5-dinitrofuran and various nitropyridine compounds as cathodes are also presented.

Previous work by the authors (1, 2) has dealt with the effect of various types of groups and their position in the molecule on the cathode potential of aromatic nitro and nitroalkane compounds during current flow. As an extension of this work, a study of the electrochemical characteristics of heterocyclic nitro compounds and their use as cathodes in primary cells has been made and is presented in this paper.

Apparatus and Technique

A technique previously described by the authors (3) has been used to measure the operating potential during current flow and the coulombic capacity of the various heterocyclic nitro compounds. This technique consists in discharging at a constant current, in a large volume of electrolyte, a 0.5-g sample of the heterocyclic nitro cathode material mixed with 0.05 g of Shawinigan acetylene black. The change in cathode potential with time was measured with a L&N type-K potentiometer, using a saturated calomel reference electrode. Measured potentials were corrected for the *IR* drop associated with the apparatus and electrolyte by means of an oscillographic technique.

All half-cell potential data reported in this paper are referred to the normal hydrogen scale and include a liquid junction potential, which in most cases is small and can be neglected.

For most of the measurements an aqueous magnesium bromide electrolyte and a magnesium anode were used. For studying the effect of *p*H on potential, a zinc anode was employed with the acidic NH_4Cl-$ZnCl_2$-H_2O and basic NaOH-H_2O electrolytes.

Experimental Data and Discussion of Results

Nitropyridine and Nitroquinoline Compounds

A number of heterocyclic compounds possess the type of stability found in benzene. Among the more common heterocycles, pyridine is less easily substituted than benzene and, in general, surpasses it in aromatic character (4). On the other hand, the resonance energies of thiophene (31 kcal) and furan (23 kcal) indicated that these compounds are less stable than benzene (39 kcal) and pyridine (43 kcal) (5). The chemical reactivity of thiophene and furan, in general, is in good agreement with this fact.

Because substitution of aromatic compounds usually takes place through attack by electron seeking groups, positions that have the greatest electron density will be substituted most readily. However, a nitro group on a position of high electron density is more difficult to reduce than one on a position of low electron density (1, 2) and, therefore, one would expect the cathode potential of aromatic heterocyclic nitro compounds to be greater for those compounds which are less easily substituted, i.e., for the more highly aromatic systems such as pyridine.

The effect of aromaticity and group substitution on the electrode potential of heterocyclic nitro compounds was determined by half-cell potential studies of a number of nitropyridine and nitroquinoline compounds discharged continuously in 250 g/l $MgBr_2 \cdot 6H_2O$ electrolyte at a rate of 0.005 amp/g. The half-cell discharge curves are presented in Fig. 1-5, and theoretical capacity and electrode efficiency data for these compounds are given in Table

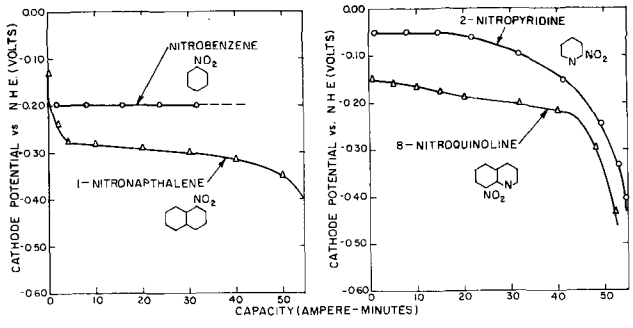

Fig. 1. Half-cell potential studies of various heterocyclic nitro compounds discharged in 250 g/l $MgBr_2 \cdot 6H_2O$ electrolyte at a rate of 0.005 amp/g.

Table I. Theoretical capacities and electrode efficiencies of various nitropyridine and nitroquinoline compounds

Compound	Theoretical capacity, amp-min/g	Experimental capacity,* amp-min/g	Electrode efficiencies, %
nitrobenzene	78.4	—	—
2-nitropyridine	77.7	51.5	66.3
4-hydroxy-2-nitropyridine	69.0	56.8	82.3
2-chloro-5-nitropyridine	60.9	46.9	77.0
2-hydroxy-5-nitropyridine	69.0	57.0	82.6
2-hydroxy-3-cyano-5-nitropyridine	58.5	50.6	86.5
2-amino-5-nitropyridine	69.3	60.6	87.6
2-amino-3-nitropyridine	69.3	57.8	83.4
4-amino-3-nitropyridine	69.3	65.5	94.5
4-nitropyridine	77.7	43.2	55.6
4-nitropyridine-N-oxide	69.0	32.8	47.5
m-dinitrobenzene	114.9	88.0	76.6
3, 5-dinitropyridine	114.0	71.1	62.4
2-hydroxy-3, 5-dinitropyridine	104.4	80.2	76.8
2-chloro-3, 5-dinitropyridine	94.6	50.4	53.3
1-nitronaphthalene	55.8	54.4	97.5
8-nitroquinoline	55.4	51.3	92.6
6-nitroquinoline	55.4	53.7	96.9
5-nitroquinoline	55.4	45.0	81.2
5-nitroisoquinoline	55.4	48.0	86.6
6, 8-dinitroquinoline	88.1	43.3	49.1

* Capacity calculated on the basis of a −0.40 v end potential.

I. The theoretical capacities were computed by means of Faraday's Law, assuming a 6-electron change per nitro group, and the electrode efficiencies were calculated from the data in Fig. 1-5, using a −0.40 v end potential to compute the capacities.

Figure 1 shows half-cell discharge data for nitrobenzene and 2-nitropyridine along with their corresponding bicyclic compounds, 1-nitronaphthalene and 8-nitroquinoline. The higher potential of 2-nitropyridine as compared with nitrobenzene is understandable in terms of resonance theory. In pyridine, the nitrogen atom has a greater attraction for electrons than has a carbon atom and decreases the availability of electrons. Thus, the effect of resonance in pyridine is to bring electrons from the α or 2 and γ or 4 positions to the nitrogen atom, which decreases the electron density at these positions relative to that at the β or 3 positions. The inductive effect is also operative, and because electrons are removed from the β positions of pyridine as well, this position too has a lower electron density than found in benzene. The nitropyridines then, because of the lower electron density in the vicinity of the reducible nitro group, should have a greater affinity for electrons and operate at higher cathode potentials than comparable nitrobenzene derivatives.

The effect induced by the nitrogen atom is similar to that found in nitrobenzene as evidenced by the fact that it is about as difficult to substitute on pyridine as on nitrobenzene. If this behavior is assumed to be caused by the similar ring electron densities of pyridine and nitrobenzene, it would be expected that the cathode potential of 2-nitropyridine would be comparable to that of o-dinitrobenzene. Half-cell

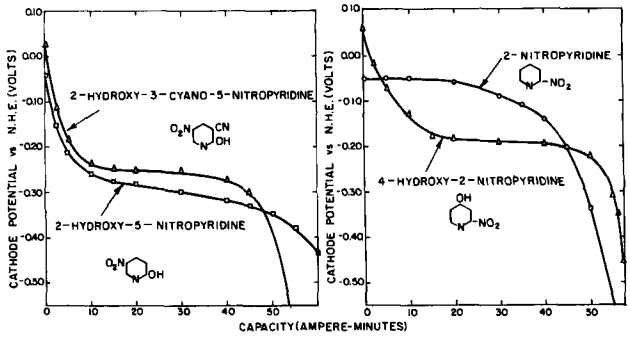

Fig. 2. Half-cell potential studies of various nitropyridine derivatives discharged in 250 g/l $MgBr_2 \cdot 6H_2O$ electrolyte at a rate of 0.005 amp/g.

discharge studies of o-dinitrobenzene under similar conditions of discharge confirm this reasoning.

Figure 1 also shows that the simple monocyclic nitro compounds, nitrobenzene and 2-nitropyridine, operate at higher potentials than their corresponding bicyclic compounds. These results are consistent with the stronger aromatic character of the monocycles as compared with the bicylic compounds. Because quinoline is related to naphthalene similarly to the way pyridine is related to benzene, the higher operating potential of 8-nitroquinoline as compared with 1-nitronaphthalene is to be expected.

In Fig. 2 are half-cell discharge data for various nitropyridine derivatives discharged at a rate of 0.005 amp/g in magnesium bromide electrolyte. These results indicate that the effect of substituent groups and their position in the molecule on the potential of nitropyridine compounds closely parallels their effect on the potential of nitrobenzene derivatives. For example, the presence of the electron-repelling hydroxyl group in 4-hydroxy-2-nitropyridine causes the cathode potential of this compound to be 0.15 v lower than the potential of 2-nitropyridine. The magnitude of this effect is comparable to that found for the corresponding nitrobenzene derivatives. Similarly the substitution of an electron attracting —CN group in the -3 position of 2-hydroxy-5-nitropyridine results in a compound, 2-hydroxy-3-cyano-5-nitropyridine, with a higher operating potential than the parent compound.

The half-cell potential-time discharge curves of these hydroxy nitropyridine compounds show a striking similarity to those of the hydroxy aromatic C-nitroso compounds (6). As is the case with the latter compounds, the high initial operating potentials of the hydroxy nitropyridines decrease rapidly during the first 10 amp-min of discharge and then assume a constant value for the remainder of the discharge.

This behavior can be explained in the following way: both the 2- and 4-hydroxy pyridines are tautomeric with the pyridones: e.g.,

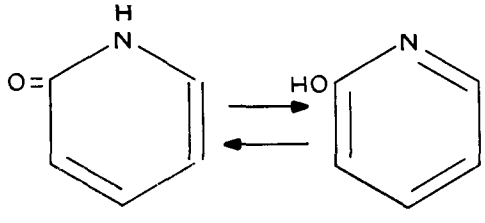

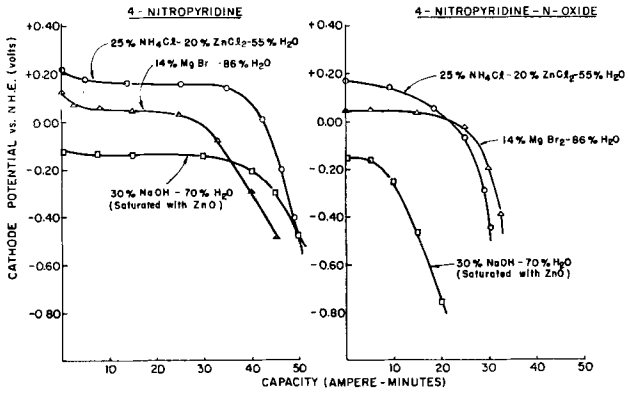

Fig. 3. Half-cell potential discharge curves of 4-nitropyridine and 4-nitropyridine-N-oxide discharged at a rate of 0.005 amp/g in various aqueous electrolytes.

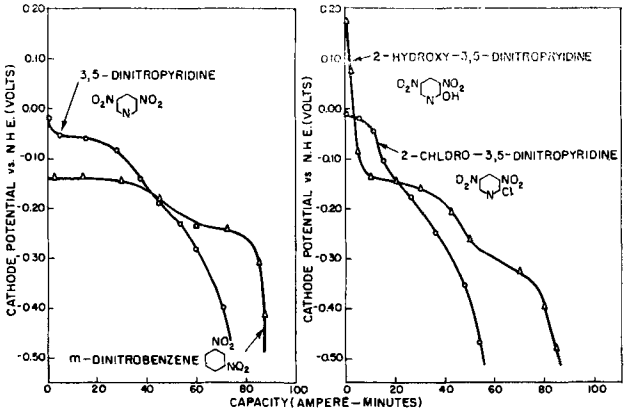

Fig. 4. Half-cell potential studies of various dinitropyridine compounds discharged in 250 g/l $MgBr_2 \cdot 6H_2O$ electrolyte at a rate of 0.005 amp/g.

and it is believed that the high initial potential of these compounds is a result of the pyridone structure. However, during the discharge, hydroxyl ion is formed as a consequence of the cathodic reduction reaction, and a neutralization reaction occurs with time between the hydroxypyridine form and the alkaline electrolyte with the formation of the strongly electron-repelling phenoxide ion. At this point, the cathode potential is due to that of the hydroxypyridine salt, and it remains constant at the lower potential throughout the remainder of the discharge.

The higher potential of 4-hydroxy-2-nitropyridine as compared with that of 2-hydroxy-5-nitropyridine is attributed to the fact that the nitro group in the former compound is on a position of lower electron density than the nitro group in 2-hydroxy-5-nitropyridine and is thus more readily reduced. This behavior is apparent when the possible resonance structures of pyridine are considered Thus, it would be expected that 2- and 4-nitropyridine compounds would operate at higher cathode potentials than comparable 3-nitropyridine compounds.

In Fig. 3 the high cathode potential of 4-nitropyridine compounds is demonstrated by the half-cell potential discharge curves of 4-nitropyridine and 4-nitropyridine-N-oxide obtained by discharging these compounds at a rate of 0.005 amp/g in aqueous $MgBr_2$, NaOH, and NH_4Cl-$ZnCl_2$ electrolytes. The curves show that both compounds operate at about the same potential, indicating the effect of the N-oxide group on the electrode potential to be very small. In general, the electrode potentials of these 4-nitropyridine compounds increase with decreasing electrolyte pH, a result similar to that found for the aromatic nitrobenzene compounds. However, unlike the aromatic nitrobenzene compounds which have poor electrode efficiencies in strongly basic electrolyte, 4-nitropyridine operates at an efficiency of 62.7% in this electrolyte.

Figure 4 gives half-cell potential discharge data for various 3,5-dinitropyridine compounds discharged continuously in a 250 g/l $MgBr_2 \cdot 6H_2O$ electrolyte at a rate of 0.005 amp/g. The data show that the dinitropyridine compounds operate at higher potentials than their corresponding mononitropyridine compounds. For example 2-hydroxy-3,5-dinitropyridine, for its first discharge step, operates at a potential approximately 0.14 v higher than that of 2-hydroxy-5-nitropyridine. In addition to their higher operating potentials, the dinitropyridine compounds have higher theoretical ampere-minute capacities than the mononitropyridine compounds and consequently show more promise for use as cathode materials in dry cells.

The data in Fig. 4 illustrate that the effect of substituted groups on the potential of 3,5-dinitropyridine is similar to that found for the aromatic dinitrobenzene and mononitropyridine compounds. The 0.08 v lower potential of m-dinitrobenzene as compared with 3,5-dinitropyridine also agrees with theory.

The half-cell potential discharge curves of various nitroquinoline compounds given in Fig. 5 show that the various isomeric mononitroquinoline compounds operate at comparable potentials of about −0.15 to −0.20 v for most of their discharge life. As expected, the cathode potential of 6,8-dinitroquinoline is 0.1 v higher than the potentials of 6- and 8-nitroquinoline.

The electrode efficiencies of the nitropyridine and nitroquinoline compounds are in general quite high as indicated by the data in Table I. For the 3-(or 5-) nitropyridine compounds efficiencies of 77-95% are obtained, while the nitroquinoline compounds operate at electrode efficiencies ranging from 81-97%.

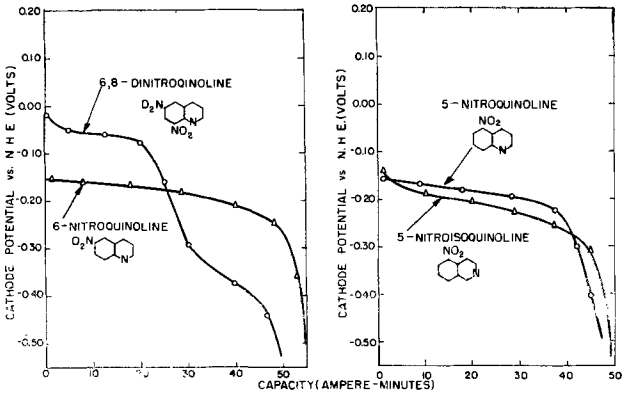

Fig. 5. Half-cell potential studies of various nitroquinoline compounds discharged in 250 g/l $MgBr_2 \cdot 6H_2O$ electrolyte at a rate of 0.005 amp/g.

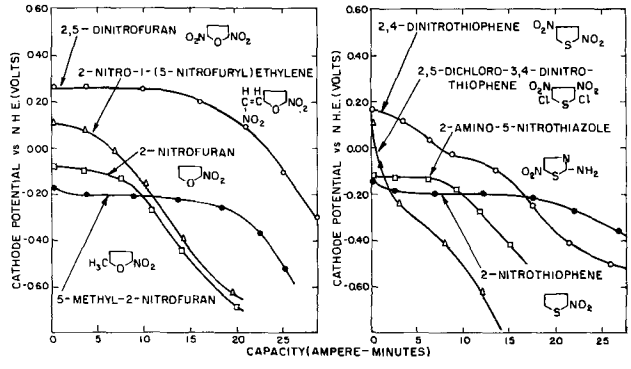

Fig. 6. Half-cell potential studies of various nitrofuran and nitrothiophene compounds discharged in 250 g/l $MgBr_2 \cdot 6H_2O$ electrolyte at a rate of 0.005 amp/g.

However, the more strongly oxidizing 2- and 4-nitropyridine and dinitropyridine compounds have lower efficiencies.

Nitrofuran, Nitrothiophene, and Other Five Membered Heterocyclic Nitro Compounds

In Fig. 6 are half-cell potential discharge curves of various nitrofuran and nitrothiophene compounds. Despite the weakly aromatic character of furan as compared with benzene and thiophene, 2-nitrofuran operates at a higher cathode potential than either nitrobenzene or 2-nitrothiophene under similar conditions of discharge. The apparent anomalous behavior of 2-nitrofuran may be explained by the fact that furan is not a true aromatic compound, and any generalization based on aromatic behavior would not be pertinent for this compound. For example, furan behaves like a typical diene in the Diels-Alder reaction, while ring cleavage by mineral acid shows its vinyl ether character. However, resonance energy considerations show that furan has some characteristics of a typical aromatic substance as well. It is thus apparent that the unsaturation of the furan nucleus will frequently manifest itself as a diene or vinyl ether, rather than as a true aromatic system typified by benzene.

The data in Fig. 6 also illustrate the effect of substituted groups on the potential of 2-nitrofuran. The cathode potentials of 2-nitrofuran derivatives increase as the 5-position is substituted with increasingly stronger electronegative groups, i.e., in the order $—CH_3$, —H, $—CH{=}CHNO_2$, $—NO_2$. As with the other nitro compounds studied, the effect of substituent groups on the cathode potential of 2-nitrofuran can be explained by their effect on the electron density in the vicinity of the reducible nitro group.

It is significant that the increase in potential caused by the addition of a $—NO_2$ group to the -5 position of 2-nitrofuran is 0.15-0.20 v greater than the increase found for the addition of a $—NO_2$ group to the ortho, para, or meta position of nitrobenzene. In this respect the nitrofurans behave more like the nitroalkanes than like the aromatic nitro compounds. Moreover, the nitrofurans, like the nitroalkanes, have exceedingly poor electrode efficiencies in the $MgBr_2$ electrolyte, giving values ranging from 16-31% for the four compounds studied.

Table II. Theoretical capacities and efficiencies of various five membered heterocyclic nitro compounds

Compound	Theoretical capacity, amp-min/g	Experimental capacity,* amp-min/g	Electrode efficiencies, %
nitrobenzene	78.4	—	—
2-nitrofuran	85.5	13.6	15.9
2, 5-dinitrofuran	122	30.7	25.2
2-nitro-1-(5-nitrofuryl) ethylene	52.4†	14.2	27.1
2-methyl-5-nitrofuran	75.8	23.2	30.6
2-nitrothiophene	74.8	31.6	42.2
2, 4-dinitrothiophene	111	20.9	18.8
2, 5-dichloro-3, 4-dinitrothiophene	78.8	7.5	9.5
2-amino-5-nitrothiazole	67.0	14.5	21.6
1-nitronaphthalene	55.8	54.4	97.5
6-nitroindazole	59.1	51.9	87.8
6-nitrobenzimidazole	59.1	51.8	87.6
5-nitroindazole	59.1	16.5	27.9
5-nitrobenzotriazole	58.9	61.5	100
5-nitro-2-benzimidazol-ethiol	49.5	43.0	86.9

* Capacity calculated on the basis of a −0.40 v end potential.

† Theoretical capacity calculated on the basis of the reduction of furan nitro group only.

Figure 6 also gives half-cell potential discharge curves for various nitrothiophene derivatives and for 2-amino-5-nitrothiazole. Because thiophene undergoes the typical substitution reactions of aromatic compounds and is more reactive than benzene, its nitro derivative would be expected to operate at a lower cathode potential than nitrobenzene. However, the discharge curves in Fig. 1 and 6 show that both 2-nitrothiophene and nitrobenzene operate at comparable potentials of −0.20 v in the magnesium bromide electrolyte. The effect on the cathode potential of additional $—NO_2$ and —Cl groups on the thiophene nucleus is similar to that found with other nitro compounds as evidenced by the high cathode potentials of 2,4-dinitrothiophene and 2,5-dichloro-3,4-dinitrothiophene. However, the data in Table II show that these compounds operate at extremely poor electrode efficiencies.

The thiazoles, which are structurally similar to thiophene and to pyridine, show reactions similar to

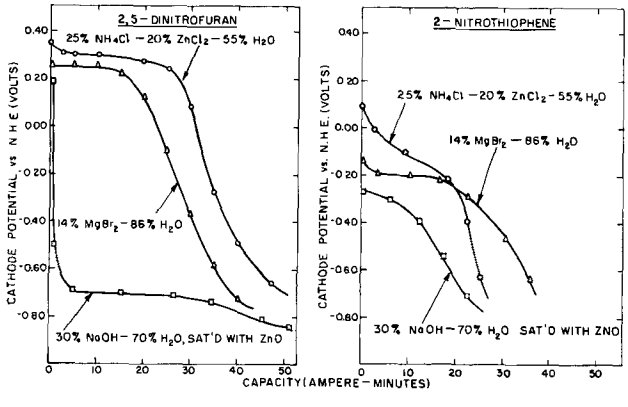

Fig. 7. Half-cell potential curves of 2,5-dinitrofuran and 2-nitrothiophene discharged at a rate of 0.005 amp/g in various aqueous electrolytes.

pyridine rather than those of thiophene. This behavior is particularly apparent in the resistance shown toward substitution reactions and is evidenced by the higher cathode potential of 2-amino-5-nitrothiazole as compared with nitrobenzene and 2-nitrothiophene.

Half-cell potential discharge studies were made on 2,5-dinitrofuran and 2-nitrothiophene to determine the effect of pH on the operating potential and capacity of these compounds. Figure 7 shows that the cathode capacity of 2,5-dinitrofuran increases only slightly with decreasing pH and is considerably less than the theoretical capacity (122 amp-min/g) of this compound. Similarly, 2-nitrothiophene shows no improvement in capacity with the more acidic NH_4Cl-$ZnCl_2$ electrolyte and actually shows a slight decrease. The poorer capacities obtained from these compounds in the strongly basic NaOH electrolyte are similar to those found for the aromatic nitro and nitroalkane compounds and can be attributed to the presence of side products which are formed by the condensation of the primary reduction products and to the poor stability of these compounds in this electrolyte.

In general the effect of decreasing electrolyte pH is to increase the cathode potential in agreement with theoretical considerations. It is interesting to note that the effect of pH on the cathode potential of 2,5-dinitrofuran is small, a relationship similar to that found for the nitroalkanes (2) but different from that found for the aromatic nitro compounds. The behavior of 2-nitrothiophene in this respect is closer to that of the aromatic nitrobenzene compounds.

In addition to the simple 5-membered heterocyclic compounds, each of the heterocyclic compounds can be fused to a benzene ring to give bicyclic systems which are comparable to naphthalene and quinoline. The half-cell potential discharge curves of various bicyclic heterocyclic nitro compounds are presented in Fig. 8. In general, these compounds, which contain two or three nitrogen atoms in the 5-membered ring, operate at potentials higher than that of 1-nitronaphthalene but lower than that of the nitroquinolines. As with the nitroquinoline compounds high electrode efficiencies are obtained with these bicyclic heterocyclic nitro compounds.

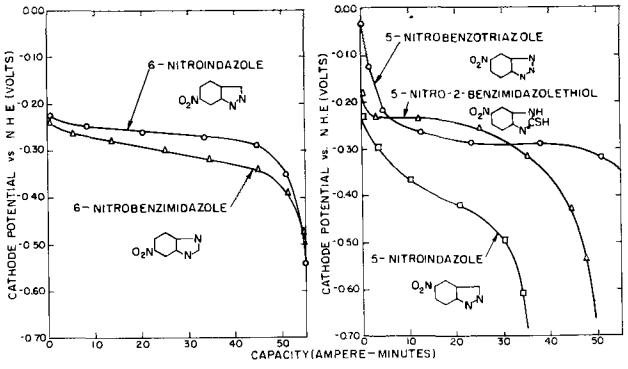

Fig. 8. Half-cell potential studies of various bicyclic heterocyclic nitro compounds discharged in 250 g/l $MgBr_2 \cdot 6H_2O$ electrolyte at a rate of 0.005 amp/g.

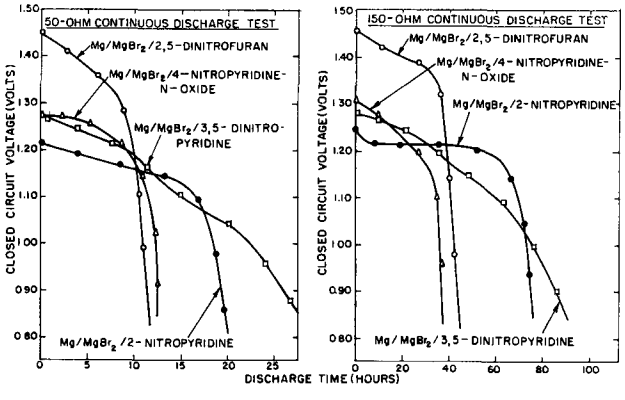

Fig. 9. AA-size magnesium dry cells containing various heterocyclic nitro compounds as cathodes discharged continuously through 50- and 150-ohm resistances.

Experimental Dry Cell Data

Experimental dry cells containing various heterocyclic nitro compounds as cathodes were assembled in the usual manner, using an AA-size can of impact-extruded magnesium AZ10A alloy and a magnesium bromide electrolyte. The cathode mix (weighing approximately 5 g) consisted of two parts by weight of Darco G-60 carbon black to one part by weight of the nitropyridine compounds. For cells containing 2,5-dinitrofuran as the cathode, two parts of the nitro compound was blended with one part by weight of Shawinigan acetylene black.

The performance characteristics of these Mg/$MgBr_2$/heterocyclic nitro AA-size cells on a 50- and 150-ohm continuous discharge test are shown in Fig. 9. The operating voltages of these cells closely parallel their half-cell potentials after corrections are made for the half-cell potential of the magnesium anode, which operates at a potential of about 1.3 v in this electrolyte. From the limited shelf-life data available, it appears that the cells containing the nitropyridine cathodes can be stored for extended periods of time without an appreciable decrease in cell performance, while the 2,5-dinitrofuran cells do not have an appreciable shelf life.

The use of heterocyclic nitro compounds as cathodes in dry cells appears to offer some advantages over the nitrobenzene compounds in that many of them operate at higher potentials at comparable electrode efficiencies. At present, these compounds are not as readily available as the nitrobenzene derivatives, being more difficult to synthesize; however, they offer a vast new source of potential cathode materials for future use. For example, considering only the pyridine compounds, almost every type of benzene compound has its analog in the pyridine series, and the number and types of pyridine derivatives are potentially as extensive as those in the benzene system.

Acknowledgment

The authors wish to acknowledge the support of this research by the Power Sources Division of the U. S. Army Signal Research and Development Laboratory under Contract No. DA-36-039-sc-78048. They also wish to express their appreciation to Dr. W. B. Hardy, of American Cyanamid Company, and Dr. K. J. Hayes, of the Norwich Pharmacal Com-

pany, for supplying many of the compounds used in this investigation.

Manuscript received Feb. 12, 1960. This paper was prepared for delivery before the Columbus Meeting, Oct. 18-22, 1959.

Any discussion of this paper will appear in a Discussion Section to be published in the June 1961 JOURNAL.

REFERENCES

1. R. Glicksman and C. K. Morehouse, *This Journal*, **105**, 299 (1958).
2. R. Glicksman and C. K. Morehouse, *ibid.*, **106**, 288 (1959).
3. C. K. Morehouse and R. Glicksman, *ibid.*, **103**, 94 (1956).
4. L. F. Fieser and M. Fieser, "Organic Chemistry," p. 847, D. C. Heath and Co., Boston (1950).
5. L. Pauling, Gilman's "Organic Chemistry," Vol. II, pp. 1968-1969, John Wiley & Sons, Inc., New York (1947).
6. R. Glicksman and C. K. Morehouse, *This Journal*, **105**, 613 (1958).

Discharge of a Lead-Acid Cell through an R-L Circuit

J. J. Lander[1] and E. E. Nelson

Naval Research Laboratory, Washington, D. C.

ABSTRACT

Submarine cells of the lead-acid type were discharged through resistance-inductance circuits. The data are analyzed to show no contribution to voltage loss other than *IR* losses in the cell during the initial voltage transient; consequently, a method is provided for the determination of the internal resistance. Circuit geometry is an important factor determining the types of discharge curves which can be obtained.

It has been desirable for various reasons to determine the internal resistance and other electrical characteristics of lead-acid storage cells (1-5). Experimental determinations of the internal resistance have been more or less uncertain because of presumed effects contributed by polarization phenomena other than *IR* drop. In this work, measurements involving cell discharges through a resistance-inductance series circuit are shown which lead to a determination of the internal resistance of a fully charged cell.

Theory

When a constant voltage is discharged through a resistance-inductance circuit, current builds up with time and levels off to a constant value depending on the resistance and the inductance in the circuit, according to the equation

$$E = L\, dI/dt + RI \qquad [1]$$

If this relation is applied to the circuit shown in Fig. 1, it can be shown that the voltage change measured across V_T, after the switch is closed, will be given by the differential equation

$$dV_T/dt = -\left(\frac{R_o + R_I}{L}\right) V_T + \text{const.} \qquad [2]$$

At the instant the switch is closed, all the energy supplied by the voltage source is contained in the term $L\, dI/dt$, the value of I being zero. As time proceeds and I builds up, the voltage V_T will fall off logarithmically from its open-circuit value and approach a constant value as dI/dt approaches zero. If R_I is unknown, its value could be determined by measuring the voltage V_T and current with time. It would be given by dividing the current at any time into the difference between the open-circuit value of V_T and its value at the corresponding time. R_I might also be obtained from the slope of the dV_T/dt vs. V_T line if R_o and L were known.

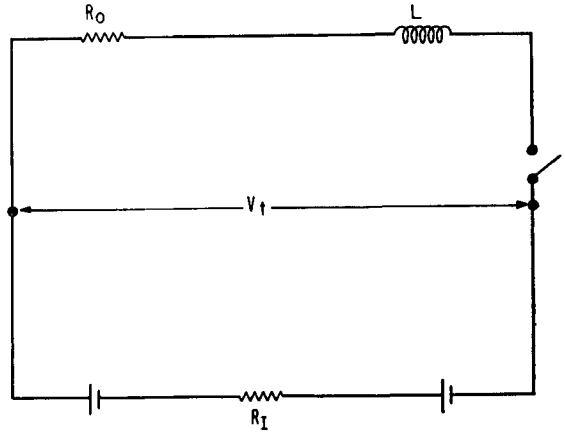

Fig. 1. An R-L series circuit

It might be assumed that a lead-acid cell discharging through an R-L circuit could be represented for some initial time interval by the circuit given in Fig. 1. The two potential sources would correspond to the positive and negative plates and V_T, the voltage measured across the cell terminals. It is not to be supposed that this circuit would represent the cell over a whole period of transient voltage, because other kinds of polarization besides *IR* drop are known. These would render the voltage source nonconstant, and Eq. [2] would not be adequate. If, however, the additional polarization should be slow to develop compared to the time necessary for the inductance field to be established, the proposed circuit would be a good representation of the initial voltage transient.

[1] Present address: Delco Remy Division, General Motors Corporation, Anderson, Indiana.

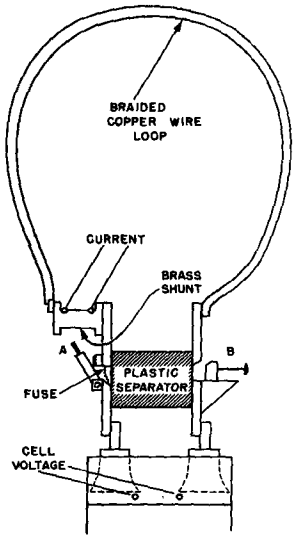

Fig. 2. Cell top and switch

Experimental Work

Experimental work consisted in discharging a fully charged submarine cell (~ 7000 amp-hr nominal capacity) through resistances of known values, while cell voltage and voltage drop across another small resistance in series were recorded as a function of time. The resistance consisted of ½ and 1 in. braided copper cables, or lengths of these in parallel, in series with a short, heavy brass tube of resistance 1.4×10^{-6} ohms. This tube was provided for measuring current. A switching device was mounted on the cell terminals as shown in Fig. 2. The cables were arranged in big loops, 4-5 ft in diameter to supply the inductance. It was attempted to keep the inductance loop relatively constant. Resistances were measured by running currents of about 100 amp through appropriate parts of the circuit and measuring voltage drops with a precision potentiometer.

In Fig. 2, A is a heavy six-bladed knife switch used to open the circuit; a fuse was placed in parallel to take the load when the switch was opened and then burn out to break the discharge circuit. The circuit was closed by driving the wedge switch B into its seat in the mounting. B was designed to make the circuit quickly and completely. All mechanically contacting parts were silver-plated to reduce contact resistance. Under best conditions the total resistance of the switch mounting could be reduced to $15\text{-}20 \times 10^{-6}$ ohms.

Procedure for making a run was as follows. The cell was charged to full gassing and then allowed to sit on open circuit overnight for the voltage to become steady. The shunt resistors were clamped into place with both switches open and their resistance values measured. Voltage connections were made to the recorder from the proper places in the discharge circuit; the knife switch was closed and the wedge switch slammed home. Current was allowed to run for the desired period; the circuit was broken and the cell charged for another run.

Cell voltages (V_p) were measured at the tops of the plates inside the cell, because preliminary data showed that measurements made across the cell terminals included enough inductance contribution

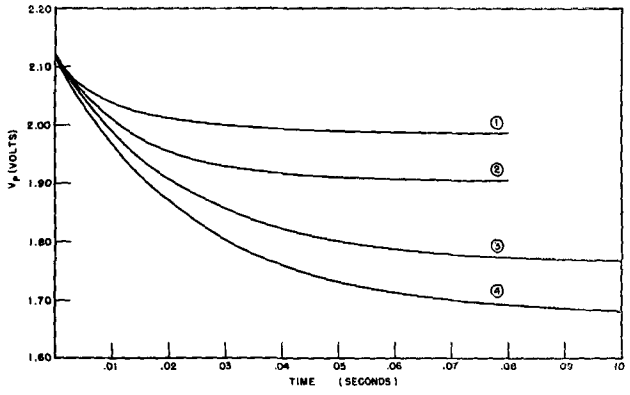

Fig. 3. Cell voltage vs. time

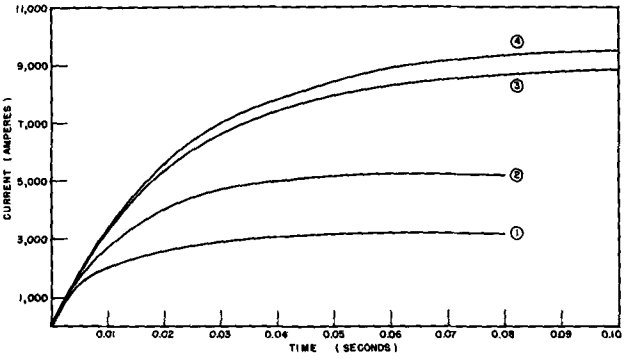

Fig. 4. Current vs. time

to render results very difficult to analyze quantitatively. Similarly, the short, heavy, brass tube was used so no appreciable inductance would be included in the current measurement.

A Brush recorder, type BL-202, was used to measure voltages. Time could be established to within 0.002 sec. This was considered to be of sufficient precision because the initial transients existed for times of 0.04-0.10 sec, depending on the L/R ratio, and because the measured voltages rose (from zero, in the case of current) and fell away (from OCV, in the case of cell voltage) very smoothly.

Data

Figures 3 and 4 show voltage decay and current rise curves over the first 0.1 sec or so, for the cell shorted through external shunts having resistances: 171, 193, 354, and 624×10^{-6} ohms. These data were all checked once and duplicate traces checked almost exactly when superimposed.

Discussion and Conclusion

The slopes of the voltage-time curves were measured and are shown plotted against the cell voltage in Fig. 5. The curves are linear; therefore Eq. [2] describes the discharges over these transient periods, i.e., these portions of the discharge data represent a constant potential driving current through an R-L circuit.

Presumably, the cell voltage might be constant over the ranges included in Fig. 5 and yet include some initial contribution, other than IR_l, to voltage decay. Therefore, the curves of Fig. 6 are shown where the voltage drop from open circuit is plotted against several values of current for each discharge.

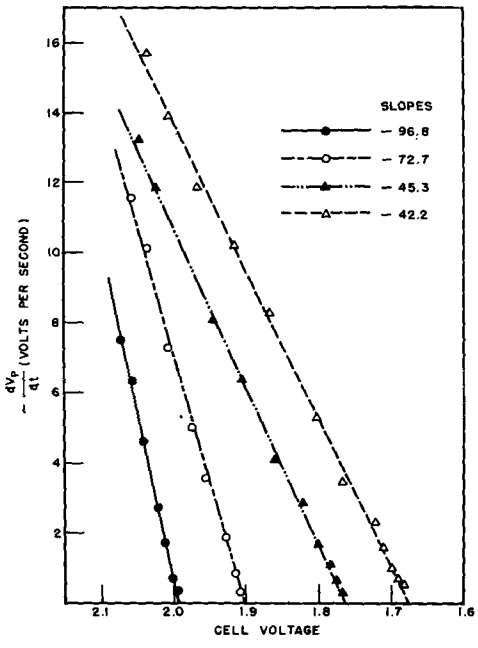

Fig. 5. $-dV_p/dt$ vs. cell voltage

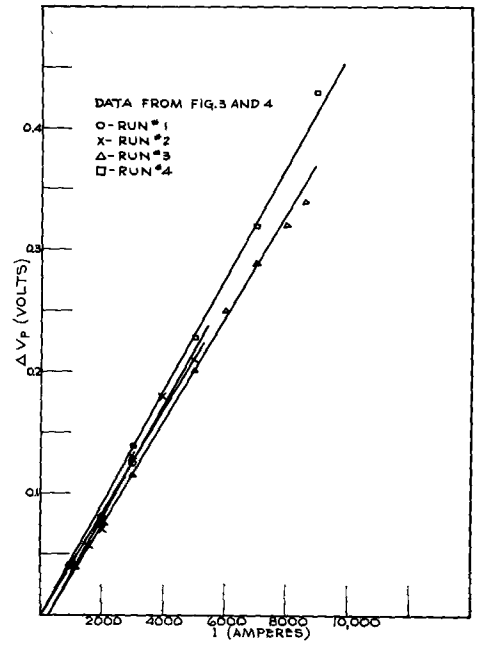

Fig. 6. Change in cell voltage vs. current, all runs

The curves are linear and nearly superimposable for each pair of runs and extrapolate through zero within 0.01 v.

It is concluded that there are no substantial (i.e., outside experimental error) contributions to voltage loss within the cell from sources other than *IR* loss over the discharge periods. The internal resistance obtained from the slopes of the curves of Fig. 6 has the value 43.7 ± 3.8 x 10^{-6} ohm. The resistance of the risers and lugs was measured during current flow and it contributes 10 x 10^{-6} ohm to the cell resistance measured at the tops of the lugs outside the cell, so total resistance of this cell in the fully charged condition was 53 x 10^{-6} ohm.

Values of inductance of the one-turn loop were estimated to be 5-8 x 10^{-6} henry (6). Values calculated from the slopes of the curves of Fig. 5, knowing R_o and R_I, ranged between 5 and 7 x 10^{-6} henry.

One run was made in which time was extended out to 2 sec, during which cell voltage and single electrode potentials were measured. For this run, no polarization was evident at the negative plate after 0.1 sec, the total contribution from sources other than IR_I loss being located at the positive plate. With somewhat over 9000 amp flowing, positive plate polarization amounted to 0.05 v at 2 sec, and it was still increasing slowly when the run was stopped at about 5 sec.

Discharge Voltages Measured at the Cell Terminals

It has been mentioned that cell-voltage taps were located at the tops of the plates inside the cell to avoid contributions from the $L\ dI/dt$ term. One set of data will be presented to illustrate the effect of including such a contribution with the voltage taps at the cell terminals.

The circuit was rearranged to approach a short-circuit condition by removing the cables and swinging the short, heavy, current-measuring brass tube between the tops of the plates forming the switch mounting, so the external resistance consisted of the switch mounting and the brass tube in series. Reference to Fig. 2 will aid in getting the picture. The inductance loop was then bounded by the plates of the cell, the cell risers and lugs, the plates and switches comprising the switch mounting and the brass tube. The inductance of the loop was estimated to have a value of about 0.3 x 10^{-6} henry. For this run a different cell was used than was used for obtaining the previous data. It had a different number of plates but had the same nominal capacity.

The data for the run is given in Fig. 7. The shunt voltage curve (current) rose smoothly from zero to a value corresponding to 34,300 amperes.[2] The cell

[2] A word should be said about current density. The gross positive plate area is 64,000 cm^2 for this cell. Particle size measurements indicate the actual area of the active material could be as high as 3000 x the gross area, so current density can be in the range 0.5 to 1.7 x 10^{-4} amp/cm^2 depending on current distribution.

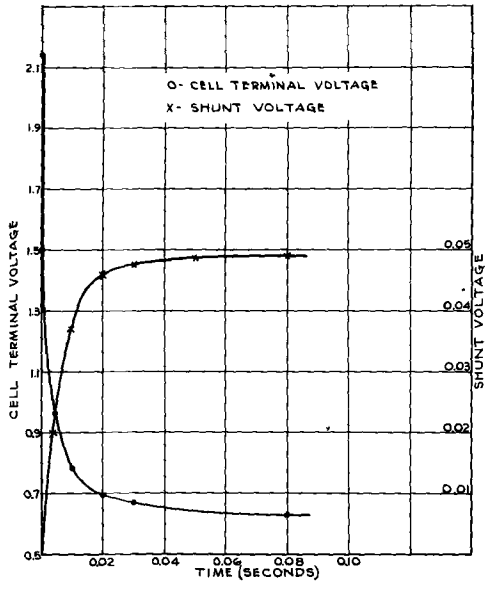

Fig. 7. Cell discharge data, voltage measured at cell terminals.

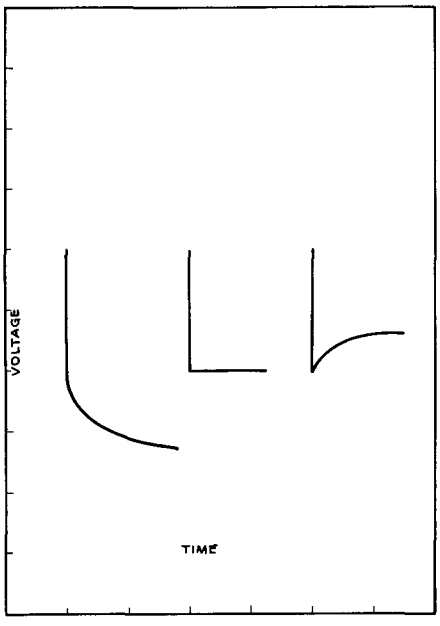

Fig. 8. Types of discharge curves possible in R-L circuits

voltage, however, fell immediately (i.e., within 0.002 sec) to a value of about 1.5 v, thereafter decaying smoothly to a value of 0.63 v.

Now, when the location of the cell voltage taps in relation to the geometry of the inductance loop is considered, it appears that the initial voltage drop could include 1/3-1/2 the initial $L\ dI/dt$ term. Furthermore, at zero time there can be no contribution from IR loss inside the cell because $I = 0$, or from electrochemical polarization because no current has passed. The conclusion that the initial voltage drop corresponds to an inductance contribution is inescapable.

The circuit inductance can be obtained from the time constant, i.e., t, when $I = 0.632\ I$ max. and total R in circuit from the equation: $L = tR$. t is 0.06 sec and R is approximated from the data assuming that when I levels off there is substantially no electrochemical contribution to polarization. If so, R_I is 43.7 x 10^{-9} ohm, R_o is 18.1 x 10^{-6} ohm, and L is 0.37 x 10^{-6} henry. Then, the initial voltage drop of 2.12-1.50 or 0.62 v is equal to $L_I\ dI/dt$, where L_I is the inductance contribution to the initial voltage drop measured at the terminals. dI/dt at zero time is 5.1 x 10^5 amp/sec from Fig. 7 and, therefore, L_I is 0.12 x 10^{-6} henry, i.e., within the estimated range of 1/3-1/2 of total L based on the circuit geometry.

One further point is to be made: by judicious selection of resistances in the latter circuit, polarization curves of the types illustrated in Fig. 8 could have been obtained, and this in a circuit containing R-L elements only. Of course, time constants would vary, depending on R, so the curves are illustrative only.

Manuscript received July 9, 1959. This paper was prepared for delivery before the Columbus Meeting, Oct. 18-22, 1959.

Any discussion of this paper will appear in a Discussion Section to be published in the June 1961 JOURNAL.

REFERENCES

1. E. Willihnganz, *Trans. Electrochem. Soc.*, **79**, 243, 253 (1941).
2. E. Willihnganz, "The Cold-Test Voltage of the Storage Battery," National Lead Co. Research Lab., Brooklyn, N. Y. (1944).
3. B. G. Bingham, Naval Research Lab. Report, No. 3707, June 30, 1950.
4. J. H. Kluck, Naval Research Lab. Report, No. 3839, July 27, 1951.
5. J. J. Lander and E. E. Nelson, Naval Research Lab. Report, No. 4347, May 10, 1954.
6. The Radio Amateur's Handbook, p. 460, American Radio Relay League, W. Hartford, Conn. (1945 ed.).

The Silver-Silver Oxide Electrode

B. D. Cahan, J. B. Ockerman, R. F. Amlie, and P. Rüetschi

Carl F. Norberg Research Center, The Electric Storage Battery Company, Yardley, Pennsylvania

ABSTRACT

An a-c square wave technique was used to study resistance and double-layer capacity during film formation on silver electrodes in KOH solutions. The peak in the voltage-time curve at constant current anodization is shown to coincide with complete surface coverage by Ag_2O and is not an ohmic resistance, but rather an overvoltage effect. Evidence for the existence of an unstable higher oxide than AgO (or additional oxygen) during oxygen evolution is presented. Microvolumetric gas measurements with large area electrodes on open-circuit decay also support this conclusion. The duration of the upper voltage plateau of the voltage-time curve during discharge of AgO electrodes is determined by contact phenomena among individual AgO particles, in particular by separation and passivation of the remaining AgO by insulating surface layers of Ag_2O.

Increased interest in the silver-silver oxide electrode has prompted a number of investigations about this system. However, the recent literature (1-15) shows a number of contradictions in the interpretation of the observed phenomena, in particular with regard to the presence of oxides higher than AgO on the electrode, and with regard to the shape of the voltage-time curves during constant current anodization and discharge of silver in KOH electrolyte.

It was decided, therefore to apply the a-c square-wave technique which was developed recently (16) to study films on lead electrodes. This technique in-

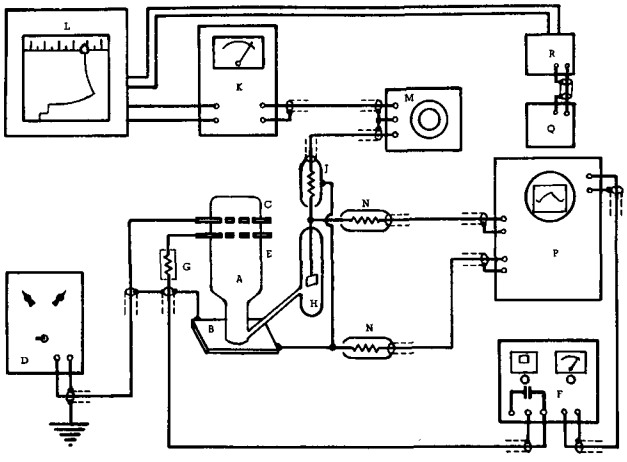

Fig. 1. Block diagram of electronic circuit: A, electrolytic cell; B, sample; C, upper platinum electrode; D, constant current supply; E, lower platinum electrode; F, square wave generator; G, noninductive resistor; H, reference electrode; J, 9 mΩ scope probe; K, electrometer; L, high speed recorder; M, bias box; N, 4 mΩ scope probes; P, oscilloscope; Q, camera; R, relay.

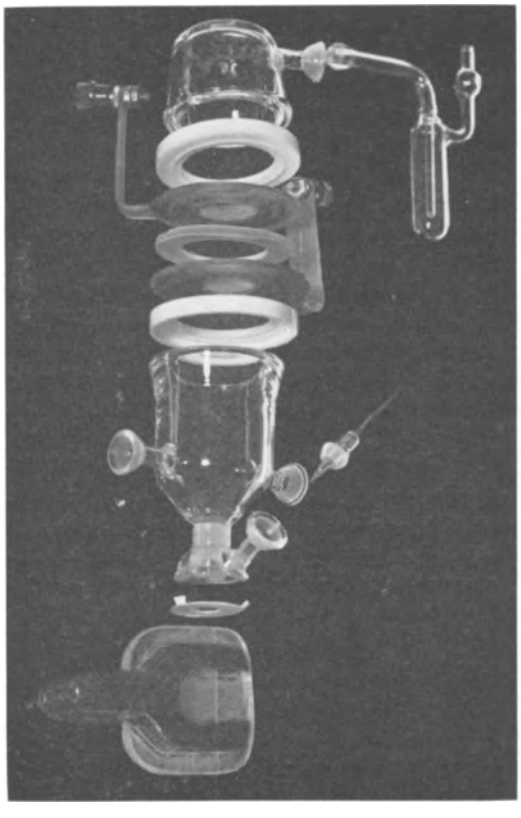

Fig. 2. Glass cell for the study of films at electrochemical interfaces.

volved the superposition of an a-c square wave current on the polarizing d-c constant current.

Experimental

The experimental set-up is illustrated schematically in Fig. 1. It shows the electrolytic cell, with separate auxiliary electrodes for the supply of a-c and d-c currents, and the recording equipment to follow the a-c and d-c response of the test electrode through a reference electrode. The instrumentation has been described in detail (16).

Figure 2 is a photograph of the cell. The test electrode, consisting of a sheet of silver, was clamped against the bottom of the cell with a thin Teflon gasket to prevent leakage. An area of 1 cm^2 was exposed to the electrolyte. A special micro reference-electrode was constructed in the following manner. A 28 gauge platinum wire was bent into a flat loop, 2 mm in length, and one end was pinch-sealed into a 3 mm Pyrex tube. The loop was heavily gold coated by placing gold chloride crystals on it and decomposing them by heating, and then fusing the gold into the surface of the platinum. Contact to the platinum wire in the tube was made by filling the tube with soft solder and by inserting a copper wire into the molten solder. The gold was then wetted with mercury such that it filled the loop. Mechanical cleaning of the gold-coated loop improved the wetting with mercury. This reference electrode was then placed into the KOH electrolyte to be used and anodized briefly. Microelectrodes prepared in this way gave potentials within 0.1 mv of a standard HgO reference electrode. The microelectrode was placed into the Luggin capillary, which intersected the side wall of the electrolytic cell within 0.3 mm of the electrode surface. This minimized the ohmic drop in the electrolyte during measurements of electrode potentials and provided for an undisturbed linear electrical field. Since the microelectrode was only 3 mm from the electrode surface, frequency dispersion and capacitive pick-up were minimized.

Figure 3 shows examples of oscilloscope traces obtained with this equipment. The traces shown here were selected in order to demonstrate the advantage of using a micro reference-electrode over a macro-electrode and the advantages of a differential oscilloscope input over a single ended one. The traces are voltage-time curves. The sweep speed was 20 μsec/cm. The voltage scale was 5 mv/cm. The square wave current used had a frequency of 6250 cps and was 10 ma peak to peak.

Trace 1 was obtained using a conventional macro reference electrode and differential oscilloscope input (type 53/54 D Tektronix plug-in preamplifier). Here the electrolyte path between the reference

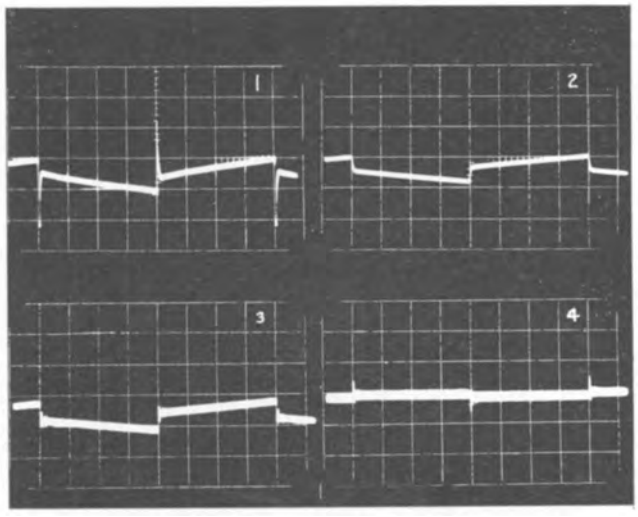

Fig. 3. Oscilloscope traces of voltage-time curves. Abscissa: time (20 μsec/cm); ordinate: voltage (5 mv/cm).

electrode and the working electrode was a Luggin capillary 8 cm long. Clearly visible is the overshoot of the trace due to capacitive pick-up. The duration of the transient spike at the moment of current reversal is between 2-3 μsec. This obscures the determination of initial slopes of the traces.

Trace 2 shows a similar curve, but taken with a microelectrode. It can be seen that the transient spikes are completely eliminated. The rise-time of the oscilloscope preamplifier was about 1 μsec in the 5 mv/cm range used here, and the reference electrode shows a perfect frequency response for this rise time. [When a wider band pass amplifier was used (type 53/54 B Tektronix plug-in unit), the rise time of the traces was found to be 0.1 μsec, or as good as the rise time of the square wave current used.] This shows that the arrangement used here is capable of following extremely fast electrochemical phenomena.

Trace 3 shows the effect of using a single-ended preamplifier (type 53/54 D Tektronix unit, used single ended) instead of a differential amplifier. The traces show extensive ringing and noise pick-up. At the low voltage signal levels used here even the resistance of the copper wires of the cable shields and the ground return paths represent considerable impedances. Even though all ground connections are made at the working electrode, high-frequency cable oscillations are detectable and a-c ground loops are set up.

Trace 4 was obtained by connecting the single ended amplifier between the square wave generator ground and the working electrode, which were short circuited by the cable shield. Trace 4 represents the difference between trace 2 and 3. In trace 2 the effects of all ground loops and spurious pick-up have been eliminated or cancelled electronically.

Pure silver sheet (99.99%) was etched in dilute nitric acid, washed with triple-distilled water, and air dried. The sample was cathodized at 3 ma/cm² in 30% KOH at 28°C for several minutes whereby hydrogen was evolved to remove any surface films of silver oxide. The current was reversed and the electrode anodized. The potentials were recorded and pictures were taken with the camera on the oscilloscope to determine the double layer capacity and resistance at rapid intervals during the anodization period of 5 min. Then the current was reversed and the oxide film discharged.

In a second phase of this investigation of the silver-silver oxide system, a microvolumetric study of oxygen evolved during the open-circuit decay of oxygen overvoltage was made. The oxygen evolved at constant temperature and pressure was measured as a function of time simultaneously with the decay of potential. The experimental set-up for this study has been described recently (17).

A standard AgO storage battery plate as produced by the Industrial Division of The Electric Storage Battery Company, containing 7 g of silver, was charged over prolonged periods of time at 50 ma in 30% KOH. The current was then interrupted and the potential allowed to decay to 0.52 v vs. Hg/HgO or 20 mv positive to the reversible AgO/Ag_2O potential. The plate was then charged at various

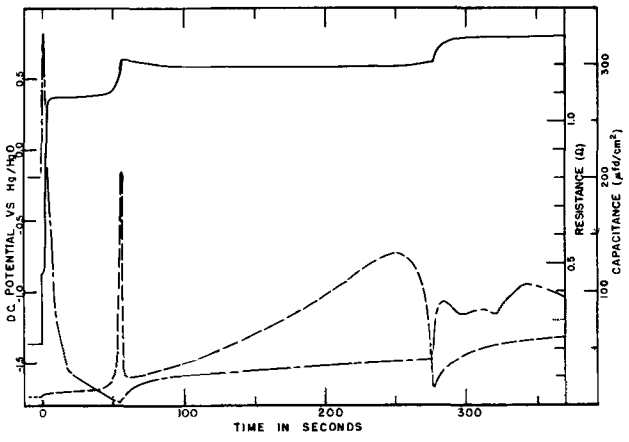

Fig. 4. Electrode potential (solid line), ohmic resistance (dashed line), and double layer capacity (dotted-dashed line) of silver during anodization at 3 ma/cm² as a function of time.

constant currents from 10 ma to 250 ma and the build-up of oxygen overvoltage recorded. After 24 hr of overcharge the currents were interrupted and the cell sealed simultaneously. The gas evolved during overvoltage decay was measured by the displacement of a drop of liquid in a calibrated capillary.

Results

The anodization curve of a 1 cm² sheet silver electrode is shown as the solid line in Fig. 4. The curve starts out at hydrogen evolution at 3 ma/cm². At $t = 0$ the current was reversed and the potential rose rapidly. After a sharp rise of 450 mv there was a slight arrest and then the potential rose smoothly to the Ag/Ag_2O potential at about +0.35 v.

After about 40 sec, the potential increased to a peak of +0.62 v, and decreased subsequently to about +0.57 v. The potential rose again after 250 sec to +0.6 v, after which a sharp break occurred, and the potential increased to +0.8 v. At the point of the sharp rise a cloud of fine gas bubbles was seen rising in the electrolyte.

The electrode film resistance calculated from the oscilloscope traces as recorded by the camera is plotted as a dotted line. The initial resistance is very low, about 0.03 Ω, and is due primarily to the gas bubbles adhering to the surface, and reducing the effective cross section of the electrolyte. As the current is reversed, the resistance shows a slight jump, but remains relatively constant at 0.04 to 0.05 Ω for about 40 sec.

At this time, the resistance builds up quite rapidly to a very high value of 0.8 Ω, and probably higher, indicating a rapid passivation of the surface. At the moment the potential reaches its peak, the resistance falls off such that within 1 sec the resistance has fallen to 0.1 Ω. During the course of the Ag_2O/AgO voltage plateau the resistance increases smoothly to a point about 30 sec before the third step in the voltage-time curve, or where O_2 is evolved. Here, rather than increasing as at the beginning of the Ag_2O/AgO plateau, the resistance takes a sharp dip, falling to a value of 0.06 Ω. After the oxygen evolution starts, the resistance builds

up smoothly as the oxide film thickness continues to increase slowly.

The curve showing the differential capacitance (as determined from the initial slope of the voltage-time oscillographs) is plotted as a dot-dash line. This curve reflects in a general way the inverse of the resistance-time curves, with several noteworthy exceptions. The initial capacity during H_2 evolution is about 200 μfd/cm^2, indicating a roughness factor of about 10 (assuming a double layer capacity of 20 μfd/cm^2 of true surface area). The momentary high capacity after reversal shows that some highly reversible reaction is in progress, but after the first 10-15 sec the capacity decreases nearly linearly to very low values of 1-2 μfd/cm^2. After the Ag_2O/AgO plateau is reached the capacity rises rapidly to 25 μfd/cm^2 and then more slowly to about 40 μfd/cm^2. When oxygen evolution starts the capacity increases abruptly and erratically, rising to a peak and decaying, rising to a peak and decaying, rising again, etc.

The discharge curve of a specimen that had been held at the oxygen evolution potential at 3 ma/cm^2 for 3 min is shown by the solid line in Fig. 5. The potential falls in about ½ sec to the Ag_2O/AgO plateau, but this drop is *not* instantaneous. The AgO plateau lasts for 100 sec, at 3 ma/cm^2 and then drops to the Ag_2O/Ag discharge potential. This second plateau lasts for 170 sec (longer than the first plateau) and then the potential falls off rapidly. A slight arrest is noted, at −0.75 v and then the potential drops to the H_2 evolution value.

The resistance curve during discharge shows a very different behavior from that obtained on anodization. The resistance of 0.3 Ω at oxygen evolution shows an initial rise which levels off at about 0.5 Ω. A more gradual increase sets in, which slowly accelerates until values as high as 2.5 Ω or more are reached. The resistance breaks down completely within 1/6 of a second, or the repetition rate of the camera we used, at the moment when the potential drops to the lower voltage plateau. The resistance falls to 0.04 Ω and gradually decreases to unmeasurably low values during the Ag_2O/Ag plateau.

After a sharp initial peak, the capacitance decreases about linearly as passivation progresses, decreasing to 1 or 2 μfd/cm^2 at the transition point. As the Ag/Ag_2O step progresses, the capacitance increases more or less linearly to very high values (greater than 4000 μfd/cm^2) and drops off sharply at the end of the second voltage plateau. A further peak in capacitance occurs during the small potential arrest, and then the capacitance decreases rapidly at H_2 evolution. It might be noted that the capacitance at this point is about 400 μfd/cm^2 as compared to 200 at the start of the run, indicating a roughening of the surface by a factor of 2.

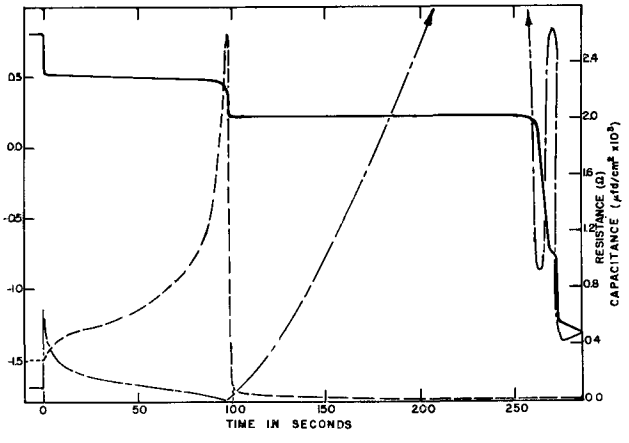

Fig. 5. Electrode potential (solid line), ohmic resistance (dashed line), and double layer capacity (dotted-dashed line) of a silver oxide film (produced by previous anodization of silver in KOH) during discharge at 3 ma/cm^2, as a function of time.

The results of the microvolumetric studies during oxygen overvoltage decay are shown on Fig. 6. These results were obtained with porous large-area electrodes. Figure 6A shows the plots of electrode potential vs. time on a logarithmic scale, for open-circuit decay from three different prepolarizing currents. Also shown is a plot of oxygen evolved vs. time during overvoltage decay on open circuit. Figure 6B shows a similar curve for the decay of oxygen overvoltage on PbO_2 in sulfuric acid. The results for PbO_2 (Fig. 6B, 6D, and 6F) are included here for purposes of comparison only, because they are representative of the decay of overvoltage on an inert electrode (17). Similar curves are obtained for decay of oxygen overvoltage on nickel in KOH, decay of hydrogen overvoltage on Zn and Cd in KOH, and Pb in H_2SO_4.

Figure 6C is a plot of the electrode potential during oxygen overvoltage decay vs. relative excess of oxygen, or vs. $V_T - V_X$, where V_T is the total volume of oxygen evolved to a potential 20 mv above the open-circuit potential, and V_X is the volume of oxygen evolved to any intermediate potential. Figure 6D shows a similar plot for decay of oxygen overvoltage on PbO_2 (17). Figure 6E illustrates a charging curve for build-up of oxygen overvoltage on AgO. The large-area electrodes were charged after being allowed to decay to a potential 20 mv above the reversible open-circuit potential, at different currents. Similar charging curves are shown in Fig. 6F for PbO_2.

Discussion

These results permit a detailed analysis of the mechanisms of the silver oxide electrode. In particular, the effects of the resistance of the surface films on silver are brought out clearly. The lower oxide, Ag_2O, has a very high electrical resistivity. Ag_2O powder was compressed into a hard, shiny pellet at 62,500 psi. The resistance was measured with an electrometer ohmmeter to be $7 \cdot 10^8$ Ω cm. (Using this value, a 1 cm^2 monolayer would have a calculated resistance of about 1 Ω. The extrapolation is, of course, very approximate, since a monolayer has different properties from bulk material.) From the length of the Ag/Ag_2O plateau in Fig. 4 and a surface roughness factor of about 10, the thickness of the Ag_2O film produced during the plateau is roughly 50-100 monolayers thick. It is apparent that the surface film of Ag_2O is nonuniform and that at the moment of complete coverage, the resistance must rise to relatively high values. This causes the sharp peak in the resistance curve.

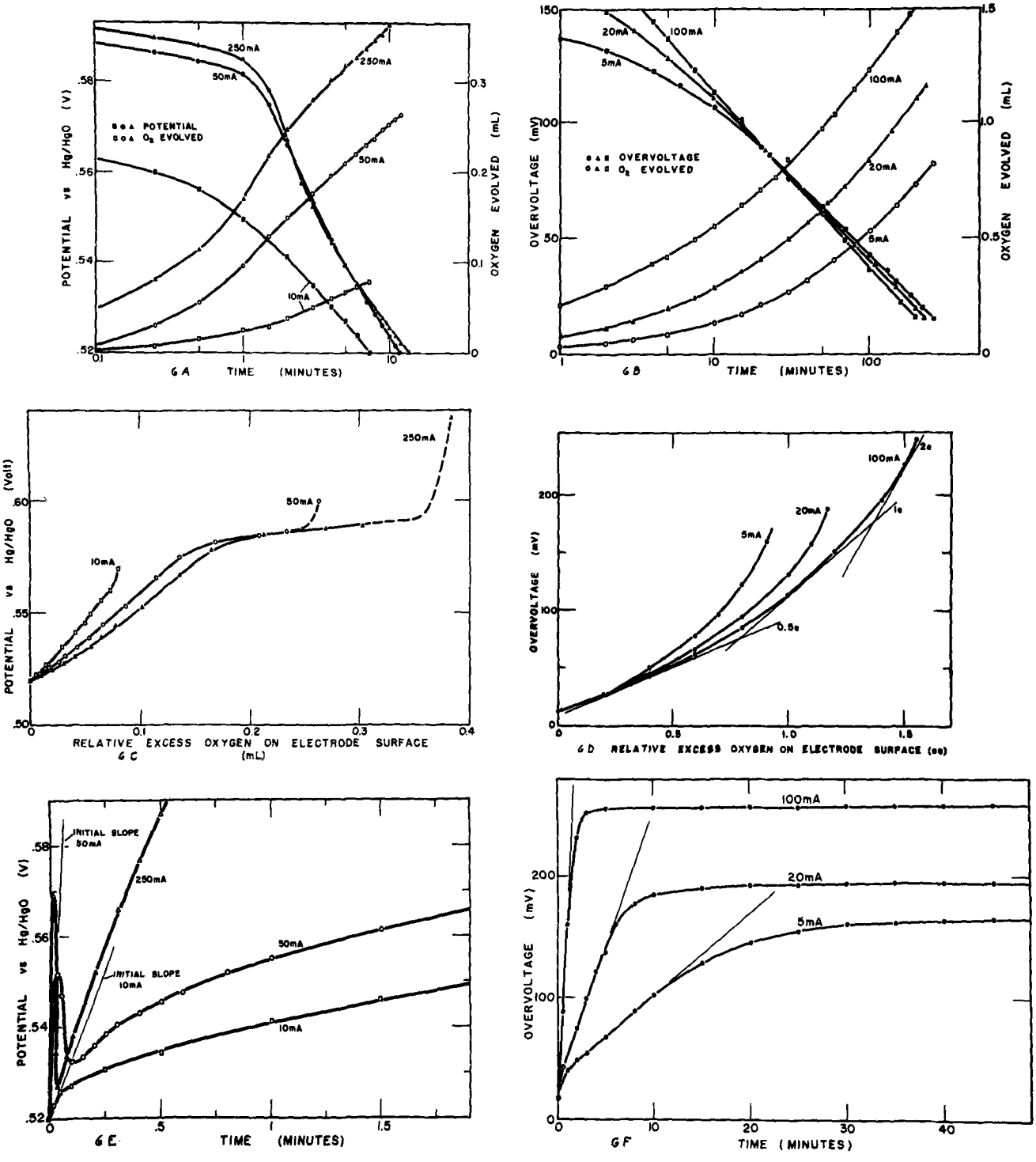

Fig. 6. Comparison of overvoltage and gas evolution data on AgO and PbO_2 electrodes. Fig. 6A, overvoltage decay and gas evolution during open-circuit decay of an AgO electrode in KOH. Fig. 6B, overvoltage decay and gas evolution during open-circuit decay of a PbO_2 electrode in H_2SO_4. Fig. 6C, electrode potential of AgO in KOH during decay as a function of gas evolved. Fig. 6D, electrode potential of PbO_2 in H_2SO_4 during decay as function of gas evolved. Fig. 6E, charging curves for oxygen overvoltage build-up on AgO electrodes. Fig. 6F, charging curves for oxygen overvoltage build-up on PbO_2 electrodes.

The peak observed in the voltage-time curve at the beginning of the AgO step is not directly due to an ohmic resistance effect since the ohmic resistance is in the order of 1 Ω and would produce a voltage increase of only 3 mv at 3 ma/cm². The peak is much higher and is produced rather by a concentration of the current into small localized areas, where the conversion of Ag_2O to AgO can proceed. This causes an increased overvoltage for the conversion reaction. The points where Ag_2O first converts to AgO are those where the Ag_2O film is thinnest and which were covered last. From these points the conversion spreads until the Ag_2O film is substantially oxidized. Simultaneously a further attack of metallic silver takes place. Any Ag_2O which is formed during this stage must be rapidly oxidized and can have only a transitory existence.

The resistivity of AgO was measured in the same

way as for Ag_2O, and was found to be $5 \cdot 10^8$ Ω cm. This is five orders of magnitude smaller than for Ag_2O.

During the upper plateau 0.6 coulombs of electricity are used in forming a film of AgO of "average" thickness of approximately $5 \cdot 10^{-6}$ cm. Since the resistivity is $5 \cdot 10^8$ Ω cm, the resistance of the film should be of the order of 0.25 Ω. This is of the order of the resistance actually measured, 0.53 Ω. This resistance value shows that there *cannot* be at any time during anodization a significant complete interface layer of Ag_2O present. On open circuit, a heavier film of Ag_2O can be present, formed by local action cells between AgO and Ag.

It is pointed out here that the limiting film thickness roughly of $5 \cdot 10^{-5}$ cm is of particular importance for the manufacturing of porous silver oxide electrodes for silver-zinc batteries. It is evident that only particles with a diameter less than 10^{-4} cm (1 μ) are readily and completely converted from metal to oxide.

At the end of the AgO plateau the resistance drops to values of 0.08 Ω. This drop should not be interpreted as a physical rupture of the layer and an exposure of silver to the electrolyte, because the oxidation of metallic silver has been shown to be small once a complete AgO film is formed, and ruptures therefore should not occur. It is proposed that a further incorporation of oxygen in the AgO film has taken place, producing a highly unstable film of a higher oxide than AgO. It is not clear how the additional oxygen is adsorbed in the individual crystallites. However, in any case, the resistivity of the film is changed.

Although little accurate data is available, it is often observed that when a metal oxide exists in several valence states, the resistivity decreases with increasing valence state. For example, PbO has a resistivity of $2\text{-}5 \cdot 10^7$ Ω cm and PbO_2 of 1 to $5 \cdot 10^{-4}$ Ω cm. Similarly, AgO has much lower resistivity than Ag_2O, and a possible higher oxide would have an even lower resistivity. Although this rule is not without exceptions, it could possibly account for the sharp drop in resistance observed at 250 sec in Fig. 4. Only very small parts of the AgO surface film need be converted to a highly conducting compound in order to produce the observed effect.

The rise in potential at the point of oxygen evolution is not due to an ohmic-resistance passivation, but rather to oxygen overvoltage on the limited number of sites of the higher, unstable oxide, concentrating the current to small local areas.

The capacitance peak at the beginning of the anodization curve shows that the reaction is here very reversible. The linear decrease during the first voltage plateau is due to a decrease in the available surface area. The capacity during the AgO step is small. This indicates that the surface film is now conductive, and that the capacitance is again due to the solid-liquid double layer. The erratic behavior of the capacitance during oxygen evolution is due to the instability of the higher silver oxide sites which may vary in number and size.

During discharge of the silver oxide film, shown in Fig. 5, the resistance is low at the beginning and increases quickly as the higher silver oxide sites disappear. The further increase in resistivity is due to build-up of Ag_2O on the surface toward the electrolyte, blocking the underlying AgO from reaction. The resistance rises to values greater than 2.5 Ω. When the electrode is substantially covered with Ag_2O, the local high current density polarizes the electrode to a potential where metallic silver can be produced. At this point, the resistance drops sharply due to the formation of filamentary crystals of silver, providing good electrical contact. The first voltage plateau during discharge is always observed to be substantially shorter than the second plateau, although the film consisted initially of almost pure AgO, and the total capacity to the end of the second plateau corresponds to a two-electron change. As explained above, this is due to a covering of AgO by Ag_2O. As the passivating layer of Ag_2O is converted to silver, further AgO can be discharged, by formation of more Ag_2O from a local cell of Ag and AgO. The energy corresponding to the 250 mv difference between the two plateaus is lost internally as heat. The electrochemical reactions for the oxidation of Ag and the reduction of AgO are fast. Thus internal local action in an electrode between Ag and AgO should proceed rapidly. The utilization of AgO in discharge of silver-zinc cells is illustrated in Fig. 7. Two standard commercial cells were made using chemically produced AgO in the positives. In one of these cells (upper circuit), a special inert conductive matrix[1] was incorporated which could establish electric contact to each individual AgO particle. In this manner, the passivation due to Ag_2O was greatly minimized, and all the AgO was utilized at the

[1] Subject matter of patent application.

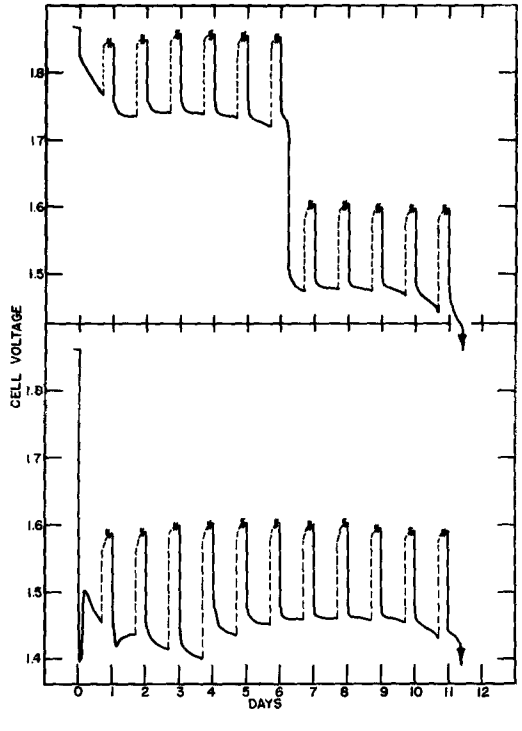

Fig. 7. Discharge curves of commercial silver-zinc cells with and without conductive, inert matrix in the silver electrode. The solid line is the cell voltage during discharge. The dotted line represents the recovery of cell voltage on open circuit.

higher voltage plateau, at close to 100% efficiency.

These cells were discharged for 6 hr/day and allowed to recover overnight. The discharge is shown in Fig. 7 by the solid line and the recovery by the dotted line. The initial sharp drop in voltage for the lower cell shows the insulating effect of the Ag_2O film, which quickly covered the surface of the AgO electrode. The voltage recovered somewhat as soon as some silver was produced. Overnight, most of the silver was reoxidized by the remaining AgO.

The upper curve is for an identical cell but with the conductive matrix. The discharge occurs at the higher plateau for the theoretical time, namely one half of the discharge. This results in an increase of 10% in the watt-hour output.

The decay of oxygen overvoltage on open circuit on an inert electrode is in general expected to follow, after an initial time period, a linear relationship with the logarithm of time, having a slope equal to the negative of the Tafel slope (17). It is noticed in Fig. 6A that the decay curve from 10 ma charge shows this normal behavior, while the decay curves from 50 and 250 ma show a characteristic inflection. The curves for evolved oxygen show similar inflections. The curves approach the same slope toward the end of decay only. The electrode potential tends to remain higher than normal for an initial period of time. Figure 6C shows this even more clearly. Several tenths of a cubic centimeter of oxygen are evolved while the potential remains at 0.585 ± 0.005 v, independent of the value of the prepolarizing current. This quantity of oxygen corresponds to 10 micromoles. No such potential plateau is observed for a "normal" electrode like PbO_2 (Fig. 6D).

The decay from 10 ma/cm^2 for AgO (Fig. 6C) also shows no such arrest, indicating that the charging potential was not sufficiently high to produce the higher oxide.

The arrest in oxygen overvoltage decay on AgO has been observed by other investigators (2, 15) but has been interpreted sometimes to be caused by hydroxyl-hydroperoxide ion couples and/or hydroxyl-oxygen couples (8, 15). This interpretation does not explain the high conductivity of the film at the point of oxygen evolution and, furthermore, the potential of such couples would not coincide with the plateau observed.

The charging curves of large-area AgO electrodes (Fig. 6E) which had previously been kept slightly above the Ag_2O/AgO potential, but below the potential of the plateau mentioned above, show a sharp initial peak unlike the smooth build up of oxygen overvoltage on PbO_2. These peaks possibly correspond to a nucleation phenomena for the higher oxide or the active sites of oxygen evolution.

Conclusions

1. The mechanism responsible for the peak in the anodization curve of Ag in KOH solution at the beginning of the AgO step (Fig. 4) is due to passivation, forcing the currents to small areas and producing a high overvoltage. It is *not* due directly to an ohmic resistance.

2. The reason for the shortness of the AgO step on discharge of an AgO electrode is an isolation of AgO by an Ag_2O film which is highly resistive.

3. By special electrode formulation the length of the AgO plateau can be extended to the theoretical length of ½ of the discharge time.

4. Evidence is presented for the existence of a conductive, unstable oxide of silver with an oxidation state higher than AgO. Because of its transitory nature, identification by means of x-ray diffraction techniques is difficult, if not impossible.

5. The use of an adequately designed cell and microreference electrode, together with a differential amplifier, permits single electrode studies at high frequencies, with electrode voltage rise-times better than 0.1 μsec.

Acknowledgments

The authors are indebted to Captain C. G. Grimes, Director of Research of The Carl F. Norberg Research Center of The Electric Storage Battery Company, for the permission to publish this paper.

Manuscript received Feb. 26, 1960. This paper was prepared for delivery before the Columbus Meeting, Oct. 18-22, 1959.

Any discussion of this paper will appear in a Discussion Section to be published in the June 1961 JOURNAL.

REFERENCES

1. A. Hickling and D. Taylor, *Discussion Faraday Soc.*, **1**, 277 (1947).
2. P. Jones, H. R. Thirsk, and W. F. K. Wynne-Jones, *Trans. Faraday Soc.*, **52**, 1003 (1956).
3. A. B. Neiding and I. A. Kazarnovskii, *Dokl. Akad. Nauk SSSR*, **78**, 713 (1951).
4. T. P. Dirkse and G. J. Werkema, *This Journal*, **106**, 88 (1959).
5. P. Rüetschi and P. Delahay, *J. Chem. Phys.*, **23**, 556 (1955).
6. T. P. Dirkse, *This Journal*, **106**, 453 (1959).
7. B. N. Kabanov and D. I. Leikis, *Z. Elektrochem.*, **62**, 660 (1958).
8. C. P. Wales and J. Burbank, *This Journal*, **106**, 885 (1959).
9. Yu. V. Pleskov, *Doklady Akad. Nauk. SSSR*, **117**, 645 (1957).
10. K. Nagel, R. Ohse, and E. Lange, *Z. Elektrochem.*, **61**, 795 (1957).
11. F. Bonk and A. B. Garret, *This Journal*, **106**, 612 (1959).
12. T. I. Borisova and V. I. Veselovskii, *Zhur. Fiz. Khim.*, **27**, 1195 (1953).
13. T. I. Borisova, *Trudy Sov. Elektrokhim. Akad. Nauk. SSSR Otdel Khim Nauk* 1950, 386 (1953).
14. I. N. Pospelova, A. A. Rakov, and S. Ya. Pshezhetskiy, *Zhur. Fiz. Khim. SSSR*, **30**, 1433 (1956).
15. T. P. Dirske, *This Journal*, **106**, 920 (1959).
16. B. D. Cahan and P. Rüetschi, *ibid.*, **106**, 543 (1959).
17. P. Rüetschi, J. B. Ockerman, and R. Amlie, *ibid.*, **107**, 325 (1960).

The High-Temperature Aqueous Corrosion Resistance of the Uranium-5% Zirconium -1½% Niobium Alloy

J. E. Draley, S. Greenberg, and W. E. Ruther

Argonne National Laboratory, Lemont, Illinois

ABSTRACT

The uranium-5% zirconium-1½% niobium alloy shows good corrosion resistance, as gamma quenched, in water to about 315°C. Optimum heat treatment results in a rate of about 6 mg/cm²/day at 290°C. Moderate aging, e.g., 400°C for 2 hr, results in reduced corrosion rates in the initial stages of corrosion; however, corrosion resistance can be destroyed by overaging. After protracted exposure, samples fail; this is believed due to absorbed corrosion product hydrogen.

Operation of heterogeneous water-cooled nuclear reactors at high temperatures would be facilitated if the fuel were corrosion resistant. Since unalloyed uranium corrodes very rapidly in high-temperature water, considerable effort has been devoted to the development of corrosion resistant alloys of reasonably low alloy content and to the understanding of the corrosion mechanism. Much of this work has been summarized (1-5).

The development of a group of "distorted" alpha phase alloys of relatively low alloy content has been described (6). In this class, niobium has appeared to be the most valuable alloying element. Its loss of as-quenched corrosion resistance during heat treatment can partly be prevented by the ternary addition of zirconium. This paper is concerned with the detailed corrosion behavior of the uranium-5% zirconium-1½% niobium alloy.

This alloy was chosen as the fuel for the Argonne Experimental Boiling Water Reactor. The properties of a fissionable material are profoundly affected by nuclear radiation. Its effect on the corrosion behavior, as well as on some physical and mechanical properties, of this alloy has been described in detail elsewhere (7-9). It is sufficient to mention here that only small amounts of radiation greatly increase the corrosion rate of relatively resistant material.

Experimental Procedure

Alloys were vacuum melted and cast by the Foundry and Fabrication Group of the Argonne Metallurgy Division. The compositions of all those studied during this investigation, together with the crucible and mold material, are given in Table I.

Most samples were gamma quenched by heating at 1000°C in vacuum (suspended in tantalum wire basket) and quenching in Woods Metal at 125°C. Other samples were gamma treated by heating to 850°C in liquid metal or salt and quenching in various media. The method of heat treatment is indicated in the data.

Relatively low-temperature treatments subsequent to quenching are referred to as aging treatments. Because of the wide variation in times and temperatures of aging, three methods were used: (*a*) sample in an evacuated ampoule placed in electric oven (low temperatures, long times); (*b*) sample placed in Vycor tube furnace with flowing argon or helium (low and medium temperatures, short and medium times); and (*c*) sample immersed bare in liquid metal (high temperature, short time).

Table I. Composition of alloys tested†

Alloy	Zr	Nb	C, ppm	N, ppm	Si, ppm	Crucible material‡
H-203-T	3.93	1.77	10	35	200	
B	4.70	1.73				Magnesia
H-317-T	5.40	1.57	65	46	50	
B	5.36	1.60	23	26	60	Magnesia
H-416-T	4.88	1.71	25	11		
B	4.81	1.67	22	10	100	Graphite
H-419-T	5.80	1.80	15	13	200	
B	4.95	1.62	78	34	150	Graphite*
L-157-T	7.00	1.60	64	41	100	
B	6.00	1.65	43	134	100	Magnasite*
L-170-T	5.70	1.95	12	10		
B	5.20	1.60	21	16	100	Magnasite*

† Unless otherwise indicated, composition is given as weight per cent. Analyses by Chemistry Division, ANL.

‡ Most casting was done into a water-cooled copper mold.

* Denotes those which were cast into heated graphite molds.

Samples were air cooled after aging. There were enough samples aged by two of these methods to indicate that the method used was not a significant variable.

Samples are described by the original casting number and the location (when known) with relation to the ingot, indicated as T (top), B (bottom), or C (center). Preparation of the material is described as c (as cast) or r (rolled). Thus L-170B-r indicates the bottom section of casting L-170 in the rolled condition. Compositions are given in weight per cent.

The high-temperature corrosion tests were conducted in stainless steel autoclaves, placed in forced convection ovens. In most tests, samples were insulated from electrical contact with a stainless steel

holder by means of synthetic sapphire rods. Some corrosion tests performed in the Argonne Reactor Engineering Division are also reported here. In these tests the alloy samples were allowed free contact with the bodies of the stainless steel test autoclaves. There was no noticeable effect of such contact.

Before the first period of test, samples were wet-ground to 400 grit metallurgical paper. Whenever the sample shape made this procedure impractical, it was electropolished in a perchloric-acetic acid (1 to 10) bath. Results indicate that there was no significant difference in corrosion behavior caused by this difference in procedure. Surface areas were measured, after which the samples were degreased in methyl alcohol, washed in distilled water, and weighed. After each test period each sample was cleaned of loose oxide with wet Kleenex, dried under vacuum, and weighed. Since very little of the corrosion product remained on the sample, weight losses closely approximated actual metal corroded. These values were plotted as a function of time, and the slopes of the curves so obtained are described as the "corrosion rate" (areas used in the computations were the original sample areas). These rates are expressed as mg/cm²/day (mcd).

Distilled water was used as the corroding medium unless otherwise indicated. This water was double distilled, passing through a cation exchange resin between the two distillation steps. The resistivity of the water was equal to or greater than one megohm-cm at the tap. The autoclave was filled with this water, heated to boiling, and the water discarded. The sample and its holder were placed in the autoclave; water was then added and again heated to boiling. A water sample was withdrawn and the autoclave sealed while the water was still boiling. The specific resistance of this water sample was measured as a check on water quality and cleanliness of the autoclave. The value was typically several hundred thousand ohm-cm. Fresh water was added in this way for each exposure so that during long tests the water was replaced each time the sample was examined.

Hydrogen analyses were performed in an apparatus in which the uranium alloy sample was heated into the gamma phase region (about 850°C). By means of two Toepler pumps the hydrogen was passed, through a paladium valve, into a calibrated volume where its pressure was measured. That the evolution of hydrogen is complete has been demonstrated by corroborative analyses run by combustion. For analyses of samples after corrosion test, the corrosion product was sometimes removed by grinding the samples clean, and sometimes it was left on and simply dried by evacuation at room temperature. For a few cases where both procedures were used on similar samples, the results were the same, inferring that the drying procedure adequately removed moisture, so that errors from this source are unlikely.

For metallographic examination the majority of samples were electroetched with the Ames solution at 15-30 ma/cm² at room temperature. This solution consists of eight parts (by volume) concentrated phosphoric acid, five parts ethyl alcohol, and five parts ethylene glycol. In some cases, electroetching was carried out in a 10% (by weight) chromic acid solution at room temperature using a current density of 10-15 ma/cm².

Results

Heat Treatment

Necessity for gamma quench.—The uranium-zirconium-niobium system has been thoroughly studied and analyzed (10, 11). The discussion here is limited to that necessary for an understanding of the relationship between heat treatment and corrosion resistance.

Between 677°C and the melting point the alloy (5 Zr + 1½ Nb) consists of a single phase (gamma). A two-phase (beta plus gamma) region exists in the narrow temperature range of 666°-677°C. Below 666°C, the structure depends on the heat treatment received by the material.

Alpha uranium is orthorhombic and lacks high-temperature corrosion resistance. The beta phase has a complex structure of tetragonal symmetry. Gamma uranium has a body-centered cubic lattice and has shown good corrosion resistance when retained by alloying.

Isothermal quenching from the gamma to the beta-plus-gamma region (and holding there for, say, 24 hr) followed by rapid quenching to room temperature produces alpha plus a martensitic (distorted alpha) phase. This structure is not corrosion resistant.

If the above procedure is followed except that the temperature of the isothermal quench is reduced to about 660°C, the room temperature structure consists of normal alpha and retained (metastable) gamma. This structure also lacks corrosion resistance.

Rapid quenching from the gamma phase to temperatures close to room temperature produces the martensitic (distorted alpha) structure. This structure is corrosion resistant. It is not known if the alloying elements are present as a submicroscopic dispersion or are in supersaturated solution. However, a second phase has not been detected at 2000X. This treatment and resulting structure is necessary for high-temperature corrosion resistance.

The rate of quench is very important. One typical method of heat treatment consists of holding the sample at 1000°C for 1 hr and then quenching in molten Woods Metal at 125°C. In one such operation the sample caught up in such a position that only about one-half was immersed in the Woods Metal. A subsequent three-day corrosion test at 300°C resulted in almost complete disintegration of that part of the sample which was not immersed.

Additional experiments confirmed the importance of quenching rate. A series of samples were heated in lead at 800°C and quenched in water, molten Woods Metal at about 125°C, oil, and liquid nitrogen. The first two groups of samples were satisfactory in water at 290°C. The latter two disintegrated in less than four days. It is indicated that the rate of quenching in oil and liquid nitrogen is lower than some critical required value. In the latter case

this is probably due to the presence of a vapor blanket.

Corrosion-resistant material is produced by quenching from temperatures in the range 725°-1000°C. The materials tested apparently were homogeneous at these temperatures, since corrosion behavior was independent of time at temperature during gamma treatment, in the range of a few minutes to 5.5 hr.

Aging characteristics.—The aging characteristics of the alloy are of importance from the point of view of particular uses. Of equal interest is the fact that a study of the aging process can lead to an understanding of the nature of the corrosion resistance and the mechanism of the loss of corrosion resistance.

Overaging destroys the corrosion resistance of the alloy. Failure of the alloy can take place either by complete disintegration or by cracking or spalling into several pieces. The latter is apparently a stage in the former. If an apparently sound piece which has cracked off is subjected to a short additional exposure, further severe cracking or complete disintegration usually takes place. This statement refers to cracking into several relatively equivalent pieces and not to minor chipping from the bulk of a sample.

As an arbitrary measure of the aging resistance of the alloy it was decided that a sample was resistant to the given combination of time and temperature if it did not fail in either of the above ways in two weeks of testing in degassed, distilled water at 290°C.

In Fig. 1, the area above the curve represents heat treatments which caused failure in less than two weeks. Combinations of time at temperature below the curve did not cause failure as it has been defined. This curve is based on castings H-317, H-416, H-419, and L-170 in the as-cast and rolled conditions. Samples were quenched from 1000°C (in vacuum) and aged in vacuum, argon, helium, or molten lead. Aging for times insufficient to cause "failure" reduced short-time corrosion rates, with the optimum close to 2 hr at 400°C. This effect is illustrated in Fig. 2. Satisfactory samples had a dark brown surface uniformly interspersed with shallow pits.

As the time of exposure was increased the corrosion rates of gamma quenched and gamma quenched

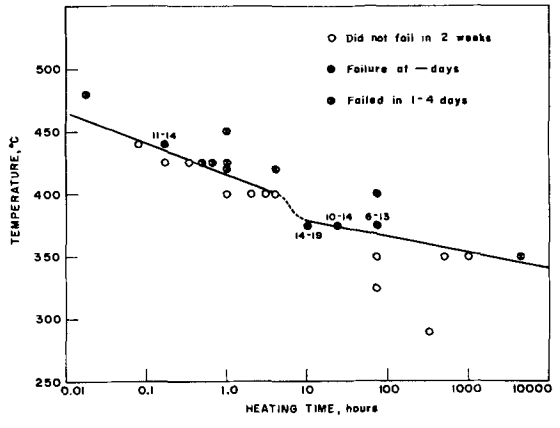

Fig. 1. Effect of heat treatment on corrosion life at 290°C of gamma quenched U-5% Zr-1½% Nb alloys.

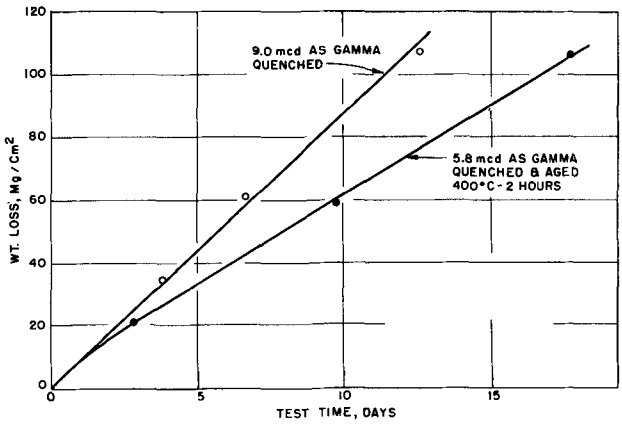

Fig. 2. Short-time effect of aging on corrosion rate of L170BC in water at 290°C.

and aged material generally became equal. In some cases the corrosion rate of gamma quenched material decreased (Fig. 3, curve 3). (This figure is also used to illustrate other ideas and will be referred to again.) It also appears that aging at 400°C decreased the corrosion life of the few samples tested for sufficient times.

To eliminate the possibility that aging occurred during test, cast samples of alloy H-317 were tested as quenched, as quenched and aged at 400°C for 2 hr, and as quenched and aged at 290°C for 312 hr. All samples showed appreciable periods of approximately equal corrosion rates.

Effect of hydrogen.—The standard heat-treatment procedure includes heating in a vacuum tube furnace at 1000°C. Considerable gas (believed to be largely hydrogen) is evolved in this process. In an effort to learn whether corrosion behavior is influenced by this gas, adjacent samples from the same rolled ingot were treated in vacuo and in molten lead.

The corrosion of these samples in water at 290°C is shown in Fig. 4. The sample heat treated in helium was included to reproduce the thermal history of the vacuum-treated sample. It is inferred that the gas content of the metal, as received, is detrimental to its corrosion properties.

A similar conclusion can be deduced from the corrosion of the sample quenched from salt (the

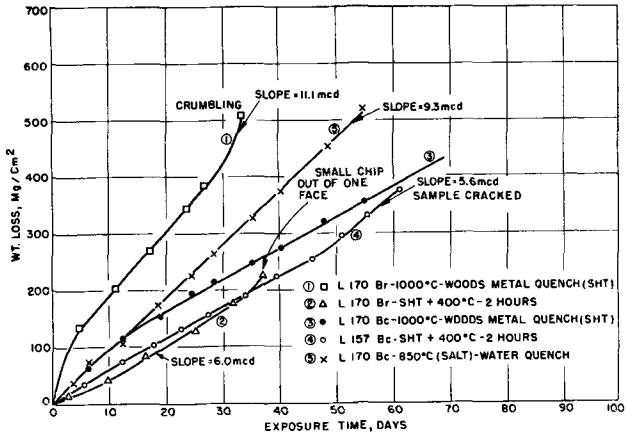

Fig. 3. Effect of heat treatment on corrosion resistance of U-5% Zr-1½% Nb alloys.

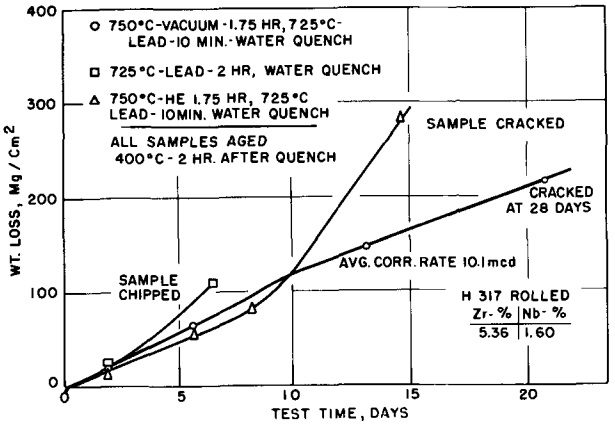

Fig. 4. Effect of gas removal on corrosion in water at 290°C of U-5% Zr-1½% Nb alloy.

eutectic of Li_2CO_3 and K_2CO_3), as shown in Fig. 3, curve 5. For the first twelve days its corrosion rate was the same as the sample, differing only by having the vacuum heat treatment. Subsequent to that time, however, the salt-treated sample continued to corrode at the same rate while the corrosion rate of the vacuum-treated sample decreased by 40%. The hydrogen content of this particular salt-treated sample was not determined; however, similar samples given the same treatment contained about 35 ppm hydrogen. Vacuum-treated metal contains little or no hydrogen.

Hydrogen can also be introduced into the sample by exposing it as the cathode in a hydrogen discharge tube. Such a sample (after 24-hr bombardment) was cracked after exposure to water and steam (because of autoclave leakage, part of the test involved a steam exposure) at 300°C for three days. A similarly tested, but nonbombarded, sample corroded in the normal manner.

Hydrogen analyses of corroded samples show direct correlation with the amount of metal corroded. In Table II such data have been treated to show the per cent of the hydrogen produced which was absorbed in the alloy. After a short initial period the percentage of hydrogen absorbed remained constant for similar samples from the same piece.

When samples from different sources were corroded, there was not always the same fraction of the produced hydrogen absorbed into the metal. It is interesting to observe in Table III, however, that the rate at which the hydrogen accumulated was approximately the same for all the samples, independent of their corrosion rates. The data from the second sample show that "loading" the material with hydrogen (by treatment in salt) before corrosion caused a higher corrosion rate. However, the absolute rate of hydrogen pickup by the sample (during corrosion) was not increased. As indicated above, an identical sample of the "loaded" material continued to corrode at the initial rate for at least 55 days, so that the shorter exposure time for the second sample in Table III does not invalidate the argument.

Table II. Hydrogen build-up as function of corrosion time (Water, 290°C; Alloy H-416C-c, gamma quenched, aged 2 hr at 400°C)*

Time, hr	Metal corroded, mg	H_2 in corroded sample, ppm	% of total H_2 produced that is found in sample
113	234	4.0	1.14
274	692	6.5	0.71
401 (Chip out of sample)	848	7.6	0.69
642 (Sample cracked into 3 pieces)	1127	13.9	0.71

* Four identical samples were tested for the times indicated. Initial hydrogen content (after heat treatment) was 0.9 ppm.

Table III. Hydrogen absorption in corroding alloy (Water, 290°C)

Sample and heat treatment	Test time, days	Average corrosion rate, mcd	% of H_2 produced that entered metal	Rate of hydrogen build-up in metal, $\mu g/cm^2$/day	Condition after test
H-416C-c Gamma quenched from vacuum, aged 400°C, 2 hr	26.7	8.6	0.7	1.09	Cracked
L-170B-c Gamma quenched from salt	18.9	9.4	0.6	0.95	No cracks
H-419B-r Gamma quenched from vacuum, aged 400°C, 2 hr	48.9	6.7	0.96	1.07	Cracked
L-170B-c Gamma quenched from vacuum	47.9	6.5	0.97	1.06	No cracks

Although the rate of hydrogen pickup was approximately the same, the corrosion-induced cracking was not. Assuming that this type of cracking is caused by corrosion product hydrogen, it must be supposed that high local hydrogen concentrations in the metal cause it, rather than the total amount present. The following experimental results support this hypothesis.

A quenched and aged specimen contained 0.9 ppm hydrogen. After about eleven days of testing at 290°C the sample was cut in half and analyzed for hydrogen. The results were 5.7 and 8.1 ppm (±0.1 ppm). It is significant that the piece with the higher hydrogen content had a subsurface crack which was revealed in sample preparation.

The salt-treated sample referred to in Table III contained about 35 ppm hydrogen after heat treatment. Very likely this was uniformly distributed in the body-centered cubic gamma uranium during the treatment. After an additional hydrogen build-up of 8 ppm during the corrosion test there was no evidence of cracking. Thus a total quantity of hydrogen which causes cracking in a sample in which it is not uniformly distributed did not cause cracking here. Perhaps the original (uniformly distributed) hydrogen enhanced the diffusion of the corrosion product hydrogen so that it too was uniformly distributed.

Table IV. Effect of aging on corrosion in water at 290°C and on hydrogen absorption

Sample*	Aging time at 400°C, hr	Corr. rate, mcd	Hydrogen content after 3-day test, ppm	Appearance of sample after test
1	0	13.5	60	Dull. Pitted
2	1	337†	832	Sample cracked into irregularly shaped piece and slurry. This piece in good condition.
3	2	450†	1220	Same as above.
4	3	616†	1340	Same as above.
5	4	—	—	Completely disintegrated.

* L-170BC—quenched from salt at 850°C.

† Based on remaining piece.

A group of samples which had been simultaneously quenched from salt were aged in a helium atmosphere at 400°C for various periods of time and tested for 71 hr in degassed, distilled water at 290°C. The aging times bracketed that for optimum corrosion resistance of a vacuum-treated sample, i.e., approximately 2 hr. Results are shown in Table IV.

The as-quenched sample reacted typically, indicating that the samples were adequately quenched. The behaviors of the aged samples were completely different from that of vacuum quenched and similarly aged metal in that the corrosion resistance was destroyed.

It seems likely that during the aging process the hydrogen concentrated, perhaps at grain boundaries. These concentrations might act as nuclei for further local hydrogen build-up, especially if the hydrogen is present as hydride. The analytical samples consisted of small pieces of metal close to cracked surfaces. As expected, very high hydrogen contents were found. It is also possible that the hydrogen content of the specimen increased the rate of transformation of the strained alpha to normal alpha, with resultant increase in corrosion.

When the hydrogen content of the alloy becomes greater than its solubility, it has been expected that a hydride phase will form. Efforts to observe such a phase in a number of samples of the sort previously discussed were unsuccessful. It was therefore attempted to obtain higher total hydrogen content as follows. A sample of L-170B-c was quenched from salt at 850°C and aged in helium at 400°C for 3 hr. It was then exposed to degassed, distilled water at 290°C for 24 hr. At the end of this period the sample had a rough, heavily pitted, irregular surface; it had corroded at an average rate of 2126 mcd. The hydrogen content was 1100 ppm. The unexpectedly high corrosion rate (as compared with data in Table IV) could have been due to an inadequate quench. However, the object of obtaining a sample with high hydrogen content for metallographic study was achieved.

The sample was examined metallographically after heat treatment, after corrosion, and after hydrogen analysis.[1] The respective hydrogen contents

[1] The hydrogen analysis produces a slow cooled alloy and the resultant structure is very complex. The sample was therefore gamma quenched and aged after analysis in order to produce a structure more conducive to evaluation.

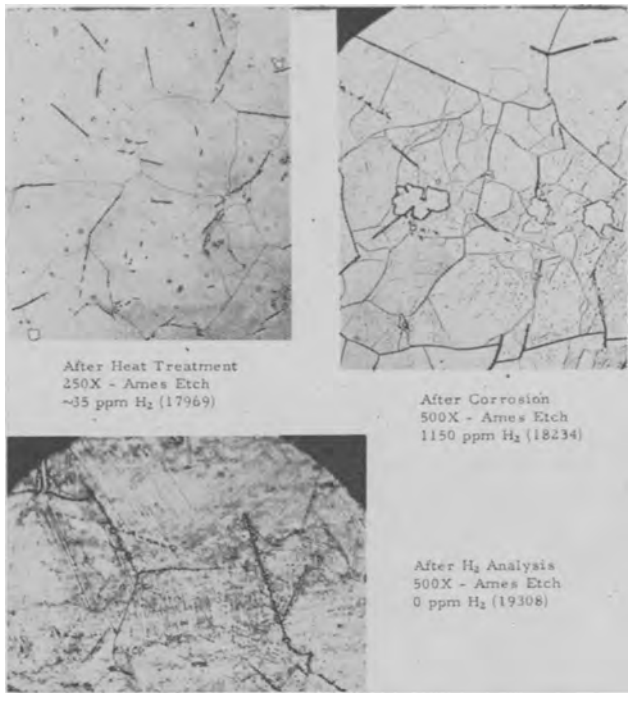

Fig. 5. Effect of hydrogen on structure of U-5% Zr-1½% Nb alloy.

were approximately 35, 1100, and 0 ppm. The photomicrographs appear in Fig. 5. Only the sample with the high hydrogen content has what may be described as a "salt and pepper" effect. This structure has been found in this alloy only in samples containing high hydrogen contents. It is therefore inferred that the structure is hydride.

The difficulty of forming the (proposed) hydride is in line with the report that the addition of as little as 0.5% zirconium to 10.5 and 12% molybdenum alloys virtually eliminates the precipitation of hydride (4).

It would be desirable to identify the new phase as the hydride in a more rigorous manner, for instance by x-ray or neutron diffraction. However, the highest hydrogen concentrations produced to date are below the threshold (2000 ppm or greater) of detection and identification by these methods. The particles are too small to be identified by standard microfocus x-ray equipment.

Effect of temperature.—Water temperature affects both the corrosion rate and the useful life of this alloy. As indicated earlier, simultaneous aging may occur at sufficiently high temperatures. Figure 6 is

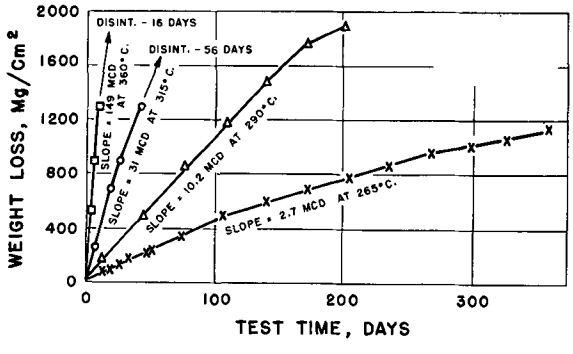

Fig. 6. Effect of temperature on aqueous corrosion behavior of gamma quenched alloy (H203r).

representative of tests performed by the Reactor Engineering Division. The effects of temperature on corrosion rate and life are illustrated.

Discussion

Structural Aspects

The quenched alloy has a martensitic "strained alpha" structure. Although optical metallography up to 2000X shows only a single phase structure, we have postulated a sub-microscopic second phase. Such a structure is possible if the rate of cooling is not great enough to prevent some decomposition before the temperature of the martensitic transformation is reached (12).

Moderate aging would complete precipitation of the second phase, if it were not already complete, and cause a slight growth of the second phase particles already present. We have attempted to confirm or disprove the existence and growth of the second phase by means of the optical microscope, x-ray diffraction, and electron microscope techniques.

Optical metallography has not been fruitful in revealing the relations between aging and corrosion behavior. Moderate aging produces a "cellular" structure within the martensite. Severely overaged samples, i.e., 475°C for 3 min, show what appears to be gross precipitation at grain boundaries. These changes are illustrated in Fig. 7, 8, and 9.

Several comments should be made concerning these figures. The dark lines are probably borides. This casting had an unusually high boron content, i.e., 15 ppm. The "overaged" sample also had the "cellular" structure, but it was impossible to show both the "cellular" structure and grain boundary effect with one etch, i.e., a longer etching time was required to develop the "cellular" structure. Neither the "cellular" structure nor the grain boundary precipitation could be shown to exist on the as quenched sample. The grain boundary effect was revealed only on the "overaged" sample.

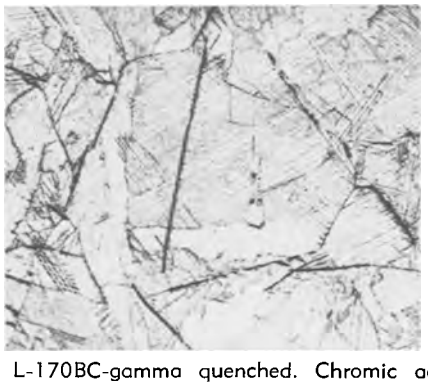

Fig. 7. L-170BC-gamma quenched. Chromic acid etch, VHN-382, 30 kg. Magnification 500X before reduction for publication.

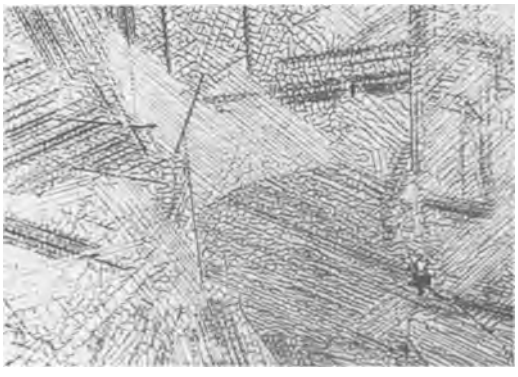

Fig. 8. L-170BC-gamma quenched and aged 400°C, 2 hr (moderate aging); Ames etch, VHN-566, 30 kg. Magnification 500X before reduction for publication.

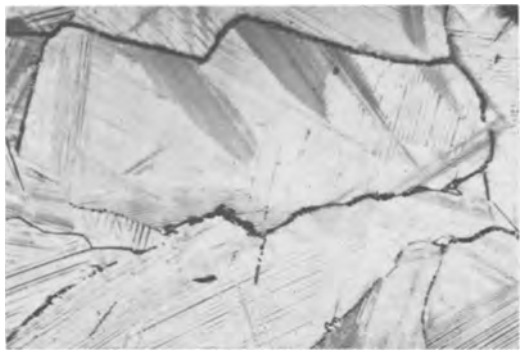

Fig. 9. L-170BC-gamma quenched and aged 475°C, 3 min (overaged), Ames etch, VHN-563, 30 kg.

X-ray diffraction results for a group of quenched and aged samples are more interesting. In Table V it is indicated that a significant return toward the lattice parameters of α-uranium accompanies increased aging. At the same time enough line sharpening was observed to indicate strain relief. These observations are consistent with the hypothesized growth of a fine precipitate. It would thus appear that agglomeration of the precipitate and return of the lattice dimensions to those of α-uranium are responsible for loss of corrosion resistance.

Etched surface textures, as revealed by electron microscopy (using direct, i.e., negative, carbon replicas) suggest that a precipitate is present in the as-quenched alloy, and that particle size increases as the alloy is aged. Figures 10, 11, and 12 are representative of quenched and aged samples, as seen at high magnification.

Any theory relating corrosion resistance to structure must explain the observation that resistance of the zirconium-niobium ternaries to aging is considerably greater than that of binary alloys containing up to about 6% niobium (6). There are at least two ways to explain the beneficial effect of zir-

Table V. (13) Effect of aging on lattice parameters and corrosion resistance

Aging† Temp, °C	Time	2θ Angle for (111)	Corrosion resistance at 290°C*
As-quenched		39.1	Good
425	10 min	39.3	Good
425	20 min	39.3	Good
425	40 min	39.35	Bad
425	2 hr	39.4	Bad
425	4 hr	39.5	Bad
440	5 min	39.35	Good
475	3 min	39.4	Bad
(α-Uranium)		39.5	Bad

* Good and bad indicate no failure and failure, in two weeks' exposure to water, respectively.

† All alloys quench from 1000°C.

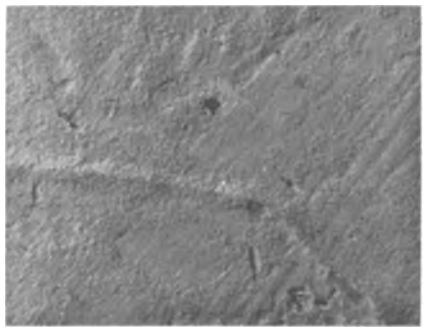

Fig. 10. L-170BC-gamma quenched, Ames etch, 16,100X —5227B.

Fig. 11. L-170BC-gamma quenched and aged 400°C, 15 min, Ames etch, 16,100X—5282A.

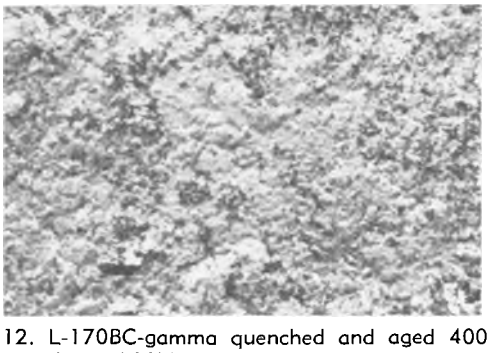

Fig. 12. L-170BC-gamma quenched and aged 400°C, 6 hr, Ames etch, 16,100X—5326C.

conium as an additive to the uranium-niobium binary alloy. In the first, the addition of several per cent of zirconium will augment the grain refining action of the niobium and will very likely slow down agglomeration of the second phase during aging. Hence the distribution of the second phase will perhaps be more favorable initially, and the unfavorable effects of overaging will be retarded.

The second explanation deals with the nature of the second phase formed. At equilibrium the ternary alloy consists of alpha uranium and about 10% γ_1 (10), which is gamma uranium saturated with niobium and zirconium. The corresponding structure of the niobium binary alloys is α-uranium and γ_2 (niobium saturated with uranium). γ_2 is not found in the ternary system. It is entirely possible that the γ_1 phase agglomerates slower than the γ_2 phase; hence the ternary alloy overages more slowly.

Role of Hydrogen

Aqueous corrosion of uranium.—It is considered helpful to discuss some aspects of the mechanism of the aqueous corrosion of uranium and then to show how the situation is modified by alloying. The results of this investigation will be used to support the belief that hydrogen produced as a product of the corrosion reaction has a considerable influence on corrosion behavior.

As unalloyed uranium corrodes in air-saturated distilled water at room temperature it forms a thin continuous and protective film of uranium dioxide. Samples of the metal in this environment develop typical interference-color films, and the progress of corrosion can be estimated from the apparent film thickness. After sufficiently long exposure, however, points of local breakdown of this film are observed. At these points the corrosion product is fine granular uranium dioxide. Where this type of product is formed, the rate of corrosion is considerably higher. With further exposure these points of breakdown gradually spread, and it is inferred that eventually most of the surface would be corroding at the more rapid rate characteristic of the situation where the relatively unprotective corrosion product is formed (1). It is considered, and the idea is developed in a publication by two of us (14), that these points of local breakdown represent places at which corrosion product hydrogen reacts beneath the protective film to form uranium hydride. This hydride then prevents bonding between the oxide film and the metal. Since this bonding appears to be a necessary requirement for the stability of thin oxide films of this type, the corrosion product takes its more stable form, a mass of fine crystals.

It is essential that there be some oxygen dissolved in the water in order to have the protective film. The means by which the oxygen acts cannot be stated unequivocally, but it appears reasonable to suppose that oxygen adsorbed on the protective oxide film will prevent the entry of hydrogen into the film and, hence, will prevent access of hydrogen to the uranium surface. The fact that breakdown ultimately occurs indicates that the prevention of the entry of hydrogen into the oxide film is not complete. In the absence of dissolved oxygen, corrosion always proceeds on initially clean metal at the rate characteristic of the situation where there is no stable protective film (1).

As the temperature is increased it is perhaps more difficult to prevent the access of some of the hydrogen to the metal surface, and the solubility of oxygen in the water is reduced. Consequently there is a temperature above which the formation of the highly protective film is not observed on unalloyed uranium. In air-saturated water this temperature is about 60°-70°C. The addition of hydrogen peroxide to the water apparently increases this temperature somewhat (1).

Alloying.—By the addition of more than a minimum amount of zirconium the apparent sensitivity to the hydrogen effect can be considerably reduced, so that the protective film forms in boiling distilled water on a uranium-5% zirconium alloy (15, 16). The behavior of this alloy in boiling distilled water can be described in exactly the same terms as was the corrosion of unalloyed uranium in air-saturated distilled water at room temperature. Ultimately local breakdown of the oxide film occurs, and the film

does not form if oxygen is rigidly excluded from the water.

There are three mechanisms which appear reasonable as explanation for the effect of the alloying zirconium. In the first the incorporation of zirconium into the UO_2 lattice could make an inherently more stable film and could also make the process of hydrogen migration through it more difficult. That this is at least reasonable is indicated by the fact that the presence of zirconium in the oxide produced on these alloys has been observed to reduce the UO_2 lattice dimensions (16).

The second proposal for the protective action of zirconium is that a zirconium-containing phase in the surface layers of the metal acts as a getter for that hydrogen which does reach the metal surface. If, then, this zirconium phase is distributed in such fashion that it can getter all of the hydrogen reaching the surface, no uranium hydride should be formed, at least until the zirconium becomes saturated. According to this picture the ultimate breakdown of the oxide film occurs when this saturation is effected. Presumably the zirconium-rich phase can absorb hydrogen only at a given maximum rate. Oxygen might be effective by maintaining the rate of arrival of corrosion product hydrogen below this limit.

If the alloy content is increased so that the total rate at which the zirconium-rich phase can absorb hydrogen at the surface is equal to or greater than the rate at which hydrogen gets there (without any retardation, as by oxygen), then there should be no requirement for dissolved oxygen. 7.5% zirconium is apparently sufficient for this purpose in boiling water (15). Some gettering action by zirconium is indicated in uranium alloys, since it has been reported (4) that as little as 0.5% zirconium virtually eliminates the formation of internal hydride crystals during corrosion in gamma-phase alloys.

The third alternative considers that hydrogen diffuses rapidly into the strained phase (martensitic). Hence the entire surface would be gettering the hydrogen. This proposal is in accord with the fact that the strained lattice has larger parameters than the normal alpha structure (Table V). In other studies (17, 18), increasing lattice parameters (by tension) has been observed to cause the rate of hydrogen diffusion to increase, sometimes strikingly.

As previously noted (16), the altered properties of the oxide appear to be insufficient to explain the observed phenomena. There would be no obvious explanation for the sensitivity of the 5% alloy to oxygen in boiling water, nor would it be clear why there should be a critical minimum zirconium content to achieve corrosion resistance. The proposals relating to the disposal of hydrogen are therefore preferred and will be emphasized in the remainder of this discussion. Of these, the one based on the action of the precipitated phase is preferred. In addition to the observed activity of zirconium (as a getter) referred to above, the greater effectiveness of increased percentages of zirconium seems more readily explained on the basis of this hypothesis. (The martensitic transformation always seems to be at least nearly complete, as indicated by x-ray diffraction and the observed topography of corroded specimens.)

A fine random dispersion of the second phase is desirable for its most efficient operation. Improved dispersion of the second phase produced by aging the quenched material is accompanied by some production of normal α-uranium. This perhaps explains the reduced corrosion lifetime of those aged samples which have lower corrosion rates. Perhaps niobium is better than zirconium both as a hydrogen getter and as a grain refiner, explaining its observed superiority as an alloying constituent (1).

Damage by hydrogen.—Presumably the niobium and/or zirconium do not do a perfect job in providing protection. It is assumed that a small amount of hydrogen is available to the surface uranium. Very possibly this influences the corrosion rate, either by the formation of a small amount of uranium hydride or perhaps even by some disruption of the oxide by gaseous hydrogen formed beneath it.

When samples of the alloy described in this report are corroded in water they frequently become pock-marked or etched. Sometimes such localized corrosion is observed to make rather deep pits. This is probably an indication of the presence of impurity phases; whether the interface between such phases and the matrix are preferred sites for hydride formation is not known, but might be suspected. Subsequent reaction with the water could change the hydride to oxide.

It is known that some hydrogen diffuses into the metal. Thus, a constant rate of hydrogen pickup by corroding samples was observed, in terms of micrograms of hydrogen per square centimeter of corroding surface. It is presumably this hydrogen which initiates the formation of cracks (perhaps by formation of internal hydride) after prolonged corrosion exposure. The growth of oxide within the cracks probably leads to rupture and ultimate failure by a wedging action.

Both reduction of the corrosion rate and increase of the corrosion lifetime might be induced by the use of more efficient material (for hydrogen disposal), or its better distribution. In addition, it would be desirable to have the hydrogen in the metal uniformly distributed. This should provide increased corrosion lifetimes over those now observed for the reference alloy. Both objectives are perhaps at least partly achieved in those alloys in which the gamma phase is stabilized. The body-centered cubic gamma phase has a much higher multidirectional hydrogen diffusion rate than does the α-uranium; it might also provide a more efficient surface for the formation and liberation of hydrogen. Active cathodes on its surface should provide additional benefit, and apparently do (3).

Acknowledgment

The cooperation and interest of the following were of great aid in this study: C. R. Breden and A. H. Roebuck of the Reactor Engineering Division, ANL, directed the experiments on the long-time corrosion tests; G. Dragel performed the corrosion tests and is responsible for some of the photomicrographs;

E. J. Silk, on loan to the Metallurgy Division from Babcock and Wilcox, is responsible for some of the photomicrographs and aided in their interpretation.

Manuscript received Dec. 18, 1959. This paper was prepared for delivery before the Columbus Meeting, Oct. 18-22, 1959. Work on the paper was performed under the auspices of the USAEC.

Any discussion of this paper will appear in a Discussion Section to be published in the June 1961 JOURNAL.

REFERENCES

1. J. W. McWhirter and J. E. Draley, "Aqueous Corrosion of Uranium and Alloys: Survey of Project Literature," ANL-4862 (May 1952).
2. J. T. Waber, "A Review of the Corrosion of Uranium and Its Alloys," LA-1524 (Nov. 1952).
3. R. K. McGeary, *et al.*, "Development and Properties of Uranium Base Alloys Corrosion Resistant in High Temperature Water. Part I, Alloys without Protective Cladding," WAPD-127 (April 1955).
4. E. W. Cawthorne, *et al.*, "Corrosion in 650°F Degassed Water of Uranium-Molybdenum Alloys Containing Impurity Additions," BMI-1045 (Oct. 1955).
5. J. E. Draley "Preliminary Report on Low Columbium: Uranium Corrosion Resistant Alloys," ANL-5078 (June 1953).
6. J. E. Draley, S. Greenberg, and W. E. Ruther, "The High Temperature Aqueous Corrosion of Uranium Alloys Containing Minor Amounts of Niobium and Zirconium," ANL-5530 (Oct. 1956).
7. J. H. Kittel, S. Greenberg, S. H. Paine, and J. E. Draley, *Nuclear Sci. and Engrg.*, **2**, 431 (1957).
8. S. Greenberg and J. E. Draley, *ibid.*, **4**, 319 (1958).
9. S. Greenberg, *ibid.*, **6**, 159 (1959).
10. A. E. Dwight and M. Mueller, "The Constitution of the Uranium-Niobium Binary and the Uranium-Zirconium-Niobium Ternary Alloys," ANL-5581 (Dec. 1957).
11. A. E. Dwight, "Kinetic Transformations in the Uranium Rich Uranium-Niobium and Uranium-Niobium-Zirconium Alloy Systems," ANL-5582, to be published.
12. Morris Cohen, "Phase Transformation in Solids," Chap. 17, "The Martensitic Transformation," John Wiley & Sons, Inc., New York (1951).
13. M. Mueller, Private communication (May 1955).
14. J. E. Draley and W. E. Ruther, *This Journal*, **104**, 329 (1957).
15. H. A. Pray and W. E. Berry, "Corrosion of Uranium Alloys in High Temperature Water," BMI-874 (Oct. 1953).
16. J. E. Draley, J. W. McWhirter, F. Field, and J. Guon, "The Corrosion of Low Zirconium-Uranium Alloys in Boiling Water," ANL-5030 (April 1953).
17. D. P. Smith, "Hydrogen in Metals," University of Chicago Press, Chicago (1948).
18. M. W. Burkart, Editor, "The Corrosion Mechanisms of Uranium Base Alloys in High Temperature Water," WAPD-127-Part III (Oct. 1956).

Inhibition of Acid Attack on Steel by Heavy Metal Ions

Joseph A. Shropshire

Products Research Division, Esso Research and Engineering Company, Linden, New Jersey

ABSTRACT

Ions of lead, tin, and cadmium were shown to inhibit the dissolution of steel in acid solutions in the absence of metal plating. A mechanism was postulated whereby sulfide ions produced by metal dissolution combined with the heavy metal ions to form a protective coating on the dissolving surface. Analytical studies indicated that both lead and tin ions were removed from acid solutions in contact with iron filings, in quantities too great to be explained by adsorption. Studies on the effect of increased acid concentration and varying sulfur content of the dissolving metal tended to substantiate the mechanism. The order of effectiveness of inhibition of ions of lead, tin, and cadmium was shown to coincide with the order of solubility of the respective metal sulfides.

Although the effect of foreign ions on the corrosion resistance of various metals has been studied extensively for a number of years, some controversy remains concerning the action of certain metal cations in reducing the attack on iron and steel by nonoxidizing acids. The action of As^{+++} in this respect has been recognized for many years (1, 2). More recently, Sn^{++} has been shown to exhibit an effect similar to arsenic in 1*N* H_2SO_4 and 1*N* HCl (3). As yet, however, no completely satisfactory mechanism to explain these phenomena has been advanced. The present work studies the effect produced by Sn^{++}, Pb^{++}, and Cd^{++} on the acid dissolution of steel and proposes a mechanism for inhibition applicable to these ions as well as to As^{+++}.

The rate of dissolution of iron or steel in a nonoxidizing acid such as H_2SO_4 or HCl has been shown to increase in the presence of certain ions capable of being reduced at local cathode potentials (3-5). In contrast, the presence of As^{+++} or Sn^{++} greatly reduces the attack on steel by 1*N* H_2SO_4 or 1*N* HCl. The action of As^{+++} has been attributed by previous investigators (2) to the high hydrogen overvoltage of metallic arsenic. Gatos (3) has established, however, that the presence of metallic arsenic alone on the steel sample does not cause a decrease in rate of dissolution. He has further studied the effects of As^{+++} and Sn^{++} and concludes that the inhibition is due to the following reactions at anodic sites on the metal surface:

$$Sn^{++} \rightarrow Sn^{++++} + 2e^-$$

$$5As^{+++} \rightarrow 3As^{+++++} + 2As^\circ$$

These reactions are postulated to compete with and suppress the primary reaction, the oxidation of iron.

In the present study, a comparison of the effects of Sn^{++} and Pb^{++} on the corrosion of steel in 1*N* HCl solution has been made. These two ions were chosen in light of the oxidation mechanism proposed to account for the effect of Sn^{++}, and the fact that Pb^{++}, while similar to Sn^{++} in most respects, differs greatly in oxidation stability. Thus the respective standard oxidation potentials indicate that Pb^{++} should not inhibit in the manner proposed for Sn^{++}.

$$Sn^{++} \rightarrow Sn^{++++} + 2e^- \qquad E^\circ = +0.15 \text{ v}$$

$$Pb^{++} \rightarrow Pb^{++++} + 2e^- \qquad E^\circ = +1.69 \text{ v}$$

Experimental Procedure

Weight loss measurements.—Corrosion rates were determined by conventional weight loss measurements. Two types of metal specimens were used: (*a*) SAE 1010 steel coupons measuring 1 x 1.5 x 1/16 in., (*b*) disk-shaped specimens (3/4 in. diameter, 1/8 in. thick) of vacuum melted electrolytic iron to which had been added varying amounts of sulfur. Elemental analysis of the 1010 steel gave the following results: C, 0.08%; S, 0.019%; P, 0.01%; Cu, 0.007%; Mn, 0.25%. Analyzed sulfur contents of the electrolytic iron samples ranged from 0.001 to 0.021%. Corrosion tests were carried out individually in stoppered Erlenmeyer flasks containing 500 ml of test solution. Specimens were suspended vertically from a small glass rod through a 1/8 in. hole near the top of the metal coupon. Prior to immersion, the test specimens were sand-blasted, scrubbed with powdered detergent, rinsed with cold water and acetone, and finally degreased with benzene and desiccated. All corrosion tests reported in this paper were carried out at 25.0° ± 0.5°C, and all test times were of the order of 20 hr.

Baker's Analyzed lead chloride and metallic tin were used to prepare the necessary stock solutions, and test solutions were obtained by appropriate dilution. The simple deaeration of test solutions (as used in Fig. 1) was effected by prolonged bubbling with nitrogen, after passing the gas through identical solutions for vapor content equilibrium. After bubbling of nitrogen was stopped, a slow stream of the gas was passed over the top of the solutions during weight loss runs. Constancy of rate for the dissolution reaction was established independently by following the cross-sectional area change of a 1010 steel probe via resistance measurements.

Experimental Results and Discussion

Effect of Sn^{++} and Pb^{++} on the Corrosion of Steel in 1N HCl

Both Pb^{++} and Sn^{++} inhibit the dissolution of steel in 1*N* HCl. The results of the rate studies, shown in Fig. 1, indicate that Pb^{++} is just as effective as Sn^{++}, and that, in fact, the data for both metal ions fall on the same curve. At this low *p*H, dependence of rate on the state of aeration was neither expected nor found. Microscopic inspection (500X) revealed no plating of metal in either case at these low ion concentrations and high acidity. (Later studies indicated that metal plated under similar conditions formed crystals which were easily visible at this magnification.) Utilizing standard methods, measurement of the potential of 1010 steel in 1*N* HCl as a function of plumbous ion concentration indicated no significant change from the value found in 1*N* HCl alone. The identical nature of the inhibition curves for Pb^{++} and Sn^{++} and the fact that oxidation to the plumbic state is impossible under such mild conditions suggest that most of the inhibition in both cases is attributable to a different mechanism than that previously proposed.

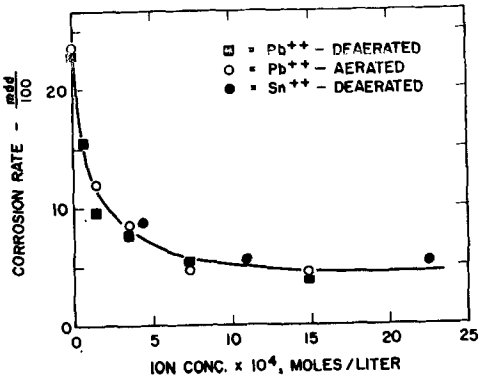

Fig. 1. Corrosion rate of 1010 steel in 1N HCl as a function of stannous and plumbous ion concentration.

Ion Removal Studies

Since no metal plating was observed, it was felt that the inhibition evidenced by both stannous and plumbous ions could be due to protection of the metal surface by the formation of an impervious layer of material. Studies were therefore carried out to determine if stannous and plumbous ions were removed from acid solution by contacting with iron filings. Two methods of contacting were employed: [1] percolation of 50 ml of the M^{++} — 1*N* HCl solutions through 30.0 g of Fisher 20 mesh iron filings (0.10% S) contained in a column with a glass wool filter, and subsequent analysis for changes in M^{++} concentration, and [2] agitation of 50 ml of the M^{++} — 1*N* HCl solutions with 30.0 g of Fisher 20 mesh iron filings in a separatory funnel, immediate filtration through glass wool, and subsequent analysis. Contact times in both cases averaged 5 min. Metal ion concentrations of the test solutions were identical to those which were shown to inhibit acid attack on steel.

Analyses for Pb^{++} were carried out by the dithizone method with final colorimetric determination. Tin determinations were made by a low concentra-

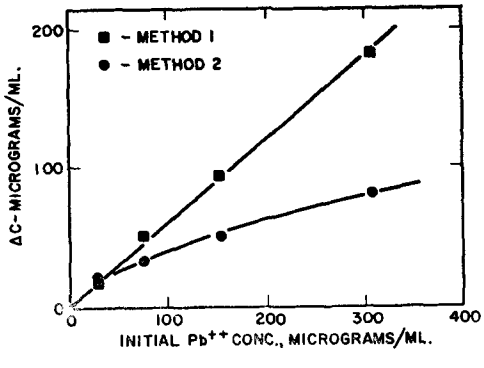

Fig. 2. Removal of plumbous ion from 1N HCl solution by contacting with iron filings. T = 25°C.

tion air-free iodine titration with complete reduction to the stannous state in a closed system with a carbon dioxide atmosphere. Due to analytical difficulties encountered at low concentrations, studies on tin were carried out at a single ion concentration known to give effective inhibition. All duplicate determinations agreed within 1%.

The change in lead ion concentration caused by contacting with iron filings is shown in Fig. 2, and the data obtained for Sn^{++} at a single concentration are given below:

Method	Initial Sn^{++} conc $\mu g/ml$	ΔSn^{++} conc $\mu g/ml$
1	534	320
2	534	249

The results indicate that more than half the metal ion can be removed from solution. If a surface area for the iron filings of 500 cm^2 is assumed (estimated on the basis of 30.0 g of spheres of radius 0.042 cm and density 7.86 g/cm^3), the amount of, e.g., Sn^{++} removed from solution corresponds to approximately three hundred times that needed for monolayer coverage of the surface. Thus, the removal of ions cannot be ascribed to adsorption phenomena. If metal ions were plated during this contacting process, the amount of ions removed would not be expected to decrease with agitation of the system. These facts led to the belief that metal ions were removed from the solution by precipitation as an insoluble species.

Mechanism

Examination of the possible reactions which could occur in the system led to the postulate that the steel (or iron) has a sulfur content sufficient to precipitate the sulfides of both lead and tin. Common steels have a sulfur content of 0.02-0.05%, the sulfur being in the form of metal sulfides. Dissolution of the surface of the metal in acid solution then results in the formation of hydrogen sulfide in the immediate vicinity of the surface. The hydrogen sulfide equilibrium is such that in 1*N* HCl solution, in which the dissociation is suppressed, sulfide ion concentrations of the order of 10^{-23} moles/liter can exist (6). Solubility products of plumbous and stannous sulfides (1.0×10^{-29} and 8×10^{-29}, respectively) (7) show that this sulfide ion concentration is sufficient to initiate the precipitation of the metal ions, even from 0.0001M solutions. Such sulfide concentrations are not grossly in excess since these divalent metal halides ionize incompletely (e.g., $[PbCl]^+ \rightarrow Pb^{++} + Cl^-$; $K_2 = 0.03$) (8). The increase of sulfide ion concentration in the layer adjacent to the surface should cause the solubility limits of the heavy metal sulfides to be exceeded at distances near enough to the surface to create a protective layer. The formation of such a layer would naturally depend on the distance from the surface at which precipitation occurs, and thus become a combined function of sulfide ion diffusion and metal ion concentration. This layer is looked on as being a barrier to diffusion of the participants in the partial reactions occurring at the surface, thus causing the over-all rate of dissolution to decrease. A further consequence of the buildup of sulfide ion in the diffusion layer is that a heavy metal ion approaching the surface would probably be converted to the sulfide before approaching closely enough for electron transfer, i.e., reduction to the metal, to occur. Direct reduction of the sulfides of lead and tin is considerably more difficult than reduction of the ions themselves and, thus, is not a likely reaction (9).

Table I. Corrosion rate of 1010 steel in 1N HCl in the presence of Cd^{++}

Molarity Cd^{++}	Rate— mdd / 100	Relative rate
0.00	23.8	1.00
0.01	12.8	0.54
0.10	10.7	0.45

Since the heavy metal sulfides exhibit a marked tendency toward colloid formation when precipitated from dilute solution, it is possible that agitation of the solutions while contacting with iron filings could result in precipitation of the sulfides at greater distances from the surface and in concentrations at which colloid formation would be favored. Thus a nonfilterable dispersion could give rise to the observed variation in ion removal by the two methods used. (It is felt that the "ion removal" data are such that adsorption as well as metal plating are improbable as explanations. It must be realized, however, that these data provide no positive evidence of sulfide formation.)

Cadmium Ion

If the sulfide formation mechanism as postulated above is the correct one, cadmium ion should also act as an inhibitor for the corrosion of steel in 1*N* HCl solutions. For cadmium, the solubility product of the sulfide (1.4×10^{-28}) (7) is such as to make it a borderline case, i.e., a lesser degree of inhibition is to be expected. More important, the second ionization constant for $CdCl_2$ as reported by Harned (8) is 0.01. Thus the $CdCl_2$ concentration required to produce precipitation of the sulfide in a solution approximately 1*N* with respect to Cl^- is increased one hundredfold. Results of weight loss measurements carried out in the presence of cadmium ion at two concentrations (Table I) indicate that concentrations of cadmium ion up to one hundred times those used for Pb^{++} and Sn^{++} produce only a 50% inhibition, and thus, the foregoing conclusions are qualitatively confirmed.

Effect of Solution Acidity

The degree of inhibition afforded by Sn^{++} and Pb^{++} was found to be greatly reduced in 3*N* HCl solution, as shown in Fig. 3. This evidence reinforces the sulfide mechanism, since the increase in acidity causes a sharp increase in the solubility of the sulfides of tin and lead. It is doubtful that the observed decrease in effectiveness of the metal ions would occur if metal plating were a major factor here, since the increase in acidity from 1*N* HCl to 3*N* HCl would result in a change of hydrogen discharge potential at a cathodic site of only a few millivolts. The same change in acidity, however, causes a ninefold decrease (ideally) in the sulfide ion concentration in the acid solution.

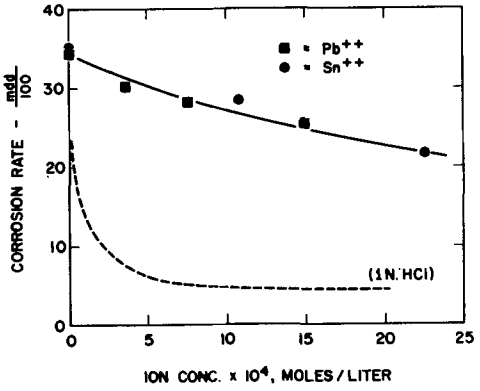

Fig. 3. Corrosion rate of 1010 steel in 3N HCl as a function of stannous and plumbous ion concentration.

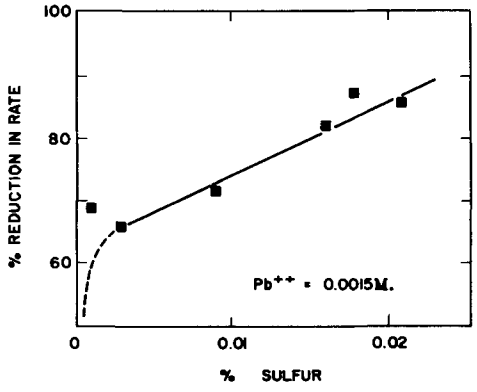

Fig. 4. Effect of sulfur content of electrolytic iron specimens on corrosion rate in IN HCl —0.0015M Pb^{++}. Per cent reduction calculated against rate in IN HCl alone.

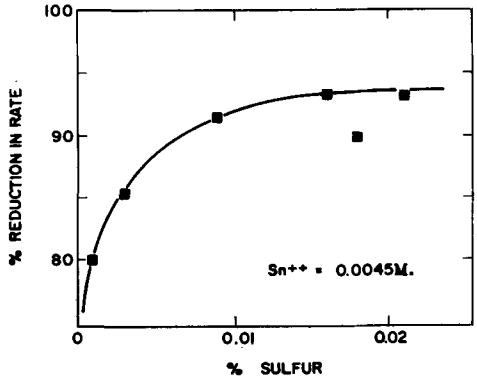

Fig. 5. Effect of sulfur content of electrolytic iron specimens on corrosion rate in IN HCl —0.0045M Sn^{++}. Per cent reduction calculated against rate in IN HCl alone.

The rate of dissolution of 1010 steel in 3*N* HCl in the presence of 0.01 mole/liter of cadmium ion was found to be 92% of the rate of dissolution in pure 3*N* HCl. This is undoubtedly due to the fact that cadmium forms the most soluble sulfide of the metals investigated. It is to be expected that cadmium ion would exhibit no effect whatsoever in solutions of slightly greater acidity.

Effect of Sulfur Content of the Metal

If the postulated sulfide formation mechanism is correct, it follows that sulfur content of the metal should play a determining role in the inhibition. Accordingly, a series of vacuum melted electrolytic iron samples which differed only in sulfur content was obtained. Weight loss measurements were carried out on these samples in 1*N* HCl alone and in 1*N* HCl containing low concentrations of Pb^{++} and Sn^{++}. The results of this study indicate that high levels of inhibition are obtained, and that the degree of inhibition in both cases increases with sulfur content of the sample (Fig. 4 and 5).

It is of interest to note that a saturation level is obtained with the use of a Sn^{++} concentration somewhat higher than that of Pb^{++}. Such a level admits to several possible explanations in light of the proposed mechanism. It is possible that maximum surface coverage has been realized and that the remaining attack represents reaction occurring by diffusion of reactants through the sulfide layer. Alternatively, it could be assumed that the majority of impurities and the majority of attack are centered about the grain boundaries of the metal lattice and that while this attack is inhibited by sulfide formation, a residual dissolution remains at crystal faces.

The apparent inconsistency of the data at 0.001% S in Fig. 4 is explained by the fact that microscopic examination (500X) revealed relatively large crystals of lead on this sample only. This observation conforms to the previous hypothesis that metal plating should not occur in the presence of an appreciable amount of sulfide ion. The plated lead in itself appears to be an effective inhibitor, probably due to its high overvoltage for hydrogen discharge. It is of interest to note that this behavior was observed only with Pb^{++}, which is reduced only slightly more easily than Sn^{++}.

The plating of metal ions at very low sulfur contents was reconfirmed by the observation that both lead and tin were plated from their 1*N* HCl solutions on electrolytic iron powder (trace sulfur) which had been sintered into coupons with a density of 6.5 g/cm³.

Conclusion

The presence of plumbous, stannous, and cadmium ions has been shown to inhibit the dissolution of iron and steel in 1*N* HCl. With the exception of iron specimens with extremely low sulfur content, no evidence of plating of any of the metals on the iron or steel samples has been detected. Both plumbous and stannous ions are removed from acid solutions in contact with iron filings, in amounts dependent on the mode of contacting. The removal of plumbous ion is linear with initial ion concentration. As yet, no satisfactory explanation for the linearity can be advanced. The inhibition afforded by Pb^{++} and Sn^{++} is markedly decreased by small increases in acidity of the solutions, and has been shown to be dependent on the sulfur content of the dissolving metal.

In view of these facts, it is postulated that the dissolution of a steel surface in a strong nonoxidizing acid produces sufficient sulfide ions to precipitate the respective heavy metal sulfides at the surface. This metal sulfide formation probably occurs at distances from the surface which are too great for iron discharge, and thus precludes metal plating. The precipitated layer of sulfide then restricts diffusion to and from the surface and causes a decrease in rate of the partial reactions. Since As^{+++} forms a sulfide which is insoluble even in strong acid solu-

tion, it is believed that the well-known inhibition effects of As^{+++} are accounted for by a similar mechanism. The concentration of ions required for maximum effectiveness appears to increase in the order $As^{+++} < Pb^{++} \simeq Sn^{++} < Cd^{++}$. This order is in agreement with the respective metal sulfide solubility products (7).[1]

A puzzling factor in the experimental results is that corrosion rates characteristic of each metal ion concentration were obtained after the first few minutes of reaction. The continued release of sulfide ions during the period of reaction would be expected to increase the thickness of the protective layer and thus cause a decrease of corrosion rate with time. It is possible that the film is established quite rapidly at the period when reaction rate is high and that subsequent reaction by slow diffusion of ions through the film does not add measurably to the "effective" film thickness. This would occur if the metal sulfide formed in the latter case by diffusion of $S^{=}$ through the film were loosely bound at relatively large distances from the surface.

It should be emphasized that, in accord with Gatos' observations on Sn^{++}, no plating of tin, lead, or cadmium on ordinary steel coupons was observed in these systems. Observation of the plating on electrolytic iron specimens and on steel coupons in less acid systems indicated that the metal deposits were semi-adherent and crystalline, and that even the most minute deposits were readily observable under the microscope.

Oxidation at anodic sites, as postulated by Gatos, is certainly not a factor in the inhibition evidenced by plumbous ion, although it could play a minor role in the case of Sn^{++}. Cadmium ion, at low concentrations, is probably stable in acid solutions insofar as reduction is concerned, and cannot conceivably function by the oxidation mechanism previously postulated for Sn^{++}.

The inhibition effects produced by As^{+++}, Sn^{++}, Pb^{++}, and Cd^{++} through formation of a sulfide layer at a dissolving steel surface are, of course, limited to a definite range of acidity. The upper limit of this range is governed by the solubility of the respective metal ion sulfides, being greatest for As^{+++} and lowest for Cd^{++}. The lower limit of the range is largely determined by the *p*H at which the sulfide in the test metal specimen becomes soluble in the corroding medium.

It should be mentioned that many metal ions (e.g., Cu^{++}) form sulfides of such low solubility as to make inhibition by this mechanism possible. However, if the system is capable of causing deposition of a low-overvoltage metal, either through reduction of the ions themselves or sulfides, then the concurrent increase in local cell current and subsequent galvanic cell action overshadows any possible inhibition effects. For Ni^{++}, indications exist that, dependent on the metal ion concentration of the system, both phenomena may occur (3).

[1] The author can find no published value for the solubility product of As_2S_3. However, it is well known that HgS and As_2S_3 are the most insoluble of the heavy metal sulfides (10).

Acknowledgments

The author gratefully acknowledges the helpful suggestions of Dr. J. S. Batzold, Dr. J. O'M. Bockris, and Dr. P. J. W. Debye during the course of this investigation.

Manuscript received Sept. 8, 1959.

Any discussion of this paper will appear in a Discussion Section to be published in the June 1961 JOURNAL.

REFERENCES

1. U. R. Evans, "Metallic Corrosion, Passivity and Protection," p. 536, Edward Arnold & Co., London (1948).
2. A. Wachter, R. S. Treseder, and M. K. Weber, *Corrosion*, **3**, 406 (1947).
3. H. C. Gatos, *ibid.*, **12**, 322t (July 1956).
4. W. R. Buck and H. Leidheiser, *ibid.*, **14**, 308t (1958).
5. H. C. Gatos, *This Journal*, **103**, 286 (1956).
6. H. T. S. Britton, "Hydrogen Ions," Vol. II, p. 115, Chapman & Hall Ltd., London (1942).
7. H. H. Uhlig, Editor, "Corrosion Handbook," p. 1138-9, John Wiley & Sons, Inc., New York (1948).
8. H. S. Harned and B. B. Owen, "The Physical Chemistry of Electrolytic Solutions," 3rd ed., p. 560-1, Reinhold Publishing Co., New York (1958).
9. W. M. Latimer, "Oxidation Potentials," 2nd ed., pp. 148, 153, Prentice-Hall, Inc., New York (1952).
10. P. C. L. Thorne and E. R. Roberts, "Inorganic Chemistry," p. 545, Interscience Publishers, New York (1949).

Addendum

H. A. Laitinen, R. P. Tischer, and D. K. Roe wish to add the following acknowledgment to their paper "Exchange Current Measurements in KCl-LiCl Eutectic Melt" which was published in the June issue of the *Journal*, Vol. 107, pp. 546-555 (1960):

This work was supported by the office of Ordnance Research, U. S. Army.

Bridged Complexes and the Deposition of Tin-Nickel Alloys

Robert L. Rau[1] and John C. Bailar, Jr.

Department of Chemistry and Chemical Engineering, University of Illinois, Urbana, Illinois

ABSTRACT

The method of continuous variations has been used to determine the nature of the complex in solutions containing tin(II), nickel(II), and fluoride ions. This indicates the formation of $SnF_4^=$, which in turn forms $NiSnF_4$. Other complexes of the type $NiSnF_x^{4-x}$, where x is 1, 2, or 3, have been shown to form, also. These complexes may contain one or more fluoride bridges. There is no indication of complex formation in the absence of fluoride.

Since the introduction of a bright tin-nickel alloy plate by Parkinson in 1951, much interest has been aroused in the nature of the species responsible for the nearly constant one to one atomic ratio of tin-nickel in the plate.

Parkinson (1) has shown that tin and nickel are deposited in roughly equal atomic proportions, over a wide range of conditions, from solutions containing stannous chloride, nickel chloride, sodium fluoride, ammonium fluoride, and enough hydrochloric acid to give the solution of *p*H of 2.5. This plate is the intermetallic compound NiSn, which has been unattainable by any other method (2).

A more detailed study of the electrolyte used in the plating process has led to several interesting qualitative conclusions (3). When the cathode potential was plotted against current density for a series of solutions containing a constant amount of stannous chloride and increasing amounts of sodium fluoride, it was observed that the cathode potential became increasingly negative, indicating complex formation between stannous and fluoride ions. A similar study using nickel chloride in place of stannous chloride indicated little or no complexing between nickel and fluoride ions. A third study, in which increasing amounts of nickel chloride were added to a solution containing constant amounts of stannous chloride, sodium fluoride, and ammonium bifluoride, indicated that the addition of nickel chloride caused the potential at which tin plates out to become more negative. It was suggested that this could be due to the formation of a complex containing both tin and nickel.

Davies (4) has studied the interaction between fluoride and stannous ions by determining the effect of a change in fluoride ion concentration on the nature of the alloy deposit. The solutions studied had a constant nickel concentration but contained varying amounts of stannous and stannic tin (the latter being due to the air oxidation of the stannous ion). At low fluoride concentrations the deposits obtained had a matte surface and a tin content higher than that of the bright alloy, but with fluoride concentrations above certain critical values the typical bright appearance of the tin-nickel alloy was obtained. The fluoride concentration range in which this change took place was quite narrow. The bright tin-nickel alloy could be obtained only from solutions in which each stannous ion was associated with four fluoride ions and each stannic ion with six fluorides ions.

Further studies (4) have indicated that $SnF_6^=$ is more stable than $SnF_4^=$ and is not involved in the deposition of the tin-nickel alloy. If the tin-nickel electrolyte contains an insufficient amount of fluoride to complex all the stannous and stannic ions, there is uncomplexed stannous ion in the electrolyte, and the bright alloy is not deposited.

By comparing the transport numbers of the metallic ions in the electrolyte with calculated values for the simple metallic ions, the existence of a tin(II)-fluoride complex seemed to be confirmed (5). For solutions containing nickel chloride, the difference between the experimental and calculated values of the transport number of Ni(II) suggested that the nickel ion was part of a negatively charged ion. Since there is no evidence for complex formation between nickel(II) and fluoride in aqueous solution (6), Brook, *et al.* suggested that Ni(II) was associated with the stannous fluoride complex.

In spite of the reluctance of nickel(II) to form fluoride complexes, some combination of $SnF_4^=$ with Ni(II) seems to occur, but conclusive evidence for this has not been established. It was the object of this investigation to determine the nature of the species formed in the tin-nickel electrolyte, using the method of continuous variations (7-9) with refractive index as the measured property.

Experimental

The Zeiss dipping refractometer, which was used in this investigation, does not give a direct reading of refractive index, but for our purposes it was not necessary to convert the readings to refractive index values. The instrument is easily read to ± 0.03 scale units; if desired, these can be converted to refractive index values having an accuracy of 0.00002 units.

In a typical study, solutions approximately 0.1M were prepared by direct weighing of analytical grade reagents. In some cases concentrations were determined analytically (10). Portions of these so-

[1] Present address: Minnesota Mining and Manufacturing Co., St. Paul, Minn.

lutions were measured into glass stoppered flasks in such a manner that the first flask contained 90% by volume of solution A and 10% of B. The second flask contained 80% of A and 20% of B and so on up to 10% of A and 90% of B. In every case the total volume was 10 ml.

After the solution had been in a thermostat for 30 min, it was placed in the refractometer cup, the prism of the refractometer was put in position, and the assembly was immersed in the water bath for 20 min prior to reading. All readings were taken at 25°C.

The continuous variation curves were obtained by plotting the solution readings (n) minus the reading of pure water (n_o) vs. volume per cent of the two constituents. The deviation curves were obtained by plotting the difference between the values used in the continuous variation curves and the values obtained by assuming no interaction between the constituents against per cent composition. Such a plot gives a maximum deviation at the point corresponding to the ratio in which the two constituents react.

Preparation of solutions.—To eliminate the possibility of atmospheric oxidation of the stannous ion, the distilled water was boiled and saturated with nitrogen. All stannous solutions were stored under an atmosphere of nitrogen and were used within 24 hr after preparation.

To duplicate the optimum plating conditions (4), all solutions were brought to a *p*H of 2.5. In the preparation of standard stannous solutions, it was necessary to add acid to prevent hydrolysis. This gave the solution a negative *p*H. If, however, two moles of fluoride ion were added per mole of stannous ion, it was possible to prepare stannous solutions of *p*H 2.5. A Beckman model G *p*H meter was used.

In cases in which ammonium fluoride was a constituent of the solution, it was necessary to take into account the two ionization constants of hydrofluoric acid (11) in order to prepare an acid solution having a known unassociated fluoride ion concentration.

Continuous Variation Studies

Study No. 1—$SnCl_2$:$2NH_4F$ vs. NH_4F—In order to determine the nature of the complex formed between stannous and fluoride ions, a continuous variation study of $SnCl_2$:$2NH_4F$ vs. NH_4F was undertaken (Fig. 1). The deviation curve shows a maximum at 33% $SnCl_2$:$2NH_4F$, indicating a [Sn(II) + $2F^-$]:F^- reaction ratio of 1:2; the complex must have the composition $SnF_4^=$.

Study No. 2—$NiCl_2$ vs. NH_4F—The data are plotted in Fig. 2. The figure shows no deviation, indicating no reaction between the constituents under the existing conditions.

Study No. 3—$SnCl_2$:$4NH_4F$ vs. $NiCl_2$—This study was undertaken to determine whether there is any interaction between the constituents in a solution containing Sn(II), Ni(II), and F^- (Fig. 3). The deviation curve indicates a [Sn(II) + $4F^-$]:Ni(II) reaction ratio of 1:1.

Study No. 4—$SnCl_2$:$3NH_4F$ vs. $NiCl_2$—In order to determine whether four fluoride ions are necessary for Sn(II) and Ni(II) to become part of the same species, a solution containing Sn(II) and F^- in the ratio 1:3 was used in a continuous variations study. The deviation curve shows a maximum (and thus indicates compound formation) at a ratio of [50% Sn(II):$3F^-$] and 50% Ni(II).

Studies 2, 3, and 4 were repeated using SnF_2 and $Ni(ClO_4)_2$ instead of the chlorides. Where a greater difference in successive readings was desired, an

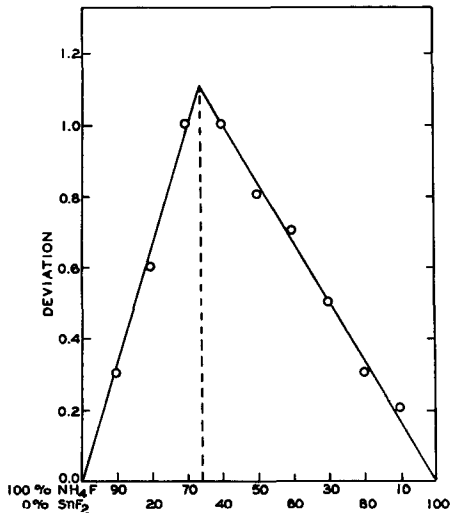

Fig. 1. 0.1M SnF_2($SnCl_2$:$2NH_4F$) vs. 0.1M NH_4F

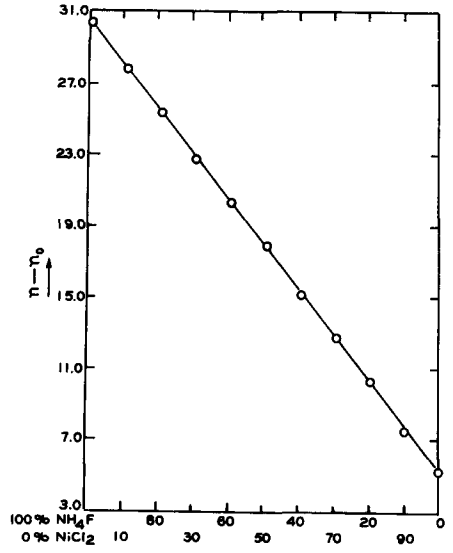

Fig. 2. 0.1M $NiCl_2$ vs. 0.1M NH_4F

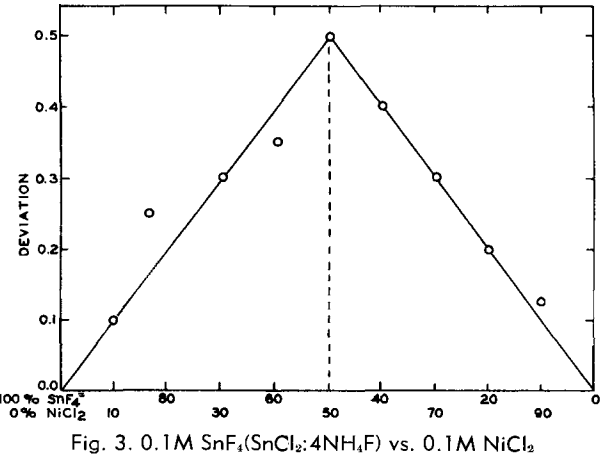

Fig. 3. 0.1M SnF_4($SnCl_2$:$4NH_4F$) vs. 0.1M $NiCl_2$

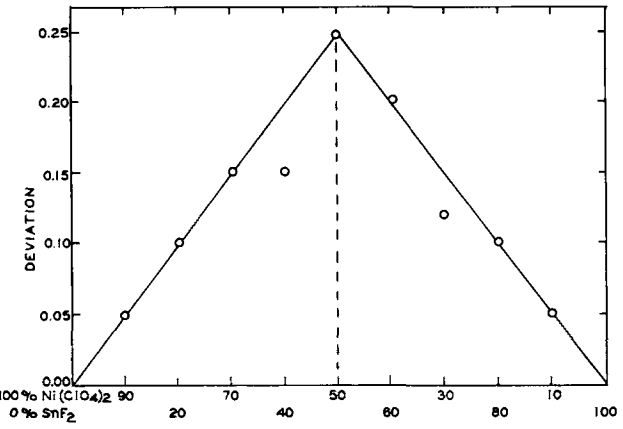

Fig. 4. 0.1M SnF_2 vs. 0.1M $Ni(ClO_4)_2$ + $NaClO_4$

inert salt such as $NaClO_4$ was added to one of the solutions. In all cases the results were exactly the same as those obtained with chloride ion present.

Study No. 4a—SnF_2 vs. $Ni(ClO_4)_2$ + $NaClO_4$—The data obtained using a solution of Sn(II) and F^- in a ratio of 1:2 as one of the constituents are plotted on Fig. 4. The curve shows a maximum deviation at 50% SnF_2 and 50% $Ni(ClO_4)_2$.

Study No. 5—SnClF vs. $Ni(ClO_4)_2$ + $NaClO_4$—To determine whether one fluoride ion is sufficient to allow Sn(II) and Ni(II) to become part of the same complex, a study of tin(II) chlorofluoride vs. nickel perchlorate was undertaken.

A 0.1M solution of tin(II) chlorofluoride (12) had a *p*H of 2.3 due to partial hydrolysis of the stannous ion. The nickel perchlorate solution was brought to a *p*H of 2.3 by the addition of perchloric acid.

After standing for 30 min the SnClF solution became slightly turbid, so the refractometer was immersed in the solutions for only 10 min. The readings for 100% SnClF before and after the formation of the turbidity did not change by more than the maximum experimental error. Figure 5 shows a maximum deviation at 50% SnClF and 50% $Ni(ClO_4)_2$ indicating a SnF^+:Ni(II) reaction ratio of 1:1.

Study No. 6—$SnCl_2$ vs. $NiCl_2$—To ascertain whether the presence of fluoride ions is necessary for the formation of the complex species, a continuous variation study of tin(II) chloride vs. nickel chloride was undertaken.

To prevent the hydrolysis of the stannous ion, the calculated quantity of stannous chloride was dissolved in a solution of 25 ml of water containing 2 ml of concentrated hydrochloric acid. The resulting solution had a *p*H less than zero. The nickel chloride solution was prepared in a similar manner.

The curve (Fig. 6) shows no deviation, indicating no reaction between stannous chloride and nickel chloride under existing conditions.

Discussion

In order to explain the constant composition of the tin-nickel alloy which is obtained over a wide range of conditions, several investigators have postulated the existence of a tin-nickel complex (3, 4). Except for the work previously cited, however, no

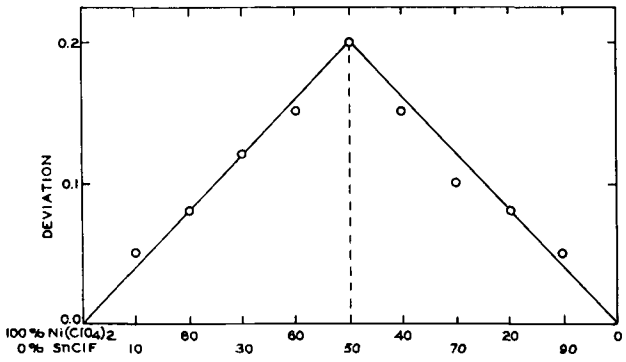

Fig. 5. 0.1M SnClF vs. 0.1M $Ni(ClO_4)_2$ + $NaClO_4$

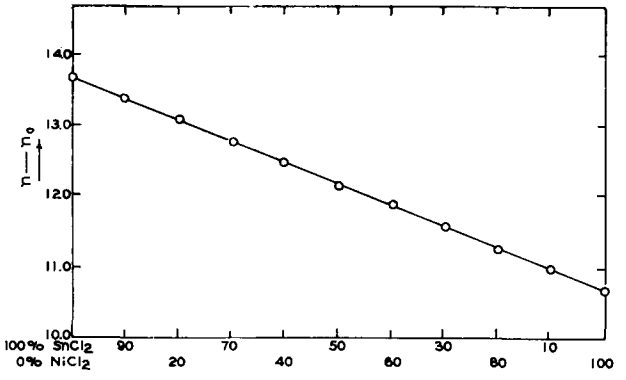

Fig. 6. 0.1M $SnCl_2$ vs. 0.1M $NiCl_2$

evidence has been offered in support of this hypothesis.

Study No. 1 indicates a [Sn(II) + $2F^-$]:F^- reaction ratio of 1:2, which is consistent with the formation of $SnF_4^=$. Davies (4) and Brook (5) have postulated the existence of $SnF_4^=$ from experimental data obtained by entirely different methods.

Study No. 2 indicates that Ni(II) forms no complex with fluoride ions under the conditions investigated. Similar results have been obtained by other investigators (6), although there have been some claims of complex formation between Ni(II) and fluoride (13).

Study No. 3 indicates that Sn(II) and Ni(II) are present in a 1:1 ratio in the complex species. If we assume that the only anions associated with either tin(II) or nickel(II) are the fluoride ions of $SnF_4^=$, the formula for the complex is $NiSnF_4$. Davies (4) and Brook have postulated the existence of such a complex.

If a metal ion and a complexing agent form a series of complexes for which the successive stability constants do not differ greatly, a solution of the constituent ions may contain appreciable amounts of all the possible complexes (14). If such a relationship exists in the tin(II)-fluoride system, a solution of constituent ions may contain SnF_3^-, SnF_2, and SnF^+ as well as $SnF_4^=$. The existence of all of these complexes has not been definitely established, but studies of tin(II) chloride and bromide systems indicate the simultaneous existence of successive complexes. Duke and Courtney (15) obtained values for the stability constants of $SnCl^+$, $SnCl_2$, $SnCl_3^-$, and $SnCl_4^=$, and concluded that an acid solution of the constituent ions contains some of each of these complexes. The determination of stability constants of Sn(II)-Br^- complexes led Vanderzee (16) to a

similar conclusion; the stability constants of the bromide complexes are smaller than those of the chloride complexes. We should therefore expect a solution of tin(II) and fluoride ions to contain all the ions $SnF_n^{(2-n)}$ (where n = 0, 1, 2, 3, and 4), each of these being more stable than the corresponding chloride or bromide complex. The concentration of each complex would be determined by the ratio of the concentrations of the tin and fluoride ions and the relative stability constants of the various complexes.

The electrolyte used by Parkinson in his studies of the tin-nickel alloy doubtless contains some of each of the possible tin(II)-fluoride complexes. The continuous variation studies reported here indicate that even one fluoride ion is sufficient to bind a tin(II) ion and a nickel(II) ion into a complex in which the metal ions are present in a 1:1 ratio.

Study No. 6, in which stannous chloride and nickel perchlorate were the constituents, showed no deviation from the "no reaction" curve, and it is assumed that $SnCl_2$ and Ni(II) do not form a complex under the conditions studied. It should be pointed out, however, that the conditions of Study No. 6 are not identical to those of previous studies. Because of the absence of fluoride ions, it was necessary to keep the *p*H below 2.5 in order to prevent the hydrolysis of the stannous ion.

As previously shown, $SnF_4^=$ is the predominant species in solutions containing an excess of fluoride ion, but other tin(II)-fluoride complexes may be present in the commercial electrolyte. Evidence for the formation of a 1:1 tin(II)-nickel(II) complex was obtained in all cases in which fluoride ions were present, but in the absence of fluoride ions there was no indication of tin-nickel complex formation. The conclusion that fluoride ions are necessary for complex formation is consistent with previous observations that the bright alloy plate cannot be obtained from solutions which do not contain fluoride (4).

The consistent 1.1 ratio of Sn(II):Ni(II) obtained in the continuous variation studies can be explained most easily by assuming that fluoride ions serve as bridging groups between the metals. Fluoride ions have not previously been shown to serve as bridging groups, but compounds which may contain fluoride bridges are known. Under extreme thermal conditions, the fluorides and chlorides of some alkaline earth elements combine to form compounds of the type $CaF_2 \cdot CaCl_2$, $SrF_2 \cdot SrCl_2$, and $BaF_2 \cdot BaCl_2$ (17). The complex $[Co(NH_3)_4BeF_4]^+$ (18) probably contains fluoride bridges.

From the continuous variation studies, we have concluded that only one fluoride ion is necessary for bridging in the tin-nickel complex, but we cannot be sure that only one fluoride ion acts as a bridging group when more are available.

Throughout this discussion it has been assumed that nickel(II) does not form complexes with fluoride ions, but that in the presence of a tin(II)-fluoride complex some type of association takes place. Apparently, no other similar cases have been reported, and we can offer no explanation for this seemingly inconsistent behavior. Because the phenomenon is of both theoretical and practical importance, other examples are being sought in the hope that they will shed light on the nature of the bonding in such mixed complexes. Fluoride complexes of Ni(II) have been reported, but their existence is not shown by the method of continuous variations. Evidently the conditions prevailing in this work were not conducive to their formation.

The formation of a tin(II)-nickel(II)-fluoride complex does not preclude the simultaneous existence of the individual ions in the electrolyte. Cuthbertson, *et al.* (3) have shown that complex species as well as the individual ions are present in the commercial electrolyte. It is, therefore, not illogical to assume the existence of the equilibria

$$NiSnF_x^{4-x} \rightleftharpoons Ni^{+2} + SnFx^{2-x}$$
$$\updownarrow$$
$$Sn^{+2} + X\,F^-$$

Under normal conditions, the simple ions are not discharged because their potentials are too high. If the concentrations of the constituent ions are high enough, the equilibrium shifts in favor of the formation of $NiSnF_x^{4-x}$, but in dilute solutions very little of the tin-nickel complex is formed. Electrolysis of such a solution would not be expected to give the tin-nickel alloy.

Manuscript received Oct. 2, 1959.

Any discussion of this paper will appear in a Discussion Section to be published in the June 1961 JOURNAL.

REFERENCES

1. N. Parkinson, *J. Electrodepositors' Tech. Soc.*, **27**, 129 (1951).
2. H. P. Rooksby, *ibid.*, **27**, 153 (1951).
3. J. W. Cuthbertson, N. Parkinson, and H. P. Rooksby, *This Journal*, **100**, 107 (1953).
4. A. E. Davies, 4th International Conf. on Electrodeposition and Metal Finishing, April 1954.
5. P. A. Brook, A. E. Davies, and J. W. Price, *J. Appl. Chem.*, **5**, 81 (1955).
6. E. R. Sheffer and E. M. Hammaker, *J. Am. Chem. Soc.*, **72**, 2575 (1950).
7. H. W. Bond, Thesis, University of Illinois (1938).
8. P. F. Cundy. Thesis, University of Illinois (1939).
9. N. Costachescu and T. Apostoi, *Ann. Sci. Univ. Jassy*, **7**, 101 (1912); *J. Chem. Soc.*, (Abs. of papers), **102**, II, 528 (1912).
10. "Scott's Standard Methods of Chemical Analysis," **1**, 1207 (1925) D. Van Nostrand Co., New York (1939).
11. H. H. Broene and T. De Vries, *J. Am. Chem. Soc.*, **69**, 1644 (1947).
12. W. H. Nebergall, G. Baseggio, and J. C. Muhler, *J. Am. Chem. Soc.*, **76**, 5533 (1954).
13. A. Kurtenacker, W. Finger, and F. Hey, *Z. anorg. Chem.*, **211**, 281 (1933).
14. I. V. Tananayev and E. N. Duchman, *Bull. Acad. Sci. U.S.S.R.*, Div. Chem. Sci., **6**, 591 (1947), (Russian) *C. A.*, **42**, 4025i (1948); K. E. Kleiner, *J. Gen. Chem. U.S.S.R.*, **21**, 19 (1951) (English); A. K. Babko and K. E. Kleiner, *J. Gen. Chem. U.S.S.R.*, **17**, 1259 (1947) (English Summary); C. Brosset and B. Gustaver, *Svensk Kem. Tidskr.*, **54**, 185 (1942) (English); C. Brosset and J. Orring, *Svensk Kem. Tidskr.*, **55**, 101 (1943) (English).
15. F. R. Duke and W. G. Courtney, *J. Sci.*, **24**, 397 (1950).
16. C. E. Vanderzee, *J. Am. Chem. Soc.*, **74**, 4806 (1952).
17. G. A. Buhalova and A. G. Bergman, *J. Gen. Chem.*, U. S. S. R., **21**, 1723 (1951) (English).
18. A. B. Ray, S. Banerjie, and H. Ray, *J. Indian Chem. Soc.*, **31**, 731 (1954).

Retention of Chloride in Zinc Sulfide during Phosphor Preparation

A. Kremheller, S. Faria, P. Goldberg, and D. J. Bracco

General Telephone & Electronics Laboratories Inc., Bayside, New York

ABSTRACT

A concentration cell procedure, based on the method of Furman and Low, is employed to study chloride retention in zinc sulfide powders. Amounts of 0.001% by weight of chloride in 1 g of zinc sulfide can be determined quantitatively. Zinc sulfide powders with physically admixed or coprecipitated chloride are processed in open boats with variations in firing time and temperature; the retained chloride is determined. The chloride retained after displacement of surface chloride is defined as "'volume chloride." It is found that the retention of volume chloride in zinc sulfide is similar whether zinc chloride or sodium chloride is used as the flux; a peak concentration is observed in both cases after processing near 500°C. The experimental results are interpreted and found significant in elucidating the mechanism of the incorporation of chloride into zinc sulfide powder during phosphor preparation.

Although Tiede and Schleede (1) and recently Riehl and Ortmann (2) report that they have obtained luminescent zinc sulfide phosphors without employing a fluxing agent, commercial zinc sulfide phosphors are usually prepared with a fluxing agent, such as zinc chloride or sodium chloride. The presence of flux exerts a pronounced influence on the luminescence emission, crystal structure, and particle size. It is well known that the use of chloride flux has a beneficial effect during zinc sulfide phosphor preparation; however, the particular mechanism by which the chloride enhances the luminescence emission is not yet fully understood.

Schleede and Gantzckow (3) propose that a thin film of flux dissolves small particles of the base material with subsequent precipitation on large particles, and that the thin film sets up strain and disorder in the host lattice during cooling. The resulting lattice imperfections are considered by these authors as the cause of luminescence.

Guntz (4) is probably the first researcher who considers the possibility of flux action within the volume of the phosphor. Following a suggestion by Gugel (5), Smith (6) shows that the flux is able to form a solid solution with the base material. Kroeger and Hellingman (7) assume that chloride, i.e., the flux anion, is incorporated substitutionally into the host lattice. They find by quantitative chemical analysis 2 to 27 x 10^{-5} g atoms of chloride per mole of zinc sulfide in various phosphor samples. Their investigations aim at correlating the incorporated coactivator with the activator concentration and the luminescence mechanism; however, the authors point out that experimental difficulties lead to a ± 50% error in the determination of incorporated chloride, especially, since a certain part of the chloride may be too tightly bound for removal. Bube (8) was aware of this difficulty and removed 10% of the sample with nitric acid to dispose of occluded surface chloride before conducting a quantitative chloride analysis: in this case the possible error is given as ± 20%. There are some objections to Bube's procedure of removing surface chloride, in that small particles, corners, edges, specific crystallographic planes, and similar singularities may dissolve preferentially. Some chloride may still be held by surface forces. This fraction may not be completely removable by fractional dissolution and water washing; reprecipitation may also occur.

Froelich (9) observes that much of the initially added activator remains with the zinc sulfide phosphor after processing while almost all flux is lost, although it is apparent that coactivators have a beneficial effect on the phosphor obtained.

An attempt is made in the present paper to define and determine the amount of volume chloride that becomes incorporated into zinc sulfide during the process of phosphor preparation. The present study is considered as the first step in investigating and establishing the mechanism by which chloride helps to change a finely divided, nonluminescent zinc sulfide powder into a well crystallized, brightly luminescent phosphor. While the final objective of the investigation will be an attempt to correlate quantitatively the amount of chloride on and within the base material with luminescence emission and related properties of phosphors, this introductory exploration should establish a procedure for chloride determination and present some data on the quantitative chloride retention in zinc sulfide powder during phosphor preparation.

Experimental

In studying the incorporation of chloride into a phosphor, it is necessary to distinguish between chloride on the external surfaces and that which becomes incorporated into the volume. Palumbo and Levine (10) have shown that washing zinc sulfide powder with water until the filtrate shows no chloride does not assure that the surface is free of chloride. In a typical example, a sample of zinc sulfide powder precipitated in the presence of chlo-

ride may contain more than 1% by weight of chloride after water washing. The authors (10) find, however, that on leaching the water-washed sample with sulfate solution an appreciable fraction, for instance 30%, of the chloride appears in the leachate. It seems reasonable to assume that the sulfate ions displace chloride ions from the surface of zinc sulfide powder, so that the chloride remaining after displacement washing can be defined as volume chloride, i.e., that which is retained on enclosed internal surfaces and in the host crystal lattice. Accordingly, the determination of volume chloride is an experimental process during which the sample approaches asymptotically, after successive leachings with sulfate ion, a constant amount of retained chloride which is called volume chloride. The latter is, therefore, defined experimentally as the amount retained when the filtrate does not contain any detectable chloride, and when the retained chloride is found constant after additional displacement washings.

Chloride is determined by the concentration cell method of Furman and Low (11); this technique may also be employed in determining the concentration of other halides. The analysis is conducted by measuring the emf between two silver-silver chloride electrodes (Fig. 1) which are suspended in chloride solutions of different concentrations. One electrode is immersed in a chloride solution of concentration x and the other in a solution of concentration $0.01 + x$, where x is the chloride to be determined and the concentrations are in moles per liter. Electrochemical theory leads to the following equation at 25°C:

$$E = 0.0591 \log \frac{2(x + 0.01)}{x + (x^2 + 4P_o/f^2)^{1/2}} \qquad [1]$$

where E is the emf, x is moles of chloride per liter, P_o is the solubility product of AgCl in pure H_2O, and f is the activity coefficient. The value of the activity coefficient is found experimentally by using a solution with $x = o$ and measuring the emf. A graph of Eq. [1] facilitates the determination of x. For chloride analysis, zinc sulfide is washed in deionized water to remove the zinc sulfate and is then dissolved in hot dilute nitric acid. The acid solution is digested until the hydrogen sulfide is expelled; the sulfur which forms is removed by filtration. The volume is adjusted to 100 ml; two 25-ml aliquots are taken, to one 5 ml of water are added, to the other 5 ml of 0.06M NaCl. The aliquots are then placed into the arms of the concentration cell and the emf is measured. Bancie-Grillot and Grillot (12) indicate that chloride is lost if hot $4N$ HNO_3 is employed in dissolving zinc sulfide; however, in this laboratory careful checks with blanks containing known amounts of added chloride have shown no loss within the limit of chloride detection.

The results obtained by the concentration cell technique have been found to be reproducible and accurate. As little as 0.001% by weight of chloride in 1 g of zinc sulfide can be determined; the limit of detection is 0.0005%. In many cases gravimetric analyses have been run on selected zinc sulfide samples, with results that confirm the usefulness of the concentration cell procedure.

The zinc sulfide powders, zinc chloride, and sodium chloride used in these experiments are free of heavy metals to the limit of spectrographic detectability. Some of the zinc sulfide powders contain coprecipitated chloride in amounts specified below. The zinc sulfide described as chloride-free contains 0.0015 ± 0.0005% (Fig. 2) by weight of chloride. During phosphor preparation the samples are held in transparent quartz boats and heated in transparent quartz combustion tubes in an atmosphere of helium. Conductivity-grade deionized water is used for washing. The zinc sulfate used for leaching and the nitric acid for dissolution of zinc sulfide powder contain no chloride to the limit of detectability.

Results

The amount of added halide has a marked influence on the luminescence intensity and spectral distribution of the emission. Accordingly, it appears desirable to study quantitatively the history of added chloride during zinc sulfide phosphor syntheses. The mechanism by which chloride carries out its function of enhancing luminescence has not yet been established. Previous investigators have examined only the finished product. Our results show that the phosphor passes during its preparation through stages in which the amount of incorporated

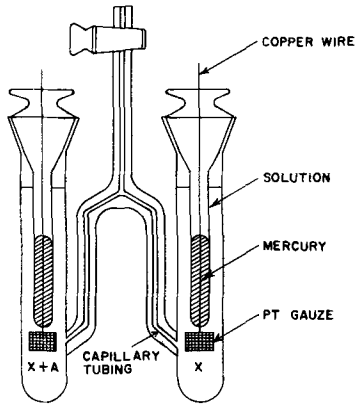

Fig. 1. Concentration cell with silver-silver chloride electrodes.

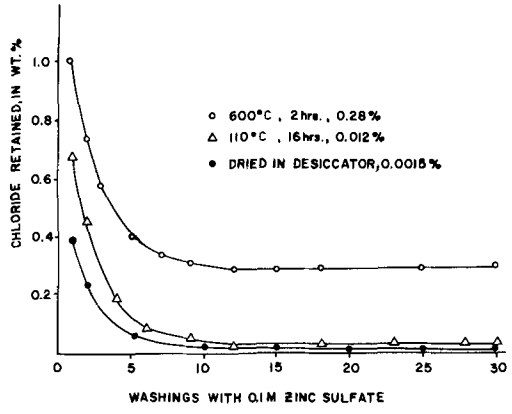

Fig. 2. Volume chloride retained after successive leachings with 0.1M zinc sulfate solution.

volume chloride is several orders of magnitude higher than that in the final phosphor. Data will be presented on the incorporation and retention of chloride in the volume of zinc sulfide as found during various steps of phosphor preparation from zinc sulfide powders with physically admixed or coprecipitated chloride coactivator.

Experimental definition of volume chloride.—Chloride-free zinc sulfide is mixed with 5% by weight of zinc chloride in solution. To check possible effects at room temperature, the slurry is placed in a vacuum desiccator at 25°C until it is completely dry. The dried mixture is then divided into eight 2-g portions. The first portion is leached once with 35 ml of 0.1M zinc sulfate, a second portion is leached twice with successive 35 ml portions of solution, and the remaining portions are leached in the same way for 5, 10, 15, 20, 25, and 30 times, respectively. The powder was separated from the leach solution by filtering through fritted glass filters and successive water washings. After separation, each portion is dissolved in nitric acid and the chloride content is determined as described above. The portion that had been leached only once contains 0.39% by weight of chloride, and after twenty leachings the retained amount decreases gradually (Fig. 2) to a constant value of 0.0015% by weight of chloride. Since this is the chloride content of the chloride-free zinc sulfide, it can be concluded that none of the added chloride became incorporated into the volume on drying at 25°C.

The same study is repeated on samples which are processed in a quartz combustion tube in one case for 16 hr at 110°C, and in another case for 2 hr at 600°C. After leaching, the samples are dissolved and their chloride contents are determined. Figure 2 indicates the number of times each sample has been leached and the resulting asymptotically attained volume chloride. It is seen that, in contrast to the result obtained by drying at room temperature, chloride is now incorporated into the volume of zinc sulfide powder during the heat treatment.

Influence of duration of heat treatment.—The amount of chloride incorporated into the volume of zinc sulfide, when zinc sulfide with physically admixed zinc chloride is heated at 600°C for 2 hr, is found above to be 0.28% by weight. In order to determine how the amount of incorporated volume chloride depends on the duration of heat treatment, zinc sulfide samples with 5% by weight of zinc chloride are heated at 750°C for 1, 4, 10, 20, and 30 min, and for 1, 2, 3, 4, and 8 hr. These samples are treated as above to determine the volume chloride. The data, which are presented in Fig. 3, show that chloride incorporation proceeds very rapidly. A peak value is attained within the first 10 min of heat treatment at this temperature. Thereafter, chloride begins to leave the volume as the sample remains at temperature. It should be noted that the amount of chloride in the volume of zinc sulfide after processing at 750°C for 2 hr is smaller than that incorporated during processing at 600°C for the same time. This result indicates the importance of the firing temperature, as discussed in the next part.

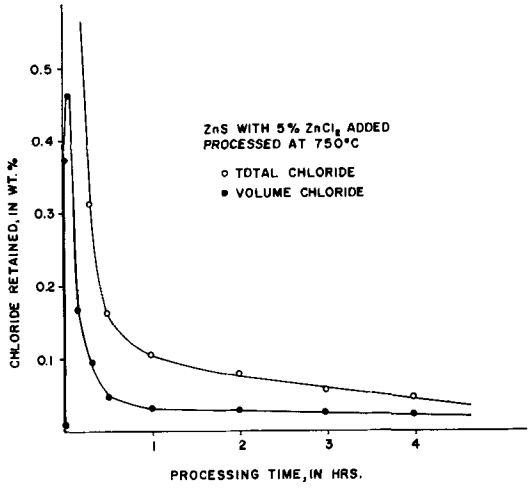

Fig. 3. Retention of total chloride and volume chloride as a function of processing time at 750°C.

Influence of the temperature of heat treatment.—It has been shown above that chloride is incorporated into the volume of zinc sulfide when heated with 5% zinc chloride. It is qualitatively clear from the above data that the amount of volume chloride incorporated first increases with temperature and then decreases as the temperature increases further. The present study is concerned with the quantitative nature of this temperature dependence. Zinc sulfide with 5% zinc chloride admixed is heated for 2 hr at various temperatures between 200° and 1100°C. External surface chloride is removed by the zinc sulfate leaching procedure, and the chloride content of the samples is determined; data are given in Fig. 4.

The peak value for the incorporation of chloride into the volume of zinc sulfide occurs near 500°C. The chloride retention curve rises about linearly to a maximum, and falls off so that the volume chloride diminishes to about 0.01% by weight at 800°C and to about 0.003% at 1100°C.

Usually a chloride other than zinc chloride is employed in phosphor synthesis; therefore chloride retention has been investigated when sodium chloride is added as the flux. The zinc sulfide samples with sodium chloride admixed are prepared in the same way as those containing zinc chloride. However, the amount of sodium chloride is changed to

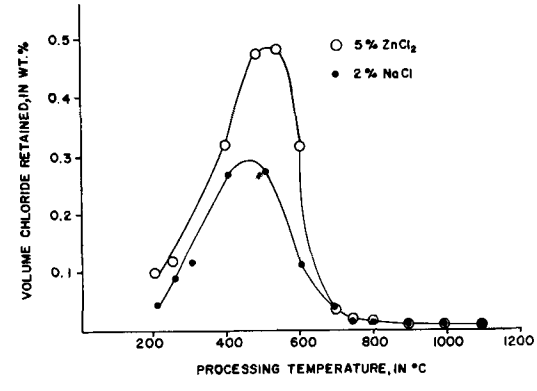

Fig. 4. Retention of volume chloride as a function of processing temperature for $ZnCl_2$ and NaCl addition; processing time is 2 hr.

2% by weight to approach a flux concentration often used in commercial practice. The zinc sulfide powders with the admixed sodium chloride are heated for 2 hr in the temperature range from 200° to 1100°C. The heat-treated powders are leached with zinc sulfate and then analyzed for volume chloride as before. The data, which are presented in Fig. 4, show the same general dependence of volume chloride on processing temperature as observed with zinc chloride, which has a much lower melting point than sodium chloride.

Retention of volume chloride in zinc sulfide containing coprecipitated chloride.—Chloride may be added to zinc sulfide either as a chloride salt after zinc sulfide precipitation from solution, as described above, or as coprecipitated[1] chloride formed when zinc sulfide is precipitated in the presence of a soluble chloride. In the latter case, amounts of about 1% by weight of chloride become incorporated into the volume of zinc sulfide during its formation.

As another, complementary part of studying the history of chloride incorporation during phosphor preparation, it appears of interest to observe the retention of volume chloride when coprecipitated chloride is present in the volume of zinc sulfide powder. For this purpose, zinc sulfide is prepared by passing hydrogen sulfide through a solution of zinc chloride acidified to pH 2.5 with hydrochloric acid. The zinc sulfide precipitate is filtered and leached with zinc sulfate solution until it attains a constant chloride content after several successive washings. The constancy of chloride is determined by analysis of the zinc sulfide sample as well as by the absence of chloride in the filtrate. The zinc sulfide prepared by this method contains 0.82% by weight of chloride which is all present in the volume.

Samples of zinc sulfide containing coprecipitated chloride are placed in quartz boats and heated in a quartz combustion tube at 400°C for 1, 4, and 16 hr, respectively, in an atmosphere of helium. Each specimen is leached twenty times with 0.1M $ZnSO_4$ after heating and then is dissolved to determine the chloride content. Figure 5 presents the data; almost all the volume chloride remains in zinc sulfide under the above processing conditions. The same experiment is performed by maintaining the zinc sulfide powder with coprecipitated chloride for various periods of time at 600°, 800°, and 1100°C, as shown in Fig. 5. It is found that the amount of retained volume chloride decreases rapidly with increasing processing temperature. The amounts of chloride remaining incorporated in the volume after heating for 4 hr at 600°C are comparable to the amounts of volume chloride incorporated when the chloride is introduced in the form of zinc chloride or sodium chloride by physical admixture.

[1] The term "coprecipitated" is used in the sense as given by I. M. Kolthoff and E. B. Sandell, Textbook of Quantitative Inorganic Chemistry, The MacMillan Co., New York, 1948, pp. 110-112.

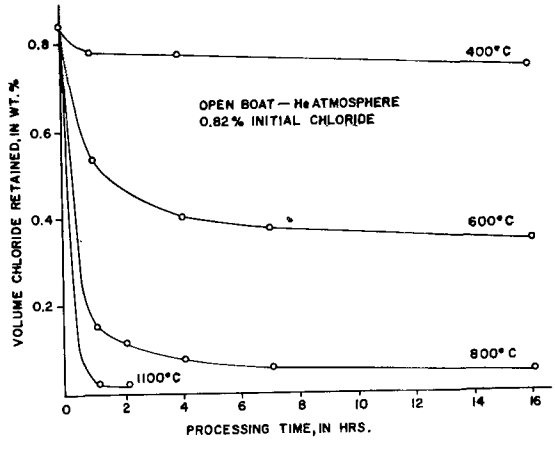

Fig. 5. Retention of coprecipitated volume chloride as a function of processing time and temperature.

Discussion

As part of the present investigation, it has been found that it is possible to define volume chloride as chloride not removed by successive leachings. One obtains reproducible values of volume chloride; these values depend on the conditions to which zinc sulfide powders containing either physically admixed or coprecipitated chloride have been subjected.

Following the explanation of Leverenz (13) for particle growth of Zn_2SiO_4, one can explain the incorporation of chloride into the volume of zinc sulfide as an attendant effect of particle growth. The admixed chloride coats the surface of the zinc sulfide grains which grow together and include chloride on contiguous surfaces. Chloride included in intergranular boundaries cannot be removed by leaching with sulfate ions and is, therefore, volume chloride as above defined. As the temperature increases (Fig. 4) to about 500°C, the number of intergranular boundaries also increases so that additional chloride becomes incorporated. When the processing temperature is increased above 500°C, the walls of the intergranular boundaries may start to sinter together so that chloride is expelled. At high temperatures many grain boundaries disappear, and particle growth takes place. A part of the volume chloride is then displaced to the external surface and volatilizes, while some may be retained on interior surfaces and some may become incorporated into the host lattice.

Sodium chloride flux shows essentially the same behavior as zinc chloride with respect to chloride incorporation into zinc sulfide. However, the two fluxes differ considerably in physical properties, such as vapor pressure and melting point. The similarity in behavior may indicate that chloride incorporation into the volume of zinc sulfide is essentially a property of the host material and the chloride ion, and to a lesser extent a property of the flux cation. The fact that zinc chloride has a lower melting point than sodium chloride, yet shows the same temperature dependence of chloride incorporation, tends to cast doubt on a mechanism of flux action that depends on the dissolving (3) of zinc sulfide by the fluxing agent. This result is in agreement with Bube (8) who finds that the amount of chloride retained is the same regardless of whether sodium chloride or hydrochloric acid is present during preparation of a copper-activated zinc sulfide phosphor. The concentration of retained chloride is about the same whether it is present origi-

nally as a coprecipitate or is admixed with the sulfide before firing. For this reason one is led to suspect that the actual mode of retention is the same in both cases.

As shown in Fig. 4, the volume chloride is a function of firing temperature for a given firing time. The volume chloride does not, however, by itself, determine the obtainable luminescence; maximum luminescence is usually obtained by firing at temperatures well above 500°C. Therefore, if a numerical correlation between the amount of incorporated chloride and luminescence is to be expected, one must consider the volume chloride to be composed of at least two kinds, one of which is effective in promoting luminescence. One hopes that future explorations will make it possible to distinguish between the various fractions of volume chloride, so that quantitative correlation with luminescence can be established. A first goal (14) will be to differentiate between lattice chloride and internal surface chloride.

Acknowledgment

Grateful acknowledgment is made to A. K. Levine for many helpful discussions, R. Bastian for conducting some additional chloride analyses, and J. T. Ragusin for valuable assistance with the experimental work.

Manuscript received March 14, 1960. This paper was prepared for delivery before the Cincinnati Meeting, May 1-5, 1955.

Any discussion of this paper will appear in a Discussion Section to be published in the June 1961 JOURNAL.

REFERENCES

1. E. Tiede and A. Schleede, *Berichte*, **53B**, 1921 (1920).
2. N. Riehl and H. Ortmann, *J. Phys. Radium*, **17**, No. 8-9, 620 (1956).
3. A. Schleede and H. Gantzckow, *Z. Phys. Chem.*, **106**, 37 (1923).
4. A. A. Guntz, *Ann. Chim.*, **5**, 157 (1926).
5. V. M. Gugel, *Bull. Acad. Sci. USSR*, Ser. Phys., **9**, 539 (1945).
6. A. L. Smith, *J. (and Trans.) Electrochem. Soc.*, **96**, 75 (1949).
7. F. A. Kroeger and J. E. Hellingman, *ibid.*, **93**, 156 (1948); **95**, 68 (1949).
8. R. H. Bube, *J. Chem. Phys.*, **19**, 985 (1951).
9. H. C. Froelich, *This Journal*, **100**, 280 (1953).
10. D. T. Palumbo and A. K. Levine, *ibid.*, **102**, 181 (1955).
11. N. H. Furman and G. W. Low, *J. Am. Chem. Soc.*, **57**, 1585 (1935).
12. M. Bancie-Grillot and E. Grillot, *Compt. rend.*, **237**, 171 (1953).
13. H. W. Leverenz, "Luminescence of Solids," John Wiley & Sons, Inc., New York, (1950).
14. A. Kremheller and A. K. Levine, The Release of Chloride from Zinc Sulfide by Grinding, paper presented at The Electrochemical Society Meeting, San Francisco, May 1956.

Study of Ball Milling and the Determination of Lattice Chloride in Zinc Sulfide

A. Kremheller, S. Faria, and A. K. Levine

General Telephone & Electronics Laboratories Inc., Bayside, New York

ABSTRACT

Ball milling, followed by displacement washing, permits a distinction to be made between lattice chloride and internal surface chloride as parts of volume chloride. The surface area, which is determined by gas adsorption methods, increases rapidly in the beginning and then in a linear manner as a function of milling time. The extent of linearity between surface area and milling time is considered to be a measure of crystallinity. The data indicate that the maximal amount of lattice chloride becomes incorporated at a processing temperature near 700°C after a processing time of 2 hr. Zinc sulfide gradually loses its ability to luminesce under ultraviolet (u.v.) irradiation during milling; the logarithm of the luminescence emission is about proportional to the newly formed surface. It appears that the luminescence centers consist of lattice regions of about 0.2 μ in diameter, as is indicated by the observed minimal size of luminescent particles. The luminescence emission of milled samples can be restored by reprocessing, although the degree of restoration is highly sensitive to impurities introduced during milling.

Lenard and Klatt (1) were probably the first to observe that photoluminescence is considerably decreased during the destruction, e.g., by crushing, of phosphor particles. Wecker (2), Frey (3), and Broser and Reichardt (4) among others have confirmed this observation. Many researchers (5) have attempted to correlate the decay of luminescence intensity during phosphor destruction with the particle size, extent of destruction, and related parameters. However, some conclusions which have been attained are confounded by the method of particle size determination, as zinc sulfide particles usually agglomerate if they are below 1 μ in diameter. For instance, Frey (3) concludes from microscopic observations that the grain size of zinc sulfide approaches a constant value of 4 μ during ball milling, although he observes small particles (about 0.1 μ) when an electron microscope is used. Short and

Steward (6) attempt a correlation between photoluminescence intensity and crystal structure changes during grinding of zinc-cadmium sulfides. They find that the residual photoluminescence is an exponential function of the retained hexagonal structure fraction. Broser and Reichardt (4) were probably the first to consider the surface increase during ball milling of zinc sulfide phosphors. They determined the surface change and degree of destruction of the phosphor particles by an optical procedure based on reflection.

Results on grinding of zinc sulfide are only incidental to the present investigation, which is mainly concerned with a distinction between chloride present on internal surfaces and within the lattice. Zinc sulfide particles are destroyed in order to expose the incorporated volume chloride. The various fractions of chloride have been discussed in a previous publication (7), in which the need for determining lattice chloride and its possible implication on luminescence properties of zinc sulfide also have been indicated. The present paper consists essentially of the continuation of previous researches looking into the mechanism of flux action during zinc sulfide phosphor preparation. The present incidental results on ball milling appear, however, to be of such general interest in considering the mechanism of photoluminescence that their inclusion seems desirable.

Experimental

The zinc sulfide powder, processing procedure, and fluxing agent used have been specified in a previous publication (7) which also explains the determination of small amounts of chloride by the concentration cell procedure.

The ball milling is performed in 4-oz glass bottles with screw caps; 0.5 in. diameter procelain balls are employed for crushing the zinc sulfide particles. The speed of the ball mill, the number of balls, and the sample size are kept constant in all experiments. Dry milling is employed to avoid the decomposition of zinc sulfide which takes place, for instance, in the presence of water. It is found that the chloride contamination introduced by milling for 300 hr is below the limit of detectability, i.e., 0.0005% by weight, by the concentration cell procedure (7); however, amounts near 10 ppm each of copper, iron, lead, and silicon are detected. These impurities affect the restoration of luminescence during refiring of ball milled samples, as will be shown.

A simplified gas adsorption method (8) was employed for determining the newly formed surface area after ball milling. The simplified procedure reduces the time for one surface area determination by a factor of about ten when compared with the general Brunnauer-Emmett-Teller (B.E.T.) method, makes routine determinations feasible, and permits one to obtain a quantitative measure of the extent of destruction of phosphor particles during ball milling. Optical and electron microscope studies, as well as the general B.E.T. gas adsorption method, have been employed to confirm and supplement results obtained by the simplified method.

A semi-quantitative measure of the blue, green, and red luminescence intensity was obtained with a laboratory plaque tester (9) in which u.v. radiation from two germicidal lamps excites the phosphor to be tested. The emission from the phosphor is filtered, and the emission within the corresponding spectral range is measured with a photomultiplier tube, thus permitting a comparison of the luminescence emission from different phosphor samples to be made. We have found this method to be accurate, and the results are reproducible within ± 2%.

Results

Ball Milling and Surface Area

The average particle diameter of zinc sulfide decreases during milling, but the rate of decrease diminishes with milling time, as shown in Fig. 1. In this figure, three different initial particle sizes are represented; the size in microns is given for average equivalent spherical diameters. If one assumes that the crystallites are perfect, Rittinger's law (10) applies. This law states that the work consumed in particle-size reduction is directly proportional to the area of the newly formed surface. If the material is hard, which means that the cohesive forces are large, much work is needed to expose a given surface area.

The determination of the particle size is quite difficult and represents only an average value that is confounded by the fact that the particles are actually not spherical and are distributed over a variety of shapes according to their sizes (11). An improved sensitive index of the effect of milling is therefore the increase in surface area with milling time. Figure 2 represents this relationship. It is interesting to observe that the curves consist of two distinct regions. During the initial milling period the specific surface area increases rapidly, while there exists a linear relationship with extended milling times. The slope in the linear part is very nearly the same in all five cases, and the fracture of particles is still proceeding at the same rate after 100 hr of ball milling. The increase in specific surface area is larger for smaller particles than for the larger ones during the initial part of milling.

These results are readily amenable to an interpretation. The data can be explained tentatively by assuming that during the early stages of milling the increase in surface area is predominantly due to the breaking of particle aggregates, such as fracture along grain boundaries and similar imperfections,

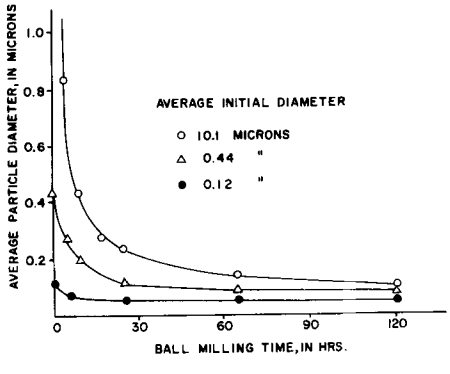

Fig. 1. Dependence of average particle diameter on milling time.

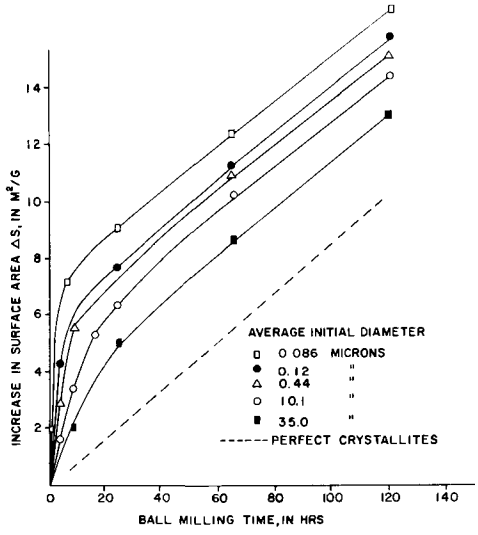

Fig. 2. Increase in surface area with milling time for various initial particle sizes.

while in the later stages of milling it is the fracture of single crystallites that is dominant. This explanation is also in agreement with the sequence of the curves in that the large particles can be expected to exhibit better crystallinity and fewer imperfections than the small ones. Generally, it may well be feasible to compare the crystallinity and degree of perfection of crystalline materials by evaluating these relationships, as given in Fig. 2.

Distinction between Internal Surface Chloride and Lattice Chloride

When the agglomerates and crystallites are broken up, the surface area of the powder increases. A portion of the volume chloride becomes exposed, and this can be replaced by displacement washings with zinc sulfate solution. Most of the chloride that becomes removable is exposed in the early stages of milling when agglomerates and imperfections are broken up. There will also be some loss of lattice chloride during the initial stage of ball milling; however, this amount can be estimated readily. If one assumes that the lattice chloride is uniformly distributed throughout the lattice, e.g., in a 1-g sample, one finds that about 1% of the volume chloride present will be exposed as lattice chloride if the increase in specific surface area is 10 m^2/g. On the other hand, if a portion considerably larger than 1% of the volume chloride becomes displaceable, essentially internal surface chloride must be exposed. In addition, one may expect also from Fig. 2 that mainly internal surface chloride becomes exposed during the initial stages of milling when agglomerates break up.

In a practical case, one would expect therefore that a diagram of the volume chloride as a function of the increase of specific surface area Δs will initially show an amount of chloride exposed per newly formed specific surface area, which is determined essentially by internal surface chloride which becomes displaceable; one can see this exemplified in Fig. 3. However, during subsequent milling essentially lattice chloride becomes exposed when the single crystallites fracture. The sample represented

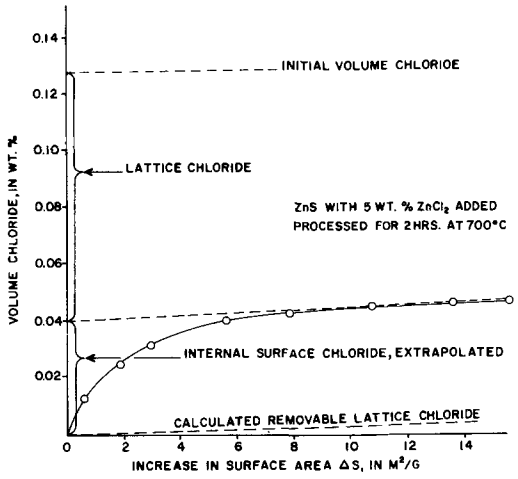

Fig. 3. Distinction between chloride on internal surfaces and within the lattice.

in Fig. 3 was processed for 2 hr at 700°C after 5% by weight of zinc chloride as a flux had been added. The volume chloride is 0.127% by weight, as indicated by the dashed horizontal line. After milling is started one finds that an increasing amount of chloride becomes exposed as the surface area is increased. After the increase in specific surface area is about $\Delta s = 10$ m^2/g, the amount of exposed chloride becomes a linear function of Δs. Since single crystallites rather than agglomerates fracture on further milling, it appears likely that lattice chloride is essentially exposed from here on. The straight part of the curve can be extended toward the ordinate of Fig. 3, so that an extrapolation to indicate the amount of lattice chloride present becomes possible. It is assumed in this estimate that the lattice chloride is uniformly distributed within the lattice and is exposed at a linear rate from the start of milling. In the sample shown in Fig. 3, the amount of internal surface chloride is found to be about 0.04% by weight, so that the incorporated lattice chloride amounts to 0.09%.

Other samples were treated in the same manner in order to distinguish between lattice chloride and internal surface chloride as parts of volume chloride. Results are given in Table I. The amount of internal surface chloride decreases as the crystallinity is improved at elevated processing temperatures. The lattice chloride concentration appears to have a peak near 700°C, although one could hardly draw definite conclusions because the determination of lattice chloride is not possible in a direct manner after sample processing at 500°C. In this case the slope does not change as in Fig. 3, but one obtains the impression that internal surface chloride is exposed even after a ball milling time of 350 hr. The

Table I. Chloride retained in zinc sulfide processed with 5% by weight of zinc chloride for 2 hr

Processing temp, °C	Wt % of chloride in Volume	Lattice	Internal surfaces
600	0.303	0.08	0.22
700	0.13	0.09	0.04
800	0.017	0.014	0.003
900	0.0065	0.0055	0.001
1000	0.0030	0.0025	0.0005

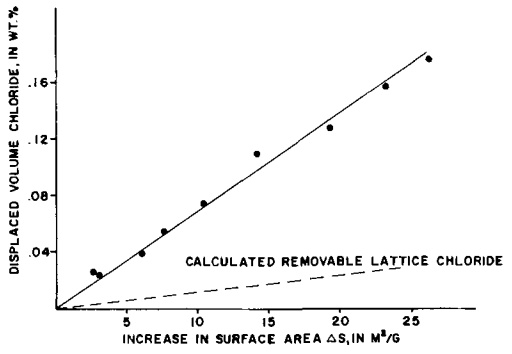

Fig. 4. Removal of coprecipitated volume chloride from precipitated zinc sulfide after milling.

behavior of this sample is very similar to that of zinc sulfide containing coprecipitated chloride,[1] as seen in Fig. 4.

The chloride flux, which is beneficial in preparing zinc sulfide phosphors, may also be present in the coprecipitated form. This is common commercial practice, for the same quality of phosphor is attained with a smaller amount of coprecipitated chloride as with admixed flux. It therefore appears valuable to know the way in which chloride is distributed in this case. A zinc sulfide powder containing 0.80% by weight of coprecipitated chloride was carefully washed with zinc sulfate solution until the amount of volume chloride was at the constant value of 0.73%. Portions of this material were milled for successive periods after which the surface increase and the amounts of displaceable chloride were determined. Figure 4 represents the amount of exposed volume chloride as a function of the increase in surface area during milling. The largest Δs corresponds to 350 hr of milling, during which time about 20% by weight of the initial volume chloride is rendered displaceable. From the nearly linear character of the curve one can surmise that all the chloride rendered displaceable is of one type. If this were uniformly distributed lattice chloride, one should expect a relationship between Δs and exposed chloride as shown by the dashed line in Fig. 4. When this is compared with the experimental results plotted in the upper line, it appears that the coprecipitated chloride is not uniformly distributed within the lattice. The data can be taken to mean that the chloride lies for the most part on internal surfaces of tightly agglomerated particles of the precipitated zinc sulfide powder. This incidental result is of importance to analytical chemists who are concerned with the manner in which coprecipitated ions are incorporated into a precipitate.

When the same zinc sulfide powder is processed for 2 hr at 700°C, one finds about 0.25% by weight of volume chloride of which about one half is lattice chloride. Therefore, the incorporation of volume chloride into the lattice is very similar in this case to that observed with zinc sulfide containing physically admixed chloride flux.

Decay of Luminescence Intensity during Milling

Several experimental samples of a luminescent zinc sulfide phosphor were milled for various lengths

[1] "Coprecipitated" is used in the sense as indicated in ref. (7).

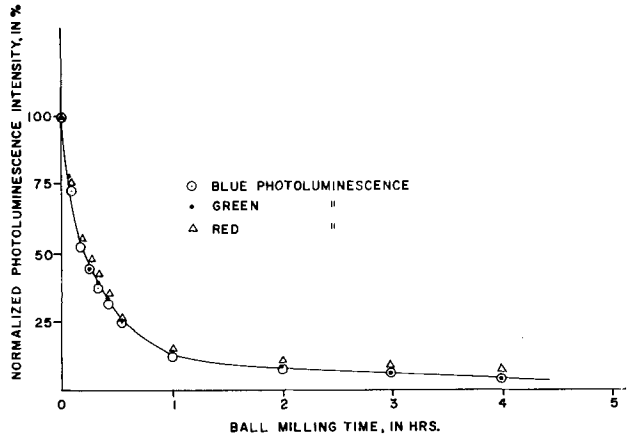

Fig. 5. Decay of photoluminescence intensity of zinc sulfide phosphor during milling.

of time; results are presented in Fig. 5. The blue and green photoluminescence emission decay somewhat faster than the red component. This different behavior of the red part of the emission after ball milling was also observed by Wecker (2). One finds that the ability to luminesce is essentially destroyed during the first 10 hr of milling when the agglomerates are broken up and the internal surfaces (cf. Fig. 2) are exposed.

Therefore, it appears that the exposure of internal surfaces may be intimately connected with the decay of luminescence intensity during the milling process. This consideration led us to plot the logarithm of the luminescence intensity B as a function of the increase of surface area Δs exposed during the ball milling. The resulting Fig. 6 indicates that the luminescence decreases about exponentially with increasing surface area. This means that the decrease in luminescence with the change in Δs is proportional to the instantaneous luminesence emission, i.e., $dB/d(\Delta s) = -aB$.

Another interesting result is that no particles below 0.2 μ were found to be photoluminescent in these very extensive experiments. It appears that a

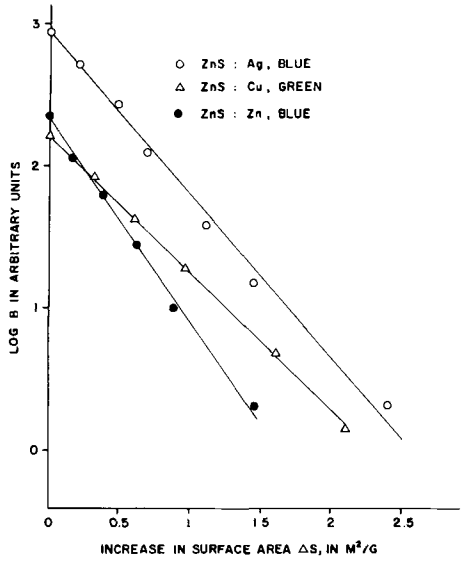

Fig. 6. Logarithm of the photoluminescence intensity B as a function of the increase in surface area Δs during milling.

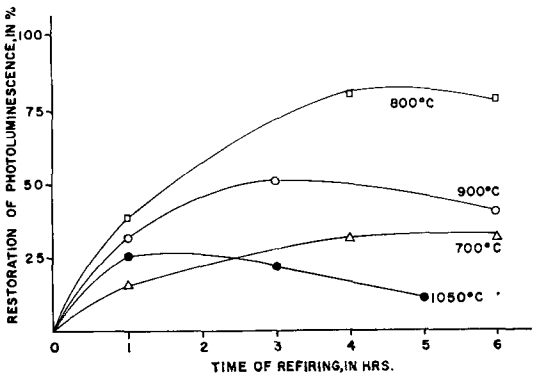

Fig. 7. Restoration of photoluminescence intensity by refiring after milling.

minimum cell size is required for photoluminescence; this is in agreement with conclusions stated by other authors (12-15).

Restoration of Luminescence Emission after Milling

Some experiments have been conducted to explore the restoration of photoluminescence by heat treatment of the milled phosphor. Figure 7 presents some data on recovery of photoluminescence by reprocessing at various temperatures. The extent of restoration is given in per cent of the green luminescence emission before milling as a function of processing time, and the temperature as parameter. If a sample that becomes nonluminescent during milling is held at 800°C for 4 hr the original luminescence is nearly restored, while on extended firing the intensity decreases again. The luminescence recovery was found to be optimum at 800°C. The restored luminescence intensity can be further increased by about 20% if chloride flux, such as 2% by weight of zinc chloride, is admixed or if the sample is quenched rapidly after refiring.

The average particle size increases during the refiring process, as can be determined readily by the gas adsorption method or by microscopic observation (11). The particle size also increases, however, in cases where the restoration of luminescence emission is counteracted by other processes, such as the diffusion of "killer" impurities introduced during ball milling; the extent of this contamination is indicated above. The degree of luminescence recovery and especially the maxima found for various processing temperatures and times become self-evident if impurity diffusion is assumed, as can be seen from Fig. 7. It appears likely that the degree of contamination was smaller in our samples than in those used by Broser and Reichardt (4), since they obtain maximum restoration with a 30-min heat treatment at 500°C.

Summary and Discussion

A study of the mechanism of flux action on the luminescence behavior of zinc sulfide has led to a method that permits one to distinguish between internal surface and lattice chloride. Previous investigations have led to ambiguous results because difficulties arose from the presence of occluded and internal surface chloride. The present study is based on the displacement of chloride ion by sulfate ion, surface area determination by the simplified gas adsorption method, and the use of milling as a means of exposing lattice chloride and internal surface chloride.

It was found that the internal surfaces are exposed mainly during the initial stages of milling, so that internal surface chloride becomes exposed preferentially and can be removed by ion-exchange washings. The slope of the curve of displaceable chloride as a function of the increase in specific surface area gradually approaches a constant value with additional milling, when essentially lattice chloride is rendered displaceable. Simple extrapolation permits one to obtain a quantitative estimate of the amounts of lattice chloride and internal surface chloride.

The instantaneous luminescence intensity of milled zinc sulfide phosphors is found to be an exponential function of the increase in specific surface area. The decrease in luminescence occurs essentially during the exposure of internal surface chloride. When luminescence emission is no longer perceptible, about 80% of the original lattice chloride is still incorporated within the phosphor lattice. It may therefore be concluded that the presence of lattice chloride alone is not sufficient for photoluminescence. A possible correlation may exist between the occurrence of luminescence and the requirement of a certain minimum cell size, since no photoluminescent particles have been observed below 0.2 μ in diameter. It appears possible that the exposure of internal surfaces is accompanied by the creation of trapping levels that lead to the observed decrease in luminescence with the increase in specific surface area.

Acknowledgment

Grateful acknowledgment is made to D. J. Bracco for many helpful discussions, and to J. T. Ragusin for valuable assistance with the experimental work.

Manuscript received March 14, 1960. This paper was prepared, in part, for delivery before the San Francisco Meeting, Apr. 29-May 3, 1956.

Any discussion of this paper will appear in a Discussion Section to be published in the June 1961 JOURNAL.

REFERENCES

1. P. Lenard and V. Klatt, *Ann. Physik*, **12**, 439 (1903).
2. F. Wecker, *ibid.*, **42**, 561 (1942); **43**, 607 (1943).
3. F. Frey, *ibid.*, **2**, 147 (1948).
4. I. Broser and W. Reichardt, *Z. Physik*, **134**, 222 (1953).
5. H. Meier, *Z. Elektrochem.*, **60**, 1007 (1956).
6. M. A. Short and E. G. Steward, *Z. Physik. Chem.* (Neue Folge), **13**, 298 (1957).
7. A. Kremheller, S. Faria, P. Goldberg and D. J. Bracco, *This Journal*, **107**, 749 (1960).
8. D. T. Palumbo, F. M. Starkweather, and D. J. Bracco, "A Simplified Gas Adsorption Method for the Determination of the Surface Area of Fine Powders," presented at The Electrochemical Society Meeting, Cincinnati, May, 1955.
9. K. H. Butler and R. W. Mooney, Private communication.
10. P. Rittinger, "Lehrbuch der Aufbereitungskunde," Berlin (1867).
11. Results on "Particle Growth during Phosphor Preparation" will be published in the near future.

12. P. D. Johnson and F. E. Williams, *J. Chem. Phys.*, **18**, 1477 (1950).
13. I. O. M. Poltorak and A. V. Lavrov, *Zhur. Fiz. Khim.*, **29**, 1254 (1955).
14. A. Smekal, "Ueber den Aufbau der Realkristalle," Bologna (1927).
15. A. J. Dekker, "Solid State Physics," p. 410, Prentice Hall, Inc., New York (1959).

Donor Concentration at the Surface of a Diffused N-type Layer on P-type Germanium

R. Glang[1] and W. B. Easton[2]

Diamond Ordnance Fuze Laboratories, Washington, D. C.

ABSTRACT

Four methods of evaluating the donor concentration at the surface of a diffused N-type layer on P-type germanium have been investigated. All methods assumed a complementary error function (erfc) distribution in the diffused layer. The methods required the use of experimental data for junction depth and sheet resistivity, and of published data for diffusion coefficients of group V elements and electron mobilities in germanium. The methods were applied to calculate the donor concentrations at the surfaces of a number of diffused samples. Under diffusion conditions, which were expected to result in an erfc impurity distribution, the actual concentration profile in the vicinity of the junction was shown to deviate from the erfc law. Due to this deviation, one of the methods of calculating the surface concentration was ruled out. With the other three methods, calculated surface concentrations agreed within a factor of 2 or 3. The disagreement is mainly caused by lack of precise information in respect to the electron mobilities in the diffused layer. Therefore, all the methods represent approximations only.

The preparation of diffused PN-junctions has become a widely used technique in the fabrication of semiconductor devices (1, 2). The electrical characteristics of these devices depend to a large degree on the properties of the diffused layer (3). Therefore, a quantitative knowledge of these properties is essential to the design of devices as well as to the experimental direction of the diffusion process. Some of these properties, for instance the junction depth and the sheet resistivity of the layer, are amenable to direct experimental determination. The concentration of the diffused impurity at the surface, however, cannot be measured directly; it has to be derived from other measured parameters. This concentration is generally referred to as surface concentration. There are several ways of determining the surface concentration (4), and the actual choice of the method will depend on the types of experimental data which are available.

The following discussions concern a special case of the diffusion process, characterized by the diffusion of a donor element from a source of constant vapor pressure into P-type germanium of uniform acceptor concentration. The diffusion temperature is maintained constant during the entire experiment. Furthermore, it is assumed that the indiffusion is not complicated either by a rate-determining layer or by evaporation from the germanium surface. If Fick's second equation of diffusion is solved for these boundary conditions, the complementary error function (erfc) is obtained as the general type of the impurity distribution (5):

$$N(x) = N_0 \text{erfc}\ (x/2\sqrt{Dt}) \qquad [1]$$

where $N(x)$ is the concentration of donors in the germanium at a certain distance, x, from the surface; N_0 is the donor concentration immediately at the surface; t is the diffusion time; and D is the diffusion coefficient of the donor element in germanium.

Figure 1 shows the concentration profile of the donors and, in addition, the initial acceptor concentration A, as functions of x. At a certain depth w, where these concentrations are equal and no excess charge carriers are available, the PN-junction is formed; at this depth

$$N(w) = A \qquad [2]$$

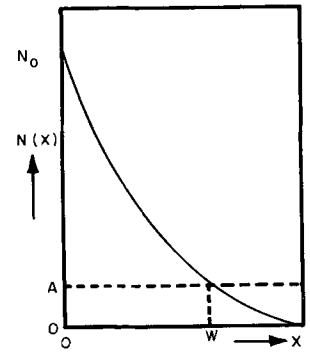

Fig. 1. Concentration of donors N(x) and initial concentration of acceptors A as a function of distance x from the surface of a diffused layer.

[1] Present address: International Business Machines Corp., Kingston, New York.

[2] Present address: Cornell University, Ithaca, New York.

Determination of the Surface Concentration

1. From the erfc distribution.—The simplest treatment of the problem of the surface concentration is obtained by substituting Eq. [2] in Eq. [1] and solving for N_0:

$$N_0 = \frac{A}{\text{erfc}(w/2\sqrt{Dt})} \qquad [3]$$

Values of the diffusion coefficients D for group V donor elements in germanium have been published frequently (6-10). The junction depth w can be determined experimentally, for instance by the techniques described by Bond and Smits (11). The initial acceptor concentration A can be obtained from Hall measurements on the P-type material prior to diffusion. Unfortunately, this simple method was found to be completely unsatisfactory, as will be shown and explained later on.

2. By differential etching.—N_0 may also be expressed in terms of conductivity of the surface layer. Four-point-probe measurements (12, 13) on diffused layers can be expressed in terms of the sheet conductivity σ_s of the entire diffused layer. Since the carrier concentration in the layer varies with depth, the total sheet conductivity is the integral of the differential

$$d\sigma_s = e \cdot \mu(N_x) \cdot n(x) \cdot dx \qquad [4]$$

where $\mu(N_x)$ is the electron mobility at a certain distance x from the surface and is a function of the total impurity concentration N_x at that depth; e is the electron charge. Assuming that all donors are ionized and that a fraction of them equal to the number of acceptors is not available for the conduction process,

$$n(x) = N(x) - A \qquad [5]$$

To obtain the sheet conductivity of a layer of finite thickness, Eq. [4] is integrated. For this purpose, the layer which is closest to the surface and extends into a depth Δx, small compared to the total junction depth w, will be considered. Within this shallow layer, an average value $\bar{\mu}$ can be used to approximate the mobility. Furthermore, the error function is expanded into a series, of which only the first term has to be considered as long as $x/2\sqrt{Dt}$ is small compared to 1. Then

$$N(x) \cong N_0\left[1 - \frac{2}{\sqrt{\pi}} \cdot \frac{x}{2\sqrt{Dt}}\right] \qquad [6]$$

With these simplifications, the sheet conductivity of the first surface layer of thickness Δx follows from integration of Eq. [4].

$$\Delta\sigma_s = e \cdot \bar{\mu}\left[N_0 \cdot [\Delta x - \frac{(\Delta x)^2}{2\sqrt{\pi Dt}}] - A\Delta x\right] \qquad [7]$$

Equation [7], solved for the surface concentration, yields

$$N_0 = \frac{\frac{\Delta\sigma_s}{e \cdot \bar{\mu}} + A\Delta x}{\Delta x - \frac{(\Delta x)^2}{2\sqrt{\pi Dt}}} \qquad [8]$$

Frequently it will be tolerable to further simplify this expression by neglecting second order terms.

The numerical solution of Eq. [8] requires knowledge of the differential sheet conductivity $\Delta\sigma_s$. This information is obtained by measuring the sheet conductivity of the diffused layer with a four-point-probe, then briefly etching the surface and taking another four-point-probe measurement on the new surface. The difference between the two sheet conductivities is $\Delta\sigma_s$. The thickness Δx of the removed surface layer may be determined either by using a calibrated etch or by another junction depth measurement after the etch. Attempts to derive Δx from the difference in the weight of the unetched and etched sample did not give satisfactory results. The average mobility in Eq. [8] has to be estimated either on the basis of a Hall measurement (14, 15) on the diffused layer, or by comparing the average resistivity $\Delta x/\Delta\sigma_s$ of the removed layer with resistivities obtained from published mobility data (16-18).

3. From average mobility approximations.—It is also possible to relate the surface concentration to the total sheet conductivity of the layer, if one succeeds in integrating Eq. [4] over the entire junction depth, i.e., from zero to w. This integration can be done algebraically by using the simplifying approximation of a constant average mobility throughout the entire layer. Obviously, this assumption will affect results more seriously than it did in the foregoing method, where it was applied for a thin sublayer only. With this simplification, the sheet conductivity of the diffused layer is represented by

$$\sigma_s = e\bar{\mu} \cdot [N_0 2\sqrt{Dt} \int_0^{w/2\sqrt{Dt}} \text{erfc } u\, du - \text{erfc}(x/2\sqrt{Dt})\, d(x/2\sqrt{Dt} - \int_0^w A\, dx] \qquad [9]$$

The first integral term can be transformed according to

$$\int_0^z \text{erfc } u\, du = \frac{1}{\sqrt{\pi}} - \int_z^\infty \text{erfc } u\, du \qquad [10]$$

Numerical values of the function $\int_z^\infty \text{erfc } u\, du$ have been published by Kaye (19), who uses the symbol "ierfc z" for this first repeated integral of the complementary error function. Introducing his symbol, with the understanding that

$$z = w/2\sqrt{Dt} \qquad [11]$$

and, furthermore, substituting the more commonly used sheet resistivity ρ_s for the sheet conductivity, where

$$\rho_s = \frac{1}{\sigma_s} \qquad [12]$$

the surface concentration follows from Eq. [9]

$$N_0 = z \cdot \frac{\frac{1}{w \cdot \rho_s \cdot e \cdot \bar{\mu}} + A}{1/\sqrt{\pi} - \text{ierfc } z} \qquad [13a]$$

For numerical solution, A, w, z, and ρ_s are determined as before. The product

$$w \cdot \rho_s = \bar{\rho} \qquad [14]$$

represents the average resistivity of the layer. Since data relating the electron mobility to the donor concentration are published for germanium (16-18) one may derive a graph giving μ as a function of the resistivity. This graph may be used to estimate the average mobility in the layer from the experimental value of the average resistivity as given by Eq. [14].

A more elegant way of interpreting Eq. [13a] requires a Hall measurement instead of a resistivity measurement on the diffused layer. The Hall measurement yields the average excess carrier concentration directly in the following terms:

$$\bar{n} = \frac{3\pi}{8} \cdot \frac{H \cdot I}{w \cdot e \cdot V_H} \qquad [15]$$

where H is the magnitude of the magnetic field, I is the current through the sample, and V_H is the measured Hall voltage. The average electron concentration $\bar{n}$ is given by:

$$\bar{n} = \frac{1}{w \cdot \rho_s \cdot e \cdot \bar{\mu}} \qquad [16]$$

and when substituted in Eq. [13a] leads to:

$$N_0 = z \cdot \frac{\bar{n} + A}{1/\sqrt{\pi} - \text{ierfc } z} \qquad [13b]$$

Further simplifications of Eq. [13a] or [13b] are possible, since A in most practical cases will be very small compared to $\bar{n}$. In addition, the term ierfc z converges rapidly to zero; for $z = 1.6$, for instance, the value of ierfc z is only 1% of $1/\sqrt{\pi}$, and therefore may be neglected.

4. From computer approximations.—The accuracy of the method described in the foregoing paragraph is limited by the assumption of a constant average mobility over the entire layer. Better results are to be expected if the variation of the mobility within the layer is considered. This consideration necessitates the use of a computer. For diffused layers in silicon and various types of impurity distributions, Backenstoss (20) has computed and published curves which relate the surface concentration to the average layer resistivity $\bar{\rho} = \rho_s \cdot w$. For germanium, however, similar data have not been published. In the following discussion, the individual steps of the computation process, which has been applied to obtain analogous curves, are outlined briefly. Only diffused N-layers on P-type germanium and erfc-distributions are considered.

In the general conductivity equation

$$\frac{1}{\bar{\rho}} = \frac{1}{\rho_s \cdot w} = \frac{1}{w} \cdot e \cdot \int_0^w \mu(N_i)[N(x) - A]\, dx \qquad [17]$$

$N(x)$ is assumed to be given by Eq. [1]. The mobility $\mu(N_i)$ is taken from the data of Conwell (17). This implies the assumption that the total impurity concentration approximately equals the excess donor concentration: $N_i \simeq N(x) - A$, which is true only if $N(x)$ is large compared to A. The integral was evaluated by Simpson's rule, using an IBM 704 computer. The computation is greatly simplified by the change of variable, $x = wu$. On substituting the latter and Eq. [1] in Eq. [17]

$$\frac{1}{\bar{\rho}} = e \cdot \int_0^1 \mu\,(N_0 \text{ erfc } zu - A) \cdot [N_0 \text{erfc}(zu) - A] \cdot du \qquad [18]$$

where $z = w/2\sqrt{Dt}$. The value of z is determined by assuming Eq. [1] as a first approximation for $x = w$, and solving for z by Newton's iteration method. This procedure defines an effective diffusion coefficient D, which has the advantage of making the resistivity a function only of the initial and surface concentrations. It will be shown later on that Eq. [1] does not give a true picture of the impurity distribution in the region close to the junction, and therefore the effective diffusion coefficient will not be a true value. However, diffusion coefficients of group V elements in germanium, published by different authors (6-10), vary within rather wide limits. Therefore, for the problem at hand, the effective D-value is certainly as good as one of the published values.

The complementary error functions used in the calculations were evaluated by means of the Rand approximation (21) of the form:

$$\text{erfc } y = \frac{2}{\sqrt{\pi}} \int_y^\infty \exp(-v^2)\, dv =$$

$$[1 + a_1 y + a_2 y^2 + a_3 y^3 + a_4 y^4 + a_5 y^5]^{-8}$$

An unsuccessful attempt was made to find a simple approximation for $\mu(n)$ or $n \cdot \mu(n)$. The latter was found to be approximately proportional to $(\log n)^4$, but the approximation was not close enough for computation. The values of $\mu(n)$ were therefore taken from Conwell's graph (17) in which they are plotted as a function of log n. The mobilities were found during computation by four-point Lagrange interpolation. The values of the average conductivity of the diffused layer, $1/\bar{\rho}$, were computed for various values of A and N_0. Results are shown in Fig. 2. The truncation and round-off errors in the calculation are negligible. Sources of possible errors are therefore the mobility data and the use of Eq. [1] to compute z.

Application of Methods and Discussion of Results

Numerous diffusion experiments were conducted in accordance with the conditions stated in the introduction. The source of the diffusing impurity and the wafers to be treated were kept together in a covered quartz boat, which was located in a vacuum tube furnace and heated to varied diffusion temperatures. The diffusion tube containing the boat was mantled by a graphite cylinder to pick up RF energy from an induction coil. Heating and cooling periods prior to and after the experiment were in the order of only 10 min. The diffusing donor im-

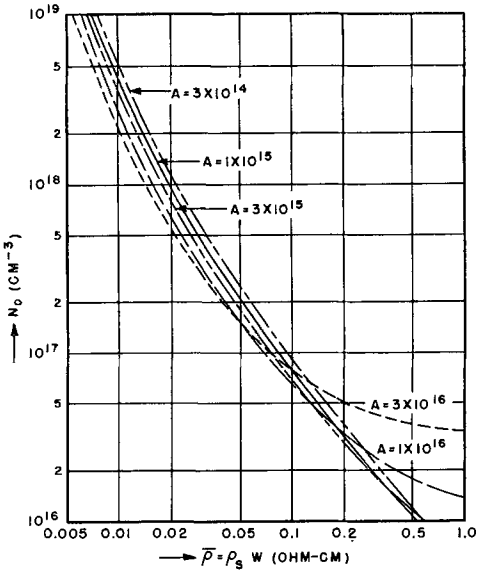

Fig. 2. Surface concentration N_0 vs. average resistivity $\bar{\rho}$ for several initial acceptor concentrations A; computed for diffused N-type layers with an erfc distribution in germanium.

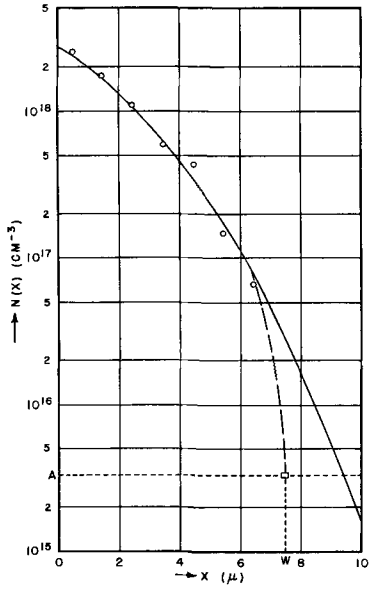

Fig. 3. Actual impurity distribution N(x) (circles, dashed line, and square) and ideal erfc distribution (solid line) vs. distance x from the surface of a diffused N-type layer on P-type germanium. Arsenic indiffusion: 1 hr at 800°C.

purity was arsenic obtained by evaporation from powdered master alloys containing arsenic in germanium.

Numerical values of the diffusion coefficients were based on data given by Smits (6); only in the computer approximations were effective D-values used. Junction depths were determined by angle lapping the diffused sample, depositing copper to delineate the junction, and subsequently making interference depth measurements (11). The average mobilities needed for solution by methods 2 and 3 were estimated from the average resistivity, again using the mobility data published by Conwell. In one case, the mobility was determined experimentally by Hall measurement on the diffused layer.

Experimental data and results of the calculations for 13 samples diffused in various runs are listed in Table I. On comparing the surface concentrations shown in the last four columns of the table, the most striking fact is that all values obtained by direct evaluation of the erfc equation (method 1) are unreasonably small. In order to investigate this phenomenon further, a few diffused layers have been analyzed by a method which has been mentioned by Smits (4). It consists of etching away the diffused layer in small steps and taking four-point-probe conductivity measurements between steps. In this way the average donor concentrations for each individual sublayer can be evaluated. In the immediate neighborhood of the junction, measurements are not possible, because the resistance of the remaining and extremely thin layer becomes very high and unreproducible.

An example of such a layer analysis is shown in Fig. 3. The circles indicate concentrations derived from measurements. The solid line is an erfc curve, calculated to fit the experimental points most closely.

Table I. Parameters of germanium diffused with arsenic

Sample No.	Diffusion time, min	Diffusion temp, °C	A[a], 10^{15}/ccm	w[b], 10^{-4} cm	ρ_s[c], ohm/sq	Surface concentration N_0 10^{17}/ccm Calculated by methods 1	2	3	4
H5-48-34	60	800	3	7.5	11.3	0.6	36	17	54
H5-61-36	360	700	3	5.6	17.6	1.2	20	15	36
V21-30-46	60	800	2	5.8	29.3	0.2	—	4.4	12
P1-47	60	750	5	2.6	120	0.2	—	1.7	3.5
P1-48	40	750	5	1.5	154	0.1	—	2.1	5.6
P1-49	40	750	5	1.5	169	0.1	—	1.8	4.8
P1-50	40	750	5	1.5	210	0.1	—	1.4	3.4
P1-51	242	800	10	10.6	22.9	0.6	2.7	2.6	4.7
P1-52	241	800	10	10.4	30.9	0.6	3.3 5.8[d]	1.8 4.0[d]	3.0
SM1-53	30	750	1.5	2.0	115	0.1	—	2.6	7.0
SM1-54	61	800	1.5	6.6	65	0.2	—	1.3	2.6
SM1-55	37	800	1.5	3.8	90	0.1	—	1.5	3.7
SM1-56	45	800	1.5	3.8	116	0.1	—	1.0	2.5

[a] Initial acceptor concentration.
[b] Depth at which A = donor concentration $N(w)$.
[c] Sheet resistivity.
[d] Derived from Hall measurements.

The small square indicates the depth where the junction was determined to be located, using the angle lapping technique. From this figure, it can be seen that the true impurity distribution in the vicinity of the junction deviates strongly from the erfc curve; the true distribution in this vicinity is indicated by a dashed line. This deviation is larger than a possible error in the junction depth determination.

Other samples which have been investigated in the same way gave similar results. In the numerical evaluation of Eq. [3], too small a value of w will give an erfc value which is too high and, therefore decrease N_0. This effect has been observed in all cases and, therefore, it must be concluded that for diffusion conditions, as explained previously, the resulting impurity distribution follows the erfc curve in the major part of the layer, but deviates strongly in the neighborhood of the junction. Since the determination of the surface concentration by method 1 depends strongly on the validity of the erfc law exactly at the junction, this method is not suitable for a reasonable estimate of N_0.

The mechanism which causes this deviation of the impurity distribution is not fully understood. On a few samples, which had been used for a layer analysis, the acceptor concentration A was determined by Hall measurement after the diffused layer had been etched off completely. It was found that A was larger than it had been prior to diffusion, in one extreme case by a factor of two. This may be an indication of simultaneous indiffusion of copper during the diffusion process. It is well known that copper is a rapidly diffusing acceptor impurity in germanium, and the complete exclusion of traces of copper from the surface of the sample during the cleaning operations is extremely difficult (22). Copper atoms in the order of 10^{16}/ccm in the layer may at least partially account for the observed deviation in the distribution of excess donors. Near the surface the contamination with copper is negligibly small compared to that with arsenic. In greater depths, however, the arsenic concentration decreases and eventually becomes even smaller than the copper concentration. This happens close to the junction, and that is the region where the deviations appear.

The fact that the impurity distribution does not exactly follow the erfc law raises the question of how this deviation affects the other methods of calculation. There is obviously no influence on the differential etching method because all measurements involve only the region nearest to the surface of the diffused layer. The accuracy of this method therefore depends entirely on the accuracies of the estimate of the mobility and the thickness of the etched-off layer. Results are nearly independent of the value of the diffusion coefficient, since in Eq. [8], D occurs in a second order term only. This deviation certainly influences the results of methods 3 and 4 in some degree. However, these methods involve integration over all donors in the diffused layer. The small region near the junction, where the deviation from the erfc law becomes noticeable, does not contribute a substantial fraction of the total integral. Therefore, the effect of this deviation will be minor.

The accuracy of methods 2, 3, and 4 is limited mainly by the lack of precise information about the electron mobility in various parts of the diffused layer. The mobility data of Conwell, used for most of the calculations, refer to samples of homogeneous doping with no concentration gradient and as little compensated impurities as possible. Therefore, these values may not hold well for the diffused layers. For example, the electron mobilities for concentrations between 10^{19} and 5.10^{17}/ccm should range from 3000 to 1500 cm^2/v sec, according to Conwell. The average Hall mobility, however, has been measured on a sample of corresponding concentrations and was found to be only 930 cm^2/v sec. Because of the mobility values used for most of the calculations, results may be in error by a factor in the order of two. On the other hand, it may very well be that the experimental mobility value is too low, because the Hall measurements were made on N-type layers adjoining P-type bulk material, and the measured voltage depends on the effectiveness of the junction as an insulator between different regions. If a small leakage current passes through the junction, the Hall voltage will be affected by the presence of holes in the P-type region.

The rather crude assumption of a constant mobility throughout the entire layer is reflected in the last two columns of Table I. All data obtained according to method 3 are smaller than those of method 4 by a factor of about 2.5, whereas the values of the differential etching method are somewhere in between.

On comparing the surface concentrations of different samples calculated by the same methods, minor differences will be noted. These differences are due to the fact that master alloys with slightly varying amounts of arsenic, in the order of 10^{19}/ccm, have been used as sources of the diffusant. The first two samples listed in Table I, i.e., those bearing the designation "H5—", were diffused in the presence of a master alloy which was richer in arsenic than the other sources by a factor of about 10.

Summary and Conclusions

Four methods have been investigated in order to obtain data of the surface concentrations in diffused layers. These methods are not equally suitable for the purpose. The first method involves a junction depth measurement and the assumption of an erfc distribution extending throughout the entire layer and into the junction region. It leads to numerical results which disagree by more than one order of magnitude with resistivity and Hall measurements and with all calculations based on these measurements. The complete experimental analysis of diffused layers, by determining sheet conductivities and excess electron concentrations of individual partial layers, indicates that the distribution of donors in the neighborhood of the junction deviates from the erfc distribution. Therefore, the erfc equation fails to give true values of the surface concentration.

The remaining three methods rely on the fact that the conductivity of the diffused layer is related to the number of excess electrons in the N-type region. The fraction of the conductivity which is due to

carriers in the deviating part of the distribution curve is either not involved (method 2), or is negligibly small compared to the total quantity (methods 3 and 4). Therefore, these methods are not sensitive to deviations of the donor distribution in the region of the junction. Their accuracy depends, rather, on how closely the true relation between excess electron concentration and conductivity of the layer can be approximated. These methods allow fairly accurate calculations of the surface concentration. The major limitation of method 3 is that it employs the concept of a constant mobility. However, the relation between electron concentration and conductivity requires knowledge of electron mobilities in the diffused layer, and these are amenable to experimental determination only to a limited extent. Therefore, in the preceding calculations, the electron mobilities had to be estimated by comparison with data referred to germanium of similar but not exactly the same impurities as in the diffused layers. Consequently, these three methods can give only an estimate of the surface concentration. Considering the uncertainty in the mobility data as the main source of error, the surface concentrations obtained by either method 2 or 4 should not deviate from the true value by a factor larger than 2.

Manuscript received Jan. 12, 1960.

Any discussion of this paper will appear in a Discussion Section to be published in the June 1961 JOURNAL.

REFERENCES

1. L. P. Hunter, "Handbook of Semiconductor Electronics," Chap. 7, p. 12, McGraw-Hill Book Co., Inc., New York (1956).
2. F. J. Biondi, "Transistor Technology," Vol. III, p. 64ff, D. Van Nostrand Co., Inc., New York (1958).
3. *Ibid.*, p. 245 ff.
4. F. M. Smits, *Proc. IRE*, **46**, 1055 (1958).
5. *Ibid.*, p. 1049 ff.
6. *Ibid.*, 1052.
7. K. B. McAfee, W. Shockley, and M. Sparks, *Phys. Rev.*, **86**, 137/38 (1952).
8. C. S. Fuller, *Phys. Rev.*, **86**, 136/37 (1952).
9. J. A. Burton, *Physica*, **20**, 845 (1954).
10. W. Bösenberg, *Z. Naturforsch.*, **10A**, 285 (1955).
11. W. L. Bond and F. M. Smits, *Bell System Tech. J.*, **35**, 1209 (1956).
12. L. B. Valdes, *Proc. IRE*, **42**, 420 (1954).
13. F. M. Smits, *Bell System Tech. J.*, **37**, 711 (1958).
14. O. Lindberg, *Proc. IRE*, **40**, 1414 (1952).
15. L. J. van der Pauw, *Philips Research Repts.*, **13**, 1 (1958).
16. H. E. Bridgers, J. H. Scaff, and J. N. Shive, "Transistor Technology," I, p. 79, D. van Nostrand Co., Inc., New York (1958).
17. E. M. Conwell, *Proc., IRE*, **40**, 1331 (1952).
18. P. P. Debye and E. M. Conwell, *Phys. Rev.*, **93**, 693 (1954).
19. J. Kaye, *J. Math. Phys.*, **34**, 119 (1955).
20. G. Backenstoss, *Bell System Tech. J.*, **37**, 699 (1958).
21. C. Hastings, Jr., "Approximations for Digital Computers," p. 186, Princeton University Press, Princeton, N. J. (1955).
22. L. P. Hunter, "Handbook of Semiconductor Electronics," Chap. 7, p. 15, McGraw-Hill Book Co., Inc., New York (1956).

A Study of the Thorium-Tungsten-Boron System

Douglas T. Pitman and Dilip K. Das

Spencer Laboratory, Raytheon Company, Burlington, Massachusetts

ABSTRACT

A phase diagram for the Th-W-B system has been determined by x-ray diffraction of samples fired to a brightness temperature of 1800°C and furnace-cooled. A ternary compound was found with a probable composition of $ThWB_4$. This compound is monoclinic with lattice parameters: a = 12.25, b = 3.75, c = 6.14Å, and $\beta = 104.1°$. The stability of the thorium and tungsten borides and their reaction with ThO_2 were also investigated.

The hexaborides of the alkaline earth and rare earth metals and thorium with the general formula MB_6 have been investigated by Lafferty (1). He found that these borides had certain desirable properties that might make them good thermionic emitting materials. The hexaborides were found to be unstable in the presence of refractory metals such as Mo and W, and certain precautions had to be used to prevent their decomposition. However no work has been reported on the Th-W-B ternary system and the stability of the tungsten borides and thorium borides in the presence of thorium or boron. This information would be of importance for the design and conception of high-temperature cathodes and the interpretation of the emission mechanisms. The phase diagram of W-B has been reported by Kiessling (2) and Brewer, *et al.* (3). It has four intermediate phases: W_2B_5, W_2B, and a high- and low-temperature form of WB. The Th-B system has been reported in the literature by various authors (3-6) and has two intermediate phases: ThB_4 and ThB_6. Th and W do not form any compounds or solid solution and their eutectic composition is about 8 atomic per cent (a/o) tungsten with a melting point of 1475°C (7). Also of interest is the role of ThO_2 as an impurity in the thorium and its effect on the phases present in the ternary diagram.

Experimental

The ternary compositions were synthesized by reactive sintering of pressed powder compacts. The boron obtained from U. S. Borax Research Corporation had a maximum impurity of less than 0.4%. Westinghouse thorium had a maximum impurity

Table I. Spectrographic analysis of B, Th, W, and ThB_4

o/o	B	Th	W	ThB_4
Al		0.3-0.03	0.001-0.0001	0.3-0.03
B		0.003-0.0003		
Ba			0.001-0.0001	
Ca	0.001-0.0001	0.3-0.03	0.01-0.001	0.001-0.0001
Cr		0.001-0.0001	0.001-0.0001	0.003-0.0003
Cu	0.01-0.001	0.01-0.001	0.01-0.001	0.001-0.0001
Fe	0.01-0.001	0.1-0.01	0.03-0.003	0.1-0.01
Ga		0.003-0.003		
K			0.01-0.001	
Mg	0.01-0.001	0.3-0.03	0.01-0.001	0.003-0.0003
Mn	0.1-0.01	0.03-0.003	0.03-0.003	0.003-0.0003
Na			0.001-0.0001	
Ni			0.003-0.0003	
Pb		0.01-0.001	0.001-0.0001	
Si	0.3-0.03	1.00-0.10	0.01-0.001	0.03-0.003
Sr			0.001-0.0001	
Ti	0.003-0.0003		0.003-0.0003	
Zn			0.001-0.0001	

content of less than 2.2%. X-ray diffraction analysis showed that there was about 1.0% thoria in the thorium. The tungsten was obtained from Fansteel Metallurgical Corporation with a purity better than 99.8%. The particle size of these materials was less than 100 mesh. Spectrographic analyses of the starting materials B, Th, and W are given in Table I.

Ten-gram samples were weighed out and thoroughly spatulated. Five grams was then pressed at 10,000 psi to form a compact with a ¼ in. diameter and a thickness of about ½ in. These compacts were vacuum-fired to a brightness temperature of 1800°C for ½ hr and furnace cooled at a pressure of 10^{-4}-10^{-5} mm Hg. The sample temperature dropped from 1800° to 700°C in about 90 sec after the heat was turned off.

The small furnace in which the compacts were fired was placed inside a vacuum bell jar. The heater was a 1 in. diameter by 1½ in. long helix of six turns made from 0.080 in. tungsten wire. Three molybdenum heat shields were mounted around the heater coil. A viewing port was cut into the shields to allow the temperature of the sample to be measured with an optical pyrometer. The sample rested on a ThO_2 disk of a special design to give a minimum contact area between the compact and the disk. The disk was placed on a molybdenum pedestal that brought the sample up to the middle of the heater coil directly in line with the viewing port in the molybdenum radiation shields. This experimental arrangement avoided contamination of the sample and the loss of boron by diffusion into the container. Temperatures were measured with a L&N optical pyrometer, and all temperatures reported in the body of the paper are brightness temperatures. As many as three compacts could be fired simultaneously without physical contact between the individual specimens.

X-ray diffractometer traces or Debye-Scherrer powder photographs were made of all the fired samples in order to identify the crystalline phases. The powder photographs were taken with a 114.59 mm radius camera. Filtered copper Kα radiation was used for all x-ray work. Several samples were examined in the diffractometer using a high temperature camera (8) capable of reaching 2000°C in a vacuum of 10^{-5} to 10^{-6} mm Hg.

Table II. Phase analysis of Th-W-B system

Sample No.	Composition (mole %) intended Th	W	B	Heat treatment Br Temp, °C	Time, min	Crystalline phases present as identified by x-ray diff.*
1	7.9	61.4	30.7	1800	30	W_2B, Th, W
2	25.0	50.0	25.0	1800	30	W_2B, Th, W
3	49.5	32.9	17.6	1800	30	Th, W_2B, W
4	50.0	25.0	25.0	1800	30	Th, W_2B
5	50.0	20.0	30.0	1800	30	Th, W_2B
6	50.0	14.4	35.6	1800	30	Th, W_2B
7	35.0	10.0	55.0	1800	30	$ThWB_4$, Th, ThB_4
8	20.0	30.0	50.0	1800	30	W_2B, $ThWB_4$, Th
9	20.0	20.0	60.0	1800	30	$ThWB_4$, W_2B
10	12.5	25.0	62.5	1800	30	WB, $ThWB_4$, ThB_4
11	15.1	23.9	61.0	1800	30	$ThWB_4$, WB
12	16.6	16.7	66.7	1800	30	ThB_4, $ThWB_4$, WB
13	18.0	18.5	63.5	2100	30	$ThWB_4$, WB
14	22.5	15.0	62.5	2100	30	$ThWB_4$
15	23.5	12.5	64.0	1800	30	$ThWB_4$, ThB_4
16	21.0	10.5	68.5	1800	30	$ThWB_4$, ThB_4
17	17.3	13.8	68.9	1800	30	ThB_4, $ThWB_4$, WB
18	21.0	13.0	66.0	1800	30	$ThWB_4$, ThB_4, WB
19	25.0	3.0	72.0	1800	30	ThB_4, $ThWB_4$
20	18.7	6.0	75.3	1800	30	ThB_4, $ThWB_4$, WB
21	12.7	11.1	76.2	1600	30	W_2B_5, ThB_4
22	13.6	4.7	81.7	1600	30	ThB_6, ThB_4, W_2B_5
23	12.0	20.2	67.8	2100	30	ThB_4, WB

* All the samples have ThO_2 present in an amount of not more than 3%.

Results and Discussion

The phase equilibrium data used to determine the Th-W-B ternary diagram are given in Table II. This table lists the composition in atomic per cent, the firing temperature and time, and the crystalline phases as identified by x-ray diffraction.

Figure 1 is the proposed ternary diagram as determined by this experiment.

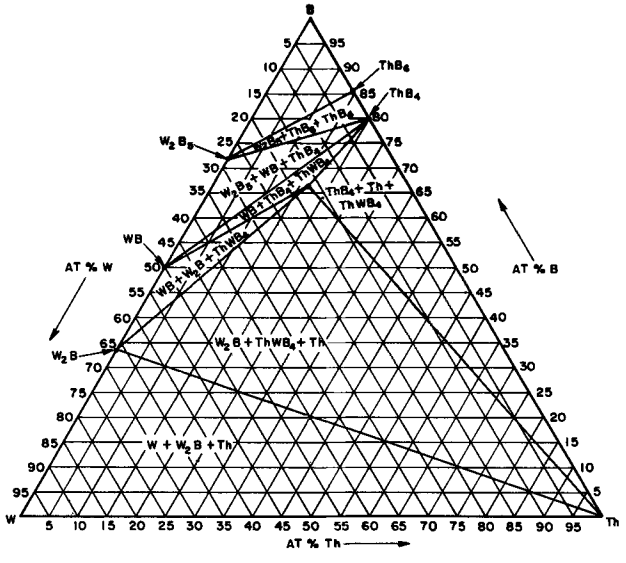

Fig. 1. Phase diagram of the system Th-W-B based on samples fired at 1800°C and furnace cooled.

It is known from the binary phase diagrams that the homogeneity ranges of WB and W_2B_5 are 48-51 a/o and 66.6-68.0 a/o B, respectively, while the homogeneity ranges of the other existing phases are too narrow to be measured. The assumption was made that all the compounds and elements in the binary systems could be represented as points on the ternary phase diagram.

The initial samples were chosen in order that their composition would fall on the intersections of lines drawn in the ternary field for all possible combinations of phase co-existence. This reduced the number of fired samples needed to establish the phase diagram. The analysis of these strategic samples showed which two phases could or could not co-exist, thus determining the locations and contents of every three-phase field, barring the existence of ternary compounds in these regions.

A ternary compound was found which could be represented by the formula $ThWB_4$. A number of samples were required to ascertain its composition. This phase was found to co-exist with W_2B, WB, ThB_4, or Th. Since the lattice constants did not vary with composition the homogeneity range is believed to be very narrow.

The ternary phase has the approximate composition $ThWB_4$ based on the following evidence. The sample, 50 m/o ThB_4 and 50 m/o W, was fired in the usual manner. Weight loss during the firing was found to be 2 w/o. The composition of the evaporant was found to be Th and B. X-ray diffraction and metallographic examination of this sample showed it to be primarily the ternary phase with a combined total of less than 2 w/o ThO_2 and WB. Also using the molecular formula, $ThWB_4$, and calculating the theoretical density on the basis of two molecules per unit cell, (crystal structure studies are described in the next paragraph), good agreement is obtained between the calculated and measured density. For the reasons above the most probable composition is $ThWB_4$.

Small crystals of the ternary phase could be obtained on the surface of samples which were in the vicinity of $ThWB_4$ in the phase diagram by firing them to 2100°C. Precession photographs were made using a small crystal 0.05 mm by 0.15 mm (Mo Kα, λ = 0.7107 Å). These photographs showed $ThWB_4$ to be monoclinic with a = 12.25 Å, b = 3.75 Å, c = 6.14 Å and β = 104.1°. The probable space groups are P_2, $P_{2/m}$, or Pm. The x-ray density, assuming two molecules per unit cell, is 5.6 g cm^{-3} while the measured density is 5.8 g cm^{-3}. The pycnometric value of the density is high because of the presence of a small amount of WB. The melting point of this phase is 2175° ± 25°C which is lower than the melting points of the surrounding borides: ThB_4, W_2B, and WB.

The diffraction data and the calculated hkl values for monoclinic $ThWB_4$ are presented for comparison along with those of ThO_2 and ThB_4 in Table III. It was also found that other refractory metals such as Mo or Re react with ThB_4 to form ternary compounds which are isomorphous with $ThWB_4$.

In the presence of W, ThB_4 is unstable with the result that W_2B is always the first product formed along with free Th. This reaction was examined by means of the high-temperature camera mounted on the Geiger counter diffractometer. It was found that in a 50 m/o W and 50 m/o ThB_4 sample, W_2B first appeared at a temperature of 1100°C with a decrease in the intensity of ThB_4 and W lines. As the temperature was raised the amount of W_2B continued to increase until at 1600°C the W_2B began to decrease with the formation of $ThWB_4$. Holding the sample at this temperature for 1 hr showed the components to be $ThWB_4$ with a small amount of W_2B. As the temperature was further increased to about 1800°C WB started to appear and $ThWB_4$ decreased slightly in intensity indicating that both B and Th were evaporating off from the surface.

Table III. X-ray diffraction data for $ThWB_4$, ThB_4, and ThO_2

$ThWB_4$			ThB_4			ThO_2*		
hkl	I/I_o	d	hkl	I/I_o	d	hkl	I/I_o	d
200	3	5.92	110	4	5.159			
			001	61	4.091			
010	41	3.748	200	53	3.636			
			210	77	3.252	111	100	3.234
			111	7	3.200			
400	100	2.963	201	61	2.718	200	35	2.800
211	5	2.655	211	100	2.546			
			310	14	2.301			
$40\bar{1}$, $40\bar{2}$	30	2.423	221	32	2.177			
$41\bar{1}$	81	2.324	002	19	2.046			
$51\bar{1}$, $60\bar{1}$	32	2.033	311	21	2.008	220	58	1.980
			112	4	1.905			
103, 402	9	1.880	321	7	1.809			
020	20	1.873	202	19	1.783			
601	12	1.753	410	40	1.765			
			212	32	1.731			
113	3	1.682	330	12	1.714	311	64	1.689
$61\bar{2}$	7	1.676	411	35	1.619	222	11	1.616
$60\bar{3}$	9	1.612	222	7	1.601			
$32\bar{1}$	18	1.587	331	19	1.581			
$71\bar{1}$, $42\bar{1}$	24	1.582	312	5	1.528			
$80\bar{1}$	22	1.532	430	2	1.455			
800	3	1.483	322	4	1.436			
$70\bar{3}$	12	1.480	510	3	1.428	400	8	1.400
711	20	1.422	431	7	1.371			
			511	7	1.347			
			412	32	1.337			
			332	16	1.314	311	26	1.284

* Data from Swanson and Tatge, National Bureau of Standards Circular 539.

Boron reacted with ThO_2 to form ThB_6 at a temperature of less than 1600°C. When the temperature was raised to 2100°C, ThB_6 disappeared and was replaced by ThB_4, with two moles of boron reacting with excess ThO_2.

Firing ThB_4 in contact with ThO_2 at 2300°C resulted in no reaction, reduction, or solid solution,

contrary to the postulations by Brewer, *et al.* (3). The phase ThX_2, which was reported by Brewer to be a solid solution between ThO_2 and ThB_4, was not found in any of the samples examined during this investigation, and it is quite probable that this phase involves some element other than B.

ThB_6 fired to 1600°C in vacuum showed no decomposition. The apparent instability that Brewer proposes for ThB_6 may be partly due to diffusion of boron into the molybdenum boride crucible that he used.

WB fired in contact with ThO_2 to 2100°C showed no apparent reduction of the ThO_2. X-ray examination revealed WB, W_2B, and ThO_2 to be present in the sample.

X-ray examination of mixtures of W_2B and ThO_2 fired to 1800°C showed only W_2B and ThO_2.

$ThWB_4$ was found to be inert to ThO_2 at a temperature of 2100°C.

During this investigation pure ThB_4 and ThB_6 were prepared. The preparation of ThB_4 by firing powder compacts of the elements was found to be mainly a problem of obtaining equilibrium. This was achieved by regrinding and refiring the sample. In the case of ThB_6, boron was lost when the reaction became strongly exothermic at 1050°-1150°C. To compensate for the loss of boron in the resultant ThB_6-ThB_4 mixture, a calculated amount of B was added to convert all the samples to ThB_6 on refiring at 1800°C. The calculations were based on a calibration curve obtained with the x-ray diffractometer from known mixtures of the two compounds. The impurities of the synthesized ThB_4 and ThB_6 were those of the elemental starting materials although substantially reduced by the vacuum firing. The amount of ThO_2 which was the main impurity in the Th has been practically eliminated. The spectrographic analysis of the ThB_4 is included in Table I for comparison.

Acknowledgments

The authors are indebted to Dr. L. Lesensky for his encouragement and helpful discussion during the course of this investigation. They also wish to acknowledge the efforts of Dr. L. E. Alexander who took and interpreted the precession photographs of the ternary phase and Mr. N. J. Aubert and Mr. W. Y. Tye for their skilled assistance.

Manuscript received Aug. 21, 1959. Portions of this paper have been presented at the Nineteenth Annual Conference on Physical Electronics held at the Massachusetts Institute of Technology on March 26-28, 1959.

Any discussion of this paper will appear in a Discussion Section to be published in the June 1961 JOURNAL.

REFERENCES

1. J. M. Lafferty, *J. Appl. Phys.*, **22**, 299 (1951).
2. R. Kiessling, *Acta. Chem. Scand.*, **1**, 893 (1947).
3. L. Brewer, D. L. Sawyer, D. H. Templeton, and G. H. Dauben, *J. Am. Ceram. Soc.*, **34**, 173 (1951).
4. A. Zalkin and D. H. Templeton, *Acta Cryst.*, **6**, 269 (1953).
5. R. Kiessling, *Acta Chem. Scand.*, **4**, 163, 209 (1950).
6. F. Bertaut and P. Blum, *Compt. rend*, **234**, 2631 (1952).
7. H. A. Wilhelm, A. S. Newton, A. H. Doane, and G. Neher, "Thorium Metallurgy," CT-3714 (February 1946).
8. D. K. Das and D. T. Pitman, Pittsburgh Diffraction Conference (Nov. 1959).

Theory of Faradaic Distortion

K. B. Oldham

King's College, University of Durham, Newcastle upon Tyne, England

ABSTRACT

The passage of a pure a.c. across an electrode gives rise to a cell potential containing sinusoidal components of frequencies which are multiples of the fundamental. The first harmonic is predominant and expressions are here derived for its amplitude and phase angle. The magnitude of the effect is similar to that of faradaic rectification, but its measurement may offer advantages over the latter in the determination of the kinetic parameters of some electrode reactions. The effect of the double layer is considered, and an apparatus is described which enables faradaic admittance, rectification, and distortion to be measured simultaneously.

Two effects of the passage of an alternating current across an electrode have been employed to determine the rates of the two electrode reactions and their dependence on potential. The first of these effects, faradaic admittance (1), is usually exploited by placing the cell[1] in one arm of an a-c bridge: the kinetic parameters are calculated from the magnitudes of the resistance and capacitance which must be inserted into a balancing arm to achieve a null signal across the bridge (2, 3). The second effect, faradaic rectification (4), is assessed by measuring the change in d-c potential which the alternating current produces, either directly (5, 4) or by supplying the cell with an intermittent high-frequency signal, the resultant square-wave potential being nullified by application of an intermittent current (6, 7). A third effect is now described: this too may be employed for the determination of the kinetic parameters of the electrode reaction.

[1] The design of the cell is such that one electrode remains depolarized. One method of achieving this result is to employ two electrodes similar in all respects except area, of which one electrode has incomparably more than the other. The equilibrium potential of such a cell is, of course, zero and therefore if the passage of a current through the cell causes a change v in the potential of the smaller electrode, the cell potential is directly equal to v plus an ohmic potential V_o caused by the passage of the current through the resistance R_s of the cell solution. The potential across a cell having chemically dissimilar electrodes is, however, equal to the sum of three terms, $(v + V_o + V_e)$, V_e being the equilibrium potential of the polarizable electrode versus the reference (depolarized) electrode.

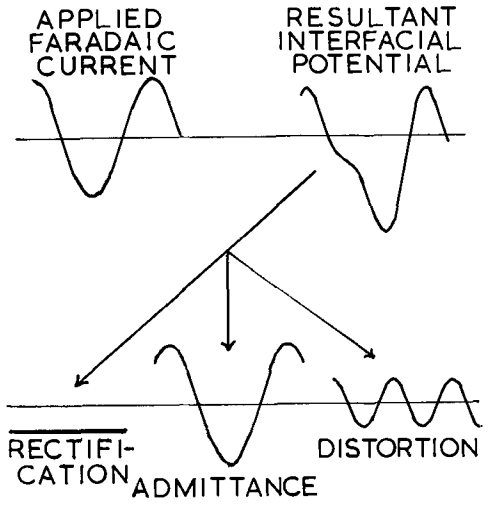

Fig. 1. Wave forms of the applied faradaic current (a pure sine wave) and the resultant interfacial potential. The latter contains three major components having the wave forms shown in the three lower diagrams.

If the instantaneous anodic magnitude of the faradaic component of the applied alternating current is $I \cos \omega t$, its effect is to change the electrode potential from its equilibrium value E_e to $(v + E_e)$. It will be shown in the *Mathematical Derivation* below that v has the form

$$v = \Psi + V \cos(\omega t + \theta) + V_2 \cos(2\omega t + \theta_2) + (\text{much smaller terms}) \quad [1]$$

and the unknowns Ψ, V, θ, V_2, and θ_2 in this equation will be evaluated there. The upper two diagrams in Fig. 1 show typical plots of the quantities $I \cos \omega t$ and v against time; the three lower diagrams correspond to the three leading terms on the right hand side of Eq. [1] into which v can be resolved. The d-c potential Ψ, which has been termed the redoxokinetic potential (8), arises from faradaic rectification. The ratio V/I is termed the faradaic impedance of the electrode and since θ turns out to take values between 0 and $-\pi/4$, this impedance is best represented by a pure resistance in series with a Warburg impedance (1). The third term on the right hand side of [1] arises in the same way as Ψ: from the nonlinearity of electrode reaction rate with potential, and it is suggested that the effect giving rise to this harmonic content in v be termed "faradaic distortion." The primary object of the present communication is the derivation of an expression for V_2, the amplitude of the faradaic distortion.

Electrode Reaction

Established expressions for the cathodic and anodic currents associated with the electrode reaction

$$\mathrm{Ox} + ne^- \rightleftharpoons \mathrm{Rd}$$

are

$$\vec{i} = nA\mathbf{F}ka_o \exp\{-\alpha n\mathbf{F}E/RT\} \quad [2]$$

and

$$\overleftarrow{i} = nA\mathbf{F}ka_o' \exp\{(1-\alpha)n\mathbf{F}E/RT\} \quad [3]$$

where a_o and a_o' are the activities of Ox and Rd at the electrode surface. E is the potential of the electrode vs. the standard Ox/Rd electrode and k is a standard rate constant (9), being equal to the actual rates of both forward (cathodic) and reverse reactions at a standard Ox/Rd electrode in equilibrium. The term α denotes the transfer coefficient of the forward reaction.[2]

If equilibrium is established at the electrode, the surface activities will be equal to a and a', the bulk activities of Ox and Rd; moreover, the forward and reverse currents are then equal to each other and to the quantity termed the equilibrium exchange current I_e. Therefore,[3]

$$a \exp\{-\alpha n\mathbf{F}E_e/RT\} = I_e/nA\mathbf{F}k = a' \exp\{(1-\alpha)n\mathbf{F}E_e/RT\} \quad [4]$$

For many purposes I_e is a more convenient kinetic parameter than k, but it must be appreciated that the equilibrium exchange current (unlike the standard rate constant k) is itself a function of the activities of Ox and Rd and, to a lesser extent, is also dependent on the concentrations of other constituents of the solution.

In the next three sections, cases are considered in which Rd is a pure phase of invariant activity. The reaction $Cu^{2+} + 2e^- \rightleftharpoons Cu$ occurring at a copper electrode would be an example: in such situations it is usual to set the invariant activity equal to unity.

The bulk activity a of Ox may be set equal to fC, where C is the concentration (mole cm^{-3}) of Ox in the bulk of the cell solution[4] and f is its activity coefficient.[5] In such cases equation [4] shows that the relationship between I_e and C is $I_e = nA\mathbf{F}k(fC)^{1-\alpha}$.

The section *Soluble Reductant Case*, below, deals with the more general case in which the activity of Rd is not constant. Examples of such reactions include $Fe^{3+} + e^- \rightleftharpoons Fe^{2+}$ and $Cd^{2+} + 2e^- \rightleftharpoons Cd(Hg)$. For such cases Eq. [4] gives $I_e = nA\mathbf{F}k(f'C')^{\alpha}(fC)^{1-\alpha}$, where C' is the bulk concentration and f' the activity coefficient[5] of Rd.

Mathematical Derivation

Let it be supposed that at time $t = 0$ the circuit is made and that for $t > 0$ the faradaic cell current is given by

$$i = I \cos \omega t + (\text{transients important only at small } t) \quad [5]$$

If r represents the dimension normal to the electrode

[2] Equations [2] and [3] may be applied directly only to electrode reactions which take place in a single step. Nevertheless, these equations often apply in cases where the reaction mechanism is complex, although the terms k and α no longer have the simple significances ascribed to them in the text. Approximate expressions for the apparent k and α terms may be deduced by constructing the mechanism's equivalent reaction pair (10).

[3] Note that Eq. [4] also embodies the Nernst equation for the system.

[4] The present theory is limited to cases in which the cell solution is of high ionic strength. Furthermore, if Ox is an ion, C must be much less than the ionic strength. These restrictions are needed to ensure that transport of Ox shall be by diffusion and not by migration. A high concentration of supporting electrolyte is also useful in reducing R_s and in keeping the double layer capacity constant.

[5] The activity coefficient of Ox (and also that of Rd in cases where the latter dissolves in the cell solution) will be effectively constant in a solution of high ionic strength,[4] even though the concentration of Ox is subject to local variation. Moreover, if a series of experiments is conducted in which the bulk concentration C of Ox is varied, it would be natural to maintain the ionic strength constant throughout the series: thus f would be constant from one experiment to the next as well as within any one experiment.

surface,[6] $C(r, t)$ will signify the concentration of Ox at a distance r at time t. It will be assumed that the surface concentration can be represented by the Fourier series

$$C(0, t) = \sum_{j=0}^{\infty} \mu_j \cos j\omega t + \sum_{j=1}^{\infty} \lambda_j \sin j\omega t \qquad [6]$$

where the μ's and λ's are undetermined coefficients.

Fick's second law of diffusion, $\partial C(r, t)/\partial t = D\partial^2 C(r, t)/\partial r^2$, must apply to the system,[4] D being the diffusion coefficient of Ox. Solution of this equation under the boundary condition [6] and the initial condition $C(r, 0) = C = C(\infty, t)$ is[7]

$$C(r, t) = C + \mu_o \operatorname{erfc} [r/2(Dt)^{1/2}]$$

$$+ (2/\pi^{1/2}) \sum_{j=1}^{\infty} \int_{r/2(Dt)^{1/2}}^{\infty} \{\mu_j \cos (j\omega t - j\omega r^2/4Dp^2)$$

$$+ \lambda_j \sin (j\omega t - j\omega r^2/4Dp^2)\} \exp (-p^2)\, dp$$

On differentiation (13), this gives

$$\partial C(r, t)/\partial r = -(\pi Dt)^{-1/2} \exp (-r^2/4Dt) \sum_{j=0}^{\infty} \mu_j$$

$$+ (2/\pi^{1/2}) \sum_{j=1}^{\infty} \int_{r/2(Dt)^{1/2}}^{\infty} (j\omega r/2Dp^2) \cdot \exp (-p^2)$$

$$dp \{\mu_j \sin (j\omega t - j\omega r^2/4Dp^2) - \lambda_j \cos (j\omega t - j\omega r^2/4Dp^2)\} \cdot$$

which may be evaluated for $r = 0$, $t > 0$, since the integral then has a zero lower limit.[8] The expression thus obtained for the surface concentration gradient is

$$\partial C(0, t)/\partial r = -(\pi Dt)^{-1/2} \sum_{j=0}^{\infty} \mu_j$$

$$- \sum_{j=1}^{\infty} (j\omega/2D)^{1/2} \{(\mu_j + \lambda_j) \cos j\omega t - (\mu_j - \lambda_j) \sin j\omega t\}$$

From Fick's first law of diffusion, an expression may now be derived relating the concentration gradient at the electrode surface to the flux of Ox and hence to the anodic faradaic current in the form $i = -nA\mathbf{F}D\, \partial C(0, t)/\partial r$. Comparison of this equation with [5] shows that $\mu_j = 0 = \lambda_j$ for $j = 0$, $j \geq 2$ and that $\mu_1 = \lambda_1 = I/nA\mathbf{F}(2D\omega)^{1/2}$, whence [6] becomes

$$C(0, t) = C(1 + Q \sin \omega t + Q \cos \omega t) \qquad [7]$$

where $Q = I/nA\mathbf{F}C(2D\omega)^{1/2}$. Clearly, since $C(0, t)$ cannot be negative, $Q \leq 2^{-1/2}$; however, it will be convenient to place a more severe restriction on Q, *viz.* $Q \leq 0.1$.

[6] The electrode need not be planar provided its radius of curvature is everywhere large compared with the "diffusion layer thickness" (11). This latter quantity may be taken as the value of r at which the amplitude of the concentration oscillations has fallen to 1% of its surface value. Now, the concentration amplitude can be shown (2-4) to be proportional to $\exp[-r(\omega/2D)^{1/2}]$, and taking $D = 10^{-5}$ cm^2 sec^{-1}, $\omega/2\pi \geq 10$ cps, we see that the diffusion layer cannot exceed 2.5×10^{-3} cm in thickness. A lower limit to the radius of curvature might thus be set at 0.1 mm.

[7] The analogous problem in heat conduction is considered by Carslaw and Jaeger (12).

[8] Rejecting small values of t, the limit may be taken to approach zero before the integrand. The integration is then carried out with the aid of transformations akin to those discussed by Carslaw and Jaeger (14).

The current $I \cos \omega t$ must be equal to the difference $(\overleftarrow{i} - \overrightarrow{i})$ obtained by subtracting Eq. [2] from [3]. Therefore, since a' is equal to unity and f is constant,[5]

$$I \cos \omega t = nA\mathbf{F}k \exp \{(1 - \alpha)n\mathbf{F}(E_e + v)/RT\}$$

$$- nA\mathbf{F}ka[C(0, t)/C] \exp \{-\alpha n\mathbf{F}(E_e + v)/RT\}$$

This equation may be simplified by substituting for $C(0, t)$ from Eq. [7] and for E_e and k from [4]. The result is

$$I \cos \omega t = I_e \exp \{(1 - \alpha)n\mathbf{F}v/RT\}$$

$$-I_e(1 + Q \sin \omega t + Q \cos \omega t) \exp \{-\alpha n\mathbf{F}v/RT\} \qquad [8]$$

It will be convenient to define a new parameter y by $y = I/I_eQ$. This new parameter is dimensionless and can take values between 0 and $+\infty$; it is a measure of the ability of the electrode reaction to keep pace with the alternating electrode potential. At low y values the electrode is able to follow the potential variation, whereas at high values of y this is not possible and $C(0,t)$ assumes an almost constant value; the changeover between these two extremes occurs in the vicinity of $y = 1$.

Provided that $n\mathbf{F}v/RT << 1$, *i.e.*, if the total magnitude of the perturbation v never exceeds a few millivolts, a simplification of the exact Eq. [8] may be achieved by making series expansions of the two exponential terms and rejecting all but the first few members of these series. However, since both faradaic distortion and faradaic rectification are second order effects, the retention of only two terms, *viz.*

$$\exp \{-\alpha n\mathbf{F}v/RT\} \approx 1 - \alpha n\mathbf{F}v/RT \qquad [9a]$$

$$\exp \{(1 - \alpha)n\mathbf{F}v/RT\} \approx 1 + (1 - \alpha)n\mathbf{F}v/RT \qquad [9b]$$

is inadequate to give a reliable expression for v. Nevertheless, as a first approximation, it is instructive to insert the approximations [9] into Eq. [8]. This approach yields[9]

$$n\mathbf{F}v/RT \approx [(y + 1)Q \cos \omega t + Q \sin \omega t](1 + \alpha Q \sin \omega t + \alpha Q \cos \omega t)^{-1}$$

$$\approx [(y + 1)Q \cos \omega t + Q \sin \omega t](1 - \alpha Q \sin \omega t - \alpha Q \cos \omega t)$$

$$\approx (y+1)Q \cos \omega t + Q \sin \omega t - \tfrac{1}{2}\alpha(y+2)Q^2 - \tfrac{1}{2}\alpha yQ^2 \cos 2\omega t - \tfrac{1}{2}\alpha(y+2)Q^2 \sin 2\omega t \qquad [10]$$

Recalling that $Q \leq 0.1$ and that $0 < \alpha < 1$, inspection of Eq. [10] will show that the rms values of the two terms $(y+1)Q \cos \omega t$ and $Q \sin \omega t$ always account for more than 87% of the rms value of $n\mathbf{F}v/RT$. Therefore, approximation [9a] can be vastly improved by adding a third term in which $n\mathbf{F}v/RT$ is replaced by the two most important terms in [10], *i.e.*,

$$\exp \{-\alpha n\mathbf{F}v/RT\} = 1 - \alpha n\mathbf{F}v/RT + \tfrac{1}{2}\alpha^2[(y+1)Q \cos \omega t + Q \sin \omega t]^2$$

[9] It will be noted that the inclusion of additional terms in the binomial expansion of $(1 + \alpha Q \sin \omega t + \alpha Q \cos \omega t)^{-1}$ would have introduced additional harmonics (terms in $\sin 3\omega t$, $\cos 4\omega t$, etc.) of very small amplitude, but would not have affected the magnitude of any of the five final terms in [10] by more than 1%.

A similar improvement may be made to [9b] and if these amended equations are then inserted into expression [8], the following result can be obtained

$$n\mathbf{F}v/RT = (y+1)Q\cos\omega t + Q\sin\omega t$$
$$-\tfrac{1}{2}[(1+y+\tfrac{1}{2}y^2)-\alpha(y+y^2)]Q^2$$
$$+\tfrac{1}{2}[\alpha(y+y^2)-(y+\tfrac{1}{2}y^2)]Q^2\cos 2\omega t$$
$$-\tfrac{1}{2}(1+y-\alpha y)Q^2\sin 2\omega t + \text{terms in } Q^3$$

This expression for v is readily transformed into [1] and the five unknowns in the latter equation are thus found to be

$$\Psi = -(RTQ^2/4n\mathbf{F})(y+z+yz+2)$$
$$V = (RTQ/n\mathbf{F})(y^2+2y+2)^{1/2}$$
$$\theta = -\operatorname{arccot}(1+y)$$
$$V_2 = (RTQ^2/4n\mathbf{F})(y^2+2y+2)^{1/2}(z^2+2z+2)^{1/2}$$
$$\theta_2 = -\operatorname{arccot}\frac{y+z+yz}{y+z+2}$$

where $z = (1-2\alpha)y$.

The expressions given above for V and θ have been derived previously (4). The equation for Ψ is in agreement with that given by Barker, Faircloth, and Gardner (6), but differs from an expression derived earlier by the present author (4), which was in error (15). For fast electrode reactions y approaches zero and therefore $\Psi = -RTQ^2/2n\mathbf{F} = -n\mathbf{F}V^2/4RT$. This last relationship has been experimentally verified for the $Hg_2^{2+} + 2e^- \rightleftharpoons 2Hg$ reaction (4).

Magnitude of the Distortion

It is convenient to express V_2 in terms of the amplitude V of the fundamental interfacial potential. In this form the amplitude of the first harmonic potential (the faradaic distortion) is given by

$$V_2 = \frac{n\mathbf{F}V^2}{4RT}\left(\frac{z^2+2z+2}{y^2+2y+2}\right)^{1/2} \qquad [11]$$

This equation predicts that if $V = 10$ mv, $T = 300°K$, and $n = 2$, then the magnitude of V_2 will lie between 0 and 2 mv, depending on the magnitudes of the parameters k, α, C, f, D, and ω.

For a given system at constant temperature, Eq. [11] shows that V_2 depends on V and ω only, varying directly as V^2 but showing a complicated dependence on frequency. Figure 2 shows how the ratio V_2/V^2 varies with y for various values of α. Since y is proportional to the square-root of ω, a change in y from 0.1 to 10 corresponds to a ten-thousandfold increase in frequency. The shape of the curves in Fig. 2 is seen to be very dependent on α, especially when the latter is greater than 0.5. If the transfer coefficient exceeds 0.64, the curves exhibit minima at characteristic values of y. It will be apparent that I_e and α may readily be determined if a curve of the type shown in Fig. 2 is constructed. An apparatus which enables V_2 to be measured as a function of ω at constant V is described below.

The faradaic distortion method of determining the kinetic parameters of an electrode reaction shares with faradaic rectification the advantage over the classical a-c method (faradaic admittance) that a knowledge of the double-layer capacity is not needed; uncertainties associated with the double-layer often lead to difficulties when a-c studies are made at electrodes other than mercury (3, 16). Faradaic distortion offers two advantages over faradaic rectification in the determination of α and I_e. First, as a comparison of Fig. 2 and 3 shows, curves of V_2 against frequency are far more characteristic of α than the corresponding plots of Ψ. Second, whereas several effects can be envisaged which might cause spurious d-c potentials to exist across the cell, thereby interfering in the measurement of Ψ, only one effect[10] other than faradaic distortion is likely to introduce alternating potentials of frequency ω/π. On the other hand, faradaic rectification does not suffer from the severe limitations which are the subject of the next section.

The close parallelism between faradaic distortion and faradaic rectification is illustrated by a comparison of the values acquired by V_2 and Ψ in the limiting cases $y << 1$ and $y >> 1$. In the former case $V_2 = n\mathbf{F}V^2/4RT = -\Psi$ while in the latter, $\Psi = (2\alpha-1)n\mathbf{F}V^2/4RT = \pm V_2$.

[10] If the double-layer capacity is potential dependent, then the passage of an a.c. across the electrode will introduce harmonic frequencies in the interfacial potential. The first harmonic is the most serious and its amplitude is $(V^2/4c)(\partial c/\partial E)$. This effect is unlikely to interfere in the determination of faradaic distortion except in the vicinity of the electrocapillary maximum, where the double-layer capacity does change appreciably with potential (17).

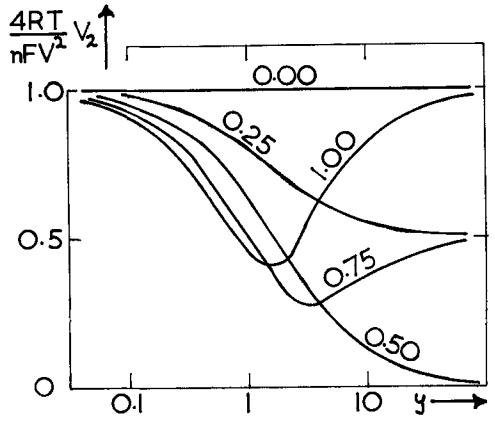

Fig. 2. Dependence of faradaic distortion on the parameter y (proportional to the squore root of frequency) for values of the transfer coefficient α = 0.00, 0.25, 0.50, 0.75, 1.00.

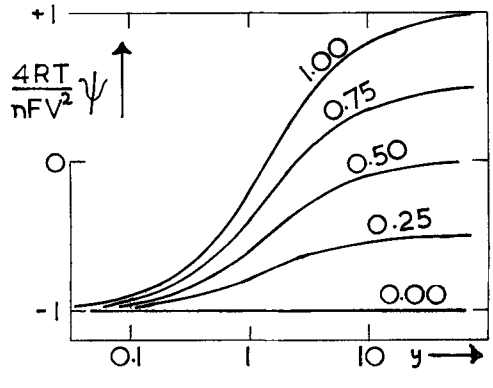

Fig. 3. Dependence of faradaic rectification on the parameter y for values of the transfer coefficient α = 0.00, 0.25, 0.50, 0.75, 1.00.

Effect of the Double Layer

As yet the fact has been ignored that, in addition to the faradaic path, an alternative route, the charging and discharging of the electrical double layer, is accessible to a.c. crossing the electrode/solution interface. Usually this nonfaradaic path is considered as a pure capacity,[11] proportional to electrode area but otherwise constant (19); its capacitance will be equated to cA.

The production by faradaic distortion of an alternating potential of frequency ω/π across the electrode interface will cause a current of the same frequency to flow across the double layer capacity. However, this harmonic current must be shunted back via the faradaic path, as illustrated in Fig. 4, since no harmonic frequencies are present in the current flowing in the external circuit. The presence of this harmonic component in the faradaic current cannot be ignored unless the nonfaradaic impedance is much greater than the faradaic impedance; if this is not the case, the appropriate correction terms must be inserted into Eq. [5] and the entire derivation of V_2 repeated. The result is

$$V_2 = \frac{n\mathbf{F}V^2}{4RT} \cdot \left(\frac{z^2+2z+2}{y^2+2y+2} \right)^{1/2} \cdot \frac{x}{[(y+2^{-1/2})^2+(x+2^{-1/2})^2]^{1/2}} \qquad [12]$$

where $x = n^2\mathbf{F}^2D^{1/2}C/RTc(2\omega)^{1/2}$. Also,

$$\theta_2 = \operatorname{arccot} \frac{(y+2^{-1/2})(y+z+2)-(x+2^{-1/2})(y+z+yz)}{(x+2^{-1/2})(y+z+2)+(y+2^{-1/2})(y+z+yz)}$$

The term x is a measure of the ratio of the nonfaradaic impedance to the faradaic.[12] Therefore, for a sufficiently large x value [12] reduces to Eq. [11]. However, as x becomes small V_2 decreases and this may be interpreted as the shorting out of the faradaic distortion by the decreasing double layer impedance.

[11] However, Bockris and Conway (18) regard the nonfaradaic path as equivalent to a condenser with a relaxing dielectric. In their terms, the present treatment is only valid at frequencies low enough that $1/\omega$ is large compared with the relaxation time of the dielectric.

[12] In fact, $2x$ is the ratio of the reactances of the two paths.

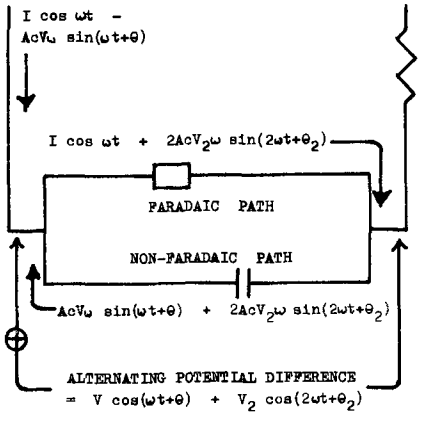

Fig. 4. Distribution of currents between the faradaic and nonfaradaic paths. The resistor shown represents the solution resistance R_s.

Inspection of Fig. 2 shows that $y \leq 10$ covers the region most useful for the determination of kinetic parameters by faradaic distortion. In this region the final fraction in [12] exceeds 0.95 if $x \geq 35$. Taking the following representative values: $T = 298°K$, $c = 39$ μfd. cm^{-2} (20), $n = 2$, and $D = 10^{-5}$ cm^2 sec^{-1}; this restriction becomes $C/\omega^{1/2} \geq 4 \times 10^{-8}$ mole sec$^{1/2}$ cm^{-3}. On the other hand, the final fraction in [12] is less than 0.1 if $x \leq 0.11$ which implies $C/\omega^{1/2} \leq 1.2 \times 10^{-10}$ mole sec$^{1/2}$ cm^{-3}. The practical consequences of these limitations are shown below.

C (mole cm^{-3}):	10^{-9}	10^{-8}	10^{-7}	10^{-6}	10^{-5}	10^{-4}
Double layer effect can be ignored and Eq. [11] is obeyed for frequencies less than	....	...	1.0 cps	100 cps	10 kc/s	1.0 Mc/s
Double layer capacity effectively shorts out all faradaic distortion if the frequency is in excess of	10 cps	1.0 kc/s	100 kc/s	10 Mc/s	....	....

Three conclusions can be drawn immediately. First, faradaic distortion will not interfere in conventional admittance measurements provided low enough concentrations (about 10^{-6} M) are employed: higher concentrations can be tolerated provided a low frequency limit is set at a value greater than 10 cps.[13] Second, since the double layer shorting effect becomes very pronounced at low concentrations, the analytical applications of faradaic rectification (7, 21) are unlikely to be paralleled by similar developments of faradaic distortion. Third, if faradaic distortion is to be employed quantitatively (to measure k or α, for example), the concentration range available will be seen to be severely limited. An audio-frequency bridge has a range of about 10 cps to 10 kc/s and the table shows that full use can be made of this range only for concentrations greater than 10^{-5} mole cm^{-3}. An upper concentration limit (about 0.1 M, i.e., $C = 10^{-4}$) is set by the requirement that the Ox concentration shall be much less than the supporting electrolyte.[4] Taking all factors into consideration it would appear that the faradaic distortion method is a useful one for determining kinetic parameters over a thousandfold range of reaction rates, suitable exchange current densities ranging from about 20 ma cm^{-2} to 20 amp cm^{-2}. Although this range is rather narrow, it does encompass some important electrode reactions: thus the $Cu^{2+} + 2e^- \rightleftharpoons Cu$ reaction is reported to have $I_e/A \approx 2$ amp cm^{-2} at $C = 10^{-5}$ mole cm^{-3} in an acidified KNO_3 solution (22).

Soluble Reductant Case

Cases in which Rd is not a pure phase but is a species soluble in the cell solution (or in the electrode in the case of amalgam electrodes) can be treated in a manner which exactly parallels the method described above under *Mathematical Deri-*

[13] In any case, since V_2 is proportional to V^2, a lower percentage of distortion can always be realized by decreasing the signal across the cell.

vation. Since no new principles are involved it will suffice to present the results; these are

$$\Psi = -(RT/4n\mathbf{F})(Q^2-Q'^2)(Y+Z+YZ+2)$$

$$V = (RT/n\mathbf{F})(Q+Q')(Y^2+2Y+2)^{1/2}$$

$$\theta = -\operatorname{arccot}(1+Y)$$

$$V_2 = (RT/4n\mathbf{F})(Q^2-Q'^2)(Y^2+2Y+2)^{1/2}(Z^2+2Z+2)^{1/2}$$

$$\theta_2 = -\operatorname{arccot}\frac{Y+Z+YZ}{Y+Z+2}$$

where $Q' = I/nA\mathbf{F}C'(2D'\omega)^{1/2}$, $Y = I/I_e(Q+Q')$, and $Z = (1-2\alpha)Y(Q+Q')/(Q-Q')$. Each of these equations reduces to the corresponding equation already given above as Q' tends to zero. The above expression for Ψ differs from that obtained previously by the present author (4) but is in agreement with equations derived by Barker (7) and (for the special case $C = C'$, $D = D'$) by Doss and Agarwal (23, 5). The equations for V and θ are well established (2, 3). The expression for the amplitude of faradaic distortion can be cast into a particularly simple form when $CD^{1/2} = C'(D')^{1/2}$:

$$\pm V_2 = \frac{n\mathbf{F}V^2}{4RT}\cdot\frac{(1-2\alpha)Y}{(Y^2+2Y+2)^{1/2}} = \frac{(1-2\alpha)VI}{4I_e}$$

Moreover, θ_2 then equals θ, showing that the fundamental interfacial potential is perfectly in phase with its first harmonic.

Again, the double layer affects V_2 and θ_2. The equation analogous to [12] is

$$V_2 = \frac{n\mathbf{F}V^2}{4RT}\left(\frac{Z^2+2Z+2}{Y^2+2Y+2}\right)^{1/2}\frac{X}{[(Y+2^{-1/2})^2+(X+2^{-1/2})^2]^{1/2}}$$

and

$$\theta_2 = \operatorname{arccot}\frac{(Y+2^{-1/2})(Y+Z+2)-(X+2^{-1/2})(Y+Z+YZ)}{(X+2^{-1/2})(Y+Z+2)+(Y+2^{-1/2})(Y+Z+YZ)}$$

where $X = n\mathbf{F}I/RTAc(2\omega)(Q+Q')$.

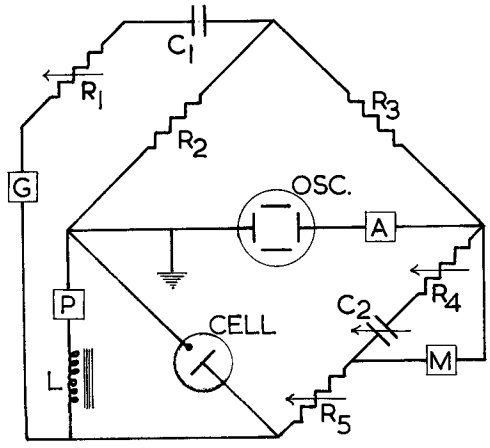

Fig. 5. Circuit for measuring all three faradaic effects. Suitable component values are G: 10 c/s-10 kc/s, 100 v; R_1: 0-100kΩ; C_1: 1 μfd; R_2: 5 kΩ; R_3: 5 kΩ; A: 10000 X; R_4: 0-100Ω; C_2: 0-5 μfd; M: 10 mv f.s.d.; R_5: 0-10Ω; P: to read to 10 μv; L: 10 H.

Measurement

The circuit shown in Fig. 5 permits the amplitude V_2 of faradaic distortion to be measured without the use of filter networks or tuned amplifiers. Faradaic rectification may also be measured with this apparatus and, provided that the double layer capacity is known, the faradaic admittance can be determined as well. Rough measurements with a circuit of this type have confirmed the predicted parallelism between faradaic rectification and distortion.

The pure sinusoidal potential produced by G, a generator of variable frequency and high voltage output, is fed through the high resistance R_1 to produce a pure a.c. of frequency $\omega/2\pi$. Since R_2 and R_3 are equal resistors, if R_4 and C_2 are adjusted[14] so that the impedance of the R_4-C_2-R_5 arm is identical in both phase angle and magnitude to the impedance of the cell, no signal of frequency $\omega/2\pi$ will appear across the amplifier A and cathode ray oscilloscope OSC. However, a signal of the harmonic frequency ω/π remains and if the resistance of R_2 is much greater than the cell impedance, the whole of the distortion voltage V_2 will be developed across the A-OSC arm. V_2 can be calculated from the height of the oscilloscope trace if the gain of A and the sensitivity of OSC are known.

A series of measurements of V_2 at a constant known value of V, the fundamental alternating interfacial potential, but varying frequency can be made by adjusting R_5 to equal the solution resistance R_s. With the bridge balanced the a-c millivoltmeter M then measures V directly and R_1 can be repeatedly adjusted to give any predetermined M reading.

The potentiometer P enables Ψ to be measured, V_e being subtracted if necessary.[1] The choke L restricts the passage of a.c. through P and d.c. is prevented from flowing through the cell by P being balanced and by the presence of the condensers C_1 and C_2.

Symbols

A	area of the electrode, cm²
C,C'	bulk concentrations of Ox and Rd, mole cm⁻³
$C(r,t)$	concentration of Ox at a distance r from the electrode surface at time t, mole cm⁻³
D,D'	diffusion coefficients of Ox and Rd, cm² sec⁻¹
E	potential of the electrode vs. standard Ox/Rd electrode, v
E_e	equilibrium (null) value of E, v
$\mathbf{F}$	the faraday, 9.65 × 10⁴ coulomb equivalent⁻¹
I	amplitude of applied faradaic a.c., amp
I_e	equilibrium exchange current, amp
Ox	an electroreducible species
Q,Q'	dimensionless parameters defined in sections on *Mathematical Deviation* and *Soluble Reductant Case*
R	gas constant, 8.32 joule mole⁻¹ deg⁻¹
Rd	an electroöxidizable species formed by reduction of Ox
R_s	resistance of the cell solution, ohm
T	absolute temperature, °K
V	amplitude of that component of the interfacial potential having the fundamental frequency ($\omega/2\pi$), v
V_2	amplitude of that component of the inter-

[14] Under certain conditions a parallel arrangement of R_4 and C_2 may be more convenient.

	facial potential having the harmonic frequency (ω/π), v
V_e	equilibrium cell potential, v
V_o	potential generated by the passage of current through R_s, v
X,Y,Z	dimensionless parameters defined in section *Soluble Reductant Case.*
a,a'	bulk activities of Ox and Rd, treated as dimensionless
a_o,a_o'	surface activities of Ox and Rd, dimensionless
c	double layer capacity per unit area, farad cm^{-2}
e^-	an electron
f,f'	activity coefficients of Ox and Rd, liter $mole^{-1}$
$\overleftarrow{i}, \overrightarrow{i}$	anodic and cathodic currents resulting from the faradaic reaction at the electrode surface, amp
j	a running index
k	standard rate constant, mole cm^{-2} sec^{-1}
n	number of faradays needed to reduce one mole of Ox, equivalent $mole^{-1}$
p	an integration variable
r	normal distance from the electrode surface, cm
t	time, sec
v	total interfacial potential, v
x,y,z	dimensionless parameters defined in sections *Mathematical Deviation* and *Effect of the Double Layer*
α	transfer coefficient of the cathodic reaction
θ	phase angle by which the fundamental component of the interfacial potential leads the faradaic current
θ_2	phase angle by which the harmonic component of the interfacial potential leads the faradaic current
λ,μ	surface concentration amplitudes, defined by Eq. [6], mole cm^{-3}
Ψ	potential due to faradaic rectification, sometimes termed the redoxokinetic potential, v
ω	angular frequency of the applied current, sec^{-1}

Manuscript received Oct. 12, 1959.

Any discussion of this paper will appear in a Discussion Section to be published in the June 1961 JOURNAL.

REFERENCES

1. D. C. Grahame, *This Journal*, **99**, 370C (1952).
2. J. E. B. Randles, *Discussion Faraday Soc.*, **1**, 11 (1947).
3. P. Delahay, "New Instrumental Methods in Electrochemistry," Chap. 7, Interscience Publishers Inc., New York (1954).
4. K. B. Oldham, *Trans. Faraday Soc.*, **53**, 80 (1957).
5. K. S. G. Doss and H. P. Agarwal, *Proc Indian Acad. Sci.*, **34**, 263 (1951).
6. G. C. Barker, R. L. Faircloth, and A. W. Gardner, *Nature*, **181**, 247 (1958).
7. G. C. Barker, *Anal. Chim. Acta*, **18**, 118 (1958).
8. K. S. G. Doss and H. P. Agarwal, *J. Sci. Ind. Res. India B*, **9**, 280 (1950).
9. J. E. B. Randles, *Trans. Faraday Soc.*, **48**, 828 (1952).
10. K. B. Oldham, *J. Am. Chem. Soc.*, **77**, 4697 (1955).
11. L. L. Bircumshaw and A. C. Riddiford, *Quarterly Rev.*, **6**, 157 (1952).
12. H. S. Carslaw and J. C. Jaeger, "Conduction of Heat in Solids," Chap. II, Oxford University Press, London (1947).
13. G. A. Gibson, "An Elementary Treatise on the Calculus," p. 458, MacMillan, London (1933).
14. H. S. Carslaw and J. C. Jaeger, *Op. cit.*, footnote on page 47.
15. M. Fleischmann and K. B. Oldham, *Ann. Reports*, **55**, 67 (1958).
16. H. A. Laitinen and R. A. Osteryoung, *This Journal*, **102**, 598 (1955).
17. I. M. Kolthoff and J. J. Lingane, "Polarography," p. 110, Interscience Publishers Inc., New York (1941).
18. J. O'M. Bockris and B. E. Conway, *J. Chem. Phys.*, **28**, 707, (1958).
19. D. C. Grahame, *J. Am. Chem. Soc.*, **68**, 301 (1946).
20. D. C. Grahame, *ibid.*, **71**, 2975 (1949).
21. K. S. G. Doss, K. Sundararjan, U. H. Narayanan, and S. Visvanathan, *Electrochim. Acta*, **1**, 22 (1959).
22. P. J. Hillson, *Trans. Faraday Soc.*, **50**, 385 (1954).
23. K. S. G. Doss and H. P. Agarwal, *Proc. Indian Acad. Sci.*, **35**, 45 (1952).

Correction

In the paper by M. P. Korver, R. S. Johnson, and N. C. Cahoon, "Study of the Recuperation Reaction in the Leclanché Dry Cell," which appeared on pp. 587-591 of the July JOURNAL, the line drawings for Figures 1 and 2 on pp. 588 and 589 were reversed. The captions for the figures are correct, however.

The Electrolytic Formation and Dissolution of Oxide Films on Platinum

H. A. Laitinen and C. G. Enke

Noyes Chemical Laboratory, University of Illinois, Urbana, Illinois

ABSTRACT

The extent of surface oxidation of a smooth platinum electrode and the electrode capacitance were measured for various conditions of anodization. The electrolytic formation of the surface platinum oxide is shown to be a highly irreversible reaction. A mechanism which involves a hydroxyl radical intermediate of the oxygen evolution reaction is proposed for the surface oxide formation reaction. This mechanism is supported by the shapes of the anodic and cathodic charging curves on platinum and the interrelationships of the electrode potential, the electrode capacitance, and the extent of surface oxidation. From these same interrelationships it was also concluded that the steady-state evolution of oxygen occurs on a surface which has at least one atom of oxygen per surface platinum atom and that the rate-determining step in the oxygen evolution reaction is the electrolytic discharge of oxygen-containing radicals which are adsorbed on the electrode surface. The surface oxide is reduced at potentials several hundred millivolts cathodic to the potential required to form the oxide. The reduction of the surface oxide is shown to be a first order reaction. The rate of the reduction increases with increasingly cathodic electrode potential.

It has been well substantiated that a surface oxidation occurs on a platinum electrode which is functioning as an anode in water solutions (1-17). The surface oxide thus formed on platinum has the unusual ability to transfer charge from the metal to a reactant in the solution without an appreciable increase in the thickness of the film. The film is electron conducting rather than ion conducting, and therefore does not grow beyond one or two atomic layers. The presence of the surface oxide alters the behavior of platinum indicator electrodes to such an extent that almost all investigators using such electrodes have had to adopt a standard anodic or cathodic pretreatment in order to obtain reproducible results. The formation of the surface oxide layer has been shown to affect considerably the results obtained with platinum indicator electrodes in potentiometry (14), chronopotentiometry (1), polarography (10), and kinetics determinations (18). A knowledge of the chemical nature of the surface oxide as well as the mechanism of its formation is a prerequisite to the understanding of the behavior of platinum indicator electrodes.

Historically, three experimental approaches have been taken in an effort to arrive at a conclusion regarding the composition of the surface oxide on platinum. These are cathodic stripping (3-5, 7-9, 15, 17,), chemical attack (2), and potentiometry 10-12, 16). In the first case, the number of coulombs of electricity required to completely reduce the surface oxide is determined. If the exact electrode area and the number of platinum atoms per square centimeter are known, and if it is assumed that the oxide is a monomolecular film, the oxidation state of the oxidized platinum surface can be calculated. Because of the assumptions required for such calculations, the results are indicative but not conclusive. In the case of the chemical attack the oxide film is dissolved and the solution analyzed spectroscopically for platinum(II) and platinum(IV). Here one must be certain that during the chemical attack the oxidation state of the platinum has not been changed. Finally, the potentials of the plateaus in the anodic and cathodic charging curves have been equated to the thermodynamic standard potentials of Pt-PtO or Pt-PtO_2 to demonstrate the existence of these species on the electrode surface. Giner (8) has discounted all such comparisons by pointing out the physical and chemical differences between a monomolecular layer of PtO on platinum and crystalline platinum(II) oxide [and similarly platinum(IV) oxide]. Such a monolayer may be regarded as identical to a chemisorbed oxygen atom layer. Furthermore, it will be shown here that the reaction of the formation of the surface oxide is so irreversible that it is incapable of determining the potential of the platinum electrode even under conditions of no electrode current.

Cathodic and Anodic Charging Curves

It is worthwhile at this point to make a critical evaluation of the interpretation of the shapes of the cathodic and anodic charging curves on platinum. Typical charging curves for oxygen and hydrogen free solutions are shown in Fig. 1. Potentials in this figure and throughout the paper are referred to the normal hydrogen electrode. A constant anodic current is passed while the potential of the electrode is followed as a function of time (or coulombs). The potential rises slowly (region Ha) until all the hydrogen adsorbed on the electrode has been oxidized. The potential then rises rapidly through region Ca

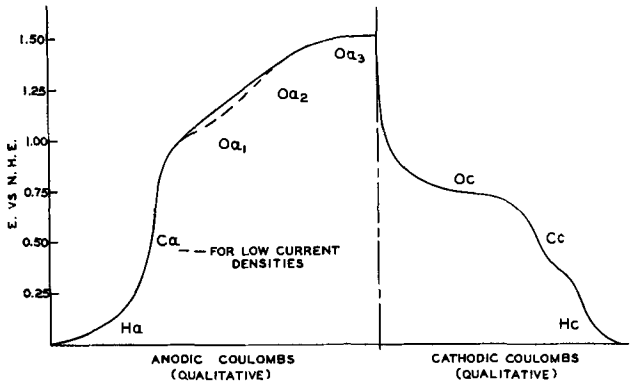

Fig. 1. Anodic and cathodic charging curves

where the only process is the charging of the electrical double layer. At about 0.9 v an anodic process begins and the potential increases more gradually through regions Oa_1 and Oa_2. Eventually the oxygen evolution potential is reached, causing a leveling off of the potential (region Oa_3). If the current is reversed and the electrode thus anodized is now made the cathode, the cathodic charge curve of Fig. 1 is observed. The potential drops very rapidly to about 0.7 v where there is a plateau (region Oc) due to the reduction of the substance formed during regions Oa_1 and Oa_2 of the anodization. When all of the oxidation product has been reduced, the potential drops rapidly again through region Cc and then enters the hydrogen evolution region Hc.

The shapes of the cathodic and anodic charging curves on platinum were one of the first indications of a surface oxidation (5) and they have been of interest to many investigators subsequently (3, 4, 6-9, 11, 15-17). A comparison of the anodic and cathodic charging curves shows that they are not the same shape. If the difference in their shapes were the effect of polarization due to a slow reaction, the curves would become more similar as the current density is decreased. However, very low current density studies (15-17) have shown that the hysteresis is not decreased significantly with decreasing current density. Such an intrinsic hysteresis suggests a reaction which is so irreversible that the oxidation and reduction occur by different mechanisms.

A comparison of the charging curves also shows that the region Oa_1-Oa_2 is always larger than the region Oc indicating that more electricity is used to form the oxide than is required to remove it. Vetter and Berndt (15) who found a ratio of anodic to cathodic coulombs of nearly two postulated the oxidation of water to the oxide during the anodization and the reduction of the oxide to hydrogen peroxide during the cathodization. However, no chemical evidence for the presence of hydrogen peroxide has been reported. Other investigators using slightly different conditions have not observed a ratio of anodic to cathodic coulombs of two. Furthermore, it is unlikely that the oxidation of water to oxide would occur at a higher potential than the reduction of the oxide to peroxide. Another explanation lies in the possibility of a mixed anodic process where a reaction (such as the evolution of oxygen) occurring simultaneously with the oxide formation reaction consumes some of the electricity.

The following mechanism for the electrolytic formation and dissolution of the surface oxide on platinum gives a satisfactory explanation of the shapes of the anodic and cathodic charging curves. When a constant anodic current is applied to the platinum electrode, any hydrogen present at the electrode surface will be oxidized. When the hydrogen has been exhausted the first step in the oxidation of the water occurs. The oxidation product (which is an intermediate in the oxygen evolution reaction) may react with the surface platinum atoms to form a surface oxide, or it may react to evolve oxygen. In this way the unoxidized portion of the electrode surface on which the oxidation of water can occur most readily decreases, causing an increase in the potential due to increased polarization (region Oa_1). When the entire surface of the platinum has reacted with the oxygen evolution intermediate, the oxidation of water must take place on the oxidized platinum surface. The presence of the oxide partially counteracts the positive charge of the platinum thus causing the oxidation of water to occur at a higher electrode potential (region Oa_2). Giner and Lange (19) observed a substantial increase in the work function and a corresponding decrease in the volta potential of platinum when the surface was oxidized, showing that the oxygen imparts a negative charge to the surface. When sufficient intermediate has been formed on the surface of the oxidized platinum, the intermediate will be further oxidized to oxygen and the steady-state oxygen evolution region of the charging curve is reached (region Oa_3). At higher current densities the break between regions Oa_1 and Oa_2 is not observed because the increased polarization overvoltage causes the electrode potential to become sufficient to oxidize the water on portions of the oxide layer before the entire platinum surface has become oxidized.

When the current is reversed making the oxidized electrode the cathode, the potential follows the reduction of the surface oxide and then, when the oxide is exhausted, the potential drops to the hydrogen evolution potential.

Experimental

The cell.—Perchloric acid electrolytes of different concentrations were used exclusively. Perchloric acid was chosen because it was not expected to influence the surface reactions on platinum either by direct chemical interference or by adsorption. If the acid concentration was high enough, the solution was effectively buffered. Unless otherwise stated, the solution was continuously swept with a stream of purified nitrogen in order to keep the solution free from dissolved oxygen and hydrogen. The presence of oxygen is undesirable because it affects the open-circuit potential of an oxidized electrode, and it acts as a depolarizer when treating the electrode cathodically. Hydrogen reacts chemically with the oxygen on the platinum electrode surface and acts as a depolarizer for anodic electrode treatment.

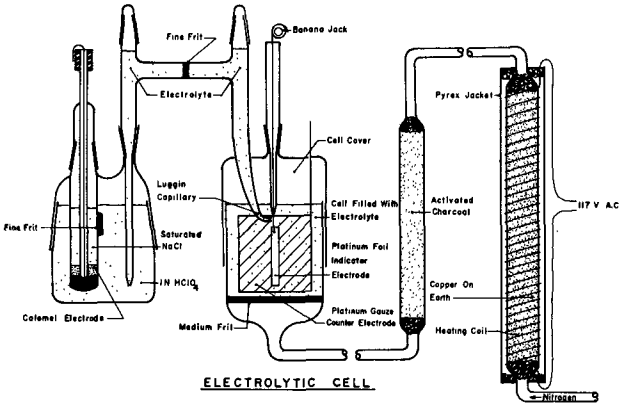

Fig. 2. Electrolytic cell

The cell arrangement is shown in Fig. 2. The cell itself was a filter funnel of 50-ml capacity, provided with a medium porosity glass frit. The indicator electrode was a 36 x 2.5 mm piece of 3 mil platinum foil welded to a 30-ga platinum wire sealed in a soft glass tube. Within the soft glass tube, the platinum wire was silver-soldered to a No. 20 ga copper wire connected to a banana jack.

The platinum foil electrode was cut from a 50-cm^2 piece of previously unused platinum foil. The surface roughness of this foil was determined in the laboratory of Professor Norman Hackerman at the University of Texas by the gas adsorption method (20). Professor Hackerman has perfected an apparatus to work with small areas making this determination economically practical on platinum. The results obtained in his laboratory on the platinum foil indicate a roughness factor of 1.12 within 10% accuracy. The true indicator electrode area was 2.0 cm^2 since both sides of the foil were exposed. The counter electrode was a platinum gauze cylinder placed concentrically around the indicator electrode. The calomel electrode was connected to the cell through an elaborate salt bridge which was designed to prevent any significant diffusion of chloride ions from the calomel compartment into the measurement cell during the course of an experiment. The cell arm of the salt bridge terminated in a luggin capillary which was placed up against the indicator electrode. The other arm of the salt bridge had a drawn-out tip which was immersed in a compartment of 1*N* $HClO_4$. This compartment served to connect the arm of the salt bridge to the frit on the side of the calomel compartment as well as to reduce the concentration gradient of chloride ions between the calomel and the salt bridge. The nitrogen which was bubbled through the cell electrolyte was passed first through a heated column of of copper-on-earth and then through a column of activated charcoal packed with glass wool. The copper-on-earth was prepared in this laboratory by M. S. Chao according to the method of Meyer and Ronge (21).

The equipment.—Figure 3 shows a block diagram of the equipment used in this investigation. A complete description of each piece of equipment and its operation is available (22). The constant current source was used to obtain constant current anodic

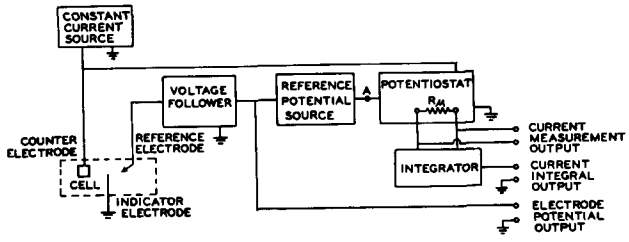

Fig. 3. Complete instrumentation

or cathodic charging curves. The voltage follower allowed the electrode potential to be followed accurately on a recorder or oscilloscope without drawing more than 10^{-10} amp from the indicator electrode. When the potentiostat was turned on, the voltage applied to the counter electrode was such that the potential at point A (Fig. 3) was equal to that of the indicator electrode. Thus the potential between the reference electrode and the indicator electrode was precisely equal and opposite to the potential of the reference potential source. The current required to maintain this electrode potential was measured by measuring the potential across R_m and the time integral of the current was obtained at the output of the integrator. A system of relays was arranged so that when a key was pressed, a signal would trigger the oscilloscope sweep and shortly thereafter the reference potential would change by a preset value of 10 mv. Using a Tektronix Model 502 Dual Beam Oscilloscope, it was possible to observe the number of coulombs necessary to effect this potential change (at the integral output) as well as the shape of the current-time curve. The potentiostat was capable of rising to an output of 50 ma in as little as 50 μ sec.

Surface Oxide Determination by Cathodic Stripping

Chronopotentiometry was used to determine the extent of surface oxidation of the platinum indicator electrode. The indicator electrode was grounded and the saturated calomel reference electrode was connected to either the oscilloscope or the recorder. The constant current source, which was connected between the counter electrode and ground, was turned on and the potential of the indicator electrode was recorded as a function of time. The shape of the curve was that of the cathodic chronopotentiogram shown in Fig. 1. The amount of charge per unit area, Q/A, of oxide on the platinum surface was calculated by multiplying the current density by the time required to reach the middle of region Cc. A current density of 15 $\mu a/cm^2$ was used. This current density was chosen because it was at least one hundred times the current withdrawn by the potential measuring circuit. It is very likely that current densities in the region of 100 $\mu a/cm^2$ would cause the apparent amount of surface oxidation to be decreased due to premature polarization to the hydrogen evolution potential. However, no difference in the quantity of surface oxidation measured was observed between determinations using cathodic current densities of 15 and 30 μa. The cathodic current was turned off as soon as the electrode potential reached the potential of the inflection point of

the region Cc. This procedure avoided the evolution of hydrogen. The discharge of hydrogen on the platinum was observed to have an effect on subsequent anodizations.

If the surface oxidation is thought of as a compound or mixture of compounds obeying the law of small whole numbered ratios of atomic constituents, it is desirable to be able to convert millicoulombs per square centimeter to atoms of oxygen per surface atom of platinum. To make this conversion it is necessary to know the number of surface atoms of platinum per square centimeter. Using the lattice constants in Wyckoff (23) for crystalline platinum one calculates 1.3 x 10^{15} atoms/cm^2 for the 100 plane and 1.5 x 10^{15} atoms/cm^2 for the closest packed 111 plane. If one takes the two-thirds power of the number of platinum atoms per cubic centimeter as calculated from the density of platinum, 1.5 x 10^{15} atoms/cm^2 is obtained. The predominant crystal face on a polycrystalline surface would be the 111. Using 1.5 x 10^{15} atoms/cm^2 it was calculated that about 0.5 millicoulombs/cm^2 are required to provide each surface platinum with an oxygen atom. An accuracy of 10% is all that should be claimed for this number.

Potentiostatic Formation of Surface Oxide

Two methods are available for controlling the anodic treatment given to the electrode: namely, electrolysis at constant anodic current and electrolysis at constant anodic potential. Both methods were tried in this study. It was found that the constant potential anodization yielded a more reproducible quantity of surface oxidation as determined by cathodic chronopotentiometry. If the quantity of oxide on the electrode surface is a function of the anodization potential, the better reproducibility of the constant potential is reasonable. The potential of the electrode follows the shape of the anodic chronopotentiogram, as shown in Fig. 1, during constant current anodization. The steady-state potential of the electrode (region Oa_3) is reached slowly, and therefore only at long times are the two anodization methods equivalent. Another consideration is the shape of the steady-state anodic current-voltage curve. In the region of interest which is negative to the rapid evolution of oxygen, the current increases slowly with increasing potential. It would be difficult then to obtain a reproducible steady-state potential (and thus a reproducible surface oxidation) by applying a constant current.

Constant potential anodization was used throughout this work. With the indicator electrode grounded, the calomel reference electrode was connected to the input of the voltage follower. The reference potential source was connected between the output of the voltage follower and the input of the potentiostat. The potential was established within milliseconds after turning on the potentiostat.

Effect of Varying the Time of Anodization

The quantity of oxide on the surface of the electrode was measured as a function of the time of anodization at a given potential. The purpose of this experiment was to determine how long it takes the surface coverage to come to a constant value at a given applied potential. Before each anodization, the electrode had been freed of oxide by the previous chronopotentiometric determination and then allowed to drift until the open-circuit potential reached a steady value. This potential was between 0.8 and 0.85 v. The cathodic constant current was switched on immediately after the potentiostat was turned off. The quantity of oxide per square centimeter vs. the time of anodization was determined for five potential values. Results are shown in Fig. 4. Each of the curves shown actually has a point on the origin of the graph, but the initial rise is too steep to be shown. The potentiostat could pass 1 millicoulomb in 20 msec, a time very short compared to 1 sec, the shortest time interval plotted.

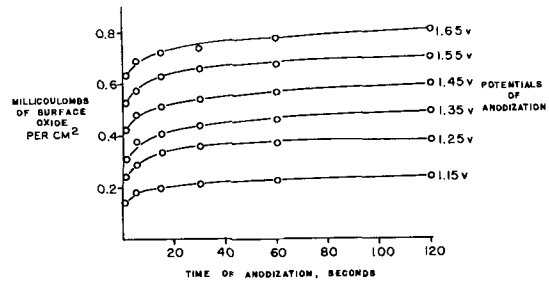

Fig. 4. Variation of amount of surface oxide with time of anodization at constant potential.

The amount of oxide on the surface increased quite rapidly during the first 15 sec of anodization at each potential. The subsequent increase in surface oxide was gradual. Apparently some slow process was causing a slow increase in the oxidation. Since steady-state coverage was not reached within a reasonable time of anodization, an anodization time of 30 or 60 sec was chosen for subsequent experiments. An anodization of 30 sec yielded a coverage which was at least 90% of that for a 2-min anodization.

Post-Anodization Behavior of Electrode

When the potentiostat was turned off after an anodization, the electrode did not remain at the anodization potential. The electrode potential dropped suddenly at first and then decreased slowly to about 0.85-0.95 v. The time required to reach a steady-state open-circuit potential increased with increasing potential of anodization. For an anodization at 0.95 v, steady state was reached in about 10 min. For anodizations at 1.3-1.7 v, over an hour was required to reach steady state. Despite the large drop in potential during an hour, the amount of surface oxide decreased by only about 0.2 millicoulombs/cm^2. Approximately the same amount of oxide was lost during an hour regardless of the anodization potential. The range studied was from 1.15 to 1.75 v. In this case the electrode was anodized for 3 min at each potential.

Experiments were also performed relating the decay of the open-circuit potential and the surface coverage for shorter times. The electrode was anodized for 30 sec at 1.25 v, 1.45 v, or 1.65 v. After the potentiostat had been turned off, the open-circuit

potential was followed for an amount of time t_d. At time t_d the constant cathodic current was applied and the quantity of oxide was determined. Thus the open-circuit potential and the surface coverage were determined for various values of t_d up to 15 min for all the three anodization potentials. The potential fell off rapidly during the first minute of drift. The drop in potential was 0.2 v for the 1.25-v anodization, 0.3 v for the 1.45-v anodization, and 0.35 v for the 1.65-v anodization. A decrease in surface charge was not noticeable for the first minute. At the end of five min, 0.015 millicoulombs had been lost; after 15 min, 0.045 millicoulombs were lost. The absolute value of the oxide loss was the same for all three anodization potentials. If the surface coverage decay is linear at 0.045 millicoulombs/cm^2/15 min, at the end of an hour, the amount lost would be 0.18 millicoulombs/cm^2. This value is in reasonable agreement with the result cited for a 1-hr drifting time. It was thus demonstrated that an electrode may be left at open circuit after the anodization for times up to 1 min without appreciably affecting the amount of surface oxide.

The lack of correlation between oxide loss and potential decay throws considerable doubt on the notion that the post-anodization open-circuit potential is a function of the type or quantity of oxide on the electrode surface. It has been claimed that the potential decay is caused by the decomposition of an unstable surface oxide whose presence affects the open-circuit potential (16). If this were the reason for the potential decay, the rate of loss of the surface oxide would decrease as the quantity of unstable oxide decreases. Furthermore, it seems unlikely that the amount of unstable oxide on the platinum would be independent of the potential of anodization or the quantity of total oxide on the electrode surface.

In the mechanism of the oxide formation suggested in the discussion of the charging curves above, the potential of the electrode during anodization is controlled by the oxygen evolution process and not by a redox couple established between the platinum and the oxide layer. The anodic potential, then, would be dependent on the partial pressure of oxygen. In solutions swept free of oxygen, when the anodization is stopped, the electrode potential will drop rapidly as the oxygen diffuses away from the electrode surface. Eventually the oxygen partial pressure becomes so small that the oxygen-water couple can no longer establish an electrode potential. It is experimentally observed that the open-circuit potential of a platinum electrode, oxidized or reduced, eventually drifts to about 0.8 v. This potential is established by a very slow exchange since it is immediately polarized several tenths of a volt by an applied current density of a half-microampere per square centimeter. This explanation of the potential decay is supported by an experiment reported by Giner (8) who noted that the open-circuit potential of a partially oxidized platinum electrode is increased about 200 mv when the solution is saturated with oxygen. The extent of electrode oxidation was not increased by the presence of the oxygen gas, which shows that the oxidation process requires the passage of an electrical current.

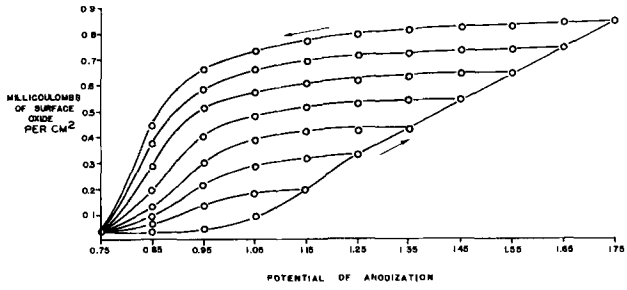

Fig. 5. Variation of amount of surface oxide with potential and direction of potential change.

The slow disappearance of oxide from the electrode surface will be shown later to be due to the diffusion of the oxygen atoms from the electrode surface to the interior of the platinum along grain boundaries. Such a diffusion satisfies the observed conditions of being a potential independent process, of being a process independent of the extent of surface oxidation (once a significant portion of the first oxidation product has formed), and of being a very slow process.

Effect of the Anodization Potential

The electrode was anodized for 30 sec, allowed to remain at open circuit for 30 sec, and then the quantity of surface oxide was determined chronopotentiometrically. The number of millicoulombs of oxygen per square centimeter as a function of the potential of anodization is shown as part of Fig. 5. The quantity of oxide increases with increasing potential of anodization. Between about 1.2 v and 1.75 v the amount of surface oxide increases linearly with potential.

The hysteresis curves of Fig. 5 result from the following experiment. The electrode was anodized for 30 sec and then the electrode potential was reduced to a lower value for 30 sec. The electrode was left at open circuit for 30 sec and then the quantity of oxide was determined. It was found that the quantity of oxide which was present at the first anodization potential remained when the potential was decreased except at potentials below 0.95 v where the surface oxide began to be removed. To determine whether or not this hysteresis might be caused by a slow equilibrium a reduced electrode was put at 1.05 v for 1 hr without obtaining an increase in surface oxide over that shown in Fig. 5. The electrode was also preanodized at 1.45 v for 1.5 min and then put at 1.05 v for 1 hr. The quantity of oxide was only 0.135 millicoulombs less than that shown in Fig. 5 for the same pretreatment with a 30-sec anodization at 1.05 v. The loss of surface oxide at a reduced potential was less than that of an oxidized electrode left at open circuit for the same period.

This hysteresis substantiates several interesting conclusions reached earlier on other bases. (*A*) The electrode potential is not determined by the degree of surface oxidation. (*B*) To reduce a substance on an electrode, electrons must be supplied to the electrode either from an oxidation occurring on the same electrode or from an external current source.

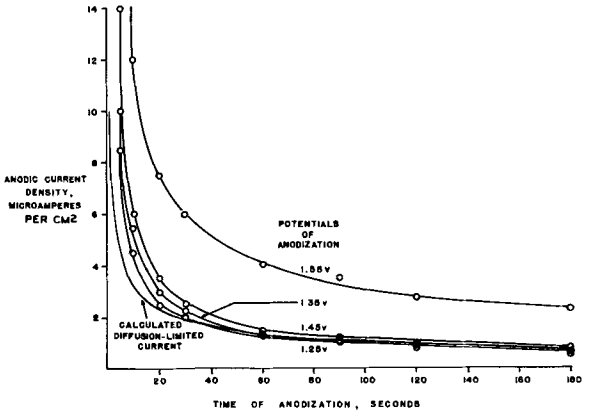

Fig. 6. Anodic current density as function of time

When the surface oxide is not reduced at open circuit, it may be due to the lack of an electron source. When the surface oxide is not reduced when the potentiostat is still connected, it is proof that the oxide is not reduced at the potential applied. (*C*) Since two steps are not observed in the oxide removal curves, that oxidation in excess of one oxygen per platinum is reduced at the same potential and thus probably by the same mechanism as the lower oxide.

Anodic Current as a Function of Anodization Time

When a constant anodic potential was applied to the unoxidized electrode, the current was very large but rapidly decayed to a small value. A plot of the current as a function of the time of anodization is shown in Fig. 6 for four potentials of anodization. Note that the current for the anodizations at 1.25, 1.35, and 1.45 v are almost identical after the first 60 sec of anodization. The current for the anodization at 1.55 v is much higher than that for the other potentials at all times. Apparently the process which requires current at the longer times of anodization is independent of potential. The anodic current at 3 min for anodizations from 1.25 to 1.45 v was also independent of the rate of stirring in the cell as provided by the nitrogen bubbling.

We suggest that an explanation for this behavior may be the diffusion of oxygen atoms into the platinum. Evidence of the penetration of platinum by oxygen has been presented in the literature (9, 24). The diffusion of a surface oxygen atom into the electrode interior would leave a vacancy on the electrode surface which requires current to become refilled. The rate of diffusion would decrease with increasing time of anodization, as was observed. The rate of diffusion would be independent of potential as long as the surface is saturated with oxygen atoms. The greatly increased current at 1.55 v is due to the evolution of oxygen. The solution of Fick's laws for the boundary condition of constant surface concentration is $i = n\mathbf{F}C^\circ \sqrt{D/\pi t}$. A surface concentration of one oxygen per platinum corresponds to a concentration C° of 0.11 moles/cm³. For an observed i equal to 0.8 μa/cm² at t = 180 sec, D is equal to 10^{-18} cm²/sec. This estimate must be regarded as very crude because a linear diffusion model is assumed for what is probably a grain boundary diffusion.

A value for the diffusion coefficient of oxygen in platinum has not been reported previously. The activation energy E for self-diffusion in the platinum lattice has been determined as 68.2 kcal/g-atom (25). The diffusion coefficient D is obtained from the relation $D = D_o \exp(-E/RT)$ where D_o is a constant which can be estimated as 1. Thus the self-diffusion coefficient of platinum at room temperature has a value of about 10^{-49} cm²/sec. The activation energy of self-diffusion along grain boundaries in silver (which has the same crystal structure as Pt) is about 0.45 times the activation energy of lattice diffusion (25). The self-diffusion of Pt along grain boundaries can thus be estimated to be within several orders of magnitude of 10^{-22} cm²/sec. Considering the smaller size of an oxygen atom than a platinum atom the uncertainties in the estimation made above, and the effect of chemical bond formation, the observed value of 10^{-18} cm²/sec for the grain boundary diffusion of oxygen in platinum at room temperature is a reasonable one. The theoretical current due to the replacement of diffused oxygen atoms for D = 10^{-18} cm²/sec is plotted on Fig. 6.

The grain boundary diffusion of oxygen atoms is preferred by the authors over the loss of surface oxygen into the solution for the following reasons: (*A*) The loss of surface oxidation by combination of bonded (chemisorbed) oxygen atoms requires the rupture of platinum-oxygen bonds, a process not likely to be independent of the electrode potential or of the extent of surface oxidation in excess of one oxygen per surface platinum atom. (*B*) Recent photomicrographic evidence (26) indicates preferential attack of grain boundaries upon severe anodic treatment of platinum.

Photographic records were made of oscilloscopic measurements of the electrode current during the first 0.1 sec of anodization at constant potential. The potential was established on the electrode within 2 msec. The area under the current-time curve, expressed as coulombs, was always larger than the amount of surface oxide determined chronopotentiometrically after a 30-sec anodization at that same potential. Anodization potentials from 0.95 to 1.75 v were studied. In some cases the current-time integral was equivalent to as much as twice the quantity of oxide found on the surface after a 30-sec anodization. The ratio would be even greater if the quantities of surface oxide for a 1-sec anodization (Fig. 4) were used.

The fact that considerably more current was used for an anodization than could be accounted for by the amount of oxide formed substantiated the notion that another process occurs while the oxide layer is being formed. At potentials of 1.45 v and lower, the anodization current at long times can all be accounted for by the diffusion of oxygen along the platinum grain boundaries. Therefore, the reaction that occurs during the formation of the surface oxide is inhibited by the formation of the oxide. If the concurrent process is the evolution of oxygen, the overvoltage of oxygen evolution on platinum is thus explained.

Double Layer Capacity as a Function of Potential

The potentiostat was turned on to apply a constant potential to the indicator electrode. The current-integrator was connected, and the step potential was set at 10 mv. The output voltage of the current-integrator was measured on the oscilloscope. Using the second beam of the oscilloscope, the electrode current was also observed. The initiation of the potential step triggered the oscilloscope sweep. No current other than the double layer charging current was observed over the entire potential range except at high anodic and cathodic potentials where oxygen and hydrogen evolution occur, respectively. The step potential was applied in both directions with the same results.

Currents lower than 1 μa could not be observed with the equipment employed because of the noise level of the potentiostat and the voltage follower. For a reaction which is as irreversible as Fig. 5 shows the oxide formation to be, the rate of the reaction would be expected to be too slow for the reaction current to be observed with this equipment. Thus the kinetic parameters of the oxide formation reaction are not obtainable with the potential step apparatus used here. Only the double layer charging current will be integrated by the current-integrator when the integration is performed over very short times (10^{-3} sec).

The double layer capacity was measured by the method described above. The current integrator was calibrated for this purpose using a decade of large standard capacitors. The double layer capacity was shown to be a function of potential, with a distinct hysteresis behavior depending on the direction of potential change. The relationship is shown in Fig. 7. The minimum capacity of the electrode was about 20 μf/cm^2. The capacity rose as the potential increased until a value of about 60 μf was reached at about 1.25 v. The capacity varied between 60 and 55 μf for potentials above 1.25 v. The capacity remained high as the potential was decreased until the potential had reached a value of about 0.95 v. The capacity then rapidly returned to the minimum value. The similarity between the capacity-potential curve (Fig. 7) and the surface oxide-potential curves (Fig. 5) is obvious. It is evident that the presence of the surface charge causes the double layer capacity to increase up to three times its normal value.

It has been postulated by Llopis and Colum (27), who also observed this capacity hysteresis, that the reason for the increase of the electrode capacity of a

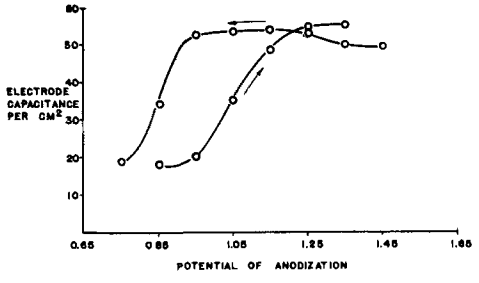

Fig. 7. Hysteresis behavior of electrode capacitance

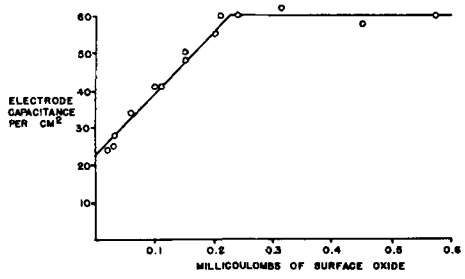

Fig. 8. Relation between electrode capacitance and amount of surface oxide.

platinum electrode at the beginning of surface oxide formation is due to the presence of dipoles such as Pt . . . O at the electrode solution interface. The negative end of the dipole may be adsorbed oxygen or some other intermediate in the oxygen evolution reaction. The capacity across this dipole would be of such a magnitude that the relative effect of the ionic double layer in the solution would be small. Furthermore, a large portion, if not all, of the potential gradient between the electrode and the solution would be developed across the dipole at the electrode surface.

Dependence of Double Layer Capacity on Surface Oxidation

Electrode capacities were again measured for the various conditions of anodizations and preanodization studied in the section above. After each capacity was measured, the current-integrator was disconnected as quickly as possible, the potentiostat was turned off, and the amount of charge on the electrode surface was determined chronopotentiometrically. Figure 8 shows the results of this experiment. The double layer capacity was found to be a linear function of the amount of surface oxide until a capacity value of 55-60 μf was reached. The double layer capacity then remained constant, independent of the amount of surface oxide. The line drawn on Fig. 8 was determined by an analysis by the method of least squares.

On the basis of the explanation advanced above for the increase in the electrode capacity as a result of the electrode oxidation it is possible to account for the capacity vs. surface charge curve (Fig. 8). For an unoxidized electrode in 1*N* perchloric acid at about 0.8 v, the double layer capacity is about 20 μf/cm^2. Highly polar groups, which might be represented as $Pt^+ \ldots O^-$ (27), $Pt^+ \ldots OH$, or $Pt^+ \ldots OH_2^+$ may exist at the metal-solution interface of the "oxidized" metal surface. These dipoles replace the water molecules and ions which form the electrical double layer at the reduced electrode surface. To account for the experimentally observed increase in electrode capacity from 20 to 60 μf/cm^2, a threefold increase in capacity due to the presence of the highly polar groups is required. For a partially covered surface, the total electrode capacity may be thought of as many capacitors in parallel (sites of hydroxyl adsorption and dipole formation) and some of low value (a double layer formed of ions and water molecules). The electrode capacity is thus a linear function of the fraction of the sur-

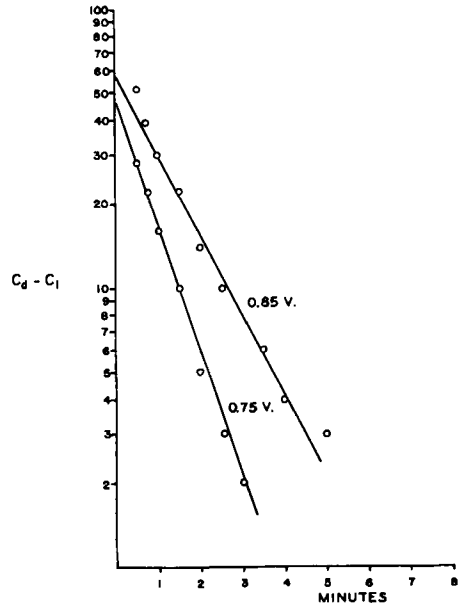

Fig. 9. Decay of surface capacitance in unstable region

face which is covered by the dipoles as demonstrated by Fig. 8.

It can be further postulated that the dipole at the electrode surface is primarily Pt...O, that is, that the electric field across the dipole is largely across the planes of the Pt^+ and O^- atoms, respectively, and is independent of the state of protonation or hydration of the O^- atom. If the surface oxidation continues and the $Pt^+...O^-$ dipole becomes a $Pt^{++}...O^=$ dipole, the capacity will not change. The permittivity of the dipole has a linear dependence on the ratio of the dipole moment to the electric field strength. When the $Pt^+...O^-$ dipole becomes a $Pt^{++}...O^=$ dipole, the dipole moment is doubled, but so is the electric field strength across the dipole. If the permittivity remains unchanged, the capacity will also remain unchanged. This explanation of the electrode capacity accounts for the linearity of capacity with surface oxidation until a surface charge of 0.25 millicoulombs (equivalent of one electron per surface platinum) has been reached as well as the constant electrode capacity observed for higher surface charge.

The postulation of the formation of the polar group as an explanation for the capacity increase is preferred over explanations involving the usual ionic double layer. One reason for this preference is that the capacity is a function of electrode oxidation (Fig. 8), but independent of potential since points on Fig. 8 were taken from both the oxide formation and dissolution curves. There is an electrode potential difference of about 200 mv between equivalent oxidation states on the oxide formation and dissolution curves. The ionic double layer capacity is known to vary with potential and therefore cannot appreciably affect the electrode capacity which is measured for the oxidized surface. The ionic double layer capacity also varies with ionic strength but, as it will be shown later, the electrode capacity of an oxidized electrode is independent of ionic strength.

Rate of Surface Oxide Dissolution

The fact that the double layer capacity is a linear function of the surface coverage was used to advantage to determine the rate of surface oxide dissolution. The electrode was put at 1.25 v until the double layer capacity came to a steady-state value (requiring about 1 min). The electrode potential was then shifted suddenly to 0.85 v and the double layer capacity was followed as a function of time. The capacity jumped to a value higher than that measured at 1.25 v and then dropped off and eventually reached a steady-state value. When the steady-state value of capacity was subtracted from all of the measured capacity values and the logarithm of the difference was plotted against time (Fig. 9), a straight line resulted. The same experiment was repeated using a removal potential of 0.75 v. Another straight line of steeper slope resulted. The conclusions to be drawn from these experiments are that the dissolution reaction is a first order reaction, and that the rate of dissolution increases with increasing cathodic electrode potential. The "half-life" of the oxide is 1 min at an electrode potential of 0.85 v and 2/3 of a minute at 0.75 v.

Effects of Acidity and Ionic Strength

Perchloric acid of 0.01M concentration was used in the cell and salt bridge for some measurements. The surface oxide was measured as a function of potential and the dissolution potential curve for anodization at 1.25 v was made. The results were identical to those shown in Fig. 5 except that the potential axis was shifted 0.12 v in the increasing positive direction. In other words, an anodization of 1.25 v in 0.01M $HClO_4$ corresponds to an anodization of 1.37 v in 1M $HClO_4$.

The double layer capacity measurement at the lower electrolyte concentration was rather difficult to make. The increased solution resistance caused the potentiostat to respond slowly due to the potential drop in the solution between the electrode and the luggin capillary. For this reason the capacity could be measured only roughly. If the experimental error is taken to be 10%, the capacity-potential curve is the same as that for 1M $HClO_4$ (Fig. 7) except for the same potential shift which was noted above for the surface oxide. The capacity-charge relationship observed in 1M $HClO_4$ solutions was also reproduced within 10% for 0.01M $HClO_4$ solutions.

The independence of the electrode capacity over a hundredfold change in ionic strength is another indication that the electrode capacity is not determined by the ionic double layer. The electrode capacity must then arise from the highly polar nature of the adsorbed surface layer.

Conclusions

On the basis of the observed anodic behavior of the platinum electrode, a mechanism for the surface oxidation and oxygen evolution reactions can be proposed. The first step is the formation of an oxygen evolution intermediate which is adsorbed on the electrode surface. The choice of an intermediate

is limited because only one electron is used in its formation from water. Possible intermediates are $\cdot OH$, $\cdot O^-$, $\cdot OH_2^+$. The hydroxyl radical has been chosen to represent the intermediate in the reaction equations.

$$Pt + H_2O \rightleftharpoons Pt...OH + H^+ + e^- \quad [1]$$

The Pt...OH thus formed[1] can further react in either of two ways. First, an oxygen evolution reaction may be written which removes the surface hydroxyl, presumably through the intermediate formation of surface $\cdot OOH$, forming a bare platinum site:

$$Pt...OH + H_2O \rightarrow Pt...OOH + 2H^+ + 2e^-$$

$$Pt...OOH \rightarrow Pt + O_2 + H^+ + e^- \quad [2a]$$

Second, the surface hydroxyl may be converted to a surface oxygen atom which is firmly held

$$Pt...OH \rightarrow PtO + H^+ + e^- \quad [2b]$$

Bare platinum sites produced by reactions [2a] are reoxidized by reaction [1], so that eventually all the surface is covered with firmly held PtO. Subsequently oxygen evolution must occur on the PtO surface, as has been also postulated by Llopis (27). Once again, surface hydroxyl formation may be postulated, with competitive reactions to form oxygen molecules, or to further oxidize the surface.

An important consideration here is the finding of Rosenthal and Veselovskii (13) by isotope experiments that oxides formed at lower potentials (0.8-1.2 v) do not appear in oxygen gas subsequently evolved from the surface. Oxides formed at higher potentials were found to make a partial contribution to oxygen molecules formed at the surface. This finding suggests that the first oxygen atom per surface platinum atom is held more firmly than additional oxygen atoms. Moreover, the oxygen evolution reaction cannot involve combination of oxygen atoms if one of the atoms is of the firmly held type, and the present finding of the stability of even the higher surface oxidation at open-circuit forces the rejection of an atom-combination mechanism for oxygen evolution.

A similar reaction sequence as postulated above for a bare platinum surface may be written for oxygen evolution at a PtO surface, in which the PtO bonds are not disrupted:

$$PtO + H_2O \rightarrow Pt^o...OH + e^- + H^+ \quad [3a]$$

$$Pt^o...OH + H_2O \rightarrow Pt^o...OOH + 2e^- + 2H^+ \quad [3b]$$

$$Pt^o...OOH \rightarrow PtO + H^+ + e^- + O_2 \quad [3c]$$

According to the above mechanism the oxidation of the platinum surface occurs only when oxygen is being evolved concurrently. From the principle of microscopic reversibility it follows that the formation of the oxide is energetically possible at potentials less positive than the potential of oxygen evolution, but it appears that the oxide is not formed at an appreciable rate except in the presence of the oxygen evolution intermediates. In order to dissolve the surface oxide, however, it would be necessary to put the electrode at a potential for which the oxide is unstable. At such a potential, the instantaneous rate of oxide dissolution would be proportional to the instantaneous quantity of oxide on the surface. A first order reduction of the surface oxide was confirmed experimentally. The hysteresis of the potential vs. surface oxidation curve is direct evidence that oxide formed at potentials of 1.2-1.7 v is reduced only at potentials of about 0.95 v and below. The standard potential of the surface oxide formation on platinum would be closer to the reduction potential than to the oxidation potential, that is, about 0.8-0.9 v.

[1] Reaction [1] has been postulated by Bockris and Huq (28) as being the rate-controlling process.

Manuscript received Feb. 1, 1960.

Any discussion of this paper will appear in a Discussion Section to be published in the June 1961 JOURNAL.

REFERENCES

1. F. C. Anson and J. J. Lingane, *J. Am. Chem. Soc.*, **79**, 1015 (1957).
2. F. C. Anson and J. J. Lingane, *ibid.*, **79**, 4901 (1957).
3. M. Becker and M. Breiter, *Z. Elektrochem.*, **60**, 1080 (1956).
4. M. Breiter, C. A. Knorr, and W. Volkl, *ibid.*, **59**, 681 (1955).
5. J. A. V. Butler and G. Armstrong, *Proc. Roy. Soc.*, **A137**, 604 (1932).
6. B. V. Ershler, *Discussions Faraday Soc.*, **1**, 269 (1947).
7. A. L. Ferguson and M. B. Towns, *Trans. Electrochem. Soc.*, **83**, 271, 285 (1943).
8. J. Giner, *Z. Elektrochem.*, **63**, 386 (1959).
9. A. Hickling, *Trans. Faraday Soc.*, **41**, 333 (1945).
10. I. M. Kolthoff and N. Tanaka, *Anal. Chem.*, **26**, 632 (1954).
11. J. K. Lee, R. N. Adams, and C. E Bricker, *Anal. Chim. Acta*, **17**, 321 (1957).
12. G. Radlein, *Z. Elektrochem.*, **61**, 727 (1957).
13. K. I. Rosenthal and V. I. Veselovskii, *Doklady Akad. Nauk S.S.S.R.*, **111**, 637 (1956).
14. J. W. Ross and I. Shain, *Anal. Chem.*, **28**, 548 (1956).
15. K. J. Vetter and D. Berndt, *Z. Elektrochem.*, **62**, 378 (1958).
16. S. E. S. El Wakkad and S. H. Emara, *J. Chem. Soc.*, **1952**, 461.
17. Ts. I. Zalkind and B. V. Ershler, *Zhur. Fiz. Khim.*, **25**, 565 (1951).
18. S. Glasstone and A. Hickling, *Chem. Revs.*, **25**, 407 (1939).
19. J. Giner and E. Lange, *Naturwissenchaften*, **40**, 506 (1953).
20. S. Brunauer, P. H. Emmett, and E. Teller, *J. Am. Chem. Soc.*, **60**, 309 (1938).
21. F. R. Meyer and G. Ronge, *Angew. Chem.*, **52**, 637 (1939).
22. C. G. Enke, Doctoral Dissertation, University of Illinois (1959).
23. R. W. G. Wyckoff, "Crystal Structures," Interscience Publishers, New York (1948).
24. A. D. Obrucheva, *Zhur. Fiz. Khim.*, **26**, 1448 (1952).
25. C. E. Birchenall, *Metallurgical Revs.*, **3**, 235 (1958).
26. D. G. Davis, Jr., *Talanta*, **3**, 335 (1960).
27. J. Llopis and F. Colum, "Proceedings of the International Committee on Electrochemical Thermodynamics and Kinetics, Eighth Meeting, 1958," pp. 414-427, Butterworths, London.
28. J. O'M. Bockris and A. K. M. S. Huq, *Proc. Roy. Soc. (London)*, **A237**, 277 (1956).

Technical Notes

Electrode Assembly for Electrochemical Measurements

Milton Stern[1] and A. C. Makrides

Metals Research Laboratories, Union Carbide Metals Company,

Division of Union Carbide Corporation, Niagara Falls, New York

The isolation of electrical contacts from the test solution is a common problem in electrochemical measurements. It may be circumvented in some cases by using leads of the same material as the electrode. Such an arrangement, however, produces an ill-defined current density distribution and introduces an extraneous vapor-metal-solution interface.

Electrical connections are masked frequently with tape, wax, or thermosetting plastics. All these substances contaminate the solution to some degree. Wax is probably least objectionable. In corrosive solutions, however, it often causes preferential attack next to the masked surface. Contamination of solution can be avoided with wire electrodes sealed in glass. The method is limited to tungsten and platinum since only these metals give leakproof seals. These difficulties may be eliminated with a demountable electrode assembly in which only glass and a fluorinated plastic (Teflon), besides the electrode, are exposed to solution. The assembly has been used with considerable success for several years in these Laboratories.

A diagram of the assembly is shown in Fig. 1. The electrode is tapped, threaded, and attached to a stainless steel rod through a Teflon washer machined to a narrow edge at the end next to the electrode. The rod is isolated from solution with a heavy-wall glass tube ground at the lower end at an angle of approximately 60°. The assembly is made leakproof by tightening a nut at the top of the steel rod. Sufficient pressure is exerted to produce liquid-tight seals at both the glass-Teflon and Teflon-electrode junctions. A thin Teflon washer is used between the retaining nut and the tube to avoid cracking the glass.

An assembly will remain leakproof for several weeks and has been used in boiling acid solutions. Although Teflon washers can be used more than once, they are deformed to a certain extent after each run and have to be replaced after a few runs. Their life can be extended by remachining the lower edge.

The glass tube is attached eccentrically to a ground glass joint which is inserted, again eccentrically, in a second ground glass joint on the cell (see insert in Fig. 1). The distance between electrode and a Lugin capillary probe can thus be easily adjusted within rather wide limits. Mercury or water-sealed joints are used to avoid contamination from lubricant.

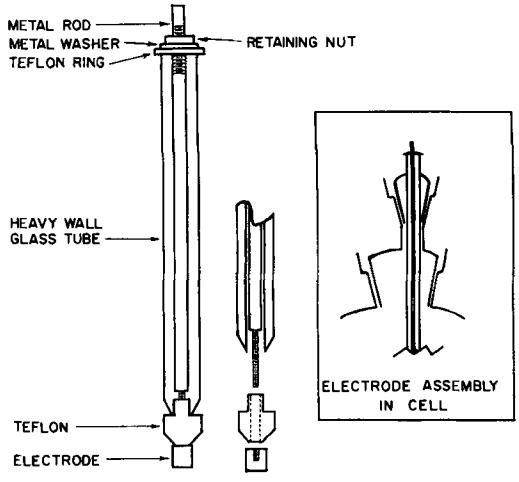

Fig. 1. Electrode assembly

A number of modifications of the basic design have been employed. For example, in experiments with a rotating electrode, a cylindrical sample was secured to the steel rod in the usual way and recessed and threaded at the lower end. A V-shaped Teflon section, which rode in a glass cup fused to the bottom of the cell, was attached at this end. The Teflon bearing minimized eccentric motion of the electrode and isolated the bottom surface of the cylinder from solution. At the top of the assembly, an inverted steel cup rotating in a pool of mercury sealed the system from the atmosphere while providing electrical contact to the electrode.

The basic assembly described above can be used with any metal or semiconductor electrode which can be attached securely to a metal rod. It can be used in practically every common test solution since only glass and Teflon come in contact with solution. Furthermore, it can be cleaned in any of the usual ways, for example, with a saturated chromic-sulfuric acid solution (cleaning solution).

Manuscript received May 9, 1960.

Any discussion of this paper will appear in a Discussion Section to be published in the June 1961 JOURNAL.

[1] Present address: Speedway Laboratories, Linde Co., Indianapolis, Indiana.

Identification of the Diffusing Species in Uranium Oxidation

J. G. Schnizlein, J. D. Woods,[1] J. D. Bingle, and R. C. Vogel

Chemical Engineering Division, Argonne National Laboratory, Lemont, Illinois

As part of an extensive study of the kinetics of uranium oxidation, experiments have been designed to establish whether uranium or oxygen diffuses through the oxide film during the oxidation reaction at 200°C in 200 mm oxygen. Two distinctly different types of marker experiments have been used to demonstrate the same conclusion.

In the first method, metallographic examination was used to establish whether an inert marker would become buried in the oxide and whether or not two impinging oxide films would fuse together. Other investigators (1-4) have shown that in cases of metal ion diffusion during oxidation, as with copper (1), an inert marker will become buried in the oxide. Similarly, two oxide surfaces growing against one another will fuse into a continuous oxide layer (2). The lack of burial of a wire or lack of fusion of the impinging oxides is generally accepted as indication of the absence of metal-ion diffusion.

The second method used involved an alpha-counting technique to locate a marker of enriched uranium. Although the use of inert markers in metal oxidation studies is common, the use of a radioactive isotope of the metal as a marker is a recent (5), extremely useful innovation. The metal isotope marker is not inert but becomes a part of the oxidation process, thereby avoiding the danger of altering the reaction under examination. In these experiments an enriched uranium film was sputtered onto the surface of normal uranium. The higher percentage of uranium-234 and -235 gives the marker considerably more alpha activity than normal uranium. After oxidation the active marker can be located by direct counting of the surface. The location of the marker indicates whether uranium or oxygen is the diffusing species.

Experimental

The uranium specimens were cubes 1 cm on an edge prepared by the Metallurgy Division of Argonne National Laboratory from high-grade biscuit metal. The metal contained approximately 250 ppm total analyzed impurities. The cubes were β-quenched to assure uniform grain structure and random orientation. The oxidation of the samples was conducted at constant temperature and constant pressure in an apparatus in which the consumption of oxygen was measured volumetrically.

Metallographically determined marker.—Two uranium cubes were polished through 1-μ diamond paste and wired together with 640-μ diameter (22-gauge) Inconel wire with a 25-μ (1-mil) platinum wire separating the cubes near one edge. Thus, a V-shaped space was left between the cubes ranging in width from zero to approximately 30 μ.

[1] Special Scientific Employee in 1957 from Drake University.

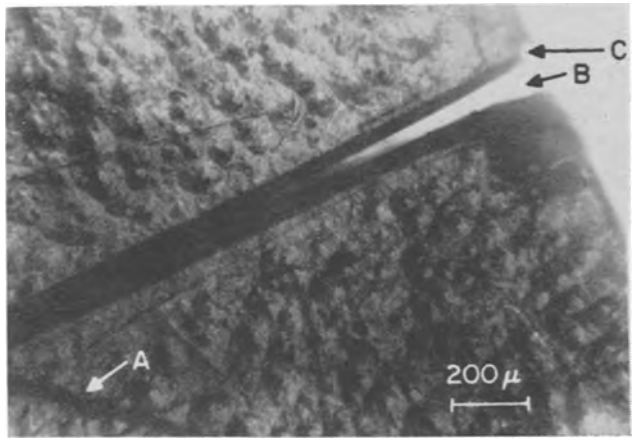

Fig. 1. Open V-shaped space between oxidized uranium cubes. A, 25 μ diameter platinum wire (out of focus); B, V-shaped space still unfilled with oxide; C, notch on edge of oxidized cube.

The sample was then oxidized at 200°C in 200 mm oxygen until the oxygen consumed was equivalent to 5150 μg/cm^2. The study of the kinetics of oxidation (which will be published at a later date) indicates that uranium dioxide is produced under these conditions and that an essentially linear oxidation rate is achieved after a brief, much lower initial rate. After cooling in vacuum, microscopic examination (Fig. 1) showed that the V-shaped space between the cubes was still not closed by oxide. The 25-μ platinum wire (A) can be seen, out of focus, in the corner opposite the open edge (B). The interesting notch (C) in the oxide at the edge of the cube should be noted. This is an indication of the absence of uranium diffusion in the oxidation mechanism (6, 7). Other related uranium oxidation experiments have shown even more clearly than Fig. 1 that the raised surfaces of the oxide are approximately of the same dimensions as those of the original sample, with notches clearly evident at each edge.

An additional oxidation of 12,500 μg/cm^2, to a total of 17,650 μg/cm^2, was completed to close the gap. Examination of the edge of the oxide contact was not satisfactory because of the notch developed on each cube edge. To obtain a cross-section view the sample was mounted in "Scotchcast," a low-temperature thermosetting plastic. After polishing through 600 grit silicon carbide paper, the section was examined.

A view of the cross section showing the platinum wire (A) separating the two cubes and locating the original metal surfaces is presented in Fig. 2. It is obvious that the two oxides have not fused, in fact, the oxide layers (C and D) from the first and second oxidations are distinctly separate. The thickness of these oxide layers is approximately proportional to

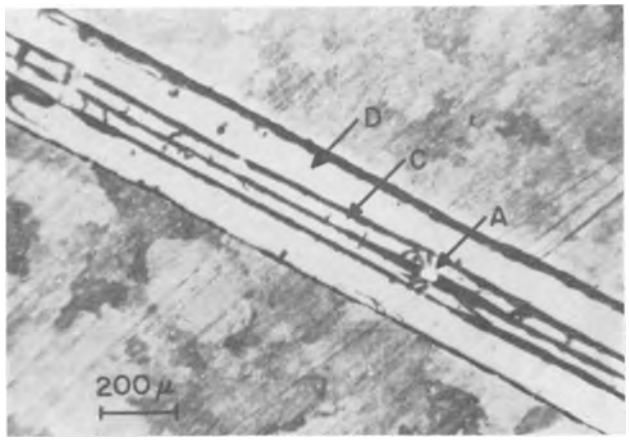

Fig. 2. Cross section of impinging oxide from two uranium cubes. A, cross section platinum wire; C, oxide produced in first oxidation; D, oxide produced in second oxidation.

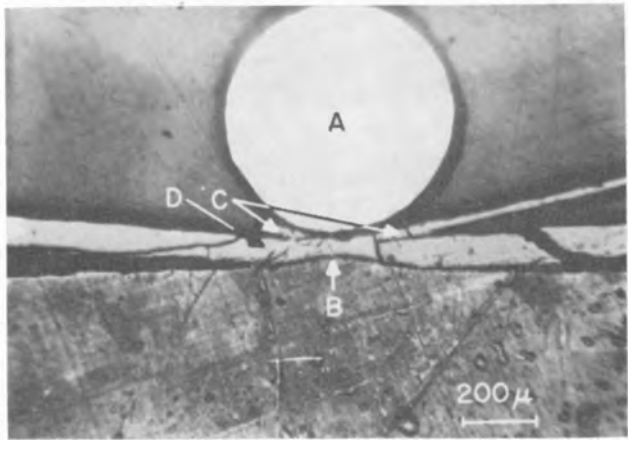

Fig. 3. Cross section of Inconel binding wire on oxidized uranium cube. A, originally 640 μ diameter Inconel wire; B, hump in uranium surface where partial protection is afforded by wire; C, oxide produced in first oxidation; D, oxide produced in second oxidation.

the extent of each oxidation. Two other interesting observations are: (*a*) the metal surfaces are now parallel instead of forming the V-shape of the original assembly, and (*b*) the 25-μ diameter platinum wire (A) has been flattened into an oval cross section approximately 17 x 38 μ. Both of these observations demonstrate the tremendous pressure of the oxide film as the gap was closed.

Figure 3 illustrates the lack of burial of the 640-μ diameter Inconel binding wire (A). It appears that the uranium was partially protected during the oxidation so that a hump (B) is observed in the surface. The oxide produced during the first oxidation (5,150 μg/cm²) becomes diminishingly thin under the wire (C), whereas that produced during the second oxidation (D) (12,500 μg/cm²) is continuous. There is no tendency of the oxide to grow up around the wire.

Radioactive marker.—For the experiments utilizing the marker of enriched uranium, two approaches were used. In the first, the active marker was initially on the exterior of the cube. After oxidation the activity should either remain on the surface or be distributed through the oxide, depending on whether oxygen or uranium was the diffusing species. In the second, the sputtered film of enriched uranium was covered with a film of normal uranium. In this case, if oxygen were diffusing, the activity would remain buried as a thin band, whereas if uranium diffused, the activity would be distributed throughout the oxide.

The normal uranium cubes were polished through 1-μ diamond paste and then electropolished. The sputtering of the enriched uranium marker onto the cubes was accomplished in a vacuum bell-jar with a glow discharge in 25-μ argon pressure using 30 to 50 ma at 2.2-2.6 kv. Although there was not any way of measuring the actual thickness of the sputtered films, previous experiments would indicate that, under the conditions used, the films of enriched uranium were approximately 1 μ thick. In the second approach this 1-μ film of enriched uranium was covered with several microns of normal uranium.

The samples were oxidized at 200°C in 200 mm oxygen. The oxidation was continued to approximately 1000 μg/cm², or a thickness of 8 μ, assuming ideal density and uniform oxidation.

The oxidized samples were hand polished on 2/0 emery paper and one face of the cube was counted with an alpha-beta-gamma proportional counter after successive polishing strokes. Although this polishing technique was only semiquantitative, experience indicated that approximately four strokes removed 1 μ of oxide. The shape of the curve obtained by plotting counts per minute vs. number of strokes (Fig. 4) clearly indicates the location of the marker in each case.

Discussion of Results

Each of two types of marker experiments demonstrate conclusively that oxygen, rather than uranium, diffuses through the oxide layer during the course of oxidation at 200°C in 200 mm oxygen.

In the metallographically determined marker experiment, all of the observations indicate an absence of uranium diffusion through the oxide. The most noteworthy of these observations are: (*a*) the lack of tendency for the oxide to grow up around the Inconel binding wire; (*b*) the lack of fusion of the

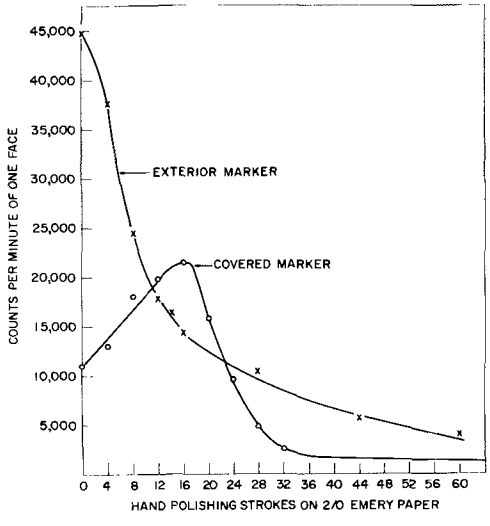

Fig. 4. Activity within the oxide layer: enriched uranium marker experiment.

oxides layers impinging on each other; and (c) the notch in the oxide which occurs at an edge of the cube.

Both approaches to the radioactive marker experiment also demonstrate that oxygen is the diffusing species since uranium diffusion would have caused the active marker to be distributed throughout the exterior oxide. In the first case, the initially exterior enriched uranium marker remained on the outside surface and was readily polished off. In the second case, the covered enriched marker remained covered and in a narrow band. The uniform increase of activity as the sample was polished would be expected as the alpha-absorbing oxide was removed from the enriched marker.

Acknowledgment

The authors wish to express their indebtedness to S. Rothmann of the Metallurgy Division, Argonne National Laboratory, for his aid in the uranium sputtering technique.

Manuscript received Feb. 29, 1960. Work was performed under the auspices of the U. S. Atomic Energy Commission.

Any discussion of this paper will appear in a Discussion Section to be published in the June 1961 JOURNAL.

REFERENCES

1. A. O. Dravnieks and H. J. McDonald, *J. (and Trans.) Electrochem. Soc.*, **93**, 177 (1948).
2. J. Chirigos and D. E. Thomas, WAPD-53 (1952).
3. C. E. Birchenall, *Ind. Eng. Chem.*, **46**, 893 (1954).
4. O. Kubaschewski and B. E. Hopkins, "Oxidation of Metals and Alloys," pp. 85-86, Academic Press, Inc., New York (1953).
5. J. Bardeen, W. H. Brattain, and W. Shockley, *J. Chem. Phys.*, **14**, 714 (1946).
6. O. Kubaschewski, *loc cit.*, p. 207.
7. H. Inouye, ORNL-1565 (1953).

Further Studies of Leveling Using Radiotracer Techniques

Seward E. Beacom and Bernard J. Riley

Research Laboratories, General Motors Corporation, Warren, Michigan

In a previous paper (1), it was shown by radiotracer techniques that the organic addition agent, sodium allyl sulfonate, which imparts leveling characteristics to a bright nickel plating solution, is preferentially adsorbed onto the peaks of an irregular surface. This was considered to be verification of a part of leveling theory which assumes that the leveling process is initiated by this preferential adsorption on peaks.

The cathodes, which were machined to exhibit a surface of alternate peaks and valleys, had rather large peak-to-peak separations (0.16 cm) and peak-to-valley heights (0.077 cm). Because of questions which have been raised about making interpretations based on cathodes of these dimensions, it seemed important to determine experimentally the limit to which this concept of preferential adsorption could be extended. Thus, a series of machined cathodes of decreasing surface roughness has been prepared and plated in solutions containing the addition agent tagged with S-35. Within the limits of the techniques available, the results show that the concept of preferential adsorption may be extended to include those surfaces which more nearly approach a microprofile dimension.

To establish further the reliability of the results being reported, it was considered desirable to show that the radioactivity observed in the deposits comes from the pure S-35 isotope only and not from some other radioactive impurity. Also, it seemed necessary to show, by an exchange study, that the observed activity comes directly from the sulfonate part of the tagged addition agent and not indirectly by way of an exchange with the sulfate ions present in the plating bath. The results of the investigation demonstrate that the observed activity is due to the presence of pure S-35 and that it comes directly from the sulfonate group.

Experimental and Results

Radiochemical purity of sodium allyl sulfonate.—Several samples of sodium allyl sulfonate tagged with S-35 were prepared (1) and the chemical purity verified by infrared analysis.

To assure that there was no complicating radiochemical impurity present in the compound, decay measurements were carried out over a period of approximately eight months. The agreement of the experimentally obtained half-life value of 87.4 days with the accepted published value of 87 days indicated that, within the limits of counting statistics, there was no appreciable radioactive impurity present.

As further evidence of the presence of pure S-35, a determination of the energy value of the isotope was obtained using the standard technique of the absorption curve. The average half-thickness corresponded to an energy of 0.172 Mev as calculated from the published range energy value (2). This energy agrees, within experimental error, with the literature value of 0.167 Mev.

Plating cell.—Some trouble with stirring patterns, edge effects, and addition agent depletion had been experienced with the 80 ml cell used previously (1). A new round cell, 13.97 cm in diameter by 8.89 cm high, and holding a liter of plating solution, was constructed from Lucite. To accommodate the anode and cathode, slots 2.54 cm wide by 0.32 cm deep were cut vertically into opposite sides of the cell. When used with a propeller stirrer rotating at 100 rpm, edge effects and stirring patterns have been virtually eliminated, and many plating runs can be made before addition agent depletion becomes serious.

Further work on grooved cathodes.—The surface features of representative machined cathodes, as well as the Precision Reference Specimens of Surface Roughness (3), are recorded in Table I. The sulfa-

Table I. Cathode data

Cathode	Machined cathodes Peak-to-peak separation, cm	Machined cathodes Peak-to-valley height, cm	Number of peaks/cm of width
A	0.058	0.028	17
B	0.086	0.043	12
Precision reference-specimens of surface roughness			
SR(350)[a]	0.039	0.0041	26
SR(125)[b]	0.0096	0.0011	102

[a] 350-μin. average roughness.

[b] 125-μin. average roughness.

Table II. Plating, counting, and autoradiographic data

Foil No.	Cathode	Foil thickness, cm	Counts, cpm/cm^2 Top[a]	Counts, cpm/cm^2 Bottom[b]	Exposure time, hr	Detail
87	A	0.0049	3885	3197	25	Good
81	B	0.0052	4732	5137	25	Excellent
85	SR(350)	0.0054	4170	3416	93	Excellent
86	SR(125)	0.0054	4914	4870	93	No detail

Bath composition and plating conditions: nickel sulfate, 300 g/l; nickel chloride, 30 g/l; boric acid, 30 g/l; proprietary wetting agent, 5 ml/l; sodium allyl sulfonate (total) 2 g/l; N-allyl quinaldinium bromide, 4 mg/l; *pH* of 3.0; temperature, 60°C; mild agitation; current density, 7 amp/dm^2; activity in bath, 1.1 × 10^6 cpm/ml of solution.

[a] Surface of foil next to solution during plating.

[b] Surface of foil next to grooved cathode during plating.

mate nickel-plated brass cathodes of known roughness were cleaned, passivated, and then plated in the radioactive plating bath. The plate was removed as a foil which was thoroughly rinsed, dried, and retained for examination of radioactivity (1). A summary of the plating conditions and the counting and autoradiographic data is given in Table II. All autoradiography was done with Eastman Kodak Autoradiographic A film. Figure 1 is the autoradiogram and densitometer trace for foil number 85 which was chosen as representative of the results obtained. It is apparent from this autoradiogram that

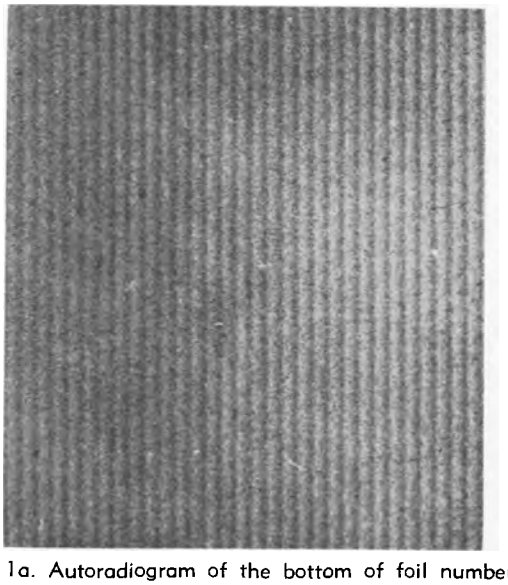

Fig. 1a. Autoradiogram of the bottom of foil number 85 with 26 peaks/cm of width.

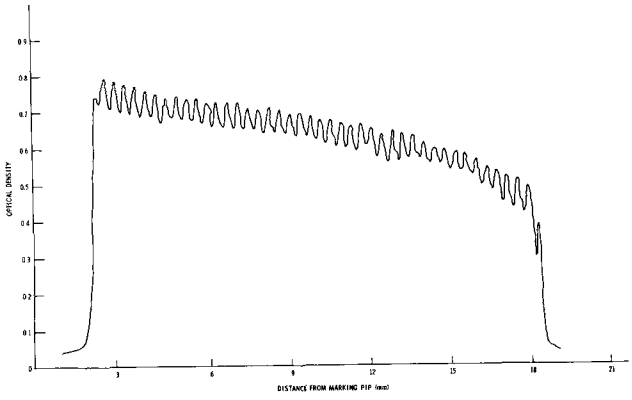

Fig. 1b. Densitometer trace of the autoradiogram shown in Fig. 1a.

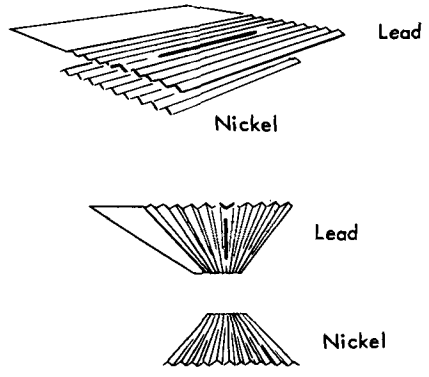

Fig. 2. Sketch of slitted lead foil counting arrangement. The heavy line on the accented peak locates the slit.

the degree of surface roughness does not affect the results within the limits of resolution of the film. Due to this limitation, however, it has not been possible to obtain a satisfactory autoradiogram from the 125-μin. specimen.

Figure 2 shows a stylized sketch of the slit-counting arrangement which has been used to supplement autoradiography (1). Matching slitted lead foils were prepared for the machined cathodes listed in Table I. Data from the counting profiles of portions of the foils, as shown in Table III, also indicate preferential adsorption on the peaks. It was not possible

Table III. Lead slit counting data

Peak	Top	Recess	Bottom	Obverse of peak	Obverse of recess
		Cathode A			
301		240		219	200
316		279		257	254
305		281		347	323
291		232		278	301
294		293		395	326
286		270		359	308
425		327		383	315
		Cathode B			
692		664		720	685
642		514		628	555
570		568		652	502
535		524		679	517
521		494		569	576
487		484		637	534
549		493		553	528
499		484		536	527

Table IV. S-35 tagged sulfate plating and counting data

Foil No.	Activity, cpm/ml of soln.	Counts Top[a]	Counts Bottom[b]	Counts per minute/cm² Top[a]	Counts per minute/cm² Bottom[b]
93	7.5×10^5	58	69	6	7
94	7.5×10^5	52	56	6	6
95	1.5×10^6	86	97	9	10
96	1.5×10^6	89	86	9	9
97	3.0×10^6	165	181	18	19
98	3.0×10^6	144	152	15	16
99	6.0×10^6	238	280	25	30
100	6.0×10^6	240	260	25	28

[a] Surface of foil next to solution during plating.

[b] Surface of foil next to cathode during plating.

to prepare slitted lead foils for examination of the Precision Reference Specimens of Surface Roughness.

Sulfate ion exchange.—Using S-35 tagged sulfate (as H_2SO_4), 1 in.² steel shim stock samples were plated under conditions identical to those used with the S-35 tagged sodium allyl sulfonate. The radioactive H_2SO_4, with a specific activity of 50 mc/ml, was added in increasing amounts to the bright nickel plating bath. The starting concentration of 7.5 x 10^5 cpm/ml of plating solution represented an activity which was close to that used for the S-35 tagged sodium allyl sulfonate experiments. A summary of the results is given in Table IV. At an activity level of 1.5 x 10^6 cpm of the tagged sulfate per milliliter of plating solution, approximately 9 cpm/cm² of sulfate pickup is observed. This is compared with the 5000 cpm/cm² pickup from the tagged sodium allyl sulfonate at the same level of activity. It appears from the small amount of sulfate activity recovered that the exchange reaction, if it occurs at all, must be quite negligible, and that the source of activity found in the deposits comes directly from the sulfonate and not by exchange from the sulfate ions. The very low remaining activity due to sulfate may result from a slight general surface adsorption of sulfate ion.

Discussion

The concept of the preferential adsorption of addition agents on the peaks of irregular surfaces which is verified experimentally in this work is additional support for results previously reported (1). It seems likely that this adsorption produces at least in part the polarization effects, noticed by other investigators, which may lead to the leveling phenomenon.

Experimental work in this laboratory has shown that leveling occurs on surfaces which have an average surface roughness of 125, 50 and 20 μin. If leveling theory is correct, then it seems reasonable to assume that preferential adsorption also occurs on the peaks of these surfaces which possess a more nearly microprofile dimension. It appears that only experimental difficulties have prevented verification of this assumption.

Manuscript received March 16, 1960.

Any discussion of this paper will appear in a Discussion Section to be published in the June 1961 JOURNAL.

REFERENCES

1. S.E. Beacom and B. J. Riley, *This Journal*, **106**, 309 (1959).
2. C. Coryell and N. Sugarman, "Radiochemical Studies: The Fission Products," Vol. I, p. 18, McGraw-Hill Book Co., Inc., New York (1951).
3. J. D. Thomas, *Proc. Am. Electroplaters' Soc.*, **43**, 60 (1956).

Electrochemiluminescence at a Silicon Anode in Contact with an Electrolyte

Allen Gee

Semiconductor Division, Texas Instruments Inc., Dallas, Texas

In the study of stain films on single-crystal silicon, emission of light has been observed during the anodic oxidation of the film. This film can be formed from the substrate either electrochemically when HF is the electrolyte by the method of Turner (1) or chemically by the method of Archer (2). This note deals principally with the chemically formed film designated as Type I amorphous silicon by Archer because luminescence is more easily observed.

Experimental

A slice of 5 ohm-cm, boron-doped, p-type silicon having 1.2 cm² of its 111 face exposed is sealed with wax to the bottom of a polyethylene cell. Two ohmic contacts to the silicon are made on the under side. After the cell is filled with electrolyte, a platinum electrode and a saturated calomel electrode are inserted from the top. A constant current source is connected between one ohmic contact and the platinum electrode. The voltage between the other ohmic contact and the calomel electrode is fed to a recorder.

Before forming the film, the chemically polished surface of the silicon is treated for a few seconds with a slow etch (10 volumes 70% HNO_3 to 1 volume 49% HF) and then thoroughly rinsed with water. The film is grown by treatment with a 49% HF solution containing about 0.1% HNO_3 until a blue interference color is visible.

Results

With almost any neutral or acid electrolyte, the voltage of the film-covered silicon electrode at constant anodic current increases with time in the manner shown in Fig. 1. The plateau between 0.5 and 1 v represents a region where ready oxidation occurs. Visible light is emitted in the last half to the last fourth of this region, and passivation, indicated by

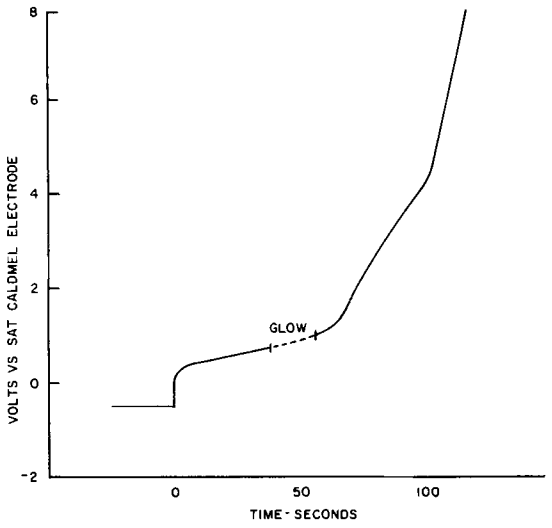

Fig. 1. Voltage of 5 ohm-cm p-type silicon anode coated with Type I film in 1M H_2SO_4. Current density, 1.6 ma/cm² after time zero. Period of luminescence shown on curve.

the sharp voltage rise, always sets in as soon as the luminescence disappears. On the same scale, a film-free silicon electrode gives a near vertical trace.

The faint, reddish glow usually starts at a single point, expands to cover the entire surface, and then contracts to a point away from the area where it started. On some occasions, various areas of the surface glow successively. The luminescence is responsive to short pulses of current, and the pattern of glow is not changed by current interruptions. Color of the emitted light has not been found to vary perceptibly and is not a function of the electrolyte. In subdued lighting, a rather bright flash is seen when the current density is 10 ma/cm². In near darkness, a prolonged glow is detectable at 0.2 ma/cm².

Attempts to obtain quantitative data to correlate with such parameters as the thickness of the film (2) have been disappointing. For many measurements, the entire plateau of Fig. 1 corresponds to the passage of 30-100 millicoulomb/cm². Within such wide limits, the exact procedure for forming the film is not critical.

Luminescence occurs in any indifferent electrolyte such as 1M solutions of KCl, LiCl, H_2SO_4, HNO_3, and acetic acid. Basic solutions (such as 1M NH_4OH), as well as 1M KF, or 20% NH_4HF_2 dissolve the film so that the film-free characteristics are obtained. When the electrolyte is HF, no luminescence or passivation occurs, but light is emitted when the electrolyte is 0.5M KF in acetic acid buffer.

Treatment of the film with most oxidizing agents (dilute solutions of dichromate, permanganate, copper salts; 30% H_2O_2, 70% HNO_3, Br_2 vapor) decreases the amount of oxidizable materials as measured anodically and reduces or eliminates the luminescence. Neutral or acid persulfate and reducing agents in general have little effect. Allowing the film to dry in room air for 16 hr does not alter its properties.

The emission of light accompanies anodic oxidation and is not the result of local heating. By making contact to the film with mercury instead of an electrolyte, current can be passed through the film without evidence of glow. Passage of 25 ma/cm² through the film in either direction for several minutes does not produce any significant change in the subsequent anodic behavior.

The original blue film becomes scarcely visible after anodic treatment. A fresh amorphous silicon film can be grown without etching off the anodized film. When formed in this manner, normal anodic behavior is observed except that the interference colors are now only slightly affected. Unlike the original film, the anodized film seems not to dissolve in dilute bases with evolution of gas even though there is a slight change in appearance.

Passage of cathodic currents until hydrogen evolution is visible has little effect on the original film and does not reduce the anodized film. A p-type semiconductor electrode is known (1, 3) to offer lower resistance to current flow in the anode direction. Application of 60 cycle power instead of d.c. to the silicon electrode produces the same luminescence effect for a comparable level of rectified current.

The amorphous silicon film formed anodically in 49% HF simply by shorting the silicon to a platinum electrode exhibits different and more erratic properties. Luminescence has been detected only at current densities greater than 5 ma/cm² and sometimes not at all.

Luminescence has not been observed on film-covered n-type silicon. Since only a few samples of silicon have been examined, no definite statement relating the phenomenon to the nature of the substrate can yet be made. Further efforts are directed toward locating the region within the film from which light is emitted and toward elucidating the mechanisms involved.

Manuscript received April 29, 1960.

Any discussion of this paper will appear in a Discussion Section to be published in the June 1961 JOURNAL.

REFERENCES

1. D. R. Turner, *This Journal*, **105**, 402 (1958).
2. R. J. Archer, Second Conf. on Semiconductor Surfaces, Washington, D. C., Dec. 1959.
3. W. H. Brattain and C. G. B. Garrett, *Bell System Tech. J.*, **34**, 129 (1955).

A PNP High-Frequency Silicon Transistor

W. A. Little

Texas Instruments Inc., Dallas, Texas

NPN high-frequency silicon transistors were described originally by Tanenbaum and Thomas (1), and more recently a switching transistor was described by Aschner, *et al.* (2). The need for complementary-type switching transistors has led to the development of a PNP silicon double-diffused transistor which is described in this paper. The essential features of this transistor are shown in Fig. 1. Solid-state diffusion techniques are used to obtain the high degree of control required for high-frequency devices. Oxide masking techniques are used to provide exposed emitter and base areas at the surface and to control the emitter geometry. Contact of the exposed regions is obtained by evaporated metal stripes. Electrical characteristics of transistors prepared in this manner are described.

Fabrication

Transistors are fabricated by starting with 1-3 ohm-cm p-type silicon wafers that have been lapped and optically polished flat to provide a uniform surface. An n-type layer with a surface concentration of between 10^{17} and 10^{19} atoms/cm^3 is diffused into the parent p-type material to a depth of 4-5 μ. This is accomplished by an open-tube diffusion process similar to the one described by Frosch and Derick (3). Red phosphorus is used as a diffusant to obtain these values of surface concentration.

This base layer diffusion actually is done in two steps as is shown schematically in the diagram of Fig. 2, which is adapted from Fig. 2 of Aschner, *et al.* (2). First, a thin concentrated n-layer is deposited on the silicon wafer. In the second step, the source of phosphorus is removed from the combustion tube and wet oxygen is used to grow an oxide layer 5000-8000Å thick. During this time, the n-layer is diffused into the wafer to the desired depth.

The purpose of the oxide layer is to provide a mask against the subsequent emitter diffusion on portions of the exposed surface where direct contact to the base region is required. In order to produce the selective mask to accomplish this, a photographic process is used to remove the oxide selectively. This is the same type of process that is used to form the etched wiring of printed circuit boards. A photosensitive liquid, termed the resist, is applied to the surface of the oxidized silicon wafer. Upon drying, this liquid forms a thin photosensitive coating which adheres strongly to the oxide coating of the wafer. The resist coating may then be exposed using ultraviolet light and contact printing, through an ordinary film negative which contains the desired pattern. The resist is then developed in trichloroethylene. The portions of the resist that were protected by the opaque regions of the film negative

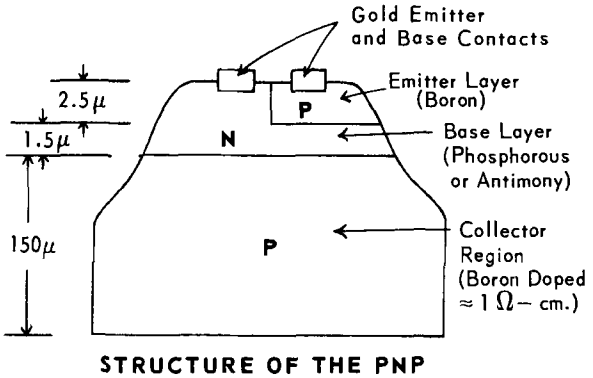

STRUCTURE OF THE PNP TRANSISTOR

Fig. 1. Geometry of PNP transistor

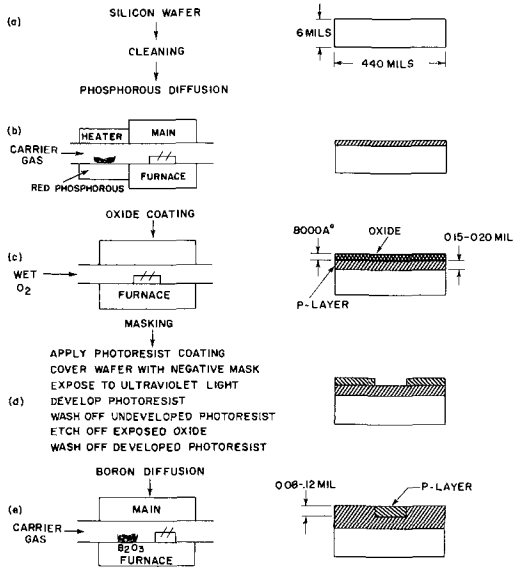

Fig. 2. Detail of diffusion and oxide masking techniques

Fig. 3. Photomicrograph of an oxide masked double-diffused wafer. The junctions have been exposed by bevel lapping and polishing at an angle of about 5° and staining the p regions.

and, hence, were not exposed to the ultraviolet light, are washed away by the developer. The resist pattern thus forms a protective coating over the oxide which limits the attack of etches to those regions not covered by the resist. If the sample is placed in a weak etch, the oxide in these regions will be removed completely down to the silicon substrate. Then the developed resist can be removed easily with an organic solvent, leaving the desired oxide diffusion mask. In addition to producing extremely sharp, well-defined patterns the photo resist process allows a quick and simple method of changing device geometry merely by changing the film negative pattern. In the evaluation units fabricated to date, a simple bar pattern has been used, ultimately leading to a wafer having alternate base and emitter regions exposed.

After the wafer has been prepared with the oxide mask of suitable geometry, a diffused p-type layer 2 μ to 3 μ deep with a surface concentration of approximately 10^{20} atoms/cm^3 is superimposed on the n-layer. This is accomplished by means of an open tube diffusion process in which the source of diffusant (boric acid) was placed in the furnace beside the silicon wafers.

To illustrate the degree of control obtained in this process, a photomicrograph is shown in Fig. 3. This was made by lapping and polishing the wafers at an angle of five degrees to the surface and staining the emitter and collector with a hydrofluoric-nitric acid etch (4) to delineate the junctions clearly. In Fig. 3 it can be seen that the collector and emitter junctions are quite planar. Also, any imperfections are much less than the layer thicknesses. This photograph shows the alternately exposed emitter and base regions produced by oxide masking. Interference microscopy (5) techniques were used in measuring the thickness of the thin diffused layers.

The next step is the metal evaporation of emitter and base stripes through a mask. In order to secure proper placement of the metal stripes, the evaporation mask must be indexed with respect to the negative mask used in preparing the wafers for emitter diffusion. Close control of the vacuum deposition is necessary to secure placement of the stripes on the desired area about 0.5-1 mil from the line marking the boundary between base and emitter.

After alloying the gold emitter and base stripes in an r.f. heater at about 750°-850°C, the squares are ready for mesa masking and etching. The remainder of the fabrication process follows standard procedures for dicing of squares into individual units, bonding the collector to the header, bonding leads to the base and emitter stripes, and encapsulating the units. Figure 4 is a photomicrograph of a completed device showing emitter and base stripes and the bonded leads.

Electrical Characteristics

Electrical characteristics of a PNP silicon high-frequency transistor prepared by the techniques described above are presented here. During fabrication of experimental devices, base widths were deliberately varied from about 1 to 2 μ. The characteristics described below are for an intermediate

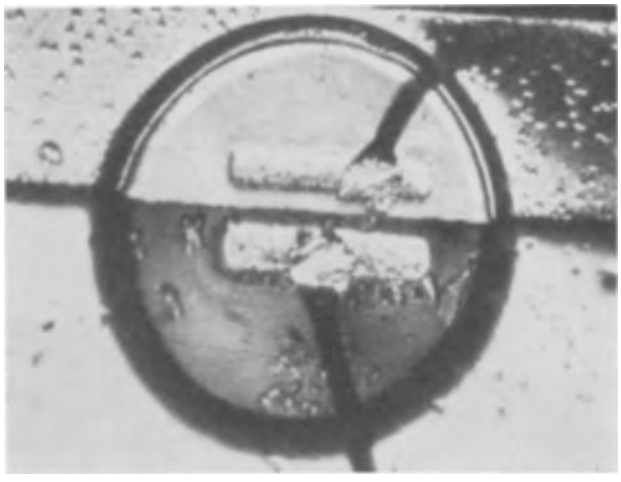

Fig. 4. Photomicrograph of completed unit showing the gold stripes and bonded leads.

base width of 1-½ μ. In such a device, typical collector-base breakdown voltage was of the order of 35 v, while the emitter-base breakdown voltage was 9 v. At a typical d-c bias condition of 10 ma emitter current, with collector-base voltage $V_{CB} = 6$ v, the d-c forward current transfer ratio h_{FE} was 35, and the d-c forward voltage drop V_{BE} was of the order of 0.8 v.

High-frequency characteristics of a typical device are illustrated by Fig. 5. The common-emitter current transfer ratio h_{fe}, shown as a function of frequency, decreases inversely with increasing frequency to a value of 1 at a frequency (f_T) of 200 mc. Common-emitter input resistance $R_e(h_{ie})$, also shown in Fig. 5, decreases with increasing frequency and appears to approach a limiting value of the order of 45 ohms at high frequencies. Hence, this value can be taken as essentially equal to the high-frequency base resistance of the unit. Collector transition capacitance at a reverse bias of 6 v is approximately 3 pf, whereas the emitter transition capacitance (at reverse bias of 3 v) is somewhat larger—3.8 pf. This reflects the fact that, even though the emitter-base area is less than the collector-base area, the emitter-base junction gradient is considerably steeper than that at the collector-base junction.

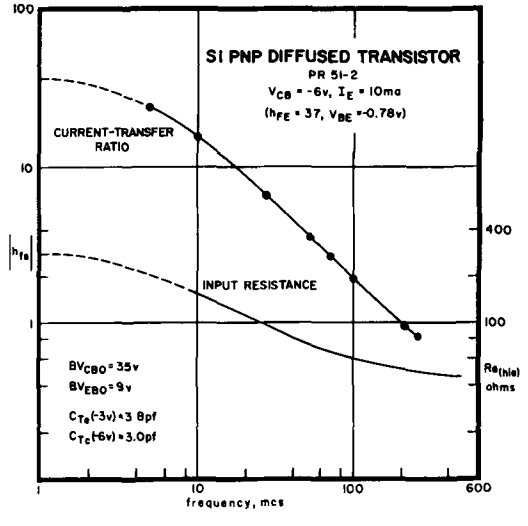

Fig. 5. The current transfer ratio and input resistance vs. frequency for a typical unit.

Acknowledgments

The writer is grateful for the helpful discussions and suggestions of R. L. Pritchard, and wishes to thank Jay W. Lathrop, L. E. Barnes, and R. L. Martin for assistance with experiments. Thanks are also due to George Pierson for measuring the parameters for the experimental transistors.

Manuscript received March 24, 1960. This paper was presented at the Washington, D. C., Meeting of Electron Devices, 1959.

Any discussion of this paper will appear in a Discussion Section to be published in the June 1961 JOURNAL.

REFERENCES

1. M. Tanenbaum and D. E. Thomas, *Bell System Tech. J.*, **35**, 1 (1956).
2. J. F. Aschner, C. A. Bittmann, W. F. Hare, and J. J. Kleimack, *This Journal*, **106**, 415 (1959).
3. C. J. Frosch and L. Derick, *ibid.*, **104**, 547 (1957).
4. C. S. Fuller and J. A. Ditzenberger, *J. Appl. Phys.*, **27**, 544 (1956).
5. W. L. Bond and F. M. Smits, *Bell System Tech. J.*, **35**, 1209 (1956).

Technical Review

Report of the Chlor-Alkali Committee of the Industrial Electrolytic Division for the Year 1959

Nelson J. Ehlers

Columbia-Southern Chemical Corporation, Pittsburgh, Pennsylvania

Clifford A. Hampel

Skokie, Illinois

Chlorine-Caustic

Production and Sales

Chlorine and caustic soda production in the U. S. was at an all-time high in 1959. With about 4,285,000 ton production of chlorine, the increase above 1958 was nearly 19%. U. S. capacity as reported by The Chlorine Institute was near 14,100 TPD at the end of the year, which means the industry operated at 83% of capacity in 1959. Apparent per capita consumption was 48.2 lb, an all-time high and double that of 1949.

After a substantial chlorine production increase in 1959, it is felt by many that prospects for future growth are good. Recent publicized estimates of growth indicate from 7 to 8.5% per year growth from 1960 to 1970. Another source estimates an increase of 70% in chlorine and 50% in caustic soda during the ten-year period.

Canadian chlorine production in 1959 was about 287,000 tons as compared to 268,000 in 1958. Indications are that about 305,000 tons will be produced in 1960.

Caustic soda production in the U. S. increased 17% above 1958, for a total of about 4,675,000 tons in 1959. The apparent per capita consumption was 50.0 lb, an all-time high, which was nearly twice that of 27.3 in 1949. Lime soda caustic production data are not available, but it is estimated such production was some 300,000 to 325,000 tons for the year.

Even though caustic is being converted to soda ash on a relatively small scale, soda ash continues to be converted to lime soda caustic. Some sources believe that caustic was more in excess during 1959 than in the previous year.

Table I. U.S. sources of chlorine

	1959 (preliminary)		1958	
	Tons	%	Tons	%
Cl_2 equiv. of NaOH	3,997,200	93.3	3,319,042	92.1
Cl_2 equiv. of KOH	58,900	1.4	48,736	1.3
Cl_2 equiv. of Na	172,500	4.0	169,857	4.7
Cl_2 equiv. (others) *	56,400	1.3	66,903	1.9
Cl_2 total gas produced	4,285,000	100.0	3,604,538	100.0

* By difference.

About 75% of the capacity of chlorine in 1959 was in diaphragm cells, 19% was in mercury cells, 5% in sodium cells, and less than 1% in nonelectrolytic processes. Two-thirds of the capacity added in 1959 was in diaphragm cells and one-third in mercury cells.

Estimated sources of chlorine comparing 1959 with 1958 appear in Table I.

New Plants and Expansions

U. S. chlorine capacity increases amounted to about 760 TPD in 1959 as compared to 640 TPD in 1958, and are believed to be as shown on p. 792.

Diamond Alkali completed modernization of facilities at Painesville, Ohio, using Diamond diaphragm cells to replace Tucker-Windecker cells, while Frontier Chemical at Wichita, Kans., completed modernization using Hooker S-3B cells. Chlorine producing plants of Gulf at Port Arthur, Texas, and West Virginia Pulp & Paper at Luke, Md., were shut down in January 1959.

Increased facilities for 1960 and 1961 are believed to be as shown on p. 792.

1959 Increase

Company	Site	Type Cells	Quantity, TPD
Diamond Alkali Co.	Deer Park, Texas	DeNora Mercury Cells	200
Jefferson Chemical Co.	Port Neches, Texas	Hooker S-3B Cells	150
Stauffer Chemical Co.	Niagara Falls, N. Y.	Hooker S-3M Cells	30
Weyerhaeuser Timber Co.	Longview, Wash.	DeNora Mercury Cells	80
Wyandotte Chemicals Corp.	Geismar, La.	Diamond Diaphragm Cells	300

1960-61 Increase

Company	Site	Type Cells	Quantity
Dow Chemical Co.	Plaquemine, La.	—	Expansion
Food Machinery & Chemical Corp.	S. Charleston, W. Va.	Hooker S-3B	Modernization and modest expansion
Hooker Chemical Corp.	Niagara Falls, N. Y.	Uhde Mercury	100 TPD
Kolker Chemical Corp.	Newark, N. J.	Hooker S	50 TPD
Olin Mathieson Chemical Corp.	McIntosh, Ala.	Mathieson (E-11) Mercury	125 TPD
Olin Mathieson Chemical Corp.	Niagara Falls, N .Y.	Mathieson (E-11) Mercury	About 50% increase
Pennsalt Chemicals Corp.	Wyandotte, Mich.	Gibbs	Modernization
Stauffer Chemical Co.	Henderson, Nev.	Hooker S	45 TPD

An estimate of chlorine capacity by companies appeared in the *Chemical & Engineering News,* December 14, 1959, p. 38.

The Canadian capacity at the end of 1959 is estimated by The Chlorine Institute of about 950 TPD. Western Chemicals Ltd., Duvernay, Alta., brought a 20 TPD diaphragm cell expansion on line in 1959. Consolidated Mining & Smelting Co. has announced plans for construction of a $2.6 million chlorine-alkali plant at Trail, B. C. Canadian Industries Ltd. has announced conversion of a number of mercury cells from NaOH to KOH. Pennsalt is apparently firming up its plans for a plant in the Vancouver, B.C., area.

Markets and End-Use Patterns

There does not appear to have been a major change in the end-use patterns for chlorine and caustic during 1959. The use of chlorine dioxide for bleaching in the pulp and paper industry is gaining in importance and is affecting chlorine usage.

The present use of chlorine in the extraction of titanium, zirconium, hafnium, columbium, and tantalum suggests the need for serious consideration of its use in the recovery of other metals. DuPont is using titanium tetrachloride for the production of titanium dioxide at its New Johnsonville, Tenn., plant. The general interest in this use for titanium tetrachloride could lead to a substantial use of chlorine in the future.

Table II. Chlorine—caustic soda end-use pattern*

Chlorine	%	Caustic soda	%
Chemicals	80.7	Chemicals	32.4
Pulp & paper	15.9	Rayon, film	14.9
Sanitation	3.2	Pulp & paper	11.4
Others	0.2	Soap, cleaners	6.0
		Petroleum refining	5.4
		Textiles	5.4
		Net exports	5.3
		Others	19.2
Total	100.0	Total	100.0

* Courtesy of Diamond Alkali Co.

The end-use pattern of caustic remains quite diversified. The alkali industry is watching the nylon-rayon battle for supremacy in the tire industry. Rayon remains the largest single use of caustic soda. The further application of caustic in the pulp and paper industry looks promising.

Table II gives a recent estimated end-use pattern for chlorine and caustic soda in 1959.

Technical Developments

With recent price reductions in power rectification units of silicon and germanium, the trend toward this type of unit will continue, especially where cell amperages are high and circuit voltages are low.

The interest of industry in platinum-titanium anodes for diaphragm and mercury cells continues. Articles of interest appeared in *Chemical Week,* December 12, 1959, p. 67, and *Chemical Week,* December 26, 1959, p. 50. The patent situation is not yet clear. Test installations exist but it is doubtful if any chlorine producer in the U. S., Canada, or England has made a decision at present for a large-scale installation.

For the first time in the U. S., liquid chlorine is being transported from a producer to a consumer in a tank truck (see *Chemical Week,* March 19, 1960, p. 31). Barge shipments of chlorine to large consumers on the Gulf and Atlantic shores, as well as on inland waterways, continue to increase.

The Chlorine Institute, Inc., continues a most aggressive program for the safe handling of chlorine in transportation and in producing and consuming plants.

Monsanto Chemical Co. continues to offer the DeNora cell for recovery of chlorine from hydrochloric acid. Although considerable interest has been shown, it is doubtful if a large-scale installation has been initiated at present.

Among articles of interest appearing recently, which have not otherwise been cited, were: "Chlorine Output Hits New High," *Chemical & Engineering News,* Dec. 14, 1959, p. 38; "Confidence Keys Chlorine Makers Outlook," *Chemical Week,* March 7, 1959, p. 113; "Chemical Forecast—1964," Chemical Market Research Association Report—*Oil,*

Paint & Drug Reporter, Sept. 28, 1959, pp. 44 and 47; "Alkalis and Chlorine Industry—Outlook for 1960 and Review of 1959," *U. S. Dept. of Commerce, BDSA, Chemical & Rubber Div.*, ER-59-86; "Cell Users Get New Fuel for Old Debate," *Chemical Week*, March 5, 1960, p. 95; "Graphitized Anodes in the Electrolysis of Aqueous Chloride Solutions," V. V. Stender and O. S. Ksenzhek, *J. Applied Chem., USSR*, **32** (1), 111 (1959);[1] "Influence of Electrolyte Composition on the Distribution of Current Inside a Graphite Anode and on Its Internal Wear," B. M. Bulygin, *J. Applied Chem., USSR*, **32** (1), 122 (1959).[1]

Among U. S. patents of interest which issued recently are: 2,868,711, electrolytic cell; 2,870,074, electrolysis of alkali metal chloride brine; 2,872,291, process and apparatus for the decomposition of alkali metal amalgams; 2,872,403, electrolytic cell; 2,884,-310, production of alkali metal hydroxides by ion exchange; 2,887,448, fused salt cell; 2,898,284, mercury cathode chlorine cell; 2,919,238, fused salt electrolytic cells.

Soda Ash

The U. S. production of soda ash increased about 13% from 1958 to 5,611,600 tons in 1959, thus reversing the downward trend since 1956. The only year of higher production was in 1956. The apparent per capita consumption was 61.6 lb for 1959, which was equal to the average of the years 1949 to 1959 inclusive. It is evident the per capita consumption of soda ash has not changed since the early 1940's. The U. S. industry operated at about 80% capacity in 1959; 12.7 % of the production was "natural soda" and 87.3% was "synthetic."

Diamond Alkali is engaged in a modernization program of its soda ash producing facilities at Painesville, Ohio. Dow Chemical Co. continues to operate its plant at Freeport, Texas, converting electrolytic caustic to soda ash. Dow is reported to be studying the possibility of increasing its capacity to produce soda ash. Considerable interest in the trona deposits in Wyoming has been indicated by several producers and potential producers of soda ash. Food Machinery & Chemical Corp. continues to expand in soda ash in Wyoming, and capacity is now in the 550,000 ton per year range.

Miscellaneous Chemicals

Potassium hydroxide.—Production of KOH (88-92%) increased about 21%, from 76,870 tons in 1958 to 92,869 tons in 1959. The trend toward high-purity KOH from mercury cells continues.

Chlorates.—The American Potash and Chemical Corp. began an expansion of its sodium chlorate facilities at Aberdeen, Miss., which will increase capacity to 25,000 tons per year. Hooker Chemical Corp. placed an additional circuit on line at its Columbus, Miss., plant, bringing capacity there to over 24,000 tons per year. Pennsalt Chemicals Corp. announced plans to expand its Portland, Oreg., sodium chlorate plant by 25%. The formation of the Penn-Olin Chemical Corp. was announced with the intent to construct a 25,000 ton per year sodium chlorate plant at Calvert, Ky. The new plant of Standard Chemical Ltd. at Beauharnois, Que., was placed in operation during late 1959. A review of markets for chlorates and perchlorates during 1958 and 1959 was published in *Chemical and Rubber*, August 1959.

Sodium chlorate production in 1959 was 87,665 tons, which was an increase of about 30% above the 67,249 ton production in 1958. Production has more than doubled since 1954.

Perchlorates. —Continued interest in solid-fueled missiles and the use of ammonium perchlorate as an oxidizer led to the announcement of plans by Pennsalt Chemicals Corp. to expand its plant at Portland, Oreg., by several thousand tons per year. During 1960, the Navy declared the ammonium perchlorate plant at Henderson, Nev., which is operated by the American Potash and Chemical Corp., as surplus to its needs, and arrangements are being made for disposal.

Miscellaneous Metals

Aluminum.—The production of aluminum in this country continues to grow. The primary production in 1959 of 1,953,000 tons set a new record; it was 25% above 1958 and 16% above 1956, the previous peak year for aluminum. Canada showed a decrease of 46,000 tons, or 7% less than 1958 production, during the past year.

At the end of 1959, total domestic capacity amounted to 2.4 million tons. New production facilities in 1959 included: (*a*) Ormet Corp. started its fifth and last pot line at its 180,000 ton per year plant at Clarington, Ohio; (*b*) Kaiser Aluminum & Chemical Corp. installed two new lines to complete its 145,000 ton per year plant at Ravenswood, W. Va.; and (c) Reynolds Metals Co. completed three lines at its new plant at Massena, N. Y., each having a capacity of 33,000 tons per year.

New aluminum prices established in December are 26¢ per lb for pig and 28.1¢ per lb for ingot.

Magnesium.—Consumption of primary magnesium reached about 44,000 tons in 1959, an increase of some 25% over 1958. While primary production of magnesium has been increasing steadily since 1958, the production rate of some 3,000 tons per month at the end of the year is still less than the consumption rate, although this production rate will be increased during 1960.

Alabama Metallurgical Corp., a new producer, began production of magnesium by the ferrosilicon reduction of dolomite last fall. This year, it should reach its anticipated capacity of 6 to 7,000 tons per year. The company is jointly owned by Calumet & Hecla and Brooks & Perkins.

The brightest possibility for significant expansion of the nonmilitary use of magnesium lies in its use in the engines of the lightweight automobiles. Expectations are that total consumption of primary magnesium will reach 45-50,000 tons in 1960, but the automotive die-casting outlet may cause an increase above this figure.

Sodium.—The production of sodium reached 112,-019 tons in 1959, only slightly more than the 1958 output and still much less than the 133,000 tons made in 1957. It is evident that with the production

[1] Reference pages of the English translation.

capacity at about 200,000 tons per year, the sodium industry faces for some time to come the problem of idle plant capacity.

Titanium.—During the first half of 1959, production and consumption of titanium sponge were at rates slightly greater than the 1958 average annual rate. In the second half of 1959, the steel strike cut the consumption of titanium sponge, and the production rate dropped accordingly. Imports of titanium sponge were about three quarters of the 1958 rate. In spite of the handicap of the steel strike, production of mill products increased. According to BDSA, in the near future consumption of titanium mill products will be reduced because of the cancellation of some defense aircraft programs which would have consumed substantial quantities of mill products. The growing use of titanium in construction of civilian aircraft, in missiles, and in the chemical process industries will only partly compensate for this loss. Therefore, consumption and production of titanium mill products in 1960 may be lower than in 1959. Growth in these uses and in other civilian applications is confidently expected in the future. Recently, ICI mentioned growth in the use of titanium in surgical implants, and suggests the use of titanium in nuclear applications because of the rapid dissipation of radioactivity which is formed when titanium is exposed to intense radiation. The development of new titanium alloys with improved qualities continues at a high rate.

An article of interest appears in *Chemical Engineering,* Feb. 22, 1960, p. 66

The Bureau of Mines and the Business and Defense Services Administration report the following figures:

	Sponge			Mill Products
	Production tons	Imports tons	Consumption tons	Shipments tons
1955	7,398	567	4,145 (est.)	1,898
1956	14,595	2,048	10,936	5,166
1957	17,249	3,532	8,221	5,658
1958	4,585	2,072	4,147	2,594
1959*	3,898	1,563	3,953	3,211

* Based on estimate, 10 months.

Zirconium.—The three companies, Carborundum Metals Co., Mallory-Sharon Metals Corp., and Columbia-National Corp., continue to supply zirconium sponge to the Atomic Energy Commission under contract. Columbia-National temporarily discontinued operations in December, 1959, because of a sponge quality problem with the AEC. The production of these three producers remains a little above 2,200,000 lb per year, and no future expansion of sponge producing facilities is planned at the present time.

Manganese.—The consumption of manganese metal derived by the electrolytic process amounted to 12,732 tons in 1959. This quantity would have been greater but for the long steel strike which began in July. At that time, the consumption had reached about 9,000 tons. Over 80% of this metal is used in the preparation of steel ingots, chiefly of the stainless variety.

Lithium.—The drastic cutback in the preparation of boron high-energy fuels caused the cessation in the production of lithium, as intermediate in the process, at the Olin Mathieson Chemical Corp. plant at Model City, N. Y. This plant had sufficient capacity to be a major producer of lithium by the electrolysis of fused lithium chloride admixed with potassium chloride in Downs type cells.

Beryllium.—Pure beryllium metal is made in the United States by the reduction of beryllium fluoride with magnesium. Both producers, Brush Beryllium Co. and Beryllium Corp., reported higher production of the metal in 1959 over 1958. It is estimated that production reached about 150,000 lb in 1959, compared with 50,000 lb in 1958, and it is expected that the figure will approach 300,000 lb in 1960 (*Chemical Week,* Feb. 20, 1960). Chief outlets for beryllium are in nuclear and space applications.

Chromium.—The electrolysis of ammonium chromium sulfate solution continues to be the premier source of the highest purity chromium metal. Production in 1959 probably reached about 2,000 tons, the reported capacity of the Union Carbide Metals Co.'s Marietta, Ohio plant.

Tantalum and columbium.—Tantalum production was estimated to be well over 300,000 lb in 1959, a sizable increase over the 1958 figure. Most of the metal is obtained either by the electrolysis of fused potassium fluotantalate or by sodium reduction of this and other tantalum compounds. Most of the metal is consumed in electronic applications, chiefly as capacitors. The production and use of columbium, found in all tantalum ores, are still small, probably around 60,000 lb in 1959.

Prices for tantalum were cut toward the end of the year. Capacitor grade powder dropped to $49.80 per lb from $58.60, and sheet tantalum is priced at $59.16 per lb.

Manuscript received May 31, 1960. This paper was prepared for delivery before the Chicago Meeting, May 1-5, 1960.

Any discussion of this paper will appear in a Discussion Section to be published in the June 1961 JOURNAL.

Separation of the Defect Concentration and Diffusion Coefficient in Diffusion-Limited Scaling Reactions[1]

Arthur J. Rosenburg[2]

Lincoln Laboratory, Massachusetts Institute of Technology, Lexington, Massachusetts

ABSTRACT

In diffusion-limited scaling reactions the rate constant is proportional to the quantity DC_0, where D and C_0 are the diffusion coefficient and the solubility of the defect whose motion through the growing scale is essential to continued reaction. In order to separate D and C_0, recourse is usually made to an independent measurement of one or the other, which is a difficult and frequently unreliable procedure. A new technique is proposed which permits the accurate and simultaneous determination of D and C_0 from reaction rates alone. The method is based on the controlled interruption of a scaling reaction and possesses a rigorous internal check. It is applicable in principle to any such reaction, and the necessary mathematical formulation is presented in a convenient analytical form. Conventional experimental techniques can be used when $C_0 >> 10^{17}$ cm^{-3}. The treatment is illustrated for the oxidation of InSb.

In diffusion-limited scaling reactions, of which the oxidation of metals provides the most familiar examples, direct contact of the reactants is prevented by the formation of a protective scale at the reaction interface. Once such a scale is formed, continued reaction is made possible by the motion of atomic defects through it. Thus, in the oxidation of a metal surface

$$yM + \frac{z}{2} O_2 = M_yO_z \qquad [1]$$

the formation of a nonporous film of M_yO_z on the surface prevents direct access of the oxygen to the underlying metal, but the diffusion of metal or oxygen defects, interstitial atoms or lattice vacancies, charged or uncharged, through the film lets the reaction proceed. One such defect predominates in a given oxide, and the rate at which the film continues to grow is given by (1, 2)

$$dX/dt = k\,X^{-1} \quad k = \Omega D(C_0 - C_1) \qquad [2]$$

where C_0 is the equilibrium concentration of the defect at the interface where it originates, and C_1 is the equilibrium concentration at the interface where the reaction is completed. D is the diffusion coefficient of the defect and is assumed to be independent of concentration. X is the film thickness, and Ω is the increase in the volume of the film which occurs when one defect completes its reaction.[3] Equation [2] assumes that space-charge effects at the boundaries of the oxide can be neglected. This is always the case for uncharged defects, and holds for charged defects when $X >> (\kappa\, kT/8\pi e^2 C_0)^{1/2}$ where κ is the dielectric constant of the oxide (usually ≈ 10), e is the electronic charge, and the other symbols have their usual meanings.

Upon integration Eq. [2] gives the familiar parabolic growth law

$$X^2 = 2kt \qquad [3]$$

It applies in principle to all reactions which are controlled by the diffusion of defects through a scale which deposits at the interface between the reactants. The reactants may be solids, liquids, or gases, and the scale may be solid or liquid, but solid scales at gas-solid, gas-liquid, liquid-solid, or liquid-liquid interfaces are most frequently encountered.

Since C_0 is generally much larger than C_1, and Ω is usually known, measurements of the parabolic rate constant k give the product DC_0 directly. By itself, however, this quantity is of little theoretical value. In order to separate D and C_0, which have fundamental significance, independent measurements of D or C_0 are required. These measurements are not only very difficult to make but are inconclusive unless differences in sample structure and purity are demonstrably negligible.

It is the purpose of this article to discuss a simple experimental method for simultaneously determining the quantities D and C_0. The method uses reaction rate measurements only and is applicable in principle to any scaling reaction described by Eq. [2].

Theory of Interrupted Kinetics of Diffusion-Controlled Scale Formation

We shall consider the generalized reaction

$$aA + bB = S \qquad [4]$$

where the product S forms a flat, nonporous scale which separates the reservoirs containing A and B. It is assumed that a defect enters the A/S interface ($x = 0$) and diffuses to the S/B interface ($x = X$) where it completes the reaction with B causing an increase, Ω, in the volume of the scale. Since the

[1] The work reported in this paper was performed at Lincoln Laboratory, a center for research operated by Massachusetts Institute of Technology with the joint support of the U. S. Army, Navy, and Air Force.

[2] Present address: Materials Research Division, TYCO Incorporated, Waltham, Mass.

[3] If, for instance, the defect is a metal atom, Ω is $1/y$ times the volume of an M_yO_z molecule.

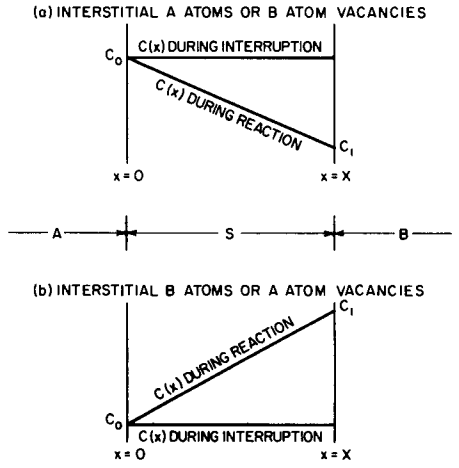

Fig. 1. Concentration of defects in a scale (S) interposed between A and B during the reaction $aA + bB = S$. In each case it is assumed that the supply of B can be interrupted while that of A is held constant.

diffusion of the defect controls the over-all rate, the reaction at each surface goes to equilibrium. The equilibrium concentration of the defect at $x = 0$ is C_0 while that at $x = X$ is C_1 (Fig. 1a). At intermediate positions in the scale the concentration is $C(x)$; if the diffusion coefficient of the defects is independent of $C(x)$, the latter is a linear function of x as shown in Fig. 1a.

Assume that the film has reached a thickness, X, and that its rate of growth is given by Eq. [2]. Let the concentration of B in its reservoir be reduced to a concentration which puts reaction [4] at equilibrium. (In a metal oxidation this would correspond to reducing the oxygen pressure to the dissociation pressure of the oxide.) The defects continue to enter the film at $x = 0$ but are no longer removed at $x = X$. Their concentration approaches C_0 throughout the film, and the reaction stops (Fig. 1a).

If the concentration of B is now suddenly raised to its value prior to the interruption, the flow of defects is resumed and the original concentration distribution is re-established. If C_0X is large enough, the restoration of the concentration gradient should resolve itself as a relatively fast initial uptake of B followed by a gradual return to the rate observed prior to the interruption.

Mathematically, the rate after the interruption can be treated as follows. In addition to requiring that D is independent of $C(x)$ and that the surface is flat, it is assumed that $X >> \Omega\, C_0$ (so the increase of X during this phase of reaction is negligible), and that defects can be created or destroyed only at $x = 0$ and $x = X$. Then at a given temperature,

$$\frac{\partial C(x)}{\partial t} = D\frac{\partial^2 C(x)}{\partial x^2} \qquad [5]$$

with the boundary conditions that

$$\left.\begin{aligned} &C(x) = C_0 \text{ for all } x && \text{when } t = 0\\ &C(x) = C_0 \text{ at } x = 0\\ \text{and}\quad &C(x) = C_1 \text{ at } x = X \end{aligned}\right\} \quad \text{when } t > 0 \qquad [6]$$

where t is measured from the readmission of B to the system. The equation is readily solved by standard techniques (3) giving

$$C(x) = C_0 - \frac{(C_0 - C_1)x}{X} + \frac{2}{\pi}\sum_1^\infty \frac{C_1\cos n\pi - C_0}{n}$$

$$\sin\frac{n\pi x}{X}\, e^{-D'n^2t} + \frac{4C_0}{\pi}\sum_0^\infty \frac{1}{2m+1}\sin(2m+1)$$

$$\pi\frac{x}{X}\, e^{-D'(2m+1)^2t} \qquad [7]$$

where $D' = D\pi^2/X^2$.

By taking the derivative of $C(x)$ with respect to x, evaluating it at $x = X$, and integrating from $t = 0$ to $t = t$, one obtains an expression for Δ, the number of defects crossing unit area at $x = X$ in time t.

$$\Delta = D\int_0^t \left(\frac{\partial C}{\partial x}\right)_{x=X} dt = \frac{D(C_1 - C_0)t}{X}$$

$$-\frac{2X}{\pi^2}\sum_1^\infty [C_1 - C_0(-1)^n]\left[\frac{1}{n^2}\right]$$

$$[e^{-D'n^2t} - 1] + \frac{4C_0X}{\pi^2}\sum_0^\infty \frac{1}{(2m+1)^2}[e^{-D'(2m+1)^2t} - 1] \qquad [8]$$

For most practical purposes $C_1 >> C_0$ and Eq. [8] reduces to

$$\frac{\pi^2\Delta}{XC_0} = 2\sum_1^\infty \frac{(-1)^n}{n^2} - 4\sum_0^\infty \frac{1}{(2m+1)^2}$$

$$- D't + 2\sum_1^\infty \frac{(-1)^n}{n^2}\, e^{-n^2D't}$$

$$+ 4\sum_0^\infty \frac{1}{(2m+1)^2}\, e^{-(2m+1)^2D't} \qquad [9]$$

Equation [9] has been solved numerically with the results given in Table I. The equation has two simple limiting forms. At the beginning of the reaction

$$\Delta = Bt^{1/2} \quad (t << X^2/D) \qquad [10]$$

where

$$B = 1.12\, D^{1/2}\, C_0 \qquad [10a]$$

Later in the reaction

$$\Delta = Q + Rt \quad (t > X^2/2D) \qquad [11]$$

where

$$Q = XC_0/3 \qquad [11a]$$

and

$$R = DC_0/X \qquad [11b]$$

Therefore, while direct rate measurements can at best give the product DC_0/X (Eq. [2] or [11b]) the

Table I. Numerical solution for the diffusion equation of interrupted kinetics, Eq. [9]

$$\frac{\Delta}{XC_0} = \frac{2}{\pi^2}\sum_{1}^{\infty}\frac{(-1)^n}{n^2} + \frac{4}{\pi^2}\sum_{0}^{\infty}\frac{1}{(2m+1)^2} + \frac{Dt}{X^2} - \frac{2}{\pi^2}\sum_{1}^{\infty}\frac{(-1)^n}{n^2}e^{-n^2D\pi^2t/X^2} - \frac{4}{\pi^2}\sum_{0}^{\infty}\frac{1}{(2m+1)^2}e^{-(2m+1)^2D\pi^2t/X^2}$$

Dt/X^2	$(Dt/X^2)^{1/2}$	Δ/XC_0
0.02026	0.1422	0.159
0.03040	0.1744	0.195
0.04053	0.2011	0.226
0.05066	0.2250	0.253
0.06079	0.2466	0.276
0.07092	0.2664	0.299
0.08115	0.2845	0.320
0.09118	0.3020	0.339
0.1013	0.3183	0.357
0.1114	0.3338	0.375
0.1216	0.3485	0.392
0.1317	0.3629	0.408
0.1418	0.3765	0.423
0.1621	0.4026	0.453
0.1824	0.4272	0.480
0.2026	0.4501	0.507
0.2229	0.4720	0.532
0.2432	0.4930	0.556
0.2837	0.5325	0.603
0.3242	0.5694	0.647
0.3647	0.6038	0.691
0.4053	0.6366	0.733
0.5066	0.7117	0.837
0.6079	0.7795	0.939
0.7092	0.8422	1.041
0.8105	0.9002	1.142
0.9118	0.9549	1.243
1.0132	1.0065	1.344

interrupted rate measurements give additional expressions for $D^{1/2}C_0$ (Eq. [10a]) and XC_0 (Eq. [11a]). A separation of D and C_0 is thus effected; in terms of the parameters in Eq. [10] and [11] one obtains

$$C_0 = \frac{0.8}{X}\frac{B^2}{R} \qquad [12]$$

$$C_0 = 3Q/X \qquad [13]$$

$$D = 1.25\left(\frac{RX}{B}\right)^2 \qquad [14]$$

It is clear from Eq. [12] and [13] that the parent Eq. [9] is overdetermined, since three independently measurable experimental quantities, B, Q, and R, must be quantitatively described with only two adjustable parameters, D/X^2 and XC_0. The entire formalism thus possesses the rare and wondrous quality of a rigorous internal check.

Experimental Procedure

The use of interruption kinetics depends on the feasibility (i) of reducing the concentration of B to its equilibrium value, and (ii) of measuring the arrival of defects at the S/B interface. Both are quite easily accomplished.

(i) The supply of B to the B reservoir can simply be cut off. The reaction then automatically proceeds to equilibrium, the scale acting as a sink for the residual B. If the reservoir is large, it may be evacuated or flushed with inert gas or liquid (depending on the system) and then closed off. The scale then acts as a source of B (by partial decomposition) and the concentration again adjusts to the equilibrium value. In most cases the latter is small enough so that the required decomposition is negligible.

(ii) When a defect reaches the outer interface it immediately reacts with a stoichiometric number of B atoms. The two kinds of atomic defects which can originate at $x = 0$ are interstitial A atoms or B atom vacancies. When the former reach $x = X$ they will combine with $\frac{b}{a}$ atoms (cf. Eq. [4]) while the latter will combine with one B atom. In either case the depletion of B atoms from the freshly filled B reservoir gives a direct measure of the arrival of defects at $x = X$. Δ_B, the total depletion of B atoms from the B reservoir after time, t, thus gives a direct measure of Δ, the quantity in Eq. [9]-[11]. It should be noted that one may determine Δ by measuring the increase in X, but this will generally be very difficult.

The question naturally arises as to what procedure should be used to measure Δ if the defects originate at the S/B surface, but, as before, the B concentration is the only quantity which can be varied and measured. The defects which can arise at the S/B interface are B interstitial atoms or A atom vacancies. Their concentration distribution before and after the interruption of the supply of B is compared in Fig. 1 with the case where the defects originate at the A/S interface. The obvious difference lies in the relative magnitudes of C_0 and C_1.

It turns out, however, that Eq. [9] is completely symmetrical and, with suitable changes in sign, describes each of the four cases equally well. Procedures (i) and (ii) are thus applicable regardless of the defect type, and the measurement of Δ_B again gives a direct measure of Δ. In order to make the treatment entirely general we shall redefine C_0 in Eq. [9]-[13] to mean the equilibrium concentration of the mobile defect at the interface where it originates when the reaction is proceeding normally. This may or may not correspond to the concentration during the interruption.

Since Δ_B is the quantity which is actually measured, it is convenient to use it directly. If Δ_B is substituted for Δ in Eq. [9], [10], and [11], then, instead of obtaining C_0 from Eq. [12] and [13], one obtains C_0^B whose relation to C_0 is summarized in Table II. The value of D is entirely independent of the units of Δ.

Use of Eq. [9]-[14]

The most convenient way to use Eq. [9]-[14] will be illustrated with recent data obtained on the oxidation of the intermetallic compound InSb where a thin protective scale of In_2O_3 is formed (4). A monocrystalline specimen exposing 4.0 cm^2 of flat surfaces was oxidized at 342°C and 0.3 mm oxygen until the total oxygen uptake was 5.76 x 10^{17} atoms cm^{-2}. The sample enclosure was evacuated and

Table II. Relation between C_0 and C_0^B in the reaction $aA + bB = S$

Defects originating at A/S interface	
1. Interstitial A atoms	$C_0 = \frac{a}{b} C_0^B$
2. B atom vacancies	$C_0 = C_0^B$
Defects originating at S/B interface	
3. Interstitial B atoms	$C_0 = C_0^B$
4. A atom vacancies	$C_0 = \frac{a}{b} C_0^B$

closed off for 15 hr without changing the temperature. Oxygen was then readmitted and the uptake measured by following the small pressure change at constant volume with a thermistor manometer. The results are plotted vs. $t^{1/2}$ and t in Fig. 2a and 2b.

As expected Fig. 2a is linear at small times, while Fig. 2b becomes linear at the longer times, and the rate approaches the value observed just prior to the interruption. The intercept of Fig. 2a is not zero. The value of the intercept, designated Z, can be treated as an additive constant for which a correction must be made in any expression containing Δ_B.

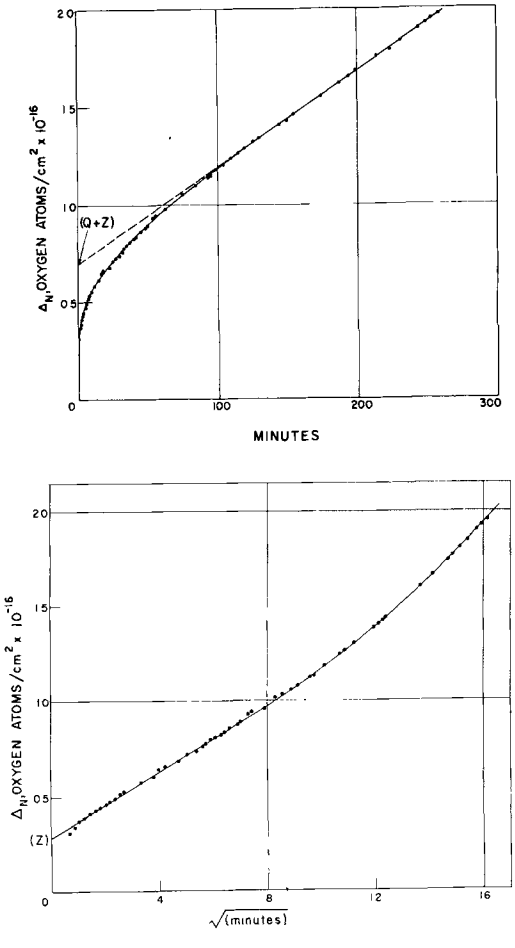

Fig. 2a (top), Fig. 2b (bottom). Interrupted oxidation of InSb. The uptake of oxygen was measured after a 15-hr interruption of the reaction at 342°C, p_{O_2} = 0.3 mm, and X ~1.24 x 10^{-5} cm. The time is measured from readmission of oxygen. The solid curves represent the solution of Eq. [9], modified by the inclusion of the additive constant, Z (see text).

From Fig. 2a and 2b one finds B, the slope of Fig. 2a to be 8.60 x 10^{14} oxygen atoms cm^{-2} min$^{-1/2}$; R, the slope of Fig. 2b to be 4.92 x 10^{13} oxygen atoms cm^{-2} min^{-1}, and Q, the intercept of Fig. 2b minus Z, to be 4.04 x 10^{15} oxygen atoms cm^{-2}. From Eq. [14] one obtains D/X^2 = 4.09 x 10^{-3} min^{-1}. From Eq. [13] one obtains XC_0^B = 1.212 x 10^{16} oxygen atoms cm^{-1}. From Eq. [12] one obtains XC_0^B = 1.202 x 10^{16} oxygen atoms cm^{-1}. The close agreement of the two independent values of XC_0^B provides the most important confirmation of the diffusion mechanism, and presages an excellent over-all description of the data by Eq. [9].

Substituting the value of D/X^2 and the average value of XC_0^B into the column headings of Table I, one obtains values of Δ_B vs. t and $t^{1/2}$ for the entire range of t. Adding Z to these values of Δ_B, plotting the results, and drawing a smooth curve through the points, gives the solid curves in Fig. 2a and 2b. The applicability of Eq. [9] is clearly verified in this case.

Values of D/X^2 and XC_0^B are thus obtained without reference to the chemistry or the thickness of the scale. Knowing X, one can obtain D directly. In order to determine C_0, however, one must know both X and the identity of the defect. The quantity X may be determined independently, or by using the total oxygen uptake combined with the stoichiometry of the scale and its molecular volume. For In_2O_3 the uptake of 5.8 x 10^{17} oxygen atoms cm^{-2} corresponds accordingly to *ca.* 1.24 x 10^{-5} cm.[4]

For reasons which are described elsewhere (4) it is believed that the mobile defects are interstitial In^{+3} cations arising at the $InSb/In_2O_3$ interface. Thus $C_0 = \frac{2}{3} C_0^B$. One obtains, accordingly[3] D = 1.04 x 10^{-14} cm^2 sec^{-1}, C_0^B = 1.22 x 10^{21} oxygen atoms cm^{-3}, C_0 = 8.1 x 10^{20} In^{+3} ions cm^{-3}.

Practical Considerations

(i) The length of time for which the reaction is interrupted must exceed X^2/D if the equilibrium concentration is to be attained throughout the film.

(ii) The quantity $Q^B = XC_0^B/3$ must be considerably larger than the sensitivity limit of the analytical technique. For gaseous reactions the sensitivity of microgravimetric methods is usually about 10^{15} atoms, while standard low-pressure manometric techniques (thermistor or Pirani gauge) permit measurements of 10^{14} atoms. For practical film thicknesses (< 10 μ) and surface areas (< 10 cm^2), C_0^B must exceed *ca.* 10^{17} cm^{-3}. The use of larger areas, thicker films, or very low-pressure techniques, although less convenient, would extend the practical limit of C_0^B to substantially lower values. For practical reasons it is also evident that $DC_0^B t_{min}$ must be smaller than $XC_0^B/3$ where t_{min} is the minimum time before which a measurement can be made after the readmission of B to the system.

(iii) When $XC_0^B/3$ is less than 10^{15} atoms cm^{-2},

[4] The geometric surface area to which the data is normalized is a factor, F, ("roughness factor") less than the true area. If $F \approx 1.3$ as is believed to be the case for chemically polished InSb, the corrected values of X, D, C_0^B, and C_0 are 9.5 x 10^{-6} cm, 6.15 x 10^{-15} cm^2 sec^{-1}, 1.57 x 10^{21} cm^{-3}, and 1.05 x 10^{21} cm^{-3}, respectively.

one may encounter spurious effects due to chemisorption. Since chemisorption usually proceeds much more rapidly than the diffusion reaction described by Eq. [9], it will contribute an additive constant to Δ_B in a manner analogous to that observed in Fig. 2a.[5]

[5] In the case of InSb the effect is not thought to be associated with simple chemisorption of oxygen (4).

Manuscript received Feb. 26, 1960.

Any discussion of this paper will appear in a Discussion Section to be published in the June 1961 JOURNAL.

REFERENCES

1. C. Wagner, *Z. Phys. Chem.*, **B21**, 25 (1933).
2. N. Cabrera and N. F. Mott, *Rep. Prog. Phys.*, **12**, 163 (1948).
3. J. Crank, "The Mathematics of Diffusion," p. 42 ff, Oxford (1956).
4. A. J. Rosenberg, *J. Phys. Chem.* (in press).

The Electrical Properties of Some Natural Waxes

Thomas D. Callinan and Ann M. Parks

International Business Machines Corporation, Yorktown Heights, New York

ABSTRACT

The dielectric constants and dielectric loss factors of Carnauba, Ouricuri, and American Montan wax determined over a temperature range of —60° to 90°C and at frequencies of 0.1, 1, 10, and 100 kc, indicate that the component omega-hydroxy acid esters rotate in the solid state in the temperature region 25°-70°. Furthermore, from dipole measurements, the molecules were found to possess a trans-trans configuration.

Recent advances in dielectric spectroscopy (1) suggested that this might prove a valuable tool in the determination of the nature of waxes. By dielectric spectroscopy is meant the elucidation of certain properties of materials in terms of their molecular and atomic constituents through an analysis of their dielectric constants and dielectric losses over a broad temperature (—100° to 200°C) and broad frequency (dc to 10^{10} cps) range. From the discipline as it now stands, it is possible to establish the presence and magnitude of permanent electric moments in the component molecules and to determine whether association exists. Certain peaks and troughs in the loss spectra may also be related directly to the molecular structure.

Using this technique, it has been found possible to establish the essential molecular structure of such naturally occurring waxes as Carnauba, Ouricuri, and Montan wax and to suggest why they behave the way they do in certain circumstances. In each case, the dielectric constant and dielectric loss factor were determined at frequencies between 100 and 100,000 cps at temperatures in the range —60° to 98°C, and the dipole moments of each were calculated from measurements made on benzene solutions of the waxes.

Materials

The Carnauba wax used in these tests was derived from a genus of palm known as *Copernicia Cerifera Martius*. The wax was obtained from mature leaves and bears the commercial designation "North Country No. 3" and the provincial name "Gordierosa." The solid was a hard, brown material which melted abruptly at 79°C. It has a specific gravity at 25°C of 0.9988. Chemically, Carnauba wax is a mixture of alkyl esters (85%) and uncombined acids, alcohols, lactides, and hydrocarbons. Approximately 40% of the wax consists of omega-hydroxy acid esters having the formula:

$$HO—C_nH_{2n}C(O)O\,C_mH_{2m}+1$$

where n and m may be 18, 20, 22, or 28, (2). No effort was made to separate the components of Carnauba wax as it was the purpose of the work to study the material as a mixture.

Ouricuri wax is derived from the undersurface of the leaves of the palm tree known as *Attalea Excelsa Martisu*. It is a hard, dark brown solid, having a specific gravity at 25°C of 1.06661 and melts at 69°C. The wax is considered to have the following composition: alkyl esters (myricyl cerotate) and hydroxy esters total 61%, free wax acids 11%, resin acids 4%, resinols 15%, hydrocarbons 7%, and residue 2% (2).

Montan wax is a brown-black solid extracted from a California lignite. It has a specific gravity of 1.020 at 25°C and melts at 77°C. It is considered to be composed of esters of wax acids (53%) including hydroxy acids. It resembles, therefore, the Carnauba and Ouricuri waxes, (2).

Some of the properties of these waxes are tabulated in Table I.

Experimental Methods

Each wax was melted and poured into an Elliott cell (3) previously heated in an air oven to 100°C. In actual practice the cell was modified by drilling holes in the base so that dry nitrogen gas could be passed around the electrodes and sample during measurement. This effectively eliminated interference by moisture condensation in the 0°C region. The assembled and filled cell was removed from the oven and allowed to cool to room temperature. Dielectric properties were then determined from

Table I. Select properties of waxes

Chemistry	Montan	Ouricuri	Carnauba
(A) Alkyl esters, %	53	61	85
(1) Hydroxy acid esters, %	12-14	—	55
(B) Hydrocarbons, %	3	7	3
Specific gravity	1.020	1.0661	0.9988
Penetration, 150 g/ 5 sec/25°C	0.06	0.10	0.08
Melting point, °C	77	69	79
Acid value	50-55	21-24	3

measurements on the General Radio 1610-A capacitance bridge network. Measurements were made as the samples slowly cooled from 95° to 25°C and as they warmed from −60° to 25°C.

The resistance of each wax sample was measured in the Elliott cell on a General Radio Type 544-B megohm bridge in the temperature range of 25°-95°C. Results are expressed in terms of the volume resistivity of the sample in order to correct for the resistance in the cell itself.

Dipole moments were calculated from measurements on dilute benzene solutions of the waxes. The density of each solution was measured on a Seederer-Kohlbusch density balance and the refractive index measured on a Spencer Refractometer at 24°C. The dielectric constant was measured in a two terminal Balsbaugh cell with a volume of 75 cc, at 24°C and 10,000 cps frequency. This frequency is believed to be above the range of ionic vibrations in the molecules, and the polarization calculated is a result of induced and orientation polarizations. The molar polarization and refraction were calculated according to the Clausius-Mosotti (4) and Debye (5) equations. This method involves use of the relationships

$$P = \frac{\epsilon' - 1}{\epsilon' - 2} \cdot \frac{M_1N_1 + M_2N_2}{d}$$

$$\text{and } R = \frac{n^2 - 1}{n^2 + 2} \cdot \frac{M_1N_1 + M_2N_2}{d}$$

where P is the molar polarization, ϵ' the dielectric constant, d the density, M and N refer to the molecular weights and mole fractions of solute and solvent, R is the molar refraction, and n is the refractive index.

By linear extrapolation of the molar polarization to infinite dilution the dipole moment of the molecules is calculated from the relationship $M = 0.0128 \sqrt{(P-R)\,T}$, where T is expressed in absolute degrees.

Dielectric Properties of Carnauba Wax

The dielectric constants ϵ' and dielectric loss factors ϵ'' of Carnauba wax are listed in Table II and are shown graphically in Fig. 1. At very low temperature, the dielectric constant of Carnauba wax is low (2.16-2.29) and differs only slightly at different frequencies. As the temperature rises the dielectric constant increases at first slowly (0.006/degree) and then more rapidly (0.02/degree) until a temperature is reached at which the dielectric constant passes through a maximum and decreases with further increases in temperature. Concomitant with these changes in dielectric constant, there are changes in dielectric loss factor. All pass through a maximum at different temperatures depending on the frequency.

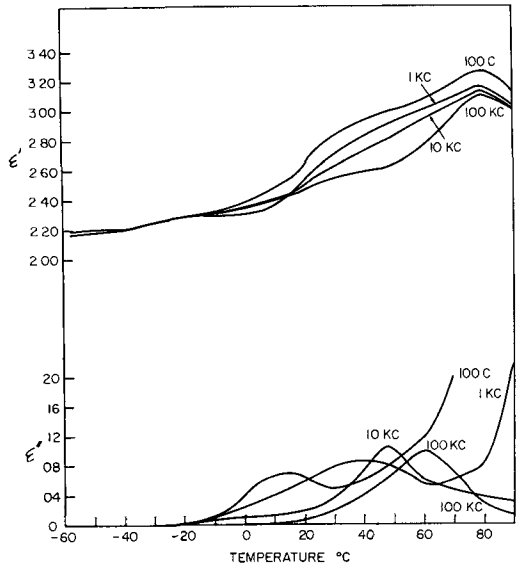

Fig. 1. Variation of dielectric constant ϵ' and dielectric loss factor ϵ'' of Carnauba wax with temperature at 100, 1,000, 10,000, and 100,000 cps.

Table II. Carnauba wax

Frequency (cps), temp, °C	100 ϵ'	100 ϵ''	1000 ϵ'	1000 ϵ''	10,000 ϵ'	10,000 ϵ''	100,000 ϵ'	100,000 ϵ''
−58	2.17	0.000	2.16	0.000	2.19	0.000	2.19	0.000
−50	2.18	0.000	2.18	0.000	2.20	0.000	2.20	0.000
−20	2.30	0.000	2.29	0.000	2.28	0.000	2.28	0.000
−5	2.34	0.010	2.29	0.000	2.33	0.000	2.33	0.000
18	2.59	0.066	2.48	0.004	2.46	0.016	2.44	0.016
21	2.69	0.060	2.57	0.061	2.52	0.023	2.49	0.019
31	2.84	0.050	2.72	0.080	2.64	0.040	2.55	0.020
40	2.94	0.060	2.85	0.081	2.72	0.070	2.58	0.040
48	2.98	0.080	2.91	0.080	2.79	0.105	2.62	0.060
60	3.07	0.120	3.00	0.055	2.94	0.060	2.76	0.100
79	3.26	0.435	3.16	0.080	3.13	0.060	3.10	0.030
95	3.13	1.90	3.04	0.217	3.03	0.029	3.02	0.014

At higher temperatures the dielectric loss factors show runaway tendencies at low frequencies reaching values greater than the maxima obtained at lower temperatures.

Dielectric Properties of Ouricuri Wax

The dielectric constant ϵ' and dielectric loss factor ϵ'' of Ouricuri wax as a function of frequency and temperature is shown graphically in Fig. 2 based on the data listed in Table III. At low temperatures and all frequencies the dielectric constants and dielectric loss factors are again low.

As was observed above the temperature coefficient of change in dielectric constant changes markedly at about 25°C from 0.003/degree to 0.02/degree. It then passes through a maximum in the vicinity of the melting point of the wax, when determined at frequencies higher than 1 kc. Runaway characteristics are observed above 50°C, but below this temperature the dielectric loss factor curves pass through a maximum at a characteristic temperature for each frequency.

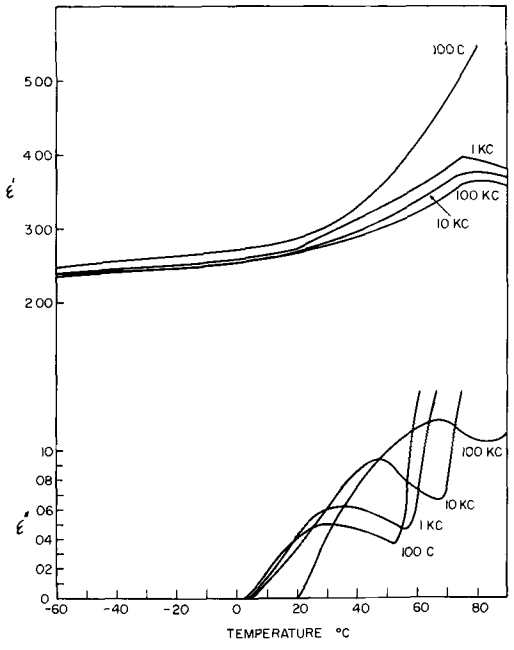

Fig. 2. Variation of dielectric constant ϵ' and dielectric loss factor ϵ'' of Ouricuri wax with temperature at 100, 1,000, 10,000, and 100,000 cps.

Table III. Ouricuri wax

Frequency (cps), temp, °C	100 ϵ'	100 ϵ''	1000 ϵ'	1000 ϵ''	10,000 ϵ'	10,000 ϵ''	100,000 ϵ'	100,000 ϵ''
—60	2.47	0.000	2.40	0.000	2.38	0.000	2.39	0.000
—50	2.54	0.000	2.43	0.000	2.40	0.000	2.40	0.000
—5	2.68	0.000	2.56	0.000	2.52	0.000	2.52	0.000
18	2.84	0.036	2.71	0.046	2.66	0.030	2.64	0.000
22	2.90	0.044	2.76	0.053	2.70	0.040	2.68	0.008
42	3.37	0.043	3.19	0.060	3.05	0.089	2.95	0.080
48	3.44	0.040	3.28	0.056	3.14	0.093	3.00	0.100
68	4.54	1.70	3.63	0.290	3.55	0.067	3.36	0.120
75	5.15	7.30	3.96	1.17	3.74	0.180	3.62	0.112
80	5.43	11.50	3.92	1.40	3.74	0.209	3.63	0.108
93	6.58	19.48	3.88	2.11	3.69	0.274	3.58	0.110

Dielectric Properties of Montan Wax

The dielectric constant ϵ' and dielectric loss factor ϵ'' of American Montan wax are listed in Table IV and are shown graphically in Fig. 3. The dielectric constant remains low and increases only slowly (0.008/°C) on passing from —60° to 25°C. Above this temperature there is a rapid increase resulting in an apparent dielectric constant of 16 at 98°C; this is accompanied by and attributable to very high losses. These losses are so high that they swamp the usual maxima in the dielectric constant at the melting point; the only suggestion of it existing comes from the definite plateau which occurs at 100,000 cps. Again, however, each loss curve passes through a maximum at a definite temperature.

Comparison of Electrical Properties

For the sake of comparison and to interpret the dielectric loss spectra the volume resistivity of each wax as a function of temperature is shown in Fig. 4. In each case the resistance remains constant until the wax begins to melt. At this point the resistance decreases rapidly and levels out again in the liquid.

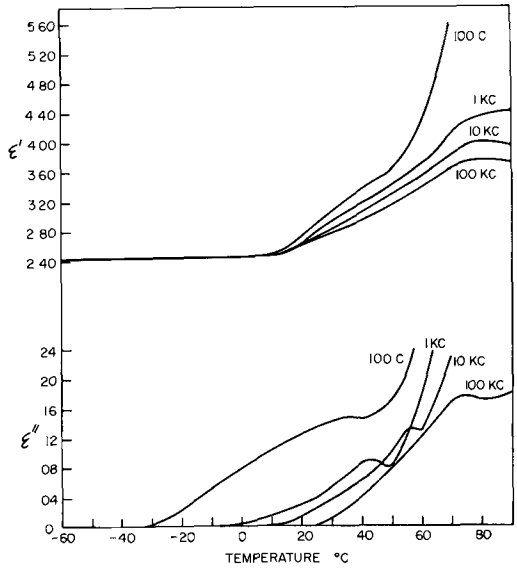

Fig. 3. Variation of the dielectric constant ϵ' and dielectric loss factor ϵ'' of American Montan wax with temperature at 100, 1,000, 10,000, and 100,000 cps.

Table IV. American No. 16 Montan wax

Frequency (cps), temp, °C	100 ϵ'	100 ϵ''	1000 ϵ'	1000 ϵ''	10,000 ϵ'	10,000 ϵ''	100,000 ϵ'	100,000 ϵ''
—60	2.44	0.000	2.42	0.000	2.43	0.000	2.43	0.000
—40	2.44	0.000	2.43	0.000	2.45	0.000	2.43	0.000
—10	2.44	0.052	2.43	0.000	2.43	0.000	2.43	0.000
0	2.44	0.080	2.43	0.006	2.43	0.000	2.43	0.000
5	2.44	0.092	2.43	0.010	2.43	0.000	2.43	0.000
18	2.66	0.122	2.57	0.027	2.55	0.009	2.55	0.000
24	2.90	0.134	2.80	0.036	2.67	0.025	2.79	0.000
35	3.20	0.144	3.04	0.070	2.77	0.050	2.86	0.024
42	3.40	0.148	3.20	0.088	3.10	0.068	3.00	0.048
50	3.62	0.17	3.44	0.080	3.28	0.100	3.15	0.080
60	4.23	1.15	3.68	0.18	3.54	0.13	3.37	0.12
70	5.58	6.10	4.12	0.82	3.84	0.23	3.66	0.17
80	—	—	4.36	2.32	3.99	0.38	3.75	0.17
90	—	—	4.42	3.70	3.96	0.52	3.72	0.18

As expected from this data since Carnauba shows the lowest conductivity in the liquid form it also has the lowest dielectric losses. In the same manner

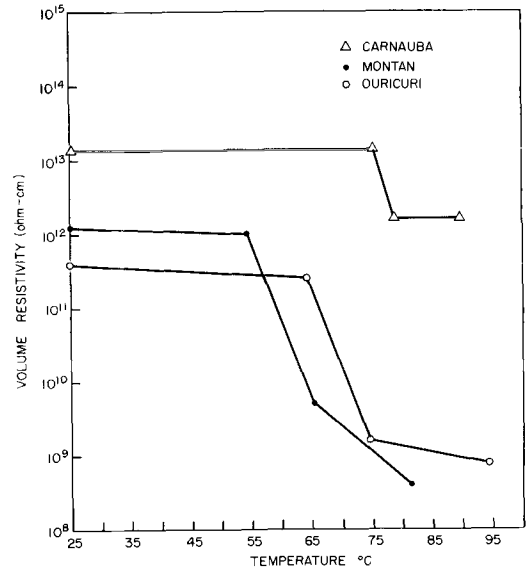

Fig. 4. Volume resistivity vs. temperature of the waxes

Table V. Dipole moments of the waxes

Wax	Mole fraction	ϵ', at 10,000 cps	Extrapolated polarization, P, cc	Molar refraction	Dipole moment, esu-cm, $X10^{-18}$
Carnauba	5×10^{-6}	2.2768	2040	1568	4.8
$M = 920$	1×10^{-5}	2.2772			
	5×10^{-5}	2.2780			
Ouricuri	4×10^{-6}	2.2811	4200	3037	7.5
$M = 848$	9×10^{-6}	2.2803			
	4×10^{-5}	2.2839			
	9×10^{-5}	2.2855			
Montan	1×10^{-5}	2.2763	885	472	4.5
$M = 834$	2×10^{-5}	2.2780			
	1×10^{-4}	2.2800			
	2×10^{-4}	2.2833			

Ouricuri shows less conductivity than Montan and lower dielectric losses. In the solid waxes, however, the order of increasing conductivity is Carnauba, Montan, Ouricuri, but Ouricuri generally shows the lowest losses. Correlation in this region is difficult, however, due to the presence of maxima in the loss curves.

Because of the temperature and frequency dependence of the dielectric constants of the waxes, relatively high dipole moments are indicated. The results of these measurements are shown in Table V. Montan and Carnauba have essentially the same dipole moments, but that of Ouricuri is considerably higher. As was shown above Ouricuri also has the highest dielectric constant at 24°C followed by Montan and Carnauba. Calculation of the theoretical dipole moment for various configurations of a planar omega-hydroxy acid ester such as is present in the waxes leads to the conclusion that these esters must be arranged predominately in a trans-trans configuration. This arrangement is shown in Fig. 5 and predicts a moment of 4. 3D on the basis of known bond moments and angles (6a). The opposite configuration, the cis-cis form in which the hydroxyl hydrogen and the alkyl group of the esters are on the same side of the chain as the carbonyl predicts a moment of only 0.25D. Combination of the *cis* and *trans* forms lead to theoretical moments of 2.65D.

The dielectric properties of the waxes at 25°C are reproduced graphically in Fig. 6. The Ouricuri wax

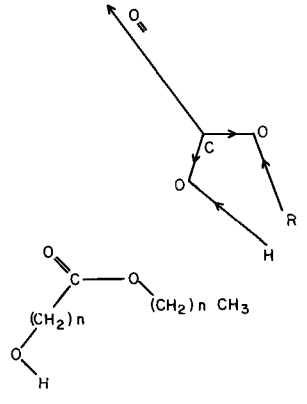

Fig. 5. Vectoral representation of trans-trans omega-hydroxy acid ester.

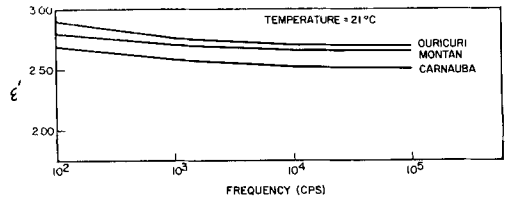

Fig. 6. Comparison of the dielectric constants ϵ' of the waxes

shows the highest ϵ' throughout the frequency range with Montan wax and Carnauba wax placing second and third in that order.

All three natural waxes were found to possess dielectric constants which were highly dependent on temperature and two discrete regions where the temperature coefficient of dielectric constant differed. Both Fitzgerald (7) and Stempel (8) have shown that the waxes remain crystalline to within six degrees of their respective melting points.

Conclusions

In view of the fact that the change in the temperature coefficient of the dielectric constant being discussed occurs well below the melting points of the waxes, a mechanism analogous to that observed on abrupt melting of organic crystals does not apply. This leaves us with the explanation of molecular rotation similar to that found in water and some organic crystals.

Molecular rotation has been also reported to occur in a number of long-chain compounds such as primary alcohols. These compounds are known to exist in alpha and beta forms, and rotation takes place about the axis of the chain in the alpha or high-temperature form (9). That this mechanism also applies to the three waxes under consideration is confirmed by the similarity of their dielectric behavior to that observed in 1-docosanol, a material previously shown to exhibit molecular rotation (6b). In this case the dielectric constant is strongly temperature dependent and shows a fivefold increase in the temperature coefficient of change in dielectric constant at about 26°C, a temperature well below its melting point.

Since the three waxes are composed largely of omega-hydroxy acid esters, the mechanisms of the effects determined dielectrically are interpreted to be as shown in Fig. 7. The molecules tend to align themselves in an orderly fashion. At very low temperatures there is high cohesion between parallel chains and strong head-to-head attraction between hydroxyl groups. As the temperature rises the hydrogen bonding between hydroxyl groups is reduced so that the molecules can rotate around the molecular

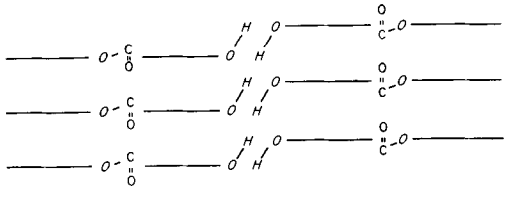

Fig. 7. Molecular arrangement of omega-hydroxy acid esters in wax crystals.

axis but remain in an orderly bundle. At elevated temperatures the cohesion between chains is reduced and the material melts. The noted differences between the three waxes are believed to be caused by differences in the relative amounts of esters and other materials present.

Manuscript received Feb. 15, 1960. This paper was prepared for delivery before the Philadelphia Meeting, May 3-7, 1959.

Any discussion of this paper will appear in a Discussion Section to be published in the June 1961 JOURNAL.

REFERENCES

1. A. R. V. Hippel, "Dielectric Materials & Applications," John Wiley & Sons, Inc., New York (1954).
2. A. H. Warth, "The Chemistry & Technology of Waxes," Reinhold Publishing Co., New York (1956).
3. M. A. Elliott, A. R. Jones, and L. B. Lockhart, *Ind. Eng. Chem., Anal. Ed.*, **19**, 10 (1947).
4. O. F. Mosotti, *Mem. Soc. Ital. Sc. (Modena)*, **14**, 49 (1850); R. Clausius, "Die Mechanische Warmetheorie," Vol. II, p. 94, Vieweg, Verlag, Brunswick, Germany (1879).
5. P. Debye, "Polar Molecules," Chemical Catalog, New York (1929).
6. C. P. Smyth, "Dielectric Behavior and Structure," McGraw-Hill Book Co., Inc., New York (1955) a, Chap IX; b, Chap. V.
7. E. Fitzgerald, Private communication.
8. N. Stempel, Private communication.
9. S. Glasstone, "Textbook of Physical Chemistry," 2nd ed., p. 424, D. VanNostrand & Co., New York (1946).

Factors Influencing the Luminescent Emission States of the Rare Earths

L. G. Van Uitert

Bell Telephone Laboratories, Incorporated, Murray Hill, New Jersey

ABSTRACT

The number of electronic states from which luminescent emission by rare earth ions can be observed is dependent on the extent to which the host lattice perturbs their f-orbital electrons. Among others, perturbing influences may stem from the following sources: (*a*) coulombic affinities of the ions or molecules surrounding the rare earth ions for the electrons they share with the latter; (*b*) concentration effects, i.e., exchange coupling; (c) thermal effects, i.e., vibronic interactions.

Results obtained on metal organic complexes, hydrates, fluorides, and tungstates are compared. The effects on emission of the rare earth ion concentration in the tungstates are compared for europium, terbium, dysprosium, and erbium at room temperature, and the influences of thermally excited interactions on the emission of erbium are demonstrated.

In principle, emission should be observable from all of the excited states of the rare earth ions when they are not influenced by their surroundings. Of course, this condition cannot be fully realized in the solid state. However, different environments have markedly different influences on the rare earths. In the case of europium, for example, the number of states from which emission is observed varies from one in its chelate compounds to four in its oxides (1-3). Even in a given structure, the number of states from which emission is observed can be quite dependent on the rare earth concentration (4, 5) and thermal effects (6). In this paper, the influences of a number of environments on the luminescent emission of several of the rare earths are compared, and the factors which appear to be responsible for the relationships observed are discussed.

Materials

Members of the series $Ca_{1-2x}Na_xRE_xWO_4$, where RE = europium with $x = 3 \times 10^{-5}$, 10^{-4}, 5×10^{-4}, 10^{-2}, 10^{-1}, and 0.50; RE = terbium with $x = 10^{-4}$, 10^{-3}, 10^{-2}, 5×10^{-2}, 0.2, and 0.5; RE = dysprosium with $x = 5 \times 10^{-6}$, 10^{-4}, 10^{-3}, 5×10^{-3}, 10^{-2}, 10^{-1}, 0.25, and 0.50; and RE = erbium with $x = 10^{-5}$, 3×10^{-5}, 10^{-4}, 10^{-3}, 10^{-2}, 3×10^{-2}, 10^{-1}, 0.25, and 0.50, were prepared by crystallization from a $Na_2W_2O_7$ flux, as previously described (7). The crystals obtained by this method are nearly perfect in structure compared to those obtained by sintering techniques and therefore are suitable for making emission intensity comparisons. Emission from samples of a given composition grown at various rates, and hence of quite different crystallite size, compares in intensity to within a few per cent of one another under the measuring conditions employed.

Measurements

Measurements were made employing a Gaertner high dispersion spectrometer with an AMINCO photomultiplier microphotometer which employed a 1P22 photomultiplier tube. The system was calibrated against a tungsten lamp to give relative values of brightness of the emitting surface in units of power per unit wave-length range. Emission was excited by illuminating a sample 1 in. long by ½ in. wide by ¼ in. deep with a 3660Å rich H4 spotlight through a Corning 5874 filter. All of the intensity measurements are relative to 100 for the 5450Å peak of a comparable sample of $Na_{0.5}Tb_{0.5}WO_4$.

Table I

Process	Ionization potential, ev	Reference
$La \rightarrow La^{+}$	5.61	(10) p. 137
$La^{+} \rightarrow La^{2+}$	11.4	(10) p. 138
$La^{2+} \rightarrow La^{3+}$	19.2	(10) p. 139
$H_2O \rightarrow H_2O^{+}$	12.6	(11) p. 265
Organic-O $\rightarrow$ Organic-O^{+}	>10	(11) p. 265

Table II

Process	Electron affinity, ev	Reference
$F \rightarrow F^{-}$	4.27	(12) p. 161
$O \rightarrow O^{-}$	3.1	(11) p. 40
$O \rightarrow O^{=}$	—7.28	(12) p. 161

Discussion

The number of electronic states from which luminescent emission by rare earth ions can be observed may be expected to depend on the extent to which the host lattice perturbs their electron envelopes. The number of emitting states observed does not appear to be as critically dependent on geometric considerations as the crystal field splitting or the relative strengths of the emission lines. Among others, the perturbing influences may stem from the following sources: (*a*) the coulombic affinities of the ions or molecules surrounding the rare earth ions for the electrons they share with the latter; (*b*) concentration effects, i.e., exchange coupling; (c) thermal effects, i.e., vibronic interactions.

Coulombic Affinities

There is considerable evidence that bond strength, which may be expected to bear directly on perturbing influences, increases with an increase in the affinity of one or both of the bonded atoms for the electrons shared (8, 9). As a first approximation one may consider the electron affinities or ionization potentials of the ions or molecules surrounding the rare earth ions in the several host lattices to provide a measure of the extent to which these surroundings may perturb the f-orbital electrons of the rare earths. A comparison of the values given in Tables I and II shows that the third ionization potential of lanthanum, which may be considered to be representative of the rare earths, is larger than the ionization potentials of H_2O or organic oxygen and is much larger than the electron affinities of fluorine or oxygen. Hence, one cannot ascribe full possession of the electrons about these molecules and ions to themselves when they are bonded to trivalent rare earth ions. Electron diffraction work carried out on beryl ($Be_3Al_2Si_3O_{18}$) by Bragg and West (13) has shown that in the silicates the silicon and oxygen atoms are closer to the Si^{+} and O^{-} ionic states than to the Si^{4+} and O^{2-} states. Hence, one may expect the ionization potential of oxygen to depend on the central cation when it is part of an anionic group such as $WO_4^{=}$.

In a similar manner, the electron affinity of an organic oxygen atom is dependent on the nature of the molecule of which it is part. Coulson (14) has shown that for carbon-carbon bonding one may expect an increase in the electron affinities of the carbon entities as the s-character of their σ bonds increases in the order sp^3 (single bonding), sp^2 (double bonding), and sp (triple bonding). This is a consequence of the fact that the s-orbital lies lower energetically than do the p-orbitals. It may be expected that a similar increase in the multiple bond character of isoelectronic oxygen would result in its having an increased electron affinity. Hence, one may expect a stronger bonding of ketonic oxygen (double bonded to carbon) to the rare earth ions than occurs with ethers or alcohols. Further, one might expect an additional increase in bonding strength to the rare earths through the oxygen atoms of chelating agents such as acetylacetone by the development of resonance structures and a reduction in entropy.

The above considerations, in conjunction with the observations given below, suggest that the following environments diminish in perturbing influence in the order: O—O chelates, ketones and hydrates, fluorides, high central charge anionic groups ($WO_4^{=}$), less covalent oxides. In the case of europium, one emission state (17,300 cm^{-1}) is active in the chelate (1, 15), and an additional state (19,000 cm^{-1}) is observed in the hydrate (1); a third (21,500 cm^{-1}) is apparent in the fluoride (3), and a fourth (24,200 cm^{-1}) in the tungstate (5) and calcium oxide (16). In a like manner, one emission state (20,700 cm^{-1}) is observed for terbium in the chelate, hydrate (1), and fluoride (3); a second is found in the tungstate (4); and there are possibly three or more when terbium is combined with aluminum oxide (4, 17). Erbium does not luminesce in the chelate or hydrate but exhibits two main emission states (15,300 and 18,400 cm^{-1}) in the fluoride (3) and a third (24,500 cm^{-1}) in the tungstates (6) and calcium oxide (16). Parallel patterns are observed for a number of the other rare earths.

Concentration Effects

Increasing the rare earth concentration can produce effects quite comparable to those found on changing the host environments. This is readily observed by comparing members of the series $Ca_{1-2x}Na_xRE_xWO_4$. Figure 1 shows the dependencies of the intensities of emission from the 26,500 and 20,700 cm^{-1} states of terbium on the concentration of terbium in the above tungstates and of the 20,700 cm^{-1} state of terbium when it is substituted totally or in part for yttrium in yttrium hexa-antipyrene tri-iodide (4). These values are represented

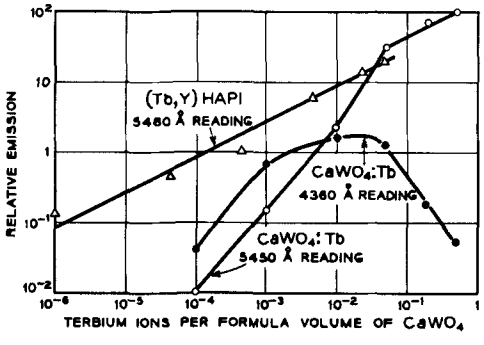

Fig. 1. Relative emission vs. the concentration of terbium

by the intensities measured for the emission peaks at 4360 and 5450Å in the tungstates and 5480Å in the antipyrene complexes, respectively. The metal ions are separated by 14Å in the antipyrene complexes; hence, they can be considered to be isolated from each other. Therefore, it is reasonable to employ the curve for the antipyrene complexes as a reference for the dependence of emission intensity on concentration for strongly bonded terbium ions.

In the dilute materials, the emission from the tungstates is much weaker than that from the antipyrene complexes. However, at high terbium concentrations, the tungstates compare favorably to terbium hexa-antipyrene tri-iodide and take on the emission characteristics of its yttrium substitution series in its intensity dependence on concentration and number of emission states. This is equivalent to a change from a relatively ionic to a more covalent or stronger bonding environment and appears to be related to the development of exchange coupling between the paramagnetic rare earth ions.

Figure 2 shows the dependencies of the intensities of emission from the 24,200, 21,500, 19,000, and 17,000 cm^{-1} states of trivalent europium (represented by the values measured for the peaks at 4312, 5105, 5545, and 6140Å, respectively) on europium concentration. The relationships shown suggest that the emission from 24,200 cm^{-1} is quenched by the pairing of europium ions (they occur in neighboring calcium sites) and emission from 21,500 and 19,000 cm^{-1} is quenched by the association of three or more europium ions (5).

In contrast to the behavior exhibited by europium, the intensities of emission from 24,500, 18,400, and 15,300 cm^{-1} exhibited by erbium vary uniformly (as shown in Fig. 3 which is discussed below) instead of quenching sequentially with increasing concentration. This provides supporting evidence that the quenching observed for terbium and europium is not due to an emission and reabsorption process.

The spectrum of dysprosium in calcium tungstate which is observed in the visible range is due to emission from an electronic state (2, 3) at 21,000 cm^{-1}. The dependence of the intensity of emission from this state (represented by the values measured for the strongest peak which is at 5750Å) on dysprosium content is shown as part of Fig. 4. Dysprosium luminesces a bright yellow at a 1% concentration but is completely quenched in $Na_{0.5}Dy_{0.5}WO_4$. The quenching observed in this case also appears to be due to exchange coupling.

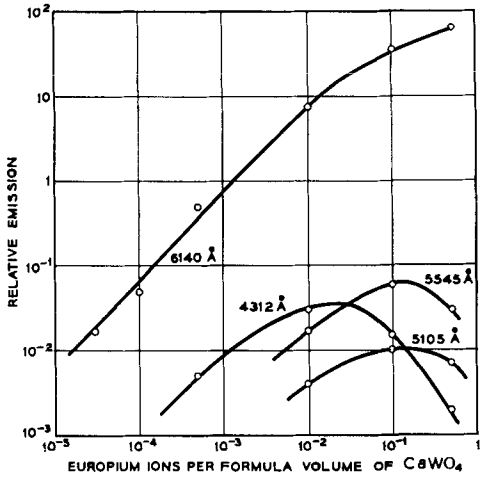

Fig. 2. Relative emission vs. the concentration of europium

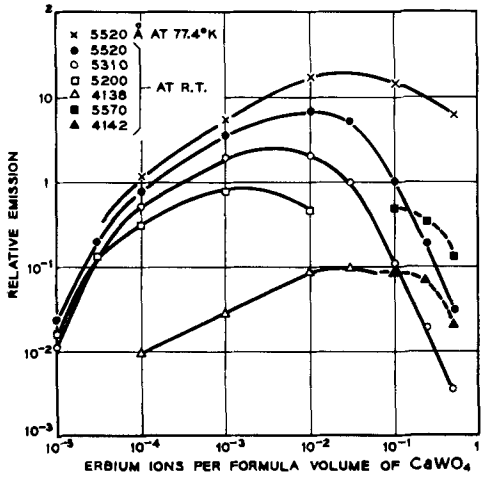

Fig. 3. Relative emission vs. the concentration of erbium

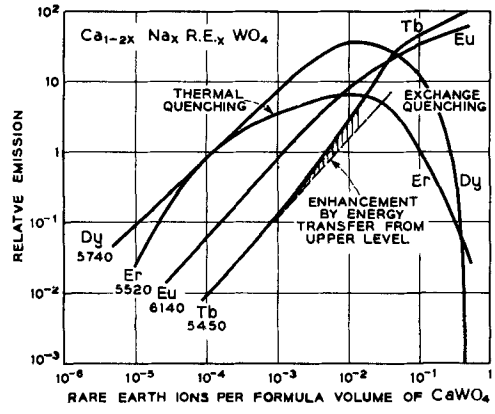

Fig. 4. Relative emission vs. rare earth concentration

Thermal Effects

Thermal effects play an important role in the emission spectra of erbium in the scheelite structure. Besides the three main emission states at 15,300, 18,400, and 24,500 cm^{-1}, erbium shows strong emission from thermally excited levels at 18,830, 19,080, and 19,200 cm^{-1} at room temperature (6). In $Na_{0.5}Er_{0.5}WO_4$, emission from the above states is quenched at room temperature, thus allowing emission from states that are probably just below those at 18,400 and 19,200 cm^{-1} to be seen. At 77°K emission from the thermally excited states is no longer observed, but emission from the high erbium content samples is again very bright (6). Figure 3 shows the dependencies of the intensities of emission from the 18,400, 24,500, 18,830, and 19,200 cm^{-1} levels of erbium (represented by the values measured for the peaks at 5520, 4138, 5310, and 5200Å, respectively) on erbium concentration at room temperature. It also shows the comparable data for levels which are presumed to lie just below those

at 18,400 and 19,200 cm^{-1} (represented by the values measured for the peaks at 5570 and 4142Å, respectively). The comparable data for the peak at 5520Å at 77°K are also given.

The relationships observed show that emission from the thermally excited states of erbium is quenched by increasing the concentration of erbium as well as by lowering the temperature. However, while the emission from the principal excited states is also quenched by increasing the concentration of erbium at room temperature, lowering the temperature reduces the effectiveness of this quenching mechanism and bright emission is obtained from these levels. The effects noted are quite probably due to vibronic interactions and their dependence on temperature. Since the peaks at 5570 and 4142Å do not show the same concentration or thermal dependencies as their close neighbors, they may originate from levels which, while only a few wave numbers below the dominant levels, do not couple thermally to the lattice in the same way.

Comparisons

Figure 4 presents a comparison of the dependencies of emission at room temperature on rare earth concentration for the dominant excited states of the several rare earth ions discussed. The curve for the emission measured for the 6140Å peak of europium appears to be a reliable reference for the following reasons: (*A*) The dilute materials show an almost linear dependence of emission on europium concentration. The deviation observed at high concentration is consistent with the change in environmental conditions discussed in the case of terbium. (*B*) The aggregate emission from the excited states, other than that at 17,000 cm^{-1}, is never more than a few per cent of the latter. Thus, possible emission enhancement due to energy transfer from higher levels as a result of changing environmental conditions would not be significant. (*C*) Emission from the 17,000 cm^{-1} level of europium does not appear to be quenched by concentration or thermal effects in these compositions.

The curve for dysprosium shows the same linear dependence as the one for europium at low concentrations. The rapid decrease in emission as the dysprosium concentration increased above 10^{-2} provides an excellent example of concentration quenching. This effect, as well as the quenching of emission from the higher energy states of terbium and europium, is not altered by reducing the temperature to 77°K.

Concentration quenching of emission from the higher of two energy states can occur so as to permit energy transfer to the lower, thus enhancing emission from it. The data for terbium provide an example of such a transfer. Figure 1 shows that at low terbium concentrations the emission from 26,500 cm^{-1} (as indicated by the data for the peak at 4360Å) is about three times as bright as that from 20,700 cm^{-1} (represented by the data for the peak at 5450Å). As the terbium concentration is increased from 10^{-3} to 5×10^{-2}, both curves deviate from linearity, the curve for the peak at 4360Å in a direction which indicates a relative loss in brightness and the curve for the peak at 5450Å in a direction which indicates a relative gain in brightness. The latter curve is readily compared to the curve for the 6140Å peak of europium in Fig. 4. The arithmetic sum of the two terbium emission curves provides a resultant curve that is symmetrical with that for the 6140Å peak of europium.

The curve in Fig. 4 for the emission at room temperature for the erbium peak at 5520Å shows the effects of a quenching process which has a strong thermal dependence. This curve deviates strongly from linearity at concentrations of erbium as low as 10^{-4}, in addition to showing strong quenching effects above 10^{-2}, as do the curves for dysprosium and the higher emitting states of terbium and europium.

Acknowledgments

The author is indebted to C. G. B. Garrett, D. L. Wood, A. D. Liehr, K. Nassau, and J. H. Scaff of these Laboratories for helpful discussions and comments.

Manuscript received April 4, 1960. This paper was prepared for delivery before the Chicago Meeting, May 1-5, 1960.

Any discussion of this paper will appear in a Discussion Section to be published in the June 1961 JOURNAL.

REFERENCES

1. O. Deutchbein and R. Tomaschek, *Ann. Phys.*, (5) **29S**, 311 (1937).
2. H. Gobrecht, *ibid.*, (5) **28S**, 673 (1937).
3. N. Chatterjee, *Z. Phys.*, **113**, 96 (1939).
4. L. G. Van Uitert and R. R. Soden, *J. Chem. Phys.*, **32**, 1161 (1960).
5. L. G. Van Uitert and R. R. Soden, *ibid.*, **32**, 1687 (1960).
6. L. G. Van Uitert and R. R. Soden, *ibid.*, in press (1960).
7. L. G. Van Uitert and R. R. Soden, *J. Appl. Phys.*, in press (1960).
8. W. Gordy, *J. Chem. Phys.*, **14**, 305 (1946).
9. A. D. Walsh, *J. Chem. Soc., London*, **1948**, 398.
10. C. E. Moore, "Atomic Energy Levels," National Bureau of Standards, V3 (1958).
11. Y. K. Syrkin and M. E. Dyatkina, "Structure of Molecules in the Chemical Bond," Interscience Publishers, New York (1950).
12. T. Moeller, "Inorganic Chemistry," J. Wiley & Sons, Inc., New York (1955).
13. W. L. Bragg and J. West, *Proc. Roy Soc*, **A111**, 691 (1926).
14. C. A. Coulson, V. Henri Memorial Volume, Desuer, Liege (1948).
15. V. V. Kuznetsoug and A. N. Sevchenko, *Akad. Nauk. Izv.*, **23**, No. 1, 2 (1959).
16. G. Urbain, *Ann. Chim. Phys.*, [8] **18**, 222 (1902).
17. M. Ch. de Rohden, *Ann. Chem.*, **3**, 338 (1915).

Electroluminescence—A Disorder Phenomenon

D. W. G. Ballentyne

Harlow Research Laboratories, Associated Electrical Industries Limited, Harlow, Essex, England

ABSTRACT

In general, electroluminescence is considered to occur at a junction between a semiconducting crystal and a metal or electron rich material. The present work indicates that electroluminescence only occurs in zinc sulfide powders containing both sphalerite and wurtzite. This observation suggests that electroluminescence is a disorder phenomenon associated with stacking faults in the crystal.

Two types of electroluminescence have been observed. Certain substances (e.g., SiC, GaP, etc.) (1) emit light when subjected to a direct electric field applied between electrodes in contact with the surface of the crystal. This emission, carrier injection electroluminescence, is simply explained by the recombination of injected carriers at p-n junctions. The second type of electroluminescence, intrinsic electroluminescence (2), gives rise to the sustained emission of light on the application of an alternating field to the phosphor suspended in a dielectric. In this case, carrier injection is not possible, and the effect has been explained by the acceleration of carriers in an exhaustion barrier in the phosphor, say zinc sulfide activated with copper, at an interface with an electron rich layer of copper sulfide. Such a mechanism does not explain fully certain observations. Many workers have observed that light can be emitted internally from a crystal (2, 3). Steward, *et al.* (4) showed that the electroluminescent emission from a ZnS platelet occurred in bands parallel to birefringent-colorless bands denoting regions of wurtzite and sphalerite. Ultraviolet emission occurred throughout the crystal, and it was concluded that the emission in this case was associated with stacking faults in the c-direction. McKeag and Steward (5) reported a new method of preparing a zinc sulfide phosphor, which consisted of prefiring ZnS at 1200°C, activating with copper at 700°C. The material was electroluminescent throughout the body of the crystal. The copper necessary for the activation entered the crystal most effectively at the refiring stage which was the temperature where the transformation from the hexagonal to cubic zinc sulfide occurred most readily. There existed a correlation between electroluminescence and disorder.

In the present work (6) it is intended to show that in all cases investigated electroluminescent phosphors consist of mixtures of sphalerite and wurtzite. This structure is associated with a redistribution of trapping levels with the removal of the deep traps. An electroluminescent phosphor has been prepared without the addition of a substance capable of forming an electron rich layer. This phosphor also has a disordered structure.

Experimental Results

Two types of general electroluminescent phosphors were prepared. One type of phosphor was prepared according to the Froelich (7) method at 1100°C, while the other group was prepared according to the Butler (8) method at 800°C. Various activators, copper, silver, and manganese, and various coactivators, aluminum, gallium, indium, and thallium, were added. The crystal structure of the phosphors was determined using a 9 cm Unican Powder camera in conjunction with a Raymax 60 x-ray set.

In Fig. 1 the diffraction photographs of a series of phosphors fired at 1100°C in wet H_2S are given. The phosphors A, B, and C containing less than 10^{-4} g Cu/1 g ZnS are totally hexagonal in structure and are not electroluminescent. Phosphors D and E containing copper in excess of 10^{-3} g Cu/1 g ZnS contain both cubic and hexagonal zinc sulfide. These phosphors are electroluminescent. In the actual case

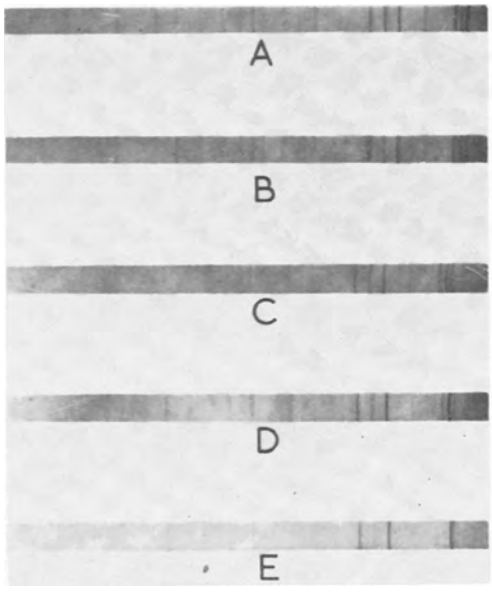

Fig. 1. X-ray powder photograph of a series of phosphors fired at 1100°C in wet H_2S. A, 1 g ZnS 1 x 10^{-6} g Cu 1 x 10^{-4} g Al; B, 1 g ZnS 1 x 10^{-5} g Cu 1 x 10^{-4} g Al; C, 1 g ZnS 1 x 10^{-4} g Cu 1 x 10^{-4} g Al; D, 1 g ZnS 1 x 10^{-3} g Cu 1 x 10^{-4} g Al; E, 1 g ZnS 1 x 10^{-2} g Cu 1 x 10^{-4} g Al.

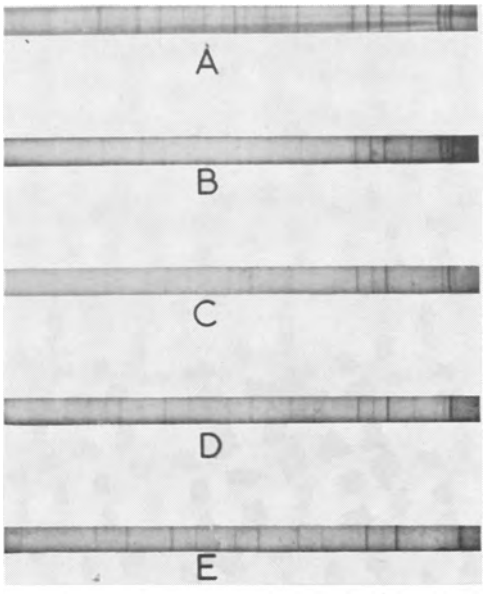

Fig. 2. X-ray powder photograph of a series of phosphors fired at 1100°C in wet H_2S. A, 1 g ZnS 2 x 10^{-4} g Cu 1 x 10^{-4} g Al; B, 1 g ZnS 4 x 10^{-4} g Cu 1 x 10^{-4} g Al; C, 1 g ZnS 6 x 10^{-4} g Cu 1 x 10^{-4} g Al; D, 1 g ZnS 8 x 10^{-4} g Cu 1 x 10^{-4} g Al; E, 1 g ZnS 1 x 10^{-3} g Cu 1 x 10^{-4} g Al.

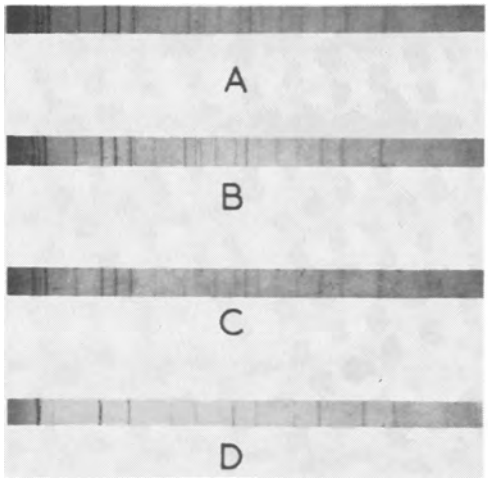

Fig. 3. X-ray powder photograph of a series of phosphors fired at 1100°C in wet H_2S. A, 1 g ZnS 1 x 10^{-5} g Ag 1 x 10^{-4} g Al; B, 1 g ZnS 1 x 10^{-4} g Ag 1 x 10^{-4} g Al; C, 1 g ZnS 1 x 10^{-3} g Ag 1 x 10^{-4} g Al; D, 1 g ZnS 1 x 10^{-2} g Ag 1 x 10^{-4} g Al.

given the concentration of aluminum coactivator was 10^{-4} g Al/1 g ZnS. The same result is obtained for aluminum concentrations varying between 10^{-2} g Al to 10^{-6} g Al/1 g ZnS. The replacement of aluminum by gallium or indium gives similar results. In Fig. 2 the diffraction photographs for a series of phosphors with copper concentrations between C and D in Fig. 1 are given. Up to a concentration of 6 x 10^{-4} g Cu/1 g ZnS the material is hexagonal, above this concentration it consists of a mixture of two phases and only in these cases are the phosphors electroluminescent. It was thought that the correlation between electroluminescence and crystal structure might be fortuitous as copper sulfide precipitation onto the crystallites occurs at approximately the same concentrations. A study of silver phosphors indicates that this is not the case. The

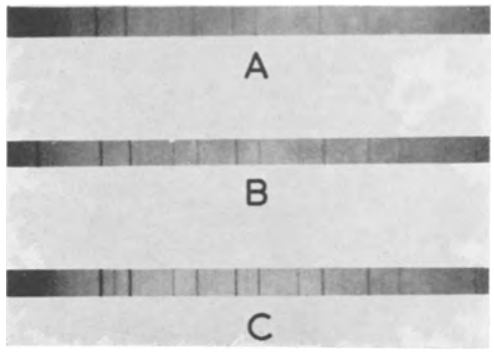

Fig. 4. X-ray powder diffraction photograph of a series of phosphors fired in argon at 800°C. A, 1 g ZnS 1 x 10^{-3} g Cu 1 x 10^{-3} g KCl; B, 1 g ZnS 1 x 10^{-3} g Cu 1 x 10^{-3} g NH_4Cl; C, 1 g ZnS 1 x 10^{-3} g Cu 1 x 10^{-3} g NH_4Cl 1 x 10^{-2} g Pb.

body color of a series of phosphors whose diffraction patterns are shown in Fig. 3 indicates that silver precipitation occurs at 10^{-4} g Ag/1 g ZnS. The mixed phases only occur in the phosphor containing 10^{-2} g Ag/1 g ZnS, and only this phosphor is electroluminescent. There was a further possibility that electroluminescence was a property of cubic zinc sulfide, and that it was the appearance of this phase rather than the formation of a mixture which caused the emission in the cases considered above.

Figure 4 shows the diffraction photographs of three typical so-called cubic zinc sulfide electroluminescent phosphors prepared below the transition point (1024°C). The best of these phosphors is C, and inspection shows that this phosphor has the most clearly defined hexagonal phase. It may be concluded, therefore, that in the so-called cubic electroluminescent zinc sulfide phosphors two phases are necessary for the emission, and the addition of the various substances during the preparation facilitates the growth of the hexagonal phase in the sphalerite temperature range.

Thermoluminescence experiments show that the appearance of electroluminescence and disorder in zinc sulfide is accompanied by a major change in the trapping states in the phosphor. Figure 5A gives the glow curves for the phosphors whose diffraction patterns are given in Fig. 1. It can be seen that the nonelectroluminescent phosphors containing less than 10^{-4} g Cu/1 g ZnS have trapping levels which cause a maximum in the glow curve at −100°C and a "tail" which extends to room temperature. The electroluminescent phosphors, on the other hand, have much shallower traps and the deeper traps have disappeared or no longer give rise to radiative transitions. This trend is shown more clearly in Fig. 5B for phosphors containing the same copper concentration (10^{-6} g-10^{-2} g) but with 10^{-2} g Al instead of 10^{-4} g Al/1 g ZnS. In this case the photoluminescent phosphors have a glow curve consisting of two peaks, one at −100°C, and one nearer room temperature at approximately −40°C. The electroluminescent phosphors again have a much narrower glow curve peak with a maximum between −120°C and −140°C.

Similar results have been obtained for all the other phosphors investigated, although the position

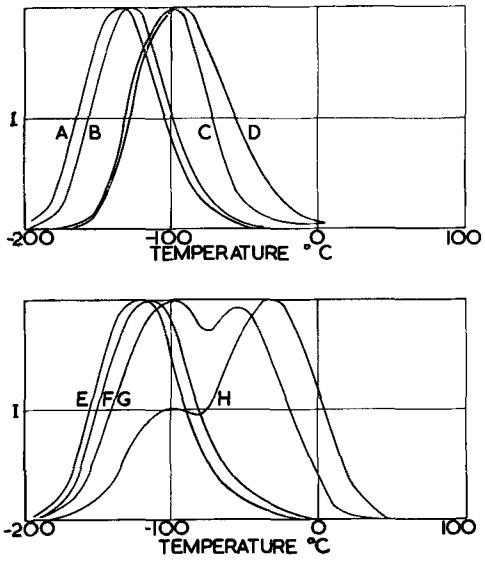

Fig. 5. Thermoluminescence curves of phosphors containing between 10^{-5} and 10^{-2} g Cu (D→A and H→E) with 10^{-4} and 10^{-2} g Al, respectively.

of the glow curve maximum does not appear to be so important as the absence of traps which extend the glow curve to room temperature.

These results appear to indicate, therefore, that electroluminescence occurs in crystals in which there are regions of both wurtzite and sphalerite. It may, therefore, be a property of the disordered region between the two types of crystal. If this is the case, then it should be possible to prepare an electroluminescent phosphor by disordering zinc sulfide by some other means than adding excess copper sulfide. Such a phosphor is described below.

During investigations into thallium-activated phosphors 10% TlCl was added to zinc sulfide and the phosphor was fired at 800°C in a stream of wet H_2S. The resulting phosphors were shown by spectroscopic means to contain no thallium ion; at the temperature of the experiment it had all sublimed. This phosphor was brilliantly photoluminescent and moderately electroluminescent in the green due presumably to vacancies. Exhaustive analysis did not indicate the presence of copper or thallium. The body color, off-white, also showed that an excess of electron-rich material which hitherto had been thought to be necessary for electroluminescence was not present. Figure 6 shows that the crystals of phosphor consisted of a mixture of hexagonal and cubic zinc sulfide. That this phosphor is electroluminescent is shown by the brightness against voltage and frequency curves. The brightness variation may be expressed by the usual relation

$$B = A_o \sqrt{F} \exp\left(-b/\sqrt{v}\right)$$

Discussion

Conventional electroluminescent phosphors have been shown to consist in all cases of the two phases of zinc sulfide, wurtzite, and sphalerite. It would appear possible that electroluminescence can occur without the addition to the phosphor of a material that could act as an electron source.

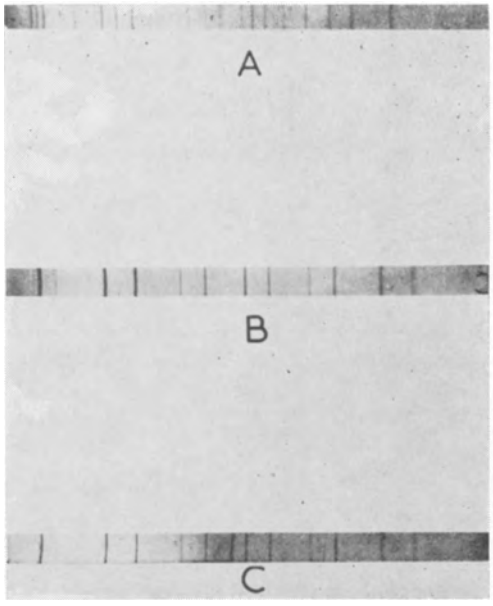

Fig. 6. X-ray powder photograph of: A, hexagonal zinc sulfide; B, 0.9 g ZnS 0.1 g TlCl fired at 800°C in H_2S; C, cubic zinc sulfide.

It is difficult to see, however, where the field for the acceleration of the electrons sufficient to ionize the luminescent centers can arise in such a system. The band gap energy between the two forms of zinc sulfide is small (0.01 ev), but Merz considers that the impurities may cause the band gap to widen to 0.1 ev. The observation of high photovoltages in zinc sulfide single crystals (9) shows experimentally that high fields must exist in these crystals, although the mechanism is obscure. In view, however, of these results, it may not be amiss to suggest the possibility that electroluminescence is a recombination effect at what is essentially a p-n junction. The original objections to this approach, the low threshold and the minority carrier being a hole, is not now important. The threshold of electroluminescence has been shown to depend on the method of detection of the light emitted, and Destriau has been able to go down to levels 0.01 of that visible to the dark adapted eye and still detect light. Wood's (10) observation of p-type conduction in cadmium sulfide doped with copper shows that p-type conduction in the II-VI compounds is not so unlikely as has been hitherto thought.

However, it must be admitted that no explanation of the biphase effect in electroluminescence is satisfactory, and at present the experimental results only are reported.

Acknowledgments

The author would like to thank Dr. M. E. Haine and the A.E.I. (Woolwich) Research Laboratories for permission to publish these results. Further, he would like to acknowledge with gratitude the help of his colleagues during the course of this work.

Manuscript received March 7, 1960.

Any discussion of this paper will appear in a Discussion Section to be published in the June 1961 JOURNAL.

REFERENCES

1. See, for example, G. Destriau and H. Ivey, *Proc. I.R.E.*, **44**, 1911 (1956).

2. G. Destriau, *Phil. Mag.*, **38**, 700 (1947); P. Zalm, *Philips Research Reports*, **11**, 353 (1956).
3. See, however, D. Frankl, *Phys. Rev.*, **100**, 1105 (1956).
4. M. A. Short, E. G. Steward, and T. B. Tomlinson, *Nature*, **177**, 240 (1956).
5. A. H. McKeag and E. G. Steward, *This Journal*, **104**, 41 (1957).
6. D. W. G. Ballentyne, *J. Physics & Chemistry of Solids*, **10**, 272 (1959).
7. H. C. Froelich, *This Journal*, **100**, 496 (1953).
8. H. H. Homer, R. M. Rulon, and K. H. Butler, *ibid.*, 100, 566 (1953).
9. W. J. Merz, *Helv. Phys. Acta*, **31**, 6 (1958).
10. J. Woods, Birmingham Symposium on Dielectric Devices, 1959.

On the Mechanism of Chemically Etching Germanium and Silicon

D. R. Turner

Bell Telephone Laboratories, Incorporated, Murray Hill, New Jersey

ABSTRACT

The electrode potential of germanium or silicon in a chemical etching solution is a function of solution pH, rate of etching, physical condition of the surface, conductivity type, and resistivity. The results suggest that excess holes and electrons are produced at the surface of the semiconductor during chemical etching. Holes are injected at cathode sites, but only a portion of these holes are consumed at anode sites since the anode reaction involves current multiplication.

Semiconductors such as Ge or Si are chemically etched in aqueous solutions containing an oxidizing agent such as nitric acid and an anion such as F^- which is capable of forming water-soluble complexes with the semiconductor. The etching process is actually electrochemical in its action, that is, there are anode and cathode sites on the surface of the semiconductor with local cell currents flowing between them. Semiconductor material goes into solution at the anodic sites while the oxidizing agent is reduced at the cathodic areas. The rate of chemical etching is determined by the magnitude of the corrosion current. If the etching process is nonpreferential and material is removed uniformly, any given area on the surface of the semiconductor must continually alternate between being anode and cathode. When one spot is anodic much more than it is cathodic, an etch pit will form at that point. Experience has shown that this is most likely to occur at grain boundaries and dislocations at the surface of the single crystal. Conversely, hillocks are formed on areas that are cathodic more than they are anodic.

The average current density between local anode and cathode areas during chemical etching can be estimated from the rate of etching. Assuming that the surface while etching is half anode and half cathode and that Ge or Si goes into solution with a valence of 4, the average corrosion current density in amp/cm^2 is given by:

$$i = 2\Delta\epsilon d \qquad [1]$$

where Δ is the etch rate in cm/sec, ϵ is the electrochemical equivalent in coulombs/g, and d is the density of the semiconductor in g/cm^3. The rate of chemically etching n-type Si in HF-HNO_3 mixtures has been determined by Robbins and Schwartz (1). A plot of some of their data along with the equivalent corrosion current density derived from Eq. [1] is shown in Fig. 1. Similar results should be obtained for p-type Si specimens. The etch rate can be converted into inches per minute by multiplying by the factor 2.36 x 10^{-3}. The maximum rate of etching occurs when the ratio of HNO_3 to HF in the solution is 1 to 4.5. Klein (2) has studied the rate of chemically etching silicon in HNO_3-HF mixtures under carefully controlled conditions of temperature and stirring. He also found that maximum etching rate occurred when the HNO_3/HF mole ratio was about 1 to 4.5. The significance of this ratio will be discussed later. The maximum Si etch rate is about 28 μ/sec which corresponds to about 190 amp/cm^2 average corrosion c.d. This is a tremendous current density, but even more amazing is the fact that an n-type silicon electrode biased anodically in a suitable electroetching solution will pass just a few μa/

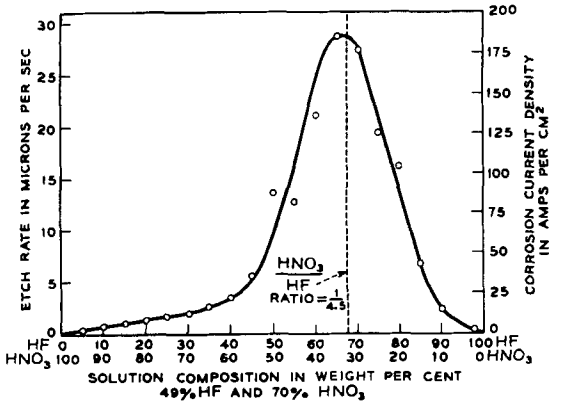

Fig. 1. Rate of chemical etching Si and equivalent corrosion C.D. vs. solution composition, HF + HNO_3 mixtures. Etch rate vs. solution composition data from Robbins and Schwartz (1).

cm^2. This means the maximum chemical etch rate is higher by a factor of 10^8 than the maximum electrolytic etch rate. In order to obtain a better understanding of this phenomenon, potential measurements were made on Ge and Si electrodes in etching and nonetching solutions.

Potential measurements always require two electrodes. If the second electrode is a standard reference electrode, i.e., its potential is known and is constant during the experiment, then the single electrode potential of a semiconductor can be determined from the measured cell voltage. Semiconductor electrodes differ from metal electrodes in that an appreciable part of the single electrode potential may be located inside the semiconductor. In analyzing the potential measurements made on Ge and Si it will be necessary to consider the potential within the semiconductor as well as that at the semiconductor-solution interface.

Experimental Studies on Electrode Potentials

Bars of n- and p-type Ge and Si were used as electrodes. The size, geometry, and surface orientation of the electrodes did not affect the measured potentials within the limit of experimental reproducibility—about ± 0.005 v. Ohmic contacts were made to the Ge by abrading one end, tinning and soft soldering it to a Cu wire. The Si electrodes were abraded at one end and then coated with nickel by the "electroless process" (3) before soldering to the Cu wire. Prior to the potential measurement, each electrode was bright etched in C.P.-4 etching solution (for Si the bromine is omitted), rinsed in deionized water, and blotted dry with filter paper. The electrodes were held vertically during a measurement so that only the tip end of the semiconductor was immersed. Unless otherwise indicated, the solutions were unstirred and initially at room temperature. All potential measurements were made against a saturated KCl calomel reference electrode, hereafter referred to as S.C.E.

Since many of the electrolytes used contained HF or strong alkali, polyethylene containers were used instead of glass. The electrolyte was separated from the saturated KCl solution and the reference electrode by a polyethylene syphon fitted with a filter paper plug. Electrode potential measurements were made with either a Millivac Type MV-17C d-c voltmeter, a L&N X-Y recorder, or a Sanborn Type 151 recorder depending on the experiment and the kind of data desired.

Single electrode potential measurements were made in a variety of solutions, some etching and others nonetching. The results of potential measurements in some of the solutions are shown in Fig. 2. The solutions listed are arranged in their approximate order of increasing *p*H from left to right: (A) conc. (16*N*) HNO_3, (B) CP-4 without Br, (C) 32% conc. HNO_3 + 68% (48%) HF, (D) Landgren's etch (4) — 3% $KMnO_4$ + 97% conc. HNO_3,[1] (E) 48% HF, (F) sat. KCl, and (G) 1N KOH. All per cent compositions in this paper are weight per cent values. The potentials of n- and p-type Ge electrodes are indicated by the small letters while the capital letters are for Si electrodes. These are average values of measurements made on 3 to 5 different electrodes. The spread of the data is indicated where it is more than ±0.02 v. Whenever the electrode potential was photosensitive, the cell was shielded from room light.

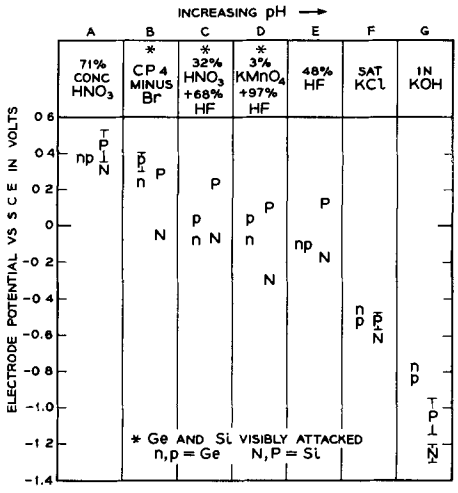

Fig. 2. Electrode potentials of n- and p-type Ge and Si in various etching and non-etching solutions. Unstirred at room temperature.

Figure 2 shows three things: (*a*) increasing *p*H shifts the electrode potential in the negative direction; (*b*) an appreciable potential difference is observed between n and p-type Ge and Si when the solution rapidly corrodes the semiconductor; and (c) p-type Ge or Si is always positive in potential with respect to n-type when a potential difference does exist. The effect of *p*H on the electrode potential of Ge has been observed many times before (5, 6). Cretella and Gatos (7) have observed n-type Ge to be positive in potential with respect to p-type Ge in nitric acid solutions more dilute than 6*N*. This effect cannot always be duplicated. The surface pretreatment appears to be more of a factor than the nitric acid solution. In rapidly etching solutions, however, the results are reproducible and p-type Ge is positive relative to n-type Ge. In etching solutions where the rate of corrosion is controlled by the mass transfer of one of the reacting species to or from the surface stirring increases the etch rate and it also may shift the electrode potential. The effect of stirring on the electrode potentials of Ge and Si are discussed later. If the solution does not attack the semiconductor at an appreciable rate, there is no potential difference between n- and p-type electrodes of either Ge or Si. Electrolytes B, C, and D in Fig. 2 visibly attack both Ge and Si, as evidenced by gas evolution and rapid electrode dissolution. The potential difference between n- and p-type Si in 48% HF is attributed to a slow corrosion process which is made possible by dissolved oxygen. Solution G (1*N* KOH) also attacks Si but only slowly at room temperature. When the electrolyte corrodes the semiconductor at a sufficiently rapid rate, light has no effect on the measured electrode potentials. The potential of Ge and Si in etching solutions is

[1] Solution rapidly etches p-type portions of a silicon single crystal containing p- and n-regions with little effect on n-type regions.

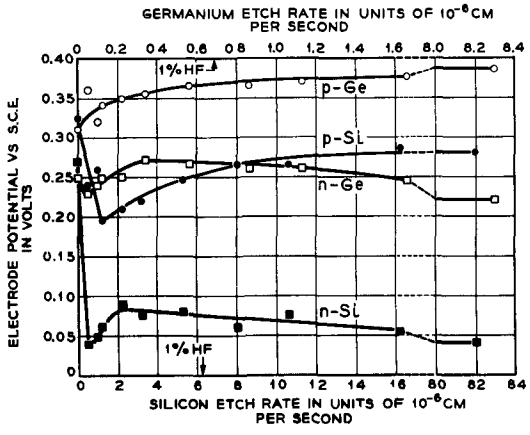

Fig. 3. Effect of etch rate on the electrode potentials of n- and p-type Ge and Si in HF-HNO_3 mixtures. Rate of etching increased by adding HF to HNO_3.

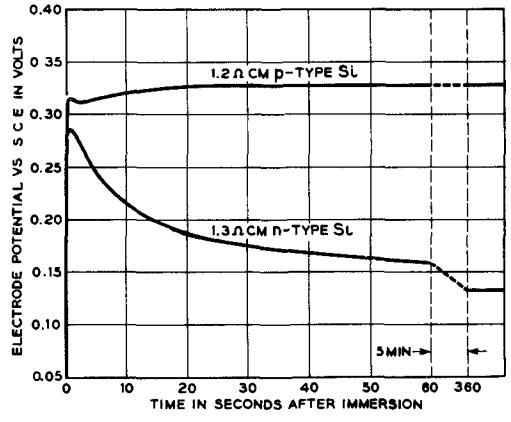

Fig. 4. Electrode potential-time curves for lapped n- and p-type Si immersed in 10% HF + 90% HNO_3.

also a function of the equilibrium hole density in the semiconductor, as is shown later.

A fresh solution of concentrated HNO_3 does not chemically etch Ge or Si at an appreciable rate. The etch rates increase rapidly with additions of HF as shown by Cretella and Gatos (7) for Ge and Robbins and Schwartz' for Si (see Fig. 1). It is of interest to observe the change in the single electrode potential of a semiconductor when the electrolyte changes from an essentially nonetching solution to an etching one. This experiment was carried out by measuring the electrode potentials of 0.8 ohm cm n- and 3.5 ohm cm p-type Ge and 0.7 ohm cm n- and 1.2 ohm cm p-type Si first in concentrated HNO_3 and then with various additions of HF. In concentrated HNO_3 alone the electrode potentials are extremely light-sensitive. For this reason, all light was excluded from the cell. Instead of plotting electrode potential against the amount of HF added, it is more meaningful to show the relation between the electrode potential and the rate of etching as given in Fig. 3. The etch rate for a solution composition 1% (49%) HF + 99% concentrated HNO_3 is indicated for both Ge and Si. The etch rate for Ge in conc. HNO_3 solutions containing from 0 to 10% (49%) HF was determined experimentally from weight loss measurements with four specimens, two n-type and two p-type. Robbins and Schwartz's[1] data, Fig. 1, was used for Si. Note that Si etches about ten times faster than Ge in comparable HF-HNO_3 mixtures. One drop (~ 0.04 cc) of 49% HF produces a large shift in the potential of n- and p-type Si and n-type Ge toward the negative direction. p-Type Ge changes slightly in the positive direction. As the etch rate increases with more HF, the electrode potentials of n-type Ge and Si rise and then decrease again while the potentials of p-type Ge and Si increase. The electrode potentials of all the electrodes reach relatively stable values in solutions containing about 10% HF + 90% HNO_3, where the etch rate is 63 x 10^{-6} cm/sec on Si and 6.7 x 10^{-6} cm/sec on Ge. At this rate of etching the photovoltaic effect is completely absent.

Another interesting experiment was to abrade the surface of semiconductor electrodes and record the change in potential with time as the damaged surface layer was chemically etched away. This was done with 1.3 ohm cm n- and 1.2 ohm cm p-type Si electrodes. The surfaces were abraded by lapping on a glass plate with No. 600 silicon carbide and water. Typical electrode potential-time curves after immersion in 10% (49%) HF + 90% concentrated HNO_3 are shown in Fig. 4. Initially the electrode potentials of abraded n- and p-type Si are about the same. As the damaged surface layer is etched away, the potentials drift apart. The largest potential change occurs with the n-type Si electrode. p-Type Si reaches a stable potential in about 30 sec while the potential of n-type Si becomes stable after 6 min. A potential measurement of this kind may be useful in determining when all the abraded surface material has been removed by etching.

Single electrode potentials of n- and p-type Ge and Si in HNO_3 + HF acid mixtures were also measured as a function of material resistivity. To get reproducible results it was necessary to use freshly prepared solutions. The electrode potentials against the resistivity, ρ, and the equilibrium bulk hole density, p, at 300°K, are shown on a semilog plot in Fig. 5 and 6. The p values were determined from the resistivities using the relation:

$$\frac{1}{\rho} = q\mu_n n + q\mu_p p$$

where q is the charge on the electron, μ_n is the electron mobility, n is the equilibrium bulk electron

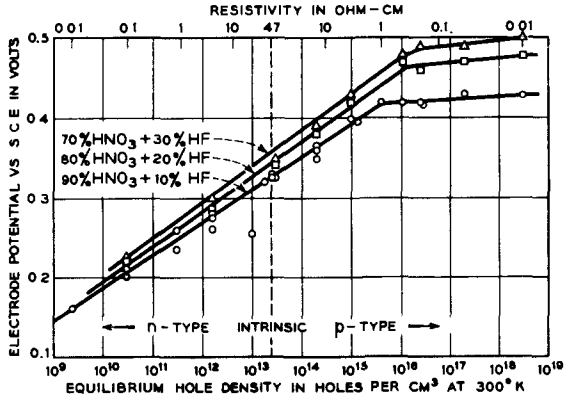

Fig. 5. Electrode potentials of Ge in HNO_3-HF mixtures vs. resistivity and equilibrium hole density.

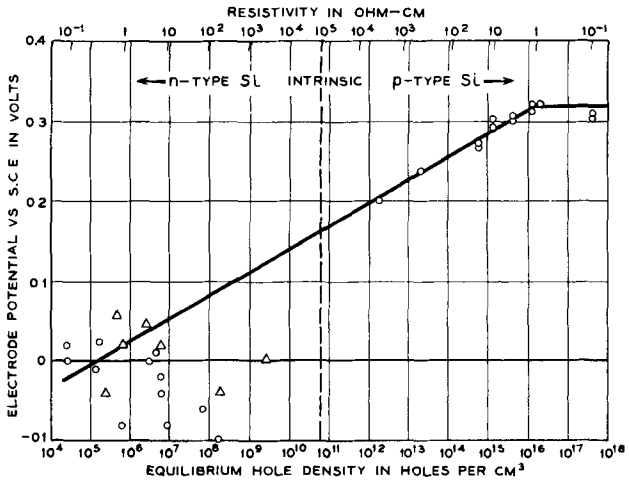

Fig. 6. Electrode potentials of Si in 90% conc. HNO_3 + 10% conc. HF vs. resistivity and equilibrium hole density.

density, and μ_p is the hole mobility. Electron and hole mobilities were obtained from Prince's (8) data and n was derived from the relations: $np = 6.25 \times 10^{26}/cm^6$ at 300°K for Ge and $np = 4.6 \times 10^{21}/cm^6$ at 300°K for Si.

Electrode potentials of Ge were measured in 90% HNO_3 + 10% HF, 80% HNO_3 + 20% HF, and 70% HNO_3 + 30% HF. The measured potentials were fairly stable in freshly prepared 90% HNO_3 + 10% HF, but in the other solutions, where the rate of etching was more rapid, the potentials fluctuated probably because of the stirring effect produced by a greater rate of gas evolution. Most of the data show a linear relation between the electrode potential and the logarithm of the equilibrium hole density with a slope of 0.04 up to about $p \sim 10^{16}$ holes/cm^3. Above 10^{16} holes/cm^3, the electrode potential becomes almost constant. The reason for this limiting potential effect is discussed later. Although there is some difficulty in obtaining a reasonably accurate potential measurement at the higher etching rates, it is clear that at a given equilibrium hole density the electrode potential increases with the etching rate. The difference is most apparent in the region where the potential levels off.

The variation of the electrode potential of Si with p in 90% HNO_3 + 10% HF is different from the Ge results in some respects, as can be seen in Fig. 6. The data obtained with p-type Si electrodes have the same form as p-type Ge except that the slope of the best straight line through the points is about 0.03 instead of 0.04. The results with n-type Si are quite different from those of n-type Ge. The points are widely scattered and there does not appear to be a consistent relation between E_{Si} and p. It was thought at first that perhaps minority carrier lifetime was an important factor. Several uncompensated Si specimens were obtained with reasonably good lifetimes for the resistivity. These results are the triangular points in Fig. 6 and are also widely scattered. An extrapolation of the line from the p-side to the n-side shows the extent of deviation and that there are a few points near the line.

Discussion

An interpretation of the electrode potential measurements on Ge and Si in etching and nonetching solutions should aid in elaborating the mechanism of chemical etching Ge and Si. It will be convenient to discuss the three parts of the measured electrode potentials: (a) the contact potential between the copper wire attached to the semiconductor by means of an ohmic contact and the semiconductor bulk (E_I), (the contact potential is defined as the potential difference in the work functions of the metal and the semiconductor), (b) the potential drop across the space-charge layer between the semiconductor bulk and the surface (E_{II}) (this is called the surface potential, Ψ_s, by physicists), and (c) the potential across the semiconductor-electrolyte interface (E_{III}).

The contact potential E_I between the copper and the semiconductor varies with the position of the Fermi level in the semiconductor bulk; that is, the nature of the doping. The contact potential can be considered to be constant in the electrode potential measurements on a given semiconductor specimen at room temperature. In nonetching solutions, that is, when there is essentially no charge transfer across the semiconductor-electrolyte interface and the semiconductor is at equilibrium, $E_I + E_{II}$ is also a constant regardless of the conductivity type and semiconductor resistivity. This is due to the fact that the Fermi level at the surface of a semiconductor in solutions is determined not by the bulk charge carrier density but by the charge density at the surface. This is illustrated in Fig. 7. The Fermi level at the surface is at a fixed position relative to the valence and conduction bands, that is, Φ_s is independent of the bulk properties of the semiconductor (9, 10). This means that the potential difference ΔE_{II} between n- and p-type material is exactly equal but opposite in sign to the contact potential difference ΔE_I. In nonetching solutions, therefore, changes in the measured electrode poten-

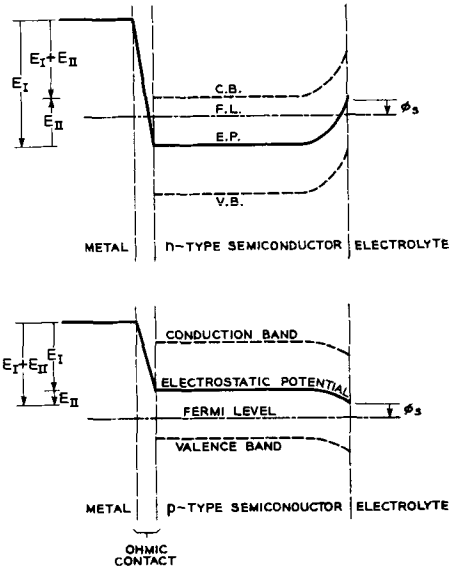

Fig. 7. Energy level diagrams for an n- and p-type semiconductor in contact with a metal and an electrolyte.

tial can be due only to changes in the interfacial potential (E_{III}).

Potential differences between n- and p-type Ge or n- and p-type Si are observed when the electrodes immersed in a nonetching electrolyte are illuminated with light or when they are immersed in a chemical etching solution without light. Under these conditions the surface region of the semiconductor is not at equilibrium. The photovoltaic effect of semiconductor electrodes in solutions has been observed many times (11, 12). It is attributed to hole-electron pairs produced by light energy in the surface region. These extra hole-electron pairs change the Fermi level at the surface of the semiconductor with respect to that of the bulk, that is, E_{II} changes. The measured electrode potential of semiconductors changes when illuminated with light (11, 13). The sign and magnitude of the potential differences between n- and p-type electrodes in etching solutions as shown in Fig. 5 and 6 are essentially the same as those obtained in the photovoltaic effect. This suggests that holes and electrons are produced at the surface of the semiconductor during chemical etching. Several other observations tend to support this interpretation: (*a*) the photovoltaic effect disappears even at moderate rates of chemical etching; (*b*) the rectifying characteristic of a broad-area p-n junction is completely eliminated if either side of the junction is exposed to an etching solution; (c) a Ge or Si diode, with masked leads, generates a considerable amount of power (~ 0.3 milliwatt/cm of exposed junction length) when immersed in C.P.-4 solution; and (*d*) the saturation current density of n-type Ge or Si made anodic in a chemical etching solution increases in proportion to the rate of etching (14). These effects can be explained satisfactorily only by assuming that large numbers of holes and electrons are produced at the surface of semiconductors during chemical etching.

The mechanism of chemically etching Ge and Si must include a source of excess holes and electrons. As stated earlier, chemical etching of semiconductors is an electrochemical process with local anode and cathode areas. Semiconductor dissolution takes place at the anode sites, while the oxidizing agent is reduced at the cathode areas. It has been well established that the anodic dissolution reaction at Ge and Si electrodes consumes holes (11). Brattain and Garrett (11) also found that when they anodically biased an n-type Ge electrode to the saturation current region and then injected holes with light, the total dissolution current increased between 1.4 to 1.8 times the current due to hole injection. Turner (15) has suggested that the mechanism for the anodic dissolution of Ge involves the diffusion of two holes to the surface with a return flow of two electrons for each atom dissolving. This would give a current multiplication factor of 2. Beck and Gerischer (9), however, have found that the current multiplication factor is near 2 only when holes are consumed as fast as they arrive at the anode surface. If holes can diffuse to the surface or holes are injected into the surface region faster than they are consumed in the anode reaction, then the current multiplication factor may be less than 2.

If a semiconductor such as Si is chemically etched in a HNO_3-HF acid mixture, the reaction at the anode sites is the dissolution of silicon as follows:

$$Si + 2H_2O + ne^+ \rightarrow SiO_2 + 4H^+ + (4-n)\,e^- \qquad \xrightarrow{6HF} \quad H_2SiF_6 + 2H_2O \quad [2]$$

where e^+ represents a hole and n is the average number of holes required to dissolve 1 Si atom; n may range from 2 to 4 depending on the current multiplication factor. A Si dissolution valence of four is assumed for the process which is probably correct for HNO_3-rich solutions. In HF-rich solutions, there is evidence that Si dissolution is divalent (12, 16, 17). It is also assumed that Si dissolves by first forming an oxide which then reacts with HF to form the water-soluble silicofluoride complex.

The main function of the oxidizing agent in the chemical etching solution is not to oxidize the semiconductor as is sometimes proposed (1) (Ge and Si are readily oxidized in most oxygen-containing systems) but to provide an easily reduced material for the cathode reaction. In the absence of an oxidizing agent (including oxygen) and metal ions more noble than the semiconductor, the only cathode reaction possible is the discharge of hydrogen ions. The hydrogen discharge reaction can only proceed at a very slow rate, however, because of hydrogen overvoltage. This limits the chemical etching rate to a negligible value.

Oxidizing agents do more than provide an easily reduced material at semiconductor electrodes. They modify the distribution of mobile charge carriers in the surface region so that the Fermi level at the surface is nearer the valence band than it is the conduction band. This is illustrated in Fig. 7. The electron transfer process in the reduction of the oxidizing agent involves the transfer of an electron from the valence band to the ion being reduced. It is equivalent to hole injection. This concept was formulated independently by Gerischer and Beck (9, 18) and Dewald (10). Both have obtained experimental evidence in support of this mechanism. Pleskov (19), using a novel technique of working both sides of a Ge electrode electrochemically, has confirmed their observations.

The reduction of HNO_3 is a complicated reaction involving several steps (20, 21). Cretella and Gatos (7) have shown that the mechanism proposed by Vetter (20) for the cathodic reduction of HNO_3 on a Pt electrode also applies to Ge. The over-all reaction can be written as follows:

$$HNO_3 + 2H^+ \rightarrow HNO_2 + H_2O + 2e^+ \qquad [3]$$

Holes injected into the semiconductor by the cathodic reduction of the oxidizing agent supply the holes required for the anodic dissolution part of the chemical etching process. Combining Eq. [2] with two times Eq. [3] (for charge balance) gives the following over-all reaction for chemically etching silicon in HNO_3-HF mixtures:

$$Si + 2HNO_3 + 6HF \rightarrow H_2SiF_6 + 2HNO_2 + 2H_2O + (4-n)e^+ + (4-n)e^- \quad [4]$$

Each atom of Si dissolving uses up to 2 molecules of HNO_3 and six of HF. The activation energy (~ 4 kcal/mole) (2, 22) for the over-all reaction indicates that the kinetics of the process is diffusion-controlled. Therefore, if the rates of diffusion and convection of HNO_3 and HF from the solution bulk to the Si surface are approximately equal, the maximum etching rate should occur when the mole ratio of HNO_3 to HF is 1/3 [solution composition: 42% by wt (70%) HNO_3 + 58% by wt (49%)HF].

Schmid and Spahn (21, 23) found that HNO_3 reduces beyond nitrous acid, HNO_2, to nitric oxide, NO, when copper is chemically etched in HNO_3. For this mechanism, the over-all cathodic reduction of nitric acid is

$$HNO_3 + 3H^+ \rightarrow NO + 2H_2O + 3e^+ \quad [5]$$

Robbins and Schwartz (1, 24) have assumed that HNO_3 reduces to NO as in Eq. [5] when Si is chemically etched in HNO_3-HF mixtures. However, they also propose that the anode reaction product is SiF_4. As a result, their over-all anode-cathode reaction for etching silicon in HNO_3-HF mixtures gives a 1/3 mole ratio as in Eq. [4] which is only fair in agreement with the results shown in Fig. 1. An excellent agreement is obtained, however, if H_2SiF_6 is assumed to be the anode reaction product instead of SiF_4. The over-all etching reaction obtained by combining Eq. [2] and [5] (Eq. [2] is multiplied by 3 and Eq. [5] by 4 for the necessary charge balance) is as follows:

$$3Si + 4HNO_3 + 18HF \rightarrow 3H_2SiF_6 + 4NO + 8H_2O + 3(4-n)e^+ + 3(4-n)e^- \quad [6]$$

The mole ratio of HNO_3 to HF for this reaction is 4/18 or 1/4.5. This agrees very well with the HNO_3-HF composition which gives the maximum rate of etching shown in Fig. 1 [33% by wt (70%)HNO_3 + 67% by wt (49%)HF]. Klein (2) obtained a maximum etching rate on Si at about the same solution composition. Robbins and Schwartz (1) have properly concluded that to the left of the maximum, where the HF concentration is relatively low, the rate of etching is controlled by the diffusion and convection of HF to the Si surface. The arrival of HNO_3 at the Si surface becomes rate determining in solutions with compositions to the right side of the maximum in Fig. 1.

The number of excess holes and electrons produced in chemically etching Si, as shown in Eq. [4] and [6], depends on the rate of etching and the current multiplication factor $\left(\alpha = \frac{4}{n}\right)$ in the anode reaction. If n is 2, then $\alpha = 2$; but if 4 holes are consumed in dissolving 1 Si atom, then $\alpha = 1$ and no excess holes and electrons are produced. Potential measurements on Ge and Si electrodes in chemical etching solutions indicate that $\alpha > 1$, since the potential is a function of the conductivity type and resistivity as shown in Fig. 5 and 6. The measured electrode potential, except for n-type Si, is shown to be a logarithmic function of the equilibrium hole density. At present, the author does not have a satisfactory interpretation of the results obtained with n-type Si. The material lifetime or the total impurity density were found not to be a factor. Dewald (10) has shown that holes are the potential-determining carriers at semiconductor electrodes in etching solutions. The hole density just inside the space-charge layer (p_1) is large on n-type as well as p-type electrodes. For very strongly p-type samples (equilibrium hole densities $p > \sim 10^{16}$ holes cm^{-3}), p_1 is not appreciably different from the equilibrium hole density and the measured electrode potential becomes almost constant. The limiting potential effect should occur at higher p values if the rate of hole generation at the surface increases. This is confirmed by the results shown in Fig. 5 since the etch rate increases with larger amounts of HF.

The potential (E_{III}) at the semiconductor-electrolyte interface can best be illustrated with typical anode and cathode potential-current curves as shown in Fig. 8. In order to simplify the diagram, the IR drops in the local corrosion circuits were not included. In HNO_3-HF mixtures the cathode reaction is the reduction of HNO_3 according to Eq. [5], while the anode reaction is the dissolution of the semiconductor, Eq. [2]. The case illustrated in Fig. 8 is the condition where the etching rate is determined by the mass transfer of HF to the surface. The intersection of the anode and cathode curves determines the etching or corrosion current, and the measured potential of the electrode. In concentrated HNO_3 without HF, the corrosion current is essentially zero and the measured potential is the open-circuit potential of the cathode reaction—the reduction of nitric acid on the semiconductor. When HF is added, the anode reaction proceeds at a much higher rate before polarization sets in, curve A_2. The etching rate on Ge or Si increases markedly and the measured electrode potential changes in the negative direction. When the measured electrode potential is appreciably far from the open-circuit anode or cathode potential it is often called a mixed corrosion potential. The large initial poten-

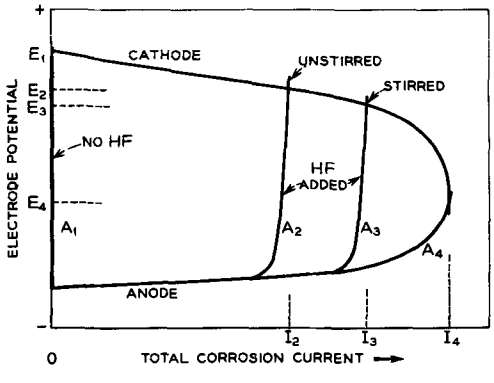

Fig. 8. Typical electrochemical polarization curves for local anodes and cathodes on Ge or Si in HNO_3 with and without HF additions.

tial change in Fig. 3 which occurred when a small amount of HF was added to HNO_3 is attributed to a large change in the mixed interfacial potential. Subsequent changes in the electrode potential at higher etch rates with more HF as shown in Fig. 3 are complicated by changes in E_{II} (inside the semiconductor) due to the excess holes and electrons produced. Stirring increases the supply of the rate-determining material to the surface of the semiconductor. This increases the corrosion current and shifts the electrode potential, as shown in Fig. 8. The potential change with stirring is easily demonstrated by simply jiggling the electrode. When HF is the rate-determining material the potentials of both n- and p-type Ge (or Si) always shift in the negative direction and when HNO_3 is the controlling factor, the potentials become more positive with stirring. Current I_4 and potential E_4 represent the values obtained when the mass transfer of HNO_3 and HF are equally rate determining. As previously mentioned, this occurs on Si at the maximum rate of etching when the HNO_3/HF ratio is about 1-4.5.

Summary and Conclusions

The chemical etching of semiconductors is really an electrochemical process. Semiconductor dissolution takes place at local anode sites while the oxidizing agent is reduced at local cathode areas. The total anodic current always equals the total cathodic current. The average anode and cathode current density calculated from rates of etching data is in the order of amperes per square centimeter. The rate of etching is controlled by the mass transfer of an ionic or molecular species in the electrolyte to the surface of the semiconductor. It is not limited by the supply of holes or electrons in the semiconductor surface. In fact an excess of holes and electrons are produced at the surface. The large number of holes required to maintain the semiconductor dissolution reaction rate at amperes per square centimeter are supplied by hole injection at nearby cathodic areas. Due to a current multiplication effect in the anode reaction, an equal number of excess holes and electrons are produced at the semiconductor surface. These excess holes and electrons modify that part of the measured electrode potential which is just inside the surface of the semiconductor.

Acknowledgments

The author is grateful to Miss A. D. Mills and D. D. Bacon for their help in obtaining the germanium and silicon electrode material used in this work. He is also indebted to U. B. Thomas, J. F. Dewald, and D. L. Klein for their aid in interpreting the data and suggestions as to the best way to present the material.

Manuscript received March 30, 1960. This paper was prepared for delivery before the Chicago Meeting, May 1-5, 1960.

Any discussion of this paper will appear in a Discussion Section to be published in the June 1961 JOURNAL.

REFERENCES

1. H. Robbins and B. Schwartz, *This Journal*, **106**, 505 (1959).
2. D. L. Klein, Recent News Paper, Electrochem. Soc. Meeting, Chicago (1960).
3. M. V. Sullivan and J. H. Eigler, *This Journal*, **104**, 226 (1957).
4. C. R. Landgren, U. S. Pat. 2,847,287, Aug. 12, 1958.
5. M. L. Nichols and S. R. Cooper, *Ind. and Eng. Chem. Anal. Ed.*, **7**, 350 (1935).
6. W. W. Harvey and H. C. Gatos, *This Journal*, **107**, 65 (1960).
7. M. C. Cretella and H. C. Gatos, *ibid.*, **105**, 487 (1958).
8. M. B. Prince, *Phys. Rev.*, **92**, 681 (1953); **93**, 1204 (1954).
9. F. Beck and H. Gerischer, *Z. Elektrochem.*, **63**, 943 (1959).
10. J. F. Dewald, "Semiconductors," Chap. 17, Reinhold Publishing Corp., New York (1959).
11. W. H. Brattain and C. G. B. Garrett, *Bell System Tech. J.*, **34**, 129 (1955).
12. A. Uhlir, *ibid.*, **35**, 333 (1956).
13. W. W. Harvey and H. C. Gatos, *J. Appl. Phys.*, **29**, 1267 (1958).
14. D. R. Turner, To be published.
15. D. R. Turner, *This Journal*, **103**, 252 (1956).
16. D. R. Turner, "Surface Chemistry of Metals and Semiconductors," H. C. Gatos, Editor, John Wiley & Sons, Inc., New York (1960).
17. R. J. Archer, *J. Phys. Chem. Solids*, In press.
18. H. Gerischer and F. Beck, *Z. Phys. Chem.*, **13**, 389 (1957).
19. Iu. V. Pleskov, *Akad. Nauk. SSSR, Doklady*, **126**, 111 (1959).
20. K. Vetter, *Z. Phys. Chem.*, **194**, 199 (1950).
21. G. Schmid, *Z. Elektrochem.*, **63**, 1183 (1959).
22. H. Robbins and B. Schwartz, Electrochemical Society Meeting, Oct. (1960).
23. G. Schmid and H. Spahn, *Z. Metallkunde*, **46**, 128 (1955).
24. H. Robbins and B. Schwartz, *This Journal*, **107**, 108 (1960).

Preparation of Boron by Fused Salt Electrolysis

Nelson P. Nies

U. S. Borax Research Corporation, Anaheim, California

ABSTRACT

The preparation of elemental boron by fused salt electrolysis was investigated using various electrolytes composed of B_2O_3 dissolved in mixtures of alkali metal and magnesium chlorides, fluorides and oxides, with a graphite crucible anode and a steel cathode at about 850°C. The best product purity, 97.5%, was obtained with a bath containing KCl, KF, and B_2O_3, treated with HCl gas. This electrolyte has the advantage that it is not as volatile as previously used baths containing KBF_4. Lower purities were obtained with baths containing sodium or magnesium salts. An approximate phase equilibrium diagram is given of the liquid system KCl-KF-B_2O_3.

Elemental boron has been prepared by (*a*) thermal reduction of boric oxide with metals (1, 2), (*b*) thermal reduction of boron halides or fluoborates with metals or hydrogen (2-5), (*c*) thermal dissociation of boron halides or hydrides (5-8), and (*d*) fused salt electrolysis. In the first of these methods the highest purity has been obtained by the use of magnesium powder (Moissan process); most commercial boron has been produced by this means. However, the purity of Moissan boron (without further treatment) is usually less than 92%, and this method is limited economically by the cost of the magnesium and the excess B_2O_3 used. Methods (*b*) and (*c*) are capable of producing higher purity boron but also have been limited economically by the cost of raw materials. The electrolytic method is not so limited by raw material costs and was believed worthy of further investigation.

Early work on the electrolysis of alkali borates, reviewed by Andrieux (9), resulted in impure products and low yields. Kahlenberg (10) electrolyzed fused KBF_4 and stated that operation was satisfactory except for contamination of the product with copper from oxidation of the cathode. He also attempted the electrolysis of a KF-B_2O_3 bath but was unsuccessful because of attack on his containers. He reported a product analyzing 100% B from a nonfluoride bath containing KCl, K_2O, and B_2O_3, but, as will be shown, this result could not be confirmed in the present work.

Andrieux (11) reported that in the electrolysis of borates, the product of highest purity, about 85% B, was obtained when the cation present was magnesium. Cooper (12) reported a maximum purity of 96.7% B by electrolysis of a KF-KBF_4-B_2O_3 bath and 99.5% B with KCl-KBF_4 and KCl-KBF_4-B_2O_3 baths. Cooper's electrolytes containing B_2O_3 are analogous to those used in aluminum production. Andrieux and Deiss (13), Ellis (14), Miller (15), Murphy, Tinsley, and Meenaghan (16), Fullam (17), and Stern and McKenna (18) have also electrolyzed baths containing KBF_4. These investigators also obtained their maximum purity by using KBF_4. In most cases they did not reach the maximum purity reported by Cooper.

The use of KBF_4 leads to appreciable loss of boron and fluoride by volatilization, because of its tendency to decompose on heating [v.p. 182 mm at 800°C(19)]. The purpose of the present work was to find, if possible, a bath which would be more stable than those containing fluoborates and which would produce a comparable product.

Experimental

A graphite crucible, of inside diameter 254 mm, inside depth 380 mm, with walls 76 mm thick and with a close-fitting shell of 6.4 mm (¼ in.) Inconel was used as a bath container and as the anode. This was enclosed in a brick furnace heated with a gas burner. The cathodes used were either cylindrical or flat. The flat cathodes were made by welding 5 mm x 127 mm or 152 mm Armco iron plates together with ⅜ in. spacers between them, to form a hollow cathode which could be cooled by blowing compressed air into it. The cylindrical cathodes were made from mild steel pipe closed at the bottom, with a tube inside the cathode extending almost to the bottom for cooling with compressed air at the end of a run. It was found helpful in preventing attack on the cathodes to have tubes for air cooling welded to the cathode above the bath level. A layer of frozen electrolyte was put on the upper part of the cathode, above the bath level, by momentarily dipping the cathode in the bath before bolting it in place for the electrolysis, and this layer was maintained during electrolysis by passing a current of air through these tubes. To start a run, the crucible was filled with about 35 kg of the mixed ingredients (technical grade) and heated until fused and the desired temperature was reached. The cathode was then bolted to a water-cooled copper cathode holder and lowered into the bath. The bath was not covered and no protective atmosphere was used. The current was supplied by Edison batteries. In some experiments the potential was applied to the cathode before placing it in the

bath; this procedure usually resulted in a layer of electrolyte between the black deposit and the cathode. In most experiments, therefore, the current was not turned on until a few minutes after lowering the cathode into the bath, in order to permit melting of the layer of frozen salt which formed at first on the surface of the cathode. Any black scum on the surface of the bath was removed by skimming at frequent intervals. It was found desirable at the end of a run to decrease the current to about 25-40 amp and cool the cathode by passing compressed air through it for a few minutes before raising the cathode from the bath, in order to increase adherence of the deposit to the cathode. The product generally formed on the surface of the cathode as a smooth black deposit (occasionally rough in places) containing about 25% elemental boron and 75% electrolyte. The deposit often showed a tendency to ignite in spots just after removal of the cathode from the bath. If this occurred it was quickly extinguished by covering with granular sodium chloride. On soaking the cathode in water the deposit disintegrated and was easily removed from the cathode. In some cases, the deposit was removed by hammer and chisel, in order to separate the smooth parts of the deposit from the rough. Any parts which appeared different, such as the deposits on the edges and sides of a flat cathode, were separated also. These portions of the crude deposit were extracted with boiling water, digested overnight with hot concentrated HCl, washed and dried at 110°C. The products were practically amorphous to x-rays.

For analysis, a freshly dried 0.2-g sample, was either fused with 10 g of sodium carbonate (20) or dissolved in mixed acids (21); B_2O_3 was determined by titration by the usual method, using mannite.

Data on selected runs with various electrolytes are given in Table I.

Discussion

One of the first bath compositions investigated (Run 1) was the KCl-K_2O-B_2O_3 bath, which had been stated by Kahlenberg (10) to give pure boron. In this nonfluoride bath some alkalinity is necessary to dissolve the B_2O_3. Only a very low yield of 65% boron could be obtained with this bath.

Replacement of KCl partially (Run 2) or completely (Run 3) by KF in these alkaline baths gave a somewhat better but still unsatisfactory purity, 78-79% B. If the alkalinity was increased to 32.5% (Run 4), no deposit at all was obtained. These poor results with alkaline baths may have been due to oxidation of the deposit by carbonate, which was present in alkaline baths in higher concentrations than in nonalkaline baths (Runs 3, 4, 6).

Better results were obtained with electrolytes not containing added alkalinity. Electrolytes com-

Table I. Summary of experiments on the electrolytic production of elemental boron

Run No.	Bath components, wt %				pH of 0.33% solution	Hr	Avg temp, °C	Volts	Amp	Average cathodic current density, amp·dm^{-2}	Current efficiency, %	Product purity, % B
	KCl	KF	K_2O	B_2O_3								
1	59	0	21	20	—	2	882	4.3-5.4	560-780	87	1	65.0
2	23.5	31.5	21.5	23.5	—	3	857	4.2-5.3	570-800	98	31	79.3
3[a]	0	50	20	30	—	3	849	4.5-5.5	495-775	96	55	78.0
4[b]	0	43	32.5	24.5	—	3	882	3.5-4.6	500-775	81	0	—
5[c]	56	36		8	—	1.3	810	5.3-5.7	580-605	135	34	80.4
6[d]	11.5	73.5		15	—	2.0	850	3.8-4.7	600-740	99	81	87.8
7	71	21.5		7.5	—	1.5	845	3.9-4.7	505-650	81	40	83.5
8	44	33		23	7.6	1.5	860	3.6-3.8	255-300	74	67	87.0
9[e]	43.5	32		24.5	4.7-4.9	1.5	860	3.5-3.7	280-300	79	58	93.3
10[e,f]	91	7.2		1.8	3.4	1.5	840	4.0-4.2	285-310	82	62	90.4
11[e]	46.5	30.0		23.5	4.9	1.5	871	3.6-3.8	290-300	79	47	96.0
12[e]	44	41		15	7.1-7.2	2.0	812	3.1-3.2	310-370	87	57	94.7
13	0	92.5		7.5	—	3.0	896	3.4-4.1	595-940	107	58	84.0
14	0	69.5		30.5	—	3.0	802	4.9-5.6	515-710	92	67	86.5
15[g]	0	85		15	5.6-5.7	2.5	877	2.6-3.2	310-355	87	28	90.7
		KBF_4										
16[h]	70	22		8	3.8	2.0	827	3.5-3.7	295-360	84	79	95.0
		NaCl	NaF									
17[e]	20.5	32	27.5	20	8.1	2.0	909	2.7-3.4	295-340	84	56	85.9
18[e]	0	39	36	25	7.7-7.9	1.0	836	3.7-3.9	340-370	93	27	79.4
	MgF_2	KF										
19[i]	11	79		10		4	906	2.5-3.2	315-360	48	18	84.3

[a] Run 3: Analysis of electrolyte for CO_2: before run, 0.42%; after run, 0.19% CO_2.
[b] Run 4: Analysis of electrolyte for CO_2: before run, 0.43%; after run, 0.23% CO_2.
[c] Run 5: KCl-KF eutectic (m.p 605°C) + B_2O_3.
[d] Run 6: CO_2 content of electrolyte at start of run, 0.012%.
[e] Runs 9-12; 17 and 18: Electrolyte acidified with gaseous HCl before electrolysis.
[f] Run 10: HCl was passed into this bath for 2½ hr, causing a second liquid of composition 21% KCl, 31% KF and 48% B_2O_3 to form at the bottom of the crucible.
[g] Run 15: Gaseous HF passed into bath before electrolysis.
[h] Run 16: Cooper (12) electrolyte.
[i] Run 19: Product contained 2.3% Mg.
Note: Cathode dimensions: Runs 1-4, 6, 7, 13, 14, 19: flat, 12 × 2 cm, immersed 23 cm; Run 5: cylindrical, 9 cm diameter, immersed 12 cm; Runs 8-12, 15-18: cylindrical, 6 cm diameter, immersed 23-24 cm.

posed of KCl, KF, and B_2O_3 (runs 5-8) gave products ranging up to a maximum of 91.6% boron in the coarser fraction of Run 8. In these experiments the + 100 mesh fraction of the product was usually of higher purity than the finer fractions. When a flat cathode was used, the deposit at the edges, where the current density was greater, generally gave a somewhat higher purity than that on the flat sides. This bath composition gave poor results under some conditions such as low temperatures and low KF or B_2O_3 concentrations. A KF/KCl ratio equal to that of the eutectic in the system KF-KCl also gave poor results (Run 5).

It is known that fused halides exposed to the atmosphere will gradually become alkaline. Since the above experiments indicated that an increase in electrolyte alkalinity gave a poorer quality product, neutralization with HCl was attempted. It was found that the alkalinity could be eliminated by bubbling HCl gas into the fused salt bath through a graphite tube. A convenient means of controlling the addition of the gas was to determine the *p*H of a 0.33% solution of the electrolyte. By electrolysis of these acid-treated baths (Runs 9-12) it was possible to produce boron of markedly increased purity. The highest over-all product purity reached was 96% B in Run 11. Coarser fractions of the products were again of higher purity than the finer fractions and reached 97.3-97.5% B in several runs. Boron of good purity was obtained with electrolytes of which the *p*H of the 0.33% solution ranged from 4.8 to 7.2, and the KCl:KF:B_2O_3 proportions by weight were 47:30:23, 57:30:13, 42:38:20, and 45:40:15.

Figure 1 is a phase equilibrium diagram of the liquid system KCl-KF-B_2O_3. The numbers shown are examples of the product purity obtained with acid-treated baths of various proportions of these components. In Run 10, the HCl was passed into the fused bath for 2½ hr, which apparently caused a loss of HF from the bath and resulted in separation of the bath into two liquids, represented by the ends of the tie line in Fig. 1.

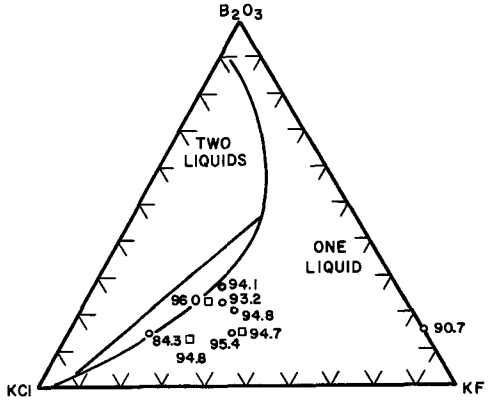

Fig. 1. Phase diagram for the liquid system KCl-KF-B_2O_3 at approximately 800°-900°C (wt %), showing the per cent boron in the product obtained by HCl treatment and electrolysis of various electrolyte compositions. Squares represent products in which the +100 mesh fraction consisted of 97.3-97.5% boron.

For reasons not fully understood, lower purities and "blistering" of the deposits were sometimes observed. A cause of this may be the partial burning of the deposit which sometimes occurred in spots just after removal of the cathode from the bath.

Other electrolyte compositions were investigated. Electrolytes of B_2O_3 dissolved in KF were tried over a range of B_2O_3 concentration up to the composition B_2O_3:2KF suggested by Kahlenberg (10). An attempt was made to acidify these baths by passing in gaseous HF. The HF was absorbed, but less readily than HCl. The maximum product purity obtained with this acidified bath was 90.7% (Run 15) compared with 86.5% without addition of acid (Run 14).

Cooper's (12) electrolyte KCl-KBF_4-B_2O_3 gave typically 93.5-95.5% purity under our conditions. An example is Run 16.

Electrolytes containing sodium salts were tried, HCl being passed in as before (Runs 17, 18). Sodium salts did not absorb either HCl or HF well enough to become acidic. These experiments gave lower product purities than the potassium salts and thus confirm Cooper's (12) statement that sodium salts are detrimental. Metallic sodium was observed in the deposit and on the surface of the bath in some cases, especially where the operating temperature was below the boiling point of sodium, 880°C.

Also, electrolytes composed of KF, MgF_2, and B_2O_3 were tried (Run 19) but the purities were only 82-84% B and the products contained appreciable amounts of magnesium.

Acknowledgment

The author wishes to thank Dr. E. W. Fajans for helpful discussions, and Vincent Morgan, L. E. Hiebert, L. L. Thomas, and S. A. Sorenson for their contributions to the experimental work.

Manuscript received March 21, 1960. This paper was prepared for delivery before the New York Meeting, April 27-May 1, 1958.

Any discussion of this paper will appear in a Discussion Section to be published in the June 1961 JOURNAL.

REFERENCES

1. E. Weintraub, *Trans. Am. Electrochem. Soc.*, **16**, 165 (1909).
2. J. S. Spevack and A. Kurtz, A. E. C. Report A-1246 (1944).
3. H. Haag (to Hermann C. Starck A. G.) U. S. Pat. 2,794,708, June 4, 1957.
4. D. R. Stern and L. Lynds, *This Journal*, **105**, 676 (1958).
5. C. F. Powell, I. E. Campbell, and B. W. Gonser, "Vapor Plating," pp. 106-111, John Wiley & Sons, Inc., New York (1955).
6. H. L. Johnston, H. N. Hersh, and E. C. Kerr, *J. Am. Chem. Soc.*, **73**, 1112 (1951).
7. E. J. Prosen, W. H. Johnson, and F. Y. Pergiel, *J. Res. Nat. Bur. Stds*, **61**, 247 (1958).
8. L. V. McCarty and D. R. Carpenter, *This Journal*, **107**, 38 (1960).
9. J.-L. Andrieux, *Rev. Met.*, **32**, 487 (1935).
10. H. H. Kahlenberg, *Trans. Am. Electrochem Soc.*, **47**, 30 (1925).

11. J.-L. Andrieux, *Ann. Chim.*, **12**, 423 (1929).
12. H. S. Cooper (to Walter M. Weil), U. S. Pat. 2,572,248 and 2,572, 249, Oct. 23, 1951.
13. J.-L. Andrieux and W. J. Deiss, *Bull. Soc. Chem.*, **1955**, 838.
14. R. B. Ellis (to Callery Chem. Co.), U. S. Pat. 2,810,683, Oct. 22, 1957.
15. G. T. Miller, *This Journal*, **106**, 815 (1959).
16. H. F. Murphy, R. S. Tinsley, and G. F. Meenaghan, Bull. Virginia Polytech. Inst., Eng. Exp. Sta. Series No. 115 (1957).
17. H. T. Fullam, Doctoral Dissertation Series, Pub. No.: 20,381, pp. 136-7, University Microfilms, Ann Arbor, Mich. (1956).
18. D. R. Stern and Q. H. McKenna (to American Potash & Chemical Corp.) U. S. Pat. 2,892,762, June 30, 1959.
19. J. H. deBoer and J. A. M. van Liempt, *Rec. Trav. Chim.*, **46**, 124 (1957).
20. H. Blumenthal, *Anal. Chem.*, **23**, 992 (1951).
21. C. A. Hampel, "Rare Metals Handbook," p. 81, Reinhold Publishing Co., New York (1954).

Catalytic Activity and Electronic Structure of Rhodium-Palladium-Hydrogen Cathodes in Acid Solution

James P. Hoare[1]

Scientific Laboratory, Ford Motor Company, Dearborn, Michigan

ABSTRACT

Hydrogen overvoltage measurements were made on a series of rhodium-palladium alloy cathode beads. Two phases, α and β similar to those in the Pd-H system, are considered in the Rh-Pd-H system. Mechanisms for the hydrogen producing reactions on rhodium, palladium, and rhodium-palladium alloy cathodes are discussed. From low current density measurements the catalytic activity of the cathode surface for the hydrogen reaction was determined. It appears that vacancies in the *d*-band of the catalyst metal are necessary for strong bonds between the absorbed hydrogen and the surface but it is the density of states at the Fermi level that determines how strong the chemisorbed bonds are. The catalytic activity is directly related to the heat of absorption and so to the *d*-band structure.

In recent years much interest has been generated in establishing relationships between the surface properties of metallic catalysts and the electronic structure of the bulk metal (1). It has been suggested that on a metal such as palladium, containing vacancies in the *d*-band, hydrogen is adsorbed with a greater heat of adsorption than on an alloy of palladium and gold in which the number of *d*-band vacancies has been reduced (2).

Hydrogen overvoltage measurements were carried out on a series of Pd-Au (3) and Pd-Ni (4) alloys. The results of these investigations indicated that the surface catalytic activity of the electrode is directly associated with the number of vacancies in the *d*-band of the bulk metal through the heat of adsorption of hydrogen on the metal as pointed out by Conway and Bockris (5). It was, therefore, indicated (2, 3, 5, 6) that for metals on which the slow discharge step or Volmer mechanism (7) is rate determining the catalytic activity should increase (2, 3) as the number of holes is increased. However, for those metals on which an H-atom desorption step is rate controlling, such as the slow combination or Tafel mechanism (8) and the so-called electrochemical or Horiuti mechanism (9), the reverse should be true.

In order to test this theory further and possibly to determine whether the catalytic activity is related to the number of holes or to the density of states in the *d*-band it was desired to find a series of alloys in which the number of holes could be increased. An obvious system is that of Rh-Pd. Although the phase diagram of this system is not available, still the two metals have very similar atomic dimensions and both form face-centered cubic crystals (10). Therefore, it is not unlikely that they are completely miscible in one another. Since Rh has one less electron than Pd, additions of Rh to Pd should form a series of alloys with an increasing number of vacancies in the alloy *d*-band. It is with this system that the present investigation is concerned.

Experimental Methods

A series of Rh-Pd alloys of the following compositions were made by melting the required amount of Pd, 99.7% pure, with that of Rh, 99.8% pure, in an induction furnace under a hydrogen atmosphere. These compositions are: 1, 2, 5, 10, 15, 20, 50, and 90 atomic per cent (a/o) rhodium. A portion of the alloy, welded to a Pt wire which served as the electrical contact, was melted to form a small bead. The alloy bead and the Pt lead were imbedded in polyethylene in such a manner that only a hemisphere of the alloy bead was exposed. The exposed apparent surface area of the beads, measured geometrically, ranged between 0.09 and 0.04 cm^2.

The cylindrical cell, shown in Fig. 1, was made of Teflon and was designed to hold about 25 ml of solution. A large piece of Pt gauze lined three quarters of the inner wall and served as the anode, while a rather small piece of Pt gauze served as the reference electrode. The cell top was fitted with a Teflon tube which provided the hydrogen inlet, a

[1] Present address: Research Labs., General Motors Corp., Warren, Mich.

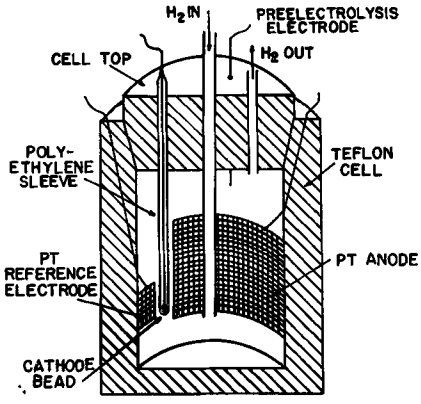

Fig. 1. Teflon cell

short tube for the hydrogen outlet, the polyethylene covered cathode bead and platinum lead, and a hole through which the pre-electrolysis electrode (a Pt wire) could be placed.

The water was triply distilled from an all-quartz still, and all purification techniques were the same as those described before (11, 4). Overvoltage measurements on the alloy beads were carried out with an electronic current interrupter in electrolytically purified 2*N* sulfuric acid solution vigorously stirred with purified hydrogen in the same way as was done in the case of the bright Pd bead (11). Potential measurements were recorded only when the pulse from the current interrupter indicated clean surface (12) conditions (high pseudo-capacitance) (13). The temperature was 25° ± 1°C, and individual points could be reproduced within ± 2.5 mv. The potential η (positive in the direction of anodic polarization) is an electrode potential or overpotential measured by reference to a reversible Pt/H_2 electrode in the same solution.

Results and Discussion

Two series of experiments were carried out on the Rh-Pd alloy beads.

The α-Rh-Pd-H *System.*—In the first series of experiments, the Rh-Pd alloy cathode was anodized at a relatively high current density (0.3 amp/cm^2) for about 30 min. The circuit was broken and the open-circuit potential of the bead vs. a Pt/H_2 electrode in the same solution was followed as a function of time. When the ternary system, Rh-Pd-H, had reached a steady state and the potential had been constant for at least 12 hr, this steady-state value was recorded. Then by means of a constant current source and a high-value series resistor (20 to 60 megohm), the alloy bead was first slightly cathodized stepwise and the time independent (constant for at least 10 min) values of the potential η were recorded for each step. Afterwards, the cathodic current was reduced stepwise to zero and was continued in like manner in the anodic direction. The points on the curves in Fig. 2 are the average values for at least three cycles of increasing and then decreasing the current over the complete current range shown in Fig. 2. These points were reproducible within ± 0.5 mv.

The potential η observed at zero current may be interpreted as a mixed potential derived from two

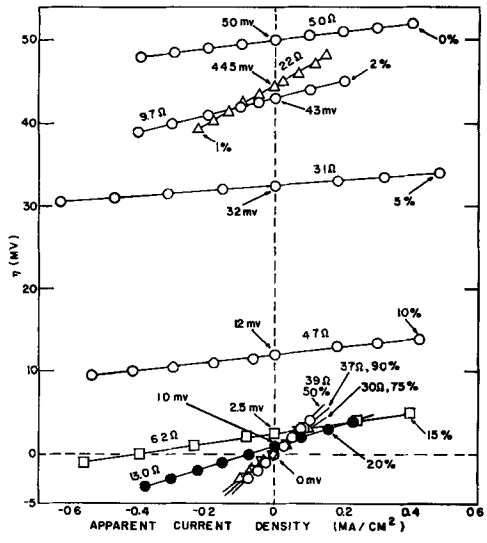

Fig. 2. Apparent current density i vs. electrode potential or overpotential η referred to a Pt/H_2 electrode in the same solution (2N H_2SO_4). Anodic currents to the right, anodic polarizations upward. Linear current density range for Rh-Pd alloys. Atomic per cent Rh indicated on graph together with open-circuit potentials. The slope $d\eta/di$ is given for each alloy in ohm cm^2 (25°±1°C).

phases existing in the Rh-Pd-H system analogous to the α and β phases found in the Pd-H system (14). If, in this region, the mixed potential is determined by the α-phase analogue of the Rh-Pd-H system (hereafter designated as α-Rh-Pd-H), then this steady-state potential is, for practical purposes, identical to the equilibrium potential (15) for the saturated α-phase. Since it has been shown (16) that in the Pd-H system a bead-type of electrode similar to that used in this investigation exhibits the potential of a Pd cathode in the α-phase of maximum composition for periods of time greater than a week, these electrodes are good approximations to a pure α-phase electrode. There may or may not be small amounts of the β-phase also present, but the electrochemical properties are determined by the dominant α-phase.

In the low current density region where a linear relationship between the current density i and electrode potential or overpotential η exists, the slope of the i vs. η curve may be taken as a measure of the rate of the hydrogen reaction k occurring at the electrode (17), i.e., k will be defined as equal to $di/d\eta$. A plot of the rates of reaction obtained from the reciprocal of the slopes of the curves in Fig. 2 for the hydrogen reaction proceeding on the α-Rh-Pd-H cathodes is shown by the triangles in Fig. 3. These experiments were also repeated for a pure Pd bead on which k was observed to be 0.20 mho cm^{-2} in agreement with the value of 0.13 mho cm^{-2} found earlier for α-Pd (18).

The β-Rh-Pd-H *System.*—In the second series of experiments, the Rh-Pd beads, after strong anodization, were cathodized at current densities of the order of 300 ma cm^{-2} for about 90 min. This treatment converted the cathodes completely to the β-Rh-Pd-H phase. Cathodic overvoltage measurements were taken as before (11). Results are shown in Fig. 4. Overvoltage measurements were also

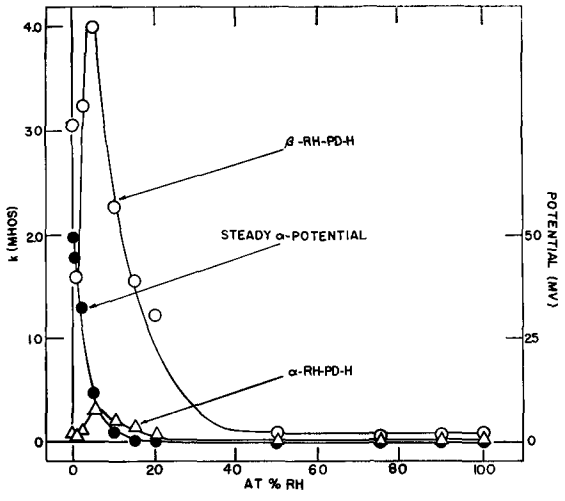

Fig. 3. Rate k (mhos/cm²) of the hydrogen reaction at α-Rh-Pd-H (△) and β-Rh-Pd-H (O) alloy electrodes as a function of atomic per cent Rh in the Rh-Pd alloy. Steady α open-circuit potentials (●) referred to Pt/H_2 in the same electrolyte (2N H_2SO_4). For β open-circuit potentials, see Table I.

made on a pure Pd and pure Rh bead; these results are included in Fig. 4 and are similar to those found in the literature (11, 19).

In general, it is seen that these data may be placed in two groups. In the first group are the data for high Pd-content cathodes up to 15 a/o Rh. The curves are composed of three sections: the low current or non-Tafel region, a Tafel region in which b is about 0.04 v, and a second Tafel region in which b is about 0.12 v. The high Rh content alloys, from 50 to 100 a/o Rh, form the second group. These curves have only one Tafel region whose b-slope is 0.12 v in addition to the non-Tafel region. Parsons (20) has discussed the mechanisms of electrochemical kinetics in terms of Tafel b-slopes. A slope of 0.04 v found on the high Pd-content alloys as well as on pure Pd (11) is consistent with the electrochemical mechanism on a sparsely covered surface. Although a unique mechanism for a slope of 0.12 v is not available (20), it is felt that the data for high Rh-content cathodes are more easily interpreted in terms of the slow discharge mechanism for the same reasons offered in the case of Pd-Ni alloys (4).

A mixed mechanism is exhibited by the data taken on the 20 a/o Rh cathode shown in Fig. 4. These data seem to correspond to a transition state between the high Rh-content and high Pd-content cathodes. Here a Tafel region with a b-value of 0.075 v is observed which could be explained by a mechanism in which both the slow discharge and the electrochemical steps are equally slow and are equally rate determining.

From a plot of η vs. i at low current densities, the rate k for the hydrogen reaction proceeding on a β-Rh-Pd-H cathode was determined in the same way as for the α-Rh-Pd-H cathode electrodes above. These linear plots did not pass through zero potential for the high-Pd content cathodes at zero current density. This same behavior was noted in the Pd-H (11), Au-Pd (3), and Ni-Pd-H (4) systems and may be interpreted similarly (11) as due to the partial pressure of the dissolved hydrogen. The

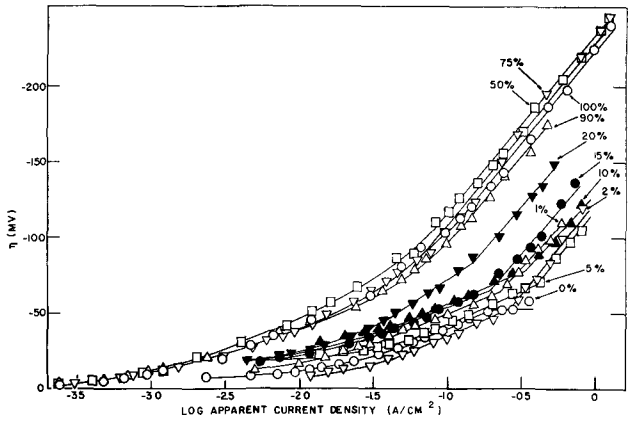

Fig. 4. Log i vs. η for cathodic polarization of β-Rh-Pd-H systems. The atomic per cent Rh in the Rh-Pd alloy is indicated on each curve; 25°±1°C.

curves for the high Rh-content alloys all pass through zero at zero current density. These curves are not shown, but the values for k and for the zero current intercepts η_0 are given in Table I along with the Tafel b-slopes of the high current density regions (Fig. 4).

A plot of k for β-Rh-Pd-H as a function of atomic % Rh is shown by the circles in Fig. 3. In the case of the high Pd-content cathodes, the rate is considerably higher for the β than for the α-analogue. However, the rate is approximately the same in the two cases for the high Rh-content cathodes which is to be expected if these alloys dissolve negligible quantities of hydrogen. The smooth curve drawn through these points would indicate, then, that the hydrogen solubility limit occurs at about 30 a/o Rh. Both curves exhibit a pronounced maximum at about 5 a/o Rh.

Catalytic activity and electronic structure.—The magnetic susceptibility and the low-temperature specific heat of Pd-Rh alloys have been measured (21). A maximum is found in the susceptibility-composition curve at about 5 a/o Rh. This is interesting since one obtains an alloy with a magnetic susceptibility greater than that of either pure substance. From the specific heat data, the electronic heat coefficient γ was determined, and a plot of γ as a function of the alloy composition also exhibits a maximum at about 5 a/o Rh. The fact that both quantities have a maximum value for the same

Table I. Cathodic polarization data for the β-Rh-Pd-H system in 2N H_2SO_4 at 25°C

Alloy composition a/o Rh	k, mhos/cm²	Zero current intercept, η_0, mv	b_1, v	b_2, v
0	3.03	7.1	0.040	—
1	1.59	17.8	0.040	0.117
2	3.24	19.9	0.041	0.122
5	4.00	19.5	0.042	0.119
10	2.26	15.4	0.040	0.122
15	1.67	16.2	0.042	0.119
20	1.23	15.4	0.075	0.116
50	0.093	0	—	0.118
75	0.080	0	—	0.120
90	0.083	0	—	0.122
100	0.095	0	—	0.120

alloy composition suggests that the density of states at the Fermi level for the alloy is at a maximum value.

It has been assumed that the electrode mechanism on the high Pd-content cathodes is electrochemically controlled and, therefore, that a H-atom desorption step is rate determining. As the number of holes in the d-band is increased by additions of Rh to Pd, the heat of adsorption of hydrogen should increase and the rate of reaction k should decrease (2). This is observed. The reaction rates are higher for all β-Rh-Pd-H cathodes where all holes in the d-band have been filled with electrons from dissolved hydrogen than for the corresponding α-Rh-Pd-H cathodes where all the holes have not been filled as shown in Fig. 3. Apparently this is not the complete picture since each curve in Fig. 3 shows a maximum at an alloy concentration of 5 a/o Rh, suggesting that the rate of the hydrogen reaction on Rh-Pd-H alloy cathodes is also a function of the density of states at the Fermi-level energy of the hydrogen-free Rh-Pd alloys.

Such an interpretation of the data requires that a direct relationship exist between the activation energy and the heat of adsorption of hydrogen, which is not self-evident. By a theoretical analysis of the shape of the energy surfaces involved and by an inspection of the pertinent experimental data, Rüetschi and Delahay (22) were able to show a linear relationship between the hydrogen reaction occurring at Ni, Ag, and Hg cathodes and the heat of adsorption on these metals. However, this gives an expression opposite in sign to that found for Pd-H alloys (2). The rate-determining step on Ni, Ag, and Hg is found to be the slow discharge of a hydrogen ion from the double layer (23). In this case, as the number of holes in the d-band are decreased and, consequently, the heat of adsorption of hydrogen decreased, the rate of reaction should decrease (2) as found by Oikawa (24) for a series of Ni-Cu alloy cathodes. This was observed by Rüetschi and Delahay as shown in Fig. 2 of ref. (22).

Recently, from theoretical considerations, Parsons (25) and Gerischer (26) have come to the similar conclusions that the plot of the logarithm of the rate of the hydrogen reaction at equilibrium conditions, (when the overvoltage η is zero) i.e., the exchange current density i_o, as a function of the energy of adsorption of hydrogen, gives a similar type of curve no matter which step is rate determining. This indicates that the reaction mechanism cannot be determined alone by the sign of the relationship between changes in the rate with changes in the energy of adsorption. This is not held by Conway and Bockris (5). It is to be remembered, though, that Parsons considers a noble metal cathode surface to be highly covered with atomic hydrogen and assumes that the shape of the Morse curve is rigid and does not change as the energy of adsorption changes. Shuldiner and Hoare (3, 4, 11, 27) consider such surfaces to be sparsely covered with atomic hydrogen.

It should also be noted that Parsons, Bockris, and Delahay consider the changes in reaction rate with changes in heat of adsorption obtained from studies of overvoltage on a series of different metal cathodes, while Schuldiner and Hoare (2) observe these changes on continuous series of alloy cathodes. In these latter cases, abrupt changes or even discontinuities in the properties of the cathode surface are less likely.

It is interesting to note that the influence of the density of states on the rate of reaction is such that the activation energy decreases as the density of states in the hydrogen-free Rh-Pd alloys increases. It is not unreasonable to consider that changes in the density of states in the bulk material would change the energy of the surface states which in turn would cause changes in the activation energy of the reaction occurring at the surface.

It is suggested, then, that the presence of holes in the d-band of the Rh-Pd alloy cathodes makes possible the formation of strong chemical bonds between the chemisorbed hydrogen atoms and the metallic atoms of the cathode surface (5); that there is a direct correspondence between the heat of adsorption of hydrogen and the activation energy of the hydrogen reaction; and that, once a strong bond is formed, how strong the bond is or how much energy resides in the bond is a function of density of states at the Fermi-level energy in the bulk hydrogen-free alloy in such a manner that, as the density of states increases, the bond becomes less strong.

For the alloys above about 30 a/o Rh there is not any essential difference between the two curves since these alloys do not dissolve significant quantities of hydrogen and, hence, do not form α- and β-type phases but only one single solid Rh-Pd phase. As suggested above, the slow discharge mechanism is rate controlling on these cathodes. As Rh is added and the number of holes increases, the rate on the high Rh-content cathodes should increase since now the slow discharge mechanism is rate determining. The data in column 2 of Table I does show a trend in that direction. Even though this slight increase may be within the limits of experimental error, the amount of the increase for the high-Rh-content cathodes may actually be very small and difficult to detect because of experimental difficulties. This is true since Rh with about two holes in the d-band per atom is in such great excess in this range of alloy composition (50 a/o Rh) that the percentage of change in the number of holes in the alloy d-band with additions and subtractions of Pd having only 0.6 hole per atom would be very small.

Finally, the initial drop in the rate curves in Fig. 3 from the value for pure Pd is surprising and unexpected. The rate for the 1% Rh cathode was checked twice with new beads, and the value shown was reproduced each time. Although a quantitative explanation for this is not available at this time, a qualitative one may be found in Parsons' work (25). He shows on theoretical grounds that i_o is proportional to $1/p^n$, where p is the partial pressure of molecular hydrogen and n has a value between 0 and 1. If the magnitude of the intercept η_o (Table I) is proportional to the excess partial pressure of

dissolved hydrogen above the equilibrium partial pressure, then it is seen that this partial pressure increases in going from pure Pd to 1 a/o Rh in Pd. Therefore, the rate should drop, since $p > 1$. For higher Rh-content alloys there is little or no change in η_o, and this effect is not observed.

Acknowledgments

The author wishes to express his gratitude to Dr. A. Arrott and Dr. A. W. Overhauser of the Physics Department for most helpful and interesting discussions and to Dr. J. E. Goldman, Manager of the Chemistry and Physics Departments, for his many well-taken comments and faithful support during the course of this work. The author is also indebted to Dr. F. E. Hoare of Leeds University for his fruitful suggestions, to Dr. G. Parravano of the University of Michigan for his most interesting criticism, to the Metallurgy Department of the Ford Scientific Laboratory for the preparation of the alloys, and to the Analytical Section of the Physics Department for the analysis of the alloys.

Manuscript received Jan. 22, 1960.

Any discussion of this paper will appear in a Discussion Section to be published in the June 1961 JOURNAL.

REFERENCES

1. O. Beeck, *Discussions Faraday Soc.*, **8**, 118 (1950); A. Couper and D. D. Eley, *ibid.*, **8**, 172 (1950); D. A. Dowden, *J. Chem. Soc.*, **1950**, 242.
2. S. Schuldiner and J. P. Hoare, *J. Phys. Chem.*, **62**, 504 (1958); Electrochemical Mechanisms of Nobel-Metal Hydrogen Systems, Part III, Electronic Configuration and Catalytic Activity, NRL Report 5171, July 1958.
3. S. Schuldiner and J. P. Hoare, *J. Phys. Chem.*, **61**, 705 (1957).
4. J. P. Hoare and S. Schuldiner, *ibid.*, **62**, 229 (1958).
5. B. E. Conway and J. O'M. Bockris, *J. Chem. Phys.*, **26**, 532 (1957).
6. J. Horiuti and M. Polanyi, *Acta Physicochem. U.R.S.S.*, **2**, 505 (1935).
7. T. Erdey-Gruz and M. Volmer, *Z. physik Chem.*, **A150**, 203 (1930).
8. J. Tafel, *ibid.*, **50**, 641 (1905).
9. J. Horiuti and G. Okamoto, *Sci. Pap. Inst. Phys. Chem. Res. Tokyo*, **28**, 231 (1936).
10. C. J. Smithels, "Metals Reference Book," 2nd ed., Vol. I, p. 196, Interscience Publishers Inc., New York (1955).
11. J. P. Hoare and S. Schuldiner, *This Journal*, **102**, 485 (1955).
12. S. Schuldiner, *ibid.*, **99**, 488 (1952); S. Schuldiner and J. P. Hoare, *J. Chem. Phys.*, **26**, 1771 (1957).
13. D. C. Grahame, *Chem. Rev.*, **41**, 441 (1947).
14. S. Schuldiner, G. W. Castellan, and J. P. Hoare, *J. Chem. Phys.*, **28**, 16 (1958).
15. J. P. Hoare, G. W. Castellan, and S. Schuldiner, *J. Phys. Chem.*, **62**, 1141 (1958).
16. J. P. Hoare, *This Journal*, **106**, 640 (1959).
17. P. Dolin, B.Ershler, and A. Frumkin, *Acta Physiochem. U.R.S.S.*, **13**, 779 (1940).
18. J. P. Hoare and S. Schuldiner, *This Journal*, **104**, 564 (1957).
19. J. P. Hoare and S. Schuldiner, *J. Chem. Phys.*, **25**, 786 (1956).
20. R. Parsons, *Trans. Faraday Soc.*, **47**, 1332 (1951).
21. F. E. Hoare and J. Preston, *Nature*, **180**, 334 (1957).
22. P. Ruetschi and P. Delahay, *J. Chem. Phys.*, **23**, 195 (1955).
23. I. A. Ammar and S. A. Awad, *J. Phys. Chem.*, **60**, 1290 (1956); J. O'M. Bockris and E. C. Potter, *J. Chem. Phys.*, **20**, 614 (1952); A. N. Frumkin, *Discussion Faraday Soc.*, **1**, 57 (1947).
24. M. Oikawa, *Bull. Chem. Soc. Japan*, **28**, 626 (1955).
25. R. Parsons, *Trans. Faraday Soc.*, **54**, 1053 (1958).
26. H. Gerischer, *Bull. Soc. Chim. Belg.*, **67**, 506 (1958); H. Gerischer and W. Mehl, *Z. Elektrochem.*, **59**, 1049 (1955).
27. S. Schuldiner, *This Journal*, **106**, 891 (1959).

Fused Salt Polarography Using a Dropping Bismuth Cathode

Raymond J. Heus and James J. Egan

Brookhaven National Laboratory, Upton, New York

ABSTRACT

An apparatus is described which is suitable to study fused chlorides by the polarographic technique. Dropping bismuth is used in a way analogous to dropping mercury. Polarographic waves are shown for $PbCl_2$, $ZnCl_2$, and $CdCl_2$ in a LiCl-KCl eutectic melt at 450°C. The method serves as an analytical tool at high temperatures, besides yielding physicochemical information such as diffusion coefficients by application of the Ilkovic equation.

Many studies have been made on fused salts using the polarographic technique (1-8). In general solid wire microelectrodes have been used to measure concentrations which were found to be proportional to the limiting current. The dipping platinum microelectrode has been used by Flengas (9), and Chovnyk used derivative polarography at wire microelectrodes (10). Nachtrieb and Steinberg used a dropping mercury electrode to study low melting nitrate melts (11).

The dropping mercury electrode has not been employed at temperatures greater than 220°C, due to the high vapor pressure of mercury. Aside from gallium (12), no metal other than mercury has been employed as a dropping electrode, but dropping electrodes should prove useful since they have been so successful in lower temperature studies.

In order to expand the range of temperatures at which dropping electrodes can be used, the following work was undertaken using molten bismuth at 450°C as the electrode material. Bismuth is an adequate metal for this purpose since its chloride is not too stable, the element is liquid over a large temperature range with a low vapor pressure, and it

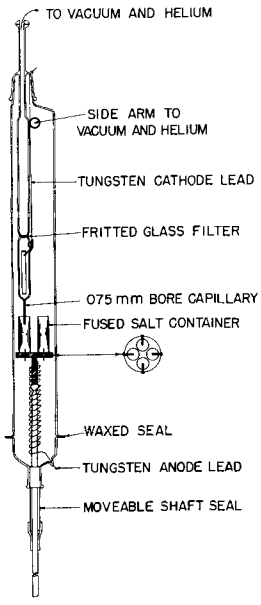

Fig. 1. Dropping bismuth polarographic cell with four fused salt cups.

has a melting point of 271°C. Other metals however can probably be used instead of bismuth depending on the experimental conditions.

Finally, the advantages of the dropping electrode include a constantly renewed surface which is important when ions are being reduced to metals at the electrode, and a shape which enables a mathematical treatment of the mass transport at this electrode (Ilkovic equation). When proper care is taken, the dropping electrode seems to obey these equations better than other electrodes, probably because of the thin diffusion layer which exists at dropping electrodes (13a).

Experimental Details

The apparatus used for obtaining polarograms is shown in Fig. 1. Since it was imperative to exclude oxygen from both the bismuth (the formation of an oxide causes plugging of the capillary) and the fused salt, the capillary and salt cup were contained in a vacuum-tight Vycor tube 70 cm long and 64 mm in diameter. Ground glass ball joints connected the container and the space above the capillary to separate sources of both helium and high vacuum. This arrangement allows one to regulate the pressure difference across the capillary to any value between 0 and 1 atmosphere.

The capillaries were made by drawing Pyrex tubing to a small bore, care being taken to obtain a thick wall so the end could be cut off at 90° to the bore. The particular capillary to be used was then selected by examination using a microscope. Capillaries with a 0.075-mm bore and a 10-cm length were found best suited for experiments. One could produce a slow drop time with this size, and the bore was large enough not to plug easily. Before the bismuth entered the capillary it was filtered through a coarse Pyrex frit located above the capillary.

The fused salt was held in four Pyrex cups which also contained bismuth pool anodes. A tungsten wire was sealed into the bottom of each cup and cleaned electrolytically to insure good electrical contact. The tungsten wires also served to hold the salt cups on a stand which could be raised and lowered to the desired height by a moveable shaft seal. This shaft seal was constructed from "trubore tubing" which was lubricated with a high vacuum grease to keep the container tight to a vacuum better than 10^{-5} mm Hg. Electrical contact to the dropping bismuth cathode was made by sealing a tungsten wire through the inner Pyrex tube as shown. To assure a good electrical contact with the bismuth pool, a tantalum ribbon was spot welded to the tungsten wire.

In an attempt to make the capillary section of use in more than one experiment, a tantalum foil "pillow" was added to this compartment. When the bismuth solidified upon cooling, the pillow would collapse and the glass would not break. Unfortunately, bismuth remaining in the capillary itself would more often than not break the capillary upon expansion.

A wire wound nichrome resistance furnace surrounding the outer Vycor container was used to heat the contents to approximately 450°C. The temperature was measured with a chromel-alumel thermocouple attached to the outside of the Vycor container and was controlled with a recording potentiometer. A sight port through the cylindrical furnace enabled one to view the dropping electrode and the salt cups for manipulation at high temperature.

The current through the cell was measured by recording the voltage drop across a standard resistor (200 or 250 ohm) in series with the cell. A Brown automatic recorder with 25 mv full scale and a pen speed of 3.5 sec full scale was used. The potential applied across the cell varied linearly with time at the rate of 0.3 v/min. This was accomplished by driving a Helipot with a synchronous motor and a Graham variable speed transmission, the source of voltage being a 2-v storage battery.

After each run the entire salt content of the cell was weighed, dissolved, and analyzed for Pb, Cd, or Zn using aqueous polarographic techniques.

The LiCl-KCl eutectic (41 mole % KCl) used as solvent was prepared as follows. The powdered materials, in a weight ratio to form the eutectic mixture, were put above a fine Pyrex frit and attached to a source of high vacuum and purified helium. The contents were heated under vacuum just below the melting point for approximately 24 hr then melted under vacuum for another hour and forced through the frit into capsules by applying an atmosphere of helium pressure over the molten salt. The capsules were then evacuated and sealed off for later use in experiments.

The solute salts were prepared independently. The $PbCl_2$ was used as obtained from the manufacturer. The $CdCl_2$ powder was desiccated for one day under vacuum. The $ZnCl_2$ powder was heated under dry HCl, then melted, and finally evacuated and sealed off in a capsule until used. The bismuth metal was also pretreated before it was loaded into

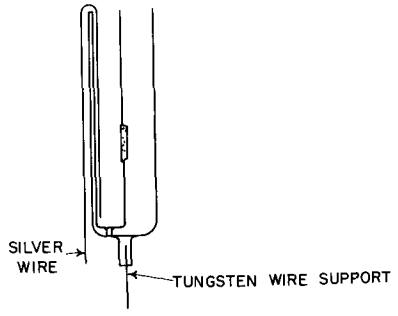

Fig. 2. Fused salt cup using a Ag|AgCl reference electrode

the apparatus by melting and filtering it through a coarse glass frit.

In order to use the half cell Ag|AgCl in LiCl-KCl (eutectic), as a working anode instead of the bismuth pool, the cup shown in Fig. 2 was constructed and replaced the cups shown in Fig. 1. Here a small tube containing a fine Pyrex frit was sealed into one of the ordinary salt cups. A 2 wt % solution of AgCl in KCl-LiCl (eutectic) was added to this tube along with a Ag wire. The remainder of the cup was filled with the solution to be examined. The tungsten wire merely served to hold the cup on its platform and the Ag wire was the anode. Unfortunately, the fine frit would sometimes allow appreciable amounts of AgCl to diffuse through it. The silver chloride would then react with the bismuth pool collected at the bottom of the larger compartment to produce bismuth trichloride. This bismuth trichloride would then be reduced at the dropping electrode and interfere with the shape of the polarograms under investigation. For this reason the bismuth pool anode was used in most experiments.

Experimental Results

Polarograms obtained with the apparatus are shown in Fig. 3, 4, and 5 and Fig. 8. Figure 3 is a polarogram taken on the solvent salt alone giving a background current of 9 μa. This current decreases slightly at larger drop times. An estimate of the reducible impurity content of this salt from the polarogram puts it at about 0.5 millimoles/liter. Figure 4 is a polarogram of $PbCl_2$, whereas Fig. 5 shows a polarogram of $CdCl_2$ in the eutectic mixture. In all of these curves it can be seen that the solvent salt starts to be reduced at around −0.8 v with respect to the bismuth pool.

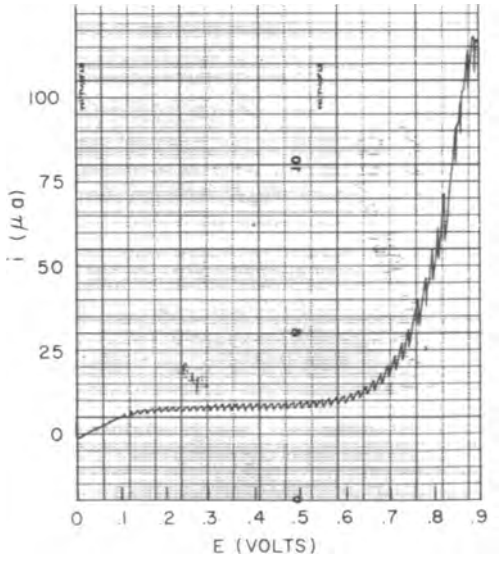

Fig. 3. Polarogram of LiCl-KCl eutectic (blank) using a drop time of 2.7 sec. Potential negative to bismuth pool anode here and in Figs. 4, 5, 8.

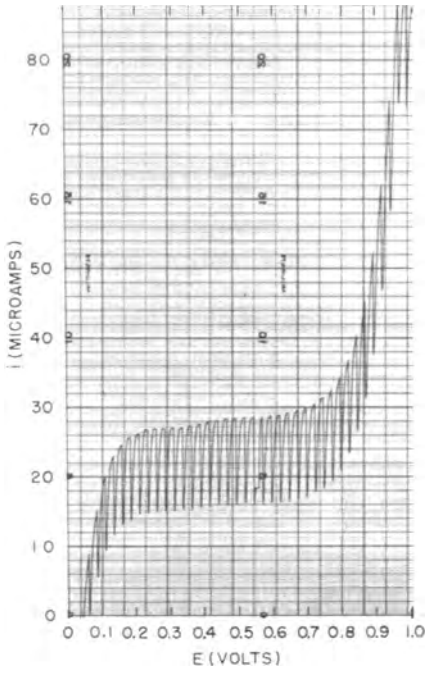

Fig. 4. Polarogram of a 1.8 millimole/liter $PbCl_2$ solution in LiCl-KCl eutectic at a drop time of 4 sec.

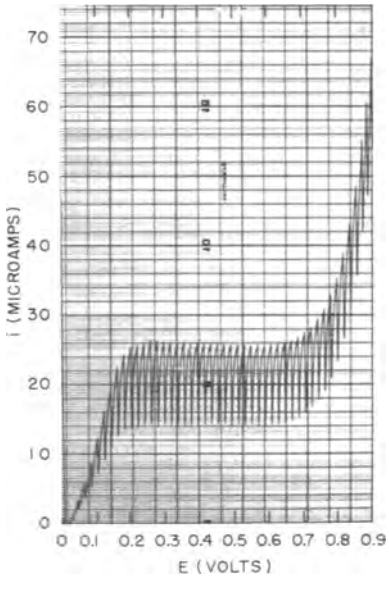

Fig. 5. Polarogram of a 3.4 millimole/liter $CdCl_2$ solution in LiCl-KCl eutectic at a drop time of 3.1 sec.

In the polarogram of $PbCl_2$ there is a small negative current which arises before a voltage is applied to the cell. This is probably due to a mixed potential arising from the reaction

$$2Bi(\text{dropping electrode}) + 3PbCl_2(\text{LiCl-KCl}) = 2BiCl_3(\text{LiCl-KCl}) + 3Pb(Bi)$$

which takes place to a small extent when the fresh bismuth solution comes in contact with the salt

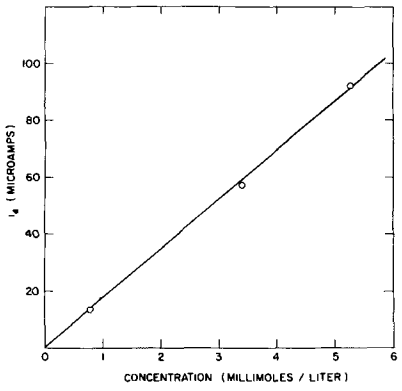

Fig. 6. Concentration dependence of the diffusion current for $PbCl_2$ at a drop time of 4 sec.

solution. Since $CdCl_2$ is more stable than $PbCl_2$ (14), this effect is negligible in the $CdCl_2$ polarogram.

The concentration dependence of the diffusion current is shown in Fig. 6 and 7 for $PbCl_2$ and $CdCl_2$ where a correction has been made for the current from the solvent alone. The diffusion current was taken at the maximum current of each drop. Concentrations were calculated using the density data of Van Artsdalen and Yaffe (15). A straight line is obtained within 5% for concentrations from 0.5 to 5 millimolar. This precision can probably be improved by further purification of the solvent salt and the use of more advanced electrical circuitry techniques.

Figure 8 shows a polarogram of $PbCl_2$ and $ZnCl_2$ in the eutectic mixture with a very fast drop time. Here the limiting current is not diffusion controlled (note the large currents obtained in comparison to those using large drop times), the Ilkovic equation fails and one readily obtains maxima as evidence with the Zn^{++} wave. It was found however that the limiting current was proportional to the concentration even at these fast drop times.

Discussion

The Ilkovic equation for bismuth drops at 450°C is

$$i_d = 880\, n\, D^{1/2} C\, m^{2/3} t^{1/6}$$

where i_d is the diffusion current in microamperes, measured at the maximum current of each drop, t the drop time in seconds, m the mass of the flowing bismuth in mg/sec, D the diffusion coefficient in cm^2/sec, and C the concentration in millimoles/liter. This equation is derived using the density of liquid bismuth at 450°C which is 9.8 g/cm^3 (16). Since the diffusion current i_d is inversely proportional to the two-thirds power of the density of the flowing metal (13b), the above equation is obtained from the corresponding equation for mercury by multiplication of the mercury constant 706 by the two-thirds power of the density ratio of mercury to bismuth $(13.69/9.8)^{2/3}$.

Diffusion coefficients were calculated from this equation by measuring m and t. Knowing the values of i_d and C as shown in Fig. 6 and 7, the values of D were found to be 1.7×10^{-5} cm^2/sec and 1.8×10^{-5} cm^2/sec for $PbCl_2$ and $CdCl_2$, respectively, at 450°C.

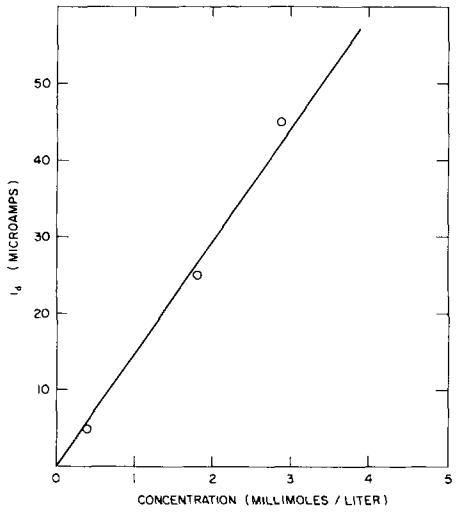

Fig. 7. Concentration dependence of the diffusion current for $CdCl_2$ at a drop time of 3.1 sec.

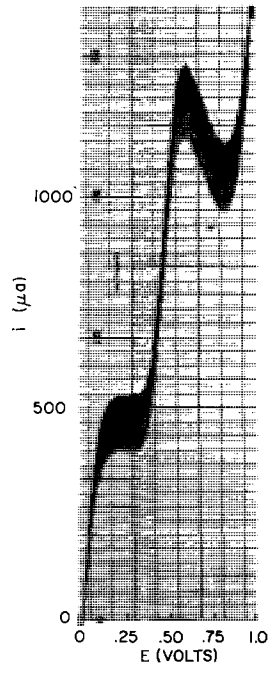

Fig. 8. Polarogram of a solution containing 3.6 millimoles/liter $PbCl_2$ and 8.5 millimoles/liter $ZnCl_2$ in the eutectic mixture at a drop time of 0.8 sec.

Since Laitinen and co-workers (17, 18) have obtained the diffusion coefficients for $PbCl_2$ and $CdCl_2$ in this eutectic mixture from chronopotentiometric measurements, a check was available to see that the Ilkovic equation was applicable. These workers obtain values for D of 2.0×10^{-5} cm^2/sec and 1.7×10^{-5} cm^2/sec for $PbCl_2$ and $CdCl_2$, respectively. The agreement is considered satisfactory and within the limits expected in light of the assumptions made in obtaining the Ilkovic equation and the experimental accuracy of the measurements reported here.

Other elements may also be examined using dropping bismuth electrodes. Although the LiCl starts to be reduced at −0.8 v with respect to the bismuth pool due to its low activity coefficient in bismuth (19) and its high concentration in the salt

mixture, it is estimated that all chlorides less stable than manganese and more stable than gallium (14) can be investigated with pure dropping bismuth electrodes. Use of alloy electrodes might extend the range of elements which can be studied.

In these experiments it was found that when the concentration of reducible ion exceeds 7 or 8 millimoles/liter, polarographic maxima would interfere with the measurements. As expected the maxima occurred more readily at faster drop times. No attempt was made to find a maximum suppressor for these systems.

Acknowledgments

The authors would like to thank Mr. L. Bowditch, Dr. K. Rowley, Miss Elinor Norton, and Dr. F. T. Miles, for their help during the course of this work, and especially Dr. R. H. Wiswall, Jr., who originally suggested this problem. They also thank Dr. R. A. Osteryoung for helpful suggestions concerning the importance of drop time in obtaining a diffusion controlled process.

Manuscript received March 31, 1960. Work on this paper was done under the auspices of the U.S.A.E.C.

Any discussion of this paper will appear in a Discussion Section to be published in the June 1961 JOURNAL.

REFERENCES

1. Y. S. Lyalikov and V. I. Karmazin, *Zavadskaya Lab.*, **14**, 138, 144 (1948).
2. Y. S. Lyalikov, *Zhur. Anal. Khim.*, **5**, 323 (1950); **8**, 38 (1953).
3. Y. K. Delimarski, *Uspekhi Khim.*, **23**, 766 (1954).
4. N. G. Chovnyk, *Doklady Akad. Nauk. SSSR*, **87**, 1033 (1952).
5. N. G. Chovnyk, *Zhur. Fiz. Khim.*, **30**, 277 (1956).
6. I. D. Panchenko, *Ukrain. Khim. Zhur.*, **21**, 468 (1955).
7. E. D. Black and T. DeVries, *Anal. Chem.*, **27**, 906 (1955).
8. H. A. Laitinen and H. C. Gaur, *This Journal*, **104**, 730 (1957).
9. S. N. Flengas, *J. Chem. Soc.*, **1956**, 534.
10. N. G. Chovnyk, *Doklady Akad Nauk. SSSR*, **95**, 599 (1954).
11. N. H. Nachtrieb and M. Steinberg, *J. Am. Chem. Soc.*, **70**, 2613 (1948); **72**, 3558 (1950).
12. P. A. Giguare and D. P. Lamontagne, *Science*, **120**, 390 (1954).
13. I. M. Kolthoff and J. J Lingane, "Polarography," Interscience Publishers, 2nd ed, New York (1952); (a) p. 43-44; (b) p. 40.
14. H. A. Laitinen and C. H. Liu, *J. Am. Chem. Soc.*, **80**, 1015 (1958).
15. E. R. Van Artsdalen and I. S. Yaffe, *J. Phys. Chem.*, **59**, 118 (1955).
16. A. Journiaux, *Bull. Soc. Chim.*, **51**, 677 (1932).
17. H. A. Laitinen and W. S. Ferguson, *Anal. Chem.*, **29**, 4 (1957).
18. H. A. Laitinen and H. C. Gaur, *Anal Chim. Acta*, **18**, 1 (1958).
19. J. J. Egan and R. H. Wiswall, Jr., *Nucleonics*, **15**, 104 (1957).

Brief Communications

The JOURNAL accepts short technical reports having unusual importance or timely interest, where speed of publication is a consideration. The communication may summarize results of important research justifying announcement before such time as a more detailed manuscript can be published. Consideration also will be given to reports of significant unfinished research which the author cannot pursue further, but the results of which are of potential use to others. Comments on papers already published in the JOURNAL should be reserved for the Discussion Section published biannually.

Submit communications in triplicate, typewritten double-spaced, to the Editor, Journal of The Electrochemical Society, 1860 Broadway, New York 23, N. Y.

Irreversible Thermodynamics in Electrochemistry

Andre J. deBethune

Chemistry Department, Boston College, Chestnut Hill, Massachusetts

ABSTRACT

The Onsager thermodynamics of irreversible processes provides a unified approach to the study of electrolytic systems out of equilibrium, such as concentration cells with transference, the initial and final emf's of thermal cells, and thermal diffusion (Soret effect) of ions. For concentration cells, the method justifies the classical results obtained by Nernst from equilibrium considerations. For nonisothermal systems, the product S^*dT is the thermodynamic driving force of a process, where S^* is the entropy transported reversibly from the "hot" to the "cold" heat reservoir (in the limiting case of equal temperatures) by the occurrence of a reversible process in the system. The emf of a concentration cell, the initial emf of a thermal cell, and the Soret coefficient, all properties of systems out of equilibrium, are determined, according to the Onsager relations, by the ratios of the reversible fluxes of matter to electricity, of entropy to electricity, and of entropy to matter, respectively, as they occur in systems completely at equilibrium.

The transport entropy S^* can become, according to circumstances, the entropy S^*_I of electrical transport, or the entropy S^*_D of diffusion transport. S^*_I in turn involves the entropies S^*_E of electrochemical transport (for the electrode reactions) and S^*_M of migration transport (for the thermal liquid junction). The contribution of an ion (or electron) to S^*_E and to S^*_M gives rise to the ionic entropies of electrochemical transport S^*_{Ei} and of migration transport S^*_{Mi}, respectively. The latter contributes also to S^*_D. The sum $\overline{S}_i = S^*_{Ei} + S^*_{Mi}$ is known as the entropy of the moving ion and is measurable for a single ionic species. The initial thermal emf involves the transport entropy S^*_I, the Soret coefficient involves S^*_D, while the final thermal emf involves $S^*_I \pm t_g S^*_D$ where t_g is the transference number of the ion to which the electrodes are not reversible.

For the hydrogen ion, $S^{*\circ}_E(H^+) = -4.48$ cal/deg, if S^*_M is taken as zero in a saturated potassium chloride salt bridge. For other ions, $S^{*\circ}_{Ei} = S^\circ_i - z_i\ 4.48$, and the mass action dependence is normal. For most ions, S^*_{Mi} appears to be small, i.e., about 0-3 cal/deg, and the mass action dependence is abnormal and low. In dilute solutions, S^*_{Mi} shows a Debye dependence on concentration. These facts are consistent with the electrostatic interpretation of S^*_{Mi} as the entropy of depolarization of the solvent dielectric when the ion moves away. For ions transferred by a chain mechanism (H^+ and OH^-), S^*_{Mi} is significantly larger. The transport of ions across biological membranes plays an important role in life processes. Since living systems are not necessarily uniform in temperature, ionic transport entropies may have a role to play in the function of the biological cell.

The classic application of thermodynamics to a cell out of equilibrium is Nernst's (1) well-known law for the emf of an isothermal concentration cell with transference, derivable from chemical potentials (free energies), and expressible in terms of ionic transference numbers t_i and ionic concentrations c_i (in ideal solutions) or ionic activities a_i.

Another example of a cell out of equilibrium is a thermal cell (electrochemical thermocouple) consisting of two identical electrode-electrolyte systems maintained at two different temperatures. A thermal cell develops a measurable emf, usually several tenths of a millivolt per degree, directly proportional to the applied temperature differential over not too wide temperature ranges. Thermal cells have been investigated experimentally, since the pioneering work of Bouty (2), by Richards (3), Kolthoff (4), Sorensen (5), and Lange (6), among others. The subject has been reviewed by Lange (7) and by deBethune, Licht, and Swendeman (8, hereinafter referred to as deBLS). Under usual experimental conditions, the emf developed, known as the *initial thermal emf,* has been found stable whenever free convection maintains constancy of the electrolyte concentration across the temperature gradient.

Thermal cells may be subject to thermal diffusion in the electrolyte (Soret effect) (9). This tends to concentrate strong electrolytes, usually in the cold region (10), by several tenths of one per cent per degree (11). The development of these concentration gradients, if not prevented by convection, further affects the emf, which gradually shifts to a new stationary value, the *final thermal emf.* Such

emf shifts were demonstrated experimentally by Agar and Breck (12) in a cell whose electrolyte was wholly contained within the pores of a sintered Pyrex disk, to prevent convective remixing of the thermally diffused solute. The emf shift, of the order of hundredths of a millivolt per degree, followed a first order law with a half-life of about 10 min in their cell, and was essentially complete in 1-2 hr.

The thermodynamic theory of the *initial emf* of a thermal cell has been given by Eastman (13a) and by Wagner (13b) from Carnot's theorem, in terms of certain transport entropies designated by deBLS (8) as the *ionic entropy of electrochemical transport* S^*_{Ei} and the *ionic entropy of migration transport* S^*_{Mi}.[1] These ionic entropies are not separately determinable (without assumptions) for a single ionic species.

Temkin and Khoroshin (14) combined Eastman's theory (13a) of the Soret effect with Nernst's concentration cell equation to obtain an expression for the *final emf* of a thermal cell. While the *initial thermal emf* depends not only on the ion r to which the electrodes are reversible, but also on the gegenion g, Temkin and Khoroshin proved that the *final thermal emf* is independent of the gegenion, [a fact which was experimentally verified by Agar and Breck (12)]. They further proved that the sum $S^*_{Ei} + S^*_{Mi}$, which they denote as the entropy of the moving ion (Entropiya dvizhushchikhsya Iona) $\overline{\overline{S}}_i$, is an experimentally determinable quantity for a single ionic species, provided a value can be assigned to $\overline{\overline{S}}$ for the electrons.

The thermodynamic relations governing electrolytic systems out of equilibrium, such as concentration cells, thermal cells, and thermal diffusion, can be derived in an elegant manner by the methods of irreversible thermodynamics and the Onsager reciprocal relations (15). Treatments along such lines have already been given by Prigogine (16), deGroot (17a), Holtan (17b), Kirkwood (18), van Rysselberghe (19a), Haase (19b), Harned and Owen (20), and Agar (21).

In the present paper, we shall apply the Onsager thermodynamics from a particularly simple point of view, namely, from a consideration of those fluxes that are macroscopically measurable, the flux I of electricity, J of entropy, and K of solute. These fluxes are measurable, I by an ammeter, J by a calorimeter, and K by chemical analysis. The conjugate driving forces are also measurable, so that the method is a powerful one for expressing theoretical relationships between measurable entities under certain nonequilibrium conditions.

General Description of Thermodynamic System

Consider an electrolyte containing a single binary solute, one molecule of which dissociates into $\nu = \nu_+ + \nu_-$ ions of valence z_+ and z_- (with sign). Electroneutrality demands that $\nu_+ z_+ + \nu_- z_- = 0$, while the magnitude of the $\nu_i z_i$ product for either ion will be denoted by β. The molality of the solute is m, its thermodynamic mean ion activity $a_\pm$, and its chemical potential $\mu(\text{salt}) = \nu_+\mu_+ + \nu_-\mu_- = \mu^\circ + \nu RT \ln a_\pm = \mu^\circ + \nu RT \ln \nu_\pm m\gamma_\pm$.

The cell can be represented schematically by

$$\begin{gathered}\text{Cu}(T_1, V)/\text{Electrode } (T_1)/\text{Electrolyte } (T_1, a)/\\ \text{Electrolyte } (T_2, a + da)/\text{Electrode } (T_2)/\\ (\text{Cu}(T_2)/\text{Cu}(T_1, V + dV)\end{gathered} \quad [1]$$

where T_1 and T_2 denote the temperatures of two large separate heat reservoirs No. 1 and 2 in contact with different portions of the system, and $T_2 = T_1 + dT$ and $dT \geqq 0$. The electrical potentials are V and $V + dV$ in the left and right terminals, respectively. The two ionic species will be denoted by the indeces i and j in general, the ion to which the electrodes are reversible by r, the gegenion of r by g. Let the current I be positive when it flows through the cell from left to right. The entropy flux J (in calories·deg^{-1}·sec^{-1}) will be taken positive from the hot (T_2) to the cold (T_1) heat reservoir. The ionic fluxes K_i (in gram ions·sec^{-1}), and the solute flux K (in moles·sec^{-1}), defined as $\Sigma K_i/\nu$, will be taken positive through the liquid junction from right to left. The current I at the liquid junction can be expressed by $\mathbf{F}(K_- - K_+)$ for 1,1-salts and by $-\mathbf{F}\Sigma z_i K_i$ in general.

The irreversible rate of production of Clausius' uncompensated entropy (22, 23) from all these fluxes can be expressed by

$$\dot{S} = IX_I + JX_J + \Sigma K_i X_i \geqq 0 \quad [2]$$

where the driving forces are $X_I = -dV/T$, $X_J = dT/T$, $X_i = d\mu_i/T = R\,d \ln a_i$. The two ionic terms are conveniently coalesced to

$$K_+X_+ + K_-X_- = (K_+ + K_-)\,R\,d \ln a_\pm = KX_K \quad [3]$$

where $X_K = d\mu(\text{salt})/T = \nu R\,d \ln a_\pm$. Equation [2] then becomes

$$\dot{S} = IX_I + JX_J + KX_K \geqq 0 \quad [4]$$

The three fluxes may be expressed by phenomenological equations

$$I = L_{II}X_I + L_{IJ}X_J + L_{IK}X_K \quad [5]$$

$$J = L_{JI}X_I + L_{JJ}X_J + L_{JK}X_K \quad [6]$$

$$K = L_{KI}X_I + L_{KJ}X_J + L_{KK}X_K \quad [7]$$

where the L's are generalized admittances (reciprocal resistances). By the Onsager reciprocal relations, the conjugate cross-admittances are equal, i.e., $L_{IJ} = L_{JI}$, $L_{IK} = L_{KI}$ and $L_{JK} = L_{KJ}$.

Apply Eq. [5] to the cell when the temperature and concentration are both uniform (X_J and $X_K = 0$). A current I flowing is then the resultant only of an externally applied emf $-dV = TX_I$, and Ohm's law shows that $L_{II} = T/r$ where r is the total resistance of the circuit, including any "polarization resistances" of the electrodes. In general, however, Eq. [5] shows the current I as the resultant of three emf's: an externally applied emf $dE_{\text{ext}} = -dV = L_{II}X_I r = TX_I$; a thermally induced emf $dE_{\text{th}} = L_{IJ}X_J r = TL_{IJ}X_J/L_{II}$; and a concentration emf $dE_{\text{conc}} = L_{IK}X_K r = TL_{IK}X_K/L_{II}$.

[1] In Eastman's terminology, the absolute ionic entropy, and the entropy of transfer, respectively. See Appendices I and II for nomenclature of transport entropies.

At the potentiometric balance point, $I = 0$, and

$$-TX_I = TL_{IJ}X_J/L_{II} + TL_{IK}X_K/L_{II} \quad [8a]$$

or

$$-dE_{ext} = dV = dE_{th} + dE_{conc} \quad [8b]$$

i.e., we have the ordinary condition for potentiometric balance, in which the observed potential difference dV between the two terminals is a measure of the combined electromotive forces intrinsic to the system. These emf's are to be considered positive, following the Lewis-Stockholm convention (24), whenever they tend to drive positive electricity through the cell from left to right.

Isothermal Concentration Cells

Take cell [1] at uniform temperature ($X_J = 0$). From Eq. [8],

$$-TX_I = dV = dE_{conc} = TL_{IK}X_K/L_{II} \quad [9]$$

By the Onsager relations, this becomes,

$$dE_{conc} = (L_{KI}/L_{II})\nu RT\, d\ln a_{\pm}. \quad [10]$$

Suppose now that the cell is brought to a state of uniform concentration ($X_K = 0$), and a small external emf applied (dV negative). The current flowing is $I = L_{II}X_I = \beta\mathbf{F}/\tau$ if τ is the time required for the passage of β faradays of positive electricity through the cell from left to right. The simultaneous flux of solute through the cell from right to left is $K = L_{KI}X_I = (K_r + K_g)/\nu$. The ionic fluxes from right to left are $K_r = \beta(1 - t_r)/z_r\tau$ for the ion to which the electrodes are reversible, and $K_g = -\beta t_g/z_g\tau$ for the gegenion, where the t_i's are Hittorf transference numbers. Since $t_r + t_g = 1$, the solute flux becomes

$$K = (\beta t_g/\tau\nu)(1/z_r - 1/z_g) \quad [11]$$

Since $\nu_i z_i = \pm\beta$ (for $z_i = \pm$), $1/z_r - 1/z_g$ is equal to $\pm(\nu_r + \nu_g)/\beta$ for $z_r = \pm$, so that

$$K = \pm t_g/\tau \quad (\text{if } z_r = \pm) \quad [12]$$

The ratio $L_{KI}/L_{II} = (K/I)_{X_J = X_K = 0} = \pm t_g/\beta\mathbf{F}$. Equation [10] then yields Nernst's expression for the emf of a concentration cell with transference

$$dE_{conc} = \pm t_g(\nu RT/\beta\mathbf{F})\, d\ln a_{\pm} \quad (\text{if } z_r = \pm) \quad [13]$$

This equation is derived here as a consequence of the Onsager relations. The emf of an isothermal concentration cell is expressible in terms of the measurable quantities t_g and $a_{\pm}$ and is a fully significant thermodynamic quantity, as discussed by Guggenheim (25).

It is of theoretical interest to decompose the concentration emf [13] into the sum of (a) the difference of the electrode potentials dE_{el}; plus (b) the liquid junction potential dE_{lj}. Neither of these two terms is exactly measurable, and neither is unambiguously calculable from fully significant quantities. Yet both are approximately measurable, e.g., by the use of two saturated potassium chloride calomel electrodes (SCE) immersed in the two electrolyte compartments of the cell, and both can be calculated from any arbitrarily selected definition of single ion activities, such as that implicit in the Debye theory (26).

To clarify the point at issue, postulate an *ideal reference electrode* (IRE), *which can be defined conceptually as an unpolarizable electrode having zero thermal temperature coefficient* (8) *and zero liquid potential at the junction of its salt bridge with any electrolyte.* Two such IRE's are immersed in the two electrolyte compartments of cell [1], and connected by two leads of the same kind of metal to the isothermal potentiometric slide wire to which the two terminals of cell [1] are already connected. The potentials in the two IRE leads are V' and $V' + dV'$, respectively. Then at potentiometric balance for all four electrodes, $dE_{lj} = dV'$, while $dE_{el} = [(V + dV) - (V' + dV')] - [V - V'] = dV - dV'$.

It is convenient to consider the current I and the two ionic fluxes K_r and K_g

$$I = L_{II}X_I + L_{Ir}X_r + L_{Ig}X_g \quad [14]$$

$$K_r = L_{rI}X_I + L_{rr}X_r + L_{rg}X_g \quad [15]$$

$$K_g = L_{gI}X_I + L_{gr}X_r + L_{gg}X_g \quad [16]$$

At the balance point, $I = 0$, and

$$-TX_I = dV = dE = TX_r(L_{Ir}/L_{II}) + TX_g(L_{Ig}/L_{II}) \quad [17]$$

By the Onsager relations, this becomes

$$dE = TX_r(L_{rI}/L_{II}) + TX_g(L_{gI}/L_{II}) =$$

$$TX_r\,(K_r/I)_{X_r = X_g = 0} + TX_g\,(K_g/I)_{X_r = X_g = 0} \quad [18]$$

Consider now a cell at uniform concentration ($X_r = X_g = 0$). The current I is $\beta\mathbf{F}/\tau$, as before. The two electrode reactions together yield the ionic fluxes $K_r = \beta/z_r\tau$ and $K_g = 0$. This gives for the difference of the electrode potentials

$$dE_{el} = TX_r/z_r\mathbf{F} = (RT/z_r\mathbf{F})\, d\ln a_r \quad [19]$$

At the liquid junction, the two ionic fluxes are $K_i = -t_i\beta/z_i\tau$ so that the junction potential becomes

$$dE_{lj} = T\,\Sigma(-t_i/z_i\mathbf{F})X_i = (-RT/\mathbf{F}).$$

$$\Sigma\,(t_i/z_i)\, d\ln a_i \quad [20]$$

In contrast to Eq. [13], neither [19] nor [20] are fully thermodynamically significant since they involve nonfully significant single ion activities. They can be made approximately significant by adopting a rule for the definition of single ion activities, either (a) Scatchard's practical rule (27) "We will define single ion activities as those measured with the use of a saturated potassium chloride bridge" as in pH or pCl measurements (28, 29) or (b) a theoretical rule, consistent with the Debye theory whereby $a_i = \nu_i m\gamma_i$ and $\gamma_i = \gamma_{\pm}^{-z_i/z_j} = \gamma_{\pm}^{\nu_j/\nu_i}$. Where this latter rule is adopted, [19] becomes

$$dE_{el} = (RT/z_r\mathbf{F})\, d\ln m[1 + (\nu_g/\nu_r)\,.$$

$$(d\ln\gamma_{\pm}/d\ln m)] \quad [19']$$

and [20] becomes

$$dE_{ij} = (-RT/\mathbf{F})\Sigma(t_i/z_i)\, d\ln m\,.$$
$$[1 + (\nu_j/\nu_i)(d\ln\gamma\ /d\ln m)] \qquad [20']$$

where $j = g, r$ when $i = r, g$. The right hand sides of both [19'] and [20'] now involve only fully significant quantities.

Equations [13], [19], and [20] are identical with the classical expressions derived from chemical potentials by the application of the reversible thermodynamics of isothermal processes to concentration cells with transference, in spite of the fact that these cells are not at equilibrium. The Onsager relations show why the application of reversible relations to a nonequilibrium situation nevertheless yields correct results. The coefficients of the chemical potential gradients TX_K, or TX_r and TX_g, in the emf equations [10], [17] and [18], become, by the Onsager relations, flux ratios of matter to electricity of the form K/I. However, these flux ratios are to be taken, in each case, in a cell that is completely at equilibrium (X_J and X_K's all equal to zero). The flux I is therefore a reversible flux of electricity in the strict thermodynamic sense, and the K's are the conjugate reversible fluxes of matter. It is the ratio of the reversible fluxes K/I in an equilibrium cell (whose emf is zero) which determines, together with the actual chemical potential gradients, the observable emf of the actual nonequilibrium concentration cell.

Initial EMF of Thermal Cells

Take cell [1] at uniform concentration ($X_K = 0$). From Eq. [8],

$$-TX_I = dV = dE_{th} = TL_{IJ}X_J/L_{II} \qquad [21]$$

By the Onsager relations, this becomes

$$dE_{th} = (L_{JI}/L_{II})\ dT \qquad [22]$$

Suppose now that the cell is brought to uniform temperature ($dT = 0$) and a small external emf applied (dV negative). The current flowing is $I = L_{II}X_I = \beta\mathbf{F}/\tau$, as before. At the same time, the entropy flux is $J = L_{JI}X_I = S^*_I/\tau$ if S^*_I is the entropy transported from the right heat reservoir (No. 2) to the left heat reservoir (No. 1), when β faradays of positive electricity are transferred through the cell from left to right. S^*_I may be termed the entropy of electrical transport. The ratio $L_{JI}/L_{II} = (J/I)_{X_J=X_K=0} = S^*_I/\beta\mathbf{F}$. From [22], one obtains therefore for the initial thermal emf

$$dE_{th} = (S^*_I/\beta\mathbf{F})\ dT \qquad [23]$$

The ratio J/I is, once again, the ratio of two reversible fluxes occurring in an equilibrium cell (whose emf is zero). This ratio determines, together with the actual temperature gradient, the observable emf of the actual nonequilibrium thermal cell. As defined here, the thermal emf is positive whenever the hot electrode is the (+) terminal of cell [1].

The entropy S^*_I is the entropy transported isothermally and reversibly from one heat reservoir to the other by a reversible flow of electricity, in the absence of a temperature gradient. The transport of entropy occurs by a threefold mechanism. (i) The reaction at the right electrode absorbs a quantity of heat Q^*_E from its heat reservoir (No. 2) while the equal and opposite reaction at the left electrode evolves an equal quantity of heat to its heat reservoir (No. 1). The entropy transported is $S^*_E = Q^*_E/T$ and is denoted as the *entropy of electrochemical transport.* (ii) The migration of ions through the electrolyte is accompanied by the absorption of a quantity of heat Q^*_M (Eastman's "heat of transfer") from the electrolyte in the right compartment, and the evolution of an equal quantity of heat to the electrolyte in the left compartment. An equal amount of heat then enters the right electrolyte from the right heat reservoir (No. 2) and leaves the left electrolyte to the left heat reservoir (No. 1), to keep the temperature constant. The entropy transported is $S^*_M = Q^*_M/T$ and is denoted as the *entropy of migration transport.* (iii) The migration of β moles of electrons from the T_1 zone to the T_2 zone of the right-hand Cu terminal of cell [1] transfers heat from the No. 1 to the No. 2 heat reservoir. Dividing this heat by T, one obtains the entropy transported from No. 2 to No. 1 as $-\beta S^*_M$ (E^- in Cu). Thus

$$S^*_I = S^*_E + S^*_M - \beta S^*_M(E^- \text{ in Cu}) \qquad [23a]$$

For the passage of β faradays of positive electricity through the cell from left to right, the reaction at the right electrode may be written as β times

$$\Sigma\omega_k A_k + (1/z_r)A_r + E^-(\text{Cu}, T_2) = 0 \qquad [24]$$

where A_r is the ion to which the electrode is reversible, and the A_k denote neutral substances whose stoichiometric coefficients ω_k may be positive or negative. Thus for Ag/Ag^+ electrodes, reaction [24] is: $Ag^+ - Ag + E^- = 0$; for $Pb/PbSO_4$ electrodes: $\frac{1}{2}PbSO_4 - \frac{1}{2}Pb - \frac{1}{2}SO_4^= + E^- = 0$. The corresponding *entropy of electrochemical transport* S^*_E is, for β faradays,

$$S^*_E = \beta\{-\Sigma\omega_k S_k - (1/z_r)S^*_{Er} - S^*_E(E^- \text{ in Cu})\} \qquad [25]$$

where S_k is the partial molal third law of entropy of the neutral species A_k, and S^*_{Er} is the partial molal entropy of electrochemical transport of the ion r. $S^*_E(E^-$ in Cu) is the electrochemical transport entropy of the electrons in Cu, or in general, in the nonisothermal metallic terminal arm of the cell.

The *entropy of migration transport* can be expressed by

$$S^*_M = \Sigma(-t_i\beta/z_i)S^*_{Mi} \qquad [26]$$

where S^*_{Mi} is the entropy of migration transport of the ion i (also known as its "entropy of transfer," see Appendix II). The total entropy transported by the current becomes

$$S^*_I = -\beta\Sigma\omega_k S_k - (\beta/z_r)S^*_{Er} - \Sigma(t_i\beta/z_i)S^*_{Mi} - \beta\bar{\bar{S}}(E^- \text{ in Cu}) \qquad [27]$$

where $\bar{\bar{S}}$, the entropy of the moving electrons (14), has been written for the sum $S^*_E + S^*_M$ for the electrons in Cu. The only electronic term appearing in the thermal emf is the entropy $\bar{\bar{S}}$ of the moving electrons in the nonisothermal metallic terminal arm of the cell. In Richard's (3) study of the calomel electrode, this was Hg; in Agar and Breck's (12) work, Pt; in the bulk of thermal cell studies, it has been Cu.

Now remove the two electrolyte compartments from cell [1], and allow the two electrodes to touch. Cell [1] becomes the thermocouple: Cu-Electrode. The equivalent value of S^*_E becomes $S^*_E(E^-$ in Electrode$) - S^*_E(E^-$ in Cu) for 1 Faraday. The equivalent of S^*_M becomes $S^*_M(E^-$ in Electrode). Therefore, for the whole thermocouple, Eq.[23] and [23a] yield[2]

$$\mathbf{F}(dE/dT)_{\text{couple}} = \mathbf{F}(dV/dT) = S^*_I = \bar{\bar{S}}(E^- \text{ in Electrode}) - \bar{\bar{S}}(E^- \text{ in Cu}) \qquad [28]$$

A comparison of Eq. [27] and [28] shows that the emf of a thermal cell does not contain a thermocouple emf as such, contrary to earlier statements (3, 8) that it does. But it does contain the entropy $\bar{\bar{S}}$ of the moving electrons in the nonisothermal metallic arm of the cell. No electronic term of the electrode metal itself appears, and the thermoelectric power of the terminal metal relative to the electrode metal makes no direct contribution to the thermal cell emf.

When thermal cells are measured with Cu terminals, and a "thermocouple correction" applied to the data [as in Carr and Bonilla's (30a) study of the Ni electrode], the net effect of the correction, by Eq. [28], is to transform the electronic term in [27] from that of Cu to that of the electrode metal itself. There seems to be no particular advantage to such a procedure, however. The better practice, experimentally and theoretically, would seem to be to *standardize on one metal for the nonisothermal metallic arm of all thermal cells.* In practice, this metal might as well be chosen as Cu.

Equation [28] gives a method for evaluating the entropy $\bar{\bar{S}}$ of moving electrons in different metals, relative to that in a standard metal, usually chosen to be Pb. From the magnitude of thermocouple emf's (microvolts per degree), such entropies amount to microvolt-faradays per degree, i.e., hundredths or tenths of a calorie per degree. Temkin and Khoroshin (14) evaluated the "absolute" value of $\bar{\bar{S}}(E^-)$ in Cu and Pt from the third-law integral

$$\bar{\bar{S}}(E^-) = -\mathbf{F}\int_0^T \sigma dT/T \qquad [29]$$

where σ is the "absolute" Thomson coefficient of the metal, i.e., the heat capacity of the *unit of* positive electricity in the metal (30b). Their results are, in microvolt-faradays per degree,

$$\bar{\bar{S}}(E^- \text{ in Cu}) = -1.95 - 0.005\,(T - 300) \quad (T > 240°\text{K})$$

$$\bar{\bar{S}}(E^- \text{ in Pt}) = 4.54 + 0.044(T - 300) \quad (T > 220°\text{K})$$

Thus, at 298°K, $\bar{\bar{S}}(E^-$ in Cu$) = -1.94\ \mu\text{v}\mathbf{F}$/deg $= -0.045$ cal/deg. The electronic term could then be eliminated completely in [27] by adopting for the nonisothermal terminal arm a metal whose Thomson coefficient is virtually zero, e.g., Pb(30c). In practice, it is more convenient to use copper experimentally. The third-law value for the electrons in Cu is so small that it could, without significant error, be set equal to zero. This we shall do, and we shall thereby adopt a slightly different electronic standard from that of Temkin and Khoroshin. We shall arbitrarily set $\bar{\bar{S}}(E^-$ in Cu) equal to zero at all temperatures. The electronic term in [27] may then be omitted, provided the thermal cell is measured with nonisothermal terminal arms of copper.

Thus for a thermal $Ag/AgNO_3$ cell ($\beta = 1$)

$$\mathbf{F}(dE_{\text{th}}/dT) = S^*_I = S(\text{Ag}) - S^*_E(\text{Ag}^+) + t_-\,S^*_M(\text{NO}_3^-) - t_+\,S^*_M(\text{Ag}^+) \qquad [30]$$

and for a thermal $Al/Al_2(SO_4)_3$ cell ($\beta = 6$)

$$6\mathbf{F}(dE_{\text{th}}/dT) = S^*_I = 2S(\text{Al}) - 2S^*_E(\text{Al}^{+3}) + 3t_-\,S^*_M(\text{SO}_4^{=}) - 2t_+\,S^*_M(\text{Al}^{+3}) \qquad [31]$$

The initial thermal emf depends on the ion to which the electrodes are reversible, and also on the gegenion. The migration terms in [30] and [31] determine the thermal liquid junction potential (tljp), the other terms the effect of temperature on the electrode potentials. Neither of these quantities is separately measurable, without assumptions. Both are conceptually measurable by the use of two IRE's, as defined above.

The two transport entropies S^*_{Ei} and S^*_{Mi} for an ion do not coincide with one another, and neither do they coincide with its conventional partial molal ionic entropy S_i (based on the standard $S°(H^+) = 0$ at all temperatures). S^*_{Ei} is the entropy transported between heat reservoirs by an ion when it sheds its hydration sheath in being consumed at one electrode and picks up a new hydration sheath in being produced at the other electrode. S^*_{Mi} is the entropy transported by the ion when it drags its hydration sheath with it across the cell. Neither of these entropies is separately determinable for a single ionic species (without assumptions). Neutral combinations are determinable, and also the sum $\bar{\bar{S}}_i = S^*_{Ei} + S^*_{Mi}$ for a single ion (see below).

The standard entropy of electrochemical transport of the hydrogen ion was shown by deBLS (8) to be $S^{*\,\circ}_E(\text{H}^+) = -4.48 \pm 0.5$ cal/deg at 25°C, from the thermal temperature coefficient of the

[2] Comparison of [28] with classical expressions for the thermoelectric power shows that $S^*_I = \mathbf{F}\pi/T$, where π is the Peltier heat, i.e., the heat absorbed by the thermocouple when the unit of positive electricity crosses the junction from "Electrode" to Cu. The temperature derivative of the thermoelectric power yields $d^2V/dT^2 = dS^*_I/\mathbf{F}dT = C^*_I/\mathbf{F}T = [\bar{\bar{C}}(E^-$ in Electrode$) - \bar{\bar{C}}(E^-$ in Cu$)]/\mathbf{F}T = -[\sigma(\text{Electrode}) - \sigma(\text{Cu})]/T$, where C^*_I is the heat capacity of electrical transport, $\bar{\bar{C}}$ the heat capacity of the moving electrons, and σ the Thomson coefficient. Thus $\bar{\bar{C}}(E^-$ in Cu$) = -\mathbf{F}\sigma(\text{Cu})$. Over wide ranges of temperature, thermocouple emf's satisfy the empirical equation $V = at + \frac{1}{2}bt^2$. S^*_I is then equal to $\mathbf{F}(a + bt)$ and $C^*_I = \mathbf{F}Tb$. Constancy of b implies that $\bar{\bar{C}}/T$ is a constant.

standard hydrogen electrode which is + 0.871 millivolts per degree when measured with a saturated potassium chloride bridge (8, 31). This result is based on the assumption that S^*_M can be set equal to zero in such a bridge ("saturated KCl bridge rule").

The standard entropy of electrochemical transport $S^{*\circ}_{Ei}$ of any other ion should then be

$$S^{*\circ}_{Ei} = S^\circ_i + z_i \ (-4.48 \text{ cal/deg}) \quad [32]$$

Concentration effects on thermal emf's (8) indicate that the ionic entropy S^*_{Ei} has substantially the same mass-action dependence as the ordinary entropy S_i, i.e.,

$$S^*_{Ei} = S^{*\circ}_{Ei} - R \ln a_i - RT(d \ln a_i/dT) \quad [33]$$

Ionic entropies of migration transport S^*_{Mi} are discussed in greater detail below. For many ions, the values appear to be quite small, about 0-3 cal/deg. For H^+ and OH^-, they are significantly larger, about 10 cal/deg. For many salts, the tljp's should not exceed a few hundredths of a millivolt per degree and should make only small contributions to total cell emf's of several tenths of a millivolt per degree (see below). In strong acids and bases, the tljp's appear to be large, about − 0.35 and + 0.5 mv/deg, respectively, referred to KCl as zero (8). These two values are qualitatively consistent with the Soret effect (below) in that the cold end of the thermal liquid junction dipole takes on the charge of the faster ion (H^+ or OH^-).

Thermal Diffusion (Soret Effect)

Take cell [1] and remove both electrodes. This effectively makes $X_I = 0$. In the steady state of thermal diffusion, $K = 0$, and

$$X_K = -(L_{KJ}/L_{KK})X_J \quad [34]$$

By the Onsager relations, this becomes

$$X_K/X_J = -L_{JK}/L_{KK} = -(J/K)_{X_I=X_J=0} \quad [35]$$

Now bring the cell to uniform temperature ($X_J = 0$), and let there be a small chemical potential gradient (X_K positive), such that the solute flux $K = 1/\tau$, if τ is the time required for 1 mole of solute to diffuse across the liquid boundary from right to left, under the impulsion of X_K, in a cell (without convection) so large that this amount of diffusion does not significantly alter the chemical potential gradient. The concurrent flux of entropy is $J = S^*_D/\tau = (\nu_+ S^*_{M+} + \nu_- S^*_{M-})/\tau$, where S^*_D, the *entropy of diffusion transport,* is the entropy transported from the right heat reservoir No. 2 to the left heat reservoir No. 1 by the passage of 1 mole of solute through the liquid boundary from right to left. Equation [35] then transforms to

$$X_K/X_J = \nu RT(d \ln a_\pm/dT) = -(J/K)_{X_I=X_J=0} = -S^*_D/1 \text{ mole}. \quad [36]$$

The Soret coefficient can be defined as the relative change in solute activity (or concentration) per degree change in temperature, i.e., either

$$d \ln a_\pm/dT = -S^*_D/\nu RT \quad [37a]$$

or

$$d \ln m/dT = -S^*_D/\{\nu RT[1 + (d \ln \gamma / d \ln m)_T]\} \quad [37b]$$

If the entropy of diffusion transport S^*_D is positive, the Soret coefficient is negative, i.e., strong electrolytes concentrate in the cold region. This is the situation normally observed. Soret coefficients usually amount to minus a few tenths of one per cent per degree, the corresponding values of S^*_D are then a few calories per degree per mole. Values for S^*_D for a number of salts are listed in Table I.

Consider two thermal cells identical in every respect, except in the nature of the gegenion g. Then from Eq. [23] and [27], it can be shown that the difference between the initial thermal emf's of the two cells, containing the two electrolytes 1 and 2, is

$$F(dE/dT)_{\text{th},1} - F(dE/dT)_{\text{th},2} = t_{r2} S^*_{Mr}/z_r + t_{g2} S^*_{Mg2}/z_{g2} - t_{r1} S^*_{Mr}/z_r - t_{g1} S^*_{Mg1}/z_{g1} = \pm t_{g1} S^*_{D1}/\beta_1 \mp t_{g2} S^*_{D2}/\beta_2 \quad (\text{if } z_r = \pm) \quad [38]$$

Equation [38] provides a convenient method of evaluating the entropy S^*_D of one salt relative to that of another salt with which it has a common ion, from observations of initial thermal emf's. The vanishing of electrode terms from Eq. [38] implies

Table I. Entropies of diffusion transport S^*_D (cal/deg.mole) at 25°C

KCl: 0.0025 *m*, 2.21[d]; 0.005 *m*, 1.88[d]; 0.01 *m*, 1.72[a], 1.68[d], 3.15(34.7°)[d]; 0.02 *m*, 1.58[d]; 0.05 *m*, 0.91[a]; 1 *m*, 0.37[b], 1.20(35°)[b], 2.02(45°)[b]; 2 *m*, 0.86[b], 0.087(15°)[b], 1.63(35°)[b], 2.31(45°)[b]; 3 *m*, 1.26[b], 0.52(15°)[b], 1.97(35°)[b], 2.61(45°)[b]; 4 *m*, 1.70[b], 1.06(15°)[b], 2.28(35°)[b], 2.86(45°)[b].

KBr: 0.0025 *m*, 2.15[d]; 0.005 *m*, 1.98[d]; 0.01 *m*, 1.87[a], 1.85[d], 3.15(34.7°)[d]; 0.02 *m*, 1.68[d]; 0.05 *m*, 1.05[a].

KI: 0.0025 *m*, 0.27[d]; 0.005 *m*, 0.10[d]; 0.01 *m*, −0.09[ad], 1.27(34.7°)[d]; 0.02 *m*, −0.27[d]; 0.05 *m*, −0.65[a].

NaCl: 0.0025 *m*, 3.12[d]; 0.005 *m*, 2.62[d]; 0.01 *m*, 2.60[a], 2.58[d], 3.80(34.7°)[d]; 0.02 *m*, 2.08[d]; 0.05 *m*, 1.81[a].

NaBr: 0.0025 *m*, 3.09[d]; 0.005 *m*, 2.82[d]; 0.01 *m*, 2.74[a], 2.70[d]; 0.02 *m*, 2.42[d]; 0.05 *m*, 1.94[a].

$AgNO_3$: 0.01 *m*, 4.20[a], 4.16[d], 5.33(34.7°)[d]; 0.014 *m*, 3.92[d]; 0.1 *m*, 2.90[b], 4.95(45°)[b]; 0.2 *m*, 2.81[b], 4.24(45°)[b]; 0.5 *m*, 2.79[b], 3.99(45°)[b]; 1 *m*, 3.14[b], 3.86(45°)[b].

$\frac{1}{2}CdSO_4$: 0.01*m*, 3.85[c]; 0.033 *m*, 3.08[c]; 0.09 *m*, 2.35[d]; 0.1 *m*, 2.43[c], 2.41[b], 3.36(45°)[b]; 0.18 *m*, 2.08[b], 2.94(45°)[b]; 0.34 *m*, 1.76[c]; 0.37 *m*, 1.69[b], 2.45(45°)[b]; 1 *m*, 1.22[b], 1.86(45°)[b]; 1.04 *m*, 1.32[c]; 2.1 *m*, 1.14[c].

$TlClO_4$: 0.005 *m*, 2.55[d]; 0.01 *m*, 2.35[d]; 0.02 *m*, 2.18[d]; 0.05 *m*, 2.85[c], 1.98[d]; 0.1 *m*, 1.73[c]; 0.15 *m*, 2.18[c]; 0.2 *m*, 1.58[c]; 0.26 *m*, 1.54[c].

$\frac{1}{2}Tl_2SO_4$: 0.04 *m*, 5.22[d]; 0.1 *m*, 4.03[c].

0.1 *m* solutions[c]: $TlNO_3$: 1.69; $TlOCOCH_3$: 6.17; $\frac{1}{2}Tl_2CO_3$: 4.27; $\frac{1}{2}Cd(ClO_4)_2$: 1.1; $\frac{1}{2}Cd(NO_3)_2$: 0.77; $\frac{1}{2}CdCl_2$: 0.70.

0.01 *m* solutions[d]: KF: 4.56; NaF: 5.48, 6.72(34.7°); NaI, 0.77, 2.05(34.7°); LiF: 2.83, 4.13(34.7°); LiCl: −0.067; LiBr: 0.047, 1.10(34.7°); LiI: −1.94, −0.23(34.7°); RbCl: 2.75; CsCl: 2.78; $(C_2H_5)_4NCl$: 10.36; KNO_3: 1.66(34.7°); $NaNO_3$: 1.64; $\frac{1}{2}K_2SO_4$; 4.6, 5.9(34.7°).

[a] Agar, conductimetric (21); [b] Longsworth, optical (11); [c] Agar and Breck, initial and final thermal emf (12); [d] Agar and Turner, conductimetric (51).

Table II. Differences of thermal liquid junction potentials (mv/deg) and entropies of diffusion transport S^*_D (cal/deg. mole) computed from them by Eq. [38]. 0.01 molal or normal electrolytes, except where noted. Reference values in parentheses.

Electrolyte	Δtljp	S^*_D	Electrolyte	Δtljp	S^*_D
KCl	$+0.011 \pm 0.003^{aa}$	—	$\frac{1}{2}CdCl_2$	$+0.03^{al}$	0.4
KCl(1*M*)	$+0.024 \pm 0.003^{aa}$	—	Et_4NCl^e	-0.114^{ak}	11.6
KCl	$(0.000)^a$	$(1.72)^f$	KBr	$(+0.0039)^{am}$	(1.87)
KCl(1*M*)	$(0.000)^a$	$(0.37)^g$	LiBr	$+0.0367^{bn}$	0.18
HCl	-0.340^{ah}	10.5	NaBr	-0.0058^{bn}	2.69
HCl(1*m*)	-0.344^{ah}	9.7^g	NH_4Br	$+0.0336^{bn}$	0.27
LiCl	$+0.04^{ai}$	−0.24	Me_4NBr^e	-0.072^{bn}	7.32
LiCl(1*M*)	$+0.046^{aj}$	-3.0^g	Et_4NBr^e	-0.0985^{bn}	11.9
NaCl	-0.007^{ak}	2.56	$n\text{-}Pr_4NBr^e$	-0.1024^{bn}	16.6
NaCl (1*m*)	-0.033^{ah}	2.54^g	$n\text{-}Bu_4NBr^e$	-0.1019^{bn}	19.5
NH_4Cl	$+0.01^{ai}$	1.25	$n\text{-}Am_4NBr^e$	-0.1011^{bn}	22.8
NH_4Cl(1*m*)	$+0.026^{ah}$	-0.86^g	KI	$(-0.0405)^{am}$	$(-0.12)^f$
RbCl	-0.016^{ak}	2.42	LiI	$+0.0275^{ck}$	−2.12
RbCl(1*m*)	-0.088^{ah}	4.42^g	NaI	-0.0165^{ck}	0.83
CsCl	-0.0265^{ak}	2.90	KOH	$+0.445^{anq}$	15.17
CsCl(1*m*)	-0.078^{ah}	3.96^g	LiOH	$+0.0901^{dn}$	12.57
$\frac{1}{2}CaCl_2$(1*N*)	-0.08^{al}	5.8^g	NaOH	$+0.0440^{dn}$	15.46
$\frac{1}{2}SrCl_2$	-0.01^{al}	2.5	Me_4NOH^e	$+0.0252^{dn}$	20.2
$\frac{1}{2}SrCl_2$(1*N*)	-0.08^{al}	5.8^g	Et_4NOH^e	$+0.0342^{dn}$	26.8
$\frac{1}{2}BaCl_2$	-0.02^{al}	3.0	$n\text{-}Pr_4NOH^e$	$+0.0644^{dn}$	29.7
$\frac{1}{2}BaCl_2$(1*N*)	-0.08^{al}	5.3^g	$n\text{-}Bu_4NOH^e$	$+0.0748^{dn}$	33.6
$\frac{1}{2}MgCl_2$	$+0.02^{al}$	0.9	$n\text{-}Am_4NOH^e$	$+0.0813^{dn}$	36.3
$\frac{1}{2}ZnCl_2$	$+0.01^{al}$	1.5	KNO_3	$(-0.0219)^{am}$	$(0.76)^f$
$\frac{1}{2}ZnCl_2$(1*N*)	$+0.02^{al}$	-0.8^g	$AgNO_3$	-0.123^{apq}	5.85

[aa] Referred to "saturated KCl," i.e., observed thermal emf's of calomel and silver chloride cells in 1*M* and 0.01*M* KCl, Richards (3), Kolthoff and Tekelenburg (4), Bernhardt and Crockford (41), Salvi (42), Young (43), Goyan (43), and Levin and Bonilla (47), *minus* calculated thermal emf's of deBLS (8), based on "saturated KCl bridge rule."
[a] Referred to KCl of the same concentration.
[b] Referred to KBr of the same concentration.
[c] Referred to KI of the same concentration.
[d] Referred to KOH of the same concentration.
[e] Me, methyl; Et, ethyl; Pr, propyl; Bu, butyl; Am, amyl.
[f] Reference values of S^*_D for 0.01*m* electrolytes from Agar (21), cf. Tables I and III(b).
[g] Referred to Longsworth's (11) $S^*_D = 0.37$ cal/deg for 1 *m* KCl (Table I).
[h] Bernhardt and Crockford (41).
[i] Khoroshin and Temkin (14).
[j] Salvi (42).
[k] Goyan, Young, and Preston (43).
[l] Richards (3).
[m] Computed from reference values of S^*_D via Eq. [38].
[n] Goodrich, *et al.* (44).
[p] Burian (45), Khoroshin and Temkin (14), Lange and Hesse (46).
[q] Observed thermal emf's in KOH and $AgNO_3$ electrolytes, *minus* calculated thermal emf's of deBLS (8), based on "saturated KCl bridge rule," and corrected to KCl of the same concentration by means of [aa] values above.

that the activity of the ion *r* is the same in the two electrolytes. Clearly, this assumption is valid only for dilute solutions of the two salts, at the same concentration of the ion *r*, and at the same ionic strength. Under this assumption, the difference of the initial thermal emf's given by [38] is simply the difference of the thermal liquid junction potentials (tljp's) of the two salts.

In Table II are listed such differences of tljp's between the electrolytes listed and certain reference electrolytes chosen to be KCl, KBr, KI, and KOH, as determined from observed values of initial thermal emf's (except for values in parentheses which are computed from the reference S^*_D values via Eq. [38]). A positive sign means that the hot end of the thermal liquid junction dipole is more positively charged than that of the reference electrolyte.

The transference numbers utilized in Eq. [38] have been taken, or estimated, from MacInnes (48), Harned and Owen (20), or from the sources of the thermal emf data. The S^*_D values listed in Table II have then been computed from observed Δtljp's and from certain reference S^*_D values (in parentheses) taken from Tables I and III(b).

While the accuracy of the method is limited, as discussed by Tyrrell, *et al.* (49), *e.g.*, an uncertainty of ± 0.01 mv/deg in the Δtljp yields uncertainties in S^*_D ranging from ± 0.5 cal/deg when the relevant transference number is ½, up to ± 2 cal/deg when the transference number drops to 1/10th, nevertheless, the results are in fair agreement with those of other methods [Tables I and III(a)(b)], and are of interest since they yield a number of new values of S^*_D for electrolytes not previously determined.

In dilute solutions, the entropy S^*_D of diffusion transport behaves as an additive ionic property (21). This permits the evaluation of the entropy of migration transport of an ion, relative to that of some standard ion. Such conventional single ion values of $S^*_{M_i}$ are given in Table III, relative to $S^*_M(Cl^-) = 0$ at all concentrations. Column (a) gives Eastman's estimates of 1928, intended by him as absolute values. Column (b) is taken from Agar's work. Columns (c) and (d) are based on the values of S^*_D deduced from the Δtljp's in Table II, except for the reference values in parentheses, and for certain values based on Table IV as noted.

The concentration dependence of S^*_D has been

Table III. Conventional single ion entropies of migration transport $S^*_{M_i}$ (cal/deg) at 25°C based on $S^*_M(Cl^-) = 0$.

Ion	$S^*_{M_i}$ (a)	(b)	(c)	(d)	Ion	$S^*_{M_i}$ (a)	(b)	(c)	(d)
H^+	9.3	10.4	10.5	9.7	OH^-	—	—	13.5	—
Li^+	0.1	−0.084	−0.3	−3.0	F^-	—	2.92	—	—
Na^+	0.9	2.61	2.55	2.54	Cl^-	0.0	(0)	(0)	(0)
K^+	1.0	1.72	(1.72)	(0.37)	Br^-	—	0.134	(0.15)	—
Rb^+	1.1	2.79	2.4	4.4	I^-	—	−1.84	(−1.84)	—
Cs^+	—	2.82	2.9	4.0	NO_3^-	—	−0.96	(−0.96)	—
Ag^+	—	5.16	6.8	—	$\frac{1}{2}SO_4^=$	—	2.925	2.7[f]	0.0[f]
NH_4^+	0.0	—	0.7	−0.9	ClO_4^-	—	—	1.0[f]	−3.0[f]
$\frac{1}{2}Mg^{++}$	—	—	0.9	—	CH_3COO^-	—	—	3.3 (0.1m)[f]	
$\frac{1}{2}Ca^{++}$	—	—	—	5.8	$\frac{1}{2}CO_3^=$	—	—	1.5 (0.1m)[f]	
$\frac{1}{2}Sr^{++}$	—	—	2.5	5.8	Tl^+	—	—	3.1 (0.1m)[f]	
$\frac{1}{2}Ba^{++}$	—	—	3.0	5.3	$\frac{1}{2}Cd^{++}$	—	—	1.35[f]	1.05[f]
$\frac{1}{2}Zn^{++}$	—	—	1.5	−0.8					
$\frac{1}{2}Cd^{++}$	—	0.935	0.4	—					
Me_4N^+[e]	—	6.71	7.0	—					
Et_4N^+[e]	—	10.44	11.7	—					
n-Pr_4N^+[e]	—	—	16.3	—					
n-Bu_4N^+[e]	—	—	19.7	—					
n-Am_4N^+[e]	—	—	22.7	—					

(a) Eastman (32) for 0.02N.
(b) Agar (12, 21) for 0.01m.
(c) This study, estimated from Table II for 0.01m. Reference values in parentheses.
(d) This study, estimated from Table II for 1 M. Reference values in parentheses.
[e] Me, methyl; Et, ethyl; Pr, propyl; Bu, butyl; Am, amyl.
[f] Interpolated or extrapolated from data of Table IV; single ion values based on "saturated KCl bridge rule," instead of chloride ion standard.

discussed by Agar (21). It decreases with increasing concentration (Table I) in dilute solutions, but much less rapidly than a normal mass-action dependent entropy would, and it seems to attain a finite limiting value at infinite dilution. In concentrated solutions of KCl and $AgNO_3$, S^*_D increases with increasing concentration! The derivative $dS^*_D/d \ln a_\pm$ is very close to $-R$ in $CdSO_4$ and to $-\frac{1}{2}R$ in $TlClO_4$, instead of the mass-action value $-2R$ for salts with $\nu = 2$.

In very dilute solutions ($m < 0.02$), S^*_D decreases as a linear function of the square root of the molality. The derivative $dS^*_D/d\sqrt{m}$ has values, in cal/deg. (unit of molality)$^{1/2}$, of −6.0 to −6.5 in dilute KCl, NaCl, KBr, NaBr, and KI; and of −26 in $CdSO_4$. These values are discussed again below in connection with the electrostatic interpretation of the ionic entropy of migration.

Final EMF of Thermal Cells

Restore the two electrodes to cell [1], and allow a Soret steady state to be established. This makes $K = 0$ while $X_K \neq 0$. At potentiometric balance, $I = 0$. Equations [5], [6], and [7] can then be solved, with elimination of X_K, to yield

$$(-X_I/X_J)_{\text{final}} = dV/dT = dE_{\text{fin}}/dT$$
$$= [L_{IJ}/L_{II} - (L_{IK}/L_{II})(L_{KJ}/L_{KK})]/$$
$$[1 - (L_{IK}/L_{II})(L_{KI}/L_{KK})] \quad [39]$$

This expression involves four distinct admittance ratios, three of which have already been evaluated. The fourth admittance ratio is L_{KI}/L_{KK}. This can be equated to $L_{IK}/L_{KK} = (I/K)_{X_I = X_J = 0}$, i.e., it is equal to the ratio of the flux of electricity to the flux of matter in the liquid boundary, in the absence of any applied emf (no electrodes) and of a temperature gradient. However, the flux of matter under such conditions occurs by diffusion of electroneutral groups of ions and does not give rise to an electric current at all. Therefore $I/K = 0$ in the boundary, and this fourth admittance ratio is zero. Equation [39] simplifies to

$$(-X_I/X_J)_{\text{fin}} = L_{IJ}/L_{II} - (L_{IK}/L_{II})(L_{KJ}/L_{KK}). \quad [40]$$

The validity of Eq. [40] can be confirmed by noting that the admittance ratios can be replaced by driving force ratios, e.g., $L_{ab}/L_{aa} = -(X_a/X_b)_{a = X_c = 0}$, so that

$$(-X_I/X_J)_{\text{fin}} = (-X_I/X_J)_{I = X_K = 0} + (-X_I/X_K)_{I = X_J = 0} \cdot (X_K/X_J)_{K = X_I = 0} \quad [41]$$

The latter expression is obviously equivalent to

$$(dV/dT)_{\text{fin}} = (\partial V/\partial T)_{d \ln a = 0} + (\partial V/RT\, \partial \ln a)_{dT = 0} \cdot (RT\, \partial \ln a/\partial T)_{dV = 0} \quad [42]$$

i.e., the final thermal emf is equal to the initial thermal emf L_{IJ}/L_{II} plus a term which is exactly the isothermal emf of the concentration cell that the Soret effect has created.

We have already established that $L_{IJ}/L_{II} = S^*_I/\beta\mathbf{F}$; $L_{IK}/L_{II} = \pm\, t_g/\beta\mathbf{F}$ (if $z_r = \pm$); and $L_{KJ}/L_{KK} = S^*_D/1$ mole. Therefore Eq. [40] transforms to

$$dE_{\text{fin}}/dT = S^*_I/\beta\mathbf{F} \mp t_g S^*_D/\beta\mathbf{F} \quad (\text{if } z_r = \pm) \quad [43]$$

By introducing values for S^*_I (Eq. [27]) and S^*_D, Eq. [43] further transforms to

$$dE_{\text{fin}}/dT = (1/\beta\mathbf{F})\{-\beta\Sigma\omega_k S_k - (\beta/z_r)S^*_{Er} - \beta\bar{\bar{S}}(E^- \text{ in Cu}) - t_r(\beta/z_r)S^*_{M_r} - t_g(\beta/z_g)S^*_{M_g} \mp t_g \nu_r S^*_{M_r} \mp t_g \nu_g S^*_{M_g}\} \quad (\text{if } z_r = \pm). \quad [44]$$

Since $\mp\, \nu_r = -\beta/z_r$ and $\mp\, \nu_g = +\beta/z_g$ for $z_r = \pm$, the terms involving the migration transport

entropy of the gegenion g vanish, while the two corresponding terms for the ion r coalesce to $-(\beta/z_r)S^*_{Mr}$. The final emf therefore reduces to

$$dE_{\text{fin}}/dT = (1/\beta\mathbf{F})\{-\beta\Sigma\omega_k S_k - \beta\bar{\bar{S}}(E^- \text{ in Cu}) - (\beta/z_r)\bar{\bar{S}}_r\} \quad [45]$$

All properties of the gegenion have vanished from Eq. [44] and [45], while the ion r contributes the sum $S^*_{Er} + S^*_{Mr} = \bar{\bar{S}}_r$, denoted by Temkin and Khoroshin (14) as the "entropy of the moving ion." This sum thus becomes a measurable thermodynamic property of a single ion, provided a value can be assigned to the electronic term, as discussed above.

For example, for a thermal Ag/Ag^+ cell, the final emf, with the electronic term neglected is given by $dE_{\text{fin}}/dT = (1/\mathbf{F})\,[S(\text{Ag}) - \bar{\bar{S}}\,(\text{Ag}^+)]$. For a thermal $Hg/Hg_2SO_4/Al_2(SO_4)_3$ cell, it is $dE_{\text{fin}}/dT = (1/6\mathbf{F})[6S(\text{Hg}) - 3S(Hg_2SO_4) + 3\bar{\bar{S}}(SO_4^=)]$.

A comparison of Eq. [43] and [23] show that the *final* minus the *initial* thermal emf of a cell is equal to $\mp\ t_p S^*_D/\beta\mathbf{F}$ (if $z_r = \pm$). This provides an electrochemical method of measuring the entropy S^*_D of diffusion transport, and the associated Soret coefficient (12).

It is of theoretical interest to decompose the measurable final thermal cell emf [45] into formal expressions for the electrode potential difference and the liquid junction potential, since these two quantities are at least conceptually measurable by the use of two IRE's, as defined above. The liquid junction potential in the final state of the thermal cell can be formally expressed by evaluating Eq. [40] for the liquid boundary processes only. In the boundary $L_{IJ}/L_{II} = L_{JI}/L_{II} = (J/I)_{x_J=x_{K=0}} = -\Sigma t_i (\beta/z_i)S^*_{Mi}/\beta\mathbf{F} = (t_-\nu_- S^*_{M-} - t_+\nu_+ S^*_{M+})/\beta\mathbf{F}$; and $L_{IK}/L_{II} = L_{KI}/L_{II} = (K/I)_{x_J=x_{K=0}} = -t_i(\beta/z_i)/\nu\beta\mathbf{F} = (t_-\nu_- - t_+\nu_+)/\nu\beta\mathbf{F}$, provided K is taken as $(K_+ + K_-)/\nu$; while L_{KJ}/L_{KK} as evaluated above is already a boundary quantity equal to $S^*_D/1$ mole $= (\nu_+ S^*_{M+} + \nu_- S^*_{M-})/1$ mole. The substitution of these expressions into Eq. [40] gives, for the final thermal liquid junction potential,

$$dE_{lj,\,\text{fin}}/dT = \nu_+\nu_-(S^*_{M-} - S^*_{M+})/\nu\beta\mathbf{F} \quad [46a]$$

For example, in sodium chloride electrolyte, this becomes $(1/2\mathbf{F})[S^*_M(\text{Cl}^-) - S^*_M(\text{Na}^+)]$, and in aluminum sulfate $(3\cdot 2/5\cdot 6\mathbf{F})[S^*_M(SO_4^=) - S^*_M(\text{Al}^{+3})]$.

By subtracting [46a] from [45], neglecting the electronic term, one obtains the difference of the electrode potentials for the final state of the thermal cell in the form

$$dE_{el,\,\text{fin}}/dT = S^*_E/\beta\mathbf{F} - S^*_D/\nu z_r\mathbf{F} \quad [46b]$$

The first term in [46b] gives the effect of temperature on the electrode potentials, without liquid junction potential and without thermal diffusion. The second term gives the further effect of the thermal diffusion concentration gradient on the electrode potentials. This second term takes the form, in a thermal Ag/AgCl/NaCl cell, $(1/2\mathbf{F})[S^*_M(\text{Na}^+) + S^*_M(\text{Cl}^-)]$; in a thermal $Al/Al_2(SO_4)_3$ cell, $-(1/5\cdot 3\mathbf{F})[2S^*_M(\text{Al}^{+3}) + 3S^*_M(SO_4^=)]$.

Table IV. Transport entropies of Tl^+ and Cd^{++} ions and gegenions (cal/mole.deg) from the data of Agar and Breck (12)

$S^\circ(\text{Tl}^+) = 30.4$; $S^\circ(\text{Cd}^{++}) = -14.6$ (33)

Electrolyte	$\bar{\bar{S}}_+$	pa_+	S^*_{E+}	S^*_{M+}	S^*_{M-}
$TlClO_4$, 0.05m	35.8	1.403	32.3	3.5	—0.6
$TlClO_4$, 0.1m	33.9	1.132	31.1	2.8	—1.1
$TlClO_4$, 0.15m	34.0	0.982	30.4	3.6	—1.4
$TlClO_4$, 0.20m	33.3	0.879	29.9	3.4	—1.8
$TlClO_4$, 0.26m	32.5	0.800	29.6	2.9	—1.4
$TlNO_3$, 0.1m	34.0	1.151	31.2	2.8	—1.1
$TlOCOCH_3$, 0.1m	34.0	1.131	31.1	2.9	3.3
Tl_2CO_3, 0.05m	33.9	1.138	31.1	2.8	3.0
Tl_2SO_4, 0.05m	34.0	1.138	31.1	2.9	2.3
$CdSO_4$, 0.005m	—8.96	2.602	—11.7	2.7	5.0
$CdSO_4$, 0.017m	—10.99	2.248	—13.3	2.3	3.9
$CdSO_4$, 0.05m	—12.47	1.973	—14.6	2.1	2.8
$CdSO_4$, 0.17m	—13.93	1.684	—15.9	2.0	1.6
$CdSO_4$, 0.52m	—14.78	1.458	—16.9	2.1	0.6
$CdSO_4$, 1.05m	—14.64	1.327	—17.5	2.9	—0.6
$Cd(ClO_4)_2$, 0.05m	—12.27	1.835	—15.2	2.9	—0.4
$Cd(NO_3)_2$, 0.05m	—11.87	1.842	—15.2	3.4	—0.9
$CdCl_2$, 0.05m	—10.07	2.406	—12.6	2.5	—0.5

Values of the Ionic Transport Entropies

Values of the entropy $\bar{\bar{S}}_i$ of the moving ion have been obtained for Cd^{++} and Tl^+ by Agar and Breck (12) from measured final thermal emf's, and are listed in Table IV. The corresponding entropies S^*_D of diffusion transport, from the difference of final and initial thermal emf's, are given in Table I. In Table IV, $pa_+ = -\log a_+$ where $a_+ = \nu_+ m\gamma_+$, γ_+ is calculated by the rule $\gamma_+ = \gamma_\pm^{-z_+/z_-}$, and $\gamma_\pm$ is interpolated from Latimer (33). The entropy of electrochemical transport S^*_{E+} is computed from entropy data (33) via the "saturated KCl bridge rule" of deBLS (8), Eq. [32] and [33], neglecting the third term in $d\ln a_i/dT$. The entropies of migration transport for the two ions are then computed from $\bar{\bar{S}}_+$ and S^*_{E+} (Table IV), and S^*_D (Table I).

For both Cd^{++} and Tl^+ ions, the mass-action dependence of $\bar{\bar{S}}_+$ parallels that of S^*_{E+}, so that S^*_{M+} is apparently independent of concentration: $S^*_M(\text{Tl}^+) = 3.1 \pm 0.3$ cal/deg; $S^*_M(\text{Cd}^{++}) = 2.5 \pm 0.4$ cal/deg. The migration transport entropies of the anions do vary with concentration, and can be expressed within the range of concentrations studied by the approximate relations: $S^*_M(ClO_4^-) = -3.7 + (\frac{1}{2}R')pa(ClO_4^-)$; $S^*_M(SO_4^=) = -6.6 + R'pa(SO_4^=)$, where $R' = 2.303\,R$ and $pa_i = -\log a_i$. The mass-action dependence for sulfate is normal, while that for perchlorate contains the surprising coefficient $\frac{1}{2}R'$ instead of R'. Thus the concentration effect on S^*_{Mi} ranges from apparently no dependence for Tl^+ and Cd^{++}, to half mass-action dependence for ClO_4^-, to full mass-action dependence for $SO_4^=$. Values of S^*_{M-} for other anions are as follows: 0.1 m NO_3^-, —1.1, —0.9; 0.1 m CH_3COO^-, 3.3; 0.05 m $CO_3^=$, 3.0; 0.1 m Cl^- (in $CdCl_2$), —0.5. The several anion values, calculated above from the KCl bridge rule, show reasonable agreement between the Tl^+ and

Table V. Transport entropies of various ions (cal/deg) from the data of Khoroshin and Temkin (14)

Ion	$\bar{\bar{S}}^\circ_i$	$S^{*\circ}_{Ei}$	$S^{*\circ}_{Mi}$
H^+	5.2	—4.48	9.7
Li^+	—1.4	—1.1	—0.3
Na^+	10.8	7.7	3.1
K^+	20.0	20.0	0.0
NH_4^+	21.4	22.49	—1.1
Ag^+	20.8	13.19	7.6
$\frac{1}{2}Mg^{++}$	—18.15	—18.6	0.45
$\frac{1}{2}Ca^{++}$	—7.75	—11.1	3.35
$\frac{1}{2}Sr^{++}$	—4.95	—9.2	4.25
$\frac{1}{2}Ba^{++}$	—0.15	—3	2.85
$\frac{1}{2}Zn^{++}$	—15.95	—17.20	1.25
F^-	7.8	2.2	5.6
Cl^-	19.5	17.7	1.8
Br^-	23.4	23.77	—0.4
NO_3^-	42.0	39.5	2.5
ClO_4^-	46.8	47.7	—0.9
$\frac{1}{2}SO_4^=$	3.2	6.53	—3.3

the Cd^{++} series and are not inconsistent with the conventional values of Table III (referred to chloride as zero).

Values of the moving ion entropies $\bar{\bar{S}}_i$ have also been deduced by Khoroshin and Temkin (14) from the ingenious suggestion that initial thermal emf's measured in aqueous LiCl should be virtually the same as final thermal emf's, since S^*_D for dilute LiCl is virtually zero (Table III). This led them to a value of 19.5 cal/deg for $\bar{\bar{S}}^\circ(Cl^-)$. From this, they deduced values for other ions from the relation

$$\Sigma\nu_i\bar{\bar{S}}_i = \Sigma\nu_i S_i + \Sigma\nu_i S^*_{Mi} \qquad [47]$$

where S_i is the conventional ionic entropy. Equation [47] is valid for any neutral ion combination for which $\Sigma\nu_i S_i = \Sigma\nu_i S^*_{Ei}$. The final summation in [47] is, of course, S^*_D for a neutral electrolyte. By taking S_i and S^*_D data from various sources, Khoroshin and Temkin obtained the values of $\bar{\bar{S}}^\circ_i$ given in Table V. Standard entropies of electrochemical transport $S^{*\circ}_{Ei}$ have been computed from conventional entropy data (33) by means of the "saturated KCl bridge rule," Eq. [32]. The migration transport entropy $S^{*\circ}_{Mi}$ is then obtained by difference. The values given in Table V are only approximate, but, on the whole, they are fairly consistent with data given in Tables I through IV.

Ionic Transport Entropies

To distinguish between the ionic entropies of electrochemical transport S^*_{Ei} and of migration transport S^*_{Mi}, it is necessary to consider the interaction between an ion and its environment. Eastman (34) divides the vicinity of an ion "into three concentric regions of gradually differing properties. First, there is the 'ion-cavity,' within which there are no solvent molecules." The thickness of the ion-cavity has been estimated (35) as 0.10Å for anions and 0.85Å for cations, in addition to the crystallographic ionic radius. Next comes the hydration (solvation) layer, described by Eastman in these words: "immediately outside of the ion cavity the (polar) molecules of solvent are strongly attracted and oriented. The inner layers of solvent molecules in this second region, and those extending out from it to varying distances in different cases, are held so strongly by the central ion as to form a complex with it, acting in processes of diffusion, as a single molecule. The third region comprises all the rest of the outer space. In this [third] sphere the solvent molecules are still subject to forces of compression and orientation, diminishing with distance from the center of the complex, and not sufficiently strong to bind these molecules to the ion."

Let one mole of the ion i be associated with n_2 moles of bound solvent (in Eastman's second region) and n_3 moles comprising the remainder of the (unbound) solvent (Eastman's third region). Let S_2 and S_3 be the partial molal entropies of the solvent in these second and third regions, and S_1 the molal entropy of the solvent in the absence of any ions. The compression and orientation of solvent molecules by electrostatic attraction between the ion and the dipoles of the solvent result in S_2 being significantly less, and S_3 somewhat less, than S_1.

When one mole of an ion is transferred from the right to the left electrolyte compartment by the agency of the two electrode reactions, the entropy transported from the right (No. 2) to the left (No. 1) heat reservoir includes the quantity $(n_2 + n_3)S_1 - n_2S_2 - n_3S_3$, *i.e.*, the gain in entropy of the solvent upon its release from the ordering influence of the electric field of the ion, corresponding to the absorption of heat in the breaking of ion-solvent bonds in the second region and in the relaxation of compression and orientation forces in the third region. The entropy of transport for one molal unit of the electrode reaction might therefore be expressed as $S^*_E = S(M) - S_{ic}(M^+) + (n_2 + n_3)S_1 - n_2S_2 - n_3S_3$, where $S_{ic}(M^+)$ is the partial molal entropy of the ion-cavities of M^+. The entropy of electrochemical transport of the ion M^+ becomes $S^*_E(M^+) = S_{ic}(M^+) + n_2(S_2 - S_1) + n_3(S_3 - S_1)$, *i.e.*, it includes entropy terms pertaining to the binding of solvent molecules in the second region and to the orientation and compression of the solvent in the third region.

When one mole of an ion is transferred from the right to the left electrolyte compartment by migration, "the aggregate comprising the first and second regions above remains mostly intact and takes part in no . . . entropy changes. But as the ion moves it leaves behind material which had been under its influence in the third sphere, and brings under its influence solvent molecules not previously so strongly affected. A relaxation occurs, therefore, in the region from which it goes, with an attendant increase of entropy and absorption of heat. The reverse effects appear in the region into which it moves. It is, therefore, these changes in the third sphere that give rise" (Eastman, 34) to the ionic entropy of migration transport $S^*_M(M^+)$ which may be equated to $n_3S_1 - n_3S_3$, i.e., to the gain in entropy of the solvent in the third region upon its release from the electric field of the ion. On this model, the entropy of the moving ion $\bar{\bar{S}}(M^+)$ becomes

$S_{ic}(M^+) + n_2(S_2 - S_1)$, *i.e.*, it includes the solvent entropy terms of the second region only, the region that moves with the ion.

The total entropy of the solvent n_3S_3 in the third region in the presence of the ion, relative to its entropy n_3S_1 in the absence of the ion, can be calculated at infinite dilution from a simple electrostatic model, on the assumption that the solvent in the third region can be treated as a continuous medium of dielectric constant ϵ. Consider a charge q located in a dielectric ϵ and a concentric sphere of radius r so chosen that the surface of the sphere lies well into the dielectric region. The total electrostatic potential energy of the electric field outside the sphere is $q^2/2\epsilon\, k_o r$ where k_o is a constant equal to 1 esu or $10^{-9}/8.988$ amp.sec.volt^{-1}.m^{-1} (36). This energy may be equated to the electrostatic free enthalpy G of the polarized dielectric outside the sphere, whose entropy therefore becomes $-dG/dT = -(q^2/2k_o r)d(1/\epsilon)/dT$. The latter may be taken equal to $n_3(S_3 - S_1)$ and therefore to $-S^*_{Mi}$. Gurney (37) suggests that the dielectric constant may be represented by the empirical formula $\epsilon = \epsilon_0 \exp(-T/\theta)$ where $\epsilon_0 = 305.7$ and $\theta = 219°K$ for water. The derivative $d(1/\epsilon)/dT = 1/\epsilon\theta = 5.83 \times 10^{-5}$ deg^{-1} for water at 25°C. Upon substitution of appropriate numerical values, the ionic entropy of migration is calculated as

$$S^*_{Mi} = +(9.68\ z_i^2/r_A) \text{ cal/deg.mole} \quad [48]$$

at infinite dilution. Taking the crystal radius (38) of K^+ at 1.33Å, plus 0.85Å for the ion cavity, plus 2.80Å as the approximate diameter of one water molecule, a total radius of 5.0Å is estimated for the sphere "bounding" the second from the third regions. S^*_{Mi} can then be calculated as 1.94 cal/deg for K^+ ion at infinite dilution, a value which is of the right order as compared with the conventional single ion value of Table III. However, Eq. [48] cannot be used for any accurate calculation of S^*_{Mi} since the appropriate third region radius, and the short range dielectric constant, are uncertain. Agar (21) has shown that little correlation exists between conventional values of S^*_{Mi} and ionic crystal radii.

At finite concentration, the potential surrounding an ion is reduced by multiplication by the Debye-Hückel factor, $\exp(-\kappa r)$, and Eq. [48] should be multiplied by the same factor. The derivative $dS^*_{Mi}/d\kappa$ becomes $-9.68\ z_i^2\exp(-\kappa r)$ cal.Å/deg. For 1, 1-salts in water at 25°C, and very dilute solutions where $\exp(-\kappa r) \approx 1$, the derivative $dS^*_{Mi}/d\sqrt{m}$, in cal/deg. (unit of molality)$^{1/2}$, $= -3.18$. For both ions of the salt, $dS^*_D/d\sqrt{m}$ is twice this or -6.36 in satisfactory agreement with observed values of -6.0 to -6.5 reported above for several 1, 1-salts. For $CdSO_4$, the limiting slope should be $2^2 \cdot 2$ or 8 times this, about -51. The observed slope in the most dilute solutions for which there are data, -26, appears to be rapidly approaching this limiting value.

Thus Eastman's interpretation of the entropy of migration S^*_{Mi} as being primarily the entropy of relaxation of the polarized dielectric of the solvent in the third region, when the ion departs, appears to be well founded. On this basis, the migration transport entropy of an ion should always be positive, and, according to Eq. [48], multiplied if necessary by the Debye-Hückel factor to take care of interionic attractions, it should always be small, around 1 to 3 cal/deg for univalent ions.

However, electrostatics does not tell the whole story. Agar (21) points out that where an ion breaks up the structure of the water, its presence may actually increase the entropy of the solvent in the third region, and this would lead to negative migration entropies as reported above for several ions (Tables III to V).

To quote Eastman once more: "The conception of solvated ions . . . takes into account only the electrical effects . . . . Several factors . . . neglected . . . may be of importance in certain cases. Any sort of chemical bonding in the ion aggregate may greatly affect the spheres of influence about the central charge, and so alter the heat [entropy] effects attending its diffusion. This kind of thing may differentiate, for example, between positive and negative ions in their orienting and bonding effects on water molecules. The hydrogen nuclei of the solvent may form a sort of hydrogen bond (39) with electrons of the outer shell of negative ions, a type which is not possible between oxygen atoms and most positive ions. The effect of such bonds, if extensively formed, would be to increase region two at the expense of three, with consequent lessening of the heat of transfer [and of the entropy of migration]. The possibility that either ion of the solvent [H^+ or OH^-] may be transferred, in effect, by a chain mechanism, must also be considered in solutions of acids and bases. For if this occurs, not only the energy represented in the third sphere above, but that of the second as well, a very much larger quantity, would be involved in the heat of transfer." There is evidence that S^*_{Mi} for H^+ and OH^- is considerably larger (about 10 cal/deg) than for other ions, as discussed above.

The large values obtained for the conventional entropy of migration S^*_{Mi} of the tetraalkylammonium ions (Table III) appear surprising at first, since Eastman's students (44) had speculatively expected values close to zero, and had even used this hypothesis as a basis for evaluating a set of S^*_{Mi} values, which proved inconsistent with known values of S^*_D from the Soret effect (Table I). The large values actually obtained point to another mechanism than just the electrostatic one discussed above. The hydrocarbon chains must exert some ordering influence on the neighboring water structure, perhaps by the formation of "icebergs" (44). The removal of the alkyl chains by migration of the ions then allows a disordering of the water structure left behind, i.e., a "melting of the icebergs" (44), with a consequent absorption of heat and a positive entropy of migration. The increment in S^*_{Mi} for every

four CH_2 groups added to the ion appears to be around 4 cal/deg, in going from methyl to amyl, i.e., about 1 cal/deg/CH_2 group added. This entropy effect is still small as compared with the intrinsic molal entropies of the materials involved, i.e., about 8.1 cal/deg for CH_2 (from the entropy difference between ethanol and methanol) and 16.7 cal/deg for H_2O. Thus Eastman's students speculations regarding the smallness of the entropy of migration of the tetraalkylammonium ions may still be justified as regards an individual linkage within the ion, even though it is not justified for the huge ion as a whole.

If one attributes the same value of 1 cal/deg to the migration of the methyl (CH_3) group, as well as to CH_2, a residual conventional value of about 3 cal/deg is obtained for the migration entropy of the N^+ core of the R_4N^+ ions, i.e., a value which is quite consistent with that of other simple ions such as Na^+, K^+, Rb^+, and with the electrostatic values, Eq. [48], as well.

The values for divalent ions (Tables III to V) are considerably smaller than what one would expect from the electrostatic relation [48] alone. Undoubtedly, the Debye-Hückel drop-off at finite concentration is already much more significant in this case, as may be the structure-breaking properties of the ion on the solvent, which would tend to lead to negative values of the migration transport entropy.

Summary

The application of the Onsager thermodynamics to electrochemical systems out of equilibrium permits a unified approach to the problems of concentration cells with transference, thermal diffusion in electrolytes, initial and final emf's of thermal cells. For isothermal concentration cells, the method confirms the classical results of Nernst derived from equilibrium considerations of free energy. For non-isothermal systems, the method brings out the entropy S^* transported from hot to cold heat reservoirs (in the limit of equal temperatures), multiplied by the applied temperature differential dT, as the characteristic thermodynamic driving force of a process. For an ion, the entropy transported is different when the ion is transported by electrode reactions and when it is transported by migration. This gives rise to the ionic entropies of electrochemical transport S^*_{Ei} and of migration transport S^*_{Mi}, respectively. Values of the ionic transport entropies can be estimated from data on initial and final thermal emf's and Soret coefficients. For an ion, the standard value of $S^{*\circ}_{Ei} = S^\circ_i - z_i(4.48$ cal/deg) while the nonstandard values of S^*_{Ei} show a normal mass action dependence on concentration. For many ions, except H^+ and OH^-, S^*_{Mi} appears to be small and positive, *i.e.*, about 0-3 cal/deg. Such values are in semi-quantitative agreement with calculations based on Eastman's model of the ionic entropy of migration as the electrostatic entropy of depolarization of the solvent dielectric when the ion moves out. The concentration dependence of S^*_{Mi} does not follow the law of mass action, but it appears to follow the Debye-Hückel relations in dilute solutions. The establishment of better values for the ionic transport entropies remains a challenging task.

Ionic transport across biological membranes is an important process in the release of energy by living systems (18, 40). Holtan (17b) has shown by qualitative experiments that large thermal emf's (of the order of 10^{-2} volts per degree) can be developed in colloidal mixtures and in nerve fibers. He has suggested that such thermal emf's may contribute to the initiation of nerve impulses. The role of ionic transports arising from possible local thermal gradients resulting from metabolic energy release in living systems, needs to be explored, and may be hoped to shed some light on the mechanism of the living cell as a thermodynamic engine. "Where is the way to the dwelling of light?" (Job 38: 19).

Acknowledgment

The author wishes to express his gratitude to the International Nickel Company, Inc., of New York, for a Grant-in-Aid in support of this work.

Manuscript received Dec. 28, 1959.

Any discussion of this paper will appear in a Discussion Section to be published in the June 1961 JOURNAL.

APPENDIX I

Glossary of Transport Entropies Used in This Paper

S^*: the entropy of transport, the entropy transported reversibly from the right heat reservoir No. 2 (normally the hot one) to the left heat reservoir No. 1 (normally the cold one) by the occurrence of some reversible process in the cell (system), in the limiting case of a vanishing temperature difference between the heat reservoirs.

S^*_I: the entropy of electrical transport, i.e., the entropy transported between heat reservoirs, as above, by the flow of a positive current through the cell from left to right.

S^*_E: the entropy of electrochemical transport, i.e., the contribution to S^*_I of the two equal and opposite electrode reactions.

S^*_M: the entropy of migration transport, i.e., the contribution to S^*_I of the current transported by ionic migration through the solution.

S^*_D: the entropy of diffusion transport, i.e., the entropy transported between heat reservoirs, as above, by the flow of solute across the liquid junction from right to left.

S^*_{Ei}: the ionic entropy of electrochemical transport, i.e., the contribution of an ion (or electron) to S^*_E.

S^*_{Mi}: the ionic entropy of migration transport, i.e., the contribution of migration (or diffusion) of an ion (or electron) to S^*_M or to S^*_D.

$\overline{\overline{S}}_i$: the entropy of the moving ion, i.e., the sum $S^*_{Ei} + S^*_{Mi}$.

Ionic index $_r$: the ion to which the electrodes are reversible; $_g$: the gegenion of $_r$.

APPENDIX II

Comparative Nomenclature for the Three Ionic Transport Entropies Appearing in the Equation $\bar{\bar{S}}_i = S^*_{Ei} + S^*_{Mi}$

Author	$\bar{\bar{S}}_i$	S^*_{Ei},[1]	S^*_{Mi}
This paper	Entropy of moving ion $\bar{\bar{S}}_i$	Ionic entropy of electrochemical transport S^*_{Ei}	Ionic entropy of migration transport S^*_{Mi}
Eastman (13a)	—	Absolute partial molal ionic entropy $\bar{S}_i$	Ionic entropy of transfer S^*_i (= heat of transfer Q^*_i/T)
Temkin and Khoroshin (14)	Entropy of moving ion $\bar{\bar{S}}_i$ (Entropiya dvizhushchikhsya iona)	Entropy of a single ion S_i	Ionic entropy of transfer S^*_i (= heat of transfer Q^*_i/T)
Agar (12, 21)	Transported entropy $\bar{\bar{S}}_i$	Partial molal ionic entropy S_i	Ionic entropy of transport S^*_i (= heat of transport Q^*_i/T)
deGroot (17a)[2]	Entropy of transfer S^*_i	Ionic entropy S_i	Reduced heat of transfer Q^{**}_i/T
Haase (19b)	Überführungsentropie S^*_i	Partielle molare Entropie der solvatisierten ionenart S_i	Überführungswärme Q^*_i/T
Domenicali (50)[2]	Transport entropy per particle S^*	—	—

[1] $S^*_{Ei} = S_i + z_i(-4.48$ cal/deg) where S_i is the conventional partial molal ionic entropy, Latimer (33), and z_i is the ionic charge (with sign).

[2] de Groot defines a "heat of transfer" Q^*_i, and Domenicali a "transport heat" Q^*_i, where $Q^*_i = T\bar{\bar{S}}_i + \mu_i$.

REFERENCES

1. W. Nernst, *Z. physik. Chem.*, **4**, 129 (1889).
2. E. Bouty, *J. Phys.*, **8**, 289, 341 (1879); **9**, 306 (1880); **10**, 241 (1881).
3. Th. W. Richards, *Z. physik Chem.*, **24**, 39 (1897).
4. I. M. Kolthoff and F. Tekelenburg, *Rec. trav. chim.*, **46**, 18 (1927).
5. S. P. L. Sorensen and K. Linderstrom-Lang, *Compt. rend. trav. lab. Carlsberg*, **15**, [6], 1 (1925).
6. E. Lange and Th. Hesse, *Z. Elektrochem.*, **37**, 238 (1933).
7. E. Lange, Handbuch Experimental Physik, **12**, 327 (1932); *Z. physik. Chem.*, **209**, 162 (1958).
8. A. J. deBethune, T. S. Licht, and N. Swendeman, *This Journal*, **106**, 616 (1959).
9. Ch. Soret, *Ann. chim. phys.*, [5], **22**, 293 (1881).
10. E. D. Eastman, *J. Am. Chem. Soc.*, **50**, 289 (1928).
11. L. G. Longsworth, "Soret Coefficients of Electrolytes," pp. 183-199 in "Structure of Electrolytic Solutions," W. J. Hamer, Editor, John Wiley & Sons, Inc., New York (1959).
12. J. N. Agar and W. G. Breck, *Trans. Faraday Soc.*, **53**, 167 (1957); W. G. Breck and J. N. Agar, *ibid.*, **53**, 179 (1957).
13. (a) E. D. Eastman, *J. Am. Chem. Soc.*, **48**, 1482 (1926); **50**, 283, 292 (1928). (b) C. Wagner, *Ann. Physik*, [5] **3**, 629 (1929); **6**, 370 (1930).
14. M. I. Temkin and A. V. Khoroshin, *Zhurn. fiz. khimii*, **26**, 500 (1952); A. V. Khoroshin and M. I. Temkin, *ibid.*, **26**, 773 (1952).
15. L. Onsager, *Phys. Rev.*, **37**, 405 (1931); **38**, 2265 (1931).
16. I. Prigogine, "Etude Thermodynamique des Phenomenes Irreversibles," Chap. XII, Desoer, Liege (1947).
17. (a) S. R. deGroot, "Thermodynamics of Irreversible Processes," North Holland Publishing Co., Amsterdam (1951); (b) H. Holtan, Jr., "Electric Potentials in Thermocouples and Thermocells," Thesis, Utrecht (1953).
18. J. G. Kirkwood, "Transport of Ions through Biological Membranes," pp. 119-127, in "Ion Transport across Membranes," H. T. Clarke and David Nachmansohn, Editors, Academic Press, New York (1954.)
19. (a) P. van Rysselberghe, *J. Phys. Chem.*, **57**, 275 (1953); "Electrochemical Affinity," Hermann, Paris (1955); (b) R. Haase, *Z. physik. Chem., N. F.*, **11**, 379 (1957).
20. H. S. Harned and B. B. Owen, "Physical Chemistry of Electrolytic Solutions," 3d ed., Reinhold Publishing Co., New York (1958).
21. J. N. Agar, "Thermal Diffusion in Electrolyte Solutions," pp. 200-223 in *op. cit.*, W. J. Hamer, editor, reference (11); J. N. Agar, *Rev. Pure Applied Chem. (Roy. Aust. Chem. Inst.)*, **8**, 1 (1958).
22. R. J. E. Clausius, "Mechanische Wärmetheorie," Chap. 10, Vieweg und Sohn, Braunschweig (1876).
23. A. J. deBethune, *Ind. Eng. Chem.*, **50**, 129 (1958).
24. G. N. Lewis and M. Randall, "Thermodynamics and the Free Energy of Chemical Substances," McGraw-Hill Book Co., New York (1923). J. A. Christiansen and M. Pourbaix, *Compt. rend. 17th Conf. I.U.P.A.C.* (Stockholm 1953), pp. 82-84, Maison de la Chimie, Paris (1954). T. S. Licht and A. J. deBethune, *J. Chem. Education*, **34**, 433 (1957).
25. E. A. Guggenheim, "Thermodynamics," North Holland Publishing Co., Amsterdam (1949).
26. P. Debye and E. Hückel, *Physik. Z.*, **24**, 185, 305 (1923).
27. G. Scatchard and R. C. Breckenridge, *J. Phys. Chem.*, **58**, 602 (1954); G. Scatchard, *Science*, **95**, 30 (1942); *Rev. Sci. Instruments*, **26**, 395 (1955).
28. R. G. Bates, "Electrometric pH Determinations," John Wiley & Sons, Inc., New York (1954).
29. M. Stern, H. Shwachman, T. S. Licht, and A. J. deBethune, *Anal Chem.*, **30**, 1506 (1958).
30. (a) D. S. Carr and C. F. Bonilla, *This Journal*, **99**, 475 (1952); (b) G. Borelius, W. H. Keesom, C. H. Johansson, and J. O. Linde, *Proc. Acd. Sci. Amsterdam*, **33**, 1, 17 (1930); **35**, 10, 25 (1932); (c) G. P. Harnwell, "Principles of Electricity and Electromagnetism," McGraw-Hill Book Co., New York (1939).
31. H. A. Fales and W. A. Mudge, *J. Am. Chem. Soc.*, **42**, 2434 (1920).
32. E. D. Eastman, *ibid.*, **50**, 295 (1928).
33. W. M. Latimer, "Oxidation Potentials—The Oxidation States of the Elements and their Potentials in Aqueous Solutions," 2nd Ed., Prentice Hall, New York (1952). National Bureau of Standards, "Selected Values of Chemical Thermodynamic Properties," Circular 500 (1952).

34. E. D. Eastman, *J. Am. Chem. Soc.*, **50**, 285 (1928).
35. W. M. Latimer, K. S. Pitzer, and C. M. Slansky, *J. Chem. Phys.*, **7**, 108 (1939); A. J. deBethune, *ibid.*, **29**, 616 (1958); **31**, 847 (1959).
36. A. J. deBethune and J. J. Perez, *Am. J. Phys.*, **24**, 584 (1956).
37. R. W. Gurney, "Ionic Processes in Solution," McGraw-Hill Book Co., New York (1953).
38. L. Pauling, "Nature of the Chemical Bond," 2nd Ed., Cornell University Press, Ithaca (1942).
39. W. H. Rodebush and W. M. Latimer, *J. Am. Chem. Soc.*, **42**, 1419 (1920).
40. H. T. Clarke and D. Nachmansohn, Editors, "Ion Transport across Membranes," Academic Press, New York (1954).
41. H. A. Bernhardt and H. D. Crockford, *J. Phys. Chem.*, **46**, 473 (1942).
42. G. R. Salvi, Thesis, Boston College (1960).
43. University of California Theses: M. B. Young (1935); F. M. Goyan (1937); R. G. Preston (1941).
44. J. C. Goodrich, F. M. Goyan, E. E. Morse, R. G. Preston, and M. B. Young, *J. Am. Chem. Soc.*, **72**, 4411 (1950).
45. R. Burian, *Z. Elektrochem.*, **37**, 238 (1931).
46. E. Lange and Th. Hesse, *ibid.*, **38**, 428 (1932).
47. H. Levin and C. F. Bonilla, *This Journal*, **98**, 388 (1951).
48. D. A. MacInnes, "Principles of Electrochemistry," Reinhold Publishing Co., New York (1939).
49. H. J. V. Tyrrell and G. L. Hollis, *Trans. Faraday Soc.*, **48**, 893 (1952); H. J. V. Tyrrell and R. Colledge, *ibid.*, **50**, 1056 (1954).
50. C. A. Domenicali, *Rev. Modern Physics*, **26**, 237 (1954).
51. J. N. Agar and J. C. N. Turner, *Proc. Roy. Soc.*, **A255**, 307 (1960).

Entropy of the Moving Cuprous Ion in Molten Cuprous Chloride from Thermogalvanic Potentials

Ambrose R. Nichols, Jr.[1] **and Cecil T. Langford**

Scientific Research Laboratory, Convair Division of General Dynamics Corporation, San Diego, California

ABSTRACT

Potentiometric measurements have been made on a thermogalvanic cell consisting of copper electrodes immersed in molten cuprous chloride in which there was a temperature gradient. The difference in temperature ΔT between the electrodes was varied from 30° to 70°C and the average temperature of the cell T_{avg} was varied from 462° to 588°C. Over these ranges the emf was proportional to ΔT, and $\Delta E/\Delta T = -0.436$ mv/°C, the hot electrode being the (—) terminal of the cell. From this value, the entropy of the moving cuprous ion in the melt was calculated for three different temperatures.

Thermogalvanic potentials in aqueous solutions have been studied rather extensively beginning with the work of Richards (1) who measured the temperature coefficient of the calomel electrode. It was not until about 1930 that studies were initiated in the electrochemistry of fused salts, but very little work was done in the field for the next twenty years. In the early 1950's there was a resurgence of interest, and as is evident from a recent bibliography compiled by Janz (2), an enormous amount of work has been done during the past eight years on the electrochemistry of fused salts. As is also evident from this same bibliography, practically all of the investigations in this field have been made with systems at uniform temperature throughout.

Much of the recent work with fused salts has been concerned with the development of reference electrodes constructed in such a manner that liquid junction potentials are practically eliminated. Senderoff and Brenner (3) used a coarse asbestos plug in the tube connecting the two half-cells, but apparently sufficient diffusion took place to introduce an unknown boundary potential into their measurements. Others, including Delimarskii (4), and Bockris, *et al.* (5), have used thin diaphragms of soda glass or Pyrex, but these are not suitable for use at high temperatures and, except in the case of concentration cells, do not lend themselves to exact thermodynamic analysis. Some very precise recent work in this field is described in a series of papers by Flengas and Ingraham (6) who developed a reversible silver-silver chloride reference electrode for use at high temperatures. The side-arm tube of the silica half-cell contains a single asbestos fiber (as opposed to a coarse plug) carefully sealed into the tube in a specified manner (6a). By using the same solvent (an equimolar mixture of NaCl-KCl) in the two half-cells with very low concentrations of the solutes (AgCl in the standard, and MCl_n in the other half-cell) the measured emf is, for all practical purposes, free from any liquid junction potential. In their most recent paper (6f) these authors give an emf series for several metals with corresponding standard electrode potentials referred to their standard Ag-AgCl electrode. Throughout their work they have determined the effect of temperature on the emf of each cell studied. The emf measurements, however, are made under isothermal conditions. It would be possible to calculate reaction entropies from their results but impossible to determine entropies of transport.

Many investigators have studied thermogalvanic potentials in aqueous solutions, but the most comprehensive treatment of the subject is given in a

[1] Professor of Chemistry, San Diego State College, San Diego, California.

recent paper by deBethune, Licht, and Swendeman (7) who give references to 28 earlier contributions, clarify the concepts of isothermal and thermal temperature coefficients of standard electrode potentials, and compute values for both of these, at 25°C, for nearly 300 electrodes. Their treatment of the thermodynamics of thermocells is applicable to fused electrolytes and we shall utilize their notations later in discussing our own results.

Reinhold (8) has measured the emf of a large number of thermocells with solid electrolytes. Among them was a cell analogous to ours and we shall compare his results with those obtained in this study. He also found (8c) that the temperature coefficient of the emf of an isothermal cell could be calculated from the thermal coefficients of related thermocells. Holtan (9), who reinvestigated and extended some of Reinhold's work, found a theoretical basis for the correspondence between thermocells and isothermal cells observed by Reinhold.

The present investigation involved measurements of the emf of a thermogalvanic cell consisting of copper electrodes immersed in molten cuprous chloride in which there was a temperature gradient. It was observed experimentally that the *hotter electrode* was the *negative* (−) *terminal*. The cell may be represented diagramatically as

$$(+)\mathrm{Cu(s)} \;|\; \underset{T_1}{\mathrm{CuCl(l)}} \;|\; \underset{T_2}{\mathrm{Cu(s)}}\,(-) \qquad [1]$$

where $T_2 > T_1$. Following the customary convention in thermocells, where a positive emf means that the hot electrode is the (+) terminal (7-9, 12, 14, 15), the sign of the emf of cell [1] is negative. It will be noted that this sign convention agrees with that of the I.U.P.A.C. (10) when the thermocell is diagrammed with the hot electrode on the right. When the outside circuit is closed and the cell operates spontaneously, the electrode reactions are

$$\text{at the hot electrode:} \quad \mathrm{Cu(s,}T_2\mathrm{)} = \mathrm{Cu^+}(T_2) + e^-(T_2), \qquad [2]$$

$$\text{at the cold electrode:} \quad e^-(T_1) + \mathrm{Cu^+}(T_1) = \mathrm{Cu(s,}T_1\mathrm{)}. \qquad [3]$$

If the temperature difference is neglected there is no net over-all chemical reaction but, physically, cuprous ions are transported from the hot electrode to the cooler one inside the cell, and electrons are transported from the hot to the cooler electrode in the outside circuit. Such a cell is analogous to a metallic thermocouple in that the molten electrolyte may be regarded as having replaced one of the dissimilar metals. For this reason some investigators have referred to cells of this type as galvanic thermocouples.

Experimental

A cell, made of Vycor glass, was placed inside a stainless steel container that fitted snugly in an electrically heated muffle furnace from which the door had been removed. The arrangement is shown in Fig. 1; Fig 2 is a sketch of the thermogalvanic cell. The container protruded 12.7 cm beyond the front of the furnace, and a temperature gradient

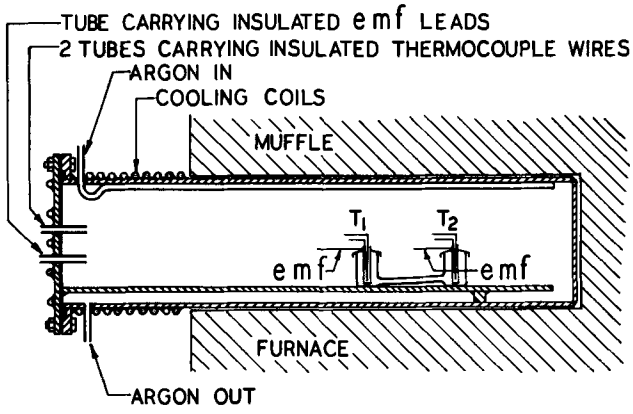

Fig. 1. Thermogalvanic cell assembly

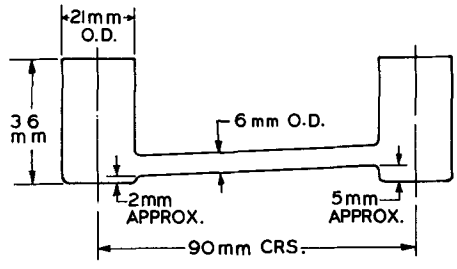

Fig. 2. Thermogalvanic cell made of Vycor glass. Hotter compartment on the right.

was maintained inside it by passing cooling water through coils that surrounded the front parts of the vessel. The tube connecting the two cell compartments was placed at a slight angle to the horizontal to minimize convection currents in the molten salt when the right hand compartment was made the hotter one by placing it toward the rear of the furnace. Powdered cuprous chloride was added to the cell until the connecting tube was full and each of the electrode compartments was about half full. The cuprous chloride was Baker and Adamson's Reagent, A.C.S. grade, dried to constant weight at 110°C without further purification. Preliminary experiments in which vacuum dried, freshly precipitated, cuprous chloride was used gave identical results with those reported here.[2] Electrodes were made from 5-cm lengths of 0.635-cm copper rod. A 0.318-cm hole was drilled from one end of the rod to within 0.16-cm of the other end, giving an open cylinder into which an insulated Pt-Pt + 10% Rh thermocouple was inserted. The junction rested on a single "fish-spine" insulator at the bottom of the cylinder. The cell compartments were covered with crucible lids. A copper electrode for each compartment was inserted through a hole in the center of the lid. When the bottom of the electrode rested on the bottom of the cell compartment the electrode protruded above the lid about 1.3 cm.

The thermocouple wires passed from the electrode through the face-plate of the container and protruded for a distance of 5 cm beyond it. Platinum and platinum + 10% rhodium lead wires ex-

[2] Apparently any Cu^{++} present in the Reagent grade CuCl is reduced by the metallic Cu electrodes, as reported by Flengas and Ingraham (6f).

tended from the front of the face-plate to a near-by Dewar flask where junctions between them and copper lead wires were maintained at the temperature of melting ice. The noble metal lead wires were connected to the corresponding thermocouple wires by means of a compression connector fabricated from a block of micarta that was attached to the outside of the face-plate. Insulated external copper leads passed from the potentiometer through the face-plate for a distance of about 5 cm. These were joined with copper connectors to short lengths of copper wire that were attached to the electrodes. Because of the continuous copper leads from the copper electrodes to the binding posts of the potentiometer, the observed emf was free from any metallic thermocouple voltage. Three double-pole, double-throw switches permitted the three circuits from inside the furnace to be passed either to a 6-point Brown recording potentiometer or to a L & N Type K-2 potentiometer. During a run, air was excluded from the heated cell by passing a stream of oxygen-free argon continuously through the stainless steel container. Argon from a commercial cylinder was passed over copper turnings heated to 350°C in a combustion tube furnace, before it was admitted to the furnace.

At the start of a run, a temperature controller in the heating circuit of the muffle furnace was set to bring the cell to a temperature considerably above the melting point of cuprous chloride. When the first "temperature plateau" was reached, two or three sets of voltages were measured at 10-min intervals, by means of the L & N Type K-2 potentiometer. The Type K-2 readings to the nearest microvolt were recorded and used in the calculations. The controller was then set for the next desired temperature plateau which would be attained in about 30 min. A particular set of voltages was obtained quite rapidly by manipulating the three double-pole, double-throw switches so that the circuit from the thermocouple in the hotter electrode, that from the cooler electrode, and the circuit from the thermogalvanic cell were switched, in turn, from the recording potentiometer to the Type K-2 instrument. Prior to the switching operation each of the three voltages was being printed on the strip chart at intervals of 27 sec and the values could be estimated to 0.01 mv. It was possible, therefore, to preset the Type K-2 potentiometer to a value quite near the actual voltage so that the final balancing required only a few seconds. Indeed, the three voltages could be determined on the Type K-2 in less than 2 min.

It will be observed from Table 1 that the temperature of the electrodes did not remain entirely constant during the two or three sets of readings that were taken at each so-called temperature plateau. During the ascending part of the temperature cycle the furnace cooled slightly at a plateau, while the reverse was true during the descending part of the cycle. It was not deemed necessary to obtain closer temperature control since, for a given set of readings, the actual temperatures of the electrodes and the corresponding emf of the thermogalvanic cell were measured essentially simultaneously.

Table I. Thermogalvanic potentials for the Cell Cu | CuCl(*l*) | Cu (T_1 T_2) in run No. 1. Hotter electrode (T_2) observed to be the negative (—) terminal

Temp, Plateau No.	Δt, °C	Avg $t = (t_2 + t_1)/2$, °C	$\Delta E/\Delta t$, mv/°C
1	29.5	509.1	—0.436
1	30.0	507.6	—0.431
1	29.5	506.7	—0.440
2	31.5	528.9	—0.443
2	31.6	528.4	—0.441
3	33.8	551.8	—0.431
3	34.1	551.6	—0.428
3	33.6	550.7	—0.435
4	35.4	581.9	—0.427
4	34.9	581.6	—0.434
5	36.4	550.9	—0.434
5	36.4	551.4	—0.434
6	37.8	523.8	—0.428
6	38.2	524.4	—0.423
7	36.9	495.5	—0.443
7	37.1	495.7	—0.441
		Average	—0.434
		Standard deviation of the set	0.006

Results and Discussion

If an aqueous solution of a substance is placed in a temperature gradient, a gradual change in concentration will, in general, take place because of thermal diffusion of the solute. This phenomenon is known as the Soret (11) effect, and the steady state finally attained is the so-called Soret equilibrium. When a solution of an ionic material constitutes the electrolyte of a thermogalvanic cell the emf will, in general, vary from an initial value E_i before the composition of the solution has had time to alter appreciably, to a final value E_s corresponding to the Soret equilibrium or steady state, as shown experimentally by Agar and Breck (12). In a series of papers, Eastman (13) suggested that the emf of such a cell is related to certain entropy changes that occur when it operates, and he introduced the concepts of entropy of transfer S^* and heat of transfer Q^* for those species that move between the electrodes. He proposed the following equation (13c) for the initial emf,

$$-\mathbf{F}(dE_i/dT) = \Delta S_R + \Delta S^*, \qquad [4]$$

where ΔS_R is the entropy gained by the electrode system at the higher temperature in the electrode reaction caused by one Faraday of positive electricity passing reversibly from the electrode to the electrolyte, and ΔS^* is the net entropy of transfer of the ions. $\Delta S^* = t_c S^*_c - t_a S^*_a$, where t_c and t_a are the transport numbers for the cation and anion, respectively.

More recently Temkin and Khoroshin (14), in a theoretical study of thermogalvanic cells, have developed an equation for the steady-state emf E_s. They show that, in so far as the ions are concerned, the heat of transfer of the potential-determining ion only is involved and the effects of the other ions

contained in the solution may be neglected. Their equation [24], with minor changes in symbols, is, for electrodes reversible to positive ions of valence n

$$-n\mathbf{F}(dE_s/dT) = \Delta S_R + Q^*_t/T + nQ^*_{e^-}/T \quad [5]$$

Q^*_t is the heat of transfer of 1 mole of the positive ion with respect to which the electrode is reversible, and $Q^*_{e^-}$ is the heat of transfer of one equivalent of electrons from the electrode. ΔS_R is the change in entropy during the transfer of the ion from the electrode into the solution and is identical with Eastman's ΔS_R in Eq. [4], *i.e.*, it is the increase in entropy for the chemical reaction that occurs reversibly at the hotter electrode when n Faradays of positive electricity pass from electrode to electrolyte. Thus, for reaction [2], the above authors would write

$$\Delta S_R = \bar{S}(\mathrm{Cu^+}) - S(\mathrm{Cu}) \quad [6]$$

where, in the general case, $\bar{S}$ is the partial molal entropy of the positive ion in the solution to which the electrode is reversible. As pointed out by deBethune, *et al.* (7) the ionic entropy involved in this reaction is also an entropy of transport, and is not equal to the conventional $\bar{S}$ for a single ion. They suggest that it be called the ionic entropy of electrochemical transport and be designated by the symbol $S^*_{E_t}$. Also, they suggest that the entropy ΔS_R absorbed by the reaction at the hot electrode be referred to as the entropy of electrochemical transport and designated S^*_E. For the entropy transported through the cell by electrolytic migration, *i.e.*, the net entropy of transfer ΔS^*, they propose the term entropy of migration transport represented by S^*_M.

In terms of the latter concepts, we write for reaction [2]

$$S^*_E = S^*_E(\mathrm{Cu^+}) - S(\mathrm{Cu}) \quad [7]$$

an expression which is equivalent to ΔS_R in Eq. [4] and [5]. Also, S^*_M is identical with Eastman's ΔS^* in Eq. [4] and $S^*_{M_t}$ is the same as Temkin and Khoroshin's Q^*_t/T in Eq. [5].

Temkin and Khoroshin (14) introduced a quantity $\bar{\bar{S}}$, which they called the entropy of the moving ion, and defined it by the equation

$$\bar{\bar{S}} = \bar{S} + S^* \quad [8]$$

where $S^* = Q^*/T$. In terms of the newer concepts and nomenclature discussed above, $\bar{S}$ should be replaced by $S^*_{E_t}$, and S^* by $S^*_{M_t}$, hence for the ionic processes occurring in cell [1] (electrochemical transport and migration transport) Eq. [8] should be written,

$$\bar{\bar{S}}(\mathrm{Cu^+}) = S^*_E(\mathrm{Cu^+}) + S^*_M(\mathrm{Cu^+}) \quad [9]$$

According to Khoroshin and Temkin (15), when the Soret effect is zero $E_t = E_s$. In cell [1] the molten electrolyte consists of only one component, hence no concentration gradient can develop. The measured thermal emf, therefore, is an initial one which is also indefinitely stable, and should be given by both the Eastman Eq. [4], and by the Temkin-Khoroshin Eq. [5]. If we rewrite Eq. [4] in terms of the newer concepts as discussed above, and add a term for the entropy of the moving electron, which Eastman (13c) neglected, we have,

$$-\mathbf{F}(dE_t/dT) = S^*_E + S^*_M + \bar{\bar{S}}_{e^-(\mathrm{Cu})} \quad [10]$$

or

$$-\mathbf{F}(dE_t/dT) = S^*_E(\mathrm{Cu^+}) - \bar{\bar{S}}(\mathrm{Cu}) + t_c S^*_M(\mathrm{Cu^+}) - t_a S^*_M(\mathrm{Cl^-}) + \bar{\bar{S}}_{e^-(\mathrm{Cu})} \quad [11]$$

Similarly, for Temkin and Khoroshin's Eq. [5], for the passage of one faraday, we have

$$-\mathbf{F}(dE_s/dT) = S^*_E(\mathrm{Cu^+}) - S(\mathrm{Cu}) + S^*_M(\mathrm{Cu^+}) + \bar{\bar{S}}_{e^-(\mathrm{Cu})} \quad [12]$$

For copper electrodes in molten cuprous chloride $t_a = 0$ and $t_c = 1$, hence Eq. [11] reduces to Eq. [12] and either may be used with the temperature coefficient of the thermopotential of cell [1]. Upon combining Eq. [9] with Eq. [12] and rearranging, the following equation for the entropy of the moving cuprous ion is obtained

$$\bar{\bar{S}}(\mathrm{Cu^+}) = -\mathbf{F}(dE_s/dT) + S(\mathrm{Cu}) - \bar{\bar{S}}_{e^-(\mathrm{Cu})} \quad [13]$$

Table I gives detailed results for run number 1, and Table II summarizes the results of three separate runs comprising 56 measurements of electrode temperatures and corresponding cell potentials. It was thought the $\Delta E/\Delta T$ might vary with the average temperature of the cell or with the magnitude of ΔT, or with both, but no such variations were observed. In a particular run, ΔT was changed only slightly but the temperature of the furnace was raised through 40°-80°C and then lowered through 80°-120°C during which cycle the values for $\Delta E/\Delta T$ fluctuated around the average shown in the last column with no detectable trend. In run No. 3 the temperature difference between the electrodes was deliberately increased by placing the cell farther toward the front of the furnace where the temperature gradient was greater. Although ΔT was about doubled, $\Delta E/\Delta T$ remained constant over the temperature cycle shown. The average value for $\Delta E/\Delta T$, for all 56 measurements, is -0.436 mv/deg C and may be used for dE_s/dT giving a value of 10.05 cal/deg for the first term on the right of Eq. [13].

The average temperature of the melt varied from about 462° to 588°C (15° below 477° in run No. 2,

Table II. Summary of thermogalvanic potentials for the cell Cu | CuCl(*l*) | Cu for three runs. Hotter electrode (T_2) observed to be the negative (—) terminal

T_1 T_2

Run No.	No. temp plateaus	No. of measurements	Temp cycle for hotter electrode t_2, °C	Variation in $\Delta t = t_2 - t_1$, °C	Average $\Delta E/\Delta T$, mv/°C	Standard deviation (set), mv/°C
1	7	16	522-600-514	30-38	—0.434	0.006
2	7	18	555-596-477	30-33	—0.437	0.006
3	7	22	530-618-519	63-70	—0.437	0.005

Average $\Delta E/\Delta T$ for 56 observations = -0.436 mv/°C

Standard deviation of the set = 0.006 mv/°C

Table III. Effect of temperature on the entropy of the moving cuprous ion as calculated by Eq. [13]

Avg. temp of cell, °K	$F(dE/dT)_{th}$, cal/deg mole Cu^+	$S(Cu)$, cal/deg g-atom	$\bar{\bar{S}}_{e^-(Cu)}$, cal/deg equiv	$\bar{\bar{S}}(Cu^+)$, cal/deg mole Cu^+
735	—10.05	13.50	—0.095	23.65
798	—10.05	14.04	—0.102	24.19
861	—10.05	14.55	—0.109	24.71

to 30° below 618° in run No. 3) and the average of these values is 525°C. The last two terms on the right of Eq. [13] are evaluated from the literature for a temperature of the melt of 525°C. Temkin and Khoroshin (14) give the following equation for the entropy of the moving electrons in copper:

$$\bar{\bar{S}}_{e^-(Cu)} = -[1.95 + 0.005\,(T\text{-}300)]\ \text{microvolt-faradays/degree-equiv},\ T \geqq 240°K. \quad [14]$$

This yields $\bar{\bar{S}}_{e^-(Cu)} = -0.102$ cal/deg at 798°K. Giauque and Meads (16) have determined the molal entropy of copper and give the value $S(Cu, 298.1°) = 7.961$ cal/deg. Kelley (17) gives the following equation for the molal heat capacity of copper from 298° to 1357°K,

$$C_p = 5.41 + 1.50 \times 10^{-3}\,T \text{ cal/deg} \quad [15]$$

from which we calculate $S(Cu, 798) - S(Cu, 298) = 6.08$ cal/deg. This gives $S(Cu, 798) = 14.04$ cal/deg.

If the above values are substituted in Eq. [13] we have, at 525°C,

$$\bar{\bar{S}}(Cu^+, 798°K) = 10.05 + 14.04 + 0.10 = 24.19 \text{ cal/deg} \quad [16]$$

Similar calculations for the lowest (462°C) and the highest (588°C) average temperatures of the melt have been made. These results and the above are summarized in Table III.

The following thermocell with solid electrolyte was studied by Reinhold (8c):

$$(+)Cu(s) \,|\, \underset{T_1}{} \, CuCl(s) \,|\, \underset{T_2}{} \, Cu(s)(-) \quad [17]$$

T_2 was kept constant at 400°C and T_1 was varied from 113° to 400°C. From his equation for dE/dT as a function of ΔT we calculate, for $\Delta T = 30°C$, $dE/dT = -0.846$ mv/deg. From theoretical considerations applicable only to solid electrolytes, Holtan (9) calculates, for the same cell with T_1 between 300° and 400°C, $\Delta E/\Delta T = -0.82$ mv/deg. These values are about double our value of — 0.436 mv/deg obtained for cell [1] with molten CuCl. In this connection it is interesting to note that Holtan (9) obtained similar results for the cell,

$$(+)Ag \,|\, \underset{T_1}{} \, AgCl \,|\, \underset{T_2}{} \, Ag(-) \quad [18]$$

thermopotentials for which he measured with both solid and molten AgCl. His observed temperature coefficient of the thermopotential for molten AgCl was approximately half that for the solid electrolyte.

It is possible, by the relationship observed by Reinhold (8c) and confirmed theoretically by Holtan (9), to calculate the temperature coefficient of the thermopotential of the cell,

$$(+)Cl_2(g) \,|\, \underset{T_1}{} \, CuCl(l) \,|\, \underset{T_2}{} \, Cl_2(g)(-) \quad [19]$$

which we may designate as $(\Delta E_{19}/\Delta T)_{th}$. The measured coefficient of cell [1], $(\Delta E_1/\Delta T)_{th} = -0.436$ mv/deg, and the temperature coefficient of the emf of the isothermal cell

$$(-)Cu(s)\,|\,CuCl(l)\,|\,Cl_2(g)(+) \quad [20]$$

can be derived from results of Hamer, Malmberg, and Rubin (18), who calculated the emf of cell [20] at several temperatures up to 1500°C. From a plot of their values of E vs. T we have obtained, by graphical methods, the slope of the curve at $T = 525°C$ and find $(\Delta E_{20}/\Delta T)_{isoth} = -0.220$ mv/deg at 525°C. By Reinhold's rule, which has been demonstrated by deBethune, *et al.* (7) and by Holtan and Krogh-Moe (19), these coefficients are related as follows

$$(\Delta E_{20}/\Delta T)_{isoth} = (\Delta E_{19}/\Delta T)_{th} - (\Delta E_1/\Delta T)_{th} \quad [21]$$

Upon substituting in Eq. [21] the measured value for cell [1] and the derived value for cell [20] we find,

$$(\Delta E_{19}/\Delta T)_{th} = -0.656 \text{ mv/deg at } 525°C \quad [22]$$

The result obtained in Eq. [22] is probably only approximate since it depends not only on the accuracy of our measurements for cell [1], and the reliability of the thermodynamic data used by Hamer, *et al.* in calculating emf's for cell [20], but also on the errors inherent in the graphical differentiation of their results.

Manuscript received Dec. 15, 1959.

Any discussion of this paper will appear in a Discussion Section to be published in the June 1961 JOURNAL.

REFERENCES

1. T. Richards, *Z. Physik. Chem.*, **24**, 39 (1897).
2. G. J. Janz, "Electrode Processes, E.M.F." in "Bibliography on Molten Salts," pp. 24-30, Rensselaer Polytechnic Institute, Troy, N. Y. (1958).
3. S. Senderoff and A. Brenner, *This Journal*, **101**, 31 (1954).
4. Yu. K. Delimarskii, *Zhur. Fiz. Khim.*, **29**, 28 (1955).
5. J. O'M. Bockris, G. J. Hills, D. Inman, and L. Young, *J. Sci. Instr.*, **33**, 438 (1956).
6. S. N. Flengas and T. R. Ingraham, (a) *Can. J. Chem.*, **35**, 1139 (1957); (b) **35**, 1254 (1957); (c) **36**, 780 (1958); (d) **36**, 1103 (1958); (e) **36**, 1063 (1958); (f) *This Journal*, **106**, 714 (1959).
7. A. J. deBethune, T. S. Licht, and N. Swendeman, *This Journal*, **106**, 616 (1959); A. J. deBethune, *ibid.*, **107**, 829 (1960).
8. H. Reinhold, (a) *Z. anorg. Chem.*, **171**, 181 (1928); (b) *Z. phys. Chem. (B)*, **11**, 321 (1931); (c) H. Reinhold and A. Blachny, *Z. Electrochem.*, **39**, 290 (1933).
9. H. Holtan, Jr., Electric Potentials in Thermocouples and Thermocells, Thesis, Utrecht, (1953).
10. T. S. Licht and A. J. deBethune, *J. Chem. Education*, **34**, 433 (1957).
11. C. Soret, *Ann. chem. phys.*, [5] **22**, 293 (1881).
12. J. N. Agar and W. G. Breck, *Trans. Faraday Soc.*, **53**, 167 (1957).
13. E. D. Eastman, (a) *J. Am. Chem. Soc.*, **48**, 1482 (1926); (b) **50**, 283 (1928); (c) **50**, 292 (1928).

14. M. I. Temkin and A. V. Khoroshin, *Zhur. Fiz. Khim.*, **26**, 500 (1952).
15. A. V. Khoroshin and M. I. Temkin, *ibid.*, **26**, 773 (1952).
16. F. W. Giauque and P. F. Meads, *J. Am. Chem. Soc.*, **63**, 1897 (1941).
17. K. K. Kelley, Bull. 476, U. S. Bureau of Mines, p. 63 (1949).
18. W. J. Hamer, M. S. Malmberg, and B. Rubin, *This Journal*, **103**, 8 (1956).
19. H. Holtan, Jr., and J. Krogh-Moe, *Acta Chem. Scand.*, **9**, 1022 (1955).

Cathodic Processes on Passive Zirconium

Robert E. Meyer

Chemistry Division, Oak Ridge National Laboratory, Oak Ridge, Tennessee[1]

ABSTRACT

Measurements were made of the rates of reduction of various oxidizing agents on passive zirconium in acid solutions of sodium sulfate at temperatures ranging from 25° to 85°C. The oxidizing agents included in these experiments were oxygen, hydrogen ion, and cupric ion and hydrogen peroxide in the presence of oxygen. The kinetic orders of reduction were determined from potentiostatic experiments in which the current was determined as a function of concentration. Unit and fractional orders were observed with oxygen reduction, and fractional orders from about 0.5 to 0.65 were observed for Cu^{++} and H_2O_2. Possible mechanisms are suggested in which charge transfer through the film is assumed to play a predominant role.

The study of electrochemical reduction on the surface of film-covered electrodes has received comparatively little attention. The usual goal in studies of reduction processes is to measure rates on bare metals, and therefore care is taken to remove any films that may be present. It is clear, however, that the presence of a film can markedly influence the reduction processes at the surface by affecting the energetics of the reaction at the double layer, or by imposing a barrier to charge transfer through the film, or both. The study of reduction processes on film-covered electrodes is important to the field of corrosion for the corrosion of metals that form surface films over the entire surface of the metal must necessarily involve the reduction of the oxidizing agent on the surface of the film.

Zirconium is known to form a film, presumably of ZrO_2, when in contact with O_2 in aqueous solution. The standard potential (1) for the half-reaction $Zr + 2H_2O = ZrO_2 + 4H^+ + 4e^-$ is −1.43 v. It is evident from this potential that ZrO_2 is thermodynamically stable under potentials at which such oxidizing agents as O_2, H_2O_2, and H^+ are easily reduced. Furthermore, measurements made in O_2-saturated 0.1*M* Na_2SO_4 (pH ~ 4) showed that the rate of formation of ZrO_2 at potentials in the vicinity of SCE falls off to values on the order of 10^{-8} to 10^{-9} amp/cm^2 after a few days (2). Therefore it should be possible to study reduction processes on film-covered zirconium without significant interference from the film-forming reactions. It is found, in practice, that determinations of reduction rates are reasonably reproducible on a given sample, and therefore it is safe to conclude that the effect of reduction experiments on the surface of the electrode is slight.

[1] Operated by Union Carbide Corporation for the U. S. Atomic Energy Commission.

In the experiments described here, attention was centered on the reduction of H^+, O_2, and Cu^{++} and H_2O_2 in the presence of O_2. It was found that reasonable steady states could not be achieved with Cu^{++} and H_2O_2 if attempts were made to remove O_2. All measurements were made on electrodes after the corrosion reaction had decayed to a negligible rate.

Theory

For the present purposes the following equation will be assumed as representing the reduction current at an electrode:

$$i_c = K \pi_i (a_i^{p_i}) \exp \frac{-\alpha_c z_c E F}{RT} \qquad [1]$$

where i_c is the reduction current density, $\pi (a_i^{p_i})$ is the product of the activities of the reactants raised to the appropriate orders p_i, $\alpha_c z_c$ is the product of the transfer coefficient and the charge number, and E is the potential of the electrode measured with respect to the reference electrode. The value of K will depend on the particular reference electrode chosen. From experimental data, one can determine K, the orders, and the product $\alpha_c z_c$, and therefore determine information of mechanistic significance.

The product $\alpha_c z_c$ is determined from the slope of the log-current density vs. potential plot and is calculated from the derivative:

$$\frac{\partial \log i_c}{\partial E} = \frac{-\alpha_c z_c F}{2.303\, RT} \qquad [2]$$

The orders are determined in experiments in which the electrode is held at constant potential and the activity of a reactant is increased by progressive additions of concentrated solutions. The orders are calculated from the derivative (3):

$$\frac{\partial \log (i_c - i_{c,o})}{\partial \log a_i} = p_i \qquad [3]$$

where $i_{c,o}$ is the initial current density before additions of the reactant. Actually all of the desired information can be obtained either from a series of galvanostatic (constant i) experiments at various activities or by a series of potentiostatic experiments at various potentials. However, if the electrodes vary somewhat in their properties from day to day, it is better to do both types of experiments since αz factors can be obtained more accurately from galvanostatic experiments and orders can be determined more precisely from potentiostatic experiments.

Experimental

Preliminary experiments showed that great precautions had to be taken in order to obtain reproducible data. In particular, the electrodes had to be prepared carefully and the solution and cells thoroughly freed from impurities.

The electrodes were cylinders machined from ¼ in. crystal-bar zirconium and had an area of 2.2 cm². Before use they were cleaned, chemically polished in H_2O-HNO_3-HF solution, rinsed in boiling triply distilled water, and vacuum annealed for several hours at 750°-800°C. Immediately before use they were removed from vacuum, mounted on Teflon holders, and placed in the cell. Such a procedure involved a few minutes' exposure to air, and therefore the electrodes undoubtedly had a thin oxide film on their surface before being introduced into the cell.

All solutions were made from triply distilled water, one distillation of which was made from alkaline permanganate. The sodium sulfate used was doubly recrystallized and the sulfuric acid was prepared by dilution of the C.P. grade. Solutions were pre-electrolyzed for at least 24 hr before use between platinum electrodes with a current of 5-10 ma. The potential of the platinum cathode was well below the lowest potential used on the zirconium electrodes.

The cells were made from Pyrex and Teflon and no greases, waxes, or other sources of surface-active impurities were used in the cell. The cells were thoroughly cleaned before use, and in most of the experiments the final rinse water and the water used for the solutions was distilled directly into the cell.

Potentials were measured by a L&N model 7664 pH and emf meter coupled to a 10-mv Brown recorder. This apparatus was calibrated periodically with a potentiometer and had an accuracy of ± 1 mv on a 1000-mv scale and ± 0.5 mv on a 100-mv scale. Currents were measured by this same unit by measuring the potential drop across precision resistors. In the constant-potential determinations of the orders, an electronic potentiostat developed at this laboratory was used.

Results

Oxygen reduction.—All measurements of oxygen reduction were made in 0.1*M* Na_2SO_4 of varying pH at temperatures in the interval 25°-88°C. Measure-

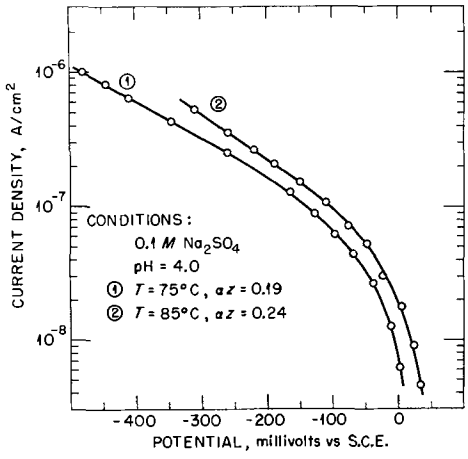

Fig. 1. Oxygen reduction on passive zirconium

ments at the lower temperatures were sluggish, and therefore most of the galvanostatic work was done at 75° and 85°C (Fig. 1). In all cases steady-state values only were used in calculating Tafel slopes. In general, points were taken after the potential showed no drift (< 1 mv) in a period of 5-20 min, depending on the current densities. Slow drifting occurred occasionally but was usually eliminated if the solution were changed and freshly pre-electrolyzed solution admitted. In preliminary experiments, almost all of the samples gave values of αz between 0.18 and 0.35 with 0.25 being an approximate average. In order to obtain a better estimate of $\alpha_c z_c$, three electrodes were prepared under carefully reproduced conditions. These samples showed $\alpha_c z_c$ values of 0.28, 0.32, and 0.33 one day after initial immersion at 75°. There was evidence that at very low current densities, i.e., below ~ 10^{-7} amp/cm², the Tafel slope changed to give a somewhat higher $\alpha_c z_c$. The exact value could not be determined precisely because the potentials at these current densities were too close to the rest potential.

The determination of the reaction order at high concentration of O_2 was carried out potentiostatically by passing pure He, mixtures of He and O_2, and pure O_2 through the cell. At low concentrations of O_2, varying quantities of O_2 were introduced into the cell by anodic evolution on Pt with a closed cell (using an external cathode). Constant current density was used so that the total amount of oxygen present was proportional to the total charge passed. Some of the results are shown in Fig. 2 and 3. In

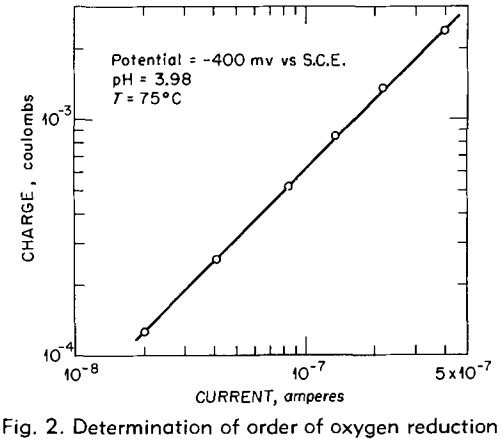

Fig. 2. Determination of order of oxygen reduction

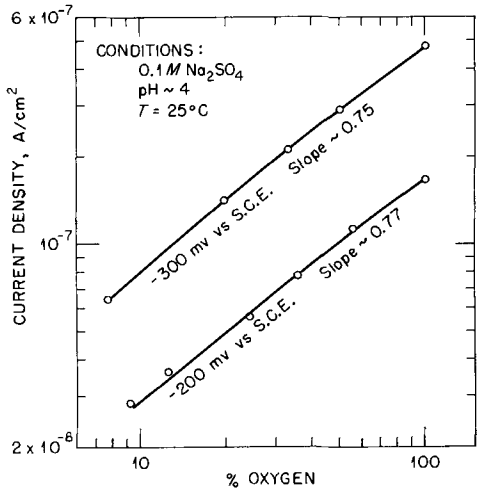

Fig. 3. Determination of order of reduction of oxygen

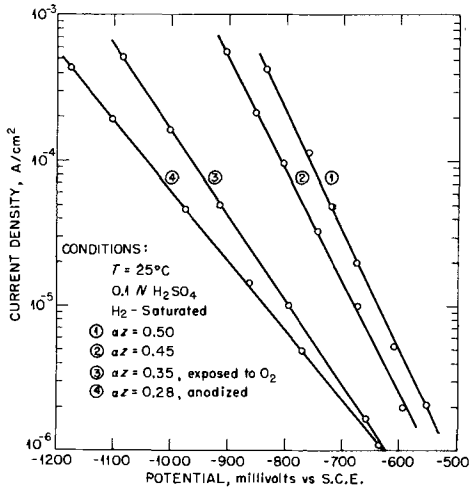

Fig. 4. H^+ reduction on zirconium

Fig. 2, current density is obtained by dividing by 2.2 cm^2, the electrode area. All of the results taken together showed that, for a given electrode under constant conditions, fractional orders of from 0.7 to 0.8 were obtained at high current densities and unit orders were observed at low current densities. For an electrode at 75°, the order slopes changed from unity to fractional in the region 2-5 x 10^{-7} amp/cm^2.

The effect of changing the *p*H at low current densities was to increase the potential by approximately *RT/F* for every *p*H unit decrease in the pH range 2-5. At higher current densities the change was complicated by drifting but the change seemed to be less than *RT/F*. The application of Eq. [3] did not give reproducible orders.

An attempt was made to determine the limiting current due to diffusion with a sample that was unusually stable. By limiting polarization at high current densities to a few minutes, it was possible to estimate roughly the limiting current density as 150 μa/cm^2 for O_2 saturated solutions at 75° (concentration $\approx$ 5 x $10^{-4}M$ and *p*H = 2.75).

In order to check for any possible *IR* drop during polarization, current decay measurements were made with an oscilloscope (Tektronix 536). Using a sensitivity of 1 mv/cm and a current density of about 5 x 10^{-7} amp/cm, no detectable *IR* drop was observed when the current was interrupted.

Hydrogen ion reduction.—The reduction of hydrogen ions was carried out in hydrogen-saturated solutions on electrodes treated in various ways as described below. Unless otherwise mentioned all experiments were carried out at 25°C in H_2-saturated 0.1*N* H_2SO_4. Most of the electrodes were introduced directly into H_2-filled solution-free cells and solution was added only after H_2 was passed through the cell for several hours.[2] When H_2-saturated solution was admitted to the cell, the initial potentials of the zirconium electrode were well below the reversible H_2 potential because of the corrosion reaction $Zr + 2H_2O \rightarrow ZrO_2 + 2H_2$. However, the rate of this reaction decreased rapidly with time and, after an hour, polarization measurements were began. Usually linear Tafel plots were obtainable with electrodes treated this way and two examples are shown as curve No. 1 and 2 in Fig. 4. In general, the slopes were such as to give αz factors of 0.4-0.5, which is frequently observed in hydrogen-evolution experiments on other metals.

If oxygen were admitted to the cell, the potential would rise rapidly before leveling off. After several days the O_2 was removed and Tafel plots such as is shown as No. 3 of Fig. 4 were obtained. A similar effect was produced by anodizing in the absence of O_2 as shown by curve No. 4. Both of these curves show linear Tafel plots but low $\alpha_c z_c$ factors (0.35 and 0.28, respectively).

The effect of *p*H was investigated by preparing an alkaline 0.1*M* Na_2SO_4 solution and decreasing the *p*H by the progressive addition of small quantities of H_2-saturated 2*N* H_2SO_4. The temperature was 25°C and the electrodes were exposed only to H_2-saturated solution before the effect of *p*H was investigated. The electrode therefore had only that small amount of film that would be formed by reaction with hydrogen ions. Results are shown in Fig. 5. In alkaline solution there was no change in current at constant potential with change in *p*H and in acid solution a change of about 60 mv/*p*H unit was observed at constant current. The pH was measured by forcing out several milliliters of solu-

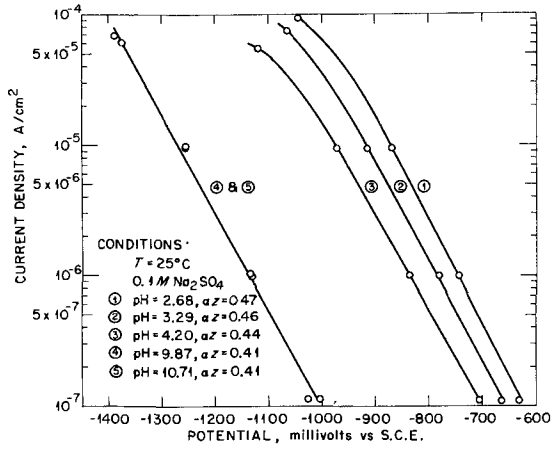

Fig. 5. pH Dependence of H^+ reduction on zirconium

[2] The H_2 was purified with an all Pyrex train containing Drierite, Hopcalite (for CO removal), Ascarite, liquid nitrogen traps, and hot catalyst (either Pd or Cu).

tion through a Teflon valve into an O_2-free container and using a glass electrode with a Beckman Model G pH meter. Results are consistent with discharge from H_2O in basic solution and discharge from hydrogen ions in acid solution.

Reduction of Copper II and H_2O_2.—As mentioned above, the Cu^{++} and H_2O_2 reduction experiments were carried out in the presence of O_2. Because of the decomposition of H_2O_2 at 66°C, the oxygen could not be removed completely in the H_2O_2 experiments. Temperatures had to be maintained at 66°C or higher because at lower temperatures the rates were too slow to measure accurately. The concentrations were changed by precisely measuring out small quantities of concentrated stock solutions of known concentration. Electrodes were prepared in the manner described above, and the corrosion reaction was allowed to decay for several days before measurements were made. All experiments were carried out at constant ionic strength (0.1*M* Na_2SO_4).

Results are shown in Fig. 6 and 7. The order of reduction of Cu^{++} as determined from the slope $\partial \log (i—i_o)/\partial \log a$ varied from 0.66 to 0.61. The orders with respect to H_2O_2 reduction were also fractional, but the slopes varied from about 0.40 to 0.66 as shown in Fig. 7. A possible explanation for these unusual orders is presented below. Tafel slopes could not be measured directly in this case since reasonable steady states were not attained in the absence of oxygen. Potential-current curves taken in the presence of oxygen represent the reduction of both O_2 and Cu^{++} (or H_2O_2) and there may be interaction between them. The Tafel slope can be estimated roughly by taking current-potential points from lines of constant concentration in Fig. 6 and 7. Using this method the slope for copper reduction varied from somewhat greater than RT/F ($\alpha_c z_c \approx 1$) at low current densities to almost $3RT/F$ ($\alpha_c z_c \approx 1/3$) at high current densities and for H_2O_2 the slope was about $4RT/F$.

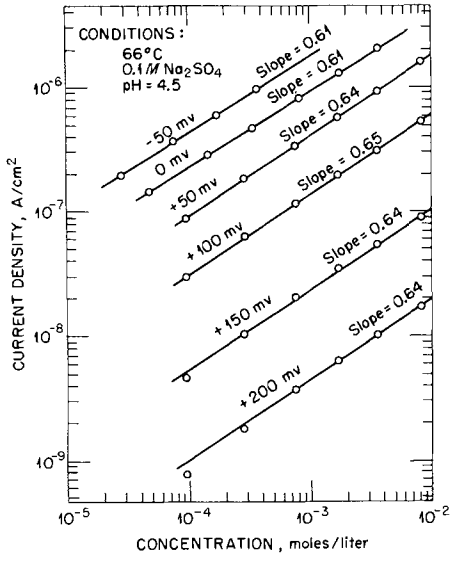

Fig. 6. Reduction of copper(II) on passive zirconium

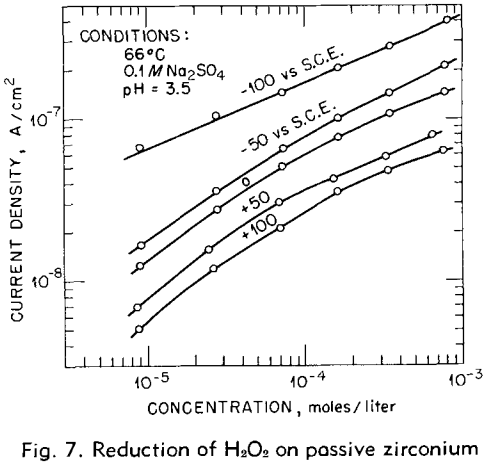

Fig. 7. Reduction of H_2O_2 on passive zirconium

Discussion

In the discussion of these results, it is important to keep in mind that the results described here may be valid only for films prepared as described above. Films which are prepared by higher temperature gaseous oxidation or by anodizing to high voltages are not necessarily similar in kinetic properties to those described here.

The films formed in these experiments are not assumed to be uniform, since the various inhomogeneities at the surface should cause local variations in the nature and amount of the film. This lack of uniformity may cause large variations in current density across the surface of the electrode[3] but it does not invalidate the use of Eq. [1]. This point has been discussed in detail by Posey (3).

Pores or cracks are sometimes suggested as being present in films of this sort. However, at the potentials of these experiments any exposure of bare metal through defects of this type is unlikely. It must be remembered that these potentials are almost 2 v above the equilibrium potential of the reaction $Zr + 2H_2O \rightarrow ZrO_2 + 4H^+ + 4e^-$ and that zirconium is an extremely reactive metal. The arguments against the existence of pores in passive films on iron have been given by Vetter (4) and similar arguments apply to zirconium. Further, the limiting current measurements show that the effective area of the electrode is not significantly smaller than the apparent area. Thus, the experimental figure of 150 $\mu a/cm^2$ should be compared to values of from 80 $\mu a/cm^2$ to 4×10^3 $\mu a/cm^2$ calculated from the well-known equation, $i_l = zFDC/l$ where D is the diffusion coefficient, C is the concentration in moles/cm³, and l is the thickness of the diffusion layer. Values of $D = 2 \times 10^{-5}$ cm²/sec, $z = 4$, $C = 5 \times 10^{-7}$ moles/cm³, and l varying from 0.05 to 10^{-3} cm were taken. Since the experimental measurement was taken under conditions of slight stirring (a slow stream of gas bubbles at the side of the cell), it is clear that the effective area is of the same order of magnitude as the apparent area. This observation is difficult to reconcile with any hypothesis which suggests that only a few pores or singularities are responsible for charge transfer through the film.

Any mechanism of reduction must however take into account the fact that the presence of this film may cause charge transfer through the film to affect

[3] This may also be a cause of the difference observed in different specimens since it is clearly impossible to duplicate the surface of a given specimen.

the over-all kinetics. For very thick films of high resistivity, the film barrier can simply be regarded as *IR* drop, but for the thin films considered here (20-100Å) such an explanation cannot be used. For the reasons described below, it seems better to interpret the data given here on the basis of a potential barrier within the film such that the current, which is assumed to be electron current, is given by the exponential expression, $I \sim \exp -\alpha V/kT$.

According to the original Mott-Cabrera (5) theory of thin film formation on metals, an electric field is formed across the film by electrons which leave the metal surface and find their way to O_2 adsorbed on the surface. The rate-determining step is assumed to be the movement of metal ions through the metal-oxide interface under the influence of the field. However, as Cabrera points out later (6) the transport of electrons through film will also be under the influence of this field, and for all but the thinnest films, the transport of the electrons should also affect the rate.

In the case of zirconium it was shown by the author (2) that a rate law in reasonable agreement with experiment can be derived under the assumption that both ion transport (an anodic process) and the reduction of oxygen were rate-determining. The assumption was made that the reduction current was proportional to $\exp(-\alpha_c z_c V_f/kT)$ where V_f is the potential across the film. The resulting rate-time expression is roughly hyperbolic in rate and time but does not permit a simple exact analytical expression. The important point here is that a fit of the data is obtained if the reduction process is considered a function of the potential across the film and that it too is rate-determining.

Because of the above considerations it is felt that a reduction process on these zirconium electrodes involves charge transfer through the film as well as the usual charge transfer process at the interface. Furthermore, the fractional orders and the unusually low αz factors obtained from the reduction experiments can be best explained from the above assumptions. Before this can be explained the formal mathematics must be stated.

For the purpose of describing these kinetics two cases of a dual-barrier model are used. Case I assumes that, if a reduction process is occurring at a steady-state, two potential-dependent reactions occur at equal rates, the one corresponding to the film reaction and the other to the surface double layer reaction. The rates of the individual reactions can be represented by the two equations:[4]

$$i = K_f \pi_i (a_{i,f}^{p_{i,f}}) \exp(-\alpha_f z_f V_f/kT) \qquad [4]$$

$$i = K_s \pi_j (a_{j,s}^{p_{j,s}}) \exp(-\alpha_s z_s V_s/kT) \qquad [5]$$

where V_f and V_s are the separate potential drops affecting the two different barriers. The activities for the solution reaction are to be taken as the ordinary solution activities. Depending on the nature of the film reaction, the activities in Eq. [4] may represent the effective concentration of electrons, holes, etc., or in some cases may represent the concentration of adsorbed species on the surface of the electrode. Thus, if the film reaction were the transfer of an electron over the potential barrier to adsorbed oxygen, the reaction rate would depend on the number of electrons striking the barrier, the number of O_2 molecules adsorbed, and the probability of electron transport across the barrier.

The over-all measured potential E will be equal to $V_f + V_s + V_k$ where V_k is the constant sum of all of the other potential drops occurring in the measuring circuit. Combining this relation with Eq. [4] and [5] by eliminating V_f and V_s one obtains:

$$i = K_t [\pi_{i,f}(a_{i,f}^{p_{i,f}})^{\frac{\alpha_s z_s}{\alpha_f z_f + \alpha_s z_s}}] [\pi_{j,s}(a_{j,s}^{p_{j,s}})^{\frac{\alpha_f z_f}{\alpha_f z_f + \alpha_s z_s}}] \exp\frac{-\alpha_t z_t E}{kT} \qquad [6]$$

where

$$\alpha_t z_t = \frac{\alpha_f z_f \alpha_s z_s}{\alpha_f z_f + \alpha_s z_s}$$

and

$$K_t = \left(\exp\frac{\alpha_f z_f \alpha_s z_s V_k}{(\alpha_f z_f + \alpha_s z_s) kT}\right) K_f^{\frac{\alpha_s z_s}{\alpha_s z_s + \alpha_f z_f}} K_s^{\frac{\alpha_f z_f}{\alpha_s z_s + \alpha_f z_f}}$$

Therefore

$$\frac{\partial \ln i}{\partial E} = \left(\frac{-\alpha_f z_f \alpha_s z_s}{\alpha_f z_f + \alpha_s z_s}\right) \times \frac{1}{kT} \qquad [7]$$

and

$$\frac{\partial \log i}{\partial \log a_{i,f}} = \frac{p_{i,f}\alpha_s z_s}{\alpha_f z_f + \alpha_s z_s} \qquad [8]$$

and

$$\frac{\partial \log i}{\partial \log a_{j,s}} = \frac{p_{j,s}\alpha_f z_f}{\alpha_f z_f + \alpha_s z_s} \qquad [8a]$$

Equation [6] predicts that the apparent orders as measured by $\partial \log i/\partial \log a$ will be the true order p multiplied by a fraction. This will be true only if all activities are completely independent of each other so that the activity in question can be varied without affecting the values of the activities at either of the barriers. If an activity affecting one barrier is a function of the activity of a reactant of the other, i.e., if $a_s = f(a_f)$, then

$$\left(\frac{\partial \log i}{\partial \log a_f}\right)_E = \frac{p_i \alpha_s z_s}{\alpha_f z_f + \alpha_s z_s} + \frac{p_j \alpha_f z_f}{\alpha_f z_f + \alpha_s z_s}\left(\frac{\partial \log a_s}{\partial \log a_f}\right)_E \qquad [9]$$

If a_s is proportional to a_f, the derivative $\partial \log a_s/\partial \log a_f$ will be unity and, if both p's are unity, the over-all order will be unity.

Although the order determinations were carried out at constant over-all potential, it is still possible that V_f and V_s may have varied, subject to the condition that their sum is constant. If the solution concentration of the oxidizing agent is increased,

[4] One might justifiably object to the use of this rate equation for the film reaction. In this derivation, it is to be regarded purely as a formal equation giving the current as a function of the activities and the potential for a film at constant thickness. The constants K_f and α_f are not necessarily analogous in their theoretical interpretation to K_s and α_s in the rate equation representing the surface reaction.

this will cause an increase in current at the double layer (or through the film if it is adsorbed and affects the film barrier). In order that a steady state be maintained, the potentials V_f and V_s must readjust. The effect of this is described mathematically by Eq. [8], in which it is shown that the apparent order will be p multiplied by a fraction.

Using Eq. [8a], it is possible to predict that lowering $\alpha_f z_f$ will lower the apparent order. Since it was observed experimentally that the thicker the film the lower the $\alpha_t z_t$ coefficient for H^+ and O_2 reduction, it was assumed that this was due to a decrease of $\alpha_f z_f$. Therefore a specimen was anodized to a light blue color (16 v) and reduction of Cu^{++} was carried out with this electrode. The log a vs. log $(i—i_o)$ slope was not linear, but in no portion of the curve was the slope greater than 0.3, as would be predicted qualitatively from Eq. [8a].

Alternatively the fractional orders may be explained by the assumption of an adsorption isotherm such that the activity at the surface is not directly proportional to the activity in the bulk of the solution. This however seems somewhat more arbitrary than the explanation involving the dual barrier. Also, one would have to assume that the same adsorption isotherm holds for H_2O_2 and Cu^{++} since they both give about the same order.

Equation [7] also predicts that the observed $\alpha_t z_t$ will generally be smaller than either $\alpha_s z_s$ or $\alpha_f z_f$. The unusually low transfer coefficients observed in these experiments may be explained on this basis. Thus, if $\alpha_f z_f = \alpha_s z_s = 0.5$, $\alpha_t z_t$ will be 0.25. For O_2 reduction, it is possible to calculate that $\alpha_s z_s = 1.2$ and $\alpha_f z_f = 0.4$, using the fact that the observed order, 0.75, $= \alpha_s z_s/(\alpha_s z_s+\alpha_f z_f)$ and the observed $\alpha_t z_t$, 0.31, $= (\alpha_s z_s \alpha_f z_f)/(\alpha_f z_f+\alpha_s z_s)$. Here it is arbitrarily assumed that oxygen affects the film barrier. The experimental determinations of the apparent order and the apparent Tafel slope are, however, not considered precise enough to warrant accurate calculations of $\alpha_f z_f$ and $\alpha_s z_s$.

The second case that might occur in this system is that which occurs when one of the reactions is essentially at equilibrium. In this case a Nernst-like expression may be used for the potential of the barrier at equilibrium and the normal rate equation for the other. A steady potential across the barrier at equilibrium will be achieved if the activities affecting this barrier remain constant. For the barrier at equilibrium, we may write

$$V_1 = V_{1,0} + \frac{RT}{nF} \ln \frac{\pi a^r_{1,ox}}{\pi a^s_{1,red}} \qquad [10]$$

The standard rate equation, e.g., Eq. [4] or [5], along with the relation $V_1 + V_2 = V_t$ gives:

$$i = K_2(\pi_3 a_2^{p_2}) \left(\frac{\pi a^r_{1,ox}}{\pi a^s_{1,red}} \right)^{\frac{\alpha}{n}} \exp \frac{+\alpha z V_{1,0}}{kT} \exp \frac{-\alpha z V_t}{kT} \qquad [11]$$

The following derivatives are obtained from Eq. [11]:

$$\frac{\partial \log i}{\partial \log a_2} = p_2 \qquad [12]$$

$$\frac{\partial \log i}{\partial \log a_{1,ox}} = r \frac{\alpha}{n} \qquad [13]$$

and

$$\frac{\partial \ln i}{\partial V_t} = -\frac{\alpha z}{kT} \qquad [14]$$

Thus it is possible to obtain either unit or fractional orders in this case depending on whether the added constituent affects the barrier at equilibrium or not. It must be emphasized that the added constituent cannot affect any of the other activities; otherwise Eq. [12] and [13] are not valid.

It is therefore possible for the models proposed here to account for the fractional orders and low values of αz without resorting to unusual adsorption isotherms. Furthermore, the postulate of two barriers seems quite reasonable on film-covered electrodes of this type. There is not enough experimental evidence, however, to say fairly conclusively that these models are valid, or further to give explicit mechanisms for the reduction of the various oxidizing agents. The primary purpose of the presentation was to show that it is possible to obtain these effects from the two-barrier model.

It should be pointed out that two of the effects that do not seem to conform to Case I can be explained by assuming that Case II applies at low current densities. Thus, the fact that unit order is observed with oxygen reduction at low current densities can be explained by assuming that oxygen is adsorbed at the interface and that the rate-determining step is the transfer of electrons through the film barrier to the O_2 at the surface with the ultimate formation of a negatively charged oxygen-containing species, perhaps OH^-. Charge transfer through the surface is effected by a slight perturbation of the equilibrium OH^- (ads.) + $H_3O^+ \rightleftarrows 2H_2O$. The amount of OH^- adsorbed would probably be relatively constant since most of the oxide ions exposed to solution would probably react to form OH^-. At high current densities this equilibrium would be polarized and Case I would apply. This equilibrium also agrees with the observed pH dependence.

Similarly the change of the Tafel slope of Cu^{++} reduction may indicate a change from Case I to Case II with the difference that Cu^{++} (aq.) may not be adsorbed but may affect only the outer barrier. In both of these cases there is not enough experimental evidence to propose specific mechanisms.

The precise mechanism of charge transfer through the film is open to speculation since little is known concerning the structure and semiconducting properties of these films. For the reasons described above, cracks or pores were rejected as a mechanism for charge transfer. Tunnel effect should be extremely dependent on thickness and its effects are probably slight for the stable films present after a day's exposure to O_2. The data on H_2 evolution, however, show large changes in current at constant potential. It is suggested, therefore, that the initial

film present on the samples used in the H_2 overvoltage work is relatively transparent to electrons because of the tunnel effect. The growth of the oxide on the surface then causes a sharp reduction in the rate of tunneling.

In order for electrons to be transferred through the stable films formed by anodizing or exposure to O_2, electrons must *surmount* the barrier imposed by the field in the film. This of course results in very low rates at room temperature and even at 88°C the electrodes will reach rates of about 10^{-9} amp/cm^2 at open circuit after several days. The important parameter here is therefore the height of the potential energy barrier and the rate of transfer should therefore not be so sensitive to changes in thickness. To a good approximation therefore, the rate of transfer will be given by $i = K \exp - eV/kT$ where eV represents the height of the potential energy barrier.

Acknowledgment

The kind encouragement and helpful discussions of Dr. G. H. Cartledge, Dr. F. A. Posey, and Dr. A. L. Bacarella, all of this Laboratory, are gratefully acknowledged.

Manuscript received Jan. 18, 1960. This paper was prepared for delivery before the Chicago Meeting, May 1-5, 1960.

Any discussion of this paper will appear in a Discussion Section to be published in the June 1961 JOURNAL.

REFERENCES

1. W. M. Latimer, "Oxidation Potentials," p. 271, Prentice-Hall, New York (1952).
2. R. E. Meyer, *This Journal*, **106**, 930 (1959).
3. F. A. Posey, *ibid.*, **106**, 571 (1959).
4. K. J. Vetter, *Z. Elektrochem.*, **55**, 274 (1951).
5. N. Cabrera and N. F. Mott, *Repts. Prog. Phys.*, **12**, 163 (1948-49).
6. N. Cabrera, "The Oxidation of Metals," in "Semiconductor Surface Physics," p. 327, University of Pennsylvania Press, Philadelphia (1957).

Technical Note

Crystallographic Data on Beta-$Sr_2P_2O_7$

C. W. W. Hoffman and R. W. Mooney

Chemical and Metallurgical Division, Sylvania Electric Products Inc., Towanda, Pennsylvania

The tin-activated alkaline-earth pyrophosphates have been studied by three groups of workers (1-3) with the discovery of several phosphors. Calcium, strontium, and barium pyrophosphate occur in polymorphic modifications and Ranby and co-workers (1) showed that α-modifications were orthorhombic and probably isomorphous. It was also suggested that β-$Ca_2P_2O_7$ and β-$Sr_2P_2O_7$ were probably isomorphous although no crystallographic data were given. Recent work (3) has shown that there is a relationship between the emission and perhaps the excitation spectra of the three tin-activated α-modifications as well as a marked similarity between the excitation and emission spectra of β-$Ca_2P_2O_7$:Sn and β-$Sr_2P_2O_7$:Sn.

In a recent publication, Corbridge (4) working with single crystals of β-$Ca_2P_2O_7$ showed that it was tetrahedral with space group $P4_1$, and cell dimensions: a = 6.66Å and c = 23.86Å. Assuming a similar tetrahedral unit cell for β-$Sr_2P_2O_7$, it turned out to be a straightforward task to index its Debye-Scherrer pattern resulting in a = 6.920Å and c = 24.79Å. Table I lists the observed intensities and the slightly refined d-spacings, (omitting a very weak line at d = 3.30 which has been found to be in error), from a recent publication (5). It is evident that the calculated d-spacings based on the proposed unit cell account very well for the pattern.

Table I. X-ray powder data for β-$Sr_2P_2O_7$

I	d (obs)	d (calc.)	hkl
12	4.86	4.89	1 1 0
		4.80	1 1 1
5	4.54	4.55	1 1 2
9	4.20	4.21	1 1 3
8	3.544	3.548	1 0 6
32	3.460	3.460	2 0 0
44	3.427	3.427	2 0 1
60	3.333	3.333	2 0 2
25	3.193	3.192	2 0 3
20	3.156	3.157	1 1 6
		3.153	1 0 7
100	3.099	3.099	5 0 8
		3.095	2 1 0
45	3.076	3.071	2 1 1
35	3.023	3.021	2 0 4
	3.006	3.003	2 1 2
25	2.902	2.898	2 1 3
22	2.870	2.869	1 1 7
20	2.839	2.838	2 0 5
11	2.772	2.769	2 1 4
11	2.652	2.653	2 0 6
15	2.626	2.625	2 1 5
10	2.475	2.477	2 1 6
		2.475	2 0 7
15	2.439	2.435	2 2 1
12	2.403	2.400	2 2 2
6	2.344	2.346	2 2 3
17	2.307	2.307	3 0 0
6	2.278	2.276	2 2 4
9	2.225	2.222	3 0 3
12	2.186	2.188	3 1 0
26	2.161	2.162	3 0 4
		2.155	3 1 2
		2.155	2 0 9
8	2.110	2.115	3 1 3
		2.105	2 2 6
25	2.063	2.066	5 1 2
		2.064	3 1 4
23	2.016	2.015	2 0 10
		2.014	3 0 6
		2.013	2 2 7
8	1.937	1.935	2 1 10
		1.934	3 1 6
		1.933	3 0 7
12	1.924	1.920	2 2 8
	1.918	1.919	3 2 0
8	1.901	1.903	1 1 12
		1.897	3 2 2
11	1.824	1.833	3 2 4
		1.829	2 2 9
		1.822	2 1 11
10	1.791	1.790	3 2 5
		1.788	3 1 8
10	1.743	1.741	3 2 6
11	1.678	1.678	4 1 0
		1.675	4 1 1
12	1.667	1.666	4 0 4
5	1.634	1.634	4 0 5
		1.632	3 2 8
6	1.594	1.596	4 0 6
6	1.557	1.555	4 1 6
		1.554	4 0 7
6	1.521	1.521	4 2 3

The sample of β-$Sr_2P_2O_7$ had been prepared by heating $SrHPO_4$ for several hours at 650°C giving a material whose analysis agreed generally with the theoretical composition of $Sr_2P_2O_7$ (5). Assuming, as

with β-$Ca_2P_2O_7$, 8 $Sr_2P_2O_7$ groups per unit cell a theoretical density of 3.91 g/cm^3 results, in good agreement with the experimental value of 3.86 g/cm^3 (5). In view of the marked similarities between the β-$Ca_2P_2O_7$ and β-$Sr_2P_2O_7$ powder patterns, it is likely that the compounds have the same space group, namely $P4_1$, although single crystal work would be required to definitely establish the space group of β-$Sr_2P_2O_7$.

Acknowledgment

The authors are indebted to Mr. R. C. Ropp for the preparations of several β-$Sr_2P_2O_7$ samples.

Manuscript received May 18, 1960.

Any discussion of this paper will appear in a Discussion Section to be published in the June 1961 JOURNAL.

REFERENCES

1. P. W. Ranby, D. H. Mash, and S. T. Henderson, *Brit. J. Appl. Phys.*, Supplement #4, 518 (1955).
2. A. H. McKeog and E. G. Steward, *ibid.*, Supplement #4, 526 (1955).
3. R. C. Ropp and R. W. Mooney, *This Journal*, **107**, 15 (1960).
4. D. E. C. Corbridge, *Acta Cryst.*, **10**, 85 (1957).
5. R. C. Ropp, M. Aia, C. W. W. Hoffman, T. J. Veleker, and R. W. Mooney, *Anal. Chem.*, **31**, 1163 (1959).

Technical Review

The Structure and Relaxation of Dielectrics

Charles P. Smyth

Frick Chemical Laboratory, Princeton University, Princeton, New Jersey

It is the aim of this paper to examine the reasons for the behavior of simple dielectric materials at high frequencies, in particular, in relation to their structures. It is a well-known fact that the dielectric constant and loss of a simple dielectric material depends on its polarizability. For molecular materials, nonpolar molecules give low dielectric constant and zero loss, and molecules with permanent dipole moments give dielectric constants to liquids which are larger, the larger their moments, and the greater their number per unit volume. The loss, which normally occurs only in a certain frequency region, depends on the same quantities, as well as on the frequency. In the region of loss, the dielectric constant falls off rapidly with increasing frequency. This behavior has been described and explained by the familiar Debye theory (1).

In order that these simple relationships may hold, the molecules must have freedom to orient in the alternating electric field used to measure the dielectric constant and loss. It is for this reason that most molecular solids have low dielectric constants and zero losses. However, many crystalline solids composed of symmetrical molecules have been found (2) to behave much like liquids for some distance below the melting point in a so-called "rotator state," and the orientational freedom of the polar segments of large molecules and polymers may result in similar behavior.

The static or low-frequency dielectric constant is observed when the dielectric material is in equilibrium with the applied field. Under the influence of the field, the polar molecules or segments rotate toward an equilibrium distribution of molecular orientation with a resultant polarization of the dielectric. When the polar molecules are very large, or the viscosity of the material is very great, or the frequency of the alternating field is very high, the rotary motion of the molecules is not sufficiently rapid for the attainment of equilibrium with the field. The displacement current then acquires a conductance component in phase with the field, and dielectric loss occurs. The lag in the attainment of the equilibrium is termed dielectric relaxation, which may be defined as the exponential decay with time of the polarization when the applied field is removed. The phenomenon may be treated in terms of a relaxation time, defined as the time in which polarization is reduced to $1/e$ times its value at the instant the field was removed, e being the natural logarithmic base. This definition leads to the relationship that the relaxation time is the reciprocal of the critical angular frequency at which the loss is a maximum. The lag of the molecular dipoles behind the field increases with increasing frequency until the dielectric constant has decreased to a value which receives no contribution from dipole orientation.

The formal relationships between dielectric constant, loss, relaxation time, and frequency of field are largely independent of the mechanism of relaxation. The dielectric relaxation time is obtained by various methods from the measured values of dielectric constant and loss (1). If the dielectric is a dilute solution of polar molecules in a nonpolar solvent, the macroscopic relaxation time thus obtained may be regarded as the molecular relaxation time. If, however, each polar molecule is surrounded immediately by other polar molecules, the change in local internal field caused by the turning of one molecule requires the neighboring molecules to assume new orientations, with consequent longer relaxation time for the dielectric as a whole, the

macroscopic relaxation time. No generally satisfactory relationship between the two relaxation times has as yet been obtained, but an approximate relationship derived independently by O'Dwyer and Sack (3) and by Powles (4) requires the ratio of the macroscopic to the molecular relaxation time to lie between 1 and 1.5. Experiment has shown (5) that the ratio lies within this range for a large number of molecules, while an extension of the range to 0.9-2.0 would include most of the molecules which have been examined. For approximate consideration of the magnitudes of the relaxation times, the difference between the macroscopic and the molecular values can evidently be neglected in most cases, but, in detailed consideration of structural effects, account should be taken as far as possible of the difference. In his early treatment (1) Debye derived a much used and abused equation for the relaxation time τ on the assumption that the orienting dipole was in a spherical molecule of radius a moving in a continuous viscous fluid of internal friction coefficient η:

$$\tau = \frac{4\pi\eta a^3}{kT}$$

where k is the gas constant per molecule and T is the absolute temperature.

When, in early work, several observed values of the relaxation time and the macroscopic viscosity were substituted in this equation, molecular radius values of the right order of magnitude were obtained, the apparent agreement being facilitated by the cube root relationship involved. The development of the equation by Perrin (6) and others in more elaborate form to make it applicable to ellipsoidal molecules gave good agreement with measurements on aqueous solutions of proteins (7). It is to be noted that, in these solutions, the solvent molecules are so small in comparison with the solute as to give an approximation to the continuous viscous fluid assumed by Debye. The full significance of these results for protein solutions is, however, uncertain because it has been shown (8) that proton fluctuations, rather than molecular orientation may be at least partially responsible for the observed behavior (7). When the relaxation times of small, nearly spherical molecules of known radius were measured and used to calculate the coefficient of internal friction or microscopic viscosity, the values found for the latter were only 0.008-0.06 of the macroscopic viscosity, and little parallelism was observed between the internal friction coefficient and the macroscopic viscosity (9). The extreme departure from predicted behavior was observed for t-butyl chloride and dibromodichloroethane in the "rotator" crystalline state, in which the apparent coefficient of internal friction was lower than that of the substance in the liquid state (10). In these cases, the orienting polar molecules are surrounded by molecules of the same or nearly the same size and not by the continuous fluid postulated by Debye.

This behavior may be further illustrated by some recent measurements and calculations (11) on solutions of several polar molecules, which, for the present purpose, may be regarded as rigid. The relaxation times were calculated from the molecular dimensions and the macroscopic viscosity by Fischer's (12) modification of the Perrin equation (6). The calculated value for t-butyl chloride in heptane solution is 25 times the observed at 20°, while, for the solution in Nujol, which has a macroscopic viscosity 257 times that of heptane, the calculated value is 3870 times the observed. For the slightly larger camphor molecule, the ratio is 10.5 in heptane and 2110 in Nujol solution while, for the large and somewhat flat molecule of 1-chloronaphthalene the ratio is 4.4 in heptane and 188 in Nujol solution. The macroscopic viscosity is almost without significance when the polar molecule is spherical and can rotate without displacement of its neighbors, but increase in molecular asymmetry and size increases the extent to which the polar molecule must displace its neighbors in order to rotate and so increases the dependence on viscosity. The long molecule of 4-bromobiphenyl, which has the dipole in its long axis, has a relaxation time in Nujol solution so long that, when measured at a wave length of 1.2 cm, the loss is very small and the dielectric constant is close to the optical dielectric constant, which receives no contributions from the permanent molecular moment. For the Nujol solutions of this molecule, the calculated relaxation time is 19.5 times the observed while, for those in heptane, the ratio is down to 2.1. For all these solutions, the departure of the calculated from the observed relaxation times is less wide, the lower the viscosity and the higher the temperature, which causes the viscosity to be lower. These results indicate that the larger the solute molecules and the smaller the solvent, the better the agreement between the calculated and the observed relaxation times.

Meakins (13) has recently concluded from a number of measurements that, when the polar solute molecule is at least three times as large as the solvent molecule, the solutions give good agreement with the unmodified Debye theory. Measurements (14) on benzene solutions of a large disk-shaped porphyrazine molecule having about 10 times the volume of the solute molecule give fair agreement with the unmodified Debye theory, but a shift of the molecular dipole from the plane of the disk to a direction perpendicular to it increases the relaxation time to 2.5 times the value, an increase not predicted by the unmodified Debye relation. It appears, therefore, that the relaxation times of molecules at least three times as large as the molecules surrounding them may be roughly proportional to the macroscopic viscosity, but dipole direction within the molecule and molecular shape must be taken into account (5, 14). The use of mutual viscosity instead of macroscopic viscosity gives much worse agreement for these solutions of large molecules, although it has been found to lessen the discrepancies between theoretical and observed behavior for some solutions of smaller molecules (15).

Although dielectric loss is proportional to the square of the permanent dipole moment of the

molecule (1), the dipole moment does not occur in the simple Debye equation for the relaxation time. However, the dipole moment affects the relaxation time indirectly through its effect on the intermolecular forces which influence the viscosity. Atomic and molecular polarizability exert somewhat similar effects upon the viscosity and, hence, upon the relaxation time. The Debye equation requires proportionality of the relaxation time to the molecular volume, and a very rough proportionality has been observed (16). The actual effect of change in molecular volume may be large because of its effect on viscosity, in addition to its direct effect on the relaxation time. In spite of the extreme departures of relaxation times of solutions from proportionality to viscosity which have been pointed out, a very definite tendency of the relaxation times of pure liquids to increase with viscosity has been observed (17, 18), so much so that it is frequent practice in comparing relaxation times to use a so-called reduced relaxation time, τ/η, the ratio of the relaxation time to the viscosity.

The specific effects of molecular structure and shape may be illustrated by examples (18). As shown by the Stuart-Briegleb atomic models, fluorobenzene and pyridine depart only a little from the form of the symmetrical benzene molecule, fluorobenzene showing a slight protusion at the fluorine atom and pyridine a slight indentation at the nitrogen atom. The relaxation times of these molecules are nearly the same, although the measured viscosity of pyridine is 47% larger than that of fluorobenzene. Attachment of a methyl group to benzene lowers the viscosity slightly from 0.65 to 0.59 centipoise, while a similar substitution in the 4-position of pyridine lowers the viscosity still less. The protrusion of the methyl group raises the molecular relaxation time of 4-methylpyridine 83% above that of pyridine. It is higher than that of the similarly shaped toluene molecule by 56%, as compared to a difference of 59% in the viscosities. The substitution of methyl groups on the pyridine molecule in the 2- and 6- and in the 2-, 4-, and 6-positions alters the viscosity only slightly but raises the relaxation time greatly, so that 2,4,6-trimethylpyridine has a molecular relaxation time about 6 times that of pyridine. Substitution on the side chain of the toluene molecule raises the viscosity by 15% and doubles the relaxation time, but substitution of a second methyl group in the ortho position of toluene raises the viscosity by 37% and the relaxation time by 59%. The viscosity of *i*-propylbenzene is 16% higher than that of ethylbenzene, while the relaxation time is 42% higher.

In the monohalogenated benzenes, increasing size of the halogen and consequent increase in its polarizability and in the intermolecular forces increase both the viscosity and the molecular relaxation time. Benzonitrile and nitrobenzene, when compared to the monohalogenated benzenes, show somewhat longer relaxation times than would be expected on the basis of their viscosities and molecular volumes. Their larger dipole moments, 4.39 x 10^{-18} for benzonitrile and 4.21 x 10^{-18} for nitrobenzene, may account for this through increased intermolecular action not adequately taken into account in the calculation of the molecular relaxation time. In dilute solution in benzene, relaxation times (10^{-11} sec.) have been found as follows: chlorobenzene, 0.75; bromobenzene, 1.02; nitrobenzene, 1.15. The comparatively small differences between these values and between them and the value for toluene show the importance of the liquid viscosities and the dipole-dipole interactions in causing the much larger differences between the pure liquids which are observed (19).

It is natural to expect that a nonspherical molecule should have different relaxation times around different axes of rotation. Perrin (6) has calculated that, for an ellipsoidal molecule with its permanent moment along one axis, the dispersion is the same as if the molecule were spherical, although the value of the relaxation time is different, while, for an elongated ellipsoid of revolution having a moment perpendicular to the axis of revolution, the single relaxation time is almost the same as that for a sphere of the same volume. If, however, the permanent moment does not lie in an axis of symmetry, more than one relaxation time results. The loss peaks associated with the different relaxation times are normally so close together that a single somewhat broadened and flattened loss maximum is observed. It has been common practice to represent the dependence of the dielectric loss on the frequency by an equation giving a distribution of relaxation times around a most probable value (1). In the equation of Cole (20) and Cole the extent of the distribution is represented by an empirical constant, which is 0 when there is but a single relaxation time and 1 when the number of different relaxation times approaches infinity. For nearly spherical molecules, the constant is zero or close to it. Variation in the environment of the polar molecules may result in some distribution of relaxation times. However, in the mixed solvent, Nujol, the roughly ellipsoidal molecule of 4-bromobiphenyl shows (11) but one relaxation time, in conformity with the Perrin theory, which is frequently not obeyed so well.

It is usually impossible to distinguish experimentally between the different distribution functions. The dielectric losses of the pure alkyl bromides were satisfactorily analyzed in terms of a Cole-Cole distribution (20) of relaxation times around a most probable value for each liquid (21). Recently, however, Professor K. Higasi in the writer's laboratory has carried out an analysis in terms of a distribution of relaxation times between two limiting values (22), one corresponding to the rotation of the terminal CH_2Br group around its C-C bond and the other to the end-over-end rotation of the entire molecule in its extended form. The intermediate relaxation times correspond to orientation by twisting of segments around the other C-C bonds of the molecular chain. This method of analysis is an equally good representation of the experimental results and, for these molecules, is much more logical from the point of view of struc-

ture than the Cole-Cole distribution. Dipole orientation in polymers may occur by mechanisms resembling those just discussed for the alkyl bromides, but the much greater sizes of the molecules provide a greater variety of possible segmental orientation with consequent distribution of relaxation times, so that the loss-frequency curves commonly extend over very wide frequency ranges and have extremely flat maxima.

The presence of movable polar groups, such as CH_3O, CH_2Cl, and NH_2 in otherwise rigid molecules provides a possibility of dipole orientation by a single intramolecular rotation as well as by molecular rotation. The relaxation times observed for such substances are normally the result of two overlapping absorption regions, which can be clearly distinguished only by measurements at several frequencies extending into the region of millimeter waves. Measurements at 3 mm have been combined with those at longer wave lengths to show the existence of only one dielectric absorption region for rigid polar molecules, such as methylquinolines, while alcohols show additional absorption regions (23). Water shows but a single value of the relaxation time in this region with no distribution, but the high value, 6.0, of the apparent optical dielectric constant proves the presence of further considerable absorption at shorter wave-lengths, a conclusion at least qualitatively consistent with the infrared absorption spectrum.

From the practical point of view, it is evident that the dielectric loss of a material, like the dielectric constant, is greater, the greater the number of polar molecules per unit volume and the larger their polarities, provided that the molecules are free to orient in an applied electric field. The frequency region within which the loss is considerable lies within a hundredfold range of frequency or two logarithmic decades when the material has a single relaxation time. When there is a distribution of relaxation times, the frequency region of loss is extended and the maximum loss is lowered. The location of the region of loss is moved to higher frequency, the higher the temperature, the smaller the molecules, and the lower the resistance to molecular or polar group rotation. For large molecules surrounded by small, the measured macroscopic viscosity may give a fair measure of this resistance to orientation, but, for small molecules, the resistance is much lower than indicated by the viscosity, which, in such cases, frequently has little significance. Loss then occurs at higher frequencies than those predicted from the viscosity.

Manuscript received March 2, 1960

Any discussion of this paper will appear in a Discussion Section to be published in the June 1961 JOURNAL.

REFERENCES

1. C. P. Smyth, "Dielectric Behavior and Structure," Chap. I, II, McGraw-Hill Book Co., New York (1955).
2. *Ibid.*, Chap. V.
3. J. J. O'Dwyer and R. A. Sack, *Australian J. Sci. Research*, **A5**, 647 (1952).
4. J. G. Powles, *J. Chem. Phys.*, **21**, 633 (1953).
5. R. C. Miller and C. P. Smyth, *J. Am. Chem. Soc.*, **79**, 3310 (1957).
6. F. Perrin, *J. Phys. Radium*, **5**, 497 (1934).
7. Ref. (1), Chap. XIII.
8. J. G. Kirkwood and J. B. Shumaker, *Proc. Nat. Acad. Sci.*, **38**, 855 (1952).
9. C. P. Smyth, *J. Phys. Chem.*, **58**, 580 (1954).
10. J. G. Powles, D. E. Williams, and C. P. Smyth, *J. Chem. Phys.*, **21**, 136 (1953); D. E. Williams, Thesis, Princeton University (1956).
11. O. F. Kalman and C. P. Smyth, *J. Am. Chem. Soc.*, **82**, 783 (1960).
12. E. Fischer, *Physik. Z.*, **40**, 645 (1939).
13. R. J. Meakins, *Trans. Faraday Soc.*, **54**, 1160 (1958).
14. D. A. Pitt and C. P. Smyth, *J. Am. Chem. Soc.*, **63**, 582 (1959).
15. D. A. Pitt and C. P. Smyth, *J. Phys. Chem.*, **81**, 783 (1959).
16. A. D. Franklin, W. M. Heston, Jr., E. J. Hennelly, and C. P. Smyth, *J. Am. Chem. Soc.*, **72**, 3447 (1950).
17. P. L. McGeer, A. J. Curtis, G. B. Rathmann, and C. P. Smyth, *ibid.*, **74**, 3541 (1952).
18. C. P. Smyth, *Proc. Nat. Acad. Sci.*, **42**, 234 (1956).
19. See also R. W. Rampolla and C. P. Smyth, *J. Am. Chem. Soc.*, **80**, 1057 (1958).
20. K. S. Cole and R. H. Cole, *J. Chem. Phys.*, **9**, 341 (1941).
21. E. J. Hennelly, W M. Heston, Jr., and C. P. Smyth, *J. Am. Chem. Soc.*, **70**, 4102 (1948).
22. Cf. H. Fröhlich, "Theory of Dielectrics," pp. 93-95, Oxford University Press, London (1949).
23. R. W. Rampolla, R. C. Miller, and C. P. Smyth, *J. Chem. Phys.*, **30**, 566 (1959).

June 1961 Discussion Section

A Discussion Section, covering papers published in the July–December 1960 JOURNALS, is scheduled for publication in the June 1961 issue. Any discussion which did not reach the Editor in time for inclusion in the December 1960 Discussion Section will be included in the June 1961 issue.

Those who plan to contribute remarks for this Discussion Section should submit their comments or questions in triplicate to the Managing Editor of the JOURNAL, 1860 Broadway, New York 23, N. Y., *not later than March 1, 1960.* All discussion will be forwarded to the author(s) for reply before being printed in the JOURNAL.

The Cathodic Behavior of AgO in Alkaline Solutions

Thedford P. Dirkse

Calvin College, Grand Rapids, Michigan

ABSTRACT

A study has been made of the discharge of AgO to determine why only a part of the discharge capacity of AgO is delivered at the potential of the AgO-Ag_2O couple and to determine the role of oxygen in this process. The difference in discharge capacity of electrodes produced by constant-current and by constant-potential anodization also has been studied. A mechanism involving the transport of $O^=$ ions through the electrode material and the reaction of these ions with the electrolyte is presented.

When a fully charged silver-zinc battery is discharged, the voltage-time curve usually has two levels (Fig. 1). The higher of these is generally attributed to the presence of AgO in the silver electrode. However, the processes occurring when AgO is discharged are not well understood. The capacity delivered at this higher level on discharge is usually but a fraction of that theoretically available. Furthermore, this capacity appears to depend on a variety of circumstances, some of which are unknown. In recent years several facts have been brought to light in connection with this capacity. A good deal of the capacity available as AgO on the electrode is delivered at a voltage level corresponding to that of Ag_2O (1, 2). The exact amount delivered at this lower voltage level depends on the current density. It also has been shown that the capacity of AgO delivered at this higher voltage level decreases on stand with no loss in total capacity (3). Recently, Wales and Burbank (4) have shown that during certain periods of discharge the reduction of AgO to Ag_2O and that of Ag_2O to Ag likely proceed simultaneously. Their results fail to give any evidence for the presence of solid solutions of AgO in Ag_2O on discharge.

A second problem associated with the cathodic behavior of AgO arises from the fact that oxygen can be added to AgO without changing the emf of the substance (5). This added oxygen does not alter the x-ray diffraction pattern of AgO except to make it more diffuse.

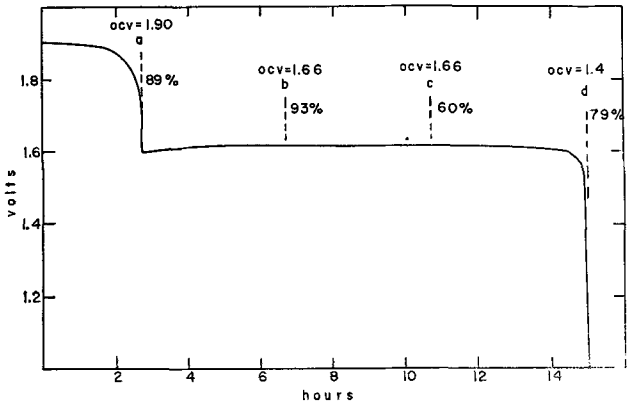

Fig. 1. Voltage-time curve for the discharge of an AgO-Zn-40% KOH cell at room temperature. Percentages are discharge efficiencies.

The present work was carried out to obtain more information on the cathodic behavior of AgO and to investigate more thoroughly the role of oxygen in this process.

Experimental and Discussion

The experimental techniques used in this work were the same as those described earlier (5). When electrodes were to be weighed they were first soaked in distilled water for at least 8 hr, then dried in a stream of purified nitrogen at room temperature, and finally placed in a desiccator for at least 24 hr. All these operations were carried out in the absence of light. After this, the electrodes were weighed and the change in weight was considered to be due to changes in oxygen content. Where possible the electrode was finally reduced to Ag and weighed. The weight of Ag at this time agreed, within experimental error, with the weight at the beginning of the charging process.

Oxygen content.—In the work reported earlier (5) it was shown that when silver is treated anodically in KOH solutions the addition of oxygen to form Ag_2O and AgO follows Faraday's laws. When the gassing potential is reached some oxygen is still added to the electrode. This was determined by weighing the electrode before and after such gassing treatment. At constant-current charging the oxygen added during gassing often corresponded to about 10% of the current passed. Apparent current densities of 0.25 to 2.5 ma/cm^2 were used, yet there was no stoichiometric evidence for complete transformation of all the Ag to AgO even though these electrodes were allowed to remain at the gassing potential for periods of up to 10 hr.

With constant-potential charging, oxygen also can be added to the silver electrode even when the potential is kept below that needed for gassing. Products having oxygen contents corresponding to $AgO_{1.5}$ have been prepared in this manner.

The question then arises whether the oxygen added to the electrode during gassing on constant-current charging or during prolonged constant-potential charging at a potential about 100 mv

below the gassing potential contributes to the discharge capacity of the electrode.

To check this, a commercially prepared sintered Ag electrode, 1.5 x 3.8 cm, weighing 2.4 g, was charged at 0.1 amp in 40% KOH. Its capacity was determined by charging up to the gassing potential and then allowing it to stand 20 hr before being discharged. The discharge capacity exactly equaled the charge input (0.68 amp-hr). The electrode then was given a series of cycles in which it was charged at the same rate and allowed to remain at the gassing potential for 8 to 15 hr. It was discharged immediately after each of these charges, and the discharge capacity was only 3% larger than the previous charge input up to the gassing potential. Thus while prolonged gassing on constant-current charge does add oxygen to the electrode as noted above, this oxygen contributes very little to the discharge capacity. In all these instances, however, there was no complete conversion to AgO. Since this electrode accepted 0.68 amp-hr of charge, its composition when charged corresponded to about $AgO_{0.5}$. Since there definitely was AgO present, as determined by x-ray diffraction and by observation of the discharge voltage-time curve, free silver also was present.

Wales and Burbank (4) observed that prolonged gassing on constant-current charge appeared to produce more perfectly crystalline AgO. This suggests that when the electrode reaches the gassing potential on charge the surface has not been completely converted to crystalline AgO. During gassing more oxygen is added to the surface, forming more completely crystalline AgO. Perhaps it is this oxygen that gives the small increase in discharge capacity which is obtained on prolonged gassing.

This oxygen, however, is not the only oxygen added during the gassing period. The weight gained during gassing is larger than that corresponding to the extra discharge capacity. Earlier work (6) has shown that, when an electrode is charged at constant-current and is allowed to charge at the gassing potential for several hours or more, appreciable amounts of oxygen can be added. This oxygen is held firmly by the electrode material, but it does not add correspondingly to the discharge capacity. Moreover, this oxygen is released on discharge. For example, a sintered Ag electrode, 3.8 cm square and weighing 6.2 g, was charged at a constant-current of 0.04 amp in 15% KOH for 3 days. It was then soaked in distilled water and dried overnight in an oven at 60°C. The weight gain corresponded to a product having the composition $AgO_{0.8}$. This electrode was stored dry in the dark for 2 years and then charged again, this time at 0.7 amp in 40% KOH for 24 hr. It was gassing profusely during the latter part of the charge. When it was soaked in distilled water much gas was evolved. It was then dried for 24 hr at 60°C. There was a slight gain in weight, corresponding to less than 1% of the charge applied. After 3½ weeks the electrode was discharged at 0.1 amp in 42% KOH. After 10 hr the voltage *vs.* Zn fell below 1 v and the discharge was terminated even though there was still visible evidence of oxides on the plate. The electrode again was soaked in distilled water and dried for a day at 60°C. The loss in weight was 0.57 g. Assuming that this loss was due to oxygen, this corresponds to 1.9 amp-hr. Yet only 1 amp-hr had been removed during the discharge. Apparently, about 0.27 g oxygen escaped as bubbles during the discharging process, but no attempt was made to observe this.

Changes do occur if the electrode is stored for some time. Several electrodes similar to the one just described were charged at constant-current and were stored dry for 1 to 2 years. None of them was completely converted to AgO, and none lost weight during this storage. With some, the open-circuit voltage (ocv) after storage was that associated with Ag_2O. Others, however, gave an ocv associated with AgO. Thus, this dry storage does not necessarily lead to complete conversion of AgO to Ag_2O (reaction [1]).

$$AgO + Ag \rightarrow Ag_2O \qquad [1]$$

This reaction does take place when electrodes are stored in electrolyte or even in water. Figure 2 is a picture of electrodes which had been partially discharged. The white portions are Ag whereas the darker portions are oxides of silver. One such electrode was placed in electrolyte, and after about 3 weeks all the Ag had been oxidized to Ag_2O. In such a situation, Eq. [1] represents the net effect of a local cell reaction consisting of a AgO cathode and a Ag anode. This reaction may take place rapidly at first, but as Ag_2O is produced the internal resistance of the local cell is increased and the reaction slows down.

These electrodes did not deliver their total available capacity after storage. After discharge, such

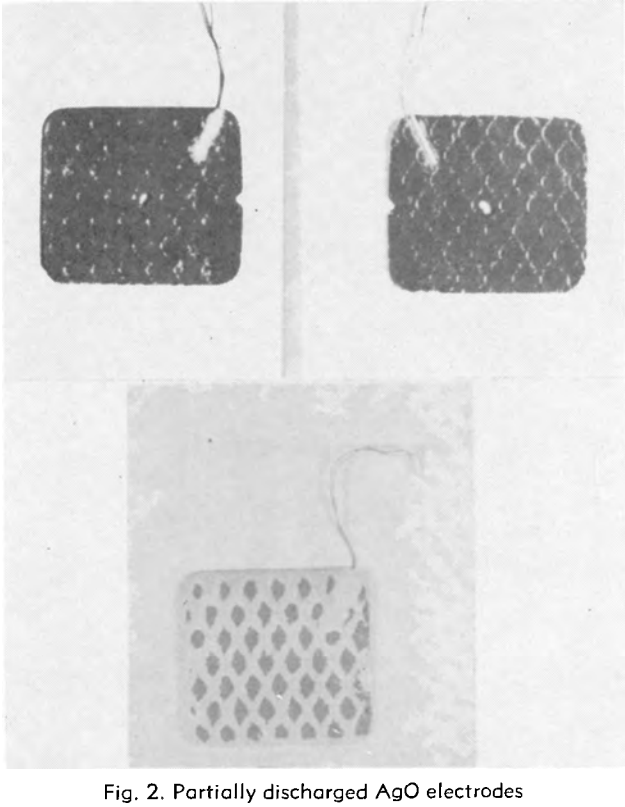

Fig. 2. Partially discharged AgO electrodes

an electrode was heavier than it was before being charged, indicating that discharge had not removed all the oxygen from the electrode material. With one charged electrode, 25% of the theoretical discharge capacity (calculated from oxygen content) was unavailable after storage. This phenomenon has been noted with other electrodes also.

An attempt was made to follow this change during storage by x-ray analysis. Freshly charged electrodes gave good sharp patterns for AgO. In some electrodes there were also areas giving good Ag_2O patterns. After dry storage for 1.5 years the electrodes still gave the AgO pattern, but it was weak and the lines were broader. This indicates a deterioration of the crystallinity of the oxide structure and is likely due to diffusion of oxygen ions to areas of lower oxygen content. There was no loss of oxygen. This diffusion during storage apparently also affects the current path through the electrode, and this may be responsible for the reduction in capacity. The current path is altered, as will be noted later, so that some of the oxygen in the interior of the electrode cannot escape from the silver lattice.

With constant-potential charging (at potentials slightly below the gassing potential) large amounts of oxygen can be introduced into the silver lattice. This oxygen may exceed the stoichiometric ratio of AgO, and yet many of the physical properties are the same as those of AgO (5). It has been suggested that at least part of this oxygen is physically adsorbed rather than chemically bound. This idea is consistent with the following results.

A small electrode was charged in 30% KOH at a constant potential of 350-400 mv above the reversible potential of Ag-Ag_2O. After charge its composition was $AgO_{0.47}$. After standing one week it was discharged in 42% KOH at about 1 ma/cm^2. At intervals the discharge was interrupted, the electrode was dried, weighed, and x-rayed. Then it was inserted in the cell and the discharge continued. The x-ray patterns showed the same variations as have been reported earlier (4). Discharge results are given on Fig. 1. The electrode was weighed at points a, b, c, and d. The loss in weight was considered to be due to a loss of oxygen. This was justifiable since the weight of the silver on the electrode at the end of the discharge was within 0.3% of that on the electrode at the beginning of the experiment. The theoretical weight loss was calculated from the ampere-hours of discharge. This value divided by the actual weight loss was called the discharge efficiency. The discharge efficiency at point a on Fig. 1 refers to the interval from the beginning of discharge to point a, that at point b refers to the interval between a and b, etc. Perhaps as the electrode discharges, adsorbed oxygen escapes in a mechanical fashion from the lattice. On the basis of the efficiencies, this is more easily accomplished toward the end of the discharge.

Three other electrodes were prepared on platinum grids. They were made by pasting the grid with moist Ag_2O, air drying, and thermally reducing them at 550°C to Ag. Then they were subjected to constant-potential charging until they had an oxygen content greater than AgO. Two of them (A and B) were stored dry for 3 months at room temperature and the third was stored dry for 1.5 years after 4 months' storage in the dark in 30% KOH. None of these electrodes lost any appreciable weight over this period of time. This shows that the extra oxygen is bound rather firmly to the silver. Their emf values and x-ray diffraction patterns were those of AgO. There was nothing to indicate a new type of oxide, *e.g.*, Ag_2O_3.

Electrodes A and B were discharged at a very low current density in 28% KOH. Typical discharge curves were obtained, although relatively little discharge capacity (2% and 15% of the total) was obtained at the higher voltage level. Electrode C was discharged in 40% KOH at an 11 hr rate. No discharge capacity was obtained at the voltage level corresponding to AgO. The ocv, however, was 1.9 v *vs.* Zn.

The fact that so little discharge capacity was obtained at the higher level in each case may at first seem to be normal. These electrodes stood for some time before being discharged, and it has been shown that standing reduces the amount of capacity delivered at the high voltage level but does not reduce the total discharge capacity (3). This has been attributed to the fact that on stand reaction [1] takes place (4). If this is the case, there must have been more than a trace of unoxidized silver present in the charged electrodes. It follows then that constant-potential charging does not bring about complete conversion to AgO even though the composition of the material can be represented by $AgO_{1.5}$. It can be argued that reaction [2] takes place at the platinum

$$2AgO \rightarrow Ag_2O + 1/2\ O_2 \qquad [2]$$

grid and that the formation of the Ag_2O increases the internal resistance of the electrode so that the discharge voltage is polarized to the Ag_2O-Ag level. This reaction then would take place in the dry state since these electrodes were stored dry. Ohse (7) noted a lack of evidence for this reaction in 1N KOH.

A comparison was made of the capacity obtained to that theoretically available. The theoretical capacity was calculated on the basis of both silver and oxygen content. Results are given in Table I.

It is obvious that all the oxygen present in these electrodes was not useful for discharge purposes. This also follows from the fact that with electrode C, *e.g.*, the loss in weight of oxygen during discharge was 130% of that corresponding to the actual capacity obtained. Some of this oxygen was apparently released from the electrode during dis-

Table I. Capacity of "AgO" electrodes

Electrode	Composition	% Theoretical capacity on basis of		
		O_2	Ag^{++}	Ag^{+++}
A	$AgO_{1.6}$	56	91	60
B	$AgO_{1.5}$	55	85	57
C	$AgO_{1.2}$	23	27	18

charge without entering into the discharge reaction. The small value for per cent theoretical capacity is due to the prolonged storage of this electrode, as noted earlier in this paper. Since electrode C had a 4 month wet stand it is very possible that reaction [1] proceeded to a significant extent. This could build up sufficient Ag_2O to increase the internal resistance of the electrode, alter the current path within it, and thus bypass some of the oxide during the discharge reaction.

If one assumes that the silver present in the electrode was all in the divalent state, then the actual discharge capacity still is less than theoretical. At the current densities used one would expect practically 100% discharge/charge efficiency. The fact that the actual discharge capacity is less than theoretical supports the idea that some unoxidized silver was present in the charged electrodes. It also makes unnecessary the suggestion that trivalent silver is present in the electrodes. These results support the idea that divalent silver is the highest oxidation state of silver in the charged electrodes. Furthermore, even prolonged constant-potential charging fails to convert all the silver to the divalent state.

It follows from these results that the oxygen content of the electrodes charged by the constant-potential method is no measure of the oxidation state of the silver. This method of charging may be rather inefficient. Although the weight of oxygen added to the electrode follows Faraday's laws (5), the discharge of such an electrode does not necessarily give a capacity equal to the oxygen content. This oxygen is strongly held and not readily released from the dry solid at room temperature. On discharge it appears to be released as the positive charge on the silver atoms (ions) is decreased. It may be forced out of the electrode as the lattice changes from AgO to Ag_2O. As this reduction takes place the silver ions move closer together leaving less room for occluded oxygen. Furthermore, the reduced charge on silver ions decreases the power to attract or adsorb oxygen atoms.

With constant-current cycling the discharge capacity generally equals the charge input up to the gassing potential (8). The weight of oxygen added during charge at moderate rates follows Faraday's laws (5). Prolonged gassing does result in the addition of oxygen and a small increase in discharge capacity. This indicates that the oxygen added during normal charging is a good measure of the state of oxidation of silver. With prolonged gassing, however, much of the oxygen added appears to be merely physically adsorbed.

Polarization.—One of the questions in connection with the discharge of AgO is the extent of polarization. Less than half the discharge capacity of an electrode usually is delivered at the higher voltage level. This raises the possibility that the AgO→Ag_2O process is polarized to such an extent that it operates at the lower potential of Ag_2O→Ag.

The extent of this polarization was studied by an interrupter method (9). Electrodes in which the surface is almost completely AgO showed very little polarization in the initial stages of discharge. A rapid increase in polarization was noted as the AgO was converted to Ag_2O and this polarization at times was so great that it caused the discharge of AgO to take place at a potential below that of Ag_2O (9). After this the potential rose to that of the Ag_2O→Ag process. The point at which the voltage drops to that of the Ag_2O→Ag level seems then to be determined by the current density on the surface layer of AgO. When this exceeds a certain value the potential drops. This drop in potential also is influenced by the formation of increasing amounts of Ag_2O. This highly resistive material may bring about an *IR* drop in the electrode itself.

With small wire electrodes on which but thin films of oxide were produced, about 40% of the discharge was obtained at the higher voltage level over a modest range of current densities. Conceivably this fact can be used to indicate that the fall of potential from the higher to the lower level is determined more by the resistance of the Ag_2O formed than by the increase of current density on the AgO. Since only thin films of oxide are produced, the resistance of the Ag_2O is not as great as with thicker films. Under these conditions the fall in potential occurs at a later stage in the discharge. It also may be that a greater fraction of the AgO present is on the surface and therefore the higher voltage level on discharge lasts relatively longer.

In Fig. 2 the pattern of the silver spots is the same as that of the grid of the electrode, indicating the importance of the current path in the discharge process. Furthermore, this suggests that the electrical resistance is an important factor in this process.

This polarization also is due in part to the electrolyte. This was shown by varying the KOH concentrations. At an apparent current density of about 1 ma/cm^2 the polarization amounted to 3, 6, and 32 mv in 1*N*, 0.5*N*, and 1.0*N* KOH, respectively. These values are corrected for the *IR* drop in the solution.

Mechanisms.—In discussing possible mechanisms for the cathodic behavior of AgO one should know whether the discharge reaction proceeds from the grid to the electrode-electrolyte interface or in the opposite direction. The discharge reaction is the removal of $O^=$ ions from the electrode material. To determine where in the electrode this process begins, the silver oxides were pressed into pellets about 1.25 cm diameter and 0.65 cm thick. They were discharged in a cell shown on Fig. 3. Only a small

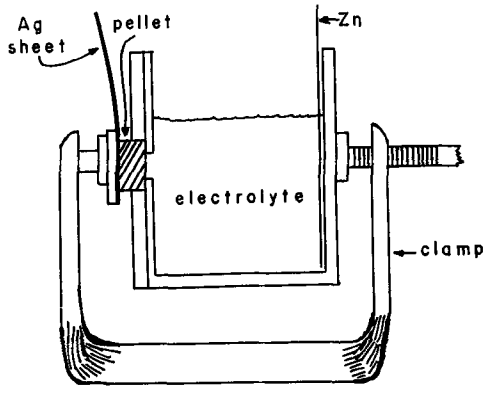

Fig. 3. Cell for use with pelletized electrodes

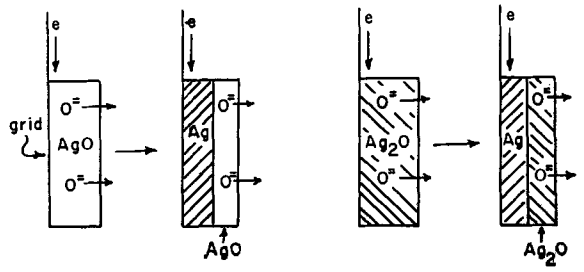

Fig. 4. Mechanism for the reduction of AgO

surface area was exposed to the electrolyte, and the grid (the Ag sheet) was completely outside the cell case. The electrolyte did seep into and penetrate the pellet.

Pellets of both Ag_2O and AgO were prepared and discharged at 35 ma/cm², considering only the surface area exposed to the bulk electrolyte. In either case the material was reduced to Ag during discharge and gave the capacity calculated from its weight, i.e., 231 ma-hr/g of Ag_2O and 432 ma-hr/g of AgO. When the material was discharged only long enough to deliver about half the discharge capacity of the material, it was found that with the Ag_2O pellet the reduced Ag was at the grid and not at the electrolyte. With the AgO pellet the same thing occurred. In fact, there was almost a plane surface that separated the Ag from the unreduced oxide. This plane was practically at the mid-point of the pellet. Furthermore, the unreduced oxide was AgO and not Ag_2O. This was determined by x-ray analysis, and it is possible that small amounts of Ag_2O were present. However, the bulk of the material was AgO. This suggests that on discharge the removal of $O^=$ ions proceeds from the grid toward the electrode-electrolyte interface (Fig. 4). Moreover, no large amounts of Ag_2O need be produced during the discharge of the AgO.

During the discharge of AgO small amounts of Ag_2O may be formed at the electrode-electrolyte interface as the $O^=$ ions are removed from the electrode by the electrolyte. X-ray evidence (4) indicates that this occurs, and the extent of this Ag_2O formation would depend on the current rate. This Ag_2O will be formed then because $O^=$ ions are removed from the surface at a faster rate than they are transported through the electrode material. The current path available is a significant factor since the $O^=$ ions begin to migrate from the areas where the current enters the electrode (Fig. 2).

Because the polarization of AgO is determined to some extent by the concentration of the KOH, it is apparent that some solvent or solute species are involved in this cathodic process. The species available are OH^-, K^+, and H_2O.

The cathodic process involves the removal of $O^=$ ions from the oxide. As the silver is reduced these ions are ejected from the electrode material. It is unlikely that the negatively charged OH^- ions would be responsible for this removal of the negatively charged oxygens. They would, no doubt, be repelled from the electrode.

It is possible that the free H_2O molecules are involved in this process. During discharge the H part of the molecule would be oriented toward the electrode and then the following process could occur

$$\begin{matrix} Ag = O & H \\ & \diagdown \\ & \quad O \\ & \diagup \\ Ag = O & H \end{matrix} + 2\,e \rightarrow Ag_2O + 2\,OH^- \qquad [3]$$

If this explanation is correct, then the cathodic polarization should increase with increase in KOH concentration. In a dilute solution more H_2O molecules would be available for reaction. However, as noted above, no such effect was observed.

Since, as indicated earlier, it is unlikely that the OH^- ions are involved, one is left with the K^+ ions as the reacting species. These ions are hydrated in solution, probably $K(H_2O)_4^+$ (10). Conceivably, these ions are drawn to the electrode with the H atoms oriented toward the electrode surface and then reaction [3] takes place. The charge on the K^+ ion aids in attracting the $O^=$ ions of the solid. It also weakens the O — H bonds in the H_2O. Thus the H_2O molecules bound to the K^+ ions are more reactive than the uncombined H_2O molecules. Attempts were made to determine the effect of substituting Na^+ ions for K^+ ions by using 0.1*N* NaOH solutions and also 7M solutions of $NaC_2H_3O_2$ and $KC_2H_3O_2$. However, any differences observed were within the limits of experimental error.

In summary, the cathodic reaction of AgO involves the removal of $O^=$ ions from the lattice by the H_2O molecules that are bound to the K^+ ions. This reaction occurs at the electrode-electrolyte interface. The amount of interfacial area is extensive because the KOH solution permeates the bulk AgO so thoroughly. As reaction proceeds, $O^=$ ions from the interior of the lattice migrate to this interface. Thus there are two factors responsible for the polarization of the AgO: (*a*) the reaction of $O^=$ ions with hydrated K^+ ions; and (*b*) the transport of $O^=$ ions through the electrode material. If the second process is not as fast as the first one, then the $O^=$ ion concentration at the electrode-electrolyte interface is reduced and the emf of the electrode decreases.

Acknowledgment

This work was supported by the Office of Naval Research. Thanks are also due to the Yardney Electric Company and to the M. Ames Chemical Works for furnishing some of the materials used in this work, and to Dr. W. C. Vosburgh for his help in preparing this manuscript.

Manuscript received March 30, 1960.

Any discussion of this paper will appear in a Discussion Section to be published in the June 1961 JOURNAL.

REFERENCES

1. I. A. Denison, *Trans. Electrochem. Soc.*, **90**, 387 (1946).
2. J. C. White, T. P. Dirkse, and R. T. Pierce, *ibid.*, **90**, 467 (1946).
3. C. P. Wales, NRL Report 5167, Aug. 11, 1958, Naval Research Laboratory, Washington, D. C.
4. C. P. Wales and J. Burbank, *This Journal*, **106**, 885 (1959).
5. T. P. Dirkse, *ibid.*, **106**, 920 (1959).

6. T. P. Dirkse and L. A. Vander Lugt, "A Study of the Oxides of Silver," Techn. Report No. 4 on Contract No. N onr-1682(01), June 30, 1957, Calvin College, Grand Rapids, Mich.
7. R. W. Ohse, *Z. Elektrochem.*, **63**, 1063 (1959).
8. T. P. Dirkse and J. De Vries, Paper presented at Electrochemical Society Meeting, Columbus, Oct. 20, 1959.
9. T. P. Dirkse and G. J. Werkema, *This Journal*, **106**, 88 (1959).
10. G. W. Brady and J. T. Krause, *Norelco Reporter*, **5**, 111 (1958).

Relation of Electron Configuration to Passivity in Cr-Ni-Fe Alloys

H. G. Feller and H. H. Uhlig

Corrosion Laboratory, Department of Metallurgy

Massachusetts Institute of Technology, Cambridge, Massachusetts

ABSTRACT

Critical current densities for passivity were measured for single phase Cr-Ni-Fe alloys as a function of Cr content for 20%, 40%, 50% and 60% Ni compositions. Major discontinuities in slope approximate the ratio 12/88 for Cr to Fe in the 20 and 40% Ni alloy series, and 14/86 for Cr to Ni in the 50 and 60% Ni alloy series. These ratios correspond to observed critical compositions for passivity in the Cr-Fe and Cr-Ni binary systems. Additional discontinuities occur at the critical binary Cr to Fe ratio in the 50 and 60% Ni series. This behavior is interpreted in terms of separate electron interaction in the ternary system between Cr and Fe distinct from interaction between Cr and Ni. Flade or activation potentials become more active with increasing Cr content, corresponding to increased stability of passivity. In accord with greater stability, average time for breakdown of passivity increased exponentially with Cr content.

The austenitic Cr-Ni-Fe stainless steels are passive alloys of which the 18% Cr, 8% Ni, balance Fe alloy (18-8) is an important example. These alloys, including the ferritic and martensitic Cr-Fe stainless steels, must contain a minimum of 12% Cr in order to exhibit optimum passivity or corrosion resistance. This critical concentration of Cr has been related to the tendency of an "unfilled" *d* band (or uncoupled *d* orbitals) of Cr to fill (or become coupled) with electrons donated by Fe, a process which is assumed to be just complete at 12%. Larger amounts of alloyed Cr correspond to residual uncoupled electrons or vacancies in surface atoms of Cr accounting for an alloy best able to chemisorb its environment, e.g., $O_2 + H_2O$, and become passive in a manner similar to pure chromium. Below 12% Cr, the *d* orbitals of Cr are coupled and the alloy has chemical properties more nearly resembling Fe, i.e., it is not passive. Similar electron interaction occurs in other binary transition metal alloys, a summary of known relations having been presented recently by one of us (1).

Electron interaction in relation to passivity has also been described for the ternary Mo-Ni-Fe and quaternary Cr-Fe-Ni-Mo passive alloys (2). It was in the interest of exploring this matter further using relatively pure ternary alloys instead of commercial compositions that this investigation was initiated. The Cr-Fe-Ni system is ideally suited to such a study because the phase diagram shows (3) that the alloys at low temperatures (650°C), are solid solution, face-centered cubic, over a wide range of composition. Metallographic examination of several alloys prepared for the present investigation confirmed that they were single-phase.

Measurement of Passivity

Passive behavior of the alloys was evaluated by measuring critical anodic current densities to produce passivity. Data of this kind provide a better criterion of the relation between alloy composition and passivity than do corrosion rates, as was discussed previously by Bond and Uhlig (4). A discontinuity in slope of critical current density plotted with composition, or minima in values of current density are observed at a relatively specific alloy composition. This critical composition has been found to be insensitive to *p*H or temperature of environment in the case of the Cr-Fe alloys (5), or to *p*H in the case of the Cr-Ni alloys (4), whereas similar alloy compositions corresponding to discontinuities in slope or to minima in corrosion rates tend to shift with environment. The discontinuity in slope of critical current densities for the Cr-Fe alloys, for example, comes at 10-12% Cr. This is also the critical composition derived from corrosion rate measurements of these alloys in water or in the atmosphere, but in acids or alkalis, passivity occurs at lower or higher Cr percentages.

The electrochemical mechanism of passivation (6-8) makes it clear why this is so. It has been shown, for example, that stainless steels achieve passivity whenever the anodic current density accompanying corrosion reaches or exceeds the critical current density. The same relation is expected to hold for other passive alloys. But the cathodic

reaction rate varies with environment and shifts the corrosion rate accordingly, thereby inducing passivity at higher or lower alloy compositions depending on the actual rate and the value of the critical current density in a particular environment. The influence of the cathodic reaction is eliminated by relying instead on critical current densities as a measure of the ease or difficulty with which an alloy becomes passive. In addition, constant renewal of the alloy surface by anodic dissolution during measurements avoids compositional changes caused for example by redeposition of ions in solution.

The important consideration from the present standpoint is that discontinuities in the critical current density for passivity are observed as a function of Cr content in the Cr-Ni-Fe alloy system as for the Cr-Fe system. These discontinuities can be interpreted in terms of electronic interaction between components of the alloy, similar to interactions hypothesized previously for the binary Cr-Fe, Cr-Ni, and other alloy systems (1).

Preparation of Alloys, Experimental Procedure

Alloys were prepared from electrolytic Fe and Cr, and from carbonyl Ni, melted in vacuum (10^{-5} mm Hg) by induction in high-purity alumina crucibles. No deoxidizers were added. Casting was carried out in a helium atmosphere by drawing the melts into 7 mm Vycor tubes and quenching in water. The helium was purified by passage over titanium sponge at 800°C, then through a liquid N_2 cold trap. In general, a single series of alloys was prepared by withdrawing a portion of the initial composition melt and quenching, then adding additional calculated amounts of Ni and Fe for the next composition, melting, withdrawing a portion, etc. This procedure was repeated several times. Ingots were homogenized in silica tubes in a helium atmosphere at 1050°C for 20 to 50 hr. Chips were then machined for chemical analysis of Ni and Cr and the remaining alloy was lightly cold-swaged to approximately 5 mm diameter rods. The swaged rods were annealed at 1050°C for 30 min and air-cooled. Representative analyses of 16 alloys showed a carbon content of 0.01-0.02%, and 5 representative samples showed a nitrogen content of 0.007-0.008%.

Electrodes measuring 1 to 2 cm long by 3.4 mm diameter were machined from the annealed rods with a small diameter stem at one end to which a nickel wire was silver-soldered. The wire was enclosed by a Pyrex tube, with a Teflon gasket insuring that only the alloy specimen came into contact with the electrolyte. The surfaces were abraded, using successively finer emery paper to 3/0 grit. After degreasing with benzene, the electrode was inserted into the cell, the latter being arranged so that pickling and washing, and final introduction of electrolyte could be carried out without exposing the electrode surface to air. The pickle was either dilute HNO_3 in the case of low Cr alloys, or dilute H_2SO_4 in the case of high Cr alloys. Deaerated electrolyte and deaerated distilled water for washing were contained in 5-gal carboys connected to the cell by glass tubing. Deaeration was accomplished by bubbling through nitrogen, first purified by passing over copper turnings at 450°C. After pickling of the electrode, the cell was filled and emptied 3 times with water and twice with electrolyte. The electrode was finally pickled anodically for 10 min with electrolyte in the cell using about 1/20th to 1/10th the current density required for passivation. Measurement of critical current density followed immediately.

The cell was all-glass with sealed-in glass electrical connections, separated into two halves by a ground glass joint. It contained two Pt cathodes spaced equally on either side of the test electrode to insure uniform current density. The test electrode fitted into the cell by means of a ground-glass joint. The reference cell was Ag-AgCl in 0.1*N* KCl, connected to a salt bridge filled with H_2SO_4 the tip of which (asbestos fiber sealed in glass) was located near the electrode surface.

The electrolyte for all measurements was deaerated 1.28*N* H_2SO_4 whose *p*H was about 0.4. Measurements were carried out in a constant temperature room maintained at 25° ± 0.5°C.

Critical current densities were determined by measuring times to reach a steady passive potential for a series of current densities, each above the critical value. The reciprocal of these times $1/t$ were then plotted with current densities i in accord with the relation:

$$i - i\ (\text{Crit.}) = K/t$$

where K is a constant equal to the coulombs required for passivation and i (Crit.) is the critical current density for passivity below which passivity is not achieved no matter how long the time. Applied current was obtained from 30 dry cells operating through a high resistance so as to maintain a constant value. The current densities chosen were within a factor of 2 or 3 times the critical current density, over which range the above equation is known to hold.

Potentials were also measured in 1.28*N* H_2SO_4 at which passivity decays spontaneously to an active potential on shutting off the anodic current. These are called "activation" or Flade potentials. A typical decay curve for the 4.8% Cr, 20% Ni, balance Fe alloy, as recorded by a high-input-resistance recorder, is shown in Fig. 1. In general, decay curves were obtained by first polarizing the electrodes to the passive region and holding for ½ to 1 min in order to allow the passive film to form. If insufficient time was allowed, no Flade potential was observed. Based on many measurements, it was found that the Flade potential was independent of time held at the passive potential; however, time to reach the Flade potential after shutting off the current increased the longer the electrode was maintained in the passive state. Flade (9) also observed much earlier that, when iron was held in the passive state for a long period, the time observed for decay tended to be longer.

Results

Critical current densities for 15 alloys all containing 20% Ni (average = 20.1% with a maximum

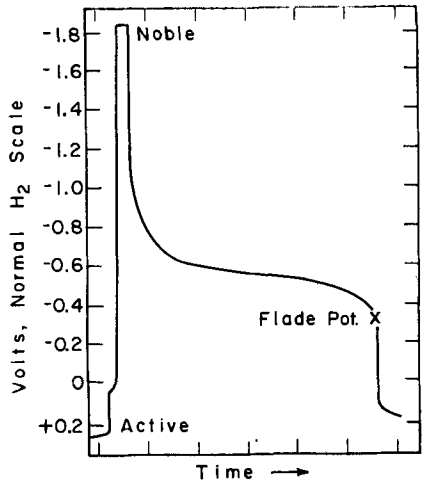

Fig. 1. Recorded potential decay of passivated 4.8% Cr, 20% Ni, balance Fe alloy in deaerated 1.28N H_2SO_4, 25°C.

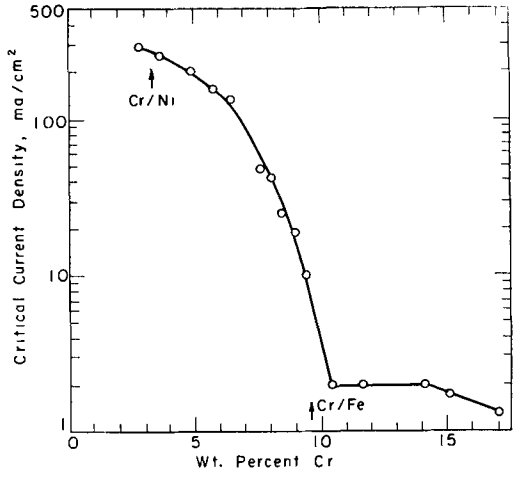

Fig. 2. Critical current densities for passivity of 20% Ni alloys in 1.28N deaerated H_2SO_4, 25°C.

deviation of 0.6%) and variable Cr and Fe are shown in Fig. 2. It is noted that alloys within the low Cr range require current densities in the order of 100-300 ma/cm² for passivation, whereas for alloys of greater than 10.5% Cr, current densities only about 1/100th as large are required. Optimum conditions for passivity can be said to initiate, therefore, at a minimum of 10.5% Cr. Although the corrosion rate corresponding to a critical current density of 2 ma/cm² is approximately 5,000 mdd, which is a high rate, in more dilute acids, of course, the critical current density and corresponding corrosion rate would be much lower. It should also be noted that the current density required to maintain passivity, corresponding to the steady-state corrosion rate of passive alloys, is much less than the critical current density. The important consideration is that as Cr content increases, the critical current density falls markedly and, at 10.5% Cr, achieves relatively low values which remain low for higher Cr compositions. This is typical of the behavior of Cr-Fe and other alloys as they progress from the active to the passive range of composition. The value 10.5% Cr, therefore, is a unique or critical composition.

Similar data for 40% (av. = 40.1%, max. deviation of 0.5%), 50% (av. = 50.0%, max. deviation of 0.6%) and 60% (av. = 60.0%, max. deviation of 0.7%) Ni alloys are shown in Fig. 3, 4 and 5. Major changes in slope occur as for 20% Ni alloys, but with some additional smaller changes in slope also apparent. A possible cause for these smaller changes will be discussed later.

Flade potentials for 20 and 60% Ni alloys are summarized in Fig. 6, each point representing an average of several determinations. Values for 40 and 50% Ni show a similar scatter, with all values for low Cr alloys starting at about −0.45 v to the normal H_2 electrode and ending at about 0 to −0.15 v for 15-20% Cr alloys. The value for the Flade potential E_F of Fe in H_2SO_4 of pH 0.4, as calculated from the relation (5) $E_F = -0.63 + 0.059\ pH$, is

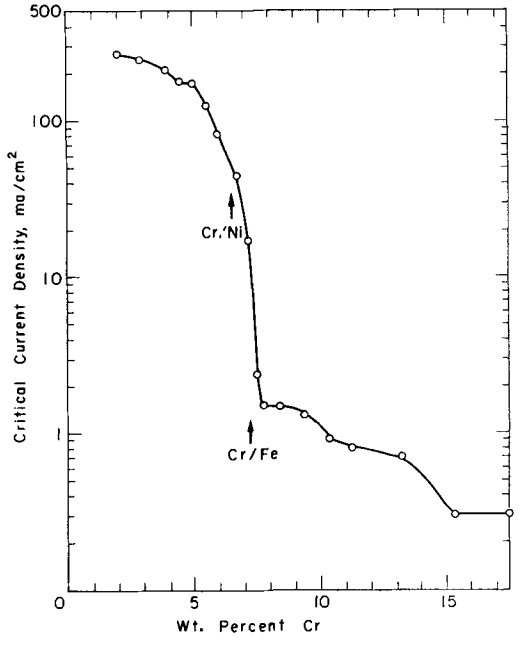

Fig. 3. Critical current densities for passivity of 40% Ni alloys in 1.28N deaerated H_2SO_4, 25°C.

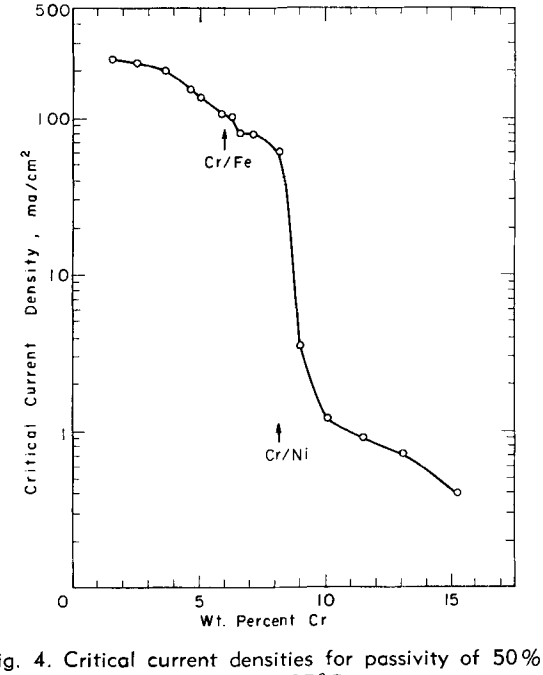

Fig. 4. Critical current densities for passivity of 50% Ni alloys in 1.28N deaerated H_2SO_4, 25°C.

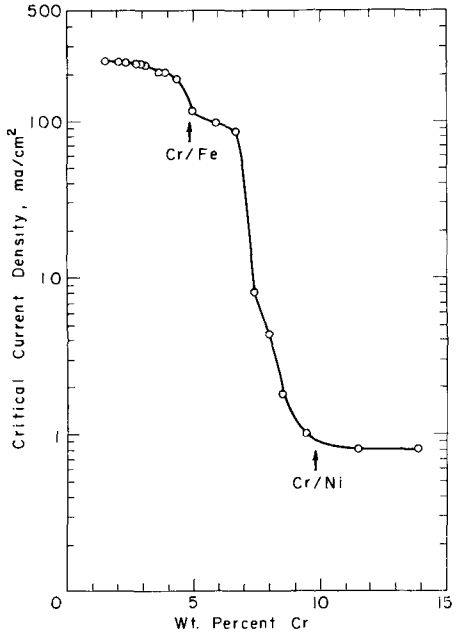

Fig. 5. Critical current densities for passivity of 60% Ni alloys in 1.28N deaerated H_2SO_4, 25°C.

equal to −0.61 v. The less noble values for the alloys indicate that their passivity is more stable than that of iron. The standard Flade potential (pH = 0) for Cr, by way of example, is +0.2 v. Some potentials of Fig. 6 fall off the best curve through all the points. It may not be coincidence that these marked deviations occur mostly at alloy compositions corresponding to discontinuities in slope of critical current density as observed in Fig. 2 and 5. The extent to which the two sets of data can be correlated is not entirely clear, however, and any attempt in this direction would probably require additional measurements on alloys of composition falling in between present compositions.

The over-all shape of the Flade potential curves in Fig. 6, allowing for deviations mentioned above, are similar to those reported for the Cr-Fe alloys in H_2SO_4 by Rocha and Lennartz (10). There is a

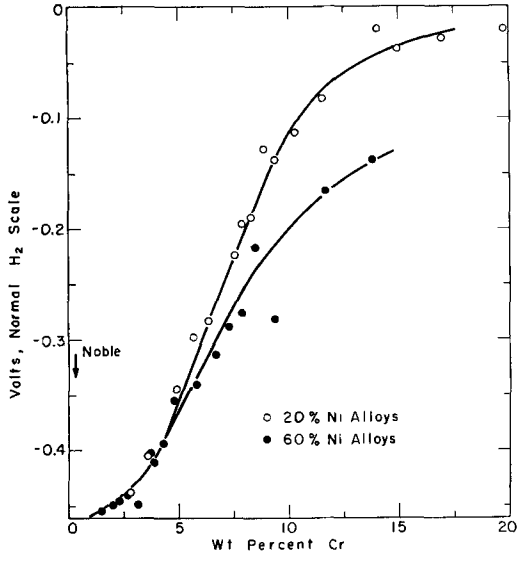

Fig. 6. Activation or Flade potentials of Cr-Ni-Fe alloys in 1.28N deaerated H_2SO_4, 25°C.

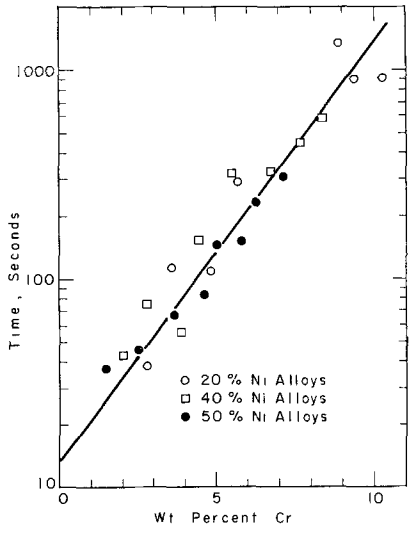

Fig. 7. Relation of Cr content of Cr-Fe-Ni alloys to time for breakdown of passivity in 1.28N deaerated H_2SO_4, 25°C.

bending of the curve both at low and high Cr compositions with relatively steep rise in the region of the critical Cr composition.

Time t_0 in seconds required for passivity to break down increases with Cr content, as Fig. 7 shows, in accord with the approximate relation $\log t_0 = 0.2$ (% Cr) + 1.15. The recorded data are for the 20, 40, and 50% Ni alloy series where the time held at the passive potential in each instance was 15-20 sec. Values for the 60% Ni series also fall on the best straight line through all the points but with greater scatter in the 1 to 3% Cr range. It is concluded that without any Cr, the median life of the passive film in 1.28*N* H_2SO_4 is about 14 sec, which is consistent with the observed behavior of passive iron, including probably also the Fe-Ni alloys. The prolonged life of the passive film as Cr content increases is consistent with the more active values of the Flade potential for higher Cr alloys, which, as mentioned before, parallel increased stability of passivity.

Discussion

Major changes in the slope of critical current densities plotted with respect to per cent Cr presumably can be interpreted in terms of a more protective oxide film initiating at the critical Cr compositions, or alternatively in terms of a stronger bond between discharged OH^- (or O_2) and the base metal, leading in either case to a passive film. A stronger bond between adsorbate and adsorbent would be expected to occur for compositions in which the *d* orbitals of Cr are uncoupled. Under such conditions, corresponding to Cr compositions above the critical value, the observed critical current density is low and tends to change only slightly with increasing % Cr, as shown in Fig. 2 through 5. For compositions corresponding to coupled *d* orbitals of Cr, critical current densities are much higher and the change with alloy composition is greater.

Although a passive film hypothesized to consist of metal oxide may meet the immediate *qualitative* requirements for an explanation of critical Cr compositions in the stainless steels, no quantitative evaluation has been offered by proponents of this

Table I. Calculated values for critical % Cr for passivity in Cr-Ni-Fe alloys

% Ni	Donor electrons from Fe only	Ni only	Fe and Ni
20	9.6%	3.3%	12.5
40	7.2	6.5	12.9
50	6.0	8.2	13.2
60	4.8	9.8	13.4

viewpoint. On the other hand, an evaluation is possible in terms of the electron configuration theory which proposes that the vacant surface *d* orbitals of Cr should be completely coupled by electrons from Fe at 12 wt % Cr or less in the Cr-Fe alloys, or when the weight ratio of Cr/Fe equals 12/88. Assuming that this ratio is maintained in the Cr-Ni-Fe alloys, the following expression is derived for critical per cent Cr for passivity assuming electrons donated only by Fe: Crit. % Cr = 12/88 (100 − Crit. % Cr − % Ni) or Crit. % Cr = 0.120 (100 − % Ni).

On the other hand, if the surface *d* orbitals of Cr are coupled by electrons donated from Ni only, the corresponding value is: Crit. % Cr = 14/86 (% Ni), where 14/86 is the empirical ratio for passivity observed for the Cr-Ni alloys based on observed critical current densities (4). A third case can be considered for which electrons are donated both from Fe and Ni. Using the same empirical ratios for Cr/Fe and Cr/Ni, this leads to: Crit. % Cr = 14/86 (% Ni) + 12/88 (100 − Crit. % Cr − % Ni) = 0.023 (% Ni) + 12.0.

The calculated values for critical Cr compositions are summarized in Table I, and are also indicated for the first 2 cases cited above on Fig. 2 through 5.

For 20% Ni alloys, it is seen in Fig. 2 that the major predicted change of slope at 9.6% Cr for the case of donor electrons from iron comes close to the observed change in slope at about 10.5% Cr. There is no observed change in slope at 3.3% Cr for the case of donor electrons from Ni. For 40% Ni, the predicted change of slope at 7.2% Cr for donor electrons from Fe again comes close to the observed value at 7.6% Cr. Because of the rapidly changing slope in this region, it is not possible to observe whether a change in slope also results from donor electrons from Ni predicted to occur at 6.5% Cr. Furthermore, it is not certain that the slight discontinuity in slope observed at 5% Cr is real.

For 50% Ni alloys, the observed change in slope at about 10% Ni lies to the right of the predicted values based on donor electrons from either Fe or Ni. The observed value, however, comes closer to the predicted value based on donor electrons from Ni equal to 8.2% Cr than it does to the value based on electrons from Fe. In this connection, some significance may attach to the fact that alloys at 50% Ni contain more Ni than Fe. It should be noted in Fig. 4 that a slight change in slope also occurs close to the value of 6% Cr predicted for donor electrons from Fe. This slight change of slope becomes more pronounced in the 60% Ni alloy series in Fig. 5 where the change can no longer be ascribed to possible variations of measurement. The predicted change based on donor electrons from Fe is at 4.8% Cr compared to an observed value of 4.5 to 5% Cr. The major change of slope at about 9.5% Cr now comes close to the predicted value of 9.8% Cr based on donor electrons from Ni. It appears, therefore, that in alloys containing less than 50% Ni, the major critical composition corresponds to electrons donated to Cr from Fe, whereas above 50% Ni, the critical composition corresponds to electrons donated by Ni.

There is no strong evidence that donor electrons come from both Fe and Ni, even though this might be expected on fundamental grounds. The predicted values of critical per cent Cr for donor electrons from both metals lie definitely to the right of the observed major changes in slope. It should be noted that any small changes in slope of critical current density as a function of composition in this higher chromium range fall within the experimental errors of measurement since the maximum change on the logarithmic scale as plotted amounts to only a few ma/cm^2. The same situation does not apply to changes of slope in the lower chromium composition range where deviations from a smooth curve through the observed points amount to tens or hundreds of ma/cm^2.

The primary features of the critical current density curves are described reasonably well, therefore, by the separate electron interaction between Cr and Fe distinct from interaction between Cr and Ni. Furthermore, the critical compositions in the ternary system approximate in each case the critical composition typical of the corresponding binary system. Further experiments are needed to establish whether similar relations can be expected in other passive alloy systems.

Acknowledgment

The authors are grateful for support of this research by the Shell Oil Company Foundation Inc.

Manuscript received April 13, 1960. This paper was prepared for delivery before the Houston Meeting, Oct. 9-13, 1960.

Any discussion of this paper will appear in a Discussion Section to be published in the June 1961 JOURNAL.

REFERENCES

1. H. H. Uhlig, *Z. Elektrochem.*, **62**, 700 (1958).
2. H. H. Uhlig, *Trans. Electrochem. Soc.*, **85**, 207 (1944).
3. Metals Handbook, p. 1261, A.S.M., Cleveland (1948).
4. A. Bond and H. Uhlig, *This Journal*, **107**, 488 (1960).
5. P. King and H. Uhlig, *J. Phys. Chem.*, **63**, 2026 (1959).
6. N. Tomashov, *Corrosion*, **14**, 229t (1958).
7. M. Stern, *This Journal*, **105**, 638 (1958).
8. H. Uhlig and P. King, *ibid.*, **106**, 1 (1959).
9. F. Flade, *Z. physik. Chem.*, **76**, 513 (1911).
10. H. Rocha and G. Lennartz, *Arch. Eisenhüttenw.*, **26**, 117 (1955).

Dissolution of Iron in Sulfuric Acid and Ferric Sulfate Solutions

A. C. Makrides[1a]

Metals Research Laboratories, Union Carbide Metals Company,
Division of Union Carbide Corporation, Niagara Falls, New York

ABSTRACT

Dissolution of iron in sulfuric acid solutions containing ferric sulfate is described by the superposition (without distortion) of the partial processes of hydrogen evolution, reduction of ferric ion, and anodic dissolution of iron. Reduction of ferric ion occurs at a diffusion-limited rate. Derived relations between electrode potential and the concentration of ferric sulfate, the linear flow velocity, and time are verified. A comparison of potential-current density curves obtained by polarization and from addition of ferric sulfate suggests that adsorption of ferric ion, if any, has no appreciable effect on iron dissolution

Corrosion or dissolution of metals in environments found in practice often involves a reaction proceeding at a rate limited by diffusion. For example, the corrosion rate of iron in nearly neutral aerated salt solutions is determined, to a large extent, by the rate of diffusion of oxygen to the iron-solution interface. Similarly, dissolution of nickel in acid solution is accelerated by oxygen which apparently is reduced as fast as it diffuses to the interface. A study of such systems is of interest therefore not only in general electrochemical theory but also in developing methods for minimizing corrosion in industrial processes.

It is essential in a study of a heterogeneous reaction proceeding at a diffusion-limited rate to control mass transport to the interface precisely and reproducibly. The rotating cylinder electrode (1-3) meets these requirements and possesses the advantage of a uniform mass transport rate over the whole of its lateral surface. An application of the rotating electrode to dissolution of iron in ferric sulfate solutions is presented here. The results are discussed on the basis of the Wagner-Traud postulate of superposition of partial processes together with elementary hydrodynamic considerations.

Electrochemistry of Iron Dissolution

Iron dissolves in aqueous acid solutions through an electrochemical mechanism (4-6). In moderately concentrated acid solutions and in the absence of reducible substances other than hydrogen ions, the partial processes are described by

$$\eta_c = -\, b_c \log \frac{i_c}{i_{oc}} \quad \text{for } 2H^+ + 2e^- \rightarrow H_2 \qquad [1]$$

and

$$\eta_a = b_a \log \frac{i_a}{i_{oa}} \quad \text{for } Fe \rightarrow Fe^{++} + 2e^- \qquad [2]$$

where the η's are overpotentials associated with current densities i_a and i_c and the i_o's are exchange current densities. At the steady state,

$$i_a = i_c = i_{corr} \qquad [3]$$

at a common electrode potential. The corresponding overpotentials are

$$\eta_c = E_{corr} - E_c^{rev} \qquad [4]$$

$$\eta_a = E_{corr} - E_a^{rev} \qquad [5]$$

where E_{corr} is the corrosion or dissolution potential and E^{rev} the reversible potential for each partial process.

If another reducible substance is introduced in the solution, the partial cathodic current is the sum

$$i_c = i_H + i_r \qquad [6]$$

where i_H is the partial current of hydrogen evolution and i_r the reduction current of the added oxidant. Only the case where i_r is equal to the limiting diffusion current, i_d, is considered here.

Equation [6] expresses the basic assumption of this development, viz., that the partial processes taking place during dissolution can be superimposed without interference. The only restriction imposed is that at the common electrode potential the sum of all cathodic processes equals the sum of all anodic processes. An electrochemical description of dissolution based on this assumption was given first by Masing (7) and in detail by Wagner and Traud (8).

Dependence of the dissolution potential on i_d.—The diffusion current depends on the concentration of oxidant and its diffusion coefficient, and on the flow rate. It is similar to an anodic current applied externally since it is independent of the electrode potential. This analogy is developed below.

If $i_d >> i_H$, then

$$i_c \cong i_d \qquad [7]$$

and the corrosion current for an electrode dissolving under these conditions is given by the diffusion current, while the potential is determined by the anodic polarization curve (Eq. [2]). Formally,

$$i_d = i_{corr} = i_a$$

and

$$\eta_a = E - E_a^{rev} = b_a \log \frac{i_d}{i_{oa}}$$

[1a] Present address: Research Department, Socony Mobil Oil Company, Inc., Dallas, Texas.

or

$$E = b_a \log \frac{i_d}{i_{oa}} + E_a^{rev} \qquad [8]$$

Therefore, it is possible to obtain the anodic polarization curve for the electrode by determining E as a function of i_d.

If $i_d \sim i_H$, both hydrogen discharge and oxidant reduction must be considered. Proceeding similarly to the above

$$E = b_a \log \frac{(i_d + i_H)}{i_{oa}} + E_a^{rev} \qquad [9]$$

with i_H a function of potential. Equation [9] reduces to [8] at sufficiently positive potentials where i_H becomes negligible.

Dependence of potential on concentration.—If the dependence of i_d on the concentration of oxidant, C_{ox} (moles cc^{-1}), is known, we can immediately write down E as a function of C_{ox}. Since under most conditions $i_d >> i_H$, Eq. [8] rather than [9] is used in what follows.

The diffusion-limited current is

$$i_d = n\mathbf{F}\frac{dj}{dt} = n\mathbf{F}kC_{ox} \qquad [10]$$

Here, j is the number of moles of oxidant transported across a unit area of metal-solution interface, t the time in seconds, n the number of equivalents per mole of oxidant, $\mathbf{F}$ Faraday's constant, and k the rate constant in cm/sec. For turbulent flow, and in excess of an indifferent electrolyte (constant ionic strength), k may be assumed independent of C_{ox} (9). From Eq. [8] and [10]

$$E = b_a \log C_{ox} + b_a \log \frac{n\mathbf{F}k}{i_{oa}} + E_a^{rev} \qquad [11]$$

Therefore, at constant k and i_{oa}, the potential is a linear function of the logarithm of the concentration of depolarizer with a slope equal to the Tafel slope of the anodic polarization curve.

Time dependence of the dissolution potential.—The change of E with time can be calculated from Eq. [8] and [10]. The potential of an electrode immersed in a solution originally C_{ox} in oxidant moves in a cathodic (active) direction as oxidant is depleted by reaction. The rate at which oxidant is used is given by Eq. [10]. From Eq. [8]

$$\frac{dE}{dt} = \frac{b_a}{2.30(i_d)}\frac{d(i_d)}{dt}$$

with i_{oa} independent of time. Noting that

$$dj = -\frac{V_s d(C_{ox})}{A}$$

where V_s is the solution volume and A the surface area of the electrode, we have from Eq. [10] for constant k (fixed flow),

$$\frac{d(i_d)}{dt} = n\mathbf{F}k\frac{d(C_{ox})}{dt} = -n\mathbf{F}k^2\frac{A}{V_s}C_{ox}$$

Substituting above and using Eq. [10]

$$\frac{dE}{dt} = \frac{-A}{2.30V_s}k\,b_a \qquad [12]$$

The potential is therefore a linear function of time with a slope given by Eq. [12]. If dE/dt and b_a are known, k can be obtained from Eq. [12].

Dependence of potential on hydrodynamic flow conditions.—Equations [8] and [10] yield a relation between E and k from which we may derive the dependence of the potential on various hydrodynamic parameters. Some useful relations are given below.

The rate constant of a diffusion-controlled reaction occurring at a cylindrical electrode in turbulent flow is

$$k = \frac{D}{\delta} = (C_1)\,V\,(R_d)^{-\beta}\,(Pr)^{-\gamma} \qquad [13]$$

where D (cm^2/sec) is the diffusion coefficient of the oxidant, δ (cm) the effective thickness of the boundary layer, and V (cm/sec) the linear velocity. R_d is Reynolds number, $d_i V/\nu$ with d_i (cm) the diameter of the electrode and ν (cm^2/sec) the kinematic viscosity, and Pr is Prandtl's number, ν/D. Equation [13] is based on an extended Reynolds momentum-mass transfer analogy (the Chilton-Colburn analogy) and is in good agreement with experiments [2] with $C_1 = 0.079$, $\gamma = 0.644$, and $\beta = 0.2$ to 0.3. As noted previously (3), β depends on the range of Reynolds numbers and on the roughness of the electrode. For hydrodynamically rough surfaces β approaches zero, while for smooth electrodes $\beta \cong 0.3$ at small Reynolds number ($\sim 10^3$) and $\cong 0.2$ at large Reynolds numbers ($\sim 10^5$).

Two useful relations can be derived from Eq. [13]. At constant C_{ox}, from Eq. [8] and [10]

$$E = b_a \log k + b_a \log \frac{n\mathbf{F}\,C_{ox}}{i_{oa}} + E_a^{rev}$$

And from Eq. [13]

$$E = b_a \log V^{(1-\beta)} + (\text{Constant}) \qquad [14]$$

Therefore, the potential varies linearly as the logarithm of the velocity at any constant C_{ox} with a slope of $b_a(1-\beta)$.

At constant potential, from Eq. [8],

$$i_a = i_d = \text{const}$$

And from Eq. [10] and [13]

$$(\text{Constant})_1 = n\mathbf{F}k\,C_{ox} = n\mathbf{F}\,(\text{Constant})_2\,V^{(1-\beta)}\,C_{ox}$$

Rearranging,

$$-\log C_{ox} = (1-\beta)\log V + (\text{Constant}) \qquad [15]$$

The value of β for a particular experimental arrangement can be obtained from a log-log plot of the oxidant concentration against the linear velocity at constant potential.

Relations [1], [2], [8], [10], [11], [12], [14], and [15] have been verified for iron electrodes in ferric sulfate solutions 0.5N in sulfuric acid.

Experimental

The experimental arrangement reported previously (3) was modified to reduce the concentration

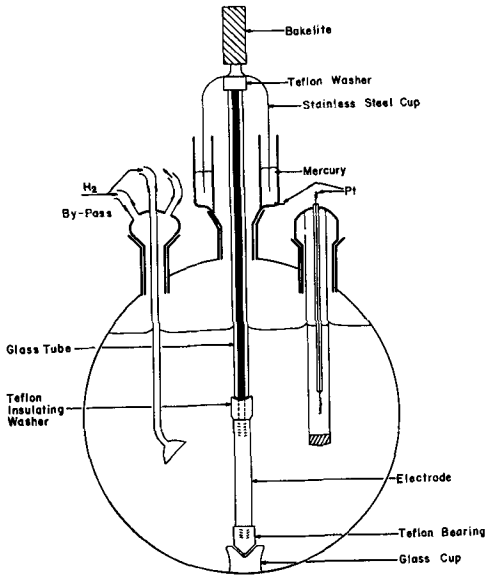

Fig. 1. Reaction cell

of oxygen in solution and to make it easier to vary the rotational speed.

The cell is shown in Fig. 1. The electrode, generally a cylinder 1 cm in diameter and about 4 cm long, was attached to a stainless steel shaft isolated from the solution with a glass tube. A Teflon washer gave a water-tight seal at the point of attachment of specimen to shaft and also isolated the top surface of the cylinder from solution. At the other end of the cylinder, a Teflon bearing riding in a glass cup fused to the cell minimized eccentric motion and at the same time isolated the lower surface of the cylinder from solution. Smaller electrodes, about 1 cm^2 in surface area, were used in polarization studies. In these cases, the Teflon washer at the top was extended to leave only about 0.3 cm of the electrode exposed to the solution.

The steel shaft ended in an inverted steel cup which rotated in mercury and sealed the system from the atmosphere. Electrical contact to the electrode was made through the mercury pool.

Hydrogen, purified over copper at 500°C and through sodium plumbate, concentrated sulfuric acid, triply distilled water, a drying tower, and a cold trap, was passed through the solution prior to a run and over the solution during a run.

Potentials were measured against S.C.E. and platinized platinum with a high impedance L&N pH meter connected to a multiple range, adjustable zero, Dynamaster Bristol recorder. Alternatively, a Rubicon potentiometer was used together with a galvanometer of 0.007 μa/mm sensitivity. A capillary probe with a bridge filled with solution of the same acid concentration was used in polarization measurements. The bridge led to an external S.C.E. A greaseless, closed, stopcock prevented mixing of (air-saturated) solution outside the cell with solution in the cell, but had sufficient conductivity when wetted with solution to maintain electrical contact. Constant current was obtained through appropriate resistances from two banks of three 45-v batteries arranged in series to give 135 v.

Greaseless ground glass joints were used to avoid possible contamination from lubricant. Although some air probably diffused into the cell, any contribution from dissolved oxygen to the cathodic current was negligible (see below).

Electrodes were rotated with a Bodine motor at speeds continuously variable up to 4000 rpm. The motor was electrically insulated from the electrode by a short Bakelite sleeve, friction-fitted on the upper part of the shaft (Fig. 1). Rotational velocities were measured to 0.2% with both a Jaquet tachometer (via an auxiliary shaft driven through an 18:1 reduction gear) and a stroboscope.

Through a ground glass joint (not shown in Fig. 1) small amounts of a concentrated solution of $Fe_2(SO_4)_3$ were added to the solution from a precision ($\pm$0.01 ml) buret equipped with a greaseless Teflon stopcock.

Analytical reagent-grade ferrous sulfate was recrystallized twice, washed with absolute alcohol and anhydrous spectroscopic-grade ether, and dried. Ferric sulfate was prepared from ferrous sulfate by oxidation with hot, concentrated sulfuric acid. Ferric sulfate solutions also were prepared from recrystallized C.P. ferric sulfate. Water was triply distilled, one distillation being carried out of dilute, alkaline potassium permanganate. The reaction vessel and all glass parts were cleaned with a saturated solution of potassium dichromate in concentrated sulfuric acid (cleaning solution) and rinsed with triply distilled water prior to use. Water drained uniformly and with zero contact angle from glass surfaces cleaned in this way.

Electrodes were prepared from Ferrovac E iron (99.92+ iron). They were abraded with 2/0 emery paper, washed with reagent-grade carbon tetrachloride, left to dry, etched in 1:3 HNO_3, washed with distilled water, etched in 1:3 H_2SO_4, and washed again.

Concentrations of various solutions were determined by analysis. The cell was thermostated at 30.0 $\pm$ 1°C.

Results and Discussion

Dissolution in Sulfuric Acid

In 0.52*N* H_2SO_4 the steady-state dissolution potential changed by less than 0.2 mv on varying the speed from zero to 4000 rpm (200 cm/sec). Concentration overpotentials therefore were negligible for both partial processes. Also it may be inferred that the partial current for reduction of any trace of oxygen present in solution was negligible in comparison with the corrosion current.[1]

Metal dissolution in acid alone is described by Eq. [1]-[5], i.e., by specifying the exchange current and Tafel slope for hydrogen evolution and for metal oxidation. These parameters were not always reproducible with iron. In general, electrodes belonged to one of two sets: (i) the steady-state corrosion potential was about —0.510 to —0.520 v vs.

[1] It was suggested (3) that an observed dependence of potential on rotational speed in solutions which were thought to be air-free was attributable to an electrokinetic effect. It is apparent that some dissolved oxygen must have been present in these solutions. As with other oxidants, the partial current for oxygen reduction increases and the dissolution potential becomes more positive when the flow velocity is increased.

S.C.E., the corrosion current about 400 μa/cm^2, b_a = 0.050 to 0.060 v, and b_c = 0.095 to 0.105 v; (ii) the corrosion potential was —0.495 to —0.505 v vs. S.C.E., the corrosion current about 2200 μa/cm^2, b_a = 0.030 to 0.040 v and b_c = 0.095 v. The hydrogen exchange current was considerably larger than in (i) (see below).

The time dependence of the corrosion potential differed for (i) and (ii). For set (i), E_{corr} increased from about —0.550 to —0.515 in about 3-4 hr and remained essentially constant at about this value. For set (ii), the drift continued, although at a smaller rate, for at least 24 hr. The corrosion current increased during this time to the value given above.

The cause of these differences is obscure. The rather wide variation in results obtained in electrochemical studies (4-6, 9-12) with iron and other metals of Group VIII, notably nickel, has been ascribed variously to impurities in solution, impurities in the metal, or to solution of hydrogen in the metal (10, 11). It is possible that some impurities, e.g., carbon and sulfur, have a pronounced effect on the kinetics of dissolution even if present in very small quantities. Since the system was designed primarily for the study of dissolution in solutions with oxidants, results for dissolution in acid alone are limited. The work reported for acid solutions is considered preliminary to a more extensive study with a more suitable experimental arrangement.

The variability of b_a made it necessary in most cases to obtain polarization curves prior to a run in order to compare anodic slopes observed directly and by addition of ferric sulfate. In other cases, the corrosion rate and corrosion potential were used to characterize the electrode.

Figure 2 gives anodic and cathodic polarization curves typical of electrodes belonging to set (i). The reversible H^+/H_2 potential was —0.275 v vs. S.C.E. Hydrogen overpotentials were

$$\eta_c = -(0.105) \log \frac{i_c}{2.2 \times 10^{-6}} \qquad [16]$$

with i_c in amp/cm^2. From $b_c = 2.30\ RT/\alpha_c F$, the transfer coefficient α_c, is 0.57. For the anodic polarization curve

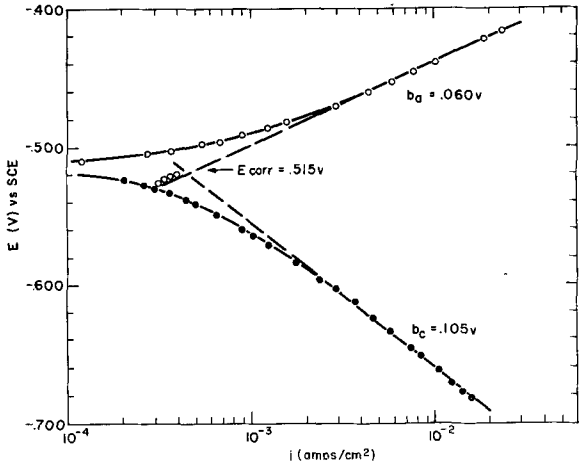

Fig. 2. Polarization diagram for iron in 0.52N H_2SO_4 at 30°C. The diagram is typical of set (i). The electrode was in solution for 10 hr E_{corr} = —0.515 v.

$$E = -0.320 + 0.060 \log i \text{ vs. S.C.E.} \qquad [17]$$

The reversible potential for Fe/Fe^{++} was not known, since activity coefficients for ferrous sulfate were not available. The standard potential for Fe/Fe^{++} is $E' = -0.68$ vs. S.C.E. With an estimate of $E_a^{rev} \cong -0.80$ ($a_{FeSO_4} \cong 10^{-4}$), $i_{oa} \cong 10^{-8}$ amp/cm^2 at this $FeSO_4$ concentration.

The dissolution rate may be obtained by extrapolation of either the anodic or cathodic polarization curves to the dissolution potential (6). At E = —0.515 v, η_c = —0.240 v and from Eq. [16]

$$i_c = i_{corr} = 4.1 \times 10^{-4} \text{ amp/cm}^2$$

A similar extrapolation of the anodic curve to E = —0.515 v yields $i_a = i_{corr} = 5.6 \times 10^{-4}$ amp/cm^2. Alternatively, following Wagner and Traud (8) and Stern (12), i_{corr} may be determined from the slope of the E vs. i_{appl} curve at small values of i_{appl}. If, for example, the electrode is polarized cathodically

$$i_{appl} = i_c - i_a \qquad [18]$$

For convenience, the steady-state dissolution potential (instead of the reversible potential) may be taken as the reference potential so that

$$i_c = i_{corr} \exp(-2.30\ \epsilon/b_c)$$
$$i_a = i_{corr} \exp(+2.30\ \epsilon/b_a) \qquad [19]$$

where $\epsilon = E - E_{corr}$. Substituting [19] in [18]

$$i_{appl} = i_{corr}\left[\exp\left(\frac{-2.30\epsilon}{b_c}\right) - \exp\left(\frac{2.30\epsilon}{b_a}\right)\right] \qquad [20]$$

Expanding around ϵ = 0, neglecting higher terms for small ϵ, and rearranging we obtain the equation given by Stern (12)

$$i_{corr} = \frac{b_a b_c}{2.30\ (b_a + b_c)\ (\epsilon/i_{appl})} \qquad [21]$$

Figure 3 shows a plot of ϵ vs. i_{appl} at small ϵ, from which $i_{corr} = 4.1 \times 10^{-4}$ amp/cm^2.

Figure 4 gives results typical of electrodes belonging to set (ii). The curves drawn through the open triangles were obtained 4 hr after immersion of the electrode in the solution, while the curves through the full triangles were obtained 24 hr after

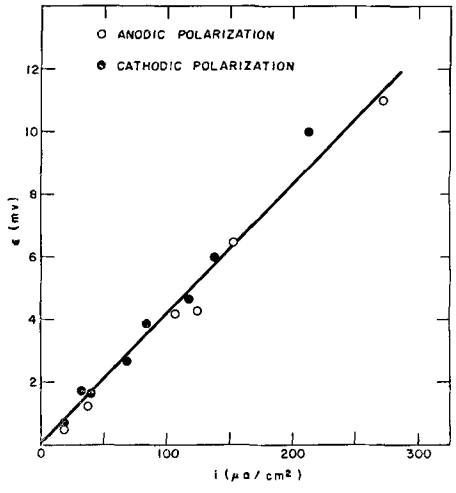

Fig. 3. Polarization data at small applied current densities in 0.52N H_2SO_4 at 30°C.

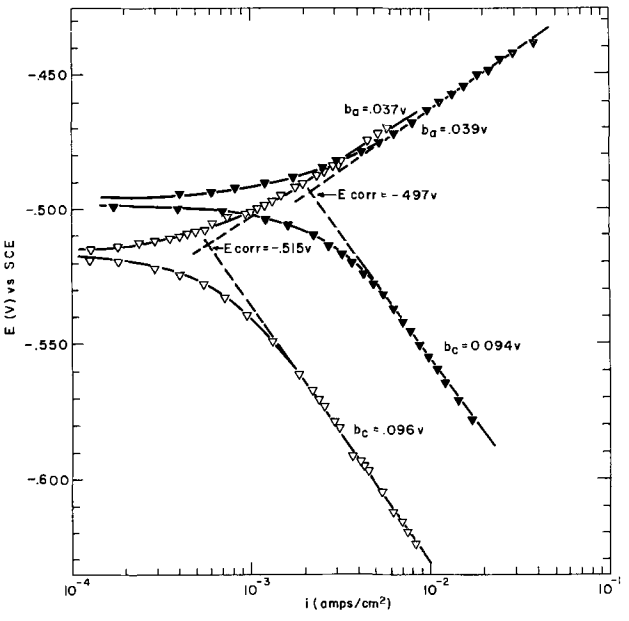

Fig. 4. Polarization diagram for iron in 0.52N H_2SO_4 at 30°C. The diagram is typical of set (ii). Curves through open points were obtained 4 hr after the electrode was in solution, and those through the full points after 20 hr in solution.

immersion. Hydrogen overpotentials for the two cases are

$$\eta_c = -0.096 \log \frac{i}{2 \times 10^{-6}}$$

and

$$\eta_c = -0.094 \log \frac{i}{1 \times 10^{-5}}$$

The anodic polarization curve was essentially unaltered during this time. The two sets of results are described by

$$E = -0.385 + 0.038 \log i \text{ vs. S.C.E.}$$

which yields on assumptions similar to those made above, $i_{on} \cong 10^{-11}$ amp/cm². Therefore, the shift of the corrosion potential to more noble values and the increased corrosion rate result essentially from the increase of the hydrogen exchange current.

Dissolution in Ferric Sulfate Solutions

The behavior of iron electrodes in ferric sulfate solutions paralleled that on anodic polarization. Data with electrodes belonging to set (i) are presented in Fig. 5 which shows the dependence of potential on the concentration of ferric sulfate over the range of velocities 50 to 200 cm/sec. The potential is a linear function of the logarithm of ferric ion concentration at potentials sufficiently removed from the corrosion potential. According to Eq. [11], the slope of the linear sections of these plots should be equal to b_a. Values of b_a determined in this way range from 0.057 to 0.066 v while 0.060 v was measured directly (see Fig. 2).

Rate constants at various velocities are required for comparison of results from anodic polarization and from addition of ferric sulfate. Rate constants were determined by withdrawing 5 ml portions of the solutions at various times and analyzing for iron. Equation [10] was used in the integrated form

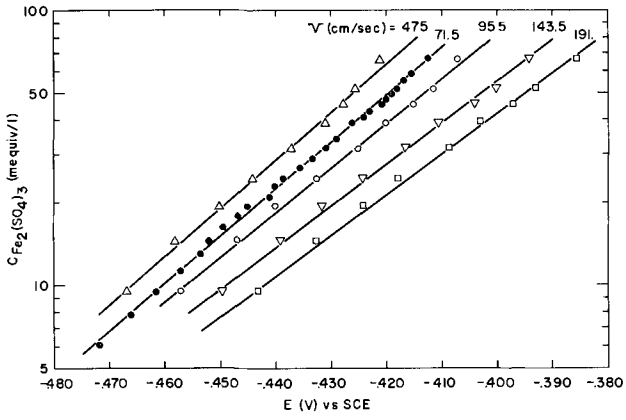

Fig. 5. Electrode potential as a function of ferric sulfate concentration at various linear velocities. The slopes are, from left to right, 0.057, 0.058, 0.062, 0.066, and 0.066 v.

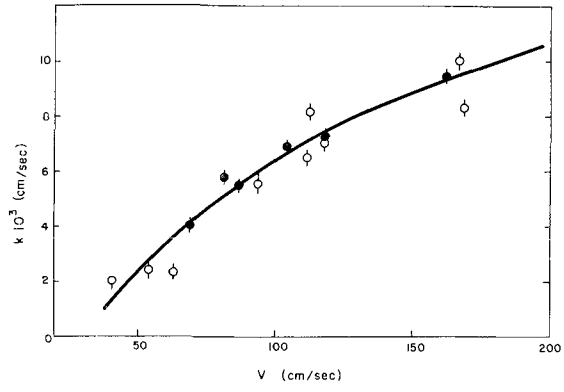

Fig. 6. First order rate constants as a function of velocity in 0.52N H_2SO_4 at 30°C. Values shown by open circles were calculated from the change (determined by analysis) of ferric ion concentration with time using Eq. [22]; solid circles were obtained from the time dependence of the dissolution potential and from the anodic Tafel slope (b_a = 0.060 v) using Eq. [12].

$$k = \frac{2.30\ V_s}{A\ t} \log (C°/C) \qquad [22]$$

Results are shown in Fig. 6. Rate constants cannot be computed from Eq. [13] since the diffusion constant of ferric ion in 0.5*N* H_2SO_4 solution is not known. From experimental values of k, with β = 0.20 (see below), and $\nu = 0.87 \times 10^{-2}$ cm²/sec, we find from Eq. [13] $D \cong 3 \times 10^{-6}$ cm²/sec. The estimated equivalent thickness of the boundary layer is then $\delta = D/k \cong 0.5 \times 10^{-3}$ cm at V = 100 cm/sec.

Potential-current density curves obtained by anodic polarization and from addition of ferric sulfate are compared in Fig. 7. Points obtained by the two methods differ by less than 10 mv at any current density.

Dependence of Dissolution Rate and Potential on Flow Velocity

According to [15], a plot of log C vs. log V at constant potential is linear with a slope of $(1-\beta)$. Data from Fig. 7 are plotted in Fig. 8 at E = const = — 0.420 v vs. S.C.E. Over the limited range of velocities used (50-200 cm/sec), $(1-\beta)$ = 0.80 or β = 0.20. Using this value for β, it is expected from Eq. [14] that a plot of log V vs. E at constant C is linear with a slope of 0.80 b_a. Figure 9 gives such

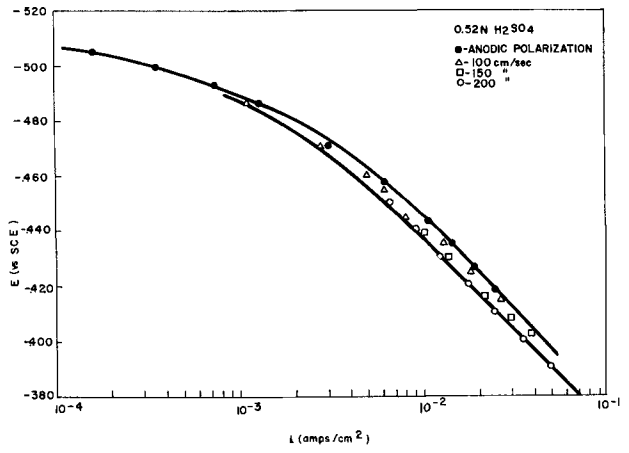

Fig. 7. Comparison of anodic curves obtained directly and by addition of $Fe_2(SO_4)_3$ for electrodes of set (i).

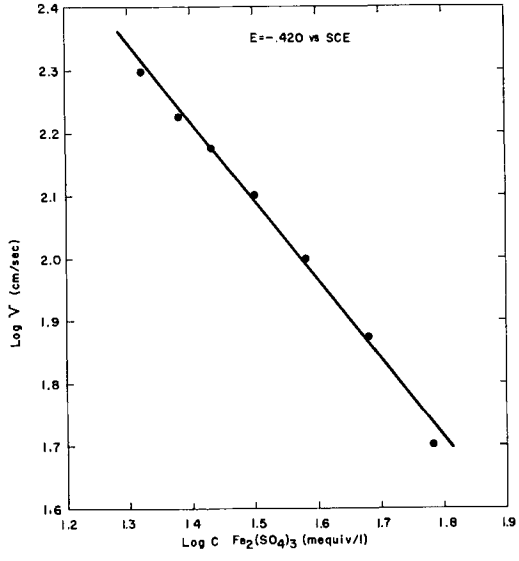

Fig. 8. Plot from data given in Fig. 5 at constant potential

plots for an electrode having a mean value of b_a = 0.060 v ($E_{corr} = -0.521$) at 34.6, 46.1, and 67.5 mequiv/l of $Fe_2(SO_4)_3$. The observed mean slope of 0.044 is in good agreement with a calculated value of 0.048 v.

Time Variation of Potential

The change of potential with time at various flow velocities is given in Fig. 10. From the slope, dE/dt, and with b_a = 0.060 v, rate constants were obtained from Eq. [12]. These are shown as solid circles in Fig. 6. The good agreement with k's found by analysis confirms the validity of Eq. [12].

Electrodes of set (ii).—Figure 11 shows the dependence of potential on ferric ion concentration for electrodes belonging to set (ii). The slope of the linear section of the curve is 0.040 v. Results were similar to those described above. The smaller Tafel slope of the anodic curve led however to relatively smaller changes of potential.

General Discussion

Although the anodic reaction for dissolution of iron in sulfuric acid solution followed a Tafel relation, both the slope and the exchange current varied

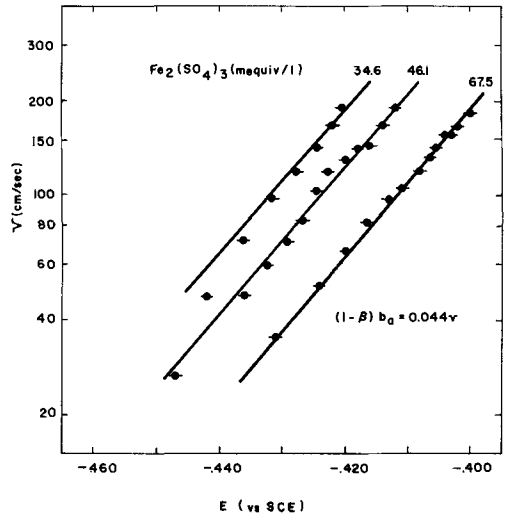

Fig. 9. Dependence of electrode potential on velocity at constant $Fe_2(SO_4)_3$ concentration in 0.52N H_2SO_4 at 30°C.

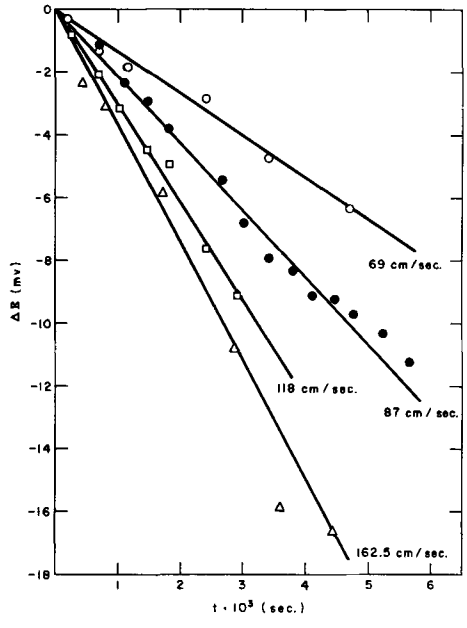

Fig. 10. Change of potential with time at various flow velocities.

within rather wide limits. As noted above, Tafel slopes were generally either about 0.035 or 0.060 v; exchange currents were smaller by 10^3 for electrodes having the former slope.

Reported Tafel slopes for the Fe/Fe^{++} couple also vary widely. Roitar, Jura, and Polujan (13) found for "electrolytic iron" in 1.25M $FeSO_4$, b_a = 0.060 or 0.075 v, depending on the history of the electrode, with $i_o \cong 3 \times 10^{-6}$ amp/cm². Stern and Roth (14) reported b_a = 0.068 v in 4% NaCl at pH of 1.5. Okamoto, Nagayama, and Sato (11) found b_a = 0.10 with Armco iron in 0.3N H_2SO_4. Hoar and Hurlen (15) determined b_a = 0.030 and $i_o \cong 3 \times 10^{-11}$ amp/cm² in 0.5M $FeSO_4$ + 0.1M $NaHSO_4$. Bonhoeffer and Heusler (16) obtained b_a = 0.030 in perchlorate solutions, a value also reported by Kaesche (17) in similar solutions.

Pronounced time dependence of the anodic polarization curve is also generally observed and is frequently associated with an open hysteresis loop

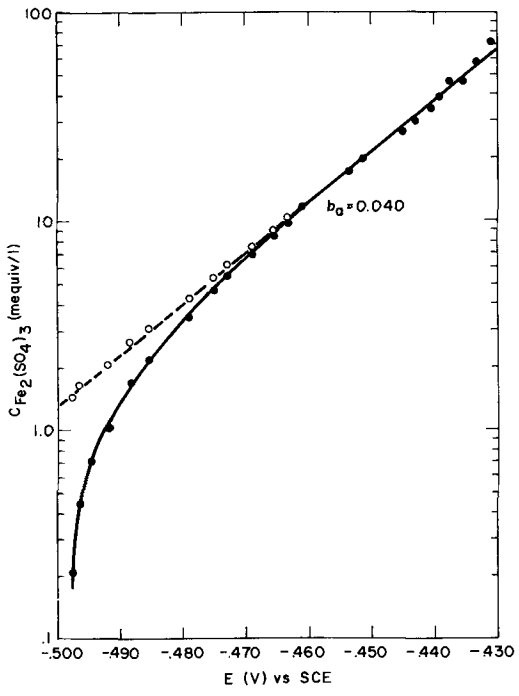

Fig. 11. Electrode potentials as a function of $Fe_2(SO_4)_3$ concentration at V = 58 cm/sec. Data are typical of electrodes of set (ii). Open circles were calculated from Eq. [27] as explained in text.

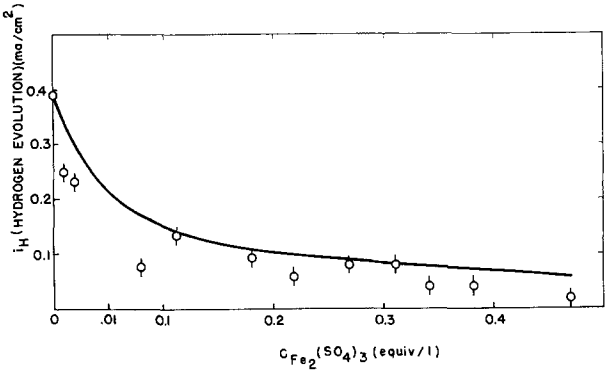

Fig. 12. Rate of hydrogen evolution as a function of $Fe_2(SO_4)_3$ calculated from Eq. [28]. Points are experimental average rates given in ref. (21).

(6, 11). The curve traced on decreasing the current density falls below the curve obtained on increasing the current, the corrosion potential being displaced after a cycle to a more negative value. A similar drift toward lower overpotentials, particularly at high current densities, was observed here. In obtaining anodic polarization curves, each current setting was held for about 1 min during which time the potential decreased by about 1 mv. The electrode returned to a potential 10-15 mv more negative than E_{corr} after anodic polarization and drifted to within a few millivolts of E_{corr} in about 15 min.

A number of hypotheses have been advanced to account for the anodic behavior of iron. It has been suggested repeatedly (4, 11, 18) that the extent of adsorption of atomic hydrogen on the surface of an iron electrode decreases with increasing (more noble) potential. It is possible to account for some of these effects on the assumption that an adsorbed film of hydrogen interferes with the rate of the $Fe \rightarrow Fe^{++}$ reaction. Alternatively, adsorption of hydroxyl ion and its variation with potential (19) have been postulated.

Anodic overpotentials for iron are relatively large, the exchange current being of the order of 10^{-8} -10^{-11} amp/cm^2. It is probable that small amounts of impurities have a pronounced effect on dissolution kinetics. One expects dissolution to proceed mainly at sites where metal cations are in states of higher energy than at the rest of the surface (20). These may be at subgrain boundaries, dislocations, edges of incomplete layers, etc. As ions from such sites dissolve, near neighbors are placed in positions energetically favored for dissolution. However, these sites are probably also preferred for adsorption of impurities. It is thus probable that impurities in quantity far less than a monolayer may have a large effect on the anodic partial reaction. Some impurities may be introduced from the dissolving electrode. Okamoto, Nagayama, and Sato (11), for example, suggest that sulfide ions produced from sulfur inclusions in Armco iron may be responsible for the anodic hysteresis loop. It is probable that the divergent results quoted above are a consequence of extraneous impurities and are not characteristic of clean iron electrodes. It should be noted, however, that impurities present in quantities sufficient to affect the anodic partial reaction may have a relatively small or even negligible effect on processes, such as reduction of ferric ion, which proceed over essentially the whole of the electrode surface.

Dissolution in Ferric Sulfate Solutions

Previous work (1, 3) has shown that reduction of ferric ion on iron and mild steel in acid solution proceeds at a diffusion-limited rate. The first order kinetics, the dependence of the rate on flow velocity, and the absolute magnitude of the rate constants ($\sim 10^{-3} - 10^{-2}$ cm/sec) are all in accord with the assumption that dissolution is limited only by the rate of diffusion of ferric ion to the interface.

It is in general possible to determine the anodic partial curve from the dependence of potential on the concentration of oxidant when the oxidant is reduced at a diffusion-limited rate (Eq. [11]). The question to be answered experimentally is whether the oxidant, ferric ion in this case, modifies the anodic partial curve or the reduction kinetics for hydrogen evolution.

The anodic partial curve is not changed by ferric ion. Although the anodic slope was variable, values obtained with the same electrode by anodic polarization and from the dependence of potential on the ferric ion concentration coincided closely. It may be concluded that ferric ion has no specific effect on the anodic partial curve.

The absence of specific effects is not surprising. If reduction occurs at a rate limited by diffusion, a concentration gradient of an equivalent thickness δ is established in the steady state.[2] If sufficient in-

[2] The equivalent thickness of the boundary layer is obtained by assuming that the concentration of the diffusing species changes linearly with distance from a value of zero at the interface to its bulk concentration at δ. The physical thickness of the boundary layer may be approximated with sufficient accuracy for the purpose of this discussion by δ.

different electrolyte is present, changes of ionic strength caused by ferric ion may be neglected. Ferric ion could then influence the kinetics of metal dissolution or of hydrogen reduction either by adsorption in the fixed part of the electrical double layer or through reaction with some intermediate formed in either process.

There is no apparent intermediate in the anodic process with which ferric ion could interact. At the same time, adsorption of ferric ion is unlikely since it is precisely in the region of the Helmoltz layer that its concentration approaches zero ($C \cong (10^{-5} C_{bulk}) \cong 10^{-6}$ to 10^{-7} equiv/l). The concentration gradient for ferrous ion is, of course, opposite to that for ferric ion. However, the results show that the local excess of ferrous ion had little effect on the anodic curve.

Ferric ion could modify the hydrogen evolution reaction (h.e.r.) by reacting with adsorbed hydrogen atoms formed when hydrogen is discharged. Interference effects, if any, will be significant in the neighborhood of the corrosion potential. At more positive potentials the h.e.r. reaction becomes negligible.

The two most likely mechanisms for the h.e.r. on iron are slow discharge and the adsorbed hydrogen-hydrogen ion reaction.[3] These may be written as

$$H_3O^+ + e \rightarrow H_{ads} + H_2O \qquad [23]$$

and

$$H_3O^+ + H_{ads} + e \rightarrow H_2 + H_2O \qquad [24]$$

with

$$H_2O + H_{ads} + Fe^{+++} \rightarrow H_3O^+ + Fe^{++} \qquad [25]$$

possible in the presence of ferric ion.

If we denote the rate by v, and if [23] is rate controlling, i.e., $v_2 > 10\ v_1$, the over-all rate of h.e.r. is unaffected by [25] in the range $i_d \sim V_3 \sim V_{h.e.r.}$. Similarly, if [24] is slow and [23] fast, again [25] is negligible for $V_{h.e.r.} \sim V_3$. In either case, the stationary concentration of H_{ads} is not changed to any appreciable extent by reaction [25]. Only if [23] and [24] are comparable in rate will reaction [25] have an appreciable effect on the h.e.r. It is shown below that no effect was detected.

It must be emphasized that the possible effects on the h.e.r. discussed above are in addition to the expected decrease in rate at the more positive potentials in ferric sulfate solutions. This decrease is, of course, allowed for in superposing partial processes.

It has been proposed (21) that ferric ion reduction and hydrogen evolution are competitive not because of indirect reduction (process [25] above) but through competition between ferric and hydrogen ions for available adsorption sites. The suggestion was based on an interpretation of the dissolution rate of mild steel in stagnant ferric sulfate solutions (21).

Let us examine the dependence of the dissolution rate of ferric ion concentration, particularly in the range $i_d \sim i_H$. The dissolution rate (equiv/cm²/sec) is

$$\text{(dissolution rate)}\ F = i_a = i_d + i_H$$

If we choose the dissolution potential in the absence of ferric ion as the reference potential, then

$$i_a = i_{corr} \exp\ (2.30\ \epsilon/b_a) \qquad [26]$$

or

$$\epsilon = b_a \log\ (i_a/i_{corr})$$

where i_{corr} is the dissolution rate in acid alone. But from $i_a = i_d + i_H$,

$$i_a = i_d + i_{corr} \exp\ (-2.30\ \epsilon/b_c) \qquad [27]$$

and substituting [26] into [27]

$$i_a = i_d + i_{corr}\ (i_{corr}/i_a)^{b_a/b_c}$$

from which

$$i_a - i_{corr}\ (i_{corr}/i_a)^{b_a/b_c} = i_d = nFk\ C_{Fe^{+++}} \qquad [28]$$

Possible interference effects may then be looked for (a) in the rate of reduction of ferric ion as a function of $C_{Fe^{+++}}$ and (b) in the rate of hydrogen evolution as a function of $C_{Fe^{+++}}$. We have already shown (22) that within the range 0.01 to 0.467 equiv/l for which data are given in (21), the rate of ferric ion reduction is proportional to the ferric ion concentration with an average rate constant of 1.75×10^{-4} cm/sec.[4]

The rate of hydrogen evolution is given in Eq. [28] by the second term on the left-hand side. From (21), $i_{corr} = 0.39$ ma/cm² and $b_a = 0.060$ v. The curve given in Fig. 12 was calculated using the value of k given above and assuming $b_c = 0.100$ v. The points shown are experimental values given in Table II of ref. (21). The curve lies somewhat above a "least squares" line but is in fairly good agreement with the average rates of hydrogen evolution found in (21).[5]

Equation [27] can be used to determine whether the cathodic partial reactions are additive. At any given concentration of ferric ion, the rate of hydrogen evolution can be calculated if it is assumed, as above, that the two processes are independent. Figure 11 shows the results of this calculation. Here, $i_{corr} = 390\ \mu$a/cm² at $E_{corr} = -0.500$ vs. S.C.E., and $b_c = 0.100$ v. For each concentration i_d was calculated from the rate constant ($k = 3.1 \times 10^{-3}$ cm/sec) and i_H was obtained from the second term on the r.h.s. of Eq. [27]. Anodic currents obtained in this way were converted to equivalent concentrations of ferric ion and are shown as open circles on the same figure. They fall, within experimental error, on the line extrapolated from high concentrations of ferric ion ($i_d >> i_H$). It may be concluded that hydrogen evolution and ferric ion reduction do not interfere with each other.

Conclusions

An analysis of changes of electrode potential with concentration and flow velocity shows that the Tafel line for the Fe/Fe^{++} couple is unaffected by ferric ion. Specific effects expected if adsorption of ferric ion took place are not found. The overpotential curve

[3] It is not likely that a combination of absorbed hydrogen atoms is the slow step for the h.e.r. on iron since the Tafel slope is about 0.1 v.

[4] For the experimental conditions employed in (21), a dependence of the reduction rate on $(C_{Fe^{+++}})^{5/4}$ is expected (23). However, experimental scatter made it impossible to distinguish between a 5/4 power and linear dependence (see (22)).

[5] A decrease of the rate of hydrogen evolution with time was observed in (21). The experimental points shown are, therefore, average rates over 5 hr.

for hydrogen evolution is also apparently unaffected but the experimental evidence is less extensive in this case. These conclusions may be extended to other systems where reduction occurs at a rate limited by diffusion. In general, it is unlikely that the oxidant will have a specific effect, either on the anodic reaction or on hydrogen evolution, since its concentration approaches zero at the interface. Specific effects may appear however if the reduction products adsorb on the electrode.

Acknowledgment

The author thanks Mr. R. Aikin who skillfully assisted in the experimental part of this work. Helpful discussions with Dr. M. Stern are gratefully acknowledged.

Manuscript received March 23, 1960.

Any discussion of this paper will appear in a Discussion Section to be published in the June 1961 JOURNAL.

REFERENCES

1. C. V. King and W. H. Catchart, *J. Am. Chem. Soc.*, **59**, 63 (1937); C. V. King and P. L. Howard, *Ind. Eng. Chem.*, **29**, 75 (1937); C. V. King and L. Weidenhammer, *J. Am. Chem. Soc.*, **58**, 602 (1936); M. B. Abramson and C. V. King, *J. Am. Chem. Soc.*, **61**, 2290 (1939); C. V. King, "Pittsburgh International Conference on Surface Reactions," p. 5, Corrosion Publishing Co., Pittsburgh (1948).
2. M. Eisenberg, C. W. Tobias, and C. R. Wilke, *Chem. Eng. Progr.*, **51**, [16] (1955); *This Journal*, **101**, 306 (1954).
3. A. C. Makrides, N. Komodromos, and N. Hackerman, *This Journal*, **102**, 363 (1955); A. C. Makrides and N. Hackerman, *ibid.*, **105**, 156 (1958).
4. O. Gatty and E. C. R. Spooner "The Electrode Behaviour of Corroding Metals in Aqueous Solutions," p. 253, Oxford (1938) (and references therein).
5. K. Bonhoeffer and W. Jena, *Z. Elektrochem.*, **56**, 585 (1952).
6. M. Stern, *This Journal*, **102**, 609 (1955).
7. G. Masing "Dic Korrosion Metallischer Werkstoffe," by O. Bauer, O. Kröhnke, and G. Masing, Vol. 1, p. 45, Leipzig (1936) [quoted by C. Wagner and W. Traud, see ref. 8].
8. C. Wagner and W. Traud, *Z. Elektrochem.*, **44**, 391 (1938).
9. J. N. Agar, *Discussions Faraday Soc.*, **1**, 26 (1947).
10. A. M. Azzam, J. O'M. Bockris, B. E. Conway, and H. Rosenberg, *Trans. Faraday Soc.*, **46**, 918 (1950); J. O'M. Bockris and E. C. Potter, *J. Chem. Phys.*, **20**, 614 (1952).
11. G. Okamoto, M. Nagayama, and N. Sato, "International Committee of Electrochemical Thermodynamics and Kinetics" 8th Meeting Madrid 1956, p. 72, Butterworths (1958).
12. M. Stern, *Corrosion*, **14**, 440 (1958).
13. W. Roitar, W. Jura, and E. Polujan, *Acta Physichochim.*, **10**, 389 (1939).
14. M. Stern and R. M. Roth, *This Journal*, **104**, 390 (1957).
15. T. P. Hoar and T. Hurlen, "International Committee of Electrochemical Thermodynamics and Kinetics," 8th Meeting Madrid 1956, p. 445, Butterworths (1958).
16. K. Bonhoeffer and K. Heusler, *Z. Phys. Chem.*, **8**, 390 (1956).
17. H. Kaesche, *Z. Elektrochem.*, **63**, 492 (1959).
18. K. Bonhoeffer, Paper presented at ECS Meeting, San Francisco, April 30, 1956.
19. K. E. Heusler, *Z. Elektrochem.*, **62**, 582 (1958).
20. T. P. Hoar, "Modern Aspects of Electrochemistry, No. 2", J. O'M. Bockris, Editor, p. 270, Academic Press, New York (1959).
21. H. C. Gatos, *This Journal*, **103**, 286 (1956).
22. A. C. Makrides, *ibid.*, **103**, 706 (1956).
23. C. Wagner, *J. (and Trans.) Electrochem. Soc.*, **95**, 161 (1946).

Inhibition of Metal Dissolution by Ferric Sulfate

A. C. Makrides and Milton Stern

Metals Research Laboratories, Union Carbide Metals Company,

Division of Union Carbide Corporation, Niagara Falls, New York

ABSTRACT

Iron-chromium alloys are passivated in acid solution at a critical ferric sulfate concentration which depends on acid normality and flow velocity. Smaller concentrations of ferric ion increase the dissolution rate of active electrodes by providing a cathodic partial process occurring at a diffusion-limited rate. Once passivity is achieved, however, considerably less than the critical ferric ion concentration is required to maintain the electrode passive. The dependence of the electrode potential on the concentration of ferric ion is quantitatively related to the anodic polarization curve of the electrode. Polarization curves obtained in the active region coincide with curves derived from studies with ferric ion. The inhibitor concentration required to produce passivity is directly proportional to the anodic critical current density, while the primary passive potential is not changed by ferric ion. These results suggest that adsorption of ferric ion is not responsible for inhibition by this ion.

A number of oxidizing substances inhibit metal dissolution by inducing a transition from the active to the passive state (1). A characteristic electrochemical difference between the action of these substances and that of nonoxidizing inhibitors is the change of electrode potential which they produce. Oxidizing inhibitors displace the mixed potential in the positive (noble) direction by about 1 v, while nonoxidizing inhibitors produce changes which may be of either sign and which rarely exceed 0.1 v.

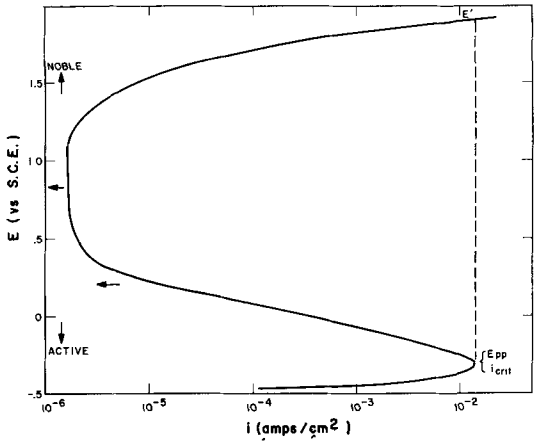

Fig. 1. Schematic polarization curve typical of iron-chromium alloys (series 400 stainless steels). Dashed curve shows transition to oxygen evolution with constant current source. Full curve is obtained in a potentiostatic experiment. E_{pp} is the primary passive potential and i_{crit} the critical current density. Arrows at left indicate decreasing current with time in this potential region.

It is generally agreed that nonoxidizing inhibitors reduce the dissolution rate by forming an adsorbed film at the metal-solution interface (2). Conflicting mechanisms have been proposed for inhibition by oxidizing substances. It has been suggested (3) that oxidizing inhibitors induce passivity by adsorption. It is possible however to give an account of inhibition in which specific effects, such as expected from a model postulating adsorption, are not assumed (1). A study of inhibition by ferric ion was carried out to determine whether specific effects are, in fact, present. As shown below, the results are consistent with the generalized description given in (1). It may therefore be concluded that inhibition is not related to adsorption of ferric ion.

Passivating inhibitors.—The anodic polarization curve of a number of common metals and alloys (1, 4, 5) is of the general type shown in Fig. 1. The full curve is the result of a potentiostatic and the dashed curve of a galvanostatic experiment.

With no applied current, the electrode dissolves at some rate i_{corr} corresponding to a mixed potential E_{corr}. If the electrode is polarized anodically with a constant current source, the rate of the anodic partial reaction increases smoothly with potential until at some current i_p a large, discontinuous potential jump occurs (from E_{pp} to E' on the diagram). Oxygen evolution takes place at E'. However, if a polarization curve is obtained by controlling the potential and allowing the current to vary, potentials intermediate between E_{pp}, the primary passive potential (6), and E' are attainable. At first, the steady-state current decreases in this potential region. After some low value is reached, it becomes more or less independent of potential over an interval of several tenths of a volt. Oxygen is again evolved at sufficiently positive potentials.

In general, several hours are required to achieve a steady state at potentials more positive than E_{pp}. In some cases time dependent results are also observed at potentials somewhat more negative than E_{pp}.

The reversible potential of a redox couple whose oxidized form is an inhibitor lies in the passive potential region. Since a mixed potential in the passive region can be maintained with such redox couples, stable inhibition (small dissolution rate) is observed when the metal is passivated either externally or by the added redox couple. The redox couple may displace the potential to the passive region when its reduction rate exceeds some current equivalent i_p'.

A specific effect by an inhibitor can be detected experimentally by comparing anodic polarization curves with and without inhibitor. If the inhibitor alters the anodic reaction in some specific way, then at any given potential the anodic partial current will be less than that indicated by the anodic curve determined in the absence of inhibitor. If this is the case, one expects i_p to differ from i_p'. Further, the potential, say E_{pp}', at which the inhibitor induces a transition to a passive state should also differ from E_{pp}. If, on the contrary, the inhibitor has no specific effect, the anodic partial current will depend only on the potential. Therefore, $i_p' = i_p$ as well as $E_{pp}' = E_{pp}$. This study was directed toward determining these quantities with and without ferric sulfate.

Experimental

Previous work (7, 8) established that ferric ion is reduced on iron and mild steel at a rate limited only by diffusion. Since it appeared probable that this would also be true for the iron-chromium alloy used here, it was essential to control the rate of mass transport to the interface precisely and reproducibly. A rotating, cylindrical electrode was chosen since it satisfied these requirements and possessed the advantage of a uniform mass-transport rate over the whole of its lateral surface.

The experimental arrangement was described in detail previously (8). Briefly, electrodes of various projected surface areas were rotated at equivalent linear velocities up to 200 cm/sec in hydrogen- or argon-saturated sulfuric acid solutions. Small amounts of a concentrated solution of ferric sulfate were added from a precision buret.

Only glass and Teflon were in contact with solution. Greaseless ground glass joints were used to avoid possible contamination from lubricant.

Ferric sulfate was prepared from ferrous sulfate by oxidation with hot, concentrated sulfuric acid. Solutions were also prepared from recrystallized C. P. ferric sulfate. Water was triply distilled, one distillation being from dilute, alkaline potassium permanganate. The reaction vessel and all glass parts were cleaned with a saturated solution of potassium dichromate in concentrated sulfuric acid (cleaning solution) and rinsed with triply distilled water prior to use. Water drained uniformly and with zero contact angle from glass surfaces cleaned in this way.

Potentials were measured against S.C.E. and platinized through a high impedance L&N pH meter connected to a multiple-range, adjustable-zero, Dynamaster Bristol recorder. Alternatively, a Rubicon potentiometer was used together with a galvanometer of 0.007 μa/mm sensitivity. A capillary probe

with a bridge filled with solution of the same acid concentration was used in polarization measurements. The bridge led to an external S.C.E. A greaseless, closed stopcock prevented mixing of (air-saturated) solution outside the cell with solution in the cell, but had sufficient conductivity when wetted with solution to maintain electrical contact. Constant current was obtained through appropriate resistances from two banks of batteries, each consisting of three 45 v cells arranged in series to give 135 v.

Potentiostatic measurements were conducted with an Analytical Instruments Company potentiostat, an electromechanical device. It was necessary to use the same material for the test electrode and for a potentiostat reference electrode and to place the two electrodes in the same solution, since this potentiostat does not operate properly if a high impedance exists between the electrodes. Auxiliary electrodes of the same material as the test electrode were placed directly in the cell. Electrodes were cut from a bar of an iron-chromium alloy (stainless steel 410) of the following per cent composition: 12.39 chromium, 0.09 carbon, 0.44 manganese, 0.024 phosphorus, 0.022 sulfur, 0.27 silicon, 0.24 nickel, 0.07 molybdenum, and 0.12 copper. They were abraded with 2/0 emery paper, washed with reagent-grade carbon tetrachloride, left to dry, etched in 1:3 HNO_3, washed with conductivity water, etched in 1:3 H_2SO_4, and washed again.

Concentrations of various solutions were determined by analysis. The cell was thermostated at 30° ± 1°C.

Results and Discussion

General observations.—Electrodes were active in hydrogen-saturated sulfuric acid solutions with potentials in the neighborhood of −0.490 v *vs.* S.C.E. The corrosion potential increased with time at first, but drift became negligible (< 2 mv/hr) after about 3 hr of immersion. Electrodes were aged therefore for at least 3 hr before a run.

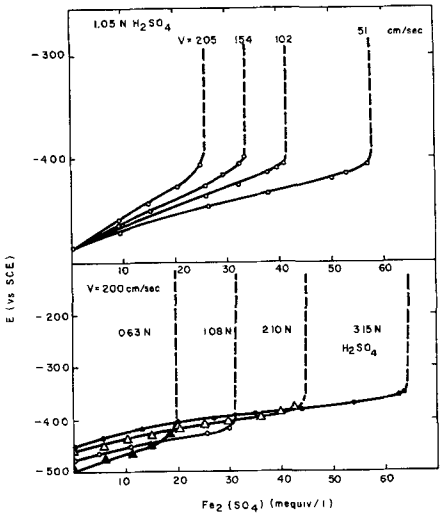

Fig. 2. Electrode potentiol as a function of ferric sulfate concentration at (top figure) various velocities in solutions of constant acidity and (bottom figure) in solutions of varying acidity at constant velocity. Dashed lines indicate discontinuous transition to potentials about +0.4 v vs. S.C.E. Tronsitions to passive potentials were irreversible (see text).

The potential moved in the anodic direction when ferric sulfate was added (Fig. 2). About a minute was required to establish a steady state after each increment in ferric ion concentration. A discontinuous transition from active to noble potentials occurred at a critical ferric ion concentration. The increase of potential was about 0.8 v. The critical concentration varied with flow velocity and acid normality as shown in Fig. 2.

Once passivity (noble potential) was produced, the electrode remained passive when the flow velocity was decreased. In the cases studied here, the electrode remained passive even when the rotational velocity was reduced to zero.

Passive specimens could be activated by cathodic polarization. The current required for activation increased with the amount of ferric ion in solution and with rotational velocity.

Detailed studies of the active region, of the transition to a passive potential, and of the passive potential region are presented below.

Active potential region.—Anodic polarization curves were obtained with a constant current source, with a potentiostat, and by following the potential as a function of ferric ion concentration.

For an electrode dissolving at a rate i_{corr} in a hydrogen-saturated acid solution

$$i_a = i_H = i_{corr} \qquad [1]$$

Here i_a is the partial anodic current corresponding to metal dissolution and i_H the partial cathodic current corresponding to hydrogen evolution. Both i_a and i_H are functions of potential.

If the electrode is polarized anodically by a constant current source, then

$$i_a = i_{appl} + i_H \qquad [2]$$

at a potential E more positive than the corrosion potential, E_{corr}. Since i_H decreases exponentially with potential, at sufficiently positive potentials

$$i_a \simeq i_{appl} \qquad [3]$$

where i_{appl} is the externally applied current. At sufficiently positive potentials, therefore, an anodic polarization curve obtained with a constant current source coincides with the anodic partial curve for the metal.

The same remarks apply to a polarization curve obtained with a potentiostatic device in this potential region.

If another reducible substance is introduced in the solution, the cathodic partial current, i_c, is the sum of the hydrogen evolution current and of the reduction current of the added oxidant. If reduction of oxidant occurs at a diffusion-limited rate, then

$$i_a = i_c = i_H + i_d \qquad [4]$$

where i_d is the limiting diffusion current and is independent of potential. At large flow velocities and large concentrations of oxidant, $i_d >> i_H$ and

$$i_a = i_c \simeq i_d \qquad [5]$$

A plot of potential against i_d under these conditions yields the anodic partial curve for the metal. Specific effects attributable to the oxidant (or to its reduction product) may be detected by comparing anodic partial curves obtained in this way with curves measured directly (Eq. [3]).

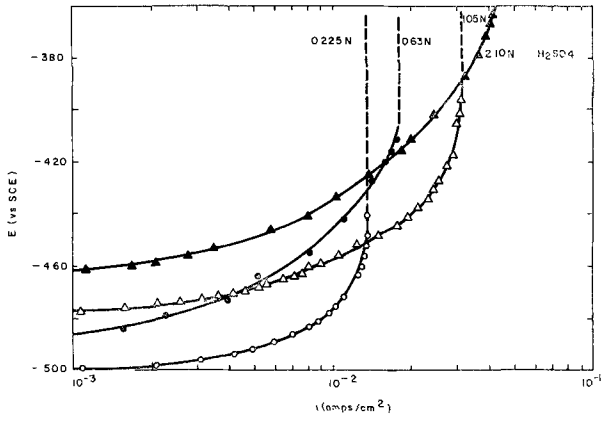

Fig. 3. Polarization curves with a constant current source in solutions of varying acidity. Dashed lines indicate transitions to potentials where oxygen is evolved ($> +1.0$ vs. S.C.E.).

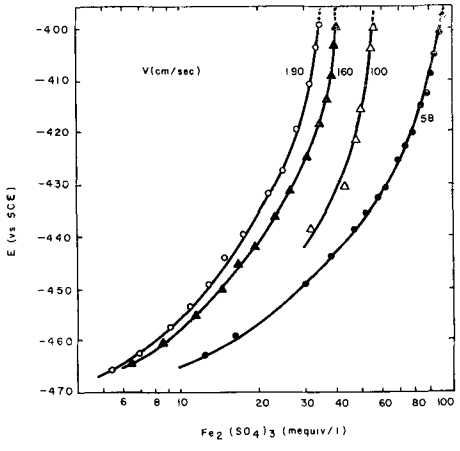

Fig. 4. Potential as a function of ferric sulfate concentration in N H_2SO_4 at various velocities.

Polarization curves obtained with a constant current source are shown in Fig. 3. Results were not time dependent in the active region, even at potentials close to the primary passive potential. Electrodes polarized for long periods (30 min) at a current density only 0.2 ma/cm^2 less than the critical did not show any tendency to become passive and the potential did not drift. In general, each current setting was held for 3 min, the same time interval used in runs with the potentiostat.

Figure 4 shows the dependence of the potential on concentration of ferric ion in the active region. The curves are similar to the polarization curves of Fig. 3. The primary passive potential, taken as the most positive potential observed before a transition to a passive state occurred, was essentially that found with a constant current source.

The reduction current for ferric ion must be known as a function of concentration and flow velocity in order to compare results of Fig. 4 with those of Fig. 3. If ferric ion is reduced at a diffusion-limited rate (see below)

$$i_d = \frac{n\mathbf{F}V_s}{A}\frac{dc}{dt} = n\mathbf{F}kC_{ox} \qquad [6]$$

Here n is the number of equivalents per mole of oxidant, $\mathbf{F}$ Faraday's constant, C_{ox} the concentration of oxidant, A the (projected) surface area, V_s the volume of solution, t the time, and k a rate constant. The rate constant depends on various hydrodynamic parameters but is independent of the nature of the electrode since the diffusion gradient is entirely within the liquid phase. Reaction rate constants used here were determined for the same experimental conditions from the dissolution rate of iron electrodes in ferric sulfate solutions (see ref. 8).

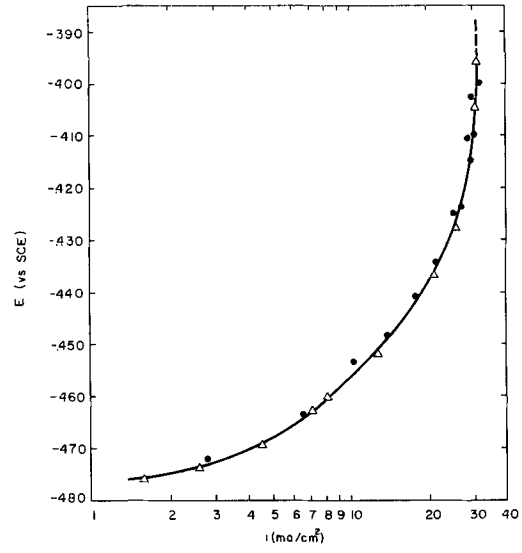

Fig. 5. Comparison of polarization curves obtained with a constant current source (triangles) and indirectly from the dependence of potential on $Fe_2(SO_4)_3$ concentration (circles). In the latter case, current densities were calculated from Eq. [6].

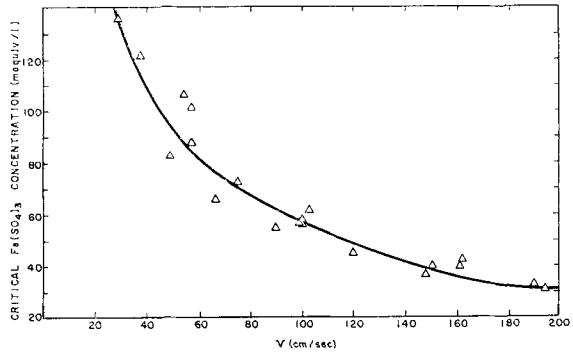

Fig. 6. Critical $Fe_2(SO_4)_3$ concentration required for passivity in N H_2SO_4 as a function of velocity. Points shown were obtained with six different electrodes.

Anodic polarization curves in N H_2SO_4 obtained with a constant current source and from Eq. [5] and [6], using constants given in ref. (8), are compared in Fig. 5. Essentially the same curve is obtained by either method.

Transition to a passive potential.—A discontinuous transition to a potential in the passive region occurs at a ferric ion concentration which depends on acid normality and flow velocity. The critical ferric ion concentration in N H_2SO_4 is plotted as a function of flow velocity in Fig. 6.

If the critical current density required for passivating the electrode is independent of the ferric ion concentration, then from Eq. [6]

$$i_p' = n\mathbf{F}kC_{crit} = \text{(constant)} \qquad [6a]$$

Table I. Comparison of the equivalent critical current density for passivity calculated from mass transfer and measured by anodic polarization

Type 410 stainless steel in N H_2SO_4 at 30±1°C

Velocity, cm/sec	Critical $Fe_2(SO_4)_3$ concentration, mequiv/l	k* cm/sec	Calculated equivalent critical current density, i_p', ma/cm²
55	107	2.8	29
58	102	3.2	31.5
58	90	3.2	28
67	66	4.0	25.5
75	71	4.6	31.5
90	55	5.7	30
100	57	6.4	35
103	61	6.6	39
120	44	7.6	32
148	36	8.8	30.5
161	41	9.3	37
162	43	9.4	39
182	30	10.0	29
190	34	10.4	34
194	31	10.5	31.5
			Average 32 ± 3

Measured critical anodic current, i_p
by constant current polarization: 31, 31, 28, 27, 32
Average 30 ± 2
In all cases $E_{pp} = E_{pp'} = -0.395 \pm 0.005$ *vs.* S.C.E.

* In 0.5N H_2SO_4 solutions.

where C_{crit} is the concentration of ferric ion required to produce passivity.

For turbulent flow, the rate constant is given by [see ref. (8)]

$$k = (\text{Constant})\ V\ (R_d)^{-\beta}\ (Pr)^{-\gamma} \qquad [7]$$

Here V is the linear flow velocity, R_d is Reynolds number, $\frac{Vd_i}{\nu}$, with d_i the diameter of the electrode and ν the kinematic viscosity, and Pr is Prandtl's number, ν/D, with D the diffusion coefficient of ferric ion. For the conditions employed here [see ref. (7)]

$$k = (\text{constant})\ V^{0.80}$$

Substituting in Eq. [6a]

$$C_{crit} = (\text{Const.})\ V^{-0.80} \qquad [8]$$

A log-log plot of C_{crit} against the velocity (Fig. 7) has a slope of −0.79 in good agreement with Eq. [8]. Equivalent current densities required for passivity were calculated from Eq. [6a] and are given in Table I. The equivalent current density for passivity is independent of the concentration of ferric ion and differs by less than 10% from the critical current density found by anodic polarization. The rate constants used in calculating i_p' were determined in 0.5N H_2SO_4. Rate constants in N H_2SO_4 are probably smaller, mainly because of a decrease of the activity coefficient of ferric ion. The higher mean value of i_p' is probably due to somewhat larger rate constants in 0.5 than in N H_2SO_4.

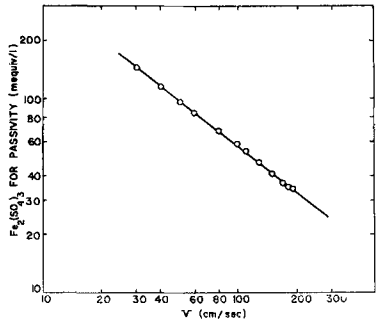

Fig. 7. Critical $Fe_2(SO_4)_3$ concentration for passivity as a function of velocity plotted according to Eq. [8]. The slope of the log-log plot is −0.79.

The conclusions drawn from Table I were confirmed by anodically passivating electrodes in solutions containing less than the critical ferric ion concentration. If ferric ion has no specific effect, the sum of the equivalent reduction current for ferric ion and of the applied current should be constant and equal to the critical current. Table II shows this to be true and also shows that the primary passive potential is not changed by ferric ion (see also Table I).

Table III compares equivalent current densities for passivity with ferric sulfate to critical current densities determined by anodic polarization for various acid normalities. Primary passive potentials are also given.

Passive potential region.—When the critical ferric ion concentration is exceeded, the electrode becomes passive with a mixed potential positive with respect to S.C.E. The potential depends on the ferric ion concentration and to a small extent on the normality of H_2SO_4, but is independent of flow velocity. It drifts slowly to more positive values, reaching a steady state after about 100 hr. At concentrations of the order of 0.010 equiv/1, the mixed potential is negative to the reversible Fe^{+++}/Fe^{++} potential, but it essentially coincides with the reversible potential at larger ferric ion concentrations (0.10 equiv/1).

The time dependence of the mixed potential in the passive region is probably caused by a decrease

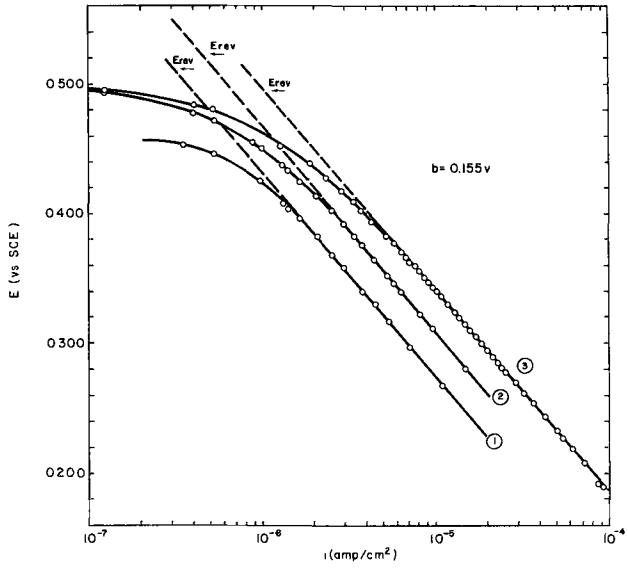

Fig. 8. Cathodic polarization curves of ferric sulfate on passive electrodes. Arrows indicate the reversible potential for the Fe^{+++}/Fe^{++} couple measured with a platinized platinum electrode. Curves 1 and 2 were obtained with solutions 0.0011M in ferrous ion and respectively 0.0138M and 0.0288M in ferric ion. For curve 3, $[Fe^{++}] = 0.005M$ and $[Fe^{+++}] = 0.066M$. Exchange currents are (from 1 to 3) 3.3, 4.3, and 8.1 × 10^{-7} amp/cm² while the Tafel slope is for all cases 0.155 v. The solution was N in H_2SO_4.

Table II. Comparison of measured critical anodic current density to the sum of the current density equivalent to ferric ion reduction and the applied anodic current

Type 410 stainless steel at 30 ± 1°C

V = 100 cm/sec; k = 6.4 cm/sec

H_2SO_4	$Fe_2(SO_4)_3$ concentration, mequiv/l	Equivalent $Fe_2(SO_4)_3$ reduction current, ma/cm²	Applied anodic current densiy, ma/cm²	Sum of equivalent and applied current densities, ma/cm²	Measured critical anodic current density, ma/cm²	Primary passive potential, E_{pp}, vs. SCE
0.63N	8.0	5	12	17		—0.405
	16.0	10	10	20		±0.005
	29.5	19	0	19	16	
	6.4	4	17	21		
	12.8	8	12	20		—0.410
	19.2	12	9.5	21.5		±0.005
	25.5	16	6.0	22		
	35.0	22	0	22	20	

Table III. Comparison of the equivalent critical current density for passivity calculated from mass transfer and measured by anodic polarization at various H_2SO_4 concentrations

Type 410 stainless steel at 30 ±1°C

Concentration H_2SO_4, N	Velocity, cm/sec	Critical $Fe_2(SO_4)_3$ concentration, mequiv/l	Calculated equivalent critical current density i_p', ma/cm²	Average measured critical current density i_p, ma/cm²	Primary passive potential with ferric sulfate, v vs. S.C.E.	Primary passive potential from anodic polarization, v vs. S.C.E.
0.225	—	—	—	13.5	—	—0.440
0.63	50	82	18			
	75	43	20			
	100	30	19			
	150	26	22	18	—0.415	—0.410
1.05	50-200	—	32*	30*	—0.395	—0.395
2.10	105	72	47			
	155	54	48			
	200	47	49	43	—0.370	—0.360
3.15	75	108	50			
	105	97	64	55	—0.345	—0.350

* Averages from Table I.

in the rate of oxidation of the passive electrode. In similar studies with type 304 stainless steel it was found (9) that the oxidation rate at constant potential was inversely proportional to time. This observation suggested a logarithmic oxidation law for the increase in thickness of the passive film. It is believed that type 410 stainless steel behaves similarly, although no detailed observations were made.

Cathodic polarization curves for reduction of ferric ion on passive electrodes were determined after the electrode had reached a steady state. Curves for various ferric ion concentrations are given in Fig. 8. At any given potential the current increases with ferric ion concentration. The Tafel slope is 0.155 v and is independent of ferric ion concentration. The Tafel curves measured here are similar to the ones reported by Stern (10) for 304 stainless steel.

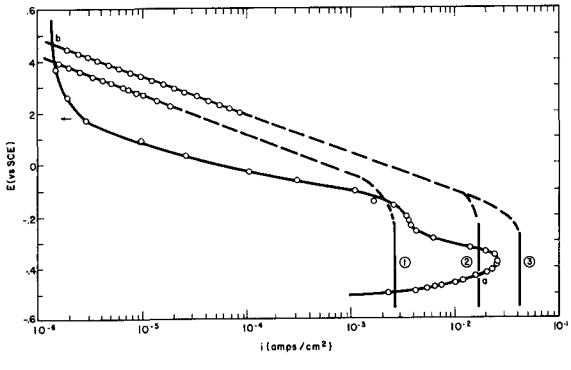

Fig. 9. Superposition of reduction curves for ferric ion and of the anodic polarization curve of Type 410 stainless steel in N H_2SO_4. Reading from curve 1 to 3, 0.010M Fe^{+++} at 55 cm/sec, 0.066M Fe^{+++} at 55 cm/sec, and 0.066M Fe^{+++} at 100 cm/sec. The upper sections of the reduction curves were determined by cathodic polarization on passive electrodes, while the solid lines at lower right are limiting diffusion currents obtained from Eq. [6] (see text). The dashed lines connecting the two are extrapolated from the passive region.

Potentiostatic curves.—Figure 9 gives a potentiostatic anodic polarization curve for type 410 stainless steel in N H_2SO_4. The primary passive potential is —0.380 v; the critical current density 28 ma/cm². These are to be compared with —0.395 v and 30 ma/cm² determined by polarization with a constant current source (see Table I). At each potential setting positive to E_{pp}, the current decreased rapidly at first and then changed slowly with time. The points shown were taken at 3-min intervals at which time the initial rapid change had come to an end.

Polarization curves for reduction of ferric ion are also shown in Fig. 9. The experimentally measured curves are connected with dashed lines calculated from the Tafel constants (slope and exchange current) and from the measured limiting diffusion current. It should be noted that the diffusion current is independent of the nature of the electrode and is a function only of the concentration and flow conditions.

General Discussion

Results shown in Figure 9 account completely for both the accelerating and the inhibitive effect of

ferric ion. Starting with a specimen freely corroding in acid solution, the figure indicates that ferric ion in concentration less than the critical increases the dissolution rate by providing an additional cathodic reaction which occurs at a rate limited by diffusion. The dissolution rate increases with increasing concentration and flow velocity until some critical current, i_p', is exceeded. This current is the same as the critical current found by anodic polarization (either potentiostatically or from a constant current source). When this critical current is exceeded, the electrode becomes passive with a dissolution rate of about 10^{-4} to 10^{-7} amp/cm^2.

At small concentrations and flow velocities two mixed potentials, indicated by points a and b on Fig. 9, are stable. The potential assumed by the system on addition of ferric ion depends on its previous state. Thus, if the electrode is originally active, ferric ion displaces the potential to (a), while if the specimen is already passive, potential (b) is stable. These observations account for the widely different concentrations required to produce and to maintain passivity. Thus, ferric ion causes a transition to a passive state only if its reduction rate exceeds i_p, which is in this case about 3 x 10^{-2} amp/cm^2. However, the reduction current necessary to maintain the electrode passive is only about 10^{-6} amp/cm^2, and decreases with time to probably less than 10^{-7} amp/cm^2.

An electrode in state (a) may be displaced to state (b) by polarization with an external source. When the sum of the applied anodic current and the equivalent reduction current exceed i_p (see Table II), the electrode undergoes a transition to a passive state which is maintained, since it is stable, even when the applied current is reduced to zero. Similarly, if the electrode is at potential (b), it may be activated by a cathodic current and remains active at (a) even after the applied current is reduced to zero. However, when the reduction rate of ferric ion exceeds the critical current density, the system is no longer bistable. In this case, the only stable mixed potential is in the passive region.

Figure 9 describes adequately the stainless steel-ferric sulfate system both at potentials more active than E_{pp} and in the neighborhood of the reversible Fe^{+++}/Fe^{++} potential. No experimental information is available, however, for ferric ion reduction at potentials between E_{pp} and about +0.1 v *vs.* S.C.E. An extrapolated curve is shown in this potential region in Fig. 9. This extrapolation is only approximate since the Tafel parameters for reduction are probably not the same on passive and active surfaces. It is likely that on active surfaces the exchange current is several powers of ten larger than on passive electrodes. An increase in exchange current shifts the reduction curve for ferric ion to the right, *i.e.* to lower overpotentials at any given current density. The dashed line must therefore be considered as giving a lower limit for the current at any given potential. The limiting current densities indicated by vertical solid lines in Fig. 9 are, of course, independent of the surface state of the electrode; their magnitudes were determined in separate experiments.

The starting point of this investigation was the attempt to determine whether adsorption of an oxidizing inhibitor, such as ferric ion, played a significant role in inhibition. If inhibitor ions are specifically adsorbed, changes in the composition of the surface state of the metal brought about by adsorption will be manifest in the anodic polarization curve of the metal. The results above clearly show that ferric ion produces no detectable change in the anodic behavior of stainless steel 410. It may be concluded that adsorption of ferric ion is unrelated to inhibition by this ion.

Acknowledgment

The authors thank Mr. R. E. Aikin for his assistance in the experimental part of this work.

Manuscript received March 23, 1960.

Any discussion of this paper will appear in a Discussion Section to be published in the June 1961 JOURNAL.

REFERENCES

1. M. Stern, *This Journal*, **105**, 638 (1958).
2. A. C. Makrides and N. Hackerman, *J. Phys. Chem.*, **59**, 707 (1955).
3. H. H. Uhlig and A. L. Geary, *This Journal*, **101**, 215 (1947).
4. N. Y. Bune and Y. M. Kolotyrkin, *Doklady Akad. Nauk S.S.S.R.*, **111**, 1050 (1956).
5. C. Edeleanu, *Metallurgia*, **50**, 113 (1954); *Nature*, **173**, 737 (1954).
6. N. D. Greene, Submitted to *This Journal*.
7. A. C. Makrides, N. Komodromos, and N. Hackerman, *This Journal*, **102**, 363 (1955); A. C. Makrides and N. Hackerman, *ibid.*, **105**, 156 (1958).
8. A. C. Makrides, *ibid.*, **107**, 869 (1960).
9. M. Stern, *ibid.*, **106**, 376 (1959).
10. M. Stern, *ibid.*, **104**, 600 (1957).

Correction

On page 666 of the August 1960 issue of the JOURNAL in the paper by S. Uno Falk "Investigations on the Reaction Mechanism of the Nickel-Cadmium Cell," the approximate values of the temperature coefficients of the emf and the electrode potentials should be:

dE/dT	dE_a/dT	dE_k/dT
Pocket cells	Pocket cells	Pocket cells
−0.00030	−0.00006	−0.00024
Sintered cells	Sintered cells	Sintered cells
−0.00018	−0.00014	−0.00004 v/°K

The Influence on the Oil Dielectric Strength of the Gas Pressure in Equilibrium with the Oil

Paolo Gazzana-Priaroggia and Giuseppe Palandri

Research Laboratories, Società Italiana Pirelli, Milan, Italy

ABSTRACT

A laboratory investigation of the influence of gas pressure on the electrical breakdown of thin oil, as used in oil-filled cables, was carried out at gas pressure between about 5 x 10^{-6} mm Hg and 1000 mm Hg. The test cell consisted of a glass container enclosing a platinum sphere gap (0.5 mm). Tests were carried out at ambient temperature. The results of this investigation showed that the dielectric strength of the oil is absolutely independent of the gas pressure, provided a perfect equilibrium is reached between the gas dissolved in the oil and the free gas remaining in the cell above the oil surface.

The influence of dissolved gas on the dielectric strength of oil has been discussed often and some data have been published giving the relation between oil dielectric strength and gas pressure (1, 2). These experimental results, of course, refer only to gas dissolved in the oil and not to gas in the form of bubbles or films.

This matter is not only of scientific but also of practical interest with regard to the problem of degassing oils used as impregnants of high-voltage electrical equipment. Published data, however, were not obtained under conditions of most interest to the present authors and they therefore undertook this study. For practical reasons it was decided to study the behavior of thin mineral oil as used in oil-filled cables under 50-cycles stress and to use dry air in the range of 5 x 10^{-6} mm Hg to about 1000 mm Hg.

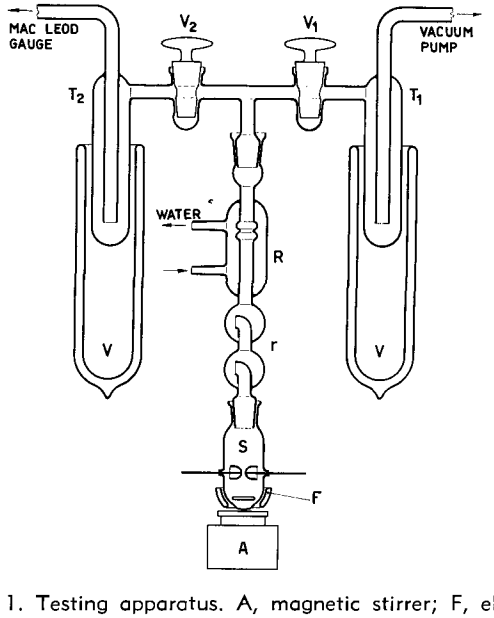

Fig. 1. Testing apparatus. A, magnetic stirrer; F, electric heater; S, sphere gap cell (platinum hemispheres 10 mm diameter, 0.5 mm gap); R, condenser; r, reflux condenser; V, Dewar vessels containing solid CO_2; T_1, T_2, cold traps; V_1, V_2, vacuum tight valves.

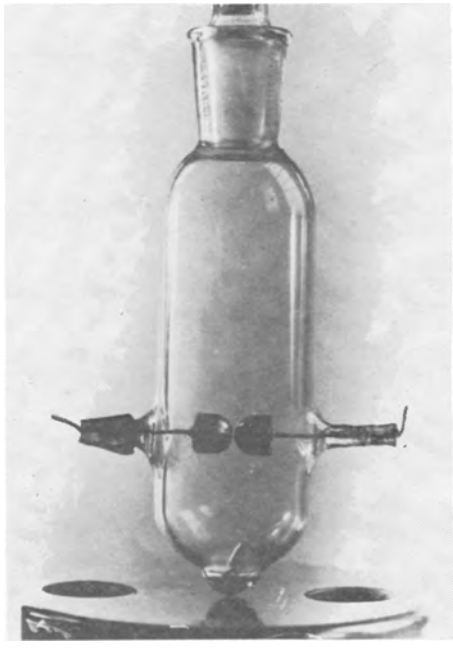

Fig. 2. Sphere gap cell

The apparatus is shown schematically in Fig. 1. Detail of the sphere gap cell S is given in Fig. 2.

Preparation of Tests

From the first test it appeared evident that to obtain sufficiently consistent results a certain cleanliness of the oil was necessary. To this end 55 cm^3 of clean, dry oil were introduced into the sphere gap cell. This oil had been filtered previously under vacuum through a glass filter. The sphere gap cell then was connected to the remainder of the testing apparatus. The oil was degassed by heating and stirring under vacuum at 110°C. To avoid fractionation of the oil while it was being degassed, the condenser R and the reflux condenser r were introduced into the vacuum circuit between the sphere gap cell S and the vacuum traps T.

The evacuation of the sphere gap cell was carried out by means of a diffusion pump for pressures below 10^{-3} mm Hg and with a mechanical pump, for

higher pressures. The absolute pressure was measured by means of a MacLeod gauge directly connected to the apparatus through a cold trap. To make sure that no moisture was present in the oil, the oil was degassed thoroughly and then saturated with dry air before reaching the desired pressure by pumping.

Each pressure was obtained and kept constant during the test by means of a vacuum limiter inserted in the vacuum circuit.

Test Results

The oil subjected to the investigation was the NJ 2 thin oil produced by Italian Standard Oil, having a viscosity of 25 centistokes at 20°C. 50-cycle a-c dielectric strength measurements were made as a function of the absolute pressure starting from 6 x 10^{-6} mm Hg, which was the highest vacuum obtainable with the present equipment, up to atmospheric pressure. The voltage was applied starting from 10 kv and then increasing it in steps of 10 kv/min.

From the first test it became evident that a considerable spread of results was obtained unless the greatest care was taken to make sure that the gas dissolved in the oil was in complete equilibrium with the free gas present in the sphere gap cell above the oil surface. If the saturation pressure of the oil was higher than the pressure of the free gas, the dielectric strength results obtained were considerably lower than the results obtained when a perfect equilibrium was reached. To overcome this difficulty, after the desired absolute pressure value was reached, the oil was left to cool down to the ambient temperature and kept under the desired pressure value with continuous stirring for about 24 hr before making any dielectric strength test.

To limit to as much as possible the influence of the static head of the oil, the oil level was kept at the minimum value necessary to obtain complete covering of the platinum spheres. This requirement determined the amount of 55 cm^3 of the oil which was mentioned before. The static head above the center point of the gap was 30 mm.

The results obtained are shown in the diagram of Fig. 3, in which average values and spread of results are indicated. For each pressure 10 different tests were made. No subsequent tests were made on an oil sample after the first discharge. This was done to avoid trouble due to gas evolution from the oil following breakdown since this could alter the pressure equilibrium. As can be seen, the average dielectric strengths lie on a straight line parallel to the abscissa, having on ordinate value of 400 kv/cm rms. All tests were carried out at ambient temperature (18°+25°C).

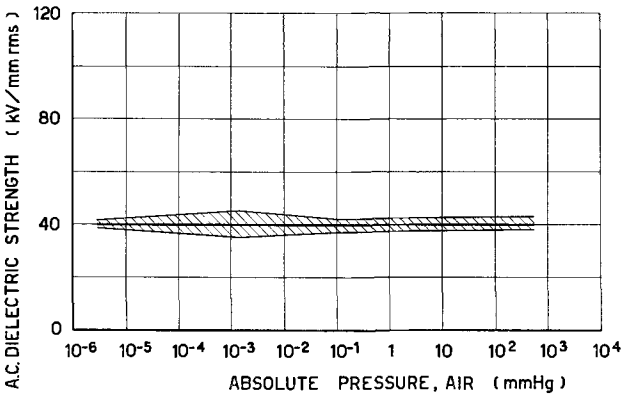

Fig. 3. A-C dielectric strength of thin cable oil vs. absolute air pressure.

Interpretation of Results

The values obtained for the average dielectric strength of about 400 kv/cm rms are lower than the results obtained by other investigators on pure liquid hydrocarbons under controlled physical conditions (3, 4). However, the consistency of the results obtained in the tests described in the present paper indicates that the tests were certainly governed by a well-determined breakdown mechanism. The conclusion could be that this mechanism differs from the breakdown mechanism ruling the tests described by the above-mentioned investigators.

It seems to the authors that an explanation may be found in the fact that the breakdown mechanism of absolutely pure dielectric liquids probably is ruled only by the movement of electrons, accelerated by the electrical field, which ionize the oil molecules; on the other hand the breakdown mechanism with which the tests described above are concerned probably is ruled by particles much bigger than electrons such as molecular aggregates or submicroscopic impurities, still accelerated by the electrical field but unable to ionize the oil molecules.

Two facts are of great importance in understanding these tests: (*a*) the breakdown is practically independent of the saturation pressure of the oil provided a perfect equilibrium is reached between the gas dissolved in the oil and the free gas above the oil surface; and (*b*) the breakdown strength is lowered when the saturation pressure is higher than the pressure of the free gas.

These two facts, combined with the assumption made above that particles much bigger than electrons are responsible for the breakdown of oils as used in industrial apparatus, have suggested the following theory:

A charged particle in suspension in the oil is accelerated by the electrical field and tends to cavitate the liquid in its wake; if the saturation pressure of the gas dissolved in the oil is equal to the pressure of the free gas acting on the oil surface, this tendency is very much reduced. Breakdown occurs when the movement of the particle becomes quick enough to create a cavitation in which gaseous ionization may take place.

Within the conditions of the present investigation it can be concluded that, when this particular state is reached, ionization occurs whatever the pressure of the gas dissolved in the oil, provided this is not higher than a pressure approximately equal to the atmospheric pressure.

Tests not reported in this paper indicate that when the gas pressure is higher than atmospheric the breakdown strength does not remain constant but tends to rise above 400 kv/cm rms. This suggests that in this condition gaseous ionization does not follow immediately when the cavitation onset level is attained but that a higher field is required to pro-

duce bubbles of such a dimension to cause ionization of the gas evolved in the cavity.

Acknowledgment

The authors are grateful to Pirelli S.p.A. for permission to publish the present paper and to Mr. Mazzola for carrying out the laboratory tests.

Manuscript received Feb. 23, 1960. This paper was prepared for delivery before the Philadelphia Meeting, May 3-7, 1959.

Any discussion of this paper will appear in a Discussion Section to be published in the June 1961 JOURNAL.

REFERENCES

1. F. M. Clark, *J. Franklin Inst.*, **215**, 39 (1933).
2. F. M. Clark, *Elec. Eng.*, p. 50 (January 1935).
3. B. Salvage, The Inst. of Electrical Engineers, *Monograph 2*, (May 15, 1951).
4. T. J. Lewis, *Proc. Inst. Elec. Eng.*, **100**, part II, 141 (1953).
5. P. K. Watson and J. B. Higham, *ibid.*, **100**, part II, 168 (1953).
6. J. L. Maksiejewski and H. Tropper, *ibid.*, **101**, part II, 183 (1954).
7. K. A Macfadyen, *British J. Appl. Phys.*, **6**, 1 (1955).
8. A. H. Sharbaugh, J. K. Bragg, and R. W. Crowe, *J. Appl. Phys.*, **26**, 434 (1955).
9. T. J. Lewis, *ibid.*, **27**, n. 6, 645 (1956).
10. (Laboratoria N. V. Philips' Gloeilampenfabrieken, Eidenhoven, Holland)—J. A. Kok and M. M. G. Corbey, Applied Scientific Research B 6, p. 197-206 (1956).

Electropolishing in Cyanide Electrolytes

F. Sullivan and E. H. Newton

Arthur D. Little, Inc., Cambridge, Massachusetts

ABSTRACT

Mirrorlike polished surfaces can be obtained on silver, sterling silver, gold alloys, copper, and brass by electropolishing in cyanide electrolytes. The optimum current density and agitation rate to obtain a brilliant polish varies widely with the metal being polished. For silver and silver plate a current density range of 1.1-2.8 ASD at 45 cm/min is necessary; for copper and brass the range is 2-8 ASD at 1300-2600 cm/min. Agitation is not critical in gold alloy electropolishing because the very high current density (>250 ASD) induces copious gassing. Rapid periodic movement of sterling silver into and out of the polishing bath within a current density range of 10-16 ASD is required to mirror polish this alloy.

Anyone who has observed the anodes in a copper or silver cyanide plating bath may have noted the different appearance they assume at various times, dull and etched, bright or filmed. These surface changes represent the three conditions important in characterizing the events taking place at the anode during electropolishing, that is, the etching region, the polishing region, and the permanent film region of the voltage-current density relationship.

This paper covers details of the commercial electropolishing of silver plate and pilot plant studies on the electropolishing of sterling. Laboratory electropolishing of gold alloys, copper, and brass is also discussed. All of the studies were carried out in cyanide electrolytes.

The relationship between most of the operating variables encountered in polishing cyanide soluble metals in cyanide electrolytes is most conveniently expressed in the form of voltage-current density or polishing curves. The information necessary to construct a polishing curve is obtained by noting the current passing through the cell and the appearance of the anode while increasing the voltage at 0.2 v increments. In order to start with a uniform surface, a light etch is first produced on the anode. The anode is removed at each voltage step and the degree of etch or polish determined.

Electropolishing of Silver Plate

One series of experiments designed to determine the effect of agitation rate on the shape of the polishing curve was carried out in a bath which was 0.3M with respect to silver cyanide, free potassium cyanide, and potassium carbonate (1). The anode was a silver-plated copper panel rotated at various speeds.

Figure 1 shows typical polishing curves for silver plate at three agitation rates. The polishing zone is indicated by the dotted lines at the letter P. In this area the anode was mirror bright all over. Below the polishing zone the silver surface was dull and etched. Above the polishing zone, the anode assumed a cloudy blue appearance. The broadest polishing range occurred at the intermediate agitation rate. With no agitation the polishing range was very

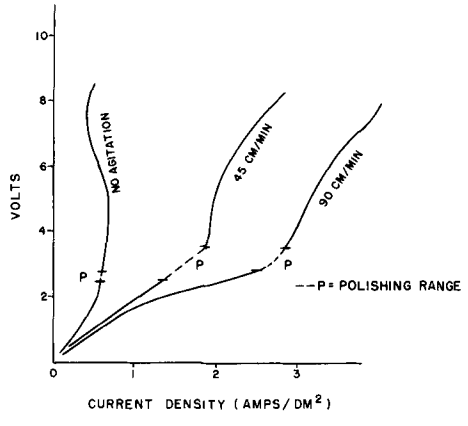

Fig. 1. Typical polishing curves for silver plate at various agitation rates. Bath composition: silver (as metal), 32.4 g/l; KCN (free), 19.5 g/l; K_2CO_3, 42 g/l.

narrow and operating in this range was impractical. At the higher agitation rate the polishing range also narrowed.

Temperatures ranging from 10°-50°C had only minor effects on the polishing results obtained. In general, the higher the temperature the higher the current density at a given voltage. This would be expected from the increased conductivity. While good polishes could be obtained at higher temperatures, the results showed no improvement over those obtained at room temperature. At the higher temperatures, polishing was more difficult to control because of slight etching action after the current had been cut off. Cyanide breakdown was more rapid at higher temperatures. At low temperatures, throwing power appeared somewhat improved.

Commercial electropolishing of silver plate.—Silver plate has been electropolished commercially by several large silver companies on both continuous and batch installations (2). Electropolished surfaces of high quality have been produced on such materials as costume jewelry, novelties, holloware, and flatware. The electropolishing solution most generally used commercially is shown in Table I (3). The cathodes may be either silver or stainless steel with an area at least twice than of the anodes. The work should pass through the bath by either straight line or reciprocal motion at a rate of approximately 45 cm/min. The voltage is generally between 2.5 and 3.5, but these limits may be extended in either direction where conditions demand. The current density is in the range of 1.1-2.8 amp/dm^2 (4).

When the correct polishing conditions exist, a uniform brown film forms on the anode remaining there throughout the polishing cycle. The agitation must be smooth to protect this anodic film which is essential for optimum leveling and brightness. It is believed that this polishing film permits the selective dissolution of the projections or irregularities in the plate thus producing leveling and brightening.

In the continuous flatware process used by a large silver company, spoons, forks, and other articles are mounted in racks and conveyed through a typical cleaning and plating cycle (5). After the plating rinse and pre-dip operations, they pass through an electropolishing bath of the composition previously described. The work moves through the bath at approximately 45 cm/min and remains in the solution about 20 sec. Rinse and pre-dip cycles are advisable, because without these, the drag-in of silver plating solution will rapidly change the composition of the polishing bath and necessitate frequent analysis and adjustment.

Table I. Bath composition and conditions for electropolishing silver plate

Composition	Grams/liter
Silver (as metal)	32.8
Free potassium cyanide	19.5
Potassium carbonate	41.5
Polishing conditions	
Voltage	2.5-3.5
Current density	1.1-2.8 amp/dm^2
Agitation rate	45 cm/min
Temperature	ambient

Holloware.—Silver-plated holloware has also been successfully electropolished by several large silver companies. Articles such as trays, coffee pots, creamers, Paul Revere bowls, baby cups, and many other items have been polished commercially with excellent results. In general, polishing conditions are essentially the same as those for polishing flatware, except the polishing time usually ranges from 1 to 1½ min and the agitation should be reciprocal. Articles to be electropolished should be racked so as to allow the least resistance or turbulence as they pass through the bath.

In articles such as deep bowls, it may be necessary to adjust the distance between the cathodes and anode to obtain maximum throwing power. In some instances internal anodes are necessary for polishing deeply recessed surfaces.

In a few cases, "thieves" have been used to protect certain areas from receiving too much current. These points of high current density, unless shielded, will have a smoky blue appearance.

Advantages and Limitations.—Let us consider a few of the advantages of electropolishing silver. Hand buffing is a slow, expensive, dirty operation. By electropolishing, wheel finishing costs can be reduced from 20 to 100% depending on the class of the article. The 100% figure may sound a bit strange but in costume jewelry and some special lines wheel finishing has been eliminated completely. Electropolishing is ideal for intricate shapes or filagree work where buffing is extremely difficult or impossible. The saving in refining costs compared to the savings realized by refining of buffing dust is appreciable. The silver removed from the work plates out on the cathodes and is recovered in pure metallic form.

Electropolishing in cyanide is a short operation, and many pieces can be processed at one time. Finished articles have more silver more uniformly distributed on them than their buffed counterparts. If properly carried out, it is possible to obtain as high a luster by the removal of 2% of the silver deposit as would be possible by removing 5-10% by hand buffing.

One of the outstanding advantages in electropolishing holloware is the excellent brightness which results in difficult to buff areas such as the inside of handles. The saving in finishing costs and the other advantages previously mentioned in the electropolishing of flatware also apply to holloware.

Although in certain applications a saleable finish can be produced directly from the tank, electropolishing does not necessarily eliminate all finishing operations. Electropolishing cannot exactly duplicate a finished buffed surface. In the field of flatware, for instance, esthetic requirements often demand that the brilliant electropolished glitter be toned down or softened. This would necessitate a wheel operation.

The quality of the plate and the conditions of the basis metal have a marked influence on the resulting polish. The amount of silver removed is generally so small that imperfections in the base

are not eliminated. In fact, the high luster tends to accentuate flaws. Good pre-plate finishing and a smooth electrodeposit are prerequisites for good electropolishing.

There was considerably more interest in electropolishing silver plate ten years ago than at the present time. The popularity of electropolishing now appears to have diminished appreciably due to the advent of several of the modern proprietary bright silver plating baths. Electropolishing does, however, have its place in certain applications such as the continuous production of silver flatware where control of the polishing bath is not as critical as the control of the bright plating bath.

Sterling Silver

In the laboratory sterling silver has been electrolytically polished to a specular brightness in a cyanide bath. Mirror bright polishes have been obtained on flatware, holloware, costume jewelry, and other commercially produced sterling articles (6). Because of certain difficulties which will be discussed later, the electropolishing of sterling has not yet progressed beyond the pilot plant stage.

The bath composition was only slightly different from that used for electropolishing silver plate, but the form and speed of agitation differ greatly. The recommended bath is shown in Table II and was operated at room temperature. The anode, or work, was agitated by repeated immersions and withdrawals from the solution. The cycle of anode movement may be termed a stroke, and the work was lifted clear of the solution with each stroke. This had the effect of cutting the current on and off. The best polishing occurred at current densities between 10 and 16 amp/dm^2 at a potential of from 2.5 to 12 v. The agitation was at least 20 strokes/min and the polishing time approximately 1½ min. Articles were positioned on the racks so as to produce the least turbulence.

The exact reason for the marked improvement in the polishing of sterling silver when repeatedly removed from the solution is not known. Exposure of the film to air may allow the cupric ion formed by evolution of oxygen during the anodic process to be reduced by the cyanide to the more stable cuprous state. Removal of the work from the bath and the consequent draining of excess cyanide could assist in reestablishing the polishing film. The film formed on copper during polishing in cyanide solutions is not as readily dissolved as the film formed on silver. Consequently, the rate of agitation during the polishing of alloys containing copper

Table II. Bath composition and conditions for electropolishing sterling silver

Composition	Grams/liter
Silver (as metal)	32.8
Free potassium cyanide	26-32
Potassium carbonate	41.5
Polishing conditions	
Voltage	2.5-12
Current density	10-16 amp/dm^2
Agitation rate	20-100 strokes/min
Temperature	ambient

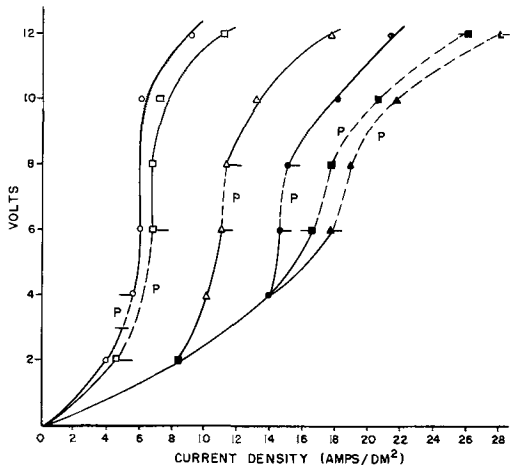

Fig. 2. Polishing curves for sterling silver at various agitation rates. - - P = polishing range; length of stroke = 26 cm. Agitation rate: ○, 10 strokes/min; □, 20 strokes/min; △, 40 strokes/min; ●, 60 strokes/min; ■ 80 strokes/min; ▲, 100 strokes/min.

must be considerably higher than during the polishing of pure silver to increase the cyanide ion concentration of the anodic film. Agitation in the solution without the dunking action is not sufficient to polish sterling. Figure 2 shows typical polishing curves for sterling silver at various agitation rates. Good polishing was noted only in the dotted areas designated by the letter P. Below this area is the etch region and above is the permanent film zone. At the higher agitation rates, the polishing range is extremely broad.

Interrupting the current without withdrawal of the anode from the solution will result in semi-bright etched surfaces. For example, a piece of sterling with an area of 24 cm^2 was immersed in a bath at 5 v, and the current was turned on and off at a rate of 30 times/min. A brown film appeared and disappeared with the current. At the end of 2 min the sample was semi-bright and etched. Turning the current on and off 60 times/min did not improve the brightness.

A series of experiments was carried out to determine the behavior of sodium and potassium salts in sterling silver polishing baths. Three compositions were investigated: (*a*) containing mixed sodium and potassium salts, (*b*) containing all sodium salts, and (c) containing all potassium salts. Figure 3 shows the effect of these cations on the shape and position of the polishing curve. The potassium bath (No. 3) polished at a lower voltage but higher current density than the other two solutions. The composition containing all sodium ions produced the poorest polish. The best polish was noted in the straight potassium bath.

An interesting application is in controlling the weight of sterling while polishing takes place. In the laboratory seven sterling silver soup spoons were suspended from a rack and repeatedly immersed and withdrawn from the polishing bath at a rate of 30 times/min. Five volts was applied at a current density of 15 amp/dm^2. The original weight of the spoons was 304.3 g, but after several minutes of operation the weight was reduced to 278.3 g. The

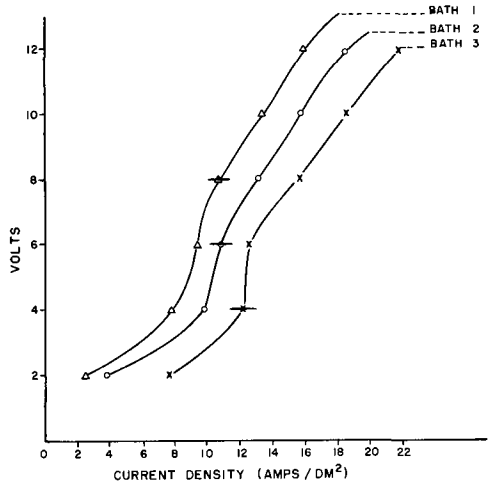

Fig. 3. Polishing curves for sterling silver in various bath compositions; polishing above line, etch region below line; agitation, 60 strokes/min. Composition (g/l): bath 1, 2, 3, AgCN, 40.2; bath 3, KCN, 26; bath 1,2, NaCN, 19.6; bath 1,3, K_2CO_3, 41.5; bath 2, Na_2CO_3, 31.8.

spoons were all very bright and required no mechanical buffing to attain further brilliance.

The sterling silver polishing bath will remove fire scale. This method has many obvious advantages over the nitric acid solution commonly used for this purpose.

Pilot plant studies.—In a 100-gal sterling polishing bath installed at one of the large sterling silver companies, thousands of pieces of flatware and holloware were electropolished to determine the utility of the bath. The brightest polishes were obtained on flatware, and more than 5000 pieces were processed. Although bright polishes could be obtained, difficulty was encountered in pit removal. For example, in manufacturing flatware from heavy wrought material the forming hammer closes up many defects present in the stock. Electropolishing tends to open up these defects. In polishing holloware, the immersing and withdrawing operation sometimes created drainage and racking problems. However, after a 6-month operating period, the bath was still performing well, a fact which indicates that there was no stability problem.

As a result of this study and subsequent laboratory work, it is felt that the process is most suitable for polishing specialty items such as trays or coffee pots and small articles such as costume jewelry. Approximately 1 hr of finishing time could be saved by electropolishing large sterling trays, and 20 min could be saved by electropolishing coffee pots. Since only a few hundred of these items were made per year, the savings from electropolishing these articles did not justify installing the process. Other applications which appear more promising are weight reduction and the removal of fire scale.

Other Metals

Electropolishing of gold alloys.—The investigation into the electropolishing of gold alloys was carried out as part of a general program for determining the anodic behavior of metals in cyanide solutions. Most of the work was done in 3*N* potassium cyanide solutions to avoid complicating reactions. No attempt was made to develop a practical polishing bath.

All the tests were run in 2-l beakers containing 1 l of solution; a new solution was used for each experiment. Four sheet copper cathodes 8.3 cm x 6.4 cm were hung symmetrically around the sides of the beaker. The samples used were silver-gold and copper-gold binary alloys, (18, 16, 12, and 10 karat). All of the copper-gold alloys looked like copper. The silver alloys varied in color from the bright yellow brass of the 18 karat to the silvery color of the 10 karat. Anodes were 2.54 x 5.08 x 0.16 cm. The cathode to anode ratio was approximately 8:1. The cathode to anode distance was 4.3 cm.

For most of the tests the sample was rotated at 22 rpm in a circle of 4.45 cm diameter which corresponds to a linear speed of approximately 310 cm/min.

The potential was increased stepwise from 0 to 20 v. Each voltage was applied for 30 sec, and readings were taken on the ammeter at the start and after equilibrium had been reached. After every few points the voltage was dropped to the etching region and a very light etch given to the surface so that the previous condition of the surface would not influence the results. In the very high current density regions (220-330 amp/dm^2) the time at each point was shortened to 20 sec so the sample would not be dissolved too rapidly. A small microscope lamp was used to illuminate the specimen while in the bath. The sample was removed from the bath, washed, and dried at each point when any change was observed.

Complete polishing over the whole surface of the samples was obtained only at the higher voltages and current densities. (16-20 v, 240-350 amp/dm^2). All the alloys polished like pure gold in 3N potassium cyanide. No good polishing was observed in the voltage range where copper or silver are ordinarily polished.

Voltage-current density curves on these alloys showed only slight differences. With the copper alloys at a given voltage, slightly higher current densities were obtained with decreasing gold content. With the silver alloys the curves showed no correlation with gold content. Figure 4 shows a typical polishing curve for a binary gold alloy.

Individual cases varied somewhat, but to reach the polishing range the general pattern as the voltage was increased was as follows: 1, Linear rise of the current with voltage. No films are present in this region and the surface of the anode is etched; 2, polarization point at which film formation begins; 3, polarizing region in which soluble or loosely adherent films are present. In this region the anode has an etched surface with or without edge polishing; 4, more sloping, less polarized region usually accompanied by soluble films with the surface of the anode partly polished; 5, second etch region with no films and a linear rise of current with voltage; 6, partly polished region with no films and a linear rise of current with voltage; 7, polishing region. Surface of the anode is completely polished. Vigorous gassing is present in this region at both the cathode and anode.

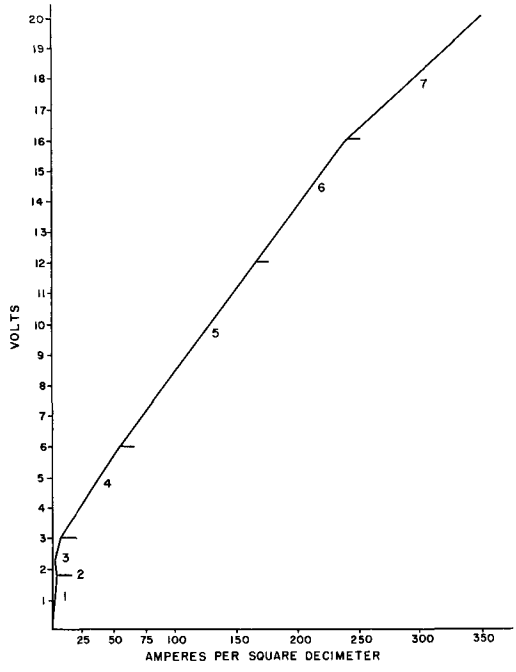

Fig. 4. Typical polishing curves for binary gold alloys; bath composition, 3N KCN; agitation rate, 310 cm/min. Appearance of gold surface: 1, etch; 2, start of film formation; 3, etch and/or edge polishing; 4, part polish, part etch; 5, etch; 6, part polish, part etch; 7, polish.

Agitation of the work was not critical. Comparisons of data obtained in experiments in which the work was not agitated with experiments in which the work was rotated in one direction at 310 cm/min showed only slight differences.

Although all the tests were started at room temperature, no attempt was made to control temperature so by the time a complete curve was plotted, the solution had been warmed up to about 45°C. One experiment was carried out in the reverse order starting with 20 v at room temperature and ending at the low voltage and higher temperature. No significant difference was noted between the curve prepared from this data and the previously described curve. This indicates that temperatures from 20° to 45°C have little or no effect on the polishing curve.

Although most of the work was carried out in 3*N* potassium cyanide solutions, concentrations of 0.3*N*, 1*N*, and 7*N* were also studied. None of these polished as well as the 3*N* solution.

Experiments were also performed with 3*N* sodium cyanide and 3*N* barium cyanide instead of potassium cyanide. The sodium cyanide gave a slightly improved polish at high current densities and voltage. The barium cyanide solution polished similar to the potassium cyanide bath. Current density-voltage curves for these cyanides closely resembled the 3*N* potassium cyanide curve.

Very little change in the quality of polish or current density-voltage curves was obtained by adding the following materials to the 3*N* potassium cyanide bath: additional potassium gold cyanide, copper cyanide, potassium ferrocyanide, potassium ferricyanide. However, the addition of 30 g/l potassium tartrate shifted the polishing range to a lower

Table III. Bath composition and conditions for electropolishing copper and brass

Bath composition:	Grams/liter
Copper cyanide	31
Zinc cyanide	47
Potassium cyanide	126
Polishing conditions:	
Voltage	1.8-3.4
Current density	2-8 amp/dm^2
Agitation rate	400-2600 cm/min
Temperature	25°-30°C

voltage. Between 5 and 10 v and at 55-110 amp/dm^2, a good polish was obtained over the whole surface. With the 3*N* potassium cyanide bath alone, no polish or only part polish-part etch was obtained in this range. At higher voltages and current densities, the tartrate-potassium cyanide bath acted the same as plain potassium cyanide.

Brass and copper polishing.—In the laboratory copper and brass have been electropolished to mirror brightness in cyanide polishing baths. The most brilliant finishes were produced on brasses containing 70% or more copper. Leaded brass could not be polished satisfactorily.

The electropolishing solution which we have found most effective is shown in Table III. Polishing was carried out at a current density of 2-8 amp/dm^2 at agitation rates ranging from 1300-2600 cm/min. The extremely high rate of agitation was a major problem. On a curved surface where there is streamlined flow, mechanical agitation was possible. However, with flat surfaces and odd shaped items, very fast hand agitation was necessary to produce good polishing. We were unsuccessful in our attempts to duplicate the hand agitation by mechanical means.

Figure 5 shows the effect of three agitation rates on the polishing curves obtained by electropolishing short lengths of red brass pipe in the above bath. The initial "free cyanide" was about 50 g/l and the *p*H was 12. The pipe was agitated by rotating it in a circular path 7.6 cm in diameter. No polishing occurred at the lowest agitation rate. The best mirrorlike polish was obtained at 2600 cm/min at the knee of the curve, that is, between 2.3 and

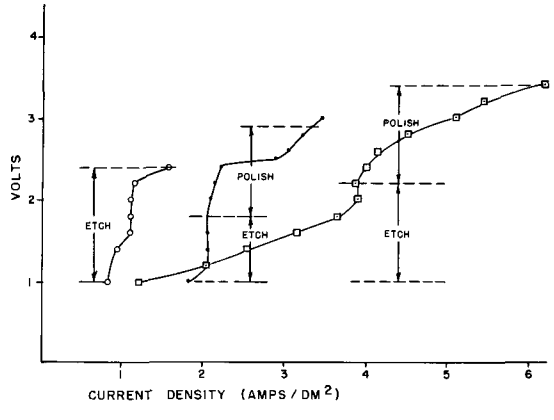

Fig. 5. Polishing curves for red brass at three agitation rates. Bath composition: copper cyanide, 31 g/l; zinc cyanide, 47 g/l; potassium cyanide, 126 g/l; agitation rate: ⊙ 400 cm/min; • 1300 cm/min; dotted square 2600 cm/min; temperature, 27°C.

Table IV. Bath composition and conditions for electropolishing 70/30 brass

Bath composition:	
Potassium cyanide	75 g/l
Potassium tartrate	20 g/l
Potassium ferrocyanide	20 g/l
Potassium dihydrogen phosphate	20 g/l
Conc. ammonium hydroxide	4 ml/l
Operating conditions:	
Voltage	5-6
Current density	25-50 amp/dm^2
Agitation rate	very fast hand
Temperature	50°-60°C
Time	3-5 min

2.5 v at about 4 amp/dm^2. Under these conditions 68% of the metal lost from the polished anode plated out on the copper cathodes.

Pure copper may also be polished in the above bath. An additional stability problem was encountered because the copper tended to build up in the solution while the zinc was being depleted. The addition of a zinc anode remedied this, permitting brass to plate out during the electropolishing operation, thus maintaining the desired solution balance. Occasional readjustments of the copper and zinc concentration and close control of "free cyanide" were necessary for continued operation of the bath.

The quality of an electropolished surface depended to a great extent on the grain size of the metal. The effect of grain size of 70/30 brass on the resulting polish was noted in a series of experiments carried out in the polishing bath shown in Table IV. The composition of this solution departed considerably from that used in previous research and was similar to the type of bath used in brightening or stripping solid gold rings (7). The bath was operated at a higher temperature and current density than the bath described previously. Brass did not plate out at the cathode so periodic analysis of the bath was necessary for continued operation.

Five panels of 70/30 brass with grain sizes varying from 0.010 to 0.075 mm and hardnesses ranging from ½ hard, ¼ hard, and soft were polished for 3 to 5 min using very fast hand agitation. A uniform polish could be produced only on panels that were bent into a semicircle. Although all panels were polished to some degree, rolling marks were not completely removed in any case. The panels with the smallest grain sizes were polished to a mirror bright state. The polish on the larger grain size brass samples was decidedly inferior. The hardness of the panels had no effect on the quality of the polish.

Acknowledgment

The investigation of the electropolishing of silver, sterling silver, and gold alloys was sponsored by Oneida Limited. The authors wish to thank Arthur D. Little, Inc., and Oneida Limited for permission to publish this data.

Manuscript received May 11, 1960. This paper was prepared for delivery before the Columbus Meeting, Oct. 18-22, 1959.

Any discussion of this paper will appear in a Discussion Section to be published in the June 1961 JOURNAL.

REFERENCES

1. S. E. Eaton (to Oneida Ltd.), U.S. Pat. 2,610,144, Sept. 9, 1952.
2. D. Gray and S. E. Eaton, *Metal Finishing*, **45**, 60 (1947).
3. S. E. Eaton (to Oneida Ltd.), U.S. Pat. 2,416,294.
4. S. E. Eaton (to Oneida Ltd.), U.S. Pat. 2,610,143, Sept. 9, 1952.
5. D. Gray, *Metal Finishing*, **47**, 55 (1949).
6. F. Sullivan (to Arthur D. Little, Inc.), U. S. Pat. 2,661,330, Dec. 1, 1953.
7. J. B. Kushner, *Prods. Finishing*, p. 44, Nov. 1942.

Particle Growth during Zinc Sulfide Phosphor Preparation

A. Kremheller[1] and S. Faria

General Telephone and Electronics Laboratories, Incorporated, Bayside, New York

ABSTRACT

The influence of processing conditions, such as time and temperature, and the effect of fluxing agents on the particle size and concomitant properties observed during zinc sulfide phosphor preparation are reported. The particle size increases exponentially with the reciprocal firing temperature and as the square root of the firing time when phosphors are prepared in open boats; the activation energy and frequency constant depend on the flux employed. A particle size anomaly is observed when zinc sulfide powder containing zinc chloride is processed near 1000°C in sealed quartz vials. This anomaly, which can be ascribed to the Hedvall effect, is accompanied by anomalies in chloride retention and crystal structure.

Commercial zinc sulfide phosphors are usually prepared by heat treatment of the host material in the presence of an activator and a coactivator (1). The average particle size of the zinc sulfide crystallites increases during this treatment, and the final particle size depends on the processing conditions and the additives. Tiede and Schleede (2) observed that the fluxing agent promotes crystal growth at low temperatures by lowering the melting point of the base material. A few years later Schleede and Gantzckow (3) proposed that a thin film of the fluxing agent dissolves small particles of the base material, and that subsequent precipitation takes

[1] Present address: Republic Aviation Corp., Farmingdale, N. Y.

place on large particles with concomitant increase of the average particle diameter.

Work and Odell (4) discussed particle size and the growth mechanism during heat treatment of zinc sulfide powder and observed that the development of pigment properties of zinc sulfide is closely related to changes in particle size. The authors indicated that their experimental data agree quite well with the theory of growth by vaporization; they also pointed out that the theoretical considerations are quite similar for particle growth by dissolution and subsequent reprecipitation. They found that the particle size is primarily a function of the processing temperature, and only secondarily of time. Leverenz (5) established that zinc sulfide crystals grow in approximate proportion to exp $(-E/kT)$, where E is the activation energy connected with the growth process. The growth rate decreases with increasing time because the crystals approach a size distribution that is determined largely by the temperature and by the nature and sizes of the initial particles. Bube (6) confirms that the particle size varies exponentially with the reciprocal of the processing temperature and finds an activation energy of 1.3 ev for the host material without additives. Shionoya and Amano (7) showed that the change of the particle volume with processing time is proportional to the reciprocal processing temperature. The proportionality constant is considered to contain the activation energy, which is nearly three times as high without as with the fluxing agent. They found that the increase of the particle volume with time t is constant at constant temperature, which is not in agreement with our results (8) which lead to a $t^{3/2}$ dependence, as explained in the discussion section.

The present paper deals with the influence of time and temperature of heat treatment and the effects of various additives on particle size, crystal structure, and luminescence of zinc sulfide powder. This includes processing in open boats and sealed quartz vials, study of the final product, and elucidation of the growth mechanism as a function of experimental conditions. The implications of the experimental data as to the influence of the various processing parameters on particle growth and related properties are discussed.

Experimental

The zinc sulfide powder and the additives used in these experiments were essentially free of heavy metals to the limit of spectrographic detectability. The zinc sulfide powder contained about 0.45% by weight of sulfate and less than 0.002% of chloride.

The samples are kept in transparent quartz boats and heated in transparent quartz combustion tubes in an atmosphere of helium during open-boat processing; the linear flow rate was about 1 cm/min. Another series of experiments was conducted with sealed evacuated quartz vials containing the base material and the source of the coactivator. The purpose of using sealed vials was to keep the flux concentration constant during the heat treatment.

A simplified gas adsorption method, microscopic counting, x-ray analysis, and electron photomicrography were employed in determining the particle size and the crystal structure, as discussed previously (9). The same publication (9) also describes a semi-quantitative method which was employed in the present investigation to obtain a measure of photoluminescence intensity. The determination of chloride has been discussed in some detail in a previous publication (10). This method permits one to determine quantitatively amounts of 0.001% by weight of chloride in 1 g of zinc sulfide; results have been found to be reproducible and accurate.

Results

Particle growth studies are of interest by themselves and are a first step in controlling the particle size so that phosphors of a given particle size can be prepared. For instance, a given particle size can be attained by processing the powder at low temperature for a long time or at high temperature for a short time; proper selection of processing conditions will depend on other requirements on the final product.

While the processing conditions are important with respect to particle growth, it is well understood that the initial particle size and the size distribution also have to be considered, especially, when zinc sulfide powder is processed at low temperature and/or for very short times. For this reason, our experimental conditions have been selected in such a manner that the initial particle size can essentially be neglected with respect to the final size. In the present study the average initial particle diameter was 0.02 μ, and the final diameter was at least ten times as large.

In order to study the influence of the flux and processing conditions without additional complications, activators were not added. The experiments and results are arranged in two sections. The first part presents phosphor processing in open boats, while the second part deals with the study of material preparation in sealed quartz vials.

Phosphor Preparation in Open Quartz Boats

Zinc sulfide powder without flux addition was processed at temperatures from 200° to 1250°C for up to 40 hr in open boats. It was found that the average particle size increases exponentially with the reciprocal of the processing temperature, as is implicit for a typical case in Fig. 1. In another series of experiments, the processing temperature was

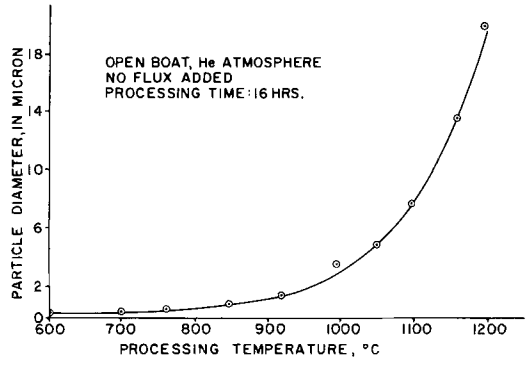

Fig. 1. Average particle diameter as a function of processing temperature.

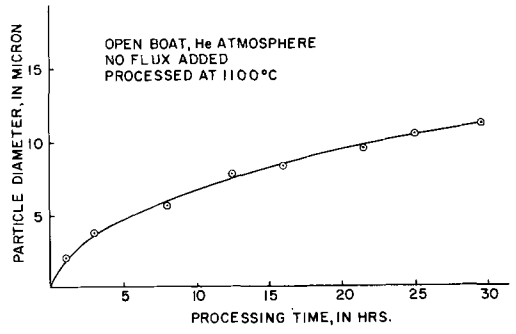

Fig. 2. Increase of average particle diameter with processing time.

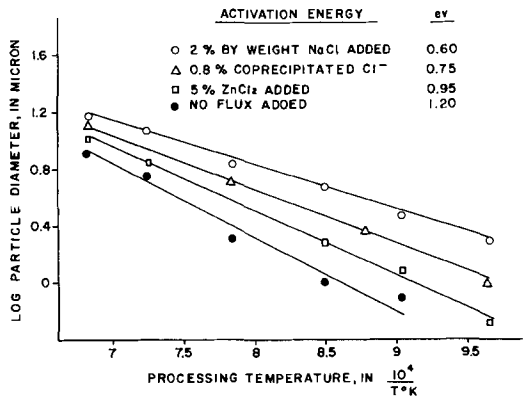

Fig. 3. Dependence of average particle diameter on reciprocal processing temperature; fluxing agent as the parameter.

kept constant and the processing time was varied. A typical result of this study is presented in Fig. 2. The curve corresponds to the hypothesis that the particle size increases with the square root of the processing time. Accordingly, the average particle diameter X can be expressed[2] as a function of processing temperature T and time t by the equation:

$$X \cong At^{1/2} \exp(-a/T) \qquad [1]$$

Equation [1] contains the constants A and a, which are found to be $A = 3.15 \times 10^4$ micron hr $^{-1/2}$ and $a = 1.25 \times 10^4$ °K, when no coactivator is added.

X-ray diffraction analysis indicates that the originally cubic zinc sulfide powder is transformed into the hexagonal form when processed above 1100°C. At processing temperatures below 900°C the processed material is cubic, while amounts of hexagonal phase that increase with the temperature are found in the intermediate interval. The samples exhibit some luminescence if they are processed above 1000°C.

In another series of experiments, various amounts and kinds of fluxes were added. It was found that the fluxing agent changes the constants A and a in Eq. [1]. Effective fluxing agents lower the value of a, which may be interpreted as a decrease in the activation energy needed for the growth process. Figure 3 represents data that are in good agreement with Eq. [1]; the experimental points are plotted for zinc sulfide without flux and with 2% by weight of NaCl processed for 2 hr at various temperatures. The constants in Eq. [1] are $A = 2 \times 10^3$ micron hr$^{-1/2}$ and $a = 7.5 \times 10^3$ °K when 2% NaCl is used as the additive. The same Eq. [1] is obeyed when 5% by weight of zinc chloride or 0.8% of coprecipitated chloride are present (see also Fig. 3).

Phosphor Preparation in Sealed Quartz Vials

In order to keep the concentration of the fluxing agent constant, zinc sulfide powders with flux addition were heat-treated in sealed quartz vials. In one series of experiments a constant amount of various halides was added before processing for 3 hr at 850°C. The purpose of this study was to compare qualitatively the influence of various halide anions and of the cations zinc and sodium on particle growth and attendant properties. Figure 4 shows photomicrographs of zinc sulfide processed with 0.007 gram atom of halide per mole zinc sulfide. Zinc sulfide with sodium halide leads to a growth habit in the form of triangular plates, while zinc halides lead to spherical polyhedra, similar to those observed without coactivator. Table I presents data on these samples. It is seen that the average particle diameters of samples with sodium halide addition are larger than those with zinc halide addition. The sodium halides favor the formation of cubic structure; however, one also observes that the cubic samples are larger in particle size than the partially hexagonal samples. It appears that flux action leading to large particles requires that the sodium halide be liquid. While there are considerable variations from sample to sample in various properties, the zinc halides are essentially as effective as the sodium halides with respect to the photoluminescence intensity.

Another series of experiments yielded quite unexpected results, when 0.25% by weight of zinc chloride was physically admixed to zinc sulfide in sealed vials which were subsequently heat-treated for various times and temperatures. Equation [1] is not valid in this case, because one observes a peak in particle size as a function of processing temperature near 1000°C, as shown in Fig. 5. The curve in Fig. 5 shows the dependence of the particle size on the temperature of processing from 800° to 1200°C for a processing time of 4 hr; the curves for 2, 8, and 16 hr, which are not shown, vary in absolute particle size while their general shape is the same. The anomalous peak near 1000°C is accompanied by anomalous behavior with respect to the crystal structure and the amount of retained volume chloride,[3] as shown in Fig. 5. It was found that these

[2] The left side of Eq. [1] is equal to $(X^2 - X_0^2)^{1/2}$ which has been approximated by X since $X > X_0$.

[3] See definition of "volume chloride" in ref. (10).

Table I. Some properties of zinc sulfide powders with 0.007 g atom of halide per mole of zinc sulfide added, and processed in sealed, evacuated quartz vials for 2 hr at 850°C

Halide added	Average particle diameter, μ	Ratio of hex.: cubic	Blue photoluminescence, relative	Melting point of halide, °C
NaF	1	1:9	44	992
NaCl	10	0:10	680	801
NaBr	14	0:10	647	755
NaI	8	0:10	357	651
ZnF_2	<1	2:8	2	872
$ZnCl_2$	1	2:8	765	262
$ZnBr_2$	<1	3:7	790	394
ZnI_2	3	0:10	753	446

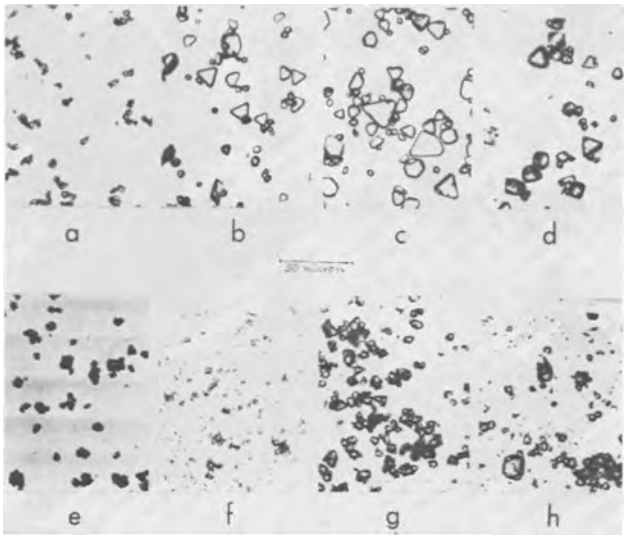

Fig. 4. Zinc sulfide powders with 0.007 g atom of halide per mole of zinc sulfide added and processed for 3 hr at 850°C in sealed quartz vials; the added halides are: a, NaF; b, NaCl; c, NaBr; d, NaI; e, ZnF_2; f, $ZnCl_2$; g, $ZnBr_2$; and h, ZnI_2.

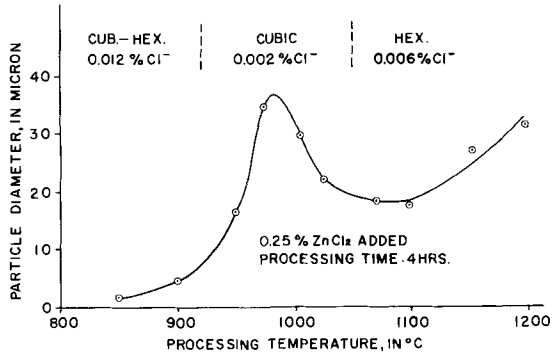

Fig. 5. Anamalous particle growth and attendant chloride retention and crystal structure in sealed quartz vials.

zinc sulfide phosphors contain some hexagonal structure even at processing temperatures below 950°C, while the pure hexagonal structure occurs above 1050°C and pure cubic structure is found in the intermediate range. The amount of retained volume chloride is lowest in the region of the anomalous peak. It appears that the anomaly near 1000°C can be explained as being due to the Hedvall[4] effect (11), since one observes a considerable amount of randomness in the crystal structure of zinc sulfide crystals (especially for those of cubic structure) that are annealed at this temperature (12). The degree of randomness was found to be enhanced considerably during annealing in the presence of halide when compared with samples containing no additives. A series of samples without additives was used as a blank; in this case the anomalous growth peak was absent.

It appears that the randomness in the crystal structure seems to facilitate crystal growth near 1000°C while the degree of incorporation of chloride is actually decreased. One may also conclude that the low concentration of volume chloride in particles processed near 1000°C can be interpreted by assuming that the growth rate is increased by randomness while the diffusion or incorporation of chloride is lowered. It is also possible that chloride is incorporated by diffusion alone and that the diffusion rates in hexagonal and cubic zinc sulfide may differ. In that case one would expect to find the largest amount in the smallest particles because of their large surface area and in those of hexagonal structure because of their open structure. These observations appear to be closely connected with the fact that chloride influences the cubic-hexagonal structure equilibrium (12).

[4] The Hedvall effect ascribes similar anomalies to the increased chemical reactivity near a transition point.

Summary and Discussion

As part of commercial phosphor preparation zinc sulfide powder is submitted to a heat treatment process during which the particle size increases. The average particle diameter is found to increase with the square root of the processing time and exponentially with the reciprocal of the temperature during phosphor preparation in open boats. The growth process is related to the tarnishing reaction, corrosion processes, and similar diffusion-limited growth phenomena (13). For instance, the same exponential dependence of the growth rate on the temperature has been found by Keck (14) for the growth of selenium films in vacuum. The time dependence of particle growth with $t^{1/2}$ has been found, for instance, for $Ba(OH)_2$ on BaO by Jahoda (15) and for germanium oxide films by Lukes (16).

The growth Eq. [1] can be derived theoretically if one considers the particle growth as a quasi-chemical reaction (17). The derivation, which is not discussed here, leads to an expression for a diffusion-limited process. Constant a in Eq. [1] can be interpreted as being equal to the activation energy E for the growth process divided by the Boltzmann constant k. The constant A is then found to be proportional to the concentration of molecules, ions, or atoms in the gaseous phase and inversely proportional to the concentration of mobile molecules in the solid substance. These concentrations and the activation energy may be modified by the presence of additives, so that one would expect, in agreement with our experiments, a variation in a and A with the kind of additive employed. Since additives that are solids at the processing temperature do not affect the particle growth significantly (see NaF-addition in Table I), one may assume that the vapor pressure of the additive must be fairly high in order to be effective in stimulating particle growth. The concentration of the additive appears not to be critical, because in open boats a considerable amount of the additive is lost (10) with processing time and temperature, and the values of a and A in the growth Eq. [1] do not change, as can be seen in Fig. 3.

It is interesting to find that Shionoya and Amano (7) obtained activation energies without an additive and with 2% NaCl added, which are about 2 to 3 times larger than our values. The explanation of this discrepancy is quite simple, since one finds that they consider the particle volume rather than the diameter. In this case the growth Eq. [1] is essentially raised to the third power, so that the activation energy for volume growth should be three times

that for linear growth. According to Eq. [1] the volume should be proportional to $t^{3/2}$, while Shionoya and Amano (7) found a linear dependence between particle volume and the processing time t. It appears that the difference in time dependence can be ascribed to the limited range of experimental conditions that Shionoya and Amano (7) considered.

The other series of experiments in sealed quartz vials which led to the observations of the anomalous behavior near 1000°C has been discussed in the result section. The Hedvall effect (11) offers a possible explanation for the growth anomaly; however, there has to be some additional influence and/or interaction to account for the anomalies in crystal structure and chloride incorporation in the case of sealed vials, because none of the above three anomalies has been observed when processing was conducted in open boats.

It is quite apparent that many problems in this field require further study. The present experimental investigation has led to a growth equation which explains certain results. On the other hand, it is also clear that the growth Eq. [1] can only be considered to be an approximation which does not apply in certain cases. It is expected that future investigations will lead to a better understanding of the anomalous behavior, the growth process and phosphor preparation which may finally contribute to the synthesis of novel or improved phosphor materials.

Acknowledgment

Grateful acknowledgment is made to D. J. Bracco, A. K. Levine, P. Goldberg, V. C. Brophy, C. F. Tufts, and other colleagues for their generous contributions and many helpful discussions. Thanks are due J. T. Ragusin for valuable assistance with the experimental work.

Manuscript received April 25, 1960. This paper was presented in part at the Cincinnati Meeting, May 1-5, 1955.

Any discussion of this paper will appear in a Discussion Section to be published in the June 1961 JOURNAL.

REFERENCES

1. H. W. Leverenz, "Luminescence of Solids," John Wiley & Sons, Inc., New York (1950).
2. E. Tiede and A. Schleede, *Berichte*, **53**, 1921 (1920).
3. A. Schleede and H. Gantzckow, *Z. physik. Chem.*, **106**, 37 (1923).
4. L. T. Work and I. H. Odell, *Ind. Eng. Chem.*, **25**, 411, 543 (1933).
5. H. W. Leverenz, *Science*, **109**, 183 (1949).
6. R. H. Bube, *J. Chem. Phys.*, **20**, 716 (1952).
7. S. Shionoya and K. Amano, *J. Chem. Soc. Japan*, **77**, 303 (1956).
8. A. Kremheller, D. J. Bracco, and P. Goldberg, Particle Size and Structure of Fired Zinc Sulfide Powders, presented at the Cincinnati Meeting, May 1955.
9. A. Kremheller, S. Faria, and A. K. Levine, *This Journal*, **107**, 753 (1960).
10. A. Kremheller, S. Faria, P. Goldberg, and D. J. Bracco, *ibid.*, **107**, 749 (1960).
11. J. A. Hedvall and L. Leffler, *Z. anorg. u. allgem. Chem.*, **234**, 235 (1937).
12. A. Kremheller, *Sylvania Technologist*, **8**, 11 (1955).
13. C. Wagner, *Z. physik. Chem.*, **B21**, 25 (1933).
14. P. H. Keck, *J. Opt. Soc. Am.*, **42**, 221 (1952).
15. F. C. Jahoda, *Phys. Rev.*, **107**, 1261 (1957).
16. F. Lukes, *Czechosl. J. Phys.*, **8**, 491 (1958).
17. G. N. Lewis and M. Randall, "Thermodynamics and the Free Energy of Chemical Reactions," McGraw-Hill Book Co., New York (1923).

Electroluminescence Maintenance

W. A. Thornton

Lamp Division, Westinghouse Electric Corporation, Bloomfield, New Jersey

ABSTRACT

The maintenance of several electroluminescent phosphors, mainly of the ZnS:Cu,Cl type, has been investigated. Data are given illustrating its dependence on phosphor properties, such as copper and chlorine additions, firing temperature and particle size, on conditions of operation, and on lamp construction. Changes in properties other than light emission and recent maintenance improvements are described.

Electroluminescence (1, 2) shows a characteristic slow decrease in light emission, in common with all other practical light sources, over long periods of operation of the lamp. Improvements in the maintenance of electroluminescence have kept pace with increases in brightness and efficiency and have required knowledge of the dependence of electroluminescence maintenance on phosphor properties, conditions of operation, and lamp construction. It is the purpose of this paper to describe the influence of these factors on electroluminescence maintenance. Electroluminescent phosphors have not changed basically from the type discovered by Destriau (3, 4) in 1936, and consist typically of zinc sulfide activated by copper and chlorine. The ZnS:Cu,Cl and ZnS:Cu,Mn,Cl phosphors are in most general use, and it is to these that the data to follow primarily refer.

Electroluminescence maintenance has been the subject of three previous papers. Observations on photoluminescence, dark capacitance and conductance, photoconduction, wave form, and low-temperature deterioration of light emission were related by Thornton (5) (Paper I) to the typical maintenance (brightness-time) curve by assuming field-diffusion of traps or donors within the phosphor

crystal. Roberts published a paper (6) (Paper II) based in part on results obtained much earlier (7), in which he gives an empirical relation accurately describing typical brightness-time behavior, gives some data on voltage and frequency dependence of maintenance, and also concludes that deterioration is due to physical processes within the phosphor grain. Deep traps appearing in the phosphor crystal during deterioration are ascribed by Thornton (8) (Paper III) to incoming oxygen ions; the presence of the deep traps was indicated by thermoluminescence measurements and by the fact that brightness-voltage changes with deterioration could be reproduced by firing into the phosphor deep-trap-producing impurities such as In, Cd, and Ga, and could be removed temporarily simply by heating the deteriorated lamps. That oxygen is involved was indicated by similar thermoluminescence behavior of oxygen (9) in ZnS, by the fact that the brightness-voltage changes with deterioration could also be reproduced by firing small amounts of ZnO into the ZnS phosphor, and by the appearance of free zinc (10) on the phosphor crystals during electroluminescence deterioration.

Most of the data presented in this paper were obtained from conventional electroluminescent lamps which consist of phosphor powder dispersed in a plastic dielectric material (polyvinyl chloride acetate) at room temperature. When organic materials are used as the dielectric, the lamp is subjected to temperatures no greater than 50° to 100°C. Therefore, all the data presented here are characteristic of electroluminescent phosphor powders as prepared. In the case of ceramic lamps, which are subjected to processing temperatures in the neighborhood of 600°-700°C, profound changes occur in the phosphor during this processing and its electroluminescence properties are altered; no consideration is given here to the ceramic type of electroluminescent lamp.

II. Results

A. Dependence of Maintenance on Phosphor Properties

1. Copper and chlorine additions.—ZnS:Cu,Cl phosphors showing blue electroluminescence are known to have much poorer maintenance characteristics than similar phosphors of the same type which show green emission. It is of interest, practically, to determine the dependence of electroluminescence maintenance on the proportions of added copper and chlorine in phosphors[1] made at constant firing temperature and covering a wide range of copper and chlorine additions. The phosphor samples, about forty in all, were sprayed on conducting glass. The phosphor/plastic (Ucilon[2]) weight ratio was unity, gross thickness of the finished lamps was about two mils, and they were coated with evaporated aluminum to form the rear electrode. The lamps were mounted in good thermal contact with a massive metal base and operated together, from a single power supply and simultaneously, in an air-conditioned room (temperature about 70°F., R.H. about 30%). The temperature of the lamps did not rise significantly above room temperature. The deterioration to be described is the "intrinsic" deterioration characteristic of the phosphor rather than that due to its environment. Light output measurements during deterioration were made with an RCA 931-A photomultiplier and battery box for long-time stability. No spectral shift with deterioration was detected (see Section D-3). Initial brightness measurements were made in a castor-oil cell, 60 μ thick, using the Ultrasensitive Spectra Brightness Meter.[3] Cell thickness reproducibility is better in the oil cells than in the sprayed lamps, although brightness readings among the sprayed lamps agreed well with those obtained with the oil cell. All of these measurements were made at 4000 cps, the frequency at which electroluminescent maintenance was determined.

The percentages of added impurities are plotted as ordinate and abscissa, respectively, on logarithmic scales in Fig. 1. In this figure are plotted contours of equal maintenance, in per cent of initial brightness, after operation at 150 v, 4000 cps. Contours plotted for short and long periods of operation show the same configuration. Electroluminescence maintenance improves rapidly with increase of both copper and chlorine additions. The contours are roughly symmetrical about the line of equal copper and chlorine additions; this is the line of unity slope in Fig. 1. Furthermore, again roughly, a schematic representation of these contours may be given as in the inset of Fig. 1. This implies that, for a given maintenance characteristic, certain equal additions of copper and chlorine are required. For example, for 10% maintenance, an addition of 0.5 mole % of copper and 0.5 mole % of chlorine is required. Further additions of chlorine (at constant copper) or of copper (at constant chlorine) will not improve the maintenance; instead a greater addition of both is required. Since the contours show no sign of closing, it may be assumed that further maintenance improvement may be realized by greater impurity addition. This is of interest practically only if maintenance is the only requirement. To a marked degree, there is a correlation between better main-

[1] Supplied by W. Lehmann.

[2] Metal and Thermit Corporation, Rahway, N. J.

[3] Manufactured by Photo Research Corporation, Hollywood, Calif.

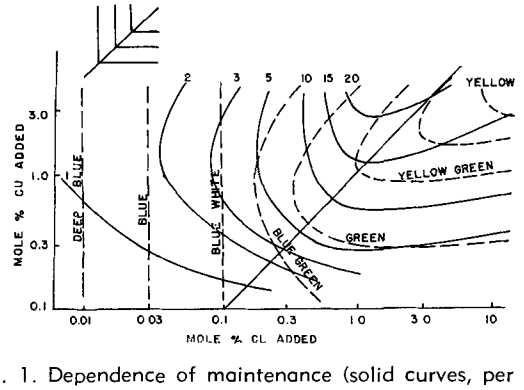

Fig. 1. Dependence of maintenance (solid curves, per cent of initial brightness, 150 v, 4000 cps) and visual color (dashed curves) on copper and chlorine additions. Inset: schematic diagram of same data.

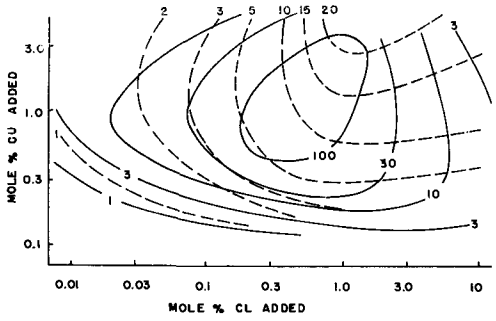

Fig. 2. Dependence of maintenance (dashed lines, per cent of initial brightness, 150 v, 4000 cps) and brightness (solid lines, oil cell, 200 v, 4000 cps, arbitrary units) on copper and chlorine additions.

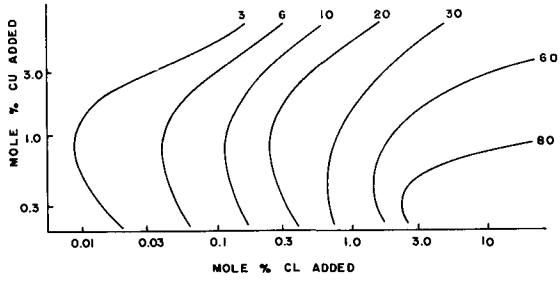

Fig. 3. Dependence of integrated thermoluminescence (—195°C to room temperature, arbitrary units) on copper and chlorine additions.

tenance and longer wave-length emission, as shown in Fig. 1. Here are plotted the maintenance contours and also visual color contours which, although subjective, are correct in their gradation from apparent shorter to longer wave lengths. The maintenance and color contours are not coincident. This means, for example, that there is a definite procedure for obtaining a green-emitting phosphor of optimum maintenance (in this case, by extrapolation to 10 mole % copper and 2 mole % chlorine added). While the blue-emitters are always poorer in maintenance, Fig. 1 demonstrates simple matching of a required color to optimum maintenance and hence the best blue emitter is chosen easily. Note that the color contours of Fig. 1 follow the simple schematic diagram even more closely, and hence the same discussion applies.

The third important characteristic is brightness. Contours of equal brightness (in arbitrary units proportional to ft-L) are given in Fig. 2. Initial brightness contours (not shown) for the sprayed cells which were deteriorated had the same configuration; the plotted brightness data were obtained from oil cells. Figure 2 includes the maintenance contours already described. In the blue region, the brightness and maintenance contours are approximately coincident; that is, maximum brightness and maximum maintenance for a certain color occur at about the same point. In the green and yellow-green regions the contours are not at all coincident, but at least the high brightness contours are elongated in the direction of best maintenance so that not much brightness is sacrificed in realizing good maintenance. Brightness and maintenance are often equally important, and the total light emitted throughout the operating life of the lamp (lumen-hours) is the criterion. Peak "lumen-hours" is obtained in the green and falls off by a factor of twenty toward the yellow; hence, the effect is due neither to decreasing luminosity (since luminosity rises slightly in this range, 5200-5650Å) nor to poorer maintenance but is a marked physical effect. In the blue regions, fortunately, a ridge occurs at about 1 mole % copper along which maximum lumen-hours can be chosen for a given color.

As discussed in Section III, density of trapping sites is thought to be related to the maintenance of a phosphor. For this reason, the thermoluminescence of each phosphor in this series was measured by integrating the thermal glow, between —195°C and room temperature, following equal irradiation at 365 mμ at the lower temperature. In Fig. 3 the total light output due to thermoluminescence (release of trapped electrons followed by recombination) is plotted in arbitrary units.

As a matter of interest, the yellow-emitting ZnS:Mn,Cu,Cl phosphors show similar contours and as wide a maintenance variation as the ZnS:Cu,Cl type described above, depending also on copper and chlorine additions. For samples of yellow phosphors of this type with various copper and chlorine additions, the time to half brightness at 4000 cps ranged from 4 to 350 hr. The initial brightness of the best maintenance phosphor was about 60% of that of the brightest yellow phosphor.

2. Firing temperature.—A series of blue-white ZnS:Cu,Cl phosphors[4] was fired at various temperatures. The experimental procedure was identical to that described in the previous section. The maintenance of those phosphors fired at higher temperatures was much better than the maintenance of those fired at 950°C and below (Table I). The brightness units are proportional to foot-lamberts; maintenance is given in per cent of initial brightness after 24 hr at 150 v, 4000 cps. Comparing the variations with firing temperature with the corresponding contours of Fig. 1, the increasing firing temperature appears to have the effect of causing increased retention of copper. The practical result is a blue-white phosphor of much improved maintenance.

Part but not all of the maintenance improvement with increasing firing temperature is undoubtedly due to the increase in particle size with increasing temperature, as shown in Table I. The dependence of maintenance characteristics on particle size is described in the next section.

3. Particle size.—Any alteration of the phosphor (impurity addition, firing temperature, etc.) re-

[4] Supplied by A. Wachtel.

Table I. Phosphor characteristics as a function of firing temperature

Firing temp, °C	Initial brightness, B	Maintenance, M, %	B x M	Average particle size, μ
650	7.2	1.2	9	2.5
800	5.3	1.2	6	2.5
950	4.9	2.7	13	3
1100	11.0	5.1	56	5
1250	9.5	11.0	104	8

Table II. Phosphors for which effect of particle size on maintenance was determined

B	Blue	ZnS: Cu, Cl
BG	Blue-green	ZnS: Cu, Cl
G	Green	ZnS: Cu, Cl
YG	Yellow-green	ZnS: Cu, Cl
Y (1)	Yellow	ZnS: Cu, Mn, Cl
Y (2)	Yellow	ZnS: Cu, Mn, Cl

sults, in general, in a change in mean particle size also. Efficiency (11) and brightness (11, 12) have been shown to depend on mean particle size. The maintenance of output also depends on particle size. Therefore an observed variation in maintenance, for instance, cannot be attributed entirely to a certain alteration of the phosphor if a particle size change also is induced by the alteration. This section describes a determination of the dependence of maintenance on particle size alone, in order that this effect of particle size may be allowed for in determining true maintenance variation due to phosphor alteration.

From each of the six phosphors listed in Table II five or six fractions were separated out by water settling. Several particle size determinations were made by microscope and the apparent mean particle size averaged to obtain the nominal particle diameter used in plotting the data. These nominal particle sizes are very approximate, and only the large differences in the mean diameter of the fractions make the determination meaningful. Although the number of particles considerably coarser than the nominal size was negligible, there were small numbers of fines present in the coarser fractions. The nominal average particle sizes designated are estimated to be within about 15% of the true average in the case of most of the 30 fractions; one or two fractions, however, consisted of particles of approximately two different diameters, and these were discarded. Each fraction apparently consists of a bell-shaped distribution similar in shape to the original phosphor. Such a distribution is well suited to this maintenance study, since any actual electroluminescent phosphor of interest practically will have such a distribution.

The dependence of maintenance of the phosphors on particle size is shown in Fig. 4. All of the curves are seen to extrapolate approximately through the origin. The dependence of the blue phosphor is nearly linear to 12 μ; it is characteristic of the blue phosphors, having relatively low copper and chlorine additions, that the range of particle size is limited. The dependence of the other phosphors is also quite linear to about 12 μ, and then the maintenance becomes fairly constant at larger particle size. The slight apparent decrease in maintenance of the largest particles in some cases may not be real, but may be due to the presence of a few fine particles as already noted.

Thus, the particle size effect is considerable. On the other hand, particle size is by no means the major consideration in electroluminescence maintenance. Modified firing procedures have been shown to lead to maintenance improvement factors of as much as twenty; no difference in average particle diameter of the original and such modified phosphors is apparent by microscope. Maintenance also has been shown to depend very strongly on copper and chlorine additions during phosphor preparation (Section A-1.); in the array of samples studied, the maintenance of electroluminescence brightness varied by a factor of 50 while the particle size ranged over a factor of 2 or 3. In a method of maintenance improvement over conventional blue phosphors by use of other coactivators (13) the maintenance differs by a factor of 18 while the particle diameter ratio is roughly 2. Higher firing temperatures improve the maintenance of a blue phosphor by a factor of ten while the particle size is increased by a factor of three (Section A-2). Hence, in the last four examples, the particle size effect on maintenance is a minor one, compared to the over-all maintenance variations cited.

4. Emission color variation with particle diameter. —In certain phosphors of the ZnS:Cu,Cl type a definite shift occurs in emission color with variation of particle size from the same phosphor batch. The emission spectra of the five particle size fractions of the blue-green phosphor of Table II are given in Fig. 5 together with mean particle diameter as determined by microscope. The shift of emission toward the blue with increasing particle size is not consistent with the general improvement in maintenance of phosphors the longer wave length their emission color. Small and large particles from the same batch are apparently activated differently, and emission color indicates that the smaller particles are more highly activated. Maintenance has been shown to depend very strongly on activation (per cent addition of copper and chlorine) and also to

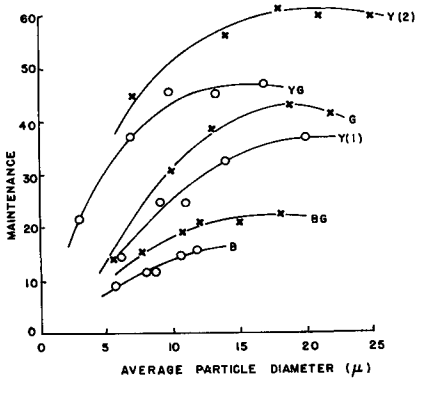

Fig. 4. Dependence of maintenance (per cent of initial brightness, 120 v, 4000 cps) on particle diameter.

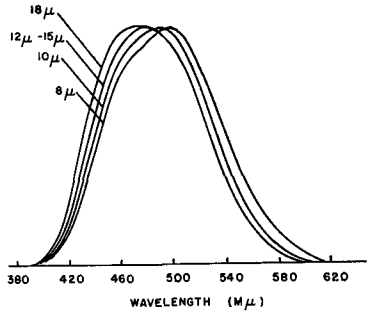

Fig. 5. Variation of emission color with particle size from the same lot of phosphor. Blue-green ZnS:Cu, Cl.

depend somewhat on particle size. These dependences, as determined, are slightly inaccurate due to the interrelation of activation and particle size.

The emission color of the blue and deep yellow-green phosphors (near the extremes of the color range of ZnS:Cu,Cl class) does not vary with particle size, very likely because (*a*) the blue fine particles contain only active blue luminescence centers and so the coarse particles can emit no bluer light, and (*b*) the coarse yellow-green particles contain only active yellow-green luminescence centers so the finer particles can emit no yellower light. The possibility that the yellower emission from smaller particles might be due to their stronger absorption of blue emission, was eliminated by the following experiment. A large-particle fraction (20-30 μ diameter, blue-green emission) was crushed to an average diameter of 1 or 2 μ. No change in the electroluminescence emission spectrum occurred within experimental error due to this mechanical reduction in particle size, and it differed significantly from the spectrum of the original small-particle fraction (4-6 μ diameter, green emission) of the same phosphor batch.

B. Dependence of Maintenance on Conditions of Operation

1. Frequency.—It is well known that electroluminescent phosphors deteriorate more rapidly at higher frequencies (5, 6). This behavior is true generally, with no known exceptions. It was suggested[5] that, at least approximately, a universal deterioration curve results from plotting the per cent of initial brightness against the total number of cycles of operation, rather than the hours of operation. The validity of such a universal deterioration curve was determined for the phosphors in Table II. Figure 6 shows the data plotted in terms of cycles of operation. A universal curve can be drawn approximately for frequencies higher than 1000 cps, but at lower frequencies significant deviations from the universal curve occur. On the basis of these curves, a parameter useful for describing the maintenance properties of an electroluminescent phosphor is the high-frequency half-life under dry conditions, defined as the number of cycles of operation at frequencies greater than 1000 cps after which light emission has been reduced to half the initial value.

[5] By E. A. Sack, Westinghouse Research Laboratories, Pittsburgh, Pa.

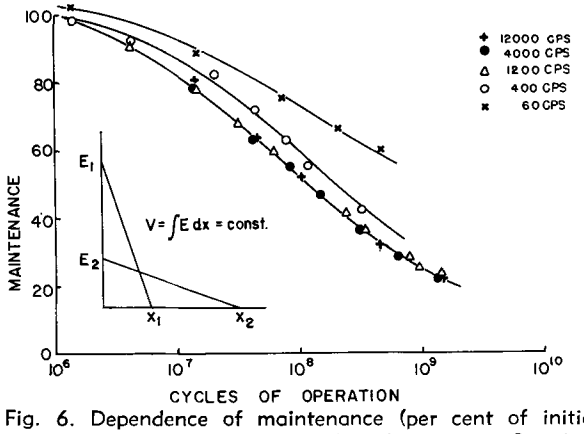

Fig. 6. Dependence of maintenance (per cent of initial brightness) on total number of cycles of operation. Standard green phosphor, 200 v. Inset: Field distribution at (1) high and (2) low frequency.

All the phosphors showed low-frequency deviations from the universal curve which satisfactorily described deterioration above 1000 cps. These deviations ranged from a factor of two in half-life for the phosphor with blue emission to a factor of ten with the yellow-green. Generally, these deviations are in the direction of longer half-life (in cycles) at lower frequency; the blue phosphor, however, showed a shorter half-life in cycles at low frequency. The yellow-emitters showed low-frequency deviations which were intermediate between the blue and yellow-green.

The frequency dependence of maintenance is therefore very strong, covering a range in half-life even greater than the range of frequencies of operation.

It might be expected that if two identical lamps are operated, one at a high frequency and one at a low frequency and at the same applied voltage, that the brightness of the high-frequency lamp would initially be much greater than that of the low-frequency lamp but would eventually fall below; this would follow if the lumen-hour capabilities of the two lamps were about equivalent. It is observed, however, that of two identical lamps operated at the same voltage and different frequencies, the brightness of the lamp operated at the higher frequency never falls below that of the lamp operated at lower frequency. Lamps operated at high frequency, although they have deteriorated to a small percentage of initial brightness, are still brighter than identical low-frequency lamps. The brightness-time curves of these lamps approach each other more and more closely after a period of operation but apparently do not cross even after very long times. Such behavior suggests fast-deterioration and slow-deteriorating components of light emission, the latter being relatively independent of frequency. The presence of two components is particularly marked in the case of an improved-maintenance yellow phosphor described in Section E and in Fig. 14.

2. Voltage (field strength).—It is not unreasonable to expect that an increase in voltage and field strength will lead to more rapid deterioration of the phosphor since the light output is higher. Roberts (6) reported, however, that the maintenance of certain lamps improved slightly with increase in field strength. A determination of the voltage dependence of maintenance was made for blue and green ZnS:Cu,Cl phosphors and a yellow-emitting ZnS:Mn,Cu,Cl phosphor. Some of the results are given in Table III. At low frequency (60 cps) the maintenance of the blue phosphor improves with increasing field strength. At intermediate frequency (400-4000 cps) the blue and green phosphors deteriorate slightly more rapidly at higher field strengths, and the yellow phosphor shows no voltage dependence within experimental error. Thus, electroluminescence maintenance does not depend appreciably on the field strength experienced by the phosphor. The greatest observed variation in half-life over the range of useful voltage is no more than a factor of two or three; this is to be compared

Table III. Dependence of maintenance (half-life) on applied voltage for various phosphors and frequencies

	Initial brightness, arb. units	Voltage	Half-life, hr
	1300	400	380
	700	310	290
Blue	400	230	210
60 cps	50	150	150
	8	75	180
	1600	370	1.0
	1300	340	1.3
Blue	1050	300	1.3
4000 cps	240	203	1.4
	9	95	1.1
	770	370	2.2
	580	340	3.5
Green	320	300	2.6
4000 cps	100	200	3.5
	6	92	5.0
	600	400	14
	380	360	14
Yellow	250	317	14
4000 cps	60	212	16
	2	97	12

to the variation of 1000 to 1 due to frequency. There is little disadvantage, therefore, in operating a lamp close to breakdown in order to obtain maximum brightness, since the maintenance is about that observed at much lower voltages. Conversely, maintenance cannot apparently be improved significantly by reducing the field strength on the phosphor.

3. Temperature.—Electroluminescence deterioration proceeds (5) at a rate too slow to measure if the phosphor is maintained at liquid nitrogen temperature (−195°C). On the other hand, the maintenance is poorer at temperatures higher than room temperature than it is at room temperature. This behavior is illustrated by Fig. 7.

4. Humidity.—It is well known generally in electroluminescence work that moisture has a strong deleterious effect on the maintenance of output. Atmospheric water vapor is perhaps the most important adverse influence on electroluminescence maintenance from the point of view of practical

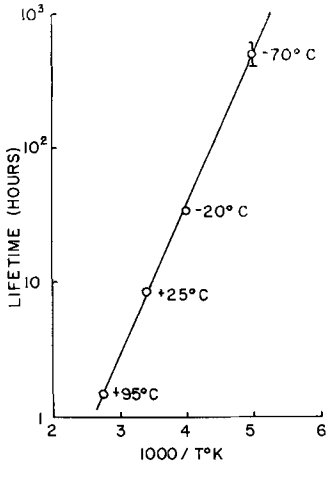

Fig. 7. Dependence of lifetime (time to half of initial brightness) on temperature. Standard green phosphor, 150 v, 4000 cps.

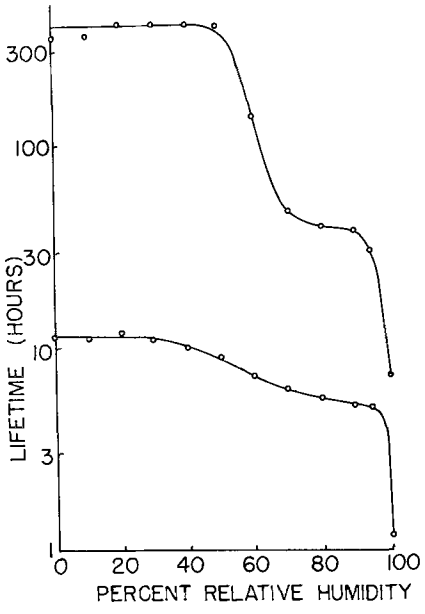

Fig. 8. Dependence of lifetime (hours to half of initial brightness) for two green ZnS:Cu, Cl, phosphors as a function of per cent relative humidity. 4000 cps, PVCA dielectric, 23°C.

application. Operation at zero humidity is certainly the ideal condition for obtaining information on the intrinsic maintenance behavior of a phosphor, and this has been done for much of the testing reported in this paper. For experimental unprotected lamps, when the relative humidity of the air-conditioned laboratory rose above 30% the lamps were always operated in a closed vessel of the desiccator type at zero humidity. The dependence of lifetime on per cent relative humidity is shown in Fig. 8 for a standard and an improved green ZnS:Cu,Cl phosphor. The curves shown were obtained with sulfuric acid solutions, and similar results were obtained with saturated solutions of solid materials. The reduction in lifetime from low to high humidity (excluding 100%) is by a factor varying from 2 to 10. The deterioration observed when a phosphor is operated in a vacuum (10^{-5} mm Hg) either with or without plastic dielectric[6] is similar to what is observed if a lamp is operated in air at zero humidity or in 100% humidity so long as perfect protection from moisture is achieved; the plastic dielectric apparently serves only to slow the ingress of moisture somewhat. Moisture has apparently no detectable adverse effect on the phosphor so long as voltage is not applied; if the phosphor layer is thoroughly dried before operation, the maintenance is unaffected. Storage of an already aged phosphor under humid conditions, or even wetting it, will show no adverse effects so long as the phosphor is dried before the field is applied.

Zinc selenide electroluminescent phosphors which emit in the red have been found to show far better

[6] As long as no moisture is present, the nature of the dielectric material seems to have no effect whatsoever on the maintenance characteristics of a given phosphor. Various waxes, epoxy resin, nitrocellulose, Lucite, polyvinyl chloride acetate (PVCA) which was generally used in the lamps described in this report, castor oil, air, and vacuum led to very similar rates of deterioration so long as the humidity was low or zero. This conclusion does not apply (a) to solid dielectric materials which are not stable with time, such as plastics containing volatile plasticizers, or (b) to glass dielectrics during the firing of which the phosphor is altered because of the higher temperatures necessary.

maintenance than zinc sulfides. It has been found also that the electroluminescence of a selenide phosphor is remarkably maintained in the presence of moisture.

5. *Two lifetimes from electroluminescent lamps.* —An electroluminescent lamp deteriorated at high frequency and low voltage to a fraction of its initial brightness may show no evidence of deterioration under low frequency and high voltage excitation. In other words, a lamp excited to brightness L_0 at high frequency and low voltage (HFLV) can be quite completely deteriorated and then can be excited to L_0 again by the same LFHV conditions which produced an equivalent brightness L_0 initially. When excited by the low frequency and high voltage, the phosphor is as fresh as initially and an entirely new "lifetime" is begun. The first deterioration has little or no effect on the rate of the second deterioration. Coarse (15 μ) particles and fine (3 μ) particles show the same behavior; namely, deterioration at a high frequency is not seen at a much lower frequency as long as the operating voltage is higher than that at which the deterioration took place; this will usually be the case in practice since higher voltage is required to reproduce a given brightness at lower frequency. A typical pair of frequencies at which the two "lifetimes" may be obtained is 60 and 4000 cps. Since newer coarse phosphor powders show very reasonable maintenance at frequencies as high as 10,000 cps, the first high-frequency "lifetime" can be long enough to be practically valuable. The purpose of this section is to illustrate this behavior by means of the maintenance contours to be described, and to show that the sequence HFLV followed by LFHV operation is the correct one to obtain the two "lifetimes" from an electroluminescent lamp.

One lamp made with standard green phosphor was deteriorated for 400 hr at high frequency (20 kcps) and low voltage (60 v rms) to 20% of initial brightness. This operating point is indicated by the cross in Fig. 9, which is a maintenance contour in frequency and voltage of the deteriorated lamp. The heavy lines and plotted points are apparent maintenance, in per cent of initial light output, as measured under frequency and voltage conditions other than those at which deterioration took place; that is, brightness was measured, before and after deterioration, at each combination of voltage and frequency. Note, for example, that this lamp shows no sign of deterioration at 160 v, 60 cps and that its light output under these conditions is equal to the initial light ouput before the original deterioration at HFLV.

The dashed lines of equal light emission illustrate the well-known observations (*a*) that the frequency dependence of electroluminescence becomes negligible at low voltage, where the voltage dependence of emission is strong, and (*b*) that the frequency dependence is strong at high voltage, where the voltage dependence is weak.[7] A change in operating conditions from HFLV to LFHV operation is more or less parallel to the equal-brightness lines; hence, light output under the latter conditions can be equal

[7] An explanation of these interdependences is given in ref. (14).

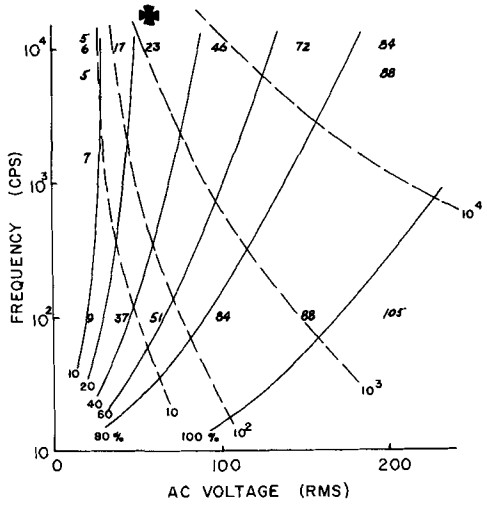

Fig. 9. Apparent maintenance (solid lines, per cent of initial brightness) at voltage and frequency other than that at which deterioration took place. Cross indicates conditions of deterioration (see text for time of deterioration). Dashed lines are initial brightness in arbitrary units. Standard green phosphor.

to or greater than the initial light output at the conditions under which deterioration took place.

Another lamp was deteriorated at a lower frequency (60 cps) and a higher voltage (150 v rms). For this case of initial LFHV operation, which resulted in deterioration of electroluminescence to 12% of initial, subsequent operation under the opposite HFLV conditions makes little difference in the observed state of deterioration, and no advantage is gained. Improvement results only by moving to lower frequency or higher voltage or both as in the previous case, but even then the recovery is not large (from 12% to about 30%).

Reasons based only on the mechanism of electroluminescence have led to the view (8) that an increase in frequency of excitation leads to more marked localization of the light-emitting and deterioration processes of electroluminescence. In a study of the field quenching of alpha particle scintillations, Alfrey and his associates (15) have obtained further and independent evidence that localization of the electric field is greater at high frequency. It is generally accepted that low voltages lead to greater localization of the high-field region or, put in another way, that with increase in voltage the high-field region extends farther and farther into the crystal (6). Such behavior will lead to maximum localization of deterioration effects if excitation is at high frequency-low voltage (HFLV), to the upper left in Fig. 9. Following deterioration under such conditions, marked recovery takes place if frequency is reduced or voltage increased or both. This is because in either case the light-emitting high-field region is extended into fresh regions of the phosphor crystal and the deterioration becomes proportionally less evident. In fact, in the voltage and frequency region below and to the right of the 100% line in Fig. 9, the active region extends so far into fresh parts of the crystal that the reduced emission from the original small region of excitation

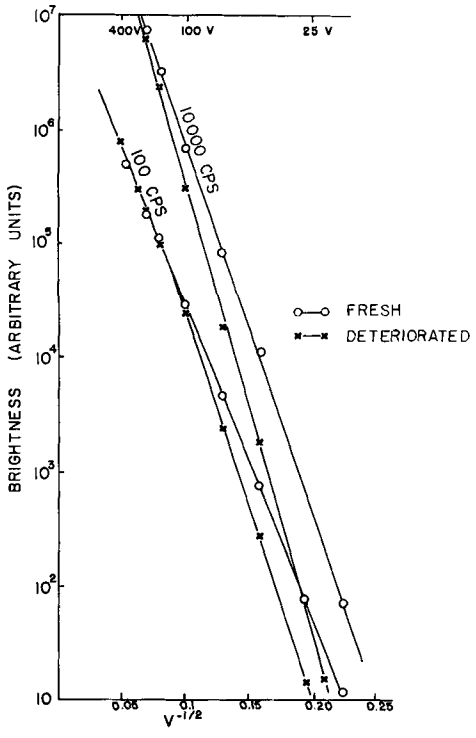

Fig. 10. Change in brightness-voltage dependence with deterioration (at 20,000 cps, 60 v, 15 hr). Standard green phosphor.

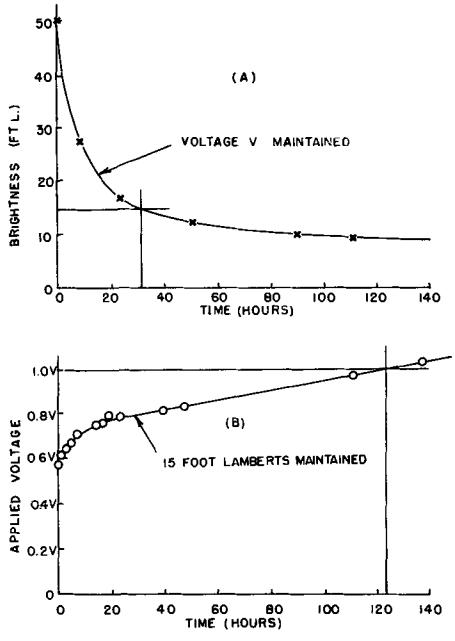

Fig. 11(A). Maintenance characteristic for constant voltage operation (4000 cps). Standard green phosphor.

Fig. 11(B). Maintenance characteristic for constant brightness operation (4000 cps). Standard green phosphor.

is masked, and deterioration effects are no longer seen. That the deterioration in the original active region is nonuniform is suggested by the observation that further localization of the active region by increasing the frequency or reducing the voltage from the conditions under which the deterioration took place, leads to even poorer apparent maintenance.

6. Localization of the electric field.—Further evidence that the excitation region in the phosphor is contracted by decrease in voltage or an increase in the frequency and expanded by an increase in voltage or a decrease in frequency appears in Fig. 10. The lamp from which the data for this figure were obtained was deteriorated at 20,000 cps and 60 v for 15 hr. Following this, the voltage-brightness characteristics were compared at 10,000 cps and at 100 cps with those for the fresh lamp. At 10,000 cps the effect of the deterioration is seen up to 400 v, but at 100 cps the effect is observed only up to 100 v. Apparently the "extent" of the high-field (excitation) region coincides with the volume of the phosphor crystal which was deteriorated at 100 v, 100 cps and at 400 v, 10,000 cps.

7. Constant brightness operation.—In lamp applications where there is a brightness control and where the desired brightness is less than the maximum brightness obtainable, operation is expected to be at constant brightness. Deterioration with operation is corrected for implicitly by resetting the brightness control (voltage) to a different setting as deterioration proceeds. The question was raised[8] whether a lamp operated at constant brightness would have a longer useful life than an identical lamp operated, as usual, at constant voltage. The question is made meaningful only if some restriction is made, such as that the rated voltage of the lamp should not be exceeded. Increasing the voltage during life should, by extending the excitation region into fresh parts of the phosphor crystal, result in longer life (see Section B-5 and B-6). This was confirmed by the results shown in Fig. 11. Operation was at 4000 cps. Two similar lamps were used, in each case V being the rated voltage at which the lamp brightness was initially 50 ft-L. The "desired" brightness was chosen at 15 ft-L. Figure 11 (A) represents a lamp operated at constant rated voltage V. This lamp deteriorated to 15 ft-L after about 30 hr of operation at 4000 cps, a typical maintenance figure for an early green-emitting ZnS:Cu,Cl phosphor. Figure 11 (B) represents the other lamp operated at the constant "desired" brightness of 15 ft-L. The applied voltage was about 0.6 v initially and rose to a value of V in about 120 hr. The useful life of the constant brightness lamp was therefore about four times that of the lamp operated at constant voltage. At the end of its "life" each lamp was operating at voltage V and a brightness of 15 ft-L. In one case the useful life is terminated by too low a brightness at rated voltage, and in the other case by too high a voltage to maintain rated brightness.

This increase in lifetime by constant brightness operation was confirmed[9] also at 400 cps. Different dielectric materials and lamp thicknesses were tested. The dielectric material had no effect. Lamp thickness does, however, have a strong effect; the thicker the lamp and the higher the breakdown voltage, the smaller the advantage in constant brightness operation. The reason is as follows: At a

[8] By S. Goldfarb, Wright Air Development Center, Dayton, Ohio.

[9] Data from R. W. Wollentin.

given required brightness the brightness-voltage dependence is stronger for the thicker lamp since the required field strength is lower. Therefore the initial voltage is a larger fraction of the final voltage, the voltage increase during life is smaller, and the utilization of fresh phosphor regions due to the voltage increase is less marked. The effect on lifetime is large indeed, since the thick lamps last only twice as long as with standard (constant-voltage) operation, while the lifetime of the thinner lamps is four times as long. This effect is beneficial, since lamps normally will be operated as near breakdown as possible to realize maximum brightness at minimum voltage (thin lamps), and such operation will lead to maximum improvement in lifetime due to constant brightness operation. In such a case, the maximum voltage obviously must not exceed the breakdown voltage of the lamp.

8. External series impedance.—The impedance of electroluminescent lamps is dependent on frequency and voltage of excitation (11, 16). The impedance of these lamps increases during life (see Section D below), and this effect is greatest with low frequency and high voltage operation. The impedance increase occurs in the phosphor powder itself; the dielectric material does not change its electrical properties with life if the lamp is properly finished and cured. Therefore, an added fixed impedance in series with the lamp will divide the voltage in such a way that the effective voltage on the lamp will automatically increase during life as the impedance of the lamp (phosphor) increases. This increase in effective voltage will tend to compensate for the normal decrease in brightness with life. Lamps were made with a poor maintenance blue phosphor in order to obtain the results in a short time, and were operated at 400 cps. Table IV identifies the series element, the total voltage applied to the lamp and series impedance combination, and the time in hours for the brightness to decay to half the initial brightness. Similar experiments have been conducted at 60 cps and increases in half-life of about five times have resulted from the addition of a series resistor equal to the initial impedance of the lamps.

It is interesting to note that operation of a lamp with a series impedance is inherently stable. The impedance of the lamp (phosphor) decreases with increasing field strength. Therefore, as the lamp impedance increases due to operation and the effective voltage across the lamp increases, this increase leads in turn to a reduction in lamp (phosphor) impedance at the new higher field strength. The effect is a type of negative feedback ensuring stability of operation. It should be borne in mind that the dielectric embedding material itself acts as an impedance in series with the phosphor crystals. At low phosphor concentrations where, on the average, each phosphor crystal is isolated in the dielectric, the maintenance is better than at high concentrations where each crystal is effectively in contact with one or more others and the series impedance effect is absent. Under certain conditions the maintenance is expected to improve upon addition of a clear coat, for the same reason. These effects are described in later sections.

9. Pre-aging effects.—Pre-aging at rated voltage and frequency leads to apparent improvements in maintenance since early deterioration is more rapid than later, and the "initial" brightness is then defined as that after some deterioration (the pre-aging) has taken place. Pre-aging is feasible so long as excess brightness is available. Pre-aging, at voltages and frequencies other than those under which the lamp is to be run, can lead to the same maintenance improvement in a much shorter time.

An improvement in 400 cps maintenance is associated with a certain cost in initial 400 cps brightness. This relation is given roughly in Table V, where L_o is the initial brightness and L_a is the brightness after aging, both measured under operating conditions rather than pre-aging conditions, and holds approximately regardless of the conditions of pre-aging. Various pre-aging conditions necessary to achieve the maintenance improvement in 1 and 2 of Table V are given in Table VI. Hence, for example, the 400 cps half-life of a lamp can be

Table IV. Effect of series impedance on maintenance

Lamp	Element	Total voltage	Half-life, hr
1	None	300	11
2	70 × 10³ ohm	540	37
3	100 × 10³ ohm	640	43
4	130 × 10³ ohm	750	80 (extrapolated)
5	None	220	10
6	0.006 mf	400	32
7	0.003 mf	660	50

Table V. Relation of loss in initial brightness to half-life improvement by pre-aging

	Brightness ratio L_a/L_o, 400 cps	Half-life improvement factor
1	0.80	2
2	0.60	5
3	0.40	10
4	0.20	25

Table VI. Pre-aging conditions for specified half-life improvement

Frequency, cps	Voltage	Time, hr
Condition 1, 80% of initial output,* doubled half-life		
400	210	6
400	80	130
1200	240	3
1200	100	40
4000	280	1
4000	140	9
12000	280	0.3
12000	160	3
Condition 2, 60% of initial output* 5 × half-life		
400	160	130
400	360	6
1200	180	40
1200	400	3
4000	210	9
12000	250	3

* Measured under the aging conditions 250 v, 400 cps, rather than the pre-aging conditions.

improved by a factor of five at a reduction of 40% in initial brightness and this pre-aging can be accomplished in times varying from 3 to 130 hr depending on the frequency and voltage used for pre-aging.

C. Dependence of Maintenance on Lamp Construction

1. Phosphor concentration.—It has been customary to use a phosphor/plastic-dielectric weight ratio which yields maximum initial brightness within breakdown voltage requirements. It was found that this weight ratio also has an effect on maintenance and so this factor must be considered when arriving at an optimum ratio.

A set of lamps made with standard green phosphor and PVCA dielectric and utilizing a wide range of phosphor/plastic weight ratios (while maintaining constant lamp thickness) was subjected to accelerated life test at 4000 cps. At low phosphor concentrations or weight ratios, the maintenance is constant, independent of concentration. At a certain higher concentration the maintenance worsens rather abruptly and then remains constant at the poorer value for still higher phosphor concentrations. The corresponding half-life is reduced by a factor of two or three at high phosphor concentrations. Because of this peculiar result, these experiments were repeated by spraying an entirely new series of lamps. The results were essentially the same. The experiments were repeated for the third time to obtain more data in the transition region. These results are given in Fig. 12. The curve marked $t_{1/2}$ is the half-life in hours taken from the actual maintenance curve for operation at 120 v, 4000 cps. The transition is continuous as the phosphor/plastic weight ratio changes. The curve marked L_o is the initial brightness in ft-L at 120 v, 400 cps. Above a ratio of 5.0 some arcing occurs. The curve marked $L_o t_{1/2}$ is the product of L_o and $t_{1/2}$ and is indicative of the total light output during the life of the lamp.

2. Phosphor layer thickness.—It is intended only to re-emphasize here that the maintenance variation due to different applied voltages on lamps of constant thickness is also to be expected when lamps of various thicknesses are to be operated at a certain predetermined voltage. As shown in the preceding and following sections, phosphor concentration and

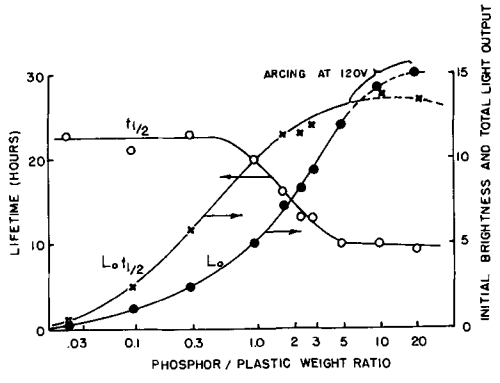

Fig. 12. Dependence of maintenance (hours to half of initial brightness at 120 v, 4000 cps), initial brightness (ft-L at 120 v, 4000 cps) and the product of these, in arbitrary units, on phosphor/plastic weight ratio. Standard green phosphor, constant thickness lamps.

Table VII. Dependence of maintenance on number of clear coats

No. clear coats	Half-life, cycles	Half-life, hr at 400 cps	Breakdown brightness, arb. units	Breakdown voltage, v
0	0.4×10^8	60	11	200
1	0.41	60	16	240
3	0.51	70	23	350
10	0.7	100	22	500
30	1.4	200	17	700
100	2.4	330	—	—

clear coat thickness must be identical among lamps in which this phosphor layer thickness or field strength effect is to be utilized or studied.

3. Clear coat thickness.—A clear coat is a layer of clear dielectric material containing no phosphor and is often applied to a lamp before or after the phosphor/plastic layer has been laid down. The half-life of conventional sprayed lamps has been observed to increase with the number of clear coats up to a factor of six times the half-life of an identical phosphor layer with no clear coat. Identical lamps consisting only of a thin phosphor/plastic layer were sprayed. Some were reserved as controls and the others were sprayed with from 1 to 100 very thin clear coats of PVCA lacquer-thinner solution. All lamps were operated at 150 v, 4000 cps. Table VII gives the half-life in number of cycles to half-brightness, the breakdown brightness, and the breakdown voltage as a function of the number of clear coats applied over the identical phosphor-plastic base layer. This indicates that in the particular case where a certain brightness is desired and excess voltage is available, maximum maintenance is obtained by utilizing as high a voltage as possible and increasing the clear coat to phosphor-layer ratio until the desired brightness is obtained. Previous indications that clear coats improve maintenance have sometimes been attributed to better moisture protection. The above experiments were carried out in an air-conditioned laboratory in about 30% relative humidity. The effect of clear coats on maintenance may also be that the clear coat behaves as a series impedance (primarily a capacitance) and the maintenance improvement may be the same as that observed when a series capacitor is connected to the lamp (see Section B-8).

D. Changes in Other Properties with Deterioration

1. Electrical properties.—In the fresh electroluminescent phosphor layer, both the capacitance and the conductance increase with increasing voltage (16). This behavior changes, however, with deterioration of the lamp (Fig. 13). The voltage dependence of both capacitance and conductance in the fresh lamp has largely disappeared in the deteriorated lamp, and this is observed over a wide range of frequencies of measurement and of deterioration. The reduction at high voltage of conductance leads to a reduction in power dissipation at high voltage; little change in either is observed at low voltage. The changes in power absorption and light emission during deterioration lead to drastically reduced efficiencies at low voltage. At high

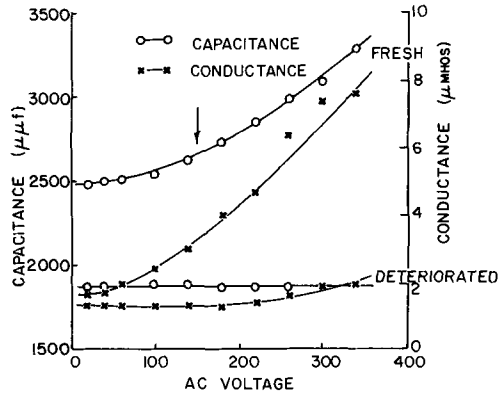

Fig. 13. Variation in capacitance and conductance for fresh and deteriorated lamps. Arrow indicates voltage at which deterioration took place. Standard green phosphor. 4000 cps, 150 v, 1000 hr.

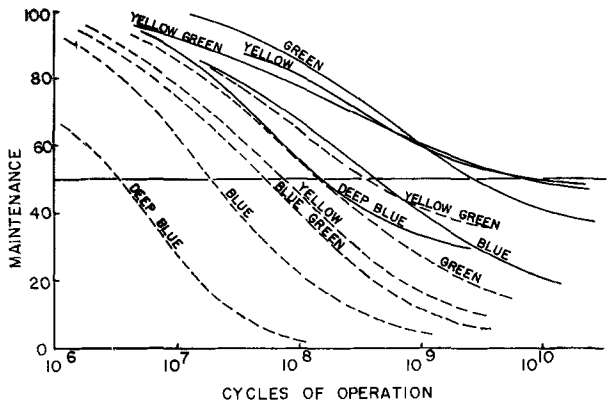

Fig. 14. Comparison of maintenance (per cent of initial brightness) characteristics of standard phosphors (dashed curves) and improved phosphors (solid curves), 150 v, 4000 cps.

voltage the efficiency can remain quite unchanged or can increase appreciably; this effect is a shift of peak efficiency toward higher voltage due to deterioration, and is another manifestation of the localization of deterioration effects in the phosphor crystal.

The gradual decrease with operation of the capacitance (5, 6) and conductance of a phosphor layer may be related directly to the electroluminescence process. Three cells were operated singly while in a bridge circuit for 120 hr at 150 v, 4000 cps. Cell A was a conventional sprayed phosphor-plastic layer of green-emitting ZnS:Cu, Cl phosphor. Cell B was similar except that no plastic dielectric was present. Cell C consisted of clear plastic dielectric with no phosphor, and the electrical characteristics of this cell did not change with operation. Components of the capacitance and of the conductance decrease roughly in proportion to the decrease in light output for both the conventional phosphor-plastic sprayed layer and the water-settled layer of phosphor powder alone.

2. Frequency response.—High-frequency deterioration depresses the light output more strongly in the frequency region where deterioration took place than at lower frequencies. Low-frequency deterioration depresses the brightness about equally at all frequencies. This observation also is related to the localization of electric field with increasing frequency discussed in Sections B-5 and B-6.

3. Emission spectrum.—No change in emission spectrum of ZnS:Cu, Cl phosphors with deterioration has ever been observed. In the case of conventional green-emitting phosphors, a quantitative search for such a spectral change was made and none found beyond slight discrepancies which could be attributed to darkening of the plastic dielectric material. The emission spectra of twelve phosphors (including ZnS:Cu, Cl emitting from the deep blue to yellow-green, ZnSSe:Cu,Cl emitting in the yellow, red ZnSe:Cu, Cl, blue-green ZnS:Cu, Pb, Cl, and yellow ZnS:Cu, Mn, Cl) were compared when fresh and after long deterioration to a few per cent of initial brightness. Only the ZnSe:Cu, Cl phosphor appeared to shift slightly, toward longer wave lengths. The other phosphors showed no detectable change in emission spectrum.

D. Recent Maintenance Improvements

The phosphors described in this paper are predominantly conventional ZnS:Cu, Cl phosphors in which emission color shifts from the deep blue to the yellow-green as copper and chlorine additions are increased. The yellow-emitting manganese-activated ZnS:Cu, Mn, Cl phosphors behave much like those without manganese in their maintenance behavior, the manganese serving primarily to shift the blue or green "normal" emission to a relatively invariant yellow (17). The maintenance characteristics of earlier standard phosphors (dashed curves) are summarized in Fig. 14, where per cent of initial brightness is plotted against cycles of operation; the data were obtained at 150 v, 4000 cps, low humidity, and the resulting "universal curves" describe the maintenance behavior at frequencies of about 1000 cps or higher (Section B-1). Recent improvements in maintenance of the same basic phosphors have been made possible by alterations in activation and by modified firing procedures. These improved phosphors, covering the same range of emission color, are represented by the solid curves in Fig. 14; the same operating conditions as above were used in obtaining the data. These maintenance improvements do not usually sacrifice initial brightness. The old and new deep blue and greenish blue phosphors are about equivalent in brightness, the improved-maintenance green phosphors are often brighter than the original, and the improved maintenance yellow in Fig. 14, for example, has half the initial brightness of the original yellow shown, while its half-life is 100 times longer. This particular phosphor involves only an increase in Cu-Cl addition in accordance with Section A-1. The small losses in initial brightness as maintenance improves, as in the case of the yellow phosphor, are gradual and a compromise can be made at any point; however, integrated light output over the life of the lamp (lumen-hours) improves very rapidly indeed as maintenance improves. In fact, it is a property of some of the recent phosphors that a relatively high plateau of light emission is reached after long oper-

ation, as in the case of the improved yellow of Fig. 14. Obviously if the point of leveling off is near 50%, as in this example, the half-life, or time to half of initial brightness, is not a useful parameter for measuring maintenance since (a) minor differences in phosphors would lead to large variations in this quantity, and (b) defining the useful life to include deterioration to levels somewhat less than 50% of initial would increase it by a large factor.

Taking the improved green phosphor as an example, 1000 cps operation leads to a half-life of 750 hr. Because the high-frequency half-life in cycles is about doubled for 400 cps operation and roughly ten times greater for 60 cps operation of this type of phosphor (Section B-1), the corresponding extrapolated half-lives are 3750 hr at 400 cps, and 12,000 hr at 60 cps; such behavior requires good moisture protection and great patience to measure.

III. Discussion

The improvement in maintenance with increasing equal copper and chlorine additions can be explained as follows. The normal trapping or donor sites are associated with Cu-Cl centers in strongly electroluminescent ZnS:Cu, Cl phosphors. Excess chlorine (lower right hand region in Fig. 1-3) leads to phosphorescence and deeper traps which are detrimental to electroluminescence. The greater the copper-chlorine addition to the phosphor, the higher the expected concentration of normal traps or Cu-Cl centers, and the less rapid the quenching of electroluminescence either by a given rate of incoming deeper traps (8) or depletion of normal traps by outward diffusion (5). That the density of normal traps and good maintenance are strongly correlated is shown by Fig. 3, even though the deep traps, contributing to phosphorescence and not to electroluminescence, confuse interpretation in the low-copper high-chlorine region (lower right) of the figure. As the concentration of Cu-Cl centers increases, the electroluminescence brightness reaches a peak and then drops off (Fig. 2), perhaps due to self-quenching by the centers (concentration quenching), but maintenance apparently continues to improve. The degree of deterioration of electroluminescence after a period of operation is very likely related to the ratio of the concentration of deep traps which have appeared to the concentration of normal traps.

Maintenance improves with increasing particle diameter. If deterioration is due to the introduction of a foreign substance from the surface into the crystal volume, or to the escape from the volume to the surface of some entity necessary to electroluminescence, then an increase in the rate of deterioration with increase in surface to volume ratio is to be expected; experimentally the rate of deterioration is proportional to this ratio for all but the largest particle sizes.

Maintenance depends strongly on frequency and very little on voltage. An increase in frequency reduces the crystal volume experiencing the field and increases the maximum electric field in the crystal; therefore the rate of field-diffusion is increased and the volume affected by it is reduced and deterioration becomes more rapid. In the schematic inset of Fig. 6, E_1 and X_1 refer to the maximum field and extent at high frequency. As the active charge density decreases with deterioration, the slope dE/dX decreases and the field configuration approaches that of the low frequency case (E_2, X_2). Hence the light output also decreases toward that characteristic of low frequency excitation but never drops below since E_2 will always be less than E_1. An increase in voltage increases the maximum field but also increases the extent of the field so, although the rate of diffusion is greater, the volume into or out of which the diffusion takes place is also increased and the net effect on maintenance may be small. In the case of the blue phosphor (Section B-2) the copper-chlorine addition is relatively small so the volume concentration n of trapping or donor sites is expected to be small. It follows from Poisson's relation that the extent of the field will increase more rapidly with voltage if n is small. This blue phosphor (Table III) actually maintains output better at high voltages than at low voltages (at low frequency) as if in fact the excited crystal volume increased more rapidly with voltage than the rate of field-diffusion causing deterioration.

The temperature dependence of deterioration is very strong. If the diffusion of ions is involved, the electroluminescence half-life should be related to the ionic mobility (5) and should show an exponential temperature dependence. This dependence of half-life on temperature is shown experimentally in Fig. 7 and corresponds to an activation energy of about 0.1 ev.

In Section B-5 it was shown experimentally that electroluminescence deterioration is at least somewhat nonuniform, since contraction of the excitation region by reducing the voltage or increasing the frequency leads to a progressively smaller fraction of the light emission originally observed under the same conditions. This is to be expected. Any decrease of the positive charge density (the ionized donor or trapping sites active in the electroluminescence process) due either to incoming deeper traps or depletion of the normal traps by field-migration outward will reduce the field gradient gradually during deterioration and, at constant voltage, expand the high-field region into fresh parts of the phosphor crystal. Hence contraction of this region, as above, confines the excitation to phosphor parts which have been deteriorated the longest.

Evidence for the localization (8) of the electric field with increase in frequency was given in Sections B-5, B-6, and D-2. The pre-aging data of Section B-9 also indicate this effect. To pre-age a lamp to a given fraction of its initial brightness (measured at an arbitrary voltage and frequency) the voltage also must be increased if the frequency is increased; the contraction of the excitation region at the higher frequency must be counteracted by its expansion at higher voltage. Further evidence for this effect is implicit in the data of Sections B-1 and B-2. The blue phosphor, the only one showing better maintenance at high voltage (high fields),

also shows better maintenance as a longer half-life in terms of cycles of operation at high frequency (high fields). The other phosphors have longer half-lives in cycles at low frequency (low fields) and at low voltage (low fields). Incidentally, it was noticed recently that in his major 1947 paper (4) on electroluminescence, Destriau developed an analytical expression predicting higher active fields at higher frequencies of excitation.

The absence of even a slight shift in emission color, as deterioration proceeds to a point where brightness is only a few per cent of initial, suggests that the luminescence centers are not destroyed during electroluminescence deterioration for the following reason. All of the ZnS:Cu, Cl phosphors emit in both of the well-known blue and yellow-green emission bands of this type of phosphor; the blue-green and green emitters of this class, in particular, show substantial components of emission in both of these bands. If the blue and green centers differ significantly in their physical or electrical configuration, and if the motion of one constituent of the centers is involved in electroluminescence deterioration, then one of the centers is likely to be more vulnerable to destruction than the other by the deterioration process. No such effect seems to exist within the experimental error of a few per cent. On the other hand, the trapping and release of electrons is now considered to be an indispensable part of the electroluminescence process (14, 18-21). One theory (14) of electroluminescence in zinc sulfide explains the bulk of typical experimental data by considering only the trapping and release process without dealing explicitly with either recombination at the centers or the ionization process. If this trapping process is quenched by either or both the mechanisms described in Papers I or III, the electroluminescence brightness will deteriorate without destruction of the centers; as already pointed out, the maintenance of photoluminescence suggests that the luminescence centers remain intact.

In Section B-1 it was pointed out that some phosphors show a very definite slowly deteriorating component of light emission after long operation, and that probably all phosphors show this to some degree. In Fig. 15 the brightness-time data of a typical phosphor have been fitted by assuming

$$L = \frac{L_1}{1 + t/t_1} + \frac{L_2}{1 + t/t_2}$$

where $L_1 + L_2 = L_0$ and t_1 and t_2 are the widely different half-lives of the two components; here, $L_1 = L_2 = L/2$, $t_1 = 6$ hr and $t_2 = 97$ hr. In some cases according to such an analysis, the long-lived component deteriorates extremely slowly and is also a major fraction of the initial brightness; an example is the improved maintenance yellow phosphor of Fig. 14.

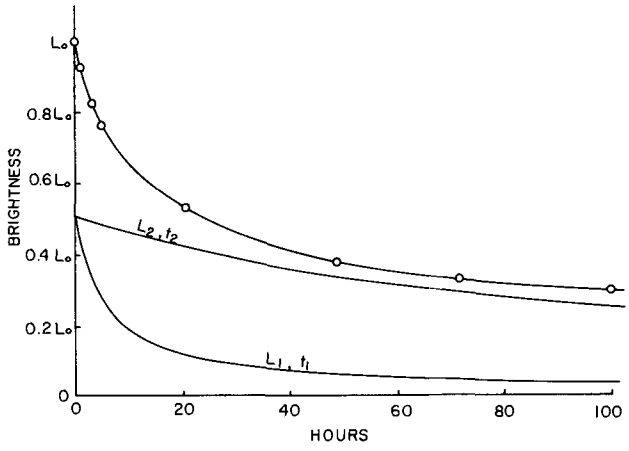

Fig. 15. Resolution of normal maintenance characteristic into short-lived and long-lived components. Standard green phosphor, 150 v, 4000 cps.

Acknowledgment

It is a pleasure to acknowledge the cooperation and valuable assistance of the author's associates. He wishes to thank particularly J. VanBroekhoven, W. Lehmann, and A. Wachtel for kindly supplying many of the phosphors, R. L. Fitzmaurice for making the countless lamps and for help in obtaining the data, J. M. Grasso and R. M. Potemski for their assistance, and H. F. Ivey for continued encouragement and helpful discussion.

Manuscript received March 24, 1960. This paper was prepared for delivery before the Chicago Meeting, May 1-5, 1960. Much of the work described in this paper was carried out under Contract AF33(616)5811 from the Wright Air Development Center.

Any discussion of this paper will appear in a Discussion Section to be published in the June 1961 JOURNAL.

REFERENCES

1. H. F. Ivey, *IRE Trans. Electron Devices*, Vol. ED-6, p. 203, April, 1959 (complete bibliography).
2. G. Destriau and H. F. Ivey, *Proc. IRE*, **43**, 1911 (December 1955) (Review Paper).
3. G. Destriau, *J. Chim. Phys.*, **33**, 587 (1936).
4. G. Destriau, *Phil. Mag.*, **38**, 700, 774, 800, 885 (1947).
5. W. A. Thornton, *Bull. Amer. Phys. Soc., II*, **1**, 301 (1956); *J. Appl. Phys.*, **28**, 313 (1957) (Paper I).
6. S. Roberts, *J. Appl. Phys.*, **28**, 262 (1957) (Paper II).
7. S. Roberts, Unpublished work (1952).
8. W. A. Thornton, Papers presented at Electrochemical Society Meeting, New York City, April 27-May 1, 1958, and at International Symposium on Solid-State Physics, Brussels, June 2-7, 1958. (Paper III).
9. W. Hoogenstraaten, *This Journal*, **100**, 356 (1953).
10. F. A. Kröger and J. A. M. Dikhoff, *ibid.*, **99**, 144 (1952).
11. W. Lehmann, *ibid.*, **105**, 585 (1958).
12. P. Goldberg, *ibid.*, **106**, 34 (1959).
13. P. M. Jaffe, To be published.
14. W. A. Thornton, *Phys. Rev.*, **102**, 38 (1956).
15. G. F. Alfrey, I. Cooke, and K. N. R. Taylor, Paper presented at International Symposium on Solid-State Physics, Brussels, June 2-7, 1958. G. F. Alfrey and K. N. R. Taylor, *J. Electronics and Control*, **4**, 417 (1958).
16. W. Lehmann, *This Journal*, **103**, 24 (1956).
17. H. C. Froelich, *J. Opt. Soc. Amer.*, **43**, 320 (1953).
18. P. Zalm, Philips Research Repts., **11**, 353 415 (1956).
19. G. F. Alfrey and J. B. Taylor, *Proc. Phys. Soc. (London)*, **66B**, 775 (1955).
20. P. D. Johnson, W. W. Piper, and F. E. Williams, *This Journal*, **103**, 221 (1956).
21. C. H. Haake, *J. Appl. Phys.*, **28**, 117, 245 (1957); *This Journal*, **104**, 291 (1957); *J. Opt. Soc. Amer.*, **47**, 881 (1957).

Determination and Identification of Impurities in Silicon from Low-Temperature Hall Data

R. T. Bate

Battelle Memorial Institute, Columbus, Ohio

and L. R. Weingarten and D. J. Shombert

Research Laboratory, Merck, Sharp and Dohme, Rahway, New Jersey

ABSTRACT

Low-temperature measurements of the Hall effect have been used to determine donor and acceptor concentrations and in some cases to identify the major impurity in silicon. A simple apparatus for making these measurements with liquid helium is described. Typical results are presented and correlated with lifetime data at room temperature. Interpretation of the Hall coefficient measurements is discussed, and a simplified analysis of the case of the two types of donor impurity is suggested.

Experimental Apparatus

Low-temperature Hall measurements have been used by many workers to study impurity levels in silicon.[1, 2] This paper describes the use of such measurements to evaluate high-purity Merck silicon.

Figure 1 shows the Dewar used for these measurements, which is relatively simple in design. The liquid nitrogen Dewar which serves as a radiation shield has been omitted for clarity. The Dewar, made of Pyrex, is arranged so that four samples can be run at one time, and these are fastened to a relatively massive brass block which is surrounded by a tube containing helium gas at 1 atm. Outside this is a reflux column, in which the helium pressure can be varied to control the transfer of heat from the samples to the liquid helium bath above. The gasket seal at the top of this column is arranged so that the pressure cannot cause an explosion as the Dewar warms. Under proper conditions, the samples will warm from 20° to 80°K in 5-6 hr. Measurements are made by d-c potentiometry, and the magnetic field is monitored by NMR.

Theory of Hall Effect

In extrinsic silicon, the Hall coefficient in a homogeneous rectangular sample is given by Eq. [1], [2], and [3], shown below

$$R = 10^8 \frac{V_H T}{IH} \frac{\text{cm}^3}{\text{coulomb}} \qquad [1]$$

$$R_n = \frac{r_c}{ne}, \frac{1}{e} = 6.25 \times 10^{18} \text{ coulomb}^{-1} \qquad [2]$$

$$R_p = \frac{r_v}{pe} \qquad [3]$$

V_H is the Hall voltage, I is the current in amperes, T is the thickness in cm, and H is the magnetic flux density in gauss; p and n are the hole and electron concentrations, respectively, and r_v and r_c are the respective Hall coefficient factors. These factors depend in general on crystal orientation, impurity

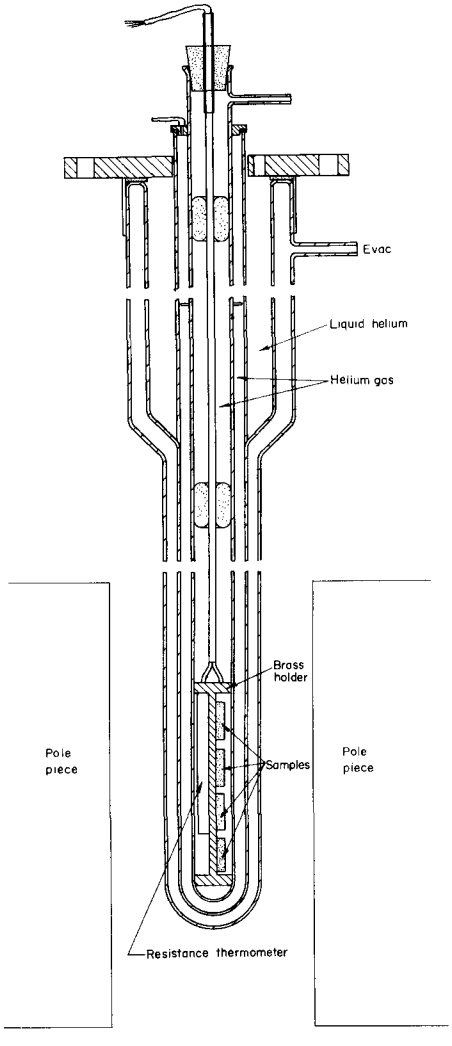

Fig. 1. Dewar for Hall measurements

[1] A method of determining the degree of compensation of p-type silicon from magnetoresistance measurements of liquid nitrogen temperature has been proposed also (1).

[2] References to much of this work are given in the review articles by Burton (2) and Kohn (3).

concentration, temperature, and magnetic field. If they can be determined, then the hole or electron concentration can be deduced directly from Hall measurements.

A discussion of the Hall coefficient factor for p-type silicon has been given by Beer and Willardson (4), and Gold and Roth (5) have studied n-type silicon. In p-type material, this factor is quite sensitive to ionized impurity scattering; however, the effect of impurity scattering in n-type material has not been calculated in terms of the exact conduction band structure. In high-purity silicon, the Hall coefficient factors are probably near unity below 40°K for reasonably strong magnetic fields. This assumption has been justified for p-type silicon by the careful work of Klein and Straub (6). Since our analysis of the Hall data required consideration only of the region below 40°K and the exhaustion region, correction for the Hall coefficient factor was necessary only in the determination of the exhaustion carrier concentration. The effect of impurity scattering in the exhaustion region in p-type material can be included by assuming initially that $r_v = 1$ at all temperatures and by calculating an approximate impurity concentration. This concentration is used then to calculate an impurity mobility from which the Hall coefficient factor can be evaluated by the method of Beer and Willardson. The Hall coefficient factor so determined then is used to correct the exhaustion carrier concentration.

The electron or hole concentration in extrinsic material is given by Eq. [4] or [5] below:

$$\frac{n(n+N_a)}{N_d-N_a-n} = A_c T^{3/2} \frac{\Sigma_i N_d^i f_d^i \exp(-\epsilon_d^i)/KT}{\Sigma_i N_d^i f_d^i}, \qquad A_c = 2.78 \times 10^{15} \frac{\text{deg}^{-3/2}}{\text{cm}^3} \quad [4]$$

$$\frac{p(p+N_d)}{N_a-N_d-p} = A_v T^{3/2} \frac{\Sigma_i N_a^i f_a^i \exp(-\epsilon_a^i)/KT}{\Sigma_i N_a^i f_a^i}, \qquad A_v = 5.62 \times 10^{14} \frac{\text{deg}^{-3/2}}{\text{cm}^3} \quad [5]$$

where N_a and N_d are the total acceptor and donor concentrations and N_a^i, f_a^i, and ϵ_a^i are the concentration, Fermi factor, and activation energy for a particular species of acceptor, N_d^i, f_d^i, and ϵ_d^i are the corresponding quantities for a particular donor. The Fermi factor for an impurity is just the probability that it is not ionized and for an acceptor is given by

$$f_d^i = \{1 + \tfrac{1}{4} \exp[(\epsilon_F - \epsilon_a^i)/KT]\}^{-1}$$

and for a donor by

$$f_d^i = \{1 + \tfrac{1}{2} \exp[(\epsilon_F - \epsilon_d^i)/KT]\}^{-1}$$

where ϵ_F is the Fermi energy. These equations are derived under the following assumptions: (*a*) only singly ionized (*i.e.*, groups III and V) impurities are present; (*b*) classical statistics hold; (*c*) no local interaction between impurities occurs; (*d*) excited bound states of carriers on impurities can be ignored (7); (*e*) the spin-orbit splitting of the degenerate ground state of the electron at the impurity site and perturbations of the band structure by the impurity can be assumed negligible (7); (*f*) the ground state of a donor is assumed doubly degenerate and that of an acceptor fourfold degenerate; and (*g*) impurity band conduction is not important. Under these assumptions, a unique activation energy can be defined which is just equal to the energy necessary to excite an electron from the valence band into the ground state of an acceptor or from the ground state of a donor into the conduction band.

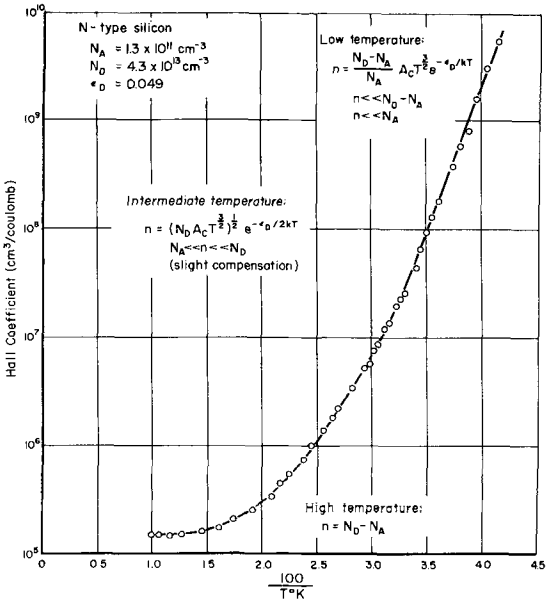

Fig. 2. Temperature dependence of Hall coefficient of n-type silicon.

Results and Discussion

Since the activation energies are known (8) for most singly ionized impurities in silicon, it is theoretically possible to identify those impurities and to determine the total donor and acceptor concentrations by fitting Hall data to these equations.

Figure 2 shows a temperature plot of the Hall coefficient for an n-type sample in which one donor (arsenic) seems to be predominant. This leads to the familiar situation in which three approximately linear regions appear on a semilog plot of the Hall coefficient *vs.* reciprocal temperature. The equations for the carrier concentration in each of these regions are given in the figure. The intermediate linear region occurs only in relatively uncompensated samples. The slope in this region is just half that in the low temperature region (neglecting the $T^{3/2}$ factor). The transition between these two regions occurs when the carrier concentration is approximately equal to the minority impurity concentration.

The fact that the intermediate linear region is observed in an n-type sample of this purity is rather surprising, since it suggests a very low boron concentration. Note from Fig. 2 that the analysis yields an acceptor concentration of the order of 10^{11} cm^{-3}. It is not clear whether this figure indicates the true boron content or whether some of the boron has become electrically inactive, possibly because of local interaction with some other impurity or defect.

The Hall plots for many undoped n-type samples show approximately linear regions between 20° and 40°K which correspond to activation energies in the

Table I. Activation Energies for Group III and Group V Impurities in Silicon

Group III acceptors	ev	Group V donors	ev
B	0.046	P	0.044
Al	0.057	As	0.049
Ga	0.065	Sb	0.039
In	0.16	Bi	0.067

For two donors whose activation energies differ by $\Delta\epsilon_1$ plot ln $(T^{3/2}R)$ *vs.* $1/T$ at low temperature:

$$\text{Slope} = 1/k\left[\epsilon_1 + kT\ln\left(\frac{N_1}{N_d} + \frac{N_2}{N_d}e^{\Delta\epsilon/kT}\right)\right]$$

range 0.039-0.049 ev. As can be seen from Table I, this range includes three relatively closely spaced levels associated with antimony, phosphorus, and arsenic. The behavior of the Hall coefficient in relatively uncompensated samples can be explained if it is assumed that two or three of these impurities are present. If $N_a << N_d$, the low-temperature slope of a plot of $T^{3/2}$ x the Hall coefficient *vs.* reciprocal temperature for the case of two donors in an n-type sample is $1/k[\epsilon_1 + kTln(N_1/N_d + N_2/N_d \exp^{\Delta\epsilon/KT})]$ where N_1 is the concentration of the donors with the lower activation energy, N_2 is the concentration of those with the higher activation energy, and $\Delta\epsilon$ is the difference of their activation energies. This slope is somewhat temperature dependent, but it always lies between the slopes expected for donor one alone and donor two alone. Assuming that the average experimental slope is given approximately by its value at 25°K, we can define an effective activation energy for a pair, and the carrier concentration at 25°K then is given by an equation which is of the same form as the relation for a single donor. Thus the total donor and acceptor concentrations for the case of two donors can be determined from the Hall coefficient at 25°K, the slope of the $T^{3/2}R$ plot at 25°K, and the exhaustion Hall coefficient in the same way they are found in the case of a single donor. This procedure is valid only provided $n(25°K) << N_a << N_d$ because the relative populations of the two levels are influenced by compensation.

For the case of two donors, the effective activation energy is easy to compute, and Fig. 3 shows a plot for the pairs, Sb-P, P-As, and Sb-As as a function of relative concentration. If measurements are made carefully, these plots can be used to estimate the relative concentrations for different pairs which might be present.

Figure 4 shows a Hall plot for two p-type samples. The low-temperature slopes are both characteristic of boron, but number two, which is from a zone refined crystal, still exhibits the intermediate temperature characteristic at the lowest temperatures. This is indicative of extremely low compensation.

Table II gives a summary of the results of Hall and room temperature lifetime measurements on some single crystal silicon samples.

Conclusions

The activation energies of the p-type samples investigated were all characteristic of boron, and the

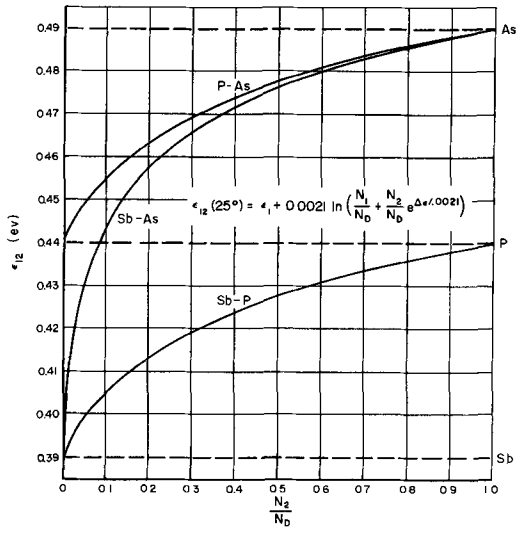

Fig. 3. "Effective" activation energy for pairs of donors in silicon at 25°K.

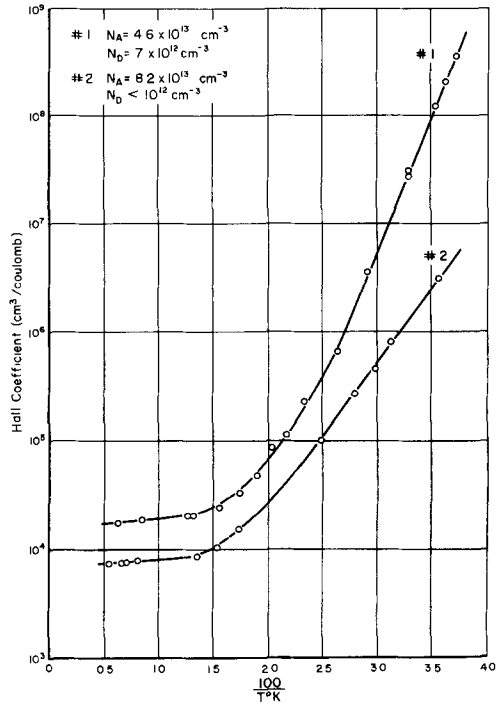

Fig. 4. Temperature dependence of Hall coefficient for two p-type silicon samples.

"effective" activation energies of the n-type samples were in the range 0.039-0.049 ev. It is concluded from this that the major acceptor impurity in all the samples investigated is boron and that it is present in concentrations of about 10^{13} cm^{-3}. The major

Table II. Lifetime Data on Some Single Crystal Silicon Samples

Sample	N_a, cm^{-3}	N_d, cm^{-3}	$N_a + N_d$, cm^{-3}	Lifetime, μ sec
B-95-5A	2.6×10^{13}	1.3×10^{13}	3.9×10^{13}	150
B-21-25B	8.3×10^{12}	$<10^{12}$	8.3×10^{13}	800
50-EX-126C	1.0×10^{13}	5×10^{12}	1.5×10^{13}	>1000
50-EX-122B	8.9×10^{12}	$<10^{12}$	9×10^{12}	600
B-15-17B	7×10^{12}	1.4×10^{13}	2.1×10^{13}	500
50-EX-126B	2.4×10^{13}	2.4×10^{13}	4.8×10^{13}	100
50-EX-122A	1.2×10^{13}	5.4×10^{13}	6.6×10^{13}	200
50-EX-111	1.6×10^{13}	3.2×10^{13}	4.8×10^{13}	600

donor impurities appear to be phosphorus, antimony, and arsenic, and their concentration is apparently reduced to less than 10^{13} cm^{-3} in some zone refined material.

Acknowledgment

The authors are indebted to J. J. Duga and F. J. Reid for making some of the Hall measurements, and to H. Leonard for sample preparation.

Manuscript received Feb. 11, 1960.

Any discussion of this paper will appear in a Discussion Section to be published in the June 1961 JOURNAL.

REFERENCES

1. Long, Motchenbacher, and Myers, *J. Appl. Phys.*, **30**, 353 (1959).
2. J. A. Burton, *Physica*, **20**, 845 (1954).
3. W. Kohn, "Solid State Physics," F. Seitz and D. Turnbull, Editors, Vol. 5, p. 257, Academic Press, New York (1957).
4. A. C. Beer and R. K. Willardson *Phys. Rev.*, **110**, 1286 (1958).
5. L. Gold and L. M. Roth, *ibid.*, **107**, 358 (1957).
6. C. A. Klein and W. D. Straub, Private communication.
7. E. H. Putley, *Proc. Phys. Soc.*, **72**, 917 (1958).
8. E. M. Conwell, *Proc. IRE*, **46**, 1281 (1958).

A Modified Closed Box System for the Diffusion of Boron in Silicon

R. S. Yatsko and J. S. Kesperis

U. S. Army Signal Research and Development Laboratory, Fort Monmouth, New Jersey

ABSTRACT

A modified closed box diffusion system has been investigated over a wide range of conditions. Boron layers have been diffused in silicon from B_2O_3-SiO_2 sources ranging from concentrations of 0.2% B by weight to pure B_2O_3. Nonmelting source conditions have been varied to melting source conditions yielding surface concentrations ranging from 10^{18} to 10^{21} carriers/cc. Some effects of environmental atmospheres and materials are discussed. Applications to photovoltaic devices and double diffused transistors are described.

Boron diffusion is by far the most common approach today in the achievement of precision controlled p-type areas in silicon semiconductor devices. Yet methods currently in use for obtaining desirable surface concentrations of boron utilize widely varying diffusion techniques. Even techniques for the production of diffused areas of similar doping content and depth vary widely from one user to the other.

It is the objective of this paper to discuss the investigation of a general diffusion system for boron, capable of reproducibly attaining particular surface concentrations in the range 10^{18} to 10^{21} atoms/cc by using only simple variations of source concentration, temperature, and time. Experimental data, the capabilities, and limitations of this process are discussed, and although a complete investigation of the system is not presented, the results obtained have already been successfully applied to various semiconductor devices at these laboratories and should serve as useful information to those concerned with the design and fabrication of silicon devices.

Experimental

Figure 1 shows a typical diffusion boat consisting of quartz with provisions for holding a small platinum box in the center which carries the source material. Two center posts contain the box and separate it from two end compartments which carry the silicon wafers. The boat is constructed by sealing off tubular quartz and cutting a longitudinal section off, such that approximately ¾ of the cross-section area remains on the boat. The cut edges of the boat are carefully lapped flat with a 600 grit. A quartz flat plate acts as a cover plate. A 0.003 in. platinum sheet, equal in area to the quartz flat, acts as a gasket between the lapped edges and the cover plate. It is this gasket which forms a partial seal for the diffusion process. A single annealing process at 1100°C was sufficient to allow the platinum gasket to form on the contours of the quartz boat. The gasket could then be used many times with the same boat during subsequent diffusion runs with no further forming treatment. During the actual diffusion run, platinum wire was wrapped tightly about the entire assembly to prevent any movement of the parts during insertion and removal from the furnace.

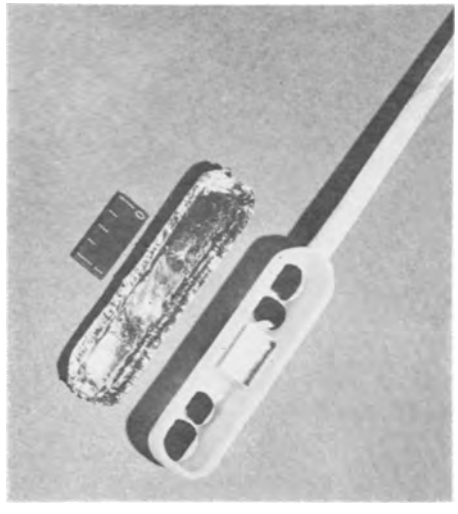

Fig. 1. Modified closed box showing quartz boat containing Pt source box and polished Si wafers. Formed Pt gasket is shown at left.

The boat thus constructed has only a partial seal and differs from a sealed capsule in this respect. However, the disadvantage of a finite leak rate was

not found to be significant as far as achievement of desired surface concentrations was concerned; the obvious advantages of ease in loading and re-use made it quite preferable to a sealed capsule technique.

Silicon wafers were polished carefully to a mirror finish using Linde A abrasive in an automatic bowl feed polisher. Diffusion was carried out in a Kanthal wound furnace using alundum tubes sealed off carefully at each end, with provisions for the insertion of the boat and dry argon gas.

Junction depths were measured by standard angle lapping and staining techniques (1). Evaluation of surface concentrations were made with four-point probe resistance measurements and the published data of Backenstoss (2).

Effects of system materials and environmental atmospheres.—The $B_2O_3SiO_2$ source is reactive with quartz and must be isolated from the quartz in the system. Initial attempts to use a high purity graphite modified closed box resulted in very nonuniform silicon surface layers that could not be removed by HF, dilute NaOH, or boiling HNO_3 followed by HF rinses. Furthermore, a significant erosion of the actual silicon surface was observed. These difficulties are eliminated by the use of either an all-platinum system (with provisions for holding the silicon on quartz flats) or an all-quartz system with a platinum container for the source as was adopted for these experiments.

The nature of the surrounding atmosphere and particularly the presence of the water vapor is of major importance in a closed box system which is not sealed totally against leaks. Early attempts to use the modified closed box with a surrounding air ambient consistently produced diodes with very low forward inflection voltages. Solar converters produced in this manner gave corresponding open-circuit voltages in the 0.3-0.4 v range. It became necessary to make the diffusion tube air tight and to flush the system carefully with argon which was passed through two liquid nitrogen traps to insure an acceptable level of dryness. The incorporation of these methods improved the reproducibility of electrical characteristics and resulted in normal inflection voltages.

Preparation of the diffusion source.—Four selected sources were prepared for diffusion from boric and silicic acids. Compositions ranged from the equivalent of pure boron oxide to 0.2% boron in the following manner: pure B_2O_3, $4B_2O_3$-$1SiO_2$, $1B_2O_3$-$1SiO_2$, and 0.2% B. The composite sources were prepared by mixing boric and silicic acid powders together, adding distilled, deionized water, drying over low heat with constant stirring. The source was then placed in a platinum source box and sintered at the diffusion temperatures under a dry argon atmosphere.

Diffusion from composite oxide sources must be preceded by a suitable sintering at either the diffusion temperature or at temperatures slightly higher in order to obtain consistent diffusion results. The sintering or "bake out" process is used to dry and homogenize the source and at the same time probably acts to saturate the quartz box with boron. As can be expected, nonmelting oxide sources are much more difficult to homogenize than melting sources. Consistent diffusion results have been obtained with melting sources after 1.5-2 hr of bake out, depending on the diffusion temperature and SiO_2 concentration in the source, while bake out times of 6 to 7 hr were necessary with nonmelting oxide sources. Thurston (3) and co-workers have studied the bake out time required for 0.1% B sources by experimentally comparing the diffusivities of phosphorus and boron in silicon dioxide. Although boron showed five times the diffusivity of phosphorus in silicon dioxide, bake out of nonmelting boron-silicon dioxides required 7 hr while nonmelting phosphorus-silicon dioxide sources required only 3 hr. It was also found that when fresh sources of B_2O_3-SiO_2 were used in an already used quartz capsule, an additional 7 hr bake out was necessary. On the basis of these experiments, the saturation of the source and quartz capsule could not explain effectively the unusually long bake out time required for nonmelting B_2O_3-SiO_2 sources.

Results and Discussion

Runs 1 and 2 in Table I show the range of results obtained for diffusions at 1129°C with a 0.2% B nonmelting source. Runs 3 to 5 show the results at 1218°C. Surface concentrations varied only by one-half order of magnitude between these temperature extremes. Reproducibility of penetration and doping at a given temperature was very good. These diffusions were characterized by very uniform post diffusion oxides with a maximum oxide thickness of 2800Å at 1218°C for 30-min diffusion time. Excellent uniformity of surface concentration was found over the entire area of the diffused wafers.

In order to obtain high surface concentrations at temperatures practicable for device manufacture, it was found necessary to increase the B_2O_3 in the source. It was determined that the order of 0.2% B represented the maximum concentration for nonmelting conditions in the source at 1200°C. An order of magnitude increase in boron concentration produced partial melting at temperatures as low as 1125°C. Progressive increases in the B_2O_3 concentration changed the appearance of the baked out source from a white powder (0.2% B) to an agglomeration of small hemispherical globules (2% B), through a series of uniformly white translucent glasses to 50% B_2O_3, followed by an increase in the transparency of the melt as the pure B_2O_3 glass was approached. The change in source appearance from nonmelting to melting conditions was accompanied by a sharp departure in appearance of the post diffusion oxides. It was found impossible to maintain uniformity in the grown oxide with melting sources. These variations in oxide thickness were accompanied at certain temperatures with nonuniformity in sheet resistance over the area of the diffused wafer, but in most cases, very uniform results were obtained.

Diffusion from 50% B_2O_3 sources had to be carried out at 1125°C or higher in order to obtain uniform sheet resistances over the entire wafer area. Runs 6 and 7 (Table I) show the variation in sheet resistance obtained on two wafers at 1100°C. Variations

Table I. Tabulation of data summarizing obtainable surface concentrations under various conditions of diffusion source and temperature

Run	Source	Bulk carrier conc.	Time, min	Temp, °C	Sheet res., ohms/square	Junction depth, μ	Surface conc., carriers/cc
1	0.2% B	7×10^{15}	30	1129	1015	0.5	6×10^{18}
2	0.2% B	7×10^{15}	30	1129	1380	0.45	4×10^{18}
3	0.2% B	7×10^{15}	30	1218	134	2.3	9×10^{18}
4	0.2% B	7×10^{15}	30	1218	130	2.2	1×10^{19}
5	0.2% B	7×10^{15}	30	1218	145	2.3	8×10^{18}
6	50% B_2O_3	9×10^{15}	15	1100	17-29	1.1	2×10^{20}
7	50% B_2O_3	9×10^{15}	15	1100	82-104	1.1	3×10^{19}
8	50% B_2O_3	7×10^{15}	25	1125	7.0	1.9	3×10^{20}
9	50% B_2O_3	7×10^{15}	25	1125	3.4	2.3	4×10^{20}
10	50% B_2O_3	7×10^{15}	20	1125	3.9	1.9	4×10^{20}
11	50% B_2O_3	7×10^{15}	20	1125	9.0	1.8	2×10^{20}
12	50% B_2O_3	8×10^{15}	15	1200	0.82	4.0	8×10^{20}
13	50% B_2O_3	8×10^{15}	15	1200	1.0	3.6	8×10^{20}
14	50% B_2O_3	8×10^{15}	15	1200	0.94	3.9	8×10^{20}
15	50% B_2O_3	8×10^{15}	15	1200	1.8	3.8	5×10^{20}
16	50% B_2O_3	8×10^{15}	15	1200	0.85	3.2	1×10^{21}
17	80% B_2O_3	8×10^{15}	15	1125	5.5	1.5	3×10^{20}
18	80% B_2O_3	8×10^{15}	15	1125	4.6	1.9	3×10^{20}
19	80% B_2O_3	8×10^{15}	15	1125	8.3	1.8	2×10^{20}
20	80% B_2O_3	8×10^{15}	15	1125	7.3	1.5	4×10^{20}
21	80% B_2O_3	8×10^{15}	15	1125	5.2	1.6	4×10^{20}
22	B_2O_3	8×10^{15}	150	1000	15.5	1.3	2×10^{20}
23	B_2O_3	8×10^{15}	150	1000	14.2	1.3	2×10^{20}
24	B_2O_3	8×10^{15}	150	1000	17.6	1.2	1.5×10^{20}
25	B_2O_3	8×10^{15}	150	1000	18.8	1.2	1.5×10^{20}
26	B_2O_3	8×10^{15}	150	1000	15.2	1.3	2×10^{20}
27	B_2O_3	8×10^{15}	150	1000	19.2	1.2	1.5×10^{20}
28	B_2O_3	8×10^{15}	150	1000	14.3	1.3	2×10^{20}

of one order of magnitude in surface concentration were observed from wafer to wafer at 1100°C. Uniform sheet resistances were obtained at 1125°C and higher, with a much greater reproducibility in surface concentration. Runs 8 to 11 show the range of diffusion results for 25 min and 20 min diffusion time at 1125°C. Higher surface concentrations were obtained at 1200°C with the 50% B_2O_3 source. Runs 12 to 16 list the data obtained from the five wafers diffused at 1200°C.

In order to determine whether an increase in boron concentration would result in higher surface concentrations at 1125°C, five runs were made with an 80% B_2O_3 source (Runs 17-21). No significant difference was observed in surface concentration between the two sources at 1125°C. At 1200°C the difficulty encountered in removing postdiffusion oxide layers from the 80% source made a comparison with the 50% source impossible.

It was found that the postdiffusion oxides became more difficult to remove with longer diffusion times. Although no difficulties were encountered with the 50% and 80% source at 1125°C for diffusion times of 15 min to ½ hr, deep diffusions of 4 hr duration produced surface layers very difficult to remove. Diffusions for 4 hr at 1200°C produced surface layers which were impossible to remove. Diffusions from pure B_2O_3 sources had to be performed at temperatures below 1025°C to prevent pitting and erosion of the silicon surface. However at 1000°C, no difficulties were encountered for diffusion times as long as 2.5 hr.

Runs 22-28 list the data from 7 control runs made at 1000°C for 2.5 hr with pure B_2O_3 as the source. Excellent control of sheet resistance and penetration was obtained.

Fabrication of solar cells.—Five solar cells were fabricated utilizing the pure B_2O_3, 1000°C process. Since doping levels of 2×10^{20} were obtainable by this process, it was thought that the relatively low temperature required would be the least deleterious to the lifetime in the device, and this was the basis for choosing this as the beginning process in determining the optimum modified closed box process for solar cell fabrication. The diffused cells were given electroless nickel contacts to both p- and n-sides, followed with a solder dip. A polystyrene coating was placed over the active area to reduce reflection. Evaluation was conducted with a tungsten filament light source, filtered through a water bath to reduce the infrared. The illumination was calibrated to a radiation rate of 84.4 mw/cm^2. The total dark current series resistance amounted to 0.2 ohm. Surface concentrations and junction depths were as shown in Table I for the pure B_2O_3 runs. Results are indicated in Table II. Figure 2 shows the comparative light output current-voltage characteristics for cells 1 and 5 which represent the performance extremes from this group.

Application to Transistor Fabrication

The technique was applied to the fabrication of the emitter region of a p-n-p transistor. Table III

Table II. Tabulation of output efficiency data of 5 solar cells fabricated by diffusion from a pure B_2O_3 source at 1000°C

Cell	Area, cm^2	E_{cc}, v	E_{mp}, v	I_{mp}, ma	P_{mp}, mw	Efficiency, %
1	1.80	0.560	0.442	38.5	17.0	11.2
2	1.44	0.555	0.420	32.3	13.8	11.2
3	1.67	0.550	0.409	37.2	15.2	10.8
4	1.71	0.550	0.420	38.1	16.0	11.1
5	1.50	0.550	0.420	32.3	13.6	10.7

Table III. Tabulation of data showing results of emitter diffusions using a modified closed box system

Run	Source	Time, min	Temp, °C	Sheet res., ohms/square	Junction depth, μ	Surface conc, carriers/cc	Junction depth base diffusion, μ	Base width, μ
1	80% B_2O_3	12	1120	6.0	1.4	3.5×10^{20}	2.4	1.0
2	80% B_2O_3	12	1120	4.0	1.4	4.0×10^{20}	2.4	1.0
3	80% B_2O_3	12	1120	6.0	1.3	4.0×10^{20}	2.4	1.1
4	80% B_2O_3	12	1120	4.5	1.3	3.5×10^{20}	2.4	1.1
5	50% B_2O_3	15	1125	11.3	1.4	2.0×10^{20}	2.5	1.1
6	50% B_2O_3	15	1125	11.2	1.4	2.0×10^{20}	2.5	1.1
7	50% B_2O_3	15	1106	15.5	1.0	2.0×10^{20}	2.5	1.5
8	50% B_2O_3	15	1106	14.4	1.1	2.0×10^{20}	2.5	1.4
9	50% B_2O_3	15	1106	15.7	1.1	2.0×10^{20}	2.5	1.4
10	Pure B_2O_3	150	1000	7.9	1.3	2.0×10^{20}	2.5	1.2
11	Pure B_2O_3	150	1000	8.0	1.3	2.0×10^{20}	2.5	1.2
12	Pure B_2O_3	150	1000	10.2	1.2	2.0×10^{20}	2.4	1.2
13	Pure B_2O_3	150	1000	10.3	1.2	2.0×10^{20}	2.4	1.2
14	Pure B_2O_3	150	1005	5.4	1.5	2.0×10^{20}	2.5	1.0
15	Pure B_2O_3	150	1005	6.2	1.6	2.0×10^{20}	2.5	1.0

shows results obtained for a number of emitter diffusion runs. The base region into which the boron emitters were diffused was diffused previously with antimony. The antimony depth of diffusion was approximately 2.5 μ and the surface concentration ranged from 1×10^{19} atoms/cc to 2×10^{19} atoms/cc. It was necessary to diffuse the boron emitters to shallow depths in order to maintain a thin base region. The aim was to diffuse the boron emitters to depths varying from 1.0 to 1.5 μ, attain a surface concentration greater than 10^{20} atoms/cc, and obtain masking in regions where the boron was not desired. Examination of Table III reveals that the sheet resistance of the group of wafers diffused with the 80% source ranged from 4 to 6 ohms/square. Diffusion depths varied from 1.3 to 1.4 μ for the temperature and time used, and the surface concentration achieved ranged from 3×10^{20} to 4×10^{20} atoms/cc for the temperature used. Diffusions with the 50% source were performed at two different temperatures, 1125° and 1106°C. At 1125°C the diffusion depths obtained were 1.4 μ and the sheet resistance was 11.2 ohms. At 1106°C the diffusion depths varied from 1.0 to 1.1 μ and the sheet resistances from 14.4 to 15.7 ohms. A surface concentration of 2×10^{20} atoms/cc was obtained at both temperatures at which the diffusions were made. Pure B_2O_3 was used for lower temperature diffusions. A surface concentration of 2×10^{20} atoms/cc was achieved at the temperature used. Sheet resistances varied from 8 to 10 ohms/square and junction depths ranged from 1.2 to 1.3 μ. No difficulty was encountered in removing the oxides from any of the diffused samples. Masking of boron where desired can be obtained by choosing a suitable combination of diffusion conditions and oxide thickness. For the diffusion conditions listed and an oxide thickness of approximately 1800Å complete masking of boron was achieved. The three melting sources have been used for forming emitters in fabricating a high-frequency p-n-p transistor. The nonmelting source is an excellent technique for forming a base region in a n-p-n or n-p-i-n structure.

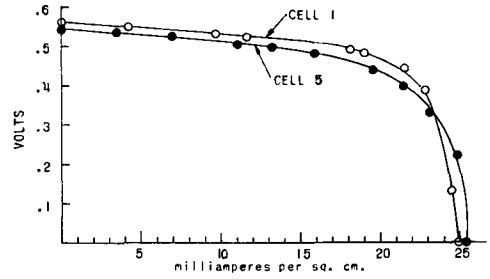

Fig. 2. Output current-voltage characteristics for cells 1 and 5 under 84 mw/cm² illumination.

Summary

The box technique described herein can be utilized with good advantage on many areas of silicon device technology. Specifically, the excellent control and uniformity of nonmelting sources (0.2% B max) is ideally suited for formation of base areas in n-p-n transistor structures where concentrations over 1×10^{19} carriers/cc are not required. Highly doped areas, 5×10^{20}-1×10^{21} can be obtained easily with the 50% B_2O_3 source. Moderate doping in the 1×10^{20}-5×10^{20} range is best obtained with the 50% and 80% B_2O_3 sources. Where low diffusion temperatures are required, pure B_2O_3 sources can consistently yield doping levels of 2×10^{20} at 1000°C. Consistently reproducible high efficiency solar converters in the 11% efficiency range are being made from pure B_2O_3 sources. Higher conversion efficiencies may be possible by increasing the surface concentration by diffusion from a composite source at higher temperatures, but this remains to be seen.

Emitter junctions have been made by three different diffusion sources, 80% B_2O_3, 50% B_2O_3, and pure B_2O_3. All three sources met specific device p n p requirements of doping (2×10^{20} min), successful oxide masking of the base, and ease of emitter oxide removal. The specific process for a particular device will depend of course on the best device yield as well as on meeting the design specifications.

General observations of the process can be summarized as follows: (*a*) long time diffusions (4 hr) with composite sources produced very tenacious surface layers and irregular junctions; (*b*) a minimum SiO_2 concentration of 50% was required for diffusion at 1200°C or above; (*c*) 50% sources required temperatures of 1125°C min for best repro-

ducibility of diffusion results; and (*d*) diffusion from pure B_2O_3 sources must be restricted to a maximum temperature of 1025°C to minimize surface erosion and pitting. At 1000°C, no difficulties are encountered.

Acknowledgment

The authors wish to thank Dr. Howard Loar of Bell Telephone Laboratories, Murray Hill, New Jersey, for the helpful discussions on the effects of environmental atmospheres on boron diffusions, and Messrs. J. Mandelkorn and A. LaRocque, USASRDL, for their helpful comments during the course of this work. Particular indebtedness is due Mr. W. Pharo, USASRDL, whose careful growth and preparation of silicon material made this work possible.

Manuscript received March 21, 1960. This paper was prepared for delivery before the Houston Meeting, Oct. 9-13, 1960.

Any discussion of this paper will appear in a Discussion Section to be published in the June 1961 JOURNAL.

REFERENCES

1. C. S. Fuller and J. A. Ditzenberger, *J. Appl. Phys.*, **27**, 544 (1956).
2. G. Backenstoss, *Bell System Tech J.*, **37**, 699 (1958).
3. M. O. Thurston ond J. Tsai, O.S.U. Research Foundation, Contract DA-36-039, sc-83874, Rpt 896-3 (1959).

Properties of PbSe Prepared by Powder-Metallurgy Techniques

J. F. Miller and R. C. Himes

Battelle Memorial Institute, Columbus, Ohio

ABSTRACT

The application of powder-metallurgy techniques to the preparation of bulk specimens of lead selenide was studied; both the hot-press and the press-and-sinter methods were employed. Compacting pressure, sintering temperature sintering time, and the particle size of the powder were treated as variables. Electrical and thermoelectric properties, densities, and microstructures of the specimens were studied.

Sound specimens of near-theoretical density and with electrical and thermoelectric properties similar to those of the best of cast lead selenide were prepared successfully by the hot-press method. Densities of hot-pressed specimens, which were highest for those prepared at 750°C, 8100 psi, were observed to decrease with sintering temperature in the range 750°-450°C, and with compacting pressure in the range 8100-2000 psi. The pressed-specimen density was not affected appreciably by variations of sintering time (in the range 5 min-5 hr at 750°C) or variations of the particle size of the powder (in the range —60 to —200 mesh). Electrical properties of specimens with densities in the range 90-98% of theoretical, which were prepared by both the hot-press and the press-and-sinter methods, did not change significantly as density varied in this range.

Lead selenide is a potentially useful semiconductor for several types of applications. Among these are applications which make use of (*a*) its thermoelectric properties, and (*b*) the (high) positive temperature coefficient of resistance of doped lead selenide in the extrinsic temperature range. However, when conventional casting techniques are used to prepare lead selenide circuit elements, several difficulties are encountered. Unless temperature and environment are controlled precisely, there is a pronounced tendency for pores or voids to form in the castings. If cooling rate is low enough to induce reasonable crystal growth, doping elements segregate. Both of these phenomena tend to produce electrically heterogeneous castings. In addition, when special shapes are required, they often cannot be cast at all or cannot be cast with the desired degree of precision. Use of powder-metallurgy techniques was seen as one possible means of satisfactorily circumventing these difficulties, providing specimens with acceptable physical and electrical properties could be prepared in this manner.

In this investigation of the application of powder-metallurgy techniques to the preparation of lead selenide, both the hot-press and the press-and-sinter methods were employed. Compacting pressure, sintering temperature, sintering time, and particle size of the powder were treated as variables. Electrical and thermoelectric properties, densities, and microstructures of the specimens were studied to evaluate the processes.

Experimental Procedures

The lead selenide used in this research was prepared initially by reacting high-purity (99.999%) lead and selenium in the molten state in evacuated, sealed, quartz containers. The master batch of n-type material, which was used in the majority of the experiments, was doped with 0.25 at. % excess lead and 0.025% by weight of bismuth. To ensure that this material would be as nearly uniform as possible, it was quenched in room-temperature oil from the molten state. The p-type lead selenide employed was from an ingot which was cast by the Bridgman method and doped with 0.02% by weight of arsenic.

Except as is otherwise noted, the powders were prepared, classified as to particle size, loaded into

the pressing equipment, and were pressed in an atmosphere of dry argon. The powder-metallurgical specimens prepared were cylinders ⅝ in. in diameter by approximately ½ in. long.

Hot pressing was done in inductively heated graphite dies. Design and operation of the hot-pressing apparatus has been described by Bourke, *et al.* (1). Hot pressing was done at three temperatures, 750°, 600°, and 450°C; at three compacting pressures, 8100, 4000, and 2000 psi; and for various sintering times in the range 5 min-5 hr. Powders of three particle-size ranges were used: −200 mesh; −100 + 200 mesh; and −60 + 100 mesh.

Specimens prepared by the press-and-sinter method were first compacted in latex tubes under 100,000-psi hydrostatic pressure. The compacts then were transferred to quartz tubes, which were evacuated and sealed with a minimum of free (vapor) space. The specimens were sintered at temperatures of 450°, 600°, and 750° for a period of 5 hr.

For anneal treatment, cast specimens also were sealed in close-fitting, evacuated quartz tubes. Similar cooling rates were established following the heat-treatment step in all three processes (*i.e.*, hot press, press and sinter, and anneal) so that specimens would be comparable in this respect.

Electrical measurements were made on bridge-type Hall specimens to which Chromel leads were attached by spot welding. Both d-c and a-c Hall measurements were made. In cases where both types of measurements were made on a given specimen, values for resistivity, Hall coefficient, and mobility obtained from the a-c data were generally lower (*e.g.*, mobilities lower by 5-10%) than those from the d-c measurements. A qualitatively similar change was noted in d-c values when procedure was altered from that of making measurements after a steady-state condition had been obtained to that of making measurements as soon as possible after current and magnetic field had been turned on. It is likely that the differences arise because of the relatively large Peltier effect in this high-Z material.[1]

Thermoelectric properties were determined by use of the "Z-meter" (2). This device makes possible reasonably accurate measurements of both the Seebeck coefficient and thermal conductivity of such small (1.5 cm long) specimens as were available for this research.

Densities were determined gravimetrically by the hydrostatic method and were measured with respect to both ethanol and methanol. It was found that water, which was initially tried as a reference fluid, does not "wet" lead selenide perfectly, and as a result yields scattered, low values. With the technique employed, multiple measurements were made yielding mean density values to which probable errors of less than ±0.01 g/cm³ could be ascribed in every case.

In preparing the specimens for metallographic examination, Murakami's electrolytic etch, containing 22 parts $K_3Fe(CN)_6$, 5 parts NaOH, and 945 parts water by weight, was used to bring out grain boundaries.

[1] The thermoelectric figure of merit $Z \equiv \alpha^2/K\rho$, where α is the Seebeck coefficient; K, thermal conductivity; and ρ, electrical resistivity.

Experimental Results and Discussion

Electrical properties.—The preparation, electrical properties, and densities of the powder-metallurgical specimens are summarized in Table I. (In this table, data on several of the specimens are repeated one or more times to facilitate comparisons.) Properties of specimens of the cast material (first group in table) are also given. Measured electron mobilities (Hall) for the cast lead selenide are low, presumably because of high concentrations of grain boundaries and defects in this quenched material. Heat treatment similar to that given the powder-metallurgical specimens in preparation (*i.e.*, anneal at 750°C for 5 hr, see specimen 74B-1) failed to change electrical properties significantly, however.

In general, electrical properties of the powder-metallurgical specimens compare favorably with those of the cast polycrystalline material and with those of polycrystalline and single-crystal lead selenide which are reported by others (3, 4). Resistivities and Hall mobilities for the powder-metallurgical specimens are similar to those for cast polycrystalline and single-crystal lead selenide of like purity that has solidified progressively and slowly from the molten state. Seebeck coefficients and temperature dependencies of Seebeck coefficient and resistivity in the range 300°-575°K, which were studied for a number of the powder-metallurgical specimens, were also similar to those for cast lead selenide.

For the n-type material, electrical properties vary somewhat from specimen to specimen. However, no correlation is apparent between the relatively minor variations in electrical properties observed and changes made in conditions under which the samples were prepared.

For the p-type lead selenide, resistivity and Hall coefficient of the hot-pressed specimen are significantly lower than those of the cast starting material, while on the other hand, mobility in the specimen remained quite good. Since just one experiment with p-type lead selenide was conducted in this exploratory study, it is not possible to say whether the changes noted are inevitably to be expected in hot pressing p-type material or are to be expected only under certain experimental conditions and/or with specific doping agents.

Density.—For a majority of the n-type hot-pressed specimens, determined densities are higher than both the theoretical value calculated from x-ray data and the measured density of sound specimens of similarly doped cast lead selenide. In addition, in a number of cases, measured densities are also higher than can be accounted for, even though consideration is given to concentrations of excess lead and bismuth which are present. The possibility of an effect of pressure on the lattice is suggested.

Density of both the hot-pressed and the pressed-and-sintered specimens varied in a normal manner with respect to sintering temperature and compacting pressure. Density of the 5-hr hot-pressed specimens decreased as sintering temperature was reduced in the range 750°-450°C (with pressure held constant, consider specimens 79-81), and as compacting pressure was reduced in the range 8100-

Table I. Preparation and properties of powder-metallurgical lead selenide specimens

Specimen	Method	Remarks	Specimen preparation: Size of powder particles, mesh	Compacting pressure, psi	Sintering: Temperature, °C	Sintering: Time, hr	Room-temperature properties: Electrical properties: Resistivity, 10^{-3} ohm-cm	Hall coefficient, cm^3/coulomb	Hall mobility, cm^2/v-sec	Carrier concentration, $10^{18}/cm^3$	Density: Measured value, g/cm^3	Density: Per cent of theoretical[a]
			Cast N-type (starting material) lead selenide									
74A	Cast-quench	From lower end of ingot	—	—	—	—	0.92	−0.74	840	8.5	—	—
74B	Cast-quench	From middle of ingot	—	—	—	—	0.52	−0.32	620	20	—	—
74C	Cast-quench	From upper end of ingot	—	—	—	—	1.1	−0.60	550	10	—	—
74B-1	Cast-quench-anneal	74B, annealed at 750°C, 5 hr	—	—	—	—	0.64[b]	−0.46	770	14	—	—
36	Cast-Bridgman drop		—	—	—	—	—	—	—	—	8.25	99.8
			Variable—temperature									
79	Hot press		−200	8,100	750	5	1.46	−1.7	1200	3.7	8.30	100.4
80	Hot press		−200	8,100	600	5	2.09	−2.1	1000	3.0	8.28	100.2
81	Hot press		−200	8,100	450	5	2.18	−2.2	1000	2.9	8.23	99.6
76	Hot press		−200	8,100	750	2.5	1.36	−1.6	1200	3.9	8.27	100.1
84	Hot press		−200	8,100	600	2.5	1.67	−2.1	1300	3.0	8.29	100.3
							1.57[b]	−1.8	1100	3.5	—	—
			Variable—time									
79	Hot press		−200	8,100	750	5	1.46	−1.7	1200	3.7	8.30	100.4
76	Hot press		−200	8,100	750	2.5	1.49[b]	−1.7	1100	3.7	8.27	100.1
82	Hot press		−200	8,100	750	(5 min)	1.29	−1.5	1200	4.2	8.27	100.1
78	Hot press		−100 + 200	8,100	750	5	1.40	−2.0	1400	3.1	8.31	100.6
							1.36[b]	−1.7	1200	3.7	—	—
75	Hot press		−100 + 200	8,100	750	1.5	1.27	−1.5	1200	4.2	8.30	100.4
80	Hot press		−200	8,100	600	5	2.09	−2.1	1000	3.0	8.28	100.2
84	Hot press		−200	8,100	600	2.5	1.67	−2.1	1300	3.0	8.29	100.3
			Variable—atmosphere									
77	Hot press	Powder ground and loaded in argon	−60 + 100	8,100	750	5	1.28	−1.5	1200	4.2	8.29	100.3
86	Hot press	Powder ground and loaded in air	−60 + 100	8,100	750	5	1.33	−1.5	1100	4.2	8.30	100.4
			Variable—pressure									
79	Hot press		−200	8,100	750	5	1.46	−1.7	1200	3.7	8.30	100.4
90	Hot press	Powder ground and loaded in air	−200	4,000	750	5	1.24[b]	−1.6	1300	3.9	8.21	99.3
91	Hot press	Powder ground and loaded in air	−200	2,000	750	5	1.62[b]	−1.7	1000	3.7	7.67	92.8
			Variable—size of powder particle									
79	Hot press		−200	8,100	750	5	1.46	−1.7	1200	3.7	8.30	100.4
78	Hot press		−100 + 200	8,100	750	5	1.40	−2.0	1400	3.1	8.31	100.6
77	Hot press		−60 + 100	8,100	750	5	1.28	−1.5	1200	4.2	8.29	100.3
			Press-and-sinter method									
89A	Press and sinter		−200	100,000	750	5	1.11	−1.2	1100	5.2	7.48	90.5
89B	Press and sinter		−200	100,000	600	5	1.38	−1.6	1200	3.9	8.04	97.3
89B							1.31[b]	−1.3	1000	4.8	—	—
89C	Press and sinter		−200	100,000	450	5	1.74	−1.8	1000	3.5	8.12	98.2
			P-type lead selenide									
24	Cast-Bridgman drop		—	—	—	—	4.73[b]	+4.9	1100	1.3	—	—
92	Hot press	Powder ground and loaded in air	−200	8,100	750	5	1.17[b]	+1.4	1200	4.5	8.25	99.8

[a] Theoretical value 8.265 g/cm^3; calculated from precision x-ray lattice constant (a_0 = 6.1265 ± 0.0003A.
[b] A-c measurements.

2000 psi (with temperature held constant, consider specimens 79, 90, 91). For the press-and-sinter method, in which samples were initially compressed to near-theoretical density, density of the sintered specimens decreased as firing temperature was increased through the range 450°-750°C. In the ranges studied, density did not vary appreciably with hot-press time (5 min-5 hr at 750°C, 2.5-5 hr at 600°C) or particle size (−60 to −200 mesh).

The study was not sufficiently comprehensive to permit a full evaluation of combined effects of the variables. However, if the hot-press process variables are considered singly, it may be noted that near-theoretical densities were attained at minimums of 8100 psi compacting pressure, 600°C sintering temperature, and 5 min hot-press time; densities roughly equal to that of cast material were attained at minimums of 4000 psi compacting pressure, and 450°C sintering temperature.

Density of the p-type specimen, which was hot pressed for 5 hr at 750°C, is significantly lower than that of similarly treated n-type material. The excess lead, which was present in the n-type material, apparently has a salutary effect on the sintering process. The sintering of p-type lead selenide, which may proceed by different mechanisms, should be the subject of a separate study.

It is considered significant that, although densities of the sintered specimens ranged down to about 90% of theoretical, electrical properties did not change appreciably, Such low-density powder-metallurgical materials, because of the possible effect of the high concentrations of grain boundaries and voids (*i.e.*, lattice discontinuities) on thermal conductivity, may possess superior over-all thermoelectric properties.

Microstructures.—Microstructures of the hot-pressed lead selenide specimens, Fig. 1, show clearly the effects of variation of sintering temperature and time on average grain size, and of variation of compacting pressure on density.

At 750°C, 8100 psi, (Fig. 1a) considerable growth of crystals was obtained in the course of a 5-hr treatment, but at 450°C under otherwise similar conditions (Fig. 1b) little or no crystal growth occurred. However, some crystal growth is seen to have occurred in only 5 min at the higher temperature (Fig. 1c). In photomicrographs 1a, d, and e, the decrease in average grain size and density (*i.e.*, increase in concentration and size of voids) as compacting pressure is decreased from 8100 to 2000 psi may be seen. Differences between 8100 and 4000 psi are slight, but at 2000 psi both density and average grain size are considerably reduced.

Even though an extremely high compacting pressure (100,000 psi) was used in the press-and-sinter method, crystals present in the specimens were small and densities were relatively low (Fig. 1f).

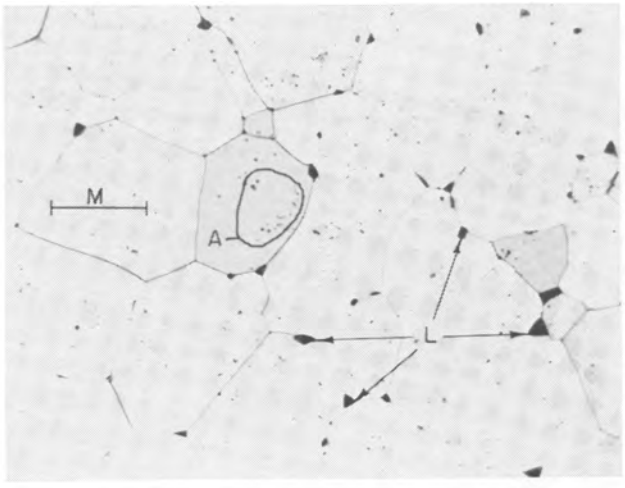

Fig. 1. Microstructures of powder-metallurgy specimens of lead selenide: M, maximum initial particle diameter; L, lead-rich phase; A, fine structure includes (a) deposits of the lead-rich phase, (b) some etch pits, and (c) some deposits of an oxide phase; V, voids. Fig. 1a. Specimen 79, —200 mesh powder, hot pressed at 8100 psi, 750°C, 5 hr. Magnification of microstructures 250X before reduction for publication.

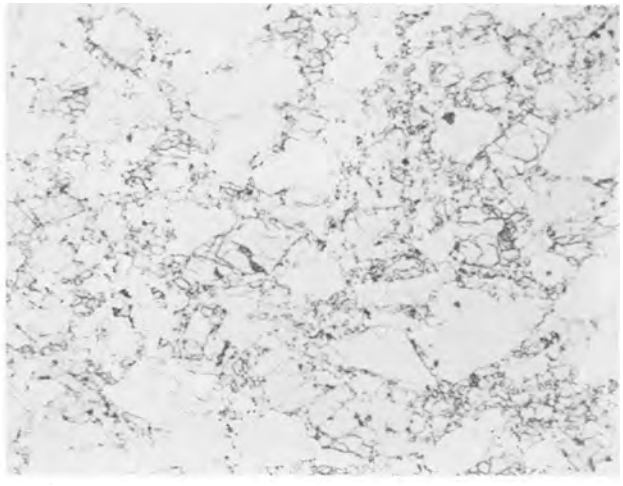

Fig. 1b. Specimen 81, —200 mesh powder, hot pressed at 8100 psi, 450°C, 5 hr.

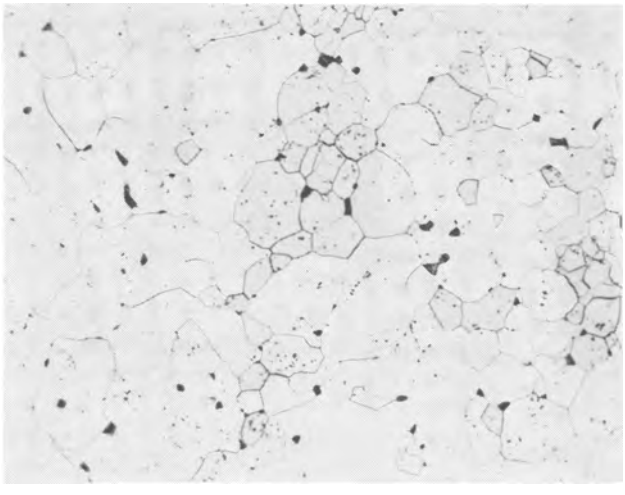

Fig. 1c. Specimen 82, —200 mesh powder, hot pressed at 8100 psi, 750°C, 5 min.

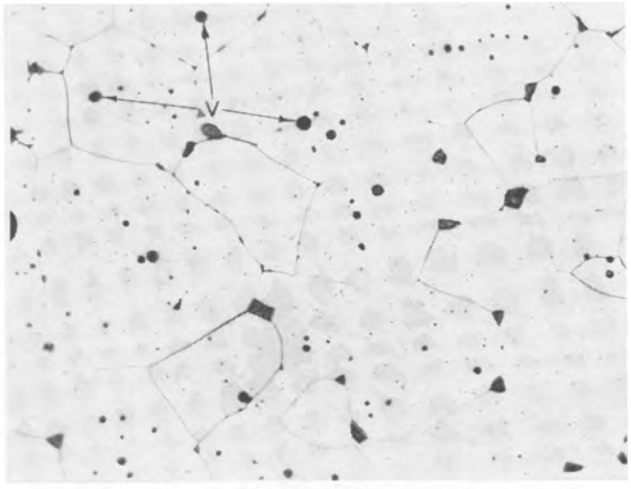

Fig. 1d. Specimen 90, —200 mesh powder, hot pressed at 4000 psi, 750°C, 5 hr.

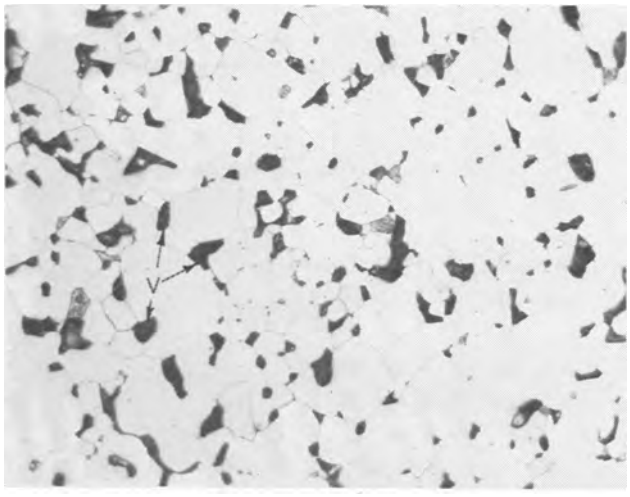

Fig. 1e. Specimen 91, —200 mesh powder ground and loaded in air, hot pressed at 2000 psi, 750°C, 5 hr.

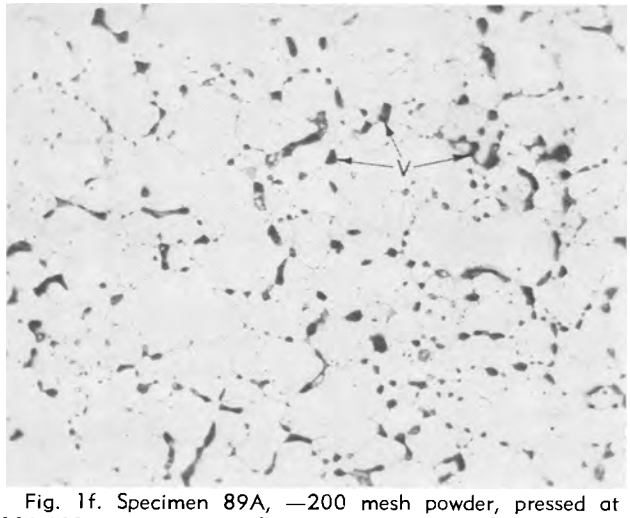

Fig. 1f. Specimen 89A, —200 mesh powder, pressed at 100,000 psi, sintered 750°C, 5 hr.

With a similar heat treatment, larger crystals and higher densities were obtained by the hot-press method (Fig. 1a, d).

The majority of the specimens were prepared from powder which was ground and handled in argon. Nevertheless, small inclusions of an oxidic

Table II. Thermoelectric properties of hot-pressed and of cast n-type lead selenide

	Hot-pressed	Cast
	Specimen 77, −60 + 100-mesh powder hot pressed at 750°C, 8100 psi, 5 hr	Specimen 35, Bridgman drop at ½ in./hr
Z-meter measurements		
Mean temperature, $\overline{T}$, °K	297.4	298.4
Resistivity, ρ, ohm-cm	1.18×10^{-3}	7.7×10^{-4}
Seebeck coefficient, α, μv/°K	−168	−135
Thermal conductivity, K, watt/cm °K	0.020	0.021
Thermoelectric figure of merit, Z, $°K^{-1}$	$1.2_4 \times 10^{-3}$	$1.1_3 \times 10^{-3}$
Hall measurements		
Resistivity, ρ, ohm-cm	1.28×10^{-3}	8.4×10^{-4}
Hall coefficient, R_H, cm^3/coul	−1.5	−0.89
Hall mobility, μ, cm^2/v-sec	1200	1100
Carrier concentration, n, cm^{-3}	4.2×10^{18}	7.2×10^{18}

phase were found in all specimens. However, metallographs showed that concentrations of this phase were considerably higher in specimens which were prepared from powder that was exposed to air in the course of grinding and loading operations.

Thermoelectric properties.—Thermoelectric properties of a typical high-density hot-pressed lead selenide specimen, which are given in Table II, indicate that material with a good thermoelectric figure of merit can be prepared by this method. It should be noted that these favorable indications have been obtained without any effort to optimize the powder-metal product with respect to thermoelectric properties. As has been suggested previously, thermoelectric properties of low-density powder-metallurgical lead selenide may be of special interest and should be the subject of future studies.

Conclusions

Sound specimens of n-type lead selenide with electrical and thermoelectric properties similar to those of cast lead selenide can be prepared by hot pressing.

Near-theoretical densities can be obtained by hot pressing for only 5 min at 750°C, 8100 psi, and for 2.5 hr at 600°C, 8100 psi. Density of the specimens decreases with sintering temperature in the range 750°-450°C, and with compacting pressure in the range 8100-2000 psi. No appreciable effect on density is produced by variation of sintering time (in the range 5 min-5 hr at 750°C, 2.5-5 hr at 600°C). Variation of size of powder particle in the range −200 to −60 mesh likewise produces no noticeable effect.

Electrical properties of hot-pressed p-type lead selenide deviate from those of the cast starting material to a greater degree than do those of the n-type material. Density of the p-type material is significantly lower than that of n-type material which is hot-pressed under similar conditions.

Specimens produced by the hot-press method contain larger crystallites and are of higher density than those prepared by the press-and-sinter method (100,000 psi). Specimens with densities in the range 90-98% of theoretical can be prepared by both methods. Anomalously high densities (above 100% of theoretical) can be attained by hot pressing. Of possible significance is the fact that electrical properties of the lead selenide that is doped suitably for thermoelectric use do not change appreciably as density varies in the range covered in this investigation.

Acknowledgments

The authors wish to express their thanks to J. E. Mock, who prepared the specimens, F. J. Reid and B. Paris, who made the electrical measurements, and J. L. McCall, who prepared the metallographs.

Manuscript received April 29, 1960. This investigation was supported by The Selenium and Tellurium Development Committee.

Any discussion of this paper will appear in a Discussion Section to be published in the June 1961 JOURNAL.

REFERENCES

1. R. C. Bourke, R. Simon, and E. H. Lougher, Abstract of paper presented at Spring Semiconductor Symposium, The Electrochemical Society, Chicago, May 2, 1960.
2. T. C. Harman, J. H. Cahn, and M. J. Logan, *J. Appl. Phys.*, **30**, 1351 (1959).
3. E. H. Putley, *Proc. Phys. Soc. (London)*, **68B**, 22 (1955).
4. R. S. Allgaier and W. W. Scanlon, *Phys. Rev.*, **111**, 1029 (1958).

Brief Communications

The JOURNAL accepts short technical reports having unusual importance or timely interest, where speed of publication is a consideration. The communication may summarize results of important research justifying announcement before such time as a more detailed manuscript can be published. Consideration also will be given to reports of significant unfinished research which the author cannot pursue further, but the results of which are of potential use to others. Comments on papers already published in the JOURNAL should be reserved for the Discussion Section published biannually.

Submit communications in triplicate, typewritten double-spaced, to the Editor, Journal of The Electrochemical Society, 1860 Broadway, New York 23, N. Y.

Kinetics of the Formation of the Iron-Tin Alloy $FeSn_2$

Robert P. Frankenthal[1] and Alexei W. Loginow

Applied Research Laboratory, United States Steel Corporation, Monroeville, Pennsylvania

ABSTRACT

The kinetics of the formation of the iron-tin alloy $FeSn_2$ have been studied at temperatures below and above the melting point of tin (232°C). At all temperatures studied, the growth obeyed the parabolic-rate law. This is indicative of a diffusion mechanism. An Arrhenius plot of the data gives a straight line below the melting point of tin and a straight line above the melting point of tin, with a sharp break at the melting point. The activation energy is the same below and above the melting point of tin and is 29.3 ± 1 kcal/mole. The kinetics of the growth were also studied as a function of various properties associated with the tin plate: tin-coating weight, steel base, and the type of pickle to which the steel base was subjected prior to electroplating of the tin. No effect due to any of these variables was found.

At temperatures up to 496°C, iron and tin react to form the intermetallic compound $FeSn_2$ (1). This compound will form not only above the melting point of tin (232°C) but also below it (2), contrary to the findings of Davies and Hoare (3). Little data have been published on the rate and mechanism of formation of this alloy: Seybolt (4) measured the rate of alloying when steel is immersed in a bath of molten tin at constant temperature and found the parabolic-rate law to be obeyed. This is indicative of a diffusion mechanism. Thwaites (2) has studied the formation of the alloy and its metallography as a function of the rate of change of temperature, at temperatures above the melting point of tin. He also reported a few results on the formation of the alloy at constant temperatures below the melting point of tin. Lambert (5) studied the alloy-growth rate on commercial tin plate at temperatures below the melting point of tin. However, because of the short times investigated and the thin tin coatings on his samples, he was not able to determine whether the alloy grew by a diffusion mechanism; also, his experiments were done with an initial alloy coating present and this unnecessarily complicated the calculations. He also stated that according to the phase diagram, at temperatures below the melting point of tin the alloy FeSn must be formed; however, this was not verified by analysis. Moreover, Stoll and Birch (6) have not been able to observe by electron diffraction any patterns other than that of $FeSn_2$ on alloys formed at temperatures up to 260°C.

The present work represents an analysis of the rate of formation curves at constant temperatures below and above the melting point of tin and the effect of temperature on the rate of formation of the alloy. Since the alloying was performed on steel covered with an electroplated tin coating, the effect of (*a*) variations in the thickness of the tin coating, (*b*) the steel base, and (*c*) surface preparation of the steel prior to electroplating on the rate of formation of the alloy were also examined.

[1] Present address: E. C. Bain Laboratory for Fundamental Research, United States Steel Corporation, Monroeville, Pa.

Experimental

The samples were prepared by electroplating the tin onto Type L (low metalloid; % Fe > 99) steel sheets from a phenolsulfonic acid electrolyte to thickness of 0.29 mg/cm², 0.50 mg/cm², 0.72 mg/cm², and 1.05 mg/cm². The tin plate with a coating of 0.72 mg/cm² was prepared with four different pickling treatments of the steel base prior to electroplating, to determine whether steel preparation had any effect on the rate of alloy formation. All pickling treatments were performed at room temperature (approximately 27°C): (*a*) electrolytic pickle in 5% H_2SO_4, 1.5 sec cathodic, 1.5 sec anodic; (*b*) electrolytic pickle in 5% HNO_3, 1.5 sec cathodic, 1.5 sec anodic; (*c*) 5-sec dip in 5% H_2SO_4; (*d*) 5-sec dip in 5% HNO_3. The steel came from four different coils produced in different steel mills at different times to determine coil to coil variations on the rate of alloy formation.

The alloys were prepared by heating the samples in a constant-temperature oil bath for various times ranging from 2 sec to 6 hr, these times being dependent on the temperature under study, which ranged from 175° to 316°C. The melting point of tin is 232°C. The temperature of the oil bath was controlled to ±0.5°C for temperatures up to 260°C. At the higher temperatures, the control was ±2°C. Upon removal from the oil bath, the samples were quenched immediately to room temperature in water or in an organic liquid. The quantity of alloy formed was determined coulometrically by the method of Kunze and Willey (7), as was the tin coating weight of the material used. In this method, the tin and the alloy are anodically stripped at constant current in 1M HCl. When all the tin has been stripped and again when all the alloy has been stripped, the potential of the sample, as measured with a silver-silver chloride reference electrode, becomes more positive. The potential-time behavior of the sample was followed on a recorder (chart speed of 30 in./min). From the measured time required to strip the tin and the alloy and from the

known current, the quantity of tin and alloy present could be calculated making use of Faraday's Laws of electrolysis. It was possible to determine the alloy to ± 0.002 mg/cm^2 by this means.

Results and Discussion

The rate of alloy growth at all temperatures studied decreased with time, as would be expected if the parabolic-rate law were obeyed; this is typical for alloying reactions and is indicative of a diffusion mechanism. Seybolt (4) found this in his study of the tin-iron system above the melting point of tin. Therefore, the data were plotted (Fig. 1 and 2) according to the parabolic-rate law, w^2 vs. t, where w is the quantity of alloy formed at time t. Linear plots are observed, but they do not go through the origin as would be expected if the parabolic-rate law were obeyed from the beginning of the reaction ($t = 0$). This type of phenomenon is frequently observed in gas-metal reactions, such as oxidation (8) or sulfidization reactions (9), and is attributed to an

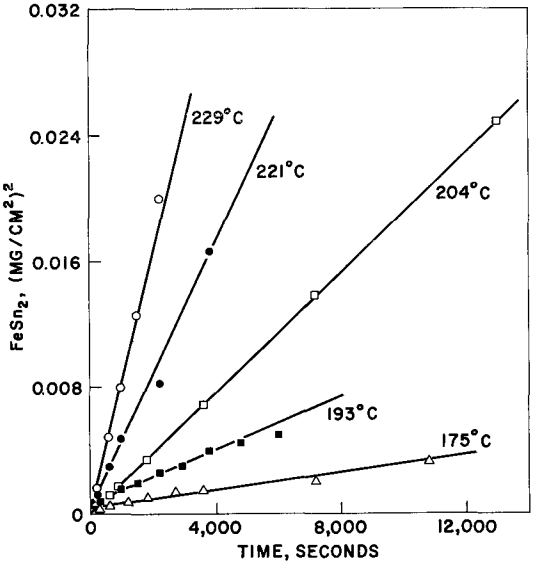

Fig. 1. Rate of growth of $FeSn_2$ at temperatures below the melting point of tin: parabolic plot.

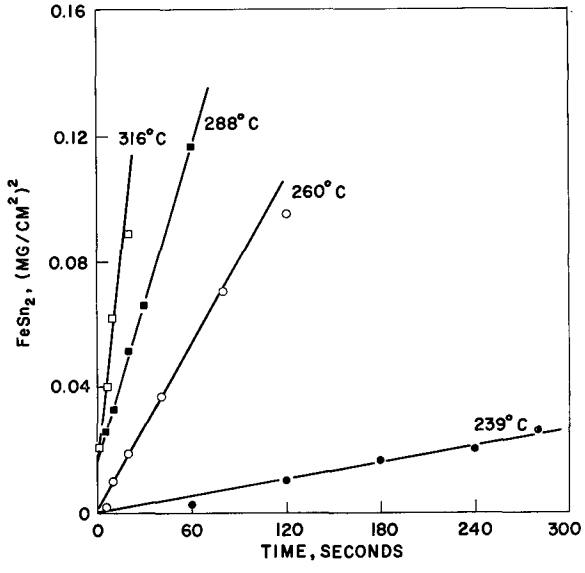

Fig. 2. Rate of growth of $FeSn_2$ at temperatures above the melting point of tin: parabolic plot.

Table I. Parabolic-rate constant as a function of temperature

Temperature	k × 10^6, mg^2/cm^4/sec
175	0.26
192	0.62
193	0.89
193	0.61
202	1.46
203	2.12
204	1.92
221	4.7
222	5.8
229	8.3
239	10.3
245	17.2
260	39.
260	88.
288	167.
316	495.

interface reaction between the metal and the gas that establishes the initial reaction layer, after which diffusion through the reaction layer becomes rate-controlling. It would be natural to expect the same situation to exist in this study since the conditions are analogous, except that either a solid-solid or a solid-liquid reaction exists at the interface instead of a solid-gas reaction. The mathematics of the metal-gas reaction were treated initially by Fischbeck (10) and by Wagner (11) and more recently by Dravnieks and Samans (9), who assumed first-order kinetics for the interface reaction. This approach was applied to the data obtained in these studies in the hope of determining the rate of the interface reaction. However, the data did not follow this relationship and thereby indicated that the interface reaction did not obey simple first-order kinetics. No further attempt was made to study the interface reaction.

Parabolic-rate constants for the diffusion reaction at the various temperatures, the slopes of the plots in Fig. 1 and 2, are given in Table I. An Arrhenius plot of the log of the parabolic-rate constant vs. the reciprocal of the absolute temperature is shown in Fig. 3. Table I and Fig. 3 include data not shown in previous figures. Two straight lines with a sharp break at the melting point of tin are observed. The

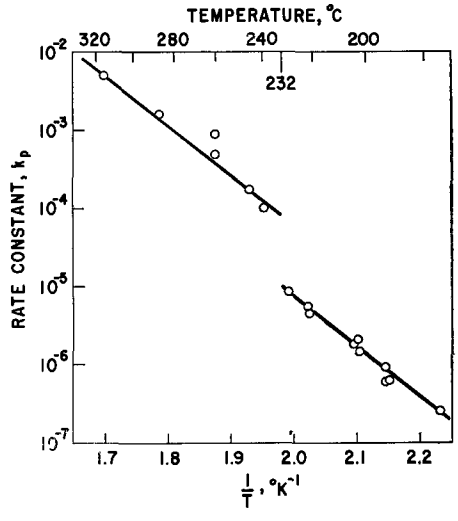

Fig. 3. Rate of formation of $FeSn_2$ with temperature.

calculated activation energy below and above the melting point is the same within experimental error and is 29.3 ± 1 kcal/mole. This value is in good agreement with the value of 28.6 kcal/mole [2] found by Seybolt (4). No similar results for analogous systems have been found in the literature. The sharp increase in the reaction rate above the melting point of tin is believed due to increased contact area at the Sn-Fe interface, compared with solid tin electrodeposited on iron.

The intercepts of the parabolic plots on the ordinate, Fig. 1 and 2, average at approximately 0.006 mg/cm^2. From the density of $FeSn_2$ (12), 7.74 g/cm^3 and the lattice parameters (13) of the alloy, a = 6.53Å and c = 5.33Å, this is calculated to be equivalent to a thickness of 11 unit cells of the alloy, which does not seem to be an unreasonable thickness, at which the interface reaction ceases to be rate-determining and the diffusion reaction commences to be rate-determining.

Tin-coating weight.—In early experiments, it was observed that some of the tin was dissolved from the samples in the oil bath, but it was not known how this affected the results. Hence, the effect of the thickness or weight of the tin coating on the rate of growth of the alloy was studied. Results are shown in Fig. 4 for 204° and 239°C. It is apparent that there is no effect except possibly at the high alloy weight levels for the 0.29 mg/cm^2 plate, in which case the results are low. These are low because there was insufficient tin on the plate (some having dissolved in the oil bath) to form more alloy, as evidenced by the fact that these samples had no free tin left on them when they were removed from the oil bath.

Steel base.—Data in Fig. 3 were obtained using the steel from the four different coils described previously. Alloy-growth studies with each steel were made at temperatures below and above the melting point of tin. Since the data from each of the coils lie on the observed lines, it is concluded that coil to coil variations do not affect the kinetics or mechanism of the growth of the alloy.

Pickle.—Figure 5 shows the effect of the various pickling treatments prior to electroplating on the rate of formation of the alloy layer at 202° and 240°C. No effect is evident, although these different treatments undoubtedly affect the surface of the steel in different manners.

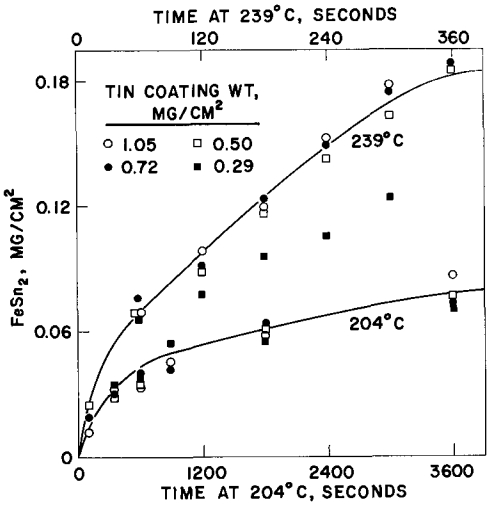

Fig. 4. Formation of $FeSn_2$ as affected by tin-coating weight.

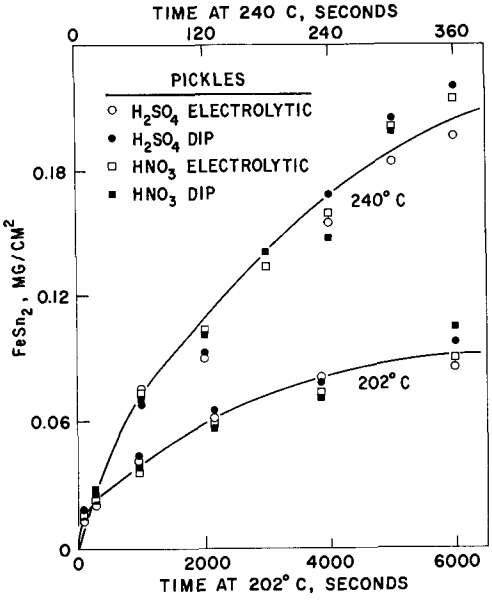

Fig. 5. Formation of $FeSn_2$ as affected by pickling conditions.

Summary

The kinetics of the formation of the iron-tin alloy $FeSn_2$ have been studied at temperatures below and above the melting point of tin (232°C). At all temperatures studied, the growth obeyed the parabolic-rate law. This is indicative of a diffusion mechanism. An Arrhenius plot of the data gives a straight line below the melting point of tin and a straight line above the melting point of tin, with a sharp break at the melting point. The activation energy is the same below and above the melting point of tin and is 29.3 ± 1 kcal/mole. The kinetics of the growth were also studied as a function of various properties associated with the tin plate: tin-coating weight, steel base, and the type of pickle to which the steel base was subjected prior to electroplating of the tin. No effect due to any of these variables was found.

Acknowledgment

The authors wish to thank Drs. R. T. Davis, Jr., and C. Luner for their helpful discussions and Messrs. R. F. Higgs and E. C. Brendlinger for preparing the tin plate used in these studies.

Manuscript received April 22, 1960.

Any discussion of this paper will appear in a Discussion Section to be published in the June 1961 JOURNAL.

[2] Seybolt reported an activation energy of 14.3 kcal/mole. However, his rate constants were calculated from the slope of a w vs. $t^{1/2}$ plot and are thus equal to the square root of the rate constants calculated from a w^2 vs. t plot; the activation energy calculated from the former rate constants will be equal to one-half that calculated from the latter rate constants.

REFERENCES

1. O. E. Romig, *Metal Progress*, **42**, 899 (1942).
2. C. J. Thwaites, *J. Iron Steel Inst.*, **183**, 244 (1956).
3. J. E. Davies and W. E. Hoare, *ibid.*, **168**, 134 (1951).
4. A. U. Seybolt, *Trans. ASM*, **29**, 937 (1941).
5. W. N. Lambert, *Corrosion*, **11**, 454 (1955).

6. P. J. Stoll and H. J. Birch, Private communication.
7. C. T. Kunze and A. R. Willey, *This Journal*, **99**, 354 (1952).
8. O. Kubaschewski and B. E. Hopkins, "Oxidation of Metals and Alloys," p. 42, Fig. 18a, Butterworth Scientific Publications, London (1953).
9. A. Dravnieks and C. H. Samans, *This Journal*, **105**, 183 (1958).
10. K. Fischbeck, L. Neundenbel, and F. Salzer, *Z. Elektrochem.*, **40**, 517 (1934).
11. C. Wagner and K. Grunewald, *Z. physik. Chem.*, **B40**, 455 (1938).
12. R. A. Covert and H. H. Uhlig, *This Journal*, **104**, 537 (1957).
13. H. Nowotny and K. Schubert, *Metallforsch.*, **1**, 17 (1946).

Properties of Vanadium-Columbium Alloys

S. T. Wlodek

Metals Research Laboratory, Union Carbide Metals Company,

Division of Union Carbide Corporation, Niagara Falls, New York

ABSTRACT

The development of a series of vanadium-columbium alloys is described. The exploitation of this alloy system allows the design of high-strength, low-density compositions possessing good aqueous corrosion resistance in boiling, oxidizing, or reducing acids and sufficient oxidation resistance to allow their fabrication by conventional hot-working techniques in air. In the warm-worked condition, the spectrum of properties measured under inert atmosphere conditions (strain rate 0.005^{-1} sec) includes ultimate tensile strengths of 120,000 to 35,000 psi over the temperature range of 700°-1000°C and stress-rupture properties at 700°C corresponding to 100-hr life at stresses in excess of 100,000 psi. Tensile strengths as high as 70,000 psi at 1000° and 40,000 psi at 1200°C were observed at higher rates of loading in the warm-worked and stress-relieved conditions.

The high melting point (1900°C) and low density (6.1 g/cc) of vanadium suggest a material of promising mechanical properties at elevated temperature with an advantageous strength-to-weight ratio for applications where such a factor would be of importance. Unfortunately, the high melting point of pure vanadium is not accompanied by the expected degree of high-temperature strength (1). This drawback, common to the other VB periodic group refractory metals, columbium and tantalum, is offset by the excellent room-temperature fabricability and ductility down to liquid nitrogen temperature. Vanadium possesses good liquid metal corrosion resistance, and because all of its short-lived isotopes decay without emitting excessively strong decay products it is often regarded as a promising structural material for nuclear applications. Of all the refractory metals, however, pure vanadium is probably the least resistant to oxidation and aqueous corrosion. The low melting point of V_2O_5 (660°C), the main oxidation product on a vanadium-base material, produces such catastrophic rates of reaction above 660°C, that the hot-working of vanadium is a most uneconomical procedure. The protection of a vanadium-base material against oxidation by means of coatings is also made a most difficult, if not impossible, problem. The poor corrosion resistance of vanadium, in either oxidizing or strongly reducing acids or high chlorine concentrations, limits its application in chemical environments.

Attempts at improving the properties of vanadium by alloying have involved the use of titanium with further additions of a third element, such as: chromium, aluminum, or silicon for strength, and oxidation resistance, as well as carbon for improved fabricability. These studies, performed primarily by Rostoker, Yamamoto, and Riley (2), and recently fully summarized by Rostoker (3), have resulted in an appreciable improvement over the properties of pure vanadium. Ultimate tensile strengths of 130,000-90,000 psi and 100-hr rupture strengths of 100,000-10,000 psi were obtained in the temperature range 500°-700°C. A different system of alloys based on the vanadium-titanium binary and containing additions of tantalum, columbium, molybdenum, or carbon in amounts not exceeding 1 weight per cent (w/o) has been proposed by Smith and Van Thyne (4) for applications requiring medium strength combined with high fabricability and good aqueous or liquid metal corrosion resistance.

It is the purpose of this paper to present some preliminary results on the oxidation resistance, mechanical properties, and aqueous corrosion behavior of a family of alloys based on a vanadium-columbium system in the region of 20-50 w/o columbium.

The vanadium-columbium phase diagram portrays a system of complete solid solution with a minimum in the liquidus at 1810°C, corresponding to a composition of 35 w/o columbium (5). Of all the elements that are completely miscible with vanadium, columbium possesses the largest degree of atomic mismatch combined with complete solid solubility. The high-melting points of this alloy system and the large atomic size difference between vanadium and columbium suggest a system with good high-temperature properties. The complete miscibility of vanadium and columbium suggests a minimum loss in fabricability on alloying with a maximum increase in strength. Although the columbium-vanadium system is of the liquidus minimum type, a

Table I. Analyses of materials

	Vanadium, %	Columbium, %
Carbon	0.043	0.030
Oxygen	0.090	0.070
Hydrogen	0.001	—
Nitrogen	0.038	0.030

characteristic often associated with systems that undergo clustering or disproportionation at some lower temperature, no evidence of the formation of a second phase was ever observed in this study. Even in columbium-vanadium alloys containing 20-50 w/o columbium and annealed for up to 100 hr at a temperature range of 700-900°C only single-phase structures were observed. This is in agreement with the work of Wilhelm, *et al.* (6), who similarly failed to find the sigma phase reported by Rostoker and Yamamoto (7).

Turning now to the oxides, the Cb_2O_5-V_2O_5 system may be roughly described as a simple peritectic type with appreciable amounts (about 20 vol %) of Cb_2O_5 being soluble in V_2O_5 at 600°C. The addition of Cb_2O_5 to V_2O_5 raises the melting point of vanadium pentoxide to the point that an equimolar mixture of V_2O_5 and Cb_2O_5 is completely solid at temperatures up to 950°C. The greater affinity of columbium for oxygen and the complete miscibility of columbium and vanadium metal all indicated the possibility that columbium might increase the oxidation resistance of vanadium by promoting the formation of a higher melting point oxide.

These were the reasons for considering this study as being a likely approach to a series of vanadium-base alloys possessing better mechanical properties and superior oxidation resistance.

Preparation of Alloys

Commercial-grade vanadium and columbium as produced by Union Carbide Metals Company with the analyses given in Table I were used throughout this study. The other alloying elements employed were also of commercial purity.

All aqueous corrosion and some oxidation samples were prepared by the nonconsumable arc melting of 70-g, 2-in. diameter buttons. The charge was prepared by compacting the vanadium and columbium as 10-mesh powders with the titanium being added in the same form. Additions of aluminum, silicon, and chromium were made by means of the intermetallic compounds Al_3Cb, $CbCr_2$, or $CbSi_2$, these master alloys having been prepared previously by melting the elemental powders. After compaction, the charge was melted four times, twice on each side, on a water-cooled copper hearth using a tungsten electrode, the melting operation being carried out in an atmosphere of pure argon with currents in the order of 200-500 amp at 24-26 v.

Wrought material for mechanical property and certain oxidation studies was obtained from consumable 1½-in. diameter 800-g ingots. The consumable electrodes were formed by welding together five 4-in. long bars of the alloy composition, the bars having been previously prepared by nonconsumable, tungsten electrode melting using the same technique described above for buttons. Satisfactory ingots with an equiaxed as-cast grain size were prepared by d-c arc melting with currents of 600-1000 amp and in an atmosphere of 120 mm Hg of argon. After dressing, these ingots were extruded in air at temperatures of 1100°-1200°C. To keep the extrusion times as short as possible, induction heating was used to preheat the billets, and the actual extrusion, at a 4-to-1 ratio, was performed in a fast-acting, flywheel activated, impact-extrusion press at speeds of 40-100 ips. Subsequent hot-working to ⅜-in. diameter was performed by swaging in the temperature range of 1000°-1100°C or by cold-working at room temperature. An argon atmosphere was used for preheating the billets prior to the extrusion and swaging operations. All fabricating procedures were performed in air; no canning or in-plant coating techniques were used.

As given in Table II, this technique of wrought sample preparation produced compositions close to the nominal analysis with a slight amount of oxygen pickup from the swaging operation.

The fabrication of most of these alloys, below about 1100°C, is tantamount to warm-working. For 0.5-hr annealing times, the recrystallization temperature of binary vanadium alloys containing 30-40 w/o columbium is about 1150°C. Very little grain growth occurs as the annealing temperature is increased to 1300°C. The recrystallization temperature for the vanadium-columbium-titanium ternary alloys, especially if modified with quaternary aluminum or silicon additions, is somewhat lower, ranging as low as 1100°C for the 50% V-40% Cb-10% Ti alloy to 1050°C for the 45% V-40% Cb-10% Ti-5% Al composition. The microstructures

Table II. Sample analyses of consumable arc melted alloys

	V	Cb	Ti	Al	Si	C*	O*	N*
Nominal	60.0	40.0	—	—	—	—	—	—
Analyzed	59.78	39.60	—	—	—	0.050	0.26	0.023
Nominal	50.0	40.0	10.0	—	—	—	—	—
Analyzed	49.89	40.00	9.40			0.039	0.23	0.020
Nominal	49.0	40.0	10.0	—	1.0	—	—	—
Analyzed	50.23	38.70	9.00		0.90	0.080	0.23	0.022
Nominal	45.0	40.0	10.0	5.0	—	—	—	—
Analyzed	45.15	39.80	9.20	4.73	—	0.030	0.20	0.020

* Carbon, oxygen, and nitrogen analyses obtained on wrought material after tensile testing. Additional pickup of oxygen probably occurred during creep-rupture testing. The above oxygen levels were the maximum observed. Values as low as 0.15 w/o oxygen were sometimes encountered.

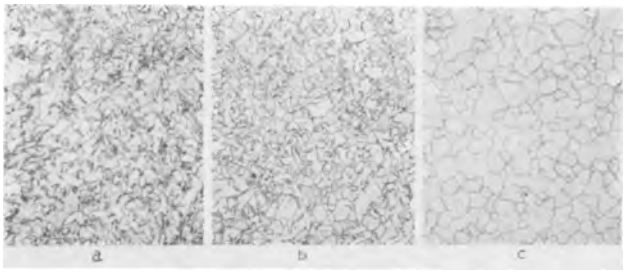

Fig. 1. 60% Vanadium-40% columbium alloy, all etched in 1 HF:1 HNO_3:3 glycerol. Magnification 100X before reduction for publication. (a) Swaged at 1000°C, annealed 0.5 hr at 1000°C, hardness 243 VPH; (b) swaged at 1000°C, annealed 0.5 hr at 1100°C, hardness 242 VPH; (c) swaged at 1000°C, annealed 0.5 hr at 1200°C, hardness 210 VPH.

illustrated in Fig. 1 for the 60% V-40% Cb composition as-swaged at 1000°C and annealed for 0.5 hr at 1000°, 1100°, and 1200°C exemplify the structure of these alloys. All the compositions given in Table II were single phase. The amount and extent of slip bands shown in Fig. 1 were characteristic of the warm-worked state, with deformation twins being readily observed in the compositions cold-worked at room temperature. Both types of deformation markings were less prevalent in titanium-containing alloys.

Corrosion Testing

Corrosion tests were performed on as-cast specimens of columbium-vanadium binary alloys over the range 20-50 w/o columbium with and without ternary titanium additions at the 10-20 w/o level. As shown in Fig. 2, the addition of columbium to vanadium greatly increased the corrosion resistance to boiling 65% HNO_3, boiling 5, 10, and 15% HCl, and boiling 10, 20 and 30% H_2SO_4 solutions. Further improvements, especially in regard to the corrosion resistance in boiling 65% HNO_3, were obtained on the addition of columbium in the presence of 10 and 20% titanium. The addition of titanium to the vanadium-columbium base, however, was found to increase the rate of corrosion in HCl and H_2SO_4 solutions. The addition of 20-50 w/o columbium, with and without further titanium additions, improved the room-temperature resistance to wet chlorine attack at room temperature to the point that corrosion rates of less than 1 mil/year were obtained. All these data were derived from 48-hr duplicate tests with the exception of the chlorine corrosion data which were obtained from 90-hr periods.

With the exception of boiling 65% HNO_3 solutions, where vanadium-columbium-titanium alloys behaved best, the most corrosion-resistant composition studied was the 50% Cb-50% V alloy. Exhibiting a corrosion rate in 65% HNO_3 of 17 mils/year, this composition corroded in boiling 5, 10 and 15% HCl at rates of 8, 50, and 83 mils/year, respectively. In addition, the 50% V-50% Cb alloy was found to corrode in boiling H_2SO_4 solutions of 5, 10, 20, and 30% concentration by weight at rates of 11, 17, 31, and 63 mils/year. By means of a bar diagram of the type first introduced by Stern and Bishop (8) the over-all corrosion resistance of the 50% V-50% Cb alloy is compared with other corrosion-resistant alloys and pure vanadium in Fig. 3. In this type of diagram, the total area below each horizontal bar denotes the range of environments in which that composition resists attack. Although the nature of this diagram is highly qualitative, the over-all degree of corrosion resistance possessed by the 50% V-50% Cb alloy is evident. This ability to withstand oxidizing or reducing acids in the presence or absence of chlorides is an appreciable improvement over pure vanadium, which, as shown in Fig. 3, is only able to withstand relatively dilute reducing solutions and relatively low chloride environments.

Oxidation Testing

The rate of oxidation of vanadium-columbium alloys containing from 20 to 40 w/o columbium with or without further additions of titanium, silicon, chromium, and aluminum in ternary or quaternary combinations was evaluated by means of continuous weight-gain measurements and intermediate exposure tests involving the subsequent measurement of the amount of metal consumed.

Continuous weight-gain measurements were obtained in an atmosphere of pure and dry oxygen at 700°, 800°, and 900°C. Test samples consisted of as-cast parallelepipeds (1.5 x 0.8 x 0.8 cm) abraded

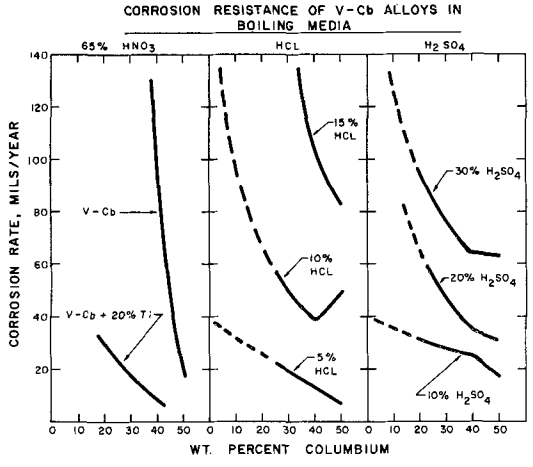

Fig. 2. Effect of columbium additions on the corrosion of vanadium in boiling 65% HNO_3, HCl, and H_2SO_4. Effect of a 20% titanium addition on the behavior of a V-Cb alloy in 65% HNO_3 is also shown.

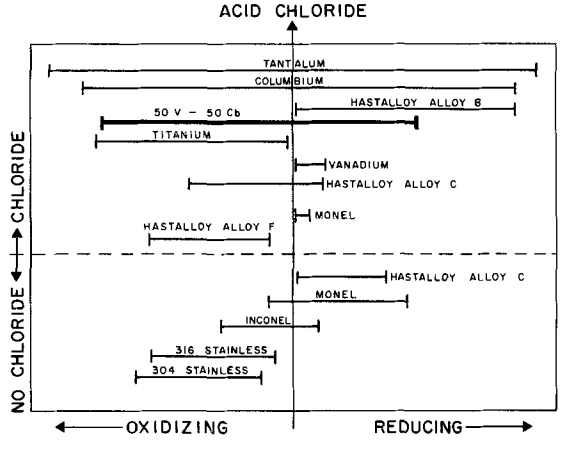

Fig. 3. Comparison of corrosion resistance of 50V-50Cb to other materials (8). Each alloy exhibits adequate corrosion resistance in all environments below its solid line.

Table III. Oxidation rates of vanadium-columbium alloys

Alloy composition, w/o				Rate of steady-state oxidation* in pure oxygen, mg/cm²/hr		
V	Cb	Ti	Other	700°C	800°C	900°C
70	30	—	—	14.4	32.6†	Liquid
60	40	—	—	9.8	57.4	64.0†
50	50	—	—	8.7	312.0	510.0†
50	30	20	—	6.4	18.2	41.3
50	40	10	—	7.2	9.0	18.8
40	40	20	—	13.1	54.2	115.0
55	40	—	5 Al	10.5	18.8	38.6†
55	40	—	5 Cr	20.5	15.0	24.9†
55	40	—	5 Si	20.9	58.8†	Liquid
50	35	10	5 Al	8.6	9.6	20.0
55	30	10	5 Si	18.0	13.1	14.9
48	40	10	2 Si	7.1	14.1	48.7
45	40	10	5 Si	7.7	12.2	18.7

* Rate of steady-state reaction, often attained after about 5.0 hr of oxidation.
† Some liquid phase present at some period during oxidation process.

under kerosene through 0000 emery paper and then rinsed in benzene before testing. The sample was suspended from one arm of a Mauer (9) automatically recording, gravimetric balance by means of a quartz rod and a platinum sling. Pure dried oxygen at a flow rate of 22.4 l/hr was passed over the specimen, the resulting increase in weight being recorded to the nearest 1.0 mg. The average length of the oxidation test was of the order of 6-8 hr.

The most significant results obtained in the rate measurements are tabulated in Table III in terms of the instantaneous oxidation rate exhibited by the alloy after 5.0 hr exposure, an interval which allowed some semblance of steady-state kinetics to be achieved. This method of comparing oxidation rates had to be adopted in view of the varying kinetic forms of oxidation exhibited by vanadium-base alloys. As shown in the weight gain *vs.* time plots in Fig. 4, various combinations of reaction rates were observed during oxidation even at 700°C.

On the basis of these results, it was possible to conclude that, while the addition of columbium to vanadium does suppress the formation of a liquid oxide, a maximum reduction in oxidation rate can be obtained only by the addition of titanium,

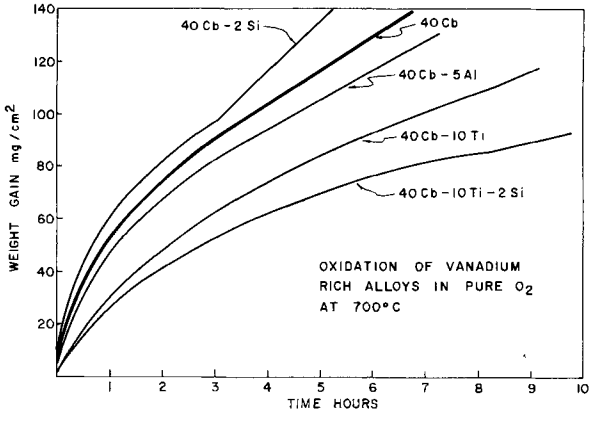

Fig. 4. Oxidation of columbium containing vanadium alloys as characterized by weight-gain values at 700°C.

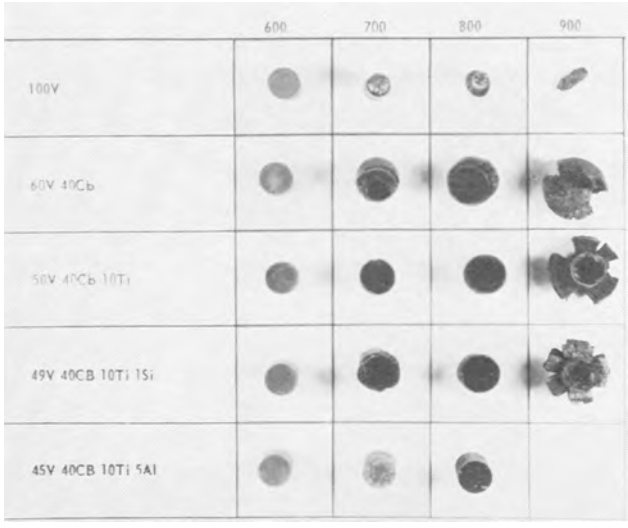

Fig. 5. Appearance of ⅜-in. diameter samples after 5.0 hr exposure in air.

especially in the presence of small amounts of silicon or aluminum.

Oxidation measurements by means of metal loss techniques, wherein the decrease in sample diameter after oxidation is measured, were made on pure vanadium and four alloys. The alloys were:

60% V-40% Cb
50% V-40% Cb-10% Ti
49% V-40% Cb-10% Ti-1% Si
45% V-40% Cb-10% Ti-5% Al

These compositions were selected on the basis of the weight-gain measurements described above to combine the minimum oxidation rate with a single phase structure. Tests were performed on wrought ⅜-in. diameter specimens over a temperature range of 600°-900°C for time periods of up to 10 hr at 900°C and up to 100 hr at lower temperatures. The 45% V-40% Cb-10% Ti-5% Al alloy was also evaluated at 1000°C. The visual appearance of some of the samples after oxidation is portrayed in Fig. 5. Following exposure in undried static air at the proper temperature and time combination, oxidation products were removed by abrasion and etching in a 20% KOH-5% $KMnO_4$ solution, and the amount of metal consumed, the metal loss, was measured with a micrometer to the nearest mil (0.001 in.). The decrease in sample diameter in terms of metal loss expressed in mils per side is plotted for a constant 5-hr period of air exposure against temperature in Fig. 6. Figure 7 presents the rate of oxidation of pure vanadium and a 50% V-40% Cb-10% Ti alloy as well as the 49% V-40% Cb-10% Ti-1% Si and 45% V-40% Cb-10% Ti-5% Al alloys at 700°C.

These measurements indicate a reduction in oxidation rate for the quaternary alloys and for the simple V-Cb-Ti ternary that approaches a five- to sevenfold improvement over pure vanadium. The rate of oxidation of the 45% V-40% Cb-10% Ti-5% Al alloy is particularly outstanding for a vanadium-base composition with no liquid oxide being observed at temperatures up to 1000°C. Liquid vanadium pentoxide was definitely noted on the other compositions tested at 900°C, and in the case of the

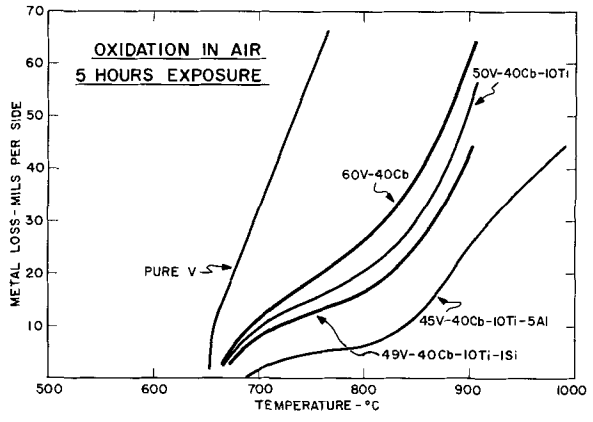

Fig. 6. Effect of temperature on oxidation of vanadium-columbium alloys.

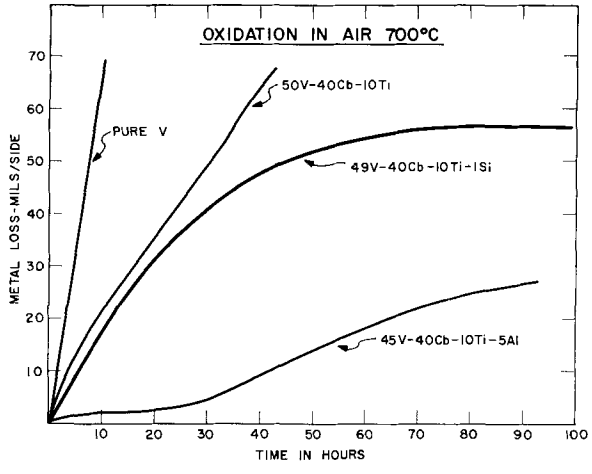

Fig. 7. Oxidation of vanadium-columbium alloys as characterized by a size decrement value at 700°C.

60% V-40% Cb alloy, small amounts of liquid oxide were observed on samples exposed at 800°C. The appearance of liquid vanadium pentoxide during the oxidation of these alloys is to some extent time-dependent, becoming more pronounced as the oxidation process proceeds. In all samples examined, no subscale surface hardening of the type encountered in columbium-base alloys or pure vanadium was noticed.

Mechanical Properties

The determination of the mechanical properties of vanadium-columbium alloys was focused primarily on the compositions of promising oxidation and corrosion resistance.

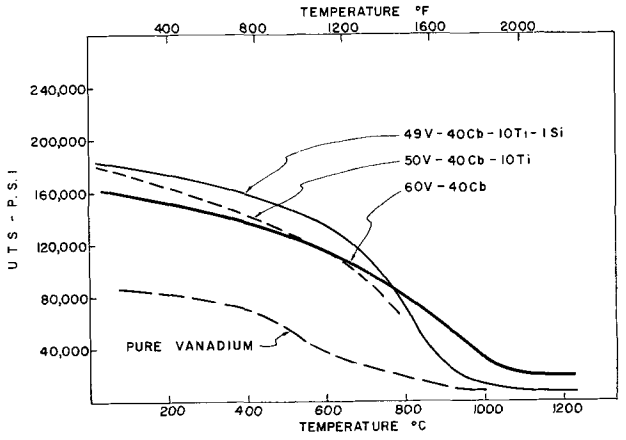

Fig. 8. Effect of temperature on tensile strength of alloys tested at 0.005^{-1} sec.

Tensile tests were performed on wrought materials using a button-head type miniature tensile specimen, with all tests being performed in vacuum. The tensile properties of as-swaged vanadium-columbium alloys with and without further additions of titanium, silicon, and aluminum are presented in Table IV for room temperature, 700° and 1000°C. These data augmented by results obtained at 1200°C are plotted in Fig. 8 for the stronger alloys in the as-swaged condition. The as-swaged condition is equivalent to warm-worked material for all alloys with the possible exception of the 45% V-40% Cb-10% Ti-5% Al composition. The effect of cold-work on the mechanical properties of the 70% V-30% Cb and 50% V-40% Cb-10% Ti alloys is presented in Table V, which also includes data on the effect of heat-treatment on the properties of warm-swaged vanadium-columbium alloys. All alloys studied could be cold-swaged at room temperature after a primary breakdown by extrusion. The high compressive strength of these materials, however, produced very frequent die failures during swaging, and since cold working did not affect the mechanical properties appreciably, the production of cold-swaged material was limited. Cold work decreased the room-temperature ductility of these materials without producing appreciable elevated temperature strengthening, even at temperatures well below the recrystallization temperature. Annealing warm-worked material in the temperature range of 1100°-1300°C tended to produce some reduction in mechanical properties which was more than made up by increased room-temperature duc-

Table IV. Tensile properties of vanadium-columbium alloys*

				R.T.			700°C			1000°C			
V	Cb	Ti	Other	U.T.S. psi × 10^{-3}	0.2% Y.S. psi × 10^{-3}	E %	U.T.S. psi × 10^{-3}	0.2% Y.S. psi × 10^{-3}	E %	U.T.S. psi × 10^{-3}	0.2% Y.S. psi × 10^{-3}	E %	Density lb/in.^{3}
70	30	—	—	Brittle failure			127.0	91.1	24.0	—	—	—	—
60	40	—	—	Brittle failure			102.3	91.0	7.4	34.8	30.8	8.0	0.25
50	40	10	—	Brittle failure			91.8	84.2	15.8	—	—	—	0.24
49	40	10	1% Si	182.0	140.0	3.0	121.0	88.4	22.3	12.8	8.85	74.0	0.23
45	40	10	5% Al	Brittle failure			91.2	69.0	5.3	7.9	5.9	142.0	—

* All impact extruded 4:1 reduction at 1100°-1200°C followed by 50% reduction by swaging at 1000°C. All tests performed at 0.005^{-1} sec strain rate.

Table V. Effect of processing variables on mechanical properties*

Alloy composition, w/o V	Co	Ti	Swaged condition†	Annealed Temp, °C	Time, hr	R.T. U.T.S. psi × 10⁻³	R.T. 0.2% Y.S. psi × 10⁻³	R.T. E %	700°C U.T.S. psi × 10⁻³	700°C 0.2% Y.S. psi × 10⁻³	700°C E %	1000°C U.T.S. psi × 10⁻³	1000°C 0.2% Y.S. psi × 10⁻³	1000°C E %	1200°C U.T.S. psi × 10⁻³	1200°C 0.2% Y.S. psi × 10⁻³	1200°C E %
70	30	—	30% C.W.	—	—	Brittle failure			128.6	109.6	5.2	—	—	—	—	—	—
70	30	—	50% 1100°C	—	—	Brittle failure			130.2	112.0	6.0	70.1	63.7	89	23.2	22.4	43.6
70	30	—	50% 1100°C	1100	0.5	124.1	125.6	2.2	—	—	—	—	—	—	—	—	—
70	30	—	50% 1100°C	1200	0.5	123.8	118.2	2.0	121.7	90.7	69.0	68.2	65.0	72	—	—	—
70	30	—	50% 1100°C	1300	0.5	123.6	114.7	5.0	126.0	90.7	25.0	—	—	—	—	—	—
60	40	—	50% 1000°C	1000	0.5	143.3	136.9	2.0	—	—	—	—	—	—	—	—	—
60	40	—	50% 1000°C	1100	0.5	154.6	141.6	62.5	140.2	131.8	40.5	68.3	63.0	35.3	22.8	22.3	14.0
60	40	—	50% 1000°C	1300	0.5	125.8	115.3	7.7	—	—	—	—	—	—	19.8	19.0	21.1
50	40	10	40% C.W.	—	—	181.0	177.2	4.0	86.7	75.5	2.8	—	—	—	—	—	—

* All tests performed at 0.02^{-1} sec strain rate.
† Preceded by extrusion 4:1 reduction at 1100°-1200°C.

tility. The sparsity of data makes even these comments questionable, but the generalization that the room-temperature ductility of these materials can be increased by the proper heat-treatment is definite. This, of course, is valid only for conditions of tensile loading applied at the strain rate used (0.005-0.02^{-1} sec). Although the tensile properties of the vanadium-columbium type of alloys are not affected appreciably by variations in strain rate within this spectrum of rate of load application, much higher rates of loading will decrease the ductility parameters and markedly increase the ultimate tensile strength. This has been observed even at 1200°C. The ultimate tensile strength of a warm-worked 60% vanadium-40% columbium alloy will vary from some 20,000 psi to 40,000 psi at 1200°C as the strain rate is increased from 0.02^{-1} sec to 0.20^{-1} sec.

The concluding step in these mechanical studies involved creep-rupture tests on as-swaged 60% V-40% Cb, 50% V-40% Cb-10% Ti, and 49% V-40% Cb-10% Ti-1% Si compositions. All tests were performed at 700°C in an atmosphere of pure helium gettered by a titanium collar placed around the creep-rupture specimen. The stress-rupture properties of these alloys at 700°C are shown in Fig. 9. Stress levels for a 100-hr life to rupture of 110,000 psi for the 60% V-40% Cb alloy, 85,000 psi for the 50% V-40% Cb-10% Ti alloy, and 90,000 psi for the 49% V-40% Cb-10% Ti-1% Si, were reflected in a correspondingly high creep resistance. As given in Table VI, the 100,000 psi minimum

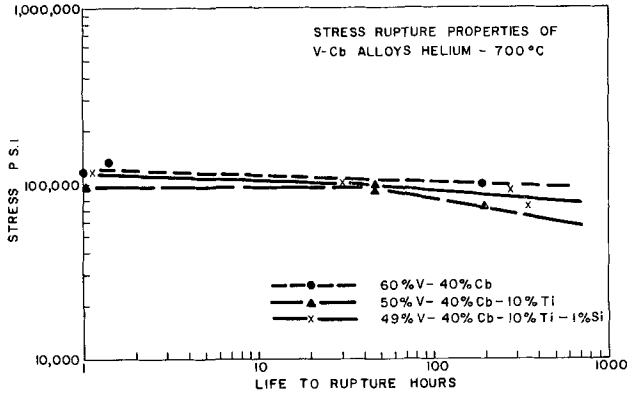

Fig. 9. Stress-rupture properties of some V-Cb alloys tested in helium.

Table VI. Creep properties of V-Cb alloys* at 700°C

Alloy composition w/o	Minimum creep rate (in./in./hr) for 75,000 psi	90,000 psi	100,000 psi
60 V-40 Cb	—	—	1.05×10^{-4}
50 V-40 Cb-10 Ti	3.58×10^{-5}	1.15×10^{-4}	1.0×10^{-4}
49 V-40 Cb-10 Ti-1 Si	8.0×10^{-5}	1.7×10^{-4}	1.85×10^{-4}

* As-swaged at 1000°-1100°C.

creep rate of the vanadium-columbium alloys at 700°C varied from 1.0 to 1.85×10^{-4} in./in./hr.

The high mechanical properties of the 60% V-40% Cb and the 49% V-40% Cb-10% Ti-1% Si alloys are even more attractive when compared with the properties of other materials on the strength-to-density basis. Such a comparison is presented in Fig. 10 where the strength-to-weight ratio of these two compositions is compared to the same ratio for the strongest iron-, titanium-, and molybdenum-base alloys. In this plot, the ultimate tensile strength of the vanadium-columbium alloys refers to the warm-worked condition as evaluated at a strain rate of 0.005^{-1} sec. If data obtained at strain rates of 0.20^{-1} sec had been used, the 60% V-40% Cb composition would approach the strength-to-weight ratio of the molybdenum-0.5 titanium alloy at 1200°C (2192°F).

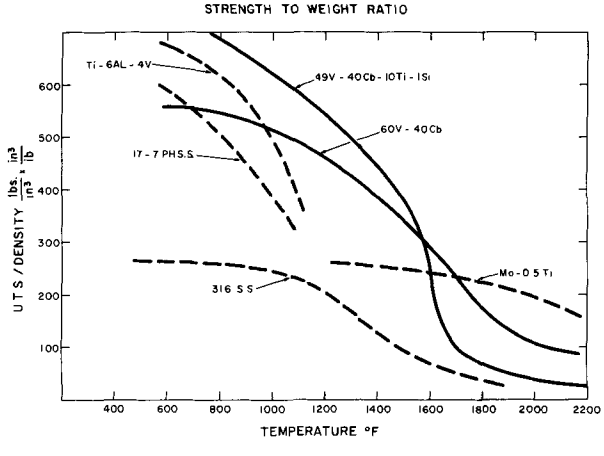

Fig. 10. Comparison of tensile properties of some commercial alloys and the vanadium-columbium compositions on a strength-to-weight basis.

Summary and Discussion

The aqueous corrosion and oxidation resistance as well as the high-temperature strength that can be imparted to vanadium by columbium additions present an appreciable improvement over other vanadium base systems (3, 4). Relatively simple alloys such as the 50% V-50% Cb or 60% V-40% Cb compositions exhibit degrees of corrosion resistance and elevated temperature strength that compare favorably with the best materials in present day commercial use. More complex alloys as exemplified by the 45% V-40% Cb-10% Ti-5% Al begin to show a level of oxidation resistance that would at least assure reliability in a coated structure, while even the simple binary combinations exhibit sufficient resistance to liquid V_2O_5 formation to allow their fabrication at elevated temperatures without cumbersome canning or coating procedures. None of these alloys, of course, is oxidation resistant enough above 660°C to permit prolonged service in air.

The degree to which columbium additions will increase the high-temperature strength of vanadium is an excellent example of the solid solution strengthening that can be imparted by adding a solute of high solubility that produces the maximum amount of lattice strain for a minimum decrease of the solvent's melting point. The small loss in fabricability and the retention of ductility after recrystallization that is made possible by such a strengthening mechanism are also beneficial. Nevertheless, the alloys are highly strain-rate sensitive, a condition that can be improved at the expense of strength by titanium additions.

The solubility of Cb_2O_5 in V_2O_5 and the resultant increase of the melting point of the vanadium pentoxide are partially responsible for the observed improvement in oxidation. Equally significant is the complete intersolubility that exists in the metallic phase and higher affinity of columbium for oxygen. Both of these latter two factors are believed to promote the inclusion of columbium in the oxide phase. A further reduction in reaction rate can be obtained by titanium and aluminum additions.

The observed increase in corrosion resistance is probably a reflection of the passivity inherent to columbium, a property which for this metal is usually associated with the presence of a protective film.

In closing, it may be noted that, although each of these possible mechanisms requires a high level of columbium in terms of weight per cent, the atomic concentration of columbium is roughly one-half of that expressed on a weight basis. The properties exhibited by these vanadium-columbium alloys can, therefore, be correctly ascribed to a vanadium-rich system and regarded as a further development in the alloy systems of this refractory metal.

Acknowledgment

The author is indebted to Mr. C. R. Bishop for the corrosion results presented here and to Mr. J. L. Wilson for his help and advice in the fabrication of these alloys.

Manuscript received May 9, 1960. This paper was prepared for delivery before the Chicago Meeting, May 1-5, 1960.

Any discussion of this paper will appear in a Discussion Section to be published in the June 1961 JOURNAL.

REFERENCES

1. J. W. Farrell, Paper presented at The Electrochemical Society Symposium on Vanadium, May 1-5, 1959, in Chicago.
2. W. Rostoker, A. S. Yamamoto, and R. E. Riley, *Trans. A.S.M.*, **48**, 560 (1956).
3. W. Rostoker, "The Metallurgy of Vanadium," John Wiley & Sons, Inc., New York (1958).
4. K. F. Smith and R. J. Van Thyne, Metallurgical Society Conferences, Reactive Metals, **2**, 403 (1959); Interscience.
5. M. Hansen and K. Anderko, "Constitution of Binary Alloys," 2nd ed., McGraw-Hill Book Co., New York (1958).
6. H. A. Wilhelm, O. N. Carlson, and J. M. Dickinson, *Trans. A.I.M.E.*, **200**, 915 (1954).
7. W. Rostoker and A. Yamamoto, *Trans. A.S.M.*, **46**, 1136 (1954).
8. M. Stern and C. R. Bishop, *ibid.*, **52**, 239 (1960).
9. F. A. Mauer, *Rev. Sci. Instr.*, **25**, 598 (1954).

Correction

Subject to the publication of the paper "Oxidation of Niobium in the Temperature Range 350°-750°C" by D. W. Aylmore, S. J. Gregg, and W. B. Jepson in the June 1960 issue of the Journal, the authors have been informed by Messrs. Murex Ltd. that the figure for the carbon content of the niobium (Batch A) was incorrectly quoted. The correct value is 0.01%.

Technical Notes

NMR Measurements of the Knight Shift in Conducting PbO_2

D. A. Frey and H. E. Weaver[1]

Instrument Division, Varian Associates, Palo Alto, California

According to the quantum mechanical model, nuclei possessing units of angular momenta and a nonzero magnetic moment are allowed only discrete orientations in an applied magnetic field. In the case of the Pb^{207} isotope where the nucleus has a spin of ½ units, there are two separate field-dependent energy levels. The energy of these levels is given by

$$E = \vec{\mu} \cdot \vec{H}$$

or

$$\nu = \gamma H_0 \text{ for the transition frequency,}$$

ν being the frequency, μ the magnetic moment, H the value of the magnetic field, and γ the gyromagnetic ratio for a given nucleus.

By varying the applied magnetic field, H, and simultaneously irradiating the sample containing the isotope under investigation with an oscillating magnetic field of frequency, ν, an NMR (nuclear magnetic resonance) absorption of energy from the rf-field may be detected when the value of the field-frequency satisfies the relation, $\nu = \gamma H_0$. NMR techniques have a wide range of application in the study of the molecular environment and its influence on the resonance character of the nuclei in an external magnetic field.

The effective magnetic field at the nucleus may differ from that of the applied field because of the influence of the external field on the environmental electrons of the nuclei, be they valence or conduction electrons. The magnitude and sign of the "chemical shifts" associated with a particular compound containing the resonating nucleus can easily be measured via the techniques of NMR. In the case of nuclei of high atomic number these relative shifts can amount to several per cent of the applied field (1). For conductors this "chemical shift" has the name Knight shift (1) after its discoverer.

Lead dioxide has long been known to be a conductor of electricity but until recently (2, 3) little quantitative data were available on its physical properties. In an earlier note Piette and Weaver (4) measured the resonance of Pb^{207} in PbO_2 and other lead compounds relative to that in the metal and found that the data were indeed consistent with the concept that PbO_2 does behave as a metal. Thomas (2) measured the conductivity and Hall coefficient for rather dense samples of PbO_2 and found that the carriers were electrons and that the temperature coefficient of conductivity is negative. Rüetschi, *et al.* (3) have measured the electrochemical properties of both α- (orthorhombic) and β- (tetragonal) forms of PbO_2. They have made extensive measurements on the effect of oxygen removal from PbO_2 on the electrical properties of both allotropic forms. It has been established that PbO_2 never has the stoichiometric composition, but rather shows an oxygen deficiency yielding a mixture with a formula more like $PbO_{1.98 \text{ to } 1.98}$. The lack of stoichiometric composition is generally felt to be the origin of the conductivity.

Lead dioxide is generally available in powder form with particle sizes of less than 1 μ. In this form it is ideally suited for NMR at 8 mc/sec and even EPR (electron paramagnetic resonance) at 9000 mc/sec, since the particles are smaller than the skin depth. Nuclear and electron resonance techniques are the "noncontacting" type, thereby requiring essentially no sample preparation and specifically no electroding.

Piette and Weaver (4) have measured the chemical shift of Pb^{207} in several representative lead compounds, in particular commercial PbO_2 (presumably β-form) relative to the resonance in lead metal. Rocard, *et al.* (5) reported later on a similar set of measurements, but with some variation in the Knight shift in PbO_2 compounds depending on the assay. They ascribed these differences to impurity content. Accordingly a series of experiments were designed to investigate the variation of the chemical shift (or Knight shift) of the Pb^{207} resonance in as many different forms of PbO_2 as were available. This note then deals exclusively with NMR and EPR measurements in PbO_2 and Pb metals.

Instrumentation

In those room-temperature measurements involving NMR a standard Varian V4200 wide line spectrometer was employed. A standard probe with the Dewar insert with associated transfer Dewar and heat exchanger were employed for measurements made at other than room temperature. By adjusting the flow rate of dry nitrogen gas, the temperature of the sample could be continuously varied from room temperature down to −185°C. For the EPR measurements a standard V4500 spectrometer plus cryogenic accessories were used. The magnet employed was V4012-3B with 2⅝ in. air gap with associated current stabilization.

[1] Present address: Physik-Institut Der Universität Zurich, Zurich, Switzerland. Dr. Weaver is on leave of absence from Varian Associates.

Table I. Summary of PbO_2 NMR measurements at room temperature

Compound	Knight shift	Relative intensity
β-PbO_2 B & A 95%	$0.58 \pm 0.02\%$	1.00
β-PbO_2 B & A 90%	$0.56 \pm 0.02\%$	0.52
β-PbO_2 E S B —	0.63 ± 0.02	0.67
β-PbO_2 N L Co.	$0.62 \pm 0.02\%$	0.55
α-PbO_2 E S B	0.48	—

Measurements

The NMR experiments performed fell into two major classifications: (i) room-temperature measurements as a function of sample preparation and crystal symmetry, (ii) measurement of the Knight shift as a function of temperature, and thermal decomposition of PbO_2 with increased temperature above 200°C. EPR experiments were designed merely to detect a resonance.

Nuclear magnetic resonance.—NMR measurements of the Knight shift relative to Pb metal were made on all available samples. Table I indicates that at least two separate shifts appear to have been observed for the β group and a third for the α sample. Since the Knight shift in the PbO_2 resonance is dependent on the density of conduction electrons near the top of the Fermi distribution, Knight shift values for these samples can be said to correspond qualitatively with their conduction properties. However, the mechanism by which conduction electrons are made available is not completely understood.

Oxygen deficiency rather than impurity content probably is responsible for the conduction electron density, hence the fluctuations among the β group. It is noteworthy that both the 90% and 95% B & A samples have approximately the same Knight shift (relative to the metal), while the ESB and NL Co. samples have considerably higher values.

To obtain further quantitative information, first moments indicative of the relative intensities were calculated from the resonance curves obtained from each of the β samples, normalizing the B & A 95% moment (or intensity) to one. In Fig. 1 (a-e) are shown typical traces of the lead resonance in various available forms of PbO_2. The signal-to-noise of ESB-α-PbO_2 (Fig. 1e) was particularly poor because of a small amount of sample. Microscopic examination of the samples at an optical magnification of 800 gave no conclusive information regarding the relative particle size which would affect the density of the sample and hence the signal-to-noise obtained from a given volume.

Variations in NMR Knight shift measurements were also used as an indication of the change in PbO_2 conductivity with thermal decomposition. Table II clearly shows a decrease in the Knight shift (or an increase in the shift relative to the metal) as the thermal decomposition progresses. This suggests that the compound goes through the transition from conductor to semiconductor before becoming an insulator in the form of PbO. It is interesting to note that further loss of oxygen (prior to an actual crystal phase change) does not improve the conduction properties, which at best is anomalous in light of the model proposed: *viz.*, it is just this initial oxygen deficiency that is responsible for the conductivity.

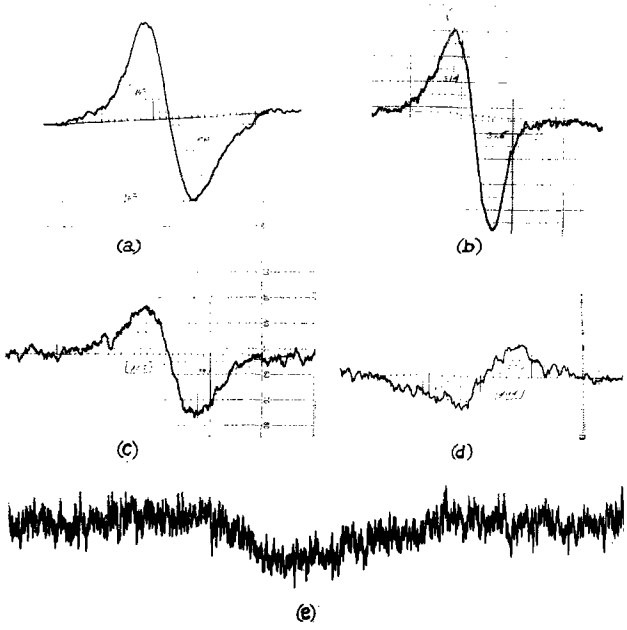

Fig. 1. Representative NMR traces of PbO_2 at 7.5 Mc/s. (a) B & A β—PbO_2 95%; gain x-10-2; (b) ESB β—PbO_2; gain x-10-3; (c) B & A β—PbO_2, 90%; gain x-10-3; (d) NL Co. β— PbO_2; gain x-10-4; (e) ESB α-PbO_2; gain x-10-4.

Electron paramagnetic resonance.—Since the particle size of the PbO_2 samples was less than the skin depth even at microwave frequencies it seemed worthwhile to investigate them for possible electron resonance. The resonance, if detected, could stem then either from paramagnetic impurity, presumably transition elements in a favorable environment, or from the conduction electrons themselves. Accordingly samples were prepared and a series of experiments were made from room temperature down to less than 2.0°K.

To date the results have been inconclusive. Lines which might be ascribed to the β-PbO_2 seem not to follow an expected pattern. Further, because of the excessive width of the observed resonance the amplitude is small and hence the attendant signal-to-noise is poor. The lack of a well-defined conduction electron resonance is not at all surprising in light of the proposed mechanism of oxygen deficiency to account for the conductivity. This model implies that there is a rather large concentration of "free" lead ions interstitially located in the regular PbO_2 lattice,

Table II. Summary of relative NMR shifts for heat-treated samples of β— B & A (95%) PbO_2

Temperature, °C	Shift* relative to untreated samples (gauss)
Room	0.0
200	—2.2
285	—6.5
330	—12.7
360	—15.3

* A negative shift implies a shift in the resonance toward higher fields.

and the presence of these "foreign" atoms could cause severe inhomogeneous temperature-independent broadening of the resonant line thereby making the resonance impossible to detect. Such seems to be the case. No resonance was detected in the lead metal powders.

Conductivity.—An experiment was performed with the low-temperature facilities at the Westinghouse Research Laboratories with β-PbO_2 commercial grade in an attempt to detect a superconducting transition. None was observed down to a temperature of 1°K (6).

Conclusion

From these data it is evident that the chemical shift associated with the resonance of Pb^{207} is indeed a Knight shift characteristic of a conductor. A series of controlled experiments measuring the NMR Knight shift relative to Pb metal as the oxygen-lead ratio is varied might well yield much more conclusive data.

Manuscript received May 11, 1960.

Any discussion of this paper will appear in a Discussion Section to be published in the June 1961 JOURNAL.

REFERENCES

1. For an excellent review of the technique of MNR see G. E. Pake, "Solid State Physics," Vol. II, p. 2, Academic Press Inc., New York (1956); W. D. Knight, *ibid.*, p. 93.
2. U. B. Thomas, *J. (and Trans) Electrochem. Soc.*, **94**, 42 (1948).
3. P. Rüetschi and B. D. Cahan, *This Journal*, **105**, 369 (1958).
4. L. Piette and H. Weaver, *J. Chem. Phys.*, **28**, 735 (1958).
5. J. Rocard, M. Bloom, and L. Robinson, *Can. J. Phys.*, **37**, 522 (1959).
6. P. C. Chester, Private communication.

Determination of the Standard Free Energy of Formation of Lead Selenide

Cabell B. Finch[1] and J. Bruce Wagner, Jr.

Department of Metallurgy, Yale University, New Haven, Connecticut

In conjunction with diffusion studies in this laboratory on the semiconducting compounds, PbS, PbSe, and PbTe, measurements have been carried out to determine the standard free energy of formation of lead selenide. Following the suggestions of Wagner (1-5), a galvanic cell involving a solid electrolyte

$$Pb(s) \mid PbCl_2 + 1\%\ KCl(s) \mid PbSe(s), Se(l) \qquad (I)$$

was used. The virtual cell reaction of cell (I) on passing two faradays is

$$Pb(s) + Se(l) = PbSe(s) \qquad [1]$$

The lead selenide was prepared by synthesis from its elements. Lead, 99.999% pure, was reacted with 99.99+% selenium by a method used for the synthesis of cuprous sulfide (4). The synthesized PbSe was mixed with an excess of the pure selenium and pressed into pellets at a pressure of about 350 kg/cm^2. The solid ionic electrolyte, $PbCl_2$ + 1% KCl, was prepared as described elsewhere (6) and pressed into pellets. Crucibles to contain the molten selenium coexisting with PbSe were made by drilling a hole in one side of the electrolyte pellet. The galvanic cell was assembled by placing a 99.999% lead pellet in a graphite crucible. The crucible of electrolyte which contained the PbSe pellet with excess selenium was placed on top of the lead pellet. Glass wool or asbestos was packed between the walls of the graphite and electrolyte crucibles in order to prevent vapor transport of selenium to the pure lead. A graphite electrode was placed in contact with the PbSe pellet and the entire cell was placed in a glass tube under argon as described in ref. (3).

A controller maintained the temperature better than ±1°C and the temperature was measured with a chromel-alumel thermocouple which was calibrated previously against the melting points of lead, zinc, and aluminum. The electromotive force measurements were consistent on increasing and decreasing the temperature between 200° and 300°C, and

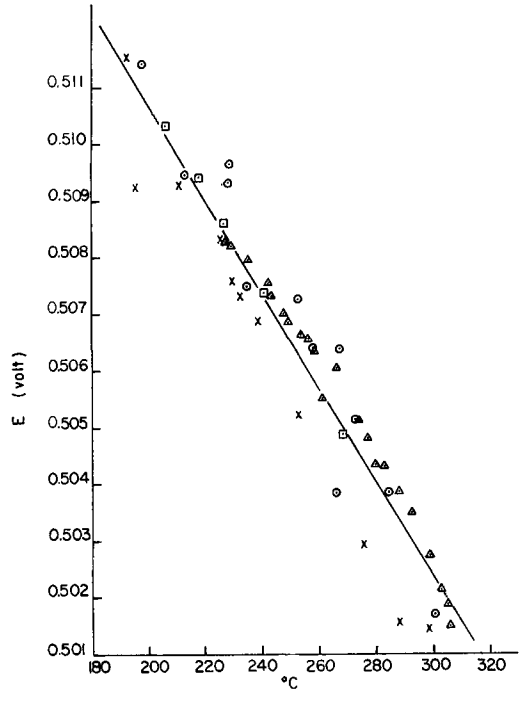

Fig. 1. EMF vs. temperature for the cell, Pb(s) | $PbCl_2$ + 1% KCl | PbSe(s), Se(l)

[1] Present address: Oak Ridge National Laboratory, Oak Ridge, Tenn.

the results of four separate experiments are shown in Fig. 1. Using a least squares analysis of all these data the standard free energy of formation of lead selenide in the range of 200° to 300°C may be expressed by the equation

$$\Delta G^\circ = -nFE = [-23{,}352 + 3.8(t - 250)] \text{ cal} \quad \text{(II)}$$

where **F** is the Faraday constant, E the electromotive force, and t the temperature in °C.

All but two of the emf data, one at the high temperature and one at the low temperature, lie between ±1.5 mv of the least square curve. This corresponds to ±69 cal in ΔG°. Thus with a temperature variation of ±1°C the total estimated accuracy is better than ±80 cal in ΔG°.

Below about 200°C, the attainment of steady values was very sluggish. Above about 300°C, the vapor pressure of selenium was sufficiently high that vapor transport sometimes caused contamination of the lead pellet. At the end of each experiment, the lead was examined for selenium contamination and any results obtained under these conditions were discarded. In addition, the higher temperatures favored plastic deformation of some of the cell components causing short circuits. Therefore the present measurements were restricted to the range of 200° to 300°C. The present value of the standard free energy of formation agrees well with unpublished data of Lorenz and Wagner (5).

Acknowledgment

The authors wish to thank Professor Carl Wagner for advice and the Office of Naval Research for financial support.

Manuscript received May 18, 1960.

Any discussion of this paper will appear in a Discussion Section to be published in the June 1961 JOURNAL.

REFERENCES

1. C. Wagner, Proc. of the Seventh Meeting of the International Committee of Electrochemical Thermodynamics and Kinetics, Lindau (1955), p. 361 [Published as a separate paper without changes in pagination by Butterworths Scientific Publications (1957)].
2. K. Kiukkola and C. Wagner, *This Journal*, **104**, 308 (1957).
3. K. Kiukkola and C. Wagner, *ibid.*, **104**, 379 (1957).
4. J. B. Wagner and C. Wagner, *J. Chem. Phys.*, **26**, 1602 (1957).
5. G. Lorenz and C. Wagner, Unpublished research at the Massachusetts Institute of Technology (1956).
6. J. B. Wagner and C. Wagner, *This Journal*, **104**, 509 (1957).

Microalloy Junction for Silicon

L. Maissel

Research Division, Philco Corporation, Philadelphia, Pennsylvania

The development of the germanium microalloy junction (1) brought about considerable improvement in the frequency response of transistors made by electrochemical techniques (2); its main features are high injection efficiency and very shallow depth of penetration (approximately 0.001 mil). It consists, basically, of an indium-gallium dot alloyed at as low a temperature as possible.

In searching for a similar contact for silicon it was first necessary to analyze the general requirements for a satisfactory microalloy junction. By definition, the metal used in forming the junction must be such as to dissolve only a small percentage of its own volume of semiconductor when alloying takes place. The metal semiconductor phase diagram should, therefore, be of the general form of Fig. 1.

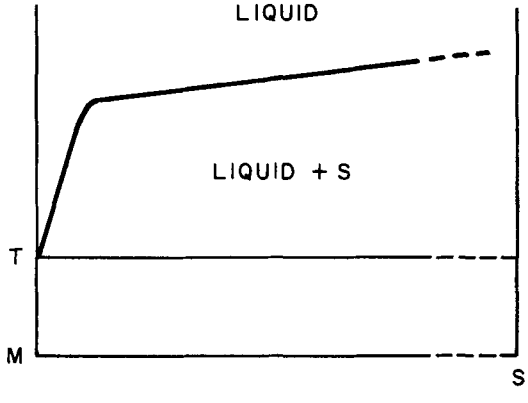

Fig. 1. Metal semiconductor phase diagram

In the case of germanium the metals that have this type of liquidus curve are indium, bismuth, lead, and gallium. Gallium cannot be used in practice because of its low melting point. Any of the other three would be suitable if it were not for the requirement that the microalloy junction must possess high injection efficiency as well as shallow penetration. This means that a small percentage of some suitable dopant must be included with the alloying metal. The only two dopants that are sufficiently soluble in germanium, to give a high injection efficiency junction, are aluminum and gallium. The former is, however, almost completely immiscible at all temperatures with all three of the possible alloying metals. Gallium is immiscible with bismuth and lead but, fortunately, not with indium. The indium-gallium combination is thus the only one suitable for a germanium microalloy[1] if alloying is allowed to proceed to equilibrium.

Similar reasoning applied to silicon indicates that either tin or antimony might be suitable metals for microalloying. The former, however, has shallow penetration only at relatively low temperatures (below 600°C) where dopant solid solubilities are also low. Antimony has shallow penetration below 800°C and has the additional advantage of also being a donor element with reasonable solid solubility in silicon at these temperatures.

Accordingly, an attempt was made to make an

[1] Microalloy junctions also can be formed by using a very rapid heating cycle, so that equilibrium and hence full penetration is not reached. However, it will be shown that nonequilibrium alloying is unsuitable for silicon.

alloyed junction of pure antimony in silicon. Initial attempts failed because of "balling up" of the antimony during alloying. That this was not surprising can be seen from the following considerations

If a given liquid is to wet a solid, it is a necessary (although not sufficient) condition that the surface tension of the solid must exceed that of the liquid. The surface tension of liquid antimony is approximately 350 dynes/cm; the values for solid silicon and solid silicon dioxide are approximately 600 dynes/cm and 300 dynes/cm, respectively (3). Thus the condition for antimony wetting is satisfied by silicon but not by its oxide. In view of the invariable presence of a thin oxide layer on the surface of silicon the net effect is that antimony will not wet silicon.

Since the surface tension of almost all liquid metals is greater than 300 dynes/cm it would seem that very few metals should ever wet silicon. However, the oxide film is generally of a porous nature so that metal and silicon are in fact in direct contact in a limited number of places. If the metal and the silicon have a eutectic reaction then, as long as the temperature is kept below the melting point of the pure metal (but above the eutectic point) fusion can begin in the regions of direct metal-to-silicon contact. The liquid so formed spreads out as it dissolves silicon so that the oxide film is undercut and, eventually, dislodged. In the absence of a eutectic reaction it should still be possible to promote wetting of the silicon by the metal provided the latter can be constrained from "balling up" long enough for the process of oxide film undercutting to become effective.

Direct mechanical constraint of the liquid antimony by suitable jigging was not considered feasible because of the extremely delicate nature of the electrochemically formed base region. Several other ways of achieving the required constraint were explored. Alloying was attempted in an oxidizing atmosphere in the hope that the skin of antimony oxide that formed prior to the melting of the antimony would be tough enough to hold it in position. Some success was obtained but results were not reproducible. A layer of refractory metal was tried in place of the oxide but this invariably broke contact with the silicon and simply floated on the surface of the antimony.

Alloying of antimony to silicon then was attempted by use of the technique of "dip alloying." The principle behind this method is as follows: suppose silicon, with a dot of plated antimony on its surface, is plunged into a fused salt bath. Provided the melting point of the bath is greater than that of antimony, the crust of salt that freezes on the surface of the cold silicon when it first enters the bath will still be solid when the antimony reaches its melting point. During the brief period before the crust remelts the antimony is thus constrained by a tough close-fitting jacket, so that wetting can occur by the mechanism discussed above. A number of salt baths were investigated for use in this connection and successful alloying of antimony to silicon was obtained in both KCl and KBr. Most compounds that were tried had to be rejected because they reacted with either antimony or silicon or both.

In order to establish that a true microalloy junction was being formed during dip-alloying, a number of test transistors were fabricated as follows: blanks of 5 ohm-cm p-type silicon were jet-etched to a thickness of approximately 0.4 mil. Dots of antimony 20 and 40 mils in diameter were then jet-plated onto opposite sides of the etch pit from an ethylene glycol solution containing 10 g SbF_3 and 60 g HF per liter. After dip-alloying in KCl for 30 sec at 800°C, units were rinsed in deionized water (to remove KCl) and were then clean-up etched. Whereas the antimony dots had shown only weak rectification before alloying, the alloyed units exhibited alpha-values of approximately 0.9. To measure the junction thickness, punch-through voltages before and after alloying were compared. These measurements showed the depth of penetration to be approximately 2×10^{-6} in., about twice that of a typical germanium microalloy junction. The feasibility of microalloying silicon was thus demonstrated.

Acknowledgments

The author wishes to thank Mr. V. C. Sirvydas for his assistance in the fabrication of the punch-through units.

Manuscript received April 11, 1960.

Any discussion of this paper will appear in a Discussion Section to be published in the June 1961 JOURNAL.

REFERENCES

1. A. D. Rittman, G. E. Messenger, R. A. Williams, and E. Zimmerman, *I.R.E. Trans.* on Electron Devices 49, April 1958.
2. J. W. Tiley and R. A. Williams, *Proc. I.R.E.*, **41**, 1706 (1953).
3. A. Bondi, *Chem. Rev.*, **52**, No. 2 (1953).

Electrolytic Production of Zirconium in a Fused Salt Voltaic Cell

Meyer L. Freedman

Refractory Metals Laboratory, General Electric Company, Cleveland, Ohio

The production of refractory metal powders by electrolysis of their compounds in molten salt solutions has been investigated intensively because of the valuable properties of high purity and coarsely crystalline form which may be obtained (1). The low oxygen, carbon, and nitrogen contents which can be achieved are particularly valuable for titanium, zirconium, boron, silicon, and beryllium, since these metals cannot be purified readily during processing. Also, because of their particle sizes, the electrolytically produced metal powders are consolidated more readily by conventional metallurgical processing than the metal sponges produced by chemical reduction. These advantages apply in part

alloyed junction of pure antimony in silicon. Initial attempts failed because of "balling up" of the antimony during alloying. That this was not surprising can be seen from the following considerations

If a given liquid is to wet a solid, it is a necessary (although not sufficient) condition that the surface tension of the solid must exceed that of the liquid. The surface tension of liquid antimony is approximately 350 dynes/cm; the values for solid silicon and solid silicon dioxide are approximately 600 dynes/cm and 300 dynes/cm, respectively (3). Thus the condition for antimony wetting is satisfied by silicon but not by its oxide. In view of the invariable presence of a thin oxide layer on the surface of silicon the net effect is that antimony will not wet silicon.

Since the surface tension of almost all liquid metals is greater than 300 dynes/cm it would seem that very few metals should ever wet silicon. However, the oxide film is generally of a porous nature so that metal and silicon are in fact in direct contact in a limited number of places. If the metal and the silicon have a eutectic reaction then, as long as the temperature is kept below the melting point of the pure metal (but above the eutectic point) fusion can begin in the regions of direct metal-to-silicon contact. The liquid so formed spreads out as it dissolves silicon so that the oxide film is undercut and, eventually, dislodged. In the absence of a eutectic reaction it should still be possible to promote wetting of the silicon by the metal provided the latter can be constrained from "balling up" long enough for the process of oxide film undercutting to become effective.

Direct mechanical constraint of the liquid antimony by suitable jigging was not considered feasible because of the extremely delicate nature of the electrochemically formed base region. Several other ways of achieving the required constraint were explored. Alloying was attempted in an oxidizing atmosphere in the hope that the skin of antimony oxide that formed prior to the melting of the antimony would be tough enough to hold it in position. Some success was obtained but results were not reproducible. A layer of refractory metal was tried in place of the oxide but this invariably broke contact with the silicon and simply floated on the surface of the antimony.

Alloying of antimony to silicon then was attempted by use of the technique of "dip alloying." The principle behind this method is as follows: suppose silicon, with a dot of plated antimony on its surface, is plunged into a fused salt bath. Provided the melting point of the bath is greater than that of antimony, the crust of salt that freezes on the surface of the cold silicon when it first enters the bath will still be solid when the antimony reaches its melting point. During the brief period before the crust remelts the antimony is thus constrained by a tough close-fitting jacket, so that wetting can occur by the mechanism discussed above. A number of salt baths were investigated for use in this connection and successful alloying of antimony to silicon was obtained in both KCl and KBr. Most compounds that were tried had to be rejected because they reacted with either antimony or silicon or both.

In order to establish that a true microalloy junction was being formed during dip-alloying, a number of test transistors were fabricated as follows: blanks of 5 ohm-cm p-type silicon were jet-etched to a thickness of approximately 0.4 mil. Dots of antimony 20 and 40 mils in diameter were then jet-plated onto opposite sides of the etch pit from an ethylene glycol solution containing 10 g SbF_3 and 60 g HF per liter. After dip-alloying in KCl for 30 sec at 800°C, units were rinsed in deionized water (to remove KCl) and were then clean-up etched. Whereas the antimony dots had shown only weak rectification before alloying, the alloyed units exhibited alpha-values of approximately 0.9. To measure the junction thickness, punch-through voltages before and after alloying were compared. These measurements showed the depth of penetration to be approximately 2×10^{-6} in., about twice that of a typical germanium microalloy junction. The feasibility of microalloying silicon was thus demonstrated.

Acknowledgments

The author wishes to thank Mr. V. C. Sirvydas for his assistance in the fabrication of the punch-through units.

Manuscript received April 11, 1960.

Any discussion of this paper will appear in a Discussion Section to be published in the June 1961 JOURNAL.

REFERENCES

1. A. D. Rittman, G. E. Messenger, R. A. Williams, and E. Zimmerman, *I.R.E. Trans.* on Electron Devices 49, April 1958.
2. J. W. Tiley and R. A. Williams, *Proc. I.R.E.*, **41**, 1706 (1953).
3. A. Bondi, *Chem. Rev.*, **52**, No. 2 (1953).

Electrolytic Production of Zirconium in a Fused Salt Voltaic Cell

Meyer L. Freedman

Refractory Metals Laboratory, General Electric Company, Cleveland, Ohio

The production of refractory metal powders by electrolysis of their compounds in molten salt solutions has been investigated intensively because of the valuable properties of high purity and coarsely crystalline form which may be obtained (1). The low oxygen, carbon, and nitrogen contents which can be achieved are particularly valuable for titanium, zirconium, boron, silicon, and beryllium, since these metals cannot be purified readily during processing. Also, because of their particle sizes, the electrolytically produced metal powders are consolidated more readily by conventional metallurgical processing than the metal sponges produced by chemical reduction. These advantages apply in part

also to vanadium, columbium, tantalum, chromium, molybdenum, and tungsten.

Electrolytic extraction has not been utilized more widely for the refractory metals because of problems inherent in the anode reactions. The anodic generation of corrosive gas at high temperature may require the use of graphite containers sometimes resulting in high maintenance costs (2). Anodic polarization effects may be troublesome especially with fluoride salts (3). The problems resulting from anode reactions can be largely eliminated by the use of soluble anodes (4). Cell corrosion and anode effects are avoided, but the process then becomes one of electrorefining rather than electrowinning.

Sodium metal can be used for obtaining all of the refractory metals as sponges or fine powder by high-temperature reduction of their appropriate compounds (5). The use of sodium metal as the soluble anode in a fused salt cell should eliminate corrosion problems while generating *in situ* the current required for effecting the cathodic reduction. Refractory metals could thus be produced with the desirable properties of electrolytic powders while avoiding the difficulties of fused salt electrolysis.

Production of metal powder by this voltaic cell action was observed while experimenting with the sodium reduction of K_2TaF_7. A nickel crucible was filled with a bottom layer of K_2TaF_7, a middle layer of NaCl-KCl eutectic, and a top layer of sodium metal. The layers were separated by porous diaphragms made from Monel screen. After melting under argon, large flakes and crystals of tantalum metal were found adhering to the lower diaphragm and to the crucible wall beneath the unreacted tantalum salts. Spectrographic analysis of the washed tantalum showed it to contain less than 0.01% of copper, iron, or nickel as major impurities. The metal flakes were soft, ductile, and easily compacted into mechanically strong pellets.

The voltaic cell metals extraction phenomena was investigated on a larger scale with the apparatus shown in Fig. 1. The 10 cm diameter stainless steel container was placed in a pot furnace. Vacuum drying of the loaded cell before melting was accomplished by the use of a steel cover and rubber gasket which rested on the flange. A charge of 650 g of equimolar C.P. NaCl-KCl provided a 6 cm layer of molten salt at 750°C. Access of air was prevented by a stream of argon. After melting the salt, the cathode was lowered to the cell bottom and 25 to 50 g of sodium metal was added to the cell by melting through a porous stainless steel filter to remove oxides. Five grams of vacuum dried technical grade K_2ZrF_6 was then added to the cathode chamber to give a concentration in the molten salt of about 3% by weight. Additional 5-g portions were added at 30-min intervals during the course of the reaction. At the conclusion of a run the cathode was raised slowly to permit drainage of molten salt and then cooled under argon in the upper chamber. The cathode was then dismantled and the zirconium crystals separated from adhering salts by boiling first with water and then with dilute HCl.

A number of cathode arrangements were tried. With a basket made of 40 mesh Monel screen, the zirconium deposited only on the cell bottom and baffle wall. Thick pads of zirconium crystals formed on both the inside and exterior of a hollow cathode made from perforated nickel foil. The cathode shown in Fig. 1 was constructed from a 5 cm diameter nickel tube which was perforated with two rows of closely spaced 0.6 cm holes. A porous nickel diaphragm covered these holes and was folded over the end of the tube to support a sheet nickel bottom plate. The diaphragm was made by filling the openings of 40 mesh Monel screen with a paste of nickel powder, drying, and sintering in hydrogen at 1100°C.

In one run, 40 g of K_2ZrF_6 was added over a 4-hr period and 11.5 g of washed zirconium crystals were obtained for a yield of 89%. The addition of 50 g of K_2ZrF_6 in 3 hr reduced the cathode yield to 80% of theoretical. The metal was deposited as a thick pad of dendritic crystals over the interior walls and bottom of the cathode. This permitted drainage of

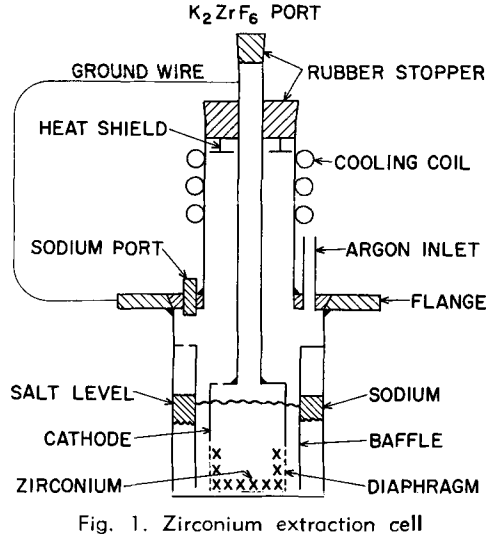

Fig. 1. Zirconium extraction cell

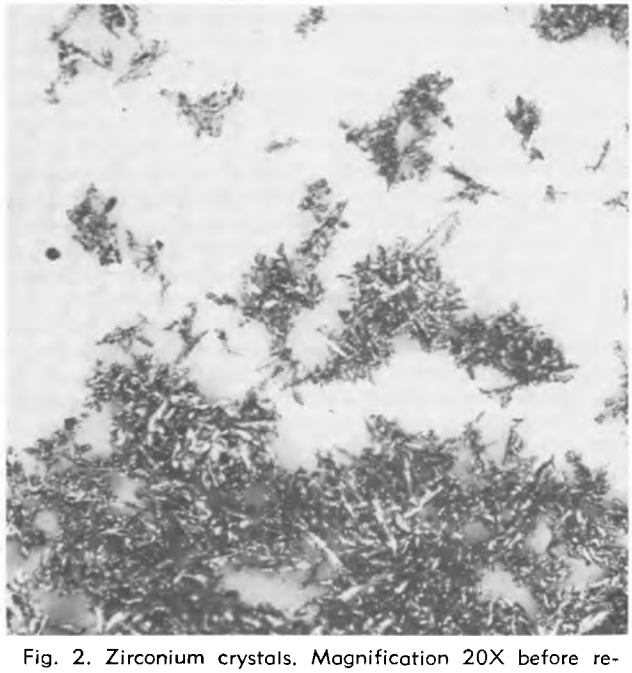

Fig. 2. Zirconium crystals. Magnification 20X before reduction for publication.

molten salts so that a weight of salt equal to only about twice that of the zirconium was retained by the cathode. The recovered metal powder was a silvery gray color with a bulk density of 0.9 g/cc. Figure 2 shows the dendritic form of these zirconium crystals. A 100 mesh screen retained approximately 50% so the average particle size was estimated as 150 μ. A qualitative spectrochemical analysis indicated only traces of iron and nickel impurities. While the particle size is similar to that reported for electrolytic zirconium (6) the dendritic form is more pronounced. Compaction to 80% of theoretical density was obtained on pressing at 50 tons/in.^{2}. The sample thus compares favorably in this respect to hydride zirconium powders (7). A Rockwell B hardness of 90 was determined on a pellet which had been further consolidated by electron beam melting. This value is well within the range for commercially pure zirconium.

The design of this experimental cell did not permit successful reuse of the salt charge. The zirconium obtained in the second run with the same salt bath was a mixture of dendritic crystals and fine black powder similar to the powder obtained by direct reduction of K_2ZrF_6 with sodium. During the time required for the removal of one cathode and the insertion of a second, atomic sodium had apparently diffused into the bulk of the molten salt. This then reacted directly with the K_2ZrF_6 as it was added to the new cathode. For continuous use of the salt bath, provision must thus be made for sealing off the sodium compartment between runs. Otherwise, a second porous diaphragm might be used to restrict the atomic diffusion of sodium while permitting ionic transport.

The anode slit height, fixed by the distance between the bottom of the baffle and the cell bottom, was also found to greatly influence the character of the extracted zirconium. A slit height of approximately 2 mm was generally used. A voltmeter connected in place of the ground wire then registered 0.6 v with the cathode raised slightly above the cell bottom during a run. When the anode slit height was increased to 5 mm the volt meter registered nearly zero. Zirconium was still deposited on the interior surface of the cathode in good yield. However, instead of dendritic crystals, the metal now consisted of irregular gray flakes having rough pebbled surfaces. The zirconium in this form prevented the drainage of molten salt from the cathode at the end of the run and was also difficult to wash free of salt. With the enlarged anode slit the concentration of atomic sodium in the molten salt adjacent to the cathode must have been nearly as high as the concentration within the sodium compartment. Under these conditions, the outer surface of the cathode itself would serve as the anode.

While fluoride salts were used in these experiments, the voltaic cell process should be more advantageous with a chloride feed. In the absence of fluorides, a porous ceramic diaphragm could be used to enclose the cathode volume while a porous metallic diaphragm would confine the sodium. Continuous operation could then be obtained with solid cathodes and molten NaCl.

Other methods have been reported for using molten inert salts in the production of refractory metal powders by sodium reduction. Thus, Vaughan partially submerges a metal grid in a fused salt bath containing a refractory metal halide and sprays sodium metal upon the grid (8). The sodium is claimed to wet the grid and to be carried along the grid surface beneath the melt where it reacts to form crystals of the refractory metal. Dean produces large crystals of refractory metals by reacting very dilute solutions of sodium and refractory metal halides in a molten salt medium (9).

Manuscript received May 25, 1960.

Any discussion of this paper will appear in a Discussion Section to be published in the June 1961 JOURNAL.

REFERENCES

1. G. L. Miller, Powder Metallurgy (1958) No. 1/2 p. 53.
2. G. T. Miller, *J. Electrochem. Soc.*, **106**, 815 (1959).
3. C. L. Mantell, "Industrial Electrochemistry," p. 477, McGraw-Hill Book Co., Inc., New York (1950).
4. R. S. Dean, "Electrolytic Titanium," Chicago Development Corp., Riverdale, Md. (1957).
5. M. Sittig, "Sodium," p. 230, Reinhold Publishing Corp., New York (1956).
6. M. A. Steinberg, M. E. Sibert, E. Wainer, *J. Electrochem. Soc.*, **101**, 63 (1954).
7. H. Hausner, Ed., "Powder Metallurgy in Nuclear Engineering," H. Hirsch, Chapter IV, p. 51, American Society for Metals, Cleveland, Ohio (1958).
8. J. L. Vaughan (To National Research Corp.) U. S. Pat. 2,847,298, Aug. 12, 1958.
9. R. S. Dean (To Chicago Development Corp.) U.S. Pat. 2,875,038, Feb. 24, 1959.

June 1961 Discussion Section

A Discussion Section, covering papers published in the July–December 1960 JOURNALS, is scheduled for publication in the June 1961 issue. Any discussion which did not reach the Editor in time for inclusion in the December 1960 Discussion Section will be included in the June 1961 issue.

Those who plan to contribute remarks for this Discussion Section should submit their comments or questions in triplicate to the Managing Editor of the JOURNAL, 1860 Broadway, New York 23, N. Y., *not later than March 1, 1960.* All discussion will be forwarded to the author(s) for reply before being printed in the JOURNAL.

Technical Feature

Fuel Cell Thermodynamics

Andre J. deBethune

Chemistry Department, Boston College, Chestnut Hill, Massachusetts

ABSTRACT

A simple fuel cell, operated reversibly, puts out, either electrochemically or in osmotic-mechanical form, an amount of useful work equal to the chemical potential (free enthalpy, Gibbs free energy) $-\Delta G$ released isothermally by the fuel plus oxygen upon their combination. This may be larger than the corresponding Carnot output $(-\Delta H)\,(T_h - T_l)/T_h$ of the same amount of fuel used to fire a reversible heat engine.

A coupled (regenerative) fuel cell regenerates the cell reagents by decomposing the reaction products at a high temperature (obtainable from a nuclear reactor). It thus acts as a heat engine in converting heat from the nuclear reactor into useful work. Its reversible work output, given by the summation of $-\Delta G$ for all isothermal steps, is exactly equal to that predicted from the heat inputs by Carnot's theorem in integral or differential form, for any fuel cell reaction, and for zero and finite values of ΔC_p for the cell reaction. The useful work output of an idealized practical irreversible fuel cell cycle is also given.

Simple Fuel Cell

A simple fuel cell (1) puts out directly and isothermally as useful work (2) the chemical potential released by a fuel (reductant) plus oxygen (oxidant) upon their conversion to combustion (reaction) products. If the cell operates electrochemically, the useful work output appears as electrical work, which is, under reversible conditions, equivalent to the charging up of a condenser. If the cell operates through semi-permeable membranes as an osmotic reaction engine, the useful work may appear in mechanical form, equivalent to the lifting up of weights (2, 3). Living systems function through the mechanism of osmotic membranes (4). The biological cell might therefore be described thermodynamically as an osmotic-mechanical fuel cell.

The maximum (reversible) useful work output $W_{u\,max}$ of the reaction

Fuel (reductant) + oxidant
= combustion (reaction) products [1]

conducted isothermally in a fuel cell, operating at a temperature T_f, is equal to the chemical potential (free enthalpy) released $-\Delta G_f$. In contrast, the same amount of fuel, firing a conventional power plant, yields a maximum useful work output equal to the heat (enthalpy) released $-\Delta H_h$ (at a high temperature T_h) multiplied by the Carnot efficiency $(T_h - T_l)/T_h$, where the low temperature T_l cannot ordinarily be less than ambient. The ratio of the first to the second of these work outputs, *i.e.*, the "fuel cell gain ratio," may be expressed in the form

$$\text{"Fuel Cell Gain Ratio"} = \frac{(-\Delta H_l) + T_f \Delta S_l - \int_l^f \Delta C_p\, dT + T_f \int_l^f \Delta C_p\, d\ln T}{(-\Delta H_l) - \int_l^h \Delta C_p\, dT} \cdot \frac{T_h}{T_h - T_l} \quad [2]$$

where h, f, and l refer to the temperatures T_h, T_f, and T_l, respectively, and the integrals contain summations of all enthalpies or entropies of transition that may be involved. In the special case where the reaction entropy ΔS_l and heat capacity ΔC_p are both zero, expression [2] shows that fuel cell operation permits a complete recovery of the reaction enthalpy drop $-\Delta H_l$ as useful work, without Carnot limitation.

Liebhafsky (1) discusses the thermodynamics of the reaction

$$H_2(g) + \tfrac{1}{2}O_2(g) = H_2O(g) \quad [3]$$

From his data and from Latimer (5), one can obtain the figures: $W_{u\,max}$(fuel cell) $= -\Delta G^\circ_{298} = 54{,}635$ cal per molal reaction unit at 298°K. By comparison, $W_{u\,max}$(power plant) $= -\Delta H^\circ_h (T_h - T_l)/T_h$. This has the values (taking $T_l = 298$°K)

T_h (°K)	400	500	1,000	2,000
$W_{u\,max}$ (power plant) (cal)	14,080	23,500	41,600	51,200

Thus the comparative advantage of the fuel cell is marked, especially at low temperatures, but tends to diminish, or even turn to a disadvantage, at

higher temperatures (1). The latter difficulty tends to arise especially for negative values of ΔS and ΔC_p, as shown by Eq. [2]. The simple fuel cell is free from the Carnot-efficiency limitation of the fuel-fired power plant, since it yields its work isothermally. The thermodynamic price paid, in either case, is the permanent conversion of a quantity of fuel to combustion products. The desirable thermodynamic properties for a simple fuel cell reaction are ΔG negative, ΔS zero or positive, ΔC_p zero or positive.

These thermodynamic properties are related to the reversible cell emf E as follows

$$-\Delta G = -\Delta H + T\Delta S = n\mathbf{F}E \qquad [4]$$

$$\Delta S = n\mathbf{F}(dE/dT) \qquad [5]$$

$$\Delta C_p = n\mathbf{F}T(d^2E/dT^2) \qquad [6]$$

These quantities can be evaluated from electrode potentials (5, 6), and from their temperature coefficients (6), and second temperature coefficients (7). An illustrative calculation is given below for reaction [3].

The following numbers give standard Gibbs-Stockholm (8) electrode potentials $V°$, and their first and second isothermal temperature coefficients (6, 7), for hydrogen and oxygen electrodes.

	$V°$, v	$(dV°/dT)_{isoth}$, mv/deg	$(d^2V°/dT^2)_{isoth}$, μv/deg^2
$H_2 = 2H^+ + 2E^-$	0.0000	0.000	0.000
$2H_2O(l) = O_2 + 4H^+ + 4E^-$	+1.229	−0.846	+0.552
$2H_2O(g) = O_2 + 4H^+ + 4E^-$	+1.185	−0.230	−0.173

For cell reaction [3], the above numbers yield $E° = 1.185$ v, $dE°/dT = -0.230$ mv/deg, and $d^2E°/dT^2 = -0.173$ μv/deg^2 at 25°C. The reaction entropy $\Delta S°$ is therefore $2\mathbf{F}(-0.230$ mv/deg$) = -10.6$ cal/deg, while $-\Delta G° = 2\mathbf{F}(1.185$ v$) = 2.370$ v$\mathbf{F} = 54.6$ kcal, and $-\Delta H° = -\Delta G° - T\Delta S° = 57.8$ kcal. The reaction heat capacity $\Delta C_p°$ is $2\mathbf{F}(298°\text{K})(-0.173$ μv/deg$^2) = -2.38$ cal/deg.

For a similar cell reaction with liquid water as the final product, $E° = 1.229$ v, $dE°/dT = -0.846$ mv/deg, and $d^2E°/dT^2 = +0.552$ μv/deg^2. The reaction entropy $\Delta S°$ is now $2\mathbf{F}(-0.846$ mv/deg$) = -39.0$ cal/deg, while $-\Delta G° = 2\mathbf{F}(1.229$ v$) = 56.7$ kcal, and $-\Delta H° = 68.3$ kcal. The reaction heat capacity $\Delta C_p°$ is now $2\mathbf{F}(298°\text{K})(+0.552$ μv/deg$^2) = +7.59$ cal/deg at 25°C.

Coupled (Regenerative) Fuel Cell

An electrochemical (or an osmotic-reaction) cell can be coupled with a high temperature source of heat (*e.g.*, a nuclear reactor) to decompose the combustion (reaction) products and regenerate the reactants of reaction [1]. Such a device is also termed a fuel cell (1), although in this case, cell reaction [1] no longer is the primary source of energy but is merely a step in a cycle that converts heat from the high temperature source into work. Such a coupled fuel cell is not ordinarily a simple Carnot cycle (*i.e.*, a cycle of two isothermals and two adiabatics), but if it is operated reversibly, it has a useful work output determined exactly by Carnot's theorem in either integral or differential form. This was proved to be true for the integral form by Liebhafsky (1) for the case where ΔC_p is zero. He also proved this to be approximately true, by a numerical example, for an idealized practical case in which only the heat exchanges during the warming-cooling portions of the cycle were allowed to be irreversible.[1]

For complete reversibility, the output of a regenerative fuel cell obeys Carnot's theorem in differential form exactly, even when ΔC_p is not zero. This can be proved by considering the following cycle of operations

$$\mathrm{M} + \mathrm{X} = \mathrm{MX} \text{ (at } T_l) \qquad [\mathrm{A}]$$

$$\mathrm{MX}(T_l) = \mathrm{MX}(T_h) \qquad [\mathrm{B}]$$

$$\mathrm{MX} = \mathrm{M} + \mathrm{X} \text{ (at } T_h) \qquad [\mathrm{C}]$$

$$\mathrm{M} + \mathrm{X}(T_h) = \mathrm{M} + \mathrm{X}(T_l) \qquad [\mathrm{D}]$$

All reactants and products are in their arbitrarily chosen standard states. All steps are completely reversible. Reaction A has a useful work output $W_{uA} = -\Delta G_A$. For a reversible reaction, the heat input $Q_A = T_l\Delta S_A$. The enthalpy change (2) is $\Delta H_A = Q_A - W_{uA}$. The thermodynamic properties of step A are summarized in Table I.

[1] Liebhafsky's efficiency of 73.3%, compared with a Carnot efficiency of 75%, should have been reported as 71.8%.

Table I. Thermodynamic properties of the four-step regenerative fuel cell cycle A-B-C-D

Step	ΔG	ΔH	ΔS	W_u	Q
A	ΔG_A	$T_l\Delta S_A + \Delta G_A$	ΔS_A	$-\Delta G_A$	$T_l\Delta S_A$
B and D combined	$\int_l^h \Delta C_p dT$ $-\Delta S_A(T_h - T_l)$ $-T_h\int_l^h \Delta C_p d\ln T$	$\int_l^h \Delta C_p dT$	$\int_l^h \Delta C_p d\ln T$	0	ΔH_{BD}
C	$-\Delta G_A$ $+\Delta S_A(T_h - T_l)$ $-\int_l^h \Delta C_p dT$ $+T_h\int_l^h \Delta C_p d\ln T$	$-\Delta H_A$ $-\int_l^h \Delta C_p dT$	$-\Delta S_A$ $-\int_l^h \Delta C_p d\ln T$	$-\Delta G_C$	$T_h\Delta S_C$
Cycle	0	0	0	$-\Delta G_A - \Delta G_C = -\Delta S_A(T_h - T_l)$ $+\int_l^h \Delta C_p dT - T_h\int_l^h \Delta C_p d\ln T$	

The heating and cooling steps B and D are in general not adiabatics, but they can be conducted as reversible heatings or coolings in the usual fashion, *i.e.*, by the conceptual use of an infinite number of heat reservoirs whose temperatures differ by intervals of dT. The heat absorbed in step B is then $\int_l^h C_p(\mathrm{MX})\,dT$, while the heat released in step D is $\int_h^l C_p(\mathrm{M}+\mathrm{X})\,dT$. Both integrals are understood to contain any heats of transition that may be involved. The net heat absorbed in heating and cooling combined is $\int_l^h \Delta C_p\,dT$ where $\Delta C_p = C_p(\mathrm{MX}) - C_p(\mathrm{M}) - C_p(\mathrm{X})$. At constant pressure, the useful work output is zero (2). The other thermodynamic properties of steps B and D combined are given in Table I, and all integrals are understood to contain summations of all enthalpies or entropies of transition.

At the high temperature T_h, the decomposition of MX, reaction C, has a further useful work output (which may in actual cases be negative, *e.g.*, as for an electrolytic decomposition and separation of M and X) equal to $-\Delta G_C$. The thermodynamic properties of step C are given in Table I.

For the whole cycle, the total useful work output, equal to the net heat input from all sources, is

$$W_u(\text{cycle}) = \oint dQ = -\Delta G_A - \Delta G_C$$
$$= -\Delta S_A(T_h - T_l) + \int_l^h \Delta C_p\,dT - T_h\int_l^h \Delta C_p\,d\ln T \quad [7]$$

According to Carnot's theorem in differential form, the useful work of the cycle should be given by

$$W_u(\text{cycle}) = \int_l^h dQ\,(T - T_l)/T \quad [8]$$

where dQ is an infinitesimal amount of heat received reversibly by the system from a heat reservoir at temperature T. Equation [8] can be expanded to give

$$W_u(\text{cycle}) = Q_C(T_h - T_l)/T_h + \int_l dQ_{B+D}\,(T - T_l)/T \quad [9]$$

where $dQ_{B+D} = \Delta C_p\,dT$. Evaluation of the two terms in Eq. [9] leads to the expression already given in Eq. [7]. Thus the work output of the cycle satisfies Carnot's theorem exactly, for a reversible operation throughout.

In practice, one of the chief sources of irreversibility in a regenerative fuel cell lies in the heat exchanges during heating and cooling (1). These can be minimized by having ΔC_p as close to zero as possible. The desirable thermodynamic properties for a regenerative fuel cell reaction are therefore

ΔG_A negative

ΔS_A negative

ΔC_p as close to zero as possible.

Finally, it is of interest to write expressions for the useful work output of a regenerative fuel cell cycle in which the two isothermal steps are reversible, while the heating and cooling steps are allowed to be irreversible. This is a much closer approximation to the actual situation for ΔC_p different from zero than the completely reversible cycle discussed above. From a consideration of the entropy-temperature diagram (9), it can be shown that this work is $S^*(T_h - T_l)$ where S^* is the quantity of entropy which falls reversibly through the temperature drop from T_h to T_l in driving forward the operation of one cycle. The useful work will therefore be $(-\Delta S_A)(T_h - T_l)$ or $\Delta S_C(T_h - T_l)$, whichever is smaller. For ΔC_p negative, the useful work output is

$$(-\Delta S_A)(T_h - T_l) = -\Delta G_A - \Delta G_C$$
$$-\{\int_l^h \Delta C_p\,dT - T_h\int_l^h \Delta C_p\,d\ln T\} \quad [10]$$

For ΔC_p positive, the useful work output is

$$\Delta S_C(T_h - T_l) = (-\Delta S_A - \int_l^h \Delta C_p\,d\ln T)(T_h - T_l) =$$
$$-\Delta G_A - \Delta G_C - \{\int_l^h \Delta C_p\,dT - T_l\int_l^h \Delta C_p\,d\ln T\} \quad [11]$$

In both Eq. [10] and [11], the expressions in braces represent the dissipated energy of the irreversible cycle, a quantity which is always positive.

Manuscript received Jan. 30, 1960.

Any discussion of this paper will appear in a Discussion Section to be published in the June 1961 JOURNAL.

REFERENCES

1. H. A. Liebhafsky, *This Journal*, **106**, 1068 (1959).
2. A. J. deBethune, *Ind. Eng. Chem.*, **50**, 129 (1958).
3. J. H. van'tHoff, *Z. physik. Chem.*, **1**, 481 (1887).
4. H. T. Clarke and D. Nachmansohn, "Ionic Transport across Membranes," Academic Press, New York (1954).
5. W. M. Latimer, "Oxidation Potentials—The Oxidation States of the Elements and their Potentials in Aqueous Solutions," 2nd ed., Prentice Hall, New York (1952).
6. A. J. deBethune, T. S. Licht, and N. Swendeman, *This Journal*, **106**, 616 (1959).
7. A. J. deBethune and G. R. Salvi, Unpublished results.
8. J. Willard Gibbs, "Equilibrium of Heterogeneous Substances (1875-1878)" in "Collected Works, Vol. I—Thermodynamics," pp. 332-349, Longmans Green, New York (1928); "Electrochemical Thermodynamics (1887)," *ibid.*, pp. 406-412; "On the Equations of Electric Motion (1899)," *ibid.*, p. 429. J. A. Christiansen and M. Pourbaix, Compt. Rend. 17th Conf. I.U.P.A.C. (Stockholm), pp. 82-84, Maison de la Chimie, Paris (1954). T. S. Licht and A. J. deBethune, *J. Chem. Educ.*, **34**, 433 (1957).
9. J. Willard Gibbs, "Graphical Methods in the Thermodynamics of Fluids (1873)" in "Collected Works, Vol. I—Thermodynamics," pp. 9-12, Longmans Green, New York (1928).

Diffusion Theory of Polarization and Recuperation Applied to the Manganese Dioxide Electrode

Allen B. Scott

Union Carbide Consumer Products Company, Parma, Ohio and

Department of Chemistry, Oregon State College, Corvallis, Oregon

ABSTRACT

The behavior of MnO_2 electrodes during and following cathodic discharge is accounted for on the basis of diffusion of the reduction product into the solid electrode. A solution of the diffusion equation predicts the general form of the discharge and recuperation curve satisfactorily. A method for determining the electrode surface area and diffusion coefficient is given and results of some preliminary experiments outlined.

Polarization and recuperation processes in oxide electrodes have received much attention in recent years, particularly those in manganese dioxide primary cell cathodes. Vosburgh (1) recently reviewed current theories of the MnO_2 electrode and has given a comprehensive bibliography. Of the mechanisms proposed, that which appears to have been originally advanced by Coleman (2) seems to have the greatest body of experimental and logical support, at least in the case of discharge at moderate current density in electrolytes having *p*H in the middle range. Coleman proposed that polarization and recuperation resulted from the accumulation of lower (hydrous) oxide on the surface and its subsequent diffusion into the solid MnO_2 and suggested that the diffusing entities were protons and electrons. He applied Fick's law to the process in order to find a relation between drain and capacity of actual electrodes; his development was complicated by allowance for the transport of the lower oxide by the electric field as well as by ordinary diffusion, although he recognized that only the latter might actually occur. Simple calculations given later show that transport by the field is insignificant. Easily available solutions for the diffusion equation, applied to a simplified model of the electrode, lead to equations for both polarization and recuperation well in accord with experiment.

Kozawa (3) reduced MnO_2 with a known amount of Mn^{++} ion and concluded that the lower oxide produced remained primarily on the surface, and that diffusion of the lower oxide into the MnO_2 was not of importance. However, his calculations were based on surface area measured by the BET method with nitrogen, and it is probable, as is shown later, that the surface presented to the electrolyte was smaller than the BET area by 5 to 10 times. In such a circumstance, the lower oxide comprised perhaps as much as the equivalent of 20 layers, and the samples were already in late stages of recuperation when potentials were measured.

The MnO_2 electrode is very nearly reversible to H^+ ion, its potential decreasing by about 0.06 v with a unit increase of *p*H. The primary electrochemical reaction for the electrode operated at moderate current densities is thus

$$MnO_2 + H^+ + e = MnOOH \qquad [1]$$

Mn^{++} is found in the electrolyte (4, 5) during discharge (except during early stages at pH > 7.5) but is undoubtedly produced by secondary chemical reactions. For example ΔF at 25°C for the consecutive reactions

$$MnOOH + H_2O = Mn^{+++} + 3OH^-$$
$$2Mn^{+++} + H_2O = Mn^{++} + MnO_2 + 4H^+$$

is -26.0 kcal at pH $= 7$ and Mn^{++} activity $= 0.01$, according to approximate data given by Latimer (6). Alternatively MnOOH may decompose in the solid state, ΔF° for the reaction

$$2MnOOH = Mn(OH)_2 + MnO_2$$

being estimated (6) at -10 kcal. $Mn(OH)_2$ would dissolve readily at *p*H $= 7$. Thus there appears to be no necessity to assume the reduction to divalent manganese as a primary step except perhaps at high current density or excessively low *p*H.

A complete theory of polarization and recuperation would have to take cognizance of a great variety of secondary reactions[1] as well as the role of carbon; for the present, it seems that more will be gained by restricting consideration to the process [1], polarization and recuperation occurring by the mechanism of Coleman.

Diffusion Theory of Polarization and Recuperation

The bobbin of a dry cell is a complicated electrochemical system, and for our purposes it will be preferable to simplify the arrangement of components to the following:

Carbon/Black/MnO_2/Solution

Conduction is entirely electronic in the carbon and the black, and almost entirely electronic in MnO_2, since MnO_2 has a conductivity between 0.1 and 0.01

[1] A theory of the effect of the removal of Mn^{++} from the electrode during discharge in acid electrolytes on polarization and recuperation has been developed by Yoshizawa and Vosburgh, (7).

ohm^{-1} cm^{-1} at room temperature (8) which certainly cannot arise from ionic migration. The electrochemical reaction, therefore, takes place at the MnO_2-solution interface. The field in the MnO_2 is very low; for example, at a current density of 1 ma cm^{-1}, taking the MnO_2 conductivity to be 0.01 ohm^{-1} cm^{-1}, the field is only 0.1 v cm^{-1}. This result shows that any migration of ions which occurs within the MnO_2 must take place as the result of chemical potential gradients rather than electric potential gradients. By comparison, if we assume unit activity coefficient, a change in mole fraction of MnOOH from 0.5 at the surface to 0.1 at a point 1 μ inside the surface of MnO_2 undergoing cathodic reduction results in a mean chemical potential gradient of 4 x 10^7 joule mole^{-1} cm^{-1}, which would exert the same effect as an electric field of 420 v cm^{-1}.

During discharge the following processes occur. Protons are transferred from solvent molecules to oxide ions on the MnO_2 surface under the influence of the negative potential of the cathode. At the same time, electrons are stably trapped on neighboring Mn^{+4} ions, reducing them to Mn^{+3}. The dilution of MnO_2 with MnOOH in the form of a solid solution reduces the MnO_2 activity and thus the electrode potential decreases as the reaction proceeds. Johnson and Vosburgh (9) studied the potential of electrodes made of mixtures of MnO_2 and MnOOH which were presumably allowed to come to equilibrium, 50 days being allowed for interdiffusion of the two solids, and found that the emf could be represented by

$$E = E^\circ + 0.073 \ln \frac{\text{mole \% } MnO_2}{\text{mole \% MnOOH}} \qquad [2]$$

at 25°C. The difference between the factor 0.073 and the theoretical value 0.059 is ascribed to the use of mole per cents rather than activities. E° varies with pH; the average at pH = 7.5 was found to be 0.416 v with respect to saturated calomel.

Recuperation consists of the diffusion of protons and electrons toward the interior under the driving force of the chemical potential gradient.

A quantitative theory for the polarization and recuperation can be obtained readily by the use of the foregoing model. Consider the MnO_2 to consist of a semi-infinite solid, bounded by the plane $x = 0$. The region $x < 0$ is occupied by solution. During discharge at constant current density, F_0 equivalents of MnOOH are produced per unit area per unit time. The diffusion problem can be solved by analogy to a problem in heat transfer, namely, the case of linear heat flow in a semi-infinite solid, initially at zero temperature, with a constant flux of heat across the boundary surface. Equations of interest in the present application, after throwing into a form suitable for mass transfer, are the following (10).

At $x = 0$, that is, on the surface of the MnO_2, the concentration of MnOOH as a function of time is

$$C = \frac{2F_0}{(D\pi)^{1/2}} \{t^{1/2} - (t-T)^{1/2}\} \qquad [3]$$

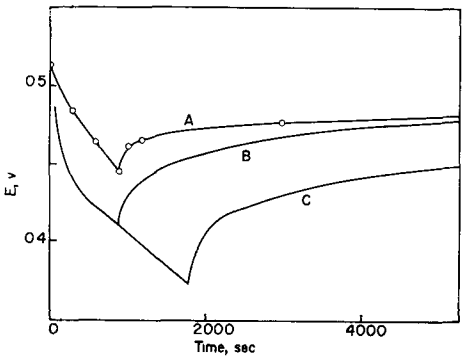

Fig. 1. Discharge and recuperation curves for the MnO_2 electrode. B, C, calculated; A, experimental (Ferrell and Vosburgh).

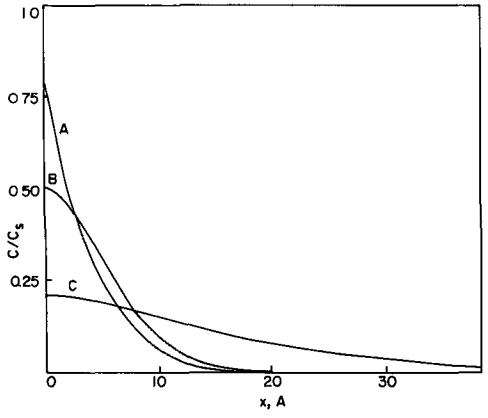

Fig. 2. Variation of MnOOH concentration with distance from surface. A, 1800 sec, discharged stopped; B, 2200 sec; C, 8200 sec.

and within the solid the concentration of MnOOH as a function of x, the distance from the surface, at any time t is

$$C = \frac{2F_0}{D^{1/2}} \left[t^{1/2} \left(\text{ierfc} \frac{x}{2(Dt)^{1/2}} \right) - (t-T)^{1/2} \left(\text{ierfc} \frac{x}{2D^{1/2}(t-T)^{1/2}} \right) \right] \qquad [4]$$

Here D is the diffusion coefficient for protons, accompanied by electrons, in the solid (assumed constant for the present), t is the time following start of the discharge, and T is the time at which the discharge stops and recuperation begins.[2] For $t<T$ the terms involving $t - T$ are to be taken as zero.

Using discharge and recovery curves such as those of Ferrell and Vosburgh (11) as a guide, the following values of the constants were arbitrarily assigned:

$F_0 = 1 \times 10^{-12}$ eq cm^{-2} sec^{-1} ($i = 9.5 \times 10^{-8}$ amp cm^{-2})

$D = 1.2 \times 10^{-18}$ cm^2 sec^{-1}

The concentration of MnOOH when pure, computed from the density, is 5.47 x 10^{-2} eq cm^{-3}. That of MnO_2 is 5.70 x 10^{-2} eq. cm^{-3}. The concentration of MnO_2 is given approximately by

$$C_{MnO_2} = 5.47 \times 10^{-2} - C_{MnOOH} \text{ eq cm}^{-3}$$

With these values and Eq. [2], [3], and [4], the curves of Fig. 1 and 2 were computed for discharge at pH = 7.5.

Figure 1 shows the variation in E with time for a discharge at current density 9.5 x 10^{-8} amp cm^{-2}, the

[2] ierfc (y) is defined by

$$\text{ierfc}(y) = \pi^{-1/2} \exp(-y^2) - 2y \pi^{-1/2} \int_y^\infty \exp(-z^2)\, dz.$$

discharge being discontinued at $T = 900$ sec and at $T = 1800$ sec. Recuperation occurs very rapidly on first stopping the discharge, but the rate of recuperation declines with time. Figure 2 shows the calculated distribution, as a function of the distance from the surface, of the MnOOH produced. Curve A represents the situation at the time of discontinuance of the discharge, curve B, 400 sec later, and curve C, 6400 sec later. It is evident that the surface was nearly saturated at 1800 sec, C_s indicating the concentration corresponding to pure MnOOH. In fact, from [3] it may be calculated that the surface would have been saturated after 2800 sec of continuous discharge.

Curve A of Fig. 2 shows clearly why the initial part of the recuperation is very rapid. The concentration gradient at the surface is extremely high during discharge; after the discharge stops the steep gradient at the surface is rapidly leveled (curve B), after which the potential rises much more slowly.

In Fig. 1 is also shown typical data of Ferrell and Vosburgh (11) for the discharge of an electrolytically deposited MnO_2 electrode at pH near 7.5, to be compared with the form of the calculated curve. The ordinates are not particularly significant, as the initial potential of MnO_2 is quite variable and further the choice of E° in Eq. [2] is somewhat arbitrary. Diffusion in the solid is seen to be adequate to account for the chief aspects of the discharge and recuperation.

It is to be noted that the slope of the calculated curve is greater than that of the observed curve after an extended period of recovery. This is almost certainly the result of assuming the solid to be semi-infinite. In the actual material composed of small, highly irregular particles, there will be many regions where advancing diffusion fronts will overlap, thus retarding diffusion.

There are two additional assumptions in the theory which require comment. First, it has been assumed that D is independent of C. It would appear, however, that D should be proportional to the concentration of unoccupied sites for protons, *i.e.*, proportional to C_{MnO_2}, and thus its variability would make itself felt wherever the concentration of MnOOH becomes large.

Second, the solid is not a continuous medium, and consequently the surface, instead of being a geometrical plane, is a region of finite thickness, namely about half the unit cell edge[3] (there being two MnO_2 formulas per cell). When D = 0 the rate of increase of concentration in the surface layer during discharge is not infinite, as given by Eq. [3], but is $F_0/1$ where 1 is the thickness of the surface layer. As D and t increase, the effects of the discontinuous structure diminish, and the surface concentration, instead of increasing linearly with time, becomes proportional to $t^{1/2}$.

If E is plotted against time for a constant-current discharge, the time required to saturate the surface with MnOOH, indicated by t_s, is located approxi-

[3] There is no unique way to compute the thickness of the surface layer of MnO_2, as this depends on the crystal plane assumed to lie parallel to the surface; further, the value would depend to some extent on the fraction of MnO_2 reduced to MnOOH.

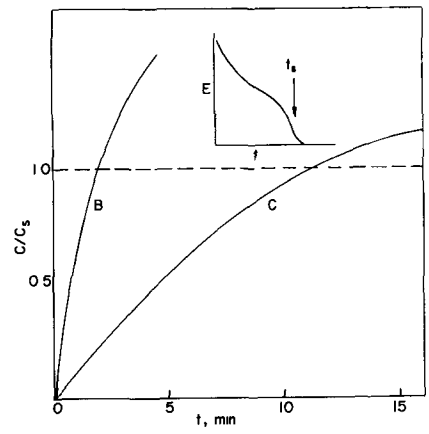

Fig. 3. Growth of MnOOH concentration at surface. A, location of t_s, the saturation time; B, t_s = 1.8 min; C, t_s = 11 min.

mately at the second inflection (inset, Fig. 3). If the discharge is very rapid,

$$C_s = \frac{F_0}{1} t_s \qquad [5]$$

In case the surface area of the oxide is unknown, F_0 may be determined in this manner, and from it, by use of the known current, the surface area may be found. Having the surface area, the oxide may be discharged at a lower rate, for which Eq. [3] may be expected to hold and

$$C_s = \frac{2F_0}{(D\pi)^{1/2}} t_s^{1/2} \qquad [6]$$

This provides a method for the measurement of D.

Experimental

To illustrate the application of the theory, some simple experiments were carried out. Using a modification of the Utilization Test (12) discharge tests were performed on electrolytic MnO_2 of surface area 63.9 m^2/g, determined by the BET method. Figure 4 shows the results of three such experiments. In an even layer against the face of a large graphite electrode, 0.706 g of MnO_2 was pressed. The electrode was made the cathode at a current of 200 ma, with an electrolyte of NH_4Cl and NH_3 at pH = 7.0 and a zinc anode. The potential of the cathode with respect to a saturated calomel electrode was measured by

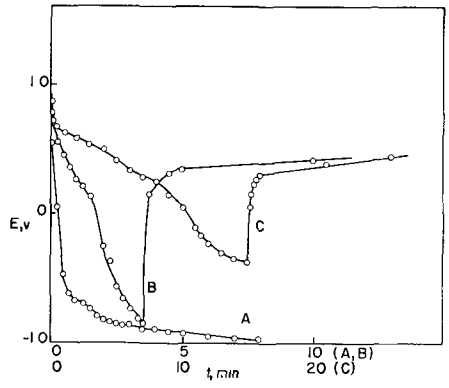

Fig. 4. Discharge of MnO_2. A, virgin sample, 200 ma; B, after recharging, discharged at 50 ma; C, after recharging, discharged at 10 ma.

means of a vacuum-tube voltmeter. An inflection at 1.8 min is barely discernible in curve A.

The oxide was then recharged, by making it the anode at 200 ma for 4 min, at 100 ma for 6 min, and allowing it to stand on open circuit until the voltage was steady. Upon cathodic discharge at 50 ma (curve B), the inflection was again observed at 1.8 min, but it was more pronounced. The polarization in the early part of the discharge was much diminished. At 3.5 min the current was discontinued and the recuperation was observed. Curve C was obtained, after again recharging the oxide, using a current of 10 ma.

Taking the thickness of the surface layer as one-half the mean unit cell edge for $\beta-MnO_2$, or 1.94Å, and assuming [5] to apply to the 50 ma discharge, $F_0 = 9.8 \times 10^{-12}$ eq cm^{-2} sec^{-1}, and the effective surface area is 5.4 m^2 or 7.7 m^2/g. This is only about 12% of the surface area measured by the BET method. As previously mentioned, this result has an important bearing on the experiments of Kozawa. D from [6] is 2.7×10^{-17} cm^2 sec^{-1}. This should be taken as a rough approximation only, on the basis of these preliminary experiments.

The effects of diffusion are apparent at 10 ma, where t_s is greater than 5 times t_s for the 50 ma discharge. A schematic plot of concentration at $x = 0$ *vs.* t is given in Fig. 3 for experiments B and C. It would assist in verifying the diffusion theory if further simple experiments of this kind were carried out to establish if $F_0 t_s^{1/2}$ were constant at higher values of $t_s^{1/2}$. The value of D could then be established.

The potential at t_s is not clearly defined. Equation [2] predicts a sigmoid discharge curve, E going to $-\infty$ at t_s; however, at $t > t_s$, E would be governed by a second relation involving MnOOH and $Mn(OH)_2$. Practically, E at t_s should be about that reported by Kozawa (3) for the Mn_2O_3 electrode, or 0.23 v with respect to the saturated calomel electrode. The observations reported here indicate that a large part of the polarization during the 200 ma discharge of the virgin MnO_2 was activation polarization. At the lower current densities, after recharging the oxide, E at t_s was still about 0.2 v less than that of the Mn_2O_3 electrode. Whether there is activation polarization under these conditions may be decided by means of an oscillographic method; however, previous results (1) make this appear unlikely. In any case, the choice of t_s is probably not much affected by the magnitude of E.

Acknowledgment

It is a pleasure to acknowledge the valuable contributions of G. E. Evans and J. A. Krumhansl who suggested the application of the physics of solids to the electrode process, of N. C. Cahoon and M. P. Korver who made available the utilization test equipment and provided much useful information concerning the theory of discharge and recuperation, and of D. R. Allenson and A. W. Smith with whom beneficial discussions were held.

Manuscript received April 5, 1960.

Any discussion of this paper will appear in a Discussion Section to be published in the June 1961 JOURNAL.

REFERENCES

1. W. C. Vosburgh, *This Journal*, **106**, 839 (1959).
2. J. J. Coleman, *Trans. Electrochem. Soc.*, **90**, 545 (1946).
3. A. Kozawa, *This Journal*, **106**, 79 (1959).
4. N. C. Cahoon, *ibid.*, **99**, 343 (1952).
5. A M. Chreitzberg, D. K. Allenson, and W. C. Vosburgh, *ibid.*, **102**, 557 (1955).
6. W. M. Latimer, "Oxidation Potentials," Prentice-Hall, New York (1952).
7. S. Yoshizawa and W. C. Vosburgh, *This Journal*, **104**, 339 (1957).
8. R. Glickman and C. K. Morehouse, *ibid.*, **103**, 149 (1956).
9. R. S. Johnson and W. C. Vosburgh, *ibid.*, **100**, 471 (1953).
10. H. S. Carslaw and J. C. Jaeger, "Conduction of Heat in Solids," p. 56, Oxford (1947).
11. D. T. Ferrell and W. C. Vosburgh, *This Journal*, **98**, 334 (1951).
12. N. C. Cahoon, *ibid.*, **99**, 343 (1952).

Aluminum Reactions with Water Vapor, Dry Oxygen, Moist Oxygen, and Moist Hydrogen between 500° and 625°C

P. E. Blackburn and E. A. Gulbransen

Chemistry Department, Research Laboratory, Westinghouse Electric Corporation, Pittsburgh, Pennsylvania

ABSTRACT

The rate of reaction between water vapor and aluminum is greater than that between the metal and oxygen. Mixtures of water vapor with either oxygen or hydrogen react with the metal at the same rate as does water vapor alone. Hydrogen blisters are formed in the metal in the presence of water vapor, but none is observed when water is absent. Blister formation in water vapor is not detected if the metal is first reacted with HCl solution.

Relatively little study has been given the reaction between water vapor and pure aluminum, although considerable research has been done on aluminum oxidation in air, oxygen, and liquid water. Oxidation of the metal in oxygen within the temperature range 350°-550°C was measured by Gulbransen and

Wysong (1). They found a parabolic rate from 350° to 475°C and a linear oxidation rate above this temperature region. Smeltzer (2) has measured oxygen reaction rates of metallographically polished and annealed aluminum between 400° and 600°C. He fitted his data to two parabolic rate constants which apply to thin and thick films. The oxide film was observed to grow very slowly above a weight gain of 35 to 40 $\mu g/cm^2$.

The barrier oxide thickness of films formed on aluminum in dry and moist atmospheres from room temperature to 600°C has been measured by Hunter and Fowle (3). Their method consisted of measuring the voltage necessary to produce normal leakage through the oxide film. The barrier oxide formed between 25° and 500°C was found to be amorphous, while a thicker crystalline film was discovered above 475°C. The thickness of each type of barrier oxide is a linear function of the temperature. For crystalline forms the thickness reaches 205Å at 600°, and for amorphous films it is 55Å at 500°. The oxide layer in excess of the barrier film is porous.

Plumb (4) has measured the specific surface area of aluminum with various surface preparations. The procedure required determining the thickness of a known amount of oxide deposited anodically on aluminum. The specific area relative to the apparent area decreased with oxide thickness. Surface roughness of 25 for rough abrasion, 6 for metallographic polish, 2 for chemical polish, and 2.5 for as-rolled samples were observed at oxide thicknesses of about 30Å.

Draley and Ruther (5) studied the reactions of both commercial 2 S aluminum and the pure metal with liquid and gaseous water. They have observed the presence of blisters in specimens oxidized in liquid water. Although these blisters usually contained corrosion products, some were found to be gas filled. Samples exposed to liquid water for two weeks at 290°C were completely destroyed. A cycle of decomposition resulted from water filling the blisters succeeded by further attack producing more blisters. Draley and Ruther have postulated a mechanism for blister formation. Briefly, protons from the reacting water diffuse through the oxide film to the metal, balancing the charge of aluminum cations moving to the gas-oxide interface. The protons are then reduced to hydrogen atoms, some of which diffuse into the metal where they combine in rifts and cavities to form hydrogen molecules. The molecular hydrogen pressure expands the soft metal, forming blisters. Vacuum fusion analyses of oxidized samples showed that the gas filling the blisters was hydrogen. It is proposed that impurities with low hydrogen overvoltage potentials catalyze the combination of hydrogen atoms within the metal. Alloys containing additions of such elements were found to resist water attack. It is suggested that these added materials catalyze formation of hydrogen molecules at the oxide metal interface. Hydrogen molecules cannot diffuse into the metal, since only atomic hydrogen is believed to diffuse.

Carlson (6) has found that intergranular attack of aluminum at 100°C is considerably less in hydrochloric acid than in distilled water.

Coriou, *et al.* (7) found that pure aluminum was severely corroded in liquid water above 200°C. Blisters formed in the pure aluminum resulted in an appreciable expansion of the metal. Practically all of the blisters were formed in grain boundaries since there was little change in the volume of aluminum single crystals.

The present research was proposed to study the reaction of aluminum in water vapor and in mixtures of water vapor with hydrogen or oxygen.

Experimental Procedure

Apparatus.—The apparatus used for this study consisted of a vacuum system made of Pyrex tubing and metal Alpert (8, 9) valves. The apparatus was evacuated with two-stage oil diffusion pumps separated from the "clean" system by crackers. A Bayard-Alpert (10) gauge and a mercury manometer, separated from the system by a null manometer, were used to measure pressures within the apparatus. Samples were heated inside a mullite furnace tube, which was sealed directly to the Pyrex system.

A Kanthal resistance furnace which heated the mullite tube was held to within ± 0.5°C by a L & N controller. Bake out ovens enclosed the system, permitting degassing or maintenance of temperature above the condensation point of water wapor.

An all-quartz microbalance was constructed of small rods. Sensitivity was increased by using a girder type beam which weighed less than half a gram. Fine quartz filaments, sealed directly to the beam and quartz frame, were employed in vertical suspension at the fulcrum and at each end of the beam. This balance had a sensitivity of 321 $\mu g/cm$ where the position of the beam could be read with a traveling microscope to ±0.0005 cm.

Gases.—Either spectroscopically pure oxygen obtained from Linde Air or tank hydrogen diffused through a palladium tube was admitted to a mixing bulb from which it could be added to the system as a

Table I. Spectrographic analysis of aluminum

Treatment	Cu	Fe	Mg	Mn	Si	Al
	parts per million					
Chemically polished	10	20	20	10	10	balance
Chemically polished and vacuum annealed	20	<10	20	10	10	balance
H_2O (blisters)	20	10	15	10	10	balance
H_2O and O_2 (blisters)	20	15	15	10	10	balance
H_2O and H_2 (blisters)	<20	<10	<10	<10	<10	balance
1M HCl-H_2O (no blisters)	20	10	10	10	10	balance

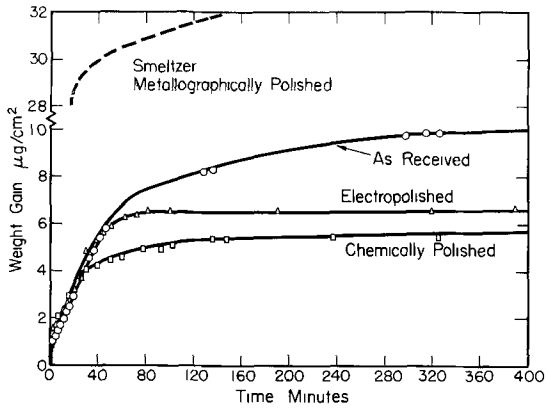

Fig. 1. Oxidation of vacuum annealed aluminum in 0.1 atm of oxygen at 600°C.

single component gas or mixed with water vapor. Water vapor was generated from a bulb of degassed distilled water.

Samples.—Two types of very pure rolled aluminum were kindly furnished by the Kingston Laboratories of Aluminium Limited. Table I compares spectrographic analyses of polished and annealed materials with those of reacted samples.

The effects of three types of surface treatment on oxidation behavior are compared in Fig. 1. The greater apparent oxide thicknesses formed on the "as-received" and on Smeltzer's metallographically polished sample are attributed to greater surface roughness for these samples (see Results and Discussion).

The electrochemical polish was carried out in a solution consisting of one part perchloric acid and 5 parts methanol at 10°C and 25 v. The chemical polishing solution was 6% nitric acid and 94% phosphoric acid, used at a temperature of 95°C. The sample was washed in 55°C distilled water. Oxidation behavior of the two specimens appeared to be similar. All of the remaining experiments were made with chemically polished samples.

Procedure.—The procedure consisted of suspending a polished specimen in the furnace tube from one end of the balance beam. After evacuating and degassing the system, the specimen was degassed and annealed at 600°C for one hour. The pressure in the system varied between 10^{-5} and 10^{-6} during the degassing treatment. The samples lost an average of 1 μg of gas per cm² during the annealing process. The furnace was adjusted to the desired temperature, gases were admitted from the mixing bulb, and the change in weight with time was observed.

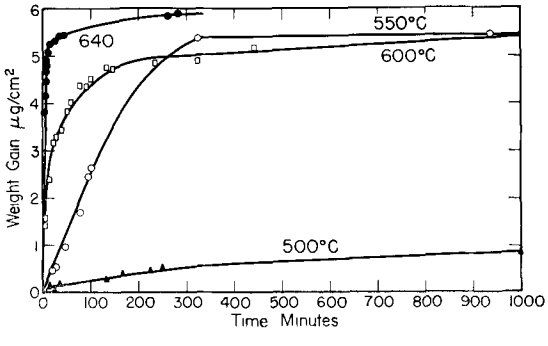

Fig. 2. Oxidation of aluminum in 0.1 atm O_2 between 500° and 640°C.

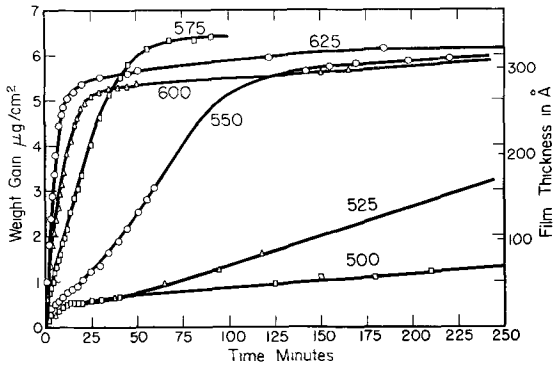

Fig. 3. Oxidation of aluminum in 0.1 atm water vapor

Results

Kinetics.—Figure 2 shows the weight gain *vs.* time curves obtained for samples oxidized in 0.1 atm of oxygen at 500, 550, 600, and 640°C. For the latter three temperatures the reaction consists of a relatively fast oxidation rate up to a weight of 5 to 6 μg/cm², where the rate becomes very slow. The 500° measurement was considerably slower than the higher temperature experiments. In these cases, as in the remainder of the kinetic studies, the data failed to conform to any of the theoretical curves, *i.e.*, linear, parabolic, cubic, logarithmic, or inverse logarithmic.

The oxidation of aluminum in 0.1 atm of water vapor for samples reacted at 25° intervals from 500° to 625°C is shown in Fig. 3. Here the extent of rapid oxidation is again between 5 and 6 μg/cm². No significance is attached to the apparently greater oxide thickness on the 575°C measurement. It is believed to be due to a larger surface roughness as a result of pitting during chemical polishing. After 24 hr the 500° measurement reached 6.0 μg/cm² while the 525° measurement was at 7.1 μg/cm². Assuming smooth surface and formation of Al_2O_3, the oxide depth is 53Å for each microgram of oxygen reacting per square centimeter. Film thicknesses based on these assumptions are given in Fig. 3. The slower rate then begins at about 300Å. However, Plumb has shown that chemically polished aluminum has a surface roughness of between 1.5 and 2.0, so the onset of the lower oxidation rate is actually between 170 and 220Å when the room temperature film of 20Å is added. Hunter and Fowle indicate that crystalline barrier films for aluminum oxide vary between 170 and 205Å over this temperature range. It is apparent that rapid oxidation ceases once the barrier oxide layer has formed. The lower rate is thus due to growth of a porous oxide over the barrier oxide. This mechanism applies to both oxygen and water vapor corrosion. The difference between this data and Smeltzer's may be attributed to a difference in surface roughness. According to Plumb the surface roughness of abraded samples may vary between 6 and 25, depending on the method and grit size used. Smeltzer's values for the extent of aluminum oxidation would fall in line

with a barrier oxide thickness of 200Å if average surface roughnesses of 8 to 10 are used for his specimens.

Apart from the extent of oxidation described above, other features of the kinetic curves are less readily explained. Between 575° and 625°C the rapid rate from 1 to 5 $\mu g/cm^2$ appears to be almost linear, whereas between 500° and 550°C there is an upward curvature. The latter effect is characteristically observed in nucleation and growth controlled reactions. The rate over the first 0.5 to 1 $\mu g/cm^2$ is seen to be much more rapid than the subsequent weight gain. In this region the amorphous barrier layer described by Hunter and Fowle may be formed. These authors observed that the amorphous layer grows much faster than the crystalline film.

Samples oxidized in oxygen and water vapor gave identical electron diffraction patterns, indicating that the reaction in water vapor above 500°C results in a nonhydrated oxide film. This is consistent with the thermodynamics of alumina hydrates, compounds which are unstable at these temperatures.

Blister formation.—All of the 10-mil samples oxidized in water vapor developed blisters within the metal large enough to form easily visible mounds on the surface. Blisters were formed either on grain boundaries or along lines parallel to the rolling direction. A photomicrograph of the surface of a sample oxidized in water vapor at 600°C clearly shows swellings on the grain boundaries (Fig. 4).

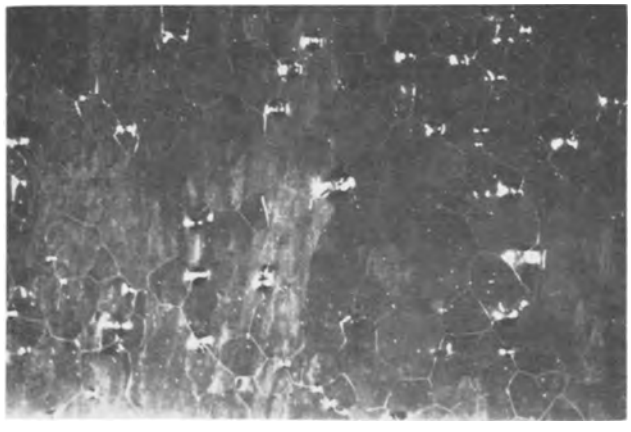

Fig. 4. Surface of aluminum oxidized in 0.1 atm water vapor at 600°C. Magnification 25X before reduction for publication.

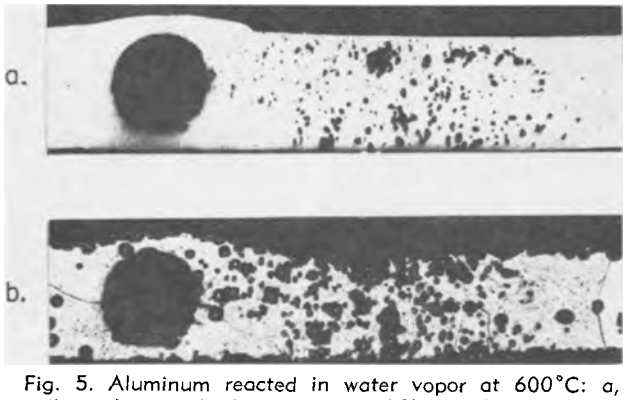

Fig. 5. Aluminum reacted in water vapor at 600°C: a, metallographic polish; b, etched in 10% HF. Magnification 100X before reduction for publication.

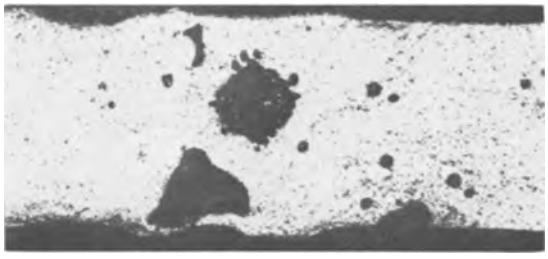

Fig. 6. Aluminum reacted in water vapor at 600°C, etched in 10% HF. Magnification 200X before reduction for publication.

No blisters formed on any of the samples oxidized in oxygen. Cross sections of water vapor samples (Fig. 5) show that, in addition to large blisters which swell the metal, there are many small cavities. Cross sections of as-received British specimens revealed the presence of small cavities and occasionally some large ones. It was observed that large cavities in water vapor reacted samples could be classified into two categories: (*a*) smooth walled blisters which swelled the metal, and (*b*) nondeforming cavities with walls constructed of a series of many small pits (Fig. 6). Since as-received specimens had both small cavities and the second type of large cavity, it was not possible to tell whether blisters appearing in the reacted specimens were already there or were increased by the reaction. The large smooth walled cavities resulted from the water vapor reaction since they were found only after samples had been oxidized in water vapor.

Although small blisters appear in as-received specimens, their presence in reacted samples occurs to a much greater extent. It would seem that small blisters, as well as large cavities, may form during the reaction.

The total hydrogen content of samples after reaction in water vapor (Table II) is less than 0.6% of the total weight gain, while the hydrogen content of water is 11% by weight. Thus, if the presence of hydrogen is due to reaction with water, only a small fraction of the available hydrogen enters the sample. Since the blister formation appears to be limited to impurity sites, either in grain boundaries

Table II. Gas analysis of aluminum vacuum fused at 700°C

Treatment	H_2	H_2O	CO and N_2	CH_4
	Moles/g of Al x 10^6			
As-received	1.13±0.08	0.011	0.025	0.025
Chemically polished	0.72±0.15	0.008	0.006	0.004
Annealed for 1 hr at 600°C	0.47±0.07	0.011	0.019	0.006
Oxidized in oxygen	0.40	0.011	0.038	0.013
Oxidized in water vapor	1.08±0.68	0.031	0.029	0.010
As-received*	1.21±0.25	—	0.027	0.063
Oxidized in moist air (blisters)*	1.26	—	0.043	0.035
Treated in HCl and oxidized in moist air (no blisters)*	0.35	—	0.036	0.017
Solubility at 600°C in 1 atm hydrogen	0.014			

* 40-mil French sheet; all others, 10-mil British sheet.

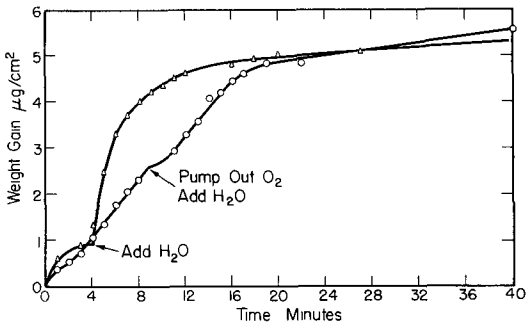

Fig. 7. Effect of oxide film on aluminum reaction at 600°C. △, sample A, very few blisters visible on surface; ○, sample B, one blister visible on surface.

or at inclusions, this low yield of hydrogen is not surprising.

The effect of an oxygen formed oxide layer on the water vapor reaction is shown in Fig. 7. Two samples were oxidized in oxygen; sample A for 3 min followed by addition of water vapor, sample B for 9 min followed by removal of oxygen and addition of water vapor. For the first case the reaction rate was sharply accelerated with addition of water vapor. In both cases the extent of oxidation was the same as in either water vapor or oxygen alone. The oxygen formed oxide layer appears to suppress formation of blisters which swell the metal, since there were very few in sample A and only one in sample B. There are two possible explanations for this finding. First, hydrogen may diffuse less readily through an oxygen formed film. Second, hydrogen pickup, which occurs simultaneously with formation of the oxide layer, is decreased in an amount proportional to the thickness of the oxygen formed film. The latter interpretation is derived from the fact that the total oxide thickness is the same whether it is formed in oxygen or in water vapor.

Before water vapor was added to these two specimens, 0.9 μg of oxygen per cm^2 reacted with sample A, and 2.5 μg of oxygen per cm^2 was taken up by sample B. If hydrogen pickup is proportional to the amount of oxide formed during the water vapor reaction, the second explanation implies that blisters would not be formed from hydrogen evolved from a μg/cm^2 oxygen pickup. Another water vapor sample was reacted until the weight gain reached 3.4 μg/cm^2. This specimen was covered with blisters somewhat smaller than those on samples oxidized

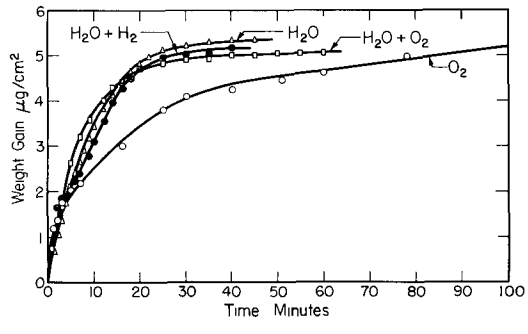

Fig. 8. Effect of corrosive atmosphere on aluminum oxidation rate at 600°C.

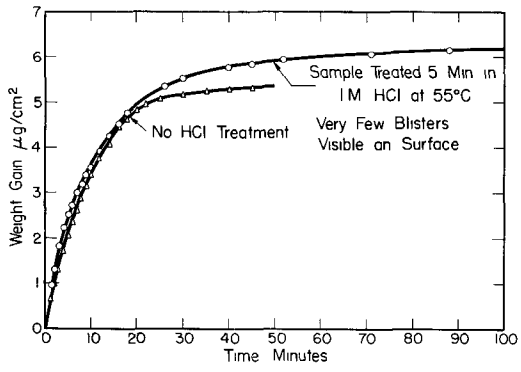

Fig. 9. Effect of treatment in HCl solution on aluminum water vapor reaction at 600°C.

to 5.5-6.0 μg/cm^2. Thus, the chief inhibitor of blister formation appears to be the resistance to hydrogen diffusion offered by oxygen formed oxide films.

The addition of oxygen or hydrogen to water before reacting it with aluminum made no apparent change in either reaction kinetics or blister formation. This is consistent with earlier observations (1) that the aluminum oxidation rate is independent of oxygen pressure. Here the oxygen partial pressure was varied between 10^{-1} and 10^{-24} atm. The rate of reaction in water vapor or in mixtures of water vapor with hydrogen or oxygen was about twice that in oxygen alone. Figure 8 presents reaction rates for samples oxidized at 600°C by the various treatments.

The suppression of intergranular attack by HCl additions to water, observed by Carlsen, was tested here. Samples were treated with HCl solutions at 55°C, washed in distilled water, annealed in vacuum, and reacted with water vapor. The kinetics of the reaction (Fig. 9) were the same as for samples without the HCl treatment, but no blisters were observed.

Table II shows the effect of HCl treatment on hydrogen content of French aluminum oxidized in moist air at 600°C. The hydrogen content of samples treated in HCl before reaction with water vapor is lower than any of the other samples tested. This is further evidence, although of a negative character, that the blisters are filled with hydrogen.

The role played by HCl in the suppression of blisters is not clearly understood from the available information. If impurities in the metal are important

Table III. Vaporization and solubility of chlorides

	Boiling point, (11) °C at 1 atm	Boiling point, (11) °C at 10^{-4} atm	Solubility, (12) g/100 g soln at 50°C
$AlCl_3$	447	142	32
Al_2Cl_6	180	77	—
$CuCl_2$	—	—	45
Cu_3Cl_3	1595	423	(1.5)
$FeCl_2$	1025	(512)	42
Fe_2Cl_6	319	172	76
$MgCl_2$	1418	677	37
$MnCl_2$	1190	562	50
$MnCl_3$	(627)	(262)	*
$SiCl_4$	57	—	*
Si_2Cl_6	139	—	*

* Unstable.

in the mechanism of blister growth, then treatment in HCl solution may result in removal of some of the impurities. This could occur either by solution of their chlorides during preparation or by vaporization of the chlorides during the degassing and annealing at 600°C. Table I gives results of spectroscopic analysis of samples following various reactions. The boiling points of the chlorides at 10^{-4} atm (10) and solubility of the chlorides in water (11) are found in Table III. There appears to be very little difference in the level of impurities in various samples. All the chlorides are water soluble, and iron, silicon, and aluminum chlorides have extremely high vapor pressures at the annealing and reaction temperature. Copper, magnesium, and manganese chlorides evaporate at a lower rate.

It is also possible that HCl suppresses blister formation by reacting with aluminum to form a chemisorbed layer of $AlCl_3$. Such a barrier may inhibit the diffusion of hydrogen.

Discussion

Since the as-received material held a considerable amount of hydrogen, the cause of the blisters is difficult to uncover. From Table II, however, it may be seen that a very low hydrogen content is found in chemically polished and vacuum annealed samples. The amount of hydrogen does not change with reaction in oxygen, whereas water vapor reaction significantly increases the hydrogen content. The rather wide scatter in these values is a function of sample size. Each specimen weighed about 0.3 g, and thus liberated only a few tenths of a microgram of gas for vacuum fusion analysis.

The data from this study are in general agreement with Draley and Ruther's experimental results. It may be noted that these earlier authors did not locate the blister with reference to grain boundaries. It is believed that their specimens came of material of much smaller grain size, making the relationship between grain boundaries and blisters obscure. Although these results appear to substantiate the Draley and Ruther theory, further work is necessary to clearly establish mechanism of blister formation.

Grace and Seybolt (13) studied the selective oxidation of aluminum in an iron-aluminum alloy between 700° and 900°C in hydrogen-water vapor mixtures. Since their study was on an alloy, their results are not applicable to our work on pure aluminum. In spite of this, there are some points which are worth mentioning. First, Grace and Seybolt made no correction for surface roughness, which could have been from 2 to 10. Second, they assume an initial weight gain of 2 to 3 $\mu g/cm^2$ (uncorrected surface area) during the first 15 min. In our work almost all of the oxide formed during the first 15 min at temperatures above 600°, *i.e.*, about 3.5 $\mu g/cm^2$ (area corrected for surface roughness). Third, Grace and Seybolt determined an oxygen pressure dependence by varying the water pressure in a constant pressure of hydrogen. This dependence was near the 1/7 power of water vapor-hydrogen ratio where H_2O/H_2 was varied by three orders of magnitude. In this study the oxygen pressure was varied by a factor of 10^{23} with no apparent change in the rate of aluminum oxidation. The suggestion may be made that the pressure dependence observed by Grace and Seybolt is due to the water vapor pressure and not to the H_2O/H_2 ratio.

The Grace and Seybolt study gives a much lower rate of reaction than that which one would find by extrapolation of this data to their temperature range. They also found parabolic oxidation which was not found here (with the possible exception of the initial 50Å film). In view of these differences it would appear that the selective oxidation of the iron-aluminum alloy cannot be treated as if it were aluminum alone oxidizing at a higher temperature.

Thermodynamic calculations were made for the 600°C reaction,

$$H_2O = H_2 + 1/2\ O_2 \qquad [1]$$

The minimum partial pressure of oxygen in water and hydrogen and the lowest partial pressure of hydrogen in water and oxygen may be computed for reaction [1]. The mixed gases each contained 0.1 atm of water with an equal amount of hydrogen or oxygen.

Although the thermodynamic oxygen pressure was varied from 10^{-1} to $10^{-24.9}$ atm and the thermodynamic hydrogen pressure was varied from $10^{-12.5}$ to 10^{-1} atm, there was no apparent change in either the kinetics of the oxide growth or the formation of hydrogen blisters.

These calculations indicate that the reaction rate is independent of oxygen partial pressure. Vacancy diffusion is therefore excluded as a rate-controlling mechanism both by the failure of the curves to obey the parabolic rate law and by the absence of pressure sensitivity.

Conclusions

Aluminum reacts rapidly with water vapor above 500°C to form a crystalline oxide layer about 200Å thick. The rate of reaction beyond this oxide thickness is extremely low. The mechanism of reaction is rather complex, involving the formation of a thin amorphous barrier layer which crystallizes and thickens. Inasmuch as the kinetic curves fail to fit theoretical curves it is not possible to determine the method of oxide formation. Hydrogen and oxygen additions to the water vapor appeared to have no effect on the kinetics.

Hydrogen-filled blisters formed in the metal along rolling lines and between grain boundaries when water vapor was present in the gas phase. Hydrogen or oxygen added to the water vapor had no effect on blister formation.

Acknowledgment

The authors are grateful to Professor Duval for his helpful suggestions, to W. M. Hickam for developing a microgas fusion analysis for use here, and to J. Senko for the spectroscopic analysis.

Manuscript received Dec. 21, 1959. This paper was prepared for delivery before the Ottawa Meeting, Sept. 28-Oct. 2, 1958. This study was supported by the U.S.A.E.C. under subcontract to Bettis Plant.

Any discussion of this paper will appear in a Discussion Section to be published in the June 1961 JOURNAL.

REFERENCES

1. E. A. Gulbransen and W. S. Wysong, *Phys. Coll. Chem.*, **51**, 1087 (1947).
2. W. W. Smeltzer, *This Journal*, **103**, 209 (1956).
3. M. S. Hunter and P. Fowle, *ibid.*, **103**, 482 (1956).
4. R. C. Plumb, *ibid.*, **105**, 502 (1958).
5. J. E. Draley and W. E. Ruther, "Experiments in Corrosion Mechanism: Aluminum at High Temperatures," ANL-5658, Apr. 1957; also J. E. Draley and W. E Ruther, *This Journal*, **104**, 329 (1957).
6. K. M. Carlsen, *ibid.*, **104**, 147 (1957).
7. H. Coriou, L. Grall, J. Hure, D. Lelong, and J. Herenguel, *Rev. Met.*, **53**, 775 (1956).
8. D. Alpert, *Rev. Sci. Instr.*, **22**, 536 (1951).
9. D. Alpert, C. G. Matland, and A. O. McCoubrey, *ibid.*, **22**, 370 (1951).
10. R. T. Bayard and D. Alpert, *ibid.*, **21**, 571 (1950).
11. L. L. Quill, "The Chemistry and Metallurgy of Miscellaneous Materials, Thermodynamics," pp. 196-207, McGraw-Hill Book Co., New York.
12. A. Seidell, "Solubilities of Inorganic and Metal Organic Compounds," D. Van Nostrand Co., Inc., New York (1940).
13. R. E. Grace and A. U. Seybolt, *This Journal*, **105**, 582 (1958).

Dissolution of Copper in Sulfuric Acid Solutions

D. P. Gregory[1] and A. C. Riddiford

Department of Chemistry, The University of Southampton, United Kingdom

ABSTRACT

When copper disks rotate in sulfuric acid solutions, the observed rate of dissolution is first order with respect to the concentration of dichromate ion used as a depolarizer. By studying the effect of temperature and stirring speed at high and low acid concentrations, the process is shown to be determined completely by the rate of transport of dichromate ion to the reacting surface. This has been confirmed by studying the effect of different surface preparations, by measuring the rate of reaction of brass and amalgamated copper with these solutions, and by comparing the observed values with the theoretical rates. The effect of blocking off progressively larger areas of the working surface is reported.

From a number of studies of the dissolution of copper in acid solutions containing a suitable depolarizer (1-12), it appears that in some cases the surface process is so slow that the observed rate is a measure of the dissolution process occurring at the interface, whereas in others the observed rate is determined partly or wholly by a transport process. It is difficult to draw any general conclusions concerning the conditions under which one might expect to be able to study the surface process itself inasmuch as some of the investigations were purely qualitative in nature, and most of the others were confined to very narrow ranges of experimental conditions; but the results as a whole do suggest that the extent to which transport processes obscure the surface reaction is governed by the *p*H of the solution and by the concentration and nature of the species used as a depolarizer.

Published results leave little doubt that varying the type of depolarizer used may have a very marked effect on the character of the dissolution process. In the case of molecular oxygen, for example, the recent, detailed study of the dissolution of polycrystalline copper in sulfuric acid solutions (12) has shown that the observed rate is free from any measure of transport control. At the other extreme, the work of King and his co-workers (5, 6, 8) and of Buben and Frank-Kamenetskii (9) makes it fairly certain that the rate of dissolution in acid solutions of ferric salts is controlled entirely by the rate of transport of ferric ion to the interface under the chosen experimental conditions. Intermediate between these extremes are cases where the observed rate is controlled jointly by both the surface process and a transport process, *e.g.*, the dissolution of copper cylinders in an acetate buffer containing *p*-benzoquinone (10).

Much less is known concerning the effect of varying the concentrations of acid and depolarizer. Van Name and Hill (2) studied the dissolution of a number of metals in sulfuric acid solutions containing either ferric alum or the dichromate ion as depolarizer, and in hydrochloric acid solutions containing ferric chloride. In each case, they studied the effect of varying the concentration of acid and concluded that, whereas the observed rate is purely transport controlled at high concentrations, there is a general tendency for the surface process to begin to affect the over-all rate as the concentration of acid is diminished. The work of Lu and Graydon (12) provides the only other study of the effect of *p*H on the rate of dissolution of copper. In this case, as mentioned above, sulfuric acid solutions containing molecular oxygen were used, and the observed rate is a measure of the dissolution process at the copper/solution interface. Varying the concentration of acid has very little effect on the rate as long as the acid is present in excess; above *p*H 1, however, the rate declines rapidly as the concentration

[1] Present address: "Shell" Research Ltd., Thornton Research Centre, Chester, U. K.

is decreased, probably as a result of film formation on the surface of the copper.

This investigation provides the only detailed information available concerning the effects of varying the concentration of the depolarizer and the temperature. The study of these effects demonstrated the absence of any measure of transport control and thus enabled Lu and Graydon to suggest a possible mechanism for the dissolution process when oxygen is used as a depolarizer. For this reason, however, it throws little light on the general problem of deciding the conditions under which one might expect to be able to study the surface process, and it therefore seemed desirable to make a detailed study of the effect of a different depolarizer on the rate of dissolution of copper in sulfuric acid solutions.

The dichromate ion was chosen since it appeared possible that the observed rate might be controlled jointly by the surface process and by one of the transport processes at low acid concentrations. From the results of Van Name and Hill (2), the observed rate is purely transport controlled at sulfuric acid concentrations of 0.25M and above, whereas King and Weidenhammer (5) have indicated that the rate of dissolution of copper in 0.1M acetic acid solutions may be controlled by a slow surface process when the concentration of dichromate ion is less than 0.1M. The present study has been made using the rotating disk system, and particular attention has been paid to experimental conditions for which the rates of the transport processes may be calculated (13, 14).

Experimental

The main features of the apparatus have been described elsewhere (14). Disks were cut from ANALAR grade copper foil (*ca.* 0.15 mm thick) and were fixed to a brass former with black wax as shown in Fig. 1. The brass former fitted closely over the end of the stirring shaft and was held in place by a locking pin. The exposed brass of the former and the upper surface of the disk were protected from attack by a coating of black wax applied in hot benzene solution. This was shown to be impervious to acid dichromate solutions. Mounting the disks in this way was found to be more satisfactory than the previous method whereby disks were cut from thick foil and mounted on metal or perspex studs (14). In addition to minimizing edge effects, a fresh disk could be used for each run, easing the task of securing a reproducible surface for processes which may not be entirely transport controlled.

Experimental solutions were warmed to the thermostat temperature and degassed before being transferred to the reaction vessel. In the vessel, a stream of nitrogen ($O_2 < 0.05\%$) was bubbled through the solution for at least 5 min to maintain it free from atmospheric oxygen. During this period, the disk was mounted on the stirring shaft and, with the motor running, a beaker containing a solution identical with that in the reaction vessel was brought up to immerse the disk. All bubbles were removed from the under surface, and the copper was subjected to a preliminary etch for 5 min ±5 sec in an attempt to secure a reproducible surface. On removal of the beaker, the motion of the disk threw off most of the adhering liquid. The disk then was immersed in the reaction vessel, the underside of the disk was inspected to ensure that no bubbles had been trapped, and the nitrogen delivery tube was raised above the surface of the solution to maintain a slight positive pressure of nitrogen within the vessel.

Samples were withdrawn at 5-min intervals, run into excess ferrous ammonium sulfate solution, and back-titrated with standard dichromate solution. At the end of the run, the disk was removed from the solution, washed, stripped from the former, and its mean diameter measured using vernier calipers. The unit rate constant, k_1, was evaluated graphically from the first order expression (14): $k_1 t = (2.303 \Sigma V. \Delta\log c)/A$, where t is the time in min, A is the apparent area of the underside of the disk, and $\Delta\log c$ denotes the difference in the logarithm of the concentration of dichromate, c, at the beginning and end of an interval during which the volume is V.

The following were chosen as standard conditions: a disk rotating at 146 rpm in a solution 1.0M in sulfuric acid and 3.0 x 10^{-2}M in potassium dichromate, at 25°. In most cases, runs were performed at least in duplicate for each set of experimental conditions, and standard runs were conducted at frequent intervals as a check. In general, the rate constants for any set of conditions seldom differed by more than 3%, and frequently agreed to within 1%. Figure 2 exemplifies the good first order plots obtained.

The diffusion coefficient of dichromate ion under various conditions and the kinematic viscosity of

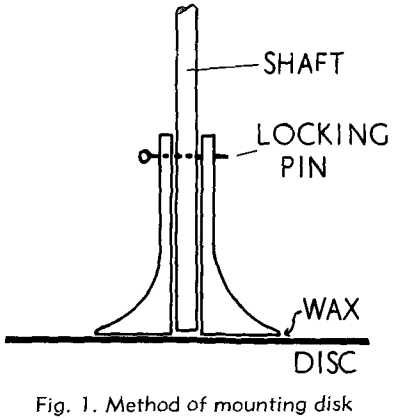

Fig. 1. Method of mounting disk

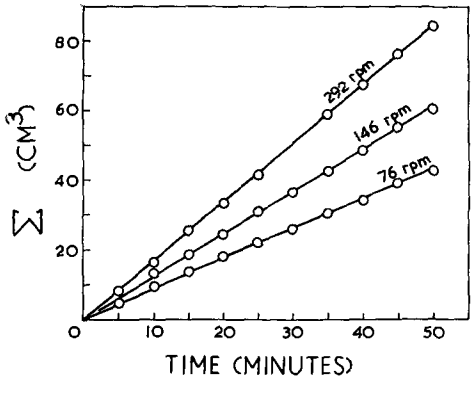

Fig. 2. Representative first order plots, 1.0M H_2SO_4, 3.0 x 10^{-2}M $K_2Cr_2O_7$, 25°.

Table I. Rate constants in 1.0M H_2SO_4 (146 rpm; 25°)

Initial conc. dichromate, M	k_1, cm min^{-1}	Mean k_1, cm min^{-1}
7.5×10^{-4}	0.137, 0.139, 0.137	0.138
1.5×10^{-3}	0.136, 0.136	0.136
3.0×10^{-3}	0.131, 0.128, 0.133, 0.132	0.131
6.0×10^{-3}	0.126, 0.124	0.125
1.2×10^{-2}	0.130, 0.137	0.134
1.5×10^{-2}	0.131, 0.130	0.131
1.8×10^{-2}	0.131	0.131
3.0×10^{-2}	0.132, 0.130, 0.129, 0.131	
	0.132	0.131

the solutions were determined by methods described elsewhere (14).

Results and Discussion

Solutions 1.0M in sulfuric acid.—When the ratio of the concentration of sulfuric acid to that of the dichromate ion is high, the rate of dissolution of copper is first order with respect to the concentration of dichromate ion. This is shown both by the linearity of the kinetic plots, examples of which are shown in Fig. 2, and by the fact that variation of the initial concentration of dichromate ion over a wide range is without significant effect upon the observed rate constant (Table I).

The extent to which the observed rate is governed by the transport of a solute species to the surface may be determined by comparing k_1, the observed unit rate constant, with k_T, the unit rate constant computed from the extended Levich theory (14). On this theory,

$$k_T = (0.554 D^{2/3} \nu^{-1/6} \omega^{1/2}) / [0.8934 + 0.316 (D/\nu)^{0.30}] \text{ cm sec}^{-1} \quad [1]$$

where D (cm^2 sec^{-1}) is the diffusion coefficient of the solute species, ν (cm^2 sec^{-1}) is the kinematic viscosity of the solution, and ω (rad. sec^{-1}) is the angular velocity of the disk.

Application of this equation to the experimental results shows that for solutions 1.0M in H_2SO_4 the observed rate is determined by the transport of dichromate to the copper surface. Thus, Fig. 3 shows the effect of varying the rate of stirring over the range 73-292 rpm for a solution 3.0 x 10^{-2}M in dichromate ion at 25°. The full line is the slope computed from Eq. [1] using the directly determined values $D_{25} = 9.07 \times 10^{-6}$ cm^2 sec^{-1} and $\nu_{25} = 1.01 \times 10^{-2}$ cm^2 sec^{-1}. Figure 4 shows the effect of varying the temperature between 15° and 45° for the same dichromate concentration, and a speed of 146 rpm. Again, the full line is the plot computed from the extended theory using the additional data $D_{45} = 1.39 \times 10^{-5}$ cm^2 sec^{-1} and $\nu_{45} = 6.83 \times 10^{-3}$ cm^2 sec^{-1}. In both cases, the theoretical slopes are slightly higher than the best straight lines through the points, but the deviation, which amounts to no more than 2%, lies within the limits of experimental error.

In confirmation of this conclusion that the surface process exerts no influence on the observed rate under these experimental conditions, supplementary experiments under the standard conditions showed that amalgamated copper disks (mean $k_1 = 0.133$ cm min^{-1}) and brass disks (mean $k_1 = 0.130$ cm min^{-1}) dissolve at the same rate as copper (mean $k_1 = 0.131$ cm min^{-1}).

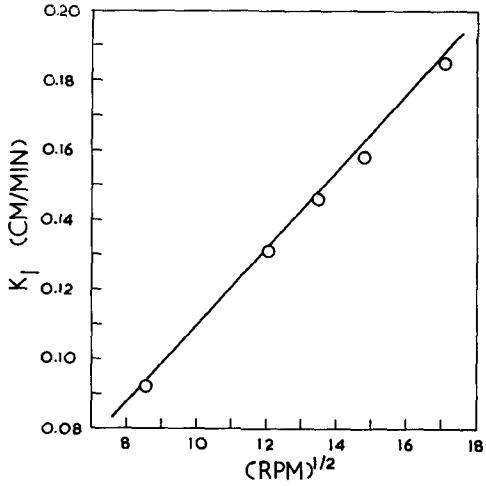

Fig. 3. Effect of stirring, 1.0M H_2SO_4, 3.0 x 10^{-2}M $K_2Cr_2O_7$, 25°.

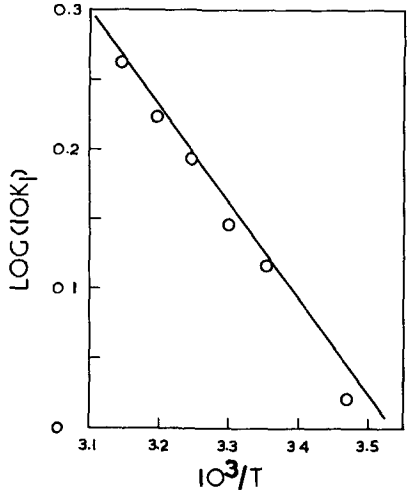

Fig. 4. Temperature coefficient, 1.0M H_2SO_4, 3.0 x 10^{-2}M $K_2Cr_2O_7$, 146 rpm.

Interesting results were obtained when the dependence of the observed rate on the method of preparation of the copper surface was studied. It has been suggested (13, 15) that roughening the surface should be without effect on the rate of transport controlled processes provided that the degree of roughening is not so large that the critical Reynolds number for the onset of turbulence is exceeded, whereas the rate of processes controlled by the surface reaction should increase. To test this suggestion, copper disks were coated cathodically with a spongy copper deposit and others were cut from a sheet of copper which had been ground with 100 grade carborundum powder. Under standard conditions, rather poor reproducibility was obtained for runs using the plated disks, probably because of the difficulty experienced in coating the upper surface and edges of the disk with black wax. The plated surface was so porous that the wax tended to be absorbed and to run over onto the lower working surface. Nevertheless, the observed rate constants ($k_1 = 0.128$, 0.132, 0.136 cm min^{-1}) are in fair agreement with the standard value. In the case of the

ground surfaces, however, the first order plots showed a high initial rate, which decreased with time and finally settled down to the standard rate.

A change from a high initial rate to a lower rate is sometimes due to a shift from transport control toward control by the surface process. In the present case, however, the lower (standard) rate is in excellent agreement with the theoretical value computed from Eq. [1], so that another explanation must be sought. It is possible that the irregularities produced on the surface by the carborundum treatment set up a small degree of local turbulence with a corresponding increase in the initial rate. Bircumshaw and Riddiford (15) reported a marked increase in the rate of dissolution of zinc in iodine solutions when jewellers rouge, used as a polishing agent, was embedded in the metal surface. Again, there was no question of control by the surface process. King (16) has reviewed other studies in which enhanced transport controlled rates have been found for roughened or etched surfaces.

In the present system, a similar effect was noted when small gas bubbles were inadvertently trapped on the underside of the disk. As in the case of bubbles trapped under zinc disks rotating in iodine solutions (14), the observed rates were higher than the standard value. Examination of the disks after withdrawal from the reaction vessel showed markings following the fluid flow lines at the surface of the disk (13) and resembling the tracks made by drops of liquid on a rotating disk (17). Microscopic examination of the marking caused by one such bubble, or surface obstruction, is shown in Fig. 5. It will be seen that a trough has been etched around the protected part of the copper surface, penetrating the 0.15 mm thick disk in one place, and along a "tail" following the flow line. The trough is very much larger than the surface obstruction and, if due to local turbulence, is certain to increase the observed rate.

The initial concentration of acid.—The effect of varying the initial concentration of acid over the range 0.01-1.53M was studied at 146 rpm and 25°

Fig. 5. Enlargement of marking caused by surface obstruction. Magnification 30X before reduction for publication.

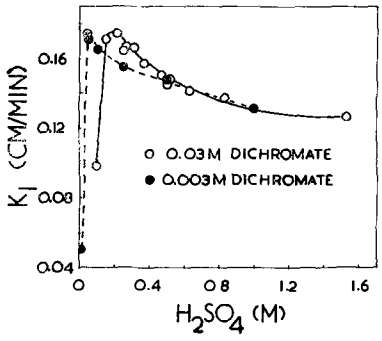

Fig. 6. Dependence on concentration of acid, 25°, 146 rpm

for both low (3×10^{-3}M) and high (3×10^{-2}M) dichromate concentrations. The mean values of k_1 are shown in Fig. 6, and it will be seen that the concentration of dichromate ion is without effect provided that the acid concentration is greater than *ca.* 0.5M.

At very low acid concentrations, there is a marked decrease in the rate. The first order kinetic plots were no longer linear, and the rate constants were estimated from the initial slopes. Acid-soluble films were formed on the disks, suggesting acid "starvation" under these conditions. From the stoichiometry of the over-all reaction, the acid, expressed as moles H_2SO_4, is consumed at a rate seven times faster than the rate at which dichromate ion is reduced. Dissolution in any solution for which the initial acid/dichromate ratio is less than 7 will be hindered eventually by a shortage of acid; on the other hand, if the initial ratio is greater than 7, this trouble will not be experienced. In the present case, an initial ratio of 7 corresponds to 0.2M H_2SO_4 for the high, and 0.02M H_2SO_4 for the low dichromate concentrations. The actual breakdowns occur in these regions (see Fig. 6). No further study of this region was made, since more interest attached to the reason for the divergence of the curves at moderate acid concentrations.

When the initial acid concentration is 0.25M, the divergence is very marked, although there can be no question of a deficiency of acid in the sense dis-

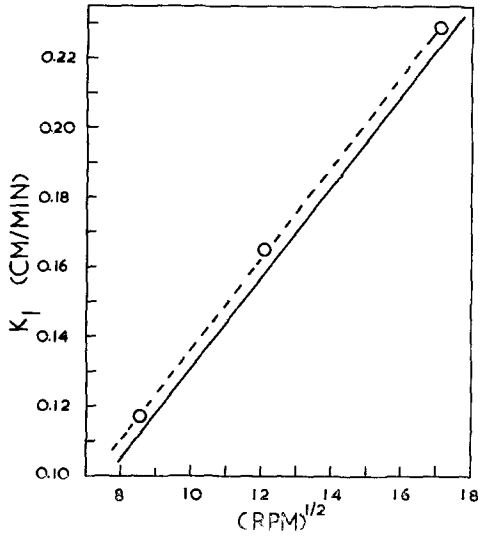

Fig. 7. Effect of stirring, 0.25M H_2SO_4, 3.0×10^{-2}M $K_2Cr_2O_7$, 25°.

cussed above. A brief study of the effect of stirring speed was made for this acid concentration using 3 x 10^{-2}M dichromate, and the results are shown in Fig. 7. The mean value of the observed rate constant is accurately proportional to the square root of the stirring speed, showing that under these conditions the process is also transport controlled. Consideration of Eq. [1] shows, however, that another factor is now influencing the rate. The determined values for the diffusion coefficient of dichromate ion at 3.0 x 10^{-2}M and 3.0 x 10^{-3}M, respectively, are identical within the limits of experimental error (D_{25} = 1.16 x 10^{-5} cm^2 sec^{-1}) for this acid concentration and lead to theoretical values for k_T at 146 rpm of, respectively, 0.158 and 0.157 cm min^{-1}. This is in good agreement with the observed value (0.155 cm min^{-1}) for the lower dichromate concentration. The observed value for the higher dichromate concentration (0.165 cm min^{-1}) is distinctly higher than the theoretical value, as indeed are the observed values at other stirring speeds. The full line in Fig. 7 indicates the theoretical slope computed from Eq. [1].

Since Eq. [1] predicts the maximum rate at which dichromate ions can be transported to the surface by the combined effect of diffusion and convection, it must be assumed that, at 3.0 x 10^{-2}M dichromate concentration, the transport process has been speeded up in some way; a shift toward control by the surface process would be marked by a decrease in the observed rate.

In general, ions may be transported to a surface in three ways, by diffusion, convection, and by migration under the influence of an electrical potential gradient (18). At high acid concentrations, when the relative concentration of dichromate ion is small, ionic migration will be negligible, and Eq. [1] will be applicable. If there is insufficient acid or foreign ions to suppress ionic migration through the electrical double layer, however, the rate of transport of dichromate ion will be increased. To check this explanation and to eliminate the effect, a series of runs were conducted using solutions to which sodium sulfate had been added.

Effect of adding sodium sulfate.—The initial concentration of sulfuric acid was varied over the range 0.1 to 1.0M. For runs in which the initial acid concentration was less than 1.0M, sodium sulfate was added to bring the total concentration of sulfate and bisulfate ions to 1.0M. In each case, the initial concentration of dichromate ion was 3.0 x 10^{-2}M, and the runs were performed at 25° and 146 rpm. The mean values of the observed rate constant are shown in Fig. 8, which may be compared with Fig. 6.

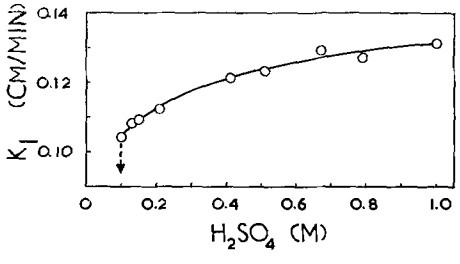

Fig. 8. Dependence of rate on concentration of acid, with added Na_2SO_4, 3.0 10^{-2}M $K_2Cr_2O_7$, 25°, 146 rpm.

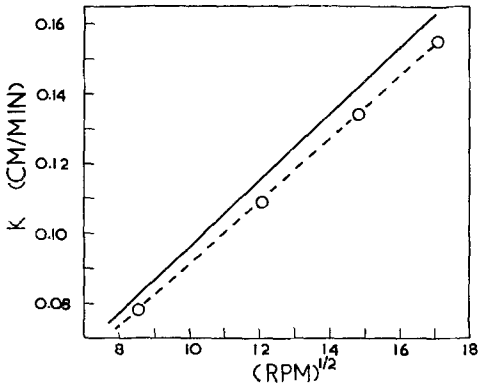

Fig. 9. Effect of stirring, 0.15 H_2SO_4, 0.85M Na_2SO_4, 3.0 x 10^{-2}M $K_2Cr_2O_7$, 25°.

The marked fall-off at very low acid concentrations is still observed, but the general trend now has altered. The observed rate constant now decreases with decreasing acid concentration due to the marked increase in the kinematic viscosity of the solution.

It is of particular interest to note that the value for a solution 0.21M in sulfuric acid and 0.79M in sodium sulfate (k_1 = 0.112 cm min^{-1}) is the same as that found for runs under the same conditions except that the initial concentration of dichromate was 3.0 x 10^{-3}M, *i.e.*, the divergence apparent in Fig. 6 has been eliminated by the added electrolyte. The observed value is, however, distinctly lower than that predicted by Eq. [1].

Since the addition of sodium sulfate increases the viscosity of the solution, the rate of the transport process is retarded, so that a shift toward surface control may be ruled out. The reason for the discrepancy between the observed and computed values may be traced to the fact that Eq. [1] is limited to the case of electrolyte solutions containing not more than three ion species.[2] In the absence of sodium sulfate, and with sufficiently high acid/dichromate ratios, it has been shown that the present system approximates closely to the theory. The presence of a large excess of sodium sulfate, however, introduces another ion species, and the theory is inapplicable.

In order to study the characteristics of this case, tests for transport control were applied to a solution 0.15M in sulfuric acid, 0.85M in sodium sulfate, and 3.0 x 10^{-2}M in dichromate.[3] The effect of varying the stirring speed at 25° is shown in Fig. 9, in which the full line is the slope computed from Eq. [1] using the determined values D_{25} = 7.71 x 10^{-6} cm^2 sec^{-1}, ν_{25} = 1.19 x 10^{-2} cm^2 sec^{-1}. It is seen to be distinctly higher than the experimental slope. The effect of varying the temperature at 146 rpm is shown in Fig. 10. From the slope, the apparent energy of activation is 3.4 kcal mole^{-1}, in good agreement with

[2] For this case, the problem of calculating the concentration profile through the transport boundary layer can be separated from the problem of determining the variation of the electrical potential through the double layer (19). When more than three ion species are present, however, this separation is not possible, and the path to a complete solution of the transport equations is barred by formidable mathematical difficulties. Nevertheless, the dependence of k_T on D, ν and ω is dimensionally of similar form to Eq. (1), but the number of proportionality must be determined by experiment (13).

[3] In the presence of added sodium sulfate, acid starvation is not detected until the acid/dichromate ratio is reduced to 7/2. The sodium sulfate decreases the rate both by increasing the viscosity of the solution and by eliminating ionic migration through the double layer. At this lower rate, for 0.15M H_2SO_4, acid exhaustion is not approached over the time intervals studied.

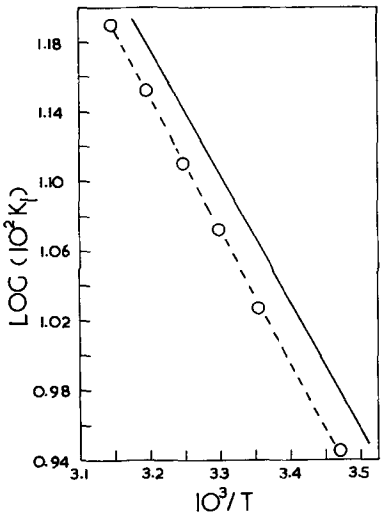

Fig. 10. Temperature coefficient, 0.15M H_2SO_4, 0.85M Na_2SO_4, 3.0 x 10^{-2}M $K_2Cr_2O_7$, 146 rpm.

the value found from Fig. 4. Again, the full line is the plot computed from Eq. [1] using the additional values $D_{45} = 1.20 \times 10^{-5}$ cm^2 sec^{-1}, $\nu_{45} = 7.96 \times 10^{-3}$ cm^2 sec^{-1}.

Figures 9 and 10 suggest that, for these conditions

$$k_T = \text{const. } D^{2/3} \nu^{-1/6} \omega^{1/2} \text{ cm sec}^{-1} \qquad [2]$$

where the constant is less than the value given by Eq. [1]. On dimensional grounds, the only effect of increasing the number of ion species beyond three should be a change in the number of proportionality. In this case, the mean value for the constant in Eq. [2] is found to be 0.562, *ca.* 7% lower than the value 0.605 predicted by Eq. [1].

That the process is indeed transport controlled under these conditions was checked by studying the effect of deliberately roughening the surface. For solutions 3.0 x 10^{-2}M in dichromate at 146 rpm and 25°, grinding the surface with carborundum gave a mean value for k_1 of 0.105 cm min^{-1} compared with the value 0.109 cm min^{-1} obtained with the standard surface. It is of interest to note that these runs with roughened surfaces gave linear first order plots without the initially high rates found in the absence of added sodium sulfate. Presumably, the high viscosity of the sodium sulfate solutions diminishes the local turbulence.

Edge effects.—For the dissolution of zinc disks rotating in aqueous iodine solutions (14), the observed rate constants at low stirring speeds were found to be higher than those predicted by Eq. [1]. It was pointed out that this could be explained equally well either by the assumption that the thickness of the disks gave rise to edge effects, or by assuming a contribution to the observed rate by natural convection.

In the present investigation, this effect is not observed, as will be seen from Fig. 3, 7, and 9, k_1 being accurately proportional to the square root of the stirring speed over the same range as that studied with the zinc disks. The very much thinner disks used in this investigation make it fairly certain that the earlier observations were in fact due to edge effects. Experiments with rotating disk cathodes have confirmed this view.

Blocking off the working surface.—It has been reported that the use of inert Perspex center studs is without effect on the observed rate of dissolution of zinc disks rotating in iodine solutions, although the exposed area of the stud amounted to *ca.* 4% of the working surface of the disk (14). Since the copper/dichromate reaction has been shown to be transport controlled under standard conditions, a similar effect should be found for this system. Progressive enlargement of an inert patch at the center should be without effect on the observed rate up to a certain point. Beyond this point, the exposed copper will be unable to cope with all the dichromate supplied by normal and radial transport, and this will result in a decrease in the observed rate. This decrease will become more marked as the blocked area is increased.

In general, the temperature coefficient of a surface process is larger than the temperature coefficient of the transport process (20). The effect of increasing the temperature will be a relative increase in the rate at which the exposed copper can cope with the dichromate supplied, and the breakdown point should then occur at a larger value of the blocked area.

To test these views, black wax was used to block off circular patches at the center of the copper disks, care being taken to ensure that the blocked off circles were concentric with the disks. Runs were carried out at 25° and 45° under otherwise standard conditions, and the mean values for k_1, computed per unit area of the *total* surface of the underside of the disk, are shown in Fig. 11. It will be seen that at 25° there is no significant effect on k_1 until the area blocked off exceeds *ca.* 10% of the total area; above this value there is a marked decrease. At 45°, the breakdown occurs at a higher value, *ca.* 15%.

Further study of this effect is desirable, but it would be better to use an inert electrode for the purpose since, when the disk is attacked, a step is formed at the edge of the blocked area which may promote a measure of local turbulence.

Acknowledgment

The authors thank Professor Cecil V. King for providing them with a manuscript copy of his review article in advance of publication, and they are grateful to the Department of Scientific and Industrial Research for an award to D. P. G.

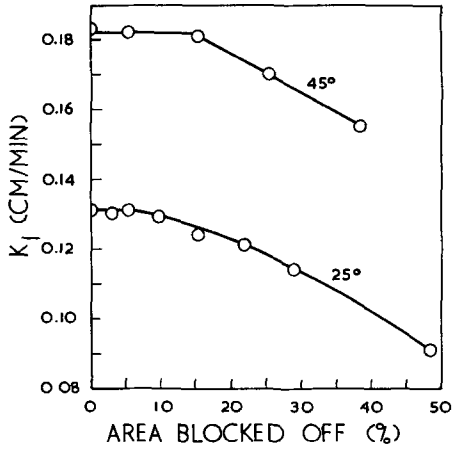

Fig. 11. Effect of blocking off working surface

Manuscript received May 27, 1960; revised manuscript received Aug. 22, 1960. This paper was prepared for delivery before the Houston Meeting, Oct. 9-13, 1960.

Any discussion of this paper will appear in a Discussion Section to be published in the June 1961 JOURNAL.

REFERENCES

1. V. H. Veley, *J. Soc. Chem. Ind.*, **8**, 858 (1889); *Phil. Trans.*, **182A**, 279 (1891).
2. R. G. Van Name and D. U. Hill, *Am. J. Sci.*, (4) **42**, 301 (1916).
3. R. Glauner and R. Glocker, *Z. Metallkunde*, **20**, 144 (1928); *Z. Krist.*, **80**, 377 (1931); R. Glauner, *Z. physik. Chem.*, **142A**, 67 (1929).
4. E. S. Hedges, *J. Chem. Soc.*, **1930**, 561.
5. C. V. King and L. Weidenhammer, *J. Am. Chem. Soc.*, **58**, 602 (1936).
6. C. V. King and P. L. Howard, *Ind. Eng. Chem.*, **29**, 75 (1937)
7. A. T. Gwathmey and A. F. Benton, *Trans. Electrochem. Soc.*, **77**, 211 (1940).
8. C. V. King and L. Appleton, *ibid.*, **77**, 219 (1940).
9. N. Ya. Buben and D. A Frank-Kamenetskii, *Zhur. Fiz. Khim.*, **20**, 225 (1946).
10. M. Hochberg and C. V. King, *This Journal*, **97**, 191 (1950).
11. T. G. Owe Berg, *Z. anorg. u. allgem. Chem.*, **265**, 332 (1951); **266**, 118, 130 (1951); **269**, 210, 218 (1952).
12. B. C.-Y. Lu and W. F. Graydon, *Canad. J. Chem.*, **32**, 153 (1954).
13. L. L. Bircumshaw and A. C. Riddiford, *Quart. Rev.*, **6**, 157 (1952).
14. D. P. Gregory and A. C. Riddiford, *J. Chem. Soc.*, **1956**, 3756.
15 L. L. Bircumshaw and A. C. Riddiford, *ibid.*, **1951**, 598.
16. C. V. King, Review entitled "Dissolution of Metals," presented at a symposium of The Electrochemical Society, 1959.
17. B. E. Dixon, A. A. W. Russell, and J. E. L. Swallow, *Brit. J. Appl. Phys.*, **3**, 115 (1952).
18 C. W. Tobias, M. Eisenberg, and C. R. Wilke, *This Journal*, **99**, 359C (1952).
19. V. Levich, *Acta physicochim. U.R.S.S.*, **17**, 257 (1942).
20. A. C. Riddiford, *J. Phys Chem.*, **56**, 745 (1952).

Microtopography of Oxide Films Formed on Tantalum

R. E. Pawel, J. V. Cathcart, and J. J. Campbell

Metallurgy Division, Oak Ridge National Laboratory,[1] Oak Ridge, Tennessee

ABSTRACT

Optical and electron microscopy were used to characterize the surface of tantalum specimens oxidized at temperatures ranging from 300° to 700°C. At the lower temperatures, the initial stages of oxidation were shown to consist of an aggregation of oxide platelets visible on the surface as crystallographically dependent, acicular structures extending from the grain boundaries. At higher temperatures, nodular growths were observed whose nucleation was not a grain-boundary phenomenon. Continued oxidation at temperatures of 500°C and above produced blistering and cracking of the oxide layer. The oxide platelets were shown to have grown during oxidation and not during cooling from the reaction temperature. At higher temperatures, both platelets and nodules served as preferred sites for blister and crack formation in the oxide and thus played an important role in the transition from the protective to the nonprotective stage of oxidation of tantalum.

Previous work (1, 2) has shown that the gaseous oxidation of tantalum takes place in a nonuniform fashion, characterized at least in the initial stages by the formation in the metal of discrete platelets of oxide resembling a typical Widmanstätten structure. The tendency for tantalum to react in such a heterogeneous manner illustrates the need for consideration of oxide morphology in any interpretation of the oxidation mechanism.

Oxidation rate measurements of Cathcart, *et al.* (1) have shown that the oxide film formed on tantalum in pure oxygen at atmospheric pressure is initially protective but becomes nonprotective as the oxidation proceeds beyond a critical point. The rate of oxidation finally approaches a constant value for longer oxidation periods. This general rate behavior is identical to that observed for niobium (3). Electron optical observations on oxidized specimens of both metals show that the onset of the nonprotective portion of the rate curves may be correlated to the formation of small blister-like cracks on the surface of the oxide. Presumably, these cracks permit easy access of oxygen to the reaction zone, resulting in the marked increase in oxidation rate.

While remarkable similarities exist in the oxidation rate curves for niobium and tantalum and in the physical and chemical properties of the two metals and their oxides, there are significant differences in the morphology of the oxide films formed on these metals, especially in the early stages of oxidation. The oxidation of niobium in the protective region is characterized by the formation of a reasonably uniform oxide film and the development of a normal sequence of interference colors as the oxide thickens. However, the initial stages of tantalum oxidation show the aforementioned platelet struc-

[1] Operated for the U. S. Atomic Energy Commission by the Union Carbide Corporation.

ture, and well-defined interference colors are not observed. It is of interest to observe that other gas-tantalum reactions, notably those with sulfur (4) and nitrogen (5), also produce a platelet structure.

In the present investigation, an effort has been made to characterize the morphology of the early stages of tantalum oxidation.

Specimen Preparation

Tantalum specimens (nominal analysis: 99.71% Ta-0.15% Nb-0.03% Fe-0.03% C-0.05% W) were cut from 0.5 mm sheet in the form of coupons, 1 x 2 cm. In most of the work reported here, the specimens were preannealed in vacuum for 1 hr at 1200°C; some specimens were strain annealed for longer periods at 1200° and 1300°C to produce a larger grain size. The specimens were mechanically polished through 0.3-μ levigated alumina and finally electropolished in a 90% H_2SO_4-10% HF solution. The specimens were then placed in quartz reaction tubes and annealed at a pressure of approximately 2×10^{-6} mm Hg at the reaction temperature for approximately 16 hr prior to oxidation. This method of specimen preparation yielded surfaces which appeared smooth in the light microscope, and which, upon oxidation, gave consistently reproducible results. Except as noted, all oxidations were performed in dry oxygen at atmospheric pressure.

The surface topography of the oxidized tantalum specimens was examined by both optical and electron microscopy. Both direct and indirect carbon replicas were used for electron microscopy, the indirect method (preshadowed carbon replica of a stripped parlodion intermediate) being used exclusively with the heavier oxide films. Each method yielded essentially identical results on a given specimen.

Mode of Platelet Formation

The resemblance of the platelet structure to the patterns observed in many precipitation systems suggested the possibility that the platelets were formed during cooling from the reaction temperature rather than during oxidation. This possibility was investigated using "hot" direct replication and hot-stage optical microscopy.

In a hot replication experiment, the specimen was oxidized in air at 400°C on a small hot plate in the vacuum evaporator. After oxidation, the system was evacuated and, with the specimen still at 400°C, a direct carbon replica, preshadowed rather heavily with gold or palladium, was made of the surface. After cooling, this replica was removed and the specimen re-replicated in the normal fashion. Electron micrography showed that essentially the same structure existed before and after cooling from the reaction temperature. The presence of shadows in the hot replica was regarded as conclusive evidence that the platelets were present at the reaction temperature.

The results of the hot-stage microscope studies served to confirm that the platelets formed during oxidation. Although the magnification and resolution of the microscope were not sufficient to permit observation of fine details, the general progress of the air oxidation at 400°C could be followed. First, a gradual darkening of several grains in the specimen was seen as platelets became visible in other lighter grains. Many platelets were observed to grow after nucleation at grain boundaries. As oxidation continued, the platelets frequently developed small feather-like subplatelets. No detectable changes in topography occurred as the specimens were cooled to room temperature in vacuum.

It should be indicated that the specimens used in this phase of the study were all oxidized in air and that the temperature control was poorer than with the standard apparatus; however, the morphology of these specimens compared favorably with that of the more carefully oxidized samples.

Oxide Morphology

The first stages of tantalum oxidation were studied over the temperature range 300°-700°C. Particular attention was paid to the initial growth behavior and its possible influence on the onset of blistering or rupturing of the oxide film. It has been suggested that the large oxide-metal volume ratios and the predominance of anion diffusion in the oxides lead to the generation of significant stresses in the oxide films formed on niobium and tantalum (1, 3). The phenomenon of highly localized crack formation in the oxide films can then be interpreted as resulting from the severe, localized deformation of the existing oxide by the forces exerted when fresh oxide is formed in a partially restricted region such as a cavity at the oxide-metal interface. The geometry associated with an oxide platelet is such that it is reasonable to expect that directional stresses would develop at such a site and lead ultimately to the formation of a crack or a blister in the oxide film. Thus, the manner in which platelet growth occurs may influence the oxidation kinetics markedly.

Only the very initial stages of oxide formation occurred on specimens oxidized at 300°C for times varying up to 95 hr. In the electron microscope, the oxide appeared as fine needles originating in the grain boundaries and extending into the grains along definite crystallographic directions as shown in Fig.

Fig. 1. Typical grain-boundary platelet growth on tantalum oxidized at low temperature. Note "bubble raft" background texture. Annealed 1 hr at 1200°C; oxidized 95 hr at 300°C; indirect replica. REF: J. V. Cathcart, R. Bakish, and D. R. Norton, This Journal, in press. Magnification 16,800X before reduction for publication.

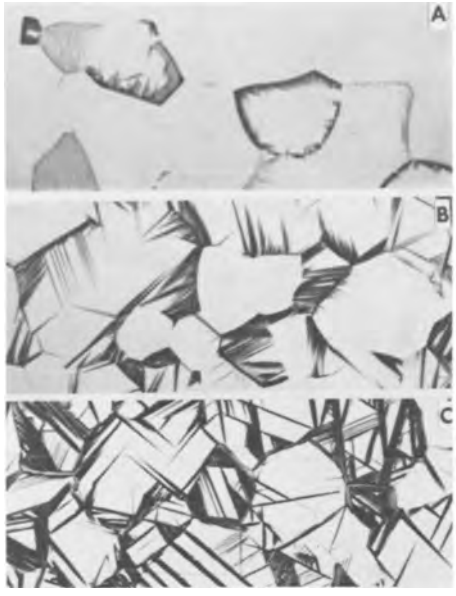

Fig. 2. Early stages of oxidation on coarse grain size tantalum at 500°C. Annealed 16 hr at 1200°C; oxidized (a) 15 min, (b) 30 min, and (c) 1 hr at 500°C. Magnification 500X before reduction for publication.

1. The "bubble-raft" structure discernible in Fig. 1 was found to be present on electropolished surfaces prior to oxidation and occurred as a result of electropolishing. Use of this fine-structure as a marker has been reported by one of us (1). At 400° and 500°C, the growth process was similar although the rate of oxidation was much greater. Prolonged oxidation at 500°C resulted in the formation of blister-like cracks in the oxide. Optical micrographs of tantalum specimens after oxidation at 500°C in the pre-blister range are shown in Fig. 2. The importance of grain-boundary nucleation in the oxidation process and the course of the subsequent growth of the platelets are illustrated.

Glancing-angle x-ray diffraction patterns obtained from specimens oxidized for times up to 8 hr at 500°C indicated that Ta_2O_5 was the major oxide formed under these conditions. After 15 min of oxidation, only a few extremely faint lines, other than the metal lines, were observed. After 1 hr of oxidation, corresponding to the time required to develop the platelet structure shown in Fig. 2c, the pentoxide lines were quite evident. The intensity of these lines increased during growth of the platelets. Very weak lines in the diffraction pattern could not be attributed with certainty to any known lower oxide of tantalum.

Fig. 4. Cross section of oxidized tantalum specimen showing growth of platelets into the metal. Annealed 1 hr at 1200°C; oxidized 6 hr at 500°C; indirect replica. Magnification 6900X before reduction for publication.

As oxidation continued at 500°C, randomly distributed blisters and cracks appeared on the surface, as shown in Fig. 3. Although the platelet structure in this micrograph is rather obscure, the size, shape, and position of the blisters do not seem to coincide with the traces of the platelets on the surface of the specimen. An electron micrograph of a cross section of a tantalum specimen oxidized at 500°C is presented in Fig. 4. The edge of the specimen is distorted; however, the platelets are seen to have grown into the metal to an appreciable depth. The largest platelets extend approximately 5 μ into the metal.

At 600°C a change in the basic oxide morphology was observed. On some grains, nodular oxide growths were interspersed with platelets. In some instances, the nodular growths showed crystallographic character and even the tendency to develop in the manner of a platelet. These characteristics are

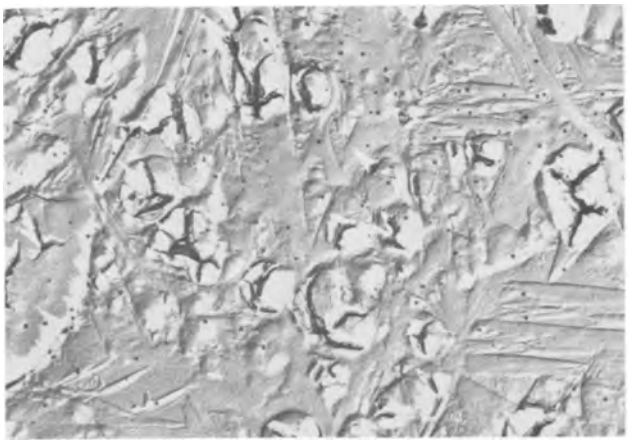

Fig. 3. Blister-like cracks observed on oxidized tantalum surface after prolonged oxidation. Annealed 1 hr at 1200°C; oxidized 7 hr at 500°C; indirect replica. Magnification 9600X before reduction for publication.

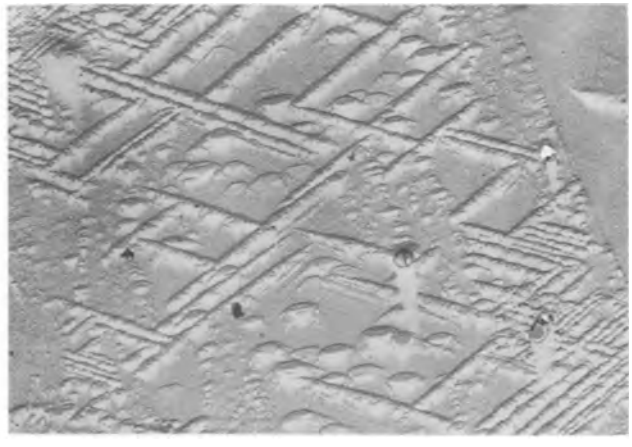

Fig. 5. Platelets and nodules formed on single grain on oxidation at 600°C. Annealed 1 hr at 1200°C; oxidized 1 min at 600°C; direct replica. Magnification 6900X before reduction for publication.

Fig. 6. Blister-like cracks appearing in grain after prolonged oxidation at 600°C. Annealed 1 hr at 1200°C; oxidized 15 min at 600°C; indirect replica. Magnification 6900X before reduction for publication.

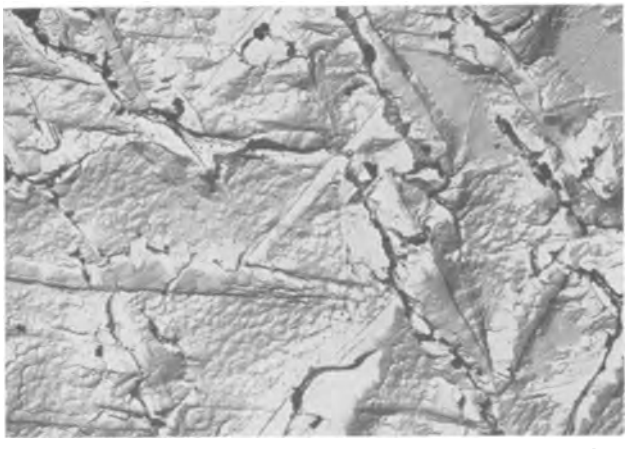

Fig. 7. Elongated cracks appearing along platelets after prolonged oxidation at 600°C. Annealed 1 hr at 1200°C; oxidized 15 min at 600°C; indirect replica. Magnification 6900X before reduction for publication.

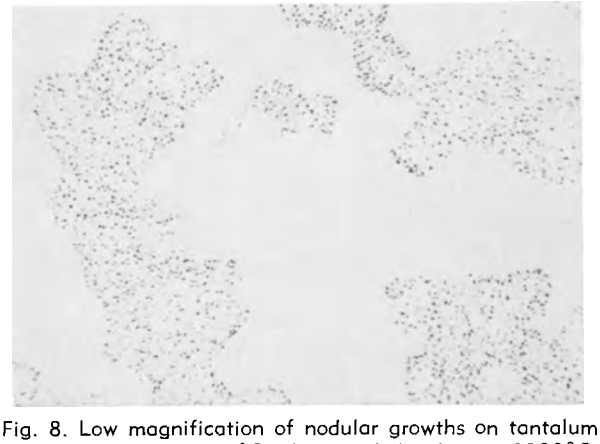

Fig. 8. Low magnification of nodular growths on tantalum surface oxidized at 700°C. Annealed 16 hr at 1200°C; oxidized 6-10 sec at 700°C. Magnification 500X before reduction for publication.

illustrated in Fig. 5. On the basis of longer (15 min) oxidation experiments at 600°C, nodular growths were found to be preferred sites for blister formation. Certain grains, originally exhibiting dense nodular formations, became blistered and oxidized much more heavily than adjacent grains where the oxide was present predominantly in platelet-type structures. Moreover, at this temperature, there appeared to be a more definite relation between the platelet growths and crack formation. In former platelet areas of these specimens, the fissures were elongated and closely followed the traces of the platelets. Even during earlier stages of oxidation at this temperature, blisters tended to form at intersections of platelets. Figures 6 and 7 are examples of crack formation in the two types of areas. Figure 6 also illustrates the extreme difference in oxidation behavior from grain to grain which was observed in these specimens.

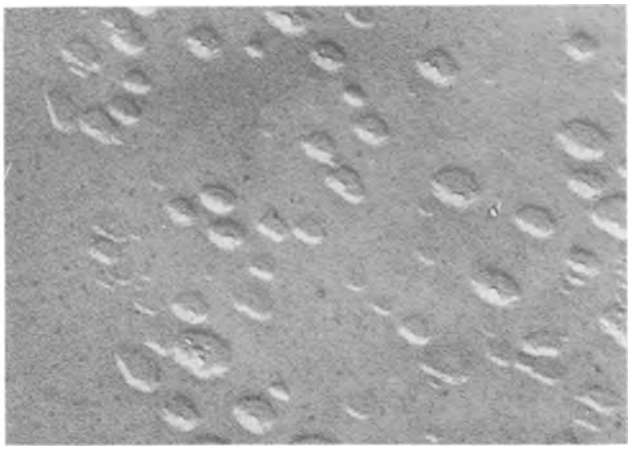

Fig. 9. Nodular growths on tantalum surface oxidized at 700°C. Annealed 16 hr at 1200°C; oxidized 6-10 sec at 700°C; indirect replica. Magnification 9600X before reduction for publication.

At 700°C the nodular growth was even more pronounced, and the first stages of oxidation consisted almost entirely of nodular-type attack. Figures 8 and 9 are typical optical and electron micrographs of these features.

Conclusions

The results of this investigation serve to illustrate the complex behavior of the initial stages of gaseous oxidation on tantalum surfaces. While the mechanism for platelet formation is not yet known, the fact that they contribute importantly to the oxidation process, at least at higher temperatures, has been demonstrated. On the basis of the results obtained, the following conclusions appear justified:

1. Oxide platelet formation on tantalum occurred at the temperature of oxidation and involved a highly directional growth process. At any one time during oxidation a wide spectrum of platelet sizes existed. X-ray data indicated Ta_2O_5 as the predominant oxide.

2. At lower temperature, the nucleation of platelets occurred primarily at grain boundaries, but at 600°C and higher, nodular growths were observed whose nucleation did not involve a grain-boundary process.

3. At lower temperatures, no direct correlation was observed between the platelet structures and blister formation in the oxide. At higher temperatures, both nodules and platelets served as preferred sites for blisters and elongated cracks.

4. Tantalum, especially at the higher temperatures, exhibited a pronounced dependence of first-stage oxidation rate on crystallographic orientation.

Acknowledgment

The authors wish to thank W. O. Harms of the University of Tennessee for his aid in the preparation of this paper. The assistance of W. H. Bridges and H. R. Tinch of the Metallography Group of this laboratory is also gratefully acknowledged.

Manuscript received May 9, 1960. This paper was prepared for delivery before the Houston Meeting, Oct. 9-13, 1960.

Any discussion of this paper will appear in a Discussion Section to be published in the June 1961 JOURNAL.

REFERENCES

1. J. V. Cathcart, R. Bakish, and D. R. Norton, *This Journal*, **107**, 668 (1960).
2. R. Bakish, *ibid.*, **105**, 71 (1958).
3. J. V. Cathcart, J. J. Campbell, and G. P. Smith, *ibid.*, **105**, 442 (1958).
4. J. V. Cathcart and J. B. Wagner, Unpublished research.
5. R. Bakish, *This Journal*, **105**, 574 (1958).

The Difference Effect and the Chunk Effect

G. A. Marsh and E. Schaschl

Research Center, The Pure Oil Company, Crystal Lake, Illinois

ABSTRACT

The negative difference effect in the case of steel can be explained in terms of corrosion by removal of blocks or "chunks" of metal containing perhaps only a few atoms. The "chunk effect" also explains the observed fact that, under conditions of high corrosion rate, minimum protective current can be much less than the calculated corrosion current. It is suggested that the chunk effect and anodic polarization occur on the same piece of metal. Either the positive or the negative difference effect may be observed depending on the corrodent.

Positive Difference Effect

The positive difference effect has been considered one of the supporting pillars of the electrochemical theory of aqueous corrosion. This effect was first recognized and named by Thiel and Eckell (1), who worked with aluminum dissolving in sodium hydroxide solution.

Thiel and Eckell reasoned that, when a metal is made an anode in an electrolytic cell, its rate of corrosion should be the sum of (*a*) local action as observed in the absence of external current, and (*b*) the corrosion rate equivalent to the applied current (utilizing the electrochemical equivalent of the metal in question). In actual tests with aluminum, however, they found the observed corrosion rate to be *less* than the sum of the components (*a*) and (*b*). To state their observation quantitatively, let I_o equal the freely corroding rate,[1] I_u equal the observed corrosion rate occurring on application of I_x, and I_x equal the externally applied current.

From Faraday's law I_x, when positive (anodic), results in an equivalent corrosion rate. To rephrase Thiel and Eckell's discovery, they expected to find

$$I_o + I_x - I_u = 0 \qquad [1]$$

Actually, they found

$$I_o + I_x - I_u = \Delta \qquad [2]$$

Δ was a positive number which they called the "difference effect." (Later they found that Δ could be negative in some cases; this discovery led to the use of the terms "positive" and "negative" difference effect.) Furthermore, Δ was linear over a certain range of I_x, so

$$\Delta = KI_x \qquad [3]$$

Since I_u and I_x are expressed as current densities, Eq. [2] and [3] can be combined:

$$I_u = I_o + I_x (1 - K) \qquad [4]$$

K is a slope; if it has a value of +1, the applied current will have no effect on measured corrosion rate. Where the positive difference effect has been observed, K lies between 0 and 1.

For small values of I_x, linearity of the curve I_u *vs.* I_x is often obtained, permitting one to obtain K from easily measured quantities:

$$K = \frac{I_o - I_{u1}}{I_{x1}} + 1 \qquad [5]$$

where the subscript 1 applies to one particular value of applied current.

The constant K was believed by Müller (2) to have fundamental significance regarding the mechanism of the anodic process. As K is independent of applied current, it must depend only on the system of metal/solution being studied.

Straumanis (3, 4) has explained the positive difference effect in terms of anodic polarization. According to his view, the positive difference effect is pronounced if there is interference with the delivery of electrons to the local cathode, or if there is interference with dissipation of ions into the corrosive agent. We believe that the latter effect is the more likely one. So with increasing anodic current, whether originating in local cells or externally applied, there is increasing anodic polarization which

[1] Corrosion rates in this paper are stated in terms of the equivalent current densities. Applied currents are also stated as current densities.

decreases the driving force for local action and gives rise to the observed positive difference effect.

The positive difference effect is *observed* only upon application of anodic current, but the phenomenon responsible for it takes place at zero applied current as well as at applied anodic currents. That anodic polarization occurs in freely corroding metals (*e.g.*, steel) is apparent from the fact that the current required for cathodic protection of a specimen showing the positive difference effect is greater than the corrosion current of the freely corroding metal. If there were no anodic polarization, the protective current would necessarily equal the corrosion current.

Negative Difference Effect

Müller (2) and Kroenig and Uspenskaja (5) found that the difference effect was negative for some metal-corrodent combinations. They and others (4, 6, 7) explained this as the result of disruption of a surface film. According to this theory, application of positive current to a specimen gradually breaks down its shielding film, thus exposing more metallic surface to attack by the corrodent and thus increasing local action. In some cases these investigators observed flaking of films in systems in which the negative difference effect was found.

Relationship between Cathodic Protection and Positive and Negative Difference Effects

In local action, assuming the local anodes do not polarize, the anodic current (*i.e.*, I_o) is equal to the current of the local cathodes. External cathodic current can be substituted for the local cathodic current. The current I_p required for cathodic protection is then identical to I_o. Thus I_p is a measure of the actual electronic current given up in the anodic process.

Anodic polarization, always present to some extent, requires I_p to be greater than I_o. Actual I_p/I_o ratios for numerous cases reported in the literature average about 1.2, indicating that for common cases such as soil corrosion there is almost but not quite complete cathodic control. Since I_p/I_o ratios above unity indicate some degree of anodic polarization, if one applied anodic current to a specimen which displayed an I_p/I_o ratio of 1.2 one should expect the positive difference effect to be evident.

For many cases the I_p/I_o ratio turns out to be far *less* than unity (8). These cases are found (for steel) in highly corrosive solutions, *viz.*, low *p*H or high dissolved oxygen concentration with a high degree of agitation. Under these same conditions of *p*H and dissolved oxygen, the negative difference effect is observed upon application of anodic current.

The low I_p/I_o ratio is not explained readily by the film-breakdown theory of the negative difference effect. The negative difference effect by definition drops to zero as applied anodic current becomes zero; Δ is not defined for negative values of I_a.

To explain the facts observed upon application of negative current, *i.e.*, cathodic protection, it is not enough for the potential of cathodic areas to be changed (in proportion to the current) to the open-circuit potential of the anodes. If such a proportional change occurred, I_p/I_o would remain at or slightly greater than unity. In order for the I_p/I_o data to be explained in terms of films, the potential of cathodic areas must change much faster than the applied current. The area or the efficiency of the cathodes must be affected by negative current. Or, alternatively, the application of negative current must result in the growth of a film over the anodic areas. But the system is under essentially cathodic control; variations in anodic area should have little effect on the cathodic reaction. Also, application of negative current would not be expected to stabilize an anodic film on steel. Indeed, the negative current should cause the reduction of films such as oxides that we normally associate with steel.

Under violently corrosive conditions where films are least likely to be present the negative difference effect is very pronounced. Under conditions of partial aeration, low velocity, neutral *p*H, where such films should be more stable on steel, the negative difference effect is *less* pronounced; under static conditions most favorable to film stability (*e.g.*, soil corrosion), the negative difference effect is absent altogether. Thus, the facts do not support the film breakdown theory of the negative difference effect in the case of steel. (This in no way suggests that the film breakdown theory may be invalid for other metals.)

Dissolution by "Chunks"

External current just sufficient for cathodic protection merely takes the place of local cathodic current, which in turn is essentially equal to the local anodic current. A low I_p/I_o ratio indicates that much more metal is being dissolved under freely corroding conditions than can be accounted for by local anodic current. To explain the low I_p/I_o ratio found when steel corrodes at high rates, the authors suggested that corrosion of steel under these conditions might proceed with the removal of "chunks" of iron containing several atoms (8). Dissolution by chunks would also explain the negative difference effect.

Relatively little work has been done on the difference effect in steel. So far particles of free iron have not been observed, perhaps because they are of only atomic dimensions. But dissolution by chunks has been observed in other metals.

Straumanis (9) points out that Al displays the negative difference effect when dissolving anodically in KCl-HCl solution. He writes: "The self-dissolution of the Al . . . increases with [application of anodic current]. After interruption of the current, H_2 evolution decreases and a cloud of white dust appears . . . . Very small hydrogen-evolving particles can be seen floating in the electrolyte, which evidently were separated from the Al together with the scale." Straumanis does not say what the particles might be, but we believe they are most likely tiny fragments of aluminum released from the parent metal by undermining.

Roald and Streicher (10) actually found "blocks" of aluminum of the order of 0.005 mm in length when certain Al alloys were dissolved in HCl. Similarly, Hoey and Cohen (11) and Higgins (12) found free Mg metal particles in the corrosion products

when Mg was dissolved anodically in NaCl solutions. Hoey and Cohen suggested that "local corrosion and/or undermining of metallic magnesium at the anode are appreciable and may, in fact, account for the observed low anodic current efficiencies of magnesium." Vermilyea (13) dissolved silver anodically and found "anode slime" composed of minute particles of metallic silver. If corrosion rate and applied current data had been taken by these workers, they would necessarily have observed the negative difference effect.

Generalized picture of corrosion rate as a function of applied current.—It has been mentioned above that the film disruption theory is inadequate to explain the low I_p/I_o ratio encountered with steel in high corrosion rate conditions, and that dissolution by chunks explains not only this but also the negative difference effect. If corrosion occurs by chunks in anodic dissolution, would it not occur in the same manner during free corrosion? To explain the low I_p/I_o effect one must assume that it does. Then

$$I_u = I_x + I_a + I_b \qquad [6]$$

where the applied current I_x results in corrosion in strict accordance with the Faraday equivalent, the rate I_a is the true local action rate, and the rate I_b is due to corrosion by chunks, *i.e.*, the "chunk effect" rate. If I_x is zero, $I_u = I_o$; the observed corrosion rate equals the freely corroding rate. Under this condition

$$I_o = I_{oa} + I_{ob} \qquad [7]$$

In this case I_{oa} and I_{ob} are the particular local action and chunk effect rates occurring together which are measured as the freely corroding rate.

For corrosion under cathodic control, the protective current

$$I_p = I_{oa} \qquad [8]$$

because the current consumption of the local cathodes is completely satisfied by the external current, so that no local action is possible. Since I_u is zero when current I_p is applied, (by definition of I_p) it follows from Eq. [7] that I_b must be zero also when I_p is applied. Therefore the chunk effect varies with applied current. The variation is believed to be more or less linear with applied current, inasmuch as I_u *vs.* I_x curves for steel are essentially linear.

Figure 1 depicts theoretical relationships between the observed corrosion rate and applied current for several types of conditions. The 45° line DBM represents the theoretical Faraday equivalence for corrosion under cathodic control. The line AB represents cathodic protection of a common corrosion system under partial anodic control (the ratio of currents AJ/DJ for steel in typical soils appears to be about 1.2). Since anodic polarization is involved, line BL (representing the extension of line AB) depicts the metal corroding with a positive difference effect, namely, the distance ML. The freely corroding rate in each case is I_o.

The line EB represents cathodic protection in cases where the ratio I_p/I_o is much less than unity. (As analyzed above, partial anodic control explains why I_p/I_o can be greater than unity, while the chunk effect explains why this ratio can be less than unity.) Ideally, I_p equals the true local action I_{oa}. The corrosion rate I_{ob} due to chunk effect is

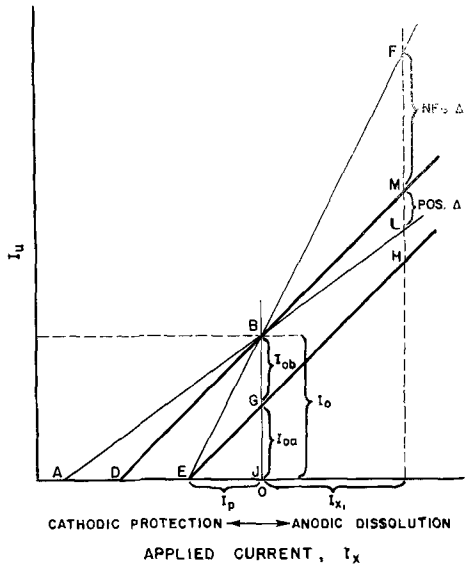

Fig. 1. Generalized corrosion rate—applied current relationships. Point B is the freely corroding rate in each case. Points E, D, and A are minimum protective currents. Points F, M, and L are observed corrosion rates with a given anodic current I_{x1}. The particular curve followed is dependent on the corrodent and the metal.

$$I_{ob} = I_o - I_p \qquad [9]$$

From Eq. [9] the chunk effect rate can be computed from the freely corroding rate and the minimum protective current. However, the freely corroding rate is merely one arbitrary point on the corrosion rate *vs.* applied current curve. If this curve is extended, (EBF on Fig. 1), a region is entered where the measured corrosion rate is greater than the Faraday equivalent rate. The true local action on application of anodic current is represented by point H; the observed corrosion rate is represented by point F. The distance FM is, by Thiel and Eckell's definition, the negative difference effect. The part of the corrosion rate occurring by chunk effect is represented by the distance FH.

Figure 1 illustrates that the chunk effect may be a fundamental property of a corroding system, while the negative difference effect is one of several possible manifestations of this property. If the chunk effect occurs, it does so even at zero applied current; that is, it occurs while the metal is freely corroding. The negative difference effect on the other hand by definition is nonexistent at zero applied current.

In Fig. 1 the curve EBF, corrosion rate *vs.* applied current, is represented as a straight line. It is recognized that none of the curves other than the Faraday equivalent is necessarily an exact straight line over the whole range of I_x. In the case of steel, however, I_u appears to be quite linear both with negative and positive values of I_x, at least up to I_x values equal to I_o. If corrosion rate varies linearly with applied current, the part of the freely corroding rate that is due to local action, I_{oa}, can be readily obtained:

$$I_{oa} = \frac{I_o I_{x1}}{I_{u1} - I_o} \qquad [10]$$

where I_{u1} is the observed corrosion rate when a current I_{x1} is applied to the corroding specimen. I_{oa} is also numerically equal to the current I_p required for cathodic protection.

This leads to a calculation of chunk effect ratio, C, which is the fraction of the freely corroding rate that is due to chunk effect:

$$C = \frac{I_{oh}}{I_o} = 1 - \frac{I_{x1}}{I_{u1} - I_o} \qquad [11]$$

The chunk effect ratio can also be computed by combining Eq. [9] and [11]:

$$C = \frac{I_o - I_p}{I_o} \qquad [12]$$

The difference effect can be determined experimentally as:

$$I_o + I_{x1} - I_{u1} = \Delta \qquad [13]$$

and since I_{u1} is larger than the sum of $I_{x1} + I_o$, the difference effect Δ is negative. From the Thiel and Eckell slope K (Eq. [5]) it is seen that K and the chunk effect ratio C are related:

$$C = \frac{-K I_{x1}}{I_{u1} - I_o} \qquad [14]$$

Up to this point the cases of corrosion with anodic polarization (positive difference effect) and corrosion with chunk effect have been considered as occurring separately. In a general case anodic polarization and the chunk effect occur simultaneously on the same piece of metal. If the decrease in local action rate exactly equals the rate at which the chunks are leaving the metal, there will be no measurable departure from the Faraday equivalence (line DBM of Fig. 1). Ordinarily, the two effects would not be equal: either the positive difference effect or the chunk effect is predominant and is observed depending on the nature of the corrodent.

Experimental

Demonstration of the negative difference effect in the case of steel.—The negative difference effect was observed as an incidental effect in experiments with dissolved oxygen concentration cells. From the standpoint of studying concentration cells the mode of generation of cell current is important; but here we are concerned with cell current merely as an externally applied current, I_x. This applied current could just as well have been obtained by using an external cathode and current source. A suitable apparatus is shown schematically in Fig. 2. The solutions used contained NaCl at various concentrations, with known dissolved oxygen concentrations between 0 and 6.5 ppm. The pH of the solutions was adjusted with NaOH or HCl at frequent intervals. The electrodes were electrical resistance probes (14) of SAE 1010 mild steel, unannealed. They were etched prior to use by immersion for 10 sec in 6*N* HCl containing 1% ferric chloride. Following this, the probes were washed in water and acetone, dried, and stored temporarily in a desiccator until used.

In such a dissolved oxygen concentration cell, the cell current depends mainly on the degree of aeration and agitation in each zone. By suitable choice of conditions the current density on the anode could be made as high as 170 μa/cm^2 (160 ma/ft^2). To compute the difference effect in such experiments one had only to obtain the freely corroding rate I_o of the unconnected probe in the anodic compartment of the cell, add the cell current I_x, and subtract the corrosion rate I_u of the anodic connected probe. Corrosion rates were obtained with the probes *in situ* by means of a corrosion meter (14). The difference effect using this method is measurable in terms of loss of metal rather than in terms of the generation of hydrogen as in most previous experiments.

As a further refinement, one could interrupt the cell current at any point and apply cathodic protection in small increments while continuously measuring the corrosion rate, thereby obtaining the minimum current needed for cathodic protection. Using steel probes initially 25 μ thick (0.001 in.) one could measure thickness changes of the order of 0.05 μ (0.2 μ in.) by means of the changes in electrical resistance.

The results with neutral solutions show a trend in the direction of negative difference effect, the effect becoming quite pronounced at low pH (Fig. 3). It is significant that some of the runs of Fig. 3

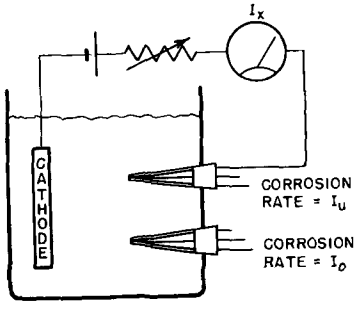

Fig. 2. Apparatus for studying corrosion rate—applied current relationships. Electrical resistance corrosion probes were used to determine the corrosion rates. The polarity of the battery could be reversed to permit study of cathodic protection.

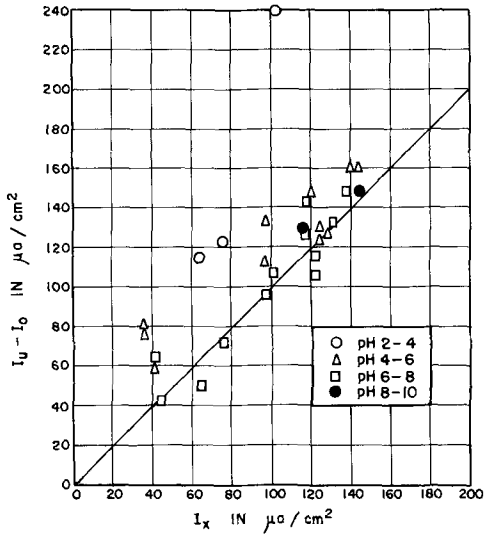

Fig. 3. Effect of pH on difference effect of steel, various NaCl solutions. Each point represents a separate run. By Thiel and Eckell's definition, points lying above the 45° line of equivalence indicate a negative difference effect; points lying below the line indicate a positive difference effect.

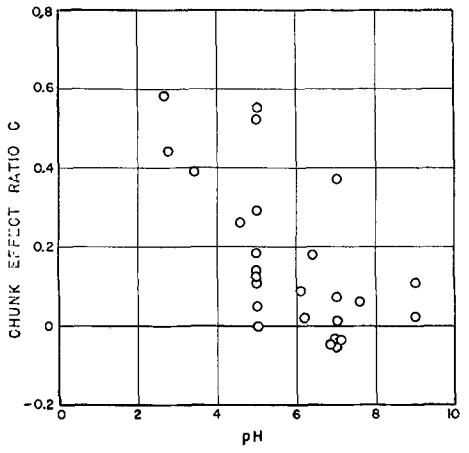

Fig. 4. Variotion of chunk effect with pH. Dato used in plotting Fig. 3 were replotted in terms of chunk effect rotio C calculated from Eq. [11]. Note the pronounced increase in C at low pH.

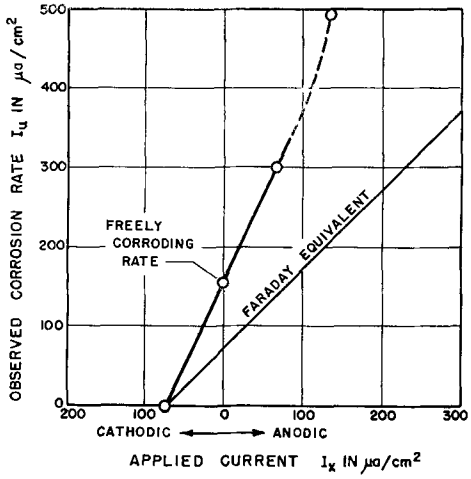

Fig. 5. Chunk effect of steel dissolving in dilute HCl, pH 2. Based on the Faraday equivalent of the cathodic protection current, about half the freely corroding rate is attributable to corrosion by more than one atom at a time.

were made in oxygen-free solutions. Thus while oxygen appears to be necessary in order to obtain the negative difference effect in, say, magnesium (5), there is no such restriction in the case of steel.

In Fig. 4, the data of Fig. 3 were replotted in terms of the fraction of the freely corroding rate due to chunk effect (C) as a function of pH. It is seen that at low pH values C may be greater than 0.5, indicating that over half of the corrosion rate is attributable to the chunk effect mechanism. This result is in general agreement with I_p/I_o data tabulated in ref. (8).

In Figs. 3 and 4 each point represents a single run with a cell of certain composition; I_x is the cell current, and $I_u - I_o$ is the difference in two measured corrosion rates. At low values of I_x, the quantities I_u and I_o are not very different, so that scatter of the data is inevitable. With a given set of conditions the cell currents were reproducible within a few microamperes; the corrosion rates in the low range were reproducible within about 2 $\mu a/cm^2$.

To illustrate the improvement in the quality of data when a single specimen was used to obtain several I_u *vs.* I_x points, an experiment was carried out in which a steel electrical resistance probe was immersed in an aqueous solution of pH 2. The freely corroding rate was determined and was converted into equivalent current; then cathodic current was applied in increments until the protective current was reached. Next the freely corroding rate was again determined and found to be the same as it was at the start of the experiment. Anodic current was again applied and a new corrosion rate was measured. The results are plotted in Fig. 5.

Based on the freely corroding rate (equivalent to 153 $\mu a/cm^2$) and the protective current (75 $\mu a/cm^2$) the chunk effect ratio C for the system of Fig. 5 was about 0.5. The measured corrosion rate was linear with applied current up to a high anodic current.

After the probe of Fig. 5 had been made anodic for a period long enough to obtain the corrosion rate, the anodic current was turned off and the protective current was again determined. This current (82 $\mu a/cm^2$) was still essentially the same as before the anodic treatment, indicating that the local action current had not been affected by the treatment. The freely corroding rate increased slightly when measured before and after the treatment.

This phenomenon occurs consistently when steel is made highly anodic at low pH: I_o increases after each treatment while I_p remains constant. Disruption of a shielding film would explain the increase in I_o but not the constancy of I_p. If more area is exposed for local action, more protective current should be required. These facts indicate that the chunk effect increases as corrosion proceeds, if the corrosion rate is very high.

Table I lists data obtained with a smooth mild steel probe immersed in dilute HCl of pH 2. Both I_o and I_p were obtained at intervals after applying anodic current. The local action current as reflected by I_p remained practically constant. "Blank" probes, not subjected to anodic current, maintained constant values of I_o and I_p over the period of the experiment; the values were reproducible within about 3 μa per cm^2. However the I_o of the anodically treated probe doubled during the experiment. The difference effect

Table I. Effect of applied anodic current on minimum protective current and on freely corroding rate—steel corroding in HCl, pH 2

Elapsed time, hr	I_0, $\mu a/cm^2$	I_x, $\mu a/cm^2$	I_u, $\mu a/cm^2$	I_p, $\mu a/cm^2$	C from Eq. [12]	C from Eq. [11]	K
0	153	—	—	75	0.44	—	—
1	—	73	307	—	—	0.48	—0.7
2	—	151	527	—	—	0.53	—1.1
3	230	—	—	82	0.64	—	—
4	—	43	484	—	—	0.81	—4.2
5	291	—	—	87	0.70	—	—

slope K decreased from -0.7 to -4.2, but K could be calculated only for the periods of time in which anodic current was being applied. The chunk effect ratio C, calculated from either Eq. [11] or [12], showed a gradual increase, with a reasonably good fit of values obtained by the two methods.

From this type of experiment, K appears to be of little value in depicting the mechanism of corrosion. If K in the example above is some measure of the disruption of a shielding film, one must ask why I_p does not vary with K. The chunk effect hypothesis on the other hand might aid in the study of mechanism. The gradual increase in C indicates that, as corrosion proceeds under conditions of high corrosion rate, a greater per cent of the freely corroding rate takes place by removal of more than one atom at a time. As I_p is essentially constant, this is not likely due to an increase in cathodic surface area, but rather to the geometric pattern by which the lattice dissolves.

Summary

Theories of film shielding of anodic areas do not explain adequately the negative difference effect and the relationship between minimum protective current and freely corroding rate in the case of steel. These effects can be explained by supposing that under certain conditions corrosion proceeds partly through removal of chunks of metal containing perhaps only a few atoms. This is believed to occur over the whole range of applied currents from cathodic protection to high anodic currents. The chunk effect is most pronounced (in steel) under conditions which yield high corrosion rates. In experiments at pH 2, for example, about 50% of the observed corrosion rate could be attributed to the chunk effect mechanism.

It is suggested that the chunk effect and anodic polarization occur on the same piece of corroding metal. Thus either the positive or the negative difference effect may be observed, depending on the corrodent.

Manuscript received Feb. 5, 1960; revised manuscript received Sept. 9, 1960. This paper was prepared for delivery before the Houston Meeting, Oct. 9-13, 1960.

Any discussion of this paper will appear in a Discussion Section to be published in the June 1961 JOURNAL.

REFERENCES

1. A. Thiel and J. Eckell, *Korrosion u. Metallschutz*, **4**, 121 (1928); **4**, 145 (1928).
2. W. J. Müller, *Trans. Electrochem. Soc.*, **76**, 167 (1939).
3. M. E. Straumanis, *Korrosion u. Metallschutz*, **14**, 67 (1938).
4. M. E. Straumanis and Y. N. Wang, *This Journal*, **102**, 304 (1955).
5. W. O. Kroenig and V. N. Uspenskaja, *Korrosion u. Metallschutz*, **11**, 10 (1935).
6. N. D. Tomashoff, "Corrosion of Metals with Oxygen Depolarization," book condensed and translated in *Light Metals*, **11**, 505 (1948).
7. M. A. Streicher, "Pittsburgh International Conference on Surface Reactions," p. 105, Corrosion Publishing Co. (1948).
8. E. Schaschl and G. A. Marsh, *Corrosion*, **13**, 243t (1957)
9. M. E. Straumanis, *This Journal*, **105**, 284 (1958).
10. B. Roald and M. A. Streicher, *ibid.*, **97**, 283 (1950).
11. G. R. Hoey and M. Cohen, *ibid.*, **105**, 245 (1958).
12. W E. Higgins, *ibid.*, **105**, 757 (1958).
13. D. A. Vermilyea, *ibid.*, **105**, 547 (1958).
14. G. A. Marsh and E. Schaschl, *Oil and Gas J.*, **54**, No. 29, 135 (1955).

Symbols Used

- Δ — Thiel and Eckell's difference effect.
- K — Thiel and Eckell's slope constant.
- I_x — Applied current density.
- I_w — Observed corrosion rate expressed as equivalent current density.
- I_o — Freely corroding rate expressed as equivalent current density.
- I_p — Minimum protective current density.
- I_a — Local action current density.
- I_b — Chunk effect corrosion rate expressed as equivalent current density.
- I_{oa} — Local action current density under the condition of zero applied current.
- I_{ob} — Chunk effect corrosion rate at zero applied current.
- C — Chunk effect ratio.

Correction

In the September 1960 issue of the JOURNAL on page 768 of the paper by K. B. Oldham "Theory of Faradaic Distortion" the term "C +" was omitted from Eq. [6]. Equation [6] should read

$$C(0, t) = C + \sum_{j=0}^{\infty} \mu_j \cos j\omega t + \sum_{j=1}^{\infty} \lambda_j \sin j\omega t \qquad [6]$$

Flash Conductivity in Solution of Triphenylamine in n-Hexane

H. Rüppel, U. Krog, and H. T. Witt

Physikalisch-chemisches Institut der Philipps-Universität, Marburg/Lahn, Germany

ABSTRACT

A method is described for detecting short-lived charged primary products (ions, electrons) produced in photochemical reactions. The photochemical reaction is initiated by a light flash in an electric field of approximately 1000 v/cm. Photochemical changes produced in the solution are measured by a current impulse which occurs between the electrodes. The method is applicable for organic solutions which have a very small conductivity in the dark. Solvents such as hexane, benzene, and toluene may be used. The method was applied to detect light-produced short-lived radical ions of triphenylamine and similar substances in n-hexane. The electrical detection of flash conductivity in the case of triphenylamine was examined optically by measuring the transient absorption band of the photoproduct by flash photometry.

Ultraviolet radiation of a wave length $\lambda > 200$ mμ generally causes no additional conductivity in liquid organic media. That is to say, organic liquids either have no absorption bands in this spectral range (*e.g.*, hexane) or only such absorption bands as lead to excited electron states and not to the splitting off of an electron (*e.g.*, benzene). When there are ionization bands the radical ions produced in the liquid generally have a very short lifetime. Therefore the stationary amount of charge carriers produced by steady light is so small that an additional conductivity cannot be detected readily.

Conditions may be more favorable if, instead of steady light, the light of an electronic flash is used. Flash light is about 1000 times more intense than steady light, and, if ionization bands exist, it may be expected that flash light will give rise to a brief but measurable conductivity in the organic liquid. This conductivity phenomenon has been designated by us as "flash conductivity" (1).

Detection of flash conductivity was first attempted in the system triphenylamine in liquid n-hexane. According to Lewis and Lipkin (2) it is probable that there is an ionization of triphenylamine by u.v. with $\lambda > 200$ mμ. On irradiating a solid solution of triphenylamine at 90°K by u.v. light, Lewis discovered a new absorption band at 660 mμ. Comparing this with the known absorption spectrum of the radical ion of triparatolylamine, he assumed that he had produced a triphenylamine positive ion. Furthermore, according to the electron gas model of Kuhn (3) one could even expect the triphenylamine to have an absorption band in the visible spectral range. There had been, however, no direct electrical proof for the ionization ion in the solid solution. In the *liquid* solution the triphenylamine radical ion had not been detected either electrically or optically.

For the detection of the triphenylamine positive ion in liquid solution it had to be demonstrated that flash excitation of the triphenylamine solution gives rise to: (*a*) a brief additional conductivity, and (*b*) a transient absorption band in the visible red.

Methods of Measurement

A schematic drawing of the arrangement for measuring flash conductivity is shown in the upper part of Fig. 1. The triphenylamine solution was placed between the electrodes of a quartz cell. The electric field was approximately 1000 v/cm. If charge carriers are produced by the flash, they will move in the electric field during their lifetime, inducing a current impulse on the electrodes. The current impulse can be amplified by the pulse amplifier (PA) and indicated on the oscilloscope (CRO).

The current impulse comes about as follows. Every charge carrier produced by the flash moves in the electric field E with a velocity $u = v \cdot E$, where v is the mobility of the charge carrier. During its lifetime τ, the charge carrier travels a distance $s = v \cdot E \cdot \tau$. By this means a definite charge q is induced on the electrodes,

$$q = e \cdot s/d = e \cdot (v \cdot E \cdot \tau)/d \qquad [1]$$

where e is the electrical charge of the particle and d the distance between the electrodes.

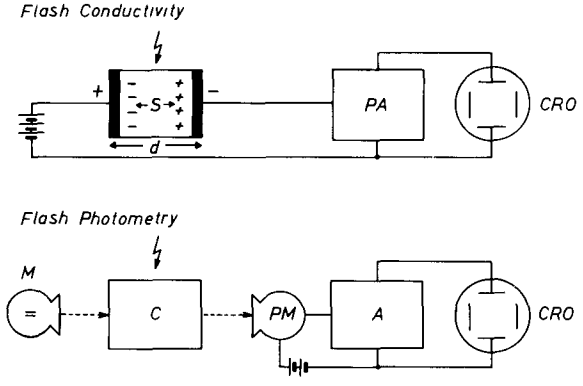

Fig. 1. Upper part: schematic drawing of the electrical arrangement (flash conductivity), d—distance between the electrodes, s—distance the charge carrier travels in the electric field during its lifetime, PA—pulse amplifier, CRO—cathode-ray oscilloscope; lower part: schematic drawing of the optical arrangement (flash photometry); M—measuring light source, C—quartz cell, PM—photomultiplier, A—amplifier.

If the production of ions per flash results in a total charge Q_o, then the current impulse at the amplifier input is given by the expression

$$Q = Q_o \cdot (v_+ + v_-) \cdot E \cdot \tau / d \qquad [2]$$

where v_+ is the mobility of the positive and v_- that of the negative charge carrier. This simple equation is valid if $(v_+ + v_-) \cdot E \cdot \tau << d$ (1).

The lower limit of measurement is fixed by the noise of the preamplifier tube. In the present case the noise level corresponded to a charge of approximately 5000 electrons. Substituting this value for Q and the known values for E, d, and v (4) one obtains a given lower limiting value of the product $Q_o \cdot \tau$, $(Q_o \cdot \tau)_{min} \approx 5 \cdot 10^3$ e·sec, which is just within the limit of measurement. Thus, the flash conductivity method is very sensitive. Assuming an ion lifetime of 10^{-1} sec, a concentration of about 10^{-18} mole/l [1] can be detected, or, in the other extreme, at a given ion concentration of 10^{-7} mole/l, ions with a lifetime of 10^{-12} sec can be detected.

In the lower part of Fig. 1 a schematic drawing of the optical arrangement for flash photometry is shown, the principle of which was reported by Norrish and Porter (5) and by Davidson and co-workers (6). A beam of monochromatic measuring light (M) passes through the quartz cell (C) and falls onto a photomultiplier (PM). If the flash produces photochemical changes in the solution which give rise to a new absorption band, the photomultiplier will detect a change in the intensity of the measuring light. The corresponding current variation in the photomultiplier output can be amplified (A) and indicated on the oscilloscope (CRO). The lower limit of measurement is fixed by the noise of the photomultiplier cathode. The theoretical value of the resolution limit is practically reached by our arrangement (7). At a signal risetime of $\approx 10^{-5}$ sec an absorption change of 0.1% is detectable.

Results

Electrical measurements.—Excitation of the triphenylamine solution in n-hexane with unfiltered flash light produced the expected current impulses. The current impulses rise linearly with the electric stress E, indicating that the lifetime of the ion is small enough to satisfy the condition for Eq. [2], or, in this case, $\tau << 1$ sec. In order to determine which of the absorption bands of the triphenylamine (see Fig. 3, solid curve) gives rise to ionization, the light of the flash was filtered. Measurements indicated that ionization accompanies absorption only in the u.v. absorption with $\lambda < 250$ mμ. Other parameters such as concentration of triphenylamine, oxygen content of the solution, etc., were also varied. The results of these measurements confirmed expectations (1).

Flash conductivity could also be detected in n-hexane solutions of diphenylamine, tetramethyl-paraphenylendiamine, and both types of chlorophyll. (Under equal experimental conditions the electrical signal in the case of chlorophyll is about three times larger than with triphenylamine. The order of magnitude of the current impulse is Q $\approx$ 10^{-13} amp sec.) On the other hand, exciting a solution of benzene in n-hexane with u.v. light of the spectral range $\lambda > 200$ mμ produced, as had been expected, no electrical signal (see above).

[1] The volume of the quartz cell was approximately 0.1 l.

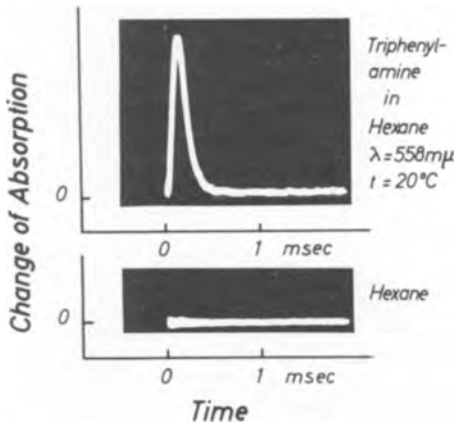

Fig. 2. Change of absorption vs. time as received on the oscilloscope. Upper part: increase of absorption was produced by irradiating triphenylamine in n-hexane with the intensive light of an electronic flash. Concentration of triphenylamine: $3 \cdot 10^{-5}$ mole/l. Wavelength of the measuring light, 558 mμ ($\Delta\lambda$ = 17mμ); temperature, 20°C; electrical energy of the flash discharge, 240 j; length of the quartz cell, 10 cm. The maximum of the absorption change corresponds to a decrease of transmission of approximately 6%. Lifetime of the photoproduct (triphenylamine positive ion) $\tau < 10^{-4}$ sec. Lower part: Response of the optical arrangement on flash light excitation of pure n-hexane.

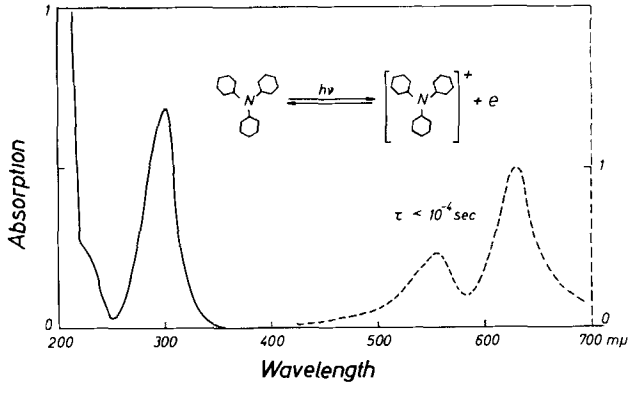

Fig. 3. Absorption vs. wave length. Solid line: normal absorption spectrum of triphenylamine in n-hexane; dashed line: transient absorption spectrum received by flash photometric measurements on illuminating triphenylamine in n-hexane by intensive flash light. (Preliminary measurements; position and relative heights of maxima may be submitted to some change.) Temperature: 20°C. Electrical energy of the flash discharge, 240 j; flash duration, approximately $2 \cdot 10^{-4}$ sec; lifetime of the photoproduct (triphenylamine positive ion) $\tau < 10^{-4}$ sec. (Both absorption spectra are plotted in arbitrary units.)

Optical measurements.—In addition to the electrical detection of charged photoproducts in the triphenylamine solution, there was also a brief appearance of a new absorption band. This may be due to the triphenylamine positive ion. The optical signal measured at a wave length of 558 mμ is shown in the upper part of Fig. 2. It was received on the oscilloscope when the intensive flash light excited the triphenylamine solution. The time course of the optical signal corresponds approximately to that of the flash light emission, indicating that the lifetime of the transient photoproduct is shorter than 10^{-4} sec. The entire transient absorption spectrum could be

traced from measurements taken at various wave lengths. The main peak of the new absorption band lies in the spectral range around 650 mμ[2](Fig. 3, dashed curve). According to the experimental work of Lewis (2) as well as to the calculations of Kuhn (3) based on the electron gas model, there is good evidence for the triphenylamine radical ion to show an absorption band in this spectral range. Thus, the transient absorption band observed on exciting the triphenylamine solution may be ascribed to the triphenylamine positive ion.

Experimental.—The measurements have been described in their essential features without regard to experimental difficulties. Owing to its high sensitivity, the apparatus is very subject to interference, most of which is caused by the intensive flash discharge. Measurements are disturbed by the electromagnetic field and by the sound and any random light of the flash. The latter causes electrode effects in the cell or false light signals on the photomultiplier. Nearly all of these troubles may, however, be handled appropriately.[3]

Conclusions

The method of using flash conductivity may be extended to quantitative measurements, *i.e.*, it may be used to measure ionization potentials, which have, until recently, been little known in the liquid state.

Finally, there is one circumstance which remains to be discussed. In a system such as triphenylamine in liquid or rigid solution it is not clearly known where the separated electron stays during its lifetime.[4] It might, therefore, be desirable to investigate systems with a definite electron acceptor present. There are donor-acceptor systems in which an electron transfer takes place from the photo-excited electron state:

$$A^* + B \rightarrow A^+ + B^- \rightarrow A + B$$

[This scheme has been used to explain the quenching of fluorescence of certain organic compounds (9)]. Owing to the high sensitivity it should be possible to detect such an electron transfer electrically in the apparatus described above. Reactions of this kind are the subject of our current investigation.

[2] Independent of the flash photometric measurements (Fig. 1) the transient absorption curve (Fig. 3, dashed line) was measured recently by us also using the method of flash spectroscopy (5).

[3] More details of the experimental technique are described in ref. (1) and (7).

[4] Tentative ideas are discussed by Lewis (2), Linschitz (8), and especially by LeBlanc (4) (see also paper by O. H. LeBlanc, Jr., presented at the Philadelphia Meeting of the Society, May 6, 1959.

Acknowledgment

The authors wish to thank Miss Rilla Spangler, West Chester, Pa., and Mr. Günter Eckel, Marburg/Lahn, for helpful suggestions regarding the textual revision of this manuscript. Grateful appreciation for research support is expressed to the Research Corporation, New York, and the Deutsche Forschungsgemeinschaft, Bad Godesberg.

Manuscript received March 1, 1960. This paper was prepared for delivery before the Philadelphia Meeting, May 3-7, 1959.

Any discussion of this paper will appear in a Discussion Section to be published in the June 1961 JOURNAL.

REFERENCES

1. H. Rüppel and H. T. Witt, *Z. physik. Chem. N. F.*, **15**, 321 (1958).
2. G. N. Lewis and D. Lipkin, *J. Am. Chem. Soc.*, **64**, 2801 (1943).
3. H. Kuhn, *Chimia*, **9**, 237 (1955).
4. O. H. LeBlanc, Jr., *Insulation*, **5**, 6, 26 (1959).
5. R. G. W. Norrish and G. Porter, *Nature*, **164**, 658 (1949).
6. N. Davidson, R. Marshall, A. E. Larsh, and T. Carrington, *J. Chem. Phys.*, **19**, 1311 (1951).
7. H. T. Witt, R. Moraw, and A. Müller, *Z. physik. Chem. N. F.*, **20**, 193 (1959).
8. H. Linschitz, M. G. Berry, and D. Schweitzer, *J. Am. Chem. Soc.*, **76**, 5833 (1954).
9. Th. Förster, "Fluoreszenz organischer Verbindungen," p. 221 ff, Vandenhoeck & Ruprecht, Göttingen (1951).

Electrodeless Passage of Direct Current through an Electrolyte

Abner Brenner

National Bureau of Standards, Washington, D. C.

ABSTRACT

An experimental setup is described for directly observing the electrical migration of a dye in a conducting system without electrodes. Direct current was produced in a continuous circuit of electrolyte, which included the dye solution, by means of a transformer and a mechanical commutator.

The passage of direct current between electrodes immersed in a conducting solution produces two phenomena: chemical reactions at the electrodes and mass transport of the solute. If one looks at this process phenomenologically, one is tempted to ask naively whether the mass transport would occur if current were passed through the solution in such a way that no electrode reactions occurred. To perform this experiment it would be necessary to produce direct current in an electrolyte without using electrodes.

On the basis of the currently accepted theories of the structure of electrolytes, it seems obvious that electrical migration[1] would occur even in the ab-

[1] Ionic or electrical migration is considered to be the flux of dissolved matter, in accordance with Faraday's law, through an electrolyte as a result of the flow of current.

sence of electrolysis. The ions in solution, being charged particles, would move in the electric field that is applied across the solution. However, the possibility could be envisioned that in the absence of electrolysis the positive and negative ions consort together as dipoles and the current then could be carried by a flow of electrons or holes as in a semiconductor or metal. As an example, the conduction of electricity through the solution of an alkali metal in ammonia is supposed to occur by a flow of electrons.

Even though current theory predicts that electrical migration would occur in the absence of electrolysis, the auther considered that direct observation of the predicted phenomena would make an interesting experiment. An additional element of interest was provided in designing the apparatus for producing direct current in the electrolyte without using electrodes.

In looking into the literature of the electrodeless passage of current through an electrolyte, the author found the subject was a rather old one. It had been the center of lively discussion and controversy 60 years ago and then had been forgotten. The author learned of the early literature somewhat by accident. In the course of preparing the J. W. Richards Memorial Lecture, the author learned that both Richards, the first president of The Electrochemical Society, and Carl Hering, the fourth president of the Society, published papers on the subject. Richards (1, 2) believed that conduction through an electrolyte occurred by the same mechanism as "metallic conduction" and that electrical migration was a secondary phenomenon which resulted from the chemical changes that occurred at the electrodes. According to his view, in the absence of electrolysis there should be no electrical migration.

Richards also attempted to show that current could be passed through an electrolyte without causing chemical changes. His experiment, which involved zinc electrodes immersed in solid zinc chloride, was unsatisfactory, because the current used was so small that evidence of electrolysis could not be detected. It was severely criticized.

Hering was of the opinion that the electrodeless passage of current through a solution would not produce any phenomena radically different from those obtained with the passage of current introduced through electrodes. He did not actually do any experimental work on the problem, but he described (3, 4) various types of unipolar devices that would achieve the electrodeless flow of current.

Marvin (5) constructed a unipolar device which, however, did not yield sufficient current for experimental purposes. By introducing two copper electrodes into the circuit he was able to obtain a deflection of a galvanometer. His other experiments involved the use of alternating current. Both he and others (6) have shown that an alternating magnetic field can induce an alternating current in a continuous tube of electrolyte. The presence of the current in the electrolyte was demonstrated by its magnetic field or by its heat effect. The electrodeless measurement of the conductivity of electrolytes by making a tube of electrolyte one element of a transformer is now in routine use (7). Experiments with induced alternating currents give no direct information on transport of material in the absence of electrodes.

The major part of the effort in this investigation was expended on the construction of apparatus and the development of a method for detecting electrical migration produced by small currents of the order of microamperes. The objective of the investigation was to set up an experiment which would permit one to observe, qualitatively, electrical migration in the absence of electrolysis. However, a comparison between the effects of the induced direct current and a current introduced by electrodes put the experiments on a semiquantitative basis.

Apparatus

Electrical and mechanical.—The apparatus consisted of three parts: a transformer, a commutator, and an electrolyte system. The apparatus is shown diagrammatically in Fig. 1 and 3 and a photograph is shown in Fig. 4.

The transformer core was originally part of the control equipment on an electric furnace and had large secondary windings that carried several hundred amperes. All windings were removed and the core was wound with a primary consisting of several hundred turns of No. 12 copper wire and a secondary consisting of a rubber tube, about 4 cm inside diameter and 8 meters long, filled with a saturated ammonium nitrate solution. This salt solution was chosen because it is a fairly good conductor and is not very corrosive.

The method of producing the direct current in the electrolyte circuit was periodically to reverse a direct current passing through the primary coil of the transformer. This ordinarily would produce an alternating current in the tube of electrolyte, but by breaking the circuit in the latter at the proper time the reversal of current was prevented. The appara-

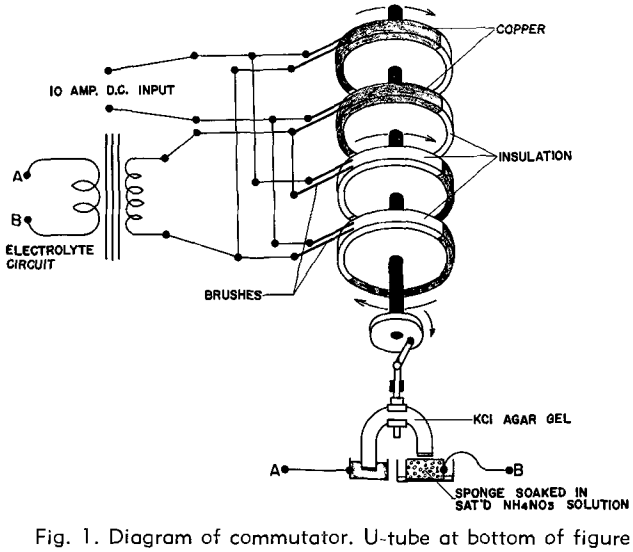

Fig. 1. Diagram of commutator. U-tube at bottom of figure closes electrolyte circuit by being brought into contact with a sponge saturated with ammonium nitrate solution. The U-tube moves vertically up and down in synchronization with the rotation of the commutator wheels. The current through the primary is reversed when the junctions between the copper and insulating parts of the wheels pass under the four pairs of brushes.

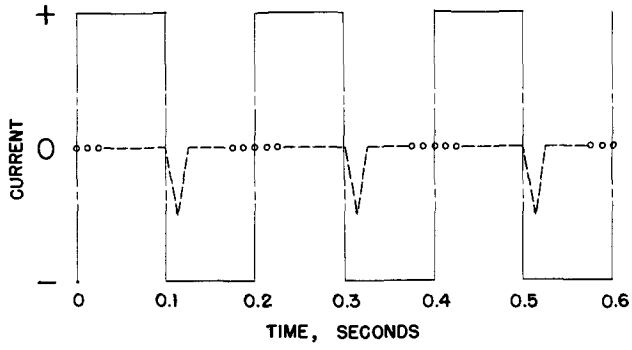

Fig. 2. Schematic representation of the currents in the primary winding of the transformer and in the secondary winding comprising the tube of electrolyte. ————, Current through primory; — — — current through secondary; o o o o, open circuit in secondary.

tus corresponds to a mechanical half-wave rectifier. The principle of operation is made clear with the aid of Fig. 1 and 2. The commutator consisted of four wheels with half of the periphery of each covered with copper and the other half with insulation. Two adjacent copper brushes contacted each wheel. When the junctions between the copper and the insulating segments passed the four pairs of brushes, the current through the primary coil was reversed.

The circuit in the electrolyte was made and broken by a U-tube containing potassium chloride solution in agar-agar gel. The tube was given a vertical reciprocating motion by a crank attached to the same shaft as the commutator wheels. The U-tube (see Fig. 4) was closed at both ends with porous glass diaphragms which served to retain the agar-agar gel during operation of the device. When the U-tube was in its lowest position, it pressed against a sponge saturated with ammonium nitrate solution and thereby completed the electrolyte circuit shown diagrammatically in Fig. 3.

The commutator operated in three steps: Step 1. The electrolyte circuit is closed by the U-tube (connected to the crank) pressing against the sponge. Figure 1 shows the arrangement of components just prior to closing the circuit for step 1. The closing or

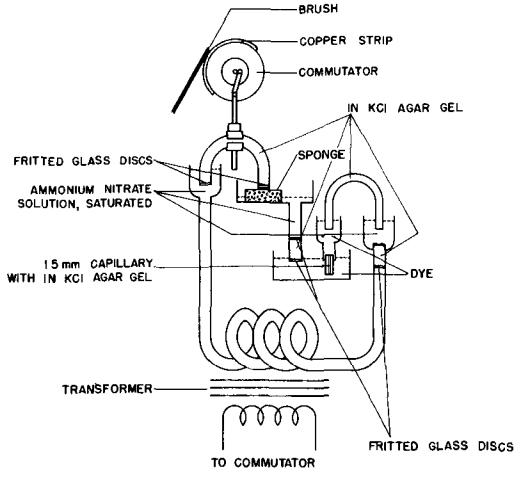

Fig. 3. Diagram of electrolyte circuit. A direct current is produced in the circuit by means of cyclically reversing the current though the primary of the transformer and interrupting the current in the secondary by means of the vertically actuated U-tube.

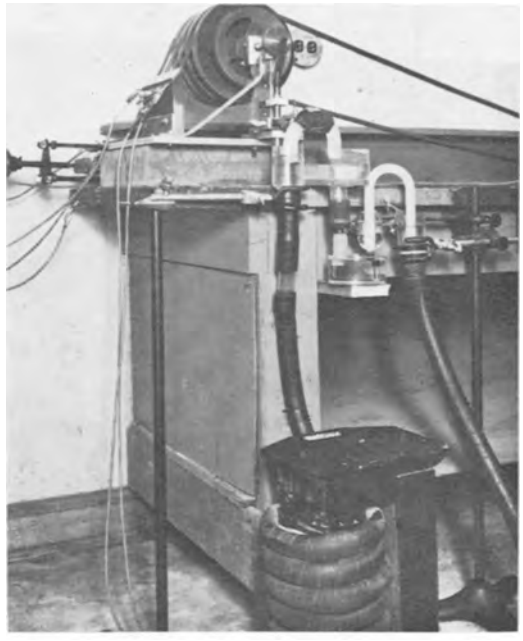

Fig. 4. Photograph of the apparatus

opening of the electrolyte circuit does not produce a flow of current through the electrolyte. Step 2. The junctions on the wheels pass under the brushes and cause the current to reverse through the primary. This change of magnetic flux induces a current in the electrolyte circuit. Step 3. The U-tube is raised from the sponge, which motion breaks the electrolyte circuit. Shortly thereafter the junctions on the wheels again pass under the brushes, causing the current through the primary to reverse to its original direction. Since the electrolyte circuit was broken previously, this produces no current in it. The positions of the brushes and the U-tube are now again as shown in Fig. 1 and the cycle is ready for a repetition.

The commutator was operated at about 300 rpm. The current in the primary was about 10 amp. The current in the electrolyte was measured roughly by intercalculating a microameter and two cadmium electrodes immersed in cadmium chloride solution into the electrolyte circuit. The latter consisted of the tube of ammonium nitrate solution, the dye solutions, and the 1.0M potassium chloride solution in the capillary. The current flowed in pulses having a peak value of 300 μ amp. The voltage was about 0.5 v.

The success of the transformer device depended largely on the use of the U-tube and sponge to break the electrolyte circuit. At first, various types of revolving and reciprocating stopcocks were used to break the circuit. However, they were unsuccessful for two reasons. The film of solution that formed around the plug prevented the circuit from being broken efficiently and the plugs galled and caused the cocks to leak. The use of Teflon plugs did not solve the problem. Another important factor in the operation of the apparatus was the reversing of the current through the primary instead of merely breaking the circuit. Reversing the primary current increased the current in the electrolyte circuit about fivefold.

Apparatus for observing ionic migration.—Since only small currents were generated in the electrolyte, a sensitive method of observing electrical migration was necessary. The moving boundary method was found to be unsuitable. The method adopted was to observe the movement of a dye, erythrosine B, (the di-sodium salt of tetraiodofluorescein) into a capillary containing a gel.

The size of the capillary was important. Preliminary experiments had shown that in a capillary about 0.5 mm in diameter, the migration caused by a current of 25 μamp in 15 min was readily detected. With still smaller capillaries, probably the migration effects of even smaller currents can be detected. However, the minimum size of the capillary that could be used in the experiment was limited by the small voltage that was available, and the gain in sensitivity was offset by the reduction in current due to the high electrical resistance of the solution in the capillary. On the other hand, a large capillary decreased the sensitivity of the experiment because of increased amount of dye diffusing into the capillary. This could be greater than that carried in by electrical migration. The optimum inside diameter of the capillary was 1.5 mm. The capillary was filled with an agar gel containing about 2% agar-agar and 1.0*N* in potassium chloride. A more dilute solution of potassium chloride would have been preferable, since it would carry less current at the junction with the dye solution. However, the resistance of a 0.1*N* solution of potassium chloride in the capillary was too high.

The use of the capillary filled with agar gel also involved a mechanical problem, because the thread of gel readily became detached from the capillary wall and occasionally even slipped out of the tube. To obviate this difficulty the capillary surface was roughened with glass powder in the following manner. A drop of mineral oil was allowed to flow through the capillary and wet the surface. Then glass powder was drawn through the tube by connecting one end to a vacuum line and placing the other end near a small quantity of powder. Finally, the capillary was heated several hours at 600°C to cause the glass powder to fuse to the wall. Capillaries about 20 cm long were prepared and pieces about 2 cm long which were used in the experiments were cut off with a diamond wheel.

The capillary was connected to the funnel shaped piece of glass shown in Fig. 4 by a rubber stopper or tube. The entire current in the electrolyte circuit passed through the capillary.

Procedure

The experiments themselves were simple and required little time. A 0.01M solution of erythrosine was poured into that vessel to which the capillary was attached, and the lower end of the capillary protruding from the end of the vessel was immersed in a beaker of the dye solution. In this manner both ends of the capillary were in contact with the dye. In Fig. 4 the dye solution has been omitted. The circuit between the beaker of dye solution and the solution in the electrolyte coil was completed with another U-tube filled with potassium chloride-agar gel.

Table I. Summary of experiments

Comparison of the electrical migration of erythrosine B with and without conventional electrodes. Dye solution, 0.01M. Solution in capillary was 1.0M potassium chloride and contained about 2% of agar. Diameter of capillary, 1.5 mm. Thirty minute run at about 300 rpm. Peak current, 300 μamp.

	Description of experiment	Migration of dye,* mole × 10^{-8}
1.	Electrodeless	6.0
2.	Electrodeless. Direction of current opposite to that of No. 1	6.7
3.	Current, 150 μamp, from an external source introduced by electrodes	6.0
4.	Current, 90 μamp, from an external source introduced by electrodes	3.4
5.	Induced direct current as in No. 1 and No. 2, except that Cd electrodes were placed in the electrolyte circuit	2.8
6.	Control. Diffusion of dye into capillary without current	1.4

* All electrical migration experiments were corrected by subtracting 1.4 × 10^{-8} moles of dye as determined by control experiment No. 6.

Since during the experiment dye diffused into the capillary tube, it was necessary to make a control experiment to correct for it. This was done by immersing another piece of capillary in the dye solution for the same length of time as the duration of the experiment. No current flowed through the control capillary.

Induced current was passed through the system for 30 min, which time was adequate to produce appreciable migration of dye into the main capillary. Both the main and the control capillaries were removed from the dye solution and rinsed. The ends containing the dye were cut off and placed in small test tubes containing 7 ml of water, and the gel was dissolved by heating. The concentration of dye in the solution was measured with a spectrophotometer, and the content of dye in the capillary was calculated.

Since the color of the dye is due to the anion, during current flow it migrated into one end of the main capillary and away from the other end. However, diffusion caused some dye to enter the latter end, but the amount was only about one-third that in the control capillary. The content of the dye in the control capillaries was reproducible within the limits of the measurement of the dye concentration.

Three types of experiments were made. These are listed in Table I. Experiments 1 and 2 dealt with electrical migration in the absence of electrodes. Experiments 3 and 4 involved the use of electrodes and permitted a comparison with the electrical migration of experiments 1 and 2. Experiment 5 was made with induced direct current, but cadmium electrodes were placed in series with the electrolyte circuit.

Results

The data in the table show that the electrical migration of the dye was roughly about the same in the presence or absence of electrodes. This was of the order of 6 x 10^{-8} moles. The current was not

measured during the electrodeless experiments so that a qualitative comparison with experiments 3 and 4 was not possible. However, the currents in the latter experiments were of about the same order of magnitude, since the peak value of the induced current was about 300 μamp.

Comparison of experiments 3 and 4 shows that the electrical migration into the capillary was approximately proportional to the current, so that the capillary method is valid as a comparative method of studying electrical migration.

To make certain that no geometrical or extraneous effects were involved in the electrodeless experiments, the currents in experiments 1 and 2 were made to flow in opposite directions. In one experiment the dye migrated into the upper end of the capillary and in the other into the lower end.

The amount of migration obtained in experiment 5 with cadmium electrodes in the circuit was less than in experiments 1 and 2. This indicates that the current during this experiment must have been less than that in 1 and 2. This could have been caused by the resistance of the additional electrolyte in the circuit (the cadmium chloride solution) and a microameter or by variations in the performance of the equipment.

The amount of electrical migration of the dye in all of these experiments indicated that it was carrying only about one-thirtieth of the current. This is understandable, since the dye, which was only 0.01M, was migrating into a capillary containing 1M potassium chloride. Hence, at the juncture of the two solutions, the major portion of the current must have been carried by the potassium chloride solution.

Since the induced direct current produced normal electrical migration, it was of interest to determine whether it also produced normal electrolysis. The induced direct current was passed through a copper wire and a platinum wire, serving as anode and cathode, respectively, immersed in a copper sulfate solution. A copper deposit was obtained in an amount roughly corresponding to the current that passed.

Summary

An apparatus was devised for producing a direct current in an electrolyte without the use of electrodes. With this apparatus it was possible to observe the electrical migration[2] of a dye in a capillary.

Acknowledgment

The author acknowledges the patient and skillful assistance of O. V. Hurst in constructing the mechanical and electrical parts of the induced current apparatus and the assistance of J. L. Sligh in performing the experiments involving the passage of current through the gas phase.

Manuscript received June 13, 1960; revised manuscript received Aug. 9, 1960. This paper was prepared for delivery before the Columbus Meeting, October 18-20, 1959.

[2] It has been suggested that the movement of the dye, instead of being due to ionic migration, might be caused by electroosmosis of water through the capillary. This possibility cannot be completely discounted, but it is unlikely, since the movement of water in solutions as strong as the one in the capillary (1.0M) is considered to be due to ion hydration and not to electroosmosis.

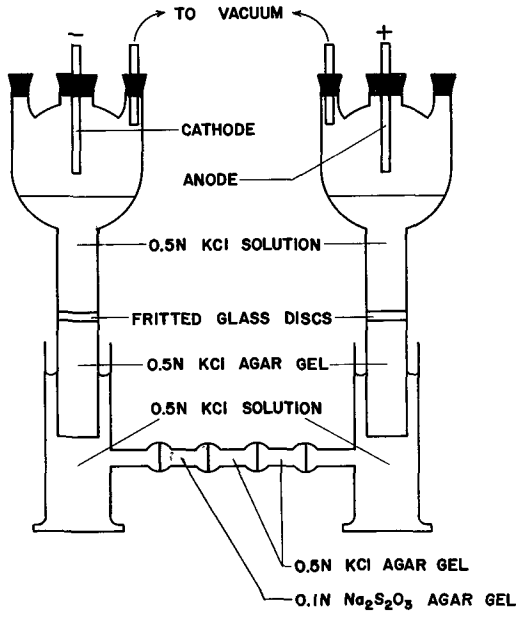

Fig. 5. Diagram of the circuit used for studying the migration of thiosulfate ion in a system provided with a gaseous discharge.

Any discussion of this paper will appear in a Discussion Section to be published in the June 1961 JOURNAL.

REFERENCES

1. J. W. Richards. *Trans. Am. Electrochem. Soc.*, **6**, 152 (1904).
2. J. W. Richards, *ibid.*, **19**, 119 (1911).
3 Carl Hering, *Trans. Am. Inst. Elec. Eng.*, **19**, 309 (1902).
4. Carl Hering, *Trans. Am. Electrochem. Soc.*, **13**, 273 (1908).
5. A. B. Marvin, *ibid.*, **3**, 347 (1903).
6. A. N. M. Hopkins, Discussion, *ibid.*, **3**, 356 (1903); B. Experiment Über Elektrolytische Leitung ohne Elektroden Hs. Behn-Eschenburg, *Z. Elecktrochem.*, **5**, 402 (1899).
7. A. Electrodeless Conductivity System, Industrial Instruments Inc. U.S. Pat. 2,542,057; B. Miroslav Salamon and Peter Svitok, *Chem. Prumysl*, **6**, 10 (1956); C. Raymond Calvert, J. A. Cornelius, V. S. Griffiths, and D. Irwin Stock, *J. Phys. Chem.* **62**, 47 (1958).
8. Alfons Klemenc, *Chimia*, **6**, 177 (1952).

APPENDIX

Electrical Migration in an Electrolyte in Contact Only with a Gas

Another method of passing current through an electrolyte without immersing electrodes in the liquid is to pass the current through the gaseous space above the liquid. The experimental arrangement for this is shown in Fig. 5. It is well known that the chemical effects at the solution-gas interface are several times greater than the amount predicted by Faraday's law (8). Hence, it was of interest to determine whether the electrical migration in the electrolyte was normal or greater than normal.

Metallic electrodes were suspended several centimeters above the surface of the electrolyte which was contained in a closed vessel, and the system was pumped down to a pressure of about 1 cm. A discharge through the gas phase was obtained with a few hundred volts. The current was set at 0.1 amp, although larger currents could have been obtained. The current passed from the metallic electrodes through the gas and the electrolyte which was contained in tubes. To prevent the electrolyte from being forced into the evacuated chambers, a KCl-agar gel was placed in the circuit in contact with a fritted glass partition.

The migration of ions in the electrolyte was investigated by using a gel containing sodium thiosulfate. The migration of the thiosulfate across a boundary into a KCl-agar gel was determined by titration with a standard iodine solution. The amount of thiosulfate that migrated in the system with the gas discharge was compared with that which migrated in a conventional system provided with metallic electrodes. The amounts were the same within the experimental precision which was about 5%.

Formation of Phosphor Films by Evaporation

L. R. Koller and H. D. Coghill

Research Laboratory, General Electric Company, Schenectady, New York

ABSTRACT

Three processes for making ZnS phosphor films are described. One process for ZnS activated with Cu, Ag, or Mn involves evaporation of powder phosphor onto a room-temperature substrate followed by heat treatment of the film in an H_2S + HCl atmosphere. A process for ZnS:Mn alone involves the single step of evaporating the phosphor onto a substrate held between 250° and 400°C. The third process involves evaporating the phosphor in a single step onto a heated substrate in a uniformly heated enclosure such as the "Hot Wall Bell Jar." A fourth process used for silicate, phosphate, and borate phosphors involves a reaction during the course of evaporation between ZnF_2 and a heated substrate.

Thin continuous films of phosphors a few microns thick are useful for practical applications as well as for investigation of cathodo, photo, and electroluminescent phenomena. One method of preparing such films is by evaporation *in vacuo*. The technology of forming phosphor films by evaporation is relatively new. DeBoer (1) patented a process for evaporating ZnS and $CaWO_4$ x-ray intensifying screens in 1934 although it is questionable whether his films would be considered luminescent by present standards. Williams (2) prepared a number of different kinds of phosphor films by evaporation in 1947. He found that efficient films of manganese-activated zinc fluoride could be evaporated but that zinc sulfide, zinc sulfoselenide, and zinc cadmium sulfide films failed to show appreciable luminescent efficiency. More recently Koller (3), and Feldman (4) described methods for making sulfide and fluoride phosphor films. Feldman also described methods for making oxygen containing phosphors. Rychlewski (5) patented methods for forming films of ZnS as well as some oxygen containing phosphors. All three of these methods involve heat treatment at some stage of the process. Studer and Cusano (6) have formed films of a variety of ZnS:Se phosphors by a different but related procedure, namely, vapor reaction.

Although ZnS and some other host lattice materials may be readily evaporated *in vacuo* and condensed again in the form of thin transparent films, these films are not necessarily luminescent (with the possible exception of ZnF_2). The formation of a phosphor film imposes the additional requirement that the film be crystalline and contain activator and coactivator materials in suitable lattice sites and concentration.

Since the vapor pressures of the various constituents of a phosphor differ widely, the condensate (*i.e.* the film) will not have the same composition as the phosphor material evaporated. Furthermore the composition of the condensate will change during the course of the deposition as the phosphor composition changes due to this fractional distillation. These effects result in a gradation of composition throughout the depth of the film.

The composition of the film is also affected by the difference in accommodation coefficients of the phosphor components. Not every molecule which arrives at the substrate surface remains there. Many are reflected from the surface and condense on the relatively cold wall of the bell jar. The composition of the film will depend on the relative accommodation coefficients of the phosphor constituents which in turn are functions of the temperature of the substrate. Accordingly, the composition of a film will depend in a rather complex way on the nature of the material being evaporated, the length of time during which the evaporation has been in progress and the temperature of the evaporator and the substrate.

From these considerations it can be seen that the optimum conditions for forming films of any given phosphor will depend on the nature of the phosphor and that no one method will be satisfactory for all phosphors.

The procedures for forming phosphor films may be broadly classified as follows.

Two-step processes: (a) simultaneous evaporation of host lattice and activator materials and condensation on room-temperature substrate followed by heat treatment; (b) sequential evaporation of host lattice and activator materials (order immaterial), both condensed on room-temperature substrate followed by heat treatment.

One-step processes: simultaneous evaporation of host lattice and activator onto heated substrate.

Reaction processes: phosphor formed in one step by reaction of a compound with a heated substrate.

Apparatus

All of the two-step processes and some of the one-step processes were carried out in a vacuum system with an 18 in. bell jar exhausted by a 6 in. oil diffusion pump. The system had no cold trap. During the course of an evaporation the pressure maintained was about 10^{-4} mm.

A number of different types of evaporators made of tungsten wires and tungsten foil were used. The most versatile and useful was a foil boat formed by folding a strip of 0.001 in. tungsten foil lengthwise and clamping the ends. A boat ⅜ in. high 1¾ in. long is heated to a temperature of 1673°K by a current of 60 amp with a drop of about 3.2 v. Tungsten was the most satisfactory material for evaporating sulfide phosphors and did not react significantly with them. It also had less copper impurity present than either platinum or molybdenum. Platinum was used for evaporating fluoride phosphors.

The heater for the substrate consisted of a bank of four 500-w tubular quartz infrared lamps mounted on a reflector and placed a few inches above the substrate.

Most of the materials evaporated were in the form of crystalline powders. In order to keep these from jumping out of the boat and sputtering, they were compressed into pellets by means of a small hydraulic press. These compact pellets could be evaporated at the rate of about 0.05 g/min with very little sputtering.

Preparation of Surface

Most of the films were deposited on 2 in. diameter Pyrex disks. The glass was cleaned with a mild abrasive, rinsed in distilled water, and air dried. Other cleaning methods appeared to give equally satisfactory results.

Evaporation

After the preliminary heating of the substrate, films were formed by evaporating the phosphor at rates of about 0.05 g/min with the source 3-6 in. from the substrate. Films were usually deposited to a thickness of about 2μ. The film growth could be monitored by observation of the interference color.

The effect of the vapor pressures of the constituents on the composition is illustrated by the analysis of ZnS:Mn films formed by evaporating a ZnS:Mn phosphor having an Mn content of 0.1%. By means of a slide changer, films were collected during the first, second, and third minutes of evaporation. The Mn/Zn ratios in these films were 0.003, 0.007, 0.011, respectively, compared with 0.001 for the original material. Thus the Mn/Zn ratio in the film was greater than that of the source material and increased progressively during the course of the evaporation. A number of analyses of other ZnS:Mn films showed a Mn/Zn ratio of as much as ten times that of the original film. Thus in addition to a variation in activator concentration with film thickness, ZnS:Mn films tend to have an over-all higher Mn content than the source material.

The effect of the accommodation coefficient on film composition is illustrated by some experiments on evaporation of a ZnCdS phosphor onto substrates at various temperatures. The same evaporation procedure was followed in successive runs. The substrate temperature is given in the first column of Table I. In these experiments the substrate temperature was not constant but increased during the course of the evaporation due to the heating effect of the evaporator. The second column gives the cadmium to zinc ratio. The source material had a cadmium to zinc ratio of 9/1. Table I shows the marked decrease in the Cd/Zn ratio with increasing substrate temperature. The maximum at the low temperature end of the range was not investigated further.

Table I.

Substrate temp, °C	Cadmium to zinc ratio
190-250	6.4/1
250-280	8.1/1
280-330	4.2/1
330-370	2.2/1
430	2.1/1

Two-step process for zinc sulfide phosphors activated with Ag, Cu, *and* Mn.—Evaporation of sulfide phosphors and condensation on a glass substrate at or near room temperature results in clear transparent films. The presence or absence of activator has relatively little effect on film formation. The films formed in this way, however, are not luminescent. Electron diffraction shows them to be amorphous. In order to convert these films to phosphors they must be crystallized by heat treatment. This is accomplished by heating them in an atmosphere of H_2S + 10% HCl at about 650°C for ½ hr. This treatment converts them from the nonluminescent amorphous state to the luminescent crystalline state. Electron diffraction shows that after this heat treatment the films are hexagonal and microcrystalline with the crystal size of the order of 1000Å. After this treatment, the films have a matte surface. They become quite transparent if polished.

The HCl vapor is necessary in order to introduce Cl coactivator into the lattice simultaneously with the recrystallization as it is probable that Cl coactivator is lost during the evaporation process. A higher concentration of HCl than 25% results in excessive attack on the film while less than 2% is not effective. The H_2S flow is regulated at about 2 ft³/hr. The optimum time of heating is about ½ hr. Shorter times result in significantly less efficient films while heating up to several hours does not result in any further improvement. No activation is obtained below 550° or above 750°C. The lower limit is probably determined by the rate of diffusion of activator and coactivator. The upper limit is probably determined by the retention of chlorine by the phosphor which Goldberg and Kremheller (7) found to be a maximum at 650°C.

Attempts to introduce Cl by evaporation of AgCl or $ZnCl_2$ simultaneously with the ZnS were not successful.

Attempts were made to use Al as a coactivator for ZnS:Ag by evaporating Al onto the surface of the film and then heat treating *in vacuo* or dry nitrogen. Amounts of Al less than 1% of the weight of the film were ineffective. Larger amounts resulted in moder-

ate bluish-green luminescence. The films remained clear, transparent, and colorless although similar films without the Al subjected to the same heat treatment developed a matte etched surface.

Indium and gallium coactivators only resulted in weak orange luminescence when added to ZnS:Ag.

The method of introduction of the activator is relatively unimportant. It may be introduced simultaneously with the deposition of the ZnS by evaporating a standard powder phosphor. It may be mixed with the ZnS, or it may be evaporated from a separate boat in the form of a salt or the pure metal either simultaneously with, prior to or after the ZnS evaporation. The over-all activator phosphor ratio must be correct however; hence the evaporation conditions must be determined empirically.

The temperature of the substrate on which the phosphor is deposited is crucial. Films deposited *in vacuo* on a substrate at a temperature above about 100°C are crystalline but they are nonluminescent (with the exception of ZnS:Mn) and do not become luminescent when heat treated (at 650°C) in H_2S + 10% HCl. A possible explanation is that in the crystallized material diffusion of chlorine at this temperature takes place mainly along the grain boundaries, and not through the body of the crystals. Heat treatment (below 650°C) is only effective in activating sulfide films provided they are initially in the amorphous condition corresponding to deposition at substrate temperatures below 100°C.

This two-step procedure has proved to be effective for making photo and cathodoluminescent Zn and Cd sulfide films with Ag, Cu, and Mn activators having brightnesses 1/5 to 1/10 of the corresponding phosphors.

One-step process for Mn *activated* ZnS.—Manganese activated ZnS differs from the Cu and Ag activated Zn sulfides in that it can be formed by a one-step process. This consists of evaporating the phosphor material and depositing it on a substrate in the range from 250° to 400°C. This results, without any further treatment, in a cathodo and weakly photoluminescent film. The reason for this difference in behavior between the Mn and the Ag and Cu activated phosphors is that the luminescence is the result of electron transitions between levels in the Mn center while in the other phosphors the transition is from the conduction band to the center. The latter process requires a higher degree of perfection of the host lattice than is obtained by crystallization at 250°C. At higher substrate temperatures the chlorine coactivator is lost as pointed out in the previous section.

One-step process for ZnS *phosphors—"Hot Wall Bell Jar."*—The ideal condition for forming phosphor films is to deposit them on a substrate at a temperature high enough so that the incident molecules will have sufficient mobility to form an ordered structure. With sulfide phosphors evaporated in an ordinary bell jar the substrate temperature is limited to not much above 300°C. This is because of the re-evaporation or reflection from the heated substrate. At 400°C this is so great that only very thin films are formed while at 600°C no deposition takes place at all. This is in spite of the fact that at 600°C

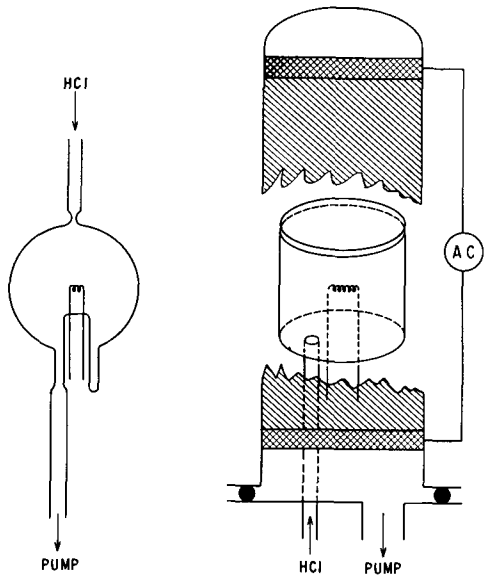

Fig. 1a. Bulb for evaporation on heated wall; Fig. 1b. Hot wall bell jar.

the rate of evaporation of ZnS is only of the order of 10^{-11} g/cm²/sec. In order to form films on surfaces at elevated temperatures it is necessary to carry out the evaporation in a vessel whose walls are uniformly at the substrate temperature. In any ordinary bell jar system the walls and the base are usually at a substantially lower temperature than the substrate and so act as a sink for ZnS.

This difficulty can be avoided by depositing the film on the wall of a uniformly heated spherical bulb with an evaporator at the center. This arrangement is shown in Fig. 1. The evaporator consists of a helical tungsten filament in which is placed a pellet of the phosphor. The bulb is pumped continuously and is in an oven to maintain a uniform wall temperature. A small flow of HCl is maintained through the bulb to make up for the loss of coactivator during the evaporation of the phosphor. The loss of host lattice material or activator through the connection to the pump is negligible, but the chlorine is more volatile and it is necessary to introduce some to make up for the losses. The HCl flow required is about 10,000 μl/g of phosphor evaporated.

To the extent that the bulb walls are at uniform temperature there is no tendency for the different phosphor components other than the coactivator to separate out, and the composition of the deposit will be the same as the material evaporated. The relatively high temperature of the walls during deposition insures diffusion of the activator uniformly throughout the film.

By this procedure Cu, Ag, and Mn activated ZnS phosphor films were made by evaporation of commercial powder phosphors. A number of sulfoselenide phosphor films have also been prepared in the same way. The films show both cathodo and photoluminescence when deposited at 650°C. As the deposition temperature is lowered, both of these decrease in efficiency but the effect on the photoluminescence is more marked. At 500°C the latter is negligible while the cathodoluminescence is still fairly efficient. Below this temperature the cathodoluminescence also falls off rapidly.

The phosphors prepared in this way show approximately the same emission and excitation spectra as the corresponding powder phosphors. Their brightness is 1/5 to 1/10 of that of the powders under the same excitation. The decay rate of the luminescence is usually higher for the films than for the corresponding powders.

While this procedure is very effective in forming films, the samples on curved bulb walls are unsuitable for many applications. Accordingly a system was devised for depositing the films on flat 2 in. diameter Pyrex disks. This system is shown schematically in Fig. 1b. It consists essentially of a small quartz chamber closed at the top and bottom by glass disks which seat against ground shoulders. The upper disk is the sample to be coated, the lower one is perforated for evaporator filament leads and HCl inlet tube. This chamber is essentially a demountable bulb. It is placed in a small quartz bell jar. The bell jar is coated on the outside with a conducting tin oxide coating having a resistance of about 30Ω between the silver paste ring electrodes. By passing a current through this coating the walls may be heated rapidly and uniformly to as much as 700°C. The bell jar is sealed by an "O" ring. The base plate is water cooled and an additional metal ring on top of the bell jar flange is also water cooled to protect the "O" ring.

Various cathodo, photo, and electroluminescent sulfoselenide phosphors have been made with this apparatus.

Reaction process for forming oxygen containing phosphors.—A number of oxygen containing phosphors may be formed by reaction of a vaporized substance with a heated substrate in a single step. One of these is Zn_2SiO_4:Mn. This is formed by reaction of ZnF_2:Mn with a heated substrate consisting of a high silica content glass such as fused quartz, Vycor, Pyrex, or Corning No. 1710. The glass substrate is maintained at a temperature in the 550°-650° range while ZnF_2:Mn is evaporated from a platinum evaporator filament. The ZnF_2 reacts with the SiO_2 of the glass according to the reaction

$$2ZnF_2 + 2SiO_2 \rightarrow Zn_2SiO_4 + SiF_4$$

The SiF_4 is volatile and is pumped out of the system leaving a layer of Zn_2SiO_4 well bonded to the glass. As the evaporation continues, the willemite becomes covered with a layer of ZnF_2. Thus the deposit consists of two layers; the Zn_2SiO_4 next to the glass and on top of this layer of ZnF_2. The ZnF_2 can be readily dissolved in NH_4OH leaving the insoluble film of willemite. The two-layer system of a yellow phosphor on top of green phosphor may also be used as a penetron (8, 9). This reaction method of forming willemite permits the formation on Pyrex or other high silica glasses at temperatures several hundred degrees below those required when the phosphor is formed by the two-step process.

Rottgardt (10) has described a related method of forming silicate phosphors by evaporating a fluoride onto a silicate base and subsequently carrying out the reaction by heat treatment in air.

An analogous process may be used to form a zinc borate phosphor. In this case a borate glass is used as the substrate and ZnF_2 again is evaporated. Since good borate glasses with sufficiently high melting points are not available this process is carried out with a borate glass glaze on the surface of No. 7052 FN glass. The resultant phosphor is a red cathodoluminescent zinc borate with an overlying layer of ZnF_2:Mn. The latter may be dissolved off in NH_4OH without damage to the zinc borate.

An analogous process can also be used with phosphate glasses. These, however, are low melting and unsatisfactory for many purposes. An alternative process is possible here. This is to first evaporate a layer of ZnF_2:Mn onto a Pyrex substrate at, say, 300°C, which is low enough to avoid reaction with the glass but high enough to insure good adhesion. The temperature is then raised to 550°C and a pellet of P_2O_5 is evaporated. This reacts with the ZnF_2 to form $Zn_3(PO_4)_2$:Mn.

Summary

A considerable number of zinc cadmium sulfoselenide phosphor films can be made by vacuum evaporation of commercial powder phosphors. Luminescent films of zinc sulfide activated with Cu, Ag, or Mn may be formed by deposition at room temperature followed by heat treatment in a suitable atmosphere. The same phosphors may be formed in a single step by evaporation onto a heated substrate in the "Hot Wall Bell Jar."

Manganese activated ZnS may also be formed in a single step by deposition on a substrate between 250° and 400°C.

Zinc silicate, phosphate, and borate may be formed in a single step by reaction of zinc fluoride with a heated substrate.

Manuscript received June 15, 1960; revised manuscript received July 20, 1960. This paper was prepared for delivery before the Chicago Meeting, May 1-5, 1960.

Any discussion of this paper will appear in a Discussion Section to be published in the June 1961 JOURNAL.

REFERENCES

1. J. H. deBoer and C. J. Dipple, U. S. Pat. 1,954,691, April 10, 1934.
2. F. E. Williams, *J. Opt. Soc. Am.*, **37**, 302 (1947).
3. L. R. Koller, Electrochem. Soc., Spring Meeting (1957).
4. C. Feldman and M. O'Hara, *J. Opt. Soc. Am.*, **47**, 300 (1957); C. Feldman and M. O'Hara, *ibid.*, **48**, 816 (1958); C. Feldman, *J. Soc. Motion Picture & Tel. Eng.*, **67**, 455 (1958).
5. T. Rychlewski, U.S. Pat. 2,898,225, Aug. 4, 1959; T. Rychlewski, U.S. Pat. 2,903,378, Sept. 8, 1959.
6. F. J. Studer and D. A. Cusano, *J. Opt. Soc. Am.*, **45**, 493 (1955).
7. P. Goldberg, D. J. Bracco, and A. Kremheller, *This Journal*, **102**, 79C (1955).
8. L. R. Koller and H. D. Coghill, *J. Appl. Phys.*, **29**, 1064 (1958).
9. C. Feldman, *J. Opt. Soc. Am.*, **47**, 790 (1957).
10. J. Rottgardt, U.S. Pat. 2,876,129, March 3, 1959.

Thermoelectric and Crystallographic Properties of Ag_2Se

J. B. Conn and R. C. Taylor

Research Laboratories, Merck Sharp and Dohme, Rahway, New Jersey

ABSTRACT

Silver selenide has been prepared by fusion techniques and found to be a good thermoelectric material. The Seebeck coefficient, resistivity, and thermal conductivity have been measured as a function of temperature. The effect of doping with 30 different elements and compounds at different doping concentrations has been studied. The inter-relationships between the thermoelectric properties have been examined and are discussed. The crystal lattice of silver selenide has been determined, and the subcell and superstructure are elucidated.

During the past few years, this laboratory has been engaged in a study of thermoelectric materials. In the course of these investigations, the excellent properties of silver selenide were discovered. A thorough examination of the material was made, including crystallographic studies, temperature dependence of its thermoelectric properties, and effect of alloying and doping on these properties.

The semiconducting properties of silver selenide have been put to use in thermopiles by Schwarz (1). His n-type material was a silver sulfide-silver selenide alloy with a figure of merit of 0.9×10^{-3} deg^{-1}. The corresponding p-type material was an alloy of silver, copper, tellurium, and selenium with a figure of merit of 1.0×10^{-3} deg^{-1}. Resistivity and Hall effect of silver selenide have been studied by Mooser and Pearson (2) and by Busch and Junod (3). The energy gap and room-temperature electron mobility were also determined by Busch and Junod to be 0.075 ev and 2000 cm^2/v-sec, respectively. They found the material to show metallic behavior above the transition temperature of 133°C. They observed no measurable ionic conductivity. Miyatani (4) measured the properties of silver selenide via the emf of the galvanic cell $Ag/AgI/Ag_2Se/Pt$ and at 130°C determined the electron mobility to be 810 cm^2/v sec and the effective electron mass to be 0.11 m. Junod (5) recently published an extensive investigation of the crystallographic and semiconducting properties of silver selenide, silver sulfide, and copper selenide, including conductivity, Hall effect, Seebeck coefficient, and other properties.

Materials

Starting materials were sufficiently pure so that further purification was not considered necessary. Selenium was obtained in 99.999+% purity from American Smelting and Refining Company. Silver of 99.99+% purity from American Smelting and Refining and of 99.9999% purity from Consolidated Mining and Smelting Company of Canada, Ltd. was used. Doping materials were of a similar high purity.

Preparation.—All samples were prepared in 12 mm 1D quartz tubes which had been carbon-coated prior to introduction of the materials. Carbon-coating was accomplished by pyrolysis of acetone vapor (using nitrogen as a carrier gas) on the inside surface of the quartz tube at about 900°C. Carbon-coating had the reducing properties which are found so advantageous in graphite crucibles and so prevented reaction of oxides with the quartz. At the same time the undesirable absorption of selenium vapor into graphite was eliminated by substitution of the thin carbon coating. The materials were then introduced into the quartz tube in the desired composition, the tube evacuated to about 10^{-5} mm and sealed. The tube was kept at 1050°-1100°C for 16 hr followed by a 3-hr cooling period in the furnace, or a 24-hr drop time through a temperature gradient. No difference in properties was found between ingots prepared by the two different methods, nor were we able to produce more than slightly oriented ingots because of the phase change at 133°C. Ingots weighed about 40 g. After removal from the quartz tubes, the ingots were machined for measurement. Samples were found to be homogeneous, with clean, but slightly pitted surfaces. Except in the few cases where the quartz tubes cracked in cooling (and this was invariably found to be due to insufficient carbon coating) the ingots were free of surface oxidation. In most cases the ingots were malleable and easily machined. A few of the samples which had been doped with excess sulfur, selenium, tellurium, or silver iodide were found to be brittle; apparently the high vapor pressure of these doping agents produces internal cracks in the ingot. Many of the ingots were annealed at 125°C for 48 hr with no apparent effect.

Measurements

The samples were cut to approximately ¾ in. long and faced off on a lathe. Two rings were machined into the surface of the sample and into these rings platinum wires were tightly wound to act as the probe for a-c resistivity measurements. The sample was then placed between two resistance wire wound graphite heaters, and pressure for thermal and electrical contact was applied to the unit by a vise type jig. A temperature gradient of 5°-15° was maintained across the length of the sample by

power supplied from a d-c source to the resistance heaters. At thermal equilibrium ΔT was determined from two thermocouples placed through the center of each heater and in contact with the sample. The thermal emf was measured from the copper leads of each thermocouple. Measurements were made with a L&N type K-3 potentiometer. The measurement temperature was taken as the average between hot and cold ends of the sample.

Resistivity as a function of temperature was determined by means of current contacts made to the sample through the graphite heaters; the potential drop was measured across the platinum probes.

Thermal conductivity data were obtained by placing the sample between a copper sink in contact with an ice-water reservoir and a resistance heater; ΔT was measured with thermocouples placed in the sink and heater about 1 mm from the sample contact. The heat lost by conduction through the sample to the cold sink was balanced by the input to the heater, the temperature of which was kept within 1°C of ambient. K is calculated from the resistance and the current required to keep the heater at ambient.

Crystallographic Investigations

An extensive study of the structure of low-silver selenide was published by Boettcher, *et al.* (6). The unit cell was described as tetragonal, a = 7.06Å, c = 4.98Å, the axial ratio changing with temperature. The lattice was deduced as essentially selenium packing, with silver atoms occupying random sites in the interstices.

Numerous samples of cast silver selenide have been subjected to x-ray diffraction study during the course of this work, and the patterns were sensibly the same, save for crystal ordering. However, far too many reflections were present to be accounted for on the basis of Boettcher's tetragonal axes. On the other hand, an assignment was arrived at on the basis of a 4-molecule orthorhombic unit cell, a = 4.344Å, b = 7.111Å, c = 7.790Å; this reproduced nearly all of the observed reflections exactly, the exceptions being occasional split lines, one member of which could not be incorporated unless all axes were doubled. This suggested the existence of a superstructure, but its nature remained in doubt until completion of the experiment described below.

It was decided to attempt direct preparation of crystalline low-silver selenide by wet process at room temperature, involving reaction of a water-soluble silver salt with a soluble selenide. Since the silver chalcogenides are soluble in alkali cyanide solutions, it was anticipated that interaction of potassium silver cyanide with potassium selenide would provide a crystallization medium for silver selenide. Accordingly, a concentrated solution of silver(I) oxide in potassium cyanide, having composition $K_3Ag(CN)_4$, was added gradually to a freshly prepared strongly alkaline solution of the stoichiometric amount of potassium selenide under stirring and nitrogen atmosphere. The precipitate produced at first was black and finely divided, but when about half of the silver cyanide reagent had been added, a rapid transformation set in, with conversion to a gray, coarse, and very bulky solid. After completion of the metathesis, the product was collected, washed, and dried *in vacuo*.

Under the microscope the particles were seen to consist of globular rosettes of lustrous minute prisms; the x-ray diffraction pattern was essentially that of all other low-silver selenide samples but was exceptionally bright, and showed a wealth of detail not previously observed. The analytical data were surprising and at first sight very disappointing: the Ag/Se ratio was 2.28, a large divergence from the stoichiometric. It was noticed however, that this ratio is 16/7 within the accuracy of the microanalytical determination.

For $Ag_{16}Se_7$, F. W. 2278.8,	Calc.	Found
Ag	75.75	76.1
Se	24.25	24.4
	100.00	100.5

The x-ray diffraction data were then worked up (Norelco Wide-Range Diffractometer, CuKα radiation). The spacings fit an orthorhombic unit cell, a = 8.630Å, b = 14.13Å, c = 15.50Å, and containing $4Ag_{16}Se_7$. The calculated density is 8.00; observed pyknometrically, 7.96. The subcell contains $4Ag_2Se$; the superstructure is derived from it by a systematic vacancy at every eighth selenium lattice site. The formation of this defect phase is all the more striking when it is recalled, as stated above, that it began to crystallize in the presence of a large excess of selenide ion.

Inspection of the phase diagram for the system Ag-Se, as published by Hansen (7), shows that a homogeneous phase of composition $Ag_{16}Se_7$ cannot be attained from a melt, since a liquid miscibility-gap intervenes. Indeed, when the powder was melted in sealed quartz under vacuum, the resulting ingot was coated with silver. Evidently, when high-silver selenide, which is stoichiometric, is cooled through the transition, it can only approximate the structure of the true low-temperature phase.

The question concerning the tetragonal phase described by Boettcher becomes even more puzzling in view of the recent publication of Junod (5) who states that his x-ray diffraction data were in complete agreement with Boettcher. The present authors have had opportunity to discuss this matter with members of the research staffs of other organizations, who also have studied low-silver selenide; they found as we did, that the system is not tetragonal. In fact, one group arrived independently at an orthorhombic axial assignment in close agreement with our own data for the subcell. It can only be surmised that if the tetragonal phase does exist, it must be a metastable transitional form.

Thermoelectric Properties

Stoichiometric silver selenide.—Silver selenide is a semiconducting material with orthorhombic symmetry at room temperature. At 133°C it undergoes a transition to a cubic lattice. The melting point is 897°C. According to the phase diagram (7), the range of miscibility in the liquid state of excess silver or selenium in silver selenide extends from 32 to 44.5 at. % selenium. Beyond these limits a layered ingot results on cooling from the melt.

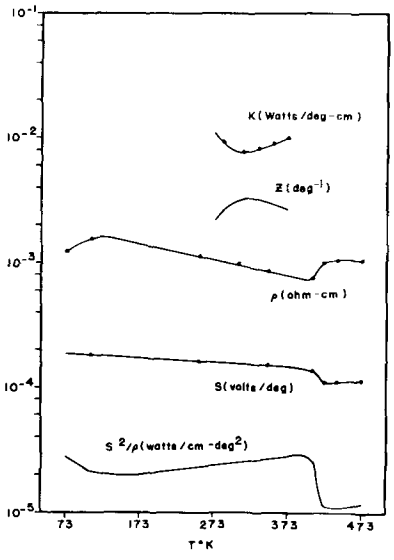

Fig. 1. Variation of thermoelectric properties of stoichiometric silver selenide with temperature.

The variation of the thermoelectric properties of silver selenide with temperature is shown in Fig. 1. The Seebeck coefficient shows a linear decrease from −167° to 120°C, then falls sharply at the transition temperature of 133°C, followed by a slow rise to 220°C. The data of Junod (5) show an increase in Seebeck coefficient to about 0°C followed by a decrease to the transition point, then a sharp break at the transition point. While our studies indicate a decrease in Seebeck coefficient of only about 40 μv/°C through the transition point, those of Junod show a decrease of about 80 μv/°C.

Silver selenide exhibits typical nondegenerate semiconductor behavior in its resistivity, which decreases with increasing temperature from −180°C to the transition point. Here a sudden increase in resistivity occurs followed by a slow rise. Thus the cubic high-temperature form exhibits the behavior of a metal or degenerate semiconductor, as reported by Junod. His data, while being in substantial agreement with ours, show a decrease in resistivity through the transition point, this being followed by a slow increase.

Table I. Room temperature properties of Ag_2Se

R(cm^3/coulomb)	μ(cm^2/v-sec)	n(cm^{-3})
2.2	2050	2.8×10^{18}
S(μv/°C)	ρ(ohm-cm)	k(watts/deg-cm)
−150	10.2×10^{-4}	0.009

The thermal conductivity curve shows a minimum at room temperature. An increase occurs as the temperature increases due to the presence of transport processes other than those associated solely with electrons or phonons, such as ambipolar diffusion. The increase as temperature decreases is a result of reduced phonon-phonon interactions. A maximum figure of merit, in excess of 3.0×10^{-3} deg^{-1} occurs at about 40°C.

A summary of the room temperature properties of stoichiometric silver selenide are shown in Table I. These values are found to be in close agreement with those of Junod.

Effect of doping.—The thermoelectric properties are listed in Table II. With the exception of Cu, AgI, and the group IIB elements, doping agents had very little effect on Ag_2Se. In many cases, the thermoelectric properties are identical for a particular element at the doping levels of both 0.1 and 0.5 mole %, indicating that Ag_2Se is saturated with respect to that element at <0.1 mole %. This low solubility of most foreign materials in Ag_2Se is a prime factor in its insensitivity to doping. It is obviously impossible to p-dope silver selenide, a phenomenon which has been observed in other cases such as ZnSb (8).

The reproducibility of Seebeck coefficient for duplicate ingots, with very few exceptions, has been excellent. Reproducibility of resistivities was not

Table II. Properties of doped Ag_2Se

	S, μv/°C	ρ, × 10^4 ohm-cm	K, watts/deg-cm	Z, × 10^3 deg^{-1}		S, μv/°C	ρ, × 10^4 ohm-cm	K, watts/deg-cm	Z, × 10^3 deg^{-1}
Stoich	−150	10.2	0.0092	2.4	0.1 Ga	−118	4.9	0.0119	2.4
0.5 Cu	−52	2.2	0.0254	0.5	0.5 Ga	−113	4.7	0.0125	2.2
0.5 Ag	−122	6.2	0.0113	2.1	0.1 In	−114	5.4	0.0121	2.0
0.1 Au	−151	10.5	0.0094	2.3	0.5 In	−118	5.1	0.0129	2.1
0.5 Au	−139	8.5	0.0101	2.2	0.1 Tl	−151	13.0	—	—
0.1 S	−153	13.5	0.0090	1.9	0.1 Zn	−123	6.6	0.0099	2.3
0.5 S	−142	8.9	0.0100	2.3	0.5 Zn	−124	6.3	0.0124	2.0
0.5 Se	−151	9.8	0.0089	2.6	0.1 Cd	−98	4.6	0.0152	1.4
0.5 Te	−152	12.0	0.0093	2.1	0.5 Cd	−73	3.2	0.0167	1.0
0.1 Ge	−118	6.6	0.0115	1.8	0.1 Hg	−66	2.7	0.0226	0.7
0.5 Ge	−125	6.5	0.0108	2.2	0.5 Hg	−35	2.5	—	—
0.1 Sn	−150	12.0	0.0091	2.1	0.1 Fe	−110	4.8	0.0122	2.1
0.5 Sn	−120	5.3	0.0115	2.4	0.1 Co	−119	5.8	0.0108	2.3
0.1 Pb	−120	5.9	0.0109	2.2	0.1 Pd	−151	9.7	0.0094	2.5
0.5 Pb	−121	5.8	0.0125	2.0	0.1 V	−117	5.5	0.0119	2.1
0.1 P	−136	7.6	0.0104	2.3	0.1 Cr	−149	9.4	0.0091	2.6
0.1 As	−152	10.6	0.0104	2.1	0.1 Mn	−104	4.6	—	—
0.5 As	−124	5.6	0.0114	2.4	0.1 Re	−145	10.6	0.0094	2.1
0.5 Sb	−114	5.5	0.0121	2.0	0.5 Li	−127	6.0	0.0104	2.6
0.1 Bi	−119	6.2	0.0105	2.2	0.1 AgI	−60	3.1	—	—
0.5 Bi	−122	5.9	0.0117	2.2	0.5 AgI	−23	1.8	0.0552	0.05
0.1 Al	−147	9.0	—	—	0.01 $MoSe_2$	−149	10.1	0.0097	2.3
					0.03 $MoSe_2$	−149	9.4	0.0098	2.4

quite as good, especially in the case of stoichiometric Ag_2Se, where Seebeck coefficient for six samples is within the limit of −146 to −153 μv/°C while ρ covers a range of 7.7 to 13.3 ohm-cm.

The effects of the various doping agents can be considered from the viewpoint of the periodic groups of elements. Only the effect on one parameter need be discussed, since the value of one determines the values of the others, as will be seen in the following sections.

Elements of groups IB and IIB are the only ones to show a large effect on the thermoelectric properties. In group IB, the order of effect is Cu > Ag > Au. In group IIB, the order is reversed, being Hg > Cd > Zn. The order in the group IIB elements parallels the energy gaps of the selenides of these elements, as shown in Table III.

In both cases metallic behavior is approached as one goes from Zn to Cd to Hg. The energy gap of Ag_2Se is 0.075 ev (3). The compound Au_2Se does not form. The energy gap of Cu_2Se is not known but is most likely lower than that of Ag_2Se, since the Seebeck coefficient and resistivity of Cu_2Se are lower than those of Ag_2Se. Thus in the group IB elements, metallic behavior would be approached in the order Au-Ag-Cu, as shown in Table IV. The implication of the reverse trends in the two groups in their doping action on Ag_2Se is that the elements form their normal bond patterns rather than entering in simple isomorphous replacement.

Group VIA has no effect whatsoever, the Seebeck coefficient remaining in the range of −150 μv/°C at both doping levels for S, Se, and Te. If, as mentioned previously, elements form their normal selenide bonds, this would explain the lack of effect of the VIA elements. Groups IIIA (Al, Ga, In, Tl), IVA (Ge,Sn,Pb), and VA (P,As,Sb,Bi) all behave similarly, lowering the Seebeck coefficient to the range of −120 μv/°C at 0.5 mole %. Apparently all but Sn and As saturate Ag_2Se at less than 0.1 mole %, accounting for the leveling of Seebeck coefficient at −120. The transition elements displayed widely divergent effects on the properties, no trends being obvious.

As shown in Fig. 3 and 4, the samples mainly fall into two groups, one with a Seebeck range of 115-125 μv/°C and the second with a range of 145-155 μv/°C. The average figure of merit of 18 materials in the 145-155 range is 2.4 x 10^{-3} deg^{-1}, with six of the samples exceeding 2.5 x 10^{-3} deg^{-1}. The average Z in the 115-125 range, for 19 alloys is 2.2 x 10^{-3} deg^{-1}, with only one exceeding 2.5 x 10^{-3} deg^{-1}.

Table III

Element	S of Ag_2Se at 0.5 mole % doping level	Energy gap of selenide, ev
Hg	−35	HgSe = 0.16
Cd	−80	CdSe = 1.74
Zn	−126	ZnSe = 2.58

Table IV

Element	S of Ag_2Se at 0.5 mole % doping level	Energy gap of selenide, ev
Cu	−51	Cu_2Se < 0.075
Ag	−122	Ag_2Se = 0.075
Au	−139	Au_2Se —

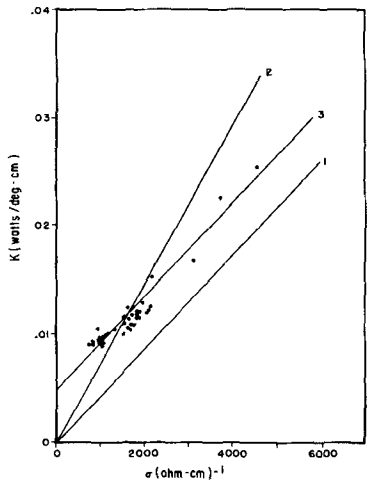

Fig. 2. Electrical conductivity vs. thermal conductivity for stoichiometric and doped samples of silver selenide at room temperature. Curve 1, Wiedeman Franz law, nondegenerate semiconductor, $Kel\rho = 4.35 \times 10^{-6}$ v^2/deg. Curve 2, Wiedeman Franz law, metals, $Kel\rho = 7.35 \times 10^{-6}$ v^2/deg. Curve 3, silver selenide.

Relationship between K and σ.—The relationship between thermal and electrical conductivity at room temperature is shown in Fig. 2. Line 1 represents the Weidemann-Franz ratio for nondegenerate semiconductors (<2.5 x 10^{19} carriers cm^{-3}), where $Kel/\sigma = 4.35 \times 10^{-6}$ V^2/deg. Line 2 is the Wiedemann-Franz ratio for metals (or degenerate semiconductors) where $Kel/\sigma = 7.35 \times 10^{-6}$ V^2/deg. Line 3 is that for the experimentally determined values for Ag_2Se, stoichiometric and doped, where K is the sum Kel + Kph. It is seen that a straight line relationship exists between K and σ for silver selenide which parallels the Wiedemann-Franz law for nondegenerate semiconductors. Since Ag_2Se is then a nondegenerate semiconductor, the ratio $Kel/\sigma = 4.35 \times 10^{-6}$ V^2/deg must hold. Extrapolation of the data to $\sigma = 0$ yields a Kph value of 0.0046 watts/deg-cm. By reducing the thermal conductivity values of the silver selenide samples 0.0046 watt/deg cm, it is found that the line for Ag_2Se and that for nondegenerate semiconductors coincide. The average product $Kel\rho$ for all samples is 4.37 x 10^{-6} V^2/deg, as necessitated by the Wiedemann-Franz law. Any deviation from line 3 for any silver selenide samples can be attributed theoretically to some degree of structure doping, which would then alter the lattice contribution, Kph, from its value of 0.0046 watt/deg-cm. Deviation of the product $Kel\rho$ from 4.35 x 10^{-6} V^2/deg is then a measure of the crystal disorder, except at very high conductivities where the materials become degenerate.

Relationship between S and σ.—The relationship existing between Seebeck coefficient and electrical conductivity is shown in Fig. 3. A large scattering exists at the high conductivity end of the line. As doping agents inject a higher concentration of carriers, electrical conductivity increases and Seebeck coefficient decreases. The values of $S^2\sigma$ remain within the region of 2-3 x 10^{-5} watts/cm-deg^2, for materials with Seebeck coefficients between −90

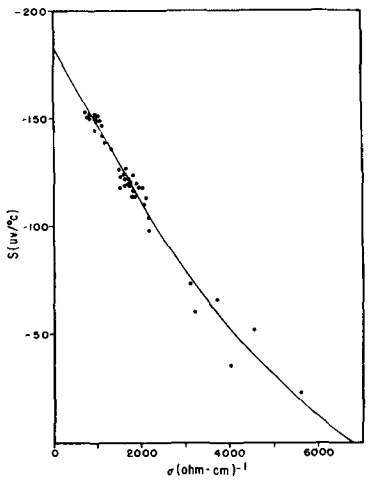

Fig 3. Electrical conductivity vs. Seebeck coefficient for stoichiometric and doped silver selenide at room temperature.

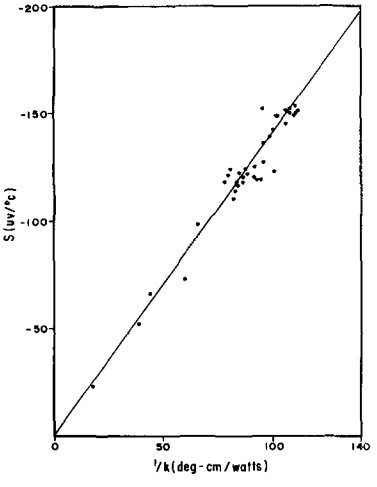

Fig. 4. Thermal resistivity vs. Seebeck coefficient for stoichiometric and doped samples of silver selenide at room temperature.

and −150 μv/°C. The highest values of $S^2\sigma$ are found in the Seebeck coefficient range of −120 μv/°C; however, their Z values are lower than those in the −150 μv/°C range due to higher thermal conductivity.

Relationship between S and K.—The product of Seebeck coefficient and thermal conductivity is remarkably constant at 1.4, resulting in a straight line passing through the origin when Seebeck coefficient is plotted against thermal resistivity, as shown in Fig. 4. The constancy of this product suggests a considerable phonon drag term in the Seebeck coefficient, the product being (Sel + Sph) (Kel + Kph). If no phonon term were present for S, the product would not be expected to be constant any more than it would be for ρ (Kph + Kel), since one term would be entirely electronic, and the other both electronic and phonon. Thus the product Sel σ is probably constant as is Kel ρ. However, the problem of determining Sel presents far more difficulty than does Kel since only a certain proportion of the phonon activity contributing to K will contribute to S. A wavelength requirement for phonons must be met before they will contribute to S. This requirement is that only phonons which have wave lengths not less than the electron wave length will contribute to S.

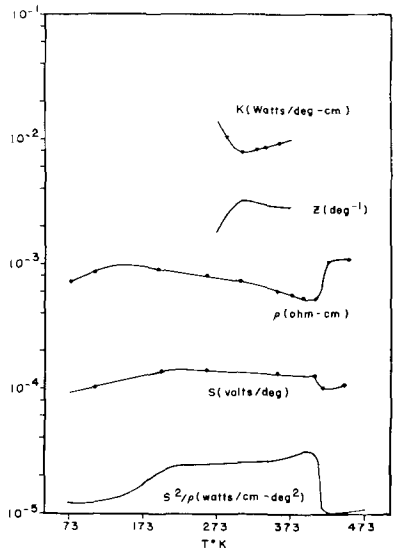

Fig. 5. Variation of thermoelectric properties with temperature of silver selenide doped with 0.1 mole % P.

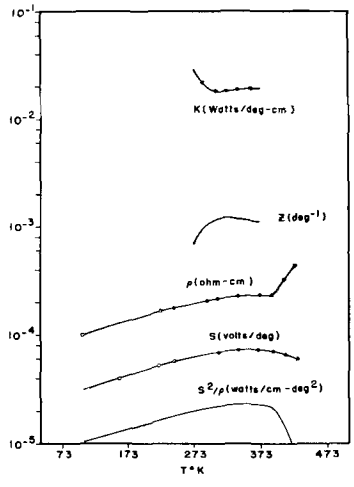

Fig. 6. Variation of thermoelectric properties with temperature of silver selenide doped with 0.1 mole % Hg.

Phonons satisfying this requirement possess a much longer free path length than the bulk of the phonons, and these phonons possess the most marked directional properties along the temperature gradient (9). Therefore the effect of dragging of electrons by such phonons is particularly large. The number of phonons possessing these long wave lengths is probably extremely dependent on crystal perfection. Normally a phonon wave length ranges from one to a few atomic distances, while electronic wave lengths may easily exceed 10 atomic distances.

Effect of temperature on doped Ag_2Se.—The temperature dependence of Seebeck coefficient, resistivity, and thermal conductivity of silver selenide doped with 0.1 mole % phosphorus and 0.1 mole % mercury was investigated. The results are shown in Fig. 5 and 6. The Seebeck coefficient for phosphorus-doped Ag_2Se increases fairly rapidly with temperature to a maximum at about −40°C and then falls slowly to the transition temperature where a sharp drop occurs, followed by a rise to 175°C. In the mercury-doped sample, the Seebeck coefficient increases with temperature to a maximum at 95°C, followed by a decrease at the transition point which is more

gradual than for the stoichiometric or phosphorus-doped samples.

In its resistivity, phosphorus-doped Ag_2Se behaves in a fashion similar to the stoichiometric material except that degenerate conduction exists below −120°C. Mercury-doped Ag_2Se, on the other hand, acts as a degenerate semiconductor throughout the entire temperature range as would be expected from its low resistivity.

The variation of thermal conductivity and figure of merit with temperature is similar to that for Ag_2Se. Thermal conductivity minima in all cases occur at about room temperature. It can be seen that the high-temperature increase in thermal conductivity is much more gradual for the mercury-doped sample. Since this material is degenerate, ambipolar diffusion, if it occurs at all, will have much less effect at higher temperatures due to the larger number of excess carriers present.

Stoichiometric and mercury-doped silver selenide alike display a maximum figure of merit at about 40°C. However, the maximum figure of merit for mercury-doped Ag_2Se is only 1.2×10^{-3} deg^{-1} as against 3.3×10^{-3} deg^{-1} for the undoped compound. Phosphorus doping shifts the maximum to about 30°C and is 3.2×10^{-3} deg^{-1}.

Conclusions

Silver selenide has been found to be a good thermoelectric material. It has a figure of merit of the order of 3×10^{-3} deg^{-1} in the vicinity of room temperature. It has been found impossible to p-dope silver selenide. The stoichiometric material shows the best thermoelectric properties, no improvement being obtained by doping. The compound is nondegenerate from −167°C to the transition point of 133°C, after which its behavior is metallic. Doping was found to occur by formation of normal bond patterns. Kph for silver selenide is 0.0046 watt/°cm, and it is believed that a phonon drag term exists in the Seebeck coefficient. The material becomes degenerate if doped with mercury. The favorable combination of electrical and thermal conductivities characteristic of low-Ag_2Se is ascribed to the existence of a crystal superstructure based on an orthorhombic defect phase having composition $Ag_{16}Se_7$.

Acknowledgments

The authors wish to thank Dr. G. V. Downing and associates for measurements of the thermoelectric parameters.

Manuscript received May 9, 1960. This paper was prepared for delivery before the Houston Meeting, Oct. 9-13, 1960.

Any discussion of this paper will appear in a Discussion Section to be published in the June 1961 JOURNAL.

REFERENCES

1. E. Schwarz, *Research* (London), **5**, 407 (1952).
2. E. Mooser and W. B. Pearson, *Phys. Rev.*, **101**, 492 (1956).
3. G. Busch and P. Junod, *Helv. Phys. Acta.*, **30**, No. 6, 420 (1957).
4. S. Miyatani, *J. Phys. Soc. Japan*, **13**, 317 (1958).
5. P. Junod, *Helv. Phys. Acta.*, **32**, 567 (1959).
6. A. Boettcher, G. Haase, and H. Treupel, *Z. Angew. Phys.*, **7**, 478 (1955).
7. M. Hansen, "Constitution of Binary Alloys," 2nd Ed., pp. 49-51, McGraw-Hill Book Co., Inc., New York (1958).
8. A. F. Ioffe, "Semiconductor Thermoelements and Thermoelectric Cooling," p. 63, Infosearch Ltd., London (1957).
9. *Ibid.* p. 33.

Separation of Sulfur, Selenium, and Tellurium from Arsenic

J. M. Whelan, J. D. Struthers, and J. A. Ditzenberger

Bell Telephone Laboratories, Incorporated, Murray Hill, New Jersey

ABSTRACT

Three methods have been investigated for separating trace amounts of sulfur present in high-purity arsenic. These are: (*a*) vacuum sublimation, (*b*) sublimation in a hydrogen stream, and (c) distillation of arsenic from an arsenic-lead solution. The last method is somewhat more effective than the second. The first was unsatisfactory. The lead process yielded arsenic containing the following atom fractions of sulfur, selenium, and tellurium; 1×10^{-9}, $\leq 2.7 \times 10^{-8}$, and $\leq 2 \times 10^{-8}$, respectively. Concentrations of these impurities were measured with the aid of radiotracer techniques.

Arsenic of high purity is required for the preparation of the semiconductors InAs and GaAs. The atom fractions of sulfur and selenium in available "semiconductor grade" arsenic are in the range 0.2 to 5×10^{-6}. These impurities are donors in the above semiconductors which cannot be removed readily by zone refining because of their unfavorable distribution coefficients (1-5). The donor concentrations, $\sim 2 \times 10^{16}$ cm^{-3}, in better samples of InAs and GaAs can be attributed to the residual amounts of sulfur and selenium in the arsenic.

A number of methods have been proposed to reduce further the concentration of sulfur in arsenic. These are: (*a*) vacuum sublimation (6), (*b*) sublimation in H_2 (5, 7), (c) condensation into Pb followed by distillation (7), (*d*) repeated oxidation and reduction with carbon (8), and (*e*) H_2 reduction of redistilled $AsCl_3$ (9). These methods have been

evaluated primarily by differences in the carrier concentrations and mobilities of InAs samples made from the initial and purified As. This evaluation is subject to a number of uncertainties such as the purity of the indium and contamination associated with the InAs preparation. However, the Pb condensation-distillation proposed by Harman, Stambaugh, and Goering was somewhat more promising than the others. An atom fraction of sulfur in the arsenic equal to 9×10^{-7} would account for the net donor concentration in their InAs. Compensation or other donor impurities would either raise or lower this estimate.

We re-examined the vacuum sublimation, H_2 sublimation, and Pb condensation-distillation methods for their relative efficiencies for reducing the sulfur content in arsenic. As will be described, we found the Pb condensation-distillation to be more effective than the others. Quantitative results are given later to indicate the residual concentrations of sulfur, selenium, and tellurium in arsenic purified by this method. Concentrations of the above impurities were measured by radiotracer techniques. By the use of radioactive tracers it is possible to determine concentrations of sulfur, selenium, and tellurium which are lower by several orders of magnitude than can be determined by chemical, spectrographic, or spectrophotometric methods. Sulfur[35] was obtained as BaS in $Ba(OH)_2$ solution and converted to As_2S_3 for arsenic doping. Radioactive Se and Te were used directly after irradiation at the Brookhaven reactor in a flux of 8×12^{12} neutrons/cm^2/sec for 31 days. Beta counting was used for the powdered arsenic samples containing sulfur and tellurium. Gamma counting was used for those samples containing selenium.

The three methods used for separating trace amounts of sulfur from arsenic are based on the relative vapor pressures of arsenic and the sulfur species. At low concentrations, ~ 1 ppm, sulfur is probably present in arsenic as a solute, As_2S_2. The relative difference in vapor pressure of this sulfide and arsenic (1.0 and 0.4 atm, respectively, at 565°C) is probably too small for the degree of separation desired under ideal conditions by a single sublimation. Sublimation in hydrogen favors the reduction of the sulfide in the vapor phase to $H_2S(g)$ and $As_4(g)$. Arsenic is condensed in the exhaust hydrogen stream. It is desirable to use a high ratio of H_2 to As_4 partial pressures to shift the equilibrium to the right for the reaction: $As_2S_2(g) + 2H_2(g) = \frac{1}{2} As_4(g) + 2H_2S(g)$. The third method consists of dissolving arsenic in lead followed by distillation from the resulting solution. Many metals form stable sulfides with low vapor pressures. Lead was a particularly good choice because it does not form arsenides. This facilitates the arsenic recovery by distillation.

Experimental

The first series of experiments were intended to determine the relative effectiveness of the three processes for separating small amounts of sulfur from arsenic. Arsenic, containing an estimated sulfur concentration of 1-10 ppm, was mixed with an amount of radioactive sulfur equivalent to 2 ppm of the arsenic. This mixture was sublimed twice to mix the tracer sulfur with that originally present. The arsenic was condensed as a rod during the second sublimation. The end and center sections were analyzed to determine their relative sulfur concentrations. Absolute concentrations were not obtained because of the uncertainty of the sulfur concentration originally present in the arsenic. Intermediate sections of the arsenic rod were used for the separation experiments described below. The initial sulfur concentrations of these sections were taken as averages of the appropriate end and center sections. One section of the above rod was sublimed in a sealed quartz tube 50 cm long which had been previously evacuated. This tube was heated uniformly to 600°C and then one end cooled to 350°C. The resulting temperature gradient was maintained for 58 hr. Arsenic condensed in the cold end to form a rod 22 cm long. The rod was then divided into five approximately equal sections. The first and last section corresponded to the coldest and hottest sections of the rod, respectively. Sulfur concentrations of the five sections are listed in the first column of Table I. The initial sulfur atom fraction is 1.6 α where α is a constant having a value between the limits 10^{-5} to 10^{-6}. As previously mentioned, the uncertainty in the value of α arises from the uncertainty in the sulfur concentration of the arsenic before doping with tracer sulfur. After sublimation, the first and last sections to condense had atom fractions of sulfur equal to 2.7 α and 1.0 α, respectively. The small difference between these concentrations illustrates the limitations of simple vacuum sublimation for separating trace amounts of sulfur from arsenic.

A second arsenic sample in which the sulfur atom fraction was 1.4 α was sublimed in a hydrogen stream at 450°C. The hydrogen at 1 atm was first passed through a charcoal trap at 78°K and then over the arsenic at 450°C at a rate of approximately 400 cc/min. From the time required to sublime the arsenic, we estimated the ratio of H_2 to As_4 pressures to be between 100 and 200 to 1. The atom fraction of sulfur in the arsenic collected in the exhaust stream was 0.004 α, a substantial reduction from 1.4 α in the starting material.

The sulfur atom fraction in the arsenic used for the Pb-condensation-distillation experiment was 2.0 α. This arsenic was condensed into lead at 550°C contained in a sealed tube. The weight ratio of arsenic to lead was 1:2. It was then distilled from the solution at 535° and condensed into a cooler region

Table I. Relative effectiveness of vacuum sublimation, H_2 sublimation, and Pb condensation-distillation for separating trace amounts of sulfur from arsenic

	Vacuum sublimation	Sublimation in H_2	Pb condensation and distillation
Initial atom fraction of S in As	1.6 α	1.4 α	2.0 α
Final atom fraction of S in As	1st fraction 2.7 α 2nd fraction 1.6 α 3rd fraction 1.4 α 4th fraction 1.5 α 5th fraction 1.0 α	0.044 α	<0.001 α
	$10^{-5} > \alpha > 10^{-6}$		

of the tube. The atom fraction of the sulfur in the recovered arsenic was equal to or less than the detection limit, 0.001 α. These results are summarized in Table I.

The lead condensation-distillation was somewhat more effective than sublimation in hydrogen for removing small amounts of sulfur from arsenic. The latter method would not be expected to be as good for separating small amounts of selenium and tellurium from arsenic because of the lower stability of H_2Se and H_2Te. Lead selenide and telluride are stable. They were expected to have low vapor pressures when diluted with a large excess of lead at temperatures in the range of 600°-700°C. The experiments described below illustrate the effectiveness of the lead method for separating trace amounts of sulfur, selenium, and tellurium from arsenic. The example for sulfur differs from the previous one in that isotopic dilution effects were greatly reduced.

The arsenic used in these experiments was supplied by American Smelting and Refining Co. Estimated atom fractions of sulfur, selenium, and tellurium in the arsenic are $\sim 2 \times 10^{-6}$, $\sim 10^{-7}$, and $< 10^{-7}$, respectively. Those for sulfur and selenium were furnished by the supplier and that for tellurium was based on the failure to detect it by mass spectrographic means (10). Dilution errors associated with tracer techniques were minimized by first doping the arsenic with the large amount of the appropriate tracer impurity in comparison to that originally present. An amount of radioactive sulfur as As_2S_3 equivalent to 500 times the sulfur originally present was sealed in an evacuated quartz tube with the first arsenic sample. This was sublimed and condensed six times from one end of the tube to the other at approximately 600°C to insure adequate mixing. The sample was then crushed and resublimed to form a rod. After discarding the ends of this rod, the remainder was divided into five sections. The end and center sections were analyzed for their sulfur content. Averages of these were used to estimate the concentration of the two remaining pieces prior to purification by distillation from lead. The minimum and maximum atom fractions of sulfur were 1.1 and 3.9×10^{-6}. These figures combined with those in Table I show that sublimation is a satisfactory method for reducing the atom fraction of sulfur in impure arsenic to $\sim 10^{-6}$.

Radioactive elemental selenium was mixed with another arsenic sample in the same manner as that described above for mixing arsenic and As_2S_3. The minimum and maximum limits for the atom fraction of selenium in this sample were 1.0 and 1.7×10^{-4}. The large amount of selenium in the final arsenic suggests that simple sublimation is relatively ineffective for separating even moderate amounts of selenium from arsenic.

Tellurium doped arsenic was prepared by subliming twice a mixture equivalent to an atom fraction of radioactive tellurium of 10^{-6}. The tellurium atom fraction in the center portion of the final arsenic prior to the purification was between 1.3 and 2.4×10^{-7}.

Each of the arsenic samples prepared for purification was sealed in an evacuated quartz tube with twice its weight of high-purity lead and placed in a vertical tubular furnace. The bottom of the tube containing the lead was maintained at 600°C and the upper portion between 600° and 650°C. The arsenic dissolved in the lead overnight. Following this, the thermal gradient of the furnace was readjusted to give a uniform temperature of 600°C. Arsenic was distilled from the solution by gradually withdrawing the tube from the furnace and allowing the arsenic to condense in the upper colder section. This section containing the arsenic was sealed off and an additional amount of arsenic was distilled and condensed after increasing the temperature of the lead solution to 700°C. The arsenic fractions distilled from the lead at 600° and 700°C were analyzed for sulfur, selenium, and tellurium. Atom fractions of sulfur, selenium, and tellurium in the arsenic distilled from the lead solution of 600°C were 1.1×10^{-9}, $\leq 2.7 \times 10^{-8}$ and $\leq 2 \times 10^{-8}$, respectively. The major errors in concentrations of sulfur, selenium, and tellurium found in the purified arsenic result from errors in the preparation of the comparison standards and from the statistical fluctuations inherent in counting data. It is estimated that the analytical data are accurate to within ±25%. The average arsenic yield was 65% when distilled from the solution at 600° and 84% at 700°C. However, the atom fractions of sulfur and selenium in the fractions distilled from the solution of 700°C were substantially higher, 6.6×10^{-8} and 7.4×10^{-7}, respectively. No change was observed in the tellurium concentration of the condensate even when the temperature of the lead solution was raised to 760°C. These results are summarized in Table II. The weights of the initial doped arsenic samples varied between 1.5 and 5 g. Increasing the amount of arsenic to 250 g and maintaining the 1:2 weight ratio of arsenic to lead has raised the average yield distilled from the lead solution of 600°C to 85%.

Discussion

Lead has a vapor pressure of $\sim 10^{-3}$ mm at 600°C. Therefore, one expects to find a small concentration

Table II. Effectiveness of Pb condensation and distillation for separating sulfur, selenium, and tellurium from arsenic

	Sulfur	Selenium	Tellurium
Initial atom fraction	1.1 to 3.9×10^{-6}	1.0 to 1.7×10^{-4}	1.3 to 2.4×10^{-7}
Atom fraction in As distilled from Pb bath at 600°C	1.1×10^{-9}	$\leq 2.7 \times 10^{-8}$	$\leq 2 \times 10^{-8}$
Atom fraction in As distilled from Pb at 700°C	6.6×10^{-8}	7.4×10^{-7}	$\leq 2 \times 10^{-8}$

of lead in the arsenic after separation of sulfur, selenium, and tellurium. Before using the arsenic to prepare GaAs, it is resublimed twice. The lead concentration after this is ~ 1 ppm. Concentrations of 1 ppm of lead in arsenic are not nearly as serious as similar concentrations of sulfur and selenium, because the lead can be readily removed from GaAs by zone refining. Its distribution coefficient is < 0.02 (4).

The results in Table II indicate that even lower concentrations of sulfur and selenium in arsenic could be obtained by distilling the arsenic from the lead solution at a lower temperature. The only disadvantage to using a lower temperature is the reduction in arsenic yield due to a lower arsenic vapor pressure. Distillation below 550°C would require a more dilute solution of arsenic in lead in accordance with the As-Pb phase diagram. This would further reduce the arsenic yield.

Assuming arsenic is the only source of sulfur, selenium, and tellurium in GaAs or InAs, the equivalent concentrations in these compounds to those in Table II would be 2×10^{13}, $\leq 6 \times 10^{14}$, and $\leq 4 \times 10^{14}$ atoms cm^{-3}, respectively. Weisberg and Rosi noted a difference in the electrical properties of InAs made from arsenic distilled from lead when the lead arsenic solution was first equilibrated at 600° and 750°C prior to distillation from the solution at 600°C (5). The InAs made from arsenic equilibrated at the higher temperature had a net donor concentration of 1.4×10^{16} whereas arsenic equilibrated at 600°C yielded InAs with a net donor concentration of 2.7×10^{16} cm^{-3}. These differences are not likely to be due to differences in the sulfur and selenium concentrations in the two arsenic samples in light of the data in Table II.

Conclusion

Simple sublimation is not a satisfactory method for separating trace amounts of sulfur from arsenic. Sublimation in hydrogen is somewhat less effective than distillation of arsenic from a lead-arsenic solution. The latter method has been used to reduce the atom fractions of sulfur selenium and tellurium in arsenic to 1×10^{-9}, $\leq 2.7 \times 10^{-8}$, and $\leq 2 \times 10^{-8}$, respectively.

Manuscript received May 17, 1960; revised manuscript received Aug. 22, 1960. This paper was prepared for delivery before the Columbus Meeting, Oct. 18-22, 1959.

Any discussion of this paper will appear in a Discussion Section to be published in the June 1961 JOURNAL.

REFERENCES

1. E. Schillmann, *Z. Naturforsch.*, **11a**, 463 (1956).
2. T. C. Harman, H. L. Goering, and A. C. Beer, *Phys. Rev.*, **104**, 1562 (1959).
3. R. Gremmelmairer, *Z. Naturforsch.*, **11a**, 511 (1956).
4. H. C. Gatos, Editor, "Properties of Elemental and Compound Semiconductors," p. 141, Interscience Publishers, New York (1960).
5. *Ibid.*, p. 25.
6. J. Richards, see R. Barrie, F. A. Cunnell, J. T. Edmond, and I. M. Ross, *Physica*, **20**, 1087 (1954).
7. T. C. Harman, E. P. Stambaugh, and H. L. Goering, Paper delivered at Electrochemical Soc. Meeting, Cleveland (1956).
8. D. P. Enright, Naval Ordnance Laboratory Report 6024 (1958).
9. R. H. Harada and A. J. Strauss, *J. Appl. Phys.*, **30**, 121 (1959).
10. A. J. Ahearn, Bell Telephone Laboratories, Private communication.

Electrolytic Vanadium and Its Properties

D. H. Baker, Jr.,[1] and J. D. Ramsdell

U. S. Bureau of Mines, Boulder City, Nevada and Reno, Nevada, respectively

ABSTRACT

The fused salt electrorefining technique has been applied successfully to vanadium. The electrolyte was sodium chloride containing 3-6% vanadium as vanadium dichloride. Current efficiency was approximately 91%. Oxygen and nitrogen impurities were reduced by two thirds of the amount contained in the feed material. The hardness of the product was reduced from 97 Rockwell B to 35 R_B. Arc melted ingots could be given a 99% cold reduction by rolling before edge cracking appeared.

Growing interest and the industrial need for purer metals and improved alloys for application under high-temperature and high-speed conditions has demanded the elimination and/or control, as far as possible, of impurities.

As a part of this program of intensified research, the Federal Bureau of Mines Reno Metallurgy Research Center and the Boulder City Metallurgy Research Laboratory have undertaken a joint investigation to produce and evaluate high-purity vanadium.

In the past few years the Bureau of Mines has developed and proved the technical feasibility of fused salt electrorefining of metals such as titanium (1), beryllium (2), hafnium (3), zirconium, to remove impurities, such as O_2 and N_2, as well as certain other elements.

Fused salt refining of vanadium was considered because the gaseous impurities, nitrogen and ox-

[1] Present address: U. S. Bureau of Mines, Washington 25, D. C.

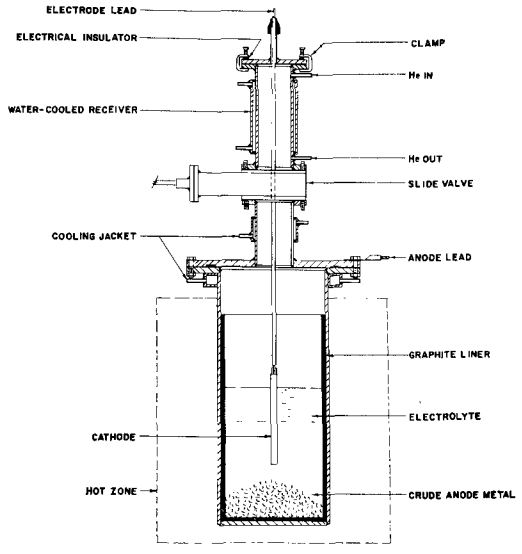

Fig. 1. Schematic drawing of cell

ygen, which can be controlled by this technique, have serious effects on vanadium's physical properties. Commercially, the production of low nitrogen-oxygen vanadium is an expensive, complicated and time-consuming process by any of the standard reduction techniques.

Since the fused salt electrorefining technique has shown the ability to control gaseous impurities in other reactive metals such as titanium and has been scaled up to a 10,000-amp cell, the technique offered a means of improving the quality of technical grade vanadium at something approaching a commercial scale.

This investigation was undertaken to ascertain the feasibility of applying the fused salt electrorefining method to the production of a metal product exceeding the purity of present commercial vanadium metal (99.5 V). The principal specific object was to improve the ductility of the final product by removing oxygen and nitrogen.

Description of Process

Input material.—The anode, or feed material, is commercially produced vanadium metal having a Rockwell B hardness of 97 and containing, according to the producer, 99.5% V, 0.30 Fe, 0.18 O_2, 0.03 N_2, 0.006 H_2, and 0.03 Cr.

Equipment.—Figure 1 is a schematic diagram of the 12-in. diameter electrolytic cell used. This cell was identical to those used for refining titanium metal, except for a graphite liner to minimize iron contamination of the bath. A receiving chamber and valve system permitted the introduction and removal of the cathode without disturbing the inert atmosphere of the cell proper.

External heat was used to maintain the electrolyte at an operation temperature of about 800°C.

Vanadium metal, crushed to $-\frac{1}{2}$ in., was charged to the bottom for the anode. On the basis of experience gained in operating similar cells on other metals, the minimum ratio of the cathode to the anode area was fixed at 1:3. Under higher anode areas, exceeding the minimum, more operative stability was obtained. The cathode used in the 12-in. diameter cell was a $\frac{3}{4}$-in. diameter iron rod.

Vanadium chloride was applied to the 60-lb sodium-chloride bath through the reaction of chlorine gas and a small amount of admixed hydrogen chloride with the granular anode metal contained in the cell bottom. The reaction of hydrogen chloride alone with the vanadium anode material was extremely slow. The hydrogen evolved from the hydrogen chloride passed from the chlorinator and through the bath assisting in the purification of the sodium chloride. The off gas was permitted to escape from the cell through an oil bubbler.

Working procedure.—The cathode, cleaned and burnished, was introduced into the cell through the receiving chamber above the bath compartment. The receiving chamber was evacuated and charged with inert gas (helium), after which the cathode was lowered into the bath through a valve. Prior to use, the cathodes were stored in a drying oven under controlled low-humidity atmosphere.

Upon completing the cathode placement, the appropriate voltage was applied for the particular test, and the refining process was conducted.

On completion of the "run," the cathode, bearing the product metal, was withdrawn into the upper cell chamber, previously evacuated and charged with inert gas, to cool before final removal from the cell.

Deposits were leached with a 2-3% HCl solution to dissolve the entrained salts and subjected to agitation in a high speed mechanical agitator to separate the metal crystals. Salt-free metal crystals were then washed with acetone to assist in the rapid removal of moisture and sized through the appropriate screens.

Testing the product.—The general quality of the product was quickly determined on the basis of hardness tests alone for preliminary "run" evaluation purposes. Individual run products shown to be similar by chemical and hardness evaluation were composited for further study. Compacts of the crystalline vanadium powders weighing 10-70 g were melted into buttons or cigar-shaped ingots in a tungsten electrode arc furnace under helium. Ingots were homogenized by remelting five times, being turned over after each melt. Samples were also taken for complete analysis or for semiquantitative analysis. Hardness was found to correlate reasonably well with the degree of purity. The relation of hardness to oxygen content is shown in Fig. 2.

Investigations

A total of 127 cycles or runs were made in the 12-in. cell before the graphite liner failed terminating the operation. The specific factors contributing to the failure of graphite were primarily the result of stresses arising from thermal cycles of the iron container and graphite liner. No evidence of corrosion or reaction with the graphite were detected as illustrated by the metal analysis of less than 0.01% carbon.

When the cell was placed in operation, the electrolyte contained 2.8% soluble vanadium. The first three cycles were made for the purpose of conditioning the electrolyte, a total of 68 amp-hr at 0.2 v. Very fine, needle-like, crystals of cathode metal were discarded because of iron contamination.

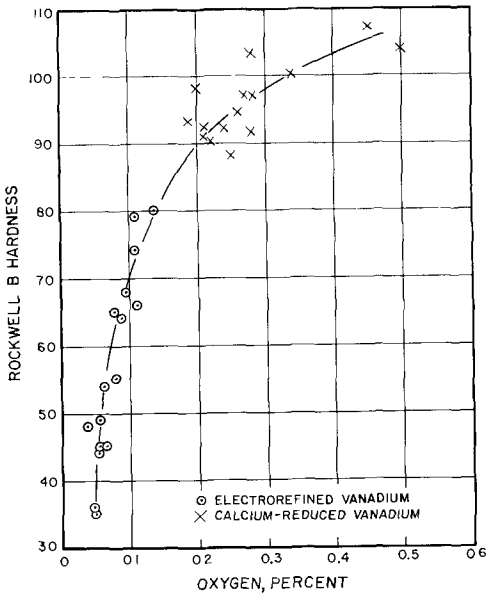

Fig. 2. Effect of oxygen on the hardness of arc-melted vanadium.

The metal product from the fourth run tested 95 R_B in hardness and there was a progressive improvement in succeeding cycles with a hardness as low as 35 on the +35 mesh fraction. Vanadium metal produced in the following 60 cycles of operation was separated into four sieve products as shown in Table I. Approximately 72% of the cathode metal produced was coarser than 80 mesh standard Tyler. The total deposited metal had a weighted average hardness of 52 R_B.

Production of soft, coarsely crystalline, cathode metal is affected by the anode area in addition to other factors. A large anode area with fresh metal surface results in a high quality product; the effect is shown in Table II. Hardness of the metal product decreases very quickly after the addition of anode material.

Table I. Typical screen and hardness distribution of vanadium deposits

	Screen size, standard Tyler mesh			
	+35	−35 +80	−80 +150	−150
Weight, %	27	45	16	12
Hardness, R_B	36	46	55	62

Table II. Effect of metal addition on product hardness

Test cycle	Hardness	Remarks
28	63	Deposit prior to 900 g addition of anode metal.
29	54	First deposit after addition.
30	60	
31	49	
32	51	
33	50	
50	84	Deposit prior to 1100 g addition of anode metal.
51	60	
52	65	
53	60	
54	59	

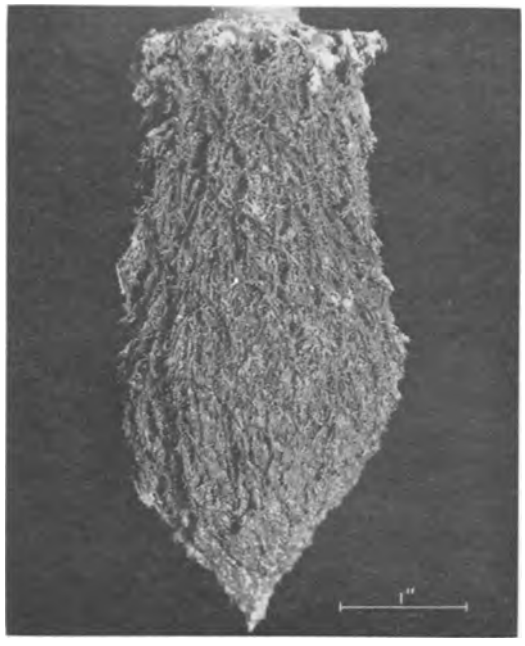

Fig. 3. Vanadium cathode deposit, as removed from the cell, produced 0.45 v.

Coarse crystalline metal was produced at applied voltages between 0.4 and 0.7 v. The bath contained 3.0% vanadium as the dichloride and was at a temperature of at least 800°C. Figure 3 illustrates the coarser deposits obtained at 0.45 v. Deposits produced at very low voltages (less than 0.3 v) or above 1.0 v contain much finer crystals. Voltages above 2.0 v would cause electrowinning from the bath with the evolution of chlorine gas, chemical attack on the iron of the cell, and iron contamination of the bath and the product. A typical range of analyses of the refined metal is C < 0.01%, Fe 0.003-0.05% O_2 0.04-0.10%, N_2 < 0.002%.

Current efficiencies for 100 cycles or runs were nearly all within the range of 88-94% with an average of 91%, based on the assumption that vanadium is transported at a valence of 2. At the average current efficiency, 522 amp-hr will deposit 1 lb of vanadium metal.

The first 100 runs with the 12-in. cell were made at voltages from 0.2 to 1.5 v and with initial current densities from 100 to 3500 amp/ft^2. No major importance can be given to the calculated current density because the cathode area begins to increase the instant metal deposits. The currents are kept within the limits from 2 to 68 amp by choice of immersion depth of the cathodes used.

Vanadium metal can be purified in respect to O_2 and N_2 by the fused salt electrorefining technique. Reduction of these gaseous impurities was in the order of two thirds, hardness was reduced from 97 Rockwell B to a low of 35 R_B.

Primary Fabrication

Arc-melted electrorefined vanadium is characterized by large randomly oriented grains. Within the grains are configurations (revealed by conventional etching techniques) in the form of pits and sub-boundaries similar to structures associated with dislocation sites.

After melting, the 10-g buttons were easily cold rolled to 0.005 in. sheet, a total reduction of 98%, with no intermediate anneals. Electrorefined vanadium shows a hardness increase of approximately 55 V.h.n. greater than its original annealed hardness when cold reduced 65%. Most of the hardening occurs in the 0-15% cold work range, approximately 27 V.h.n. for a reduction of 5% and about 38 V.h.n. for a reduction of 15%. Above 15% reduction range, hardening increases at a reduced rate with increasing amounts of deformation.

The large columnar grains of the larger arc-melted ingots deformed nonuniformly, and whenever annealing was preceded by heavy reductions recrystallization produced a banded structure that persisted during grain growth. After considerable experimental work with various sequences of flat rolling, swaging, square rolling, and cold pressing, a schedule of cold pressing and square rolling followed by annealing was adopted for initial large ingot breakdown of approximately 75% reduction in area. Although some banding was still present, this working sequence produced optimum grain structure and retained enough cross-sectional area for further testing.

Recrystallization

For recrystallization studies, these bars were further cold-rolled from 5 to 65% reduction in area. To protect the specimens from gaseous contamination during annealing, they were sealed in Vycor capsules, and were annealed for 1 hr at temperatures of 200° to 1000°C. The effect of temperature on the Vickers hardness for one lot of electrolytic vanadium is shown in Fig. 4.

For all reductions heated to temperatures in the range of 200° and 400°C, an increase in hardness of 3-15 V.h.n. over that of the cold worked metal is noted. As the temperature is increased above 400°C, hardness decreases rapidly for all reductions until the prior to deformation hardness is reached. The return to pre-deformation hardness occurs for annealing temperatures in the range of 900°-1000°C and corresponds to the temperature range for the beginning of grain growth. In general, for annealing temperatures between 900° and 1000°C, the 65% cold worked metal show an increase in hardness while the 5% cold work specimens show a continuing decrease in hardness. The 35% cold worked specimens exhibit both increasing and decreasing hardness in this annealing range (900°-1000°C). A similar high-temperature hardening effect was noted by Pugh (4) for 80% cold reduced vanadium annealed above 1200°C.

An anomaly occurs in the temperature range of 600° to 800°C, in the hardness *vs.* annealing temperature curve for all reductions in general; it is most pronounced for the low reductions. According to Lacy and Beck (5), this anomaly is attributed to an aging mechanism similar to strain aging in steel and titanium. Rostoker, *et al.* (6) noticed this same anomaly for high percentages of cold work rather than for the low reductions as noted in this investigation. It appears, if this anomaly is due to strain aging, that decreasing the quantity of interstitial impurities in vanadium reduces the amount of deformation necessary to promote strain aging in this temperature range.

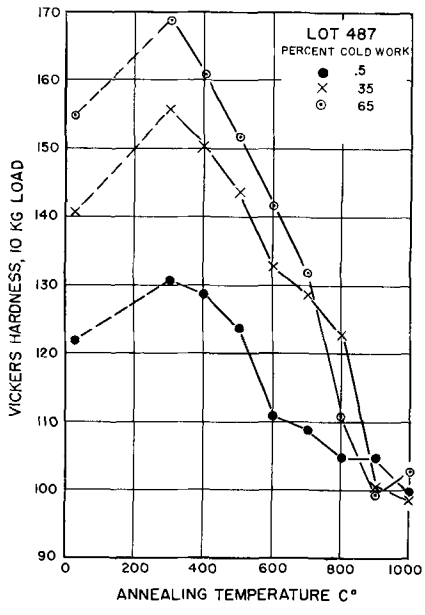

Fig. 4. Effect of temperature on the Vickers hardness of electrorefined vanadium.

The rapid decrease in hardness for the 35, 50, and 65% cold worked metal annealed in the range of 700°-800°C corresponds to the terminus of the mentioned anomaly and also to the initial microscopic evidence of recrystallization for these same reductions.

Microscopic evidence of recrystallization by nucleus growth for vanadium cold-reduced 65% is first observed for the 700°C anneal; recrystallization by nucleus growth for reductions of 35-50% is first observed for the 800°C anneal. Recrystallization is essentially complete for these three reductions after a 900°C anneal. The 35% reduction is near the minimum critical deformation necessary to promote nucleus growth rather than grain coarsening. Grain coarsening was observed for reductions of 5, 15, and 25%. Lacy and Beck (5) report metallographic recrystallization occurring in 60% extruded vanadium for annealing temperatures in excess of 750°C, while Nash, *et al.* (7) noted that metallographic evidence of recrystallization for iodide vanadium cold work 90% was present for annealing temperatures between 650° and 700°C.

Grain growth is evident in all reductions for annealing temperatures in excess of 900°C and is continuous except for the 5% cold-worked metal, which exhibits extreme discontinuous grain growth between 900° and 1000°C.

Mechanical Properties

Tensile data for vanadium cold rolled 50% and annealed at 950°C is plotted as a function of oxygen content in Fig. 5. Oxygen is used as a parameter since the authors observed it to have a greater and more consistent effect on the strength and hardness than other impurities found in high-purity vanadium.

Strength and hardness are plotted as straight line functions of oxygen content. As oxygen content increases from 0.047 to 0.109 w/o, tensile strength

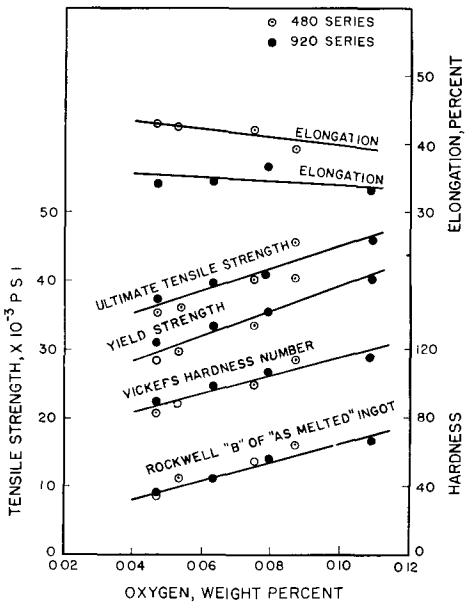

Fig. 5. Comparison of the effect of oxygen content, tensile strength, hardness, and elongation of electrorefined vanadium.

increases from 35,000 to 46,000 psi while hardness increases from 83 to 116 V.h.n. Ductility as measured by tensile elongation (33-43% in 1 in.) is not appreciably influenced by oxygen content.

Approximately 60% of the tensile specimens tested exhibited a yield phenomenon similar to that noted by Lacy and Beck (5) that consists of an upper and lower yield point which differ on an average of 2,000 psi.

An indication of the significance of oxygen rather than nitrogen, which was once thought to be the major hardener and strengthener of vanadium, becomes more apparent by individual comparisons.

Lot	O_2	N_2	Y.S.	U.T.S.
A	0.093	0.016	45,600	53,000
J	0.084	0.014	41,800	48,600
B	0.055	0.014	30,000	37,200

Comparison of the above lots indicates that the tensile and yield strengths decrease progressively with decreasing oxygen content and constant nitrogen content.

Lot	O_2	N_2	Y.S.	U.T.S.
K	0.107	0.004	46,700	53,000
488	0.087	0.003	40,500	45,900
H-I	0.062	0.003	36,000	43,200

Comparison of lots K, 488, and H-I again indicates that the tensile and yield strengths decrease with lower oxygen content and constant nitrogen content of a much lower level than for lots A, J, and B.

Lot	O_2	N_2	Y.S.	U.T.S.
A	0.093	0.016	45,600	53,000
K	0.107	0.004	46,700	53,000

In this comparison, despite the very marked difference in nitrogen content, the tensile and yield strengths remain practically constant.

Lot	O_2	N_2	Y.S.	U.T.S.
486	0.053	<0.001	28,900	36,100
B	0.055	0.014	30,000	37,200
H-I	0.062	0.003	36,000	43,200

A comparison of lots 486, B and H-I shows that the tensile and yield strengths are consistent at very similar oxygen contents and very dissimilar nitrogen contents. In this case, the oxygen level is nearly one-half that of the previous comparisons of lots A and K. These comparisons indicate, within the limits of the compositions investigated, that the influence of oxygen on the mechanical properties is much more pronounced than that of nitrogen.

Further study is required to obtain more direct correlation of properties with oxygen and/or nitrogen content as these elements appear to be most potent in their specific influence.

Physical Properties

Thermal expansion properties were independent of impurity content and the derived value for the coefficient of thermal expansion at 20°C is 8.84 x 10^{-6}/°C.

Resistivity correlated well with other properties measured for the respective lots of electrolytic vanadium. Resistivity decreased with increasing purity and decreasing strength. The values obtained varied from 22.6 to 25.2 microhm-cm at 26°C, which are, in general, lower than those previously reported for vanadium: 24.8-26.0 microhm-cm.

These Bureau of Mines investigations have shown that the fused salt electrorefining technique offers a feasible means of controlling the quantity of gaseous impurities, such as O_2 and N_2, in vanadium metal to low levels consistently. The study also has shown that the properties of electrorefined vanadium are considerably different from those exhibited by commercially available vanadium because of the reduction of impurity content. The oxygen content more than any other single impurity showed the most marked affect on hardness strength and workability.

Manuscript received June 6, 1960; revised manuscript received Aug. 26, 1960. This paper was prepared for delivery before the Chicago Meeting, May 1-5, 1960.

Any discussion of this paper will appear in a Discussion Section to be published in the June 1961 JOURNAL.

REFERENCES

1. J. R. Nettle, D. H. Baker, Jr., and F. S. Wartman, Bureau of Mines Rept. of Investigations 5315, 1957, 43 pp; D. H. Baker, Jr. and J. R. Nettle, Bureau of Mines Rept. of Investigations 5481, 1959, 11 pp; O. Q. Leone, J. R. Nettle, and D. H. Baker, Jr., Bureau of Mines Rept. of Investigations 5494, 1959, 20 pp.
2. M. M. Wong, F. R. Cattoir, and D. H. Baker, Jr., Bureau of Mines Rept. of Investigations 5581, 1959, 9 pp.
3. D. D. Blue and D. H. Baker, Jr., Electrorefining of Vanadium, Chromium, Zirconium, and Hafnium, Paper presented at the Second United Nations International Conference on the Peaceful Uses of Atomic Energy, Geneva, Switzerland, June 1958, 17 pp.
4. J. W. Pugh, Discussion to Lacy and Beck, *Trans. Am. Soc. Metals*, **48**, 579 (1956).
5. C. E. Lacy and C. J. Beck, *ibid.*, **48**, 579 (1956).
6. W. Rostoker, D. J. McPherson, and M. Hansen, WADC Technical Report 52-145, Part 2, 1954.
7. J. W. Nash, H. R. Ogden, R. E. Durtschi, and I. E. Campbell, *This Journal*, **100**, 272 (1953).

On the Vacuum Sintering of Tungsten Ingots

J. W. Pugh and L. H. Amra

Refractory Metals Laboratory, General Electric Company, Cleveland, Ohio

ABSTRACT

A furnace for vacuum sintering tungsten is described, and results obtained from tungsten sintering experiments are discussed. The rate of densification at various temperatures is given special emphasis, but microstructure, hardness, fabricability, and purity are also examined. Temperatures from 1800° to 3100°C and times from 0.25 to 8.00 hr were employed. Results indicate that sintered densities at least as high as 82.5% of theoretical density are necessary for successful fabrication, and that densities as high as 97.0 have structures which are readily fabricable. High-temperature vacuum sintering is found to produce very pure tungsten, commensurate in this respect with the best arc cast tungsten.

The sintering of tungsten is not a new process. In the first decade of this century at least seven ingenious techniques were employed to consolidate tungsten so that it could be used for electric lamp filaments (1). The technique devised by Coolidge in 1909 was the most successful (2). His process which involved sintering pressed powder ingots in hydrogen and fabricating them to wire by swaging and drawing at progressively lower temperatures is essentially the one being used today. Little interest in vacuum sintered tungsten has been reported, although several advantages over hydrogen sintered metal might be expected.

Some of the most promising alloying elements for tungsten alloys are Ti, Zr, Hf, Cb, and Ta. These elements are all hydride formers, and their addition to tungsten requires consolidation in an inert atmosphere. High vacuum is perhaps the easiest and most satisfactory answer to this requirement. Moreover, vacuum offers the additional advantage of deoxidation since the vapor pressure of tungsten oxide is quite high at sintering temperatures and the vapor pressure of tungsten is relatively low. The sintering process can take effective advantage of this relatively unique situation because the vapor can be removed readily through the porous network of the compacted ingot. It is also true, of course, that the equilibrium of any purification reaction which results in gas evolution would be shifted favorably in vacuum.

In view of the foregoing, a vacuum sintering furnace was constructed, and some basic data on the vacuum sintering of tungsten were obtained.

Procedure

A schematic diagram of the furnace employed for these experiments is shown in Fig. 1. This furnace provides for heating compressed powder ingots by means of their own electrical resistance. 720 KW of powder is available between a stationary top electrode and a movable lower electrode, both of which are water cooled. Expansion and contraction of ingots during sintering is compensated for by means of a feed back device which involves a strain gauge, amplifier, and electrode drive mechanism. Vacuum of about 10^{-4} mm pressure is maintained by means of a 25 cm, (10 in.) oil diffusion pump and a Kinny 3.12 cubic meter/min, (110 ft^3/min) mechanical pump. An auxiliary 0.42 cubic meter/min (15 ft^3/min) mechanical pump is used for rough pumping the system.

Tungsten powders having a Fisher Sub-sieve size of 4.53 μ were compressed in a double acting hydraulic press at pressures of 1.89 metric tons/cm^2 (12 TSI) to form ingots having the dimensions 0.95 x 0.95 x 61.0 cm (⅜ x ⅜ x 24 in.). The green ingots were presintered 1 hr at 1200°C in hydrogen so that they had a presintered density of 11.5 g/cc. They were then placed in the vacuum sintering furnace and brought to the prescribed sintering temperature at the rate of 20°C/min. After prescribed times at temperature, each ingot was cooled rapidly to room

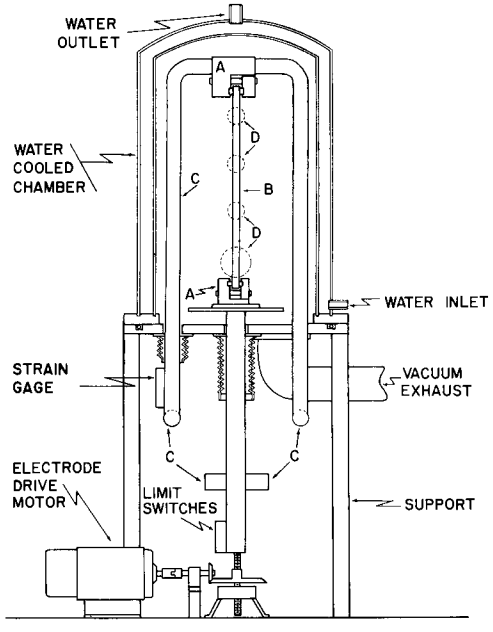

Fig. 1. Schematic representation of vacuum sintering furnace: A, electrodes; B, ingot; C, lead; D, sight port positions.

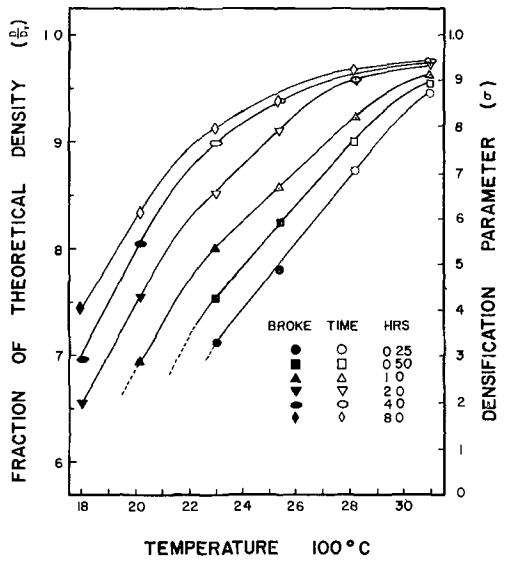

Fig. 2. Effect of temperature on the densification of tungsten ingots

temperature. The initial cooling rate in each case was approximately 500°C/min.

After the ingots were sintered, they were evaluated for density, microstructure, fabricability, and purity. Fabrication testing consisted of attempting to swage each ingot to 40% reduction in area after heating it to 1600°C.

Results and Discussion

Figure 2 indicates the effect of temperature on sintered density for various times at temperatures. The parameter plotted as the ordinate is the one commonly used to describe the degree of densification in sintered ingots: the density of the ingot (D) divided by the density of completely consolidated tungsten D_T. The Densification Parameter (σ) at the right is the densification achieved for the ingot divided by the maximum densification possible.

$$\sigma = \frac{D - Do}{D_T - Do}$$

where Do is the density of the ingot before sintering. The solid data point symbols in Fig. 2 represent ingots which could not be swaged satisfactorily. Apparently an ingot must attain more than 82.5% of its theoretical density before it can be fabricated in this way.

These data are plotted in another way in Fig. 3. Here the densification parameter is plotted as a function of time for each of the five temperatures employed. Figure 3 was used to plot the relationships shown in Fig. 4. Here the logarithm of sintering time is shown as a function of reciprocal absolute temperature for five different states of constant densification. These relationships are apparently straight lines and the empirical Arrhenius equation,

$$t = A \exp\left(\frac{\Delta H}{RT}\right)$$

is suggested. Here t is time, A is a constant, R is the gas constant, T is absolute temperature, and ΔH is the apparent activation energy for sintering. Note

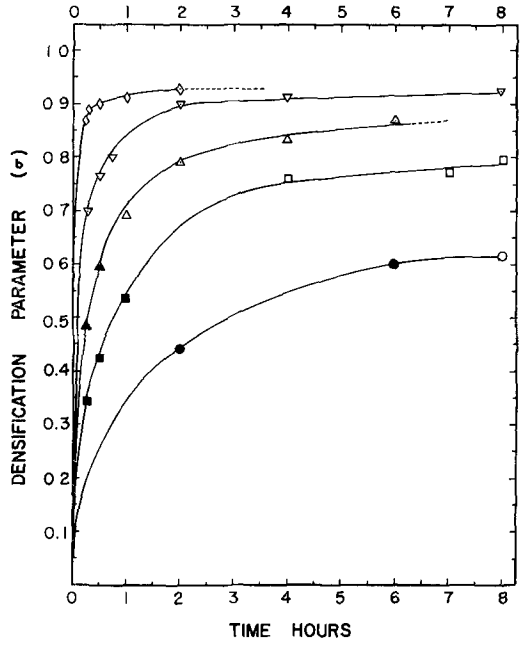

Fig. 3. Effect of time on the densification of tungsten ingots

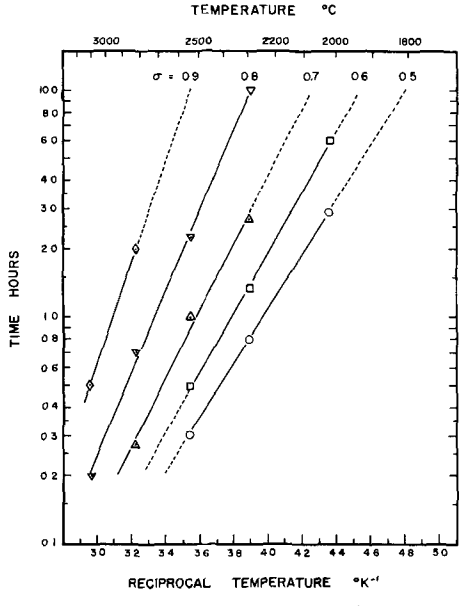

Fig. 4. Time-temperature relationships for vacuum sintered tungsten

that while these relationships are straight, they are not parallel and that the apparent activation energy changes from about 55 kcal/mole for a densification parameter of 0.5-105 kcal/mole for a parameter of 0.9. The precision of these determinations is not great, and the interpretation of these activation energies in terms of rate processes and mechanisms is not within the scope of this investigation. It does seem clear, however, that the effective or apparent activation energy as obtained from Fig. 4 increases with densification. A similar result for pre-reduced copper powder sintered in vacuum has been reported by Jordan and Duwez (3). Figure 5 shows how grain size increases as a function of time for three sintering temperature, and Fig. 6 permits a comparison of three microstructures which resulted from 2-hr treatments at the same three temperatures. The increase in pore size observed with

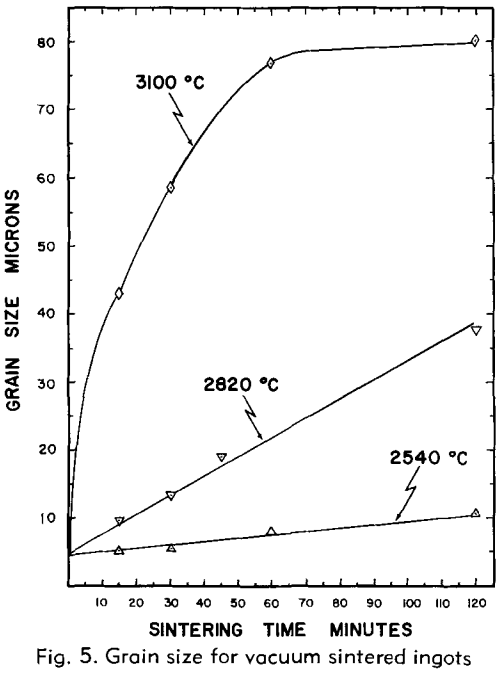

Fig. 5. Grain size for vacuum sintered ingots

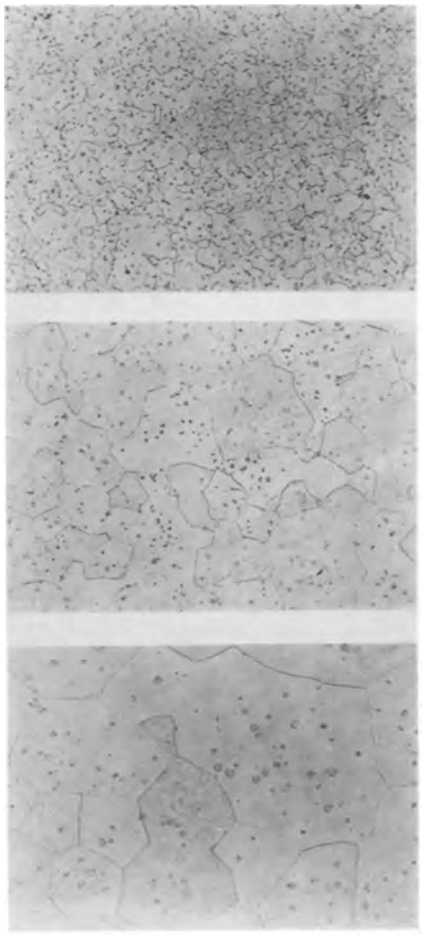

Fig. 6. Microstructures of tungsten ingots vacuum sintered 120 min. (a) (top) 2540°C; (b) (center) 2820°C; (c) (bottom) 3100°C. Magnification 250X before reduction for publication.

increasing density agrees with the findings of Rhines, Birchenall and Hughes (4). Figure 7 shows the effect of density on the hardness of the sintered ingots. Rockwell A measurements were taken first on each ingot. Diamond Pyramid Hardness was made on seven ingots to provide the relationship shown here.

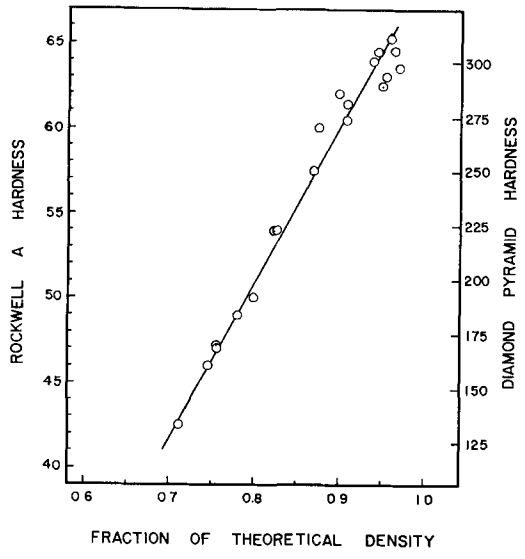

Fig. 7. Hardness of vacuum sintered tungsten

Table I. Gas analysis of sintered tungsten

No. of ingot	Conditions of sintering		Gas content, ppm*		
	temp, °C	time, min	O_2	N_2	H_2
333W17	3100	120	2	1	0
337W21	2820	122	8	2	1
315W7	2820	30	12	2	1
339W23	2540	360	6	1	0
336W20	2540	120	5	1	1
343W26	2020	120	57	5	2

* All results are ±5 ppm.

Table II. Data on sintered tungsten

Sintering conditions		Density			
Temp, °C	Time, min	g/cc	% theor.	Hardness, R "A"	Grain count, g/mm²
1800	120	Hg		25	
1800	480	14.40	74.6	46	
2020	120	14.65	75.6	47	
2020	198	14.85	77.0		
2020	360	16.00	82.6	54	
2020	480	16.10	83.4		
2300	15	13.76	71.2	42.5	
2300	30	14.57	75.4	47.2	
2300	60	15.46	80.0	50.0	
2300	240	17.34	89.8		
2300	420	17.42	90.0	62.0	
2300	480	17.65	91.3		
2540	15	15.05	78.0	49.0	
2540	30	15.95	82.5	54.3	33,500
2540	60	16.75	87.0	57.5	
2540	120	17.60	91.0	60.5	8,700
2540	240	17.94	93.7		
2540	360	18.24	94.5	64.5	
2820	15	16.85	87.3	60.0	10,600
2820	30	17.39	90.0	61.0	5,700
2820	47	17.70	91.0	61.4	
2820	120	18.49	95.7	62.4	700
2820	240	18.56	96.0	65.2	
2820	480	18.70	96.7		
3100	15	18.26	94.5	63.9	540
3100	18	18.42	95.5	63.0	
3100	30	18.44	95.5		
3100	60	18.60	96.4	64.5	
3100	120	18.75	97.0	63.5	334

Of special interest are the vacuum gas analysis results shown in Table I. The improvement in impurity content with time and temperature is remarkable. The oxygen content of the ingot sintered for 2 hr at 3100°C is perhaps comparable to the best arc-cast ingot analysis. This comparison is inexact because both products are so pure that they extend the analysis technique to its limit of resolution.

Conclusion

Table II provides a summary of the data obtained in these experiments. The information available here is sufficient to permit the programming of vacuum sintering treatments for tungsten with confidence. There are a number of unexplored avenues of practical experimentation remaining. For example, it would be most useful to know the effect of particle size and size distribution on sintering kinetics. It would also be of interest to know the effect of a variety of impurities on sintering kinetics and on gas content.

Manuscript received April 20, 1960. This paper was prepared for delivery before the Houston Meeting, Oct. 9-13, 1960.

Any discussion of this paper will appear in a Discussion Section to be published in the June 1961 JOURNAL.

REFERENCES

1. C. J. Smithells, "Tungsten," Chemical Publishing Co., Inc., New York (1953).
2. W. A. Coolidge, *J. AIEE*, p. 953 (1910).
3. C. B. Jordan and P. Duwez, *Trans. AIME*, **188**, 943 (1950).
4. F. N. Rhines, C. E. Birchenall, and L. A. Hughes, *ibid.*, **188**, 378 (1950).

Liquidus Curves for Aluminum Cell Electrolyte

III. Systems Cryolite and Cryolite-Alumina with Aluminum Fluoride and Calcium Fluoride

Anne Fenerty[1] and E. A. Hollingshead

Aluminium Laboratories Limited, Arvida, Quebec, Canada

ABSTRACT

Liquidus curves have been determined by means of cooling curves and visual examination of the cooling melt. The binary systems of cryolite with aluminum fluoride and calcium fluoride gave, respectively: peritectic point at 30% aluminum fluoride and 739°C, eutectic point at 40% aluminum fluoride and 694°C; eutectic point at 26% calcium fluoride and 945°C. In the system cryolite-alumina-calcium fluoride the ternary eutectic point was at 2.9% alumina, 21% calcium fluoride and 933°C. (Compositions are in weight per cent). Diagrams are given for the cryolite-rich part of the systems cryolite-calcium fluoride, cryolite-alumina-aluminum fluoride, cryolite-alumina-calcium fluoride, and cryolite-alumina-aluminum fluoride-calcium fluoride.

In the two preceding papers (1, 2) liquidus diagrams were reported for cryolite-alumina and for cryolite and cryolite-alumina with sodium fluoride, sodium chloride, and aluminum fluoride. The object of the present paper is to present additional data, a revised liquidus diagram for cryolite-alumina-aluminum fluoride, and liquidus diagrams for the cryolite-rich part of the systems cryolite-calcium fluoride, cryolite-alumina-calcium fluoride, and cryolite-alumina-aluminum fluoride-calcium fluoride.

Foster (3) recently reported the determination of the cryolite-alumina phase diagram by quenching methods. His results, except for pure cryolite, agree within the experimental error with those obtained in this laboratory (1) by cooling curves and visual examination of the cooling melt, the techniques used to obtain the results presented in this paper.

For the melting point of pure cryolite Foster (4) found 1004°C through quenching methods with a thermocouple calibration based in part on 992°C for the melting point of sodium fluoride. Both these are lower than the corresponding values of 1009° and 994°C found in this laboratory (2) by the cooling curve method. For comparison Grjotheim (5) found 1008.5° and 994.5°C, respectively, by the cooling curve method. Dworkin and Bredig (6) found 995°C for sodium fluoride, while Sense and others (7) found 996°C from the intercept of the vapor pressure-temperature curves of the liquid and solid. On the other hand much higher values for both cryolite and sodium fluoride, 1027° and 1012°C, respectively, were found by O'Brien and Kelley (8) from heat content measurements. It has already been noted (9) that too high a melting point was obtained in this way for nickel chloride, 1030°C *vs.* 1009° from cooling curves.

Materials

Hand-picked natural cryolite containing no visible impurities was crushed to −100 mesh or, preferably, to −20 mesh. The principal impurities in the two lots used were 0.01 and 0.02% iron and 0.01 and 0.04%

[1] Present address: Flint, Michigan.

silicon respectively. The alumina, produced experimentally, had a loss on ignition at 1000°C of 0.08% and contained 0.03% Na, 0.03% Ca, 0.03% Fe, 0.03% Si, 0.02% Ti, and 0.14% F. The aluminum fluoride was purified by vacuum distillation of Alcan dry-process aluminum fluoride. It contained 0.23% cryolite, 0.03% aluminum sulfate, 0.02% iron, 0.02% silicon, 0.01% manganese, and 98.4% aluminum fluoride (based on total fluorine content). The calcium fluoride was reagent-grade, from J. T. Baker Chemical Co. It had a loss on ignition at 110°C of 0.3-0.4% and contained 98-99% calcium fluoride (based on total fluoride content).

Method

The apparatus and methods were substantially as described in the first paper (1). The 150-g samples were made up by weight, thoroughly mixed, heated to about 100°C above the melting point, and stirred at about 100 rpm until clear and during the determination of the freezing point.

Primary freezing points were determined by the cooling-curve method when the first appearance of crystals in the melt, as observed through a telescope, corresponded to the primary break in the cooling curve. In general this was so on the cryolite side of the eutectic point. On the alumina side of the eutectic point and on most melts containing 25% or more of calcium fluoride or aluminum fluoride the primary freezing point was obtained by the visual method. In this method the temperature at which crystals first appear in the slowly cooled melt is determined. For final determinations rates of cooling of 0.1-0.15°C/min were used and the melt was observed every 5-15 min. The failure of the cooling-curve method to detect the primary crystallization of alumina is attributed to the steepness of the liquidus curve (low heat of crystallization and small percentage of crystals forming per unit decrease in temperature), and to the sluggishness with which alumina crystallizes.

The platinum, 10% rhodium-platinum thermocouples were all made from the same two spools of wire. One of them was calibrated in pure silver, in copper-silver eutectic alloy (799.0°C), and in standard samples of aluminum and copper certified by the National Bureau of Standards. Each thermocouple was checked periodically at the freezing point of reagent-grade sodium chloride, 801°C.

Accuracy

Two or more determinations were usually made for each composition and the mean or median value selected. With the cooling-curve method this value should not be in error by more than 3°C.

With the visual method duplicate values usually differed by less than 10°C. They would tend to be low because it was not possible to make a proper correction for supercooling. An upper limit for this correction was determined for one composition (cryolite—11% alumina) by cooling slowly until crystals appeared, then heating slowly with continuous stirring to determine the lowest temperature at which they would redissolve. This was found to be 10°-14°C higher than the mean temperature (972°C) at which the crystals appeared. Since some superheating must be required to redissolve, the negative bias of the visual method is probably less than 10°C.

For melts containing 25% or more aluminum fluoride results by the visual method were less reproducible than indicated above. This may be attributed in part to the greater steepness of the liquidus curve on the alumina side of the eutectic point. Changes in melt composition, as indicated by weight loss, were similar to those for cryolite-alumina melts.

Results

The liquidus diagram for cryolite-aluminum fluoride, reported in the preceding paper (2), was redetermined and slightly higher liquidus temperatures obtained. The revised values for the peritectic point are 739°C and 30% aluminum fluoride (weight per cent), for the eutectic point 694°C and 40% aluminum fluoride. It was verified by the visual method that on the aluminum fluoride side of the eutectic point the liquidus temperature rises rapidly to 860°C at 45% aluminum fluoride. This contradicts Grjotheim's finding (5) by the cooling-curve method that there is a maximum of 731°C at 45.2% aluminum fluoride corresponding to the compound $NaAlF_4$.

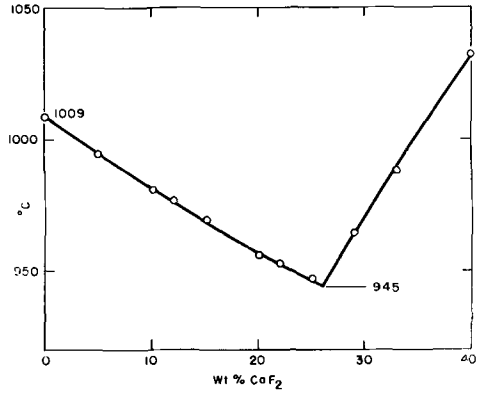

Fig. 1. Liquidus diagram for cryolite-calcium fluoride

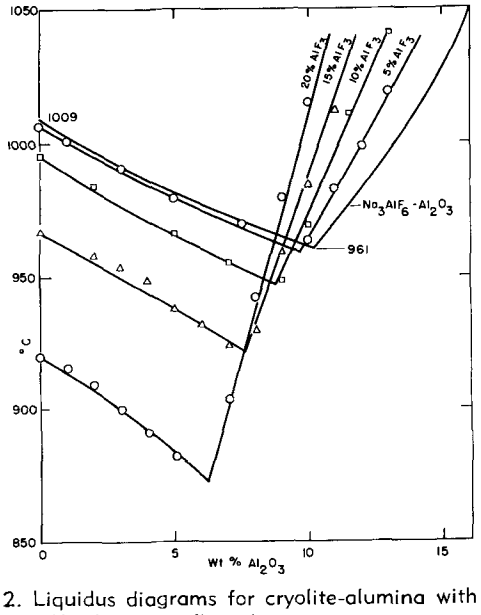

Fig. 2. Liquidus diagrams for cryolite-alumina with 5, 10, 15, and 20% aluminum fluoride.

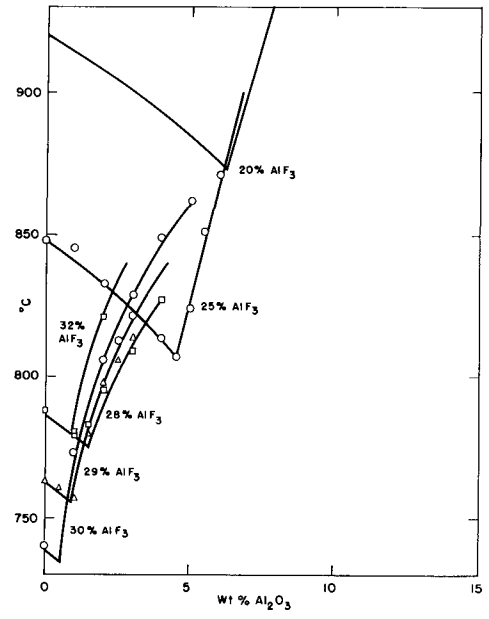

Fig. 3. Liquidus diagrams for cryolite-alumina with 25, 28, 29, 30, and 32% aluminum fluoride.

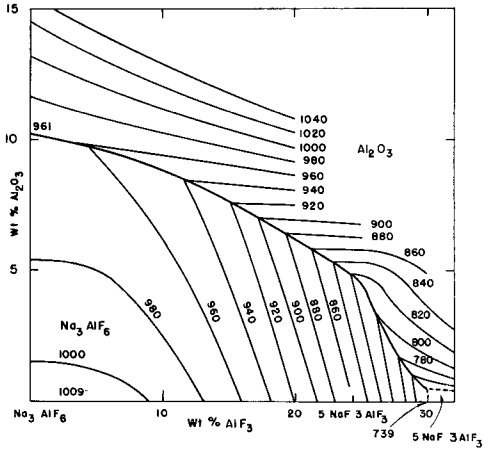

Fig. 4. Liquidus diagram for cryolite-alumina-aluminum fluoride

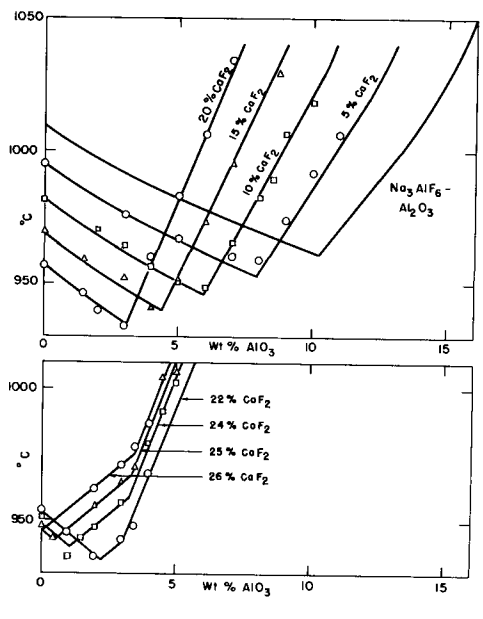

Fig. 5. Liquidus diagrams for cryolite-alumina with 0, 5, 10, 15, 20, 25, and 26% calcium fluoride.

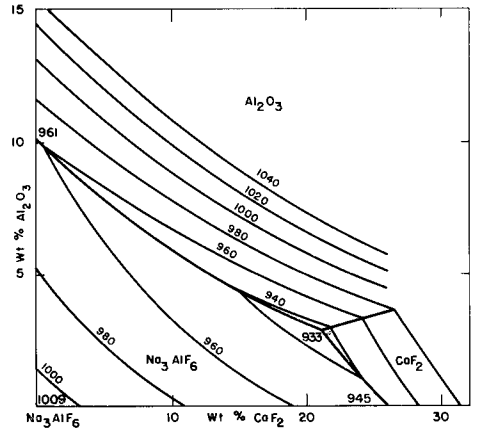

Fig. 6. Liquidus diagram for cryolite-alumina-calcium fluoride.

The liquidus diagram for cryolite-calcium fluoride (Fig. 1) was found to have a eutectic point at 26% calcium fluoride and 945°C This is in good agreement with the 25.5% calcium fluoride and 942°C obtained by Gupalo (10).

In the ternary system cryolite-alumina-aluminum fluoride sections were determined at 5, 10, 15, 20, 25, 28, 29, 30, and 32% aluminum fluoride, and the results are plotted in Fig. 2 and 3. The ternary diagram (Fig. 4) is based on these, on the revised diagram for cryolite-aluminum fluoride (see above), and on the diagram for cryolite-alumina (1) redrawn with the eutectic point at 10.2% alumina and 961°C. This ternary diagram replaces the preliminary diagram presented in the preceding paper (2). The eutectic line separating the fields of crystallization of cryolite and alumina and the isothermal contours indicating the solubility of alumina show a gradual reduction in alumina content with increasing aluminum fluoride content up to 25% of the latter. Beyond this they show a much more rapid decrease in alumina content.

Kostyukov's (11) diagram for this system, based presumably on measurements by the cooling-curve method which does not adequately detect the crystallization of alumina, gives alumina solubilities which are much too high. Thus the peritectic point, at which the melt is saturated with respect to alumina, cryolite, and chiolite, is given as 5.7% alumina, 27.8% aluminum fluoride and 710°C. Also the ternary eutectic point, at which the melt would be saturated with respect to alumina, chiolite, and aluminum fluoride, is given as 3.9% alumina, 36.8% aluminum fluoride and 678°C. The more recent work of Fuseya and Takeda (12), carried out by the cooling-curve method, gave alumina contents higher than those of Kostyukov. For comparison the present work indicates that the alumina content at the ternary peritectic and eutectic points is less than 1%. It may be noted too that the results of both these laboratories for the eutectic point in the system cryolite-alumina (16 and 18% alumina, respectively) are also in error.

For the ternary system cryolite-alumina-calcium fluoride the results for sections taken at 5, 10, 15, 20,

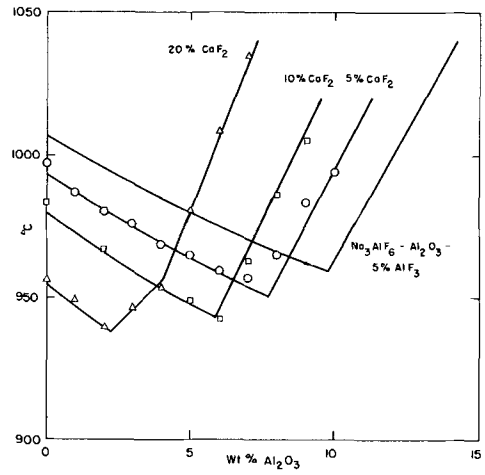

Fig. 7. Liquidus diagrams for cryolite-alumina 5% aluminum fluoride with 5, 10, and 20% calcium fluoride.

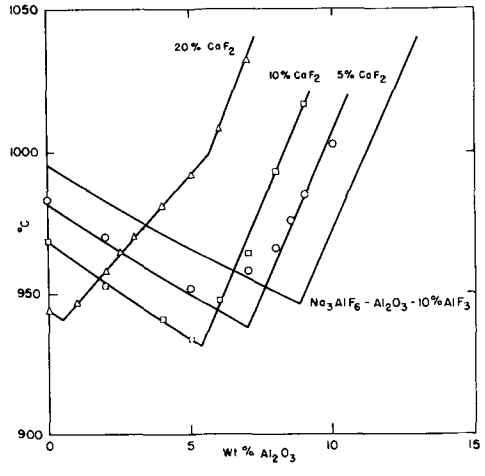

Fig. 8. Liquidus diagrams for cryolite-alumina-10% aluminum fluoride with 5, 10, and 20% calcium fluoride.

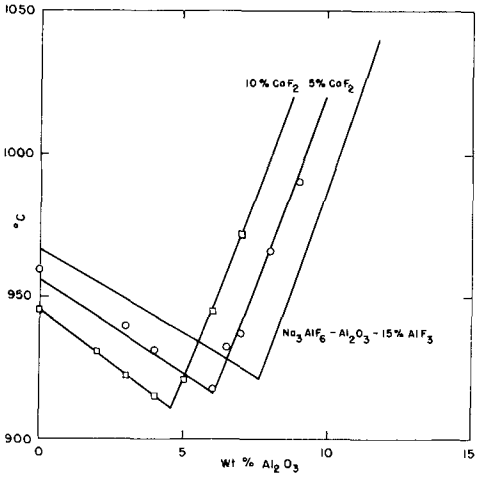

Fig. 9. Liquidus diagrams for cryolite-alumina-15% aluminum fluoride with 5 and 10% calcium fluoride.

22, 24, 25, and 26% calcium fluoride are plotted in Fig. 5. The ternary diagram, based on this and on the diagrams for cryolite-calcium fluoride and cryolite-alumina, is given in Fig. 6. It is a simple eutectic diagram with the ternary eutectic point at 2.9% alumina, 21% calcium fluoride and 933°C.

Henry and Lafky (13) determined the percentage of alumina which would dissolve in cryolite-calcium

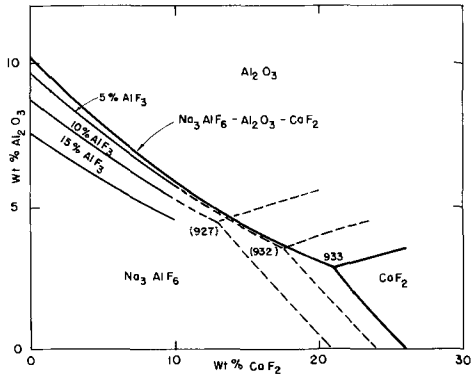

Fig. 10. Eutectic lines for cryolite-alumina-calcium fluoride with 5, 10, and 15% aluminum fluoride.

fluoride melts on prolonged stirring at a given temperature. Values at 1000°C interpolated from their results and from the present work are compared below:

	0% CaF_2	5% CaF_2	10% CaF_2	15% CaF_2
Henry and Lafky	12.0	10.3	8.5	6.8
This work	13.2	10.8	8.9	7.2

Their results are consistently slightly lower than those of the present investigation which is not unexpected in view of the methods used. Gupalo's (10) result for the ternary eutectic, 10.5% alumina, 13.6% calcium fluoride and 923°C, is quite different from that given above. Again the most likely explanation is failure to detect the initial crystallization of alumina.

The effect on the system cryolite-alumina of combined additions of 5, 10, or 15% aluminum fluoride and 5, 10, or 20% calcium fluoride was determined; results are plotted in Fig. 7, 8, and 9. Figure 10, based on these, shows the effect of 5, 10, and 15% aluminum fluoride on the eutectic lines of the system cryolite-alumina-calcium fluoride taken from Fig. 3. The field of crystallization of calcium fluoride is shifted to much lower percentages of calcium fluoride. For example, the addition of 10% aluminum fluoride shifts the ternary eutectic point from 21% calcium fluoride to approximately 13%.

In this quaternary system Abramov, Kostyukov, and Kulakov (14) have examined the pseudoternary section chiolite-alumina-calcium fluoride, which was not done by the present authors. However, in view of the method used (cooling curves and optical identification of the primary crystals) and of the discrepancy between Kostyukov's results and those reported here for the ternary system cryolite-alumina-aluminum fluoride, their alumina solubilities are most likely to be too high.

Manuscript received May 31, 1960.

Any discussion of this paper will appear in a Discussion Section to be published in the June 1961 JOURNAL.

REFERENCES

1. N. W. F. Phillips, R. H. Singleton, and E. A. Hollingshead, *This Journal*, **102**, 648 (1955).
2. N. W. F. Phillips, R. H. Singleton, and E. A. Hollingshead, *ibid.*, **102**, 690 (1955).
3. P. A. Foster, Jr., *J. Am. Ceram. Soc.*, **43**, 66 (1960).
4. P. A. Foster, Jr., *J. Phys. Chem.*, **61**, 1005 (1957).
5. Kai Grjotheim, *Kgl. Norske Videnskab. Selskabs Skrifter*, **1956**, No. 5, 1-90.

6. A. S. Dworkin and M. A. Bredig, *J. Phys. Chem.*, **64**, 269 (1960).
7. Karl A. Sense, C. A. Alexander, R. E. Bowman, R. W. Stone, and R. B. Filbert, Jr., *J. Phys. Chem.*, **61**, 384 (1957).
8. C. J. O'Brien and K. K. Kelley, *J. Am. Chem. Soc.*, **79**, 5616 (1957).
9. J. W. Johnson, Daniel Cubicciotti, and C. M. Kelley, *J. Phys. Chem.*, **62**, 1107 (1958).
10. I. P. Gupalo, Investigation of the equilibrium diagram, density and viscosity of the system cryolite-alumina-calcium fluoride, Leningrad Phys. Inst., 1952 (From A. I. Belyaev, M. B. Rapoport and L. A. Firsanova, Metallurgie des Aluminiums, Vol. 1, Berlin, VEB Verlag Technik, 1956).
11. A. A. Kostyukov, Investigation of the equilibrium diagram of the system consisting of the fluorides and oxides of aluminium and sodium. Leningrad Polytech. Inst., 1949. (Same source as ref. 10).
12. Giichiro Fuseya and Bunshichi Takeda, *J. Electrochem. Soc. Japan*, (Overseas Ed.), **27**, E 139 (1959).
13. J. L. Henry and W. M. Lafky, *Ind. Eng. Chem.*, **48**, 126 (1956).
14. G. A. Abramov, A. A. Kostyukov, and I. B. Kulakov, *Trudy Leningrad. Politekh. Inst. im M. I. Kalinina*, No. 188, 45 (1957).

The Structure of Cryolite-Alumina Melts

Perry A. Foster, Jr. and William B. Frank

Alcoa Research Laboratories, Physical Chemistry Division, Aluminum Company of America, New Kensington, Pennsylvania

ABSTRACT

The integrated cryoscopic equation, Temkin's formulation for ionic melts, and recent findings on the constitution of molten cryolite are employed to evaluate several reaction mechanisms for the solution of alumina in cryolite. The reaction mechanism that emerges as the most probable from a plot of -log a_c *vs.* $1/T$ is $3F^- + Al_2O_3 = 3/2\ AlO_2^- + 1/2\ AlF_6^{3-}$. The deviation from linearity of the plot for this reaction at high alumina contents can be attributed to some dimerization of the AlO_2^- ions to give $Al_2O_4^{2-}$ ions.

There is no method available for the direct structural evaluation of molten salts comparable to x-ray diffraction in the study of solids. A technique frequently used is to employ the integrated cryoscopic equation

$$-\ln\ a_i = (\Delta H_f/R)\,(1/T - 1/T_o) \qquad [1]$$

where a_i is the activity of the solvent, ΔH_f the cryoscopic heat of fusion of the pure solvent, T the liquidus temperature in °K, and T_o the melting point of pure solvent.

The use of this equation presupposes that ΔH_f is independently known, that ΔH_f does not vary with temperature ($\Delta C_p = 0$), that a reliable phase diagram exists from which liquidus temperatures are known over a range of compositions, and that there is no solid solubility.

Various reaction mechanisms are now hypothesized between the solvent and the solute which will permit an evaluation of the solvent activity in the liquid (a_i).For ideally behaving simple salt systems, where the solvent and solute do not dissociate, the activity of the solvent (a_i) may be equated to its weighed-in mole fraction (N_o). This criterion has been used as a test of ideality in certain molten salt systems (1). In a system such as that considered in this report, where the solvent (cryolite) dissociates on melting, knowledge of the products of dissociation and the degree of dissociation as a function of temperature is required. This information is now available for cryolite.

If the solvent activity is calculated from a reaction mechanism which properly describes the constituents present, and the system behaves ideally, a plot of $-\ln a_i$ vs. $1/T$ will be a straight line, the slope of which corresponds to the known ΔH_f.

Properties of Molten Cryolite

Dissociation of cryolite.—It is now known that cryolite dissociates partially to simpler compounds on melting. From calculations based on densities of NaF-AlF_3 melts, Frank and Foster (2) arrived at a scheme of dissociation to sodium fluoride and sodium tetrafluoaluminate, as follows:

$$Na_3AlF_6 \rightleftarrows 2NaF + NaAlF_4 \qquad [2]$$

The equilibrium constant for the reaction can be written:

$$K_D = a^2_{NaF} \cdot a_{NaAlF_4}/a_{Na_3AlF_6} \qquad [3]$$

Grjotheim (3, 4) arrived at the same scheme by an independent method, involving calculations based on a cryoscopic study of the NaF-AlF_3 system. The actual value of the dissociation constant at the melting point obtained by these two methods differs somewhat because of different approximations in the calculations. Nevertheless, this concept of molten cryolite explains so many observations of cryolite behavior that there is little doubt that the mechanism is correct.

Temperature dependence of the cryolite dissociation constant K_D.—In order to carry out the cryoscopic calculations over a range of cryolite-alumina compositions, it was necessary to know the extent of dissociation of molten cryolite as a function of temperature. The dissociation constant was determined

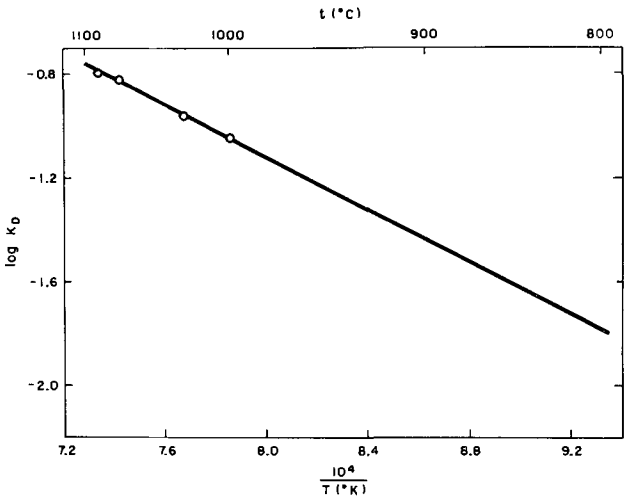

Fig. 1. Dissociation constant of cryolite as a function of temperature.

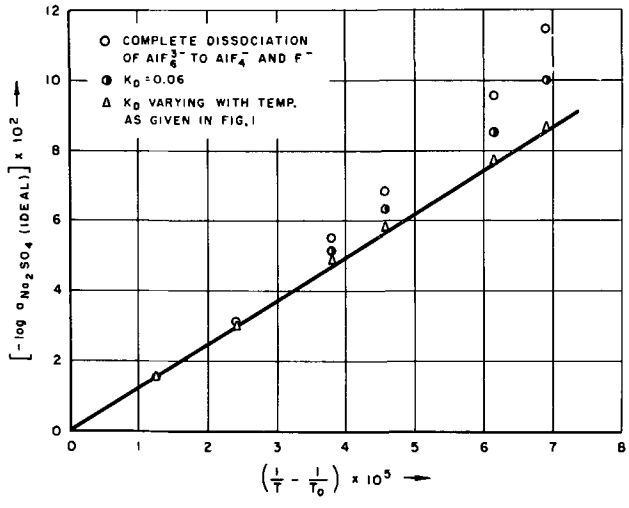

Fig. 2. Sodium sulfate activity as a function of temperature for the system Na_2SO_4-Na_3AlF_6.

by Frank and Foster (2) at four temperatures from 1000° to 1090°C. A plot of log K_D *vs.* $1/T$ was linear and the heat of dissociation was calculated from the slope as 22.5 kcal/mole (Fig. 1).

Since the validity of calculations in the cryolite-alumina system is dependent on accurate knowledge of the cryolite dissociation, it was important to test the values of K_D in another system involving cryolite as one of the binary constituents. Grjotheim (5) reported on a cryoscopic study of the Na_2SO_4-rich side of the Na_2SO_4-Na_3AlF_6 system. The purpose of the work was to substantiate the selection of the dissociation scheme of cryolite to NaF and $NaAlF_4$ and his value of 0.06 for the dissociation constant. Results are shown in Fig. 2, where $-\log a_{Na_2SO_4}$ is plotted against $(1/T - 1/T_0)$.

The solid line represents the known calorimetric heat of fusion of sodium sulfate. The open circles give the conformity to this line when the added cryolite is considered to be completely dissociated at all concentrations. The half-filled circles show the improved conformity when Grjotheim's dissociation constant of 0.06 is used over the range of temperatures of the investigation. The triangles show the almost perfect agreement that is obtained when the variation of K_D with temperature, extrapolated from the values of Frank and Foster (2), determined in the temperature range 1000°-1090°C to the temperature of the Na_2SO_4-Na_3AlF_6 system, 800°-880°C, is used. The agreement gives confidence in the use of this information on the degree of dissociation of cryolite for further calculations in the cryolite-alumina system with liquidus temperature of 962°-1004°C.

Heat of fusion of cryolite.—Two recent calorimetric determinations of the heat of fusion of cryolite gave values of 27.91 (6) and 27.64 (7) kcal/mole. An average of 27.8 kcal is employed here. It is now recognized that this is not only the heat of fusion but also includes a heat effect due to the partial dissociation of cryolite. The true cryoscopic heat of fusion ΔH_f, for undissociated cryolite becomes

$$\Delta H_f = \Delta H_F - \alpha\,\Delta H_D \qquad [4]$$

where ΔH_F is the calorimetric heat of fusion, 27.8 kcal; α the degree of dissociation at the melting point (0.35) (from ref. 2); and ΔH_D the heat of dissociation, 22.5 kcal, for reaction [2] with reactants and products in the liquid state. A value of 19.9 kcal/mole of undissociated cryolite is obtained from Eq. [4]. This value determines the slope of the line that a given reaction scheme of cryolite and alumina must reproduce if it is to be considered valid.

The assumption that the cryoscopic heat of fusion of cryolite is independent of temperature can be shown to be valid by correcting the heat content data (6, 7) for dissociation. The four measurements of the heat content of cryolite above the melting point by O'Brien and Kelley (6) and the three measurements by Albright (7) indicate that the apparent heat capacity of the liquid is greater than the heat capacity of the solid. However, when allowance is made for the temperature dependence of dissociation and the heat of dissociation as determined by Frank and Foster (2), the heat capacities of solid and liquid cryolite are almost identical. Therefore, the assumption of a constant ΔH_f should not lead to significant error.

Activities in Cryolite-Alumina Melts

The liquidus temperatures of the cryolite-alumina system are taken from the recent work of Foster (8). These temperatures range from the melting point of cryolite (1004°) to the eutectic temperature (961°C). Only the quantity a_i, the activity of the undissociated cryolite in the melts, remains to be evaluated in Eq. [1].

Temkin ionic model for molten salts.—Temkin's formulation (9) for the activity of a component in an ionic melt is accepted. According to that model, the activity of a component M_iA_i is given by

$$a_{M_iA_i} = (n_{M_i^+}/\Sigma_i n_{M_i^+}) \cdot (n_{A_i^-}/\Sigma_j n_{A_j^-}) = X_{M_i^+} \cdot X_{A_i^-} \qquad [5]$$

where $n_{M_i^+}$ is the number of cations of species M_i, $\Sigma_i n_{M_i^+}$ the total number of cations, $n_{A_i^-}$ the number of anions of species A_i, $\Sigma_j n_{A_j^-}$ the total number of anions, $X_{M_i^+}$ the cation fraction, and $X_{A_i^-}$ the anion fraction.

The ion fractions are raised to the appropriate power indicated by the number of times a given ion

appears in the formula of the component being considered.

In mixtures of components that have a common monovalent cation, such as Na^+ in most of the cases considered in this report, the cation fraction X_{Na^+} equals unity; and it can be shown from [5] that the activities of the individual components reduce to their anion fractions X_{A_j}.[1]

Method of calculation.—From [5] it follows that the activity of cryolite a_c can be expressed as

$$a_c = X^3_{Na^+} \cdot X_{AlF_6^{3-}} \qquad [6]$$

When sodium is the only cation present in the melt, Eq. [6] can be simplified to

$$a_c = X_{AlF_6^{3-}} \qquad [7]$$

The value of the anion fraction for undissociated cryolite $X_{AlF_6^{3-}}$ is determined by the degree of dissociation α as follows. Consider the equilibrium

$$AlF_6^{3-} \rightleftarrows AlF_4^- + 2F^-$$

$$K_D = (X_{AlF_4^-}) \cdot (X_{F^-})^2/(X_{AlF_6^{3-}}) \qquad [8]$$

This expression is equivalent to Eq. [3] where K_D had been expressed in terms of activities of components rather than anion fractions.

For one mole of cryolite before dissociation, at equilibrium the number of moles of AlF_4^- is α; of F^-, 2α; of AlF_6^{3-}, $1-\alpha$; the total moles of anions, $1+2\alpha$.

The expressions for the anion fractions become:

$$X_{AlF_4^-} = \alpha/(1+2\alpha)$$
$$X_{F^-} = 2\alpha/(1+2\alpha)$$
$$a_c = X_{AlF_6^{3-}} = (1-\alpha)/(1+2\alpha) \qquad [9]$$

These anion fractions are substituted into Eq. [8] to give

$$K_D = 4\alpha^3/(1-\alpha)(1+2\alpha)^2 \qquad [10]$$

Since K_D is known as a function of temperature, α can be calculated, and the cryolite activity can be determined from Eq. [9].

When alumina is added to cryolite, the degree of dissociation α changes to some new value α_i that is different for different possible reaction schemes. The ion fractions, expressed as X_i, are now written in terms of both α_i and N_i, where N_i represents the weighed-in mole fractions of the starting components. The weighed-in mole fractions of cryolite and alumina are N_0 and N_1, respectively ($N_0 + N_1 = 1$).

For any isoplethal composition, values for T and K_D are known. An equation similar to Eq. [10] is utilized to obtain α_i. This quantity is now used in an equation similar to Eq. [9] to calculate a_c (cryolite activity). —Log a_c can now be plotted against $1/T$ for each reaction mechanism. If the chosen mechanism is the proper one and the system behaves ideally, this plot should be a straight line whose slope is $\Delta H_f/(2.303R)$.

[1] The existence of a common monovalent cation permits equating the anion fraction to the simple mole fraction. This was done by Frank and Foster (*loc. cit.*) in the study of the constitution of cryolite.

Table I. Isoplethal compositions with related liquidus temperatures and cryolite dissociation constants

Wt % Al_2O_3	Weighed-in mole fraction of cryolite N_0	Weighed-in mole fraction of Al_2O_3 N_1	Liquidus temperature t °C	$10^4/T$	Cryolite dissociation constant K_D
0	1.0000	0	1004	7.830	0.0925
3.25	0.9353	0.0647	990.4	7.914	0.0845
5.16	0.8992	0.1008	981.4	7.971	0.0792
8.12	0.8459	0.1541	970.5	8.041	0.0729
10.50	0.8054	0.1946	961.6	8.099	0.0684

Possible mechanisms for the solution of alumina in cryolite.—Some of the schemes for the reaction of alumina with cryolite that have been proposed in the literature are presented below. In all but the first case, alumina is considered to be completely consumed in the formation of some new oxygen-containing species. In each case, the equilibrium between cryolite, sodium fluoride, and sodium tetrafluoaluminate is maintained. The reaction to form the oxygen-containing constituent influences this equilibrium by consuming and/or forming one of the three species, and by changing the total number of moles present.

List of Schemes

I. Simple solution, without ionization
II. $5/2AlF_6^{3-} + Al_2O_3 = 3/2AlO_2F_2^{3-} + 3AlF_4^-$
III. $AlF_6^{3-} + Al_2O_3 = 3AlOF_2^-$
IV. $AlF_6^{3-} + Al_2O_3 = 3/2Al_2O_2F_4^{2-}$
V. $Al_2O_3 = AlO^+ + AlO_2^-$
VI. $3F^- + Al_2O_3 = 3/2AlO_2^- + 1/2AlF_6^{3-}$
VII. $3F^- + Al_2O_3 = 3/4Al_2O_4^{2-} + 1/2AlF_6^{3-}$

Results

Details of the calculations for the individual schemes are given in the Appendix. The numerical values for the quantities N_0, N_1, and K_D corresponding to each liquidus temperature are listed in Table I. The values for the cryolite activity calculated for each of the seven schemes are given in Table II. The linearity of the plot of log a_c *vs.* $1/T$ and the agreement of its slope to the cryoscopic heat of fusion (19.9 ± 1.0 kcal) provide the criteria by which the schemes are evaluated. Figure 3 presents a graphical comparison of the schemes with the dashed line representing the cryoscopic heat of fusion of cryolite.

Table II. Cryolite activities for reaction schemes

Alumina content wt %	Cryolite activity a_c Scheme I	Scheme II	Scheme III	Scheme IV	Scheme V	Scheme VI	Scheme VII
0	0.3806	0.3806	0.3806	0.3806	0.3806	0.3806	0.3806
3.25	0.3670	0.3372	0.3196	0.3528	0.3429	0.3507	0.3689
5.16	0.3604	0.2986	0.2876	0.3362	0.3228	0.3314	0.3586
8.12	0.3478	0.2224	0.2399	0.3062	0.2914	0.2959	0.3345
10.50	0.3373	0.1544	0.2044	0.2800	0.2674	0.2651	0.3099

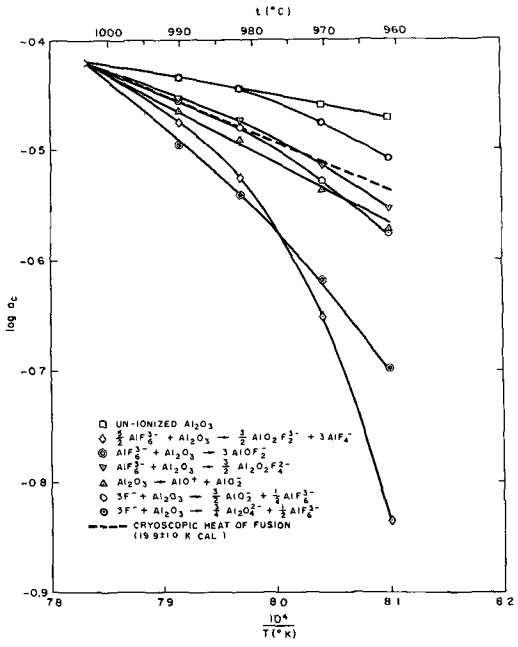

Fig. 3. Cryolite activities as a function of temperature in the system cryolite-alumina.

Scheme I, in which alumina is considered as a molecular solute, produces points falling on a line whose slope gives a low value for ΔH_f of 7.5 kcal. Schemes II, III, and V are rejected because they give high values of ΔH_f of 25 to 40 kcal in the dilute region where the curves are somewhat linear. Scheme IV ($Al_2O_2F_4^{2-}$) approximates the expected slope at low alumina concentrations. However, even the initial slope of 17.5 kcal is outside the expected error in the heat of fusion for cryolite. Scheme VII ($Al_2O_4^{2-}$) gives a low value for ΔH_f of 7.5 kcal in dilute solutions. Scheme VI (AlO_2^-) is the only scheme that reproduces the heat of fusion line in the dilute region. The points up to 5% alumina fall essentially on a line whose slope corresponds to a cryolite heat of fusion of 19.7 kcal. At higher alumina contents there is considerable deviation.

Discussion

Scheme I which produced a line whose slope gave a low value of 7.5 kcal for the heat of fusion can also be ruled out by other experimental evidence. In cryolite-alumina melts, complete exchange occurs rapidly between the aluminum of aluminum oxide and that of cryolite (10). The density of fused cryolite decreases upon the addition of the more dense aluminum oxide (11). A reaction between cryolite and alumina, rather than a physical solution of alumina in cryolite, is indicated.

Scheme VI (AlO_2^-) showed good agreement with the cryoscopic heat of fusion for alumina contents up to 5 wt %. The existence of the anion AlO_2^- in cryolite alumina melts was suggested by transport number determinations (10), viscosity and density measurements (12) in cryolite alumina melts. Sodium aluminate has been identified by x-ray powder diffraction patterns in NaF-Al_2O_3 melts quenched from above the liquidus.

It may not be unreasonable to expect that the observed deviation at higher alumina contents is due to interaction between AlO_2^- ions that gives rise to partial dimerization ($Al_2O_4^{2-}$). In the soda-alumina system, sodium aluminate ($Na_2O \cdot Al_2O_3$) is a well-established compound melting at 1650°C. The nature of its ions in the molten state is not known. Both AlO_2^- and $Al_2O_4^{2-}$ are possible anions; however, calculations of a possible equilibrium between AlO_2^- and $Al_2O_4^{2-}$ over the composition range from pure cryolite to the eutectic temperature led to an unreasonable variation in the equilibrium constant for the monomer-dimer reaction.

Although the evaluation contained in this paper cannot be interpreted as conclusive evidence of the validity of a single reaction mechanism, it is of interest to note that several proposed mechanisms can be ruled out and that the mechanism suggested by this investigation is in agreement with other experimental evidence.

Manuscript received April 22, 1960. Revised manuscript received Aug. 3, 1960.

Any discussion of this paper will appear in a Discussion Section to be published in the June 1961 JOURNAL.

REFERENCES

1. H. Flood, T. Forland, and A. Nesland, *Acta Chem. Scand.*, **5**, 1193 (1951).
2. W. B. Frank and L. M. Foster, *J. Phys. Chem.*, **64**, 95 (1960).
3. K. Grjotheim, *Kgl Norske Vidensk. Selskabs Skrifter*, **1956**, No. 5.
4. J. Brynestad, K. Grjotheim, and S. Urnes, *Z. Elektrochem.*, **63**, 707 (1959).
5. K. Grjotheim, T. Halvorsen, and S. Urnes, *Can. J. Chem.*, **37**, 1170 (July, 1959).
6. C. J. O'Brien and K. K. Kelley, *J. Am. Chem. Soc.*, **79**, 5616 (1957).
7. D. M. Albright, Thesis, Carnegie Institute of Technology (1956).
8. P. A. Foster, *J. Am. Ceram. Soc.*, **43**, 66 (1960).
9. M. Temkin, *Acta Physicochim., U.R.S.S.*, **20**, 411 (1945).
10. L. M. Foster and W. B. Frank, *J. Phys. Chem.*, **61**, 1531 (1957).
11. J. D. Edwards, C. S. Taylor, L. A. Cosgrove, and A. S. Russell, *This Journal*, **100**, 508 (1953).
12. G. A. Abramov, M. M. Vetyukov, I. P. Gupalo, A. A. Kostyukov, and L. N. Lozhkin, "Theoretical Bases of Electrometallurgy of Aluminum," Metallurgy Publishing House (1953).
13. T. Forland, H. Storegraven, and S. Urnes, *Z. anorg. u. allgem. Chem.*, **279**, 205 (1955).
14. J. F. Boner, *Helv. Chim. Acta*, **33**, 1137 (1950).
15. W. D. Treadwell, *Schweiz, Arch. angew. Wiss. u. Tech.*, **6**, 69 (1940).
16. M. Rolin, *Ann. phys.*, **6**, Series 12, 970 (1951).
17. M. Frejacques, *Bull. soc. franc. electriciens*, **9**, 684 (1949).

APPENDIX

The documentation for the complex anion product and the mathematical expressions for the cryolite activity and dissociation constant are given here.

Scheme I.—A conceivable but unlikely mechanism for the incorporation of alumina in croylite is the simple solution of un-ionized Al_2O_3 molecules. In treating this case, the Temkin model must be abandoned since there is no meaning to an "ion fraction." The cryolite activity is equated to its mole fraction, considering all components in the molecular form. At equilibrium

$$a_{Na_3AlF_6} = (N_0 - N_0\alpha_i)/(2N_0\alpha_i + 1) \qquad [1]$$

The degree of dissociation α_i is calculated from the following expression for the dissociation constant

$$K_D = \left(\frac{\alpha_i}{1-\alpha}\right)\left(\frac{2N_0\alpha_i}{2N_0\alpha_i + 1}\right)^2$$

Scheme II.—Forland (13) investigated the equilibrium between carbon dioxide and molten mixtures of sodium fluoride, cryolite and aluminum oxide. The results were explained by assuming that alumina dissolves as a complex ion containing two oxygen atoms for each aluminum. Although it was difficult to determine the number of fluorine atoms in the complex, Forland suggested that two was the most probable number. The formation of this anion can be written as

$$(5/2)\,AlF_6^{3-} + Al_2O_3 \rightarrow (3/2)\,AlO_2F_2^{3-} + 3AlF_4^-$$

The anion fraction of cryolite becomes:

$$X_{AlF_6^{3-}} = (N_0 - N_0\alpha_i - (5/2)N_1)/(N_0 + 2N_0\alpha_i + 2N_1) \quad [2]$$

The value of α_i to be employed in Eq. [2] is obtained from the following expression for the dissociation constant

$$K_D = \left(\frac{2N_0\alpha_i - 6N_0 + 6}{7N_0 - 2N_0\alpha_i - 5}\right)\left(\frac{2N_0\alpha_i}{N_0 + 2N_0\alpha_i + 2N_1}\right)^2$$

Scheme III.—Boner (14) interpreted the alumina-cryolite phase diagram and x-ray analysis of the phases in equilibrium as evidence for the existence of $AlOF_2^-$. The formation of this anion can be written as

$$AlF_6^{3-} + Al_2O_3 \rightarrow 3AlOF_2^-$$

The anion fraction for this reaction becomes

$$X_{AlF_6^{3-}} = (N_0 - N_0\alpha_i - N_1)/(N_0 + 2N_0\alpha_i + 2N_1) \quad [3]$$

The values of α_i are obtained from the following expression for the dissociation constant

$$K_D = \left(\frac{N_0\alpha_i}{2N_0 - N_0\alpha_i - 1}\right)\left(\frac{2N_0\alpha_i}{N_0 + 2N_0\alpha_i + 2N_1}\right)^2$$

Scheme IV.—Treadwell (15) proposed the formation of the oxyfluoride ion $Al_2O_2F_4^{2-}$ in cryolite-alumina melts. The formation of this anion can be written as

$$AlF_6^{3-} + Al_2O_3 \rightarrow (3/2)\,Al_2O_2F_4^{2-}$$

The cryolite anion fraction becomes

$$X_{AlF_6^{3-}} = (N_0 - N_0\alpha_i - N_1)/(N_0 + 2N_0\alpha_i + (1/2)N_1) \quad [4]$$

The following expression provides the values of α_i to be employed in Eq. [4].

$$K_D = \left(\frac{N_0\alpha_i}{2N_0 - N_0\alpha_i - 1}\right)\left(\frac{2N_0\alpha_i}{N_0 + 2N_0\alpha_i + (1/2)N_1}\right)^2$$

Scheme V.—Rolin (16) concluded, from the results of a cryoscopic study of the cryolite-alumina system, that the dissociation of alumina can be represented by the equation

$$Al_2O_3 \rightarrow AlO^+ + AlO_2^-$$

The cryolite anion fraction becomes

$$X_{AlF_6^{3-}} = (N_0 - N_0\alpha_i)/(N_0 + 2N_0\alpha_i + N_1) \quad [5]$$

The following equation is solved for α_i,

$$K = \left(\frac{\alpha_i}{1-\alpha_i}\right)\left(\frac{2N_0\alpha_i}{N_0 + 2N_0\alpha_i + N_1}\right)^2$$

and $X_{AlF_6^{3-}}$ is calculated by substituting this value of α_i into Eq. [5]. However, in this case the expression does not represent the activity of the solvent, cryolite, since the cation fraction is not unity and must be evaluated also.

The cation fraction of sodium can be expressed as

$$X_{Na^+} = (3N_0)/(3N_0 + N_1) \quad [6]$$

The cation-anion fraction product becomes

$$a_c = X_{Na^+}{}^3 \cdot X_{AlF_6^{3-}}$$

Substitution of expressions for anion and cation fractions, (Eq. [5] and [6]) yields

$$a_c = \left(\frac{3N_0}{3N_0 + N_1}\right)^3\left(\frac{N_0 - N_0\alpha_i}{N_0 + 2N_0\alpha + N_1}\right)$$

Scheme VI.—Transport number determinations (10) in cryolite-alumina melts and viscosity and density measurements (12) suggest the existence of the aluminate ion. The formation of this anion can be written as

$$3F^- + Al_2O_3 \rightarrow (3/2)\,AlO_2^- + (1/2)\,AlF_6^{3-}$$

The cryolite anion fraction becomes

$$X_{AlF_6^{3-}} = (N_0 - N_0\alpha_i + (1/2)N_1)/(N_0 + 2N_0\alpha_i - N_1) \quad [7]$$

From the following expression for the dissociation constant, values for α_i are obtained

$$K_D = \left(\frac{N_0\alpha_i}{N_0 - N_0\alpha_i + (1/2)N_1}\right)\left(\frac{2N_0\alpha_i - 3N_1}{N_0 + 2N_0\alpha_i - N_1}\right)^2$$

Scheme VII.—Frejacques (17) postulated the existence of the compound $Na_2Al_2O_4$ in cryolite-alumina melts. The formation of the anion of this compound may be written as

$$3F^- + Al_2O_3 \rightarrow (3/4)\,Al_2O_4^{2-} + (1/2)\,AlF_6^{3-}$$

The cryolite anion fraction becomes

$$X_{AlF_6^{3-}} = (N_0 - N_0\alpha_i + (1/2)N_1)/(N_0 + 2N_0\alpha_i - (7/4)N_1) \quad [8]$$

The values of α_i to be used in Eq. [8] are obtained from the following expression of the dissociation constant

$$K_D = \left(\frac{N_0\alpha_i}{N_0 - N_0\alpha_i + (1/2)N_1}\right)\left(\frac{2N_0\alpha_i - 3N_1}{N_0 + 2N_0\alpha_i - (7/4)N_1}\right)^2$$

Technical Notes

On the Role of the Oxygen Concentration Cell in Crevice Corrosion and Pitting

G. J. Schafer, J. R. Gabriel,[1] and P. K. Foster

Department of Scientific and Industrial Research, Dominion Laboratory, Wellington, New Zealand

Uhlig (1) states that contact corrosion of stainless steels ". . . proceeds by a mechanism identical to that described . . . for pit growth." In the case of stainless steel others also have recognized the similarity between crevice corrosion and pitting (2), but it does not appear to have been suggested to date that the two processes are identical for any metal in any electrolyte. Possibly because of the obvious difficulties associated with measurements on pits or crevices, relatively few fundamental investigations appear to have been attempted. However, Ulanovskii and Korovin (3) showed that the solution in stainless steel crevices corroding in sea water reached pH values of about 3 while Rozenfeld and Marshakoff (4) showed that the solution pH in corroding aluminum crevices also falls below that of the bulk of the solution. (They also suggested that this low pH is more important than differential aeration after corrosion has been initiated.)

The acid nature of the solution in pits has been demonstrated for a number of metals (5, 6) and Hoar's acid theory (7-9) is at present probably the most generally accepted explanation of the pitting attack on many metals.

So it can be said that in all cases investigated, the solution pH fell at sites of local corrosion.

No oxygen concentration measurements in corroding pits and crevices have been located by the authors, but Evans and others have postulated that crevice corrosion is initiated by local exhaustion of oxygen (or inhibitor) in a crevice (10-12) while May (13) concluded that the pitting of copper in waters containing chloride was dependent on the interaction of anodically produced cuprous chloride with oxygen diffusing towards the anode, and Streicher (2) attributed stainless steel pitting to the joint action of differential acid and oxygen concentration cells.

Thus, while there is no direct evidence, it is widely held that pitting and particularly crevice corrosion are influenced by the action of differential aeration cells.

Another mechanism known as the metal ion concentration cell is well established in the literature but has been shown to be invalid (14) (see also Appendix I).

[1] Present address: Atomic Energy Research Establishment, Harwell, England.

In the present work it is suggested that pitting and crevice corrosion are identical processes, each depending on the conjoint action of the acid mechanism and differential aeration. To support this hypothesis two arguments are advanced against a differential aeration cell mechanism as the sole agent responsible for any localized corrosion.

1. Unless oxygen is used up at anodes, a self-supporting steady-state system depending solely on differential aeration is impossible. This is shown as follows: The differential aeration cell mechanism assumes that oxygen concentration on a particular anode is smaller than on adjacent cathodes. Oxygen concentration on an anode must therefore either be constant or reach a minimum value.

Consider a steady-state differential aeration system in which oxygen is transported by diffusion only, oxygen is used up only at cathode areas, no oxygen is evolved anywhere, and anodes of finite area exist.

Let C be the oxygen concentration.

At anodes no oxygen is consumed or produced, so $\text{grad}_n C = 0$ on the anode surface. It follows that C cannot be constant on the anode because if so, calculation of C and ∇C at a point close to the anode by Taylor's series would show that C and ∇C had not changed on moving off the surface. The Taylor series calculation then could be repeated for a point a little further away and so on, until it was shown that C = constant everywhere and $\nabla C = 0$ everywhere. This corresponds to the case where no corrosion action takes place and is of no interest.

Since oxygen flow is always toward cathodes, there can be no minimum of C on an anode surface, and any minima of C must be on cathodes. Since oxygen concentration is a continuous function of position, this implies that, for any anode-cathode interface in the type of system considered, there must be points on the cathode side of the interface (perhaps only very close to the interface) where the oxygen concentration is smaller than the concentration at some place on the anode side of the interface (perhaps relatively far from the interface). But this is contrary to hypothesis because it is implicit in the concept of a differential aeration cell that oxygen concentration must always be greater at cathodes than at anodes.

The only way to resolve this difficulty while retaining the requirement of steady state is to assume either that only point anodes exist, or that oxygen is consumed at anodes. The former assumption is untenable because infinite anode current densities would occur, hence oxygen must be consumed at anodes.

However, the oxygen which must be used at anodes in general represents anode corrosion due to local microcell action. Hence local microcell action at anodes is essential for the working of a self-supporting differential aeration cell and must contribute to the dissolution of metal. In other words, if the current flowing between the anodic and cathodic regions were measured, it would not be found to account for all of the observed corrosion.

2. The differential aeration mechanism itself, if considered in detail, leads to differential acid concentrations. For if a differential aeration mechanism causes localized corrosion, the *p*H of the solution at anodic areas must become lower than the *p*H of the solution at cathodic areas due to the preponderance of metal ion production and oxygen depolarization at the two respective surfaces.

It is therefore postulated that after the mechanism which determines the site of corrosion initiation has ceased to operate (*i.e.*, as soon as localized attack has begun), for any particular metal in a certain medium, exactly the same mechanism operates in the case of pitting and crevice corrosion. So in many cases of crevice corrosion it is probably an acid mechanism which chiefly accounts for the localized nature of the attack. The local exhaustion theory accounts mainly for the position at which attack is initiated.

It may be noted that the operation of an acid mechanism corrosion cell *ipso facto* produces a differential aeration effect because the microcell corrosion due to acid conditions uses up oxygen. So if, for example, a pit is initiated on a piece of stainless steel either by oxygen starvation or by acid attack (other things being equal), the final corroding systems should be identical.

Important factors such as active-passive cells (*e.g.*, stainless steels) and oxygen-absorbing anodic corrosion products (*e.g.*, copper) have not been discussed here because, while they may influence the relative importance of the differential aeration and the differential acid concentration cells, the above arguments are basically unaffected.

Conclusion

It is proposed that the crevice corrosion mechanism must, like pitting (2, 15), be divided into two stages. A differential aeration or inhibitor exhaustion mechanism is decisive in determining the locations at which crevice corrosion is initiated. After initiation, however, continued crevice corrosion depends also on the acid mechanism frequently used to explain the autocatalytic nature of pitting.

The presence of oxygen as a depolarizing agent is still essential, but not in the sense of a differential aeration mechanism. The following example illustrates this point. Copper corrodes only very slowly in oxygen-free HCl, but if oxygen is added corrosion occurs rapidly (1). Thus oxygen is necessary as a depolarizing agent for the corrosion of copper in HCl, but differential aeration plays no part.

Pitting is considered to be merely a limiting case of crevice corrosion, the difference being that macroscopic geometrical factors determine the initiation sites of crevice corrosion, while random microscopic factors usually determine the sites of initiation of pitting corrosion. For any particular metal, steady-state pitting and crevice corrosion occur by identical mechanisms involving the conjoint action of differential acid concentrations and differential oxygen (or other depolarizer) concentrations.

Acknowledgments

The authors wish to thank Mr. A. McNabb and other members of the Applied Mathematics Laboratory, Wellington, for helpful discussions, and the Director for permission to publish this work.

Manuscript received July 25, 1960.

Any discussion of this paper will appear in a Discussion Section to be published in the June 1961 JOURNAL.

REFERENCES

1. H. H. Uhlig, "Corrosion Handbook," John Wiley & Sons, Inc., New York (1948).
2. M. A. Streicher, *This Journal*, **103**, 375 (1956).
3. I. B. Ulanowskii and Iu. M. Korovin, *J. Appl. Chem. (U.S.S.R.)* (English translation), **31**, 1352 (1958).
4. I. L. Rozenfeld and I. K. Marshakoff, *J. Phys. Chem. (U.S.S.R.)*, **31**, 2328 (1957).
5. T. Hagyard and J. R. Santhiapillai, *J. Appl. Chem.*, **9**, 323 (1959).
6. W. Feitknecht, *Chem. and Ind.*, **1959**, 1102.
7. T. P. Hoar, *Trans. Faraday Soc.*, **33**, 1152 (1937).
8. T. P. Hoar, *ibid.*, **45**, 683 (1949).
9. T. P. Hoar, *Discussions Faraday Soc.*, No. 1, 299 (1947).
10. U. R. Evans, "Metallic Corrosion Passivity and Protection," p. 496 *et seq.*, Edward Arnold & Co., London (1946).
11. U. R. Evans and D. E. Davies, *J. Chem. Soc.*, **1951**, (3), 2607.
12. U. R. Evans, L. C. Bannister, and S. C. Britton, *Proc. Roy. Soc.*, **A131**, 355 (1931).
13. R. May, *J. Inst. Metals*, **82**, 65 (1953-1954).
14. G. J. Schafer and P. K. Foster, *This Journal*, **106**, 468 (1959).
15. P. M. Aziz and H. P. Godard, *Ind. Eng. Chem.*, **44**, 1791 (1952).
16. I. K. Marshakoff and I. L. Rozenfeld, *J. Phys. Chem. (U.S.S.R.)*, **33**, 219 (1959).
17. I. L. Rozenfeld and I. K. Marshakoff, *ibid.*, **30**, 2724 (1956).

APPENDIX I

The experiments of Marshakoff and Rozenfeld on copper crevice corrosion (16) call for some comment. It has been proved that the metal ion concentration cell cannot be a cause of steady-state crevice corrosion (14), (or, for that matter, any other type of localized corrosion), but Marshakoff and Rozenfeld concluded that metal ion concentration cells were in fact operative in their experiments.

We agree with their interpretation, but we consider that the experiments were designed wrongly, and while in the cases of the other metals investigated this has only quantitatively influenced the results, in the case of copper it has lead to wrong conclusions.

Our objection is that the electrolyte used in many of the experiments (and in particular the experiments on copper) was far too aggressive.

Crevice corrosion is not a serious hazard in situations where the electrolyte causes general attack of freely

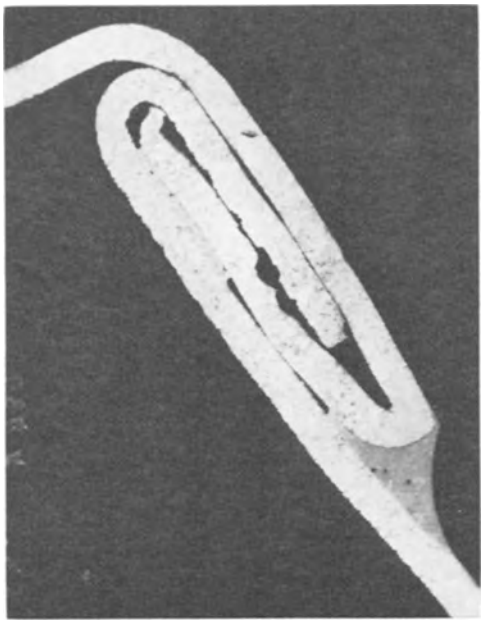

Fig. 1. Section of a brazed seam from a copper water tank. Slight general attack of the copper on the inside surface has occurred. There is no special corrosion at the crevice mouth, but the copper has been attacked locally at a number of places inside the crevice. Specimens of this kind, where crevice corrosion has occurred in the absence of interfering effects are relatively rare in our experience. Magnification 9X before reduction for publication.

exposed metal (*e.g.*, copper in 2*N* NaCl solution). As shown by Marshakoff and Rosenfeld in the cases of iron (17) and copper (16) immersed in 2*N* NaCl solution, corrosion in the crevices is less severe than corrosion of the freely exposed metal surfaces, and the electrical coupling of crevices to freely exposed metal produces only small changes in this state of affairs. Thus the crevice corrosion mechanisms are inevitably masked to a greater or lesser extent by the general corrosion taking place.

Crevice corrosion is most serious and most apparent when the freely exposed metal is relatively immune to attack and metal dissolution occurs predominantly at crevices. Only under such conditions (which usually involve a much less aggressive medium than 2*N* NaCl) is it likely that mechanisms can be successfully investigated, because the interfering general corrosion is absent.

We consider the metal ion concentration effects observed by Marshakoff and Rozenfeld to be a *result* of the general corrosion caused by the aggressive electrolyte, inside and outside the copper crevice and not the *cause* of any corrosion. In the absence of the aggressive electrolyte their experimental results would have been quite different.

A further objection to the metal ion concentration cell mechanism is that it offers no explanation for the local nature of the attack at the crevice mouth referred to by Marshakoff and Rozenfeld. In a high conductivity electrolyte such as 2*N* NaCl or sea water, corrosion would be expected to spread evenly over large areas of freely exposed metal surrounding a crevice. Also crevice corrosion of copper does not always occur at the crevice mouth (Fig. 1).

Electrodeposition of Pure Copper

Sidney Barnartt

Research Laboratories, Westinghouse Electric Corporation, Pittsburgh, Pennsylvania

Electrodeposition is attractive as a method of preparing copper plates having known added impurities. Such copper test plates are useful for oxidation to cuprous oxide semiconductors in the study of rectifiers and photovoltaic cells. As a starting point, however, a method of electrodepositing high-purity copper is necessary. The present report deals with this phase. After sufficient purity is achieved, certain metallic impurities may be incorporated one at a time by addition of an appropriate salt to the electrolyte.

Smart, Smith, and Phillips (1) have described the complex purification method used by the American Smelting and Refining Company (ASR). This involved ferric hydroxide precipitation, sulfide precipitation, electrodeposition from a sulfate solution, oxidation of the molten metal, electrodeposition from a nitrate solution, and finally melting in a high-purity graphite crucible. A much simpler procedure on a smaller scale, involving one electrodeposition step and no subsequent melting, is reported here. Data on the degree of purity attained are presented.

Procedure

The electrolyte used was $CuSO_4$-0.6M, H_2SO_4-0.8M. This was prepared from $CuSO_4 \cdot 5H_2O$ (tested-purity reagent from a single manufacturer's lot number), redistilled water, and distilled H_2SO_4 obtained by fractional distillation in all-Pyrex stills. The copper sulfate was first dissolved in water, and a solution of

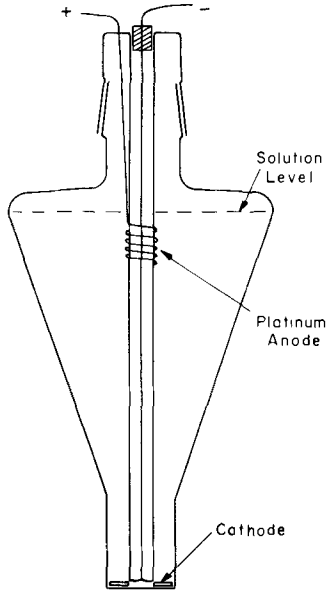

Fig. 1

reagent grade $Na_2S \cdot 9H_2O$ added to a concentration of 6 x 10^{-4}M. After heating to 70°C and cooling overnight, the mixture was decanted and filtered by suction through a fritted Pyrex filter ("ultrafine" porosity). The H_2SO_4 was then added and the volume adjusted.

Electrodeposition was carried out at 30°C and a cathode current density of 50 ma/cm^2. The Pyrex cell used is shown in Fig. 1 and was a modified inverted Erlenmeyer flask having a flat bottom. The cap of the cell held the platinum wire anode which surrounded a central vertical tube, into the bottom of which a platinum lead was sealed and protruded sufficiently to contact the cathode washer at its inner edge. The cathode diameters, 1.3 cm inner x 3.8 cm outer, closely matched the diameters of the central tube and catholyte well. The cylindrical catholyte well was 5.1 cm high and contributed to uniformity of current distribution over the cathode. All deposits were approximately 180μ in average thickness. After being stripped from the base metal and trimmed to 3.6 cm OD x 1.5 cm ID, they had a thickness variation of less than ±5%.

The cathode was a stainless steel washer having rounded edges. It was preplated with copper to a thickness of 2μ in an auxiliary acid copper bath, purified copper was deposited to the desired thickness, and then the edges of the deposit were cut to release the copper disk. The latter was treated anodically in an alkaline cyanide solution to dissolve 2.5μ of copper, thus removing the preplate layer. Final cleaning before analytical or residual resistivity measurements comprised "bright dip" in HNO_3-H_2SO_4-HCl solution followed by 10% HNO_3, redistilled water, and absolute alcohol.

Copper deposition from the acid sulfate electrolyte used resulted in a reduction of the $CuSO_4$ concentration and an increase in H_2SO_4 concentration. The solution was readjusted to the original composition after each washer was plated by removing 50 cc of the electrolyte and adding 50 cc of a purified replenishing solution having the appropriate $CuSO_4$ and H_2SO_4 concentration. By this means the solution composition was maintained constant to within ±2.5%.

Spectroscopic analysis was used for determination of metallic impurities in the copper. Arc-spectra of 50 mg samples were obtained and compared with similar spectra for high-purity copper standards.[1] Oxygen was determined on 0.7-g samples by the vacuum-fusion method, and sulfur on 1.5-g samples by a combination vacuum-fusion and mass-spectrometric procedure as described by Hickam (2, 3). Residual resistivity measurements were made on strips cut from the electrodeposit, which were vacuum annealed at 900°-940°C for 15 hr at a pressure of 10^{-6} mm Hg. On each sample resistivities measured at 4.2° and 1.9°K agreed within ±1%.

Results

The cathodic copper deposits 180 μ thick had very smooth, matte surfaces. Analyses of these deposits are given in parts per million (ppm) in Table I. Over 30 elements not listed in the table were found to be absent in the relatively sensitive arc spectra obtained. The indicated purity is 99.999+%, similar as far as is known to that of the elaborately purified ASR copper. Analytical data reported for the latter (1) are listed in the table for comparison. Actual measurements of oxygen concentration were not reported for the ASR metal, but this certainly would be less than our value of 3 ppm because ASR copper was melted in high-purity graphite as a final step.

Table I. Copper analyses, ppm

Element	Electrodeposited copper (this report)	ASR copper (1)
O	3	
S	<1	<1
Fe	<1	<0.7
As	<0.3	<2
Sn	0.2	<1
Ag	<0.1	<0.3
Pb	0.05	<1
Sb	<0.05	<1
Bi	<0.03	<0.1
Cr	Not detected	<0.5
Te		<2
Se		<1
Ni	Not detected	<1
Si	Detected*	<0.1
Mg	Detected*	
Mn	Detected*	
Zn	Detected*	

* At limit of detectability, no standards available.

Table II. Residual resistivities of polycrystalline copper

Copper used—reference	Vacuum-annealing temperature, °C	$10^3\rho_{4.2°}/\rho_{273.2°}$
Electrodeposited—this report	900-940	1.6-2.0
ASR—MacDonald and Pearson (4)	(as cast in graphite)	9.8
ASR—Kropschot, Garber, and Blatt (5)	950	1.85
ASR—White and Woods (6)	530	1.62
ASR—Powell, Roder, and Hall (7)	400	0.65
ASR—White and Tainsh (8)	530	0.56

Our residual resistivity measurements are compared in Table II with measurements on ASR copper, which has been studied by several authors.[2] The latter values vary over a wide range. It has been shown that the residual resistivity of high-purity copper is markedly dependent on annealing temperature and on slightly oxidizing or reducing conditions during the annealing procedure (4, 9), as well as on impurities unintentionally introduced. For annealing temperatures of 900°-950° the residual resistivities of the two types of copper are in excellent agreement, even though the ASR metal had been melted previously while the electrodeposited was not. This would indicate the same effective impurity concentration, but the agreement is probably fortuitous. Thus one can conclude only that the low value of residual resistivity found for the electrodeposited copper indicates high purity; a reliable purity rating relative to ASR copper is not possible from the data in Table II.

[1] Adam Hilger Ltd. (Johnson Matthey Ltd., England).

[2] It is assumed that the high-purity ASR copper obtained by each of these groups was metal prepared by the method of Smart, Smith, and Phillips (1).

Because of the high purity achieved, the simplified preparation described herein provides an attractive starting point for laboratory studies on copper having controlled added impurities, the impurities being added to the plating bath.

Acknowledgment

The collaboration of M. P. Garfunkel on residual resistivity measurements is gratefully acknowledged. Analytical data were contributed by Miss J. Senko, W. M. Hickam, and W. F. Harris.

Manuscript received July 1, 1960.

Any discussion of this paper will appear in a Discussion Section to be published in the June 1961 JOURNAL.

REFERENCES

1. J. S. Smart, A. A. Smith, and A. J. Phillips, *Trans. A.I.M.E.*, **143**, 272 (1941).
2. W. M. Hickam, *Anal. Chem.*, **24**, 362 (1952).
3. W. M. Hickam, ASTM Publication 149, p. 17 (1953).
4. D. K. C. MacDonald and W. B. Pearson, *Acta Met.*, **3**, 392 (1955).
5. R. H. Kropschot, M. Garber, and F. J. Blatt, *Phys. Rev. Letters*, **2**, 91 (1959).
6. G. K. White and S. B. Woods, *Phil. Trans.*, **A251**, 273 (1959).
7. R. L. Powell, H. M. Roder, and W. J. Hall, *Phys. Rev.*, **115**, 314 (1959).
8. G. K. White and R. J. Tainsh, *Phys. Rev.*, **119**, 1869 (1960).
9. S. T. Sekula, *Phys. Rev. Letters*, **3**, 416 (1959).

Some Observations on the System ZnS-AlP

Arrigo Addamiano

Lamp Research Laboratory, General Electric Company, Nela Park, Cleveland, Ohio

Zinc sulfide phosphors with phosphorus activator and chlorine coactivator have been described by McKeag and Ranby (1). More recently Apple (2) has shown that, under special conditions (presence of Cu activator), phosphorus and other group V elements can behave as coactivators in zinc sulfide. We have made some observations on the related system ZnS-AlP. Our work is in agreement with the investigations mentioned above and with the theory of charge compensation of Kröger and Dikhoff (3).

Interest in the system ZnS-AlP was motivated by the close similarity in crystal structure of the two substances, accompanied by a large difference in the band gaps (3.7 e.v. for ZnS, and 3.0 e.v. for AlP). The low-temperature modification of zinc sulfide has the cubic zinc-blende structure with a cell edge (4) of 5.4060Å. Aluminum phosphide also crystallizes with the zinc-blende structure and a lattice parameter (5) $a_o = 5.451$Å. The bonds in these compounds are at least partly covalent, and a comparison of the tetrahedral covalent radii of the atoms, as given by Pauling (6), (Zn 1.31Å; Al 1.26Å; P 1.10Å; S 1.04Å) shows relatively small differences.

For the study of the solubility of AlP in ZnS we used luminescent grade zinc sulfide (prefired in H_2S) and aluminum phosphide prepared as described in another paper (5). Intimate mixtures of fine powders of the two substances, with different molar content of AlP (0.5; 1.0; 5.0; 10; 20; 40; 60; 80%) were sealed in fused silica tubes in an argon atmosphere (measuring 200 mm at room temperature) and were fired 24 hr at 900°C. When the furnace was cool the tubes were extracted and the products obtained examined by x-ray diffraction using a GE-XRD3 diffractometer. For comparison x-ray data were collected also for pure ZnS and AlP, and for the unfired mixtures. Emission spectra under 3650Å and other optical data for the fired mixtures were obtained using a grating spectrophotometer.

The analysis of the x-ray diffraction data was delicate because most of the low-θ lines of zinc blende and aluminum phosphide overlap, while the high-θ lines are relatively weak. For a content of aluminum phosphide between 10 and 80 mole % the patterns of β-ZnS and AlP are clearly discernible, the high-θ reflections well resolved, and no other lines are present. For a content of AlP less than 10% the pattern of AlP does not show up either above the background in the fired samples or in the unfired mixtures. Yet, since no shift of the high-θ lines appears in the pattern of zinc sulfide, the conclusion is reached that the solubility of AlP in ZnS is very small, probably about 1 mole % or less. This conclusion is in agreement with the finding of McKeag and Ranby (1) who did not find "any significant deviation in structure" for their phosphorus activated zinc sulfide phosphors as compared to unactivated zinc sulfide.

To further check this point we have reacted a mixture of Zn_3P_2 and Al_2S_3 in a sealed quartz tube in an argon atmosphere at 900° for 24 hr. X-ray analysis of the products so obtained showed that an almost complete reaction had occurred, with disappearance of the patterns of Zn_3P_2 and Al_2S_3 and appearance of the patterns of AlP and ZnS.[1]

As for the emission spectra under u.v. (3650Å) irradiation, a bright yellow emission is present at liquid air temperature in all the fired mixtures for concentrations of AlP up to 80%. At room temperature, however, the yellow band appears only in the samples with small amounts of AlP added(up to about 10%), the brightness being a maximum in the interval 0.5-1.0% AlP. The maximum in the emission curve in the yellow region is at about 5750Å. A typical emission curve is shown in Fig. 1. Except for a shift of the emission peak, which may be due,

[1] A trace of zinc metal was also found. This is believed to be due to reaction between excess aluminum present in the commercial Al_2S_3 used and either Zn_3P_2 or ZnS.

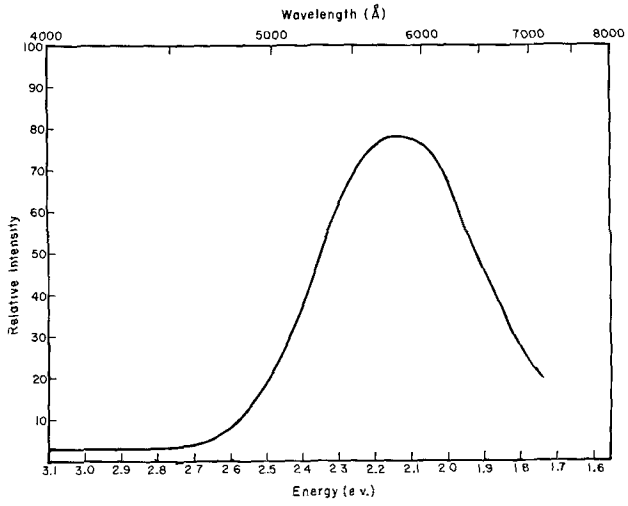

Fig. 1. Emission spectrum for ZnS:P,Al phosphors prepared with 1 mole % AlP added. Excitation by $\lambda = 3650$Å.

at least in part, to differences in experimental conditions, this emission closely resembles that observed by McKeag and Ranby in ZnS:P,Al phosphors prepared at 900°-1000°C. This similarity in the emission spectra of ZnS:P,Cl and ZnS:P,Al lends strong support to the theory of charge compensation (3) according to which a trivalent cation (Al) as coactivator should behave in the same way as a monovalent anion (Cl) coactivator.[2] It can be assumed that in ZnS:P,Al phosphorus substitutes for sulfur and aluminum substitutes for zinc.

[2] Note: It should be noted that, as mentioned by Apple (2), ZnS:P without coactivator is practically nonluminescent when prepared in H_2S at 950°.

We may summarize the results of the present investigation by saying that ZnS:P,Al phosphors with yellow emission can be prepared by diffusion of AlP in ZnS at 900°. In spite of the similarities in crystal structure and covalent atomic radii between ZnS and AlP the solubility of AlP in ZnS is very limited, probably not in excess of 1 mole %. The existence of ZnS:P,Al phosphors with emission similar to that of ZnS:P,Cl phosphors brings further support to the theory of charge compensation and shows that in ZnS:P,Al phosphors, P is the activator and Al the coactivator atom.

Acknowledgments

The author wishes to thank Dr. Eugene Apple for criticism and suggestions, Dr. Ralph M. Potter for his assistance in the measurement of the emission spectra and for critically reading the paper, and Miss Jeanette R. Cooper for the x-ray data.

Manuscript received July 13, 1960.

Any discussion of this paper will appear in a Discussion Section to be published in the June 1961 JOURNAL.

REFERENCES

1. A. H. McKeag and P. W. Ranby, *J. (and Trans.) Electrochem. Soc.*, **96**, 85 (1949).
2. E. F. Apple, *This Journal*, **106**, 271 (1959).
3. F. A. Kröger and J. Dikhoff, *Physica*, **16**, 297 (1950).
4. A.S.T.M. File Index, Card No. 5-0566.
5. A. Addamiano, *J. Am. Chem. Soc.*, **82**, 1537 (1960).
6. L. Pauling, "The Nature of the Chemical Bond," 2nd ed., p. 179, Cornell University Press, Ithaca, N. Y. (1940).

High-Temperature Base-Tab for Silicon

Leon Maissel[1]

Research Division, Philco Corporation, Philadelphia, Pennsylvania

In the course of recent work in silicon transistor development, the need arose for a base-tab that could be attached to the silicon blank early in the manufacturing process so as to serve as a holder for the silicon during subsequent steps. As temperatures in excess of 800°C occurred during one or more of these steps, it was not possible to use a conventional gold solder which fuses at approximately 360°C.

The following are the general requirements for a satisfactory base-tab solder: (i) It should readily wet the semiconductor when melted in contact with it. The existence of a eutectic reaction between solder and semiconductor guarantees this. (ii) It should be sufficiently ductile so that considerable mismatch between its coefficient of thermal expansion and that of the semiconductor can be accommodated without undue strain being introduced in the joint. Conversely, if it has a coefficient of expansion close to that of the semiconductor, it need not be so ductile. (iii) It should "dope" the region near the tab to the same type (n or p) as the rest of the semiconductor; otherwise a rectifying junction may be formed. Correct doping can be insured in practice by including a trace of suitable impurity in the solder. (iv) It should substantially reduce the minority carrier lifetime in the vicinity of the junction. Without this quality the junction, although nonrectifying, may still not be entirely ohmic. For a sufficiently potent lifetime killer, condition (iii) disappears.

Also the material of the tab itself should match the semiconductor reasonably well with regard to coefficient of expansion but, as is the case for the solder, considerable mismatch can be accommodated if the latter is sufficiently ductile.

Gold satisfies these requirements very well, but in choosing a solder having more favorable high-temperature properties than gold, platinum was considered to have the most promise. It has a eutectic reaction with silicon at 830°C (1) and possesses high ductility (2). Its effect on minority carrier lifetime in silicon was not known, but it is not one of the

[1] Present address: IBM Corp., Product Development Lab., Poughkeepsie, N. Y.

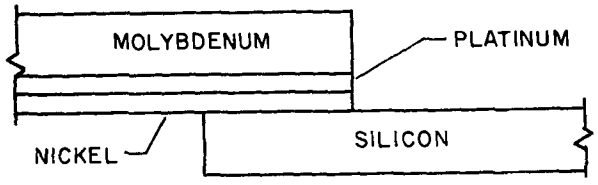

Fig. 1

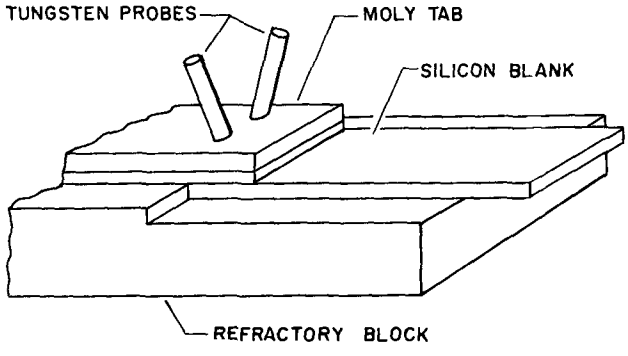

Fig. 2

recognized dopants so that it should be possible to satisfy condition (iii) for both n- and p-type silicon. Molybdenum was selected for the tab itself, having a coefficient of expansion fairly close to silicon (3) over the temperature range concerned as well as a high melting point.

Preliminary experiments showed that molybdenum could be bonded to silicon by means of platinum, but that the resulting joint had unexpectedly poor thermal properties. It was postulated that platinum ductility was being reduced by the formation of intermetallic compounds with silicon. In an attempt to reduce this effect, a number of additives to the platinum were investigated, and it was found that the introduction of a nickel layer about one third the thickness of the platinum produced a joint that was substantially strain-free and capable of temperature cycling over a wide range. This result was also somewhat unexpected since a pure Si-Ni-Mo joint was found to crack immediately on cooling. The fact that the Ni-Pt bond was much more strain-free than that using pure Pt suggested that either the Ni-Pt was more ductile than pure Pt, that the Ni-Pt matched the silicon more closely in expansion coefficient, or that Ni was suppressing the formation of Si-Pt intermetallic compounds as postulated above. Evidence against the first two mechanisms was provided by the fact that a bond formed between elements in the order Si-Pt-Ni-Mo was almost as badly strained as the straightforward Si-Pt-Mo bond, whereas the Si-Ni-Pt-Mo bond was substantially strain-free. Figure 1 shows in cross section the structure that was found best suited for joining a 5-mil molybdenum tab to a 5-mil silicon blank.

In order to prepare the tabs and bond them in a reproducible manner the following scheme was devised.

First, 5-mil Mo sheet was cleaned by scrubbing in detergent. It was then anodized in a mixture of concentrated sulfuric and phosphoric acids, dipped in a strongly alkaline solution (in this case, Lectrite N.F.) and, after rinsing, immediately given a chrome strike coat (100 to 1, CrO_3 to H_2SO_4). This was followed by a Ni strike from a standard Wood's bath after which the Pt (approximately 0.2 mils as in Fig. 1) was deposited from a solution of Platanex III.[2] The Mo was plated on both sides to protect it against oxidation during its subsequent life as a base-tab.

Following the Pt, a layer of Ni (approximately 0.1 mil thick as in Fig. 1) was deposited from a standard Watt's bath (on one side of the Mo only). The Mo sheet was cut into strips 75 mils wide and 200 mils long and bonding to the Si blanks (75 x 150 x 5 mils) was effected as illustrated in Fig. 2.

The Si blank was dipped in HF, rinsed in deionized water, dried in dry filtered air, and then laid on a refractory block, the moly-tab being pressed against it by means of two tungsten rods (or probes) as shown. Heat was produced by passing current between the probes for a pre-set period of time. For consistent results it was necessary to perform the operation in an inert atmosphere. Nitrogen does not qualify as an inert atmosphere in this instance. It was extremely important to be certain that pressure was applied uniformly by the two tungsten probes; otherwise the solder wetted only in the area of highest pressure and, in some cases, even penetrated to the other side of the Si. Optimum results were obtained by heating at approximately 1,000°C for 10-15 sec. A suitable material for the refractory block was difficult to find, the only really satisfactory one being carbon. Because of the mechanical weakness of pure carbon, in practice a block of alundum, having its surface coated with graphite, was used. The graphite coating had to be renewed frequently.

Low resistance ohmic contact could be made to p-type but not to n-type Si by this process. Spectrographic analysis of the Ni deposited from a Watt's bath showed that it contained approximately 0.05% boron. This was not surprising in view of the large quantity of boric acid in the Watt's bath. Because of the high distribution coefficient of boron, this amount was sufficient to insure ohmic contact to p-type Si and rectifying contact to n-type Si. In order to pursue this still further the 0.1-mil Ni layer was deposited from the following bath (4): $NiSO_4 \cdot 6H_2O$, 175 g/liter; $NiCl_2 \cdot 6H_2O$, 50 g/liter; H_3PO_4, 50 g/liter; H_3PO_3, 1.3 g/liter. In addition, 14 g of $NiCO_3$ were neutralized with approximately 50 g of H_3PO_3 and added to this solution.

Nickel deposited from this solution contained about 1% of phosphorus and, as expected, base-tabs prepared in this way gave low resistance contacts to n-type Si and high resistance ones to p-type Si.

Table I gives results obtained with various combinations of base-tab and silicon type. Tabs were attached as described above at opposite ends (but on the same face) of a silicon blank, and the measured resistance was compared with that calculated from the geometry of the system, the resistivity of the silicon being known from four-point probe measurements. Resistance measurements were at 3 v.

Besides satisfying the electrical requirements for base-tabs (as shown in Table I) the units were also

[2] Platinum plating solution marketed under that name by the Sel-Rex Corporation.

Table I

Silicon type	Buffer acid	Measured R ohm	Calculated R ohm	Approximate contact resistance ohm/cm²
Resistivity type				
0.2 ohm-cm p	Boric	1.2	1.1	0.001
1 ohm-cm p	Boric	45	41	0.05
5 ohm-cm p	Boric	200	180	0.25
1 ohm-cm n	Boric	20,000	50	250
1 ohm-cm n	Phosphoric	150	50	1.2
1 ohm-cm p	Phosphoric	1,500	45	18

given thermal and mechanical shock tests similar to those used for testing the conventional gold alloy base-tabs, for example, repeated plunging into liquid nitrogen from room temperature. In all cases, mechanical and thermal strength was found to be at least as good as for the conventional tabs. Silicon blanks could not be separated from their tabs until the temperature exceeded 800°C. If the pulling force was limited to the blanks' own weight they remained attached to the tabs at and above this temperature, presumably because of surface tension.

Acknowledgments

The author wishes to thank Mr. H. A. Cassel for his assistance during several phases of this work and Mr. R. Duva of Sel-Rex Corporation for valuable advice on platinum plating.

Manuscript received July 18, 1960.

Any discussion of this paper will appear in a Discussion Section to be published in the June 1961 JOURNAL.

REFERENCES

1. M. Hansen, "Constitution of Binary Alloys," 2nd ed., p. 1140, McGraw-Hill Book Co., New York (1958).
2. R. F. Vines, "The Platinum Metals and Their Alloys," p. 31, International Nickel Co., Inc., New York (1941).
3. L. Maissel, *J. Appl. Phys.*, **31**, 211 (1960).
4. A. Brenner, D. E. Couch, and E. K. Williams, *J. Research Natl. Bur. Standards*, **44**, 109 (1950).

Copper Sulfide Creep on Porous Electroplate

M. S. Frant

Research Division, AMP Inc., Harrisburg, Pennsylvania

The spread of silver sulfide from a pore site on a porous gold electroplate after exposure to sulfur vapor has been reported recently by Egan and Mendizza (1). They found that the silver sulfide creep effect was specific for gold electroplate and did not occur on rhodium or palladium plate.

This paper reports that similar creepage phenomenon has been observed on tin electroplate over copper, and that copper sulfide apparently will creep over a variety of other covering metals. Figure 1 shows samples of tin-plated copper returned from field service in a location in which sulfides were known to be present. To the naked eye the pore sites appear as small black spots. However, under magnification (Fig. 1a) the characteristic "flowery" appearance can be seen. In Fig. 1b another feature is shown: the central black area is surrounded by a thinner brown region. The outer brown region often has spots at a periphery which are black also. It has not been established whether the chemical composition of this region is different, whether the color difference can be attributed only to a difference in the film thickness, or whether it represents other pore sites.

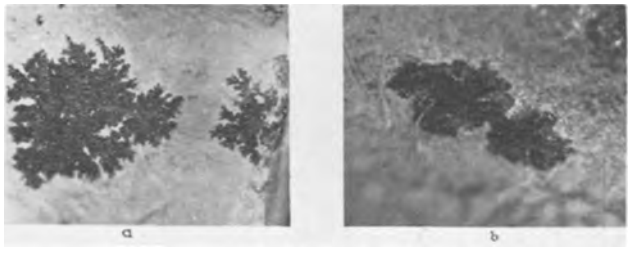

Fig. 1. Copper sulfide spots on tin-plated copper samples returned from field service. Area shown: 7.8 mm².

Figure 2a shows similar black spots surrounded by the brown area on samples which had been in storage for over a year in brown kraft boxes, but which had not otherwise been exposed to an adverse environment.

Microchemical spot tests (2) were positive for copper and sulfides, negative for other likely metals and anions. To confirm, similar tin-plated copper specimens were suspended over powdered sulfur at 60°, a technique which had been used previously for evaluating antitarnish treatments on silver. Exposures of two to three days led to spots identical in appearance to the samples returned from the field, and giving the same chemical tests.

To establish that the black spots occur at pore sites, two experiments were performed. First, tin-plated specimens were deliberately scratched before exposure to sulfur vapor. Figure 2b shows such a

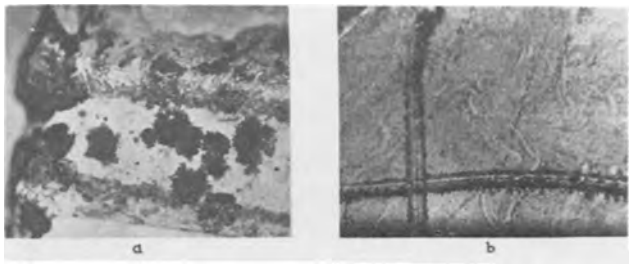

Fig. 2. a. Copper sulfide spots on tin-plated copper which had been stored in brown kraft boxes; Fig. 2b, Copper sulfide growing from scratches in tin-plated copper held 24 hr over sulfur at 60°. Areas shown: 7.8 mm².

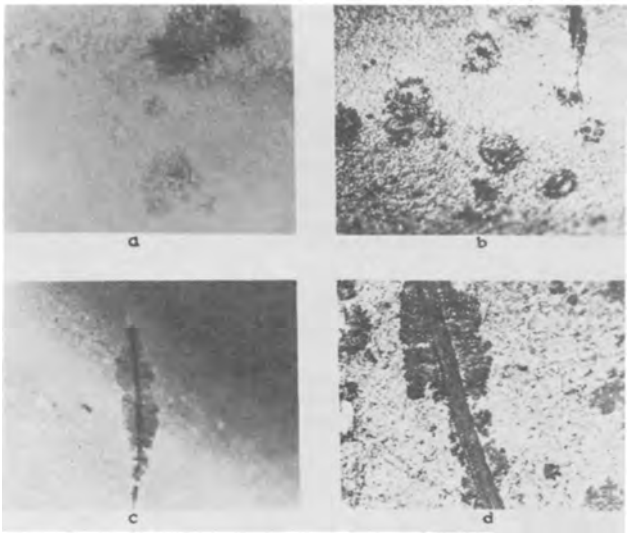

Fig. 3. Copper sulfide spots on (a) nickel-plated copper; (b) nickel-plated brass covered with palladium; (c) tin-plated silver solder; and (d) gold-plated copper. Areas shown: 7.8 mm^2, except for (c) which was 20X before reduction for publication.

Fig. 4. Copper sulfide growth from scratch in nitrocellulose lacquer on copper after 24 hr over sulfur at 60°. Area shown: 7.8 mm.

scratch after exposure. The black film can be seen spreading out from the scratch. Second, tin-plated copper samples were pressed against filter paper pads, soaked in ammonia-ammonium persulfate solution (3) which gives a blue color at pore sites. The samples were then washed, dried, and exposed to sulfur vapor. Good correlation was found.

Similar creepage phenomena have been noted on nickel-plated copper (see Fig. 3a), nickel-plated brass covered with palladium[1] (Fig. 3b), tin-plated silver solder (80% Cu, 20% Ag) (Fig. 3c), and gold-plated copper (Fig. 3d). The samples of nickel and palladium plate do not show as much of the "flowery" appearance or color differences as tin plate and gold plate. Interference colors were widely observed on gold-plated samples; spots would develop overnight on gold plate which was as much as 1 μ (40 millionths of an inch) thick.

[1] The palladium coating was approximately 2.5μ (100μ in.) thick and was applied by an electroless process using tetrammine palladous chloride through the courtesy of R. F. Vines, International Nickel Co.

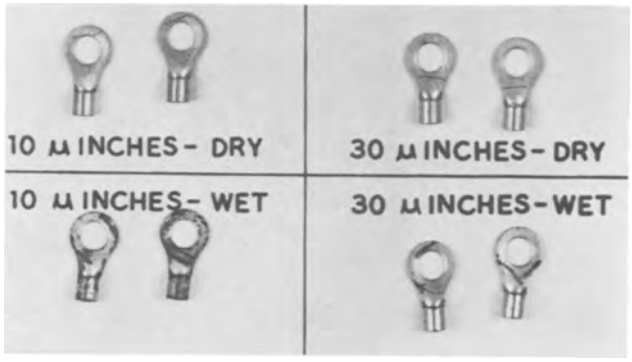

Fig. 5. Effect of moisture and gold thickness on growth on copper sulfide films. Shown are gold-plated specimens having 10 and 30 μ in. average thickness, and the results of 18 hr in a closed container with sulfur which either contained several per cent of water or had been dried overnight over P_2O_5.

To determine whether the outer metallic plating entered into a chemical reaction with the growing film, specimens of O.F.H.C. and electrolytic copper were coated with nitrocellulose or acrylic lacquers, the lacquer scratched, and the sample exposed to sulfur vapor. After several days a growth of copper sulfide (Fig. 4) could be clearly observed spreading out on top of the lacquer.

The effect of moisture on the growth rate is rather striking. After it was observed that sulfur samples and containers seemed to lose their ability to produce spots after a number of cycles, replicate tests were run on sulfur which had been dried and on sulfur containing several per cent of water. The typical result is shown in Fig. 5, in this case for gold-plated copper. The accelerating effect of moisture has been reported for H_2S attack on copper by Shklovsky (4), and for the reaction of sulfur with silver by Smith (5).

The fact that the copper sulfide films will grow on a variety of metals and on a nonmetal suggests that the surface material does not enter into the chemical reaction. Further, the spreading of a sulfide over a presumably nonconducting lacquer film must occur by a different mechanism than that proposed by Gensch and Wagner (6) for the spreading of a silver iodide film along a tantalum surface, since they attributed the spreading to the relatively easy flow of electrons through the substrate on which the spreading occurs. The differences in amount and appearance of the films on the various metals may be attributable to differences in pore size, or to the presence of an adsorbed water layer which would aid in the spread of the film.

The available literature (7) indicates that the formation of copper sulfides occurs by simultaneous diffusion of sulfur inward and copper outward, with the latter effect predominating. Such a mechanism would be consistent with the observations reported here.

The precautionary statement of Egan and Mendizza (1) on the practical importance of this phenomenon should now be extended to a much wider range of metals. Gold, nickel, and tin, on copper or copper alloy substrates are among the most widely used combinations for electrical contacts and terminations. In sulfiding atmospheres, contact failure due to sulfide formation may occur by creepage out

from pores even when "sulfide-resistant" platings are employed.

Manuscript received May 23, 1960.

Any discussion of this paper will appear in a Discussion Section to be published in the June 1961 JOURNAL.

REFERENCES

1. T. F. Egan and A. Mendizza, *This Journal*, **107**, 353 (1960).
2. F. Feigl, "Spot Tests," pp. 89, 280, Elsevier Publishing Co., Amsterdam (1954).
3. M. S. Frant, *Plating*, **45**, 157 (1958).
4. I. S. Shklovsky, *Trudy Inst. Fiz, Khim., Akad. Nauk SSSR, Issledovaniya po Korrozii Metal.*, **1**, 241 (1951).
5. J. W. Smith, *J. Chem. Soc.*, **1931**, 860; *Bull. soc. chim.* **7**, 706 (1940).
6. C. Ilschner-Gensch and C. Wagner, *This Journal*, **105**, 198 (1958).
7a, L. Czerski and S. Patzau, *Arch. Gornictwa i Hutnictwa* 2, 353 (1954); b, Y. Suge and S. Sonoike, *J. Appl. Phys. (Japan)*, **20**, 152 (1951); c, for silver, see U. Croatto, *Gazz. chim. ital.*, **79**, 458 (1949).

Brief Communication

Electronic Analysis of the Fe-Ni System

S. Yamaguchi

The Institute of Physical and Chemical Research, Tokyo, Japan

In the present study, an electron beam was applied to the crystallographic and the thermomagnetic analysis of the Fe-Ni system. Invar (Ni: 36% by weight) whose Curie point was known to be 120°C was used for the experiments described below. Invar powder was prepared by filing from an ingot. The particles of Invar were held by magnetic attraction on the sharp edge of a razor blade (5 x 5 mm) of hard steel whose remanence was known to be about 10,000 gauss. In this way the magnetic induction of the Invar particles was kept saturated. To study electron diffraction, an electron beam was allowed to graze these Invar particles as indicated in Fig. 1.

Experimental procedure.—The following process was carried out to investigate the magnetic states of the Invar particles as a function of their temperature. The diffraction pattern was first photographed with the specimen kept cool. Here care was taken not to preheat the specimen with the electron beam. Exposure to the electron beam (wave length 0.0299Å and current 0.1 ma) could be reduced to little more than the time necessary for photographing the diffraction pattern (only 0.5 sec). Second, a diffraction pattern from the specimen preheated with the electron beam for 2 min without interruption was superimposed on the first pattern from the cool specimen. In this process, the position of the photographic plate as well as the wave length and the current of the incident beam were kept constant. A double diagram obtained in this way is shown in Fig. 2.

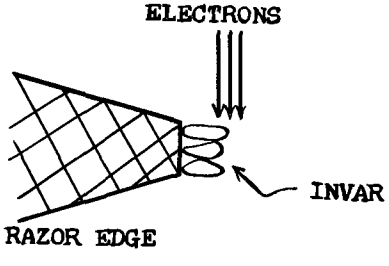

Fig. 1. Arrangement of the Invar specimen relative to the incident beam.

Analysis of the diagram.—In Fig. 2 there is evident an eccentricity between the diffraction rings corresponding to the cold and hot states of the austenitic specimen. This eccentricity means that the Lorentz effect of the cold specimen on the electron beam is distinguishable from that of the hot specimen. It is possible to calculate the difference between the magnetic induction in the two states (ΔB) from the ring eccentricity measurable in Fig. 2 (ΔZ). We have a relation between ΔB and ΔZ:

$$\Delta B = \frac{h}{eL\lambda l} \cdot \Delta Z \qquad [1]$$

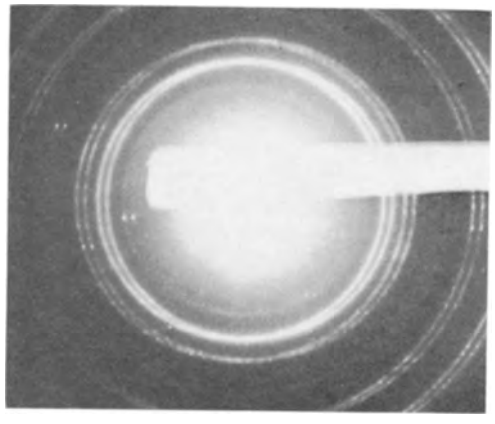

Fig. 2. Double diagram from the cold and from the hot specimen showing the difference of the Lorentz effect; wave length: 0.0299Å; camera length: 495 mm; Positive enlarged 4 times before reduction for publication.

where h is Planck's constant (6.6×10^{-27} erg. sec), e is the electron charge (1.6×10^{-20} emu), L is the camera length (495 mm), λ is the wave length of the electron beam (0.0299Å), and l is the magnetic field region traversed by the electron beam.

In Fig. 2 we measure $\Delta Z = 0.04$ cm. We obtain, therefore,

$$\Delta B \cong 4000 \text{ gauss}$$

according to Eq. [1]. Here $l \cong 3\ \mu$ was assumed.[1]

Discussion of results.—This ΔB-value is understandable as being the difference between the saturation induction of Invar and the remanence of the razor edge. It is plausible that the temperature of the specimen irradiated with the beam for 2 min was above 120°C, *i.e.*, the Curie temperature of Invar. If this is true, then the ΔB-value here measured (4000 gauss) should equal the difference between the saturation induction of Invar at room temperature ($B_s \cong 15000$ gauss) and the remanence of the razor edge ($B_r \cong 10000$ gauss). There is indeed found to be a rough agreement between them ($B_s - B_r \cong \Delta B$).

It was observed during the present experiment that some of the Invar particles fell from the razor edge when they were irradiated with the rather strong beam. As the temperature of these particles here exceeded the Curie temperature (120°C), they followed the normal influence of gravity. In Fig. 2 there are found some weak rings corresponding to Fe_3O_4. The ferromagnetic inclusion of the high Curie point (575°C) material (2) played a rôle in holding the Invar particles on the razor edge, even after they had reached the Curie point (120°C). In fact, according to electron microscope studies it is plausible that the temperature of the object could reach 500°-600°C only with some difficulty (3).

Supporting experiments.—Figure 3 is a double diagram in which the diffraction pattern of the specimen irradiated with the electrons (0.0299Å, 0.1 ma) for 2 min and that irradiated for 4 min were superimposed by means of a double exposure technique. In this diagram there is no ring eccentricity due to the Lorentz effect, since the temperature of the specimen always exceeded the Curie point so that it behaved paramagnetically.

Figure 4 is a double diagram which consists of the diffraction pattern of the specimen irradiated with a very weak electron beam (0.0299Å, 0.03 ma) for 2 min and that irradiated for 4 min. It was possible to observe a crystalline pattern even from paraffin with this weak beam (4). Since the melting point of paraffin was about 50°C, the temperature of the Invar specimen was kept under this temperature

[1] The l-value was estimated as follows. The diffraction pattern of the specimen in its ferromagnetic state below the Curie point (*e.g.*, Fig. 3) and that of a nonferromagnetic gold foil were superimposed by means of a double exposure technique (1) The ring eccentricity here measured made it possible to calculate l in Eq [1], since ΔB in this equation was equal to the saturation induction of Invar (15000 gauss)

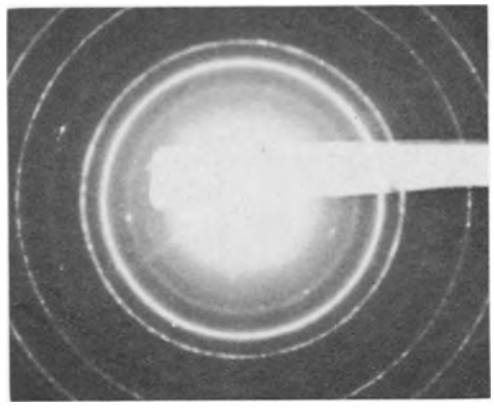

Fig. 3. Double diagram from the hot specimens heated over the Curie point (120°C). No ring eccentricity.

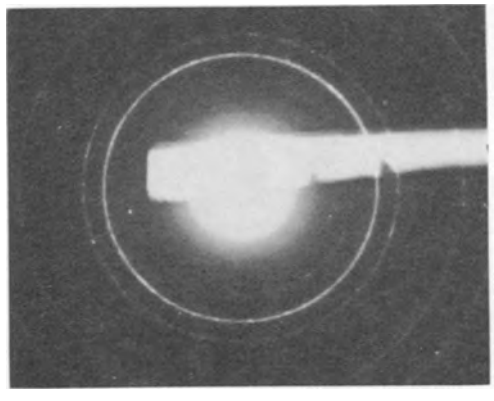

Fig. 4. Double diagram from the cold specimens kept at 50°C. No ring eccentricity.

in the case of Fig. 4. In Fig. 4 there is found no ring eccentricity. It is therefore concluded that the two magnetic states of the specimen shown in Fig. 4 are also below the Curie point.

Conclusion

In the present study, an electron beam was utilized for heating the specimen as well as for its diffraction and magneto-analysis. As the temperature of the specimen heated with the electronic irradiation can be controlled, it is possible to study the magnetic transition of the Fe-Ni system by the present process.

Manuscript received June 10, 1960.

Any discussion of this paper will appear in a Discussion Section to be published in the June 1961 JOURNAL.

REFERENCES

1. S. Yamaguchi, *This Journal*, **107**, 55 (1960).
2. R. M. Bozorth, "Ferromagnetism," p. 723, D. Van Nostrand Co., Princeton, N. J. (1956).
3. Cf. V. E. Cosslett, "Practical Electron Microscopy," p. 264, Butterworths Scientific Publications Ltd., London (1951).
4. S. Yamaguchi, *Z. angew. Phys.*, **8**, 221 (1956); *Z. Phys.*, **134**, 618 (1953).

Technical Feature

Plasma Thermionic Converters

E. W. Salmi

Los Alamos Scientific Laboratory, Los Alamos, New Mexico

Within the last year or so, a great deal of attention has been given to a method of direct conversion of heat energy to electricity which is generally termed "thermionic conversion." There are several variations on the approach to this problem. At Los Alamos, we have been concerned primarily with the cesium plasma diode, which we have also called a "plasma thermocouple." This work was initiated as part of the advanced nuclear propulsion studies under the Rover Program.

Before going into our experimental program let us examine the manner in which a plasma can be used for generating electricity. The word plasma usually is associated with the Sherwood project. While the fusion reaction requires temperatures in the millions of degrees, it is possible to generate plasmas at much lower temperatures. In fact, several gaseous elements form plasmas at temperatures around 2000°C. Of all the available elements, cesium with an ionization potential of 3.87 v is ionized the most easily. One can produce a plasma by introducing a little cesium vapor into a metal container and heating everything to about 2500°K. This is illustrated in Fig. 1. If the cesium pressure is at 0.1 mm Hg, then about 10% of the atoms will be ionized. This is strictly thermal ionization and does not depend on the nature of the container walls. The plasma will be electrically neutral so that the numbers of electrons and ions per unit volume are equal. However, in thermal equilibrium the mean velocities of the electrons and ions will not be equal. In a cesium plasma the mean velocity of the electrons is some 500 times the mean velocity of the ions and, therefore, the electron current across any arbitrary boundary will be 500 times the ion current. Under these circumstances if a small probe is introduced into the plasma as illustrated in Fig. 1, one will draw an electron current which is of the order of 500 times the ion current. The next question is, what voltage does one obtain? This is illustrated in Fig. 2. The left-hand side of the graph shows what the electrostatic potential diagram would be in the steady state (1, 2). The electrochemical potential for the electrons is constant and uniform everywhere. The electrochemical potential is the sum of the chemical potential and the electrostatic potential. Since the chemical potential of an electron in a metal is generally different from the chemical potential of an electron in a plasma there will exist an electrostatic potential difference, equal to the difference between the chemical potentials of the electrons in the metal and the plasma, as indicated in Fig. 2. On the right-hand side are shown two of the many possibilities which may arise at the probe-plasma interface. If the probe is cooled, a monolayer of cesium may form on its surface, resulting in a work function of about 1.8 v as indicated. In the upper right-hand side the case is illustrated in which the probe draws no net current. The electron current and ion current are equal. In order to reduce the electron current into the probe there must exist an

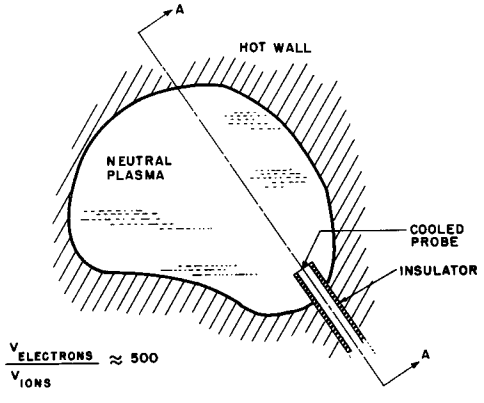

Fig. 1. Idealized model

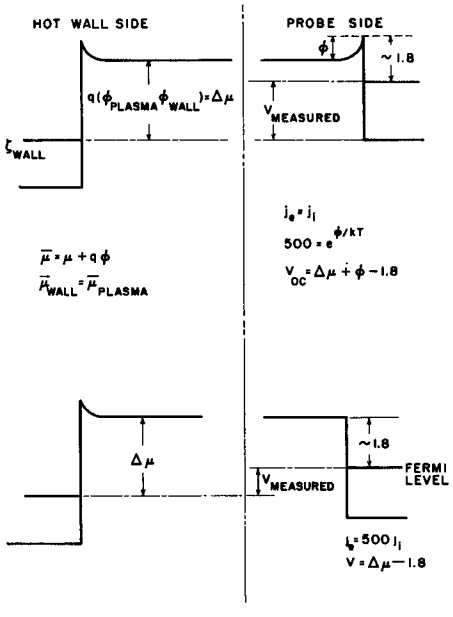

Fig. 2. Electrostatic potential diagrams

electrostatic sheath potential in the plasma at the probe-plasma interface. This potential, ϕ, must reduce the electron current by a factor of 500. Hence, we have the equation

$$500 = \exp\left(\frac{\phi}{kT}\right)$$

for the "open circuit" case (3). If a voltmeter is placed between the probe and the hot metal container one will obtain a voltage which is

$$V = \Delta\mu + \phi - 1.8$$

By lowering the voltage of the probe one begins to draw current to the probe and around the external circuit. Lowering the sheath potential ϕ increases the electron current. The particular case for which ϕ has been reduced to zero is illustrated in the lower right hand side of Fig. 2. The probe is at the same potential as the plasma and the electron current will be 500 times the ion current. These currents can be calculated from the thermodynamic equilibrium equations. The expected voltage is

$$V = \Delta\mu - 1.8$$

since in this case ϕ is zero. The power output of the device would then be the voltage V times the net current.

The above conditions are rather idealistic. However, the calculations for a cesium pressure of 0.1 mm of Hg and a temperature of 2500°K give a current of 50 amp/cm^2 and a voltage of 1.7 v. The resulting power output would be about 80 watts/cm^2. This is the type of performance one can hope for.

The experiments to date have not approached this idealistic model. In most experiments the geometry has consisted of two flat plates, so that the probe is not a small perturbation of the system but becomes one-half of the container. The cesium near the collector is, therefore, not near equilibrium with the hot walls. Also, since the hot wall is only one-half the container and must supply all the electrons which are picked up by the collector one runs into electron emission limitations from the hot wall. Despite these experimental difficulties 30 watt/cm^2 has been observed by increasing both the cesium pressure and emitter temperature (3). With this geometry the maximum short circuit current was about 60 amp/cm^2.

There have been various modifications in the experimental geometry, some of which have tended to approach the idealized model (4). In trying to interpret the data some difficulty is encountered in determining the area of the collector. Although this area is uncertain, it is believed that in several types of experiments the observed values corresponded to as much as 50 watts/cm^2. Along with this value a short circuit current of 130 amp/cm^2 was measured.

These are some of the results which have been achieved in the laboratory and most of the results have been reported in various articles. In all this work the heat source has been electrical.

About a year ago there was performed the first test in a reactor which utilized fission as a heat source. The results of this experiment also have been reported previously (5). The cell design used was complex to the point of being of little value as part of a reactor. Since the first experiment, attempts have been made to simplify the construction and to develop a cell which would be useful as a part of a reactor. In Fig. 3 is shown what is called a "triple-cell experimental rod," a device now being tested in the Omega West Reactor. The diameter across the rod is about ⅝ in. This rod consists of three cells stacked in series. Each cell consists of an emitter, or in keeping with our idealized model, a hot wall of UC:ZrC. Next comes a Cs vapor-filled gap of about 1 mm width and then a collector. Fissions in the enriched UC:ZrC keep the emitter temperature at about 2100°C. Depending on the Cs pressure and other variables, the collector runs at about 400°C. Since the Omega West Reactor is a water tank reactor, the cell will be in cool flowing water. A layer of thermal insulation is placed outside the collector which establishes the temperature gradient between the 400°C collector and the 40°C water. The water also carries away the waste heat from the cell. The emitter is held in place by a thin Nb tube which is attached to the adjacent cell so that the cells are in series. The collectors are electrically separated by small insulator spacers which are also shown in Fig. 3.

In the experimental cell there is shown a Cs bath, the temperature of which may be varied for experimental purposes. In order to establish a uniform Cs pressure in the three cells, a series of small holes are drilled into the collector at the junctions between cells. In an actual reactor the Cs pressure would be at a fixed known value and a Cs pool would be established at the bottom end of the rod and kept at a fixed temperature by the bottom cell.

Once this experimental rod has been developed one can see how to develop a reactor. Instead of stacking three cells, 10 or 20 cells can be placed in series, forming a rod about 2 ft in length. This is now a fuel element for a reactor. Several hundred of these rods can be put into a standard type of water tank reactor and it will become critical. By adding electrical connectors and putting in various control rods,

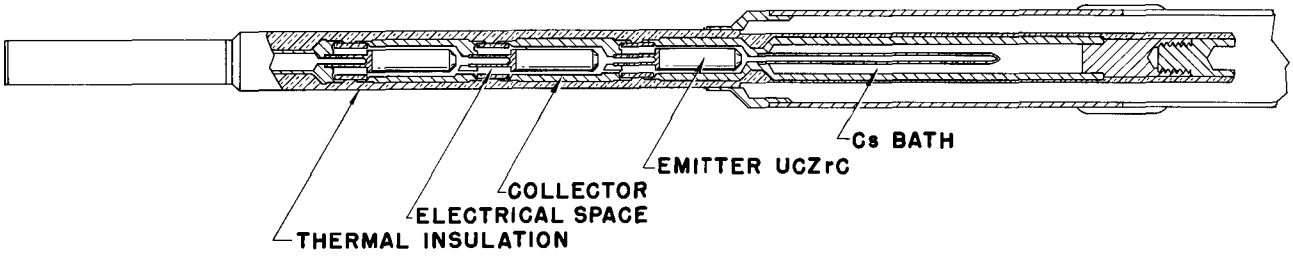

Fig. 3. Triple-cell experimental rod

one has a reactor which generates electricity directly.

Aside from the simplicity of this type of reactor there is another fundamental property of the cell which has not been mentioned. This is the temperature of the probe or collector. Normally the collector temperature is run near equilibrium with the Cs vapor pressure temperature. In some electrically heated experiments the collector temperature was increased to about 1500°K. Under these circumstances the open-circuit voltage did drop. However, the current at lower voltages remained constant, and as a result the power output also remained constant. If this remains true in further experiments, the device will be ideally suited for outer space application. A fundamental difficulty in outer space is the necessity of dumping waste heat by means of thermal radiation. If one can dump the waste heat at a high temperature, the radiator problem will be greatly reduced.

Although very attractive, outer space applications do not exhaust the potential of the thermionic converter. The reactor described earlier consisting of a bundle of rods in a tank of water may have a particular appeal in maritime propulsion and in special situations such as remote installations, if it can meet reasonable lifetime and efficiency requirements.

Present reactors fall into many different categories: fast, thermal, gas cooled, water cooled, breeders, and so forth. The same variety of direct conversion reactors is, in theory, possible using the plasma cell in one of its many forms as the fundamental building block.

Finally, a particularly interesting application of the water moderated reactor is in commercial power production. It will be recalled that the heat thrown off by the collector of the thermionic cell is still at a relatively high temperature. This heat can be used to produce steam in the usual manner and to run turbines with the further production of electrical power. This use of the plasma cell as a "topping cycle" should push up the over-all efficiency of atomic power plants to a very interesting value in the years to come.

Manuscript received April 21, 1960. This work was performed under the auspices of the Atomic Energy Commission.

Any discussion of this paper will appear in a Discussion Section to be published in the June 1961 JOURNAL.

REFERENCES

1. K. G. Hernquist, M. Kanefsky, and F. H. Norman, *RCA Review*, **19**, 244 (1958).
2. H. W. Lewis and J. R. Reitz, *J. Appl. Phys.*, **30**, 1439 (1959).
3. Pidd, G M. Grover, E. W. Salmi, Roehling, and Erickson, *J. Appl. Phys.*, **30**, 1861 (1959).
4. W. A. Ranken, G. M. Grover, and E. W. Salmi, to be published in *J. Appl. Phys.*
5 G. M. Grover, *Nucleonics*, **17**, 54 (1959).

Technical Review

Practical Neutron Activation Analysis for the Electronic Scientist

J. P. Cali and J. R. Weiner

United States Air Force Cambridge Research Laboratories, Air Research and Development Command, Bedford, Massachusetts

ABSTRACT

Neutron activation analysis is an extremely sensitive analytical method for determining trace impurities in semiconductor materials. Theoretical aspects are discussed, and procedures are outlined. Parameters which determine sensitivity are considered, as well as the techniques whereby they may be varied to increase sensitivity. Tables are included which list elements that can be determined by neutron activation analysis, their half-lives, and minimum detectable amounts. Also tabulated are elemental matrix materials of electronic interest together with naturally occurring associated impurities which are determined by neutron activation analysis and other methods. These matrices are also ranked according to extent of flux perturbations, degree of self-activation, and ease of chemical separation.

Since the advent of transistors, thermoelectric, and other semiconductor materials whose electronic properties are wholly or principally dependent on minor constituents, the importance of trace impurity analysis is apparent. With today's increased specialization, the need for communication between related fields of interest has become necessary. For this reason, it is hoped that this paper will familiarize the electronic scientist with some of the aspects of the determination of trace impurities by the relatively

new and ultra-sensitive method of neutron activation analysis.

Neutron Activation Analysis

Description of method.—Neutron activation analysis, as an important and practical analytical method, became feasible only with the advent of the nuclear reactor, because, as will be shown, a high flux of neutrons is necessary to achieve the desired detection sensitivity. Many excellent references exist which give the general principles of the method (1-3, 5). It is, in fact, the extreme sensitivity of this method which makes it valuable as an analytical tool for the determination of trace impurities in concentrations too low to be detected by more conventional methods as, for example, emission spectroscopy.

The principal nuclear reaction occurring when a stable isotope of an element is irradiated with thermal neutrons is the n, γ reaction. The resulting product nucleus is, in general, a radioactive species of the same element one mass unit higher than the original stable nucleus. Decay of the product nucleus is usually by beta or gamma emission, although other modes of decay are possible, *e.g.*, K-capture or alpha emission. Because radioactive atoms can be detected in relatively small numbers, the possibility exists for a sensitive method of detection. The subject of competing nuclear reactions to give the same product nucleus as that formed by the n, γ reaction, and the question of second order reactions, while interesting, are not covered here; the interested reader may find a full account in the cited general references.

In practice, the material of interest is irradiated in a reactor, exposing all impurities and the matrix to an intense flux of thermal neutrons. Depending on the reaction cross section, number of atoms present, time of irradiation, and other quantities covered in Eq. [1] below, the n, γ products of the impurities and matrix are formed in varying amounts. It is now necessary to separate each activity; this is usually done by employing radiochemical separations. The separated radioactivities are then counted and from a knowledge of the various parameters involved, a calculation leads to the concentration of the original impurity which gave rise to the induced, measured activity. The various parameters involved are related as follows:

$$m = \frac{AD(t)}{\phi N f \sigma (1 - e^{-\lambda t})} \qquad [1]$$

where m is the minimum detectable mass, in g, of the trace element; A is the atomic weight of the trace element in g/g at.; $D(t)$ is the minimum detectable disintegration rate, in disintegrations/sec, of the activated impurity. Also, in this term are corrections for assay (aliquoting) and losses due to incomplete recovery during the radiochemical separations (chemical yield); ϕ is the thermal neutron flux, in thermal neutrons/sec cm^2; N is Avogardo's number (6×10^{23} at./g at.); f is the fractional abundance of the target nuclide; σ is thermal neutron reaction cross section in cm^2/ target at.; and $(1 - e^{-\lambda t})$ is the saturation factor, where t is the time of irradiation, in sec, λ is the decay constant of the activity produced, in reciprocal sec.

The actual procedure which would be used in the analysis of a trace impurity in a semiconductor is now considered. Although the method is of general applicability, a specific example is used for clarity, namely, the determination of trace arsenic in silicon metal. The steps are:

1. Weigh out a gram or so of silicon. Place in a quartz needle a weighed out small amount of pure arsenic.
2. Etch (if the state of material allows) the silicon to remove surface contamination.
3. Place the silicon and the quartz needle in a suitable irradiation container.
4. Irradiate in a nuclear reactor for 5 days at highest possible flux.
5. Open the irradiation capsule. Re-etch the silicon and dissolve in suitable reagents (in this case nitric-hydrofluoric acid mixture) and add a known amount of stable arsenic (about 10 mg).
6. Use suitable radiochemical procedures to separate the arsenic (which now carries with it the induced radioactive arsenic) from all other possible induced activities (not quite so hard as it seems, since group separations, scavenging, etc., remove interfering activities in a few steps).
7. Obtain the carrier arsenic in suitable form and weigh. Mount in a suitable way and count the radioactive arsenic. Compare this count with a portion of the radioactive arsenic standard from the quartz needle. Make all corrections to the unknown count for chemical yield, assaying, weight of sample, and finally compute the mass of trace arsenic by the following:

$$M_{As} = \frac{M_{std} \times C_{As}}{C_{std}}$$

where M_{As} and M_{std} refer to the masses of the unknown arsenic and the weighed or standard arsenic, respectively, and C_{As} and C_{std} refer to the counting rate of the unknown arsenic and the known arsenic, respectively.

Theoretical sensitivity.—The sensitivity for any given element is defined as the minimum amount which can be determined under a given set of conditions. These conditions are given either directly from Eq. [1] or are implicit in it and are: 1, magnitude of the thermal neutron flux of the reactor in which the material is irradiated; 2, thermal activation cross section of the target nuclide; 3, length of time the sample is irradiated; 4, half-life of the radioisotope produced by the n, γ reaction on the target nuclide; 5, efficiency of the radiation detector in measuring the radiation produced from the decaying radionuclide; 6, amount of high cross-section material in the sample which might interfere in the separation of the desired element, or more seriously, cause flux attenuation and self-shielding; 7, loss of activity due to radiochemical separations and/or aliquoting procedures; 8, minimum amount of activity required to measure accurately the half-life, and in certain cases, the maximum beta energy of the radionuclide; 9, amount of sample available for

analysis; and 10, time required from end of irradiation to the measurement of the induced activity.

From this list, it can be seen that several of these conditions can be varied in order to attain greater sensitivity of detection should this be required. Increased sensitivity is attained by irradiation at higher neutron fluxes for longer periods of time, assuming for the latter condition, of course, that saturation has not occurred (conditions 1 and 3); by increasing the efficiency of the detection of the measured radiation, as for example, using an internal flow counter *vs.* a Geiger counter (condition 5); by increasing the amount of matrix material under irradiation (condition 9); by decreasing the loss of activity due to chemical manipulations, assaying, and aliquoting procedures (condition 7); and finally, for those induced activities having short half-lives, reducing the elapsed time from the end of irradiation to the measurement of the activity (condition 10). Conditions 2, 4, and 6 are absolutely invariant and, for a given radiation measuring system, and as a practical matter, so is item 8.

Practical sensitivity.—In the previous section, those factors which affect the sensitivity of the neutron activation method have been considered from a theoretical viewpoint. In this section, a list of elements which can be determined by this method, giving practical minimum detectable amounts, without, however, considering the effect of the matrix, which is taken up in a later section, are shown in Table I.

The minimum detectable amounts are computed for the following conditions: 1, thermal flux: 10^{13} neutrons/sec cm^2; 2, minimum detectable activity: 10 distintegrations/sec. This is, in general, the amount of radioactivity required to confirm the half-life and maximum beta energy of the measured radionuclide. However, from practical considerations, losses of 50% each for aliquoting and chemical yield are included. This requires then, 40 disintegrations/sec before these losses yield the required 10 disintegrations/sec [$D(t) = 40$ d/s]; 3, 1-g sample size; 4, time of irradiation is until saturation occurs, or five days, whichever is first. Saturation is considered attained when the value of $e^{-\lambda t}$ is 0.05 or less; 5, no consideration in the calculations is made for loss of activity by decay after irradiation. For isotopes having a half-life greater than 12 hr this factor may be neglected; for those less than 12 hr, but greater than 2 hr, a correction lowering the sensitivity by several percent would have to be applied, but is not considered here.

Table I gives a list of those elements easily determined by this method, showing both the nuclear reaction of interest together with the half-life of the produced nuclide. In general, only elements giving induced activities with half-lives greater than 2 hr have been considered. However, for special cases, half-lives greater than a few minutes can be determined using special techniques. The rare earth elements, although extremely sensitive, have not been included, as they are not of general electronic interest, except in other rare earth matrices where the extremely high cross sections of the matrix make for a very difficult analysis.

The minimum detectable amount has been calculated from Eq. [1]. It should be noted, however, as is not the case for many similar compilations, that this calculation is extremely conservative, giving values which are readily obtainable in any laboratory, assuming of course, that the matrix material is not of high cross section, which problem is discussed next.

Table I. Elements determinable by N.A.A.*

Element	Nuclear reaction of interest	$t_{1/2}$	Minimum detectable amount, μg
Na	$Na^{23}(n,\gamma)Na^{24}$	14.97h	3×10^{-4}
Si	$Si^{30}(n,\gamma)Si^{31}$	2.63h	5.8×10^{-2}
P	$P^{31}(n,\gamma)P^{32}$	14.22d	5×10^{-3}
S	$S^{34}(n,\gamma)S^{35}$	87d	0.5
Cl	$Cl^{37}(n,\gamma)Cl^{38}$	37.29m	1.7×10^{-3}
K	$K^{41}(n,\gamma)K^{42}$	12.52h	3.4×10^{-3}
Ca	$Ca^{44}(n,\gamma)Ca^{45}$	164d	1
Sc	$Sc^{45}(n,\gamma)Sc^{46}$	83.9d	3.3×10^{-4}
Cr	$Cr^{50}(n,\gamma)Cr^{51}$	27.8d	6×10^{-3}
Mn	$Mn^{55}(n,\gamma)Mn^{56}$	2.576h	2.9×10^{-5}
Fe	$Fe^{58}(n,\gamma)Fe^{59}$	45.1d	1.5
Co	$Co^{59}(n,\gamma)Co^{60}$	5.24y	5×10^{-3}
Ni	$Ni^{64}(n,\gamma)Ni^{65}$	2.564h	2×10^{-2}
Cu	$Cu^{63}(n,\gamma)Cu^{64}$	12.80h	1.4×10^{-4}
Zn	$Zn^{68}(n,\gamma)Zn^{69}$	13.8h	2.4×10^{-3}
Ga	$Ga^{71}(n,\gamma)Ga^{72}$	14.3h	2.4×10^{-4}
Ge	$Ge^{76}(n,\gamma)Ge^{77}$	11.3h	7×10^{-2}
As	$As^{75}(n,\gamma)As^{76}$	26.4h	1×10^{-4}
Se	$Se^{74}(n,\gamma)Se^{75}$	121d	5×10^{-2}
Br	$Br^{81}(n,\gamma)Br^{82}$	35.87h	3.4×10^{-4}
Sr	$Sr^{88}(n,\gamma)Sr^{89}$	51d	2.4
Y	$Y^{89}(n,\gamma)Y^{90}$	64.2h	7×10^{-4}
Zr	$Zr^{96}(n,\gamma)Zr^{97}$	17.0h	0.2
Mo	$Mo^{98}(n,\gamma)Mo^{99}$	66h	1×10^{-2}
Ru	$Ru^{102}(n,\gamma)Ru^{103}$	39.8d	2×10^{-2}
Pd	$Pd^{108}(n,\gamma)Pd^{109}$	13.5h	2×10^{-4}
Ag	$Ag^{109}(n,\gamma)Ag^{110m}$	253d	1×10^{-3}
Cd	$Cd^{114}(n,\gamma)Cd^{115}$	53h	3×10^{-3}
In	$In^{113}(n,\gamma)In^{114}$	50d	6×10^{-3}
Sn	$Sn^{120}(n,\gamma)Sn^{121}$	27.5h	2×10^{-2}
Sb	$Sb^{121}(n,\gamma)Sb^{122}$	2.8d	3×10^{-4}
Te	$Te^{126}(n,\gamma)Te^{127}$	9.4h	5×10^{-3}
Cs	$Cs^{133}(n,\gamma)Cs^{134}$	2.07y	3×10^{-3}
La	$La^{139}(n,\gamma)La^{140}$	40.2h	1×10^{-4}
Hf	$Hf^{180}(n,\gamma)Hf^{181}$	44.6d	5×10^{-3}
Ta	$Ta^{181}(n,\gamma)Ta^{182}$	115d	2×10^{-3}
W	$W^{186}(n,\gamma)W^{187}$	24h	1×10^{-4}
Re	$Re^{185}(n,\gamma)Re^{186}$	89h	3×10^{-5}
Os	$Os^{192}(n,\gamma)Os^{193}$	31h	2×10^{-3}
Ir	$Ir^{193}(n,\gamma)Ir^{194}$	19h	2×10^{-5}
Pt	$Pt^{196}(n,\gamma)Pt^{197}$	18h	6×10^{-3}
Au	$Au^{197}(n,\gamma)Au^{198}$	2.70d	2×10^{-5}
Hg	$Hg^{202}(n,\gamma)Hg^{203}$	47d	1×10^{-2}
Tl	$Tl^{203}(n,\gamma)Tl^{204}$	3.56y	0.1
Pb	$Pb^{208}(n,\gamma)Pb^{209}$	3.30h	4.8
Bi	$Bi^{209}(n,\gamma)Bi^{210m}$	5.01d	0.1

* Only for the conditions set forth in this paper. Special cases are not considered.

Matrix Problem

In order to obtain reasonable sensitivity in the use of this method, fairly large sample weights are desirable. This can, however, pose three problems, not necessarily or usually mutually exclusive: (*a*) the effect of neutron beam perturbations by materials of high absorption cross section; (*b*) the problem of handling a large amount of induced radiation of the matrix; and (c) the ease with which the matrix is chemically separated from the trace impurities. These criteria are discussed in order and finally tabulated for a group of matrices in Table II.

Table II. Matrices for N.A.A. ranked according to perturbation, induced activity, and ease of chemical separation effects

Group No.	Criteria of group: Total flux perturbations		Induced activity for standard irradiations given		Half-life of induced activity	Elements arranged in descending order of ease of separation
A	5% or less	and either	less than 10 mc	or	less than 12 hr	Si, C, Pb, Ba, Bi, Mg, Ti
B	5% or less	and either	10-1000 mc	or	greater than 12 hr	Ni, Te, Sn, Fe, Zn, Ge
C	5% or less	and	greater than 1000 mc	and	greater than 12 hr	As, Se, Cu, Y, La, Cr, P, Ga
D	5% to 90%	and either	10-1000 mc	or	greater than 12 hr	Mo
E	5% to 90%	and	greater than 1000 mc	and	greater than 12 hr	Hg, W, Ta
F	greater than 90%					Re, Gd

Total flux perturbation effect.—There are two simultaneous and different perturbation effects which occur when an absorbing material is placed in a neutron flux. The first is the attenuation, sometimes referred to as self-shadowing, of the neutron beam as it is absorbed progressively in its passage from the surface to the interior of the sample. Depending upon the neutron absorption and reaction cross sections, the interior of a given sample will "see" less of the unperturbed flux than will the exterior portions. When the cross sections are sufficiently high, the evaluation of this effect becomes important. The second perturbation effect is that caused by the flux gradient resulting when a neutron absorbing material is placed in an unperturbed neutron field. This effect, like the first, is directly concerned with the cross sections of the absorbing material and is similarly difficult to evaluate; in general, it will vary from reactor to reactor.

In any given situation, these perturbation effects must be determined empirically, but for the purposes of this paper, the approach given in reference (6) by Lewis of the Materials Testing Reactor, Idaho Falls, Idaho, is used. In reference to Table II, materials have been grouped according to total flux perturbations, using calculations similar to that of the cited reference. Flux perturbations of less than 5% are negligible and occur in those matrices easiest to work with, other effects being equal; perturbations between 5 and 90% give a range of materials intermediate in difficulty; and finally, those materials whose total perturbation effects are greater than 90% are not recommended for neutron activation analysis, except in very special and unusual circumstances.

Induced radiation effect.—As was explained, not only the trace impurities, but also the matrix material will become radioactive upon irradiation. The quantity of radiation induced in the trace components is negligible when considered from the handling and health safety aspects, but the radiation induced in a gram or more of high cross-section matrix material is significant. The usual radioanalytical laboratory can handle up to 10 millicuries of activity, using only general laboratory equipment and minimal lead shielding, remote handling equipment or other specialized gear. From 10 to 1000 millicuries of activity can be handled by experienced personnel, but requires a complete and well equipped "hot" or high level laboratory. Above 1000 millicuries of activity, only trained people working in the best environment should be considered. Remote handling equipment, especially designed fume hoods, proper shielding, and automatic radiation detection devices are mandatory for working at this level of radiation.

Concurrently with the radiation intensity, the half-life of the induced activity must be considered. For short-lived activities, the intensity of the induced radiation will fall off rapidly and it is then possible to wait for a short period before starting the radiochemical separation process. Materials whose activities have half-lives less than 12 hr are considered to be in this category.

Ease of chemical separation effect.—A very unfavorable matrix element, considering the first two effects only, may under certain conditions be reconsidered should its chemical properties be such that it is easily, rapidly, and specifically removed by chemical manipulations from the induced trace activities. In Table II the elements in each group have been arranged in descending order according to this effect.

Table II has taken all these considerations into account and lists a group of elements of present or possible future electronic interest, according to the criteria given.

In general, should the element of interest fall into Groups A, B or C then no great problems should arise and activation analysis can be successfully done. Sensitivities generally will be as in Table I since 1-g samples are usually feasible within this class. Elements falling into Groups D and E will require considerable attention and complete "hot" facilities. The difficulty of working with these classes is great but not insurmountable, and the sensitivities for the trace impurities will probably decrease by a factor of approximately 10, since smaller samples will undoubtedly have to be used.

Elements classified in Group F present great difficulty and, because very small sample sizes must be used, it is probable that other methods of analysis will yield more sensitive results.

Summary

In Table III, a group of elements of present or potential electronic interest have been listed. The trace impurities tabulated are those found, usually in the part per million range, upon careful spectrographic analysis of the highest purity materials available at present.

An illustration shows how the information contained in this paper could be used by the electronic scientist.

Table III. Matrices of electronic interest and naturally occurring associated impurities

Matrix element	Associated impurities: Determination by N.A.A.	Associated impurities: Determination by other methods*
Carbon	Si, Na, Fe	Mg
Magnesium	Zn, Fe, Mn, Pb, Si, Ca, K, Na, Cu, Ni, Ag, Sn	Al
Silicon	Ga, In, P, As, Sb, Fe, Cu, Zn	B, Al
Phosphorus	Ca, Fe	
Titanium	Sn, Si, Fe, Ca, Na, Cu	Al, Mg
Chromium	Fe, Ca, Cu, Si, Ni	Al, Mg, Ti
Iron	Si, Mn, Ni, Cu, Ag, Na, Cr, Mo	Al, Mg, Ti
Nickel	Fe, Si, Na, Ca, Cu, Ag, Mo, Cr	Al, Mg
Copper	Si, Ca, Pb, Ag, Ni	Mg
Zinc	Pb, Ca, Cu, Fe, Na, Si, Ag, K	Al, Mg, Ti
Gallium	Sn, Pb, Tl, Cu, Ag, Na, Ca	Mg
Germanium	Ca, Cu, Ag	Mg
Arsenic	K, Na, Fe, Si, Ag	
Selenium	Si, Na, Fe, Ni, Ag, Ca, Cu, Mn, Te	Al, Mg, Ti
Yttrium	Fe, Si, Na, Cu, Ag	Al, Mg, Tb, Dy
Molybdenum	Si, Fe, Na, Ca, Cu	Mg
Tin	In, Ge, K, Ag, Ca, Fe, Pb, Si, Na, Bi, Cu, Zn, As	Al, Mg
Tellurium	Ag, Mn, Ca, Si, Na, Cu, Fe, Pb, Se	Mg
Barium	Ca, Fe, Si, Cu, Mn, Na, Sr	Al, Mg, Ti
Lanthanum	Ca, Si, Sn, Fe, Pb, Cu, Na	Mg, Pr, Nd
Gadolinium†	Pb, Ca, Si, Fe, Na, Cu	Mg, Tb, Sm, Eu
Tantalum	Cu, Na, Si	Al, Nb
Tungsten	Mo, Fe, Ca, Si, Cu, Na	Mg
Rhenium†	Fe, Si, Ca, Na, Cu	Mg
Mercury	Cu, Ag, Ca, Na	Mg
Lead	Cu, Ca, Fe, Si, Ag	Al, Mg
Bismuth	Fe, K, Si, Ca, Cu, Pb, Ag, Na	Al, Mg

* Magnesium, aluminum, titanium, and certain rare earths can be done using special techniques under carefully controlled conditions.
† These elements are not recommended for N.A.A.; they fall into Group VI.

PROBLEM; Determine in the part per million range (or lower) the Periodic Group III impurities in silicon carbide.

1. Consider first the matrix. Use Table II to determine the ease with which an analysis could be performed. (Note: when considering compounds, treat each element separately.) In reference to Table II, both silicon and carbon are in Group A, presenting no problem for activation analysis. A compound such as bismuth telluride, where the bismuth falls into Group A, but the tellurium falls into Group B, would be considered to be a Group B classification.

2. Consider the sensitivities of the trace impurities to be analyzed. Table I shows boron and aluminum absent; therefore, other methods would have to be considered for those two elements. However, gallium, indium, and thallium all fall within the sensitivities required.

3. In normal high-purity material (before further purification) what is the expectation of finding these elements? Consider Table III. Here they are absent in carbon, but both gallium and indium are found in silicon. It should be realized, however, that this Table III considers impurities at the spectroscopic level, generally about 1 ppm.

A whole group of materials of electronic interest has been covered. Most of the II-IV compounds are represented, *e.g.*, magnesium silicide, magnesium stannide, and magnesium plumbide. Many of III-V compounds, such as gallium arsenide and indium antimonide, are represented. The semiconductor metallics, germanium, silicon, and silicon carbide, are given. The thermoelectrics are represented by bismuth telluride and bismuth selenide.

In a general survey of this type, it is impossible, practically, to cover every possible permutation of trace and matrix element. However, it is hoped enough general and specific information has been imparted to the electronic scientist so that he may better understand the problems encountered in the important area of electronic materials.

For those interested in obtaining more details, the following extensive bibliographies by Meinke (7, 8), are cited.

An excellent handbook on activation analysis has been prepared by Koch and is invaluable for workers in this field (4).

Manuscript received Feb. 2, 1960; revised manuscript received Aug. 10, 1960.

Any discussion of this paper will appear in a Discussion Section to be published in the June 1961 JOURNAL.

REFERENCES

1. G. E. Boyd, *Anal Chem.*, **21**, 335 (1949).
2. H. Brown, *et al.*, *Science*, **109**, 347 (1949).
3. D. J. Hughes, "Pile Neutron Research," Addison-Wesley Publishing Co., New York (1953).
4. R. C. Koch, "Activation Analysis Handbook," Nuclear Science and Engineering Corp., Pittsburgh, Pa. (1958).
5. G. W. Leddicote, *et al.*, *Nucleonics*, **8**, 62 (1951).
6. W. B. Lewis, *ibid.*, **13**, 82 (1955).
7. W. W. Meinke, *Anal. Chem.*, **28**, 736 (1956).
8. W. W. Meinke, *ibid.*, **30**, 686 (1958).

Discussion Section

This Discussion Section includes discussion of papers appearing in the JOURNAL of the Electrochemical Society, Vol. 106, No. 6 (June 1959), and Vol. 107, No. 1, 3, and 6 (January, March, and June 1960). Discussion not available for this issue will appear in the Discussion Section of the June 1961 JOURNAL.

Chemical Etching of Silicon, I. The System HF, HNO_3, and H_2O

Harry Robbins and Bertram Schwartz (pp. 505-508, Vol. 106, No. 6)

B. A. Irving[1]: The authors present measurements of the etch rate of silicon in mixtures of nitric-hydrofluoric acids of various concentration and interpret these in terms of a two-stage diffusion-controlled reaction involving thermal and chemical autocatalysis. However, the chemical kinetic basis of this interpretation seems misleading. This discussion seeks to clarify some points in this and to show how an empirical rate expression may be deduced in accord with all the experimental observations.

Chemical autocatalysis takes place when one of the products of a chemical reaction is able to catalyze the reaction itself. Cretella and Gatos,[2] in a paper published after Robbins and Schwartz's paper had been submitted, report investigations of an analogous autocatalytic process, the oxidation of germanium by nitric acid. Nitrous acid produced by the oxidation acts as an intermediate catalyst. Similar reaction schemes, based on the results of Vetter,[3] can be written for the oxidation of silicon. The initial slow reaction is with HNO_3 or NO_3^- to produce nitrous acid.

$$2\epsilon^- \text{ (from Si)} + 3H^+ + NO_3^- \rightarrow H_2O + HNO_2 \quad [1]$$

The nitrous acid reacts with more nitric acid to give N_2O_4 which rapidly can oxidize silicon and eventually produce a double quantity of nitrous acid.

$$HNO_2 + HNO_3 \rightarrow N_2O_4 + H_2O \text{ slow} \quad [2]$$

$$N_2O_4 \rightarrow 2NO_2 \quad [3]$$

$$2\epsilon^- \text{ (from Si)} + 2NO_2 \rightarrow 2NO_2^- \quad [4]$$

$$2NO_2^- + 2H^+ \rightarrow 2HNO_2 \quad [5]$$

The initial reaction [1] soon becomes swamped and the rate of oxidation then is determined by the availability of HNO_2 and, hence, by the amount of reaction already taken place. It is, therefore, an exponential function of time. When the rate has reached a certain value, however, there is adequate HNO_2 and the availability of HNO_3 becomes a limiting factor. The rate then becomes constant in time with HNO_3 (or equally H^+ and NO_3^-) diffusing to the surface at a steady rate and the surface concentration of HNO_2 is maintained constant, the balance between the net rate of production by the reaction and the rate of loss by out-diffusion.

The difference between the etch rate of ground and polished surfaces lies in the time required for the steady-state etch rate to be reached. The activation energy for the reaction [1] and [4] on ground surfaces (containing many dislocations) is expected to be less than for a more perfect etched or carefully polished surface,[4] and, therefore, the catalyzed reaction gets started more readily. Adding nitrous acid (nitrite or nitrogen oxides) similarly helps initiate the catalyzed reaction.

The way the steady-state etch rate varies with concentration (the measured etch rate-concentration function) reflects the availability of nitric acid (HNO_3) at the surface since reported etch rates are "steady-state" values. The diffusion gradient of HNO_3 (or H^+ and NO_3^-) will be affected by increases in the bulk nitric acid concentration, tending to increase the concentration at the surface. The increase in rate expected from this also increases the concentration of HNO_2 at the surface which increases the rate still more. Similarly, the heat of reaction increases the rate, as a higher etch rate is equivalent to higher rate of liberation of heat and, hence, an increased surface temperature. This, in turn, affects the diffusion rates to and from the surface in the way outlined by Robbins and Schwartz. The diffusion gradient, the surface concentration of nitrous acid, and surface temperature are all power functions of the bulk concentrations. The etch rate will, therefore, be some power function of the nitric acid concentration. The index is expected to be greater than 1 but not necessarily integral. A plot of log (etch rate) against log (nitric acid concentration) at 80% hydrofluoric acid concentration, taken from Robbins and Schwartz's Fig. 2, is shown in Fig. 1 published here. This has a slope about 2 and indicates an etch rate approximately proportional to the square of the nitric acid concentration.

The second stage of the dissolution process is the reaction of the oxidized silicon with hydrofluoric acid to give soluble silicofluoride ions or silicon tetrafluoride.

$$Si - 4\epsilon^- + 6F^- \rightarrow SiF_6^{2-} \quad [6a]$$

$$Si - 4\epsilon^- + 4F^- \rightarrow SiF_4 \quad [6b]$$

The reaction may be written with either F^-, or HF, or HF_2^-, all of which exist in hydrofluoric acid solutions.[5] This reaction is not chemically catalyzed but is, of course, hastened by a rise of temperature. The reaction is not expected to be kinetically of sixth or fourth order as the numerous addition steps will not necessarily have equal rates and the slowest step will be rate determining. A plot of log (etch rate at 60% nitric acid concentration) against log

[1] Research Lab., Associated Electrical Industries, Aldermaston Court, Aldermaston, Berkshire, England.
[2] M. C. Cretella and H. C. Gatos, *This Journal*, 105, 487 (1958).
[3] K. J. Vetter, *Z. physik. Chem.*, 194, 199 (1950).
[4] N. Cabrera, "Semiconductor Surface Physics," p. 342, University of Pennsylvania Press, Philadelphia (1957).
[5] *See*, for instance, review by H. R. Leech, Supplement to Mellors' "Treatise on Inorganic Chemistry," pp. 111-119, Longmans Green & Co., New York (1956).

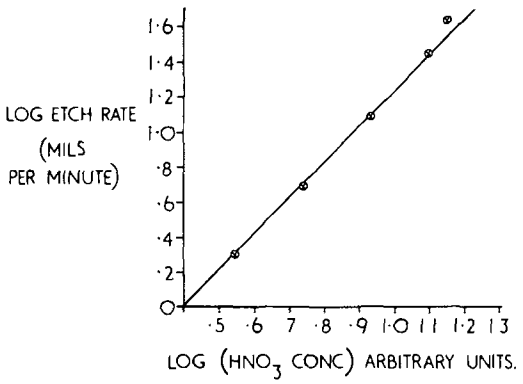

Fig. 1

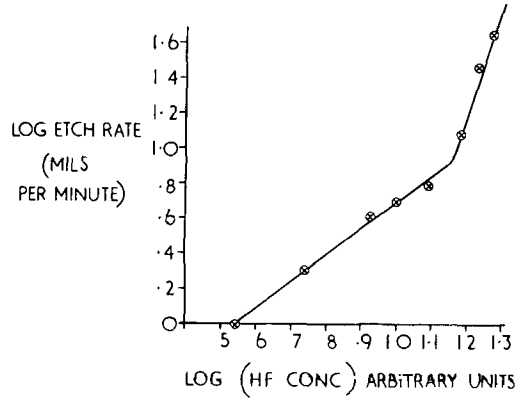

Fig. 2

(hydrofluoric acid concentration), taken from Fig. 2 of Robbins and Schwartz's paper, is shown in Fig. 2 published here. The slope is about 3/2 on the left and rises to about 6 at the right, though the latter figure is doubtful. The rate is approximately proportional to the 1.5 up to 6 power of the nominal hydrofluoric acid concentration.

Combining the two partial rate expressions gives: Rate $\propto$ (nitric acid concentration)^2 (hydrofluoric acid concentration)^n, $n = 1.5 \rightarrow 6$ [7]

The approximate linear plots of Robbins and Schwartz's Fig. 3 can be explained using the above rate expression. If the fraction of nitric acid is x, then the fraction of hydrofluoric acid is $(1 - x)$ and rate $\propto x^2 (1 - x)^n$, $n = 1.5 \rightarrow 6$; therefore: log (rate) $= 2 \log x + n \log (1 - x) +$ const.

Plots of $2 \log x + n \log (1 - x)$ against x for x between 0.1 and 0.9 give curves of the general form shown in Robbins and Schwartz's Fig. 3. The position of the maximum etch rate depends on the value of n and can be estimated by differentiating the rate expression, equating to zero and solving for x. A value of $n = 4.5$ gives a maximum at $x = 0.3$ in agreement with the "no added water" curve of Robbins and Schwartz's Fig. 3. This value for n is reasonable because the acid strengths correspond to the portion of Fig. 2 where the slope is about 4.5. A value of about 6 would be applicable in the strongest acid mixtures and 1.5 for the diluted etchants (etch rate 1-2 ml/min). The position of the maximum varies accordingly from $x = 0.25$ for the most concentrated acids ($n = 6$) to $x = 0.56$ for the diluted etchants ($n = 1.5$). This is in accord with Robbins and Schwartz's results for various levels of added water.

It is seen, therefore, that, although the reaction is diffusion controlled, an empirical rate expression [7] can be deduced which is in satisfactory agreement with all the experimental results and which is to be preferred to the exponential function indicated by Robbins and Schwartz. This expression should not be interpreted stoichiometrically, but the reactions taking place may be inferred by comparison with other data on the reduction of nitric acid and the composition of acidic fluoride and silicofluoride solutions.

Harry Robbins and Bertram Schwartz: In our discussions of the chemical etching of silicon[6,7] in work subsequent to that being discussed by Mr. Irving, we have considered several alterative mechanisms for the oxidation process. One of these is similar to the mechanism discussed by Mr. Irving. We feel that the situation is considerably more complex than that outlined by him, and are inclined to consider that the mechanism of Abel and Schmid[8] makes a substantial contribution to the over-all reaction. This mechanism involves the oxidation of silicon by HNO_2 as the oxidant. The HNO_2 is formed autocatalytically in a two-step reaction as follows:

$$HNO_3 + HNO_2 \rightleftarrows N_2O_4 + H_2O \qquad [1]$$

$$N_2O_4 + 2NO + 2H_2O \rightleftarrows 4HNO_2 \qquad [2]$$

The NO for the reaction is available, since it is the reduction product of HNO_2. We also feel that the direct reaction of HNO_3 with silicon is also possible under certain conditions, so that there exist several parallel paths for the oxidation step. In our study of the temperature dependence of the reaction, we have found at least two "activation energies" that we have associated with the oxidation step, and which lend support to the possibility that more than one oxidation mechanism may be important in the over-all reaction.

The steady-state reaction via HNO_2 need not involve the diffusion of HNO_3 to the silicon surface as implied by Mr. Irving. Reactions [1] and [2] may well take place within the boundary layer, since the HNO_2 at the silicon surface may be depleted by reaction with the silicon, so that the concentration of HNO_2 will be a maximum within the boundary layer. Under this condition, the situation becomes exceedingly complex, involving concentration gradients of NO, HNO_2, N_2O_4, and HNO_3 within the boundary layer, and complicated interactions between these species, as suggested by Spahn and Schmid.[9]

The situation is complicated still further by the oxide removal process, and by the probability that the reaction is not strictly diffusion controlled over the entire range of compositions of etching solution we have considered. Under the latter condition, as we have discussed elsewhere,[7] the practice of using bulk solution concentration values in a rate equation cannot be justified, but it becomes necessary to take

[6] H. Robbins and B. Schwartz, *This Journal*, **107**, 108 (1960).
[7] H. Robbins and B. Schwartz, *This Journal*, Manuscript submitted for consideration for publication.
[8] E. Abel and H. Schmid, *Z. physik. Chem.*, **132**, 55 (1928).
[9] G. Schmid and H. Spahn, *Z. Metallk.*, **45**, 128 (1955).

cognizance of the actual concentrations existing at the surface of the semiconductor, and the nature of the surface itself may then also influence the kinetics. These and other problems have made exceedingly difficult the derivation of a kinetic expression that would be valid over even a very limited range of compositions.

With respect to the kinetic expression derived by Mr. Irving, we wish to note first that the expression will be valid only on the no-added water line, and cannot be used in the form presented where the sum of the weight fraction of HF and HNO_3 does not equal 1. We have also plotted the expression

$$\log R = 2 \log X + n \log (1-x)$$

as a function of x, for values of $n = 6$ and $n = 4.5$, and it was seen that the curves were only a very crude approximation to the data published. Furthermore, if one takes the empirical rate expression

$$\log R = 2 \log x + n \log (1-x) + \log A$$

where A is the constant of proportionality in the expression

$$R = A\, x^2\, (1-x)^n$$

and calculates A by inserting the values of the measured etch rates on the no added-water line, the values of A so obtained vary by as much as three orders of magnitude. We are, thus, not inclined to agree with Mr. Irving that the empirical expression is in satisfactory agreement with the experimental data.

Electrolytic Reduction of Thorium Oxide

L. H. Meyer, (pp. 43-47, Vol. 107, No. 1)

J. R. Chalkley[10]: It would seem necessary to refer to the problem of oxyhalide formation in the systems Dr. Meyer has been considering.

In the fused chloride system, it has been shown that thorium oxychloride plays a vital role in the electrolysis.[11] Thorium oxide does not dissolve in the NaCl-KCl eutectic melt, but the oxychloride is soluble. (It is also soluble in water.) It decomposes at low Th^{4+} concentrations into the oxide and tetrachloride, and it has a low decomposition potential, depositing a finely divided mixture of metal and oxide. The oxychloride is formed by dissolving thoria in melts containing higher concentrations of thorium tetrachloride, and it is necessary that these higher concentrations should be avoided in any chloride cell used for the electrolytic reduction of thoria. But, even at the lower concentrations, it has been shown conclusively that $ThOCl_2$ is formed as a direct product of the anode reaction (anodic chlorination), and that its rate of decomposition (to ThO_2 and $ThCl_4$) is not sufficiently rapid to prevent its appearance in the catholyte and the deposition of a fine, low-grade deposit.

It is misleading to draw direct conclusions from the anode gas analysis; theoretically, chlorine would be expected to be evolved if an inert anode could be used. As evidence for this, it is easily demonstrated that oxygen will displace chlorine from a thorium tetrachloride melt. The graphite anode, however, plays an important part in the electrolysis as illustrated by the following equations, which also show that chlorine is the primary product in the anode:

$$ThOCl_2 \rightleftharpoons ThO^{++} + 2Cl^-$$

$$ThCl_4 \rightleftharpoons Th^{4+} + 4Cl^-$$

At the anode:

$$Cl^- \rightarrow Cl$$

$$ThO_2 + 2Cl + C \rightarrow ThOCl_2 + CO_2$$

$$ThO_2 + 4Cl + C \rightarrow ThCl_4 + CO_2$$

It is interesting to note that chlorination with molecular chlorine under similar conditions forms only the tetrachloride directly, the oxychloride being formed during the later stages by the back-reaction:

$$ThO_2 + ThCl_4 \rightleftharpoons 2ThOCl_2$$

It would not be justifiable to extend this behavior to cover similar reactions in the fluoride system, since it is known that many oxides are appreciably soluble in fused fluoride melts. On thermodynamic evidence, oxygen would then be the primary product at the anode, but, on present evidence, the possibility of oxyfluoride formation in the melt cannot be discounted.

The fused chloride system has been shown to be unfavorable for the operation of a direct oxide electrolytic process. Nevertheless, the two-stage process in which thoria is directly and completely chlorinated in situ in the melt and then electrolyzed[12,13] is, over-all, equivalent to the oxide electrolytic process. Very high efficiencies are obtained by this process, and, as with most fused chloride systems, the following advantages over the corresponding fluoride systems are shown:

(*A*) Lower operating temperatures.

(*B*) Easier leaching conditions due to higher chloride solubilities. 'Stripping' of thorium from the melt is advocated, but thorium in leach liquors is effectively recovered by oxalate precipitation.

(*C*) Less corrosive conditions, giving a wider choice of refractory and insulator materials.

Influence of Electrode Surface Conditions on the Electrical Strength of Liquefied Gases

D. W. Swan and T. J. Lewis (pp. 180-185, Vol. 107, No. 3)

A. H. Sharbaugh[14]: It is gratifying to note the general agreement of Dr. Lewis' values for the electric strength of *liquid* nitrogen and our measurements on *gaseous* nitrogen at high pressures. We observed values of the order 1.8 mv/cm at densities which are about one-quarter of the liquid density.[15] Thus, it would appear that there is no marked discontinuity in electric strength in passing from the gaseous to liquid phase.

[10] Impregnated Diamond Products Ltd., Tuffley Crescent, Gloucester, England.

[11] J. R. Chalkley and W. H. Cleaver, "Examination of an Anodic Chlorination Process for the Preparation of Thorium from Thoria," *Atomic Energy Research Estab.*, Report X/M 185, 1959.

[12] A. R. Gibson, J. H. Buddery, J. R. Chalkley, and R. P. Marshall, "Thorium Metal Production by a Chlorination Process," *Proc. 2nd. Intern. Conf. Peaceful Uses Atomic Energy, Geneva 1958*, 4, pp. 237-242.

[13] A. R. Gibson and J. R. Chalkley, "Production of Thorium Metal," *Bull. Inst. Mining Met.*, 69 (Part 6), 281 (1960).

[14] Research Lab., General Electric Co., P. O. Box 1088, Schenectady, N. Y.

[15] *1957 Ann. Rep., Conf. on Elec. Ins.*, p. 32.

I should like to call attention to two earlier examples of the influence of the anode properties on the measured values of electric strength of hydrocarbon liquids. The first was observed in n-hexane where we measured a decrease of about 10% in the electric strength when a smooth flat stainless steel anode was roughened by grit blasting.[16] The "hill-to-valley" depth of the roughened surface was of the order of 10% of the 70μ gap separation. A second example was reported for some measurements in benzene where solutions with different concentrations of electrolyte were employed as anodes. In this case, the effect was interpreted as being due to the space-charge enhancement of the applied field by positive ions emitted from the anode.[17]

Molecular Structure and the Electrical Strength of Liquid Hydrocarbons

T. J. Lewis (pp. 185-191, Vol. 107, No. 3)

P. K. Watson[18]: The model which has been proposed appears to have at least two notable defects: It indicates that the mechanism of breakdown in liquids takes place by means of an electron multiplication process, and it implies that the breakdown strength of a liquid should be virtually independent of an applied hydrostatic pressure.

Now, on the basis of our recent experiments on high-field conduction currents in hexane in the microsecond region, we have concluded that there is no significant multiplication process in hexane even at fields of 1.3 mv/cm.[19]

Moreover, recent experiments have indicated that the breakdown strengths of liquids are strongly pressure dependent, even for pulses as short as 1 μ sec.[20]

Obviously, there is a correlation between electrical breakdown strength and some parameter associated with molecular structure, but the relationship must be more indirect than Dr. Lewis has indicated.

A. H. Sharbaugh[21]: By analogy with Townsend-type breakdown in gases, a theory of liquid breakdown which involves an electron multiplication (α-process) predicts that the value of the product $\alpha\delta$ will be approximately constant for wide ranges of gap width δ and ionization coefficient α. At *constant* δ, we have observed a 50% decrease in the electric strength E_b of liquid hexane when the electrode area is increased from $\sim$ 0.2 to 3 cm^2.[22] Since α, if it exists, would be expected to be a strong function of E, it is difficult to reconcile this experimental observation with the hypothesis of a multiplication process for breakdown in liquid hexane.

[16] *1955 Ann. Rep., Conf. on Elec. Ins.*, p. 16.
[17] *J. Appl. Phys.*, 25, 382 (1954).
[18] Research Lab., General Electric Co., P. O. Box 1088, Schenectady, N. Y.
[19] A. H. Sharbaugh and P. K. Watson, "High-Field Conduction Currents in Liquid Hexane under Pulse Conditions," Abstract No. 20, ECS Meeting, Philadelphia, Pa., May 1959.
[20] K. C. Kao and J. B. Higham, "Effects of Hydrostatic Pressure, Temperature, and Voltage Duration on the Electric Strengths of Hydrocarbon Liquids," Abstract No. 11, ECS Meeting, Philadelphia, Pa., May 1959.
[21] Research Lab., General Electric Co., P. O. Box 1088, Schenectady, N. Y.
[22] *1955 Ann. Rep., Conf. on Elec. Ins.*, p. 16.

T. J. Lewis: The statement by Dr. Watson, that the model implies that breakdown occurs by an electron multiplication process and should be independent of an applied hydrostatic pressure, is not really correct. The criterion set up is one for the necessary field to overcome various loss processes and so provide some electrons of sufficient energy to contribute effectively to the next stage in the breakdown sequence.

Only when all the succeeding stages of the breakdown (some of which may be pressure dependent) are maintained in a reasonably constant manner, i.e., C constant, will comparison between experiments be possible in terms of this criterion. Such a situation should arise for a series of similar hydrocarbons.

One should not proceed too far by analogy with gas discharges in expecting clearly measurable values of α since the actual value might be small or only significant when breakdown is imminent or even masked by the other processes embodied in C. Even when α is small, however, the liquid still can exert a marked influence through the loss process envisaged.

The results mentioned by Dr. Sharbaugh, in which a decrease in strength of n-hexane is observed when the electrode area is increased at constant gap width, provide evidence, I believe, not for liquid mechanisms but for quite a different aspect of the subject. It should be recalled that these measurements were made using the microsecond pulse technique. Under these conditions, an analysis of the variation of strength with area according to the concepts outlined in Abstract 13[23] will indicate that the observations are exactly in agreement with a statistical model of the breakdown process and do not, therefore, shed any light on the possibility of a multiplication process.

A New Statistical Theory for the Breakdown of Liquid Hydrocarbons

B. W. Ward and T. J. Lewis (pp. 191-195, Vol. 107, No. 3)

Oliver H. LeBlanc, Jr.[24]: It has been shown experimentally by Goodwin and Macfadyen and by Crowe that the time lags observed with application of short pulses are directly proportional to the electrode spacing. This seems to me to be clear evidence that the time lag must be formative and not statistical.

P. K. Watson[25]: For a time lag to be ascribed to a statistical process, similar to the well-known effect in gases, it is necessary to postulate the nature of the event for which one is waiting. In the gaseous case, this event is the arrival of an initiating electron, and Dr. Lewis has suggested that, by invoking a similar phenomenon for liquids, one can explain the dependence of breakdown strength upon pulse width in the microsecond region.

[23] "A New Statistical Theory of the Breakdown Process and the Reinterpretation of Pulse Breakdown Measurements in Liquid Hydrocarbons" by T. J. Lewis, ECS Meeting, Philadelphia, Pa., May 1959.
[24] Research Lab., General Electric Co., P. O. Box 1088, Schenectady, N. Y.
[25] Research Lab., General Electric Co., P. O. Box 1088, Schenectady, N. Y.

This hypothesis is not, in fact, consistent with the experimental facts:

(*A*) The currents which are observed in liquids, under microsecond pulses of voltage, at fields in the range 1 to 1.5 mv/cm, are of the order of milliamp per cm^2.[26] Assuming a value for electron mobility of the order of 10^{-3} cm/sec/v/cm,[27] this gives an electron emission rate of 10^{13} electrons/sec/cm^2 from the cathode. It is difficult to see how such a copious emission can be consistent with statistical time lags in the microsecond region.

(*B*) If, however, one supposes that the probability of an electron initiating a breakdown is very small (say 1 in 10^6 or so), then it might be argued that the experimental evidence is still consistent with a statistical time lag, in that one is awaiting the emission of a very large number of electrons from the cathode. This again, however, is at variance with the observed facts: If, as has been suggested, the electron emission from the cathode is a field-assisted thermionic process (Schottky emission), then one would expect any statistical time lags to be strongly temperature dependent. In fact, the experiments of Kao and Higham indicate that the time lags are independent of temperature.[28]

Finally, it may be thought that the electrons are field emitted: In this case, however, one would expect a marked reduction in time lag if, by some means or other, one were able to increase the field needed to cause breakdown. This can be done by changing the hydrostatic pressure applied to the liquid, and Kao and Higham find that in hexane, for example, there is no change in the critical time lag, in going from atmospheric pressure, up to 25 atm, despite a very marked increase in the breakdown strength.

Thus, one is forced to conclude that the observed time lags in liquids are not consistent with a statistical model.

T. J. Lewis: The present theory does not preclude the existence of a formative time lag. In fact, it states that both statistical and formative times exist and that the latter is expected to be dependent on the electrode spacing, thus leading to the results obtained by Goodwin and Macfadyen and by Crowe. The important result, which may not have been adequately presented in the paper but which can be properly developed in a full treatment, is that the formative time is not that associated with the "knee" of the electric stress-pulse duration curve, but is a much smaller quantity.

Dr. Watson's concluding comment is that the observed time lags in liquids are not consistent with a statistical model. I submit that the experimental evidence obtained by many different workers employing short-duration pulses is overwhelmingly to the contrary. The reasons are:

(*A*) When a proper statistical analysis is made both of the method used and the results obtained for the electric strength as a function of pulse duration, the existence of a statistical process becomes very evident. Failure to take account of the nature of the experimental method has led to erroneous conclusions in the past.

(*B*) If a step-function voltage pulse is employed instead of microsecond pulses, the breakdown time lag can be measured directly and has obvious random fluctuations.

We have made measurements on n-hexane under both categories (*A*) and (*B*) above to confirm this, and it is important to note that it is *not* necessary to postulate the nature of the random process in order to establish these experimental facts.

However, it is profitable to proceed further by enquiring into the nature of the random events which give rise to the effects noted. In the paper, I have attempted to do this by postulating a random process of rate *IW* which is partly cathode and partly liquid dependent. It would be wrong to assume at this stage more than the property that *IW* increases with field, provided all other conditions remain constant. It is certainly not justifiable to dismiss the evidence for a statistical time lag as Dr. Watson does, simply because *I* in the presence of hydrocarbon does not conform to vacuum emission laws.

If *I* is identical with the electron emission rate from the cathode and that is, in the worst case, 10^{13} electrons/sec and concentrated on a single emission site, then it is true than *W* would need to be $< 10^{-6}$ to give time lags of the right order. Further consideration indicates that this is not at all unlikely. In fact, values of *W* very much less than this are probable, if only the most energetic electrons in the liquid are capable of initiating a breakdown. Even when *W* is of this order of smallness, one is not awaiting the emission of a large number of electrons since any electron, even the first, may lead to breakdown.

The form of *IW* chosen in the paper to illustrate the theory was unfortunate in that it did not indicate that large changes in *I* and *W* can be tolerated provided *IW* remains of the right order of magnitude.

[26] A. H. Sharbaugh and P. K. Watson, "High-Field Conduction Currents in Liquid Hexane under Pulse Conditions," Abstract No. 20, ECS Meeting, Philadelphia, Pa., May 1959.
[27] O. H. LeBlanc, *J. Chem. Phys.*, In press; "Electron Drift Mobility in Liquid n-Hexane," Abstract No. 22, ECS Meeting, Philadelphia, Pa., May 1959.
[28] K. C. Kao and J. B. Higham, "Effects of Hydrostatic Pressure, Temperature, and Voltage Duration on the Electric Strengths of Hydrocarbon Liquids," Abstract No. 11, ECS Meeting, Philadelphia, Pa., May 1959.

The System BaO-TiO_2-P_2O_5: Phase Relations, Fluorescence, and Phosphor Preparation

D. E. Harrison (pp. 217-221, Vol. 107, No. 3)

Mary V. Hoffman[29]: The x-ray data presented in this paper for the compound 2BaO: TiO_2: P_2O_5 differ considerably from those obtained by Ranby, Mash, and Henderson[30] and more recently in this laboratory (Table I). The pattern as presented apparently was obtained on material recrystallized from the melt. This method results in considerable crystal growth, and, with this compound, in severe orientation. A more representative pattern is ob-

[29] Luminescent Materials Lab., Lamp Metals and Components Dept., General Electric Co., Cleveland, Ohio.
[30] P. W. Ranby, D. H. Mash, and S. T. Henderson, *Brit. J. Appl. Phys.*, Supplement No. 4.

Table I. X-ray diffraction pattern: $2BaO \cdot 1TiO_2 \cdot 1P_2O_5$

From paper		From low-temperature firing	
d	*I/I*	*d*	*I/I*
8.34	30	8.40	16
		4.70	20
		4.51	22
		4.29	3
4.17	80	4.17	27
3.90	25	3.90	75
		3.75	8
3.59	10	3.60	100
		3.50	7
		3.36	22
		3.23	31
2.84	5	2.84	18
2.78	100	2.79	47
2.73	10	2.72	33
2.65	3	2.65	29
2.39	3	2.39	27
		2.35	9
		2.33	15
2.28	3	2.28	10
2.25	3	2.25	14
		2.20	17
2.19	3	2.19	14
2.14	5	2.14	31
		2.08	8
		1.99	13
		1.96	7
1.94	3	1.94	10
		1.90	5
		1.87	11
		1.79	8
1.75	10	1.75	20
		1.72	7
		1.69	5

tained by firing at low temperatures, preferably at or below 1000°C. Noticeable orientation will occur in material fired at 1090°C. The differences in the patterns are large enough to obscure positive identification, since the orientation tends to suppress those lines which distinguish 2:1:1 from the similar pattern of $Ba_2P_2O_7$. The x-ray data were obtained on a General Electric diffractometer, XRD-5, using CuK radiation, nickel filter.

An Investigation of the Reaction between Aluminum and Water

W. J. Bernard and J. J. Randall, Jr. (pp. 483-487, Vol. 107, No. 6)

F. J. Burger and D. M. Cheseldine[31]: This paper confirms a number of results which we obtained in the course of work carried out under Canadian Government Contract DRB 700129, "Development of Aluminum Electrolytic Capacitor, ECRDC Project C44." These were summarized in the First and Second Quarterly Reports of November 1958 and February 1959, respectively.

In our investigation, two methods were used to determine the degree of hydration of the product of the reaction of hot deionized water on aluminum.

In one method, the volume of hydrogen evolved during the reaction was measured directly and correlated with the weight increase of the aluminum specimen. The ratio of these two quantities varies according to the degree of hydration of the oxide formed, as illustrated, e.g., by equations [1] and [2], which represent the formation of mono- and trihydrates, respectively.

$$2Al + 4H_2O = Al_2O_3 \cdot H_2O + 3H_2 \quad [1]$$

$$2Al + 6H_2O = Al_2O_3 \cdot 3H_2O + 3H_2 \quad [2]$$

Calculations show that for a weight increase of 1 mg the volume of hydrogen at NPT is 1.02 cc in the case of monohydrate formation, and 0.66 cc in the case of trihydrate.

In a typical experiment, a specimen of 99.99% pure, etched aluminum foil (measuring 2 in. x 2 in. x 0.0035 in., and having attached to one of its sides a tag 2 in. long by ¼ in. wide) was immersed in deionized water ($\rho_{25°C} > 10^6$ ohm-cm) at 90°C, as follows.

The weighed specimen was placed under an inverted short-stemmed glass funnel and secured by leading the tag out through the stem of the funnel and turning its end over. Funnel and foil then were completely immersed in the hot water and an inverted burette filled with water placed over the stem of the funnel to collect the evolved hydrogen. After a suitable reaction time (say 1 hr), the foil was quickly removed from the water, dried either at 110°C or *in vacuo* at room temperature, and reweighed.

The volume of hydrogen, measured at room temperature and atmospheric pressure and corrected for 0°C, was found to be 32 cc.

Corrections for barometric pressure, water vapor pressure, and losses due to solubility of hydrogen in water were not applied. The corresponding weight increase of the foil specimen after drying under vacuum at room temperature was 43.5 mg, *i.e.*, a weight increase of 1 mg was accompanied by evolution of approximately 0.74 cc of hydrogen (NPT). The hydration calculated from these figures is 2.4 moles H_2O and 1 mole of Al_2O_3. The mean value obtained by this method from 7 separate experiments was 2.8 moles of water.

In our second series of experiments, applying the method of Lewis and Plumb[32] in which the oxide is stripped in an aqueous solution containing 2% CrO_3 and 5% H_3PO_4 at 85°C, we found a somewhat lower figure for the hydration. In these experiments, too, the same type of etched, 99.99% pure Al foil was used. Foil specimens were immersed in boiling deionized water for 5, 30, and 60 min. The times required for stripping these layers were about 10, 30, and 40 min, respectively. The weight changes observed, namely, first, after boiling and, second, after stripping the aluminum foil, are shown in Table I published here. In each of these cases, the foil was

Table I. Weight changes on, first, boiling and, second, stripping 4-sq.-in. etched aluminum foil

Reaction time (min)	5	30	60
(*A*) Weight increase after boiling (mg)	60.8	98.2	119.2
(*B*) Weight loss after stripping (mg)	98.3	159.8	193.6
Ratio $\frac{(A)}{(B)}$	0.62	0.63	0.63

[31] The Telegraph Condenser Co., (Canada) Ltd., 50 Bertal Rd., Toronto 15, Ont., Canada.

[32] J. E. Lewis and L. C. Plumb, *This Journal*, 105, 499 (1958).

dried in vacuo at room temperature for ½ hr before weighing.

The composition of the reaction product is shown to be independent of reaction time in the range covered by reference to the bottom line of the table which lists the ratio of combined oxygen and hydrogen (weight increase) to hydrated alumina (weight loss). The mean of this ratio, being 0.63, corresponds to 2.1 moles H_2O per mole of alumina, the values for mono- and tri-hydrate being, respectively, 0.55 and 0.665.

Both methods, therefore, support the view that the hydrate formed is not mono-hydrate as has been commonly assumed hitherto, but is of a higher order.

Growth of Single Crystal Silicon Overgrowths on Silicon Substrates

Albert Mark (pp. 568-569, Vol. 107, No. 6)

R. C. Sangster[33]: Very similar work was reported by Sangster, Maverick, and Croutch.[34] The lead paragraph reads as follows: "A study has been made of the feasibility of growing Si crystals by the reaction of gaseous $SiBr_4$ with H_2 at the surfaces of hot Si seed filaments. The immediate objective has been to produce deposits of a purity and a crystal perfection sufficient for semiconductor device purposes. An ultimate objective has been the deposition of arbitrary, complex, p-n junction structures by control of the types and amounts of impurities deliberately introduced into the process gas stream. This is a partial report covering the more interesting observations and results." Included were descriptions of the apparatus used, an analysis of the deposition process with respect to both the fundamental phenomena involved and the effects of process variables, microphotographs of epitaxial single crystal silicon deposits, description of the optimum experimental conditions, and some preliminary electrical results on epitaxially grown p-n junction structures. The authors feel that the current interest in techniques of this sort is quite justified and long overdue. We hope that Mr. Mark's contribution will help stimulate further activity in this field.

[33] Central Research Labs., Texas Instruments Inc., P. O. Box 1079, Dallas 21, Texas.
[34] R. C. Sangster, E. F. Maverick, and M. L. Croutch, *This Journal*, 104, 317 (1957).

June 1961 Discussion Section

A Discussion Section, covering papers published in the July–December 1960 JOURNALS, is scheduled for publication in the June 1961 issue. Any discussion which did not reach the Editor in time for inclusion in the December 1960 Discussion Section will be included in the June 1961 issue.

Those who plan to contribute remarks for this Discussion Section should submit their comments or questions in triplicate to the Managing Editor of the JOURNAL, 1860 Broadway, New York 23, N. Y., *not later than March 1, 1960.* All discussion will be forwarded to the author(s) for reply before being printed in the JOURNAL.

Some Practical Aspects of Copper Refining in a Multiple System Tank House

M. A. Mosher

Raritan Copper Works, Perth Amboy, New Jersey

Weird Character of the Tank House

In this day of rapid revolution, startling innovation, and overnight obsolescence in industrial processes and equipment, the electrolytic copper tank house stands and has stood for nearly three-quarters of a century as a fixed and stubborn example of resistance to radical change. In the great copper, zinc, and nickel industries so completely dependent on it, the tank house seems to be considered a fundamental thing, comparable in our physiology to the process of metabolism, and in nature to "Old Man River" who "just keeps rollin' along."

The typical copper tank house with its hundreds of cells and thousands of electrodes and millions of gallons of circulating solution, is for the greater part of each 24-hr day a quiet and unspectacular place, with only the faint purring of pumps and the gentle flow of electrolyte through the tanks to indicate that it is actually functioning. Almost unique among the great producing units of modern industry, the tank house makes most of its production in majestic and peaceful silence, in marked contrast to the ceaseless roar of furnaces, the din of machinery, and the noisome reactions of large chemical processes.

Of course there are a few hectic hours in each day when a tank house, like a restless infant, has to be fed and changed, but that is only to keep it healthy and behaving properly.

The Tank House Boss

In line with these unique characteristics of the operation, long exposure to tank house work tends to develop a rather peculiar type of chief operator or superintendent, and having been one of these, I will briefly describe him for you, even though by comparison with the masterful and dynamic operators of other types of processes, he may seem drab and uninteresting.

He tends to become a slave of the established routine which he has worked out, the hard way, to get the best results. He learns to live with and keep alert to a staggering number of small easily overlooked operating details, because he knows from bitter experience that disregard of any of them may upset his whole show. He is slow to arrive at conclusions about process difficulties because he knows that dozens of inter-related factors are involved in every operating crisis he has to deal with. He develops a militant aversion to any radical innovations or changes in his methods of operation because he feels their adoption may result in complications which will jeopardize vital production. And, finally, he develops a great patience in the face of operating adversity, realizing that, in most cases of process sickness in a tank house, there is no miracle-drug cure.

Contrary as these characteristics of a good tank house operator may seem, there is much justification for them in tank house work for the following reasons:

1. The tank house process is essential for economically providing the standardized high-purity product on which his company or division depends for its existence. This is a tremendous responsibility for its operator, and consciousness of this fact naturally makes him conservative and jealous of his time-proven methods and procedures.

2. The tank house operator knows that it takes months or even years successfully to work out worthwhile changes or innovations, because every move must be made with care and patience to avoid upsetting the scheduled flow of large-scale continuous production.

3. No matter how eagerly the tank house operator may want process improvement through research, he knows from many a disappointment that the best of research results can fail miserably when applied to full-scale commercial operation. In fact there are few other industrial operations where laboratory or small-scale tests will provide so little usable data for full-scale application.

Tank House Improvements

You may wonder why I have tried to give you a picture of the typical tank house superintendent, but through it I think we have arrived at the main reason why changes and improvements in tank house operation for the past half century have been somewhat limited in scope, and chiefly in the area of construction materials, physical arrangement, and improved mechanical equipment for handling anode input and cathode production. These advances can be listed as follows:

Improved building walls and roof construction, using such materials as glazed hollow tile and Porete roof slabs that afford insulation against loss of heat and minimize condensation when outside temperature is low.

Conversion to reinforced concrete cell construction to replace wood.

Improved types of solution line insulation to provide protection against the passage of stray electrolytic current, such as the use of plastic pipe and tubing to replace lead and rubber.

Use of heat exchangers constructed of corrosion-proof materials, in place of lead pipe heating coils. This more efficient solution heating equipment has made possible an increase of about 10°F (5.6°C) in the accepted temperature for electrolyte entering the cells.

Larger cells to permit the use of higher circuit amperage and to reduce the number of unit loads of anodes and cathodes to be handled by crane.

Improved addition agents and better addition agent control.

Improved methods for inspection of cells in operation, particularly the introduction of the Gaussmeter for the detection of shorted cathodes.

Continuous filtration of make-up solutions.

Improved pump design and construction, using stabilized stainless steel.

The racking of anodes at the casting furnace and the mechanical washing and loading of cathode production in the tank house were introduced about 35 years ago. At about the same time the method of stripping starting sheets was changed from horizontal to vertical handling. That about sums up the improvements in mechanical handling since overhead electric cranes for tank-load lifts were introduced in the early 1900's.

Present Day Equipment and Operation

The general acceptance and adoption of most of these advancements by the various refineries in the last two decades has resulted in a fair degree of standardization in both equipment and operation. We can therefore discuss these accepted essentials of present day tank house equipment and operation with assurance of their almost general application.

Our discussion will be confined to the Walker Multiple System lay-out with the electrodes in parallel in each cell and the cells themselves in series in the electrolytic circuit. In the original Walker system current was passed from tank to tank by means of a conductor bar of small cross section placed on the common partition between adjacent tanks. The contact end of the cathode rods of the first tank rested on the conductor bar in alternation with the contact lugs of the anodes in the second tank. This arrangement has been largely superseded by the Whitehead contact which eliminates the conductor bar by having the contact end of the cathode rods rest directly in a slot in the contact lug of the anodes. As much as 5 mv of *IR* drop per cell is saved by this direct contact.

Electrolytic Cells

Two general types of reinforced concrete construction have proved satisfactory. One type comprises the assembly of precast slabs to form a row or tier of cells with partitions common to two tanks. The use of replaceable planks of heavy wood for the bottoms of these cells is generally favored. The precast concrete elements are so fitted and interlocked that only a few bolts and stays are required to make the entire tier a rigid construction unit. All types of cells have a bottom outlet for the removal of electrolytic slime, and in many designs another outlet is provided in the end wall of the cell a few inches above the bottom for the decantation of electrolyte prior to the removal of slime. Bottom outlets discharge into a system of launders which convey the slime slurry by gravity to pumps in the cellar. The other type of construction is the cast-in-place monolithic tier of reinforced concrete.

Insulating slabs of glass or stoneware are placed between the tank bottoms and the supporting piers which rise from a 7 to 8 ft cellar. Tiers or rows are usually designed in pairs as sections. The section is the operating unit in practically all tank houses, as the electrolytic current bus bars are so arranged that the current can be conveniently applied to or cut off from it to permit removal or replacement of anodes, cathodes or electrolyte.

Eight-pound 6% antimonial lead is still universally used for cell linings, but there is considerable testing and experimentation with several types of acid-resisting plastic materials.

Solution Lines and Tanks

Solution lines for conveying electrolyte to and from the cells have traditionally been of lead with lengths of insulating rubber tubing at the cell inlet and outlet. However, polyvinyl tubing is replacing rubber in many tank houses and there have recently been several installations in which p.v.c. pipe and p.v.c. lined launders have replaced lead pipe and lead linings. Increasing use of plastics in place of lead has resulted from the need to eliminate conducting paths through which destructive current can stray from the electrolytic circuit.

Lead-lined steel or steel skeleton tanks are still favored for storage, settling, and mixing of tank house solutions, although there have been many trial installations of plastic-lined tanks.

Pumps

Centrifugal pumps of all types, both horizontal and vertical, are in general use, but lead construction has been almost entirely abandoned in favor of stabilized stainless steel alloys. Use of the latter metal makes it necessary to protect fully the pumps from electrolytic corrosion resulting from stray current which gives the pump positive polarity.

Electrolyte—Composition and Temperature

The aqueous solution of copper sulfate and sulfuric acid used in electrolytic copper refining can vary widely in chemical composition, specific gravity, and temperature and still give satisfactory results in the production of high-purity cathode copper.

The content of these electrolyte constituents is usually adjusted to compensate for the presence of contaminating salts which accumulate from the solution of anode impurities. For example, sulfuric acid content can range from 150 to 220 g/l, but in most tank houses is maintained near 200 g/l since this concentration has a high electrical conductivity and usually avoids the anode polarization which results from the reduced solubility of impurity salts caused by high acid content. Likewise copper content as sulfate may range from 40 to 55 g/l but is usually maintained at 45 g/l. This content insures pure copper deposition, yet allows for the presence of reasonable amounts of soluble impurities. The copper content of the electrolyte tends to increase by about 1.5% of the copper deposited. A sufficient amount of electrolyte is therefore continually passed through plating-out or liberator cells equipped with lead anodes. This maintains the desired level of copper content in the entire body of electrolyte, and the copper thus removed is of normal high purity.

The beneficial effect of temperature in maintaining solubility of the salts is important. Electrolyte temperature can range from 120°F (48.9°C) to 150°F (65.6°C) and most tank houses use 140°F (60°C) or higher at the cell inlet to insure high solubility as well as to lower specific gravity, which facilitates movement of the electrolyte through the cell.

Of the soluble impurities which accumulate from normal corrosion of the anode, arsenic, antimony, bismuth, and nickel give the operator the most concern and make it necessary for him to keep close control of copper and acid content as well as temperature. Of these four anode impurities, nickel remains almost entirely soluble in the electrolyte. Much of the arsenic, antimony, and bismuth forms complex compounds, probably arsenates, which are insoluble and precipitate with the slime. While the electrolyte can safely tolerate nickel up to 20 g/l and arsenic up to 15 g/l, antimony and bismuth can become troublesome when they exceed 0.5 g/l. Difficulty with

electrolytic impurities can be minimized by reducing the sulfuric acid content to as low as 125 g/l, and holding copper content down to 45 g/l. The total amount of soluble impurity elements should not be permitted to exceed 30 g/l.

Any appreciable amount of soluble selenium and tellurium, introduced through return solutions from the leaching of electrolytic slime, can cause havoc in the tank house, since these elements cement out on the cathode surfaces and destroy the continuity of crystal growth. The result is a coarse, granular deposit which in extreme cases becomes nonadherent and falls from the cathode.

It should be noted that soluble impurities in the electrolyte appreciably increase its resistivity and can become a significant factor in the cost of electric power.

Electrolyte Purification

Except for minor modifications, the general procedure for removing arsenic, antimony, and nickel to maintain reasonable electrolyte purity is as follows:

The required volume of electrolyte is diverted continuously through liberating cells for plating out the copper. The solution is then further electrolyzed in outdoor tanks to deposit arsenic and antimony. The resulting high-acid nickel-bearing solution is evaporated to approximately 60° Be', which precipitates the nickel as a crude sulfate. With proper washing and centrifuging this product is marketable. The resulting "black acid" and wash waters are returned to the electrolyte, or subjected to acid distillation to remove iron, calcium, magnesium, sodium, and potassium salts. It is possible to remove appreciable amounts of calcium and magnesium salts by isolating batches of decopperized solution and letting these salts crystallize out at outdoor temperature.

Electrolyte Conditioning

Early in the development of electrolytic copper refining it was found that the electrolyte required certain additions to produce consistently firm and relatively smooth cathode deposits free from entrapped impurities and sprouting growths which would short circuit to the anodes. Common salt to introduce chloride ions was the first of these additions and is supposed to have been adopted after the benefits of an accidental intake of sea water for solution make-up had been noted at an east-coast refinery. Most refineries now add salt or hydrochloric acid to maintain a chlorine content of 0.02 to 0.035 g/l. The exact function of the chloride ion is not well understood, but it precipitates dissolved silver and improves the physical characteristics of the cathode deposit. Several refineries have noted difficulty with sandy, nonadherent cathode deposit when chlorine content was permitted to fall below 0.008 g/l.

Organic additions are also necessary in order to obtain a fine-grained, firm cathode deposit which remains relatively free from sprouts and protrusions during many days of plating. Animal glue, a complex protein, has long served as the most effective organic addition agents, apparently due to the slight cathode polarization which it causes. Other organic compounds work well in conjunction with glue but not to the extent of displacing it entirely. Among these are casein, thiourea, and sulfonated products such as goulac and bindarene from sulfite liquors, and Avitone, a sulfonated petroleum derivative. Orzan A, an ammonium ligno-sulfonate and Separan, a flocculating agent, are also used by certain refineries. These sulfonated compounds appear to modify the action of glue, tending to decrease its polarization effect and counteracting the excessive hardness and sprouting of the deposit which can result from an overdose of glue alone. Several refineries find that an addition of light petroleum oil emulsified in electrolyte is beneficial in tempering the action of glue. Each refinery has developed from experience an organic addition agent formula which gives the best results under its own process conditions, and the amounts added vary widely. Per ton of cathode deposition, glue additions range from 0.01 to 0.3 lb, the usual amount being about 0.1 lb. Modifying agents are added in a ratio of 2, 3, or 4 times the weight of glue. Addition agents are dissolved or emulsified in relatively large volumes of water and continuously introduced in the circulating electrolyte reservoirs, preferably by mechanical reagent feeders.

Daily evaporation of water from the electrolyte averages 2-3% of the total volume being heated and circulated through the cells. This evaporation has to be carefully and continuously replaced, either with clean water or "make-up" solution, which results from the washing of cathodes and anode scrap, or from the leaching and washing of electrolytic slime. Make-up solution must be thoroughly blended and kept warm, so that it will mix readily when added continuously to the circulating electrolyte. If water is required in addition to available make-up solution, it should be clean and warm and added in a small stream at a point where it will mix in thoroughly. Making up evaporation is a critical item in tank house operation, since careless addition of solution or water causes localized dilution of the electrolyte. This can quickly upset the proper functioning of all cells receiving it.

The cathode surfaces in cells receiving diluted electrolyte even for a short period will show areas of needle or whisker-like copper deposit, which will later develop into short-circuiting growths.

Electrolyte Heating

Low pressure steam is universally used by means of heat exchangers, immersion heaters, or closed coils. Depending on building construction and climate, steam requirements average roughly one pound for each pound of cathode production. It is important that during cold weather building ventilation be regulated to maintain a minimum temperature of 80°F (26.7°C).

Karbate (resin-bonded carbon) tubes are used for conducting the electrolyte through heat exchangers. Stabilized stainless steel jackets carry the stream in immersion or plate coil heaters, and lead pipe is used for closed coils. The Karbate tube heat exchanger has been in favor in recent years because of its compactness and high rate of heat transfer.

Whatever the type of heating apparatus used, the condensate water is usually collected and utilized through a separate hot water system for all process washing and electrolyte make-up purposes. This avoids eventual contamination of the electrolyte with prolonged use of raw water and is an important factor in the economy of using steam for heating.

Electrolyte temperature much below 120°F (48.9°C) will, with most refinery electrolytes, permit salting-out of sulfates and bring on anode polarization which upsets the electrolysis by increasing the cell voltage to the decomposition voltage of the copper sulfate electrolyte. When this occurs the operators dub the cells "crazy."

Circulation of Electrolyte

The heated electrolyte must circulate through each cell at a rate which will prevent too great a loss of temperature between the inlet and outlet and maintain the proper ion concentrations at the electrode surfaces. For good operation this temperature drop is seldom permitted to exceed 10°F or 5.6°C. The required rate of flow

varies with the size of the tank and the room temperature but usually falls within the range of 3.5-6 gal/min. Excessive rate of flow tends to interfere with the settling of the electrolytic slime which sloughs from the anodes.

Once a satisfactory rate of electrolyte flow has been established, it is most important that it be maintained constantly and kept uniform in all cells. Otherwise not only the electrolyte temperature, but the beneficial effects of the organic addition agents will vary from cell to cell.

In most refineries the circulating electrolyte is pumped to a head tank from which it feeds by gravity to the sections of electrolytic tanks. Some refineries, however, pump directly into the supply lines. In this case care must be taken to avoid intake of air at the pump, as air entrained in the electrolyte will form small bubbles on the cathode surfaces and prevent copper deposition wherever they cling, thus having the effect of increasing the current density.

Anodes

The impure anodes, cast from blister or converter copper after it has been furnace refined to remove sulfur, usually have a copper content of 99+%. Oxygen content is usually within the 0.10 to 0.30% range, and in most cases the percentages of the various impurity elements, exclusive of silver, are in the second or third decimal place. Silver plus gold seldom exceeds 30 oz/ton or 0.10%.

In different refineries, anode dimensions vary from 27 to 36 in. in width, from 31 to 39 in. in length, and from 1¼ to 2 in. in thickness. Anodes are universally cast flat with two ears or lugs at one end. This permits them to be hung vertically, and the longer of the two lugs acts as the conductor for the inflow of current. Weight per anode ranges from 440 to 700 lb, and anode life under electrolysis is scheduled at from 21 to 42 days, leaving a scrap remainder of 12 to 20%. Scrap anodes are washed free of adhering slime and returned to the anode furnace for remelting.

In most refineries anode life is about 4 weeks, during which period the cells produce two sets of deposited cathodes. This affords an economical operating schedule and permits the use of a standard rotation for taking out cathode production, replacing anodes, and removing slime from the cells. In some cases where nodularized cathode deposition results from the requirement to electrolyze with high current density or with troublesome anode impurities, it is necessary to plate three or four sets of cathodes during the life of the anode.

After casting, anodes are hung by their lugs and evenly spaced in racks which hold a cell load, so that they can be placed in the cells in unit crane lifts of several tons. While in the racks it is important that the individual anodes be plumbed to hang vertically. This is accomplished by a slight bending of the lugs, using a heavy hammer. Also at this time the contact area of the long lugs is cleaned or polished.

Cathodes

The thin starting sheets of electrolytic copper which are hung between the anodes, and in most refineries at each end of the cell, are usually produced as a 24-hr deposit on smooth, oiled plates or blanks of hard rolled copper which are themselves hung as cathodes in special cells operated for this purpose. In order to eliminate the necessity for surface oiling, there has been considerable experimentation with stainless steel blanks, but passivity to corrosion has been found to decrease with use, and surface repolishing becomes necessary. A deposited sheet, 0.02 to 0.03 in. thick, is peeled from each side of each blank every working day. After stripping, the blanks are re-oiled if necessary and returned to their cells. Strips cut from the same sheet deposit are formed into loops and affixed to each sheet by punching or spot welding so that a copper rod can be threaded through them. These rods support the sheets when they are later hung in the production cells; they also serve as current conductors.

The anodes used in the cells for depositing sheets are usually 2 in. wider and 1 in. longer than the anodes in production tanks. This insures adequate deposition around the edges of the blanks even after 75% of the anode has been corroded away. Starting sheets are usually 2 in. wider and 1 in. longer than the anodes used in production cells. This avoids the formation of a heavy border of deposition during the early days of production plating while the regular anodes still retain their full area.

Before being hung in production cells as cathodes, starting sheets must be "flapped" or flattened so that they will hang straight and not touch the adjacent anodes. In most refineries the flapping is done by hand, but machines are being developed which perform both flattening and affixing of loops.

To permit effective flattening, the sheets must be soft and pliable and free of springiness. The deposition surface must be free of roughness which would promote nodular growth. As a result of these requirements, the composition and conditioning of the electrolyte for the starting sheet cells must be controlled closely and handled through a circulation separate from those which supply the production cells. It is best to use only glue as addition agent. Due to the presence of oil on the blanks, the amount of glue necessary may be 0.2-0.3 lb/ton in order to insure a smooth, tough, fine-grained deposit. Copper content of starting sheet electrolyte is usually maintained between 45 and 50 g/l and acid content between 180 and 190 g/l. The temperature of the electrolyte entering cells should be no less than 140°F (60°C). Cathode current density in excess of 23 amp/ft² tends to cause rough deposition.

Production Cathodes

In the production cells, the starting sheets are spaced carefully in relation to the adjacent anodes, and anode lugs and cathode rod ends are all checked for good current contact. With electrolyte up to normal level and at proper temperature and flow, the section is ready for operation. Current is applied, and deposition continues until the scheduled growth of the cathodes has been completed. Current is then shut off from the section of cells and the cathodes are withdrawn by crane, thoroughly washed with hot water by immersion or spray, and loaded for transportation to furnaces or the market.

The copper content of the completed cathode should be 99.98+% with the percentages of most of the impurity elements in the fourth decimal place. Sulfur and iron content as high as 0.002% can be tolerated. Silver content should not exceed 0.35 oz/ton.

Cathode Current Density

The amount of current through each cell can be set to obtain the desired production of cathode deposit within a fairly wide range of current density. For economic reasons the operation is seldom carried on at less than 10 amp/ft² of cathode surface. Under high production demand, many refineries have operated at 25 or 26 amp/ft², but 15 to 20 amp/ft² is generally preferred. Higher current density tends to produce a rougher deposit and often causes excessive short circuiting from sprouting cathode growths.

Cathode Current Efficiency

Current efficiency is considered a measure of good tank house operation since it is an index of the production obtained for the investment in power and labor, the two chief items of operating cost. Under ideal conditions 1 amp deposits 0.06274 lb of copper per 24-hr day per cell. Using the average of hourly amperage readings taken during the life in days of the cathodes in a cell or section of cells, a theoretical weight of deposition is calculated. When the completed cathodes are removed they are weighed, and the net weight of deposition is divided by the calculated theoretical deposition. A current efficiency of 90% is considered good, but many refineries average 94% or better. The chief cause of reduced current efficiency is short circuiting between adjacent cathodes and anodes. Another cause of lowered efficiency is stray current loss through tank linings and solution lines, which, however, seldom exceeds 2 or 3%.

Power Yield

Since power is measured and paid for in kilowatts, some concern has to be given to the voltage component by minimizing resistances wherever possible in the electrolytic circuit. The source of d-c power is located as close as possible to the cell room, main bus lines are of ample size, anode-to-cathode spacing is set at the minimum which will avoid short-circuiting, and all conductor contacts are kept clean. Both electrolyte temperature and acid content are maintained at values which reduce electrolyte resistivity. As current density is increased, power yield tends to decrease, and this explains why most refineries prefer to operate at moderate current density provided it will enable them to meet their production requirements. Power yield varies widely among different companies in a range of from 6 to 12 lb of copper per kilowatt hour.

Scheduling

The section of tanks, made up of two tiers or rows through which the electrolytic current flows across and back again to the main bus, is the normal unit of operation in the tank house. The tiers are seldom more than a foot apart, and to permit the current to leave the main bus bar and flow across the first tier and return to the bus across the second tier, there is a gap in the bus bar similar to the space between the tiers. This gap is easily bridged by dropping a short piece of bus bar across it and clamping it to maintain good contact. This short piece of bus is called a "lock" or "jumper" and when it is clamped in place the section is "locked out" or "jumpered"; the current is shunted past the section through the lock. This permits removal of completed cathodes and anode scrap, the cleaning of tanks, and finally reloading with new anodes and starting sheets. A scheduled removal of completed cathodes is called a "pulling" or "drawing." When only full-grown production cathodes are removed to be replaced with starting sheets, it is often called a "copper." When both cathodes and fully corroded anodes or scrap are removed and the slime cleaned from the tanks, the drawing is called a "mud."

It is highly desirable for smooth tank house operation to be able to pull the sections on a regular schedule so that they are unloaded and reloaded in the same rotation, cycle after cycle. Such a schedule evens out the work for the loading and unloading crews as well as for the inspection groups who keep the cells operating properly while under electrolysis. To establish and operate a pattern schedule efficiently it is necessary that the anodes be of uniform weight, that current amperage be held closely to the designated figure, and that the ampere efficiency be maintained at a predetermined satisfactory figure. The latter requirement is the most difficult to control since it involves consistently good performance of both the loading and inspection crews as well as the maintenance of uniformly satisfactory conditioning and circulation of electrolyte. Within limits it is possible to adjust a pattern schedule to an increase or decrease in production requirements, but a full cycle is required to complete the adjustment.

Where it is not possible to maintain a regular schedule due to uncontrollable variations, it is general practice to schedule section pullings approximately two weeks in advance.

Cell Inspection and Correction during Electrolysis

All of the items of tank house materials, equipment, and procedure center around the proper operation of the individual cells under electrolysis, so that their inspection and the prompt correction of any malfunctioning become of paramount importance. Competent and sustained good performance on the part of both supervision and operators assigned to cell inspection is most essential.

Satisfactory electrolysis requires that the flow of current be equal and uniform through each anode and cathode in the cell. To achieve this, two things are necessary: first, all electrode contacts must be kept clean for good conduction and, second, cathodes and anodes must be kept evenly spaced with no contact in the cell, either above or in the electrolyte.

Whenever these conditions are not maintained, the distribution of current among the electrodes becomes uneven due to their being in parallel. The current which faulty electrodes fail to receive is taken by electrodes with good contact, resulting in wide variations in current density. Cathodes operating under high current density develop undesirable surface growths which may result in short-circuiting contacts, through which the current flow is excessive and deposits no copper. The ampere efficiency of the cell is lowered proportionately.

The same condition develops when starting sheets come in contact with adjacent anodes because of surface irregularities or poor spacing. To the operator all anode-to-cathode contacts are known as "shorts" or "hot sheets" as the supporting rod of a shorted cathode becomes hot to the touch due to the excessive current it is carrying.

To perform their inspection and correction work, the operators, designated as "inspectors," "metermen," "hotsheetmen," or "section men," work on top of the tanks, their weight being suported by the closely spaced cathode rods.

The meterman uses a millivoltmeter whose terminals are connected to two copper prongs attached to a 3-ft stick so that he can walk along each cell and make contact with the prongs between each anode and cathode just beneath the surface of the electrolyte. Because of the parallel arrangement, normal anode-to-cathode voltage is approximately the same as the cell voltage and ranges from 0.18 to 0.35 v. When the meterman observes a low reading he chalk-marks the electrodes involved so that the condition causing it can be corrected by a hotsheetman. He usually checks the cathode rod by touch, and, if it is cool, the cathode rod or anode lug contact is fouled. If the rod is hot, the cathode is shorted to one or the other of its adjacent anodes.

Until a few years ago the hotsheetman detected shorted cathodes by going over the cells and touching all cathode rods to locate those which were hot. This method has been largely superseded by the use of the Gaussmeter, which is mounted on a stick and passed over the cathode rods as the operator proceeds along the cell. The stronger magnetic field surrounding the rod of a shorted

cathode with its excessive current flow shows a high reading on the Gaussmeter.

As promptly as possible after faulty contacts have been located and marked, the section men make the necessary corrections. Contacts are wiped or shined with sandpaper. While they are still not too heavy, usually up to the fourth day of deposition, shorted cathodes are lifted out of the electrolyte for correction. The operator uses a flat iron blade or "knife" to remove shorting growths and smooth out any irregularities. Corrected cathodes are returned with special care as to spacing to avoid recurrence of the shorting.

It is highly essential that inspection and correction work be performed thoroughly and competently during the first three or four days of deposition. A section of cells with new starting sheets may have as high as 25% of shorts and faulty contacts. In order to obtain proper over-all current efficiency shorts should be reduced to less than 3% for the fourth day of deposition.

In order to check their performance properly, hotsheetmen usually work in small groups or in pairs on designated sections of cells. The work is laid out so that all cells can be gone over for correction at least twice, and the sections of young copper three or four times each day. Most refineries confine the correction work to the day shift, but some find it worthwhile to have a small crew of competent operators follow up on the second shift to give additional attention to sections of young cathodes. A single meterman usually can check by millivoltmeter the sections of cells covered by several groups of hotsheetmen. One voltmeter inspection per section per day is considered adequate.

It should be noted that too much inspection can defeat its own purpose since the additional walking on the cathode rods may move them out of alignment and cause new shorts. This is especially true when the cathodes are still light in weight.

Recommendations

This tedious review of some of the hundreds of little details involved in good tank house operation has touched only lightly on the electrochemistry of the copper refining process. Competent research has done a good job of keeping abreast of the needs of the various refiners for special adaptations and modifications of the basic process to suit it to their individual requirements for the production of pure electrolytic copper from their particular type of crude blister. I hope I have made clear what I stated at the outset, that despite the world's dependence on tremendous tonnages of electrolytically refined copper, the techniques of good tank house operation have seen little change in recent times and still depend to a great extent on hand labor performed under rather unfavorable working conditions.

With the decreasing availability of the required type of labor and the constantly increasing rate of wages, especially in this country, it is time that more serious consideration be given to radical improvements in tank house operation, particularly to the problem of efficient cell performance during electrolysis. Here are a few suggestions of things to come and many of them are on the drawing boards or being developed on the job at the present time:

1. Anodes with uniformly good physical characteristics. This means positive control of weight within narrow limits during casting, sound lugs of uniform thickness, and perfect flatness so that they hang vertically when racked in tank loads. They must be free of blisters, protrusions, and fins, and the contact surface of the long lug should be ground or shined to clean metal.
2. Starting sheets should be produced, stripped, flattened, looped with rods in place and hung in racks by mechanical means to eliminate the present arduous hand-handling. It is not too much to suggest that means could be devised to place them in the cells by crane a tank-load at a time, instead of one at a time by hand.
3. Improved control facilities should be installed to insure proper conditioning and supply of electrolyte so that composition, clarity, temperature, and flow can be held within narrow limits of variation with a minimum of hand juggling.
4. Anode scrap as well as cathode production should be washed, bundled, and loaded out by mechanical means.
5. In the construction of tank house buildings more consideration should be given to insulation against variations in outside temperature, and adequate ventilation facilities should be provided to improve working conditions and to minimize vapor condensation as well as variations in humidity and rate of evaporation.
6. Full advantage should be taken of the rapid development of acid-resisting steels and plastics to replace iron and lead in tank house equipment. In this connection, cells should be fully protected on the outside as well as inside, especially when made of concrete.

We have taken a brief look into the aging anatomy, complex functions, and obvious needs of the tank house, the work-horse of the copper industry. If doing so has been mildly interesting to the uninitiated, a little helpful to the embryo operator, and a bit provocative to the tank house graduate, it will more than have served its modest purpose.

Feature Section

Electrochemistry as We Enter the Sixties

Presidential Address*

William C. Gardiner

Since this is the first meeting of The Electrochemical Society in the 1960's, I propose to compare electrochemistry today and our Society as it is today with electrochemistry and the Society at the start of previous decades. This should be of interest to all of you at this time.

I have reviewed the Proceedings of the Society for the annual meetings in the springs of 1910, 1920, 1930, 1940, and 1950. It may be necessary to remind some of you that these dates do not coincide with the tenth, twentieth, and so on, anniversaries of the Society because it was founded in 1902.

It was very interesting for me to read about the activities of our predecessors. The pages are filled with the names of men who contributed greatly to the science and technology of electrochemistry as well as other fields.

In 1910, President Leo H. Baekeland, known to all of you as the inventor of Bakelite, opened the meeting in Pittsburgh with a talk on "Science and Industry." He gave a forceful discourse on the merits of the scientist and engineer and their contributions to progress and industry, giving enlightenment on what a research scientist can do and the way he works. He would still be far from satisfied with the recognition given to scientists and engineers in America.

On Friday, a special train carried the members around to various steel mills and other plants in the Pittsburgh area. It was reported that, at the informal dinner in the evening, "Section 'Q' was strongly in evidence, enjoying itself with its usual ABANDON." On Saturday afternoon, a General Public Meeting was held in Carnegie Music Hall where Professor Joseph W. Richards spoke on "What the Electrochemical Industries are Accomplishing."

In 1920, Professor Wilder D. Bancroft of Cornell was President, and opened the meeting in the Rogers Building at M.I.T. with a paper on "Contact Catalysis" in which he reviewed the theories of catalysis as of that time. He then conducted a "Symposium on Colloid Chemistry." On Friday, joint sessions were held with the A.I.E.E. on "Electrically Produced Alloys" in the morning and then, in the afternoon, *eight electric cars* took the guests to General Electric at Lynn, Mass. It was reported that "A printed itinerary gave all the details of the visit with great accuracy, and it was carried according to plan with military precision." Afterward, the informal dinner was graced by the presence of "our esteemed friend, Professor Elihu Thompson."

On Saturday, they met at Harvard University where Professor T. W. Richards welcomed the Society. He said that there was an historical reason for visiting Harvard occasionally because Benjamin Thompson, later to become Count Rumford, walked ten or more miles from North Woburn to Harvard Hall to hear John Winthrop's lectures on natural philosophy. About 30 years later, Count Rumford founded The Royal Institution where Davy and Faraday did their great work in electrochemistry. It is to be regretted that we no longer take advantage of meeting on the campuses of some of our leading universities.

By 1930, the Presidential Address had become an evening affair when Dr. Francis C. Frary spoke in St. Louis on "Research as a Vocation." He pointed out that character and temperament are more important than an applicant's technical training, and discussed the value of intellectual integrity, personality, imagination, and curiosity. These are inherent in the character of a good researcher. Training can improve such things as observation, manipulation, attention to detail, accuracy, care in observing and recording data, clarity of thought, and expression; broad training is desirable on fundamentals of science, languages, and mathematics

I noted several other items of interest that occurred at the St. Louis Meeting in 1930. There was final acceptance of the formal resolution for incorporation of the Society. Also, the Joseph W. Richards Memorial Fund was established by a gift of Dr. E. G. Acheson to meet the expenses incurred by inviting and entertaining distinguished guests from foreign countries. We might regret that this fund is so small, because we are inviting more and more foreign scientists to participate in our meetings and can do so only through the benevolence of our National Science Foundation.

In the spring of 1940, we met at Galen Hall, Wernersville, Pa. Professor H. Jermain Creighton of Swarthmore, in his talk on "Forty Years of Electrochemistry," reviewed the development of electrochemical theory. The Society was struggling to recover from the depression, and he challenged 100 fellow members to bring in two new members apiece to bring the number of members back to the pre-depression level. Our membership has increased but we have lost the pleasure of being able to meet in such beautiful surroundings.

When we met in Cleveland in 1950, Professor A. L. Ferguson quoted from letters that he had solicited from former Presidents of the Society and others in speaking on "What the Society Would See if It Looked in a Mirror." He analyzed opinions that had been expressed on the training of electrochemists, on the professional standing of electrochemistry, electrochemists, and our JOURNAL. He noted that there were 337 Charter Members in 1902 and that the membership had risen to 2279 in 1921, then decreased in the depression to 1156 in 1936. It was more or less static from 1936 to 1942 but had increased to 2000 in 1950. He thought that the diverse interests of industrial and academic people had

* Delivered at the Chicago Meeting, May 3, 1960.

caused the loss of both to either purely engineering or purely scientific societies. However, the management of The Electrochemical Society had been revised to become more representative of all groups. Professor Ferguson regretted the inadequate facilities for training electrochemists in universities and the general lack of appreciation of the importance of electrochemistry in their departments of chemistry.

The character of our meetings has changed tremendously. In the first four decades, we all met together and there was only one activity at a time. There was much more opportunity for people of different interests to meet and learn about the other fellow's problems. Plant trips were a big feature of the programs. Five Divisions were operating in 1940 but they still could plan their activities without overlapping. By 1950, there were nine Divisions, and simultaneous technical sessions were in operation. We still have nine Divisions but, at this meeting, there are as many as seven simultaneous sessions. Plant trips are becoming rare. Besides the conflict with technical sessions, I think that this is due partly to having to restrict our meetings to the larger cities where traffic problems and distances discourage local committees from planning trips. I wonder whether this is a good trend. I remember that I have gained considerable benefits from such trips, myself.

Publication of our JOURNAL, formerly called the TRANSACTIONS, is one of the most important functions of the Society. As you look at the books on the shelf, there is not a very obvious change through the years except for a change in color and a change in dimensions. However, the content of new scientific knowledge in our JOURNAL has changed considerably. The annual volume of the world's scientific literature is enormous so we must limit manuscripts to original work reported as concisely as possible. Our editors are necessarily very critical and exacting. In 1910, there were 24 papers presented and published. At this meeting in 1960, 214 papers are scheduled. I cannot say how many will be eligible for publication. The papers of special symposia are now being published in book form so that those who wish may obtain the complete collection. This permits publication of reviews by experts without burdening the JOURNAL. During the first four decades, published articles averaged 14 pages and preprints were distributed before the conventions. The necessity for economy has reduced preprints to abstracts and the average length of a published paper in 1950 was 7 pages and, so far this year, it has averaged 5.3. We must reduce every paper to the minimum required for the clear presentation of new material.

The editorial burden is carried by 14 Divisional Editors assisting the Technical Editor. These men are experts in their field but rely further on specialists to review each paper. In addition, there are the News Editor, the Book Review Editor, and over all, the Editor. All of this is done on a voluntary basis by members of our Society. I am sure that most of you, from time to time, have contributed in this way. I have heard criticisms of our JOURNAL to the effect that the quality of papers is not high or that publication takes too long. I know that these matters are also of chief concern to our editors and that they are continually striving to improve the JOURNAL as a service to you. It is also your JOURNAL. It publishes the papers you write and edit. This is a democratic institution, so he who can do better should not hide his light under a bushel but should volunteer his services. Our Managing Editor and her assistant are staff employees. Someday we may be affluent enough to enlarge our staff with people who are qualified to do the technical editing. This might reduce the time required to prepare a paper for publication.

What are electrochemists working on to contribute in the 1960's? In reading the program of this meeting, I see many contributions to the Electronics industry; electrolytic capacitors, luminescence, semiconductors (new materials, theory, preparation, and device technology). In Electrothermics and Metallurgy, I see papers on refractory metals, rhenium, vanadium, and iron. The Industrial Electrolytic and Theoretical Electrochemistry Divisions have a joint symposium to discuss electrochemical engineering as a unit process.

What are the contributions of electrochemistry to the space age? Electrothermics and metallurgy have contributed refractory materials for nose cones and the many special alloys in rockets. Fused salt electrolysis produces titanium, beryllium, and other "rare" metals. Some of the exotic high-energy fuels, fluorine, hydrogen, and hydrazine, depend on electrochemical production or electrochemically produced raw materials. New light batteries power the electronic circuits, printed electrochemically and utilizing electrolytic capacitors, transistors, and other semiconductor devices for their guidance and broadcasting systems.

And can we dream about a few advances that will be made in the sixties! Our fastest growing Division (Electronics) will discover new and better phosphors, new semiconductors to give more efficient rectifiers and transistors. Electrothermics and Metallurgy will contribute cheaper "rare" metals and alloys. Electrolytic cells may reach capacities of half a million amperes. Electrodeposition will be extended to the "rarer" metals. The Battery people will make the fuel cell practical as well as develop many special batteries. Corrosion will be better understood and, I hope, markedly reduced. And, finally, we expect the Theoretical Division to extend our knowledge of electrochemistry in all its branches and lead us into new fields yet to be discovered.